2013 IFCS-EFTF Proceedings

This conference marks the 60th anniversary of the IEEE Ultrasonics, Ferroelectrics, and Frequency Control Society and is a joint meeting of four related groups. This year we have the 6th joint meeting between the International Frequency Control Symposium (IFCS) and the European Frequency and Time Forum (EFTF), and the 3rd joint meeting between the International Symposium on the Applications of Ferroelectrics (ISAF) and the Piezoresponse Force Microscopy Workshop (PFM). These proceedings includes papers from IFCS and EFTF.

A prime focus of these ongoing meetings is to establish progress through communication and collaboration. That communication is the core reason we publish these proceedings. A total of 268 papers are presented in this joint IFCS and EFTF product covering 6 major areas:

- Materials, Resonators, and Resonator Circuits
- Oscillators, Synthesizers, Noise, and Circuit Techniques
- Microwave Frequency Standards
- Sensors and Transducers
- Timekeeping, Time and Frequency Transfer, and GNSS Applications
- Optical Frequency Standards and Applications

I would like to thank all the authors for their contributions to this year's proceedings.

Sincerely,

Aaron Partridge, IFCS/EFTF Editorial Chair
Founder and Chief Scientist, SiTime Corp.
Sunnyvale California.

UHF Quartz MEMS Oscillators for Dynamics-Based System Enhancements

R.L. Kubena, D.J. Kirby, Yook-Kong Yong*, D.T. Chang,
F.P. Stratton, H.D. Nguyen, R.J. Joyce, R. Perahia,
H.P. Moyer, & R.G. Nagele
HRL Laboratories, LLC, Malibu, CA, 90265 USA
*Rutgers Univ., Piscataway, NJ
Email: rlkubena@hrl.com

Abstract— **Processes for fabricating full wafers of UHF quartz MEMS oscillators bonded to Si have been developed at HRL over the past several years. These devices have shown state-of-the-art noise and stability along with extremely small vacuum packaged die size of less than 3 mm^2. An interesting by-product of the high frequency, small size, and wafer-scale fabrication of these devices is that several novel dynamics-based enhancements can be considered. These include the use of nonlinear dynamics for reducing oscillator phase noise at CMOS capable voltages and co-integration with more complex structures for sensing vibration and serving as a local timing reference for reducing thermally-induced sensor drifts. Several of these novel concepts made possible by wafer-scale MEMS-based processing will be reviewed.**

Keywords- Quartz MEMS, phase noise, duffing, nonlinear operation, vibration compensation, force rebalance, frequency locking, ovenization, and Si Disk Resonator Gyro.

I. INTRODUCTION

A long standing goal of RF MEMS is to allow large-scale integration of both active and passive components on chip for reduced size, weight, and costs. These goals have driven much of the research for Si MEMS devices based on processing and material compatibility with analog and digital Si electronics. However, it was realized almost a decade ago, that MEMS-based processing can be applied to many other resonator materials, including quartz [1], AlN [2], and diamond [3]. These other material systems provide several advantages that can enhance their usefulness in a variety of markets. In particular, piezoelectric quartz has been universally used for many decades as a timing standard in most all commercial and military communication and navigation systems. As such, there is a wealth of knowledge in designing, packaging, and performance testing quartz oscillators that can aid in developing new devices.

In addition to some of the obvious advantages of size and costs for directly integrated quartz resonators on Si-based circuits, quartz MEMS processing allows several new capabilities to be considered. These include adding more functionality to the resonator and the control electronics to explore new ways to improve the overall system performance. Moreover, one can also integrate quartz resonators with other structures and sensors to provide "system-on-chip" capability and then use each sensor in an optimal fashion to reduce overall system errors. This synergy with multiple sensors co-located on a single chip and sensing similar dynamic environmental inputs provides the system designer with a new tool to improve the system performance. In this paper, we will first briefly review the status of quartz MEMS devices and their performance and then review several of these new ideas.

This work was sponsored in part by DARPA'S MTO office under the DEFYS program, issued by DARPA /CMO under contract No. HR0011-10-C-0109. The views and conclusions contained in this document are those of the authors and should not be interpreted as representing the official policies, either expressly or implied, of DARPA or the U.S. Government.

II. UHF QUARTZ MEMS

A. Fabrication and Packaging

The process flow for integrating UHF quartz resonators to Si substrates has been described previously [1], so it will not be repeated here in detail. In summary, ebeam evaporated Al is first deposited and patterned on a piezoelectric quartz wafer for top-side metallization, and the quartz is then fusion bonded at low temperature to a Si handle wafer. Grinding and CMP (Chemical Mechanical Polishing) are used to thin the quartz to the desired thickness for shear-mode operation. Vias are then plasma etched in the quartz and bottom-side Al electrode metal, via, and bond metals are applied and patterned. A photoresist layer is then used as a mask for plasma etching to define the quartz resonator. The wafer is then bonded to a Si-based substrate using Au/In eutectic bonding which allows subsequent higher temperature processing. Finally, the Si handle wafer is removed by SF_6 plasma etching, thereby releasing the resonators.

The devices at this point in the processing are shown in Figures 1 and 2. Note the spacing between the bottom of the quartz and the substrate is typically between 5 to 8 microns. We have been processing 3" quartz wafers to date, but larger quartz wafers up to 6" in diameter are expected to be available in the future. A Si capping wafer with a recessed cavity is then

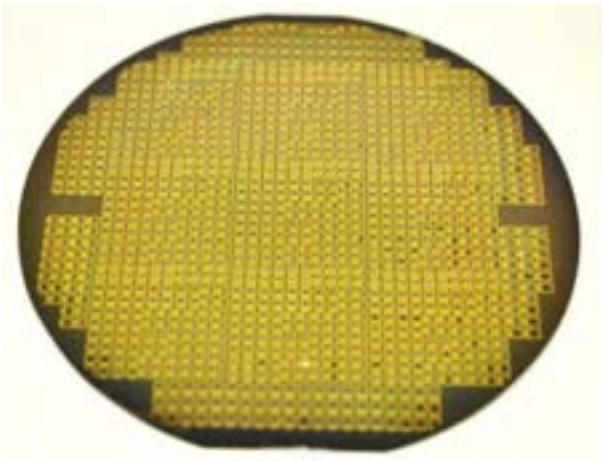

Fig. 1. Completed AT-cut UHF quartz resonators on a 3" Si wafer before encapsulation..

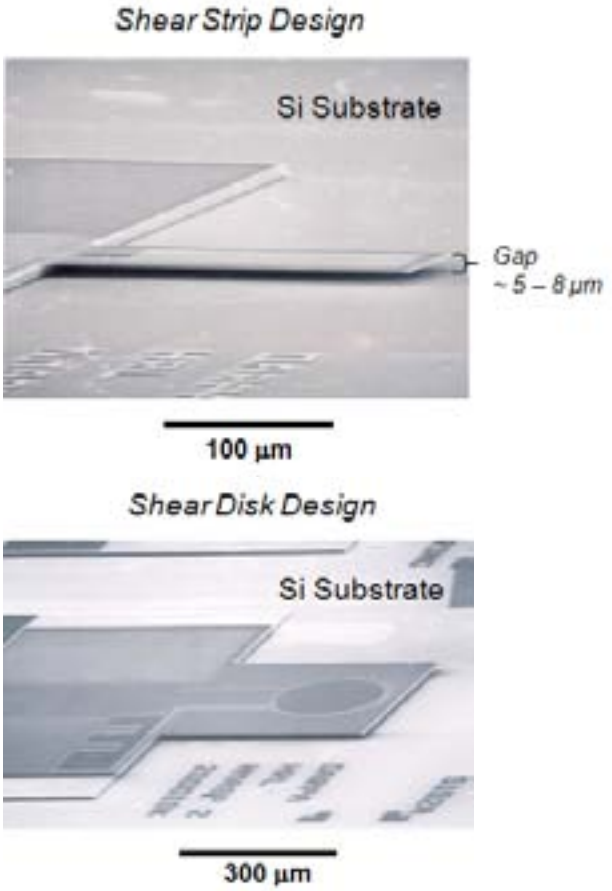

Fig. 2. SEM microphotographs of rectangular quartz strip (top) and disk (bottom) designs bonded to a Si substrate.

patterned with a Au/In or Au/Sn bonding layer and bonded to the base wafer in a roughly 10^{-4} to 10^{-5} Torr vacuum for packaging at wafer level. The capping wafer is then plasma etched to define the bond pad slits, and the wafer is singulated by sawing. The capped and singulated die are shown in Figure 3. The typical die size for UHF quartz resonators in the 300 – 1000 MHz frequency range is ~ 1.5 x 1.5 mm^2.

B. Resonator and Oscillator Test Results

Our devices have been tested with an Agilent admittance meter (model E4991A) as resonators on a probe station and have been hybridized as surface mount components in Pierce and Clapp oscillator and VCOs (voltage controlled oscillators). A typical admittance characteristic for an AT-cut, shear-mode,

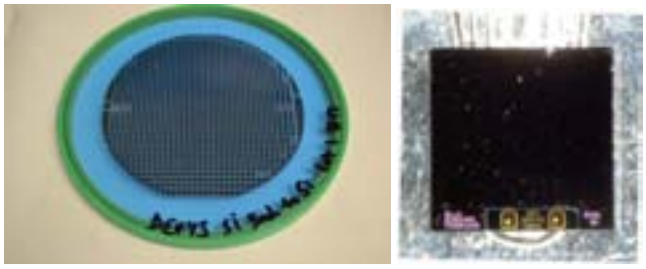

Fig. 3. Singulated die at wafer level (left) and close-up of die (right) after vacuum packaging.

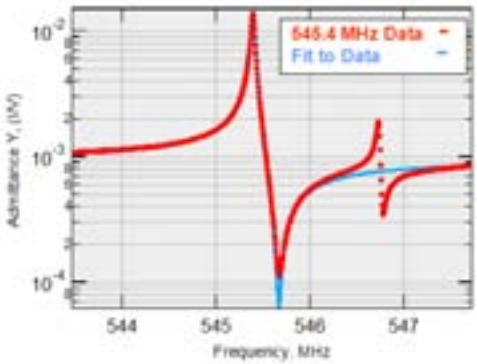

Fig. 4. Admittance plot of AT-cut strip resonator in air. Quartz plate dimensions: 225 x 80 µm, Al electrode dimensions: 160 x 50 x 0.08 µm.

545 MHz strip resonator in air is shown in Figure 4 showing a Q of 14.8 K, R_1 = 70 Ω, C_o = 2.8 x 10^{-13} F, C_1 = 2.8 x 10^{-16} F, and a L_1 = 3.0 x 10^{-4} H. This gives an f x Q product of 8.0 x 10^{12}. f x Q products >1.0 x 10^{13} can be obtained for resonant frequencies near 1 GHz. We have noted that at UHV frequencies, there is no difference in the equivalent circuit values for resonators operated in air or vacuum.

The f/T profile of a 367-MHz 200-µm-diameter disk resonator is shown in Figure 5 and follows the expected "S" shape profile for an AT-cut angle of 35° 18'. After a bake-out in air at >100° C, the hysteresis was about 1 ppm. For stable hysteresis <<1 ppm, two things are required: (1) hermetic or vacuum packaging to remove and prevent contamination from forming on the electrodes and (2) stress isolation from the mounts. Recent COMSOL models [4, 5] of the effects of stress propagation from the mounts to the electrodes over temperature have shown that for quartz resonators it is important to reduce the thermally-induced stress in the active regions to <100 kPa. This is particularly important for very thin UHF designs. Temperature dependent stress can rotate the f/T curves and stress relaxation can produce hysteresis. Stress isolation can be accomplished in the design of the resonator.

Both Pierce and Clapp oscillators have been constructed for testing the phase noise of these resonators. A picture of a Clapp VCO is shown in Figure 6, and its phase noise is plotted in Figure 7. In Figure 7, we also plotted the phase noise of a 16-

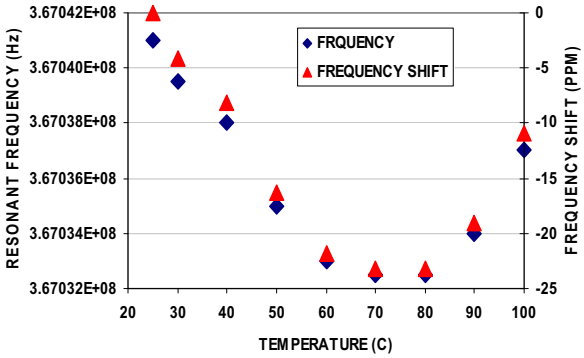

Fig. 5. f/T profile of a 200-um-diameter disk resonator in air after a >100° C bake.

Fig. 6. A 705-MHz Clapp VCO using a capped AT-cut quartz MEMs resonator.

MHz Vectron quartz VCC1 series XO multiplied up to 705 MHz with a noiseless multiplier. One can see that for high offset frequencies, the phase noise for the quartz MEMS VCO is lower. At 10 Hz offset, the commercial HF part is about -8 dB better. Thus, for portable communication applications, if one wishes to minimize power by not employing a frequency synthesizer or PLL, these UHF oscillators offer new capabilities with reasonably good performance. Commercial testing of these oscillators has demonstrated the ability to acquire and track GPS signals with roughly 300 times less local oscillator power than is currently used in existing systems [6]. One of the key issues in moving to low noise 1-GHz operation is integrating the resonator with an appropriately designed high gain, low noise amplifier.

III. Nonlinear Performance Enhancements

A. Operation Near a Bifurcation Point

Drive level dependency [7] has been well studied for quartz resonators and is believed to result (ignoring heating effects) from a nonlinearity in the elastic modulus in the crystal. This nonlinearity can be described with an additional term in the standard electrical harmonic oscillator equation:

$$\frac{V}{L} = \ddot{q} + \frac{\omega_0}{Q}\dot{q} + {\omega_0}^2 q(1 + \beta q^2) \qquad (1)$$

where β describes the degree of third-order nonlinear behavior of the elastic modulus. At high drive levels, this nonlinearity

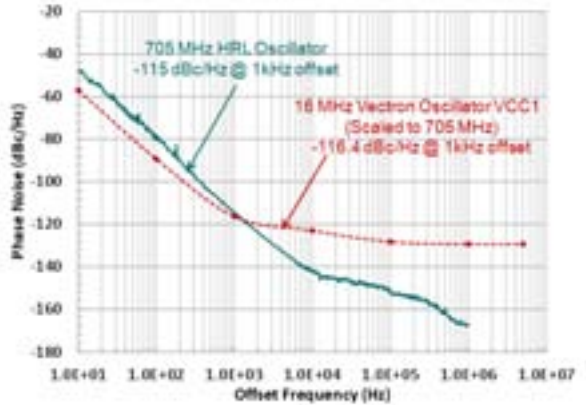

Fig. 7. Phase noise of the 705-MHz Clapp VCO shown in Fig. 6. For comparison, the phase noise of a commercial Vectron 16-MHz VCC1 series XO is shown by multiplying its phase noise to 705 MHz with a noiseless multiplier.

distorts the normal admittance profile and increases the phase slope of the resonator. This increase in phase slope is equivalent to an increase in Q, and thus one could expect the contribution of phase noise from the electronics would be reduced if the oscillator operates near the region where the phase slope approaches infinity (the bifurcation point). This is the basis of the Yurke [8] model for "amplifier-noise evasion" in oscillators using a nonlinear resonator. The key to using this concept in real world oscillators is (1) driving the resonator to a high enough amplitude to reach the bifurcation point, (2) controlling the circuit's operating point to find and stabilize the operation of the loop near a region of high phase slope, and (3) preventing amplitude noise in the drive signal from adding phase noise (AM to PM noise conversion).

The first step in studying this effect is determining the drive level necessary to reach the bifurcation point. As shown in Figure 8, for a 995-MHz resonator, the resonator becomes highly nonlinear near a drive level of 400 mV (peak) and shows a corresponding 125 ppm frequency shift. For comparison, similar voltage drive levels were applied to a

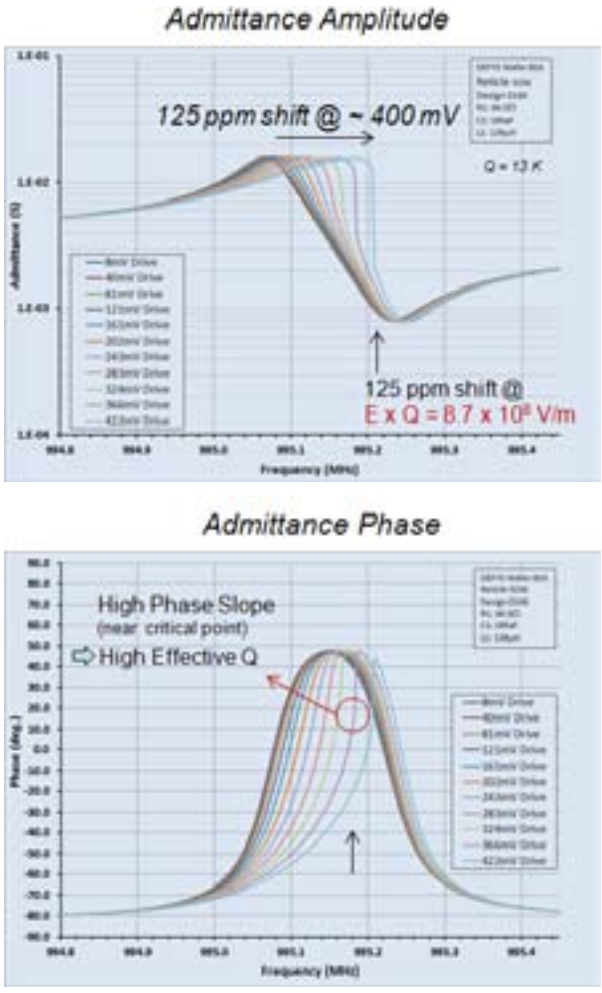

Fig. 8. Admittance amplitude (top) and phase (bottom) of a 100-µm-diameter disk resonator with a fundamental mode resonance at 995 MHz. The resonator reaches the bifurcation point at a drive level of approximately 300 - 400 mV (peak).

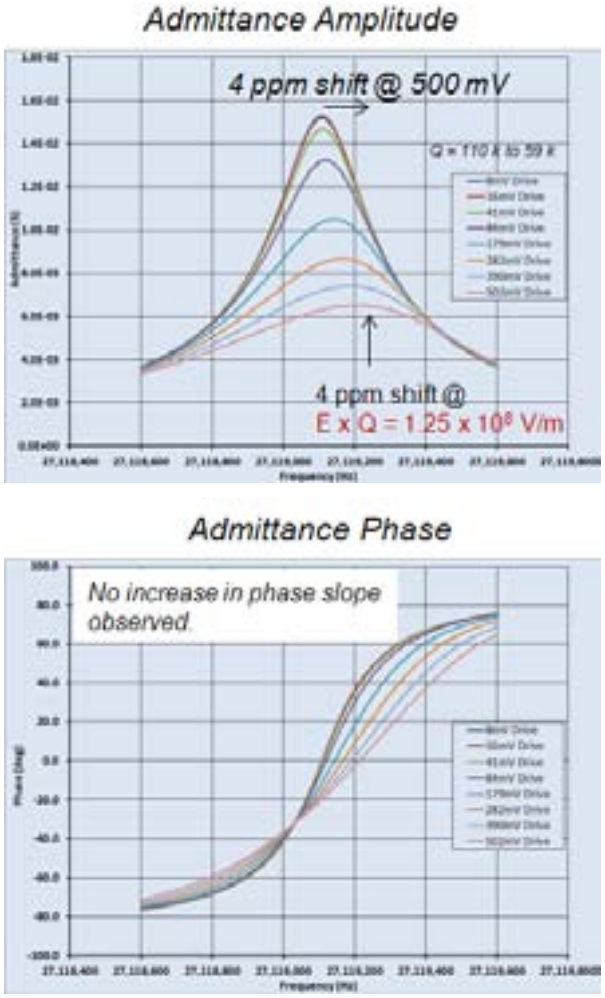

Fig. 9. The admittance amplitude (top) and phase (bottom) of a commercial 27-MHz miniaturized resonator (Epson FA-180T). Note the phase slope decreases as the drive level is increased. Voltages are peak values.

commercial HF resonator from Epson (model # FA-180T) operating at 27 MHz. The results are shown in Figure 9. For this resonator, a 500 mV (peak) drive produces much less nonlinearity and a frequency shift of only 4 ppm. (This part also shows a drop in Q as the drive voltage is increased.) From equation (2) below, it can be shown that a constant electric field (E) applied to devices with different thicknesses produces the same degree of nonlinearity for a similar Q. We have found that E x Q is a useful metric for determining the degree of nonlinearity exhibited by a resonator since it represents the degree of local strain in the crystal. For the 995-MHz resonator at a drive level of ~ 400 mV, E x Q = 8.7 x 10^8 V/m while for the 27-MHz resonator at a drive level of 500 mV, E x Q = 1.25 x 10^8 V/m. Thus, UHF resonators seem ideally suited for nonlinear studies and operation at voltages <1 volt.

In order to study "amplifier-noise evasion", we constructed a breadboard control loop [9] in which the phase and gain in the loop around the resonator could be varied while the amplitude of the resonator admittance was measured in closed loop operation using a high speed differential probe configuration.

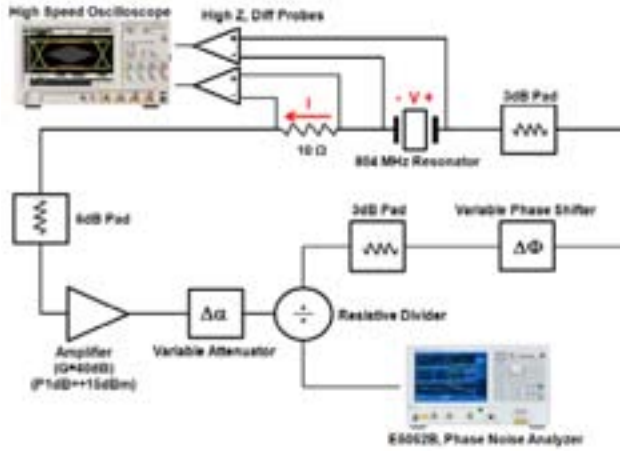

Fig. 10. Breadboard circuit for measuring the amplitude of the admittance of the resonator in closed loop operation while adjusting the gain and phase of the electronics to sweep the frequency of operation.

This allowed us to predetermine the best open- loop phase slope operating point for the resonator and then to adjust the phase and gain of the loop to sweep the frequency and measure the phase noise at various operating points. This set-up did not provide ideal conditions for the lowest phase noise measurements but was constructed to allow a wide range of operating points to be evaluated for relative phase noise improvements. The circuit is shown in Fig. 10, and the resulting admittance and phase noise plots are shown in Fig. 11

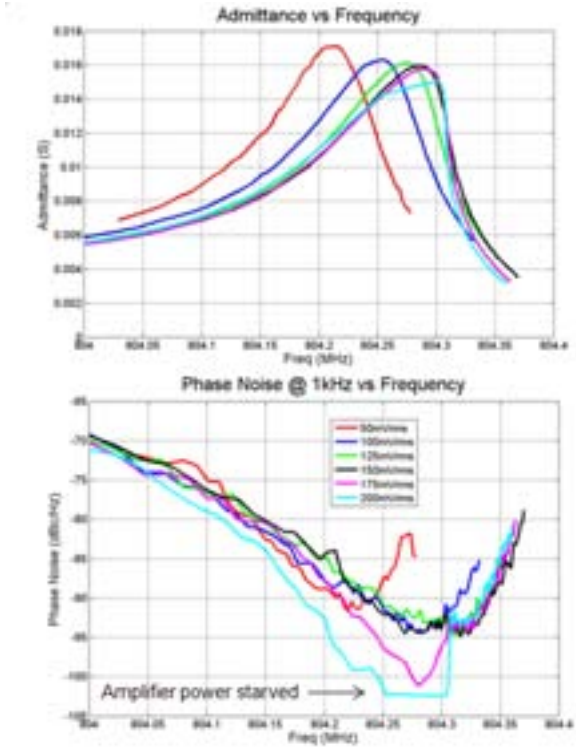

Fig. 11. Amplitude of admittance (top) and phase noise (bottom)of a nonlinear 804-MHz AT-cut oscillator at 1 kHz offset versus frequency showing a sharp drop in phase noise near the expected high phase slope region of the resonator admittance curve.

for an 804-MHz resonator. As seen in the closed-loop admittance plot, the gain of the amplifier at 804 MHz was starting to saturate even when the attenuator was completely removed from the loop near the bifurcation point. However, a sharp drop in phase noise was seen at a point near the highest phase slope. We believe this is the first strong evidence of noise evasion for quartz oscillators. In the future, we will need to redesign the loop with higher gain stages to further study this encouraging new result.

B. Nonlinear Modal Coupling

It is very common for quartz oscillators to be operated not only at the fundamental shear-mode resonance but also at the third and fifth overtones. These overtones usually do not fall directly at a third or fifth harmonic of the fundamental frequency, but particular electrode and plate design can bring the overtone mode frequencies close to the harmonic frequencies. We have studied the possibilities of nonlinear mode coupling from the fundamental to higher order overtones with a Matlab Simulink model. The initial governing two-dimensional equations [10] for this study are as follows:

$$C_{66}u_{1,22} + \eta_{66}\dot{u}_{1,22} + e_{26}\varphi_{,22} - \rho\ddot{u}_1 = -\gamma[(u_{1,2})^3]_{,2} \quad (2)$$

$$e_{26}u_{1,22} - \varepsilon_{22}\varphi_{,22} = 0 \quad (3)$$

$$C_{66}u_{1,2} + \eta_{66}\dot{u}_{1,2} + e_{26}\varphi_{,2} \pm 2\rho' h'\ddot{u}_1 = -\gamma(u_{1,3})^3 \text{ at } X_2 = \pm h \quad (4)$$

$$\varphi = \pm\frac{1}{2}Ve^{i\omega t} \text{ at } X_2 = \pm h \quad (5)$$

$$\gamma = \frac{1}{2}C_{22} + C_{266} + \frac{1}{6}C_{6666} \quad (6)$$

where C_{ik} is the elastic shear-mode stiffness matrix, η_{ik} is the damping matrix, e_{ik} is the piezoelectric matrix, ρ is the quartz density, γ is the nonlinear third-order coefficient containing the second, third and fourth order elastic constants, u is the displacement, ε is the dielectric matrix, 2h is the quartz plate thickness, 2h' is the electrode thickness, φ is the electric potential, and V is the applied voltage. The x_1 axis is in the shearing direction and the x_2 axis is normal to the quartz plate.

One can now assume both the fundamental and third overtone modes with amplitudes A_1 and A_2, respectively, are present at the same time and substitute a dual eigenmode solution into equation (2):

$$u_1(X_2,t) = A_1(t)\,Sin(\frac{\pi X_2}{2h}) + A_2(t)\,Sin(\frac{3\pi X_2}{2h}) \quad (7)$$

If ones then multiplies the resulting equation by each eigenmode solution and integrates through the thickness, one obtains the following nonlinear coupled equations of motion:

where ω_1 and ω_2 are drive frequencies in the neighborhood of the natural fundamental and third overtone frequencies, ω_{n1} and ω_{n2}, respectively. The expressions in equations (8) and (9) are defined as the following, which can be derived from the linear equations except for the gamma terms:

Table of expressions

$$\omega_{n1} = \eta_1\sqrt{\frac{\overline{C}_{66}}{\rho}}(1-\frac{4k_{26}^2}{\pi^2}-R),\ \omega_{n2} = \eta_2\sqrt{\frac{\overline{C}_{66}}{\rho}}(1-\frac{4k_{26}^2}{9\pi^2}-R),\ \eta_1 = \frac{\pi}{2h},\ \eta_2 = \frac{3\pi}{2h},\ \gamma_1 = \frac{\eta_1^2\gamma}{\overline{C}_{66}},\ \gamma_2 = \frac{\eta_2^2\gamma}{\overline{C}_{66}},$$

$$\overline{C}_{66} = C_{66} + \frac{e_{26}^2}{\varepsilon_{22}},\ k_{26}^2 = \frac{e_{26}^2}{\overline{C}_{66}\varepsilon_{22}},\ R = \frac{2\rho' h'}{\rho h},\ K_1 = \frac{-e_{26}V_1e^{i\omega t}}{2h(C_{66}-2\rho' h'\omega_1^2 h)},\ K_2 = \frac{-e_{26}V_2e^{i\omega t}}{2h(C_{66}-2\rho' h'\omega_2^2 h)}$$

By solving equations (8) and (9) in a Matlab model, one can study the nonlinear coupling between the two modes for various drive levels and different frequency matching conditions between the two modes. We have found that if the fundamental mode is driven strongly into a nonlinear regime while the third overtone is very lightly excited, the third overtone mode can be pumped to a higher amplitude and the Q (defined by the full-width at half-maximum of its response curve or the phase slope) is predicted to be higher. The results are shown in Figure 12 for a ~ 1.6 GHz third overtone device. Several curves are shown for the pumped third overtone mode for different frequency matching conditions. For $f_{n2} = 3f_{n1}$, the Q enhancement is predicted to be ~ 8X. For $f_{n2} = 3f_{n1}$ + 800 kHz, the Q enhancement is predicted to be 4X. As the voltage on V2 is increased, the Q enhancement is decreased. The origin of this predicted increase in Q is still being studied. The model assumes a constant f x Q product of ~ 1 x 10^{13} Hz for the fundamental and third overtone modes. Thus, the third overtone is being pumped with a drive with a three times higher Q. This may explain part of the Q enhancement. Experiments are currently being performed at HRL with mode matching to within 100 ppm to verify these predictions.

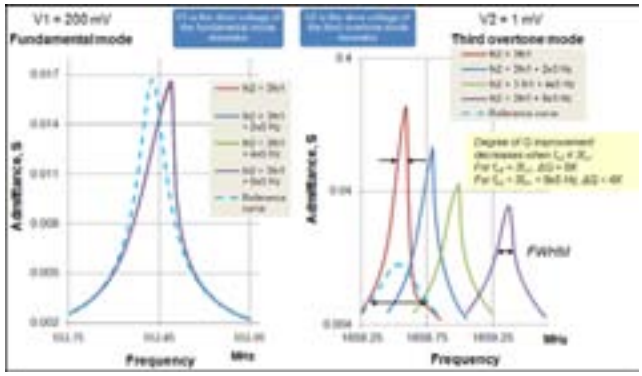

Fig. 12. The admittance curves for the nonlinear coupling of the fundamental to third overtone modes when V1 is driven with a 200 mV peak voltage and V2 is driven with a 1 mV peak voltage.

$$\ddot{A}_1 + \frac{\omega_{n1}}{Q_1}\dot{A}_1 + \omega_{n1}^2 A_1(1+\gamma_1(\frac{3}{4}A_1^2 + \frac{9}{4}A_1A_2 + \frac{27}{2}A_2^2)) = -\frac{8K_1h\omega_1^2}{\pi^2} \quad (8)$$

$$\ddot{A}_2 + \frac{\omega_{n2}}{Q_2}\dot{A}_2 + \omega_{n2}^2 A_2(1+\gamma_2(\frac{3}{4}A_2^2 + \frac{1}{6}A_1^2 + \frac{27A_1^3}{2A_2})) = \frac{8K_2h\omega_2^2}{9\pi^2} \quad (9)$$

IV. Sensor Synergy for Improved Performance

The ability to define complex structures both on and around the quartz resonator using quartz MEMS processing is very useful for mitigating system errors in navigation and communication systems [11]. As an example, a precise clock can be used to correct for thermal drifts in navigation sensors. A set of IMU sensors can be used to detect motion and reduce vibration induced phase noise errors in clocks. Autonomous IMUs can correct for errors in GPS location when GPS signals are not available, and GPS timing signals can be used to correct for local clock inaccuracies. These are just a few examples of the synergistic interplay that is possible when devices are allowed to communicate. If these devices share a common package or housing, thermal gradients can be minimized while vibration compensation can be simplified. In this section, we will give an overview and initial modeling results for a few of these topics.

A. Dynamical Control for Reduced Vibration Sensitivity

Vibration sensitivity of clocks is of primary concern when the clock is located in a moving vehicle. We have tested our UHF oscillators on a shaker table to determine their vibration sensitivity. Care was used to reduce stray capacitance changes during the measurements, but all extraneous signals have likely not been eliminated due to our hybrid board construction as seen in Figure 6. Figure 13 shows the measured out-of-plane gamma for a 645-MHz oscillator using a 200-µm-disk design with a 0.5 g peak sinusoidal input. The measured out-of-plane (along the y axis of quartz) gamma was typically ~ 5.0 x 10^{-10}/g. Predicted vibration sensitivities from quartz models for 500-MHz designs and 0.5 g inputs have yielded 1.8 x 10^{-10}/g, 9 x 10^{-13}/g, and 3.0 x 10^{-15}/g in the y, x, and z axes, respectively. Thus, reducing the out-of-plane vibration sensitivity is of particular interest.

One method that is currently being developed is to add additional electrodes to the underside and top of the quartz plate for capacitance sensing and force rebalance. This allows active force rebalancing of the inertial forces on the quartz plate in the out-of-plane direction. A schematic of the new design is shown in Figure 14. FEA COMSOL analysis has been used to calculate the tip cantilever displacement for several designs from 500 MHz to 1 GHz fundamental operation. The results are shown in Figure 15. For the design parameters given in this figure, the change in the capacitance for 1 g acceleration is between 1 – 5 aF. Fortunately, these capacitance values are commonly detected by circuits used for MEMS accelerometers. Assuming a differential capacitance detection system as shown in Figure 14 with a bandwidth of 1 kHz and a clock drive of ±1 volt @ 1 GHz, we calculate that a detection noise floor of between 4 to 1 mg is possible for resonators with fundamental shear-mode resonances between 500 MHz to 1 GHz, respectively. Thus, within the constraints of the typical dimensions of a UHF quartz shear-mode resonator, a combined accelerometer/resonator structure is possible. A small sub-10 µm gap between the quartz resonator and the substrate and cap is needed to maintain the required acceleration sensitivity and low operating voltages.

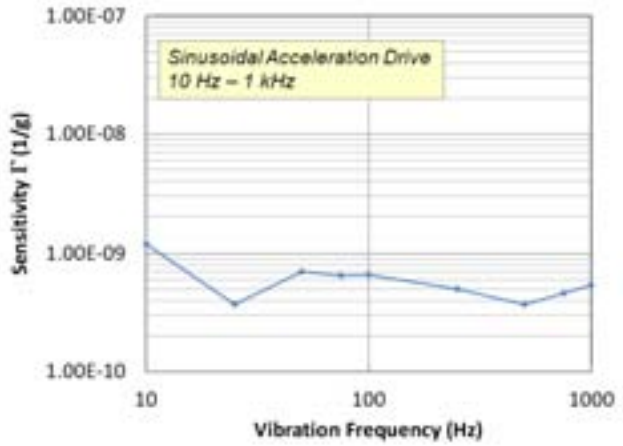

Fig. 13. The out-of-plane (y axis) vibration sensitivity of a 645-MHz oscillator with a 0.5 g peak sinusoidal input.

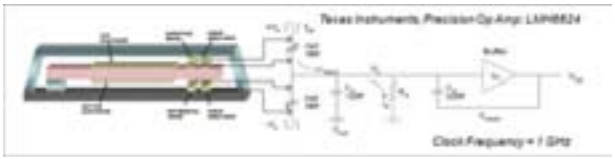

Fig. 14. Schematic of a new design in which the quartz plate serves as both a UHF resonator and an accelerometer with mg sensitivity for force rebalancing of inertial forces on the clock.

B. Frequency Locking for Sensor Ovenization

Another interesting combination of sensors and oscillators on chip is the use of a precision clock for the thermal control of inertial units [12]. For typical Si-based gyroscopes, the uncompensated frequency sensitivity to temperature is roughly -30 ppm/ºC, being due to the change in the elastic constant of Si. In addition, measurements of the bias drift over temperature for the Si Disk Resonator Gyro (DRG) [13] have shown 5-10 deg./hr/º C sensitivity. Since similar temperature-induced drift

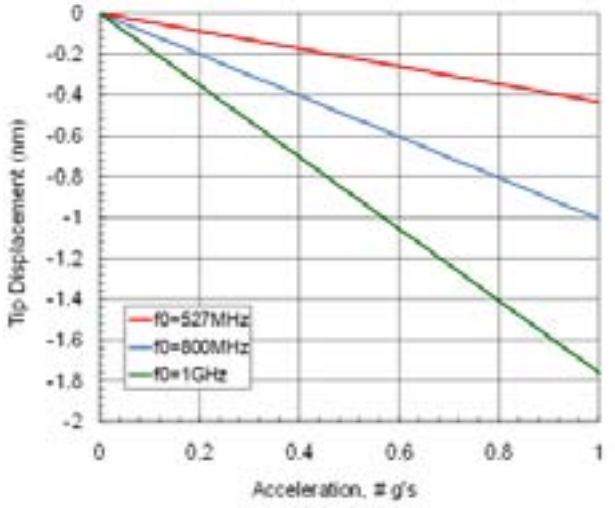

Fig. 15. Tip displacement of several shear-mode resonators as a function of resonance frequency. The quartz plate is 380 x 165 µm^2 and the capacitance sense electrodes are assumed to be 65 x 130 µm^2. The gap spacing between the capacitance sense electrodes on the quartz resonator and the substrate and cap wafer is taken as 5 µm.

is a major factor limiting many applications of MEMS gyros, controlling the temperature in a small ovenized housing is highly beneficial.

The common approach to controlling the temperature of a resonator is by using a thermistor or RTD sensor in the package for monitoring the temperature and then using a heater element in a servo loop. Due to inaccuracies in the temperature sensor itself and temperature gradients between the resonator and the sensor, these approaches are usually limited to controlling the temperature to within 1 – 10 mK. However, quartz manufacturers developed years ago a self-temperature sensing mechanism with high accuracy using two resonant modes of a resonator [14]. This technique relied on the temperature sensitivity differences between the two modes to sense the temperature of the resonator without the need of a separate sensor. For example, the fundamental mode and the third overtone mode of a shear-mode SC-cut resonator have different f/T profiles and the difference $3f_{n1} - f_{n2}$ can be used as the error signal for ovenization. This approach was developed for the microcomputer compensated crystal oscillator (MCXO).

Using this idea, we have designed and are fabricating an integrated Si Disk Resonator Gyro (DRG) and a quartz SC-cut shear-mode resonator in which the difference in the temperature sensitivity of the resonators can be used for ovenization control. The integrated structure is shown in Figure 16. The quartz resonator sits within the base pedestal of the Si DRG and on a common heater for both resonators. This provides maximum coupling from the heater to the resonators, minimizes thermal gradients, and minimizes the total size of the package. If the resonant frequency of the gyro is then locked to that of the quartz clock by means of a thermal feedback loop as shown in Figure 17, the gyro is effectively thermally stabilized [12]. For a short-term stability of the clock of 3 x 10^{-9} over temperature and a frequency stability of the gyro of -30 ppm/^{o}C, one can stabilize the effective temperature of the gyro to 100 μK. This is measured at the gyro itself and provides a highly robust method for improving the bias drift and turn-on to turn-on bias stability over temperature.

V. Conclusions

We have shown that microfabrication techniques that are commonly used in MEMS processing can be applied to piezoelectric quartz resonators for a wide variety of new studies and applications. The use of wafer-scale processing allow the device designer to incorporate new features that rely on small structures and gaps, high electric fields produced with low supply voltages, tightly coupled control electrodes, and co-integration with other sensors. In these cases, novel nonlinear dynamics can be explored as well as dynamical control of vibration and thermal instabilities. The synergistic use of multiple navigation and timing units co-located on a single chip for error correction schemes provides new possibilities for advanced communication and navigation systems.

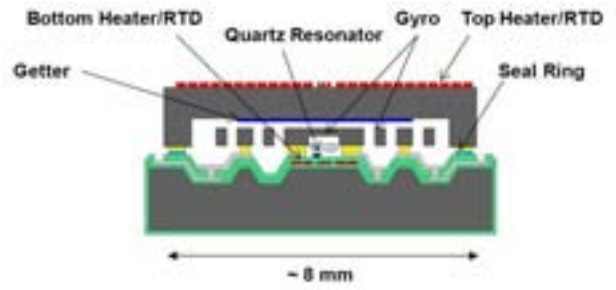

Fig. 16. An integrated Si DRG and a quartz clock in a common ovenized housing for locking the frequency of the gyro to that of the quartz clock with minimal thermal gradients for high accuracy loop control.

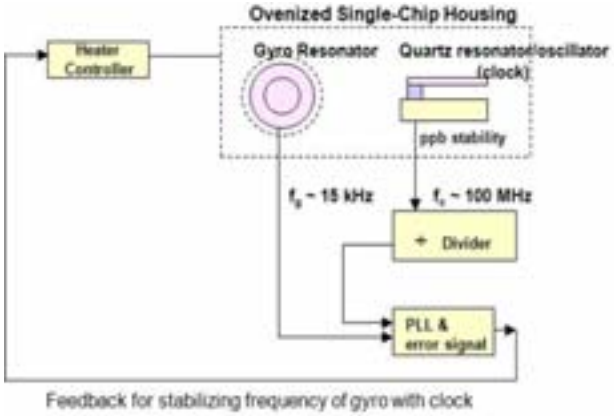

Fig. 17. A heater-based servo loop for controlling the effective temperature of the gyro based on the much higher stability of the ovenized SC-cut quartz clock.

References

[1] R. L. Kubena, et al., "Next generation quartz oscillators and filters for VHF-UHF systems," Proc. 2006 IEEE International Microwave Symposium, San Francisco, Ca., June 11-16, 2006.

[2] F. Zhang, et al., "A 2.6 GHz, 25 fs jitter, differential chip scale oscillator that is <1 mm^2 in area and 0.25 mm tall," Proc. 2012 IEEE International Frequency Control Symposium, Baltimore, MD., May 21-24, 2012.

[3] J. E. Butler, et al., "Diamond materials for MEMS and NEMS structures and devices," Proc. of NanoTech 2003, San Francisco, Ca., Feb. 23-27, 2003.

[4] Y. K. Yong, R. L. Kubena, D. J. Kirby, R. Perahia, and D. T. Chang, "Modeling approach to analyze bonding stress in UHF quartz resonators," unpublished.

[5] D.J. Kirby, et al., "Optimizing UHF quartz MEMS resonators for high thermal stability," unpublished.

[6] Commercial testing performed by Rockwell Collins.

[7] M. S. Patel, Y. K. Yong, M. Tanaka, T. Imai, "Drive level dependency in quartz resonators," Proc. 2005 IEEE International Frequency Control Symposium, Vancouver, BC, Canada, Aug. 29-31, 2005.

[8] B. Yurke, D.S. Greywall, A. N. Pargellis, and P.A. Busch, "Theory of amplifier-noise evasion in an oscillator employing a nonlinear resonator," *Phys. Rev. A*, vol. 51, no. 5, pp 4211-4229, May 1995.

[9] H. P. Moyer, et al., "Nonlinear behavior of an UHF quartz resonator in an oscillating system," Proc. 2012 IEEE International Frequency Control Symposium, Baltimore, MD., May 21-14, 2012.

[10] Y. K. Yong and J. F. Chen, "Resonator Q increase and noise reduction in third overtone thickness shear resonators by the nonlinear characteristics of their fundamental thickness shear mode," Proc. 2012 IEEE International Frequency Control Symposium, Baltimore, MD., May 21-24, 2012.

[11] R. L. Kubena, "MEMS-on-chip inertial navigation system with error correction," US Patent #8,151,640, issue date April 10, 2012.

[12] R. L. Kubena, "Frequency locking of resonators for improved temperature control of gyroscopes," US Patent #8,402,824, issue date Mar. 26, 2013.

[13] W. Snapp, et al., “Mesoscale Disk Resonator Gyroscope for Far Target Locator,” JNC 2012 Joint Navigation Conference, Colorado Springs, Co., June 12-15, 2012.

[14] J. R. Vig, “Quartz crystal resonators and oscillators – a tutorial”, rev. 8.5.3.6, resonator self-temperature sensing, p. 2-18, Jan. 2007.

Nonlinear Dynamics in Aluminum Nitride Contour-Mode Resonators

Nicholas Miller and Gianluca Piazza
Department of Electrical and Computer Engineering
Carnegie Mellon University
Pittsburgh, Pennsylvania, USA, 15213
Email: njmiller@andrew.cmu.edu

***Abstract*—In this work we discuss the self-heating dynamics of aluminum nitride contour mode resonators. The self-heating introduces a quadratic coupling between the resonator motion and its temperature. This coupling produces a nonlinear frequency response identical to the Duffing resonator in steady-state. However, since the thermal relaxation rate is much smaller than the mechanical relaxation rate the dynamics of the resonator differ from the conventional Duffing resonator.**

***Keywords*—Aluminum nitride contour-mode resonator, nonlinear, self-heating, MEMS.**

I. Introduction

In the past several years aluminum nitride (AlN) contour mode resonators (CMRs) have recieved a great deal of attention as a candidate technology for the monolithic integration of high-quality passive elements in radio frequency (RF) circuits [1]–[6]. Monolithic intregration promises to enable compact, low-power, and reconfigurable or agile RF devices that exhibit unprecidented performance. AlN resonators are CMOS compatible, possess low motional resistance due to large electromechanical coupling coefficients, and have fundamental frequencies set by lithographically defined dimensions [1]. The low motional resistance of these resonators allows for integration with existing 50Ω based RF systems and lithographically defined frequencies allows for integration of multi-frequency systems [7]. Moreover, AlN CMRs have been demonstrated with frequencies in the GHz range with an $f \cdot Q$ product of $\sim 4.6 \cdot 10^{12}$ in air [1], [2], [8]. These attributes make AlN CMRs amenable to monolithic integration and a strong candidate for the construction of reconfigurable RF systems.

AlN CMRs consist of a film of AlN sandwiched between two metal patterned layers. The resonator considered in this work is a rectangular device excited by apodized interdigitated electrode on the top layer, see figure 1 [9]. The bottom metal layer is left floating.

One important aspect of AlN CMRs is a relatively large temperature coefficient of frequency (TCF). Values around -20 to -30 ppm/°C are typical and thus AlN CMRs require temperature compensation for some applications [6], [10]. This same temperature sensitivity has been shown to be the leading source of a softening nonlinear behavior exhibited by AlN CMRs [11], [12]. In [11] it was illustrated that the measured resonator admittance exhibits a softening behavior, but that the amount of bending in the resonance depends on the rate of frequency sweep employed in the measurement. In [12] it was shown that self-heating AlN CMRs can be described with a Duffing resonator model. However, this analysis was performed in the quasi-static limit. Both works show that the nonlinearity arises from self-heating. In this work we consider the complete dynamic model of a self-heating AlN CMR and discuss the response of the resonator to a frequency sweep through resonance and its relationship to the sweep rate. In addition, we illustrate that while the self-heating nonlinearity appears similar to the Duffing nonlinearity in the quasi-static case, its dynamics are different. This has important ramifications for some appliciations. For example, the ability of these resonators to evade amplifier noise in oscillators using the techniques described in [13].

AlN CMRs can be described by an equivalent lumped-element circuit: the modified Butterworth Van Dyke (MBVD) model. The lumped-parameter circuit is shown in figure 2 and the fitting of this model to an AlN CMR is shown in figure 3. It is at this level of abstraction that we begin our analysis. However, for a discussion of the reduction of the distributed model to a lumped-parameter ODE the interested reader is direct to [1] and references therein. For these devices Joule heating reduces the Young's modulus of the AlN film, changing the motional lumped parameters (R_m, C_m, and L_m) according to the power dissipated by the resonator [1], [12]. We have indicated this modification to the MBVD model by using variable circuit elements in figure 2.

Our discussion of the nonlinear dynamics of AlN CMRs is arranged as follows. In section II we describe the self-heating model of an AlN CMR. We analyze this model using perturbation techniques in section III. The results of this section are compared with measurements in section IV. Discussion and conclusions are given in section V.

II. Extended MBVD model

We begin with the MBVD circuit model shown in figure 2 and allow L_m, R_m, and C_m to be functions of the resonator temperature deviation from ambient, T. The charge equations for this circuit are

$$L_m \ddot{q}_m + \epsilon \left(R_m + R_s\right) \dot{q}_m + \frac{1}{C_m} q_m = \epsilon V - \epsilon R_s \dot{q}_0, \quad (1)$$

$$(R_0 + R_s)\dot{q}_0 + \frac{1}{C_0} q_0 = V - R_s \dot{q}_m, \quad (2)$$

This material is based on work supported by the Defense Advanced Research Project Agency under the MTO-DEFYS program, award # FA86501217264.

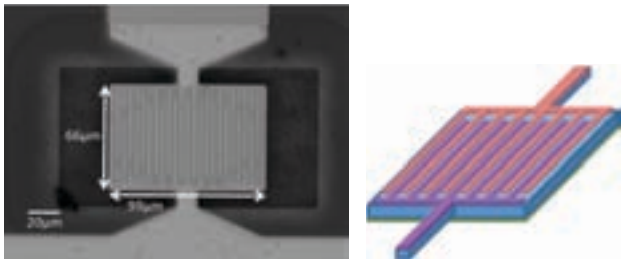

(a) (b)

Fig. 1: Microscope image (a) and cartoon diagram (b) of an aluminum nitride (AlN) contour-mode resonator (CMR). The microscope image shows an apodized resonator [9]

where q_m is the charge on capacitor C_m, q_0 is the charge on capacitor C_0, and V is the voltage applied across the terminals of the circuit. ϵ is a book-keeping parameter marking the terms we will treat as perturbations in section III. We assume that temperature changes are relatively small and so we keep only the first order change in L_m, R_m, and C_m. Thus, we have

$$L_m \approx L_m^{(0)} + \epsilon L_m^{(1)} T, \tag{3}$$

$$R_m \approx R_m^{(0)} + R_m^{(1)} T, \tag{4}$$

$$C_m \approx C_m^{(0)} + \epsilon C_m^{(1)} T. \tag{5}$$

Following [12], we augment the MBVD model with a lumped parameter temperature model for the resonator

$$C_{\text{th}} \dot{T} = -\epsilon \frac{T}{R_{\text{th}}} + \epsilon P_{\text{diss}}, \tag{6}$$

where C_{th} is the resonator heat capacity, R_{th} is the thermal resistance between the resonator and ambient, and P_{diss} is the power dissipated through the resistive elements. P_{diss} is maximum at resonance and in this case the current flows mostly through the mechanical branch of the circuit, the upper branch in figure 2. Thus, for simplicity, we keep only this current in our expression for the dissipated power. Moreover, The principle component of R_m should dominate the variation due to temperature, and so we drop $R_m^{(1)}$ in P_{diss} as well. Accordingly, we approximate the dissipated power as

$$P_{\text{diss}} \approx (R_m^{(0)} + R_s) \dot{q}_m^2. \tag{7}$$

Equations (1)-(7) complete the extended MBVD model. The introduction of temperature dependent coefficients, equations (3)-(5), and the form of (7) introduce a nonlinear coupling between the charge equation (1) and the temperature equation (6). The nonlinear coupling between the resonator and its temperature makes this system difficult to treat exactly. However, these resonators exhibit a separation of time scales due to their large quality factors, making them accessible by perturbation analysis.

III. Envelope Equations

In this section we treat equations (1)-(7) as a weakly nonlinear resonator employing the method of averaging [14]. The terms that we will treat as perturbations have already been marked by ϵ. We consider the primary resonance with weak forcing, and thus we choose

$$V = V_0 \cos \omega t, \tag{8}$$

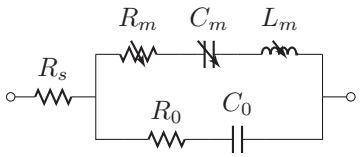

Fig. 2: Modified Butterworth Van Dyke (MBVD) circuit model with nonlinear motional elements.

with ω being close to the resonator's natural frequency. Next we employ the coordinate change

$$q_m = a_0 u e^{i\omega t} + \text{c.c.}, \tag{9}$$

$$\dot{q}_m = i\omega a_0 u e^{i\omega t} + \text{c.c.}, \tag{10}$$

where a_0 is the characteristic amplitude of oscillation, u is the complex amplitude of the resonator, and c.c. stands for the complex conjugate of the preceding terms. Application of this coordinate transformation places equations (1), (2), and (6) in a form amenable to perturbation analysis.

For this system q_0 is a 'fast' variable and is enslaved to the 'slow' evolution of u. Accordingly, we substitute equations (8) and (10) into (2) and solve for q_0 under the assumption that u is constant. This gives

$$q_0 = \frac{C_0}{2} \frac{V_0 - 2i\omega R_s a_0 u}{1 + i\omega C_0 (R_0 + R_s)} e^{i\omega t} + \text{c.c.}. \tag{11}$$

From equaiton (11) we find that the admittance of the resonator is given by

$$Y = \frac{i\omega}{1 + i\omega C_0 (R_0 + R_s)} \left(C_0 + (1 + i\omega C_0 R_0) \frac{2 a_0 u}{V_0} \right). \tag{12}$$

To arrive at an approximate equation for the 'slow' evolution of the resonator's complex amplitude and temperature we substitute equation (11) into equations (1) and (6) and then drop the fast oscillating terms. Moreover, when we substitute for $\dot{q}_0$, we take the time derivative of the $e^{i\omega t}$ term, but not the time derivative of u. The reason being that the slow evolution of u makes this term in $\dot{q}_0$ negligible. In addition, it is convenient to introduce a scaling of both temperature and time in order to simplify the resulting equations. We therefore introduce the the non-dimensional time variable, $\mathfrak{t}$, and the non-dimensional temperature, τ. The relationship between t and $\mathfrak{t}$ and T and τ is given in table I. From this point onward we will use the overdot, $\dot{\square}$, to indicate the derivative with respect to $\mathfrak{t}$ and we also set $\epsilon = 1$ since this book-keeping parameter has served its purpose for the perturbation analysis [14]. Thus we arrive at an approximate set of resonator equations,

$$\dot{u} = -(1 + i\sigma) u - (\delta + i) u \tau + \nu, \tag{13}$$

$$\dot{\tau} = -\frac{1}{\gamma} \tau + |u|^2, \tag{14}$$

where, as we stated above, u is the non-dimensional complex amplitude of oscillation and τ is the non-dimensional resonator temperature. In addition we have introduced the reduced parameters in table I.

To show that a self-heating AlN CMR gives a Duffing-like frequency response, we solve for the fixed points of

$t = \frac{1}{\rho}\mathfrak{t}$	$a_0 = \frac{T_0 \rho C_{\text{th}}}{2\omega^2 (R_m^{(0)} + R_s)}$	$\rho = \frac{R_m^{(0)} + R_s + \omega^2 C_0^2 (R_0 + R_s)(R_m^{(0)} R_s + R_m^{(0)} R_0 + R_0 R_s)}{2 L_m^{(0)} (1 + \omega^2 C_0^2 (R_0 + R_s)^2)}$
$T = T_0 \tau$	$\delta = \frac{T_0 R_m^{(1)}}{2\rho L_m^{(0)}}$	$\sigma = \frac{\omega}{2\rho} - \frac{1}{2\rho\omega L_m^{(0)} C_m^{(0)}} - \frac{\omega C_0 R_s^2}{2\rho L_m^{(0)} (1 + \omega^2 C_0^2 (R_0 + R_s)^2)}$
$T_0 = \frac{2\rho\omega (C_m^{(0)} L_m^{(0)})^2}{L_m^{(0)} C_m^{(1)} + L_m^{(1)} C_m^{(0)}}$	$\gamma = \rho R_{\text{th}} C_{\text{th}}$	$\nu = \frac{V_0}{4 i \omega \rho L_m^{(0)} a_0} \frac{1 + i\omega C_0 R_0}{1 + i\omega C_0 (R_0 + R_s)}$

TABLE I: Reduced parameter definitions.

equations (13) and (14). It is easiest to solve for the frequency response by assuming that $|u|$ is known and solve for the frequency detuning, σ, the phase of the resonator, $\angle u$, and the temperature τ. The result is

$$\sigma = -\gamma|u|^2 \pm \sqrt{\left|\frac{\nu}{u}\right|^2 - (1 + \delta\gamma|u|^2)^2}, \tag{15}$$

$$\angle u = \angle\nu \mp \tan^{-1}\left(\sqrt{\frac{|\nu|^2}{(|u| + \delta\gamma|u|^3)^2} - 1}\right), \tag{16}$$

$$\tau = \gamma|u|^2. \tag{17}$$

The frequency response described by equations (15)-(17) matches the conventional Duffing frequency response [14] when $\delta \to 0$. This slight difference arises from the nonlinear damping imposed by the temperature variations of the motional resistance, R_m.

While the quasi-steady state frequency response of equations (13) and (14) appears similar to that of the Duffing resonator, the added temperature dynamics cause the resonator to behave differently in non-steady-state situations. For most AlN CMRs the temperature dynamics are much slower than the resonator amplitude dynamics. In our formulation this is manifested by the condition $\gamma \gg 1$. Accordingly, when the resonator is probed by a frequency sweep the temperature dynamics can reveal themselves during the sweep even though the sweep rate is much slower than the resonator's mechanical relaxation rate. This was observed in [11]. In order to explore this further, we suppose that σ changes in time as it will during a frequency sweep. In addition, we suppose that γ is indeed large and therefore the dynamics of u are much faster than that of τ. To arrive at a simple model for the swept resonator we solve (13) for the quasi-static fixed point $u(\mathfrak{t}, \tau)$ and insert this solution into (14). This gives a simplified model for the swept resonator

$$\dot{\tau} = -\frac{1}{\gamma}\tau + \frac{|\nu|^2}{(1 + \delta\tau)^2 + (\sigma(\mathfrak{t}) + \tau)^2}, \tag{18}$$

$$u(\mathfrak{t}, \tau) = \frac{\nu}{(1 + \delta\tau) + i(\sigma(\mathfrak{t}) + \tau)}. \tag{19}$$

While equation (18) is difficult to solve, we can again employ a perturbation approach to obtain an approximate solution for a linear frequency sweep in the weak heating limit. In this case we use a direct perturbation scheme. First we let $\sigma(\mathfrak{t}) = \sigma_0 + r\mathfrak{t}$. Then we let $\tau = \tau_0 + \epsilon\tau_1$ and $|\nu|^2 \to \epsilon|\nu|^2$. The zero$^{\text{th}}$ order equation is $\dot{\tau}_0 = -\tau_0/\gamma$. We will assume that equilibrium has been obtained prior to sweeping, and thus $\tau_0 = 0$. The first order equation is

$$\dot{\tau}_1 = -\frac{1}{\gamma}\tau_1 + \frac{|v|^2}{1 + (\sigma_0 + r\mathfrak{t})^2}. \tag{20}$$

$L_m = 19.146\ \mu\text{H}$	$C_m = 1.2768$ fF	$R_m = 57.082\ \Omega$
$C_0 = 160.09$ fF	$R_0 = 16.976\ \Omega$	$R_s = 9.4207\ \Omega$
$a_0 = 6.3 \times 10^{-15}$	$\gamma = 1.5876 \times 10^{-4}$	$\delta = 0.01$

TABLE II: Resonator parameter values.

The solution to (20) is

$$\tau(\mathfrak{t}) \approx \frac{|\nu|^2}{r} \operatorname{Im}\left[e^z \left(\Gamma(0, z_0) - \Gamma(0, z)\right)\right], \tag{21}$$

$$z(\mathfrak{t}) = \frac{i - \sigma(\mathfrak{t})}{r\gamma}, \tag{22}$$

where $\Gamma(0, z)$ is the incomplete Gamma function. For $\sigma_0/r\gamma \ll -1$, that is starting the sweep sufficiently far from resonance, the solution depends very weakly on the starting frequency, σ_0. In this case, the Gamma function $\Gamma(0, z_0)$ can be dropped and we have

$$\tau(\mathfrak{t}) \approx -\frac{|\nu|^2}{r} \operatorname{Im}\left[e^z \Gamma(0, z)\right]. \tag{23}$$

This solution is appropriate for very weak driving such that the self-heating is small. When the resonator is driven strongly equation (18) must be solved numerically. This can be done readily using commonly available numeric solvers.

IV. Experimental Results

The self-heating dynamics of the resonator can be exposed via a rapid frequency sweep using a vector network analyzer (VNA) under high power. The VNA employed for this work was the Agilent N5230A. The resonator we employed is shown in figure 1 (a). The low power admittance of the resonator is shown in figure 3. From this admittance data we fit the linear MBVD parameters using least squares regression. The parameters are shown in the top two rows of table II.

Under higher power the peak of the admittance plot bends toward lower frequencies, a softening behavior similar to a Duffing resonator. However, when the VNA sweep rate is increased the admittance plot changes. This is illustrated in figure 4 which shows a zoomed in view of the admittance peak as a function of the normalized frequency detuning. The black dashed line shows the fixed points for the resonator system, *i.e.* equations (15)-(17). The blue, red, and green lines are the numeric solutions to the sweeping model, equation (18), and the blue, red, and green marks are the measured data. The nonlinear resonator parameters a_0, γ, and δ were fit to the data shown. The fourth nonlinear parameter, e.g. T_0

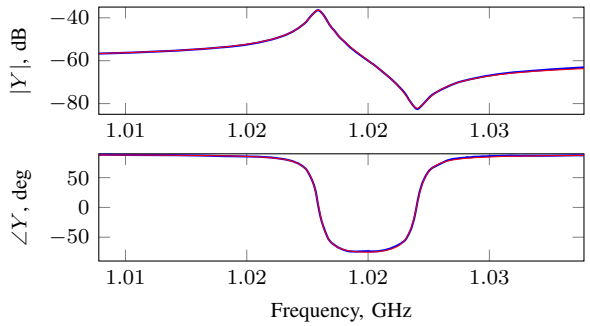

Fig. 3: Resonator admittance for low power. The blue curve is the measured admittance and the red curve is the admittance of the MBVD model.

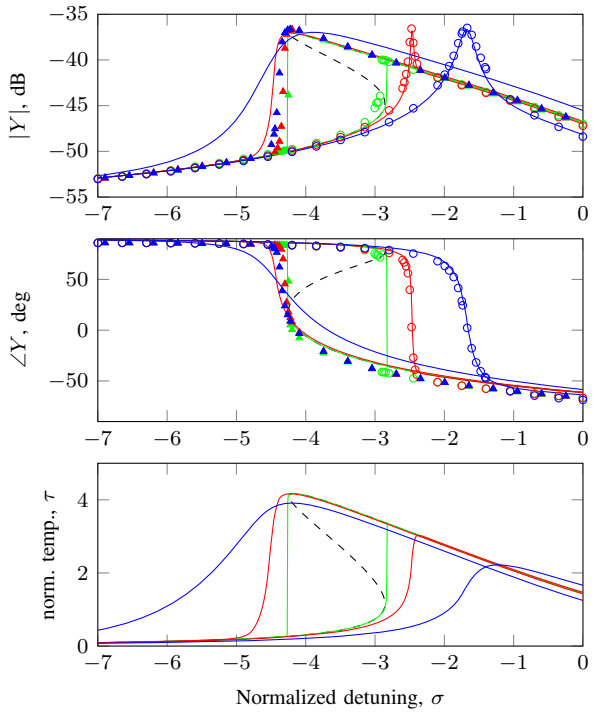

Fig. 4: 11dBm sweeps at 2.7 GHz/sec sweep up, ○, and down ▲, 0.28 GHz/sec sweep up, ○, and down ▲, and 3.4 MHz/sec sweep up, ○, and down ▲. The detuning range shown corresponds to a frequency range of 3.375 MHz. The drive power was 11 dBm.

could not be fit because the resonator temperature could not be measured during the sweep. The figure illustrates how the sweep response adiabatically tracks the steady-state solution for a slow sweep, see the green line and marks for 3.4 MHz/sec sweep rate. However, for a fast sweep (0.28 and 2.7 GHz/sec) the temperature lags the steady-state solution and so does the admittance. The sweeps upward in frequency show a very nice agreement with the model. The sweep down, however, falls from the peak more rapidly than the model predicts. This is a strange phenomenon because the relaxation time of the resonator appears different as the frequency is swept up or down. This phenomenon is currently unexplained and requires further investigation.

V. Conclusions

In this work we examined the nonlinear dynamics of a self-heating AlN CMR using perturbation techniques. We demonstrated that the resonator exhibits a Duffing like response in steady-state, but differs from the conventional Duffing resonator due to the slowness of the temperature dynamics. The temperature dynamics can be revealed via rapid frequency sweeps using a VNA. Using perturbation analysis to predict the response to the VNA frequency sweep we obtained good agreement with experimental results.

References

[1] G. Piazza, P. Stephanou, , and A. Pisano, "Piezoelectric aluminum nitride vibrating contour-mode mems resonators," *Journal of Microelectromechanical Systems*, vol. 15, pp. 1406–1418, 2006.

[2] P. Stephanou and A. Pisano, "Ps-4 ghz contour extensional mode aluminum nitride mems resonators," *Ultrasonics Symposium, 2006. IEEE*, pp. 2401–2404, 2006.

[3] G. Piazza, "Integrated aluminum nitride piezoelectric microelectromechanical system for radio front ends," *Journal of Vacuum Science & Technology A: Vacuum, Surfaces, and Films*, vol. 27, pp. 776–784, 2009.

[4] M. Rinaldi, C. Zuniga, C. Zuo, and G. Piazza, "Super-high-frequency two-port aln contour-mode resonators for rf applications," *IEEE Transactions on Ultrasonics, Ferroelectrics and Frequency Control*, vol. 57, pp. 38–45, 2010.

[5] C. Zuo, J. V. der Spiegel, and G. Piazza, "1.05-ghz cmos oscillator based on lateral-field-excited piezoelectric aln contour-mode mems resonators," *IEEE Transactions on Ultrasonics, Ferroelectrics and Frequency Control*, vol. 57, pp. 82–87, 2010.

[6] A. Tazzoli, G. Piazza, M. Rinaldi, J. Segovia, C. Cassella, B. Otis, J. Shi, K. Turner, C. Burgner, K. McNaul, D. Bail, and V. Felmetsger, "Piezoelectric nonlinear nanomechanical temperature and acceleration insensitive clocks," *Proc. SPIE 8373, Mirco- and Nanotechnology Sensors, Systems, and Applications*, vol. 83730A, 2012.

[7] G. Piazza, P. Stephanou, and A. Pisano, "Single-chip multiple-frequency aln mems filters based on contour-mode piezoelectric resonators," *Journal of Microelectromechanical Systems*, vol. 16, pp. 319–328, 2007.

[8] M. Rinaldi, C. Zuniga, and G. Piazza, "5-10 ghz aln contour-mode nanoelectromechanical resonators," *Micro Electro Mechanical Systems, 2009. MEMS 2009. IEEE 22nd International Conference on*, pp. 916–919, 2009.

[9] M. Giovannini, S. Yazici, N.-K. Kuo, and G. Piazza, "Spurious mode suppression via apodization for 1 ghz aln contour-mode resonators," *Frequency Control Symposium, 2012 IEEE International*, pp. 1–5, 2012.

[10] C. Lin, T. Yen, Y. Lai, V. Felmetsger, M. Hopcroft, J. Kuypers, and A. Pisano, "Temperature-compensated aluminum nitride lamb wave resonators," *IEEE Transactions on Ultrasonics, Ferroelectrics and Frequency Control*, vol. 57, pp. 524–532, 2010.

[11] A. Tazzoli, M. Rinaldi, and G. Piazza, "Experimental investigation of thermally induced nonlinearities in aluminum nitride contour-mode mems resonators," *IEEE Electron Device Letters*, vol. 33, pp. 724–726, 2012.

[12] J. Segovia-Fernandez and G. Piazza, "Thermal nonlinearities in aln contour mode resonators," *submitted*, 2013.

[13] B. Yurke, D. Greywall, A. Pargelliz, and P. Busch, "Theory of amplifier-noise evasion in an oscillator employing a nonlinear resonator," *Physical Review A: Atomic, Molecular, and Optical Physics*, vol. 51, pp. 4211–4229, 1995.

[14] A. Nayfeh and D. Mook, *Nonlinear Oscillations*. Wiley-VCH, 1995.

Close-in Phase Noise Reduction in an Oscillator based on 222 MHz Non-linear Contour Mode AlN Resonators

J. Segovia-Fernandez, C. Cassella, G. Piazza
Department of Electrical and Computer Engineering
Carnegie Mellon University
Pittsburgh, USA
jsegovia@andrew.cmu.edu; piazza@ece.cmu.edu

***Abstract*—Phase Noise noise reduction in oscillators can be accomplished by using nonlinearly driven resonators locked into a particular nonlinear state that fulfill specific frequency and phase conditions. In this work, we experimentally demonstrate this theory by showing a substantial improvement of the close-in phase noise (lowered by as much as -20dBc/Hz @ 100Hz) of a 222 MHz oscillator that incorporates a nonlinearly driven AlN contour mode resonator (CMR).**

I. Introduction

Microelectromechanical Systems (MEMS) resonators are considered a promising alternative to quartz and surface acoustic wave (SAW) resonators for building stable oscillator circuits for modern sensing and communication applications. Major advantages of the MEMS technology are its compatibility with semiconductor fabrication techniques, which permit its integration with integrated circuit (IC) devices, and its relatively small form factor, which enables new functionalities in a given chip area. On the other hand, the use of miniaturized devices in electronic applications comes with limitations in terms of power handling. As the device size shrinks, MEMS resonators exhibit a larger nonlinear behavior. Although this could be seen as a disadvantage for the implementation of oscillators, a study [1] has first claimed that introducing a nonlinear resonator in the feedback loop can improve the output Phase Noise (PN). It is suggested that by locking the non-linear device into a particular operating state (referred here as critical operating state (COS)) the PN introduced by the amplifier and filtered by the resonator can be evaded [1].

AlN Contour Mode Resonators (CMRs) are an emerging class of piezoelectric MEMS devices exhibiting high quality factor (Q) and low motional resistance at high frequencies (f_r), which make them good candidates for the implementation of frequency references in RF front-end systems [2]. A previous study [3] on 1GHz AlN CMRs has demonstrated that by driving the resonator at a relative high power and with a slowly modulated input (slower than the device thermal time constant (τ_{TH})) pronounced nonlinearities associated with thermal effects are present. Lower frequency AlN CMRs also exhibit the same kind of non-linearity. In this work a 222.5 MHz resonator with Q=3000 is used as a frequency reference in an oscillator circuit. In this particular case, when the resonator is driven nonlinearly, the measured resonance response shows the combined impact of thermal effects and variable damping [4]. These two phenomena are here exploited for the synthesis of a low PN oscillator.

Specifically, we demonstrate a clear improvement of the PN close-in of a 222 MHz oscillator that incorporates a nonlinearly driven AlN CMR. The oscillator circuit of this paper is built by using coaxial electronic components. The experiments reveal that the offset frequency (f_{off}) up to which the PN is reduced is limited by the device τ_{TH}, hence related to the thermal non-linearities of the CMR. Finally, a modified Lesson equation is used to explain the PN reduction achieved by locking the resonator around the COS.

II. Nonlinear AlN Contour Mode Resonator (CMR) Characterization

The resonator used in the oscillator circuit of this work is known as a one port AlN CMR, whose principle of operation was previously introduced in [5]. An AlN plate is sandwiched between a bottom metal plate and a patterned top electrode. The number of electrodes is equivalent to the number of fingers (n) (or sub-resonators). Each electrode is alternatively connected to signal and ground voltages, which generate an electric field across the piezoelectric material. Hence, a lateral strain is induced in the direction of the finger width (Fig. 1). The resonance frequency (f_r) of this type of resonator is set by two parameters: the width of the finger (W), that is related to the wavelength of the first mode of vibration (λ), and the acoustic velocity of the resonator stack $(Y/\rho)^{1/2}$.

The AlN CMR was fabricated by a three masks process as described in [3]. For the device employed in this study the AlN thickness is set to be 1 µm, and both electrodes are

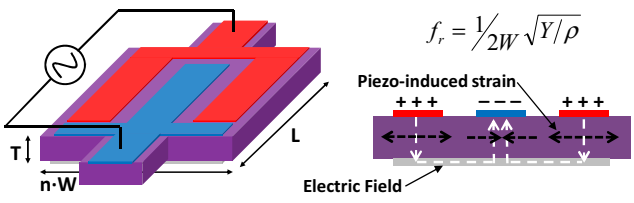

Fig. 1. Schematic representation of an AlN CMR made to vibrate if by applying opposite potentials to adjacent electrodes.

This work was supported by the DEFYS DARPA contract #FA8650-10-1-7030

selected to be around 100 nm thick. The choice of metals for this specific resonator is Pt for the bottom plate, which is used to attain AlN films with a good c-axis orientation, and Al for the top electrodes, which is selected to reduce the series resistance induced by the smaller electrodes. The top view dimensions of the 222 MHz resonant plate are 60 μm (width) by 140 μm (length). *n* is equal to 3 and the width of each finger is 20 μm. The anchors' geometry is optimized to achieve a high quality factor (*Q*) according to previous studies on anchor losses in AlN CMRs [6]. Thus, both anchor length and width are set to be 20 μm, which is equal to λ/2 (Fig. 2).

The resonance response of AlN CMRs is described by the Modified Butterworth Van Dike (MBVD) model (more detail about the circuit can be found in [3]). To experimentally extract the electrical response of the 222 MHz resonator this was mounted on a PCB and connected in series between input and output SMA connectors (this is the same configuration that will be used in the oscillator circuit). One port is then connected to an Agilent N5230A network analyzer (VNA) and the other port is 50 Ω terminated (Fig. 3). The reflection coefficient (S_{11}) is recorded on the VNA and translated into the admittance magnitude (Y_{11}). The *Q* can be directly computed from this measurement as the ratio $f_r/\Delta f_{-3dBs}$ when the device is subjected to small power levels (below -5dBm the device is working in the linear regime). If the device is instead subjected to an increasing power level, the reported admittance manifests a Duffing-like response, which is indicative of a pronounced nonlinear behavior (Fig. 4).

Experimental protocols for characterizing the nonlinear performance of AlN CMRs have been developed for 1GHz devices in [3]. In that work, both Amplitude-frequency (A-f) and 3rd order intermodulation distortion (IMD3) measurements were performed to extract the nonlinear elastic coefficient (α), and fit the recorded admittance for different power levels. The analysis also revealed that the origin of the elastic nonlinearities was mostly thermal when the input was slowly modulated (the input was kept constant for longer than the device τ_{TH}).

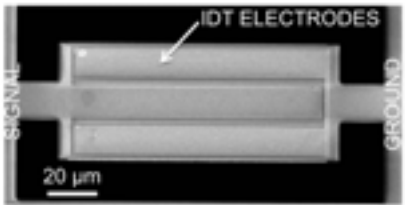

Fig. 2. SEM image of the 222MHz AlN CMR used in the oscillator circuit.

Fig. 3. 222MHz AlN CMR wire bonded on a 2 port FR4 circuit board (PCB).

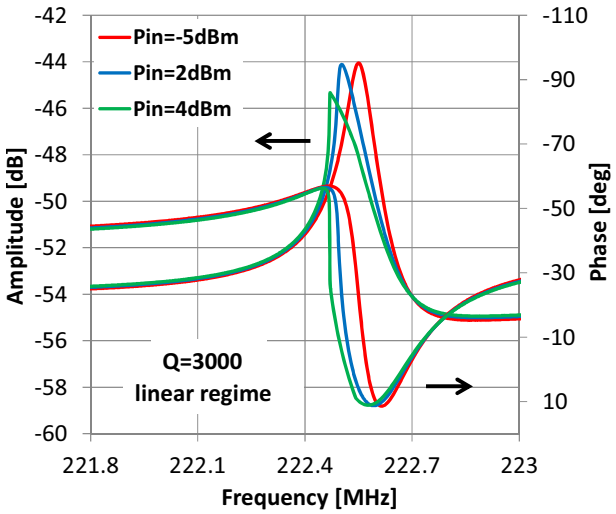

Fig. 4. Tested admittance response (amplitude and phase) of the 222MHz AlN CMR wirebonded on a PCB for different values of input power (Pin=-5dBm, 2dBm, and 4dBm).

It is important to note that the 222 MHz AlN CMR tested here exhibited a certain deviation from the typical Duffing-like behavior. On Fig. 3 we can see that as P_{in} is increased the frequency shift of the peak is also accompanied by a reduction of its magnitude. This phenomenon indicates the dual source of nonlinearities. In fact, not only elastic nonlinearities (related to thermal effects) are at play, but also a variable damping [4]. Although the origin of the latter is still unclear, we believe it has a direct impact on the oscillator performance. We identify the COS as the set of points for which we observe close to infinite phase to frequency slope. Fig. 4 shows the forward and backward sweeps of the amplitude and phase of the 222 MHz resonator for P_{in}=4 dBm. Since the direction of the sweeping does not almost alter the resonance profile we can claim that the COS condition is roughly fulfilled for a large range of phases in this particular case.

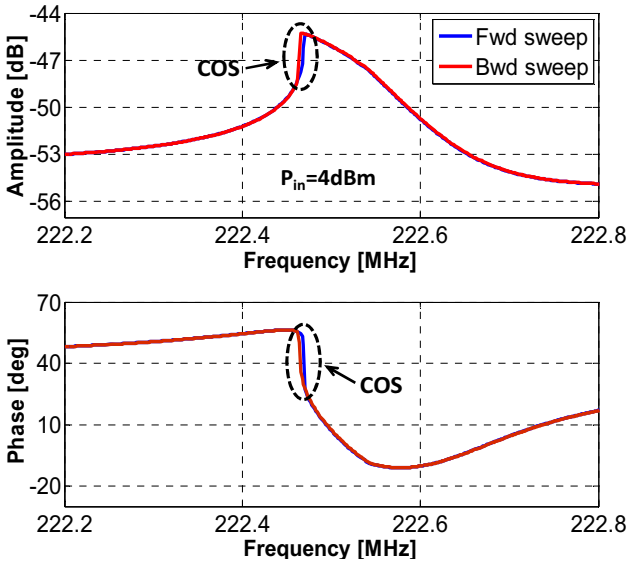

Fig. 5. Amplitude and phase of the admittance response of the 222 MHz AlN CMR mounted on a FR4 circuit board when Pin=4dBm and the frequency is swept back and forward.

III. Nonlinear Oscillator Phase Noise

A. Oscillator Setup

The 222 MHz oscillator of this study is built by using coaxial electronic components (Fig. 5). The AlN CMR is mounted on a 2-port PCB (Fig. 3) that is connected in series with the rest of components in the circuit. The design of the strip lines and the selection of the 2 ports connectors are optimized in order to reduce the parasitic capacitances of the PCB. All the discrete elements, SMA connectors, and cables are chosen to have the characteristic impedance equal to 50 Ω for matching purposes. An external DC power supply is used to bias the RF amplifier (Mini-circuits ZKL-1R5+) and the output is taken from one of the power divider (M/A-COM T-1000) terminals. To close the loop, the other terminal is connected to the phase shifter (ATM P1213)

B. Phase Noise Experiments

The experiments are carried out by setting the DC bias of the RF amplifier to 6V, therefore ensuring enough gain to both sustain oscillations and drive the resonator nonlinearly. The phase shifter is manually tuned in steps of 5° to increase the circuit delay and, hence, lock the oscillator into different oscillation frequencies (f_{osc}) along the nonlinear resonance curve of the 222 MHz AlN CMR. Table I summaries the output power (P_{out}) and the f_{osc} recorded on the Signal Source Analyzer (SSA) for each phase delay ($\Delta\theta$). Assuming that the only element in the circuit that changes the response with frequency is the resonator, we can also identify its f_r by looking at the maximum P_{out} recorded (the higher is the admittance the lower are the losses in the loop). Consequently, we find that f_r=222.434MHz and this value corresponds to $\Delta\theta$=10° (these values are highlighted by a red box in Table I). Furthermore, we confirm that the P_{in} sent to the resonator is around 4 dBm (this value coincides with P_{out} as the losses in the phase shifter and the cables are approximately the same of those components that connect the power divider with the SSA).

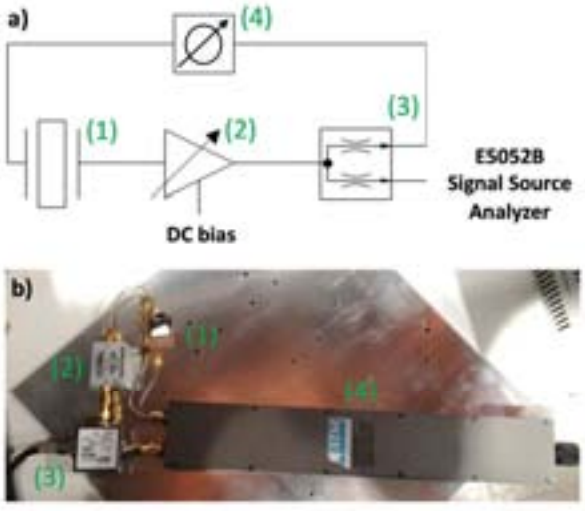

Fig. 6. a) Circuit schematics and b) actual oscillator setup including the (1) AlN CMR mounted on a PCB, (2) RF amplifier, (3) power divider, and (4) phase shifter.

TABLE I. Summary of Output Powers and Oscillation Frequencies corresponding to different Phase Delays in the 222MHz Oscillator.

$\Delta\theta$ (°)	P_{out} (dBm)	f_{osc} (MHz)
0	3.36	222.501
5	3.78	222.470
10	4.04	222.434
15	4.01	222.422
20	3.88	222.413
25	3.79	222.407
30	3.68	222.399
35	3.63	222.393
40	3.62	222.384

Fig. 6 reports the oscillator PN versus the offset frequency (f_{off}) measured for different values of $\Delta\theta$. A dramatic reduction in the PN close-in (f_{off}<1 kHz) is observed when $\Delta\theta \geq 15°$ (this corresponds to $f_{osc}<f_r$ according to Table I). Considering that the power in the AlN CMR is $P_{in} \approx$ 4dBm, we can conclude that for a range of values of the phase shift the resonator is operated in the COS (see Fig. 4). Thus, the effective improvement of PN translates to a change of slope that goes from $1/f^4$ to $1/f^2$ for close-in offsets. Moreover, the experimental results show that the AlN CMR τ_{TH} limits the maximum f_{off} up to which the PN improvement can occur. This confirms the thermal origin of the nonlinearities of the 222MHz AlN CMR. We confirmed that for lower DC biases the power driving the resonator is also lower and no PN improvement is observed.

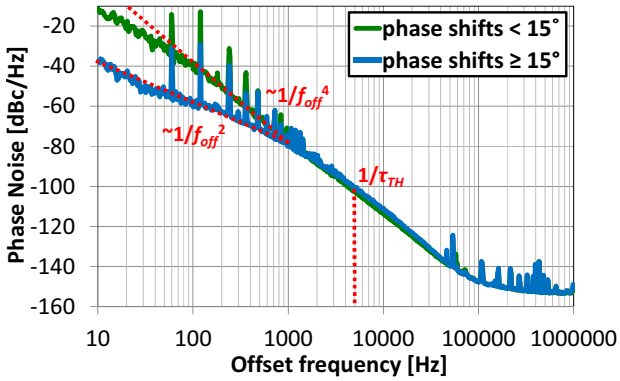

Fig. 7. a) Circuit schematics and b) actual oscillator setup including the (1) AlN CMR mounted on a PCB, (2) RF amplifier, (3) power divider, and (4) phase shifter.

IV. Discussion and Analysis

The previous experimental results show an evident PN slope reduction for close-in offsets that changes from $1/f_{off}^4$ to $1/f_{off}^2$. To provide an intuitive explanation of this phenomenon we resort to a modified version of the Lesson equation that is used to model the PN in closed loop oscillators [7]. Equation (1) describes the oscillator as a first-order filter, which integrates any phase modulations

generated in the circuit (*i.e.* amplifier) when f_{off} is below the Leeson frequency (f_L).

$$S_{\emptyset}(f_{off}) = S_{\theta}(f_{off})\left[1 + {f_L}^2/f_{off}^2\right] \quad (1)$$

where $1/2S_{\emptyset}(f)$ is the single sideband power spectral noise density that is recorded on the SSA, $S_{\theta}(f_{off})$ is the power spectral noise density of the circuit noise. f_L depends on the relaxation time of the resonator (τ) and directly affects the frequency stability of the oscillator with respect to any phase fluctuations generated in the circuit [8].

$$\tau = 1/2\pi f_L = \partial\varphi/\partial\omega \quad (2)$$

where $\partial\varphi/\partial\omega$ is the phase to frequency slope of the resonator admittance at f_{osc}. In the linear regime and when f_{osc}=f_r, (2) becomes $\partial\varphi/\partial\omega = Q/\pi f_r$. In this case, f_L is inversely proportional to Q. For a linear resonator, (1) states that PN lowers if a higher Q resonator is available. When the resonator is locked into the COS region, τ tends to a very large value (ideally infinite), and f_L approaches 0. This non-linear phenomenon effectively lowers the output PN, as if the oscillator was made insensitive to any PN generated externally to the resonator. Under this condition (1) is reduced to:

$$S_{\emptyset}(f_{off}) = S_{\theta}(f_{off}) \quad (3)$$

Comparing (1) and (3), we can observe that the PN in the close-in region goes from ${1/f_{off}}^2 S_{\theta}(f_{off})$ to $S_{\theta}(f_{off})$. This perfectly matches with the case of this study if we assume that the PN produced in our circuit is $S_{\theta}(f_{off}) \propto {1/f_{off}}^2$.

To confirm that the amplifier was the dominant source of noise in the circuit ($S_{\theta}(f)$), we later substituted this amplifier by a lower noise version. Then, we made sure that the power applied to the resonator was enough to drive the device nonlinearly and tuned the phase shifter to reach the COS condition. However, even thought the recorded PN was lower for all f_{off} (-107dBc/Hz @ 1kHz and $1/f_{off}^3$ at the close-in (f_{off}<10kHz)), no change of slope in the close-in region was observed. In this case, the PN was limited by the resonator frequency fluctuations. This confirmed the origin of $S_{\theta}(f_{off}) \propto {1/f_{off}}^2$ as related to the amplifier and proved the concept of amplifier noise evasion by using a nonlinear resonator in the oscillator.

V. CONCLUSION

In this paper we have demonstrated reduction of the close-in phase noise (slope change from $1/f_{off}^4$ to $1/f_{off}^2$) for a 222 MHz oscillator by operating a nonlinearly driven AlN CMR in a particular nonlinear state. To prove the concept, we have built the oscillator by using external coaxial components, which allowed us to separately control the phase and driving power in the circuit. The experimental data also showed the impact of the thermal effect on the resonator nonlinear behavior (PN noise improvement was limited to frequency offsets < τ_{TH}). A simple and intuitive way to explain the experiments was also presented by modifying the conventional Leeson theory.

REFERENCES

[1] B. Yurke, D.S. Greywall, A.N. Pargellis, and P.A Busch, "Theory of amplifier-noise evasion in an oscillator employing a nonlinear resonator," *Phys. Rev. A51*, pp. 4211-4229, (1995).

[2] G. Piazza, P. J. Stephanou, A. P. Pisano, "Piezoelectric Aluminum Nitride Vibrating Contour- Mode MEMS Resonators", *Journal of MEMS*, vol. 15, no. 6, pp. 1406-1418, 2006.

[3] J. Segovia-Fernandez, G. Piazza, "Thermal Nonlinearities in Contour Mode AlN Resonators", *Journal of Microelectromechanical Systems*, in press.

[4] R. Lifshitz, and M. C. Cross, "Nonlinear dynamics of nanomechanical and micromechanical resonators". In Review of Nonlinear Dynamics and Complexity, H. G. Schuster, ed., Vol. 1. pp. 1–52.

[5] G. Piazza, P. J. Stephanou, and A. P. Pisano, "One and two port piezoelectric higher order contour-mode MEMS resonators for mechanical signal processing," *Solid-State Electron*, vol. 51, no. 11-12, pp. 1596–1608, 2007.

[6] J. Segovia-Fernandez, M. Cremonesi, C. Cassella, A. Frangi, and G. Piazza, "Experimental Study on the Impact of Anchor Losses on the Quality factor of Contour Mode AlN Resonators," unpublished.

[7] D. B. Leeson, "A simple model of feedback oscillator noises spectrum," *Proc. IEEE,* vol. 54, pp. 329–330, Feb. 1966.

[8] E. Rubiola, Phase Noise and Frequency Stability in Oscillators. Cambridge University Press, 2009.

MEMS-based Mechanical AGC for Oscillator Circuits

Andreja Erbes[†*], Xueyong Wei[‡] and Ashwin A. Seshia[†]
[†]Engineering Department, University of Cambridge, Cambridge, United Kingdom
[‡]School of Mechanical Engineering, Xi'An Jiaotong University, Xi'An, China
[*]Email: ae279@eng.cam.ac.uk

***Abstract*—This paper investigates a nonlinear amplitude saturation behavior in an electrostatically transduced, silicon MEMS disk resonator operating in its secondary elliptical bulk-mode ($SEBM$) at 3.932 MHz towards its implementation as an all-mechanical automatic gain control (AGC) element. The nonlinear vibration behavior of the $SEBM$ mode is experimentally observed in open-loop testing such that above a threshold small signal drive voltage at a given polarization voltage, the vibration amplitude of the $SEBM$ mode saturates. We also study this nonlinearity in an oscillator circuit designed such that the driving power level at the resonator input can be manually tuned as the circuit operates. The measurements of the voltage amplitudes show a clear transition from the linear to the nonlinear saturation region as the driving power is increased. Short-term frequency stability measurements were also conducted for different v_{ac} and the resulting Allan deviation plots show an improvement in the short-term stability from 1.4 ppb in the linear region to 0.4 ppb in the amplitude saturation region.**

I. Introduction

The demand for high performance and reduced size wireless communication devices has pushed current research interests towards the design and development of low power, small footprint and single chip CMOS integrated wireless-transceivers. The potential of Micro Electro Mechanical Systems (MEMS) technology to meet some of these requirements has led to the recent development and adoption of micro-mechanical resonators for operation as timing references [1]. Such micro-resonators, unlike their traditional quartz crystal counterparts, are manufactured using standard semiconductor manufacturing techniques and offer considerably smaller form factor as well as shorter lead times. Electrostatically transduced MEMS resonators have also been shown to provide high mechanical quality factors (Q) and low static power dissipation, making them attractive alternatives to quartz based timing references. The small size of silicon micro-resonators also comes at a cost of a reduced power handling capacity, which is limited by nonlinear effects of the transduction mechanism and mechanical nonlinearities, affecting the achievable signal-to-noise ratio.

However, these inherent nonlinearities can potentially be engineered to achieve useful properties in certain applications. In this paper, we investigate a nonlinear amplitude saturation behavior in an electrostatically transduced, Si MEMS disk resonator (Fig. 1), operating in its secondary elliptical bulk-mode ($SEBM$) at 3.932 MHz (Fig. 2) towards its implementation as an all-mechanical automatic gain control (AGC) element. The nonlinear vibration behavior of the $SEBM$ is experimentally observed in open-loop testing such that above a threshold small signal driving voltage v_{ac}, the vibration amplitude of the mode saturates. Such nonlinear clamping behaviors have been reported in other MEMS resonators in [2] and [3]. In this work, the amplitude clamping behavior was also studied in a closed-loop configuration where the driving level of the MEMS resonator can be manually adjusted. The performance of this MEMS-based oscillator circuit was then characterized in the linear and nonlinear oscillation region, respectively. We experimentally measure an improvement in the oscillator short-term frequency stability as the resonator is set in the nonlinear region. These results indicate that the amplitude clamping effect in nonlinear micro resonators can potentially be applied in MEMS based oscillator circuits as a mechanical AGC to simplify the circuit configuration as well as retain excellent short term frequency stability.

II. Amplitude Saturation

A. Open-loop characterization

Experiments were performed on Si disk resonators which have a radius of 750 μm, 25 μm thickness and an electro-mechanical transduction air gap of 2 μm (as shown in Fig. 1). The chosen mode of operation is the in-plane $SEBM$ mode at 3.932 MHz. In order to trigger this mode, the body of the device is grounded, while a small signal v_{ac} in combination to a V_{DC} bias voltage is set on the drive electrodes, driving the bulk disk in mechanical vibration. The motional current was sensed through the Sense Electrodes which were biased with the same V_{DC} potential. The BAW micro-resonator was electrostatically addressed using high V_{DC} (typically $>$ 60 V) and v_{ac} ($>$5 dBm output power) and achieved measured quality factor values $Q \approx$ 0.5x10^6 in vacuum (p_0 = 30 mTorr).

Figure 3 shows a series of experimentally measured S_{21} responses of the disk resonator, after a numerical feed-through parasitic cancellation, when operating in the vicinity of the $SEBM$ mode with V_{DC} = 100 V and varying v_{ac} (1.22-2.82 Vp-p). From Fig. 3, when v_{ac} = 1.22 Vp-p, the amplitude response of the resonator is just at the edge of the linear region of operation. However, when we increase the small signal power further, keeping V_{DC} constant, the curves begin to level off indicating an amplitude saturation effect of the generated motional current (i.e. the amplitude of vibration). Furthermore, there is a frequency broadening of the clamping region as the ac component is further increased from 1.35 Vp-p to 2.82 Vp-p. The precise mechanism behind this particular amplitude saturation behavior is yet to be determined. Possible explanations include the parametric [2] or amplitude-dependent nonlinear excitation [3] of a coupled mode of oscillation.

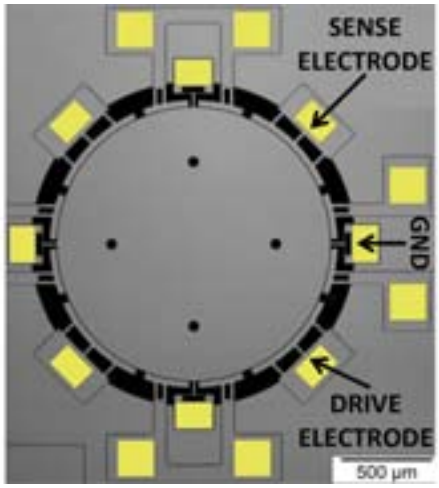

Fig. 1. Micrograph of the electrostatically transduced 3.932 MHz silicon disk resonator.

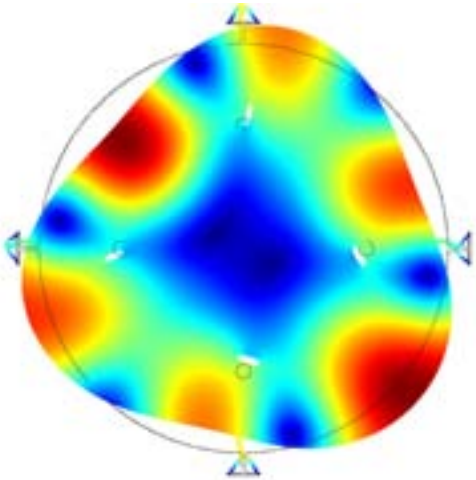

Fig. 2. FEM mode shape analysis of the micro-resonator at 3.932 MHz.

Further experiments are underway to ascertain the origin of the clamping mechanism when the in-plane $SEBM$ is driven into the nonlinear region.

This nonlinear amplitude saturation effect recorded during open-loop characterization can be used as a soft-voltage limiter / all-mechanical AGC, when implemented in an oscillator closed-loop circuit topology.

III. Amplitude and Frequency Stabilization

A. Oscillator Test Circuit

In order to experimentally verify that this particular nonlinear behavior can be used in an oscillator circuit as a soft limiter, we developed a closed loop oscillator topology where the oscillations are self sustained at the $SEBM$ mode. The schematic of this oscillator circuit is shown in Fig. 4. The MEMS resonator is implemented in a feedback loop where the Driving Amplitude Control unit is used to manually tune the value of the driving v_{ac} voltage which is fed to the resonator. For each value of v_{ac}, the Oscillation Amplitude unit measures the amplitude of the signal after the Gain Stage v_{output} (which

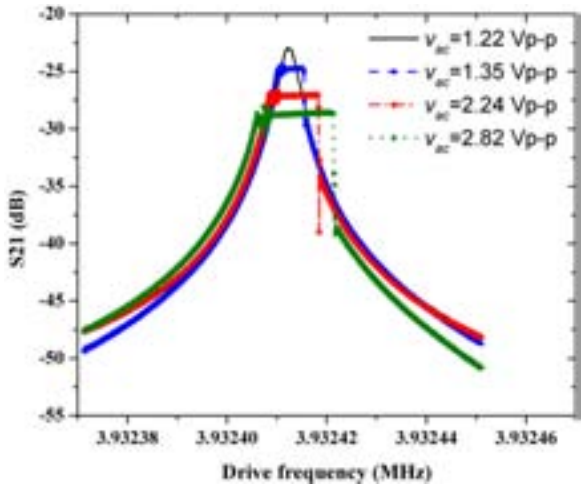

Fig. 3. Measured S_{21} parameter of the disk resonator at the $SEBM$ mode for different drive v_{ac} and V_{DC} = 100 V. The transmission characteristics demonstrate an amplitude saturation behavior when $v_{ac} > 1.35$ Vp-p.

corresponds to the resonator's amplitude of vibration), while a frequency counter (Agilent 53230A) simultaneously records the frequency stability of the oscillator. The Driving Amplitude Control unit is implemented using an AD8611 comparator circuit, driving the MEMS resonator with a square-wave signal of peak-to-peak voltage v_{ac}.

B. Amplitude stabilization

Figure 5 plots the measured Mean Output Amplitude v_{output} as a function of the Driving amplitude control voltage v_{ac} in the range of 0.75-2.8 Vp-p with a fixed polarization voltages V_{DC} at 60 V, 100 V and 120 V respectively. The circuit configuration of Fig. 4 can successfully lock itself into the $SEBM$ mode as we vary the values of v_{ac} and V_{DC}. Fig. 5 shows a clear transition of the oscillator amplitude from the linear to the nonlinear saturation region as the driving power increases for large V_{DC} = 100 V and 120 V. This transition point is consistent with the behavior measured in open-loop testing. From the open-loop measurements of Fig. 3 for a bias voltage of 100 V, the amplitude clamping behavior starts to appear at a $v_{ac} > 1.22$ Vp-p. In the closed-loop circuit, this transition occurs for a driving $v_{ac} > 1.25$ Vp-p. The threshold v_{ac} marking the transition between the linear / nonlinear regime is observed at lower driving voltages as the DC-bias is increased: v_{ac} = 1.25 Vp-p for V_{DC} = 100 V, v_{ac} = 1.15 Vp-p for V_{DC} = 120 V. This suggests that the nonlinear transition point is dependent on the product $v_{ac}V_{DC}$ which is proportional to the applied force on the resonator.

The slope of the output amplitude curve is not completely flat as a function of v_{ac} as we see from Fig. 3 and Fig. 5. This may be due to the unavoidable presence of the feed-trough parasitic capacitance between the input and output stages of the resonator. However, the benefit of this nonlinear amplitude saturation behavior is that the resonator amplitude will saturate before the circuit nonlinearities start becoming dominant.

C. Short-term frequency stability

The short-term frequency stability of an oscillator is a critical figure-of-merit. Nonlinear operation of a resonator as

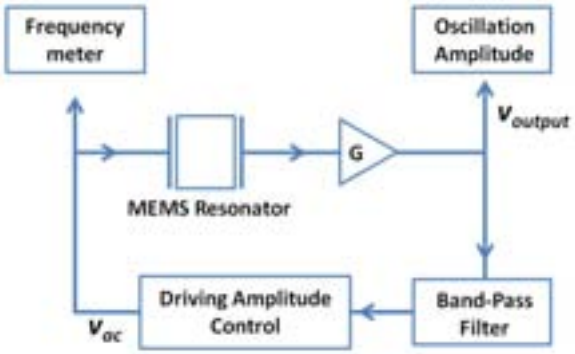

Fig. 4. Schematic of the closed-loop configuration implemented with the disk resonator and used to lock into the $SEBM$ mode.

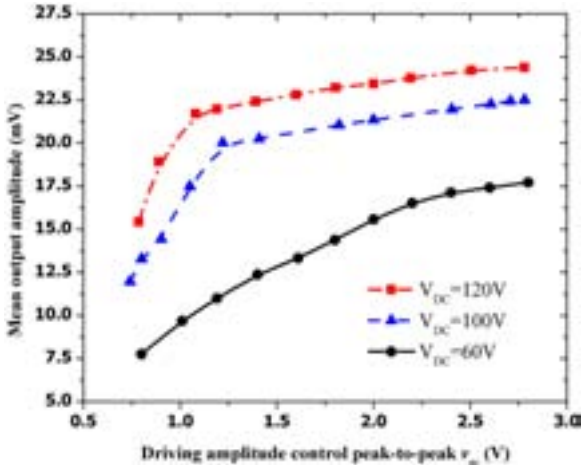

Fig. 5. Oscillation amplitude v_{output} for different drive v_{ac} in the closed loop configuration of Fig. 4.

opposed to the linear-regime is usually avoided because of the amplitude-frequency (a-f) correlation. This has been known to impact the frequency stability of the oscillator due to mixing and up-conversion of low frequency noise onto the carrier and the interaction between amplitude noise and phase noise [4]. However, it has been reported in [5] that driving a double-ended-tuning fork MEMS resonator into the nonlinear regime can result in improved frequency stability due to amplitude and frequency stabilization resulting from internal resonance of a coupled higher order mode. Since the disk resonator presented in this paper operates in a strongly nonlinear regime where amplitude clamping occurs, the question arises as to whether this impacts on the frequency stability.

To experimentally assess the short-term frequency stability of the oscillator as v_{ac} is varied, we produced two-point modified Allan deviation plots using the measurements obtained from the frequency counter. The Allan deviation $\sigma_y(\tau)$ measures the fractional frequency fluctuations of the oscillator for different averaging periods τ and can be expressed as

$$\sigma_y(\tau) = \sqrt{\frac{1}{2(N-1)} \sum_{i=1}^{N-1} \left(y_{i+1}^{\tau} - y_i^{\tau}\right)^2} \qquad (1)$$

where y_i^{τ} is the average normalized frequency fluctuation $(\delta f_i / f_0)$ over the ith interval of length τ.

The resulting Allan deviation plots (Fig. 6) as a function of the drive v_{ac}, show an improvement in the short-term stability (at τ = 0.5s averaging time) from 1.4 ppb in the linear region (v_{ac} = 1.2 Vp-p) to 0.4 ppb for operation in the amplitude saturation region (v_{ac} = 1.6-2.4 Vp-p) at a polarization voltage of V_{DC} = 100 V.

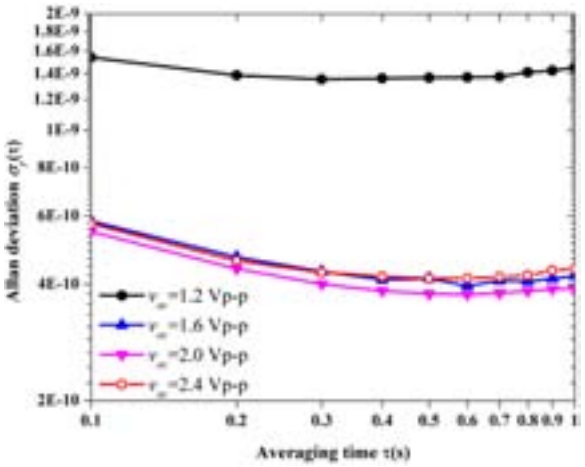

Fig. 6. Allan deviation plots for different drive v_{ac} and V_{DC} = 120 V

IV. Conclusion

A 3.932 MHz disk resonator with nonlinear amplitude clamping behavior was demonstrated in this work. This nonlinear clamping was experimentally demonstrated in open-loop characterization measurements and shows a threshold driving power v_{ac} value for which the amplitude of vibration of the resonator in the $SEBM$ mode saturates. This effect was used to produce an all-mechanical amplitude gain control mechanism where the closed-loop voltage amplitude saturates at similar levels to the ones measured in open-loop testing. Furthermore, the MEMS-based oscillator retains excellent short-term frequency stability measures even though the micro resonator is driven into a complex nonlinear region. There is a 3.5X improvement in the short term frequency stability between the linear region and the nonlinear saturation region. These results show the potential of utilizing such amplitude clamping effects in micro-resonators to produce oscillator circuits where the AGC element can be implemented by the MEMS resonator itself. Such a passive implementation enables a simpler oscillator circuit topology and allows for lowering the power dissipation of such circuits.

Acknowledgment

The authors would like to gratefully acknowledge the Qualcomm European Research Studentships in Technology as well as the UK Engineering and Physical Sciences Research Council for financial support and the IEEE UFFC society for providing travel support for the presentation of this paper.

REFERENCES

[1] C.-C. Nguyen, "MEMS technology for timing and frequency control," *Ultrasonics, Ferroelectrics and Frequency Control, IEEE Transactions on*, vol. 54, no. 2, pp. 251 –270, feb. 2007.

[2] C. van der Avoort, R. van der Hout, J. J. M. Bontemps, P. G. Steeneken, K. L. Phan, R. H. B. Fey, J. Hulshof, and J. T. M. van Beek, "Amplitude saturation of mems resonators explained by autoparametric resonance," *Journal of Micromechanics and Microengineering*, 2010.

[3] L. Lipiäinen, A. Jaakkola, K. Kokkonen, and M. Kaivola, "Nonlinear excitation of a rotational mode in a piezoelectrically excited square-extensional mode resonator," *Applied Physics Letters*, vol. 100, no. 15, p. 153508, 2012.

[4] V. Kaajakari, J. Koskinen, and T. Mattila, "Phase noise in capacitively coupled micromechanical oscillators," *Ultrasonics, Ferroelectrics and Frequency Control, IEEE Transactions on*, vol. 52, no. 12, pp. 2322 –2331, dec. 2005.

[5] D. Antonio, D. Zanette, and D. Lopez, "Frequency stabilization in nonlinear micromechanical oscillators," *Nature Communications*, vol. 3, 2012.

A 1 GHz SAW Oscillator on Epitaxial GaN/Si Substrate: Toward Co-Integrated Frequency Sources

Marc Faucher
IEMN, UMR CNRS 8520
Villeneuve d'Ascq, France
marc.faucher@isen.iemn.univ-lille1.fr

Jean-Michel Friedt
SENSeOR SAS,
Besançon – Mougins, France

Gilles Martin
FEMTO-ST, UMR CNRS-UFC-ENSMM-UTBM 6174
Besançon, France

Sylvain Ballandras
frec|n|sys SAS
Besançon, France

Abstract— **GaN is an attractive material for the fabrication of various integrated devices combining several physical effects (semi-conductors, piezoelectric and optic parts, etc.). This work is dedicated to the investigation of GaN for the fabrication of surface acoustic wave oscillators. The first functional two-port resonators have been designed and built on 1.8 µm thick GaN epitaxial layers grown on (111) Silicon. An analysis of the obtained results has been achieved and a set of elastic constants has been fitted to meet the best possible agreement between theory and experiments. Comparison between experimental and theoretical transfer functions has been also exploited to refine the estimation of the wave characteristics. An oscillator has been finally built using the obtained resonators to assess the interest of this material for this kind of application and to prepare future development on this basis.**

Keywords- RF Oscillator; SAW Resonator; Epitaxial GaN; Silicon (111); Layered substrate

I. INTRODUCTION

SAW-resonator based oscillators are fabricated for embedded applications such as Radar and local oscillators for space missions requiring frequency transposition for telecommunications. Although rather compact, these discrete devices contribute to on-board charge and are currently poorly suited to co-integration. The possibility for providing ultimately compact sources able to operate on the same board than most radio-frequency circuits would yield a major advance for integrated time-frequency systems.

Previously on GaN, SAW transducers has already been demonstrated [1,2], as well as actuators and other resonant devices based on the 2-DEG [2-5]. In this paper, we focused the use of Gallium Nitride (GaN) on Silicon Si(111) epitaxial layers for the fabrication of SAW resonators with low losses and good resonance peak dynamic range, a prerequisite for the design of oscillators. Devices have been designed on a 1.8 µm thick GaN. Exploiting the analysis of the obtained results, a set of elastic constants has been fitted. Double-port SAW resonators have been designed and fabricated using this data base. Comparison between experimental and theoretical transfer functions has allowed for refining the estimation of the wave characteristics. An oscillator has been finally built using the obtained resonators to assess the interest of this material for this kind of application.

SAW resonators have been processed using E-beam lithography with a 2 µm period, yielding resonators operating near 1 GHz with Q factor close to 2000 and insertion losses better than 12 dB. Two port resonators were inserted in a feed-back loop oscillator based on a low-noise HX2400 amplifier, enabling short term measurements as well as phase noise extraction. A short term stability of 10^{-7} per second has been measured, clearly penalized by the temperature sensitivity of the SAW (about -30 ppm.K^{-1}). A phase noise figure of -115 dBc/Hz was found at 10 kHz from the carrier and a floor level of -165 dBc/Hz was finally measured. Although these figures are not the best achievable using this material, they are really promising as High Electron Mobility Transistors (HEMTs) are currently manufactured on the same substrate, allowing for future development of co-integrated SAW oscillators.

II. UPDATING THE WAVEGUIDE PROPERTIES

The first step of the presented development did consist in the fabrication of a single-port SAW resonator to adjust the physical constants representative of the substrate (and more particularly the GaN layer). The S_{11} response of the resonator was measured and compared to the predicted device response using a mixed matrix model. The simulation parameters then have been updated to refine the theoretical description of the guided mode properties on such a compound substrate. As shown by the comparison between Figure 1 and Figure 2, the theory/experiment agreement has been optimized considering the S_{11} base line (representative of the resistive losses and other sources of quasi-static damping), the phase velocity (across the resonance frequency), the stop band width (reflection coefficient on a single obstacle) and the magnitude of S_{11} (representative of propagation losses). Only the secondary lobes are poorly predicted from a spectral point of

view (which may be explained by the lack of knowledge of the actual layered substrate structure).

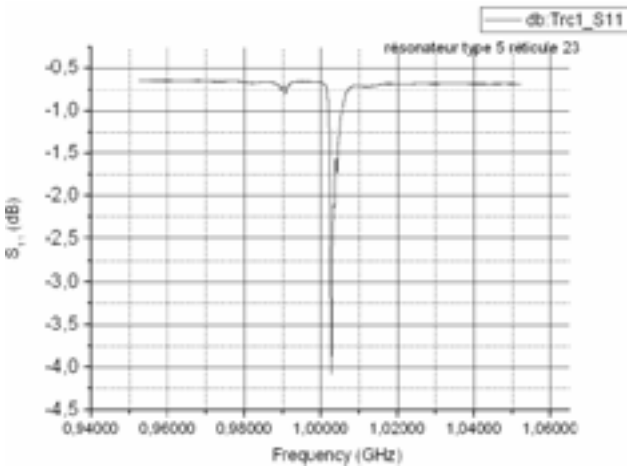

Figure 1 Experimental S_{11} response of the first single-port resonator built on the GaN/Si substrate

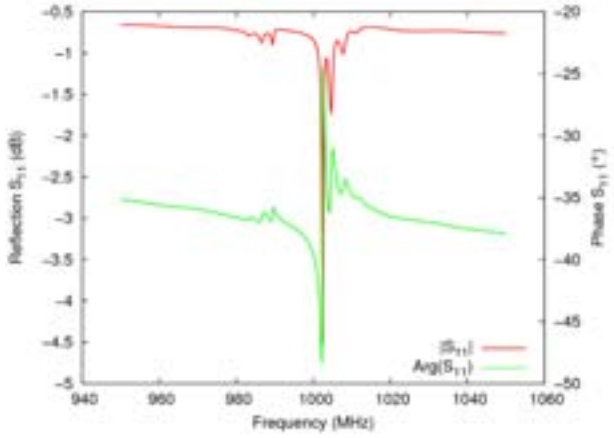

Figure 2 Theoretical prediction of the single-port resonator reflection coefficient S_{11} corresponding to the configuration of after model updating

The simulation of Figure 2 has been achieved considering material coefficients already used in **Error! Reference source not found.**. Some parameters however had to be updated to fit the experimental results of Figure 1. Particularly, the reflection coefficient on a single obstacle has been increased by 20% (yielding a value of 1.8%), the attenuation has been set to 7.5×10^{-3} dB/λ (initially equal to 10^{-3}), the conductance was significantly increased and the phase velocity adjusted to 4050 $m.s^{-1}$. Finally, a 20Ω contact resistance has been accounted for to fit the experimental base line and magnitude, which is a pretty high value that could be explained by the presence of the two dimensional electron gas (2DEG) near the SAW propagation region, or by residual conductivity at the material surface. These updated parameters did allow for a re-computation of the dispersion properties of the GaN/Si(111) waveguide as shown in . The main changes considering the initial predicted dispersion is the slight increase of velocity and decrease of coupling factor, the shape of the curve is kept identical. The use of a 1.8 µm GaN reveals optimal for promoting the coupling coefficient when operating at 1 GHz, allowing for values in excess of 0.2%. Therefore, the double-port resonator dedicated to the oscillator application has been fabricated considering this condition.

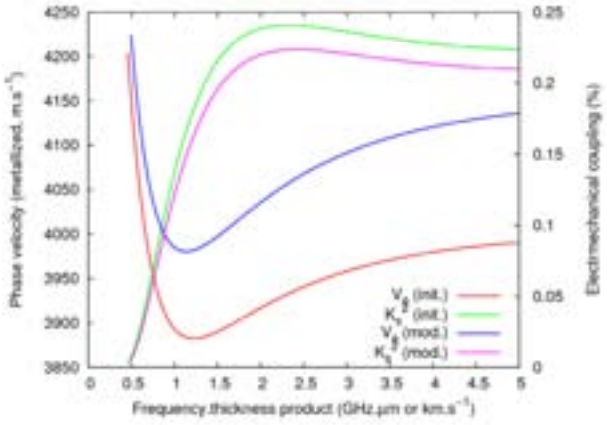

Figure 3 Dispersion curve of the Rayleigh-like wave propagating atop GaN/Si(111): phase velocity and coupling factor versus frequency-thickness product relative to the GaN – 1.8 µm thick GaN is optimal at 1 GHz for maximizing the coupling factor and at 2 GHz for frequency reproducibility

III. FABRICATION OF THE RESONATORS

The fabrication process starts from a GaN epitaxial layer grown by MOCVD on a (111) high resistivity silicon substrate. The structure is the standard one in HEMT processing, including a 1900 nm nucleation layer and buffer, followed by a 25nm Aluminum-Gallium Nitride (AlGaN) barrier. The first step consists in opening large areas in a positive optical resist that will include the whole SAW design. Then, the etching of the entire AlGaN barrier and of 100nm of GaN is performed using a Cl_2/BCl_3 plasma in order to remove the 2DEG and ensure enough electrical insulation under the transducers.

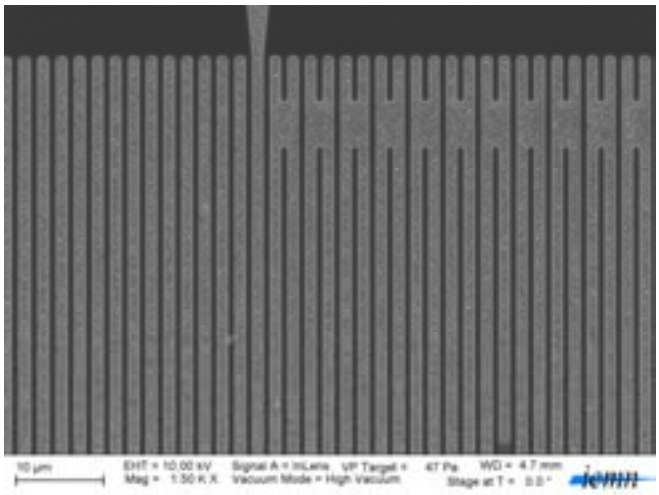

Figure 4 SEM view of a detail of the double-port resonator built on GaN/Si(111) - one can note Al residues after etching which pollute the device surface and hence may be a reason of the observed limited Q factors

As a second step, we deposited a 200 nm thick Al by evaporation. This layer was then patterned using e-beam lithography with PMMA resist in order to define the inter-digitated transducers as well as reflectors of the SAW resonator. Careful attention was paid to the proximity correction by taking information account the whole epitaxial stack and the design. Al was then etched using a Cl_2/BCl_3 plasma, followed by resist stripping in an O_2 plasma. The designed transfer function is shown in Figure 5 and the corresponding experimental measurements are reported in Figure 6 and Figure 7.

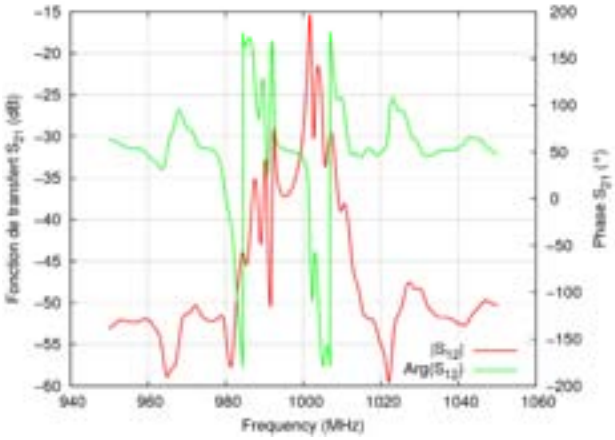

Figure 5 Transfer function of the double-port SAW resonator computed considering the updated parameter of section II

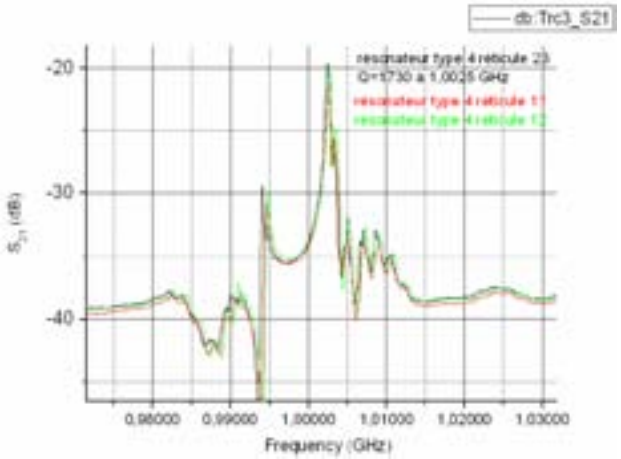

Figure 6 Experimental tranfer function of a first set of double-port resontaors with Insertion losses slightly below 20 dB and Q factor above 1700

Although the overall shape of the transfer function is correctly predicted (resonance at the end of the stop band near 1.002 GHz and a stop band width of about 8 MHz), the side lobes are not reliably predicted which tends to indicate that the structure operation has to be better understood. As shown, two sets of devices have been fabricated to provide resonators for the oscillator tests. The first devices exhibited insertion losses imposing two amplifier stages to reach a loop gain large enough to meet Barkhausen conditions. Therefore, a second run was managed to allow for improving the quality of the devices (mainly reducing surface pollution as shown in Figure 4), yielding a spectacular improvement of insertion loss with experimental values below 10 dB. In that later case, a single amplifier stage is enough to operate the oscillator.

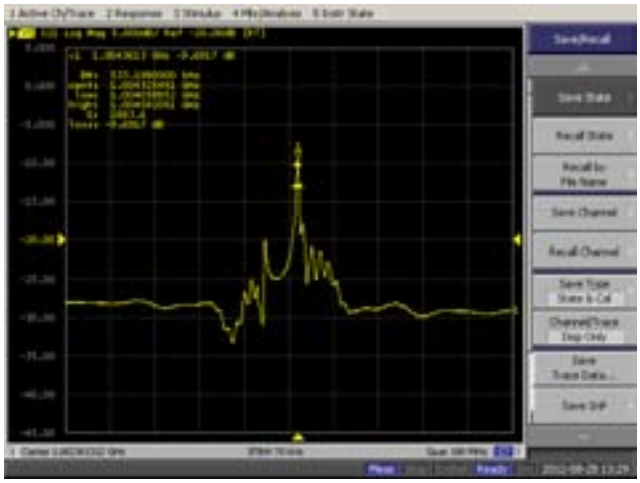

Figure 7 Experimental transfer function of the second set of double port resonators, with improve insertion losses and Q factor close to 1900

IV. Oscillator Fabrication and Characterization

As explained in Introduction, a feedback loop oscillator has been manufactured to allow for testing the quality of the developed GaN/Si resonator frequency stabilization. The resonators were encapsulated in a TO-8 package compatible with vacuum sealing and bonded onto a test board allowing for an easy implementation of the oscillator (in laboratory conditions, as shown in Figure 8). Although the resonator did actually filter the frequency efficiently, a SAW filter was added in the loop to suppress high frequency level feedback mainly introduced by the TO-8 package. Due to the fact that only small parts of GaN/Si were available and not suited to saw-dicing techniques, the use of such a package was inescapable.

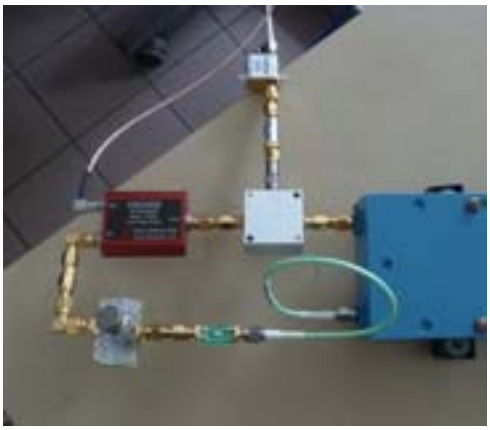

Figure 8 Experimental oscillator setup including the To-8 packaged resonator, a low noise HX2400 holtzworth integrated amplifier, a phase-shifter and a coupler allowing for collecting the signal to be characterized – a 1 GHz SAW filter is inserted to suppress high frequency level feedback

As already mentioned, a single stage of amplification was required using resonators exhibiting IL less than 10 dB. A low-noise HX2400 amplifier was then selected, enabling short term measurements as well as phase noise extraction. A short term stability of 10^{-7} per second has been measured, clearly penalized by the temperature sensitivity of the SAW (about -30 ppm.K^{-1}). Note that this stability was recently improved using a 500 MHz GaN/Si resonator stabilized oscillator, yielding a short term stability of 3.10^{-9} per second (Figure 9).

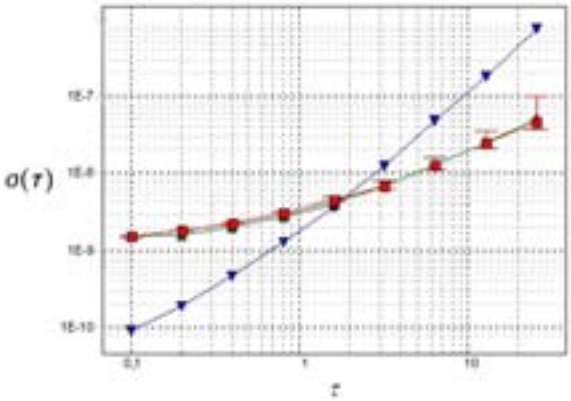

Figure 9 Short term stability of a 500 MHz oscillator stabilized with a GaN/Si SAW resonator based on a material composition similar to the 1GHz device

A phase noise figure of -115 dBc/Hz was found at 10 kHz from the carrier and a floor level of -165 dBc/Hz was finally measured. One can note that the phase noise level passes below -160 dBc/Hz at 500 kHz from the carrier. It is clear that any possibilities to improve the Q factor of the resonator will impact this figure of merit. It has been shown in the paper that routes can be followed in that purpose, by improving the device overall quality but also by a better understanding of its operation, allowing for an optimized design of the SAW device and an improved

VI Conclusion

In this paper, we have shown the possibility to stabilized a feedback loop oscillator with double port SAW resonators built using E-beam lithography on epitaxial GaN grown on (111) Silicon. The devices have been analyzed to try and optimized the next generation of resonators built on such substrates. Although the first results are not meeting the state-of-the-art characteristics of SAW resonators on single crystal, the quality was good enough to obtain phase noise figure better than -160 dBc/Hz at 1 MHz from the carrier. Several tracks are currently considered to improve the Q factor of the resonator and hence this figure of merit.

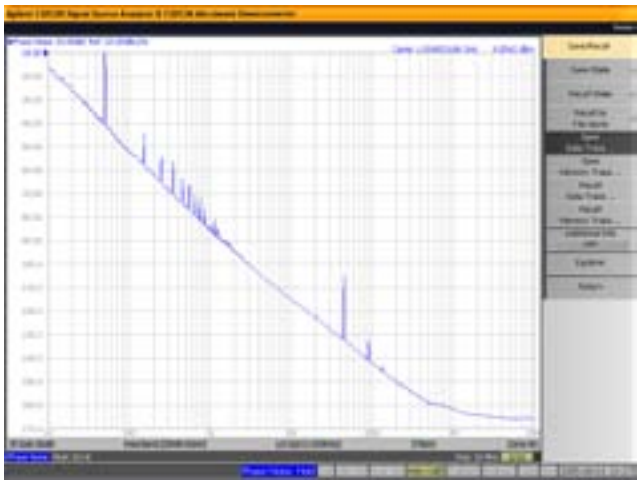

Figure 10 Phase noise of the 1 GHz oscillator of with a noise floor in the vicinity of -165dBc/Hz at 1 MHz from the carrier

The results demonstrate that a GaN-based SAW can be fabricated with acceptable performances on a wafer where the 2DEG can be kept at chosen areas and removed under the SAW. This allows preserving the epitaxial wafer surface for the definition of ohmic contacts and gates. As a consequence, simple process flows can be envisaged in order to co-integrate an amplifier, the next step toward monolithic oscillators.

Acknowledgment

This work was partly supported by the French RENATECH network and its IEMN technological facility.

References

[1] F. Calle, J. Grajal, J. Pedros, Active SAW devices on 2DEG heterostructures, Electronics Letters 40 , 1384, 2004.

[2] King-Yuen Wong, Wilson Tang, Kei May Lau, Kevin J. Chen, Surface acoustic wave device on AlGaN/GaN heterostructure using two-dimensional electron gas interdigital transducers,Appl. Phys. Lett. 90, 213506 (2007)

[3] K. Brueckner, F. Niebelschuetz, K. Tonisch, S. Michael, A. Dadgar, A. Krost, V. Cimalla, O. Ambacher, R. Stephan, and M. A. Hein, "Two-dimensional electron gas based actuation of piezoelectric AlGaN/GaN microelectromechanical resonators" , Appl. Phys. Lett.93, 173504 (2008)

[4] Marc Faucher, Yvon Cordier, Matthieu Werquin, Lionel Buchaillot, Christophe Gaquiere, Didier Theron, "Electromechanical Transconductance Properties of a GaN MEMS Resonator With Fully Integrated HEMT Transducers",IEEE/ASME Journal of Microelectromechanical Systems - 01/2012; 21(2):370-378.

[5] A.Ansari, V.J.Gokhale, V.A. Thakar, J.Roberts, M.Rais-Zadeh, Gallium nitride-on-silicon micromechanical overtone resonators and filters, proc IEDM 2011,pp 20.3.1

[6] S. Camou, Th. Pastureaud, D. Schenck, S. Ballandras, V. Laude, "Guided elastic waves in GaN-over-Sapphire" El. Letters, Vol. 37, pp. 1053-1055, 2001

.

Tunable Opto-Electronic Oscillator for Ultra-Wide-Band Transceivers

Danny Eliyahu, Wei Liang, Elijah Dale, Anatoliy A. Savchenkov,
Vladimir S. Ilchenko, Andrey B. Matsko, David Seidel, and Lute Maleki
OEwaves Inc., 465 North Halstead Street, Suite 140, Pasadena, CA 91107, U.S.A.
E-mail: Andrey.Matsko@oewaves.com

***Abstract*—We study both theoretically and experimentally an RF photonic frequency source featuring low phase noise, low power consumption, compact size, and wideband tunability. Performance parameters of the oscillator are superior to existing tunable electronic oscillators and synthesizers operating in the 2-35 GHz band, with the close-in phase noise at least 20 dB lower than what is currently achieved with free running tunable RF oscillators.**

***Index Terms*—Optical whispering gallery mode resonator, opto-electronic oscillator, phase noise, voltage controlled oscillator**

I. Introduction

Conventional approaches serving multioctave electronic devices typically employ several fixed frequency sources along with phase lock loops (PLLs) to cover the entire spectral range. This approach is complex and results in limited spectral purity of the generated signal, and leads to an overall increase in the size weight and power (SWaP). For example, existing electronic phase locked dielectric resonator oscillators (PLDROs) are on the order of 2x2.5 inch in footprint with 1–2 Watts of DC power consumption. These devices do not have multi-octave tunability. Their phase noise degrades at high RF frequencies because of reduction of the quality factor of the dielectric resonator. These oscillators also have high acceleration sensitivity. In this paper we describe a novel photonic oscillator based on optical whispering gallery mode (WGM) microresonator that removes all the mentioned PLDRO shortfalls. A major feature of the proposed oscillator architecture is the inherently low acceleration sensitivity, a parameter of significance for all mobile platforms. The successful fabrication of the device supports the development of novel ultra-wideband receivers for communications and radar. The oscillators are also suitable for radar and communication systems supporting small platforms, such as Unmanned Vehicle Systems.

II. Schematic of the Oscillator

The oscillator described below takes advantage of the technology of opto-electronic oscillator (OEO). The OEO is based on an opto-electronic feedback loop that directly converts light energy to spectrally pure microwave or RF oscillation, and has been described in detail in the literature. The oscillator is driven with a continuous wave laser that acts as the source of energy. An important feature of the OEO architecture is that the phase noise does not degrade with increasing oscillation frequency, in contrast to electronic oscillators.

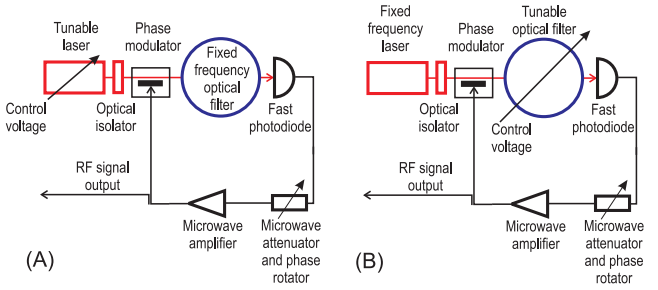

Fig. 1. Schematic of the tunable opto-electronic oscillator. (A) Tunability is achieved due to tunability of the laser frequency. (B) Tunability is achieved due to tunability of the optical resonator frequency. The resonator can be tuned much faster than the laser.

The novel tunable OEO configuration described here is shown in Fig. 1a. Light from an agile tunable semiconductor laser is fed into a broadband phase modulator, then to an ultra-high-Q optical microresonator, and then to a fast photodiode, to produce an electric signal. The signal from the photodiode is amplified before being fed back to the phase modulator to complete the OEO loop. Self-sustained oscillation starts when amplification in this feedback loop exceeds the loss. The narrow optical bandwidth of the resonator (less than 10 kHz) provides the filter function required for the loop. The change in the laser frequency provides the tunability of the oscillator. The spectral purity depends on the Q of the circuit ensured by the optical microresonator. This configuration eliminates supermodes in the noise spectra associated with fiber OEOs.

The device does not require the laser light to pass through the ultra-high-Q optical resonator, as was required in all previous implementations of resonator-based OEOs. Only one modulation sideband passes the resonator mode. Aside from simplification of the architecture, this feature allows improving the linearity of the optical part of the opto-electronic loop. Moreover, it allows reducing the resonator size leading to reduction of the vibration sensitivity of the system. It was noted previously that a phase modulator can be used in a microresonator-based OEO loop [1]; however the realization that the free spectral range of the resonator can significantly exceed the oscillation frequency, if the oscillator configuration shown in Fig. 1 is utilized, is novel.

It was also shown previously that tunable OEOs can be realized using an optical phase modulator and a phase-shifted

fiber Bragg grating (PS-FBG) [2]. The tunability is achieved using a tunable laser source in the OEO loop. The system described here is novel in the sense that it involves a high-Q microresonator that has narrower bandwidth and lower acceleration sensitivity compared to the Bragg grating. It is possible to reduce the phase noise of the OEO due to narrow bandwidth of the resonator modes; while a stable passively mode-locked fiber laser was used to stabilize the OEO in [2]. In addition, agile tunability of the microresonator-based OEO can be achieved by tuning the frequency of the microresonator-based filter, Fig. 1b, if the microresonator is made of an electro-optical material.

The oscillator can be locked to an external frequency reference using a standard PLL. The same loop can be used to tune the oscillator to a desirable frequency Fig. 2. The tuning speed and phase noise of such an oscillator depends upon the bandwidth of the PLL loop. If the bandwidth exceeds 1 MHz, the oscillator will tune to a desired frequency in less than a microsecond. However, within the locking bandwidth, its phase noise will be limited to the phase noise of the PLL oscillator. To achieve the intrinsic low phase noise performance of the oscillator, the bandwidth of the PLL should be much narrower, e.g. 100 Hz. Such a bandwidth will restrict the settling time for the low phase noise of the device to 10 ms.

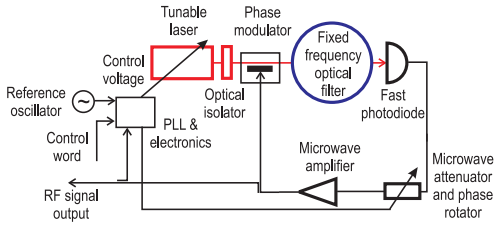

Fig. 2. A phase lock configuration for the tunable opto-electronic oscillator.

A major feature of the oscillator is that the packaged device will have extremely low acceleration sensitivity. The acceleration sensitivity of high performance microwave oscillators primarily results from coupling of vibration disturbances to the high-Q element of the device. The acceleration coupling is increased by resonances corresponding to the actual size of the cavity, which typically range from one to a few inches. This effect severely degrades the performance of the oscillator and diminishes its usefulness. The only remedy currently available is to isolate the oscillator from sources of vibration, which adds to the size and complexity, and reduces the range of applications of high performance microwave oscillators to the laboratory environment. By contrast, crystalline WGM microresonators have mm-scale dimensions, very high mechanical frequencies, and high mechanical Q and, thus, experience a small acceleration for a given applied force. Previous studies indicate that with microresonators the acceleration sensitivity along the resonator plane (x-y plane) is less than 10^{-12}/g, and is basically negligible. In the z-direction, the acceleration sensitivity of a 25-micron thick WGM resonator was calculated to be in range of 10^{-12}/g.

A feature of the WGM resonator is that light is coupled in via the evanescent wave. Fixing the amount of light coupling in a vibration environment can appear a major challenge for the stability of the oscillator, it has, however, been demonstrated that the proposed design for the widely tunable OEO architecture is highly stable in frequency below the level of 10^{-11}/g. This is significantly smaller than the acceleration sensitivity of synthesizers and PLLs used for generation of microwave signals over frequency bands much smaller than the target of the present task.

Finally, an advantage of the proposed oscillator is that its operational frequency can, fundamentally, reach W-band and higher without degradation of the spectral purity of the generated signal. This happens because the quality factor of the oscillator feedback loop does not degrade with the oscillation frequency.

III. Theory

The use of phase modulators in OEOs is unusual since phase modulated light does not produce RF signal on a photodiode. The OEO described here oscillates since the WGM resonator transforms phase modulation to amplitude modulation. In what follows we show that the transformation occurs because of both microresonator-based phase rotation and absorption of the light. Surprisingly, the absorption is not essential here. The microresonator can be overloaded significantly to operate as lossless reflective filter and still enable OEO operation.

Let us consider an OEO shown in Fig. (2). Light emitted by a tunable laser is phase modulated, filtered with a fixed frequency optical filter, and demodulated on a fast photodiode. The photocurrent is phase shifted, amplified, and fed back to the phase modulator. The basic idea of the device operation is that the change of the laser frequency with respect to the frequency of the optical filter results in tuning of the RF transfer function of the opto-electronic loop.

An amplitude transfer function of a fixed frequency optical resonator is

$$F(\omega) = \frac{E_{out}}{E_{in}} = \frac{\gamma_1 - \gamma_2 + i(\omega_0 - \omega)}{\gamma_1 + \gamma_2 + i(\omega_0 - \omega)}, \qquad (1)$$

where ω is the spectral frequency, ω_0 is the frequency of the resonance, E_{in} and E_{out} are the complex amplitudes of the electric field of the input and output light waves, γ_1 and γ_2 are the parameters of the resonance determining the contrast, $1 \geq C \geq 0$, $C = 1 - (|E_{out}|^2/|E_{in}|^2)|_{\omega=\omega_0} = 4\gamma_1\gamma_2/(\gamma_1 + \gamma_2)^2$, and bandwidth $\Gamma = \gamma_1 + \gamma_2$ of the resonance. It is worth noting, that the model describes a WGM resonator with a single coupler, if γ_1 is the intrinsic and γ_2 is the loading-related bandwidths. In the case of significant overloading of the resonator mode, $\gamma_2 \gg \gamma_1$, the contrast of the resonance is nearly zero, $C \to 0$, while phase shift introduced by the mode is not zero.

Let us assume that the input light is both amplitude and phase modulated and that the modulation depth is small, so

the amplitude of the electric field can be presented as

$$E_{in} = E_0\left(1 + a\cos\Omega t\right)e^{-i(\omega t + b\sin\Omega t)} \approx \quad (2)$$
$$E_0 e^{-i\omega t}\left[1 + \left(\frac{a}{2} - \frac{b}{2}\right)e^{i\Omega t} + \left(\frac{a}{2} + \frac{b}{2}\right)e^{-i\Omega t}\right],$$

where a and b are the amplitude and phase modulation coefficients, respectively.

For the amplitude of the light exiting the resonator we find

$$E_{out} = E_0 e^{-i\omega t}\left[F(\omega) + \left(\frac{a}{2} - \frac{b}{2}\right)F(\omega-\Omega)e^{i\Omega t} + \left(\frac{a}{2} + \frac{b}{2}\right)F(\omega+\Omega)e^{-i\Omega t}\right]. \quad (3)$$

The modulated light is sent to a photodiode with resistance ρ and responsivity R, so the photocurrent i_{PD} is equal to $i_{PD} = RP_{out}$, where P_{out} is the optical power at the photodiode (PD). We are interested in the first modulation harmonic of the exiting power (other harmonics are present as well). The photo current is given by

$$\left.\frac{i_{PD}}{RP_0}\right|_{\exp(\pm i\Omega t)} = \frac{1}{2}\left[(a-b)F(\omega)F^*(\omega-\Omega) + (a+b)F^*(\omega)F(\omega+\Omega)\right]e^{-i\Omega t} + c.c. \quad (4)$$

The power of the RF signal from the PD is

$$P_{RF} = \frac{1}{4}\rho R^2 P_0^2\left|(a-b)F(\omega)F^*(\omega-\Omega) + (a+b)F^*(\omega)F(\omega+\Omega)\right|^2 \quad (5)$$

Therefore, the corresponding normalized RF transfer function is given by

$$G_{ph} = \left|F(\omega)F^*(\omega-\Omega) - F^*(\omega)F(\omega+\Omega)\right|^2, \quad (6)$$
$$G_a = \left|F(\omega)F^*(\omega-\Omega) + F^*(\omega)F(\omega+\Omega)\right|^2. \quad (7)$$

for the cases of pure phase and amplitude modulation, respectively. Function G_a always has a minimum at $\Omega = \pm(\omega_0 - \omega)$, so the amplitude modulation is not suitable for the OEO operation. Spectral dependence of G_{ph} on the modulation frequency Ω is shown in Fig. 3.

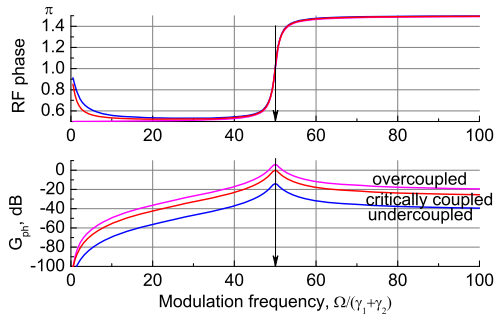

Fig. 3. RF power transfer function and phase shift found using Eq. (6) for various parameters of the resonator. Overcoupled regime corresponds to $\gamma_1 = 0.1$ and $\gamma_2 = 0.9$; undercoupled – $\gamma_1 = 0.9$ and $\gamma_2 = 0.1$; and critically coupled – $\gamma_1 = 0.5$ and $\gamma_2 = 0.5$.

The maximal RF transfer occurs in the case of the overcoupled resonator, when the modulation sidebands are not absorbed. Therefore, the absorption of a modulation sideband does not play any role in the device operation. The RF frequency of the maximum transmission is equal to the frequency detuning between the laser frequency and the frequency of the resonator mode. It means that all slow drifts of the laser frequency will be imprinted at the RF signal. A stable laser is needed to achieve good RF phase noise at low offsets. The modulation sidebands enter the filter, while the carrier does not. This process determines the spectral width of the RF transfer function.

The performance of the oscillator can be improved if one uses an optical fiber delay line along with the resonator. A complex optical transfer function of the resonator with a single optical coupler and the fiber delay line is

$$F(\omega) = \frac{\gamma_1 - \gamma_2 + i(\omega_0 - \omega)}{\gamma_1 + \gamma_2 + i(\omega_0 - \omega)}e^{i\omega\tau}, \quad (8)$$

where τ is the fiber delay time.

The amplitude of the electric field after the phase modulator is

$$E_{in} \simeq E_0 e^{-i\omega t}\left[1 - \frac{b}{2}e^{i\Omega t} + \frac{b}{2}e^{-i\Omega t}\right], \quad (9)$$

where b is the (small) phase modulation coefficient, E_0 is the complex amplitude of the input light, and Ω is the yet unknown RF oscillation frequency. It is easy to find from Eq. (8) and Eq. (9) that the normalized frequency transfer function of the RF photonic loop is

$$H(\Omega) \simeq \frac{\gamma_1 + \gamma_2}{\gamma_1 + \gamma_2 - i(\Omega - \omega_0 + \omega)}e^{i\Omega\tau}. \quad (10)$$

The oscillation frequency is given by

$$\arg[H(\Omega)] = -\psi_0, \quad (11)$$

where ψ_0 is the RF phase shift introduced by the electronic part of the loop. Assuming

$$\Omega\tau = (\Omega - \Omega_f)\tau + 2\pi N, \quad (12)$$

where N is integer, $\Omega_f\tau = 2\pi N$, $(\Omega - \Omega_f)\tau < 2\pi$, $\gamma_1 + \gamma_2 \gg |\Omega - \omega_0 + \omega|$, and $\psi_0 = 0$, we arrive at the conventional frequency puling condition for the oscillation frequency

$$\Omega_0 = \frac{\omega_0 - \omega}{1 + \tau(\gamma_1 + \gamma_2)} + \frac{\Omega_f\tau(\gamma_1 + \gamma_2)}{1 + \tau(\gamma_1 + \gamma_2)}. \quad (13)$$

The oscillator can be continuously tuned by changing the frequency of the microresonator without a fiber delay line in the loop. The tuning is also possible if a fiber delay line is introduced. However, the addition of the delay line requires tuning not only the microresonator optical filter, but also the RF phase shifter. Without a phase shifter the oscillator can be tuned quasi-continuously by hopping from one frequency to another as determined by the delay of the fiber link.

The phase noise of the oscillator is found from

$$\mathcal{L}(f) = \left|\frac{1}{1-H(\Omega_0+2\pi f)}\right|^2 \left[\frac{2q\mathcal{R}P\rho + Fk_BT}{P_{RF}} + \frac{\kappa}{f} + \frac{(2\pi f)^2}{(\gamma_1+\gamma_2)^2+(2\pi f)^2}(\mathcal{L}_{laser}+\mathcal{L}_{WGMR})\right]. \quad (14)$$

where P_{RF} is the demodulated averaged RF power at the photodiode output, q is the charge of an electron, $\mathcal{R}$ is the responsivity of the photodiode, ρ is the resistance of the photodiode, P is the overall DC optical power at the photodiode, F is the noise factor of the amplifiers placed after the oscillator, k_B is Boltzmann constant, T is the ambient temperature, κ is the flicker noise parameter, $\mathcal{L}_{laser}$ and $\mathcal{L}_{WGMR}$ are the phase noise values for the laser and the WGMR, respectively. Phase noise $\mathcal{L}_{WGMR}$ results from interaction of the resonator with the environment as well as with the voltage source used for TOEO tuning. Both the laser and resonator phase noise penetrate to the oscillator phase noise due to strong dispersion introduced by the WGM the modulation sideband interacts with.

The phase noise of the generated RF signal includes thermal noise, shot noise, and flicker noise on one hand, and by the phase noise of the laser as well as the microresonator, on the other. Without the microresonator the laser phase noise is cancelled at the photodiode since both the carrier and the modulation sidebands equally depend on the noise. The resonator de-correlates the noise in a modulation sideband resulting in increase of the noise of the generated RF signal. The phase noise of the laser determines the phase noise of the TOEO if there is no fiber loop. Introduction of the fiber loop results in suppression of the overall phase noise.

IV. Experiment

We assembled the OEO shown in Fig. 1b. The measured transfer function of the open OEO loop (proportional to G_{ph}) is shown in Fig. 4a. The measured RF signal of the oscillating OEO is shown in Fig. 4b.

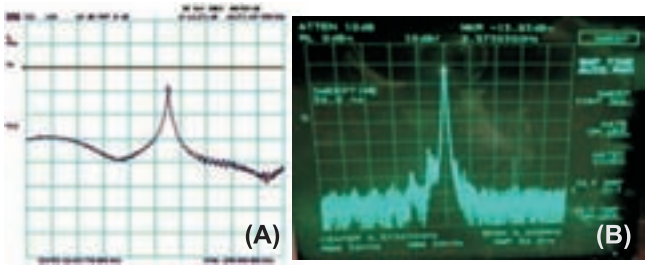

Fig. 4. (A) Transfer function of the open OEO loop as seen at the screen of network analyzer. (B) RF spectrum of the operating OEO as seen at the screen of RF spectrum analyzer.

We used a Koheras Adjustik laser operating at 1549.75 nm with output power of 9.4 mW to pump the oscillator; a phase EOM (EOspace, 16 GHz 3dB bandwidth); a 40 GHz u2t photodiode; a Hittite RF amplifier; and 220 m of SMF-28 optical fiber. These components were mounted on an optical breadboard for demonstration of the TOEO operation and for its characterization.

The tunable optical filter was based on a packaged lithium tantalate WGMR. The resonator was fabricated by mechanical polishing of a cylindrical Z-cut $LiTaO_3$ preform. It had 650 μm in diameter and 100 μm in thickness (69.62 GHz FSR). The unloaded bandwidth was around 1 MHz, the loaded bandwidth was 11 MHz. Modes with horizontal polarization were exited by the laser, and the mode contrast was at about 90-95%. The resonator was packaged with a TEC and a thermistor and pigtailed with PM fibers. Two optical isolators (one at the input and one at the output of the resonator) were also installed. The resonator pads were traced and wire-bonded to a K connector on the package. The microresonator had gold electrodes mounted on its top and bottom surfaces. The frequency tuning was achieved by applying DC voltage to the electrodes.

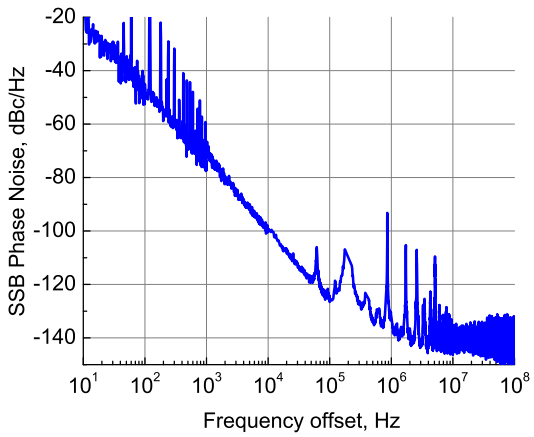

Fig. 5. Measured single sideband phase noise of the TOEO with 220 m of single mode fiber link added between the resonator and the photodiode (offset from 8.44 GHz).

We studied the phase noise of the oscillator (Fig. 5) with an OEwaves phase noise measurement system. As expected, the phase noise was determined by the phase noise of the pump laser. The contribution of the high frequency phase noise resulting from the resonator is estimated to be negligible compared with the contribution from the laser noise.

V. Conclusion

We have introduced and studied a novel tunable opto-electronic oscillator based on a high-Q optical microresonator and a phase modulator.

References

[1] K. Volyanskiy, P. Salzenstein, H. Tavernier, M. Pogurmirskiy, Y. K. Chembo, and L. Larger, "Compact optoelectronic microwave oscillators using ultra-high Q whispering gallery mode disk-resonators and phase modulation," *Opt. Express*, vol. 18, No. 21, pp. 22358-22363, October 2010.

[2] W. Li and J. P. Yao, "Wideband frequency-tunable optoelectronic oscillator incorporating a tunable microwave-photonic filter based on phase-modulation to intensity-modulation conversion using a phase-shifted fiber-Bragg grating," *IEEE Trans. Microw. Theory Tech.*, vol. 60, no. 6, pp. 1735-1742, June 2012.

Kerr Frequency Comb-Based K_a-band RF Photonic Oscillator

Vladimir S. Ilchenko, Jerry Byrd, Anatoliy A. Savchenkov, Danny Eliyahu,
Wei Liang, Andrey B. Matsko, David Seidel, and Lute Maleki
OEwaves Inc., 465 North Halstead Street, Suite 140, Pasadena, CA 91107, U.S.A.
E-mail: Andrey.Matsko@oewaves.com

***Abstract*—We report on the realization of a packaged RF photonic oscillator based on Kerr optical frequency comb generated in an ultra-high Q crystalline whispering gallery mode (WGM) resonator. The oscillator produces spectrally pure RF signals in K_a frequency band, characterized with single sideband phase noise of -110 dBc/Hz at 10 kHz. The stability of the free running oscillator is characterized with Allan deviation of 10^{-10} at 1 s. We also argue that usage of hyperparametric gain based on cubic nonlinearity of the host material of an optical microresonator as part of an Opto-Electronic Oscillator (OEO) loop allows achieving generation of low noise RF signals in microrezonator-based OEOs.**

***Index Terms*—Optical whispering gallery mode resonator, opto-electronic oscillator, phase noise**

I. Introduction

An Opto-Electronic Oscillator (OEO) [1], [2] is used to produce low noise RF signals by optical means. A conventional OEO includes a laser, an electro-optical modulator (EOM), one or multiple optical delay lines, a fast photodiode, an RF filter, and an RF amplifier. The continuous wave (cw) light of the laser is modulated by the EOM. The modulated signal passes the optical delay line(s) and is transformed to an RF signal with the photodiode. The RF signal is filtered, amplified and fed back to the modulator. As a result, a closed RF circuit is created. The oscillation starts when the RF amplification exceeds the integral loss in the circuit. Some elements of the circuit can be merged or replaced, e.g. a directly modulatable laser can be used, and an optical bandpass filter can be utilized instead of the RF filter.

An OEO has an advantage over electronic oscillators due to the optical delay line which becomes an effective ultra-narrow-band filter for the RF signal. The Leeson frequency [3] of the OEO, determined by the length of the delay line, can be very small, at a level that is unattainable in conventional microwave and mm-wave frequency RF oscillators. As a result, an OEO can produce high frequency RF signals with extremely low phase noise. For instance, an OEO generating a stable 10 GHz signal with phase noise of -163 dBc/Hz at 6 kHz offset from the carrier was demonstrated [4].

The long optical delay line used in the fiber-based OEOs results in peaks in the power spectral density of phase noise of the oscillator. The peaks appear at frequencies corresponding to the free spectral range of the opto-electronic loop. This is an undesirable feature in certain applications where the phase noise noise at higher Fourier frequencies can fold back to increase the noise at lower frequencies. The use of the long fiber also restricts the reduction in the size of the packaged oscillator and requires isolation from the external environment. A high-Q optical resonator or an atomic transition instead of the fiber delay line can be used to eliminate these undesirable features [5]. The application of high-Q optical resonators adds value to the system if resonators are not only used for buffering the RF signal and cleaning the supermode spectrum, but also to replace the EOM. Electro-optic modulators based on high-

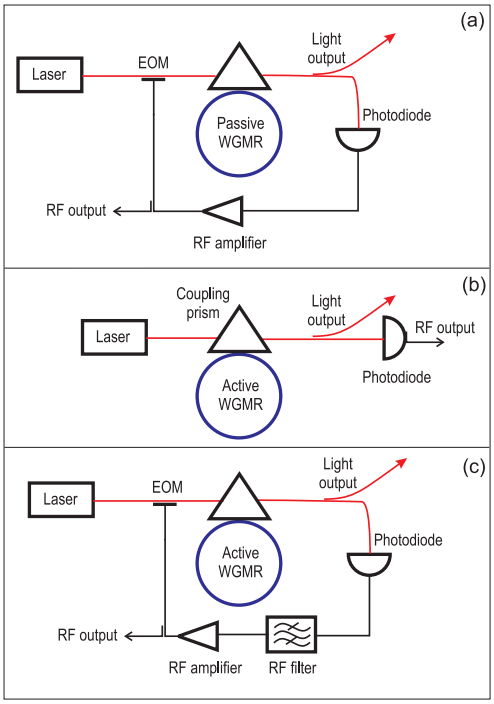

Fig. 1. Possible schemes of opto-electronic oscillators based on microresonators. Here EOM stands for electro-optical modulator, and WGMR – for a whispering gallery mode resonator.(a) A scheme of conventional microresonator-based OEO. The microresonator works as an energy storage element and RF filter. The oscillation occurs at the frequency proportional to the free spectral range (FSR) of the resonator. (b) A scheme of a self-oscillating microresonator-based OEO, e.g. a hyper-parametric RF photonic oscillator or Kerr frequency comb based RF photonic oscillator. The resonator is pumped with continuous wave light. Optical harmonics are generated in the microresonator due to a nonlinear optical process, e.g. four-wave mixing. The oscillation occurs at the frequencies proportional to the resonator FSR. (c) A schematic of the Kerr comb based oscillator. Both nonlinearity of the resonator and an electronic loop are involved.

Q crystalline whispering gallery mode (WGM) resonators combine all the above mentioned functions making an extra-compact OEO feasible [6]. Moreover, the resonant tunable single sideband (SSB) modulator [7] makes fabrication of tunable, compact OEOs possible [8].

It is known that Coupled Opto-Electronic Oscillators (COEO) allow achieving phase noise much lower compared with phase noise of conventional OEOs having the same length of optical fiber involved [9]–[13]. A COEO is a regenerative device that involves both optical and RF gain (active optical and RF loop), while OEO has a passive optical loop and active RF loop. The COEO is more efficient since its effective RF quality (Q-) factor depends on the width of the optical spectrum generated in the active optical loop and is much larger compared with the effective Q-factor of the passive optical fiber loop of the same length usually used in an OEO.

It was shown recently that RF photonic oscillators can be created without usage of an RF feedback loop. These oscillators are based on nonlinear processes within the optical microresonator. Examples include a hyper-parametric [14] as well as Kerr frequency comb [15] based RF photonic oscillators [16], a mode-locked (Raman) laser [17], an opto-mechanical oscillator [18]–[21], a strongly-nondegenerate RF-optical parametric oscillator [22], etc. The devices generate optical harmonics with frequencies slightly different from the frequency of the optical pump taking energy from the optical pump. No RF amplification is involved. The demodulated optical signal becomes a source of stable RF signal.

The optical hyper-parametric oscillator as well as a Kerr frequency comb generator is a product of cubic optical nonlinearity of the material of which the resonator is made, and is generated by pumping one of the resonator modes with a continuous wave coherent light. Kerr frequency comb generation is a unitary process, and can occur in a resonator where the only losses are related to coupling to the external world. In such a case the repetition frequency of the comb does not depend on either frequency or power of the pump light, and the comb becomes an ideal oscillator that does not require any stabilization. The phase noise of the repetition rate of such a comb is given by Leeson formula with oscillator bandwidth coinciding with the bandwidth of the optical modes of the nonlinear resonator and the phase noise has only f^{-2} and f^{0} spectral frequency components.

In practice, contact of the resonator with the environment as well as finite absorption in the resonator host material spoils the stability conditions, and the repetition rate of the comb becomes dependent on parameters of the pump light. We demonstrate a packaged Kerr frequency comb based oscillator producing spectrally pure RF signals in K_a frequency band, characterized with single sideband phase noise of -110 dBc/Hz at 10 kHz. The stability of the free running oscillator is characterized with Allan deviation of 10^{-10} at 1 s. This kind of performance is one of the best ever demonstrated with small volume K_a band oscillators, however the measured noise is much larger than one would expect in an ideal system.

To regain the stability, locking the laser to the resonator mode becomes necessary. An important feature of the Kerr comb is that it is enough to stabilize only a single point in its frequency spectrum to obtain its stable operation. Since the frequency of one comb line coincides with the frequency of the pump laser, and the comb repetition rate is fixed by the properties of the monolithic resonator generating the comb, the entire Kerr comb is stabilized once the frequency of the pump laser is stabilized to an external reference. There is no need to generate an octave spanning Kerr comb to stabilize it. We discuss our progress in experimental realization of the frequency stabilization scheme.

We also show theoretically that usage of optical hyper-parametric gain based on cubic optical nonlinearity of the nonlinear optical microresonator being a part of an Opto-Electronic Oscillator (OEO) loop allows achieving generation of low noise RF signals in microrezonator-based OEOs. Spectral purity of those signals is better compared with the spectral purity of signals generated in similar RF photonic oscillators that have linear optical microrezonators in their loops (Fig. 1a); and, spectral purity of the Kerr frequency comb based RF photonic oscillators based on the self-oscillating nonlinear optical microresonators (Fig. 1b). We suggest a scheme of the RF photonic oscillators relying on the active optical microresonators (Fig. 1c) and explain its principle of operation.

II. Phase Noise of a Packaged K_a-band RF Photonic Oscillator

We fabricated and studied a free running K_a Kerr comb RF photonic oscillator. We fabricated a WGM resonator with 35 GHz free spectral range (FSR) from a commercially available z-cut MgF_2 optical window and pumped the resonator with light from a 1550 nm distributed feedback (DFB) laser. The Kerr comb generation was observed when the cw pump power exceeded 0.1 mW. We pumped the resonator with 5 mW of light and collected 2.8 mW of light exiting the resonator on a fast photodiode characterized with responsivity of 0.55 A/W. The comb generated a 35 GHz RF signal with -22 dBm power at the output of the photodiode.

We used an Agilent signal analyzer and a 40 GHz frequency counter, both locked to a reference Rb clock, to measure the Allan deviation of the K_a-band signal. In addition, we used an OEwaves phase noise measurement system to measure phase noise of the RF signal generated by the comb oscillator. The resultant phase noise and Allan deviation are shown in Fig. (2a) and (2b), respectively.

Theoretically, the shot noise limited floor of the single sideband phase noise is given by equation

$$\mathcal{L}(f) = \frac{2q\rho_{pd}\mathcal{R}P + Fk_BT}{2P_{RF}}\left[1 + \left(\frac{\delta\nu_{S21}}{2f}\right)^2\right], \qquad (1)$$

where P is the optical DC power absorbed at the photodiode, P_{RF} is the demodulated RF power at the photodiode, q is the charge of an electron, F is the integral noise figure of the photodiode and RF amplifier inserted after the photodiode, k_B is the Boltzmann constant, T is the room temperature,

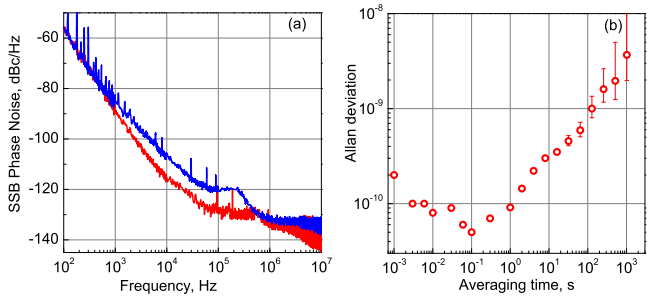

Fig. 2. Characteristics of a free running Kerr comb. Single sideband (SSB) phase noise, (a), of the 35 GHz RF signals generated by free running optical Kerr frequency combs on a fast photodiode. The blue curve is taken using $x4$ frequency divider and OEwaves phase noise test system. The red curve is taken by the measurement of the frequency beat between two nearly identical comb oscillators. The Allan deviation for the 35 GHz comb is shown in panel (b). The WGM resonator temperature is stabilized using a thermistor and a TEC.

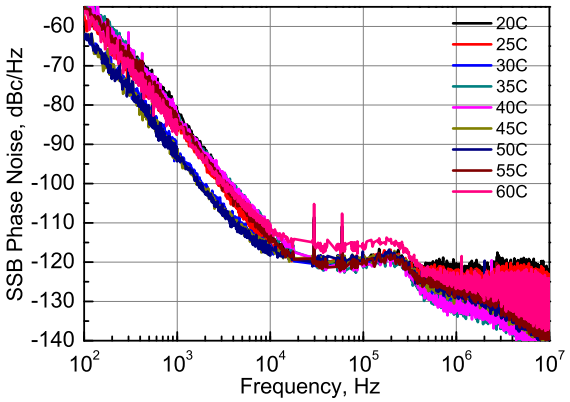

Fig. 3. Characteristics of a free running Kerr comb at different temperatures of the oscillator package. Single sideband (SSB) phase noise of the 35 GHz RF signals generated by free running optical Kerr frequency comb on a fast photodiode. The WGM resonator temperature is stabilized using a thermistor and a TEC.

$\delta\nu_{S21}$ is the full width at the half maximum (FWHM) of the S_{21} of the photonic system (usually coinciding with the FWHM of the mode), and f is the linear spectral frequency. Assuming that $\rho_{pd} = 50$ Ohm, $\mathcal{R} = 0.55$ A/W, $P \approx 5$ mW, $P_{RF} \approx 6$ μW, $F = 3$, $T = 295$ K, and $\delta\nu_{S21} = 10^5$ Hz we find $\mathcal{L}$(f=10 kHz)$\simeq -124$ dBc/Hz. The noise floor approaches -144 dBc/Hz. This is more than 10 dB smaller compared with the observed noise. The difference can result from additional noise introduced by the pump laser.

We also measured thermal dependence of the oscillator phase noise. The temperature of the oscillator package was varied from 20^{o}C to 60^{o}C. Change of the phase noise is shown in Fig. (3). In accordance with the measurement, the phase noise stays below -110 dBc/Hz at 10 kHz for the entire frequency range.

III. Correlation between carrier frequency and repetition rate of the Kerr comb oscillator

We studied the behavior of a free running Kerr frequency comb oscillator to illustrate the correlations between frequency

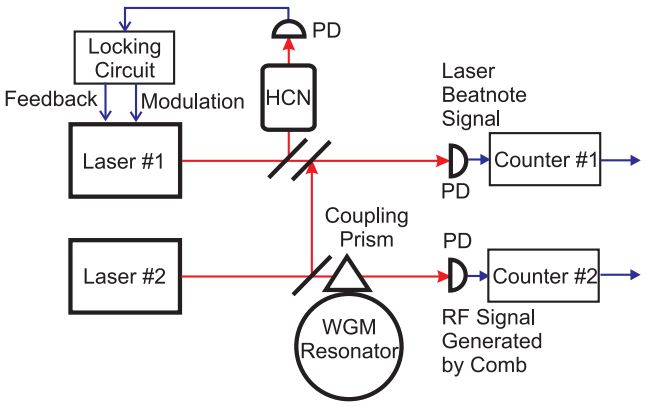

Fig. 4. Schematic of the experimental setup used to observe correlation between the drift of the optical comb harmonics and the Kerr comb repetition rate. The comb repetition rate is measured directly via the RF signal generated at the output of a fast photodiode (PD). A separate laser locked to an HCN transition using PDH technique is utilized to measure the optical frequency. The beat frequency between two lasers is set to be approximately 50 MHz.

of the optical pump locked to a mode of a nonlinear resonator and comb repetition rate. The measurement setup is shown in Fig. (4). This correlation enables the stabilization method of the comb suggested above: it is enough to stabilize only a single point in its frequency spectrum to obtain stable clock operation. The second stabilization point corresponds to locking of the laser to the mode of the resonator. In this system the frequency of one comb line coincides with the frequency of the pump laser, while the comb repetition rate is fixed by the properties of the monolithic resonator generating the comb. Thus, the entire Kerr comb is stabilized once the frequency of the pump laser is stabilized to an external reference and the same time locked to a mode of the resonator; there is no need to generate an octave spanning Kerr comb to stabilize it. In this respect, it is in principle enough to have only two harmonics in the comb (a.k.a. a hyper-parametric oscillator [14]) to realize a stabilized clock. It is even advantageous to use a narrower comb for the stabilization purpose since the narrow comb is not impacted by the variations of the group velocity dispersion and the quality factors of the resonator modes, which may cause undesirable correlation between the comb repetition rate and the pump laser noise.

To establish that a stabilized oscillator could indeed be realized with this scheme, we must verify that the change in the RF frequency, ω_{RF}, corresponds to the change of the optical frequency, ω_0. The stabilization would only be possible if the optical drift is related to the RF drift by their frequency ratio ω_0/ω_{RF} at any instant of time. To examine this, we simultaneously measured both the optical frequency of the pump light and the RF frequency generated by the comb.

We locked a 1550 nm DFB laser to the P9 molecular line of HCN vapor in a sealed cell and used the laser as a reference oscillator (Fig. 4) to measure the frequency of the pump laser involved in comb generation. The laser locked to the cell had stability (Allan deviation) of 3×10^{-11} at 50 s averaging time (τ), beyond which the Allan deviation drifted as $\tau^{1/2}$. This

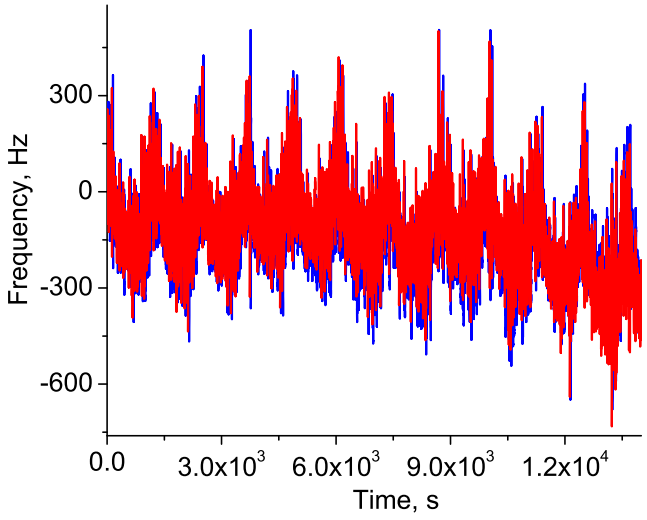

Fig. 5. Experimental observation of correlation between the Kerr frequency comb repetition rate (RF frequency) and the pump frequency using setup shown in Fig. 4. Simultaneously measured drift of the optical pump frequency (blue) and RF frequency (red). The optical frequency is shifted by a constant value and scaled by a constant ratio: $(\omega_0 - 6.4918 \times 10^7)\omega_{RF}/\omega_0$ Hz. The RF frequency is shifted by a constant value: $-(\omega_{RF} - 2297)$ Hz.

reference stability was adequate to observe any drift of the laser that was locked to the resonator mode up to 10^3 s.

We then switched off direct temperature stabilization of the resonator (only the temperature of the platform was stabilized) and observed simultaneous drift of the pump laser frequency and comb repetition rate (RF frequency), with the magnitudes of the shifts following the frequency ratio ω_0/ω_{RF}. RF and optical frequencies were simultaneously recorded for one day and then compared. The result of this measurement is shown in (Fig. 5). Again, the optical and RF frequencies drifted together and the ratio of their drift was ω_0/ω_{RF}. This experiment confirmed that by reducing the drift of the optical frequency and locking it to an atomic transition, the RF frequency produced by the comb could be stabilized. We were unable to measure the degree of correlation quantitatively since our frequency counters had relative frequency drift.

IV. Conclusion

We report on packaging of K_a band Kerr frequency comb RF photonic oscillators and also discuss possible ways of frequency stabilization of the oscillators. Our preliminary measurements show that the frequency of the pump light and the repetition rate of the Kerr frequency comb produced by a nonlinear optical microresonator are correlated if the frequency of the pump light is locked to the corresponding mode of the microresonator.

Acknowledgments

The authors acknowledge support from Defense Sciences Office of Defense Advanced Research Projects Agency under contract No. W911QX-12-C-0067 as well as support from Air Force Office of Scientific Research under contract No. FA9550-12-C-0068.

References

[1] X. S. Yao and L. Maleki, "Optoelectronic microwave oscillator," J. Opt. Soc. Am. B, vol. 13, n. 8, pp. 1725-1735, Aug. 1996.

[2] X. S. Yao, L. Maleki, and D. Eliyahu, "Progress in the Opto-Electronic Oscillator - A Ten Year Anniversary Review," in 2004 IEEE MTT-S Int. Microwave Symp. Dig., vol. 1, June 2004, pp. 287-290.

[3] E. Rubiola, *Phase noise and frequency stability in oscillators,* Cambridge: Cambridge University Press, 2008.

[4] D. Eliyahu, D. Seidel, and L. Maleki, "Phase noise of a high performance OEO and an ultra low noise floor cross-correlation microwave photonic homodyne system," Proc. of 2008 IEEE International Frequency Control Symposium, May 2008, pp. 811-814.

[5] D. Strekalov, D. Aveline, N. Yu, R. Thompson, A. B. Matsko, and L. Maleki, "Stabilizing an optoelectronic microwave oscillator with photonic filters," Journal of Lightwave Technology, vol. 21, no.12, pp. 3052-3061, Dec. 2003.

[6] A. B. Matsko, L. Maleki, A. A. Savchenkov, and V. S. Ilchenko, "Whispering gallery mode based optoelectronic microwave oscillator," J. Mod. Opt., vol. 50, no. 1517, pp. 2523-2542 Oct. 2003.

[7] A. A. Savchenkov, W. Liang, A. B. Matsko, V. S. Ilchenko, D. Seidel, and L. Maleki, "Tunable optical single-sideband modulator with complete sideband suppression," Opt. Lett., vol. 34, no. 9, pp. 1300-1302, Apr. 2009.

[8] A. A. Savchenkov, V. S. Ilchenko, W. Liang, D. Eliyahu, A. B. Matsko, D. Seidel, and L. Maleki, "Voltage-controlled photonic oscillator," Opt. Lett., vol. 35, no. 10, pp. 1572-1574, May 2010.

[9] X. S. Yao and L. Maleki, "Dual microwave and optical oscillator," Opt. Lett., vol. 22, pp. 1867-1869, 1997.

[10] X. S. Yao, L. Davis, and L. Maleki, "Coupled optoelectronic oscillators for generating both RF signal and optical pulses", J. Lightwave Technol., vol. 18, pp. 73-78, 2000.

[11] N. Yu, E. Salik, and L. Maleki, "Ultralow-noise mode-locked laser with coupled optoelectronic oscillator configuration," Opt. Lett., vol. 30, pp. 1231-1233, 2005.

[12] E. Salik, N. Yu, and L. Maleki, "An ultralow phase noise coupled optoelectronic oscillator," IEEE. Photon. Technol. Lett., vol. 19, pp. 444-446, 2007.

[13] A. B. Matsko, D. Eliyahu, P. Koonath, D. Seidel, and L. Maleki, "Theory of coupled optoelectronic microwave oscillator I: expectation values," J. Opt. Soc. Am. B, vol. 26, pp. 1023-1031, 2009.

[14] A. A. Savchenkov, A. B. Matsko, D. Strekalov, M. Mohageg, V. S. Ilchenko, and L. Maleki, "Low threshold optical oscillations in a whispering gallery mode CaF_2 resonator," Phys. Rev. Lett., vol. 93, art. no. 243905, 2004.

[15] P. Del'Haye, A. Schliesser, O. Arcizet, T. Wilken, R. Holzwarth, and T. J. Kippenberg, "Optical frequency comb generation from a monolithic microresonator," Nature (London), vol. 450, pp. 1214-1217, 2007.

[16] A. A. Savchenkov, A. B. Matsko, V. S. Ilchenko, I. Solomatine, D. Seidel, and L. Maleki, "Tunable optical frequency comb with a crystalline whispering gallery mode resonator," Phys. Rev. Lett., vol. 101, art. no. 093902, 2008.

[17] W. Liang, V. S. Ilchenko, A. A. Savchenkov, A. B. Matsko, D. Seidel, and L. Maleki, Passively Mode-Locked Raman Laser, Phys. Rev. Lett. vol. 105, art. no. 143903, 2010.

[18] T. Carmon, H. Rokhsari, L. Yang, T. J. Kippenberg, and K. J. Vahala, "Temporal behavior of radiation pressure-induced vibrations of an optical microcavity phonon mode," Phys. Rev. Lett., vol. 94, art. no. 223902, 2005.

[19] T. J. Kippenberg, H. Rokhsari, T. Carmon, A. Scherer, and K. J. Vahala, "Analysis of radiation-pressure induced mechanical oscillation of an optical microcavity," Phys. Rev. Lett., vol. 95, art. no. 033901, 2005.

[20] K. J. Vahala, "Back-action limit of linewidth in an optomechanical oscillator," Phys. Rev A, vol. 78, art. no. 023832, 2008.

[21] A. B. Matsko, A. A. Savchenkov, V. S. Ilchenko, D. Seidel, and L. Maleki, "Optomechanics with surface-acoustic-wave whispering-gallery modes," Phys. Rev. Lett., vol. 103, art. no. 257403, 2009.

[22] A. B. Matsko, V. S. Ilchenko, A. A. Savchenkov, and L. Maleki, "Highly nondegenerate all-resonant optical parametric oscillator," Phys. Rev. A, vol. 66, art. no. 043814, 2002.

Fiber Ring Resonators with Q Factors in Excess of 10^{10} for Time and Frequency Applications

K. Saleh, A. Fernandez, O. Llopis
CNRS ; LAAS ; Université de Toulouse
7 av. du Colonel Roche, BP 54200, 31031 Toulouse, France

G. Cibiel
CNES, 18 avenue Edouard Belin, 31410 Toulouse, France

***Abstract*—The design of ultra high Q factor fiber ring resonators is described. The resonators are characterized with a microwave frequency modulation technique, which allows a precise measurement of their performance. Optoelectronic oscillators are then realized. The phase noise performance is compared to the results obtained with lower Q factor resonators, and the relatively high intra-cavity bandwidth noise is discussed.**

Keywords—Microwave-optics; optoelectronic oscillator; optical resonator; optical fiber; phase noise

I. INTRODUCTION

In the field of low phase noise microwave sources, the opto-electronic oscillator (OEO) is now very popular. Since the first delay line feedback OEOs in the 1990s [1,2], based on optical fiber spools of a few kilometers, the design of these systems has evolved towards more compact oscillators based on optical resonators. These resonators can be whispering gallery mode resonators, such as mini disk monocrystaline resonators [3-5], passive fiber loop resonators [6,7] or active fiber loops resonators, i.e. coupled optical and electronic oscillator (COEO) [8,9].

Recent work [7] has shown the capability of fiber ring resonators (FRRs) of featuring very high optical quality factors (Q_{opt}). These FRRs are compact and easy to use. However, their high quality factor, combined with significant intra-cavity power enhancement factor, lead to the generation of nonlinear optical effects inside the resonator, especially Rayleigh and Brillouin scattering [10]. When the FRR is used to stabilize the frequency of an optoelectronic oscillator (OEO), these nonlinear optical effects degrade the OEO phase noise. In order to eliminate a great part of these effects, an optical isolator has been inserted inside a 100 m long FRR that featured a Q_{opt} of $2\ 10^9$. The use of this FRR to stabilize the frequency of a 10 GHz OEO has resulted in a phase noise level as low as -52 dBc/Hz at 10 Hz offset frequency [7]. The investigations described in this paper tried to extend the performance of such a system to higher Q factors, in order to reach a lower phase noise level for the OEO. However, even if we have been successful in increasing the Q factor of our resonators above 10^{10}, the resulting phase noise is higher than the one obtained with the resonator with Q_{opt} of $2\ 10^9$. This problem is discussed and some hypothesis on the origin of this noise are given.

II. OEO BASED ON FIBER RING RESONATORS

The fiber ring resonator structure is depicted in Figure 1. It uses one or two optical couplers, preferably two if a filtered output is needed (resonator used in transmission mode). The parameters which can be optimized to get the desired Q factor and insertion losses values are the coupling coefficients (and couplers residual losses), the residual losses of all the elements of the loop (including fiber splices) and the fiber type. Of course, a trade-off has to be found between high Q factor and low insertion losses.

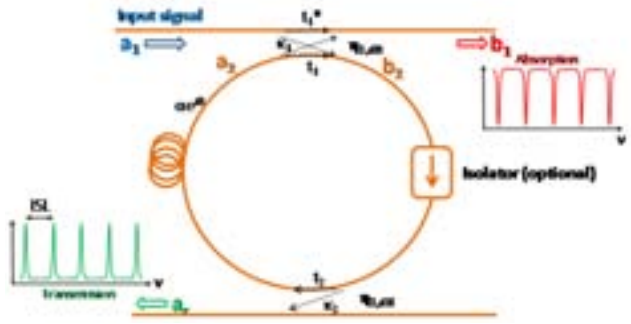

Figure 1 : Fiber ring Resonator topology

The previously realized ring resonators were in the range of 20 m to 100 m length. Because it is the optical resonator bandwidth which is preserved in the microwave application, the microwave Q factor of the OEO is degraded by the ratio of the microwave to optical carrier frequency, which is about 20 000 for a 10 GHz application (optical carrier at 194 THz, or 1550 nm) . Therefore Q_{opt} must be higher than 10^9 in order for this technology to be competitive with the best microwave resonators, which means a fiber ring larger than 10 m and a low coupling factor, or a fiber ring of 100 m if lossy elements are included in the loop. With this approach, most of our designs were based on 20 m fiber rings, featuring Q factors of about $3\ 10^9$, using either SMF fiber or PM fiber. A 100 m ring has also been designed, using PM fiber and including an isolator in order to prevent the growing up of Stimulated Brillouin Scattering (SBS), which appears at relatively low input power because of the large intra cavity power enhancement factor inside the resonant loop.

These resonators have been used to stabilize various OEOs. All the OEOs have the same topology, which is described in previously published papers [7,10] and depicted in Figure 2. The laser is first locked to the resonator frequency thanks to a Pound Drever Hall (PDH) feedback loop ; the oscillation is started thanks to a second loop which is a microwave loop including one or two amplifiers, a phase shifter and a dielectric resonator filter centered at 10.2 GHz.

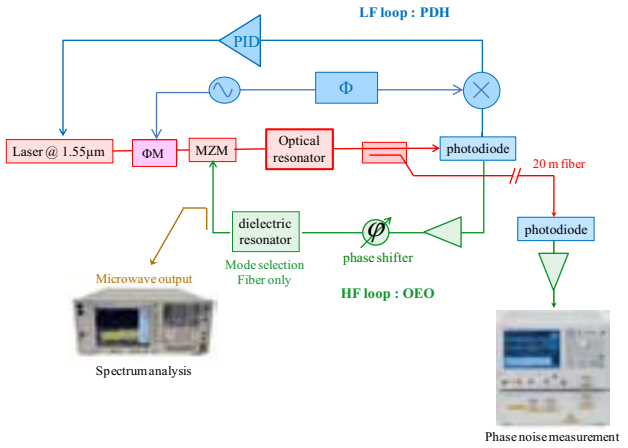

Figure 2 : OEO topology, including a PDH laser stabilization loop and an microwave oscillation loop.

The phase noise results obtained on 10.2 GHz OEOs realized using this system are depicted in Figure 3. In each case, the oscillator system is the same and only the optical resonator is removed and replaced by another. Three types of resonators are used in the OEOs described in this Figure : a mini-disk of CaF_2, a 20 m ring resonator (two spectra plotted, for different optical input power in the resonator) and the 100 m ring resonator which includes an isolator.

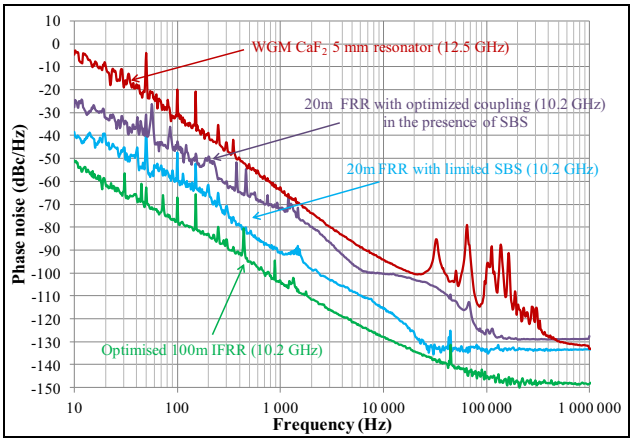

Figure 3 : Phase noise of previously realized OEOs, stabilized with the same PDH circuit, including one OEO based on a CaF_2 mini-disk ($Q = 10^8$), one OEO realized with a 20 m FRR ($Q = 3.5\ 10^9$) and one OEO stabilized with a 100 m FRR which includes an isolator ($Q = 2\ 10^9$).

The best result is obtained with the 100 m FRR OEO, featuring -52 dBc/Hz at 10 Hz offset, and -128 dBc/Hz at 10 kHz. With this resonator, we have been able to remove the main nonlinear optical effects limiting the performance of the 20 m FRR OEO. The phase noise of this oscillator is only limited by the RF amplifiers phase noise, and the measured spectrum can be described by a Leeson type approach.

III. Ultra High Q Resonators Design

Our goal was then to increase again the Q factor of our FRR, above 10^{10} (which means an equivalent Q factor at 10 GHz above 500 000). To this purpose, two ways can be followed : realizing a 100 m long FRR without isolator in the loop, or realizing a much longer FRR, such as a 1000 m FRR, and keeping the isolator which prevents some of the optical nonlinear effects (particularly the growing up of SBS).

In such a design, a trade-off has to be found between Q factor enhancement and the optical losses through the resonator (high Q means low coupling, which induces losses). Optical losses higher than 5 dB means RF losses higher than 10 dB, which are added to the losses of the microwave to optical and optical to microwave conversion which are generally high. We have thus chosen to limit optical IL to about 5 dB. The resonator is modeled either using an equivalent circuit approach on ADS software, or using a dedicated Matlab approach (both give the same results). The resonator performance is simulated varying the coupling factors of the optical couplers (the other parameters being the residual losses of the optical devices provided by the devices manufacturers).

For the 100 m resonator without isolator, a coupling factor close to 1 % meets our requirements in Q and insertion losses (IL). In the case of the 1000 m resonator, a coupling factor of about 10 % is necessary to maintain relatively low IL. This coupling factor also corresponds to the maximum intra cavity power enhancement factor.

The resonators have then been realized, and included in metallic boxes with passive thermal isolation. The devices characterization is performed still using the PDH stabilization loop : the laser is stabilized on one resonance, and the lateral resonances are measured using a microwave vector network analyser (VNA), i.e. the green loop in Figure 2 is replaced by the VNA.

Figure 4 depicts the transmission curve (S_{21}) obtained on the 100 m resonator (actually, more precisely, it is a 120 m resonator). A Q_{opt} of $1.25\ 10^{10}$ has been measured, with optical IL of 7.5 dB (a bit degraded compared to our simulation).

Figure 5 depicts the same measurement performed on the 1000 m resonator. In this case, a Q_{opt} of $1.7\ 10^{10}$ has been reached, with optical IL of 4.1 dB, which was perfectly in agreement with our simulated data. The measured S_{21} phase curve is also depicted in this figure (it is this parameter which stabilizes the oscillator), and the high slope looks very clean and can be easily measured using our microwave modulation technique.

IV. OEOs with Q in Excess of 10^{10}

These two resonators have then been included in the OEO system described in Figure 2. A 10.2 GHz oscillation has been obtained, and its phase noise has been measured.

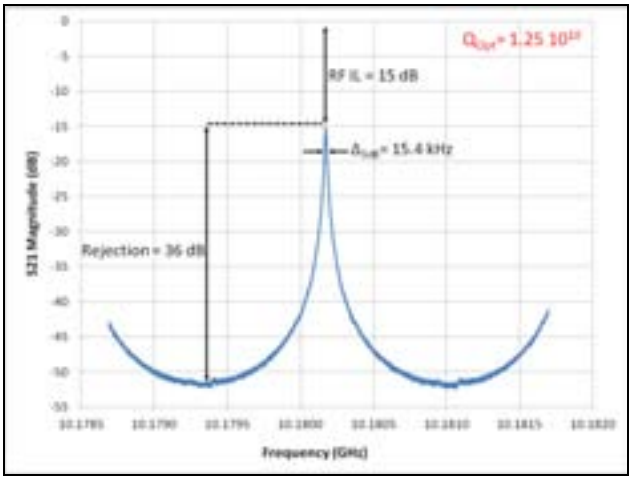

Figure 4 : Measurement of the transmission response near 10.2 GHz of the 120 m resonator, using the PDH lock and a frequency modulation approach (microwave network analyser).

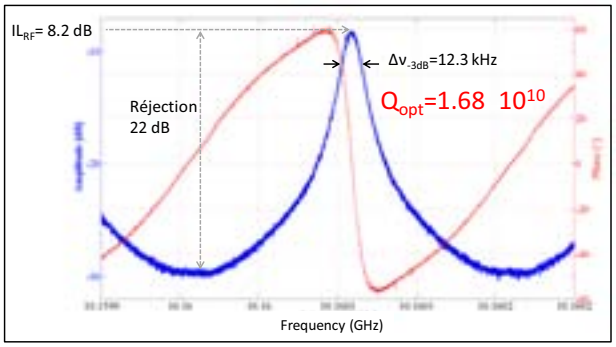

Figure 5 : Measurement of the transmission response of the 1000 m resonator, using the PDH lock and a frequency modulation approach (vector network analyser). The measured Q factor and IL are in this case identical to the ones simulated. The S_{21} phase response is also depicted in this figure.

The phase noise of the 120 FRR OEO is depicted in Figure 6. As shown in the figure, a sudden increase of the noise is observed inside the resonator half bandwidth. We were expecting such a phenomenon, because this resonator is not protected against optical nonlinear effects, and the intra cavity power enhancement factor is huge. We have attempted to reduce its influence by reducing the resonator optical input power, but the best phase noise level we could get with the PDH locking still going on was -40 dBc/Hz @ 10 Hz, which has to be compared to the -52 dBc/Hz @ 10 Hz obtained with the preceding 100 m FRR with a Q factor 6 times lower (but made of PM fiber and including an isolator).

We were more confident in the 1000 m FRR OEO, because of the isolator in the loop, but once again a sudden increase of the noise is observed inside the resonator half bandwidth, has shown in Figure 7. Also shown in this figure is the effect of a reduction of the resonator input power : the changes observed in the carrier to noise ratio outside the resonator bandwidth are proportional to this power, but the phase noise improvement inside the cavity is not (but there is effectively an improvement at low power). The FSR for this resonator is also very small : 200 kHz, which means that the dielectric resonator filter is no more sufficient to filter only one resonant mode. However, at low optical power, we still were able to get a single oscillation, even if the lateral modes can be seen on the spectra every 200 kHz offset.

For this 1000 m FRR OEO, the best phase noise results is -27 dBc/Hz @ 10 Hz and -105 dBc/Hz @ 10 kHz, which is still far from the best result described in section II. The reason may lie in two points : either the 1000 m section between two isolators is too large to prevent the built up of Rayleigh scattering noise, or a polarization noise is predominant because conventional SMF fiber has been used in this design instead of PM fiber (because of the cost of 1000 m PM fiber).

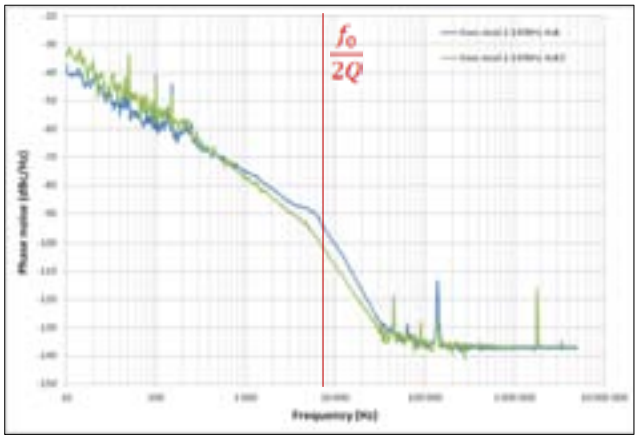

Figure 6 : Phase noise of the 10.2 GHz OEO based on the 120 m resonator ($Q = 1.25\ 10^{10}$). The two curves correspond to two different loop parameters. A large increase of the noise is clearly seen inside the resonator half bandwidth.

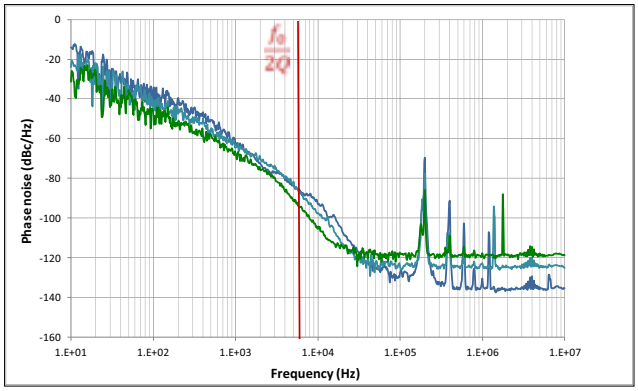

Figure 7 : Phase noise of the 10.2 GHz OEO based on the 1000 m resonator ($Q = 1.7\ 10^{10}$). Again, a large increase of the noise is clearly seen inside the resonator half bandwidth, in spite of an attempt of reducing the intra cavity power (the three spectra presented correspond to different optical power levels at the resonator input).

V. CONCLUSION

Optical resonators with Q factor in excess of 10^{10} have been successfully designed and realized using the fiber ring resonator approach. The stabilization of a laser on one resonance has been demonstrated, using the Pound Drever Hall

technique. The measurement of the resonators characteristics have thus been performed thanks to a microwave modulation and a vector network analyser. The measured data (Q factor, insertion losses, out of band rejection…) are very close to the simulated data for these ultra high Q resonators.

OEOs have then been realized with these two resonators and an approach based on the PDH laser stabilization on the resonator. The measured phase noise spectra show a sudden increase of the noise inside the resonator half bandwidth, which is the signature of a noise induced by the resonator itself.

Further studies will try to cancel this parasitic noise contribution, and also to improve the performance of the best OEO realized up to now, which was based on a 2 10^9 Q factor resonator.

ACKNOWLEDGMENT

This study is sponsored by the French National Space Centre (CNES) and the "Direction Générale de l'Armement" (DGA), French MoD procurement agency, under the contract ANR-11-ASTR-0029 MINOTOR.

REFERENCES

[1] X.S. Yao, L. Maleki, "High frequency optical subcarrier generator," Electronics Letters, vol. 30, Issue 18, pp. 1525-1526, Sept. 1994.

[2] X.S. Yao, D. Eliyahu, L. Maleki, "Progress in the optoelectronic oscillator – a ten year anniversary review," IEEE Microwave Theory and Tech. Symp. Digest, vol. 1, pp. 287-290, Jun. 2004.

[3] A. A. Savchenkov, E. Rubiola, A. B. Matsko, V. S. Ilchenko, L. Maleki, "Phase noise of whispering gallery photonic hyper-parametric microwave oscillators", Optics Express, March 2008, Vol. 16, No. 6, pp. 4130-4144.

[4] V. S. Ilchenko, J. Byrd, A. A. Savchenkov, A. B. Matsko, D. Seidel, L. Maleki, "Miniature Oscillators Based on Optical Whispering Gallery Mode Resonators", Proc. of the 2008 IEEE Int. Freq. Control Symp., pp. 305-308.

[5] P.-H. Merrer, K. Saleh, O. Llopis, S. Berneschi, F. Cosi, G. Nunzi Conti, "Characterization technique of optical whispering gallery mode resonators in the microwave frequency domain for optoelectronic oscillators", Applied Optics, Vol. 51, Issue 20, pp. 4742-4748, July 2012.

[6] P. H. Merrer, A. Bouchier, H. Brahimi, O. Llopis, and G. Cibiel, "High-Q Optical Resonators for Stabilization of High Spectral Purity Microwave Oscillators", proc. of the 2009 IEEE EFTF-IFCS, pp. 866–869, (2009).

[7] K. Saleh, P.H. Merrer, O. Llopis, G. Cibiel, "Optoelectronic oscillator based on fiber ring resonator: overall system optimization and phase noise reduction", 2012 IEEE International Frequency Control Symposium (IFCS), 21-24 may 2012.

[8] X. S. Yao, L. Davis, L. Maleki, "Coupled optoelectronic oscillators for generating both RF signal and optical pulses", Journal of Lightwave Technology, Vol. 18, Issue 1, Jan. 2000, pp. 73 – 78.

[9] N. Yu, E. Salik, L. Maleki, "Ultralow-noise mode-locked laser with coupled optoelectronic oscillator configuration", Optics Letters, May 2005, pp. 1231-1233.

[10] K. Saleh, O. Llopis, G. Cibiel, "Optical Scattering Induced Noise in Fiber Ring Resonators and Optoelectronic Oscillators", Journal of Lightwave Technology, vol. 31, no. 9, pp. 1433,1446, May 1, 2013.

Experimental characterization of optoelectronic oscillators based on optical mini-resonators

Rémi Henriet, Aurélien Coillet, Patrice Salzenstein, Khaldoun Saleh, Laurent Larger, Yanne K. Chembo

Franche Comté Electronique Mécanique Optique Thermique Sciences et Technologies (FEMTO-ST), Centre National de la Recherche Scientifique (CNRS), route de Gray, F25030 Besançon, France

***Abstract*—The fabrication process of whispering gallery mode disk resonators is presented with different characterization techniques in order to monitor roughness and optical quality factor. This type of resonators is then used as the reference frequency element to stabilize the oscillation frequency of an optoelectronic oscillator. Experimental results are provided and demonstrate the efficiency of the method.**

Keywords-component; Optoelectronic oscillator, phase noise, delay line, optical resonator

I. INTRODUCTION

We develop an optoelectronic oscillator [1] (OEO) based on intensity modulation and a high-Q disk resonator. In this OEO, the resonant element is a 5 mm diameter crystalline whispering-gallery-mode resonator [2] (WGM). It selects the microwave oscillating frequency as an optical storage energy element. This resonator also filters the microwave modulation signal. The generated oscillating frequency corresponds to the free spectral range (FSR) of the mini-resonator (in the range 10–11 GHz) [3]. Therefore no delay-induced spurious peaks are present in the spectrum, in contrast with the classical optoelectronic oscillator where the storage element consists of an optical fiber delay line [4, 5]. This resonator features a high quality factor which has been characterized using the cavity ring-down method (CRD) [6]. Another advantage of our system resides in its compactness allowing for efficient control of the temperature. We present experimental results related to the temporal dynamics and phase noise performance of WGM-based OEO. The analysis proceeds by matching the theoretical and experimental results [7]. Power spectrum is given and the generated microwave signal stands 50 dB above the filtered noise of the RF amplifier. We hereafter provide a discussion relatively to its main features.

II. MANUFACTURING THE OPTICAL MINI-RESONATOR

A. Choice of the resonator

In Whispering Gallery Mode (WGM), the light confinement is achieved by total internal reflection on air crystalline interface. The photon life time in WGM cavity – and therefore the delay of the oscillator loop – allows to determine the Q factor. This parameter is defined by the absorption of the disk and the surface losses. To achieve very low absorption losses, the use of a crystalline-resonator is a good choice. The laser light wave is efficiently coupled into and out of the resonator by evanescent field through two tapered optical fibers in an add-drop configuration. Such coupling method offers accurate performance, a good mechanical stability and the coupling efficiency can be easily controlled.

Such high Q-factor resonator is then used to achieve a low phase noise of the OEO. The resonator can be a micro-sphere [9] but we rather prefer disk-resonators. MgF_2 [10], CaF_2 [11], Quartz and fused silica [3] resonators have been studied and each of them provides its own advantages and limitations. In order to prepare the optical resonator, we use a dedicated process and instrumentation, and give the adequate shape to the resonator by polishing and performing several treatments as illustrated on Figure 1. The resonator smoothness is then characterized. Tapered optical fibers are also fabricated in the laboratory. When the laser light wave is coupled into the resonator and the laser wavelength is scanned, resonance peaks are detected and can be then characterized via the CRD technique as reported in reference [6].

Figure 1. Polishing a mini-resonator

B. Manufacturing process

The diameter of the resonator is chosen in the range 5-6 mm in order to get a FSR in the range of 10 GHz. The manufacturing process is divided in two steps: the grinding and the polishing. The grinding generates the geometry of an optical guide: a rim of 50 micrometer on the circumference of the disk. It is realized using silicon carbide and on a very stable support to minimize the geometry default and increase the speed of grinding. The polishing represents the decreasing in the optical guide roughness. It is realized with a sub-micron diamond powder on felt. The hardness of the disk increases the time of each step. This process allows obtaining a very low roughness, 2 nm, and thus a very high Q factor.

Typical roughness obtained is given in Figure 2.

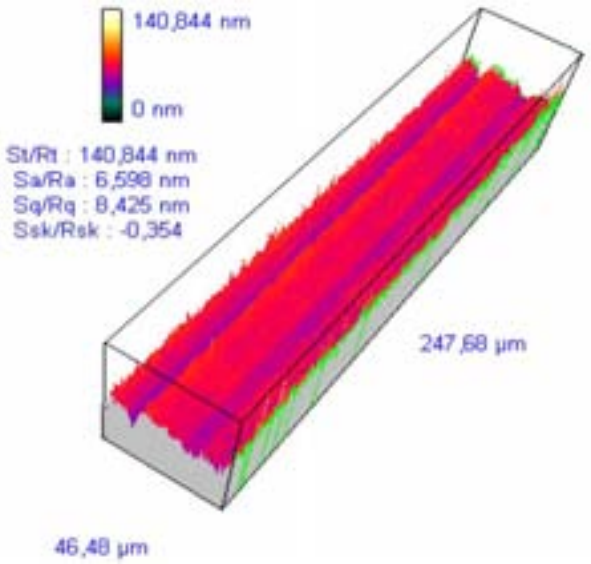

Figure 2. Average surface roughness is 6.5nm

III. Experimental study of the OEO

In order to evaluate the OEO performances if the above resonator is included, the setup given in Figure 3 is used [12]. The optical path is in thin red, while the electric path is in thick black. Inserts show the spectra of the optical fields E(t), F(t) and G(t) at the input, interior and output of the WGM resonator, respectively. The spectral lines are separated by the frequency Ω_M which corresponds to the FSR of the resonator. The through port of the coupling fibers is used to monitor the optical spectra with the OSA, in both the transient and stationary regimes. In the open-loop configuration (no oscillations), this through port is also used to perform the CRD measurement using an oscilloscope, thereby enabling the determination of the intrinsic and in-coupling quality factors. In the electric branch, a fast oscilloscope enables to resolve the temporal dynamics of the microwave V (t), whose complex envelope is V(t) (or A(t) in the dimension form). An ESA also enables to monitor the corresponding RF spectrum.

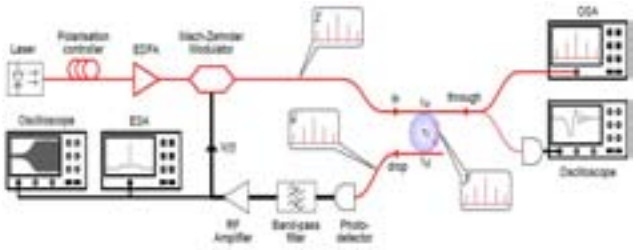

Figure 3. Experimental setup for characterizing the disk-resonator and the realized OEO. EDFA: Erbium-doped amplifier; ESA: Electrical spectrum analyzer; OSA: Optical spectrum analyzer.

We show on figure 4 the coupling of a laser lightwave into the resonator through a tapered fiber.

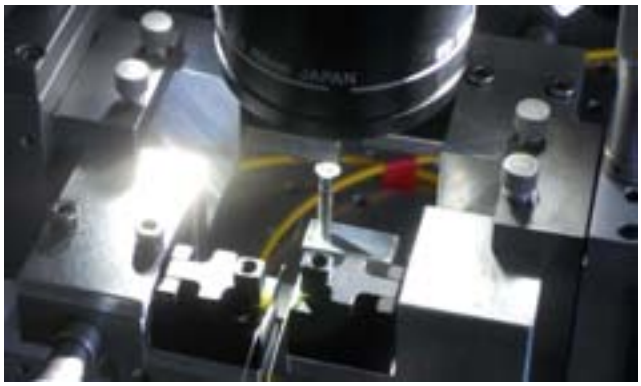

Figure 4. A 5.5 mm diameter disk-resonator coupled in transmission mode to two tapered fibers. The resonator acts like a band-pass filter with a high quality factor

The high Q resonator is then characterized by the CRD technique. Figure 5 presents an example of the ringing diagrams that can be obtained.

It has to be underlined that the key parameters are determined by fitting the measured trace to an adequate simulated trace corresponding to the researched Q-factor for the resonator characterized at 1550 nm.

Figure 6 shows the power spectrum of the OEO. The 10.41 GHz oscillation frequency corresponds to the FSR of the resonator [12]. This microwave signal is strong, and stands 50 dB above the filtered noise of the microwave amplifier.

Authors acknowledge the support of the French National Research Agency (ANR) grant "ANR-2010-BLAN-0312-02" and the French National Space Agency (CNES) grant "SHYRO R&T LN-0001-004".

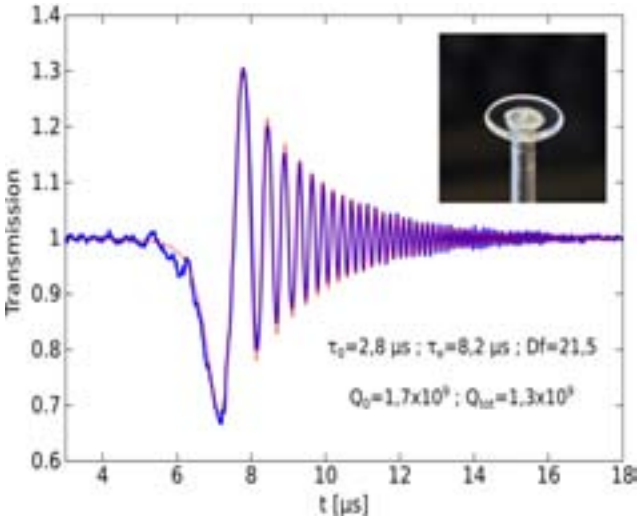

Figure 5. Characterization of a resonator designed and manufactured at the laboratory

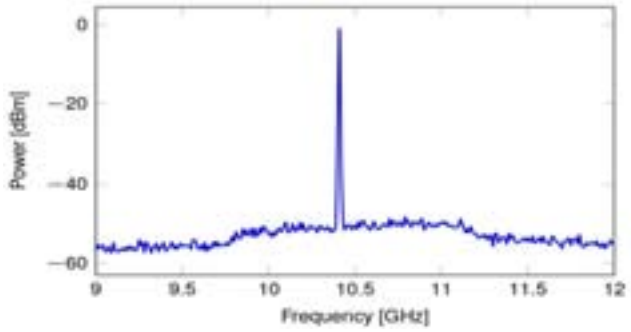

Figure 6. Characterization of a resonator designed and manufactured at the laboratory

On the other hand, the laser wavelength must be stabilized onto one of the resonator's resonances to be able to maintain a stable performance of the oscillator. Different stabilization techniques are possible [13], and we are currently setting up a Pound-Drever-Hall laser stabilization loop [14,15]. The next step will be therefore the characterization of the OEO in terms of phase noise.

IV. Conclusion

We presented here the different fabrication steps of WGM resonators and their characterization. The first experimental results of an optoelectronic oscillator (OEO) based on a high-Q disk resonator are also presented. We are currently working on the stabilization of the system, especially on the laser stabilization onto the resonator, in order to be able to characterize the phase noise performance of this OEO.

References

[1] L. Maleki, "The optoelectronic oscillator," Nature Photonics, vol. 5, N°12, pp 728–730, 2011.

[2] V. S. Ilchenko, X. S. Yao, L. Maleki, "High-Q microsphere cavity for laser stabilization and optoelectronic microwave oscillator," Proceedings of SPIE, vol. 3611, pp. 190–198, 1999.

[3] K. Volyanskiy, P. Salzenstein, H. Tavernier, M. Pogurmirskiy, Y. K. Chembo, L. Larger, "Compact Optoelectronic Microwave Oscillators using Ultra-High Q Whispering Gallery Mode Disk-Resonators and Phase Modulation," Optics Express, vol. 18, n°21, pp. 22358–22363, 2010.

[4] X. S. Yao, L. Maleki, "High frequency optical subcarrier generator," Electronics Letters, vol. 30, n°18, pp. 1525–1526, 1994.

[5] K. Volyanskiy, J. Cussey, H. Tavernier, P. Salzenstein, G. Sauvage, L. Larger, E. Rubiola, "Applications of the optical fiber to the generation and to the measurement of low-phase-noise microwave signals," J. Opt. Soc. Am. B, vol. 25, n°12, pp. 2140-2150, 2008.

[6] Y. Dumeige, S. Trebaol, L. Ghisa, Thi Kim Ngan Nguyen, H. Tavernier, P. Féron, "Determination of coupling regime of high-Q resonators and optical gain of highly selective amplifiers," J. Opt. Soc. Am. B, vol. 25, n°12, pp. 2073–2080, 2008.

[7] Y. K. Chembo, K. Volyanskiy, L. Larger, E. Rubiola and P. Colet, "Determination of phase noise spectra in optoelectronic microwave oscillators: a Langevin approach," IEEE J. of Quantum Electron., vol. 45, pp. 178–186, 2009.

[8] P. Salzenstein, E. Pavlyuchenko, A. Hmima, N. Cholley, M. Zarubin, S. Galliou, Y. K. Chembo and L. Larger, "Estimation of the uncertainty for a phase noise optoelectronic metrology system", Physica Scripta, vol. T149, 014025, 2012.

[9] A. Chiasera, Y. Dumeige, P. Féron, M. Ferrari, Y. Jestin, G. Nunzi Conti, S. Pelli, S. Soria and C. Righini, "Spherical whispering-gallery-mode microresonators," Laser & Photonics Reviews, vol. 4, pp. 457–482, 2010.

[10] H. Tavernier, P. Salzenstein, K. Volyanskiy, Y. K. Chembo and L. Larger, "Magnesium Fluoride Whispering Gallery Mode Disk-Resonators for Microwave Photonics Applications," IEEE Photonics Technology Letters, vol. 22, n°22, pp. 1629–1631, 2010.

[11] I. S. Grudinin, V. S. Ilchenko and L. Maleki, "Ultrahigh optical Q factors of crystalline resonators in the linear regime," Phys. Rev. A, vol. 74, 063806, 2006.

[12] A. Coillet, H. Henriet, P. Salzenstein, K. Phan Huy, L. Larger L. and Y. K. Chembo, "Time-domain Dynamics and Stability Analysis of Optoelectronic Oscillators based on Whispering-Gallery Mode Resonators," IEEE Journal of Selected Topics in Quantum Electronics, vol. 19, n°5, 6000112, 2013.

[13] P. Salzenstein, V. B. Voloshinov and A. S. Trushin, "Investigation in acousto-optic laser stabilization for crystal resonator based optoelectronic oscillators," Optical Engineering, vol. 52, n°2, 024603 2013.

[14] R. W. P. Drever, J. L. Hall, F. V. Kowalski, J. Hough, G. M. Ford, A. J. Munley and H. Ward, "Laser phase and frequency stabilization using an optical resonator". Appl Phys B, vol. 31, n°2, pp. 97–105, 1983.

[15] E. D. Black, "An introduction to Pound-Drever-Hall laser frequency stabilization," Am. J. of Phys., vol. 69, n°1, pp. 79–87, 2001.

High Spectral Purity Microwave and Terahertz Oscillator

Gwennaël DANION, Goulc'hen LOAS, Ludovic FREIN, Cyril HAMEL, Anthony CARRÉ, Steve BOUHIER, Marc VALLET, Marc BRUNEL, Antoine ROLLAND, Mehdi ALOUINI, François BONDU
IPR, UMR6251
CNRS / Université de Rennes 1
Rennes, France
gwennael.danion@univ-rennes1.fr,
francois.bondu@univ-rennes1.fr

Frédéric CLEVA, Jean-Pierre COULON, Mourad MERZOUGUI, Alain BRILLET
ARTEMIS, UMR7250
CNRS / Université de Nice Sophia Antipolis/ OCA
Nice, France

Alexandre BECK, Guillaume DUCOURNAU, Mohamed ZAKNOUNE, Christophe COINON, Xavier WALLART, Emilien PEYTAVIT, Tahsin AKALIN, Jean-François LAMPIN
IEMN, UMR 8520
CNRS / Université de Lille 1
Lille, France

Grégoire PILLET, Loïc MORVAN, Ghaya BAILI, Jérôme BOURDERIONNET
THALES Research and Technology
Palaiseau, France

***Abstract*— We report on the design of an ultra stable microwave/THz oscillator and on the realization and the characterization of its laser source. The tunable oscillator is expected to show below -150 dB rad^2/Hz phase instability at an offset frequency of 10 kHz for a 30 GHz carrier frequency, as well as 18 GHz, 100 GHz, 400 GHz and 1 THz carrier frequencies.**

Keywords: millimeter and sub-millimiter wave oscillator, frequency stabilization, optical to microwave conversion, THz, ultra low phase noise.

I. INTRODUCTION

The OSMOTUS project (2012-2014) consists into the realization of two microwave/THz oscillators with a very low phase instability, below -150dB rad^2/Hz at an offset frequency of 10 kHz for a 20 GHz carrier frequency. We use the photomixing of two optical frequencies generated by a two-axis dual frequency dual polarization laser. The two laser frequencies will be stabilized on an ultra-low-expansion (ULE) cavity since they are the best resonators in the optical range [1]-[2]. This setup will transfer the exceptional stability from the optical domain to the microwave and terahertz one. Two identical setups will measure the submillimeter phase spectral purity.

II. DUAL-FREQUENCY TUNABLE LASER SYSTEM

A. Two-Axis Dual Frequency Laser

The dual-axis 1550 nm laser is pumped by a polarized and single mode 800 mW diode at 980 nm. This pump, polarized at 45° with respect to horizontal and vertical axes, is spatially split thanks to a birefringent YVO_4 crystal, so that the active medium is pumped by two 2-mm spaced beams. The plano/concave dual axis cavity includes an active medium, one etalon and one electro-optical element per axis, and an YVO_4 crystal recombining the two orthogonal polarization eigenstates (see Fig. 1). The active medium is a 1.5-mm-long phosphate glass co-doped Er/Yb. The high reflectivity coating on the external face of the active medium is the input coupler M1; the internal face of the active medium has a high reflectivity coating at 980 nm. The resonator is closed by the output coupler M2, whose curvature had been chosen in order to facilitate the single mode operation: a good compromise is obtained with a 4 cm radius. The 0.5% transmission of this coupler enables the laser to operate far from the threshold, reducing favorably noises; the laser delivers a with few mW output power per axis. The single mode operation is obtained and controlled on each axis by 40-µm thick etalons with 30% reflection on each side. The rough tunability of each optical frequency is realized by tilting the etalon. We are thus able to sweep each optical frequency by steps of the 1.7 GHz of the free spectral range of the laser cavity; this allows the beat note to be tunable from DC to about 900 GHz [3]-[4].

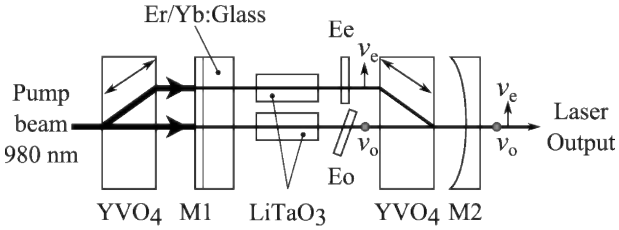

Figure 1. Two-axis dual frequency laser

The frequency of each polarization, with a measured (10^4/f) Hz/Hz$^{1/2}$ frequency noise spectral density, will be further stabilized on one of the resonances of a Fabry Perot cavity. The frequencies are both continuously and independently tunable thanks to the lithium tantalate ($LiTaO_3$) electro-optic crystals, using both thermo-optic (600 MHz/°C) and electro-optic (1.1 MHz/V) effects. The measured relative intensity noise spectral density of one optical axis is displayed on the blue curve on figure 2.

B. Amplifier System

The OSMOTUS performance requires tens of mW for the frequency stabilization, the amplitude stabilization and the beat note generation. The power fluctuations have to be stabilized in order to reduce the AM/PM couplings in the cavity and in the electronic components. Each polarization is independently amplified by a fiber system. Our amplifier system is composed of an erbium doped fiber amplifier (EDFA) and a semiconductor optical amplifier (SOA) per polarization axis (see Fig. 2).

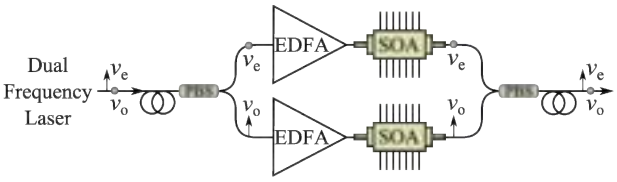

Figure 2. Amplifier system; PBS: polarization beam splitter; EDFA:Erbium doped fiber amplifier; SOA: Semiconductor optical amplifier

Since the EDFA is operated in deep saturation, it provides a constant 10 mW output power into the SOA, which is then also saturated. In that condition, the SOAs deliver a constant output power of 60 mW per polarization axis, with an amplifier system noise factor of 6 dB. Furthermore, a gain-saturated SOA decreases the intensity noise of a laser [5]. As shown on the Figure 2. the output relative intensity noise (RIN) of one axis of the dual frequency laser is reduced by 20 dB, including at the relaxation oscillation of the laser at 100 kHz, without stabilization electronics. The SOA driving currents will permit to independently stabilize the polarization amplitudes with a few hundred kilohertz bandwidth. We have checked that the amplifier system does not add any noticeable frequency noise.

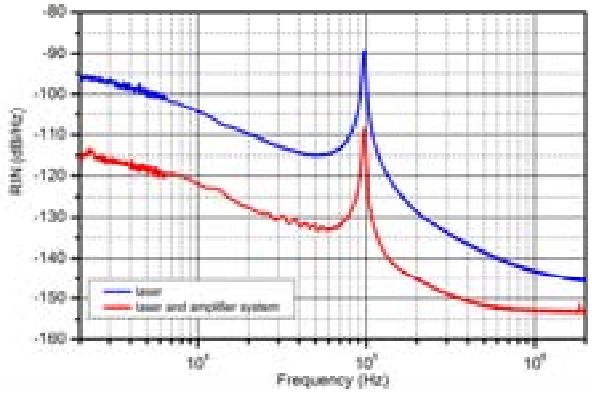

Figure 3. RIN of laser and laser with amplifier

III. Stabilization And Microwave/THz Generation

The two optical frequencies of the laser described above will be stabilized onto two resonances of one Fabry-Perot cavity with the Pound-Drever-Hall scheme. The cavity spacer is made with an ultra-low expansion ceramic (ULE). The cavity is placed in vacuum. This is today the best relative dimensional stability compact resonator, limited by the thermal fluctuations of the spacer and of the mirrors [6]-[9]. The two laser frequencies sense the same cavity length fluctuations so that the best possible relative frequency stability of the beat note is limited by the relative dimensional stability and by the shot noise of each polarization. For a 10 GHz beat note, the beat note frequency noise should be limited by the optical shot noise. For a 1 THz beat note, the cavity stability should limit the beat noise phase noise at 10 Hz offset frequency to –90 dB rad²/Hz.

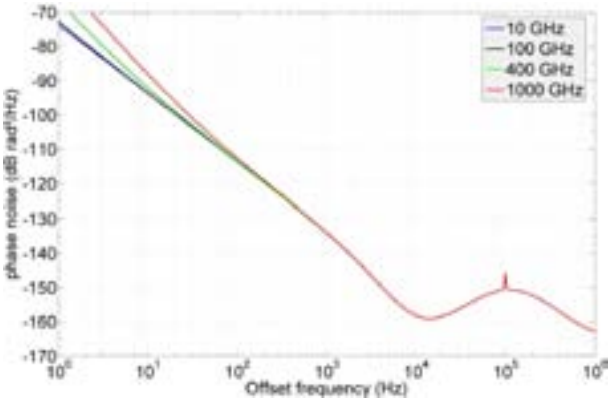

Figure 4. Expected phase noise of ultra stable oscillator

A 75% fraction of the beam transmitted by the cavity is used to stabilize the amplitude of the laser, and a 25% fraction is sent on a polarizer and a photomixer for optical to millimeter wave conversion. In the submillimeter frequency range the photomixer is an optimized UTC photodiode. The AM/PM conversion is a known limiting factor to the

stability of some optical resonators [10]. A first coupling is the opto-thermal conversion in the cavity: the power fluctuations are absorbed by the mirrors and thus induce fluctuations of the cavity length by dilation of the mirrors and by index modification with temperature. In our setup, this effect will be made negligible at a 1 Hz frequency offset by stabilization of the optical carrier at the 8.10^{-9}/sqrtHz level, already demonstrated out of loop. Static biases on the frequency stabilization error signal could give AM/PM couplings: we predict to correct for these by tuning the offsets of the error signals. Photodiodes and amplifiers also give AM/PM couplings at levels of about 10 rad/W; these couplings should be negligible with our level of amplitude stability.

IV. Conclusion

The system will be tunable from DC to THz by steps of 1.5 GHz, which is the free spectral range of the ULE cavity. Two laser/cavity systems are on development. Their phase noise performance will be evaluated by beat note of the two millimetre or THz outputs. At a 10 GHz beat note frequency, our system should have state of the art phase noise performance both at 1 Hz and 10 kHz offset frequencies. Furthermore, the phase noise of the sub millimetre carrier is relatively independent of its carrier frequency: at 18 GHz, 100 GHz, 400 GHz, 1 THz, we hope to exceed the state of the art. At 400 GHz, we use uni-travelling-carrier photodiode (UTC-PD). At 30 GHz, we expect to obtain -80 dB rad^2/Hz at 1 Hz offset frequency, and below -150 dB rad^2/Hz at 10 kHz offset frequency.

Acknowledgment

This work is supported by the Agence Nationale de la Recherche (OSMOTUS ANR-2011-BS03-010-01).

References

[1] F. Bondu, P. Fritschel, C.N. Man and A. Brillet : Ultrahigh Spectral Purity Laser for the VIRGO Experiment, Optics Letters 21, 1996, 582-584

[2] M. Notcutt, L.-S. Ma, J. Ye and J. Hall : Simple and compact 1-Hz laser system via an improved mounting configuration of a reference cavity. Opt. Lett., 30, 2005, pp 1815-1817

[3] M. Alouini, M. Brunel, F. Bretenaker, M. Vallet, and A .Le Floch : Dual tunable wavelength Er:Yb:glass laser for terahertz beat frequency generation, IEEE Photon. Technol. Lett. **10** 1554-1556 (1998).

[4] P.Laporta, S.Taccheo, S.Longhi, O.Svelto, C.Svelto : Erbium-ytterbium microlasers: optical properties and lasing characteristics, Optical Materials 11, 1999,269-288.

[5] S.-J. Kim, J.-H. Han, J.-S. Lee, and C.-S. Park, "Intensity noise suppression in spectrum-sliced incoherent light communication systems using a gain saturated semiconductor optical amplifier," IEEE Photon. Technol.Lett., vol. 11, no. 8, pp. 1042–1044, Aug. 1999.

[6] M. Zhu and J. L. Hall : Short and long term stability of optical oscillators, Frequency Control Symposium, 1996 46th, proceeding of the, pp 44-45

[7] S. Matsuura, P. Chen, G. A. Blake, J. C. Pearson and M. H. Pickett, A tunable cavity-locked diode laser source for terahertz photomixing, IEEE Trans. Microwave Theory Tech., 2000 **48**, 380-387

[8] L. Aballea and L. F. Constantin : Optoelectronic difference-frequency synthesizer: terahertz waves for high resolution spectroscopy, Eur. Phys. J. Apll. Phys. 45, 21201 (2009).

[9] Q.-F. Chen, A. Nevsky and S. Schiller : Locking the frequency of lasers to an optical cavity at the $1.6x10^{-17}$ relative instability level

[10] J.-Y. Vinet : "On special modes and thermal issues in advanced gravitational wave interferometric detectors", Living Reviews in General Relativity 2009

Inverse Relationship Between the OEO *Q*-factor and Vibration Sensitivity

James P. Cahill, Gary M. Carter, and Curtis R. Menyuk
Dept. of Computer Science and Electrical Engineering
University of Maryland: Baltimore County
Baltimore, MD, USA
jcahill1@umbc.edu

Justin Pritchett, Ryan Sorenson, Morris Berman, Olukayode Okusaga, and Weimin Zhou
U.S. Army Research Laboratory
Adelphi, MD, USA

Abstract—**External vibrations induce phase noise in low noise oscillators such as the OEO (opto-electronic oscillator). The *g*-sensitivity quantifies the efficiency of this process. In fiber-based OEOs, vibrations of the fiber spool dominate the generation of phase noise. In this case, we observe decreasing *g*-sensitivity with increasing *Q*-factor (i.e., fiber length). This result indicates the interplay of two effects. First, only a portion of the optical fiber is affected by vibrations of the spool, even though the entire spool is subjected to vibrations. For the spools that we studied, the effective length is less than 500 m. Second, as the *Q*-factor increases, an OEO "filtering" effect reduces the phase noise that is induced by a constant magnitude perturbation. These results can be used to optimize the *g*-sensitivity of fiber-based OEOs by either reducing it for low phase noise RF generation or increasing it for sensing applications.**

Keywords-Microwave oscillator, vibration sensitivity, opto-electronic oscillator,

I. INTRODUCTION

The OEO is a delay line oscillator that exploits the advantages of the optical transfer of microwave signals [1]. It is a cost-efficient and frequency-agile source of low phase noise microwave signals whose noise level is comparable at frequencies below 50 kHz to what the best dielectric resonant oscillators can produce [2]. However, as with any high-quality oscillator, environmentally-induced noise from sources such as vibrations can be detrimental to the phase noise of the microwave signal. The transduction gain relating the strength of the external vibration to the phase noise it induces is called the vibration (or *g*-) sensitivity.

In fiber-based OEOs, high *Q*-factor cavities can be achieved using long fiber paths—up to several kilometers. Such a length of fiber is commonly managed by winding the fiber to a spool. In this case, external vibrations affect the phase noise primarily through perturbations of the fiber spool, rather than through direct perturbations of the fiber [3]. Consequently, it is important to characterize the effects of the fiber spool on the OEO *g*-sensitivity.

We present evidence that the *g*-sensitivity of a fiber-based OEO decreases as the fiber length wound to a single spool increases. This decrease is the result of two effects. First, the coupling between the fiber and spool diminishes as more fiber is wound to the spool. Consequently, only a portion of the fiber effectively experiences the vibration, and the magnitude of the vibration-induced perturbation remains constant with increasing fiber length. In the spools that we tested, the length that corresponds to this perturbation—the effective length of the fiber—is less than 500 meters. Second, the power of the phase noise induced by a constant magnitude perturbation decreases as the *Q*-factor (i.e., the fiber length) of the cavity increases. As a consequence, the OEO filters the phase noise.

We can exploit these effects to alter the *g*-sensitivity of fiber-based OEOs. For applications requiring high purity microwave signals, we can decrease the *g*-sensitivity by both lowering the coupling between the spool and the fiber (e.g. by adding padding [4] or by altering the spool geometry) and by increasing the total fiber length. Alternatively, as reported in [5], OEOs can also be used as sensors. In this application, we must increase the *g*-sensitivity while maintaining low phase noise floor levels. In this case, it is necessary to increase the spool-to-fiber coupling, while optimizing the total fiber length.

II. VIBRATIONS IN A FIBER SPOOL

External vibrations induce stresses and strains in the fiber spool that couple into the fiber. The stresses and strains interact with the fiber, altering the round-trip time of the RF signal in an OEO, which causes phase noise. In this section, we are concerned with the scaling of changes in the round-trip time, $\Delta\tau$, as the total fiber length of the OEO, l, increases.

Vibration-induced stresses and strains affect light traveling through the fiber via three mechanisms [6]: physical length changes of the fiber, perturbations of the material index of refraction via the strain-optic effect, and perturbations of the waveguide index of refraction via deformation of the fiber core. Each of these processes will induce $\Delta\tau$ in the OEO that will scale similarly with fiber length.

If the coupling between the fiber and spool is everywhere equal, the perturbation of the round-trip time, $\Delta\tau_{\text{nom}}$, referred to here as the nominal round-trip time, will be proportional to the total length of fiber, l. Hence, we write

$$\Delta\tau_{\text{nom}} \propto l. \tag{1}$$

We found experimentally that the perturbations to the round-trip time are almost constant for the lengths measured, indicating that the spool-to-fiber coupling is not the same at every point in the fiber. For this reason, it is useful to define an effective fiber length that experiences the vibration.

$$l_v \equiv l\,(\Delta\tau/\Delta\tau_{\mathrm{nom}}), \tag{2}$$

where $\Delta\tau$ is the actual perturbation in the fiber delay. From (1), we infer

$$\Delta\tau \propto l_v. \tag{3}$$

We will use (3) to characterize the phase noise.

III. Vibration-Induced Phase Noise

We briefly review the effect of a sinusoidal vibration on the phase noise of an OEO [7].

A sinusoidal frequency change with a peak-to-peak amplitude, Δf, and frequency, f_v, manifests itself in the oscillator phase noise as a sideband at f_v. The single sideband phase noise, $L(f_v)$, at this frequency is

$$L(f_v) = (f_{\mathrm{osc}}/2f_v)^2\,(\Delta f/f_{\mathrm{osc}})^2. \tag{4}$$

We consider an OEO with round-trip time τ and fiber delay length l. The round-trip time determines the oscillating frequency of the OEO via the relation $f_{\mathrm{osc}} = m/\tau$, where m is an integer that denotes the cavity mode that is oscillating. Consequently, we can represent a fractional change in the round-trip time as a fractional frequency change. Hence:

$$\Delta f/f_{\mathrm{osc}} = -\Delta\tau/\tau. \tag{5}$$

We may combine this result with (4) to relate the single sideband phase noise, $L(f_v)$, to the vibration-induced change in the round-trip time. We obtain

$$L(f_v) = (f_{\mathrm{osc}}/2f_v)^2\,(\Delta\tau/\tau)^2. \tag{6}$$

To determine how $L(f_v)$ scales with length, we first note that the round-trip time of an OEO is dominated by the propagation time of the signal within the optical fiber. Hence, we can replace the total round-trip time with $\tau = nl/c$, where n is the optical fiber's index of refraction and c is the speed of light in the vacuum. Using this relation with (3), we find

$$L(f_v) \propto (l_v/l)^2. \tag{7}$$

Thus, a sinusoidal vibration induces a sideband in the OEO phase noise at the vibration frequency. The sideband's power spectral density (PSD) is proportional to the square of the effective fraction of the fiber that is coupled to the spool vibrations.

IV. Results

Our physical model predicts that the effective length of fiber affected by spool vibrations will be constant for long fiber lengths. To demonstrate this result experimentally, we expose only a portion, l_s, of the fiber delay of an OEO to a sinusoidal vibration. We then increase the portion of the fiber that is exposed to the vibration, while keeping the total fiber length constant. By varying the length of fiber exposed to the vibration, we can determine whether the perturbation to the fiber delay depends on the total length of fiber exposed to the vibration.

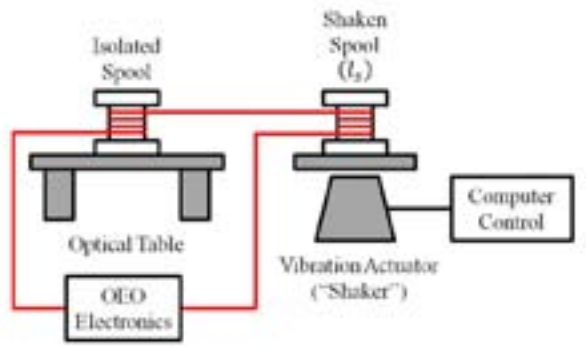

Figure 1. Schematic of experimental apparatus used to measure the effective round-trip time perturbation. Total fiber length is held constant while the length on the shaker is increased.

The setup for this experiment is shown in Fig. 1. We concatenate two fiber spools to form the entire OEO delay, but affix only one of the spools to a shaker. We apply a sinusoidal vibration to the spool on the shaker, while passively isolating the other spool from acoustics and vibration. We measure the phase noise of the microwave signal, and we record the peak that appears at the frequency of the vibration tone. We then repeat the measurement, increasing l_s while keeping the total fiber length constant. Equation (7) indicates that the phase noise sideband will be proportional to l_v^2. Because of diminishing coupling between the fiber and spool, we expect l_v to be constant.

Fig. 2 shows the experimental results. Fitting the log of the data to a linear regression yields a slope of approximately –0.3. The shallow slope indicates that for the lengths tested, the phase noise sideband is constant to within our experimental error. This result is consistent with the hypothesis that the mechanical coupling between the fiber and spool has effectively saturated. In the spools tested here, this saturation occurs at a length shorter than 500 meters.

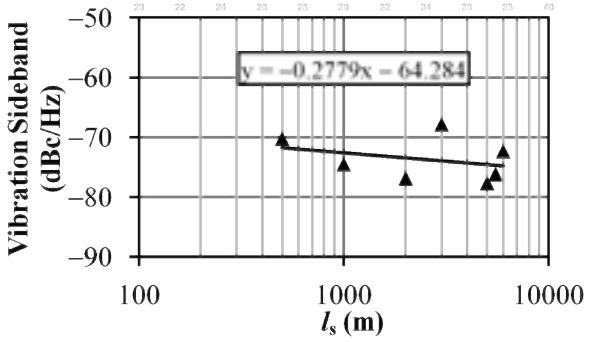

Figure 2. PSD of the vibration-induced phase noise peak for a fixed length OEO. The independent variable is the length of fiber that is exposed to vibration.

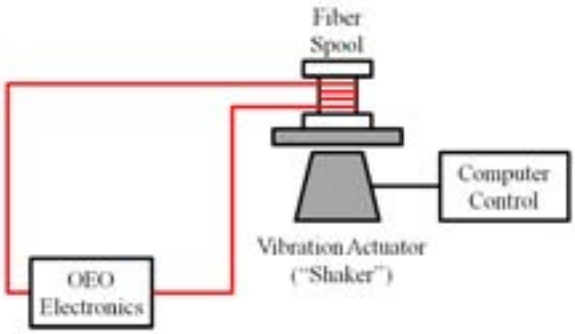

Figure 3. Schematic of experimental apparatus used to measure the length dependence of *g*-sensitivity. Total fiber length is varied.

Because we have shown that l_v is approximately constant, Eq. (7) predicts that the *g*-sensitivity of the OEO will decrease as the total fiber length increases. To test this hypothesis, we expose the entire fiber delay of an OEO to a sinusoidal vibration and measure the phase noise of the microwave signal. Fig. 3 shows the experimental setup. Again, we record the magnitude of the vibration sideband. We repeat the measurement for OEOs of different lengths of fiber. The fiber spools used in this experiment are the same as the earlier experiment.

Fig. 4 shows the experimentally measured values for the PSD of the vibration-induced microwave phase noise peak for OEOs of different delay length. These results demonstrate that as the OEO fiber delay increases, the magnitude of the vibration-induced peak decreases. When the data are converted to a logarithmic scale and fit to a linear regression, the resulting slope is approximately −2.2, so the PSD is proportional to $l^{-2.2}$. This result is consistent with (7) to within the accuracy of our experiments.

In conclusion, we have demonstrated two features of the OEO *g*-sensitivity. First, although mechanical coupling between the fiber and spool dominates the vibration-induced phase noise, the interaction is approximately independent of fiber length for the lengths measured. This result implies that the mechanical coupling diminishes when the fiber wound to the spool rises above a critical value. For the spools tested, this value is less than 500 meters. Second, as implied by the first result, the *g*-sensitivity of the OEO decreases with increasing fiber delay. These results can be used to decrease the *g*-sensitivity of fiber-based OEOs used for low phase noise RF generation or to increase the *g*-sensitivity of OEOs that are used for sensing applications.

ACKNOWLEDGMENTS

The authors thank A. Frydman for his support and helpful discussions.

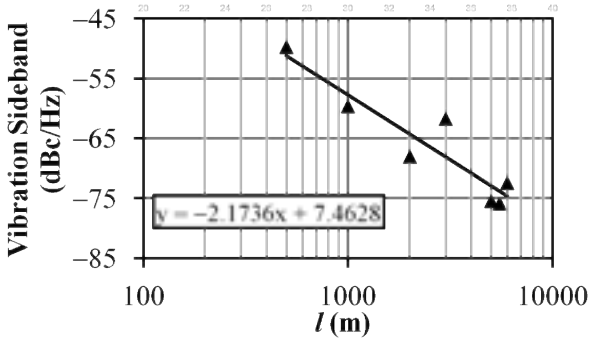

Figure 4. PSD of the vibration-induced phase noise peak for OEOs with different fiber delay lengths.

REFERENCES

[1] X. S. Yao and L. Maleki, "Optoelectronic oscillator for photonic systems," *IEEE J. Quantum Electron.*, vol. 32, no. 7, pp. 1141–1149, July 1996.

[2] X. S. Yao and L. Maleki, "Multiloop optoelectronic oscillator," *IEEE J. Quantum Electron.*, vol. 36, no. 1, pp. 79—84, Jan 2000.

[3] N. Ashby, D. A. Howe, J. Taylor, A. Hati, and C. Nelson, "Optical fiber vibration and acceleration model," in Proc. of *FCS, 2007 IEEE International Joint with EFTF*, pp. 547–551, May 2007.

[4] J. Taylor, C. Nelson, A. Hati, N. Ashby, and D. Howe, "Residual vibration-induced pm noise of a rigid optical fiber spool," in Proc. of *40th Annual PTTI Mtg.*, pp. 549—558, 2008.

[5] O. Okusaga, J. Cahill, J. Pritchett, R. Sorenson, M. Berman, W. Zhou, G. M. Carter, and C. R. Menyuk, "The optoelectronic oscillator as an acoustic sensor," in Proc. of *UFFC, 2013 IEEE International Joint with FCS*, 2013 (to be published: paper # IFCS-EFTF4-C2-2).

[6] C. D. Butter and G. B. Hocker, "Fiber optic strain gauge," *App. Opt.*, vol. 17 no. 18, pp. 2867—2869, Sept. 1978.

[7] A. Hati, C.W. Nelson, and D.A. Howe, "Vibration-induced PM Noise in Oscillators and its Suppression," *Aerial Vehicles*, Thanh Mung Lam, Ed. 2009, Ch. 13, pp. 259—286.

Scattering of Cold Atom Coherences by Hot Atoms: Background Gas Collision Shifts of Primary Fountain Clocks

Kurt Gibble
Department of Physics
The Pennsylvania State University
University Park, USA

***Abstract*—We theoretically analyze frequency shifts of cold-atom clocks due to background gas collisions. Because nearly all collisions with room-temperature background gases that transfer momentum eject cold atoms from a clock, the frequency shifts for cold atoms are significantly different than those of room-temperature clocks. From general arguments, measurements of the loss of Ramsey fringe amplitude can usefully bound this source of systematic error.**

Keywords—atomic clock, background gas collision, frequency shift

I. SUMMARY

This paper briefly summarizes a recent theoretical analysis [1] of the frequency due to background gas collisions with ultracold clock atoms. Several primary cesium fountain frequency standards report an uncertainty of 1×10^{-16} for the frequency shift due to background gas collisions [2-4]. It contributes noticeably to a number of overall uncertainty budgets, as low as 2.1×10^{-16} [4], and can be the largest single contribution in the uncertainty budget. These uncertainties are estimated using the measured pressure shift for H_2 in room-temperature Cs cell clocks [5]. Because any momentum transferred to a cold atom almost always prevents it from being detected (Fig. 1), room-temperature measurements do not describe the frequency shifts of ultracold atoms.

We analyze the quantum scattering and show that the interference scattering in the forward direction, with no change in momentum, dominates the background gas shift of cold atoms [1]. For H_2, the frequency shift of a room-temperature clock has the opposite sign as that of a cold atom clock, and is about an order of magnitude larger. Highly polarizable gases, including background Cs vapor, produce similar shifts for cold atoms as H_2. We show that the frequency shift and the loss of Ramsey fringe amplitude due to background gas collisions with cold clock atoms scale in the same way, allowing the background gas shift to be bounded to $\approx\pm4\times10^{-17}$. Measuring the loss of Ramsey fringe amplitude or using calculated shifts [1] can reduce the background gas shift in uncertainty budgets so that it no longer contributes significantly.

Financial support from NASA, NSF, and Penn State.

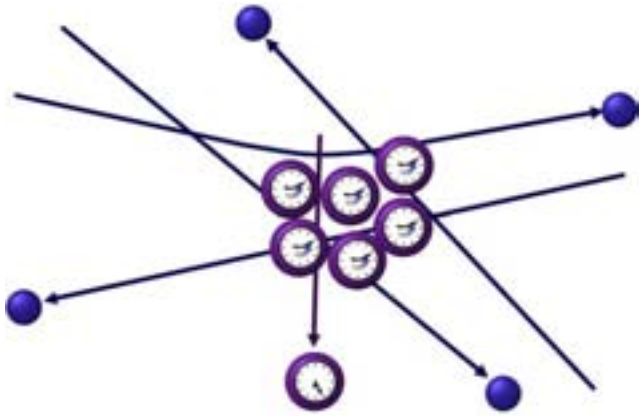

Fig. 1. Background gas collisions with cold clock atoms eject clock atoms so that they are not detected. Nonetheless, undeflected cold atom coherences experience a phase shift due to the scattering. The frequency shifts of undeflected cold clock-atoms are due to long-range collisions with polarizable background gases.

ACKNOWLEDGMENT

We gratefully acknowledge discussions with M. Cole, I. Iordanov, J. Sofo, and K. Szymaniec.

REFERENCES

[1] K. Gibble, "Scattering of Cold Atom Coherences by Hot Atoms: Frequency Shifts from Background Gas Collisions," Phys. Rev. Lett. vol. 110, 180802 (2013).

[2] S. Weyers, U. Hübner, R. Schröder, "Uncertainty evaluation of the atomic caesium fountain CSF1 of the PTB," Chr. Tamm, and A. Bauch, Metrologia vol. 38, p. 343-352, 2001.

[3] R. Li, K. Gibble and K. Szymaniec, "Improved accuracy of the NPL-CsF2 primary frequency standard: evaluation of distributed cavity phase and microwave lensing frequency shifts," Metrologia vol. 48, p. 283-289, 2011.

[4] J. Guéna, M. Abgrall, D. Rovera, P. Laurent, B. Chupin, M. Lours, G. Santarelli, P. Rosenbusch, M. E. Tobar, R. Li, K. Gibble, A. Clairon, and S. Bize, "Progress in Atomic Fountains at LNE-SYRTE," IEEE

Trans. Ultrasonics, Ferroelectrics, and Freq. Control, vol. 59, p. 391-410, 2012.

[5] See C. W. Beer and R. A. Bernheim, “Hyperfine pressure shift of 133Cs atoms in noble and molecular buffer gases,” Phys. Rev. A vol. 13, p. 1052-1057, 1976.

Nanoscale Resonant Sensors with 1D Carbon Nanostructures

A Review of Carbon Nanotube Based NEMS Devices

Zenghui Wang
Electrical Engineering
Case Western Reserve University
Cleveland, OH 44106, USA

***Abstract*— Carbon-based low-dimensional nanostructures, such as graphene and carbon nanotubes, have outstanding mechanical properties and can be implemented as novel nanomechanical devices. Such devices, owing to their miniature sizes and the unique physical properties of the materials, make excellent candidates for physical sensors. In this paper, we will focus on the state-of-the-art nanomechanical resonators made of carbon nanotubes, and evaluate their potential as ultra-sensitive sensors. Specifically, we will describe nanotube resonator mass sensors with the best ones achieving single-proton mass sensitivity, and a nanotube resonant sensor for detecting surface processes such as adsorption and phase transition.**

Keywords—nanoelectromechanical systems (NEMS); carbon nanotube; resonator; sensor; surface adsorption

I. Introduction to Carbon Nanostructures

Carbon nanostructures have been under intensive study for the last two decades. The three most commonly studied forms, graphene (2D), carbon nanotube (1D), and fullerene (0D) can all be viewed as derivatives from the 3D form, graphite (Fig. 1(a)).

The 1D form, carbon nanotube, can be either single-walled or multi-walled, depending on the number of cylindrical layers (Fig. 1(b)). Single-walled nanotube (SWNT) typically have diameter around 1nm, and its length can range from tens of nm to a few cm. The high aspect ratio, nanoscale size, and outstanding physical properties make it a unique choice for building resonant NEMS devices.

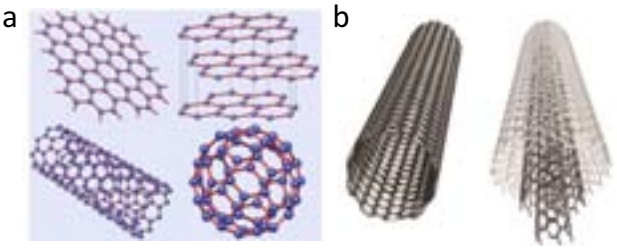

Fig. 1. Schematic of different forms of carbon nanostructures. (a) Graphite (upper right) and its derivatives (counter-clockwise): graphene, carbon nanotube, and fullerene. (b) Single-walled (left) and multi-walled (right) nanotubes.

II. Unique Properties of NEMS Based on Carbon Nanostructures

A. Ultra-Low Mass in Motion

The low mass of the carbon nanostructures make them particularly attractive for various sensing applications such as mass spectroscopy and ultra-low force detection. NEMS devices fabricated with conventional top-down approaches, on the other hand, are limited by the capability of the available lithography techniques and are therefore unlikely to surpass the chemically derived nanostructures. For example, a graphene resonator, made of just a single sheet of carbon atoms, is practically the thinnest resonator one can achieve, and has the lowest possible areal mass density. Similarly, a SWNT resonator is made of a single carbon molecule that is typically 1 nm in diameter and hollow inside. In the near future it is not expected that lithography technique can produce miniature devices comparable with a SWNT resonator in size and mass.

B. Pristine Resonator Surfaces

Carbon nanostructures used in the NEMS devices can have pristine surfaces free from harsh chemical processing. For example, mechanically exfoliated single layer graphene is a single crystal with its both surfaces (note that it has only two surfaces) well defined with the hexagonal honeycomb lattice. Similarly, chemically grown carbon nanotube is a graphene-rolled-up tube and its curved surface well resembles that of graphene. In contrast, top-down fabricated NEMS devices experience processing steps such as Reactive Ion Etch (RIE) and the resulting surfaces can be much rougher, with side walls being very different in surface morphology than the top/bottom sides. Therefore, NEMS based on bottom-up derived nanostructures are particularly suitable for studying surfaced-related phenomena thanks to their pristine surfaces.

III. Sensing Applications

In this section we survey the studies on sensing applications (with a focus on mass sensing) of NEMS based on carbon nanotubes, and compare their performance (mainly mass sensitivity) with conventional top-down fabricated (with lithography technique) NEMS devices to illustrate the unique advantages of carbon nanostructures.

A. Mass Sensing with NEMS Devices

Mass sensing with resonant devices are based on the frequency downshift of a resonator upon the loading of additional masses. A unique advantage of this technique is that it doesn't require the measured particle to be charged (and thus can resolve neutral species), in contrast to conventional mass spectrometry.

To the first order, the mass of the add-particle (the mass to be measured, which is added to the moving part of the resonator during measurement) can be related to the change in resonance frequency f via

$$\frac{\Delta m}{m_0} \approx \frac{\Delta f}{f_0} \tag{1}$$

where f_0 is the initial resonance frequency, Δf is the frequency downshift upon mass loading, m_0 is the initial mass of the resonator, and Δm is the mass of the add-particle. Note that Eq. (1) only gives an order-of-magnitude estimate; the detailed relation depends on many factors such as the resonance mode shape and attachment position of the add-particle.

From this simple relationship it is clear that a smaller m_0 is desirable for achieving a smaller Δm. Therefore, for improved mass sensitivity it is natural to use resonators with small m_0. As technology advances, NEMS devices with smaller sizes continue to be realized, along with continued improvements in achieved Δm.

Doubly clamped beam resonator (see Fig. 2 for illustration) is a commonly used geometry for NEMS devices. One of the main advantages is that the ability to pass an electrical current through the resonator allows direct electrical readout of the mechanical motion, making such devices widely used in different sensing applications.

In 2004, a Caltech group realized attogram (10^{-18}g) mass sensing with a lithography-defined doubly clamped SiC resonator (14μm×670nm×260nm) at T≈17K [1]. This sensitivity corresponds to a few thousands of Au atoms. In 2006 the same group achieved zeptogram (10^{-21}g) mass sensitivity (tens of Xe atoms) by employing a further miniaturized SiC resonator (2.3μm×150nm×70nm) [2]. Similar devices are also used in bio-sensing experiments, demonstrating single-molecule sensitivity [3], [4].

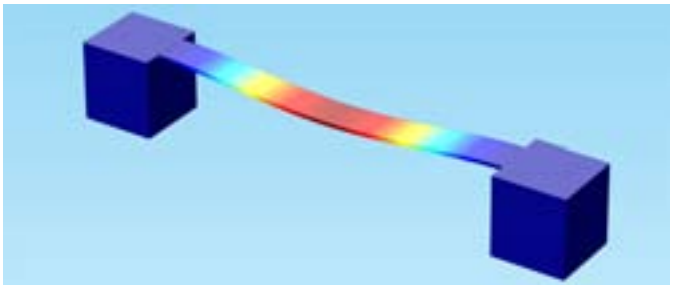

Fig. 2. Schematic of a doubly clamped resonator (in its fundamental resonace mode). For top-down fabricated devices, the suspended part is typically a rectangular beam.

B. Carbon-Nanotube Resonators

The first electrically-tunable SWNT resonator was realized in 2004 by a Cornell group [5]. The device was fabricated by mechanically clamping (and thus electrically contacting) both ends of a SWNT and then suspending the middle segment of it. The resulting doubly clamped device (Fig. 3(a)) is a field-effect transistor (FET), whose conductance between source and drain can be modulated by the voltage on the gate.

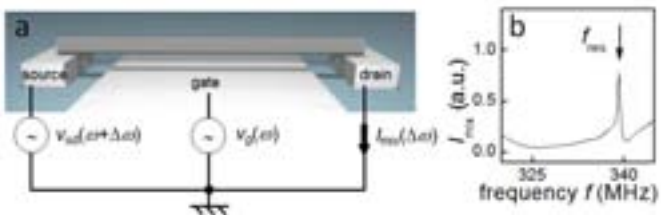

Fig. 3. SWNT resonator. (a) Schematic of a device. (b) An example of mechanical resonance signal in the mixing current.

Mechanical resonance of the suspended carbon nanotube is actuated and detected electrically. An AC signal with angular frequency ω, $V_g(\omega)$, is applied between the SWNT and the underlying gate, generating an AC force at the same frequency and drives the mechanical vibration.

Due to the much smaller capacitance between the SWNT and the gate (compared with the parasitic capacitance between the source/drain contacts and gate electrode), it is difficult to directly read out the mechanical motion signal at frequency ω. Therefore a down-mixing technique is used. In short, a bias signal at a slightly-offset frequency $\omega+\Delta\omega$, $V_{sd}(\omega+\Delta\omega)$, is applied between the source and drain electrodes. The conductance of the SWNT FET is modulated by its mechanical motion at frequency ω. The current through the SWNT is the product of the bias and the conductance, resulting in a term at the intermediate frequency $\Delta\omega$ in the current, $I_{mix}(\Delta\omega)$, which can be detected with a lock-in amplifier. At mechanical resonance, the large motion amplitude leads to large modulation of the device conductance and consequently large modulation in the mixing current. A typical resonance signal in I_{mix} is shown in Fig. 3b. The resonance frequency of the SWNT resonator can be tuned by applying a DC gate voltage, which changes the tension of the SWNT.

C. SWNT Resonator Mass Sensing

In 2008, two research groups independently performed mass sensing experiments with doubly-clamped nanotube resonators. The Caltech group built a SWNT resonator (500nm in length and 1nm in diameter) to detect adsorption of individual Xe and Ar atoms. By fitting measured time-dependent adsorption curve to a statistic model, the researchers are able to weigh the mass of individual Ar atoms, corresponding to a mass sensitivity better than 0.085zg (their measured mass of an Ar atom) [6]. The CIN2 group used a similar structure (900nm long SWNT resonator with 1.2nm diameter) to detect mass loading from evaporated Cr atoms. Resolution of 1.4zg is achieved at low temperature [7]. Atomic mass sensitivity based on singly-clamped nanotube resonator is also demonstrated [8].

As shown in Eq. (1), to further improve mass sensitivity (decrease Δm), one needs to use a smaller device (decrease m_0) and increase the quality factor Q of the resonator (to get better resolution in $\Delta f/f_0$). Accordingly, in 2012 the same CIN2 group built an ultra-short (150nm) nanotube resonator with Q up to 2000, and achieved mass sensitivity of 1.7yg (a single proton) after annealing the device with electrical current [9]. It is worth note that the same group also built a very long (4μm) SWNT resonator with very low spring constant, and achieved force sensitivity of 12zN/Hz$^{1/2}$ [10].

D. Discussion on NEMS Resonator Mass Sensing

Table 1 lists the NEMS mass sensing experimental work discussed above. For SiC devices the dimension is listed as length×width×thickness, and for nanotube resonators it is length×diameter.

TABLE I. NEMS RESONATOR MASS SENSING

Ref	*Device Dimension*	m_0(g)	f_0 (MHz)	Q	Δm(g)
[1]	14μm×670nm×260nm	9.9×10^{-12}	32.8	3000	2.53×10^{-18}
[2]	2.3μm×150nm×70nm	7.3×10^{-14}	190	5000	7×10^{-21}
[3]	1.7μm×120nm×100nm	9.2×10^{-14}	450	2000	1.7×10^{-20}
[6]	500nm×ϕ1nm	1×10^{-18}	300	200	8.5×10^{-23}
[7]	900nm×ϕ1.2nm	2.5×10^{-18}	167	1665	1.4×10^{-21}
[8]	254nm×ϕ2.09nm	2.33×10^{-18}	328.5	1000	3×10^{-22}
[9]	150nm×ϕ1.7nm	6×10^{-19}	2000	1000	1.7×10^{-24}

Clearly both smaller m_0 and higher Q are both important for achieving high mass sensitivity. Top-down fabricated NEMS resonators generally have higher Q, but to further decrease the device size it requires advancement in fabrication technology, such that smaller devices with well-defined surfaces (to retain the high Q) can be made. On the other hand, NEMS devices based on carbon nanostructures (such as SWNT) naturally has ultimately small m_0 which is ideal for sensing applications.

Figure 4 plots the relationship between Δm and m_0 for all the work listed in Table 1. From (1) one can see that, under similar experimental techniques/settings (e.g. measurement bandwidth, equipment resolution, statistical technique, etc.), $\Delta m \propto m_0$ for devices with similar Qs. One such trend line is shown in Fig. 4, and the overall behavior of the data points agree well with this expected trend. Devices with higher Qs have better mass sensitivity (smaller Δm) and appear lower on the plot, and vice versa. This is also apparent from Fig. 4: all the top-down fabricated SiC NEMS have higher Qs and appear below the overall trend line, while most nanotube resonators have lower Qs and are on the other side of the line.

On the other hand, from Eq. (1) one can also see that $\Delta m \propto 1/Q$ if all the other experimental parameters remain the same. We plot in Fig. 5 Δm *versus* Q for all the work listed in Table 1, together with a trend line of $\Delta m \sim 1/Q$. It clearly shows that all the SiC resonators are above the line (has larger Δm) due to their larger m_0 values, while the SWNT devices appear well below the line. Indeed, the effect from m_0 is so dominant such that the dependence of Δm on Q cannot be seen at all from this plot.

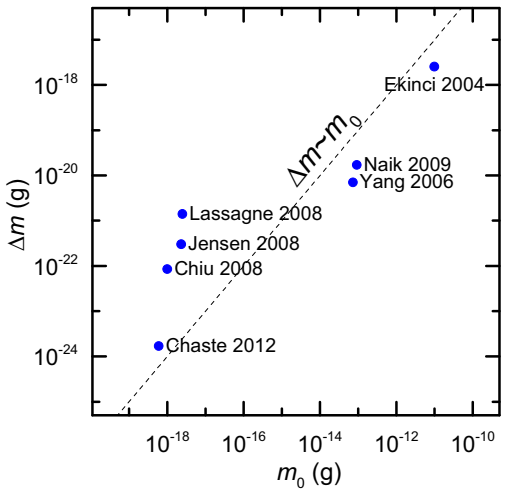

Fig. 4. Mass sensitivity Δm versus resonator intrinsic mass m_0 for all the work listed in Table 1. The dashed line represents linear dependence between Δm and m_0.

The observations imply that under the current technology, in order to improve the sensitivity of these resonant mass sensors, it is much more effective to build NEMS devices based on carbon nanostructures and utilize their ultralow mass. The milestone of achieving yoctogram sensitivity with SWNT resonator clearly demonstrates this fact.

For future work towards improved NEMS mass sensing, there are two main approaches. The first one is to continue improving the Q for NEMS devices based on carbon nanostructures. The first tunable SWNT resonator has a Q of 80[5]; over the years this number has been well improved, and devices with Q up to 10^4 has been reported [11]. Among SWNT mass sensing works, the recent yoctogram sensitivity device has a Q of ~2000 [9]. On the other hand, making SWNT devices compatible with large scale fabrication processes would greatly enhanced the feasibility of these ultra-sensitive devices in realistic applications. This may take significant effort. The other pathway is to further downsize top-down fabricated NEMS devices while maintaining their high Q. This requires novel lithography techniques and advancement in etching processes. In addition, multimode sensing can be used to detect the mass and position of the add-particle in real time, offering new possibilities [4].

IV. SURFACE SCIENCE STUDIES

In this section we describe the surface science studies (focusing on surface adsorption) with NEMS resonators based on 1D carbon nanostructures, and demonstrate its uniqueness (mainly detecting phase transition in the adsorbed layer) compared to conventional top-down fabricated (with lithography technique) NEMS devices.

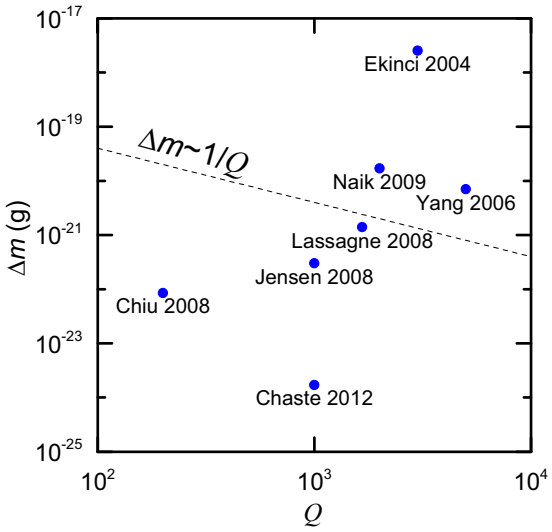

Fig. 5. Mass sensitivity Δm versus resonator quality factor Q for all the work listed in Table 1. The dashed line represents linear dependence between Δm and $1/Q$.

A. *Surface Adsorption Processes*

The study of surface adsorption typically involves answering the following question: under a given condition, when a surface is exposed to a vapor of a different material, what happens on the surface? The detailed answer depends on various parameters such as temperature, pressure, the type of materials involved, the morphology of the surface, etc. Further complications can come from non-equilibrium conditions (e.g. the temperature of the surface is different from that of the vapor) or co-adsorption (different types of adsorbates exist concurrently).

Surface adsorption involves many different physical processes. When a gas atom/molecule impinges on a surface, it may or may not adsorb. The probability is described by the sticking coefficient. Upon adsorption, the atom/molecule can still leave the surface if it has sufficient thermal energy, and the process can be characterized by the desorption rate. The adsorbates can also diffuse alone the surface.

Besides these dynamic processes, the equilibrium states are also extensively studied. A common measure of such equilibrium states is the surface coverage, which provides information about the phase of the adsorbed surface layer. In many adsorption systems, various phases and phase transitions have been identified and studied, revealing a plethora of physics phenomena in these 2-Dimensional (2D) systems.

A common way to describe phase behavior in adsorption system is by using isotherm, which plots the coverage of adsorbates (corresponding to the density of the adsorbed layer) versus 3D gas pressure under a given temperature. From such plots one can derive the entire phase diagram. The relationship between an isotherm plot and a phase diagram is illustrated in Fig. 6.

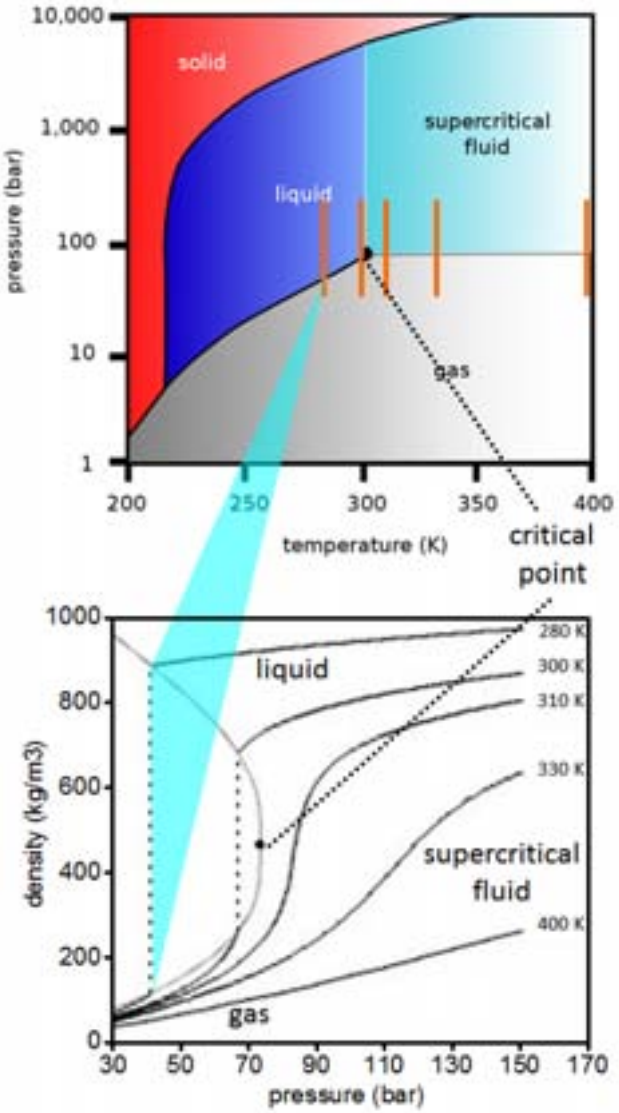

Fig. 6. Phase Diagram (top) and isotherm (bottom) of CO_2 in 3D space. The phase diagram delineates the phase boundaries. Taking vertical (constant temperature) slices (orange lines) in the phase diagram and plotting the order parameter of the system (density) versus temperature for each of these slices, one obtains the isotherm plot. Each isotherm curve represents a vertical slice in the phase diagram. First order phase transitions are represented by vertical steps in the isotherm (highlighted triangle), and the profile of these steps outlines the vapor-liquid phase-coexistence region, with its tip being the critical point.

B. *Surface Adsorption Studies with NEMS Devices*

Lithography-fabricated NEMS devices have been used to study surface adsorption. The mass sensing studies[1], [2] are essentially adsorption experiments at the low coverage limit. Indeed, these devices are well-suited for studying the dynamic processes: the high resonance frequency leads to high operation speed, and the high Qs provide high resolution for detecting small frequency shift. Indeed, the same Caltech group has studied the diffusion process of Xe atoms adsorbed on the surface of a SiC resonator, by monitoring the frequency

noise in the resonance signal arise from the adsorbate fluctuation [12].

C. Adsorption on SWNT Resonator Surface

In addition to the above mentioned advantages of NEMS devices, SWNT resonators further benefit from the pristine surface that comes with the as-grown carbon nanotube, which offer additional opportunities for surface adsorption study. The pristine nanotube surface provides an ideally homogeneous substrate for studying phase behaviors. This is important for observing well-defined phase transitions, as inhomogeneity in the substrate leads to difference in adsorbate-substrate interaction, and thus breaks the simultaneity of phase transition among different adsorption sites.

SWNT resonators with as-grown pristine surfaces have been used to map out the phase behavior of Ar, Kr, and ^{4}He adsorbed layers on nanotube surfaces for different temperature ranges[13], [14]. Multiple low-dimensional phases and phase transitions are observed.

Such adsorption experiments are to certain extent similar to the mass sensing experiments, except they probe a wide range of surface coverage: from the 0 coverage limit (as in mass sensing experiments) to more than one complete monolayer. Most studies are conducted between 0 and 1 layer to reveal the phase transition within the first monolayer. Experiments at higher coverage usually show layer-to-layer condensation instead of phase transition.

In order to reach one complete monolayer, the adsorption experiments are setup up differently than the mass sensing studies (where an oriented nozzle directs the atomic/molecular beam towards the NEMS device resonating in high vacuum). To study the equilibrium states, a stable 3D vapor pressure is necessary to maintain the adsorbed layer on the surface. Therefore, in adsorption experiments, the entire device chamber is gradually pressurized with the adsorbate gas, and resonance of the NEMS device is recorded for each pressure.

An example of adsorption experimental data is shown in Fig. 7. At the low pressure limit (left side) the resonance frequency f_{res} (altitude of the dark curve) slowly decreases, as in the mass sensing experiments. As pressure continues to increase, the decrease in resonance frequency accelerates, until at a certain point it suddenly takes a huge leap to a much lower value. This suggests a large, sudden change in the density of the adsorbed layer (and thus the mass of the resonator) over a very small pressure range, signifying a strong 1$^{\text{st}}$ order phase transition, like the vapor-liquid condensation in the case of 3D matter.

The frequency shift can be converted to the adsorbates coverage on the nanotube surface by assuming that f_{res} varies as $\rho^{-1/2}$ (ρ being the overall density of the resonator). Therefore, the value

$$\phi = \frac{\Delta\rho/m_{ads}}{\rho_0/m_C} = \frac{m_C}{m_{ads}}\left[\left(\frac{f_0}{f_{res}}\right)^2 - 1\right] \qquad (2)$$

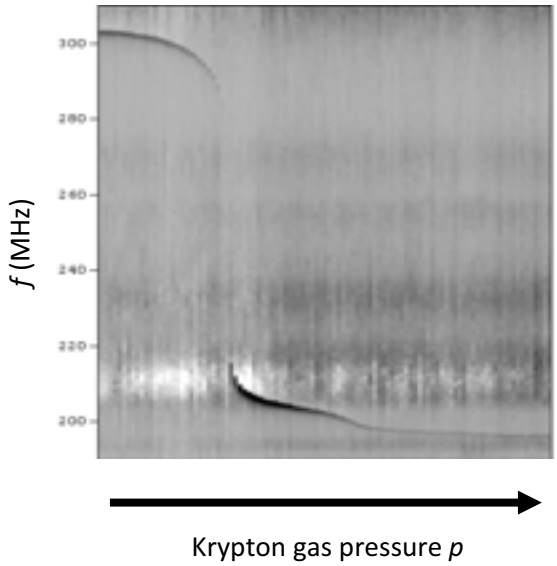

Fig. 7. Example of an experimental adsorption data set. The data is taken with a SWNT resonator exposing to Kr gas with gradually increasing pressure at 77K. The verticle axis is frequency f, the horizontal axis is time (with pressure linearly increasing), and the grey scale represents the measured mixing current. The mechanical resonance shows up as the a sharp (dark) feature at a paticular frequency (the resonance frequency f_{res}) for each verticle data column. Sudden jump in f_{res} represents sudden change in the total density of the resonator, indicating strong phase transition in the adsorbed layer.

gives the ratio of the number of adsorbed atoms to carbon atoms in the layer. Here m_C and m_{ads} are the masses of the carbon atom and adsorbate atom, respectively.

Using Eq. (2) the experimental data in Fig. 7 can be converted to the coverage-pressure isotherm, as shown in Fig. 8. By examining a family of such isotherms under different temperatures, various phases and phases transitions are identified and studied[13], [14].

D. Discussion on NEMS Resonator Surface Adsorption

The small mass and high surface-to-volume ratio make NEMS devices highly sensitive to surface adsorptions, providing an ideal platform for studying both the dynamic processes and equilibrium states.

Furthermore, NEMS resonators based on carbon nanostructures benefit from their pristine surfaces and are capable of resolving various phase transitions within the first adsorbed monolayer, generating new knowledge about this low-dimensional system. Furthermore, the pristine nanotube resonator surface allow exotic phases specific to adsorption systems (unavailable in 3D matters) to be observed. The so-called "Commensurate Solid" (CS) provides an example.

Figure 9 illustrate the CS phase of Kr monolayer adsorbed on a graphitic surface, where the adsorbate atoms are registered with specific locations on the substrate. In this arrangement there is 1 Kr atom per 6 C atoms, and the coverage of CS is fixed at 1/6, which has been observed with SWNT resonators[13]. More interestingly, the fact that SWNT is a seamless roll-up of a graphene sheet imposes additional requirement for a seamless CS coverage: the adsorbate atoms

must also fold onto themselves upon rolling (see Fig. 9 for comparison). This requires that the roll-up vector of the nanotube (*N*,*M*) is a lattice vector in the CS lattice: $N\boldsymbol{a}_1+M\boldsymbol{a}_2.=X\boldsymbol{b}_1+Y\boldsymbol{b}_2$, where *X* and *Y* are both integers.

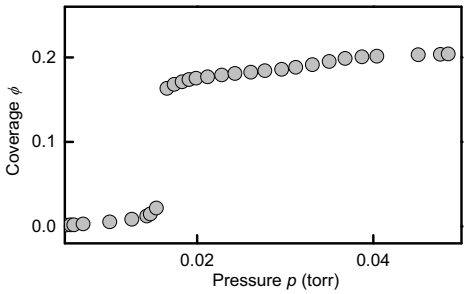

Fig. 8. Coverage isotherm generated using Eq. (2) with the data in Fig. 7. The vertical axis is the numerical coverage (number of adsorbed Kr atom per C atom), and the horizontal axis is 3D Kr pressure. Phase transition appears as vertical step in the isotherm (sudden density increase).

Simple math show that this can occur only when (*N*–*M*)/3 is an integer, where (*N*,*M*) is the nanotube's roll-up vector. This coincides the requirement for an SWNT to be metallic[15]. This also implies that only 1/3 of the SWNT may have a seamless coverage of CS phase of adsorbed Kr atoms. These unique properties suggest opportunities for studying new adsorption phenomena on nanotube surfaces.

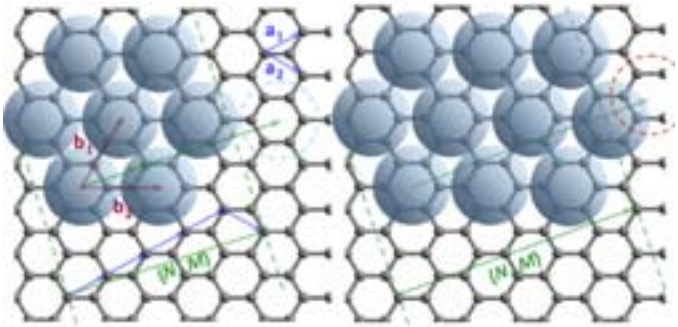

Fig. 9. Schematic of commensurate solid (CS) phase on nanotube surfaces. Large translucent circles represent Kr atoms, and the honeycomb structure underneath represents the graphitic surface of SWNT. $\boldsymbol{a}_1$ and $\boldsymbol{a}_2$ are the basis vectors of the SWNT hexagonal lattice, while $\boldsymbol{b}_1$ and $\boldsymbol{b}_2$ are the basis vectors for the Kr CS lattice. (*N*,*M*) is the roll-up vector of the nanotube: it determines how a graphene sheet is rolled-up into a nanotube, with a given C atom fold seamlessly onto its counterpart $N\boldsymbol{a}_1+M\boldsymbol{a}_2$ away. In order for a SWNT to have a seamless CS coverage, $N\boldsymbol{a}_1+M\boldsymbol{a}_2$ must also be a lattice vector in the $\boldsymbol{b}_1$ $\boldsymbol{b}_2$ basis such that a Kr atom can also fold perfectly into another Kr atom (left), instead of landing in the wrong position after folding (right).

V. Conclusion

Carbon nanostructure-based NEMS resonators have demonstrated unique capabilities in addition to all the benefits offered by a conventional NEMS resonator. Specifically, the ultra-low mass of carbon nanotube facilitates ultra-sensitive mass sensing with SWNT resonators, achieving yoctogram mass sensitivity. The pristine surface of as-grown SWNT enables detailed study of surface adsorption on the resonator, revealing exotic phases and phase transitions in this low-dimensional system. Future development in large-scale fabrication of such resonant devices can lead to practical use of carbon nanostructure in applications such as mass spectroscopy, force detection, and gas sensing.

References

[1] K. L. Ekinci, X. M. H. Huang, and M. L. Roukes, "Ultrasensitive nanoelectromechanical mass detection," *Appl. Phys. Lett.*, vol. 84, pp. 4469–4471, May 2004.

[2] Y. T. Yang, C. Callegari, X. L. Feng, K. L. Ekinci, and M. L. Roukes, "Zeptogram-scale nanomechanical mass sensing," *Nano Lett.*, vol. 6, pp. 583–586, April 2006.

[3] A. K. Naik, M. S. Hanay, W. K. Hiebert, X. L. Feng, and M. L. Roukes, "Towards single-molecule nanomechanical mass spectrometry," *Nat. Nanotechnol.*, vol. 4, pp. 445–450, July 2009.

[4] M. S. Hanay, S. Kelber, A. K. Naik, D. Chi, S. Hentz, E. C. Bullard, E. Colinet, L. Duraffourg, and M. L. Roukes, "Single-protein nanomechanical mass spectrometry in real time," *Nat. Nanotechnol.*, vol. 7, pp. 602–608, September 2012.

[5] V. Sazonova, Y. Yaish, H. Ustunel, D. Roundy, T. A. Arias, and P. L. McEuen, "A tunable carbon nanotube electromechanical oscillator," *Nature*, vol. 431, pp. 284–287, July 2004.

[6] H. Y. Chiu, P. Hung, H. W. C. Postma, and M. Bockrath, "Atomic-scale mass sensing using carbon nanotube resonators," *Nano Lett.*, vol. 8, pp. 4342–4346, November 2008.

[7] B. Lassagne, D. Garcia-Sanchez, A. Aguasca, and A. Bachtold, "Ultrasensitive mass sensing with a nanotube electromechanical resonator," *Nano Lett*, vol. 8, pp. 3735–3738, November 2008.

[8] K. Jensen, K. Kim, and A. Zettl, "An atomic-resolution nanomechanical mass sensor," *Nat. Nanotechnol.*, vol. 3, pp. 533–537, July 2008.

[9] J. Chaste, A. Eichler, J. Moser, G. Ceballos, R. Rurali, and A. Bachtold, "A nanomechanical mass sensor with yoctogram resolution," *Nat. Nanotechnol.*, vol. 7, pp. 301–304, April 2012.

[10] J. Moser, J. Güttinger, A. Eichler, M. J. Esplandiu, D. E. Liu, M. I. Dykman, and A. Bachtold, "Ultrasensitive force detection with a nanotube mechanical resonator," *Nat. Nanotechnol.*, vol. 8, pp. 493–496, July 2013.

[11] A. Eichler, J. Moser, J. Chaste, M. Zdrojek, I. Wilson-Rae, and A. Bachtold, "Nonlinear damping in mechanical resonators made from carbon nanotubes and graphene," *Nat. Nanotechnol.*, vol. 6, pp. 339–342, June 2011.

[12] Y. T. Yang, C. Callegari, X. L. Feng, and M. L. Roukes, "Surface adsorbate fluctuations and noise in nanoelectromechanical systems," *Nano Lett.*, vol. 11, pp. 1753–1759, April 2011.

[13] Z. Wang, J. Wei, P. Morse, J. G. Dash, O. E. Vilches, and D. H. Cobden, "Phase transitions of adsorbed atoms on the surface of a carbon nanotube," *Science*, vol. 327, pp. 552–555, January 2010.

[14] H.-C. Lee, O. E. Vilches, Z. Wang, E. Fredrickson, P. Morse, R. Roy, B. Dzyubenko, and D. H. Cobden, "Kr and ^{4}He adsorption on individual suspended single-walled carbon nanotubes," *J. Low Temp. Phys.*, vol. 169, pp. 338–349, December 2012.

[15] J. C. Charlier, X. Blase, and S. Roche, "Electronic and transport properties of nanotubes," *Rev. Mod. Phys.*, vol. 79, pp. 677–732, May 2007.

Micro-Electro-Mechanical Resonant Tilt Sensor with 250 Nano-Radian Resolution

Xudong Zou, Pradyumna Thiruvenkatanathan and Ashwin A. Seshia

Nanoscience Centre, Department of Engineering, University of Cambridge, United Kingdom
Email: xz280@cam.ac.uk

***Abstract*—This paper reports a high-resolution frequency-output MEMS tilt sensor based on resonant sensing principles. The tilt sensor measures orientation by sensing the component of gravitational acceleration along a specified input axis. A combination of design enhancements enables significantly higher sensitivity for this device as compared to previously reported prototype sensors. The MEMS tilt sensor is calibrated on a manual tilt table over tilt angles ranging over 0-90 degrees with a relatively linear response measured in the range of ±20°(linearity error <2.3%) with a scale factor of approximately 50.06 Hz/degree. The noise-limited resolution of the sensor is found to be approximately 250 nano-radians for an integration time of 0.8 s, which is over an order of magnitude better than previously reported results [1].**

Keywords—MEMS, resonant sensors, tilt sensing.

I. INTRODUCTION

Tilt sensors or inclinometers are widely utilized in many fields such as alignment of machinery, attitude control systems, user interfaces in smart phones, slope monitoring in tunnels and embankments and in wearable devices. Many of these applications require small size, low power and in some cases high performance. Recently, a number of MEMS tilt sensors based on various principles such as thermal convection, piezo-resistance, optical or capacitive sensing [2-6] have been reported providing advantages of reduced size, weight and power and batch manufacturability. However, these solutions are often limited in terms of sensitivity and resolution particularly for low bandwidth applications.

In this paper, we report on a resonant MEMS tilt sensor design for enhanced sensitivity. The mechanical element of the tilt sensor is fabricated in a silicon-on-insulator MEMS (SOI-MEMS) foundry process. The device is vacuum packaged using a custom process following wirebonding to a standard leadless chip carrier. The tilt sensor is then calibrated on a manual tilt table over tilt angles varying from 0-90 degrees demonstrating a relatively linear scale factor of 50.06 Hz/degree in the range of ±20°. This result demonstrates approximately a factor of 6 sensitivity enhancement on a similar device reported by our group last year [1]. A low-noise DC polarization voltage source is used to bias the resonant element. The vacuum packaged sensor chip is then co-integrated together with an oscillator circuit on a single PCB to provide frequency output readout with a noise-limited resolution of approximately 250 nano-radians for an integration time of 0.8 s – an order of magnitude improvement in device resolution over previously reported results.

II. SENSOR DESIGN

We have previously reported on a prototype resonant MEMS tilt sensor [1] demonstrating a scale factor of 8.08 Hz/degree for tilt angles in the range of ±20°. The topology (Fig.1) and operation principle (Fig.2) of the sensor remains similar to the previous device and is briefly introduced below. The mechanical design of the tilt sensor consists of a proof mass suspended by an arrangement of four identically designed flexural beams. A force leverage mechanism couples (and amplifies) the inertial force on the proof mass onto two double-ended tuning fork resonant strain gauges located on either side of the mass. When the sensor is subjected to an angular tilt about the sensing axis, the change in the gravitational force displaces the suspended proof-mass inducing independent axial tensile and compressive stresses on the two DETFs, the magnitudes of which are proportional to the sine of tilt angle. The output of the device is measured by recording the resonant frequency shift of the DETFs which is proportional to the axial force acting on the tines. The differential measurement of frequency enables a first-order cancellation of common-mode effects such as temperature.

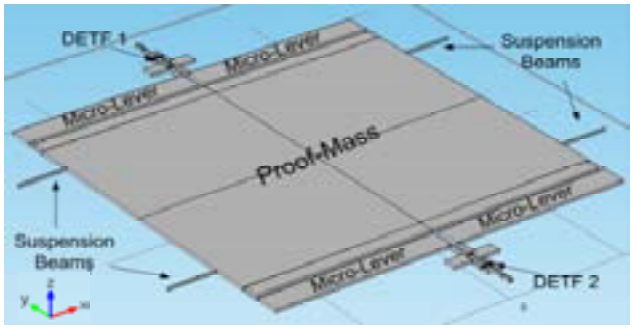

Fig. 1. Topology of the resonant tilt sensor.

The sensitivity of MEM resonant tilt sensor can be estimated from:

$$\Delta f_{out}(\theta) = S_{\mathrm{Re}s} \times EA_{Lvr} \times M_{proof} \times g \times \sin\theta \qquad (1)$$

where S_{Res} is the scale factor of DETF resonant sensing element in unit of '*Hz/N*', EA_{Lvr} is the effective force amplification factor provided by the micro-levers, M_{Proof} is the proof-mass, θ is the tilt angle and g is the magnitude of the gravity acceleration. Δf_{out} is the differential frequency shift output of the tilt sensor. In order to enhance the sensitivity of the tilt sensor, several design modifications were made to the design reported previously [1] to increase the S_{Res}, EA_{Lvr} and M_{Proof}, respectively.

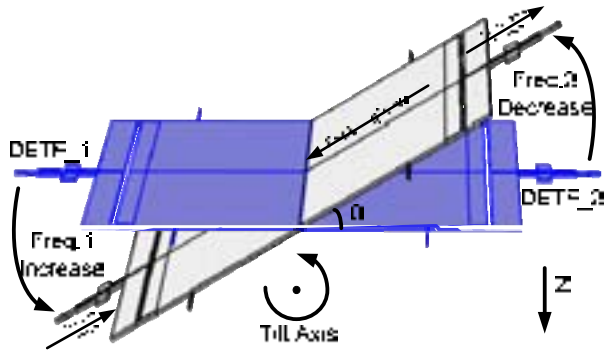

Fig. 2. Schematic illustrating the operation of the tilt sensor.

A. DETF sensing element

Two DETFs form the sensing elements of this device. The scale factor of DETFs sensing element is given by:

$$S_{Res} = \frac{\Delta f}{F_{Axial}} \approx \frac{1}{2\pi} \cdot 0.293 \left(\frac{L_T^2}{E t_T w_T^3} \right) \cdot \sqrt{E \left(\frac{w_T}{L_T} \right)^3 \cdot \frac{1}{\rho \left(A_{Ele} + 0.375 \cdot L_T w_T \right)}} \quad (2)$$

Where F_{Axial} is the axial force load on the free end of DETF sensing element, E is the modulus of elasticity of the material, ρ is the density of the material, L_T, w_T and t_T are the length, width and thickness of the DETF tine beam and A_{Ele} is the area of attached parallel-plate driving/sensing electrodes. As shown in Eq. 2, the scale factor is determined by material properties and device geometry. For single-crystal silicon devices, the relationship between the scale factor and device dimensions may be written as:

$$S_{Res} \propto \frac{L_T^{7/2}}{t_T w_T^{3/2} \left(A_{Ele} + C_2 \cdot L_T w_T \right)^{1/2}} \quad (3)$$

The thickness of the device layer is specified by the manufacturing process. The scale factor enhancement reported in this work arises from in the new tilt sensor was realized by narrowing the beam width and reducing the size of electrodes.

B. Micro-levers

The micro-lever is a mechanical force amplifier that couples the inertial force on the proof mass axially onto the DETFs. The effective amplification factor of micro-lever (EA_{Lvr}) is defined by Eq. 4:

$$EA_{Lvr} = \frac{F_{Axial}}{M_{proof} g \cdot \sin\theta} \quad (4)$$

The effective amplification factor of micro-lever is not only determined by the design of micro-lever but also influenced by the mechanical suspension and DETF design, and can be estimated as:

$$EA_{Lvr}\left(A_{Lvr}\right) \approx \frac{k_{vt} A_{Lvr}}{k_{sus} A_{Lvr}^2 + k_{vt}} \quad (5)$$

The maximum value of the effective amplification provided by the lever is:

$$Max(EA_{Lvr}) = \frac{A_{Lvr}}{2}, \text{ when } A_{Lvr} = \sqrt{\frac{k_{vt}}{k_{sus}}} \quad (6)$$

Here the A_{Lvr} is the lever amplification factor, which is determined by the geometry of the micro-lever, k_{sus} is the flexure stiffness of the proof mass suspension along the sensing axis and k_{vt} is the axial stiffness of the DETFs. As shown in Eq. 5 and Eq.6, for a specific design of the DETF sensing element and suspension, where k_{sus} and k_{vt} are fixed, there is an optimum lever geometry to maximize the effective amplification factor as implemented in device presented in this work. Moreover, as the maximum EA_{Lvr} is determined by the ratio between the axial stiffness of the DETFs and the flexure stiffness of the suspension, a more flexible suspension is designed to further increase the sensitivity to tilt angle.

C. Proof-mass

Increasing the proof-mass is the most straight forward method to enhance the sensitivity. Limits on the proof-mass dimensions are imposed by the fabrication process, material properties and the design area as well as considerations of sensor robustness (e.g. response under sudden shock). The dimensions of the designs presented here were largely restricted by constraints imposed by the foundry process.

III. Scale Factor Calibration

The device is fabricated in a SOI-MEMS foundry process (MEMSCAP Inc., USA) with a device layer thickness of 25 µm. The micro-fabricated chips are mounted onto standard chip carriers and then vacuum packaged using a custom process. The optical micrograph for a packaged sensor chip with wire-bond is shown in Fig. 3.

The vacuum packaged sensor chip is co-integrated with frequency tracking oscillator circuits (Fig.4) on a single PCB and mounted on a manual tilt table to calibrate the scale factor. As shown in Fig. 5, the tilt sensor and manual tilt table were placed on a suspended platform which is adjusted parallel to the ground. The frequency of oscillator output signal was

measured and recorded using a frequency counter (Agilent 53230A).

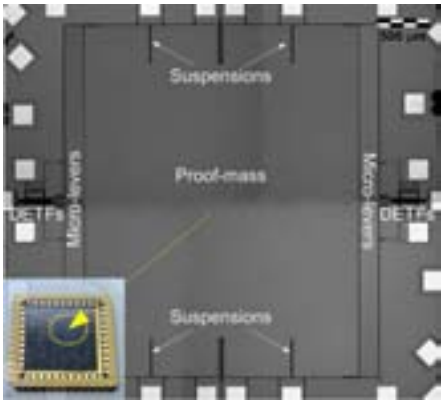

Fig. 3. Optical micrograph of the MEMS sensor element (inset: wire-bonded vacuum packaged chip).

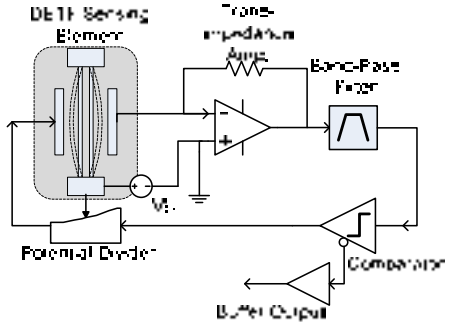

Fig. 4. Electro-mechanical frequency tracking oscillator circuit schematic.

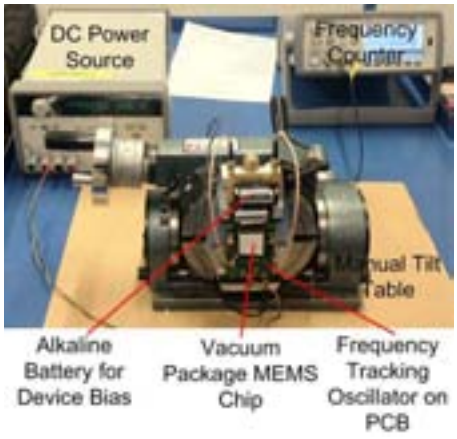

Fig. 5. Experimental calibration set- up.

Fig. 6 shows the output frequency variation of DETF_1 (see Fig. 2) observed in a 0^o-90^o tilt test with 10^o increment for each step. The dashed line is the fitting curve for the mean frequency shift of the tilt sensor for each calibration point. The output frequency shift of the oscillator is seen to vary as a sinusoidal function of the tilt angle and is in agreement with the analytical model presented in Eq. 1. The tilt test results also indicate that the new sensor provides a relatively linear response in the range of $\pm 20^o$ with a differential scale factor of approximately 50.06 Hz/degree, compared to the value of 8.08Hz/degree reported previously [1].

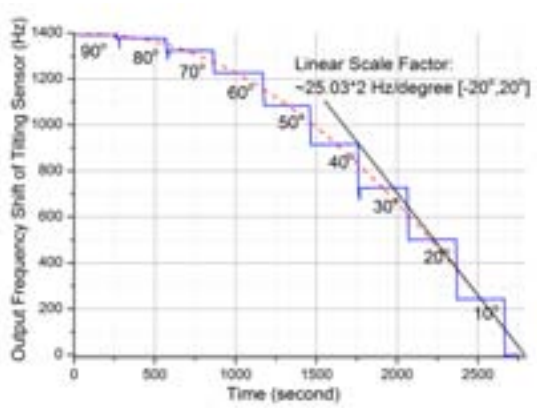

Fig. 6. Output frequency shift response versus tilt angle.

IV. Resolution Analysis

Improving the resolution of the resonant tilt sensor not only requires increasing the scale factor but also optimizing the noise floor. As the frequency shift of the DETFs induced by tilt angle change is tracked by an oscillator circuit, the noise floor of resonant tilt sensor can be derived from the frequency stability of the oscillator output. The noise-limited tilt angle resolution of MEM resonant tilt sensor within the linear tilt angle range is defined as:

$$\theta_{\min} = \left(\frac{\Delta f_n}{f_0}\right) \cdot \frac{\bar{f}_0}{S_{Tilt}} \tag{7}$$

Where the $(\Delta f_n/f_0)$ is the frequency stability of the output signal of frequency tracking oscillator with invariant acceleration input, normally represented in units of ppm (part per million) or ppb (part per billion), $\bar{f}_0$ is the average output frequency of the oscillator over the period of measurement and S_{Tilt} is the scale factor of the tilt sensor.

A. Voltage-Frequency Noise Conversion

The frequency stability of the electro-mechanical oscillator can be influenced by several factors. In this section, we consider limitations arising from voltage-to-frequency (V-F) noise conversion impacting on the frequency stability of the oscillator. V-F noise conversion may arise from the nonlinearities in the mechanics and the electrostatic transduction of the DETF sensing element. The mechanical nonlinearity of DETF converts the noise and drift of the AC driving signal into a corresponding frequency shift [7]. In the oscillator implementation described here, a comparator is employed to limit the amplitude of the drive signal (see Fig.4) and the impact of the AC V-F noise conversion is expected to be small. The parallel-plate electrostatic actuation in the DETF sensing element introduces a frequency pulling effect that is

dependent on the magnitude of DC polarization voltage [8]. Due to the non-linear electrostatic actuation, low-frequency voltage noise and drift in the DC polarization voltage can result in a shift in the oscillator output frequency. If the fluctuation in the DC polarization voltage is defined as $V_P(t)=V_{P0}+\Delta V_P(t)$, the frequency shift induced by the polarization voltage may be expressed as

$$\Delta f_{0\_DC}^2(t) \approx G_{DC}(f_0, V_{P0}, g_{Elc}, t_{Elc}) \cdot \Delta V_P^2(t) \qquad (8)$$

where G_{DC} is a coefficient determined by the resonant frequency of DETF, the geometry of the parallel-plate actuator and the level of DC polarization voltage. The DC polarization voltage limited resolution of MEM resonant tilt sensor can then be estimated as:

$$\theta_{\min\_DC}^2(B) = \left(\frac{f_0^2}{S_{Tilt}^2}\right) \int_{1/\tau_d}^{B} \left(\frac{1}{f_0^2}\right) G_{DC} S_{DC}(f)\, df \qquad (9)$$

where $S_{DC}(f)$ is the power spectral density of the DC polarization voltage noise, B is the measurement bandwidth which is related to the reciprocal of the counter gate time, τ_d is the time-scale over which drift starts to impact the output frequency and f is the Fourier Frequency in the integral of Eq. 10.

B. Experimental Results

To study the influence of DC polarization voltage on the frequency stability of the sensor output, two successive measurements were made on a tilt sensor with the sensitive axis oriented normal to the gravity field. In the first measurement, the DC polarization voltage was supplied by an alkaline battery. In the second measurement, the DC polarization voltage was supplied from a conventional low-noise regulated DC power supply (Agilent E3631A). The magnitude of the polarization voltage was set to be identical in both cases. The oscillator output was logged on a frequency counter and modified Allan deviation calculations were carried out. The results of this calculation are plotted in Fig. 7. When the DETF sensing element was polarized by the regulated DC power source, the short-term frequency stability floor of the oscillator is found to be approximately 19.5 ppb for an averaging time of 1.6 seconds. When the DETF sensing element was polarized using a battery, the short-term frequency stability floor of the oscillator is found to be about 6.7 ppb for an averaging time of 0.8 seconds. It is known that batteries normally has lower noise level than the conventional DC power source [9], so this experiment demonstrates that the influence of DC polarization voltage noise on the frequency stability of the oscillator. For the tilt sensor using batteries as DC polarization source, the equivalent angle resolution is approximately 250 nano-radian, which is over an order of magnitude better than previously reported results [1].

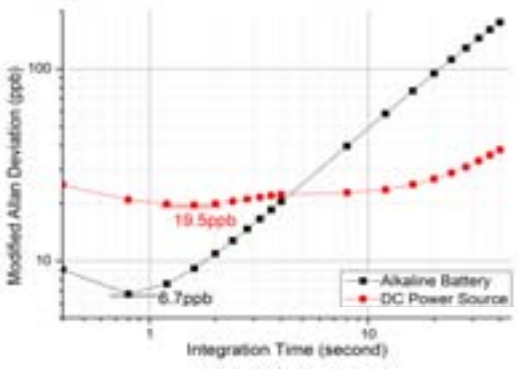

Fig. 7. Modified Allan deviation results for the freqency tracking oscillator with different DC polarization sources.

However, it should also be noted that the output frequency of the tilt sensor polarized by batteries shows larger long-term drift comparing to the tilt sensor polarized by a regulated DC power supply.

V. CONCLUSION

This paper demonstrates an improved high-resolution resonant MEMS tilt sensor with a measured scale factor of 50.06 Hz/Degree for a ± 20 degree tilt angle range. The noise-limited resolution of the device is found to be 250 nano-radian for a 0.8 second averaging time employing a battery-based DC polarization source, demonstrating over an order of magnitude improvement in resolution over previous prototypes.

References

[1] X. Zou, P. Thiruvenkatanathan and A.A. Seshia, "Micro-electro-mechanical resonant tilt sensor," Frequency Control Symposium (FCS), 2012 IEEE International, 21-24 May 2012.

[2] J. Choi and S. Kong, "Fabrication and Characteristics of Micro-Electro-Mechanical-System-Based Tilt Sensor," Japanese journal of applied physics, vol. 48, p. 06FG05, 2009.

[3] J. Ho, K. Chang Jin, and K. Seong Ho, "An optimized MEMS-based electrolytic tilt sensor," Sensors & Actuators: A. Physical, vol. 139, pp. 23-30, Sept. 2007.

[4] L. Jinxing, K. Fusao, L. Xuefeng, K. Kunitomo, and T. Ueda, "Characterization of a quartz MEMS tilt sensor with 0.001° BA precision," in International Solid-State Sensors, Actuators and Microsystems Conference, 2009 (Transducers 2009), Denver, CO, USA, pp. 308-310.

[5] P. M. Moubarak and P. Ben-Tzvi, "Design and Analysis of a new Piezoelectric MEMS Tilt Sensor," 2011 IEEE International Symposium on Robotic and Sensors Environments (ROSE 2011), pp. 83-88, 2011.

[6] B. V. Amini, R. Abdolvand, and F. Ayazi, "Sub-micro-gravity capacitive SOI microaccelerometers," Transducers '05, Digest of Technical Papers, Vols 1 and 2, pp. 515-518, 2005.

[7] T.A. Roessig, R.T.Howe,and A.P. Pisano, "Nonlinear mixing in surface-micromachined tuning fork oscillators," *Proceedings of the 1997 IEEE International Frequency Control Symposium,* pp.778-782, 28-30 May 1997.

[8] V. Kaajakari, M.Tomi, O.Aarne, and S. Heikki. "Nonlinear limits for single-crystal silicon microresonators." *Journal of Microelectromechanical Systems,* 13, no. 5 pp 715-724, 2004.

[9] M. Horak and V.Papez, "Very low noise DC power supply," , *Proceedings of the 2012 International Conference on Applied Electronics (AE)*, pp.99-102, 5-7 Sept. 2012.

Frequency Scaling of Molybdenum Disulfide (MoS_2) Two-Dimensional (2D) Nanomechanical Resonators

Jaesung Lee*, Zenghui Wang, Philip X.-L. Feng*
Department of Electrical Engineering & Computer Science, Case School of Engineering
Case Western Reserve University, Cleveland, OH 44106, USA
*Email: jaesung.lee@case.edu, philip.feng@case.edu

***Abstract*—Molybdenum disulfide (MoS_2) is a layered material that has attractive potential for enabling ultrascaled two-dimensional (2D) nanostructures and nanosystems for future electronics, optoelectronics, and sensors applications. It also has superb mechanical properties, being ~30 times stronger than steel and has intrinsic strain limit up to ~10–20%. These make MoS_2 a particularly interesting material for building novel 2D nanoelectromechanical systems (NEMS). Here we demonstrate ultrathin 2D NEMS resonators based on drumhead-structured MoS_2 diaphragms suspended on circular microtrenches, vibrating at high and very high frequencies (HF & VHF). We show that the resonance frequency can be tuned by adjusting parameters such as built-in tension and dimensions of the MoS_2 devices. In combination with analytical and computational modeling, we identify in these devices the elastic transition regime between the membrane and plate limits, which leads to a clear roadmap for frequency scaling of MoS_2 NEMS resonators.**

Keywords—nanoelectromechanical systems (NEMS); two-dimenstional (2D) crystal; molybdenum disulfide (MoS_2); resonator; thermomechancial noise, frequency scaling

I. Introduction

Nanoelectromechanical devices and systems (NEMS) made of atomically-thin layers of crystalline materials have unique properties and advantages that come from the ultra-low mass and great flexibility of the motional parts of the devices. Graphene NEMS, for example, have been extensively studied and demonstrated great potential. Meanwhile, building NEMS devices by using different 2D materials that have unique electronic and optical properties [1-4] can lead to novel devices suitable for different applications. For most of the last decade, however, graphene has been the only 2D material under significant attention. The recently emerging 2D material MoS_2 is particularly attractive for its compelling physical properties. For example, MoS_2 has a layer-number-tunable band-gap: it evolves from an indirect-gap semiconductor in bulk to a direct-gap semiconductor in monolayer [2]. To date, extensive efforts have mainly been focused on studying the electronic and optical properties of 2D MoS_2 structures [1-4]. Recently, initial experiments have demonstrated that 2D MoS_2 also has excellent mechanical properties [5], which make it one of the strongest and most stretchable and flexible 2D semiconducting materials. In this work, we demonstrate high frequency and very high frequency (HF/VHF) nanomechanical resonators based on very thin suspended MoS_2 diaphragms. In addition, by combining measurement results with theoretical modeling, we present a roadmap that describes the frequency scaling capability of drumhead resonators based 2D MoS_2.

II. Device Fabrication and Measurement

Drumhead-shaped 2D MoS_2 resonators are fabricated using photolithography and mechanical exfoliation. Circular microtrenches of different dimensions are patterned onto wafers with ~290nm-thick thermally-grown SiO_2 on Si with photolithography followed by buffered oxide etch (BOE). We peel off bulk MoS_2 by mechanical exfoliation to achieve devices of different thicknesses. After exfoliation, MoS_2 flakes covering predefined microtrenches form drumhead-structured nanomechanical resonators. We use optical microscope to search and identify suspended MoS_2 structures and later (after measurements of resonances) perform atomic force microscopy (AFM) studies to measure the thicknesses of MoS_2 flakes.

Thermomechanical motions of the MoS_2 nanomechanical drumhead resonators are carefully measured by employing an ultra-sensitive laser interferometry system (Fig. 1). We use a 50× microscope objective to produce a ~1μm laser spot on the device, which enable us to measure the mechanical motion of the devices with a displacement sensitivity at the level of ~30fm/$Hz^{1/2}$. All the measurements are performed at room temperature (T~300K) and in moderate vacuum (p~6mTorr). We use a 632.8nm He-Ne laser, and we control the laser power on the device to be below ~0.7mW to minimize heating effect. This laser power level yields good responsivity in the motion transduction, and does not generate noticeable heating.

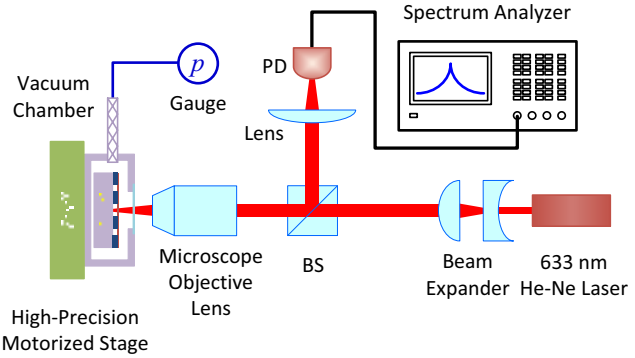

Fig. 1. Schematic of the laser interferometry motion detection system, with thermomechanical resonances spectra analysis. All measurements are performed in moderate vacuum (~6mTorr), and at room temperature (~300K).

III. Experimental Results and Discussions

We investigate the intrinsic thermomechanical resonances of the devices arising from the Brownian motions. Without any external drive, we measure the thermomechanical noise spectrum of the devices using this specially engineered, highly sensitive optical interferometry system. We then fit the measured results to a damped harmonic resonator model to estimate measured quality (Q) factor and the frequency-domain displacement spectral density [6]

$$S_{x,th}^{1/2}(\omega)=\left(\frac{4k_BT\omega_0}{M_{eff}Q}\cdot\frac{1}{\left(\omega^2-\omega_0^2\right)^2+\left(\omega\omega_0/Q\right)^2}\right)^{1/2}. \quad (1)$$

Here, k_B is the Boltzmann constant, M_{eff}, ω_0, and Q are the effective mass, angular resonance frequency, and measured quality factor of the resonance mode, respectively.

To calculate the thermomechanical motion amplitude using Eq. (1), it is necessary to determine M_{eff}, which depends on the mode shape of the resonance. Here we calculate effective masses of circular plate and membrane resonators for their out-of-plane vibrations. For fully clamped circular plate, the mode shape of fundamental mode (m=0, n=1) as a function of normalized radius (0<r<1) can be written as

$$Z_{01}(r)=J_0(\beta_{01}\cdot r)-\frac{J_0(\beta_{01})}{I_0(\beta_{01})}\cdot I_0(\beta_{01}\cdot r), \quad (2)$$

where J_0 is the 0th order Bessel function J, and I_0 is the 0th order extended Bessel function I. For the fundamental mode, $\beta_{01}^2=10.216$. The normalize displacement is defined as

$$u_{01}(r)=\frac{Z_{01}(r)}{\max(Z_{01})}, \quad (3)$$

and the effective mass can be calculated by using

$$M_{eff,01}=M\cdot\frac{1}{\pi}\int_0^1 2\pi r\cdot\left[u_{01}(r)\right]^2 dr. \quad (4)$$

Here M is the total mass of the resonator. Using Eq. (4) we calculate the effective mass of a circular plate to be $M_{eff,01}=0.1828M$ for the fundamental out-of-plane mode.

Similarly, for a circular membrane, the mode shape is

$$Z_{01}(r)=J_0(\beta_{01}\cdot r), \quad (5)$$

where $\beta_{01}=2.405$. The calculated an effective mass for its fundamental mode is $M_{eff,01}=0.2695M$. Using Eqs. (1)–(5) we are able to estimate the thermomechanical resonant noise spectral density of the devices and thus determine the signal transduction responsivity and displacement sensitivity.

Figure 2 shows examples of measured thermomechanical resonance spectra from relatively larger devices (diameter d~6μm) with different thicknesses (t~10–50nm). The measured thermomechanical resonance of device #1 (Fig. 2 (a)–(c), with diameter d≈5.7μm and thickness t≈13nm) has resonance frequency f≈11.54MHz in the HF band, with Q≈105. Another device, device #2 (Fig. 2(d)–(f), with d≈6.2μm and t≈48.8nm), exhibits thermomechanical resonance at f≈16.76 MHz with Q≈180. We have tested devices of a wide range of thickness (t~2–68nm, corresponding to ~3–97 layers).

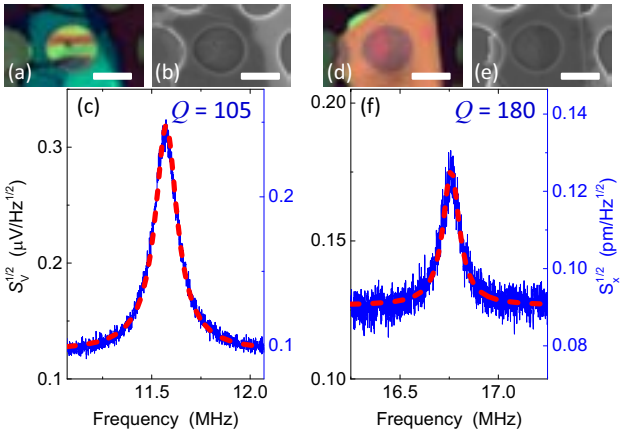

Fig. 2. HF MoS_2 nanomechanical resonators – device images & measured thermomechanical resonances. For each device, optical microscope image, SEM image, and resonance characteristics are shown. (a)–(c) Device #1 (d≈5.7μm and t≈13nm). (d)–(f) Device #2 (d≈6.2μm and t≈48.8nm). From the color and contrast in the optical images, approximate device thicknesses can be estimated (we have verified with AFM). All scale bars are 5μm.

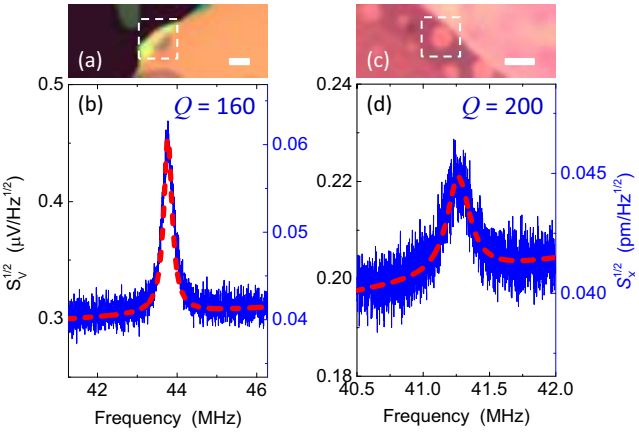

Fig. 3. VHF MoS_2 nanomechanical resonators based on MoS_2 drumheads with smaller diameters. Optical image and mechanical resonance are shown for both devices. (a)–(b) Device #3 (d≈2.5μm and t≈57.5nm). (c)–(d) Device #4 (d≈1.6 μm and t≈2.8nm). All scale bars are 2μm.

We have also measured thermomechanical resonances from relatively smaller devices (Fig. 3). Device #3 (d≈2.5μm and t≈57.5nm) shows resonance in the VHF (30–300MHz) band with f≈43.77MHz and Q≈160. Device #4 (d≈1.6 μm and t≈2.8nm) also displays resonance in the VHF band with f≈41.27MHz and Q≈200. In measurements of both devices, a displacement sensitivity of $S_x^{1/2}$≈42fm/Hz$^{1/2}$ is achieved.

IV. Frequency Scaling

We further investigate the frequency scaling capability of these HF and VHF MoS_2 2D nanomechanical resonators. We

theoretically calculate the fundamental resonance frequencies for circular drumhead resonators and compare with measured results. For a tensioned circular drumhead resonator (clamped on perimeter edge) with finite flexural rigidity D, the resonance frequency can be calculated with the expression [7, 8]

$$\omega_{mn} = \left(k_2^{mn}\frac{d}{2}\right)\sqrt{\frac{16D}{\rho d^4}\left[\left(k_2^{mn}\frac{d}{2}\right)^2 + \frac{\gamma d^2}{4D}\right]}. \quad (6)$$

Here, ω_{mn} is the angular frequency for the resonance for a specific mode (m,n) (with m and n being the numbers of nodal diameters and nodal circles), d is diameter of the diaphragm, ρ is the areal (2D) mass density (kg/m^2), and γ is the built-in tension (force per unit length, in N/m, as in surface tension) of MoS_2 resonator. $D=E_Y t^3/[12(1-\nu^2)]$ is the flexure rigidity, with E_Y being the Young's modulus, t the thickness of the MoS_2, and ν the Poisson's ratio. k_2^{mn} is a mode-dependent parameter which can only be precisely determined numerically.

In the limit of an ideal membrane, the built-in tension dominates, and $\gamma d^2/D \to \infty$. Eq. (6) then simplifies into

$$\omega_{mn} = \frac{\left(k_2^{mn} d\right)}{d}\sqrt{\frac{\gamma}{\rho}}. \quad (7)$$

Eq. (7) gives the 'membrane limit' of a drumhead resonator, which shows dependence on both the built-in tension and dimensions of the device. Here, we use 2D surface tension γ (force per unit length, N/m), which is suitable to 2D material-based resonator, instead of the other form of tension (force, in N) or stress (force per unit cross-sectional area, in Pa or N/m^2) which are more suitable for 3D structures. In addition, we used ρ, the 2D mass density, for the same reason.

In the other limit of an ideal plate, the bending rigidity dominates, and $\gamma d^2/D \to 0$. Eq. (6) then becomes

$$\omega_{mn} = \frac{\left(k_2^{mn} d\right)^2}{d^2}\sqrt{\frac{D}{\rho}}. \quad (8)$$

This is the well-known expression for circular plate resonators. Both limits are plotted as dashed lines in Fig. 4 for d=6μm devices. In the transition regime between the membrane and plate limits, ($k_2^{mn}d/2$) can be approximated with a double exponential expression.

$$\left(k_2^{mn} d/2\right) = \alpha + (\beta - \alpha)e^{\left[-\eta e^{\delta \ln(x)}\right]}, \quad (9)$$

where $x=\gamma d^2/(4D)$. For the fundamental resonance mode (m=0, n=1), the numerical parameters are α=5.7832, β=10.215, η=0.1148, and δ=0.4868 [8]. Compared to the numerical solution, the error from using this approximation (Eq. (9)) is below 3.8% in the entire range of x for the fundamental mode.

Using Eqs. (6) and (9), we calculate resonance frequency of the fundamental mode for MoS_2 drumhead resonators with different diameters and thicknesses. To calculate the areal mass density of MoS_2 resonators, we use 5.06g/cm^3 for the 3D mass density and 0.7nm as the monolayer thickness [2, 4]. In literature there are a number of different Poisson ratios reported for MoS_2, from 0.125 [9] to 0.25 [10] and 0.27 [11]. Here we use Poisson's ratio ν=0.165 [12], same as that for graphene. Indeed, in our estimation, ν very little affects the resonance frequency. This is because when the device is in the ideal membrane limit, resonance frequency does not depend on Poisson's ratio. In the ideal plate limit, ν only affects the flexure rigidity D, and the variation in resonance frequency due to different ν values is always below 2.5%. We use Young's modulus of E_Y=0.2TPa [5,9,13], and the resulting frequency values are consistent with our experimental data. In Fig. 3, we display calculated resonance frequency using built-in tension values γ=0.1–0.5N/m (except for d=0.5μm), as typically observed in mechanically exfoliated flakes [5]. For d=0.5μm devices, we show an additional curve with a tension γ=4.2N/m, which can lead to GHz resonators if the MoS_2 diaphragm is thinner than 3 layers. This tension level corresponds to a strain of only 3% in monolayer and 1.5% in bilayer, still far below the intrinsic strain limit of this material [5,13]. The calculation results are plotted in Fig. 4 together with the experimental results from more than 20 measured devices.

From Fig. 4 we observe that, when the device is sufficiently thin, the resonator is operating in the membrane regime, and can have great frequency tunability through the built-in tension of MoS_2. On the other hand, thick devices mostly operate in the plate regime. In our measurements, data from the larger-diameter (d~6μm) devices agree well with the 6μm curves, and data from the smaller-diameter (d~2μm) devices match the 2μm curves. Data points from some incomplete diaphragms are below the curves for the d~2μm devices. For devices with d=2~6μm and thickness of t=10–20 layers of MoS_2, even with very small tension (γ=0.1–0.5N/m), they are already in the 'crossover' transition regime from plate to membrane.

Besides thickness and tension, lateral device size also has strong effect on the resonance frequency. In Fig. 4 the smaller devices (red circles) clearly have much higher frequencies (note the log scale) than the larger ones. Indeed, all these devices operate in a higher radio frequency band (VHF versus HF). This signifies that reducing the lateral dimension is also an effective means for achieving higher frequencies in MoS_2 nanomechanical resonators. In Fig. 4 we also plot the calculation results for d=0.5 μm devices (the green curve family at the top). It shows that given this small size, 1GHz devices can be achieved for devices thicker than 20 layers.

To further appreciate the strong effect from lateral device size, we plot resonance frequency versus device diameter in Fig. 5. The log-log plot again clearly demonstrates the different power law dependences on diameter in the ideal membrane and plate limits (dashed lines). As expected, part of the 10 layer curve (thin solid line) lies in the transition region between the two limits, while the 100 layer curve (thick line) is mostly in the ideal plate limit. The strong and monotonic dependence of resonance frequency on device diameter signified in this plot, regardless device thickness and the regime it operates in, again suggests that smaller diameters are effective to attaining resonance frequencies in the UHF band.

The results in Fig. 4 and Fig. 5 demonstrate frequency scaling of MoS_2 resonators through dimension engineering. Designing smaller-diameter devices and engineering higher

built-in tension for thinner devices can both lead to higher resonance frequencies. For instance, for a 0.5μm diameter device, a moderate built-in tension level of 4.2N/m (strain $\varepsilon \approx 1.5\%$ for bilayer and $\varepsilon \approx 3\%$ for monolayer) can realize GHz flexural mode MoS_2 resonators for devices less than 3 layers.

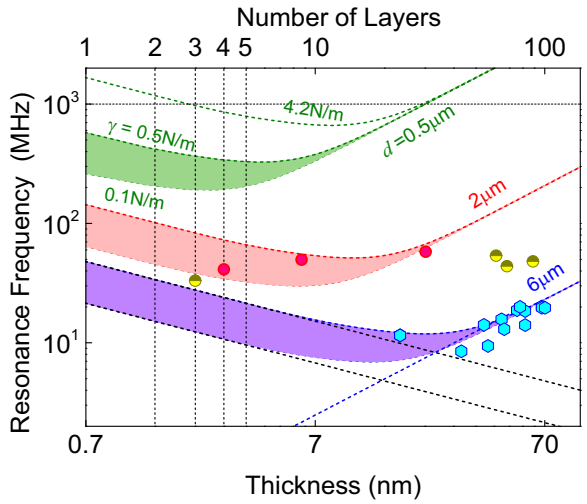

Fig. 4. Frequency scaling and elastic regimes for drumhead MoS_2 2D nanomechanical resonators. Blue, red, and green lines represent calculated fundamental flexural-mode resonance frequencies for devices with d=6μm, 2μm, and 0.5 μm, respectively. The regions with filled colors represent the γ=0.1–0.5N/m built-in tension range for each device size. Black and blue dashed lines respectively show the membrane and plate limits for d=6μm devices. Blue hexagons represent measured devices with larger diameters (~6μm). Red circles represent devices with smaller diameter (~2μm). Half-covered yellow circles denote d~2μm devices with incomplete drumheads.

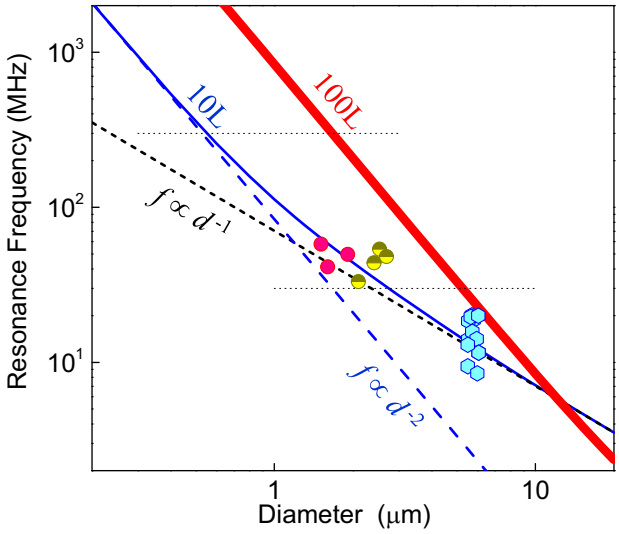

Fig. 5. Frequency scaling of drumhead-shaped MoS_2 2D nanomechanical resonators. Resonance frequency versus device diameter for devices with different thickness (in units of MoS_2 monolayer) are plotted. The red and blue solid lines represent devices of 100 layers and 10 layers, respectively. The blue and black dashed lines stand for ideal plate and membrane (with 0.3N/m built-in tension) limits, respectively. Horizontal dotted lines mark the onsets of VHF and UHF bands. Experimental data are the same as shown in Fig. 4.

V. Conclusions

In summary, we have demonstrated drumhead-structured HF/VHF 2D nanomechanical resonators based on suspended MoS_2 nanosheets with different sizes and thicknesses. Using an ultrasensitive optical interferometric readout technique with exceptional displacement sensitivity as good as ~30fm/Hz$^{1/2}$, we have measured thermomechanical resonances arising from the undriven intrinsic Brownian motions of resonators, the smallest motions from the devices. We also systematically investigate frequency scaling of the MoS_2 resonators and elucidate the membrane and plate limits, as well as the elastic transition regime in between. Combining analysis with experimental results, we identify the built-in tension levels in these exfoliated MoS_2 structures. These results offer guidelines for engineering 2D nanomechanical resonators with desired resonance frequencies, via size scaling and tension control.

Acknowledgment

We are grateful to Case School of Engineering and the T. Keith Glennan Fellowship for financial support. We thank K. He, J. Shan, and R. Yang for helpful discussions.

References

[1] K. S. Novoselov, D. Jiang, F. Schedin, T. J. Booth, V. V. Khotkevich, S. V. Morozov, and A. K. Geim, "Two-dimensional atomic crystals," *Proc. Nat. Aca. Sci.*, vol. 102, pp. 10451-10453, June 2005.

[2] K. F. Mak, C. Lee, J. Hone, J. Shan, and T. F. Heinz, "Atomically thin MoS_2: a new direct-gap semicondcutor," *Phys. Rev. Lett.*, vol. 105, pp. 136805, September 2010.

[3] B. Radisvljevic, A. Radenovic, J. Brivio, V. Giacometti, and A. Kis, "Single-layer MoS_2 transistors," *Nat. Nanotechol.*, vol. 6, pp. 147-150, January 2011.

[4] A. Splendiani, L. Sun, Y. Zhang, T. Li, J. Kim, C.-Y., Chim, G. Galli, and F. Wang, "Emerging photoluminescence in monolayer MoS_2," *Nano Lett.*, vol. 10, pp. 1271-1275, March 2010.

[5] S. Bertolazzi, J. Brivio, and A. Kis, "Stretching and breaking of ultrathin MoS_2," *ACS Nano*, vol 5, pp. 9703-9709, November 2011.

[6] J. Lee, Z. Wang, K. He, J. Shan, and P. X.-L. Feng, "High frequency MoS_2 nanomechanical resonators," *ACS Nano*, vol. 7, pp. 6086-6091, June 2013.

[7] T. Wah, "Vibration of circular plates," *J. Acoust. Soc. Am.*, vol. 34, pp. 275-281, July 1962.

[8] H. Suzuki, N. Yamaguchi, and H. Izumi, "Theoretical and experimental studies on the resonance frequencies of a stretched circular plate: application to Japanese drum diaphragms," *Acoust. Sci. Technol.*, vol. 30, pp. 348-354, March 2009.

[9] M. R. Lovell, M. M. Khonsari, and R. D. Marangoni, "A finite element analysis of the frictional forces between a cylindrical bearing element and MoS_2 coated and uncoated surfaces," *Wear*, vol. 194, pp. 60-70, June 1996.

[10] Q. Yue, J. Kang, Z. Shao, X. Zhang, S. Chang, G. Wang, S. Qin, and J. Li, "Mechanical and electronic properties of monolayer MoS_2 under elastic strain," *Phys. Lett. A*, vol. 376, pp. 1166-1170, Faburary 2012.

[11] J. L. Feldman, "Elastic constants of 2H-MoS_2 and 2H-$NbSe_2$ extracted from measured dispersion curves and linear compressibilities," *J. Phys. Chem. Solids*, vol. 37, pp. 1141-1144, Faburary 1976.

[12] O. L. Blakslee, D. G. Proctor, E. J. Seldin, G. B. Spence, and T. Weng, "Elastic constants of compression-annealed pyrolytic graphite," *J. Appl. Phys.*, vol. 41, pp. 3373-3382, August 1970.

[13] T. Li, "Ideal strength and phonon instability in single-layer MoS_2," *Phys. Rev. B*, vol. 85, pp. 235407, June 2012.

Aluminum Nitride Nano-Plate Infrared Sensor with Self-Sustained CMOS Oscillator for Nano-Watts Range Power Detection

Yu Hui, and Matteo Rinaldi
Dept. of Electrical and Computer Eng.
Northeastern University
Boston, MA, USA
hui.y@husky.neu.edu; rinaldi@ece.neu.edu

Abstract—This paper presents, for the first time, a fast (thermal time constant of 1.3 ms) and sensitive (responsivity of 310 Hz/μW) Infrared detector consisting of an Aluminum Nitride (AlN) nano-plate resonator (NPR) connected to a compact and low power CMOS self-sustained oscillator (fabricated in the AMIS 0.5 μm CMOS process) as a direct frequency readout. A high performance (quality factor Q = 1283 and electromechanical coupling coefficient k_t^2 = 1.56%) MEMS resonant structure based on a thin AlN (250 nm thick) NPR coated with Si_3N_4 (100 nm thick) as IR absorber was fabricated and tested, showing a measured temperature coefficient of frequency (TCF) of -35 ppm/K and FEM simulated temperature rise factor of 72.5 mK/μW. Thanks to the high electromechanical performance of the MEMS resonator, a compact and low power (2.3 mW) self-sustained CMOS oscillator circuit was used as a direct frequency readout, enabling the demonstration of a novel uncooled IR detector with a low Noise Equivalent Power (NEP) of 3.5 nW/Hz$^{1/2}$.

Keywords—Aluminum Nitride; MEMS Resonators; Infrared Sensor; MEMS-CMOS Oscillator.

I. INTRODUCTION

With the recent advance in Micro/Nano-Electro-Mechanical Systems (MEMS/NEMS) technologies, miniaturized sensors with high sensitivity and low detection limit have been developed. In particular, MEMS resonators have been successfully used in detecting mass [1], gas flow [2] and specific chemical agents [3], showing extremely high sensitivity. The exclusive advantage of MEMS/NEMS resonant detectors is the combination of high sensitivity to external perturbation (extremely reduced overall volume) and low noise performance (intrinsically high quality factor Q). MEMS resonant IR detectors based on gallium nitride [4] and quartz [5] resonators have been recently demonstrated showing promising performance. However, complex, cumbersome, power hungry and expensive electronic readouts, based on open-loop measurements involving the use of a network analyzer, have been employed so far to measure the resonance frequency or impedance change of such resonant MEMS IR detectors, which has prevented these technologies to meet the stringent miniaturization, cost and power requirements typical of commercial and military IR imaging and sensing applications.

In this work, a step stone towards the development of MEMS resonant IR thermal detectors characterized by high sensitivity, low detection limit, fast response and compact readout was set by demonstrating an Aluminum Nitride (AlN) piezoelectric MEMS-CMOS oscillator. For the first time, an ultra-thin (250 nm thick) AlN piezoelectric resonator (differently from gallium nitride and quartz, ultra-thin and high quality AlN film can be deposited directly on Silicon substrates by low-temperature sputtering process) working at a higher order lateral-extensional mode [6], whose resonance frequency is highly sensitive to external temperature fluctuation, was integrated with a thin Si_3N_4 film (100 nm thick) as an effective long wavelength IR absorber [7]. The high electromechanical performance (quality factor Q = 1283 and electromechanical coupling coefficient k_t^2 = 1.56%) of the AlN NPR, enabled the direct connection of the resonant device to a compact and low power self-sustained CMOS oscillator circuit as direct frequency readout. This first prototype shows an IR responsivity of 310 Hz/μW, thermal time constant of 1.3 ms, noise equivalent power (NEP) of 3.5 nW/Hz$^{1/2}$ and a power consumption of 2.3 mW , indicating the great potential of the AlN MEMS resonant IR detector technology for un-cooled IR imaging and sensing.

II. DESIGN AND SIMULATION

The core element of the IR detector proposed in this work is an AlN nano-plate resonator, working at a higher order lateral-extensional mode of vibration. The resonance frequency of the AlN NPR, f_0, is determined by the pitch of the interdigital electrode, W_0 (Fig. 1), defined as:

$$f_0 = \frac{1}{W_0}\sqrt{\frac{E_{eq}}{\rho_{eq}}} \quad (1)$$

where E_{eq} and ρ_{eq} are the equivalent Young's modulus and density of the material stack of the resonator. The temperature sensitivity of the resonator arises from the temperature dependence of the equivalent Young's modulus (E_{eq}) of the material stack forming the resonator [8]. For AlN nano-plate contour-mode resonators, the typical value of temperature coefficient of frequency (TCF) is in the range of -30 ~ -50 ppm/K.

This work was supported by DARPA Young Faculty Award contract No. N66001-12-1-4221.

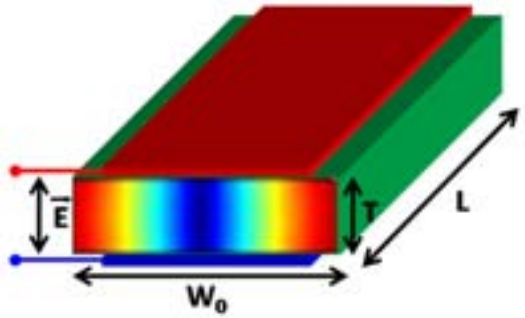

Fig. 1. 3D schematic of the AlN nano-plate resonator. 2D FEM simulated displacement of AlN plate under vertical electric field was superimposed to the AlN film.

IR detectors are typically characterized by two key parameters: noise equivalent power (NEP), and thermal time constant τ, and they can be defined as

$$NEP = \frac{\Delta f_n}{R} \tag{2}$$

$$\tau = R_{th} \cdot C_{th} \tag{3}$$

where Δf_n is the noise induced frequency fluctuation, R is the responsivity, R_{th} is the thermal resistance and C_{th} is the thermal capacitance. For high performance IR detectors, the noise equivalent power and thermal time constant need to be as small as possible. Therefore, the product of NEP and τ can be considered as a device figure of merit for device design and optimization, and can be expressed as

$$NEP \cdot \tau \propto \frac{c \cdot \rho_{eq}}{\eta \cdot TCF} \frac{T^2}{Q \cdot \sqrt{P_c}} \tag{4}$$

where c is the thermal capacity, η is the IR absorption coefficient, P_c is the input power to the resonator. Besides the material properties, (4) clearly shows that fast and low detection limit thermal detectors can be implemented using high quality factor AlN nano-plate resonators with thickness, T<1 μm.

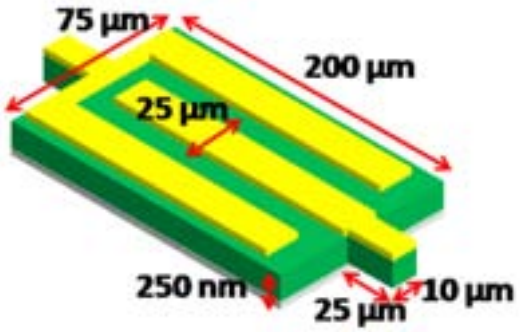

Fig. 2. Optimized dimensions of the AlN nano-plate resonator (the bottom interdigital electrode is shown on top here for clarity).

Based on the aforementioned analysis, an optimized design of an AlN nano-plate resonant structure was proposed (Fig. 2). The thermal time constant and the temperature rise factor (thermal resistance) of the proposed AlN NPR IR detector were estimated by 3D Finite Element Method (FEM) simulation using COMSOL Multiphysics. The thermal conductivity and the heat capacity of AlN were set to be 80 W/(m·K) and 740 J/(Kg·K), respectively. The 3D FEM simulation results are shown in Fig. 3. A thermal time constant as small as 1.3 ms was achieved, thanks to the overall reduced volume of the resonant structure (reduced thermal mass). The temperature rise factor (thermal resistance) of the AlN NPR was found to be 72.5 mK/μW, which guarantees high sensitivity of the device to absorbed IR power.

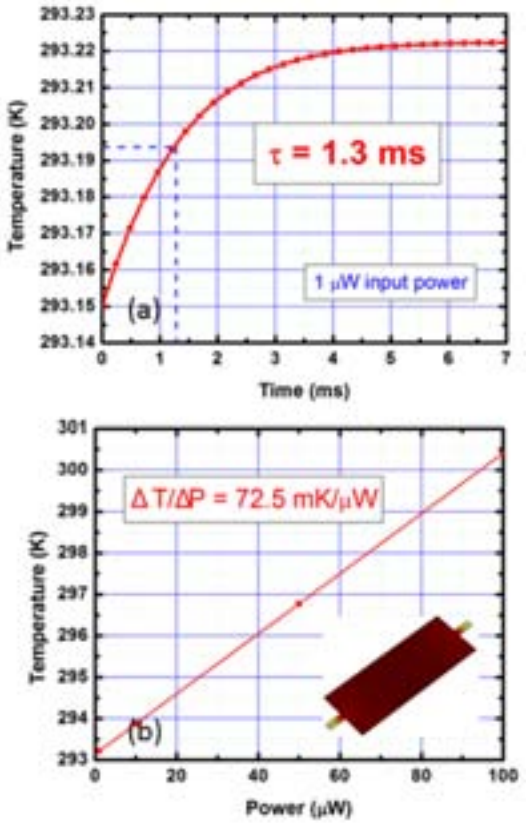

Fig. 3. 3D FEM simulation of the AlN NPR: (a) thermal time constant and (b) temperature rise factor. The inset in (b) shows the uniform temperature distribution across the AlN NPR.

III. EXPERIMENTAL RESULTS

The AlN nano-plate resonator was fabricated using a five-mask microfabrication process, and the detail can be found in [9]. The CMOS integrated circuit (IC) in this work was fabricated in the AMIS 0.5 μm CMOS process. The fabricated AlN NPR was wire bonded to the CMOS IC using a K&S 4523 wedge bonder. The fabricated and wire-bonded MEMS and CMOS dies are shown in Fig. 4.

The electrical performance of the fabricated AlN NPR integrated with thin Si_3N_4 IR absorber was tested by an Agilent E5071C network analyzer after a short-open-load calibration on a standard substrate. The measured admittance amplitude and phase versus frequency and Butterworth-Van Dyke (BVD) model fitting are shown in Fig. 5. The extracted mechanical quality factor Q and electromechanical coupling coefficient k_t^2 are 1283 and 1.56%, respectively. Such high electromechanical performance of the device enabled the capability to connect the MEMS resonator to a compact and low power CMOS oscillator as direct frequency readout. The

temperature coefficient of frequency of the fabricated AlN NPR was measured by a temperature controlled RF probe-station. The measured TCF was found to be -35 ppm/K. Based on the measured TCF and simulated thermal resistance (72.5 mK/μW), the responsivity of the IR detector was estimated to be ~310 Hz/μW.

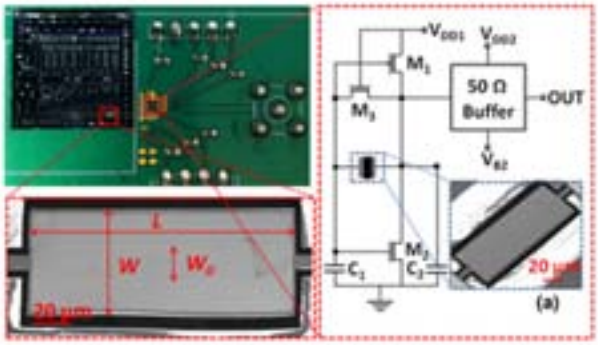

Fig. 4. (a) The fabricated AlN NPR MEMS chip wire bonded to the CMOS die (fabricated in the AMIS 0.5 μm CMOS process). (b) Scanning Electron Microscope (SEM) image of the fabricated AlN NPR; (c) Schematic of the CMOS integrated circuit (IC) as the frequency readout.

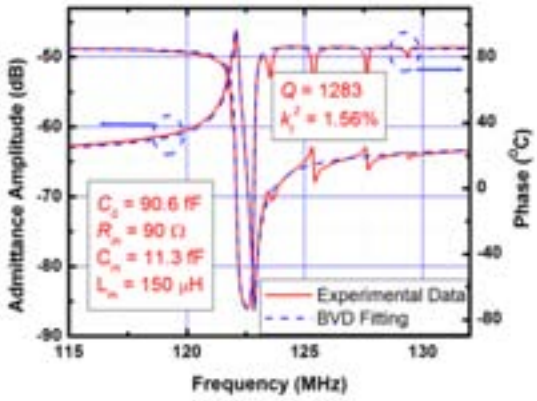

Fig 5. Measured admittance curve and BVD fitting of the fabricated AlN nano-plate resonator.

To evaluate the performance of the fabricated AlN NPR MEMS-CMOS oscillator, the Allan Deviation and phase noise of the device were measured by an Agilent 53230A frequency counter and Agilent N9010A spectral analyzer, respectively. The measured Allan Deviation versus measurement time is shown in Fig. 6 (a). A minimum Allan Deviation of 3.5 Hz was measured at a measurement time of 100 ms, indicating a noise spectral density in 1 Hz measurement time of 1.1 $Hz/Hz^{1/2}$. The phase noise was measured to be -81.1 dBc/Hz at 1 KHz offset and phase noise floor -133.5 dBc/Hz, which are comparable to what is typically achieved with conventional AlN contour-mode resonator based MEMS oscillators [10]. The Noise Equivalent Power (NEP) of the IR detector was estimated to be ~3.5 $nW/Hz^{1/2}$ by dividing the measured noise spectral density by the responsivity of the device (310 Hz/μW).

The IR radiation reflection *R* of the 100 nm Si_3N_4 thin film was measured by a Bruker HYPERION series FTIR microscope. Since the Si_3N_4 was deposited directly on top of a 100 nm thick Au layer, the transmission through the resonant structure was assumed to be ~0. The IR absorption *A* was thus calculated by 1-*R*. A broadband IR absorption higher than 25% from 8 μm to 16 μm with a peak absorption of ~38% at 14 μm was recorded for the 100 nm Si_3N_4 incorporated in the resonant body of the device. .

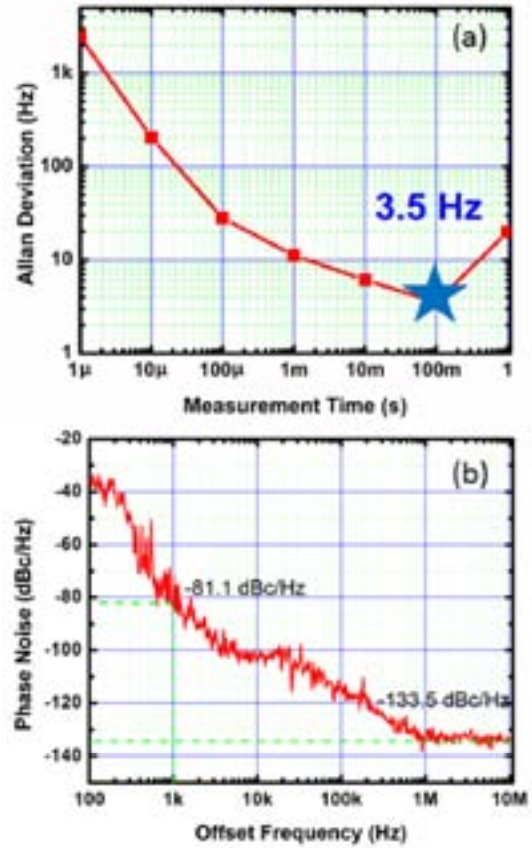

Fig. 6. Measured (a) Allan Deviation and (b) phase noise of the fabricated AlN NPR MEMS-CMOS oscillator.

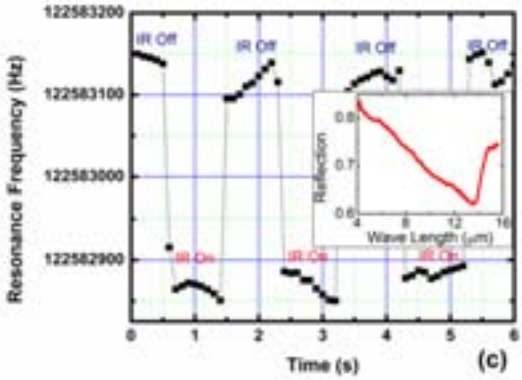

Fig. 7. IR response of the fabricated IR detector to a broad-band IR source (500nm – 25 μm radiation range). The inset shows the measured reflection of the thin Si_3N_4 film.

The IR response of the fabricated device was measured using a Cool Red Infrared light source from Ocean Optics, with a radiation spectrum from 0.5 μm to 25 μm. A ZnSe IR focusing lens was used to focus the modulated IR radiation from the IR source to the AlN NPR. The measured IR response of the device (output frequency of the oscillator versus time) is shown in Fig. 7. The resonance frequency

decreases by ~ 300 Hz when the device is exposed to IR radiation, which corresponds to an absorbed IR radiation power of ~ 1 μW.

IV. CONCLUSION

In this paper, a high performance IR detector based on an AlN nano-plate resonant MEMS-CMOS oscillator was designed, fabricated and tested. For the first time, a high electromechanical performance (quality factor Q = 1283 and electromechanical coupling coefficient k_t^2 = 1.56%) AlN nano-plate resonator integrated with Si_3N_4 thin film IR absorber was connected to a CMOS oscillator, as a low-power and compact frequency readout. The fabricated first prototype showed an IR responsivity of 310 Hz/μW, thermal time constant of 1.3 ms, noise equivalent power (NEP) of 3.5 $nW/Hz^{1/2}$, and power consumption of ~2.3 mW, demonstrating the great potential of the AlN nano-plate resonant IR detector technology for un-cooled IR imaging and sensing applications.

ACKNOWLEDGMENT

The authors wish to thank the staff of the George J. Kostas Nanoscale Technology and Manufacturing Research Center at Northeastern University where the devices were fabricated. This work was supported by DARPA Young Faculty Award contract number: N66001-12-1-4221.

REFERENCES

[1] M. Rinaldi, C. Zuniga and G. Piazza, "ss-DNA Functionalized Array of AlN Contour-Mode NEMS Resonant Sensors with Single CMOS Multiplexed Oscillator for sub-ppb Detection of Volatile Organic Chemicals ", *Proceedings of the 24th IEEE Conference on Micro Electro Mechanical Systems (MEMS 2011)*, Cancun, Mexico, 23-27 January 2011, pg. 976-979.

[2] C. Zuniga, M. Rinaldi, A. Tazzoli, G. Piazza, "Single Transistor Oscillator Based on Piezoelectric Resonant Nanochannel for Operation in Liquids", *Proceedings of the 2012 Solid-State Sensors, Actuators and Microsystems Workshop (Hilton Head 2012)*, Hilton Head Island, 3-7 June 2012, pg. 367-370.

[3] C. Zuniga, M. Rinaldi, S. M. Khamis, A. T. Johnson, and G. Piazza, "Nanoenabled Microelectromechanical Sensor for Volatile Organic Chemical Detection", *Applied Physics Letters*, vol. 94, 223122, 2009.

[4] V. J. Gokhale, J. Roberts and M. Rais-Zadeh, "Sensitive Uncooled IR Detectors Using Gallium Nitride Resonators and Silicon Nitride Absorbers", in *Proc. Solid-State Sensors, Actuators, and Microsystems Workshop (Hilton Head 2012)*, Hilton Head Island, June 3-7, 2012, pp. 46-49..

[5] M. B. Pisani, K. L. Ren, P. Kao and S. Tadigadapa, "Application of Micromachined Y-Cut-Quartz Bulk Acoustic Wave Resonator for Infrared Sensing", *J. Microelectromech.Syst.*, vol. 20, pp. 288-296, 2011.

[6] G. Piazza, P. J. Stephanou and A. P. Pisano, "Piezoelectric Aluminum Nitride Vibrating Contour-Mode MEMS Resonators",*Journal of Microelectromechanical Systems*, vol. 15, pp. 1406-1418, 2006.

[7] W. R. Knolle, D. L. Allara,"Infrared Spectroscopic Characterization of Silicon Nitride Films-Optical Dispersion Induced Frequency Shifts", *Applied Spectroscopy*, vol. 40, pp. 1046-1049, 1986.

[8] J. H. Kuypers, C. Lin, G. Vigevani and A. P. Pisano, "Intrinsic temperature compensation of aluminum nitride Lamb wave resonators for multiple-frequency references", *2008 IEEE International Frequency Control Symposium*,Honolulu, HI, 19-21 May 2008, pg. 240-249.

[9] Y. Hui and M. Rinaldi, "High Performance NEMS Resonant Infrared Detector Based on an Aluminum Nitride Nano Plate Resonator", *Proceedings of the 17th International Conference on Solid-State Sensors, Actuators and Microsystems (Transducers 2013)*, Barcelona, Spain, June 16-20, 2013, pg. 968-971.

[10] M. Rinaldi, C. Zuo, J. Van der Spiegel and G. Piazza, "Reconfigurable 4-Frequency CMOS Oscillator Based on AlN Contour-Mode MEMS Resonators", *Proceedings of the IEEE International Ultrasonics Symposium 2010*, San Diego, USA, 11-14 October 2010.

The OEO as an Acoustic Sensor

Olukayode Okusaga, Justin Pritchett, Ryan Sorenson, Weimin Zhou, Morris Berman
Sensors and Electronic Devices Division
U.S. Army Research Laboratory
Adelphi, MD, U.S.A.
Olukayode.k.okusaga.civ@mail.mil

James Cahill, Gary M. Carter, Curtis R. Menyuk
Computer Science and Electrical Engineering Department
University of Maryland Baltimore County
Baltimore, MD, U.S.A.

***Abstract*—The optoelectronic oscillator (OEO) is a radio-frequency (RF) source that utilizes lengths of optical fiber in a ring resonator to create low-phase-noise signals. In this work, we demonstrate a novel fiber-optic acoustic sensor by measuring the modulation sidebands induced on the OEO's RF signal by an acoustic tone impinging on the fiber spool in the OEO. The narrow linewidth and high oscillating frequency of the OEO results in a sensor with both high signal-to-noise ratios and high spectral resolution.**

Keywords-Optoelectronic oscillators, acoustic sensing

I. INTRODUCTION

The optoelectronic oscillator (OEO) is a radio-frequency (RF) source that utilizes the low loss-per-unit-length of optical fibers to create a ring-resonator that can generate low-phase-noise RF signals at frequencies greater than 10 GHz [1]. Fig. 1 shows a schematic diagram of an OEO. A continuous wave (CW) laser beam is passed through an optical modulator. The output from the modulator is passed through a fiber spool and then into a photodetector. The output from the photodetector is then amplified and passed through an RF bandpass filter, the output of which is connected to the RF-modulation port of the optical modulator. This configuration constitutes an optoelectronic ring-resonator in which RF signals build up from noise in the amplifiers, photodetector, and laser. Signals at frequencies that experience an integer multiple of a 2π phase rotation in one round-trip experience constructive interference and hence build up faster from one round-trip to the next than signals at other frequencies. At steady-state, the power spectral density of the OEO is given by

$$P_{\mathrm{RF}}(f)=\frac{N(f)}{1+\left|g(f)\right|^{2}-2g(f)\cos\left[2\pi f\tau+\phi(f)\right]}, \quad (1)$$

where, f is the RF frequency, τ is the round-trip time, $N(f)$ is the spectrum of the noise injected in each round-trip, $g(f)$ is the steady-state round-trip gain spectrum, and $\phi(f)$is the sum of any frequency-dependent phase fluctuations in excess of the phase delay induced by the nominal round-trip time τ. Eq. 1 shows that, at steady-state, the OEO's signal power is concentrated at frequencies that satisfy the condition:

$$f_{\mathrm{OSC}}=\frac{m}{\tau}, \quad (2)$$

where m is an integer. Low-phase-noise OEOs utilize fiber spools as long as 10 km. Hence, the round-trip time is determined almost entirely by the transmit time of the laser light through the optical fiber spool

$$\tau=\frac{nl}{c}, \quad (3)$$

where n is the effective index of refraction of the optical fiber, l is the length of the optical fiber, and c is the speed of light in vacuum. From Eq. 2 and 3 we see that the transit time through the fiber spool determines the steady-state oscillating frequency of the OEO. Therefore, external perturbations that alter the transmit time through the optical fiber will alter the oscillating frequency of the OEO.

Sound waves incident on the spools — around which the optical fiber is wound — will induce stresses that alter the round trip time in the OEO. A time-varying sound wave will result in a time-varying fluctuation of the OEO oscillating frequency. In this work, we show that we can create an acoustic sensor by measuring this acoustically-induced frequency modulation of the OEO signal. In addition, because the linewidths of our OEOs are less than 1 Hz, the resulting acoustic sensor has sub-Hertz spectral resolution.

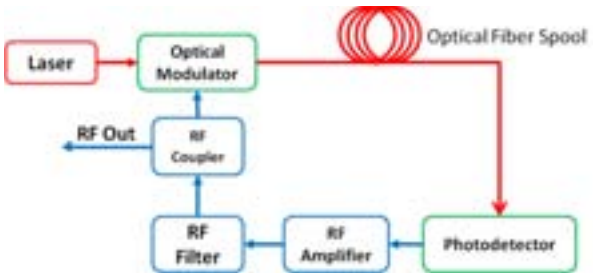

Figure 1. A schematic diagram of the optoelectronic oscillator.

II. PRESSURE WAVES IN OPTICAL FIBERS

Sound waves incident on the spools - around which the optical fiber is wound – induce stresses in the spools. These stresses

deform the spool thereby inducing strain in the optical fiber wound around the spool [2]. Strains in optical fibers can alter the transit time of light through the fiber in two ways: by either altering the physical length of the fiber; or by changing the speed of light (or the effective index of refraction) in the spool. For small perturbations, the change in transit time may be written as

$$\Delta\tau = \Delta n \frac{l}{c} + \Delta l \frac{n}{c} \tag{4}$$

where Δl is the change in fiber length, and Δn is the change in the refractive index of the fiber. Longitudinal strains induced in the fiber cause the fiber length to change, while transverse strains alter the waveguide properties of the fiber leading to a change in its effective index of refraction [2]. Finally, via the strain-optic effect, all strains lead to changes in the refractive index of the fiber material [3]. All three mechanisms contribute to the acoustic sensitivity of the OEO.

III. PHASE MODULATION

A. Optoelectronic Phase Modulation

As a result of the strain-induced changes in fiber transit time, a time varying sound wave will result in a time varying fluctuation in the OEO frequency. Eq. 1 shows that the frequencies at which the power spectral density of the OEO's RF signal is greatest are determined by the fiber transit time τ. When the fiber spool is exposed to a time varying sound wave, the frequencies at which the RF spectrum is peaked become

$$f_{\mathrm{osc}}^{'} = f_{\mathrm{osc}} + \Delta f(t) = \frac{m}{\tau + \Delta\tau(t)}. \tag{5}$$

If the unperturbed OEO's RF signal is a pure tone oscillating at f_{osc}, then the perturbed RF signal will be

$$A_0 \cos\left[2\pi f_{\mathrm{osc}} t + 2\pi\Delta f t\right], \tag{6}$$

where A_0 is the unperturbed RF signal's amplitude. If the sound wave is also a pure tone oscillating at f_a, then from Eq. 5, we may write the induced frequency shift as

$$\Delta f \approx -\frac{m}{\tau}\frac{\Delta\tau}{\tau} = -f_{\mathrm{osc}}\frac{\Delta\tau}{\tau}\cos(2\pi f_a t). \tag{7}$$

Therefore, the acoustic perturbation results in frequency modulation sidebands at offset frequencies ± f_a from the nominal oscillating frequency. These sidebands have magnitudes that are proportional to the nominal oscillating frequency and the change in transit time through the fiber. Therefore, the high oscillating frequency of the OEO (>10 GHz) improves its acoustic sensitivity.

If instead of a pure tone, the unperturbed OEO's RF signal's power spectral density is given by Eq. 1, but the OEO oscillates at a single frequency, then we may rewrite the power spectral density equation for the unperturbed OEO as

$$P_{\mathrm{RF}}(f') \approx \frac{N(f')}{\left[1 - g(f')\right]^2 - g(f')\left(2\pi f'\tau\right)^2}, \tag{8}$$

where f' is the offset from the nominal oscillating frequency. The nominal oscillating frequency of the OEOs used in this work was 10 GHz. The spectrum in Eq. 7 corresponds to a Lorentzian with a full width at half maximum given by

$$\Delta f = \frac{\sqrt{g_0}}{\pi\tau}, \tag{9}$$

where g_0 is the peak round-trip gain at steady-state. For all the OEOs used in this work, the full width at half maximum was less than 30 mHz. The modulation sidebands induced by the sound waves will also have linewidths proportional to the linewidth of the unperturbed OEO. Therefore, the narrow linewidth of the OEO potentially improves its spectral resolution.

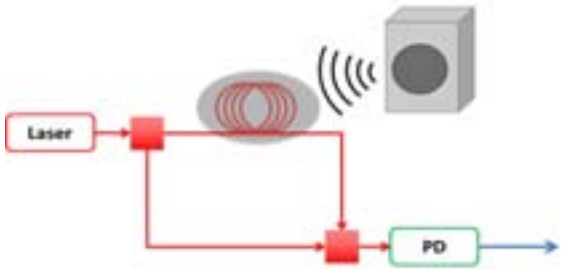

Figure 2. A schematic diagram of an asymmetric Mach-Zehnder modulator used as n acoustic sensor. The sound wave modulates the current from the photodetector "PD."

B. Optical Phase Modulation

So far we have discussed detecting RF frequency modulation induced by sound waves in an OEO. However, an optical beam, even without RF modulation, would experience similar phase modulation when transmitted through an optical fiber spool exposed to sound waves. Fig. 2 shows a schematic diagram of an asymmetric Mach-Zehnder interferometer that includes a fiber spool exposed to sound waves. The optical phase fluctuations induced in the fiber spools result in amplitude fluctuations at the output of the interferometer. Such optical interferometers are the basis of many conventional fiber-optic acoustic sensors [4]. A potential advantage of such optical sensors is that their oscillating frequencies are typically on the order of 100 THz, which may lead to greater acoustic sensitivity than an OEO oscillating at 10 GHz.

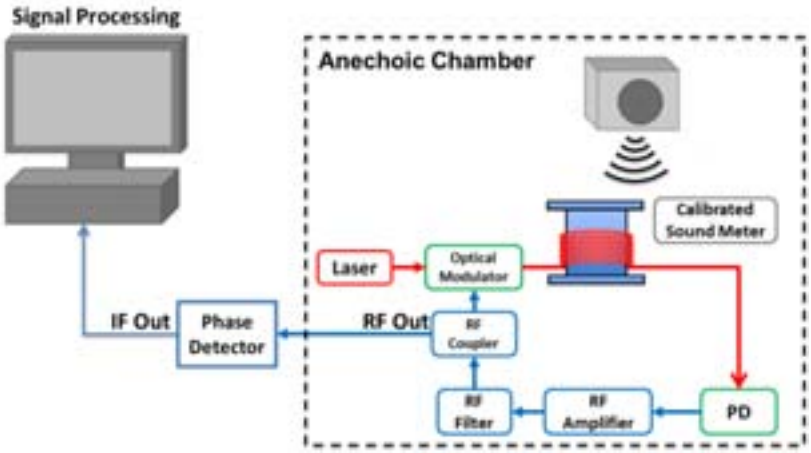

Figure 3. A schematic diagram of our OEO-based acoustic sensor experiment.

However, a potential disadvantage of conventional optical sensors is that the laser linewidths are typically many orders of magnitude greater than the linewidths of low-noise OEO. For instance, the Koheras fiber laser we used in our experiments has a linewidth of approximately 100 Hz. Therefore, conventional fiber-optic acoustic sensors may have worse frequency resolution than the OEO. In the following sections we will describe experiments we performed to test the performance of both types of acoustic sensors.

IV. Experiments

A. Experimental Setup

Fig. 3 shows a schematic diagram of our OEO-based sensor experiment. We placed an OEO in an anechoic chamber. We then played a 1 kHz tone from a speaker approximately 3 m away from the fiber spool in the OEO. We placed a calibrated sound meter next to the spool in order to determine the sound level at the spool. The sound level used in the experiments shown in this wok was 47 dBa,which was the minimum level our calibrated sound meter could detect. To measure the induced phase modulation side bands, we used a delay-line phase-noise measurement system [5]. This measurement system was isolated from the acoustic signal.

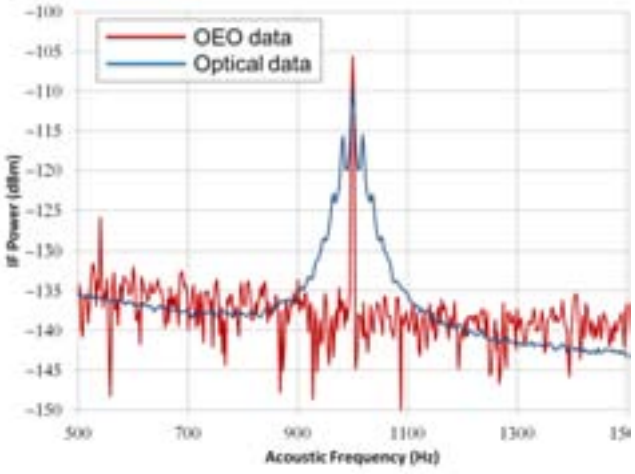

Figure 4. Phase noise plots froman OEO and an a Mach-Zehnder interferometer exposed to a 47 dBa 1 kHz acoustic signal.

We used a similar setup to that in Fig. 3 to test the conventional optical sensor. However, we replaced the OEO with the optical interferometer shown in Fig. 2. In the case of the optical interferometer, we measured the induced modulation directly from the output of the photodetector in the interferometer. In both cases we used the same laser, photodetector, and 6 km spool of Corning SMF-28e+ single-mode optical fiber to detect the acoustic signals.

B. Experimental Results

Fig. 4 shows plots of the phase noise curves of both the OEO and the optical interferometer around 1 kHz. In both cases, the acoustic signal induced a modulation sideband at 1 kHz. In the case of the OEO, the ratio between the peak of the induced sideband and the noise floor of the unperturbed oscillator at 1 kHz is 30 dB; while in the case of the optical interferometer, it was ~26 dB. In addition, the induced sideband in the optical interferometer had a linewidth of approximately 100 Hz, while the linewidth of the induced sideband in the OEO was less than 1 Hz.

V. Conclusion

In this work, we presented experimental data demonstrating the performance of the OEO as an acoustic sensor. We exposed an OEO and a conventional optical interferometer using the same laser, fiber spool, and photodetector, to a 1 kHz 47 dBa acoustic signal. Our results show that the OEO had comparable signal-to-noise ratios to those of the optical interferometer. However, the measured sideband linewidth in the OEO was two orders of magnitude lower than that of the optical interferometer. Our results show that the OEO can potentially be used as a high-spectral-resolution acoustic sensor without sacrificing sensitivity.

References

[1] X. S. Yao and L. Maleki, "Optoelectronic oscillator for photonic systems," *IEEE J. Quantum Electron.*, vol. 32, no. 7, pp. 1141–1149, July 1996.

[2] N. Ashby, D. A. Howe, J. Taylor, A. Hati, and C. Nelson, "Optical fiber vibration and acceleration model," in Proc. of *FCS, 2007 IEEE International Joint with EFTF*, pp. 547–551, May 2007.

[3] C. D. Butter and G. B. Hocker, "Fiber optic strain gauge," *App. Opt.*, vol. 17 no. 18, pp. 2867–2869, Sept. 1978.

[4] G. B. Hocker, "Fiber-optic sensing of pressure and temperature," *Appl. Opt.*, vol. 18 no. 9, pp. 1445–1448, 1979.

[5] E. Salik, "Dual photonic-delay line cross correlation method for phase noise measurement," in *Proceedings of the 2004 IEEE International Frequency Control Symposium*, pp. 303–306, 2004.

Towards a SAW Based Phononic Crystal Sensor Platform

R. Lucklum, M. Zubtsov, A. Oseev
Institute of Micro and Sensor Systems (IMOS)
Otto von Guericke University
Magdeburg, Germany

ralf.lucklum@ovgu.de

M.-P. Schmidt, S. Hirsch
Teprosa GmbH
Magdeburg, Germany

F. Hagemann
SAW Components Dresden GmbH
Dresden, Germany

***Abstract*—A Surface Acoustic Wave (SAW) sensor platform based on phononic crystals specifically designed for chemical and biosensing will be introduced. The unique feature of this sensor concept is the possibility to determine volumetric properties of analytes at volume as low as 1 nl. The sensor platform has the capability paving the way to study chemical reactions in microreactors or biomaterials directly in their physiological environment without any label.**

Keywords—phononic crystal sensor, surface acoustic wave sensor

I. INTRODUCTION (*Heading 1*)

Acoustic waves at ultrasonic frequencies are applied for sensing purposes as ultrasonic sensors and as microacoustic sensors. The typical operation principle of ultrasonic sensors is that a short ultrasonic burst travels through the medium of interest and probes its acoustic properties. Time of flight is a measure of intrinsic material parameters (density, elastic moduli, speed of sound, …) and kinematic values (acoustic path length, flow rate of the medium, …). The basic principle of operation of acoustic microsensors is based on a standing wave in a confined structure whose frequency is determined jointly by sound velocity and the dimensions of the confinement structure. Besides classical piezoelectric devices a large variety of micromachined resonators have been used as sensor platform. The resonance frequency is a measure of changes of the acoustic properties at the surface of the resonator. It does not play any role in latter context whether these changes are generated by a simple mass or thickness change of a chemically sensitive layer immobilized on the resonator surface, changes in viscoelastic properties of the coating material or viscosity changes of a semi-infinite liquid facing the resonator.

The phononic crystal (PnC) sensor concept merges the principles of operation of ultrasonic and acoustic sensors: an external ultrasonic transducer transmits an ultrasonic wave which passes the phononic crystal on its way to an ultrasonic receiver. The phononic crystal sensor itself provides a resonant feature which can be detected from its transmission behavior. Phononic crystals are periodic composite materials with spatial modulation of parameters relevant for acoustic wave propagation like elasticity, mass density or longitudinal and transverse velocities of elastic waves. The typical structure consists of periodically arranged scattering centers with elastic properties different to a homogeneous matrix surrounding the scatters. As chemical sensor the material of interest is assigned as one component that builds the phononic crystal. The promising feature of phononic crystals when working with liquids confined in a point or line defect structure is the existence of modes which cause characteristic discontinuities in the band gap. Such transmission windows are usually very narrow and easy-to-detect features in a transmission spectrum. At a well selected resonance acoustic energy is localized in the cavity which acts as point of measurement. The frequency of this resonance-based maximum transmission can be exploited for sensing purposes similar to acoustic microsensors. We have shown that the peak frequency is strongly governed by the speed of sound of the liquid and the thickness of the liquid layer. Since speed of sound is a material property secondary values like liquid composition can be deduced if a favorable relation between the primary and the secondary value exists. We recently have proven the sensor concept and have shown an application example [1-3]. The characteristic dimensions involved in phononic crystals like the lattice constant or size of the defect range from meters down to hundreds of nanometers. They are closely related to the frequency one can find the band gaps. For the band gap appearing at frequencies of 1 MHz to several 100 MHz, the required periodicity lies in range of 10 µm to 1 mm dimensions. Phononic crystal sensors can therefore be designed to meet the typical dimensions of microfluidic systems.

Higher probing frequencies are also required to gain competitive sensitivity. The appropriate device to start with the development of a miniaturized phononic crystal sensor is a Surface Acoustic Wave (SAW) delay line. Interdigital Transducers (IDT) launch and receive acoustic waves in the required frequency range. The delay line between the IDTs provides the space to place the phononic crystal. It has been further shown that band gaps exists [4]. Different realizations have been analyzed in [5]. However, these analyzes do not consider liquids as a prerequisite for a (bio)chemical sensor platform. We therefore face challenges in both design (simulation) and fabrication technology.

II. The SAW-PnC Sensor

The scheme of the prospective SAW-PnC Sensor is shown in Fig 1. A typical commercial delay line configuration consists of a set of IDTs to cover the required frequency range the delay line is designed for which is much broader than the frequency range of a single IDT. This feature is favorable for sensing purposes since a sensor must provide a reasonable output span to cover the expected variation of the input, e. g. a certain concentration range. The material is often $LiNbO_3$. A regular phononic crystal is placed between the IDTs. It consists of 8 rows of holes, the hole diameter is *D*, the lattice constant *a* which is close to ½ λ. With respect to fabrication issues the key parameter at the current stage of development is, however, the depth of the hole, *h*.

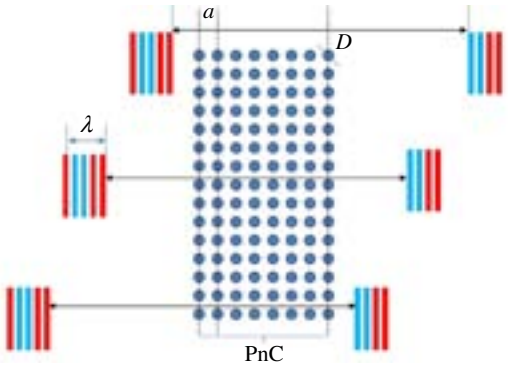

Fig. 1. Scheme of the SAW-PnC (*a* .. lattice constant, *D* .. hole diameter)

III. Simulation

Simulation has been performed with Finite Element Analysis (FEA) using Comsol™Multiphysics both in 2D and in 3D, the latter required for the analysis of the influence of the hole depth. Although the program is very powerful and allows for the implementation of the respective physics, it is not possible do model the complete device. In order to reduce computation efforts and time to an acceptable value, the computation domain does not include the electroacoustic transduction. Instead, the respective actuation has been directly implemented at the particular boundaries. For that reason there is no need for a set of IDTs as shown in Fig. 1. Furthermore, the direct search of resonances through sweeping over a large number of frequencies in the frequency range of interest is inadmissibly time consuming. We ran the sweep with appropriately adjusted sweep steps over the range where one could expect features of interest and have analyzed the displacement pattern at selected frequencies.

Fig. 2 shows the transmission curve in a larger frequency range and less frequency resolution with holes having a depth of only 2 µm (with respect to the fabricated device) and without any structure for reference. As expected, the shallow holes decrease the amplitude of the SAW but do not suppress propagation. The interesting feature is a dip at about 90 MHz which needs further evaluation.

Fig. 3 depicts the results in a smaller frequency range with higher resolution for the 2 µm hole and a hole with a depth of ¼λ. Obviously the deeper holes further decrease the displacement amplitude. A dent is appearing which may suggest the beginning of a band gap.

Fig. 4 shows the computed surface displacement profile at the two very close frequencies marked in Fig. 3. One can see on the left hand side the SAW excitation at the position of the IDTs and in the center the ¼λ holes. We observe a significant increase of surface displacement close the first hole. On the other hand we have to recognize scattering into the volume. This effect is known as Brekhovskikh-attenuation and will lead to an unwanted insertion loss. The strange pattern at the bottom of the device in Fig. 4b seems to be a computational artifact, perhaps from non-optimal boundary conditions. Further improvements in the model are required.

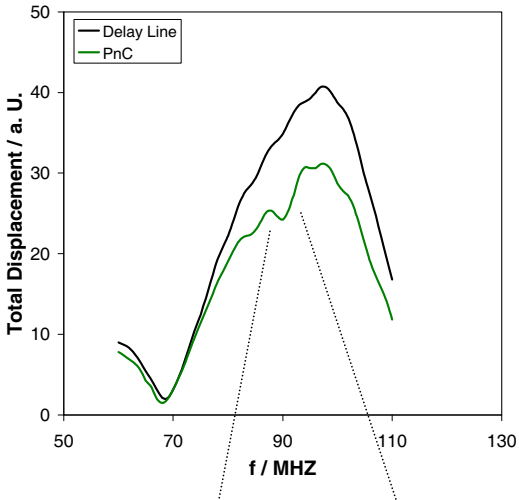

Fig. 2. Simulation of transmission of the delay line (black) and with phononic crystal structure with only shallow holes (green).

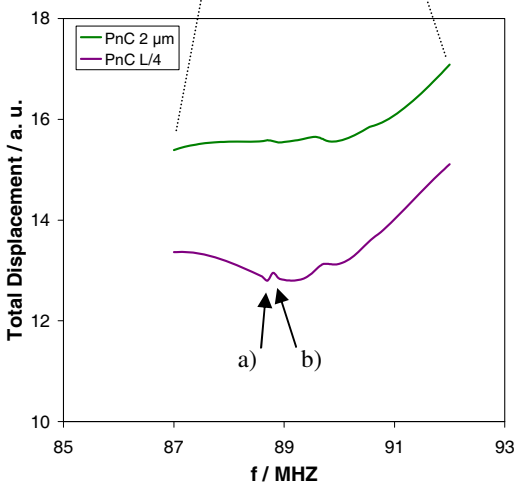

Fig. 3. Transmission analysis in a smaller frequency range with two different depths of the PnC holes (green: 2 µm, pink: ¼ λ).

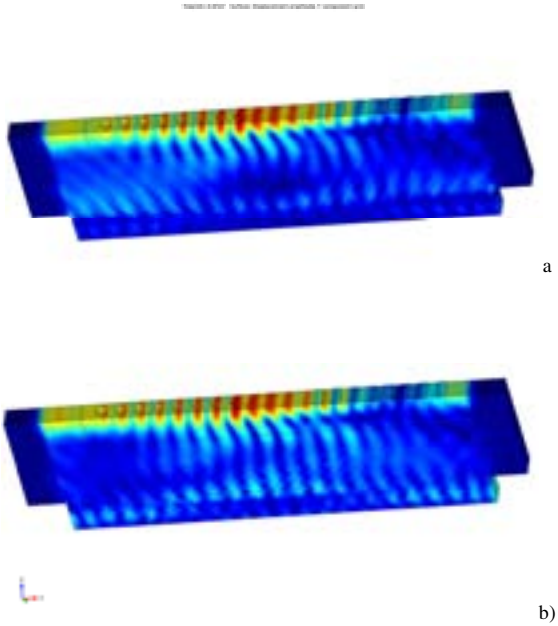

Fig. 4. Displacement at 88.7 MHz a) and 88.8 MHz. The colors illustrate positive (red) and negative (blue) Y-displacement.

IV. Technology Development

Since the preferred design elements of the phononic crystal sensor are holes and slots the development of an etching technology is required. It is far less developed for piezoelectric materials and typically based on reactive ion etching (RIE) [e.g. 6-9]. $LiNbO_3$ is the more appropriate material from the electroacoustic point of view; however, it is more challenging than quartz. We therefore have worked parallel with both substances. We further have considered two routes: etching of holes followed by realization of the IDTs and vice versa. The first variant has been applied to quartz, the second to $LiNbO_3$. The key advantage of the first variant is that hard masks can be applied without major restrictions but requires filling the etched holes for the following lithography whereas the latter one cause problems protecting the IDTs during metal etch.

Fig. 5 shows an array of etched holes as required for different SAW frequencies. A chromium/gold seed layer is deposited by PVD, lithography is based on AZ 15nXT. An Atotech electroplating process creates a nickel hard mask between the developed photoresist elements. The key dry etching process applies a mixture of SF_6/O_2. During the process a backside cooling of helium was necessary to prevent any modifications of the piezoelectric quartz structure. Finally all process residuals, the nickel hard mask and the chromium/gold layer are removed to release the structures. The side walls of the holes are sufficiently smooth and almost perpendicular. An aspect ratio h/D of one is feasible.

The $LiNbO_3$ etch has been performed with a thick photo resist only. It sufficiently protects the IDTs but the maximum etch depth is limited. The side walls are rougher than for quartz and not perpendicular. When overetching the surface of the crystal becomes rough as well. Fig. 6 shows examples.

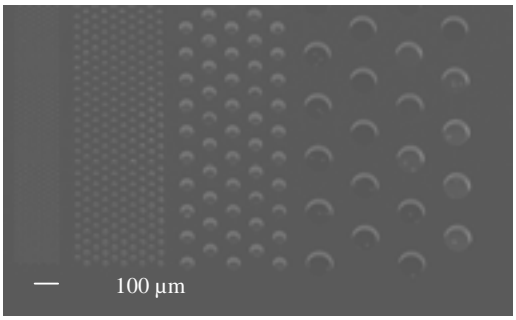

Fig. 5. SEM picture of a set of hole arrays etched into a piezoelectric quartz crystal.

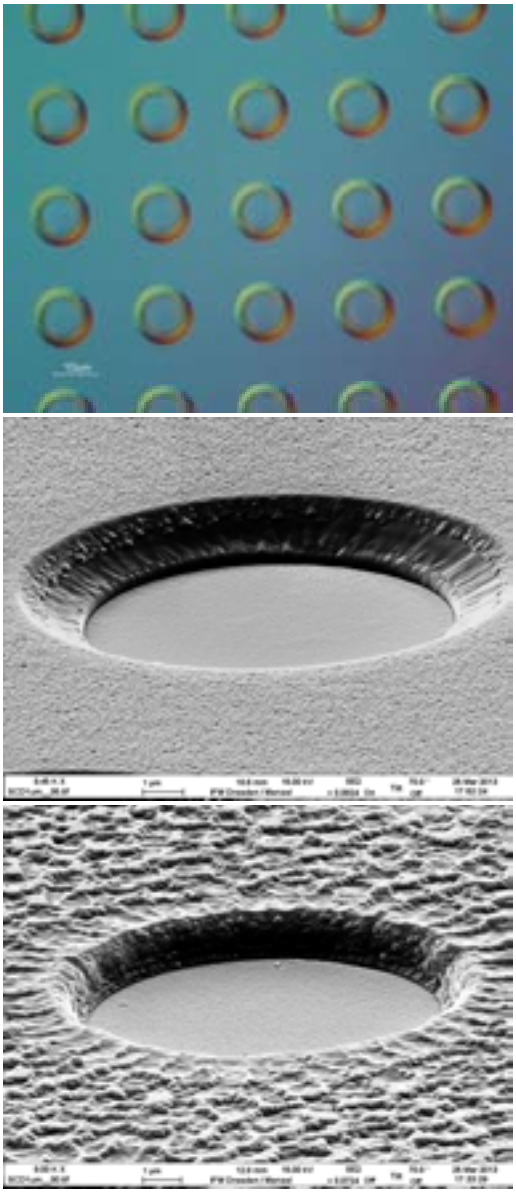

Fig. 6. SEM picture of a hole array etched into a piezoelectric $LiNbO_3$ crystal. The depth of the holes is 2 µm (a). Detail of a single hole and result from overetching are shown in (b) and (c), respectively.

V. EXPERIMENTAL

The $LiNbO_3$ crystal has been analyzed with a network analyzer before and after etching the 2 µm deep holes (Fig. 6b). A tiny but very reproducible dip appears in the transmission plot as shown in Fig. 7. The result agrees well with the simulation results although the frequency of the dip is slightly lower than in simulation. The deviation may be caused by the non-perpendicular side walls.

In conclusion, the preliminary theoretical and experimental results give good reason that a SAW PnC sensor can be realized, however, further work is required to optimize both design and fabrication technology.

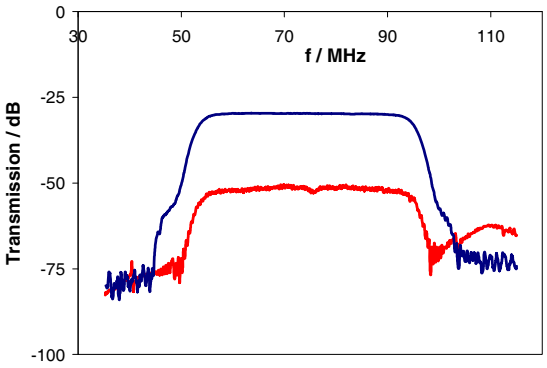

Fig. 7. Transmission measurement of a SAW delay line and a similar one after etching the holes with respect to Fig. 6b.

ACKNOWLEDGMENT

Financial support by the German Research Foundation under grant LU 605-12 is gratefully acknowledged. The authors wish to thank Dr Menzel from IFW Dresden, Germany, for his support.

REFERENCES

[1] R. Lucklum J. Li, "Phononic crystals for liquid sensor applications," Meas. Sci. Technol., 20, 124014, 2009.

[2] R. Lucklum, M. Ke, M. Zubtsov, "Two-dimensional phononic crystal sensor based on a cavity mode," Sensors Actuators B 171-172, 271-277, 2012.

[3] A. Oseev, M. Zubtsov, R. Lucklum, "Gasoline properties determination with phononic crystal cavity sensor," Sensor Actuators B, 2013, in press.

[4] V. Laude, M. Wilm, S. Benchabane, A. Khelif, "Full band gap for surface acoustic waves in a piezoelectric phononic crystal," Phys. Rev. E 71, 036607, 2005.

[5] M.B. Assouar, M. Oudich, "Dispersion curves of surface acoustic waves in a two-dimensional phononic crystal," Appl. Phys. Lett. 99, 123505, 2011.

[6] B. Zimmermann, R. Lucklum, P. Hauptmann, J. Rabe, S. Büttgenbach, "Electrical characterisation of high-frequency thickness-shear-mode resonators by impedance analysis," Sensors Actuators B 76, 47–57, 2001.

[7] D. Croux, A. Weustenraed, P. Pobedinskas, F. Horemans, H. Diliën, K. Haenen, T. Cleij, P. Wagner, R. Thoelen, W. De Ceuninck, " Development of multichannel quartz crystal microbalances for MIP-based biosensing," physica status solidi (a) 209, 892, 2012.

[8] S. Benchabane, L. Robert, J.-Y. Rauch, A. Khelif, V. Laude, "Highly selective electroplated nickel mask for lithium niobate dry etching," J. Appl. Phys. 105, 094109, 2009.

[9] Z. Ren, P.J. Heard, J.M. Marshall, P.A. Thomas, S. Yu, "Etching characteristics of $LiNbO_3$ in reactive ion etching and inductively coupled plasma," J. Appl. Phys. 103, 034109, 2008.

Absolute Phase and Amplitude Mapping of Surface Acoustic Wave Fields

Damien Teyssieux, Thomas Baron, Jean-Michel Friedt *, Gilles Martin and Pascal Vairac
FEMTO-ST Institute UMR 6174
Université de Franche-Comté, CNRS, ENSMM, UTBM
32 Avenue de l'Observatoire, F-25044 Besançon, France
* SENSeOR SAS, Besançon, France, hosted by FEMTO-ST

***Abstract*—This paper describes the development of a scanning heterodyne interferometer for acoustic wave energy mapping. A robust optical double pass interferometer setup is presented, allowing absolute phase and absolute magnitude measurements of the out-of-plane vibration component witin a 5 to 1200 MHz frequency range, only limited by the photodetector bandwidth. By using a dedicated high frequency demodulator, the system is insensitive to the low-frequency mechanical vibration. The system is here used on single-port Surface Acoustic Wave, allowing for the identification of energy distribution as a function of operating frequency and the acoustic velocity over the Bragg mirrors surrounding the resonator. We envision such an instrument as a tool for assessing acoustic energy confinement allowing for optimizing resonator quality factors aimed at providing improved frequency source stability.**

I. Introduction

Acoustic wave propagation on piezoelectric material is well-known and has led to a thriving use in filters [1], resonators [2] and sensors [3]. While accurate design tools have been developed [4], rising operating frequencies emphasize some of the one dimensional or two-dimensional limitations of the models including the effect of the busses on acoustic energy guiding and more generally of energy confinement. Furthermore, actual manufacturing of high frequency devices reaches the technological limits of lithography and electrode patterning tool, yielding the need for experimental validation of the acoustic energy distribution in the device.

Acoustic energy mapping is a rich analysis method complementary to the classical electrical S-parameters characterization since the latter is insufficient for a good acoustic phenomena understanding. Consequently, several optical setups have been developed in order to measure the surface acoustic vibration, with an emphasis on mapping speed since the faster the characterization, the less prone the measurement is to environmental disturbances and most significantly temperature drift. While magnitude detection is readily achieved by using power measurement of the signal modulated by the acoustic wave in any interferometric strategy, sufficient for energy distribution mapping, the more subtle phase information needed to extract the phase velocity is more challenging due to the slow drift inherent to the high sensitivity to environmental parameters of interferometric setups. Indeed, the challenging aspect of the basic homodyne interferometric approach is its sensitivity to the static phase and hence the slow drift over time of this component which might be suppressed using postprocessing but is best eliminated using extended modulation approaches to get rid of this slowly static phase variation. Some of the classical solutions include the Sagnac interferometer proposed by Tachizaki et al. [5], also used by Hashimoto et al. [6], or another setups by Kokkonnen et al. [7], Martinussen et al. [8], Graebner et al. [9].

In this paper, an alternative approach is proposed, using amplitude splitting heterodyne interferometry. In a first part the theory justifying this concept is proposed, followed by a description of the experimental setup. Finally some results when scanning Surface Acoustic Wave (SAW) resonators operating at 393±1 MHz are presented.

II. Theory and optical setup

A. Amplitude splitting interferometry

Generally and for out-of-plane vibration measurement, amplitude splitting interferometry is used. The Michelson interferometer [10],[11] is the most common configuration. It is based on two arms corresponding to a splitting of a beam of light, with the first acting as a reference arm (fixed path) and the second as the signal arm (movable arm). Both beams are recombined to produce an interference pattern, assuming perfect alignment, resulting in a fringe pattern corresponding to the phase difference between the two waves. This phase difference is, assuming a quadrature condition, locally proportional to the optical path difference. In the case of a monochromatic source (e.g. laser beam), and because the frequency of light waves is too high to be detected by currently available detectors, the resulting intensity is proportional to :

$$I = I_o \left[r_s + r_{ref} + 2\sqrt{r_s r_{ref}} \cos\left(\frac{4\pi \left(\Delta d - \Delta n\right)}{\lambda} \right) \right] \quad (1)$$

where r_s and r_{ref} are the reference mirror and the sample reflectivity, respectively, Δd is the optical path difference due to the object movement, Δ_n is the optical static phase difference between the sample and reference paths and λ is the wavelength of the laser. By assuming a sinusoidal out of plane surface vibration $A\cos\left(\omega t + \varphi\right)$, the resulting intensity is:

$$I(t) = I_c + 2I_o\sqrt{r_s r_{ref}} \cos\left(\frac{4\pi A}{\lambda} \cos\left(\omega t + \varphi\right) - \Phi_n \right) \quad (2)$$

This equation corresponds to a homodyne interferometer and shows that the resulting intensity depends on the sample reflectivity.

When the vibration amplitude is small compared to λ, the Bessel development of the solution of eq. (2) is simplified

[12],[13] into:

$$I'(t) \propto \cos(\Phi_n) + \frac{4\pi A}{\lambda}\cos(\omega t + \varphi)\sin(\Phi_n) \quad (3)$$

Several methods allow to stabilize the interferometer ($\Phi_n = (2n+1)\pi/2$) in order to measure an absolute amplitude and an absolute phase [14] but at the cost of increasing the system complexity. At least one significant issue with the homodyne method concerns the radio frequency leakage. In order to suppress the sample reflectivity problem and diminish radio frequency leakage problems, a frequency shift can be introduced in one of the interferometer arms [7]. This frequency shifting can be achieved by using an Acousto-Optical Modulator (AOM). In this way, the resulting interference intensity, when the vibration amplitude is small compared to λ, is [15]:

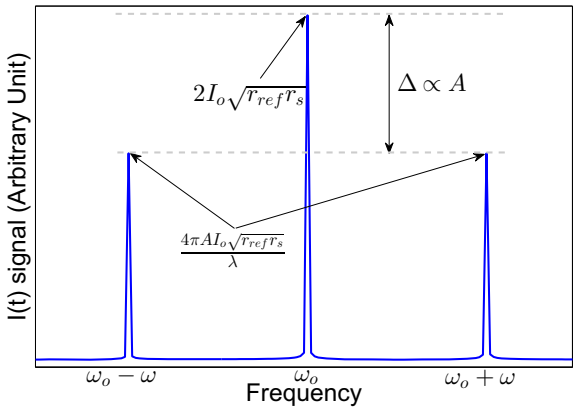

Fig. 1. Fourier Transform of the heterodyne interference signal.

$$\begin{aligned} I(t) &= 2I_o\sqrt{r_{ref}r_s}[\cos(\omega_o t + \Phi_n) \\ &+ \frac{2\pi A}{\lambda}\cos\left((\omega_o+\omega)t + \varphi + \Phi_n - \frac{\pi}{2}\right) \\ &+ \frac{2\pi A}{\lambda}\cos\left((\omega_o-\omega)t - \varphi + \Phi_n - \frac{\pi}{2}\right)] \quad (4) \end{aligned}$$

This equation corresponds to a heterodyne interferometer, where ω_o corresponds to the AOM frequency shift, resulting in a signal of interest observed as a modulation peak (ω_o) and two neighbouring peaks ($\omega_o \pm \omega$). The theoretically absolute value of Fourier Transform of $I(t)$ signal is shown in Fig.1. The absolute amplitude vibration is directly achieved by the modulation/neighbouring peak magnitude ratio (or decibel difference), independent to the sample surface reflectivity. By comparing the phases of the modulation and neighbouring peaks, the absolute phase of the surface vibration is obtained. Thus the static phase Φ_n is suppressed.

Such an approach has been selected and the associated experimental setup is described in the next section.

B. Optical setup description

The optical setup is based on a double-pass heterodyne interferometer [16]. A schematic of the interferometer is shown in Fig.2. The quarter-wave plate's (QWP) fast axis angle is adjusted at $45°$ with respect to the incoming beam linear polarization. After passing through the quarter-wave plate, the laser beam exhibits circular polarization. By passing through the Polarizing Beam Splitter (PBS), the beam is divided into

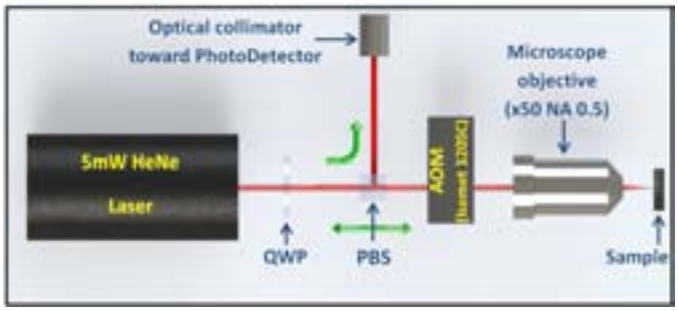

Fig. 2. Optical setup of the double-pass heterodyne interferometer (QWP: quarter-wave, plate PBS: polarizing beamsplitter and AOM: Acousto Optic Modulator)

two beams. The first beam (vertical polarization) is directed towards the optical fiber collimator, acting as the reference arm of the interferometer. The second beam (corresponding to the horizontal polarization) is directed trough the Acoustic Optical Modulator (AOM). The angle between the incident beam and the AOM is set in order to obtain the first diffraction order collinear to the laser beam (the zero order diffraction mode is not used). This beam is the signal arm of the interferometer. After reflection on the sample (by passing trough the microscope lens), the beam is phase modulated by the surface sample vibration and is directed again in the AOM and through the PBS. Due to the quarter-wave plate, the beam has a circular polarization. By using the reflexion on the laser mirror, the signal is directed towards the optical fiber collimator (vertical polarization) and interferes with the reference beam. Use of the mirror of the laser is not problematic (potentially yielding laser instability) in this case due to the frequency shift (AOM double-pass). When the vibration amplitude is small compared to λ, the interference signal of this setup is given by:

$$\begin{aligned} I(t) &= 2I_o\sqrt{r_{ref}r_s}[\cos(2\omega_o t + \Phi_n) \\ &+ \frac{2\pi A}{\lambda}\cos\left((2\omega_o+\omega)t + \varphi + \Phi_n - \frac{\pi}{2}\right) \\ &+ \frac{2\pi A}{\lambda}\cos\left((2\omega_o-\omega)t - \varphi + \Phi_n - \frac{\pi}{2}\right)] \quad (5) \end{aligned}$$

Eq. (5) emphasizes the two passes of the light beam through the AOM, yielding a $2\omega_o$ term which will vanish during the demodulation process described in the next section.

III. Demodulation

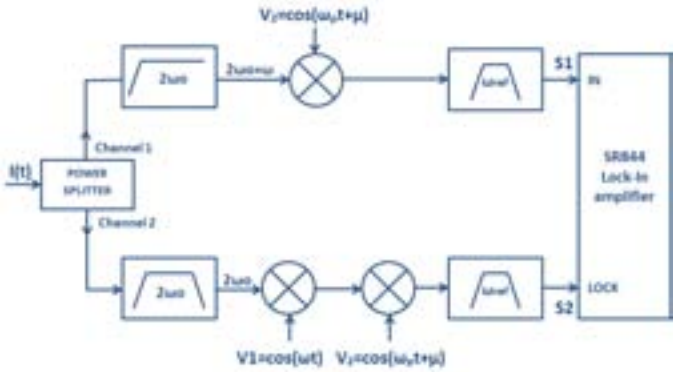

Fig. 3. Demodulation scheme: the recorded signal passing twice through the AOM is centered on a $2\omega_o$ frequency which will be out of the analysis frequency range of S_1 and S_2. ω is the SAW device operating frequency. ω_p is user selected through ω_{ref} as defined in the text.

The setup of the electronic demodulation is schematically shown in Fig.3. S is the interference signal from the interferometer (eq.5), V_1 is the sample drive signal and V_2 is a new user defined signal (from another signal generator, Fig. 3) where μ is the phase difference between V_1 and V_2. With $\omega_p = 2\omega_o + \omega - \omega_{ref}$ and after band-pass filtering at ω_{ref}:

$$S_1 = \frac{I_o\sqrt{r_{ref}r_s}\pi A}{\lambda}\cos\left(\omega_{ref}t + \Phi_n - \mu - \frac{\pi}{2} + \varphi\right) \quad (6)$$

$$S_2 = \frac{I_o\sqrt{r_{ref}r_s}}{4}\cos\left(\omega_{ref}t + \Phi_n - \mu - \frac{\pi}{2}\right) \quad (7)$$

S_1 and S_2 are detected synchronously by a RF lock-in amplifier (SR844 Stanford Research), where S_2 is the lock signal. This setup allows for a maximum detection frequency of 4.5 GHz, limited by the operating bandwidth of the RF components. ω_{ref} is set on the Lock-in frequency range ($0 - 200$ MHz for the SR844). This modulation scheme does not require the clocks of the two signal generators (V_1 driving SAW and V_2) since the drifting phase μ between these two sources is discarded when mixing in the two branches of the demodulation scheme (Fig. 3).

IV. Experiment and results

The objective of the experiments described in this section is to demonstrate the measurement of the acoustic amplitude as well as the acoustic phase of SAW devices, and more specifically a single port SAW resonator. This resonator is obtained by patterning aluminum electrodes using a lift-off process on AT-cut quartz. We select a metallization to period ratio $a/p = 0.5$ and an acoustic period λ of 8 μm. The single port resonator is constituted by one hundred interdigited electrodes in a comb layout, and one hundred Bragg reflectors acting as mirrors on each sides of the transducer. The frequency characterization using a network analyzer exhibits a strong resonance, which is well observed when measuring the acoustic vibration field at one point (Fig.4). In addition to the main resonance at 392.26 MHz, another mode at a nearby frequency is observed at 394.7MHz.

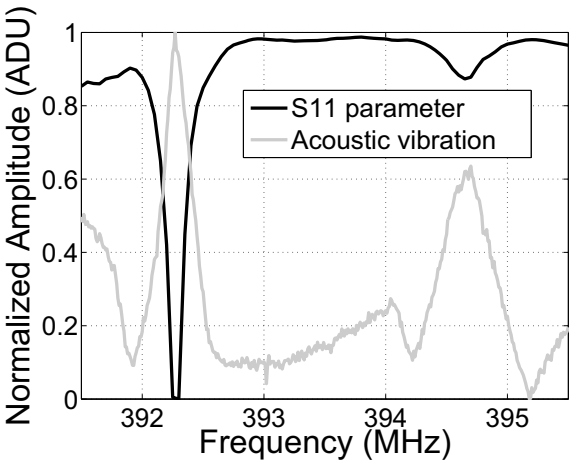

Fig. 4. Electrical reflection coefficient and single-position optical characterisation of the acoustic field magnitude of a single port reflective SAW resonator.

Based on the electrical measurement characteristics of this SAW device, optical mapping of the acoustic field characteristics is performed at both these frequencies. The result of the optical scan characterization on this resonator is shown in Fig. 5 at (a) 392.26 MHz and (b) 394.7 MHz. On the main resonance at 392.26 MHz, the maximum amplitude is well characterized as a light-colored area located over the interdigitated comb transducers. For the second resonance at 394.7 MHz, the maximum amplitude exhibits the parasitic pattern due to the refraction of the acoustic waves under the electrode busses .

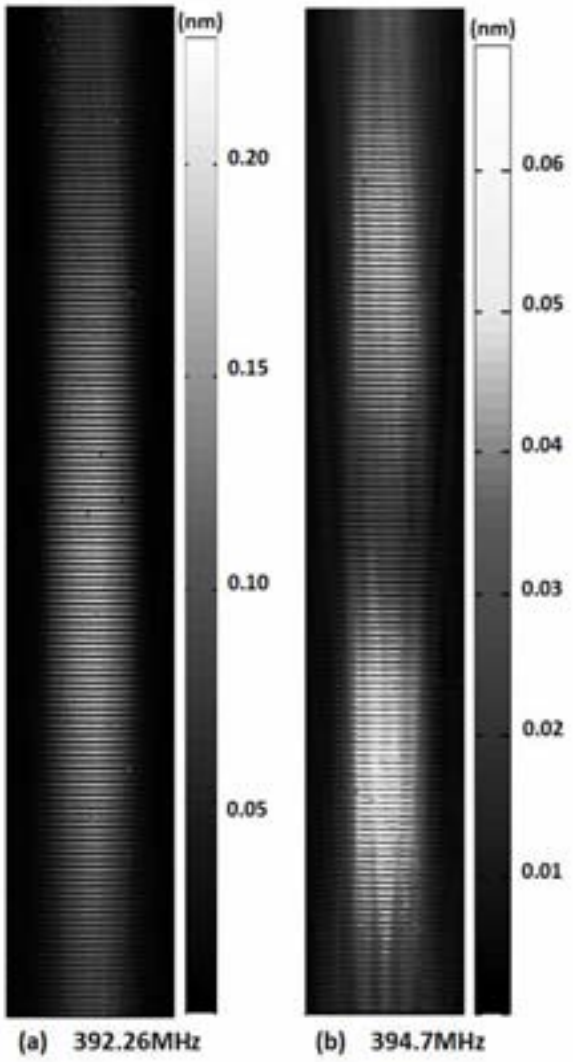

Fig. 5. Optical scan charactization of the acoustic field (out of plane component) amplitude of a single port resonator at (a) 392.26 MHz and (b) 394.7 MHz. Notice that the visual appearance of the stripes, associated with the acoustic nodes and antinodes, is associated due to aliasing of the image.

Following the optical scan characterization, phase information is extracted as shown in Fig.6. A zoom on several periods, which is possible thanks to the large size of the acoustic period and hence wide electrode spacing, exhibits the spatial distribution of the acoustic phase this device, with a 2π rotation over one mechanical period. Unwrapping this acoustic phase information along the acoustic propagation direction provides an estimate of the acoustic velocity. As shown in Fig. 7, the propagating wave over each mirror (positions 0 to 1250 and 1330 to 2400 μm) are characterized by acoustic propagation velocities of equal value but opposite sign (slope of the phase v.s distanc relationship), while the acoustic velocity cancels at the standing wave area over the acoustic cavity (positions 1250 to 1330 μm). The observed acoustic velocity, obtained

by considering that the phase φ to position x slope is given by

$$\frac{d\varphi}{dx} = 2\pi\frac{f}{c} = \frac{2\pi}{\lambda} \Rightarrow c = 2\pi f\left(\frac{d\varphi}{dx}\right)^{-1}$$

of $c = 3138.7 \pm 1$ m/s on both slopes, is consistent with the SAW device operating frequency of $c = \lambda \times f$=8 μm$\times$392.26 MHz=3138 m/s. The scanning probe measurement hence demonstrates the ability to characterize the acoustic propagation and confinement capabilities on a SAW resonator configuration, a requirement for experimentally assessing the main characteristics of a SAW design (acoustic velocity and reflection coefficient on the Bragg mirror electrodes) and understanding the cause for spurious modes or quality factor characterization beyond the basic electrical characteristics. Notice on the zoom of the slopes the ripples associated with the standing wave between adjacent interdigitated fingers. The periodicity of these ripples is 4 μm, consistent with a standing wave pattern between adjacent electrodes.

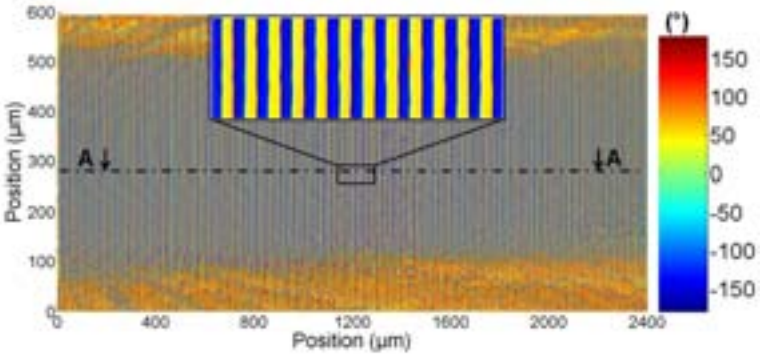

Fig. 6. Optical scan charactization of the acoustic field (out of plane component) phase of a single port resonator at 392.26 MHz.

V. Conclusion

Scanning probe mapping of the acoustic field charateristics, magnitude and most importantly phase, are demonstrated on radiofrequency surface acoustic wave devices using an amplitude splitting heterodyne interferometry approach. This method was selected for its stability and ease of optical alignment, while being insensitive to reflectivity and static phase variations as the scanning takes place. The measurement method, compatible with a use at acoustic device operating frequencies of up to 4.5 GHz, is demonstrated on a 392 MHz SAW resonator. The acoustic velocity of the wave propagating over the Bragg mirrors is observed as the slope of the unwrapped phase *v.s* position map.

Acknowledgment

This work was partly supported by the french RENATECH network and its FEMTO-ST technological facility. The authors thank the Ecole Nationale Supérieure de Mécanique et des Microtechniques (ENSMM) for funding support through the BQR grant and the Agence Nationale pour la Recherche through the Grant P2N 2010 'Phemto' . The authors also thanks Sébastien Euphrasie for his scientific suggestions.

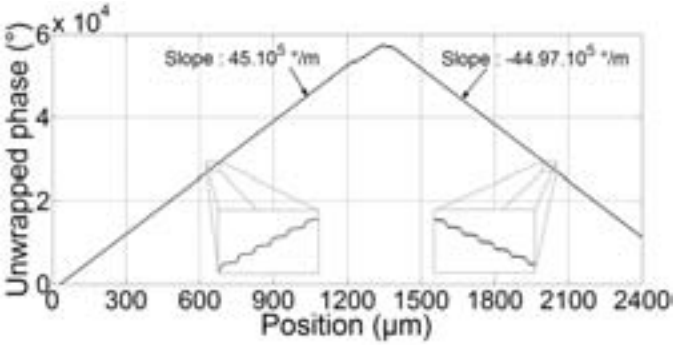

Fig. 7. Unwrapped phase along the AA cross section of Fig. 6: the acoustic cavity extends from positions 1250 to 1330 μm and is surrounded by Bragg mirrors over which the acoustic wave propagates at a velocity related to the slope of the observed linear reltionship between phase and position. Inset: zoom on the phase evolution as a function of position, exhibiting the standing wave between interdigitated transducers.

References

[1] C. Campbell, *Surface Acoustic Wave Devices and Their Signal Processing Applications*. Academic Press, 1989.

[2] G. Montress, T. Parker, and D. Andrea, "Review of SAW oscillator performance," in *Proc. IEEE Ultrasonics Symposium*, 1994, pp. 43–53.

[3] D. Royer and E. Dieulesaint, *Elastic Waves in Solids, Vol. 2*. Springer, 2000.

[4] S. Ballandras, R. Lardat, M. Wilm, T. Pastureaud, A. Reinhardt, N. Champavert, W. Steichen, W. Daniau, V. Laude, R. Armati, and G. Martin, "A mixed finite element/boundary element approach to simulate complex guided elastic wave periodic transducers," *Journal of Applied Physics*, vol. 105, p. 014911, 2009.

[5] T. Tachizaki, T. Muroya, O. Matsuda, Y. Sugawara, D. Hurley, and O. Wright, "Scanning ultrafast sagnac interferometry for imaging two-dimensional surface wave propagation," *Review of Scientific Instruments*, vol. 77, p. 043713, 2006.

[6] K. Hashimoto, K. Kashiwa, N. Wu, T. Omori, M. Yamaguchi, O. Takano, S. Meguro, and K. Akahane, "A laser probe based on a sagnac interferometer with fast mechanical scan for RF surface and bulk acoustic wave devices," *IEEE Trans Ultrason Ferroelectr Freq Control.*, vol. 58, no. 1, pp. 187–194, 2011.

[7] K. Kokkonen and M. Kaivola, "Scanning heterodyne laser interferometer for phase-sensitive absoluteamplitude measurements of surface vibrations," *Appl. Phys. Lett.*, vol. 92, p. 063502, 2008.

[8] H. Martinussen, A. Aksnes, and E. Engan, "Wide frequency range measurements of absolute phase and amplitude of vibrations in micro- and nanostructures by optical interferometry," *Opt. Express.*, vol. 15, no. 18, pp. 11 370–11 384, 2007.

[9] J. E. Graebner, B. P. Barber, P. L. Gammel, D. S. Greywall, and S. Gopani, "Dynamic visualization of subangstrom high-frequency surface vibrations," *Appl. Phys. Lett.*, vol. 78, no. 2, pp. 159–161, 2001. [Online]. Available: http://link.aip.org/link/?APL/78/159/1

[10] J. V. Knuuttila, P. T. Tikka, and M. M. Salomaa, "Dynamic visualization of subangstrom high-frequency surface vibrations," *Opt. Lett.*, vol. 25, no. 9, pp. 613–615, 2000.

[11] J. Lawall and E. Kessler, "Michelson interferometry with 10 pm accuracy," *Rev. Sci. Instrum.*, vol. 71, no. 7, pp. 2669–2676, 2000.

[12] F. Larmer, A. Schilp, K. Funk, and C. Burrer, "Experimental characterization of dynamic micromechanical transducers," *J. Micromech. Microeng.*, vol. 6, pp. 177–186, 1996.

[13] M. Abramowitz and I. Stegun, *Handbook of Mathematical Functions with Formulas, Graphs, and Mathematical Tables*. Dover Publications, 1964.

[14] L. Lipiäinen, K. Kokkonen, and M. Kaivola, "Phase sensitive absolute amplitude detection of surface vibrations using homodyne interferometry without active stabilization," *J. Appl. Phys.*, vol. 108, p. 114510, 2010.

[15] J. P. Monchalin, "Heterodyne interferometric laser probe to measure continuous ultrasonic displacements," *Rev. Sci. Instrum.*, vol. 56, no. 4, pp. 543–546, 1985.

[16] P. Vairac and B. Cretin, "New structures for heterodyne interferometric probes using double-pass," *optics communications*, vol. 132, pp. 19–23, 1996.

Towards a Large-Scale, Optical Timing Distribution System with Sub-Femtosecond Residual Timing Jitter

Michael Y. Peng, Patrick T. Callahan,
Amir H. Nejadmalayeri, Franz X. Kärtner
Dept. of Electrical Engineering and Computer Science
and Research Laboratory for Electronics,
Massachusetts Institute of Technology,
Cambridge, MA, USA

Tony D. Roberts, Philip Battle
AdvR, Inc.
Bozeman, MT, USA

Stefano Valente, Kemal Ahmed, Ming Xin,
Franz X. Kärtner
Center for Free-Electron Laser Science,
Deutsches Elektronen-Synchrotron,
Hamburg, Germany

Eric Monberg, Man Yan, Lars Grüner-Nielsen,
John M. Fini
OFS Laboratories
Somerset, NJ, USA

***Abstract* — We present here key technologies for an all-optical timing distribution system with sub-femtosecond precision. Timing distribution over a 1.2-km polarization-maintaining, fiber-optic link using balanced optical cross-correlators (BOC) for link stabilization was demonstrated for 16 days with 0.6 fs RMS timing drift and during a 3-day interval only 0.13 fs drift. Jitter characterization of two identical commercial femtosecond lasers using the BOC method verified sub-100-as timing jitter for frequencies above than 1 kHz. Preliminary operation of a fiber-coupled, hybrid-integrated BOC using periodically-poled $KTiOPO_4$ (PPKTP) waveguides indicate great potential for improved BOC timing sensitivities and overall system efficiency and robustness.**

Keywords - timing jitter; ultrafast optics; optical fiber applications; phase locked loops; nonlinear optical devices

I. INTRODUCTION

Modern X-ray free-electron lasers (FELs) [1-3] require timing distribution systems with extremely high timing stability to synchronize RF and optical sources located up to several kilometers apart. Since conventional RF timing systems have already reached a practical limit of about 50-100 fs timing precision for such long distances, next-generation timing systems [4,5] are adopting fiber-optic technology to achieve superior performance with optical signal transport and timing distribution.

Over the past decade, we have been advancing technology for a pulsed optical timing distribution system [5]. Our system consists of a femtosecond mode-locked laser tightly locked to a microwave standard and stabilized fiber links for distributing the pulsed optical timing signal to remote locations. Link stabilization is performed using compact, single-crystal balanced optical cross-correlators (BOC), which are capable of attosecond-level timing resolution. Sub-10-fs system performance over days of operation has been achieved but is limited mainly by polarization mode dispersion (PMD) in standard single-mode fiber.

The authors acknowledge financial support by the United States Department of Energy through contract DE-SC0005262, and the Center for Free-Electron Laser Science at Deutsches Elektronen-Synchrotron, Hamburg, a research center of the Helmholtz Association, Germany. S.V. acknowledges support by Italian National Civil Authority (ENAC) and University of L'Aquila through Giuliana Tamburro and Ferdinando Filauro scholarships, respectively.

In the near future, it is necessary to improve timing distribution down to sub-fs precision since current facilities, such as LCLS at Stanford, can already produce X-ray pulses shorter than 10 fs [6] and concepts for sub-fs X-ray pulse generation are already in place. Improving upon our previous work, we demonstrate here: 1) timing stabilization of a 1.2-km dispersion-compensated, polarization-maintaining (PM) fiber link with sub-fs residual timing drift over 16 days, 2) jitter measurements of two ultralow-noise, commercial femtosecond lasers for sub-100-as timing distribution, and 3) fiber-coupled, hybrid-integrated cross-correlators using periodically-poled $KTiOPO_4$ (PPKTP) waveguides for improved BOC timing sensitivities and overall system efficiency and robustness.

II. TIMING-STABILIZATION OF 1.2 KM PM FIBER LINK

Link stabilization is critical for preserving the timing precision of the pulsed optical timing signal as it propagates through the fiber link over long distances. Environmental disturbances to the fiber link (e.g. thermal fluctuations, acoustic noise, and vibrations) will induce errors in the pulse arrival times at the link output. To stabilize the link, we first measure the round-trip link timing error with high timing resolution using a BOC and then adjust correspondingly a variable delay within the link path to compensate for the detected error.

Our previous results with a 300-m stabilized fiber link using standard single-mode fiber showed that PMD limited the link stability to about 10 fs over few days of operation and caused delay jumps as much as 100 fs when the fiber was significantly perturbed [7]. To eliminate PMD-induced drifts, we collaborated with OFS in designing and fabricating a 1.2-km PM link with 3rd-order dispersion-compensation. The PM link consists of 1088 m of standard PM fiber matched to 190 m of custom dispersion-compensating PM fiber (PM-DCF). The PM-DCF has a PANDA-like geometry containing Boron stress rods with 35-μm diameters, a core index profile similar to conventional DCF, and a dispersion and dispersion slope of -104.1 ps/(nm·km) and -0.34 ps/(nm^2·km), respectively, at 1550 nm.

A. *Experimental Set-up*

The experimental set-up for timing stabilization of the 1.2-km PM link (Fig. 1) begins with a free-running Er-doped fiber laser (Menlo Systems) that outputs 160-fs pulses centered at 1560 nm with +20 dBm average power and 200 MHz repetition rate. The pulse width and repetition rate are selected to keep higher-order dispersion and fiber nonlinearity low. The set-up is divided into two sections: the in-loop, which is responsible for link stabilization, and the out-of-loop, which is for measuring the in-loop performance.

In the in-loop section, the pulses are first divided into a reference and signal path. The reference path serves as a timing reference for the in-loop BOC. The signal path consists of a voltage-controlled free-space delay, polarization optics, 1.2-km PM link, and output coupler. Since the forward and reflected pulses must propagate on the same polarization axis in the PM link, a 45° Faraday rotator is necessary to induce a 90° round-trip polarization rotation so that the reflected pulses will reach the in-loop BOC. The half-wave plate aligns the free-space polarization with the slow axis of the PM fiber. The coupled input power to the PM link was +11 dBm, which is near the onset of fiber nonlinearities. With a 90/10 output coupling ratio, the reflected power was sufficient for in-loop stabilization without the use of an optical amplifier. The timing error is detected with the in-loop BOC, which consists of a single 4-mm PPKTP crystal operated in a double-pass configuration with appropriate dichroic elements [8]. The BOC timing sensitivity was 21 mV/fs. The stabilization feedback loop consists of a PI controller (Menlo, PIC210), high voltage amplifier (Menlo, HVA150) and stacked combination of a 40-µm piezoelectric actuator (Thorlabs, PAS009) and 25-mm motorized delay stage (PI, M-112.12S) for short- and long-term stabilization, respectively. The feedback bandwidth was 20 Hz.

The out-of-loop BOC, which is used to evaluate the in-loop stabilization, monitors the timing error between the link output pulses and new pulses from the laser. The timing sensitivity of the out-of-loop BOC was 2.3 mV/fs. For long-term drift measurements, the out-of-loop voltage is sampled at 1 Hz with an A/D converter (National Instrument, cDAQ-9172). A low-pass RC filter with a 0.5-Hz bandwidth is used to improve signal-to-noise after detection. The time delay of the motor stage was also recorded simultaneously.

Temperature stabilization and vibration isolation are critical for sub-fs-level stability. Separate enclosures were built for the free-space optics and PM link. Each consisted of an external 2" layer of extruded polystyrene insulation foam and an internal Aluminum enclosure, which was temperature-controlled with a resistive heater pad and PID controller.

B. *Long-term Stabilization Results*

Sub-fs timing stabilization of the 1.2-km PM link was achieved for 16 days. Recorded data for the link drift and motor delay are shown in Fig. 2a. Although the data log for the motor delay faulted in day 13, the link stabilization remained unaffected. Overall, the motor delay corrected for over 65 ps of timing fluctuations while the timing drift remaining at the link output showed only a maximum deviation of 2.5 fs and a RMS value of 0.6 fs. This represents a suppression of timing fluctuations by a factor of more than 20,000 over 16 days, indicating that the PM fiber was effective in overcoming the previous 10-fs-level stability limit over few days of operation and eliminating large 100-fs delay jumps caused by PMD upon significant perturbation of the fiber.

Recorded data for relative changes in the internal temperatures of the PM link and free-space enclosures and ambient temperature are plotted in Fig. 2b. The strong correlation between the link drift, free-space enclosure temperature, and ambient temperature confirms that the link drift is limited by environmental fluctuations penetrating into the free-space BOCs or causing drifts in the free-running laser repetition rate. This is reasonable because the free-space

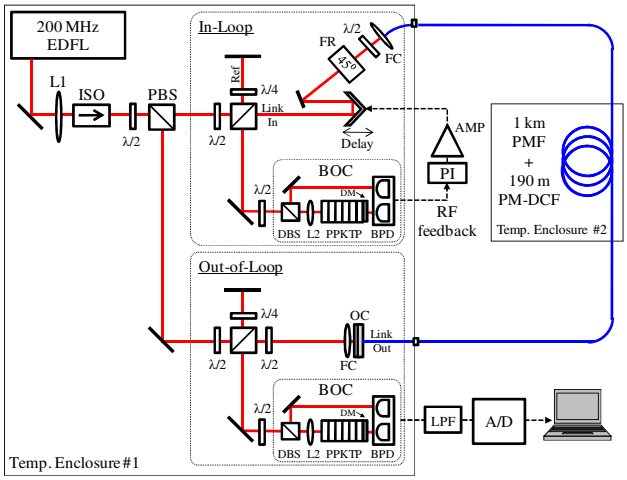

Figure 1. Schematic of the experimental set-up for the timing-stabilized 1.2-km PM fiber link; EDFL, Erbium-doped fiber laser; L1, collimator; ISO, isolator; λ/2, half-wave plate; λ/4, quarter-wave plate; PBS, polarizing beam-splitter; FR, 45° Faraday rotator; FC, fiber collimator; PMF, standard PM fiber; PM-DCF, dispersion-compensating PM fiber; OC, output coupler; BOC, balanced optical cross-correlator; DBS, dichroic beam-splitter; L2, focusing lens; PPKTP, periodically-poled KTiOPO4; DM, dichroic mirror; BPD, balanced photodetector; PI, proportional-integral controller; AMP, high voltage amplifier; LPF, low-pass filter; A/D, analog-to-digital converter

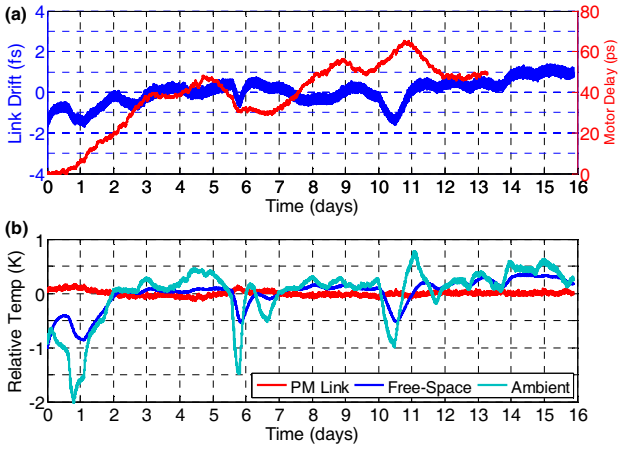

Figure 2. Long-term measurements for the timing-stabilized 1.2-km PM fiber link over 16 days; (a) link drift, as measured by the out-of-loop BOC, and time delay, as controlled by the in-loop motor stage; (b) relative changes in the internal temperatures for the PM link and free-space enclosures and ambient temperature.

enclosure is large in volume, making it difficult to isolate the enclosed optics from the environment. Resolving these issues should yield 100-as-level stability or even better; this is evident during days 11-14 when ambient fluctuations were fortuitously minimal, resulting in a RMS timing drift of only 0.13 fs.

III. ULTRA-LOW LASER TIMING JITTER MEASUREMENT

In addition to the timing link, we also demonstrate that ultralow-noise lasers for sub-fs timing systems are commercially available today. To measure their timing jitter, however, conventional methods via high-speed photodetectors and RF mixers cannot be used; excess phase noise during photodetection and limited resolution in the mixer prevent jitter characterization below 1 fs. An alternative approach is to use the BOC, which can precisely extract timing information with attosecond-level resolution by avoiding intensity-conversion noise during photodetection [8].

A. *Experimental Set-up*

The jitter measurement set-up using the BOC technique begins with two identical femtosecond lasers (Onefive, ORIGAMI), which produce 170 fs pulses centered at 1554 nm with 170 mW average power. The output pulses trains are aligned with orthogonal polarizations and combined in a polarization beam-splitter before being sent into a BOC. The relative timing jitter between the pulse trains is converted into a voltage signal with a BOC timing sensitivity of 1.3 mV/fs. The error signal is fed back to the piezoelectric tuning port of the local laser to lock its repetition rate to that of the master laser. A "loose" locked loop is implemented so that the high-frequency laser timing jitter can be observed beyond the locking bandwidth. The timing jitter spectral density is measured by directly feeding the output of BOC into a signal source analyzer (Agilent, E5052B). The measured spectrum is divided by two since we assume that the two lasers have identical and uncorrelated jitter.

B. *Results*

The timing jitter spectral density and its corresponding integrated timing jitter are given in Fig. 3. Within the locking bandwidth, the integrated jitter caused by acoustic noise below 200 Hz is suppressed to 100 as. Beyond the locking bandwidth, the integrated jitter from 1 kHz to 1 MHz is less than 70 as and from 10 kHz to 1 MHz is even less than 15 as. This extremely low timing jitter indicate that these lasers are well-suited and immediately available for sub-fs timing distribution systems spanning over kilometer distances.

IV. INTEGRATED BALANCED OPTICAL CROSS-CORRELATOR

To further improve the precision of our timing distribution system, fiber-coupled integrated BOCs are an absolute necessity. One major benefit is that an all-fiber implementation of the timing system will eliminate fs-level drifts caused by free-space beam misalignments. Second, the second-harmonic generation (SHG) conversion efficiency of the integrated BOC will be a significant improvement over that of a bulk-crystal BOC by 1-2 orders of magnitude [9]. In collaboration with AdvR, the fabrication of PPKTP waveguides was optimized by

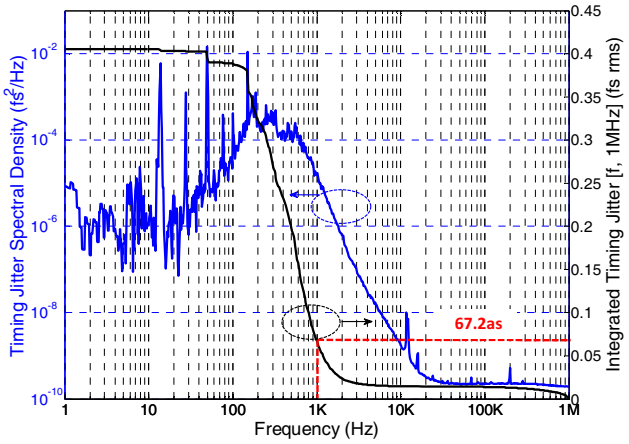

Figure 3. Measured timing jitter spectral density for an individual laser and its integrated timing jitter for the frequency range [f, 1 MHz].

decreasing the mode size and improving the poling quality, and by packaging fiber-coupled, hybrid-integrated BOCs using these waveguides.

A. *SHG Conversion Efficiency in Waveguides*

The waveguides were fabricated by Rb+ ion exchange on a KTP substrate and were diced and polished to a final length of 1 cm. An anti-reflective coating at 1550±50 nm and 775±25 nm was deposited on the front facet of the crystal, and a dichroic coating that is highly-reflective at 1550±50 nm and anti-reflective at 775±25 nm was deposited on the rear facet. Therefore, after forward propagation through the crystal, pulses at the fundamental (FH) wavelength of 1560 nm will be reflected back into the waveguide, generating another second-harmonic (SH) pulse on the return path for balanced operation of the cross-correlator. A peak normalized SH conversion efficiency of 1.76 %/[W-cm^2] was extracted at 1560 nm. The integrated BOC is expected to have a factor of 50 increase in timing sensitivity compared to the bulk-optics BOC, given the same input pulse parameters. This means that the optical power can be decreased by a factor of 50 while achieving the same signal-to-noise ratio as that of bulk-optic BOCs.

B. *Fiber-Coupled Device Operation*

We mounted the coated PPKTP waveguides in a robust fiber-coupled package. The PM fiber at the module input couples FH pulses into the waveguide and couples the reverse-generated SH out. The multi-mode fiber at the other end collects the forward-generated SH. The PPKTP module was tested in a fiber-coupled, cross-correlator configuration. Due to excess coupling loss between the PM fiber and the waveguide for the reverse-generated SH, the SH power collected on the forward path was approximately 10 dB higher than that of the reverse path. Therefore, a 10-dB attenuator was inserted to symmetrize the cross-correlation curve. Preliminary operation of the device yields a timing sensitivity of 4 mV/fs (Fig. 4). A thorough characterization of the device performance as well as packaging optimization is currently in process.

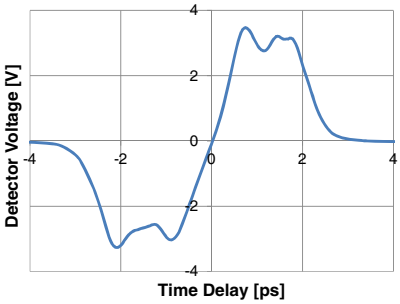

Figure 4. BOC voltage response as a function of relative pulse time delay

V. Summary of Results

In summary, we have presented key technologies towards an all-optical, fiber-based timing distribution system capable of sub-femtosecond precision. Timing distribution over a timing-stabilized 1.2-km PM link using BOCs was demonstrated for 16 days with 0.6 fs RMS timing drift and during a 3-day interval only 0.13 fs drift. Jitter characterization of two identical commercial femtosecond lasers using the BOC method verified sub-100-as timing jitter for frequencies greater than 1 kHz. Lastly, preliminary operation of a fiber-coupled, hybrid-integrated BOC using PPKTP waveguides indicate great potential for improved timing sensitivity and overall system efficiency and robustness.

References

[1] J. Arthur et al., *Linac Coherent Light Source (LCLS) Conceptual Design Report SLAC-R593*. Stanford, 2002.

[2] M. Altarelli et al., *XFEL: The European X-Ray Free-Electron Laser. Technical design report*. DESY, 2006.

[3] C. J. Bocchetta and G. De Ninno, *FERMI@ Elettra: conceptual design report*. Sincrotrone Trieste, 2007

[4] J. M. Byrd et al., "Femtosecond synchronization of laser systems for the LCLS," *Proc. Int. Particle Accelerator Conf.*, Japan, 2010, pp. 58–60.

[5] J. Kim, J. A. Cox, J. Chen, and F. X. Kärtner, "Drift-free femtosecond timing synchronization of remote optical and microwave sources," *Nat. Photonics*, vol. 2, no. 12, pp. 733–736, Dec. 2008.

[6] Y. Ding et al., "Femtosecond X-Ray Pulse Characterization in Free-Electron Lasers Using a Cross-Correlation Technique," *Phys. Rev. Lett.*, vol. 109, no. 25, p. 254802, Dec. 2012.

[7] J. A. Cox, J. Kim, J. Chen, and F. X. Kärtner, "Long-term stable timing distribution of an ultrafast optical pulse train over multiple fiber links with polarization maintaining output," *Conf. Lasers Electro-Optics,* 2009, pp. 1 –2.

[8] J. Kim, J. Chen, J. Cox, and F. X. Kärtner, "Attosecond-resolution timing jitter characterization of free-running mode-locked lasers," *Opt. Lett.*, vol. 32, no. 24, pp. 3519–3521, Dec. 2007.

[9] A. H. Nejadmalayeri, F. N. C. Wong, T. D. Roberts, P. Battle, and F. X. Kärtner, "Guided wave optics in periodically poled KTP: quadratic nonlinearity and prospects for attosecond jitter characterization," *Opt. Lett.*, vol. 34, no. 16, pp. 2522–2524, 2009.

Local Ties Control in Application of Laser Time Transfer

Jan Kodet[1,3], Ulrich Schreiber[1]
[1]Technische Universität München, Wettzell Observatory, 93444 Bad Koetzting, Germany
kodet@fs.wettzell.de

Johann Eckl[2]
[2]Bundesamt für Kartographie und Geodäsie, Wettzell Observatory, 93444 Bad Koetzting, Germany

Ivan Prochazka[3]
[3]Czech Technical University in Prague, Prague, Czech Republic

Petr Panek[4]
[4]Institute of Photonics and Electronics Academy of Sciences of the Czech Republic, Prague, Czech Republic

***Abstract*— In many fundamental physical experiments time plays an important role. The standard way for the comparison of time and frequency is the application of GNSS signals and the Two-Way Satellite Time and Frequency Transfer - TWSTFT. This technique is based on radiofrequency signal transmission. Recently, there was a rapid increase of optical time comparison development, which uses the Satellite Laser Ranging network (SLR). Currently the French project T2L2 is in operation on board of Jason 2 and the European Space Agency project ELT in support of the Atomic Clock Ensemble in Space (ACES) is under development. The goal of both projects is the time synchronization with a precision below 40 ps rms and an absolute error well below 100 ps. Comparing the results of the optical time transfer with the GNSS time comparison requires unprecedented control of the local ties between the different observation techniques. One of the possible methods is the application of the Two Way Time Transfer (TWTT) on a single coaxial cable. Such a system can be implemented using two or more event timers, which are interconnected by a standard coaxial cable. The event timers are exchanging pulses between each other and time tagging them. Out of the measured result one can evaluate the difference of time scale represented by the event timers. It was shown that such a technique can be used for time transfer with a precision of a few picoseconds of rms and an absolute error below 20 ps for distances reaching several hundreds of meters.**

We have implemented this technique for establishing and monitoring the absolute time delays between the SLR system and the time keeping laboratory on the Geodetic Observatory Wettzell. The event timers were developed at the Czech Technical University. The measurement principal is based on SAW filter excitation. The Event Timers were located in different buildings 50 meters apart and with the help of the TWTT technique, the delay between them was measured. The second input sockets of the event timers were used to monitor the respective local timescale.

Keywords—two way time transfer; event timing; time comparison;

I. INTRODUCTION

The precise and accurate time transfer is a prerequisite of a number of experiments in fundamental physics, Earth science, global navigation and many other disciplines. One of the most challenging disciplines is the time transfer ground to space. The standard techniques used recently are based on radio frequencies. They do provide nanosecond accuracies [1]. A significant improvement in time transfer accuracy between ground and space is expected to be achieved by using optical frequencies [2]. The contributors of systematic error to the overall error budget in the optical domain may be reduced to the level of 10 picoseconds.

The laser time transfer (LTT) ground to satellite is an extension of the standard measurement technique of the satellite laser ranging (SLR). A ground SLR station fires laser pulses toward the satellite and records the local times of the laser firings. On board of a satellite the laser pulses are detected and time tagged to the satellite time scale. At the same time the laser pulses are reflected by a system of a retro-reflectors back toward the ground station, which, again, detects the return pulses and time tags them to the ground time scale. The recorded data on board of the satellite is then sent to the ground using a standard telemetry channel.

Combining the laser firing times, propagation and instrumental delays and satellite arrival times, the space and the station clocks may be compared. The error in propagation time ground to space is completely compensated in a laser time transfer when combined with satellite laser ranging data at the same time. The importance of such a method is reflected in a rapid development of the time transfer projects T2L2 (France), ELT (ESA) or LTT (China).

Doing the time transfer using SLR technique requires deep understanding of the individual timing systems of each site. First of all it is important determine from which reference point the optical time transfer is performed. In case of optical time transfer actually the time transfer is realized between the satellite time scale and the time scale which is realized inside the event timer. It requires a very good synchronization of the event timing system relative to the local time scales, which we want to compare.

The simplified diagram of the Wettzell Observatory timing system is shown in Fig. 1. It consists of four buildings separated by several tens of meaters in distance. We are

operating several Cesium atomic standards, where HP1732 is considered as the master clock establishing UTC(IFAG). In addition we are operating several H-Masers which are used for Very Long Baseline Interferometry (VLBI) measurements as well as SLR observations. In each observation point the local time scale is generated out of distributed frequency sources. From a distribution of the generated 1pps signals, 1pps is sent back to the Master Clock (MC) room where the localy generated time scales are compared to the Master Clock time scale (UTC(IFAG)) every 3 hours. For measuring these time delays between the time scales the time interval counter SR620 is used measuring the delays with a resolution of 1 ns.

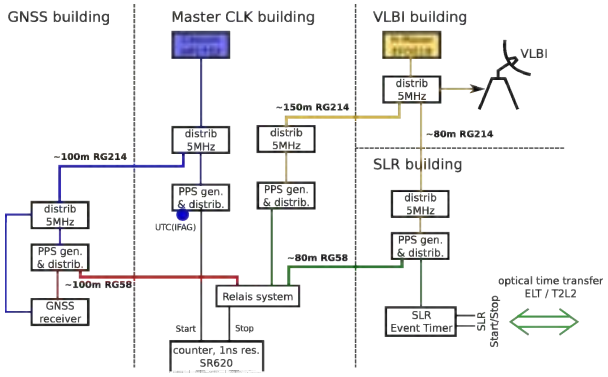

Fig. 1. The simplified block diagram of the timing sytem in Wettzell Observatory. There are several atomic clocks distributing frequency between different building, where the geodetic observation techniques are located. The time scales are generated in each building separately.

For the optical time transfer between ground and space measuring biases between local time scales with an accuracy of 1 ns can be one of the limiting factors of the entire experiment. The problem arises when all timing signals are distributed approximately 90 cm underground using cables RG214 (frequency) and RG58 (1pps) and that the annual temperature variations under ground in the same depth reaches 12 ºC. Considering the temperate dependency of the cables [3] one can conclude, that the timing delays between the local scales must be changing in an uncontrolled fashion over the year by as much as 1 ns. Such changing biases are not captured by the current measurement system.

For monitoring these biases we applied the recently introduced TWTT method, which is based on two or more interconnected event timing systems linked with a single cable [4]. This method allows a time scale comparison with picosecond precision and accuracy. We are now systematically investigating the local biases by applying this technique.

II. The Timing Device

For comparing the time scales we are using Event Timing (ET) devices which were developed at the Czech Technical University [5]-[7]. The ET allows the detection of Times of Arrival (ToA) of input pulses with respect to a local time base. The single shot precision is 700 fs RMS per channel.

Operating the device in a common laboratory environment without temperature stabilization a TDEV better than 4 fs is routinely achieved for averaging times between 300 s to 3000 s [7]. For checking the measurement performance and for experiments such as two way time transfer, a reference time mark generator has been included into the timing device. It generates low jitter pulses synchronously to the local time base. The repetition frequency of these pulses and number of generated pulses are programmable.

III. Two Way Time Transfer Principal

The technique of the Two Way Time Transfer (TWTT) via single coaxial cable was inspired by the comparison of the two event timers using pulses and a signal splitter. The pulse from a signal source is split into two equal pulses and connected to the ET A using cable C_1 and to ET B using cable C_2; The times of arrival (ToA) at both devices are measured and the time difference is computed ($Diff_1$). Then the cables are exchanged (ET A -> C_2 and ET B -> C_1) and time difference ($Diff_2$) is computed again. The time scales difference between both event timers then becomes

$$\hat{\Delta}_c = \frac{1}{2}\left(Diff_1 + Diff_2\right) \quad .$$

The advantage of exchanging the cables is that the time scale differences do not depend on the length of the cables C_1 and C_2.

Inspired by the described method we have implemented the TWTT technique according to the schema displayed in Fig. 2

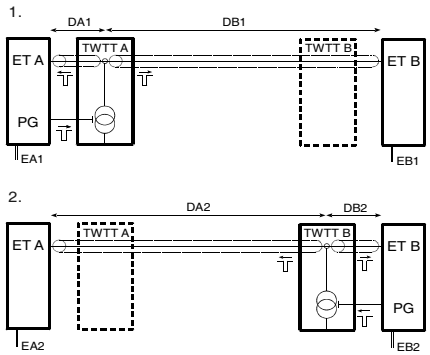

Fig. 2. Block scheme of the Two Way Time Transfer via a single coaxial cable: 1st step when the TWTT module A is generating the test pulse, 2nd step when the TWTT module B is generating the test pulse.

The operating scheme is the following: two Event Timers ET A and ET B are equipped with TWTT modules. These modules are interconnected by a single coaxial cable. The measurement is carried out in two steps. In the first step the ET A generates a pulse, using a current driver the pulse is applied to the interconnecting cable and the ToA of the received pulse is measured by both event timers (ToA_{A1} and ToA_{B1}). In the second step the role of the devices is exchanged. The ET B generates a similar pulse that propagates along the cable in opposite direction. After time tagging at both devices this yields ToA_{A2} and ToA_{B2}. The timescales difference can be then computed according as

$$\hat{\Delta} = \frac{1}{2}\left((ToA_{B1} - ToA_{A1}) + (ToA_{B2} - ToA_{A2})\right).$$

The precision of the resulting time scale difference will depend on the precision of both event timers, the reproducibility of the pulses generated by TWTT modules and on the influence of noise induced on the interconnecting cable. Experimentally it was possible to establish time scale comparisons with a precision and an accuracy of the order of 1 ps [4].

IV. EXPERIMENTS

At the Geodetic Observatory Wettzell we carried out several TWTT experiments with two ET systems. That is why only two scales could be compared at the same time. First of all it is important to note that the operation principle is comparing the time scales held inside the event timers. When a locally generated time scales realized by 1pps signals need to be compared, they must be time-tagged at second input of each of the event timing systems. To reducing systematic errors we have used the following steps to calibrate such a system up to reference point, UTC(IFAG) in our case:

1. We set the trigger levels of the ET devices to be the same in both ETs (IN1(TWTT input)/-0.180 V and IN2/0.7 V). In the same laboratory we used a common clock (frequency reference) for both devices and we measured the difference between the ETs using TWTT (ΔT_{TWTT}). Then we switched the inputs of the ETs from TWTT input to IN2, were we have connected the power spitted 1pps pulses. Exchanging the cables of the 1pps signals we have measured the difference of the event timers in the second input (ΔT_{1pps}). The difference between the ET using IN2 and TWTT input was $\Delta ET = -12.6\ ps$, measured with accuracy 2.6 ps rms.
2. As a second step we have installed the ETs in laboratories whose time scales were to be compared, the simplified scheme is in Fig. 3. The absolute calibration is divided into three steps.
   a. At first the ETs were connected to the reference points for time, namely UTC(IFAG) and $SLR_{ref.}$ with cables of the delays τ_{C1} and τ_{C2}. In this arrangement the time scale difference $SLR_{ref.}$ – UTC(IFAG) was evaluated.
   b. The cables were exchanged and the time scale difference $SLR_{ref.}$ – UTC(IFAG) was evaluated again. Out of those two measurement one can obtain the cable length difference $\Delta\tau_C = \tau_{C2} - \tau_{C1}$.
   c. The cables were connected to another output in the pulse distribution system of the 1pps and the time differences to the reference points were evaluated, ε_{UTC} and ε_{SLR}.

   The measured calibrations are summarized in TABLE I. The Time scale difference from the reference point UTC(IFAG) to $SLR_{ref.}$ can be computed according to

$$SLR_{ref.} - UTC(IFAG) = ppsDiff - \Delta\tau_C - \varepsilon_{SLR} - \varepsilon_{UTC} - \Delta ET,$$

where SLRref. – UTC(IFAG) is the time scale difference from the reference points, ppsDiff is the difference of 1pps pulses in SLR and MC.

TABLE I. SUMMARY OF TWTT CALIBRATION.

Constant name	Mean value	rms
ΔET	-12 ps	2.6 ps
$\Delta\tau_C$	10.085 ns	104 ps
ε_{UTC}	-17 ps	93 ps
ε_{SLR}	0	0

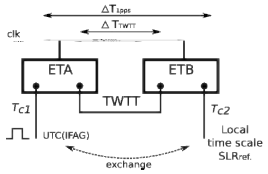

Fig. 3. Calibration of the TWTT method used in experiment, which is comparing two time scales.

The TWTT was implemented after considering several facts and additional measurements. First of all the repetition rate of sending pulses was chosen with respect of the communication speed as 500 Hz. The entire measurement loop was programmed in such a way that between two following 1pps pulses one TWTT measurement was done. To improve the precision of the TWTT measurement 32 pulses were exchanged between each ET. The single shot precision of the TWTT method using a 100 m long interconnecting cable of RG214 quality is 1.4 ps. With averaging a precision of the TWTT method of $1.4\,ps/\sqrt{32} = 0.25\ ps$ was obtained. The most important quantity is the systematic error, which is introduced by such a measurement. It can be measured connecting both devices to the same clock source. With short RF cables one can measure the time difference between the ETs using the TWTT method. In the here reported case the systematic error is negligible [4]. After that the devices were interconnecting using the long RF cable, which was used for the TWTT procedure between the buildings and the ETs offset was measured again. The difference between the measurements with short and long cable is giving the systematic error. Using the 100 m of RG214 (in our case we used this cable for interconnecting the master clock (MC) and the GNSS room) the systematic error was measured to be 7.4 ps. The MC and SLR buildings were interconnected with higher quality cable (LDF4) of a length 93 m. Measuring the systematic error caused by the TWTT signal degradation on this cable is 1.8 ps.

Up to now we have compared two time scales with UTC(IFAG). The first experiment performed was between

MC and GNSS laboratory, where the GPS receiver WTZA (Ashtech Z12T) is located. The experiment lasted several days and is shown in Fig. 4. The sudden rise of the time scales difference during 4th day was caused by an air conditioning failure. The absolute delay was compared to the absolute timing delay from the reference point of the GPS WTZA receiver up to UTC(IFAG) reference point. The delay was measured 3.4 ns higher than the old records. This discrepancy shows the need of better monitoring of the time scales, because there is not yet any plausible explanation for such a difference.

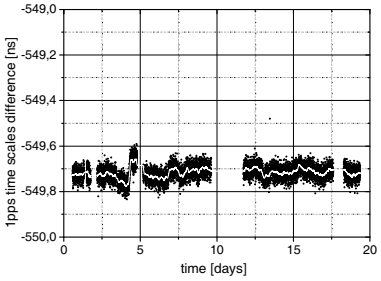

Fig. 4. Time scale comparison between Master Clock room where UTC(IFAG) is located and the GNSS laboratory where the GPS receiver WTZA (Ashtech Z12T) is located.

To show the timing stability, the time deviation of the time difference was computed, see Fig. 5. The single shot jitter of time scale difference was 22 ps rms and the TDEV falls down to 3 ps for averaging intervals $\tau > 200$ s.

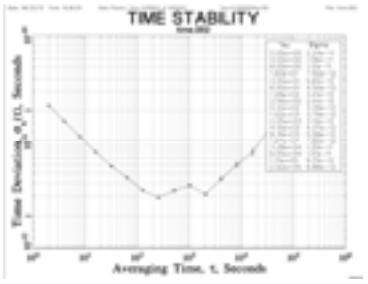

Fig. 5. Timing stability TDEV of compard UTC(IFAG) and GNSS laboratory time scales.

As a second step the entire experiment was moved to perform time comparison between UTC(IFAG) and the SLR time scale, which is important for optical time transfer. For this purpose we have developed a program, which can be used for full implementation of the measured results of time comparison into the entire ranging chain, where the epochs from the SLR measurement can be corrected. Fig. 6 shows the time difference between UTC(IFAG) and the SLR time scale. There is a significant drift of 2.5 ns/day, which is caused by the drift of the main cesium clocks HP1732 versus the H-Maser EFOS18.

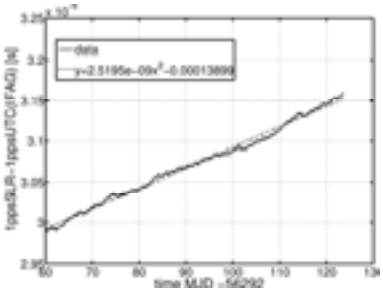

Fig. 6. Time scale comparison between Master Clock room where UTC(IFAG) is located and the SLR techniqu.

V. CONCLUSION

We have implemented the Two Way Time Transfer method in the Geodetic Observatory Wettzell for comparing the locally generated system time scales with our timing reference point UTC(IFAG). Up to now we have made two comparisons between UTC(IFAG) and GNSS laboratory and SLR as well as the absolute calibration of the suggested measuring technique. We have shown that the systematic error of the TWTT method can be kept very low. For high quality RF cables as LDF4 the systematic error can be kept as low as 1.8 ps, which is almost negligible in comparison with the single shot precision of the 1pps generation. The comparison of the time scales between UTC(IFAG) and the GNSS laboratory the time scale shows that both scales are uncorrelated for averaging times up to 200 s and the TDEV levels out at 3 ps for $\tau > 200$ s. Even though both scales are generated from the same source of frequency (Cs, HP1732) the observed drifts were caused by air-conditioning failure in GNSS laboratory.The comparison of the time scales between UTC(IFAG) and SLR shows the difference of two different sources of clocks, which generate the scales. While SLR runs from the H-Maser EFOS18, UTC(IFAG) is generated from cesium standard HP1732. A linear drift between the Cs HP1732 and H-Maser EFOS18 of 2.5 ns/day was obtained.

ACKNOWLEDGMENT

This work has been carried out by support of the Technische Universitaet Muenchen, the Bundesamt für Kartographie und Geodasie and the Czech Technical University in Prague. We acknowledge funding through the Forschergruppe DFG FOR1503.

REFERENCES

[1] P. Defraigne, M. C. Martínez-Belda, and Zhiheng Jiang, "Time transfer from combined analysis of GPS and TWSTFT data," in Proc. 40th Annual Precise Time and Time Interval, Reston, VA, USA, Dec.1-4 2008, pp. 565–576.

[2] M. R. Pearlman, J. J. Degnan, and J. M. Bosworth, "The International Laser Ranging Service," Advances in Space Research, vol. 30 (2), 2002, pp. 135–143.

[3] Catalog of Heliax Coaxial Cables, Andrew Ltd

[4] P. Panek et al, "Accuracy of two-way time transfer via a single coaxial cable", 2013 Metrologia 50 60 doi:10.1088/0026-1394/50/1/60

[5] Pánek P.; "Time Interval Measurement Based on SAW Filter Excitation". IEEE Trans. Instr. Meas, vol. 57, no. 11, pp. 2582-2588, Nov 2008

[6] Procházka, I. - Pánek, P.; “Nonlinear effects in the time measurement device based on surface acoustic wave filter excitation”. Review of Scientific Instruments. 2009, vol. 80, no. 7, p. 076102

[7] Pánek, P. - Procházka, I. - Kodet, J.; “Time measurement device with four femtosecond stability”. Metrologia. 2010, vol. 47, no. 5, p. L13-L1

Single Photons Optical Two-Way Time Transfer Providing Picosecond Accuracy

Ivan Prochazka, Josef Blazej
Dept. of Physical Electronics
Czech Technical Univ. in Prague
115 19 Prague, Czech Republic
prochazk@fjfi.cvut.cz

Jan Kodet
Dept. of Physical Electronics
Czech Technical Univ. in Prague
115 19 Prague, Czech Republic
FESG Fundamentalstation Wettzell
Technische Universitaet Muenchen
93444 Bad Koetzting, Germany

Petr Panek
Inst. of Photonics and Electronics
Academy of Sciences of Czech Rep.
182 51 Prague, Czech Republic

***Abstract*—We are reporting on a new approach to an optical two-way time transfer based on signals of individual photons. This approach enables to reach extreme timing stabilities and minimal systematic errors using existing electro-optic technologies. In our indoor experiment we have achieved sub-picosecond precison and 3 ps accuracy of a two-way time transfer via free space optical channel. The entire system is compact and simple. It is a perspective technique for space application, where it might provide picosecond accuracies over space distances.**

Keywords—photon counting; two-way time transfer; accuracy; picosecond stability

I. Introduction

The two-way time transfer is an effective way to synchronize two independent time scales with high precision and accuracy independently on the variations of the interconnecting channel [1]. In our previous work we have demonstrated electronic circuits for two-way time transfer via a single coaxial cable with picosecond accuracy and precision [2]. The experiment proved the capability of this technique to maintain picosecond stability over the periods of seconds to days. The systematic errors of the order of units of picoseconds have been achieved [3].

This technique may be effectively applied in configurations, where the sites may be interconnected by a broad bandwidth coaxial cable. Considering the performance of the top quality coaxial cables available, the picosecond performance may be accomplished over distances up to 2 km maximum. For longer distances the optical approach may be considered.

Propagation of optical signal in a free space is suffering of negligible degradation (in atmosphere) or no degradation at all in a vacuum. Photon counting approach to the signal detection is providing several additional key advantages: the reduction of most systematic errors found in commonly used multi-photon detection systems and the capability to operate with ultimately low signals. The repetitive optical signals of an average intensity as low as 1×10^{-4} photon per pulse may be detected and time tagged with sub-picosecond precision and stability.

We have designed and tested the optical analogy of the two-way time transfer using a common optical channel. The photon counting approach has been applied. The pilot experiment has been completed in our lab.

II. Principle of Operation

Optical two way time transfer (OTWTT) is a powerful technique to compare two time scales with sub-picosecond precision and a few picosecond accuracy over long distances. The principle is plotted in Fig. 1.

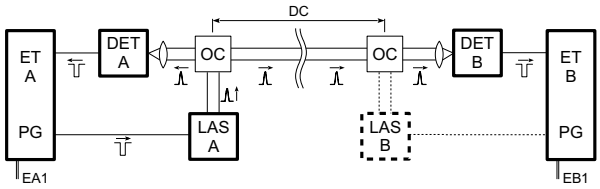

Fig. 1. Experimental scheme of optical two-way time transfer.

The operating scheme is the following: two event timers *ET A* and *ET B* are equipped with identical OTWTT modules. The event timers represent the time scales *A* and *B*. Each OTWTT module consists of an optical signal combiner *OC*, laser diode optical source *LAS* and an optical detector *DET*. These modules are interconnected by an optical channel: free space or an optical fiber. The measurement is carried out in two phases. First the part *A* is activated, as illustrated in Fig. 1. The source of optical pulse – diode laser *LAS A* is generating a ultrashort optical pulse triggered by a pulse generator *PG*. It is split by a signal combiner *OC A* and is propagating in both directions toward parts *A* and *B*. They are detected by the optical detectors and time tagged in the respective time scales *A* and *B*. The corresponding epochs *EA1* and *EB1* are recorded and stored. In the second phase the module *B* is activated, the diode laser *LAS B* is generating ultrashort uniform pulse, which is split and propagating toward both parts *A* and *B*. There they are detected and time tagged in the respective time scales. The corresponding epochs *EA2* and *EB2* are recorded and stored. Using equations

$$DS = ((EB1 - EA1) + (EB2 - EA2)) / 2 \qquad (1)$$

$$DC = ((EB1 - EA1) - (EB2 - EA2)) / 2 \qquad (2)$$

two pairs of epochs $EA\times$ and $EB\times$ can be combined producing the difference *DS* between the two time scales (1) along with the delay of the optical channel *DC* interconnecting the two

OTWTT modules (2). Reference points are defined symmetrically inside each optical signal combiner.

III. Why Single Photon Detection?

The application of single photon detection – photon counting – has a number of key advantages in comparison to a conventional optical detection of "strong" (i.e. multi-photon) optical pulses in this type of measurement:

- The detection process is inherently digital, the detector has only two output stages: photon not detected and photon detected. There is no analog signal processing (amplification, discrimination, etc.) involved. This simplifies the detector itself and reduces the problems of device stability, linearity, drifts, aging etc.
- The photon counting approach to the optical detection is based on an ultimately fast sampling of optical signal, where the sampling itself is provided by a quantum nature of light. This fact is canceling the dependence of detection delay on signal amplitude and maintains a wide dynamical range.
- Photon counting process is capable to detect ultimately low energy optical signals. In a real experiments the optical pulses of an average energy of 1×10^{-4} photons per pulse may be detected.
- Extreme detection sensitivity, high dynamical range and high timing resolution in detection of pulsed signals enable to complete the measurements under very high background photon flux and dark count rate conditions.
- Various signals – photons – from various sources and signal paths may be detected in one setup. The detected signals are identified in data analysis process.

Photon counting approach to detection of optical signals has indeed drawbacks:

The experimental result can not be obtained on the basis of a single measurement. The result may be obtained by a statistical processing of a set of a large number of individual measurements only. That is why the effects suffering of time variations much slower than a useful signal data rate may be measured. Considering the useful data rate of photon counting signals of the order of 100 readings per second, the measured effect time variations of the order of seconds and slower may be registered. Considering a nature of the time transfer experiment, this effect represents no limitation.

IV. Experiment Setup

We have designed and tested the optical two way time transfer in laboratory conditions. The experimental scheme was identical to Fig. 1.

The optical test pulses were generated by a PicoQuant diode laser type LDH-P-FA 530B which is delivering 80 ps long pulses at the wavelength of 531 nm. The epoch timing was accomplished using an in house built epoch timing systems NPET [4], which are providing sub-picosecond resolution and femtosecond timing stability [5]. A common source of frequency and time reference has been used for both epoch timing systems *A* and *B*.

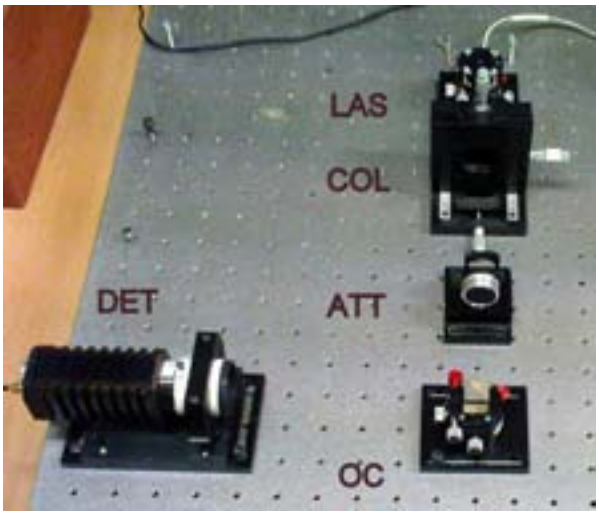

Fig. 2. The realization of experimental setup of part *A*. Optical signal is generated by laser *LAS*, collimated by a collimator *COL*, attenuated by attenuator *ATT*, split by optical signal combiner *OC* to detector *DET* and to the part *B* of experiment setup on a right side, not displayed on photo.

The optical signals were detected by photon counting detectors developed in our labs [6]. These are solid state photon counters based on silicon. They do provide more than 30 % photon detection probability, timing resolution of a single measurement better than 20 ps. Their long term and temperature stability is excellent. The temperature drift is typically 260 fs/K, the timing stability in a sense of time deviation TDEV is better than 150 fs for averaging time of seconds to days [6].

The two-way time transfer optical link was a free space path on an optical bench. The signal combiner has been realized using a modified cube beam splitter and additional neutral density attenuators. The photograph of the experimental setup of part *A* is in Fig. 2. Laser source and its collimating optics is on a top right, in a right center is a set of attenuators, bottom right is the cube beam splitter. The photon counting detector package is on the left. Please note no signal path optical shielding. The photon counting experiment has been performed in full daylight conditions.

The measurements were carried out at the repetition rate of 500 measurements per second. The optical signals intensity on the detectors inputs has been adjusted to get a useful data rate of 5 to 15 %. This optical signal intensity guarantees photon counting regime of operation. The useful data flow was typically 20 to 75 valid readings per second. The average values were evaluated for groups of 70 data points, every 1.5 second. The total background photon flux and dark count rate were rather high of the order of 0.5 Mega counts per second. Nevertheless the photons of interest have been detected, time tagged and identified.

V. Experiment Results

The example of the data acquired in one measurement series lasting 5000 seconds is plotted in Fig. 3. The histogram of mean epochs recorded on detector *A* is plotted. The resulting single shot resolution of the system is 50 ps r.m.s.

The time scales difference *DS* evaluated on the basis of these data sets is plotted in Fig. 4. The two time scales *A* and *B* were represented by a common frequency and time reference. Hence the Fig. 4 illustrates the stability of the measurement setup. The identical data set has been used to evaluate the time deviation TDEV [7]. One can conclude from Fig. 5 that at the measurement repetition rate of 500 measurements per second the time scales difference of 1 ps may be achieved within 100 – 200 seconds. Obviously higher measurement repetition rates (up to 5 kHz) will result in a same precision and accuracy in shorter time.

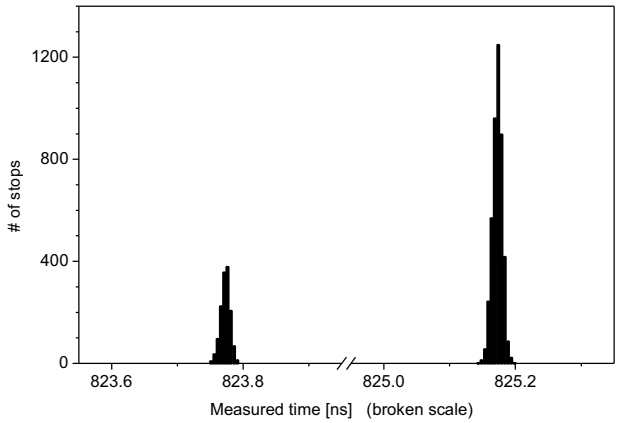

Fig. 3. Example of measured data, the histogram of mean epochs recorded on detector *DET A*.

The two-way time transfer optical path delay *DC* was evaluated to be 540 ps. This value is in an excellent agreement with the geometry of the experiment. The equivalent optical distance of reference points of modules *A* and *B* was determined as 160 ± 1 mm.

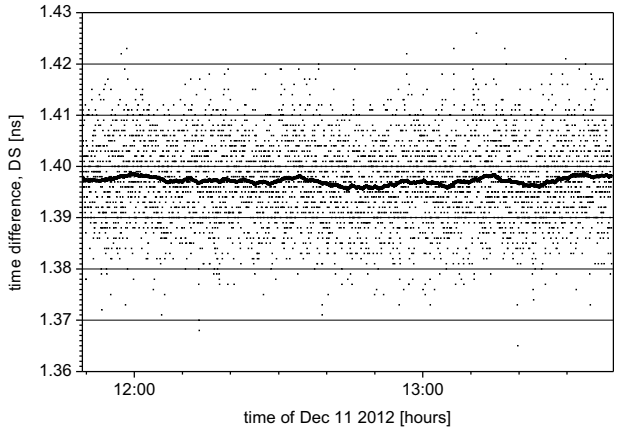

Fig. 4. The time scales difference *DS* evaluated on the basis of data sets plotted in Fig. 3 (points). And its moving average (solid line) evaluated with time window 15 min.

The measurement series were repeated over three days. The series to series data consistency was within statistical errors.

VI. Time Transfer Precision and Accuracy

The precision of the time scales difference will obviously depend on the precision of both event timing systems and on the stability of the photon counting detectors. All of those provide sub-picosecond precision. The time deviation TDEV value obtained from experimental data demonstrates this fact.

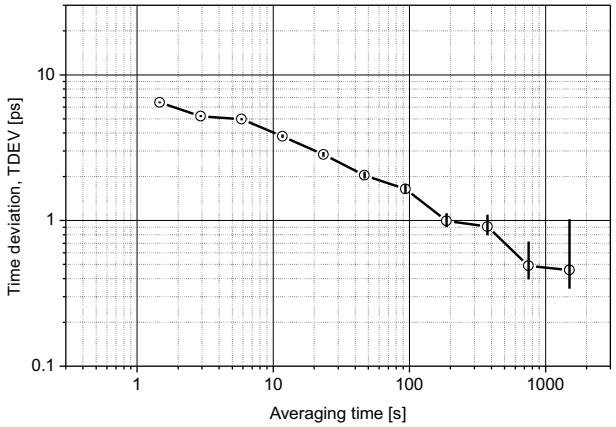

Fig. 5. The time scales difference DS in a sense of time deviation TDEV, the time scales *A* and *B* were represented by a common frequency and time reference, hence it illustrates the stability of the measurement setup

The key question is the accuracy of the time scales difference *DS*. Considering the analogy to the two-way time transfer via single coaxial cable and the detailed error analysis [3] one can conclude that the accuracy is limited by the non-symmetry of the setup, propagation of the test pulses in two directions and non-equality of response of the detectors and event timing devices to the test signals. Applying photon counting approach these non-symmetries may be kept at 1 ps level.

In optical two-way time transfer over a free space the resulting accuracy may be estimated by comparison of evaluated propagation delay *DC* with the real optical path length. According to error analysis [3] the accuracy of time scales difference *DS* is higher in comparison to optical path delay *DC*. Thus the accuracy of *DC* represents the worst case estimate of accuracy of time scales difference *DS*. The measured optical path difference *DC* was equal to the physical length of the optical path with better than 3 ps accuracy. This fact indicates the accuracy of determining *DC* at the level of 3 ps. That is why the accuracy of optical two way time transfer better than 3 ps has been achieved.

VII. Perspective Applications

One of the most promising application of this time transfer technique is an inter-satellite link. The technique described together with the existing technology is capable to provide sub-picosecond precision and a few picosecond accuracy for time scales synchronization over distances in space. Thanks to a photon counting approach miniature laser sources and transmitting and receiving optics may be used. The microchip lasers delivering pulses of micro Joule energies and collecting optics of 20 mm in diameter may accomplish optical two-way time transfer over distances up to 100 thousands kilometers. The photon counting detectors have been qualified for operation in long lasting space missions [6].

The capabilities of the technology available for space applications has been demonstrated in a satellite laser ranging experiment. The measurements have been performed at the

satellite laser ranging station in Graz, Austria [8]. The measurement repetition rate was 2 kHz. The precision of one way propagation delay ground to space to the GPS satellite in a sense of time deviation TDEV is plotted in Fig. 6.

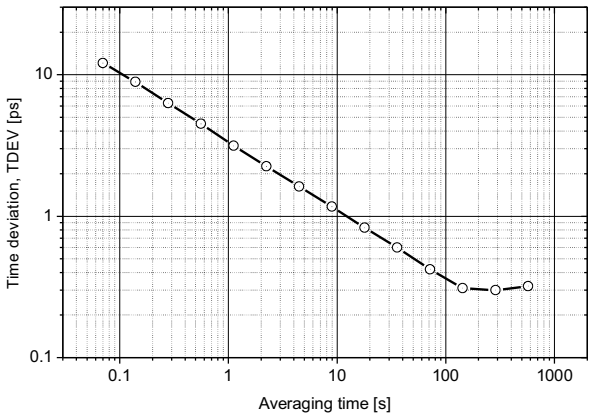

Fig. 6. One way propagation delay ground to space to the GPS satellite in a sense of time deviation, evaluated from outdoor experimental data, photon counting detection, station Graz, Austria, 2 kHz laser repetition rate. Note the values of 200 fs for averaging times of hundreds of seconds.

From Fig. 6 one may conclude that existing electro-optical technologies based on photon counting approach might support laser time transfer in space with sub-picosecond precision.

VIII. Conclusion

We have demonstrated a new approach to an optical two-way time transfer which is based on signals of individual photons. This approach enables to reach extreme timing stabilities and minimal systematic errors using existing electro-optic technologies. In our indoor experiment we have achieved sub-picosecond precision and an accuracy better than 3 ps of a two-way time transfer via free space optical channel. This technique is a perspective for space application, where it might provide picosecond accuracies over long distances. The microchip lasers delivering pulses of micro Joule energies and collecting optics of 20 mm in diameter may accomplish optical two-way time transfer over distances up to 100 thousands kilometers. The entire system is compact, rugged and simple.

Acknowledgment

This work has been carried out at the Czech Technical University in Prague with a support of research framework RVO 68407700. We are also acknowledging project DFG FOR1503.

References

[1] J. Levine, "A review of time and frequency transfer methods," Metrologia, vol. 45, pp. S162-S174, 2008.

[2] I. Prochazka, J. Kodet, and P. Panek, "Note: Electronic circuit for two-way time transfer via a single coaxial cable with picosecond accuracy and precision," Rev. of Sci. Instruments, vol 83, p. 116104, 2012.

[3] P. Panek, J. Kodet, I. Prochazka, "Accuracy of two-way time transfer via a single coaxial cable," Metrologia, vol. 50, pp. 60-65, 2013.

[4] P. Panek, I. Prochazka, "Time interval measurement device based on surface acoustic wave filter excitation providing one picosecond precision and stability," Rev. of Sci. Instr., vol. 78, pp. 78-81, 2007.

[5] P. Panek, I. Prochazka, and J. Kodet, "Time measurement device with four femtosecond stability," Metrologia 47, pp. L13-L16, 2010.

[6] I. Prochazka, J. Kodet, and J. Blazej, "Note: Solid state photon counters with sub-picosecond timing stability," Rev. of Sci. Instr., vol. 84, p. 046107, 2013.

[7] W. J. Riley, Handbook of Frequency Stability Analysis, NIST Special Publication 1065, 2008.

[8] D. Kucharski, G. Kirchner, Hyung-Chul Lim, and F. Koidl, "Optical response of nanosatellite BLITS measured by the Graz 2 kHz SLR System," Advances in Space Research, vol. 48, pp. 1335–1340, 2011.

Comparsion between Timing Methods in BeiDou Satellite Navigation System

Hai Sha，Pengpeng Li，Jianwei Zhan，Bo Xu，Gang Ou
College of Electronic Science and Engineering
National University of Defense Technology
Changsha, China
sandhai@163.com

***Abstract*—BeiDou satellite navigation provides the RDSS two-way timing and RNSS timing. In this paper, the basic principles of these two timing methods are illustrated, and the factors which affect the precision for the two methods are analyzed. Compared with the wildly used RNSS timing method, the RDSS timing method can only be used by a limited number of users, due to the limited capacity of the RDSS system, and it cannot meet the requirements of high dynamic users. However, the experimental results indicate that the RDSS two-way timing method provides higher precision than RNSS timing method.**

Keywords—BeiDou; RDSS; RNSS; timing method; error analyses

I. INTRODUCTION

BeiDou satellite navigation system can provide service of positioning, timing and short message communications based on the radio determining of satellite service (RDSS) and the radio navigation of satellite service (RNSS) for the users of China and part of Asia-Pacific region [1]. In 2020, BeiDou system will completely be established with global coverage.

In BeiDou system, there are two timing ways: RDSS two-way timing method and RNSS timing method. Because RDSS payloads were only installed in the GEO orbit satellites [2], RDSS two-way timing can only be used when one or more GEO satellites are visible. For RNSS timing, it demands four or more satellites are visible. Currently the BeiDou timing receiver has been widely utilized in electric power, communications, finance and other industries.

In this paper, the basic principles of these two timing methods are discussed. Then through analyzing the various errors, the precision is drawn in theory. Finally through the equipment test result, two timing methods are validated in respect of accuracy.

II. BASIC PRINCIPLE

A. RDSS two-way timing method

For the RDSS system, in Master Control Center (MCC), the time frame interrogation signal generated under the control of the main atomic clock (BeiDou system Time: BDT) is transmitted from the MCC to satellite via satellite transponder, and finally received by the timing user.

There are two steps in RDSS two-way timing method. In the first step, the forward propagation delay τ_{forward} from the Measure Control Center (MCC) to the user is calculated by the MCC. In the second step, the time clock error Δt is calculated by the user on receiving the forward propagation delay [3-4]. The principle is shown in Fig.1.

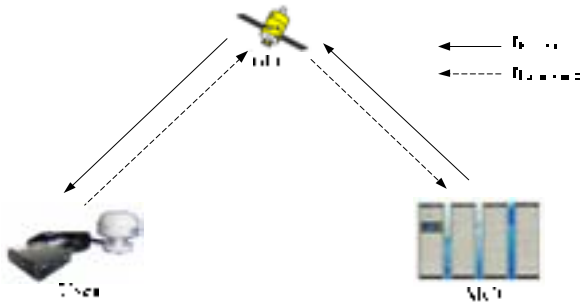

Fig. 1. Principle of RDSS two-way timing method

In the first stage, when receiving the time frame interrogation signal transmitted by the MCC, the user immediately sends the response signal. The round-trip time delay τ_{delay} between sending the interrogation signal and receiving the response signal is measured by the MCC. τ_{delay} can be expressed as follows:

$$\tau_{\text{delay}} = \tau_{\text{forward}} + \tau_{\text{backward}} \tag{1}$$

If the position of satellite and user were unchanged in the two-way transmission, τ_{forward} is equal to τ_{backward}. So the value of τ_{forward} is[3]

$$\tau_{\text{forward}} = \frac{1}{2}\left[\tau_{\text{delay}} + (\tau_{\text{forward}}^{\text{air}} - \tau_{\text{backward}}^{\text{air}}) - \tau_{\text{backward}}^{\text{equip}}\right] + \tau_{\text{forward}}^{\text{equip}} \tag{2}$$

Where $\tau_{\text{forward}}^{\text{air}}$ and $\tau_{\text{backward}}^{\text{air}}$ are respectively troposphere and ionosphere delay in forward and backward propagation process; $\tau_{\text{forward}}^{\text{equip}}$ is the equipment delay in forward propagation process from the MCC to user; $\tau_{\text{backward}}^{\text{equip}}$ is the equipment delay in backward propagation process.

In the second step, the τ_{forward} value is send to the user through the interrogation signal by the MCC. The pseudo-range ρ on receiving this interrogation signal is obtained by the user, the time clock error Δt can be obtained as follow:

$$\Delta t = \frac{\rho}{\mathrm{c}} - \tau_{\text{forward}} \tag{3}$$

B. RNSS timing method

RNSS timing can be achieved by obtaining the clock offset between local time and the BDT, which is realized by receiving RNSS signals [5]. When the position of the RNSS receiver is unknown, four or more satellite observations must be obtained to determine the extra unknown position information and time information . If position of the RNSS receiver is accurately determined, then only one satellite observations is needed to achieve the BDT. The principle of RNSS timing is shown as Fig. 2.

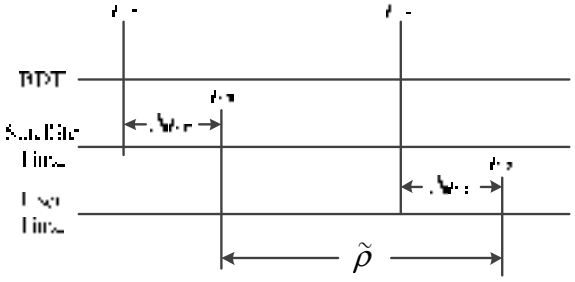

Fig. 2. Principle of RNSS timing method

Suppose the j[th] satellite observation has been obtained, the satellite time and BDT at the time instant of transmission are t_{BT} and t_{ST} respectively, while the receiver time and BDT at the time instant of receiving are t_{BR} and t_{UR} respectively.

Δt_{SB} is time error between the satellite time and BDT at the moment of signal transmission, while Δt_{UB} is time error between the receiver time and BDT at the moment of signal receiving. $\tilde{\rho}$ is the pseudorange measured by the receiver, which can be modeled as

$$\frac{\tilde{\rho}}{\mathrm{c}} = t_{\text{UR}} - t_{\text{ST}} = \frac{\rho^j}{\mathrm{c}} + \Delta t_{\text{SB}} - \Delta\tau - \Delta t_{\text{UB}} \tag{4}$$

Where ρ^j is the true distance between the satellite and the receiver; c is the speed of light. $\Delta\tau$ is time error including the satellite clock error, ionosphere error, tropospheric error, hardware delay and receiver noise. The receiver clock error can be expressed as

$$\Delta t_{\text{UB}} = \frac{\tilde{\rho}}{\mathrm{c}} - \frac{\rho^j}{\mathrm{c}} + \Delta t_{\text{SB}} - \Delta\tau \tag{5}$$

Δt_{UB} represents time error between the receiver time and the BDT, which is needed when computing the time information.

III. Analysis of Timing Precision

A. RDSS two-way timing method

The precision of RDSS two-way timing method is analysis from the formula (3). ρ contains the user measurement error; τ_{delay} contains the MCC measurement error, $\tau_{\text{forward}}^{\text{air}}$ and $\tau_{\text{backward}}^{\text{air}}$ contain the atmospheric error which composed of the troposphere and ionosphere error, $\tau_{\text{forward}}^{\text{equip}}$ and $\tau_{\text{backward}}^{\text{equip}}$ contain the device delay error. Otherwise, the position of the satellite is different on the forward and backward propagation process, which induces the approximation error.

Hence, assume that all errors are independent, the error of RDSS two-way timing method is

$$m_{\Delta t} = \sqrt{m_{\text{user}}^2 + \frac{1}{4}m_{\text{mcc}}^2 + \frac{1}{4}m_{\text{iono}}^2 + \frac{1}{4}m_{\text{trop}}^2 + \frac{1}{4}m_{\text{device}}^2 + m_{\text{app}}^2} \tag{6}$$

Where m_{user} is the user measurement error, m_{mcc} is the MCC measurement error, m_{iono} is the ionosphere delay error, m_{trop} is the troposphere delay error, m_{device} is the device delay error, m_{app} is the approximation error. According to the RDSS system parameters [1,6], the theoretic precision of RDSS two-way timing is:

$$\sqrt{10^2 + \frac{5^2+1^2+0.5^2+0.5^2}{4} + 3^2} = 10.8\text{ns}\cdot$$

B. RNSS timing method

From the formula (5), the factors which mainly affect the precision of the RNSS timing are receiver measurement error, satellite orbit error, satellite clock error, ionosphere error, tropospheric error. Suppose that the UERE value of RNSS standard positioning service is 7.1 m [6], the precision of RNSS timing is about 23.7 ns.

Meanwhile, the clock error is obtained while computing the PVT solution, then the precision of clock error σ_{t} can be expressed as:

$$\sigma_{\text{t}} = \text{TDOP} \times \sigma_{\text{UERE}} \tag{7}$$

IV. Experimental Result

In order to compare the precision of RDSS two-way timing method with that of RNSS timing method, the measurement data of these two timing method are compared.

As to the RDSS two-way method timing, the timing result is shown as Fig. 3. The timing precision is 8.1 ns, which is according to the theory analysis.

The RNSS timing test is carried out in Changsha by the high precise receiver. Because the true BDT is unknown, the variance of clock error is shown as Fig. 4, which is subtract from the frequency drift. The timing precision is equal to the variance of clock error added by system error. Meanwhile the TDOP is Fig.5.

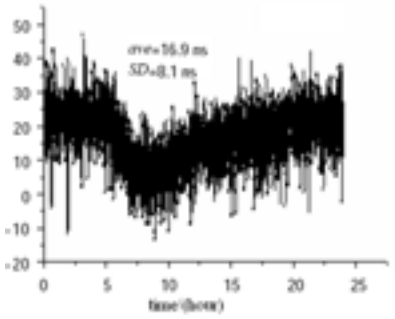

Fig. 3. Result of RDSS two-way timing in Herbin [3,4,7]

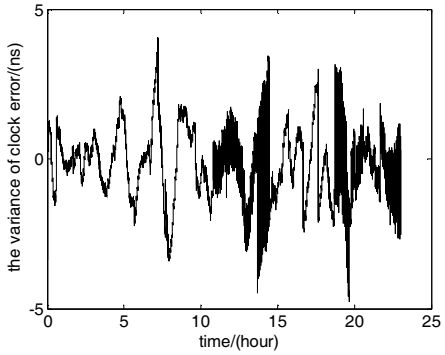

Fig. 4. Result of RNSS timing in Changsha

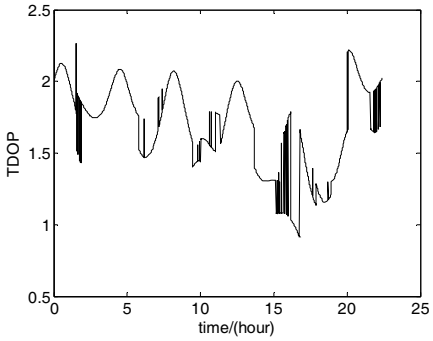

Fig. 5. TDOP value

V. CONCLUSION

The precision of RDSS two-way timing method is mainly influence by the MCC measurement error, ionosphere delay error, troposphere delay error and approximation error. The measurement data and the test result indicate that indicate that the precision of RDSS two-way timing method is about 8.1ns. The variance of clock error in RNSS timing method is about 5 ns. If considering the system error, the precision is larger than that of RDSS two-way method.

REFERENCES

[1] S.S. Tan, "The Engineering of Satellite Navigation and Positioning". Beijing: National Defense Industry Press, 2010.

[2] J. Xie, and T. Liu, "Research on Technical Development of BeiDou Navigation Satellite System", Lecture Notes in Electrical Engineering, pp. 197-209, Proceedings of the 4rd China Satellite Navigation Conference. Berlin: Springer, 2013.

[3] B.D. Li, L.J Liu, X.M Ju X. Shi and et al, "Precision Analysis of Satellite Two-way Time", Journal of Time and Frequency, 33:129-133, 2010.

[4] B. Liu, J.H. Qu, Y. Hong, L.J. Xu and et al, "Precision Analysis of RDSS Two-Way Timing", Lecture Notes in Electrical Engineering, pp. 424-433, Proceedings of the 4rd China Satellite Navigation Conference. Berlin: Springer, 2013.

[5] B.W. Parkinson, J. James, and J. Spilker, "Global Positioning System: theory and applications," American Institute of Aeronautics and Astronautics Inc., Washington DC, pp. 489-490, 1996.

[6] J.H. Zhou. "Construction and evaluating performance of the groud system in BeiDou system". Invited presentation of 4rd China Satellite Navigation Conference, Wuhan, China, 2013

[7] F. Pan, and Y. Du, "Test and evaluation of precision of RDSS experimental satellite". National Time and Frequency Conference, pp. 1-12, 2005.

.

Performances of EGNOS Network Time: An Update

Jérôme Delporte, Norbert Suard
CNES – French Space Agency
Toulouse, France
jerome.delporte@cnes.fr

Pierre Uhrich, Philip Tuckey
LNE-SYRTE
Observatoire de Paris
Paris, France

Abstract—**EGNOS is the European Satellite Based GPS Augmentation System. It generates its own time scale (ENT) that is steered to GPS time. The time offset between ENT and UTC (actually UTC(OP)) is contained in EGNOS Message Type 12. The aim of this paper is to validate the content of this message and to present the performances of ENT with respect to UTC and GPS time over more than 4 years.**

Keywords-component : EGNOS, ENT, UTC, GPS time.

I. INTRODUCTION

The European Satellite Based Augmentation System, called EGNOS (European Geostationary Navigation Overlay Service), provides to users in Europe an augmentation of three pseudo-GPS signals plus corrections/integrity information about the available GPS constellation [1] enabling to compute a safe and precise position that can be time tagged in a legal time scale (UTC). The EGNOS Open Service was declared operational in October 2009, while the Safety-Of-Life service has been operational since March 2011. EGNOS services are, at the time of writing, broadcast by 3 geostationary (GEO) satellites, whose PRNs are 120, 124 and 126.

EGNOS broadcasts the ephemerides of the GEO satellites (Message Type 9) allowing time and frequency transfer [2], although the GEO-ranging function is currently not supported by the EGNOS system. EGNOS also broadcasts in its navigation message the time difference between EGNOS Network Time (ENT) and UTC (actually UTC(OP)). This is done through an EGNOS ground station set up in Observatoire de Paris and connected to UTC(OP) [3,4].

The time offset between ENT and UTC(OP) is contained in EGNOS Message Type 12. The aim of this paper is to validate the content of this message and to present the performances of ENT with respect to UTC and GPS time. Moreover the recent improvements of UTC(OP) [5] allow to relate ENT to UTC with an unprecedented accuracy without any additional modeling.

II. EGNOS NETWORK TIME

A. ENT generation

The EGNOS Ground Segment consists of Ranging and Integrity Monitoring Stations (RIMS) equipped with Cs or Rb clocks, which are connected to a set of redundant control and processing facilities (CPF), in order to determine the integrity, ephemeris and clock differential corrections for each monitored satellite, to compute the ionosphere delays, and to generate the GEO satellite ephemeris. The GEO satellite downlinks these data on the GPS L1 frequency with a modulation and a coding scheme similar to GPS.

RIMS clock synchronization is performed using the composite clock technique in which ENT is defined as the implicit ensemble mean of a set of RIMS clocks and the synchronization process generates estimates of the time and frequency offsets of each RIMS clock relative to it [6]. ENT is then steered to GPS time using a second order, low-pass digital filter.

B. ENT requirements

All measurements and data are referred to the internal EGNOS Network Time (ENT) whose performance requirements were derived exclusively from navigation accuracy performance requirements. It is required that ENT stay within 50 ns (5σ) of GPS Time (GPST), allowing the user to combine GPS and EGNOS signals in the navigation solution. The EGNOS user shall be aware that applying EGNOS corrections to its GPS measurements will turn its time reference from GPS time into ENT.

GEO Time is the time reference of the EGNOS pseudo ranges. The [ENT - GEO Time] accuracy is specified to be less than 10 ns (3σ), after offset and frequency corrections provided in EGNOS GEO message 9, which might be of interest to realtime users. Table 1 below summarizes the EGNOS time requirements:

TABLE I. EGNOS TIME REQUIREMENTS [7]

1	[ENT - GPS time] offset ≤ 50 ns (5σ)
2	[GEO Time - GPS time] offset ≤ 50 ns (5σ)
3	[GEO Time – ENT] accuracy ≤ 10 ns (3σ)
4	[ENT - UTC(OP)] accuracy ≤ 10 ns (3σ)

C. The Message Type 12

To synchronize ENT and UTC, it was decided to install a special RIMS at Observatoire de Paris, called "RIMS-UTC" or PARA, as part of the EGNOS system. A block diagram of this RIMS can be found in [3]. The time difference [ENT – UTC] can be computed by the CPF using simply :

$$ENT - UTC = [ENT - UTC(OP)] + [UTC(OP) - UTC]$$

where [ENT – UTC(OP)] is determined by the CPF as an output of its ENT composite clock algorithm, and [UTC(OP) – UTC] is computed by CPF using a prediction algorithm. Currently this prediction is not implemented and therefore EGNOS broadcasts in its message 12 the time offset [ENT – UTC(OP)] for the real time synchronization to UTC in compliance to [8].

The Message Type 12 (MT12) contains an estimation of ENT – UTC(OP) expressed in the form of a linear model (offset A0, drift A1 and reference time t_{ot}), assumed to be valid for 86400 s, that can be extrapolated at any current time from its reception to the reception of a new set of such parameters or its validity time. The maximum broadcast interval of MT12 is 300 s [8]. However it has been shown that the accuracy of A1 is limited [9], it is therefore not recommended to use it for more than a couple of minutes beyond the reference time t_{ot}. Possible ways to improve the model are detailed in [9] and an implementation is expected to be carried out with the EGNOS v2.4.2. by 2017.

III. PERFORMANCES OF ENT

A. *UTC-ENT*

In this paragraph, we estimate the time difference UTC – ENT. This computation is carried out by :

UTC–ENT = [UTC–UTC(OP)] – [ENT-UTC(OP)]

where UTC-UTC(OP) comes from the BIPM Circular T and ENT-UTC(OP) is the daily mean coming from MT12. The uncertainty on this estimation is in the range of a few ns (quadratic sum of the uncertainties in our process and in the BIPM Circular T).

Figure 1 shows UTC-ENT from February 2008 to May 2013 as well as a linear fitting:

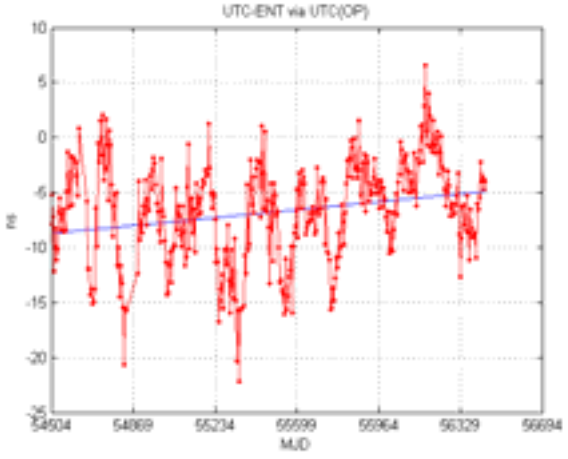

Figure 1. Esimation of UTC - ENT

ENT is therefore a real-time time scale close to UTC. The mean value of UTC-ENT over more than 5 years is -6.7 ns and the standard deviation is 4.5 ns. On top of the fluctuations, we also observe a general trend of about 0.7 ns per year, the origin of which is unclear. The stability of UTC-ENT is given in Figure 2.

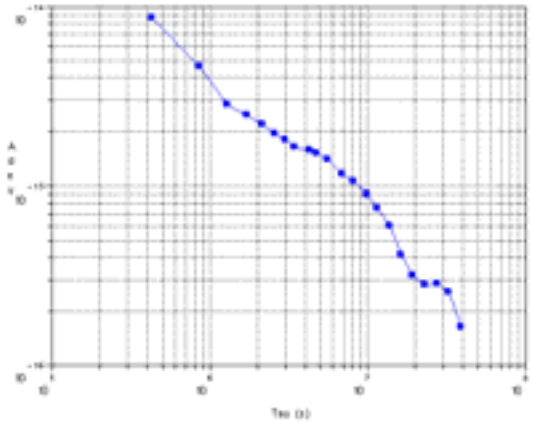

Figure 2. Allan deviation of UTC - ENT

It shall be recalled here that ENT is steered to GPST which is itself steered to UTC(USNO). Figure 3 is the time deviation of UTC-ENT.

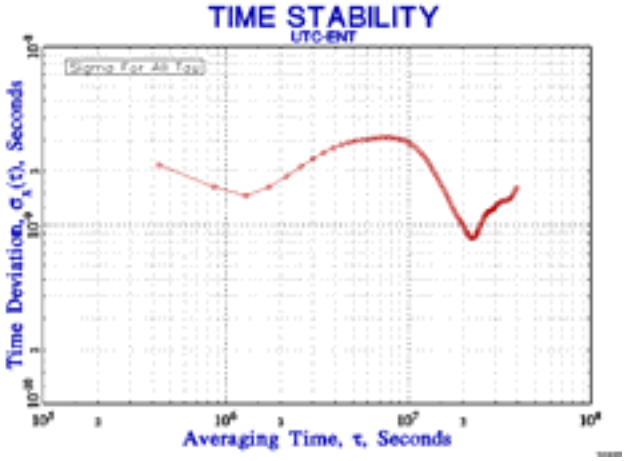

Figure 3. Tdev of UTC - ENT

B. *GPST-ENT*

In this paragraph, we estimate the time difference GPST – ENT. This computation is carried out by:

GPST–ENT = [GPST–UTC] + [UTC-ENT]

Where GPST-UTC comes from the BIPM Circular T and UTC-ENT comes from the previous computation. Figure 4 shows UTC-ENT from February 2008 to May 2013.

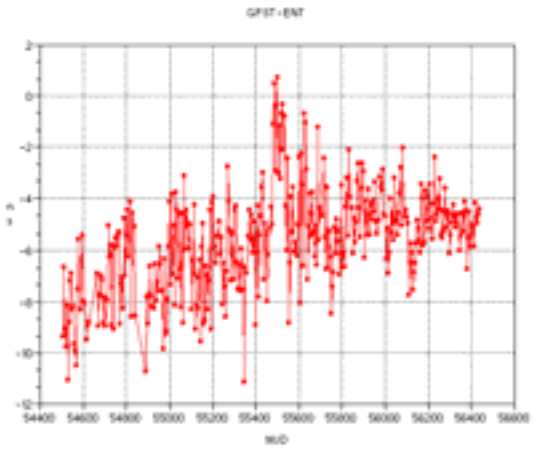

Figure 4. Estimation of GPST - ENT

ENT being steered to GPST, one may expect a zero mean value. This is not what we observe, maybe because of some remaining calibration biases. The mean value of UTC-ENT over more than 5 years is -5.7 ns and the standard deviation is 2.0 ns. According to this estimation, the requirement on the time offset ENT-GPST is met.

IV. Independent Assessment of ENT-UTC(OP)

A. Method

The method consists in an independent estimation of ENT at user level. In this case, we use the GPS measurements of a dual-frequency calibrated receiver called OPMT connected to UTC(OP). We apply EGNOS corrections and station delays on these measurements, so that we get $[ENT_{user} - UTC(OP)]_{OPMT}$ that we can compare to $[ENT - UTC(OP)]_{MT12}$.

The general model for EGNOS measurements uses the C/A pseudo-range observable (C1 observable in the RINEX files). The reference orbit and clocks come from the GPS broadcast ephemeris.

The following formulation is used (one epoch and one GPS):

$$C_1 = D^{EGNOS} + e + \left(h_{rec}^{EGNOS} - h_{GPS}^{EGNOS}\right)$$

- C_1 is the C/A pseudo-range measurement.
- D^{EGNOS} is the geometrical distance between the transmitter and the receiver L_1 centres of phase, including the troposphere delay.
- e is the ionosphere propagation delay on the L1 GPS frequency.
- h_{rec}^{EGNOS} and h_{GPS}^{EGNOS} are respectively the receiver and transmitter clock offsets expressed in the EGNOS reference time.

D^{EGNOS} is computed using the GPS broadcast ephemeris corrected with the data from the EGNOS messages. The tropospheric delay is estimated with a standard mapping function and a fixed zenith troposphere delay of 2.37 m. The receiver centre of phase is obtained using the IGS station log for OPMT station and the ITRF solution for the corresponding marker coordinates. e is estimated using the EGNOS ionosphere message. h_{GPS}^{EGNOS} is computed using the slow and fast corrections obtained from the EGNOS messages applied on the GPS broadcast clock value corresponding to a single frequency user (use of the broadcast TGD values).

Then, at a given epoch and for each GPS in view we obtain an estimation of h_{rec}^{EGNOS} from the above equation. All these estimates are averaged over a 15 minute interval to minimize the pseudo-range measurement noise effects. This produces an estimation of the offset between the receiver clock and the EGNOS time defined by the EGNOS messages.

B. The EPO (EGNOS Performance Observatory) tool

The OPMT receiver is not directly connected to UTC(OP) but to an Hydrogen Maser whose time offset is monitored versus UTC(OP) on an hourly basis. These time offset values are given in so-called LZOP files. These values can be interpolated by a simple linear model over one day for down sampling. The values of the different time propagation delays of OPMT station are extracted from the CGGTTS daily file.

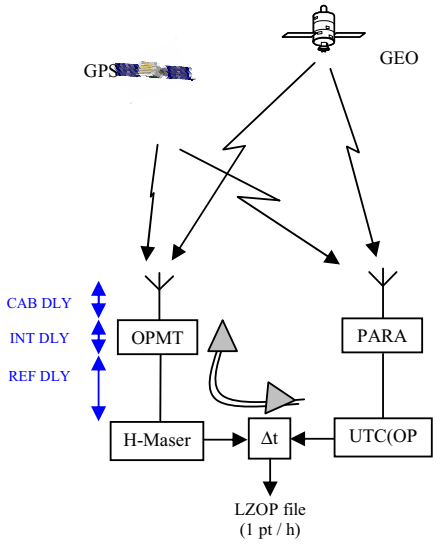

Figure 5. Independent assessment chain (OPMT), EGNOS RIMS (PARA) and their connections to UTC(OP)

Basically, the method implemented in CNES EPO tool is to determine first $[ENT_{user} - UTC(OP)]_{OPMT}$, this time difference being obtained by :

- applying the EGNOS corrections on the GPS measurements collected at OPMT (using the previously described method)

- relating ENT to UTC(OP) using the internal delays of the station OPMT

This time difference is then compared to the broadcast information at each reception time of a new valid model of MT12.

Finally, we obtain $[ENT - UTC(OP)]_{MT12}$ - $[ENT_{user} - UTC(OP)]_{OPMT}$ which is expected to be close to zero if the different calibrations of pieces of equipment and cables in the EGNOS PARA RIMS and in the independent assessment chain are correct. This analysis is automatically performed on a daily and a monthly basis.

C. *Results*

Figure 6 shows the mean daily difference $[ENT - UTC(OP)]_{MT12}$ - $[ENT_{user} - UTC(OP)]_{OPMT}$ computed as explained above from Nov 2008 to May 2013.

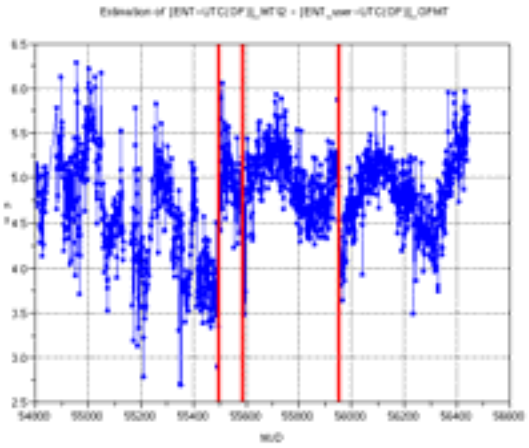

Figure 6. Mean daily difference $ENT - UTC(OP)]_{MT12}$ - $[[ENT_{user} - UTC(OP)]_{OPMT}$

The red vertical bars indicate the changes of Hydrogen Maser in the station OPMT. The stability of this mean daily difference is quite good over such long a period. We observe that the changes of Hydrogen Maser (as well as other events) have an impact at the ns level, consistent with delay calibration uncertainties at Observatoire de Paris.

The overall bias is about 4.7 ns and can be at least partly explained by :

- the uncertainty in the calibration of IGS station OPMT (estimated in the range of 3.3 ns (k=1))
- the uncertainty in the calibration of RIMS PARA and equipment used to connect it to UTC(OP)
- the difference between ENT and $ENT_{user.}$
- the potential code bias [10] between the OPMT receiver (Ashtech Z12T) and the RIMS receiver

This result however validates the requirement on the accuracy of ENT-UTC(OP).

V. UTC(OP) MODERNIZATION

LNE-SYRTE has improved the performances of UTC(OP) since October 2012. UTC(OP) is currently generated from a H-Maser steered on Primary Frequency Standards Cesium fountains [5]. Figure 7 shows the evolution of UTC – UTC(OP) since February 2008 :

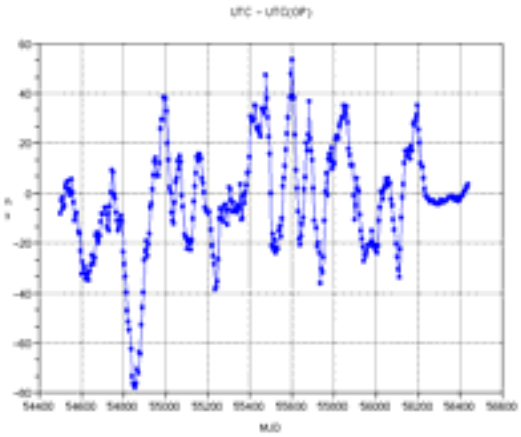

Figure 7. UTC – UTC(OP)

Since Nov 2012, UTC(OP) has been between +/- 5 ns of UTC. It is now an excellent realization of UTC and therefore the EGNOS user can obtain UTC in real-time at the level of a few ns, when applying the MT12.

ACKNOWLEDGMENT

The authors wish to thank the NTMF (CNES Navigation and Time Monitoring Facility) exploitation team for their daily work to compile the database enabling such long term analyses.

REFERENCES

[1] J. Benedicto, "EGNOS : the European Satellite Based Augmentation to GPS and GLONASS", Proceedings of ENC-GNSS 1998

[2] P. Pánek, A. Kuna, "Time and frequency transfer using EGNOS satellite system", Proc. of 43rd PTTI, 2011.

[3] P. Uhrich, D. Valat, M. Brunet, J. Maréchal, T. Beltan, N. Suard,"The French Time Reference UTC(OP) and the Connection of the EGNOS Network Time", Proceedings of EFTF 2005.

[4] J. Delporte, N. Suard, D. Sidorov, P. Uhrich et al., "EGNOS Network Time and its relationships to UTC and GPS time", proc. of PTTI 2009.

[5] G.D. Rovera at al.., "The new UTC(OP) based on LNE-SYRTE atomic fountains", submitted to this conference.

[6] I. Alcantarilla,"EGNOS Time", Presentation at the workshop 'Time and Frequency Services with Galileo', 2005.

[7] EGNOS System Requirement Document, ESA document

[8] DO2209 release D, "Minimum Operational Performance Standard for Global Positioning System/Wide Area Augmentation System Airbone equipment", section A.4.4.15.

[9] J. Simon, H. Secretan, N. Suard, J. Caro, "Robust Estimation of the Offset between UTC and SBAS Network Time", Proc. of ION GNSS 2012.

[10] R. Eric Phelts, "Effects of Signal Deformations on Modernized GNSS Signals", Journal of Global Positioning Systems (2006), Vol. 5, No. 1-2:2-10

Exponential Degrading of NTP Synchronization with Number of Network Hops

Akihiko Machizawa and Tsukasa Iwama
National Institute of Information and Communications Technology
Tokyo, Japan 184–8795
Email: machi@nict.go.jp

***Abstract*—Time synchronization using the Network Time Protocol (NTP) has increased with the growth of the Internet. There are hundreds of public NTP servers in the world. Conventional client software selects a peer/server using packet delay jitter statistics for some manually listed servers, even though it is commonly understood that the nearest NTP server should be used. We demonstrate that NTP synchronization degrades with the number of network hops. The hop count indicates the number of routers on the network path, which is where most jitter and packet loss occur. The accuracy of client time synchronization degrades exponentially with hop count. We propose a round-trip hop-counts-capable NTP server response for the accurate selection of the nearest server.**

I. Introduction

Time synchronization using the Network Time Protocol (NTP) [1] has increased with the growth of the Internet. NTP is a standard for time synchronization in an IP-based network. There are hundreds of public NTP servers across the world. Conventional client software selects a peer/server using packet delay jitter statistics for some manually listed servers, even though it is commonly thought that the nearest NTP server should be used. What is the "nearest?" There are two metrics for network distance [2]. One is delay time and the other is hop count. The hop count indicates the number of routers on the network path. Communication quality is degraded because of the hop count, because most jitter and packet loss occur at routers.

Although it is known that packet delay jitters are proportional to the square root of the hop count [3] [4], how an increasing number of hops affects NTP synchronization has not yet been reported. However, detecting the nearest server can be difficult. An IPv4 header has a Time-to-Live (TTL) field and an IPv6 header has a Hop Limit (HL) field. Since each router subtracts one count from these fields, the hop count can be estimated with the fields. Some Internet Control Message Protocol (ICMP) diagnostic tools, such as traceroute, use ICMP echo reply and ICMP time-exceeded packets to determine initial TTL/HL values as the hop count. However, such tools use a significant number of packets and are often blocked by fire walls. Furthermore, the forward and backward paths may differ. In addition, traceroute measures only the hop counts of the forward path.

In this article, we quantitatively demonstrate that client NTP synchronization accuracy degrades with the hop count. We analyze the pseudo one-way delay between clients and our NTP server (ntp.nict.jp) [5], [6] [1]. This server is a primary (stratum 1) NTP server operated by the national time authority in Japan and is used by more than ten million clients worldwide.

We propose a method to detect the nearest NTP server using round-trip hop counts (RTH). RTH is the total number of hops on the path from a client to a server (forward path) and from the server back to the client (backward path). We propose a TTL/HL reflecting method at servers to measure RTH. This method copies the TTL/HL values of incoming request packets at the servers into the field of the outgoing NTP server response packets. The TTL/HL values successively decrease by the forward and backward paths. Using this method, clients can select the nearest NTP server among the listed servers.

The remainder of this paper is organized as follows. In Section II, we examine the methodology employed to evaluate synchronization error. In Section III, we compare the degradation of NTP synchronization with the hop count and delay time. Then, in Section IV, we propose a simple and effective RTH measurement technique.

II. Methodology

A. One-way Delay and Synchronization Error

In Fig. 1, an NTP request packet from a client contains only the origin timestamp T_1. A server receives the packet at T_2. The server sends an NTP response packet to the client at T_3. The packet now contains T_1, T_2, and T_3. The client receives the packet at T_4. Timestamps T_1 and T_4 are based on the client clock, which has the offset (O) relative to the server. Timestamps T_2 and T_3 are based on the server clock and show the correct time. The network delay from the client to the server is d_1, and the delay from the server to the client is

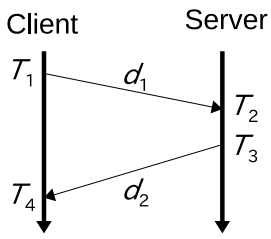

Fig. 1. Four timestamps of NTP and one-way delay

[1] http://www2.nict.go.jp/aeri/sts/tsp/PubNtp/index-e.html

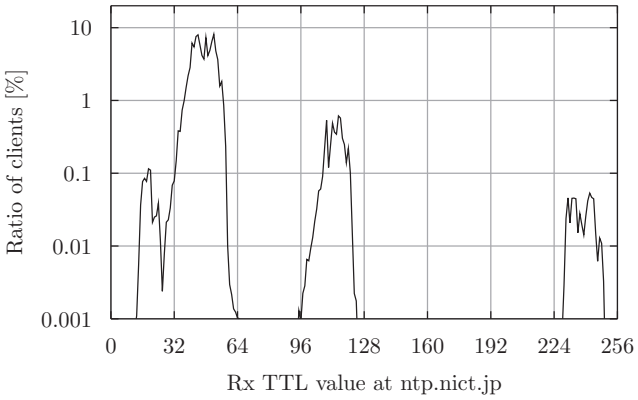

Fig. 2. Histogram of TTL/HL values in packets received by ntp.nict.jp

d_2. These four timestamps and two delays have the following relation ship.

$$T_2 = T_1 + O + d_1, \tag{1}$$

$$T_4 = T_3 - O + d_2. \tag{2}$$

If d_1 and d_2 are known, O can be computed as follows.

$$O = ((T_2 - T_1) + (T_3 - T_4) + (d_2 - d_1))/2. \tag{3}$$

Most NTP clients assume symmetric delay, i.e., $d_1 = d_2$. However, delays are actually asymmetric and dynamic. Therefore, offset estimation error is a function of network delay. The following equation, which is derived from equation (1), represents the synchronization error trend.

$$T_2 - T_1 = O + d_1. \tag{4}$$

B. Round-Trip Hop Counts Estimation

An IPv4 header has a TTL field, while an IPv6 header has a HL field. Since each router subtracts one count from these fields, the hop count can be estimated with the fields. One-way hop counts from a client to a NTP server can be estimated by capturing NTP request packets at the server. The TTL/HL values in the captured packets show the hop counts as they are decreased by one at each hop. Fig. 2 shows the distribution of TTL/HL values received by ntp.nict.jp. RTH is the total number of hops from both the forward and the backward paths. The estimated RTH is equal to two times the estimated one-way client to the server hop count.

Four groups can be seen in Fig. 2. The smallest and second smallest groups overlap. The nmap OS fingerprints database states that initial values of 32, 64, 128, and 255 are used. [2] Each group in Fig. 2 must correspond to each initial value. Hence, hop counts are estimated from the difference between each initial and received TTL/HL values. Then, based on the symmetric path assumption, RTH is estimated as two times the one-way hop count. However, we know that the forward and backward paths may be different. We will propose a real RTH estimation method in Section IV.

[2]http://nmap.org/

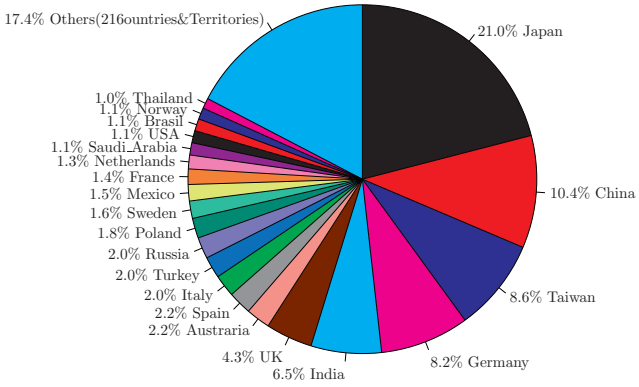

Fig. 4. Geographical distribution of clients using ntp.nict.jp (as of June 2013)

C. One-way Delay Classification

Equation (4) contains the one-way delay d_1 and the offset O. So, $T_2 - T_1$ is called as pseudo one-way delay. Clients are classified into four categories using the pseudo one-way delay, as shown in Fig. 3. Type I is normal, and the others are abnormal. Type IIa is the switching route, Type IIb is time-slotted, and Type IIc is drifted. We use data from the Type I clients.

III. Results

A. Data Collection

We use NTP response packets from ntp.nict.jp. This server receives requests from all over the world (238 countries and territories). This server is a Stratum 1 NTP server operated by the national time authority in Japan. This server has field-programmable-gate array-based high-performance hardware. Fig. 4 shows the geographical distribution of clients that access ntp.nict.jp. More than 10 million clients are distributed around the world. Therefore, the request packets for this server are suitable for analyzing the synchronization error related to the hop count. The pseudo one-way delay represents client synchronization, because it is the sum of the clock offset and network delay, as expressed by equation (4). We capture the server's response packets. The reason we use the server's response packets rather than request packets is that the response packets contains both T_1 and T_2 timestamps.

B. Results Analysis

Fig. 5 plots the standard deviation of the pseudo one-way delay between the server and clients along the estimated RTH on a semi-log scale, and Fig. 6 plots the standard deviation of the pseudo one-way delay between the server and clients along the pseudo one-way delay on a semi-log scale. We can see a stronger correlation in Fig. 5 than Fig. 6. The accuracy of client time synchronization degrades exponentially with the hop count. The regression line is expressed as follows.

$$\sigma = \sigma_0 \times \alpha^H, \tag{5}$$

$$\sigma_0 = 1.1 \times 10^{-}5\ [s], \tag{6}$$

$$\alpha = 1.25. \tag{7}$$

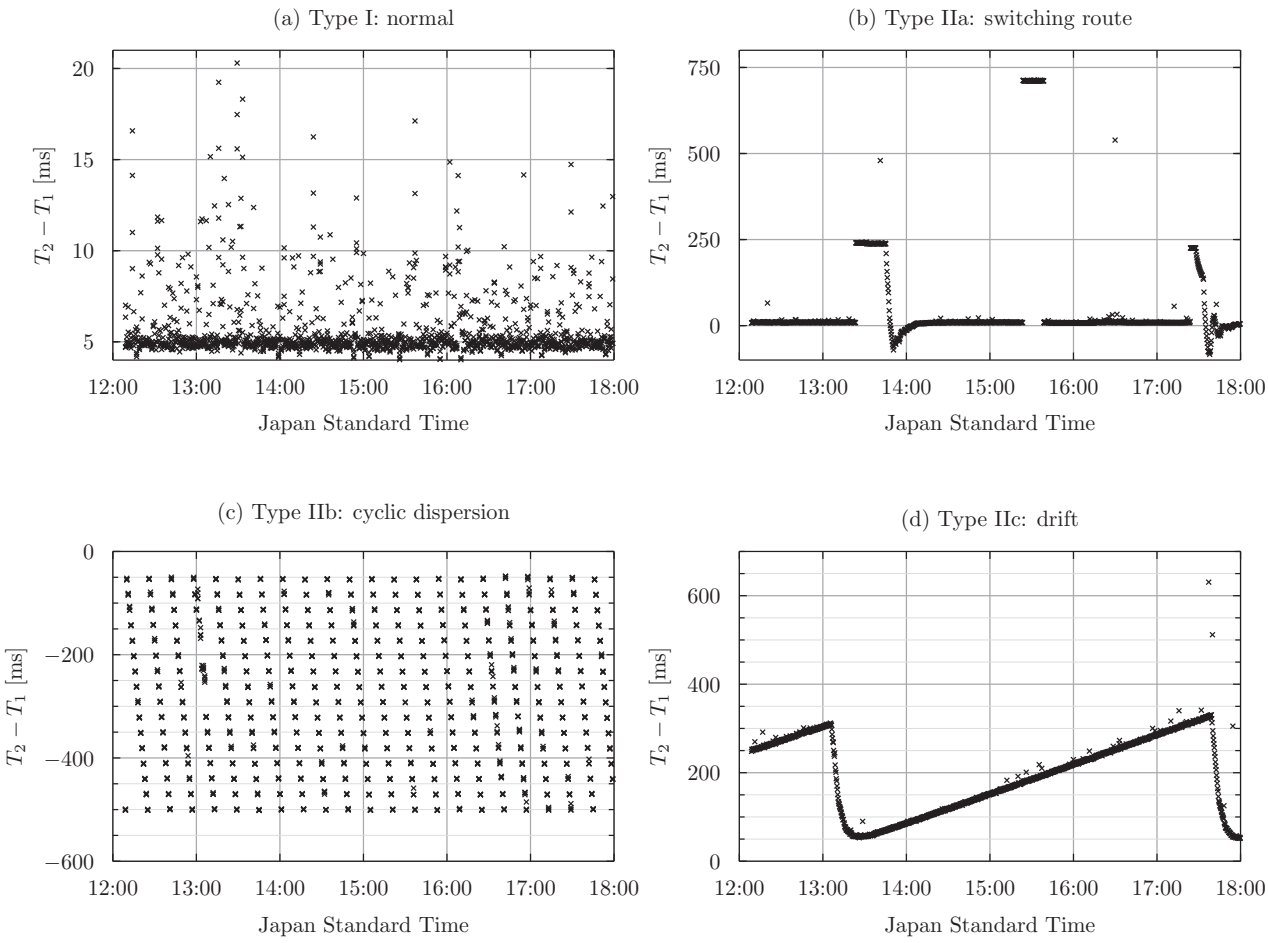

Fig. 3. Typical pseudo one-way delay.

Here σ denotes the standard deviation of the pseudo one-way delay, and H is the estimated round-trip hops.

IV. RTH CAPABLE SERVER RESPONSE

The forward path and backward path between a client and server may be different. We propose a TTL/HL reflecting method at servers to measure the exact RTH. This method copies the TTL/HL values of incoming request packets at the server into fields of the outgoing NTP server response packets. The TTL/HL values successively decrease by the forward and backward paths. Using this method, clients can select the nearest NTP server among available servers.

Fig. 7 illustrates the proposed method.

1) The client sends NTP request packets with TTL/HL values as TTL_1.
2) The server copies the TTL/HL value of the received packets (TTL_2) into the initial TTL/HL values of the response packets (TTL_3).
3) The client extracts TTL/HL values of the received server response packets as TTL_4.
4) Then, RTH can be calculated as follows.

$$RTH = TTL_1 - TTL_4. \tag{8}$$

The current recommended default initial TTL/HL value, which is published in the "IP OPTIONS NUMBERS" at the IANA web site [3], is

$$TTL_{IANA} = 64. \tag{9}$$

The value must be at least sufficiently large for the Internet's "diameter," i.e., the longest possible path. A reasonable value is approximately two times the diameter, which allows for continued Internet growth [7], [8]. If the server receives a packet with a TTL/HL value greater than or equal to TTL_{IANA}, then it recognizes that the packet is a RTH request and copies the value into the response packet. However, if the TTL/HL value of the receiving packet is less than TTL_{IANA}, the server sets the TTL/HL value as TTL_{IANA}.

The ability to select the most appropriate nearest server will lead to (1) improved client accuracy, (2) reduced network traffic, and (3) reduced power consumption. We implemented the TTL/HL reflecting function on servers associated with ntp.nict.jp (this NTP server is a multiple IP address host).

[3] http://www.iana.org/assignments/ip-parameters

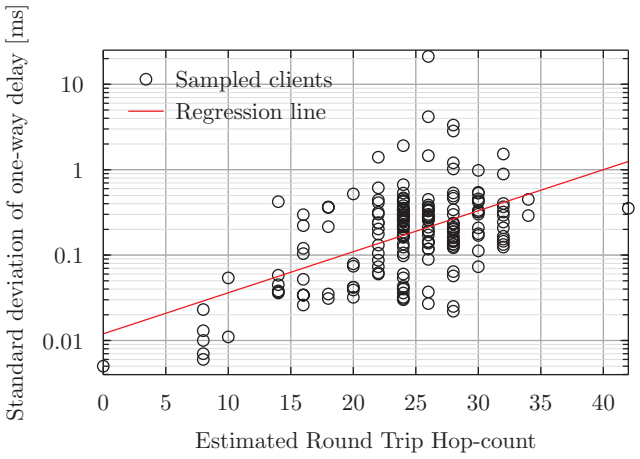

Fig. 5. Degradation of client accuracy with RTH. The standard deviation of the pseudo one-way delay from clients to ntp.nict.jp increases exponentially with increasing network distance (RTH).

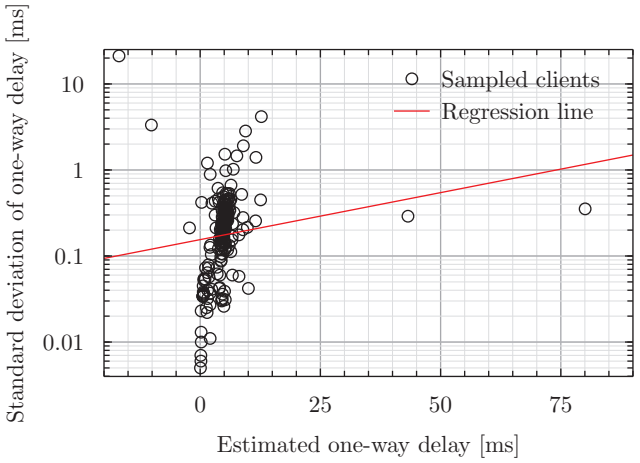

Fig. 6. Degradation of client accuracy with delay.

V. Conclusion

We showed that the accuracy of NTP client synchronization degrades exponentially with the hop count. We also proposed a TTL/HL reflecting method for the selection of the nearest server. RTH is more useful than round-trip time for NTP synchronization. The proposed method is very simple and has been implemented at ntp.nict.jp.

Selecting the nearest server will lead to (1) improved client accuracy, (2) reduced network traffic, and (3) reduced power consumption. We implemented the TTL/HL reflecting function on the servers associated with ntp.nict.jp.

In future, we plan to develop a NTP client that implements both the TTL/HL reflecting method and high-precision time stamping [9].

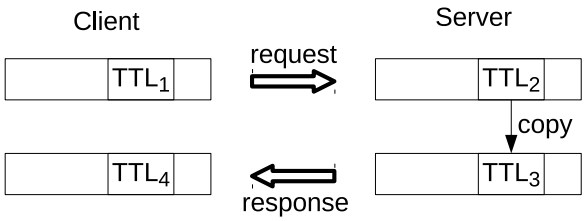

Fig. 7. Server implementation of round-trip hop function.

References

[1] D. Mills, J. Martin, J. Burbank, and W. Kasch, "Network time protocol version 4: Protocol and algorithms specification," IETF, RFC 5905, June 2010.

[2] V. Paxson, "On calibrating measurements of packet transit times," in *Proc. ACM SIGMETRICS 1998*, June 1998, pp. 11–21.

[3] C. Barry and S. Bangalore, "Synchronization in packet networks: Timing metrics and monitoring," in *Proc. Precise Time and Time Interval (PTTI)*, 2008, pp. 197–204.

[4] D. Mohl and M. Renz, "Improved synchronization behavior in highly cascaded networks," in *Precision Clock Synchronization for Measurement, Control and Communication, 2007. ISPCS 2007. IEEE International Symposium on*, 2007, pp. 96–99.

[5] H. Toriyama, A. Machizawa, and T. Iwama, "High performance ntp server using fpga," in *PTB-BIPM Workshop on the Impact of Information Technology in Metrology*, Berlin, Jun. 2007.

[6] A. Machizawa, T. Aoki, T. Iwama, H. Toriyama, K. Imamura, S. Tsuchiya, A. Kaneko, H. Maeno, and Y. Takahashi, "Development of a reliable public ntp system based on japan standard time," *Trans. IEICE*, vol. J96-D, no. 10, 2013 (in Japanese, to be published).

[7] R. Braden, "Requirements for internet hosts – communication layers," IETF, RFC 1122, 1989.

[8] J. Reynolds and J. Postel, "Assigned numbers," IETF, RFC 1700, October 1994.

[9] A. Machizawa, T. Iwama, and H. Toriyama, "Software-only implementations of slave clocks with sub-microsecond accuracy," in *Precision Clock Synchronization for Measurement, Control and Communication, 2008. ISPCS 2008. IEEE International Symposium on*, Sept. 2008, pp. 17–22.

First Spectroscopy of the $^1S_0 \rightarrow {}^3P_0$ Transition in Lamb-Dicke Confined Magnesium Atoms

A. P. Kulosa, S. Rühmann, K. H. Zipfel, D. B. Fim, T. W. Wübbena, W. Ertmer and E. M. Rasel
Institute of Quantum Optics
Leibniz University of Hanover
Hanover, Germany
Email: kulosa@iqo.uni-hannover.de

Abstract—**10^4 magnesium atoms have been trapped in an optical lattice at the predicted magic wavelength of 469 nm. The trap depth of the lattice sites is 16 E_r corresponding to a Lamb-Dicke parameter of $\eta = 0.51$. The temperature of atoms in the lattice is 10 μK. We performed magnetic field-induced spectroscopy on the strongly spin-forbidden clock transition and observed for the first time a 50 kHz broad carrier signal together with a 80 kHz broad red sideband.**

Keywords-Magnesium optical lattice clock; Lamb-Dicke spectroscopy; magic wavelength

I. INTRODUCTION

Magnesium is the 12th element in the periodic table and thus is the lightest species among the candidates for optical atomic clocks. It has three stable isotopes: the bosonic ^{24}Mg and ^{26}Mg, as well as the fermionic ^{25}Mg with a nuclear spin of I = 5/2. Most knowledge has been gained so far on ^{24}Mg which has a natural abundance of 78.99 % in an isotope mixture. Magnesium benefits from a low sensitivity to black body radiation [1] and a relatively simple electronic level structure (see fig. 1).

All relevant transitions for laser cooling and clock spectroscopy in magnesium are in the blue or UV range of the electromagnetic spectrum. Laser cooling at 285 nm in the singlet manifold has been well developed [2]. The broad transition linewidth of 78 MHz limits the final temperature in a magneto-optical trap (S-MOT) to approximately 3 mK. The intercombination line with its linewidth of 36 Hz is not suitable for magneto-optical trapping. Nevertheless, we use this transition to optically pump the pre-cooled singlet atoms into the long-lived triplet manifold. Metastable magnesium thus only occurs by laser excitation of the intercombination line as there is no decay channel from the $^1P_1$ to the triplet manifold via intermediate states like in strontium [3].

Applying a repumping laser to the $^3P_1 \rightarrow {}^3D_2$ transition, atoms are optically pumped to the $^3P_2$ state which is the starting point for our triplet MOT (T-MOT). The $^3P_2 \rightarrow {}^3D_3$ cooling transition further cools the atoms to 1 mK. Since the energy splitting of the ^{3}D states is only marginal, a second repumping laser for the $^3P_0$ state is mandatory to close the MOT cycle. All lasers operate around 383 nm.

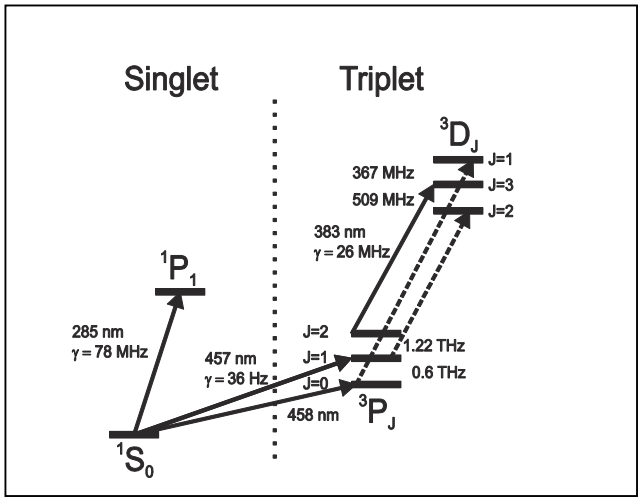

Figure 1. Partial level scheme of ^{24}Mg. The S-MOT is operated on the $^1S_0 \rightarrow {}^1P_1$ transition. The intercombination transition $^1S_0 \rightarrow {}^3P_1$ is used for transferring the atoms to the triplet manifold. Operating the T-MOT envolves three lasers: The cooling laser is acting on the $^3P_2 \rightarrow {}^3D_3$ transition, while two additional repumping lasers re-cycle atoms that have decayed to the $^3P_0$ and $^3P_1$ states. Clock spectroscopy is performed on the $^1S_0 \rightarrow {}^3P_0$ transition.

Concerning optical trapping of magnesium, it turned out that directly applying laser light at 469 nm (which is the predicted magic wavelength) to the atoms while they are in the $^3D_3$ state leads to photo ionisation. Hence, we need a far detuned trap for first trapping before we can load the magic wavelength lattice. Recently, we developed a loading scheme for an optical dipole trap (ODT) at 1064 nm for enhancing the transfer efficiency into the dipole trap, which has earlier been limited by the density of the T-MOT [4]. Atoms are continuously pumped from the singlet manifold into the dark $^3P_0$ state by not applying the relevant repumping laser. The coldest among the $^3P_0$ atoms are accumulated in the dipole trap thus creating a quasi energy filter for metastable atoms.

In this paper we report about the successful transfer of $^3P_0$ atoms into an optical lattice at the predicted magic wavelength of 469 nm and the first spectroscopy of the strongly spin-forbidden clock transition $^1S_0 \rightarrow {}^3P_0$ at 458 nm. This is a key breakthrough in order to realise a magnesium lattice clock

improving our latest frequency measurement on cold free-falling atoms [5].

II. Experimental Setup

Atoms are prepared and manipulated in a vacuum chamber made of stainless steel with a background gas pressure below 10^{-9} mBar. The S-MOT is loaded from a Zeeman-slowed thermal beam of magnesium atoms as described in [5]. In contrary to our previous work, the light at 285 nm is nowadays generated by frequency quadrupling a commercial 5 W fibre amplifier laser at 1141 nm. For long-term stability, the frequency doubled laser at 570 nm is locked to an iodine spectroscopy. The main output of the laser feeds a home-built resonant second harmonic generation (SHG) cavity allowing for the generation of up to 350 mW at 285 nm with a linewidth of 6 MHz. An acousto-optic modulator (AOM) splits the UV light into a resonant beam for Zeeman-slowing the thermal atoms and the light further prepared for magneto-optical trapping.

For pumping the atoms from the singlet to the triplet manifold we perform laser excitation on the narrow $^1S_0 \rightarrow {}^3P_1$ intercombination line. The transfer laser is a commercial laser system consisting of an amplified diode laser at 914 nm feeding a SHG cavity. The output power at 457 nm is typically 120 mW. In order to address this narrow transition, the laser is frequency-stabilised to a high-finesse cavity with F = 39000 providing a laser linewidth of 30 Hz. A detailed description of this laser system can be found in [6].

The T-MOT light at 383 nm is generated by a laser system consisting of three independent lasers for addressing the $^3P_2 \rightarrow {}^3D_3$ cooling transition and the two repumping transitions, respectively. Three master oscillator power amplifiers (MOPA) deliver 1 W optical power at 766 nm each feeding independent home-built SHG cavities (see fig. 2). The output power of each SHG is about 100 mW at 383 nm and the lasers have a linewidth of 1 MHz. For frequency stabilisation of the three MOPAs that are far from any magnesium transition and differ several hundreds of GHz in frequency (see fig. 1), we transfer the stability of a reference laser to the MOPA systems via a common transfer cavity [7,8]. Following a suggestion given by Budker et al. [9], we lift the degeneracy of higher order modes inside the cavity by slightly tilting one of the cavity mirrors thus obtaining a mode spacing of 112.5 MHz which is feasible for locking a laser with respect to an atomic transition (the remaining gap can be bridged with AOMs). The length of the cavity is controlled with a piezo-electric transducer (PZT) to which one of the cavity mirrors is attached. Long-term stability is achieved by stabilising the cavity length to an ECDL locked to the ^{39}K D_2-line at 766 nm via Doppler-free saturation spectroscopy. The MOPAs are stabilised to the transfer cavity using the Pound-Drever-Hall (PDH) method [10]. Frequency modulation sidebands are generated by laser diode current modulation around 20 MHz. Each SHG cavity is then locked to its respective MOPA light using exactly the same modulation sidebands which largely reduces the complexity in electronic stabilisation efforts.

A Ti:Sa laser giving 0.9 W of optical power with a maximum

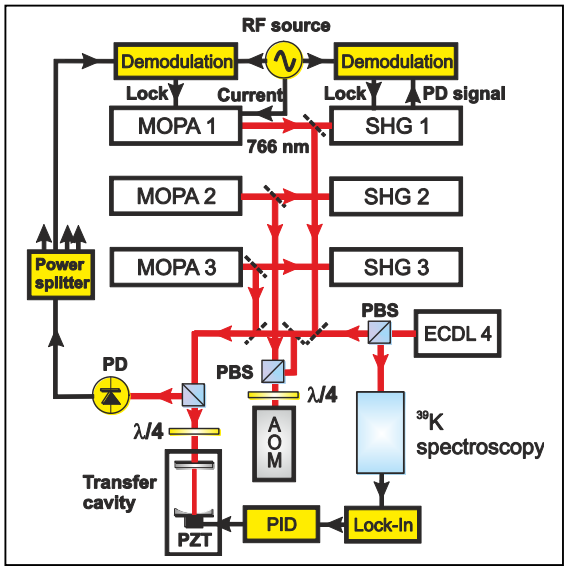

Figure 2. Schematic setup of the laser system used for operation of the T-MOT. The three independent lasers are locked to a common transfer cavity using the PDH scheme. The length of the transfer cavity is stabilised by means of a fourth laser referenced to the D_2-line of ^{39}K via Doppler-free spectroscopy. The locking scheme is shown in detail only for MOPA 1 for clarity. (PZT: piezo-electric transducer, PBS: polarising beam splitter, PD: photo diode)

tuning range of 930 – 960 nm feeds a commercial SHG cavity providing the light for the optical lattice. Long-term frequency stability of the Ti:Sa laser is obtained by stabilising it to the ultra-stable clock laser at 916 nm by means of another transfer cavity. According to the theoretical prediction of the magic wavelength for magnesium, the SHG output delivers 130 mW fibre-guided light at 469 nm to the experiment for generating the optical lattice. In order to fulfil the power requirements on Lamb-Dicke confinement, this light is enhanced in a linear build-up cavity which is set up in the horizontal plane around the vacuum chamber. Fig. 3 shows the schematic setup of the resonator. The cavity has a total length of 850 mm with a beam waist of 65 µm and consists of a curved mirror (R = 500 mm, T = 3 % around 469 nm), a plane mirror being HR-coated for the magic wavelength but AR-coated for the clock laser at 458 nm and a second curved mirror (R = 350 mm) having the same coating as the plane one. We operate with this three-mirror folded design due to two constraints on the cavity: (i) the clock laser has to be spatially overlapped with the lattice light for interrogation without being enhanced inside the cavity and (ii) the transmission of the incoupling mirror has to match the light losses per round trip inside the cavity (impedance matching) to ensure the highest possible enhancement factor. Offering a high transmission for 458 nm at the same time represents a hard-to-fulfil requirement on the mirror coating. Finally, the dipole trap beam at 1064 nm emitted by a Ytterbium fibre laser is overlapped with the lattice light in order to transfer the atoms into the optical lattice.

The maximum build-up factor of the cavity is 15, so we obtain a circulating power of 1.5 W by coupling 100 mW of light into the cavity. The corresponding trap depth is 16 E_r with E_r being

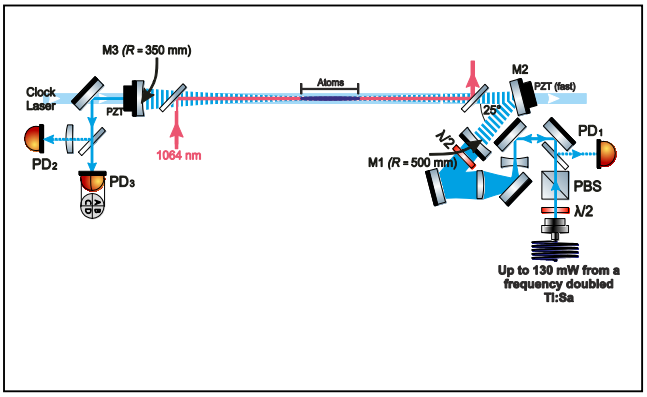

Figure 3. Schematic setup of the enhancement cavity for generation of the optical lattice. The total length of the cavity is 850 mm which is stabilized using the back-reflected light at mirror M1 (photo diode PD1). Using PD2 measuring the light leaking out of the cavity, the intra-cavity power is stabilised while a 4-quadrant photo diode (PD3) stabilises the cavity mode.

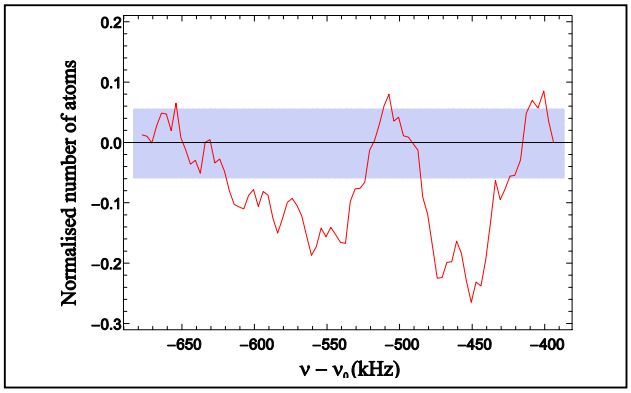

Figure 4. First spectroscopy of the clock transition. The red line is a moving average of five consecutive data points while the blue area indicates the signal standard deviation in absence of the spectroscopy laser. The carrier is observed at a detuning of -460 kHz and the red sideband at a detuning of -550 kHz.

the recoil energy (in temperature units E_r is 1.8 μK). We measured the trap frequencies to be 2π x 150 kHz which results in a Lamb-Dicke parameter of η = 0.51. The enhancement and thus the trap depth may be further increased by exchanging the view ports of the vacuum chamber as there might be a coating damage. A photo diode in front of the cavity is used for cavity length stabilisation (PD1) using the PDH scheme. PD2 is used for stabilising the circulating power inside the cavity while a 4-quadrant photo diode controls the cavity mode by giving feedback to two PZTs acting on Mirror 3 (see fig. 3).

The clock laser at 916 nm is guided via a 30 m long phase-stabilised fibre from a separate room to the magnesium experiment showing a frequency instability of 5 x 10^{-16} in 1 s averaging time. The light is amplified in the magnesium laboratory and frequency doubled to 458 nm in a commercial SHG cavity with an output power of 100 mW. The clock laser light is further fibre-guided to the experimental chamber and is aligned paraxial with the optical lattice.

III. Preparation of Atoms

The procedure of preparing metastable $^3P_0$ atoms in an ODT at 1064 nm is described in detail in [4]. For clarity, the continuous loading scheme we are using is different from stepwise loading of the S-MOT and the T-MOT with subsequent capture in the dipole trap. Instead, during the dipole trap loading, the S-MOT laser, transfer laser, T-MOT lasers and dipole laser are operating continuously, except the repumping laser for the $^3P_0$ state. Since the ODT has a maximum depth of 260 μK, we filter out the coldest $^3P_0$ atoms being captured by the potential. We trap about 10^5 atoms at a temperature of 100 μK.

In order to trap atoms in the optical lattice, the lattice light is applied additionally to the ODT, while the dipole trap and all other lasers are turned off after a period of 100 ms. Transfer of atoms to the lattice is performed with an efficiency of 10 %. The temperature of atoms in the lattice has been measured to be 10 μK.

IV. Spectroscopy of the $^1S_0 \rightarrow {}^3P_0$ Transition

In order to enhance the mHz natural linewidth of the clock transition for spectroscopy, we follow the suggestion of Taichenachev et al. [11] and apply a homogeneous magnetic field during the interrogation pulse thus creating a mixture of the magnetic $^3P_1$ state and the non-magnetic $^3P_0$ state. In order to address the transition for the first time, we apply a strong field (B = 500 G) causing ~ kHz power broadening of the line. Later on, we will require only a weak magnetic field if the transition frequency is well known.

After 1 s of preparation of atoms in the dipole trap, they are transferred to the optical lattice. In parallel, the static magnetic field is created by switching the Anti-Helmholtz MOT coils to Helmholtz configuration. During the 100 ms spectroscopy pulse, atoms in the $^3P_0$ state eventually are de-excited to the $^1S_0$ state depending on the clock laser frequency, so losses in number of atoms would indicate a spectroscopy resonance. For detection the quadrupole field is restored, atoms are released from the lattice and subsequently captured by the T-MOT for fluorescence detection. Detection in the triplet manifold is carried out with a high signal-to-noise ratio since no atoms from the background gas contribute to the signal.

Fig. 4 shows such a recorded spectroscopy sequence. The clock laser frequency was changed in steps of 300 Hz. Each data point is the result of three differential measurements (with and without the clock laser) being averaged. Furthermore, we took a moving average over five such consecutive data points to reduce the signal noise. One can clearly see a carrier signal together with a red sideband. Knowing the frequency of the $^1S_0 \rightarrow {}^3P_0$ clock transition without performing an absolute frequency measurement to be ν_0 = 655 058 646 681 860(47) Hz due to earlier frequency measurements of the $^1S_0 \rightarrow {}^3P_1$ transition [5] and the $^3P_1 \rightarrow {}^3P_0$ transition [12] we observe the carrier with 25 % of atoms being de-excited at a detuning of -460 kHz from the expected signal having a FWHM of 40 kHz. Due to the magnetic field of 500 G, a 2nd order Zeeman shift of -534 kHz is expected for the clock transition which is

in moderate agreement with the measurement. The red sideband could be observed at a frequency detuning of -550 kHz with a FWHM of 80 kHz. The broad carrier linewidth may be due to additional homogeneous broadening effects like fluctuations in the magnetic field. The width of the red sideband is subject to inhomogeneous broadening since the width of the second lattice energy band is 50 kHz. However, we do not observe a blue sideband giving rise to the assumption, that atoms occupy mostly the lowest energy band in the $^3P_0$ lattice potential.

V. Summary & Outlook

We have presented the successful loading of 10^4 metastable atoms in an optical lattice at the predicted magic wavelength of 469 nm. The atoms have a temperature of 10 μK. Performing magnetic-field-induced spectroscopy, we are able to observe the strongly spin-forbidden $^1S_0 \rightarrow {}^3P_0$ clock transition.

In order to increase the signal-to-noise ratio of the spectroscopy signal, we will, as a next step, optically pump the prepared atoms in the $^3P_0$ state back to the $^1S_0$ state, while being held by the dipole trap. Transfer to the optical lattice will thus happen in the singlet manifold and remaining metastable atoms will be blown away with resonant beams. Performing clock spectroscopy starting in the $^1S_0$ state with detection using the T-MOT afterwards promises a significant higher signal-to-noise ratio as no background atoms will contribute to the detection signal.

VI. Acknowledgment

This work was supported by the Sonderforschungsbereich 407 and the Cluster of Excellence "QUEST" (Centre for Quantum-Engineering and Space-Time Research).

References

[1] S. G. Porsev and A. Derevianko, "Multipolar theory of blackbody radiation shift of atomic energy levels and its implications for optical lattice clocks", Phys. Rev. A, vol. 74, 020502(R), 2006

[2] T. E. Mehlstäubler, *et al.*, „Observation of sub-Doppler temperatures in bosonic magnesium", Phys. Rev. A, vol. 77, 021402(R), 2008

[3] N. Poli, *et al.*, "Cooling and trapping of ultracold strontium isotopic mixtures", Phys. Rev. A, vol. 71, 061403(R), 2005

[4] M. Riedmann, *et al.*, "Beating the density limit by continuously loading a dipole trap from millikelvin-hot magnesium atoms", Phys. Rev. A, 043416, 2012

[5] J. Friebe, *et al*., "Remote frequency measurement of the $^1S_0 \rightarrow {}^3P_1$ transition in laser-cooled ^{24}Mg", New J. Phys., vol. 13, 125010, 2011

[6] J. Friebe, *et al*., "Absolute frequency measurement of the magnesium intercombination transition $^1S_0 \rightarrow {}^3P_1$", Phys. Rev. A, vol. 78, 033830, 2008

[7] P. Bohlouli-Zanjani, K. Afrousheh and J. D. D. Martin, "Optical transfer cavity stabilization using current-modulated injection-locked diode lasers", Rev. Sci. Instrum., vol 77, 093105, 2006

[8] C. E. Liekhus-Schmaltz, R. Mantifel, M. Torabifard, I. B. Burgess and J. D. D. Martin, "Injection-locked diode laser current modulation for Pound-Drever-Hall frequency stabilization using transfer cavities", JOSA B, vol. 29, issue 6, pp. 1394-1398, 2012

[9] D. Budker, S. M. Rochester and V. V. Yashchuk, "Obtaining frequency markers of variable separation with a spherical mirror Fabry-Perot interferometer", Rev. Sci. Instrum., vol 71, 2984, 2000

[10] R. W. P. Drever, *et al*., "Laser phase and frequency stabilization using an optical resonator", Appl. Phys. B, vol. 31, issue 2, pp. 97-105, 1983

[11] A. V. Taichenachev, *et al*., „Magnetic field-induced spectroscopy of forbidden optical transitions with application to lattice-based optical atomic clocks", Phys. Rev. Lett. vol 96, 083001, 2006

[12] A. Godone and C. Novero, "The magnesium frequency standard", Metrologia, vol. 30, issue 3, 163, 1993

Low-Noise 1-Micron Optical Frequency Comb Based on Diode-Pumped Solid-State Laser Technology

Stefan Kundermann, Erwin Portuondo-Campa, Jonathan Bennès, Steve Lecomte
Time & Frequency, Systems
Centre Suisse d'Electronique et de Microtechnique, Neuchâtel, Switzerland
Email: steve.lecomte@csem.ch

***Abstract*—Optical frequency combs are key instruments that have revolutionized many fields like frequency metrology and spectroscopy. Traditionally based on fiber lasers or Ti:Sapphire lasers they have been widely studied. Here we demonstrate a 1-micron optical frequency comb based on passively mode-locked diode-pumped solid-state laser technology with low-noise properties and high-reliability.**

Keywords—femtosecond laser; optical frequency comb; carrier-envelope offset frequency; relative intensity noise

I. INTRODUCTION

Optical frequency combs (OFCs) have revolutionized the way optical frequency metrology can be done since more than 10 years and are a key component in optical atomic clocks. Initially demonstrated with Ti:Sapphire lasers [1], optical frequency combs have been generated with several other laser technologies. Fiber laser technology at wavelengths of 1 µm and 1.55 µm has been the object of many efforts for improving their performances and in particular their noise properties [2]. OFCs based on passively mode-locked diode-pumped solid-state lasers (DPSSLs) have been less studied while offering excellent prospects for low-noise high-performance operation due to the low-loss laser cavity and high intra-cavity pulse energy [3]. A 1.55 µm DPSSL has been self-referenced and characterized in [4] while in [5] a self-referenced 1-micron Yb:KYW has demonstrated state-of-the-art low phase-noise microwave generation. Here we present a passively mode-locked diode-pumped Yb:glass laser that has been self-referenced and that demonstrates low-noise properties.

II. EXPERIMENTAL SETUP

The laser is passively mode-locked via a semiconductor saturable absorber mirror (SESAM) and delivers 111 fs transform-limited soliton pulses with an average output power of 205 mW at a repetition rate of 100 MHz. The pump diode is a fiber-coupled single-mode diode and the laser gain material is made of Yb-doped glass. One cavity mirror (the SESAM) is mounted on a piezoelectric transducer (PZT) for repetition rate tuning. After propagation in a 50-cm long photonic crystal highly nonlinear optical fiber (HNLF), the laser pulses generate an octave spanning supercontinuum amounting 110 mW of average power that spans from 650 nm to 1325 nm (see Figure 1). An f-2f nonlinear Michelson interferometer is fed with the supercontinuum for carrier-envelope offset frequency (f_0) detection. In contrast to the system reported in [5] no external optical amplifier is needed. A signal-to-noise ratio of up to 40 dB for f_0 (at an instrument resolution bandwidth of 91 kHz) has been detected. Prior to the injection into the HNLF, a small portion of the laser output is sampled, coupled into a single-mode fiber and detected with a fast photodiode for repetition rate stabilization via the PZT-mounted SESAM. H-maser referenced synthesizers provide the frequency reference for the stabilization of both, the repetition rate and f_0. Figure 2 presents the schematic of the experimental setup.

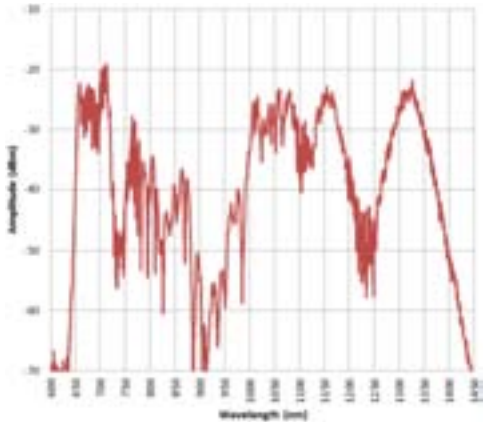

Fig. 1. Typical spectrum of the generated supercontinuum. The total average power was 110 mW.

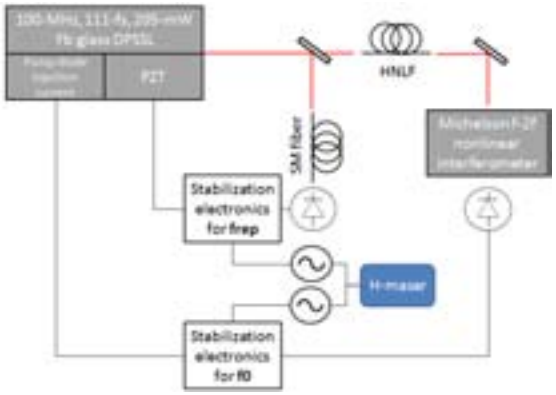

Fig. 2. Schematic of the experimental setup.

The financial support of the Canton of Neuchâtel is gratefully acknowledged.

III. RESULTS

Using standard locking electronics and feedback to the pump diode injection current, f_0 was phase locked to an H-maser referenced microwave synthesizer. The selected f_0 frequency harmonic was at 274 MHz and was first band-pass filtered and then divided by a factor 16 before being phase-compared to the reference synthesizer signal in a digital phase detector. The in-loop f_0 integrated phase noise amounts 736 mrad when integrated from 1 Hz to 1 MHz for a measured f_0 frequency of 274 MHz (see Fig. 3). The achieved integrated phase noise is comparable to the best fiber lasers. The f_0 phase-locking is very robust and lasts for days. Figure 3 shows an Allan deviation of the stabilized f_0 when compared to the reference synthesizer signal. The anticipated τ^{-1} slope is well observed. The relative intensity noise (RIN) of the laser has been also measured (Figure 4). For a free-running laser, at offset frequencies above the laser pump modulation bandwidth, shot-noise limited RIN is achieved with a level of -154 dBc/Hz. The corner frequency around 4 kHz is directly linked to the long upper-state lifetime of the ytterbium ions in the gain medium that acts as a low-pass filter to pump power fluctuations.

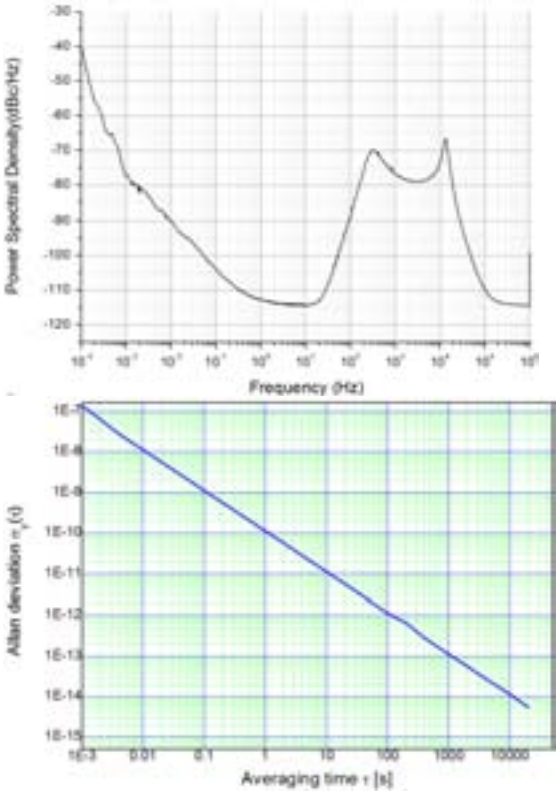

Fig. 3. Top: Phase noise power spectrum density of the divided by 16 274-MHz carrier-envelope offset frequency. The integrated phase noise amounts 736 mrad when integrated from 1 Hz to 1 MHz at a carrier frequency of 274 MHz. Bottom: Allan deviation of the stabilized f_0.

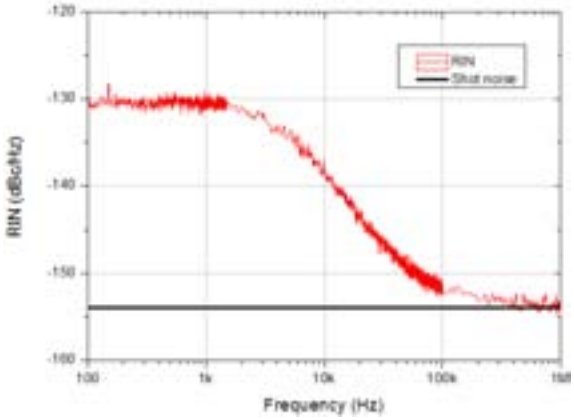

Fig. 4. Relative intensity noise (RIN) of the free running laser.

The repetition rate stabilization on an H-maser referenced synthesizer resulted in a relative frequency instability of $3 \cdot 10^{-12}$ at 1s averaging time. Figure 5 shows the Allan deviation of the free-running and H-maser referenced repetition rate of the mode-locked laser. These measurements were performed with a Symmetricom 5120A instrument based on cross-correlation.

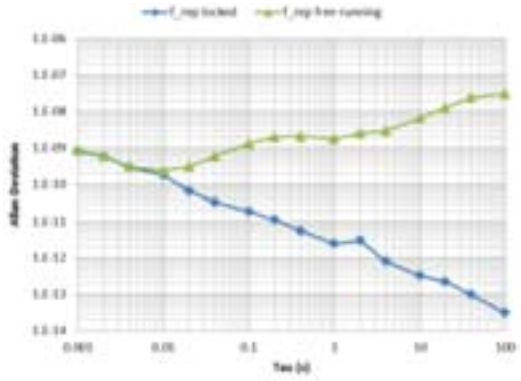

Fig. 5. Allan deviation of the free running and H-maser stabilized repetition rate of the modelocked laser.

IV. CONCLUSIONS

A low-noise 100-MHz diode-pumped Yb:glass solid-state laser has been fully stabilized. An integrated phase noise of 736 mrad has been measured for the carrier envelope offset frequency while the Allan Deviation of the repetition rate amounted to $3 \cdot 10^{-12}$ at 1 s averaging time. The relative intensity noise was limited to the photocurrent shot noise (-154 dBc/Hz) for frequencies above 100 kHz. This system was very reliable with locking periods of several days. Future work will be related to the stabilization on an optical reference and the generation of low-phase noise microwaves.

REFERENCES

[1] D.J. Jones, S.A. Diddams, J.K. Ranka, A. Stentz, R.S. Windeler, J.L. Hall, and S.T. Cundiff, "Carrier-Envelope Phase Control of Femtosecond Mode-Locked Lasers and Direct Optical Frequency Synthesis", Science, vol. 288, pp.635-639, April 2000.

[2] J.J. McFerran, W.C. Swann, B.R. Washburn, N.R. Newbury, "Suppression of pump-induced frequency noise in fiber-laser frequency combs leading to sub-radian f ceo phase excursions", Appl. Phys. B, vol. 86, pp. 219-227, September 2006.

[3] R. Paschotta, "Noise of mode-locked lasers. Part II: Timing jitter and other fluctuations", Appl. Phys. B, vol. 79, pp. 163-173, May 2004.

[4] S. Schilt *et al.*, "Fully stabilized optical frequency comb with sub-radian CEO phase noise from a SESAM modelocked 1.5-μm solid-state laser", Optics Express, vol. 19, pp. 24171-24181, November 2011.

[5] S.A. Meyer, T.M. Fortier, S. Lecomte, S.A. Diddams, "A frequency-stabilized Yb:KYW femtosecond laser frequency comb and its application to low-phase-noise microwave generation", Appl. Phys. B, published online July 5 2013.

Long Distance Phase-Coherent Link Between Near- and Mid-Infrared Frequencies

B. Argence, B. Chanteau, O. Lopez, C. Chardonnet, C. Daussy, B. Darquié, A. Amy-Klein
Laboratoire de Physique des Lasers,
Université Paris 13, Sorbonne Paris Cité, CNRS,
Villetaneuse, France
berengere.argence@univ-paris13.fr

D. Nicolodi, M. Abgrall, Y. Le Coq
[2]LNE-SYRTE,
Observatoire de Paris, CNRS, UPMC,
Paris, France

G. Santarelli[2,3]
[3]Laboratoire Photonique, Numérique et Nanosciences,
Université de Bordeaux 1, Institut d'Optique and CNRS,
Talence, France

Abstract— **We present a new method for accurate mid-infrared frequency measurements and stabilization to a near-infrared ultra-stable frequency reference, transmitted with a long-distance fibre link and continuously monitored against state-of-the-art atomic fountain clocks. We demonstrate the frequency stabilization of a mid-infrared laser with fractional stability better than 4×10^{-14} at 1 s averaging. This new stabilization scheme gives us the ability to transfer frequency stability in the range of 10^{-15} or even better, currently accessible in the near-infrared or in the visible, to mid-infrared lasers in a wide frequency range.**

Frequency transfer, high resolution spectroscopy, frequency stabilization.

I. INTRODUCTION

Ultra-high-resolution spectroscopy enables to test fundamental physics with molecules as for instance the non conservation of parity [1] or the stability of the electron-to-proton mass ratio [2]. However many of these tests rely on the availability of ultrastable and accurate laser sources emitting in the mid-infrared (MIR) where molecules exhibit rovibrational transitions. MIR laser frequency stabilization has been performed for a long time using molecular references such as CH_4 or OsO_4 [3]. However the obtained stability is at least one order of magnitude below those of visible or near-infrared (NIR) lasers stabilized to ultra-stable cavity. Moreover only a few molecular lines can be used when ultra-high accuracy is needed. It is thus very challenging to develop a frequency stabilization scheme in the MIR with performances similar to that of the visible and NIR domains.

For that purpose, we have built a frequency chain which enables to coherently transfer the stability and accuracy of an ultrastable laser emitting at 1.54 µm to the MIR spectral region (Fig. 1). This ultrastable signal is generated at LNE-SYRTE where its frequency is measured against a set of primary standards using an optical frequency comb. It is transferred from LNE-SYRTE to LPL through an optical link [4]. A second optical frequency comb is phase-locked to this signal and, using sum-frequency generation in a non-linear crystal [5], the MIR frequency is compared or phase-locked to a high-harmonic of the comb repetition rate.

In this paper, we will describe the principle of coherent frequency stability transfer between near- and mid-infrared frequencies around 10 µm and present the performances obtained with the phase-lock of a CO_2 laser. We will then give the first results of frequency stabilization obtained with a Quantum Cascade Laser (QCL).

II. EXPERIMENTAL SET-UP

The experimental setup is shown in figure 1 (a thorough description can be found in reference [6]). The ultra-stable optical reference located at LNE-SYRTE is a 1.54 µm fiber laser locked to a high finesse cavity. Its fractional frequency instability was measured to be lower than 2×10^{-15} at 1 s and 10^{-14} at 100 s (after a 0.3-Hz/s drift was removed) [7]. Its frequency is measured using a fiber fs laser centered around 1.55 µm. The laser repetition rate is phase-locked to the optical reference frequency after removal of the comb frequency offset f_0. The absolute frequency of the comb repetition rate 36^{th} harmonic (9 GHz) is continuously measured against the primary standards of LNE-SYRTE. It enables real-time correction of the ultra-stable laser frequency drift by acting on the driving frequency of an acousto-optic modulator. This results in an ultra-stable NIR reference, the frequency of which is traceable to primary standards with a 10^{-14} uncertainty after 100 s.

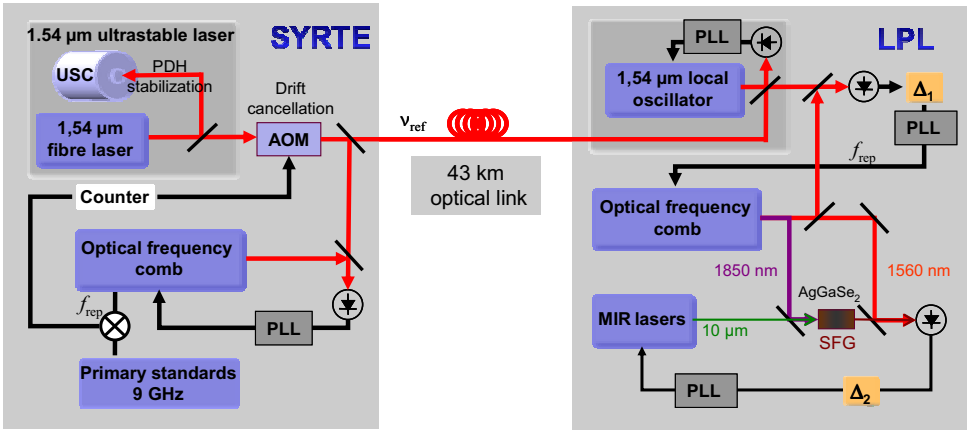

Figure 1. Experimental set-up. The MIR laser frequency can either be controlled with the beat-note Δ_2 or the OsO_4 absorption signal (see text). PLL: phase-lock loop, PDH: Pound-Drever-Hall stabilization, SFG: sum-frequency generation, AOM: acousto-optic modulator, USC: ultra-stable cavity.

This optical reference signal is transmitted to LPL through a 43-km long optical link. The free-running link exhibits a propagation instability of 2×10^{-14} at 1 s and around 10^{-15} between 100 s and 1 day. When compensated, the link instability has been measured to be roughly $10^{-15}\ \tau^{-1}$ and to reach around 10^{-18} after 10^3 s. The frequency stability and accuracy of the reference signal are thus preserved at the LPL optical link end. At LPL, a low-noise laser diode is phase-locked to the incoming signal and constitutes the local optical frequency reference ν_{ref}. The repetition rate f_{rep} of a 1.55 µm fibre fs laser is phase-locked to ν_{ref}. The beat-note Δ_2 (see Fig. 1) then compares the MIR laser frequency ν_{MIR} around 10 µm and the n^{th} harmonic of the repetition rate. This signal is generated using sum-frequency generation (SFG) of the MIR light and an additional comb output centred on 1.85 µm, generated in a non-linear fiber [5]. This comb output and the MIR laser beam are focused in a 10-mm long crystal of AgGaSe2 for type I SFG. The resulting shifted comb, centred on 1.55 µm, is combined with the 1.55 µm fs-laser output. An adjustable delay line enables to control the overlap of the pulses in the time domain. The resulting beat-note Δ_2 shows a signal-to-noise ratio of about 25-30 dB in a 100 kHz bandwidth. This beat-note is then mixed with an RF oscillator to generate the error signal to lock the MIR laser to the optical frequency comb (OFC). Resulting from the frequency difference between two modes of the same comb, Δ_2 is independent of the comb offset f_0. The MIR frequency is thus directly linked to the near-infrared frequency reference.

III. MIR FREQUENCY NOISE AND STABILITY

To characterize the phase-coherent link between the near-infrared frequency reference and the MIR frequency, we

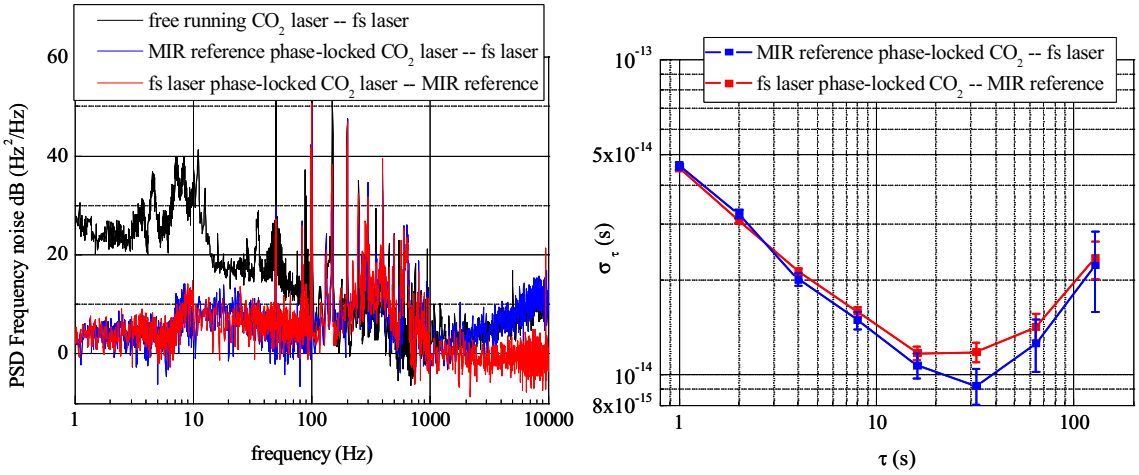

Figure 2. CO_2 laser results. *(Left)* PSD of frequency noise of the free-running CO_2 laser (black), the CO_2 laser phase-locked onto the MIR reference (blue) and onto the fs laser (red). *(Right)* Fractional frequency stability (Allan deviation) with ± 1σ error bars, same colors as the left figure.

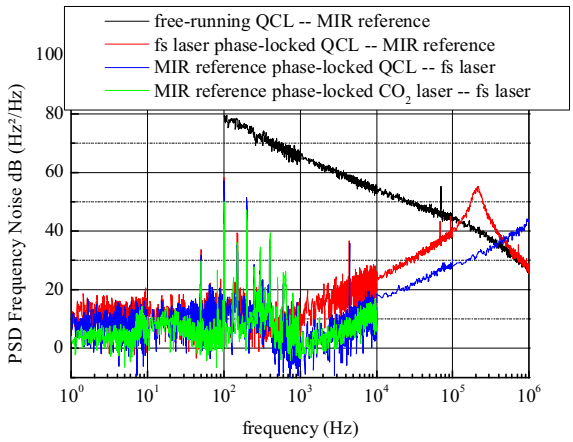

Figure 3. QCL preliminary results in terms of frequency noise. Free running QCL (black), QCL phase-locked onto MIR reference (blue) and onto fs laser (red). CO_2 laser phase-locked onto MIR reference from fig. 2 is added for comparison (green).

used a CO_2 laser stabilized onto an OsO_4 saturated absorption line as a MIR reference. Such a OsO_4-stabilized CO_2 laser constitutes the current state-of-the-art MIR secondary reference standard [3]. Corrections are applied to a PZT controlling the laser cavity length with a stabilization bandwidth of about 400 Hz limited by the PZT actuator. We first phase-lock the MIR laser onto the MIR reference and use the Δ_2 beat-note to evaluate the frequency noise and stability. Then, the MIR laser is phase-locked onto the OFC using Δ_2 and frequency stability is measured by beating with the MIR reference. Two MIR lasers have been successively phase-locked to the optical reference signal. We will first present the performances obtained with a CO_2 laser and then give the preliminary results of the QCL phase-lock.

A. CO_2 laser

Fig. 2 shows the frequency noise and stability of the CO_2 laser either locked onto the MIR reference or onto the OFC. In both cases, the results are very similar. The CO_2 laser frequency noise reaches about 3 Hz²/Hz at 1 Hz and is pretty flat (white frequency noise) until a few hundred hertz. The f slope after 1 kHz observed on the blue data is attributed to the NIR phase-locked loop. It is not observed when the CO_2 laser is locked to the OFC due to its small stabilization bandwidth of ~ 400 Hz. The right figure shows a 1s-stability lower than 5×10^{-14} with a decrease in $\tau^{-1/2}$ until a few tens of seconds. The small difference between the stabilities is due to non-stationary effects.

B. Quantum Cascade Laser (QCL)

Fig. 3 presents preliminary frequency noise results obtained with a QCL. The free-running QCL is much noisier than the CO_2 laser (about 70 dB at 100 Hz). However, the set-up allows a frequency noise reduction of about 60-70 dB at 100 Hz with a lock bandwidth of about 200 kHz when the QCL is phase-locked onto the OFC (bandwidth > 1 MHz when locked onto the MIR reference [8]). There is still some residual noise in the low frequency domain that is not suppressed. The frequency noise is indeed a little higher (less than 10 dB Hz²/Hz) than the one of the stabilized CO_2 laser. We attribute this excess noise to optical feedback in the laser and are now progressing towards its reduction. Nevertheless, these results represent to our knowledge the best ones ever obtained with a QCL.

IV. Conclusion

We have presented a coherent frequency chain able to transfer the frequency stability and accuracy from a remote ultra-stable 1.54 µm frequency reference to a MIR source. State-of-the-art results have been obtained with a CO_2 laser and we are now progressing toward the extension of this experiment to QCLs. Preliminary results give a frequency noise lower than 100 Hz²/Hz from 1 Hz to a few kHz. Moreover, this technique can be easily implemented in any laboratory receiving an ultra-stable signal and adapted to laser sources in a wide wavelength range, from 3 to 20µm.

References

[1] B. Darquié et al, “Progress toward a first observation of parity violation in chiral molecules by high-resolution laser spectroscopy”, Chirality, vol. 22, pp. 870-884, 2010.

[2] A. Shelkovnikov et al, “Stability of the Proton-to-Electron mass ratio”, Phys. Rev. Lett., vol. 100, pp. 150801-150803, 2008.

[3] V. Bernard et al, "CO_2 laser stabilization to 0.1-Hz level using external electrooptic modulation", IEEE J. of Quant. Electr., vol. 33, pp. 1282-1287, 1997.

[4] O. Lopez et al., "Cascaded multiplexed optical link on a telecommunication network for frequency dissemination," Opt. Expr., vol. 18, pp. 16849-16857, 2010.

[5] A. Amy-Klein et al, “Absolute frequency measurement of an SF6 two-photon line using a femtosecond optical comb and sum-frequency generation”, Opt. Lett., vol. 30, pp. 3320-3322, 2005.

[6] B. Chanteau. et al., “Mid-infrared laser phase-locking to a remote near-infrared frequency reference for high-precision molecular spectroscopy”, New J. Phys., vol. 15, pp. 073003, 2013.

[7] H. Jiang et al, “Long-distance frequency transfer over an urban fiber link using optical phase stabilization”, J. Opt. Soc. Am. B, vol. 25, pp . 2029, 2008.

[8] P. L. T. Sow et al, Conference given at the 68th International Symposium on Molecular Spectroscopy, FD15 paper, https://molspect.chemistry.ohio-state.edu/symposium/Abstracts/p557.pdf

Improving Frequency Control of Temperature Compensated Surface Acoustic Wave Devices

Sergey Mishin[1], Michael Gutkin[1], Alexander Bizyukov[2] , Vladimir Sleptsov[3]

[1] Advanced Modular Systems, Inc, Goleta, CA/USA, smishin@amssb.com
[2] Karazin Kharkiv National University, Kharkiv, Ukraine
[3] Moscow State Aviation Technological University Moscow, Russia
Email: smishin@amssb.com; mgutkin@amssb.com

***Abstract*—In this paper, we demonstrated improvement of frequency uniformity and stability for Temperature Compensated Surface Acoustic Wave (SAW) devices. SiO_2 has been used to obtain low Temperature Coefficient (TempCo) in SAW devices for more than three decades [1]. One of the big issues is that SAW devices have to be processed at temperatures below 300C. When low temperature SiO_2 is exposed to the ambient environment, it interacts with ambient humidity [2], [3], [5], [6]. Such interactions can change frequency of the SAW devices and can make frequency trimming with a focused Ion Beam [7], [8] extremely challenging. UV and steam treatment of SiO_2 improved trimming rate stability on the first trimming [4] and [9], but was not sufficient to provide tight frequency control required for SAW devices after the second trimming. Using silicon nitride (Si_3N_4) capping layer on top of SiO_2 showed some improvement in frequency control after trimming process. Most improvement was obtained using aluminum nitride (AlN) capping layer on top of SiO_2 followed by two trimming steps.**

Keywords-SAW, Temperature, coefficient, trimming. frequency

I. INTRODUCTION

Controlling frequency of temperature compensated devices is critical in obtaining high yielding production process. The use of SiO2 films has been recently used to improve behavior of SAW filters over the required temperature range. Unfortunately, the diffusion of the moisture into SiO2 film during exposure of the wafers to the ambient environment causes the reaction of H20 with strained Si-O bonds and formation of silanol (Si-OH). This has a great effect on the local intrinsic SiO2 film stress and leads to the reduction of compressive residual stress and progressive increase of the tensile residual film stress.

With above mentioned effect, it is impossible to obtain yield above 90% without use of frequency trimming. In this paper we address the issues with obtaining best results through a judicious use of both deposition and trimming techniques.

II. EQUIPMENT

In this research, we used Advanced Modular Systems' (AMSystems) three chamber cluster tool pictured in Figure 1 for deposition of all layers as well as frequency trimming.

SiO2 was deposited using RF diode mode from SiO2 target. We used 12" target at 1kW of RF power and frequency 13.56 MHz. Only Ar process gas had been added during SiO2 deposition.

Si3N4 film was deposited by dual AC magnetron from highly doped - highly conductive Si target. 40kHz AC power at 1kW had been applied between two Si targets. Ar and N2 were added as process gases during deposition. Deposition was done in poisoned nitride mode to get a stable and stoichiometric Si3N4 film.

Standard process for AlN deposition was used with dual AC magnetron. AC power applied between targets in a reactive deposition mode.

Standard Trimming process was performed on the deposited films. Process is established by removing film thickness of the top layer, based on frequency maps using an adjustable focused DC ion source and scanning wafer mechanism. Trimming process was used to get high yield of devices from wafer.

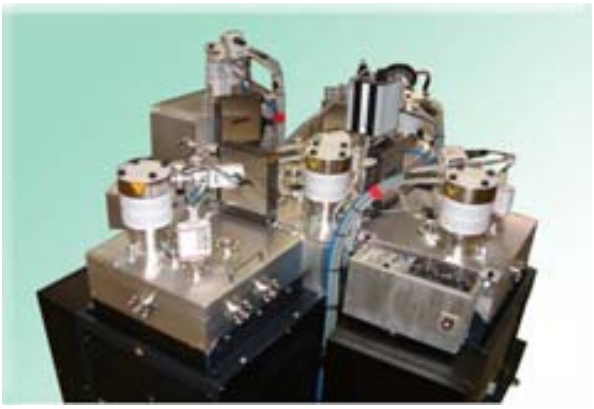

Figure 1: AMSystems Cluster Tool

III. METHODS FOR IMPROVING TEMPCO CONTROL

For several decades SAW device manufacturers attempted to utilize SiO2. Unfortunately, low temperature oxide depositions necessary for the SAW applications, combined with a need for low cost equipment, limited options available to the SAW manufacturers. Over decades many methods have been tried in order to reduce variation of frequency due to the inherent oxide interactions with ambient moisture. In this

paper we have compared few methods of protection and surface modification of the silicon dioxide films in order to prevent the physical adsorption of water vapor molecules on the surface of silicon dioxide film and reaction between Si-O bonds with H2O molecules with Si-OH formation.

To prevent physical adsorption of water vapor on Silicon dioxide film we used two different cap layers: AlN and Si3N4 films. Both films have good passivation properties, stable and have high grain density. 500A of Si3N4 or AlN films were deposited on top of SiO2 films without vacuum break. 500A was chosen to make sure that after trimming process at least 200A of the film is still remaining.

For SiO2 surface modification we used two methods:

1. High power density UV radiation
2. Annealing of SiO2 film in high humidity environment

High power density UV radiation was done by scanning wafer under excimer laser radiation. XeCl excimer laser with wavelength 308nm and power density greater than 10MW/cm2 per pulse was used for SiO2 surface modification. Surface densification under this process conditions prevented diffusion of moisture into SiO2 grain bonds.

Annealing of SiO2 film in high humidity was done at the temperatures between 250…300C in water stem with post annealing and then, drying. This process allows saturating all available Si-O bonds and eliminating further changes under exposure to the ambient.

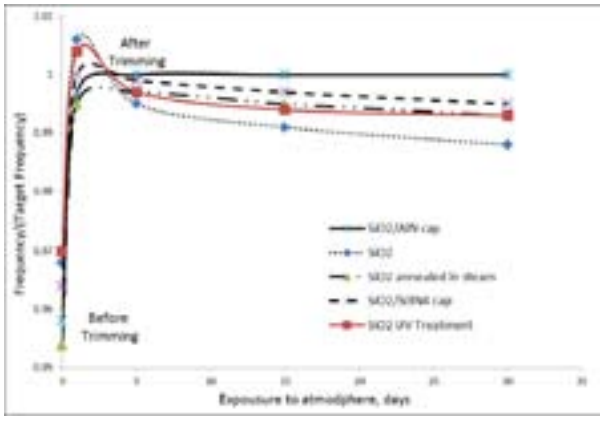

Figure 2: Average Frequency as a function of time exposure to atmosphere for different methods of SiO2 treatments and capping processes

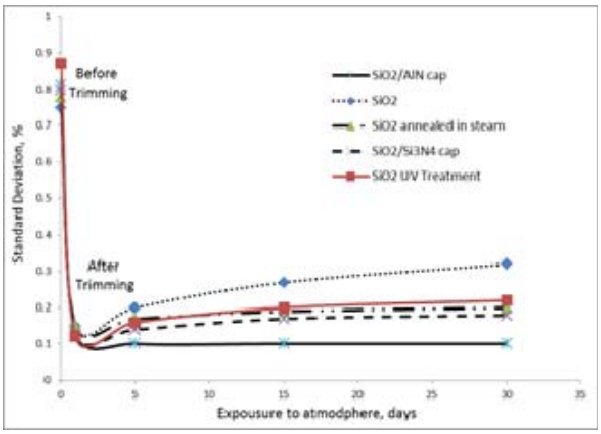

Figure 3: Cross wafer Frequency variation as a function of time exposure to atmosphere for different methods of SiO2 treatments and capping processes

Figures 2 and 3 show improvements obtained using different methods commonly used to improve frequency control in temperature compensated SAW devices.

The most successful method as we observed is to cap SiO2 with AlN without air exposure and trim it with focused ion beam. Even though this technique is adequate for a lot of devices, there is a further benefit in performing a second trim. Figure 4 shows the benefits of the two steps trimming vs. one step trimming.

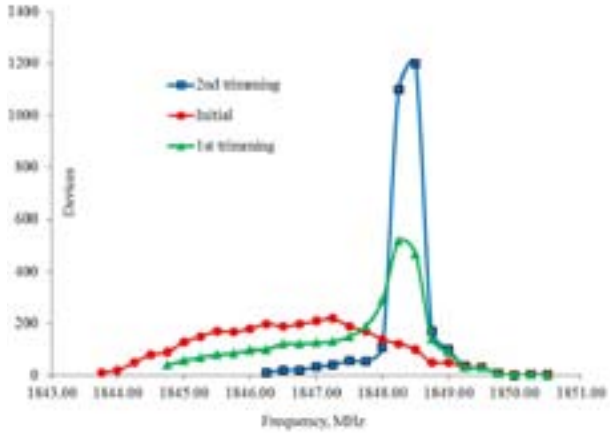

Figure 4: Two step trimming on an AlN capped temperature compensated SAW device

Depending on the initial frequency distribution, the first trim can have 5X improvement. Second trim provides another 4X improvement over the first trim. As the result the total frequency improvement can be as big as 20 times.

IV. SUMMARY

Capping SiO2 temperature compensated layer with AlN film and using two steps trimming can provide high yielding SAW devices for the tough requirements for today's RF filter needs.

REFERENCES

[1] Willingham, C.B., et.al., "Temperature Compensated Surface Wave Devices", United States Patent #3965444I. S. Jacobs and C. P. Bean, "Fine particles, thin films and exchange anisotropy," in Magnetism, vol. III, G. T. Rado and H. Suhl, Eds. New York: Academic, 1963, pp. 271–350.

[2] H.A.Naseem, et.al., "Stress and bonding characterization of PECVD silicon dioxide films",Electrochemical Society, Vol.97-10, pp.217-226,4-9 May,1997

[3] Leplan H., "Ressidual stresses in evaporated silicon dioxide thin films: Correlation with deposition parameters and aging behavior", Journal of Applied Physics, pp.962-968, 1995

[4] M.S. Haque, et.al., "Post-deposition processing of low temperature PECVD silicon dioxide films for enhanced stress stability", Thin Solid Films, Volumes 308-309, 1997, pp. 68-73

[5] Leplan H., "Kinetics of residual stress evolution in evaporated silicon dioxide films exposed to room air", Journal of Applied Physics, pp.6926-6931, 1996

[6] Parada E. G., "Aging of photochemical vapor deposited silicon oxide thin films", Journal of Vacuum Science &Technology, Volume 14, pp.436-440

[7] Quiang Zou, et.al., "High Coupling Coefficient Temperature Compensated FBAR Rsonator for Oscillator Apllication with Wide Pulling Range", 2010 IEEE International Frequency Control Symposium, pp. 646-650

[8] S. Mishin, "Improving Manufacturability of Bulk Acoustic Wave and Surface Acoustic Wave Devices", SPAWDA 2011, IEEE

[9] S. Mishin, et.al., "Production Issues in Using Silicon Dioxide Films for Temperature Compensated Bulk and Surface Acoustic Wave Devices", 2012 IEEE International Frequency Control Symposium

Investigation of the Electrode Coating Influence on the Frequency Temperature Characteristics of the Resonators Operating at the Rotated Y -Cut $Ca_3TaGa_3Si_2O_{14}$ Single Crystals

Andrey Medvedev, Aleksey Zabelin, Svetlana Bazalevskaya, Oleg Buzanov, Sergey Sakharov, Vladimir Alenkov
OAO «Fomos - Materials»
Moscow, Russia
medvedev@newpiezo.com

Alexey Dmitrienko, Alexander Blinov
JSC "Research Institute For Physical Measurements"
Penza, Russia

***Abstract*—Resonators manufactured on $Ca_3TaGa_3Si_2O_{14}$ single crystals (CTGS) operating in a thickness shear mode were investigated. The frequency temperature characteristics of the rotated Y-cut based resonators were measured. The resonators operated at the crystal elements with angle cut −21°20' have frequency deviation less than 120 ppm in the operating temperature range from −60 up to 85°C. The temperature coefficient of frequency of the second order is close to −0.022 ppm/°C^2. It is shown that maintaining turnover point of the frequency temperature characteristic within the range of ±1 °C requires accuracy of the crystal element manufacturing not worse than ±1.5 angular minutes for resonators with Ag electrodes. The dependence of the Bechmann's number on electrode thickness was calculated. It was discovered that for Ag electrode coating with electrode thickness of 200 nm, the single-response characteristic of the resonator can be obtained if the electrode size (l_x) does not exceed 12 thicknesses of the crystal element. With the limiting value of the relative electrode size equaling l_x/t =12.3, the relative resonance interval is 1%, while the capacitance ratio is 47 units.**

Keywords-$Ca_3TaGa_3Si_2O_{14}$, resonator; single crystal; bulk acoustic waves; temperature coefficient of frequency (TCF)

I. INTRODUCTION

More recently, new piezoelectric crystals that also operate at high temperatures have been introduced for wide bandwidth acoustic wave filters, frequency control, and high-temperature sensor applications. The study, production, and application of the langasite family crystals have been rapidly developing in recent years. Langasite family crystals are promising piezoelectric materials for the new generation of acoustoelectronic devices, as they can successfully replace the traditionally used ceramics and quartz. The crystals have high acoustic Q-factors, zero temperature coefficients of frequency of the first-order (TCF(1)), high coupling coefficients. Moreover, they lack phase transition up to pre-melting temperatures (Tmelt = 1470°C).

The langasite family is a group of crystals isostructural to $Ca_3Ga_2GeO_{14}$ and recently it includes around 100 compounds. The best known crystals with zero TCF(1) of the group are langasite, lanthanum gallium silicate (LGS, $La_3Ga_5SiO_{14}$), langatate, lanthanum gallium tantalate (LGT, $La_3Ta_{0.5}Ga_{5.5}O_{14}$), langanite, lanthanum gallium niobate (LGN, $La_3Nb_5Ga_{5.5}O_{14}$), calcium niobium gallium silicate (CNGS, $Ca_3NbGa_3Si_2O_{14}$), and catangasite, calcium tantalum gallium silicate (CTGS, $Ca_3TaGa_3Si_2O_{14}$). Langasite family crystals belong to the structure type of the trigonal system (space group P321, point group 32).

Temperature frequency characteristic of the temperature compensated langasite cut is a parabola. The value of temperature coefficient of frequency of the second order TCF(2) is equal to −0.058 ppm/°C^2. Frequency deviation in the operating temperature range from −60 to 85 °C is about 300 ppm. For some applications of piezoelectric devices, such frequency deviation value is not satisfactory. As a result of search for a more temperature stable material, the $Ca_3TaGa_3Si_2O_{14}$ (CTGS) single crystal was synthesized.

CTGS possesses a number of unique piezoelectric characteristics that enable its application for the development and manufacture of acoustoelectronic devices. CTGS has a small frequency deviation in the temperature range (temperature frequency coefficient of the second order is about −0.026 ppm/°C^2 [1] and −0.039 ppm/°C^2 [2]).

In this work, the influence of electrode materials and sizes on the frequency temperature characteristics of CTGS resonators operating in a thickness shear mode (TS-mode) was investigated. The Bechmann's number for CTGS resonators was also calculated.

II. EXPERIMENTAL

CTGS single crystals were grown by Czochralski method using an Ir crucible. The growth process was carried out in Ar atmosphere. The crystals were grown along the crystallographic <100> direction. The pulling rate was 0.5 − 1 mm/h and the rotation speed was 11 rpm.

Figure 1. CTGS single crystal

The orientation of CTGS single crystals and the notation system for designation crystalline plates were made according to the IEEE Standard on Piezoelectricity [3]. The plate's cuts are denoted by (YZw) Φ. In this work, we used the plates of six cuts (YZw) –25°, (YZw) –22°20', (YZw) –21°20', (YZw) –21°, (YZw) –20°30', and (YZw) –20°. The obtained crystals and plates were oriented using an X-ray diffraction. The plates were lapped with 10μm Al_2O_3. The roughness of plates was Ra<0.24 μm. We produced the round shape blanks 4.5 mm in diameter and with primary flat oriented parallel to Z′-axes. The plates' thickness was about 120 um. Electrodes of different sizes and from diverse metals (Ag and Au) were deposited. The fundamental frequency of TS-mode was about 10.7 MHz. The measurements of the temperature frequency characteristics were performed by the S&A W2200B Temperature Test System. The attenuation characteristics of the CTGS resonators were measured using Agilent E5061A specter analyzer. For the approximation of the frequency temperature characteristics, a polynomial function was used,

$$(f_r - f_0)/f_o = a + b\cdot(T - T_0) + c\cdot(T - T_0)^2 \qquad (1)$$

where b and c are the temperature coefficients of frequency of the first and second order, respectively. f_0 is resonance frequency at the reference temperature T_0, f_r is resonance frequency at temperature T.

A turnover temperature was obtained by formula,

$$T_e = -b/2c \qquad (2)$$

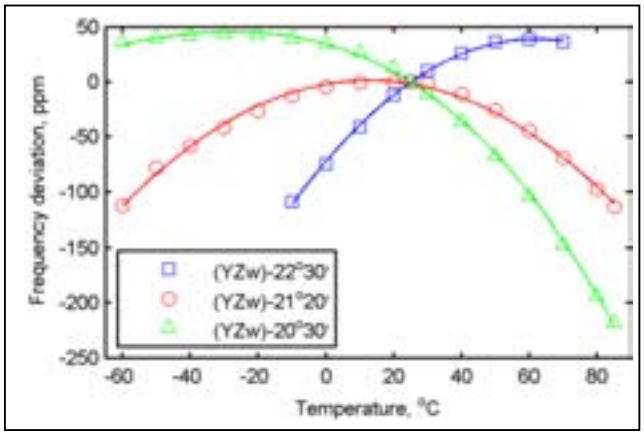

Figure 2. Frequency temperature characteristics of CTGS resonators. Electrode film is Ag, the electrode diameter is 1.75 mm.

III. RESULTS AND DISCUSSION

A. *Study of frequency temperature characteristics of CTGS resonators*

Figure 2 shows a typical frequency deviation as a function of temperature for CTGS resonators. As observed in Fig.2, resonators with Ag electrodes operating at (YZw) –21°20' cut have a frequency deviation less than 120 ppm in the temperature range from –60 up to 85°C. The value of TCF(2) is about −0.022 ppm/°C^2 which is in a good agreement with [1] and [2].

The turnover temperatures for different sizes and electrode materials were calculated by formula (2). As observed in Fig.3, for the electrode of the same size and material with angle cut varying from –25° to –20°, the dependance of frequency temperature characteristic extremum point is represented by a straight line. Inclination of lines for Au electrodes is half times bigger than that of Ag electrodes. It means that for resonators with Ag electrodes, maintaining turnover point of the frequency temperature characteristic within the range of ±1 °C requires crystal element manufacturing accuracy not worse than ±1.5 angular minutes. For resonators with Au electrodes, the accuracy should be ±1.0 angular minutes.

B. *Bechmann's number for CTGS resonators*

In [4], Tiersten applied the equations of three-dimensional linear piezoelectricity in the analysis of trapped energy resonators vibrating in coupled thickness-shear and thickness-twist modes in the vicinity of the fundamental and odd overtone thickness-shear frequencies. Based on his analysis, Tirsten derived the two-dimensional condition that generalizes the Bechmann's number $\lceil l_x/t \rceil$ for one dimension and provides the condition for the existence of only one trapped mode.

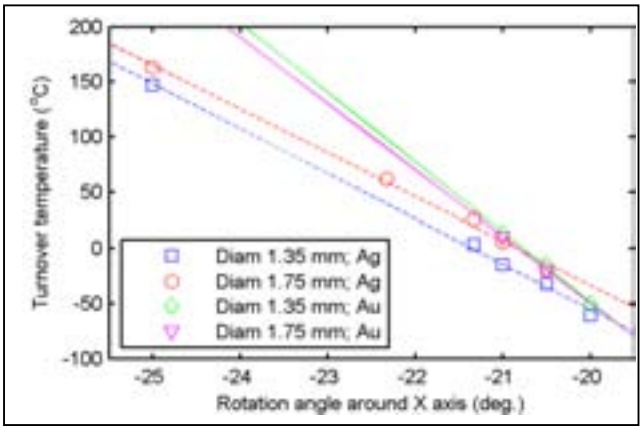

Figure 3. Turneover temperature as a function of rotation angle for resonators with different electrodes

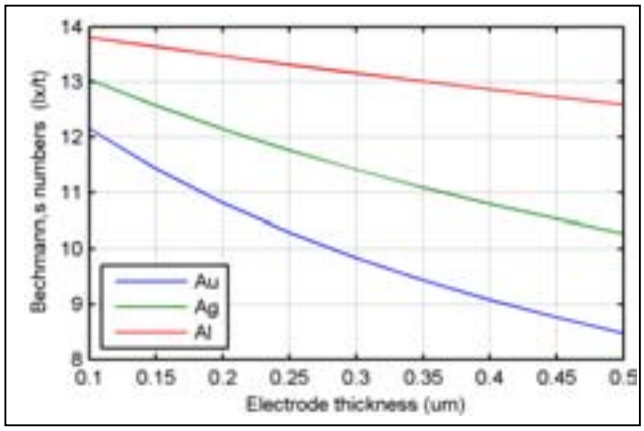

Figure 4. Bechmann's number as a function of the electrode thickness

The latter condition can be written as:

$$\left[\frac{l_x}{t}\right] \le \frac{d_B}{n\sqrt{4k_{26}^2/n^2\pi^2 + R}} \qquad (3)$$

where k_{26}^2 is coupling coefficient for this cut, n – overtone number. In this paper, we considered only the fundamental mode of the thickness shear mode ($n=1$). The dimensionless trapping parameter d_B depends on the material constants of the crystal and the electrode shape.

Loading mass R determines the frequency change after electrode deposition.

$$R = 2\rho' t'/\rho t \,. \qquad (4)$$

where - ρ , ρ' - density of the plate and electrode's material, respectevely.

Using the formulas of paper [4], values of parameters d_B were calculated. The optimum shape of electrode for (YZw) – 21°20' cut is an ellipse elongated along the X-axis. The ratio γ of the electrode size along the X axis to the electrode size along the Z′ axis is equal to 1.84. The parameter d_B value equals to 2.92. For the case $\gamma = 1$, the value of dimensionless parameter d_B is equal to 1.78.

Based on (3) and (4), the values of Bechmann's number as a function of a thickness of Al, Ag end Au electrodes were calculated. As observed in Fig.4 for the Ag electrode with thicknesses of 200 um, the relative electrode size should be less than 12 units. To specify our estimates, CTGS resonators with different electrode sizes were produced. Fig.5 shows amplitude frequency characteristic of CTGS resonators.

As observed from Fig.5, there is not any spurious resonance in the case of relative electrode sizes being less than 12.3 units. On the other hand, there is unwanted response with relative electrode size equalling 15.7 units.

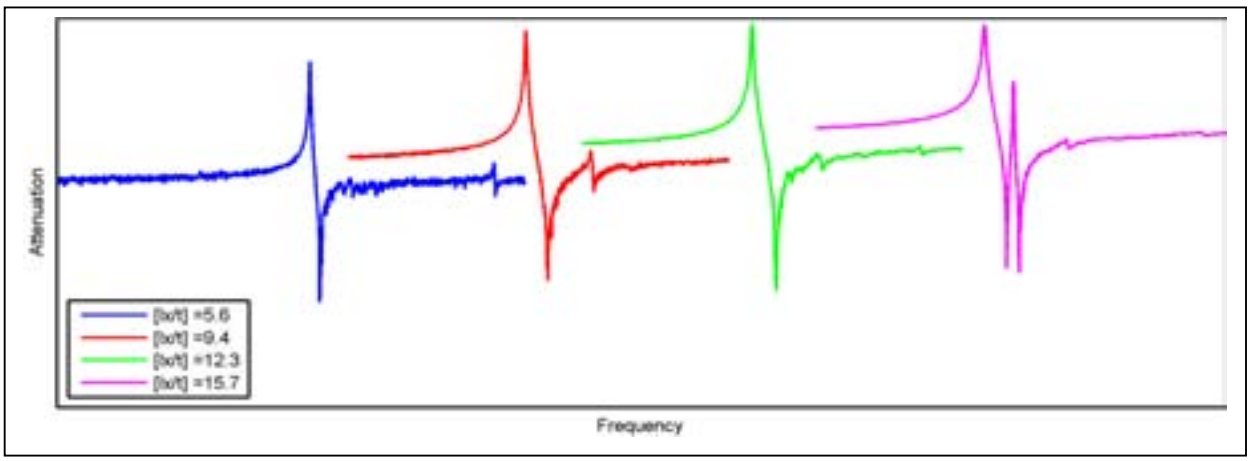

Figure 5. Amplitude frequency characteristic of CTGS resonators with different electrode sizes

TABLE I. PROPERTIES OF CTGS RESONATORS

Ratio of the electrode diameter to the plate thickness	Resonance resistance, R, Ом	Static capacitance, C_0, pF	Resonance spacing, %	Capacitance ratio, r
5.6	252	0.52	0.41	123
9.4	19	1.54	0.91	54
12.3	11	2.5	1.05	47
15.7	14	4.3	1.43	34

The measurement results for CTGS resonators are shown in the Table. The resonance spacing increases from 0.41% to 1.43% with the relative electrode size growing from 5.6 to 15.7 units.

IV. CONCLUSION

Resonators on CTGS single crystals operating in the fundamental mode of thickness shear vibration were investigated. On (YZw) –21°20' cut in operating temperature range from –60 up to 85°C, the resonance frequency deviation of less than 120 ppm was obtained. The TCF(2) is close to –0.022 ppm/°C^2.

It was shown that for resonators with Ag electrodes, maintaining extremum point temperature of the temperature-frequency characteristic within the range of ±1 °C requires crystal element manufacturing accuracy not worse than ±1.5 angular minutes.

The dependence of the Bechmann's number on electrode thickness was calculated. It was discovered that for Ag electrode coating with the thickness of 200 nm, the single response resonator can be obtained if the electrode size (l_x) does not exceed twelve thicknesses (t) of the crystal element. With the limiting value of the relative electrode size equaling l_x/t =12.3, the relative resonance interval is 1%, while the capacitance ratio is 47 units.

REFERENCES

[1] Shen Jen *et al.*:2002 IEEE Int. Freq. Con. Symp., p.307-310

[2] Fapeng Yu *et al.*:J. Appl. Phys. 109,114103 (2011)

[3] IEEE Standard on Piezoelectricity, ANSI/IEEE. Standard. 176, (1987)

[4] H.Tiersten Proc. 29. Ann. Symp. Freq. Contr., 1975, p. 71-73

IR-Reflectance Assessment of the Tilt Angle of AlN-Wurtzite Films for Shear Mode Resonators

Jimena Olivares, Mario DeMiguel-Ramos, Enrique Iborra, Marta Clement, Teona Mirea

GMME-CEMDATIC
Universidad Politécnica de Madrid
Madrid, SPAIN
eiborra@etsit.upm.es

Milena Moreira, Ilia Katardjiev

Department of Solid State Electronics
Uppsala University
Uppsala, SWEDEN

***Abstract*— In this paper we propose the use of infrared spectroscopy as an alternative technique to X-ray diffraction for the assessment of the crystal orientation of aluminum nitride thin films. Infrared scans of samples with different tilt angles of the c-axis are measured to accurately determine the structure of the longitudinal optical absorption band, which is found to be the composition of the contributions of three different populations of grains with different angles of tilt of the c-axis. A direct relationship is established between the wavenumber of these contributions and the actual angle of tilt measured through a XRD ψ-scan.**

Keywords- IR reflectance; structural analysis; AlN; tilted-grains

I. INTRODUCTION

Quartz crystal microbalances (QCM) operating in liquid media have demonstrated the potential of shear acoustic wave resonators for bio-medical applications. Since their relative sensitivity increases with frequency, resonators operating at GHz frequencies are expected to push down detection limits, as already stated in the late fifties [1]. High frequency resonators make use of piezoelectric thin films, which also offers the possibility of integrating them in a multisensory chip. For these reasons, bulk acoustic wave (BAW) resonators based on AlN or ZnO films are being developed as an alternative to QCMs for bio-chemical applications [2].

BAW resonators operating in the shear modes are preferred for sensing applications in liquid environments, because the movement of the material parallel to the surface is not hampered by the surrounding liquid, which overcomes the attenuation suffered by longitudinal modes obliged to displace the adjacent fluid in their movement normal to the surface. AlN and ZnO films deposited by sputtering crystallize in the wurtzite structure and tend to grow with the c-axis normal to the substrate. Shear modes can be excited in several ways. The most straightforward, known as lateral excitation, would be by applying an electric field parallel to the surface to excite the shear wave by virtue of the d_{15} piezoelectric coefficient. In practice, lateral excitation is achieved using coplanar electrodes on top of the c-axis oriented films, which provides an extremely weak electric field between the electrodes and, hence, a hardly noticeable shear excitation [3]. An alternative way to effectively excite shear modes is by normal excitation of films exhibiting the c-axis tilted respect to the surface normal, through the component of the electric field perpendicular to the c-axis and the d_{15} coefficient. According to theoretical studies [4], the largest electromechanical coupling factor (k_S^2) for the shear modes in AlN is achieved for a tilt angle of around 47°. Films with tilted grains are achieved by sputtering on rough substrates displaced from the center of the target so that the growth of the microcrystal along a given direction is encouraged [5]. An effective method to assess the angle of tilt of the c-axis is the XRD polar figure of the (00·2) planes, although this measurement is complex and time-consuming. A more convenient solution is the ψ-scan in a conventional Bragg-Brentano XRD configuration (see figure 1) along the Bragg angle corresponding to <00·2> direction (θ=18°); in this case, an accurate alignment of the sample in the φ orientation is required to guarantee the detection of the x-ray reflected in the tilted grains.

In this communication we propose an alternative method to detect and quantify the angle of tilt of wurtzite AlN films independently of the φ orientation through infrared (IR) measurements in the reflectance mode. The method is based on the analysis of the longitudinal optical (LO) absorption mode, which is sensitive to the angle between the c-axis and the surface of the film.

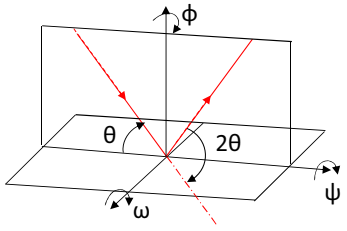

Figure 1. Geometry and nomenclature for the XRD measurements

II. THEORY

The absorption of infrared incident radiation by a polycrystalline thin film depends significantly on the geometry (angle between the incident radiation and the polarization state

and angles between the bonds and the surface) and on the nature of the phonons associated with each vibrational mode. The vibrational modes in a given material can be IR active or not, depending on its ability to absorb IR radiation. Materials with wurtzite structure, like AlN, have two types of bonds: **A1,** parallel to the c-axis, and, **E1,** nearly perpendicular to it. The phonons associated with these two bonds (or branches) split into two IR active vibrational modes: longitudinal optical (LO) and transverse optical (TO), which propagates perpendicular and parallel to the c-axis, respectively. Therefore, there are four characteristic IR active modes: **A1**(LO), **E1**(LO), **A1**(TO), and **E1**(TO), which are sketched in figure 2 together with the direction of the associated electric field (***E***) and the propagating vector (***q***). Figure 2 also shows (third row) the wave vector ***k*** and the electric field $\boldsymbol{E}_v$ of the photons in the AlN for both TO LO energy regions, assuming a horizontal AlN surface. The directions of $\boldsymbol{E}_v$ and ***k*** results from the application of Snell's laws and the actual dispersion of the refractive index in materials exhibiting a wurtzite structure shown in figure 3. The behavior of the refractive index is due to the anisotropy in the macroscopic electric field induced by polar phonons.

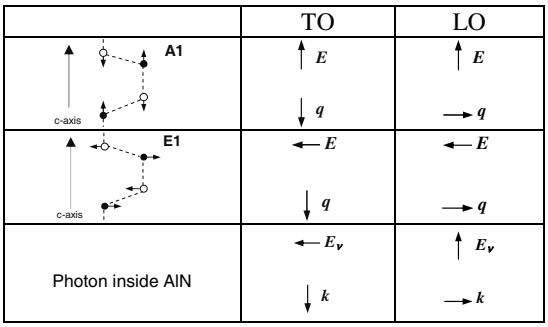

Figure 2. Schematic representation of the magnitudes involved in the absorption for the IR modes TO and LO of the branches A1 and E1. ***E*** is the direction of the electric field induced by the vibration of the polar bonds, ***q*** is the propagation vector of the phonons, $\boldsymbol{E}_v$ is the electric field of the photons and ***k*** is the wave vector of the transmitted light. It is assumed that the AlN surface is horizontal with respect to the figure.

A phonon can absorb a photon with an associated electric field ($\boldsymbol{E}_v$) and a wave vector (***k***) only if the scalar products $\boldsymbol{E}\cdot\boldsymbol{E}_v$ and $\boldsymbol{q}\cdot\boldsymbol{k}$ are different from zero. The resulting absorption bands in the IR transmittance or reflectance spectra of an AlN thin depend on these selection rules. The phonon frequencies corresponding to the LO and TO regions, $\boldsymbol{\Omega}_{LO}$ and $\boldsymbol{\Omega}_{TO}$, and the loss factor $\boldsymbol{\gamma}$ are slightly dependent on the crystal quality of the polycrystalline film and some other material parameters, such as the internal stress or the presence of impurities. The measured IR spectrum of AlN films shows a band of total reflection (*reststrahlen* band) between the TO and LO modes, in which the real part of the refractive index is null (neglecting optical losses). For AlN the wavenumbers associated to these frequencies used in this work are $k_{A1(LO)}$ = 890 cm^{-1}, $k_{EI(LO)}$=916 cm^{-1}, $k_{A1(TO)}$ = 608 cm^{-1}, and $k_{E1(TO)}$ =669 cm^{-1}.

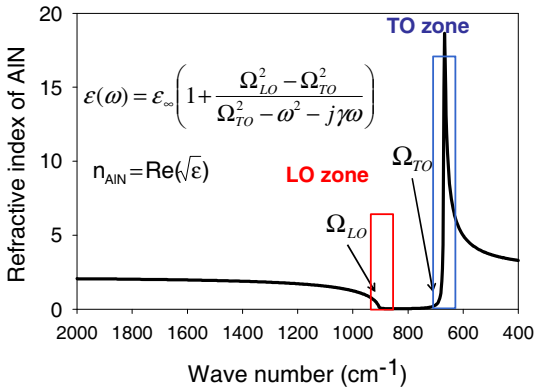

Figure 3. Dispersion of the real part of the refractive index for a wurtzite AlN film.

As shown in figure 3, the refractive index of AlN increases strongly near the TO modes and falls to almost zero around the LO modes. Therefore, according to Snell's laws, for IR light impinging the surface at any angle of incidence (different from normal or grazing), the transmitted light with an energy close to that of the TO modes travels perpendicular to the surface, whereas it moves almost parallel to the surface for energies around the LO modes. Therefore, for a pure c-axis oriented film and under normal incidence, the **A1**(TO) mode cannot absorb a photon, since the associate electric field, $\boldsymbol{E}_{A1TO}$, is perpendicular to $\boldsymbol{E}_v$. In the same way, the **E1**(LO) mode cannot be observed because the associated electric field, $\boldsymbol{E}_{E1LO}$, is perpendicular to $\boldsymbol{E}_v$. Thus, according to the selection rules sketched in figure 2, transmittance spectra can only display the **E1**(TO), whereas reflectance spectra only shows the **A1**(LO) mode; in this last case, although total reflection takes place, the light penetrates into the film to a depth of around a wavelength and can be absorbed by phonons. On the contrary, in the hypothetical scenario of grains lying with the c-axis parallel to the surface, both **A1**(TO) in normal transmittance and **E1**(LO) in normal reflectance would appear in the spectra. Finally, if the c-axis is tilted with respect to the surface normal, a band corresponding to a composition of the two modes in each zone (**A1**(TO) and **E1**(TO) for transmittance and **A1**(LO) and **E1** (LO) for reflectance) with mixed **E1** and **A1** symmetry character will appear. These composed modes, called *quasi-modes*, have vibrational energies that are a composition of those of the pure modes and their direction of propagation forms with the c-axis or the normal to the surface [6-8]. This is described by a relationship between the position of the resulting absorption bands ($\boldsymbol{\Omega}_{Q(LO)}$ and $\boldsymbol{\Omega}_{Q(TO)}$) in the IR spectrum and the angle ψ of the c-axis with respect to the surface normal [6,7]:

$$\Omega_{Q(TO)}^2=\Omega_{E1(TO)}^2\cdot\cos^2(90-\psi)+\Omega_{A1(TO)}^2\cdot\sin^2(90-\psi) \quad (1)$$

$$\Omega_{Q(LO)}^2=\Omega_{A1(LO)}^2\cdot\cos^2(90-\psi)+\Omega_{E1(LO)}^2\cdot\sin^2(90-\psi) \quad (2)$$

According to this model, the tilt angle of the grains associated to each band can be derived by measuring their position in the reflectance spectrum around the LO zone. It is important to highlight that a given tilt angle is associated to a

single absorption band whose energy is a composition of that of A1 and E1 modes in each branch.

III. Experimental

A pure Al target 15-cm in diameter was sputtered in a Von Ardenne-CS 730 pulsed-DC planar magnetron sputtering system. A standard 10-cm diameter (100)-Si substrate covered by a Ni layer was placed on the substrate holder directly under the target. The distance between the substrate and the target was about 5.5 cm. The deposition of the AlN film was carried out in two stages as described in [9]. Initially, during the nucleation stage, the discharge was operated at a pressure of 2.66 Pa for a period of 3 minutes, to grow a 100 nm-thick seed layer. After the first stage the process pressure was decreased to 0.266 Pa, which resulted in an anisotropic deposition flux at the substrate surface (excluding the center area). During this stage, a 2.5 µm-thick layer was grown.

Since the structure contains a metallic underlayer, only reflectance measurements were carried out. Infrared reflection spectra were measured with a Fourier transform infrared (FTIR) Nicolet 5-PC spectrophotometer in the 400 cm^{-1}- 4000 cm^{-1} range with a spectral resolution of 2 cm^{-1}. A spot size of 4 mm in diameter was used to measure each 5 mm along a radius of each wafer.

X ray diffraction (XRD) measurements were performed with a Supratech XPERT-PRO diffractometer using the Kα1,2 doublet of a β-filtered Cu anode. θ/2θ patterns from 10° to 40° and ψ scans from -80° to 80° around the (00·2) reflection at 2θ=36.02º. These measurements were performed along the radius of each wafer in steps of 5 mm.

IV. Results and Discussion

To extract the tilt angle of the c-axis with respect to the normal to the surface (ψ), the IR specular reflection spectra of AlN thin films were measured. Figure 4 shows the reflectance spectra of a representative 2100 nm-thick AlN film deposited on a 10 nm-thick Mo layer, both in the reflectance mode and in absorbance units. Reflectance coefficient (*R*) is related with absorbance (*A*) through: $A=Ln(-R/100)$.

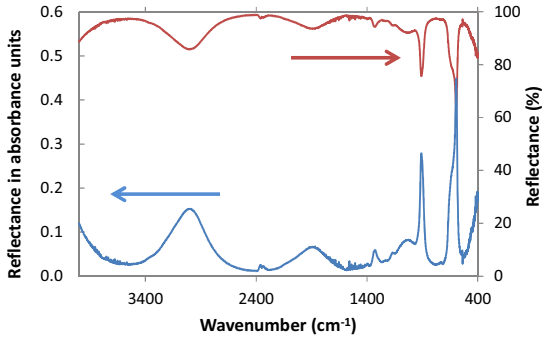

Figure 4. Reflection spectra of AlN films deposited on a Mo metallic layer in % of reflectance and in absorbance units

Interference fringes in the AlN film are clearly visible. The reststrahlen band can also be observed. At the edges of this band, the absorption modes are present as valleys in the reflectance spectrum and as peaks in the absorbance one. For the analysis, we have chosen the reflection spectrum in absorbance units and fitted the bands with Lorentzian curves. Figure 5 shows the reflectance spectra of the film of figure 4 around the reststrahlen band in absorbance units. Absorption bands in both LO and TO zones can be seen. In the TO zone the refractive index is very high and suffers a significant variation with the wavenumber (see figure 3). For this reason the interference fringes are very sharp and close to each other. In the film of the figure, the sharpest peak at 600 cm^{-1} is actually an interference fringe and not an absorption band. For thinner or thicker films, these interference fringes in the TO zone may overlap the TO modes making it difficult to extract accurate information from them. Since the sought information can be found in both TO and LO zones, the LO absorption band is a more convenient choice for a detailed analysis.

The existence of composed peaks in the LO zone suggests the existence of different populations of grains with different orientations, that is, different angles of tilt of the c-axis. It is worth noting that a single grain with a fixed tilt angle ψ yields only one quasi-LO mode at a wavenumber given by equation (2).

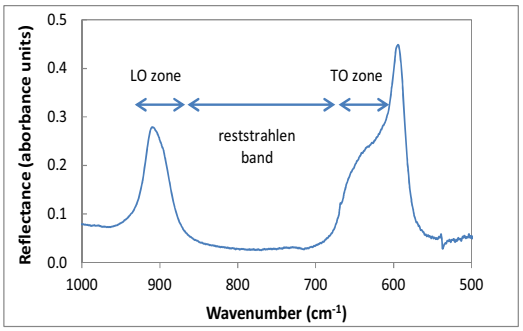

Figure 5. Detail of the reststrahlen band zone of the Ir absorbance spectra for AlN film deposited on a Mo layer.

To analyze the spectral terms of the absorption band, these were fitted using lorentzian functions together with the baseline to account for the background arising from the optical interference fringes and the reststrahlen band edge. The accuracy of the fit is increased by simultaneously fitting the composed absorption band and its second derivative, since this latter is very sensitive to the number and the position of the lorentzian terms. First, we have fitted the spectrum using two lorentzian contributions, which account for two populations of grains having two different c-axis orientations. The fitting is shown in figure 6.

Although Fig. 6(top) suggests that both position and amplitude of the band are accurately fitted, the analysis of the second derivative reveals that the fit is not correct. Fig. 6(bottom) shows the new fit achieved by adding a third lorentzian contribution revealing that, although the accuracy in the fit of the spectrum does not improve, the fit of the second derivative is more precise, which suggests that the sample contains actually three populations of differently tilted grains.

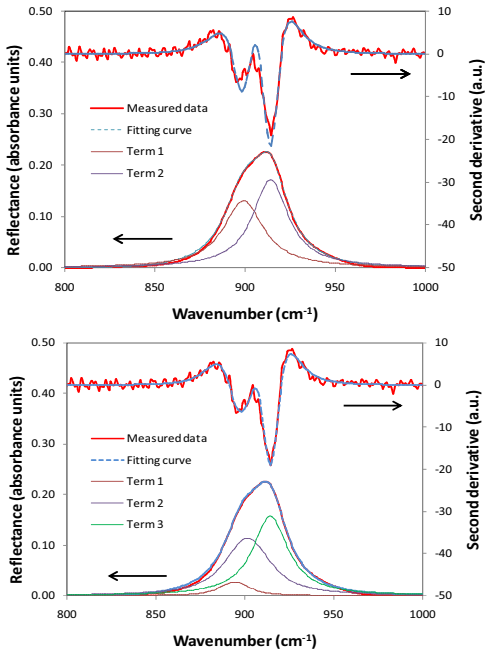

Figure 6. Comparison of the fitting of experimental data with (top) two, and (bottom) three lorentzian terms. The second derivative of the experimental data and fittings are also shown.

The values of the tilt angle for each population are 35º, 0º and 66º, as derived from wavenumbers extracted from the fitting of the spectra using equation (2). To validate these values we have analyzed the XRD-ψ scan of the samples. A typical pattern is shown in figure 7. Three angles of tilt can be observed at ψ=-34°, 0° and 65°, which are in good agreement with the abovementioned IR results.

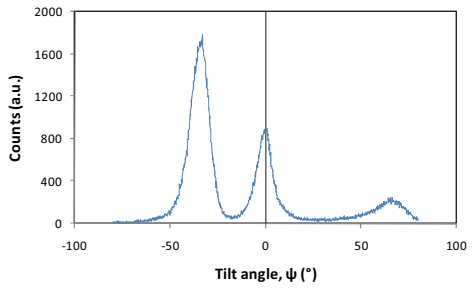

Figure 7. XRD ψ scan of the 00·2 peak of the same sample of figure 6.

To confirm the accuracy of the angle of tilt achieved through the analysis of the IR spectra we have analyzed the XRD-ψ scans of several samples containing differently tilted grains and compared the information with that obtained from the IR absorption analysis. Figure 8 shows in the theoretical relationship between angle of tilt and the position of the IR absorption band derived from eq. 2 along with the experimental data achieved using the two techniques. The excellent agreement confirms that IR spectrophotometry is an adequate technique to assess the c-axis tilt.

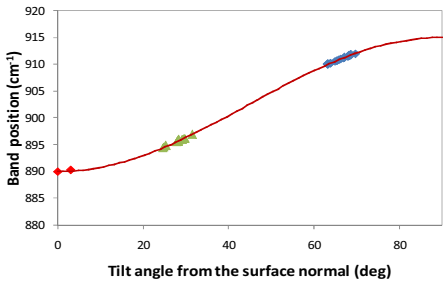

Figure 8. Relationship between the fitted band positions in the LO zone of the reflectance spectra of several AlN films and the tilt angles derived from the XRD measurements. The red line is the relation of equation (2).

V. Conclusions

In this paper we propose an accurate method for determining the structure of AlN films with grains with the c-axis tilted with respect to the normal to the surface. By fitting accurately the position of the IR absorption bands, the fine structure including the different populations of grains with different angles of tilt can be assessed. The method does not require any special experimental arrangement, which makes it a straightforward non-destructive technique to quantify the axis of tilt of non pure c-axis-oriented films.

Acknowledgment

This work was partially supported by the European Comission through the 7th Framework Programme by the *RaptaDiag* project (http://www.raptadiag.eu/), the COST action IC1208 and by the Ministerio de Economía y Competitividad del Gobierno de España through project MAT2010-18933.

References

[1] G. Sauerbrey, Z. Phys. vol.155, pp. 206-217, 1959.

[2] Martin Nirschl, Matthias Schreiter, Janos Vörös, "Comparison of FBAR and QCM-D sensitivity dependence on adlayer thickness and viscosity", Sens. & Actuat. A, vol. 165,pp. 415-421, *201*.

[3] M. Clement, E. Iborra, J. Olivares, M. de Miguel-Ramos, J. Capilla, J. Sangrador, "On the Lateral Excitation Of Shear Modes in AlN Layered Resonators", IEEE 2012 Ultrasonics Symposium, pp. 535-538, 2012.

[4] J. Bjurstrom, D. Rosen, I. Katardjiev, V.M. Yanchev, and I. Petrov, "Dependence of the Electromechanical Coupling on the Degree of Orientation of c-Textured Thin AlN Films", IEEE Trans. Ultrason. Ferroelectr. Freq. Control vol. 51, pp. 1347-1357, 2004.

[5] Milena Moreria, Johan Bjurström, Tomas Kubart, Björn Kuzavas and Ilia Katardjiev, "Synthesis of c-tilted AlN films with a good tilt and thickness uniformity", IEEE 2011 Ultrasonics Symposium, pp. 1238-1241, 2011.

[6] L. Bergman, D. Alexson, R. J. Nemanich, M. Dutta, M. A. Stroscio, C. Balkas, and R. F. Davis, "Phonon dynamics and lifetimes of AlN and GaN crystallites", MRS Internet J. Nitride Semicond. Res. vol. 4S1, pp. G6.65, 1999.

[7] C.A. Arguello, D.L. Rousseau, and S.P.S. Porto, "First-order Raman effect in wurtzite-type crystals", Phys. Rev. 181, 1351 (1969).

[8] D. W. Berreman, "Infrared absorption at longitudinal optic frequency in cubic crystal films", Phys. Rev. vol. 130, pp. 2193-2198, 1963.

[9] J. Bjurström, G. Wingqvist, and I. Katardjiev, "Synthesis of textured thin piezoelectric AlN films with a nonzero c-axis mean tilt for the fabrication of shear mode resonators", IEEE Trans. Ultrason. Ferroelectr. Freq. Control vol. 53, pp. 2095-2100, 2006.

Measurement of Independent Piezoelectric Constants of a Lanthanumgallium Silicate Family Crystals by X-ray Diffraction Method

O. Buzanov
FOMOS Materials Co.
Moscow, Russia
buzanov@newpiezo.com

D. Irzhak, D. Roshchupkin
X-ray acoustooptics laboratoty
IMT RAS
Chernogolovka, Russia
irzhak@iptm.ru

Abstract— **Independent piezoelectric strain coefficients d_{11} and d_{14} in disordered $La_3Ga_{5.3}Ta_{0.5}Al_{0.2}O_{14}$ (LGTA) and ordered $Ca_3TaGa_3Si_2O_{14}$ (CTGS) crystals of the langasite family were measured by high-resolution X-ray diffraction (HRXRD) under external electric field application which causes changes in the interplanar spacing because of the reverse piezoelectric effect. The experiment showed that the piezoelectric strain coefficients can be precisely determined by measuring changes in the interplanar spacing using the optical scheme of a triple-axis X-ray diffractometer. The measured independent piezoelectric strain coefficients d_{11} and d_{14} for LGTA and CTGS crystals were $d_{11(LGTA)}=6.455\cdot10^{-12}$ C/N, $d_{14(LGTA)}=-5.117\cdot10^{-12}$ C/N; $d_{11(CTGS)}=3.330\cdot10^{-12}$ C/N, $d_{14(CTGS)}=-15.835\cdot10^{-12}$ C/N.**

Keywords-piezoelectric coefficients; piezoelectric effect; langasite; X-ray diffraction

I. INTRODUCTION

The application of high-resolution X-ray diffraction for measuring piezoelectric strain coefficients is based on that the X-ray radiation is sensitive to changes in the interplanar spacing. The effect of external electric field applied to a crystal on the character of X-ray diffraction was first reported in 1938 [1]. It was shown that the applied electric field causes changes in the shape and angular position of diffraction peaks. The possibility of application of X-ray diffraction to measure piezoelectric constants was theoretically substantiated in 1976 [2]. Some articles present the results of measuring piezoelectric constants of various materials where the values of constants measured by X-ray diffraction differ, as a rule, from those obtained by the conventional method based on measuring the velocity of bulk acoustic waves [3-4].

Piezoelectric strain coefficients measured by HRXRD are characterized by high precision because the constants are calculated on the basis of precisely measured values of a studied crystal thickness and electric voltage applied to it. The present-day experimental facilities permit the determination of X-ray diffraction angle with an accuracy of ~0.0001°. Note, however, that there are some problems which hamper the application of HRXRD. First is the bending of a studied sample under the electric field effect. The bending is caused both by the use of thin single-crystal wafers (<500 mkm) and rigid fastening of these wafers. In double-axis X-ray diffraction this results in the shift of diffraction maxima because of changes in the interplanar spacing and bending deformation of single-crystal wafers. To avoid the bending effect, soft plastic fastening should be used and the optical scheme of a triple-axis X-ray diffractometer should be employed for investigation. When a fixed X-ray wavelength is used, the diffraction angle depends only on the interplanar spacing and can be exactly determined from the angular position of the crystal-analyzer.

The aim of this work is to measure the independent piezoelectric constants in the LGTA and CTGS crystals by high-resolution triple-axis X-ray diffraction.

II. DETERMINATION OF PIEZOELECTRIC COEFFICIENTS BY HRXRD

The equation for the reverse piezoelectric effect describes crystal deformation under external electric field as

$$r_j=d_{ij}\cdot E_i \quad (1)$$

where r_j are the components of the deformation tensor, d_{ij} are the components of the piezoelectric strain coefficients tensor, and E_i are the components of the electric field intensity vector.

According to the definition of the deformation tensor, its diagonal components are quantities which characterize relative changes in the distance between atoms of a unit cell along the three basic directions of the coordinate system [5]. So, the diagonal components of the deformation tensor correspond to a relative change in the interplanar spacing in a crystal along corresponding directions.

The relation between the X-ray diffraction angle and interplanar spacing in a crystal is determined by the Bragg equation [6]

$$2d\cdot\sin(\Theta)=n\cdot\lambda \quad (2)$$

where d is the interplanar spacing, Θ is the diffraction angle, n is the diffraction order and λ is the X-ray wavelength. The

This work was supported by Ministry of education and science of Russian Federation (contract 16.513.12.3027) and Russian Found of Basic Researches (contract 11-02-00659)

relative change in the interplanar spacing $\Delta d/d$ can be described as

$$\Delta d/d = \frac{(d+\Delta d)-(d-\Delta d)}{(d+\Delta d)+(d-\Delta d)}, \quad (3)$$

where Δd is the absolute change in the interplanar spacing d. In the case of increasing of the interplanar spacing ($d + \Delta d$), a decrease in the diffraction angle is observed in accordance with expression (2). Denote this angle as Θ^-. If the interplanar spacing decreases($d - \Delta d$), the diffraction angle would increase. Denote this angle as Θ^+. Express the terms in (3) with the terms from (2) using the designations introduced above, we obtain an expression connecting the relative change in the interplanar spacing with the change in the diffraction angle

$$\Delta d/d = \frac{\sin\Theta^+ - \sin\Theta^-}{\sin\Theta^+ + \sin\Theta^-}. \quad (4)$$

The piezoelectric strain coefficients were measured using thin single-crystal wafers with metallic electrodes formed on their surfaces. The crystallographic orientation of the plates was chosen such that the external voltage applied to the electrodes would cause compressive (tensile) deformation of the wafer in the direction normal to the vector of the electric field intensity. Using the laboratory coordinate system and denoting this direction as the x_1 axis, the electric field intensity would be

$$E_i = E_1 = U/D, \quad (5)$$

where U is the applied electric voltage and D is the single-crystal wafer thickness along x_1. Using expression (1) and taking (4) and (5) into account we obtain an expression for the piezoelectric strain coefficient d_{11}

$$d_{11} = \frac{\sin\Theta^+ - \sin\Theta^-}{\sin\Theta^+ + \sin\Theta^-} \cdot \frac{D}{U}. \quad (6)$$

Note that an applied electric field can also cause shear deformation in the presence of the corresponding components of the piezoelectric strain coefficients, which would also change the position of the Bragg maximum on the rocking curve of the crystal. Therefore, it is necessary to use the optical scheme of a triple-axis X-ray diffractometer and to determine the value of the Bragg angle from the angular position of the crystal-analyzer, which would allow the determination of compressive (tensile) deformation through excluding the effect of shear deformation.

All independent piezoelectric strain coefficients can be determined by using a set of crystal wafers cut in a certain way. However, in some cases only one crystal wafer can be used. This concerns crystals belonging to the space group of symmetry 32. The tensor of the piezoelectric strain coefficients for crystals of this symmetry group is

$$d_{ij} = \begin{pmatrix} d_{11} & -d_{11} & 0 & d_{14} & 0 & 0 \\ 0 & 0 & 0 & 0 & -d_{14} & -2d_{11} \\ 0 & 0 & 0 & 0 & 0 & 0 \end{pmatrix},$$

i.e. this tensor has only two independent components d_{11} and d_{14}. If electric field is applied to the plate of the X-cut of a crystal of the symmetry group 32 (planes (110) are parallel to the wafer surface), the crystal wafer would be subject to compressive (tensile) deformation in the x_1 and x_2 directions in accordance with expression (1). The deformation sign would depend on the orientation of the wafer in the laboratory coordinate system and direction of the applied electric field. Therefore, reflection from the planes of (*hh0*) type in the geometry of reflection diffraction and reflection from the (*h00*) planes in the transmission geometry can be used to measure the piezoelectric strain coefficient d_{11}.

To measure the second independent piezoelectric strain coefficient d_{14}, use can be made of the fact that the piezoelectric strain coefficient responsible for the crystal compression along the x_2 direction during rotation of the X-cut wafer of a crystal of symmetry group 32 around the x_1 axis changes as

$$d'_{12} = -\cos^2\alpha \cdot d_{11} + \sin\alpha \cdot \cos\alpha \cdot d_{14}, \quad (7)$$

where d'_{12} is the value of the piezoelectric coefficient in the new coordinate system and α is the angle of the wafer rotation around x_1. If the wafer is rotated at the same angle but in different directions, values of the piezoelectric strain coefficient d'_{12} would be different. This can be explained by the properties of trigonometric functions in expression (7): the **cos** function is even while **sin** is odd. The expression for d_{11} and d_{14} can be obtained from the difference in the values of piezoelectric coefficients in two coordinate systems.

$$d'_{12(+\alpha)} - d'_{12(-\alpha)} = 2\sin\alpha \cdot \cos\alpha \cdot d_{14}, \quad (8a)$$

$$d'_{12(+\alpha)} + d'_{12(-\alpha)} = -2\cos^2\alpha \cdot d_{11}. \quad (8b)$$

Thus, to measure the piezoelectric strain coefficient d_{14} it is appropriate to find the reflections from the planes normal to the (*hh0*) planes and not coinciding with planes of (*h00*) and (*00l*) type.

III. Experimental Set-Up

The independent piezoelectric strain coefficients d_{11} and d_{14} in the LGTA and CTGS crystals were measured on a Bruker D8 DISCOVER X-ray diffractometer in the triple-axis X-ray diffractometer scheme. The experimental scheme is shown in Fig. 1. The X-ray radiation was collimated with a 100 μm entrance slit. The source of radiation was an X-ray tube with a rotating copper anode ($CuK_{\alpha 1}$ radiation, X-ray wavelength $\lambda = 1.54$ Å). Ge(220) crystals with double reflection were used as a crystal-monochromator and a crystal-analyzer.

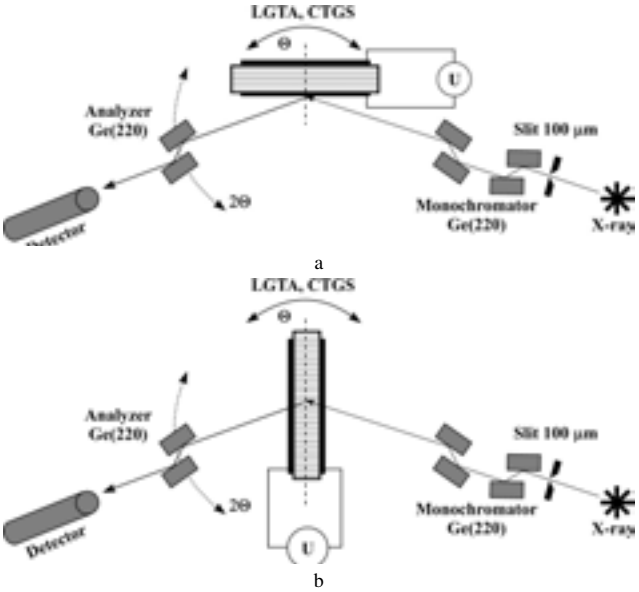

Figure 1. Experimental set-up: (a) bragg diffraction geometry, (b) laue diffraction geometry

Plates of the LGTA and CTGS X-cut (16×8×0.2 mm^3) were used in the measurements. *Al* – electrodes with thickness of 100 nm were deposited on both sides of the single-crystal wafer to apply the external electric field.

The X-ray diffraction angle was determined from the maps of diffracted intensity distribution depending on the rotation of the sample (Θ) and crystal-analyzer (2Θ).

The measurements were performed for different reflections, which radically increased the precision of the measurement results. Table I presents the reflections and corresponding Bragg angles for the studied LGTA and CTGS crystals.

TABLE I. X-RAY BRAGG REFLECTIONS FOR MEASUREMENTS OF PIEZOELECTRIC COEFFICIENTS

Reflection (*hkl*)	**Diffraction geometry**	**2Θ (°)**	
		LGTA	***CTGS***
(110)	Bragg	21.584	21.895
(220)	Bragg	43.974	44.648
(330)	Bragg	68.331	69.464
(440)	Bragg	96.969	98.867
(201)	Laue	30.531	31.119

IV. EXPERIMENTAL RESULTS

In the experiment, maps of the diffracted X-ray intensity in the 2Θ – Θ space coordinates were obtained. Figure 2 displays the maps of the diffracted X-ray intensity distribution for the (400) reflection of LGTA under applying of the external electric voltage of various polarity U= – 1800, 0, +1800 V in the diffraction scheme of Fig. 1(a).

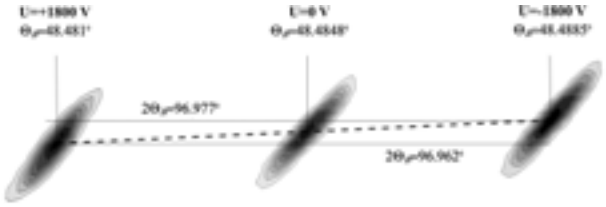

Figure 2. Experimental maps of the diffracted x-ray intensity obtained for reflection (440) and at different values of external electric voltage applied to LGTA wafer in bragg diffraction scheme of Fig. 1(a).

The figure shows that an applied electric field causes changes in the Bragg peak angular position along two coordinate axes (2Θ and Θ). In this case the fastening of the single-crystal wafer maintains its free movement under deformation and the angular movement of the diffracted intensity maximum along the 2Θ axis, corresponding to the scanning by the crystal-analyzer, is equal to the double value of the rotation angle Θ of the studied crystal.

Table II presents the results for the X-ray diffraction angles of various reflections and the values of the piezoelectric strain coefficient d_{11} for the LGTA and CTGS single crystals calculated from expression (6). The average value of the piezoelectric strain coefficient d_{11} from Table II is $d_{11(LGTA)}=6.455\cdot10^{-12}$ C/N for the LGTA crystal and $d_{11(CTGS)}=3.330\cdot10^{-12}$ C/N for the CTGS crystal.

TABLE II. DIFFRACTION ANGLES FOR DIFFERENT REFLECTIONS OF LGTA AND CTGS CRYSTALS AND PIEZOELECTRIC COEFFICIENTS d_{11}.

Reflection (*hkl*)	**LGTA**			**CTGS**		
	$2\Theta^-$ (°)	$2\Theta^+$ (°)	$d_{11}\cdot10^{-12}$ (C/N)	$2\Theta^-$ (°)	$2\Theta^+$ (°)	$d_{11}\cdot10^{-12}$ (C/N)
(110)	21.5855	21.583	6.358	21.8957	21.8943	3.331
(220)	43.9765	43.9715	6.010	44.6474	44.6446	3.312
(330)	68.335	68.326	6.428	69.4664	69.4616	3.350
(440)	96.977	96.962	6.437	98.8711	98.8630	3.330
(201)	21.5855	21.583	6.358	21.8957	21.8943	3.331

The reflection (201) was used to measure the piezoelectric strain coefficient d_{14}. The maps of the diffracted X-ray intensity distribution were obtained in the Laue diffraction geometry schematically presented in Fig. 1(b). To position the (201) plane in the reflecting mode, the single-crystal wafers of the LGTA and CTGS X-cut were rotated around the X axis by the angle α=±34.8° for LGTA and α=±35.6° for CTGS.

Figure 3 shows the maps of the diffracted X-ray intensity obtained in the diffraction scheme of Fig. 1(b) for the reflection (201) of the LGTA single-crystal wafer under electric voltage of various polarity *U*= – 1800, 0, +1800 V. The map in Fig. 3(a) was obtained at the rotation of the single-crystal wafer around the X axis by the angle α=–34.8° and that in Fig.3 (b) at α=+34.8°.

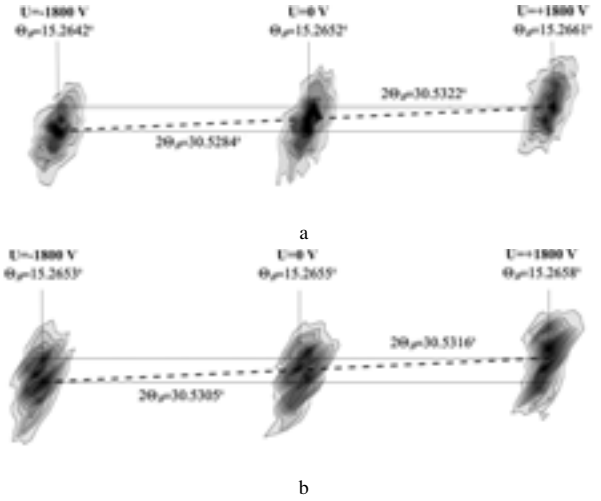

Figure 3. Experimental maps of the diffracted x-ray intensity obtained for reflection (201) and at different values of external electric voltage applied to LGTA wafer in laue diffraction scheme of Fig. 1(b): (a) α=−34.8°, (b) α=+34.8°.

The values of d'_{12} were calculated from expression (6). To calculate the d_{14} coefficient in LGTA and CTGS crystals, expression 8(a) was used, taking the rotation angle α around the X axis into account. Note that the obtained values of the piezoelectric strain coefficients allow for the sample rotation in the laboratory coordinate system. The results of d_{14} measurements in the LGTA and CTGS crystals are presented in Table III.

TABLE III. PIEZOELECTRIC COEFFICIENTS d_{14} IN LGTA AND CTGS CRYSTALS.

LGTA				CTGS			
$d'_{12(+\alpha)}\cdot10^{-12}$ (C/N)	$d'_{12(-\alpha)}\cdot10^{-12}$ (C/N)	α (°)	$d_{14}\cdot10^{-12}$ (C/N)	$d'_{12(+\alpha)}\cdot10^{-12}$ (C/N)$_i$	$d'_{12(-\alpha)}\cdot10^{-12}$ (C/N)	α (°)	$d_{14}\cdot10^{-12}$ (C/N)
1.954	6.750	34.8	-5.117	-9.681	5.229	35.16	-15.835

Comparison of the d_{11} and d_{14} values obtained in this work with those reported in other articles [7-8] shows that the data for LGTA virtually coincide while the values of the coefficients for CTGS radically differ. Note that the difference in the values of d_{11} is smaller than for d_{14} in the CTGS crystal.

V. CONCLUSION

High-resolution X-ray diffraction in the triple-axis diffractometer scheme was used to measure the independent piezoelectric strain coefficients d_{11} and d_{14} in disordered $La_3Ga_{5.3}Ta_{0.5}Al_{0.2}O_{14}$ and ordered $Ca_3TaGa_3Si_2O_{14}$ crystals of the langasite family. To measure the piezoelectric strain coefficients d_{11} and d_{14}, an external electric field was applied to single-crystal wafers, which causes changes in the interplanar spacing due to the reverse piezoelectric effect and, hence, brings about changes in the Bragg peak angular position. This approach is a direct method for measuring piezoelectric strain coefficients.

It is shown that the independent piezoelectric strain coefficients d_{11} and d_{14} in crystals of the langasite family of the space group symmetry 32 can be measured using only one single-crystal wafer of the X-cut. In this case, the piezoelectric strain coefficient d_{11} is measured using the reflection from the planes of (110) type in the Bragg diffraction geometry and the d_{14} coefficient is measured using the reflection from the planes of (201) type in the Laue diffraction geometry.

The measured values of the independent piezoelectric strain coefficients were $d_{11(LGTA)}=6.455\cdot10^{-12}$ C/N, $d_{14(LGTA)}=-5.117\cdot10^{-12}$ C/N in the LGTA crystals and $d_{11(CTGS)}=3.330\cdot10^{-12}$ C/N, $d_{14(CTGS)}=-15.835\cdot10^{-12}$ C/N in the CTGS crystals.

REFERENCES

[1] A. Němejcová and J. Brož, "The Effect of a Direct Electric Field on the Laue Diffraction Photograms", Phys. Rev. 54, pp. 379–384, 1938

[2] G. R. Barsch, "X-ray determination of piezoelectric constants", Acta Cryst. vol. A32. pp. 575-586, 1976.

[3] S. Annaka and A. Nemoto, "Piezoelectric constants of [alpha]-quartz determined from dynamical X-ray diffraction curves", J. Appl. Cryst., №10, pp. 354-355, 1977.

[4] L. H. Avanci, L. P. Cardoso, S. E. Girdwood, D. Pugh, J. N. Sherwood, and K. J. Roberts Piezoelectric Coefficients of mNA Organic Nonlinear Optical Material Using Synchrotron X-Ray Multiple Diffraction, , Phys. Rev. Lett. 81, №24, 5426-5429 (1998)

[5] Sirotin Y.I., Shaskolskaya M.P. Fundamentals of Crystal Physics. Moscow: Mir Publishers (1982)

[6] W. H. Bragg and W. L. Bragg, "The Reflection of X-rays by Crystals", Proc. R. Soc. Lond. vol. A 88, 1913

[7] Shujun Zhang, Akira Yoshikawa, Kei Kamada, Eric Frantz, Ru Xia, David W. Snyder, Tsuguo Fukuda, Thomas R. Shrout, "Growth and characterization of high temperature $La_3Nb_{0.5}Ga_{5.3}Al_{0.2}O_{14}$ (LNGA) and $La_3Ta_{0.5}Ga_{5.3}Al_{0.2}O_{14}$ (LTGA) piezoelectric single crystals", Solid State Communications, 148, pp. 213–216, 2008

[8] Xuzhong Shi, Duorong Yuan, Xin Yin, Aijian Wei, Shiyi Guo, Fapeng Yu, "Crysatl growth and dielectric, piezoelectric and elastic properties of of $Ca_3TaGa_3Si_2O_{14}$ single crystal", Solid State comm., vol. 142, pp. 173–176, 2007.

Method of Controlling Coupling Coefficient of Aluminum Scandium Nitride Deposition in High Volume Production.

Sergey Mishin[1], Michael Gutkin[1], Alexander Bizyukov[2] , Vladimir Sleptsov[3]

[1] Advanced Modular Systems, Inc, Goleta, CA/USA, smishin@amssb.com
[2] Karazin Kharkiv National University, Kharkiv, Ukraine
[3] Moscow State Aviation Technological University Moscow, Russia
Email: smishin@amssb.com; mgutkin@amssb.com

Abstract— **In this paper, we present our studies of the influence of the stress on Aluminum Nitride containing various concentrations Scandium (Sc). Coupling coefficient (kt2) was measured across the wafer and wafer to wafer as a function of stress and Sc content of the film. Previous studies demonstrate a considerable increase in kt2 as a function of Sc content of the film [1], [2], [4], [5]. Unfortunately, when deposited on 200mm wafers we observed that coupling coefficient varies significantly more than that of a standard Aluminum Nitride (AlN). Both stress and concentration of Sc must be controlled across the wafer to achieve uniform coupling coefficient acceptable for production of Bulk Acoustic Resonator (BAW) devices [3], [6], [7]. We were able to control coupling coefficient across the wafer and wafer-to-wafer by adjusting magnetic fields in dual magnetron configuration as well as adjusting concentration of Sc in our two sputtering targets.**

Keywords- component; Aluminum Nitride; Scandium; coupling coefficient; stress

I. INTRODUCTION

Most PVD deposition processes require only average stress measurement on a wafer to provide reasonable device performance. It is not uncommon to have 300MPa to 400MPa variation of stress across wafer on AlN deposition without anyone realizing it. Actually stress has a significant impact on coupling coefficient of AlN film. Local Stress variation across a wafer produces variation of piezoelectric coupling coefficient, and, as the result, dramatically reduces device yield. Similar problem can be addressed to the stress variation of AlScN film. Figure 1 shows effect of stress on AlN and AlScN films.

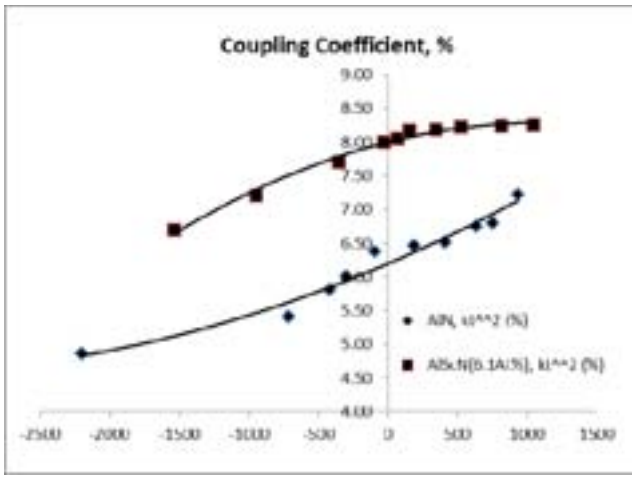

Figure 1: Variation of coupling coefficient as a function of stress for AlN and AlScN films

Tight control of coupling coefficient is essential for producing high quality devices. Using dual target magnetron configuration allows very tight control of stress and coupling coefficient across a wafer.

In this investigation we used different magnetic fields on each magnetron in conjunction with different concentrations of Sc on each target to produce the tightest control on both stress and coupling coefficient.

II. EQUIPMENT

In this investigation we used Advanced Modular Systems cluster tool with AlN and AlScN deposition chambers and ion beam trimming module (shown in Figure 2).

Both AlN and AlScN depositions use a dual magnetron with AC power applied between targets. Frequency of AC power is 40 kHz and power may vary from 3 to 10 kW. It is a reactive deposition process in deep poison mode using two aluminum or composite targets and, argon and nitrogen process gasses.

The trimming module uses DC focused ion source with argon process gas to improve thickness/uniformity of either AlN or AlScN films. Film thickness trimming/tuning is a process based on ion beam scanning across a wafer with power variation based on film thickness map. Utilization of the trimming module opens up a much wider process window for stress control because it allows to avoid spending too much effort on controlling thickness uniformity during deposition.

Simple resonators with three layer's Bragg reflector were manufactured during investigation for piezoelectric coupling coefficient measurements.

Figure 2: AMSystems cluster tool

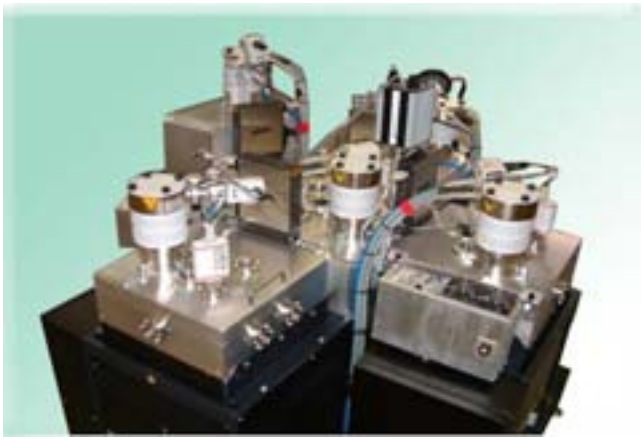

III. STRESS CONTROL

Typical stress control techniques involve either substrate bias or change in gas pressure. Unfortunately, both of these methods are capable of changing average stress on a wafer without having much effect on the local stress across a wafer.

AlN Film stress depends on magnetic field on the surface of the target (7). AlScN film stress also depends on magnetic field on target surface. Since center of the wafer receives more deposited material from the inner target and wafer edge receives more deposition from the outer target, variation of the ratio of the strength of magnetic field between inner and outer targets (magnetrons) allows controlling concentric stress uniformity. We found that in AMS system stress variation has almost perfectly radial distribution that varies with the ratio of magnetic field between inner and outer magnetrons. Figure 3 shows change in stress across a wafer as a function of the ratio of the inner to outer magnetron magnetic fields.

Figure 3: Stress variation across wafer as a function of the ratio of inner to outer target magnetic fields

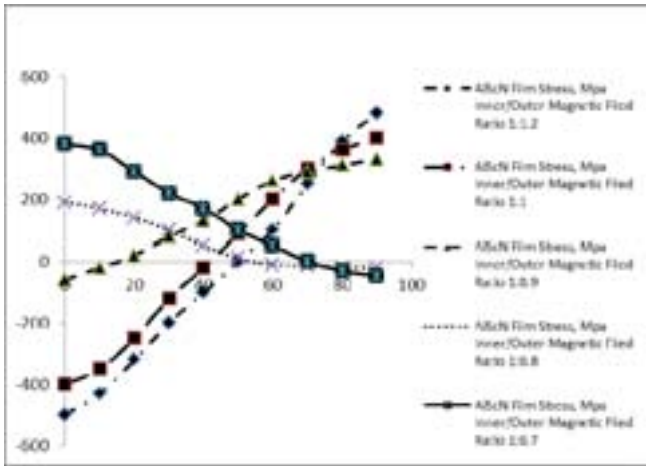

It is clear that a standard 1:1 ratio of magnetic field that produces the best results for AlN process is unacceptable for AlScN process. We found that the ratio of inner/outer of 1.0/0.8 is the best for stress control.

Placing an additional magnetic field with an adjustable strength behind a wafer as shown in Fig.4 creates a variable unbalance effect of the either inner or outer magnetron (and, as the result, increases or reduces ion bombardment) and provides an additional fine control of the film stress uniformity across a wafer (center to edge) over the target life. This magnetic field can be varied by either an electro-magnet with adjustable electrical current or a permanent magnet with a motor that can adjust the distance between the magnet and the wafer.

Figure 4. Magnetron with the enhanced magnetic field

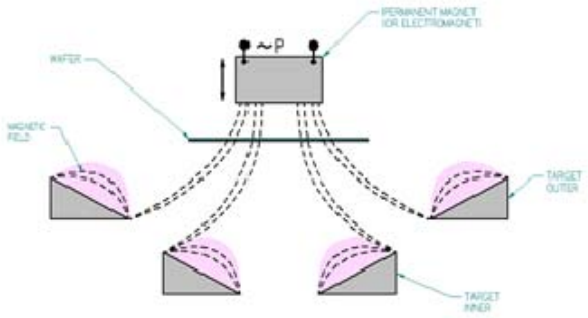

IV. COMPOSITION CONTROL

Another advantage of the dual magnetron is its capability to use targets (inner and outer) with different ratio of Sc/Al. This

method provides an additional control to obtain a uniform coupling coefficient across a wafer.

We started our study by using the same composition on both targets of about 6.1 atomic % Sc with the rest being Al. Analysis showed that deposited on the wafer film contained about 4.2% Sc. In order to achieve desired improvement of coupling coefficient we changed to 8 atomic % Sc on the inner target and varied Sc concentration on the outer targets. Figure 5 shows variation of coupling coefficient across a wafer as the inner target Sc concentration is 8% and outer target Sc concentration is varied between 0 and 8%.

Figure 5: Coupling coefficient across wafer as a function of Sc concentration in two targets

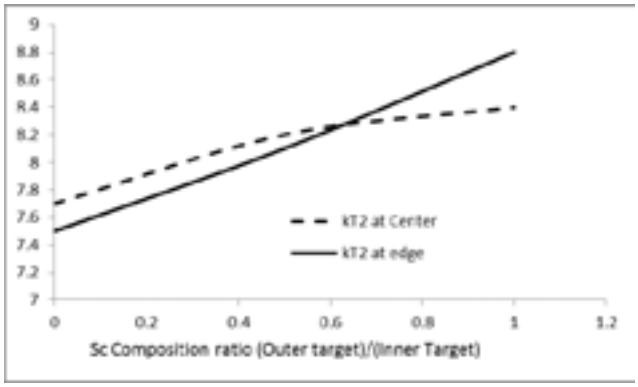

By using the same Sc concentration of inner and outer targets we get slightly higher concentration of scandium on the edge of the wafer. The optimum concentration profile is obtained with concentration of scandium of about 8% on the inner target and 4% on the outer target. It should be noted that most cost efficient method would be to use 8% Sc for inner target and pure outer aluminum target. The Coupling coefficient on the edge is only slightly lower than that in the center, but the cost of the target set is less than half of the target set with equal concentration in the inner and outer targets.

Figure 6 shows excellent control of both local stress and coupling coefficient across a wafer using optimized combination of optimum magnetic field ratio and Sc concentration.

Figure 6: Coupling coefficient and local stress on AlScN wafers

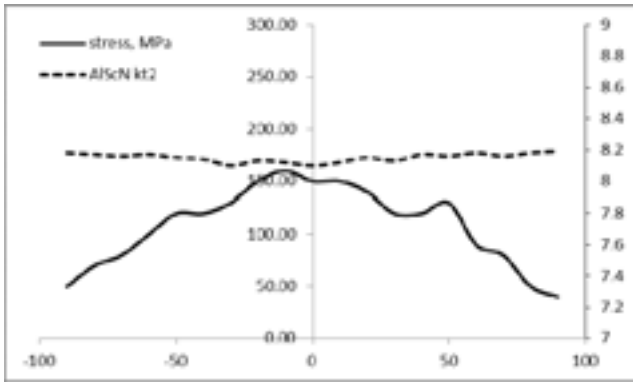

V. SUMMARY

Using dual magnetron design is highly advantageous in controlling stress and coupling coefficient in AlScN films. By adjusting magnetic field and concentration on target, it is fairly easy to obtain highly controlled coupling coefficient and stress in a high volume production environment.

REFERENCES

[1] Milena Moeira, et.al., "Aluminum scandium nitride thin-film bulk acoustic resonators for wide band applications", Vacuum, July 2011, Issue 1, pp. 23-26

[2] Morito Akiyama, "Influence of temperature and scandium concentration on piezoelectic response of scandium aluminum nitride alloy thin films", Applied Physics Letters, Oct. 2009, Vol.95, Iss. 16, pp. 2107-2107-3

[3] H.P.Lobl, et.al.. "Piezoelectric materials for BAW resonator and filters", 2001 IEEE International Ultrasonics Symposium, Atlanta, GA, Oct. 7-10,pp.807-811.

[4] Pau Muralt, et.al.. "Electromechanical properties of AlScN thin films evaluated at 2.5 GJz film bulk acoustic resonators", Applied Physics Letters 99, 2011

[5] Keiichi Umeda1, et.al.. "PIEZOELECTRIC PROPERTIES OF ScAlN THIN FILMS FOR PIEZO-MEMS DEVICES", MEMS 2013, Taipei, Taiwan, January 20 – 24, 2013

[6] Sergey Mishin, "Improving Manufacturability of Bulk Acoustic Wave and Surface Acoustic Wave Devices", IEEE SAWDA 2011

[7] Sergey Mishin, Rich Ruby John Larson, Yury Oshmyansky, "Sputtering Process for Bulk Acoustic Wave Filters", Semiconductor International, 2003

Optimization of Tether Geometry to Achieve Low Anchor Loss in Lamé-Mode Resonators

Vikram Thakar[1] and Mina Rais-Zadeh[1,2]

[1]Department of Mechanical Engineering, University of Michigan,
[2]Department of Electrical Engineering and Computer Science, University of Michigan,
Ann Arbor, USA
email: thakar@umich.edu

***Abstract*—In this paper, we study the fundamental cause of anchor dissipation in Lamé- or wineglass-mode resonators and show that by carefully optimizing the resonator tether geometry low anchor losses can be achieved, making it possible to reach the intrinsic *fxQ* limit of the resonating material. Through analytical and finite element investigation, we demonstrate that the anchor loss is most significant when the flexural-mode resonance frequency of the tether is in sync with the Lamé-mode frequency of the resonating plate. This has a significant bearing on the design of Lamé-mode resonators with release holes or temperature-compensation trenches, where the modification of the resonator structure requires modification to the tether geometry to maintain a high *Q*. We verify the predicted results through experimental measurements and present an optimized design that exhibits a mechanical *Q* of 408,270 for the fundamental Lamé mode at 41.57 MHz. The *fxQ* for this device is 1.7x10^{13}, one of the highest values reported in silicon.**

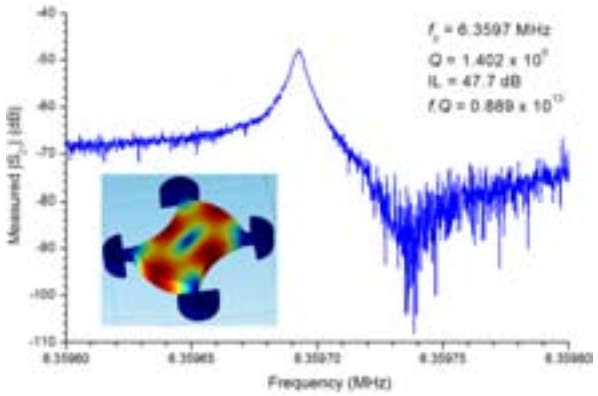

Fig. 1: Measured response of a fundamental Lamé mode at 6.3597 MHz showing a *Q* of 1.4 million.

I. Introduction

Low-loss resonators operating in the low- to mid-frequency range (kHz to few MHz) are critical in the implementation of low-power precision timing references in real time clocks and inertial measurement units (IMUs). At these frequencies, most silicon-based resonator topologies suffer from increased thermoelastic damping (TED) [1]. Due to their isochoric nature, pure Lamé-mode resonators are immune to TED and are ideally suited for such low-frequency timing applications. Straight tether supported Lamé- or wineglass-mode resonators operating in the low MHz frequency range have been shown to exhibit extremely high $f \times Q$ values on the order of 10^{13}, close to the fundamental phonon-phonon loss limit in silicon (see Fig. 1) [2], [3]. However, experimental results suggest increased anchor dissipation exists for certain tether geometries, resulting in *Q* degradation by over an order of magnitude [3]. In light of the utility of these resonators in timing applications, the design of tethers for low anchor loss is critical and merits further investigation.

Anchor loss, also known as clamping loss, has been widely investigated in a variety of resonator geometries due to its significance in the design of high-*Q* resonators. Unlike intrinsic losses which are primarily set by the material of the resonator and its operating frequency [1], [4], anchor loss is design dependent and therefore can be minimized through appropriate design choices. Analytical models estimating the clamping loss in simple beam geometries have been presented in literature [5]. Recently, more exotic ring resonators have also been analyzed for their substrate damping effects [6]. Unfortunately, most of these analytical estimates require precise knowledge of the stress profile at the anchoring area, which is difficult in the case of complex resonator geometries. In addition, the estimation of the exact *Q* may require the use of fitting parameters, which need to be extracted from measured results. Recognizing this limitation, a significant effort has been put towards the estimation of anchor *Q* using finite element methods. Bindel *et al.* applied the method of perfectly matched layers (PML) to the problem of anchor dissipation in stem-supported disk resonators [7], motivated by their utility in electromagnetic analysis [8]. Since then, there has been additional work validating the PML-based approach for anchor *Q* estimation [9]. In both these works, the finite element analysis (FEA) has been implemented using custom built codes, making it difficult to generically adopt. In this work, COMSOL®, a commercial software package, is utilized to model the anchor loss in resonators. The COMSOL

This work is supported by NASA under the Chip-Scale Precision Timing Unit project (Grant #NNX12AQ41G).

simulation parameters are chosen such that the simulated anchor *Q*s match reported analytical estimates of anchor *Q* for different beam resonance modes. This model is then used to predict the anchor loss in Lamé-mode resonators. In the subsequent analysis, it is shown that the anchor *Q* degradation is primarily due to the co-existence of the tether resonance modes near the frequency of the primary Lamé mode. This has important consequences in the design of Lamé-mode resonators with passive compensation or etch holes for wet release compatibility, as such modifications can lead to a reduction in the resonator frequency.

For the purpose of experimental verification, a 100 µm × 100 µm Lamé-mode resonator is analyzed for its tether-dependent anchor loss and a good agreement between the predicted and measured results is shown. An optimized Lamé-mode resonator is presented with a measured mechanical *Q* of 408,270 at a center frequency of 41.57 MHz, attaining an $f \times Q$ of 1.7×10^{23}, which is close to the intrinsic phonon-phonon limit in silicon [4].

II. Estimation of Anchor *Q* using Finite Element Modeling

Fig. 2 shows the finite element model of a beam using a PML to model the substrate as a semi-infinite layer [7]. The material parameters for the PML are same as those for the substrate layer, which usually are the same as those for the beam. It should be noted that the parameters of the PML are critical in achieving accurate anchor *Q* estimates. Similar to the observations in [9], the choice of alpha, *i.e.* the PML scaling factor, determines the magnitude of the simulated anchor *Q* and should be optimized for the specific resonator frequency and geometry. This idea is elaborated in Fig. 3, which shows a large variation in the simulated *Q* as a function of alpha.

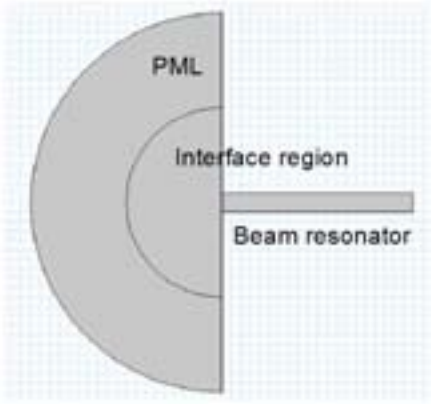

Fig. 2: Model of a beam resonator for anchor loss estimation.

From Fig. 3, we can clearly see that the minimum value of the estimated anchor *Q* converges to the analytical estimate from [5]. A similar study is performed for all the beam geometries and modes analyzed in [5]. The results are summarized in Table 1, demonstrating an excellent agreement between the analytical and the FEM estimates of minimum anchor *Q*.

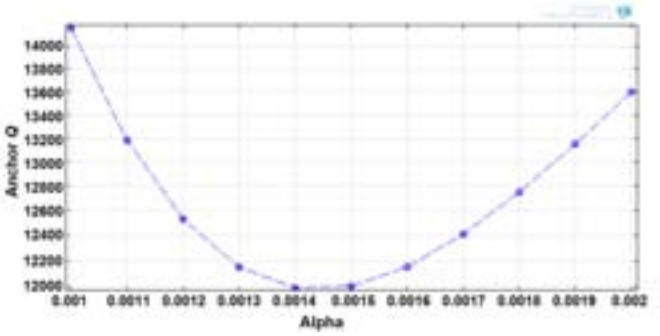

Fig. 3: Simulated anchor *Q* for a silicon beam resonator as a function of alpha. The silicon beam is 500 µm long and 7.2 µm wide. The analytical estimate of anchor *Q* for the third-order flexural mode (clamped-clamped boundary) is calculated to be 11,177 [5].

Table 1: Comparison of the simulated anchor *Q* with analytically calculated estimates for flexural modes of a silicon beam resonator [5].

Length (µm)	Width (µm)	Frequency (kHz)	Anchor *Q*	
			Analytical	*Simulated*
Fixed Free Cantilever (first-order flexure)				
700	6.45	15.94	2.6626×10^6	2.65×10^6
500	4	19	4.0684×10^6	4.1×10^6
500	5	24.59	2.083×10^6	2.1×10^6
500	6.2	30.14	1.0925×10^6	1.1×10^6
Fixed- Fixed Beam (first-order flexure)				
900	7.9	74.8	248,470	247,612
700	5.15	80.3	421,980	419,165
500	3.8	117	382,800	380,418
300	3.4	288.4	115,440	115700
Fixed- Fixed Beam (third-order flexure)				
700	8.7	740	17,365	18,940
500	6.1	1030	18,357	20,061
500	7.2	1210	11,177	11,976

III. Resonator Design

Fig. 4 shows a scanning electron microscope (SEM) image and critical tether parameters of a Lamé-mode resonator. The frequency of the fundamental Lamé mode is set by the characteristic plate length L as marked in Fig. 4 and is given as,

$$f_0 = \frac{1}{2L}\sqrt{\frac{G}{\rho}} \quad (1)$$

where G is the shear modulus (Pa) and ρ is the density (kg/m^3). Fig. 5 plots the simulated anchor *Q* loaded with the intrinsic phonon-phonon loss limit in silicon [4] as a function of tether geometry for a 100 µm × 100 µm square plate resonating in the fundamental Lamé mode.

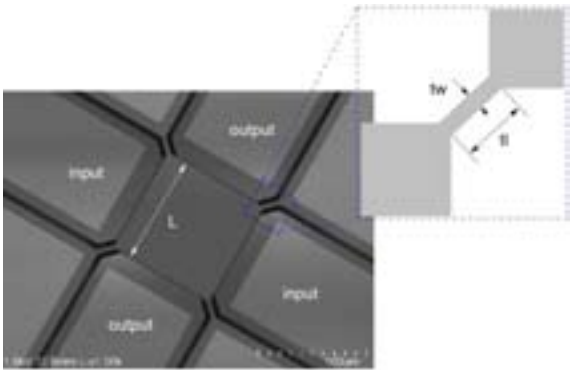

Fig. 4: (Left) A SEM image of a Lamé-mode resonator and (right) the critical tether parameters. The characteristic length L sets the frequency of the fundamental Lamé mode.

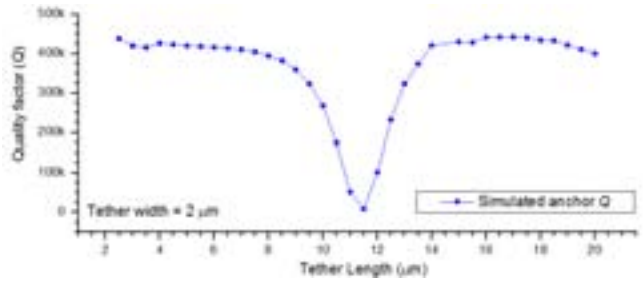

Fig. 5: Simulated anchor Q as a function of tether length for a 100 μm × 100 μm Lamé-mode resonator having a tether width of 2 μm. The simulated Q is loaded with the phonon-phonon loss limit in silicon [4]. Change graph wider

IV. Origin of Anchor Loss in Lamé Resonators

In order to support the Lamé-mode resonance, the tethers are required to undergo forced flexural vibrations. As a consequence, the anchor loss in such resonators is strongly dictated by the flexural resonance frequency of the tether which can be expressed as,

$$f_n = \frac{1}{2\pi}\beta_n^2 \frac{t_w}{t_l^2}\sqrt{\frac{EI}{\rho A}}, \qquad (2)$$

where f_n is the resonance frequency of the nth mode, β_n is the mode constant, t_w is the tether width (μm), t_l is the tether length (μm), E is the Young's modulus (Pa), I is the area moment of inertia for the tether cross-section (m^4) and A is the cross-section area of the tether (m^2). For a cantilever loaded with a mass at its free-end, the resonance frequency is found to be reduced and can be estimated using the formulation in [10]. The effect of mass loading is accounted for by the lowering of the mode constants, β_n, which affects the resonance frequency through (2). Table 2 lists the mode constants and the critical tether length at which the flexural resonance frequency for the tether equals the frequency of the fundamental Lamé-mode of a 100 μm × 100 μm square plate when the tether width is fixed at 2 μm. While the results agree well for longer tether lengths, at shorter tether lengths, the tether aspect ratio is much smaller than 10:1 and the Euler-Bernoulli approximation introduces significant inaccuracies. Inclusion of the effect of rotary inertia can help improve the accuracy of the analytical estimates. Fig. 6 plots the FEA results of the first two tether modes and their critical tether lengths.

Table 2: Analytically estimated critical tether length for a 100 μm × 100 μm Lamé-mode resonator.

	β	Critical tether length (μm)	
		Analytical	Simulated
Mode 1	0.425	1.44	3.5
Mode 2	3.925	13.34	11.5
Mode 3	7.065	24.01	23
Mode 4	10.215	34.72	34

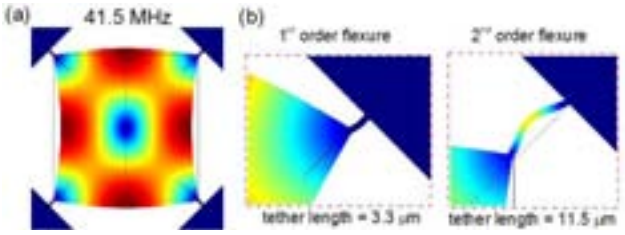

Fig. 6: (a) Fundamental Lamé mode of a 100 μm × 100 μm silicon square plate. (b) First- and second-order flexural modes of the tether. The tether width is 2 μm and the critical tether length is 3.3 μm and 11.5 μm for the first- and second-order mode, respectively. With these critical anchor dimensions, maximum anchor loss of the resonator is found.

From the presented analysis, it is clear that when the tether resonance frequency is near the frequency of the Lamé mode, the resonator Q is degraded due to the additional energy lost from the tether's resonance. In other words, to enable high-Q Lamé-mode resonators, the tether geometry should be set such that the flexural mode of the tethers is far from the fundamental Lamé-mode frequency. While a simple analytical formulation can be used to estimate the critical tether lengths FEM is preferred where accuracy is critical.

V. Experimental Verification

A. Device Fabrication

In order to experimentally investigate the dependence of the Lamé-mode anchor Q on its tether length, devices were fabricated using the process flow shown in Fig. 7. The starting substrate is a silicon-on-insulator (SOI) wafer with a 25 μm thick low resistivity (0.02 Ω.cm) device layer to enable electrostatic actuation. The choice of electrostatic actuation is made to ensure that the resonator Q is not degraded by interface losses [11].

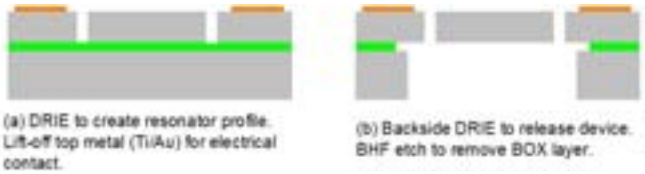

Fig. 7: Fabrication process flow used to experimentally investigate anchor loss in Lamé-mode resonators.

B. Measured Results

The fabricated devices are measured using an Agilent E5061B network analyzer in a vacuum probe station. Multiple dies of resonators were tested and the extracted

mechanical Q as a function of the tether length is plotted in Fig. 8. The data for the simulated anchor Q is overlaid for comparison. In order to obtain the unloaded resonator Q, the series electrical resistance and the resonator motional impedance is estimated using standard extraction techniques [12]. From the analysis, it is estimated that series electrical resistance of the contacts to the resonator is 3.9 kΩ.

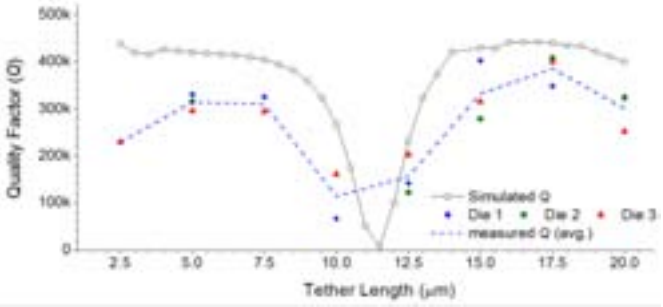

Fig. 8: Extracted unloaded Qs of multiple Lamé-mode resonators as a function of tether length for a tether width of 2 μm. The data for simulated Q is overlaid for comparison.

Fig. 9 plots the measured response of a Lamé-mode resonator with optimized tether geometry: a tether length of 17.5 μm and tether width of 2 μm. The measured Q for this device is 302,120 at 41.57 MHz. Using the extraction method in [12], the unloaded Q of the resonator is extracted to be 408,270 giving an $f \times Q$ of 1.7×10^{13}.

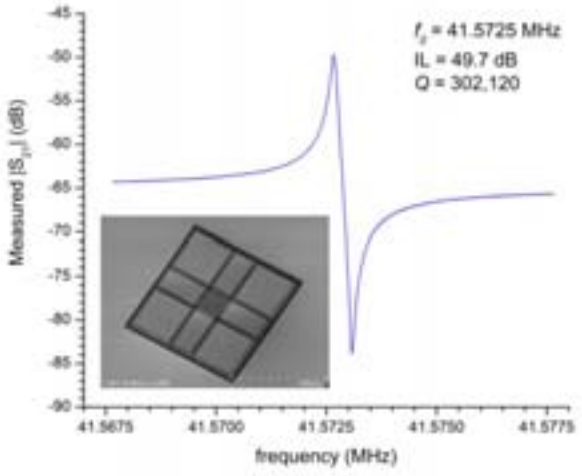

Fig. 9: Measured response of an optimized Lamé-mode resonator with an applied bias of 250 V. (Inset) SEM image of the device. The device has a tether length of 17.5 μm and tether width of 2 μm.

The results in Fig. 8 suggest that for optimum tether geometries the resonator Q is primarily limited by the intrinsic phonon-phonon interactions in silicon. Secondly, we can clearly see the accuracy of prediction using finite element methods. With the validation of the anchor loss model, a similar analysis can be performed for the tether optimization of passively compensated Lamé-mode resonators, and will aid in the development of low-power low-frequency precision timing references.

VI. Conclusion

In this paper we investigated the cause of anchor loss in Lamé-mode resonators and verified the role of the tether resonance modes in degrading the Lamé-mode resonator Q. Finite element analysis was used to estimate the resonator Q and was shown to agree well with both analytical estimates and experimental measurements. An optimized tether design was presented with an unloaded Q of 408,270 for the fundamental Lamé mode at 41.5 MHz attaining an $f \times Q$ of 1.7×10^{13}, which is close to the fundamental phonon-phonon loss limit in silicon.

For low-power low noise timing applications, it is important to design passively compensated resonators to reduce the frequency fluctuation with temperature. From the presented analysis, we can deduce that since the frequency of temperature-compensated Lamé-mode resonators is different from their uncompensated counter-parts, the optimum tether geometry will also be different. The presented tether optimization procedure will be invaluable for the design of low-loss temperature-compensated Lamé-mode resonators.

Acknowledgment

The authors acknowledge A. Peczalski and Z. Wu, both at the University of Michigan, for useful discussions. The authors also acknowledge the staff at the University of Michigan Lurie Nanofabrication Facility (LNF), a member of NNIN, for their help with device fabrication.

References

[1] S. A. Chandorkar, et al., "Limits of quality factor in bulk-mode micromechanical resonators," MEMS, Tucson, AZ, Jan. 2008

[2] J. Lee, J. Yan and A. Seshia, "Study of lateral mode SOI-MEMS resonators for reduced anchor loss," J. Micromech. Microeng. vol. 21, pp. 045010, 2011

[3] L Khine and M. Palaniapan," High-Q bulk-mode SOI square resonators with straight-beam anchors," J. Micromech. Microeng., vol. 19, pp. 015017, 2009

[4] R. Tabrizian, M. Rais-Zadeh, and F. Ayazi, "Effect of phonon interactions on limiting the f.Q product of micromechanical resonators," Transducers'09, pp. 2131-2134, Denver, CO, 2009.

[5] Z. Hao, A. Erbil and F. Ayazi, "An analytical model for support loss in micromachined beam resonators with in-plane flexural vibrations," Sensors and Actuators A, vol. 109, pp. 156-164, 2003.

[6] Z. Hao and F. Ayazi, "Support Loss in the Radial Bulk-mode Vibrations of Center-supported Micromechanical Disk Resonators," Sensors and Actuators A, Vol. 134, pp. 582-593, March 2007.

[7] D. Bindel, S. Govindjee, "Elastic PMLs for resonator anchor loss simulation," Internat. J. Numer. Methods Engrg., vol. 64, 2005.

[8] J-P. Bérenger, "A perfectly matched layer for the absorption of electromagnetic waves," J. Comput Phys, vol. 114, pp. 185–200, 1994.

[9] A. Frangi, A. Bugada, M. Martello and P. Savadkoohi, "Validation of PML-based models for the estimation of anchor dissipation in MEMS Resonators," Eur J. Mech A, vol. 37, pp. 256-265, 2013.

[10] P. Laura, J. Pombo and E. Susemihl, "A note on the vibrations of a clamped-free beam with a mass at the free end," *J. Sound Vibration*, vol. 37, no. 2, pp. 161-168, 1974.

[11] A. Frangi, M. Cremonesi, A. Jaakkola and T. Pensala, "Analysis of anchor and interface losses in piezoelectric MEMS resonators," Sensors and Actuators A: Physical, vol. 190, pp. 127-135, Feb. 2013.

[12] G. K. Ho , K. Sundaresan , S. Pourkamali and F. Ayazi "Low-motional-impedance highly-tunable I2 resonators for temperature-compensated reference oscillators", Proc. 18th IEEE Int. Conf. MEMS, pp.116 -120 2005

Mechanically Coupled SOI Lamé-mode Resonator-Arrays: Synchronized Oscillations with High Quality Factors of 1 Million

Yuanjie Xu and Joshua E.-Y. Lee
Department of Electronic Engineering
City University of Hong Kong
Kowloon, Hong Kong
joshua.lee@cityu.edu.hk

***Abstract*—In this work, we present the first demonstration of synchronized oscillations in an SOI resonator array with quality factors (Qs) in the order of 10^6 through mechanical coupling. We have fabricated arrays of up to six resonators. Our experimental results indicate that even as the length of the array is expanded, Q is maintained in the order of 10^6 at a resonant frequency of 13MHz. This yields an f•Q product of 1.3×10^{13}, which is close to that of a single Lamé mode resonator. With Q maintained at 10^6, our results show that the motional resistance reduces according to the number of resonators incorporated into the array. These results in turn suggest that mechanical coupling can be extended to even yet longer arrays for reducing motional resistance as well as improve power handling without notably diminishing Q.**

Keywords—array; mechanical coupling; motional resistance; Lamé mode; quality factor

I. INTRODUCTION

Within the field of frequency control and timing devices, micromachined electromechanical resonators have a number of attractive features that help them standout from FBARS, SAW, and quartz resonators. Some of these include the advantage of a small form factor and an easier path towards integration with integrated circuit electronics. Possibilities of where this kind of technology is heading include all-mechanical radio front-ends [1]. Due to their small size and high quality factors (Q) that can be over 10^4, radio-frequency channel selection is now a possibility [2]. Silicon-based (including polysilicon) devices have the advantage of superior mechanical characteristics that allow for high Q even in the millions to be realized [3]. While more efficient electromechanical transduction technologies like piezoelectric AlN provide a pathway to realizing devices with motional resistances approaching targets of 50Ω, the tradeoff that continues to remain is the limited Q typical of this class of devices [4]. Capacitive devices and hybrids thereof continue to exhibit the highest Qs reported in the literature [5-7]. At the same time, the drawback of capacitive transduction lies in the less than satisfactory coupling efficiency even with narrow air gaps, leading to motional resistances that are much larger than is desired [8]. In principle, for contour modes of resonance that have their eigenfrequencies defined by their lateral dimensions, the coupling area reduces when these devices are scaled toward higher operating frequencies, translating to a higher motional resistance. One approach of overcoming this loss in area that comes with designs for higher frequency is to couple multiple copies of the same resonator into an array. By summing up the individual currents from each resonator collectively, the overall motional current increases and thus reduces the net motional resistance. Due to the fabrication tolerances and high Qs, such collective summation is difficult with electrical coupling since the resonances of the each resonator will not perfectly coincide altogether. In order to synchronize their resonances, resonators can be mechanical coupled. Through careful design of the link couplers and phase combinations of the electrodes, the spurious modes can be suppressed so as to yield just a single detectable resonant peak. This has been successfully demonstrated in a polysilicon surface micromachining process based on coupled disk resonators [9]. In fact, this mechanical coupled array approach has been used in combination with more lossy AlN resonators in order to boost Q [10]. While the Qs for these polysilicon arrays are not significantly lower than those of the single disk resonator, the f•Q product of these resonators are notably lower than for single-crystal silicon (SCS) resonators [11]. Possible reasons could lie in the design (e.g. anchor loss in the quasi-nodes of the wine glass disk resonator) or in the material itself possessing greater internal frictional loss [12].

We have previously reported on SCS resonator arrays that were fabricated in SOI based on square-plates [13] and disks [14] that were excited to vibrate in the breathing mode. SCS has the advantage over polysilicon of higher piezoresistive coefficients; hence these resonator arrays could also exploit the benefits of piezoresistance to further enhance transduction. It was found that mechanical coupling did not necessarily result in greater attenuation of Q. However, these breathing mode resonators are limited by anchor losses with Qs that are far less than the highest f•Q products reported for SCS resonators. In this work, we apply the principle of mechanical coupling to the Lamé mode, known for their high Qs and low loss in order to further assess the impact of mechanical coupling on Q. Results of fabricated resonator arrays of up to 6 resonators show that Q can be maintained at a million, with no significant indication that mechanical coupling degrades Q. This allows the motional resistance to be reduced in proportion to the number of devices.

This work was supported by a grant under the Early Career Scheme from the Research Grants Council of Hong Kong (project number CityU 124312), and the Strategic Research Grant from City University of Hong Kong (project number 7002690).

II. Low Loss Features of the Lamé Mode Resonator

The nodes of the Lamé mode of a square-plate resonator are located at the corners of the plate, thus providing a convenient location to clamp the structure. Being able to clamp the plate at the nodes helps reduce anchor loss. In previous studies that compared different kinds of tether designs and their effects on Q, it was found that the choice between a T-shaped and straight tether made no significant difference to the associated Q [15]. It was also shown in a previous study that making variations to the geometry of T-shaped tethers likewise made no difference to Q [16]. These results altogether suggest that anchor loss is unlikely to be the dominant cause that limits Q.

The Lamé mode's unique isochoric mode shape means that the driving factor for thermoelastic damping (TED) is absent. The effects of this unique feature have been observed in our previous studies on the effect of etch holes on Q [17]. Hence by elimination, the observable Q of the Lamé mode is most likely determined by more fundamental dissipation effects such as Akhieser loss. In short, the unique low-loss characteristic of the Lamé mode allows us to more carefully examine the effects of attenuation from mechanical coupling in the limit of low dissipation, whereby these effects should be more obvious.

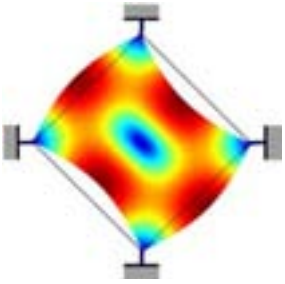

Fig. 1. Mode shape of a Lamé mode resonator simulated by finite elements in COMSOL multiphysics.

III. Lamé Mode Resonator Array

The sides of the Lamé mode square-plate resonators in this work are aligned to the <110> direction in the (100) plane. We have previously shown that this yields Qs that are twice that in the <100> direction [18]. To synchronize two resonators that are to vibrate in phase, we physically link the two resonators by a beam coupler that is half of the wavelength (λ/2) of the Lamé mode resonator. This is defined by:

$$\lambda = L\sqrt{1+\nu} \tag{1}$$

where L is the length of the square-plate and ν is the Poisson's ratio in the <110> direction. As a further measure, as is seen from Fig. 2, the electrical routing of the electrodes has been designed so as to actuate and detect both resonators in phase.

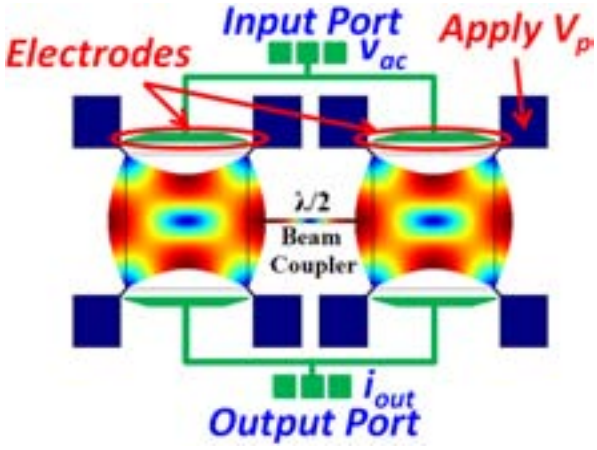

Fig. 3. Simplest configuration of a resonator array containing just two of the same resonators linked via a λ/2 beam coupler. The resonators are designed to be actuated and detected in phase by the routing of the electrodes.

Note that the schematic in Fig. 2 represents a single-ended configuration. To achieve a fully-differential configuration as the array size is doubled, we couple two sets of in-phase twin arrays (illustrated in Fig. 2) with a beam coupler that is a full wavelength (λ). This is depicted in Fig. 3 that shows an array of four resonators, which can be separated into two sections. Within each section the resonators vibrate in phase, linked by λ/2 coupler. Between the two sections, the resonators vibrate in anti-phase through the λ coupler. This phase combination is excited preferentially over other spurious modes by the design of the electrical routing of the electrodes. As shown in Fig. 3, the two sections are actuated and detected out-of-phase via two separate input ports and also two separate output ports.

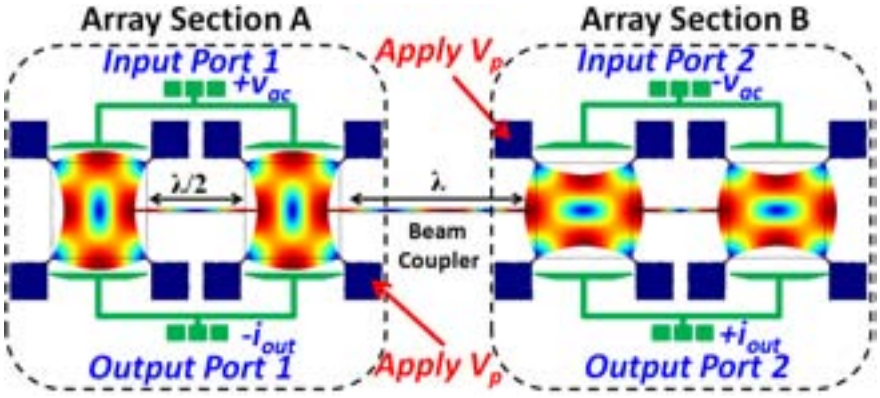

Fig. 2. Phase combination of an array of four resonators split into two sections. Within each section the resonators are in phase but between the sections the resonators are out-of-phase (AABB combination), achieved by the choice of beam coupler lengths and electrical routing of electrodes.

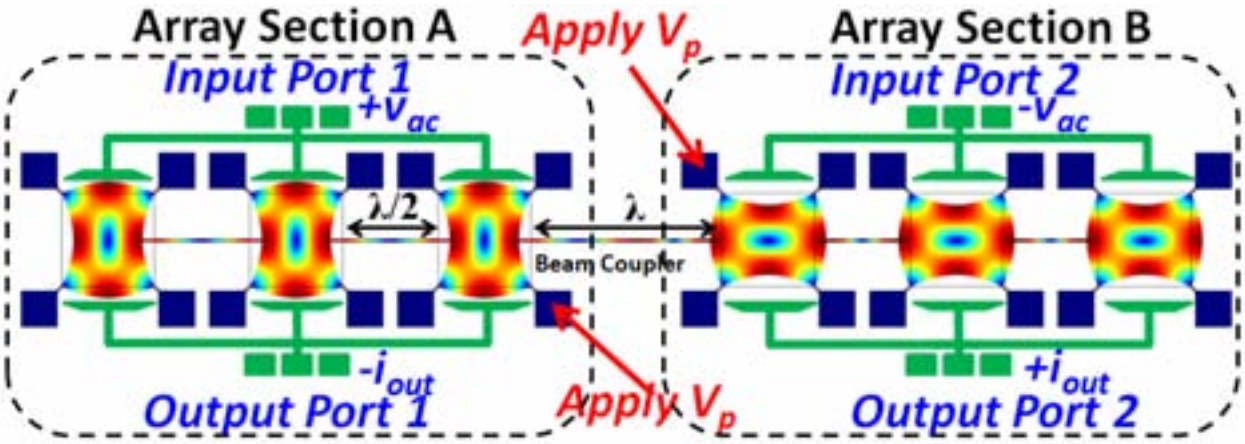

Fig. 4. An array of six resonators formed by inserting an additional resonator to each section of the 4-resonator array. Longer arrays can likewise be formed by extending the array further in the same fashion that allows the same fully-differential biasing configuration to be reused.

Based on the fully-differential mechanically coupled array configuration shown in Fig. 3 for 4 resonators, we extended the length of the array resonator up to six resonators by adding one more resonator to each section. This allows us to preserve the fully-differential biasing configuration that has the benefit of providing feedthrough cancellation. As the number count of resonators in the array increases, motional resistance should in turn decrease by the same proportion.

These devices were fabricated on a 10µm thick SOI device layer using a standard surface micromachining process, where the release of the free structure was realized by etching a trench through the substrate. The square-plate resonators had a length of 320µm, each clamped on all four corners with straight beam tethers. The above array designs were fabricated on the same die along with a single square-plate resonator for comparison (transduction gap limited to 2.5µm). Micrographs of each of these arrays are shown in Fig. 5. The electrical routing on the electrodes is marked out by the metal trace in addition to the bond pads on each anchor in order to apply a DC bias voltage.

IV. Experimental Results

The fabricated devices were electrically characterized under mTorr levels of vacuum, measuring the electrical transmission using an Agilent E5061A network analyzer. Fig. 6 shows the measured results after feedthrough has been extracted out. The resonant peaks from each measurement have been deliberately aligned for better visualization of the characteristics in relation to each other. The resonant frequency from the resonators was around 12.9MHz, with deviations in the same order that would be expected of fabrication tolerances estimated under an SEM.

The single Lamé resonator had a Q of about 1.2 million. In comparison, the resonator arrays had very similar value of Q to each other that were on average 16% lower than for the single Lamé resonator. These results show that extending the length of the array from two to six resonators reveals no conclusive trend that Q decreases as the length of the array is increased. In the results show in Fig. 6, the same source power of 10dBm was used. It can be seen that as the number of resonators in the

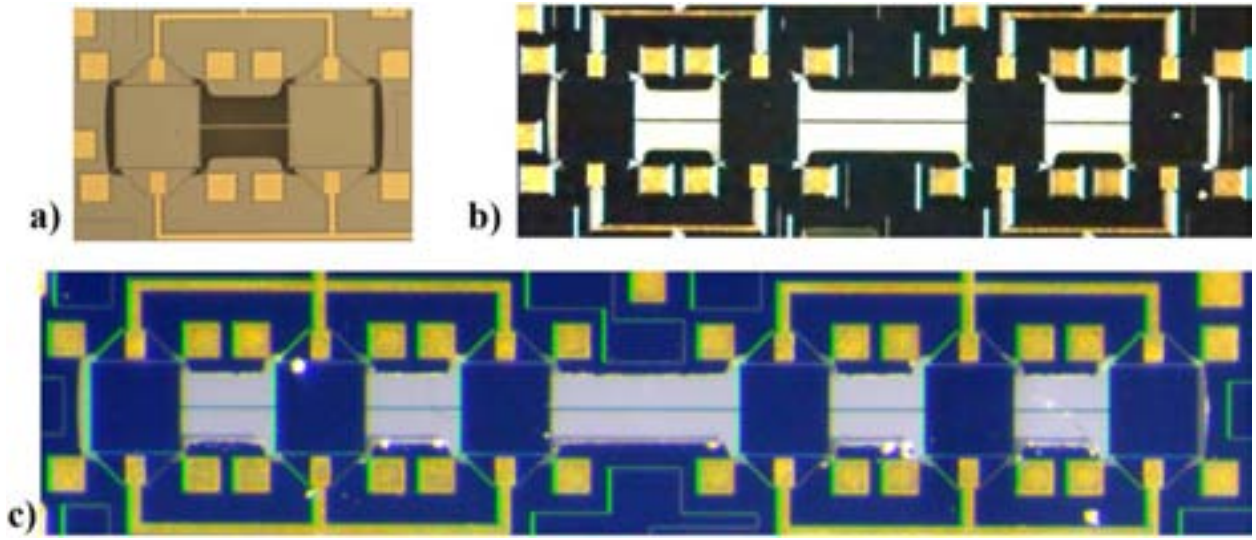

Fig. 5. Micrographs of fabricated SOI mechanically coupled resonator arrays using a standard SOI surface micromachining process comprising (a) two, (b) four, and (c) six resonators. The resonators are physically linked together by a combination of half (λ/2) and full (λ) wavelength beam couplers.

array is increased, the degree of nonlinear bifurcation (seen in the frequency shift of the peak) was reduced accordingly. This is indicative that increasing the array size could also improve the power handling capability. We have extracted the motional resistance (R_x) of each device from the measured transmission. These extracted values are summarized in Table 1 along with their respective values of Q. From Table 1, it can be seen that R_x appears to scale inversely with the number of resonators.

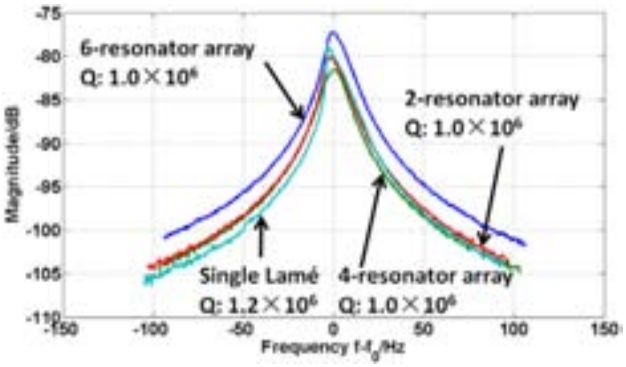

Fig. 6. Measured electrical transmission of resonator arrays as well as for a single Lamé resonator using 10dBm source power. The position of resonant peaks have been deliberately aligned for ease of comparison.

TABLE I. EXTRACTED QUALITY FACTOR AND MOTIONAL RESISTANCE OF THE ELECTRICALLY CHARACTERIZED RESONATOR ARRAYS

No. of resonators	Extracted Parameters	
	Quality factor (10^6)	*R_x (kΩ)*
2	1.03	1011
4	0.98	550
6	1.03	330

V. CONCLUSION

We have fabricated mechanical coupled arrays of low loss high Q Lamé resonators in this work to assess the attenuation in Q due to mechanical coupling. Here we have demonstrated an array of up to six resonators with a Q around a million. By a choice of the coupling beam lengths, we are able to prescribe the phase combination of the resonators in the array in order to obtain a fully-differential biasing configuration. Comparing Qs between arrays of two, four, and six resonators, no conclusive correlation between increasing the array size and degradation in Q was found. Compared to a single Lamé resonator, the Qs of the arrays were slightly lower by ~16%. It has been shown here that the motional resistance indeed scales inversely with the number of resonators in the array. This is the first time that mechanically coupled silicon resonators with Qs in the order of a million have been demonstrated. These results suggest that the approach of mechanical coupling to realize synchronized arrays could be feasible even for a low loss material like single crystal silicon and also with low damping modes like the Lamé resonant mode. Hence by coupling resonators into arrays, the motional resistance can be reduced in proportion to the length of the array. And as indicated by the results of this work, this could be achieved without significantly sacrificing the quality factor. Fabricating and characterizing even longer arrays of the Lamé mode resonators would further test the validity of this proposition.

REFERENCES

[1] C. T.-C. Nguyen, "Mechanical radio," IEEE Spectrum, vol. 46, no. 22, pp. 30-35, Dec. 2009

[2] C. T.-C. Nguyen, "MEMS-based RF channel selection for true software-defined cognitive radio and low-power sensor communications," IEEE Communications Magazine, vol. 51, no. 4, pp. 110-119, Apr. 2013

[3] J. E.-Y. Lee and A. A. Seshia, "Square wine glass mode resonator with Q of 4 million," Proc. IEEE Sensors Conf. 2008, Lecce, Italy, 26-29 Oct. 2008, pp. 1257-1260

[4] L.-W. Hung and C. T.-C. Nguyen, "Capacitive-piezo transducers for higher Q contour-mode AlN resonators at 1.2 GHz," Tech. Dig. Hilton Head 2010, SC, Jun. 6-10, 2010, pp. 463-466.

[5] S. Pourkamali, G. K. Ho, and F. Ayazi, "Low-impedance VHF and UHF capacitive silicon bulk acoustic wave resonators - Part II: Measurement and Characterization," IEEE Trans. Electron Devices, vol. 54, no. 8, pp. 2024-2030, Aug. 2007..

[6] M. Ziaei-Moayyed, D. Elata, E. P. Quévy, and R. T. Howe, "Differential internal dielectric transdution of a Lamé-mode resonator," J. Micromech. Microeng., vol. 20, 115036, 2010.

[7] D. Weinstein and S. A. Bhave, "Internal dielectric transduction in bulk-mode resonators," J. Microelectromech. Syst., vol. 18, no. 6, pp. 1401-1408, 2009.

[8] J. R. Clark, W.-T. Hsu, M. A. Abdelmoneum, and C. T.-C. Nguyen, "High-Q UHF micromechanical radial-contour mode disk resonators," J. Microelectromech. Syst., vol. 14, no. 6, pp. 1298-1310, Dec. 2005.

[9] Y.-W. Lin, S.-S. Li, Z. Ren, and C. T.-C. Nguyen, "Low phase noise array-composite micromechanical wine-glass disk oscillator," Tech. Dig. IEEE IEDM 2005, Washington, DC, 5-7 Dec., 2005, pp. 287-290.

[10] L.-W. Hung and C. T.-C. Nguyen, "Q-boosted AlN array-composite resonator with Q >10,000," Tech. Dig. IEEE IEDM, San Francisco, CA, 6-8 Dec. 2010, pp. 162-165

[11] J. E.-Y. Lee, J. Yan, and A. A. Seshia, "Low loss HF band SOI wine glass bulk mode capacitive square-plate resonator," J. Micromech. Microeng., vol. 19, 074003, Jul. 2009

[12] V. T. Srikar and S. D. Senturia, "Thermoelastic damping in fine-grained polysilicon flexural beam resonators," J. Microelectromech. Syst., vol. 11, pp. 499-504, 2002.

[13] A. Iqbal and J. E.-Y. Lee, "Piezoresistive sensing in an SOI mechanically-coupled micromechanical multiple resonator array," IEEE Trans. Electron Devices, vol. 59 , no. 11, pp. 3091-3096, Nov. 2012

[14] A. Iqbal, W. Zhang, and J. E.-Y. Lee, "Enhanced piezoresistive sensing via synchronized oscillations in a mechanically coupled disk array," Proc. Transducers 2013, Barcelona, Spain, 16-20 Jun. 2013

[15] J. E.-Y. Lee, J. Yan, and A. A. Seshia, "Study of lateral mode SOI-MEMS resonators for reduced anchor loss," J. Micromech. Microeng., vol. 21, 045010, Apr. 2011

[16] Y. Xu and J. E.-Y. Lee, "Does greater piezoresistive transduction give rise to higher anchor loss in a square-extensional mode micromechanical resonator?" Sens. Actuator A-Phys. (in press) 10.1016/j.sna.2013.01.048

[17] C. Tu and J. E.-Y. Lee, "Thermoelastic dissipation in etch-hole filled Lamé bulk-mode silicon microresonators," IEEE Electron Device Lett., vol. 33, no. 3, pp. 450-452, Feb. 2012.

[18] C. Tu and J. E.-Y. Lee, "Crystallographic effects on energy dissipation in high-Q silicon bulk mode resonators," J. Microelectromech. Syst., vol. 22, no. 2, pp. 262-264, Apr. 2013

A Parallel-Class Thermally-Actuated Micromechanical Filter with Tunable Center Frequency and Bandwidth

Cheng Tu and Joshua E.-Y. Lee
Department of Electronic Engineering
City University of Hong Kong
Kowloon, Hong Kong
mems305@gmail.com

Joshua E.-Y. Lee
Information and Communications Technology Centre
City University of Hong Kong Shenzhen Research Institute
Shenzhen, People's Republic of China
joshua.lee@cityu.edu.hk

***Abstract*—A thermally-actuated micromechanical filter with center frequency at very high frequency (VHF) range (64MHz) has been demonstrated for the first time by electrically coupling two thermal-piezoresistive (thermal actuation and piezoresistive readout) resonators. A small-signal equivalent circuit for this filter is proposed and used to analyze the measured frequency response. The filter exhibits tunability in the center frequency (72.2ppm) and relative bandwidth (0.002% to 0.004%) through the capability to tune the resonant frequency of each resonator by adjusting their bias voltages due to the Joule heating effect. Although the filter is not an optimized one, it is sufficient to achieve an out-of-band rejection of more than 10dB and ripple of less than 1dB in the pass band throughout the whole tuning range.**

Keywords- thermal actuation; micromechanical filter; parallel-resonator architecture; tunable center frequency and bandwidth

I. INTRODUCTION

In recent years, increasing efforts have been devoted to improve the performance of the micromechanical filters in order to meet the critical demand for low cost, single-chip, multi-band, multi-standard radio frequency (RF) solutions that are needed by next-generation wireless communication systems [1-6]. Compared to conventional filter implementations based on ceramic and also surface acoustic wave (SAW) technologies, micromechanical filters have significant advantages in terms of their small form factor, low cost batch-fabrication as well as compatibility with CMOS integrated circuits.

To date, two distinct transduction mechanisms technologies for micromechanical resonators have demonstrated successful realization of RF filtering function. These are based on either capacitive [1-3] or piezoelectric [4-6] transduction. Although characterized by high quality factor (Q), capacitive resonators typically suffer from high motional resistance (normally above kΩ at VHF range [1]) which leads to high insertion loss of the constructed filter referenced to 50 Ω systems. To lower the motional resistance, one common approach is to reduce the transduction gap, though this increases the complexity of the fabrication. Since the piezoelectric materials possess large electromechanical coupling coefficient, the motional resistance of piezoelectric resonators can be reduced to a few 100 Ω [5]. One of the commercially available piezoelectric filters is based on film bulk acoustic resonators (FBARs) [4]. However, the resonant frequency of FBAR is a function of film thickness, which makes multiple frequencies solution difficult to realize on a single substrate. More recently, single-chip multiple-frequency micromechanical filters based on aluminum nitride (AlN) with center frequencies in the VHF range have been successfully demonstrated. These have exhibited promising performance such as low insertion loss (4dB) and large out-of-band rejection (27dB) [6]. However, these AlN contour mode piezoelectric resonators show Qs that are typically limited to a few thousand. This is significantly lower in comparison to the level of Qs that are greater than 10,000 typical of capacitive silicon-based micromechanical resonators.

For the first time, this paper presents a thermally-actuated micromechanical filter realized by electrically coupling two identical dog-bone shaped thermal-piezoresistive resonators [7]. As a proof of concept, the filter has a modest center frequency of 64 MHz, which in principle can be scaled to yet higher frequencies. Moreover, this new class of micromechanical filters possesses a convenient tuning mechanism for its center frequency and bandwidth by adjusting the bias voltages of the constituent resonators. In addition, the fabrication process for this thermally-actuated filter is much simpler than for narrow gap capacitive devices. Compared to capacitive transduction (drive and sense), both the thermal actuation mechanism and piezoresistive readout scheme exploited here are much more efficient, allowing a significant reduction in insertion loss than if the device was activated by capacitive transduction.

II. THERMALLY-ACTUATED FILTER DESIGN

A. Structure and operation principle of the filter

Recently, thermal-piezoresistive resonators have attracted much interest by offering better frequency-scaling performance in the electromechanical transduction [7]. Fig. 1(a) depicts of the vibration mode shape of a single dog-bone resonator, which has a finite-element (FE) simulated frequency of 64.7574MHz. As the resonator vibrates, a voltage across the anchors will result in a modulated motional current due to the piezoresistive effect inherent to single crystal silicon. However, this motional current is always accompanied by a much stronger feedthrough

This work was supported by a grant under the Early Career Scheme from the Research Grants Council of Hong Kong (project no. CityU 124312), the Applied Research Grant from the City University of Hong Kong (project no. 9667062), as well as the Science, Industry, Trade and Information Technology Commission of the Shenzhen Municipality (project no. JC201105201047A).

current stemming from the resistive path between input and output ports.

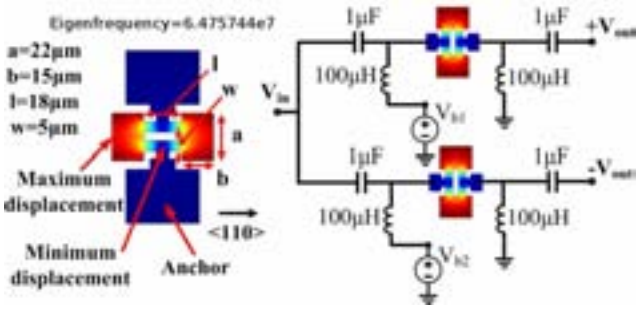

(a) (b)

Figure 1. (a) FE simulation of the mode shape of the dog-bone resonator using COMSOL. (b) Circuit schematic of the thermally-actuated filter realized by electrically coupling two dog-bone shaped in parallel configuration.

Fig. 1(b) provides a circuit schematic showing the thermal piezoresistive resonators configured as a parallel-class filter [1-2]. Two resonators are electro-thermally excited by the same AC drive voltage, but their output motional currents are sensed differentially. Since the resonators are designed to be identical, thus resulting in the same resistance (to the first order) in both current paths, significant resistive feedthrough cancellation can be achieved. This feedthrough cancellation idea was reported before in [8] where one of the resonators was inactive and used as dummy resonator. But distinct from [8], both resonators are active here to form a 2nd-order filter. It can also be seen from Fig. 1(b) that each resonator is biased with a DC voltage. By adjusting these bias voltages, the resonant frequencies of the resonators can be tuned independently, thus enable tuning of the center frequency and bandwidth of the filter.

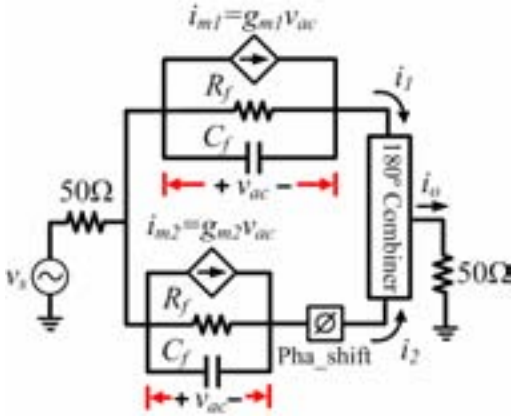

Figure 2. Small-signal equivalent circuit to capture the frequency response of the parallel-class thermally-actuated micromechanical VHF-band filter.

B. Small-signal equivalent circuit for the filter

The proposed small-signal equivalent circuit for the filter is shown in Fig. 2. The AC current in each path i_n (n = 1, 2) is a combination of the piezoresistive current $i_m = g_m(\omega)v_{ac}$, where $g_m(\omega)$ is the normalized motional conductance function and v_{ac} is the AC voltage across the resonator) and feedthrough current that is associated with a parasitic resistance R_f and capacitance C_f (Identical parasitic components are assumed for both current paths). v_s is the source voltage and i_o is output current. The motional conductance function $g_m(\omega)$ is given by [9]:

$$g_m(\omega) = \frac{\Pi}{(1-(\omega/\omega_o)^2 + j(\omega/\omega_o)/Q)} \quad (1)$$

where Π denotes a lumped parameter that describes the thermal-piezoresistive conversion in the resonator, ω_o is the angular resonant frequency and Q is the quality factor. The admittance for each path $Y_n(\omega)$ is:

$$Y_n(\omega) = \frac{i_n}{v_{ac}} = g_{mn}(\omega) + \frac{1}{R_f} + j\omega C_f \quad (2)$$

To model the phase difference between the two paths, a phase shifter is cascaded at the end of the second path. Thus, the total admittance of the two-port filter can be obtained:

$$Y(\omega) = Y_1(\omega) + Y_2(\omega)e^{jPha\_shift} \quad (3)$$

where *Pha_shift* represents the phase difference between the two paths. In the ideal case where there is no phase difference between i_1 and i_2, *Pha_shift* would simply be zero. However, a small phase difference was detected from the measurement and will be discussed in the following section.

III. MEASUREMENT AND DISCUSSION

Fig. 3 shows SEMs of a pair of 10-μm-thick dog-bone twin resonators (R1 and R2) fabricated side-by-side on the same die using a standard SOI MUMPS process. The lateral dimensions of the resonators are the same as those described in Fig. 1. The fabricated pair of devices was electrically characterized under vacuum using probe station (Janis Research ST-100) and using a network analyzer (Agilent E5061A). Short-Open-Load-Through (SOLT) calibration was performed prior to measuring the device under test. All measured results were acquired using 50Ω termination impedance.

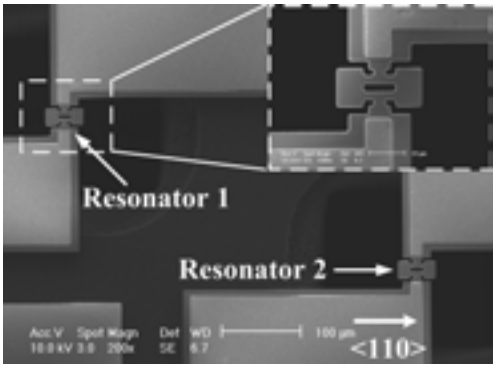

Figure 3. SEM of two 64MHz 10-μm-thick dog-bone resonators fabricated using a standard SOI MUMPS process. Both resonators are aligned along the <110> crystallographic orientation.

Fig. 4 shows the magnitude plot of the measured electrical transmission for a single resonator (R1 in this case) with bias voltage (V_{b1}) of 3.24V. The measured bias current used was 60mA. From the transmission plot we can infer that there is a high level of feedthrough that is substantial enough so as to mask the resonant peak. Fig. 5 shows the measured electrical

transmission for the parallel-class filter using the configuration shown in the circuit schematic provided in Fig. 1(b) when bias voltages V_{b1} and V_{b2} were set to be 3.24V and 0V respectively. Since no DC voltage is applied to R2 in this case, R2 serves only as a dummy in this configuration. By comparing Fig. 4 against Fig. 5, this pseudo-differential configuration provides a significant reduction in feedthrough (27.5dB), which in turn yields a larger resonant peak of 3dB. The measured resonant frequency for R1 is 64.5656MHz as shown in Fig. 5. Almost the same level of reduction in feedthrough can be found from the same pair of measurements when implemented for R2 (the magnitude plots have been omitted for brevity). However, the measured resonant frequency of R2 using the same bias voltage applied previously to R1 was found to be 64.6238MHz. This discrepancy between the resonant frequencies is less than 0.1% and is likely to stem from fabrication tolerances. The measured resonant frequencies of R1 and R2 were both lower than the value simulated by finite elements (64.7574MHz). This is expected due to the Joule heating effect involved in thermal actuation and the negative temperature dependence of Young's modulus of silicon.

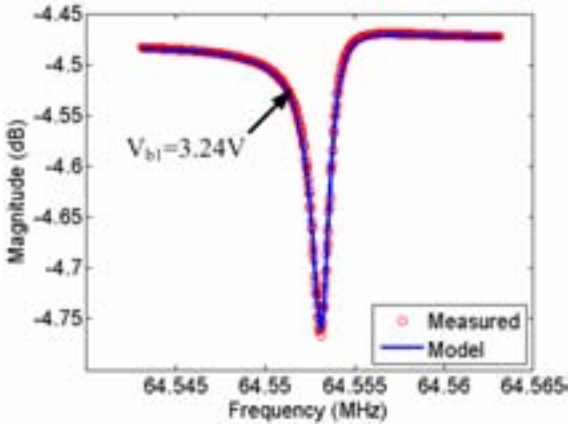

Figure 4. Measured and modeled electrical transmission (magnitude) for a single resonator (R1 in this case) with DC bias voltage V_{b1} of 3.24V, which yields a bias current of 60mA.

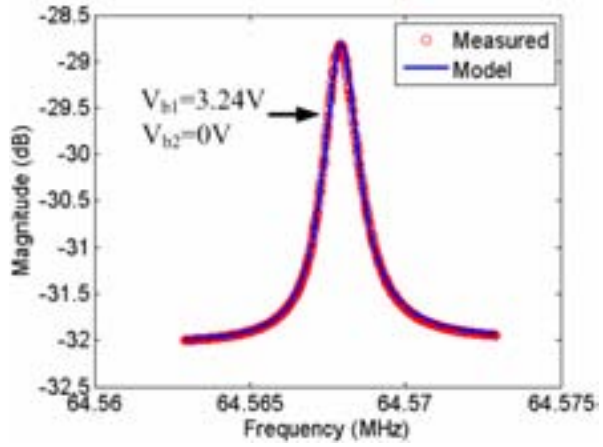

Figure 5. Measured and modeled electrical transmission (magnitude) of the filter using the configuration shown in the circuit schematic illustrated in Fig. 1(b): V_{b1} = 3.24V and V_{b2} = 0V). The measured bias current to R1 was 60mA. R2 here served as a dummy resonator.

By adjusting the bias voltages, the resonant frequencies of the two resonators can be tuned to come closer to each other to realize a bandpass filter frequency response. Fig. 6 shows one of the measured filter frequency responses (magnitude) when V_{b1} and V_{b2} were set to be 3.52V and 3.69V respectively. The corresponding measured bias currents were 60mA and 60.4mA. Compared to the previous two measurements, the bias voltage for R1 is 0.28V higher to yield same bias current (60mA). This translates to an increase in resistance by 4.7Ω. The increased resistance of R1 indicates higher ambient temperature which is caused by the additional heat generated by R2. In fact, each resonator consumes DC power of about 200mW in this case. It can also be observed that the increased ambient temperature when both resonators are actuated leads to a lower resonant frequency of R1 compared to that shown in Fig. 5.

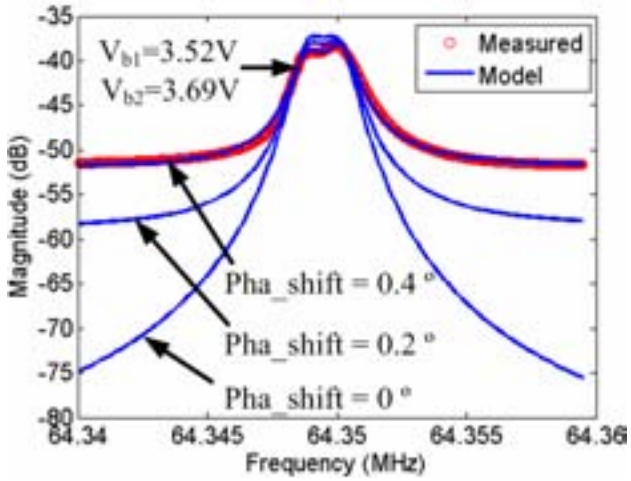

Figure 6. Measured and modeled electrical transmission (magnitude) of the filter with V_{b1} = 3.52V and V_{b2} = 3.69V. The corresponding measured bias currents were 60mA and 60.4mA for R1 and R2 respectively.

TABLE I. PARAMETERS EXTRACTED BY FITTING

Parameters extracted by fitting measured result in Fig. 5			
g_{m1}	g_{m2}	f_{o1}	Q
1.87×10^{-8}S	0S	64.5656MHz	5.16×10^{4}
Pha_shift	R_f	C_f	
-4°	64Ω	4pF	
Parameters extracted by fitting measured result in Fig. 6			
g_{m1}, g_{m2}	f_{o1}	f_{o2}	Q
1.87×10^{-8}S	64.3488MHz	64.3502MHz	5.16×10^{4}
Pha_shift	R_f	C_f	
0.4°	69Ω	6pF	

By fitting the measured result to the circuit model described in Fig. 2, the respective circuit parameters can be extracted accordingly. Table I presents the extracted circuit parameters extracted based on the measured results shown in Fig. 5 and 6. It can be seen from this table that the extracted normalized motional conductance (g_m) and Q are the same in the cases of both Fig. 5 and Fig. 6. It is also found that there always exists a phase difference between the two current paths. Interestingly,

according to the model prediction, the out-of-band rejection of the filter can be improved by a factor of more than 20dB if there is no phase difference between two paths, which is shown in Fig. 6. In addition, the extracted values of R_f successfully capture the increase in resistance observed in the measurements between actuating a single device compared to both devices at the same time.

Fig. 7 shows three measurements of electrical transmission (magnitude) of the filter when V_{b1} was kept constant at 3.52V while V_{b2} was varied. As expected, the resonant frequency of R2 is decreased with increasing V_{b2}. At the same time, it was found that the heat generated by R2 was sufficient to decrease the resonant frequency of R1 further. The downward shifts of the resonant frequencies of both devices result in a shift in the center frequency of the filter (72.2ppm). Since the variation of V_{b2} has a larger effect on the resonant frequency of R2 than on R1, the separation of the resonant frequencies and thus the bandwidth of the filter can be tuned (0.002% to 0.004%) as shown in Fig. 7. In addition, this filter exhibits out-of-band rejection of more than 10dB and little ripple in the pass band (<1dB) during the whole tuning range with the termination impedance of 50Ω.

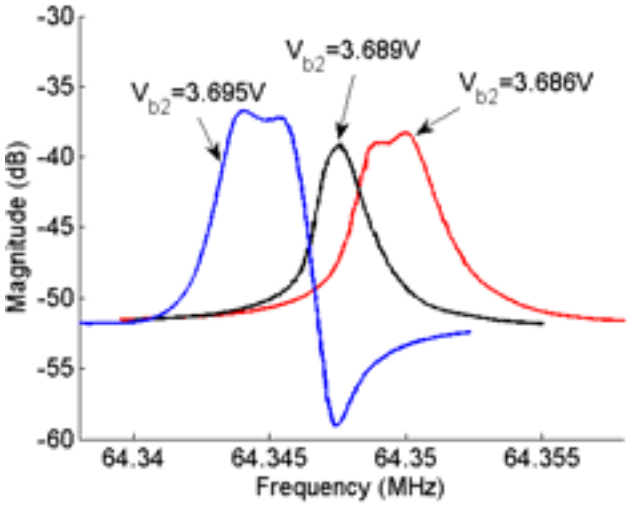

Figure 7. Measured electrical transmission (magnitude) of the filter. V_{b2} was varied to demonstrate tuning of the bandwidth while V_{b1} was kept constant at 3.52V.

Several methods to improve the performance of the filter can be explored in the future. First, two bias voltages, rather than just one bias voltage, can be adjusted at the same time to enlarge the tuning range of the center frequency and bandwidth. Second, a phase shifter could be used in either current path so as to reduce the phase difference between two paths and thus improve the out-of-band rejection of the filter. Third, the major drawback for this thermally-actuated filter is its high power consumption (about 200mW for each resonator) and the resultant heat-related issues such as the dependence of the resonant frequency on the ambient temperature. One solution for this problem is to physically scale down the resonator size towards higher operating frequencies. This will reduce the bias current required and thus DC power consumption. One actual demonstration that validates this effect of physical scaling on power reduction has been reported in [7], where submilliwatt of DC power consumption has been recorded. Hence scaling these concepts towards higher frequencies (as required of RF filtering) is also beneficial in reducing power consumption.

IV. Conclusion

A thermally-actuated micromechanical filter that employs a piezoresistive readout operating in the VHF band to lower the insertion loss is demonstrated for the first time using parallel-class configuration. A small-signal equivalent circuit of the filter is also proposed which can be used to extract the physical parameters and predict the frequency response of the filter. In addition, tunable center frequency (72.2ppm) and bandwidth (0.002% to 0.004%) are conveniently achieved by adjusting the bias voltages in this filter. With room for further optimization, this filter already exhibits an out-of-band rejection of more than 10dB and a ripple of less than 1dB in the pass band (<1dB) with 50Ω termination during the whole tuning range. Finally, several ways to improve the performance of the new filter have been briefly described.

Acknowledgment

The SEM images were taken at the City University of Hong Kong Electronic Packaging and Failure Analysis (EPA) Centre.

References

[1] S.-S. Li, Y.-W. Lin, Z. Ren, and C. T.-C. Nguyen, "A micromechanical parallel-class disk-array filter," in *Proceedings of 2006 IEEE Int. Frequency Control Symp.*, Geneva, Switzerland, May 29-June 1, 2007, pp. 1356-1361.

[2] J. R. Clark, A.-C. Wong, and C. T.-C. Nguyen, "Parallel-resonator HF Micromechanical Bandpass Filters," in *Proc. Digest of Technical Papers, 1997 International Conference on Solid-State Sensors and Actuators*, Chicago, Illinois, June 16-19, 1997, pp. 1161-1164.

[3] S. Pourkamali and F. Ayazi, "Electrically Coupled MEMS Bandpass Filters; Part I: With Coupling Element and Part II: Without Coupling Element," *Sensors and Actuators A*, Aug. 2005, pp. 307-325.

[4] R. C. Ruby, P. Bradley, Y. Oshmyansky, A. Chien, and J. D. Larson, III, "Thin film bulk wave acoustic resonators (FBAR) for wireless applications," in *Proc. IEEE Ultrasonics Symp.*, 2001, pp. 813–821.

[5] R. H. Olsson, III, C. M. Washburn, J. E. Stevens, M. R. Tuck, and C. D. Nordquist, "VHF and UHF mechanically coupled aluminum nitride MEMS filters," in *Proceedings of 2008 IEEE Int. Frequency Control Symp.*, May 19-21, 2008, pp. 634–639.

[6] G. Piazza, P. J. Stephanou, and A. P. Pisano, "Single-chip multiple-frequency AlN MEMS filters based on contour-mode piezoelectric resonators," *J. Microelectromech. Syst.*, vol. 16, no. 2, pp. 319–328, Apr. 2007.

[7] A. Rahafrooz and S. Pourkamali, "High-frequency thermally actuated electromechanical resonators with piezoresistive readout", *IEEE Trans. Electron Devices*, vol. 58, p. 1205-1214, 2011.

[8] C-C. Chen, H-T. Yu, and S-S.Li, "A balanced measurement and characterization technique for thermal-piezoresistive micromechanical resonators," in *Proc. 25th IEEE MEMS*, Paris, France, Jan. 2012, pp. 377-380.

[9] J. E.-Y. Lee and Y. J. Xu, "Direct Inference of Parameters for Piezoresistive Micromechanical Resonators Embedded in Feedthrough," Sens. Actuators A, Phys., vol. 186, pp. 257–263, Oct. 2012.

Anomalous DC-Current-Induced Attenuation of Q Factor in a Silicon Contour Mode Micromechanical Resonator

Haoshen Zhu, Cheng Tu and Joshua Lee
Department of Electronic Engineering
City University of Hong Kong
Hong Kong, China
haoshezhu2-c@my.cityu.edu.hk

Abstract—**In this work, we report the experimental observation of quality factor (Q) variation in piezoresistively sensed silicon micromechanical resonators vibrating in a lateral contour mode. By fine tuning the bias current, the gradual descending and ascending trend of Q is distinctively observable. It shows a drastic drop in Q by nearly one order of magnitude (from 10^5 to 10^4) at a certain bias current level. The observed Q variation is replicable even when applying a capacitive sensing configuration with bias current running through. This anomaly is consistently detected from multiple die samples including resonators aligned along both <110> and <100> crystal orientations in the (100) plane. A detailed quantitative study is currently underway.**

Keywords-micromechanical resonator; quality factor; piezoresistive sensing; single crystal silicon; microelectromechanical systems (MEMS).

I. INTRODUCTION

Silicon based micromechanical resonators are becoming an increasingly viable alternative to quartz resonators that are bulk sized and difficult to integrate with CMOS for the time and frequency control market. These devices are of great interests in the research community and have also come to the point of commercialization in recent years [1, 2]. Referred to as MEMS oscillators, some of these products that are based on capacitive transduction of the embedded resonator exhibit excellent phase noise and temperature stability performance competitive with existing temperature compensated crystal oscillators (TCXO) [3, 4]. For these capacitive MEMS oscillators, the relatively large motional impedance limits further improvements in phase noise (especially in the far from carrier portion), as a high-gain sustaining amplifier circuitry is normally required and imposes more thermal noise. Efforts have been made to shrink the transduction gap to deep submicron (~10nm) in order to obtain sufficient electromechanical coupling and lower the motional impedance [5, 6]. However, fabricating narrow gap increases the manufacturing complexity and may cause reliability issues (e.g. pull-in). Furthermore, for higher frequency applications, the reduction of lateral dimensions increases the challenge of sensing via capacitive transducers.

To overcome the weak coupling in capacitive transduction, piezoresistive sensing for silicon micromechanical resonators was introduced [7] and showed remarkable improvement in the transduction at the fundamental mode of 1.1GHz [8] by using the piezoresistance inherent in silicon. Moreover, NXP has recently demonstrated its MEMS oscillator product based on a piezoresistively-sensed dog-bone resonator recently [9]. This aside, the single-crystal-silicon (SCS) square-extensional (SE) mode resonator is of great interest due to its outstanding power handling and high Q. The first MEMS oscillator prototype that could meet the GSM specifications was based on the SE mode resonator [10]. Therefore, efforts have been made to improve transduction further via piezoresisitive sensing, and it has been reported that using piezoresistive readout can greatly boost the transduction of SE mode resonators [11, 12].

The small-signal model predicts that, for electrostatically-actuated piezoresisitively-sensed devices, the transconductance is proportional to the injected DC bias current, while assuming a constant Q [7]. Previously, some correlation between the Q and DC bias current was reported for dog-bone resonators, showing that the effective Q could be adjusted by changing the DC current; an effect attributed to the thermodynamic feedback mechanism [13]. Even self-sustained oscillation without any amplifying circuitry can be achieved with a proper design of the resonator and a certain amount of bias current due to this possibility of amplifying Q through the current [13, 14].

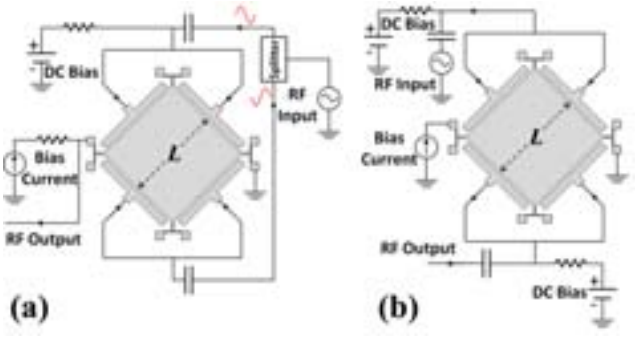

Figure 1. Schematics showing the measurement setup for SCS square-plate resonators using electrostatic actuation in combination with: (a) piezoresistive sensing; and (b) capacitive sensing.

This work was support by the strategic research grant from City University of Hong Kong (under project numbers 7002690 and 7008182) and a grant under the Early Career Scheme from the Hong Kong Research Grants Council (project number CityU 124312).

In this paper, we focus on the effect of injecting DC current on Q for SE mode resonators. The anomalous Q versus bias current profile deviates from the correlation previously found for dog-bone resonators, indicating the complex nature of the underlying thermomechanical coupling mechanisms. These results also suggest that a different mechanism is at work in the attenuation of Q in the case of the SE mode resonator.

II. Characterization Method

The square-plate resonators are surrounded by 4 electrodes with air gaps in between to perform electrostatic actuation. The T-shaped anchors function as the primary piezoresistors [11] and provides for higher Q in the SE mode of vibration. For piezoresistive sensing, the measurement setup is shown in Fig. 1a, where 2 electrodes with DC-biased AC signal are used to excite the SE-mode. The remaining 2 electrodes carry an AC signal that is out of phase in relation the other 2 electrodes to help eliminate capacitive feedthrough. Since the output current from the piezoresisitive setup involves both a capacitive and a piezoresisitive signal, to rule out a possible causal relation to piezoresistive electromechanical coupling, the devices are also characterized in a capacitive sensing setup (see Fig. 1b), but with a bias current through the device to mimic the self-heating effect in piezoresisitive sensing. From the capacitive sensing setup, the magnitude of the resonant transmission peak will also provide us with an instant indication on the change of Q as the electromechanical coupling would be independent of the bias current and the amplitude of the mechanical displacement can thus be directly associated with Q.

The square plate resonators (lateral dimension L = 800μm) were fabricated in a foundry silicon on insulator (SOI) MEMS process. Scanning electron micrographs (SEMs) of the devices are shown in the insets of Fig. 2. As the mechanical property and piezoresistive coefficients are well known to be anisotropic [15] for SCS, devices with the same dimensions but with edges aligned along different crystal orientations of interest (<110> and <100>) were fabricated alongside each other for the chief purpose of comparison. The devices were electrically probed in a cryogenic probe station and characterized via an Agilent E5061A vector network analyzer at a vacuum level ~10^{-4}mBar and room temperature.

III. Experimental Results

The resonant frequency of the SCS SE-mode resonators can be determined as follows [16],

$$f_{SE} = \frac{1}{2L}\sqrt{\frac{E_{bi}}{\rho}\left[1+\left(1-\frac{8}{\pi^2}\right)\left(\frac{\upsilon}{\upsilon-1}\right)\right]}, \qquad (1)$$

where ρ is the material density, E_{bi} is the biaxial modulus, and v is the Poisson's ratio. Due to the anisotropy of the material, the <110> and <100> resonators share the same E_{bi} (which is invariant) but have different values of v [16], given as follows:

$$E_{bi} = C_{11} + C_{12} - \frac{2C_{11}^{\ 2}}{C_{12}}$$

$$\upsilon_{<110>} = \frac{C_{11}^{\ 2} + C_{11}C_{12} - 2C_{12}^{\ 2} - 2C_{11}C_{44}}{C_{11}^{\ 2} + C_{11}C_{12} - 2C_{12}^{\ 2} + 2C_{11}C_{44}} \qquad (2)$$

$$\upsilon_{<100>} = \frac{C_{12}}{C_{11} + C_{12}}$$

where the C_{11}, C_{12} and C_{44} are elementary elastic constants of SCS. The calculated resonant frequencies are consistent with what we have measured at room temperature as well as finite element (FE) simulations, as shown in Table I. The simulated eigenmode shapes are shown in Fig. 2.

TABLE I. List of measured, calculated and simulated resonant frequency of the SE-mode resonators

Devices	Resonant Frequency [MHz]		
	Calculated	*Simulated*	*Measured*
<110> 800μm	5.470	5.447	5.453
<100> 800μm	5.299	5.310	5.310

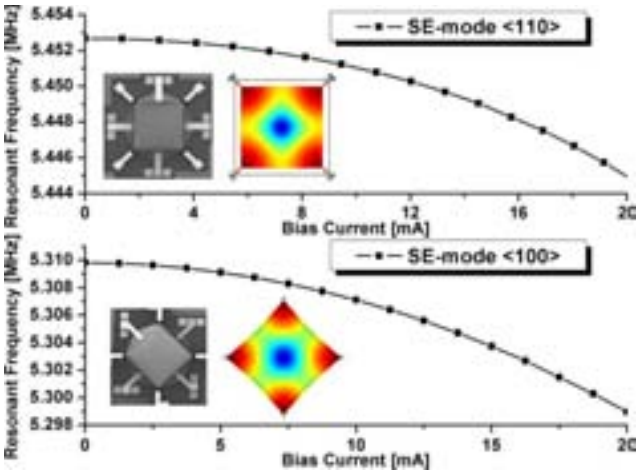

Figure 2. Measured resonant frequency vs. bias current profiles of the square-extensional (SE) mode resonators aligned along both the <110> and <100> crystal axes. Insets: SEMs of devices and FE simulated eigenmode shapes (solid lines indicate the nominal layout of the resonator; red: maximum displacement; blue: minimum displacement).

Fig. 2 shows the typical resonant frequency shift as a function of injected bias current (0 to 20mA). The measured diagonal resistance of the device is about 160Ω. The device temperature increases due to Joule heating, causing a downward parabolic drift in resonant frequency due to the negative temperature coefficient of elasticity (TCE) known for moderately n-doped SCS. As reported previously, our SE mode devices exhibit a temperature coefficient of frequency (TCf) ~-20ppm/K [16]. Associated with the TCEs of SCS, the frequency shift due to Joule heating effect is simulated via COMSOL Multiphysics. The simulated profiles of resonant

frequency versus bias current are shown in Fig. 3, indicating a downshift in frequency of ~1400ppm at 20mA for both <110> and <100> devices, which agrees well with the measurements. According to the simulations, the temperature distribution over the entire square plate is largely homogeneous (see insets in Fig. 3) with a mean temperature rise of about a 60°C for a bias current of 20mA.

Fig. 4 illustrates the variation in Q as a function of injected DC bias current for resonators with <110> crystal orientation. The measured intrinsic Qs (without bias current) are as high as 500,000 for the devices vibrating in the SE-mode. For Device 1 (D1), we first performed piezoresistive sensing with different bias currents. The measured Q is almost unaffected by varying the bias current except around 15mA bias current. As we fine tune the bias current with a step ~0.1mA, the Q (in terms of the -3dB bandwidth) as well as the maximum transmission peak height gradually decreases and then later increases, showing a severe reduction of nearly an order of magnitude at 15.2mA. The measured frequency responses with fine-tuned bias current around 15mA are shown in Fig. 5. This observation was been observed repeatedly in multiple measurements. Besides, as we switch to the capacitive sensing setup (Fig. 1b), similar trends of Q versus bias current are obtained, showing a good match with our piezoresistive sensing result. Since the coupling in capacitive transduction is not dependent on bias current, we find that the transmission level divided by Q is quite stable throughout the bias current interval. This indicates that severe dissipation is likely to be happening at a certain bias current and dampens the mechanical displacement of the resonator due to thermomechanical coupling. Multiple devices were tested and similar trends pointing to this phenomenon were found even through not exactly at the same bias current level due to fabrication variations. The profile of the measured Q against bias current of another device (D2) using capacitive sensing is also included in Fig. 4. Similar trends that include a drop in Q at around 13mA were found, illustrating that this effect can be consistently observed.

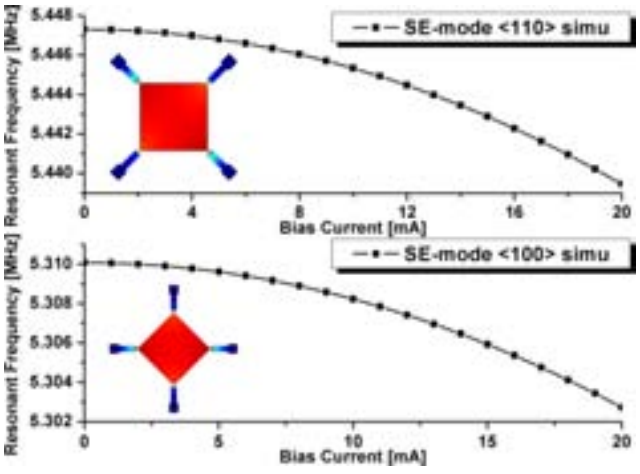

Figure 3. FE-simulated resonant frequency vs. bias current profiles of SE mode resonators aligned along both the <110> and <100> crystal axes. Insets: the simulated temperature distribution of the devices with bias current running through the structure via 2 anchors (red: highest temperature; blue: lowest temperature).

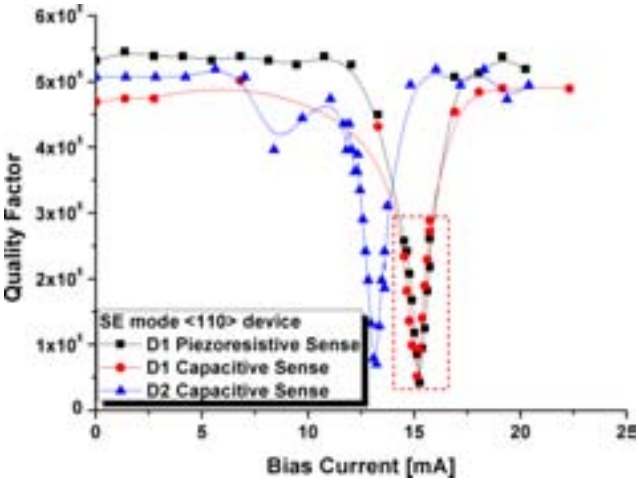

Figure 4. Q vs. bias current profile of <110> axis SE-mode resonators. Drastic Q drop at particular bias current level observed in both device D1 and D2. Similar trends of variation in Qs seen among both piezoresistive as well as capacitive sensing setup.

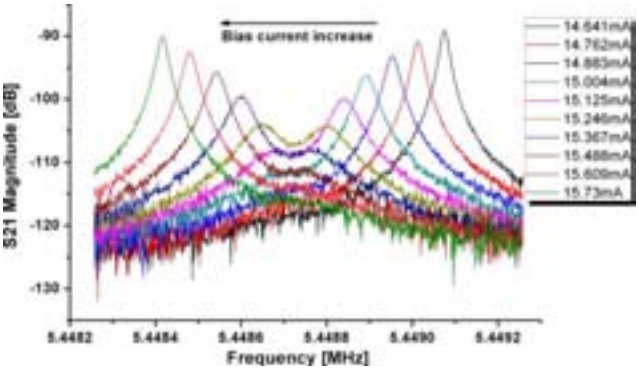

Figure 5. Measured S21 of D1 using piezoresistive sensing as bias current is fine-tuned around the Q valley. Note the significant variation in the peak magnitude of the S21.

The same measurements were carried out for the <100> devices. The measured values of Q as the bias current is swept are shown in Fig. 6. Although the resonant frequencies are different from the <110> devices due to the anisotropy of SCS, similar trends that show a drop in Q were found. Fig. 7 shows the measured frequency responses of the device as the bias current was fine-tuned at around 17mA (highlighted by the red box in Fig. 6).

The previously reported general theory of thermoelastic damping (TED) on SE mode resonator indicates that the TED limited Q is inversely proportional to the resonant frequency [17]. As such, decrease in resonant frequency due to increased joule heating should be accompanied by an inverse increase in Q that is monotonic and gradual. However, we have observed instead an abrupt change in Q, which thus cannot be accounted by the theory. This anomalous behavior, repeatedly observed in multiple experiments, may thus suggest that a more complex mechanism of thermomechanical coupling due to the injected current could be at work.

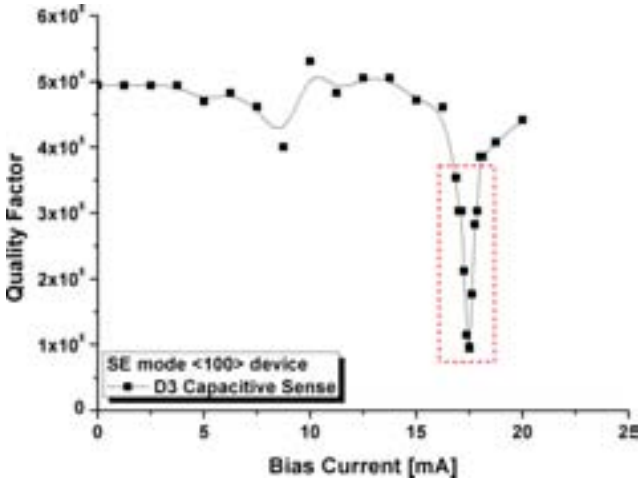

Figure 6. Q vs. bias current profile of <100> axis SE-mode resonators shown for D3 using capacitive sensing. An abrupt drop in Q is detected once again at a particular bias current level.

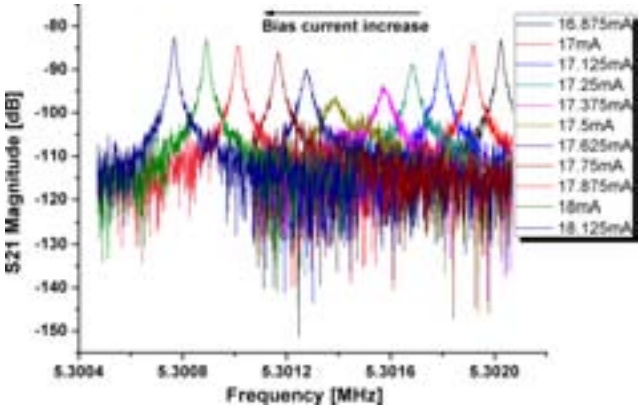

Figure 7. Measured S21 of D3 (capacitive sensing) as bias current is fine-tuned around the Q valley.

IV. Conclusion

An anomalous attenuation of Q caused by changing the DC bias current is detected and reported for the first time in SE mode microresonators. The measured Q drops by nearly an order at a certain current level. This effect is repeatedly found in multiple samples (including devices with both <110> and <100> crystal orientations) using piezoresisitive sensing, and also verified using capacitive sensing to decouple results from any causal relation with the method of piezoresistive sensing. Our study indicates a potential drawback on thermal tuning of resonant frequency since the Q can be influenced by injecting DC current as well. As demonstrated by the results reported herein, injecting a bias current can significantly reduce Q and thus hamper the transduction of the device. Understanding the underlying mechanism as such could prove to be critical for piezoresistively-transduced devices. A solid understanding of the basis of the observed anomaly would allow guidelines for designing piezoresistive resonators so as to avoid damping of Q associated with the injection of bias currents.

Acknowledgment

Partial travel expense is generously supported by IEEE-UFFC and EFTF. The SEMs were provided by G. Shan of the Department of Physics and Materials Science, City University of Hong Kong.

References

[1] C. S. Lam, “A review of the recent development of MEMS and crystal oscillators and their impacts on the frequency control products industry,” in *Proc. IEEE Int. Ultrason. Symp.*, Beijing, China, 2008, pp. 694–704.

[2] J. T. M. van Beek, and R. Puers, “A review of MEMS oscillators for frequency reference and timing applications,” *J. Micromech. Microeng.*, vol. 22, no. 1, pp. 013001-1–013001-35, 2012.

[3] H. Lee, A. Partridge, and F. Assaderaghi, “Low jitter and temperature stable MEMS oscillators,” in *Proc. IEEE Int. Freq. Contr. Symp.*, MD, May 21-24, 2012.

[4] K. J. Schopef, “TCMO: A versatile MEMS oscillator timing platform,” in *Proc. 41st Annual Precise Time and Time Interval Mtg.*, Santa Ana Pueblo, NM, 2009, pp 481-492.

[5] S. Pourkamali and F. Ayazi, “Fully Single Crystal Silicon Resonator with Deep-Submicron Dry-Etched Transducer Gaps,” in *Proc. IEEE Int. Conf. Micro Electro Mech. Syst.*, Maastricht, Netherlands, Jan. 2004, pp. 813-816.

[6] M. Akgul, et al., “Oscillator far-from-carrier phase noise reduction via nano-scale gap tuning of micromechanical resonators,” in *Digest Tech. Transducers‘09 Conf.*, Denver, CO, 2009, pp. 798–801.

[7] J. T. M. van Beek, P. G. Steeneken, and B. Giesbers, “A 10MHz piezo-resistive MEMS resonator with high Q,” in *Proc. IEEE Int. Freq. Contr. Symp.*, Miami, FL, 2006, pp. 475-480.

[8] J. T. M. van Beek, et al., “Scalable 1.1 GHz fundamental mode piezo-resistive silicon MEMS resonator,” in *Tech. Dig. IEEE Int. Elect. Dev. Mtg.*, Washington, DC, 2007, pp. 411–414.

[9] K.L. Phan, et al., "High precision frequency synthesizer based on MEMS piezoresistive resonator," in *Digest Tech. Transducers‘13 Conf.*, Barcelona, Spain, 2013, pp. 802-805.

[10] V. Kaajakari, T. Mattila, A. Oja, J. Kiihamäki, and H. Seppä, “Square extensional mode single-crystal silicon micromechanical resonator for lowphase noise oscillator applications,” *IEEE Elect. Dev. Lett.*, vol. 25, pp. 173-175, 2004.

[11] A. T.-H. Lin, J. E.-Y. Lee, J. Yan, and A. A. Seshia, "Methods for enhanced electrical transduction and characterization of micromechanical resonators," *Sens. Actuators A, Phys.*, vol. 158, no. 2, pp. 263-272, 2010.

[12] Y. Xu and J. E.-Y. Lee, "Differential-input piezoresistively-sensed square-extensional mode resonator for parasitic feedthrough cancellation," in *Digest Tech. Transducers‘11 Conf.*, Beijing, China, 2011, pp 2474-2477.

[13] P. G. Steeneken, et al., “Piezoresistive heat engine and refrigerator,” *Nat. phys.*, vol. 7, no. 4, pp. 354-350, 2011.

[14] A. Hajjam, A. Rahafrooz, and S. Pourkamali, “Temperature compensated single-device electromechanical oscillators,” in *Proc. IEEE Int. Conf. Micro Electro Mech. Syst.*, Cancun, Mexico, 2011, pp. 801–804.

[15] Y. Kanda, "A graphical representation of the piezoresistance coefficients in silicon," *IEEE Trans. Elect. Dev.*, vol. 29, pp. 64–70, 1982.

[16] H. Zhu, G. Shan, C. Tu, J. E.-Y. Lee, "Crystallographic and eigenmode dependence of TCf for single crystal silicon contour mode resonators," in *Proc. IEEE Int. Conf. Micro Electro Mech. Syst.*, Taipei, Taiwan, 2013, pp. 761-764.

[17] S. A. Chandorkar, et al., “Multimode thermoelastic dissipation,” *J. Appl. Phys.*, vol. 105, no. 4, p. 043505, Feb. 2009.

Multimode Characteristics in Mechanically-Coupled Silicon Carbide (SiC) Nanowire Array Resonators

Rui Yang*, Jaesung Lee, Zenghui Wang, Philip X.-L. Feng*
Department of Electrical Engineering & Computer Science, Case School of Engineering
Case Western Reserve University, Cleveland, OH 44106, USA
*Email: rui.yang@case.edu, philip.feng@case.edu

***Abstract*—We report on the measurements and modeling of mechanically-coupled arrays of very thin silicon carbide nanowire (SiC NW) nanomechanical resonators. The exceptional mechanical properties and attractive optical properties of SiC make it highly interesting for resonant nanoelectromechanical systems (NEMS), with resonant modes operating at high frequencies that can be exploited for resonance-based signal processing and sensing applications. In this work, we demonstrate arrays consisting of SiC NWs as narrow as 50nm, patterned by electron beam lithography and focused ion beam, on ~50–500nm SiC thin epitaxial layers and polycrystalline layers. We investigate the multimode resonances in mechanically coupled arrays. We show that by controlling the undercut ledges of suspended SiC NW arrays, we can tune the strength of mechanical coupling in such arrays and engineer their multimode resonance characteristics.**

Keywords—nanoelectromechanical systems (NEMS); silicon carbide (SiC); multimode resonance; nanowire; array; mechanical coupling; spatial mapping

I. Introduction

Resonant micro/nanoelectromechanical systems (MEMS & NEMS) have emerged as interesting candidates for components in signal processing, timing, and communication applications, because of their attractive attributes such as high quality (Q) factors, high operating frequencies, and compatibility with manufacturing of integrated circuits (ICs) [1]. Arraying and mechanical coupling in MEMS resonators have been actively pursued for attaining lower insertion losses and motional impedances in realizing devices such as filters and oscillators [2]. Recent filters demonstrated by employing mechanically coupled MEMS resonators and arrays mainly include disk arrays, beam arrays, and plate arrays, where the coupling strength between individual resonators are often determined by the dimensions and stiffness of the coupling beam [3-6].

Exploring mechanical coupling in NEMS resonators are also fundamentally and technologically important. Many cases (such as in many coupled MEMS devices) require that the mechanical coupling stiffness k_c be smaller than the device's own effective stiffness k_{eff}. This means the coupling beams or springs should be sufficiently more compliant (*i.e.*, narrower, in the case of using beams) than the individual resonators to be coupled [3]. As the device dimensions keep shrinking from MEMS to NEMS regime (*e.g.*, nanowires, nanotubes, *etc.*), however, designing and fabricating nanomechanical coupling structures with controllable coupling strength, from compliant (weak coupling) to stiff (strong coupling), become increasingly difficult, due partly to the current practical limitations in nanofabrication. Although nanowire structures have recently been used to realize novel mechanically coupled NEMS devices [7,8], these nanowire coupling structures have been enabled by advanced and expensive lithography techniques. Scaled, smaller NEMS devices may demand other techniques to enable mechanical coupling with controllable strength.

To investigate mechanical coupling in very small NEMS, here we explore the possibility of exploiting undercut ledges that are often automatically created while making suspended NEMS. We use resonant arrays of SiC NWs as the prototype systems. As shown in Fig. 1, a SiC NW array consists of a number of parallel doubly-clamped SiC NWs; the two ledges under the two clamping ports are formed by undercutting in the device release process. By engineering the width of the ledges, the coupling strength between resonators is varied.

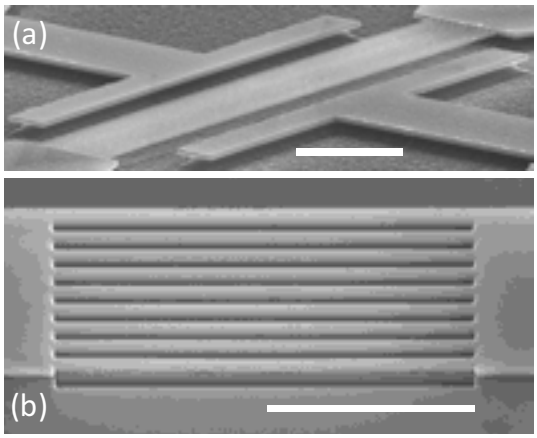

Fig. 1. SEM images of the mechanically coupled doubly-clamped SiC NW arrays fabricated by (a) EBL with metallization, and (b) FIB without metallization. *Scale bars*: (a) 2μm, (b) 10μm.

II. Device Design and Fabrication

A. Design of SiC Nanowires with Ledge Coupling

Mechanically coupled SiC NW arrays are fabricated with two different methods and studied independently. Figure 1a shows the scanning electron microscope (SEM) image of the device fabricated by using electron beam lithography (EBL),

with Al metallization on top (30–50nm thick). Each SiC NW has width of w≈50nm, length L≈10μm, and thickness t≈50nm. Figure 1b shows the SEM image of the device fabricated by focused ion beam (FIB), without metallization, and each SiC NW has w≈500nm, L≈20μm, and t≈500nm.

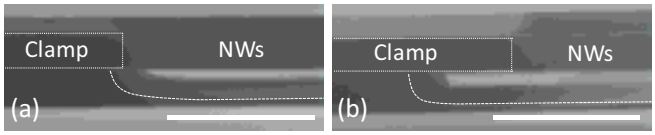

Fig. 2. SEM images of the devices with similar dimensions fabricated by FIB, with (a) narrower ledge, and (b) wider ledge, where the red dashed lines show the undercuts. *Scale bars*: 2μm.

Ledges are suspended portions of the clamping ports, thus they can provide mechanical coupling, because such suspended clamping regions are not infinitely rigid and are susceptible to motions. Figure 2 shows the SEM images of the clamping region of a FIB-enabled device with different ledge widths. The images are taken from devices with similar dimensions except the ledge width: narrower in Fig. 2a and wider in Fig. 2b. When the arrays of SiC NWs are in vibration, the ledges function as mechanical springs that couple the motions of individual NWs in the array. Intuitively, varying the width of the ledge can change the coupling strength.

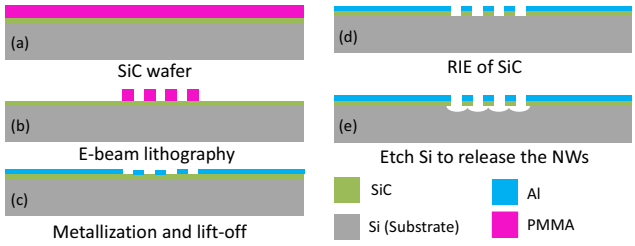

Fig. 3. Simplified fabrication process for the EBL patterned device. (a) Low pressure chemical vapor deposition (LPCVD) of SiC, and spin coating of PMMA, (b) EBL and development, (c) Al deposition and lift-off, (d) Reactive ion etching (RIE) of SiC, and (e) Isotropic etch of Si to release the SiC NWs.

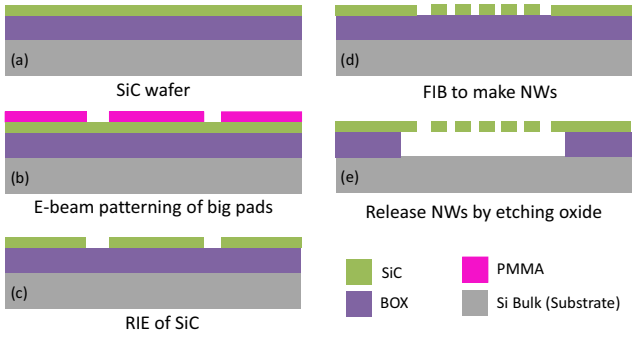

Fig. 4. Simplified fabrication process of using FIB without metallization on a novel SiC/SiO_2/Si platform. (a) LPCVD of SiC, (b) EBL for pads, (c) RIE of SiC, (d) FIB, and (e) Release the SiC NWs by etching the SiO_2 underneath.

B. *Fabrication of the Two Types of SiC Nanowires*

The fabrication of the SiC NW devices is divided into two categories: EBL and FIB. Figure 3 shows the process flow of the EBL patterned devices, while Fig. 4 shows that for the FIB defined devices. In Fig. 3, the SiC epitaxial layer is deposited directly onto Si, and is ~50nm thick. In order to facilitate out-of-plane motions, it would be better that the stiffness in the vertical direction be not higher than that in the lateral direction, thus the widths of the NWs are designed to be similar to their thicknesses. In Fig. 4, the device layer is polycrystalline 3C-SiC with a thickness t≈500nm, deposited on 500nm-thick SiO_2. So the width of the NW is designed to be w≈500nm, similar to the thickness. The width of the ledge could be simply changed by engineering the time of etching the Si (Fig. 3) or etching the SiO_2 (Fig. 4). This method provides great convenience and flexibility in tuning the strength of mechanical coupling.

III. Experimental Results

A. *Measurement System*

Detection of thermomechanical resonances of the SiC NWs is performed by using an optical interferometry with a 632.8nm He-Ne laser, as illustrated in Fig. 5. The optical signal is converted into electrical signal with a photodetector, and fed to a spectrum analyzer. Since the NWs in an array are close to each other, it is necessary to have a very small spot size to distinguish between the NWs. With the beam expander, the spot size has been reduced to ~1μm, which facilitates spatial mapping of the array of 500nm-wide NWs. The motorized X-Y stage moves the device relative to the laser spot.

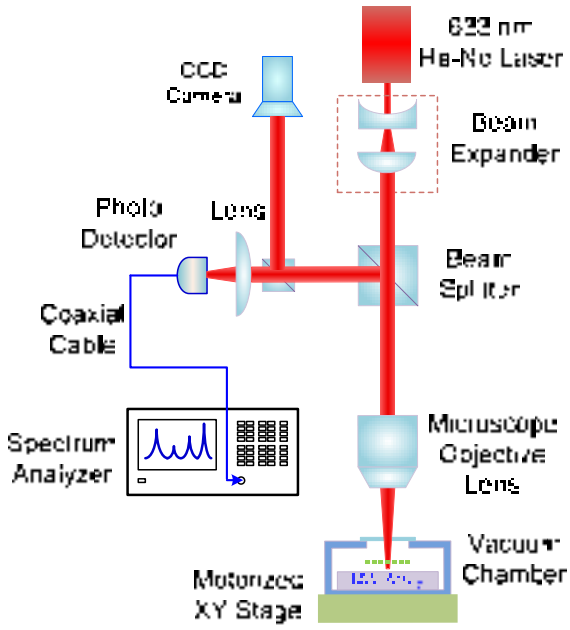

Fig. 5. Illustration of the laser interferometry system for detecting and mapping multimode resonances in the mechanically coupled arrays of SiC nanowires.

B. *Results from the EBL Device*

Figure 6 shows the measured multimode response from an array of 10 SiC NWs with individual NW dimensions L×w×t≈10μm×50nm×50nm. Sensitive detection of mechanical displacement down to the levels of Brownian motions is achieved in vacuum and room temperature. The displacement sensitivity is better than 1pm/√Hz. The resonances are shown

in Fig. 6 insets, where the fitting to the resonances shows that each mode has different *Q*. The laser spot is much bigger than the NW width (50nm) in this device. The measured resonances represent the coupled, collective motions of the arrayed NWs.

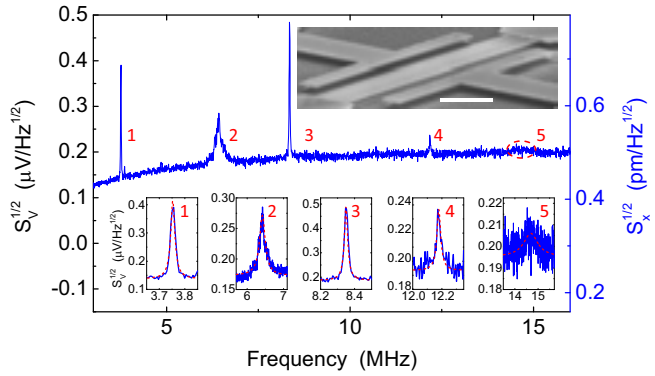

Fig. 6. Resonance spectrum measured from a SiC NW array of *N*=10. *Bottom Insets*: first 5 measured resonances (1–5) with fitting (red dashed lines). *Top Inset*: SEM image of the device fabricated by EBL. *Scale bar*: 2μm.

In order to characterize the mode shapes of the SiC NW array resonators, finite element modeling (FEM) has been performed using COMSOL. Figure 7 shows the mode shapes of the first 6 resonances with very close frequencies. The simulated device consists of 10 SiC NWs, with similar geometry to the real device, and the ledge effects are included. Mechanical coupling (via the clamping ledge) suppresses the natural modes of each individual SiC NWs, while enabling the system to exhibit new collective, coupled resonance modes.

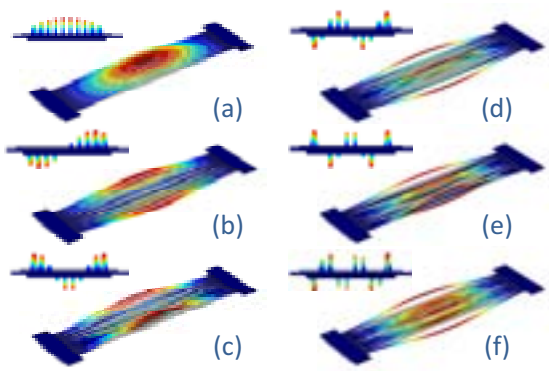

Fig. 7. (a)–(f) COMSOL simulation of the first 6 coupled modes of the array of 10 SiC NWs. *Insets*: cross-section views of the computed mode shapes.

C. *Results from the FIB Device with Narrow Coupling Ledge*

To observe the effect of the coupling ledge on the SiC NW array resonance modes, NW arrays with similar dimensions, (L×w×t≈20μm×500nm×500nm), but different ledge widths are fabricated and measured. The width of the ledge is narrow for the device measured in Fig. 8, which can be confirmed with the SEM image in the top left inset of Fig. 8a. Figure 8a shows two measured resonance spectra from two locations (indicated in the top right inset in Fig. 8a). The blue spectrum shows 3 resonances, while the red curve shows 4, and the resonance frequencies are different. The resonance amplitudes of the two resonance spectra are also different. To determine the existence of collective resonance modes, we perform mode shape mapping. This is achieved by scanning the laser spot across the NW array while recording the resonance spectrum at each position. Figure 8a bottom left inset shows the background (mapping results off any resonance), and the resulting map clearly shows the difference in the reflectivity of the surfaces, with blue area in the middle being the device area (lower reflectance). Figure 9 shows the mapping result of the four resonances, and no clear collective resonance mode is observed, presumably due to the weak coupling. Fig. 8b shows the resonance spectrum at another position, and fitting to the peaks show similar mechanical *Qs* of ~1200 and ~1250.

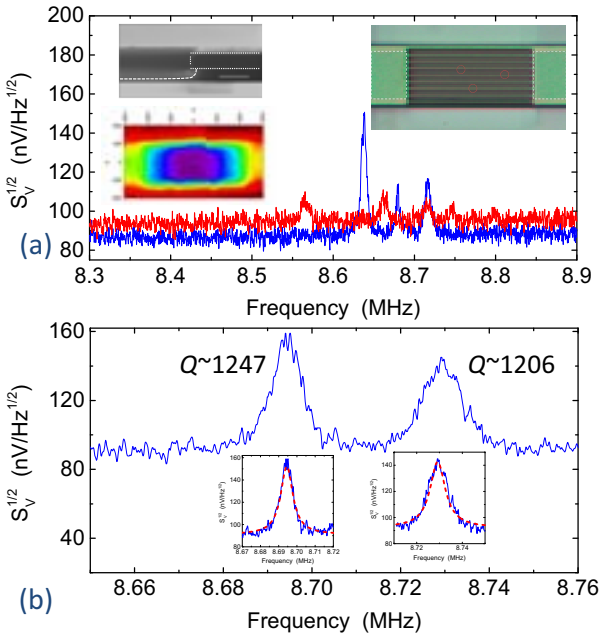

Fig. 8. Resonance spectra measured from a SiC NW array of *N*=9 patterned by FIB. (a) Data from two locations of the spots. *Top Left Inset:* SEM image of the device ledge (*Scale bar*: 1μm). *Lower Left Inset*: mapping background. *Top Right Inset*: optical image with the laser spot positions. (b) Data from the third spot location. *Insets*: fitting to the resonances.

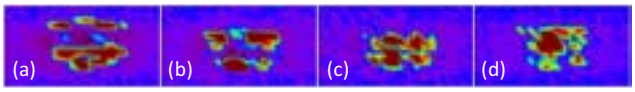

Fig. 9. (a)–(d) Spatial mapping results of the mode shapes of 4 different resonance modes shown in Fig. 8a (red curve), from low to high frequency.

D. *Results from the FIB Device with Wide Coupling Ledge*

Figure 10 shows the measured resonance spectra from another array device with similar dimensions but a wider ledge (Fig. 10a right inset). The resonance spectra show more resonance modes. We have performed spatial mapping of the mode shapes for up to 7 coupled resonance modes, as demonstrated in Fig. 11. The mapping results show that the wider ledge provides stronger coupling for this array of SiC NWs. The *Qs* of the resonances range from ~410 to ~550 (Fig. 10b), lower than the result in Fig. 8, suggesting that the wider ledge makes softer clamp, and likely have introduced more dissipation. These results clearly show that by engineering the width of the ledge, the coupling can be tuned.

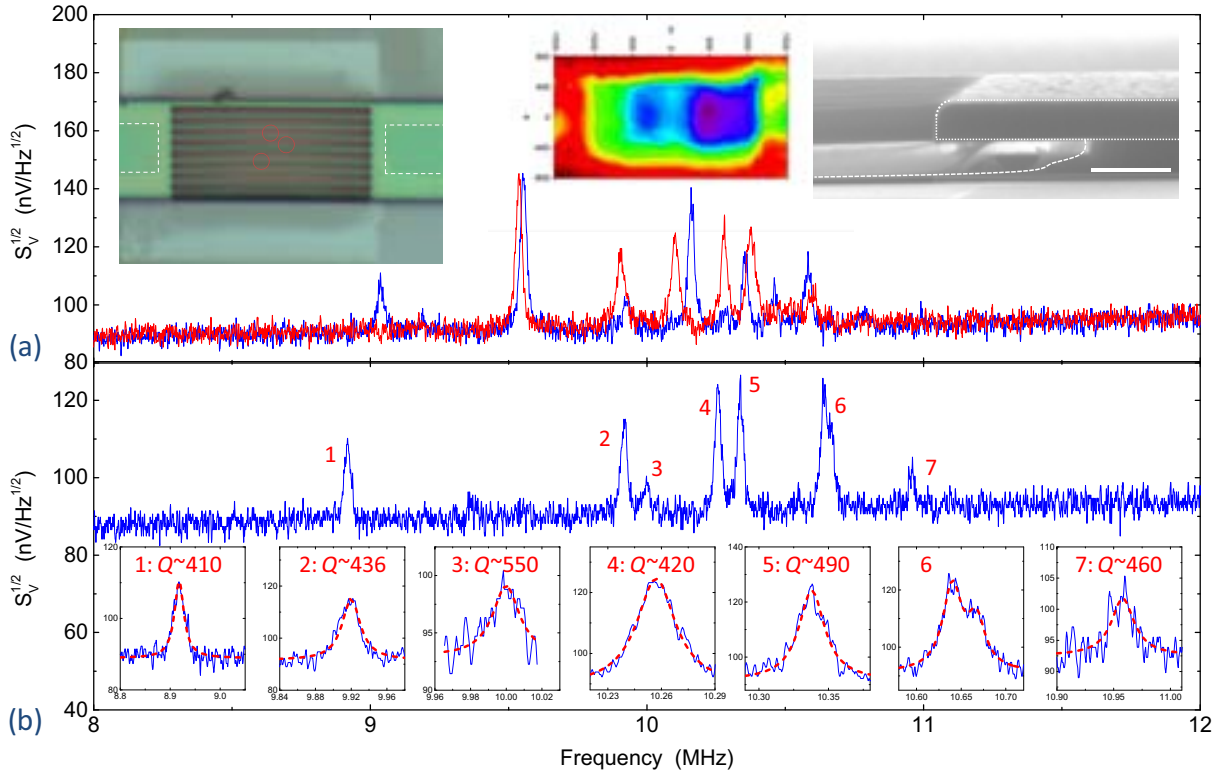

Fig. 10. Resonance spectra measured from an array device with wider ledge. (a) Data from two laser spot locations. *Left Inset*: optical image showing the laser spot positions. *Middle Inset:* mapping background. *Right Inset*: SEM image of the ledge (*Scale bar*: 1μm). (b) At another spot. *Insets*: fitting to the 7 resonances.

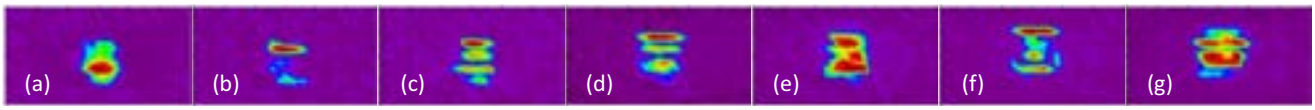

Fig. 11. (a)–(g) Optical mapping of the mode shapes for the 7 different resonance modes shown in Fig. 10b, from low to high frequency.

IV. Conclusions

Mechanical coupling among individual SiC NWs forces the arrayed system to exhibit collective resonance modes. Using laser interferometry, multimode thermomechanical resonances of high frequency resonant SiC NW arrays have been examined. Through mapping of the mode shapes of multimode resonances from devices with different ledges of different sizes, the influences of mechanical coupling in the arrays have been explored. Given the excellent mechanical, optical, chemical and thermal properties of SiC, these arrayed SiC nanodevices could be particularly interesting for sensing and signal processing applications in mesoscopic systems. The array size (N, number of NWs) can be varied to study new phenomena in large-N systems, from chaos to synchronization.

References

[1] S. Lee, C.T.-C. Nguyen, "Mechanically-coupled micromechanical resonator arrays for improved phase noise," in *Proc. of IEEE Int. Freq. Contr. Symp. (IFCS 2004)*, pp. 144-150, Aug. 2004.

[2] M.-H. Li, W.-C. Chen, S.-S. Li, "Mechanically coupled CMOS-MEMS free-free beam resonator arrays with enhanced power handling capability," *IEEE Trans. Ultrason. Ferr. & Freq. Contr.*, vol. 59, no.3, pp. 346-357, Mar. 2012.

[3] D. Weinstein, S.A. Bhave, M. Tada, S. Mitarai, S. Morita, K. Ikeda, "Mechanical coupling of 2D resonator arrays for MEMS filter applications," in *Proc. of IEEE Int. Freq. Contr. Symp. & Euro. Freq. & Time Forum (IFCS-EFTF 2007)*, pp. 1362-1365, May 2007.

[4] G.K. Ho, R. Abdolvand, F. Ayazi, "Through-support-coupled micromechanical filter array," in *Proc. of 17th IEEE Int. Conf. on MEMS (MEMS 2004)*, pp. 769-772, Jan. 2004.

[5] P.J. Stephanou, G. Piazza, C.D. White, M.B.J. Wijesundara, A.P. Pisano, "Mechanically coupled contour mode piezoelectric aluminum nitride mems filters," in *Proc. of 19th IEEE Int. Conf. on MEMS (MEMS 2006)*, pp. 906-909, Jan. 2006.

[6] S.-S. Li, Y.-W. Lin, Z. Ren, C.T.-C. Nguyen, "An MSI micromechanical differential disk-array filter," in *Proc. of IEEE Int. Solid-State Sensors, Actuators & Microsystems Conf. (Transducers 2007)*, pp. 307-311, Jun. 2007.

[7] R. Yang, T. He, C. Marcoux, P. Andreucci, L. Durrafourg, P.X.-L. Feng, "Silicon nanowire and cantilever electromechanical switches with integrated piezoresistive transducers", in *Proc. of 26th IEEE Int. Conf. on MEMS (MEMS 2013)*, pp. 229-232, Jan. 2013.

[8] R.B. Karabalin, X.L. Feng, M.L. Roukes, "Parametric nanomechanical amplification at very high frequency", *Nano Lett.*, vol. 9, no. 9, pp. 3116-3123, Aug. 2009.

Study of Phase Noise in VCXO with Inversion-Mode Varactors

Yao Huang Kao
Department of Communication Engineering
Chung Hua University
Hsinchu Taiwan ROC
Email: yhkao@chu.edu.tw

Teh Chau Liau
Department of Communication Engineering
Chung Hua University
Hsinchu Taiwan ROC
Email: thliau@chu.edu.tw

Abstract—**Voltage controlled crystal oscillators (VCXO) using CMOS varactors are investigated. The varactor is operated in the so-called inversion mode (I-Mode) with source and drain bounded together. Its capacitance is evaluated by the HSPICS-Fourier methodology. The performances of capacitance under small-signal and large-signal operations are classified. Then the frequency tuning and the related phase noise are explored. It is found that the larger the tuning coefficient has, the worse the phase noise has in I-mode varactor. The chip is fabricated by the TSMC 0.35um CMOS process. The total area including pad is 1.358 × 1.350 mm^2 and the current consumption in the core circuit is 300uA.**

Keywords- VCXO, Crystal Oscillator, Varactor, and Frequency Control, Inversion-mode

I. INTRODUCTION (HEADING 1)

Voltage controlled crystal oscillator (VCXO) is a key module in modern communication. It acts as a reference frequency in the cellular phone. [1, 2] It can also be used in the timing synchronization and clock recovery. In these applications the stringent request of phase noise is needed. CMOS process, which has the advantages of low cost and high integration, is now verified to be feasible for communication devices. The process possesses many kinds of CMOS varactor, which is used for tuning the frequency. Recently, the varactor under large-signal operation is intensively studied. [3-6] Depending on the fabrication capability, the inversion-mode (I-mode) varactor is investigated here. It has normally a steep characteristic in the C-V curve. This implies a step jump in the frequency tuning around the steep area. However, no obvious jump is observed in the measurement. It deserves us to explore intensively the basis. In this study the role of I-mode varactor through the standard process on the performance of frequency tuning and phase noise in crystal oscillators. The phase noise and tuning coefficient at different bias points are also studied. The design goal of VCXO is at 26MHz and has tuning sensitivity 25ppm/pF under loading capacitance 8pF. The parameters of the crystal are as follows: series resonant frequency fs=25.9935MHz, series capacitance Cs=4.588fF, parallel capacitance Co=1.421pF, and series resistance Rs=10Ω in 3.2×2.5mm^2 package.

The designs of varactor and VCXO are presented in section II. In section III, the performances are discussed. The experiment results are presented. Conclusions are made in section IV.

II. DESIGN OF VCXO

The schematic of the VCXO in Pierce configuration is shown in Fig. 1. [7] According to the Leeson's model, phase noise is inversely proportional to signal power. In our design, the magnitude of the signal is maximized to have rail to rail swing. The negative resistance seen into X_{in} and X_{out} by the crystal is chosen 10 times the crystal series resistance under the trade off among power, fast starting, and rail to rail swing. The aspect ratio Length/Width for each transistor is listed in the inset. m is the finger number of the gate. As the series resistance is overcome by negative resistance, the oscillation starts. According to our observation the rail to rail swing is achieved as the ratio of negative resistance to Rs is larger than seven times. The dimension of the device is listed in the table. The current consumption of the core circuit is about 300uA for low power applications. Multiple switches in capacitor bank are provided for precision control. The cascade M2 is used to reduce the effect from bias variation.

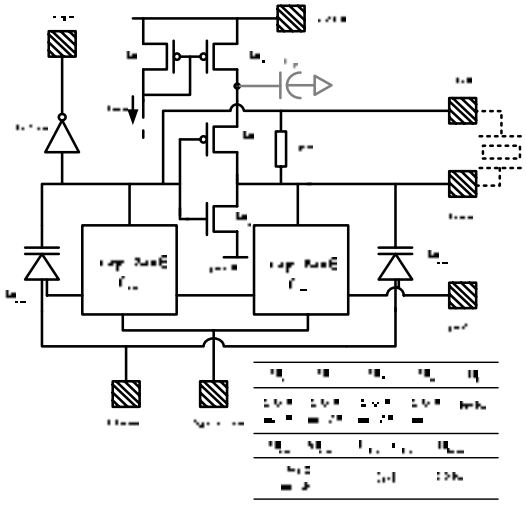

(a)

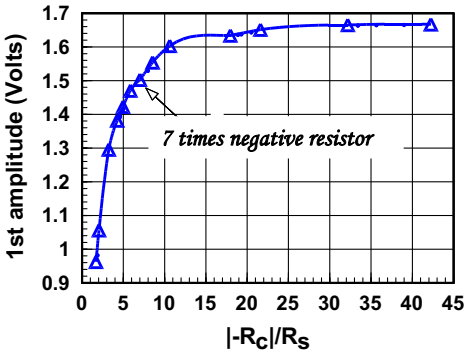

(b)

Fig. 1 (a) VCXO in Pierce configuration and (b) The dependence of the fundamental amplitude.

A. *I-mode nMOS Varactor*

Here two nMOS varactor M_{var1} and M_{var2} are used for positive voltage tuning. The structures are shown in Fig. 2a. For I-mode operation the drain and source are connected together and substrate is grounded. As the voltage Vgd>Vth, The channel beneath the gate is in inverted. The capacitance is equal to oxide layer capacitance Cox. As Vgd is decreased, the carrier in the channel is depleted. When Vgd=0, the carrier is fully depleted and the capacitance is reduced to Cox in series with Cj junction capacitance between depleted channel and N+ contact. Only strong inversion and depletion are functioned as Vgd is swept. The channel length is traded off between tuning ratio and quality factor. [6] It is suggested L= $L_{\min} \sim 3L\min$. Width is chosen from the magnitude of the capacitance. Multi-fingers in the gate is used to reduce the parasitic from the gate to source (drain) overlap. The dimension of width, channel length, and finger number under the goal of wide tuning and low phase noise are chosen as $W \times L \times m = 30\mu \times 1\mu \times 40$, respectively. The process is TSMC standard 0.35um mixed-mode with 2P4M and Polycide. For convenience, the variation of capacitance as a function V_g is shown in Fig. 2b at V_{tune}=0.8V. A nearly step change occurs around V_g=1.5V~1.6V. The ratio C_{max}/C_{min} of capacitance under small-signal is 5.77pF/1.38pF, which is obtained via spice model BSIM3.1.

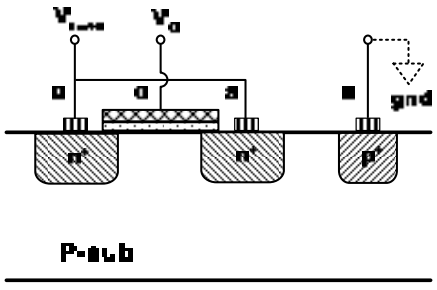

(a)

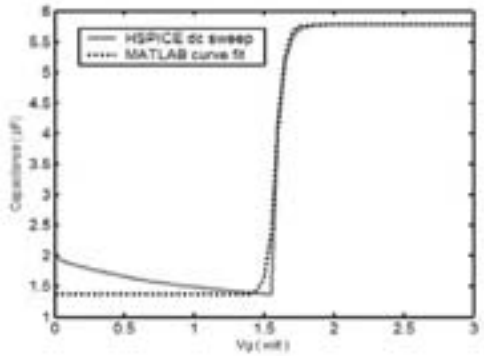

(b)

Fig. 2. NMOS varactor in (a) Inversion mode connection and (b) Variation of capacitance with V_G at V_{tune}=0.8V

B. *Large Signal Effective Capacitance*

Actually, the gate is biased at $V_g=V_{DD}/2$=1.5V and V_{tune} is changed from zero to V_{DD} within the oscillator. For reference, the capacitance under small-signal prediction is redrawn in Fig. 3a at various V_{tune}. The ac swing at the gate node is map on the figure. After power-on, however, V_g swings between zero and 3V so that the varactor is under large-signal operation. It encounters different modes of strong inversion and depletion. The partition depends on the setting of V_{tune} voltage. At V_{tune}=0.8V, the transition is located near Vg=1.5V. It results in the equal partition in the high and low value. The average value is in the middle of two limits. When the V_{tune} is set above 2V, the swing encounters only at low limit, so that the average is fixed at low limit. On the contrary, it has high limit as V_{tune} is set to zero voltage.

The effective value of capacitance is predicted from Fourier analysis of I-V waveform. A sinusoidal swing voltage is applied to the biased varactor and the current waveform is found from SPICE. From the ratio of fundamental voltage to current waveform the effective capacitance and resistance are obtained. The effective capacitance is monotonically decreased as V_{tune} is increased. More importantly, it reveals a linear shape with less steep in slope as the ac swing is increased as illustrated in Fig. 3b. Therefore, the tuning range is increased as ac swing is increased. At V_{tune}=0.8V, the transition is located near Vg=1.5V. It results in the equal partition in the high and low value. Hence the V_{tune}=0.8V is at the center of the tuning. When the V_{tune} is set above 2V, the swing encounters only at low limit, so that the effective capacitance is fixed and frequency change is not allowed.

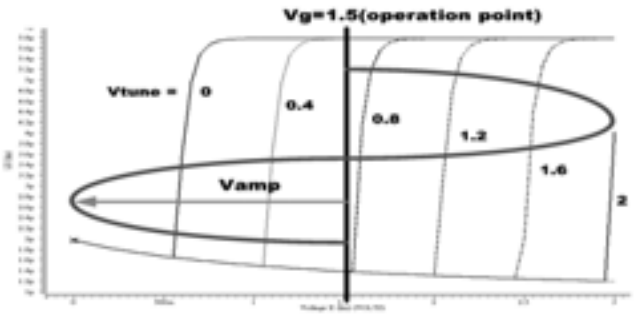

(a)

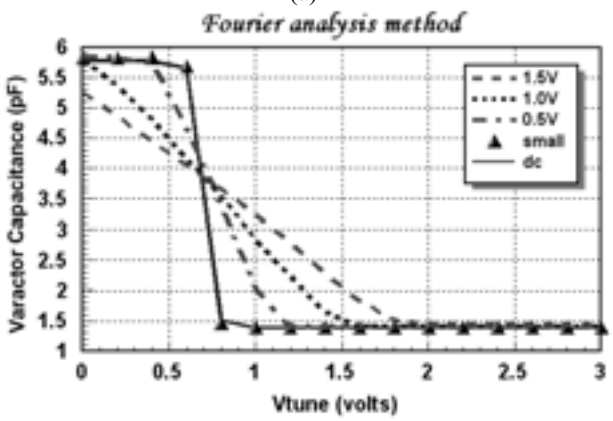

(b)

Fig. 3 (a) Instantaneous capacitance under large signal swing and (b) effective capacitance under various swings in I-mode varactor

III. Measurement Results

A. Frequency Prediction

The photo of the VCXO chip is shown in Fig. 4. The power supply is V_{DD}=3V. The tuning performances are shown in Fig. 5. The linear tuning range in I-mode occurs with V_{tune} from zero to 2V. Above 2V the tuning is almost fixed as predicted from the effective capacitance shown in Fig. 3b. The frequency deviation is from -30 to +21ppm. The maximal tuning coefficient occurs at V_{tune}=0.8V, which is at center of the linear tuning range, and is equal to 33ppm/V. The current consumption in core circuit is about 300uA and total current is 713uA.

B. Phase Noise calculation

Phase noises at different bias point are also examined. The measurements are performed with a Europtest PN9000 Phase Noise Test System with delay-line technique, which has the system noise floor around -152dBc. The performances are shown in Fig. 6a. In each figure two curves corresponding to the best and worst cases with noise level -100 and -90 dBc/Hz, respectively, at offset frequency 10Hz are illustrated. The worst case happens at the middle tuning V_{tune}=0.8V, which has maximal tuning sensitivity. The performance is better at both ends V_{tune}=0V or 3V. The difference is mainly from the tuning sensitivity. The reasons are, referred to Fig. 3a, the swing is almost in inversion region with V_{tune}=0V, where the capacitance appears as fixed Cox in I-mode. On the contrary, in the high end, the swing is almost in the depletion region V_{tune}=3V, where capacitance appears as fixed junction capacitance Cj.

The slope of phase noise near the carrier appears as $1/f^3$. It is evidenced by the 30dB difference at 10Hz or 100Hz offset as shown in Fig. 6b. The noise floor far away from the carrier is -150dBc/Hz. It might be limited by the system floor.

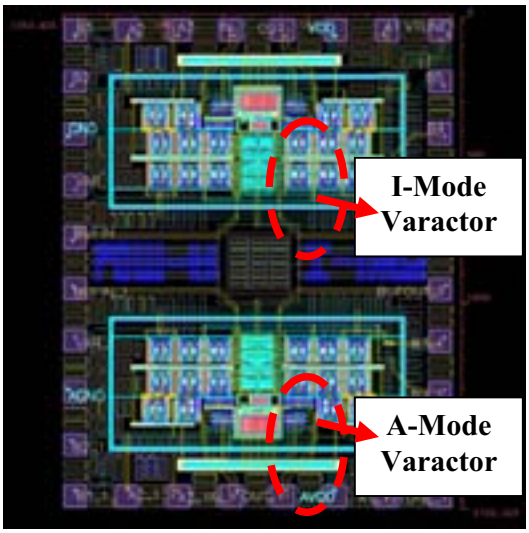

Fig. 4 Chip photograph of the VCXO

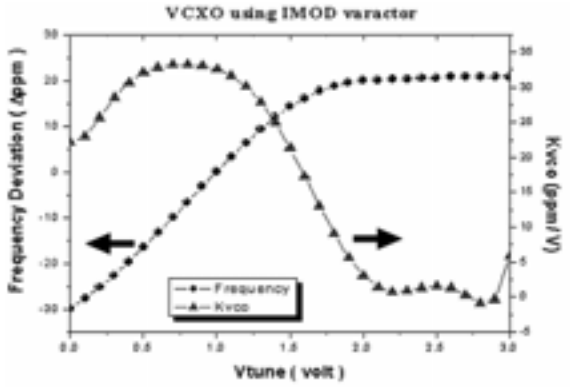

Fig. 5 Tuning capability in VCXO with I-mode varactor

As the tuning voltage is tuned at the center V_{tune}=0.8V, different regions are encountered in each swing, the noise is degraded. According to Leeson's formula, the phase noise can be described as

$$L(f_m)=10\log\left\{\left(\frac{f_o}{2Qf_m}\right)^2\left[\frac{FkT}{2P_s}\left(1+\frac{f_c}{f_m}\right)\right]+\frac{1}{2}\left(\frac{K_{vco}V_m}{2f_m}\right)^2\right\}$$

The quality factor of the tank mainly affects the $1/f_m^2$ region. So does the modulation noise voltage Vm across the varactor's terminals. It is conjectured that, for $1/f_m^3$ region, the variation of capacitance of varactor's C-V behavior plays an important role. [8] In the I-mode the lowest phase noise happens as V_{tune} is larger than 2V, in which all the swing falls in the depletion region with nearly fixed capacitance. The up-conversion effect of flicker noise is reduced. As expected, the harmonics in the I-mode is much stronger because the sharper transition from depletion to inversion region.

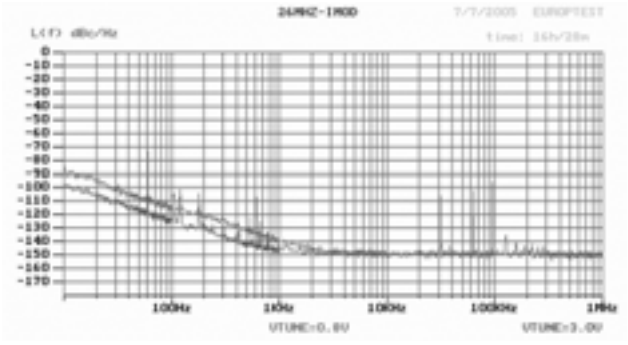

(a)

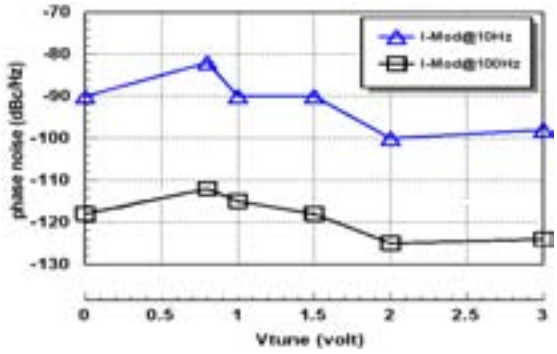

(b)

Fig. 6 Phase noise in (a) I-mode, (b) summary on V_{tune} dependence

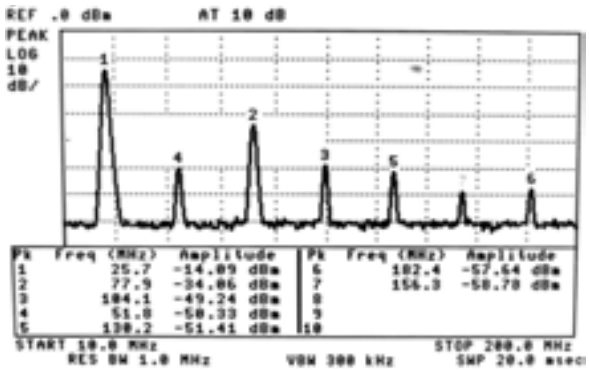

Fig. 7 Output Spectra with V_{tune}=1V

IV. Conclusions

In this work, two VCXOs at 26MHz are implemented by the TSMC standard 2P4M 0.35um CMOS process. The varactor is designed for I-mode operation. The effective capacitance in large-signal operation is indicated to have wider linear range. The performances of phase noise and tuning range are deeply discussed. The maximum tuning coefficient with 10dB worse in phase noise occurs at the middle tuning. The mechanism of degraded phase noise seems to be due to the channel transition between depletion and inversion.

ACKNOWLEDGEMT

The authors would like to thank National Chip Implementation Center and National Science Council, Taiwan, R.O.C., for chip implementation and financial support. This work was supported partly by National Science Council under the Contract NSC 99-2221-E-216 -018. The authors would also like to thank the Taiwan semiconductor manufacture company (TSMC) and chip implementation center (CIC) for the wafer fabrications.

References

[1] S. Kurogo, Y. Matsumoto, and T. Ohshima, "Analog TCXO Using Cubic Functional Voltage Generator," *IEEE International Frequency Control Symposium*, pp. 484~492, 1996.

[2] K. Nemoto and K. Sato, "2.5ppm Fully Integrated CMOS Analog TCXO," *IEEE International Frequency Control Symposium and PDA Exhibition*, pp. 740~743, 2001.

[3] E. Hegazi and A. Abidi, "Varactor characteristics, oscillator tuning curves, and AM-FM conversion," *IEEE J. Solid-State Circuits*, Vol. 38, no. 6, pp. 1033- 1043, June 2003.

[4] D. Siprak and A. Roithmeier, "Varactor Modeling Methodology for Simulation of VCO Tuning Sensitivity," *Proc. IEEE 2004 Int. Conference in Microelectronic Test Structures*, Vol. 17, pp. 273- 277, March 2004.

[5] R. L. Bunch and S. Raman, "Large-signal analysis of MOS varactors in CMOS– Gm LC VCOs," *IEEE J. Solid-State Circuits*, Vol. 38, no. 8, pp. 1325- 1332, Aug. 2003.

[6] B. Razavi, *Phase-Locking in High-Performance Systems : From Devices to Architectures*, Wiley-IEEE Press, pp. 3- 12, February, 2003.

[7] Eric A. Vittoz, Marc G. Degrauwe, and S. Bitz, "High-Performance Crystal Oscillator Circuits : Theory and Application," *IEEE J. Solid-State Circuits*, Vol. 23, no. 3, pp. 774- 783, June 1988.

[8] J. Maget, M. Tiebout, and R. Kraus, MOS Varactors with n- and p-Type gates and Their Influence on an LC-VCO in Digital CMOS, IEEE J. Solid-State Circuits, vol. 38, pp. 1139-1147, 2003.

Low Phase Noise Microwave Analog Optical Link Performance Study for High Dynamic Environment Platform

LESAGE Jean-Marc, LE PIPEC Mathieu
DGA – Information Superiority,
DGA, French MoD, Bruz,
France
jean-marc.lesage@dga.defense.gouv.fr

***Abstract*—Distribution of very low phase noise and low spurious microwave Local Oscillator (LO) is needed for most of the radar or electronic warfare applications. In this paper we study the capability to optically carry low phase noise LO, thanks to a directly-modulated optical link, while subjected to severe environmental conditions. First the optical link is compared to a coaxial cable link in terms of additive phase noise: subsequently the absolute amplitude and phase noise under random vibration are compared. It should be noticed that even in case of a wide band optical link, the phase noise floor difference between optical and coaxial cable is small even for short distance links. Secondly, the absolute amplitude and phase noise of the optical and coaxial cable link are measured with the entire optical link or only with some components of the link (10 GHz LO, optical single mode fiber (SMF), laser and photodiode) under random vibration. The phase noise degradation is almost the same when the optical or the coaxial link is under vibration and the main degradation is always due to the Local Oscillator whatever the technology is (OEO: Opto-Electronic Oscillator or traditional quartz oscillator). Some ways of improvement of optical link g-sensitivity that can be useful for OEO will be discussed. Thanks to recent experimentations done by DGA, it has been shown that very low phase noise microwave LO signals can be carried on optical link without any phase noise degradation due to the link while subjected to random vibration.**

Keywords—Opto-Electronic Oscillator; low phase noise microwave optical link ; low-g sensitivity, random vibration

I. INTRODUCTION

Nowadays, optical fibers are widely used for high speed digital link. Although optical components designed for telecommunication system are more and more efficient, they are not yet convenient for analog microwave optical link in future electronic warfare system because of the need of large bandwidth, high linearity and low noise required. Nevertheless optical links are very interesting in order to replace coaxial cable link for reasons of lower weight and cost, facility for installation, and insensitivity to electromagnetic environment.

French Mod leads a funding program in order to develop state-of-the-art microwave optical components. The links designed in this frame are very convenient because they show high-rejection of the second harmonic (H2), third harmonic (H3) and Intermodulation (IM3) over 20 GHz bandwidth.

These links can also be used for local oscillator (LO) distribution if they also show low phase noise performances. Moreover, if the link is used for airborne system, the low noise performance must not be deteriorated while subjected to high dynamic environment as for example random vibration.

In this article is firstly compared the performance of a traditional microwave cable link with a direct-modulated optical link. Secondly, these two types of links are compared under typical airborne random vibration. Finally, we extract from these experiments all the information in order to reduce the g-sensitivity of opto-electronic oscillator (OEO) because the local oscillator, whatever the technology used, remains the most sensitive component to mechanical vibration. Although opto-electronic oscillator is the most convenient technology to use in conjunction with optical microwave link, the OEO g-sensitivity must be reduced.

II. DESIGN AND PERFORMANCE OF THE STUDIED MICROWAVE OPTICAL LINK

The designed microwave direct-modulated optical link use Distributed Feed-Back (DFB) laser diode and Modified Unilateral Travelled carried (MUTC) Photodiode at 1.55 µm. The optical power of the laser is about 15 mW for a current polarization of 150 mA. The laser Relative Intensity Noise (*RIN*) floor is about - 153 dBc/Hz. The photodiode responsivity (S_{PD}) is about 0.8 A/W.

Firstly, the phase noise floor (Signal to Noise Ratio – SNR) of the otpical link is predicted thanks to a classical analytic model [1]:

$$SNR = 2\,(S_{laser} + S_{shot} + S_{th})/\,(P_m^2.S_{PD}^2.m^2) \qquad (1)$$

with P_m the fiber output optical power, m the index modulation and S_{laser} the laser amplitude noise, S_{shot} the photodiode shot noise, S_{th} the photodiode thermal noise as described as follows:

$$S_{laser} = P_m^2.S_{PD}^2.RIN \qquad (2)$$

$$S_{shot} = 2.q.S_{PD.}.\ P_m \quad (3)$$

$$S_{th} = 4.k_B.T/R \quad (4)$$

With k_B the Boltzmann's constant, q the electron charge and R the load resistance of the photodiode.

The predicted phase noise floor is about - 150 dBc/Hz when the microwave input power is at the 1 dB compression point of the link. S_{laser} mainly participate to the noise floor budget because the link is designed to be highly linear and to show large electrical dynamic range. So high power laser with low *RIN* must be used [2]. This is the most suited design for both optical RF and LO distribution.

Additive phase noise measurements are then performed in order to verify the performance of the optical link at different microwave input powers around the 1 dB compression point. The length of the optical fiber is 20 meters (with few meters more to connect the laser and photodiode) and the input microwave frequency is 10 GHz. The 10 GHz LO must be carefully chosen in order to characterize accurately the optical link added noise. A commercial synthesizer doesn't suit to added noise measurement because its amplitude and phase noise level are too high. Amplitude noise must be very low otherwise the phase quadrature doesn't show the ideal amplitude noise rejection. Phase noise must be low because of the 20 meters delay that reduces the phase noise attenuation of the source due to the quadrature. In all the experiments is used a COEO [3] which is state-of-the-art 10 GHz low phase noise oscillator. This is the reason why we show rejected relaxation peaks on the added and absolute phase noise measurements.

As shown in Fig. 1 and as expected, the optimal input power is the P1dB of the optical link and when the input power is increased or decreased, the phase noise floor is deteriorated.

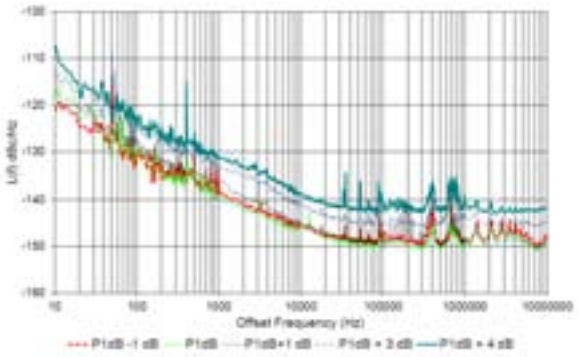

Fig. 1. Added phase noise (dBc/Hz) of the link when the input microwave power is shifted around the P1dB of the optical link

III. COMPARISON BETWEEN CABLE LINK AND OPTICAL LINK

A. Laboratory performance

Firstly are compared the two links when the input power is equal to the 1 dB compression of the optical link. The local oscillator (LO) is the same COEO used in added phase noise characterizations. The 20 meters cable losses are about 20 dB and the microwave link losses are near 30 dB because of the wide band covered by the optical link (20 GHz). So the same pre-amplifier before the links and the same amplifiers after the links are used with attenuators in order to maintain the same microwave output level in respect to Friis Formula. It is important to reach a high power output level in order to use the LO in a conversion frequency system for example. The comparison of the absolute phase noise before and after the links for input power at the P1dB is shown on Fig. 2.

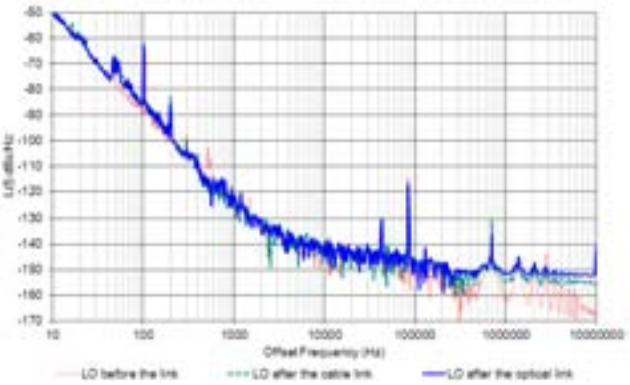

Fig. 2. Absolute phase noise of the LO only before the links, LO after the cable link and after the optical link

Concerning the phase noise floor, there is a slight difference lower than 3 dB, giving a short advantage to the coaxial cable. When no pre-amplifier is used, the input power level is decreased by 15 dB, the SNR degradation between cable and optical link increases by 5 dB. We conclude that even for low input power, the phase noise floor degradation due to the optical link is weak and acceptable for LO distribution. Of course, when the length of the link increases, the SNR of the optical link will be better than the one of the coaxial cable link.

In order to improve the noise floor, links losses have to be reduced thanks to laser and photodiode impedance matching. The bandwidth will be reduced to a few GHz which is always convenient for frequency agile LO distribution.

B. Performances under vibration

We compare the absolute phase noise of the LO at the output of the tested links when the cable or the optical fiber only or the all optical link (laser, fiber and photodiode) are under vibration. It should be noticed that no particular precautions are taken for the positioning of the classical coaxial low loss microwave cable and the classical Single Mode Fiber (SMF) in order to be representative of an airborne installation. The experiment is repeated many times as depicted in Fig.3.

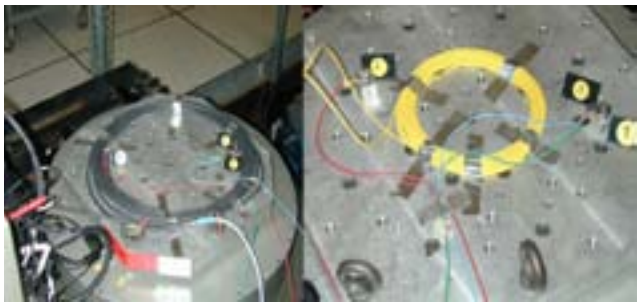

Fig. 3. Pictures of the cable and fiber vibration mounting conditions

The level of random vibration is of a few g r.m.s with typical airborne spectrum. The results are shown in Fig. 4 where the phase noise degradation is equivalent between the cable and the fiber.

The deterioration is also increased when the laser and photodiode are under vibration. But all these phase noise deteriorations are less important than the one of the LO under vibration. The COEO [3], which plays the role of LO, does not use mechanical suspension and his g-sensitivity is about few 10^{-9}/g. Whatever the used LO technology, the LO is obviously the most sensitive component of a system subjected to vibration.

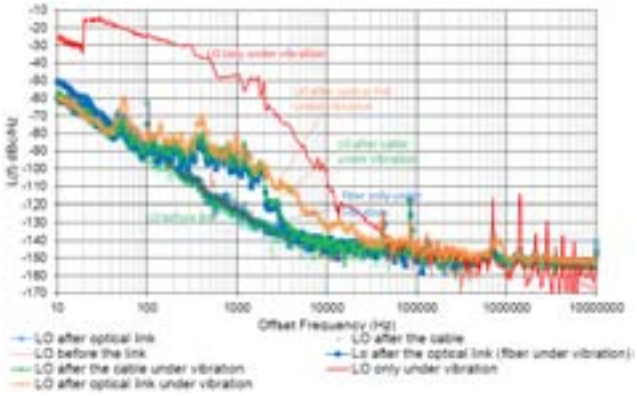

Fig. 4. Absolute phase noise (dBc.Hz) of the optical link and cable link under vibration

IV. APPLICATION TO OPTO-ELECTRONIC OSCILLATOR

As the tested optical link shows very low phase noise performance, an OEO has been built using the optical link including RF amplifier with a gain of 34 dB in order to compensate the optical link losses and narrowband filter in order to select the 10 GHz resonance frequency. The 20 meters fiber is used first and then replaced by a 1.5 kilometers one, the performances are shown in Fig. 5. The phase noise performance fits to the well-known Leeson analytical model. The 1/f added noise of the optical link with microwave amplifier is converted into $1/f^3$ absolute phase noise when the offset frequency is inferior to the Leeson frequency and the absolute noise floor is equal to the optical link SNR.

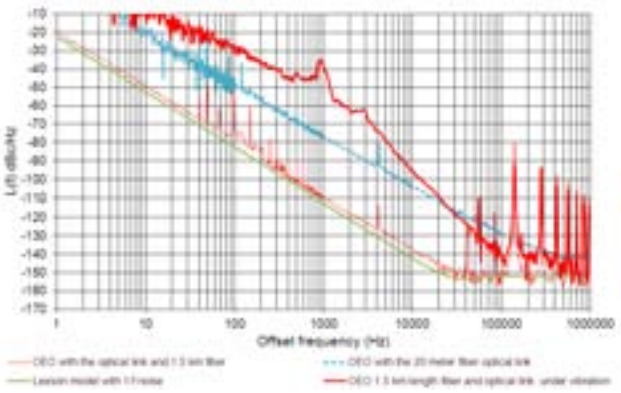

Fig. 5. Measured phase noise (dBc/Hz) of the optical electronic oscillator built with the studied optical link and 20 meters and 1.5 km fiber at 10 GHz

Although the phase noise deterioration of the optical link caused by vibration is weak (Fig4), it will become important in EOE application. Unfortunately, small phase fluctuations inside the loop directly map to larger frequency fluctuations at the output of the oscillator, thanks to Leeson model. We measure the g-sensitivity of our 1.5 km OEO at about few 10^{-9}/g. So we studied how the phase noise degradation due to the vibration can be reduced.

Firstly, we have to deal with the sensitivity of the optical fiber under vibration. Active compensation of the vibration is possible. As it is shown in [4], 1D compensation is efficient, but today, 3D compensation has not been demonstrated to our knowledge. Secondly, amplitude noise contribution may be taken into account. For an optical link with high input power (around the 1 dB compression point), the phase noise limitation is mainly due to the laser *RIN* (as predicted in the analytical model of the optical link SNR). Then optical link amplitude noise measurements under random vibration are also performed. The results are shown in Fig.6. The AM noise degradation due to the vibration must not be neglected in order to reduce the phase noise sensitivity to vibration. For instance, the photodiode must be used with an input power where the amplitude to phase noise conversion is the smallest.

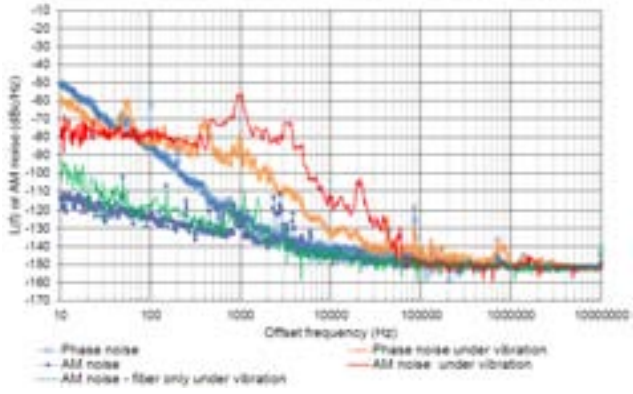

Fig. 6. Absolute phase noise and amplitude noise (dBc/Hz) of the optical link under vibration

IV. CONCLUSION AND PERSPECTIVES

Direct modulated microwave optical link designed in the frame of the DGA-funded project "ORGE" has been successfully tested in order to carry low noise LO. The noise performance is slightly degraded compared to coaxial cable link. Thanks to impedance matching of the laser and photodiode, the optical link will be appropriate to low noise microwave LO distribution.

Then, while they are subjected to random vibration, the optical link and the cable link show similar performances. Replacement of cable with optical link in airborne system can be carried out.

But when the optical link loop is closed thanks to microwave amplifier and narrowband filter in order to give a very low phase noise OEO, the phase fluctuations due to the vibration lead to larger phase noise degradation. We evaluated the g-sensitivity of state-of-the-art OEO at few $10^{-9}/g$, as much as traditional quartz oscillator without any suspension system.

In order to reduce it, on the first hand, the phase noise degradation due to the phase fluctuations of the optical fiber under vibration has to be limited or compensated thanks to 3D-accelerometer and retroaction, thanks to phase-shifter in the loop [4] for example. On the second hand, we have to keep in mind the amplitude noise degradation due to vibration.

Then, as the optical link SNR is limited by *RIN*, we may use a higher optical power laser with lower *RIN* with a photodiode at an input power where the amplitude to phase noise conversion is the smallest. The phase noise measurements of this new optical link and OEO using this link will be done under vibration soon.

ACKNOWLEDGMENT

The directly modulated optical link, designed by TSA (Thales Systemes Aéroportés) in the frame of the DGA-funded project ORGE, use semiconductor DFB laser diode and MUTC photodiode, designed by 3-5 Lab and packaged by 3S Photonics.

The authors thank also collaborators from DGA MI/MC, DGA MI/MAN/CVO and DGA IP for assistance and useful discussions.

REFERENCES

[1] Khaldoun Saleh, "High spectral purity microwave sources based on optical resonators", Thesis of the university Paul Sabatier, Toulouse III, November 2012, 29th.

[2] M.Chtioui et al "Analog microwave photonic link based on a high power directly modulated laser, a high power photodiode and passive impedance matching", Microwave Photonics 2012.

[3] D. Eliyahu, D. Seidel, and L. Maleki, " Phase Noise of a High Performance OEO and an Ultra Low Noise Floor Cross-Correlation Microwave Photonic Homodyne System", International Frequency Control Symposium, Honolulu, Hawai, p. 811 (2008)

[4] D. A. Howe, A. Hati, C. Nelson, J. Taylor, and N. Ashby "Active Vibration-induced PM Noise Control in Optical Fibers: Preliminary Studies", IEEE International Frequency Control joint the 21th European ant Time Fréquency Forum, p 552 (2007)

Evaluation of the Accuracy of the Method for Measuring State-of-the-Art Ultra-High Stability Quartz Crystal Oscillators

Patrice Salzenstein

Franche Comté Electronique Mécanique Optique Thermique Sciences et Technologies (FEMTO-ST), Centre National de la Recherche Scientifique (CNRS), route de Gray, F25030 Besançon, France

Alexander Kuna

Time and Frequency Department , Institute of Photonics and Electronics, Czech Academy of Sciences, Prague, Czech Republic

Frédéric Lefebvre

Oscilloquartz, rue des Brévard, Neuchâtel, Switzerland

***Abstract*—The accuracy of the Three-Cornered Hat method is discussed when not simultaneously applied to the determination of the contribution on short term frequency stability performed on ultra-stable quartz oscillators.**

Keywords—short term stability; ultra-stable Quartz; oscillator; non-simultaneity

I. INTRODUCTION

The best frequency stability ever measured on a quartz crystal oscillator was recently obtained.

This new Boitiers à Vieillissement Amélioré (BVA) oscillator has an estimated flicker frequency modulation (FFM) floor as lower as 2.5×10^{-14} at 5 MHz [1,2]. It leads to a significant step. To achieve such a low FFM floor, we assume that best resonators are fully characterized [3] and packed. It was obtained using a double rotated SC-cut quartz with low phase noise, good aging characteristics and low sensitivity to drive level dependency placed in appropriate thermostat in the first prototype of a double oven-controlled crystal oscillator (OCXO) realized in Switzerland by Oscilloquartz company.

We checked that the ultra-stable signal delivered by such a BVA oscillator can be distributed without any degradation of its short term stability [4]. It has to be underlined that precise measurements on oscillators were carefully performed at the Time and Frequency department in Prague in very favorable environmental conditions and deduced by three cornered hat analysis [5,6,7,8] on a dedicated system [9]. Our process for short term is analogous to what occurs for long term frequency stability characterization, but could provide questionably a precise determination of FFM floor.

The analysis proceeds by matching the theoretical and the best experimental curves not exactly simultaneously. In this paper we discuss the accuracy of our method.

II. EXPERIMENTAL RESULTS

A. State-of-the-art oscillator design

The best resonator was manufactured by Oscilloquartz Company in 2010. It was placed in appropriate thermostat [10] in the first prototype of an Oven-controlled crystal oscillator (OCXO) called 8607-C. It consists in a new BVA type oscillator where electrodes are deposited not on the resonator itself but on inner sides of two condenser discs made of adjacent slices of the quartz from the same bar, forming a three-layer sandwich with no stress between the electrodes and the vibrating element. Turnover temperature of the resonator is 88.6°C. Unloaded Q factor is 2.6×10^6. Regarding experimental phase noise measurements, QL can be given by the 1.6 Hz intercept point between 1/f slope (phase flicker noise) and $1/f^3$ slope (frequency flicker noise). $QL = 1.6 \times 10^6$.

Thermostats are especially developed by Oscilloquartz with double oven for this new model, with drastic optimization. Electronics circuits are entirely renewed to reduce contribution of the 1/f noise of the amplification elements [11], considering the goal is to decrease the 1/to curve in the time domain, where to is the integration time.

B. Frequency stability measurements

Determination of the short term frequency stability of the new oscillator is performed thanks to a Dual Mixer Time Difference Multiplication (DMTDM) [9] based 'IPE3' system developed at the Institute of Photonics and Electronics (IPE) in Prague, with a beat frequency of 5 Hz, where each measure gives 5,000 samples separated by a basic 200 ms integration time [2]. Frequency stability limit of the IPE3 bench is determined by rejecting one BVA Oscillator. Then it is possible to deduce a flicker phase of respectively 8×10^{-15} and 1.1×10^{-15} at 1 s and 13 s. Contribution of the instrumentation can be negligible between 0.2 s and 100 s where the FFM floor is expected. To determine the frequency stability of the 8607-C prototype, it is measured with two other ultra stable BVA oscillators, respectively serial number 543 and 567. The

frequency stability curves are obtained for each pair of oscillators. The contribution of each oscillator is deduced for every measure performed on each pair by the 3 cornered hat analysis [6]. One can note that, even if the two oscillators referenced 543 and 567 are much stable in terms of aging, the new one has the best FFM floor. Principle is schematically represented on figure 1.

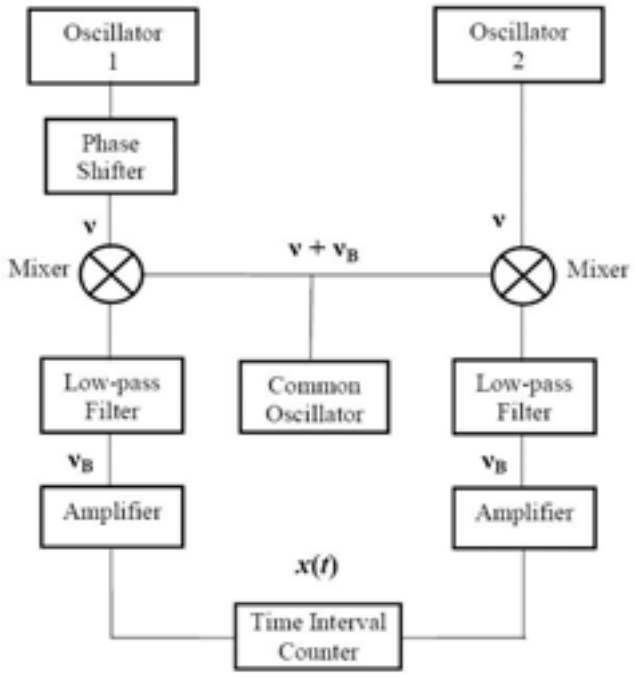

Fig. 1. Principle of DMTDM frequency stability measurement.

The experimental results are given in reference [1]: it shows that the frequency stability of the 8607-C prototype is less than 4.5×10^{-14} for integration times between 1 s and 50 s. The best obtained FFM floor is 2.5×10^{-14} for an integration time in the range 10 to 12 s.

This new prototype of 5 MHz 8607-C BVA oscillator with highly optimized double oven and low noise electronics, present the best FFM floor ever measured on a BVA quartz oscillator, at 2.5×10^{-14}, as shown on figure 2.

III. Discussion about the accuracy of the method

Estimated uncertainty for the frequency stability at 12 s is equal to $\pm$ 3×10^{-15} [12]. As we started to discuss in the introduction, we can underline that our process for short term is to be considered as analogous to what occurs for long term frequency stability characterization. But actually it could provide questionably a precise determination of FFM floor. We can have a doubt or interrogation as the analysis proceeds by matching the theoretical and the best experimental curves not exactly simultaneously. Shall we take into account the fact that we make only a single measure for one couple of oscillators, but we don't characterized the frequency simultaneously for the different couples of the 3 oscillators to be measured?

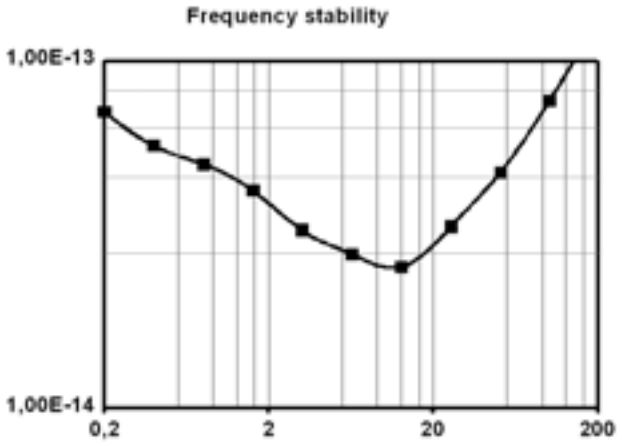

Fig. 2. Best frequency stability deduced for a 5 MHz quartz oscillator [1]. The overlapping Allan variance is given versus integration time (in s).

The Three-Cornered Hat is a well known style of hat that was popular during the late 17th century and 18th century. But in our case, it is the method used to determine the contribution to the phase noise or frequency instability by analyzing the contribution of three different pairs of oscillators. The three-cornered hat allows the extraction of stabilities for three clocks when the only available information is the time or frequency differences between the clocks [12]. Normally this method should proceed simultaneously by sampling each 200 ms integration time [2] in parallel in order the deduced contribution of each oscillator to be valid.

- To understand how the measure is performed, one should keep in mind that we work in the short term domain where the contribution of the instrumentation can be negligible between 0.2 s and 100 s, where the FFM floor is expected.
- An other important fact is the large number of samples during the acquisition. It can be considered that 5,000 samples is enough to avoid artifacts.
- We also proceed by comparing the data performed on the same pair of oscillators, but at a different time or day. Then we keep only the best reproducible measures containing successively those 5,000 samples by considering that the worse data are consequently due to external contribution. For instance the low variation of the room temperature can affect the noise.
- But we also reject the very best data to ensure the repeatability to be enough reproducible.

.With all these conditions, we simply try to get rid of the condition of simultaneity formally necessary to in the Three-Cornered Hat method. Finally we proceed as following. Three pairs of oscillators are fully characterized successively, but by performing several time, and at different moment the data acquisition. Compiling a large quantity of data, we are ready to extract from the whole dataset what is supposed to be the real contribution of each pair, when external contribution to the

noise are minimized. We assume the non-simultaneity of the measurements do not affect the right to deduce the contribution of each oscillator to the frequency instabilities.

To illustrate our method, we can see as it is analogous to how the barycenter "O", which is the point between two objects "A" and "B", respectively with a mass "M1" and "M2", where they balance each other, is determined in a triangle. In a pair the contribution of each signal generated by each oscillator to the noise is similar to a balance with different mass.

When the two mass are at equilibrium, the following condition (1) is respected:

$$(M1)x|0A| = (M2)x|OB| \quad (1)$$

In our case we consider vectorial and scalar Leibniz functions related to barycenter.

IV. Conclusion

Despite that it was not formally possible to proceed at the same time to measure the different pairs of oscillators, we assume that precise measurements on oscillators carefully performed at the Time and Frequency department in Prague in very favorable environmental conditions and deduced by the main guidelines of the three cornered hat analysis allow the validation of the best performances deduced on a 5 MHz BVA Quartz oscillator.

Acknowledgment

Authors acknowledge Ludvik Šojdr for his contribution to the measurements.

References

[1] P. Salzenstein, A. Kuna, L. Šojdr and J. Chauvin J., "Significant step in ultra high stability quartz crystal oscillators", Electronics Letters, Vol. 46, n°21, pp. 1433–1434, 2010.

[2] A. Kuna, J. Cermak, L. Šojdr, P. Salzenstein and F. Lefebvre, "Lowest Flicker-Frequency Floor Measured on BVA Oscillators", IEEE Trans. on UFFC, vol. 57, n°3, pp. 548-551, 2010.

[3] P. Salzenstein, A. Kuna, L. Šojdr, F. Sthal, N. Cholley and F. Lefebvre, "Frequency stability measurements of ultra-stable BVA resonators and oscillators", Electronics Letters, vol. 46, n°10, pp. 686-688, 2010.

[4] P. Salzenstein, N. Cholley, A. Kuna, P. Abbé, F. Lardet-Vieudrin, L. Šojdr and J. Chauvin, "Distributed amplified ultra-stable signal quartz oscillator based", Measurement, vol. 45, n°7, pp. 1937–1939, 2012.

[5] J. E. Gray and D. W. Allan, "A Method for Estimating the Frequency Stability of an Individual Oscillator," Proc. of the 28th Ann. Symp. on Freq. Contr., May 1974, pp. 243-246, 1974.

[6] D. W. Allan, "Time and frequency (time domain) characterization, estimation, and prediction of precision clocks and oscillators," IEEE Trans. on UFFC, vol. 34, n°6, pp. 647–654, 1987.

[7] P. Tavella and A. Premoli, "Estimation of Instabilities of N Clocks by Measuring Differences of their Readings", Metrologia, vol. 30, n°5, pp. 479-486, 1993.

[8] F. Vernotte, M. Addouche, M. Delporte and M. Brunet, "The three cornered hat method: an attempt to identify some clock correlations", IEEE Freq. Contr. Symp., 23-27 Aug. 2004, pp. 482- 488, 2004.

[9] G. Brida, "High resolution frequency stability measurement system," Rev. Sci. Instrum., vol. 73, n°5, pp. 2171–2174, 2002.

[10] F. Sthal, S. Galliou, P. Abbe, X. Vacheret, G. Cibiel, 'Ultra stable crystal ovens and simple characterization', Electron. Lett., vol. 43, n°16, pp. 900-901, 2007.

[11] F. L. Walls, 'The quest to understand and reduce 1/f noise in amplifiers and BAW quartz oscillators', Proc. of the 9th European Freq. and Time Forum, Besançon, France, pp. 227-240, 1995.

[12] C.R. Ekstrom and P.A. Koppang, "Error bars for three-cornered hats", IEEE Trans. on Ultrason. Ferroelec. Freq. Contr., vol. 53, n°5, pp. 876-879, 2006.

Very Low Power Consumption, Ultra Low Phase Noise, Miniature Conventional OCXO

Roman Boroditsky, Jorge Gomez
NEL Frequency Controls
Burlington, WI USA
romanb@nelfc.com gomezj@nelfc.com

Abstract **- Battery powered equipment, whether instrumentation, underwater exploration, or military require high performance frequency sources with very low power consumption for obvious reason. Current state of the art in the area of very low power consumption OCXO [1]., [2]. employs evacuation of the entire (or almost entire) electronic circuit with crystal resonator in metal enclosure and internally heating the content. Although achieving the goal of significant reduction in power consumption (60 – 80 %), this approach has some serious drawbacks. The phase noise performance of one of the implementations is average at best, of another - is outright poor. Evacuation of the entire OCXO requires very complex and tedious processes, since any minute contamination can destroy deep vacuum, needed for device to operate. The availability of die semiconductor components, a necessity for inside the vacuum, is very limited. The devices are susceptible to exposure of elevated temperatures, which might induce internal outgassing and deterioration of vacuum level. The goal of this work was to create a device, which would eliminate above mentioned drawbacks i.e. employ conventional heating technique, use off-the shelf widely available components, have comparable to evacuated devices power consumption and size, and exhibit superior phase noise performance. The goal was achieved by implementing special thermal insulation technique, and NELs ULPN technology in 20x20x10 mm package. While the steady state power consumption at room temperature is less than 250 mW, the phase noise at 10 Hz offset at <-145 dBc/Hz is better by 20 to 45 dBc than published specifications, and at -174 dBc/Hz, by 10 to 30 dBc on the floor.**

I. Introduction

The goal of this work was to design and develop a small form factor OCXO, which would have very low power consumption, suitable for operation in battery powered equipment, while possessing ultra low phase noise performance. Currently very low power consumption OCXOs described in papers and offered on the market are based on evacuation (to the deep level) of the (almost) entire OCXO circuitry with open blank crystal resonator in metal enclosure. The temperature of the entire assembly is controlled by the internal oven. This approach (to different extent) allows for significant reduction in power consumption and warm-up time of the OCXO, however it has some inherent drawbacks. Evacuation of the entire OCXO requires very complex and tedious processes, since any minute contamination can destroy deep vacuum, needed for device to operate properly. The more components and materials are involved (including inevitable organics) the more the probability of vacuum deterioration. The availability of die semiconductor components, a necessity for inside the vacuum, is very limited. The devices are susceptible to exposure of elevated temperatures above specified operating limits, which might induce internal outgassing and deterioration of vacuum level. One of the requirements for presented effort was to simplify the processes and construction and use only conventional oven design with just a crystal resonator evacuated (which are available from several vendors on the market). The phase noise performance of the above-mentioned evacuated OCXO is average in one case and outright poor for the other according to published data sheets. Substantial improvement in this department was another major purpose of presented development.

II. Design

Basic design concept is shown on Fig.1. The enclosure of the OCXO is standard in the industry miniature 20x20x10 mm^3 5-pin metal case. Internally design is based on low profile TO8 3rd overtone SC-cut crystal resonator with conventional oscillator and oven circuitry assembled on the PCB. The whole assembly is then thermally insulated from the base and the cover by NEL proprietary insulation materials. Electrical connections are made with thin wires for the same purpose of thermal insulation. The circuit design is similar to the NEL ultra low phase noise circuits, employed in larger OCXO with some minor shortcuts due to real-estate limitations. In order to maintain very low power consumption with normal operating temperature range OCXO is designed to operate at lower supply voltages either 3.3 V or 5 V DC. The experimental results shown below are for devices operating at 5 V DC power supply.

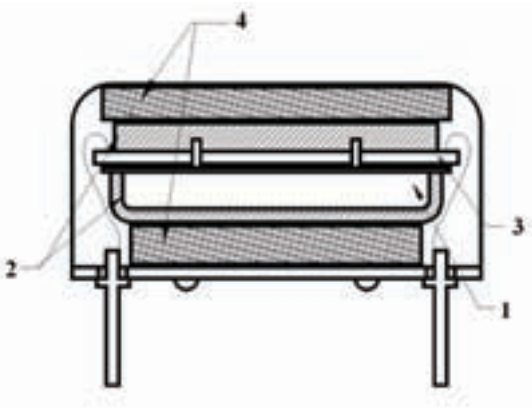

Fig. 1. Basic OCXO construction. 1 – crystal resonator; 2 – oven; 3 – PCB with circuitry; 4 – thermal insulation.

III Test results

A. Phase noise

6 units at 10.000 MHz were built and tested on 2 different instruments: DCNTS from Noise XT and 5120A-01 from Symmetricom. The plots are shown on Fig. 2. through Fig. 7.

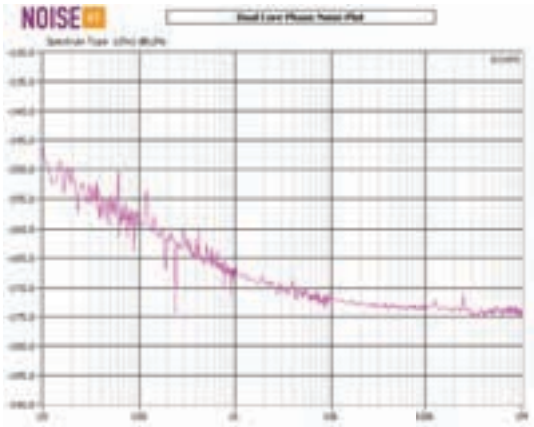

Fig. 2. Phase noise, unit #1

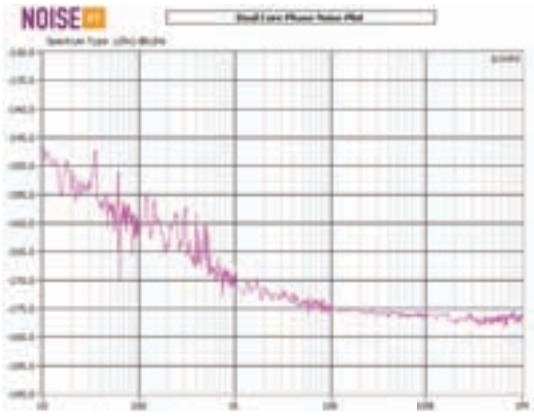

Fig. 3. Phase noise, unit #2

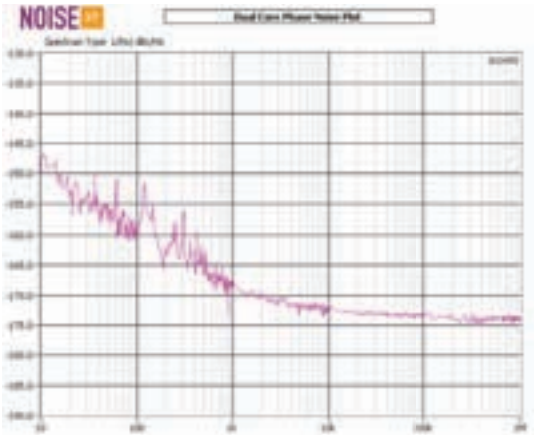

Fig.4. Phase noise, unit #3

On units #1 through unit #3 the measurements were made on DCNTS from Noise XT, on Units #4 through #6 they were made on 5120A-01 from Symmetricom. The latter has limitation on the noise floor at larger offsets (-170 dBc/Hz, guaranteed).

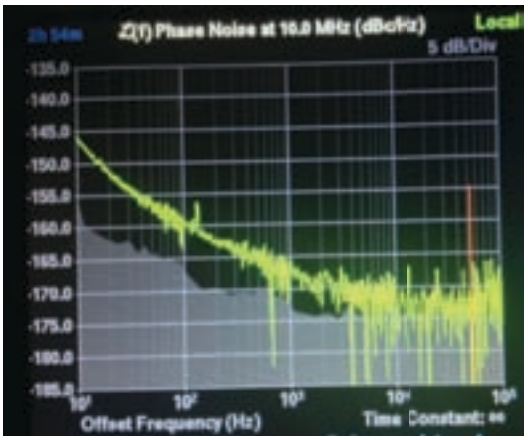

Fig. 5. Phase Noise, Unit #4

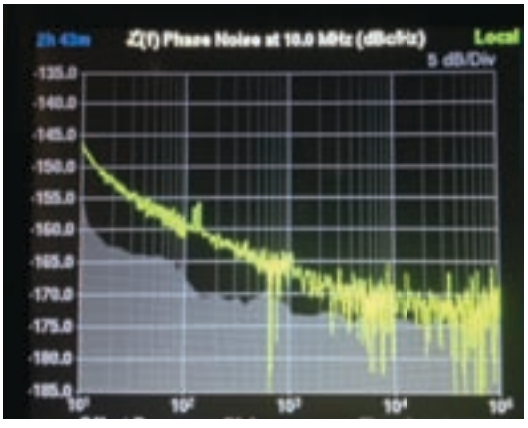

Fig. 6. Phase noise, unit #5

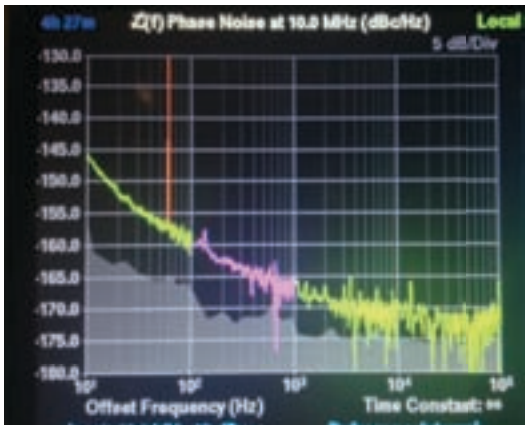

Fig.7. Phase Noise, unit #6

As one can see the phase noise of all the units is outstanding and consistent from unit to unit. It's better than -145 dBc/Hz at 10 Hz offset, close to -160 dBc/Hz at 100 Hz offset, and less than -173 dBc/Hz on the noise floor.

B. Power consumption

The data is presented in Table I.

TABLE I

POWER CONSUMPTION

Unit #	Oven Set Temperature°C	Icc at 25°C, mA	Power Consumption, mW
#1	82	52	260
#2	84	55	275
#3	80	50	250
#4	85	56	280
#5	78	49	245
#6	82	52	260

There's apparent correlation between power consumption and oven set temperature, as expected. Typical figure is about one quarter of a watt with maximum value not exceeding 300 mW at room temperature.

C. Warm-up

The warm-up data is presented in Table II.

TABLE II

Unit #	Start current, mA	Start-up power, W	Warm-up time to 0.1 ppm, s
#1	420	2.1	51
#2	400	2.0	52
#3	410	2.05	52
#4	410	2.05	53
#5	400	2.0	53
#6	420	2.1	51

While the power at start-up is rather moderate, just about 2 W, the warm-up time to the accuracy of ± 0.1 ppm (from the frequency after 1 hour) is less than 1 minute for all of the tested units.

D. Frequency Stability Over Temperature

Frequency stability curves over temperature are shown on Fig. 8. Since one of the purposes of the development was to create a building block for double oven, the oven set point was selected to attain maximum flatness in the 70°C area. Nevertheless, the overall stability in the 0°C to 75°C range did not exceed ±5 ppb.

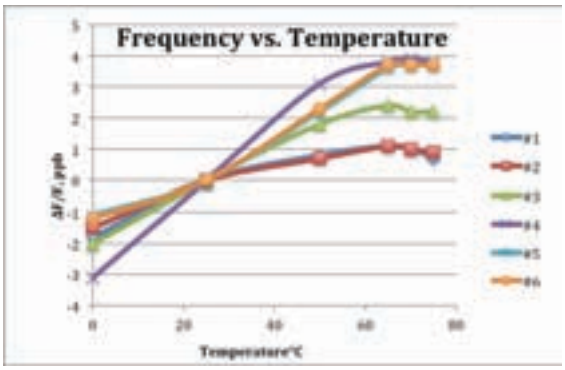

Fig. 8. Frequency Stability vs. Temperature.

E. Storage Temperature exposure

One of the important motivations for the project was to eliminate the probability of deep vacuum deterioration, and hence significant performance deterioration, after exposure to elevated temperatures. In some applications the maximum storage temperature is specified at 125°C, which may create outgassing problems in evacuated devices, where most (all) of the circuitry and structures are evacuated. All 6 units were exposed (non-operationally) to the temperature of 125°C for a total of 48 hours with data on current consumption taken after 1, 2, 4, 8, 24 hours and at the end of the experiment. The units were allowed to stabilize for about 1 hour before the measurements were taken. The frequency drift, though not documented on all units did not exceed typical for 3rd overtone SC-cut resonators retrace value after the end of the test. The current consumption data is shown on Fig. 9. Some minor fluctuations of the values can be explained by ambient temperature fluctuations in a not tightly controlled environment.

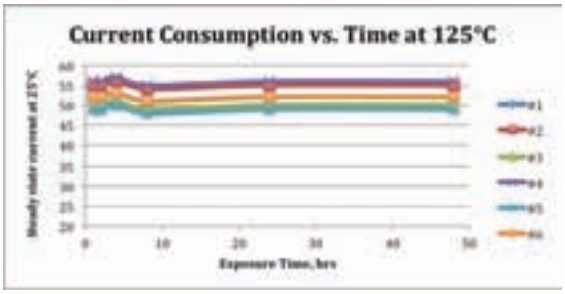

Fig. 9. Current consumption vs. time exposed to elevated temperature.

IV. Conclusions

The developed ULPN very low power consumption miniature OCXO performance met the set design goals. It exhibited outstanding phase noise, excellent stability, and very fast warm-up time, while consuming close to one quarter of a Watt power at room temperature. All is achieved with conventional technology, where only crystal resonator being sealed in vacuum, using readily available off-the shelf components. Comparison to two existing on the market evacuated OCXO (per published data sheets) is shown in Table III.

TABLE III

Device Parameter	Ex-400 from Vectron	MXO37/14 from Magic	20x20 ULPN NEL
Size, mm	21x13x7.6	20x15x10	20x20x10
Power consumption at 25°C, mW	350	150 TYP	270 TYP
Warm-up Power, W	1.5	0.7	2.0
Warm-up time to 0.1 ppm, s	120	45	60
Stability vs. Temperature, ±ppb	75	5	5
Phase noise, dBC/Hz	(20 MHz data, TYP)	TYP, MAX N/A	Average test data
@ 10 Hz	-100	-125	-147
@ 100 Hz	-130	-145	-159
@ 100 KHz	-150	-168	-174
Output power, dBm	+4	+8	+12
MAX storage temperature, °C	85	90	125

References

[1] Vectron International product data sheet http://www.vectron.com/products/ocxo/ex-400.pdf

[2] Magic Xtal Ltd product data sheet http://www.magicxtal.com/upload/uf/b52/MXO37-14.pdf

Phase Group Characteristic Based Frequency Measurement Method with Wide Band and Fast Response

Shaofeng Dong, Wei Zhou, Jinsong Zhan, Wei Hu
Department of Measurement and Instrument
Xidian University
Xi'an, China

Abstract—**As the rapid development of frequency standard, the need arises to measure frequency fast in a wide band with a high resolution. The frequency measurement instrument in commerce nowadays cannot meet the demand. And the generally existing ± 1 counting error limits the improvement of measuring precision. By analyzing the phase variation rule between every two periodic signals with different frequency, the phase group characteristics, such as phase group synchronization, are revealed in the paper. Based on the phase group characteristics and phase coincidence detection, a wide band frequency measurement method is proposed in this paper. Two adjacent phase coincidence points of the reference frequency and the measured frequency are used to generate the measurement gate, and ± 1 counting error can be eliminated effectively. Fine phase shift is used in some special situation on the reference frequency to shorten the measurement time. Experiment results show that this method achieves a precision higher than 1×10^{-13}/s in frequency standard comparison, and the typical precision of signal from 30 kHz to 100MHz achieve $6\sim8 \times 10^{-12}$/s.**

Keywords-frequency measurement; wide band; fast response; phase group characteristic

I. INTRODUCTION

With the technology progress of communication, measurement, aerospace, navigation and positioning, higher measuring precision of frequency standards is required [1], and the need arises to measure frequency fast in a wide band with a high resolution. Time-interval counting [2][3] is a basic technique of time and frequency measurement. However, ± 1 counting error generally exists in most time-frequency measuring instrument, which limits the improvement of measuring precision. Kinds of techniques designed to improve the measuring precision, such as analog interpolation, vernier, time-digital conversion [4], cannot effectively eliminate the influence of counting error. Also, the traditional frequency measurement instruments require complex frequency conversion circuits to accomplish high resolution frequency measurement in a wide band.

On the basis of analyzing the phase variation rule between every two periodic signals with different frequency, phase group characteristic and phase coincidence detection can be used to generate the measurement gate. In his paper, a wide band and high resolution frequency measurement method is proposed. And fine phase shift is used in some special situation on the reference frequency to shorten the measurement time. This method eliminates ± 1 counting error effectively, measures any frequency with high resolution and fast response in a wide range.

II. PHASE GROUP CHARACTERISTIC AND WIDE-BAND FREQUENCY MEASUREMENT METHODE

Phase processing is commonly used in high-precision and high-resolution time and frequency measurement, but the traditional phase processing is limited to the frequency comparison at the same nominal value [5][6]. For the frequency comparison between two different frequencies, frequency conversion is required, which increased the circuit complexity and cost, introduces extra noise.

Besides the periodic changes of two frequency signals, the study found, it is the regular changes of phase differences that have a significant impact on measurement, comparison and control. We characterize the regular changes of phase differences and the frequency relations of signals in terms of the greatest common factor frequency [7], the least common multiple period, equivalent phase comparison frequency [8] and so on. The phase difference variation rule between two different frequency signals is shown as Fig. 1.

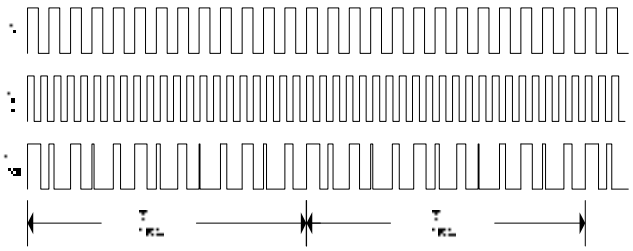

Figure 1. The phase difference variation rule between two different frequency signals.

In Fig. 1, f_{out} represents the output of phase comparison between f_1 and f_2, with f_1 used as the reference signal. It is known that the phase processing is always carried out by

Supported by the Fundamental Research Funds for the Central Universities No. K5051204003 and No. K5051304018 , the National Natural Science Foundation of China under Grant No. 10978017.

period. Because f_1 and f_2 have different frequency, it is impossible to perform phase processing continuously like the traditional way that compares phase in successive periods., the phase relationship between every two frequency signals is very complex. However, it can be seen that the same phase difference distribution appears repeatedly in each $T_{\min c}$. If all phase differences in one $T_{\min c}$ are considered as a group, the phase processing between different frequency signals can be realized in multiple periods such as the least common multiple period $T_{\min c}$. It also can be seen from Fig. 1, the phase difference between two different frequency signals reflects the periodic change characteristic with the least common multiple period $T_{\min c\,c}$ as the period. We define the phase difference in one $T_{\min c}$ as phase group, and characterize the above phenomenon as phase group synchronization. Phase group synchronization refers to the strict repeatability of the phase differences between two different frequency signals with the least common multiple period as the period. We note that, every phase group always starts at the phase coincidence point between two different frequency signals, stops at the next phase coincidence point. The start and stop points of phase group are strictly synchronous with the two different frequency signals, which means the numbers of the two compared frequency signals in one whole phase group are two integers.

Based on the phase group characteristic, a wide-band frequency measurement method is proposed in this paper. In this method, two adjacent phase coincidence points of the reference frequency f_0 and the measured frequency f_x are used to generate the measurement gate. Because f_0 and f_x are synchronized strictly with the start and stop signals of the gate, ± 1 counting error can be eliminated. In gate time, the counting numbers of f_x and f_0 are N_x and N_0, respectively, thus the measured frequency is expressed as:

$$f_x = f_0 \times \frac{N_x}{N_0}. \tag{1}$$

In this method, we can complete a wide band frequency with one high stable reference frequency signal, such as 10MHz.

III. Fine Phase Shift to Complete Fast Frequency Measurement in a Wide Band

The above wide-band frequency measurement method is based on the rapid and accurate detection of the phase coincidence between any two frequency signals. However, the frequency relation of the two compared signals has a big influence on measurement precision and response time.

For example, if the generation of phase coincidence only relies on the least common multiple period between two frequency signals, the phase coincidence point may not be able to form in the condition of complex frequency relationship between two compared signal or two signals comparing at the same frequency with a small initial phase difference, which will affect the measuring response time and accuracy of measurement.

Therefore, fine phase shift is used in this paper on one compared frequency signal, such as the reference frequency signal, to actively create phase coincidence points between the reference and measured frequency signals.

The fine phase shift on reference frequency signal is realized by a combination of wide range phase shift on chip and high resolution phase shift off chip.

A. *Wide Range Phase Shift on Chip*

Wide range phase shift on chip is realized by a high frequency clock driving a shift register. The signal to be delayed is input into the shift register, the number of shift register level is determined by the required time delay. For example, a 2.5 ns accurate phase shift can be obtained by 400 MHZ clock driving shift register.

B. *High Resolution Phase Shift off Chip*

In order to further improve the accuracy of phase shift, phase shift off chip is used. Phase shift off chip is realized by RC phase shift circuit, by adjusting the resistance R to realize the precise phase shift value control of each level.

IV. Experiment and Analysis

According to above analysis, the wide-band and fast response frequency measurement module is realized by FPGA chips combined with RC phase shift circuit. The resolution of phase shift on chip is 2.5 ns, the number of shift register is 50. The resolution of phase shift off chip is 60ps, using 42 levels RC phase shift circuits.

Based on the above phase shift resolution settings, 10 MHZ continuous frequency measurements results are shown as Fig. 2, in the condition of a high stability of 10 MHZ signal used as reference signal, measurement gate is 0.01 s.

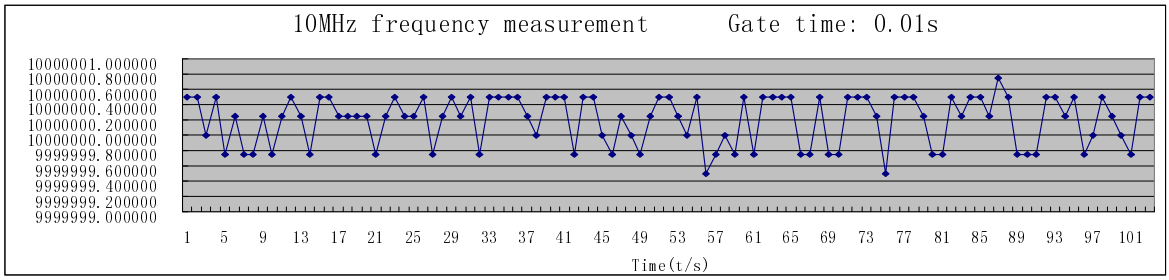

Figure 2: 10 MHZ frequency measurements results

V. CONCLUSION

Based on the phase group characteristic, this paper introduced a wide-band frequency measurement method. This method can eliminate the influence of counting error in theory and improve the measuring precision greatly. And fine phase shift on reference is used to shorten the measurement response time. Experiment results show, the method achieves a precision higher than 1×10^{-13}/s in frequency comparison, the typical precision of signal from 30 kHz to100MHz achieve $6\sim8\times10^{-12}$/s. With the improvement of phase coincidence detection resolution, phase shift precision and component response speed, the precision of this method can be further improved.

REFERENCES

[1] Th. Udem, J. Reichert, R. Holzwarth, and T. W. Hänsch, "Absolute Optical Frequency Measurement of the Cesium D1 Line with a Mode-Locked Laser," Phys. Rev. Lett.Vol.82, pp.3568-3574, May 1999.

[2] Jozef Kalisz, Ryszard Szplet, Ryszard Pelka, Andrzej Poniecki, "Single-chip interpolating time counter with 200-ps resolution and 43-s range," IEEE Transactions on Instrumentation and Measurement, vol. 46, pp. 851–856, Aug. 1997.

[3] Ryszard Szplet, Jozef Kalisz, Rafal Szymanowski, "Interpolating time counter with 100 ps resolution on a single FPGA device," IEEE Transactions on Instrumentation and Measurement, vol. 49, pp. 879–883, Aug. 2000.

[4] Kalisz, Jozef; Szplet, Ryszard; Pasierbinski, Jerzy; Poniecki, Andrzej, "Field-Programmable-Gate-Array-Based Time-to-Digital Converter with 200-ps Resolution," IEEE Transactions on Instrumentation and Measurement, vol. 46. pp.51-55, Feb. 1997.

[5] Bosco, G.C.; Garcocz, M.; Lind, K.; Pogliano, U.; Rietveld, G.; Tarasso, V.; Voljc, B.; Zachovalova´, V.N., "Phase Comparison of High-Current Shunts up to 100 kHz," IEEE Transactions on Instrumentation and Measurement,vol. 60. pp.2359–65, July 2011

[6] Schnatz, H. , Terra, O.; Predehl, K.; Feldmann, T.; Legero, T.; Lipphardt, B.; Sterr, U.; Grosche, G.; Holzwarth, R.; Ha¨nsch, T.W.; Udem, T.; Lu, Z.H.; Wang, L.J.; Ertmer, W.; Friebe, J.; Pape, A.; Rasel, E.-M.; Riedmann, M.; Wu¨bbena, T., "Phase-coherent frequency comparison of optical clocks using a telecommunication fiber link," IEEE Transactions on Ultrasonics, Ferroelectrics and Frequency Control, vol. 57. pp.175–81, Jan. 2010.

[7] Wei Zhou, "Greatest common factor frequency and its application in the accurate measurement of periodic signals," Proceedings of the 1992 IEEE Frequency Control Symposium, pp. 270-273, May 1992.

[8] Wei Zhou, Hui Zhou, Wenjing Fan, Hai Wang, Shixiang Qian, Weining Jiang, "Equivalent phase comparison frequency and its characteristics," Proceedings of the 2008 IEEE Frequency Control Symposium, pp. 468-470, May 2008.

Event Timing Device Providing Subpicosecond Precision

Petr Panek[1]
[1] Institute of Photonics and Electronics
Academy of Sciences of the Czech Republic
Prague, Czech Republic
panek@ufe.cz

Jan Kodet[2,3]
[2]Technische Universität München, Wettzell Observatory,
93444 Bad Koetzting, Germany

Ivan Prochazka[3]
[3]Czech Technical University in Prague
Prague, Czech Republic

***Abstract*—We are reporting on the latest experimental results achieved with an event timing device using a surface acoustic wave filter as a time interpolator. During the tests of the first version of the device, the noise of the filter excitation was identified as the dominant source of the measurement error. Therefore a new concept of the excitation with very low level of the noise energy was designed. This new solution led to considerable improvement of the device performance. It results from the experimental measurements that the single shot precision is repeatedly lower than 500 fs RMS when time marks generated synchronously with the time base are measured. When asynchronous time marks are split into two event timers and the resulting time difference is measured, the single shot precision is below 700 fs RMS per channel. In this case the measurement is affected not only by random errors, but also by non-linearity of the time interpolation. The temperature dependence is below 0.1 ps/K. Operating the device in a common laboratory environment without temperature stabilization, the stability TDEV better than 3 fs has been routinely achieved for range of averaging intervals from 10 s to several hours.**

Keywords—event timing; time interval measurement; time interpolation; surface acoustic wave filter

I. INTRODUCTION

All highly precise time interval and event time measurement devices are based on time interpolation between ticks of a reference time scale. An overview of traditional approaches to the time interpolation problem can be found in papers [1]-[2]. A new time interval measurement method based on a transversal SAW (Surface Acoustic Wave) filter as a time interpolator was introduced in [3]-[4]. This filter after a short excitation generates a time finite signal with highly suppressed spectra outside a narrow frequency band. It results from the sampling theorem that such a signal can be very precisely reconstructed from a finite number of its samples. This property makes the transversal SAW filter an ideal mean for the time interpolation.

The time interval measurement device using a SAW filter for time interpolation can take various forms. The simplest one is shown in Fig. 1. It measures time interval between two pulses at the single input. Each of the pulses excites a SAW bandpass filter whose output is sampled at clock ticks. The samples are then converted by an ADC (Analog to Digital Converter) and buffered. After both responses have died out, they are reconstructed from the samples and compared by means of the cross correlation to eventually estimate the time interval between the two input pulses. All the processing steps can be integrated into a simple algorithm based on fast Fourier transform. To ensure the correct operation of the interpolator, the sampled responses must not be aliased. Therefore the filter parameters must be properly chosen.

Fig. 1: Block scheme of the time measurement device using a SAW filter for time interpolation. The input pulses excite a transversal SAW band-pass filter, its output is sampled at clock ticks, the samples converted by an analog-to-digital converter and buffered. After both responses have died out, they are reconstructed from the samples and compared by means of the cross correlation to eventually estimate the time interval between the two input pulses.

An analysis of the deterministic measurement error, i.e. time interpolation nonlinearity, of this method has been given in [3]. It results from the analysis that the source of this error is an imperfect suppression of the spectra of the response outside the required band. Therefore the quality of the time interpolation depends on the stop-band attenuation of the SAW filter. It was shown that when common SAW filter parameters are considered, the resulting time interpolation error relative to clock period is very small and an accurate measurement can be achieved even with relatively low clock frequency.

A detailed analysis of random measurement errors caused by noise of excitation, noise of amplifier, quantization noise and the sampling and reference clock jitter is a subject of the paper [6]. It implies from this analysis that the noise influence is partially suppressed thanks to averaging effect because the interpolation process is not based on the only one observation but many samples taken at different times. In general, the random errors can be minimized choosing a sufficiently high center frequency of the filter and a sufficiently high clock frequency. On the other side, the filter bandwidth should be kept as small as possible. The bandwidth reduction, however, is

limited due to the increasing probability of false ambiguity solution.

Another effect which can degrade the spectral purity and the interpolation nonlinearity is the harmonic distortion of the filter response in the amplifier and the ADC. This effect was analyzed in paper [7] with a conclusion that the resulting interpolation nonlinearity has a form of a sine wave oscillating very quickly in comparison to the reference clock which was in agreement with experimental observations.

Based on the theoretical background above, a prototype of a two-channel event timing device was designed and constructed. Each channel of the device measures time of events represented by pulses at its input with respect to a common reference time scale. The architecture of one channel is in accordance with Fig. 1. An extremely good stability and reproducibility of the event timing is achieved thanks to shot-by-shot self calibration. Once the response to an input pulse has been processed, an internally generated time mark is applied to the input. This internal time mark is generated synchronously with the time base reference thus the device measures the interval between the external pulse and a selected reference clock tick and the influence of internal delays is eliminated. For the time interpolation a SAW filter with the central frequency of 525 MHz and bandwidth of 18 MHz has been used. The internal time base is based on the 100 MHz clock which serves also as the sampling signal. To make the device more flexible in usage there is an in build frequency divider and hence the input frequency 100 MHz or 200 MHz can be used. We have also succeed in implementing the computation algorithm in to the FPGA. It results in faster operation of the device, which can time-tag input pulses with repetition rate more than 10 kHz.

The experimental results achieved with this prototype were presented in [5], [7] and [8]. The resulting single shot precision was typically 900 fs RMS and the timing stability TDEV of 4 fs was achieved for averaging intervals in the range from 300 s to 2 h with the measurement repetition frequency of ~800 Hz. After adjusting the filter excitation level to the optimum, the interpolation nonlinearity was below 200 fs RMS.

II. New concept of filter excitation

During tests of the first prototype, the noise of the filter excitation was identified as the dominant source of the measurement error. The influence of this noise was estimated to be around 75 % of the overall error budget. Therefore we focused on the research of the filter excitation with the goal to design an optimal excitation concept for the new generation of the timing device.

The new exciter is a nonlinear pulse circuit activated just for a very short period. For the rest of the time its noise is effectively suppressed. The length of the excitation pulse is optimized to achieve the maximum energy spectral density of the excitation at the filter centre frequency and keeping the energy of the noise as low as possible. This solution led to considerable improvement of the device performance. The error budget estimation based on measured noise levels and the theoretical analysis [6] is summarized in Tab. 1. The error budget includes only random errors caused by noise. The influence of the dominant source of the measurement error is now negligible.

TABLE I. Error Budget

Source of error	RMS error contribution	
Noise of excitation	negligible	0 %
Noise of amplifier	235 fs	37 %
Quantization	70 fs	3 %
Clock and sampling jitter	300 fs	60 %
Overall error	390 fs	100 %

III. Experimental Results

With the aim to verify the precision and stability of the improved event timer, we have completed several experiments using test pulses generated synchronously to the local time base. First, the precision of the ToA (Time of Arrival) measurement was tested. The reference clock as well as the test pulses were generated from the MTI 260 10 MHz OCXO with a low-noise frequency multiplier [10]. The measured ToAs of 20 000 test pulses are summarized in the centered histogram in Fig. 2. The error distribution is close to Gaussian with standard deviation of 490 fs RMS. It is worth mentioning that this value does not result only from the timing precision of the tested device, but also from the jitter of the test pulses itself. Therefore this value should be understood as an upper estimation of the ToA measurement precision.

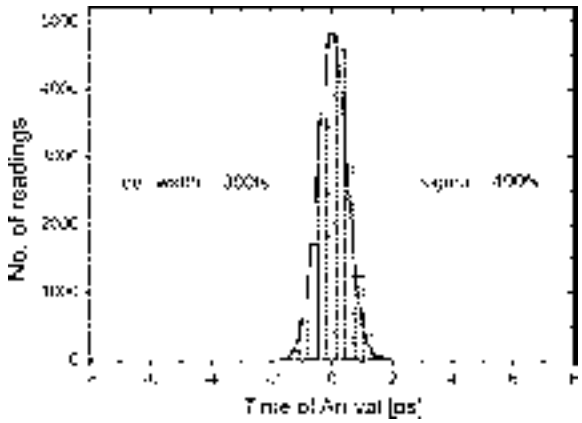

Fig. 2: Centered histogram of measured ToAs of 20 000 test pulses generated synchronously with the time base. The resulting standard deviation 490 fs includes also the time jitter of the test pulses (~300 fs RMS).

The other experiment was focused on the long-term stability of the measured ToAs and their temperature dependence. The measurement started approximately 1 hour after the device was powered on. The averages of recorded ToAs are plotted in Fig. 3. Every black point represents an average from 1000 successive measurements, i.e. all measurements from a 100 ms interval, and the white line is a 100 s moving average. Together with the ToA measurements also the surrounding temperature was recorded thus we could estimate the temperature dependence. The results are plotted in

Fig. 4. During the measurement the temperature decreased approximately by 1 K. Within the temperature range close to the common operation temperature the dependence is linear with a temperature coefficient of −169 fs/K. This value includes also a temperature dependence of interconnecting coaxial cables Huber+Suhner, SUCOFLEX 301. After this influence is corrected, the temperature dependence of the event timer itself is -70 fs/K.

The timing stability TDEV has been computed from measurements with the test pulse repetition frequency of 10 kHz. The timing stability depends not only on the event timer itself, but also on the quality of the reference clock. Therefore it was evaluated from three measurements with different clock reference sources: MTI 260 10 MHz OCXO with a low-noise frequency multiplier, Wenzel 100 MHz Ultra Low Noise OCXO, and Wenzel 100 MHz Sprinter OCXO. The length of each measurement was at least 2 hours. The resulting TDEV plots are in Fig. 5. In all three cases the TDEV dependence falls with $\tau^{-1/2}$ up to $\tau = \sim 10$ s, implying that errors of measurements acquired within an interval shorter than 10 s can be considered uncorrelated. In this region, the best results provides the clock reference generated from the MTI 260 1 OCXO with the frequency multiplier which has the lowest jitter. For averaging intervals $\tau > 10$ s the TDEV fall stops on the flicker floor which also depends on the quality of the reference clock. The best stability in this region has been achieved using the Wenzel100 MHz Ultra Low Noise OCXO. In all three cases the flicker floor was TDEV < 3 fs.

For the rest of the experiments we used 10 kHz test pulses generated from an asynchronous pulse generator. The output of the pulse generator was split to inputs of both event timers and the time difference between measured TOAs was evaluated. In this case the measurement is affected not only by random errors, but also by non-linearity of the time interpolation. The results based on 20 000 measurements are summarized in the histogram in Fig. 6. The error distribution is again very close to Gaussian. The resulting standard deviation of the time difference was 984 fs which corresponds with a ToA single shot precision of 695 fs in each channel.

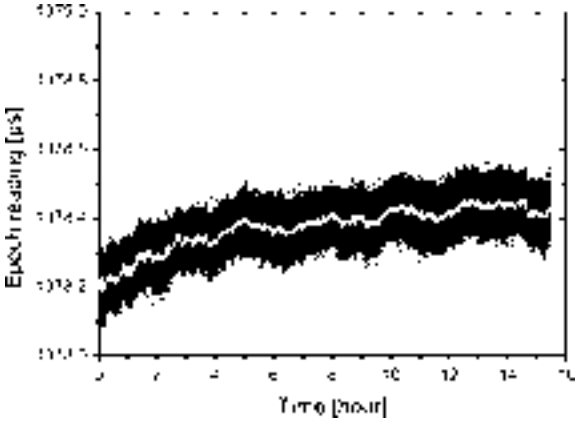

Fig. 3: The averages of recorded ToAs for 10 kHz repetition frequency of test pulses. Every black point represents an average of measurements on an interval of 100 ms, the white line is a 100 s moving average. During the measurement the temperature decreased approximately by 1 K.

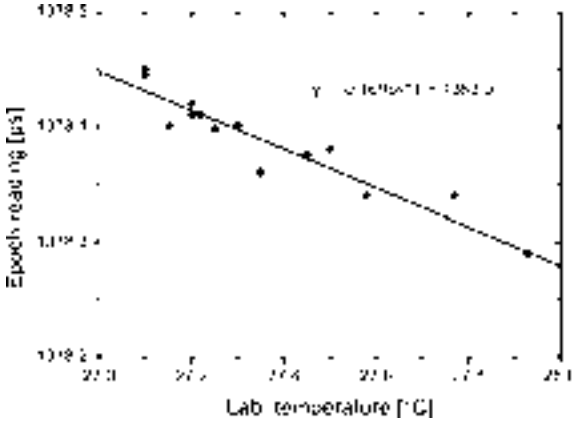

Fig. 4: Temperature dependence of the measured ToAs is −169 fs/K. After the influence of temperature dependence of interconnecting cables is corrected, the temperature coefficient of the event timer itself is -70 fs/K.

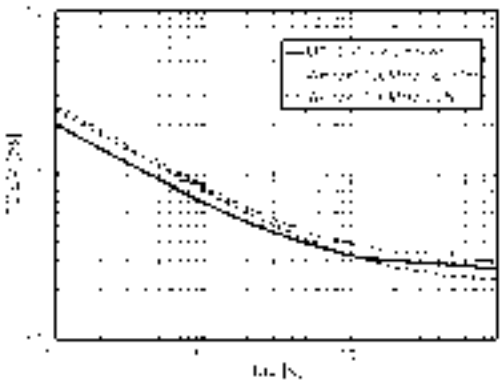

Fig. 5: Timing stability TDEV measured with three different sources of the reference clock, test pulse repetition frequency of 10 kHz, the resulting flicker floor TDEV < 3 fs in all three cases.

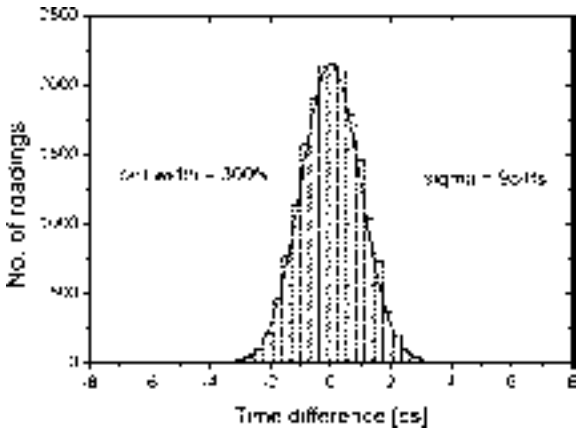

Fig. 6: Centered histogram of 20 000 time differences between ToAs measured by two event timers with the same asynchronous test pulses at the inputs. The resulting standard deviation of the time difference was 984 fs which corresponds to a single shot ToA precision of 695 fs in each event timer. In this case the measurement is affected not only by random errors, but also by non-linearity of the time interpolation.

IV. Conclusion

A new concept of the low-noise filter excitation has been designed for the event timing device using a transversal SAW filter for the time interpolation. This new solution led to considerable improvement of the device performance. It results from the experimental measurements that the single shot precision is now repeatedly lower than 500 fs RMS when time marks generated synchronously with the time base are measured. The behavior of the observed fluctuations can be well described as white noise with Gaussian distribution. When asynchronous time marks are split into two event timers and the resulting time difference is measured, the single shot precision is below 700 fs RMS per channel. In this case the measurement is affected not only by random errors, but also by non-linearity of the time interpolation. The temperature dependence of the measurements is below 0.1 ps/K. Operating the device in a common laboratory environment without temperature stabilization, the stability TDEV better than 3 fs has been routinely achieved for range of averaging intervals from 10 s to several hours.

The event timer is capable of a stand-alone operation or several event timers can create a net of timing units distributed in an area where unified time is kept using optional Two-Way Time Transfer modules [9]. A pair of event timers with a common time base can be used as a classical time interval counter.

Acknowledgment

This work has been carried out at the Czech Technical University in Prague with a support of the research framework RVO 68407700. We are also acknowledging the project DFG FOR1503.

References

[1] D.I. Porat, ”Review of sub-nanosecond time-interval measurements,” IEEE Trans. Nucl. Sci., vol. NS-20, pp.36-51, 1973.

[2] J. Kalisz, “Review of methods for time interval measurements with picosecond resolution,” Metrologia., vol.4, pp. 17-32, 2004.

[3] P. Panek, "Time interval measurement based on SAW filter excitation," IEEE Trans. Instrum. Meas., vol. 57, pp.2582–8, 2008.

[4] P. Panek, "Time interval measurement device", U.S. Patent 7 057 978 B2, Jun 6, 2006.

[5] P. Panek and I. Prochazka, "Time interval measurement device based on surface acoustic wave filter excitation, providing 1 ps precision and stability," Rev. Sci. Instrum., vol.78, pp.094701, 2007

[6] P. Panek, "Random errors in time interval measurement based on SAW filter excitation," IEEE Trans. Instrum. Meas., vol. 57, pp.1244–50, 2008.

[7] I. Prochazka and P. Panek, "Nonlinear effects in the time measurement device based on surface acoustic wave filter excitation," Rev. Sci. Instrum., vol.80, pp.076102, 2009.

[8] P. Panek, I. Prochazka and J. Kodet, "Time measurement device with four femtosecond stability," Metrologia, vol.47, pp.L13–16, 2010.

[9] P. Panek, J. Kodet and I. Prochazka, "Accuracy of two-way time transfer via a single coaxial cable," Metrologia, vol.50, pp.60-65, 2013.

[10] J. Kölbl, P. Sperber and I. Prochazka, "Frequency Source 200 MHz for Time Interval Measurements, Providing Sub-Picosecond Precision and Stability," www.eos-aus.com/img/pdfs/EOSO_Paper-200MHz_Multiplier.pdf

Sub-10 fs Jitter S-Band Oscillators and VCOs in a 1X1X0.23 mm3 Chip Scale Package

S. Gilbert[1], F. Zhang[2], R. Parker[1], M. Small[1], F. Bi[1], L. Callaghan[1], S. Ortiz[1], R. Ruby[1]
[1]Avago Technologies, San Jose, CA
[2]Marvell, San Jose, CA

***Abstract*— We present a fourth- design generation Free Running Oscillator and Voltage Controlled Oscillator using integrated bipolar circuitry in the lid wafer with a temperature-compensated FBAR resonator in the base wafer. The goal is to produce a high frequency, low-noise oscillator. Because there are ~15,000 oscillators per wafer, we can develop very sensitive testing procedures to study the oscillator behavior. For example, we have determined our frequency measurement accuracy and precision to be ~ 0.2 parts-per-million (1 σ), and our phase sensitivity floor to be less than -180 dBc/Hz. Measurements on package hermeticity, suggest that the oscillators behave with the same level of integrity as our standard FBAR filters.**

I. INTRODUCTION

Today, millions of FBAR Filters and Duplexers are sold into cell phones every year. The all-silicon package used to package these filters (providing both package integrity and hermeticity) has been utilized for the past 10 years and, to our knowledge, no part has been returned for compromised integrity or hermeticity failures. The lid wafer in the all-silicon package has, until recently, only been used to provide through-Si vias from the FBAR filter to the outside pads. The addition of circuitry to the lid enables a host of new applications. Examples include the integration of SiGe LNAs with filters to provide extremely compact filter/amplifier functionality, circuitry with integrated sensors. We call this platform; FMOS (for FBAR, Metal, Oxide and Semiconductor). Our first application is the integration of oscillator circuitry with a temperature-compensated FBAR resonator. The resulting chip-scale oscillator produces a single, well-defined frequency, and is highly sensitive (on the parts-per-million level) to package hermeticity. This allows for the design and optimization of a robust package for yield and performance, and for the testing of new markets not dominated by filtering.

The goal of this program is to demonstrate a robust, repeatable, chip-scale oscillator with superior performance.

II. DISCUSSION

FBAR resonators using traditional electrode and AlN piezo materials have a linear temperature coefficient on the order of about -27 ppm/ ^{o}C [1]. An oxide layer with a positive temperature coefficient is placed inside the bottom electrode and as part of the acoustic stack, counter balances the negative coefficient of temperature given from the AlN and metal electrodes[2,3]. These temperature compensated resonators have a zero drift linear component of frequency shift relative to temperature. We call these devices Zero Drift Resonators or ZDR.

It should be noted that although the linear component of frequency shift with respect to temperature is zero, there is both a quadratic and tertiary component. A typical quadratic term, β, as measured in the resonator ranges from -20 to -25 ppb/ ^{o}C ^{2}. In FMOS oscillators, we have obtained a better effective β with a mean of -15 to -18 ppb/ ^{o}C ^{2}, via careful tuning of the oscillator. It is critical that the Turn over Temperature (TOT) lie somewhere near the center of the commercial or industrial range (0 to 70 ^{o}C for commercial and -35 to 85 ^{o}C for industrial). Assuming TOT is in the center, the total frequency excursion for a +/- 60^{o}C swing (assuming -15 ppb/ ^{o}C ^{2}) is +/- 27 ppm. However, if the TOT is off by 40 ^{o}C (as an example), then the total frequency excursion is +/- 75 ppm (60 ^{o}C + 40 ^{o}C = 100 ^{o}C → (-15 ppb/ ^{o}C ^{2} * 10,000 ^{o}C ^{2})/2 = 75 ppm).

The third order term appears to create a ~ 10ppm perturbation on the quadratic effect on temperature and hence is ignored – for now.

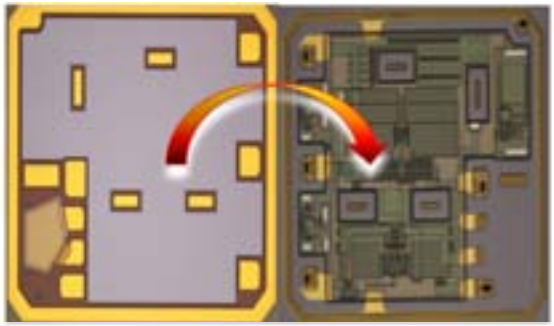

Fig.1; Optical micrograph of the base wafer containing the high Q zero drift resonator and the lid wafer containing the circuitry. The two wafers (lid and base) are bonded together and further processing forms the through vias and pads. Afterwards, the on-wafer oscillators are tested and then singulated into individual die.

Figure 1 shows an optical micrograph of a die from the base wafer (containing the ZDR) and a die from the lid wafer (containing the oscillator circuit). The two wafers are bonded together and then singulated to form the FMOS device.

III. RESULTS

There are several advantages to integrating the oscillator circuit with the resonator. One is the relative insensitivity to acceleration of a discrete oscillator using a ZDR compare to an FMOS oscillator. FMOS oscillators have about 1 ppb/g as compare to a range of 1 to 100 ppb/g for a discrete oscillator. The fact that the oscillating circuit and the resonator are 'locked' relative to each other (integrated) gives a far superior performance relative to a discrete oscillator.

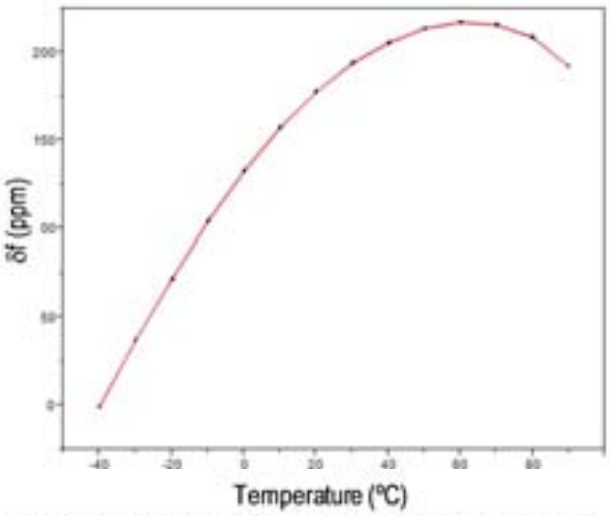

Fig.2; Change in frequency (ppm) vs Temperature. The temperature was swept between -40°C and 90°C six times. The 6 sets of data are overlaid. For this device, the TOT was60°C and the measured β was ~ -20 ppb/°C². No hysteresis is observed.

Next, having an integrated oscillator, we see repeatable δf vs temperature sweeps. Figure 2 shows δf vs. temperature for 6 temperature sweeps from -40 to 90C. Another advantage is the impedance of the circuit – as seen by the resonator – is well determined. This gives a much tighter spread in phase noise and power output power. This becomes more relevant at higher frequencies (above ~ 1 GHz). In general, variation in SMT components, pcb changes and wire bond and over mold can impact frequency repeatability, stability and apparent aging (i.e. changed in frequency over time).

Finally, we have over 15,000 oscillators on a wafer. Using a frequency counter on an ElectroGlas Probe station, one can test three Oscillators/s or 100% probe in little over 1 ½ hours per wafer. Using N-parallel probes, this number can be reduced accordingly by N (N = 1, 2, 3…). Even if only a small percent of the working oscillators are tested, one can begin to create large data bases to observe and measure trends and subtle interactions. The first test is to measure a large sample of oscillators across a wafer and, without moving the wafer, re-test. One can then plot the change in frequency of each measured resonator and plot this as a distribution. One can also un-load and re-load a wafer and measure the same oscillators again and get a sense of the measurement precision due to loading and un-loading. Figure 3 show the change in frequency for a control wafer measured six times (unloading and re-loading) spaced over 7 weeks. For a stationary wafer, the repeatability is about 200 ppb, 1σ. This precision degrades to about 1 to 2 ppm, 1σ, for load and un-load. In Fig. 3, the blue line is the first time measurement, T1, minus itself (hence 0 change). It is tempting to believe from this figure that had we used the second measurement taken at T2 (data taken a week later, red line) then the data taken at T3-T2, T4-T2, T5-T2 and T6-T2 would have been nominally a set of vertical lines. This is not the case, as each oscillator shift is random from one measurement to the next. In other words, had we used T2 or T3 etc…, as the reference frequency; this figure would still look the same! Note: we have also looked at 6 wafers measured in the same fashion and the plotted date looks similar to Fig.3. The mean is zero ppm in all these cases.

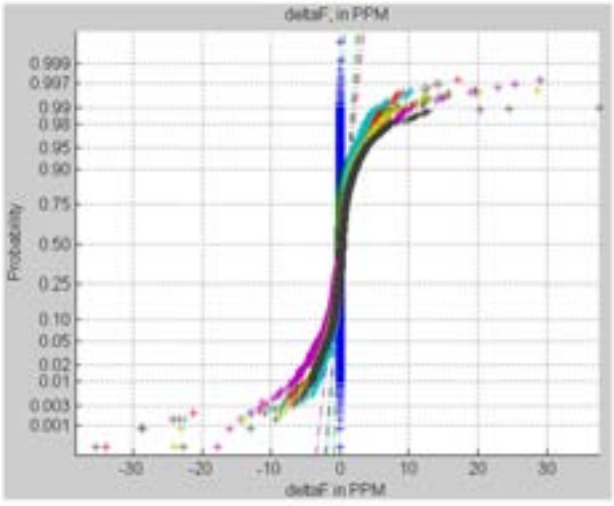

Fig. 3; Probability plots of the change in frequency for ~3000 oscillators as measured across a control wafer. The first measurement (blue) taken at time T1 is subtracted against itself (hence 0 shift). The next measurement (red) was taken at T2 (about 1 week later) and plots the change in frequency relative to the same oscillator at T1 (i.e. f2-f1). Each color represents a delta frequency measurement at T2-T1, T3-T1, T5-T1, T6-T1.

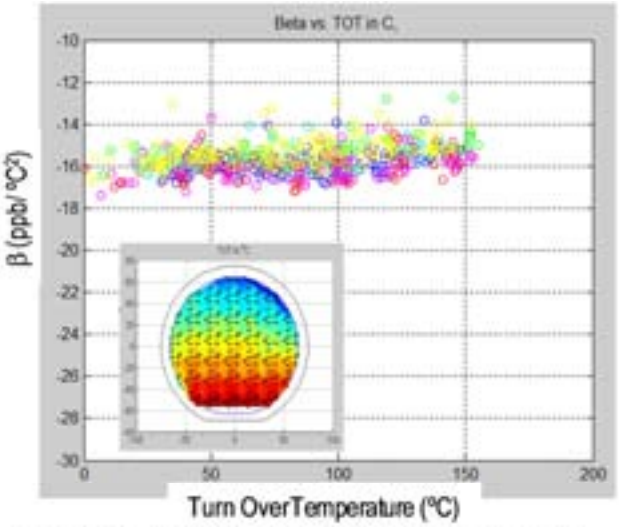

Fig.4; Parametric Plot of Turn over Temperature, TOT, (x-axes) and β (y-axes). Inset shows the TOT variation across a wafer. Here, a 'wedge' was ion milled into one of the layers to create a spread in TOT. The bottom of the wafer is ~150 °C and the top is 0 °C

We can use the ability to collect large amounts of data to study the effect of 'design' on the physical parameters of the oscillator. One key parameter of a ZDR is the quadratic coefficient of temperature, β, of our device. This property is extracted from thousands of measured oscillator frequencies over a range of temperature (from -40C to 120C). Figure 4 shows a plot of the Turn over Temperature (TOT) and β as measured over hundreds of oscillators across the wafer. It should be noted that we ion milled a 'wedge' in the thickness of the oxide, hence the TOT has a range of values across the wafer. However, it can be seen that β is steady at about -15 to -17 ppb/^{o}C ^{2} over a range of thicknesses. The data shown also includes a variety of circuit oscillator topologies. As can be seen circuit topology does not play a role in β.

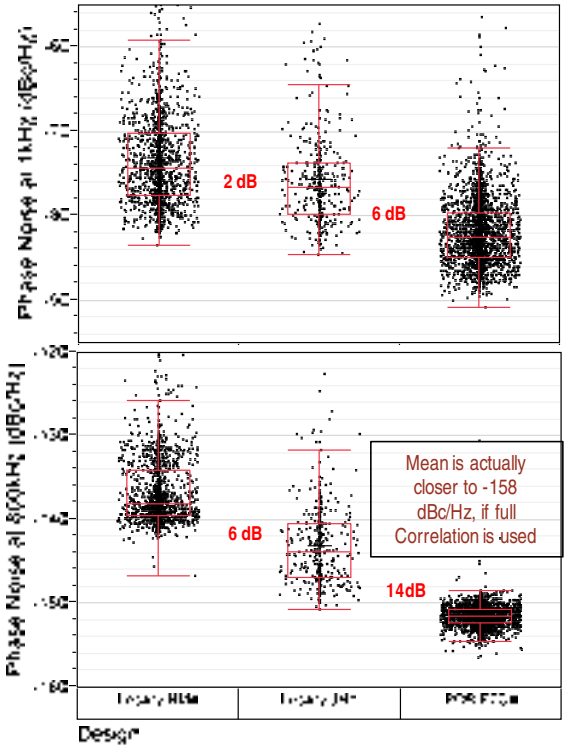

Fig.5; Phase noise measurements on ~3000 oscillators at 1 KHz offset (5a) and 800 KHz offset (5b). Plotted are the spreads in phase noise for a legacy device, the same circuit adopted to our new layout and a the final circuit topology. The delta are given in red (not shown is the improvement using correlation).

Figure 5 shows the relative improvements in phase noise (close-in at 1 KHz offset and far-from-carrier at 800 KHz) for the first design (a legacy design), a 2nd design where we optimized the layout of this legacy design and a 3rd design (labeled F7CX) using a different circuit topology. In Fig. 5, it should be noted that we originally did little or no correlation with the Agilent Signal Source Analyzer 5052B. For the newest designs, we realized that the measured phase noise floor (-156 dBc/Hz) was, in fact, the floor of the 5052B. When we turned on correlation and did long correlation times, the mean went from -153 dBc/Hz to -158 dBc/Hz, an improvement of 5 dB. The mean integrated jitter of the PORF7C devices (as measured on thousands of oscillators) is 7.5 fs (measured with correlation). The integration range for this number is 12 KHz to 20MHz. This new mean jitter performance is a factor of 4X better than published previously[4].

Figure 6 shows the phase noise plots for a device measured at -40 ^{o}C, 30 ^{o}C and 105 ^{o}C. As can be seen the phase noise is nearly constant over a wide range in temperature. We have also studied the effect of Q on the phase noise on phase noise plots. One first needs to reference Leeson's model given in (1)[5]. The model can be 'fleshed' out by observing that the onset of 'flicker noise', f_c, from the oscillating circuit is between 10 and 20 KHz, the far-from-carrier noise floor is -160 dBc/Hz.

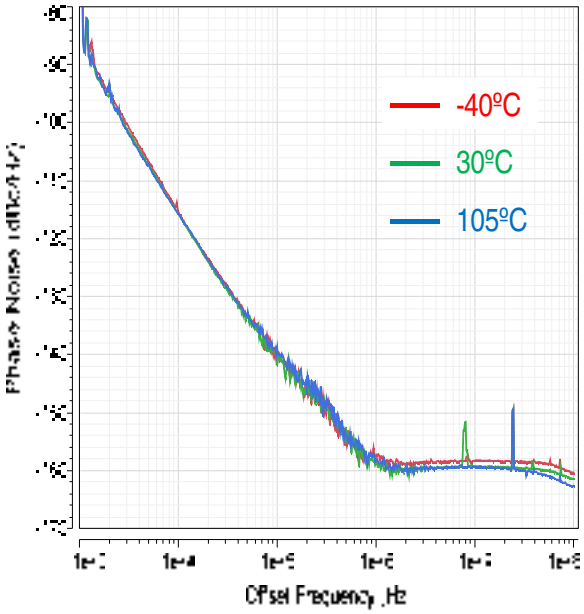

Fig.6; Phase noise of a Free Running Oscillator (F7CX) measured at 3 different temperatures. The output frequency is 2608.0 MHz and the Vcc = 3.3 V and Icc = 18 mA.

From Leeson's equation, we see that if we double the Q, we can reduce the close-in phase noise by 6 dB. In fact, a small adjustment was made in our design to optimize Q by 15%. This resulted in the measured mean of Q at 1 KHz offset improving by 1.2 dB.

$$L(f_m) = 10Log[((\frac{f_o}{2Q * f_m})^2 + 1) * (\frac{f_c}{f_m} + 1) * (\frac{2FkT}{P})] \quad (1)$$

More interesting is the effect of power injected into the resonator. In a separate set of experiments, a discrete oscillator was built using a stand-alone resonator, we were able to reduce the far from carrier average noise to -170 dBc or better. This was done by injecting more current into the resonator (~2X) and better 'tweaking' of the circuit topology. Figure 7 is the phase noise of this device. The fact that these small resonators can handle power is a testament to AlN piezoelectric resonators!

Although the phase noise at 1 KHz offset is better in the device shown in Fig 7 (vs Fig. 6), as we continue to optimize

the Q we do see that our median phase noise at 1 KHz offset on more recent runs is also about -90 dB.

A key factor to any new technology is its ability to handle extreme environmental changes. Companies have incorporated a variety of stress tests to any product to ensure that it is reliable and will work under all conditions over several years. For microcap products [6,7], our concern is that the die will lose hermeticity over time. Compromised integrity in the lid will cause failures. Running 15,000 oscillators through a variety of environmental chambers, ESD testers and thermal shock testers gives good indications (i.e. significant data) of how well the bond is and what impact a design in process, circuit or package has on the final robustness. Based on our strife data, we believe that we can deliver fully qualified parts to our customers.

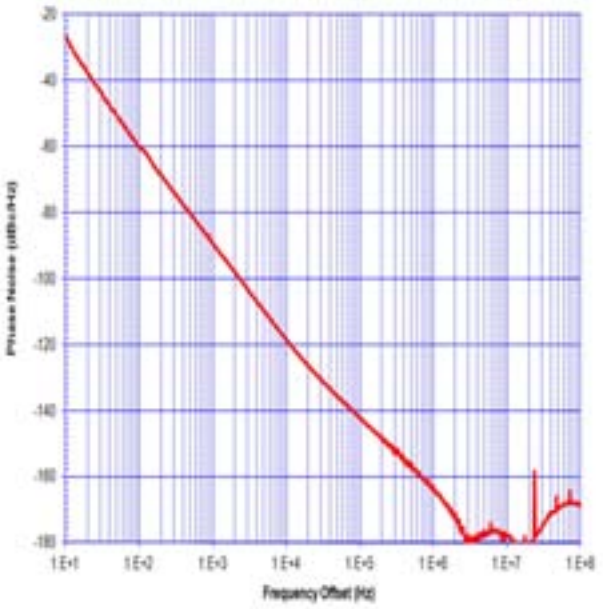

Fig.7: Phase noise of a VCO using a ZDR resonator and discrete components to make up a oscillator. The output frequency is 2500 MHz and the Vcc is 5V and Icc is ~20 mA. The Q's of the resonator in this device is comparable to the Q of the resonator shown in Fig. 6. The 5 dB difference between the two phase noise measurements at 1 KHz offset shows that other factors beside Q play a role in the close in phase noise.

IV. Conclusion

We have measured tens of thousands of oscillators and observe a mean jitter performance between 12kHz and 20MHz of 7.5 femto seconds. Output power is 2.4 dBm and the output drives 100 Ω differential. The mean phase noise of the 2608 MHz oscillator at 800 kHz offset is -158 dBc/Hz and the mean at 10 kHz offset is -118 dBc/Hz. The device draws 18.8 mA at 3.3V, and the phase noise at all frequency offsets stays within 1 dB over the temperature range from -40 to 120°C. We see a 1 to 1 correlation between resonator Q improvement and close-in phase noise: a 15% improvement in Q between two wafer lots improves close-in phase noise by 1.2 dB. Far from carrier noise is set by the power delivered to the resonator. Due to the ability of the resonator to remain linear at high powers, we have seen far-from-carrier phase noise as low as -180 dBc/Hz. The sensitivity to acceleration of these oscillators is on the order of 1 ppB/g and the start up time is measured to be less than 10 μsec.

It should be noted that the title of the paper includes VCOs as well as free running oscillators. For these devices, the only difference between the two is that for the former, we connect one pin to an external varactor and matching circuit. We have measured a tuning range of ~1400 ppm with ~2.5V tune voltage. The jitter degrades to about 20 → 25 fs (over temperature and Vtune). However, we believe we can recover the sub 10 fs jitter performance with modest redesign of the circuit. Process variation, temperature variation and Vcc pulling (and load pulling) takes up about 1000 to 1200 ppm of the tuning range, leaving enough tuning range to give the customer a guaranteed +/- 50 ppm.

Acknowledgment

The Authors would like to thank Prof. Otis for his insights and enthusiasm. We would also thank our managers and the folks in the Fort Collins IC fab for their support. And, we would like to thank the discrete oscillator team for Fig. 7

References

[1] J. Larson, et al., "Power Handling and Temperature Coefficient Studies in FBAR Duplexers for the 1900 MHz PCS Band", Ultrasonics Symposia, 2000, pp 869-874

[2] Q. Zou et al., "High Coupling Coefficient Temperature Compensated FBAR resonator for Oscillator Application with Wide Pulling Range", International Freq. Control Symp., 2010, pp 646-651

[3] Q. Zou, F. Bi, T. Lamers, R.Ruby, "Resonator device including electrodes with buried temperature compensating layer", Patent #8,436,516, Issued May 2013

[4] F. Zhang et al., "A 2.6 GHz, 25 fs jitter, Differential Chip Scale Oscillator that is <1 mm2 in area and 0.25mm Tall", International Freq. Control Symp., 2011, pp 978-982

[5] Leeson, D. B.,"A Simple Model of Feedback Oscillator Noise Spectrum", *Proceedings of the IEEE* **54** (2): February 1966, 329–330

[6] K. Wang, et al., "FBAR Rx Filters for Hand set Front End Modules with wafer level packaging", Ultrasonics Symp. 2003, pp 162-165

[7] R. Ruby, L. Kekoa, "Wafer Level Packaging of FBAR Filters", 3rd International Symposium on Acoustic Wave Devices for Future Mobile Communication Systems, March 2007, pp. 101-103

The Measurement of Transient Stability with High Resolution

Lina Bai
Department of Measurement and Instrumentation
Xidian University
Xi'an, Shaanxi, China
bailina168@163.com

Wei Zhou
Department of Measurement and Instrumentation
Xidian University
Xi'an, Shaanxi, China
wzhou@xidian.edu.cn

***Abstract*—Transient stability measurement of frequency source plays an important part in the real-time short-term stability and the characterization of distal phase noise, so its accurate measurement is of great significance. Measurement of transient noise and short-term stability of signals with the conventional digital counting methods is very difficult and the measurement accuracy is low. So we introduce a unique phase coincidence detection technology which is an important detection method and our group has worked on it for decade to measure the frequency source transient stability. When the phase difference of two signals is less than a certain value, phase coincidence detection circuit will output a narrow pulse which represents the phase coincidence, we call it the phase coincidence detection resolution threshold. When the phase difference of two signals is adjusted to the verge of coincidence detection resolution, we can judge the transient frequency stability of signals accurately from the continuity and discontinuity of the coincidence information. According to the results of multiple phase coincidence detection circuits which combine as a coincidence detection array, the phase variation in detail can be obtained. The measurement resolution depends on the stability of the coincidence detection circuit. This paper describes the principle, the experiment process and the results of transient stability measurement methods.**

Keywords—stability; Threshold; Phase coincidence detection

I. Introduction

Frequency stability measurement refers to the measurement of random fluctuation characteristics of output frequency from frequency source. The characterization of frequency stability in the time domain and frequency domain can be converted from each other. [1][2][3] The conventional time domain frequency stability measurements use the conventional counting measurement method, which the measure gate usually ranges from 1ms to 10s. [4]Measurement resolution is significantly lower in shorter gate, for example, only 10 numbers can be counted in measuring the 10 MHz frequency in the 1 μ s gate time, high precision is hard to achieve. However, the possibly short measurement gate is important to reflect the distal phase noise condition of frequency source using time domain method intuitively. So this paper proposes a new method for transient stability measurement of frequency source through the phase coincidence detection technology which has been proved as a high resolution periodic signal measurement technology[4][5][6].

II. The measurement of frequency source transient stability

A. The measurement method

With common digital method of counting measurements in measuring the signal transient noise and short-term stability, it is difficult to produce very short gate and achieve high measurement accuracy. Phase coincidence detection technology is the frequency and phase difference measurement technology that we have been developing over the years[5][6], and plays a key role in the high-resolution frequency measurement. It can detect the same information about their phases between two detected signals with identical or different nominal frequencies, such as two signals at the instant of the zero phase give particular phase coincidence information at the same time[7].It is always difficult to reach "absolute" coincidence in the implementation of phase coincidence. Thus we introduce the threshold of phase coincidence detection sensitivity, which is the value such that we recognize phase coincidence when the signal phase difference is less than it.

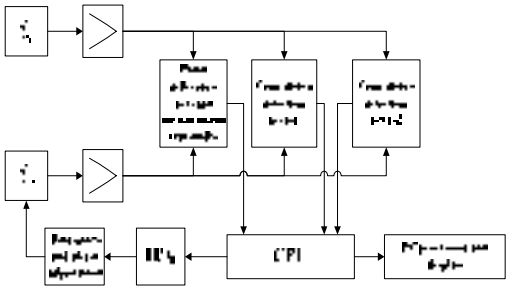

Fig. 1. Transient stability measurement block diagram.

Fig. 1 is a schematic diagram of transient stability measurement between the same nominal frequency sources, which is to regulate the phase difference between the two signals on the coincidence detection resolution threshold, to calculate the transient stability as well as time and frequency domain phase noise index from the discontinuity of the

coincidence information. The two signal frequency values can be equal or multiple. Then one can accurately measure many frequencies with a nominal value frequency.

B. Phase difference adjustment

Specific transient stability measurement block diagram shown in Fig. 1. At first, we should measure the phase difference between reference signal and measured signal. Then adjust the reference signal so that the phase difference between the reference signal and measured signal will be adjusted to the edge value of coincidence detection resolution.

In the measurement process, we can also adjust phase difference between signals to a value greater than the phase coincidence detection circuit threshold, in order to detect the degree of phase fluctuation caused by noise.

C. Coincidence detection circuit

About coincidence detection circuit, we adopt the method of D flip-flop. When the reference signal and the measured signal has a certain frequency difference and no noise influence, assume that $f_x > f_0$,($f_x < f_0$ follows the same result), we get the phase coincidence detection circuit as shown in Fig. 2.

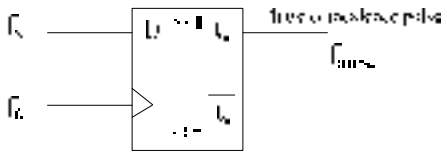

Fig. 2. .Phase coincidence detection circuit diagram.

Use the rising edge of f_0 as the clock signal, collect the f_x state as the output signal, then we get the phase coincidence detection waveform diagram as shown in Fig. 3.

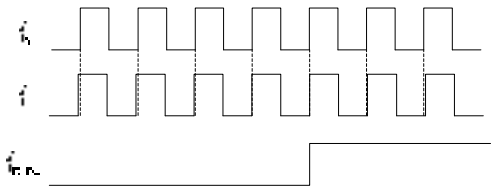

Fig. 3. Waveform diagram of phase coincidence detection.

When the nominal frequency of f_x and f_0 is the same, adjust the phase difference between the two signals to the edge of the coincidence detection sensitivity. If there is no influence of noise, it will maintain a continuous output level. But if there is noise, the phase variation will be between the inside and outside of the verge, thus the level of phase coincidence will alternate between high level and low level. The detection signal waveform diagram of one coincidence detection circuit as shown in Fig. 4, when f_x has noise.

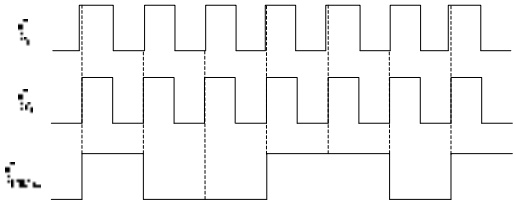

Fig. 4. Coincidence detection of "1", "0" of the signals with fixed phase difference (threshold).

In order to get more detailed quantified information, we can adopt detection circuits working in parallel with different phase coincidence detection resolution stability.

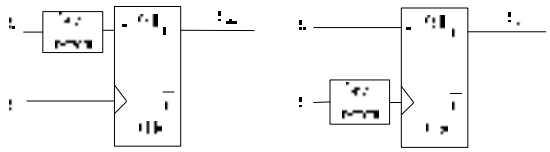

Fig. 5. Phase coincidence detection circuit of one input plus delay.

In order to quantify the change of the phase difference of the acquired signal and avoid the difficulty of getting detection circuits of different stability levels, we adopt a large number of identical phase coincidence detection devices. That is to say, 2 coincidence detection symbols in Fig. 1 represent 2 phase coincidence detection arrays. Each phase coincidence detection circuit in the array has the same degree of coincidence detection resolution stability, such as close to 1ps; but different thresholds, which means to add phase delay to one of the input signals, as shown in Fig. 5, so that each phase coincidence detector's partial coincidence information deviates from "strict phase coincidence" position, and appears a step-by-step pattern. The coincidence detection array outputs "1" and "0" selectively based on the amplitude of the noise of measured signals. It is worthwhile to mention that "1" and "0" has different quantity for the different detection circuits. So we can detect the amplitude of the noise which is closer to the actual situations as shown in Fig. 5.

Due to the use of the phase coincidence detection arrays, what we need to do is to overlap areas of noise performance from arrays. Therefore, the previous requirement of phase measurement and adjustment is greatly reduced.

D. Calculation of frequency source transient stability

Shown in Fig. 5 is the restored phase difference change curve over a short period of time. We can get the corresponding change of phase difference by using the selected sampling interval τ to intercept the curve. The average frequency value of the time τ can be obtained, the corresponding frequency stability indicators can be acquired. We generally adopt the square root of the Allan variance as a

unified representation of the time domain frequency stability. The common formula of Allen variance [9]is

$$\sigma_y(\tau) = \frac{1}{f_0}\sqrt{\sum_{i=1}^{m}\frac{(\Delta f_{i+1} - \Delta f_i)^2}{2m}} \quad (1)$$

Considering the frequency and phase relationship: $\frac{\Delta f}{f_0} = \frac{\Delta T}{\tau}$.

Formula (2) can be deduced from Formula (1).

$$\sigma_y(\tau) = \frac{1}{\tau}\sqrt{\sum_{i=1}^{m}\frac{(\Delta T_{i+1} - \Delta T_i)^2}{2m}} \quad (2)$$

Where ΔT represents the phase difference, and τ represents the duration of the corresponding period time. This formula was originally calculated for the same nominal frequency signal stability by the measurement results of phase comparison method. The deduction and change provide important foundation for the frequency stability which processed from the coincidence detection information. If we consider the response time corresponding to the period of the lower frequency signal, the coincidence detection cycle is precisely the period τ of the lower frequency signal. The change of ΔT obtained through the continuous detection of coincidence state. The ΔT_i inside is the phase difference change between the signal before and after τ.

III. Experiment and results

The schematic diagram of phase difference adjusts to the phase coincidence detection threshold is shown in Fig. 6.

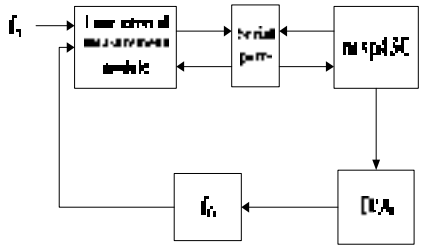

Fig. 6. Block diagram of phase difference adjustment.

Experiment process is as follows. Use time interval measurement module to measure the phase difference between standard signal and the measured signal, then msp430 microcontroller read the value of the measured phase difference through the serial port. After that, calculate the voltage value of voltage controlled oscillator, then get the analog voltage value through the D/A conversion and adjust standard oscillator phase. After taking repeated measurements and adjustments, the phase difference between the standard signal and the measured signal will be adjusted to be close to the phase coincidence detection circuit threshold.

For phase coincidence detection circuit, using a D flip-flop array plus delay to detect the phase coincidence.

When the reference signal and the measured signal have a certain frequency difference, a single coincidence detection circuit can get the phase coincidence detection signal similar to that shown in Fig. 7 Here we use a coincidence detection circuit with better performance.

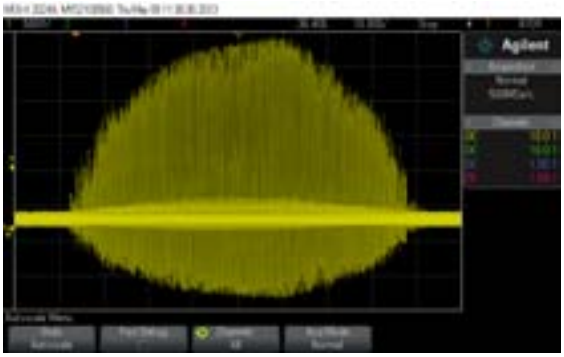

Fig. 7. Phase coincidence detection waveform of two signals with a certain frequency difference.

Experiment 1: Transient stability measurement between two 10 MHz high stability crystal oscillators. 7 sets of data are measured separately, the calculated results of the frequency stability of 100ns Allan variance are: 5.35×10^{-5}、5.45×10^{-5}、5.31×10^{-5}、5.14×10^{-5}、5.10×10^{-5}、5.11×10^{-5}、5.15×10^{-5}. Fig. 8 is the phase noise measurement result between two identical signals.

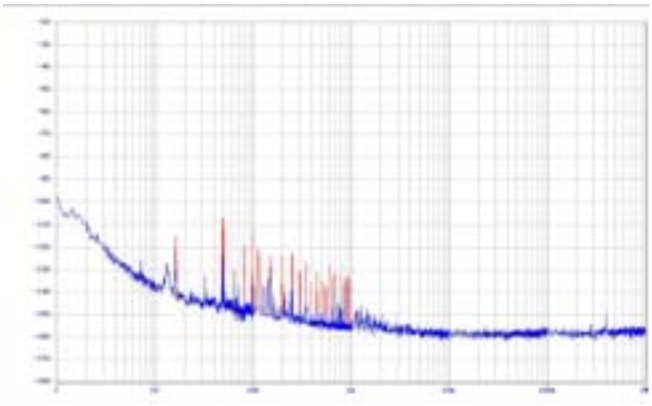

Fig. 8. The phase noise between two 10 MHz high stability crystal oscillators.

Experiment 2: Transient stability measurement between a 10 MHz high stability crystal oscillator and a 10 MHz signal output by synthesizer HP8662. 7 sets of data are measured, the frequency stability of 100ns Allan variance calculation

results are: 3.28×10^{-4}、3.44×10^{-4}、3.19×10^{-4}、3.38×10^{-4}、2.79×10^{-4}、2.69×10^{-4}、2.57×10^{-4}.

Fig. 9 is the phase noise measurement result between the two signals.

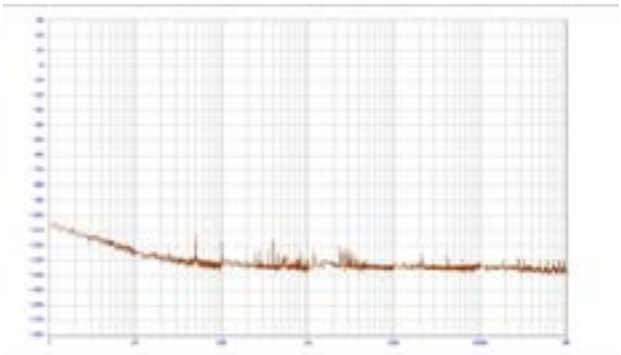

Fig. 9. The phase noise between a 10 MHz high stability crystal oscillator and a 10 MHz signal output by synthesizer HP8662.

Experiment 3: Transient stability measurement between two 18.6 MHz phase-locked crystal oscillators. 7 sets of data are measured, the calculated results of the frequency stability of 53.8ns Allan variance are: 7.95×10^{-4}、7.83×10^{-4}、8.03×10^{-4}、8.29×10^{-4}、8.79×10^{-4}、8.95×10^{-4}、1.83×10^{-3}. Fig. 10 is the phase noise measurement result between two signals.

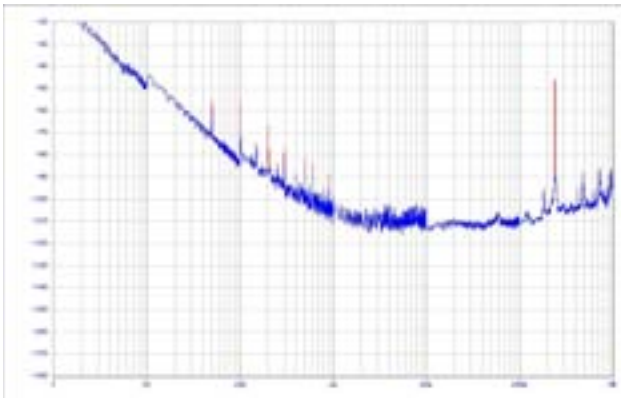

Fig. 10. The phase noise between two 18.6 MHz phase-locked crystal oscillators.

IV. CONCLUSION

Phase coincidence measurement is used mainly for high resolution frequency or phase difference measurement between signals in the past[10]. It is mainly used to capture strict phase coincidence information between the signals, we can achieve high resolution measurement between the signals under the condition that the measurement gate and signals are strict synchronous. When the signals are in the specific and stable state, the transient stability can be measured through the phase coincidence detection that reflects noise. This method makes use of periodicity of signal itself to make repeated coincidence detections, and makes use of the coincidence detection array to quantify the ups and downs of measured signal phase noise, therefore we can obtain fast response time and high resolution.

ACKNOWLEDGMENT

The word was jointly supported by the National Natural Science Foundation of China (Grant Nos. 10978017and 61201288), the Open Fund of Key Laboratory of Precision Navigation and Technology ,National Time Service Center, Chinese Academy of Sciences (Grant No. 2012PNTT05)

REFERENCES

[1] L. L. Ye, M. H. Shi, X. Q. Shen, and Y. Lou, China Science and Technology Information 12, 150(2011).

[2] X. C. Gan, and L. F. Liu, Information Technology 6, 121(2008).

[3] D. W. Allan, and Herman Dams, 29th Annual Symposium on Frequency Control Symposium, (IEEE,1975), p.404.

[4] W.Zhou, 2000 Systematic Research on High Accuracy Frequency Measurements and Control (Ph.D. Dissertation) (Tokyo: Shizuoka University).

[5] K. Elissa, "Title of paper if known," unpublished.M. Miao, W. Zhou, and B. Wang, Rev. Sci. Instrum. 83(2), 024706(2012)

[6] Z. Q. Li, W. Zhou, F. X. Chen, and C. G. Liu, Chin. Phys B 19(9), 287(2010).

[7] G. Z. Huang, Z. Q. Li, and G. W. Yin, Instrument Technology 9, 14(2010).

[8] W. Zhou, X. J. Ou, H. Zhou, B. Wang, and X. Yang, Proceedings of 2006 IEEE International Frequency Control Symposium, Miami FL, (IEEE,2006), p.260

[9] W. Zhou, X. J. Ou, H. Zhou, H. Wang, and B. Y. Qu, Time-Frequency Measurement and Control Technology (1st edn.) Xi'an:Xidian University (2006).

[10] W. Zhou, Journal of Astronautic Metrology and Measurement 12(3), 61(1993).

Phase Noises of GaN-Based Surface Acoustic Wave Oscillator

Rimantas Miškinis, Emilis Urba, Dmitrij Smirnov
Metrology Department
Center for Physical Sciences and Technology
Vilnius, Lithuania
miskinis@pfi.lt

Albertas Sereika, Romualdas Rimeika
and Daumantas Čiplys
Radiophysics Department, Faculty of Physics
Vilnius University
Vilnius, Lithuania

***Abstract*— Gallium nitride (GaN) is of interest with respect to electronics as it features both semiconducting and piezoelectric properties. We explore the possibilities for employing a GaN-based surface acoustic wave oscillator as a sensor of ultraviolet radiation, consider its thermal properties and phase noise.**

I. Introduction

Gallium nitride (GaN) as well as related semiconducting substances are of interest for application to devices which employ both semiconducting and piezoelectric properties of the structure. One of them is a surface acoustic wave (SAW) oscillator. Usually, such oscillators use a SAW delay line as a feedback circuit. In this case, the oscillation frequency is determined by the geometry of the structure and the velocity of SAW propagation. The velocity, on the other hand, is generally dependent on factors such as temperature and illumination, which offers a possibility for designing appropriate sensors.

Frequency response of a GaN-based SAW delay-line oscillator to ultraviolet (UV) illumination has been demonstrated [1, 2]. The effect has been found to be selective with respect to the wavelength of the incident light – it nearly vanishes when the wavelength exceeds 400 nm [2].

However, very important features of such oscillators – the phase noise and thermal effects – have not yet been investigated. We describe the dependences of oscillation frequency on intensity of UV illumination and ambient temperature and discuss the phase noise for a GaN-based SAW delay-line oscillator.

II. Experimental

The experimental setup of the oscillator is shown in Fig. 1. We use a layer of GaN grown by low-pressure metalorganic chemical vapor deposition on a (0001) sapphire substrate with a pair of aluminum interdigital transducers deposited on the surface of the GaN layer. Each transducer consists of 100 pairs of electrodes fabricated with the period Λ=24 μm and thus is 2.4 mm long. The distance between the central points of the transducers is 11.1 mm. Thickness of the GaN layer is 2.5 μm. The resonant frequency of the structure is 212.34 MHz. The aperture is 1.38 mm.

The two-port SAW delay line is connected to a feedback loop of a wide-band amplifier. We feed the output signal of the SAW oscillator to a SR 620 frequency counter disciplined to the 10 MHz signal of the Lithuanian national time and frequency standard HP5071A. The readings of the counter are saved every second. For UV illumination, we use a TH36 type LED (SEOUL OPTODEVICE) and a 15 W lamp of the BLB type with the radiation intensity maximum at about 365 nm.

We use a MMT-1 type thermometer resistor (with 2,2 kΩ nominal resistance) calibrated to the Lithuanian national temperature standard for measurements of temperature and a commercially available low-capacity cooler to cool the structure down and to achieve operation in a wider temperature range than naturally occurring variations of the room temperature.

III. Results

Fig. 2 shows the variation of temperature and frequency with time without cooling. As indicated on the picture, the experiment begins with UV illumination present. After some time, it is switched off. Fig. 3 shows the same magnitudes with and without cooling. The experiment begins with cooling on, in darkness (without UV radiation). Then, UV radiation is switched on. Finally, cooling stops, while UV illumination continues. The coefficients of linear dependence of oscillation frequency on temperature are the following:

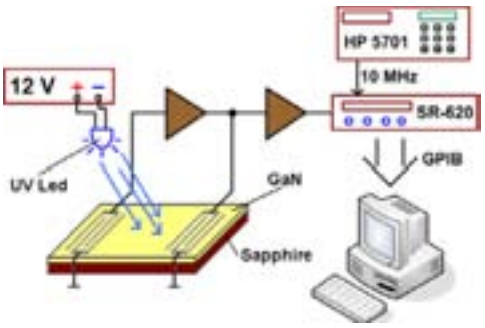

Fig.1. Experimental setup

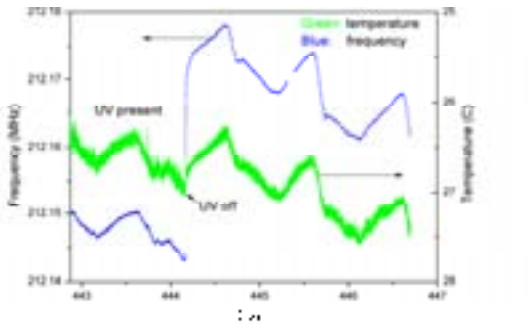

Fig. 2. Variation of temperature and frequency with time without cooling

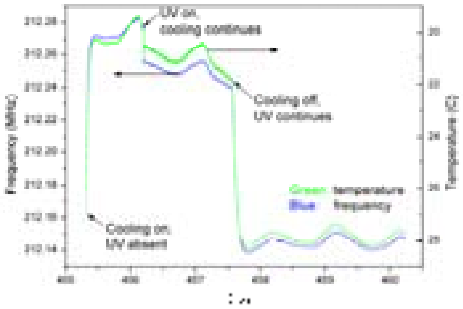

Fig. 3. Variation of temperature and frequency with time with cooling on and off

From the results of Fig. 2:

a) in the darkness: $f = 212.554$ MHz – (14271 t) Hz

b) with UV: $f = 212.475$ MHz – (12291 t) Hz

From the results of Fig. 3:

a) in the darkness: $f = 212.554$ MHz – (14031 t) Hz

b) with UV: $f = 212.585$ MHz – (15914 t) Hz,

where t is the temperature in degrees of Celsius. We can see that the coefficients of the "dark" operation are very similar in both experiments, while the coefficients under illumination differ significantly; the data are insufficient to prove that thermal sensitivity of the frequency depends on UV illumination.

Fig. 4 shows the dependence of the frequency shift on the intensity of UV illumination. It is seen that it is nonlinear, and the frequency shift at the maximum illumination intensity corresponds to that due to the change in temperature of $\sim 2\ ^{o}$C.

The spectral densities of fractional frequency fluctuations, $S_y(f)$, observed at different conditions of oscillator operation, are presented in Fig. 5 – 7. Spectral densities $S_y(f)$ were calculated using "Stable 32" software. It should be expected that different mechanisms of the phase noise can occur in such an

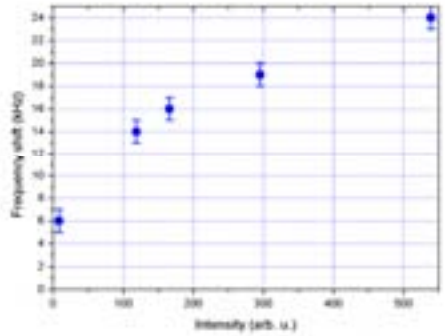

Fig.4. Frequency shift versus intensity of UV illumination

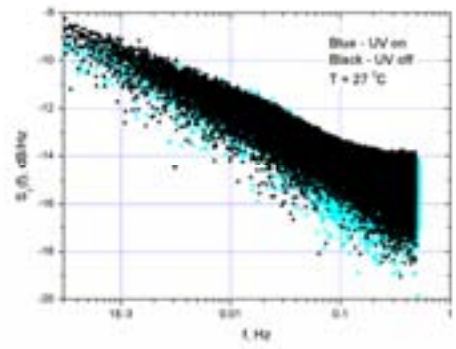

Fig. 5. Spectral densities of fractional frequency fluctuations $S_y(f)$ with the LED UV illumination on and off. Oscillator was kept at the temperature of 27 ^{0}C

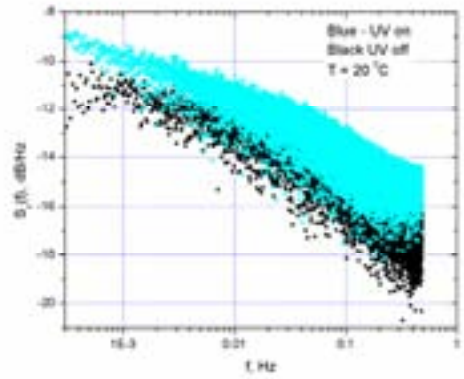

Fig. 6 Spectral densities of fractional frequency fluctuations $S_y(f)$ with the LED UV illumination on and off. Oscillator was kept at the temperature of 20 ^{0}C

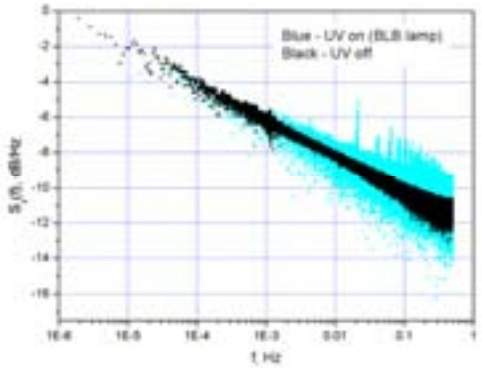

Fig. 7. Spectral densities of fractional frequency fluctuations $S_y(f)$ with the BLB lamp UV illumination on and off. Oscillator was kept at the temperature of 23 ^{0}C

experiment. However, deeper insight into this issue is necessary.

IV. Conclusion

We have demonstrated the effect that UV illumination and temperature have on oscillation frequency of GaN-based SAW delay-line oscillator. The findings imply that the frequency shift varies linearly with temperature. Therefore, using such a system as a sensor for UV illumination requires taking into account the value of temperature.

References

[1] D. Ciplys et al., GaN-based SAW delay-line oscillator, Electron. Lett., vol. 37, no. 8, pp. 545-546, April 2001.

[2] D. Ciplys et al., Visible–blind photoresponse of GaN-based surface acoustic wave oscillator, Appl. Phys. Lett., vol. 80, no. 11, pp. 2020-2022, March 2002.

Balanced SAW Oscillator in Composite Configuration with Colpitts and Cross-Coupled Pair

Yao Huang Kao
Department of Communication Engineering
Chung Hua University
Hsinchu Taiwan ROC
Email: yhkao@chu.edu.tw

I-Jhih Wu
Department of Communication Engineering
Chung Hua University
Hsinchu Taiwan ROC
Email: thliau@chu.edu.tw

Abstract—**The balanced SAW oscillator in the modified Colpitts configuration is studied. To enhance the start up a cross-coupled pair is embedded. Owing to the insulating feature of SAW resonator, the problem of latch may happen. With a careful design in the aspect ratio of CMOS transistors between main amplifier and cross coupled pair, this problem is solved. By the aid of inherent opposite polarity of cross-coupled pair appeared on the terminals of SAW resonator, the star up grows much fast as compared to the well known Colpitts oscillator. The transition period is significantly shrunk. For completeness three kinds of oscillator with single ended, balanced Colpitts, and cross coupled one are compared in terms of figure of merit (FOM) under the same magnitude across the resonator. The power consumption and phase noise are also indicated.**

Keywords- SAW, Balanced Oscillator, Cross Couple, CMOS.

I. INTRODUCTION

Clock oscillators often utilize the high quality factor and high frequency surface acoustic wave resonators (SAW) to obtain the stable frequency. As the author's knowledge, the configuration of the oscillators normally adopt the Pierce or Colpitts oscillators with single ended output. [1] The output needs an extra step to be converted to a differential pair before connected to next stages, such as mixer in receiver, divider in PLL, or phase detector in CDR as shown in Fig. 1. The differential topologies can take advantages of reduced noise, good power supply rejection ratio, and direct matching to the inputs of preceded stages. Recently two types of balanced SAW oscillators with either two parallel Colpitts or cross-coupled pair have been presented. [2-5] As compared, the former has better phase noise but suffers from the long transition due to the lack of phase inversion in initial growing. On the contrary, the latter has the inherent phase inversion, which results in fast transition. In this study a modified Colpitts architecture with embedded cross-coupled pair is presented to take the advantages of quick transition and good phase noise. The phase noise and transition time are especially investigated. In the meantime, a comparison in performances with other balanced type of Colpitts is presented.

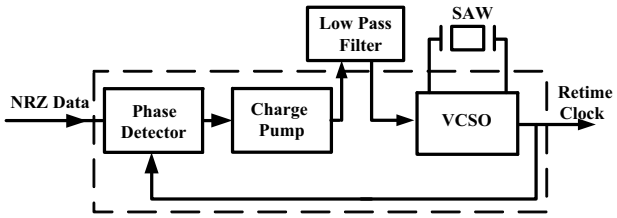

Fig. 1 Application of VCSO in giga-bit CDR

II. OSCILLATOR WITH DIFFERENTIAL OUTPUTS

The schematic of VCSO is briefly shown in Fig. 2. Two stacks in CMOS process are used for low voltage operation. M5 and M6 in combination with capacitance C1-C4 form two parallel Colpitts oscillators, which are coupled through a one-port SAW resonator. The SAW resonator exhibits a series LC resonance Ls, Cs, and Rs in parallel with a capacitance Co regarding to motional vibration and parasitic of interdigital electrodes, respectively, as shown in Fig. 3a. The parameters of equivalent circuit are listed in Table I. Under fully differential situation, the SAW resonator now is able to be re-modeled as two series resonators with center point virtually grounded as shown in Fig. 3b.

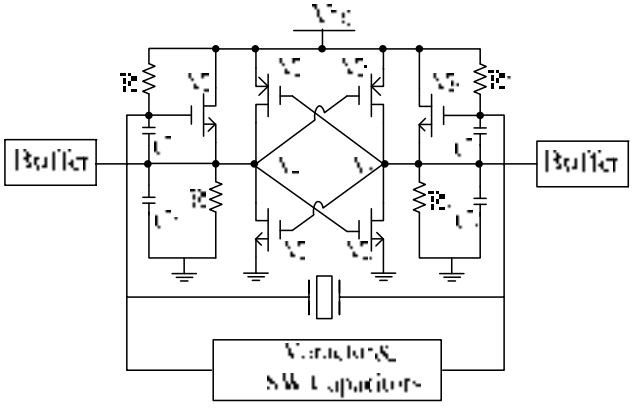

Fig. 2 Schematic of the balanced Colpitts oscillator with embedded cross-coupled CMOS pair.

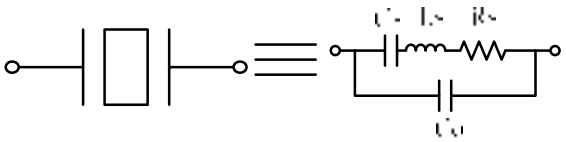

(a)

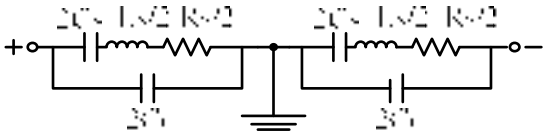

(b)

Fig. 3(a) SAW Model and (b) remodel in differential case

Table I Parameters of 425MHz SAW Resonator

Co	Rs	Ls	Cs
3.8pF	**10.53Ω**	**46.3uH**	**3.03fF**

For clearance, the capability of the balanced Colpitts oscillator is initially described. It is basically consisted of two single-ended Colpitts oscillator sharing the common SAW resonator. M5 and M6 are the main amplifiers, which combine C1/C2 and C3/C4, respectively, to form the negative resistance seen into the gate terminals. As applied to oscillator, the resonator has two operating modes. One is the series mode and the other is the parallel mode. The former has the resonator acted in series short circuit, while the latter acts as parallel circuit. Here, the latter is utilized. The SAW resonator in parallel mode provides the effective inductances to form the differential Colpitts oscillators. The frequency tuning is accomplished by the extra parallel switched capacitors and varactors. Unfortunately, the effective parasitic from the metal electrodes as illustrated in Fig. 3b now becomes 2Co, which will degrade the negative resistance as compared to that in single ended case. It causes more current consumption. The rf output power is also degraded, so as the phase noise.

It is noted that the tuning varactor is also in parallel with the SAW resonator. In some sense the larger the varactor has, the larger the tuning range has. However, this fact also degrades the negative resistance from active devices and causes low output power. Hence, a trade off exists between phase noise and tuning range. The figure of merit given by

$$FOM(dB) = 10\log\left[\left(\frac{\omega_o}{\Delta\omega}\right)^2 \frac{1}{L(\Delta\omega)\times P}\right]$$

is used to evaluate the performance, where P is the power consumption of the core circuit, $\Delta\omega$ is the offset angular frequency from the carrier, ω_o is the center frequency, and L(Δω) is the phase noise. The figures of merit (FOM) in single and balanced cases are typically around 207 and 201, respectively. The balanced one has worse phase noise.

It has been indicated that the turn-on transitions about 150us in oscillators with cross-coupled pair is faster than the previous one. [4] This is due to the nature of the phase inversion in cross coupled pair. The function of phase inversion needed by the parallel Colpitts can be easily accomplished by embedding the cross-coupled pair M1-M4 as shown in Fig. 2. M1–M4 are the cross coupled pair to enhance the negative resistance of Colpitts pair. With the pair embedded, the ac signal is amplified so that its transition is speeded. It is worth noting that, the cross-coupled pair also acts as latching in digital circuit. Therefore, the aspect ratio of the pair CMOS must be carefully traded off between latching and output power level. It is expected that the current consumption is raised, however, the output power is increased significantly. The composite configuration indeed behaves better performance in terms of FOM.

III. Performances

The layout is illustrated in Fig. 4 with die area about 0.545×0.510mm^2. The chip is fabricated by TSMC 0.18um CMOS process. V_A is the analog tuning voltage for varactor and V_B and V_C are the digital control voltage for switch bank. Due to the manufacture variation and temperature, Tuning capability is needed to overcome the frequency offset. Here, two switched capacitances are inserted to fulfill the requirement. The calculated phase noises are illustrated in Fig. 5a. For comparison the result from only cross coupled pair is included in Fig. 5b. It reveals the composite one has phase noise better than 8.9dB. The penalty in current consumption is about 1.6dB. The FOM achieves 211. It is concluded that the composite has better performance in terms of FOM. The details are listed in Table II.

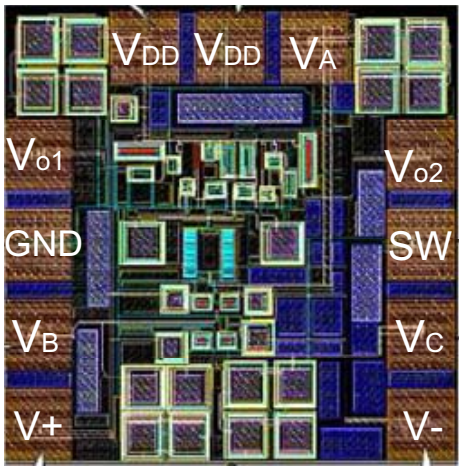

Fig. 4 Layout of the cross coupled SAW oscillator

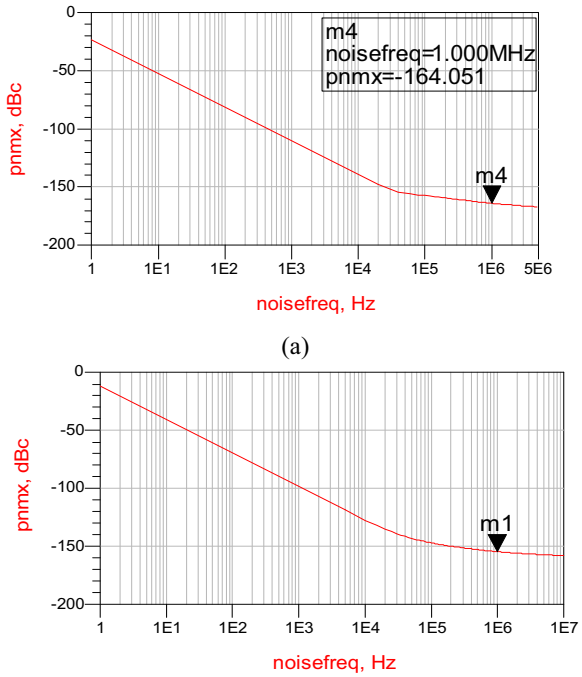

(a)

(b)

Fig. 5 Calculated Phase Noises in (a) composite oscillator with Colpitts and cross coupled pair and (b) only cross-coupled CMOS oscillator.

Table II Performances List of Two Oscillators

$FOM = 10\log\left[\left(\frac{\omega}{\Delta\omega}\right)^2 \times \frac{1}{L(\Delta\omega)\cdot P}\right]$		

IV. Conclusion

In this study a balanced VCSO using the composite configuration of Colpitts and cross coupled pair is presented. First, the comparison in single and differential Colpitts is made to indicate the effect of parasitic capacitance doubling, which causes the more current consumption. Next, the property of inverse polarity between two outputs is easily achieved by embedding the cross coupled pair. This function drives quickly the oscillator into steady state as compared to the balanced Colpitts one. The latched problem is solved by trimming the MOS size. The design is traded off between latch and phase noise. It is demonstrated that the composite configuration has better performance in terms of FOM. Our results can be extended to other high frequency and high Q resonators such as MEMS and FBAR.

Acknowledgment

The authors would like to thank National Chip Implementation Center and National Science Council, Taiwan, R.O.C., for chip implementation and financial support. This work was supported partly by National Science Council under the Contract NSC 99-2221-E-216 -018. The authors would also like to thank the Taiwan semiconductor manufacture company (TSMC) and chip implementation center (CIC) for the wafer fabrications.

References.

[1] Jon-Hong Lin and Yao-Huang Kao, A Low Phase Noise and Wide Tuning Voltage-Controlled SAW Oscillator with Surface Transverse Wave Resonator for SONET Applications, IEEE Trans. on MTT vol. 55, no. 1, pp. 60-65, Jan. 2007.

[2] M. Aissi, E. Tournier, M. A. Dubois, C. Billard, H. Ziad, and R. Plana, A 5 GHz above-IC FBAR low phase noise balanced oscillator, IEEE Radio Frequency Integrated Circuits (RFIC) Symposium, 2006 , 11-13 June 2006 Page(s):4– 28.

[3] D. Ruffieux, A high-stability, ultra-low-power quartz differential oscillator circuit for demanding radio applications, Proceedings of the 28th European Solid-State Circuits Conference, 2002. Pp. 85-88.

[4] Y. H. Kao and I. J. Wu, IEEE NEWCAS, 2011, p. 995-998.

[5] Ming-Da Tsai, Yi-Hsien Cho, and Huei Wang, “A 5-GHz Low Phase Noise Differential Colpitts CMOS VCO” IEEE Microwave and Wireless Components Letters, Vol. 15, Issue: 5, pp. 327 – 329, 2005.

Integrating Performance and Production Oriented Design of Satellite Oscillators

Harri Eskelinen
Lappeenranta University of Technology
Mechanical Engineering
Lappeenranta, Finland
harri.eskelinen@lut.fi

Pekka Eskelinen
Aalto University
School of Electrical Engineering
Espoo, Finland
pekka.eskelinen@aalto.fi

Kim Blomqvist
Aalto University
School of Electrical Engineering
Espoo, Finland
kim.h.blomqvist@aalto.fi

***Abstract*—This paper is based on background research [1] in which a manufacturability analysis was carried out for of an oscillator made for 5 GHz satellite and radar bands. The electronic circuit uses two cascaded bipolar microwave transistors in an emitter feedback amplifier configuration which is combined with a cylindrical dielectric resonator. Three miniature coupling loops are included in it, one for amplifier input, one for amplifier output via a Wilkinson power divider and another for the optional tuning varactor diode. We have formulated two research questions: Firstly, how much is it possible to increase the Q-value of the resonator by improving the manufacturing quality of its milled geometries? Secondly, is it possible to describe the required manufacturing accuracy with the Q-value added to the Product Data Management (PDM) data set? This paper focuses on the multidisciplinary aspects of the integrated performance and production oriented design of satellite oscillators. For the first time, the quality characteristic (Q-value) could be utilized directly in the mechanical PDM data of an oscillator to guide production.**

Keywords: oscillators, Q-value, PDM data

I. INTRODUCTION

In this research, three separate resonators were constructed and measured with different coupling loops. One of the resonators, shown in Fig. 1a, has a quartz plunger for the height adjustment of the dielectric disc, as indicated in Fig. 1b. The silver-coated resonator cavity itself is shown in Fig. 1c. An HP scalar network analyzer system was utilized and the resonator center frequency, insertion loss, and quality factor were measured with different vertical and horizontal disc positions.

a b c

Figure 1. a) Test resonator. b) Resonator cover showing the ceramic disc and its quartz plunger. c) Cavity interior.

II. RESEARCH METHODS APPLIED

Laboratory tests were conducted to measure the achievable surface quality and dimensional and geometric tolerances of the milled resonator cavities. To find answers to the research questions, three different research methods have been applied. Firstly, computer aided EdgeCAM simulations were used to evaluate the efficiency of the machining phases of the oscillator body and to establish the relative machining times for each machining phase. These EdgeCAM simulations were also used to evaluate the required PDM data for guiding the milling tools. Secondly, laboratory tests were conducted to measure the achievable surface quality of the resonator cavity. Thirdly, dimensional and geometric tolerances of the milled resonator cavity were measured. In this paper, the main focus is on the results dealing with the experimental evaluations of the effects of dimensional uncertainties analyzed by constructing three resonators with different coupling loops.

III. RESULTS

A. Performance aspects

In our tests, the direction convention was chosen from Fig. 1a so as to have positive x-values to the right, positive y values away from the viewer and positive z values up from the desk surface. A typical wide-band view is shown in Fig. 2 and a 3 dB width measurement example in Fig. 3. Results obtained are collected into Table 1.

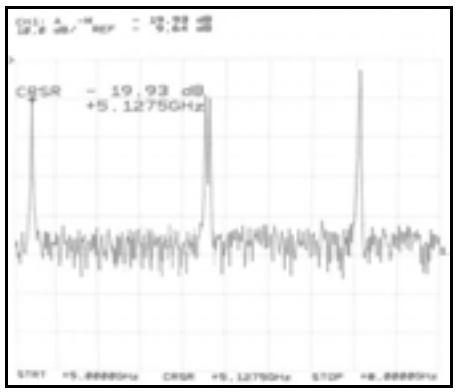

Figure 2. Wide-band spectral response of resonator I.

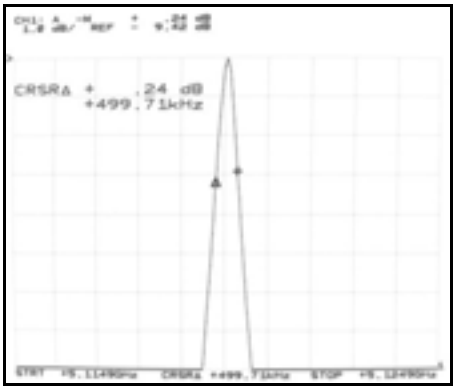

Figure 3. A close-up of the resonance characteristics revealing the 3 dB bandwidth.

TABLE I. ELECTRICAL PERFORMANCE FACTORS FOR DIFFERENT MISALIGNMENTS

Δx (mm)	Δy (mm)	Δz (mm)	f_c (GHz)	IL (dB)	Q
0	0	0	5.1196	9.52	10246
+0.5	0	0	5.1196	9.57	10225
+1.0	0	0	5.1196	9.57	10225
+1.5	0	0	5.1199	9.52	9752
+2.0	0	0	5.1201	9.65	9309
-0.5	0	0	5.1197	9.49	9770
-1.0	0	0	5.1198	9.69	10225
-1.5	0	0	5.1200	9.72	10225
-2.0	0	0	5.1204	9.98	9309
0	+0.5	0	5.1197	9.34	10246
0	+1.0	0	5.1198	9.11	9746
0	+1.5	0	5.1199	8.96	9746
0	+2.0	0	5.1204	8.70	9312
+0.5	+0.5	0	5.1199	9.12	9310
0	0	+0.5	5.1197	9.60	10246
0	0	-0.5	5.1199	9.63	10776

In order to study the effects of a non-circular cavity cross section, we added a sheet of 0.1 mm aluminum foil to cover 90 degrees of the circumference in the middle of the two active coupling probes and carefully pressed it to meet the cavity wall curvature. Other dimensional variables were kept at zero. This caused the center frequency to rise to 5.1206 GHz, the insertion loss was 10.60 dB and the Q-value dropped to 8533. If the foil was larger and covered almost 270 degrees (from probe to probe), the quality factor would be below 5000. The measured data of the two remaining test resonators is displayed in Table 2.

TABLE II. TEST RESULTS OF TWO ADDITIONAL RESONATORS.

Resonator	Notes	f_c (GHz)	IL (dB)	Q	Loop type
II	min. f	5.0468	7.66	9388	wire
II	max. f	5.0473	8.86	9858	wire
III	no cover	5.0471	4.27	6208	wire

Based on these experiments, it seems apparent that the ceramic resonator disc alignment or its position in the cavity as such are not critical compared to the circular symmetry requirement of the cavity itself. Even a very coarse mounting error of the order of 1-2 mm will only cause some de-tuning, but the quality factor will stay sufficiently high to keep the oscillator phase noise level within acceptable limits.

No measurable difference was noticed when the 0.1 mm sheet was placed inside the real active oscillator cavity, as is evident from Fig. 4 and Fig. 5. The sheet covered again one quarter of the cavity circumference. The result is partly obvious because the test system noise floor was limited by the available 100 Hz resolution bandwidth, and even with the sheet, the quality factor is above 8000. However, as was observed already with the plain resonator (see Table 1), the oscillator center frequency was changed, but surprisingly, it declined even though the resonator was tuned up. Also, the magnitude of the shift was lower, approximately 700 kHz. Nevertheless, because the entire tuning range of the oscillator (screw plus possible varactor) is only 2 MHz, it appears that the shape deformation of the cavity is also in this sense quite critical.

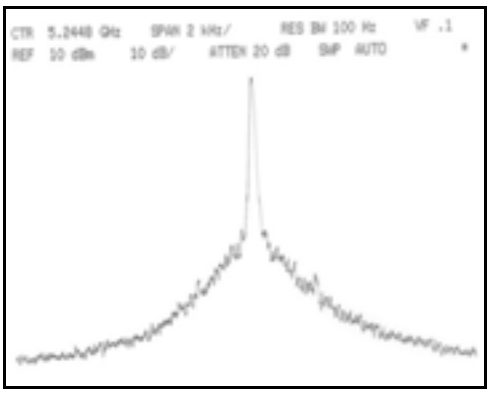

Figure 4. Oscillator spectrum without artificial shape deformation sheet.

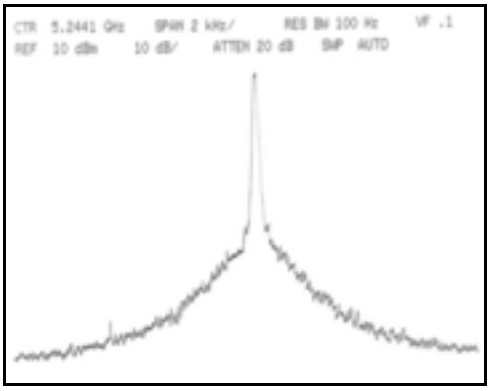

Figure 5. Oscillator spectrum with artificial 0.1 mm sheet in the cavity.

B. Production aspects

The first key observation is that both the resulting surface roughness and the geometric accuracy of the cavity seem to exceed the theoretical minimum requirements given in scientific literature. The required values for similar applications in this frequency range would be IT10 and Ra=12.8 μm [3].

However, we know that some unwanted, excessive structural inaccuracy of the construction could be caused by 1) the gluing process of the resonator buck and the quartz tube, 2) the machining challenges of these ceramic components, 3) the difficult positioning control of the power feeding loops and the resonator puck and 4) some errors of the gold coating process of the cavity (e.g. pinholes, nicks or unwanted roughness [4]). Therefore, it would be valuable to be able to produce a "buffer" against these inaccuracies by optimal handling of the machining phases of the cavity geometry. Detailed tests and analysis of the test results dealing with mechanical engineering are documented in [1] and [2]. One example of the EdgeCAM model is presented in Fig. 6.

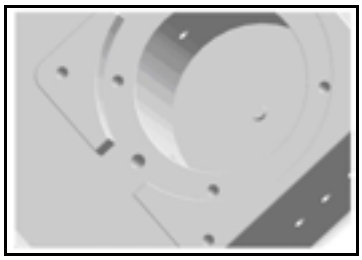

Figure 6. Example of the EdgeCAM model.

An interesting detail of the production analysis was the finding that only 20% of the machining time is spent on milling the cavity itself. Approximately 60% of the time is used for drilling and threading the small assembly holes [2].

The oscillator types which were analyzed in this paper were silver coated, but typically also gold-coated versions are used. One option for gold coating is to use a standard plating of 5ou" electrolytic gold according to MIL-G-45204 over 5ou" electrolytic nickel according to QQ-N-290. Thin layers of silicon dioxide deposited on the surfaces can also protect metals in the space environment. In addition, titanium-aluminum-nitride coatings have been tested for satellite temperature control applications [5]. Geometrical inaccuracy seems to be independent of the material selection of the coating layer. It depends rather on the selected coating process.

IV. CONCLUSIONS

A scalar network analyzer system was utilized and the resonator center frequency, insertion loss, and quality factor were measured with different vertical and horizontal disc positions. The wide-band spectral response of each resonator was established. Based on the results, the ceramic resonator disc alignment or its position in the cavity was not critical compared to the circular symmetry requirement of the cavity.

When analyzing the effects of the non-circular cavity cross section, it was noticed that e.g. 0.1 mm deflection, which covers 90 degrees of the circumference of the cavity, causes the center frequency to rise to 5.1206 GHz. Meanwhile, the insertion loss was 10.60 dB and the Q-value dropped to 8533. These tests were repeated to collect and construct the corresponding PDM data set, which illustrates the relationships between the values of the circularity and dimensional inaccuracy of the cavities and the corresponding changes of the Q-values and the center frequencies.

The findings presented in this paper are in line with the viewpoints presented by Wall and Sinnadurai [6], who identified the trends of the component industry, examined the methods of achieving "space quality", discussed the challenges of the space industry, and finally, considered the performance specifications. Our results are also supported in [7] and [8] by Lohtander, who discusses the design and manufacturing aspects of modern microwave components.

REFERENCES

[1] H. Eskelinen and M. Montonen, "Performance-integrated DFMA analysis of a satellite oscillator," in Advanced approaches to analytical and systematic DFMA analysis, H. Eskelinen, Ed., Acta Universitatis Lappeenrantaensis 509, pp. A1-A10, 2012.

[2] H. Eskelinen and P. Eskelinen, "Performance-oriented manufacturability analysis of a 5 GHz satellite oscillator", International Review of Mechanical Engineering, no. 7, vol. 6, pp. 1461-1466, 2012.

[3] H. Eskelinen and P. Eskelinen, Microwave Mechanics Components, Artech House, New York / London, 2003.

[4] D.M. Tsai and B.T. Lin, "Defect detection of gold-plated surfaces on PCBs using entropy measures," International Journal of Advanced Manufacturing Technology, no. 20, pp. 420-428, 2002.

[5] M. Brogren & al., "Titanium-aluminum-nitride coatings for satellite temperature control", Thin Solid Films no. 370, pp. 268-277, 2000.

[6] J. Wall and N. Sinnadurai, "The past, present and future of EEE components for space application: COTS – the next generation", Microelectronics International no. 3, pp. 7–16, 1998.

[7] M. Lohtander, "Observations of applying DFM(A) in MW mechanics and sheet metal work", IEEE International Symposium on Assembly and Manufacturing, Tampere Hall, Finland, paper 153, 2011.

[8] M. Lohtander and H. Eskelinen, "Review of design for manufacturing and assembly aspects to designing modern microwave and sheet metal products," Key Engineering Materials, vol. 486, pp. 9-12, 2011.

Redundant Frequency Source with Seamless Switchover

Shi Shaohua[1], Li Xiaohui[2], Fan Duosheng[1,2], Tang Sheng[3]
[1]National Time Service Center, Chinese Academy of Sciences, Xi`an, Shaanxi, China
[2]Key Lab. Of Time & Frequency Primary Standards, CAS, Xi`an, Shaanxi, China
[3]Northwest University, Xi`an, Shaanxi, China

***Abstract*—This paper describes a redundant frequency source system with seamless switchover that produces a stable and continuous output frequency signal. This system has primary and backup frequency produce links to generate the reference frequency. It has the ability to monitor the integrity of the frequency produce links and switchover seamlessly between the primary and the backup links. By use intermediate oscillator of the measurement system as a third party criterion, the autonomous monitor integrity of frequency produce links was achieved without external reference signal. The excellent short-term stability characteristics of intermediate oscillator improves the accuracy and real-time for the monitoring of sudden failure and the degradation of performance. Seamless switchover was defined as the maintenance of both output phase and frequency continuity while and after the switcher from the primary to the backup links. It was initiated when system detects a degradation of the integrity of primary links. The experiment result has been presented showing that there were no detectable change in phase and frequency after the switchover, and the jump of frequency was less than 2e-13, the change of phase less than 100ps.**

Keywords-redundant frequency standard; autonomous integrity monitoring

I. INTRODUCTION

This paper describes a redundant frequency source system to provide the reference frequency signal as the reference of high resolution electronics. In order to guarantee the reliability and stability of the frequency source of the electronic system, it usually adopts the method of redundant to deploy the frequency source, which uses multiple frequency source for the system. To ensure the reliability and continuity of the produced reference frequency signal, the system can quickly switch to other frequency sources when a certain frequency source is the degradation of performance or failure.

The research based on the research of the current redundant frequency source designs a redundant frequency source, which can achieve Seamless Switchover and is according to more than one single frequency source as reference, including the two frequency produce links of the primary and the backup. Through the high precision measurement phase difference of the output frequency signal of the primary and backup links, it designs the real-time autonomous monitoring algorithm for the integrity based on Kalman filter's model for the primary and backup links, so it can achieve independent monitoring for system integrity. And it uses the method of the phase-locked for the link output signal after the switching, to ensure that the output signal frequency of the system and the phase of the primary and backup links maintain continuously before and after switching, thereby the seamless switching of the primary and backup links for the output frequency signal is achieved.

II. SYSTEM COMPONENTS

This system is composed of the redundant frequency source, the phase measurement, the control and integrity monitoring, the generating signal of the primary and backup links, the phase-locked of the output, the system structure is shown in Figure 1.

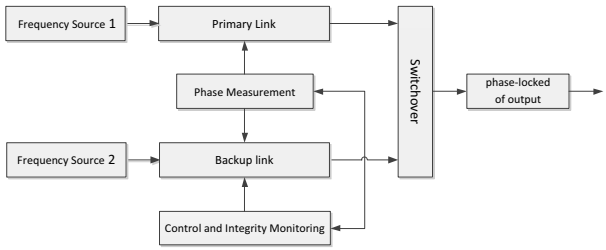

Figure 1. Schematic Diagram of Systems

The redundant frequency source includes the two atomic frequency standards, namely providing the independent frequency signal for the primary link and the backup link. The output signal of atomic frequency standard of the primary and backup links as a reference signal generate the signal of the primary and the backup, and through the switching selecting the primary signal outputs to the phase-locked loop (PLL). The primary signal final outputs after locked. The frequency signal of primary and backup links can be adjusted to achieve the seamless switching for the different frequency signal.

The phase difference measurement section real-timely measures the phase difference of output signal between the primary and backup links. And the mathematical model is done through integrity monitoring and the control part. The signal adjustment amount of the backup link is calculated, to control the output signal of the primary and backup links to maintain consistently. While the integrity of the primary link is monitored to control the seamless switching for the primary and backup links based on the monitoring results.

Supported by National Natural Science Foundation of China, No.61001076

III. THEORY OF OPERATION

A. *Signal phase mathematical model of primary and backup links*

In order to get an accurate sample of the sampled result, phase measurement method is designed based on low sampling rate. The method introduces the public oscillator as a reference source to improve the phase measurement accuracy, and through the double-balanced design structure eliminates the phase noise introduced by the common oscillator, in the case of the lower sampling rate to achieve the 0.1 nanosecond of phase measurement accuracy.

The accurate mathematical model of phase difference data is built based on obtaining accurate phase difference measurement. There are many ways of modeling, commonly used quadratic polynomial model, gray model and Kalman filter model. The Kalman filter model considers the phase bias of the system clock and the random errors. It can better describe the change of phase difference. The Kalman filter model also has the characteristics of the real-time, and it is conducive to achieve the real-timely monitoring of the phase difference.

B. *Real-time autonomous integrity monitoring algorithm of primary and backup links*

- Observations Selecting

In order to use existing equipment, the relative frequency difference of the primary link and the backup link, the relative frequency difference of the primary link and the intermediate oscillator and the relative frequency difference of the backup link and the intermediate oscillator as observations are selected. It achieves the integrity of autonomous monitoring without additional hardware.

The observations with above-mentioned are generated through the deviation measurement equipment of the primary and backup links in multi- Redundant frequency source. The observations can directly get involved in computing, and then be modeled using the Kalman filter. Then the associated detection algorithm is running to detect integrity exception and determines the abnormal attribution.

- Detection of Signal Leap

The tends of phase and frequency difference between the primary-backup links and the intermediate oscillator is real recursive fitting approximation and prediction, which uses the recent M measurement results and based on the Kalman filter model. Then the signal leap and mutation of the primary and backup links are decided according to the size of the measured frequency difference and the predicted frequency difference. The specific works is shown in Figure 2.

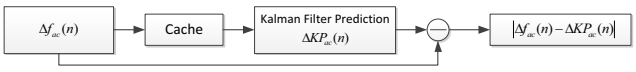

Figure 2. Detection Principle of Kalman Filter Prediction for Signal Leap

The detection threshold selection is very important in real-time autonomous integrity monitoring algorithm, it will directly affect the algorithm to detect the ability of abnormal situations. Detection threshold has relations with the abnormal state of the primary and backup links, and the tracking accuracy of Kalman filter model for the phase difference. The characteristic of the primary and backup links anomalies needs to be considered when choosing threshold, it also takes into account the impact of the Kalman filter for tracking error. By selecting the appropriate data buffer and anomaly detection threshold at a lower false alarm rate can be the case, the frequency hopping of the output signal of the primary and backup links can achieve the detection rate of 99.99% or better.

- Monitoring of Signal Degradation

Monitoring the signal degradation is achieved through using the assessment method of the signal frequency stability in design. The frequency stability of σ_{ab}^2, σ_{ac}^2 and σ_{bc}^2 of the deviation between the primary link, backup link, and the intermediate oscillator can be calculated according to the recent measurement results and the relative frequency difference, which contains the relative frequency difference of $\Delta f_{ac}(n)$ between the primary link and the intermediate oscillator, the difference of $\Delta f_{bc}(n)$ between the backup link and the intermediate oscillator and the difference of $\Delta f_{ab}(n)$ between the primary and backup links.

$$\begin{cases} \sigma_a^2 = \frac{1}{2}(\sigma_{ab}^2 + \sigma_{ac}^2 - \sigma_{bc}^2) \\ \sigma_b^2 = \frac{1}{2}(\sigma_{ab}^2 + \sigma_{bc}^2 - \sigma_{ac}^2) \\ \sigma_c^2 = \frac{1}{2}(\sigma_{ac}^2 + \sigma_{bc}^2 - \sigma_{ab}^2) \end{cases} \quad (1)$$

The obtained frequency stability needs to be processed by using tricorn, the specific algorithm is shown in Equation 1. Through the further processing, the relatively independent stability of σ_a^2, σ_b^2 and σ_c^2 of output signal between the primary and backup links and intermediate oscillator can be calculated. Through real-timely analysis and evaluation them σ_a^2, σ_b^2 and σ_c^2, the frequency stability of the primary and backup links can be derived. Thus the monitor of performance of the primary and backup links output signal can be achieved.

- Detection of Signal Loss

In the primary and backup links under normal operating conditions, the frequency difference and phase difference measuring device will output the correct measurement results. When the primary link or backup link signal is missing, the device will not output the measurement, the integrity monitoring will not be able to obtain the correct observables. Through continuously observing the phase and frequency difference measurement and selecting the appropriate threshold, at the same time using the single-step predicted values of the Kalman filter model, so the anomalies of signal missing whether the primary and backup links occurring can be determined.

C. The Precision Control Method of Primary and Backup Links Output Signal

The output signals of the primary and backup links are independent, which has a certain phase deviation and frequency deviation, and this deviation will gradually drift over time. In order to make primary and backup links maintain the consistent output signal, the primary and backup links needs to be real-timely controlled.

Before switching on the primary and backup links, the backup link has no output signal. The output signal of the backup link is directly controlled based on the phase difference measurements of the primary and backup links and remove outliers, to match the primary link consistently.

After the primary and backup links switchover, the output signal of the backup link is the system reference frequency signal. Based on the mathematical model of the phase difference established before switching, the primary link is real-timely controlled after the switch, its characteristics is consistent with the primary link before switching. Selecting the exact amount of the control in the control process, the control does not affect the stability and accuracy of the signal itself before and after.

Control in this manner, the adjustment of each control is controlled in an appropriate range. This can ensure the continuity of the signal in the control process, and guarantee the change of the signal frequency and phase within the allowable range.

D. Seamless Switchover of Primary and Backup Links

In order that the system output frequency signal is not interrupted in the primary and backup links before and after the switch, the method of output phase-locked is used to switch seamlessly in primary and backup links, so as to maintain the continuity of the system output signal. The PLL circuit is added after the primary and backup links. The output signal of switch is the reference frequency of the PLL. The signal of PLL is the final frequency signal of the system.

While the output signal of the primary link occurring phase anomalies or failures, etc is monitored, the switch will select the backup link as the output signal. The signal through precise control before switching in the primary and backup links is basically the same. And the signal switching time is very short. The PLL output signal can be remained to be not interrupted in the operating time of the switch, which uses the holding function of the PLL itself. The seamless switching for the primary and backup links can be achieved.

Using the method of the output phase lock, the system output frequency signal can be maintained continuously and without interruption. But the moment of the switch operation, the reference signal of the phase locked loop will appear transient disappearance and there may be a PLL loses lock. This leads the output signal to occur leap. The phase-locked loop enters the locked state again until the reference signal occurs, then the output signal will regain stability.

To solve the output frequency signal in the primary and backup links with switching process may cause the problem of output PLL loses lock, a PLL circuit having a holding function of the output signal of the phase-lock after switching is designed, which is shown figure 3.

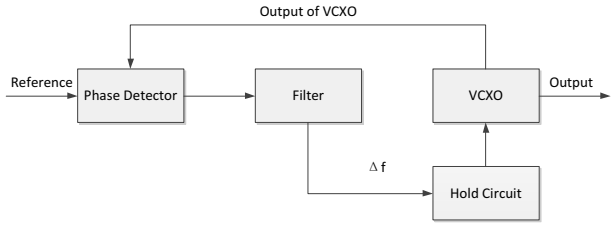

Figure 3. PLL circuit with a holding Circuit

Compared with the ordinary phase-locked loop, the PLL with the role of the holding has increased the maintaining circuit. The error controlling voltage of the loop of the loop filter output is not directly input to the voltage controlled crystal oscillator (VCXO), but by the holding circuit and then output to the VCXO, so as to control the output frequency of the VCXO.

Under the normal operating condition, the phase detector generates the adjusting voltage according to the phase difference between the reference signal and the output signal of the VCXO. The adjusting voltage processed by the loop filter generates the loop error voltage, which outputs to the VCXO through the holding circuit. When the reference signal is lost or occurs unusual, the loop will enter the state of the losing lock. In this case, the output voltage signal of the phase detector will be a large variation, this results that the output error voltage signal of the loop filter also occurs a big change. At this time the holding circuit determines the abnormality loop error voltage signal and continues to output the loop error voltage stored in history to the VCXO. The obvious changes of the output frequency signal will not occur until the reference signal is restored to the normal, the PLL enters the locked state again.

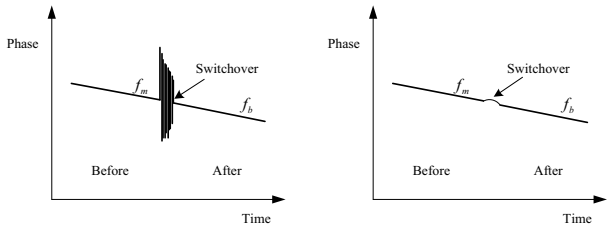

Figure 4. Output of Switchover with Different PLL

Using the function of the holding PLL to lock the output signal after switching and adopting the common PLL to lock, the switching process of the primary and backup for the output signal of the primary and backup links is shown in Figure 4. From the picture, when using the function of the holding PLL lock to output, the output signal of the system before and after switching is consistent. The large frequency and phase fluctuations do not occur. The signal of seamless switching can be achieved.

IV. THE FIRST MEASUREMENT

To measure the output signal frequency and the specific jump variables of the phase in the primary and backup links before and after switching. The master clock signal of the NTSC is a reference signal, and it is through the high-precision frequency source to generate a reference signal. Then the output signal as a test signal inputs the multi-channel phase testing instrument. Last the instrument measures the phase change volume between the test signal and the reference signal, and the time of switchover is recorded.

When the output of the system is switched from the primary link to the backup link, the moment of switching in the primary and backup links is recorded. The phase change of the test signal is calculated in the final measurement results. And the average frequency change of the signal is calculated after continually running for a period of time.

A. Result

The measurement results are shown in figure 5 and figure 6.

In Figure 5, the abscissa is the measured time in seconds; the vertical axis is the phase change value of the output signal, in units of seconds. The system carried out the four switching in the measurement process, the phase change of the switching time is indicated in the figure by a red circle. From the figure it shows that the phase change of the system before and after switching in the primary and backup links is about 0.1ns.

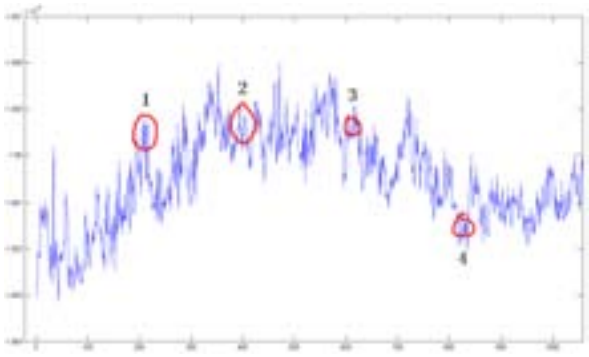

Figure 5. Phase Changes of output with Switchover

In Figure 6, the horizontal axis is the measurement time, in seconds, the figure shows that the result is the phase change from the 3800 to 14000 seconds; vertical axis is the phase change value of the output signal, in seconds, the switching time of the primary and backup links occurs in the first 4085 seconds. Seen from the figure, the initial phase value of the output signal is -7.0952μs at the switching time, after switching the phase accumulation is to -7.0937μs in 2 hours. Which is known :

$$\Delta f = \frac{-7.0937-(-7.0952)}{2\times 3600} = \frac{1.5ns}{7200s} = 2\times 10^{-13} \qquad (2)$$

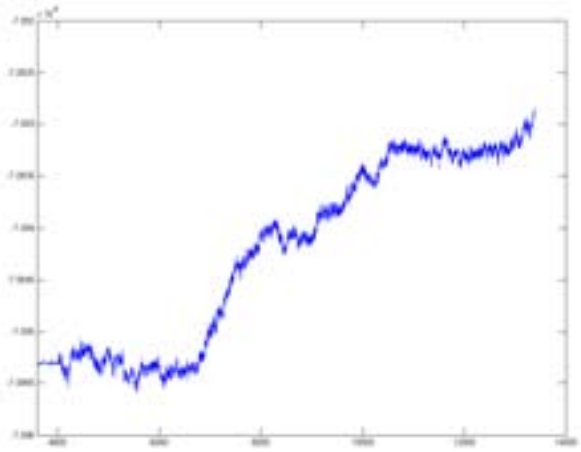

Figure 6. Signal Phase Changes with Switchover after 2 hours

It is concluded that the average frequency jump of the output signal of the system is 2×10^{-13} when the primary and backup links switchover after two hours.

V. CONCLUSIONS

The redundant frequency sources is designed in this paper, it is included the two frequency generation links with the primary and backup links. The redundant frequency sources combines with integrity monitoring method for the primary and backup links, link control strategies and the seamless switching method. It effectively simplifies the structure of the redundant frequency source, and improves its continuity and reliability of the output signal. It can generate a continuous long-term stability of high precision time and frequency signal. The redundant frequency sources meet the high reliability requirements of the current frequency source for the electronic information system.

REFERENCES

[1] JongGun Lee, YoungSeek Chung, Jinkyu Byun,etc. Multiple calibration method for high frequency surface current measurements[J]. IEEE Antennas and Propagation International Symposium, June 2007: 621-624.

[2] Muresan, M., Pitica, D., Chindris, G. Performances Evaluation of Frequency Measurement Techniques in Automotive Industry[J], 30th International Spring Seminar, 2007:187-191.

[3] S.W Lee, J Kim, Y.J Lee. Protecting Signal Integrity Against Atomic Clock Anomalies on Board GNSS Satellites[J]. IEEE Transactions on Instrumentation and Measurment, 2011, Vol60(7) : 2738-2745.

[4] Farina M, Galleani L, Tavella P, Bittanti S. A Control Theory Approach to Clock Steering Techniques[J]. IEEE Transaction on Ultrasonics Ferroelectrics and Frequency Control, 2010, Vol57(10) : 2257−2270.

[5] Galleani L, Tavella P. Detection of Atomic Clock Frequency Jumps With the Kalman Filter[J]. IEEE Transaction on Ultrasonics Ferroelectrics and Frequency Control, 2012, Vol59(3) : 504−509.

[6] Rodriguez PI, Garcia S C. Inter − Satellite Links for Satellite Autonomous Integrity Monitoring[J]. Advances in Space Research, 2011, Vol47(1) : 197−212.

Programmable Delay Controller Allowing Frequency Synthesis and Arbitrary Binary Waveform Generation

Marek Peca*, Michael Vacek, Vojtěch Michálek
Výzkumný a zkušební letecký ústav, a. s., Beranových 130, Praha – Letňany, Czech Republic
České vysoké učení technické v Praze, Břehová 7, 115 19 Praha 1, Czech Republic
*e-mail: peca@vzlu.cz

***Abstract*— Design of a programmable delay controller (PDC) within an aerospace-compatible field-programmable gate array (FPGA) fabric is presented. Although PDC is a common digital block nowadays, the possibility to use it for low-jitter arbitrary frequency generation constrained only by minimum edge-to-edge time still seems to be uncovered. The novel idea of the developed PDC is seamless line delay switching at sampling frequencies corresponding to the generated output frequency, unleashing a possibility of arbitrary binary waveform (frequency) generation. The maximum frequency is constrained only by the FPGA fabric performance, and by idle delay of available multiplexers. Glitch-free operation with no unintentional edges is employed for proper PDC control signal switching. The overall output signal jitter is composed solely of the jitter of input signal and propagation jitter of the delay elements ($\sigma_{max} = 4.1\,\mathrm{ps\,RMS}$). Measured resolution of the PDC is $\pm\Delta\tau_{max}/2 = \pm 7.5\,\mathrm{ps}$. Measured temperature drift of the PDC is $\sim 30\,\mathrm{ps\,K^{-1}}$. An ability of PDC to generate fractional frequency from the input has been demonstrated on a simplified, low-resolution variant, delivering $33.\bar{3}\,\mathrm{MHz}$ out of $50\,\mathrm{MHz}$ input.**

I. Introduction

Design of a programmable delay controller (PDC) within an aerospace-compatible, FLASH-based field-programmable gate array (FPGA) fabric will be presented. Although PDC is a common digital block nowadays, the possibility to use it for low-jitter arbitrary frequency generation still seems to be uncovered. The objective is to provide a versatile PDC block capable of generating arbitrary binary waveform constrained only by minimum achievable edge-to-edge switching time. The discussed PDC may be able to replace current building blocks such as direct digital synthesizer (DDS), phase-locked loop (PLL), micro phase stepper, or various modulators; all within purely digital circuit (FPGA, custom CMOS).

Let us call the time interval between control signal changes (updates) the sampling period T_s, and let the time interval between the consecutive edges of output signal be called the output interval T_o. Current PDC designs [1], [2], [3], [4], [5], [6], [8] operate at $T_s \gg T_o$, Fig. 1a. The key idea of our proposal is seamless PDC operation at $T_s \to T_o$, Fig. 1b. Such a development unleashes following advantages:

- generation of arbitrary binary waveform constrained only by $T_o \geq T_s$,
- generation of arbitrary frequency, constrained by $f \leq \frac{1}{2 \cdot T_s}$,
- under proper treatment, no edge will be created by the switching elements themselves; therefore, the overall jitter will be composed solely of the jitter of input signal and propagation jitter of the delay elements.

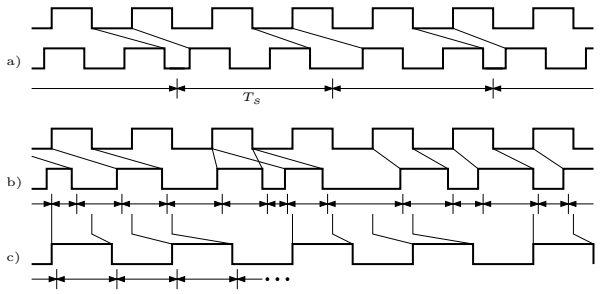

Fig. 1. Input and output waveforms for (a) ordinary PDC, (b, c) PDC allowing rapid switching

Design and implementation details of the PDC circuit are described. Performance figures, such as pass-through random jitter, achieved delay granularity, and temperature drift follow.

II. Circuit design

A. Delay line design

This section describes design of the essential PDC component: a delay line. Typical PDC based on a digital circuitry consists of fixed-length delay elements (transmission lines, gates) composed into signal path by electronic switches (multiplexers). An input signal passes through the delay elements and multiplexers to the output. The multiplexers are switched by means of another digital control signal.

The most common approach is to form the delay line as a cascade of binary elements, Fig. 2a. A favorable property of this design is that n elements may cover 2^n equidistant delay steps, provided element delays follow $K2^{-k}$ distribution, i. e. $d_{k+1} = d_k/2$. Such a delay line acts similarly to a Digital-to-Analog Converter (DAC), but working in time domain. Moreover, the conversion is monotonic by design. Since there is a lack of short delay elements within FPGA fabric, a differential

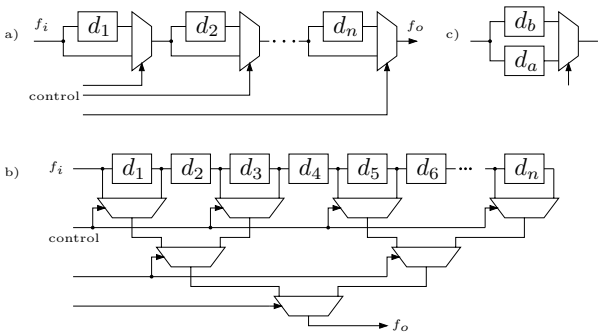

Fig. 2. PDC delay line structure: (a) cascaded design (b) tree-like design (c) fine differential delay

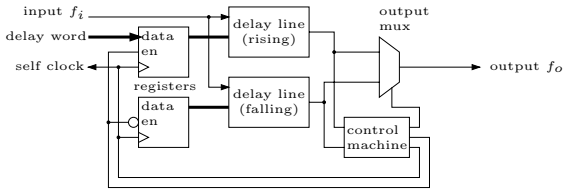

Fig. 3. Complete PDC with dual delay lines and control logic

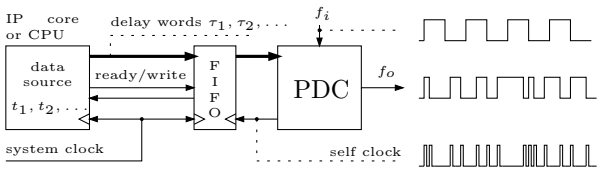

Fig. 4. Self-clocked PDC data-flow

approach to achieve very fine resolution is employed, Fig. 2c. Only $d_b - d_a$ effectively applies, allowing to push resolution down to $\sim 10^{-12}$ s level.

Another approach to delay line uses continuous, tapped line and a binary tree of multiplexers, Fig. 2b. Despite its large area consumption ($\sim 2^{b+1}$ cells for b bits), there is an advantage of uninterrupted delay line, always filled with valid, running signal. See more about its impact in Sec. II-B.

B. Control logic design

In order to achieve versatile signal generation as outlined in Sec. I., we have concluded that the multiplexer control signals should be switched at instants derived from output signal edges (of both polarity) thus operating PDC in a self-clocked manner. It is the most straightforward way to assure proper switching instants. Together with standard asynchronous FIFO, the PDC forms a circuit converting integer numeric data-stream consisting of desired output edge instants $t_1, t_2, \ldots$ into actual binary waveform, Fig. 4.

Block diagram of the PDC circuit is shown in Fig. 3. There are two identical delay lines, in order to mitigate glitches which may occur at the output of the delay line during control input reconfiguration. Just after a rising edge passes through the upper delay line, output multiplexer is switched down to the other delay line. Until next (falling) edge passes, the upper delay line may be safely reconfigured. After passage of the falling edge, the multiplexer is switched back to the upper line, and the lower delay line may be rearranged. Then, the process repeats. Both delay lines are controlled by binary delay words, one for the rising edges, other for the falling edges. The words are stored in respective registers. Loading of the registers and switching of the output multiplexer is controlled by the key part of the design, asynchronous state machine. Most importantly, it generates a non-uniform clock signal derived from the delayed edges. This clock also governs readout of the delay words from data source, i.e. a sequencer (in case of fixed sequence) or FIFO (if delays come from a complex computing system).

The most severe difficulty of the design lies in an unwanted (idle) delay between delay line reconfiguration instant and settling of output signal. In case of cascaded structure (Fig. 2a), only d_1 has always up-to-date signal at its input and inside. But $d_2 \ldots d_n$ have to absorb new input condition upon re-configuration, what may take up to $\sum_{k=2}^{n} d_k$ amount of time. Pass-through delay of all multiplexers adds up. The tree-like structure (Fig. 2b) does not suffer from such transient problem, so its settling delay belongs solely to the multiplexers.

Suppose a PDC with resolution h and maximum delay T is requested. The cascaded structure would settle in $\sim T/2$ plus delays of multiplexers. Where differential elements (Fig. 2c) are used (FPGA fine part), the common mode delay adds up. The tree-like structure exhibits unwanted delay $\log_2 T/h$ times a multiplexer delay; unfortunately, it requires $\mathcal{O}(T/h)$ macros. We see that the proposed kind of rapidly switching PDC is hard to fit into ordinary FPGA fabric.

III. Implementation

A. Delay line implementation

The delay line was implemented inside Actel/Microsemi ProASIC3E FPGA. The line is composed of two distinct parts: coarse, and fine. Two versions of delay lines, with 5 and 13 control inputs (bits), were implemented. The coarse line (5 bits) is made up of $1, 2, 4, \ldots$ combinatorial macro cells ("gates") of the same type in chain. The fine line follows differential structure, with two specially selected macros, one per a branch.

In order to obtain reasonable resolution, all the cells should be well selected as to provide fine granularity over all 2^n bit words. To our knowledge, delay models of FPGA macros are not available in open format. Therefore, we have ran place-and-route tool chain in cycle, iterating over whole macro library, and extracted delay values from SDF back-annotated files [7]. Figures were far from accurate, and lacked an important kind of information: in multiple-input cells, the delay from one input to output may depend on a state of other inputs – this has not been reflected in SDF files (although it is possible by specification [7]). Nevertheless, the obtained timing data served us well as an initial guess. In following automated analysis, every possible cell pair was coupled

with appropriately (non-)inverting multiplexer (yielding non-inverting line element). All these combinations were examined for differential delay, sorted, and shortest candidates for given differential delay were selected. Interval from zero to $\sim 0.5\,\mathrm{ns}$ has been continuously populated with $1\,\mathrm{ps}$ step. From this, candidates were picked up by hand, and subcircuit netlist has been generated. Candidate delay line, implemented into FPGA, has been measured (Sec. IV-A), and unsatisfactory cells were reassigned by hand in next iteration. This process was repeated three times.

First experimental delay line, used for performance analysis, was of 13 bit cascaded structure, 45 cells in total including multiplexers. For a frequency synthesis scenario (Sec. IV-B), 5 bit tree-like structure has been used in order to mitigate idle delay; also, elements counts were doubled to cover $50\,\mathrm{MHz}$ period.

B. Control logic implementation

PDC core controller has been designed by hand as an asynchronous state machine. An intuitive match of the machine to a set of 3-LUT macros of the ProASIC3E FPGA architecture was checked for equivalence in state encoding and transition maps to eliminate hazards. For demonstration purposes, only a fixed delay word sequence has been wired into shift-register based sequencer: approximations of $(0, T/4, T/2, 3T/4)$ for nominal input signal frequency $f_i = 50\,\mathrm{MHz}$ (Fig. 1c). The aim was to demonstrate generation of $f_o = (2/3)f_i$ frequency by the PDC.

IV. Results

A. Delay line characteristics measurements

There have been performed two fundamental experiments testing the performance of the delay line. The block diagram of measurement setup in which the PDC line resolution and linearity were measured using time interval counter (SR620 [10]) is shown in Fig. 5. The SR620 synchronous reference signal (1kpps) was connected into the FPGA fabric. Inside the FPGA, the signal is split into the PDC input and directly to the output of the FPGA chip and consequently into the A channel of the SR620. The output of the PDC was fetched into the B channel of the SR620. The time difference between the channel A and B was measured for all PDC delay line settings.

Measurement took 54 hours, pseudo-random delay words were intermixed with zero delay settings. Individual element delays have been computed from the overdetermined set of bit word to delay correspondences by least mean square fit, results are plotted in Fig. 6. Total operational line delay is $T = 8.72\,\mathrm{ns}$. Maximum step size (resolution) between adjacent delay words is $\Delta\tau_{max} = 14.9\,ps$.

Temperature in a vicinity of the FPGA chip has been measured as well. Fig. 7 shows temperature variation during experiment together with offset and PDC scale variations. In linear approximation, the offset drift is $23\,\mathrm{ps\,K^{-1}}$, the scale drift is $8.4 \times 10^{-4}\,\mathrm{K^{-1}}$, yielding $30\,\mathrm{ps\,K^{-1}}$ in the worst case.

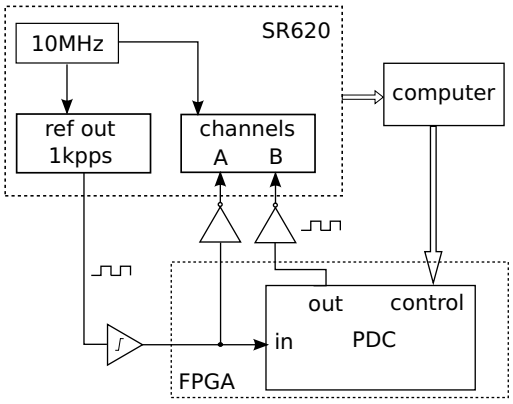

Fig. 5. PDC line resolution and linearity measurement setup

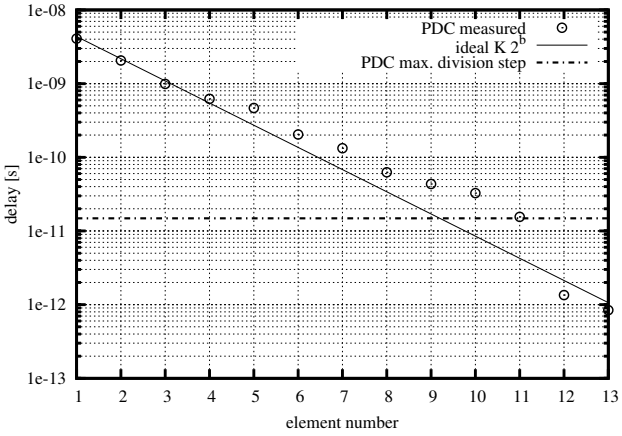

Fig. 6. PDC line resolution and linearity

The propagation jitter of the PDC was determined with the measurement setup depicted in Fig. 8. For precise jitter measurements, NPET device is employed having single shot precision of $\sigma_{NPET} = 1.0\,\mathrm{ps\,RMS}$ [9]. The NPET generates 100pps reference signal ($\sigma_{ref} = 1.2\,\mathrm{ps\,RMS}$) being synchronous with its internal clock; the reference is fed into the PDC input. The NPET measures the jitter of the reference signal propagated through the PDC for different delay settings; each single delay element is enabled at a time.

Propagation jitter of the delay line ranged from $3.9\,\mathrm{ps\,RMS}$ to $5.0\,\mathrm{ps\,RMS}$ (all delays on) for different line configurations. A jitter of signal mirrored at the output of the FPGA, but not passing through PDC, was measured $2.9\,\mathrm{ps\,RMS}$. Under assumption of independent, normal noises, jitter $\sigma_{max} = 4.1\,\mathrm{ps\,RMS}$ may be attributed to delay line in its longest configuration.

B. Frequency synthesis

Generation of $f_o = (2/3)f_i$ frequency has been performed in order to prove the concept of control logic. Input and output waveforms acquired are shown in oscilloscope screen shot Fig. 9. Waveform distortion is caused by coarse line length

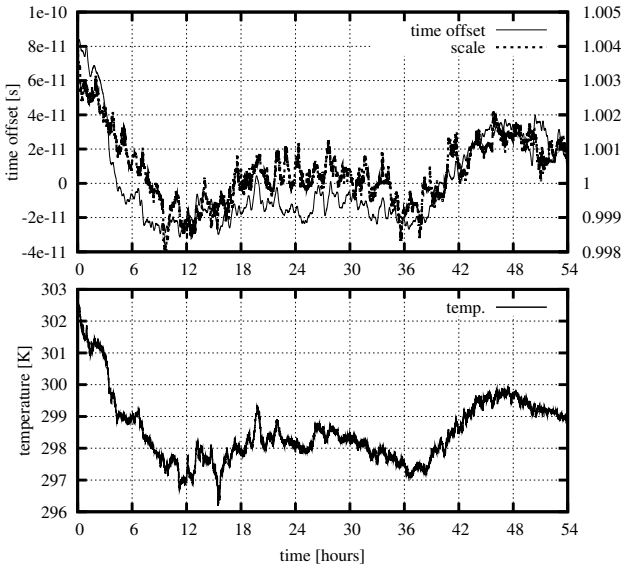

Fig. 7. Temperature and drift of PDC offset and scale

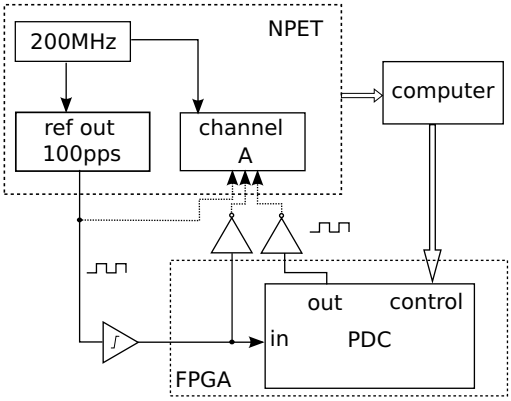

Fig. 8. PDC delay line elements jitter measurement setup

(5 bits) and unoptimized delay words.

V. Conclusion

A presumably novel type of PDC has been presented. The delay line cascaded of 13 elements exhibits a deterministic resolution $\pm\Delta\tau_{max}/2 = \pm 7.5\,\mathrm{ps}$, random jitter $\sigma_{max} = 4.1\,\mathrm{ps\,RMS}$, temperature drift $8.4 \times 10^{-4}\,\mathrm{K}^{-1}$, drift including offset up to $30\,\mathrm{ps\,K}^{-1}$. The performance is comparable to recent works [2], as well as to dedicated ECL circuits [5]. Further improvement of resolution is possible by adding more delay elements. Temperature compensation seems plausible by a measurement of reference delay line element, e. g. using ring oscillator, or Time-to-Digital Converter [11].

An ability to generate waveform differing in frequency and phase from the input signal has been demonstrated as a proof-of-concept. The effect of idle delay is severely limiting factor here, especially in an FPGA. We would like to examine pos-

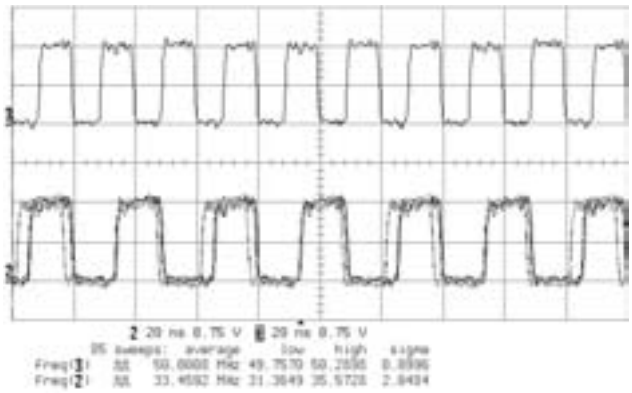

Fig. 9. Frequency synthesis by rapidly switching PDC

sible improvement by combining tree-like structure for coarse line with cascaded structure for the fine part. An implementation into ASIC shall yield significantly better performance, due to much lower multiplexer delays and unnecessity of differential delay elements.

References

[1] Z. L. M. Li, J.and Zheng and S. Wu, Dynamic range accurate digitally programmable delay line with 250-ps resolution, in 8th International Conference on Signal Processing, 2006.

[2] A. de Castro and E. Todorovich, High resolution fpga dpwm based on variable clock phase shifting, IEEE Transactions on Power Electronics, vol. 25, pp. 1115–1119, 2010.

[3] S. C. Huerta, A. de Castro, O. Garcia, and J. A. Cobos, Fpga-based digital pulsewidth modulator with time resolution under 2 ns, IEEE Transactions on Power Electronics, vol. 23, pp. 3135–3141, 2008.

[4] J. Kalisz, A. Poniecki, and K. Ryc, A simple, precise, and low jitter delay/gate generator, Review of Scientific Instruments, vol. 74, 2003.

[5] MC100EP195: 3.3 V ECL Programmable Delay Chip, ON Semiconductor. [Online]. Available: http://www.onsemi.com/PowerSolutions/product.do?id=MC100EP195

[6] M.-A. Daigneault and J. P. David, A high-resolution time-to-digital converter on fpga using dynamic reconfiguration, IEEE Transactions on Instrumentation and Measurement, vol. 60, pp. 2070–2079, 2011.

[7] Standard Delay Format Specification, version 3.0 (1995), Open Verilog International. [Online]. Available: http://www.eda.org/sdf/sdf_3.0.pdf

[8] S. Chan, Programmable delay line using configurable logic block, U.S. Patent 7049845 B1, 2004. [Online]. Available: http://www.freepatentsonline.com/7049845.html

[9] P. Panek, I. Prochazka. Time interval measurement device based on SAW filter excitation, IEEE Review of Scientific Instruments, 2004

[10] SR620: Time interval and frequency counter, Stanford Research Systems. [Online]. Available: http://www.thinksrs.com/products/SR620.htm

[11] Peca, M.; Vacek, M.; Michalek, V., "Time-to-Digit Converter Based on radiation-tolerant FPGA," European Frequency and Time Forum (EFTF), 2012 , vol., no., pp.286,289, 23-27 April 2012 doi: 10.1109/EFTF.2012.6502384

An Efficient Room Temperature Only (RTO) Trimming Solution for an Accurate Self-Compensated Oscillator (SCO)

A. Elkholy, A. Ahmed, M. Shadoufa, M. Sakr, A. El-Sayed, M. Yousef, A. Helmy, M. Essam, N. Sinoussi

***Abstract*—CMOS process variations create a major trimming challenge for a cost effective, accurate and fully-integrated CMOS LC-based reference clock generator. This work presents a new room temperature only (RTO) trimming solution for an all CMOS self-compensated oscillator (SCO) that is highly stable across temperature. Self compensation across temperature is achieved by adjusting the phase of the LC-tank at a specific temperature null (TNULL) phase where the frequency deviation across temperature is minimized. The proposed RTO trimming solution utilizes integrated heaters to thermally modulate the oscillator then uses smart algorithms to select the optimum phase setting that minimizes the frequency variation of the SCO. The integrated RTO intelligence allows trimming SCO parts in parallel with minimum testing overhead. Utilizing the RTO, the SCO achieves ±50ppm of frequency stability across temperature from -20°C to 70°C with less than one second of trimming time consumed per part.**

***Index Terms*—Single point trimming, oscillator trimming, XO replacement, self-compensated oscillator, LC oscillator, temperature null.**

I. Introduction

A reference clock generator is the heart of any electronic system. Owing to their superior frequency stability, and excellent phase noise, quartz crystal oscillators (XOs) have rightfully earned their position as the industry $de\,facto$ frequency reference since their introduction in 1919 [1]. However, XOs impose a lot of limitations on electronic systems regarding integrability and lead time which are eventually translated to increasing the overall cost of the system [2]. Driven by the continuous need for integration and cost reduction, research is eager to find a truly CMOS compatible replacement for quartz crystal oscillators [2], [3], [4], [5].

Cost is the main edge offered by the CMOS LC solution. Compared to the equivalent XOs, the cost of the CMOS LC solution is superior from two main perspectives. First of all, XOs require the presence of an extra component which is the quartz crystal (XTAL) itself. Furthermore, XOs require special, relatively expensive, packaging solutions to protect the XTAL from aging [6]. On the contrary, CMOS oscillators tolerates cheap plastic packages [4]. However, the overall cost structure of any timing solution is influenced by another important factor which is the trimming and calibration. XOs enjoy the extremely mature XTAL fabrication technology where the accurate mechanical control over the XTAL physical dimensions and cutting angle guarantees both the XOs initial accuracy and temperature dependence to an appreciable extent. For example, the AT-Cut XTAL intrinsically achieves ±50ppm across temperature from -40°C to 85°C without any compensation or trimming [7]. On the other hand, CMOS LC oscillators suffer from process variations which change the target frequency and temperature dependence. Thus, trimming is required to compensate for these variations. In order to conserve the excellent cost structure of the CMOS LC solution, trimming has to be efficient and cost effective. Hence, trimming forms one of the major challenges in having a highly accurate and fully-integrated CMOS LC based reference clock generator.

In a previous work [2], a self compensated CMOS LC oscillator (SCO) based on LC tank temperature null (TNULL) phenomenon was introduced. The design area has been reduced in [5]. However, trimming is required to achieve the target SCO performance.

This work presents a new on-chip room temperature only (RTO) trimming solution for a highly accurate SCO with minimum testing overhead. Section II highlights the basic concepts of the LC-based Self-Compensated Oscillator (SCO). Section III illustrates the main challenges of a cost effective trimming solution for the SCO, and the proposed RTO trimming solution is demonstrated. Section IV summarizes the measurements results and the overall oscillator performance. Finally, section V concludes the main points of this work.

II. LC-Based Self-Compensated Oscillators

Conventional LC oscillators exhibit thousands of PPMs of frequency deviation across temperature from 0°C to 70°C [2], [5]. The poor temperature stability of LC oscillators is justified by examining the phase versus frequency characteristic of the tank impedance across temperature which is shown in Fig. 1. LC oscillators operate with zero phase shift across the LC tank impedance leading to the frequency deviation Δf_1 annotated on Fig. 1.

However, a more desirable phase operating point (φ_{NULL}) is annotated on Fig. 1 at which the LC tank impedance exhibits minimal variation across temperature. The resulting frequency deviation (Δf_{NULL}) at φ_{NULL} is in the order of tens of PPMs which is an improvement over the conventional LC oscillator by a factor of 100 [2], [5]. Fig. 2 illustrates a hypothetical oscillator that can force the tank to operate at this non-zero phase. The phase shifter "$e^{j\varphi}$" is programmed to satisfy the condition: $\varphi = -\varphi_{NULL}$.

The reduced LC tank temperature sensitivity at the specific phase φ_{NULL} is denoted as the temperature null (TNULL)

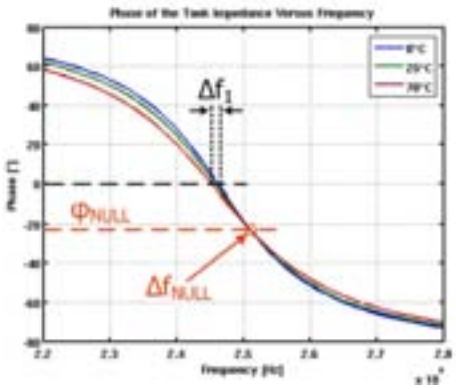

Figure 1. Phase versus frequency characteristic of the LC tank impedance at different temperatures [5].

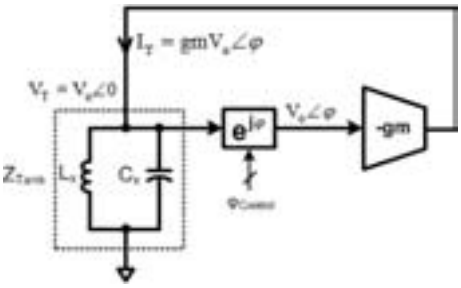

Figure 2. Block diagram of Self-Compensated LC Oscillator (SCO) [5].

phenomenon [2]. Furthermore, the oscillator that can utilize the TNULL phenomenon to achieve a stable output frequency is said to be a self-compensated oscillator (SCO) [2].

III. Room Temperature Only Trimming

A. SCO Trimming Challenges

The high sensitivity of the LC tank impedance versus temperature (Fig. 1) implies that the tank TNULL phase φ_{NULL} must be obtained with a high level of accuracy. Otherwise, the frequency stability across temperature is appreciably degraded. In order to achieve an adequate performance, measurements show that φ_{NULL} should be obtained with a maximum error of $\pm 0.1^{\circ}$. However, the exact value of φ_{NULL} varies with process, oscillation frequency and the required operating temperature range. Moreover, the absolute frequency of the oscillator varies with process and has to be adjusted to the required output frequency. Trimming is required to compensate for these variations and to set the oscillator phase to φ_{NULL} while adjusting the oscillator frequency to the required output frequency. Trimming has to be accurate, robust and cost effective.

The main challenge is that there is no direct method to measure the tank phase across temperature to determine directly the value of φ_{NULL}. The brute force trimming solution to find φ_{NULL} is to sweep the phase setting (PS) at the two extreme temperature points while measuring the frequency. The PS that minimizes the frequency difference between the two extreme temperature points is considered the optimum phase

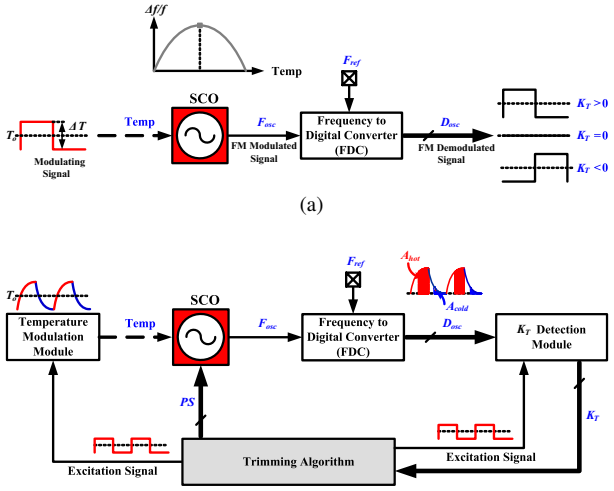

Figure 3. (a) Conceptual illustration of measuring the temperature sensitivity of the SCO by applying a thermal modulating signal, (b) Block diagram of the trimming infrastructure utilized to measure K_T of an SCO.

setting PS_{opt} or φ_{NULL} . However, this two temperature points trimming solution is very expensive due to the high cost of the two required temperature insertions, especially the cold insertion. Furthermore, a very long testing time is usually required for this large number of accurate frequency measurements. This work, proposes a single point trimming (SPT) algorithm at room temperature that enables achieving a highly accurate and cost effective SCO oscillator.

B. Single Point Trimming Basic Concepts

The main idea of the proposed SPT solution is based on estimating the oscillator temperature dependence by modulating its temperature using on-chip heaters. By applying a square wave temperature modulating signal at a temperature (T_o) as shown in Fig. 3(a), the oscillator output becomes a frequency modulated (FM) signal that depends on the frequency temperature sensitivity or slope (K_T) at this temperature. A frequency-to-digital converter (FDC) uses an accurate external reference clock to do FM demodulation to the oscillator output, where the oscillator frequency (F_{osc}) is converted into a digital word (D_{osc}) . The difference between $D_{osc}(T_o + \Delta T/2)$ and $D_{osc}(T_o - \Delta T/2)$ is utilized to estimate the value of K_T at T_o , where ΔT represents a variation in temperature around T_o. The difference between these two digital words gives an accurate digital representation of K_T that is utilized in the proposed SPT trimming algorithm.

C. Single Point Trimming Implementation

There are several non-idealities that can affect the accuracy and cost of the proposed room temperature only trimming. Practically, the thermal modulation frequency is limited by the thermal time constant of the packaged part under test. Thus, the thermal modulating square wave is low pass filtered as illustrated in Fig. 3(b). The thermal time constant is a

strong function of the die size and the package size. As the thermal modulation frequency decreases, the trimming routine becomes slower. Thus, testing cost increases impacting the overall cost of the SCO. Consequently, it becomes very important to reach PS_{opt} in a minimum number of thermal modulation cycles. This can be achieved using smart trimming algorithms.

Oscillator thermal and flicker phase noise are considered another source of non-idealities that affect the accuracy of the SPT algorithm especially when K_T approaches zero as the magnitude of the demodulated signal becomes very close to zero. Since detecting K_T depends on the difference between two frequencies, the impact of phase noise at very low frequency offsets on K_T is negligible . On the other hand, phase noise at high frequency offsets can be suppressed by incorporating an integrate and dump filter. Only parts of the heating and cooling periods are utilized by the integrate and dump filter due to the low pass filter effect induced by the slow thermal time constant of the package under test. A part of the heating period is integrated into A_{hot} and similarly another part of the cooling period is integrated into A_{cold} as shown in Fig. 3(b). The difference between A_{hot} and A_{cold} is a digital word that represents K_T more accurately in the presence of the oscillator phase noise and the large thermal time constant. Overall, trimming is only affected by phase noise at frequency offsets close to the thermal modulation frequency, thus trimming can be highly accurate.

The objective of the phase trimming algorithm is to search for PS_{opt} that adjusts the SCO K_T to a target slope control word (KCW). The selection of KCW depends on many parameters such as: operating temperature T_o, the predetermined temperature range and the desired SCO temperature dependence curve. For RTO trimming ($T_o = 25°$C), usually a value of KCW that is approximately zero is used to optimize the SCO temperature dependence for the different temperature ranges. The proposed SPT employs integrated on-chip heaters for thermal modulation to detect K_T as highlighted previously. Moreover, it utilizes smart search algorithms rather than extensive sweeps to set PS_{opt}.

A digital frequency locked loop (DFLL) is used to adjust the oscillator frequency by changing the oscillator frequency setting (FS) based on a target frequency control word (FCW). The FDC output (D_{osc}) is subtracted from FCW to give a digital word that represents the frequency error (f_e) between F_{osc} and the target frequency. f_e is then accumulated to control FS. The accumulator is loaded by an initial frequency setting (FS_{init}) to speed-up the frequency settling. The loop settles when the oscillator frequency is equal to the required frequency ($F_{osc} = FCW \times F_{ref}$) at steady-state. At the end of the trimming routine, the oscillator trimmed parameters PS and FS are programmed in a one-time programmable (OTP) read only memory (ROM) module. The OTP ROM holds the trimmed parameters in normal-operation after trimming is complete and is automatically loaded at power up.

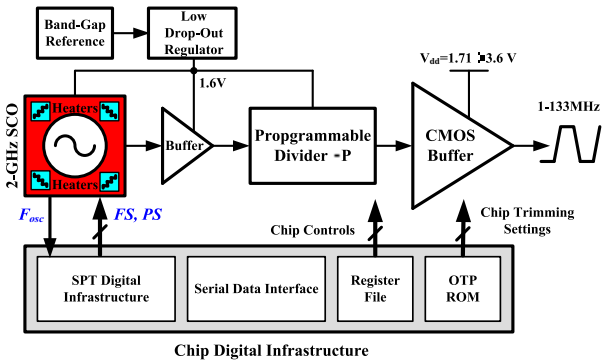

Figure 4. Chip architecture of the implemented SCO with a 1 – 133MHz CMOS output clock.

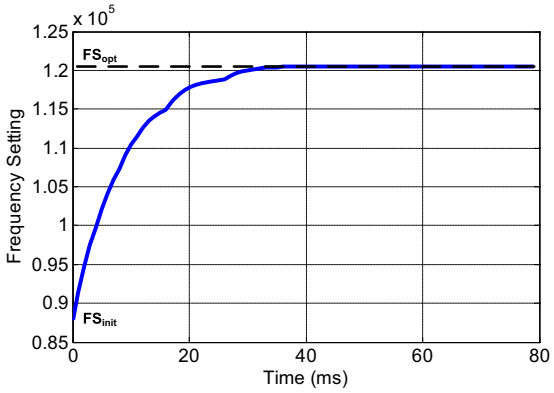

Figure 5. Measured results of FS settling from FS_{init} to FS_{opt} using DFLL.

IV. Measurement Results

The proposed RTO trimming solution was integrated with the SCO in a 0.18μm CMOS process with a single poly and 6 aluminum metal layers. The chip architecture is illustrated in Fig. 4, as in [2], where the SCO operates at 2GHz and a number of integrated heaters thermally modulate the SCO frequency during SPT. FS controls a bank of capacitors to adjust the SCO absolute frequency with an accuracy of ±2.5ppm. The SCO is followed by a programmable divider so that the output frequency ranges from 1MHz to 133MHz. The chip has a CMOS single-ended output buffer that can drive a 15pF load. The chip works with any supply voltage from 1.71V to 3.6V since an internal band-gap referenced low drop-out (LDO) regulator produces a 1.6V supply to all blocks. A serial data interface is used to communicate with the chip during testing. The die (1.55mm×1.05mm) was packaged in a 4-pin 5.0×3.2mm ceramic package and a custom DFN 5.0×3.2×0.8mm plastic package.

The proposed SPT algorithm was used at room temperature to trim 50 ceramic and 50 plastic packaged parts at the TNULL to produce 25MHz. The integrated on-chip heaters were used to modulate the SCO temperature while searching for the optimum settings of the oscillator PS_{opt} and FS_{opt} to achieve the target output frequency and temperature stability across the

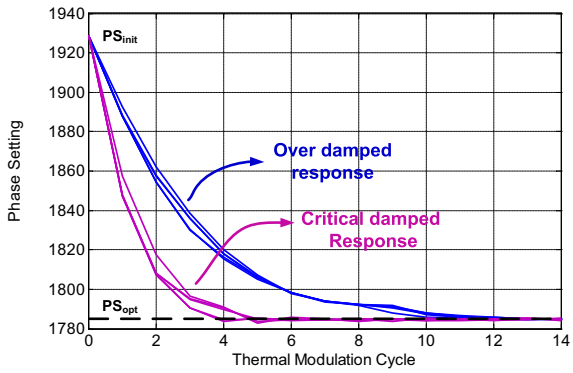

Figure 6. Measured results of trimming algorithm starting from PS_{init} to PS_{opt} using two different loop parameters, each for five iterations.

target temperature range. An accurate 1kHz reference clock was used during trimming as the reference to the FDC, thus minimal external equipment is required. Fig. 5 demonstrates measured settling behavior of FS using DFLL to reach FS_{opt}. Fig. 6 illustrates the measured settling behavior of PS to reach PS_{opt} using the proposed RTO trimming for two different loop settings, each for five iterations. By proper adjustment of trimming loop parameters, critical damped response can be achieved which minimizes the number of thermal modulation cycles used in trimming, consequently reducing the testing time and cost. The parts are trimmed in parallel such that the average trimming time consumed per part is less than 1s. The frequency stability performance was measured across temperature from -20°C to 70°C with a 10°C step. The results of the 50 parts in a non-hermetic ceramic package and the 50 plastic packaged parts are illustrated in Fig. 7 (a) and (b) respectively. All 100 parts are showing excellent frequency stability performance within ±50ppm across a (-20 – 70)°C temperature range.

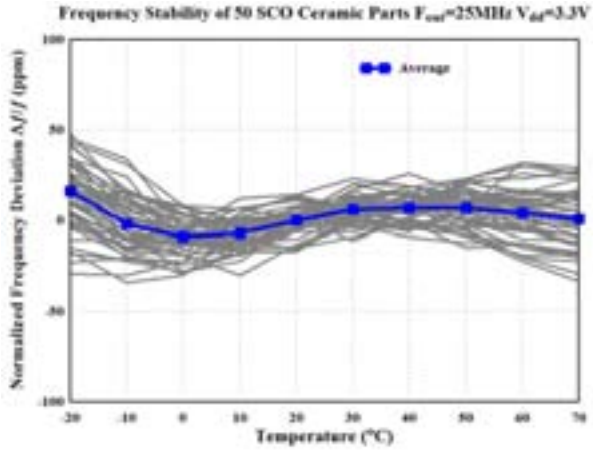

(a)

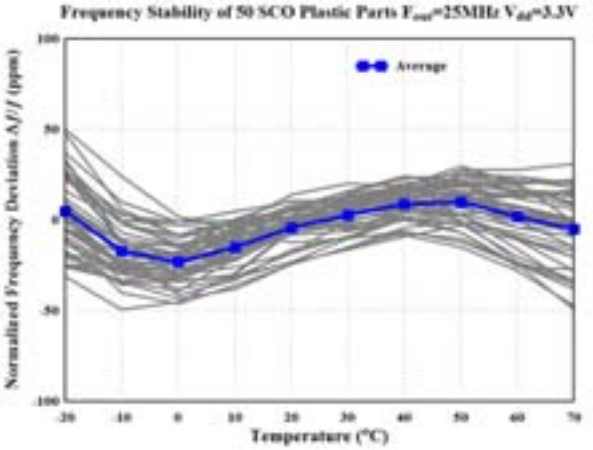

(b)

Figure 7. Normalized frequency stability across temperature of parts trimmed to 25MHz (a) 50 ceramic packaged parts and (b) 50 plastic packaged parts.

V. Conclusions

A new low cost RTO complete trimming solution for highly accurate SCO is proposed. It utilizes integrated heaters to thermally modulate the oscillator to detect the oscillator temperature dependence using on-chip FDC. Moreover, it incorporates smart search algorithms to select the optimum phase setting that minimizes the frequency variation of the SCO. The integrated intelligence offers the merit of trimming large numbers of SCOs in parallel with minimum testing overhead. Without the need for temperature insertions, the RTO solution trims the SCO to achieve $\pm 50\text{ppm}$ of frequency stability across temperature from -20°C to 70°C with less than one second of trimming time consumed per part.

References

[1] V. Bottom, "A history of the quartz crystal industry in the usa," in *Thirty Fifth Annual Frequency Control Symposium. 1981*, 1981, pp. 3 – 12.

[2] A. Ahmed *et al.*, "A highly stable CMOS self-compensated oscillator (SCO) based on an LC tank temperature null concept," in *Frequency Control and the European Frequency and Time Forum (FCS), 2011 Joint Conference of the IEEE International*, May 2011, pp. 443 –447.

[3] M. McCorquodale *et al.*, "A 25-MHz self-referenced solid-state frequency source suitable for XO-replacement," *Circuits and Systems I: Regular Papers, IEEE Transactions on*, vol. 56, no. 5, pp. 943 –956, may 2009.

[4] *Si500S Single-Ended Output Siliocn Oscillator*, Silicon Laboratories Inc., Rev. 1.1 10/11, Austin, TX.

[5] N. Sinouss *et al.*, "A single LC tank self-compensated CMOS oscillator with frequency stability of ±100ppm from -40°C to 85°C," in *Frequency Control Symposium (FCS), IEEE International*, May 2012.

[6] J. R. Vig and T. Meeker, "The aging of bulk acoustic wave resonators, filters and oscillators," in *Frequency Control, 1991., Proceedings of the 45th Annual Symposium on*, 1991, pp. 77–101.

[7] R. Bennet, *Quartz Resonator Handbook. Manufacturing Guide for at Type Units*. Defense Technical Information Center, 1960.

GRAIL USOs; Another In-Flight Quartz Radiation Experiment

Gregory L. Weaver
Space Department
Johns Hopkins University Applied Physics Laboratory
Laurel, MD, USA
gregory.weaver@jhuapl.edu

Sami W. Asmar, Kamal Oudrhiri
Radio Science Systems Group
Jet Propulsion Laboratory, California Institute of Technology
Pasadena, CA, USA

***Abstract*—The Gravity Recovery and Interior Laboratory (GRAIL) mission successfully ended in December, 2012 after an extended science phase of over 280 days mapping the gravitation field gradient of the Moon with a precision of better than 50 E-6 g's over the entire lunar surface. The mission was performed by two tandem flying spacecraft, both of which carried a Microwave Dual One-way Ranging (DOWR) instrument that together formed a highly precise relative measure of the distance between the two spacecraft as they orbited the Moon.**

The precision of the radio link maintained by the DOWR instruments was derived from the frequency stability of the ultra-stable oscillators (USOs) on-board each spacecraft. The opportunity to observe the USOs frequency throughout the GRAIL mission provides a record of not only the intrinsic performance of the oscillators, but their behavior during exposure to space conditions. We describe the effect to the frequency of each GRAIL USO, A and B, resulting from the March 7th, 2012 X5.4 level solar flare, just several days into GRAIL's science collection phase. We discuss the impact of this radiation exposure, and the asymmetric behavior of two USOs coincidentally perturbed by the same space-weather event.

Keywords—GRAIL, oscillator, space-weather, irradiation

I. INTRODUCTION

The Johns Hopkins University Applied Physics Laboratory (JHU/APL) delivered four ultra-stable oscillators (USOs) in 2010 to the Jet Propulsion Laboratory of the California Institute of Technology (JPL) for integration into the Lunar Gravity Ranging System (LGRS) of the NASA Gravity Recovery and Interior Laboratory (GRAIL) twin spacecraft. The twin GRAIL A and B spacecraft (later named Ebb and Flow) were placed into a tandem flying orbital formation over the Moon to form a single-axis gradiometer, accomplishing the primary science mission of mapping the Moon's gravitational field with sufficient accuracy to work out many long-standing questions about the Moon's cratering process, internal structure, and thermal evolution [1].

As reference sources for the LGRS, the USOs frequency stability and phase noise were one of several principal contributors to the precision and resolution of GRAIL's gravity measurements. By the mission's end in Dec. 2012, the quality of the in-flight LGRS science return allowed the resolution of lunar highland crust and maria, addressing impact, magmatic, tectonic and volatile processes shaping the Moon's near surface. This required ranging precision nearly ten times better than the base mission requirements within spatial resolution of lunar features as fine as 30 km. In terms of frequency stability, the JHU/APL USOs were found to provide Allan deviation (Adev) performance of better than 1 E-13 over 1 to 100 s time intervals, temperature coefficients of < 5 E-13 per C, and aging rates below 1 E-11 per day.

Because of the unique design of GRAIL's radio science beacon links to NASA's Deep Space Network (DSN) ground, and spacecraft inter-ranging using JPL's dual one-way ranging (DOWR) method, the in-flight frequency behavior of each USO A and B was highly resolved. This allowed incidental environment or anomalous perturbations of < 1E-12 to be attributed and characterized. The capability to resolve the in-flight oscillator frequency behavior to this degree of precision is a rare feature in deep space operations. Our paper describes the incidence of a solar flare on the GRAIL A and B spacecraft while in lunar orbit on March 7th 2012, and characterizes the coincident frequency perturbations observed on the respective USOs A and B. The observed frequency perturbations are attributed to the sensitivity of quartz resonators to irradiation by protons in the 10 to 100 MeV range.

A. *GRAIL Science Objectives and Mission*

Understanding the structure and thermal evolution of a large rocky body such as the Moon is achieved through determining its density profile from its crust to interior, and assessing surface mass concentrations (mascons) associated with early magmatism and asteroid impacts. As discussed in [1], GRAIL was focused on resolving six primary mission lunar science objectives:

1. Map the structure of the lunar crust and lithosphere.

2. Understand the Moon's asymmetric thermal evolution.

3. Determine the subsurface structure of impact basins and the origin of mascons.

4. Ascertain the temporal evolution of crustal brecciation and magmatism.

5. Constrain the deep interior structure from tides.

6. Place limits on the size of the possible inner core.

Measurements of gravity variation on planetary-scale bodies traditionally use perturbations in the orbital dynamics of satellites assessed through radiometric Doppler-based range-rate methods. The principle behind this Doppler-based method is to coordinate the frequency change observed in the radio telemetry downlink against the ground system clock to planetary surface features in a line-of-sight manner with the Earth, after the navigation solution for orbital determination is applied to remove all expected Doppler frequency shifts.

The Moon, of course, offers a complication to the single satellite Doppler-based gravity method since its synchronous orbit with the Earth prevents the far-side from observation. The GRAIL mission was designed to remove this constraint through the use of a tandem flying two satellite approach, where the change in the relative distance between the spacecraft allows the measurement of gravity by directly observing the phase between two counter-opposed one-way radio links. Fig. 1 from [2] depicts the signaling scheme used in the GRAIL mission for navigation and communication. Two Ka band (32 GHz) carrier phase tracking loop assemblies, one in each spacecraft at slightly frequency offsets, perform the inter-satellite ranging determination (KBR). Coordinately, each spacecraft sends an X-band radio science beacon (RSB) to the NASA DSN to obtain the Doppler based range rate. Since the KBRs and RSBs of each spacecraft are coherent with their respective on-board USOs, the method of DOWR was used to extract lunar gravity variation from these two radiometric observables.

GRAIL's mission design is an analogue of the proceeding Gravity Recovery and Climate Experiment (GRACE), launched in 2002, which continues to measure the gravity field of the Earth. In GRACE, the DOWR method is applied and, as GRACE flies in LEO at about 500 km in altitude, takes advantage of GPS for absolute positioning and timing synchronization. Timing synchronization error between spacecraft in the DOWR method is a key driver in the precision of extracting gravity from the radiometric observables.

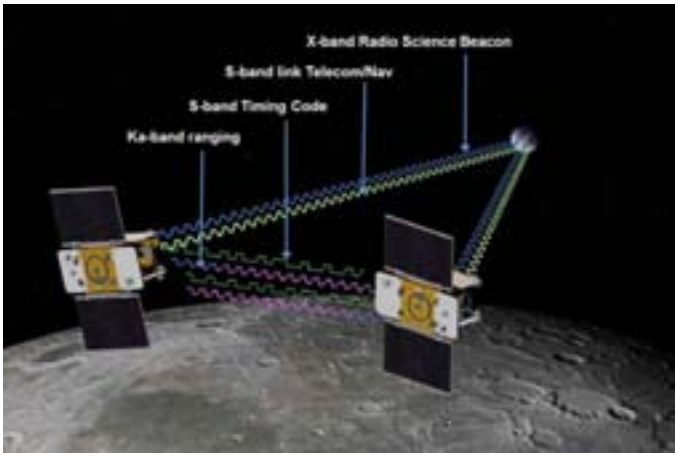

Fig. 1. Image above depicts the signaling scheme used in the GRAIL mission for navigation and communication. Two Ka band (32 GHz) carrier phase tracking loops, one in each spacecraft at slightly offset frequencies, are used for inter-satellite distance determination.

Clearly, the GRAIL LGRS could not use GPS for this purpose, and to maintain the required synchronization to better than 632 ps/Hz½ (corresponding to an error in inter-satellite distance precision of approximately 4 μm/Hz½), the LGRS design implemented an S-band inter-satellite time transfer system (TTS). [3] The performance of the TTS allowed inter-satellite synchronization to be maintained for up to 16 hours without ground link calibration. The TTS also permitted the demonstration of the first mission critical formation-flying satellite autonomous navigation around a planetary body beyond the Earth.

The primary mission of GRAIL was designed to execute three 27.3 day lunar mapping cycles over an 84 day Science Phase. The timing of the Science Phase was chosen to preserve a better than 40o sun-aspect to the spacecraft's fixed body solar panels, maintaining the highest possible power support for the LGRS. The GRAIL mission timeline from [1] is presented in Fig. 2 in a heliocentric viewpoint. GRAIL A and B launched on Sep. 10th 2011, after which they transferred to the Moon over a 107 day cruise, using the EL-1 Lagrange point. Lunar orbit insertion (LOI) occurred on Dec. 31st 2011 and Jan 1st 2012 for GRAIL A and B, respectively. Once the orbits and positions of GRAIL A and B were achieved, the Science Phase began on March 1st, 2012. The success of the initial mapping promoted an Extended Mission where the spacecraft were placed in a nearly circular orbit, 23 km in altitude. This vantage, along with the extremely-well performing instruments, allowed the measurement of lunar highland crust and maria structure, assessing the effect of dynamic processes which shaped the Moon's near surface. GRAIL A and B finished science collection on Dec. 14th at an altitude of 11 km.

B. LGRS Instrument Overview

As partially described above, the LGRS of GRAIL consists of a payload of radiometric instruments and data processing assemblies. As shown in Fig. 3, from [3] each GRAIL spacecraft USO provides a coherent frequency reference for the X-band RSB used for Doppler ranging and USO calibration, Microwave Assembly (MWA) which transmits and receives the KBR signal, and Gravity Processor Assembly (GPA) that processes phase changes to a precision of better than 10-4 cycles/Hz½ of the 32 GHz KBR signal (~1 μm/Hz½ of relative distance between the spacecraft). The GPA also maintains the timekeeping of the S-Band TTS. The LGRS operates in a continuous manner with the capability to process KBR downconverted signals into correlated baseband measurements (through synchronization provided by the TTS) at a running rate of 10 samples/s. The GPA is necessary since GRAIL must map on the far-side of the Moon with no ability to transfer or receive signals to Earth.

USOs A and B are offset in frequency by about 20.5 ppm to create a 670 kHz non-zero baseband IF signal in the MWA. The use of the non-zero baseband IF signal is identical to GRACE, and was chosen to mitigate cross interference within the MWA transmit and receive channels, while balancing the USO noise residual present in the non-zero mixing products. Direct down conversion of the KBR signals is accomplished by the comparison of the received signal to the transmitted signal,

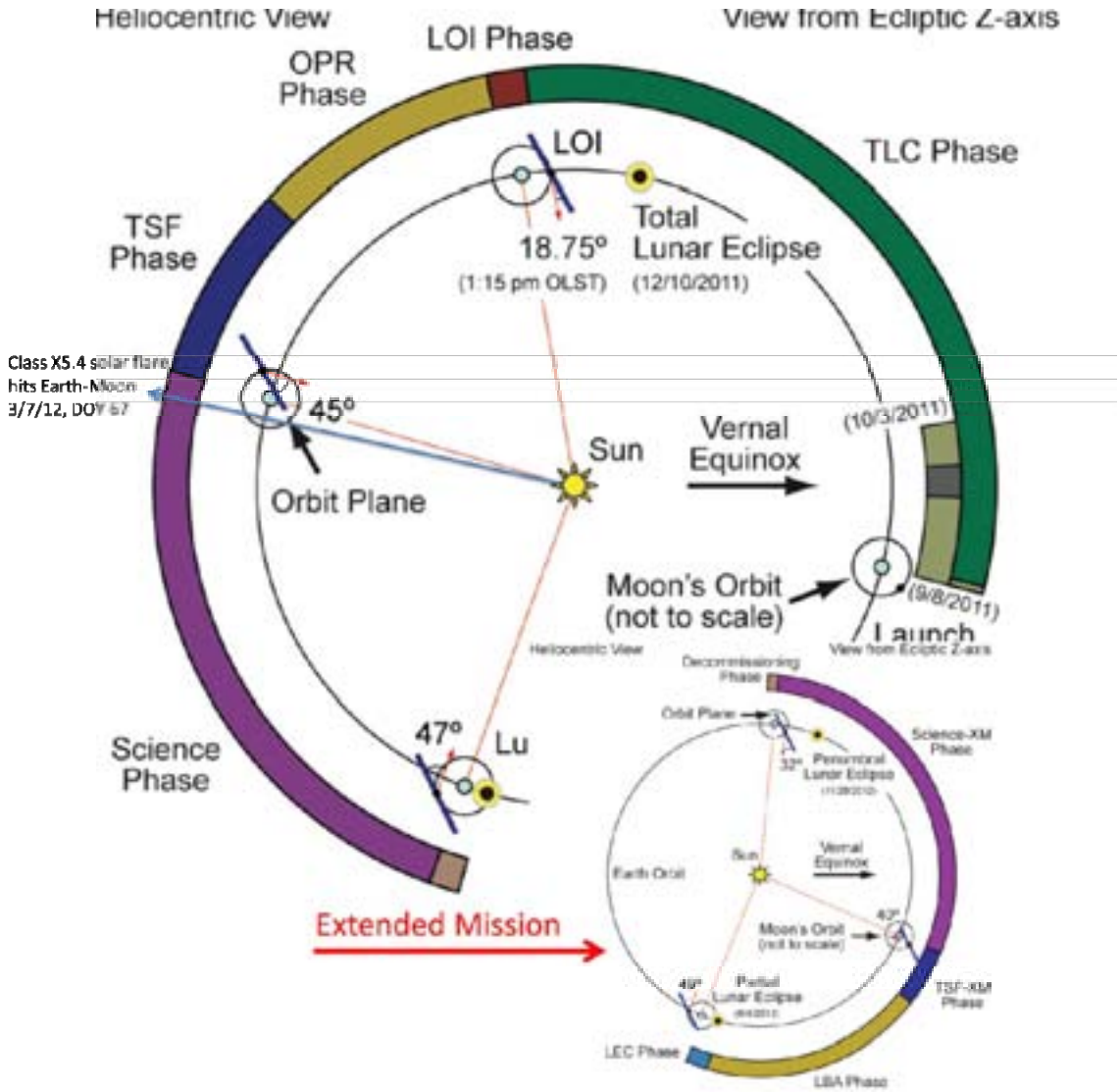

Fig. 2. The GRAIL mission timeline is presented above in a heliocentric viewpoint. GRAIL A and B launched on Sep. 10th 2011, after which they transferred to the Moon over a 107 day cruise, using the EL-1 Lagrange point. Lunar orbit insertion (LOI) occurred on Dec. 31st 2011 and Jan 1st 2012 for GRAIL A and B, respectively.

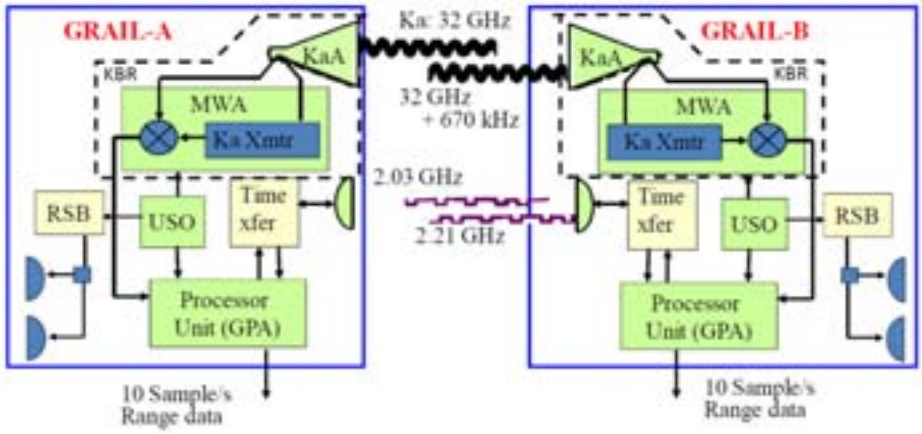

Fig. 3. Block diagram of LGRS, each GRAIL spacecraft USO provides the frequency reference for the Radio Science Beacon (RSB) used for Doppler tracking and USO calibration, Microwave Assembly (MWA) which creates and processes the ranging signal, and Gravity Processor Assembly (GPA) detects phase changes of 10-4 cycles (~1 μm of relative movement) and updates the S-Band Time Transfer System.

alternating the LO arrangement in each spacecraft's MWA. In this way, the low Fourier offset USO phase noise is cancelled in a high-pass manner, proportional to the one-way light time required to travel between the spacecraft. The change in distance or KBR phase between the two spacecraft is correlated so that the resulting IF phase information when summed in post-processing represents twice the actual distance change, which imparts one sense of the use of "dual" in the DOWR method. The doubled residual from the summed phase (two-clock) comparison is halved in post-processing when recovering acceleration.

To allow the summing of the correlated change of distance, the residual phase data associated with the clock comparison pairs, A to B and B to A, must be time coordinated. The TTS transmits a pseudorandom noise modulated signal across the link for timing information in the form of a pseudo-range measurement, equivalent to the one-way light time between the two spacecraft plus the time offset between clocks A and B. At each satellite, the received TTS signal is processed using GPS C/A code receivers inherited from GRACE. Frequency Division Multiple Access is implemented to avoid self-jamming. The two TTS transmit frequencies (2.032 GHz for spacecraft A and 2.207 GHz for spacecraft B) also avoid interference with the S-band spacecraft telecommunications and navigation downlink signals which transmit at approximately 2.280 GHz. TTS timing data is transmitted from the spacecraft as part of the instrument science data.

C. In-flight Instrument Performance and USO Verification

The 107 day cruise period of the mission design allowed for a highly desired stabilization period for the USOs, which were powered on shortly after launch, and remained powered throughout both the primary and extended mission. The long cruise using EL1 also allowed key performance evaluations of the LGRS prior to its arrival at the Moon, essentially using a gravitational quiet zone where gravity field perturbations are expected to be small. In [3], a post-launch check out on Sept. 22nd, 2011 validated the required sensitivity of the LGRS while also measuring a small relative acceleration between the spacecraft, accurately following the gravitational gradient expected from the Earth at 1 E+6 km. At the post-launch check-out, the Adev comparing the mutual stability of USOs A and B was also directly recovered by using the LGRS phase data in a novel way.

In [4], D. G. Enzer, et. al. describe the rare ability to extract the frequency stability of the paired in-flight GRAIL USOs without the need for compensation from X-band atmospheric propagation or the direct use of the DSN ground-clock for comparison. As described above, the DOWR method uses the sum of the correlated baseband phase data from spacecraft (A to B and B to A) to resolve twice the change of distance between the spacecraft.

Most conveniently, [4] derives an equation showing that, by differencing the two phase observables, successive phase differences in the two clock offsets, will form as,

$$\varphi_A^B(t) \text{ and } \varphi_B^A(t) \tag{1}$$

$$\frac{\varphi_A^B(t) - \varphi_B^A(t)}{2f_{avg}} + \frac{\Delta f}{f_{avg}} * t \tag{2}$$

where Δf is the 670 kHz KBR frequency offset, and f_{avg} is the average of the two KBR frequencies. The results calculated from (2) can be used to create the time series data necessary to directly estimate the Adev of USO A against USO B. Fig 4. from [4] plots the Adev of the relative phase offsets between USOs A and B under three conditions. The first was pre-launch prior to the integration of the science payload onto the spacecraft, where RF cabling was used to emulate a free-space link. The second was performed at the Sept. 22nd, 2011 post launch check-out described above. The third and final direct Adev measurement was made in lunar orbit just after the start of the Science Phase.

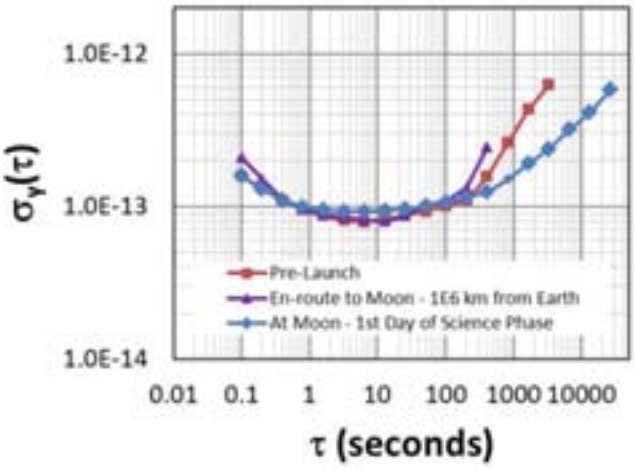

Fig. 4. The stability plotted above is the measurement of USO A against USO B at ground, and two mission conditions (en-route and on-orbit)

The USO performance shown by the three in-flight measurements is highly similar in the 1 to 100 s region, and this performance agrees well with both JHU/APL pre-ship measurements and JPL verification. The difference among the apparent drift beyond 100 s for the en-route and at-moon measurements is consistent with a maturing long-term trend as the USOs become adjusted to space conditions, revealing an apparent aging drift between the units of 2.4 E-12 per day at the start of the Science Phase. As fate would issue, this well-earned USO stabilization was to be upset 6 days later when an X5.4 level solar flare exploded from the Sun of March 7th, 2012.

II. GRAIL USO Frequency Change Observed Coincident with Solar Flare

Hereon, we describe the effect on the frequency to each GRAIL USO A and B resulting from the March 7th, 2012 X5.4 level solar flare, just several days into the Science Phase. We discuss the impact of this radiation exposure, and the asymmetric behavior of two space-oscillators coincidentally perturbed by the same space-weather event. One interesting aspect of the solar flare event was that the Moon was in a full

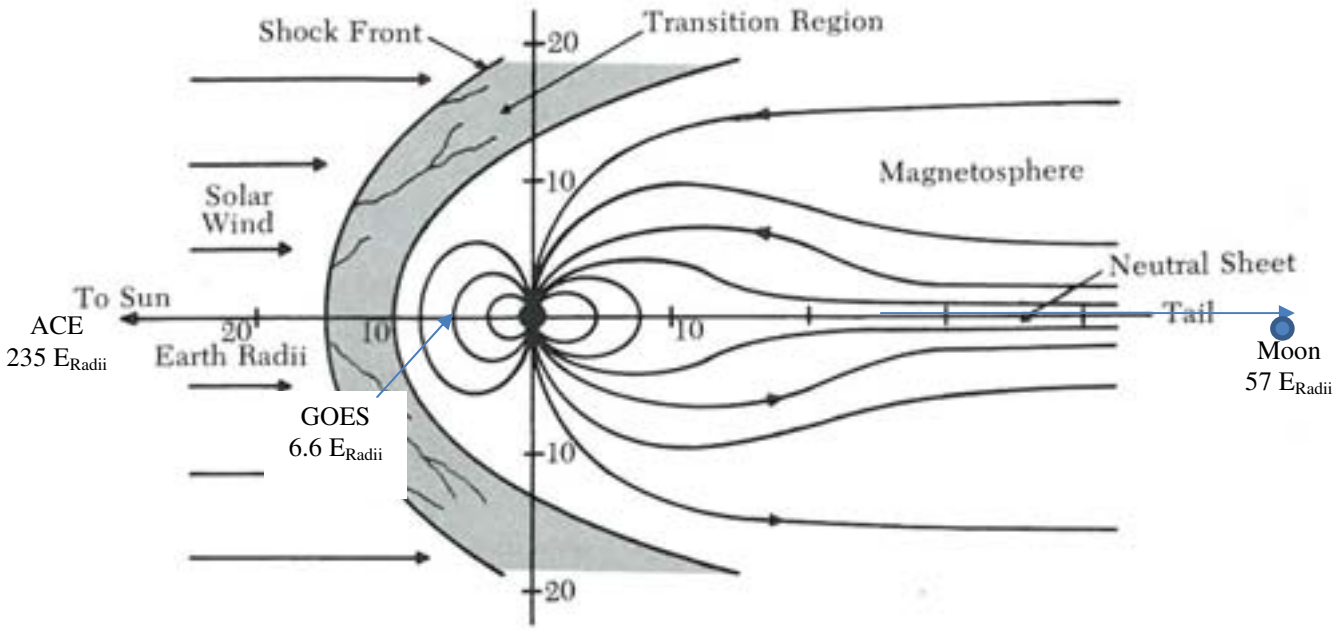

Fig. 5a. Earth magnetosphere scale cartoon showing Moon (and GRAIL spacecraft) in the magnetotail; full-moon of March 8th 2012.

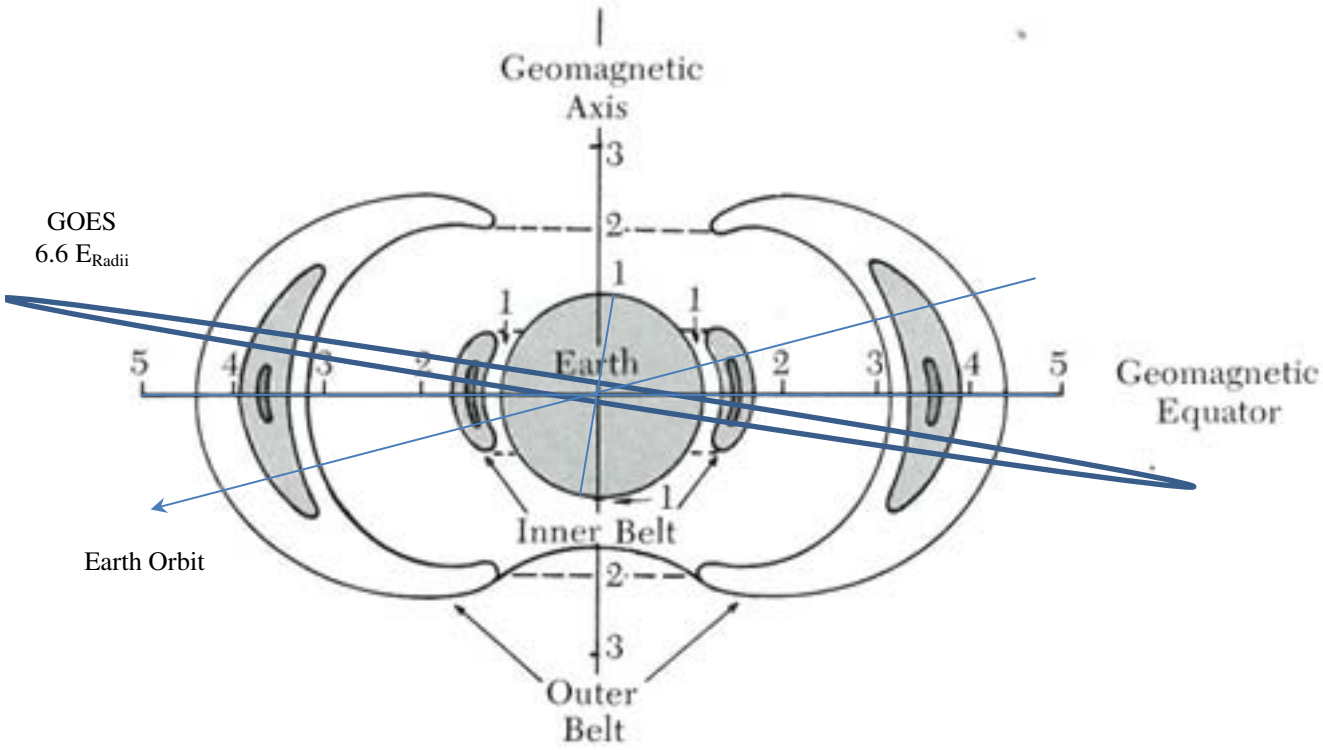

Fig. 5b. Earth Van Allen belt scale showing GOES spacecraft orbit; GOES 13 and 15 would be coming forward toward this daytime spring approximation, into the flux of the March 7th flare.

phase when the proton flux from the solar flare became incident on the Earth-Moon system, with the Moon well positioned in the Earth's magnetotail. This direct Sun-Earth-Moon alignment supports the use of Earth orbiting satellite data, collected during and after the flare for estimating particle flux, spectral energy distribution, time of flight and possibly dosimetry to GRAIL A and B.

A. *Characterization of Near-term Space weather after March 7th, 2012*

Figs. 5a and 5b show the position of the Moon (and GRAIL spacecraft), the Advanced Composition Explorer (ACE) spacecraft and the Geostationary Operational Environmental Satellite (GOES) geostationary orbit with respect to the Earth's

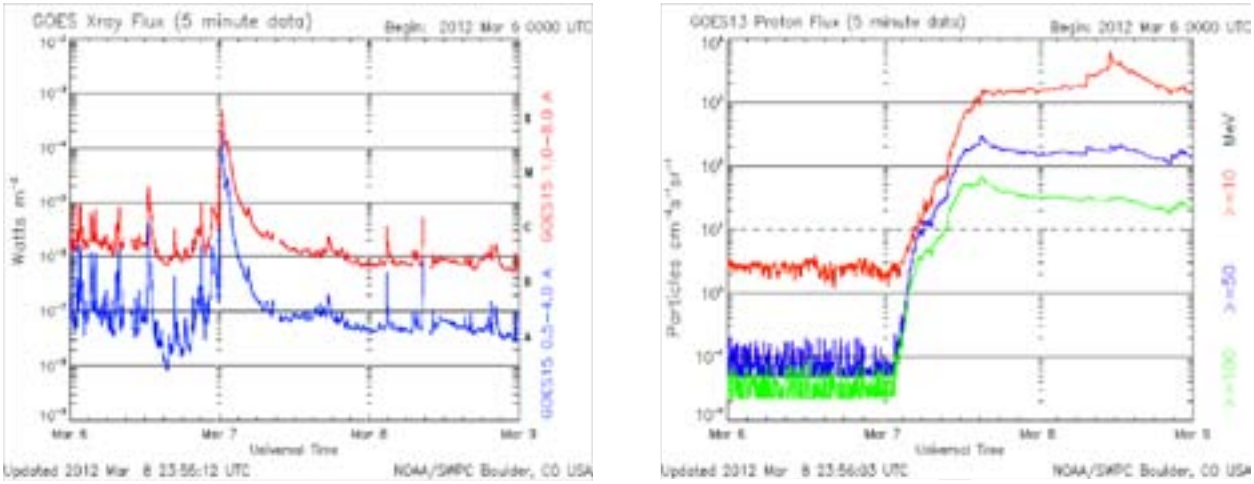

Fig. 6. GOES 15 data for X-ray flux(on-left) and GOES 13 for proton flux (on-right).

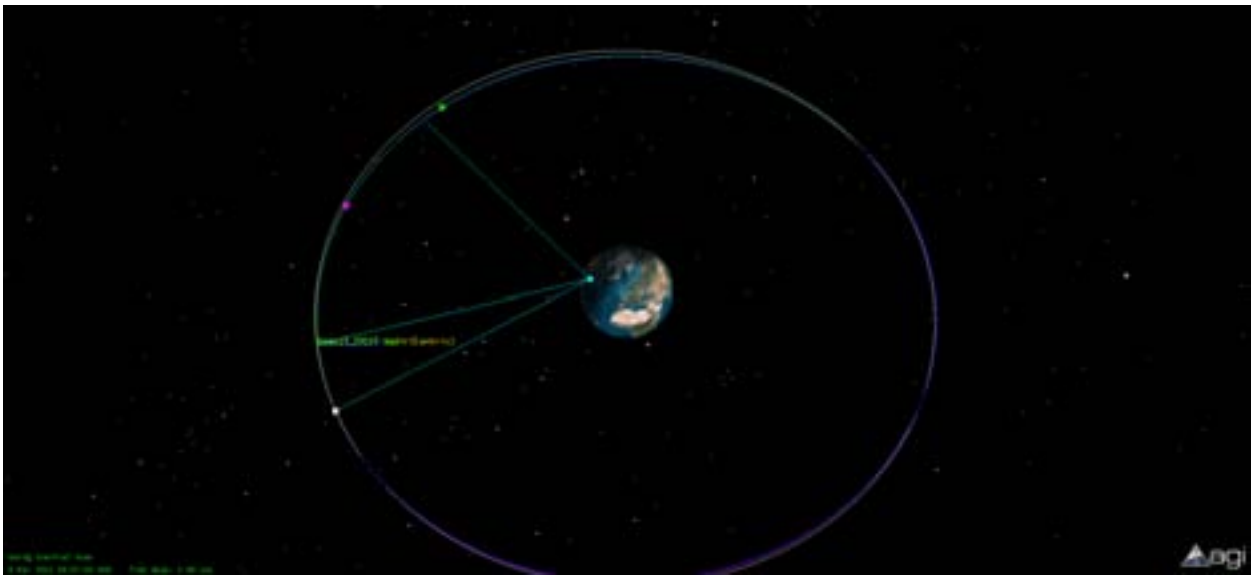

Fig. 7. Image shows position of GOES 13 on Mar 8th, 9:07 UT, sweeping into the incoming plasma front.

magnetosphere and Van Allen radiation belts. Fig. 5a is at the magnetosphere scale (measure in tens of Earth radii), while Fig. 5b is on the Van Allen belt scale (measure in Earth radii). The positions of these spacecraft are important to our observations, as we discuss the GRAIL USO frequency perturbations of Mar. 7th. ACE indicated the leading plasma edge on Mar. 7th 10:42 UT. ACE orbits the Sun-Earth L1 point approx. 1.5 million km toward the Sun from the Earth, slightly in advance of the Earth's magnetopause. GOES 15 data for X-ray flux and GOES 13 for proton flux is shown in Fig. 6. Fig. 7 shows the position of GOES 13 and 15 on Mar 8th, 9:07 UT, sweeping into the incoming plasma front.

B. USO Frequency Behavior at the Moon after Solar Flare

Fig. 8 shows short-term frequency behavior of GRAIL USOs A and B twelve hours before the solar flare, marked at almost exactly midnight of Mar. 7th (DOY 067 at 00:00 UT) and several days after the event . Inset of the chart shows the orbital position of GRAIL A and B as viewed from the Sun over the Science Phase of Mar. 4th to May 31st. The inset shows GRAIL B leading by 60 km in the early part of March. The start of the maximum rate of frequency change appears contemporaneous with the ramping proton flux detected by GOES 13. Fig. 9 shows the frequency history of the GRAIL A and B USOs about one week before the Mar. 7th flare (DOY 67) and for 30 days afterwards. The magnitude in observed frequency change in Hz at the NASA Deep Space Network (DSN) X-band downlink frequency (~8400 MHz) equates to parts in 1 E10, consistent with ionizing radiation exposure of in-flight USOs.

C. Comparison to Previous In-flight USO Exposure and Ground Irradiation Experiments

Reaction of quartz resonators (such as used in the GRAIL USOs) to ionizing radiation is well known. In 2003, an analysis of the Milstar FLT-1 on-board oscillator's frequency behavior during exposure to solar flares, described as a space experiment, was performed using space-weather data

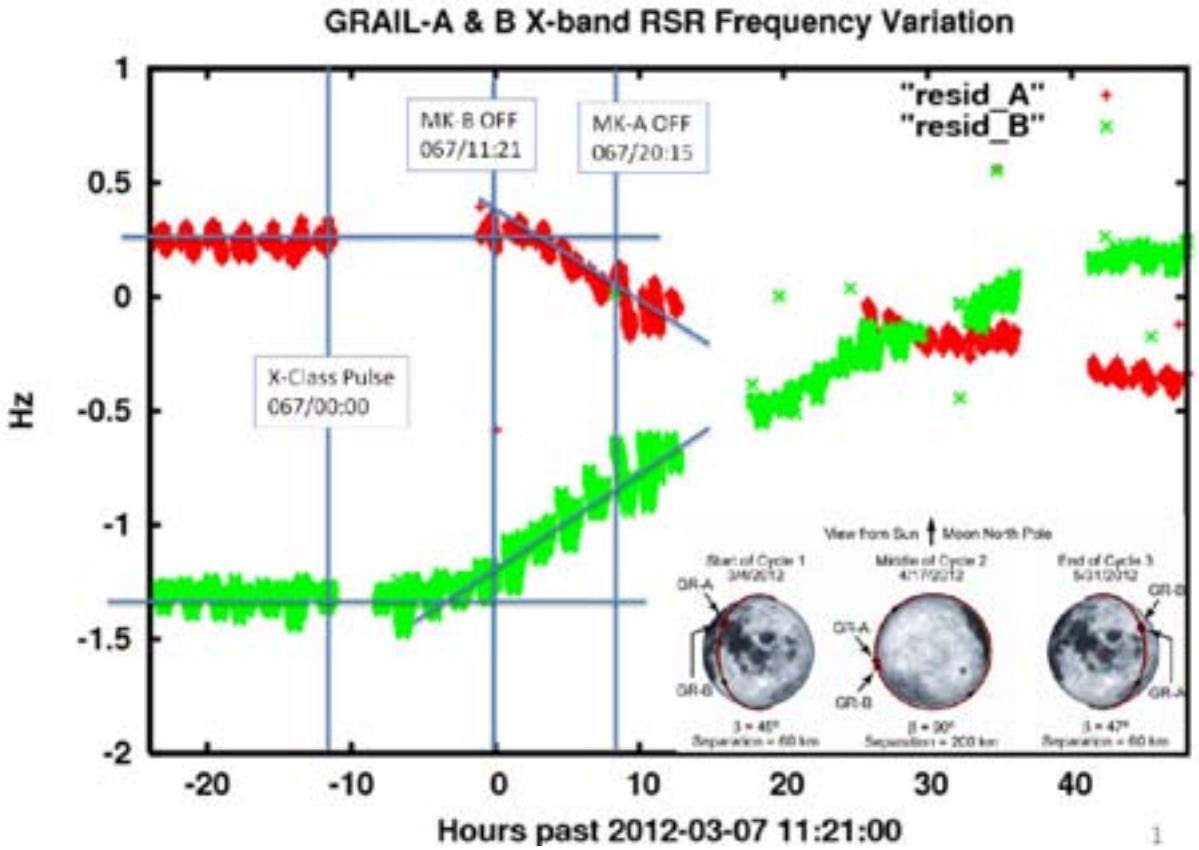

Fig. 8. Chart above shows short-term frequency behavior of GRAIL USOs A and B twelve hours before the solar flare, marked at almost exactly midnight of Mar. 7th (DOY 067 at 00:00 UT) and several days after the event . Inset of the chart shows the orbital position of GRAIL A and B as viewed from the Sun over the Science Phase of Mar. 4th to May 31st. The inset shows GRAIL B leading by 60 km in the early part of March. The start of the maximum rate of frequency change appears contemporaneous with the ramping proton flux detected by GOES 13.

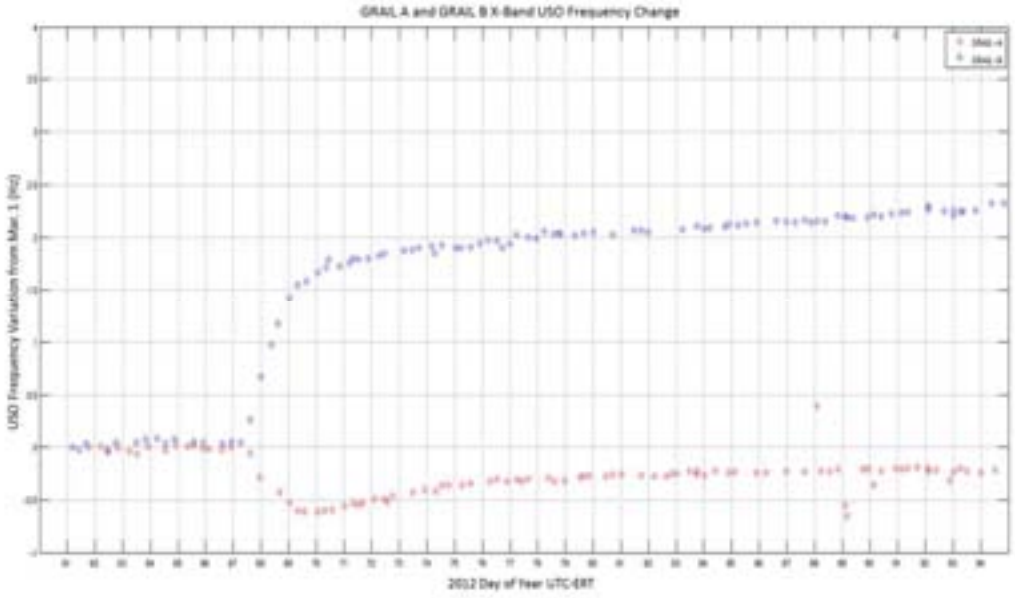

Fig. 9. Chart shows the frequency history of the GRAIL A and B USOs about one week before the Mar. 7th flare (DOY 67) and for 30 days afterwards. The magnitude in observed frequency change in Hz at the NASA Deep Space Network (DSN) X-band downlink frequency (~8400 MHz) equates to parts in 1 E10, consistent with ionizing radiation exposure of in-flight USOs.

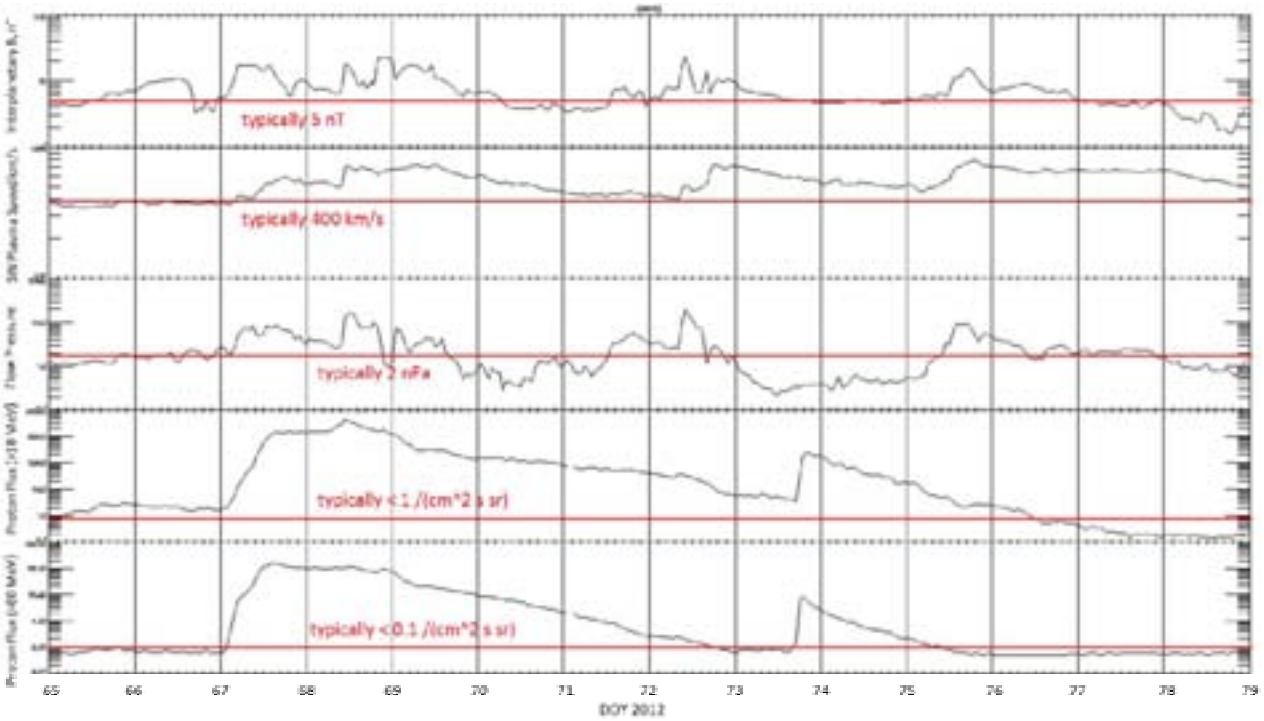

Fig. 10. chart gives a variety of solar wind parameters from NASA's OMNIWeb for the interval from Mar. 5-18, showing disturbed solar wind conditions and enhanced magnetosphere activity for much of this interval. The red overlays gives typical levels.

accumulated by the GOES [5]. Entirely similar, our observation of the GRAIL USO A and B behaviors after the Mar. 7th flare is an additional in-flight experiment with the added feature of two USOs being exposed at the same time within the same environment. Moreover, the unique frequency recovery enabled by the NASA JPL DOWR instrument removes concern that the frequency change observed at X-band by the DSN could be influenced by ionospheric perturbation due to the flare event.

Fig. 10 gives a variety of solar wind parameters from NASA's OMNIWeb for the interval from Mar. 5-18, showing disturbed solar wind conditions and enhanced magnetosphere activity for much of this interval. The red overlays gives typical levels. The correlation of the GRAIL USO A frequency change magnitude to the 10 and 80 MeV proton flux (last two plots of Fig.10) over the two weeks following the flare can be clearly distinguished, and such coordinate behavior is expected with quartz radiation sensitivity. The frequency behavior of GRAIL USO B, being opposite in sign, and not diminishing with decreasing proton flux is not inconsistent with cyclotron quartz resonator screening data.

Table 1 below shows the summary of seven quartz resonator radiation sensitivity experiments using 60 MeV proton irradiation. The proton flux ranges and frequency changes from the screening data are similar in magnitude with the solar wind data and GRAIL USO behavior described above. Also found in the screening results were varying polarities of frequency change, annealing character and irregular (non-linear) reactions [6].

TABLE I. PROTON IRRADIATION RESULTS OF QUARTZ RESONATORS FROM [6]

Exp #	Test Bed	Start Date, Time	Flux range [p/cm^2/sec]	Adjusted mean df/f per rad(Si)	Polarity	Annealing	Character
1	SC10	10/22, 9:55	2774 - 13126	-5.875E-11	-	YES	irregular: b, m
2	SC9	10/22, 14:19	3006 - 10584	5.529E-11	+	?	irregular: b, s
3	HQ23	10/22, 21:16	3007 - 9869	5.512E-11	+	NO	linear: slight b
4	P2	10/23, 7:20	3140 - 10694	1.720E-11	+	?	irregular: b, m , i
5	HQ24	10/23, 12:30	2639 - 10821	-1.906E-10	-	NO	linear: b
6	P1	10/24, 8:44	1016 - 6325	1.869E-10	+	NO	linear
7	PB	10/24, 11:18	3399 - 10197	4.541E-11	+	?	irregular: i

III. CONCLUSION

The interaction of the GRAIL USOs with the Mar 7th solar flare suggests science value in the characterization of USO radiation sensitivity prior to launch. These results continue to reveal that USO's, with properly calibrated sensitivities, can be an important adjunct to mission science collection as sensors for experiments in the deep space environment

ACKNOWLEDGMENT

We thank Dr. Timothy J. Stubbs of NASA Goddard Space Flight Center for consulting about behavior of solar wind particles at the Moon while in Earth's magnetosphere and the data of Fig. 10.

REFERENCES

[1] M. T. Zuber, D. E. Smith, D. H. Lehman, T. L. Hoffman, S. W. Asmar, M. M. Watkins, "Gravity Recovery and Interior Laboratory (GRAIL): Mapping the lunar Interior from crust to core," Space Science Reviews 10.1007/s11214-012-9952-7, 2103.

[2] S. W. Asmar, A. S. Konopliv, M. M. Watkins, J. G. Williams, R. S. Park, G. Kruizinga, M. Paik, D. N. Yuan, E. Fahnestock, D. Strekalov, N. Harvey, W. Lu, D. Kahan, K. Oudrhiri, D. E. Smith, M. T. Zuber, "The scientific measurement system of the Gravity Recovery and Interior Laboratory (GRAIL) mission," Space Science Reviews DOI 10.1007/s11214-013-9962-0, 2013.

[3] W. M. Klipstein, B. W. Arnold, D. G. Enzer, A. A. Ruiz, J. Y. Tien, R. T. Wang, C. E. Dunn, "The Lunar Gravity Ranging System for the Gravity Recovery and Interior Laboratory (GRAIL) mission," Space Science Reviews DOI 10.1007/s11214-013-9973-0, 2013.

[4] D. G. Enzer, R. T. Wang, K. Oudrhiri, W. M. Klipstein, "In situ measurements of USO performance in space using the twin GRAIL spacecraft", 2012 IEEE IFCS Proc., May 2012, Baltimore, MD, pp. 533 -537

[5] S. D. LaLumondiere, S. C. Moss, J. C. Camparo, "A "space experiment" examining the response of a geosynchronous quartz crystal oscillator to various levels of solar activity," IEEE Trans. UFFC, vol.50, no.3, pp.210-213, March 2003.

[6] G. L. Weaver, M. J. Reinhart, H. B. Sequeira, W. Stapor, "Examination of detailed frequency behavior of quartz resonators under low dose exposures to proton radiation," 2004 IEEE IFCS and Expo. Proc., Montreal, QC.

Long-Term Stability of a Hermetically Packaged MEMS Disk Oscillator

Tristan O. Rocheleau, Thura Lin Naing, and Clark T.-C. Nguyen
Dept. of Electrical Engineering and Computer Science
University of California, Berkeley
Berkeley, USA
Email: tristan@eecs.berkeley.edu

***Abstract*—A low phase noise oscillator referenced to a wine-glass disk MEMS resonator, hermetically vacuum packaged in a purpose-built packaging system, and measured in a double-oven, has provided a first long-term measurement of a MEMS disk oscillator over 10 months. After an initial burn-in period, the frequency can be seen to stabilize to within the short-term measurement variation of 300 ppb over a period of months, a significant improvement from previous studies on other MEMS resonator types, where frequency fluctuations were between 3.1 ppm and 1.2 ppm over similar time scales. Including burn-in, the total observed aging of 10 ppm is now on par with many consumer-grade quartz oscillators designed for timing applications and sufficient for target wireless sensor network applications.**

Keywords—MEMS oscillator, aging, long-term stability, hermetic packaging.

I. Introduction

MEMS-based resonators have emerged in recent years as low cost, on-chip alternatives to traditional quartz frequency references for use in timing applications [1]. Such devices offer not only valuable space savings in ever-shrinking consumer devices, such as cellular handsets, but also offer paths towards meeting the ultra-low-power requirements demanded by future wireless sensor networks [2]. While short-term stability of MEMS-based oscillators has proven to be quite good, where even the challenging GSM phase noise specifications were met some time ago [3], the long-term reliability and stability of such resonators has been largely unstudied.

Long-term frequency stability of reference oscillators is essential to maintain reliable radio communication without signals drifting into nearby bands. Typical frequency stability requirements are application-dependent and can range from tens of ppm per year to less than one ppm [4]. Cell phone requirements, for instance, remain one of the most challenging, with GSM requiring ±0.1 ppm reference oscillator stability [5]. Requirements for local-area wireless standards are much more lenient, however, with typical stability requirements of ±40 ppm [6]. Although the small size of MEMS resonators make them an exciting alternative to traditional quartz, they at the same time raise concerns of increased aging effects due to mass loading, package leaks, or stress fatiguing [7].

Some of the first published investigations on wafer-scale encapsulated resonators [8] indicated good stability, but measurements were of resonators only, not full oscillators, and were limited by experimental setup fluctuations to an accuracy of only ±3.1 ppm. Some more recent efforts have shown limited stability data of oscillators. One study [9] used an Aluminum-Nitride bulk acoustic wave resonator reference over 50 days of measurement. Here too, measurement setup fluctuations and lack of vacuum packaging, a necessary component for achieving the high Q of MEMS resonators, limited measurements to shorter time-scales and frequency fluctuations of ±1.2 ppm. Another study on a commercial device fabricated by SiTime [10] demonstrated exceptional short-term frequency stability of ±3 ppb, but only made measurements over periods of up to 15 minutes. Yet another study [11] demonstrated very close differential frequency tracking of two resonators over periods up to 30 days, but again intrinsic frequency stability was limited by measurement setup fluctuations.

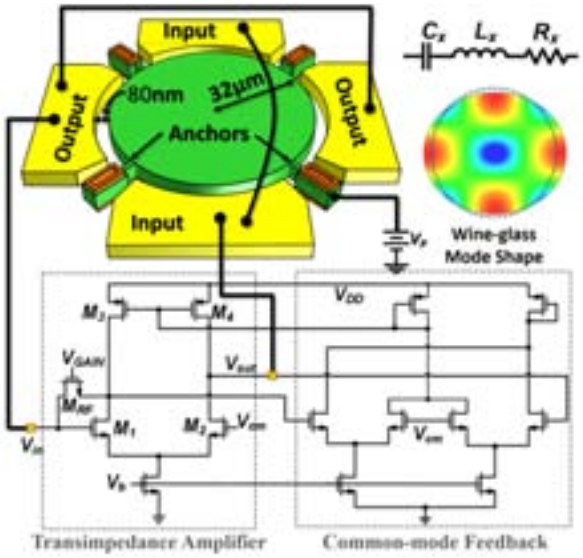

Fig. 1: Circuit schematic of the tested transimpedance amplifier-based micromechanical wine-glass disk oscillator, with the simplified equivalent circuit and mode shape for the MEMS resonator.

Meanwhile, wine-glass disk oscillators are known to exhibit exceptional short-term stability, with demonstrated phase noise below the GSM spec. [3] and superior insensitivity to vibration versus typical quartz counterparts [12]. But studies of long-term stability have until now been unpublished. To remedy this, this paper presents a first measurement of the MEMS oscillator of Fig. 1, comprised of a wine-glass disk resonator bond-wired to

This work was supported in large part by the DARPA N/MEMS S&T program.

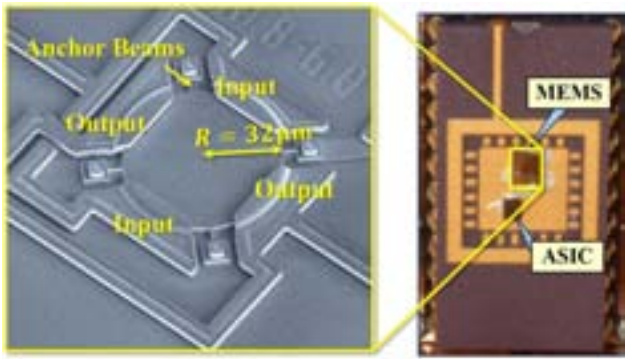

Fig. 2: SEM of the wine-glass disk resonator, left, bondwired into a DIP package with the ASIC amplifier, right.

an ASIC transimpedance amplifier and hermetically packaged in a custom-built vacuum-packaging system capable of maintaining μtorr pressures. A double-oven system maintains a constant oscillator temperature at 34°C with less than 0.001°C deviation, a key improvement over previous studies.

The long-term frequency drift of this MEMS oscillator is measured over 10 months and found to stabilize to within the short-term measurement variation of ±300 ppb over a period of months after an initial burn-in period. This marks a significant improvement from previous studies on other MEMS resonator types, where frequency fluctuations were ±3.1 ppm [8] and ±1.2 ppm [9] over similar time scales. Including burn-in, the total observed aging of 10 ppm over 10 months is now on par with many consumer quartz oscillators designed for timing applications [4] and marks performance sufficient for use in short-range wirelesss sensor networks.

II. The MEMS Oscillator

The wine-glass disk resonator used in this work, cf. Fig. 2, was fabricated using the same process as [13] and consists of a 3μm-thick, polysilicon disk with 32μm-radius supported by four beams and surrounded by electrodes separated by a tiny 80 nm capacitive gap. The resonator motion is coupled to the electrical input and output via a bias voltage V_P applied to the disk. An ac drive voltage applied to the input electrode combines with V_P to produce a force across the input electrode-to-resonator gap that drives the resonator into the compound (2, 1) mode shape, shown in Fig. 1, which comprises expansion and contraction of the disk along orthogonal axes with nodal points located at support beam attachment locations. The relationship between the drive voltage and ensuing current generated by dc-biased mechanical modulation of the electrode-to-resonator gaps at each port is aptly modeled by the equivalent *LCR* circuit shown in Fig. 1. This mode's resonance frequency is given by:

$$f_{nom} = \frac{K}{R}\sqrt{\frac{E}{\rho(2+2\sigma)}} \qquad (1)$$

where R is the disk radius, $K = 0.373$ for polysilicon structural material, and E, σ, and ρ are Young's modulus, Poisson ratio, and density of the structural material, respectively.

To form an oscillator, the resonator is placed in the feedback path of a transimpedance amplifier similar to that of [12] and consisting of a fully differential CMOS amplifier connected in shunt-shunt feedback on one arm, with output taken from the other to realize a 0° phase shift from input to output. Transistors, M_1-M_4, comprise the basic differential pair biased by a common-mode feedback circuit that preserves low output resistance and cancels out common-mode noise. The MOS transistor M_{RF} is biased in the triode region to serve as a voltage controllable shunt-shunt feedback resistor that allows convenient adjustment of the TIA gain via its gate voltage, V_{GAIN}. When gain of the TIA is greater than the motional resistance of the resonator, R_x, the positive loop gain amplifies the (initially Brownian) motion until nonlinearity in either the amplifier or resonator (or both) limits the oscillation amplitude.

The amplifier IC was fabricated in a 0.35μm CMOS technology. Although the entire die occupies an area of 900μm×500μm, the actual sustaining amplifier only consumes about 100μm×100μm. The rest of the area is consumed by an on-chip buffer used to drive 50 Ω measurement systems and by-pass capacitors for noise reduction.

III. Stable Measurement Environment

A. Packaging

Of central import in MEMS oscillator stability is packaging. For example, exposure to air is known to produce frequency shifts due to oxidation or moisture absorption even in quartz oscillators [4]. The tiny size of MEMS resonators makes environmental control even more important. For the typical resonator used here, even a single additional monolayer of atoms, from sources such as contamination or package leakage, would correspond to a frequency change of over 30 ppm.

Beyond material aging concerns, a good vacuum environment is also needed to reduce air damping and enhance resonator Q. Fig. 3 gauges the degree to which air damping affects a typical wine-glass disk resonator used in this study with a measured plot of Q versus pressure that indicates a required operating pressure of below 1mtorr to remove air damping as a relevant loss mechanism. Achieving reliable hermetic packaging at such pressures is a challenge in a laboratory environment, and a chief obstacle in past long-term studies.

Pursuant to this goal, the vacuum packaging system of Fig. 4 was constructed to facilitate hermetic sealing using AuSn solder seals with a variety of conventional ceramic packages in a vacuum environment. In this system, a heated chuck holds the ceramic package containing the bond-wired MEMS resonator and ASIC while the package lid and magnetically attach to a linear motional feedthrough.

To package an oscillator, the ASIC and MEMS die, along

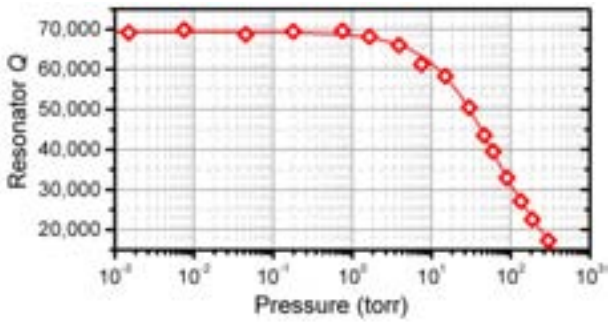

Fig. 3: Measured wine-glass disk MEMS resonator Q as a function of ambient air pressure.

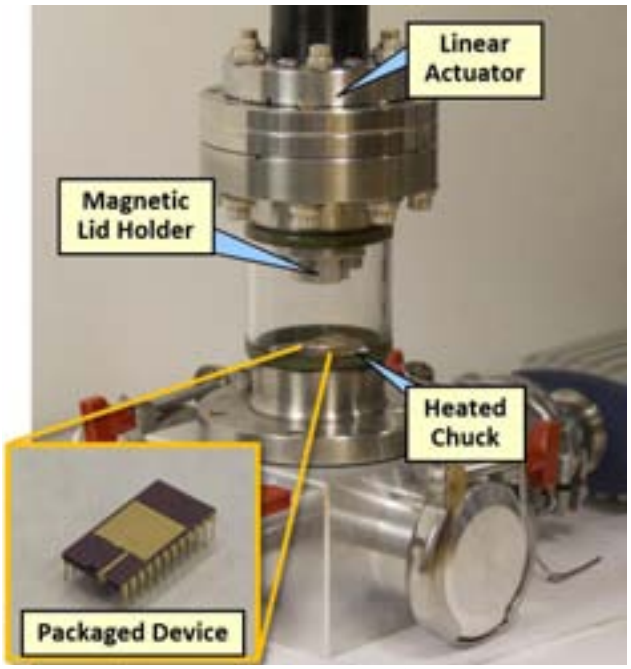

Fig. 4: Hemermetic vacuum packaging tool with zoom-in (inset) on a DIP package sealed via the tool.

with Ti metal shavings used as a getter, are first glued within the package using Ceramabond 552 high-vacuum ceramic adhesive. The package is mounted in the packaging chamber and pumped to µtorr vacuum. Following a 2 hour bakeout at 220ºC, the package lid with AuSn preform is pressed with ~10 lbs. of force against the package and heated to 350ºC for 1 minute. The package and chuck are allowed to cool to room temperature before venting and unloading. For the oscillators in this study, Kyocera KD-78382-01 24-pin dual in-line packages (DIP) and HRC-2578 lids were used.

B. Temperature Control

In order to accurately measure true aging-induced frequency drifts, the oscillator temperature environment must be very tightly controlled or compensated. For the polysilicon devices used here, the measured temperature coefficient of frequency is on the order of $T_{CF} = 21$ ppm/°C, which allows excessive frequency shifts when ambient temperature fluctuations are not compensated. In the past, two methods of temperature compensation have been applied to MEMS oscillators. Passive compensation seems to be limited to ±40 ppm total frequency shift over commercial temperature ranges [9]. On the other hand, active temperature compensation is widely used in production MEMS oscillators to provide full temperature range stability to better than ± 10 ppm [14]. But to accurately observe true frequency drift in the absence of thermal variations, an even more stable temperature environment is needed.

To this end, the work presented here employs the double-oven setup of Fig. 5 to house the measured oscillators. The outer oven consists of a Cincinnati Sub-Zero MCB-1.2 chamber which keeps the internal temperature within ± 0.1C. To further stabilize temperature, a second internal oven combines a computer controlled heating element and temperature sensor incorporated into the box used to mount the oscillator. An ultra-stable Measurement-Specialties 46007 glass-encapsulated thermistor serves as the temperature monitor and control, measured using an Agilent 34420A micro-ohm meter. This double oven was observed to hold temperature to within ~200 µK in the face of typical daily external temperature fluctuations.

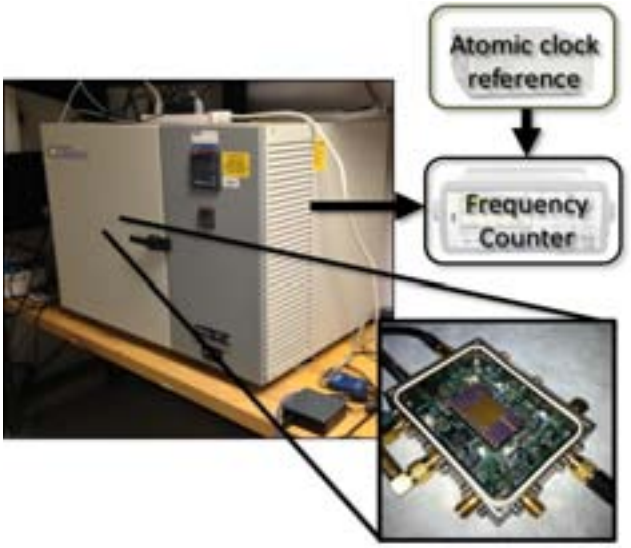

Fig. 5: Experimental measurement setup showing the oscillator mounted in the first temperature controlled oven (inset) and placed in a second environmental chamber oven for further temperature stability. The oscillator frequency is measured via a zero dead-time counter referenced to an atomic clock.

C. Frequency Measurement

When emplaced in the temperature-stable double-oven system, the oscillator output is measured using an Agilent 53230A frequency counter which allows high-resolution measurement with no dead time, i.e., no gap between measurements. For highly-stable measurements over long periods, a Stanford Research Systems FS725 atomic clock provides a frequency reference specified with ±5 ppb aging over a 20 year lifespan.

IV. Measurement Results

Fig. 6 presents typical 1 day data for the oscillator mounted in the double-oven stabilization system and demonstrates remarkable frequency stability down to ±150 ppb. Fig. 7 presents measured oscillator frequency versus time data over a 10 month aging period, exhibiting the same logarithmic decay behavior typical of quartz oscillators [4]. The increasing frequency suggests possible stress relaxation or changes to the resonator material properties over mass loading or package leaks

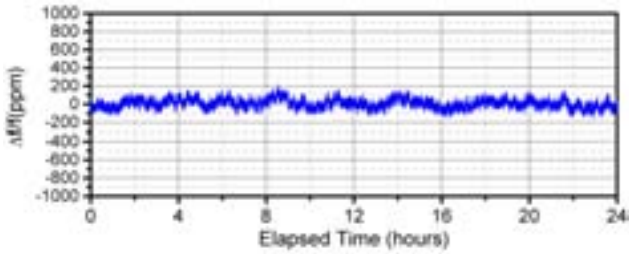

Fig. 6: Typical oscillator stability over 24 hours with a 1s averaging time.

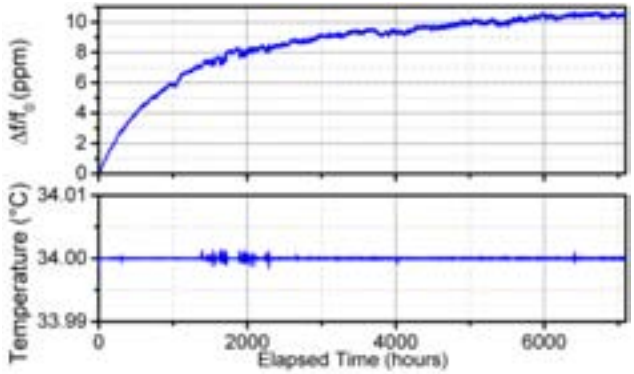

Fig. 7: Measured frequency drift and temperature stability of the MEMS oscillator. Frequency measurements were made using an Agilent 53230A frequency counter and shown here with a 100s measurement time.

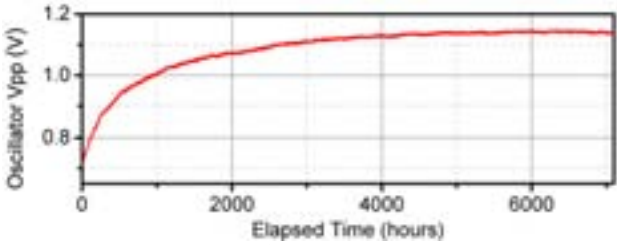

Fig. 8: Amplitude of oscillation during a long-term measurement.

as the aging mechanism. Stress relaxation in particular would be expected to contribute as both bond-wires and high-temp glue adhering the die to package would be expected to produce strain and have been observed to produce over 100 ppm/week drift in flexural mode devices [15]. Despite this, performance is good, on par even with low-cost quartz oscillators. This is not unexpected for such wine-glass devices, for which supports attached to quasi-nodal points on the resonant disk structure greatly isolate the disk from the substrate and its associated stress changes.

Interestingly, Fig. 8 presents oscillation amplitude data taken from this same time range, and shows an unexpected increase closely following the frequency drift seen. As the amplifier gain is kept fixed, this points to a surprising decrease in the R_x of the resonator over time. This again suggests that increased mass loading or air damping is not a factor here and further confirms a reliable package over the measured time span.

To better gauge the performance of this oscillator, Allan Deviation, σ_y, can be calculated from the fractional frequency shift $y_n = \Delta f / f_0$ using

$$\sigma_y^2(\tau) = \frac{1}{2}\langle(\bar{y}_{n+1} + \bar{y}_n)^2\rangle \qquad (2)$$

Fig. 9 presents Allan deviation vs. averaging time for the oscillator here. This plot closely follows typical performance of crystal oscillators [4], with decreasing Allan deviation for increasing measurement times up to approximately 1s as white phase and frequency noise are averaged out. Above 1s averaging time, the Allan deviations achieves a floor of $\sigma_y = 1.5\ x\ 10^{-8}$, competitive with typical quartz timing oscillators. As averaging time is increased, Allan Deviation remains constant till it begins to increase due to longer-term random walk noise, ultimately becoming dominated by long-term frequency drift effects.

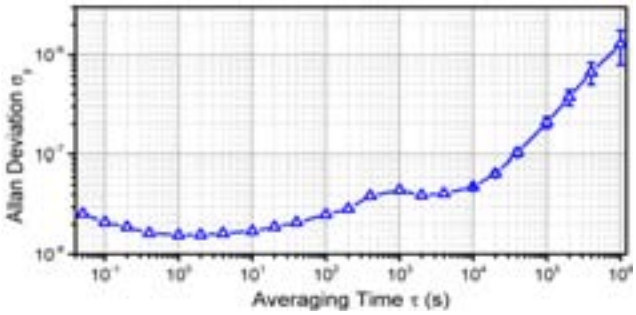

Fig. 9: Allan deviation as calculated from stability data with differing averaging times. Data with averaging time below 400s was calculated from shorter data sets taken at 0.01s sample time, while longer averaging time data was calculated from the full long-term stability data.

V. Conclusions

In this first study of long-term frequency drift in micromechanical wine-glass disk oscillators, performance is seen to be quite good, achieving stability within ± 300 ppb over a month after a burn-in period. With burn-in, the total drift is only 10 ppm over 10 months, well within required limits for many short-distance wireless communication specifications despite concerns that the small size of such MEMS resonators would lead to drift and reliability issues. Moreover, the increasing amplitude of oscillation over time suggests actual improvement in resonator quality factor and demonstrates that even simple in-house vacuum packaging is sufficient to achieve reliable operation of these MEMS devices. Whether or not Q's truly increase with time, the long-term stability measured here, together with the GSM-compliant phase noise already demonstrated in parallel work [3], elevates micromechanical wine-glass disk oscillators as some of the best MEMS has to offer, and encourages their use in small form factor, low power applications, such as the autonomous wireless sensor market, expected to grow exponentially in the coming years. More challenging cell phone reference oscillator requirements remain a target for future improvement.

References

[1] C. T. C. Nguyen, *UFFC Transactions,* vol. 54, pp. 251-270, 2007.
[2] J. M. Rabaey, J. Ammer, T. Karalar, L. Suetfei, B. Otis, M. Sheets, *et al.*, *ISSCC*, 2002, pp. 200-201 vol.1.
[3] Y.-W. Lin, S. Lee, S.-S. Li, Y. Xie, Z. Ren, and C.-C. Nguyen, *IEEE Journal of Solid-State Circuits,* vol. 39, pp. 2477-2491, 2004.
[4] J. R. Vig and T. R. Meeker, *Proceedings, FCS*, 1991, pp. 77-101.
[5] ETSI, Technical Specification 100 912
[6] IEEE, Standard 802.15.4
[7] C. L. Muhlstein, S. B. Brown, and R. O. Ritchie, *Journal of Microelectromechanical Systems,* vol. 10, pp. 593-600, 2001.
[8] B. Kim, R. N. Candler, M. A. Hopcroft, M. Agarwal, W.-T. Park, and T. W. Kenny, *Sensors and Actuators A,* vol. 136, pp. 125-131, 2007.
[9] R. Tabrizian, M. Pardo, and F. Ayazi, *Proceedings, IEEE Int. Conf. on MEMS*, 2012, pp. 23-26.
[10] L. Haechang, A. Partridge, and F. Assaderaghi, *Frequency Control Symposium*, 2012, pp. 1-5.
[11] E. J. Ng, L. Hyung Kyu, A. Chae Hyuck, R. Melamud, and T. W. Kenny, *IEEE Sensors Journal,* vol. 13, pp. 987-993, 2013.
[12] T. L. Naing, T. O. Rocheleau, R. Zeying, E. Alon, and C. T. C. Nguyen, *Proceedings, FCS*, 2012, pp. 1-6.
[13] M. A. Abdelmoneum, M. U. Demirci, and C. T. C. Nguyen, *Proceedings, IEEE Int. Conf. on MEMS*, 2003, pp. 698-701.
[14] Discera Corporation, "DSC1121 Datasheet."
[15] V. Kaajakari, J. Kiihamaki, A. Oja, H. Seppa, S. Pietikainen, V. Kokkala, *et al.*, *Proceedings, TRANSDUCERS*, 2005, pp. 916-919 Vol. 1.

All-Digital Frequency Synthesis based on Single-Bit Nyquist-Rate Sinewave Quantization with IID Random Dithering

Paul P. Sotiriadis
Department of Electrical and Computer Engineering
National Technical University of Athens
Greece
pps@ieee.org

Nikos Stamatopoulos
Department of Electrical and Computer Engineering
National Technical University of Athens
Greece
nstam@ieee.org

***Abstract*—All-digital frequency synthesis based on single-bit, Nyquist-rate, quantization of sinewave with independent and identically distributed random amplitude dithering is proposed. The output spectrum of the quantizer is derived in closed form and is related to the distribution of the random dither. Conditions for spurs-free output are derived, and the output dynamic range is defined. MATLAB simulation examples illustrate the results of the proposed approach.**

Keywords—Digital-to-frequency converter, direct digital synthesis, frequency spurs, quantization

I. INTRODUCTION

The interest in all-digital frequency synthesis (FS) has been intensified in the R.F.I.C. industry over the past few years due to the increasing challenge in the design and the extra cost of fabrication of R.F. analog and mixed-signal I.C. versus standard digital ones in modern nano-scale I.C. technologies, e.g. [1]-[3]. Efforts towards all-digital FS can be traced at least thirty years back [4][6].

Replacing a complex analog or mixed-signal frequency synthesizer with a fully digital one can result in faster concept to market cycle, lower design effort and cost and the advantage of using digital design and verification tools.

Moreover, synchronous single-bit digital outputs of all-digital synthesizers, having sinewave-like spectrum can be used as local-oscillator signals in RF chains and, they can be amplified for transmission or internal use without distortion and with very high efficiency using a switching amplifier. Also one can incorporate digital or analog phase, frequency and amplitude modulation directly in an all-digital synthesizer [7].

The proposed single-bit-output Nyquist-rate sinewave quantization scheme is practically realized by a Direct Digital Synthesizer (DDS) with a 1-Bit output Nyquist-rate Digital to Analog Converter (DAC). Dither is added to the output of the Look-Up-Table (LUT) before the hard quantization to alleviate the nonlinearity and suppress the output spurs by breaking the periodicity of the truncation error.

Note that the DAC is only virtually there representing the act of signum function, or similarly that of an MSB extractor, applied to the sum of the LUT's output with the dither.

In the above setup, single-bit quantization alone, i.e. without dithering, typically results in dense and high-power frequency spurs making the output single-bit digital signal unusable for analog and R.F. applications (although it can by used for clocking digital circuitry).

The paper derives analytically the spectrum of the single-bit dithered quantizer as a function of the dither's Cumulative Distribution Function (CDF) when the dithering sequence is formed of Independent and Identically Distributed (IID) random variables. Moreover, the noise floor power due to random dithering is derived analytically and the output dynamic range is defined and calculated explicitly.

II. DEFINITIONS AND ASSUMPTIONS

Random dithering is commonly used to suppress the spurs and shape the noise of quantization in DDS [8] and data converters [9] and to eliminate periodic patterns in fractional-N frequency dividers [10].

Here we consider the extreme case of amplitude dithered DDS with single-bit output quantization (DAC) without oversampling [9] shown in Figure 1. The cosine can be generated using a phase accumulator and a LUT, and the Zero Order Hold (ZOH) outputs a continuous-time single-bit digital waveform. All blocks are clocked by a clock reference of frequency $f_S = 1/T_S$.

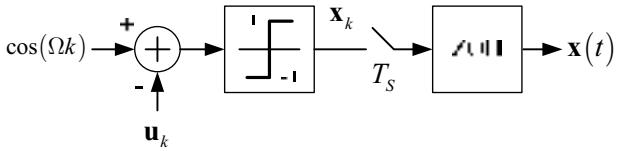

Figure 1: Dithered single-bit quantization of a sinewave

The dithering random sequence $\{\mathbf{u}_k\}$ is subtracted from the sinewave resulting in the discrete-time single-bit (± 1) signal $\mathbf{x}_k = \mathrm{sgn}\left(\cos(\Omega k) - \mathbf{u}_k\right)$ where "sgn" is the signum function.

Throughout the paper we assume that the random sequence $\{\mathbf{u}_k\}$ is formed of IID random variables having CDF $G:[-1,1]\to[0,1]$ which is continuous and has continuous second derivative in $[-1,1]$. Therefore, for every $k\in\mathbb{Z}$ and $u\in[-1,1]$ it is $\Pr(\mathbf{u}_k\le u)=G(u)$, so implicitly we assume that essentially $\mathbf{u}_k$ takes values only within $[-1,1]$. This is plausible because $\cos(\Omega k)$ does the same and hence any larger value range of the dither would be unnecessary.

It also makes sense from an application perspective to assume that $\Omega/(2\pi)$ is rational, i.e. $\Omega=2\pi w/q$ for some integer w such that $0<w<q/2$. In this case

$$\mathbf{x}_k=\operatorname{sgn}\left(\cos(2\pi wk/q)-\mathbf{u}_k\right) \tag{1}$$

and since $\{\mathbf{u}_k\}$ is an IID random sequence and $\cos(2\pi wk/q)$ has period $q/\gcd(q,w)$, the random sequence $\{\mathbf{x}_k\}$ is cyclostationary of the same period. Since q is a multiple of $q/\gcd(q,w)$, $\{\mathbf{x}_k\}$ is also cyclostationary of period q and we consider it as such in the rest of the paper to simplify notation.

A. The Period-Average Autocorrelation of $\{\mathbf{x}_k\}$

The Power Spectral Density (PSD) of a discrete-time wide-sense stationary (WSS) process is the Discrete-Time Fourier Transform (DTFT) of its autocorrelation function [11]

$$r_x(n,m)=E\{\mathbf{x}_n\mathbf{x}_m\}. \tag{2}$$

Since $\{\mathbf{x}_k\}$ is not WSS but cyclostationary of period q its PSD, $s_x(\omega)$, is commonly defined as the DTFT of its period-average autocorrelation [11]-[12], i.e., of

$$\bar{r}_x(k)=\frac{1}{q}\sum_{m=0}^{q-1}r_x(k+m,m) \tag{3}$$

and

$$s_x(\omega)=\sum_{k=-\infty}^{\infty}\bar{r}_x(k)e^{-ik\omega}. \tag{4}$$

To calculate $\bar{r}_X(k)$ we express the CDF $G:[-1,1]\to[0,1]$ as a series of Chebyshev polynomials of the first kind, i.e.,

$$G(u)=\frac{1}{2}+\frac{1}{2}\sum_{j=0}^{\infty}a_jT_j(u). \tag{5}$$

The summand and multiplying factor $1/2$ is used to simplify the algebra. Coefficients a_j are derived according to [13]

$$a_0=\frac{2}{\pi}\int_{-1}^{1}\frac{G(u)}{\sqrt{1-u^2}}du-1,\quad a_{j>0}=\frac{4}{\pi}\int_{-1}^{1}\frac{G(u)T_j(u)}{\sqrt{1-u^2}}du. \tag{6}$$

Since G was assumed continuous, its series expansion (5) converges to G everywhere in $[-1,1]$. Inversely, G can be defined using coefficients a_j as long as series (5) converges to a continuous function and G is indeed a CDF. Assuming further that series (5) is term-by-term differentiable, a necessary and sufficient set of conditions for G to be a CDF is

$$G(-1)=0,\quad G(1)=1\quad\&\quad G'(u)\ge 0\quad\forall u\in[-1,1] \tag{7}$$

Since $T_j(\pm1)=(\pm1)^j$, $j=0,1,2,\ldots$, and $T_j'(u)=j\cdot U_{j-1}(u)$, for $j=1,2,3,\ldots$, where U_j is the j-th Chebyshev polynomial of the 2nd kind [13], Eqs. (7) can be written as

$$\begin{aligned}&\sum_{j=0}^{\infty}(-1)^j a_j=-1,\quad \sum_{j=0}^{\infty}a_j=1\\ &\sum_{j=1}^{\infty}ja_jU_{j-1}(u)\ge 0\quad\forall u\in[-1,1]\end{aligned}. \tag{8}$$

Section IV illustrates how coefficients a_j are calculated for two cases of CDF G and used to derive the PSD.

III. Power Spectral Density and Dynamic Range

Using the above definitions we can express $\bar{r}_X(k)$ as a function of the coefficients a_j, $j=0,1,2,\ldots$. Specifically, we have that [14] the period-average autocorrelation $\bar{r}_X(k)$ of $\{\mathbf{x}_k\}$ is given by (9) where $\delta_0=1$ and $\delta_{k\ne0}=0$.

$$\bar{r}_x(k)=a_0^2+\sum_{j=1}^{\infty}\frac{a_j^2}{2}\cos\left(\frac{2\pi kjw}{q}\right)+\left(1-a_0^2-\sum_{j=1}^{\infty}\frac{a_j^2}{2}\right)\delta_k \tag{9}$$

Note that $\bar{r}_x$ comprises of DC term a_0^2, harmonics of $\cos(2\pi kw/q)$ and an impulse term at $k=0$. Moreover, the amplitude of the j^{th} harmonic, i.e., $a_j^2/2$, is half the square of the projection of CDF G to the j^{th} Chebyshev polynomial according to Eqs. (6). This implies that by selecting CDF G we can "shape" the period-average autocorrelation function and so the PSD of $\{\mathbf{x}_k\}$. Note however that time is discrete and the harmonics of $\cos(2\pi kw/q)$ in Eq. (9) are subject to aliasing and folding into the frequency domain $\omega\in[0,2\pi)$ simply because $\cos(2\pi kjw/q)=\cos\left(2\pi k\left((jw)\bmod q\right)/q\right)$.

A. Power Spectral Density of the Output Signal $\mathbf{x}(t)$

The output $\mathbf{x}(t)$ of the ZOH in Figure 1 is a continuous-time signal which can be written in the form

$$\mathbf{x}(t)=\sum_{k=-\infty}^{\infty}\mathbf{x}_k p\left(\frac{t}{T_S}-k\right) \tag{10}$$

where $T_S=1/f_S$ is the sampling period and pulse $p(t)$ is 1 for $t\in[0,1)$ and zero otherwise corresponding to ZOH's operation. It can be shown [14] that the PSD of $\mathbf{x}(t)$ is

$$S_x(f)=T_S\cdot\operatorname{sinc}^2(f\cdot T_S)\cdot s_x(2\pi fT_S) \tag{11}$$

where $s_x(\omega)$ is the DTFT in Eq. (4) of the period-average autocorrelation $\overline{r_x}$ and $T_S \cdot \mathrm{sinc}^2(f \cdot T_S)$ is due to the shape of the pulse $p(t)$. Combining Eqs. (4), (9) and (11), and after a lengthy algebraic manipulation we can derive the following Theorem whose proof can be found in [14].

Theorem: Following the above definitions and assumptions and further assuming that $\gcd(w,q)=1$ the PSD of $\mathbf{x}(t)$ is

$$S_x(f) = \mathrm{sinc}^2\left(\frac{f}{f_S}\right) \cdot \left(S_{HA}(f) + S_N(f) + S_{DC}(f) \right) \quad (12)$$

where HArmonics, Noise and DC components are given by

$$S_{HA}(f) = \frac{1}{4}\sum_{h=1}^{\infty} b_h \left(\delta\left(f - \frac{h}{q} f_S\right) + \delta\left(f + \frac{h}{q} f_S\right) \right), \quad (13)$$

$$S_N(f) = \frac{1}{f_S} \cdot \left(1 - a_0^2 - \frac{1}{2}\sum_{j=1}^{\infty} a_j^2 \right), \quad (14)$$

and

$$S_{DC}(f) = \frac{b_0 + 3a_0^2}{4}\delta(f) \quad (15)$$

respectively. For $h = 0,1,2,\ldots$ the power of the frequency components at $\pm(h/q) f_S$ in Eq. (13) is $b_h/4$ and

$$b_h \triangleq \sum_{r=-\infty}^{\infty} a_{I(h,r)}^2 \quad (16)$$

where $I(h,r) = |j_1 h + qr|$; constant j_1 (and k_1 which is not involved in the expression) is derived solving the Diophantine equation $wj_1 + qk_1 = 1$. Specifically coefficient b_w of the frequency components at $\pm(w/q) f_S$ is $b_w = \sum_{r=-\infty}^{\infty} a_{|1+qr|}^2$. □

Observing Eq. (16) we note that the contributions of coefficients a_j to the total power of frequency component at $\pm(h/q) f_S$ are cumulative since $a_{I(h,r)}^2 \geq 0$. Therefore, to minimize the spurs in the output we should zero as many of the coefficients a_j as possible because the smaller the set of nonzero coefficients a_j is, the smaller the set of frequency components present in $S_{HA}(f)$ will be.

Note that in order to derive coefficient b_h we first find a solution (j_1, k_1) of the Diophantine equation $wj_1 + qk_1 = 1$ using the Euclidean algorithm ("gcd" function in MATLAB). This is always possible due to our assumption that $\gcd(w,q)=1$. Any (j_1, k_1) of the infinitely many solutions is acceptable but one with absolutely small j_1, k_1 is convenient. Then we apply Eq. (16) where only j_1 is used in $|j_1 h + qr|$. The procedure is illustrated in the examples of Section IV.

B. *Noise Floor and Dynamic Range*

Typically, the desirable frequency component at the output is at frequency $(w/q) f_S$ with amplitude $\mathrm{sinc}^2(f/f_S) \cdot b_w/4$, captured by $S_{HA}(f)$ in Eq. (13). Also, the output noise (which is the only component of continuous spectrum) has PSD $\mathrm{sinc}^2(f/f_S) \cdot S_N(f)$. We define the Dynamic Range (DR) of the output as the ratio of the signal power to noise's PSD

$$DR = 10\log_{10}\left(\frac{\mathrm{sinc}^2(f/f_S) \cdot b_w/4}{\mathrm{sinc}^2(f/f_S) \cdot S_N(f)} \right) \quad \text{(dB)}$$

and after replacing the values of b_w and $S_N(f)$ we get

$$DR = 10\log_{10}\left(\frac{\sum_{r=-\infty}^{\infty} a_{|1+qr|}^2}{1 - a_0^2 - \sum_{j=1}^{\infty} \frac{a_j^2}{2}} \right) + 10\log_{10}(f_S) - 6.02 \quad \text{(dB)} \quad (17)$$

The definition of the DR can be used for other frequency components of interest as well. Also, note that the summand $10\log_{10}(f_S)$ in Eq. (17) is expected since the power of the sinewave's quantization error is spread over frequency bandwidth proportional to the sampling frequency. The use of Eq. (17) is illustrated in the examples of Section IV.

IV. Examples and Simulations

First we emphasize the importance of dithering in spurs suppression in the case of single-bit quantization by considering the case of $w = 25$ and $q = 64$ without dither. This is the limiting case of the above setup when CDF $G(u)$ is zero for $u \in [-1, 0)$ and one for $u \in (0, 1]$, i.e. $\mathbf{u}_k = 0$ with probability one. Figure 2 shows the output spectrum ignoring the weighting factor $\mathrm{sinc}^2(f/f_S)$. The spectrum is the result of MATLAB simulation and coincides completely with the theory, Eq. (12). Note that although G is discontinuous at $u = 0$ its series expansion, Eq. (5), is valid for $u \neq 0$ implying $a_{2k} = 0$ and $a_{2k+1} = 4(-1)^k / ((2k+1)\pi)$ for $k = 0,1,2,\ldots$.

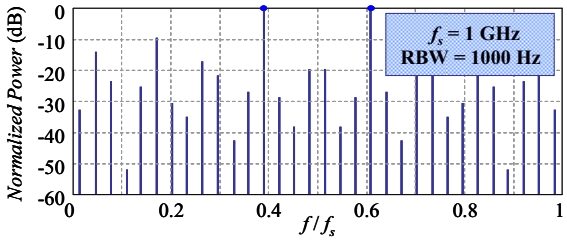

Figure 2: Spectrum of single-bit quantized sinewave without dithering when $w = 25$ and $q = 64$; ignoring the weighting factor $\mathrm{sinc}^2(f/f_S)$.

Now we consider the same case of $w = 25$ and $q = 64$ when the dithering sequence $\{\mathbf{u}_k\}$ is formed of *uniformly*

distributed IID random variables, i.e. the probability density function is constant, $G'(u)=1/2$ in $[-1,1]$ and so the CDF is $G(u)=(u+1)/2$. Since $T_1(u)=u$ we derive by inspection that $a_0=0$, $a_1=1$ and $a_k=0$ for $k=2,3,4,\ldots$.

To derive the coefficients b_h in the Theorem we find a solution of the Diophantine equation $25j_1+64k_1=1$, e.g. $(j_1,k_1)=(-23,9)$. For b_h, $h=0,1,2,\ldots$ to be nonzero, there must exist some $r\in\mathbb{Z}$ for which

$$I(h,r)=\left|j_1h+64r\right|=1 \tag{18}$$

This is because $a_1=1$ and $a_0=0$, $a_k=0$ for all $k=2,3,4,\ldots$, therefore only a_1 can contribute to b_h. Since $25j_1+64k_1=1$, a particular solution of $j_1h+64r=1$ is $(h,r)=(25,k_1)$ and so the general solution of Eq. (18) is

$$(h,r)=\pm(25,9)+\rho(64,23),\ \rho\in\mathbb{Z} \tag{19}$$

Since it is $h\geq 0$ we conclude that the (only) non zero coefficients b_h, $h=0,1,2,\ldots$ are b_{25} and $b_{\eta\cdot 64\pm 25}$, $\eta=1,2,3,\ldots$ From Eq. (16) we also get that $b_{25}=b_{\eta\cdot 64\pm 25}=1$, $\eta=1,2,3,\ldots$. So we derive that

$$S_{HA}(f)=\frac{1}{4}\sum_{\substack{h=25,\ \eta\cdot 64\pm 25\\ \eta=1,2,3,\ldots}}\left(\delta\left(f-\frac{h}{q}f_S\right)+\delta\left(f+\frac{h}{q}f_S\right)\right),$$

$S_N(f)=1/(2f_S)$ and $S_{DC}(f)=0$. The result coincides completely with the PSD derived using simulation, shown in Figure 3 where the weighted factor $\mathrm{sinc}^2(fT_S)$ is ignored.

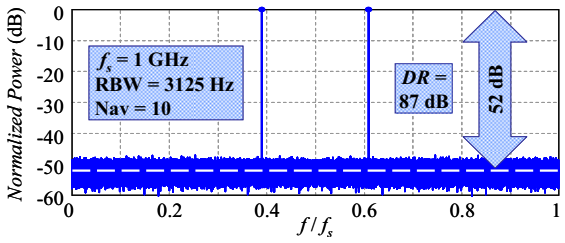

Figure 3: Spectrum of single-bit quantized sinewave with uniformly distributed dither when $w=25$ and $q=64$; the weighting factor $\mathrm{sinc}^2(f/f_S)$ is ignored. $f_S=1\,GHz$, Resolution BW = 3125 Hz and waveform averaging Nav=10 runs.

We note that there are only two frequency components in the frequency range $[0,f_S]$, the desirable one at $(25/64)f_S$ and the image of it at $((64-25)/64)f_S$ due to the discrete time nature of $\{\mathbf{x}_k\}$. The second one cannot be eliminated unless a continuous-time filter is used. Since no spurs are present we conclude that the uniform CDF results in spurs-free output. This is true in general for every integers w and q satisfying our assumptions.

Since $a_0=0$, $a_1=1$ and $a_k=0$ for $k=2,3,4,\ldots$, the dynamic range derived from Eq. (17) is expressed as

$$DR=10\log_{10}(f_S)-\ 3.01\ \text{dB} \tag{20}$$

In the PSD graph of the case $w=25$ and $q=64$ shown in Figure 3 the dashed white line indicates the averaged noise floor power. For $f_S=1\,GHz$ we get $DR\cong 87$ dB. Subtracting $10\log_{10}(RBW)$ dB, where $RBW=3125\,Hz$, to account for the resolution BW used for the simulation we get a very good match to the simulated 52 dB (Figure 3).

V. Conclusions

All-digital frequency synthesis using single-bit, Nyquist-rate quantization of sinewave and random dithering formed of independent and identically distributed random variables has been studied mathematically. The output spectrum has been calculated analytically as a function of the dither's Cumulative Distribution Function. It has been shown that uniformly distributed dither with range equal to that of the sinewave results in spurious-free output spectrum. The noise floor level due to dithering has been calculated analytically and the output dynamic range has been defined and calculated explicitly for the case of uniformly distributed dither. Examples based on MATLAB have been presented to illustrate the theory. The simulation results are in complete agreement with the theory.

References

[1] R.B. Staszewski, "State-of-the-art and future directions of high-performance all-digital frequency synthesis in nanometer CMOS", IEEE Trans. Cir. and Sys. I, Vol. 58, Iss. 7, 2011, pp. 1497-1510.

[2] H. Mair and L. Xiu, "An architecture of high-performance frequency and phase synthesis," IEEE J. Solid-State Circuits, vol. 35, no. 6, pp. 835–846, Jun. 2000.

[3] Paul P. Sotiriadis, Kostas Galanopoulos, "Direct All-Digital Frequency Synthesis techniques, Spurs Suppression and Deterministic Jitter Correction", IEEE Trans. on Circuits and Systems-I, Volume: 59 , Issue: 5, Pages: 958 – 968, May 2012.

[4] V.S. Reinhardt, "Direct digital synthesizers", Technical Report, Hughes Aircraft Co, Space and Communications Group, L.A., CA, Dec. 1985.

[5] C. E. Wheatley, III, "Digital frequency synthesizer with random jittering for reducing discrete spectral spurs," U.S. Patent 4410954, Oct. 1983.

[6] V. N. Kochemasov and A. N. Fadeev, "Digital-computer synthesizers of two-level signals with phase-error compensation," Telecommun. Radio Eng., vol. 36/37, pp. 55–59, Oct. 1982.

[7] K. Galanopoulos, P. Sotiriadis, "Modulation Techniques for All-Digital Transmitters Based on Pulse Direct Digital Synthesizers", IEEE International Frequency Control Symposium, May 2012, pp. 1-4.

[8] J. Vankka and K. Halonen, *Direct Digital Synthesizers: Theory, Design and Applications,* New york, Springer 2006.

[9] J.C. Candy (Ed.), G.C. Temes (Ed.), *Oversampling Delta-Sigma Data Converters: Theory, Design, and Simulation*, Wiley-IEEE Press, 1991.

[10] U.L. Rohde, *Microwave and Wireless Synthesizers: Theory and Design*, 1st ed. Singapore: Wiley-Interscience, 1997.

[11] J.G. Proakis, M. Salehi, *Digital Communications*, 5th Ed., McGraw-Hill Companies,Inc. , 2007.

[12] R.M. Gray, "Quantization noise spectra", *IEEE Trans. Information Theory, Vol.* 36, Iss. 6, 1990, pp. 1220-1244.

[13] J.P. Boyd, *Chebyshev and Fourier Spectral Methods*, Dover Publications, 2nd Ed., 2001.

[14] P. Sotiriadis, N. Miliou, "Single-Bit Digital Frequency Synthesis via Dithered Nyquist-rate Sinewave Quantization", to appear in the IEEE Trans. on Circuits and Systems-I (TCAS-I 13452).

Comparative Performance of Compact Schemes of Atomic Beam Longitudinal Deceleration Designed for Space-Based Frequency Standards

Zholnerov V.S
Russian Institute of Radionavigation and Time
St.-Petersburg, Russia
zholnerov@mail.ru

Vershovskii A.K.
Ioffe Phys.-Tech. Institute of Russian Academy of Science
St.-Petersburg, Russia
antver@mail.ioffe.ru

Rozhdestvenskiy Yu.V.
ITMO University
St.-Petersburg, Russia
rozd-yu@mail.ru

***Abstract*—Numerical modeling of different compact slowing schemes designed for a satellite slow-beam microwave atomic clock is presented.**

I. INTRODUCTION

Space-based frequency standards are probably the most important parts of any global navigation system. Due to their specifics, these devices must meet a number of demands, which usually are: the daily stability of 10^{-15}, volume on the order of 0.01 m^3, weight less than 10 kg, power consumption less than 100 W, and continuous operation for at least 5 years. Optical frequency standards demonstrating the unique stability of $10^{-16} \div 10^{-18}$ are extremely promising for space applications. Nevertheless, at the moment the stringent requirements listed above force us to look for simpler technical solutions, which, in particular, would not require a transfer of the stabilized frequency from the optical range. Among these, the radiofrequency standards using cold atom beams seem to have the greatest potential.

Consequently, the compaction and the energy consumption reduction of such standards together with improvement of their stability become the research priority, and one of the solutions involves the use of CPT-Ramzey resonance optical detection.

II. STATEMENT OF THE PROBLEM

Since the sensitivity of any scheme of registration of radio-optical resonance in an atomic beam is limited by the longitudinal velocity of the atoms, the longitudinal velocity of the order of 1 m/s and registration area length of at least 0.5 m are required for obtaining stability of 10^{-15}. The combination of these requirements, in turn, limits the allowable transverse velocity of the atoms in the beam.

Note that the optical preparation of the atomic beam characterized by the longitudinal velocity of 1 m/s and a divergence of 0.05 rad is a difficult task due to the limitations of the existing slowing schemes. There are two types of these schemes – one using time-dependent frequency tuning of optical radiation (so-called «laser chirping»), and other using spatially inhomogeneous magnetic field to change the frequency of the atom in order to adjust the frequency of the transition (Zeeman slowing); the latter allows a continuous beam of cold atoms to be obtained, which is considered an advantage. In practice, however, none of these schemes in their classic versions provide a longitudinal deceleration of atoms below $10 \div 20$ m/s; this limitation arises because significant time is needed for slowing the atoms from the whole initial thermal distribution to a narrow velocity peak. During a long (several ms) interaction time the atomic beam starts blurring in the transverse direction, essentially losing intensity. Since the time of longitudinal slowing of the atomic beam linearly decreases with the initial velocity of the atoms, it has been proposed to significantly reduce the upper limit v_0 of the initial velocities of the atoms that interact with the laser radiation [1].

In this case, the time of longitudinal deceleration, as well as the transverse dimension of the atomic beam, dramatically decreases, which gives hope for obtaining the number of atoms with velocities ≤ 1 m/s sufficient for registration. Of course, some loss of intensity of the atomic beam occurs in this scenario, since only the slowest part of the thermal beam interacts with the cooling light. Thus, at a speed v_0 corresponding to one-half of the average thermal velocity, about 2% of a thermal beam is effectively used; this is compensated by shorter time (and hence the shorter slowdown length and less required power), and smaller transverse dimensions of the beam of atoms in the registration area.

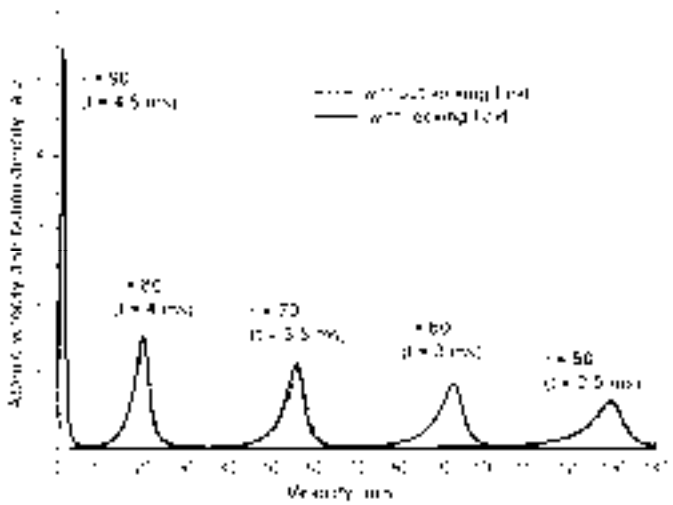

Fig. 1. Linear frequency sweeping

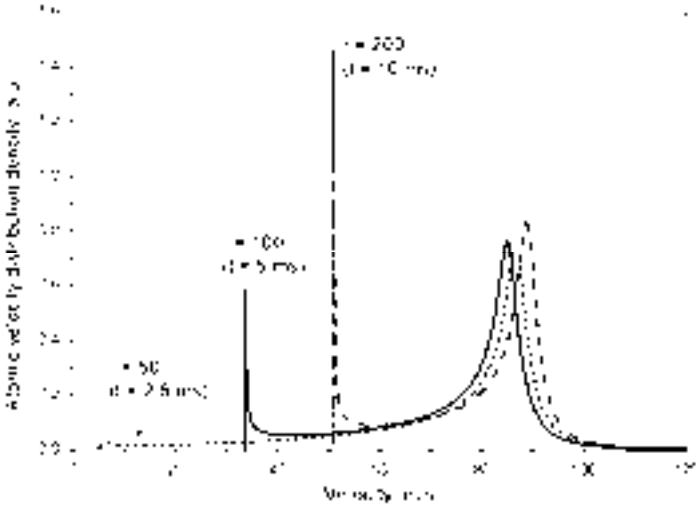

Fig. 2. Nonlinear frequency sweeping

The operating mode of such a slower will always be pulsed regardless of the method of the Doppler shift compensation, because it is necessary to let the fast atoms with $v > v_0$ leave the interaction area before the final stage of the cooling starts. Therefore Zeeman slowing method loses its main advantage – the continuity of the cooling process. On the other hand, advantages of the laser chirping methods include low energy consumption (since no strong magnetic field is needed), as well as low requirements for magnetic shielding around the registration area. In this report different versions of this method are investigated and compared.

III. The Proposed Solution

The base for modeling of longitudinal cooling process is the Fokker–Planck equation

$$\left(\frac{\partial}{\partial t}+v_z\frac{\partial}{\partial z}\right)w=-\frac{\partial}{\partial p_z}\left(F_z w\right)+\frac{\partial^2}{\partial p_z^{\,2}}\left(D_{zz}w\right), \qquad (1)$$

where $w\equiv w(v_z,t)$ is one-dimensional distribution function; $F_z=-\hbar k\gamma\dfrac{G}{1+G+(\delta+kv_z)^2/\gamma^2}$ is the light pressure force along z axis; $D_{zz}=\hbar^2k^2\gamma\dfrac{G}{1+G+(\delta+kv_z)^2/\gamma^2}$ is the pulsed diffusion coefficient; $G=2\Omega^2/\gamma^2$ is the saturation parameter; Ω is Rabi frequency; $\delta=\omega-\omega_0$ is the laser frequency $\omega=kc$ detuning from atomic transition frequency ω_0; 2γ is radiation width (FWHM) of the transition.

It is known [1], that the pulse diffusion at typical slowing times (tens ms) practically does not affect the width of the final atomic velocity distribution. Therefore we used the spatially homogeneous Liouville equation:

$$\frac{\partial}{\partial\tau}w=\frac{\partial}{\partial\tilde{v}_z}\left(f_z w\right), \qquad (2)$$

containing dimensionless variables $\tau=(\hbar k^2/m_{Rb})t=\omega_R t$, $\tilde{v}_z=(kv_z)/\gamma$, $f_z=F_z/\hbar k\gamma$.

We use the following procedure to calcule the final velocity distribution: during the first step ($\tau=0$) the initial distribution

$$w(\tilde{v}_z,\tau=0)=(\tilde{v}_z{}^3/<\tilde{v}_z>^4)e^{-\left(\frac{\tilde{v}_z}{<\tilde{v}_z>}\right)^2}, \qquad (3)$$

where $<\tilde{v}_z>$ is the most probable speed, is split to some number of small intervals $(\Delta\tilde{v}_z(t=0))_i$, and the partial number of atoms $S_i(t=0)$ is calculated for each interval. During the next step, the kinetic equations describing the action of the force f_z are solved for each interval, resulting in a new set of velocities $(\Delta\tilde{v}_z(t))_i$ corresponding to the time t. Since the total number of the atoms in each interval stays constant, the new value of atomic density $S_i(t)$ can be obtained from the old one:

$$S_i(t)=S_i(t=0)\frac{(\Delta\tilde{v}_z(t=0))_i}{(\Delta\tilde{v}_z(t))_i}. \qquad (4)$$

We started numerical simulation of longitudinal laser cooling of Rb thermal beam ($<\tilde{v}_z>=400$ m/s) on D_1 line, using one laser field with fixed detuning $\delta+k<v_z>=\dfrac{\delta}{\gamma}+\dfrac{k}{\gamma}<v_z>=\Delta+<\tilde{v}_z>=0$. In this case the model predicts a fast forming of a narrow peak in atomic distribution, and slow (tenths of second) shifting of this peak to the zero velocities. In order to increase the cooling efficiency,

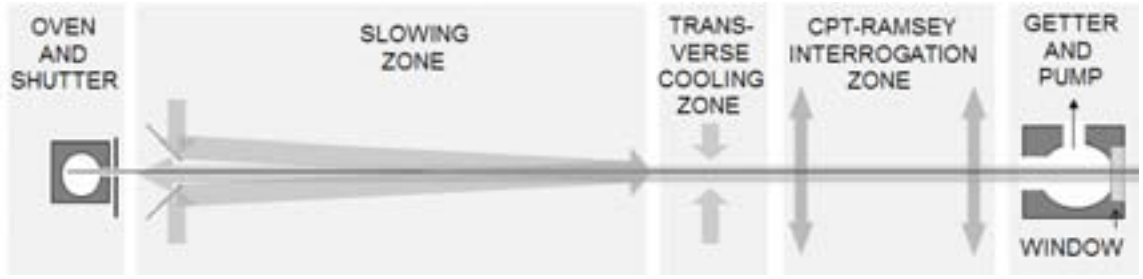

Fig. 3. Basic sheme of the atomic beam preparation/registration unit

which in our case is determined by the speed of shifting the peak to the zero velocity zone, we also modeled laser cooling with variable detuning ("chirping"): $\omega = \omega(0) + y(t)$, and, correspondingly, the light slowing force

$$F_z = -\hbar k \gamma \frac{G}{1 + G + (\delta + k v_z + y(t))^2 / \gamma^2}. \qquad (5)$$

The upper limit v_0 of the initial velocities of the atoms that interact with the laser radiation is determined by the initial detuning. For our simulation we have chosen an intermediate v_0 value: $v_0 = < \tilde{v}_z >$.

Indicated by solid lines on Fig. 1 is the evolution of the longitudinal velocity distribution of the atoms in the beam in case of the linear sweeping of the slowing light frequency $y(t) = a \cdot t$ in presence of the "locking" field, i.e. laser light propagating along the atomic beam, as was proposed in [3]. The parameters of the model were: the speed of slowing light frequency sweep $a = 3.2 \cdot 10^{12}\ c^{-1/2}$, the slowing light saturation parameter $G = 100$, the locking light saturation parameter $G_L = 3$, the locking light detuning $\delta_L = 0$.

As demonstrated in Fig. 1, it takes less than 4.5 ms to shift the atomic distribution peak to the velocity 7 m/c, and therefore the length of the slowing zone can be reduced to ~16 cm. One can chose the final speed of the beam by varying δ_L. The efficiency of the slowing process decreases drastically without the locking light, mainly because the atoms are "blown" back to the atomic source.

Indicated by dot-dashed lines on Fig. 1 is the evolution of the same distribution in the case of two counter-propagating beams symmetrically detuned from $< \tilde{v}_z >$; both frequencies are being swept linearly, as in the previous case. There is no stationary locking field in this case: the detunings of both the slowing and the locking fields are being simultaneously shifted to the zero velocities. The detunings satisfy the condition $\delta_1 + \delta_2 = 2k < v_z >$: $\delta_1 / \gamma = -260$, $\delta_2 / \gamma = -540$. It is still possible to shift the peak of the atomic distribution to the zero speed area in this configuration, but (unlike in the previous case) most atoms acquire negative v_z projection before reaching the interrogation zone.

We have also investigated variations of the methods described above, in different combinations. Fig. 2 shows the evolution of the longitudinal velocity distribution in the case of the nonlinear sweeping of the slowing light frequency: $y(t) = a t^2, a = 3.2 \cdot 10^9\ c^{-2}, \delta_L = 0$. As illustrated on Fig. 2, one (at $t < 2.5$ ms) or two (at $t > 2.5$ ms) peaks can be formed, corresponding to the roots of quadratic polynomial in the denominator of the expression describing the light pressure force; the slowing efficiency is low compared to the previous versions.

IV. Conclusion

According to the results described above, it is advisable to use linear sweeping for fast and effective cooling; presence of "locking" light beam, propagated along the atomic beam, is critical. It is possible to obtain sufficient number of atoms using slowing methods described above; short cooling time allows a rather compact beam (1.6 cm at $t = 4$ ms and initial divergence 0.02 rad) to be obtained on the interrogation zone input.

The basic scheme of the atomic beam preparation/ registration unit is shown in Fig. 3. Its drawbacks are obvious, and include: the need for an atomic beam shutter; the difficulty of forming a co-propagating "locking" beam; and the danger of covering the window (situated in the pump unit) by hot atoms. At present we are developing a modification of this construction, which promises to be free of these flaws; this modification implies placing the oven output at some angle to the unit axis, followed by selective declination of the atoms with $v < v_0$ to the unit axes. These atoms will then form an additional weak atomic beam, which will be slowed as described above.

References

[1] V. S. Zholnerov, A. K. Vershovskiy, Yu. V. Rozhdestvenskiy, "Project of a Satellite Slow Beam Atomic Clock with CPT-Ramsey Registration", Proc. EFTF-2012, Gothenburg, Sweden, p.320-322, 2012.

[2] V.G. Minogin, V.S. Letokhov, "Laser Light Pressure on Atoms" - Gordon and Breach Science Publ., New York, 248 pp, 1987.

[3] Ho Seong Lee, Sang Eon Park, Taeg Yong Kwon, Sung Hoon Yang, and Hyuck Cho. "Toward a Cesium Frequency Standard Based on a Continuous Slow Atomic Beam: Preliminary Results," IEEE Trans. Instrum. Meas., vol. 50, pp.531-534, 2001.

Medium- to Long-Term Frequency Stability of High-Performance CW Double-Resonance Rb Standard

Thejesh Bandi, Christoph Affolderbach, Gaetano Mileti
Laboratory of Time & Frequency (LTF),
University of Neuchâtel,
Neuchâtel, Switzerland
Email: thejesh.bandi@unine.ch, gaetano.mileti@unine.ch

Camillo Stefanucci, Francesco Merli*, Anja K. Skrivervik
Laboratory of Electromagnetics and Acoustics (LEMA),
École Polytechnique Fédérale de Lausanne (EPFL),
Lausanne, Switzerland
*Present address: RF division, Huber+Suhner AG,
Herisau, Switzerland

***Abstract*—We present the short-term noise budget and metrological studies on the medium- to long-term stability of our Rb standard. Our clock exhibits a short-term stability of $\sim 1.4\times10^{-13}\ \tau^{-1/2}$. The dependance of microwave power shift on light intensity, and the possibility to nullify the microwave power shift is demonstrated. The perturbing *vapor cell geometric effect* on medium- to long-term time scales, limiting the stability around 6×10^{-14} level is identified. Further required improvements are discussed.**

I. Introduction

Compact rubidium (Rb) frequency standards form the back bone of today's satellite navigation systems [1]. Recently developed laser-pumped Rb cell standards exhibit short-term frequency stabilities by at least one order magnitude better than the conventional lamp-pumped standards [2], [3].

We are developing a compact laser-pumped high-performance Rb cell standard exhibiting the performances of a passive H-maser [4], but with a reduced volume (< a factor of 10), mass (< a factor of 5) and power consumption (< a factor of 4). Our Rb cell standard is based on the Continuous-Wave (CW) Double-Resonance (DR) principle [6]. The improvement in the short-term stability of our clock has already been demonstrated [2], [5], [6], with the recent performance being a short-term stability of $\sim 1.4\times10^{-13}\ \tau^{-1/2}$ [6].

In this proceeding, we present the noise budget of the short-term clock stability. We also present a systematic metrological characterization of perturbing physical effects influencing the medium- to long-term clock frequency instability, such as the 2^{nd}-order Zeeman shift, light-shifts, microwave power shift, cavity pulling, spin-exchange shift, and the temperature coefficient shifts.

II. Experimental setup

The details of our experimental clock setup were already presented in [5]. The setup consists of three main components, (i) the frequency stabilized compact Laser Head (LH) with an overall volume and mass of < 0.9 dm^3 and < 0.6 kg, respectively, (ii) the Physics Package (PP) with an overall volume and mass of < 0.8 dm^3 and < 1.4 kg, respectively, and (iii) the low noise microwave synthesizer (Local Oscillator, LO), which is presently a rack-mount device. The laser is a DFB diode emitting at 780 nm (Rb D2 transition). The laser is frequency stabilized using an evacuated Rb reference cell that is integrated in the LH assembly. Further details on the laser head were reported in [7]. The details on the PP were reported in [5][6]. The core of this PP consists of a glass cell of 25 mm diameter that has Rb vapor and a mixture of buffer gases. Our Rb cell has two distinct parts; *cell volume*, where the ^{87}Rb vapor is interrogated with laser and microwave to obtain the DR signal, and *cell stem* that acts as reservoir for metallic Rb. This cell is situated inside a newly developed compact magnetron-type microwave resonator (V < 45 cm^3), and the details of which can be found in [8]. The details on microwave source (the LO) including the digital lock-in and clock loop electronics were presented in [3]. The phase noise of the LO was measured by cross-correlation method. At a carrier frequency of 6.8 GHz it has a noise level at -70 dBrad^2/Hz at 1 Hz Fourier frequency and noise floor at -111 dBrad^2/Hz from 10^3 Hz to 2×10^4 Hz.

III. DR signals and short-term stability noise budget

We measured a narrow DR signal linewidth of 334 Hz (FWHM) and a signal contrast of 26%. The shift in the centre frequency (from the unperturbed ^{87}Rb ground-state clock transition) mainly due to the buffer gas collisions was measured to be 3390 Hz, giving the centre frequency value of 6.834686 GHz. The error signal generated by frequency modulating the microwave frequency in the closed-clock-loop configuration gave a discriminator slope of D = 1.52 nA/Hz. The photocurrent of 1.6 μA at FWHM corresponds to an estimated shot-noise limited frequency stability of $4.9\times10^{-14}\ \tau^{-1/2}$. However, the short-term stability of our clock presently has a signal-to-noise (S/N) limit of $\sim 1.2\times10^{-13}$, mainly due to FM-to-AM conversion of laser FM noise in the atomic vapor [9]. Measurements on the noise budget limiting the short-term stability of our clock is presented in Table I.

The limit on short-term stability also includes the influences due to the intermodulation effects on the phase noise of the LO and the laser intensity and frequency fluctuations. The overall short-term clock stability can be estimated from

TABLE I. SHORT TERM NOISE BUDGET OF THE 25 MM CELL CLOCK.

Source	Instability, σ_{inst}(y) $\tau^{-1/2}$
Detector dark noise	2.5×10^{-14}
Shot-noise limit (from DR signal)	4.9×10^{-14}
Microwave noise	5.1×10^{-14}
Laser noise (microwave off)	1×10^{-13}
Total noise	1.15×10^{-13}
S/N measured (clock loop noise)	1.17×10^{-13}

the sum of the squares of the individual limits of S/N, the LO phase noise and the laser frequency and intensity fluctuations as $\sim 1.4\times10^{-13}\ \tau^{-1/2}$. This short-term stability was measured and reported in [6].

IV. MEDIUM- TO LONG-TERM STUDIES

Various physical perturbations affecting the medium- to long-term clock stability were measured and evaluated and are presented in this section.

A. 2^{nd}-order Zeeman shift on clock transition

Though the clock transition: $5\ ^2S_{1/2}|F_g = 1, m_F = 0\rangle \longleftrightarrow |F_g = 2, m_F = 0\rangle$ (in the case of ^{87}Rb) is unaffected by the magnetic field in first-order, the second-order perturbations due to magnetic field variations give rise to the 2^{nd}-order Zeeman shift [10], given as [11],

$$\Delta\nu_Z = A_0|\mathbf{B}\cdot\hat{z}|^2, \qquad \text{with } A_0 = 575.14\ \ \mathrm{Hz/G^2}, \quad (1)$$

where, $\hat{z}$ is the quantization axis direction and $\mathbf{B}$ is the resultant total magnetic field that has a contribution due to the applied quantization magnetic field $\mathbf{B_0}$, the residual field $\mathbf{B_r}$ and the field related to the noise of the magnetic shields $\mathbf{B_s}$. By considering all the above noise contributions, we estimate the influence of the 2^{nd}-order Zeeman shift on the clock frequency stability to be $\sigma_y(\tau) \approx 2.7\times10^{-15}$ up to 10^5 s integration times, however this value could degrade to the level of 10^{-14} in highly perturbed magnetic conditions.

B. Intensity & Frequency Light-Shifts (LS)

Theoretical description of the light-shift (AC Stark shift) can be found in [12], [13]. At a fixed laser frequency (i.e. when we stabilise our laser to a particular sub-Doppler transition), the clock frequency shift was measured as a function of the input laser intensity to get the intensity LS coefficient, α [13]. For the transition $|F_g = 2\rangle \rightarrow |F_e = 01\mathrm{Cross-Over}\rangle$, we measured the lowest intensity light-shift coefficient, $|\alpha|$ = 1.46 Hz·mm^2/μW.

Furthermore, when the laser intensity was kept constant, the clock frequency shift was measured as a function of laser frequency that gives the frequency LS coefficient, β [13]. At our input laser intensity I_L = 0.46 μW/mm^2, we get a frequency LS coefficient value of 82 mHz/MHz. The frequeny LS coefficient can be suppressed in the pulsed-mode. In the CW operation, it is not possible to completely suppress β, but the influence could be reduced by reducing the input laser intensity. Our measurements showed that the dependance of β on laser input intensity has a slope of 184 mHz/MHz·mm^2/μW.

C. Microwave Power Shift & dependance on light-intensity

The microwave power shift in buffer gas cell is an unavoidable phenomenon, because the atoms are relatively motionless during the microwave interaction, thereby causing the detected overall signal to be an inhomogeneous integration over the occuring spatial gradients [10][14][15]. It can be attributed to the field distribution (mode) inside the cavity. The observed shift is a weighted average of the ensemble of atoms that is dependent on each atom's position inside the cell. Therefore, the light-shift varies continuously along the path of the light beam in a buffer gas cell thereby causing inhomogeneous broadening of the resonance signal [10][16]. Hence, in a DR signal, we can say that the measured resonance frequency is a function of the applied microwave (RF) power. This inhomogeneity causes the shift on the clock hyperfine frequency and is termed as power shift, $|\mu_{PS}|$. The observed shift is dependent on light intensity and mimics the light-shift behavior, known as pseudo-light-shift effect [17].

The μ_{PS} was measured in the following method. At each fixed microwave power input, the clock frequency shift was measured as a function of laser intensity. Then, the light-shift free, meaning the pure microwave power shift value, was extracted by extrapolating to zero laser intensity, I_L. These extracted shift values at each microwave input power are plotted in Fig. 1, the slope ($\approx 4\times10^{-13}$/dBm) gives the pure microwave power shift on the clock frequency. Its effect on medium to long-term clock frequency is evaluated in Table II.

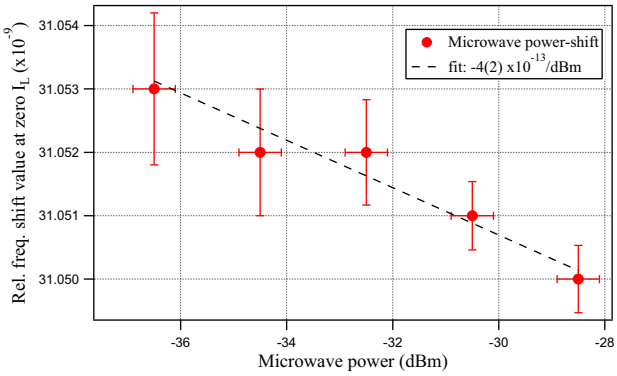

Fig. 1. Microwave power shift. The y-scaling shows relative frequency shift as the clock is referred to active H-maser.

In addition, we evaluate the dependancy of $|\mu_{PS}|$ on the input light intensity. At a smaller intensity LS coefficient of 19.5 mHz·mm^2/μW, the dependancy of input light-intensity effect on the microwave PS is well pronounced. Fig. 2 shows the microwave PS coefficient (in Hz/dBm) dependancy on the interrogating laser light intensity I_L. For instance, at an input laser intensity of $\approx$ 0.1 μW/mm^2, one can suppress the effect of microwave power shift in CW operation.

D. Temperature Coefficients

The shift due to the ^{87}Rb-buffer gas collisions is dependent on the temperature of operation of the clock [10]. A mixture of buffer gases can be used to reduce the temperature coefficient. We use a mixture of argon and nitrogen as buffer gases. Argon

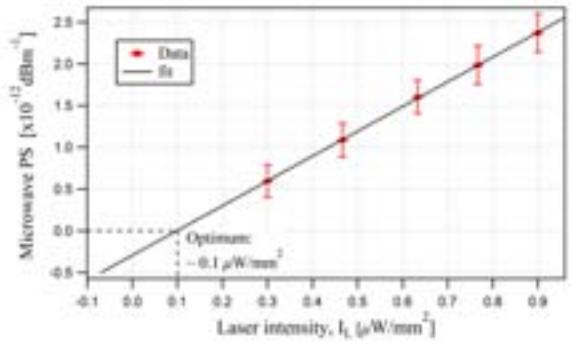

Fig. 2. Microwave power shift dependance on the input laser intensity.

has a negative linear temperature coefficient, whereas nitrogen has a positive linear temperature coefficient and due to their (much smaller) quadratic temperature coefficients, the mixture of these two at a certain temperature can give, in principle a "zero" (or inversion point) temperature coefficient [10], [18]. When the stem temperature was fixed (T_s = 321 K), a temperature coefficient value of TC_v = -1(1)$\times10^{-12}$/K has been achieved at the inversion temperature point (336 K) by a linear-fit , and the quadratic TC gives a value of -4.34$\times10^{-12}$/K^2.

The temperature coefficient was also measured as a function of the stem temperature changes, at a fixed T_v of 336 K, we get a slope of +1.22$\times10^{-11}$/K. The limits on the clock stability due to these temperature coefficients are evaluated and presented in Table II. The stem TC effect is a factor of ten higher than the cell volume TC effect. The use of BG mixtures help only to reduce the TC in the cell volume but not for the stem TC. Further studies were done to vindicate the effect due to stem TC (see Section IV-G).

E. Other perturbations

The clock frequency shift due to Rb-Rb spin-exchange collisions in the range of our operating temperatures (between 333 K to 343 K) is estimated to be ΔT_{SE} = 5$\times10^{-12}$/K. For this estimation we followed the method explained in [19].

The cavity pulling effect arises due to the feedback of the cavity on the atoms confined inside the vapor cell, because of the cavity detuning from the DR centre frequency [10]. For our magnetron-type cavity, with a measured Q-factor of ~80, the temperature dependent cavity pulling shift was estimated to be 2.9$\times10^{-14}$/K.

F. Medium- to long-term perturbations summary and contribution on clock instability

In Table II, all the above detailed perturbations are summarised along with their contributions on the clock's medium-to long-term instability at 10^4 s.

From Table II, it is clear that presently the limiting perturbations in reaching the level of 1$\times10^{-14}$ (equivalent to reach the time accuracy $<$ 1 ns/day) are the frequency LS effect $|\beta|$ and the stem TC $|TC_s|$. However, it is possible to reduce the effect of $|\beta|$ on clock frequency instability by operating our clock at lower input light intensities as explained in Section IV-B. But, we found that the stem TC arises due to our vapor cell geometric effect, as explained in the below section IV-G.

TABLE II. SUMMARY OF INSTABILITY CONTRIBUTIONS OF PHYSICAL PERTURBATIONS ON THE CLOCK TRANSITION IN MEDIUM TO LONG-TERM TIME SCALES. THE ESTIMATION IS DONE AT 10^4 S INTEGRATION TIME.

Physical effect	**Instability at 10^4 s**
Intensity LS effect, $\|\alpha\|$	9.9$\times10^{-15}$
Frequency LS effect, $\|\beta\|$	3.7$\times10^{-14}$
Microwave PS, $\|\mu_{PS}\|$	8.9$\times10^{-16}$
Cell volume TC $\|TC_v\|$ *(linear fit)*	3.5$\times10^{-15}$
Cell volume TC $\|TC_v\|$ *(quadratic fit)*	5.3$\times10^{-17}$
Stem TC $\|TC_s\|$	5.52$\times10^{-14}$
Spin ex. shift $\|\Delta T_{SE}\|$	$<$2.3$\times10^{-14}$
Cavity pulling $\|\Delta\nu_{CP}\|$	$<$ 1.5$\times10^{-16}$

G. Vapor cell geometric effect

As mentioned before, our Rb cell has two distinct parts; *cell volume*, where the ^{87}Rb vapor is interrogated with laser and microwave to get the DR signal, and *cell stem* that acts as reservoir for metallic Rb. The stem is also useful to better control the vapor pressure of the Rb inside the cell volume, and helps to increase the operation life-time of the clock.

As pointed out recently by Calosso et al., [20] a simple model of ideal gas law suggests that the temperature fluctuation in the stem results in redistribution of buffer gas particles in the entire cell; they call this effect Enhanced Temperature Sensitivity (ETS). This effect is not due to changes of interaction between Rb and buffer gas atoms, rather due to the buffer gas density variations between the cell body and the stem volumes, which is purely a geometrical effect (the stem part stays outside the microwave cavity and hence does not contribute in the microwave interrogation). In other words, one can say that the temperature gradient between the cell volume and the stem is responsible for this geometric effect. We calculated this geometric effect in our vapor cell and obtained the value 1$\times10^{-11}$/K. This calculated value matches well with the measured result of stem temperature coefficent (see Section IV-D).

V. MEASURED CLOCK STABILITY

Our clock was operated in typical ambient laboratory conditions, in air and not under vacuum. The clock's frequency stability was measured over a period of 9 days and its Allan deviation is shown in Fig. 3. The limit at 10^4 s of $\approx 6\times10^{-14}$ is in excellent agreement with the limit due to the stem temp. Coefficient, $|TC_s|$, which is attributed to the cell's geometric effect.

VI. CONCLUSIONS

DR Spectroscopic and metrological studies affecting the clock's medium- to long-term frequency stability were presented. The combined volume of our LH and PP is $<$ 1.7 dm^3, with a total mass of $<$ 2 kg. Our clock exhibits the S/N limited short-term stability of $<$ 1.4$\times10^{-13}$ $\tau^{-1/2}$. The short-term noise budget was presented showing the S/N limit. The

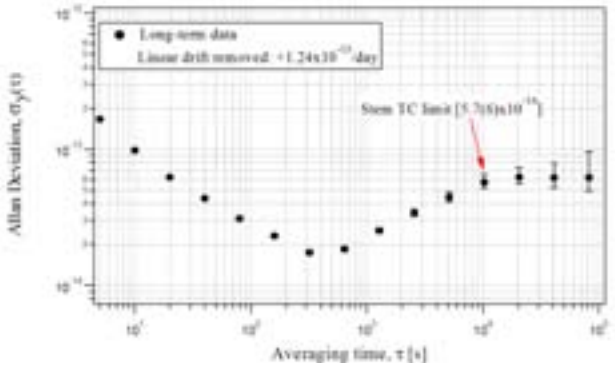

Fig. 3. Clock stability showing the limit due to stem TC at medium- to long-term time scales. This clock stability was not measured in the optimised conditions for the short-term.

Microwave power shift and its dependance on laser intensity, especially at reduced LS coefficient condition, was demonstrated. We have shown that the frequency LS coefficient (β) could be reduced by operating at lower laser input intensities. The clock's stability at 10^4 integration time is presently limited at $\sim 6\times10^{-14}$ due to the stem TC, that is characterized as the vapor cell geometric effect. By reducing the volume of the stem, we forsee to minimise the geometric effect and futhermore by operating our clock under vacuum we could reach stability levels below 1×10^{-14}.

ACKNOWLEDGMENT

This work was supported by the SNSF (grant no. 140712) and the ESA. We thank C. E. Calosso (INRIM, Italy) for the microwave synthesizer (LO). We thank F. Gruet (laser head), M. Pellaton (vapor cells), P. Scherler (CAD & PP) and M. Dürrenberger (electronics) for their technical support.

REFERENCES

[1] L. A. Mallette, P. Rochat, and J. White, "Historical review of atomic frequency standards used in space systems - 10 year update", 38^{th} Annual Precise Time and Time Interval (PTTI) meeting, 2006, pp. 69-80.

[2] T. Bandi, C. Affolderbach, C. E. Calosso, and G. Mileti, "High-performance laser-pumped rubidium frequency standard for satellite navigation", Electron. Lett., vol. 47, 2011, pp. 698-699.

[3] S. Micalizio, C. E. Calosso, A. Godone, and F. Levi, "Metrological characterization of the pulsed Rb clock with optical detection", Metrologia, vol. 49, 2012, pp. 425-436.

[4] P. Rochat et al., "The Onboard Galileo Rubidium and Passive Maser, Status & Performance, Proc. IEEE Int. Freq. Control Symposium, Vancouver, Canada, 2005, pp. 26-32.

[5] T. Bandi, C. Affolderbach, C. Stefanucci, F. Merli, A. K. Skrivervik, C. E. Calosso, G. Mileti, "Laser-pumped high-performance compact gas-cell Rb standard with $<3\times10^{-13}\ \tau^{-1/2}$ stability", Proc. of European Frequency and Time Forum (EFTF), Gothenburg, Sweden, April 24-26, 2012, pp. 494-496.

[6] T. Bandi, M. Pellaton, D. Miletic, C. Affolderbach, F. Gruet, R. Matthey, C. Stefanucci, M. Violetti, F. Merli, J.-F. Zürcher, A. K. Skrivervik, G. Mileti, "Double-resonance in alkali vapor cells for high performance and miniature atomic clocks", Proc. of IEEE International Frequency Control Symposium, Baltimore, USA, May 21-25, 2012, pp. 686-691.

[7] F. Gruet, M. Pellaton, C. Affolderbach, T. Bandi, R. Matthey, and G. Mileti, "Compact and frequency stabilized laser heads for rubidium atomic clocks". In Proc. of Int. conf. on Space Optics, 2012, no. 48.

[8] C. Stefanucci, T. Bandi, F. Merli, M. Pellaton, C. Affolderbach, G. Mileti, A. K. Skrivervik, "Compact microwave cavity for high performance rubidium frequency standards", Rev. Sci. Instrum., vol. 83, 2012, 104706.

[9] J. C. Camparo, "Conversion of laser phase noise to amplitude noise in an optically thick vapor, J. Opt. Soc. Am. B, vol. 15, 1998, pp. 1177-1186.

[10] J. Vanier and C. Audoin. "The Quantum Physics of Atomic Frequency Standards", Adam Hilger, 1:365, 1989.

[11] S. Micalizio, A. Godone, F. Levi, and C. Calosso, "Medium-Long Term Frequency Stability of Pulsed Vapor Cell Clocks", IEEE Trans. Ultrason. Ferroelectr. Freq. Control., vol. 57, 2010.

[12] B. S. Mathur, H. Tang, and W. Happer. "Light Shifts in the Alkali Atoms", Phys. Rev., 171(1), 1968,pp. 11-19.

[13] C. Affolderbach, C. Andreeva, S. Cartaleva, T. Karulanov, G. Mileti, and D. Slavov. "Light shift suppression in laser optically-pumped vapour-cell atomic frequency standards". Appl. Phys. B, vol. 80, 2005, pp. 841-848.

[14] G. Mileti, I. Ruedi, and H. Schweda, "Line inhomogeneity effects and power shift in miniaturized rubidium frequency standards", In Proc. of $6th$ European Frequency and Time Forum, 1992, pp. 515.

[15] A. Risely and G. Busca, "Effect of Line Inhomogeneity on the Frequency of Passive Rb87 Frequency Standards", In Proc. 32nd Annual Symp. on Frequency Control, 506-513. Electronic Industries Association, Washington DC, 1978.

[16] A. Risley, S. Jarvis, and J. Vanier, "The Dependence of Frequency Upon Microwave Power of Wall-coated and Buffer-gas-filled Gas Cell Rb87 Frequency Standards", J. Appl. Phys., vol. 51, 1980, pp. 4571-4576.

[17] S. Micalizio, A. Godone, F. Levi, and C. Calosso, "Pulsed optically pumped 87Rb vapor cell frequency standard: A multilevel approach", Phys. Rev. A, vol. 79, no. 013403, 2009.

[18] J. Vanier, R. Kunski, N. Cyr, J. Y. Savard, and M. Tłtu. "On Hyperfine Frequency Shifts Caused by Buffer Gases: Application to the Optically Pumped Passive Rubidium Frequency Standard". J. Appl. Phys., vol. 53, 1982, pp. 5387-5391.

[19] S. Micalizio, A. Godone, F. Levi, and J. Vanier, "Spin-exchange frequency shift in alkali-metal-vapor cell frequency standards". Phys. Rev. A, vol. 73, 033414, 2006.

[20] C. E. Calosso, A. Godone, F. Levi, and S. Micalizio, "Enhanced temperature sensitivity in vapor-cell frequency standards", IEEE Trans. Ultrason. Ferroelctr. Freq. Control., vol. 59, 2012, pp. 2646-2654.

The 2nd Harmonic Signal in Vapor-Cell Clocks & Error-Signal Quality: Does S_2 imply $dS_1/d\Delta$?

James Camparo and Gilda Fathi
Physical Sciences Laboratories
The Aerospace Corporation, 2310 E. El Segundo Blvd.
El Segundo, CA 90245, USA
james.c.camparo@aero.org

***Abstract*— How does one directly assess the quality of a Rb atomic clock signal remotely and in real time? Typically, one monitors the clock's 2nd harmonic signal, S_2, which in the quasi-static approximation is a measure of the correction signal's slope, $dS_1/d\Delta$. Unfortunately, in real vapor-cell clocks the quasi-static approximation is not valid, and the physics relating S_2 to $dS_1/d\Delta$ is complicated and not well understood. We have begun a series of studies aimed at elucidating the relationship between S_2 and $dS_1/d\Delta$, and here we present our preliminary results.**

Keywords—atomic clocks, Rabi resonance, frequency modulation, second harmonic, Rb atomic clock, vapor-cell clock

I. Introduction

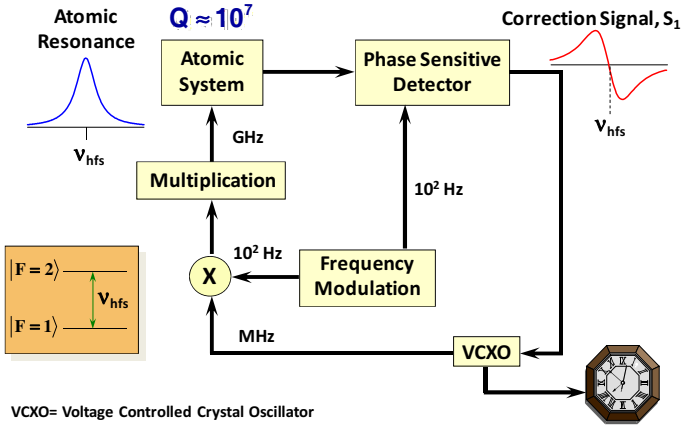

Fig. 1. The basic frequency feedback loop of a Rb atomic clock. The output frequency of a VCXO undergoes frequency modulation at some relatively low Fourier frequency (e.g., 10^2 Hz), and is then multiplied up to the microwave regime where it interacts with an ^{87}Rb vapor, causing the atomic system to undergo a state change, $|F=1\rangle \leftrightarrow |F=2\rangle$. The atoms' response to the microwave signal is monitored using phase sensitive detection (i.e., the atoms' response is demodulated at f_m), which produces a correction (or error) signal that keeps the VCXO locked to the atoms' state-transition frequency, ν_{hfs}.

In the Rb atomic clock, as illustrated in Fig. 1, the output frequency of a VCXO is multiplied up to the microwave regime, and this microwave field's frequency is modulated at f_m. Using phase sensitive detection, the atoms' response to the field is demodulated at f_m producing a 1st harmonic signal, S_1, which has a "derivative-type" shape as a function of microwave frequency. The 1st harmonic correction (or error) signal is then fed back to the VCXO, effectively locking its output frequency to the Rb atom's ground-state hyperfine transition frequency, ν_{hfs}. Specifically, defining M as the frequency multiplication factor and with $\Delta \equiv M\nu_{VCXO} - \nu_{hfs}$, the feedback loop continuously adjusts the VCXO's output frequency so that $\Delta = 0$. Clearly, the quality of the VCXO stabilization process depends on the correction signal's slope near $\Delta = 0$: $dS_1/d\Delta$, and any means of measuring $dS_1/d\Delta$ therefore provides an immediate status-of-health indicator for the clock's operation.

From an engineering perspective, the atomic dynamics that occur in an atomic clock are often conceptualized in terms of the quasi-static approximation, QSA [1]. Briefly, one assumes that the modulation period, $1/f_m$, is long compared to the time scale of atomic processes, so that the atoms effectively reach a steady state at each instantaneous frequency of the modulated microwave field. Consequently, writing $\Delta(t)$ as $\Delta_o + \delta_m g(t)$, where δ_m is the frequency modulation amplitude, Δ_o is the average microwave detuning, and g(t) is some modulation waveform (e.g., $g(t) = \sin(2\pi f_m t)$); the atoms' response to the modulated field, s(t), can be expanded in a Taylor series about Δ_o [2], yielding

$$s(t) = s(\Delta_o) + \delta_m g(t)\left.\frac{ds}{d\Delta}\right|_{\Delta_o} + \tfrac{1}{2}(\delta_m g(t))^2 \left.\frac{d^2 s}{d\Delta^2}\right|_{\Delta_o} + \ldots \quad (1)$$

For sine wave modulation, it is straightforward to show that

$$s(t) = S_o + S_1 \sin(2\pi f_m t) + S_2 \cos(4\pi f_m t) + \ldots \quad (2)$$

where

$$S_o \cong s(\Delta_o) + \left.\frac{\delta_m^2}{4}\frac{d^2 s}{d\Delta^2}\right|_{\Delta_o} \quad (3a)$$

$$S_1 \cong \delta_m \left.\frac{ds}{d\Delta}\right|_{\Delta_o} \quad (3b)$$

$$S_2 \cong -\left.\frac{\delta_m^2}{4}\frac{d^2 s}{d\Delta^2}\right|_{\Delta_o} \cong -\left.\frac{\delta_m}{4}\frac{dS_1}{d\Delta}\right|_{\Delta_o}. \quad (3c)$$

Thus, in the QSA we interpret the amplitude of the 2nd harmonic signal as a measure of the clock's correction signal slope, and therefore a measure of clock-signal quality.

However, in order to obtain large signal-to-noise ratios and narrow atomic linewidths, it is typical to operate atomic clocks under conditions such that $f_m \sim \Omega \sim \gamma$, where Ω and γ are the

This work was funded by the U.S. Air Force Space and Missile Systems Center under Contract No. FA8802-09-C-0001.

Rabi frequency and dephasing rate, respectively. Unfortunately, this regime of operation is neither quasi-static (large γ), adiabatic (large Ω), nor sudden (large f_m). Consequently, none of the standard approximations of atomic dynamics legitimately apply, notably the QSA. Therefore, while Eq. (3c) certainly provides qualitative engineering guidance, we must question its *quantitative* utility. For example, how should we interpret a sudden 10% change of S_2 in terms of $dS_1/d\Delta$? Does it imply a 10% change in $dS_1/d\Delta$, something significantly larger, something significantly smaller? In what follows, we describe our first experimental results exploring the relationship between S_2 and $dS_1/d\Delta$.

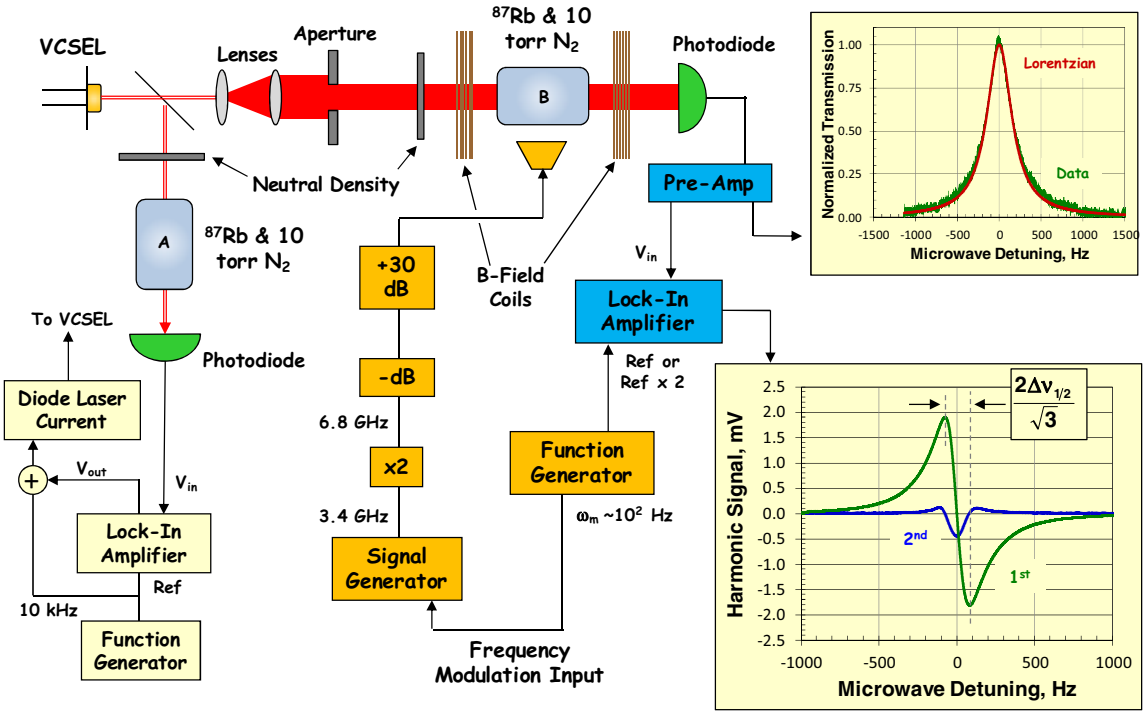

Fig. 2. Block diagram of the experimental arrangment. The block labeled "–dB" is an attenuator, and the box labeled "+30 dB" is a fixed gain amplifier. The microwaves are emitted by a 15 dB microwave horn located about 15 cm above cell B.

II. The Experiment

Figure 2 shows a block diagram of our experimental arrangement. We stabilize our VCSEL diode laser wavelength using the ^{87}Rb resonance cell on the left of the figure (cell A); this cell contains 10 torr of N_2 as a buffer gas, and is maintained at a temperature of ~37 ^{o}C. Though the Rb atomic clocks employed in GNSS and satellite communication systems use an rf-discharge lamp rather than a diode laser as their light source, we use a laser to give us better control of the light field. With the laser, we not only have the ability to vary the intensity of the light and see its effect on the 2nd harmonic signal, we can also easily vary the laser frequency. Varying the laser center frequency gives us an opportunity to mimic spectral shifts in an rf-discharge lamp's output [3], and to study the effect of such variations on the 2nd harmonic signal, which might arise as a consequence of the light shift [4].

The light intensity passing through cell A is kept very low, so that optical pumping does not occur. The laser light also passes through a second ^{87}Rb resonance cell (cell B), which again contains 10 torr of N_2 as a buffer gas. The laser light optically pumps the rubidium atoms in cell B, which is our atomic-clock signal cell, and creates a population imbalance between the atom's ground state hyperfine levels. Since the optical pumping process essentially removes atoms from the optically-absorbing hyperfine level, the laser light passing through this second cell is relatively high when the optical pumping process completes. (The optical pumping process is relatively fast, taking roughly a millisecond to complete.) If microwaves of the appropriate frequency impinge on the vapor, however, atoms are forced to return to the optically absorbing hyperfine level with a concomitant decrease in the transmitted light intensity. Consequently, as illustrated in the top graph on the right, plotting the vapor's absorption as a function of microwave frequency yields a Lorentzian absorption profile. In addition, we modulate the frequency of the microwaves in our experiment at f_m = 47.3 Hz. We can then monitor the atoms' first harmonic response to the microwaves or the atoms' second harmonic response to the microwaves using a lock-in amplifier and the appropriate reference frequency. Examples of our S_1 and S_2 data are shown in the lower graph on the right in Fig. 2. In this work, we are primarily concerned with the amplitude of the 2nd harmonic signal when the microwaves are on resonance, corresponding to locked vapor-cell clock conditions. Table I provides our experimental parameters.

For our measurement procedure, we record the in-phase and quadrature voltage components (V_I and V_Q, respectively)

of the 1st and 2nd harmonic signals, and we use these to define the harmonic signal's amplitude, A_n, and phase, θ_n (n = 1 or 2):

$$A_n = \sqrt{V_I^2 + V_Q^2} \tag{4a}$$

$$\theta_n = \tan^{-1}\left[\frac{V_Q}{V_I}\right]. \tag{4b}$$

From these data, we compute S_1 and S_2 as

$$S_1 = A_1 \cos(\theta_1 - \psi_1) \quad \text{and} \quad S_2 = A_2 \cos(\theta_2 - \psi_2), \tag{5}$$

where ψ_1 is chosen to maximize $|dS_1/d\Delta|$ on resonance and ψ_2 is chosen to maximize $|S_2|$ on resonance. The reason for including ψ_1 and ψ_2 in the computations of S_1 and S_2 is that with phase sensitive detection one routinely adjusts the reference signal's phase to maximize the in-phase component of the detector's output. Finally, we calibrate the attenuator setting to Rabi frequency using $\Delta\nu_{1/2}$ as indicated in the lower right inset of Fig. 2. Figure 3 shows $\Delta\nu_{1/2}$ plotted as a function of the relative microwave field strength, though we actually calibrate $\Delta\nu_{1/2}$ to Rabi frequency assuming linearity between the linewidth *squared* and the microwave *power* [5].

TABLE I. EXPERIMENTAL PARAMETERS

Parameter	Value
Optical Depth, NσL	1
Photon Absorption Rate, R_{ph}	25 Hz
Residual Dephasing Rate,[a] γ	46 Hz
Resonance Cell Temperature	34 °C
Laser Beam Diameter at Cell Entrance	0.4 cm
Modulation Frequency, f_m	47.3 Hz
Modulation Amplitude, δ_m	30 Hz
Axial Magnetic Field, B_z	260 mG

[a] The total dephasing rate is given by $R_{ph}/2 + \gamma$

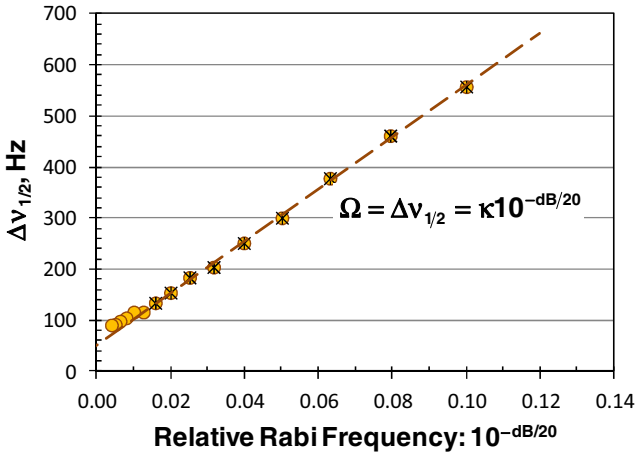

Fig. 3. This figure shows the linewidth, $\Delta\nu_{1/2}$, determined from S_1 (as illustrated in Fig. 2) plotted as a function of the relative Rabi frequency, which is determined by our attenuator setting. Since the linewidth *squared* scales with the microwave *power*, and is directly related to the Rabi frequency, we use this data to determine κ.

III. RESULTS

Our principal results are collected in Figs. 4. In Fig. 4a, we show $dS_1/d\Delta$ and $4S_2/\delta_m$ plotted as functions of the Rabi frequency; the solid lines are Gaussian fits to the data. Figure 4b shows our experimental values of $4S_2/\delta_m$ along with a full density matrix calculation of $dS_1/d\Delta$ and $4S_2/\delta_m$ [5]; there are no free parameters in the density matrix computations.

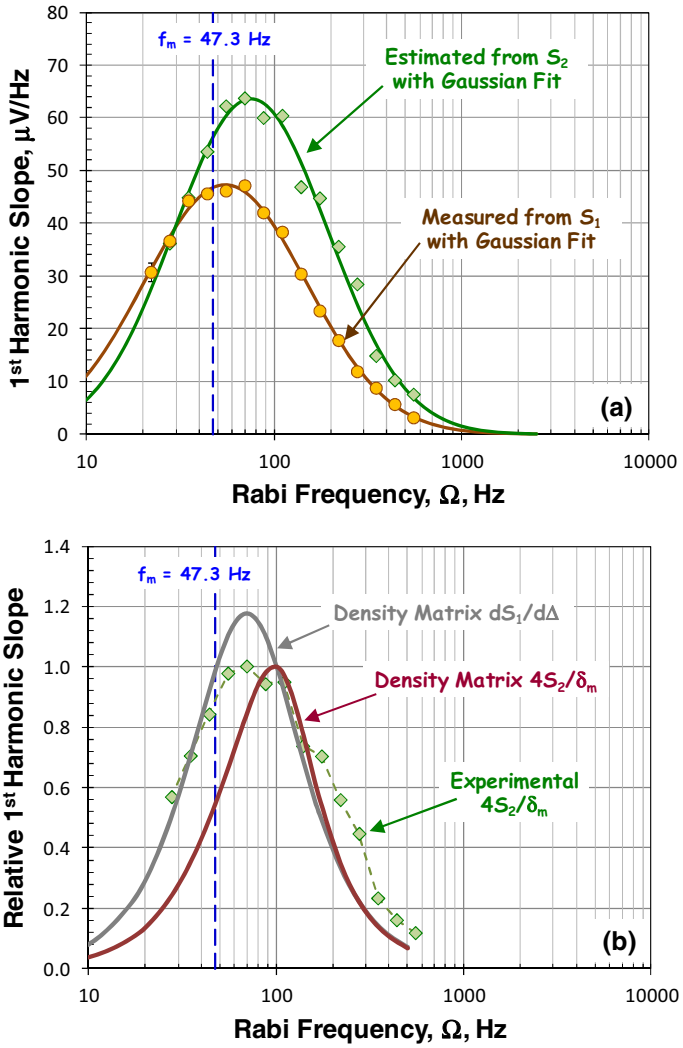

Fig. 4. (a) Experimental results of $dS_1/d\Delta$ and $4S_2/\delta_m$ as a function of Rabi frequency. The solid lines are Gaussian fits to the data. (b) A comparison of full density matrix theory with experiment. Note that the full density matrix theory is based on the Generalized Vanier Theory of the 0-0 transition lineshape as discussed in Ref. 5; there are no free parameters in the density matrix computations.

There are two things worth noting regarding the results displayed in Figs. 4a and 4b:

1. Relative to the experimental values, the theoretical values of $dS_1/d\Delta$ are too large. Additionally, relative to the experimental values, the theoretical values of $4S_2/\delta_m$ have too narrow a distribution. These observations cannot be explained by inhomogeneous broadening of the hyperfine transition. As a test, we included ~ 40 Hz of inhomogeneous broadening in the

density matrix computations with little effect on the results. At the present time, we believe the discrepancy between theory and experiment is due to spatial inhomogeneity of the Rabi frequency. Spatial variation of the Rabi frequency could arise, since the Rabi frequency is defined by a scalar product between the microwave magnetic-field vector and the static axial magnetic field, B_z. Depending on the coil geometry and the Earth's magnetic field, B_z could vary spatially.

2. Given that the peaks of $dS_1/d\Delta$ and S_2 are displaced from one another experimentally and theoretically, the $dS_1/d\Delta$ vs. S_2 relationship will only be "quasi-linear." This is illustrated more clearly in Fig. 5. Though the theoretical and experimental curves are on opposite sides of the QSA ideal result (i.e., $dS_1/d\Delta = 4S_2/\delta_m$ shown as the dashed line), they both nonetheless show that $dS_1/d\Delta$ is non-monotonic in S_2.

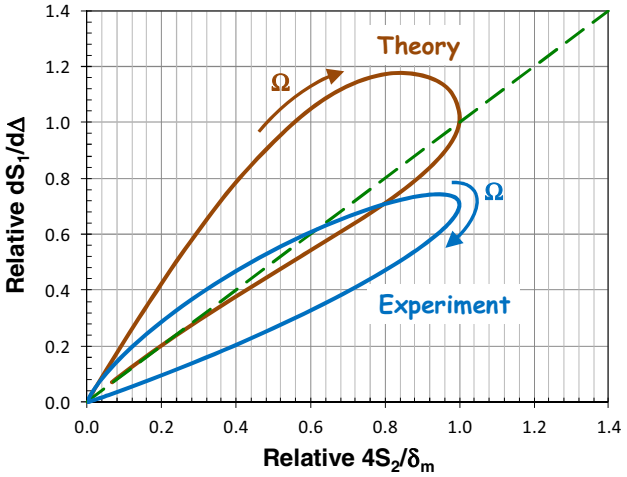

Fig. 5. The $dS_1/d\Delta$ vs $4S_2/\delta_m$ relationship. The experimental curve comes from the Gaussian fits to the data. The dashed line represents the QSA ideal: $dS_1/d\Delta = 4S_2/\delta_m$.

IV. Summary

In this paper, we have outlined our progress studying the relationship between the slope of a Rb clock's correction-signal, $dS_1/d\Delta$, and the clock's 2nd harmonic signal, S_2. Though S_2 has a "quasi-linear" relationship with $dS_1/d\Delta$, it is unfortunately non-monotonic. Moreover, the *quantitative* relationship between S_2 and $dS_1/d\Delta$ likely depends on spatial variations in the dynamics over the clock-signal's volume, arising from spatial variations in the Rabi frequency. Thus, while S_2 is certainly a *qualitative* indicator of a Rb clock's status-of-health, much more study will be required in order to develop a *quantitative* understanding of S_2's relationship with $dS_1/d\Delta$ at the basic atomic physics level. In the near term, the quantitative relationship between S_2 and $dS_1/d\Delta$ can only be defined empirically, and therefore determined on a case-by-case basis. Thus, in answer to the question posed in the title of this paper (i.e., Does S_2 imply $dS_1/d\Delta$?) at present we can only reply… Maybe.

References

[1] G. Fathi and J. Camparo, "The 2nd harmonic signal in vapor-cell atomic clocks," in Proc. 2011 Joint Conf. IEEE Internat. Freq. Control Symp. & Eur. Freq. and Time Forum. IEEE Press, Piscataway, NJ, 2011, pp. 564-569.

[2] J. Vanier and C. Audoin, The Quantum Physics of Atomic Frequency Standards Vol. 2, Adam Hilger: Bristol, 1989, pp. 1283-1305.

[3] N. Kuramochi, T. Matsuo, I. Matsuda, and H. Fukuyo, "Spectral profiles of the 87 Rb D1 line emitted from a spherical electrodeless lamp," Jap. J. Appl. Phys., vol. 16(5), pp. 673-679, 1977.

[4] S. Pancharatnam, "Light shifts in semiclassical dispersion theory," J. Opt. Soc. Am., vol. 56(11), pg. 1636, 1966; B. S. Mathur, H. Tang, and W. Happer, "Light shifts in the alkali atoms," Phys. Rev., vol. 171(1), pp. 11-19, 1968; J. C. Camparo, R. P. Frueholz, and C. H. Volk, "Inhomogeneous light shift in alkali-metal atoms," Phys. Rev. A, vol. 27(4), pp. 1914-1924, 1983.

[5] J. Camparo & R. Frueholz, "Linewidths of the 0-0 hyperfine transition in optically pumped alkali-metal vapors," Phys. Rev. A 31, 1440-1448 (1985); J. Camparo & R. Frueholz, "Saturation of the 0-0 hyperfine-transition linewidth enhancement factor in optically pumped alkali-metal vapors," Phys. Rev. A 32, 1888-1889 (1985).

Higher-order Sideband Excitation Method for Pulsed CPT Atomic Clock

Shigeyoshi Goka, Yuichiro Yano
Graduate School of Science and Engineering,
Tokyo Metropolitan University,
Hachioji, Tokyo 1920397, Japan
goka@tmu.ac.jp

Abstract— **We propose a higher-order sideband excitation method combined with pulse excitation to reduce power consumption of coherent population trapping (CPT) atomic clocks. Since higher-order sideband excitation enables reduction of radio frequency (RF), our method can significantly reduce switching power loss of an RF generator and its peripheral circuits. Experimental results show that 3rd-order sideband excitation can lead to narrow fringe width and high contrast. In addition, the relative light shift was less than one-third that with conventional excitation method.**

I. INTRODUCTION

Coherent-population-trapping (CPT)-based atomic clocks with vertical-cavity surface-emitting lasers (VCSELs) have been widely investigated to develop very small atomic references called chip-scale atomic clocks (CSACs). The power consumption of recent CSACs is nearly 100 mW, which is lower than conventional Rb atomic clocks but not low enough for portable applications. One of the main reasons of this power consumption is the switching power loss caused by parasitic capacitance in radio frequency (RF) circuits. The switching power loss accounts for the almost entire power dissipation of an RF circuit, especially in the microwave frequency range. For example, a miniaturized CPT atomic clock [1] has an RF oscillator and a related phase-locked loop (PLL) circuit power consumption of 43 mW, which is nearly half the total power (98 mW) in spite of the required RF output power being ~0 dBm (1 mW). Therefore, it is necessary to reduce the RF-related power consumption to develop lower-power CSACs. The switching power loss P_{sw} is estimated as

$$P_{sw} = f C V^2, \tag{1}$$

where, f is the frequency of the RF signal, C is the parasitic capacitance of the RF circuits, and V is the amplitude of the RF signal [2]. From Eq. (1), one or more parameters must be decreased to reduce P_{sw}. However, C and V values are determined using device parameters and required RF power, respectively. We propose a higher-order sideband excitation method to decrease the required frequency of the RF signal with pulsed CPT excitation. In our previous work [3], we reported on CPT-Ramsey resonances using a liquid crystal modulator for low power operation; therefore, our method can be applied to CSACs.

Experimental results show that 3rd-order sideband excitation can lead to narrow fringe width and high contrast. In addition, the relative light shift is less than one-third that with conventional excitation.

II. HIGHER-ORDER SIDEBAND EXCITATION

To excite the CPT resonance, two laser light fields whose wavelength is equal to the energy differences between two ground states and a common excite state are used. In conventional CPT-based atomic clocks, two lasers are generated as two first-order sidebands around the laser carrier by using the direct RF modulation of the VCSEL injection current [4]. The direct RF modulation consists of amplitude modulation (AM) and frequency modulation (FM). Although AM generates only first-order sidebands, FM generates higher-order sidebands including first-order depending on the modulation index [5]. Therefore, we can use the higher-order sidebands to excite CPT resonances at a relatively high modulation index and reduce the required RF frequency. The required RF frequency f_{RF} is expressed as

$$f_{RF} = \frac{f_{hfs}}{2n}, \tag{2}$$

where f_{hfs} is the hyper-fine splitting frequency of alkali atoms, and n is the sideband order number, which is an integer larger than 1. Table I lists the f_{RF} in higher-order sideband excitation using ^{133}Cs atoms. When n = 3, the required f_{RF} is only 1.53 GHz, which is one-third that of n = 1, and third-order sidebands can excite CPT resonance, as shown in Fig. 1.

TABLE I. REQUIRED RF FREQUENCY FOR HIGHER ORDER SIDEBANDE EXCITATION IN Cs^{133} ATOMS

Side-band order	***Required RF Frequency***	
n	***f_{RF}* [GHz]**	***Frequency Division***
1	4.60	f_{hfs} / 2
2	2.30	f_{hfs} / 4
3	1.53	f_{hfs} / 6

III. Experimental Results

A. Experimental Configureration

The measurement system for higher-order sideband excitation is shown in Fig. 2. A 895-nm VCSEL was used to excite Cs at the D_1 line. The Cs gas cell had an optical length of 20 mm and contained ^{133}Cs atoms and 1.3 kPa of N_2 buffer gas at a controlled temperature of 42.0ºC. The linearly polarized (lin||lin) laser beam of 6 mm in diameter was intensity-modulated using an acousto-optical modulator (AOM) to excite a CPT-Ramsey resonance. By using the linearly polarized laser, two Λ schemes can be formed with two pairs of ground-state hyperfine sublevels simultaneously: $|F=3, m=-1\rangle$, $|F=4, m=1\rangle$ and $|F=3, m=1\rangle$, $|F=4, m=-1\rangle$ coupled with the common excited state $|F'=3, m=0\rangle$ or $|F'=4, m=0\rangle$ [6]. The pulsed laser light field with a 1-kHz switching frequency was generated using the AOM. By adding the S/H circuit, it is possible to use the same lock-in detection system without changing the conventional measurement setup [3]. The sampling delay time T_m of the S/H circuit was set to 10 μs. The Cs standard (Symmetricom 5071A High performance tube) was used as a reference frequency source. In the experiment, the CPT characteristics with the sideband order n = 1~3 were measured because the CPT contrast of the $n > 3$ was small.

B. CPT resonances Excited by Higher Order Sidebands

Figure 3 shows the CPT resonance excited by the conventional continuous and pulsed laser light fields of the higher-order sidebands. The vertical axis is transmitted laser power normalized by the maximum value, and the horizontal axis is the detuning from the f_{RF}. Table II lists the contrast and the resonant full-width at half-maximum (FWHM) with the optimized RF power as the resonant contrast was maximized. With continuous excitation, the CPT contrast decreased and the Q values slightly decreased when n increased. This is because the higher-order wavelength components were generated by the larger frequency modulation index, which also causes the other unwanted wavelength components to decrease the CPT contrast. On the other hand, in pulsed excitation, Q values drastically increased and were not affected by n because the resonant FWHM was determined by CPT Ramsey free

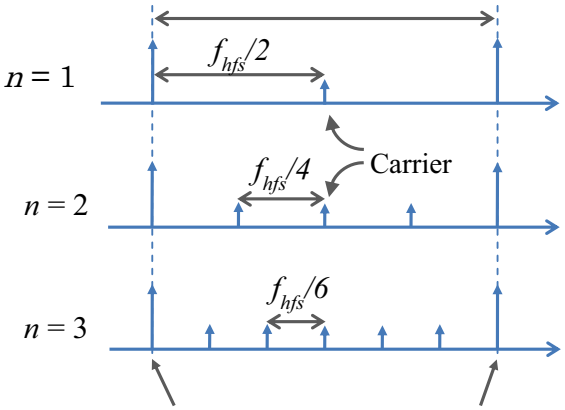

Two laser light fields for exciting CPT resonance

Fig. 1 Frequency spectrum of higher order side-bands

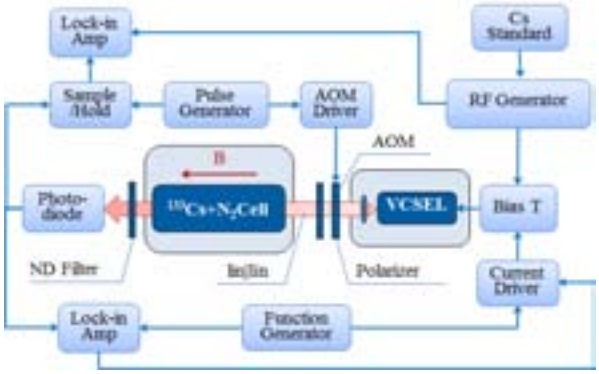

Fig. 2 Schematic of CPT mesurement system

TABLE II. Measurement Values Excited by Higher Order Sideband Pairs under Continuous and Pulse Excitation

Excitation Method	Sideband Order n	f_{RF} [GHz]	Contrast [%]	FWHM	Q value (f_{RF} / FWHM)	Figure of Merit (Q value × Contrast)	Relative Figure of Merit
Continuous	1	4.596 325	3.3	2.32 kHz	1.98×10^6	6.5×10^6	1.0
	2	2.298 162	0.7	1.09 kHz	2.11×10^6	1.5×10^6	0.23
	3	1.532 108	0.8	700 Hz	2.19×10^6	1.8×10^6	0.27
Pulse	1	4.596 325	5.3	406 Hz	1.13×10^7	6.0×10^7	9.2
	2	2.298 162	1.8	216 Hz	1.06×10^7	1.9×10^7	2.9
	3	1.532 108	1.4	142 Hz	1.08×10^7	1.5×10^7	2.3

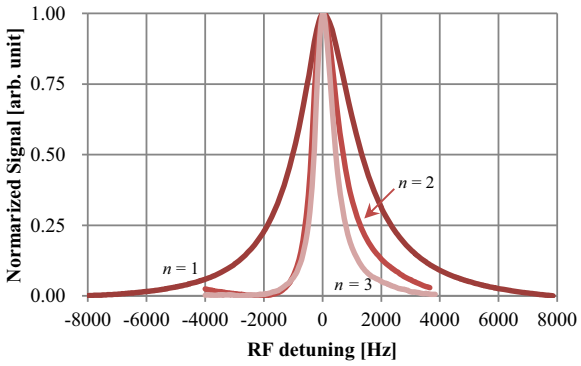

(a) Continuous excitation

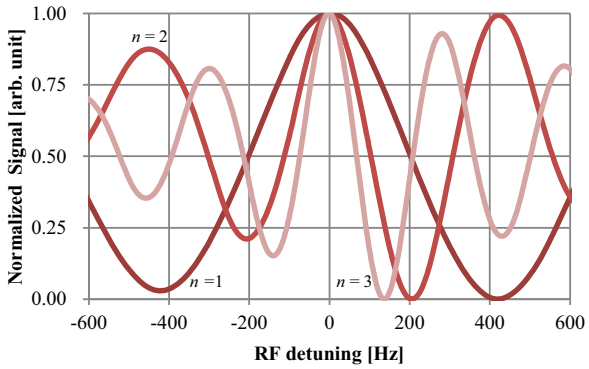

(b) Pulse excitation

Fig. 3 CPT resonances with higher order side-bands excitation

evolution time (500 μs) [7]. The Allan standard deviation $\sigma_y(\tau)$ is expressed as

$$\sigma_y(\tau) \propto \frac{1}{Q \cdot (S/N)} \tau^{-\frac{1}{2}}, \quad (3)$$

where τ is the averaging time, and the signal-to-noise ratio (S/N) is equivalent to the contrast. Since short-term stability is determined from the contrast and Q value, the figure of merit is defined as the product of the Q value and contrast. From Table II, the figure of merit of pulsed excitation (n = 3) was 2.3 times better than that of conventional continuous excitation (n = 1).

C. RF Power

The RF power dependence of contrast characteristics are shown in Fig. 4. In both excitations, there were maximal contrast values in the RF Power range of 0.3 ~ 0.5 mW. Since this RF power range was much less than the power consumption of the RF related circuit of 43 mW [1], almost all the RF electrical power was dissipated by the switching power loss. Therefore, it is possible to reduce the RF related power to 1/n.

D. Light Shift

It is well known that the light shift effect is a major limitation to the long-term stability of vapor cell-based atomic clocks [8]. Since the RF sources for each n differ, we measured the relative frequency shifts of CPT resonances, as shown in Fig. 5. The frequency shifts were observed to have a reasonably linear relationship with laser intensity; therefore, we estimated the slope of the fitted linear lines, as shown in Table III. All relative light shifts of pulsed excitation were one-third less than that of continuous excitation of n = 1. These results indicate that the higher-order excitation of n = 3 can reduce the RF frequency and relative light shift.

IV. Conclusion

We proposed a higher-order sideband excitation method combined with pulse excitation to reduce power consumption of CPT atomic clocks. Since switching power loss of RF is proportional to its frequency, lower RF frequency can reduce the power loss of an RF generator and its peripheral circuits.

Experimental results show that 3rd-order sideband excitation can lead to narrow fringe width and high contrast. In addition, the relative light shift was less than one-third that with conventional excitation. These results indicate that the proposed excitation method can improve low-power operation and frequency stabilities in CSACs.

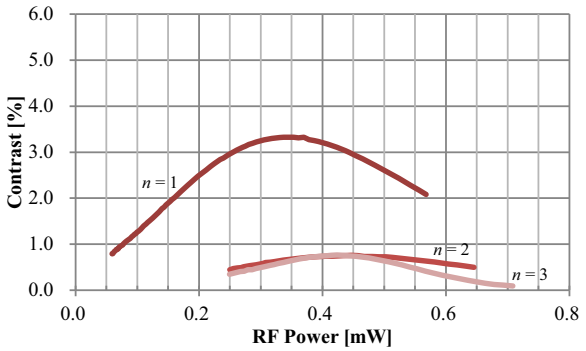

(a) Continuous excitation

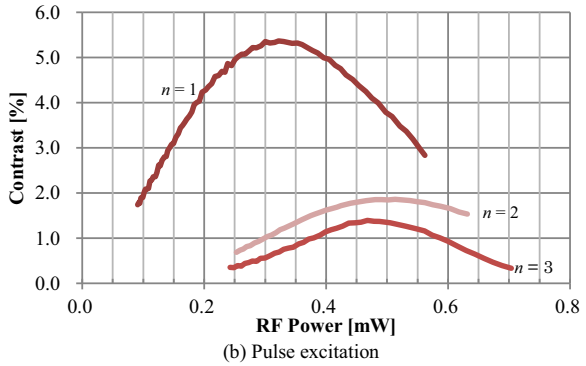

(b) Pulse excitation

Fig. 3 RF power dependence of CPT contrast

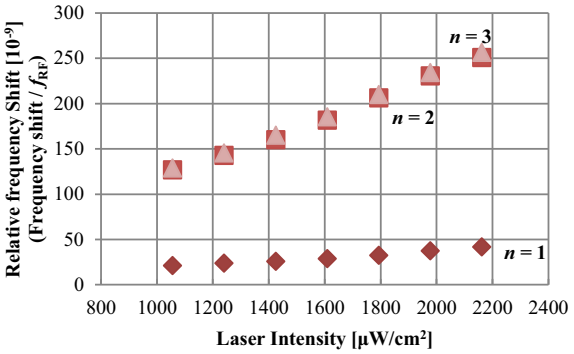

(a) Continuous excitation

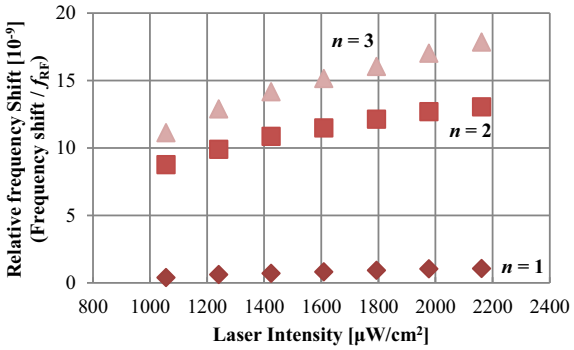

(b) Pulse excitation

Fig. 3 Relative light shift characteristics

TABLE III. RELATIVE LIGHT SHIFT ESTIMATED FROM MEASURED DATA

Excitation	Sideband order n	Relative Light Shift $[10^{-12}/(\mu W/cm^2)]$
Continuous	1	18.6
	2	115
	3	118
Pulse	1	0.602
	2	3.82
	3	5.86

ACKNOWLEDGMENT

The authors are grateful to RICOH Company, Ltd. for providing us with the Cs-D_1 VCSEL.

REFERENCES

[1] R. Lutwak, "The Chip-Scale Atomic Clock – Recent Developments," Proc. of Frequency Control Symposium, 2009 Joint with the 22nd European Frequency and Time forum, 2009, pp.573-577

[2] A. S. Sedra: *Microelectronic Circuits* (Oxford University Press, New York, 2004) 5th ed., Chap. 4, p. 345.

[3] Y. Yano and S. Goka, " Pulse Excitation Method of Coherent-Population-Trapping Suitable For Chip-Scale Atomic Clock," Jpn. J. Appl. Phys. **51**, 122401 (2012).

[4] Svenja Knappe, Robert Wynands, John Kitching, Hugh G. Robinson, and Leo Hollberg, "Characterization of coherent population-trapping resonances as atomic frequency references", J. Opt. Soc. Am. B, **18**, no.11, pp. 1545-1553 , November 2001.

[5] D. W. Fry and W. Higinbotham, "Frequency modulation theory ", Vol.11, pp.73-75, Oxford, Pergamon Press, New York, 1961.

[6] K. Watabe, T. Ikegami, A. Takamizawa, S. Yanagimachi, S. Ohshima, and S. Knappe, "High-contrast dark resonances with linearly polarized light on the D_1 line of alkali atoms with large nuclear spin", APPLIED OPTICS , **48**, no. 6, 2009, pp. 1098-1103

[7] Rodolphe Boudot, Stéphane Guérandel, Emeric de Clercq, Noël Dimarcq, and André Clairon, "Current Status of a Pulsed CPT Cs Cell Clock", IEEE Trans. Instrum. Meas. **58**, no.4, pp. 1217-1222, April 2009.

[8] J. Vanier, "Atomic clocks based on coherent population trapping: a review," Appl. Phys. B **81** (2005) pp.421-442.

Reducing the Blackbody Radiation Shift in the NIM New Fountain Design

Fang Fang[1], Kun Liu[1], Xiaoke Yan[1], Rui Suo[1], Weiliang Chen[1], Nianfeng Liu[1], Yu Zhang[2], and Tianchu Li[1]
[1] National Institute of Metrology, Beijing, P. R. China
[2] Beijing Institute of Technology, Beijing, P.R. China
E-mail: fangf@nim.ac.cn

***Abstract*—We are developing a new Cs fountain frequency standard in NIM, and shooting for the frequency uncertainty of a few parts in 10^{16}. The new fountain will run in a lab with the temperature fluctuation of 0.3K, and no active temperature control system will be added outside the flight tube. Instead, an isothermal liner will be surrounded the flight tube. It is a special type of heat pipe, made of a thin layer of vacuum tube filled with pure water. The thermal conductivity of a glass isothermal liner is about 10 times higher than that of coppers. It also works like a low pass filter reducing the temperature fluctuations of the system. The advantage of using an isothermal liner is to make the temperature of the whole interrogation region more uniform and stable. With precision standard Pt thermometers measuring the temperatures of a few locations of the flight tube, the average temperature uncertainty is less than 50 mK. The frequency shift due to the blackbody radiation can be calculated, and the relative frequency shift due to black body radiation can reach down to 7.2E-17 of this new fountain clock.**

Key words: Fountain clock, blackbody radiation, heat pipe

I. INTRODUCTION

Atomic clocks provide the most accurate measurements of the physical observables, time and frequency. Up to date, several groups' Cs fountain clocks have achieved frequency uncertainties in the low E-16 [1-5]. These capabilities offer great opportunities in a variety of precision measurements, such as realization of the second, frequency metrology, high accuracy spectroscopy, and tests of fundamental physics [6-9]. There are four main effects which will shift the energy levels of the clock transition and consequently give frequency shifts, including the cold-atomic-collision-induced density shift [10, 11], the magnetic-field-induced quadratic Zeeman shift, the Earth-gravitational-potential-induced red shift and the black-body-radiation-induced AC Stark shift [12, 13]. Theories and several new techniques have been brought to bear on the problem of estimating the spin exchange shift and microwave-power-related frequency shifts in fountain frequency standards [11, 14]. The black-body-radiation-induced frequency shift will presumably limit the accuracy that fountain clocks can achieve. NIST built a new fountain F2, which will run in a cryogenic region at a temperature of about 80 K, with an expected uncertainty far below 10^{-16}. Another way to reduce the blackbody-radiation-induced frequency shift is to improve the temperature uniformity of the flight tube and measure the temperature more accurate to reduce the temperature uncertainty.

In this Letter, we introduce the design of our new fountain NIM6. We are planning to use an isothermal liner heat pipe outside the interrogation region to improve the temperature uniformity. Heat pipes are effective thermal control devices, have been widely applied in broad areas [15]. The performance of a mock up isothermal liner is tested, and the results show reduced temperature fluctuations and better temperature uniformity with this heat pipe.

II. DESIGN OF NIM6

Atoms exposed to electromagnetic radiation during their ballistic flight will be subject to an AC Stark shift. If the thermal radiation of the vacuum enclosure gives rise to a spectral power density distribution which is equivalent to that of a black body, according to [16], the clock transition frequency is shifted by

$$\Delta\nu_{BR} = \beta\left(\frac{T}{300\,K}\right)^4\left[1+\varepsilon\left(\frac{T}{300\,K}\right)^2\right] \quad (1)$$

Here, where T is the radiation temperature of the environment expressed in kelvin. The coefficients β and ε depends on atoms and on the considered transition; up to now the theoretical accepted value of β and ε for ^{133}Cs are β=(-1.572±0.006)×10^{-14} and ε=1.4×10^{-2}. The uncertainty of this frequency shift is:

$$\delta\nu_{BR} = \Delta\nu_{BR}\cdot\frac{\delta\beta}{\beta} + 4\Delta\nu_{BR}\cdot\frac{\delta T}{T} + (2\beta\varepsilon\frac{\delta T}{T} + \delta\varepsilon\beta)\left(\frac{T}{300}\right)^6 \quad (2)$$

In equation 2, the third term is negligible at room temperatures. Reducing the temperature can reduce both first two terms, thus reducing the frequency uncertainty due to blackbody radiation. Another way to reduce the uncertainty is to reduce δT, especially when we have better knowledge of β. In the design of new fountain NIM6, we are planning to use a heat pipe and precision Pt thermometers to reduce the temperature uncertainty down to 50 mK.

The NIM6 system design is shown in figure 1. The flight tube is surrounded by 3 layers of μ-metal magnetic shield with

This work is supported by the Chinese NSF(11174260) and 973 project (2010CB922902) (sponsors)

a measured shielding factor of more than 10^4. The shields are vertical concentric cylinders with end-caps on top and bottom, each having holes for the vacuum structure, and are thermally and electrically isolated from each other and from the vacuum system. An isothermal liner will be added outside the flight tube. It is a thin layer of vacuum tube made of the fused silica, 700 mm high, filled with pure water. Three precision standard Pt100 thermometers will be added inside the isothermal liner to monitor the temperature of the flight tube.

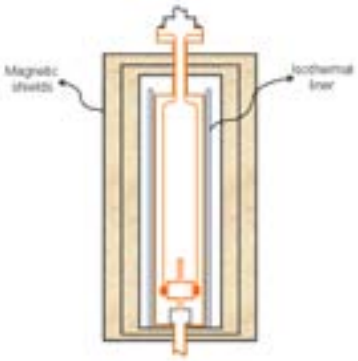

Fig.1 Schematic of the new fountain clock design. The flight tube is surrounded by 3 layers of μ-metal magnetic shield which are thermally and electrically isolated from each other and from the vacuum system. An isothermal liner will be added outside the flight tube.

The Ramsey cavity is rested on a ceramic ring. Four semi-rigid coaxial cables (one for each waveguide) connect the waveguides with vacuum feedthroughs at the top of the fountain. The Ramsey pulse power applied on the cavity is about 1 nW at the π/2 pulse. The increased temperature on the cavity due to the applied microwave was measured less than 50 mK at 100 nW input power. Thus, the temperature variations due to the Ramsey pulse are negligible at the normal running condition.

III. TEMPERATURE UNIFORMITY IMPROVEMENTS WITH ISOTHERMAL LINER

The picture of a mock up isothermal liner is shown in figure 2.

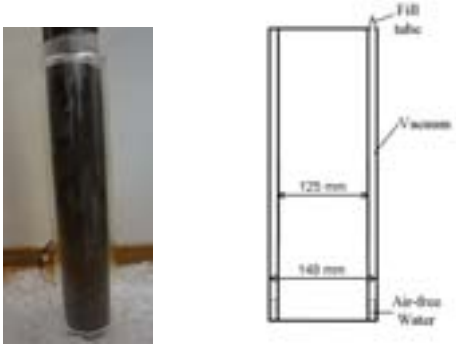

Fig.2 Picture of a mock up isothermal liner made of glass.

This mock up isothermal liner heat pipe is made of glass, has the same size as the one designed for NIM6. High purity air-free water is filled in glass vacuum tube. When there is a temperature gradient, liquid water around the hot part absorbs heat, transforms into vapor and flows toward the condensate section (cold part). This phase transitions inside the heat pipe redistribute the heat, block corresponding changes in the inner chamber temperature, regulate thermal transport and dampen temperature oscillations.

The performance of this mock-up isothermal liner is tested with a copper tube as shown in figure 2. A thin aluminum tube is placed outside the isothermal liner, and a heat tape is wrapped around it to generate temperature variations. The temperatures inside the aluminum tube and the copper tube are measured with precision standard Pt thermometers. The results are compared with the situations when the isothermal liner was taken out, and shown in figure 3.

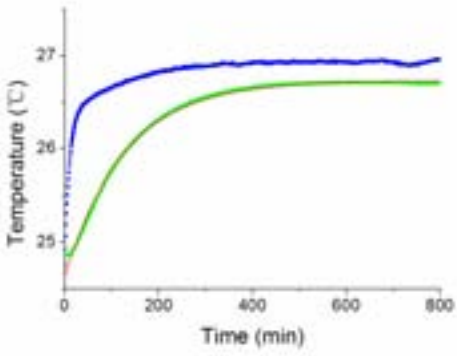

(a)

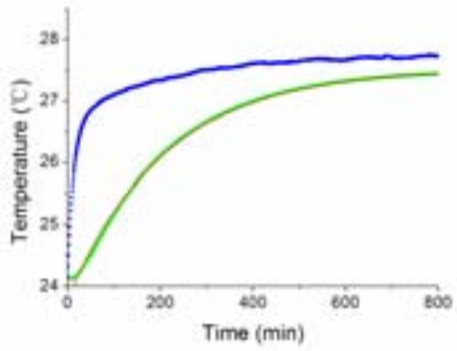

(b)

Fig.3 Comparisons of the temperature fluctuations inside the copper tube with and without the isothermal liner surrounded it. (a) shows results without the isothermal liner; (b) shows results with the isothermal liner. The blue rectangular is the temperature increasing inside the Aluminum tube (environment), the green solid circle is the temperature increasing inside the copper tube, the red solid line is the theoretical fit by an exponential curve.

From the figure, we can see that when the environment temperature increased, the temperature of the copper tube which is surrounded by the isothermal liner is increased with a slower time constant. Fitted by an exponential curve $A_1+A_2(1-$

exp(-t/τ)), the time constant τ is about 127 minutes without the isothermal liner, and about 210 minutes with the isothermal liner. This suggests that this isothermal liner works like a low pass filter, reduces the temperature fluctuations inside it.

Isothermal liners also improve the temperature gradients. This is the key benefit for NIM6 fountain clock. With improved temperature gradients and precision Pt standard thermometers, the average temperature of the flight tube can be obtained with much less uncertainty. This isothermal liner is a gravity type heat pipe. The working conditions are different for the positive and negative temperature gradient along the vertical direction. The improvements of temperature gradients with the isothermal liner are tested by wrapping the heat tape on one side to generate the temperature gradient. The results are shown in Table 1.

TABLE I. RESULTS OF THE REDUCED TEMPERATURE GRADIENT INSIDE THE COPPER TUBE WITH THE ISOTHERMAL LINER.

Temperature gradient of the environment (K/cm)	*Temperature gradient inside the copper tube (with heat pipe)*	*Temperature gradient of the environment (K/cm)*	*Temperature gradient inside the copper tube (without heat pipe)*	*Improved factor with heat pipe*
0.122	***0.011***	***0.303***	***0.011***	***2.6***
-0.0487	***-0.000432***	***-0.0645***	***-0.0051***	***6.3***

From the table, we can see that with the isothermal liner, the temperature gradient of the copper tube is improved by a factor of 6.3 when the bottom part is hot, and improved by a factor of 2.6 when the top part is hot.

IV. CONCLUSIONS

To conclude, here we have reported a new method to get a more uniform and stable temperature environment around the flight tube. At normal lab conditions, the maximum temperature fluctuation is 0.3 K, and the temperature gradient in the vertical direction is about 0.3 K/m around the fountain. With 3-layers magnetic shield and thermal isolations between them, the temperature fluctuations are reduced to be less than 0.1 K. The temperature difference between top and bottom parts of the flight tube is less than 0.1 K. With an isothermal liner, the temperature gradient can be reduced by more than a factor of 2. With precision standard Pt thermometers, which have a temperature uncertainty of less than 10 mK, and will be calibrated twice a year. For NIM6, we will use MOT to collect cold atoms. The MOT coils could heat up the MOT chamber and introduce a temperature gradient on the vacuum system. How much the isothermal liner can improve this will be tested in the future. Presumably, the total temperature uncertainty will be less than 50 mK. From equation 2, the uncertainty of blackbody-radiation-induced frequency shift is 7.2×10^{-17} with 50 mK temperature uncertainty, and keeping the total uncertainty in a few parts in 10^{16}.

REFERENCES

[1] J. Guéna, M. Abgrall, D. Rovera, P. Laurent, B. Chupin, M. Lours, G. Santarelli, P. Rosenbusch, M. E. Tobar, R. Li, K. Gibble, A. Clairon, and S. Bize, IEEE Trans. IEEE Ultrason. Ferroelectr. Freq. Control, 59, 391 (2012).

[2] K. Szymaniec, S. E. Park, G. Marra and W. Chałupczak, Metrologia 47, 363 (2010).

[3] V. Gerginov, N. Nemitz, S. Weyers, R. Schröder, D. Griebsch, and R. Wynands, Metrologia 47, 65 (2010).

[4] Y. Ovchinnikov and G. Marra, Metrologia 48, 87 (2011).

[5] S.R. Jefferts, T.P. Heavner, T.E. Parker, J.H.Shirley, Proc. of SPIE, 6673, 667309 (2007).

[6] M. Niering et al., Phys. Rev. Lett., 2000, vol. 84, pp. 5496-5499.

[7] H. Marion et al., Phys. Rev. Lett., 2003, vol. 90, 150801.

[8] Peter Wolf, Fréderic Chapelet, Sébastien Bize, and André Clairon, Phys. Rev. Lett. 96, 060801 (2006)

[9] H. Hachisu, K. Miyagishi, S. G. Porsev, A. Derevianko, V. D. Ovsiannikov, V. G. Pal'chikov, M. Takamoto, and H. Katori, Phys. Rev. Lett., 2008, vol. 100, pp. 053001.

[10] P. J. Leo, P. S. Julienne, F. H. Mies, and C. J. Williams, Phys. Rev. Lett., 2001, vol. 86, pp. 3743.

[11] K. Szymaniec, W. Chałupczak, E. Tiesinga, C. J. Williams, S. Weyers, and R. Wynands, Phys. Rev. Lett., 2007, vol. 98, pp. 153002.

[12] S. Micalizio, A. Godone, D. Calonico, F. Levi, and L. Lorini, Phys. Rev. A, 2004, vol. 69, pp. 053401.

[13] E. J. Angstmann, V. A. Dzuba, and V. V. Flambaum, Phys. Rev. Lett., 2006, vol. 97, pp. 040802.

[14] Guena J, Li R, Gibble K, Bize S, and Clairon A, 2011, Phys. Rev. Lett., 106, 130801

[15] X. K. Yan, Y. N. Duan, C. F. Ma, Z. F. Lv, Int J. Thermophys, 2011, vol. 32, 494–504

[16] T.F. Gallagher and W.E. Cooke, Phys. Rev. Lett. 1979, **42**, 835

Design and Realization of a Low Phase Gradient Microwave Cavity for a Continuous Atomic Fountain Clock

L. Devenoges, L.-G. Bernier, J. Morel
Federal Institute of Metrology
METAS
Bern-Wabern, Switzerland
laurent.devenoges@metas.ch

G. Di Domenico, A. Jallageas, M. Petersen, P. Thomann
Laboratoire Temps-Fréquence
Université de Neuchâtel
Neuchâtel, Switzerland

Abstract— **Recently, microwave phase gradients were identified as the main source of uncertainty in the continuous fountain clock. Indeed, because of its particular geometry with two interaction zones, a dedicated research effort was necessary to reduce this effect. With the help of 3D finite element simulations and ultra-precise machining, we report here on the design and realization of a new kind of low phase gradient microwave cavity. The proposed geometry based on a ring waveguide of rectangular cross-section has a theoretical spatial phase variation of 30 µrad over the interaction zones, which corresponds to a predicted relative frequency shift below 10^{-15}.**

Keywords—Atomic clock, Microwave Cavity, FE simulations, Phase Gradient, Distributed Cavity Phase Shift

I. INTRODUCTION

Fountain clocks base their measurement on time separated Ramsey RF spectroscopy [1]. A disturbance of the microwave field between the first and second interaction zones will perturb the measured frequency. Such a frequency offset $\Delta\omega$ can be expressed as $\Delta\omega = \Delta\phi/T$ with T being the free evolution time and $\Delta\phi$ a phase change in the field between the two interaction zones. Studies of this cavity-induced frequency shift started many years ago with molecular beams [2] and continued with thermal atomic beam clocks [3] and more recently with atomic fountains [4]-[10].

In pulsed atomic clocks the atomic cloud passes twice through the same micro-wave cavity [11], but nevertheless spatial phase variations in the microwave cavity result in a net phase difference and thus in a frequency shift known as distributed cavity phase shift (DCP). Recent theoretical work has shown how to model cavity phase shift in cylindrical cavities typically used in pulsed fountain clocks and how to minimize DCP [7], [12]. This work has been put to practice on a number of pulsed atomic fountains, where the DCP now has been decreased to negligible levels on the uncertainty budgets [13]-[15].

The atomic clock, which is the topic of this article, is the FOCS-2 continuous Cs fountain clock (see for example [16], [17]). In a continuous fountain clock the probed atoms follow a parabolic trajectory, passing through two spatially separated interaction zones in a microwave cavity. A first realization of such a cavity was based on the TE_{021} mode in a single coaxial cavity with the two interaction zones being in the azimuthal angles $\varphi = \pm\pi/2$ with respect to a pair of independent feeds at $\varphi = 0$ and $\varphi = \pi$. An average phase shift may exist between the two interaction zones, which produces a frequency shift known as end-to-end phase shift. It has been demonstrated that this shift can be evaluated using a reversal mechanism that exchanges the two interaction zones [17]. It was discovered though, that the DCP was too large due to the larger cavity and thus closer neighboring modes. It was estimated that the DCP had a value of about 350 µrad.

In the last year work has been done to design and build a microwave cavity better suited for use in a continuous fountain clock with a significantly smaller DCP [18]. Simulations show that with this design, phase variations across each interaction zone should be less than 30 µrad.

II. DESIGN OF THE CAVITY

The main design principle of this cavity was to reduce the mode density and the time-averaged power flow over the interaction zones. A ring waveguide cavity (L_x: 56.2 mm, L_y: 61.77 mm) has been designed with a rectangular cross-section (a: 24.9 mm, b: 14.0 mm) in which both interaction zones Z_1 and Z_2 are equidistant from the feeding ports P_1 and P_2 (see Fig.1). Its dimensions and resonance frequency $\nu_0 = 9192631770$ Hz are fixed by the atomic trajectory and the cesium clock transition. To avoid any microwave leakage out of the cavity, four cutoff waveguides parallel to the atomic beam of (9.5 mm × 58.4 mm) with more than 200 dB attenuation have been designed. Microwave power is injected through two irises (8 mm diameter) situated on the top wall of the cavity. Each feeding port, composed of waveguide sections, is excited by a coaxial line whose inner conductor acts as a coupling antenna.

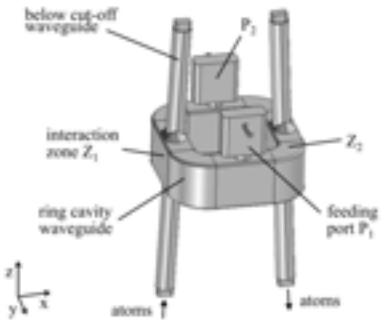

Figure 1. Scheme of the inner volume of the microwave cavity design. The ring waveguide is excited through two irises on its top wall. Two independant feeding ports P_1 and P_2 are used to balance the power flow through the interaction zones Z_1 and Z_2 (see section II and III for details).

III. Electromagnetic properties

We excite the electromagnetic mode TE_{105}, which is resonant at 9.193 GHz. Using both numerical simulations and analytical modeling (see below) we found the main characteristics of the field inside the ring waveguide. In particular, the loaded quality factor $Q_L = 6900$ was measured on the resonance curve shown in Fig.4 (-3 dB linewidth of 1.33 MHz) and the unloaded cavity factor $Q_0 = 13900$ was computed with the global coupling factor $\beta_1 + \beta_2 = 1$, which comes from the analysis of the feeding ports.

A. Finite Elements Analysis

To predict spatial phase variations of this cavity, the 3D geometry has been entirely modeled by a Finite Element Method (FEM) software. Maxwell's equations were solved numerically, assuming vacuum inside the inner volume and the boundary conditions imposed by the copper walls. The microwave field was injected through the feeding ports with a π-phase difference in between the two.

The model shows that the magnetic fields in the two interaction zones are anti-parallel. This results in an inverted Ramsey pattern with a dark central fringe [19]. The model also shows that microwave energy flows from the feeding ports to the walls along the waveguide and since the interaction regions (Z_1 and Z_2 in Fig.1) are equidistant from the ports, minimal energy will flow in these regions. Most importantly the model indicates that the phase variations across an interaction region present a saddle structure (Fig.2) with a maximum peak-to-peak phase variation of 30 µrad.

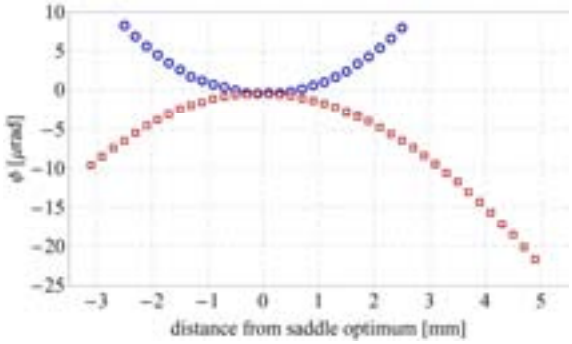

Figure 2. Modeled phase variations along the two transversal axes of the interaction zone. The circles (squares) show variations along *Oy* (*Ox*).

B. Analytical Modeling

Besides FE analysis, we developed a simple analytical model of the electromagnetic mode in the ring waveguide. We showed that the peak-to-peak phase variation over the interaction zone Δx×Δy can be computed with the following expression [19]:

$$\Delta\phi_{pp} = \sqrt{\frac{\epsilon_0}{2\sigma}}\frac{\omega^{3/2}}{4b\,c}\left(1+\frac{2\,b\,c^2\,\pi^2}{a^3\,\omega^2}\right)\left(\Delta x^2+\Delta y^2\right) \quad (1)$$

At the resonance frequency $2\pi\nu_0$ and for the waveguide dimensions (a×b) and copper conductivity ($\sigma = 5.95\times10^7$ S/m), we obtain a peak-to-peak value only limited by the losses in the walls of 30 µrad.

IV. Practical realization

The ring cavity is realized by assembling the upper and lower parts of the waveguide. All parts (cut-offs, coupling ports, half cavities) are sealed together with indium to prevent microwave leakages.

To keep phase variations close to optimum, we thoroughly studied the effect of geometric imperfections on the electromagnetic mode. We showed that mechanical tolerances on the dimensions between 5 and 10 µm and surface roughness better than $R_a = 0.025$ µm (according to ISO 4287) increase $\Delta\phi_{pp}$ less than 5%. The measurements performed on our new cavity (Fig.3) machined with state-of-the-art ultra-precise diamond milling showed that these specifications are available with a best waveguide surface roughness of $R_a = 0.012$ µm.

This work was supported by the Swiss National Science Foundation (grant 200021-141338/1).

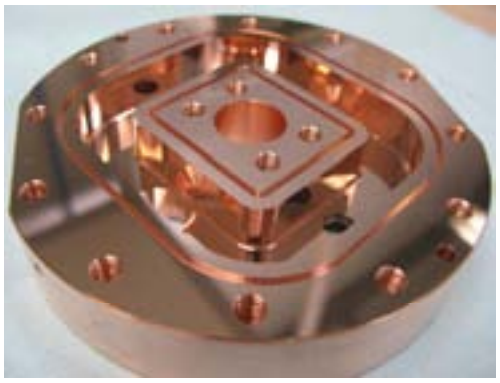

Figure 3. Picture of the inner half volume of the TE_{105} waveguide. Surfaces were machined with ultra-precise diamond miling to obtain a state-of-the-art roughness of R_a = 12 nm

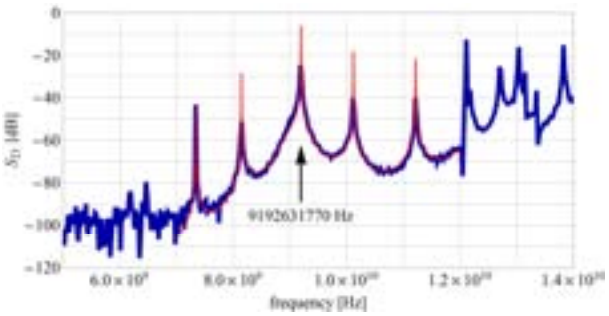

Figure 4. Cavity transmission spectrum: measurement (blue thick curve) is compared to finite element simulations (red thin curve).

V. Experimental Results

A. Frequency Spectrum

Once the cavity mounted, general properties of the waveguide (frequency spectrum and coupling and cavity factor) were measured.

The low mode density of this waveguide cavity is clearly visible on the frequency spectrum Fig.4. The closest resonances (TE_{104} and TE_{106}) are approximately 1 GHz away from the frequency of the mode TE_{105} used to interrogate the atoms. Moreover, experimental measurement (blue thick line) and numerical calculation (red thin line) of the transmission spectrum are in very good agreement.

B. Ramsey Fringes

The TE_{105} electromagnetic mode shows a π-phase difference between the two interaction zones. For this reason, Ramsey fringes exhibit a dark central fringe (Fig.5) at the Cesium resonance frequency ν_0 = 9192631770 Hz. This has been shown to have some metrological advantages [19].

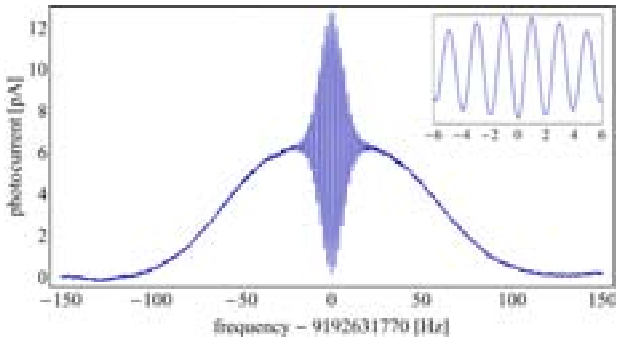

Figure 5. Ramsey fringes obtained with the new ring waveguide cavity. The inset shows the central dark fringe at 9192631770 Hz.

C. Perspectives

To evaluate the frequency shift associated with the spatial phase gradient in the microwave cavity, we are currently working on three types of experimental measurements. One experiment is to change the velocity of the cold atoms along their trajectory and thereby change where the atoms pass through the µ-wave cavities. Another experiment is to tilt the fountain in two vertical planes to probe the phase of the µ-wave field in those two directions separately. A third experiment will be to select the atomic trajectories that are being detected by blocking off part of the detection laser beam.

VI. Conclusion

We presented the design and realization of a low phase gradient microwave cavity. Numerical model based on finite elements simulation predict spatial phase variations of 30 µrad over each interaction zone. With a free evolution time of 0.52 s, both the end-to-end and distributed cavity phase shifts should be reduced to a level of 10^{-15} or below in relative units. The general electromagnetic properties of the cavity have been tested and we are currently working on the evaluation of its associated fountain frequency shifts.

Acknowledgment

We thank Dr I. Syratchev and Dr W. Wuensch at CERN for useful discussions and for their support in verifying the simulation results.

References

[1] N. F. Ramsey, "A Molecular Beam Resonance Method with Separated Oscillating Fields," Phys. Rev., vol. 78, no. 6, pp. 695–699, june 1950.

[2] S. J. Jarvis, "Molecular Beam Tube Frequency Biases due to Distributed Cavity Phase Variations," National Bureau of Standards, Technical Note 660, 1975.

[3] A. Bauch, T. Heindorff, and R. Schroeder, "Measurement of the Frequency Shift due to Distributed Cavity Difference in an Atomic Clock," IEEE Trans. Instrum. Meas., vol. 34, pp. 136–138, 1985.

[4] A. Khursheed, G. Vecchi, and A. D. Marchi, "Spatial Variations of Field Polarization and Phase in Microwave Cavities: Application to the Cesium Fountain Cavity," IEEE Trans. Ultrason., Ferroelectr., Freq. Control, vol. 43, no. 2, pp. 201–210, 1996.

[5] S. R. Jefferts, R. E. Drullinger, and A. D. Marchi, "NIST Cesium Fountain Microwave Cavities," in Frequency Control Symposium, 1998. Proceedings of the 1998 IEEE International, may 1998, pp. 6–8.

[6] P. Laurent et al., "Interrogation of Cold Atoms in a Primary Frequency Standard," in Frequency and Time Forum, 1999 and the IEEE International Frequency Control Symposium, 1999., Proceedings of the 1999 Joint Meeting of the European, vol. 1, 1999, pp. 152–155.

[7] R. Li and K. Gibble, "Phase Variations in Microwave Cavities for Atomic Clocks," Metrologia, vol. 41, no. 6, p. 376, 2004. [Online]. Available: http://stacks.iop.org/0026-1394/41/i=6/a=004.

[8] S. Yanagimachi, Y. Fukuyama, T. Ikegami, and T. Kurosu, "Numerical Simulation of Distributed Cavity Phase Shift in Atomic Fountain Frequency Standard," Japanese Journal of Applied Physics, vol. 44, no. 3, pp. 1468–1475, 2005.

[9] S. R. Jefferts et al., "On the Power Dependence of Extraneous Microwave Fields in Atomic Frequency Standards," in Frequency Control Symposium and Exposition, 2005. Proceedings of the 2005 IEEE International, august 2005.

[10] S. R. Jefferts, J. H. Shirley, N. Ashby, E. A. Burt, and G. J. Dick, "Power Dependence of Distributed Cavity Phase-Induced Frequency Biases in Atomic Fountain Frequency Standards," IEEE Trans. Ultrason., Ferroelectr., Freq. Control, vol. 52, no. 12, pp. 2314–2321, december 2005.

[11] R. Wynands and S. Weyers, "Atomic Fountain Clocks," Metrologia, vol. 42, no. 3, p. 64, 2005.

[12] R. Li and K. Gibble, "Evaluating and Minimizing Distributed Cavity Phase Errors in Atomic Clocks," Metrologia, vol. 47, pp. 534–551, 2010.

[13] J. Guéna et al., "Evaluation of Doppler Shifts to Improve the Accuracy of Primary Atomic Fountain Clocks," Phys. Rev. Lett, vol. 106, p. 130801, april 2011. [Online]. Available: http://link.aps.org/doi/10.1103/PhysRevLett.106.130801.

[14] R. Li, K. Gibble, and K. Szymaniec, "Improved Accuracy of the NPL-CsF2 Primary Frequency Standard: Evaluation of Distributed Cavity Phase and Microwave Lensing Frequency Shifts," Metrologia, vol. 48, pp. 283–289, 2011.

[15] S. Weyers et al., "Distributed Cavity Phase Frequency Shifts of the Caesium Fountain PTB-CSF2," Metrologia, vol. 49, pp. 82–87, 2012.

[16] A. Joyet, G. D. Domenico, G. Dudle, and P. Thomann, "An Alternative Approach to Primary Cs Frequency Standards,"in Proc. 22nd European Frequency and Time Forum, 2008.

[17] G. Di Domenico et al., "Uncertainty Evaluation of the Continuous Cesium Fountain Frequency Standard FOCS-2," in Frequency Control and the European Frequency and Time Forum (FCS), 2011 Joint Conference of the IEEE International, may 2011, pp. 1–5.

[18] G. Di Domenico et al., "Low phase gradient microwave cavity with two interaction zones for a continuous atomic fountain clock", IEEE Trans. Ultrason. Ferroelectr., Freq. Control, in press.

[19] C. Audoin et al., "Properties of an optically pumped cesium beam frequency standard with $\phi = \pi$ between the two oscillatory fields", IEEE Trans. Instrum. Meas., Vol. 43, no. 4, pp.515-520, 1994.

Preliminary Results of the Microwave Frequency Standard based on $^{113}Cd^{+}$ Ions

Jianwei Zhang[1,2], Shiguang Wang[1,3], Kai Miao[1,2], Zhengbo Wang[1,2], Lijun Wang[1,2,3]
[1]NIM-THU Joint Institute for Measurement Science (JMI)
[2]Department of Precision Instrument
[3]Department of Physics, Tsinghua University
Beijing (100084), People's Republic of China
Email: zhangjw@tsinghua.edu.cn

***Abstract*— The transportable microwave frequency standard based on laser-cooled $^{113}Cd^{+}$ ions is a promising to be applied in the comparison of the atomic clocks located in different places. We report the main progress of this clock including the measurements of the clock transition and the preliminary frequency stability.**

Keywords—microwave frequency standard, cadmium ions, frequency stability

I. INTRODUCTION

The frequency standards based on trapped ions were investigated by different groups and achieved great improvements in the past decades [1-6]. A project aimed at a transportable microwave atomic clock based on the laser-cooled $^{113}Cd^{+}$ ions has been carried out since 2010 in our laboratory [7]. The short-term frequency stability of this clock is expected to be $2\times10^{-14}\tau^{-1/2}$. Meanwhile, this clock can be designed to be transportable because that only one laser is needed for laser cooling, optical pump and detection. This clock is going to be applied in the comparison between the clocks located in different places, e. g. the atomic clocks at the ground stations of Beidou Navigation Satellite System. This paper reports the main progress and preliminary results of the Cd^{+} clock in the past year.

II. PROGRESS

Since the detailed description of the experimental setup can be found in [7], only a brief instruction is given here. The linear quadrupole ion trap and the technique of laser cooling are applied in this clock. The laser system is a frequency-quadrupled diode laser system from Topitca Inc. To stabilize the frequency of the laser to megahertz level, the 858 nm seed laser of this laser system is locked by comparing the frequency with an 852 nm laser stabilized to the cesium lines via a transfer cavity [8]. By the laser cooling, the velocity of ions can be slowed down and the ions can be cooled down to crystallization state. In our experiments, it is successfully demonstrated that approximately 10^4 ions are cooled to 16 mK by laser cooling [9]. Thanks to the energy level structure of the $^{113}Cd^{+}$ ions, the same laser can be used for laser cooling, optical detection, as well as optical pumping with the laser frequency blue-shifted 800 MHz by an acousto-optic modulator. During the optical pumping, the ions are prepared to the upper state of the ground-state hyperfine states. After the interaction between the microwave radiation field and the ions, the ions populated on the lower state of the ground-state hyperfine states are detected. Then the spectrum of the clock transition is obtained by measuring the population variation at different microwave frequency.

By measuring the ground-state hyperfine splitting in different magnetic fields, the clock transition in the zero field can be extrapolated. Two independent groups have measured the ground-state hyperfine splitting of $^{113}Cd^{+}$ ions [10, 11]. Based on the experimental setups, we also measure the hyperfine splitting of $^{113}Cd^{+}$ ions. On the first setup, namely JMI-1, the measured result is 15. 199 862 854 96(12) GHz [12], which precision is mainly limited by the fluctuation of the magnetic field. To solve the magnetic field problem, a box made of silicon steel is applied to shield the physics package to reduce the magnetic field fluctuation from the ambient disturbance. In the mean time, the magnetic field close to the vacuum chamber is actively controlled via a fluxgate magnetometer. On the upgraded experimental setup, JMI-2, we obtained the hyperfine splitting with better precision than previous measurement, which is 15. 199 862 855 0125(87) GHz [13]. The improvement of the measurement precision is mainly due to the following two reasons. Firstly, the magnetic field is more stable than before and measured by the $\Delta m_F=\pm 1$ transition frequencies of the ground-state hyperfine splitting, which makes the measurement error due to the Zeeman effect much smaller than the previous measurement. Secondly, the free processing time during the Ramsey interrogation is extended from 0.1 s to 2 s, which improves the measurement resolution significantly. The precision of the second measurement is limited by the frequency reference.

Recently, the preliminary stability of this clock is measured by the close-loop operation. Fig. 1 shows the schematic measurement setup. The local oscillator is an oven controlled crystal oscillator (OCXO) with an ultrahigh stability of 2×10^{-13} at 1 s. The 10 MHz output of the OCXO is feed to a microwave synthesizer to produce the 15.2 GHz microwave radiation field. The power and frequency of the microwave signal is controlled by a computer. During the detection phase, the fluorescence signal is detected by a photomultiplier tube (PMT) operating in the Geiger mode. The photon emitting rate is measured by a photon counter and the data are directed to the computer. A digital proportional-integral-derivative (PID) controller is used

This work was supported by 973 Program (Grant No. 2010CB922901) and Tsinghua University Initiative Scientific Research Program (Grant No. 20131080063).

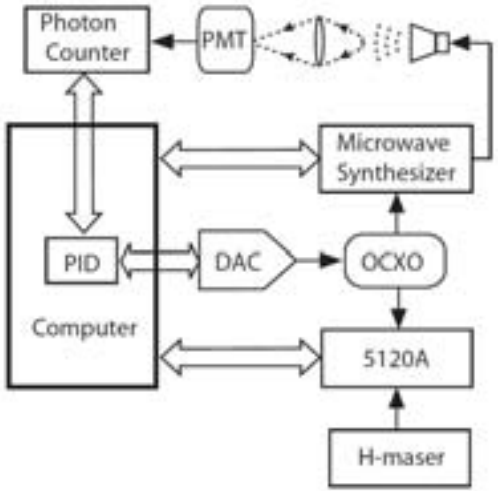

Fig. 1. Schematic experimental setup for the frequency stability measurement. PMT: photomultiplier tube, PID: proportional-integral-derivative controller, DAC: digital-to-analog converter, OCXO: oven controlled crystal oscillator, 5120A: Allan deviation test set, H-maser: hydrogen maser.

to generate the feedback signal and this signal is converted to analog signal by a digital-to-analog converter to control the frequency of the OCXO. While the clock is in close-loop operation, a part of the OCXO output is feed to an Allan deviation test set to compare with a hydrogen maser.

Fig. 2 shows the modified Allan deviation of the measurement where the linear frequency drift is removed. Because the loop time constant here is about 100 s, the stability at the averaging time less than 100 s is from the local oscillator. The stability from 100 s to 4000 s is approximately $1.5\times10^{-12}\ \tau^{-1/2}$.

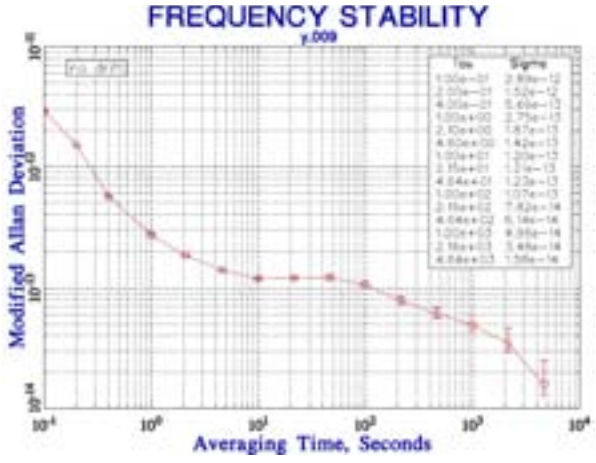

Fig. 2. Modified Allan deviation of the measured data. The period of measurement time is approximately 6 hours and the linear frequency drift is removed.

III. Conclusion and Outlook

The microwave frequency standard based on laser-cooled $^{113}Cd^+$ ions is promising to be applied in the comparison of atomic clocks located in different places. By the experimental setups at JMI, we measured the ground-state hyperfine splitting of $^{113}Cd^+$ precisely. And the preliminary frequency stability of the clock is reported. A series of upgrading of the experimental setup are planned, and an improved result is expected in the next phase.

References

[1] P. T. H. Fisk, "Trapped-ion and trapped-atom microwave frequency standards", Rep. Prog. Phys., vol. 60, pp. 761-817, 1997.

[2] D. J. Berkeland, J. D. Miller, J. C. Bergquist, W. M. Itano, and D. J. Wineland, "Laser-Cooled Mercury Ion Frequency Standard", Phys. Rev. Lett., vol 80, no 10, pp 2089–2092, 1998.

[3] J. D. Prestage, S. Chung, T. Le, L. Lim, and L. Maleki, "Liter sized ion clock with 10^{-15} stability", in 2005 IEEE International Frequency Control Symposium and Exhibition, New York: Ieee, 2005, pp 472–476.

[4] C.W. Chou, D.B. Hume, J.C.J. Koelemeij, D.J.Wineland, T. Rosenband, "Frequency comparison of two high-accuracy Al^+ optical clocks," Phys. Rev. Lett. vol. 104, pp. 070802, 2010.

[5] A. A. Madej, P. Dubé, Z. Zhou, J. E. Bernard, and M. Gertsvolf, "$^{88}Sr^+$ 445-THz single-ion reference at the 10^{-17} level via control and cancellation of systematic uncertainties and its measurement against the SI second," Phys. Rev. Lett. vol. 109, pp. 203002, 2012.

[6] Y. Huang, J. Cao, P. Liu, K. Liang, B. Ou, H. Guan, X. Huang, T. Li, and K. Gao, "Hertz-level measurement of the $^{40}Ca^+$ $4s^2S_{1/2}$-$3d^2D_{5/2}$ clock transition frequency with respect to the SI second through the Global Positioning System", Phys. Rev. A, vol 85, no 3, Mar 2012.

[7] J. Zhang, Z. Wang, S. Wang, K. Miao, B. Wang, and L. Wang, "Progress towards a microwave frequency standard based on the laser cooled $^{113}Cd^+$ ions", in Frequency Control Symposium (FCS), 2012 IEEE International, 2012, pp 1–3.

[8] S. W. Wang, J. Z. Zhang, Z. W. Wang, B. W. Wang, W. L. Liu, Y. Z. Zhao, and L. W. Wang, "Frequency stabilization of a 214.5-nm ultraviolet laser", Chin. Opt. Lett., vol 11, no 3, pp 031401–31403, 2013.

[9] S.-G. Wang, J.-W. Zhang, K. Miao, Z.-B. Wang, and L.-J. Wang, "Cooling and Crystallization of Trapped $^{113}Cd^+$ Ions for Atomic Clock", Chin. Phys. Lett., vol 30, no 1, p 013703, Jan 2013.

[10] U. Tanaka, H. Imajo, K. Hayasaka, R. Ohmukai, M. Watanabe, and S. Urabe, "Determination of the ground-state hyperfine splitting of trapped $^{113}Cd^+$ ions", Phys. Rev. A, Vol 53, pp.3982-3985, 1996.

[11] B. M. Jelenkovic, S. Chung, J. D. Prestage, and L. Maleki, "Highresolution microwave-optical double-resonance spectroscopy of $^{113}Cd^+$ hyperfine splitting of trapped ions", Phys. Rev. A, Vol 74, 022505(5), 2006.

[12] J. W. Zhang, Z. B. Wang, S. G. Wang, K. Miao, B. Wang, and L. J. Wang, "High-resolution laser microwave double-resonance spectroscopy of hyperfine splitting of trapped $^{113}Cd^+$ and $^{111}Cd^+$ ions", Phys. Rev. A, vol 86, no 2, p 022523, 2012.

[13] S. G. Wang, J. W. Zhang, K. Miao, Z. B. Wang, and L. J. Wang, "High-accuracy measurement of the $^{113}Cd^+$ ground-state hyperfine splitting at the milli-Hertz level", Opt. Express, vol 21, no 10, pp 12434–12442, 2013.

Physics of Systematic Frequency Drift of Active Hydrogen Masers with Autonomous Cavity Auto Tuning

V. I. Vasilyev, V. V. Gavrilov, A. G. Gorelov
Institute of Electronic Measurements KVARZ, Nizhny Novgorod, Russia
Email: nnipi_kvarz@sinn.ru

Abstract — **The physical model of hydrogen maser systematic frequency drift is discussed. Results of theoretical research are compared with results of experiments and long-term practical observations over drift of a hydrogen maser. One of conclusions of research is the statement that drift can change its value and a sign. The model allows to predict behavior of maser frequency with the help of maser parameters monitoring.**

Keywords - hydrogen maser; frequency drift; relaxation time; cavity auto tuning; quality factor of the spectral line.

I. INTRODUCTION

Systematic frequency change of a signal (drift) is one of the primary metrological characteristics of hydrogen maser. Minimization and prediction of drift remain an important task [1, 2]. Figures 1 shows data on long-term measurements of frequency for hydrogen maser CH1-75A. Masers are made by the Institute of Electronic Measurements KVARZ. The data show evolution of frequency of FGUP «VNIIFTRI» hydrogen clock ensemble. Drift of a hydrogen maser frequency at manufacturing does not exceed 2×10^{-15}/day, and then it decreases. In the presented plots it does not exceed 5×10^{-16}/day. It is necessary to note that drift can be of both positive and negative signs. This fact complicates understanding of a phenomenon.

Earlier a number of scientists proposed hypotheses about the drift nature, but articles had either qualitative [3] or statistical and descriptive character [2, 4]. For example, in article [2] it is considered that drift has constant linear scaling coefficient and slowly changing random component.

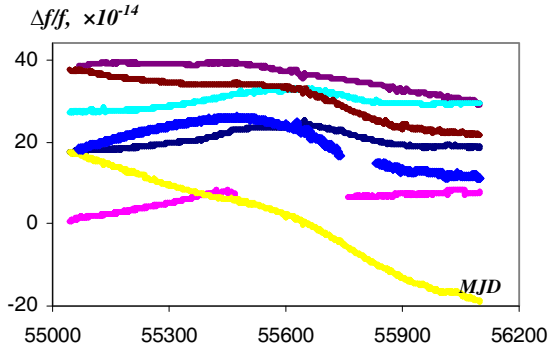

Fig1. Dependence of hydrogen masers frequency on time over four years.

II. FREQUENCY EVOLUTION OF HYDROGEN MASER

This paper presents a possibility of the theoretical description of frequency evolution for a hydrogen maser. The analysis of evolution is based on the use of the solution of the hydrogen maser differential equations in two-level approximation:

$$\begin{cases} \dfrac{d^2H}{dt^2}+\dfrac{\omega_c}{Q_c}\dfrac{dH}{dt}+\omega_c^2 H = K\dfrac{d^2M}{dt^2} & , \\ \dfrac{d^2M}{dt^2}+\dfrac{\omega_l}{Q_l}\dfrac{dM}{dt}+\omega_l^2 M = \dfrac{2\mu_B^2\omega_l\Delta N H}{\hbar} & , \\ \dfrac{d\Delta N}{dt}+\dfrac{1}{T_1}(\Delta N-\Delta N_0) = -\dfrac{2H}{\hbar\omega_l}\dfrac{dM}{dt} & , \end{cases}$$

where t – time, H – intensity of magnetic microwave field component, M – induced magnetic moment of atomic ensemble, ω_c, Q_c, V_c – angular frequency, quality factor and volume of the microwave cavity, ω_l, Q_l – angular frequency and quality factor of the spectral line, ΔN, ΔN_0 – population difference and initial population difference, η – filling factor of cavity, $K=\dfrac{\mu_0\mu_B{}^2\eta}{\hbar V_c}$ – constant, μ_B – Bohr magneton, $\hbar$ – Planck constant.

The exact solution of system is not known, therefore «a steady-state» approximation is used [4]. The importance in the solution is connected with the following parameters: T_1, T_2 – longitudinal and transverse relaxation time, $\vartheta = \phi - \psi$ – difference between oscillation phases of the microwave field and the induced magnetic moment of atomic ensemble, I – magnitude of the beam flux, $b_R = \mu_B H / \hbar$ – Rabi frequency. But this solution does not contain a drift component.

According to the approach of the articles [5, 6] as frequency evolution of a two-level quantum system being in resonant harmonic electromagnetic field, we consider the asymptotic solution of the following equation:

$$\Delta\omega_{sys} \equiv \frac{d\vartheta}{dt} = \frac{d\phi}{dt} - \frac{d\psi}{dt} \quad .$$

From the reduced equations of a hydrogen maser it is possible to derive the following time dependent equation:

$$\Delta\omega_{sys}(t) = \Delta\omega_c(t) \pm \left(K\omega_c \frac{M_0(t)}{2b_R(t)} + \Delta N(t) \frac{b_R(t)}{M_0(t)} \right) \times \sin\left(\overline{\vartheta}\right) \quad (1),$$

where $\Delta\omega_c$ – frequency detuning of cavity, $M_0(t)$ – amplitude of the induced magnetic moment of atomic ensemble, $\overline{\vartheta}$ – time averaging.

We use the ratios obtained in a «steady-state» approximation [4]. For obtaining the nontrivial solution we will consider that $\sin\left(\overline{\vartheta}\right) \approx \pm 0$. Let us specify it explicitly by using a formal small parameter ε ($0 < \varepsilon << 1$). We will derive the following solution:

$$\Delta\omega_{sys}(t) = \Delta\omega_c(t) \pm \varepsilon \left(\frac{1}{T_2(t)} + \frac{K\omega_c}{2} \frac{T_1(t)T_2(t)I(t)}{1 + T_1(t)T_2(t)b_R(t)^2} \right) \quad (2).$$

The formula shows that long-term changes of frequency are defined by slow changes of basic parameters in the course of time. The most important is dependence on a detuning of cavity. Change of frequency of the cavity directly influences frequency of a standard. Dependence on other parameters is much weaker.

To use the solution for finding of evolution of hydrogen maser frequency it is necessary to know evolution of the observable value T_1, T_2, I, b_R. If quality factor of the hydrogen spectral line Q_l at a threshold beam flux is known, it is possible to consider that $T_{2-th} \approx \frac{2Q_{l-th}}{\omega_l}$, and for a stronger beam flux to consider that $T_2 \approx \frac{1}{\chi + \beta K Q_c I}$, $T_1 \approx \frac{1}{\chi + 2\beta K Q_c I}$, where χ, β – parameters.

III. The Analysis of Solution

At correct work of automatic cavity tuning $\Delta\omega_c \approx 0 = const$ and the formula (2) appears as follows

$$\Delta\omega_{sys}(t) = \frac{K\omega_c}{2} \frac{T_1(t)T_2(t)I(t)}{1 + T_1(t)T_2(t)b_R(t)^2} + \frac{1}{T_2(t)} .$$

A. Variant

Let all parameters remain constants. Then frequency of quantum system also remains a constant.

B. Variant

On very long periods (years) polymer is not a static system, thus possessing the processes causing changes in structure and composition. It is shown in change of quality factor of the spectral line. The long-term researches made at our institute show that quality factor can change in two main directions. The first is associated with degradation of a storage bulb covering and with reduction of Q_a, the second is defined by a surface cleaning and increasing of Q_l.

Let's consider that the beam flux of hydrogen is constant, we will take value of Rabi frequency from a «steady-state» approximation:

$$b_{Rs}{}^2 = KQ_c I - \frac{1}{T_1 T_2} \quad .$$

Situation modeling at increasing (or decreasing) quality factor of the spectral line on a ratio

$$Q_l = Q_{l0} \pm a \log(t) \quad ,$$

where Q_{l0} и a – parameters, leads to the graphs represented in Fig. 2. The analysis (Fig. 3) shows that the increase in quality factor is associated with the general drift reduction.

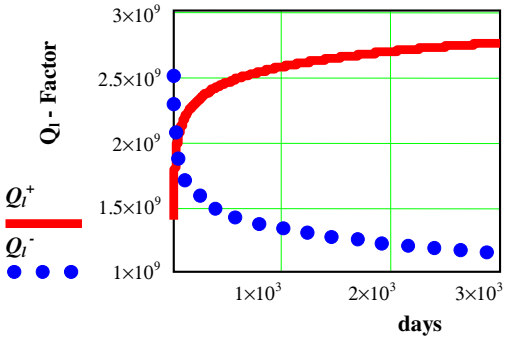

Fig.2. Modeling dependence of the spectral line quality factor on time.

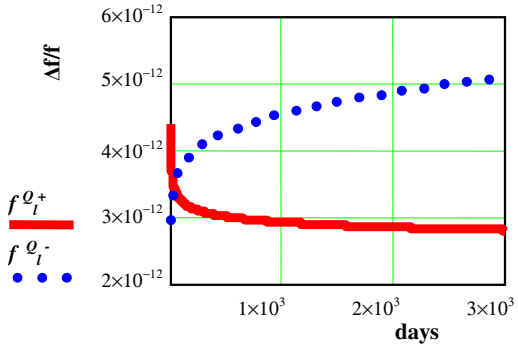

Fig.3.Modeling dependence of hydrogen maser relative frequency on time.

C. *Variant*

Let's assume that

$$b_{Ra} = z b_{Rs}, \quad z = const < 1 .$$

It means that the value of Rabi frequency differs from the value received in a «steady-state» approximation b_{Rs}. In a «steady-state» approximation it is assumed that all atoms should give energy quantum. It does not correspond to reality. In addition we will consider that the beam flux of hydrogen linearly decreases 3 times. Results of modeling at increasing and decreasing of quality factor of the spectral line are given in Fig. 4.

Sign inversion at frequency drift in variant of decreasing of quality factor is an interesting feature of Fig.4. We have drift acceleration on very long periods.

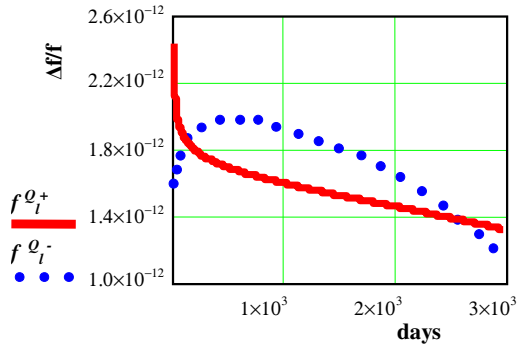

Fig.4.Modeling dependence of hydrogen maser relative frequency on time.

IV. EXPERIMENTAL RESULTS

The inner bulb surface of observable hydrogen maser is coated with fluroplastic type F-10. As experiment shows, quality factor of the line at a threshold beam flux decreases. The typical case of change of Q_l is presented in Fig.5. This phenomenon can't be presented as simple degradation of the line, because amplitude of generation increases. The fastest changes take place at the beginning.

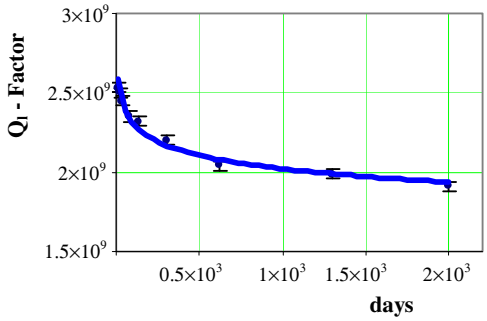

Fig.5. Change of quality factor of the spectral line at a threshold beam flux on time.

Drift decreasing at $\sin(\overline{\vartheta}) \approx \pm 0$ hypothesis examination. This hypothesis is right in a case when own frequency of the cavity is very close to the frequency of the spectral line. For hypothesis examination the CH1-75B model of new modification was used. Standard stability is presented in Fig. 6.

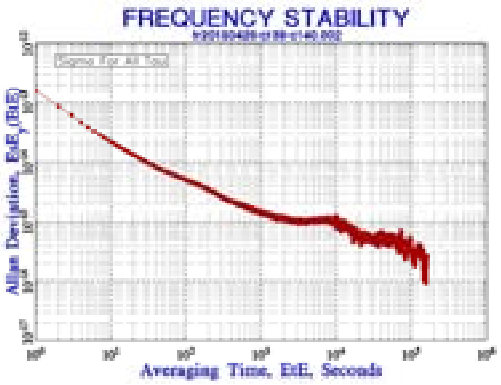

Fig.6. Hydrogen maser CH1-75B stability with removing drift.

It is possible to tune the cavity of this model with controlled accuracy. In Fig. 7 evolution of CH1-75B frequency with the microwave cavity tuned and detuned by +40 Hz are presented. After cavity detuning the frequency of a maser was compensated by $\Delta f / f = -1 \times 10^{-12}$. As the figure analysis shows, drift increased by 1.5 times from $+1.3 \times 10^{-15}$ to $+1.9 \times 10^{-15}$ per day after cavity detuning. Microwave cavity was retuned 38 days later. Frequency drift thus returned to its previous value.

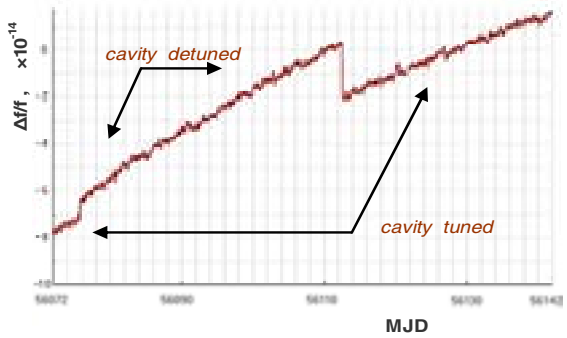

Fig.7. Evolution of output signal frequency of CH1-75B with the microwave cavity tuned and detuned by +40 Hz.

V. CONCLUSION

- The main reason for appearance of active hydrogen maser systematic frequency drift is evolution of longitudinal and transverse relaxation time of quantum system. The evolution is related to change of quality factor of the spectral line, decreasing of the beam flux of hydrogen, change of maser generation amplitude.
- Frequency drift minimization is associated with the minimization of maser operating parameters variation, for example with stabilization of hydrogen beam flux and accuracy of cavity auto tuning.
- There is a physical model helpful to predict frequency evolution on the base of maser parameters monitoring.

REFERENCES

[1] V.A. Logachev, G.P. Pashev. Estimation of linear frequency drift coefficient of frequency standards.// Proc. 50 Frequency Control Symposium, 1996, pp.960-963.

[2] Yu. Smirnov. Estimation of errors of hydrogen standards time scale preservation taking into account systematic frequency changes.// Measurement Techniques . – 2007, No.3, pp.293-297.

[3] C. Audoin, J. Vanier. The quantum physics of atomic frequency standards. – IOP Publishing, Bristol and Philadelphia. – 1989, v. 2.

[4] D. Matsakis, P. Koppang, R.M. Garvey. The long-term stability of the U.S. Naval observatory's masers.// Proc. 36 Annual Precise Time and Time Interval Meeting, 2004, pp.411-421.

[5] A.G. Chirkov, E.N. Pestov. New results of the investigations of the nature of the long term instability in quantum frequency standards and magnetometers. Non removable resonance drift.// Proc. 16 European Frequency and Time Forum, 2002, pp. E63-66.

[6] V. I. Vasilyev. Investigation of systematic frequency drift of active hydrogen frequency standards.// Proc. 6 International Symposium "METROLOGY of time and space", Moscow, 2012.

Active H-Maser with Increased Power of the Output Signal

Boyko A. I., Aleynikov M. S.
National Research Institute for Physical-Technical and Radiotechnical Measurements
FSUE VNIIFTRI
Moscow, Russia
alejnikov@vniiftri.ru

Abstract — **To improve short-time stability the amplification of the hydrogen maser output signal due to using the single-state selection and cooling the source cell is theoretically discussed. H-maser theory basic aspects are sequentially developed in the introduction part. The results of the numerical calculation active H-maser power versus magnet parameters of specific selective system and source temperature are obtained. In conclusion, the theoretic prototype of maser, that has a short-time stability achieved 2.5×10^{-14} for one second, is represented.**

Keywords - hydrogen maser ; single-state selection ; cooled source's cell.

I. INTRODUCTION

At present hydrogen masers together with ultrahigh stability oscillators [1] are the main source of a stable microwave signals. Typical short-time stability (Allan variation [2]) of this signals is estimated to be $\sigma_y \sim (1\div2)\times10^{-13}$ for 1 second. It's necessary to possess such description, for example, in atomic fountain frequency standards [3, 4] to form interrogation process. The amplification of a synthesizer based on the increased power H - maser can improve above short-time stability and ratio Signal/Noise of interrogation waveform.

One of the first idea to create active hydrogen maser with improve short-time stability was developed in the paper [5]. The gist of idea consists in using two state-selection magnets, which are separated by spin-flip region [6], instead of conventional state-selection magnet. In the new state-selection system (single-state) proposed by the authors, all of the undesirable atoms are eliminated from the hydrogen beam and, thus, only operational atoms are present in the storage bulb. Therefore, the H-maser's output power in case of single-state selection system is increased in comparison with conventional one due to spin exchange relaxation. The quantitative estimation of specific selection system will be introduced in the further statement.

In this paper the results of numerical calculation of the atomic beam's trajectories are represented. We symbolically divided it into two parts: in one of them the H-maser's power versus choice of selective system is shown, in another one - versus temperature of the hydrogen source's cell.

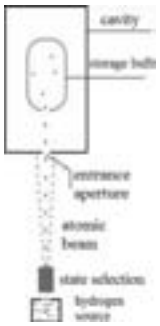

Figure 1. The design of H-maser

II. THEORY

A. General regulations

The short-time stability σ_s of hydrogen maser, which is sketchy shown in figure 1, can be written as [5]:

$$\sigma_s^2 = \frac{1}{\omega^2\tau^2}\frac{N}{S} = \frac{1}{\omega^2\tau^2}FkTB\left[\frac{1+\beta}{\beta}\frac{1}{P}\right], \qquad (1)$$

where $N = FkTB$ - equivalent noise power delivered to the receiver (F - noise figure, k - Boltzmann's constant, T - absolute temperature of the maser's storage bulb, B - equivalent bandwidth); $S = \beta P/(1+\beta)$ - the power delivered to the receiver (P - total power radiated by the hydrogen atoms in the storage bulb, β - coupling factor to the cavity); ω - circular frequency of the oscillation, τ - averaging time interval (≤ 50 s).

Here and further we suppose that hydrogen source and state selection system are the lower part of the maser and storage bulb, microwave cavity and receiver are the higher part. By-turn the maser power P in (1) can be expressed by the conventional equation [7], which contains parameters of the both maser's parts:

$$\frac{P}{P_c} = -2q^2\left(\frac{\Delta I}{I_{thr}}\right)^2 + (1-3q)\frac{\Delta I}{I_{thr}} - 1, \qquad (2)$$

where I_{thr}, P_c - threshold values of the flux and radiated power of an atomic beam, ΔI - efficient flux of the active atoms entered in the storage bulb, q - quality quantity described as:

$$q = \frac{\sigma \overline{v_r} \hbar}{2\mu_B^2 \mu_0} \frac{V_c}{V_b} \frac{1}{Q_c \eta} \frac{\Gamma_b + \Gamma_\omega}{\Gamma_b} \frac{I_{tot}}{\Delta I}, \qquad (3)$$

where σ - spin exchange cross section [8], v_r - the average relative velocity of atoms in the storage bulb, V_c, V_b - the volumes of the cavity and storage bulb, Q_c - the quality factor of the loaded cavity, η - the magnetic filling factor, Γ_b, Γ_ω - relaxation rates due to escape from the bulb and recombination on the bulb walls, I_{tot} - the total flux of atoms. The quantity q is an important parameter, which describes maser performance. If $0 \le q \le 0.17$ the oscillation will be observed. All of the quantities on the right side of (3) other than $I_{tot}/\Delta I$ can be measured; therefore, the ratio $I_{tot}/\Delta I$ determines quantity q and depends on the parameters of the lower part only. As a matter of fact, this ratio describes state selection performance.

B. Lower part of H - maser

As is well known [9], in the source hydrogen atoms are in the ground state $S_{1/2}$. The hyperfine ground state has four magnetic sublevels [$F = 1$, $m_f = 0, \pm 1$], [$F = 0$, $m_f = 0$] (F, m_f - the quantum numbers of total magnetic moment and its projection of the hydrogen atom). According to Boltzmann's temperature distribution the probability w_n of a quantum system being on level with energy E_n equals:

$$w_n \sim e^{-\frac{E_n}{kT}}$$

Since the magnetic sublevels have approximately the same energy, they are filled equally.

To create converse population in the maser's storage bulb a magnetic state-selection system is used. In the storage bulb the atoms in the state [$F = 1$, $m_f = 0$] contribute to an oscillation, but the presence of another three magnetic sublevels causes the undesirable spin exchange and the additional frequency shifts of the output waveform. To describe a state selection performance it's convenient to use parameter α:

$$\alpha = \frac{I_{10} + I_{11} + I_{1-1} + I_{00}}{I_{10} - I_{00}} = \frac{I_{tot}}{\Delta I}$$

here indices denote the quantum numbers.

This parameter is the subject of the numerical calculation of the H-maser's lower part and it describes the state-selection performance. Thus, $\alpha \ge 1$ and if the value converge to 1, there are only active atoms in the storage bulb. To calculate α we use Maxwell's velocity distribution that describes the atoms escaped from the hydrogen source [10]:

$$I(\mathrm{v}, \Theta)\, \mathrm{d}\mathrm{v}\, \mathrm{d}\Omega = \frac{2 I_0}{\overline{v}^4} v^3 e^{-\frac{v^2}{\overline{v}^2}} f(\Theta)\, \mathrm{d}\mathrm{v}\, \mathrm{d}\Omega, \qquad (4)$$

here $f(\Theta)$ - the normalized diagram of the source's direction, I_0 - the intensity of the beam at the maximum of the diagram.

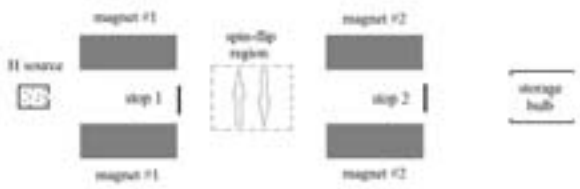

Figure 2. The H-maser's lower part with double selection

Consequently, using the equations of the atom's motion in *2N*-pole magnet [11], we may calculate atom flux $I_{F,mf}$ and, thus, α.

III. NUMERICAL CALCULATIONS

In this section we consider two problems about optimal choice of the parameters of the H-maser's lower part that is shown in figure 2. The first problem is about optimal choice of the selective system in general, and the second - source's temperature influence on the output power.

As a reference the eventual results of the numerical calculation of the conventional magnetic selective system have been discussed. Thus, let one 6-pole magnet with next parameters is used: $H_0 = (0.6 \div 0.8)$ T - field strength on the side of the gap, $r_m = (1.0 \div 2.5)$ mm - the radius of the inner magnet's hole, $l_m = (40 \div 60)$ mm - the magnet's length. The theoretical calculation of the parameter α for such selection system gives $\alpha \ge 4 \div 5$ that is insufficient satisfactory selection (there are only about (20 - 30) % active atoms in the storage bulb). For such values of the parameter α the quality quantity is $q \ge 0.07 \div 0.1$ according to the parameters of the maser's higher part. It's obvious that the output power of the H-maser with such state-selection is far from peak, and sometimes the oscillation may be complicated. So, there is a reasonable problem about improving of the state-selection efficiency.

A. State-selection system

To decrease α to 1, one should to use selective system with two magnets (Fig. 2). Usually 4-pole and 6-pole magnets are used as selective elements. The difference between 4- and 6-pole magnets consists in the magnetic field and, therefore, the force acting on the atoms, versus a radial coordinate. In the 6-pole magnet near axis the force is equal to zero, so to eliminate the undesirable atoms from the atomic beam the axis minor stops are additionally used (Fig. 2). In the 4-pole magnet this requirement is absent, because the force is not equal to zero. Thus, it's curious to compare 4- and 6-pole selective systems numerically.

Before discussing the eventual results of the calculations, a model of the hydrogen source will be described. We consider the source that consists of a system of the independent channels with the direction diagram [12]:

$$f(\Theta) = \begin{cases} \cos\Theta \left[1 - \frac{1}{2} \frac{tg\Theta}{tg\Theta_0} \right] 2\pi \sin\Theta d\Theta & 0 \le \Theta \le \Theta_0 \\ \cos\Theta \left[\frac{1}{2} \frac{tg\Theta_0}{tg\Theta} \right] 2\pi \sin\Theta d\Theta & \Theta_0 \le \Theta \le \frac{\pi}{2} \end{cases},$$

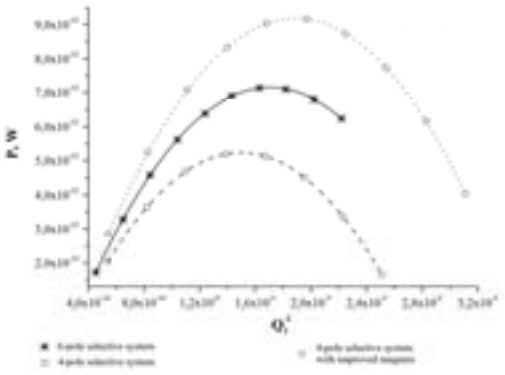

Figure 3. Atomic beam power versus inverse line Q_l

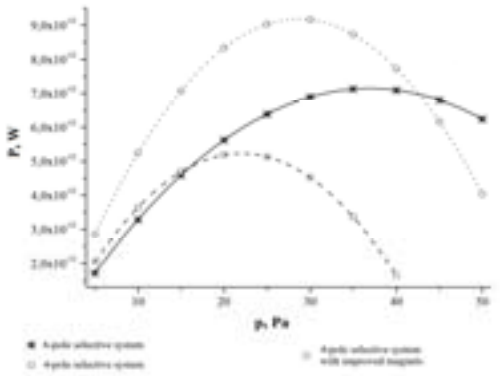

Figure 4. Atomic beam power versus pressure in source's cell

here Θ_0 = arctg(d/L) (d, L - the channel's diameter and length). The intensity maximum of the direction diagram equals $I_0 = \eta Sp\langle v\rangle/(4\pi kT)$ (η - the source's transparency, S - the source's hole cross section, p - the pressure in the source's cell, $\langle v\rangle$ - the average velocity of the atoms in the source's cell, T - the temperature of the source). Let $\eta = 0.6$, $S = \pi r^2 = \pi/4$ mm^2, $d = 40$ μm, $L = 1.5$ mm, the temperature of the source is considered to be equal 900 ^{o}K.

The relationships between atomic beam power and inverse line quality factor [13] or pressure in the source's cell are shown in figures 3 - 4. In the ordinary case the selective magnets were used with parameters: $H_0 = 0.6$ T, $r_m = 1.25$ mm for the first magnet, $r_m = 2.0$ mm - for the second, $l_m = 60$ mm. In the improved case: $H_0 = 1.0$ T, $r_m = 1.25$ mm for the first magnet, $r_m = 2.0$ mm - for the second, $l_m = 80$ mm. Parameters of the storage bulb and microwave cavity: $V_b = 3.0\times10^3$ cm^3 - the volume of the bulb, $\Gamma_{tot} = 1.15$ s^{-1} - the total density-independent relaxation rate, $T = 323$ ^{o}K - the temperature of the bulb's walls; $V_c = 17.5\times10^3$ cm^3 - the volume of the maser's cavity, $Q_c = 36.0\times10^3$ - the quality factor of the loaded cavity.

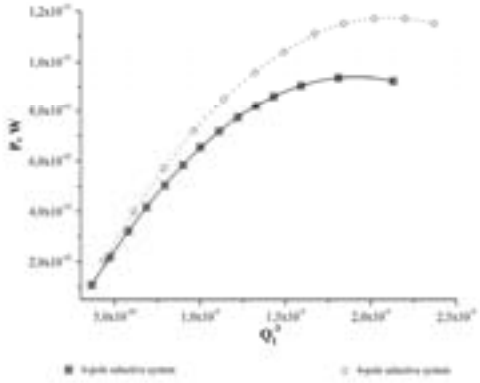

Figure 5. Atomic beam power versus inverse line Q_l

The rated values of the α for the ordinary case of the 4-pole state-selection system - 1.37, 6-pole - 1.26 and for the improved 4-pole - 1.13. The advantage of 6-pole over 4-pole state-selection in ordinary case is shown from figure 3, but in the 6-pole system stop 1 with diameter $d = 1$ mm was used and, thus, about one third of active atoms is eliminated. This fact is shown in figure 4, there 4-pole system has advantage in initial region of pressure. As a matter of fact this region (5-15 Pa) may be a principal duty of the H-maser's source. Therefore, the choice of the selective system depends on active duty of the hydrogen source. This arguments are correct in the case of the source cell's temperature $T = 900$ ^{o}K.

In the case of improved 4-pole selective system the parameter α approaches to 1 and such system eliminates practically all of the undesirable atoms. The peak power of the atomic beam is increased in 1.8 times in comparison with the ordinary case (Fig. 3-4).

B. Temperature of hydrogen source's cell

The velocity distribution (4) of atoms escaped from the source's hole represents a bell-shaped curve with essential parameter T. If the temperature T decreases, the peak of the distribution will increase and move to region of the low velocities and, thus, the state-selection performance will rise since the group of the atoms moving linearly with high velocity is absent.

The analogue of previous sections' curves represents in figure 5 with the same masers' parameters except for the hydrogen source temperature - $T = 300$ ^{o}K.

The advantage of 4-pole over 6-pole state-selection system in the case of cooled hydrogen source is shown in figure 5 (the rated values of α - 1.02 and 1.12). Moreover, the consumption of the hydrogen atoms in 4-pole system is less than 6-pole system in 1.9 times. The peak of the output waveform's power in the case of improved 4-pole system with cooled source increases in 1.3 times, than with normal source $T = 900$ ^{o}K (Fig. 3), and the consumption of the hydrogen atoms decreases in 2 times. Indeed, the improved 4-pole system with cooled source's cell is a perfect state-selection (in our case $q \sim 0.03$)

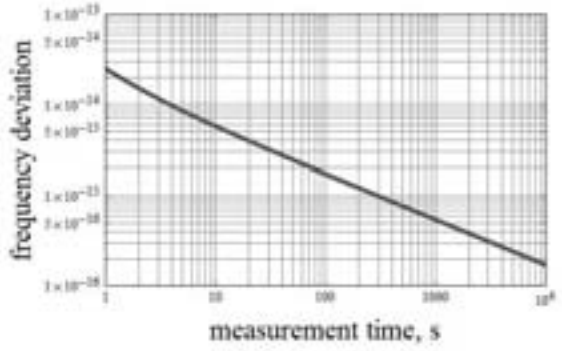

Figure 6. Predicted frequency stability versus measurement time

and in order to increase the rate of the maser's power we should vary the parameters of the H-maser's higher part.

In conclusion the conventional H-maser's frequency stability versus measurement time is lead:

$$\sigma^2(\tau) = \frac{1}{\omega^2 \tau^2} \frac{N}{S} + \left[\frac{kT}{2\tau} \right] \frac{1}{PQ_l^2} \qquad (5)$$

This relation for case of improved 4-pole selective system with cooled source is shown in figure 6 for operating point $Q_l = 1 \times 10^9$. Parameters of abstract receiver: $F = 0.8$ dB, $B = 10$ Hz.

The rated value of the short time frequency stability is 2.48×10^{-14} for one second.

IV. Conclusion

We obtained rated values of the α for various magnetic state selection system. The efficiency advantage of 6-pole using one stop over 4-pole state-selection in the case of source's temperature T = 900 ^{o}K is demonstrated, but the consumption of the hydrogen atoms in 4-pole selection is reduced by one third. In the case of source's temperature T = 300 ^{o}K the application of 4-pole state-selection is desirable. Moreover, the numerical calculation is realized: the application of improved magnets increases output power in 1.8 times, the application of cooled source - in 1.3 times.

Acknowledgment

We would like to thank Georgiy Yolkin and Fedor Rusin for many discussions. Many thanks to Igor Blinov for his contribution to the development of the project.

References

[1] R.T. Wang and G.J. Dick, " Cryocooled sapphire oscillator with ultrahigh stability ", IEEE Trans. Instrum. Meas., vol. 48, pp. 528-531, 1999.

[2] F. Riehle, " Frequency Standards. Basics and Applications ", (Transl.) Moscow FIZMATLIT, pp. 55-65, 2009.

[3] E.A. Donley, T.P. Heavner, M.O. Tataw, F. Levi, and S.R. Jefferts, " Progress Towards the Second-Generation Atomic Fountain Clock at NIST ". Proceedings of the 2004 IEEE Intern. Freq. Control Symposium and Exposition.

[4] Y. Ovchinnikov and G. Marra, " Accurate rubidium atomic fountain frequency standard ", Metrologia, vol. 48, pp. 87-100, 2011.

[5] E.M. Mattison, Robert F.C. Vessot, and W. Shen, " Single-State Selection System for Hydrogen Masers ", IEEE Trans. on Ultrason., Ferroel., and Freq. Control, UFFC-34, N. 6, 1987.

[6] S. Urabe, K. Nakagiri, Y. Ohta, M. Kobayashi, and Y. Saburi, " Majorana Effect on Atomic Frequency Standards ", IEEE Trans. on Instrum. and Measur, vol. IM-29, N. 4, 1980.

[7] D. Kleppner, H.C. Berg, S.B. Crampton, and N.F. Ramsey, " Hydrogen-Maser Principles and Techniques ", Physical Review, vol. 138, N. 4A, 1965.

[8] A.C. Allison, " Spin-Change Frequency Shifts in H-H Collisions ", Physical Review, vol. 5, N. 6, 1972.

[9] D. Kleppner, H.M. Goldenberg, and N.F. Ramsey, " Theory of the Hydrogen Maser ", Physical Review, vol. 126, N. 2, 1962.

[10] N.F. Ramsey, " Molecular beams ", (Transl.) Moscow, pp. 25-30, 1960.

[11] A.I. Pikhtelev, A.A. Ul'yanov, B.P. Fateev, " Time and frequency standards based on quantum oscillator and discriminator ", M.: Sov. radio, pp. 58-75, 1978.

[12] V.S. Troickiy, " Direction of molecular beam formed by gas current from channel ", JETP, vol. 32, N. 4, 1962.

[13] A. Boyko, G. Yolkin, N. Zhestkova, G. Kurnikov, V. Paramzin, " Hydrogen maser for frequency standard on Cs atomic fountain ", Proceed. FSUE VNIIFTRI, vol. 50, 2005.

A Waveguide Cavity for Miniature Rb Atomic Clock

Thomas Cao, Leiji Liu, Lin Yang, Xingshi Zheng
Electronic Spaceon Company
Chengdu, China
sccyh@163.com

***Abstract*—This paper is introduced a novel waveguide cavity for Rb atomic clock. In the cavity, a coupling ring shaped semi-circle imports RF signal from electronics, a screw regulator acts as a medium coupler to transmit microwave signal into absorption cell, and the both of the two parts construct a filter to suppress useless components except 6.8GHz. The RF signal can be high effectively produced in the cavity in this way. The waveguide cavity can be used to design miniature Rb atomic clock, and spread it to design chip scale atomic clock. furthermore.**

Keywords—Rb atomic clock; Waveguide cavity; coulper and transimission chipl scale atomic cloct

I. INTRODUCTION

Rb atomic clock as a frequency standard is popularly used in the aspect of telecoms, electronic instruments, etc., although Chip-Scale Atomic Clock (CSAC) based Coherent Population Trap (CPT) has been manufactured two years ago. CSAC has tiny size and very low power dissipation, but the disadvantages of high costs and lack of batch engineer applications for CSAC can not been surpassed in short term. Alternatively, Rb atomic clock with traditional gas-cell has the ad-vantages in costs and in power dissipation, and has improvements in reducing profile recent year. The means to reduce Rb atomic clock dimension is mostly to design kinds of cavity, and some progress has been made in recent year. Nowadays, introducing waveguide to the Rb atomic clock cavity design, we have realized a novel miniature waveguide cavity, and Rb atomic clock made by the cavity is lowered by three folders.

II. STUDYING ON CAVITY

A. Rb atomic clock Scheme and Cavity

Rubidium atomic clock is based on optical pumping, microwave interrogating and light intensity detecting. Rb atomic clock consists of electronics and physics package, and the latter is the key part because it will mainly decide the stability of clock. The physics package has two parts also: Rb spectrum lamp and cavity. Rb spectrum lamp to create a population inversion between the ground state hyperfine energy levels F=2 and F=1 in absorption cell inserted into cavity [1]. If the atoms of absorption cell are interrogated with microwave radiation, the change in light transmission through the cell can be checked by optical diode, and a discriminating signal in the light is to lock OCXO in the atomic clock. According to the clock operation course, enough microwave power is important, and the realization means is popularly to use cavity in which the power can be enclosed in a definite space with special model, such as TE111 or TE011. A typical scheme of Rb atomic clock is shown in figure 1.

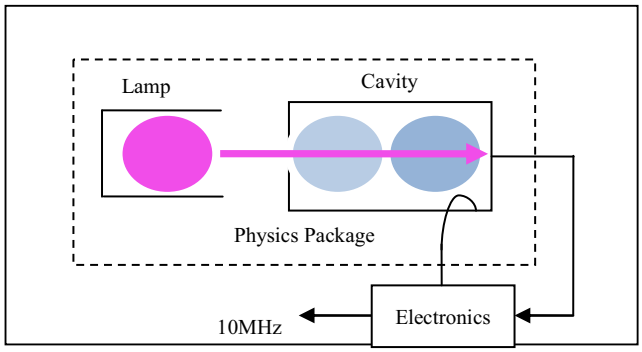

Figure 1. Cavity and Rb atomic clock diagram

In Rb atomic clock, Rb absorption cell must be enough feed with power level of microwave signal and its direction must also be parallel to the quantum axe. So, while cavity resonates at the point of 6.8GHz, the size of the cavity is a little big. Otherwise, if the no resonance occurs there, the stability of the clock will degenerate generally. Therefore, to reduce the volume of cavity is the main content of deigning miniature Rb atomic clock.

Typical means to downsize the volume is to adopt TE111 cylinder cavity. In comparison with TE011, the volume can be reduced by four folders. But the performance will worsen comparably. This cavity is popularly used in the world, and a series of Rb atomic clock have be developed and massly manufactured, including spacial high performance Rb frequency standard made by EG&G for GPS in America [2].

In order to simultaneously possess the high performance of TE011 and low size of TE111, a slot magnet cavity has been designed [3]. In the cavity, the slot and gap are respectively equivalent to capacitor and inductor according to integral parameter analysis. Therefore the resonant frequency is just decided by the size of the both part and independent on the size of cavity. Importantly, the model is approximately TE011 at an extent, and consideration of performance and volume can be realized.

A waveguide cavity, in a patent US5627497 called resonator package for atomic frequency standard by Gerold skoczen from Efratom Time and frequency Products, has been invented [4]. In the resonator package, a cylinder cavity containing absorption cell has not to be tuned and its size can not be accurately confined in a range, and a RF loop ring consisted of SRD and metal wire is shaped as a rectangle which inserts into the cavity from a hole in the profile. While to tune RF signal amplitude, the side of the loop ring must be

This work has been gotten support from National key scientific instrument and equipment development project No.2012YQ200183.

turned slowly by holding the connector, and be fixed by a screw on the optimum point where the atomic discrimination signal is maximal. The best one of the merits is that low size of cavity can be achieved, but shortage is very obvious that precession is inconvenient due to the functions of coupler and transmission are within the one loop ring. By the waveguide cavity, a kind of Rb atomic clock (model LPRO) has bee made.

B. Ttansmision-Counpler and Waveguide Cavity

Coupled strip line filters and directional couplers were presented by E. M. T. JONES and J. T. BOLLJAHN in 1956[5]. In that theory, two stripe lines are parallel each other and total effect is one of low-pass, band-pass, all-pass, or all-stop filter. Simultaneously, the signal power can been coupled and transmitted between the two strip lines. The idea from us, the combination of the stripe line filter and waveguide is to design a special waveguide cavity and reduce the cavity size more and more. While analyzing the stripe line, we found the band-pass filter could be selected to design a waveguide cavity for Rb atomic clock. The band-pass filter has the property as below.

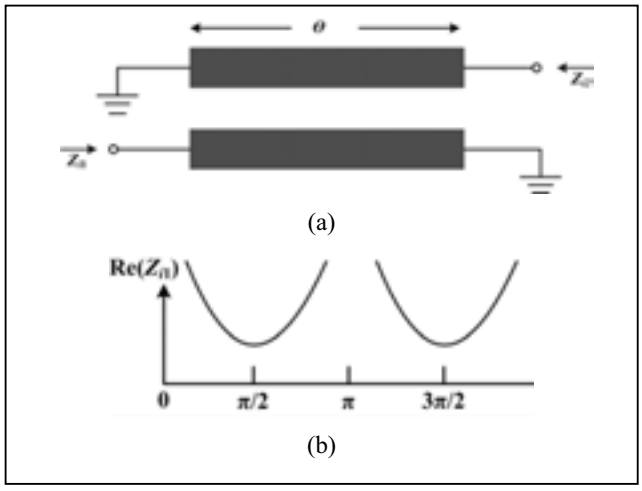

Figure 2. Coupler and transimision filter diagram. (a) abstraction construct, (b) the relation between transimission Real compoent with phase

As is known the cavity in Rb atomic clock consists of absorption cell and hole for transmitting light, which complicate the boundary condition. Therefore, computer simulation and assisting design must be used in order to achieve the optimum of mechanical parameters when we design the waveguide cavity by the above stripe line technology.

III. SIMULATING AND DESIGNING

Auxiliary computer simulation is very popularly used in researching and developing mechanical and Microwave technology and product. In this project, we will design the cavity with help of simulation, in which microwave band is about the point 6.8GHz, and the H-component been parallel to the axe of the cavity is enough strong in order to reduce the electronics power dissipation.

A. Reforming and Slimulating

The stripe line in figure 2 can not be used to design cavity for Rb atomic clock, and must be reformed. According to electromagnetic induction theory, there is alternatively transferring between H-component and E-component in space-time domain on RF signal transmitting. Regarding the cavity construct where a bottom side and cylinder profile will worsen electromagnetic field distribution from stripe lines, the one stripe line must be changed into a semicircle which is work as a coupling ring, and another one will be as a screw regulator. The both of the two lines are parallel each other also.

We have simulated the effect of the reformed construct in comparison with the stripe line in figure 2 by HFSS. The effect is in figure 3.

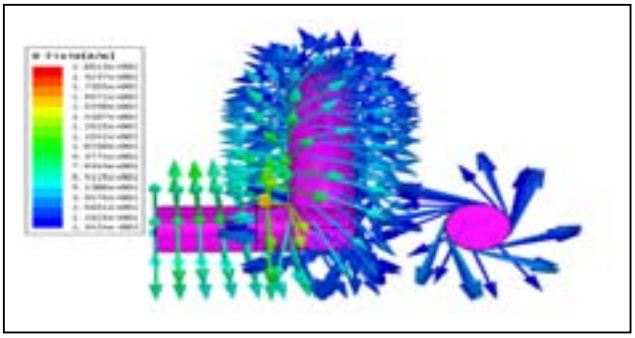

Figure 3. H-component in the Waveguide by HFSS Simulating

The above simulation is shown that H-component can transmit from the semicircle ring loop to other space, and the RF power can be coupled with the screw regulator. By this reform, big couple efficiency would be realized.

While using this construct of the reformed stripe line to design new waveguide cavity for Rb atomic clock, We have also simulated the cavity by HFSS.

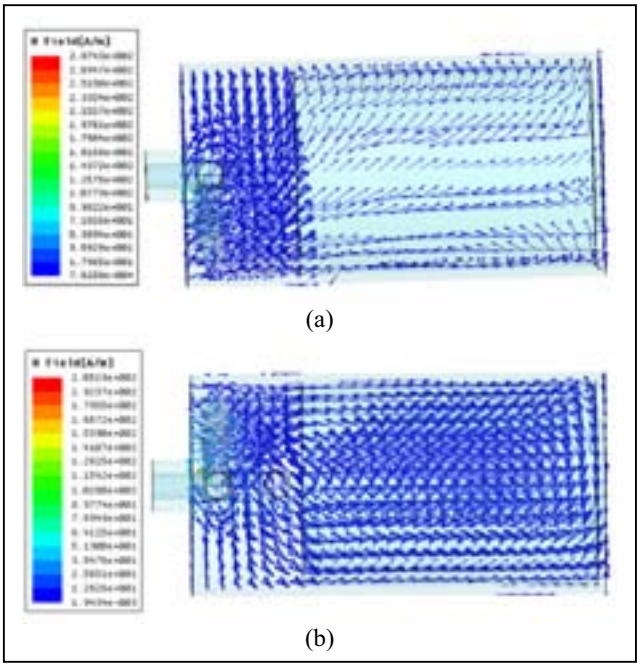

Figure 4. H-component in the Waveguide by HFSS Simulating. (a) effect without screw regulator, (b) effect with screw regulator.

B. Manufacturing and Testing

According to the above simulation, the waveguide cavity has manufactured in Spcaon. In the cavity, the screw regulator and ring loop are made of copper by coating silver. A Step-Recovery-Diode (SRD), multiplying RF signal to 6.8 GHz, is soldered on the bottom side and ring loop simultaneously. In general, the RF signal is about 60 MHz or 90 MHz.

We have tested the reflect efficiency which represents microwave transmission into absorption cell, and the curve is as below.

(a)

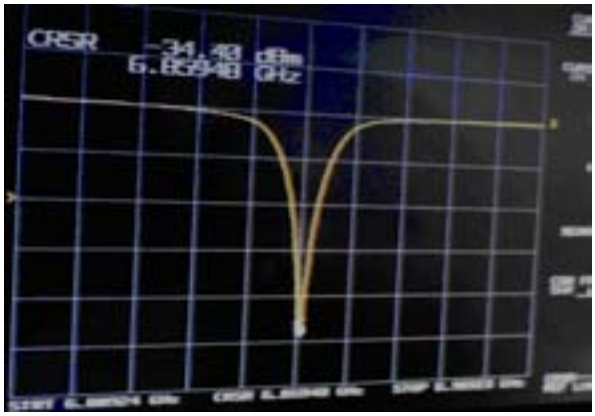

(b)

Figure 5. (a) H-component in the Waveguide by HFSS Simulating, (b) cavity reflect coeffient

From the test in figure 5, the profile of the cavity is very low, and the point of the coefficient is about 6.8 GHz. If using the cavity to design Rb atomic clock, small volume must be realized.

C. Design traditional Rb atomic clock

While the cavity was made, we have developed a miniature Rb atomic clock which is compatible with OCXO in aspect of size and pin definition。In the miniature Rb atomic clock, the cavity is heated among with OCXO, the lamp is reduced correspondingly, and final demission is just 51×51× 25 cubic millimeters. Finally, the clock is one of smallest traditional cell Rb atomic clock. The cell is made by classic procession, and the power dissipation is still big. We have tested the specification parameters of the clock [6].

D. Trying in Chi-Scale Atomic clock

Except Coherent Population Trap (CPT), another one chip-scale atomic clock has been made [7]. In that clock, its absorption cell is made by MEMS procession, and the size of the cell is just several cubic millimeters. Especially, the microwave signal is directly coupled by a circle ring loop. According to the above stripe line theory and our reforming design, the high coupling efficiency will be realized. The relative try is doing in spaceon.

IV. CONCLUTIONS

Basing stripe line coupler theory, a novel waveguide cavity has been designed where the balance between low size and high performance is realized. By this cavity design, we have firstly developed a smallest miniature Rb atomic clock which can be used to compatible with OCXO; and give an idea to develop a chip-scale atomic clock.

ACKNOWLEDGMENT

The work relative to this paper got helps from our colleagues. Wang Wenjun helped us in HFSS simulation; An Fangfan tested the miniature Rb atomic clock. Importantly, Quartzlock Company has paid many efforts to expand the international market for this clock.

REFERENCES

[1] Audoin C., Guinot B.: The Measurement of Time, Frequency and Atomic Clock, Cambridge, University Press, pp. 211-215, 2001

[2] Todd Dass etc., “Performance and Plans for the Future,” 34th Annual Precise Time and Time Interval (PTTI) Meeting, pp. 176–192.

[3] Mei etc., “miniaturized microwae cavity for atomic frequency standard,” Patent US622587B1.

[4] E. M. T. Jones and J. T. Bolljahn, “resonator package for atomic frequency standard,” Patent US5627497.

[5] R. Nicole, “Coupled-stripe-Transmission-Line Filters and Directional Couplers,” lre transactions on microwave theory and techniques, pp. 75–81, 1956.

[6] Yuanhong Cao etc., “An Ultra-Miniature Rb Atomic Clock Compatible with OCXO,” IFCS EFTF2011 Proceedings, pp. 218–222, 2011.

[7] A. M. Braun etc., “Rf-Interrogated End-State Chip-Scale Atomic Clock,” 39th Annual Precise Time and Time Interval (PTTI) Meeting. pp. 233–248.

Experimental Study on Mutual Injection Locked Vertical-Cavity Surface-Emitting Lasers

Bozhong Tan, Sihong Gu*
School of Physics,
Huazhong University of Science and Technology,
Wuhan, People's Republic of China

Jiehua Chen, Sihong Gu*
Key Laboratory of Atomic Frequency Standards
Wuhan Institute of Physics and Mathematics, CAS,
Wuhan, People's Republic of China
*Email: shgu@wipm.ac.cn

***Abstract*—recently we propose a lin⊥lin quasi-bichromatic laser scheme and experimentally realized the device. Through modulating two Vertical-Cavity Surface-Emitting Lasers (VCSELs) with same microwave and mutually injecting between two VCSELs, a lin⊥lin quasi-bichromatic laser with the 90% laser power on the two wanted frequency components is obtained. With the laser source the high quality CPT signal has been obtained. We also introduce the scheme which is promising to provide a lin ⊥ lin quasi-bichromatic laser source for the miniature CPT atomic clock.**

Keywords— Coherent Population Trapping; Atomic Clock; Vertical-Cavity Surface-Emitting Laser.

I. INTRODUCTION

The chip scale atomic clock (CSAC) based on coherent population trapping (CPT) has been widely studied[1-5], and has been applied in Global Position System (GPS), mobile communication, geodetic surveying and so on.

In the prevail CPT atomic clock, a Vertical-Cavity Surface-Emitting Laser (VCSEL) driven by a microwave modulated dc provides a lineally polarized multichromatic laser beam, which is turned with a quarter waveplate into a circularly polarized one to interact with atoms. Though the scheme suits for the miniature atomic clock it causes two main disadvantages: certain atoms are pumped into the leaky trap state[6, 7] thus make no contribution to CPT resonance, and except the two wanted frequency components the others contribute to background noise rather than CPT resonance.

Different schemes have been proposed and studied, among them the lin⊥lin bichromatic laser, which has no unwanted frequency components and eliminates the leaky trap state atoms, is a promising one. However, presently laboratory realized lin⊥lin bichromatic lasers, based on optical phase-locked loop (OPLL)[8], acoustic optic modulator (AOM)[9] and electro optic modulator (EOM)[10] etc are all with large volume and high power consumption, thus all of these setups are not suitable for the practical package atomic clock, not to speak for CSAC.

Previously we have presented a lin⊥lin quasi-bichromatic laser scheme based on master-slave injection locked VCSELs[11]. With this laser source, a very high contrast has been achieved, and the two disadvantages mentioned above can be both eliminated. Same as in [6], we define contrast as CPT signal amplitude divide by the amplitude of background light signal. However, an optical isolator used in this experiment setup makes the light source still too large to apply in a practical package atomic clock. In this paper we present our proposed mutually injection locking lin⊥lin quasi-bichromatic laser scheme and our experimental result.

This work is supported by the National Natural Science Foundation of China (NSFC) under Grant No. 11204351.

II. METHODS

The configuration of the mutually injection frequency locking lin⊥lin quasi-bichromatic laser source is depicted in Fig. 1. A 6.834GHz microwave generated by the microwave source (Agilent E8257D) is split with a power splitter (Mini-Circuits ZX10-2-71), and each the split microwave is mixed with a dc through a Bias-T. Driven by the mixed currents, both VCSELs emit multichromatic lasers with frequency distribution as that in Fig. 2.

The two orthogonal linearly polarized laser beams are combined at a polarized beam splitter (PBS) to form a lin⊥lin beam. A partial reflector reflects certain laser of each linearly polarized beam, while as the reflected beams go through the quarter waveplate twice their polarization directions are both rotated by 90 degree. Therefore, each the reflected beam goes through the PBS and injects into the other VCSEL. When there are the same frequency components between the two VCSELs' outputs, there appears injection frequency locking effect and the two VCSELs' output could be mutually frequency injection locked to each other.

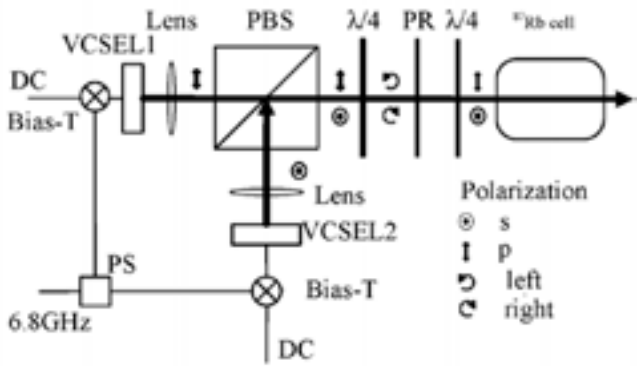

Fig. 1. Experiment setup. PBS: polarized beam splitter, PS: power splitter, PR: partial reflector.

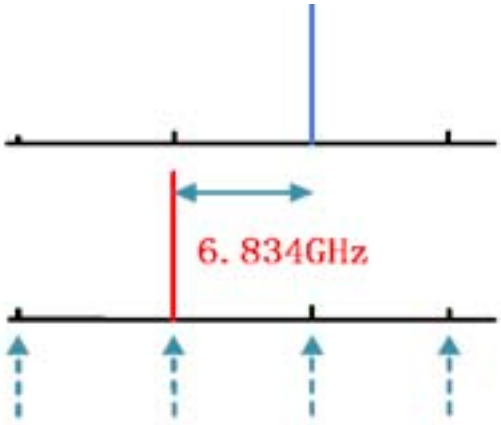

Fig. 2. Spectra of two VCSELs' outputs. The red and blue line denote the VCSELs' carriers respectively.

III. RESUALTS AND DISCUSSION

In the experiment, we used pretty weak microwave that the main power maintains in two carriers as that in Fig. 2. In order to mutually frequency lock as expected, we turned the driving current of one VCSEL to let the carrier of its output laser coincident with the first sideband of the other VCSEL's output as that in Fig. 2, and experimentally studied the mutual frequency injection locking effect[12]. With the spectral distributions of the two VCSELs's outputs are close to those of Fig. 2, and the injection ratio (defined as the laser power injected into the VCSEL divide by its output laser power), is about 0.5%, we recorded Fig. 3a, the spectrum of the mutually frequency injection locked lin⊥lin quasi-bichromatic laser, with a Fabry-Perot interferometer. From the spectrum we calculated out that the two wanted frequency components occupy about 90% of the total laser power. Under the same experimental condition, we have checked the control range by tuning wavelength of one VCSEL by changing its driving current and leaving the other VCSEL's driving current unchanged, and found that the locking range can reach 2 GHz.

It shall be mentioned that with this scheme, there will appear unwanted spectral modes from the cavity consisted of the VCSELs' high reflecting end faces when the injection is too strong. In our experiment setup, the optical length between the two VCSELs' end faces is 90 cm, therefore we recorded the cavity modes as that in Fig. 3(b) with mode spacing of 166 MHz when the injection ratio was 2.2%. According our experimental resualt, within 1% injection ratio, no obvious cavity mode was observed.

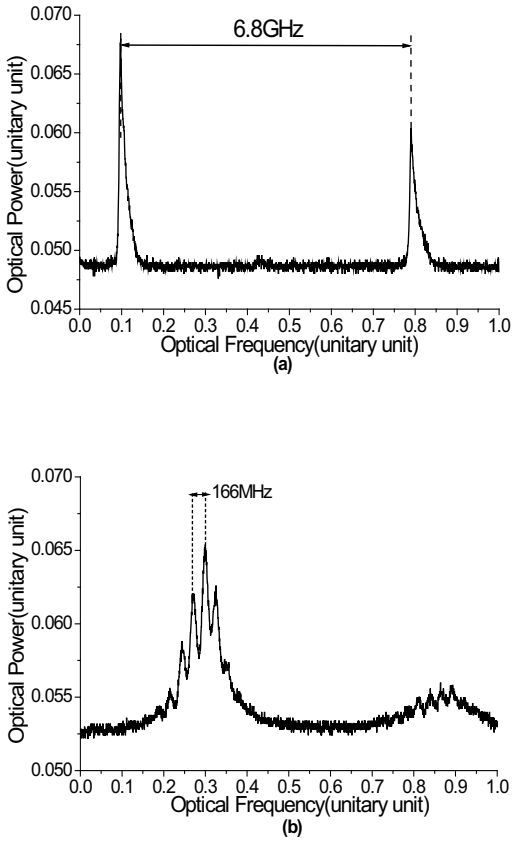

Fig. 3. The optical spectra recorded with a Fabry-Perot interferometer. The injection ratio is (a) 0.5% , (b) 2.2%.

With the experimental setup of our previous work [12], we have applied the realized lin⊥lin quasi-bichromatic laser beam to generate CPT resonance with ^{87}Rb, and obtained CPT resonance signal with contrast of 50%, while in prevail CPT atomic clock which is normally less than 5% [6].

Based on this study, we also propose a scheme as depicted in Fig. 4 for realizing a chip scale lin⊥lin quasi-bichromatic laser source. In the scheme two VCSELs are mounted on a basement such that the polarization directions of their output laser beams are orthogonal to each other, and with a birefringent crystal such as YVO4 the two laser beams are combined to form the lin⊥lin beam. With two VCSEL chips separated for less than one millimeter, according to the

refraction index a YVO4 with the thickness of less than 10 millimeter is enough to combine the two beam. Therefore, a lin ⊥lin quasi-bichromatic laser device could be integrated with about 1 cm^3. It is promising to apply this miniature laser device in the package CPT atomic clock, even CSAC.

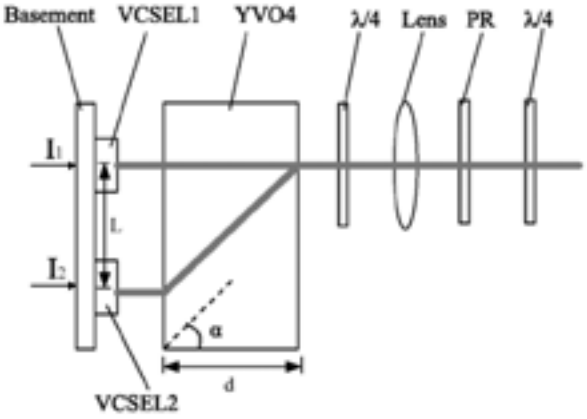

Fig. 4. The chip scale lin ⊥ lin quasi-bichromatic laser beam generator scheme.

IV. CONCLUSION

We have proposed and experimentally studied a lin⊥lin quasi-bichromatic laser beam generator scheme, and have applied the realized laser beam to obtained high quality CPT resonance signal. Based on this laser scheme, we have also proposed a miniature lin⊥lin quasi-bichromatic laser beam generator scheme, which is promising to be applied in the package CPT atomic clock even in CSAC.

REFERENCES

[1] S. Knappe, V. Shah, P. D. D. Schwindt, L. Hollberg, J. Kitching, L.-A. Liew, et al., "A microfabricated atomic clock," Appl. Phys. Lett., vol. 85, pp. 1460, 2004.

[2] R. Lutwak, "The Chip-Scale Atomic Clock - Recent developments," Frequency Control Symposium, 2009 Joint with the 22nd European Frequency and Time forum. IEEE International, pp.1075-6787, 20-24 April 2009 2009.

[3] T. Baluktsian, C. Urban, T. Bublat, H. Giessen, R. Löw, and T. Pfau, "Fabrication method for microscopic vapor cells for alkali atoms," Opt. Lett., vol. 35, pp. 1950-1952, 2010.

[4] R. Boudot, P. Dziuban, M. Hasegawa, R. K. Chutani, S. Galliou, V. Giordano, et al., "Coherent population trapping resonances in Cs--Ne vapor microcells for miniature clocks applications," J Appl. Phys., vol. 109, pp. 014912-11, 01/01/ 2011.

[5] T. Bandi, M. Pellaton, D. Miletic, C. Affolderbach, F. Gruet, R. Matthey, et al., "Double-resonance in alkali vapor cells for high performance and miniature atomic clocks," in Frequency Control Symposium (FCS), 2012 IEEE International, 2012, pp. 1-6. May 2012

[6] J. Vanier, M. W. Levine, D. Janssen, and M. J. Delaney, "The coherent population trapping passive frequency standard," Ieee T Instrum. Meas., vol. 52, pp. 258-262, Apr 2003.

[7] T. Zanon, S. Guerandel, E. de Clercq, D. Holleville, N. Dimarcq, and A. Clairon, "High Contrast Ramsey Fringes with Coherent-Population-Trapping Pulses in a Double Lambda Atomic System," Phys. Rev. Lett., vol. 94, p. 193002, 05/17/ 2005.

[8] A. M. Marino and C. R. Stroud, "Phase-locked laser system for use in atomic coherence experiments," Rev. Sci. Instrum., vol. 79, pp. 013104, 2008.

[9] B. E. Unks, N. A. Proite, and D. D. Yavuz, "Generation of high-power laser light with Gigahertz splitting," Rev. Sci. Instrum., vol. 78, pp. 083108-4, 2007.

[10] E. A. Korsunsky, N. Leinfellner, A. Huss, S. Baluschev, and L. Windholz, "Phase-dependent electromagnetically induced transparency," Phys. Rev. A, vol. 59, pp. 2302-2305, 1999.

[11] P. Yun, B. Tan, W. Deng, J. Yang, and S. Gu, "Quasi-bichromatic laser for a lin [perpendicular] lin coherent population trapping clock produced by vertical-cavity surface-emitting lasers," Rev. Sci. Instrum., vol. 83, pp. 093111-4, 09/00/ 2012.

[12] B. Tan, P. Yun, J. Yang, Y. Tian, and S. Gu, "A chip scale lin ⊥lin quasi-bichromatic laser scheme", Appl. Phys. Lett. vol. 102, pp. 161117-4, 04/22/2013

Effect of the Coherent Population Trapping on Saturated Absorption Resonances in Cs Vapor

Ersoy Sahin[1, 2], Ramiz Hamid[1], and Azad Izmailov[3]

[1] TÜBİTAK, Ulusal Metroloji Enstitüsü (UME), Gebze, Kocaeli, TURKEY
[2]Istanbul Technical University, Faculty of Science and Letters, Engineering Physics Department Maslak, Istanbul, TURKEY
[3]Institute of Physics, Azerbaijan National Academy of Sciences, H. Javid av. 33, Baku, Az-1143, AZERBAIJAN
Email: ersoy.sahin@tubitak.gov.tr

***Abstract*—We have detected and analysed interesting features of sub-Doppler resonances, which are induced in absorption of the weak monochromatic probe light beam (with the scanned frequency) by the counterpropagating two-frequency pumping radiation implementing the phenomenon of the coherent population trapping (CPT) on resonant Λ-systems of atomic levels. Our experimental investigations have been carried out on example of spectral components of the Doppler broadened D_2 line of cesium atoms. Obtained results may be used for optimization of laser frequencies stabilization on atomic transitions.**

Keywords- Sub-doppler resonance, Coherent population trapping, Laser frequency stabilization.

I. INTRODUCTION

The phenomenon of the coherent population trapping (CPT is the basis of a number of important applications: ultrahigh resolution spectroscopy, atomic clocks, magnetometers, coherent population transfer among quantum states of atoms (or molecules) and also in some others described, for example in reviews [1-3]. In particular, narrow CPT resonances are detected in absorption of a two-frequency laser radiation on three level atomic Λ-systems and also in the corresponding induced fluorescence spectrum of a gas medium. Such a resonance excitation of atoms on the Λ-system scheme is realized by means of light induced optical transitions $|1> - |3>$ and $|2> - |3>$ from long-lived levels $|1>$ and $|2>$ to the excited state $|3>$. Most given Λ-systems are not closed because of possible channels of a radiative decay of the upper state $|3>$ on "exit" quantum states, which don't interact with the resonance laser radiation [4,5]. Let us consider interaction of a nonclosed Λ-system with 2 monochromatic laser fields. Frequencies ω_1 and ω_2 of given fields are close to centers Ω_{31} and Ω_{32} of electrodipole transitions $|1> - |3>$ and $|2> - |3>$ respectively. Populations of lower levels $|1>$ and $|2>$ will dwindle at intensification of this resonance two-frequency radiation because of the light induced repumping of atoms from these levels to "exit" states after the radiative decay of the opticaly excited level $|3>$. However sharp weakening of such a repumping process takes place in consequence of a strong decrease of a population of the upper state $|3>$ under the following CPT condition [1-3]:

$$|\delta_2 - \delta_1| \le W, \qquad (1)$$

where $\delta_1=(\omega_1 - \Omega_{31})$ and $\delta_2=(\omega_2 - \Omega_{32})$ are detunings of laser frequencies. The characteristic width W of the CPT resonance in Eq.(1) is determined by intensities of laser fields and by relaxation rates of populations and coherence of lower quantum states $|1>$ and $|2>$. Under definite conditions, the value W may be much less than homogeneous widths of spectral lines of optical transitions $|1> - |3>$ and $|2> - |3>$. The population of such a nonclosed Λ-system almost completely vanishes at sufficiently intensive optical pumping at a violation of the Eq. (1). However, according to the theoretical work [6], lower long-lived levels of an open Λ-system may keep about half of the equilibrium population of an initial noncoherent molecular ensemble at the exact CPT condition $\delta_1=\delta_2$ even in the case of such strong pumping. Thus narrow high-contrast CPT peaks will arise in populations of long-lived levels $|1>$ and $|2>$ of a nonclosed Λ-system versus the detuning difference $(\delta_2 - \delta_1)$.

Recently we have carried out experimental research of such CPT resonances for nonclosed three level Λ-systems formed by spectral components of the Doppler broadened D_2 line of cesium atoms [7,8]. Given CPT resonances were detected in absorption of the probe monochromatic light beam under

action of the counterpropagating two-frequency pumping radiation. In the recent work [8] we use only one diode laser, which generates the monochromatic beam with the stabilized frequency ω_1. The second coherent radiation component (with the frequency ω_2) was obtained from this initial beam by the electro-optical modulator (EOM). The frequency difference ($\omega_1 - \omega_2$) were smoothly scanned around the microwave interval (9192.6 MHz) between hyperfine sublevels of the Cs ground term (Fig.1). In particular we have established that, at definite conditions, CPT resonances in transmission of the weak probe beam may have not only more contrast but also are essentially narrower in comparison with well-known CPT resonances in transmission of the corresponding two-frequency pumping radiation (or the light induced fluorescence of the gas medium) [8].

Unlike our previous works [7,8], now we will analyze features of sub-Doppler resonances in absorption of the weak probe beam (with the scanned frequency ω_1) counterpropagating with respect to the bichromatic pumping radiation with various fixed frequency differences ($\omega_1 - \omega_2$) near the CPT condition (1).

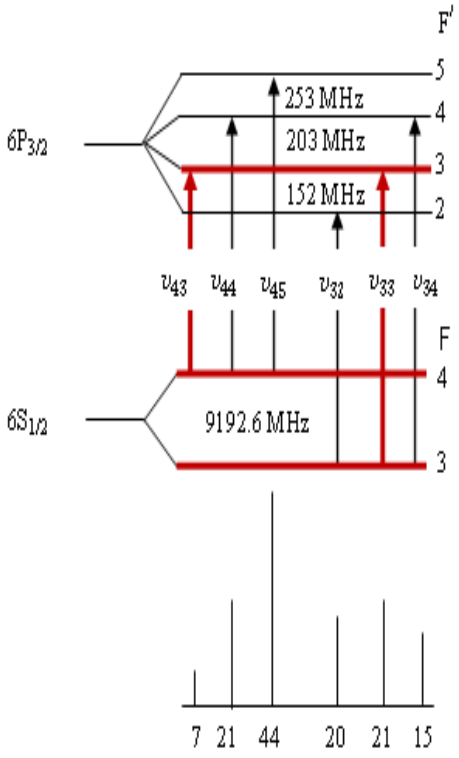

Fig. 1. Energy level scheme of the ^{133}Cs D_2 line. The relative oscillator strengths of lines, representing hyperfine transitions, are given on the bottom of the figure. CPT resonances are formed in the following 2 Λ-systems of this scheme: $6S_{1/2}(F=3) - 6P_{3/2}(F'=3) - 6S_{1/2}(F=4)$ and $6S_{1/2}(F=3) - 6P_{3/2}(F'=4) - 6S_{1/2}(F=4)$.

II. EXPERIMENTAL METHOD AND SETUP

Our experimental configuration is shown in Fig 2. The output of the external cavity diode laser (ECDL) with the frequency ω_1 was phase modulated at the ^{133}Cs hyperfine frequency 9192.6 MHz by an electro-optical modulator (EOM). The bichromatic pumping beam (with frequencies ω_1 and ω_2), which was indicated by the red color in Fig. 2, was collimated to the diameter D_{pump} = 5 mm, linearly polarized by the polarizer (P_1) and then sent to the quartz cell, containing the rarefied Cs vapor (without any buffer gas) at the sufficiently low pressure about 0.1 mPa ($3x10^{10}$ atom/cm^3). The monochromatic probe beam, which was the diameter of 1.8 mm and indicated by the green color in Fig 3., had the same parallel linear polarization after the polarizer (P_2) and propagated through the given Cs cell in the opposite direction. Both two-frequency pumping and monochromatic probe beams were overlapped in the irradiated Cs cell which was 3 cm length and diameter 2.5 cm. The cylindrical quartz Cs cell was kept at the room temperature of 22 ºC without temperature stabilization. No external magnetic field was applied on the Cs cell that was magnetically shielded. During the experiment the intensity of the monochromatic probe beam was kept constant at the sufficiently low value about 0.01 mW/cm^2 and in fact did not induce saturation and optical pumping effects in the Cs vapor. For recording of sub-Doppler resonances on different hyperfine spectral components of the Cs D_2 line (Fig.1), the laser frequency was stabilized on the transmission resonance of Fabry-perot interferometer (FPI). To avoid the amplitude fluctations of laser frequency, the FPI was modulated. Sub-Doppler resonances were recorded by using the chopper and lock-in amplifier.

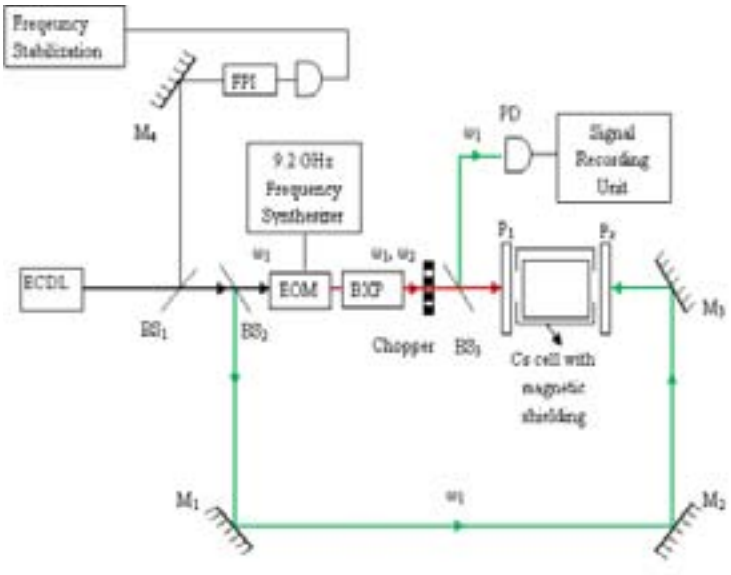

Fig. 2. Scheme of the experimental setup, which includes external cavity diode laser (ECDL), Fabry-perot interferometer (FPI), electro-optical modulator (EOM), beam splitter (BS_1, BS_2, BS_3), beam expander (BXP), mirrors (M_1, M_2, M_3, M_4), polarizers (P_1, P_2), photodiode (PD), and the Cs cell with the magnetic shielding.

III. DISCUSSION OF RESULTS

We investigated the sufficiently rarefied natural Cs vapor (without any buffer gas) where interatomic collisions were negligible. Homogeneous widths of resonance optical lines were much less than their corresponding Doppler broadening under conditions of our experiment. Then, according to the level scheme of the Doppler broadened Cs D_2 line (Fig.1), the component of the laser pumping beam with the frequency ω_1 effectively interacts with 3 various groups of atoms, whose velocity projections (along the wave vector k of this beam) are close to following values [9]:

$$V_{32} = \frac{(\omega_1 - \nu_{32})}{|k|},\ V_{33} = \frac{(\omega_1 - \nu_{33})}{|k|},\ V_{34} = \frac{(\omega_1 - \nu_{34})}{|k|}. \qquad (2)$$

We note, that narrow CPT resonances in absorption of the two-frequency pumping are formed in 2 different Λ-systems $6S_{1/2}(F=3) - 6P_{3/2}(F'=3) - 6S_{1/2}(F=4)$ and $6S_{1/2}(F=3) - 6P_{3/2}(F'=4) - 6S_{1/2}(F=4)$ (Fig.2), which correspond to atomic velocity projections V_{33} and V_{34} in Eq. (2).

The counterpropagating probe beam with the frequency ω_1 also will interact with 3 various groups of atoms whose velocity projections have opposite sign with respect to corresponding values in formulas (2). Thus 6 sub-Doppler resonances should appear in absorption of the probe beam with centers on following values of the scanned frequency ω_1: ν_{32}, ν_{33}, ν_{34}, $0.5(\nu_{32}+\nu_{33})$, $0.5(\nu_{32}+\nu_{34})$, $0.5(\nu_{33}+\nu_{34})$, in the interval between ν_{32} and ν_{34}. Fig. 3 demonstrates given saturated absorption resonances at various fixed frequency detunings $|\delta_1 - \delta_2|$ from the CPT condition (1). These detunings $|\delta_1 - \delta_2|$ are much less than the natural width γ (about 5 MHz) of the optical Cs D_2 line, however are more than the characteristic width W of the CPT resonance (1) for curves 2 and 3 in Fig.3. The curve 1 in this figure 3 corresponds to the exact CPT condition $\delta_1=\delta_2$.

The CPT phenomenon may essentially effect on the optical pumping process, which directly determines structure of saturated absorption resonances in the probe beam. Thus we directly see in Fig.3, that even small deviations $W \leq |\delta_2 - \delta_1| << \gamma$ from the equality $\delta_1=\delta_2$ lead to changes of indicated sub-Doppler resonances with the exception of the resonance with the center $\omega_1=\nu_{32}$. Indeed, the second component of the pumping radiation with the frequency ω_2 can not effect on this resonance because the dipole transition $6S_{1/2}(F=4) - 6P_{3/2}(F'=2)$ is forbidden and the CPT phenomenon are not realized on the corresponding Λ-system $6S_{1/2}(F=3) - 6P_{3/2}(F'=2) - 6S_{1/2}(F=4)$ (Fig.1). At the same time CPT leads to noticeable decrease of saturated absorption resonances with centers on frequencies $0.5(\nu_{32}+\nu_{33})$, ν_{33} and ν_{34} (Fig.3) because of the weakening of the repumping process from lower long-lived levels of corresponding Λ-systems at the CPT condition (1). However, unlike this usual situation, CPT leads to increase of the amplitude of the crossover resonance with the center $0.5(\nu_{33}+\nu_{34})$. Such nontrivial result may be caused by specific light induced redistribution of atomic populations

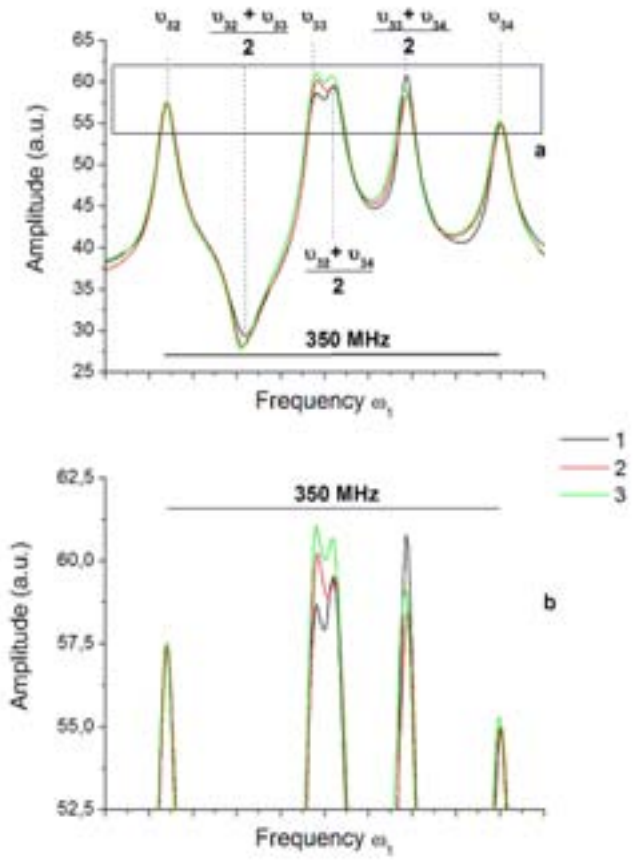

Fig. 3. Saturated absorption spectra of the probe beam versus its frequency ω_1 at the pumping intensity 7,64 mW/cm^2 and probe intensity 0.01 mW/cm^2 with corresponding beam diameters D_{pump} = 5 mm and D_{probe} = 1.8 mm for various fixed frequency detunings from the CPT condition $|\delta_1 - \delta_2|$= 0 (curve 1), 0.5 MHz (curve 2), and 1 MHz (curve 3). Figure 3b is the enlarged fragment of figure 3a enclosed in the rectangle.

between Zeeman sublevels of the ground Cs term (Fig.1) under action of the bichromatic pumping radiation.

Analyzed features of saturated absorption sub-Doppler resonances at the CPT phenomenon may be used for optimization of laser frequencies stabilization on corresponding atomic transitions.

REFERENCES

[1] E. Arimondo, "Nonabsorbing atomic coherences by coherent two-photon transitions in a three-level optical pumping," Progress in Optics, Elsevier, New York, 1996, Vol. 35, 257-354.

[2] S.E. Harris,"Electromagnetically Induced Transparency," Physics Today, July Issue, 1997, 36-42.

[3] K. Bergmann, H. Theuer, B.W. Shore, "Coherent population transfer among quantum states of atoms and molecules," Reviews of Modern Physics 70 (1998) 1003-1025.

[4] A.A. Radtsig and B.M. Smirnov, Reference Data on Atoms, Molecules and Ions, Springer, New York, 1985.

[5] H. Haken and H.Ch. Wolf, Molecular Physics and Elements of Quantum Chemistry, Springer, Berlin, 1995.

[6] A.Ch. Izmailov,"Coherent Population Trapping in the Λ system of Zeeman Degenerate Molecular Levels," Laser Phys. 15 (2005) 1543-1549.

[7] E. Sahin, R. Hamid, C. Birlikseven, G. Ozen and A.Ch. Izmailov,"High contrast resonances of the coherent population trapping on sublevels of the ground atomic term,"Laser Physics 22 (2012) 1038-1042.

[8] E. Sahin, G.Ozen, R. Hamid, M.Celik, and A.Ch. Izmailov," Coherent Population Trapping resonances on lower atomic levels of Doppler broadened optical lines," arXiv:1212.3834 [physics.atom-ph].

[9] W. Demtroder, Laser Spectroscopy: Basic Concepts and Instrumentation, Springer, Berlin, 2003.

Packageless Temperature Sensor Based on AlN/IDT/ZnO/Silicon Layered Structure

O. Legrani, O. Elmazria, M. Elhosni, A. Bartasyte and P. Pigeat
University of Lorraine, Institut Jean Lamour, UMR 7198
Centre National de la Recherche Scientifique (CNRS),
Institut Jean Lamour , UMR 7198
54506 Vandoeuvre-les-Nancy, FRANCE
ouarda.legrani@univ-lorraine.fr

S. Zghoon
National Research University
"Moscow Power Engineering Institute"
14 Krasnokazarmennaja,
111250 Moscow, Russia

***Abstract*— The possibility to generate simultaneously Surface Acoustic Wave (SAW) and Waveguiding layer acoustic wave (WLAW) in layered structures AlN/ZnO/Silicon was investigated. A delay line operating at 525 MHz was tested versus temperature in air and in contact with liquid. Experimental characterizations were also supported by modeling using the commercial software (COMSOL Multiphysics). The full delay line was simulated and liquid modeled by an additional layer on the top of AlN film.**

Keywords- AlN; packageless; silicon; temperature sensor; ZnO

I. INTRODUCTION

Devices based on wave guiding layer acoustic waves (WLAW) present a great interest in sensor application due to packageless structure, the possibility of extreme miniaturization and reduced sensibility to chemical environment. To generate isolated waves, the structures combining layers with low and high impedance in Bragg mirror configuration (ILAW-Isolated Layer Acoustic Wave) or acoustic confinement of the wave in a low-acoustic-velocity layer between two high-acoustic-velocity materials were used [1]. There are several requirements for the guiding layer: to be highly oriented and to have low surface roughness to ensure a good wave transmission and to avoid the increase of the acoustic propagation losses [2-4]. The isolated layer can be dielectric, piezoelectric or metallic and has to be stress- and crack-free and relatively thick for the confinement of the wave. Electro-acoustic properties of isolated wave, such as propagation velocity and electromechanical coupling are highly dependent on the nature, thickness and geometrical configuration of the materials composing WLAW device.

To this date, few studies have been reported in the literature on this type of structure [1, 5-7]. The successful confinement of WLAW in structures based on SiO_2 guiding layer was reported by Zhgoon et al. [1, 7]. However, more efforts need to be done to increase the coupling coefficient of such structures. Due to its low acoustic velocity and its high electromechanical coupling, zinc oxide was one of most promising material for the guiding layer. Our previous works have shown theoretically and experimentally, the possibility to generate Waveguiding layer acoustic wave in layered structures AlN/ZnO/diamond [8]. Such structures are of great interest because of their potential applications as packageless resonators, filters or sensors, based on WLAW, and as thermally compensated gas or liquid sensors, based on the combination of both SAW and WLAW. Because of its high acoustic velocity, the diamond appears to be the most suitable substrate for the production of containment structures for WLAW wave type, but it has major drawbacks including its high price and its poor compatibility with CMOS technology. In addition, the diamond growth occurs at high temperatures (700 °C - 1000 °C) inducing significant stress in the heterostructure. Therefore heterostructures with diamond are unsuitable for mass production.

The aim of this work is to evidence the potential of the AlN/ZnO/Silicon structure as low cost, CMOS compatible and packageless temperature sensor able to operate in harsh environments. Theoretical investigation was realized by using a finite element method (FEM) in order to define the best configuration and the optimized thicknesses of different layers. To achieve efficient confinement of WLAW, AlN layer was deposited on operating SAW device (IDT/ZnO/Si). The frequency response and thickness of AlN were monitored in real-time and during AlN film deposition. The second part of this paper is devoted to the experimental realization of the heterostructure with a comparison of results obtained by the simulation.

II. THEORITICAL DETAILS

Theoretical investigation was realized by a finite element method (FEM) using COMSOL Multiphysics [9]. The full delay line was simulated and liquid was modeled by an additional layer on the top of the AlN film.

$kh_{ZnO} = 1.25$ has been chosen i.e. (λ = 10 µm, thickness (ZnO) = 2 µm, thickness (AlN) > 20 µm).

The materials are described by their physical constants (elastic, piezoelectric, dielectric...), reported in literature [10-12].

The confinement of the wave was demonstrated by analyzing the field distribution of the wave in the structure notably the acoustic wave displacement profile.

III. Experimental Setup

2 µm thick ZnO films were deposited on Si (100) by rf magnetron sputtering. The pressure in the chamber was 0.002 mbar (1:1 of Ar: O_2) and the power injected in the plasma was 100 W. The distance target-substrate was fixed at 80 mm and the substrate temperature was 450°C. Then IDT were fabricated on ZnO/Si surface by using Aluminum sputtering followed by photolithography and wet etching processes. The number of IDT fingers, the aperture width (W) and the gap were set to 40, 0.4 mm and 200 µm, respectively. Finally, 30 µm of AlN were deposited on IDT/ZnO/Si by rf magnetron sputtering. AlN deposition process was optimized to avoid the AlN film cracking even in the case of thick layer. Following our experience, the key consists in working at relatively low deposition temperature (343 K). To perform electrical characterization, vacuum tight rf connectors were installed in the magnetron vacuum chamber. During AlN layer deposition, in-situ measurements of frequency and insertion losses of different modes were performed by a network analyzer (Agilent N5230A) and AlN thickness was monitored by interferential reflectometry method.

IV. Results and Discussion

1D-curves and 2D representation of modeling results for the particles displacement in AlN/ZnO/Si hétérostructure obtained for 2 µm and 12 µm of AlN thickness are shown in Fig.1 (a) and (b). The AlN thickness influences the confinement of the wave. Indeed, one can clearly observe that with 2 µm of AlN, the displacement of particles was reduced at the surface that corresponds to 30 % of confinement, at 12 µm of AlN zero displacement of particle was observed resulting in a total confinement of the wave. The addition of liquid on top of the AlN film in modeling induces no serious change in transmission signal that proves theoretically the confinement of the wave (Fig. 1(c)). The evolution of frequency response in transmission mode (S_{21}), obtained experimentally, related to the 0th, 1st and 2nd mode of acoustic wave, with AlN layer thickness is shown in Fig. 4. Before AlN deposition, only the 1st mode was observed due to the low electromechanical coupling of the other mode. At 12 µm of AlN thickness, the mode 1 starts to confine and the surface acoustic wave of 2nd mode appears. Frequency-Temperature characteristic shows a

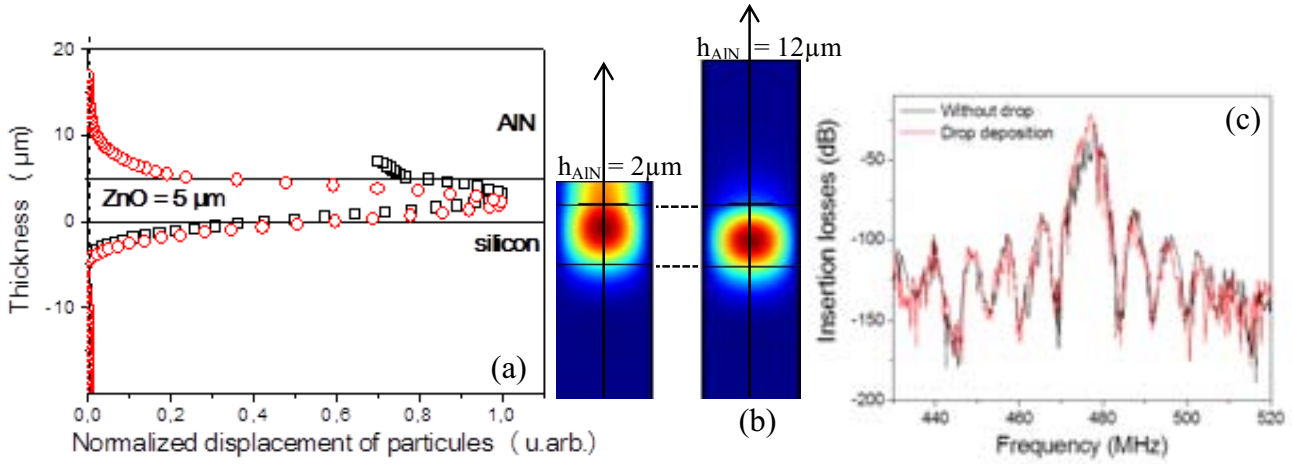

Fig.1: (a) 1D-curves and (b) 2D representation of modeling of the displacement of particles in AlN/ZnO/Si heterostructure obtained for 2µm and 12µm of AlN thickness. (c) Transmission signal of a delay-line obtained by modeling in air and with water over-layer.

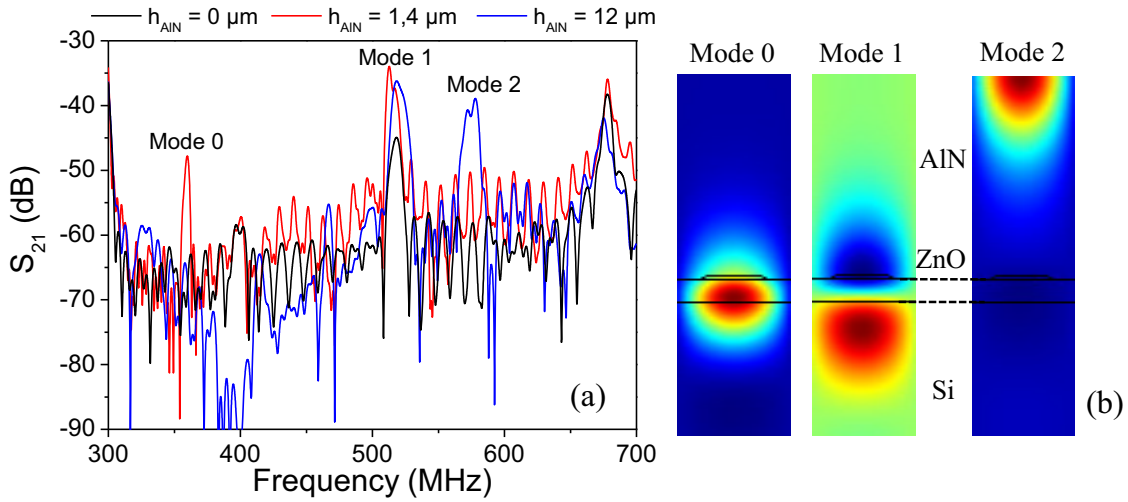

Fig. 2: (a) SAW signal (S_{21}) before and after deposition of AlN with the thickness of 1.4 and 12µm for the heterostructure AlN / ZnO / Si where kh_{ZnO} = 1.25. (b) 2D representation of modeling results for particle displacement in AlN/ZnO/Si hétérostructure obtained for 12 µm of AlN thickness for the mode 0, 1 and 2.

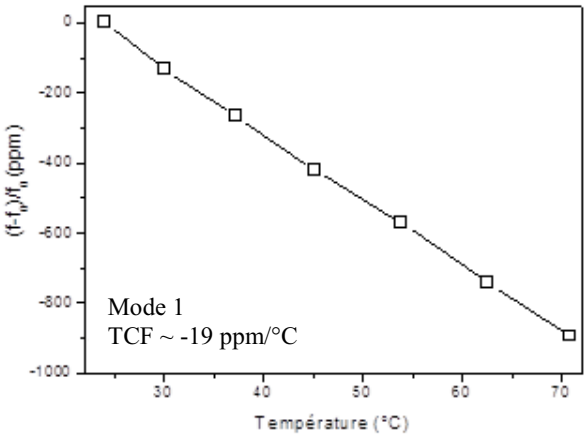

Fig 3: Relative velocity variation with temperature of AlN/ZnO/Si structure.

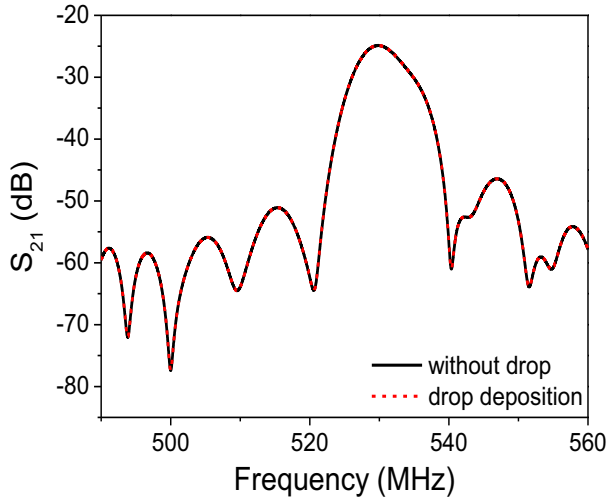

Fig. 4: Experimental test of the wave's confinement with addition of a water micro drop on the gap between the IDTs of the device.

very good linearity and a TCF value of -19 ppm/°C in air and in contact with liquid (Fig. 3). One can also observe that there is no change in transmission responses (S_{21}) collected in both conditions (Fig. 4). These results prove the total confinement of the wave in the AlN/IDT/ZnO/Si structure. Note that a Rayleigh wave on open surface is partially or completely attenuated. This study confirmed the feasibility of the AlN/IDT/ ZnO/Si structure as a packageless sensor sensitive to temperature with the ability to protect itself.

V. Conclusion

The ability to generate in the same heterostructure three propagation modes 0, 1 and 2 of the acoustic wave, the confinement of the wave in the structure and good compatibility of the results obtained in simulation to experiment have been demonstrated. The characterization of the temperature behavior of the optimized heterostructure (kh_{ZnO} = 1.25), showed its potential as a temperature sensor. The measured TCF value is - 19.1 ppm/°C. Finally the effective acoustic isolation of the wave within the heterostructure AlN / IDT / ZnO / Si has been demonstrated experimentally. Thus, this study allowed us to confirm the potential of the heterostructure AlN/IDT/ZnO/Si as the temperature sensitive device, having the ability to protect itself from air and moisture.

References

[1] K. Bhattacharjee, A. Shvetsov, and S. Zhgoon, "Packageless SAW Devices with Isolated Layer Acoustic Waves (ILAW) and Waveguiding Layer Acoustic Waves (WLAW)", IEEE Freq. Control. Symp., pp. 135–140, October 2007.

[2] O. Yamazaki, T. Mitsuyu and K. Wasa, "ZnO thin-film SAW devices", IEEE Trans. Son. Ultrason. Vol. SU-27, pp. 369-379, November 1980.

[3] Y.M. Lu, W.S. Hwang, W.Y.Liu and J.S. Yang, "Effect of RF power on optical and electrical properties of ZnO thin film by magnetron sputtering", Materials chemistry and Physics., Vol. 72 issue 3, pp. 269-272, 2001.

[4] I. Sayago, M. Aleixandre, A. Martinez, M.J. Fernandez, J.P. Santos, J. Gutiérrez, I. Gracia and M.C. Horrillo, Synthetic Metals., Vol. 148, pp. 37-41, January 2005.

[5] T.E. Parker and C.J. Dunnrowicz, United States Patent 4270105, "Stabilized Surface Acoustic Wave Device", May 1981.

[6] G.K Montress, T.E. Parker and D. Andres, "Review of SAW Oscillator performance", IEEE Ultrason. Symp., vol. 43, pp. 43-54, 1994.

[7] D.E. Cullen and R.A. Wagner, United States Patent 4213104, "Vacuum Encapsulation for Surface Acoustic Wave (SAW) Device", July 1980.

[8] O. Elmazria, S. Zhgoon, L. Le Brizoual, F. Sarry, D. Tsimbal and M.A. Djouadi, "AlN/ZnO/Diamond Structure Combining Isolated and Surface Acoustic Waves", Appl. Phys. Lett, Vol. 95, pp. 233503-3, December 2009.

[9] O. Legrani, O. Elmazria, S. Zhgoon, P. Pigeat and A. Bartasyte, "Packageless AlN/ZnO/Si Structure for SAW Devices Applications", IEEE Sensors Journal, vol. 13, p. 487-491, February 2013

[10] K. Tsubouchi, K. Sugai and N. Mikoshiba, "AlN material constants evaluation and SAW properties on A1N/A1₂0₃ and AlN/Si", IEEE Ultrason. Symp., pp.375–380, 1981.

[11] G. Carlotti, F. S. Hickernellh,. M. Liaw, L. Palmiergi, G. Socino and E. Verona, "The Elastic constants of sputtered aluminium Nitride Films", IEEE Ultrason. Symp., pp. 353–356, November 1995.

[12] G. Carlotti, G. Socino, A. Petri and E. Verona, "Acoustic investigation of the elastic properties of ZnO films", Appl. phys. Lett., vol. 51, pp. 1889–1891, October 1987.

Piezoelectric and Electroacoustic Properties of V-Doped and Ta-Doped AlN Thin Films

Enrique Iborra, Jimena Olivares, Marta Clement, Jose Capilla

GMME-CEMDATIC-ETSIT,
Universidad Politécnica de Madrid,
Madrid, SPAIN

Valeriy Felmetsger, Mikhail Mikhov

OEMGroup Inc.,
Gilbert, AZ, USA

Abstract— **In this paper we analyze the effects of doping AlN films with vanadium and tantalum to concentrations up to 6% atomic. The structure and composition of the new compounds are assessed as a function of the dopant concentration by x-ray diffraction (XRD), IR reflectance and Rutherford backscattering spectrometry (RBS). Test devices consisting on bulk acoustic wave resonators are used to assess the piezoelectric activity of the compounds as well as other material properties, such as the acoustic velocities and the piezoelectric constant. Films doped with vanadium show an overall worsening of their main properties for acoustics applications. Films doped with tantalum show variations in their wurtzite crystal structure that suggests that an improvement of the piezoelectric activity can be achieved as long as films exhibiting good crystal quality and homogeneous dipole orientation can be grown.**

Keywords—AlN doping; AlVN; AlTaN

I. INTRODUCTION

Aluminum nitride (AlN) is the preferred piezoelectric material for a broad range of thin film devices and applications requiring piezoelectric actuation, such as resonators for telecommunications RF filters, sensors, or micro-electromechanical systems. Due to its good piezoelectric properties and chemical stability, AlN is especially appropriate for operating in moderately harsh environments, such as relatively high temperatures or corrosive media. However, the increasingly demanding applications require the development of new piezoelectric materials with improved properties.

Since Akiyama [1] reported a very strong variation of the piezoelectric coefficient d_{33} when scandium (Sc) atoms were introduced in wurtzite AlN films, new compound materials based on AlN films doped with different elements have been investigated in order to develop new materials with improved piezo-acoustic properties. The addition of some chemical elements to polycrystalline AlN films has been reported to cause the deformation of their wurtzite structure and, hence, of their physical properties, which makes them suitable for some applications, such as hard coatings or electroacoustic devices. Boron, chromium, manganese, copper or scandium are some of the elements investigated to date. Not all of them provide improved properties; for example, boron-doped AlN films exhibit smaller electromechanical coupling factors in electroacoustic devices due to a decrease of the piezoelectric coefficients [2,3]. However, it has been verified that the addition of scandium produces a significant increase of the overall piezoelectric activity of the Al:Sc:N alloy [1], although other parameters, such the acoustic losses or the sound velocity, worsen [4]. Manganese and copper turn AlN into a magnetic material, but we have not found data reporting on its piezoelectric behavior [5,6]. Chromium and AlN alloys have been extensively studied because Al:Cr:N films exhibit interesting magnetic properties [7]. Regarding the piezoelectric properties, AlN films containing 6% Cr atoms exhibit an increased lattice parameter accompanied by a rise in the d_{33} piezoelectric coefficient; in contrast, the stiffness and, therefore, the sound velocity, decreases [8,9]. In a previous paper [10] we showed that doping AlN with Ti increased the lattice parameters, but some inhomogeneities appeared for doping levels above 4% atomic. In all cases, the piezoelectric response and the sound velocity decreased and the dielectric constant rose with Ti content. It is important to note that, whatever the effect of the dopant in the crystalline structure of AlN, the doped films have to fulfill the essential requisite of exhibiting a definite preferred crystalline orientation with all the dipoles pointing to the same direction in order to achieve a good piezoelectric activity. This requires a careful study of the deposition conditions of the new compound, which includes the influence of the nature of the substrate, its preconditioning, and the deposition parameters, which may vary compared to those required to grow highly oriented AlN films.

In this communication we investigate the effects of adding different amounts of vanadium and tantalum in the physical properties of the doped AlN compounds. These are deposited by co-sputtering a double coaxial target in alternate current configuration under the conditions that guarantee the best pure AlN films achievable in our equipment, which do not necessarily provide the best performing doped films. We carry out the assessment of the structural and piezoelectric properties of the doped films through Rutherford backscattering spectrometry (RBS), infrared transmission, and X-ray diffraction measurements, and frequency response of bulk acoustic wave (BAW) test resonators.

II. EXPERIMENTAL

A. Film deposition

Al:M:N (M=V, Ta) 1.1 μm-thick piezoelectric films were deposited on 150 mm-Si (100) wafers covered with a simple

acoustic reflector for the BAW test resonators used to assess the piezoelectric activity of the films. The reflector was composed of three layers of thermal SiO_2, aluminum (as low acoustic impedance film), and molybdenum (as high acoustic impedance film); their thicknesses were adjusted to achieve a resonant frequency of 3 GHz. The simulated acoustic transmittance at the resonant frequency was around -18 dB, which allowed accurately assessing the electromechanical coupling factor (k^2). The 100 nm-thick (110)-oriented Mo top layer of the reflector acted as the bottom electrode of the test devices. All the films were deposited in an Endeavor-AT cluster tool from OEM Group equipped with dual-target S-gun magnetrons [11].

The S-gun consists of two ring-shaped targets (diameters of 178 and 280 mm) mounted concentrically on the same vertical axis. The inner target is made of Al and the outer of V or Ta. Each target has its own magnetic array with opposite polarities. An alternating current power of 40 kHz applied between the two targets creates a plasma discharge at the conical face of each target. The power fed to each target can be adjusted separately by a power splitter module. Due to this dual-target arrangement, where each target alternates as a cathode and an anode, the ac powered S-gun is free from parasitic arcing and disappearing anode effects. This target configuration allows obtaining films with non-uniform composition in the radial direction, which are useful to study the variations of the properties as a function of the dopant content. Before the deposition of the $Al_{0.5-x}M_xN_{0.5}$ films, the Mo bottom electrode was treated with low energy Ar ions either in a separate RF (13.56 MHz) etch module, producing a capacitively coupled plasma, or in the deposition module (in-situ etch). Deposition processes were performed either without external heating (T<300°C) or at elevated temperatures (up to 400°C) using an external IR heater before or during deposition.

B. Film characterization

The composition of the Al:M:N films was assessed by RBS measurements. Fig. 1 shows the RBS spectra of two representative $Al_{0.5-x}M_xN_{0.5}$/Mo/Al/Mo/SiO_2/Si stacks with AlN films doped either with V or with Ta. We assumed that the N content in the films was around 50% in all cases, which was confirmed by RBS measurements. The experimental RBS spectra were fitted using SIMNRA simulation program to obtain the composition of the doped AlN layer. According to the fitting, the V and the Ta content varied between 3% and 6% atomic. RBS measurements also allowed deriving the thickness of the films assuming that the mass density did not vary significantly in the range of variation of doping.

Infrared reflection was measured with a Fourier transform infrared (FTIR) Nicolet 5-PC spectrophotometer using non-polarized light with an incident angle of 30º in the 400 cm^{-1}-4000 cm^{-1} range with a spectral resolution of 2 cm^{-1}. These spectra provide information about the chemical bonding configuration of the films and allow deducing their composition after calibrating the position of the A1(LO) band around 880 cm^{-1} with the RBS data. In previous works we related the ratio of the amplitudes A1(LO)/E1(LO) measured in pure AlN films to the presence of non-c-axis-oriented grains, which were associated to microcrystals with different polar orientation [12, 13]. For the doped films this correlation also applies. The absorption bands were fitted with lorentzian curves to accurately determine their position, amplitude and width.

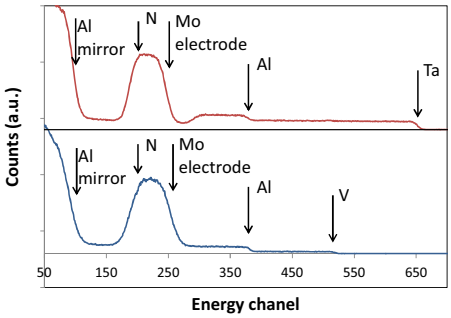

Figure 1. RBS spectra of AlVN and AlTaN representative films.

X-ray diffraction (XRD) patterns of the Al:M:N films were measured in conventional Bragg-Brentano geometry in a high intensity Supratech XPert MRD diffractometer between 2θ=10º and 2θ=80º using the Kα1,2 doublet of a β-filtered Cu anode radiation. Since all the samples were strongly c-axis oriented, the rocking curves (RC) around the (00·2) peak were also measured to assess the quality of the films through the value of their width at half maximum (FWHM).

The piezoelectric activity of the doped AlN films was assessed by measuring the electrical reflection coefficient (S_{11}) at frequencies ranging from 10 MHz to 10 GHz with an Agilent PNA N5230A network analyzer. The electrical impedance of the resonators, derived from S_{11}, was fitted with Mason's model to obtain accurate values of the material electromechanical coupling factor k_m^2. Due to the low value of the acoustic transmittance (-18 dB) the quality factor (Q) of the devices did not exceeded 20, which did not impede to achieve an accurate fitting of the impedance with frequency. Since the thickness of films, area of the resonator, dielectric constant (ε) and sound velocity (v_s) significantly influence the resonant frequency and the out-of-band response of the resonators, a careful assessment of all the geometrical dimensions of the devices was required to achieve accurate values of ε for each doped film. After the electrical characterization the thicknesses of the electrodes and the piezoelectric film were measured with a profilometer by patterning the AlN-doped films by wet etching in warm KOH using the top electrode as etching mask. The obtained values were in good agreement with those obtained from RBS measurements. The area of each device was also carefully measured with an optical microscope with accuracy better than 1% to overcome possible undercutting effects in the top electrode patterning. The method allows assessing the electro-acoustic properties of the doped-AlN films independently of the design of the test device.

III. Results and Discussion

A. Vanadium doped AlN films: AlVN

When part of the Al atoms in the AlN wurtzite structure are substituted by V atoms, the structure of the crystals changes as

a function of the V content. For low V contents the crystal structure remains being wurtzite, with slight changes in the lattice parameters. As the V content increases (above 7% atomic), the crystallinity is destroyed; the films turn from transparent to dark grey and become conductive and non-piezoelectric.

Figure 2 shows the XRD patterns of an Al:V:N layer along with that of a pure AlN film for comparison. The wurtzite structure characterized by a diffraction peak at 2θ=36º is clearly maintained in the doped layer but an additional peak at 2θ=37.52º appears. This suggests the formation of an additional phase, probably related with VN, which has the 111 XRD peak at that angle. The peaks labeled with an asterisk are the partially filtered Cuβ-components of the XRD tube.

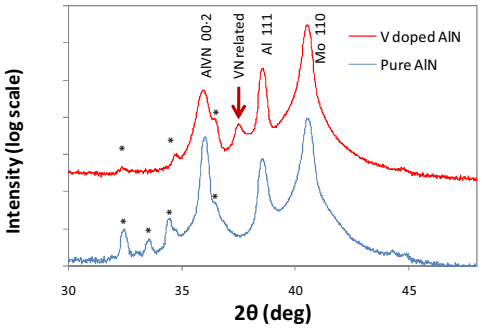

Figure 2. XRD pattern of (a) an AlVN film with a V content of 6.4% atomic and (b) a pure AlN film.

The c-parameter of the V-doped AlN films decreases from 5.02 A to 4.99 A in the composition range from 4.8% to 6.5% atomic, revealing is a very weak variation with the V content. This contrasts with the data from IR absorption that shows a shift of the LO mode to lower wavenumbers, which suggests an increase of the c-parameter of the wurtzite structure.

The electromechanical coupling factor, longitudinal acoustic velocity and dielectric constant are derived from the frequency response of the BAW devices. The best value of k_m^2 exhibited by the V-doped AlN films (2.5%) was achieved in the samples with the lowest V content (around 4.8% atomic); this value is far from the 6% routinely achieved in pure AlN films grown on identical structures. The acoustic velocity dropped from 11000 m·s^{-1} (corresponding to pure c-axis oriented AlN) to values below 9500 m·s^{-1}, as shown in figure 3.

In summary, doping AlN with V does not improve the material properties for electroacoustic devices in the range of doping studied. Both the acoustic velocity and the piezoelectric response decrease monotonously as the V content in the films increases; this is accompanied by an increase of more than 10% of the dielectric constant.

B. Tantalum doped AlN films: AlTaN

Figure 4 shows the XRD θ/2θ patterns AlN films doped with Ta contents ranging from 0% to 5% atomic. The angle of the 00·2 wurtzite reflection shifts towards lower values as the Ta content increases, which indicates an increase of the c lattice parameter.

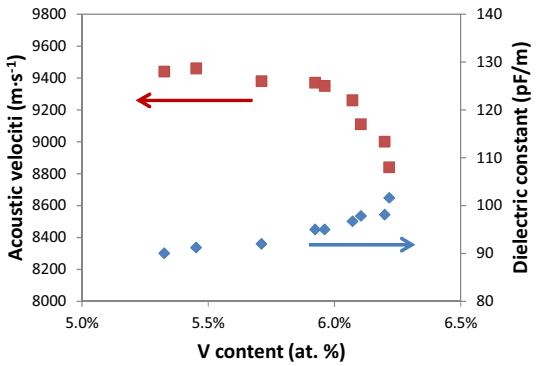

Figure 3. Acoustic velocity and dielectric constant as a function of the V content (atomic %)

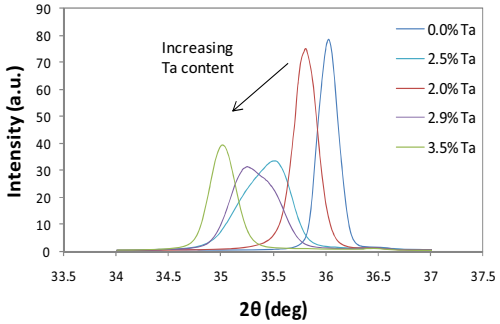

Figure 4. XRD pattern of AlTaN for various Ta contents.

It is worth noting that for intermediate Ta contents (3% and 3.2% at.) the XRD patterns show a double peak, which suggests the existence of two populations of grains with different crystal properties. This kind of inhomogeneity has also been observed in the electrical response of the test resonators that, aside from the expected main resonance around 2.8 GHz, also exhibit an additional peak at around 5 GHz, as figure 5 shows.

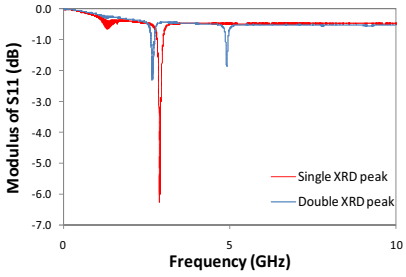

Figure 5. S11 vs frequency of two AlTaN films with and without double XRD 00·2 reflection.

The acoustic velocity and dielectric constant of the Ta-doped AlN films are represented in figure 6 as a function of the Ta content. Both tend to increase with the Ta content.

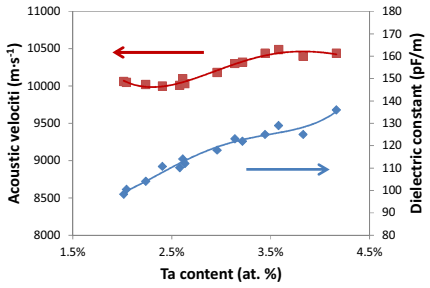

Figure 6. Acoustic velocity and dielectric constant as a functión of the Ta content (in atomic %)

Finally, the electromechanical coupling factor of Ta-doped AlN films drop dramatically from 6% to 0% as the Ta content increases. This reduction is accompanied by an significant increase of the ratio between the amplitudes of the E1(LO) and the A1(LO) modes that appear in the IR reflectance spectra, as shown in Figure 7. It has been reported in previous works [12,13] that this ratio increases significantly as the amount of grains with the c axis tilted with respect to the normal increases. This has been associated in turn to the presence of grains with opposite polarities, which accounts for the significant reduction of the piezoelectric activity.

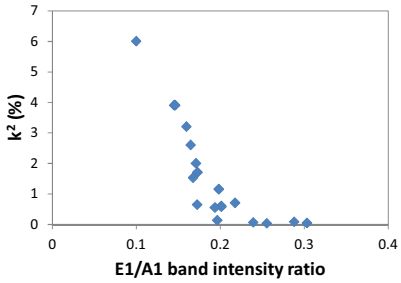

Figure 7. Electromechanical coupling factor as a function of intensity ratio of the E1(LO) and A1(LO) IR absorption bands

IV. Conclusions

We have investigated the influence of V and Ta doping on the properties of polycrystalline AlN sputtered films. In all V-doped films, new compounds with a different crystalline structure are observed. As the doping concentration increases, the relevant properties of the material for its use in electroacoustic devices worsen; the acoustic velocity and the coupling factor decrease, and the dielectric constant increases to 102 pF/m for doping levels around 6.2% atomic. At higher V contents the films become non-transparent and conductive. As for Ta doping, an increase of the *c* lattice parameter with the Ta content is observed, which suggests that an improved piezoelectric response could be achieved in this compound. However, this effect was not observed in BAW measurements that reveal, instead, a significant drop of the piezoelectric activity in most of the films. FTIR measurements reveal that this effect is very likely related to a poorly adjusted growth process (leading to grains with opposite polarities) more than to the effect of the Ta doping. Additionally, a lack of homogeneity in the crystal structure is observed at intermediate Ta content (2.5% to 3 % at.), where two kinds of compounds appear simultaneously in the films, giving rise to two resonances in BAW devices. As the Ta content increases, the sound velocity, after an initial drop, increases as well, but keeping always a value lower than that of pure AlN. The dielectric constant increases up to 140 pF/m with the Ta content. Despite the increase of the *c* lattice constant, the results so far do not allow drawing conclusions regarding the possible benefits of Ta doping. A significant improvement of the growth conditions is required in order to achieve films of better crystal quality that would allow assessing the actual effects of Ta doping.

Acknowledgment

This work was partially supported by the Ministerio de Economía y Competitividad del Gobierno de España through project MAT2010-18933.

References

[1] M. Akiyama, T. Kamohara, K. Kano, A. Teshigahara, Y. Takeuchi, and N. Kawahara, "Enhancement of piezoelectric response in scandium aluminum nitride alloy thin films prepared by dual reactive cosputtering", Adv. Mater., vol. 21, pp. 593–596, 2009.

[2] Ferenc Tasnádi, Igor A. Abrikosov, and Ilia Katardjiev, "Significant configurational dependence of the electromechanical coupling constant of B0.125Al0.875N", Appl. Phys. Lett., vol 94, 151911 (1-3), 2009.

[3] L. Liljeholm, M. Junaid, T. Kubart, J. Birch, L. Hultman, I. Katardjiev, "Synthesis and characterization of (0001)-textured wurtzite Al1-xBxN thin films", Surf. Coat. Technol., vol. 206, pp. 1033–1036, 2011.

[4] M. Moreira, J. Bjurstrom, I. Katarjev, and V. Yantchev, "Aluminum scandium nitride thin-film bulk acoustic resonators for wide band applications," Vacuum, vol. 86, pp. 23-26, 2011.

[5] Q.Y.Wu, Z. G. Huang, R. Wu, and L. J. Chen, "Cu-doped AlN: a dilute magnetic semiconductor free of magnetic cations from first-principles study", J. Phys.: Condens. Matter., vol.19, pp. 056209 (1-6), 2007.

[6] Yasushi Endo, Takanobu Sato, Ayumu Takita, Yoshio Kawamura, and Masahiko Yamamoto, "Magnetic, electrical properties, and structure of Cr–AlN and Mn–AlN thin films grown on Si substrates", IEEE Trans. Magnet., vol. 41, pp. 2718-2720, 2005.

[7] D. Kumar, J. Antifakos, M.G. Blamire, Z.H. Barber, "High Curie temperatures in ferromagnetic Cr-doped AlN thin films", Appl. Phys. Lett. Vol. 84, pp. 5004-5006, 2004.

[8] J. T. Luo, B. Fan, F. Zeng and F. Pan, "Influence of Cr-doping on microstructure and piezoelectric response of AlN films", J. Phys. D: Appl. Phys., vol. 42, pp. 235406 (1-6), 2009.

[9] V. V. Felmetsger and M. K. Mikhov, "Reactive magnetron sputtering of piezoelectric Cr-doped AlN thin films", 2011 IEEE International Ultrasonics Symposium Proceedings, pp. 835-839, 2011.

[10] E. Iborra, J. Capilla, J. Olivares, M. Clement, and V. Felmetsger, "Piezoelectric and electroacoustic properties of Ti-doped AlN thin films as a function of Ti content", 2012 IEEE International Ultrasonics Symposium Proceedings, pp., 2012.

[11] V. V. Felmetsger, P. N. Laptev, and S. M. Tanner, "Design, operation mode, and stress control capability of S-gun magnetron for ac reactive sputtering," Surf. Coat. Technol., vol. 204, pp. 840-844, 2009.

[12] E. Iborra, M. Clement, L. Vergara, A. Sanz, J. Olivares, and J. Sangrador, "Dependence of the IR reflectance LO absorption on the crystalline texture of AlN", Appl. Phys. Lett. Vol. 88, 231901, 2006.

[13] J. Olivares, S. González-Castilla, M. Clement, A. Sanz-Hervás, L. Vergara, J. Sangrador, E. Iborra, "Combined assessment of piezoelectric AlN films using X-ray diffraction, infrared absorption and atomic force microscopy", Diam. Rel. Mat. vol. 16, pp. 1421–1424, 2007.

Evaluation of the Acoustical Properties of Adhesive-free Dual Layer Piezoelectric PVDF Copolymer Transducer

Adit Decharat, Sanat Wagle, and Frank Melandsø
Department of Physics and Technology
The University of Tromsø
N-9073 Tromsø, Norway
adit.decharat@uit.no

***Abstract*—Dual layer piezoelectric transducer has been developed using an adhesive free process and characterized both experimentally and by FEM models. Our findings show an enhanced amplitude when both layers are used as a transceiver system for sufficiently large pulse width. The peak frequency obtained from Comsol modeling shows a good agreement with the experimental results.**

Keywords— Multilayer, PVDF, PEI, Ultrasonic measurements

I. Introduction

Piezo-electric transducers made from poly (vinylidenefluoride-co-trifluoroethylene) [P(VDF-TrFE)], are used in various nondestructive evaluation (NDE) and bio-medical imaging because of their broad band characteristics [1]-[5]. However, their mechanical coupling efficiency is relatively low compare to ceramic transducer. To overcome this drawback, multiple layer of piezoelectric copolymer transducer has been deployed to improve the overall performance. Conventionally, to fabricate multilayer polymer transducers from pre-polarized film, adhesive layers are used for increasing the number of layers, requiring a mechanically attaching process where the desired and a consistent thickness of each adhesive layer are difficult to achieve. Such condition, consequently, will cause a reduction of the overall acoustic response signal [4]. As far as we know, only one group has previously produced an adhesive-free multilayer transducer with few publications [5]. Therefore, there is a need for comparative evaluations on the modeling with experimental result to provide better understanding of such transducer physics, consequently improving in transducer designing. In this work, we have implemented an adhesive-free dual layer P(VDF-TrFE) ultrasonic transducer and compared our experimental results with numerical models.

II. Transducer Development and Characterization

In this section we will describe the transducer layout and the electrode structure which are common for the experimental and numerical investigations.

The proposed dual layer piezoelectric transducer was produced from two layers of P(VDF-TrFE) films (thickness 20 μm each) with intermediate conductive electrodes with thicknesses around 1 μm. The layered structure which we will refer to as a stack, are sitting on the top Polyethylenimine (PEI) backing substrate with thickness around 850 μm as shown by the schematic drawing in Fig. 1 (a). As illustrated in this figure, the acoustic wave generated by the piezoelectric film will travel down into the PEI substrate and become totally reflected when reaching the PEI/air interface. This first reflection is then detected and converted to electric signal (so-called 1st acoustic response signal) by the same piezoelectric film. To generate the wide band acoustical wave, the piezoelectric film was excited by an ultra-wide band (UWB) signal described by the 1st derivative of the Gaussian pulse expressed as

$$V(t) = \left[\frac{t - t_0}{\sigma}\right] e^{-\frac{(t-t_0)^2}{2\sigma^2}} \quad (1)$$

In this equation t_0 will be the pulse firing time while σ is the pulse width of the Gaussian distribution.

To evaluate the response from the transducer, two different modes were investigated. First, we consider sending and receiving from only a single layer (i.e. upper or lower) which we will refer to as the single layer modus. For example, if the

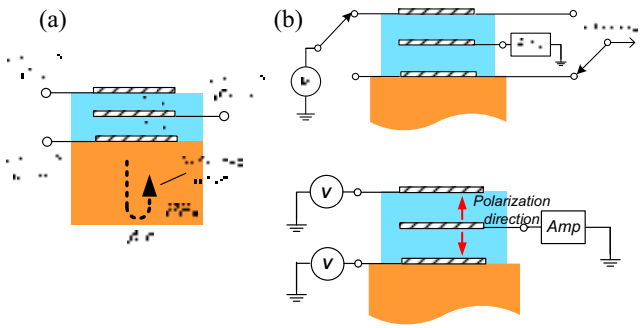

Fig. 1 Schematic drawing of transducer layout (a) and transducer evaluation mode (b).

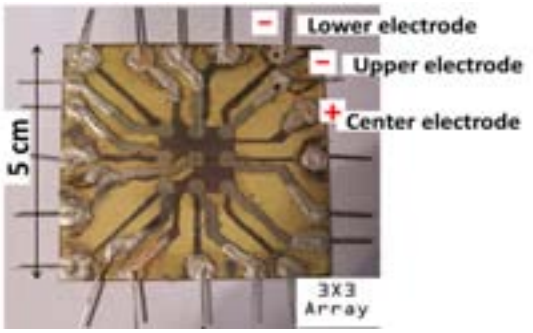

Fig. 2 Image of the prototype transducer.

upper layer is excited in single layer modus, the upper electrode will be driven by the potential given by Eq. (1), while the current is collected on the middle electrode as shown in Fig. 1(b) (Top). The lower electrode is left floating, to minimize the influence from layer that is not active.

For the second mode that we will denote as the dual layer modus, both the upper and lower electrodes are driven with the same UWB potential, while the current is detected by the middle electrode as shown in Fig 1(b) (Bottom). A number of different pulse widths σ were used in the investigation, ranging from 3.6 ns to 15 ns with a pulse amplitude of 5 Vp-p.

A. Transducer implementation

For the transducers, the P(VDF-TrFE) film was made from the fluid phase by mixing P(VDF-TrFE) powder (77:23) (in molar ration) with an appropriate amount of solvent. This solution was mixed with an ultrasonic disperser to obtain a complete dissolving of the powder**.** For the transducer conductive layer, inkjet-printable silver (Ag) ink from Sigma Aldrich was employed. The fabrication was initiated by preparing a PEI substrate with size of 5 × 5 cm. A layer of Ag ink acting as the lower electrode, was then deposited on the PEI surface by spin coating and sintered at 130 ℃ for 2 hours. The electrode was then patterned by wet chemical etching to obtain the desired electrode diameter (3 mm). The 1st layer of P(VDF-TrFE) solution was spin coated onto of the patterned electrode and degassed in 1 mbar vacuum atmosphere to vaporize the solvent. After that the sample was annealed at a temperature of 130 ℃ for 2 hours. The previous mentioned processes were then repeated to make the middle electrode, the upper P(VDF-TrFE), and the upper electrode. Then in the final step, electrical connection out of the transducer are made easy by connecting pins to the transducer edge by conductive epoxy. An image of a complete is shown in Fig. 2.

To make the P(VDF-TrFE) films piezoelectric, the sensors were polarized by applying a DC high voltage (1580 KV) between the electrodes with sample heated temperature of 100 ℃. The voltage was kept constant for 30 mins after reducing the temperature to room temperature. Dual layer transducer was polarized in opposite direction to avoid the cancellation of the acoustical signal.

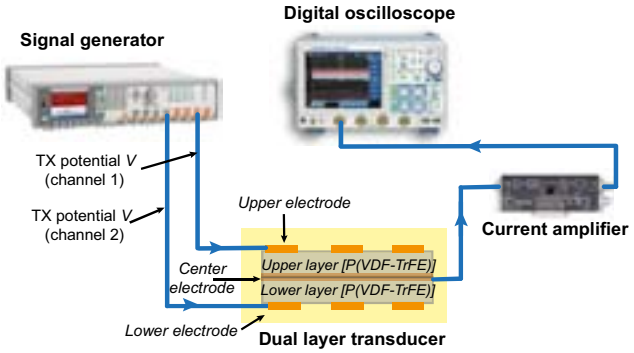

Fig. 3 Experimental setup for ultrasonic characterization.

B. Experimental Characterization

The acoustical characterization system consists of a two channel arbitrary wave generator (Agilent 81150A), a current amplifier (FEMTO DHPCA-100) and a digital oscilloscope (Yodogawa DLM 6054) as shown in Fig. 3. To generate the transmitted first derivative Gaussian signal, the time domain pulse function was specified in a Matlab program, and then uploaded on to the wave generator memory. The acoustic response signal from piezoelectric film was amplified by a low impedance current amplifier, which converts the current into output potential. Finally, this potential signal was sampled by oscilloscope capable of digitizing with up to 12-bit accuracy in high resolution.

C. Numerical Characterization

A two dimensional axisymmetric numerical simulation was developed as a time domain study in the commercial software Comsol Multiphysics. This software, which uses a Finite Element Method (FEM) to solve partial differential equations, has also previously been used to solve transducer models [6]. For our model, the elastic and piezoelectric materials are represented as linear plain strain models with loss factors 0.2 and 0.02 for PVDF and PEI, respectively, approximated by a Rayleigh damping model. A rectangular mesh with an appropriate size was chosen to solve the model. The material constant for PVDF, PEI and Silver was taken from the Comsol database and from Refs. 6 and 7.

III. Results and Discussion

In this section we have compared the experimental and numerical results, and focused on the first acoustic reflection from the backside of the PEI substrate, The acoustic response signal (ARS) from this reflection for excitation pulses with pulse widths σ=15 ns and 3.6 ns was obtained both in the experiment and in Comsol Multiphysics as shown in Fig.4. For the 15 ns pulse, the peak-to-peak voltage amplitude was found to be significant higher both in the expeiment [upper Fig. 4 (a)] and in the FEM model [upper Fig. 4(b)], when the transducer was operated in dual layer modus compared to single layer modus. However, for a 3.6 ns pulse, the opposite trend was observed as shown in the lower figures. These signals may also be transfered to the frequency domain using a Fourier transformation, yielding the responses shown in Fig. 5

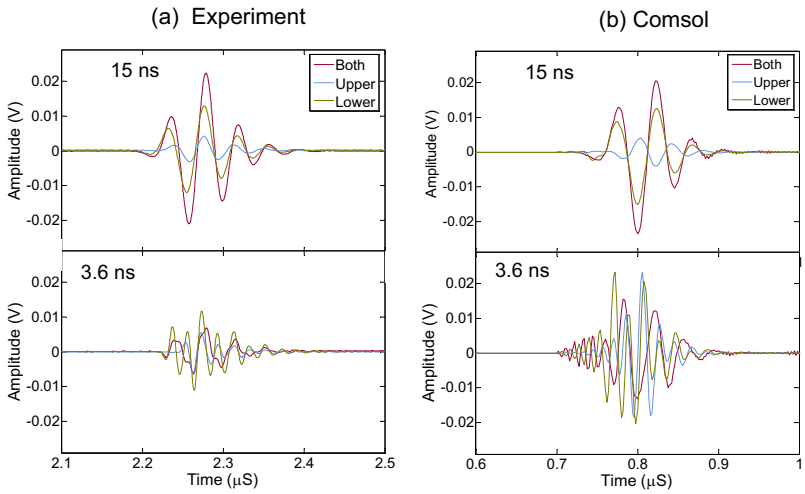

Fig. 4 The 1st acoustic response signal from experiment (a) and Comsol model (b) with pulse width 15 and 3.6 ns excitation.

(a) and (b). Here, both the experimental and numerical results yield maximum responses for the 15 ns pulse around 24 MHz. However, as the excitation pulse was shorten to 3.6 ns, the bandwidth was increased and the maximum response was splited up. The maximum response then occured around 27 MHz for the dual layer modus, and around 50 MHz for the single layer modus.

Variation in the peak-to-peak value for the ARS amplitude as a function of the pulse width was compared in Fig. 6 (a) for the experimental and numerical results. Here, we observed that the peak-to-peak amplitude obtained from the Comsol modeling was significantly higher than for the experimental results. However, both results showed similar trend in terms of the rise and fall of the ARS amplitude. Possible reasons for the observed amplitude variation can be differences in the used damping parameter of P(VDF-TrFE) and/or variation in the area of the active element for the experiment and numerical model. Moreover, a systematic study for many pulse widths has shown that the dual modus obtain the highest response for $\sigma \gtrsim 8$ ns. This behavior is most likely due to the differences in resonance frequency of the single and dual layer systems, suggesting a dual layer response frequency at around 50% of the single layer value. The estimated resonance frequencies of P(VDF-TrFE) films with thicknesses 20 and 40 μm are 15 and 30 MHz, respectively (assumng a $\lambda/4$ resonance due to rigidity of the material PEI compare to air and epoxy backing [2,3]). The speed of sound in P(VDF-TrFE) was taken as 2400 m/s in the estimate [2]. For our case, we observe that maximum amplitude of ARS for the dual layer modus was around 26 MHz and 50 MHz for the single layer modus. This indicates that the single and dual layer resonances of the developed transducer are significantly higher than $\lambda/4$, in fact closer to $\lambda/2$ resonance modes.

The variation of peak frequency of the ARS as a function of the pulse width was compared in Fig. 6 (b) for both experimental and numerical operation modes. Here, we

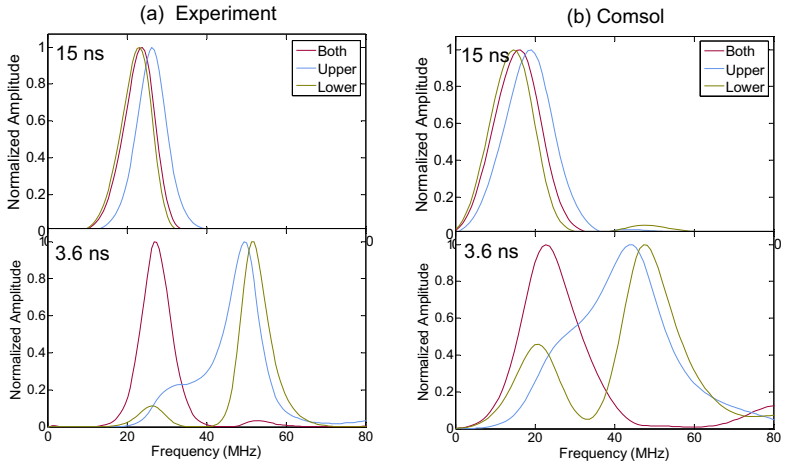

Fig. 5 Corresponding FFT of ARS from experiment (a) and Comsol model (b) with pulse width 15 and 3.6 ns excitation.

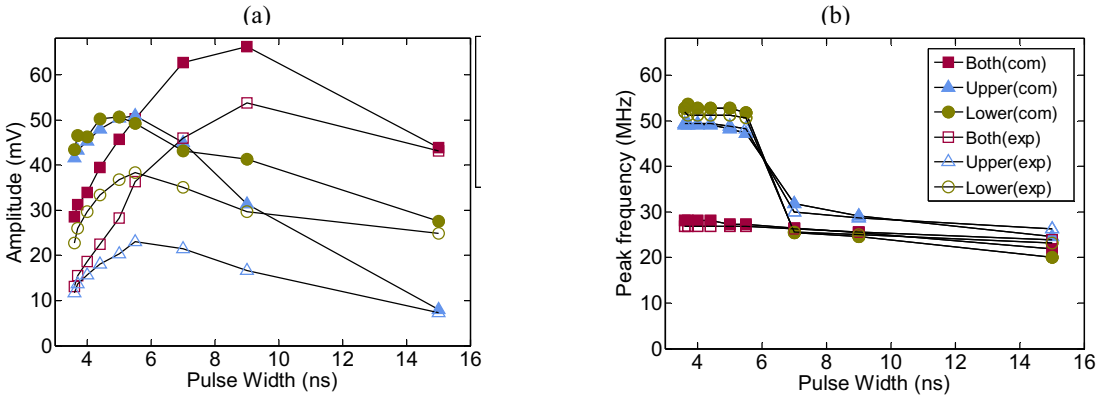

Fig. 6 (a) Relation between peak-to-peak amplitude of ARS and pulse width excitation. (b) Relation between peak frequency of ARS and various pulse width excitation. (Legends are same for fig. (a) and (b))

observed that the peak frequency obtained from Comsol modeling showed good agreement with the experimental results.

Previously, multilayer transducers produced from pre-polarized film with adhesive layers showed an increase in the sensitivity by 2.1 times (about 30 % lower than theoretically expected) when three layers of P(VDF-TrFE) were stacked and by 5 times when seven layers of P(VDF-TrFE) were stacked [4]. The dual layer transducer produced from fluid phase also showed the increase in the efficiency of the transduce [5]. The present dual transducer also showed higher efficiency (i.e. more than twice) when input pulse frequency was near to resonance frequency of the transducer.

IV. Conclusion

Adhesive free dual-layer ultrasonic transducer of P(VDF-TrFE) copolymer was developed by depositing layer by layer on the PEI polymer with the combination of different processing method from the fluid phase. The transducer was acoustically characterized by pulse/echo ultrasonic measurements and FEM models. The main findings from our study are the following:

(1) The amplitude of the acoustic response signal was higher, when transducer was operated in dual layer modus for the larger pulse widths.

(2) The frequency of the maximum amplitude of the dual layer modus was around 26 MHz and 50 MHz for single layer modus.

(3) The amplitude of the acoustic response signal shows similar trend (for rise and fall computations) but are found larger in the Comsol model than in the experimental results.

(4) The peak frequency obtained from Comsol modeling shows good agreement to experimental results.

Acknowledgment

This work was supported by The Research Council of Norway through the project ‘‘Sensors for oil and gas industry’’.

References

[1] K. Kimura, H. Ohigashi, “Generation of very high frequency ultrasonic wave using thin films of vinylidene fluoride trifluroethylene copolymer”, J. Appl. Phys., vol. 61, pp. 4749-4734, 1987.

[2] F. S. Foster, K. A. Harasiewicz, M. D. Sherar, “A history of medical and biological imaging with polyvinylidene fluoride (PVDF) transducers”, IEEE Trans. Ultrason., Ferroelect., Freq. Contr., vol. 47(6), pp. 1363 - 1371, 2000

[3] L.F. Brown, R.L. Carlson, J.M. Sempsort, “Spin-Cast P(VDF-TrFE) films for high performance medical ultrasound transducers”, Proc. Of 1997 IEEE Ultrasonics Symposium pp.1725-1727, 2007.

[4] Q. Zhang , P. A. Lewin and P. E. Bloomfield “PVDF transducers - A performance comparison of single layer and multilayer structures”, IEEE Trans. Ultrason., Ferroelect., Freq. Contr., vol. 44, pp.1148 - 1156, 1997.

[5] T. Lilliehorn, T. Blom, U. Simu, S. Johansson, M. Nilsson, M. Almqvist, “Multilayer piezoelectric copolymer transducers”, Proc. of 2005 IEEE Ultrasonics Symposium, vol. 3 pp. 1618 – 1620, 2005.

[6] E. Brodal, F. Melandsø, S. Jacobson, “Performance of an ultrasonic imaging system based on 45-MHz linear PVDF transducer array: A numerical study”, Advances in Acoustics and Vibration, Article ID 984596, doi: 10.1155/2011/984596, 15 pages, 2011.

[7] M. Fukuhara, “ Temperature dependency of elastic moduli and internal dilational and shear friction of Polyetherimide ”, J. of Poly. Sci., vol. 90, pp. 759-764, 2003.

Software Defined Radio for Passive Sensor Interrogation

J.R. Humphries and D.C. Malocha
Department of Electrical Engineering and Computer Science
University of Central Florida, Orlando, FL. 32816-2450
James.Humphries@knights.ucf.edu

***Abstract*—The software defined radio (SDR) provides a unique platform to interrogate passive, wireless sensors. The SDR platform defines many radio functions in software, rather than hardware. This allows for a very versatile interrogation platform that can be quickly reconfigured for diverse scenarios. This paper investigates the Universal Software Radio Peripheral (USRP), a commercial SDR developed by Ettus Research™, to determine its viability to interrogate passive, wireless sensors. In particular, the N200 USRP and the WBX daughterboard are considered because they allow for the greatest possible bandwidth for this platform (40MHz) and frequency tuning that is ideal for surface acoustic wave (SAW) sensor interrogation (50MHz - 2.2GHz).**

In the default operation mode, the USRP continuously streams data to and from the host computer. The host computer generates samples for transmission and processes any received samples. Synchronization of the transmit and receive chains becomes difficult due to latency in the communication medium (USB or Ethernet) between the host and USRP. While this mode is sufficient for most narrowband applications, wideband applications are more difficult to achieve because of the high sampling rates required (even in a baseband system such as the USRP). A prototype transceiver (passive tag reader) is developed by modifying the N200 FPGA to introduce new functionality to the USRP. These modifications include a custom interrogation signal generator (linear chirp) and triggering of the receiver based on the transmission state and desired listening time. These modifications are discussed and the modified transmit and receive characteristics are analyzed. Finally, a passive, wireless SAW OFC sensor is interrogated to demonstrate performance as a passive sensor transceiver.

I. Introduction

The Universal Software Radio Peripheral (USRP) is an interesting platform for a variety of wireless applications. Developed by Ettus Research™, the USRP is a versatile software defined radio (SDR) platform that can be reconfigured easily using the USRP Hardware Drivers (UHD) and software libraries such as GNU Radio. The transceiver daughterboards (RF front-end electronics) are also programmable (gain, center frequency, and port configuration) and swappable, giving the end user many options for RF characteristics.

The software radio approach has allowed the USRP to adapt to many scenarios including passive and active RADAR, cognitive radio, and OFDM [1]–[4]. Instead of an application specific design for the transceiver system, the USRP and baseband signaling approach grants the end user the ability to define the radio design using software. This approach gives access to rapid prototyping of radio systems design by quickly reconfiguring DSP, center frequencies, and sampling rates, among other specifications.

While some work has been accomplished using the USRP for RFID purposes [5], [6], little research has investigated the USRP as a platform to interrogate passive, wireless sensors. This project demonstrates modifications to the USRP which allow it to achieve the goal of communicating with passive surface acoustic wave (SAW) sensors. These functionalities are accomplished by modifying the FPGA design to introduce new functionality in the transmit and receive DSP chains. A custom chirp generator replaces the default transmit chain while a new module is implemented to synchronize timing between the transmit and receive states. These modifications are discussed and characterized in the following sections.

II. USRP and Experimental Setup

This section outlines the USRP and host computer setup that was used for this project. While many configurations are possible, the purpose of this section is to document a successful setup for the USRP platform.

A. USRP

The USRP chosen for this project is the N200 paired with the WBX daughterboard. The N (networked) series of the USRP, intended for high performance applications, is the fastest USRP in terms of sampling rates. The WBX covers this project's frequency range of interest (50MHz-2.2GHz) and has good output power (+20dBm). A brief overview of the USRP system specifications are given in Table I.

B. Host Computer and Software

The host computer used in this experiment is critical for processing high sample rates. The most important components for the host are processing speed and main memory, which prevents Ethernet packet loss. For this project, a computer was selected that utilizes a dual-core, 2.8 GHz processor with 4GB of memory and runs Ubuntu Linux, version 12.04.

Some combinations of Xilinx, FPGA source code, or UHD versions may limit performance or operation of the USRP. Xilinx 12.1 is used to build the FPGA code for the N200. Other versions of Xilinx are known to cause compatibility issues with the N200 FPGA code and can prevent the build and synthesize routines from completing efficiently. The UHD version is UHD_003.005.001-25-ge134b863. Additionally, the version of GNU Radio is 3.6.0.

TABLE I
SELECTED SPECIFICATIONS OF THE N200 USRP AND WBX DAUGHTERBOARD.

N200 USRP	
Host Interface	Gigabit Ethernet
FPGA	Xilinx Spartan 3A-DSP 1800
ADC / DAC	100 / 400 MSPS
WBX Daughterboard	
Type	Full Duplex Transceiver
Frequency Range	50MHz - 2.2GHz
Bandwidth	40MHz
Noise Figure	5-10dB
Power Output	20 dBm

III. USRP FPGA MODIFICATIONS

This section details the requirements for SAW sensor interrogation and the modifications required to achieve desired performance requirements. A custom chirp generator is implemented to replace the default transmit chain in the FPGA while another module is implemented in the receiver to synchronize with the transmit chirp. Planned updates are also discussed that will further improve the performance of the USRP.

A. Sensor Interrogation Requirements

The planned use of this transceiver is to interrogate passive, wireless SAW OFC sensors [7]. The system is based on a synchronous correlator approach using a pulsed interrogation signal [8]. The interrogator must capture the reflected signal from the target sensor and transfer the data to the host computer for post processing and data extraction. A SAW OFC sensor requires both frequency and time diversity. This leads to wideband SAW sensors (>20MHz) and time responses ranging between 1-10μs. The transmit signal must not overlap the sensor response, so the signal must be shorter than the SAW delay time. With these considerations in mind, modifications to the USRP FPGA design were implemented to transmit a 1μs linear chirp, set a listen time of 10μs, and synchronize the transmit and receive chains.

B. Modified FPGA Design

The FPGA source code is provided by Ettus and the modifications were integrated into the standard code. The existing transmit chain was removed completely since streaming TX samples are not being used and to reduce FPGA resource usage. In place of the transmit chain, a custom chirp generation module was added with outputs directly to the DAC's. Instead of replacing the whole receive chain as well, a custom module was inserted after the DDC to control the receive data flow.

1) Transmitter: A custom chirp generator was implemented to transmit a chirp of a user defined time length and bandwidth. A MATLAB script was written that allows the user to specify these parameters. The script then calculates the I and Q samples required for each clock cycle of the FPGA (assuming a 100MHz clock). Once the samples have been calculated, the script outputs the Verilog code to generate the module. The samples are output to the DAC's on the USRP in two's complement binary format.

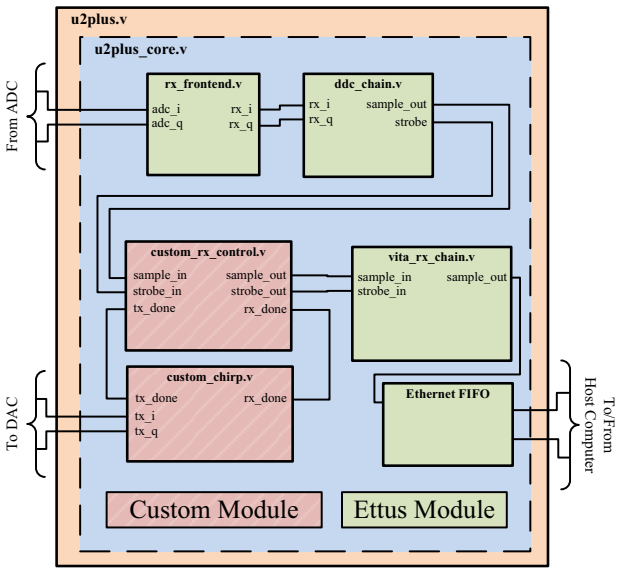

Fig. 1. Simplified block diagram of the modified FPGA design. The existing (Ettus) transmit chain was replaced by a custom chirp generator. A custom module was inserted in the receive chain to synchronize the start of the listen time with completion of transmitted chirp.

For this project, a 10MHz chirp with time length of 1μs was chosen. It is possible to generate a 50MHz bandwidth chirp in this configuration, but due to the limited sampling rate of the streaming receiver (25 MSPS), much of the chirp would be truncated from the received signal. Fig. 2 shows the I/Q samples generated for this signal.

The programmed chirp was output directly to a spectrum

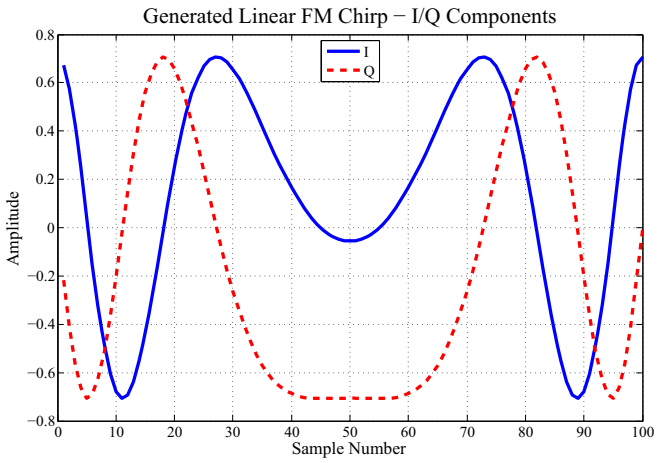

Fig. 2. A 2D representation of the generated I/Q samples for the linear FM chirp. The samples are generated at baseband and shifted up in frequency by the daughterboard. These samples are converted to binary and output directly to the DAC's.

TABLE II
CONFIGURATION OF THE USRP RECEIVE CHAIN.

USRP Receiver Configuration	
Sampling Rate	25 MSPS
T_{max} (Listen Time)	10μs
Samples per Sweep (N)	250
Δt (Resolution)	40ns
F_{max}	25MHz
Δf (Resolution)	100kHz

analyzer to compare with the predicted frequency spectrum of the signal. Fig. 3 compares the measured frequency spectrum with the predicted frequency spectrum of the generated signal. As seen in the figure, the actual transmitted signal matches well with the predicted response.

2) Receiver: A custom module was inserted between the DDC and the VITA (packet formatting) modules in the default design. Fig. 1 shows the location of this custom module (custom_rx_control.v). This module only allows samples to pass through after the transmission has completed and after a user set delay. The delay was set for 1.5μs to allow for chirp roll-off and to allow bad samples to propagate through the FPGA that were present before transmission. This module passes the strobe signal from the DDC to indicate that the output data to the VITA module is good. Fig. 4 shows an oscilloscope plot which illustrates the chirp and listening times that have been programmed. Additionally, the receiver configuration is shown in Table II. The sampling rate is currently limited by the Ethernet bus due to the constant streaming method that the default USRP configuration uses.

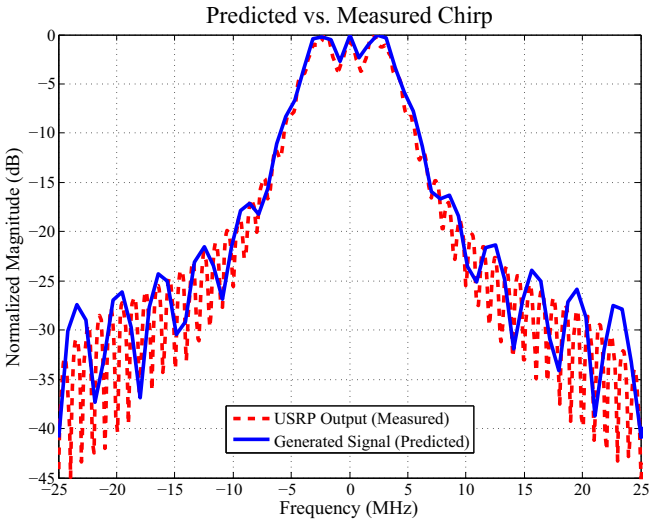

Fig. 3. Plot comparing the chirp as measured on a spectrum analyzer with the predicted frequency spectrum of the generated samples. The output at 915MHz is compared with the predicted baseband spectrum.

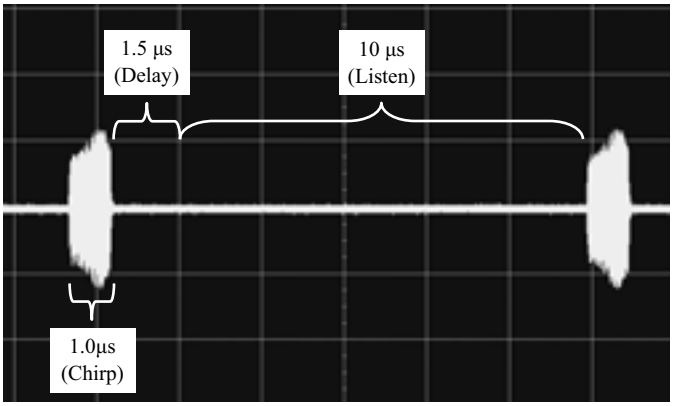

Fig. 4. Oscilloscope plot showing the chirp and listen times programmed on the N200 FPGA. Each interrogation cycle takes approximately 12.5μs to complete.

C. Planned Updates to USRP Modification

Future updates are planned to improve the functionality of the USRP as a passive sensor interrogator. These updates include improvements to the FPGA code design, better integration with the UHD, and external hardware components to improve TX/RX isolation and TX power output.

Ideally, the FPGA chirp generator would allow the user to program chirp length and chirp bandwidth. The current configuration does not allow for the chirp to be reprogrammed on the fly. Integration with the UHD drivers would allow the user programmed information to be set in the FPGA and would give run-time reconfiguration abilities.

External hardware components can be integrated with the USRP using the available MICTOR connector on the USRP mainboard. The current purpose of this connector is to connect a logic analyzer to check the FPGA logic functionality. Bypassing the current functionality would allow, for example, external TX and RX switches to be incorporated and controlled by the FPGA. This would reduce TX leakage into the RX front-end and improve extraction of sensor information. These future improvements will give a more robust transceiver that can be more easily configured for a variety of sensor designs.

IV. USRP PROTOTYPE TRANSCEIVER CHARACTERIZATION

Testing of the prototype transceiver is presented in this section. First, a wideband SAW filter was placed in-line between the TX and RX ports to test the chirp deconvolution. Finally, a passive SAW sensor is interrogated and correlated with its matched filter at 915MHz.

A. Chirp Deconvolution Through SAW Filter

A wired test was configured to test the process of deconvolving the transmitted chirp on the received signals. A wideband SAW filter was placed in-line between the transmit port and receive port on the USRP. The bandwidth of the filter is much

greater than the bandwidth of the transmitted chirp to ensure little distortion over the chirp passband.

A chirp was transmitted and 250 samples (10μs) were recorded. The chirp samples that were generated for transmission were used as the transmit signal to deconvolve and were zero padded and decimated to match the received sample number and sample rate. Fig. 5 shows the time correlation of this test. Accounting for the programmed delay on the FPGA, the time of the correlated pulse in Fig. 5 corresponds to the designed time delay of the SAW filter.

B. Passive SAW Sensor Interrogation

Characterization of the prototype system was concluded by interrogating a passive, wireless SAW OFC strain sensor at 915MHz. A single sensor is attached to a PCB dipole antenna of approximately 2dBi gain. The chirp signal is broadcast and the return signal is recorded for 10μs. The SAW delay is approximately 3μs when the system delay is taken into account.

After the samples have been saved on the host computer, the transmitted chirp is deconvolved and the sensor response is correlated with its matched filter. In this experiment, the matched filter contains only one OFC chip since the current receiver bandwidth is not large enough to capture the entire sensor spectrum. The sensor time response, frequency response, and demodulated time correlation is seen in Fig. 6. The sensor response was successfully correlated with its matched filter. Future improvements to the FPGA design will allow wider bandwidths to be utilized to improve overall sensor response with wideband designs, such as OFC.

V. Conclusion

This paper has presented the USRP as a viable platform for passive, wireless sensor interrogation. The versatility of the software radio approach allows for quick reconfiguration of many of the interrogator functions. An approach to redesign selected FPGA functions on the USRP was discussed and the modifications were detailed. The characteristics of the transmitter and receiver were shown and match well with the expected functionality. The transmitted linear FM chirp can be deconvolved using the generated signal components, which was demonstrated through a wideband SAW filter with known delay. Finally, the modified USRP was successfully demonstrated by interrogating a 915MHz, wireless SAW OFC sensor. These modifications have shown that the USRP can be adapted to function as a passive sensor interrogator platform.

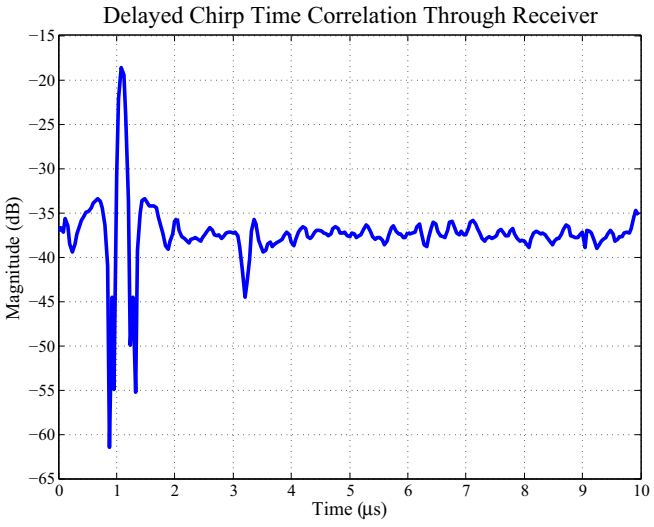

Fig. 5. Time correlation of the transmitted chirp signal through a wideband SAW filter at 915MHz. The correlation time matches the expected filter delay time of approximately 1μs when the system delay is taken into account.

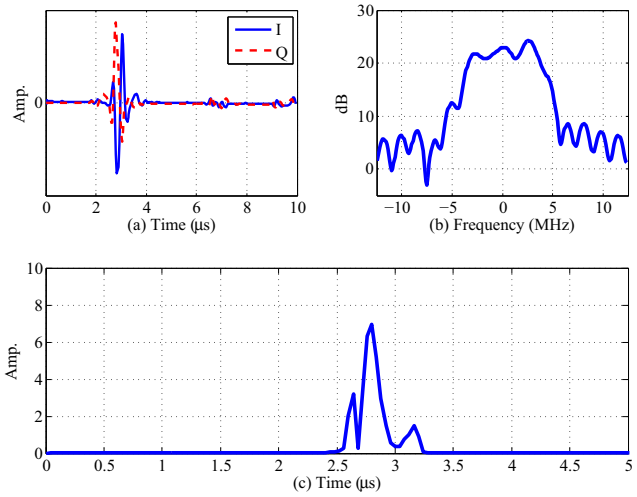

Fig. 6. (a) Received sensor response after interrogation from the transmitted chirp. (b) Frequency spectrum of the received signal. (c) Demodulated time correlation of the sensor with its matched filter.

References

[1] S. Heunis, Y. Paichard, and M. Inggs, "Passive radar using a software-defined radio platform and opensource software tools," in *Radar Conference (RADAR), 2011 IEEE*, 2011, pp. 879–884.

[2] A. Prabaswara, A. Munir, and A. Suksmono, "GNU radio based software-defined FMCW radar for weather surveillance application," in *Telecommunication Systems, Services, and Applications (TSSA), 2011 6th International Conference on*, 2011, pp. 227–230.

[3] A. Mate, K.-H. Lee, and I.-T. Lu, "Spectrum sensing based on time covariance matrix using gnu radio and usrp for cognitive radio," in *Systems, Applications and Technology Conference (LISAT), 2011 IEEE Long Island*, 2011, pp. 1–6.

[4] A. Marwanto, M. Sarijari, N. Fisal, S. K. S. Yusof, and R. Rashid, "Experimental study of OFDM implementation utilizing GNU radio and USRP - SDR," in *Communications (MICC), 2009 IEEE 9th Malaysia International Conference on*, 2009, pp. 132–135.

[5] C. Valenta and G. Durgin, "R.E.S.T. - A flexible, semi-passive platform for developing RFID technologies," in *Sensors, 2012 IEEE*, 2012, pp. 1–4.

[6] M. Buettner and D. Wetherall, "A software radio-based UHF RFID reader for PHY/MAC experimentation," in *RFID (RFID), 2011 IEEE International Conference on*, 2011, pp. 134–141.

[7] D. Malocha, D. Puccio, and D. Gallagher, "Orthogonal frequency coding for SAW device applications," in *Ultrasonics Symposium, 2004 IEEE*, vol. 2, 2004, pp. 1082–1085 Vol.2.

[8] N. Kozlovski, D. Malocha, and A. Weeks, "A 915 mhz saw sensor correlator system," *Sensors Journal, IEEE*, vol. 11, no. 12, pp. 3426–3432, 2011.

Induced Surface Roughness to Promote the Growth of Tilted-AlN Films for Shear Mode Resonators

M. DeMiguel-Ramos, M. Clement, J. Olivares, J. Capilla, J. Sangrador, E. Iborra
GMME-CEMDATIC, ETSI de Telecomunicación, Universidad Politécnica de Madrid, Madrid, Spain.
mmramos@etsit.upm.es

***Abstract*— Two methods currently used to induce surface roughness that promotes the growth of AlN tilted grains to fabricate shear mode resonators have been investigated. The first one involves the use of a rough substrate to provide tilted facets on which the AlN grains will grow with a certain angle. The second method is based on using a thin non-piezoelectric AlN seed layer that exhibits high populations of {10·3} and {10·2} planes. The influence of the power applied to the Al target and the total gas pressure during the deposition process of the AlN seed layer has been studied and correlated with the k^2_{shear} of the resonators. The best fabricated devices show a shear mode resonance frequency at around 1.45 GHz, a k^2_{shear} up to 3.64% and a Q_{shear} above 230 when operating in air, which reduces to 108 when operating in liquid.**

Seed layer; shear mode resonator; AlN; tilted grains

I. INTRODUCTION

A serious drawback of biochemical sensors based on piezoelectric resonators is the requirement of operating in liquid environments. This can be overcome by exciting shear modes that exhibit less attenuation in liquid media than longitudinal modes. Quartz has been widely used as piezoelectric material to manufacture resonators capable of operating in liquid media, because of its natural capacity to resonate in shear mode [1], [2]. Nevertheless, the difficulties encountered in the fabrication and integration of very thin crystals for operating in the GHz frequency range have boosted the search of alternative piezoelectric materials. In the last years, AlN has revealed itself as a great substitute thanks to its high acoustic velocity [3] and piezoelectric coefficients [4], and the possibility of sputtering the high quality AlN thin films required for high frequency applications [5].

To obtain AlN polycrystalline thin films with good piezoelectric performance, it is necessary that all the grains have the c-axis parallel to a given direction and the same crystal polarity [6]. This is commonly achieved by giving enough energy to the adatoms on the growing film surface, which favors the preferential growth of the {00·2} planes parallel to the surface of the substrate [7], [8]. Under these conditions, AlN microcrystals always grow normal to the surface where they are being sputtered, even if it is vertical [9]. Shear mode resonances can be achieved by transverse excitation (by means of the d_{51} piezoelectric coefficient) in AlN with microcrystals exhibiting both homogenous tilt and polar orientation. Among the different techniques developed to achieve such tilted films [10–12], the most effective is the one based on inducing a rough structure on the surface just beneath the AlN active layer [11]. On this kind of surface, if the flux of Al atoms impacting on the different facets is uniform, the grains of AlN will grow perpendicular to the facets in different directions, therefore originating a randomly-oriented AlN layer without piezoelectric response. However, if an impinging direction is encouraged (e.g. by displacing the substrate with respect to the center of the target), the grains will grow faster on the facets most exposed to the atom flux and their mean tilt angle, fixed by those planes, will be more uniform [12]. As shown in figure 1, the best possible structure to accomplish the tilted AlN grains would be a sawtooth profile of microscopic dimensions, which is unfortunately very hard to fabricate. Instead, a layer with controlled roughness is commonly used [11], [12].

Two possible approaches to control the roughness of this layer have been proposed. The first one is based on the control of the last layer of the substrate, usually the bottom electrode if it is a resonator, or the roughness of the layer just below, usually the uppermost layer of an acoustic reflector. The other method involves using a polycrystalline film, acting as seed layer, with a controlled preferred orientation that exhibits a plane with the desired tilt angle.

In this paper we have investigated the above-mentioned methods to induce surface roughness to promote the growth of tilted AlN films for shear modes resonators. The efficacy of the process involving the use of the inherited roughness of the layers below the active AlN layer has been studied and discussed. Concerning the second method, thin AlN films have been chosen as polycrystalline seed layers, because of their proven effectiveness for this purpose [11], [12]. The deposition conditions of the seed layer and their influence on the performance (electromechanical coupling factor and quality factor) of shear mode resonators have been analyzed.

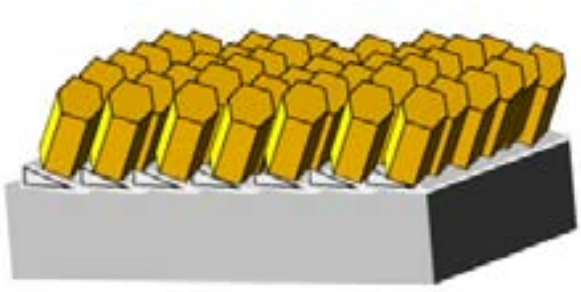

Figure 1. Sawtooth profile to promote growth of tilted grains.

II. Experimental

The deposition of AlN thin films was conducted in a custom-made ultra-high vacuum sputtering system pumped by a cryogenic pump to a base pressure of 10^{-8} Torr and provided with a transfer chamber to avoid oxygen contamination in the deposition chamber. AlN films were deposited with a 150 mm diameter 99.999% purity aluminum target located at a distance of 55 mm from the substrate holder. The 99.9999% purity gas mixture was 60% N_2 in Ar. The substrate holder could be heated to temperatures up to 600ºC and RF biased during the deposition process. The substrates consisted of (001)-oriented silicon wafers covered with an acoustic reflector made of five alternating sputtered layers of porous SiO_2 and Mo whose thicknesses were adjusted to achieve a center frequency of 2.5 GHz for the longitudinal mode and of 1.45 GHz for the shear mode. The samples selected to study the AlN seed layer had their uppermost SiO_2 layer mechanically polished with alumina slurry to a RMS roughness below 1 nm. They were covered with a 120 nm-thick iridium film that acted as bottom electrode of the resonators. Some samples were cleaned before the deposition of the AlN films by ion bombardment in a pure Ar RF discharge.

To promote the growth of AlN active layers with an effective tilt, AlN seed layers 100 nm-thick were first sputtered under the conditions that favors the growth of <10·3> or <10·2>-oriented microcrystals. The obtained tilt, combined with a good basal alignment leading to a large piezoelectric response, is the most favorable structure for shear mode generation. However, achieving in practice thick AlN films with those characteristics is a difficult task, as the energy supplied to the adatoms must be very low, which causes inevitably the appearance of inversion domains that yield, in turn, a poor piezoelectric response [13]. Therefore the strategy is based on depositing these poorly-piezoelectric polycrystalline AlN film and, without breaking the vacuum cycle, using them as a seed for the growth of the 1000 nm-thick active layer. This active layer is sputtered under a highly energetic process specially optimized to achieve the best-performing AlN piezoelectric layers in our system, which involves high power, low pressure, high temperature and substrate biasing.

After AlN deposition, a top electrode of molybdenum 150 nm-thick was deposited and patterned to fabricate resonators as test devices. The impedance of these devices as a function of the frequency (between 100 MHz and 10 GHz) was measured using an Agilent N5300 network analyzer. The resulting spectra were fitted using Mason's model to obtain the actual electromechanical coupling factor of the material (instead of the effective one, which also depends on the thickness of the other layers) [14], [15] associated to the shear mode (k^2_{shear}) and to the longitudinal mode (k^2_{long}) and their corresponding quality factors Q_{shear} and Q_{long}. The characterization of the devices and the material was conducted on samples located at 40 mm from the center of the wafer to take advantage of the abovementioned off-axis deposition.

X ray diffraction (XRD) has been used to obtain the crystal structure of the films. Conventional θ/2θ patterns and ψ scans with θ=18° (the Bragg angle for the (00·2) planes) between 80° and - 80° were measured in the radial direction of the wafer at 40 mm from the center.

Atomic force microscopy (AFM) images in contact mode were taken from selected samples to study the roughness of the substrates before the AlN deposition.

III. Results and Discussion

A. *Roughness of the uppermost layer*

To analyze the influence of the uppermost layer roughness on the orientation of the AlN grains, several deposition were made on substrates as shown in figure 2: (a) polished (RMS roughness below 1 nm) and (b) rough (RMS roughness over 12 nm). The devices fabricated on them show a clear increase of the k^2_{shear} when using the rough substrate, which indicates that higher roughness promotes the growth of tilted AlN. Polished surfaces, even when the AlN is sputtered off axis, induce a highly perpendicular growth of the grains. However, even if the same conditions are used to deposit the AlN active layer, the k^2_{shear} of the devices fabricated on different substrates varies from 1% to 2.4%, which indicates that this method is poorly reproducible and controllable, although high quality resonators have been obtained (k^2_{shear} as high as 2.4% with a Q_{shear} value of 270).

Some tests were made depositing non-oriented AlN layer, texturing it with KOH chemical etching in order to achieve a controlled surface roughness and, then, depositing an optimum AlN film again. The quality of the piezoelectric films was drastically reduced since the seed layer had to be exposed to oxygen when the vacuum cycle was broken, as already observed in previous works [16].

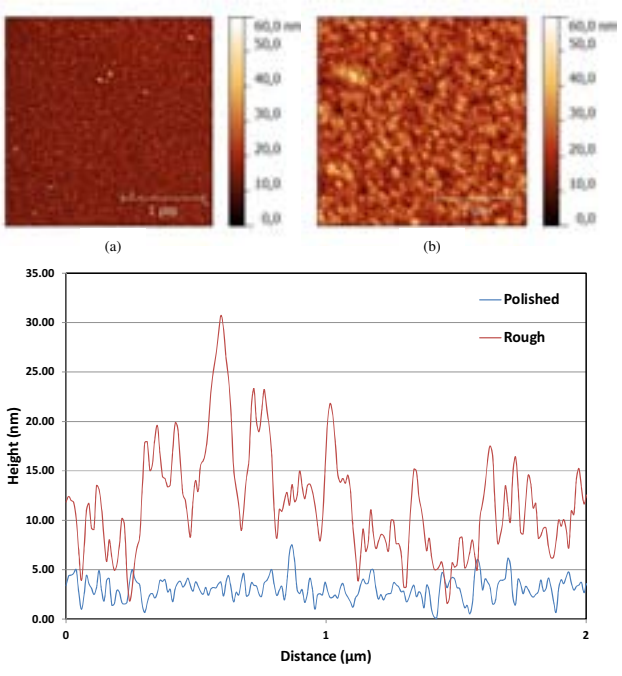

Figure 2. AFM images and profiles of (a) polished and (b) rough substrates

B. *AlN seed layer*

AlN polycrystalline seed layers with high content of <10·2> or <10·3>-oriented grains were deposited by reducing the energy supplied to the substrate during deposition through a careful control of the deposition parameters: substrate temperature (including the electron bombardment effects), ionic bombardment (caused by the self-polarization of the substrate and applied bias), cathode potential, and gas pressure. The substrate was not intentionally heated during the deposition of the seed layer and the substrate holder was not externally polarized to reduce the energy applied to the substrate. The variables tracked were the power applied to the target and the total pressure. The tilted AlN layers were grown on top of the seed layers under the sputter conditions that guarantee the best AlN films achievable in our system. The goodness of the seed layers was assessed through the value of k^2_{shear} measured in the test resonators.

Figure 3 shows the values of k^2_{shear} achieved in the test resonators for different deposition conditions of the seed layer (target power and total pressure). For the lowest pressures the k^2_{shear} values decrease when the power increases, but this tendency is reversed when the pressure rises. This behavior is due to two competitive mechanisms. A reduction in the total pressure originates an increase in the energy supplied to the substrate because the self-polarization of the substrate increases (in module), thus increasing the ionic bombardment; as a consequence the sputtered species reach the substrate with more energy as they do not completely thermalize. The energetic excess supplied at higher target power makes the AlN grains to be less tilted and the k^2_{shear} values drop because the mean tilt angle of the c-axis of the active layer is lower. At high pressures the energy supplied to the substrate is very low, due to lower substrate polarization and a complete thermalization of atoms reaching the substrate; hence, the crystallinity of the seed layer is very poor. An increase in the power applied to the target helps the crystal formation without changing the orientation tendency.

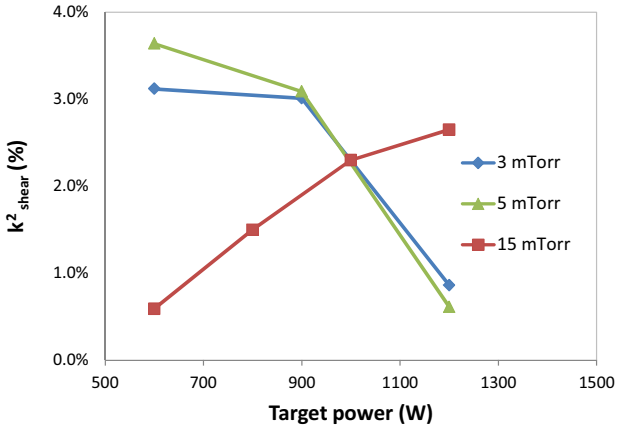

Figure 3. k^2_{shear} of the resonators as a function of the power applied to the target during the growth of the seed layer at three different total pressures.

To overcome the very demanding conditions of XRD to detect {10·2} and {10·3} we have analyzed the structure of the AlN layers by FTIR reflectance (see figure 4), which is a technique sensitive to tilt angle of the grains as we have shown in [17], [18]. The results show that the greater grain populations with orientation around <10·2> or <10·3> we get in the seed layer, the more <00·2> tilt angle we achieve in the active piezoelectric layer. Therefore k^2_{shear} increases well above the values obtained using the first method, reaching 3.64%. Figure 5 shows the longitudinal and shear resonances of a well-performing device operating in air and liquid. Notice how the longitudinal mode is strongly affected by the presence of the liquid, while the shear mode maintains Q values that still allow biosensing applications. These results are fairly reproducible and controllable compared to the results obtained in devices fabricated on rough surfaces under identical deposition conditions (see figure 6).

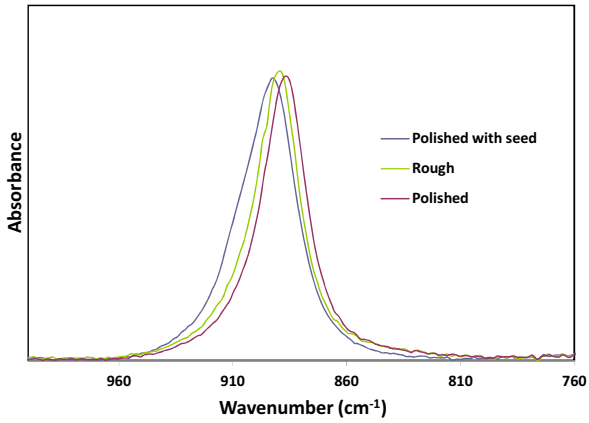

Figure 4. IR reflectance spectra of the AlN active layer deposited on top of polished substrates covered with a seed layer, polished substrates without seed layer, and rough subtrates. The position shift of the peaks towards larger wavenumbers indicates a a) 24.3°, b) 12.3° and c) 0° tilt of the AlN grains with respect to the normal to the surface.

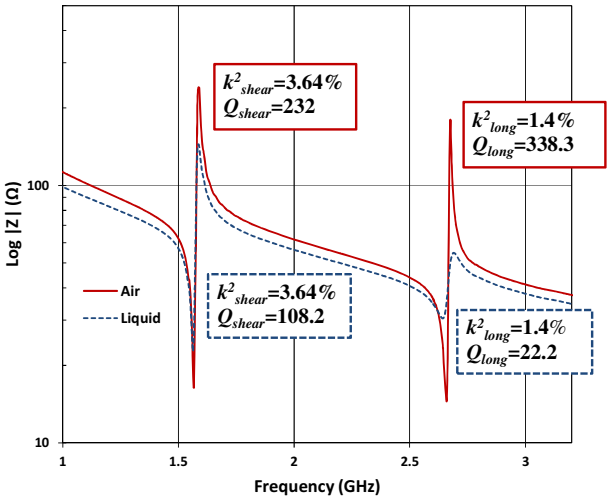

Figure 5. Impedance of the test resonator operating in air and in liquid.

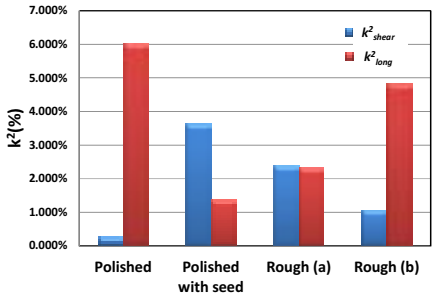

Figure 6. k^2_{shear} (blue) and k^2_{long} (red) of resonators fabricated on polished and rough substrates, with and without AlN seed layer. Notice the strong dispersion of the k^2 values of resonators fabricated on rough subtrates under the same deposition conditions.

However, the use of a non-piezoelectric seed layer generates an undesirable electrically dead layer in the resonator, which lowers its resonant frequency and worsens its performance. A metallic seed layer which could serve as bottom electrode and whose texture could be controlled like in the AlN case (e.g. W, Al or Ta) [19–21], opens the door to a promising method of new seed layers that has yet to be studied.

IV. Conclusions

We have investigated two methods to induce surface roughness that enhances the growth of tilted AlN films intended for shear mode resonators. The first method, which takes advantage of the roughness of the underlying substrates, can yield well-performing devices (k^2_{shear} up to 2.4%, Q_{shear} above 270), but in an uncontrollable way. The second method involves the use of a very thin non-piezoelectric AlN seed layer that contains inclined facets suitable for promoting the growth of tilted films; this seed layer has been achieved by sputtering at low power and moderate pressures. Combining such seed layers with an off-axis growth of the active layer we have achieved shear resonators exhibiting values of k^2_{shear} above 3.6% and Q_{shear} above 230 that have demonstrated a good performance in liquid environments.

Acknowledgment

This work was partially supported by the European Comission through the 7th Framework Program by the *RaptaDiag* project (http://www.raptadiag.eu/) and by the Ministerio de Economía y Competitividad del Gobierno de España through project MAT2010-18933.

References

[1] L. Rodríguez-Pardo, "Sensitivity, noise, and resolution in QCM sensors in liquid media," *Sensors Journal,* vol. 5, no. 6, pp. 1251–1257, 2005.

[2] M. Ferrari, V. Ferrari, and K. Kanazawa, "Dual-harmonic oscillator for quartz crystal resonator sensors," *IEEE transactions on ultrasonics, ferroelectrics, and frequency control*, pp. 241–244, 2007.

[3] G. Bu, D. Ciplys, M. Shur, L. J. Schowalter, S. Schujman, and R. Gaska, "Surface acoustic wave velocity in single-crystal AlN substrates.," *IEEE transactions on ultrasonics, ferroelectrics, and frequency control*, vol. 53, no. 1, pp. 251–4, Jan. 2006.

[4] K. Tsubouchi and N. Mikoshiba, "Zero temperature coefficient SAW delay line on AlN epitaxial films," *1983 Ultrasonics Symposium*, 1983.

[5] M. Clement, J. Olivares, E. Iborra, S. González-Castilla, N. Rimmer, and a. Rastogi, "AlN films sputtered on iridium electrodes for bulk acoustic wave resonators," *Thin Solid Films*, vol. 517, no. 16, pp. 4673–4678, Jun. 2009.

[6] J. Ruffner, P. Clem, B. Tuttle, D. Dimos, and D. Gonzales, "Effect of substrate composition on the piezoelectric response of reactively sputtered AlN thin films," *Thin Solid Films*, vol. 354, pp. 256–261, 1999.

[7] M.-A. Dubois and P. Muralt, "Stress and piezoelectric properties of aluminum nitride thin films deposited onto metal electrodes by pulsed direct current reactive sputtering," *Journal of Applied Physics*, vol. 89, no. 11, p. 6389, 2001.

[8] Y. Oshmyansky and J. Larson, "Sputtering Processes for Bulk Acoustic Wave Filters," *Semiconductor.net*, no. 805, 2003.

[9] R. Bathe, R. . Vispute, D. Habersat, R. . Sharma, T. Venkatesan, C. . Scozzie, M. Ervin, B. . Geil, a. . Lelis, S. . Dikshit, and R. Bhattacharya, "AlN thin films deposited by pulsed laser ablation, sputtering and filtered arc techniques," *Thin Solid Films*, vol. 398–399, pp. 575–580, Nov. 2001.

[10] T. Yanagitani, M. Kiuchb, M. Matsukawa, and Y. Watanabe, "Pure-shear mode BAW resonators consisting of (11-20) textured ZnO films," *Acoustics 2008 Paris*, pp. 1–6, 2008.

[11] M. Moreira and J. Bjurström, "Synthesis of c-tilted AlN films with a good tilt and thickness uniformity," *Proceedings of IEEE Ultrasonics Symposium*, pp. 1238–1241, 2012.

[12] J. Bjurström, G. Wingqvist, and I. Katardjiev, "Synthesis of textured thin piezoelectric AlN films with a nonzero c-axis mean tilt for the fabrication of shear mode resonators.," *IEEE transactions on ultrasonics, ferroelectrics, and frequency control*, vol. 53, no. 11, pp. 2095–100, Nov. 2006.

[13] E. Iborra, J. Olivares, M. Clement, L. Vergara, a. Sanz-Hervás, and J. Sangrador, "Piezoelectric properties and residual stress of sputtered AlN thin films for MEMS applications," *Sensors and Actuators A: Physical*, vol. 115, no. 2–3, pp. 501–507, Sep. 2004.

[14] E. Iborra, M. Clement, J. Olivares, J. Sangrador, N. Rimmer, and A. Rastogi, "Aluminum Nitride Bulk Acoustic Wave Devices with Iridium Bottom Electrodes," *2007 IEEE Ultrasonics Symposium Proceedings*, pp. 616–619, Oct. 2007.

[15] E. Iborra, L. Vergara, J. Sangrador, M. Clement, A. Sanz-Hervás, and J. Olivares, "Circuital model for the analysis of the piezoelectric response of A1N films using SAW filters.," *IEEE transactions on ultrasonics, ferroelectrics, and frequency control*, vol. 54, no. 11, pp. 2367–75, Nov. 2007.

[16] F. Martin, P. Muralt, M. Cantoni, and M. -a. Dubois, "Re-growth of c-axis oriented AlN thin films," *IEEE Ultrasonics Symposium, 2004*, vol. 1, no. 1, pp. 169–172, 2004.

[17] J. Olivares, M. DeMiguel-Ramos, E. Iborra, M. Clement, M. Moreira, and I. Katardjiev, "IR-reflectance assessment of the tilt angle of AlN-wurtzite films for shear mode resonators," *International Frequency Control Symposium (in press)*, 2013.

[18] J. Olivares, S. González-Castilla, M. Clement, a. Sanz-Hervás, L. Vergara, J. Sangrador, and E. Iborra, "Combined assessment of piezoelectric AlN films using X-ray diffraction, infrared absorption and atomic force microscopy," *Diamond and Related Materials*, vol. 16, no. 4–7, pp. 1421–1424, Apr. 2007.

[19] T. Ishiguro and K. Miyamura, "Controllability of Mesoscopic Surface Roughness of Sputtered Al and Al–N Films," *Materials Transactions*, vol. 46, no. 12, pp. 3037–3043, 2005.

[20] J. Dalla Torre, G. H. Gilmer, D. L. Windt, R. Kalyanaraman, F. H. Baumann, P. L. O'Sullivan, J. Sapjeta, T. Díaz de la Rubia, and M. Djafari Rouhani, "Microstructure of thin tantalum films sputtered onto inclined substrates: Experiments and atomistic simulations," *Journal of Applied Physics*, vol. 94, no. 1, p. 263, 2003.

[21] S. Kang, S. Lee, J. Park, and J. Lee, "Microstructure Control of Tungsten Film for Bragg Reflectors of Thin Film Bulk Acoustic Wave Resonators," *Journal of the Korean Ceramic Society*, vol. 40, no. 3, pp. 268–272, 2003.

GNURadio as a Digital Signal Processing Environment: Application to Acoustic Wireless Sensor Measurement and Time & Frequency Analysis of Periodic Signals

J.-M Friedt
SENSeOR, c/o FEMTO-ST Time & Frequency, Besançon, France
Email: jmfriedt@femto-st.fr

***Abstract*—The flexibility, reconfigurability and stability of software defined radio yield an attractive alternative to the analog strategy of probing acoustic transducers acting as passive sensors probed through a wireless link or to phase noise characterization of oscillators. However, developing processing blocks is a time consuming activity, yet metrology applications require a dedicated understanding of each processing step. We consider GNURadio as a means of exploiting opensource software as an optimum tradeoff between software re-usability yet compatible with an audit for assessing performance. This signal processing environment is demonstrated on two practical examples, FMCW probing of acoustic delay lines acting as sensors, and quartz tuning fork characterization. Both examples are considered as introductory setups for training and teaching yet a suitable environment for research activities.**

I. Introduction

Digital signal processing has been identified as a significant improvement over analog signal processing for a number of reasons [1], [2], including stability, flexibility and accuracy. Respectively, digital signal processing is not prone to component aging or drift over time; is reconfigurable in order to update algorithms or parameters in order to perform new functionalities on a given hardware; and provides a pre-defined, quantitative computation accuracy given the size of the handled datasets. Digital signal processing is nowadays ubiquitous and the mostly infinite computational power available yields to the trend of Software Defined Radio [3], in which general purpose radiofrequency source and sampling hardware is used for software processing of the recorded data for multiple application on a given experimental setup. Although processing power has been increasing continuously, the extensive bandwidth needed for radiofrequency (RF) sampling often remains beyond the general purpose hardware. On the other hand, most RF signal are narrowband and do not require full bandwidth sampling, so a common trend is to use an analog frontend with an amplifier and a mixer with a local oscillator to provide a zero-intermediate frequency (IF) configuration. We consider here the use of such a configuration in the context of time and frequency metrology signal processing, and most significantly consider the software environment needed to implement the associated processing algorithm, both from application and a teaching considerations since the skills for applying these concepts are mostly lacking.

II. FMCW RADAR for passive wireless sensor monitoring

Acoustic transducers [4]have been demonstrated to be relevant alternatives to silicon-based radiofrequency identification tags (RFID) when harsh environments (temperatures above CMOS operating range) or long interrogation ranges (no threshold on the received power in the case of piezoelectric substrate) are needed. By patterning electrodes on single crystal substrates, a delay line configuration aims at providing a simple means to convert the incoming electromagnetic signal to a mechanical wave whose propagation velocity on the surface of the substrate is dependent on the physical property under investigation [5]. Through direct piezoelectric effect, the pulse reflected on a mirror patterned on the substrate generates a returned electromagnetic signal: the purpose of the readout unit is to allow for a measurement of this time of flight in order to recover the physical quantity value [6].

A classical pulsed-mode RADAR approach requires large measurement bandwidths B in order to achieve time resolution $1/B$: typical pulse widths and maximum time of flight durations are respectively 100 ns and 5 μs, so that $B > 10$ MS/s is needed. Although the pulsed mode, wideband RADAR approach provides some significant range and measurement speed advantages, a simpler approach has been favored in the literature through the use of the frequency-modulated continuous wave (FMCW) RADAR approach [7]. In the latter method, a local oscillator frequency f is linearly swept along a bandwidth B within the bandpass function of the acoustic delay line. The time delayed returned τ signal is mixed and low pass filtered with the local oscillator, so that a beat signal $\Delta f(\tau) = f(t) - f(t+\tau)$ is recorded after removal of the carrier. The resulting architecture is simple and only requires low frequency sampling rates, but also introduces multiple free parameters which are best tested in a software defined radio approach. Among the parameters are the central operating frequency f and the sweep rate T: $\Delta f(\tau)/\tau = B/T$ since the frequency band B is swept linearly over a duration T.

Recently, a tutorial has been presented on the MIT OpenCourseWare web site [8] demonstrating a basic FMCW approach: this hardware platform is used as the starting point of this experiment, although the linear RF oscillator sweep and recording a no longer performed by dedicated hardware but by a personal computer sound card running GNURadio (http:

978-1-4799-0342-9/13/$31.00 ©2013 IEEE

//gnuradio.org/). The recorded signals are Fourier transformed in real time in order to display the multiple echoes returned by the acoustic delay line $\Delta f(\tau_i)$ with i an index of the echo number. In the case of the transducer we have experimented with – available from the Carithian Tech Research (CTR, Villach, Austria), $i \in [1..8]$.

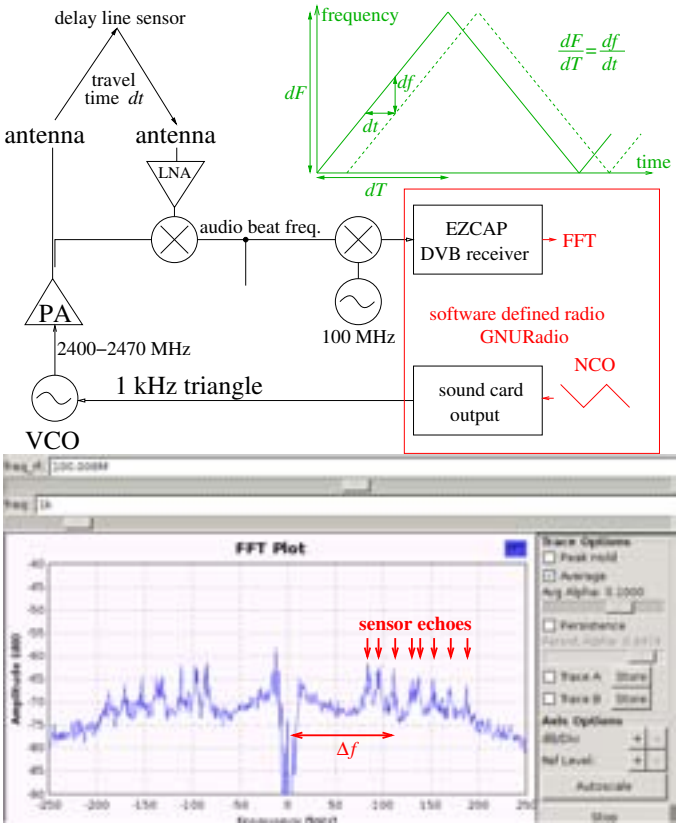

Fig. 1. Top: schematic diagram of the FMCW RADAR used to demonstrate probing a 2.45 GHz acoustic delay line acting as passive, wireless sensor. The RF hardware is based on the MIT design [8], while the signal source (triangle-shaped Voltage Controlled Oscillator – VCO – control signal) and sink (beat frequency recording and Fourier transform) are performed using the GNURadio software. Since the recording by an DVB receiver requires an input signal higher than 100 MHz, the audio beat signal is mixed with a fixed frequency oscillator to reach the requested frequency band. Bottom: real time display of the 8 echoes observed as 8 discrete frequency components of the beat signal.

Fig. 1 exhibits a screenshot of the monitored signal, in which the 8 delay line echoes are well resolved as 8-discrete beat frequencies. The software defined signal source – here a linear sweep on the output sound card – provides the flexibility to compensate for the RF oscillator non-linear frequency output with respect to the control voltage: this linearity on the whole range B is mandatory for all contributions to the beat signal to add coherently. Lack of linearity of the RF oscillator yields a given delay τ to induce variable $\Delta f(\tau)$ as the oscillator is swept and hence a broadening of the returned signal beat frequency peaks. This aspect is well demonstrated with the software defined radio as well.

For teaching purposes, the two options available to us when using widely available, commercial off the shelf analog to digital converters, are a sound card and a Digital Video Broadcast (DVB) receiver, both acting as dual I and Q channel data streams. The sound card is a high resolution analog to digital converter (typically 16 bit at least) but only provides a bandwidth up to 48 kHz (96 kHz sampling rate), while internal anti-aliasing filters prevent the monitoring of higher frequency signals. Since the CTR-delay line requires a bandwidth of at least 30 MHz and the time delay is in the 5 μs range, the sweep rate T must be $T < \frac{B \times \tau}{\Delta f(min)}$ or in this case 3.125 ms. An output frequency of 320 Hz is well within the bandpass of a soundcard output. Alternatively, higher refresh rates are achieved by sweeping the frequency source at a faster rate, hence also improving the frequency detection resolution since Δf becomes larger for a given delay τ. Since the sound card is no longer an option at higher signal frequencies and the DVB receiver only operates above 100 MHz, a frequency transposition strategy is used to bring the monitored signal in the 100 MHz range (mixing with a local quartz oscillator) before the DVB receiver demodulates the signal and provides the I/Q datastream.

III. Time & Frequency Metrology Algorithm Prototyping and Assessing Hardware Limitations

Software implementation of classical analog signal processing methods are best suited for rapid prototyping [2]. While frequency counting is intrinsically a digital method, its software implementation easily demonstrates the gains and influence on the statistics of various strategies (direct counter, reciprocal counter, sliding average functions [9], [10]). More challenging is the phase noise measurement [11]–[14], which is classically performed by mixing the test oscillator with a reference local oscillator and low-pass filtering the beat signal, possibly providing a feedback control signal for the local oscillator to track the measured oscillator frequency if long term drift is compensated for (statistics on the control signal rather than on the beat signal output itself). All these blocks are implemented as software, but the influence on the phase noise spectra as a function of the digital hardware performance often remains challenging to assess [15] .

Efficient processing of the narrowband signals considered remains a challenging aspect of the data acquisition chain: under the assumption that the oscillator under investigation is stable, sampling is not needed to meet the Shannon criteria under the hypothesis that only a narrow band around the carrier frequency holds the needed information. One such consideration yields to the fact that aliasing on purpose the measured signal to only meet the analyzed bandwidth – without the ability to reconstruct the whole signal – is enough, yet the impact on the noise level is still under consideration.

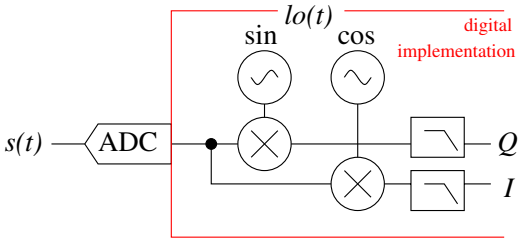

Fig. 2. Classical phase detection scheme considered here in its digital implementation.

When single sample operations are needed, such as

I/Q demodulation in which a local numerically controlled oscillator (NCO, described in the GNURadio source tree in `gnuradio-core/src/lib/general/gr_nco.h`) is mixed with the incoming signal, no stream handling functionality is needed. However, the data block size is not known and data are transmitted from one block to another asynchronously. If a minimum number of data is needed to perform a given processing step, e.g a Fourier transform, data are accumulated in a temporary array which is processed only once filled. The buffer is then freed of the processed data and the remaining values are moved to the beginning of the buffer to be processed with the next batch of data.

Phase noise analysis is the most basic processing tool for characterizing an oscillator stability. Many schemes have been devised using analog electronics, most classically mixing the oscillator output under investigation with a local oscillator assumed to exhibit better stability, low pass filtering the mixer output to get rid of the signal at the sum of the frequencies, and controlling the reference oscillator in order to keep the quadrature condition at the mixer so that $\sin(\varphi) \simeq \varphi$. In order to implement such a scheme digitally and use at best digital signal processing – flexibility in setting the local oscillator frequency, low pass filter characteristics and phase noise extraction – we assess the number of bits on which the computation has to be performed to comply with the targeted resolution. Let us assume, to justify this calculation, that we aim for phase noise resolution calculations reaching -180 dBrad^2/Hz (Fig. 3).

The phase noise S_φ defines the phase fluctuations σ_φ in a given bandwidth BW:

$$S_\varphi = \sigma_\varphi^2 / BW \text{ rad}^2/\text{Hz}$$

Considering the phase noise at carrier offset 1 to 10 MHz and 1000 points/decade, $BW = 9$ kHz in such conditions. S_φ is usually expressed in dB with $S_{dB} = 10\log_{10}(S_\varphi)$. The classical scheme of mixing the sine wave translates, in terms of digital computation [16], [17], into a product of the local numerically controlled oscillator LO and sampled signals from the oscillator under investigation s, followed by a low pass filter which we here consider to be a finite impulse response (FIR) filter with coefficients a_n:

$$I, Q = \frac{1}{N} \sum_N s_k \times LO_k \times a_{N-k}$$

where I, Q are the in-phase and quadrature coefficients obtained from two expressions of the local oscillator phase shifted by 90^o (*i.e.* expressed as cos and sin). From these two sets of coefficient, the phase is classically expressed as the argument of the complex $I + jQ$ or $\varphi = \arctan(Q/I)$.

In the low pass filter expression, the sum yields a standard deviation rising as $\sqrt{N}$ for samples affected by an additive gaussian noise, and the $1/N$ factor yields the classical decrease of the standard deviation during averaging by $1/\sqrt{N}$. This number of samples N is given by the ratio of the sampling frequency f_s to twice the maximum offset from the carrier at which phase noise is computed. Assuming a 500 Msamples/s sampling rate and a phase noise calculation at 10 MHz from the carrier, then $N = 25$.

The uncertainty of the I, Q calculation is given by the sum of the uncertainties of each term in the sum: $dI, Q = \frac{1}{N}\sum_N ds \times LO \times a_{N-k} + dLO \times s \times a_{N-k} + da \times LO \times s$. If only quantization noise is considered when representing information on M bits, then all infinitesimal terms are equal to 2^{-M} and each quantity is assumed to have been scaled to be around unity, so that this uncertainty on the computation of I and Q are dominated by $3 \times 2^{-M}/\sqrt{N}$ since the sum of the independent noise source rises as $\sqrt{N}$. We then target a given phase noise floor S_dB expressed in dB, then

$$\sqrt{BW \times 10^{S_dB/10}} = 3/\sqrt{N} \times 2^{-M}$$

$$\Leftrightarrow M = -\ln_2\left(\sqrt{N \cdot BW \times 10^{S_dB/10}}\right)/3$$

Keeping the previous assumption of $B = 500$ MHz and a targeted phase noise plot up to a 10 MHz offset from the carrier hence requiring $N = 25$, computation on 26 bits is needed to reach the targeted resolution of -180 dBrad^2/Hz. Even at -160 dBrad^2/Hz, $M = 23$ bits are needed to reach the requested computation resolution. The sum of three sources of noises rises the resolution need by 1.6 bits: if the filter can be tuned in order to prevent resolution uncertainty on its coefficients ($da = 0$) and if a square wave is used instead of the sine wave defining the NCO ($dLO = 0$), then the needed resolution becomes 25 and 21 bits respectively. However, the use of a square wave NCO brings new challenges including the rejection of unwanted harmonics and its aliases after the mixing step, while making sure than none of these aliases are brought back within the band of interest [18], [19].

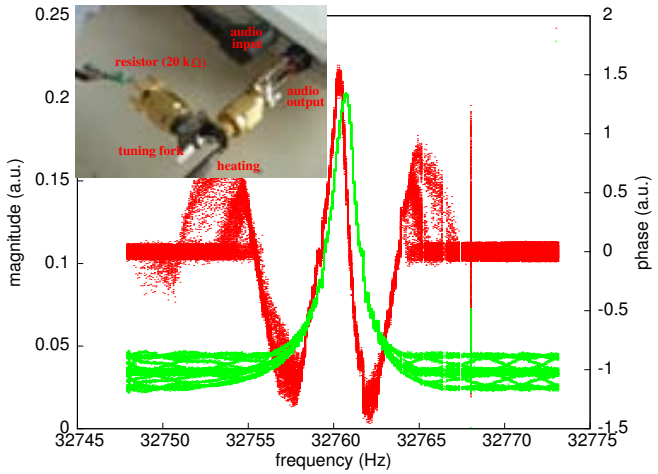

Fig. 3. Illustration of the I/Q demodulation scheme on a low frequency quartz tuning fork yielding phase (red) and magnitude (green) of the audiofrequency signal transmitted through the dipole. Notice that this experiment only requires a full-duplex sound card programmed through GNURadio as a network analyzer since the emission and recording are performed simultaneously. In this particular application, phase monitoring is used when the unpackaged tuning fork acts as a temperature sensor.

IV. Limitations of the GNURadio approach

While most digital signal processing blocks are readily available and the missing functions dedicated to time & frequency metrology are being implemented thanks to the opensource software aspect of the tool, one major limitation in terms of signal processing bandwidth is due to the software running on general purpose central processing units (CPU).

Although dedicated hardware provides FPGA-based data acquisition, the signal processing is performed on the data-flow recovered from the FPGA and not implemented on the gate matrix itself, thus reducing the processing bandwidth to the communication bus bandwidth. Hence, while this environment provides a flexible testbench for real time prototyping of signal processing algorithms, it might not be suited when large (> 100 MS/s) bandwidths are considered. Alternate solutions include on-purpose aliasing or stroboscopy [19], [20].

Nevertheless, we consider this environment best suited for getting familiar with the basics of digital signal processing of RF signals, as well as for teaching purposes since this aspect is needed to train the current and future generation of researchers interested in such a topic. The easily available hardware (sound card, DVB receiver) and the ability to add signal source blocks thanks to the opensource code makes this software most versatile.

V. Conclusion

While analog implementations of most radiofrequency signal processing schemes provide suitable results for RADAR detection of signals returned from acoustic sensors acting as passive sensors and for characterizing oscillator stability, the need to design new hardware for each new application or new frequency band is time consuming and prone to the introduction of design errors in each new hardware setup. The flexibility of software reconfigurable processing chains is well suited for such applications. However, the need for a detailed understanding of the methods implemented in each processing block is hardly compatible with the use of closed source software, and an opensource solution as offered by the GNURadio software suite is considered. Reaching the targeted resolution of low phase noise oscillator using a full software implementation in which the RF front end is solely made of a fast analog to digital converter and all further processing steps are performed by software appears challenging with current available technologies.

Acknowledgements

These activities were motivated by the Oscillator IMP LABEX grant.

References

[1] D. Mindell, *Digital Apollo: Human and Machine in Spaceflight*. The MIT Press, 2011.

[2] J. Hamkins, M. Simon, and J. Yuen, *Autonomous software defined radio receivers for deep space applications*. Wiley, 2006.

[3] P. Kenington, *RF and baseband techniques for software defined radio*. Artech House, 2005.

[4] L. Reindl and V. Plessky, "Review on SAW RFID tags," *IEEE Trans. Ultrason. Ferroelectr. Freq. Control.*, vol. 57, no. 3, pp. 654–668, 2010.

[5] R. White, "Surface acoustic wave sensors," in *Proc. IEEE Ultrasonics Symposium*, 1985, pp. 490–494.

[6] W.-E. Bulst, G. Fischerauer, and L. Reindl, "State of the art in wireless sensing with surface acoustic waves," *IEEE Trans. Industrial Electronics*, vol. 48, no. 2, pp. 265–271, 2001.

[7] S. Schuster, S. Scheiblhofer, L. Reindl, and A. Stelzer, "Performance evaluation of algorithms for SAW-based temperature measurement," *IEEE Trans. Ultrason. Ferroelectr. Freq. Control.*, 2006.

[8] G. Charvat, A. Fenn, and B. Perry, "The MIT IAP radar course: Build a small radar system capable of sensing range, doppler, and synthetic aperture (SAR) imaging," in *IEEE Radar Conference*, 2012, pp. 138–144.

[9] S. Dawkins, J. McFerran, and A. Luiten, "Considerations on the measurement of the stability of oscillators with frequency counters," *IEEE Transactions on Ultrasonics, Ferroelectrics and Frequency Control*, vol. 54, no. 5, pp. 918–925, May 2007.

[10] E. Rubiola, "On the measurement of frequency and of its sample variance with high-resolution counters," *Rev. Sci. Instrum.*, vol. 76, no. 5, p. 054703, May 2005.

[11] L. Angrisani, M. D'Apuzzo, and M. D'Arco, "A digital signal-processing approach for phase noise measurement," *IEEE Transactions on instrumentation and measurement*, vol. 50, no. 4, pp. 930–935, August 2001.

[12] J. Grove, J. Hein, J. Retta, P. Schweiger, W. Solbrig, and S. Stein, "Direct-digital phase-noise measurement," in *IEEE International Ultrasonics, Ferroelectrics, and Frequency Control Joint 50th Anniversary Conference*, 2004, pp. 287–291.

[13] L. Angrisani, A. Baccigalupi, M.D'Arco, and L. Ferrigno, "A new digital signal processing method for accurate phase noise measurement," in *11th IMEKO TC-4 Symp. – Trends in Electrical Measurement and Instrumentation*, Lisbon, Portugal, September 2001, pp. 43–.

[14] V. Ivo and H. Josef, "Phase noise measurement," in *Proceedings of the Radioelektronika*, 2001, pp. 131–134.

[15] L. Angrisani, M. D'Arco, C. Greenhal, and R. L. Moriello, "Real-time phase noise meter based on a digital signal processor," in *IMTC - Instrumentation and Measurement Technology Conference*, Sonento, Italy, April 2006.

[16] A. Hati, D. A. Howe, F. L. Walls, and D. Walker, "Noise figure vs. PM noise measurements: A study at microwave frequencies," in *Proc. of the 2003 IEEE International Frequency Control Symposium and PDA Exhibition, Jointly with the 17th European Frequency and Time Forum*, 2003, pp. 516–520.

[17] A. Hati, D. Howe, F. Walls, and D. Walker, "Merits of PM noise measurement over noise figure: A study at microwave frequencies," *IEEE transactions on ultrasonics, ferroelectrics, and frequency control*, vol. 53, no. 10, pp. 1889–1894, October 2006.

[18] M. Mishali and Y. Eldar, "Sub-Nyquist sampling," *IEEE Signal Processing Magazine*, vol. 28, no. 6, pp. 98–124, 2011.

[19] ——, "Sub-Nyquist sampling: Bridging theory and practice," *arXiv: 1106.4514v1*, 2011.

[20] C. Nelson and D. Howe, "A sub-sampling digital PM/AM noise measurement system," in *Proc. IEEE International Frequency Control Symposium (FCS)*, 2012, pp. 1–4.

Modeling and Analysis of a Liquid-Level Sensor Utilizing an Evanescent Field of a Trapped-Energy Vibrator

Ken Yamada, Tatsuya Ishioka, and Naoki Aita
Department of Electronic Engineering
Tohoku Gakuin University
Tagajo, Miyagi 985-8537, Japan

***Abstract*—Equivalent-network modeling and analysis have been presented for a liquid-level sensor that utilizes an evanescent field created by a trapped-energy vibrator. The network is constructed by modifying an electric network representing the propagation of thickness-vibration mode along the piezoelectric plate. Simulation has been performed for the sensors utilizing trapped-energy vibration modes of conventional type and the backward wave type. It is revealed that the computed results show a similar trend in variation to the experimental results that have been examined so far.**

Keywords—energy-trapping; liquid-level sensor; piezoelecytric resonator;piezoelectric sensor;equivalent-network analysis

I. INTRODUCTION

A novel approach for detecting a small-scale variation in liquid level that employs a piezoelectric thickness vibrator operating in a trapped-energy mode [1] has been studied by the authors [2]-[6]. In a trapped-energy resonator, an evanescent field is created in the surrounding region in which the vibration amplitude decays exponentially. If the evanescent region is dipped in a liquid, a depth-dependent leakage of vibration energy will occur and this causes the deterioration in the mechanical quality factor *Qm* and/or the electric conductance *G* at the resonance frequency. Because the liquid level is detected easily by observing variation in *G* of the resonator, it is desirable that the sensing device should be modeled by an equivalent electric network for simulating its operation. In this paper, a sensor is expressed by modifying an equivalent electric network proposed by Nakamura and coworkers [7],[8] which could represent the propagation of a thickness-vibration mode along the piezoelectric plate, and therefore its operation is simulated.

II. EQUIVALENT-NETWORK REPRESENTATION OF THE SENSORS AND RESULTS OF THE ANALYSES

A. *Device Using Conventional Trapped-Energy Resonator*

The sensor employing a conventional trapped-energy resonator is shown in Fig. 1(a) [2],[3]. A piezoelectric plate is supported vertically by clamping its top fringe and dipped in a liquid of which the surface level is measured. The original device studied so far was composed of a piezoelectric disk having an axisymmetric configuration with circular electrodes. However, the sensor model treated in this study is supposed to have two-dimensional geometry without taking the variations in the depth (width) direction into consideration.

This work was supported in part by a Grant-in-Aid for scientific research (C) (No. 22560340) from the Japan Society for the Promotion of Science.

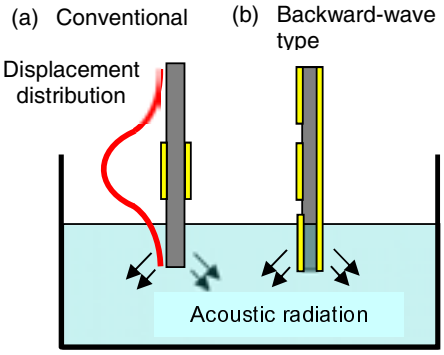

Fig. 1 Liquid-level sensors utilizing trapped-energy resonators.

Equivalent network representations for thickness vibration modes presented by Mason [9] or Krimholtz *et al*. [10] are well known and utilized widely so far. However, these networks are not applicable for vibrators operating in a trapped-energy mode. Therefore, the sensor is modeled by modifying an equivalent electric network proposed by Nakamura *et al*. [7],[8] which could represent the propagation of a thickness-vibration mode along the piezoelectric plate.

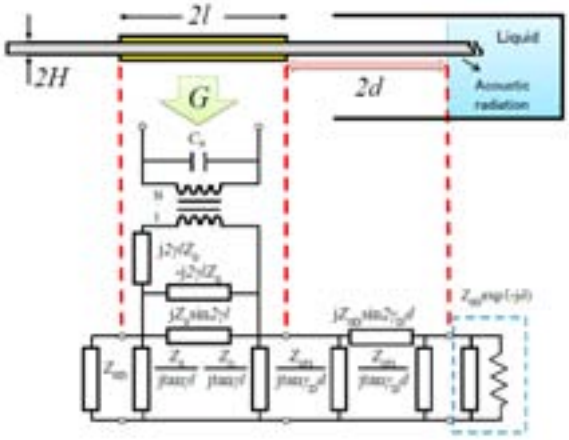

Fig. 2 Equivalent network representation for the sensor [11].

Figure 2 shows the network model [11] for the sensing vibrator with a thickness of 2*H*. Here, the sensor system is illustrated rotated by 90 ° from its original position. It has rectangular electrodes with a length of 2*l* in the direction of wave propagation and a width of unit length perpendicular to it. The central electroded region is composed of a transmission line (length: 2*l*, characteristic impedance: Z_0, wave number: γ), which is related to the electric terminal via some additional elements including a damped capacitance C_0. The section between the electrode edge and the liquid surface is expressed by a transmission line representing the unelectroded portion of length 2*d*, wave number γ_D and characteristic impedance Z_{0D}. The outermost regions are supposed to have an infinite length and are therefore expressed by the characteristic impedance Z_{0D}. In this network, Z_0 and Z_{0D} will be either real or imaginary depending on frequency. In the frequency range where energy trapping works, Z_0 is real, whereas Z_{0D} is imaginary. To take the radiation loss into account, a phase angle -δ is applied to Z_{0D} for the portion dipped in a liquid. The variation in the electric properties with the length 2*d* between the electrode edge and the liquid surface is evaluated by varying the ratio *d*/*H*.

A thickness-extensional-wave trapped-energy resonator composed of a thickness-poled $Pb(Zr,Ti)O_3$ (PZT) plate is assumed as a one-dimensional model of the sensor. Since the vibration loss is not considered intrinsically in the equivalent-network model in Fig. 2, a small amount of resistance is added at the electric port so that the resulting Q_m becomes 750. Figure 3 shows the admittance characteristic for an unloaded (free) plate computed using the network. Here, the horizontal axis is the normalized frequency Ω (=ω*H*/v_t, v_t: longitudinal wave velocity), the vertical axis is the normalized admittance $|Y|/(v_tC_0/H)$. The ratio of the electrode length 2*l* to the plate thickness 2*H* is supposed to be 9. It is noted that two inharmonic overtone modes as well as the fundamental mode are produced because the ratio *l*/*H* is large.

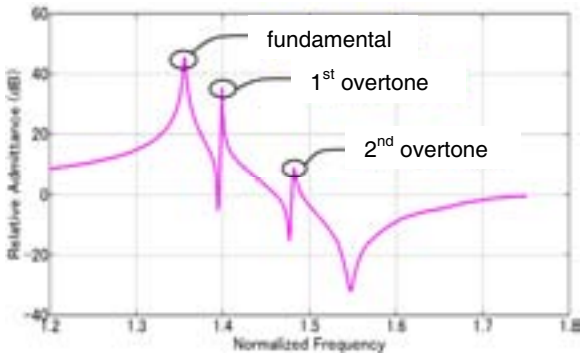

Fig. 3 Admittance characteristic computed for *l*/*H*=9.

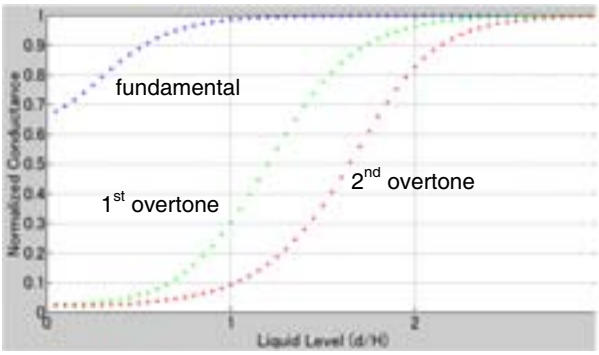

Fig. 4 Variations in *G* with the liquid level at resonances.

For sensing the liquid level, the variation in the electric conductance *G* is examined that corresponds to the variation in Q_m. Therefore, the variation in *G* with the normalized liquid level *d*/*H* is computed for the fundamental and the inharmonic modes. The result is shown in Fig. 4. Here, the vertical axis is normalized to *G* at *d*/*H*=3, and δ is assumed to be 1. It is noted that *G* decreases as the liquid surface approaches to the electrodes. The decay factor, the imaginary wave number determining the profile of the evanescent field, differs between the fundamental and inharmonic modes. For inharmonic modes, the decay factor is smaller than that for fundamental modes. Therefore, exponential decay is gentle for inharmonic modes, and the performance for liquid-level sensing is regarded as different depending on which mode is used.

B. Device using Trapper-Energy Resonator for Backward-Wave-Type Thickness Vibration

In some thickness vibration modes, the dispersion curve takes a different form, as shown in Fig. 5(a). In this case, the corresponding vibration has the cut-off regime above the cut-off frequency, and therefore it becomes a backward-wave mode. To realize energy trapping for this mode, the surrounding region should be electroded and short-circuited so that the wave number there becomes imaginary, as shown in Fig. 5(b) [5], [12]-[14]. In the trapped-energy mode of this type, spurious-free characteristics are obtained around the anti-resonance frequency rather than the resonance frequency. Therefore, the use of antiresonance may be effective for liquid level sensing.

The sensor configuration for this type of trapped-energy vibrator and the equivalent-network representation are shown in Figs. 1(b) and 6, respectively. A backward-wave-type trapped-energy resonator composed of a thickness-poled $PbTiO_3$ plate is assumed as a model. Two transmission lines representing the unelectroded gaps of the length 2*l'* are added

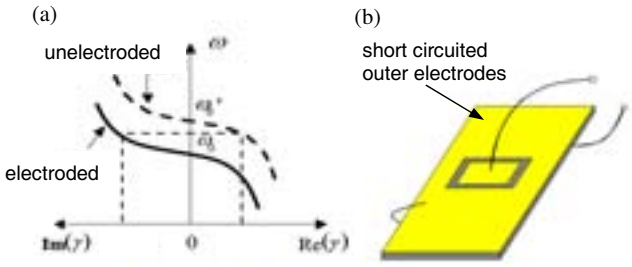

Fig. 5 (a) Dispersion curve for backward-wave thickness vibration and (b) electrode configuration for energy trapping.

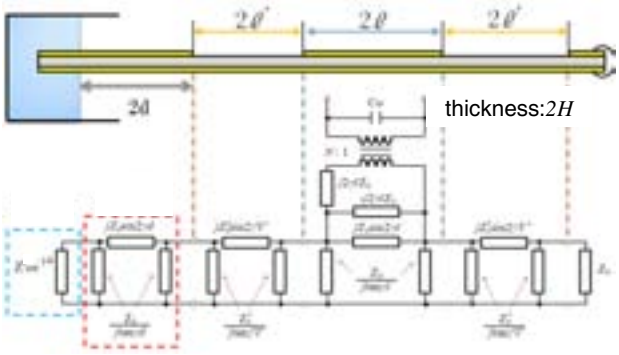

Fig. 6 Equivalent network for the sensor utilizing trapped energy vibrator of backward-wave mode.

to the network shown in Fig. 2. The outermost metallized regions are supposed to have an infinite length and are therefore expressed by the characteristic impedance Z_0. In the sensing side, however, a transmission line of the length representing the out-of-liquid portion of length $2d$, wave number γ and characteristic impedance Z_0 is added, which is terminated by $Z_0\exp(-j\delta)$.

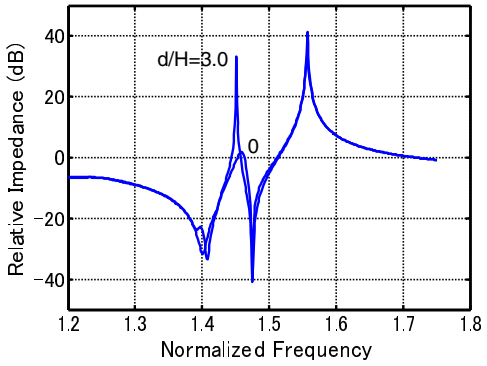

Fig. 7 Impedance characteristics computed for d/H of 0 and 3.0.

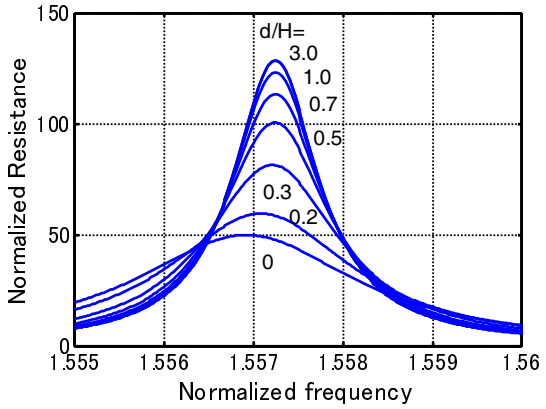

Fig.8 Variation in R with the liquid level at antiresonance.

In the trapped-energy mode of this type, spurious-free characteristics are obtained around the anti-resonance frequency rather than the resonance frequency [5], [12]-[14]. Therefore, the variations in the electric impedance characteristic are computed for d/H of 0 and 3.0. The result is shown in Fig. 7. The ratio of the center-electrode length $2l$ to the plate thickness $2H$ is supposed to be 4, and l'/H=0.5. The horizontal axis is the normalized frequency Ω (=$\omega H/v_l$, v_l: longitudinal wave velocity), and the vertical axis is the normalized impedance $|Z|/(H/v_lC_0)$. Although it is not clear enough for the fundamental mode, it is noted that smaller d/H (higher liquid level) gives a lower peak level at antiresonance frequencies.

The frequency characteristic of R, the real part of Z, is also computed for several values of d/H at the antiresonance frequency of the fundamental mode. The result is shown in Fig. 8. Here, the vertical axis is the normalized resistance $R/(H/v_lC_0)$. A gradual decrease in R is observed in accordance with the increase in the liquid level.

III. Conclusions

An equivalent network representation is presented for the liquid-level sensors operating in a trapped-energy mode thickness vibration of conventional type and backward-wave type. The variation in G and/or R with the liquid level has been computed using this network model, and it is revealed that the computed plots show a similar trend in variation to the experimental results that have been reported so far.

Acknowledgment

The authors are grateful to H. Kanno who participated in this work.

References

[1] W. Shockley, D. R. Curran, and D. J. Koneval: Proc. 17th Frequency Control Symp., 1963, p. 88.

[2] K. Yamada, H. Honda, S. Horiuchi, and T. Kinai: Jpn. J. Appl. Phys. **48** (2009) 07GB08.

[3] K. Yamada, S. Horiuchi, H. Honda, and T. Kinai: Proc. 2009 IEEE Ultrassonic Symp., p.2508.

[4] S. Seto, S. Horiuchi, and K. Yamada: Jpn. J. Appl. Phys. **49** (2010) 07HC05.

[5] K. Yamada and S. Seto: Proc. 2010 IEEE Ultrassonic Symp., p.1439

[6] K. Yamada, S. Seto, and S. Horiuchi: Proc. 2011 IEEE Ultrasonic Symp., p.1522.

[7] K. Nakamura and H. Shimizu: Denshi Tsushin Gakkai Ronbunshi **55-A** (1972) 95 [in Japanese]..

[8] K. Nakamura, H. Watanabe, and H. Shimizu: Denshi Tsushin Gakkai Ronbunshi **59-A** (1976) 985 [in Japanese].

[9] E. P. Mason: *Piezoelectric Crystals and Their Application to Ultrasonics* (D. Van Nostrand, Princeton, NJ, 1950).

[10] R. Krimholtz, D. A. Leedom, and G. L. Matthaei: Electron. Lett. **6** (1970) 398.

[11] K. Yamada, T. Koyama, and S. Seto: Jpn. J. Appl. Phys. **51** (2012) 07GC04.

[12] H. Shimizu and K. Yamada: Denshi Tsushin Gakkai Ronbunshi A **62** (1979) 8 [in Japanese].

[13] K. Yamada and H. Shimizu: Denshi Tsushin Gakkai Ronbunshi A **63** (1980) 327 [in Japanese].

[14] K. Yamada and H. Shimizu: Proc. 1984 IEEE Ultrassonic Symp., p.383.

The $GaPO_4$ Biosensor´s Affinity and its Electronic Evaluation

Milan Kolář and Jaroslav Nosek
Faculty of Mechatronics, Informatics and Interdisciplinary Studies
Technical University of Liberec
Liberec, Czech Republic
milan.kolar@tul.cz, jaroslav.nosek@tul.cz

Abstract - **This paper deals with the formation of the ASC immunocomplex at the surface of the Y-cut $GaPO_4$ resonator vibrating in thickness-shear mode. The orientation YXl (-16.4°), with the tolerance on the rotation angle ± 0.1° of the sample is used in this study. The relevant $GaPO_4$ material constants were calculated. The biochemical affinity process can be characterized by association and dissociation kinetic rate constants, by binding between a covalently immobilized small molecule and its relative antibodies. The binding curves of series resonance frequency f_s vs. time t were measured and discussed. The following tasks were considered: activation by the cystamine, glutaraldehyde, and albumine as bioactive buffer, ASC antibody solution with phosphate buffer, and regeneration of the biosensor.**

Standard frequency response of a new biosensor was evaluated by the analyzer Agilent E5100A. However, the newly developed digital processing techniques are used to precise the measurement and to evaluate the frequency changes. The Field Programmable Gate Array circuits (FPGA) open the field of digital signal processing. Our solution uses the digital down converter (DDC) for evaluation of frequency changes. The DDC consists of three components: reference complex oscillator, low-pass filter and down sampler. Complex (quadrature) oscillator works on principle of direct digital synthesis and it provides a pair orthogonal sine and cosine waveform. The complex multiplier works as mixer, its output includes images centered at the sum and difference of input frequencies. The low-pass filter is digital FIR filter and it passes the difference frequency. The down sampler reduces the sampling rate of a signal.

The digital solution gives important advantages – digital stability, controllability and small size, that allow realize the biosensor controller unit in a smaller volume. This solution reduces the cost of the biosensor unit and brings the concept of "lab on chip". The resolution of the $GaPO_4$ biosensor remains unchanged, and biosensor sensitivity is increased.

Keywords: GaPO4 biosensor; ASC formation; FPGA circuits; evaluation of frequency changes

I. INTRODUCTION

A classical realization of a biosensor is based on the AT-cut quartz resonator, vibrating in thickness-shear mode of vibration [1-8]. A process of activation of biosensor influences the resonance frequency changes vs. time. In many experiments, the resonance frequencies of the piezoelectric resonator are measured, using classical oscillator and methods.

In the last years, the outstanding properties of the quartz homeotype gallium orthophosphate ($GaP0_4$) promise new applications of this modern representative of piezoelectric single crystals with large electromechanical coupling factor [9-11]. Its coupling factor k_{26} associated with the resonators vibrating in the thickness-shear mode is approximately two times greater than that of quartz [12]. Now, the nonlinear properties of the $GaP0_4$ and methods for determination of some nonlinear constants of $GaP0_4$ were presented [12]. The outstanding properties as remarkable frequency, temperature and chemical stability of this quartz homeotype make possible to use it such as a biosensor. The increased number of the papers indicates a significance of the $GaP0_4$ too [13]. However, the use of thickness-shear mode of vibrations of the $GaP0_4$ resonator such as biosensor is relatively rare. The biosensor´s functions are closely connected to the signal processing. The field of digital signal processing is now open for modern microelectronic circuits such as FPGAs [15-16]. They are the reasons to develop our studies on $GaPO_4$ biosensors and to prepare the miniaturized sensible biosensor.

II. ROTATED Y-CUT GAPO4 RESONATOR IN OUR STUDY

In order to measure the important parameters of the $GaP0_4$ Y-cut resonators, sample plates of the orientation (YXI)-16.4° were prepared and electroded by AVL of Graz, Austria, and measured in our laboratory. The plates were 10 mm in diameter and 0.3 mm thick. The gold electrodes of 5 mm diameter were deposited on the major surfaces of the plates. The orientation of the plates was measured to ± 0.1°. The basic material parameters were calculated and transformed to the orientation (YXl)-16.4° Y-cut [12].

III. EXPERIMENTAL

A. Activation Process

Affinity interaction describes usually the formation of specific supramolecular complexes between two affinity partners. The surface of the gold-electroded resonator was firstly treated 30 min with 100 ml of acetone, and dried. Using cystamine solution (200 mg) in water, applied on the gold

TUL – Institute of Mechatronics and Computer Engineering.

electrode surface (100 µl), incubated 2 hours, then crystal unit was washed with water and air dried. Alternatively, the glutaraldehyde 3% solution 3mg/97mg in phosphate buffer with pH=7.0, applied on the gold electrode surface (100 µl), incubated 1 hour was used, then crystal unit was washed and air dried. In the third case, the albumin solution in phosphate buffer 500 µg/l ml, applied on the gold electrode surface (100 µl), incubated and stored at 4 °C 12 hours was used, then crystal unit was washed air dried. The piezoelectric unit with bio-complex as biosensor is prepared to bind with its covalent layer the antibody liquid. The frequency shifts caused by activation process are given in Table I.

TABLE I. CHANGES IN RESONANCE FREQUENCY CAUSED BY DIFFERENT MODE OF THE ACTIVATION. $GaPO_4$ RESONATOR YXL (-16.4^0).

Mode of activation	$GaPO_4$ Resonator YXl (-16.4^0)	
	fs [Hz] in the measuring cell	fs [Hz] without measuring cell
Without active surface	4 057 182	4 058 959
After treatment by acetone	4 057 663	4 059 184
After activation by cystamine	4 057 502	4 059 124
After activation by gluterdehyde	4 057 868	4 059 662
After activation by albumine	4 058 033	4 059 965

B. GaP0$_4$ Resonator´s Affinity Interactions

An important issue affecting sensor performance is the proper attachment of a biological film to the sensor surface. Several immobilization techniques have been developed and its properties studied [2], [8] to create an affinity sensor. For an affinity sensor, receptor molecules have to be immobilized on surface on the gold electrodes of the $GaPO_4$ disc. The area of the electrodes dimensions is characterized by maximum vibrations (trapped energy case). The corresponding binding molecule, if present in the sample solution, will bind specifically to the receptor of the surface. In this case the sensor directly responds to the formation of the receptor-ligand complex. When the ligand and receptor are an antigen and the relative antibody their interaction will lead to an immunocomplex. We analyzed the binding between a covalently immobilized small molecule and its relative antibodies. Formation of immunocomplex AB at the surface of the $GaPO_4$ resonator vibrating in thickness-shear mode can be characterized by association k_a and dissociation k_d kinetic rate constants. The binding curves of series resonance frequency f_s vs. time t were derived in [8]. The typical characteristics $f_s(t)$ of immunosensor shown fifth phases:

a) Relative stable background frequency $f_s(t)$ caused by presence of buffer (with their loading effect). This phase typically lasts five minutes.

b) Then, sample solution containing a mixture of antibody and analyte is injected (association phase). The antibodies with free binding sites interact with the immobiliyed ligand. A decrease of frequency *fs* is observed when a surface mass on the crystal increases (the equilibrium change *feq* is achieved eventually). This phase typically lasts about 30 minutes.

c) Reaction of biosensor with phosphate buffer. Buffer is injected again and the dissociation of immunocomplexes is observed. From this phase, the dissociation constant *kd* can be obtained. The frequency *fs* represents the amount of surface-bound irnmunocomplex at the beginning of dissociation. This phase typically lasts about 30 minutes.

d) Area of regeneration of biosensor after application of the formic acid. This phase typically lasts five minutes.

e) Terminal phase of resonator regeneration. The process of the regeneration of all covalent bonds between molecules of antibody and molecules of bioactive layer is observed. About 5 minutes.

The reaction time depends on the concentration of antibody and analyte. These results are consistent with [1] and [2].

The series resonance frequency f_s, has been determined using the standard IEEE method and Network Analyzer AGILENT E5100A in accordance to the [14]. The affinity process is presented by Fig. 1 and 2, which describes the affinity reactions of the antibody solutions ASC with phosphate buffer 1:250, or 1:100 respectively.

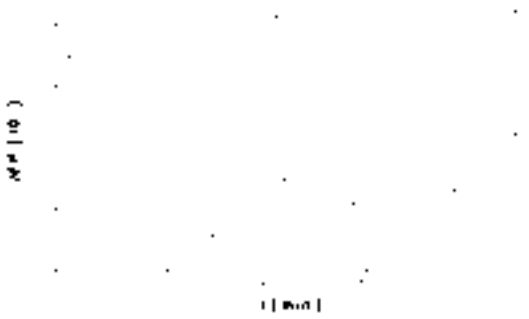

Figure 1. Affinity reaction of the biosensor with the antibody ASC 1:250. GaP0$_4$ piezoelectric resonator YXI (-16.4°).

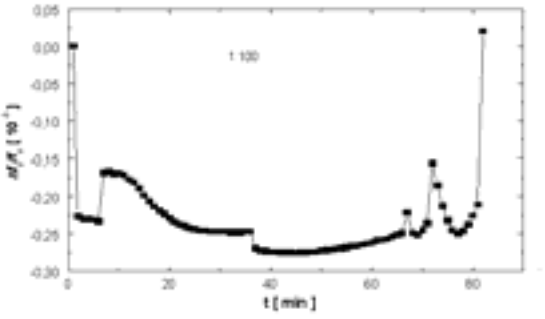

Figure 2. Affinity reaction of the biosensor with the antibody ASC 1:100.

IV. AFFINITY ELECTRONIC EVALUATION

The standard frequency response of a new biosensor was evaluated by the classical analog techniques – using analyzer Agilent E5100A (see Figure 3).

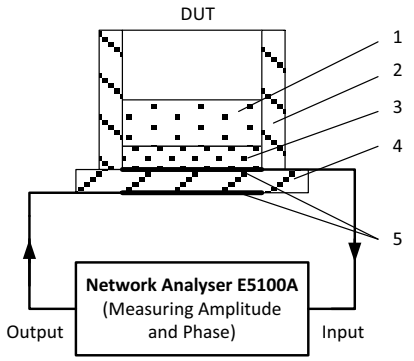

Figure 3. Block diagram of a laboratory biosensor measuring systems. 1 – Bioactive liquid, 2 – Teflon cell, 3 – Buffer, 4 – AT quartz resonator in measuring π-network, 5 – Au electrodes.

With the advent of newer larger and faster semiconductor devices has opened up the field of digital signal processing. Therefore we are made an evaluation of the signal processing (changes in resonance frequency) using digital down conversion (DDC). DDC is a technique that takes a band limited high sample rate digitized signal, mixes the signal to a lower frequency and reduces the sample rate while retaining all the information. The basic arrangement shows the Figure 4.

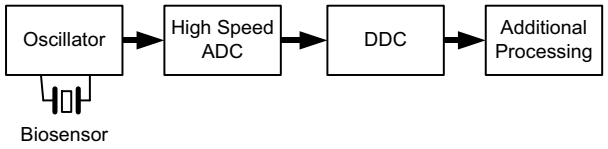

Figure 4. The basic arrangement of frequency evaluation

The signal from oscillator with biosensor (frequency about 5 MHz) is converting using fast analog-to-digital converter (ADC) to digital signal. The sample rate of an ADC must be at least twice the signal rate (the Nyquist theorem). 12-bit ADC was used for good dynamic range.

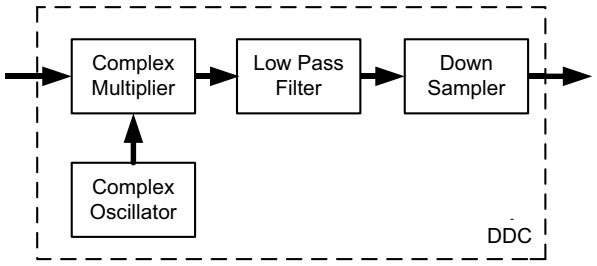

Figure 5. Block structure of DDC

Principle of the DDC is a fundamental part of many communication systems and consists of three basic subcomponents: complex numerically controlled oscillator (NCO), low-pass filter (LPF) and down-sampler (which may be integrated into the LPF). Figure 5 illustrates the block structure of the DDC.

The NCO is a digital signal generator which creates a synchronous, discrete-time, discrete-value representation of a waveform, usually sinusoidal. In our case the NCO has quadrature output (generates sine and cosine waveforms) and consists of two parts: phase accumulator (PA) and phase-to-amplitude converter (PAC) – see Figure 6. The frequency control register keeps generally N-bit word FCW. A binary phase accumulator consists of N-bit binary adder and phase register. Each clock cycle produces a new N-bit output consisting of the previous output obtained from the register summed with FCW which is constant for a given output frequency. The resulting output waveform is staircase with step size FCW (a modulo-2^N sawtooth waveform). These outputs are converted by the PAC to a sampled sinusoid or cosinusoid. PAC is designed as a memory (look-up table) - PA output word represents address.

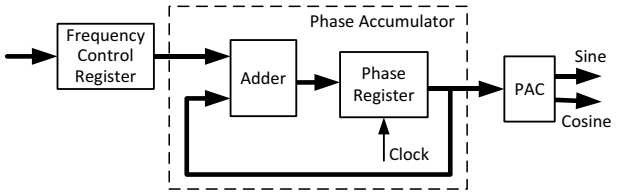

Figure 6. NCO with quadrature output

The function of the complex multiplier (mixer) is to multiply the incoming signal (from ADC) by the generated sinusoid to shift the spectrum of signal – generates sum and difference frequency. An implementation uses two multipliers, one each for the sine and the cosine. If frequencies of received signal and local tunable NCO are near, difference frequency draw to zero (spectrum centered at zero). Therefore frequency changes can measure very precisely.

The LPF pass the difference frequency while rejecting the sum frequency spectral image. LPF was implementing high speed finite impulse response (FIR) filter (4^{th} order) using registered adders and hardwired shifts. The following down sampler reduces the sampling rate of a signal for additional slower processing.

The implementation of all electronic blocks is testing on development kit which consist fast ADC, FPGA circuit (family Altera Cyclone III) and crystal reference oscillator.

V. CONCLUSION

The characteristics frequency-time correspond to the experimentally values obtained by AT-cut quartz resonator, but increasing sensitivity of the $GaP0_4$ resonator, based on the large coupling factor k_{26}, was found. The small differences in the characteristics described as a), c) and e) are caused by the process of regeneration, realized previously. The attention should be devoted to the viscoelastic interaction of liquid and resonator surface, roughness of resonator surface, controlling electronic circuit, surface tension, and different chemical interaction of resonator surface - liquid.

The digital solution gives important advantages – digital stability, controllability and small size, that allow realize the biosensor controller unit in a smaller volume. This solution reduces the cost of the biosensor unit and bringing it closer to the solutions "lab on chip". However, a resolution of the biosensor remains.

ACKNOWLEDGMENT

The authors acknowledge the Technical University of Liberec, Faculty of Mechatronics, Informatics and Interdisciplinary Studies, Piezoelectric laboratory and FPGA laboratory for support.

REFERENCES

[1] M.Mimuni, P.Skladal, M.Mascini, "A Piezoelectric Quartz Crystal Biosensor as a Direct Affinity Sensor", Analytical Letters, vol.27,8, p. 1475 (1994).

[2] P. Skládal, „Piezoelectric quartz crystal resonators applied for immunosensing and affinity interaction studies“, Methods Mol.Biol., 504, pp. 37-50, (2009). doi: 10.1007/978-1-60327-569-9_3.

[3] M. Malmquist, R. Karlsson, „Biomolecular interaction analysis: affinity biosensor technologies for functional analysis of proteins“, Elsevier, Current Opinion in Chemical Biology, vol.1, 3, pp.378-383, (Oct.1997). http://dx.doi.org/10.1016/S1367-5931(97)80077-4

[4] E. Luzi, M. Minunni, S. Tombelli, M. Mascini, „New trends in affinity sensing: aptamers for ligand binding“, TrAC, Trends Anal. Chem., vol.22, 11, pp.810– 818, (2003).

[5] S. Lofas, B. Johnsson, „A novel food hydrogel matrix on gold surfaces in surface plasmon resonance sensors for fast and efficient covalent immobilization of ligands“, J. Chem. Soc. vol.21, pp.1526–1528, (1990).

[6] M. Liss, B. Petersen, H. Wolf, E. Prohaska, „An aptamer-based quartz crystal protein biosensor“, Anal. Chem., vol. 74, pp.4488–4495, (2002).

[7] J. Horacek, P. Skladal, “Improved direct piezoelectric biosensors operating in liquid solution for the competitive label-free immunoassay of 2,4-dichlorophenoxyacetic acid",Analytica Chimica Acta, vol.347,43, (1997).

[8] M. Mascini, http://www.unifi.it/dclabi

[9] AVL Graz website, http://www.gapo-l.com, April 2010 .

[10] A. Zarka, B. Capelle, J. Detaint, D. Palmier, E. Philippot, and O. V. Zvereva, "Studies of GaP04 resonators," in Proc. 10th European Frequency and Time Forum,1996, pp.308-312.

[11] P.Krempl, J.Stadler, W.Wallnofer, W.Ellmeyer, and R.Selic, "Present State of GaP04 Research," in Proc. 5th European Frequency and Time Forum, 1991, pp. 143-147.

[12] J. Nosek, J. Zelenka, „Contribution to the electromechanical and nonlinear properties of GaP04 crystals“, IEEE Transactions on Ultrasonics, Ferroelectrics, and Frequency Control, vol.50, 6, pp.571-576, (June 2003).

[13] F.Sthal, E.Bigler, R.Bourquin, Thermal compensation in $GaP0_4$ beam resonators: experimental evidence for length extensional mode. IEEE Transactions on Ultrasonics, Ferroelectrics, and Frequency Control, vol.54, l, pp.196-197, (Jan. 2007).

[14] IEEE Standard on Piezoelectricity. IEEE 1988.

[15] T. Bijlsma, P. T. Wolkotte, G. J. M. Smit, “ An Optimal Architecture for a DDC”, in Proc. Parallel and Distributed Processing Symposium, April 2006, ISBN: 1-4244-0054-6.

[16] R. Andraka, “High Performance Digital Down-Converters for FPGA”. Xcell Journal, Issue 38, pp. 48-51, (2000).

Frequency Stability Estimation of Compass On-Board Clock Based on Smoothed Broadcast Ephemeris

Hang Gong, Wenke Yang, Hai Sha, Xiangwei Zhu, Feixue Wang
College of Electronic Science and Engineering, National University of Defense Technology,
Changsha, Hunan, P.R. China, 410073
gonghang@nudt.edu.cn

***Abstract*—For Compass and Galileo systems which are currently in their stage of construction, it is difficult to obtain precise on-board clock short-term stability for common users. In this paper, a simple estimation method based on smoothed broadcast ephemerides is proposed, which only needs observation from one single receiver. The principle of this method is discussed, followed by performance evaluation using GPS data. We conclude that the relative error of short-term stability estimated with this method is less than 10% for average time of 1~800 seconds. Short-term stability estimation of all the current 14 Compass on-board clocks are presented, with the result of approximately 6×10^{-12} at average time of 1s and 2×10^{-13} at 1000s.**

Keywords-BeiDou Navigation Satellite System (BDS/Compass); on-board clock; short-term stability estimation; precise ephemeris; smoothed broadcast ephemeris;

I. INTRODUCTION

On-board clock performance evaluation is of great significance for satellite navigation system. In the application such as satellite clock offset modeling, simulation and prediction, not only characteristics determined by the medium- and long-term stability need to be known, short-term stability parameters of satellite clock also need to be obtained.

Stability estimation of GPS satellite clock is usually implemented using IGS precise clock data, which is derived from post-processing using complex orbit determination and time synchronization (ODTS) method [1]. The sampling interval of 30s typically, even the sampling interval of 5s provided by Center for of Orbit Determination in Europe (CODE), cannot satisfy the need of shorter average time (e.g. 1s) frequency stability estimation. On the other hand, IGS products are only available for GPS and GLONASS system currently, not for BeiDou (BDS/ Compass) or Galileo system. In addition, due to limited access permission for monitoring networks observation data, there are certain difficulties for Compass and Galileo common users to obtain precise satellite clock parameters presently.

In this paper, based on the analysis of the single station estimation method of satellite clock stability in Section II, Section III proposes a method based on smoothed broadcast ephemeris. Compared with IGS clock products, the method are validated using GPS data in Section IV. Using this simple method, the short-term stability of present Compass on-board clocks is presented at the end.

II. SINGLE STATION ESTIMATION METHODS OF SATELLITE CLOCK STABILITY

For satellite *i*, the carrier phase observation equations of receiver *j* on the frequency *k* are shown as follows:

$$\varphi_k^{ij} = d^{ij} + c\left(\Delta t_S^i - \Delta t_R^j\right) + T_k^{ij} - N_k^{ij}\lambda_k + \varphi_{k0}^{ij} + s^{ij} + t_k^i + r_k^j + m^{ij} + \varepsilon_{\varphi k}^{ij} \quad (1)$$

Where φ_k^{ij} is carrier phase observation; d^{ij} is geometric distance of satellite and receiver; Δt_S^i and Δt_R^j are satellite and receiver clock offset; T_k^{ij} is atmospheric propagation delay; $N_k^{ij}\lambda$ and φ_{k0}^{ij} are integral and fractional ambiguity of carrier phase; s^{ij} is error caused by the Sagnac effect; t_k^i is transmission delay of satellite; r_k^j is receive delay of receiver; m^{ij} is multipath error; $\varepsilon_{\varphi k}^{ij}$ is measurement noise of carrier phase.

Because only relative clock offset is needed to estimate satellite clock short-term stability, we can determine the on-board clock offset with respect to receiver clock [2]. In this case, satellite clock stability can be obtained as long as the stability of receiver clock is better than that of satellite clock, which can be achieved easily.

Equations (1) show that, several errors should be corrected before the computation of satellite clock offset [2]. It should be noted that the ionospheric delay has greater impact among these errors, thus the residuals will significantly increase estimation error of frequency stability for large average time if it cannot be corrected accurately. Dual-frequency combination is one of the most effective methods, but the noise variance will be magnified when using this method.

For carrier phase observations, general dual-frequency ionosphere-free combination is as follows:

$$\varphi_{if}^{ij} = \frac{\left(\varphi_2^{ij} + N_2^{ij}\lambda_2\right) - \gamma\left(\varphi_1^{ij} + N_1^{ij}\lambda_1\right)}{1-\gamma},\ \gamma = \frac{f_1^2}{f_2^2} \quad (2)$$

Equation (2) shows that the noise variance of φ_{if}^{ij} will be larger than $\varepsilon_{\varphi 1}^{ij}$ or $\varepsilon_{\varphi 2}^{ij}$, so although estimation error of frequency

stability with large average time is improved, but the estimation error of short-term stability will correspondingly increase.

Let ionospheric delay correction on the frequency f_1 be:

$$\Delta\varphi_1 = \varphi_1^{ij} - \varphi_{if}^{ij} + \frac{N_2^{ij}\lambda_2 - \gamma N_1^{ij}\lambda_1}{1-\gamma} = \frac{\varphi_1^{ij} - \varphi_2^{ij}}{1-\gamma} \tag{3}$$

Then revise dual-frequency ionosphere-free combination to [3]:

$$\varphi'_{if} = \varphi_1^{ij} - smooth\{\Delta\varphi_1\} \tag{4}$$

Where smooth {•} is a smoothing operator.

By equations (3) and (4), carrier phase integer ambiguity solutions could be avoided, but cycle slips should be detected and repaired. On the other hand, since the ionospheric delay will not dramatically changes, smoothing $\Delta\varphi_1$ will greatly reduce the error introduced by the dual-frequency combination, so that φ'_{if} will get same noise variance as single-frequency observation, and then both short- and long-term frequency stability estimation error introduced by ionospheric delay can be reduced to minimum.

After all the errors are corrected, the satellite on-board clock offset with respect to receiver clock is as follows:

$$\Delta t_k^j = \frac{1}{c}\left(\varphi_k^j - d_k^j\right) + \Delta\varepsilon_\varphi^j \tag{5}$$

Where $\Delta\varepsilon_\varphi^{ij}$ is residual error. Receiver can obtain carrier phase observation φ_k^{ij} with high sampling rate, and then satellite clock offset with the same sampling rate can be obtained. As long as geometric distance between satellite and receiver is determined beforehand, the short-term stability of on-board clock can be estimated consequently.

Since receiver position can be accurately calibrated, the main problem to determine the geometric distance is how to obtain precise satellite position. There are three approaches to reduce calculation errors of geometric distance: Firstly, we can obtain accurate satellite position through IGS precise ephemeris products [4]; Secondly, we can accurately determine the geometric distance, such as using satellite laser ranging [5]; Thirdly, we can try to eliminate the effect of geometric distance error by two-way ranging [6] or observation fitting [7], etc. For common users, using precise ephemeris is a relatively simple method, but for Compass and Galileo systems there is no precise ephemeris available but broadcast ephemeris for the moment.

III. Estimation Methods Based on Smoothed Broadcast Ephemeris

A. *Errors of Broadcast Ephemeris*

Broadcast ephemeris is predicted results based on the post-processed satellite position data using ODTS method. The prediction error of the satellite orbit both in cross-track and along-track direction normally is 5~10m [8], but in radial direction is much smaller for it is fully observed, with only 1/3 to 1/4 of the error in cross-track or along-track directions [8], and it also changes relatively slowly, which affects the estimation of the short-term stability of the satellite clock very slightly. The error projected to receiver's line of sight direction (LOS) exhibits similar characteristic.

Taking GPS Satellite PRN14 as an example, its ECEF coordinate error of broadcast ephemeris compared with precise ephemeris on September 10, 2011 is shown in Figure 1, and its LOS direction error observed by U.S. Naval Observatory (USNO) station is also shown.

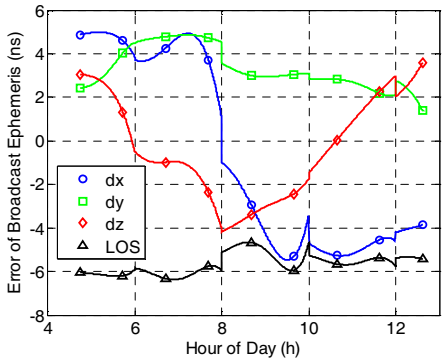

Figure 1. Broadcast ephemeris error of GPS PRN14

As shown in Figure 1, although the broadcast ephemeris absolute errors in x, y, and z-direction show marked variation up to ±6ns (approximately ±2m), but the variation of relative error in receiver's LOS direction is only 2ns. And there are much orbit jumps at the time of ephemeris update (TOE) for all direction.

Figure 2 and Figure 3 show statistical mean and standard deviation of prediction error of GPS broadcast ephemeris from September 9 to 12, 2011. It can be seen that the backward or forward prediction error within 2 hours is very small and stable, but increases radically beyond 2 hours.

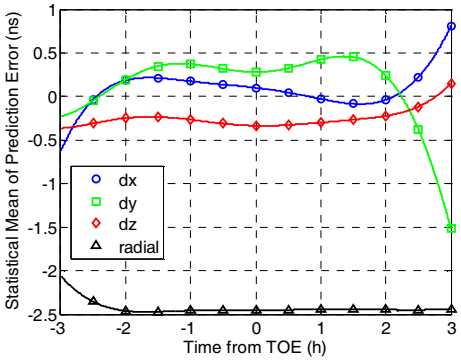

Figure 2. Statistical mean of prediction error of GPS broadcast ephemeris

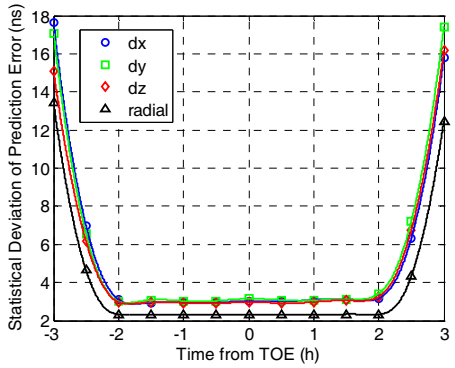

Figure 3. Statistical deviation of prediction error of GPS broadcast ephemeris

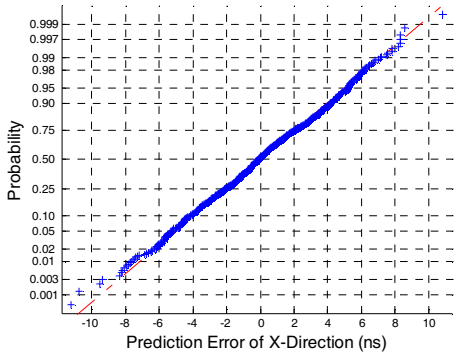

Figure 4. Lognormal probability plot of x-direction prediction error

Figure 4 shows lognormal probability statistical of x-direction prediction error within 2 hours of GPS broadcast ephemeris, which indicates that the backward and forward prediction errors are nearly normal distribution, so the prediction error of broadcast ephemeris can be modeled as:

- The prediction errors of x, y and z direction within 2 hours are distributed as $N(0,\sigma_x^2)$, $N(0, \sigma_y^2)$ and $N(0, \sigma_z^2)$ respectively;
- They are irrelevance with prediction time;

B. Smoothing Method of Broadcast Ephemeris

There are two groups of ephemeris parameters available for each observation epoch t, the TOE of the two adjacent groups of broadcast ephemeris are denoted as t_b and t_f respectively, and satellite positions calculated from the above two groups of broadcast ephemeris for t as $\mathbf{P_b}$ and $\mathbf{P_f}$, the prediction errors of $\mathbf{P_b}$ and $\mathbf{P_f}$, as $\mathbf{w_b}$ and $\mathbf{w_f}$, the actual satellite position as $\mathbf{P}$, then we have:

$$\mathbf{P_p} = \mathbf{H}\cdot\mathbf{P} + \mathbf{w} \tag{6}$$

where,

$$\mathbf{P_p} = \begin{bmatrix}\mathbf{P_b}\\ \mathbf{P_f}\end{bmatrix} = \begin{bmatrix} x_b & y_b & z_b \\ x_f & y_f & z_f \end{bmatrix},\ \mathbf{H} = \begin{bmatrix}1\\1\end{bmatrix} \tag{7}$$

$$\mathbf{P} = \begin{bmatrix} x & y & z \end{bmatrix},\ \mathbf{w} = \begin{bmatrix}\mathbf{w_b}\\ \mathbf{w_f}\end{bmatrix} = \begin{bmatrix} w_{bx} & w_{by} & w_{bz} \\ w_{fx} & w_{fy} & w_{fz} \end{bmatrix} \tag{8}$$

So the covariance of $\mathbf{w}$ is

$$\mathbf{C_w} = \mathrm{E}\left\{[\mathbf{w}-\mathrm{E}(\mathbf{w})][\mathbf{w}-\mathrm{E}(\mathbf{w})]^{\mathrm{T}}\right\} = \left(\sigma_x^2+\sigma_y^2+\sigma_z^2\right)\mathbf{I} \tag{9}$$

Then the minimum variance unbiased estimation of $\mathbf{P}$ is

$$\hat{\mathbf{P}} = \left(\mathbf{H}^{\mathrm{T}}\mathbf{C_w^{-1}}\mathbf{H}\right)^{-1}\mathbf{H}^{\mathrm{T}}\mathbf{C_w^{-1}}\mathbf{P_p} = \frac{1}{2}\mathbf{P_b} + \frac{1}{2}\mathbf{P_f} \tag{10}$$

$$\mathbf{C}_{\hat{\mathbf{P}}} = \left(\mathbf{H}^{\mathrm{T}}\mathbf{C_w^{-1}}\mathbf{H}\right)^{-1} = \frac{1}{2}\left(\sigma_x^2+\sigma_y^2+\sigma_z^2\right) \tag{11}$$

Taking GPS as an example, the broadcast ephemeris is updated every 2h. Each group of ephemeris parameters is a combination of forecasted fitting results using data of a specific time range. Thus the calculated satellite orbit parameters according to each group of ephemeris parameters jump at the time of ephemeris parameters update. A clock phase jump with amplitude of x_0 will introduce an additive overlapping allan variance as follows:

$$\sigma_y^2(\tau) = \frac{x_0^2}{(N\tau_0 - 2\tau)\tau} \approx \frac{x_0^2}{N\tau_0}\tau^{-1},\ (2\tau << N\tau_0) \tag{12}$$

where τ_0 is sampling interval and N is total sampling number.

Equation (12) shows that phase jumps will introduce additive white frequency modulation (WFM) noise, thus the orbit jumps will impact short-term stability estimation, but equation (10) could not weaken the transition, so it is needed to smooth the broadcast ephemeris in order to reduce this impact.

The prediction error model indicates that the predicted error of each group of broadcasted ephemeris is roughly the same, so it is suggested here to revise equation (10) to smooth broadcast ephemeris using linear weighted method according to the ephemeris age, namely:

$$\hat{\mathbf{P}}' = \frac{t_f - t}{t_f - t_b}\cdot\mathbf{P_b} + \frac{t - t_b}{t_f - t_b}\cdot\mathbf{P_f} \equiv k_b\cdot\mathbf{P_b} + k_f\cdot\mathbf{P_f} \tag{13}$$

Then we have:

$$\mathrm{E}\left(\hat{\mathbf{P}}'\right) = \mathrm{E}\left(k_b\cdot\mathbf{P_b} + k_f\cdot\mathbf{P_f}\right) = \mathbf{P} \tag{14}$$

$$\mathbf{C}_{\hat{\mathbf{P}}'} = \left(\mathbf{H}^{\mathrm{T}}\mathbf{C}^{-1}\mathbf{H}\right)^{-1} = \left(k_b^2+k_f^2\right)\left(\sigma_x^2+\sigma_y^2+\sigma_z^2\right) \tag{15}$$

We can see that $\hat{\mathbf{P}}'$ is still an unbiased estimation of $\mathbf{P}$, and although the estimation variance increases a bit, the satellite orbit will be smoothed.

Still taking USNO stations as example, Figure 5 shows smoothed results of GPS PRN14 broadcast ephemeris during the same time as Figure 1. It is shown that the smooth method eliminates the jumps of calculated satellite orbit, which will help to reduce the error of short-term stability estimation.

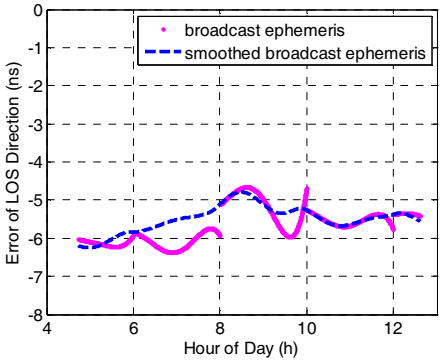

Figure 5. Smoothed broadcast ephemeris error of GPS PRN14

C. *Principle of Estimation Method*

Based on the above discussion, as shown in Figure 6, the estimation method based on precise ephemeris, broadcast ephemeris and smoothed broadcast ephemeris (denoted as PE method, BE method and SBE method respectively for the sake of simplicity) is carried out as follows:

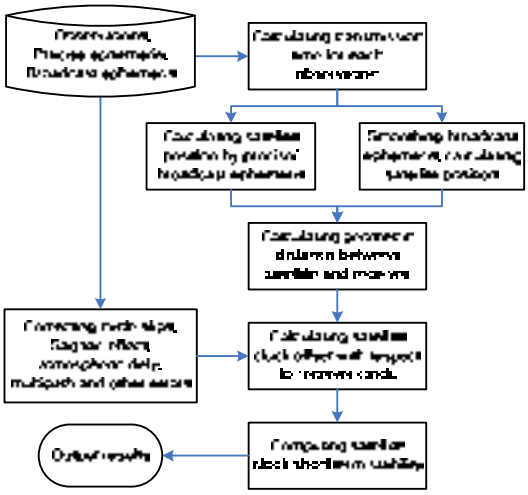

Figure 6. Principle of PE, BE and SBE method

IV. Experiments and Analysis

In this section we will use USNO station's GPS carrier phase observations published by IGS to verify these methods. This station provides GPS measurements at the rate of 1 Hz, and its receiver clock refers to a hydrogen maser which is disciplined by UTC(USNO), so that both short-term and long-term frequency stability of the receiver clock are much better than satellite on-board clock.

As a comparison of SBE method, the stability of GPS PRN14 on-board clock obtained by PE method is shown in Figure 6 firstly, along with the results of CODE precision clock product with 5s sampling interval in the same period. The experimental period is from GPST 2010-9-10 06:00:00 to 2010-9-10 12:00:00.

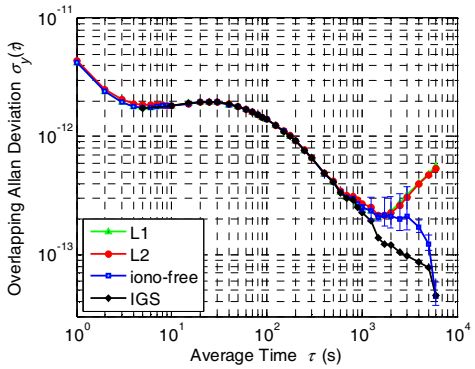

Figure 7. Frequency stability of GPS PRN14 by PE method

'L1' and 'L2' in Figure 7 are results with ionospheric delay corrected by Klobuchar model, 'iono-free' is corrected by dual-frequency ionosphere-free combination using equation (4). The above result shows that, ionosphere-free combination result is better than L1 and L2 for average time above 1000s due to correcting ionospheric delay effectively, and its short-term stability does not deteriorated within 10s average time due to noise variance smoothed. For the sake of simplicity, only dual-frequency ionosphere-free combination results will be presented in the following discussions.

Based on the same observation data of USNO station, the short-term stability estimations of GPS PRN14 on-board clock by BE and SBE method are shown in Figure 8.

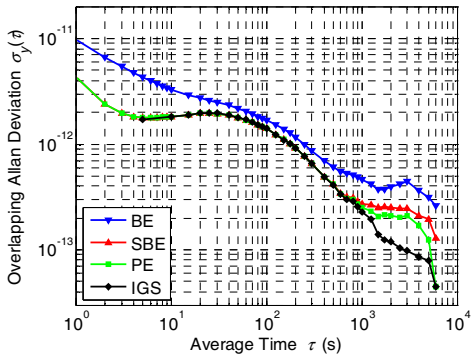

Figure 8. Frequency stability of GPS PRN14 by BE and SBE method

Taking the frequency stability calculated by IGS precise clock as true value, and the relative deviation between PE, BE and SBE method results and the corresponding true value as their estimation error. The three methods are compared with each other in Table 1 in four aspects: maximum applicable average time, maximum estimation error, and applicable GNSS systems at this stage. In which the maximum applicable average time is evaluated as the maximum average time with error less than 10%, and the maximum estimation error is evaluated as the maximum relative deviation within average time of 1000s.

TABLE I. PERFORMANCE COMPARISON OF THE THREE METHODS

	PE method	**BE method**	**SBE method**
maximum applicable average time	900s	/	800s
maximum estimation error	10.6%	148.7%	20.9%
applicable GNSS systems at this stage	GPS GLONASS	GPS GLONASS Compass Galileo	GPS GLONASS Compass Galileo

From the above table, we can draw the following conclusions:

- Orbit jumps introduced by broadcast ephemeris have a greater impact on the stability estimation, with WFM noise was introduced, leading that the results of BE method deviate from true value for all the average time, and the maximum estimation error is up to 148.7%;
- Since the influence of orbit jumps are eliminated by smoothed broadcast ephemeris, the estimation error of SBE method is greatly reduced. The result of SBE method is very close to PE method, and remarkably consistent with the true value. Its relative error is less than 10%, and even two order of magnitude less than the true value for the average time of 10~500s in particular.

V. COMPASS RESULTS

As for Compass system, precise clock is not available for validating the estimation results, and none of the results of on-board clock short-term stability is released until now, except for the stability of some satellite clock for the average time of above 100s presented by the literature [9], which is obtained from observation during February 2012 by ODTS method (denoted as ODTS results in the following discuss). In this paper, the observation data obtained from two monitoring stations (station 01 and station 03) within the same observation period are employed to estimate the short-term stability of satellite clock, and the results of the two stations are compared to validate themselves to another. As the receivers of the two stations refer to hydrogen masers which are synchronized with BDT (Compass System Time), the frequency stability of the receiver clock are better than satellite on-board clock, so the results can be used as a estimation of satellite on-board clock. In addition, ODTS results are also presented as a comparative reference.

Firstly we will compare the SBE method and ODTS results for Compass. The estimation results of SV07 on-board clock (rubidium) are shown in Figure 9, in which dual-frequency ionosphere-free combination of B1 and B3 carrier phase observations from BDT 2012-12-02 00:00:00 to 2012-12-03 00:00:00 are used. It should be noted that the frequency drift of satellite clocks are eliminated in literature [9], in order to compare with it the results of BE and SBE method in Figure 9 also eliminated frequency drift.

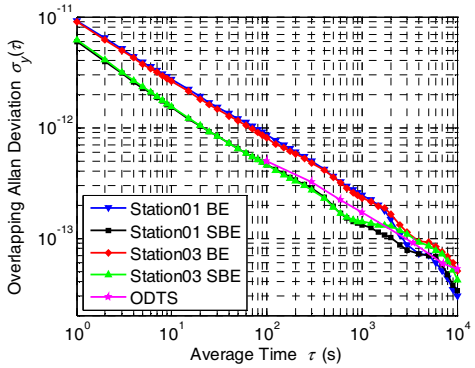

Figure 9. Frequency stability of Compass SV07 by SBE method

Figure 9 shows that the estimation results of the stations 01 and 03 by SBE method are consistent with each other, and agree well with ODTS results within the average time of less than 10000s. Since Compass broadcast ephemeris is updated once every 1 hour, orbit calculated by the broadcast ephemeris jumps frequently, but estimation error is greatly reduced after smoothing broadcast ephemeris.

Figure 10 shows stability estimation of all the 14 Compass satellite on-board clocks, in which the observation period is from BDT 2012-12-02 00:00:00 to 2012-12-04 00:00:00, but frequency drift is not eliminated in order to reflect the actual characteristics of space rubidium clock.

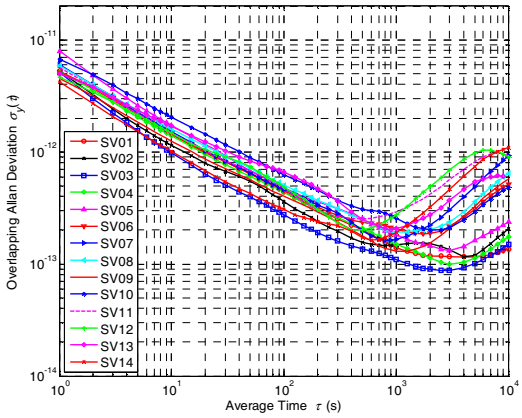

Figure 10. Frequency stability of all the current Compass on-board clocks

As can be seen from Figure 10, the stability of all the 14 on-board clocks are basically consistent for the average time of less than 1000s, and agree with ODTS results for 100~1000s, with statistical results shown in Table 2. Clocks of GEOs (SV01~SV05) are little better than that of IGSOs (SV06~SV10) or MEOs (SV11~SV14) for the average time of above 1000s.

TABLE II. FREQUENCY STABILITY ESTIMATION OF CURRENT COMPASS ON-BOARD CLOCKS

Average time (s)	SBE method	ODTS method
1	5.8×10^{-12}	/
10	1.5×10^{-12}	/
100	4.5×10^{-13}	6×10^{-13}
1000	1.7×10^{-13}	2×10^{-13}

VI. CONCLUSION

This paper proposed a simple estimation method based on smoothed broadcast ephemeris. Compared to IGS final clock product and other two methods namely PE and BE method, the performance of this method is validated using GPS observation. Experimental results indicate that the relative estimation error of this method is less than 10% for the average time of less than 800s, which is consistent with the results of PE method using precise ephemeris. Finally, the short-term stability of all the current 14 Compass on-board clocks are estimated by the proposed method, the results show that the stability of all the satellite clocks are basically consistent and agree with ODTS results. The short-term stability of current Compass on-board clocks is approximately 6×10^{-12} at average time of 1s and 2×10^{-13} at 1000s.

The proposed method in this paper provided some meaningful suggestions of short-term stability estimation and simulation of on-board clock for Compass and Galileo civil users. When the satellite on-board clock stability is better than receiver clock, the method also provides a receiver clock stability estimation approach.

REFERENCES

[1] J.M. Dow, R.E. Neilan, and C. Rizos, "The international GNSS service in a changing landscape of global navigation satellite systems," Journal of Geodesy, 83: pp. 191-198. 2009.

[2] H. Gong, W.K. Yang, Y. Wang, X.W. Zhu, and F.X. Wang, "Comparison of short-term stability estimation methods of GNSS on-board clock," Lecture Notes in Electrical Engineering, v160 LNEE, p503-513, Proceedings of the 3rd China Satellite Navigation Conference. Berlin: Springer, 2012.

[3] B.W. Parkinson, J. James, and J. Spilker, "Global Positioning System: theory and applications," American Institute of Aeronautics and Astronautics Inc., Washington DC, pp. 489-490, 1996.

[4] F. Gonzalez, and P. Waller, "Short term GNSS clock characterization using one-way carrier phase," Proc. of the 2007 Joint Conference of the IFCS and EFTF, IEEE Electron Devices Soc & Reliability Group, Geneva, Switzerland. 2007.

[5] X.F. Lu, X.L. Jia, and Z.Q. Yang, "Determination of navigation satellite clock bias using SLR and GPS dual frequency phase-smoothed pseudo-range data," Geomatics and Information Science of Wuhan University, 33: 237-240, 2008.

[6] X.H. Yang, L.M. Ma, B.Q. Sun, H. Lei, S. Le, and et al., "The method of time synchronization based on the combination of Compass GEO pseudo-range and two-way data," Proc. of 2011 Joint Conference of the IFCS and EFTF, IEEE Electron Devices Soc & Reliability Group, San Francisco, USA. 2011.

[7] J. Delporte, C. Boulanger, and F. Mercier, "Straightforward estimations of GNSS on-board clocks," Proc. of 2011 Joint Conference of the IFCS and EFTF, IEEE Electron Devices Soc & Reliability Group, San Francisco, USA. 2011.

[8] A. Roulston, N. Talbot, and K. Zhang, "An evaluation of various GPS satellite ephemerides," Proc. of the 13th International Technical Meeting of the Satellite Division of the Institute of Navigation (ION GPS-2000), Salt Lake City, UT, 2000.

[9] C.H. Han, "Time synchronization and in-orbit performance assessment of Compass on-board clocks," Invited presentation of 3rd China Satellite Navigation Conference, Guangzhou, China, 2012.

The Test and Evaluation of GPS On-board Clock

Yongliang XU
National Time Service Center/ Key Laboratory of Precision Navigation and Timing Technology of the Chinese Academy of Sciences, Xi'an, China
xuyl@ntsc.ac.cn

Wei LI
National Time Service Center/ Key Lab of Time-frequency Standard of the Chinese Academy of Sciences
Xi'an, China
kim_weili@ntsc.ac.cn

Weijin QIN
National Time Service Center/ Key Laboratory of Precision Navigation and Timing Technology of the Chinese Academy of Sciences, Xi'an, China
qwj@ntsc.ac.cn

***Abstract*—In satellite navigation system, the main time-frequency equipment of space segment is on-board clock, and its performance directly related to the pseudo code ranging and doppler effect observation precision, then affects the satellite navigation system orientation, velocity measurement and time service, so the test and evaluation of the on-board clock is very important. The methods and indicators used to evaluate the on-board clock in this paper. The performance of GPS on-board clock is evaluated based on the GPS on-board clock time difference data released by the IGS. Using Hadamard variance to evaluate the stability, the results show that the stability a day of most GPS on-board atomic clocks can reach 2×10^{-14}, in the time interval of 5 days, the stability reaches the highest level.**

I. INTRODUCTION

The satellite navigation system is based on time measurement, the main equipment depended by the time measurement is atomic clock. Master control station, all kinds of monitoring station, satellite are equipped with different amount of atomic clocks, all of the atomic clocks are synchronized to the system time. To the system, the On-board clock performance directly related to the pseudo code ranging and doppler effect observation precision, then affects the satellite navigation system orientation, velocity measurement and time service[1], so the test and evaluation of the on-board clock attach much importance. The on-board clock performance evaluation experiment had been done many times in the GPS, GALILEO and GLONASS satellite navigation systems. The similar research and experiment are carrying out in Chinese satellite navigation system.

II. THE BASIC CRITERIA FOR TESTING AND EVALUATION

In the time and frequency measurement, the frequency standard or clock to be measured is called the device under test. The measurement is a process to compared the device under test and the standard (or reference), two elements must be paid attention to as follows:

1) Reference selection

The accuracy of the reference must be at least 3 times higher than the object being measured, one order of magnitude is the best.

2) Measurement method selection

Some time comparison method is need to measure the object being measured, the error of the time comparison links must be less than the object being measured 3 times. There are two methods to meet that requirement.

(1) Choose high-precision time comparison method, to meet the requirements of testing and evaluation

(2) Optimizing the measurement method, accumulating measurement data, and use mathematical method to process the measurement data to reduce various types of errors.

III. EVALUATION METHODS OF ON-BOARD CLOCKS

1) Basic principle

According to the basic principles of testing and evaluation, the IGS precise clock difference data is used. Take the IGS integrated clock as the reference, the atomic clocks onboard as the object under test to evaluate the performance of the atomic clocks onboard.

Integrated processing the atomic clock data from all the IGS monitoring stations, more accurate and stable time scale can be obtained. Post-processing time comparison data of the atomic clock and atomic clocks onboard, the time delay error in the path used for time comparison can be well corrected to meet the requirement of the testing and evaluation of the atomic clocks onboard.

2) Testing and evaluation index analysis

The accuracy of the IGS precise satellite clock difference is better than 0.1ns[2].

To compare the uncertainty of on-board clocks using IGS precise satellite clock difference with accuracy better than 0.1ns, about $\approx 1\times10^{-15}$ frequency uncertainty will be brought one day. According to the standard of measurement uncertainty an order of magnitude higher, the index of atomic clocks onboard frequency is lower than 1×10^{-12} which meet the evaluation requirement.

The index of on-board atomic clocks frequency is lower than 1×10^{-14}(d). To evaluate the stability using IGS precise satellite clock difference with accuracy better than 0.1ns, about 1×10^{-15} stability will be brought one day. According to the standard of measurement uncertainty an order of magnitude higher, it will meet the requirement to evaluate the stability of atomic clocks onboard more than one day.

3) Index calculation model

(1) Accuracy and calculation model

Frequency accuracy refers to the consistency degree between the output frequency of device under test and the nominal frequency, it indicates the correctness of the oscillator output. The method to calculate the frequency accuracy by time difference comparison is called time difference method. The details to calculate are as follows:

$\hat{x}(t)$ is the compared atomic clocks onboard time differences, after gross error elimination of the those data, least squares linear fitting is used, and the fitting method is:

If

$$\bar{t}_i=\frac{1}{N}\sum_{i=1}^{N}t_i\ ,\quad \bar{x}_i=\frac{1}{N}\sum_{i=1}^{N}x_i(\tau)\ ,\quad \text{i=1, 2, 3……..N}$$

Draw a straight line through the point $(\bar{t}_i,\bar{x}_i)$, the equation is:

$$x(t)=\bar{x}_i+k(t-\bar{t}_i) \tag{1}$$

While

$$k=\frac{\sum(x_i-\bar{x}_i)(t-\bar{t}_i)}{\sum(t-\bar{t}_i)^2}$$

Taking zero result noted as $\hat{x}(t)$ after fitting. The atomic clocks onboard time difference data is affected by the frequency drift rate, so the data for fitting should not be too long. Make $\tau=1$, one data $\hat{x}_i(t)$ one day is obtained by fitting, i=1,2,3……N (day).

Calculating frequency accuracy by comparing the time difference data, the formula is[3]:

$$A=f(offest)=\frac{-\Delta t}{T}$$
$$=\frac{\hat{x}(t_2)-\hat{x}(t_1)}{t_2-t_1}=\frac{\hat{x}(t+\tau)-\hat{x}(t)}{\tau} \tag{2}$$

$\hat{x}(t)$ is the time difference data after processing, τ is the sampling time. A number of frequency accuracy can be obtained by using τ as sampling interval to calculate. The average of these frequency accuracy is taken as the final evaluation result.

(2) stability and calculation model

Stability characterizes the ability of the atomic clock to generate the same time and frequency within a certain time, and describes the random fluctuations of atomic clock output frequency. It does not indicate the time or frequency accuracy or not, only on whether the same value. Standard deviation of the data group is used to represent the stability in some occasions, but standard deviation can only used for stationary data. Because frequency offset contains time-varying noise, oscillator data are usually non-stationary[4][5]. For stationary data, the number of measurements increases, the mean and variance converge to the same value; for non-stationary data, the mean and variance does not converge to a certain value. Conversely, when increasing the number of measurements, the average value will be slidably changed. For this reason, some non-classical methods are used to represent time domain stability of time frequency signal. That statistical properties is called Allan variance, and it is the variance calculated by the time difference dada sampled for the second time. To overcome the linear frequency drift of the atomic clocks onboard, in this paper, Hadamard variance is used to evaluate the stability of atomic clocks onboard, it is the variance calculated by dada sampled for the third time[6]. Hadamard variance is defined as follows for the phase data:

$$H\sigma_y^2(\tau)=\frac{1}{6\tau^2(N-3)}\sum_{i=1}^{N-3}[x_{i+3}-3x_{i+2}+3x_{i+1}-x_i]^2 \tag{3}$$

The square root of the Hadamard variance is usually used to represent frequency stability, denoted as HDEV or $H\sigma_y(\tau)$.

3) Results

Using the IGS precise clock difference data from July 29, 2012 to October 27 to evaluate the performance of GPS atomic clocks onboard, the calculation result are as follows:

Table 1. The accuracy of GPS on-board clocks

Time	Satellite number	Frequency accuracy
2012.7.29~2.12.10.27 （MJD56137~56227）	G01	1.56464E-12
	G02	1.14443E-12
	G03	4.99104E-12
	G04	-2.95511E-11
	G05	-3.02479E-12
	G06	6.09588E-11
	G07	4.2496E-12
	G11	-3.90698E-12
	G12	2.04061E-12
	G13	-2.57309E-12
	G14	9.2923E-13
	G15	-6.66093E-13
	G16	-8.05873E-13
	G17	-3.25988E-12
	G18	1.82247E-12
	G19	-3.5291E-12
	G20	8.0625E-13
	G21	-2.41403E-12
	G22	5.34598E-13
	G23	-3.91266E-12
	G25	1.27853E-12
	G26	1.28926E-11
	G28	3.74722E-12
	G29	4.12023E-12
	G31	2.5029E-12
	G32	-4.07605E-12

The results of accuracy are shown as table 1, the highest accuracy is -6.66093E-13, the minimum is 6.09588E-11. Excluding the three poor clocks, as figure 1 shows, the accuracy of most GPS on-board clocks can reach the magnitude of $\pm 5\times10^{-12}$.

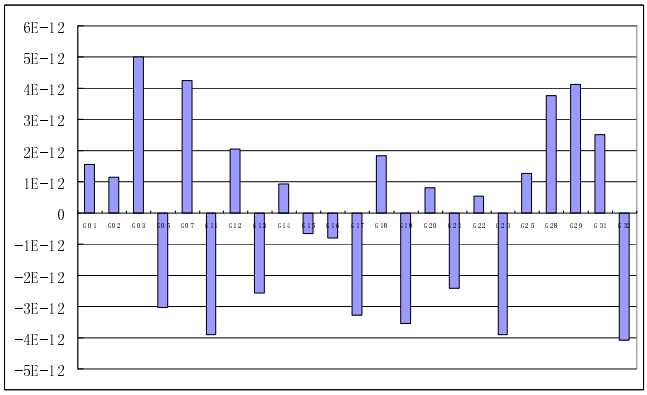

Figure 1. The accuracy of GPS on-board clocks

The results of stability of 4 on-board clocks representatively are shown as figure 2~ figure 5, their Hadamard Variance show that the stability of most GPS on-board clocks reach a level of 2×10^{-14} in one day and reaches the highest level of 6×10^{-15} in five days time interval.

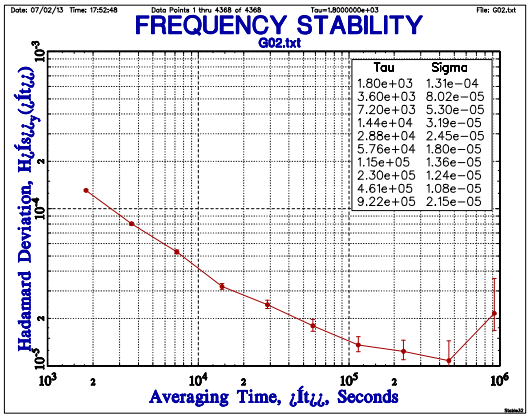

Figure 2. G02 stability (Hadamard Variance)

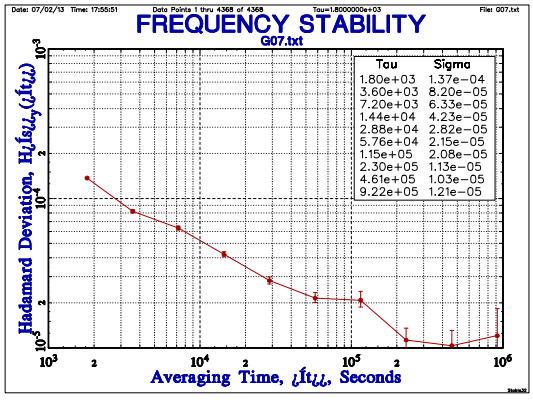

Figure 3. G07 stability (Hadamard Variance)

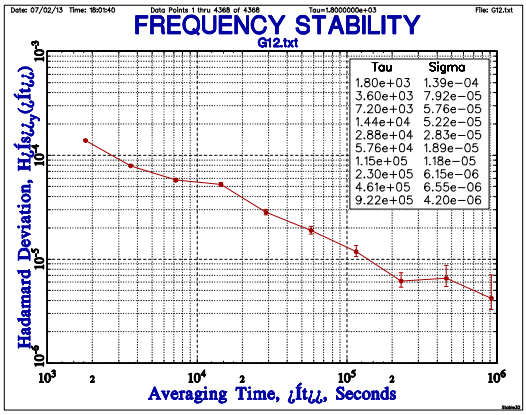

Figure 4. G12 stability (Hadamard Variance)

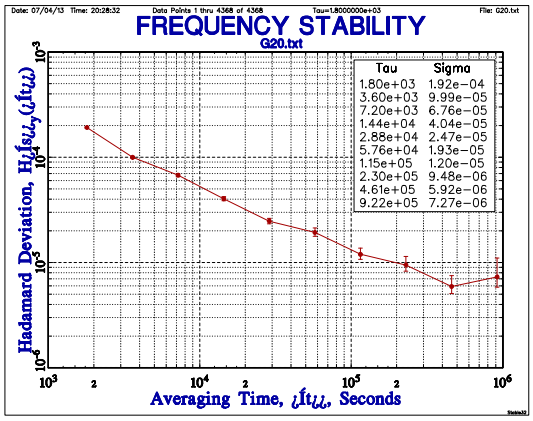

Figure 5. G20 stability (Hadamard Variance)

IV. CONCLUSIONS

Based on IGS precise clock difference data, the GPS on-board clocks performance evaluation methods used in this paper meet the basic criteria for testing and evaluation.

The evaluation results show that the accuracy of most GPS on-board clocks can reach the magnitude of $\pm 5\times10^{-12}$. The stability results evaluated by Hadamard Variance show that the stability of most GPS on-board clocks reach a level of 2×10^{-14} in one day and reaches the highest level of 6×10^{-15} in five days time interval.

Acknowledgment

We thank Dr. Yuan haibo and Dr Jia xiaolin for the help on this article.

REFERENCES

[1] Li Xiaohui, Dou Zhong. The Story of Time, Posts and Telecom Press, 2012.

[2] IGS(2008). IGS Product Availability[OL]. http://igscb.jpl.nasa.gov, 2008.

[3] Tong Baorun. The Technology of Time Unification [M]. National Defence Industry Press, 2004.

[4] P. Kartaschoff, Frequency and Time, Academic Press Inc. (LONDON), 1978.

[5] Wu Shouxian, Time Measurement, Science Press, 1983.

[6] Li Xiaohui, Yang Xuhai. The Precise Measurement of Time and Frequency, Science Press, 2010.

An FPGA Implementation of the Distributed RF Over White Rabbit

Pedro Moreira, Izzat Darwazeh
Department of Electronic & Electrical Engineering
University College London, London, UK

***Abstract*—Distributing radio frequency signals is a requirement needed in various systems such as telecommunications systems, to synchronise base stations, or in factory control floors to distribute a clock reference from the main control unit to the acquisition and actuation hardware. However, most of these distribution RF systems require dedicated links and custom-made hardware to achieve a specified performance in terms of jitter and latency. In this paper, an FPGA implementation of a distribution RF system running over the White Rabbit network is described. The White Rabbit network is a non-dedicated timing network with sub-nanosecond timing specification that uses Ethernet as communication network.**

I. Introduction

Several applications require the delivery of a stable clock reference from a central station to spatial disperse base stations. Other applications require the distribution of modulated radio frequency (RF) signals throughout several network nodes in the site. A common solution that addresses these issues is the Radio-over-Fibre (RoF) technique [1], where electro-optical modulators are used to convert a RF signal from the electrical to the optical domain that is transmitted over large distances using optical fibres. The RoF technique is normally preferred for high bandwidth applications; it also has the advantage of not requiring any sort of hardware computation. Another solution technique is the Digitized RF-over-Fibre (DRoF) [2], which uses ADCs to convert the analogue signal to the digital domain. The digital signal is then processed, typically in an FPGA, and transmitted to the receivers nodes using off-the-shelf optical transceivers optical fibres. Both RoF and DRoF are used for very high bandwidth applications using dedicated optical links at a relative high price. Recently, we have proposed a system architecture that aims to distribute RF signals over a non-dedicated Ethernet link [3], using ADCs and DACs components.

After this introductory section, this paper continues in section II with an overview of the White Rabbit network. Next, in section III, the Distribution RF architecture is outlined. Section IV describes the FGPA implementation of the proposed distributed RF system. In addition, it shows the performance, by analysing phase-noise spectra and Allan Deviation measurements, of the proposed implementation for a couple of reference RF signals. Finally, section concludes this paper with a discussion of the obtained results.

II. The White Rabbit Network

The White Rabbit (WR) project is nowadays a mature multi-lab multi-company project [4], started at European Organization for Nuclear Research (CERN). The WR project aims to use a general purpose link, Ethernet, as a network to deliver both data and timing, the WR network. It is designed for gigabit Ethernet (GbE) where general-purpose and control/timing traffic are multiplexed and managed to allow uninterrupted messages delivery. The network timing specification is to delivery sub-nanosecond timing accuracy between the master and the slave nodes. This timing specification has been reach and shown in previous works [5] [6]. Typically, the WR network is synchronised to an UTC time reference delivered from a GPS source or a Cs clock.

The WR network employs for the timing distribution two standardised protocols. The Synchronous Ethernet (SyncE), defined by ITU-T G.8261 [7], is physical layer based synchronization implementation for packet networks requiring frequency synchronization. The IEEE 1588, Precise Timing Protocol (PTP) [8], specifies a set of messages and timing stamping capabilities to synchronise the timing slaves to the grandmaster clock, previous work have shown performance of approximately 10us timing accuracy when implementing PTP [9]. In addition, WR network employs a phase measurement mechanism, the digital dual mixer time difference (DDMTD) [10], that continually measures the phase different between the master clock and the recovered clock link coming from the slave. These measurements are used to compensate the phase drifts between the transmitted master clock and recovery network clock which occur in the network link due to external environment variables. A block diagram that illustrates the WR ecosystem is shown in Fig. 1.

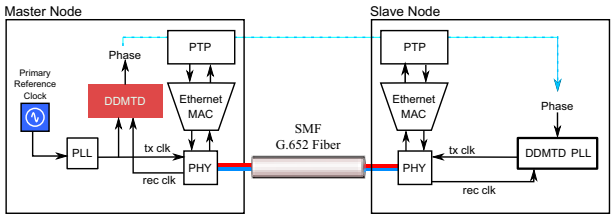

Fig. 1. WR Network System Architecture

III. Distributed Radio Frequency Architecture

The Distributed RF over white rabbit (DRF_WR) is a system architecture that takes advantage of the WR network timing specification to distribute RF clock references between nodes. An example of such system can be found at the Large Hadron Collider (LHC) where the frequency reference generated by the RF cavities is distributed to the various particles detectors to synchronise the beam with the triggering of the detectors among other functionalities. The RF frequency

generated by the cavities is not stable at a centre frequency, instead the RF frequency increases during the acceleration of the beam. The distribution of the RF signal generated by the RF cavities is realised by a dedicated and custom-made optical link with strict specification in terms of RMS jitter and latency. On the other hand, other systems require the distribution of very stable clock source such as Caesium (Cs) or Rubidium (Rb) standards over the factory control floor to synchronise its front-end equipment. In most cases this system requirement is implemented using dedicated and custom-made pieces of hardware and links that increases the cost of the system both in deployment and maintenance. For these types of applications the distributed RF over WR network has been designed as a solution leading to a more cost effective solution, as it relies on available hardware resources and on non-dedicated links. The distributed RF architecture employs a set of signal processing techniques to reduce the network bandwidth required to transmit the RF over the WR network which are detailed below.

In the transmitter (Tx) node the RF signal is digitized by means of an ADC. The ADC uses the bandpass sampling technique to directly down-convert the RF signal between DC and the Nyquist frequency without the need for passive mixers. This increases the frequency range operation of the system, which is limited by the frequency response of the ADC. To ensure that the spectrum does not overlap and corrupts the desired signal, the bandpass sampling requires that the ADC sampling rate is at least twice the bandwidth of the bandpass signal and twice the highest frequency in the bandpass signal. The digitised signal is then converted to the complex domain using a digital IQ demodulator.

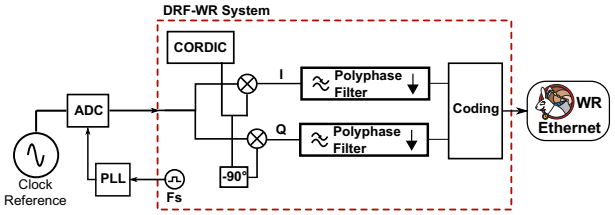

Fig. 2. Tx Architecture

The mixing frequency of the IQ demodulator is generated using the CORDIC algorithm. The CORDIC algorithm is a computationally efficient iterative arithmetic algorithm, introduced by Volder [11] in 1956.

The CORDIC algorithm relies on basic shift and adds operations which can be implemented very efficiently in hardware based designs, such as FPGAs. The CORDIC algorithm has a long latency time due it is recursive nature. However, implementing the CORDIC using pipeline architecture mitigates this issue.

The IQ demodulator down-converts the digitized signal to baseband, however, in the process it also generates a high frequency tone in the IQ signals. This high frequency tone can be removed using a digital low-pass filter (LPF). The data-rate of complex signal can be reduced to minimal specified by the Nyquist theorem, which is dependent on the bandwidth of the digitised signal. The decimation process results in savings in the bandwidth required to transmit the IQ signals to the receivers. Implementing the LPF in its direct form structures requires expensive hardware resources. To implement the filtering and decimation process in a combined and more efficient way polyphase structures are used [12]. A polyphase structure is composed by a set of filter banks each one running at the decimated frequency rate. Thus reducing the required hardware needed to implement the filtering process as each filter can share the same set of hardware resources. The decimated signal is then coded and added to an Ethernet frame. A block diagram illustrating the flow of the data processing in the Tx node is shown in Fig. 2.

In the Receiver (Rx) node, the Ethernet received data stream of the distributed RF system is decoded into the corresponding IQ components. These signals are then interpolated to restore the initial sampling rate of the sampling frequency in the Tx. The interpolated IQ components are modulated to passband by digital mixing them with the same frequency as the one applied in the Tx demodulation process. Then the up-converted IQ components are summed together to complete the modulation process. The reconstructed modulated digital signal is an identical image of the signal sampled at the Tx node. Finally, the RF signal is converted to the analogue domain by means of a DAC. An analogue LPF is added next to the DAC to remove the high frequency components generated by the conversion process. A block diagram showing the different operations realised in Rx system is shown in Fig. 2.

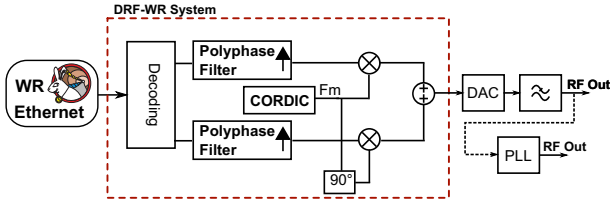

Fig. 3. Rx Architecture

For applications which require very low jitter in the reconstructed RF signal a PLL can be added in series with the analogue LPF to remove even more the remaining spurious frequency components.

IV. FPGA Implementation

To analyse the performance of the Distributed RF over White Rabbit system an FPGA implementation of the system was realized. The testing scenario aims two distribute two types of RF signals; one generated by a 10 MHz Cs clock source while the other test is to distribute a 40.078 MHz RF signal generated by a signal generator. The performance of the system is analysed by means of measuring both phase-noise spectra and Allan Deviation of the reconstructed RF signal. To realise this implementation we have used two SPEC boards plus ADC+DAC FMC cards. The SPECS are connected by 2.5 km of optical fibre (SMF G.652). The SPEC carrier card, depicted in Fig. 4, has a Xilinx SPARTAN-6 FPGA (XC6SLX45T), a FPGA Mezzanine Card (FMC) slot with low pin count (LPC) plus additional hardware [4]. The SPEC is WR compatible and it was design under open-hardware licensing.

The FMC daughter card provides a ADS62P49 dual channel 14-bit 250Msps ADC and a TI's DAC3283 dual channel

Fig. 4. The SPEC Board

TABLE I. RESOURCES REQUIRED FOR THE TX AND RX DRF CORES

Device Utilization Summary (estimated values)			
Logic Utilization	Used	Available	Utilization
Slice Registers	9133	54576	16%
Slice LUTs	14008	27288	51%
Fully used LUT-FF pairs	3022	27951	14%
Block RAM/FIFO	33	116	28%
DSP48A1s	64	58	93%
PLL_ADVs	2	4	50%

16-bit 800Msps DAC which can be clocked by an external reference, in our system it is the WR clock. The clock management and fanout is performed by TI's CDCE72010 clock synthesizer chip. Due to a hardware limitation in the FMC card we are only able to operate the DAC at 62.5 MHz; however, this limitation can be mitigated by using a PLL in series with the DAC to up-convert the signal.

The CORDIC algorithm, implemented in Tx and Rx cores, has 16 pipelined stages to achieve higher accuracy. The Tx has a decimation factor of 10, which results in using approximately 20% of the available network bandwidth. However, the selection of the above decimation factor is due to the requirements of the system which are to transmit modulated signals with a bandwidth of 2MHz. For applications that require the distribution of RF signals generated by stable clocks the required network bandwidth can be less than 0.01%. A 70-tap FIR low-pass filter with a cut-off frequency set to 2 MHz designed by the Parks-McClellan algorithm [13] was implemented in the Tx node. The implementation of the LPF and the decimation was realised with a polyphase structure. Each filter bank in the polyphase filter is composed by a 7-tap FIR. To reduce the effects of quantisation, the implementation of the filters has done using a 24-bit fix-point representation. At the Rx node the interpolation processes are designed as 70-tap FIR filter realised with a polyphase structure with 7-tap filter banks, identical to the Tx node. The current RTL implementation for the Tx and Rx DRF_WR core uses the FPGA's hardware resources as shown in Table I. The resources listed in Table I include not just the DRF_WR core but also an instantiation of the LM32 uC plus wishbone interfaces between the uC and the DRD_RF core. Nonetheless, there is further room to optimise the resources required to implement the DRF_WR core, e.g. by reducing the fix-point representation of the filters. Both Tx and Rx designs run at the required frequency of 62.5 MHz.

A. Measurements

The first set of measurements presented show the distribution of an RF clock signal generated by an Cs atomic clock, the Symmetricom Cs4000 [14]. We measured the phase noise spectrum of the RF clock signal with the Agilent's E5052B Signal Source Analyser. Fig. 5 and 6 show the phase noise spectra of the Tx input RF signal, and the reconstructed RF signal at the Rx node, respectively.

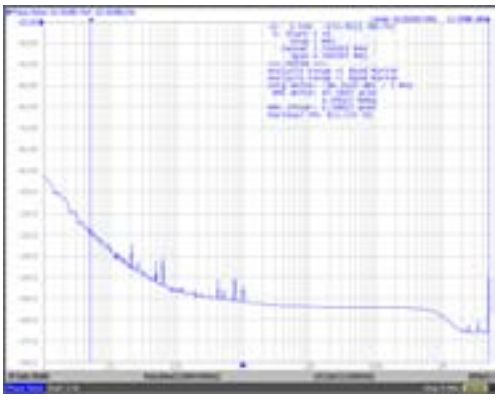

Fig. 5. Phase Noise Spectrum of the 10 MHz Tx Signal

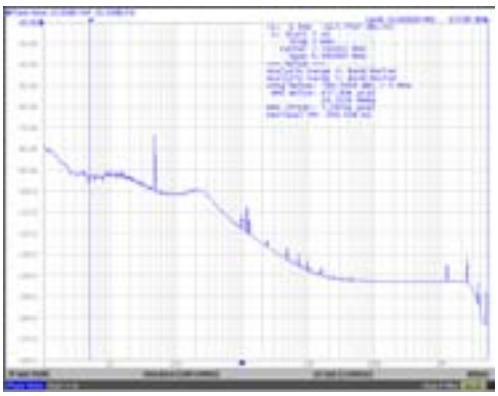

Fig. 6. Phase Noise Spectrum of the 10 MHz Rx Signal

The RMS jitter calculated in the E5052B by integrating the phase noise between the frequencies 5 Hz to 5 MHz is ~1.3ps for the Tx signal and ~7.2ps for the reconstructed signal at the Rx node. The measured phase-noise spectrum on the Rx node was done in the output of the analogue LPF, this means that the RMS jitter of the output signal can be even further reduced. This can be done by adding a PLL with narrow bandwidth in series with the LPF.

Fig. 7 and 8 show the Allan Deviation of the Tx signal the reconstructed Rx signal. The Allan Deviation is a simple and efficient measurement to verify random drift error as a function of averaging time. It can be used to determine the characteristics of different random processes.

The second set of measurements shows the distribution of a 40.078 MHz clock signal generated by a signal generator. Due to the limitation in the FMC Hardware we are not able to correctly reconstruct the 40.078 MHz. Nonetheless, this limitation is overcome by adding a PLL into the output of the DAC which up converts the RF signal to the wanted frequency.

The RMS jitter calculated between the frequencies 5 Hz to 5 MHz is ~37.9ps for the Tx signal and ~8.2ps for the reconstructed signal at the Rx node. These set of measurements indicates that the reconstructed clock signal at the Rx node is

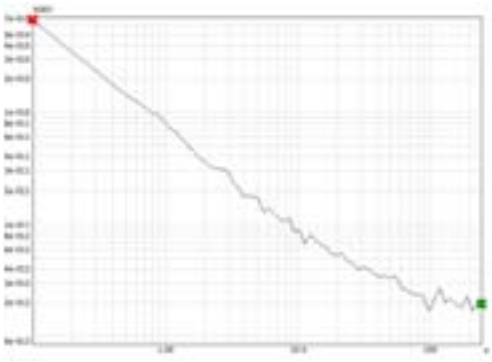

Fig. 7. Allan Deviation of the 10 MHz Tx Signal

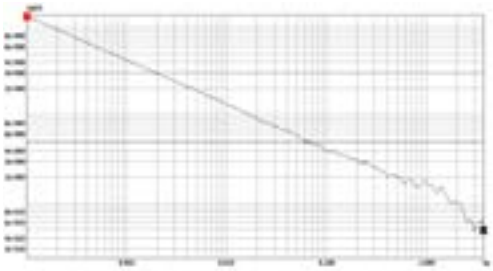

Fig. 8. Allan Deviation of the 10 MHz Rx Signal

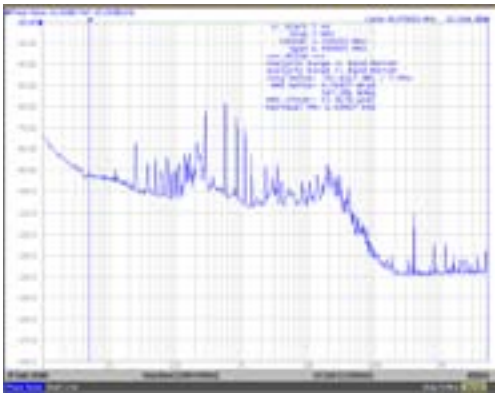

Fig. 9. Phase Noise Spectrum of the 40.078 MHz Tx Signal

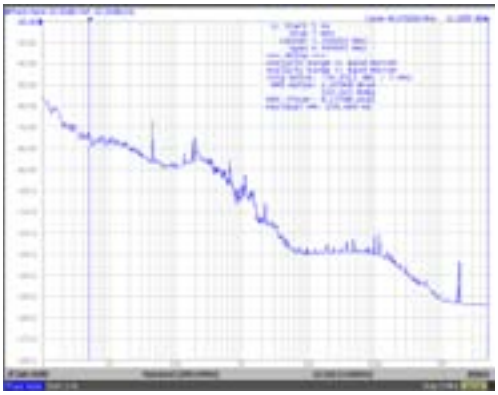

Fig. 10. Phase Noise Spectrum of the 40.078 MHz Rx Signal

more stable than the original signal sampled at the Tx. By analysing Figs. 9 and 10 it is noticeable that the high RMS jitter in Tx signal is mainly due to the frequency spurs that start ~20 Hz. These frequency spurs are filtered in the Rx signal, because of the narrow bandwidth of the PLL added.

V. Conclusion

In this paper, we have presented an FPGA implementation of the Distributed RF architecture over the White Rabbit network, a non-dedicated timing network that runs over an Ethernet link. The measurements made on the distributed signal have shown that the proposed distribution RF architecture achieves excellent performance in terms of RMS jitter and Allan Deviation.

Acknowledgement

The authors would like to thank Javier Serrano, Pablo Sanchez and Tomasz Wlostowski from CERN for their valuable comments to improve the quality of this work. In addition, the authors would like to thank the Portuguese FCT (SFRH/BD/60294/2009) for funding the PhD work of Pedro Moreira at UCL.

References

[1] J. Mitchell, M. Thakur, M. Parker, and S. Walker, "Radio-over-fibre networks: Developments from the BONE Virtual Centre of Excellence in Access," in *Future Network Mobile Summit (FutureNetw)*, Jun 2011, pp. 1–8.

[2] P. Gamage, A. Nirmalathas, C. Lim, D. Novak, and R. Waterhouse, "Design and Analysis of Digitized RF-Over-Fiber Links," *Journal of Lightwave Technology*, vol. 27, no. 12, pp. 2052–2061, June 2009.

[3] P. Moreira, J. Serrano, P. Alvarez, M. Lipinski, T. Wlostowski, and I. Darwazeh, "Distributed DDS in a White Rabbit Network: An IEEE 1588 application," in *International IEEE Symposium on Precision Clock Synchronization for Measurement Control and Communication (ISPCS)*, 2012, pp. 1–6.

[4] "Open hardware repository," http://www.ohwr.org/.

[5] P. Moreira, J. Serrano, T. Wlostowski, P. Loschmidt, and G. Gaderer, "White rabbit: Sub-nanosecond timing distribution over Ethernet," *International Symposium on Precision Clock Synchronization for Measurement, Control and Communication*, pp. 1–5, October 2009.

[6] M. Lipinski, T. Wlostowski, J. Serrano, and P. Alvarez, "White rabbit: a PTP application for robust sub-nanosecond synchronization," in *International IEEE Symposium on Precision Clock Synchronization for Measurement Control and Communication*, September 2011, pp. 25–30.

[7] ITU, *G.8261 - Timing and synchronization aspects in packet networks*, ITU Std., 2008.

[8] IEEE, *IEEE 1588-2008 Standard for a Precision Clock Synchronization Protocol for Networked Measurement and Control Systems*, IEEE Instrumentation and Measurement Society Std., 2008.

[9] D. V. J. Ridoux, "Ten Microseconds Over Lan, for Free," in *IEEE International Symposium on Precision Clock Synchronization for Measurement, Control and Communication*, 2007, pp. 105–109.

[10] P. Moreira, P. Alvarez-Sanchez, J. Serrano, I. Darwazeh, and T. Wlostowski, "Digital dual mixer time difference for sub-nanosecond time synchronization in Ethernet," *IEEE International Frequency Control Symposium*, pp. 449–453, June 2010.

[11] J. E. Volder, "The Birth of Cordic," *The Journal of VLSI Signal Processing*, vol. 25, pp. 101–105, 2000.

[12] P. Vaidyanathan, "Multirate digital filters, filter banks, polyphase networks, and applications: a tutorial," *Proceedings of the IEEE*, vol. 78, no. 1, pp. 56–93, 1990.

[13] J. McClellan and T. Parks, "A personal history of the Parks-Mcclellan algorithm," *Signal Processing Magazine, IEEE*, vol. 22, no. 2, pp. 82–86, 2005.

[14] "Cesium frequency standard," "http://www.symmetricom.com/products/frequency-references/cesium-frequency-standard/Cs4000/".

Analysis of the Sagnac Effect on the Accuracy of the Long Haul Optical Fiber Time Transfer System

Yu Longqiang ,Lu Lin , Wang Rong ,Jing Jisong ,Wu Chuanxin ,Zhu Yong,Zhang Baofu
PLA University of Science and Technology
Nanjing, China
Email: nj_lulin@163.com

***Abstract*—The influence of Sagnac effect in time transferring system over optical fiber is explained. Mathematical expression of the time deviation is deducted between any two points on the surface of the earth based on the analyses of the actual propagation path of the optical signal. To investigate the magnitude of the time deviation, we make theoretical calculation using the deducted equation when time is transferred from Prague to other four Europe cities with different directions through spherical circumference fiber links. It is demonstrated that the magnitude may reach 10^{-9}s when the transfer distance is longer than hundreds of kilometers and it is also decided by practical route of the fiber links. So accurate time compensation or calibration should be committed for the purpose of reaching subnanosecond accuracy in long-haul optical fiber time transferring system.**

Keywords—Time transfer ; Optical fiber ; Sagnac Effect ; Time Deviation

I. INTRODUCTION

In recent years, accurate time and stable frequency transfer have been studied since the existing optical communication networks can provide an alternative and complementary method to already established satellite-based ones[1-3]. Two-way time transfer is generally used to compare two geographically separated clocks with high accuracy, on the condition that the propagation time between two clocks is reciprocal [4] or the unequal propagation time can be accurately measured and compensated. However, in real fiber links, the propagation time in both directions differs due to different wavelength, temperature variation, stress and phase noise from fiber. As a result, the accuracy of the time transfer system, to a great extent, depends on the accurate measurement and compensation of the unequal propagation time including Sagnac effect.

The Sagnac effect[5,6] can be described by the following example. Two light beams sent in opposite directions around the circumference of a stationary disk using optical fibers will take the same time intervals to travel the path. If the disk is rotated with a certain angular velocity, the propagation time becomes different consequently. It is the same to the time transfer system over optical fiber of which the local clock and the remote clock are together rotating with the earth, accounting for the difference of the propagation time in both directions even if neglecting the disturbances mentioned above. In order to figure out and finally compensate this difference, we illustrate the principle of the time deviation caused by Sagnac effect and then give a mathematical expression for accurate calculation. The result of this paper will be required to be taken into consideration with the further development of the terrestrial time transfer system.

This work supported by the National Natural Science Foundation of China (NSFC) (61174199，61032005，61074065)

II. SAGNAC TIME DEVIATION

The Sagnac effect in optic fiber time transferring system can be illustrated as Fig.1. A and B are any two points on the earth. The former is the local end and the latter is the remote end. The dashed line AB (A_1B_1, A_2B_2) denotes the original optical fiber link between A and B. Simultaneous propagation processes are separated into two sequential processes to explain the phenomena more clearly as following: In time t, an optical signal is sent out from the local end A to the remote end and it arrives at B in time t_1. Then, the signal starts immediately in the opposite direction from B to A and reaches A in time t_2. So the actual bidirectional paths are A-B_1 and B_1-A_2 instead of A-B since the optical fiber is moving with the earth rotation. It is evident than bidirectional propagation times between two stations are unequal due to Sagnac effect, so calculation and compensation are needed to achieve accurate synchronization.

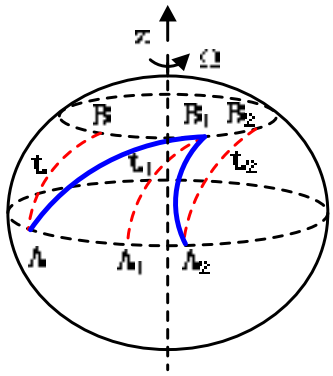

Fig. 1. The actual propagation path of the optical signals considering Sagnac effect.

If we take the travel time of A-B as the forward propagation delay, neglecting the path asymmetry analyzed above, the time compensation delay should be $(t_2-t)/2$. But in fact the forward optical signal should be delayed by t_1-t_2. That introduces a time deviation and will finally lead to a clock offset $(2t_1-t-t_2)/2$. Even though we can assert that this deviation will be very small, it may be unbearable for some applications.

To meet such demands, accurate calculation and time delay compensation is needed to modify the deviation to achieve synchronization. Besides, it is necessary to make it out that this time deviation is invariable with time for a certain time transfer system and will not affect the stability and the frequency transfer.

III. CALCULATION

To calculation the clock offset, we start from an infinitesimal of the fiber link. As is showed in Fig.2, dl is an

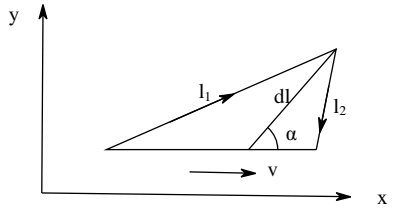

Fig. 2. The infinitesimal of the beam propagation path.

infinitesimal. l_1 is the real forward path and l_2 is the backward path. They are short enough to be thought of as linear. The vector v is the rotation speed of the earth, making an angle α with dl. If the earth is stationary, the optical signal propagates in the fiber with a speed of c/n in both directions. c, the velocity of light beam in vacuum, is 299792458 m/s. n is the index of refraction of silica optical fiber. When the earth is rotating with a linear velocity of v, the speed of the forward light and backward light no longer equals. Based on the Lorentz- Einstein transformation of speed , the modified speed of forward light is

$$u_{1x}=\frac{\frac{c}{n}\cos\alpha+v}{1+\frac{v\frac{c}{n}\cos\alpha}{c^2}}=\frac{\frac{c}{n}\cos\alpha+v}{1+\frac{v\cos\alpha}{nc}} \tag{1}$$

$$u_{1y}=\frac{\frac{c}{n}\sin\alpha\sqrt{1-\frac{v^2}{c^2}}}{1+\frac{v\frac{c}{n}\cos\alpha}{c^2}}=\frac{\frac{c}{n}\sin\alpha\sqrt{1-\frac{v^2}{c^2}}}{1+\frac{v\cos\alpha}{nc}} \tag{2}$$

and the modified speed of backward light is

$$u_{2x}=\frac{\frac{c}{n}\cos\alpha-v}{1-\frac{v\cos\alpha}{nc}} \tag{3}$$

$$u_{2y}=\frac{\frac{c}{n}\sin\alpha\sqrt{1-\frac{v^2}{c^2}}}{1-\frac{v\cos\alpha}{nc}} \tag{4}$$

We notice that the forward light and the backward light travel the same distance in the direction of the y axis. Then the difference between their propagation delays can be expressed as

$$\begin{aligned}\Delta t&=\frac{dl\cdot\sin\alpha}{u_{1y}}-\frac{dl\cdot\sin\alpha}{u_{2y}}\\&=dl\cdot\left(\frac{1+\frac{v\cos\alpha}{nc}}{\frac{c}{n}\sqrt{1-\frac{v^2}{c^2}}}-\frac{1-\frac{v\cos\alpha}{nc}}{\frac{c}{n}\sqrt{1-\frac{v^2}{c^2}}}\right)\\&=\frac{2v\cos\alpha\cdot dl}{c\sqrt{c^2-v^2}}\end{aligned} \tag{5}$$

Where v^2 is negligible compared to c^2. So the time deviation contributed by the infinitesimal is given by

$$dt=\frac{1}{2}\times\frac{2v\cos\alpha\cdot dl}{c^2}=\frac{v\cos\alpha dl}{c^2} \tag{6}$$

If the track of the fiber link L is already known, the total time deviation can be obtained by integrating Eq.(6)

$$\Delta T=\int_L dt=\int_L\frac{v\cos\alpha}{c^2}dl \tag{7}$$

From Eq.(7) we can see that the time deviation caused by Sagnac effect is independent of the fiber's refraction index. Similar conclusion has been proved by experiment [6].

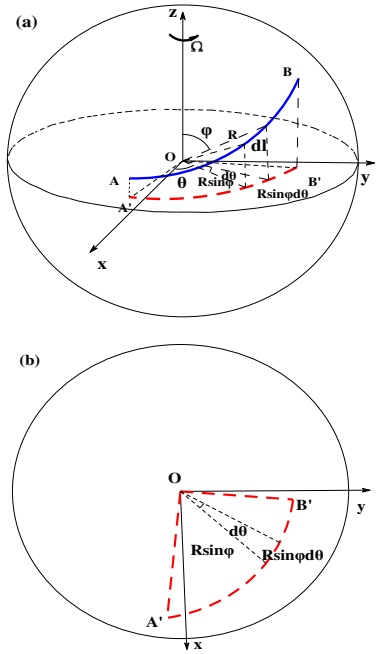

Fig. 3. The fiber link and its projection (a) on earth in spherical coordinates, (b) on the equatorial plane.

Fig 3 is the fiber link and its projection on the equatorial plane in spherical coordinates. Taking the earth as a standard sphere, we build up spherical coordinates as Fig. 3(a) shows. O is the earth's core and xoy plane corresponds to the equatorial plane. The x-axis points to the prime meridian and the z-axis points to the arctic pole. θ is azimuth angular and

φ is polar angular in spherical coordinates through the fiber link. R is the mean radius of the earth and Ω the angular velocity, R=6371 km, $\Omega=7.292\times10^{-5}$ rad/s. The curve AB denotes an arbitrary fiber link. A is the local end and B the remote end. Projecting curve AB on the equatorial plane, we get Fig. 3(b). By contrasting Fig. 2 and Fig. 3, we can reify some variables of Eq. (7) in spherical coordinates. $v=R\Omega\sin\varphi$, $\cos\alpha\cdot dl= R\ \sin\varphi\cdot d\theta$. Then the mathematical expression can be rewritten as

$$\Delta T = \int_L \frac{(R\sin\varphi)^2\Omega}{c^2} d\theta \qquad (8)$$

Eq. (8) can be used to calculate the time deviation of any time transfer system over optical fiber as long as we find out the mathematical expression of the fiber link L in spherical coordinates. Even if the course of the fiber is too irregular to denote by a definite mathematical expression, Eq. (8) still works just using numerical computation method.

It should be note that Eq. (8) can be written as

$$\Delta T = \frac{2\Omega}{c^2} \int_{L_{AB}} \frac{1}{2}\cdot(R\sin\varphi)\cdot R\sin\varphi\, d\theta \qquad (9)$$

Since $\int_{LAB} \frac{1}{2}\cdot(R\sin\varphi)\cdot R\sin\varphi\, d\theta$ equals to the pie slice area occupied by curve A′B′ and O on the equatorial plane in Fig.3 (b) which can be denoted by S, Eq. (8) can be written as

$$|\Delta T| = 2\Omega S / c^2 \qquad (10)$$

ΔT is positive if the local clock lies to the west of the remote clock, or else ΔT is negative.

TABLE I. TIME DEVIATION FROM PRAGUE TO OTHER CITIES DUE TO SAGNAC EFFECT

City	Distance(km)	Offset(ns)
London	1024.1	-3.2903
Rome	1189.3	-0.6357
Moscow	1667.3	4.7355
Stockholm	1054.3	0.6856

Table.1 shows Sagnac time deviations calculated by Eq. (8) when time is transferred from Prague to other four Europe cities with different directions through spherical circumference fiber links. It is noticeable that an east-west fiber link has a larger time offset compared to the north-south one which implies that the time deviation is also decided by practical route of the fiber links. It is showed that the time offset may reach 10^{-9}s when the transfer distance is longer than hundreds of kilometers.

IV. CONCLUSION

In this paper, the influence of Sagnac effect in time transferring system over optical fiber is explained and analyzed. Accurate equation is deducted for calculation of the Sagnac effect induced time deviation. It is showed that the time offset may reach 10^{-9}s when the transfer distance is longer than hundreds of kilometers. The result of this paper advances the time compensation mechanism in the independent terrestrial time transfer system.

REFERENCS

[1] S..Ebenhag, P.Jarlemark, R.Emardson, P.Hedekvist, K.Jaldehag, P.Löthberg. Time transfer over a 560km fiber link. Proceedings of the 22nd European Frequency and Time Forum (EFTF), 2008, 23-25.

[2] Dirk Piester, Miho Fujieda, Michael Rost, Andreas Bauch. Time transfer through optical fibers (TTTOF): First results of calibrated clock comparisons. Proc.41st Precise Time and Time Interval (PTTI) Systems and Applications Meeting,16-19, Nov 2009

[3] Vladimir Smotalacha, Alexender Kuna, Werner Mache. Time transfer in optical network. 42nd Annual Precise Time and Time Interval Meeting. 2010. 427~436

[4] Steven R. Jefferts, Marc A. Weiss, J. Levine S. Dilla, E. W. Bell, and Thomas E. Parker. Two-way time and frequency transfer using optical fibers. IEEE Transactions on Instrumentation and Measurement, vol.46, No.2, April 1997

[5] G. Sagnac, The luminiferous ether demonstrated by the effect of the relative motion of the ether in an interferometer in uniform rotation. C. R. Acad. Sci. 157,708-710,1913

[6] Ruyong Wang, Yi Zheng, Aiping Yao, Dean Langley. Modified Sagnac experiment for measuring travel-time difference between counter-propagation light beams in a uniformly moving fiber. Physics Letters. A 312, pp 7-10, 2003.

Interlaboratory Comparisons for Frequency Calibration: a First Two-Year Campaign in Italy

Franco Cordara, Diego Orgiazzi
Calibration Laboratories Department,
ACCREDIA DT
Strada delle Cacce 91, 10135 Torino (Italy)
f.cordara@inrim.it, diego.orgiazzi@tiscali.it

Valerio Pettiti
Optics Division,
INRIM – Istituto Nazionale di Ricerca Metrologica
Strada delle Cacce 91, 10135 Torino (Italy)
v.pettiti@inrim.it

Abstract — **In 2011 and 2012, ACCREDIA DT (the Calibration Laboratories Department of the Italian accreditation body) and the Time and Frequency Laboratory of the Istituto Nazionale di Ricerca Metrologica (INRIM) organized two Interlaboratory Comparisons for the Italian Accredited Calibration Laboratories, aiming to experimentally assess their calibration measurements capabilities (CMC). Two sets of instruments, preliminarily calibrated by INRIM, were circulated among the laboratories following a multi-lateral scheme with INRIM acting as pilot laboratory. The measurement results and an overall critical assessment of this exercise is provided and suggestions on possible improvements are discussed.**

Keywords: interlaboratory comparisons, frequency calibration, accreditation, GPS disciplined oscillators.

I. Introduction

In 2011 and 2012 the Calibration Laboratories Department of ACCREDIA, the Italian accreditation body, and the Optics Division of the Istituto Nazionale di Ricerca Metrologica (INRIM) organized two Interlaboratory Comparisons (ILCs) for the Italian Accredited Calibration Laboratories (ACLs).The scope of these ILCs was to experimentally assess the metrological capabilities of the ACLs in the field of frequency calibration, as requested by ACCREDIA rules and according to the ISO/IEC 17025:2005 [1].

About 80% of the ACLs accredited in this field were involved in the two ILCs, with calibration measurement capabilities ranging from 10^{-9} to 10^{-12} for the 10 MHz value, and proved to be the first successful national measurement campaign in this field and maybe also in Europe. Indeed, the instability and the limited reproducibility of the travelling frequency standards resulted in unsatisfactory results in previous experimental trials [2].

Both ILCs implemented a multi-lateral scheme having INRIM as the pilot laboratory and fulfilled the requirements of the related EA guide [3]. A set of instruments, calibrated by the Time and Frequency Laboratory of INRIM, was circulated among the ACLs. Each ACL kept the instruments for one week while performing the measurements requested by the calibration protocol before shipping them to the next one. During each circulation, that lasted about 6 months, the instruments were sent back to INRIM for an intermediate calibration. A closure calibration was also performed by the pilot laboratory at the end of each campaign to assess the consistency of instruments performances in terms of stability and repeatability.

The paper reports all the technical and logistical details of these ILCs (e.g., instrument specifications, measurements requested by the protocol, faced problems and lessons learned), together with an evaluation of the normalized errors E_n.

II. Involved Accredited Laboratories

Fig. 1 shows the geographical distribution of the eight ACLs involved in the 2011 campaign (left side) and the ten ACLs of the 2012 campaign (right side). Two ACLs were included in both campaigns, resulting then in 16 laboratories out of 20 accredited by ACCREDIA. The majority of the ACLs is equipped with a GPS-disciplined rubidium oscillator and all of them are traceable to the national time scale UTC(IT) by remote calibrations.

All ACLs were accredited for frequency calibrations and some of them also for time interval (phase/time) measurements. Their calibration measurement capabilities for the 10 MHz value are summarized in Table I.

In the 2011 ILC the ACLs were assessed in the range from 1 Hz to 1 GHz while in 2012 the measurement range was from 1 Hz to 10 MHz.

Figure 1. ACLs involved in the 2011 and 2012 ILC campaigns.

TABLE I. ACLs CALIBRATION MEASUREMENT CAPABILITIES

Quantity	Direct frequency measurement	Phase/Time measurement
Frequency	$1{,}2{\cdot}10^{-9}$ to $1{,}0{\cdot}10^{-12}$	$1{,}0{\cdot}10^{-12}$ to $2{,}0{\cdot}10^{-13}$

III. TRAVELLING INSTRUMENTS

The set of travelling instruments for both campaigns included a GPS Disciplined Oscillator (GPSDO) with a 10 MHz output frequency used as a reference standard. A signal splitter allowed for connecting the GPSDO to the same antenna already used in the ACL for its GPSDO-based frequency reference. Besides, a netbook was used to collect the travelling GPSDO relevant internal data for remote monitoring during the campaign. The sets of travelling instruments for both campaigns are shown in Fig. 2. The expanded uncertainties of both GPSDOs are reported in Table II.

In the 2011 campaign the travelling standard Fluke 910R (hereafter simply named as "GPSDO 1") provided the external reference to an Agilent 33120A function generator up to 15 MHz (sinusoidal and square waves) and to an Agilent E4428C frequency synthesizer up to 3 GHz (sinusoidal waves). Both devices were used to generate the signals to be measured by the ACLs according to the measurement protocol provided by ACCREDIA (section IV).

The two generators and the reference oscillator were replaced in 2012 by a new disciplined oscillator, the Spectra Time GPS Reference-2000 ("GPSDO 2"), also providing synthesized square waves signals in the 1 Hz to 20 MHz range. An external INRIM digital divider was also used to provide a more stable square wave signal up to 10 MHz.

Figure 2. Travelling instruments in the 2011(top) and 2012 (bottom) ILC campaigns.

TABLE II. TRAVELLING GPSDOs PERFORMANCES

ILC (GPSDO)	Frequency meas. (Tg = 100 s)	Phase/Time meas. (Tg = 1 d)
2011 (GPSDO 1)	$U_{REF} = 1{,}0{\cdot}10^{-12}$	$U_{REF} = 0{,}8{\cdot}10^{-12}$
2012 (GPSDO 2)	$U_{REF} = 5{,}0{\cdot}10^{-12}$	$U_{REF} = 0{,}7{\cdot}10^{-12}$

The characterization of the GPSDO 1 used in the 2011 ILC was performed in the pilot laboratory before starting the circulation as well as remotely during the measurement campaign. Each ACLs was asked to extract from the GPSDO 1 the time offset of its internal oscillator versus GPS Time and then send these data to INRIM by e-mail to compute its daily normalized frequency deviations versus UTC(IT). Fig. 3 graphically reports these evaluations, exhibiting a very good reproducibility of the travelling GPSDO frequency with an absolute value of its deviation versus UTC(IT) below $6{\cdot}10^{-13}$ during the whole campaign.

In the 2012 campaign, the characterization of the GPSDO 2 was made at the pilot laboratory only, as this equipment doesn't provide the data needed to remotely trace its internal oscillator to UTC(IT). The calibration results of the GPSDO 2 before the ILC are shown in Fig. 4, while Table III reports the mean frequency deviations of the GPSDO 2 as obtained from the hourly measurements performed at INRIM during the calibration sessions occurred before, in the middle and at the end of the ILC, respectively.

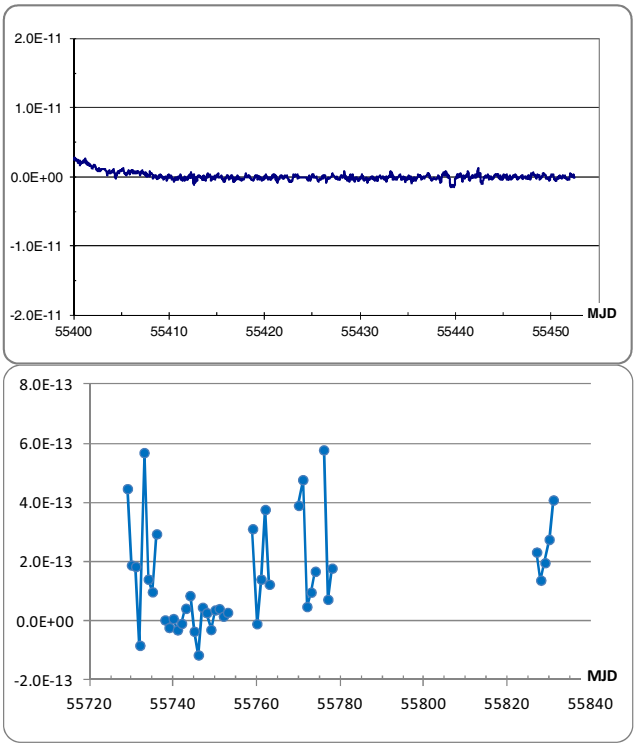

Figure 3. Normalized frequency deviation of the GPSDO 1 versus UTC(IT) during preliminary characterization in INRIM (top) and during 2011 circulation (bottom).

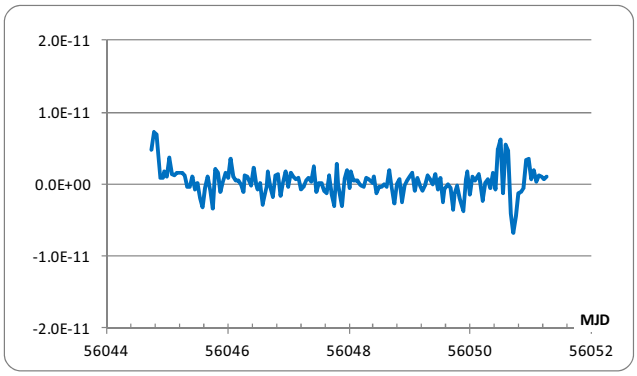

Figure 4. Normalized mean frequency deviation, over 1 hour, of the 10 MHz output of the GPSDO 2 (April 2012).

TABLE III. TRAVELLING GPSDO 2 CALIBRATION RESULTS

Period (MJD)	Frequency deviation versus UTC(IT)
56044 – 56051	$(0,3 \pm 2,0)\cdot 10^{-12}$
56142 – 56170	$(0,0 \pm 2,0)\cdot 10^{-12}$
56226 – 56238	$-(0,1 \pm 2,0)\cdot 10^{-12}$

IV. MEASUREMENT PROTOCOL

For both ILCs, ACCREDIA DT supplied a document [4] reporting the rules and the measurement protocol to be followed by the pilot laboratory and by each ACL. This document reported also all the logistical information as the travelling equipment verifications, preliminary controls and operative checks, measurements to be performed, templates for measurement reporting and communication rules with the pilot laboratory through e-mail.

Every ACL was asked to estimate the normalized frequency deviation of the 10 MHz provided by the travelling GPSDO versus its frequency standard, applying its accredited calibration procedures and in agreement with the measurement protocol. In a few cases, both direct frequency and time interval (phase/time) measurements were performed by ACLs to evaluate the frequency deviation. In addition, the measurement protocol required the calibration of the travelling generators by measuring the decimal values of the signals frequency in the range from 1 Hz to 1 GHz (ILC 2011) and from 1 Hz to 10 MHz (ILC 2012).

At the end of each ILC, the pilot laboratory and the ACCREDIA DT technical assessors analyzed the calibration results supplied by the ACLs according to the templates specified by the ILC protocol. As requested by ISO Standard [5] and EA related guide [6], the normalized errors E_n were computed:

$$E_n = (y_{ACL} - y_{REF})/(U_{ACL}^2 + U_{REF}^2)^{1/2}$$

where y_{REF} are the reference values supplied by INRIM as pilot laboratory, y_{ACL} are the values provided by the involved ACLs in their calibration certificates, while U_{REF} and U_{ACL} are the related expanded uncertainties (2σ).

The outcomes of the calibration results analysis were included in a final report drew up by ACCREDIA DT following an international guideline [7]. This final report was sent to each ACL, where every participant was identified with an anonymous code known to both ACCREDIA DT and the pilot laboratory only [8].

V. EXPERIMENTAL RESULTS

The E_n values distributions, for all the requested calibrations, are reported in Fig. 5 for both ILCs.

The distributions show a good symmetry, only slightly biased towards the negative values in 2011, indicating an overall reliability of the two ILCs. A further analysis on the data of the 2011 campaign revealed a significant asymmetry of the E_n distribution in case of low frequency signals measurements (both sine and square waves) generated by the function generator. This might be due to the Direct Digital Synthesis (DDS) technique implemented by the generator used, since it typically implies a significant short-term noise. This short-term noise could also be the reason of the higher dispersion of E_n values observed in 2012 for the measurements on the signals generated by the GPSDO 2, but not noticed on the INRIM digital divider output signals.

In spite of these minor anomalies, the computed E_n values were found always smaller than 1 except in the case of one ACL that adopted the necessary corrective actions.

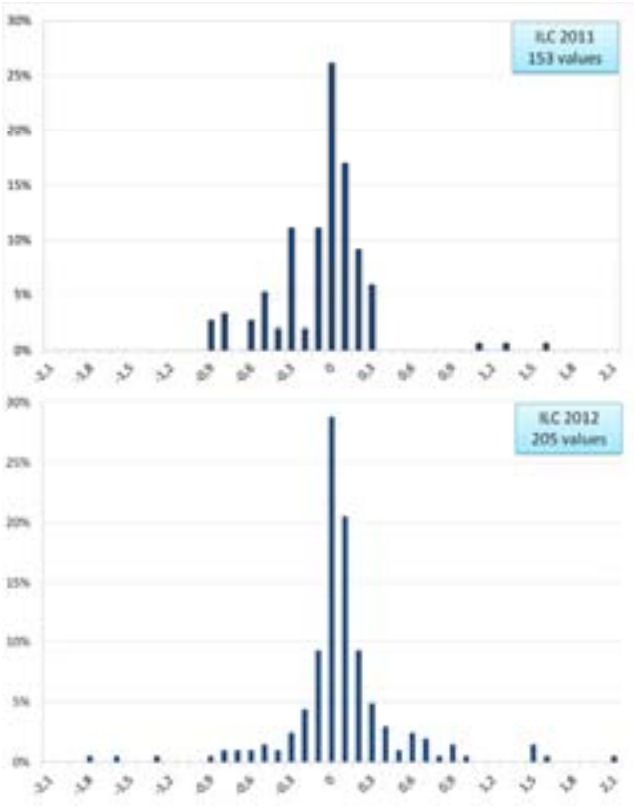

Figure 5. E_n values distribution for the 2011 ILC (top) and for the 2012 ILC (bottom).

VI. Problems Experienced

During the two ILCs no major technical problem were met, but in 2012 sudden frequency changes (of the order of 10^{-10}) of the GPSDO 2 output frequency were detected by a few ACLs. In all cases, the problem was temporary and was overcome simply by waiting one day for a new stabilization of the GPSDO frequency.

In practice the GPSDO 2 behaved as if it had been temporarily unlocked to the GPS signals, reaching again the lock condition 12 – 24 hours later. In one of these events this seemed to be related to the influence of a metallic mass set nearby the GPSDO. Investigations performed when the equipment came back to INRIM for the ILC closure, confirmed a relationship between a sudden change in frequency and a magnetic field variation. This frequency change was clearly not related to temperature changes, as a temperature effect should reflect the thermal time constant of the rubidium oscillator. Indeed, the sudden frequency jump is recovered as soon as a new steady condition is reached for the magnetic field, and the locking process gets back the nominal frequency according to the time constant of the servo system.

The sensitivity to the magnetic field was experimentally tested at INRIM moving magnetic plates close to the GPSDO 2 and continuously recording its output frequency. These operations simulated magnetic static field perturbation, changing the concentration of the Earth magnetic lines of force in proximity of the GPSDO.

While the value of the natural magnetic field, measured with a magnetic sensor for five days on the top of the workbench hosting the GPSDO and with the laboratory in quiet environmental conditions, has a mean value around 50 μT, and is stable at some μT level, when the metallic plates are set nearby the GPSDO, the magnetic sensor can detect variations of the order of more than 30 μT. But, even the metal structure of the workbench can modify locally the magnetic field. Indeed, it was observed that moving a magnetic sensor on the support plane, variations of the order of 20-30 μT could be detected.

The maximum magnetic sensitivity of GPSDO 2 showed frequency variations of the order of $1 \cdot 10^{-11}$ /μT. This results is quite in agreement with the frequency deviations of some parts in 10^{-10} observed during the campaign.

VII. Conclusions

The first successful national campaigns - and maybe one of the first in Europe - demonstrated the feasibility of an ILC to assess the metrological capabilities of accredited laboratories for frequency, at the level of 10^{-12} and below.

Some operational and logistic issues affecting similar previous experimental trials (e.g., the installation of the GPS antenna feeding the travelling GPSDO) have been overcome without significant overhead for the involved ACLs. The potential of remote monitoring the travelling equipment performance (especially the GPSDO providing the frequency reference standard) has been also successfully assessed, relying on the Fluke 910R capability to measure and archive the time offset of its internal oscillator versus the GPS Time.

Conversely, some critical points arose during the two years experience and some suggestions on possible future improvements were identified. According to the experimental analysis detailed in Section VI, the GPSDO 2 used as travelling standard in 2012 seems to be particularly sensitive to magnetic field variations, while similar devices calibrated at INRIM showed 5 to 10 times lower sensitivities. As the manufacturer specification on this subject were not supplied, it is not clear if it is an anomaly of the device used or not.

The lesson learned is that while the absolute level of the magnetic field nearby the GPSDO is not critical, since the locking mechanism compensates for this effect, what matters is the overall stability of the environment close to the device itself. According to these findings, for future exercise it is therefore strongly recommended to avoid both any movement of metallic masses in proximity of the GPSDO and occasional displacement of the GPSDO itself especially if located close to a metallic structure.

Acknowledgment

The authors wish to acknowledge the collaboration provided by the ACCREDIA DT personnel, namely its Director Mario Mosca and the Technical Officers Rosalba Mugno and Giuseppe La Paglia. Special thanks to Roberto Costa of the INRIM Time and Frequency Laboratory for the metrological support and to the staffs of all the ACLs for the outstanding effort.

The experimental contribution from Guido Pellici supporting the assessment of the magnetic field effects on the GPSDOs are also acknowledged.

References

[1] ISO/IEC 17025:2005 “General requirements for the competence of testing and calibration laboratories”.

[2] C. Calosso, V. Pettiti, F. Cordara, E. Bertacco, D. Orgiazzi “TFTS: a transfer standard for Frequency and Time Interval Inter-Laboratory Comparisons”, Proceeding of EFTF 2009, Besancon (France).

[3] EA-2/14 M:2008 “Procedure for Regional Calibration ILCs in Support of the EA MLA”.

[4] ACCREDIA DT - ILC/FREQ01-2011 and ILC/FREQ02-2012 “Protocollo per lo svolgimento di un confronto interlaboratorio (ILC) per la grandezza Frequenza” (In Italian).

[5] ISO/IEC 17043:2010 – Conformity assessment – General requirements for proficiency testing.

[6] EA-2/10 “Procedure for Regional Calibration ILCs in support of the EA MLA”, June 2008.

[7] ILAC G13:2000 “Guidelines for the competence of providers of proficiency testing service”.

[8] ACCREDIA DT - ILC Frequenza 2011 and ILC Frequenza 2012 “Relazione finale” (In Italian).

Dual-Mixer Time-Difference Measurement System using Discrete Fourier Transformation

Shinya Yanagimachi, Akifumi Takamizawa,
Takehiko Tanabe, Ken Hagimoto, Takehsi Ikegami
National Metrology Institute of Japan (NMIJ)
AIST, Tsukuba, Ibaraki 305-8563, Japan
E-mail: s.yanagimachi@aist.go.jp

***Abstract*—Simplified Dual-Mixer Time-Difference Measurement system is proposed using discrete Fourier transformation (DFT) where no sinusoidal-pulsed converter, nor zero-cross detector are necessary. The phase meter integrating the proposed method with a dead time needed to process the time difference was demonstrated with an high resolution of $\sigma_y(t=1\ s)=7x10^{-14}$ and $\sigma_y(t=10000\ s)=1x10^{-16}$. The expected truncation error due to the usage of DFT was in good agreement with the observed one. Moreover, the multi-phase meter for five oscillator was easily demonstrated where three corner hat measurement was executed, and Allan deviation of more stable oscillator that two other ones was observed at an averaging time of approximately less than 30 s.**

Keywords- component; frequency stability; noise measurement; DMTD; three-cornered hat method

I. INTRODUCTION

Precise oscillators have been contributing to the development of modern science and technology, such as the establishment of high-speed communications, navigation systems, and fundamental physics. Atomic clocks play an important role in the reliable implementation of time and frequency standards [1]. The Dual-Mixer Time-Difference(DMTD) is the most appropriate way to measure the time difference between precise oscillators with a typical standard reference signals of 5, 10, and 100MHz [2-4].

In the DMTD method, two input signals with the same nominal frequency f_0, which are usually generated by a reference signal and device under test (DUT) signal, are mixed with a common oscillator that is synchronized to the reference signal. The common oscillator has a frequency f_{beat} as an offset from f0. The output signals from two double-balanced mixers give two beat signals with a frequency typically set at a value from 1 to 100 Hz. Two sinusoidal-pulsed converters (SPCs) increase the slew rates of the two beat signals. A zero cross detector(ZCD) built in the time interval counter (TIC) determines the time interval Δt between the two beat signals with a measurement cycle of $1/f_{beat}$. Consequently, the time difference Δx between the reference and DUT signals is obtained by

$$\Delta x = \Delta t \ \mathrm{x}\ f_{beat} / f_0. \quad (1)$$

The measurement resolution of Δx, which is limited by Δt in the TIC, is enhanced by a factor of f_{beat} / f_0, and the system noise floor reaches the order of 10^{-14} at an integration time of 1s[3].

Previously, the new technique of DMTD was developed [5,6] by Anritsu CORPORATION, which is designed so that two beat signals are acquired with a par of analog-digital converters (ADCs), and digital-signal processing (DSP) to determine the time difference between tow input signals. This technique has an advantage in that the measurement system has fewer components than the conventional DMTD, as there is no need for SPCs and ZCDs in the TIC. The noise floor of the DMTD using ADCs is comparable to that of the conventional DMTD, which are expressed in terms of Allan deviation as $\sigma_y(\tau=1\ s)\sim10^{-14}$, and $\sigma_y(t=10000\ s)\sim10^{-16}$. The Anritsu group discussed in detail the degradation of the system noise floor by measuring the Allan deviation, mainly considering the hardware configuration.

For the above the new DMTD system, we propose the use of discrete Fourier transformation (DFT) as a DSP technique to determine the parameters of the precise clock. Generally, DSP is a versatile technique and helpful in many different areas where analysis of time series data is required; however, there is a truncation error to consider that can significantly affect the accuracy of the result. Most practical signals digitized by ADC are time-limited and non-periodic, and calculated results involve truncation errors.

Recently, we formulated the truncation error that causes serious error with larger frequency difference between two oscillators, while noting the specification of precise oscillator such as atomic clocks [7]. In this paper, the phase meter integrated DMTD with proposed method is demonstrated. Moreover, this method has greatly extensibility for realization of the multi-phase meter to determine the time difference during many oscillators. We also demonstrate the time difference measurement during five oscillators as well.

II. PRINCIPLE OF DMTD USING DFT

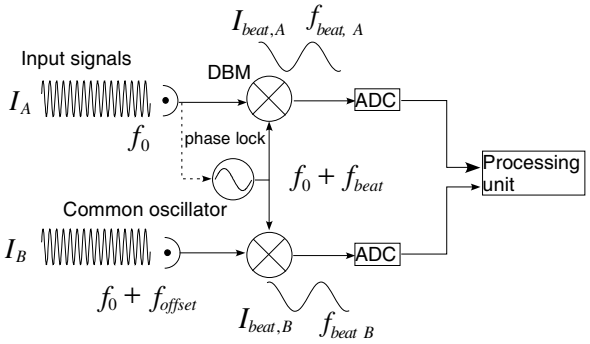

Fig. 1. Configuration of DMTD using DFT: Contrast to a conventional DMTD, SPCs and TICs are not required. Instead, two ADCs and processing unit for the DFT are used.

Figure 1 shows the configuration of the DMTD using ADCs and the DFT. The process containing the generation of two beat-down signals $I_{beat,A}(t)$ and $I_{beat,B}(t)$, using the common oscillator signal is the same as the one in the conventional DMTD. Two signals are expressed as

$$I_{beat,A}(t)=\sin(2\pi f_{\text{beat}}\, t+\theta_{\text{A}}), \tag{2}$$

$$I_{beat,B}(t)=\sin(2\pi(f_{\text{beat}}+f_{\text{offset}})t+\theta_{\text{B}}), \tag{3}$$

where $\theta_{\text{A}}=2\pi\ f_{\text{beat}}\ x_{\text{A}}$, and $\theta_{\text{B}}=2\pi\ f_0(x_{\text{A}}-x_{\text{B}})+\ 2\pi\ f_{\text{beat}}\ x_{\text{A}}$ is replaced with x_{A}, x_{B} being the time deviation of the input signal A and B respectively. Any setting of notation in this paper is the same as that defined in [7].

In order to determine $\Delta x(=x_{\text{A}}-x_{\text{B}})$, the personal computer proceeds the application the DFT to the obtained two signals through two ADCs. Two parameters are basically important: Sampling length T in a data acquisition, and sample size n. Then the Fourier spectrum $P_{\text{X}}(k)$ is obtained as a complex expression from the DFT algorithm:

$$P_{\text{X}}(k)=\Sigma_{\text{j=0}}I_{\text{beat},X}(j/n\ T)\exp(-2\pi ij/n\ k)\quad (X=\text{A, B}) \tag{4}$$

where k is the order of the harmonic spectrum, ranges from 0 to $n/2$, and can be converted into a Fourier frequency by replacing it with k/T. In the case of k=1, the frequency is the fundamental frequency of the DFT and expressed as

$$f_{\text{DFT}}=1/T \tag{5}$$

The phase $\theta_{\text{DFT},X}$ is obtained in terms of $P_{\text{X}}(l)$ as

$$\theta_{\text{DFT},X}=\tan^{-1}(\text{Im}[P_X(l)]/\text{Re}[P_X(l)])\ (\text{X=A,B}) \tag{6}$$

where k is substituted with l in Eq. (4), and l is the integer that is the nearest to the wave number of the signal acquired in the ADCs. The truncation error to be solved is closely related with this wave number, being discussed in the next section. Finally, the time difference Δx_{DFT} between two signals is calculated using the DFT from Eqs. (4), (6) as

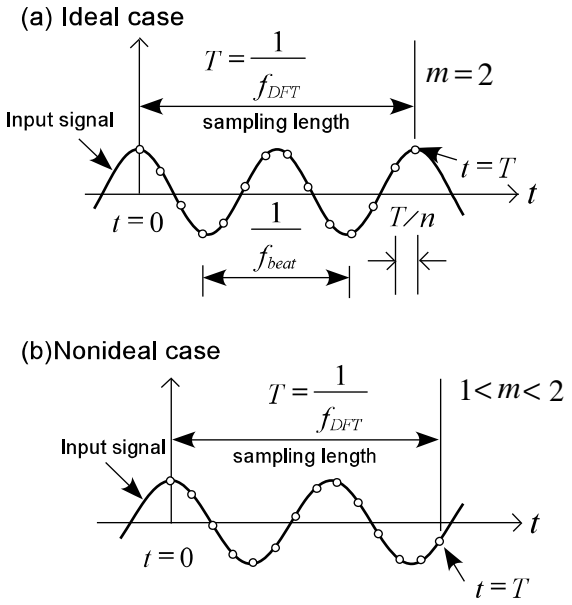

Fig. 2. Two cases of DFT (a) Ideal case and (b) non-ideal case. T(=1/fDFT): Sampling length in a data acquisition. N: Sampling number in a data acquisition. T/n: Sampling interval.

$$\Delta x_{\text{DFT}}=(\theta_{\text{DFT,B}}-\ \theta_{\text{DFT,A}})/(2\pi f_0). \tag{7}$$

III. TRUNCATION ERROR INCLUDED IN THE FOURIER SPECTRUM

Figure 2 shows a concept on the truncation error. When the signals are acquired from t=0 to T, as is drawn in two cases, DFT generally assumes that the signals continue from t=-infinity to + infinity with the acquired waveform repeated periodically. If the ratio of f_{beat} to f_{DFT} is an integer larger than or equal to 1, as an ideal case (a),

$$f_{\text{beat}}/f_{\text{DFT}}=m\ (m=1,2,\ldots..)\ , \tag{8}$$

the spectrum $P_{\text{X}}(k=m)$ gives exact information of the phase of the signal. In this ideal case, there is no discontinuity on periodical boundaries, and the real signal corresponds to the signal assumed in the DFT. If the ratio in Eq. (8) is not an interger, as non-ideal case, the information of the phase calculated from the spectrum $P_{\text{X}}(l)$ includes a truncation error due to the discontinuity on the boundaries.

Here, two beat-down signals $I_{beat,A}(t)$ and $I_{beat,B}(t)$ in Eqs. (2) and (3) is applied to DFT, then $\theta_{\text{DFT,A}}$ and $\theta_{\text{DFT,B}}$ are given by

$$\theta_{\text{DFT,A}}=\pi/2+\theta_{\text{A}}, \tag{9}$$

and

$$\theta_{\text{DFT,B}}=\pi/2+\theta_{\text{B}}+f_{\text{offset}}\{\pi T+T\sin(2\theta_{\text{B}})/(2l)\}\ , \tag{10}$$

respectively. For a detailed calculation, an appendix in [7] described. The term of the function f_{offset} originates from the truncation error, as the $(f_{beat}+f_{offset})/f_{DFT}$ is no longer an integer. By substituting Eqs. (9) and (10) for Eq. (7), the time difference that could include the truncation error is obtained:

$$\Delta x_{DFT}=\Delta x+f_{offset}/f_0\{T/2+T\sin(2\theta_B)/(4\pi l)\}. \quad (11)$$

In Eq. (11), the first term gives the exact solution, and all terms that are a function of foffset originate from the truncation error, which depends on f_{offset}, T, l, and θ_B. This behavior of the truncation error is consistent with the fact that the above four parameters change the discontinuity on all boundaries.

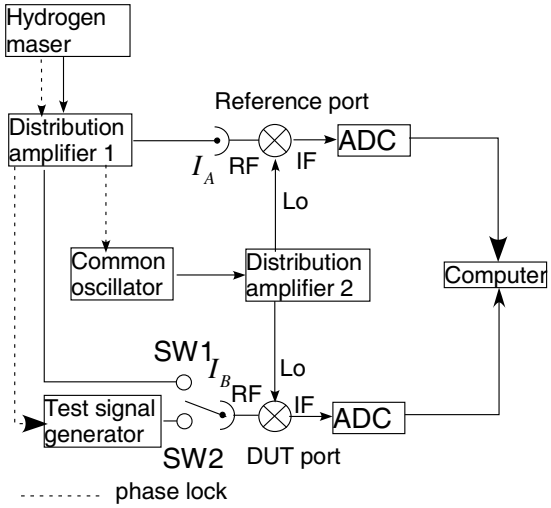

Fig. 3. Schematic diagram for experimental set up

IV. Test of Capability to Measure the Time Difference

We have demonstrated the performance and usability of the DMTD using DFT. The experimental set up is shown in Fig. 3. The Hydrogen maser reference signal I_A of 10 MHz(=f_0) passes through the distribution amplifier-1 having several output ports. The DUT signal I_B can be changed by switching SW1 and SW2. SW1 is used to investigate the system noise floor. In the use of SW2, DUT signal I_B is connected to the output from the test signal generator phase locked to the signal I_A. The test signal generator is set to produce the normalized frequency offset f_{offset}/f_0 between the two signals to simulate the signal of an atomic clock.

The common oscillator is phase locked to the signal IA and detuned by f_{beat} (62.5Hz). This signal is duplicated using distribution amplifier-2, and introduced into the local inputs of two DBMs. The two signals of $I_{beat,X}$ are obtained and simultaneously converted into digital data at a sampling length of T=0.8 s, a sampling number of n=40,000, and a time difference measurement cycle of 1 s. Two or more ADCs are supplied by NI-PCI 6143(National instruments), operated simultaneously for acquisition of multi waveform. The dead time of 0.2 s between phase measurements is reserved for processing time of the DFT on a computer, and enable us to use custom-made ADCs to easily obtain. The fundamental frequency of f_{DFT} is 1.25 Hz(=1/T), and the wave number l is 50(=f_{beat}/f_{DFT}).

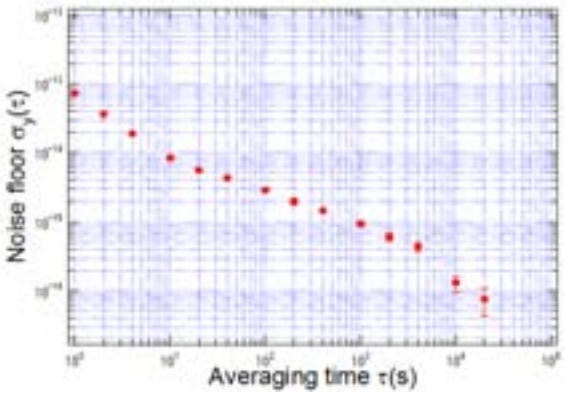

Fig. 4. System noise floor

System noise floor was observed in the case of SW1 up to an averaging time of approximately 10,000 s, which is exhibited in Fig. 4. The Allan deviation shows the performance of $\sigma_y(\tau=1\ s)=7\times10^{-14}$, and $\sigma_y(\tau=10000\ s)=1\times10^{-16}$, which is comparable to the conventional DMTD.

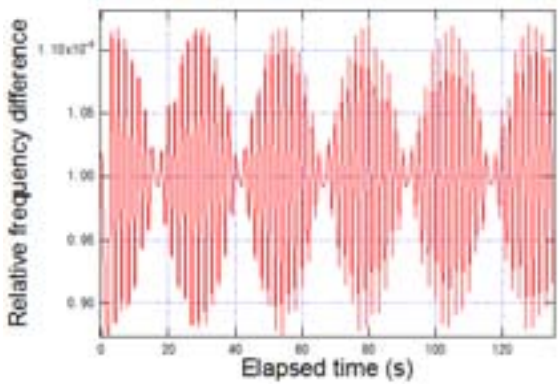

Fig. 5 Observed truncation error

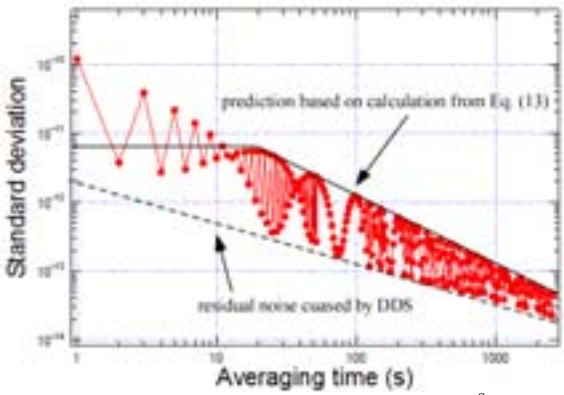

Fig. 6 Allan deviation for $f_{offset}/f_0=10^{-9}$

V. TRUNCATION ERROR APPEARED WHEN A LARGER FREQUENCY OFFSET BETWEEN TWO OSCILLATORS HAPPEN

As discussed in Sec. III, the truncation error is dependent on f_{offset}/f_0. For $f_{offset}/f_0=10^{-9}$, test signal generator was intentionally detuned so that the relatively larger truncation error occurred(Fig.5). The phase (or frequency) modulated data were observed with the center line corresponding to $f_{offset}/f_0=10^{-9}$, which should be intrinsically observed. This behavior can be explained using an error function $\Delta x_{E.F.}(T,f_{offset},l)$:

$$\Delta x_{E.F.}(T,f_{offset},l)=(T f_{offset})/(2 f_0) +\{ T f_{offset} \sin(2\theta_B)/(4\pi f_0 l)\},(12)$$

although this equation does not consider the dead time. So, the Eq. (12) does not perfectly predict the data experimentally observed. However, in perspective, the Allan deviation derived from Eq. (12) explains well the experimental result shown in Fig. 6, as is expressed by

$$\sigma(\tau)=(f_{offset}{}^2 T)/(\mathrm{sqrt}(2) l f_0), f_{offset}\tau<<1/(2\pi), \text{ or}$$

$$\sigma(\tau)= (f_{offset} T)/(2\mathrm{sqrt}(2) l\pi f_0 \tau), 1/(2\pi)<< f_{offset}\tau \qquad (13)$$

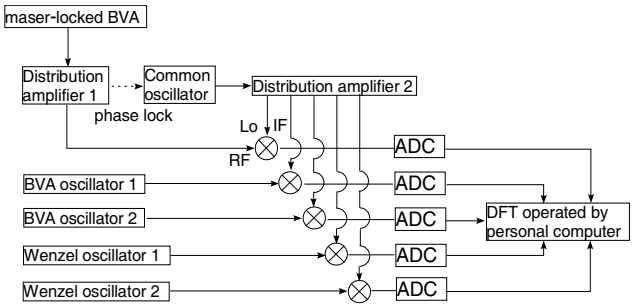

Fig. 7 Set up for multi-phase meter

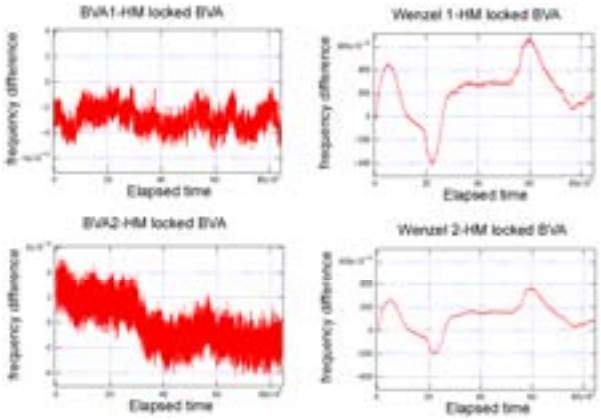

Fig 8 Observed data as a function of elapsed time

The detailed explanations, and consideration of the truncation error for the phase measurement were discussed in [7].

VI. DEMONSTRATION OF MULTI-PHASE METER

The DMTD using DFT has greatly extensibility for multi-phase meter, because the simultaneous ADCs are commercially available to easily be implemented. NI-PCI 6143 has eight ADCs so that we could measure the time difference during eight oscillators at most. Figure 7 shows a diagram of the multi-phase meter using DFT. Not so special preparation was needed comparing the DMTD measurement of two oscillators. Figure 8 is the raw data collected as the time difference during five oscillators. The two oscillators produced by Wenzel Associates, Inc. behaves similarly each other. We used three BVA oscillators, one of which is phase-locked to the Hydrogen maser, for three cornered hat measurement (Fig. 9)

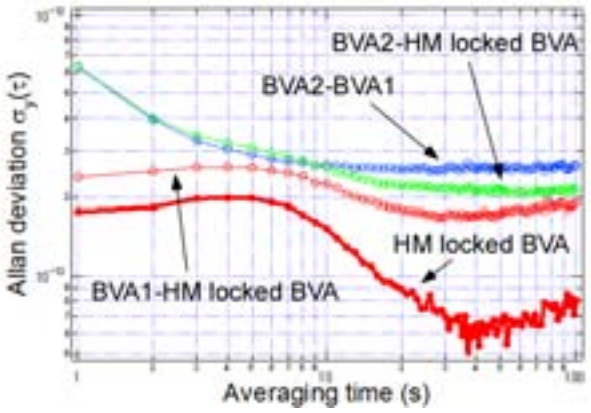

Fig. 9 Result in three cornered hat measurement

VII. CONCLUSIONS

Simplified DMTD method was proposed using Discrete Fourier Transformation, where no SPCs, nor ZCDs were needed. Truncation error was formulated to determine the time difference between two oscillators. The phase meter using DFT was implemented with not so high sampling rate by introducing dead time. The expected truncation error was in good agreement with the observed one. The multi-phase meter for five oscillators was easily demonstrated. Three corner hat measurement was also demonstrated where Allan deviation of more stable oscillator than two other ones was observed with less than approximately 30 s.

REFERENCES

[1] F. Riehle: Frequency Standards (Wiley-VCH, Weinheim, 2004) p. 387

[2] D. W. Allan and H. Daams: Proc. 29th Annu. Frequency Control Symp., 1975, p.404.

[3] S. Stein, D. Glaze, J. Levine, J. Gray, D. Hilliard, D. Howe, and A. Erb: IEEE Trans. Instrum. Meas. 32 (1983) 227.

[4] G. Brida: Rev. Sci. Instrum. 73 (2002) 2171.

[5] M. Uchino and K. Mochizuki: Electron. Commun. Jpn 87 1 (2004) 21.

[6] K. Mochizuki, M. Uchino, and T. Morikawa: IEEE Trans. Instrum. Meas. 56 (2007) 1887.

[7] S. Yanagimachi, K. Hagimoto, and T. Ikegami, "Analysis of truncation error for dual-mixer time-difference measurement system using discrete fourier transformation," 52 (2013) 03661.

Frequency Transfer Over Optical Fiber Based on Photonic RF Phase Shifter

Jianguo Shen, Guiling Wu*, Weiwen Zou, Ruihao Chen, and Jianping Chen
State Key Laboratory of Advanced Optical Communication Systems and Networks, Shanghai Jiao Tong University, Shanghai, 200240, P. R. China
*wuguiling@sjtu.edu.cn

***Abstract*—In this paper, an active phase drift cancellation scheme based on a photonic RF phase shifter for frequency transfer over optical fiber is proposed. By this scheme, a linear and stable photonic phase shifter, which is implemented with a dual parallel mach-zehnder modulator and an optical filter, is used to compensate the phase drift induced by the fiber transmission. A 1GHz reference signal transfer over 20 km single-mode fiber with sub picosecond timing jitters measured at the remote site is experimentally demonstrated using the proposed scheme.**

Keywords-photonic RF phase shifter; frequency transfer; phase compensation.

I. INTRODUCTION

Frequency transfer via optical fiber is considered to be a promising method to realize ultra-stable reference frequency remote transfer and has attracted an intensive research in recent years [1-5]. Compare to traditional satellite-based method, the stability of frequency transfer over fiber can be improved more than three orders of magnitude [1]. However, the phase drift induced by the temperature variation and mechanical perturbation during optical fiber transmission degrades the frequency stability, especially the long-term stability. Therefore, the cancellation of those phase drifts from fiber transmission is one of the critical issues in frequency dissemination via optical fibers.

Throughout the years, varieties of schemes of phase drift cancellation for frequency transfer via optical fiber have been developed. Generally, a tunable optical delay line, typically consisted of a fiber stretcher and a temperature controlled fiber spool to obtain a large range and faster respond, is adopted to compensate delay fluctuation [2-3]. Such kind of optical delay line has a large bandwidth, but is considerably bulky and power consumption. Moreover, mechanical stress on the fiber in fiber stretcher will increase the effect of the polarization mode dispersion. Additionally, a microwave phase shifter [4] or voltage control oscillator (VCO) working as a phase integrator [5-6] is employed, which features a fast tuning speed. However, VCO is band-limited while the electrical phase shifter exits nonlinear phase shift and power variation as the phase shifting.

In this letter, a novel phase drift cancellation scheme based on a linear photonic RF phase shifter for frequency transfer over optical fiber is proposed, where the phase drift originating from fiber transmission is compensated by tuning the phase of the transmitted RF signal through a linear photonic RF phase shifter. The proposed phase drift cancellation scheme is validated experimentally by a 1GHz reference signal transfer over 20 km single-mode fiber with the timing jitter less than 1ps.

II. THE PRINCIPLE OF THE PROPOSED SCHEMATIC

Fig.1 illustrates the proposed phase drift cancellation based on a photonic RF phase shifter schematically. At local site, the reference signal is applied to a well-designed photonic RF phase shifter to generate a phase-shiftable RF modulated optical signal, of which the phase can be fast tuned by simply controlling the bias voltage of the photonic phase shifter. Then, this modulation optical signal is transmitted to a remote site through an optical fiber link. At the remote site, a part of the modulated optical signal is returned through the same optical fiber link to get the phase noise induced by the fiber transmission. The phase compensation is realized by control the bias voltage with the phase error signal, which is generated by a special phase detecting sub-system and pass through the loop filter (LP).

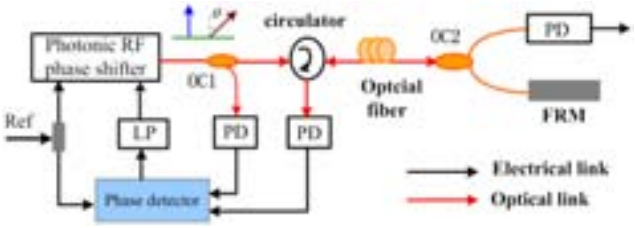

Fig.1 the schematic of the proposed phase compensation schematic

The key component in the proposed phase compensation system is a photonic RF phase shifter, which is implemented by a dual parallel mach-zehnder modulator (DPMZM) and an optical filter and shown in Fig.2. The light wave from a laser is launched into an integrated x-cut DPMZM, which is composed of two parallel sub-MZMs lying on two arms of the parent MZM, respectively. A local microwave signal from a local oscillator is applied on the sub-MZM on the top arm, and an electric up-converter (U-C) to up-convert the reference signal from a reference clock at the same time. The up-converted signal is applied to the other sub-MZM on the bottom arm. The bias voltages of the sub-MZM on the top arm and the bottom arm (DC1 and DC2) are biased at the minimum transmission point to perform optical carrier-

suppressed double sideband (CS-DSB) modulation. One sideband of the CS-DSB signal is suppressed by an optical band-pass filter (OBPF) to generate a single sideband (SSB) signal, which is detected by photo detectors to produce a phase-shifted reference signal by beating of the two signals in the same sidebands. The phase shift value of the recovered reference signal can be set by simply tuning the bias voltage of parent MZM (DC3). An EDFA is added between the DPMZM and OBPF to compensate the insert loss.

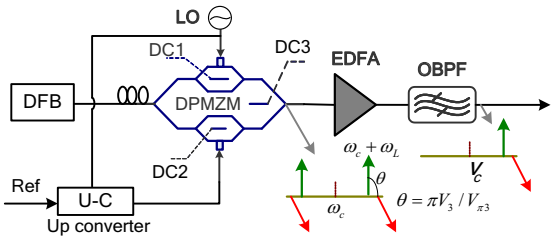

Fig.2 Schematic of the proposed photonic RF phase shifter

Under small-signal modulation, the optical field at output of the DPMZM can be expressed as follows:

$$E_1(t) = A_1 \exp[j(\omega_c t + \omega_L t - \frac{\theta}{2})] + A_1 \exp[j(\omega_c t - \omega_L t - \frac{\theta}{2})] + A_2 \exp[j(\omega_c t + (\omega_L + \omega_r)t + \frac{\theta}{2})] + A_2 \exp[j(\omega_c t - (\omega_L + \omega_r)t + \frac{\theta}{2})], \quad (1)$$

where A_1 and A_2 are the amplitude of the first sideband on the top and bottom arm, respectively; ω_c , ω_L and ω_r are the frequency of the optical carrier, local microwave and reference signal respectively; θ is the relative phase difference between the optical first sidebands on the top and bottom arm, which can be expressed as follows.

$$\theta = \pi V_3 / V_{\pi 3}, \quad (2)$$

where $V_{\pi 3}$ is the half-wave voltage of the parent MZM, V_3 is the bias voltage of the parent MZM (DC3). Assuming that the lower sidebands from the top and bottom arm are suppressed by the OBPF, we have

$$E_2(t) \propto A_1 \exp[j(\omega_c t + \omega_L t - \frac{\theta}{2})] + A_2 \exp[j(\omega_c t + (\omega_L + \omega_r)t + \frac{\theta}{2})], \quad (3)$$

Where $E_2(t)$ is the optical field of SSB signal at the output of the OBPF. A phase-shifted reference signal produced during photo detection process can be described as

$$i(t) \propto E_2(t) \times E_2^*(t) = A_1 A_2 \cos(\omega_r t + \theta) \quad (4)$$

As can be seen from Eq. (4), the optical phase is introduced to the reference signal directly and one can easily control the phase shift of the reference frequency signal linearly and continuously by tuning the bias voltage of DC3.

It is worth to note that the additional LO is used to enlarge frequency gap between the upper and lower sidebands to ensure one sideband can be suppressed completely by the optical filter. Thus, the proposed phase shifter can be for low frequency application, which corresponding to the large time delays compensation range. In fact, the LO can be replaced by the ground and the bias voltage of DC1 works at the maxim point for the high frequency application, which is realized in our previous work [7].

III. Experiment Results

A proof-concept experimental system over 20 km optical fiber based on the presented scheme is built. The optical carrier from a DFB laser with an optical power of 16 dBm is injected into a DPMZM (Photline, MXIQ-LN-40) with a usable bandwidth of 20 GHz. The bias voltages corresponding to the minimum transmission points of the two parallel sub-MZMs are 9.4 V and 9.3 V, respectively. The frequency of the local microwave signal is set at 9 GHz to ensure that the lower sideband can be suppressed completely by the consequent tunable optical band-pass filter (TOBPF, Alnair, BLV-200CL). The reference signal needed to be transferred is set at 1 GHz. Three PDs (Thorlabs, DEC010FC) with a bandwidth of 2.5 GHz is used to recover the reference signal.

Firstly, the performance of the proposed phase shifter is evaluated by testing the recovered reference signal at the PD1. Fig.3 shows the measured phase shift and power variation of the recovered reference signal as the tuning of the bias voltage (V3). A continuous and linear phase shift over 3600 is achieved when the bias voltage (V3) is tuned from -15 to 15V.

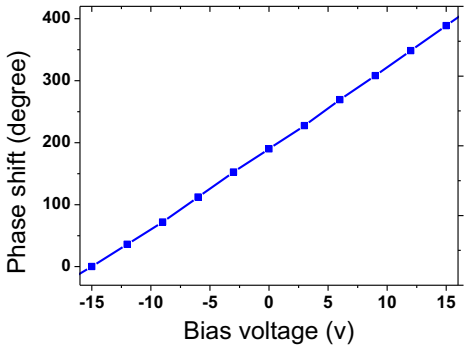

Fig.3 measured phase shift as the bias voltage tuning.

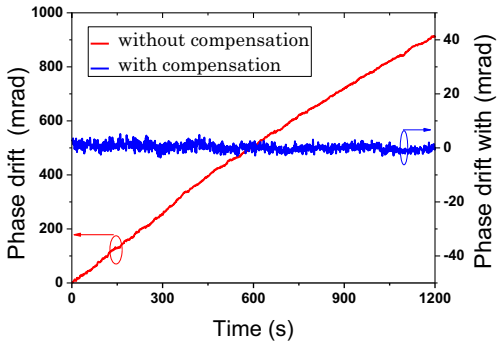

Fig.4. Phase drifts without and with phase compensation

Fig.4 shows the phases drift without and with compensation when transferring a 1GHz reference signal over 20km optical link. As can be seen, the phase drift without compensation is up to 900 mrad within 20 minutes, which mainly results from the temperature change. With the compensation based on the photonic RF phase shifter, the phase drift is less than 6 mrad or timing jitter less than 1ps (RMS).

IV. CONCLUSION

In conclusion, we proposed and experimentally demonstrated a novel phase drift cancellation scheme based on a photonic RF phase shifter for frequency transfer over optical fiber. A linear and stable photonic RF phase shifter is implemented with a DPMZM and an optical filter, which can realize phase compensation through simply tuning the bias voltage of the DPMZM. A proof-of-concept experiment of transferring a 1 GHz reference signal over 20km optical link was carried out. The timing jitter of less than 1ps is achieved with the proposed phase compensation scheme.

REFERENCES

[1] S. M. Forma, K. W. Holman, D. D. Hudson, D. J. Jones, and J.Ye D, "Remote transfer of ultrastable frequency references via fiber networks". Rev. Sci. Instrum, vol.78, pp. 021101, 2007.

[2] M. Calhoun, S. H. Huang, R. L. Tjoelker, " Stable photonic links for frequency and time transfer in the deep-space network and antenna array," Proc. IEEE, vol.95, pp.1931-1946, 2007.

[3] O. Lopez, A. Amy-Klein, M. Lours, Ch. Chardonnet, and G. Santarelli, "High-resolution microwave frequency dissemination on an 86-km urban optical link," Appl. Phys B, vol.48, pp.35-41, 2010.

[4] L. M. Zhang, L. Chang, Y. Dong, W. L. Xie, H. He, and W. S. Hu, "Phase drift cancellation of remote radio frequency transfer using an optoelectronic delay-locked lopp," Opt. Lett.vol. 36, pp.873-875, 2011.

[5] M. Fujieda, M. Kumagai, T. Gotoh and M. Hosokawa, "Ultrastable frequency dissemination via optical fiber at NICT," IEEE Trans. Instrum. Mease,vol. 58, pp.1223-1228, 2009.

[6] B. Wang, C. Gao, W. L. Chen, J. Miao, X. Zhu, Y. Bai, J. W. Zhang, T. C. Li, L. J. Wang, "Precise and continuous time and frequency synchronisation at the 5×10^{-19} accuracy level," Scientific Reports, vol.2, 556, 2012.

[7] J.G. Shen, G. L. Wu, W. W. Zou, J. P. Chen, "A Photonic RF Phase shifter based on a dual-parallel Mach-Zehnder Modulator and an optical filter," Appl. Phys. express, vol.5, 072502, 2012.

OPTIME – Time and Frequency Dissemination System Based on Fiber Optical Network – PIONIER

Ł. Buczek, J. Kołodziej, P. Krehlik, M. Lipiński, Ł. Śliwczyński
AGH University of Science and Technology
Krakow, Poland
mlipinsk@agh.edu.pl

P. Dunst, D. Lemański, J. Nawrocki, P. Nogaś
Astrogeodynamic Observatory
Space Research Centre PAS, AOS
Borowiec, Poland
nawrocki@cbk.poznan.pl

A. Czubla
Central Office of Measures, GUM
Warsaw, Poland
a.czubla@gum.gov.pl

W. Adamowicz, J. Igalson, T. Pawszak, J. Pieczerak
Orange Poland, TPSA
Warsaw, Poland
Janusz.Pieczerak@orange.com

A. Binczewski, W. Bogacki, P. Ostapowicz, M. Stroiński, K. Turza
Poznan Supercomputing and Networking Center, PSNC
Poznan, Poland
wojbor@man.poznan.pl

***Abstract*— The OPTIME project creates a long range dissemination system for transfer ultraprecise time scale and the references frequency signals in telecommunication networks. The highest accuracy signal is available only on fiber optical networks, but other type of networks can be used to transfer of signals with lower accuracy to adapt it to the needs of different user groups. Article also describes experience gained during an over-a-year experiment of connection between Central Office of Measures (GUM) in Warsaw and the Astrogeodynamic Observatory (AOS) in Borowiec.**

Keywords- Atomic clock, fiber optical network, high precision dissemination of time and frequency reference signals, time transfer.

I. INTRODUCTION

Access to ultra-precise time and frequency signals is very important for many groups of users like scientific and research communities, business or government users. Devices, which can provide such a signal (e.g. atomic clock) are not available for all of these groups of users. To ensure access high-accuracy signals other methods as satellite systems (GPS, GALILEO, GLONAS) must be used.

Next very important issue is a problem of comparison and synchronization of remote clock devices. There are only a few methods (Two-Way, PPP, L2T2) with the expected results in terms of accuracy. One of the main advantages of using fiber optical network to compare and synchronize remote devices is a very short time of receiving measurement results.

The OPTIME project proposes solution to achieve both of these issues: compare remote devices with very high accuracy and provide ultra-precise frequency and time signals to end-users. Fiber optical networks are now widely prevalent amongst research and development centers, universities, hi-tech industries or public administration so it seems to be obvious to use it as a transmission medium for time and frequency signals.

II. OPTICAL LINK GUM – AOS BOROWIEC

The idea of the OPTIME project arose as the natural consequence of the experience gained during an over-a-year operation of 421,4 km-long fiber-optic connection between Central Office of Measures (GUM) in Warsaw and the Astrogeodynamic Observatory (AOS) in Borowiec near Poznan. After some successive laboratory experiments of the time and frequency long-haul fiber-optic transfer in which the idea of the active propagation delay stabilization was evaluated the experimental link between GUM and AOS was established, basing on fiber optic infrastructure provided by PSNC – PIONIER and TPSA. The link was launched on the 27th January 2012 and as compared to other reported experimental and rather short-term installations [1], [2], [3] since that day it is in continuous operation enabling a permanent comparison of the UTC(PL) and UTC(AOS) time scales [1]. The concept of the active propagation delay in the fiber optic link was described in [5], whereas the method of joint time and frequency transfer is presented in [6]. The problem of extending the reach of the link has been discussed in details in [7] and [8].

Herein, for the first time, we are reporting on over a year comparison of UTC(PL) and UTC(AOS) atomic timescales with this system, and we refer it to the results of comparisons performed by GPS-based methods, and we also address some practical aspects of maintaining time and frequency dissemination over fiber optical network.

In Figure.1 the results of direct comparison of the UTC(AOS)-UTC(GUM) carried with usage of fiber link, the GPS PPP based on BIPM calculations and Common View (CV) C/A methods are shown. For better readability the curves for both GPS methods are shifted by ±15 ns. It is clear, that all curves are very similar and the differences between them are rather small.

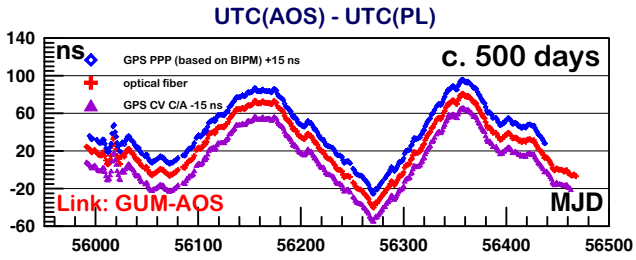

Figure. 1 Results of comparison of UTC(AOS) and UTC(PL) using: fiber optic link (middle/red), GPS PPP based on BIPM calc.(upper/blue) and GPS CV C/A (bottom/violet) methods

In Figure. 2 the differences between results obtained with the use of the fiber link and GPS PPP (BLUE) and respectively the fiber and GPS CV C/A (VIOLET) are shown.

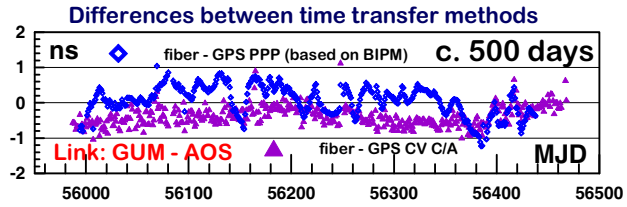

Figure. 2 Differences between time transfer methods

During the operation period in the fiber-optic link some specific events occurred. All of them are collected and listed in Table. 1. There are two types of events. One of them specified as "DLL correction" comes from the method of the time transfer stabilization [6] and may be planned. This type of event could be eliminated in the nearest future by use of automatically switched optical delay lines. The second accidental one specified as "Optical fiber break" or any type of "Breakdowns" are typical and quite commonly occurring in long-haul fiber-optic links. In our application it may be troublesome by triggering the need for new link calibration.

TABLE 1. TABLE OF EVENTS

	MJD	Event Description	Remarks
0	55963	System calibration	$\tau_{GUM-AOS}$ =2047574,25 ns
2	56080-56084	Optical fiber break	new calibration $\tau_{GUM-AOS}$ =2047351,05 ns
4	56096-56097	Optical fiber break	new calibration $\tau_{GUM-AOS}$=2047751,05 ns
5	56120-56121	Optical fiber break	no calibration required
6	56229-56230	2-hrs breakdown – unknown reason	no calibration required
7	56249-56250	Measurement breakdown at AOS	no comments
8	56330-56331	Fiber replacement	no calibration required
9	56345	Dispersion checking	OK
10	56365	Measurement reorganization	no comments
13	56464	Power supply breakdown at GUM	no comments

Nevertheless after more than one year exploitation of the link and a series of metrological experiments, it may be stated that the link is capable of transferring the highest-quality and stable 1 PPS and 10 MHz atomic reference signals for quite long distances and the technology used in the link may be used to build the wide network for time and frequency dissemination.

III. OPTIME ARCHITECTURE

The OPTIME architecture bases on three main elements. The first one is reference laboratories with reference clock devices. Each of these laboratories can provide time-frequency signals for the entire system. These reference laboratories must be leading centers with high reliability of deliver signals. The parameters of the whole system are strictly dependent on the accuracy of these laboratories.

The second element includes local repositories. Local repositories will be equipped in less precise devices like rubidium or cesium clock, which will be synchronized with references laboratories. During connection failure to reference laboratories, local repository will provide time and frequency signals until the failure will be removed. Such solution will increase the reliability of the system and minimize the effects of potential failures to end-users. Present work aims to elaboration of repository structure which enables the automatic detection of network failures and the reliable switchover to redundant and backup source of time and frequency. In order for switchover mechanism to work properly and optimally synchronization of a local repositories clock to reference laboratories is required. A concept diagram of the repository is presented in Figure 3

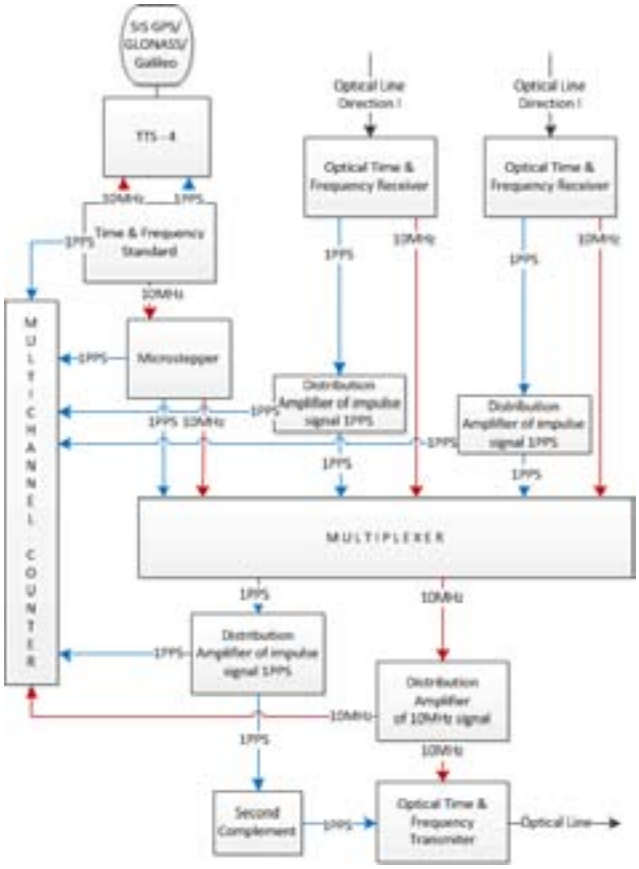

Figure. 3 Local repository diagram

The last main element of the system is dissemination network. As a backbone the OPTIME uses a fiber links provided by TPSA and PSNC – PIONIER network. All reference laboratories, local repositories and the most advanced users must be connected by optical fiber network to ensure the highest accuracy of signals. However, the OPTIME architecture also allows to use IP networks for users with less requirements.

The project plans to offer an application in the IP networks. The local repositories are going to provide 1PPS signal to a nearby located client via short distance fiber link. In the client site, 1PPS signal is going to be transformed to the RS-232 standard and supply NTP Stratum 1 server. In that way, problem of unknown time offset due to the round time trip asymmetry in IP networks is reduced. Client receives the timestamps with the time accuracy of 5us.

The project OPTIME develops the concept of national system architecture, the distribution of time and frequency. User's needs analysis was the demand for such service. Table 2 provides a first estimation of the potential needs of the division into groups of users and their requirements on the accuracy of the signals and the need for synchronization with the legal time.

TABLE 2. REQUIREMENTS FOR TIME & FREQUENCY PATTERNS

Users	Synch.	Freq. Stab.	Legal Time	Market size
SCIENCE				
T&F Lab	1ns	1.00E-15	NO	100
Opt. Astro Lab	1ns	1.00E-14	NO	100
Phys. Lab	10 ns	1.00E-17	NO	100
INDUSTRY				
Telecom.	< 3 µs	1.00E-12	YES	100 M
Mobility	< 3µs	1.00E-12	YES	100 M
Transport.	1 ms	1 µs/DAY	YES	100 K
SECURITY				
Bank/Final.	1-20 ms	-	YES	10 K
Data transfer	-	-	YES	100 K
Cryptology	1 µs	-	YES	100 K

Based on requirements analysis it is planned in future to implement national, distribution network taking advantage of the PIONIER structures – fibers. The plans assume a deployment of the local repositories in at least 21 main cites which will play the role of time and frequency distribution centers. The repositories will be supplied with at least two directions and UTC(PL) and UTC(AOS) time scales will be available in these repos.

IV. First phase of OPTIME

The first phase will focus on creation of connection between two reference laboratories and two local repositories. The first of reference laboratory will be AOS located in Borowiec with UTC(AOS), the second one will be GUM located in Warsaw with UTC(PL). Two local repositories will be created in Poznan - PSNC, and Torun - FAMO. The whole system will have fiber link more than 700 km long (see Figure 3).

Figure 3. National time and frequency distribution system – first phase.

The choice of location of local repositories was dictated by practical considerations. Poznan is a major academic center, and PSNC is an operator of PIONIER - Polish Optical Internet - a nationwide broadband optical network for e-science. Torun is a strong center of atomic, molecular and optical physics, and radio astronomy. There is one of the greatest radiotelescope located in Piwnice near Torun.

V. Opportunities for OPTIME project

The OPTIME project is planned as a demonstrator of time and frequency dissemination service. However further opportunities to develop service to include more users will be investigated. It also considers international cooperation both the exchange experiences and creates optical links to foreign partners.

Acknowledgment

The OPTIME project is co-funded be the *National Center for Research and Development* from Poland in the *Applied Research Programme*.

References

[1] O.Lopez, A.Kanj, P.E.Pottie, D.Rovera, J.Achkar, Ch.Chardonnay, A.Amy-Klein, G.Santarelli, "Simultaneous remote transfer of accurate timing and optical frequency over a public fiber network", Appl. Physics B, DOI 10.1007/s00340-012-5241-0, 07th October 2012.

[2] M.Rost, D.Piester, W.Yang, D.Feldmann, T.Wuebenna, A.Bauch, "Time transfer over optical fibers over a distance of 73 km with an uncertainity below 100 ps" , Metrologia, 49 (2012) pp. 772-778.

[3] B.Wang, C.Gao, W.L.Chen, J.Miao, X.Zhu, Y.Bai, J.W.Zhang, Y.Y.Feng, T.c.Li, L.J.Wang, "Precise and Continous Time and Frequency Synchronisation at the $5x10^{-19}$ Accuracy Level", Scientific Reports, 6-th August 2012.

[4] Ł. Śliwczyński, P. Krehlik, A. Czubla, Ł. Buczek and M. Lipiński, "Dissemination of time and RF frequency via a stabilized fibre optic link over a distance of 420 km", Metrologia 50, 133-145, 2013.

[5] Ł. Śliwczyński, P. Krehlik, Ł. Buczek and M. Lipiński,. "Active propagation delay stabilization for fiber-optic frequency distribution

using controlled electronic delay lines", IEEE Trans. Instrum. Meas , vol. 60, pp. 1480-1488, 2011

[6] P. Krehlik, Ł. Śliwczyński, Ł. Buczek and M. Lipiński, "Fiber optic joint time and frequency transfer with active stabilization of the propagation delay", IEEE Trans. Instrum. Meas., vol. 61, pp.61 2844–51, 2012.

[7] Ł. Śliwczyński, P. Krehlik, Ł. Buczek, M. Lipiński, "Frequency transfer in electronically stabilized fiber optic link exploiting bidirectional optical amplifiers", IEEE Trans. Instr. Meas., vol. 61, no. 9, pp. 2573-2580, 2012.

[8] Ł. Śliwczyński, J. Kołodziej, "Bidirectional Optical Amplification in Long-Distance Two-Way Fiber-Optic Time and Frequency Transfer Systems" IEEE Trans. Instr. Meas., vol. 62, pp. 253-262, 2013.

Interpolating Time Counter with Multi-Edge Coding

Ryszard Szplet, Dominik Sondej, Grzegorz Grzęda
Electronics Department
Military University of Technology
Warsaw, Poland
rszplet@wat.edu.pl

***Abstract*—This paper presents the design, operation and test results of an interpolating time counter with a multi-edge coding principle implemented in the second stage of interpolation. The counter is implemented in an FPGA device (Spartan-6, *Xilinx*) and provides a 2.7 ps resolution, 8 ps precision and 1 s measurement range. The development of such a high performance instrument needs to solve several design problems. The main of them are an implementation of a pattern generator and elimination of bubble errors. We designed and tested two pattern generators based respectively on look-up tables and fast carry chains. The former one is simpler for implementation while the latter allows to control parameters of the pattern signal. This control feature is especially important for the quality of T/D conversion that depends, among others, on the complexity of the pattern signal. We tested three variants of TDC based in turn on coding of three rising, three falling or six alternated edges.**

Keywords—time-to-digital conversion; time counter; multi-edge coding; two-stage interpolation

I. INTRODUCTION

Precise integrated time-to-digital converters (TDC) are typically based on the use of discrete delay lines built as chains of delay buffers [1, 2]. Due to technological spread and changes in ambient conditions, the delays of involved buffers are non-uniform. This manifests in different widths of quantization steps of TDC transfer function and ultimately deteriorates the linearity and precision of conversion. The ultra-wide steps, especially observed in FPGA-based TDCs, may be reduced in the process of conversion by detecting not a single but multiple signal transitions in a delay line [3]. This method is later called the multi-edge coding. In an integrated TDC with multi-edge coding, the leading edge of the START signal, that represents the beginning of the measured time interval, triggers the pattern generator that generates a signal with certain amount of edges. Next, this signal propagates through the time coding delay line (TCDL) that contains a tapped delay line and associated flip-flops [4]. Upon arrival of the leading edge of the STOP signal, that represents the end of the measured time interval, output states of taps of delay line are stored in flip-flops. The ordinal numbers of delay cells of TCDL, in which the transitions of pattern signal were hold, are then added up (fig. 1). The obtained total sum determines the number of the quantization step in an equivalent coding line (ECL), which is virtually created by overlapping quantization steps of the TCDL segments.

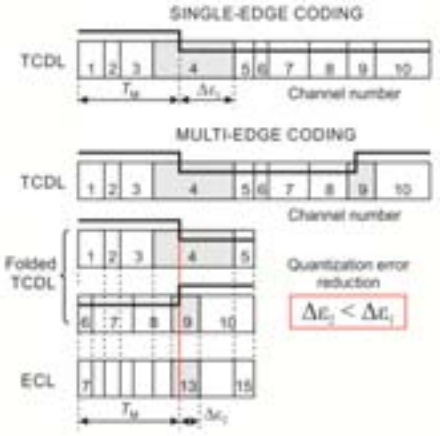

Fig. 1. The idea of multi-edge coding.

The value of measured time interval (T_M) can be calculated as:

$$T_M = \sum_{i=k}^{l} \tau_i \text{ where } l = \sum_{j=1}^{m} n_j$$

while k is the first quantization step of the ECL, n_j is the number of quantization step in the j-th segment of delay line in which the pattern signal transition is observed, τ_i is the width of the i-th bin in the ECL and m is the number of pattern transitions. In a single-edge coding method wide bins can cause a large quantization error (e.g. $\Delta\varepsilon_1$ in fig. 1). The multi-edge coding reduces such errors ($\Delta\varepsilon_2 < \Delta\varepsilon_1$) by narrowing the widths of quantization steps of TCDL. These widths, and consequently the widths of quantization steps of the ECL, are precisely evaluated during the calibration process based on a statistical code density test (SCDT) [5].

II. PATTERN GENERATORS

The multi-edge coding method requires generation of the pattern signal that is a model square signal with a certain amount of edges and possibly minimal delays between them. The shortness of the pattern is an important requirement because any increase in its length causes need for lengthening of the TCDL. This should be avoided due to larger sensitivity of longer delay lines to drifts of supply voltage and ambient temperature. Two types of pattern generators that meet the mentioned requirements are proposed.

A. LUT-based pattern generator

As the first approach we designed a pattern generator consisting of four delay buffers and a Look-Up Table (LUT) that implements the function y(a, b, c, d, e) = Σ [1, 7, 31] (fig. 2).

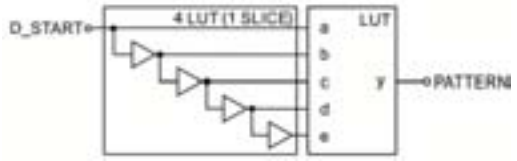

Fig. 2. Pattern generator based on Look-Up Tables.

The rising edge of the signal D_START reaches the consecutive inputs of the LUT with an incremental delay due to delays of subsequent buffers. In accordance with the implemented function, the LUT produces a square waveform with transitions that follow successive rising edges at the LUT inputs coming from the active D_START signal propagating through the chain of buffers. For the function presented above the pattern generator creates an output signal containing five edges (three rising and two falling). An important advantage of this generator is its simplicity and saving of FPGA logical resources (only two slices of *Xilinx's* Spartan-6 involved), while the main drawback is that delays between following pattern edges cannot be shorter than the delay of an elementary delay buffer.

B. Carry chain-based pattern generator

The second pattern generator has been built with the use of the carry chain structure typically implemented in modern programmable devices (fig. 3).

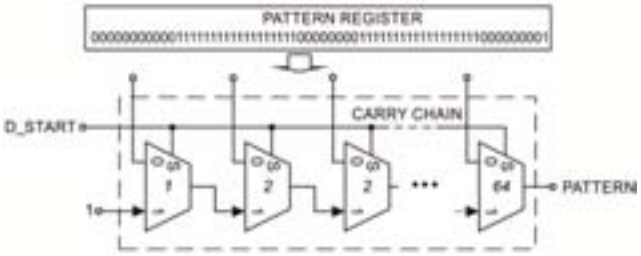

Fig. 3. Pattern generator based on carry chain structure.

The generator consists of 64 fast carry multiplexers (16 Slices in Spartan-6, *Xilinx*) connected in series and a 64-bit pattern register. Outputs of the register containing the pattern are connected to the inputs '0' of multiplexers. However, the pattern can start propagating toward the output of the carry chain only when the input signal D_START changes its state to high ('1'). The main advantage of this generator is the possibility of changing the shape of pattern by the control software without necessity of reprogramming the FPGA device.

III. BUBBLE ERRORS

The carry chains built in programmable devices together with associated flip-flops are often use for fast T/D conversion [1, 2, 4]. During tests of such a carry chain structure implemented in the Spartan-6, it has been observed that the increase in delay along the carry chain does not match the order of multiplexers, which would be expected from the schematic diagram provided by the manufacturer [6, 7]. The lack of monotonicity is a result of non-uniform propagation delays between elements of the carry chain and flip-flops. It also comes from not equal delays in the clock distribution net and from metastability effect in flip-flops. These properties can lead to appearance of bubble errors in the output code of TCDL (fig. 4).

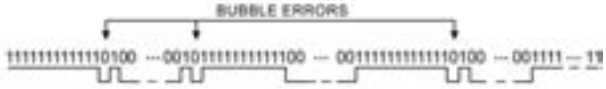

Fig. 4. An example output code with bubble errors.

In a TDC with single-edge coding such errors can be eliminated by virtual rearrangement of delay buffers in the coding line. However, in the multi-edge coding TDC both edges of the pattern signal are coded and such approach does not give proper result because the appearance of bubble errors depends also on the type of signal transition (rising/falling edge).

In order to eliminate the bubble errors an additional circuit has been developed that detects excess logic transitions in the output word of coding line and corrects them as errors (fig. 5). The circuit consists of LUTs that realize the following function y(a, b, c, d, e, f) = Σ [14, 22, 26, 38, 42, 44, 50, 52, 56].

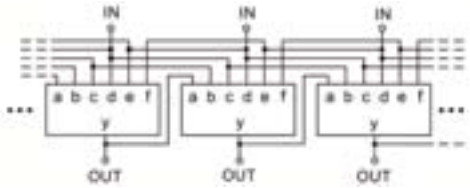

Fig. 5. Bubble error correction circuit.

The developed circuit corrects both single bubble errors (01**0**111) that may appear at the beginning and end of a coded pulse and double ones (01**00**11) at the end of the pulse. Error correction is done by swapping these '1's and '0's, which diverge from their groups.

IV. COUNTER DESIGN

Interpolation methods are typically used in time counters to obtain a high-resolution and wide measurement range [1, 4, 8]. Recently, the two-stage interpolation method, being an advanced version of the classical Nutt method [9], is the most popular. In this method the measured time interval is split into five parts. The longest one is measured by an ordinary binary counter as the integer number of the reference clock periods, which appear between leading edges of START and STOP pulses. The time intervals remaining between the leading edges of START and STOP pulses and the nearest edges of the reference clock are measured by the two-stage interpolators in respective channels START and STOP [4].

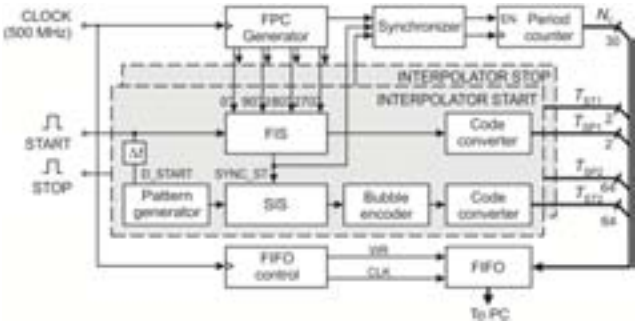

Fig. 6. Two-stage interpolation time counter.

Simplified block diagram of the designed time counter is shown in fig. 6. The first interpolation stage (FIS) has been built with the use of four double synchronizers. The main aim of the FIS is to detect the segment of four-phase clock (FPC), in which an input pulse (START or STOP) appears, and then to synchronize this signal with the nearest FPC edge. Next, this synchronized signal (SYNC_ST or SYNC_SP) is used for enabling the period counter and for further precise conversion in the second interpolation stage (SIS). Since the synchronization process takes some time (τ_{PSI}) then the input pulse (START/STOP) has to be delayed by adequate amount of time $\Delta t \approx \tau_{PSI} - \tau_G$, before it gets the pattern generator (D_START/D_STOP), while τ_G is the time needed for reliable generation of a pattern. The appearance of the active edge of D_START/D_STOP signal triggers the pattern generation and propagation of the created pattern in the SIS of corresponding channels (START/STOP). After the SYNC_ST/SYNC_SP pulse has appeared, the state of the delay line in SIS is stored in associated flip-flops.

Raw data from FIS is converted directly from the ring code to the natural binary code. Data from SIS is first corrected in the bubble encoder, and then it is appropriately converted and twofold compressed in the code converter. Finally, all measurement data from the period counter, FIS and SIS of both START and STOP channels are stored in the fast FIFO memory and then asynchronously uploaded to the computer for further analysis.

V. TEST RESULTS

A. Test setup

The experimental tests of the developed time counter were carried out in the test setup presented in figure 7, with the use of power supply voltages typical for Spartan-6 (*Xilinx*) [6] and at the room temperature of 22 ^{o}C.

To generate the reference time intervals, three generators were used consecutively, i.e.: GFT1004 (*Greenfield Technology*), 81130A (*Agilent*) and T5300U (*Vigo System*). The 10 MHz rubidium generator FS725 (*Stanford Research Systems - SRS*) and GPS-stabilized quartz generator E8-Y (*Quartzlock*) were used as the reference clock sources for the tested counter and for all time interval generators, respectively. The time counter was powered with the use of precise power suppliers 6624A (*Agilent*) and RS-75-5 (*Mean Well*). The test board with the integrated time counter and the

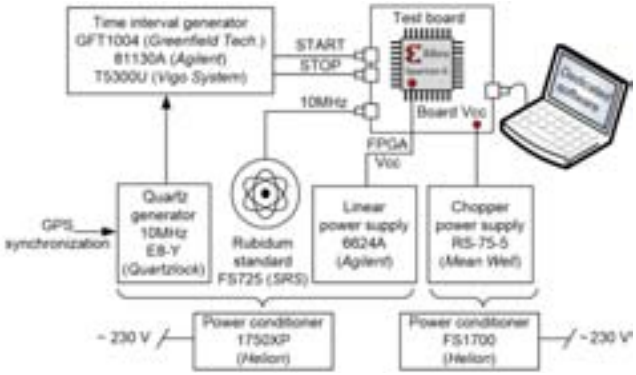

Fig. 7. Time counter test setup.

entire measurement session was controlled via USB interface with the dedicated application installed on the PC computer. Two power line conditioners FS1700 and 1750XP (*Helion*) were involved to filter deformations and noises out of the main voltage.

B. Resolution and transfer function

The first test effort was aimed at evaluation of the influence of the number of pattern edges on the counter resolution (fig. 8).

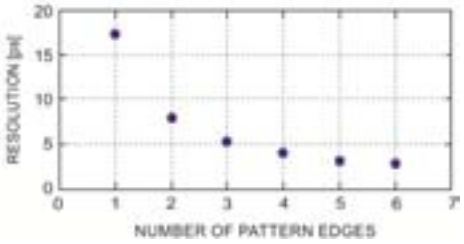

Fig. 8. The influence of the number of pattern edges on the counter resolution.

As it could be expected the resolution increases with increasing the number of pattern edges but the increase is not linear and the number of transitions larger than three gives negligible effect on the resolution (a 1.3 ps increase for 6 transitions in comparison with 4 ones). Despite the fact that any increase in the number of edges results in need of extending both the pattern and time coding lines, we decided to use a pattern consisting of six edges for further studies. It was justified by the highest resolution provided (2.7 ps). Generation of such a pattern has been done with the aid of carry chain structure (fig. 3).

Figure 9 shows bin widths, differential (DNL) and integral nonlinearity (INL) characteristics of the START interpolator. Bin width characteristic is composed of four segments corresponding to the four phases of FPC clock. A 747 quantization bins were distinguished as a result of the SCDT. Since the period of the FPC equals 2 ns then the obtained mean resolution is 2.68 ps. The extreme values of DNL and INL are 4,38 LSB (11,74 ps) and 10,40 LSB (27,87 ps), respectively. Characteristics of the STOP interpolator are similar to those presented START channel.

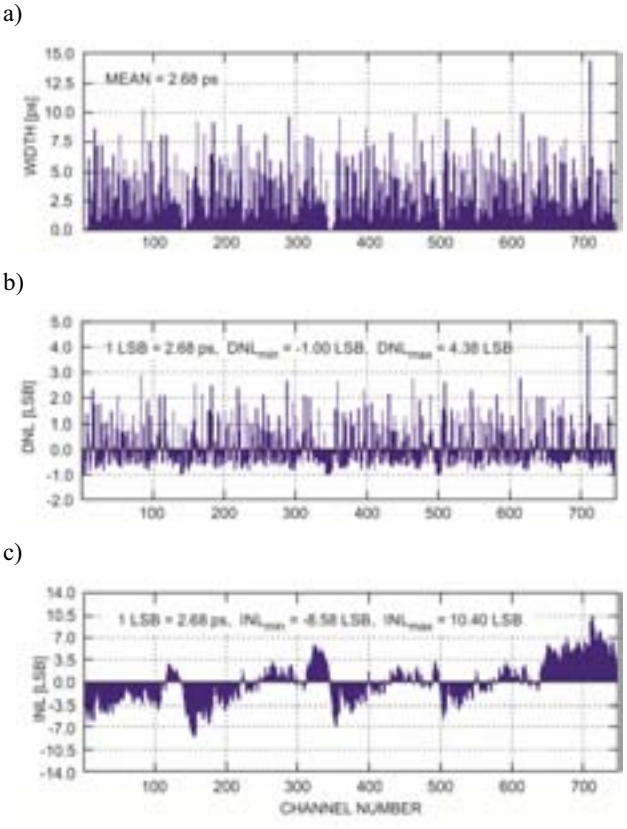

Fig. 9. Bin widths (a), differential (b) and integral (c) nonlinearities of the START interpolator.

C. Standard measurement uncertainty

In order to verify the precision of the developed time counter in its full measurement range, we first tested the precision of sources of reference time intervals. For this purposes we use a high precision oscilloscope DSA90804A (*Agilent*, noise floor < 2 ps) and evaluated characteristics of timing jitter of each time interval generator involved. Based on results of these tests, time intervals from 1 ns to 200 ns were generated by GFT1004, from 500 ns to 5 µs by 81130A, and from 10 µs to 1 s by T5300U. Measurement precision of the time counter was calculated as a standard deviation of results of 2000 measurements performed for each time interval. Figure 10 shows the measurement uncertainty achieved with and without filtration of power supply voltage. The use of power line conditioners (fig. 7) helped to lower the uncertainty level by about 0.5 ps within the range from 1 ns to 100 ns and by about 4 ps for the rest of measurement range.

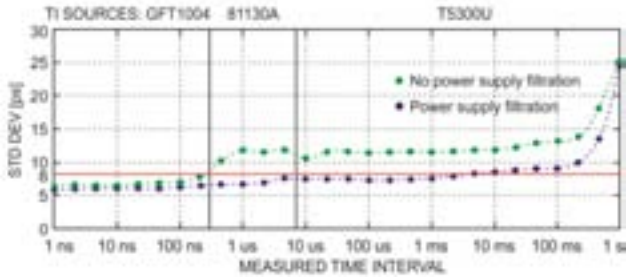

Fig. 10. Standard measurement uncertainty of the time counter.

VI. Conclusion

The use of the multi-edge coding method for T/D conversion allows to obtain a resolution value much lower than the propagation time of a single delay element in delay line. This overcomes a microelectronic technology limitation, reduces the quantization error and improves linearity of conversion. The improvement in resolution is achieved easily by increasing the number of edges of the pattern that propagates through the coding line. By applying six edges the average resolution of 2.7 ps and precision better than 8 ps for measured time intervals up to 2 ms were obtained. The high performance of the developed time counter stems also from the effective removing of bubble errors and carefully designed layout of the counter.

Acknowledgment

This work was supported by the Polish National Science Centre under contract no. UMO-2011/01/B/ST7/03278.

References

[1] J. Kalisz, "Review of methods for time interval measurements with picosecond resolution," Metrologia, vol. 41, pp. 35–51, 2004

[2] P. Napolitano, A. Moschitta and P. Carbone, "A Survey on Time Interval Measurement Techniques and Testing Methods", Proc. IEEE Instrum. Meas. Techn. Conference (I2MTC), pp. 181–186, 2010

[3] J. Wu and Z. Shi, "The l0-ps Wave Union TDC: Improving FPGA TDC Resolution Beyond Its Cell Delay," IEEE Nuclear Science Symp. Conf. Record, pp. 3440–3446, 2008

[4] R. Szplet, Z. Jachna, P. Kwiatkowski and K. Rozyc, "A 2.9 ps equivalent resolution interpolating time counter based on multiple independent coding lines," Meas. Sci. Technol. 24 (2013) 035904 (15pp)

[5] S. Cova and M. Bertolaccini, "Differential linearity testing and precision calibration of multichannel time sorters", Nuclear Instruments and Methods, vol. 77, no. 2, 1970

[6] Xilinx, Spartan-6 FPGA Configurable Logic Block User Guide, User Guide, February 2010

[7] P. Kwiatkowski, R. Szymanowski and R. Szplet, "Identification of the dynamic parameters of fast carry chains and global clock networks in Spartan-6 FPGA device", Measurement Automation and Monitoring, vol. 59, no. 8, 2013, 3 pp. (*in Polish*)

[8] S. Henzler,"Time-to-Digital Converters", Springer, 2010, 123 pp.

[9] R. Nutt, "Digital time intervals meter", Rev. Sci. Instrum. vol. 39, 1968, pp. 1342–1345

Managment and Monitoring Layer of Optical Network for Time and Frequency Transfer

J. Kołodziej, J.Stępień
AGH University of Science and Technology,
Departament of Electronics, Krakow, Poland
jacek.kolodziej@agh.edu.pl

W. Bogacki, K. Turza
Poznan Supercomputing and Networking Center,
Network Departament, PSNC, Poznan, Poland
wojbor@man.poznan.pl

Abstract — Continues operation of ultra-precise time and frequency transmission requires special monitoring, calibration and management procedures to ensure high functionality, safety, and quality of the time and the frequency dissemination. The system must deliver information to administrators, end-users, and equipment manufacturer about current state of the fiber link. In the paper a description of the essential elements of the management system and data transmission methods, based on the Internet standard protocols and preliminary test results, are presented.

Keywords— Atomic clock, fiber optical network, management and monitoring, high precision dissemination of time and frequency reference signals, network management system.

I. INTRODUCTION

The idea of design the management layer came into sight as effect of the experience carried out during an over-a-year operation of 421,4 km-long fiber-optic connection between Central Office of Measures (GUM) in Warsaw and the Astrogeodynamic Observatory (AOS) in Borowiec near Poznan. The concept of the active propagation delay in the fiber optic link used to joint time and frequency transfer was widely discussed in [1,2,3,4,5]. This optical link consists of many programmable elements (amplifiers, endpoints) and classical optical fibers belonging to PIONIER backbone and spread over many kilometers. This paper focuses on out-of-band in-fiber management of EDFA (Erbium Doped Fiber Amplifier), normally installed in locations without reliable and stabile network access. Activation and a further system monitoring require robust and safety methods of management, which are based on the telecommunication standards.

A typical network management system covers the activities, methods, procedures, and tools that assure realization of special function. It is possible to find several way of their characterization. The most common is operation, administration, maintenance, and provisioning of networked systems [6].

In the Network and Management System (NMS) the operation means all activities to improve the efficiency of network and to provide defined net services. It includes monitoring, used to remark problems as soon as possible, preferably before end users are affected. The next is *administration*, which deals with tracking of resources in the network. It uses dedicated protocols and tools to keep the network under control. The *maintenance* guarantee repairs and upgrades mechanism, when equipment must be replaced. It also involves corrective and preventive measures increasing the quality of services provided by managed network, such as adjusting device configuration parameters. The last one is *provisioning*, concerned with configuring network resources to support a given service.

Network management system collects data using several mechanisms:

- agents running in infrastructure,
- logs of activity,
- sniffers,
- monitoring on demand, executed by users.

Formerly network management was worked as network status monitor, because devices were characterized only by two states: up or down. Now a crucial part of the IT team's role is delivering services on defined level, so the performance management has become a great challenges - especially for organizations of national or international range. Several access methods supporting network and network device management exist. The well-known are CLIs (Command-Line Interface), SNMP (Simple Network Management Protocol), NETCONF (Network Configuration Protocol), custom XML (Extensible Markup Language), CMIP (Common Management Information Protocol), WMI (Windows Management Instrumentation), CORBA (Common Object Request Broker Architecture) and JMX (Java Management Extensions).

The next important thing in management is an organization of a data channel for devices maintenance. Out-of-band management (OOB), called also lights-out management (LOM), needs to use a dedicated transmission channel, what makes it robust and efficient. On the contrary, in-band management is based on software and must be a part of managed system, so it is installed on the remote sites and can work transmission device operates. This solution is simply, but it does not allow access to deep system settings (system updating, reinstallation, or fix problems that prevent the system failure during booting).

In the following paragraph standard network management system (NMS) implementation, dedicated to Optical Network for Time and Frequency Transfer is presented.

This work was co-financed with the financial resources for Research and Development from Poland in the Applied Research Program (no. PBS1/A3/13/2012).

II. Optical Network Management Architecutre for Time and Frequency Transfer

A complete remote management system of ONMTFT (stand for Optical Network Management for Time and Frequency Transfer) should manage EDFA amplifiers, reference clock transmitter and receiver from remote server (Fig.1.). Requirements for monitoring, calibration and management of the transmission line, to ensure high functionality, safety, and quality, make possible the ONMTFT functions defining:

- safe access to all active system nodes;
- reading the unit status (e.g.: name, programmable parameters);
- remote reprogramming the unit parameters (e.g.: gain)
- continues/real time and on demand monitoring node performance parameters (e.g.: temperature TEMP, input power of direction West-East P_{IW}, output power of direction West-East P_{OE}, input power of direction E-W P_{IE}, output power of direction E-W P_{OW}) (Fig. 3) [1] ;
- communication with end user (e.g.: information about system status).

Delivering necessary management data is organized by CLI protocol and out-of-band technique.

a)

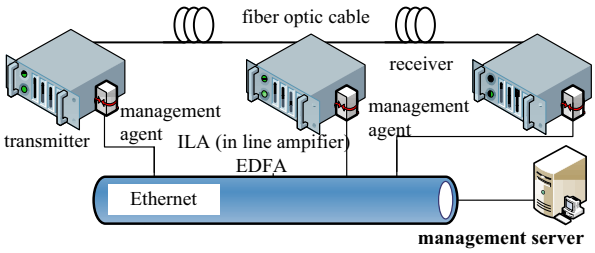

b)

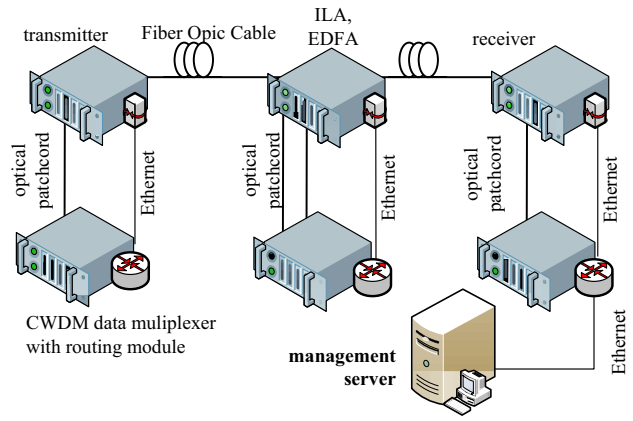

Fig. 1. Solution of out-of-band ONMTFT architecture: a) Ethernet based approach, b) "in-fiber" technique.

Implementation of the out-of-band management is usually realized, based on the Ethernet connections (Fig.1a). It is simply way of access to managed elements, but it requires additional network infrastructure. In real realization of backbone network is impossible to deliver dedicated Internet connection to ILA (In Line Amplifier) nodes. The GPRS access to network very often causes difficulties too, additionally for security reason some private network (e.g.: VLAN, VPN) is strongly recommended. Moreover management channel needs to be stable in time which is hard to achieve in GSM networks.

To eliminate this problem the remote OMTFT elements can be accessed through the time transfer link via CWDM multiplexers and routers, as shown in Fig.1b. In this case a fiber optic line is shared between time transfer link and management using in-fiber technique. A comparable solution implementing nonstandard network management procedures and dedicated to management of optical fiber link for frequency metrology was described in [8].

III. In-Fiber techniques - Nodes Arcitecture

The system of time and frequency dissemination consists of endpoints (transceiver, receiver) and regenerating nodes, included EDFA. Implementations of basic management procedures require additional management subsystem. This infrastructure (ONMTFT) contains: internal routing module (it is necessary to data exchanging between nodes and more flexible than programmable switches), Ethernet copper to fiber media converters, dedicated optical CWDM filters and optical diplexer (for physical separation of data transmission channel). The proposed hardware solution multiplexes time signal and management data using only one fiber for two functions. It is called *in-fiber* management techniques. The block diagram in Fig. 2 shows typical architecture of regenerating node. Control and status data coming from dedicated EDFA are formatted into Ethernet packet and distributed according routing table by internal routing module to media converters or local external Ethernet port. The CWDM module combines two control links (with λ_{M1} and λ_{M2} wavelengths) with time transfer carrier (λ_{C1} and λ_{C2} wavelengths) in one common fiber.

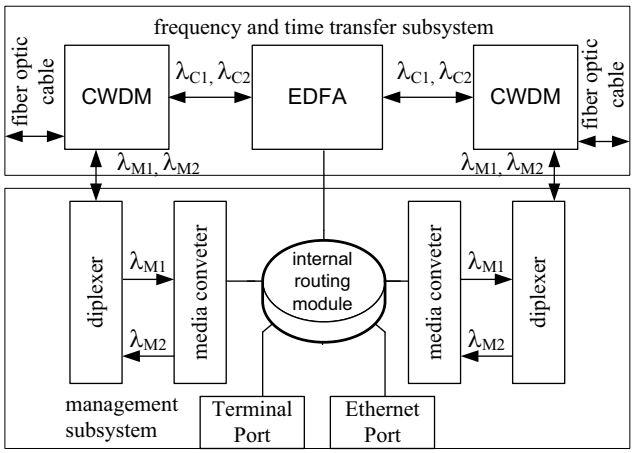

Fig. 2. Regenerating node (ILA) of fiber optic system for time and frequency transfer with management subsystem

IV. EXPERIMENTAL RESULTS

In order to verify the designed management method, presented in preceding sections, a series of measurements were arranged in the laboratory, using real telecommunication fiber link (Fig.3). The measurement results should give answer to two questions: Does a common transmission of precise time signal and management data in one optic fiber link degrade time accuracy? Does logged data of each component in the time and frequency transfer link (EDFAs, endpoints) carry information about link behavior and this information could be useful to improve time stabilization?

Answering to those problems, the test system of Time and Frequency Dissemination System with Optical Network Management for Time and Frequency Transfer, according block diagram in Fig.3, was arranged. To take closer real application of designed system, in the experiment the fibers deployed in optical cable and located in the field running along the motorway near Krakow and being the part of the TP S.A. telecommunication infrastructure, was used.

The fibers were looped-back, thus both ends of each line were accessible in the Optical Network Laboratory at AGH University of Science and Technology in Krakow. In whole line SC/APC (Angled Physical Connector) mechanical connectors were used.

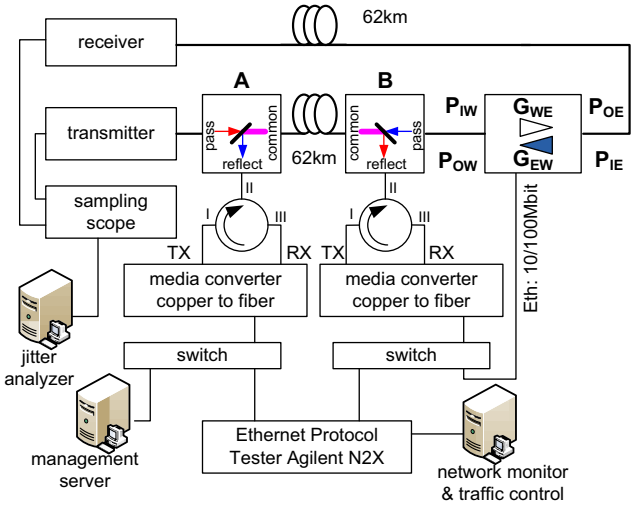

Fig. 3. Test system of Optical Network Management for Time and Frequency Transfer

In the experiments, EDFA amplifier was continuously controlled and data was recorded to the server. Managed amplifier was inserted between two 62 km long fiber spans (referred as B on Fig.3) with total attenuation equal 19.2 dB and 19.5 dB respectively. A control and status data coming from EDFA is formatted into Ethernet packets and then are transmitted over fiber by media converter. The standard small form-factor pluggable module of 1510 nm (λ_{M1}) and link budget 20 dB was applied. The optical circulator separate TX and RX signals transmitted together in circulator port II. Optic filter allows combining management wavelengths λ_{M1} and λ_{M2} (near 1510nm) with time transfer carrier (λ_{C1} and λ_{C2} wavelengths close to 1549ns) in one common fiber.

The EDFA remote pooling was executing concurrently with simulation of background 50Mbit/s network traffic, generated and measured by AGILENT N2X Network Protocol Analyzer (see Fig. 4). The maximum measured throughput between point A and B was 80Mbit/s, and this boundary is consequence of switches limitations.

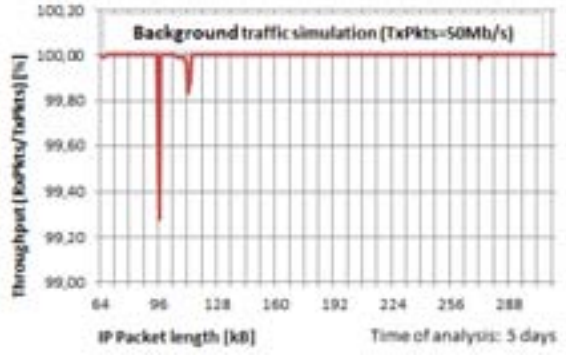

Fig. 4. Packets size test used as background traffic simulation

A set of EDFA parameters: the temperature TEMP, input power of direction West-East P_{IW}, output power of direction West-East P_{OE}, input power of direction E-W P_{IE}, output power of direction E-W P_{OW}, have been logged for 5 days, with 1 minute resolution. The behavior of EDFA gain stabilization reports graphs in Fig. 6 and in Fig.7.

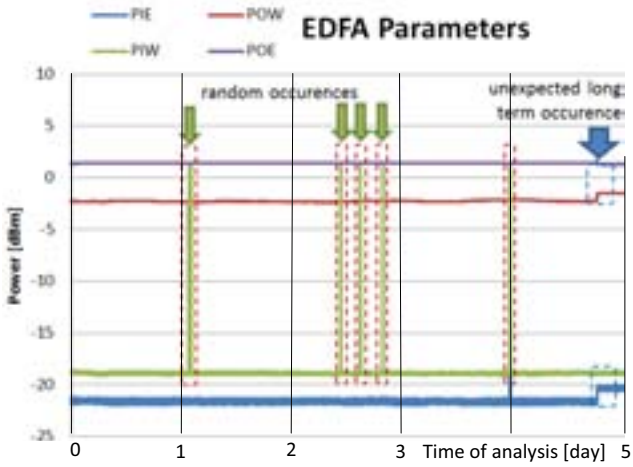

Fig. 5. Power changes in input and output of EDFA during test experiments

A short random occurrence of P_{IW} fluctuation and changes of P_{OW} and P_{IE} was observed, but its nature and its influence to time stability have not be well characterized yet.

In Fig. 7 the strong correlation between temperature and output power can be observed, however analyzes in [5] suggest that it is possible to compensate influence of temperature variance to output power. This discovery should be better investigated in future, because is related to transmitted time stability.

The time transfer accuracy was evaluated by means of Overlapping Allan Deviation (ADEV, measured using methods described in [3,7].

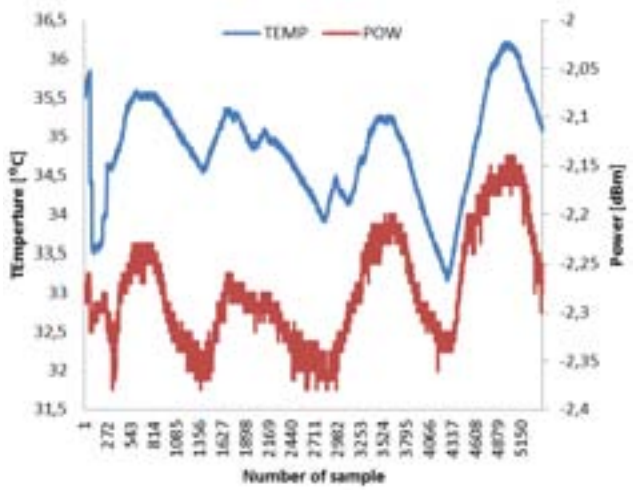

Fig. 6. Discovered correlation between output power POW and temperature TEMP

Time transfer stability with (red line) and without (blue line) management system data traffic (Fig.4.) gives similar results. It allows draw a conclusion that management facilities and in-fiber transmission do not affect time transfer accuracy.

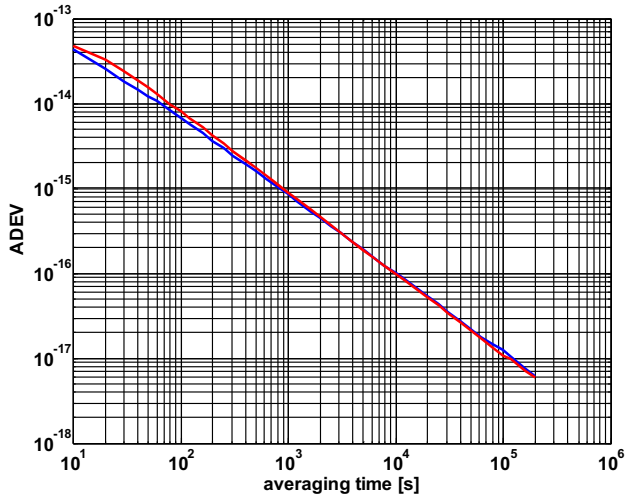

Fig. 7. Allan deviation (ADEV) with (red line) and without (blue line) running of management layer

SUMMARY

Access to ultra-precise time and frequency signals are very important for many user groups include scientific and research communities and business or government users. It requires not only infrastructure for time transfer, management layer is important too. An activating the link spread over many kilometers and keeping on its high accuracy of time transfer is impossible without reliable management system. Presented out of band in-fiber solution fulfill user expectation and could be developed in the future. The management system doesn't change *Allan deviation* of transmitted clock and allows provide additional analysis to improve performances of time transfer.

ACKNOWLEDGMENT

The authors would like to express deeply gratitude to prof. Marcin Lipiski, prof. Przemsylaw Krehlik and prof. Lukasz Sliwczynski for their valuable advices and support.

REFERENCES

[1] Ł. Śliwczyński, P. Krehlik, A. Czubla, Ł. Buczek and M. Lipiński, "Dissemination of time and RF frequency via a stabilized fiber optic link over a distance of 420 km", Metrologia 50, 133-145, 2013.

[2] Ł. Śliwczyński, P. Krehlik, Ł. Buczek and M. Lipiński,. "Active propagation delay stabilization for fiber-optic frequency distribution using controlled electronic delay lines", IEEE Trans. Instrum. Meas , vol. 60, pp. 1480-1488, 2011

[3] P. Krehlik, Ł. Śliwczyński, Ł. Buczek and M. Lipiński, "Fiber optic joint time and frequency transfer with active stabilization of the propagation delay", IEEE Trans. Instrum. Meas., vol. 61, pp.61 2844–51, 2012.

[4] Ł. Śliwczyński, P. Krehlik, Ł. Buczek, M. Lipiński, "Frequency transfer in electronically stabilized fiber optic link exploiting bidirectional optical amplifiers", IEEE Trans. Instr. Meas., vol. 61, no. 9, pp. 2573-2580, 2012.

[5] Ł. Śliwczyński, J. Kołodziej, "Bidirectional Optical Amplification in Long-Distance Two-Way Fiber-Optic Time and Frequency Transfer Systems" IEEE Trans. Instr. Meas., vol. 62, pp. 253-262, 2013.

[6] ITU-T M.3400 recommendation

[7] Ł. Śliwczyński, Ł. Buczek P. Krehlik, and M. Lipiński "Active propagation delay stabilization for fiber-optic frequency distribution using controlled electronic delay lines IEEE Trans. Instr. Meas., vol. 66 iss. 4 pp. 1480–1488.

[8] K. Predehl,G. Grosche,S. M. F. Raupach,S. Droste, Terra,J. Alnis,. Legero,T. W. Hänsch, Th. Udem,R. Holzwarth, H. Schnatz, "A 920-Kilometer Optical Fiber Link for Frequency Metrology at the 19th Decimal Place", http://www.sciencemag.org/, Science 27 April 2012:, vol. 336 no. 6080 pp. 441-444

Fiber-optic Time and Frequency Transfer based on RF Carrier Phase and Pseudorandom Noise Code

Wenke Yang, Hang Gong, Long Huang, Xiangwei Zhu, Guangfu Sun
College of Electronic Science and Engineering, National University of Defense Technology
Changsha, China
ywk@nudt.edu.cn

***Abstract*—A system based on self-made modems and off-the-shelf fiber-optic devices aiming at achieving precise fiber-optic time and frequency transfer based on radio frequency (RF) carrier phase tracking and pseudorandom noise code correlation is demonstrated. The RF carrier phase and the pseudorandom noise code are both used through the fiber-optic link in the two-way mode. The two-way transfer asymmetry caused by the different optical wavelengths for both directions, which is the case in DWDM system, is avoided by the Code Division Multiple Access (CDMA) system here. The first result of the common clock experiment shows that the measurement noise characterized as modified Allan deviation of $6.5\times10^{-11}\tau^{-3/2}$(1s to 1000s) and $2\times10^{-15}\tau^{0}$ (1000s to 10000s) with carrier phase and $2.5\times10^{-11}\tau^{-1}$ (1s to 10000s) with code.**

Keywords-RF carrier phase; pseudorandom noise code; fiber-optic; CDMA

I. INTRODUCTION

Many literatures have been reported on stable frequency transfer via optical fibers, both in optical domain [1] and RF domain [2, 3]. As to time transfer over fibers, frame detection in SDH or SONET network [4], timing code including 1PPS signal transferred using two-way Dense Wavelength Division Multiplexing (DWDM) [5] and two-way time transfer over fiber link based on commercial modems [6] have been reported.

A system based on self-made modems and off-the-shelf fiber-optic devices aiming at achieving precise fiber-optic time and frequency transfer based on radio frequency (RF) carrier phase tracking and pseudorandom noise (PRN) code correlation is proposed and the first result of common clock experiment is shown. It is different from the previous work on time transfer over fibers, for that the RF carrier phase information and PRN code are both used through the fiber-optic link in the two-way mode.

II. SYSTEM AND EXPERIMENT DESIGN

The setup of the fiber-optic time and frequency transfer system for common clock experiment is shown in Figure 1. It works like two-way satellite time and frequency transfer (TWSTFT), but the signal propagation path is replaced with optical fiber and the up and down frequency converting process for satellite transmit is replaced by the intensity modulation and the corresponding direct detect of the optical wave.

The self-made modem is composed with a transmitter unit (TU) and a receiver unit (RU). The RF carriers modulated by different PRN codes are transmitted by TU and go through the fiber-optic link with intensity modulation of 1550nm optical wave by E/O unit, and are direct detected by O/E units at both sites in two-way mode. Optical waves in both directions share the same fiber between site 1 and site 2 thanks to the optical circulators, which avoid the transmitted signals get back to the local site.

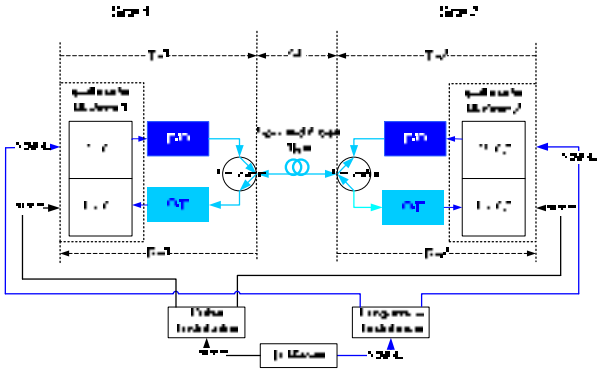

Fig. 1 The setup of the fiber-optic time and frequency transfer system for common clock experiment.

The time scale at site 1 is T_1 and the time scale at site 2 is T_2, defined at the reference end of the modems at both sites. The transmitting path delay is Tx_1 for site 1 and Tx_2 for site 2, the receiving path delay is Rx_1 for site 1 and Rx_2 for site 2. The fiber link signal path delay is SP and it is the same for both directions.

The time difference measured with PRN code correlation is shown as Eq. (1) and Eq. (2) at site 1 and site 2 respectively.

$$t_{12} = T_1 - T_2 + Tx_2 + Rx_1 + SP \tag{1}$$

$$t_{21} = T_2 - T_1 + Tx_1 + Rx_2 + SP \tag{2}$$

The time scale difference T_1- T_2 can be calculated as

$$T_1 - T_2 = \frac{1}{2}(t_{12} - t_{21}) + \frac{1}{2}(Tx_1 - Rx_1) - \frac{1}{2}(Tx_2 - Rx_2) \tag{3}$$

The carrier phase is estimated by Phase Lock Loop (PLL) which tracks the input carrier phase of RU01 and RU02 as φ_{12} and φ_{21} in circle respectively and can be written as

$$\varphi_{12} + N_{12} = \varphi_2 + (Tx_2 + Rx_1 + SP)\cdot f \tag{4}$$

$$\varphi_{21} + N_{21} = \varphi_1 + (Tx_1 + Rx_2 + SP)\cdot f \tag{5}$$

where N_{12}, N_{21} are the unknown carrier-cycle integer ambiguities of the input carrier phase of RU01 and RU02, and φ_1, φ_2 are the transmitted signal phase in circle of TU01 and TU02 respectively. f is the carrier frequency.

The time scale difference measured by carrier phase can be written as

$$\begin{aligned}(\varphi_1 - \varphi_2)/f &= (\varphi_{21} + N_{21} - \varphi_{12} - N_{12})/f \\ &+ (Tx_2 - Rx_2) - (Tx_1 - Rx_1)\end{aligned} \tag{6}$$

The experiment setup in Figure 1 is housed in a temperature controlled room with the temperature within 24±0.3°C.

III. First Result

The first result of common clock experiment is shown without calibration and the knowledge of carrier-cycle integer ambiguities. But it indicates the measurement noise of the proposed setup by PRN code correlation and carrier phase tracking.

There is no carrier cycle slips during this experiment. A continuous carrier phase measurement together with code measurement results with offset removed is shown in Figure 2.

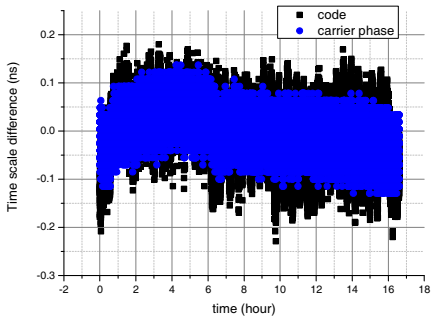

Fig. 2 Time scale difference measured with PRN code correlation and carrier phase tracking.

The code measurement result has the frequency stability as the black solid square real line, and it can be fitted as $2.5\times10^{-11}\tau^{-1}$ for averaging time 1s to 10000s as the red hollow circle dashed line in Figure 3, which shows that the flicker phase modulated noise is dominate.

The carrier phase measurement has the frequency stability as the blue solid triangle real line, and it can be fitted as $6.5\times10^{-11}\tau^{-3/2}$ for averaging time 1s to 1000s and $2\times10^{-15}\tau^{0}$ for averaging time 1000s to 10000s as the magenta hollow triangle dashed line in Figure 3, which implies that the white phase modulated noise and flicker frequency modulated noise are dominate for averaging time 1s to 1000s and 1000s to 10000s respectively.

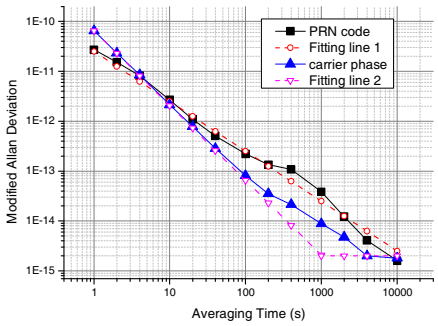

Fig. 3 The measurement noise frequency stability with PRN code and carrier phase characterized as modified Allan Deviation.

IV. Conclusions

A system based on self-made modems and off-the-shelf fiber-optic devices is proposed for time and frequency transfer with PRN code correlation and RF carrier phase tracking. The first result of common clock experiment shows the measurement noise frequency stability is $2.5\times10^{-11}\tau^{-1}$ (1s to 10000s) for code, $6.5\times10^{-11}\tau^{-3/2}$ (1s to 1000s) and $2\times10^{-15}\tau^{0}$ (1000s to 10000s) for carrier phase.

Future work will focus on the carrier-cycle integer ambiguity resolution or the combination of the code and carrier phase results, and the calibration. The noise floor for carrier phase is possibly affected by the carrier phase resolution which is limited by the hardware, which also needs more investigation.

References

[1] J. Ye, J. Peng, R. Jones, K. Holman, J. Hall, D. Jones, S. Diddams, J. Kitching, S. Bize, J. Berguist, and L. Hollberg : "Delivery of high-stability optical and microwave frequency standards over an optical fiber network", J. Opt. Soc. Am. B, Vol. 20, No. 7, 2003, pp. 1459-1467

[2] O. Lopez, A. Amy-Klein, C. Daussy et al. 86-km optical link with a resolution of $2*10^{-18}$ for RF frequency transfer, European Physical Journal D vol 48, 2008, pp. 35-41.

[3] I. S. Jacobs and C. P. Bean, High stability microwave fiber optic systems: demonstrations and applications, Proc. of the 43rd Annual Symposium on Frequency Control, 1992, pp. 310~316.

[4] Masami Kihara, Atsushi Imaoka, Two-Way Time Transfer through 2.4Gb/s Optical SDH System , IEEE Trans. Instrum. Meas., vol. 50, NO.3, Jun 2001, pp. 709-715.

[5] Atsushi Imaoka, Masami Kihara. "Accurate Time/Frequency Transfer Method Using Bidirectional WDM Transmission[J]". IEEE trans. On Instrumentation and Measurement, April, Vol. 47, No. 2, 1998, pp. 537-542.

[6] M. Rost, D. Piester, W. Yang, T. Feldmann, T. Wuebbena and A Bauch, "Time transfer through optical fibres over a distance of 73km with an uncertainty below 100 ps," Metrologia, Vol 49, 2012, pp. 772-778.

Study on the Method of Measuring and Estimating the Time Synchronization Accuracy under Constellations Autonomous Operation based on the Ground Testing System

Ren Xiaoqian, Hua Yu, Qin Weijin, Wu Haitao
National Time Service Center
Chinese Academy of Sciences
Xi'an, Shaanxi, China
renxq@ntsc.ac.cn

***Abstract*—Constellations autonomous operation capability of the satellite navigation system is one of the primary ways for improving system's survivability. It is unrealistic obviously that the satellites do not update the data to test and verify the constellations autonomous operation capability under the condition of satellite navigation system can support by the ground-monitoring system. The study of measuring and estimating constellations autonomous operation time synchronization's accuracy in condition of the satellite navigation system operate normally is so little. This paper discusses the importance of testing and verification for diffident working mode, it provides one kinds of method of measuring and estimating the time synchronization accuracy under constellations autonomous operation based on the ground testing system. In the paper, it gives the basic principle and the computational model, verifying and analysing the method by simulation data. This method provides technical support for building global satellite navigation system 's inter-satellite link.**

Keywords- Constellations autonomous operation; Measuring and Estimating; Time synchronization; Ground Testing System

I. INTRODUCTION

With the development of satellite navigation systems and navigation warfare concepts proposed, the capability of autonomous survival and operation of the satellite navigation system has become an important part of the research in the field[3]. Making the inter-satellite link to achieve the autonomous function of constellation is one of the primary means to improve the viability of the satellite navigation system[6].

GPS system has been installed the inter-satellite distance measuring equipment and on-processor in BLOCK Ⅱ R and follow-on satellite, these satellites could measure the inter-satellite distance and communicate with each other by TDMA, and autonomous computing the satellite orbits and satellite clock hourly to achieve the autonomous orbit determination and autonomous timekeeping. The indicators of GPS system on autonomous navigation is that the GPS system could make the user ranging error (URE) less than 6m on the situation of that the satellite ephemeris and satellite clock parameters couldn't be modify by the information from the injection stations on the ground[2].

The index proposed by the GPS system is derived after the processing of inter-satellite measurement data[5], which means that this index is only an estimate indicators, while the main purpose of the autonomous operation of the satellite navigation system is to improve the viability to face the extreme situation that the injection stations on the ground were destroyed in the war or other special period. It's clearly unrealistic that in order to verify the autonomous operation capability of constellation, we don't inject the revelation information to the satellite for a long time even if we have the ground-base monitoring system when we design and construct the satellite navigation. How to testing and evaluating the autonomous operation capability of navigation constellation without any affection on normal conditions is an important issue should be considered before we design and construct the satellite navigation system.

In this paper, to the above problem, a testing and evaluation method of constellation autonomous run time synchronization accuracy was put forward which based on the ground test validation system, including the basic principles and the calculation model, and the analysis is verified by simulation data, providing technical support to our construction and evaluation of global navigation satellite system inter-satellite link.

II. THE ANALYSIS OF THE MODE OF AUTONOMOUS RUNNING OF NAVIGATION CONSTELLATION

The mode of autonomous running of navigation constellation is that: without the support of ground, navigation constellation determinate orbit precisely and keep time with satellite orbit prior information by inter-satellite two-way ranging and data changing. There are two kinds of working mode[3], one is the distributed processing mode: each satellite observes all the satellites in the visible range and exchange observation data according to the sampling interval which is set by the each satellite. Each satellite determines the clock error by the latest observation data and update the navigation

message. The advantage of running mode: each satellite is relatively independent, does not affect the other satellites if someone is wrong, the disadvantage is no uniform star time reference, the absolute deviation becomes larger and hard to remove with the time pass by. Moreover, the uncertainty of ISLs link, not all the satellite can compare data with other satellites, so the deviation is larger between some satellite and other satellites.

Another is the centralized processing mode: selected one satellite as the main star, other satellites send the observation data to the main star, finishing the timekeeping calculation uniformly by the main star. The advantage of this method can easily get uniformly time benchmark, but put much dependence on the main star, selection and backup of the main star is difficulty, some satellite can not complete the comparison because of the uncertainty of the ISLs link, so it can decrease the availability of satellite.

Regardless of which processing mode, there exists the uncertainty of autonomous running of constellation of the inter-satellite links, so it is important which based on the evaluation of ground testing and without relying on the atomic on-board clocks.

III. THE METHOD OF MEASURING AND ESTIMATING THE TIME SYNCHRONIZATION ACCURACY

Constellations autonomous operate mainly based on the inter-satellite links to achieve the comparing of the satellites, and broadcast the clock error forecast. The satellite atomic clock is the main participant when the constellations autonomous operating. So, it needs a kind of technique which is not dependent on satellite clock to test and estimate the time synchronization accuracy. And the ground testing system is a system based on such a technology.

3.1 The working principle of the method of measuring and estimating the time synchronization accuracy

The ground testing system is based on a satellite transponder transmit the signal. It generates high-precision atomic clock signal on the station, and modulates to pseudo-code signal, and transmits to the all satellites on the visible range by the same carrier frequency，and transmit to the diffident satellite ground station by satellite transponder. Each station receives all time signals from diffident ground station, and determines the delay of the signal path. Thereby, it can determine the distance between the ground station to the satellite. Now, the ground testing system mainly used for time synchronization between the satellite high precision orbit determination and long-distance stations and other satellite navigation test assessment. The ranging accuracy is better than 1 cm, and the orbit determination accuracy is better than two meters, and time synchronization accuracy is better than 1 nanosecond[4].

The method of measuring and estimating the time synchronization accuracy under constellations autonomous operation based on the ground testing system is worked under the mode of transmitting and receiving signal itself. It transmits signal to the all satellites on the visible range by the same carrier frequency, and transmits to the same satellite ground station by satellite transponder, and trigger satellite local time to broadcast signal by the special carrier frequency (to make a difference from the transponder signal). The ground station receive broadcast signal and transponder signal. It can determine the deviation between the satellite time and ground standard time by comparing the deviation between the receive broadcast signal and transponder signal. Thereby, it can measure and estimate the time synchronization accuracy under constellations autonomous operation. The figure of working principle is shown in figure 1.

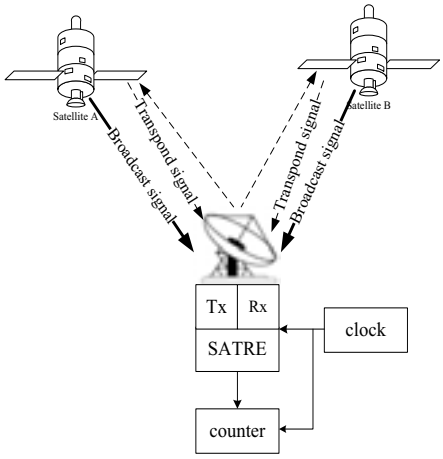

Figure 1. The figure of working principle

The ground testing system based on the satellite transponder transmit signal generate the time signal by the ground atomic clock in each satellite station. The signal of transmitting and receiving and calibrating are operated on the ground. So, it can avoid the satellite atomic clock deviation because of constellations autonomous operation, and can estimate the time synchronization accuracy under constellations autonomous operation by comparing the time deviation.

3.2 The fundamental observation equation

Assumed that the ground testing system has two ground stations, they are i and j. If the signal transmitted from i station is received successfully by the j station receiver, the time relationship formula of the signal is[4]:

$$R_{ji} = R_i^t + O_{iu} + T_i + \tau_s + R_{ji}^r + O_{jd} + I_{ji} - \Delta T_{1i} + \Delta T_{1j} \quad (1)$$

R_{ji} is j station receiver receives the i-station transmission signals delay.

R_i^t is signal delay from the i station antenna phase center (the signal transmission time) transmitted to the satellite antenna phase center (satellite receiver to signal time) .

R_{ji}^r is signal delay from the satellite antenna phase center (satellite transponder signal time) to j station antenna phase center(received i station signal time).

O_{iu} is i station signal on row ionospheric delay correction.

O_{jd} is j station signal downstream ionospheric delay correction.

T_i is i station transmitter instrument delay.

I_{ji} is j station receives the i station signal receiver instrument delay.

ΔT_{1i} is the clock offset between i station master clock relative and the ground time standard.

ΔT_{1j} is the clock offset between j station master clock relative and the ground time standard.

τ_s is the satellite transponder delay.

Assumed that the above formula has corrected the delay caused by the ionosphere, and corrected the instrumental errors. And it has taken off the effect of the earth autobiography. After the above corrections, the formula (1) can become to:

$$R_{ji} = R_i^t + \tau_s + R_{ji}^r - \Delta T_{1i} + \Delta T_{1j} \qquad (2)$$

Assumed that all the stations emit the time signal and all the stations can receive the signal transmitted from all stations. Therefore, each station can obtain N independent observation value, and the N stations have N×N observation value. If considering a pair of observation: Let i station receives j station transmitted signal, and the j station receives the i station transmitted signal. According to the equation (2), the two observation equation added to :

$$R_i^t + \tau_s + R_{ji}^r = \frac{1}{2}(R_{ji} + R_{ij}) \qquad (3)$$

The formula (3) is the pseudo distance observation equation of the i station and j station. And it is suit for any i and j (i can be equal to j).

When i is equal to j, it mean that $R_i^t = R_{ji}^r$, $R_{ji} = R_{ij}$ and it mean that each station receives only own station transmitted signal, that is the mode of transmitting and receiving signal itself. It is not difficult to obtain:

$$R_{ji}^r + \frac{1}{2}\tau_s = \frac{1}{2} R_{ii} \qquad (4)$$

The formula (4) is the pseudo distance calculation equation of ground testing system based on the transponder signal.

When satellite transponder transmit the signal from the ground station, it can design a method to trigger a signal to make satellite broadcasting the special carrier signal based on the satellite atomic clock. The time relationship formula is :

$$R_j = R^j + \tau_s^i \qquad (5)$$

It should be noted that formula (5) has been to correct the delay caused by the ionosphere and the correct instrument error, and it has taken off the effect of the earth autobiography.

R_j is j station receives the i station transmitting the signal to trigger the delay of the signal broadcast by the satellite transponder;

R^j is the delay that the Satellite broadcast signal from the satellite antenna phase center (satellite transponder i-station signal moment) to j station antenna phase center (j station receive the signal moment). It can be known that $R^j = R_{ji}^r$.

τ_s^i is the delay of i station signal to the satellite transponder to the time of the satellite broadcast signal. Let $\tau_s^i = \frac{1}{2}\tau_s$,

That formula (5) can became to :

$$R_j = R_{ji}^r + \frac{1}{2}\tau_s \qquad (6)$$

Comparing the formula (4) and (6), it can know that:

$$R_j = \frac{1}{2} R_{ii} \qquad (7)$$

In other words, the delay of the satellite broadcast signal to the receiver on the ground is equal to one half of transmitting time to receiving time under the mode of transmitting and receiving signal itself based on the ground testing system. Therefore, as long as the accurate measurement of the delay of the transmitter system to receiver system, it can calculate the starting time of the satellite broadcast signal. To compare the time offset between the satellite and the ground time standard can further analysis and estimate the time synchronization accuracy under constellations autonomous operation.

3.3 Simulation verify

To verify the validity and feasibility of the method, the paper take analysis based on the GPS data from IGS with some random errors.

Firstly, it should obtain the atomic clock data of GPS from IGS that on Taiwan station of December 20, 2010. The satellites should be observed at the same period on Taiwan station. The paper selects four satellites which are PRN4 and PRN10 and PRN17 and PRN23. The clock offset data figures are shown in figure 2.

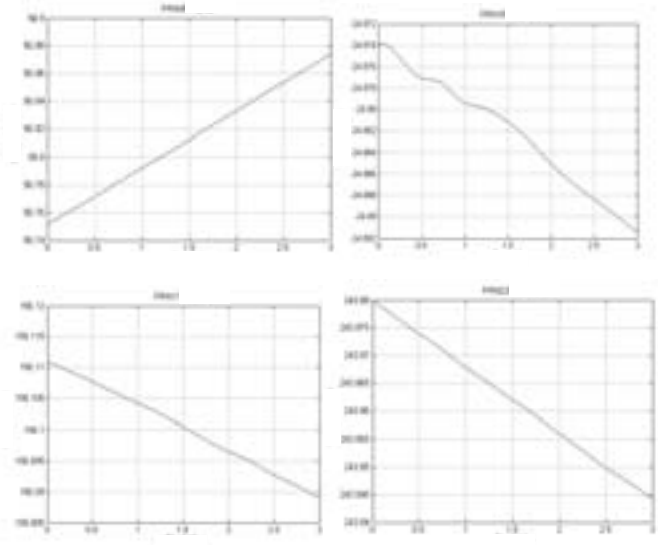

Figure 2. GPS satellite clock offset data

To use the satellite orbit data and the station coordinate, it can obtain the satellite-ground distance of the four satellites on each epoch-wise, and can convert to time offset. Because of the error less than 1 ns in the data transmission of the ground testing system, it should add a random error in simulating the satellite-ground delay. After data processing，the clock offset figure is shown in figure 3.

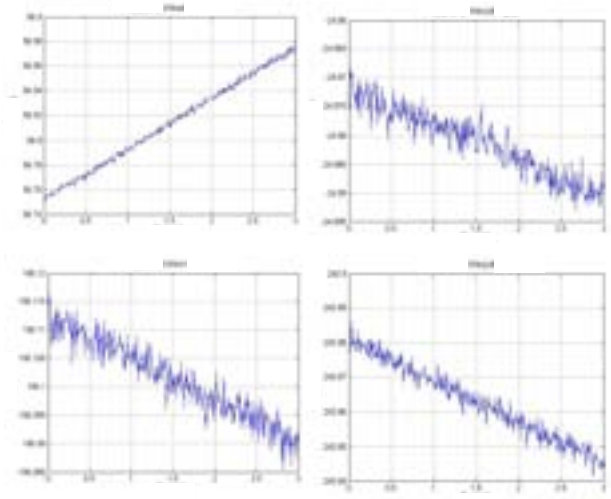

Figure 3. The clock offset after data processing

Let the above satellite data subtract the GPS system time standard data, it can obtain the figure shown in figure 4.

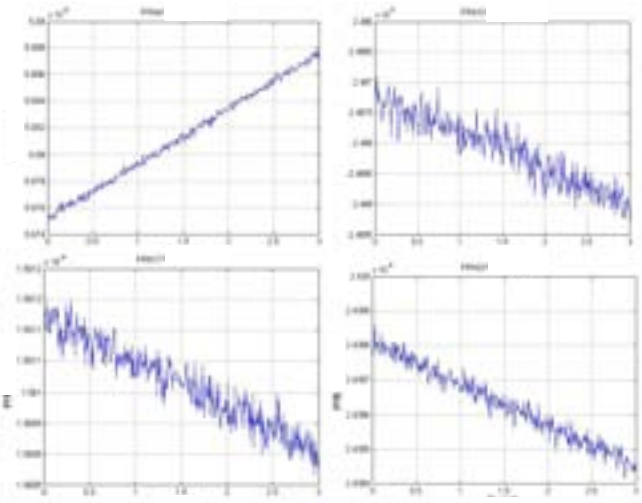

Figure 4. The data figure after subtracting the GPS time standard

The result shows that the data of PRN4 after processed have an offset of 3.57 ns (standard deviation), PRN10 is 5.53 ns, PRN17 is 6.64 ns, PRN23 is 10.5 ns. That can declare the time synchronization accuracy is less than 10 ns among the four satellite atomic clock. And it can verify the validity of the method.

3.4 The analysis of application

Now the correlative indexes of autonomous running mode of constellation of satellite navigation system are simulated or are designed by the measured data of the inter-satellite links. Which building the construction of the satellite navigation system, it is impossible not to inject the ephemeris and clock error in order to evaluate autonomous running ability, so it reduce system application. In order to cope with the extremeness of destroying ground-based monitoring system, it is necessary for evaluating the ability of autonomous running mode of constellation.

It is too high with the cost of doing experiment on the whole satellite navigation system, it is feasible for validating ability of constellation running experiment with 4-5 satellites .Choose 4-5 satellites of the same area as the simple system, cut the links between theirs and other satellites, autonomous orbit determination and time maintaining only by inter- satellite links of star-star. Evaluating it with the method, it provides the reference for answering the extremeness.

IV. CONCLUSION

With the purpose of autonomous running of navigation constellation, this paper analyses the necessity of experimenting and evaluating different working modes, advancing one kind of evaluating method of time synchronization of autonomous constellation which based on the ground-validation system. Giving the working principle , calculation model and simulation result, analysis the application value with the angle of experiment, which given the reference of building of inter-satellite links of navigation system.

REFERENCES

[1] Li Zhigang Li Huanxin, The reduction of two-way satellite time comparison, Chinese Astronomy and Astrophysics, 2003,27,226-235.

[2] M.P. Ananda, H. Bemstein, Global positioning system autonomous navigation(J), IEEE,1990,497-508.

[3] Liu Li, Zhu Linfeng, Autonomous timekeeping of navigation satellite based on inter-satellite link, 2009, P206-210.

[4] Li Zhigang, Yang Xuhai, Testing and Determining orbit based on the transponder, The conference of precision orbit and time synchronization, 2009, P80-91.

[5] Wu Haitao, Time Fundament of Satellite navigation system[M], 50-53.Science Press.

[6] Geng Liang, Wu Shiqi. Constellation Design and inter satellite link build[J]. Astronautic science and technology of China, 2000, 20(6), P62-67(Ch).

Ultra-Short Term Clock Offset Prediction for Two-Way Satellite Time Synchronization

Zhang Shengkang, Zhang Li
Science and Technology on Metrology and Calibration Laboratory
Beijing Institute of Radio Metrology and Measurement
Beijing, China
Zhangsk@126.com

Yang Yujie
Beijing Institute of Radio Metrology and Measurement
Beijing, China

Abstract—**Based on the principle of two way satellite time transfer, a time synchronization system with master-slave sturcture is established. In the system, slave sites compare their clock time with the master clock in turn. After one comparison, the slave clock offset is estimated and predicted until the next comparison period. In the paper, three clock offset prediction algorithms are discussed in detail. Their performance is evaluated and validated using measured clock offset data. The results show the linear fitting algorithm has an obvious good performance in ultra-short term prediction than quadratic polynomial method. And it's quite simple than grey system model prediction algorithm. The time synchronization system use the linear fitting algorithm for clock offset prediction in practice and has a good practical effect.**

Keywords-Two-Way Satellite Time Transfer（TWSTT）;Clock Offset Prediction; Grey System Model; Time Synchronization

I. INTRODUCTION

Two-Way Satellite Time Frequency Transfer (TWSTT) is a very high precise time & frequency remote comparison technique, which is widely used in time metrology, satellite navigation and radio measurement, etc. It is more precise than GPS common view method in time transfer, and more independent than GPS carrier phase time transfer method. Nowadays, most of the time metrology laboratories in Europe and America established the TWSTTT links. There is a TWSTT network in east Asia for remote time transfer, which is centered at NICT[1]. By means of the modem, the one pulse per second (1PPS) is modulated onto the station's intermediate frequency (IF), which is usually at 70MHz. The signal is then up-converted to the radio frequency (RF), amplified, and transmitted to the satellite. At the receiving site the RF signal is again amplified, down-converted to the IF, and demodulated by means of the modem. In TWSTT system, spread spectrum signal PN modulation is usually used, and the pseudorange of the two-way signal propagation paths are measured. Because of the reciprocity of two paths, the difference of the two measurements is the clock offset of the two stations [2].

In this paper, a high precise time synchronization system is established using TWSTT technique, which includes a master station and several slave stations. The master clock is compared with the each slave clock for a while circularly by the TWSTT system. The slave station collects and processes the comparison data, and estimates the precise parameters of the slave clock as to the master clock. Then the estimated clock parameters are used to predict the slave-master clock offset in the near future. Clock offset precise prediction with finite clock offset measurements is a very important research aspect in satellite navigation area. Considering the frequency drift of rubidium atomic clock, quadratic polynomial is used to fitting the clock offset measurements, and then to predict the clock offset after the measurement completed [3]. Cui Yongqiang, etc. [4] firstly introduced the grey system model for the satellite clock offset prediction. It's illustrated that the grey system model has better performance than the quadratic polynomial method in long term prediction. Furthermore, Lu Xiaofeng, etc. [5] presents a optimized algorithm for GM(1,1) model, which selects the grey model parameters with minimum errors by iteration method and improves the clock offset prediction performance. Zhu Xiangwei, etc. [6] presents a Kalman algorithm for satellite clock offset prediction based on GPS space based rubidium clock measurements, which improves the short term prediction performance. Zhang Qinghua, etc. [7], based on the quadratic polynomial and grey system model algorithm, furtherly put forward wavelet and ARMA methods to predict the random components. The new algorithm is quite complex and more precise. In satellite navigation field, clock offset is usually predicted on the scales of several hours to several days. However, in this paper, the clock offset algorithms are discussed on the scales of tens of minutes according to the practical requirements of the designed time synchronization system. We call them ultra-short term prediction algorithms. Several prediction algorithms are discussed and validated in practice in this paper. One of them is used in the practical synchronization system and behaves good performance.

II. TWSTT BASED TIME SYNCHRONIZATION SYSTEM

In TWSTT system, the local 1PPS signal is modulated and transmitted by the Modem & the satellite earth station facilities, and also the transmitted signal from the remote station is received and demodulated by the earth station facilities & Modem. Fig. 1 illustrates the principle of the TWSTT system. The 1PPS signal from the atomic clock in station A is splitted into two paths. One of them is to the spread

spectrum Modem A, which is transmitted to the satellite by VSAT earth station A. The other path is used as the start of a local time interval counter A. It just has the same setup in station B as station A. When the transmitted signal from B is received and demodulated, a 1PPS signal is reconstructed, which stops the time interval counter A. The readings of time interval counter at station A and B are denoted as ΔT_A and ΔT_B , and if the bidirectional propagation delay differences are ignored, then the clock offset between station A and B is given by(1),

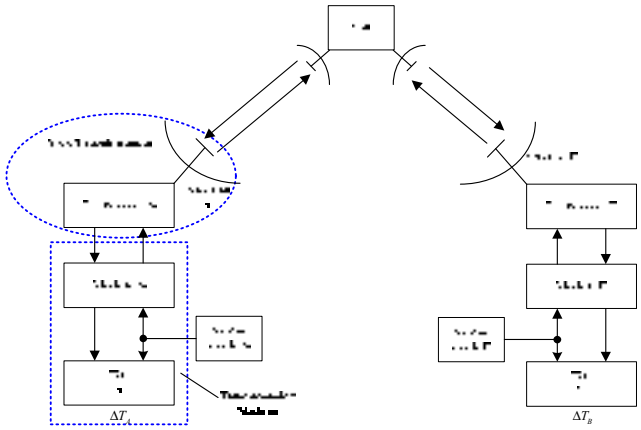

Fig. 1 Basic setup of two way satellite time frequency transfer system

$$\Delta T_{AB} = \frac{1}{2}\left(\Delta T_A - \Delta T_B\right) \qquad (1)$$

Where, ΔT_{AB} is clock offset between station A and B, ΔT_A , ΔT_B are the readings of time interval counter at station A and B, respectively.

The two way satellite time synchronization system is based on the above time transfer scheme, in which the master clock compares with the slaves in turn, as shown in Fig. 2(a). When a slave clock is comparing with the master clock, their offset is measured directly. When it is not in comparison with the master, the previous the comparison data is used to estimate the current clock offset. So the slave clock offset is gotten uninterrupted, which is informed to the user for offset compensation or synchronization, as shown in Fig. 2(b). This kinds of time division time comparsion mode reduces the master complexity and the system cost. In order to guarantee the time scale stability in the system, a hydrogen atomic clock is used as the master frequency reference. Furtherly, in order to ensure the appropriate clock offset prediction accuracy, a rubidium atomic clock is used as the slave frequency reference. Fig. 2(c) shows a segment of two-way time transfer data between the master station and a slave station, which indicates that there exists some initial clock offset and a very obvious linear drift between the two clocks.

III. ULTRA-SHORT TERM CLOCK OFFSET PREDICTING METHOD

In contrast to the clock offset predicting method in traditional satellite navigation application, this paper dicussed the predicting algorithm with shorter time and less observation data, which typically is about 10min observation data and 30min prediction length.

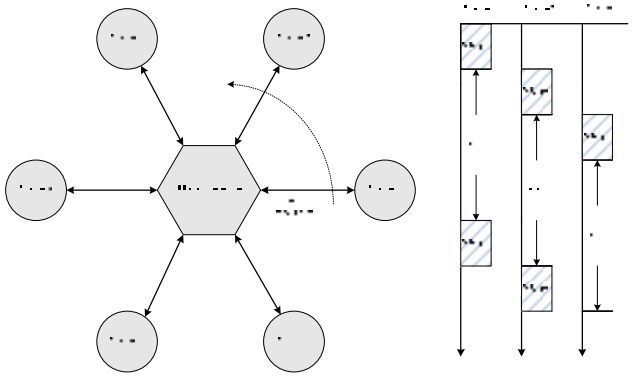

(a) time comparison process of the system (b) time synchronization flow

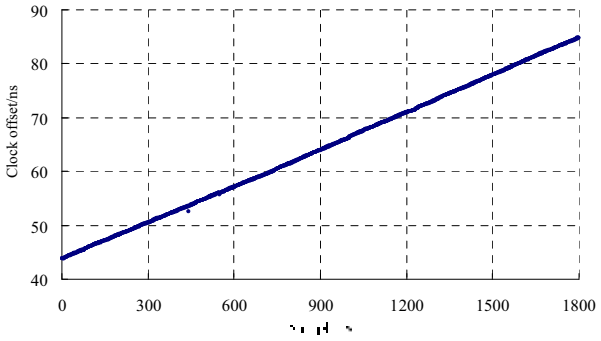

(c) TWSTT measurements between the master and a slaver

Fig. 2 Time synchronization system based on TWSTT method

A. *Quadratic Polynomial Clock Offset Predicting*

Considering the rubidium atomic clock frequency characteristics, it's time offset can be described by quadratic polynomial as (2),

$$\Delta T_k = a_0 + a_1 t_k + a_2 t_k^2 + e_k, k = 1,2,\mathrm{L}\ ,N \qquad (2)$$

Where, ΔT_k is clock offset measurements between a slave and the master, a_0, a_1, a_2 为 re initial offset, fractional clock speed and fractional clock drift, e_k is the total term of measurement noise and the random phase of atomic clock. Using those measuremets and the least square method, the fractional parameters of the slave clock can be estimated as (3),

$$\hat{\mathbf{a}} = \left(\mathbf{A}^{\mathrm{T}}\mathbf{A}\right)^{-1}\mathbf{A}^{\mathrm{T}}\mathbf{X} \qquad (3)$$

Where, $\hat{\mathbf{a}} = \begin{bmatrix} a_0 \\ a_1 \\ a_2 \end{bmatrix}$, $\mathbf{A} = \begin{bmatrix} 1 & t_1 & t_1^2 \\ 1 & t_2 & t_2^2 \\ \mathrm{L} & \mathrm{L} & \mathrm{L} \\ 1 & t_N & t_N^2 \end{bmatrix}$, $\mathbf{X} = \begin{bmatrix} \Delta T_1 \\ \Delta T_2 \\ \mathrm{M} \\ \Delta T_N \end{bmatrix}$.

Those estimated a_0, a_1, a_2 can be used to predict the clock offset for the next time segment.

B. Grey System Model Predicting[5]

GM (1,1) model is most commonly used in grey system theory. It's a differential equations model containing only a single variable, which essentially use an exponential function to fitting the clock offset cumulative time series, and uses the fitting parameters to do offset predicting. If the original data sequence of the clock offset is as (4)

$$\mathbf{X}^{(0)} = \left\{x^{(0)}(1), x^{(0)}(2), \mathrm{L}\ , x^{(0)}(k)\right\}, k = 1,2,\mathrm{L}\ , N \tag{4}$$

Do first order accumulating on data sequence $x^{(0)}(k)$, then we get (5)

$$\mathbf{X}^{(1)} = \left\{x^{(1)}(1), x^{(1)}(2), \mathrm{L}\ , x^{(1)}(k)\right\}, k = 1,2,\mathrm{L}\ , N \tag{5}$$

Where, $x^{(1)}(k) = \sum_{i=1}^{k} x^{(0)}(i), k = 1,2,\mathrm{L}\ , N$. In terms of the grey system predicting model, the clock offset predicting equation is gotten as (6),

$$x^{(0)}(k) = \left[1 - \exp(a)\right]\left[x^{(0)}(1) - u/a\right]\exp\left[-a(k-1)\right] \tag{6}$$

Where, a, u are model parameters, which satisfy (7),

$$\hat{\mathbf{a}} = \left(\mathbf{G}^{\mathrm{T}}\mathbf{G}\right)^{-1}\mathbf{G}^{\mathrm{T}}\mathbf{Y} \tag{7}$$

Where, $\hat{\mathbf{a}} = \begin{bmatrix} a \\ u \end{bmatrix}$, $\mathbf{G} = \begin{bmatrix} -\frac{1}{2}\left[x^{(1)}(1) + x^{(1)}(2)\right] & 1 \\ -\frac{1}{2}\left[x^{(1)}(2) + x^{(1)}(3)\right] & 1 \\ \mathrm{M} & \mathrm{M} \\ -\frac{1}{2}\left[x^{(1)}(N-1) + x^{(1)}(N)\right] & 1 \end{bmatrix}$,

$\mathbf{Y} = \left[x^{(0)}(2) \quad x^{(0)}(3) \quad \mathrm{L} \quad x^{(0)}(N)\right]^{T}$, $[\mathrm{g}]^{T}$ is matrix transpose.

C. Linear Fitting Predicting

Using the linear function to fit the atomic clock parameters and predicting clock offset gains little attention in satellite navigation area. However, in the short term clock offset predicting application, due to the observation time is short, clock drift may not be accurate estimated in such a short time. Linear clock offset predicting equation ignores the second order term of the clock drift as (8)

$$\Delta T_k = a_0 + a_1 t_k + e_k, k = 1,2,\mathrm{L}\ , N \tag{8}$$

According to the least square method, clock parameters are estimated as (9)

$$\hat{\mathbf{a}} = \left(\mathbf{A}^{\mathrm{T}}\mathbf{A}\right)^{-1}\mathbf{A}^{\mathrm{T}}\mathbf{X} \tag{9}$$

Where, $\hat{\mathbf{a}} = \begin{bmatrix} a_0 \\ a_1 \end{bmatrix}$, $\mathbf{A} = \begin{bmatrix} 1 & t_1 \\ 1 & t_2 \\ \mathrm{M} & \mathrm{M} \\ 1 & t_N \end{bmatrix}$, $\mathbf{X} = \begin{bmatrix} \Delta T_1 \\ \Delta T_2 \\ \mathrm{M} \\ \Delta T_N \end{bmatrix}$.

D. Experiments and Analysis

In order to verify the performance of the above-mentioned clock offset predicting algorithms, four groups TWSTT data are selected randomly, each of them is 40min length. The previous 10min data is used to estimate the fractional clock parameters, and to predicting the next 30min clock offset. The later 30min TWSTT data is used to validate the performance of the algorithms by compare the difference of predicting offset and the TWSTT data. Fig. 3 show the predicting results of quadratic polynomial algorithm, grey system model and linear fitting algorithm. It can be seen that the grey system model and the linear fitting algorithm have very good consistency of predicting trends. In the previous three plots, the quadratic polynomial algorithm presents obvious larger predicting error than the other two algorithms. Only in the fourth plot, the quadratic polynomial algorithm shows quite good performance. But the grey system model and the linear fitting algorithm always present predicting errors in the same order of magnitude and behave very good performance for predicting.

In order to quantitative analyzing the predicting performance of the three algorithms, mean prediction error (Avg.), standard deviation (Std.) and maximum prediction error (Max.) of the 30min differnces between predicting data and the measurement data are used. Tab.1 list the quantitative evaluation of the three algorithms in the four experiments. The prediction error of quadratic polynomial is basically on the magnitude of several nanoseconds, and the maximum prediction error is close to 10ns. Grey system model and linear fitting prediction algorithm have very similiar forecast accuracy, which present very stable performance in the four set of experiments.

Considering the above experimental results, in the actual time synchronization system, linear fitting algorithm has better performance than quadratic polynomial algorithm, and are more concise than the grey system model algorithm.

IV. CONCLUSION

Two way satellite time transfer technique can provide remote high precision time synchronization independent of GPS, which has an important role in radio detection, navigation and other fields and cannot be replaced. Based on the two-way satellite time transfer principle, a master-slave synchronization system is established. The system includes a master station and several slave stations. Through master-slave comparison in sequence and clock offset predicting, uninterrupted time synchronization is realized. This paper expounds the principle of two-way satellite time synchronization system, time synchronization process and scheme. Emphatically, three offset predicting algorithms are discussed in basic principles, and

validated by four sets of experiments using measured data. In conclusion, linear fitting clock offset predicting algorithm has better performance than widely used quadratic polynomial algorithm in ultra-short term prediction, and has lower complex degree than the gray system model algorithm. The linear fitting algorithm is ultimately applies in the actual synchronization system, and has very good practical effect.

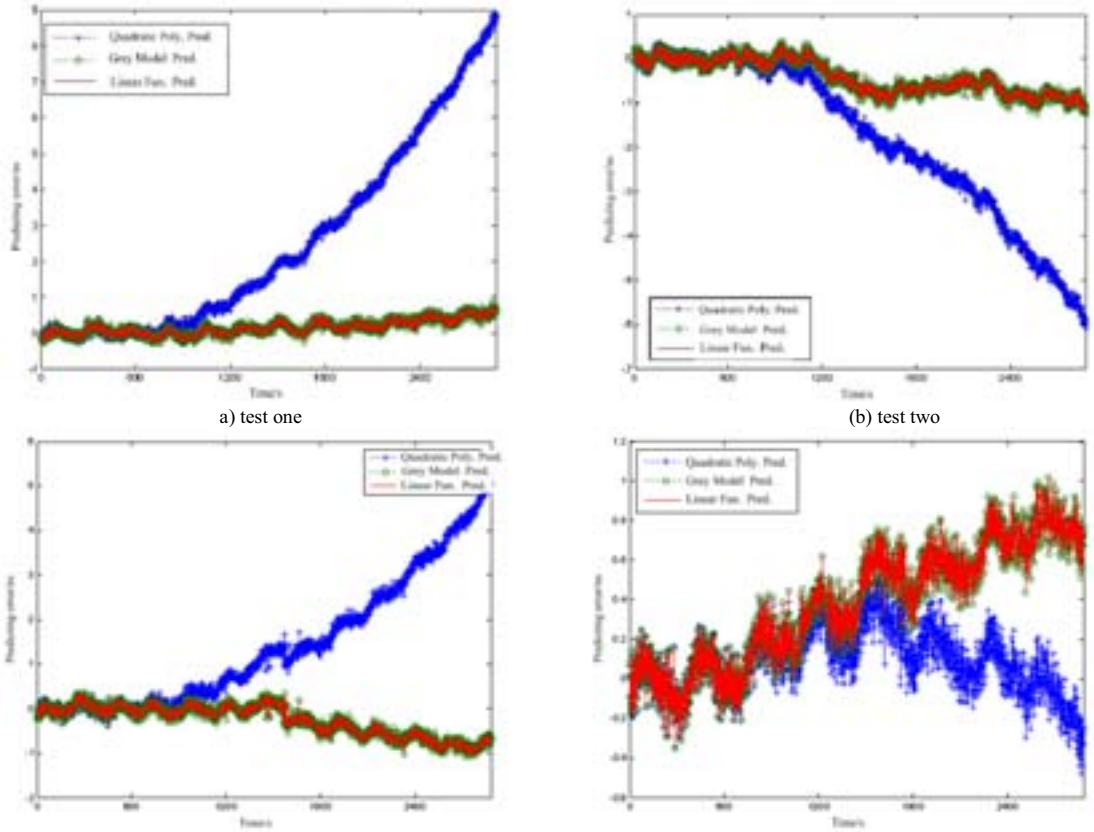

a) test one (b) test two

c) test three (d) test four

Fig. 3 comparison of the predicting performance of the three algorithms

TABLE I. PREDICTING ERROR OF THE THREE ALGORITHMS

Alg. / Seq.	Quadratic polynomial			Grey system Model			Linear fitting		
	Avg.	Std.	Max.	Avg.	Std.	Max.	Avg.	Std.	Max.
1	2.503	2.640	8.887	0.147	0.209	0.833	0.144	0.207	0.826
2	-1.804	1.790	6.099	-0.410	0.387	1.251	-0.406	0.384	1.242
3	1.420	1.465	5.255	-0.264	0.340	1.075	-0.267	0.342	1.082
4	0.090	0.160	0.530	0.379	0.298	1.020	0.380	0.299	1.022

REFERENCES

[1] W. Lewandowski, J. Azoubib, W. J. Klepczynski (1999) GPS: Primary Tool for Time Transfer. Proceedings of the IEEE. 87(1):163-172.

[2] M. Imae, M. Hosokawa, K. Imamura,et al (2001) Two-way satellite time and frequency transfer networks in Pacific Rim region. IEEE Trans. on Instrumentation and Measurement. 50(2):559-562.

[3] D. Kirchner (1991) Two-way time transfer via communication satellites. Proceedings of the IEEE. 79(7):983 -990.

[4] Elliott D., Kaplan (2006) Understanding GPS: Principles and Applications (Second Edition). Artech House

[5] Cui Xianqiang, Jiao Wenhai (2005) Grey System Model for the Satellite Clock Error Predicting. Geomatics and Information, Science of Wuhan University. 30 (5): 447-450 (in Chinese)

[6] Lu Xiaofeng, Yang Zhiqiang, Jia Xiaolin, et al (2008) Parameter Optimization Method of Gray System Theory for the Satellite Clock Error Predicating. Geomatics and Information, Science of Wuhan University. 33 (5): 492-495 (in Chinese)

[7] Zhu Xiangwei, Xiao Hua, Yong Shaowei, et al (2008) The Kalman Algorithm Used for Satellite Clock Offset Prediction and Its Performance Analysis. Journal of Astronautics. 29 (3):966-970 (in Chinese)

A Measurement Method of the GEO Satellite Local Oscillator Error

Wenfang Jing, Jin Wang, Danning Zhao
National Time Service Center, Chinese Academy Of Sciences Xi'An Lintong710600, China/ Key Laboratory for Precise Navigation, Positioning and Timing of the Chinese Academy of Sciences, Xi'an 710600, China/ University of Chinese Academy of Sciences， Beijing100039, China)

Xiaochun Lu, Jianfeng Wu
National Time Service Center, Chinese Academy Of Sciences, Xi'an Lintong710600, China/ Key Laboratory for Precise Navigation, Positioning and Timing of the Chinese Academy of Sciences, Xi'an 710600, China

***Abstract*—In recent years, Two-Way Satellite Time and Frequency Transfer (TWSTFT) method has been accredited as the most effective and high precision system. But as the frequency stabilities of today's sophisticated atomic-level clocks improve, so must the stability of a Two-Way system's method of time and frequency transfer. Carrier-phase information holds the promise of improving the stabilities of TWSTFT measurements, because of the great precision at which frequency transfers can be achieved. Many years ago, some scientists try to use carrier phase in TWSTFT, in the trial of time and frequency transferring between USNO and NIST station, some excited results proved the theory and showed the promise of carrier-phase measurement. But because of the poor stability of telecommunications GEO satellite local oscillator and some other factors, the result didn't review in other trial station. Then no further research reference was published. Based on TWSTFT system, a method for measuring the satellite oscillator frequency is presented. The radial velocity of the satellite relative to the main control station can be estimated from the relationship between the Doppler frequency shift and the frequency difference between the two stations. Then the satellite oscillator frequency can be calculated after one of the two Doppler frequencies has been measured. According to the results, the influence of transponder local oscillator can be relieved by pre-adjusting the transmitter clock. Two solutions are described to calculate the two stations velocities and satellite local oscillator. By present TWSTFT link, test campaign has been conducted with 10MChip/s PN code signal between Shanghai and Shaanxi.**

Keywords-satellite local oscillator measuring;TWSTFT; doppler frequency

I. SCOPE

Independent of GPS, TWSTFT, as one of the most accurate and precise techniques for remote time and frequency transfer, is the second widely used technique. In order to improve TWSTFT precise further, some researchers have attempted to use carrier phase observation in TWSTFT and have shown some potential [1]. For transponders onboard commercial communication satellites simply convert the input carrier with a non-coherent local oscillator, carrier phase information between transponder input and output is jammed in this process. To ensure the higher precision, the influence of satellites transponder local oscillator (STLO) should be considered. Method to measure the STLO is presented in the paper. A compensation scheme has been developed to solve the two stations velocities and satellite local oscillator.

II. THEORY

A. *Satellite Transponder*

In TWSTFT system, the GEO satellite payload is a bent-pipe signal transponder or a repeater which converts the Ground Station (GS) uplink signal to downlink signal. The bent-pipe signal transponder structure can be seen in figure 1.

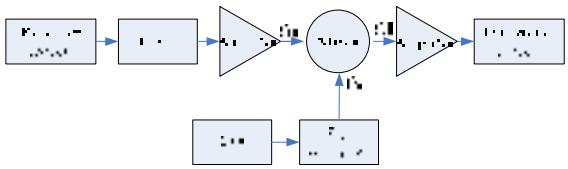

Figure 1. Satellite transponder structure

As shown in the above figure, the STLO frequency is f_{LO} , then:

$$f_s = N \cdot f_{LO} \tag{1}$$

$$f_d = f_u - f_s \tag{2}$$

In which, f_s is the transponder transforming frequency, f_u and f_d is the transponder input and output frequency separately.

B. *Frequency Transfer theory*

By the transponder, traditional TWSTFT ground station receives the signal from each other, then, space factors such as ionosphere, troposphere errors can be canceled. To enhance the system precision and use carrier phase in TWSTFT, we use the new system structure to eliminate or calculate the satellite influence. Two Way Carrier Phase (TWCP) measurement set-up is shown in figure2, in which each ground station receives the signal from the remote site and its own signal via the same

Project is sponsored by a West light Foundation of The Chinese Academy of Science (Grand No: 2012YD04) and the National Natural Sciences Foundation of China (Grand No: 11073022)

transponder. Relative to the traditional TWSTFT, TWCP has one more receiver to receive its own signal. STLO frequency can be measured by the accessorial receiver Rx2.

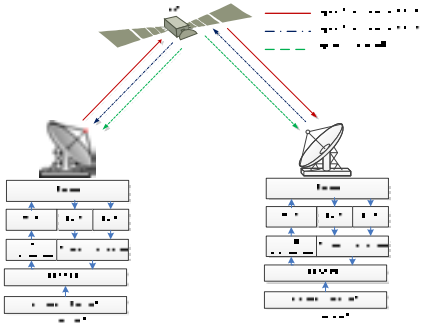

Figure 2. System frames of carrier-phase-based TWSTFT

In TWSTFT, the modem to be synchronized is equipped with a low-phase-noise hydrogen atom clock or with a Rb reference. The built-in clock, which can be controlled using a computer-based control algorithm, is synchronized to the clock on the other site of the Two-Way time link.

To achieve implementation, the one pulse per second (1 pps) is modulated onto the station's intermediate frequency (IF) by the Two-Way modem, which is usually at 70 MHz. Then the signal is up-converted to the radio frequency (RF), amplified, and transmitted to the satellite. In the satellite transponder it is retransmitted by the so-called satellite translation frequency. At the receiving site the RF signal is amplified, down-converted to the IF, and demodulated by modem.

III. MEASUREMENTS AND RESOLUTIONS

A. *Measurement equations*

Shown as Fig.2, station 1 is transmitting a signal to Station 2 and receiving its own signal relayed by a satellite. Then the signal is subject to the Doppler effects resulting from the slight motion of the satellite. The first-order Doppler coefficients are described by the following two equations.

$$k_1 = \frac{V_1}{c}\ ,\ k_2 = \frac{V_2}{c} \tag{3}$$

where V_i is a projection of the velocity vector of the satellite in the direction of Station $i(i=1,2)$ and c is the speed of light. Suppose that Station i transmits a signal with a frequency f_{txi}. At the satellite, the frequency of the received signal is centered at the Doppler-shifted frequency $\mathrm{f_{txi}} + \mathrm{k}_i \mathrm{f_{txi}}$, which is then mixed with the satellite's carrier frequency which is up-converted from the satellite's local oscillator (SLO), denoted as $\mathrm{f_s}$, and retransmitted at the carrier frequency given by the following equation:

$$\mathrm{f}_{SV} = \mathrm{f_{txi}} + \mathrm{k}_i\ \mathrm{f_{txi}} - \mathrm{f_s} \tag{4}$$

The carrier frequency is then observed Doppler-shifted at the downlink station $j(j=1,2)$ as:

$$\mathrm{f_{11}} = (\mathrm{f_{tx1}} + \mathrm{k_1 f_{tx1}} - \mathrm{f_s}) + \mathrm{k_1}(\mathrm{f_{tx1}} + \mathrm{k_1 f_{tx1}} - \mathrm{f_s}) \tag{5}$$

$$\mathrm{f_{21}} = (\mathrm{f_{tx2}} + \mathrm{k_2\ f_{tx2}} - \mathrm{f_s}) + \mathrm{k_1}\ (\mathrm{f_{tx2}} + \mathrm{k_2\ f_{tx2}} - \mathrm{f_s}) \tag{6}$$

$$\mathrm{f_{22}} = (\mathrm{f_{tx2}} + \mathrm{k_2\ f_{tx2}} - \mathrm{f_s}) + \mathrm{k_2}\ (\mathrm{f_{tx2}} + \mathrm{k_2\ f_{tx2}} - \mathrm{f_s}) \tag{7}$$

$$\mathrm{f_{12}} = (\mathrm{f_{tx1}} + \mathrm{k_1\ f_{tx1}} - \mathrm{f_s}) + \mathrm{k_2}\ (\mathrm{f_{tx1}} + \mathrm{k_1\ f_{tx1}} - \mathrm{f_s}) \tag{8}$$

The formulas can be rewritten as:

$$\mathrm{f_{11}} = \mathrm{f_{tx1}} \cdot (1 + 2k_1 + k_1^2) - \mathrm{f_s} \cdot (1 + k_1) \tag{9}$$

$$\mathrm{f_{21}} = \mathrm{f_{tx2}} \cdot (1 + k_2 + k_1 + k_1 k_2) - \mathrm{f_s} \cdot (1 + k_1) \tag{10}$$

$$\mathrm{f_{22}} = \mathrm{f_{tx2}} \cdot (1 + 2\mathrm{k_2} + k_2^2) - \mathrm{f_s} \cdot (1 + \mathrm{k_2}) \tag{11}$$

$$\mathrm{f_{12}} = \mathrm{f_{tx1}} \cdot (1 + k_2 + k_1 + k_1 k_2) - \mathrm{f_s} \cdot (1 + k_2) \tag{12}$$

Where f_{ij} is used to denote a frequency that has been transmitted by Station i and measured by Station j.

B. *Resolution of* f_s

From the formulas above, we can get the f_s related to k_1 or k_2, which is shown as follow:

$$f_s = \frac{f_{tx1}(1+k_1)^2 - f_{11}}{1+k_1} \tag{13}$$

$$f_s = \frac{f_{tx2}(1+k_2)^2 - f_{22}}{1+k_2} \tag{14}$$

$$f_s = \frac{f_{tx2}(1+k_1)(1+k_2) - f_{21}}{1+k_1} \tag{15}$$

$$f_s = \frac{f_{tx2}(1+k_1)(1+k_2) - f_{12}}{1+k_2} \tag{16}$$

C. *Resolution of* k_1 *and* k_2

With the formulas (9)-(12), to solve k_1 and k_2 is an extremely complex task. In order to reduce the resolution process and makes it easy to be implemented, a simplified method is presented. The self-closed-loop back delay of the station can be measured by receive the station itself transmitting signal. The pseudo-orange, denoted as ρ, between the station and satellite is half of the self-closed-loop back delay multiplied by the speed of light.

The Doppler can be converted to a pseudo-range rate observation given by the following:

$$V_i = \dot{\rho} = \frac{c(\Delta t_1 - \Delta t_2)}{2} \tag{17}$$

In which, $\Delta t_i (i = 1, 2)$ is the instantaneous measurement value of self-closed-loop back delay. For most TWSTFT users are national standard laboratories, each link has been installed by owners of highly accurate clock, so the station clock drift is neglected.

According to the formulas (17), k_1 and k_2 can be obtained by combined with formula (3).

D. Resolution of the difference frequency between two stations

With TWSTFT system, the two stations employ a code division multiple access (CDMA) scheme to lock onto each other and establish communication. Usually, the same uplink and downlink frequency is expected. But in fact, there is Clock offset between the two stations by a value df for the different local oscillator is used in the two stations, which can be expressed as:

$$f_{tx2} = f_{tx1} + df \tag{18}$$

By the formula (9) and (10) or (11) and (12), we can get the offset when adopted k_1 and k_2 calculated above.

$$df = \frac{f_{tx1}(1+k_1)^2 - f_{tx1}(1+k_1)(1+k_2) + f_{21} - f_{11}}{(1+k_1)(1+k_2)} \tag{19}$$

IV. TEST AND RESULTS

Measurements have been carried out at Shanghai and Shaanxi to verify function and performance. 10MChip/s PN-modulated signals on C-band have been used.

A. Observations

During the test campaign, the transponder was available continuously and transmissions were interrupted 10 to 15 minutes per hour only when the equipment is calibrated. In figures, station 1 is in Shaanxi, station 2 is in Shanghai. Here, what we concerned is the measurements of $f_{11}, f_{12}, f_{22}, f_{21}$ and ρ, which are shown in Fig.3 to Fig.6 respectively.

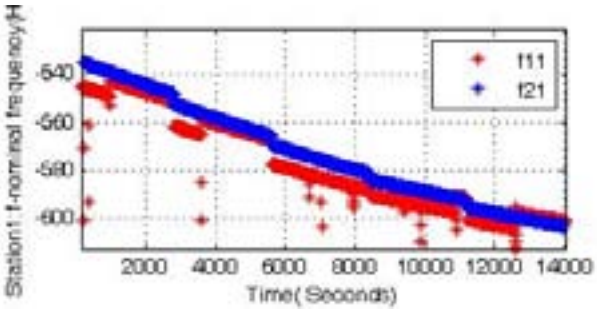

Figure 3. Frequencies received by station 1

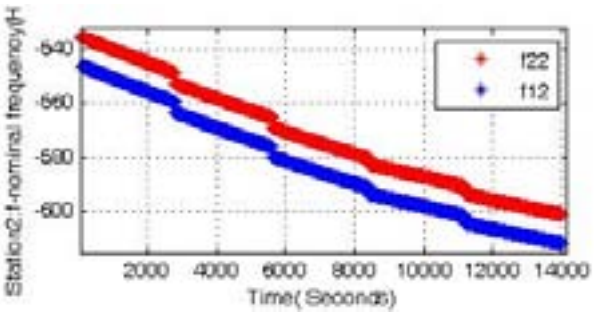

Figure 4. Frequencies received by station 2

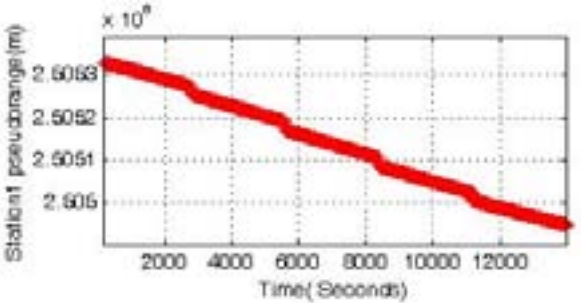

Figure 5. Pseudorange of station 1

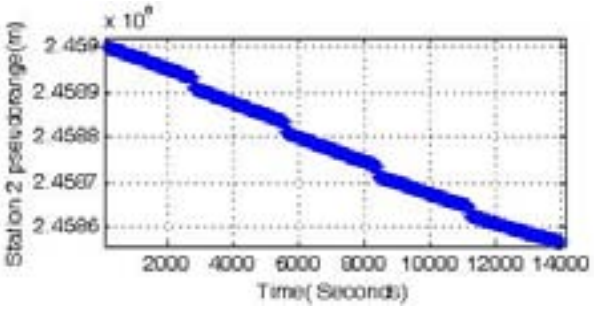

Figure 6. Pseudorange of station 2

From the figures above, we can see that the data is interrupted by the station calibration work and there are 5 hours data in the figures seen from the broken ends. About 4700 km distance difference between the station 2 and station 1 to satellite shows in the figure 5 and figure 6..

B. Resolutions

Adopting the instantaneous sample data of $f_{11}, f_{12}, f_{22}, f_{21}$ and ρ, we can draw the figures of V_i, f_s, the mean value of f_s and other calculation parameters calculated by the accordingly formulas above, which are shown in Fig.7 to Fig.10 respectively.

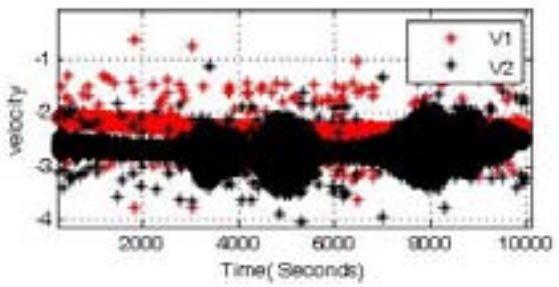

Figure 7. V_1 and V_2 calculation value

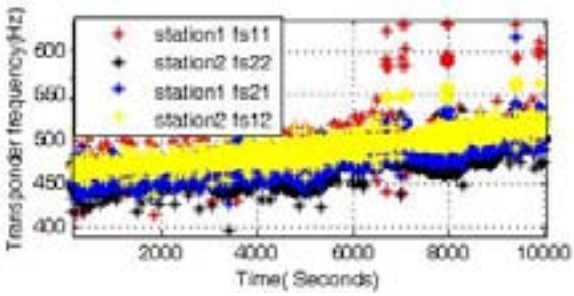

Figure 8. f_s values of formula (13) to(16)

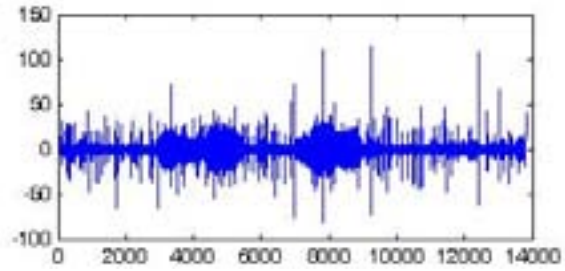

Figure 9. Stability of f_s

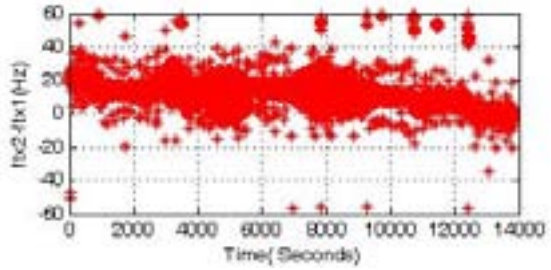

Figure 10. The frequency difference between station 1 and station 2

As the Fig.7 shows, V_1 and V_2 is surrounding 3m/s. as is consistent with the result of precise orbit method. From the figure we can see that circumstance around the station 2 is vitiated but which of station 1 is clean.

f_s values of formula (13) to(16) is shown in figure 8 which display the consistency of the results and the frequency offset 450Hz more than the nominal frequency and the offset in an upward tendency, as means the positive aging rate of the STLO. Many users calculate the Doppler by differentiating the received frequency and native nominal frequency, at this time, the STLO offset is subjected to the Doppler value, as will lead a mistake in the velocity. When knowing the STLO offset, we can pre-adjust the accordingly frequency by transmitter modem.

The figure 9 shows the stability of f_s and the figure 10 shows the frequency offset of about 20Hz between the two stations.

V. CONCLUSION

The paper suggests a simplified method of solving the satellite local oscillator and the velocity vector of the satellite in the direction of Station. The results can be used at all circumstance where there is a bent pipe transponder, such as TWSTFT, WAAS (Wide Area Augmentation System), CAPS (China Area Positioning System), and the self-closed loop link is needed. Our bench tests and live experiments have verified the coherence of the results and the experience values. For easy to calculate, the clock drift of the station, frequency offset subject to gravity and other propagation path frequency perturbations are neglected. All these would have some affects to the results which should be well understood and studied next.

ACKNOWLEDGMENT

The authors would like to thank Mr. Xiaohui Li and ZhiGang Li for their ongoing assistance with this project, and Hui Lei for his contribution to the article.

REFERENCES

[1] LI Xiao-Hui BIANYu-Jing CHEN Shu-Fang, " A Method for Accurately Measuring Satellite Oscillator Frequency at Single Station ", Journal of Time and Frequency, Vol.29 No.1,June,2006,pp.13-18,

[2] Kirchner, D. (1991), Two-way Time Transfer via Communication Satellites, Proc. IEEE 79(7),pp. 983ff

[3] W. Schäfer, A. Pawlitzki, and T. Kuhn, 2000, "New Trends in Two-Way Time and Frequency Transfer via Satellite," in Proceedings of the 31st Annual Precise Time and Time Interval (PTTI) Systems and Applications Meeting, 7-9 December 1999, Dana Point, California, USA (U.S. Naval Observatory, Washington, D.C.), pp. 505-514.

[4] Blair Fonville, Demetrios Matsakis,"Development of Carrier-phase based Two-Way Time and Frequency Transfer", 36th Annual Precise Time and Time Interval (PTTI) Meeting, pp.149-164.

[5] W. Schafer et al, "Extension of Two-Way Satellite Time- and Frequency Transfer Method to Real-Time Operation and Carrier Phase Measurements", Proceedings of the 1999 Joint Meeting EFTF – IEEE IFCS, Vol 1, April 1999, pp.203ff.

[6] Jing Wenfang, Lu Xiaochun, Wang Jin, Zhao Danning,"Research on the technology of Common-view based on the GEO Positioning System", The 2nd International Conference on Information Engineering and Computer Science 2010.pp.875-878.

Research on Calibration of TWSTFT Link by GPS

Zhiqiang Yang, Kun Liang, Qinghua Xu, Aimin Zhang
National Institute of Metrology
Beijing, China
Email:yangzq@nim.ac.cn

***Abstract*—TWSTFT is one of the most precise technique of time and frequency transfer. We research on the calibration technique of NIM TWSTFT Link by GPS time transfer system which have been calibrated. We did time and frequency transfer experiment between PTB and NIM use both TWSTFT and GPS time transfer system, process the experiment data of both system and get the time difference of them. The calibration result shown that the time difference of TWSTFT and GPS is about 1648ns, the calibration uncertainty is 5ns.**

I. INTRODUCTION

Two-way satellite time and frequency transfer (TWSTFT) is one of the most precise technique of time and frequency transfer[1,2], it has been developed into a widely used technique of time and frequency transfer between laboratories that contribute, with their atomic clocks and, in some cases, with their primary frequency standards, to the realization of International Atomic Time[3]. At present, TWSTFT is performed operationally in at least two laboratories in the United States, twelve in Europe, and seven in the Asia Pacific region[4,5]. The cooperation is organized by the CCTF Working Group on TWSTFT.

The NIM01 TWSTFT earth station was established in year 2008. National Institute of Metrology (NIM) and Physikalisch-Technische Bundesanstalt (PTB) have signed the cooperation agreement of TWSTFT in year 2009. After May of year 2009, NIM participated the Europe-Asia TWSTFT link which is organized by National Institute of Information and Communications Technology(NICT), the geostationary satellite is IS-4, and the participant laboratory include PTB, NICT, NMIJ, KRISS, NIM, NTSC, TL, OP. But the IS-4 satellite has equipment failure which is irreparable in 2010 February[6,7]. In order to continue the Europe-Asia TWSTFT link, the satellite was changed to AM2 which belongs to RUSSIA Intersputnik. After the communication experiment in 2010 August, NIM restarts the TWSTFT work. At present, the participant laboratories of Europe-Asia TWSTFT link include PTB, TL, NICT, NIM, NTSC, SU and NPLI. The results of laboratories should be processed to a specified format which follows the agreement of ITU-R SG4 [8,9,10], and be reported to BIPM.

In this paper, We research on the calibration technique of NIM TWSTFT Link by GPS time transfer system which have been calibrated. We did time and frequency transfer experiment between PTB and NIM use both TWSTFT and GPS time transfer system, process the experiment data of both system and get the time difference of them. The calibration result shown that the time difference of TWSTFT and GPS is about 1648ns, the calibration uncertainty is 5ns.

II. THE OPERATION OF NIM TWSTFT SYSTEM

TWSTFT is based on the exchange of timing signals through geostationary telecommunication satellites. It involves the transmission and reception of radio frequency (RF) signals carrying binary phase-shift keying (BPSK) modulations containing pseudorandom noise (PRN) codes. Modems generate the modulation at the intermediate frequency (IF) level which are then transmitted after up-conversion to the RF band (Ku-band or X-band are currently used). The received RF-signal is down-converted and the modem detects the modulation at the IF level. The phase modulation is synchronized with the local clock, and the modem generates a one-pulse-per-second (1PPS) output, synchronous with the BPSK sequence and named 1PPSTX. This signal represents the realization of a time scale. Each station uses a dedicated PRN code for the BPSK sequence in its transmitted signal. The receiving equipment generates the BPSK sequence of the remote station and reconstitutes a 1PPS tick from the received signal, named 1PPSRX. The difference between PPSTX and PPSRX (in general plus a constant) is measured by a time-interval counter (TIC). Following a pre-arranged schedule, a pair of stations lock on the code of the corresponding remote station for a specified period, called a session, measure the signal's time of arrival, and store the results. After exchanging the data records the difference between the two clocks can be computed.

The difference of the time scale between the laboratories is determined as follows:

$$
\begin{aligned}
TS(1)-TS(2) = &+0.5[TI(1)] \\
&-0.5[TI(2)] \\
&+0.5[SPT(1)-SPT(2)] \\
&-0.5[SCD(1)-SCU(1)] \\
&+0.5[SCD(2)-SCU(2)] \\
&+0.5[SPU(1)-SPD(1)] \\
&-0.5[SPU(2)-SPD(2)] \\
&+0.5[TX(1)-RX(1)] \\
&-0.5[TX(2)-RX(2)]
\end{aligned} \tag{1}
$$

Where,

TS(i) is Local time scale

TI(i) is Time interval reading

SPT(i) is Satellite path delay through the transponder

SCD(i) is Sagnac delay for a signal propagating from the GEO satellite to station i

SCU(i) is Sagnac delay for a signal propagating from station i to the GEO satellite

SPD(i) is Signal path downlink delay

SPU(i) is Signal path uplink delay

TX(i) is Signal delay in the transmit path of the TWSTFT station i

RX(i) is Signal delay in the receive path of TWSTFT station i

NIM earth station uses the SATRE modem which is made by Timetech Company; it has 1 transmission channel and 2 receiver channel. The diameter of antenna is 1.8 meter. The power of signal transceiver is 8W.

Figure 1. the TWSTFT earth station of NIM

There are many parameters that influence the stability of two-way time transfer system must be considered, such as transmission frequency, power level, carrier-to-noise density, and so on. For Europe-Asia TWSTFT link, NIM earth station need to arrange the transmission power close to PTB station, so that we can get a better RMS for data. The BPSK code rate of Europe-Asia TWSTFT link is 2.5Mch/s, the carrier-to-noise density reach to 55dBHz, 1pps jitter is lower than 500ps. Figure 1 shows the TWSTFT earth station of NIM.

At present, according to the pre-determined schedule, the laboratories of Europe-Asia TWSTFT link communicate once per-hour, and work 12 hours everyday. When the communicate work finish, we will process the raw data, recorded by modem, to a quadratic fit results and report to BIPM. The purpose of this format is to reduce the amount of data to be exchanged and to be able to report in one data file session results of one laboratory involving different partner stations and different satellite links. Data from more than one day may be reported in a single file. Such files allow clock differences to be calculated in an easy way.

Figure 2. the GPS antenna of NIM

There are several GPS time and frequency transfer receiver in NIM, such as septentrio, EURO160, NovAtel and so on. We also have an self-devoloped GPS time and frequency transfer receiver which has been proved to have a good performance. The TWSTFT and GPS time and frequency transfer receiver both contribute to the UTC calculate and submit compative data to BIPM everyday.

Figure 2 shows the GPS antenna array of NIM.

Figure 3. the TWSTFT and GPS control system of NIM

Figure 3 shows the TWSTFT and GPS control system in NIM laboratory.

III. THE COMPARATIVE RESULT OF NIM TWSTFT SYSTEM

The time reference of the NIM earth station is UTC(NIM). According to the schedule, the Europe-Asia TWSTFT link works from 10:30 to 22:59(UTC time) everyday. At first, from 10:30 to 10:40, the clean carrier will be transmitted, and after that, the time modulation signal will be transmitted. Every laboratory will communicate with each other once per-hour, the length of the period is 5 minute.

Figure4 shows the time difference(by TWSTFT) and frequency stability of NIM and PTB, NIM and TL, NIM and NICT, respectively. The experiment date is from MJD55930 to MJD56200. It is shown that Europe-Asia TWSTFT link is stable.

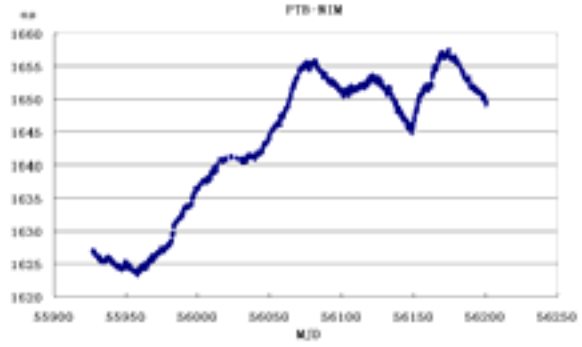

(a) Time difference between PTB and NIM

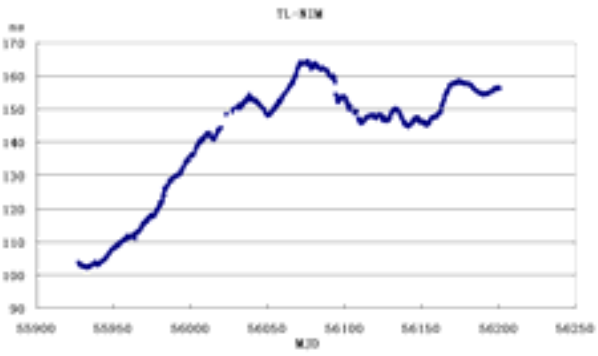

(b) Time difference between TL and NIM

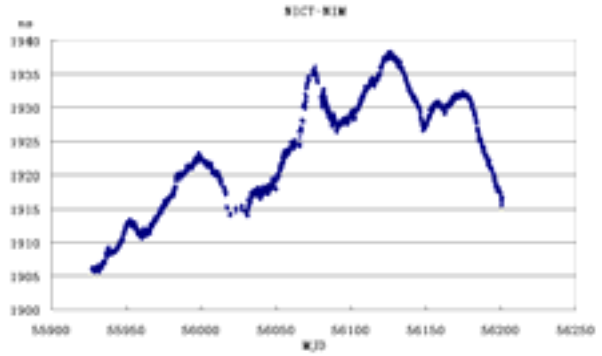

(c) Time difference between NICT and NIM

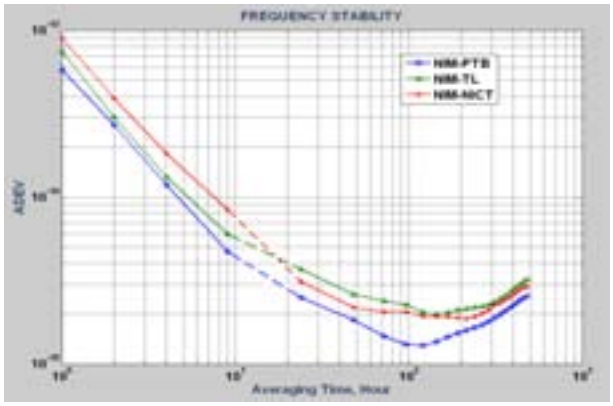

(d) The frequency stability of TWSTFT between NIM and PTB,TL,NICT

Figure 4. Experimental result of NIM by TWSTFT

Table Ⅰ summarizes the frequency stability of NIM and PTB, NIM and TL, NIM and NICT; it is shown that the one day frequency stability is better than 5×10^{-15}.

TABLE I. FREQUENCY STABILITY OF EUROPE-ASIA TWSTFT LINK

link	days			
	1	2	4	10
PTB-NIM	2.6E-15	1.9E-15	1.4E-15	2.0E-15
TL-NIM	3.8E-15	2.6E-15	2.3E-15	2.5E-15
NICT-NIM	3.1E-15	2.2E-15	2.1E-15	2.4E-15

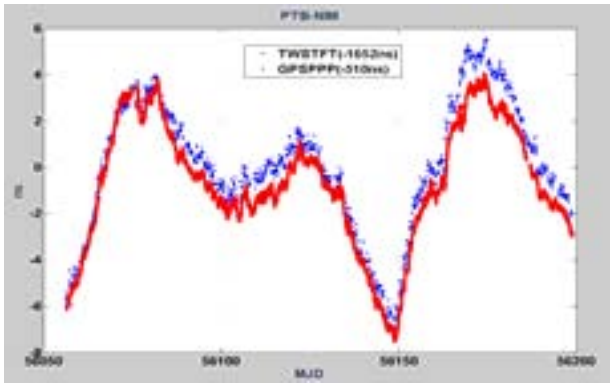

Figure 5. TWSTFT and GPS experimental result of PTB and NIM

Figure5 is TWSTFT and GPS time transfer experimental result of PTB and NIM, include GPS PPP and TWSTFT techniques. It is shown that the two time transfer techniques results are consistent.

IV. THE CALIBRATION RESULT OF TWSTFT

As we introduced before, the time and frequency transfer GPS receiver and transfer link was calibrated. We did time and frequency transfer experiment between PTB and NIM use both TWSTFT and GPS time transfer system, process the experiment data and get the time difference of them, so the TWSTFT Link is calibrated by GPS at NIM. The time difference between PTB and NIM was shown in Fig 6. The calibration result is shown in Fig 7, the experiment period is from MJD56143 to MJD56166. It is shown that the time difference of TWSTFT and GPS is about 1648ns, the calibration uncertainty is 5ns.

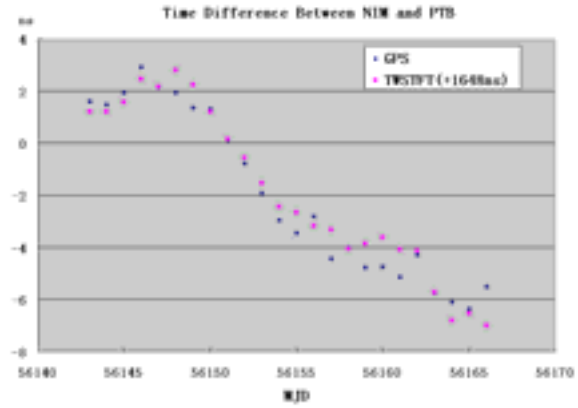

Figure 6. The time difference between PTB and NIM

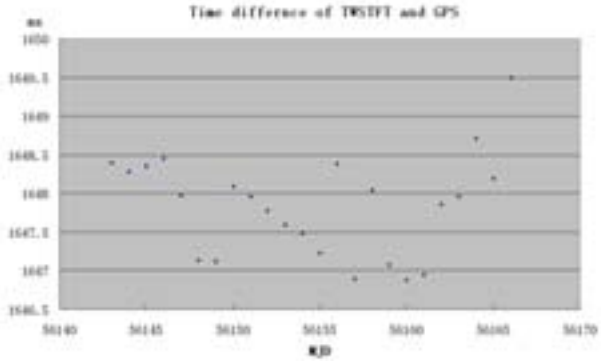

[11]

Figure 7. The calibration result of TWSTFT by GPS, the experiment period is from MJD56143 to MJD56166

V. CONCLUSIONS

The NIM01 TWSTFT earth station was established in year 2008, and participate the Europe-Asia TWSTFT link. But the TWSTFT system of NIM was not be calibrated, We research on the calibration technique of NIM TWSTFT Link by GPS time transfer system which have been calibrated. We did time and frequency transfer experiment between PTB and NIM use both TWSTFT and GPS time transfer system, process the experiment data and get the time difference of them. The calibration result shown that the time difference of TWSTFT and GPS is about 1648ns, the calibration uncertainty is 5ns.

REFERENCES

[1] Kirchner D 1991 Two-Way Time Transfer Via Communication Satellites Proc. of the IEEE 79 983-989

[2] D. W. Hanson, Fundamentals of Two-Way Time Transfer by Satellite, 43rd Annual Frequency Control Symposium, pp. 174-178, 1989

[3] Guinot B and Arias E F 2005 Atomic time-keeping from 1955 to the present Metrologia 42 S20-S30

[4] Piester D, Bauch A, Breakiron L, Matsakis D, Blanzano B, Koudelka O, 2008, Time Transfer with nanosecond accuracy for the realization of International Atomic Time, Metrologia, 45, 185-198.

[5] H. T. Lin et al., "The first two-way time transfer link between Asia and Europe", Proc. of 35th PTTI, pp. 71-79, 2003.

[6] H. Maeno et al., "Establishment of a TWSTFT link between Asia and Europe connecting NICT and PTB", Proc. of 20th EFTF, pp. 575-579, 2006.

[7] M. Fujieda et al., "Long Baseline TWSTFT Between Asia and Europe", Proc. of 38th Annual Precise Time and Time Interval (PTTI) Meeting, pp. 499-511, 2006.

[8] ITU Radiocommunication Sector 2003 The operational use of two-way satellite time and frequency transfer employing PN codes Recommendation ITU-R TF.1153-2 (Geneva, Switzerland)

[9] ITU Radiocommunication Sector 2002 ITU Handbook on Satellite Communications (3rd edition, Geneva, 2002) Section 2.3, Chapter 2 and Section AN2.1, Annex 2

[10] ITU Radiocommunication Sector, Recommendations ITU-R 524, ITU-R S.580, ITU-R S.725, ITU-R S.726, ITU-R S.728, and ITU-R S.729

Precision Analysis of Non-continuous Two-way Satellite Time Comparison

WEI Pei, YANG Xu-hai, GUO Ji, LI Zhi-gang, QIN Wei-jin
National Time Service Centre
Chinese Academy of Sciences
Xi′an, China
weipei10@ntsc.ac.cn

WEI Pei, YANG Xu-hai, GUO Ji, LI Zhi-gang, QIN Wei-jin
Key Laboratory of Precision Navigation and Timing Technology
Chinese Academy of Sciences
Xi′an, China

WEI Pei, QIN Wei-jin
University of Chinese Academy of Sciences
Beijing, China

Abstract—**As one of the high accuracy time comparison methods, Two-way Satellite Time and Frequency Transfer (TWSTFT) is one of the important methods for Bureau International des Poids et Mesures (BIPM) to organize international comparison, calculation of the International Atomic Time (TAI) and Coordinated Universal Time (UTC). Due to the interference of emitting device of TWSTFT to co-located devices of Very Long Baseline Interferometry (VLBI) or International GNSS Service (IGS) and the limitation of satellite transponder resources, the comparison is not proceed continuously. Ten consecutive days of data from C-band TWSTFT Network of National Time Service Center (NTSC) was used for analyzing the precision of non-continuous TWSTFT. The raw data of non-continuous TWSTFT was dealt with linear interpolation method. Then the result was compared with continuous TWSTFT which was seen as the true value. Finally, the influence of interval to the precision of non-continuous TWSTFT was analyzed. The comparison shows that: when the interval time is less than 2.5 days, the RMS of the difference between non-continuous and continuous TWSTFT is better than 1 ns; when the interval time is 0.5 day, the RMS is better than 0.5 ns.**

Keywords- TWSTFT; accuracy; stability

I. INTRODUCTION

As a kind of high-precision time comparison method, Two-Way Satellite Time and Frequency Transfer (TWSTFT) is the primary technique of time and frequency transfers which is used by Bureau International des Poids et Mesures (BIPM) for international time comparison [1]. Due to the symmetric signal transmission path, important sources of error such as the atmospheric delay effect can be counteract, therefore high accuracy can be obtained.

In this method, the atmospheric delay effect can be naturally eliminated since the transmit path is symmetric, thus increase the overall system accuracy. Currently, TWSTFT may be performed with 0.5 to 0.75 ns in accuracy and 0.2 ns in stability [2].

Since early 1999, TWSTFT has been used for Coordinated Universal Time (UTC) and International Atomic Time (TAI) generations. United States, Europe and Asia have formed TWSTFT networks. National Time Service Center (NTSC) participated in the Asia-Pacific TWSTFT network [3], and establishes TWSTFT links with PTB, VSL, IEN, OP, and other European timing laboratories. Moreover, NTSC formed C-band TWSTFT (TW(C)) network for continuous TWSTFT between five stations in China.

TWSTFT need to rent satellite transponders, but the transponder resource is limited, and the cost is expensive. Recently, co-locational observations with multi-methods become a trend. To construct the Very Long Baseline Interferometry (VLBI) station, International GNSS Service (IGS) station, TWSTFT station co-locationally has many advantages, such as saving the atomic clock resources and management costs. But TWSTFT need to emit signal to satellite, it will interfere the electromagnetic environment of other co-locational devices.

Due to the above reasons, the international TWSTFT is generally not consecutive. Such as the link between NTSC and National Institute of Information and Communications Technology (NICT), the official convention comparison runs 30 min, twice a week. The clock difference is obtained through interpolation [3]. In order to improve the accuracy of TWSTFT, BIPM runs TWSTFT more and more frequently: before 2004, the number of measurements was 3 points per week; since 2004, the number of measured points increased to 4 points per day; since October 2005, it increased to12 points per day in Europe-Asia area; since November 2005, it increased to 24 points per day in Asia-Pacific area [4].

TWSTFT organized by BIPM runs between timing laboratories. However, for Cs clocks or H clocks using in general engineering, the study on the difference between non-continuous and continuous TWSTFT is still on open discussion.

This work was carried out with the support of the National Natural Science Foundation of China (Grant Nos. 11033004 and 11173026).

Cs clocks and H clocks was used as time source for TWSTFT in this paper to determine the reliability of non-continuous TWSTFT in general engineering application. Interpolated results of different intervals non-continuous TWSTFT was compared with continuous TWSTFT.

For above reasons, this paper has analyzed the main error sources of TW(C), and then carried out experiment using data from TW(C) network.

II. MAIN ERROR SOURCES OF TW(C)

Fig. 1 shows the principle of TWSTFT. Station A and Station B are at the same level. The clock signal of Station A is modulated and emitted to the satellite. After receiving the signal transferred by the satellite transponder, B station demodulates the signal, and then compares with the local clock to measure the time difference between Station A and B. The process of Station B is same with Station A [1].

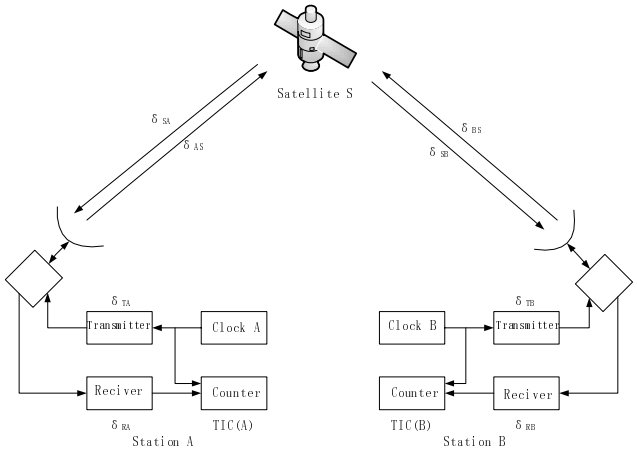

Figure. 1 Principle of TWSTFT.

TWSTFT is calculated as follows [5]:

$$TIC(A)=t_A-t_B+\delta_{TB}+\delta_{BS}+\delta_{SBA}+\delta_{SA}+\delta_{RA}+S_B \quad (1)$$

$$TIC(B)=t_B-t_A+\delta_{TA}+\delta_{AS}+\delta_{SAB}+\delta_{SB}+\delta_{RB}+S_A \quad (2)$$

Where t_A and t_B are time-scales, *TIC(A)* and *TIC(B)* are time interval readings, δ_{TA} and δ_{TB} are transmitter delays (including the modem delays), δ_{RA} and δ_{RB} are receiver delays (including the modem delays), δ_{AS} and δ_{BS} are signal path uplink delays, δ_{SA} and δ_{SB} are signal path downlink delays, δ_{SAB} and δ_{SBA} are satellite path delays through the transponder, S_A and S_B are Sagnac corrections.

Geometric path delay, ionospheric delay, tropospheric delays are included in up and down link delay [6]:

$$\delta_{AS}=(|\boldsymbol{r}_S-\boldsymbol{r}_A|)/c+\delta^{ion}_{AS}+\delta^{tro}_{AS} \quad (3)$$

$$\delta_{SB}=(|\boldsymbol{r}_B-\boldsymbol{r}_S|)/c+\delta^{ion}_{SB}+\delta^{tro}_{SB} \quad (4)$$

$$\delta_{BS}=(|\boldsymbol{r}_S-\boldsymbol{r}_B|)/c+\delta^{ion}_{BS}+\delta^{tro}_{BS} \quad (5)$$

$$\delta_{SA}=(|\boldsymbol{r}_A-\boldsymbol{r}_S|)/c+\delta^{ion}_{SA}+\delta^{tro}_{SA} \quad (6)$$

Where $\boldsymbol{r}_S$, $\boldsymbol{r}_A$ and $\boldsymbol{r}_B$ are the position vectors of satellite and stations, δ^{ion}_{AS}, δ^{ion}_{SB}, δ^{ion}_{BS} and δ^{ion}_{SA} are the ionospheric delays, δ^{tro}_{AS}, δ^{tro}_{SB}, δ^{tro}_{BS} and δ^{tro}_{SA} are the tropospheric delays, c is the speed of light in vacuum.

Herein transmission path is considered as symmetrical. So it can be considered that the geometric path delay and tropospheric delay of SA and AS, SB and BS are the same, satellite path delays through the transponder are also same. There are:

$$(|\boldsymbol{r}_S-\boldsymbol{r}_A|)/c+(|\boldsymbol{r}_B-\boldsymbol{r}_S|)/c=(|\boldsymbol{r}_S-\boldsymbol{r}_B|)/c+(|\boldsymbol{r}_A-\boldsymbol{r}_S|)/c \quad (7)$$

$$\delta_{SAB}=\delta_{SBA} \quad (8)$$

$$\delta^{tro}_{AS}=\delta^{tro}_{SA} \quad (9)$$

$$\delta^{tro}_{BS}=\delta^{tro}_{SB} \quad (10)$$

Herein that Sagnac corrections of uplink and downlink have equal value but opposite sign [7], so there is:

$$S_A=-S_B \quad (11)$$

From (1) to (11), we can obtain:

$$t_{AB}=t_A-t_B=[(TIC(A)-TIC(B))+\delta_{ion}+(\delta_{TA}-\delta_{TB})+(\delta_{RB}-\delta_{RA})]/2+S_A \quad (12)$$

Where t_{AB} is the clock difference between Station A and B which is unknown; *TIC(A)* and *TIC(B)* are time interval readings which can be obtained; δ_{TA}. δ_{TB}, δ_{RA} and δ_{RB} can be measured in advance; ionospheric delays δ_{ion} and Sagnac correction S_A can be calculated.

$$\delta_{ion}=\delta^{ion}_{AS}+\delta^{ion}_{SB}-\delta^{ion}_{BS}-\delta^{ion}_{SA} \quad (13)$$

S_A can be by accurately calculated by (14) [7,8]:

$$\delta_{Sagnac}=(\omega_e/c)R(r+h)cos(LA(e))cos(LA(s))sin(LO(s)-LO(e)) \quad (14)$$

Where ω_e is the Earth's rotation angular velocity, r is the radius of the Earth, R is the radius of the satellite orbit, *LA(e)* is latitude of the station, *LO(e)* is longitude of the station, h is height of the station, *LA(s)* is latitude of the satellite, *LO(s)* is longitude of the satellite.

Commonly, the GEO satellite is assumed to be stationary to the Earth. However, the trace of its nadir is actually changed cyclically, which affects the Sagnac correction calculation. Since the effect of the movement of GEO satellite on Sagnac correction calculation is on the level of 10^{-2} ns [9], it needs not to be considered during a sub-nanosecond time comparison.

Since the uplink and downlink signals of TW(C) differ in carrier frequency, they experience a different ionospheric delay. The total electron content (TEC) maps provided by IGS were used in ionospheric error correction in this paper [10]. TEC maps are at fixed time and geographic grid. The TEC of pierce point at requisite time is calculated by spatial four grids interpolation algorithms and proper two linear interpolation algorithms [11]. Slant TEC (STEC) can be calculated with proper mapping function, and then ionospheric delay Δ_{ion} can be calculated through (15).

$$\Delta_{ion}=(40.3\cdot STEC)/(c\cdot f^2) \quad (15)$$

Where f is carrier frequency. Since the carrier frequency of uplink and downlink are different, ionospheric delay cannot be offset. The ionosphere effect on C-band is about (0~0.5) ns range, it must be considered for time comparison at sub-nanosecond level [12].

III. TEST METHODS AND TEST RESULTS

The data used in this paper is from June 10th to June 19th, 2005. (DOY: 161-170), the reading of the time counter was recorded every second. The GEO satellite used in the experiment was Sinosat-1 telecommunication satellite (110.5°E). The ground stations were NTSC and Shanghai Astronomical Observatory (SHAO). The code rate was 20 MChips. The carrier frequency of uplink was 6.3 GHz, which of downlink was 4.1 GHz. The clock of NTSC was a HP5071A Cs atomic clock, and a SONH H atomic clock was equipped in SHAO.

Fig. 2 and Fig. 3 show the Sagnac correction and the ionospheric delay respectively during experiment.

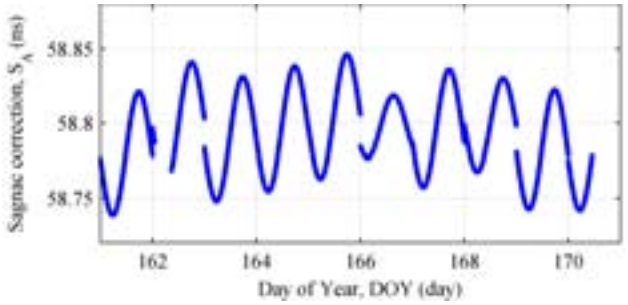

Figure. 2 Sagnac correction of TW(C).

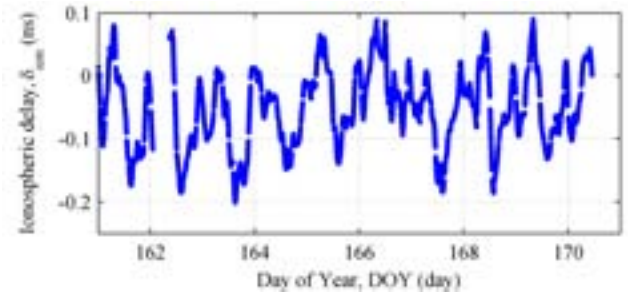

Figure. 3 The affect of ionosphere on TW(C).

The data is collected every other 0.5,1, 1.5, …… 8.5, 9 days. Each observation lasts for 1 hour and sampled 3600 data points. After interpolation processing, non-continuous TWSTFT was compared with continuous TWSTFT to find out the effect of interval on TWSTFT. Fig. 4 shows the result of continuous TWSTFT, Fig. 5 shows residuals δ of linear fit.

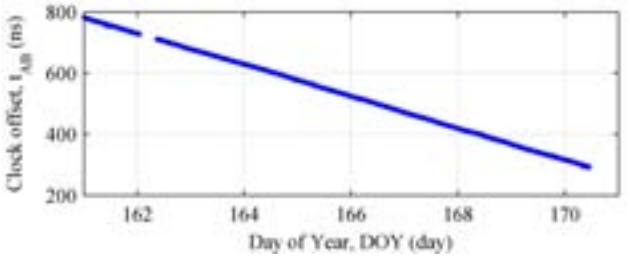

Figure. 4 Clock offset between Station A and B.

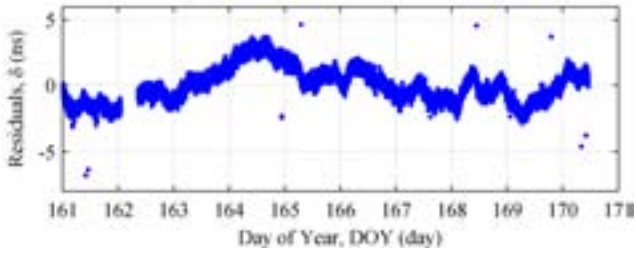

Figure. 5 Linear fit residuals of the clock offset between Station A and B.

In TAI generation, linear interpolation is used for TWSTFT. Jiang [4, 13] compared 9 kinds of smoothing-interpolation techniques by comparing to the GPS PPP as a reference. It concludes that a high-order interpolation method is better for the simple linear interpolation and the Vondrak smoothing interpolation with a filtering power of 10^5 gives the best result in most cases. In this paper, the difference between Vondrak smoothing interpolation with a filtering power of 10^5 recommended in [13] and linear interpolation was less than 0.01ns, and can both achieve the best performance when adopting different observation intervals. The improvement of Vondrak smoothing interpolation was not clear. Therefore, the traditional linear interpolation method was used in this paper. Evaluation of non-continuous TWSTFT with continuous TWSTFT is calculated as (16):

$$t^{diff}_{AB}=t^{nc}_{AB}-t^{c}_{AB} \quad (16)$$

Where t^{nc}_{AB} is the interpolation result of non-continuous TWSTFT, t^{c}_{AB} is the result of continuous TWSTFT, t^{diff}_{AB} is the difference between the 2 kinds of method.

T is the interval (*T=0.5, 1, 1.5, …… 8.5, 9 day(s)*), with every measurement lasting 1 hour (about 3600 sample points). The difference between continuous TWSTFT and non-continuous TWSTFT with different intervals is shown in Fig. 6.

Dark colored points are the measured data of non-continuous TWSTFT without interpolation. t^{diff}_{AB} of this part is 0. With the increase of the observation interval, the extent of t^{diff}_{AB} deviation from the 0 also increases. Table 1 and Fig. 7

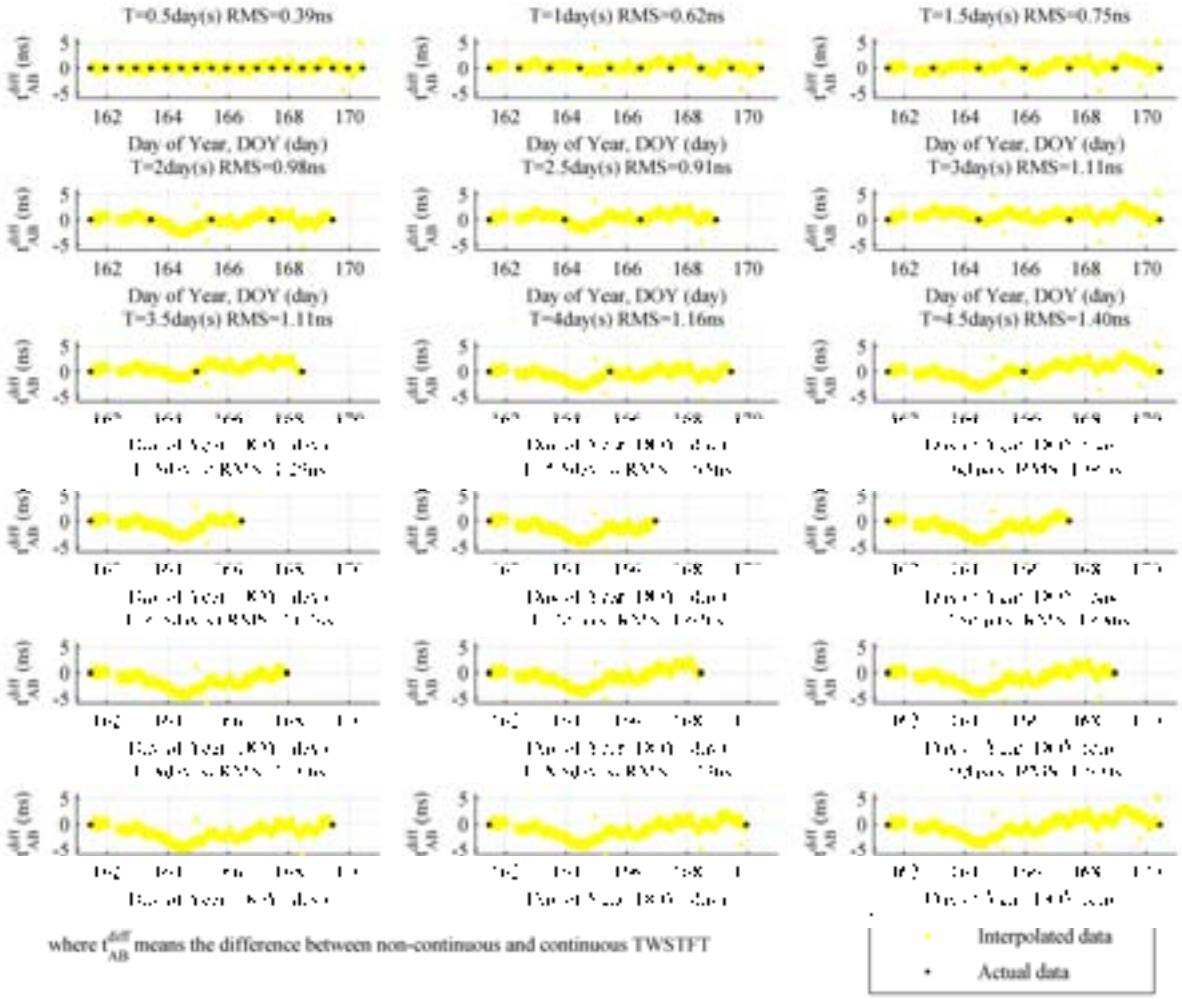

Figure. 6 The difference between continuous TWSTFT and non-continuous TWSTFT with different intervals.

depict the relationship between t^{diff}_{RMS} and the interval. where t^{diff}_{RMS} is the RMS of t^{diff}_{AB}.

Table 1 Statistically analysis for t^{diff}_{AB}.

Interval (day(s))	Max	Min	Mean	RMS
0.5	5.34	-4.22	0.04	0.39
1	5.36	-4.17	0.22	0.63
1.5	5.49	-4.56	0.30	0.75
2	2.93	-5.32	-0.26	0.98
2.5	3.71	-4.36	0.35	0.92
3	5.55	-4.32	0.87	1.12
3.5	3.31	-2.57	0.60	1.11
4	2.70	-5.53	-0.63	1.16
4.5	5.57	-4.21	0.12	1.40
5	2.77	-4.16	-0.75	1.29
5.5	1.58	-5.47	-1.55	1.95
6	2.09	-5.12	-1.11	1.67
6.5	1.42	-5.91	-1.61	2.08
7	2.94	-5.16	-0.82	1.63
7.5	2.46	-5.44	-0.98	1.68
8	1.50	-6.20	-1.62	2.10
8.5	2.57	-5.67	-0.97	1.73
9	5.55	-5.19	-0.38	1.60

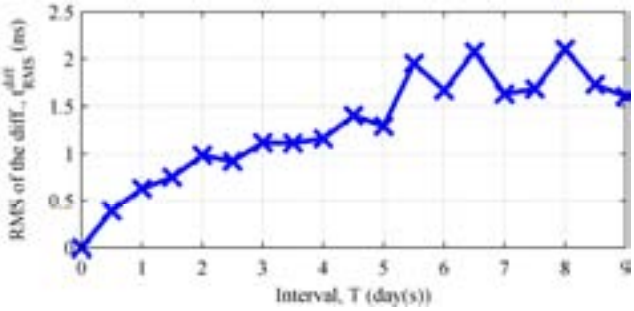

Figure. 7 The affect of interval T on t^{diff}_{RMS}.

IV. CONCLUSION

The RMS of the difference between non-continuous and continuous TWSTFT is positive correlative with the observation interval (cf. Fig. 7). When the interval is less than 2.5 days, the RMS of the difference between non-continuous and continuous TWSTFT is better than 1 ns; when the interval is 0.5 day, the RMS is better than 0.5 ns. In this paper, the accuracy will decline less than 1 ns with the interval being less than 2.5 days; In order to guarantee the reduction of accuracy being better than 0.5 ns, the observation interval should be no more than 0.5 days.

REFERENCES

[1] Li Zhigang, Li Huanxin, Zhang Hong. Reduction for the Two-way Satellite Time and Frequency Transfer [J]. Acta Astronomica Sinica, 2002, 43(4): 422-431.

[2] Li Xiaohui, et al. The precise measurement of time and frequency signal [M]. Science Press, 2010.

[3] Zhang Hong, Li ZhiGang, Li HuanXin. Measurement of the Stability of TWSTFT between NTSC and NICT [J]. Journal of Astronautic Metrology and Measurement, 2007, 27(3).

[4] Z. Jiang. Smoothing and interpolation techniques for a TW measurement series in TAI calculation. working document TWSTFT /13-09/, presented at the 13th Meeting of the TWSTFT (15-16 Nov. 2005).

[5] ITU Radiocommunication Sector, "The operational use of two-way satellite time and frequency transfer employing pseudorandom noise codes." Geneva, Switzerland, Recommendation ITU-R TF.1153-3, 2010.

[6] Wu Wenjun, Li Zhi-ang, Yang Xuhai, Lei Hui, Chen Xuan, Feng Chugang. Satellite Orbit Determination and Time Transfer Based on TWSTFT[C]. Frequency Control and the European Frequency and Time Forum (FCS), 2011 Joint Conference of the IEEE International.

[7] Wu Wenjun, Li Zhigang, Yang Xuhai, Lei hui, Chen Liang, Cheng Xuan, Feng Chugang. Sagnac Effect on Two-Way Satellite Time and Frequency Transfer [J]. Journal of Astronautics,2012,33(7):936-941.

[8] Yang Xuhai, Li Zhigang, Li Huanxin. Calculation of sagnac effect in two way satellite time and frequency transfer [J]. Chinese Journal of Scientific Instrument, 2006,S1:502-507.

[9] Wu Wenjun, Li Zhigang, Yang Xuhai, Ren Xiaoqian, Chen Liang, Lei Hui, Feng Chugang. A New Method for Satellite Motion Correction in TWSTFT[C]. Frequency Control Symposium (FCS), 2012 IEEE International.

[10] Yang Xuhai, Li Zhigang, Wu Fenglei, Li Xiaohui. Two-Way Satellite Time and Frequency Transfer Experiment via IGSO Satellite[C]. Frequency Control Symposium (FCS), 2007 Joint with the 21st European Frequency and Time Forum, IEEE International.

[11] Wu Wenjun, Li Zhigang, Li Xiaohui, Yang Xuhai, Kong Yao, Lei Hui. The Application of IGS Ionosphere Product in TWSTFT. Journal of Astronautic Metrology and Measurement, 2012,32(4):51-54.

[12] Yang Xu-hai, Li Zhi-gang, Hua Ai-hui. Analysis of Two-Way Satellite Time and Frequency Transfer with C-Band[C]. Frequency Control Symposium, 2007 Joint with the 21st European Frequency and Time Forum, IEEE International.

[13] Z Jiang. Interpolation of TW time transfer from measured points onto standard MJD for UTC generation. Proc. EFRF, 2010.

The Study on Centralized Disposing Mode Timekeeping Algorithm of Autonomous Running of Navigation Constellation

Qin weijin, Sun baoqi, Yang xuhai, Guo ji, Wei pei
National Time Service Center, Chinese Academy of Sciences
Xi'an, China
qwj@ntsc.ac.cn

Qin weijin
University of Chinese Academy of Sciences
Beijing, China
qwj@ntsc.ac.cn

Qin weijin, Sun baoqi, Yang xuhai, Guo ji, Wei pei
Key Laboratory of Precision Navigation and Timing,
Chinese Academy of Sciences
Xi'an,China

***Abstract*—The building algorithm of system time is one of the research focus of auto-navigation. This paper bases on centralized processing mode of auto-timekeeping, gives a kind of building algorithm of system time. On-board clock's weight are determined by the clock quantity which referring to the computation, change of clock velocity can reflect change of clock frequency, so it uses clock velocity instead of clock frequency for determining weight; this algorithm uses two kinds of method of predicting initial velocity: a. with the former two epochs each satellite of each day predict initial velocity, b. with the former two epochs each satellite of first day predict initial velocity. Choosing one clock as the main clock, according to defined sample interval, getting all the available clock error relative to the main clock. This paper gives the computation model of system time, testing the algorithm with IGS precise clock error(system time is IGST). The result shows: comparing to the equal weighted algorithm, the weighted algorithm has better stability. Adding prediction has a significant improvement on the system time's stability, method a: the difference between TA(weight) and TA(IGST) (International GNSS Service Time) is about 45ns, method b: the difference be-tween TA(weight) and TA(igst) (International GNSS Service Time) is about 65ns. The algorithm is in reason, it can be used for the building algorithm of system time of auto-navigation.**

Keywords-autonomous running; system time; navigation constellation; weight algorithm

I. INTRODUCTION

The basis of determining orbit and positioning of satellite is building and sustaining of system time. The basic observation of inter-satellite is distance. The trans-mitting distance of signal is velocity multiply time. Due to light velocity is 10^8, so the microsecond error can cause hundred meters error. The inter-satellite ranging of two way of radio is relatively observation, only to determine relatively clock error of inter-satellite, the absolute clock error is got by comparing to the system time. So we should build system time in order to determine the change of satellite clock relative to system time.

This paper places emphasis on the research of system time which bases on the in-ter-satellite links.

II. THE GENERATION PRINCIPLE OF SYSTEM TIME UNDER THE AUTONOMOUS RUNNING MODE

There are two kinds working mode of autonomous timekeeping of navigation satellite: centralized processing mode and distributed processing mode. The working principles of centralized processing mode: selected one satellite as the main star, inter-satellite ranging and communicating by the way of TDMA, other satellites send the observations to the main star, the relative clock error of satellite regard as the known input which is measured by inter-satellite link[1]. The time scale is established by the algorithm of atomic time. Comparing distributed processing mode, centralized processing mode can get system time easily. Based on the centralized processing mode, this paper advances the building algorithm of system time[2]. With the deviation of each satellite clock relative to the atomic time, then sends the parameter results of clock error to each satellite by communication links so that it can update the navigation information.

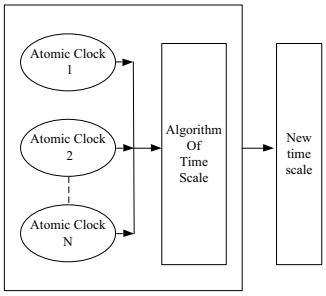

Figure 1. combinated timescale of on-board clocks

III. THE CALCULATION MODEL OF SYSTEM TIME OF CENTRALIZED PROCESSING MODE

The calculation model of system time of centralized processing mode is expressed as[3-5]:

$$TA(t) = \sum_{i=1}^{N} w_i(t) \sum_{i=1}^{N} w_i(t) h_i(t) \qquad (1)$$

$h_i(t)$ is the reading of each atomic clock, i = 1,2, • • • N, when the weight of clock i changes or the atomic clock's number of involved in the calculation changes, adding prediction in order to ensure the continuity of time scale. $h_i^{'}(t)$ is a corrective prediction, so the formula (1) can be rewritten as formula(2):

$$TA^{'}(t) = \sum_{i=1}^{N} w_i(t) \sum_{i=1}^{N} w_i(t)(h_i(t) - h_i^{'}(t)) \qquad (2)$$

The formula of corrective prediction is expressed as:

$$x_i(t_0) = TA(t_0) - h_i(t_0) \qquad (3)$$

$$h_i^{'}(t) = x_i(t_0) + y_i^{'}(t)(t - t_0) \qquad (4)$$

t_0 is the calculated moment, $y_i^{'}(t)$ is the deviation which clock i relative to the calculated time scale, or the velocity of clock i relative to the calculated time scale. Solving $x_i(t_0)$ and $y_i^{'}(t)$ is the course of epoch-wise conducting.

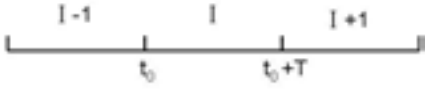

Figure 2. Epoch simple figure

choose $h_m(t_j)$ as the main clock, i=1,2,m…n, we obtain the difference between each clock and reference clock in t_j.

$$x_{im}(t_j) = h_i(t_j) - h_m(t_j) \qquad (5)$$

So we can get the calculation formula of system time of centralized processing mode:

$$x_m(t_j) = \sum_{i=1}^{N} w_i(t) \sum_{i=1}^{N} w_i(t)\{h_i^{'}(t_j) - x_{im}(t_j)\} \qquad (6)$$

$x_m(t_j)$ is the clock error which is obtained by new time scale.

3.1 The clock velocity determination

Clock velocity is obtained by linear fitting, or computed by two points:

$$y_i^{'} = \frac{x_i(t_n) - x_i(t_1)}{t_n - t_1} \qquad (7)$$

3.2 The weight determination

We use the algos weighted principle of BIPM (International rights bureau). The change of clock velocity can reflect the change of clock frequency.

This paper uses the velocity instead of frequency for determining weight. So the improved weight formula is expressed as:

$$p_i = 1 / std(y_i^{'})^2 \qquad (8)$$

In the calculation course, if we give the better clock too much weight, the time scale has too much dependence on better clock. We should restrict the weight in order to avoid the problem happening,. So we advences the maximum weight principle. Becasuse the choosing principle of maximum weight of on-board clock is not ripe, we all use the choosing principle of ground-clock:

$$w_{max}(t) = A / N \qquad (9)$$

A is an experience constant, BIPM uses 2.5, N is the clock number of involved in the calculation. When the weight exceeds the maximum, we should normalize the weight. The solution of $w_i(t)$ and $y_i^{'}(t)$ is not fixed, method changes with the da-ta changes.

IV. EXAMPLE ANALYSIS

In order to validate the rationality of algorithm, this paper downloads the data of on-board clock from IGS website, the sampling interval is 5 minutes, then carry out the simulation. Data arces from 2011.1.1 to 2011.3.1, there are 19 satellites which covering all the sampling points in the 60 days, the same sampling number assures the continuity and integrality of data and rationality of determining weight. The figure of inter-satellite as follows:

Figure 3. the figure of building inter-satellite link

All the running state of satellite involving calculating don't change in sixty days.

TABLE I. THE TYPE OF GPS ON-BOARD CLOCK(2011.1.1-3.1)

PRN	2	5	7	8	9	11	13	14	16	17
Clock type	Rb	Rb	Rb	Cs	Cs	Rb	Rb	Rb	Rb	Rb
Launch date	06 NOV 2004	17 AUG 2009	15 MAR 2008	06 NOV 1997	26 JUN 1993	07 OCT 1999	23 JUL 1997	10 NOV 2000	29 JAN 2003	26 SEP 2005
PRN	18	19	20	22	23	25	28	29	31	
Clock type	Rb	Rb	Rb	Rb	Rb	Rb	Rb	Rb	Rb	
Launch date	30 JAN 2001	20 MAR 2004	11 MAY 2000	21 DEC 2003	23 JUN 2004	28 MAY 2010	16 JUL 2000	20 DEC 2007	25 SEP 2006	

The work support by the National Natural Science Foundation Of China: the research of time transfer of GPS precise common view(No:11173026)

In order to reduce calculative burden, resampling the time interval of five minutes to the time interval of one hour. Due to the effect of measuring noise、multiple-path effect and device time-delay, the precision of relative clock error of inter-satellite link don't reach the precision of IGS clock error. So adding 1ns random noise to simulation data.

This paper chooses the PRN 05 as the reference clock, validating the algorithm from following strategy:

TABLE II. PROCESSING STRATEGY

scheme	Determine initial value of clock velocity	Determine weight	
No prediction	no	equal	weight
prediction	with the former two epochs each satellite of each day predict initial value	equal	weight
	with the former two epochs each satellite of first day predict initial value	equal	weight

4.1 The system time's algorithm without satellite prediction

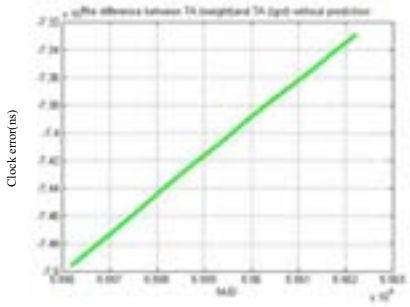

Figure 4. the difference between TA(weight) and TA(igst) without prediction

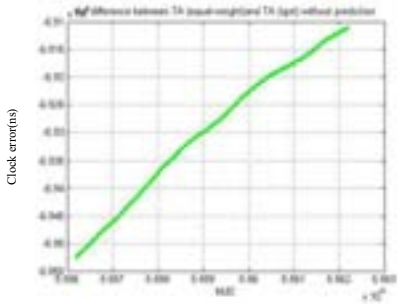

Figure 5. the difference between TA(equal-weight) and TA(igst) without prediction

Figure 4 and 5 shows distinct linear excursion without prediction, the difference between TA(weight) and TA(igst) is 1800ns, the difference between TA(equal-weight) and TA(igst) is 450ns.

4.2 The system time's algorithm with satellite prediction

This paper uses two methods for predicting initial clock velocity:

A: with the former two epochs each satellite of each day,

B: with the former two epochs each satellite of first day.

4.2.1 With the former two epochs each satellite of each day predict initial velocity

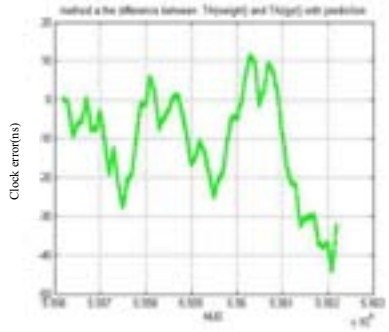

Figure 6. method a:the difference between TA(weight) and TA(igst) with prediction

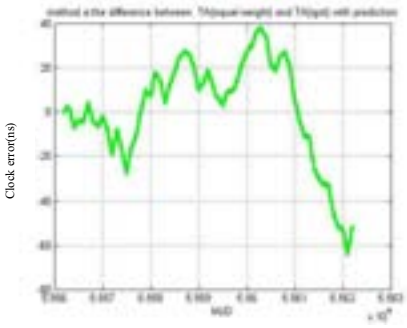

Figure 7. method a:the difference between TA(equal-weight) and TA(igst) with prediction

4.2.2 With the former two epochs each satellite of first day predict initial velocity

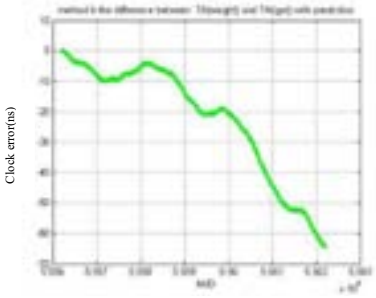

Figure 8. method b:the difference between TA(weight) and TA(igst) with prediction

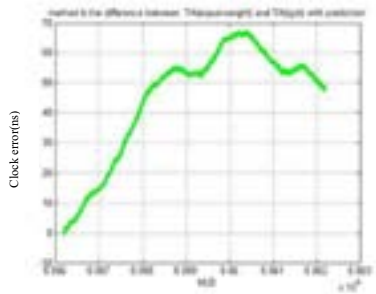

Figure 9. method b:the difference between TA(equal-weight) and TA(igst) with prediction

Figure 6-9 shows: the four figures remove linear excursion with the prediction. Method a: the difference between TA(weight) and TA(igst) is 42ns, equal is 65ns. Method b: the difference between TA(equal-weight) and TA(igst) is 65ns, equal is 68ns. The results show: the prediction method of former two epochs of each satel-lite of each day is better than the former two epochs of each satellite of first day.

4.3 Stability analysis

The designing principle of system time is obtaining the best stability[6-8]. Compare stability of system time with Hadamard deviation. Using former two epochs of each satellite of each day predicting initial velocity, it validate stability of system time from equal weight and weight[9-10].

Figure10 shows the figure of Hadamard variance of PRN05, other satellites are similar to the PRN05. It is not list for limited space. It can know: weight algorithm is more stable.

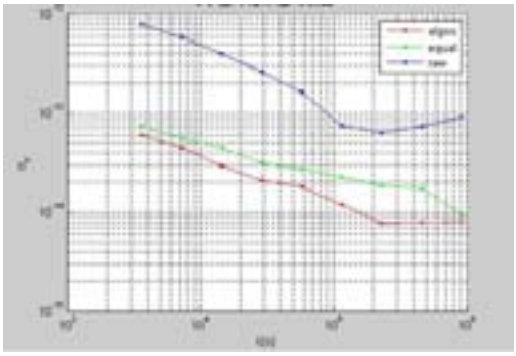

Figure 10. the Hadamard variance of three kinds of system time

V. CONCLUSION

This paper advances the building algorithm of system time of autonomous running mode.

The conclusions as follows:

(1) Prediction considers prior information of epoch-wise satellite clock, it ensures continuity and rationality of built time scale;

(2) This algorithm gives two kinds of method for predicting initial velocity:

A: former two epochs of each satellite of each day;

B: former two epochs of each satellite of first day.

The system time of Method a is more stable than method b. The reason is that: the first method considers long running condition, which is a continuous course, the second considers short running condition, which is a non-continuous course.

(3) The equal algorithm ignores the advantage and disadvantage of satellite clock so that the built system time is not ideal. The weight algorithm con-siders the advantage and disadvantage of satellite clock. Relatively, the built system time is stable and reliable. From equal algorithm and weight algorithm we know: Do not exist best algorithm of system time. We should design proper algorithm according to the intention.

REFERENCES

[1] Wu Haitao, Time Fundament of Satellite navigation system[M], 50-53.Science Press.

[2] H.Bernstein, Y.Chank, R.Frucholz and A.Wu, GPS satellite timing performance using the autonomous navigation [J], ION98b, 1998, 1705-1712.

[3] Qi Guanrong, Fundamentals of Time Science Higher Education Press, P60-62.

[4] D.W.Allan and T.K. Peppler, Ensemble Time and Frequency Stability of GPS Satellite Clocks, Proc.1988 IEEE Freq.Cont.Symp,1998,465-467.

[5] Ananda M.P, Bernstein H. Global positioning system autonomous navigation[A]. In Proceedings of IEEE Position, Location and Navigition Symposium, Las Vegas,Nevada.[C], March20-23.1990:497-508.

[6] Epstein M, Dass T. Management of phase and frequency for GPS IIRsatellites[C]. Pro-ceedings ofthe 33th Annual Precise Time and Time Interval (PTTI)Meeting, 2001.

[7] Digital Simulation and Dynamic Prediction Model of an Transact ions on Ultrasonics, Ferroelectrics, and Frequency Control,UFFC- 34, 647-654.

[8] D Piester, A Bauch, L Breakiron et. Al. Time transfer with nanosecond accuracy for the realization of International Atomic Time[J].Metrologia.2008,45(2): 185-198.

[9] Parkinson B W, Spilker J J. Global Positioning Syst em: Theory and Applicat ions (Vol. I) [M] . Published by the American Institute of Aeronauti cs and Astronaut ics, Inc. Washington, DC, 1996: 149-159.

[10] YUAN Haibo et al. Dynamic grey-autoregressive model of an atomic clock, Metrologia, 2008, 45(6).

Research On Pseudo-range Measurement Technique for CMMB system

Changjiang Huang
National Time Service Center of Chinese Academy of sciences
Xi'an , China
Key Laboratory of Precision Navigation and Timing Technology, NTSC, CAS
Xi'an , China
University of Chinese Academy of Sciences
Beijing , China
huangcj@ntsc.ac.cn

Yonghui Hu
National Time Service Center of Chinese Academy of sciences
Xi'an ,China
Key Laboratory of Precision Navigation and Timing Technology, NTSC, CAS
Xi'an , China

Huijun Zhang
National Time Service Center of Chinese Academy of sciences
Xi'an ,China
Key Laboratory of Precision Navigation and Timing Technology, NTSC, CAS
Xi'an , China

Jianfeng Wu
National Time Service Center of Chinese Academy of sciences
Xi'an ,China
Key Laboratory of Precision Navigation and Timing Technology, NTSC, CAS
Xi'an , China

***Abstract*—According to the frame structure of CMMB, A method of pseudo-range measurement with the aid of disciplined sequences for CMMB is proposed on the basis of simulating frame synchronization, carrier synchronization and sampling clock synchronization. The method adopts the pseudo-random code tracking technique and implements pseudo-range measurement on CMMB system. The simulation results show that carrier frequency offset error is less than 1e-13 and the pseudo-range measurement error is less than 6 meters when the sampling rate is 60 MHz.**

Keywords—CMMB, carrier synchronization, pseudo-range measuerment

I. INTRODUCTION

The technology of China Mobile Multimedia Broadcasting (CMMB), which has been the multimedia broadcasting standard of small-size portable electronic equipments, is winning favor of more and more users. With the development of CMMB, many research institutes and their staffs are focusing on mobile location technique by CMMB signal. CMMB, which has the advantage of a fewer station amounts and a less period of building stations because of the structure of Single Frequency Network (SFN) adopted in the ground supplementary stations, is especially suitable for navigation enhancing application to enhance and supplement the demand of GNSS navigation and orientation in China. CMMB, which adopts Orthogonal Frequency Division Multiplexing (OFDM) modulation technique, can improve largely location precision because of its favorable anti-multipath performance in the frequency selective fading channels and multi-path fading channels [1].

In signal framing structure of CMMB， both identical synchronization sequences in every beach and the continual pilots in all OFDM symbols can be used to capture and track the received signal. In the process of Pseudo-range measurement, coarse symbol timing in the time domain is carried out, and then the fraction part (F_D) and the integer part (F_I) of frequency offset are separately estimated and corrected. F_D is less than half of the sub-carrier spacing, and F_I is a multiple of the sub-carrier spacing. At last, with tracking and correcting of the sampling frequency offset in real time, the frequency offset from Doppler effects is decreased effectively.

After symbol timing and frequency synchronization, we can achieve the cross correlation between the Pseudo-random sequence of received signals and local corresponding Pseudo-random sequence in a receiver. At the same time, we track the Pseudo-random sequence by code tracking loop and achieve the time difference and pseudo-range between the base station and the receiver by the correlation peak value.

II. METHOD OF PSEUDO-RANGE MEASUREMENT

To measure Pseudo-range between a base station and a receiver in CMMB system, frequency offset must be captured , tracked and corrected in the first place, and then the sampling clock is synchronized to correct the remainder frequency offset, in the mean time, symbol timing is carried out and tracked by delay-locked loop (DLL) to measure precisely the pseudo-range.

A. frequency offset capture

Frequency offset capture includes F_D estimation which is written as $\hat{F}_D$ and F_I estimation whose value is written as $\hat{F}_I$. F_D can destroy the orthogonality among the sub-carriers and result in Inter Carrier Interference(ICI), and it can be calculated by maximum-likelihood (ML) method[2,3]. By means of the correlation of both identical OFDM disciplined

Project supported by "Western Light Talents training program of CAS" (Y305YZ1301 and "Scientific Research Equipment Development Project of CAS" (YZ201218 (Y307YR1301))

sequences with 2048 sampled values, a correlator is used to calculate the correlation of the 2048 sampled values between the selected current window and the anterior window, when the window moves continually, the coarse symbol timing is found once the correlation peak value exceeds the specified limit. The correlator can be written as:

$$Corr(n)=\sum_{k=0}^{2047} r_n(k)\cdot conj(r_n(k+2048)) \quad n=-l.....l \tag{1}$$

Where r_n is the received signal sequence, $Corr(\theta)$ is the maximum value among all the correlation values which are larger than the specified limit, and the corresponding r_θ is the synchronization sequence in the beacon, and its first sampling value is the starting position of the window. As a result, we can achieve $\hat{F}_D$ which can be written as:

$$\hat{F}_D=\frac{1}{2\pi}\arctan\frac{\mathrm{Im}\left[\sum_{k=\theta}^{\theta+2047} r_\theta(k)\cdot r_\theta^*(k+2048)\right]}{\mathrm{Re}\left[\sum_{k=\theta}^{\theta+2047} r_\theta(k)\cdot r_\theta^*(k+2048)\right]} \tag{2}$$

In a general way, after finishing the symbol timing and F_D estimation and correction, F_I is estimated [4,5]. According to the perfect characteristic of self-correlation and cross-correlation of Pseudo Random Noise (PRN) code which is demodulated by OFDM (IFFT), a correlator is used to calculate the correlation between the local sequence which is corrected by m times sub-carrier spacing and the received sequence which is corrected by $\hat{F}_D$. The integer m is adjusted continually till the correlating peak is found. The correlator can be written as:

$$sync(n)=s_l(n)\cdot\exp(\frac{-j2\pi m}{2048}) \tag{3}$$
$$k=0,1,...,2047, m=-\max,...,\max$$

Where max is specified frequency scan ranges. It is supposed that the correlating peak occurs when local signal is corrected by N times sub-carrier spacing, $\hat{F}_I$ is the algebraic product of the N and the sub-carrier spacing. Finally, both $\hat{F}_D$ and $\hat{F}_I$ are sent to the carrier numerical controlled oscillator (NCO) to finish coarse frequency synchronization.

B. frequency offset tracking

Because of Doppler effects and the instability of the oscillator, the frequency offset must be tracked in the frequency domain to finish estimating and correcting the remainder frequency offset F_d in time after finishing estimating and correcting the coarse frequency offset. In this paper, to estimate the remainder frequency offset, an effective method is used as follows [6,7]:

$$\hat{F}_d=\frac{1}{2\pi}\arctan\frac{Im\left(\sum_{k=0}^{N_b-1} Y_k'\cdot Y_k^*\right)}{Re\left(\sum_{k=0}^{N_b-1} Y_k'\cdot Y_k^*\right)} \tag{4}$$

Where Y_k is received sequence, $\hat{F}_d$ is the fraction part of frequency offset fine estimation.

All the factors such as the multi-path channel, noises, estimation errors, time delay in circuits result in large fluctuation of F_D [9]. So F_d must be corrected to make the frequency offset error which is the difference of F_d and $\hat{F}_d$ vary slowly near zero, F_d can be corrected by the F_d fine correcting model which can be given in Fig.1.

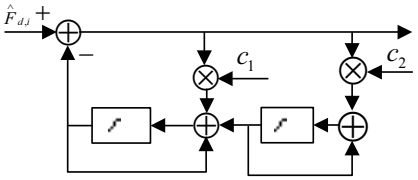

Figure 1. F_d fine correcting model

The filter coefficient c_1 and c_2 can be expressed by the freedom frequency $W_n=2\pi f_n/f_s$ and the attenuation factor η, where f_s is the sampling frequency in a disperse time system. $c_1=4\pi f_n/f_s$, $c_2=4\pi^2(f_n/f_s)$. When the model works stably, W_n and η should be satisfied with $2\eta\geq W_n$, that is $\eta\geq\pi f_n/f_s$. The bigger the value of η is, the shorter the oscillating time, but the smaller the noise attenuation extent, and the bigger the noise. So generally let η equal to the numerical value near 0.5. The value of f_n should be selected properly.

C. sampling clock synchronization

In synchronous sampling system, the joint estimation for the carrier frequency offset and sampling clock frequency offset by pilot symbols are used mostly in the frequency domain to achieve the sampling clock frequency offset estimation.[9,10] Therefore, the symbol timing error contains information about the sampling clock frequency offset. It is supposed that the sampling period is T_s, and the integer part of symbol timing offset is T_d, the fraction part is Δt, the length of the symbol is T_u, the phase deflection of K^{th} sub-carrier is ϕ_k, initial phase difference is ϕ_0, the algebraic addition of the sampling clock offset and the fraction part of frequency offset is τ, then the phase offset of k_1^{th} and k_2^{th} sub-carrier in j^{th} symbol is as follows:

$$\Delta\phi_{k21}(j)=\Delta k/T_u\times 2\pi\times\left[T_d+\Delta t(j)\right] \tag{5}$$

The phase offset between two pilots in one symbol is the function of frequency difference Δk between two pilots and

the normalized symbol timing error $[T_d + \Delta t(j)]/T_s$, where T_u is equal to NT_s.

The total timing error within the same symbol is expressed as follows:

$$\hat{\tau}_{k2,1}(j) = \frac{T_d + \Delta t(j)}{T_s} = \frac{N}{2\pi} \times \frac{\Delta\phi_{k2,1}(j)}{\Delta k} \tag{6}$$

Because of using amounts of pilots, its average is expressed as follows:

$$\hat{\tau}(j) = \frac{1}{L-1} \cdot \frac{N}{2\pi \cdot \Delta k} \sum_{n=1}^{L-1} \Delta\phi_{kn+1,n}(j) \tag{7}$$

The integer part of this average corresponds to the integer part of symbol timing errors, and the fractional part corresponds to the sampling clock frequency offset.

D. Pseudo-range Measurement Principle

The destination of pseudo-range measurement for CMMB system is to seek signal propagation time from the base station to the receiver, consequently to calculate the distance. The signal synchronization determines the pseudo-range measurement precision. Because of the noise interference, not only the top of correlation peak of synchronization sequence has a section of flat segment, but the rising and falling edges of the related triangle are not monotone, so large errors exist in the symbol timing. However, these errors can be tracked by code phase with the help of digital Delay-locked loop (DLL) technique. Fig.2 describes the block diagram of DLL module.

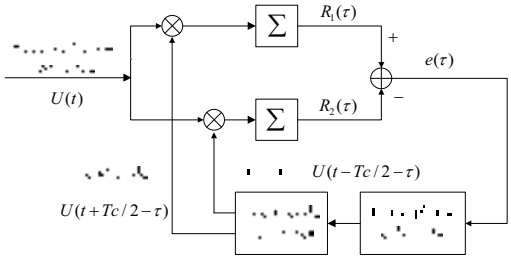

Figure 2. Block diagram of DLL module

During the measurement process, a correlator is used to find the correlation peak between the local and the received synchronization sequence bearing pseudo-random binary sequence demodulated by OFDM, and to finish coarse symbol timing. In the DLL of a receiver, the error control signal which is the difference of lead code and lag code produced by the receiver performs the code tracking by controlling code phase. Because this error control signal increases or decreases monotonously near zero, it is easy to achieve accurate symbol timing and pseudo-range measurement accuracy.

III. SIMULATION RESULT AND ANALYSIS

A. Fraction part of frequency offset Estimation simulation

The F_D estimation algorithm is simulated to assess its performance. In simulation, according to the GY/T 220.1-2006, the channel coding and modulation of synchronization sequence is generated. Fig.3 is the curves of limited representative F_D estimation errors. In the curves whose scope of the carrier frequency offset is in $(-\Delta f_b/2, \Delta f_b/2)$, the abscissa is the specified carrier frequency offset, and the ordinate is the F_D estimation error.

As can be seen from the curves that the residual frequency offset estimated by this algorithm is less than one percent of total fraction part of frequency offset.

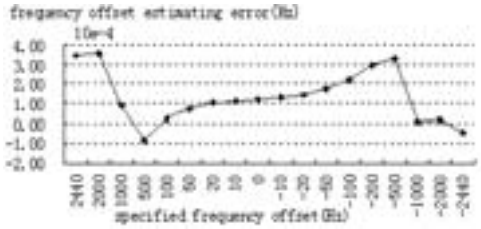

Figure 3. Curves of the fraction part of frequency offset estimation errors

B. Interpart of frequency offset Estimation simulation

Fig.4 is the effect diagram of the F_I estimation in simulation system whose local signal frequency is deviated from the actual frequency for one time of sub-carrier spacing. In Fig.4, (a) shows the correlated effect between the actual signal and local signal not corrected, and (b) shows that of actual signal and local signal corrected by one time of sub-carrier spacing. As can be seen from the diagram that actual signal is not correlated with the local signal before corrected by the integer part of frequency offset. Actually, after only finishing frequency offset correction, local signal and actual signal have maximum correlation peak.

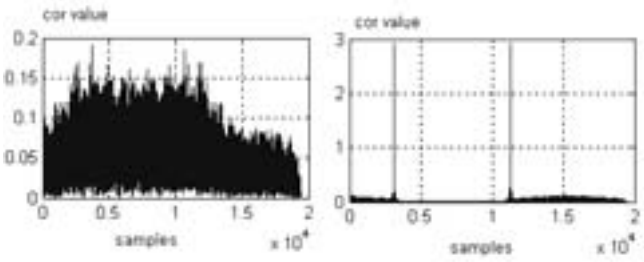

（a）not corrected by the integer part of frequency offset （b）corrected by the integer part of frequency offset

Figure 4. Eeffect diagram of the integer part of frequency offset estimation

C. frequency offset tracking simulation

In simulation, we let $f_n = 1.0e-6$, $f_s = 6e7$, $\eta = 0.5$, and track frequency offset after corrected by $\hat{F}_D$ and $\hat{F}_I$ to estimate and analyze the estimation error. Fig.5 is $\hat{F}_d$ error tracking curves. As can be seen from the curves that frequency offset estimation error after corrected by $\hat{F}_d$ converges quickly. And the estimation error changes slowly near zero.

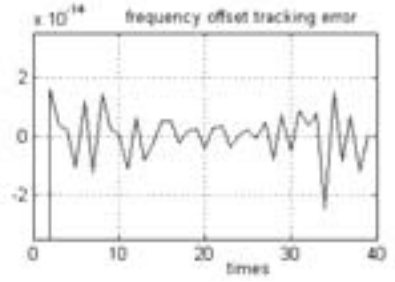

Figure 5. Tracking curves of the fraction part of frequency offset fine estimation

D. pseudo-code tracking and pseudo- range measurement

After coarse symbol synchronization and frequency offset correction, residual frequency offset is vary small, DLL is used to perform code tracking and achieve accurate symbol timing and pseudo-range measurement. In simulation, lag code gets behind lead code for 6 sampling value which is the length of one code chip, and the sampling rate is 60MHz。The simulation result shows in Fig.6, where "*" stands for the simulation wave diagram of lead code, "--" stands for that of instant code, "+" stands for that of lag code, and "o" stands for that of the difference between lead and lag code.

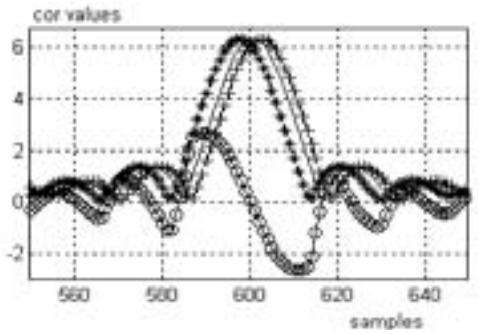

Fig.6 Diagram of DLL tracking

As can be seen from the diagram that the difference between lead and lag code has the largest change rate and a minimum of noise near zero when the instant code is correlated with the local code. It is very sensitive to control the phase of tracking code by the difference signal, so we can track precisely the phase of received code and the symbol starting position to measure precisely the pseudo-range.

IV. CONCLUSION

The traditional single carrier pseudo-range measurement tech- nique cannot be used directly in CMMB system because OFDM technique is applied. In this paper, according to the characteristic of CMMB signal, we capture and track the carrier frequency offset, estimate and correct the fraction part, the integer part of frequency offset and sampling clock frequency offset by virtue of the disciplined sequence in CMMB signal, and then further track and correct the remain frequency offset. On the basis of frequency offset correction, we use a DLL to track the pseudo-range measurement errors. Simulation results show that frequency offset tracking error is smaller than 10^{-13} Hz and pseudo-range measuring accuracy is smaller than 6 meters when the sampling rate is 60 MHz. The pseudo-range measuring method is satisfied with the measuring requirement for CMMB system.

V. ACKNOWLEDGMENT

The authors thank Yuanyuan Gao for many stimulating discussions and part simulation work during the early stages of the project leading to this paper. Thanks everyone of Project 'digital television positioning' of Timing Method and Technology Department, NTSC, CAS for their hard work. Finally thanks Professor Yu Hua for his persevering and meticulous guidance.

REFERENCES

[1] China's State Administration for Radio, Film and Television, GY/T 220.1-2006 Mobile Multimedia Broadcasting[S], 2006. (in Chinese).

[2] Mao Jianhui, Hei Yong, and Qiao Shushan. "Design of frequency and sampling clock synchronization for CMMB system"[J]. Beijing:micro-computer information,vol.24, No.8-3, 2008. (in Chinese) .

[3] Bo Ai, Jian-hua Ge and Yong Wang, "Frequency offset estimation for OFDM in wireless communications", IEEE trans. Consumer Electronics. Vol.50, No.1, pp:73-75. Feb.2004.

[4] Marco Luke, Ruggero Reggiannini. "Carrier frequency acquisition and tracking for OFDM systems". IEEE trans. Commun. Vol.44, No.11, pp.1590-1598. Nov. 1998.

[5] Jan-Jaap van de Beek, Magnus Sandell and Per Ola Borjesson. "ML estimation of time and frequency offset in OFDM systems". IEEE trans. Signal processing. Vol.45, No.7, pp.1800-1805, July.1997.

[6] Ai Bo, Wang Jintao and Zhong Zhangdui. "Synchronization technology for OFDM system". [M].Beijing: Posts & Telecommunications Press. April 2011.(in Chinese).

[7] Timothy M. Schmidl and Donald C. Cox, "Robust frequency and timing synchronization for OFDM". IEEE trans. commun. Vol.45, No.12, pp.1613- 1621, Dec.1997.

[8] Paul H.MQose, "A technique for orthogonal frequency division multi-plexing frequency offset correction". IEEE trans.Commun. vol.42, No.10, pp.2908-2914, Oct.1994.

[9] Tiejun Lv and Jie Chen. "ML Estimation of timing and frequency offset using multiple OFDM symbols in OFDM systems". GLOBECOM, pp.2280- 2284, 2003.

Real-Time Remote Calibration (RTRC) System for Time and Frequency

LIANG Kun, ZHANG Aimin
Division of Time and Frequency Metrology
National Institute of Metrology, NIM
Beijing, China
liangk@nim.ac.cn

ZUO Fei, PEI Chao
School of Electronics and Information Engineering
Beijing JiaoTong University
Beijing, China

ZHANG Side
Beijing Trust GPS Science&Technology Development Co., Ltd
Beijing, China

***Abstract*—Based on GNSS time and frequency transfer receiver of NIMTFGNSS-1 type, real-time remote calibration has been studied, and one new type of real-time remote calibration system named RTRC has been designed and implemented. The users who should be authorized can use RTRC(including one local NIMTFGNSS-1 receiver) to check and get real-time (16-minute latency) and historical data of remote calibration for their time scales and frequency standards on the web throughout the internet. Calibration uncertainties of the system for time and frequency have been evaluated as 6 ns and 2e-14 averaging one week respectively. For the user who has no time scale or frequency standard and needs either or both of them which time or frequency should be traced to UTC(NIM), National Time and Frequency Primary Standard of China, NIM can provide one low-cost rubidium clock as the accessory of NIMTFGNSS-1 receiver to make up one time scale disciplined by UTC(NIM) in real-time, its time and frequency stability averaging one day could be better than 5 ns and 3e-14 separately.**

Keywords-time and frequency; remote calibration; GNSS; atomic clock

I. INTRODUCTION

GNSS(Global Navigation Satellite System), especially GPS is one of the most useful tools for time and frequency transfer. With the quick development of GLONASS(GLObal Navigation System), BDS(Beidou Navigation Satellite System) and Galileo, GNSS time and frequency transfer becomes the more and more significant research direction. GNSS takes us the convenience of remote calibration for time and frequency. With the techniques of modern network communication, remote calibration base on GNSS time and frequency transfer in real-time is feasible.

At NIM (National Institute of Metrology, Beijing, China), real-time remote calibration(RTRC) system has been developed, and it is able to provide the timing users remote time and frequency measurement and calibration service in real-time for local time and frequency reference, and helps the metrology and timing laboratory to keep the local reference highly accurate and precise for the purposes of scientific research and metrology by remotely measuring the tiem difference between local reference and UTC(NIM)(at Changping campus) in real-time. It is easy for users to log on the website and check the real-time and historical time and frequency difference and some of their statistics.

II. DESIGN AND IMPLEMENTATION

The scheme of RTRC is illustrated as follows in Fig. 1. Each user who uses RTRC will receive one GNSS time and frequency transfer receiver of NIMTFGNSS-1[1] type(NIMGNSS-1 for short) and client software that performs the measurements and sends the instant results to RTRC central server for data storage and processing via internet. RTRC uses GNSS system as the common-view reference. NIMTFGNSS-1 and the central server are two main parts of RTRC. For user, the interface is shown in Fig. 2.

In processing, the system uses the data that are the same to CGGTTS REFSYS data of two stations every 16 min. Two stations may be the reference station NIM with UTC(NIM) and one user, or the two users. The time difference between two stations is calculated by processing of RTRC central server in real-time and the real-time or historical difference can be displayed on the webpage whenever the user logs on the RTRC web site.

If the user has no time and frequency standard, one UTC(NIM) disciplined rubidium clock with one NIMTFGNSS-1 by RTRC link can be combined as one UTC(NIM) disciplined oscillator, named NIMDO, which is provided to the user as his or her local time and frequency standard and has the advantage in the performance over GPSDO(GPS Disciplined Oscillator)[2,3]. The similar former research is NISTDO, and some detailed information can be found in [2] and [3]. NIMDO has the legal and direct traceability to UTC(NIM); its time and frequency accuracy and stability has been improved thanks to the high level reference time scale and time scale algorithm.

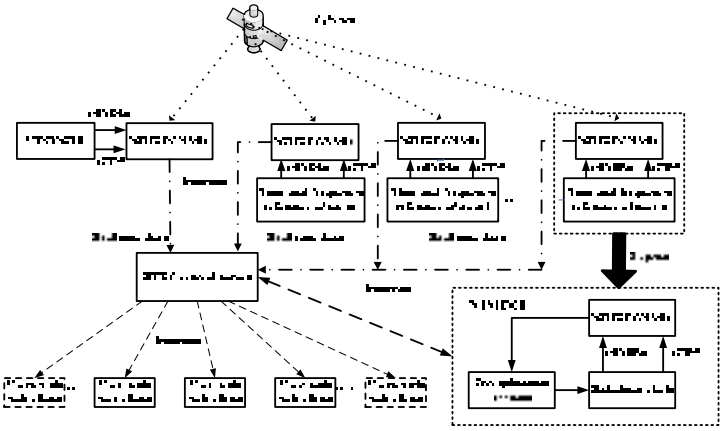

Figure 1. System scheme of RTRC

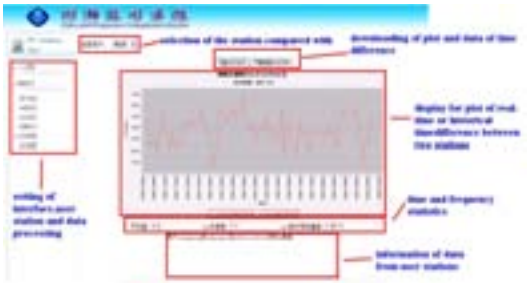

Figure 2. User interface of RTRC

III. Experiment Setup and Numric Results

Four kinds of experiments have been done for performance verification and evaluation of RTRC and NIMDO.

A. CCD(Common Clock Difference) Experiment

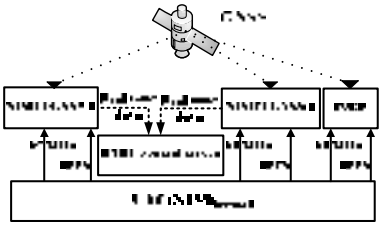

Figure 3. Schematic diagram 1

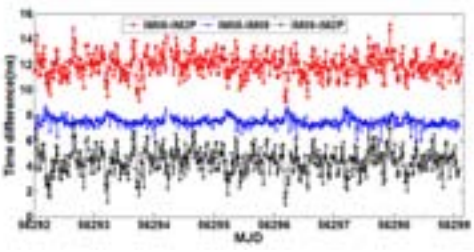

Figure 4. Results in the CCD experiment

To verify the noise level of RTRC system, the CCD experiment should be implemented. Three receivers IM08 and IM09(NIMTFGNSS-1), and IM2P(Septentrio PolaRx2eTR receiver) with the same time and frequency reference $UTC(NIM)_{hepingli}$(one cesium clock with one micro-stepper steered by UTC) at Hepingli campus of NIM, were involved in the experiment described in Fig. 3.

From Fig. 4, the standard deviations of CCD results for one week using the links of IM08-IM2P, IM08-IM09 and IM09-IM2P are 0.9 ns, 0.4 ns and 1.0 ns respectively. IM08 and IM09 have the excellent coherence with each other. Another reason for much smaller standard deviation for IM08-IM09 is that IM2P located very near to $UTC(NIM)_{hepingli}$ in the second floor is at least 20 meters far away from IM08 and IM09 located in the fourth floor, and we use more than 20 meters length radio cable for connection of two location. RTRC system uses the CGGTTS(CCTF Group on GNSS Time Transfer Standards) data indeed, so we use P3 code CGGTTS data of each link for demonstration of RTRC link noise level by post-processing.

B. Zero Baseline Experiment with the Different References

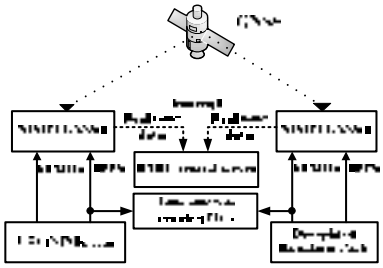

Figure 5. Schematic diagram 2

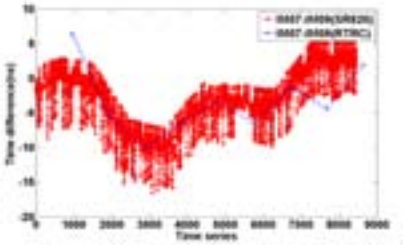

Figure 6. Comparison between RTRC and direct measurement

In Fig. 5, IM07(NIMTFGNSS-1) and IM08 at Hepingli campus with the reference to UTC(NIM)$_{hepingli}$ and the disciplined rubidium clock respectively were used to verify the calibration performance of RTRC, and in the meantime, for comparison, one local TIC(time interval counter, SRS SR620 type) was operated to measure the time difference between UTC(NIM)$_{hepingli}$ and NIMDO every second. The P3 code measurement every 16 min by RTRC is acquired from data downloading function of the system.

From Fig. 6, the trend of RTRC link agrees with that of direct measurement by TIC.

C. Long Baseline Experiment

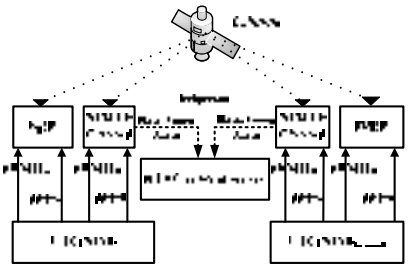

Figure 7. Schematic diagram 3

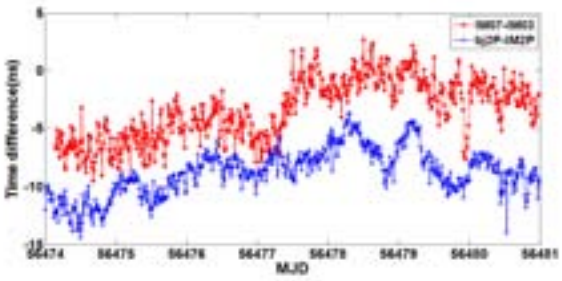

Figure 8. Comparison of two links in long baseline

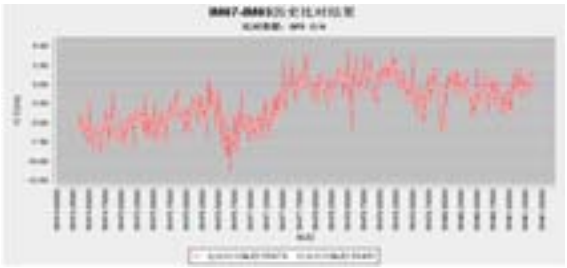

Figure 9. Real-time results by RTRC in long baseline

To show the calibration effect of RTRC directly, long baseline experiment has been implemented as shown in Fig. 6. The baseline between Hepingli campus and Changping campus is about 40 km. IM07 and IM2P referenced to UTC(NIM)$_{hepingli}$ are at Hepingli campus; IM03 and bj2P(Septentrio PolaRx3eTR receiver) referenced to UTC(NIM) are at Changping campus. The scheme of the experiment is described in Fig. 7.

Fig. 8 and 9 show the time difference between UTC(NIM)$_{hepingli}$ and UTC(NIM) with the links of IM07-IM03 by P3 code CGGTTS files, IM2P-bj2P by P3 code CGGTTS files and IM07-IM03 by C/A code measurements of RTRC in real-time from MJD 56474 to 56480. We see the quite similar results and correspondence with one another of three links. The standard deviations of time difference for three links are 1.5 ns, 1.0 ns and 1.4 ns separately. IM07 is located in the fourth floor that makes UTC(NIM)$_{hepingli}$ used for the reference of IM07 more noisy, and corresponds to the plots in Fig. 8 and 9.

D. NIMDO Performance Verification

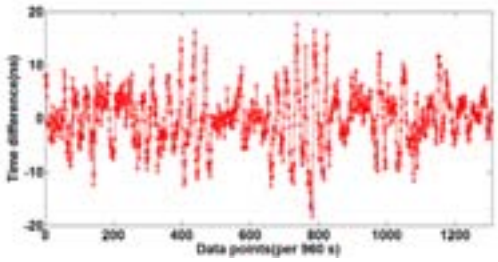

Figure 10. Time difference of NIMDO from UTC(NIM)

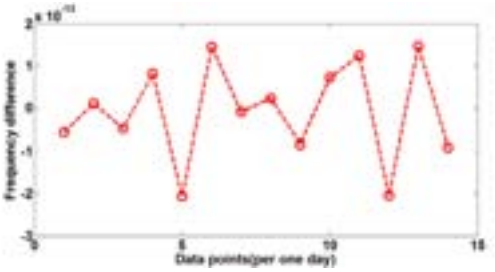

Figure 11. Frequency difference of NIMDO from UTC(NIM)

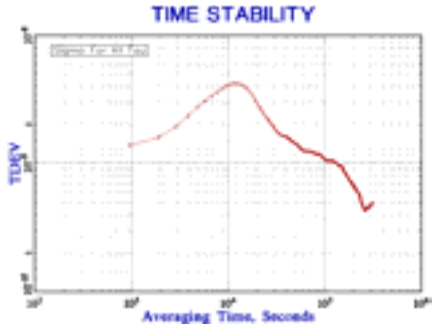

Figure 12. TDEV of NIMDO referenced to UTC(NIM)

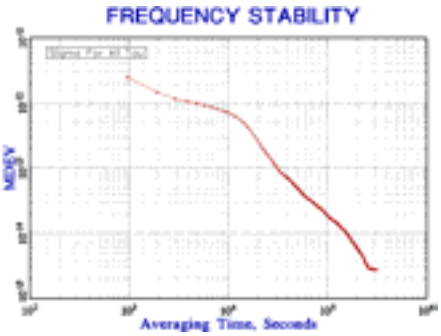

Figure 13. MDEV of NIMDO referenced to UTC(NIM)

The phase of the undisciplined rubidium clock is arbitrary and hasn't the good frequency stability because the big frequency drift. As well, the frequency accuracy would be worse and worse. For example, the direct measurement of one rubidium clock by one phase comparator for several days, its frequency stability (modified Allan deviation(MDEV)) for averaging time one hour and one day are 1.4×10^{-12} and 3.5×10^{-12} respectively, and the frequency accuracy is 1.1×10^{-10}.

Referenced to UTC(NIM), using the time difference data of about 15 days for the sampling interval 960 s by RTRC, frequency differences averaging one day were calculated, and we can reach preliminarily that in most situations the time and frequency accuracy of NIMDO could separately be within 10 ns and 1e-13 averaging one day as shown in Fig. 10 and 11; the time and frequency stability(time deviation(TDEV) and MDEV) averaging one day could be better than 5 ns and 3e-14 respectively illustrated in Fig. 12 and 13. The long frequency stability of the rubidium clock has been ameliorated due to the real-time and short latency steering to UTC(NIM).

IV. Uncertainty Analysis

Estimating the calibration uncertainty of RTRC involves evaluating the uncertainties using both Type A and Type B methods. In Type A method, we use statistical analysis by directly calculating the jitter (standard deviation) of measurement results for the link between two NIMTFGNSS-1 in the CCD experiment, and we can use the standard deviation of CCD results(0.4 ns for P3 code) shown in section 2, however, for GNSS C/A and P3 code measurements, 1.5 ns and 0.7 ns would be used usually by BIPM, and we choose the bigger one. Uncertainty evaluated by type B method, such as some theoretical analysis based on the experience, theory or authorized specification and manual, mainly includes several items as follows.

A. Calibration Uncertainty of GNSS Time and Frequency Transfer Receiver

Calibration uncertainty of GNSS time and frequency receiver using the differential method by BIPM is 5 ns, in generally. If two GNSS time and frequency transfer receivers have been calibrated, and the calibration uncertainty should be cancelled by most part of 5 ns, so the compound standard uncertainty of the time transfer link between two GNSS time and frequency transfer receivers should be less than 5.5 ns.

B. Propagation Errors

The standard uncertainty components due to ionospheric and tropospheric errors are 0.3 ns and 0.7 ns respectively which are valid for baselines up to 5000 km[4]

C. Delay Error of Cables and Converters

Evaluated by type B method, the standard uncertainty component due to the cables and the converters calibrated by VNA could be less than 0.1 ns.

D. Combined Uncertainty and Its Expension

The combined uncertainty u_c and its expension U_c can be obtained by (1) and (2) in table I.

$$u_c = \sqrt{{u_A}^2 + {u_B}^2} \tag{1}$$

$$U_c = k \cdot u_c \tag{2}$$

TABLE I. Uncertainty Budget

Source	Type	Uncertainty (ns)	
		C/A code	*P3 code*
Measurement jitter of GNSS time transfer link between two receivers	A	1.5	0.7
Uncertainty for calibration of GNSS time transfer link	B	5.5	5.5
Propagation errors(including ionospheric and tropospheric error for GNSS time transfer link)	B	0.8	0.8
Delay error of cables and converters for one GNSS time and frequency transfer receiver	B	0.1	0.1
Delay error of cables and converters for the other GNSS time and frequency transfer receiver	B	0.1	0.1
Combined uncertainty		5.8	5.7
Expanded uncertainty (k=2)		11.6	11.4

V. Conclusion and Prospect

The combined uncertainty of about 6 ns for time calibration and the corresponding uncertainty of about 2e-14 averaging one week for frequency calibration could be obtained. Preliminarily the time and frequency accuracy of better than 10 ns and 1e-13 separately averaging one day for NIMDO could be realized, and the time and frequency stability averaging one day could be better than 5 ns and 3e-14 respectively. Soon we would improve the steering algorithm and lay up five NIMTFGNSS-1 receivers at four different cities (Urumchi, Guiyang, Haerbin, and Beijing) in China to verify the effects more deeply in the longer baseline. In the near future, using GNSS real-time or near real-time precise ephemeris products, GNSS carrier phase time and frequency transfer will be studied and applied in RTRC and NIMDO to improve their performances.

Acknowledgements:

The authors thank WANG Weibo and NING Dayu from NIM for the support of hardware installation.

References:

[1]. Michael A. Lombardi, "Locking A Rubidium Oscillator to a Remote Time Scale using Real-Time Common-View GPS Measurements", Proc. of PTTI 2008, pp. 527-542, 2008.

[2]. Michael A. Lombardi, "A NIST Disciplined Oscillator", Proc. of 2010 NCSL International Workshop and Symposium, July 25-29, 2010.

[3]. LIANG Kun, ZHANG Aimin, GAO Xiaoxun,WANG Weibo, NING Dayu，ZHANG Side, "Study and Development of a New GNSS Receiver for Time and Frequency Transfer," Proc. of EFTF 2012, pp. 529-536, 2012.

[4]. Lewandowski, W. & Thomas, C., "GPS Time Transfer, " Proc. IEEE 79(7), pp991-1000

The Application of VRS in Common-view Based One-Way Timing Method

Longxia Xu
National Time Service Center, CAS
Key lab of Precision Navigation and Timing Technology
Xi'an, China
xulongxia109@163.com

Meijun Guo
National Time Service Center, CAS
Xi'an, China

Xiaohui Li
National Time Service Center, CAS
Key lab of Precision Navigation and Timing Technology
Xi'an, China

Yanrong Xue
National Time Service Center, CAS
Key lab of Precision Navigation and Timing Technology
Xi'an, China

Yinhua Liu
National Time Service Center, CAS
Key lab of Precision Navigation and Timing Technology
Xi'an, China

Abstract— **The concept of Common-View based One-way Timing Method (CV-OWTM) is proposed by the author in the IFCS conference last year. This method provides users a way to acquire the standard time with the accuracy of about 5ns. However, the CV-OWTM performs the same deficiency as the common view time transfer, that is, its timing accuracy decrease with the increase of distance between users and the reference stations. In order to solve this problem, the Virtual Reference Station (VRS) technique that used in RTK is improved and applied to CV-OWTM. Based on a potential reference stations network in China, this paper will discuss the optimal virtual correction generation algorithm for users. The number of reference stations that users adopted and the weights of involved stations both are key factors for the generation of VRS correction. For different kinds of user, combinations of different number of stations and two methods of determining weights are experimented. The optimal number of reference stations for users' application is one or three. And the distance between the user and reference station decide the weight of timing observation of this station. All in all, the application of VRS can guarantee CV-OWTM provides the timing accuracy of 5ns.**

Keywords-CV-OWTM; VRS; VRS correction; standard time; timing accuracy

I. INTRODUCTION

CV-OWTM is a new timing method proposed by the author. This method operates on network consists of several reference stations. The local time of each reference station is already synchronized with the standard time. Each station sets up receivers and monitors satellites timing signals. The observables derived from each reference stations are sent to a data processing center where generates the timing biases of each satellites in view at each reference station. The information of these biases is broadcast to users. Users who desire an accurate time use the information can get a 5ns timing accuracy.

It is not difficult to figure out that CV-OWTM has the same principle as common view time transfer. Therefore, the accuracy of this method degrades with the increasing of distance between users and the reference stations [1][2].

To guarantee the 5ns timing accuracy of CV-OWTM (Common-View based One-way Timing Method), the Virtual Reference Station technique (VRS) is adopted. VRS is initially applied in RTK to provide service in larger area. With the same purpose, the VRS is adopted to solve the fatal weakness of CV-OWTM.

II. VRS IN HERE

A. *Some Differences*

The VRS discussed herein is different from that in RTK in several aspects. The timing biases are computed according to the code observations not those of carrier phase of the reference stations. Therefore, the VRS here isn't sensitive to the movement of users and still works when users and the network are in long base line. Moreover, using the timing biases of reference stations, it is the users that calculate the VRS correction. This reduces the burden of data processing center and simplifies the communication between them. Finally, the timing biases that the data processing center broadcast contain all the errors from satellites to receiver which is different from that in RTK.

B. *Key Points*

When the VRS is applied to CV-OWTM, there are several problems should be considered. Given a fixed network, there

This work is supported by the National Science Foundation of China (11033004).

are mainly two problems need to be considered. Above all, how many timing biases of reference stations is optimal to calculate the VRS correction. The other is how to determine the weight of the selected stations. These are the two important aspect of VRS virtual observation generation algorithm.

According to a promised network consists of six reference stations, these issues are studied. Some significant conclusions are given for future research.

III. VRS VIRTUAL OBSERVATION GENERATION ALGORITHM

For CV-OWTM, clock error has no effect on its timing accuracy. The uncompensated ionospheric delay and the ephemeris error become the contributor of timing error under long base line. These two errors are both related with the distance from the user to the reference stations in CV-OWTM network. The further users away from the reference station the less relativity of timing errors in the path from satellites to users and reference stations. This characteristic of timing errors are the theory basis of the VRS [3][4].

A. VRS Algorithm

The VRS virtual correction can be expressed with the following formula (1):

$$\delta t_{vrs} = \left(\sum_{i=1}^{n} w_i \cdot \delta t_i\right) \Big/ \left(\sum_{i=1}^{n} w_i\right) \quad (1)$$

δt_i is the timing bias observed at the reference station I and w_i is its weight. n is the number of reference stations and δt_{vrs} is the VRS correction at the user position. Given the positions of the reference stations and their approximate position, users select n optimal reference stations and then compute the VRS correction themselves.

The VRS correction is virtually the result of interpolation of n timing biases of n reference stations. The user should lie in the polygon area consisted by n reference stations.

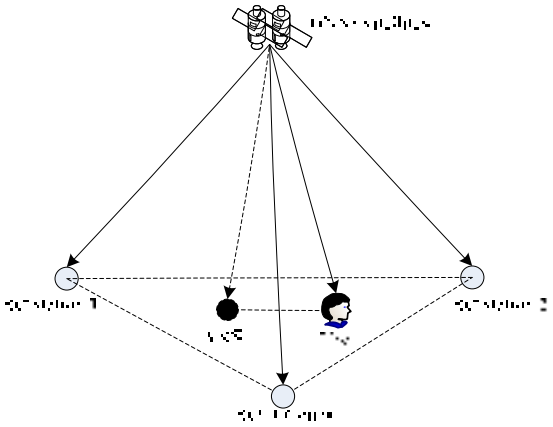

Figure 1. The principle of VRS

According to (1), the number of reference stations and their weights together determine the VRS correction. Take a promised China network for example, these two aspects are studied.

B. The Number of Reference Stations

Fig. 2 shows the distribution of the China network. Six sites are selected as the reference stations where Xi'an will also be the data processing center. If the network operates normally, it can obtain at most six sets of observations of a same satellite. Are these observations all necessary for users to compute the VRS correction?

In order to answer this question, two kinds of different locations are selected as the user positions. The first kind of users lies in the central part of the triangle with one vertex being Xi'an. The second lies in the effective range of the reference stations with the distances relative to the closest station being less than 800km.

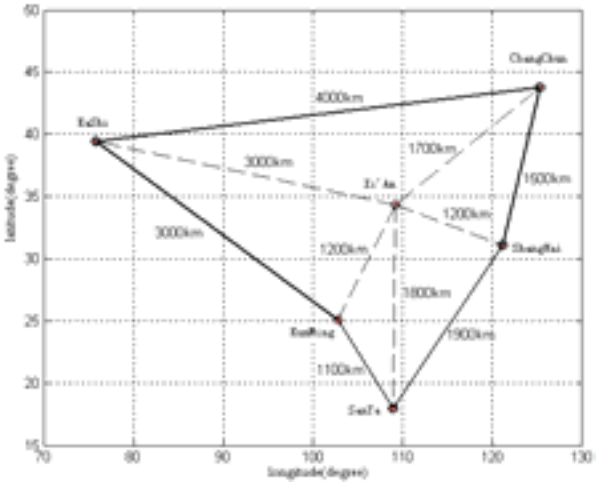

Figure 2. The network of CV-OWTM

In this paper, the correction effect of different combinations of one, three, four, five and six reference stations are compared for each kind of users. Take the user of located at Ji'nan for an example, the ephemeris and ionospheric errors together can be reduced to 2ns after applying the correction. Based on the correction results of all the first kind of users, the combination of three stations has the equivalent effect as the best result.

The distance between Shanghai and Ji'nan is about 725km which is the closest station in the network. According to the results in Table I, the user in Ji'nan can reduce the errors of ephemeris ionospheric errors to 1.23ns only with the correction provided by Shanghai station.

TABLE I. THE EFFECT OF DIFFERENT COMBINATIONS TO JI'NAN

Different combinations	User lies in Ji'nan	Correction result (ns)	
		Before	*After*
Single station	ShangHai	5.21	1.23
Three stations	Xi'an, ChangChun and ShangHai	5.04	**0.40**
Four stations	Exclude KaShi and KunMing	5.04	0.73

	Exclude SanYa and KunMing	5.21	**0.35**
	Exclude Xi'an and KunMing	5.21	0.98
	Exclude Xi'an and SanYa	5.21	0.75
	Exclude ShangHai and ChangChun	5.21	0.98
Five stations	Exclude Xi'an	5.21	1.17
	Exclude KaShi	5.06	0.91
	Exclude ShangHai	5.38	0.96
	Exclude SanYa	5.21	0.59
	Exclude KunMing	5.21	0.71
	Exclude ChangChun	5.40	1.28
Six stations	All stations	5.21	1.37

The reason why we chose the second kind of users is to test the correct effect of a single station. When users are close enough to any one of the reference stations, it may become an easy thing for the user to choose stations. In order to answer this question, we compute the correction effect of the second kind users. The results of using the correction of the nearest single station are lists in Table II. The correction results of three stations for these users are given in Table III. Comparing the results of these two tables, it is easy to answer the former question. As each station covers a specific area, users only need the correction of this station when they lie in the range of this area. The radius of the area is normally less than 1000km.

TABLE II. THE EFFECT OF SINGLE STATION TO SECOND USERS

Users	**Single station**	**Correction results (ns)**	
		Before	***After***
Akesu	Kashi	4.93	0.33
Hetian	Kashi	5.42	0.53
Xishangbanna	Kunming	9.88	1.39
Baoshan	Kunming	8.45	0.56
Hongkong	Sanya	9.29	1.30
Guangzhou	Sanya	8.86	1.75
Nanning	Sanya	9.31	1.75
Fuzhou	Shanghai	7.13	1.40
Wuhan	Shanghai	5.89	0.50
Hefei	Shanghai	5.81	0.38
Zhengzhou	Xi'an	5.64	0.28
Lanzhou	Xi'an	5.37	0.64
Chengdu	Xi'an	6.30	0.93
Huhehaote	Xi'an	5.08	0.77
Heihe	Changchun	3.29	1.51
Hulenbeier	Changchun	3.46	1.34
Beijing	Changchun	4.87	0.57

TABLE III. THE EFFECT OF THREE STATIONS TO SECOND USERS

Users	**Three station**	**Correction results (ns)**	
		Before	***After***
Akesu	Kashi,Xi'an,Kunming	4.53	0.83
Hetian	Kashi,Xi'an,Kunming	4.94	0.54
Xishangbanna	Kunming,Xi'an,Sanya	8.85	1.19
Baoshan	Kunming,Xi'an,Sanya	7.64	0.81
Hongkong	Sanya,Shanghai,Kunming	8.52	1.27
Guangzhou	Sanya,Shanghai,Kunming	7.81	0.72
Nanning	Sanya,Xi'an,Shanghai	7.72	0.79
Fuzhou	Sanya,Xi'an,Shanghai	7.21	1.16
Wuhan	Shanghai,Kunming,Sanya	5.92	1.22
Hefei	Shanghai,Changchun,Kunming	5.59	0.28
Zhengzhou	Xi'an, Shanghai,Kunming	5.31	0.55
Lanzhou	Xi'an, Changchun,Kunming	4.95	0.85
Chengdu	Xi'an, Kunming,Sanya	6.23	1.30
Huhehaote	Xi'an, Shanghai,Changchun	4.61	0.77
Heihe	Xi'an, Shanghai,Changchun	3.25	1.82
Hulenbeier	Xi'an, Shanghai,Changchun	3.40	1.70
Beijing	Xi'an, Shanghai,Changchun	4.77	0.58

C. *The Weights of Reference Stations*

As the timing biases are highly related with the distance between the users and the reference stations, two methods of determining the weights are tested.

- $w_i = 1/r_i$, $r_i = \sqrt{(x_u - x_i)^2 + (y_u - y_i)^2 + (z_u - z_i)^2}$ where (x_u, y_u, z_u) is the user position and (x_i, y_i, z_i) is the position of the ith reference station.
- $w_i = \cos(E_i - E_u)/d_i$, where E_i is the elevation of the ith reference station observe the satellite. E_u is the elevation of user observes the same satellite [5].

Thirty points are selected to compare the effects of these two weighting methods. Table IV shows the results of these two methods under the combination of three reference stations. According to the results, these two weighting methods have almost the same effect. The second weighting method not only considers the distance between user and station, but also takes the observation elevation into account. Considering the computational complexity, the first weighting method is adopted here.

TABLE IV. THE RESULTS OF TWO WEIGHTING METHODS UNDER THREE STATION COMBIANTION

Users	**Before (ns)**	**Method 1 (ns)**	**Method 2 (ns)**
Jinan	5.04	0.40	0.40
Changsha	6.31	0.53	0.53
Guiyang	7.40	0.59	0.59
Yushu	5.67	1.03	1.05
Yinchuan	4.84	0.37	0.37
Chongqing	6.52	0.96	0.96
Nanchang	6.32	0.48	0.48
Akesu	4.53	0.83	0.81

Hetian	4.94	0.54	0.52
Puer	8.51	0.91	0.91
Xishuangbanna	8.85	1.19	1.18
Baoshan	7.64	0.81	0.81
Haikou	8.56	0.47	0.46
Macao	8.48	1.25	1.24
Guangzhou	7.81	0.72	0.72
Nanning	7.72	0.79	0.79
Wuzhou	7.64	0.54	0.54
Fuzhou	7.21	1.16	0.16
Wuhan	5.92	1.22	1.22
Hefei	5.59	0.28	0.28
Nanjing	5.55	0.11	0.11
Zhengzhou	5.13	0.17	0.16
Shijianzhuang	4.87	0.52	0.52
Lanzhou	4.96	0.21	0.21
Chengdu	6.56	0.41	0.41
Huhehaote	4.61	0.77	0.77
Heihe	3.25	1.82	1.82
Hulunbeier	3.40	1.70	1.70
Beijing	4.77	0.58	0.58

IV. APPLICATION GUIDE AND CONCLUSIONS

Based on the research results derived from part III, we can summary some application guides for users. These guides virtually determine the VRS virtual correction algorithm. The implementation procedure for users is:

- Receiving the positions and timing biases of six reference stations.
- Calculating the distances respect to each station.
- If the shortest distance is less than the effective radius of the station, users only need the timing bias of this station to correct their observations.
- If the shortest distance is more than the effective radius of each station, users select three stations that are more closely. The weights of these three stations are inverse proportion to the corresponding distances.

For the stations in low latitude areas, as Sanya and Kunming displayed in Figure 3, the effective radius is smaller than those stations in middle and high areas. This is because the amplitude of ionospheric delay is large in these areas. So the residual after the ionospheric compensation is still large and change quickly.

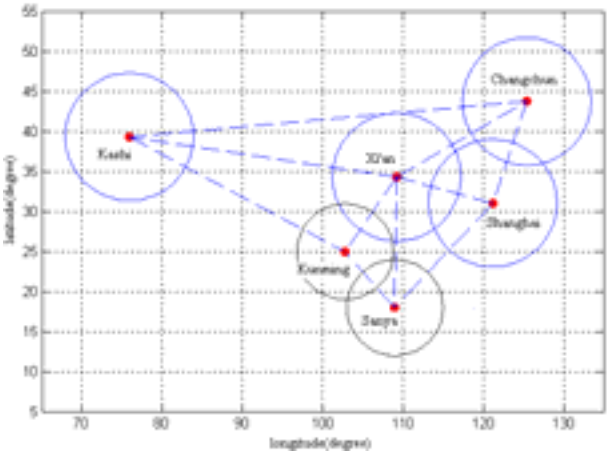

Figure 3. The effective range of each station

Finally, the VRS algorithm can eliminate the ephemeris and ionospheric delay errors and keep these errors in 2ns which guarantees the accuracy of the CV-OWTM.

The VTEC Data used in this paper are from website "http://www.dccdnc.ac.cn/dataservice/gps_tec.jsp" and the broadcast navigation message and precise ephemeris data are used to compute the ephemeris error.

REFERENCES

[1] Xu L X, "A new timing method based on common-view", 2012 IFCS Proceedings, p. 181-184, 2012.

[2] Xu L X, "Study of a new one-way timing method", Sci China: Phys Mech &Astron, vol. 55, p. 2476-2481, 2012.

[3] Kaplan E., Understanding GPS: Principles and Applications, Second Edition, Artech House, Inc., 2006.

[4] Liu Z., and Gao Y. (2001) Research toward wireless Internet-based DGPS, Proceedings of KIS 2001, Banff, Canada, June 5-8, 461-469.

[5] Erhu Wei, Hua Chai, Zhiguo An, VRS Virtual Observation Generation Algorithm, Journal of Global Positioning Systems(2006), Vol 5, No. 1-2:76-81.

A Detection Algorithm of Frequency Jumps for GNSS Satellite Clocks

Xinming Huang, Hai Sha, Hang Gong, Yiwei Wu, Gang Ou
College of Electronic Science and Engineering, National University of Defense Technology
Changsha, China
huangxinming_2007@163.com

***Abstract*—As the frequency and time reference of space satellites, satellite clock has a direct influence on GNSS service performance. Any anomaly of the atomic clock behavior on board the satellites causes errors for user position. Therefore, it is necessary to detect clock anomaly. Frequency jumps are one of the most common anomalies in atomic clocks of on-board satellites, which appear due to space radiation, temperature change and other factors. In this paper, a detection algorithm of frequency jumps based on the batch least squares residues is proposed. Performance of the new algorithm is analyzed and verified by numerical simulation. The detection algorithm of frequency jumps for satellite clocks proposed in this paper is helpful to GNSS satellite clock autonomous integrity monitoring.**

Keywords-frequency jump; least square estimation; sum test statistic

I. INTRODUCTION

As the frequency and time reference of space satellites, satellite clock has a direct influence on GNSS service performance. Therefore, it is necessary to monitor its integrity [1]. Several methods are proposed to detect anomaly of atomic clocks on board [2-5]. An extended version of the Allan variance, the dynamic Allan variance (DAVAR) [2, 3], has been used to detect anomalies in clocks, which is inapplicable to autonomous integrity monitoring of atomic clock on board due to its computational complexity and detection delay. A useful method to detect clock anomaly on board using the one-step predicted residue of Kalman filter is proposed in [4, 5]. It is effective to detect obvious anomaly bias, but ineffective for weak anomaly. Clearly, it is appreciable to provide a solution to weak frequency anomaly detection for atomic clocks on board with tolerable computational complexity and detection delay.

In this paper, clock parameters are achieved by least squares estimation. Real-time frequency residues are obtained by wiping off the trend item, and a novel sum test statistic based on residues is constructed. Performance of the new algorithm is analyzed and verified by simulation. The results show that the new algorithm has a perfect performance of detecting frequency jump.

II. THE NEW ALGORITHM

The average frequency deviation of an atomic clock, commonly modeled as a sum of white frequency noise (WFM), random-walk frequency noise (RWFN), and a slowly varying deterministic drift [5], can be written as

$$y(k) = y_{\mathrm{W}}(k) + y_{\mathrm{RW}}(k) + d(k) \tag{1}$$

Where $y_{\mathrm{W}}(k)$ is WFN, $y_{\mathrm{RW}}(k)$ is RWFN, and $d(k)$ is the time-varying drift, which can be defined as

$$d(k) = d(k-1) + d \cdot T \tag{2}$$

Where $d(0)$ equals to the standard frequency f_0, and d is the linear frequency drift, which is regarded as a constant value.

According to [5], $y_{\mathrm{W}}(k)$ has zero mean and variance given by

$$\sigma_1^2 = E[y_{\mathrm{W}}^2(k)] \tag{3}$$

The RWFN component is the solution to the random differential equation as following

$$y_{\mathrm{RW}}(k) = y_{\mathrm{RW}}(k-1) + \Delta y_{\mathrm{RW}}(k-1) \tag{4}$$

Where $y_{\mathrm{RW}}(k) = 0$, and increments $\Delta y_{\mathrm{RW}}(k)$ are statistically independent Gaussian random variables, with zero mean and variance given by

$$\sigma_2^2 = E[\Delta y_{\mathrm{RW}}^2(k)] \tag{5}$$

The frequency deviation measurements given in (1) is rewritten using matrix notation

$$\boldsymbol{y} = \boldsymbol{HA} + \boldsymbol{\varepsilon} \tag{6}$$

Where $\boldsymbol{H}=\begin{bmatrix}1 & t_1\\ \vdots & \vdots\\ 1 & t_n\end{bmatrix}, \boldsymbol{A}=\begin{bmatrix}f_0\\ d\end{bmatrix}, \mathbf{y}=\begin{bmatrix}y_1\\ \vdots\\ y_n\end{bmatrix}, \boldsymbol{\varepsilon}=\begin{bmatrix}\varepsilon_1\\ \vdots\\ \varepsilon_n\end{bmatrix}$.

It is supposed that the elements of ε have zero expectation and, for the moment, a known covariance matrix $\boldsymbol{V}(\boldsymbol{\varepsilon})$. The elements ε_i are taken as a linear combination of (independent) samples of known noise types, including WFM, RWFM.

$\boldsymbol{V}(\boldsymbol{\varepsilon})$ is expressed in terms of known covariance matrices that relate to each noise type and parameters describing the 'magnitude' of each noise type are present [6]. Each noise type is characterized by a transformation of a white noise process. The covariance matrices $\boldsymbol{V}$ for standardized WFM and RWFM, for which the transformed white noise process has unit standard deviation, are given, respectively, by confirmed by false alarm as following [7]

$$\boldsymbol{V}_{\mathrm{WFM}}=\boldsymbol{I}, \quad \boldsymbol{V}_{\mathrm{RWFM}}=\boldsymbol{W}\boldsymbol{W}^{T} \tag{7}$$

$$W=\begin{bmatrix}1 & 0 & \cdots & 0\\ 1 & 1 & \ddots & \vdots\\ \vdots & \ddots & \ddots & 0\\ 1 & \cdots & 1 & 1\end{bmatrix} \tag{8}$$

The covariance matrix $\boldsymbol{V}(\boldsymbol{\varepsilon})$ for noise arising as a linear combination of (independent) WFM and RWFM is then expressed as confirmed by false alarm as following [7]

$$\boldsymbol{V}(\boldsymbol{\varepsilon})=\boldsymbol{\sigma}^2_{\mathrm{WFM}}\boldsymbol{V}_{\mathrm{WFM}}+\boldsymbol{\sigma}^2_{\mathrm{RWFM}}\boldsymbol{V}_{\mathrm{RWFM}} \tag{9}$$

As some parameters of the measurements are unknown, it is necessary to estimate the unknown parameters. A GLS analysis is applied to obtain estimates of the normalized frequency offset f_0 and the frequency drift d together with their associated uncertainties. The estimates determined can be expressed as following

$$\hat{\boldsymbol{A}}=\begin{bmatrix}\hat{f}_0\\ \hat{d}\end{bmatrix}=(\boldsymbol{H}^T\boldsymbol{V}\boldsymbol{H})^{-1}\boldsymbol{H}^T\mathbb{V}\mathbf{y} \tag{10}$$

In order to achieve real-time detection of frequency jumps, two windows are adopted. The first window with past measurements is used to estimate the unknown parameters, while the second window with current measurements is used to construct the proposed detector.

Similar to the snapshot residual-based detection approach, a batch residual vector is obtained by taking difference between the measured and predicted frequency offsets within the second window. And a sum test statistic is built based on the batch residual vector, which is used to construct the frequency jump detector.

The batch residual vector is given as

$$\Delta\boldsymbol{y}=\tilde{\mathbf{y}}-\tilde{\boldsymbol{H}}\hat{\boldsymbol{A}} \tag{11}$$

Where $\Delta\boldsymbol{y}=\begin{bmatrix}\Delta y_1\\ \vdots\\ \Delta y_n\end{bmatrix}$, $\tilde{\mathbf{y}}=\begin{bmatrix}y_{n+1}\\ \vdots\\ y_{n+\mathrm{n}}\end{bmatrix}$, $\tilde{\boldsymbol{H}}=\begin{bmatrix}1 & t_{n+1}\\ \vdots & \vdots\\ 1 & t_{n+n}\end{bmatrix}$.

The batch residual vector follows generalized Gaussian distribution, which can be expressed as $\Delta\boldsymbol{y}$~N($\mathbf{0}$,$\mathbf{C}$). The covariance matrix of batch residual vector is expressed as (12) consequently.

$$\boldsymbol{C}=\begin{bmatrix}c_{1,1} & \cdots & c_{1,n}\\ \vdots & \ddots & \vdots\\ c_{n,1} & \cdots & c_{n,n}\end{bmatrix} \tag{12}$$

Where

$$c_{i,j}=E[(\boldsymbol{y}_{N+i}-\tilde{\boldsymbol{H}}_i\hat{\boldsymbol{A}})\cdot(\boldsymbol{y}_{N+j}-\tilde{\boldsymbol{H}}_j\hat{\boldsymbol{A}})^T] \tag{13}$$

As the residues are correlated, it is a good choice to prewhitening the residues. For any $\boldsymbol{C}$ that is positive definite, it can be shown that $\boldsymbol{C}^{-1}$ exists and is also positive definite. Consequently, it may be factored as $\boldsymbol{C}^{-1}=\boldsymbol{D}^{\mathrm{T}}\boldsymbol{D}$, where $\boldsymbol{D}$ is called the prewhitening matrix, which produces WGN. The residues prewhitened can be expressed as $\boldsymbol{Z}=\boldsymbol{D}\cdot\Delta\boldsymbol{y}$.

A frequency jump is a sudden variation in the frequency trend, which can be modeled as

$$y'(k)=y(k)+\Delta f\cdot u(k-n) \tag{14}$$

Where n is the time instant at which the frequency jump occurs, and Δf is its size, which is often a constant value. Therefore, the frequency jump detection problem can be modeled as

$$\begin{aligned} &H_0: z(n)=z'(n) && n=0,1,...,N-1\\ &H_1: z(n)=\Delta f_n'+z'(n) && n=0,1,...,N-1 \end{aligned} \tag{15}$$

Where $z'(n)$ is the nth element of the residues without frequency abnormal values, $\Delta f_n'$ is the nth element of $\Delta\boldsymbol{f}'$, which can be expressed as following

$$\Delta\boldsymbol{f}'=\boldsymbol{D}\cdot\begin{bmatrix}\Delta f\\ \vdots\\ \Delta f\end{bmatrix} \tag{16}$$

In order to improve detection performance, residues are accumulated. The new test statistic proposed for weak anomaly detection can be expressed as following

$$z = \sum_{i=1}^{n} (z_i')^2 \tag{17}$$

As prediction residues prewhitened are uncorrelated, which follow a Gaussian distribution, test statistic z follows a chi-square cumulative distribution.

Assume the probability of false alarm is P_f, and the probability of detection is P_d, the detection threshold can be confirmed by false alarm as following [7].

$$P_f = \int_{T(P_f)}^{\infty} (2^{\frac{N}{2}} \Gamma(\frac{N}{2}))^{-1} z^{\frac{N}{2}-1} e^{-\frac{z}{2}} dz \tag{18}$$

The probability of detection is given as following

$$P_d = \int_{T(P_f)}^{\infty} \frac{1}{2} (z/\lambda)^{\frac{N}{4}-\frac{1}{2}} e^{-\frac{z+\lambda}{2}} I_{\frac{N}{2}-1}(\sqrt{z\lambda}) dz \tag{19}$$

Where the noncentral parameter λ equals to $\sum_{i=1}^{N} (\Delta f_i')^2$. Performance of the test statistic can be obtained for a given probability of false alarm detection according to (18) and (19). The detection performance is decided by noncentral parameter λ, which is square sum of abnormal residues. It is obvious that parameter λ increase with large length of measurement window, which indicates better detection performance.

A frequency jumps detection method based on the new test statistic is proposed, whose implementation is shown in Fig. 1. A GLS analysis is applied to 1st window to obtain estimates of the normalized frequency offset f_0 and the frequency drift d, which are used to wipe off the trend item. A batch residual vector is obtained by taking difference between the measured and predicted frequency offsets within the second window. The residues are prewhitened by a prewhitener, and the new test statistic is acquired by accumulating the residues prewhitened. Each value of the test statistic is compared with the detection threshold, which can be confirmed by (18) with a given probability of false alarm. If value of the test statistic is bigger than the threshold, clock anomaly is decided.

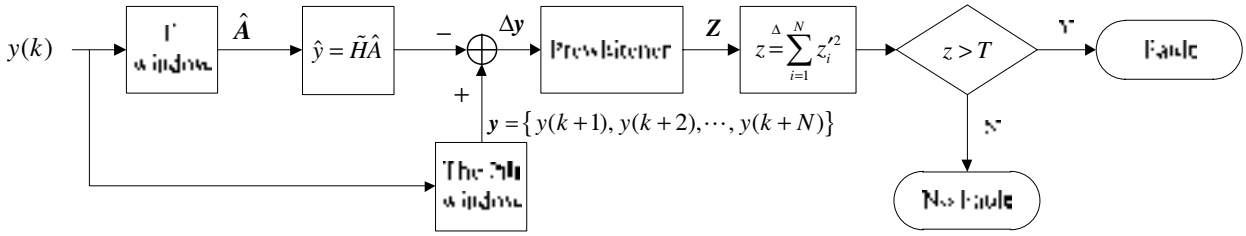

Fig. 1 Block diagram of implementation structure for frequency jumps detection

III. NUMERICAL SIMULATION

To evaluate the new detection method, numerical simulations of frequency jump detection for atomic clock is performed. The case of a rubidium clock is considered, whose variance values for a sampling time T_s=1s are given by

$$\sigma_1^2 = (5\times10^{-12})^2 \tag{20}$$

and

$$\sigma_2^2 = (5.2\times10^{-16})^2 \tag{21}$$

These values are examples of the stability reached by a space-based rubidium frequency standard following the first Galileo space clock specifications [8]. The frequency drift is given as a constant linear drift represented by

$$d = 1\times10^{-16}/s \tag{22}$$

The detection performance of the proposed detector can be confirmed by (19). In order to verify detection performance of the new detector, numerical and Mont-Carlo (M-C) simulation are verified. Numerical calculation results of fault detection probability according to formula (19) are compared with simulation results of repeat 10000 M-C simulations.

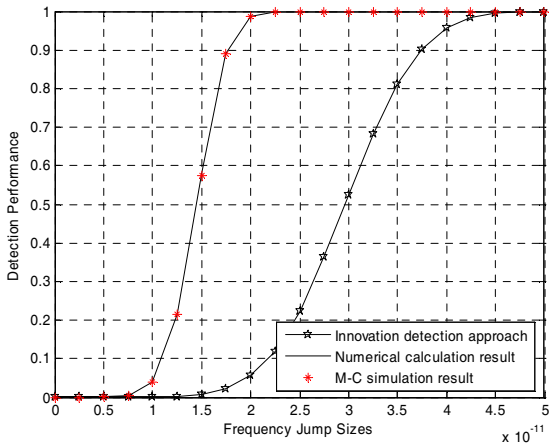

Fig. 2 Detection performances of the proposed detector

The accumulation number is 10, and the probability of false alarm is 10^{-6}. Values of P_d as a function of values of frequency jump with a constant P_{fa} are shown in Fig. 2.

It can be seen from simulation results that Mont-Carlo (MC) simulation results are highly consistent with results of the calculation formula, which illustrates the correctness of the calculation formula of detection probability. It is also obvious that detection performance of the proposed detector is better than that of innovation detection approach provided in [4, 5].

IV. CONCLUSION

A method of weak frequency detection is proposed. A GLS analysis is applied to obtain estimates of the normalized frequency offset f_0 and the frequency drift d, which are used to wipe off the trend item. A batch residual vector is obtained by taking difference between the measured and predicted frequency offsets, and a novel test statistic based on the batch residual vector is constructed. Simulation is adopted to verify detection performance of the proposed method. Such a method is simple to implement with tolerable computational complexity and detection delay. Several improvements to our method are currently been working on, such as the detection of weak frequency jumps.

REFERENCES

[1] I. Rodriquez Perez, C. Garcia Serrano, C. Catalan Catalan, A. Mozo Garcia, P. Tavella, L. Galleani, and F. Amarillo, "Inter-satellite Links for Satellite Autonomous Integrity Monitoring," *Adv. Space Res.*, vol. 47, no.2, pp. 197-212, 2011.

[2] I. Sesia, L. Galleani, and P. Tavella, "Application of the Dynamic Allan Variance for the Characterization of Space Clock Behavior," *IEEE Trans. Aero. Elec. Sys.*, vol. 47, no.2, pp. 884-895, April 2011.

[3] L. Galleani and P. Tavella, "The Dynamic Allan Variance," *IEEE Trans. Ultrason. Ferroelectr. Freq. Control*, vol. 56, no.3, pp. 450-464, 2009.

[4] L. Galleani, and P. Tavella, "Detection of Atomic Clock Frequency Jumps with Kalman Filter," *IEEE Trans. Ultrason. Ferroelectr. Freq. Control*, vol. 59, no.3, pp. 504-509, March 2012.

[5] S. Lee, J. Kim, and Y. Lee, "Protecting Signal Integrity Against Atomic Clock Anomalies on Board GNSS Satellites," *IEEE Trans. Instrum. Meas.*, vol. 60, no. 7, pp. 2738–2745, , July 2011.

[6] P. M. Harris, J. A. Davis, M. G. Cox and S. L. Shmar, "Least-squares analysis of time series data and its application to two-way satellite time and frequency transfer measurements," *Metrologia*, vol. 40, no. 6, pp. S342-S347, June 2003.

[7] S. M. Kay, *Fundamentals of Statistical Signal Processing, Volume 1: Estimation Theory*. Englewood Cliffs, NJ: Prentice-Hall, 1998.

[8] P. Waller, F. Gonzalez, S. Binda, I. Sesia, P. Tavella, I. Hidalgo, and G. Tobias, "Update on the in-orbit performance of GIOVE clocks," *in IEEE Frequency Control Symp. -European Frequency and Time Forum*, 2009, pp. 20-24.

Combination of T2L2 and GPS-CP Data: Towards an Improvement of Time Transfer Accuracy

Philippe Guillemot, Jérôme Delporte
CNES, French Space Agency
Toulouse, France
Philippe.guillemot@cnes.fr

Etienne Samain, Mytille Laas-Bourez
GeoAzur, Observatoire de la Côte d'Azur
Plateau de Calern, France

Abstract—**The Time Transfer by Laser Link (T2L2) experiment, developed by both OCA and CNES, performs ground to ground time transfer over intercontinental distances. The principle is derived from laser telemetry technology with dedicated space equipment designed to record arrival time of laser pulses at the satellite. Using laser pulses instead of radio frequency signals, T2L2 allows realizing some links between distant clocks with expected time stability of a few picoseconds and accuracy better than 100 ps.**

On the one hand, several experiments demonstrated the capability of the T2L2 system to perform time transfer with a residual accuracy in the 100 ps range [1]. Nevertheless laser operations are weather dependent and do not allow continuous comparison of remote clocks. On the other hand GPS time transfer is a worldwide, all weather and fully operational system. GPS data processing has been widely improved since the first common view / single satellite time transfer and GPS Carrier Phase techniques now allow continuous comparison with accuracy in the nanosecond range. However, carrier phase data are ambiguous and several method were developed in order to reduce them. Performances of these methods are widely demonstrated for frequency transfer and with continuous data. But some ambiguities remain as soon as there are gaps in the data and for accurate time transfer.

This work investigates the possibility to combine GPS-CP time transfer using single-difference integer ambiguity resolution [2] and T2L2 data in order to improve the resolution of the remaining GPS-CP ambiguities, in case of interruption in the data, and the accuracy of the time transfer. First we introduce the method and then we present some first results for common view time transfer in between European stations.

Keywords- Time Transfert; Space; T2L2; GPS-CP

I. INTRODUCTION

Optical time transfer is an evolution of RF techniques that takes advantage from optical signals such as higher modulation bandwidth, insensitivity to ionosphere and mono carrier schemes to improve the performances of remote clocks comparisons [3]. T2L2 is a time transfer technique based on laser ranging network at ground and on a dedicated space segment, the T2L2 instrument. Developed by CNES (Centre National d'Etudes Spatiales) and OCA (Observatoire de la Côte d'Azur), this instrument has been launched in 2008 with the Jason-2 satellite for a 3 year mission. It celebrated its fifth in orbit anniversary in June 2013 and its mission is now extended until the end of 2014.

T2L2 relies on the propagation of laser pulses between the clocks to be synchronized. It provides the capability to compare today's most stable frequency standards with unprecedented stability and accuracy. Expected T2L2 performances are in the 100 ps range for accuracy, with ultimate time stability about 1 ps over 1,000 s and 10 ps over one day. The objectives of the T2L2 experiment on Jason-2 are threefold:

- Technological validation of optical time transfer, including the validation of the experiment, its time stability and accuracy and of one way laser ranging.
- Characterization of the onboard Doris oscillator for Jason-2 purposes and a contribution to the Jason-2 laser ranging core mission.
- Scientific applications such as time and frequency metrology (comparison of distant clocks, calibration of RF links), fundamental physics (such as anisotropy of the speed of light), earth observation or very long baseline interferometry (VLBI).

Among these objectives, a special attention was paid on the assessment of the accuracy of the time transfer. This assessment had been done both in zero baseline / common clock configuration and in common view, comparing T2L2 with other technique such as GPS Carrier Phase (GPS-CP) and Two Way Satellite Time and Frequency Transfer (TWSTFT).

II. BACKGROUND

A first comparison between T2L2, GPS-CP and TWSTFT was performed between June and October 2010 during the 2nd T2L2 international campaign. Among the laser stations involved in this campaign, two sites were of a particular interest: The SYRTE / Observatoire de Paris (OP) and the Plateau de Calern / Observatoire de la Côte d'Azur (OCA). Those 2 sites were equipped with GPS receivers, TWSTFT stations, cold atoms clocks and Satellite Laser Ranging Stations. Comparison of the different T/F transfer techniques on the link between OP and OCA, regardless of absolute aspects (the links were not calibrated), showed that the noise between T2L2 and GPS or TWSTFT remained within 2 ns

during the 60 days of the campaign, with no relative drift, at least at the nanosecond level [4].

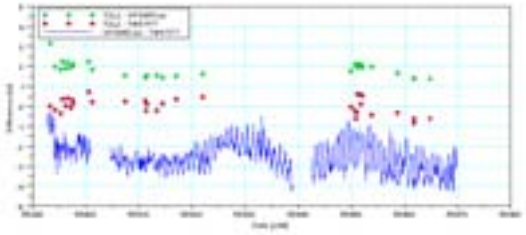

Figure 1. Comparison between T2L2, GPS and TWTFT on the link OP-OCA : T2L2-GPS (green), T2L2-TWSTFT (red) and TWSTFT-GPS (blue) (The offset between each curve was adjusted to facilitate the graph reading)

For this first comparison GPS time transfer was computed using a Carrier Phase Time Transfer / Precise Point Positioning method with ambiguity resolution on single-difference measurements developed by CNES [2]. Typical performances of the method are given in Figure 2, with frequency stability of a few 10^{-15} for integration times around 10^5 s.

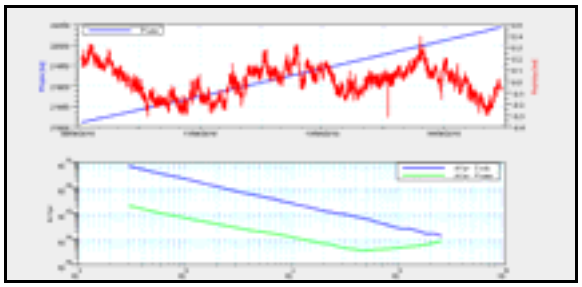

Figure 2. Typical performances of GPS Carrier Phase Time Transfer / Precise Point Positioning method with ambiguity resolution on single-difference measurements (OP/Z12-T vs OCA/GTR50 link, H-Masers)

One of the main benefits of this method is to combine phase measurements on L_1 and L_2 GPS carriers so that the phase ambiguity becomes a round number of what one calls the "Narrow Lane". The Narrow Lane is defined as

$$\lambda_c = \lambda_1\lambda_2 / (\lambda_1 + \lambda_2),$$

Where λ_1 and λ_2 are the wavelengths of the two GPS carriers. Its wavelength is 10.7 cm or 0.356758 ns. Thus, it is possible to identify, and then correct, Narrow Lane's ambiguities inside a given data set. But this correction is only relative, not absolute: An uncertainty remains and the results could be shifted by an integral number of λ_c. As far as the data set is continuous, the uncertainties are the same. Nevertheless, any gap in the data, or the necessity to process data by discontinuous batches (Figure 6), could lead to a change in this uncertainty from one data set to the next one and to induce some jumps.

Somehow, the first T2L2/GPS comparison confirms this phenomenon. The differences between T2L2 time transfer and GPS solutions extrapolated at T2L2 dates exhibit some jumps between the mean values of each period. And amplitudes of jumps are exactly an integral number of Narrow Lane wavelengths λ_c (Figure 3). We can take benefit from expected T2L2 long term stability and accuracy to identify and fix theses jumps. Since there is no other "100 ps" accurate time transfer available today (except T2L2), these jumps clearly introduce some limitation in our capability to validate this absolute and accurate comparison between T2L2 and GPS-CP time transfer.

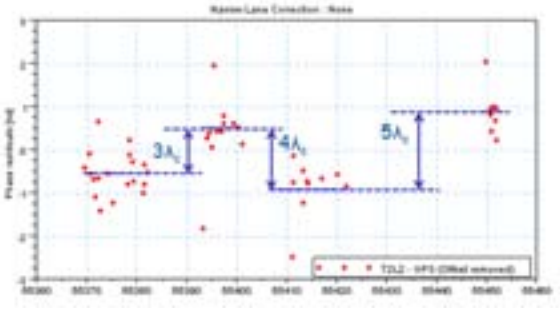

Figure 3. Difference between T2L2 and GPS ground to ground time transfer (115 ns offset removed)

III. ATTEMP TO FIX RESIDUAL NARROW LANE AMBIGUTIES

The idea there is to see if GPS data are self-sufficient to allow identification and correction of residual Narrow Lane ambiguities. Two main assumptions are done:

- First, the code time transfer is supposed to be unambiguous (with respect to Narrow Lane ambiguity) and accurate,
- Second, the Narrow Lane ambiguity introduces simple and constant "jumps" of an integral number of λ_c between code and phase solutions for the time transfer.

Two methods will be evaluated here:

- One based on a least square approach and called hereafter the 'Quadratic Fit' method,
- One based on an averaging process and called here after 'Average Differences' method.

Their aim is to identify the Narrow Lane offset NL_{Ofs} between the phase and the code, and then to remove this offset from phase data.

A. *'Quadratic Fit' method*

The method relies on the adjustment of a 2nd order polynomial within code and phase data using the least square method. But whereas all the coefficients of the polynomial are adjusted within phase data, only the zero-order coefficient (time offset) is adjusted within code data, other coefficients being the same as the ones identified using phase data. The Narrow Lane offset between code and phase is then simply the difference between the two zero-order coefficients, modulo the Narrow Lane wavelength:

- Step 1 : Phase ⇨ $P = \mathbf{a_{0p}} + a_{1p} \times t + a_{2p} \times t^2$
- Step 2 : Code ⇨ $C = \mathbf{a_{0c}} + a_{1p} \times t + a_{2p} \times t^2$
- Step 3 : $NL_{Ofs} = \text{round}((\mathbf{a_{0c}} - \mathbf{a_{0p}}) \text{ modulo } \lambda_c)$
- Step 4 : $P = P + NL_{Ofs} \times \lambda_c$

Note: In order to reduce influence of outliers during code processing (step 2), it is possible to improve the process by rejecting them (k-sigma filtering).

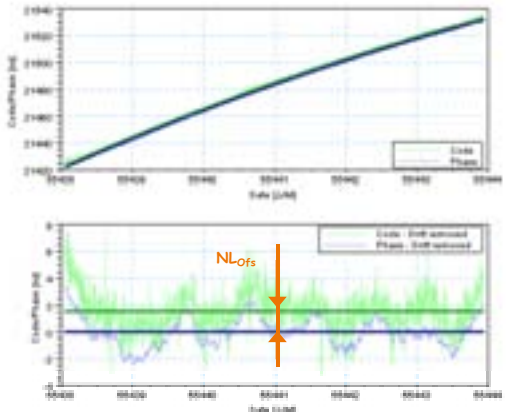

Figure 4. 'Quadratic Fit' method : Least square polynomial is performed within the full data setadjustement

B. *'Average Differences' method*

The method aims at taking advantage of the τ^{-1} behavior of the stability of the time transfer (Figure 2): For long integration periods, one can 'average' the noise on both code and phase measurement (up to reach the stability of the clocks), and it could be possible to compute the difference between code and phase time transfer with an uncertainty lower than the Narrow Lane wavelength.

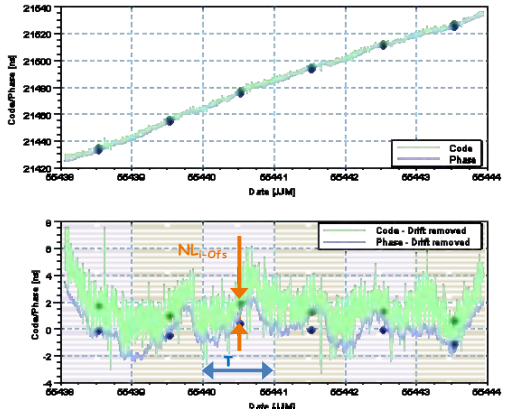

Figure 5. 'Average differences' method : Averaging on code and phase is computed for each period τ

Thus, for each adjacent window of length τ, we compute first the average code and phase values and then the offset, modulo the Narrow Lane wavelength, between these two values. At the end, the overall Narrow Lane offset between code and phase will be the median of individual offsets:

- Step 1 : Compute $\langle P_i \rangle$ and $\langle C_i \rangle$ for each period i,
- Step 2 : $NL_{i\text{-}Ofs} = \text{round}((\langle C_i \rangle - \langle P_i \rangle) \text{ modulo } \lambda_c)$
- Step 3 : $NL_{Ofs} = \text{median}(NL_{i\text{-}Ofs})$
- Step 4 : $P = P + NL_{Ofs} \times \lambda_c$

With respect to clocks and GPS-CP performances, typical length τ of the averaging window will be of some 10.000 seconds.

C. *Preliminary validation*

The validation has been performed on a 'continuous' data set, using WTZA (Wettzell, Germany) and OPMT (Paris, France) receivers between JJM 55328 and JJM 55456. We processed data by batches of 5 + 1 (overlapping) days. Such a configuration allows a simple identification and a 'manual' correction of the Narrow Lane offset, by simple difference between the 2 solutions during overlapping periods (Figure 6). Thus, resulting from this 'manual' processing, we will have our 'reference' solution (The solution is still not absolutely accurate, the Narrow Lane of the first batch being arbitrary fixed).

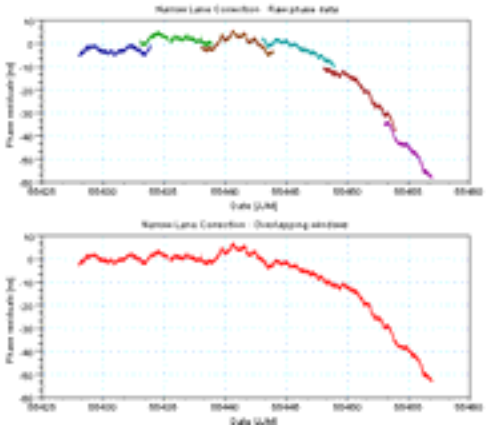

Figure 6. Data set and 'reference' solution: Phase residuals before (top, offset has been emphasized for the plot) and after (bottom) manual identification and correction of the narrow lane jumps

First results are questionable:

- Table 1 shows that each method gives a different result. Figure 7 confirms that, if the phase solution is perfectly continuous with manual corrections, some jumps remain whether we use 'Average differences' or 'Quadratic fit' methods.
- Table 1 also shows that, if the 'Quadratic fit' method seems to be rather insensitive to the filtering level, the 'Average differences' method is more sensitive to the integration time. And it is not really possible to define an optimal integration time with respect to the 'reference' solution.
- However, the standard deviation of the (code – phase) residuals (last row of Table 1) is slightly better when using our 'automated' methods than with the reference solution. Indeed, it seems to have a small differential slope between code and our phase 'reference' solution (Figure 7, top).

Batch	Ref	Quadratic fit			Average Differences		
		K=3	K=6	K=9	$\tau=10^4$	$\tau=10^5$	$\tau=10^6$
1	**0**	0	0	0	0	0	0
2	**0**	2	2	2	2	1	2
3	**3**	4	4	4	4	4	5
4	**-3**	-1	-1	-1	-1	-2	3
5	**-4**	1	1	1	1	0	0
6	**-1**	3	3	3	3	3	3
StdDev	***1.99***	***1.35***	***1.35***	***1.35***	***1.35***	***1.35***	***1.35***

Table 1. Results of the Narrow Lane identification : Each method produces each one solution (Relative comparison, the first offset is enforced to 0). The StdDev row gives the standard deviation, in ns, of the (code – phase) residuals

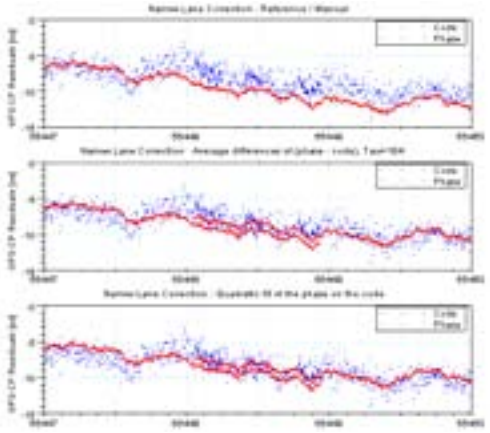

Figure 7. Zoom on an overlapping period : Whereas the 'manual' correction allows to align phase solutions, some jumps remain wthever we use 'Average difference' or 'Quadratic fit' methods

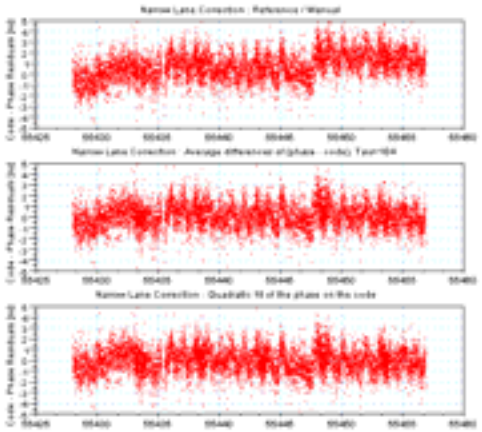

Figure 8. (Code – Phase) residuals : 'Reference' solution seems to exhibit a smal drift (top) which is not present with 'Average difference' or 'Quadratic fit' methods

This last point is confirmed by the analysis of the (Code – Phase) residuals (Figure 8): A slope appears in the reference solution (top), whereas the residuals are almost flat with 'Average difference' or 'Quadratic fit' methods. It suggests that the assumption of the consistency of code and phase solutions have to be more deeply investigated.

IV. CONCLUSION

Comparison of T2L2 and GPS-CP has demonstrated the necessity to improve the identification of Narrow Lane ambiguities to allow absolute and accurate comparison of the two systems. Different identification methods were evaluated in this paper, nevertheless the results are not reliable enough and some points need to be investigated around the consistency between code and phase solutions in GPS-CP time transfer.

This study of Code / Phase consistency can take place on two levels:

- Extending the comparison of T2L2 and GPS-CP for long batches with continuous GPS and T2L2 data set, to confirm that T2L2 can provide an independent method to identify Narrow Lane residual ambiguity. The fact that a large amount of data is now available should facilitate this analysis;
- Trying to understand the root cause of this inconsistency: does it come from the GPS measurements or from the receivers or is it introduced by the data processing?

However, it is still possible to identify Narrow Lane jumps using T2L2 as a reference, at least in a relative way. Moreover, with an accuracy better than 100 ps, T2L2 should allow an absolute identification of Narrow Lane's jumps and thus an absolute / accurate (but not really independent) comparison with GPS-CP. As soon as these will be achieved, T2L2 comparisons could permit to calibrate GPS-CP links at the 100 ps level and to improve the understanding of both the physics and the metrology involved in such CP technology.

ACKNOWLEDGMENT

The authors wish to thank the FTLRS and MeO teams from the OCA for operating the SLR stations, SYRTE staff for their welcome and support at the Observatoire de Paris, IGS, SYRTE and Wettzell teams for their GPS data and F. Mercier (CNES, GPS PPP software) for its software and support.

REFERENCES

[1] E. Samain, M. Laas-Bourez, C. Courde, P. Exertier, J.M. Torre, N. Martin, J.L. Oneto, M. Aimar, F.Pierron, Ph. Guillemot, S. Leon, "*T2L2: Ground to Ground Time Transfer*", Proceedings of the EFTF 2012, pp 36-40

[2] J. Delporte, F. Mercier, D. Laurichesse, O. Galy, "*GPS carrier phase time transfer using single-difference integer ambiguities*", International Journal of Navigation and Observation, Hindawi Publishing Corporation, Volume 2008, Article ID 2737858

[3] P. Fridelance, E. Samain and C. Veillet, "*T2L2 - Time transfer by laser link : A new optical time transfer generation*", Experimental Astronomy Vol.7 Num.3 Sept.97

[4] E. Samain, P. Exertier, Ph. Guillemot, Ph. Laurent, F. Pierron, D. Rovera, J.-M. Torre, M. Abgrall, J. Achkar, D. Albanese, C. Courde, K. Djeroud, M. Laaz-Bourez, S. Leon, H. Mariey, G. Martinot-Lagarde, JL. Oneto, J. Paris, M. Pierron, H. Viot, "*Time transfer by laser link - T2L2: Current status and future experiments*", Proceedings of the IFCS/EFTF 2011

[5] Ph. Guillemot, P. Exertier, E. Samain, F. Pierron, Ph. Laurent, M. Abgrall, J. Achkar, D. Rovera, K. Djerroud, S. Leon, "*Time Transfer By Laser Link - T2l2 : First Results Of The 2010 Campaign*", Proceedings of the PTTI 2010, pp 397-412

A Transportable Optical Lattice Clock Using ^{171}Yb

Gregor Mura, Tobias Franzen, Charbel Abou Jaoudeh, Axel Görlitz,
Heiko Luckmann, Ingo Ernsting, Alexander Nevsky, Stephan Schiller
and the SOC2 Team

Institut für Experimentalphysik
Heinrich-Heine Universität Düsseldorf
E-Mail: axel.goerlitz@uni-duesseldorf.de
http://www.soc2.eu

***Abstract*—We present first results on the spectroscopy of the $^1S_0 \rightarrow {}^3P_0$ transition at 578 nm in a transportable ^{171}Yb optical lattice clock. With the Yb atoms confined in a one-dimensional optical lattice, we have observed linewidths below 200 Hz, limited by saturation broadening. Currently the system is being upgraded towards full clock operation and use of more compact and robust subsystems.**

I. Introduction

Optical lattice clocks based on elements with two valence electrons are strong competitors in the quest for next generation time and frequency standards. Promising results have already been obtained in several stationary setups using Sr [1]–[4], Hg [5], Mg [6] and Yb [7], [8]. In particular, a record instability in the 10^{-18} range has recently been demonstrated for Yb lattice clocks [9]. However, in addition to stationary setups, transportable clocks are desirable for a variety of reasons. The ability to transport them and compare them with other frequency standards allows for a performance evaluation beyond what is possible with standards at a single institute. Furthermore, many applications, e.g. geodesy and ground stations for space missions, will benefit from transportable optical clocks. Last but not least, sending optical clocks into space will allow greatly improved tests of fundamental physics [10].

In the framework of the ESA candidate mission "Space Optical Clock", an optical lattice clock is foreseen to be operated on the ISS around the year 2018. As part of technology development towards that goal, breadboard and transportable lattice optical clock demonstrators using Sr and Yb are being developed in a EU FP7 project [11].

Our transportable Yb clock system is based on compact diode lasers (399 nm, 1156 nm frequency doubled in a PPLN waveguide, 759 nm) and a fiber laser (1111 nm frequency doubled in a PPLN waveguide), and features an intra-vacuum enhancement resonator to allow the formation of a large-volume one-dimensional optical lattice using moderate laser power. Our current experimental setup for the atom source is shown in figure 1a and comprises an optical table of $2\,\mathrm{m} \times 1\,\mathrm{m}$ for the optical and vacuum setup and approximately two standard 19" rack shelves of non-optimized electronics.

This does not include the clock laser setup shown in figure 1b, which takes up another 90 cm × 120 cm breadboard and is currently located in another laboratory. Here a commercial ECDL is frequency doubled and stabilized to sub-Hertz linewidths using a highly stable ULE cavity [12]. A phase-stabilized 300 m intra-building fiber link connects this setup to the atom apparatus, where after frequency doubling 1.5 mW are available for spectroscopy.

(a) Atom apparatus (b) Clock laser

Fig. 1: Photographs of the experimental setup, showing (a) the atom source including the lattice and cooling lasers and (b) the clock laser setup.

A. Atom source

The ytterbium atoms are loaded into the first-stage MOT on the $^1S_0 \rightarrow {}^1P_1$ transition at 399 nm with a typical time constant of 500 ms, resulting in 10^7 atoms after 2 s loading time. The second-stage MOT operating on the $^1S_0 \rightarrow {}^3P_1$ transition at 556 nm, optimized for temperature, contains several times 10^5 atoms at a temperature of around 25 µK.

From this second-stage MOT the atoms can be efficiently transferred to the optical lattice. By using an intra-vacuum enhancement resonator, we achieve a circulating laser power of 10 W, corresponding to a trap depth of 40 µK in a large volume trap (155 µm trap radius) using a moderate laser power of a few hundred mW. Due to good matching of the lattice to the volume of the postcooling MOT, we routinely achieve transfer efficiencies in excess of 20 % for atom temperatures of $\sim$ 25 µK. The addition of optical pumping on the $^1S_0 \rightarrow {}^3P_1$ transition will allow us to spin polarize the atoms. After the clock probe pulse is applied, the atoms remaining in the ground state are detected by fluorescence on the $^1S_0 \rightarrow {}^1P_1$ transition.

When operating at an appropriate oven temperature, the

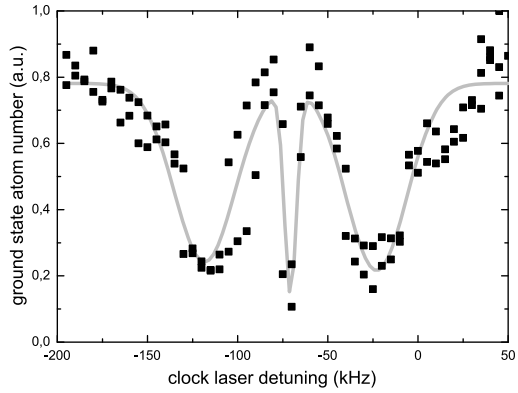

Fig. 2: Spectrum of the clock transition using the chopped lattice technique. The number of atoms remaining in the ground state after the chopped lattice sequence is plotted as function of the detuning of the clock laser.

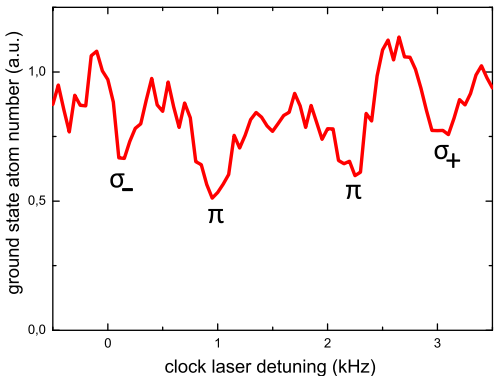

Fig. 3: Spectrum of the clock transition with the atoms held in a one-dimensional optical lattice in the presence of a magnetic bias field. The number of atoms remaining in the ground state after the clock pulse is plotted as function of the detuning of the clock laser. The four Zeeman components of the transition can be resolved.

total cycle time can be reduced to below 1 s while retaining sufficient signal from the atoms captured in the lattice.

B. Spectroscopy on the clock transition

In order to rapidly locate the clock transition, we use a *chopped lattice* technique, similar to that applied during the first frequency measurement of this transition [13]. Alternating short pulses of 578 nm light to excite the clock transition and of 556 nm light to retrap and cool the atoms allows us to achieve high contrast signals, with observed linewidths adjustable between a few kHz and hundreds of kHz. The retrapping pulses allow us to interrogate the atoms for several trap lifetimes, thus yielding a high contrast even for incoherent excitation due to loss of excited atoms. Figure 2 shows a spectrum obtained in this manner. The sharp carrier transition is clearly visible, surrounded by sidebands corresponding to motional excitations in the lattice. The sideband spacing corresponds to a trap depth of 40 µK.

Probing the transition on atoms trapped in the lattice we have successfully resolved the Zeeman components and achieved linewidths of less than 200 Hz, consistent with saturation broadening. A typical spectrum is shown in figure 3. The observed Zeeman splitting is due to a magnetic background field of ~ 2.5 G, which for clock operation will be partially compensated using the magnetic coils.

C. Next generation laser systems

Having demonstrated the capabilities required to operate our experimental apparatus as an optical clock, we are currently improving several aspects of the experimental setup, with a focus on more compact and robust subsystems. In particular, we are replacing most laser systems by more compact modules promising better performance. While several hours of hands off operation have been achieved with the previous setup, we are striving for improved reliability as well as a more compact and modular overall system.

For the first-stage cooling and detection at 399 nm we have developed a new laser system shown in figure 4, comprising two injection-locked diode lasers. For the generation of

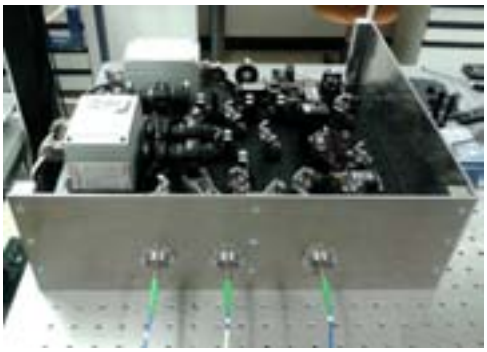

Fig. 4: New 399 nm laser system module during testing. The grey boxes contain the master ECDL and two slaves respectively. The whole system fits into a 19" rack shelf and all outputs are fiber coupled.

seed light, we are investigating several setups, among them AR coated laser diodes in an interference-filter-based ECDL design [14], developed in collaboration with the University of Hannover (LUH). The master as well as the two slave lasers and all frequency generation steps for frequency stabilization, slower and precooling MOT are contained on a $45\,\mathrm{cm} \times 45\,\mathrm{cm}$ breadboard with fiber outputs.

An interference filter based design from LUH is also currently being evaluated for the generation of the lattice light at 759 nm. Together with a new enhancement resonator providing higher finesse and tighter focusing, this self-injecting tapered amplifier will present a considerable simplification with respect to the current MOPA system consisting of a commercial ECDL and a tapered amplifier.

Our home-built 556 nm laser has already been replaced with an integrated module by Menlo Systems, which directly provides output at 556 nm employing frequency-doubling of a fiber laser, with the actual laser system requiring a volume of only 3 l. Using this system, we have successfully operated the experiment and demonstrated improved atom numbers and

stability in the postcooling MOT.

Additionally, we are currently integrating a DFB laser at $1388\,\mathrm{nm}$ into the experiment, which will be used as a repumper for the upper clock state and allow direct detection of the excited atoms. Together with further efforts to improve detection, this will lead to improved signal quality.

II. Conclusion

We have demonstrated spectroscopy of the clock transition in ^{171}Yb in a one-dimensional optical lattice. We have already observed linewidths of below $200\,\mathrm{Hz}$ and estimate an uncertainty of less than 10^{-14} to be readily achievable with minor modifications to our setup.

The current setup provides a solid foundation for a transportable ^{171}Yb lattice clock. Several ongoing modifications of the experimental apparatus will improve transportability, reliability and performance of the system and will allow rapid characterization of the system for competitive clock operation.

Acknowledgment

The research leading to these results has received funding from the European Union Seventh Framework Programme (FP7/2007-2013) under grant agreement no. 263500.

References

[1] M. Takamoto, F. Hong, R. Higashi, and H. Katori, "An optical lattice clock," *Nature*, vol. 435, no. 7040, pp. 321–324, 2005.

[2] A. D. Ludlow, T. Zelevinsky, G. K. Campbell, S. Blatt, M. M. Boyd, M. de Miranda, M. J. Martin, J. W. Thomsen, S. M. Foreman, J. Ye *et al.*, "Sr Lattice Clock at $1 \cdot 10^{-16}$ Fractional Uncertainty by Remote Optical Evaluation with a Ca Clock," *Science*, vol. 319, no. 5871, p. 1805, 2008.

[3] X. Baillard, M. Fouché, R. Le Targat, P. Westergaard, A. Lecallier, F. Chapelet, M. Abgrall, G. Rovera, P. Laurent, P. Rosenbusch *et al.*, "An optical lattice clock with spin-polarized 87 sr atoms," *The European Physical Journal D-Atomic, Molecular, Optical and Plasma Physics*, vol. 48, no. 1, pp. 11–17, 2008.

[4] N. Poli, M. Tarallo, M. Schioppo, C. Oates, and G. Tino, "A simplified optical lattice clock," *Applied Physics B: Lasers and Optics*, vol. 97, no. 1, pp. 27–33, 2009.

[5] H. Hachisu, K. Miyagishi, S. Porsev, A. Derevianko, V. Ovsiannikov, V. Pal'Chikov, M. Takamoto, and H. Katori, "Trapping of neutral mercury atoms and prospects for optical lattice clocks," *Phys. Rev. Lett.*, vol. 100, no. 5, p. 53001, 2008.

[6] J. Friebe, A. Pape, M. Riedmann, K. Moldenhauer, T. Mehlstäubler, N. Rehbein, C. Lisdat, E. Rasel, W. Ertmer, H. Schnatz *et al.*, "Absolute frequency measurement of the magnesium intercombination transition $^1S_0 \rightarrow ^3P_1$," *Phys. Rev. A*, vol. 78, no. 3, p. 033830, 2008.

[7] N. D. Lemke, A. D. Ludlow, Z. W. Barber, T. M. Fortier, S. A. Diddams, Y. Jiang, S. R. Jefferts, T. P. Heavner, T. E. Parker, and C. W. Oates, "Spin-$1/2$ optical lattice clock," *Phys. Rev. Lett.*, vol. 103, p. 063001, Aug 2009.

[8] T. Kohno, M. Yasuda, K. Hosaka, H. Inaba, Y. Nakajima, and F.-L. Hong, "One-dimensional optical lattice clock with a fermionic ^{171}Yb isotope," *Applied Physics Express*, vol. 2, no. 7, p. 072501, 2009.

[9] N. Hinkley, J. A. Sherman, N. B. Phillips, M. Schioppo, N. D. Lemke, M. P. K. Beloy, C. W. Oates, and A. D. Ludlow, "An atomic clock with 10^{-18} instability," *arXiv preprint arXiv:1305.5869*, 2013.

[10] S. Schiller *et al.*, "Einstein gravity explorer - a medium-class fundamental physics mission," *Experimental Astronomy*, vol. 23, pp. 573–610, 2009.

[11] S. Schiller *et al.*, *Let's embrace space*, Vol. II, Ch. 45, pp. 452–463. *Towards Neutral-atom Space Optical Clocks (SOC2): Development of high-performance transportable and breadboard optical clocks and advanced subsystems*, (Luxembourg: Publications Office of the European Union, 2012), ISBN 978-92-79-22207-8, doi:10.2769/31208

[12] S. Vogt, C. Lisdat, T. Legero, U. Sterr, I. Ernsting, A. Nevsky, and S. Schiller, "Demonstration of a transportable 1 Hz-linewidth laser," *Applied Physics B: Lasers and Optics*, vol. 104, 741-745, 2011.

[13] C. W. Hoyt, Z. W. Barber, C. W. Oates, T. M. Fortier, S. A. Diddams, and L. Hollberg, "Observation and absolute frequency measurements of the $^1S_0$-$^3P_0$ optical clock transition in neutral ytterbium," *Phys. Rev. Lett.*, vol. 95, p. 083003, Aug 2005.

[14] M. Gilowski, C. Schubert, M. Zaiser, W. Herr, T. Wbbena, T. Wendrich, T. Mller, E. Rasel, and W. Ertmer, "Narrow bandwidth interference filter-stabilized diode laser systems for the manipulation of neutral atoms," *Optics Communications*, vol. 280, no. 2, pp. 443 – 447, 2007.

Improved Set-Up for the Ytterbium Optical Clock at INRIM

Marco Pizzocaro*†, Filippo Bregolin*‡, Davide Calonico*, Giovanni Antonio Costanzo†, Filippo Levi* and Luca Lorini*
*Istituto Nazionale di Ricerca Metrologica (INRIM), Str. delle Cacce 91, 10135 Torino, Italy.
Email: m.pizzocaro@inrim.it
†Politecnico di Torino, Dipartimento di Elettronica e Telecomunicazioni, C.so duca degli Abruzzi 24, 10125 Torino, Italy
‡Università di Torino, Dipartimento di Fisica, Via Giuria 1, 10125, Torino, Italy

***Abstract*— We present an upgraded setup for cooling and trapping of ytterbium atoms in a optical clock experiment. The experiment aims to cool and trap ytterbium atoms in a two stage magneto-optical trap (MOT) (at 399 nm and 556 nm for the first and second stage, respectively) and to probe the narrow-line clock transition at 578 nm in an optical lattice at the magic wavelength (759 nm). We describe here the generation of all the laser sources and the design of a new physic package, including the vacuum chamber and the atomic source.**

I. Introduction

Optical lattice clock based on ytterbium are being studied and developed worldwide, for example at National Institute of Standards and Technology (NIST) [1], at the National Metrology Institute of Japan (NMIJ) [2] and at the Korea Research Institute of Standards and Science (KRISS) [3]. We present here an upgraded setup for cooling and trapping ytterbium atoms for an optical clock experiment. For the experiment ytterbium atoms have to be cooled and trapped first in a 399 nm magneto-optical trap (MOT) then in a 556 nm MOT. Finally the narrow-line clock transition at 578 nm is probed with the atoms trapped in an optical lattice at the magic wavelength (759 nm). The laser ensemble at Istituto Nazionale di Ricerca Metrologica (INRIM) is now completed and a new physic package is build, including the vacuum chamber and the atomic source.

II. Laser systems

A. Blue laser at 399 nm

In our experiment the blue 399 nm radiation is obtained by second harmonic generation (SHG) from a 798 nm titanium-sapphire (Ti:sapphire) laser using a lithium triborate (LBO) crystal, chosen to achieve high power, stability and tunability [4].

The 798 nm source is a Ti:sapphire laser pumped by a 8 W solid state pump laser at 532 nm that can be tuned from 700 nm to 970 nm and has an output power at 798 nm of 1.3 W with a linewidth < 20 kHz.

Our LBO crystal is $l = 15$ mm long, has a section of 1.5 mm $\times$ 1.5 mm, and is cut for normal incidence with antireflection coating on the faces. To increase the output power at 399 nm the crystal is placed in a bow-tie enhancement cavity, resonant at 798 nm. The cavity has been designed with two concave mirrors (radius of curvature $r = 100$ mm) around the LBO crystal leading to a beam waist inside the crystal of 35 µm [5] close to the optimum value [6]. Total length of the cavity is 715 mm, for a free spectral range of 210 MHz and the distance between the curved mirrors is 114 mm. For maximum stability and simplicity in the alignment we mounted the mirrors on top-actuated mirror mounts placed on a monolithic block of aluminum. One flat mirror is mounted on a small piezo actuator for locking of the cavity on the Ti:sapphire laser with the Hänsch-Couillaud technique. The LBO crystal is mounted on a rotational stage.

The power circulating in the enhancing cavity P_{1c} is related to the power injected in the cavity P_1 by [7]

$$P_{1c} = \frac{P_1 T_1}{\left[1 - \sqrt{(1-T_1)(1-l_{cav})(1-E_{nl}P_{1c})}\right]^2}, \quad (1)$$

where T_1 is the transmission of the input coupler of the cavity and l_{cav} represents the linear losses in the cavity, by the crystal and mirrors other than the input coupler and $E_{nl} = 7.5 \times 10^{-5}\,\mathrm{W}^{-1}$ is the effective nonlinear coefficient for LBO [6]. The optimal input coupler transmission depends on the linear losses and the input power

$$T_1 = \frac{l_{cav}}{2} + \sqrt{\frac{l_{cav}^2}{4} + E_{nl}P_1}. \quad (2)$$

We estimated a linear loss in the cavity coming from the mirrors and the coating on the faces of the crystal $l_{cav} \sim 4 \times 10^{-3}$. For a well matched input power of 1.1 W the transmission of the input coupler was chosen $T_1 = 0.012$

Figure 2 shows experimental data for the SHG power at 399 nm as a function of the input power. The output has a maximum at 0.65 W with 1.2 W of input power; the SHG efficiency is 54 %. The same figure shows also a theoretical prediction. Theory and experimental data are well matched; they slightly diverge at high power because each data point was taken without re-alignment of the optics. This system replaced a similar one that used a periodically-poled potassium titanyl phosphate (PPKTP) crystal that was found to be too absorptive at 399 nm and was delivering a maximum output power of 60 mW.

To cope for the long term frequency drift, the laser is locked to the atomic resonance by transverse spectroscopy on an auxiliary ytterbium beam. This source at 399 nm will be used for the blue MOT, for a slower beam, and for a resonant probe beam for detection since it has enough power.

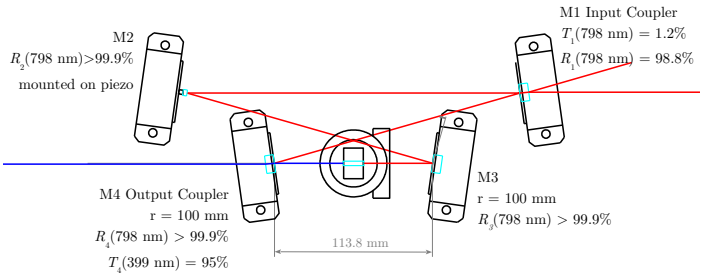

Fig. 1. Draw of the cavity for the SHG of 399 nm with the LBO crystal.

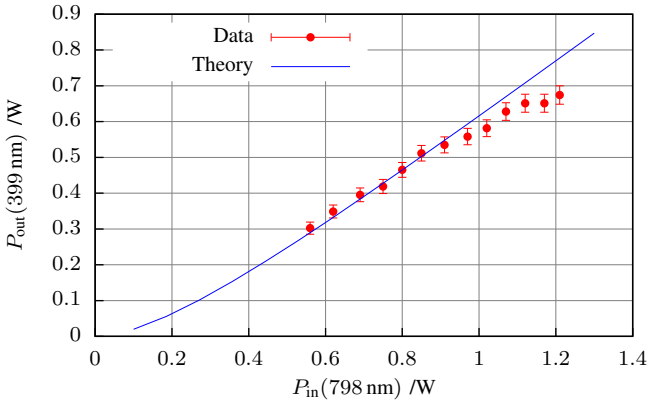

Fig. 2. SHG power as a function of input power. The continuous line is theoretically calculated for $T_1 = 0.012$ and $l_{cav} = 3.8 \times 10^{-3}$.

B. Green laser at 556 nm

The green 556 nm radiation is obtained by SHG from a 1112 nm fiber laser using a PPKTP crystal.

The 1112 nm laser source is a ytterbium doped fiber laser. It has a maximum output power of 10 mW at this wavelength and a linewidth $<$ 20 kHz. The output of the fiber laser is amplified by a fiber amplifier up to 2 W.

The amplified laser is send on the non-linear crystal using free-air optics. The PPKTP crystal is 20 mm long and used in single pass. It is held in a copper oven for temperature stabilization. The laser is focused on the crystal with a waist close to the optimum value of 35 µm [6]. Two mirrors for the visible wavelengths are used to filter the infrared light before the green is sent to the acousto-optic modulators (AOMs) and the fiber couplings needed for the experiment.

Up to 22 mW of 556 nm light has been obtained starting from 1.3 W of 1112 nm measured at the crystal. The frequency of the green laser is locked to the resonance of an ultrastable cavity.

C. Lattice laser

The Ti:sapphire laser that will be used as optical lattice is a M Squared SolsTiS pumped by a solid state pump laser at 10 W. It has a maximum output power of 3.2 W at the magic wavelength 759 nm. We have estimated its linewidth to be less than 20 kHz by comparison with another Ti:sapphire laser.

This source is able to provide large trap depths both for 1D and multidimensional lattice configurations. For example about 1 W of power in the lattice focused to a 35 µm waist gives a trap depth of $500E_r$, where E_r is the recoil energy.

D. Clock laser at 578 nm

The yellow laser at 578 nm is obtained by sum frequency generation (SFG) in a periodically-poled lithium niobate (PPLN), $LiNbO_3$, crystal, using two infrared laser sources (1030 nm and 1319 nm).

The 1319 nm source is a monolithic neodymium-doped yttrium aluminium garnet (Nd:YAG) laser with an output power of 90 mW. The 1030 nm source is an erbium fiber laser with 80 mW output power. The linewidth of both lasers is less than 10 kHz

The crystal is a waveguide, magnesium-doped, PPLN device. Infrared light of both lasers is delivered to the crystal through a polarization-maintaining fiber coupler (Y-shaped). The output of the coupler is a bare fiber, and it is simply put near to the input face of the crystal to couple the light with the non-linear waveguide (the distance is of the order of 1 µm). Being a waveguide crystal, the infrared lasers are coupled to one of 32 working channels where are tightly confined over the length of the crystal (20 mm). This design avoids problems arising from the focusing of the beam, diffraction, or walk-off angles. The output power is maximized by tuning the temperature of the crystal. We have obtained up to $P_{out} = 12$ mW of laser at 578 nm which represents the damage threshold of the crystal.

The frequency of the yellow laser is stabilized using the Pound-Drever-Hall technique on a ultra-stable cavity entirely made of Corning Ultra Low Expansion glass (ULE) and a length of 10 cm. Once locked, it has a stability of 3×10^{-15} at 1 s of integration time or a linewidth $<$ 2 Hz [8]. An improved setup using a cavity with fused-silica mirrors is planned for the near future [9].

III. Physics Package

A. Description of the chamber

Figure 3 shows a scheme of the vacuum chamber and of some of its features. The atomic source is an effusion oven at 400 °C that produces a collimated atomic beam.

The core of the design is a custom aluminum chamber for the trapping region with 6 lateral viewports (diameter 40 mm) and two larger horizontal viewports (diameter 70 mm). The other components are standard stainless steel fittings. Indium sealing is used for the viewports on the aluminum chamber (a similar solution has been adopted in the strontium optical clock at LNE-Syrte in Paris). Indium is used also between a flat-flat mating achieved using a K flange transition for sealing together aluminum and stainless steel. This solution allows for a wide area of the viewports to be available for optical access but requires only a small retaining force reducing the induced birefringence in the glass. For this reason it is preferred to Kasevich-style sealing.

Using indium-sealing, all the surface of the viewports can be coated because no flange shadows the deposition of the coating. The anti-reflection coating of the viewports is especially made by ATFilms for all the wavelengths of interest.

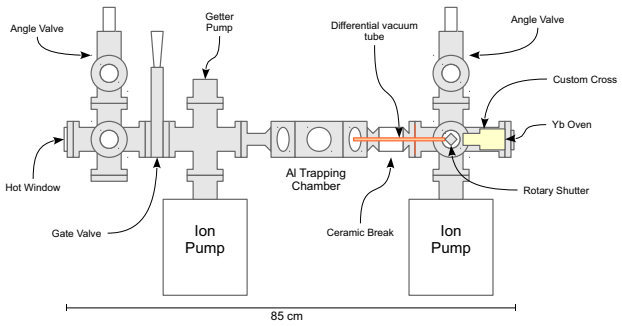

Fig. 3. Scheme of the improved vacuum chamber.

The reflectivity for the blue 399 nm is $R = 0.08\,\%$, for the green 556 nm $R = 0.1\,\%$, and for the clock laser at 578 nm is $R = 0.03\,\%$. The anti-reflection coating is especially important at the magic wavelength 759 nm ($R = 0.05\,\%$), anticipating an external enhanced cavity for the lattice.

The chamber is designed without a Zeeman slower. Instead the distance between the trapping region and the atomic source is made as short as possible to maximize the atomic flux. The distance between the oven nozzle and the MOT region is 21 cm. Considering the atomic beam divergence from the oven the flux of atoms is 5 times larger than for an hypothetical setup with the oven at 60 cm [10].

A differential-vacuum tube divides the oven side of the structure from the clean trapping region. The differential-vacuum tube has internal radius 2.5 mm and length 120 mm. It is designed to maintain a pressure ratio between the two sides of 100 both for nitrogen and hydrogen. This means that a vacuum pressure of 10^{-10} mbar in the clean side of the chamber is compatible with a pressure of 10^{-8} mbar on the oven side.

The oven is made by a stainless steel reservoir and it is heated under vacuum [11]. At the exit of the reservoir ~ 37 stainless steel capillaries are used to collimate the atomic beam. Between the oven nozzle and the differential-vacuum tube is placed a shutter that can turn off the atomic beam. The shutter is based on a rotary feedthrough, whose shaft can rotate at high speed. During clock operations the shutter will prevent scattering of the trapped atoms with the thermal beam. It will also shield the blackbody radiation from the oven and thus simplify the evaluation of the blackbody radiation shift on the clock transition.

Facing the oven nozzle, on the clean side, a window is used for a slower laser beam, counterpropagating the atomic beam. The windows is heated at 230 °C to prevent deposition of ytterbium.

Two angle valves are used for connection to turbo-molecular pumps. On both sides there is an ion pump of nominally 40 L/s speed. On the clean side there is also a non-evaporable getter pump. The getter pump is a passive pump for hydrogen (H_2) but also pumps water and carbon oxide. The getter pumping speed for hydrogen is 50 L/s.

B. Preliminary results

All the indium seals and the other flanges has been helium-checked at a level of 1×10^{-12} mbar L/s. The pressure in the trapping region is 1×10^{-9} mbar with the oven temperature 400 °C, limited by the pressure in the oven side 6×10^{-8} mbar. The atom lifetime in the lattice is expected to be ~ 3 s at this pressure, that is more than enough for clock operations. At room temperature the pressure on the trapping chamber is $< 5 \times 10^{-10}$ mbar.

With the oven at 380 °C the atomic beam flux in the trapping chamber, after the differential vacuum tube, has been measured 5×10^{10} atoms/s (for all Yb isotopes). The flux raises to 1.2×10^{11} atoms/s with the oven at 400 °C. The beam divergence in the chamber is 29 mrad, given by the capillaries in the oven nozzle and not limited by the differential vacuum tube.

C. Capture numbers and simulations

The trapping efficiency can be enhanced increasing the number of atoms with velocity lower than the capture velocity. The atomic beam from the oven can be slowed using a counter-propagating, detuned to the red, laser beam .For this purpose a Zeeman slower is usually used; a space dependent magnetic field is engineered so that the atoms are always kept on resonance while decelerated. Without the magnetic field the effect of the beam is limited because, once slowed down, atoms go out of resonance and are decelerated only for a short portion of their path.

In our setup a Zeeman slower is not used for simplicity. The simply addition of a slower beam usually improves a factor of ten the number of trapped atoms [12], [13]. Moreover a Zeeman slower is usually 50 cm long while without it is possible to keep the setup shorter.

We performed numerical simulations to investigate the possibility of exploiting the magnetic field of the MOT coils in the slowing process [10]. In our configuration the magnetic field gradient in the plane is $A_r = 0.23$ T/m. Considering the mean radius of the coils 5.5 cm we expect a maximum magnetic field of 13 mT in the plane between the coils.

We assumed a capture velocity of 30 m/s and a thermal beam at 400 °C. Considering ^{171}Yb (isotopic abundance 14.3 %), the fraction of atoms below thermal velocity (4×10^{-4}) and the measured atomic flux we obtain a capture rate in the MOT $R = 7 \times 10^6$ atoms/s without any slower beam. For a linera loss rate in the MOT $\alpha \simeq 2$ s this corresponds to a number of atoms in the MOT of $N_{\max} \sim 3 \times 10^6$.

Two example of the effects of a slower beam are simulated in fig. 4. The plots shows the trajectories in the phase space for atoms with different initial velocities 20 cm far away from the MOT center, with a fixed detuning and polarization of the slower beam. The gray thick line shows the space-dependant velocity at which the atoms are resonant with the light because of the magnetic field, given the slower detuning. The top figure shows the simpler approach. This is a simulation with detuning $\delta = -150$ MHz and polarization σ^-. With this polarization the magnetic field from the coils pushes slower atoms out of resonance and the slower is effective only far away from the MOT center. There is not enough space to slow down faster

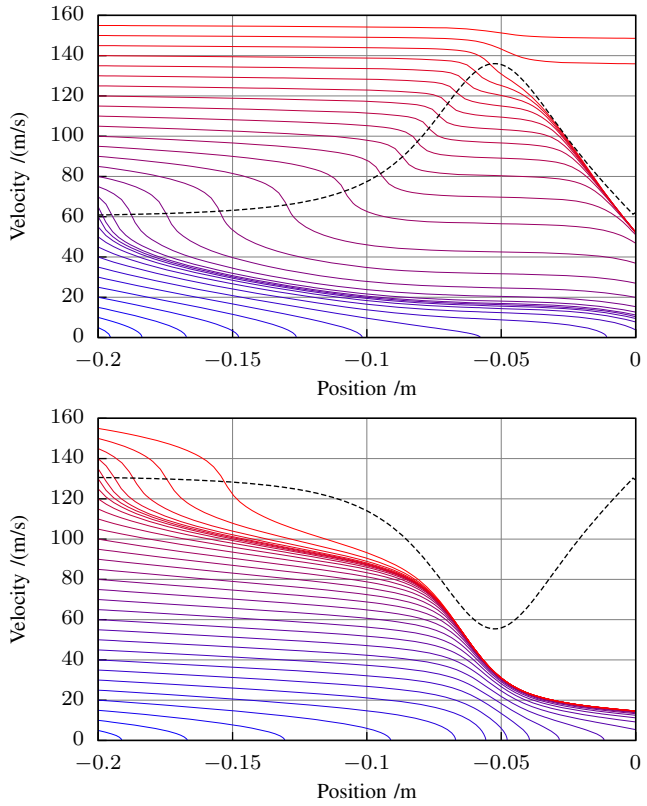

Fig. 4. Numerical simulation of the trajectories in the phase space for atoms slowed by a beam with: top, power $P = 8\,\mathrm{mW}$, waist radius $w = 4\,\mathrm{mm}$, detuning $\delta = -150\,\mathrm{MHz}$, polarization σ^-; bottom, $P = 20\,\mathrm{mW}$, $w = 4\,\mathrm{mm}$, $\delta = -330\,\mathrm{MHz}$, polarization σ^+. The thick broken line shows the velocity at which the atoms are resonant with the light, modulated by the total magnetic field of the MOT coils. The MOT is at position 0 cm with the atoms moving from left to right.

atoms brought in resonance by the magnetic field gradient of the MOT. In this configuration atoms with initial velocity $v_\mathrm{i} = 60\,\mathrm{m/s}$, usually not captured by the MOT, are brought to a velocity of $v_\mathrm{f} = 20\,\mathrm{m/s}$ that is below the capture velocity. Simulations predicts an increase of 50 for the number in the MOT respect at the case withouth the slower beam, or a fraction of atoms below the capture velocity of 2.0 % for a capture rate of $R = 3.4 \times 10^8$ atoms/s and a maximum number of atoms in the MOT $N_\mathrm{max} \sim 1.7 \times 10^8$.

The bottom figure shows a different approach, with the beam further detuned to $\delta = -330\,\mathrm{MHz}$ and polarization σ^+. With this polarization the leaking magnetic field can be used to keep atoms in resonance, achieving a makeshift Zeeman slower. This configuration is predicted to be more efficient than the previous one, with a gain in the atom number of 200, a fraction of atoms below the capture velocity of 7.6 % for a capture rate of $R = 1.3 \times 10^9$ atoms/s and a maximum number of atoms in the MOT $N_\mathrm{max} \sim 7 \times 10^8$.

Acknowledgment

The authors acknowledge for funding the EU-FP7-SPACE-2010-1 project No. 263500 (SOC2) and the EMRP program (Project SIB55-ITOC). The EMRP is jointly funded by the EMRP participating countries within EURAMET and the European Union. The authors would like to acknowledge E. K. Bertacco for the help and J. Catani for useful discussions.

References

[1] N. D. Lemke, A. D. Ludlow, Z. W. Barber, T. M. Fortier, S. A. Diddams, Y. Jiang, S. R. Jefferts, T. P. Heavner, T. E. Parker, and C. W. Oates, "Spin-1/2 optical lattice clock," *Phys. Rev. Lett.*, vol. 103, no. 6, p. 063001, Aug 2009.

[2] M. Yasuda, H. Inaba, T. Kohno, T. Tanabe, Y. Nakajima, K. Hosaka, D. Akamatsu, A. Onae, T. Suzuyama, M. Amemiya, and F.-L. Hong, "Improved absolute frequency measurement of the ^{171}yb optical lattice clock towards a candidate for the redefinition of the second," *Applied Physics Express*, vol. 5, no. 10, p. 102401, 2012.

[3] C. Y. Park, D.-H. Yu, W.-K. Lee, S. E. Park, E. B. Kim, S. K. Lee, J. W. Cho, T. H. Yoon, J. Mun, S. J. Park, T. Y. Kwon, and S.-B. Lee, "Absolute frequency measurement of $^1S_0$ ($f = 1/2$) - $^3P_0$ ($f = 1/2$) transition of ^{171}Yb atoms in a one-dimensional optical lattice at KRISS," *Metrologia*, vol. 50, no. 2, p. 119, 2013.

[4] G. Ferrari, J. Catani, L. Fallani, G. Giusfredi, G. Schettino, F. Schäfer, and P. C. Pastor, "Coherent addition of laser beams in resonant passive optical cavities," *Opt. Lett.*, vol. 35, no. 18, pp. 3105–3107, Sep 2010.

[5] T. Freegarde and C. Zimmermann, "On the design of enhancement cavities for second harmonic generation," *Opt. Commun.*, vol. 199, pp. 435–446, 2001.

[6] G. D. Boyd and D. A. Kleinman, "Parametric interaction of focused gaussian light beams," *J. Appl. Phys.*, vol. 39, no. 8, pp. 3597–3639, 1968.

[7] E. S. Polzik and H. J. Kimble, "Frequency doubling with $KNbO_3$ in an external cavity," *Opt. Lett.*, vol. 16, no. 18, pp. 1400–1402, Sep 1991.

[8] M. Pizzocaro, G. Costanzo, A. Godone, F. Levi, A. Mura, M. Zoppi, and D. Calonico, "Realization of an ultrastable 578-nm laser for an Yb lattice clock," *IEEE Trans. Ultrason., Ferroelect., Freq. Cont.*, vol. 59, no. 3, pp. 426–431, march 2012.

[9] T. Legero, T. Kessler, and U. Sterr, "Tuning the thermal expansion properties of optical reference cavities with fused silica mirrors," *J. Opt. Soc. Amer. B*, vol. 27, no. 5, pp. 914–919, May 2010.

[10] M. Pizzocaro, "Realization and characterization of optical frequency standards," Ph.D. dissertation, Politecnico di Torino, Feb. 2013.

[11] M. Schioppo, N. Poli, M. Prevedelli, S. Falke, C. Lisdat, U. Sterr, and G. M. Tino, "A compact and efficient strontium oven for laser-cooling experiments," *Rev. Sci. Inst.*, vol. 83, no. 10, p. 103101, 2012.

[12] Z. W. Barber, "Ytterbium optical lattice clock," Ph.D. dissertation, University of Colorado, 2007.

[13] D. Calonico, F. Levi, L. Lorini, G. Costanzo, M. Zoppi, M. Pizzocaro, A. Mura, E. K. Bertacco, and A. Godone, "Yb optical lattice clock at INRIM," in *Proceedings of the 24th European Frequency and Time forum*, no. P2.27, 2010.

Progress Report of an $^{27}Al^{+}$ ion Optical Clock

K. Deng, Z. T. Xu, W. H. Yuan, C. B. Qin, A. Deng, Y. L. Sun, J. Zhang, Z. H. Lu*, and J. Luo
MOE Key Laboratory of Fundamental Quantities Measurement, School of Physics,
Huazhong University of Science and Technology, Wuhan, P. R. China
*E-mail: zehuanglu@mail.hust.edu.cn

***Abstract*— An Al^{+} ion optical clock is under development at Huazhong University of Science and Technology in China. We have successfully crystallized Magnesium ions. Through micro-motion compensation and trapping parameters optimization, temperature of a trapped single ion is lowered to be around 19 mK.**

Keywords- optical clock; Al ion; laser cooling; ion trap

I. INTRODUCTION

The $^{1}S_0$ - $^{3}P_0$ transition of $^{27}Al^{+}$ at 267.4 nm has long been recognized as an excellent optical clock transition candidate. Here we give a progress report on an $^{27}Al^{+}$ ion optical clock developed at Huazhong university of Science and Technology in China. The first stage design goals for the $^{27}Al^{+}$ ion optical clock are an inaccuracy level of 10^{-17} and a stability of $10^{-16}/\sqrt{\tau}$. The implementation of the $^{27}Al^{+}$ ion optical clock will be through quantum logic spectroscopy (QLS), as first proposed by NIST [1]. A single $^{25}Mg^{+}$ ion will be trapped together with a single $^{27}Al^{+}$ ion. The $^{25}Mg^{+}$ ion acts as the logic ion and is used for sympathetic cooling and internal state detection of the $^{27}Al^{+}$ ion.

II. EXPERIMENT SETUP

In our experiment, we use a 285 nm fourth harmonic generation (FHG) laser and a 394 nm laser to photo-ionize Mg and Al atoms respectively, and we use a single 280 nm FHG laser system to cool and detect Mg ions. A 267.4 nm FHG laser is served as clock laser of Al ion, and a 267.0 nm laser as a shelving laser for the purpose of quantum logic.

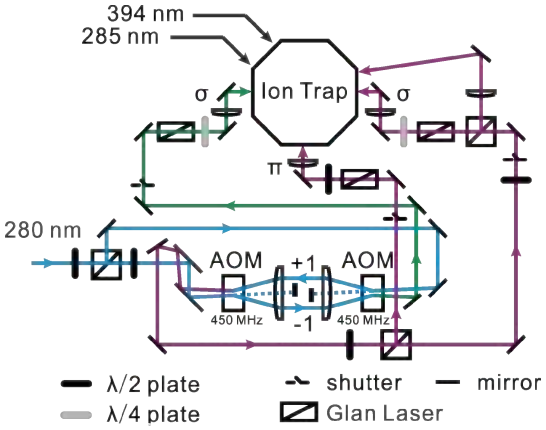

Figure 1. Experimental setup of Mg ion trapping

The 280 nm and 285 nm laser is frequency quadrupled from a 1120 nm and a 1140 nm laser respectively, and each of them can be digitally locked to a high precision wavemeter. The 560 nm second harmonic generation (SHG) of 1120 nm is locked to the transition of molecular I_2 or the wavemeter for long term stability. An electro-optic modulator (EOM) is placed between the SHG and FHG cavity of the 280 nm laser, which is used for generating 9.2 GHz sidebands [2]. The blue sideband of the laser will be used for Doppler cooling and state detection of $^{25}Mg^{+}$, while the carrier of the laser is used for Raman sideband cooling of $^{25}Mg^{+}$.

Experimental setup of Mg ion trapping is shown in Fig.1. The 280 nm laser used for laser cooling of Mg ions has been separated into two lights. Each light passes through two acoustic-optic modulators (AOMs) with a 447.5 MHz drive frequency to generate two lights with a 1.79 GHz frequency difference. The higher frequency one is further separated into three light beams. One is a σ light for Doppler cooling of $^{25}Mg^{+}$, one is a π light for Raman sideband cooling, and the third is used for micro-motion compensation of the vertical direction.

Figure 2 shows the ultrahigh vacuum system in our experimental setup. A linear ion trap, made of titanium, is placed in the center of the vacuum chamber, which is also made of titanium to reduce magnetic field influence. Two CF63 inverted viewports and two sets of custom-made image lens system are used for maximizing the fluorescence Rate. One of lens system with a 3 times of magnification is used for a photon counting PMT and the other with a 10 times of magnification is for an EMCCD.

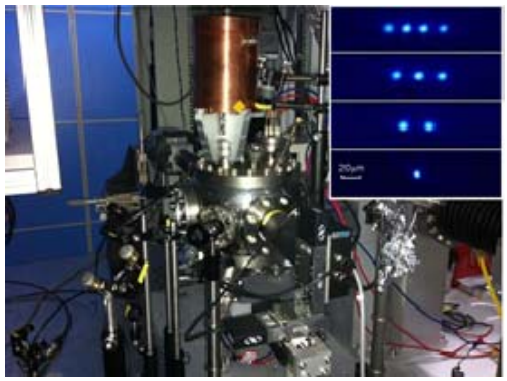

Figure 2. Vacuum system for ion trapping experiments. Inset shows pictures of crystallized Mg ions.

III. Experiment Results

Photo-ionization processing of Mg enables us to observe a strong fluorescence signal of Mg $^1S_0$ - $^1P_1$ transition during loading Mg ions. This signal ensures that the 285 nm laser is tuned to the frequency with high ionization efficiency and is also traveling through the trap center. When suitable parameters of the ion trap are set, we can successfully trap Mg ions and detect fluorescence signals with the help of the 280 nm cooling laser. Crystallized Mg ions are shown in the inset of Fig. 2. One single $^{25}Mg^+$ ion can be stably trapped.

As we know, electric potential experienced by trapped ions is not exactly the same as the ideal linear Paul trap model prediction. In fact, there exist three geometric-depended shielding factors κ_x, κ_y and κ_z for an ion trap. These shielding factors can be evaluated by finite element simulation, and also can be derived by measuring secular motion frequencies of Mg ions which are directly correlated with trap potentials.

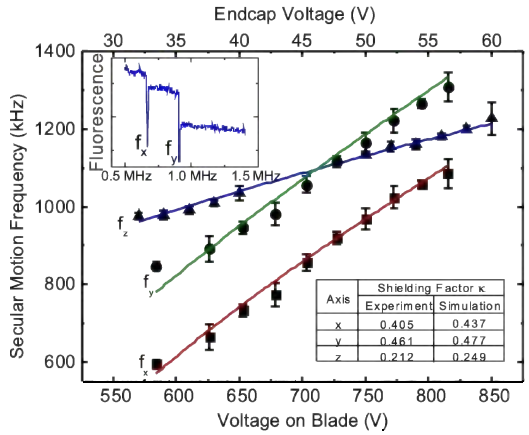

Figure 3. Shielding factors of the ion trap. Experiment results agree with finite element simulation results.

To measure secular motion frequency, we applied an alternating voltage on compensation electrodes, ions will be forced to oscillate with external oscillate electrical field. Resonance appears when the frequency of the electrical field is the same with ions' secular motion frequency. At this moment, fluorescence rate will drop greatly, as shown in the inset of Fig. 3. Shielding factors in three directions are shown in Fig. 3. Experimental results agreed with the finite element simulation results.

Single Mg ion can be trapped by reducing loading time of Mg ions. For a single Mg ion, the collected maximum fluorescence rate depends on the intensity of light and the collection efficiency of the detection system. Our collection efficiency is measured to be 0.27% which is close to the designed efficiency of 0.2%.

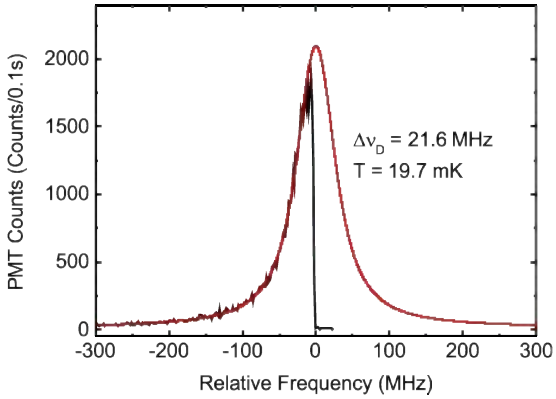

Figure 4. Spectrum of a single $^{25}Mg^+$ and its temperature estimation.

$^{25}Mg^+$ have a nuclear spin of 5/2 with hyperfine structures. Its ground state split into two levels due which is chose as a qubit for Al^+ clock transition detection. Existence of the hyperfine structure can be easily observed with the optical pumping effect, the most distinguish property between $^{25}Mg^+$ and $^{24}Mg^+$/$^{26}Mg^+$. Figure 4 shows the temperature of a trapped single $^{25}Mg^+$ ion can reach about 19 mK through micro-motion compensation and trapping parameters optimization, approaching to Doppler cooling limit.

IV. Conclusion and Outlook

We have successfully trapped single Mg ion and cooled the $^{25}Mg^+$ down to a low temperature to apply Raman sideband cooling for proposed Al^+ optical clock experiment.

Acknowledgment

The project is partially supported by the National Basic Research Program of China (Grant Number 2012CB821300), the National Natural Science Foundation of China (Grant Number 61108025 and 11174095), and the Program for New Century Excellent Talents by the Ministry of Education.

References

[1] P. O. Schmidt, T. Rosenband, C. Langer, W. M. Itano, J. C. Bergquist, and D. J. Wineland, "Spectroscopy using quantum logic," Science, vol. 309, p. 749, 2005. J. Clerk Maxwell, A Treatise on Electricity and Magnetism, 3rd ed., vol. 2. Oxford: Clarendon, 1892, pp.68–73.

[2] B. Hemmerling, F. Gebert, Y. Wan, D. Nigg, I. V. Sherstov, and P. O. Schmidt, "A single laser system for ground-state cooling of $^{25}Mg^+$," Appl. Phys. B, vol. 104, p. 583, 2011.

Progress Report on Development of Ultrastable Lasers for $^{27}Al^{+}$ Optical Clock

Yingxin Luo, Bing Ouyang, Xiaoyi Zeng, Ai Deng, Chengbin Qin, Ke Deng, Jie Zhang*, Zehuang Lu and Jun Luo
MOE Key Laboratory of Fundamental Quantities Measurement,
School of Physics, Huazhong University of Science and Technology,
Wuhan 430074, P.R. China
Email*: jie.zhang@mail.hust.edu.cn

***Abstract*—The recent progress of ultra-stable lasers used for $^{27}Al^{+}$ optical frequency standards is presented. Two diode lasers are phase stabilized to ultra-stable ULE cavities, which will be frequency quadrupled to UV as the 267.4 nm $^{27}Al^{+}$ clock laser with sub-Hz level linewidth and the 267.0 nm shelving laser with 100 Hz level linewidth for fast detection respectively. In this report, less than 3 Hz linewidth of IR lasers at 1068 nm are achieved via Pound-Drever-Hall (PDH) stabilization for the 100 Hz shelving laser application. Dynamic analysis of cavity sensitivity to vibration is also presented.**

Keywords—optical clock; ultrastable laser; dynamic analysis

I. Introduction

Optical frequency standards play important roles in high precision metrology, such as high-resolution spectroscopy and test of fundamental physics, etc. [1] [2]. Among all of them, $^{27}Al^{+}$ is one of the most promising candidates for next generation optical clock. The $^{1}S_0 - ^{3}P_0$ transition of Al^{+} ion has a natural linewidth of 8 mHz in 267.4 nm and will offer great stability in both long term and short term range. Because of this ultra-narrow transition, the clock laser is required to have a comparably narrow linewidth, and also an excellent long term stability. Moreover, for a narrow transition, its lifetime is too long to be detected, thus a shelving transition from $^{1}S_0$ to $^{3}P_1$ is needed for fast detection, as shown in Fig. 1. In this case, a shelving laser with sub-100 Hz level linewidth at 267.0 nm is also required. This report is about the recent progress on the development of ultra-stable lasers used for $^{27}Al^{+}$ optical clock.

II. Experimental Setup

To develop a shelving laser with 100 Hz linewidth, a diode laser at 1068 nm is phase locked to an ultra-stable ULE cavity (Cav1 in Fig. 2) via Pound-Drever-Hall (PDH) stabilization [3]. It is frequency quadrupled to 267.0 nm UV light for the de-shelving applications. For the clock transition, another diode laser at 1070 nm is locked to the same cavity as pre-stabilization, then to another independent cavity (Cav2 in Fig. 2) for a second stage locking. Its frequency will be quadrupled to 267.4 nm as the clock laser for $^{27}Al^{+}$.

The experimental setup is shown in Fig. 2. Two identical notched cavities are mounted inside two vacuum chambers with pressure at 10^{-8} mbar level on their optimal supporting position, where both the vibration-induced length variation and mirror tilting of the cavity are eliminated. Cavities are

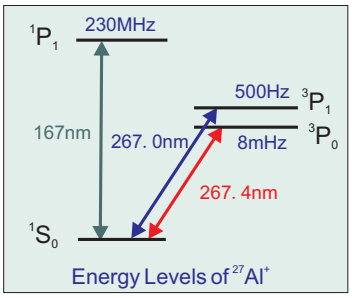

Fig. 1. Energy levels of $^{27}Al^{+}$ involved in optical clock application.

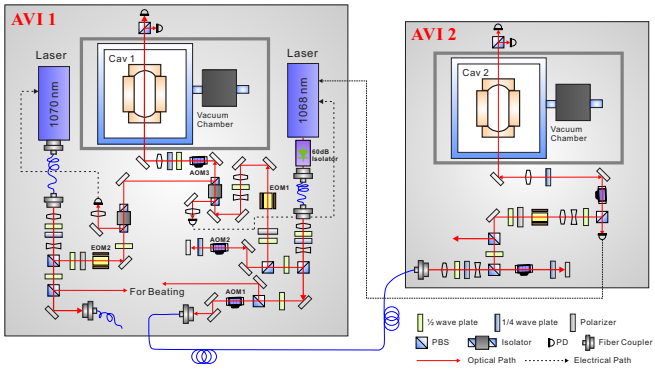

Fig. 2. Experimental setup of ultra-stable lasers for $^{27}Al^{+}$ frequency standard.

made of ultra low expansion (ULE) materials with a zero-crossing temperature of coefficient of thermal expansion (CTE) [4] around 25 °C. Both vacuum chambers are placed inside temperature controlled and acoustic-shielded boxes, with a thermal fluctuation of mK. Two active vibration isolation (AVI) platforms are applied for vibration isolation of the cavities and optics, and a vertical vibration at 10^{-7} g/$\sqrt{\text{Hz}}$ level is achieved with the AVI on. Figure 3 shows photos of the experimental setup and the cavities used in this system.

III. Experimental Results

Recently, two IR diode lasers have been stabilized to the two independent cavities respectively and beat notes of less than 3 Hz are obtained between these two lasers, indicating the shelving laser for $^{27}Al^{+}$ is ready for use. The second stage stabilization of clock laser is in progress, and a third ultrastable cavity system for beat note analysis will also be built soon.

Fig. 3. Photos of experimental setup.

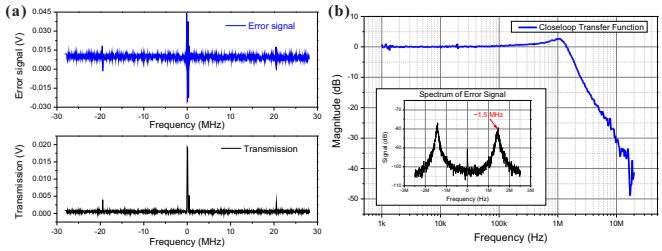

Fig. 4. (a) PDH error signal and cavity transition; (b) closed-loop transfer function of the feedback loop. The inset in (b) is the spectrum of in-loop error signal.

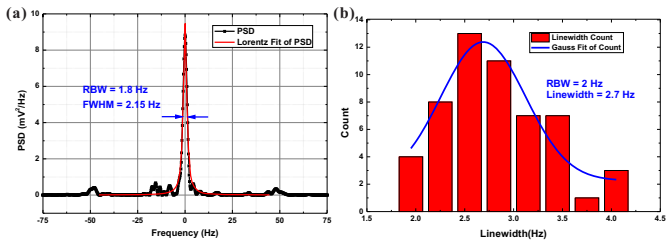

Fig. 5. (a) Laser beat note between two independent cavities; (b) histogram of linewidth distribution of beat notes from more than 50 measurements.

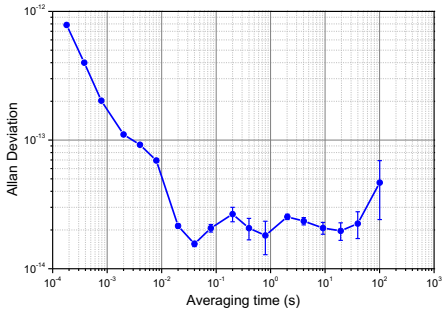

Fig. 6. Allan deviation of the beat note between two cavities.

Figure 4(a) shows PDH error signals and cavity transmission when laser frequency is scanned near resonance. In order to achieve higher signal-to-noise ratio, the modulation depth of EOM has been increased to near optimal value of about 1.08. The laser frequency is locked to the cavity with a feedback control bandwidth of about 1.5 MHz. Figure 4(b) shows the closed-loop transfer function of the system, including the cavity, detector and actuator of lasers etc., illustrating a $\sim$1.5 MHz bandwidth, with the roll-off slope of -20 dB/decade. The inset is the spectrum of in-loop error signal, where the shoulders represent the control bandwidth.

In order to study the stability of the stabled laser, we have locked the two lasers to two cavities on independent AVIs for beat note analysis, and an average linewidth of less than 3 Hz is obtained. Figure 5(a) is one of the laser beat notes, showing a linewidth of 2.15 Hz at FWHM. Figure 5(b) shows a histogram of linewidth statistical distribution of more than 50 measurements. An averaged linewidth of 2.7 Hz is obtained, indicating a linewidth of $\sim$1.9 Hz assuming two identical laser stabilization systems.

Beat note frequency is also measured with a frequency counter (Agilent, 53230A) and Allan deviations are analyzed. Stability of 2×10^{-14} at 1 s with a 0.49 Hz/s linear drift subtracted is obtained, as shown in Fig. 6. The long term stability will be further improved by searching the zero-crossing temperature of CTE of the cavities. Moreover, the residual amplitude modulation (RAM) suppression and EOM temperature stabilization will also be performed.

IV. Dynamic Analysis of Cavity Vibration Isolation

To reduce the vibration sensitivity of the ULE cavity, the cavity supporting positions are optimized according to quasi-static finite element analysis (FEA) [5]. The result is shown in Fig. 7. When mounted on this optimal position, the length variation and mirror tilting induced by vibration can be eliminated simultaneously, and the sensitivity to mounting inaccuracy is as low as 5×10^{-12} g^{-1}mm^{-1}. Cavities used in our experiments are both mounted on this optimal position for vibration insensitivity purpose. To further reveal the response of the cavity under higher frequency excitation, such as acoustic noise, we also simulated FEA dynamic analysis of the cavities' steady state response under dynamically changing loads, considering inertia and damping effects.

The ultrastable cavity has a 10 cm cylindrical ULE spacer, with a 0.5 inch bore hole along its central axis. Two 1-inch-diameter ULE mirror substrates are optically contacted to both sides of the spacer. For the FEA, spacer, mirrors and four symmetric supporting cubes are considered as a rigid body. The lower face of the support cubes are constrained in the vertical direction and free in the other two directions. The cavity is meshed with 149,000 prim elements. FEA simulations have been done using mechanical properties of ULE including mass density (2210 kg/m^3), Young's modulus (67.6 Gpa), Poisson's ratio (0.17) and Loss factor (1.64×10^{-5}). With optimized supporting positions calculated by quasi-static FEA, we performed dynamic analysis from 1 Hz to 20 kHz. Two largest resonant peaks in the vertical direction are shown in Fig. 8, which are consistent with the cavity's eigen-frequencies calculated by model analysis. The inset (a) of Fig. 8 shows that the relative deformation of the cavity length between 1 Hz to 100 Hz is in a level of 10^{-16} /g, which confirms with the quasi-static method. Vibration sensitivity of the cavity length reaches 10^{-8} /g at eigen-frequencies, as shown in the inset (b) and (c) of Fig. 8. Vibration modulation experiments are under way to examine the influence of resonant frequencies on the cavity stability.

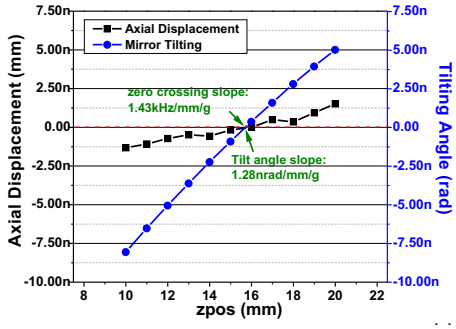

Fig. 7. Optimal mounting position of the cavity with smallest vibration sensitivity by quasi-static FEA analysis.

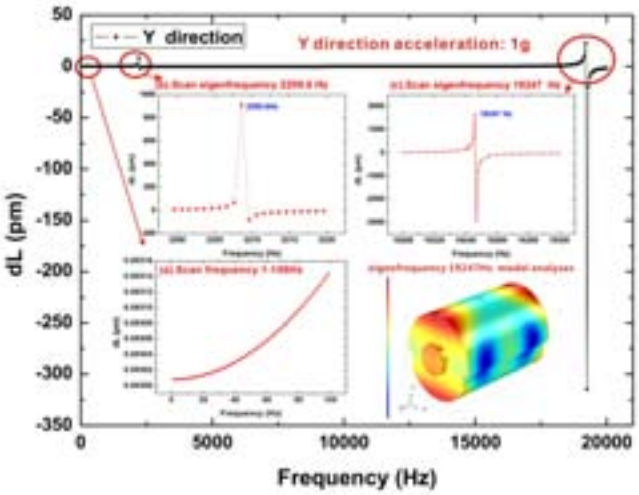

Fig. 8. Dynamic analysis of vertical vibration under optimal mounting position from 1 Hz to 20 kHz.

V. Conclusion and Outlook

In conclusion, two ultra-stable lasers for the application of $^{27}Al^{+}$ optical clock have been established and beat note of less than 3 Hz linewidth between them is obtained, one of which will be frequency quadrupled to 267.0 nm as the shelving laser. Experimental setup and the results are presented, and dynamic analysis of cavity via FEA simulations are also discussed in this report.

The second stage stabilization of the clock laser to sub-Hz level linewidth is on the way, and a third ultrastable cavity system for beat note analysis will also be built soon. Moreover, a 30 cm-long cavity with FS mirrors and a thermal compensation design [6] will be built to pursue a stability of 1×10^{-16} at 1 s for the clock laser.

Acknowledgment

The project is partially supported by the National Basic Research Program of China (Grant No.2012CB821300), the National Natural Science Foundation of China (Grant Number 61108025 and 11174095), and Program for New Century Excellent Talents by the Ministry of Education.

References

[1] T. Rosenband, D. B. Hume, P. O. Schmidt, C. W. Chou, A. Brusch, L. Lorini, W. H. Oskay, R. E. Drullinger, T. M. Fortier, J. E. Stalnaker, S. A. Diddams, W. C. Swann, N. R. Newbury, W. M. Itano, D. J. Wineland, and J. C. Bergquist, "Frequency ratio of Al^{+} and Hg^{+} single-ion optical clocks; metrology at the 17th decimal place," Science, vol. 319, pp. 1808–1812, 2008.

[2] A. D. Ludlow, T. Zelevinsky, G. K. Campbell, S. Blatt, M. M. Boyd, M. H. G. de Miranda, M. J. Martin, J. W. Thomsen, S. M. Foreman, J. Ye, T. M. Fortier, J. E. Stalnaker, S. A. Diddams, Y. Le Coq, Z. W. Barber, N. Poli, N. D. Lemke, K. M. Beck, and C. W. Oates, Sr lattice clock at 1×10^{-16} fractional uncertainty by remote optical evaluation with a Ca clock, Science, vol. 319, pp. 1805–1808, 2008.

[3] R. W. P. Drever, J. L. Hall, F. V. Kowalski, J. Hough, G. M. Ford, A. J. Munley and H. Ward, "Laser phase and frequency stabilization using an optical resonator," Appl. Phys. B, vol. 31, pp. 97–105, 1983.

[4] R. W. Fox, "Temperature analysis of low-expansion Fabry-Perot cavities," Opt. Express, vol. 17, pp. 15023, 2009.

[5] S. A. Webster, M. Oxborrow, and P. Gill, "Vibration insensitive optical cavity," Phys. Rev. A, vol. 75, pp. 011801, 2007.

[6] J. Zhang, Y. X. Luo, B. Ouyang, K. Deng, Z. H. Lu and J. Luo "Design of an optical reference cavity with low thermal noise limit and flexible thermal expansion preperties," Eur. Phys. J. D, vol. 67 , pp. 46, 2013.

Compact and Dual Ti:Sapphire Comb Lasers Pumped by Single Fiber Laser

Tze-Wei Liu[1,4], Chien-Ming Wu[2], Shinn-Yan Lin[3], Wang-Yau Cheng[4]

[1]Department of Physics, National Taiwan University, Taipei, Taiwan
[2]Institute of Photonics Technologies, National Tsing-Hua University, Hsinchu, Taiwan
[3]National Standard Time and Frequency Laboratory, Telecommunication Laboratories, Chunghwa Telecom, Taoyuan, Taiwan
[4]Department of Physics, National Central University, Chun-Li, Taiwan
Email: sylin@cht.com.tw

***Abstract*—We demonstrated two femtosecond Ti:sapphire comb laser pumped by a continuous-wave 532 nm light which is generated from a frequency doubling 1064 nm ytterbium fiber laser. To make the system small, we develop HS-CTSDL being the frequency standard.**

Keywords-frequency comb; fiber laser; Ti:sapphire; Cesium

I. INTRODUCTION

Mode locked lasers are delicate to the pumping process in terms of mode frequency stability and pulse chirping. We showed that a 1064 nm fiber laser, via a single-pass second harmonic generation, could simultaneously pump two Ti:sapphire lasers and keep them in a stable mode-locking. The SHG photorefractive effect that might cause unstable pulses was not found. Our compact dual comb lasers are significant for interdisciplinary collaborations, especially for the applications of dual comb laser spectroscopy.

Femtosecond Ti:sapphire laser was commented by J. L. Hall and T. W. Hansch as the "intelligent and beautiful princess" [1]. Indeed, Ti:sapphire oscillator plays an important role in many experiments for strengthening light properties to the extreme edge, such as ultra-low phase noise [2], ultra-short pulse duration [3], ultra-high-field [4], and broadest laser output spectrum [5], at the wavelength ranged from infrared to visible.

Optical frequency combs which had a significant impact recently in spectroscopy and metrology [6, 7] are especially sensitive to power instability, because pump power fluctuations directly affect the repetition rate and the carrier-envelope phase. Improvements in IR fiber laser technology made possible to have sufficient optical pump power in the visible region [8] using second-harmonic generation in quasi-phase-matched ferroelectric materials such as MgO-doped periodically poled stoichiometric lithium tantalate (PP-MgO:SLT) [9]. Compared to the conventional diode pump solid-state laser pump sources, fiber laser based pumps have the advantages of being more compact, lower cost, and low power consumption.

In this paper, we successfully demonstrated that two fiber-pumped ultrafast Ti:sapphire lasers could be realized. We showed the pulse quality and directly monitored the mode frequency for the comparison with conventional pumping scheme.

II. EXPERIMENTAL SETUP

The pumping source, Yb fiber laser, provided 30 W, CW, single mode 1064 nm light, which was frequency doubled by an external single pass 30 mm PP-MgO:SLT crystal [10], generating about 10 W, CW, 532 nm light in TEM00 mode. The pump beam was optimized with a pair of collimating and mode-matching lenses.

Two Ti:sapphire oscillators were assembled together on the same one cooling base, measured as 55×110 cm^2 area, allowing for using the same one temperature-regulated cooling water to keep both being in similar drift rate of lasers' mode frequencies. Several chirped mirrors and folding mirrors were installed into laser cavities to reduce the area occupation of two Ti:sapphire oscillators, which resulted in the overall size of 9.5 cm high, 31 cm length and 36 cm width.

Repetition rates of Ti:sapphire oscillators were set to be 1 GHz, and the average power of the pulse is about 700 mW [11]. Absolute mode frequency of laser was locked to one hand size cesium two-photon stabilized diode laser (HS-CTSDL) [12], and monitored its beat frequency with respect to another HS-CTSDL.

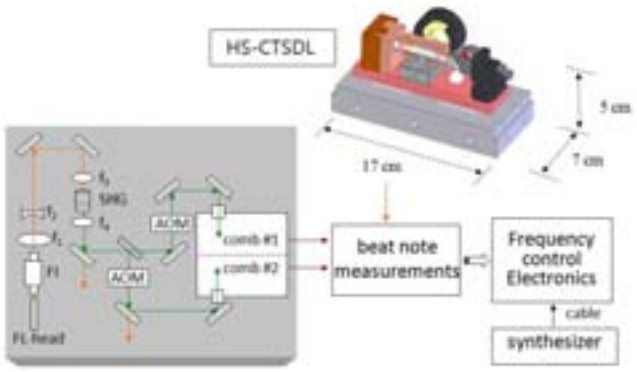

Figure 1. The experiment setup of the dual Ti:sapphire comb system pumped by a fiber laser.

III. The Effect of Pumping Source Noise

Not every fiber laser can be a good pumping source for frequency comb lasers. We compare two 1064 nm fiber lasers from different company. The first fiber laser yield 30 W maximum output power at 1064 nm wavelength, and with 2% power ripple within 100 kHz bandwidth. The second one support 20 W maximum output power at 1064 nm wavelength, and with 2% relative rms intensity noise at nominal power within 0.1 nm bandwidth.

We measured the behavior of the comb laser output pulse pumped by this two fiber lasers. The pulse output spectrums were measured by an optical spectrum analyzer, and time domain properties were measured by an autocorrelator. Both of them have about 30 nm pulse bandwidth and 26 fs pulse length. However, the mode locking of the second one is not as stable as the first one. The repetition rate of the comb laser which pumped by the second fiber laser has a messy background comparing to the other. We get beat notes from beating HS-CTSDL with these two mode locked lasers. It is about 1 MHz line width of the first one, which is about 5 times smaller than the second one, and the small line width is helpful for locking absolute frequency.

To figure out the reason of noisier output, we measured the noise spectrum of the pump light intensity by a photo detector as shown in figure 3. The standard deviation of first fiber laser's power noise is 15.2 mV while the dc output is around 1.8 V, and in the same situation, the second fiber laser's standard deviation is 49.9 mV. The second fiber laser had 35 dB higher intensity noise below 500 kHz for equivalent pump power.

This power instability would explain the less stable repetition rate and does have a direct impact on precision metrology measurements. We conclude that the second fiber laser could serve as a pump for Ti:sapphire mode-locked lasers, but to be an attractive pump source for optical frequency combs, the power stability needs to be improved.

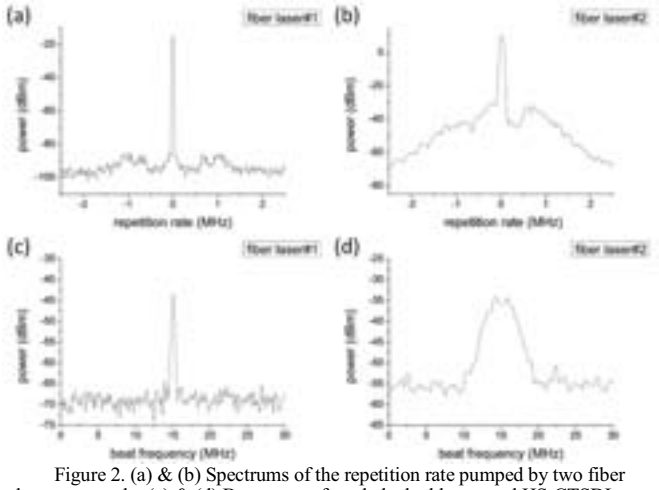

Figure 2. (a) & (b) Spectrums of the repetition rate pumped by two fiber laser separately. (c) & (d) Beat notes of mode locked lasers and HS-CTSDL.

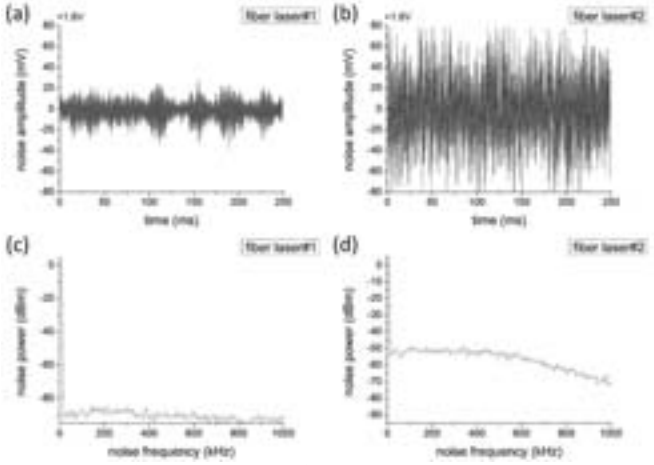

Figure 3. The intensity noise of the pump light. (a) & (b) In time domain. (c) & (d) In frequency domain.

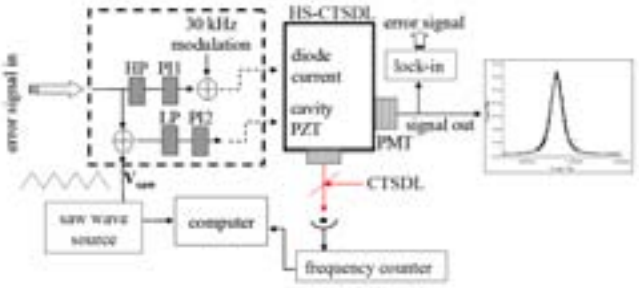

Figure 4. The experiment setup for testing mode pushing/pulling effect of HS-CTSDL

IV. Hand Size Optical Frequency References

In order to make the system small, we develop HS-CTSDL, and the biggest difference between HS-CTSDL and the other frequency stabilized laser is that the absorption cell of HS-CTSDL is put in the laser cavity.

Mode pushing/pulling effect is a big problem for intracavity One-photon spectroscopy [13, 14], and it creates lead-lag of the laser frequency. Laser frequency lead-lag, caused by the dispersion of the gain/absorption medium [14], is nonlinearly dependent on the physical length of the laser resonator. To make sure that HS-CTSDL has mode pushing/pulling effect or not, we have to record the cavity optical length synchronously with physical length.

HS-CTSDL, which has a current modulation, was locked on the cesium 6S-8S transition at the beginning. Then we add a slow saw wave to change the offset point of the PZT feedback loop while the laser kept locked (but the frequency changed). The beat frequency of HS-CTSDL and another cesium two-photon stabilized diode laser (CTSDL) is related to the cavity optical length, and the offset voltage of the PZT is related to the physical length. The result of test shows the liner relationship of offset voltage and the beat frequency, so we claim that the mode pushing/pulling effect is not obvious within our measurement precision.

Using this scheme we can also get the transition spectrum by recording beat frequency and PMT signal synchronously. Pressure shift and modulation shift of the HS-CTSDL are -2.9 kHz/0.01Pa and 3 kHz/MHz. The estimated Allan deviation [15] was deduced from a beat note measurement with two independent HS-CTSDLs stabilized to the same two-photon transition (note that figure 6(a) is just an estimated value because our lambda-type counter could not really provide appropriate sequences of frequency counting for directly deducing the Allan variance [15]) . Frequency offset of the laser is about 100 Hz/364.5 THz at 400 s sampling time, and maximum frequency discrepancy of 3.5 kHz/364.5 THz during 16 days shows the high reproducibility of the HS-CTSDL.

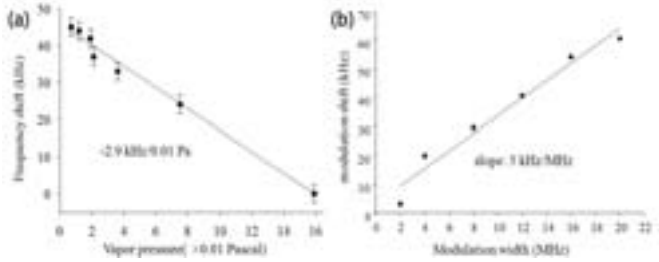

Figure 5. (a) Pressure shift and (b) modulation shift of the HS-CTSDL

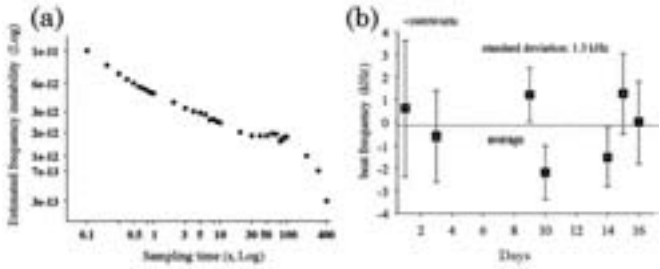

Figure 6. (a) Stability and (b) reproducibility of two HS-CSTDLs

V. RESULT

By feedback controlling the PZT (which is on the Ti:sapphire cavity mirror) and the AOM to change the cavity length and the pumping power, we can lock the repetition rate and the absolute frequency with reference to the synthesizer and HS-CTDSL. The line width of the repetition rate reduces to about 2 Hz after lock. The Allan deviation of the beat frequency was about 5×10^{-12} at 10 s sampling time.

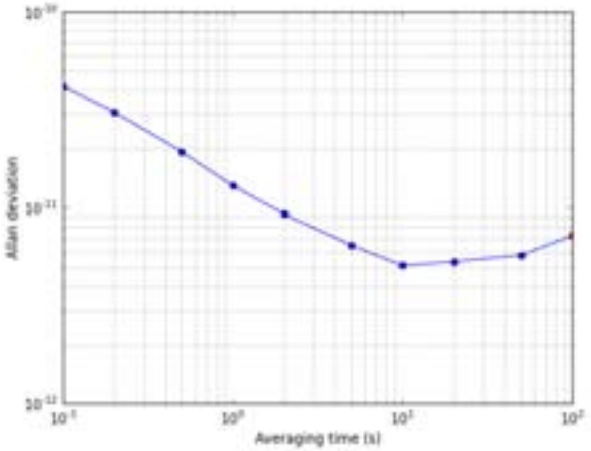

Figure 7. Allen deviation of the Ti:sapphire comb

REFERENCES

[1] J. L. Hall, and T. W. Hänsch, "History of Optical Comb Development", J. Ye, and S. T. Cundiff, *Femtosecond Optical Frequency Comb Technology*, Springer, Norwell, MA, 1, (2005).

[2] R. P. Scott, C. Langrock, and B. H. Kolner, "High-Dynamic-Range Laser Amplitude and Phase Noise Measurement Techniques", IEEE Selected Topics in quantum electronics **7**, 641 (2001).

[3] S. Giuseppe, P. Luca, and N. Mauro, "High-energy attosecond light sources", Nature Photonics **5**, 656 (2011) and references therein.

[4] S. Suckewer, "Beyond a petawatt", Nature Phys. **7**, 11 (2011) and references therein.

[5] M. Y. Sander, E. P. Ippen, and F. Kartner, "Carrier-envelope phase dynamics of octave-spanning dispersion-managed Ti:sapphire lasers", Opt. Express **18**, 4948 (2010).

[6] M. J. Thorpe, K. D. Moll, R. J. Jones, B. Safdi, and J. Ye, Science **311**, 1595 (2006).

[7] S. A. Diddams, L. Hollberg, and V. Mbele, Nature **445**, 627 (2007).

[8] G. K. Samanta, S. Chaitanya Kumar, and M. Ebrahim-Zadeh, Opt. Lett. **34**, 1561 (2009).

[9] H. Furuya, A. Morikawa, K. Mizuuchi, and K. Yamamoto, Jpn. J. Appl. Phys. Part 1 **45**, 6704 (2006).

[10] From HC PHOTONICS CORP.

[11] GIGAOPTICS, **gigajet TWIN 20c/20c**.

[12] Y. H. Chen, T. W. Liu, C. M. Wu, C. C. Lee, C. K. Lee, and W. Y. Cheng, Opt. Lett. **36**, 76 (2011).

[13] W. Jamroz, D. Hugon, T. B. Cave, A. Guest, and A. D. May, Appl. Opt. 23, 2906 (1984), and references therein.

[14] Z. Bozoki, J. Sneider, G. Szabo, A. Miklos, M. Serenvi, G. Nagy, and M. Feher, Appl. Phys. B 63, 399 (1996).

[15] S. T. Dawkins, J. J. McFerran, and A. N. Luiten, IEEE. Trans. Ultrason. Ferroelect. Freq. Contr. 54, 918 (2007). We used an Agilent 53132A counter here, which is a lambda-type counter, and our beat note was around 160 MHz.

Optical Frequency Measurement Comparison Using Fiber Laser Combs Between CMS and NMIJ

Jin-Long Peng, Ren-Huei Shu, and Tze-An Liu
Center for Measurement Standards
Industrial Technology Research Institute
Hsinchu, Taiwan
jlpeng@itri.org.tw

Hajime Inaba, Kazumoto Hosaka, Masami Yasuda, Daisuke Akamatsu, Atsushi Onae, and Feng-Lei Hong
National Metrology Institute of Japan
National Institute of Advanced Industrial Science and Technology
Tsukuba, Japan
f.hong@aist.go.jp

***Abstract*—An Er-fiber laser comb with repetition frequency of 250 MHz made by the Center for Measurement Standards (CMS), Taiwan was shipped to the National Metrology Institute of Japan (NMIJ) to compare with the NMIJ fiber laser comb by simultaneously measuring the frequency of an optical cavity-stabilized Nd:YAG laser at 1064 nm. The measured average frequency difference is 32 mHz and corresponds to a relative difference of 1.1×10^{-16}, which is limited by the measurement time. Furthermore, method for determining the comb mode number using two combs with large difference of repetition rate is proposed.**

Keywords-optical frequency measurement; optical frequency comb; mode-locked laser; frequency standard; fiber laser

I. INTRODUCTION

Mode-locked (ML) femtosecond laser functioning as an optical frequency comb has revolutionized optical frequency metrology over a decade [1]. Due to this revolutionary technique, the practical realization of SI-meter has also been modified. Traditionally, various frequency-stabilized lasers have been recommended by the Bureau International des Poids et Mesures (BIPM) for the practical realization of meter [2]. National Metrology Institutes (NMIs) bring their frequency-stabilized lasers to join a key comparison initiated by the meeting of the Comité Consulative des Longeurs (CCL) to demonstrate the equivalence of national realization of the SI-meter. Nowadays, many NMIs use the laser comb to measure the frequency of the recommended lasers in their own labs to realize the SI-meter traceable to the SI-second. Validating the measurement capability of the laser comb in different NMIs is an important issue in the mutual recognition. Two independent laser combs phase-locked to a common microwave frequency standard and measuring a common optical frequency is the most direct way to validate the measurement capability of the frequency comb.

Among the different ML laser combs, ML fiber laser comb is popular in many labs due to its compactness and free-of-alignment and is suitable for transportation to perform the comb comparison. Comb comparison using fiber laser combs to measure the frequency of a an iodine-stabilized He-Ne laser at 633 nm has been demonstrated by the National Metrology Institute of Japan (NMIJ) and the National Metrology Institute of Australia (NMIA) [3]. The Center for Measurement Standards (CMS), which is the NMI of Taiwan, has also made self-referenced fiber laser combs for the optical frequency measurement [4, 5]. Recently, one of the fiber laser combs developed by CMS was shipped to NMIJ to validate the measurement capability of the fiber laser combs of CMS and NMIJ at 1064 nm. In this paper, the results of the comb comparison are reported. Furthermore, method for determining the mode number of the beating comb line using two combs with large difference of repetition rate is proposed.

II. FIBER LASER COMB DEVELOPED BY CMS

The CMS comb is similar to the previous construction [5]. Here, we simply describe the main difference from that system.

The fiber laser oscillator has a ring cavity mode-locked by nonlinear polarization rotation (NPR) with a polarization beam splitter (PBS) before an isolator to couple out the laser pulse from the rejection port [6]. A 38-cm-long highly doped Er-fiber is used as the gain medium. The Er-fiber is pumped by a 980 nm diode laser through a wavelength-division-multiplexing coupler. The diode laser has a maximum output power of 660 mW. The mode locked laser has a repetition rate of 250 MHz and delivers a maximum output power of 94 mW from the PBS rejection port. A piezoelectric transducer (PZT) is mounted on the fiber to control the cavity length. The PZT can tune the repetition frequency up to about 8 kHz with a maximal driving voltage of 150 V.

The output from the laser oscillator is further coupled into an optical fiber and divided to three ports by a 1×3 coupler after passing a polarization independent isolator. One port is used to detect the repetition rate and to monitor the laser oscillator. Each of the other two ports is amplified to 200 mW with an Er-fiber amplifier backwards pumped by a 980 nm diode laser with output power of 660 mW. The amplified laser pulses are then compressed by standard single mode fibers and sent to highly nonlinear fibers (HNLF) to generate two branches of octave-spanning supercontinua ranging from 1050 nm to 2200 nm. Each supercontinuum has an average power of

170 mW. One branch of the supercontinua is adopted to detect the carrier-envelope-offset (CEO) frequency using collinear self-referenced f-2f interferometer [7]. The comb lines near 2200 nm are frequency-doubled with a 0.5-cm-long periodically poled magnesium-oxide-doped lithium niobate (MgO:PPLN) and mixed with the comb lines near 1100 nm. The mixed comb lines at 1100 nm are filtered with a 10-nm-wide bandpass filter and the CEO beat signals are detected by an InGaAs photodiode. The group velocity mismatch between the 2200 nm and 1100 nm combs are compensated by splicing an 8-mm-long single mode fiber after the HNLF to optimize the beat signal. The detected CEO beat signal has a signal-to-noise ratio of 40 dB at 100 kHz resolution bandwidth. The other branch of supercontinuum is adopted for optical frequency measurement.

The fiber laser oscillator, amplifiers and the HNLF are mounted on an aluminum plated with temperature controlled by a thermal-electric cooler to maintain long term stability of the mode-locking. All the above mentioned constructions of the fiber laser comb are inside an aluminum box of A3 paper size with 6.5 cm thick. To the best of our knowledge, this is the most compact fiber laser comb with an f-2f interferometer inside and is convenient for transportation to perform the comb comparison.

III. Experimental Setup and Results of the Comb Comparison

The fiber laser comb with repetition rate of 250 MHz developed by CMS was brought to NMIJ for frequency measurement comparison. The NMIJ fiber laser comb is also based on a NPR mode-locked fiber ring laser with a repetition frequency of 87.6 MHz and is similar to the construction described in [8].

The setup for the CMS-NMIJ comb comparison is shown in Fig. 1. Both the repetition and CEO frequency of the CMS and NMIJ combs are phase-locked to the 10 MHz signal of a H_2-maser linked to the Coordinated Universal Time of NMIJ (UTC-NMIJ 10 MHz signal), which has a frequency uncertainty of 3×10^{-13} at 1 s. The 4th harmonic of the repetition frequency of the CMS comb is phase-locked to a 1 GHz reference signal multiplied from the UTC-NMIJ 10 MHz signal. The 10th harmonic of the repetition frequency of the NMIJ comb is mixed with a 900 MHz source multiplied from the UTC-NMIJ 10 MHz signal to generate a difference frequency of 24 MHz. This difference frequency is then phase-locked to a synthesizer (Stanford Research Systems DS345). The CEO frequencies of the two combs are stabilized to two other synthesizers (Agilent Technologies E4400B) and are monitored by two frequency counters (Pendulum CNT-90). All the synthesizers are referenced to the UTC-NMIJ 10 MHz signal.

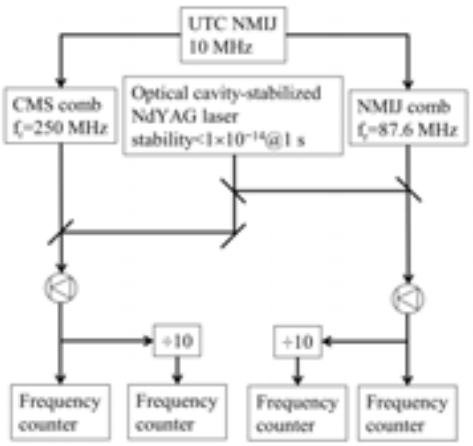

Figure 1. Experimental setup for the comb comparison.

To measure a common optical frequency, the two combs are mixed with an optical cavity-stabilized Nd:YAG laser operating at 1064 nm. The frequency stability at 1 s of the Nd:YAG laser is less than 1×10^{-14}. The two beat signals are then counted by two frequency counters (Pendulum CNT-90) simultaneously. The two beat signals are also divided by 10 and measured with another two frequency counters (Pendulum CNT-90) to check cycle-slip from the counters. If the counting of the beat signal does not match with that from the 1/10 of the beat signal, cycle-slip has happened and that data point is deleted. All the counters are referenced to the UTC-NMIJ 10 MHz signal and have a measurement time setting of 1 s.

The optical frequency of the Nd:YAG laser is calculated from the measured beat frequencies, CEO frequencies and the settings of the repetition frequencies. The mode numbers of the two combs are determined by slightly changing the repetition frequency of the NMIJ comb as demonstrated in [3]. Fig. 2 shows the measured frequency differences of the two combs. The average of the difference frequencies is 32 mHz, which corresponds to a relative difference of 1.1×10^{-16}. This is much lower than the uncertainty of the microwave frequency standard. Therefore, the absolute frequency measurement capability of the fiber laser combs is limited by the accuracy of the local reference. An NMIJ fiber comb had also been shipped to NMIA to compare the frequency measurement of an iodine-stabilized He-Ne laser at 633 nm in 2006. The NMIA comb is a commercial fiber laser comb with 100 MHz repetition rate and also has a ring cavity mode-locked with

Figure 2. Measured frequency difference between the two combs.

NPR. The measured frequency difference was 38 mHz [3], which corresponds to a relative difference of 8×10^{-17}. These comparison results validate that the NPR-based fiber laser comb can perform optical frequency measurement with a much smaller uncertainty than that of the current microwave frequency standards.

IV. Determination of the Mode Number Using Two Combs with Large Difference in Repetition Rate

To measure the frequency of a laser under measurement (LUM) using a mode-locked laser comb, the mode number of the beating comb line must be determined. Besides using a wavelength meter to offer a precise *a priori* knowledge of the frequency of the LUM, mode number can be determined by measuring the beat frequencies at various repetition rates [9, 10]. Peng et al. developed methods based on two combs with repetition rate difference of kHz to measure the mode number, which can be independent of the frequency fluctuations of the LUM [11-13]. Inaba et al. demonstrated the comb mode determination using two combs with large difference in repetition rate [3], which is also used in previous section to determine the mode number for measuring the frequency of the Nd:YAG laser. But, they need long measurement time of 1000 s to average down the uncertainty of the beat frequency difference. In this section, we propose another method that can determine the mode number in short time for two combs with large difference in repetition rate.

This method relies on measuring the beat frequencies at three different repetition rates f_{r11}, f_{r12} and f_{r13} of comb1, where two repetition rates f_{r11} and f_{r12} are close enough to have the same beating comb mode, while keeping the repetition rate of comb2 unchanged. For simplicity, assume that the offset frequencies are zero and the signs of the beat frequencies are determined to be positive. Thus, the frequency of the LUM can be expressed as:

$$f_L = n\cdot f_{r11} + f_{b11} = k\cdot f_{r21} + f_{b21}, \quad (1)$$

$$f_L = n\cdot f_{r12} + f_{b12} = k\cdot f_{r21} + f_{b22}, \quad (2)$$

$$f_L = (n+m)\cdot f_{r13} + f_{b13} = k\cdot f_{r21} + f_{b23}, \quad (3)$$

where f_{b1x} and f_{b2x} are the beat frequencies measured at repetition rate f_{r1x} of comb1 with $x=1$, 2, and 3, and at single repetition rate f_{r21} of comb2; n and k are the mode number of the beating comb line of comb1 and comb2, respectively; m is the mode number shift of comb1 when the repetition rate is changed from f_{r11} to f_{r13}. From (1), (2) and (3), the mode number shift m and the mode number n can be derived as

$$m = \frac{\frac{(f_{b21}-f_{b11})-(f_{b22}-f_{b12})}{f_{r11}-f_{r12}}(f_{r11}-f_{r13})+(f_{b11}-f_{b21})-(f_{b13}-f_{b23})}{f_{r13}}, \quad (4)$$

$$n = \frac{m\cdot f_{r13}+(f_{b21}-f_{b11})-(f_{b23}-f_{b13})}{f_{r11}-f_{r13}}. \quad (5)$$

The mode number difference m is calculated with (4) first and then substituted into (5) to get n. Both n and m are independent of the frequency fluctuations of the LUM since the two beat frequencies in all parentheses of (4) and (5) are measured simultaneously. They depend only on the relative fluctuation between the two comb lines beating with the LUM. Equations (4) and (5) is similar to (6) and (5) in [12], which are derived for two combs with about kHz difference in repetition rate. Since the two combs are phase-locked to a common highly stable microwave frequency standard, therefore, the mode number can be determined using short average time of 1 s similar to that demonstrated in [12].

Actually, the term $[(f_{b21}-f_{b11})-(f_{b22}-f_{b12})]/(f_{r11}-f_{r12})$ in (4) is equal to the mode number n, and (4) and (5) has the same form in such kind of substitution. But, this term is not used to calculate the real n in this proposal, because $f_{r11}-f_{r12}$ is small and it needs long measurement time to average down the uncertainty of the beat frequency difference to be much less than f_{r11}-f_{r12}, which was as demonstrated in [3]. This term is only used as an approximate mode number for the calculation of m in (4).

Since only the beat frequency between comb2 and the LUM appears in (4) and (5), the repetition frequency of comb2 can be any other values different from comb1 as long as the beat frequency can be effectively separated for measurement. This idea was not available during the comb comparison. The demonstration is realized with two other fiber laser combs with repetition rates of 500 MHz and 400 MHz and is published elsewhere [14].

V. Conclusions

We have shown that mode-locked Er-fiber laser combs phase-locked to a common microwave frequency standard have the capability to compare an optical frequency at 1064 nm with an uncertainty of 1.1×10^{-16}, which is smaller than the uncertainty of the best microwave frequency standard. Therefore, the absolute frequency measurement capability of the laser comb is limited by the microwave reference. In addition, we have proposed a method to determine the mode number of the beating comb line with short average time of 1 s when two laser combs with large difference in repetition rate are used for measuring the optical frequency.

Acknowledgment

J.-L. Peng thanks Yuh-Chuan Cheng for her contribution to the electronics used in the CMS fiber laser comb. F.-L. Hong thanks M. Onishi, T. Okuno, and M. Hirano of Sumitomo Electronics Inc. for providing them with the front-end components.

References

[1] Th. Udem, R. Holzwarth, and T. W. Hänsch, "Optical frequency metrology," Nature, vol. 416, pp. 233-237, March 2002.

[2] T. J. Quinn, "Practical realization of the definition of the metre, including recommended radiations of other optical frequency (2001)," Metrologia, vol. 40, pp. 103-133, April 2003.

[3] H. Inaba, Y. Nakajima, F.-L. Hong, K. Minoshima, J. Ishikawa, A. Onae, H. Matsumoto, M. Wouters, B. Warrington, and N. Brown, "Frequency measurement capability of a fiber-based frequency comb at 633 nm," IEEE. Tran. Instru. Meas., Vol. 58, pp. 1234-1240, April 2009.

[4] J.-L. Peng, H. Ahn, R.-H. Shu, H.-C. Chui, and J. W. Nicholson, "Highly stable, frequency-controlled mode-locked erbium fiber laser comb," Appl. Phys. B, Vol. 86, pp. 49-53, January 2007.

[5] J.-L. Peng, T.-A. Liu, and R.-H. Shu, "Self-referenced Er-fiber laser comb with 300 MHz comb spacing," Proceedings of the 2009 IEEE International Frequency Control Symposium jointly with the 22nd European Frequency and Time Forum (IFCS/EFTF), pp. 344-346, 2009.

[6] K. Tamura, C. R. Doerr, L. E. Nelson, H. A. Haus, and I. P. Ippen, "Technique for obtaining high-energy ultrashort pulses from an additive-pulse mode-locked erbium-doped fiber ring laser," Opt. Lett., Vol. 19, pp. 46-48, January 1994.

[7] T. schibli, K. Minoshima, F.-L. Hong, H. Inaba, A. Onae, H. Matsumoto, I. Hartl, and M. E. Fermann, "Frequency Metrology with a turn-key all-fiber system," Opt. Lett., vol. 29, pp. 2467-2469, November 2004.

[8] H. Inaba, Y. Daimon, F.-L. Hong, A. Onae, K. Minoshima, T. R. Shibli, H. Matsumoto, M. Hirano, T. Okuno, M. Onishi, and M. Nakazawa, "Long-term measurement of optical frequencies using a simple, robust and low-noise fiber based frequency comb," Opt. Express, vol. 14, pp. 5223–5231, June 2006.

[9] L.-S. Ma, M. Zucco, S. Picard, L. Robertsson, and R. S. Windeler, "A new method to determine the absolute mode number of a mode-locked femtosecond laser comb used for absolute optical frequency measurements," IEEE J. Sel. Top. Quantum Electron., vol. 9, pp. 1066-1071, July/August 2003.

[10] J. Zhang, Z. H. Lu, Y. H. Wang, T. Liu, A. Stejskal, Y. N. Zhao, R. Dumke, Q. H. Gong, and L. J. Wang, "Exact frequency comb mode number determination in precision optical frequency measurements," Laser Phys., vol. 17, pp. 1025-1028, July 2007.

[11] J.-L. Peng and R.-H. Shu, "Determination of absolute mode number using two mode-locked laser combs in optical frequency metrology," Opt. Express, vol. 15, pp. 4485-4492, April 2007.

[12] J.-L. Peng, T.-A. Liu, and R.-H. Shu, "Optical frequency counter based on two mode-locked fiber laser combs," Appl. Phys. B, vol. 92, pp. 513-518, September 2008.

[13] T.-A. Liu, R.-H. Shu, and J.-L. Peng , "Semi-automatic, octave-spanning optical frequency counter," Opt. Express, vol. 16, pp. 10728-10735, July 2008.

[14] J.-L. Peng, T.-A. Liu, and R.-H. Shu, "Determination of mode number using two laser combs with large difference in repetition rtae," in Proceeding of the 2013 Asia-Pacific Radio Science Conference, in press

Lasing of Cesium Four-level Active Optical Clock

Zhichao Xu, Wei Zhuang, Yanfei Wang, Dongying Wang, Xiaogang Zhang, Xiaobo Xue,
Duo Pan, Jingbiao Chen

State Key Laboratory of Advanced Optical Communication System and Network,
School of Electronics Engineering and Computer Science, Peking University, Beijing 100871, China

Email: jbchen@pku.edu.cn

***Abstract*—We are setting up an experiment to investigate an active optical clock scheme in four-level configuration with Cesium atoms. The 1469 nm Cesium active optical clock output in a bad cavity laser regime is generated and the wavelength is measured to be 1469.500 nm by using spectrometer. The 1469 nm lasing threshold and output power is measured when changing 455 nm pumping laser power and frequency. The 1469 nm Cesium active optical clock output multi-threshold is observed when changing bad-cavity length. We also sweep the bad-cavity length and measure the 1469 nm Cesium active optical clock output frequency using a wavelength meter, proving the cavity-pulling reduction due to the bad-cavity effect.**

Keywords—active optical clock; four-level configuration; bad-cavity

I. INTRODUCTION

To push the linewidth of optical clock from Hz to mHz is a main topic for current clock development [1]. Active optical clocks [2-5] theoretically have the potential of mHz linewidth, thus expected will provide much better stability than that of passive optical clocks. In a three-level configuration [2, 6], the pumping laser directly affects the frequency of clock transition. In order to greatly reduce the light shift of clock transition caused by pumping laser, an optical clock scheme in four-level configuration with Cesium atoms is proposed [7-12].

In this paper, we are setting up an experiment to investigate active optical clock in 4-level configuration with Cesium atoms. The Cesium active optical clock output at the wavelength of 1469 nm is observed. As the power and frequency of the 455 nm pumping laser is changed, the 1469 nm lasing threshold and output power is measured. The 1469 nm Cesium active optical clock output multi-threshold is observed when changing bad-cavity length and the 1469 nm Cesium active optical clock output frequency is measured using a wavelength meter to prove the cavity-pulling reduction due to the bad-cavity effect.

II. EXPERIMENTAL SETUP

The melting temperatures of alkali atoms, like Cs and Rb, are very low, and the laser diode for related wavelength of atomic transitions are commercially available, thus to set up 4-level Cs or Rb active optical clock experiment with thermal cell or magneto-optical trap is economic.

A homemade external-cavity diode laser at 455 nm is employed as the pumping laser. The related energy levels of

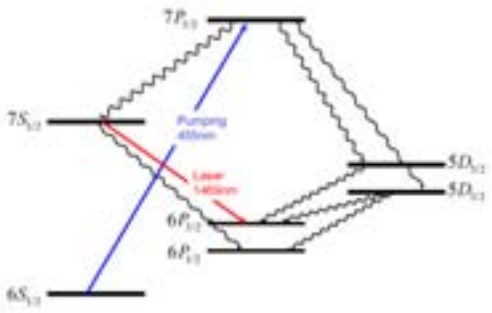

Fig. 1. The related energy levels of cesium.

cesium is shown in Fig. 1. The 455 nm external-cavity produces ~12 mW of optical power; 10 mW reaches the Cesium cell and 0.8 mW is used for saturated absorption spectrum of cesium between $6S_{1/2}$ (F=4) and $7P_{3/2}$ (F'=3,4,5) [13]. The population inversion between $7S_{1/2}$ state and $6P_{3/2}$ state in a thermal cesium cell has been experimentally established with the 455 nm pumping laser [10].

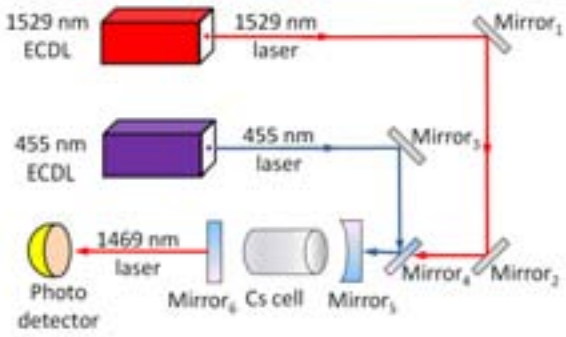

Fig. 2. Experimental setup of cesium active optical clock in four-level configuration. $Mirror_1$, $Mirror_2$ and $Mirror_3$ are highly reflecting mirrors at 1529 nm. $Mirror_4$ is coated with 1529 nm anti-reflection and 455 nm high-reflection coating. $Mirror_5$ is coated with 455 nm anti-reflection and 1469 nm high-reflection coating. $Mirror_6$ is coated with 455.5 nm high-reflection and the reflectivity of 1469 nm is 80%.

The experimental setup of cesium active optical clock is shown in Fig. 2. The cavity is composed of a concave mirror ($Mirror_5$) and a planar mirror ($Mirror_6$). $Mirror_5$ is coated with 455 nm anti-reflection and 1469 nm high-reflection coating. The radius of curvature is chosen to be 500 mm. $Mirror_6$ is coated with 455 nm high-reflection and the reflectivity of 1469 nm is 80%. The Cesium cell is 5 cm long and the cavity is 8.5 cm long. The cavity length can be swept by the piezoelectric ceramic transducer (PZT) fixed behind $Mirror_6$. The temperature of the Cesium cell is controlled around 123 ℃ and the transmission of the cesium cell at 1529 nm is measured to be 60%. A 1529 nm external-cavity diode laser is used to calibrate the cavity. Due to the loss of the cesium cell in the cavity, the finesse of the cavity is calculated to be 2, which agrees well with the experiment result indicated in Fig. 3. The free spectral range (FSR) is 1.76 GHz and the corresponding sweep voltage of the bad-cavity PZT for a single free spectral range is approximately 125 V. The cavity bandwidth is then measured to be 880 MHz. The 455 nm pumping laser is introduced into the cavity to generate Cesium active optical clock output at 1469 nm and the pumping laser power is 10 mW.

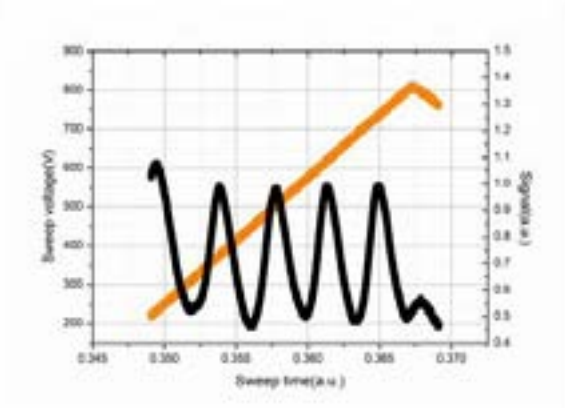

Fig. 3. Bad cavity calibration using 1529 nm laser. The sweep voltage of the bad-cavity PZT is represented by the orange line while the transmission signal of 1529 nm laser is represented by the black line. The finesse of the cavity is 2 and the free spectral range is 1.76 GHz..

III. RESULTS

Since the Cesium active optical clock output at the wavelength of 1469 nm is observed, we measured the lasing threshold and output power when changing the 455 nm pumping laser power (as shown in Fig.4) and frequency (as shown in Fig. 5).

Fig. 4 shows the measured lasing threshold and output power of Cesium active optical clock when the 455 nm pumping laser power is being changed. The frequency of 455 nm pumping laser is locked to the frequency between the saturated absorption spectrum of cesium $6S_{1/2}$ (F=4) - $7P_{3/2}$ (F'=5) and the crossover resonance corresponding to the cesium $6S_{1/2}$ (F=4) - $7P_{3/2}$ (F'=4,5) transition. Therefore the pumping laser is kept resonant with the cesium 455 nm transition and a maximum 1469 nm Cesium active optical clock output is observed (as shown in Fig. 5). The bad-cavity length is also kept in resonance with the 1469 nm Cesium active optical clock output wavelength (as shown in Fig. 6). Then the 455 nm pumping laser power is changed and the lasing threshold and output power of the Cesium active optical clock is measured. As indicated in Fig. 4, the 1469 nm Cesium active optical clock output has a threshold when the 455 nm pumping laser power equals to about 1.4 mW. When the pumping laser power is less than 1.4 mW, only weak

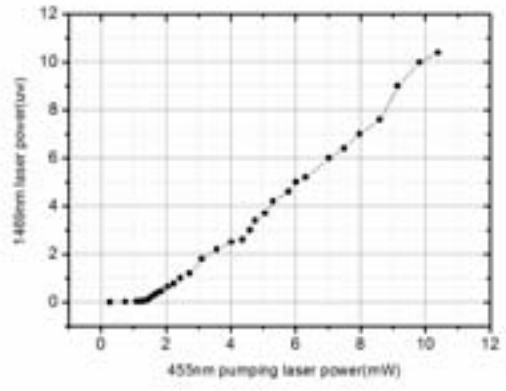

Fig. 4. 1469nm lasing threshold and output power of Cesium active optical clock when changing 455 nm pumping laser power. The frequency of pumping laser is locked to the cesium 455 nm transition and the bad-cavity length is kept in resonance with the 1469 nm Cesium active optical clock output.

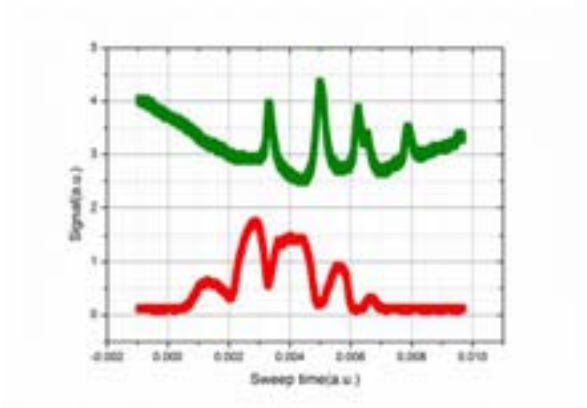

Fig. 5. 1469nm lasing threshold and output power of Cesium active optical clock when changing 455 nm pumping laser frequency. The power of 455 nm pumping laser is 10 mW and the bad-cavity length is kept in resonance with the 1469 nm Cesium active optical clock output. The green curve shows the saturated absorption spectrum and the red curve represents the corresponding 1469 nm output power of Cesium active optical clock.

fluorescence can be observed. As the 455 nm pumping laser power is increased to more than 1.4 mW, 1469 nm Cesium active optical clock output is then observed and the increase of 1469 nm Cesium active optical clock output power is proportional to the increased 455 nm pumping laser power.

Fig. 5 shows the measured lasing threshold and output power of Cesium active optical clock when the 455 nm pumping laser frequency is being changed. The power of 455 nm pumping laser equals to 10 mW and the length of the bad-cavity is kept in resonance with the 1469 nm Cesium active optical clock output wavelength.

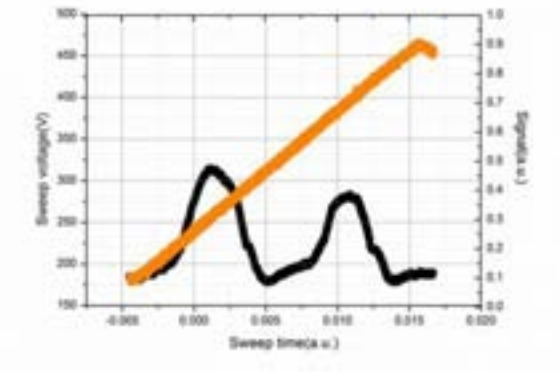

Fig. 6. 1469 nm Cesium active optical clock output multi-threshold when changing bad-cavity length. The frequency of pumping laser is locked to the cesium 455 nm transition and the incident pumping laser power is 10 mW. The sweep voltage of the bad-cavity PZT is represented by the orange line while the 1469 nm output signal of Cesium active optical clock is represented by the black line.

In Fig. 5 the green curve shows the saturated absorption spectrum and the red curve represents the corresponding 1469 nm output power of Cesium active optical clock. The 1469 nm output power indicated by the red curve has its dip where the saturated absorption spectrum shown by green curve has its peak. This can be attributed to the saturation effect of 455 nm pumping laser in the cesium cell of the bad-cavity. As shown in Fig. 2, the planar mirror of the bad-cavity ($Mirror_6$) is coated with 455 nm high-reflection. The 455 nm pumping laser will be reflected back and overlap the incident pumping laser beam in the cesium cell. When the peak of the 455 nm saturated absorption spectrum appears, the number of cesium atoms excited by the 455 nm pumping laser will decrease due to the saturation absorption in the cesium cell of the bad-cavity, resulting in the reduction of 1469 nm Cesium active optical clock output power.

Fig. 6 shows the measured lasing multi-threshold and output power of Cesium active optical clock when the length of the bad-cavity is being changed. The frequency of pumping laser is locked to the cesium 455 nm transition and the incident pumping laser power is 10 mW. The sweep voltage of the bad-cavity PZT is represented by the orange line while the 1469 nm output signal of Cesium active optical clock is represented by the black line. The measured sweep voltage of the bad-cavity PZT for a single free spectral range at 1469 nm is approximately 125 V, in accordance with the result of 1529 nm laser shown in Fig. 3. We also measured the wavelength of Cesium active optical clock output using a spectrometer. The central wavelength is measured to be 1469.500 nm as indicated in Fig.7.

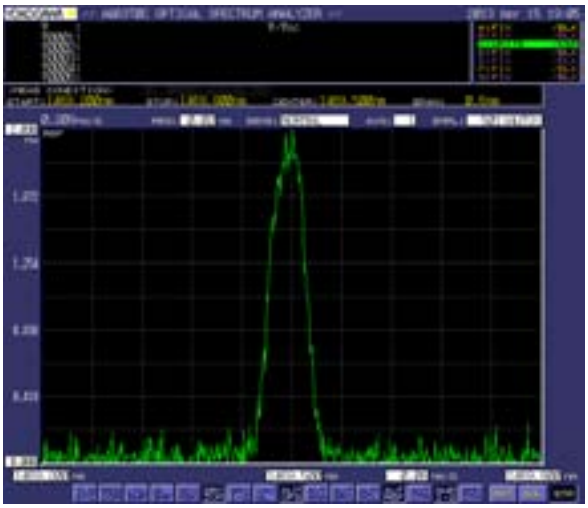

Fig. 7. 1469 nm Cesium active optical clock output wavelength measurement using spectrometer.

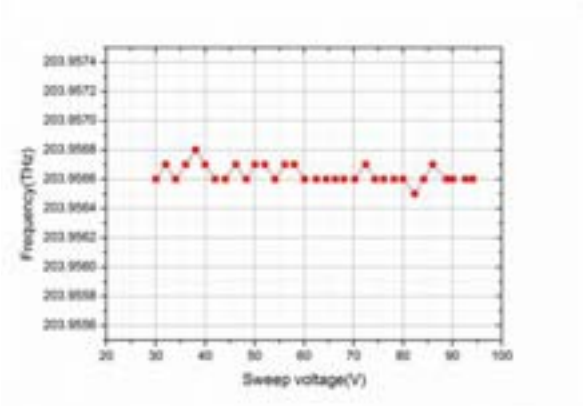

Fig. 8. 1469 nm Cesium active optical clock output frequency when changing bad-cavity length

Fig. 8 shows measured 1469 nm Cesium active optical clock output frequency when changing bad-cavity length. The sweep voltage of the bad-cavity PZT is gradually increased from 30 V to 96 V, more than half a free spectral range of the bad-cavity (the sweep voltage of the bad-cavity PZT for a single free spectral range is measured to be 125 V). In this progress the 1469 nm Cesium active optical clock output frequency is measured using the Advantest TQ8325 Digital Optical Wavelength Meter (with the resolution of 100 MHz). The measured linewidth of 455 nm transition can be as narrow as 1.4 MHz, approaching the natural linewith 1.2 MHz [13]. So right now, the linewidth of the gain is limited by saturation

broadening. The saturation intensity of Cesium 455 nm transition is I_s=1.66 mW/cm^2, while the power of 455 nm pumping laser is 10m W and the beam size is about 0.84 mm^2. The intensity of 455 nm pumping laser in the Cesium cell is then calculated to be 1.19 W/cm^2 and the saturation parameter is 717. Therefore, the gain linewidth, which is limited by saturation broadening, is 32.4 MHz, nearly 1/30 of the cavity linewdith (880 MHz). The 1469 nm Cesium active optical clock output is hence in the bad-cavity laser region. As indicated in Fig. 8, the sweep range of the bad-cavity is 900 MHz while the fluctuation range of 1469 nm Cesium active optical clock output frequency is only about 300~400 MHz, which proves the cavity-pulling reduction of the 1469 nm Cesium active optical clock output due to the bad-cavity effect.

IV. CONCLUSION

In summary, we are setting up an experiment to investigate active optical clock in 4-level configuration with Cesium atoms. We observed the 1469 nm Cesium active optical clock output and measured the wavelength to be 1469.500 nm using a spectrometer. The 1469 nm lasing threshold and output power is measured when changing the power and frequency of the 455 nm pumping laser. The 1469 nm Cesium active optical clock output multi-threshold is also observed when sweeping the bad-cavity length. The 1469 nm Cesium active optical clock output frequency is measured using a wavelength meter when sweeping the bad-cavity length and the cavity-pulling reduction due to the bad-cavity effect is observed. This work was supported by the National Natural Science Foundation of China (10874009 and 11074011)

REFERENCES

[1] D. Yu and J. Chen, “Optical Clock with Millihertz Linewidth Based on a Phase-Matching Effect”, Phys. Rev. Lett., vol. 98, p. 050801, (2007).

[2] J. Chen and X. Chen, “Optical lattice laser,” 2005 IEEE Freq. Contr. Symp., p. 608, (2005.).

[3] J. Chen, “Active Optical Clock,” Chinese. Science. Bulletin. vol. 54, p. 348, (2009).

[4] D. Yu and J. Chen, “Laser theory with finite atom-field interacting time,”Phys. Rev. A, vol. 78, p. 013846, (2008).

[5] Y. Wang, “Optical clocks based on stimulated emission radiation,” Chinese Science Bulletin, vol. 54, p. 347, (2009).

[6] D. Meiser et al.,“Prospects for a millihertz-linewidth laser,” Phys. Rev.Lett., vol. 102, p. 163601, (2009).

[7] Zhang TongGang, Wang YanFei, Zang XiaoRun, Zhuang Wei & Chen JingBiao, "Active optical clock based on four-level quantum system" Chinese. Science. Bulletin. Vol. 58, p. 2033, (2013).

[8] Zhang Shengnan, Wang Yanfei, Zhang Tonggang,Zhuang Wei, and Chen Jingbiao, “A Scheme of Potassium Atom Four-Level Active Optical Clock”, Chin. Phys. Lett. Vol. 30, p. 040601 (2013).

[9] Zang Xiaorun, Zhang Tonggang, Chen Jingbiao,"Magic Wavelengths for a Lattice Trapped Rubidium Four-Level Active Optical Clock", Chin. Phys. Lett. Vol. 29(9), p. 090601 (2012).

[10] Wang YanFei, Wang DongYing, Zhang TongGang, Hong YeLong, Zang ShengNan, Tao ZhiMing, Xie XiaoPeng & Chen JingBiao, "Realization of population inversion between 7S1/2 and 6P3/2 levels of cesium for four-level active optical clock", Science China Physics, Mechanics & Astronomy, Vol. 56 No. 6: p. 1107－1110 (2013).

[11] Yanfei Wang, Shengnan Zhang, Dongying Wang, Zhiming Tao, Yelong Hong, and Jingbiao Chen ,“Nonlinear optical filter with ultra-narrow bandwidth approaching the natural linewidth”, Optics Letters, Vol. 37, p. 4059-4061 (2012).

[12] Yanfei Wang, Xiaogang Zhang, Dongying Wang, Zhiming Tao, Weizhuang, and Jingbiao Chen,“Cs Faraday optical filter with a single transmission peak resonant with the atomic transition at 455 nm”, Optics Express, Vol. 20, p. 25817- 25825 (2012).

[13] Wang Dongying, Wang Yanfei, Tao Zhiming, Zhang Shengnan, Hong Yelong, Zhuang Wei, Chen Jingbiao, "Cs 455nm Nonlinear Spectroscopy with Ultra-narrow Linewidth", Chin. Phys. Lett. Vol. 30, No. 6, p. 060601 (2013).

Dispersion Detection of Optical Clock Transition in Thermal Atomic Beam

Xiaogang Zhang, Xiaobo Xue, Duo Pan, Shengnan Zhang, Wei Zhuang, Jingbiao Chen

School of Electronics Engineering and Computer Science,
Peking University, Beijing 100871, China

Email: jbchen@pku.edu.cn

***Abstract*—In order to develop small optical clock for various transportable applications with better stability and accuracy than that of commercial small Cs clock and H-maser clock, our group has proposed a small Ca atomic beam clock scheme with electron-shelving detection. Its potential stability was experimentally demonstrated recently. Here, we first demonstrated the dispersive detection of 657 nm transition via the Faraday rotation effect of 423 nm transition based on a thermal Ca atomic beam, this alternative detection method can effectively detect the clock signal by the ground state atoms after the clock laser interrogation. The Faraday anomalous dispersion optical filter of 423 nm transition can reach a maximum transmission of 10%. With a magnetic field of 84 G, the observed 3.3% of the ground state atoms has been excited to the $\sigma^{\pm}$ level of metastable $^3P_1(m=\pm1)$ state, which are separated 176.6 MHz to m=0 level.**

Keywords—electron-shelving detection; dispersive detection; the Faraday anomalous dispersion optical filter.

I. INTRODUCTION

In the past several years, many research groups have improved the performance of the optical atomic clock, especially based on laser cooled ions and neutral atoms. During the processing of the improvement, the compactness of the optical atomic clock also plays a key role. In order to develop small optical clock for various transportable applications with better stability and accuracy than that of commercial small Cs clock and H-maser clock, our group has proposed a small Ca atomic beam clock scheme with electron-shelving detection[1-3]. Its potential stability was experimentally demonstrated recently.

Optical filter, especially the narrow bandwidth optical filter has a great advantage on optical communication and sensing system. Additionally, the Faraday anomalous dispersion optical filter (FADOF), which has high transmission with narrow bandwidth, has been used on many areas.

In this paper, based on electron-shelving detection[4-5] and FADOF technology, we first demonstrated the dispersive detection of 657 nm transition via the Faraday rotation effect of 423 nm transition. This alternative detection method via FADOF[6] can effectively detect the clock signal by the ground state atoms after the 657 nm clock laser interrogation. The experimental system based on a thermal Ca atomic system is more convenient and transportable.

II. EXPERIMENTAL SCHEMATIC

The schematic diagram of the experimental setup is showed in Fig.1. And Fig. 2 shows the relevant Ca energy levels. The system detects the 657 nm clock signal of Ca atoms by the 423 nm transition signal after the clock laser interrogation. Because 1S0-1P1 transition and $^1S_0$-$^3P_1$ transition use the same ground state atoms, the detection technology can effectively detect the clock signal and improve the detection efficiency massively. The energy level will be split into three magnetic levels due to the additional external magnetic field. In this system, Ca atoms are loaded in a reservoir which is in vacuum. The whole vacuum system are pumped off to 10^{-6} Pa and heated to 850 ˚C. The temperature of the vacuum system is monitored using the thermocouple. When the vacuum system is heated to 807 ˚C, Ca atoms would be evaporated and becomes atomic beam. Then, the 657 nm clock signal laser is reflected to interact with Ca atomic beam. The 657 nm laser is Littrow's external cavity diode laser. Before the interaction, a λ/4 plate can change the polarization of the 657 nm laser and change the transition levels. With this interaction, the ground state of Ca atoms will be pumped to the $^3P_1$ state. Then, we detect the clock signal by 423 nm laser. The 423 nm laser is also Littrow's external cavity diode laser. Here, we detect the 423 nm signal by the Faraday rotation effect in a FADOF configuration. A folded seven-beam traveling wave configuration is employed to improve transmission efficiency. As showed in Fig.2, two high reflection mirrors are applied to realize the seven-beam configuration. The 423 nm laser beams are nearly perpendicular to the atomic beam. Two crossed Glan-Taylor prisms are set on both sides of the atomic beam. A λ/4 plate is placed between two Glan-Taylor prism. In this way, the stress-induced birefringence of vacuum windows can be compensated. Besides, a magnetic field of up to maximum 100 G is induced into the system. The magnetic field is perpendicular to the atomic beam and aligned to parallel to the resonant laser beam.

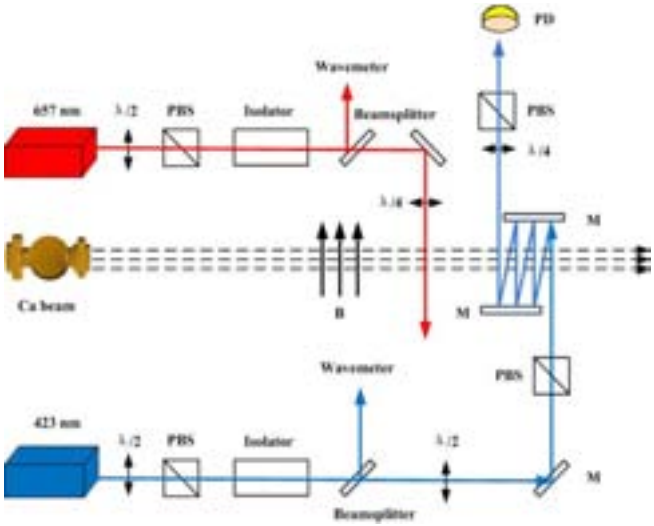

Fig. 1. The diagram of experimental setup. Lasers of 657 nm and 423 nm are the external cavity diode lasers at structure configuration of Littrow. Ca metals atoms are loaded in a reservoir which is in vacuum. The vacuum system are pumped off to 10^{-6} Pa and heated to 850 ˚C. PBS, Glan-Taylor prism; M, high reflection mirror for 657 nm and 423 nm; PD , photodiode.

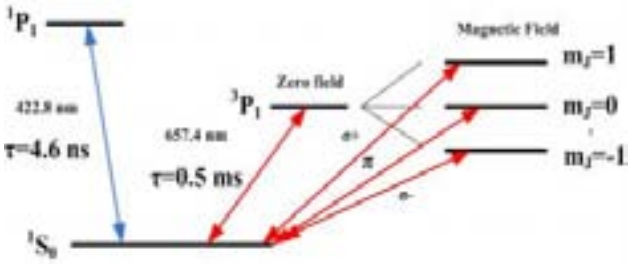

Fig. 2. Relevant Ca energy levels.

III. Experimental Results

As illustrated in Fig.3, the Faraday effect transmission spectrum of 423 nm in red line has a signal peak at the center of the resonance transition. The blue line is the fluorescence detection in another vacuum system for a reference. The laser of the fluorescence detection is strictly perpendicular to the atomic beam. The Faraday effect transmission spectrum of 423 nm has Doppler broadening. The magnetic field is set to 84 G, which is produced by passing 2.5 A of dc current through the a pairs of magnetic coils. The 423 nm laser power is 0.73 mW. The linewidth of the red line is 248 MHz and the intensity is 3.2 V. The maximum transmission efficiency [6] of the Faraday effect is 10%. In this case, the transmission efficiency is 3.9%. In order to interrogate atoms with the 657 nm clock signal, we lock the 423 nm laser to the atomic resonance transition by another vacuum system. The locking time can be more than 1 hour. Then we scan the 657 nm laser by introducing a triangular wave to the PZT of the ECDL laser. The transmission spectrum of the 657 nm clock signal is showed in Fig. 4. The upper blue line in Fig. 4 is the fluorescence detection signal in another vacuum signal as a reference. The π transition of 657 nm is chosen by aligning the polarization of the laser to parallel to the direction of the magnetic field. The lower red line in Fig. 4 is the dispersion detection. Because the polarization of laser beam is always perpendicular to the direction of the magnetic field in this vacuum system, the $\sigma^{\pm}$ transition is chosen to demonstrate this detection method in principle. In Fig. 4, the left spectrum is the σ^- transition and the right one is the σ^+ transition. The $\sigma^{\pm}$ transitions are separated 176.6 MHz to m=0 level. The 657 nm laser's power is set to 8.1 mW. The signal intensity of each is 0.054 V and the linewidth is 86.7 MHz. Fig. 5 shows us the single σ^- transition by rotating the λ/4 plate, where is before the incidence of 657 nm laser. The signal intensity becomes 0.108 V, which is doubled, but the linewidth is the same to the $\sigma^{\pm}$ transition. Comparing the 657 nm signal to the 423 nm signal, we can see that 3.3% of the ground state atoms has been excited to the metastable 3P1(m=±1) state by $\sigma^{\pm}$ level and detected here.

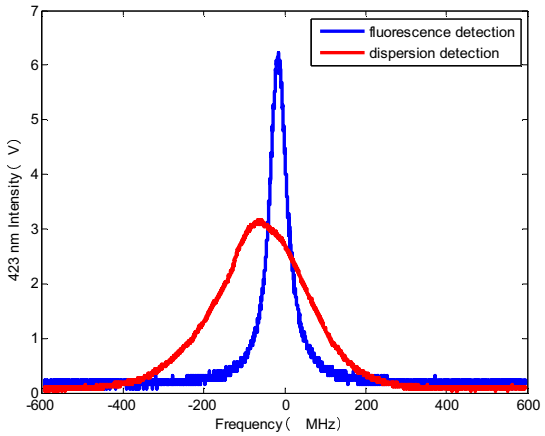

Fig. 3. Dispersion detection of 423 nm. Red (Wider): the transmission of the Faraday effect of 423 nm; Blue (Narrower): the fluorescence detection of 423 nm in another vacuum system for a reference.

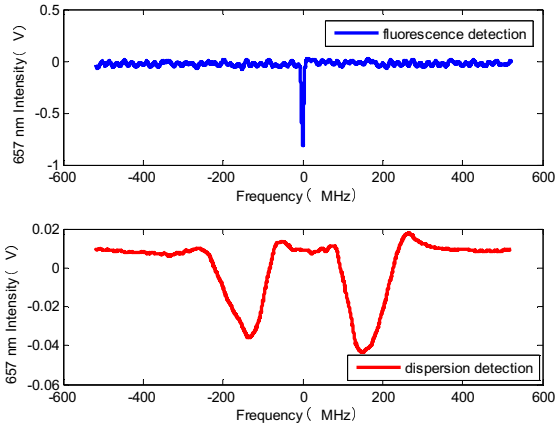

Fig. 4. Dispersion detection of 657 nm clock signal. The 423 nm laser was locked to the atomic transition center. Scanning the 657 nm laser, the upper blue line is the fluorescence detection signal of 657 nm, which is the π transition of Ca atoms. The lower red line is the dispersion detection signal of 657 nm, which is the $\sigma^{\pm}$ transition.

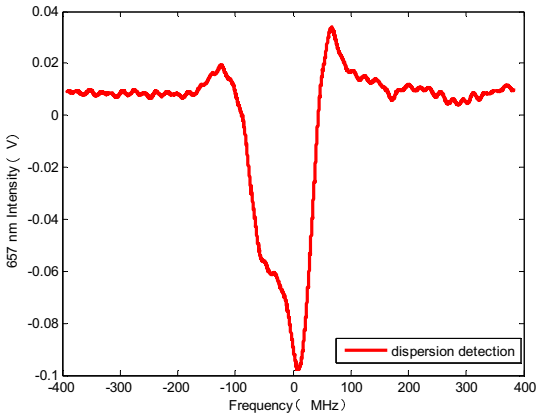

Fig. 5 The single 657 nm σ^- transition signal of the dispersion detection.

IV. CONCLUSION

In conclusion, we first demonstrated the dispersive detection of 657 nm transition via the Faraday rotation effect of 423 nm transition in a thermal Ca atomic beam. The Faraday anomalous dispersion optical filter[6] of 423 nm transition can reach a maximum transmission of 10%. With a magnetic field of 84 G, the observed 3.3% of the ground state atoms has been excited to the $\sigma^{\pm}$ level of metastable 3P1(m=±1) state, which are separated 176.6 MHz to m=0 level. In comparison with traditional atomic clocks, this new detection method provides great advantages to both integration and miniaturization.

ACKNOWLEDGMENT

This work was supported by the National Natural Science Foundation of China (10874009 and 11074011).

REFERENCES

[1] Huang Kaikai, Zhang Jianwei, Yu Deshui, Chen Zhenhui, Zhuang Wei, Chen, Jingbiao, "Application of electron-shelving detection via 423 nm transition in Calcium-beam optical frequency standard," Chin. Phys. Lett., vol. 23, pp. 3198-3201, 2006.

[2] Kaikai Huang, Donghai Yang, Jingbiao Chen, "Small compact Calcium-beam optical frequency standard in Peking university and its new scheme," Proc. of 20th EFTF, pp376-378, 27-30 March 2006, Braunschweig Germany.

[3] Xie Xiaopeng, Zhuang Wei, Chen Jingbiao, "Adiabatic passage based on the Calcium active optical clock," Chin. Phys. Lett., vol. 27, 074202, 2010.

[4] John J. McFerran and Andre N. Luiten, "Fractional frequency instability in the 10^{-14} range with a thermal beam optical frequency reference," J. Opt. Soc. Am. B, vol. 27, pp. 277-285, February 2010.

[5] J. J. McFerran, J. G. Hartnett, and A. N. Luiten, "An optical beam frequency reference with 10^{-14} range frequency instability," Appl. Phys. Lett., vol. 95, 031103, 2009.

[6] Zhichao Xu et al., "Atomic filter at 422.7 nm based on a Ca thermal atomic beam," unpublished.

Testing Optical Clock Calibration Procedures: Absolute Frequency Measurement of Rubidium 5S-7S Two-Photon Transitions

Michał Zawada*, Piotr Ablewski*, Wojciech Gawlik†, Rafał Gartman*,
Piotr Masłowski*, Piotr Morzyński*, Bartłomiej Nagórny*, Filip Ozimek‡,
Czesław Radzewicz‡, Piotr Wcisło*, Marcin Witkowski*§ and Roman Ciuryło*
*Institute of Physics, Faculty of Physics, Astronomy and Informatics, Nicolaus Copernicus University
Grudziądzka 5, PL-87-100, Toruń, Poland
Email: zawada@fizyka.umk.pl
†Institute of Physics, Jagiellonian University,
Reymonta 4, PL-30-059 Kraków, Poland
‡Institute of Experimental Physics, Faculty of Physics, University of Warsaw,
Hoża 69, PL-00-681 Warsaw, Poland
§Institute of Physics, University of Opole,
Oleska 48, PL-45-052 Opole, Poland

***Abstract*—We report the absolute frequency measurements of rubidium 5S-7S two-photon transitions with an optical frequency comb. The digital lock to the transition, the procedures of evaluating the accuracy budget and measurements of the frequency with the optical frequency comb are tested with a simple setup for the sake of comparison of two optical lattice strontium clocks. The narrow, two-photon transition, 5S-7S (760 nm) is insensitive to a magnetic field and promising candidate for frequency standard. The preformed tests yield the transition frequency with accuracy better than reported previously.**

I. Introduction

The International Committee for Weights and Measures recommended several radiations for applications including the practical realization of the metre. At the border of the visible and near-infrared ranges the BIPM recommends the $5S_{1/2}$(F=3) - $5D_{5/2}$(F=5) two-photon transition in ^{85}Rb with a standard uncertainty of 5 kHz (the relative standard uncertainty of 1.3×10^{-11}) [1]. Recent development in phase-stabilized optical frequency combs based on mode-locked femtosecond lasers allowed determination of the absolute frequency of a similar transition in Rb, $5S_{1/2}$-$7S_{1/2}$, which is 100 times weaker than 5S-5D, yet less sensitive to the stray magnetic fields. At the 5S-5D transition the rubidium atoms must be carefully shielded against the magnetic field to avoid any linear Zeeman shifts. On the other hand, the 5S and 7S levels have the same Landé g factors which cancels the linear Zeeman shifts in the 5S-7S transition. The ac-Stark effect in the 5S-7S transition is also smaller than in the 5S-5D case. All previous measurements of the 5S-7S transition [2]–[5] gave worse estimations of the absolute frequency than the measurements of the 5S-5D transition [6]–[9]. In this work we report the measurement of the absolute frequency measurements of the $5S_{1/2}$(F=2)-$7S_{1/2}$(F=2) transition in ^{87}Rb with relative standard uncertainty of 5.8×10^{-12} which is better than measured previously.

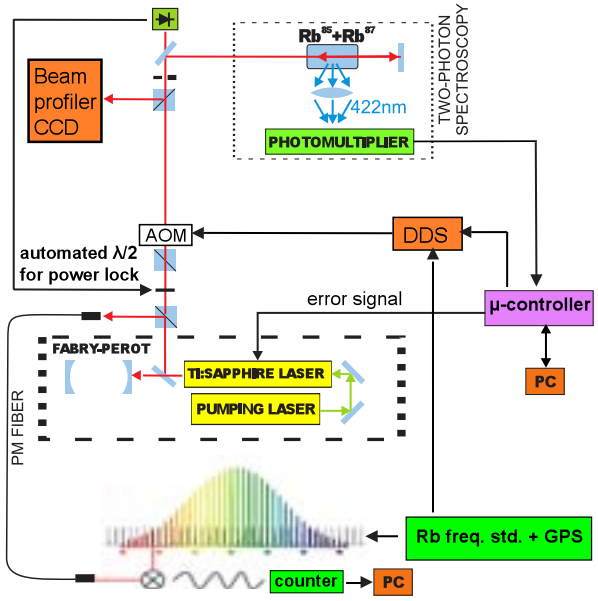

Fig. 1. Experimental setup.

II. Experimental arrangement

The experimental setup is shown in Fig.1. We have used a commercial ring-cavity titanium sapphire (TiSa) laser to study the two-photon $5S_{1/2}$-$7S_{1/2}$ transitions at 760 nm in a hot rubidium vapour cell at temperatures up to 140 Centigrades. The TiSa laser is pre-stabilised by a Fabry-Pérot cavity which narrows the laser linewidth to 300 kHz. The two-photon

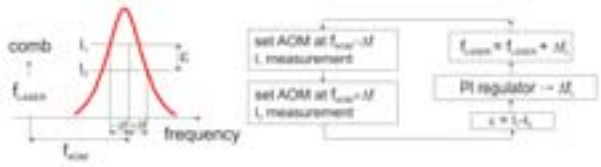

Fig. 2. The scheme of the digital lock.

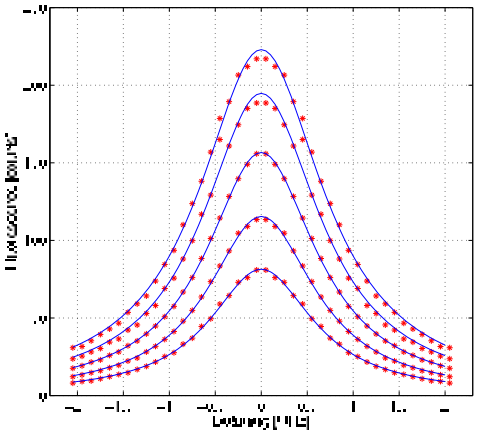

Fig. 3. The line profile for different intensities of the probing light. The Lorentz profile is fitted to the measured data.

spectroscopy signal is observed by a photomultiplier tube in the 7S-6P-5S radiative cascade, with the 6P-5S decay blue fluorescence around 421 nm.

The idea of the digital lock is depicted in Fig.2. An acousto-optic modulator (AOM) driven by a direct digital synthesizer (DDS) square-wave modulates the light frequency with the step 2Δf equal to the half-width of the line. The AOM carrier frequency f_{AOM} is chosen such that the AOM efficiency with $f_+ = f_{AOM} + \Delta f$ and $f_- = f_{AOM} - \Delta f$ is the same. The microcontroller (Atmel AT91SAM7S), which controls the DDS, counts the photomultiplier pulses. The error signal for the laser lock is calculated from the difference of the counts for f_+ and f_-. The software PI regulator in the microcontroller calculates the correction Δf_L and applies it to the TiSa laser. The power of the light sent to the rubidium cell is stabilised by the software PI regulator on the embedded PC (FOX Board G20) with a half-wave plate mounted on a piezo-driven mount and a polariser. To exclude the residual Doppler shift, the counter-propagating beams in the two-photon spectroscopy are not focused and their relative position is controlled by a CCD beam profiler camera. By changing Δf in the digital lock we can measure the line profile. Since the counter-propagating beams are not focused we can measure the line-shape of the transition broadened only by the 300 kHz laser linewidth and the light power (Fig. 3).

Part of the TiSa light is sent directly to the Er-dopped fiber optical frequency comb (Menlo FC1500-250-WG). The comb, the DDS synthesizers and counters in the experiment are locked to a microwave Rb frequency standard (SRS FS725), disciplined by the GPS (Connor Winfield FTS 375). The

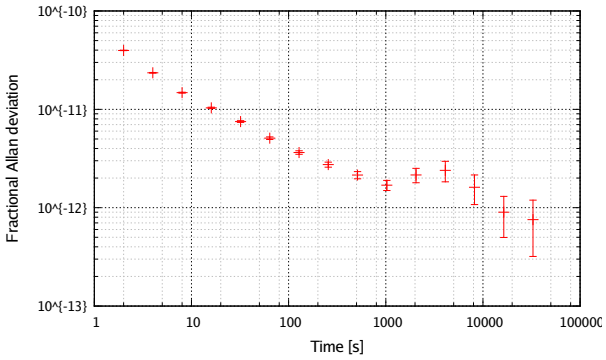

Fig. 4. Allan variance of the beat frequency between the TiSa laser and optical frequency comb.

TABLE I
ACCURACY BUDGET. (M - MEASURED, C - CALCULATED)

Effect	Shift [kHz]	Uncert. [kHz]
Pressure shift^m	-24.14	1.1
Light shift^m	0.4	1.6
Quadratic Zeeman Shift^m	0.055	0.034
Line pulling^c	0	0.01
Beam alignment (residual Doppler shift)^m	0	0.3
Second order Doppler effect^c	-0.168	0.001
DDS electronics & lock^m	-4.44	0.48
Black Body Radiation^c	-0.666	0.004
Rb frequency standard & GPS^c	0	0.4
Total:	**-29.0**	**2.0**

fractional Allan variance of the beat frequency between the locked TiSa laser and the optical frequency comb is presented in Fig. 4. After 1000 s our Rb frequency standard reaches its final stability, and our system is further disciplined by the GPS which improves the stability, as seen in the plot, after 10^4 s integration time.

III. RESULTS

Several systematic effects should be taken into account to deduce the transition frequency. The measurements are dominated by a systematic pressure shift. By measuring the absolute frequencies at different temperatures (accuracy of 0.2K), we determined the pressures [10], estimated the pressure shift coefficient in our cell as -17.82(81) kHz/mTorr (Fig. 5) and extrapolated it to zero pressure. In the same way we measured and calibrated the ac-Stark and quadratic Zeeman shifts. By measuring the absolute frequency while misaligning the probe beams we estimated the uncertainty due to the residual Doppler shift. Varying the Δf value in the DDS lock and the AOM diffraction order ($+f_{AOM}$ or $-f_{AOM}$) to cancel any residual efficiency imbalance between f_+ and f_-, we also estimated the shift of the digital lock. The black body radiation and second order Doppler shifts were calculated for a given stabilised cell temperature in the cell.

The accuracy budget for typical experimental conditions, i.e. laser intensity of 8 W/cm^2 and temperature of 128.5°C, is presented in Table I.

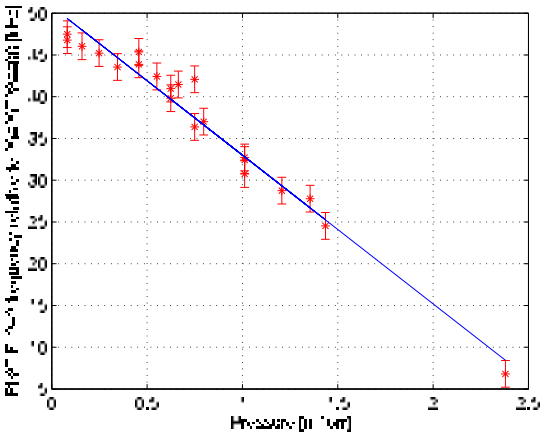

Fig. 5. Pressure shift. Frequency is relative to the best previously known value.

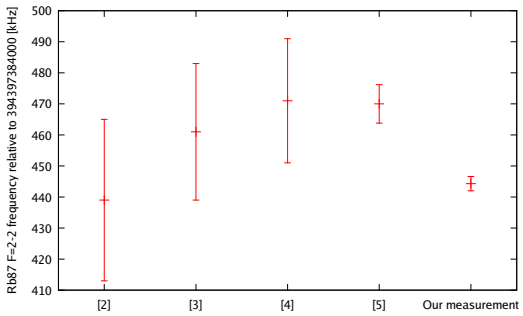

Fig. 6. Comparison with previously known values.

The absolute optical frequency for the ^{87}Rb F=2-F'=2 two-photon transition is determined to be 394397384444.3(2.3) kHz Its comparison with previously measured values is depicted in Fig. 6.

IV. Conclusion

We performed a series of measurements of the absolute frequency of the 5S-7S two-photon transitions in rubidium vapour with an optical frequency comb. The digital lock to the transition, the procedures of evaluation the accuracy budget and measurements of the frequency with the optical frequency comb, prepared for a future system of two optical lattice clocks with strontium atoms, were tested with a simple setup. Thanks to a very good long-term stability of our experimental system, we obtained higher accuracy of the 5S-7S transition frequency than any previously reported [2]–[5].

Acknowledgment

This work has been performed in the National Laboratory FAMO in Toruń and supported by the TEAM Project of the FNP, co-financed by the EU within the European Regional Development Fund.

References

[1] Bureau International des Poids et Mesures (BIPM), in Report of the 86th Meeting of the Comité International des Poids et Mesures (CIPM), (BIPM, Sèvres, France, 1997)

[2] Ming-Sheng Ko and Yi-Wei Liu, Opt. Lett., **29**, 1799 (2004)

[3] A. Marian et al., Phys. Rev. Lett. **95**, 023001 (2005)

[4] K. Pandey et al., Opt. Lett., **33**, 1675 (2008)

[5] I. Barmes et al., Phys. Rev. Lett., **111**, 023007 (2013)

[6] D. Touahri et al., Opt. Commun. **133**, 471 (1997)

[7] D. J. Jones et al., Science **288**, 635 (2000)

[8] J. E. Bernard et al., Opt. Commun. **173**, 357 (2000)

[9] C. S. Edwards et al., Metrologia **42**, 464 (2005)

[10] D. A. Steck *Rubidium 87 D Line Data*, C. B. Alcock, et al., Canadian Metallurgical Quarterly **23**, 309 (1984)

Iodine Stabilized IR Laser Sources

N. Castagna, N. Chiodo, M. Lours,
D. Holleville, Y. Lecoq, and O. Acef
LNE-SYRTE - CNRS UMR 8630
Observatoire de Paris / UPMC
61, Av. de l'Observatoire F-75014 Paris (France)
Email : ouali.acef@obspm.fr

F. Du Burck
LPL - CNRS UMR 7538 / Université Paris 13 / Sorbonne Paris Cité
99, Av. J. B. Clément F- 93430 Villetaneuse (France)
Email: frederic.du-burck@univ-paris13.fr

***Abstract*— We report on the frequency stabilization of an infrared (IR) laser emitting at 1.5 µm onto molecular iodine hyperfine transitions at 514 nm. Third harmonic generation process based on Periodically Poled Lithium Niobate non linear crystals (PPLN) is used to link the IR emission to the green region. We have developed and tested a compact experimental setup using a multi-pass iodine cell in order to meet transportable/spatial requirements. Narrow hyperfine iodine lines (FWHM ~ 300 kHz) corresponding to a quality factor Q > 10^9 are already detected and used for the IR sources stabilization purpose.**

Keywords - laser frequency stabilization, frequency tripling, second harmonic generation, molecular spectroscopy, iodine, metrology.

I. INTRODUCTION

Ultra stable optical frequency standards are of great interest for various fields such as optical communications, long distance optical links, transportable frequency standard, high resolution atomic or molecular spectroscopy, etc... Infrared lasers (IR) operating in the range 1 µm to 2 µm offer attractive possibilities for these applications regarding to their very low intrinsic phase noise, high output power, compactness and reliability in fiber mode configuration. To enhance the long term frequency stability of those lasers and to confer them a given accuracy, we must combine their use with an external frequency reference which exhibits high signal to noise ratio and linewidth as narrow as possible in same time.

Nowadays, the best performances in terms of short term frequency stability are achieved using rigid optical cavities (OC) which deliver excellent frequency discriminator and yield to impressive results in a wide range of the optical domain [1]. However, these couple laser/OC require an operative mode in a severe thermal and seismic environment, confining them to metrological laboratory activities.

Atomic and/or molecular transitions used in simple way with the saturated absorption technique constitute an elegant alternative to achieve compact experimental devices usable outside the laboratory even if the short term stability is more modest compared to the laser/OC systems. Many atomic or molecular species in coincidence with the IR sources gain curves allow already conferring levels of stability in the 10^{-11} 10^{-12} range (for example C2H2 for 1.5 µm lasers) [2]. The lines of some alkaline can also be used to stabilize these same lasers after frequency doubling [3, 4].

Molecular iodine has an absorption spectrum which extends from approximately 750 nm to 500 nm (limit of dissociation of the molecule) (Fig. 1). The atlas of iodine [5] lists some 100000 rovibrational transitions between the fundamental level (X) and the excited level (B), each of them being split in 15 or 21 hyperfine components. These molecular lines have been widely used for frequency stabilization of frequency doubled IR sources, such as Nd: YAG based systems [6, 7].

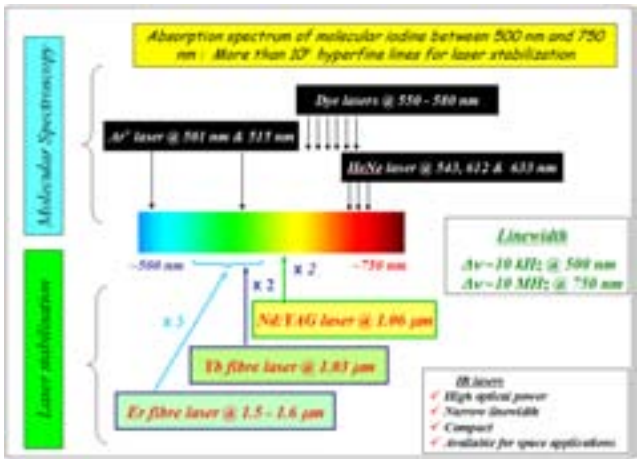

Figure 1. Laser stabilization possibilities onto molecular iodine transitions.

In this work, we report, for the first time to our knowledge, the frequency stabilization of a laser emitting in the C-band of optical telecommunications (around 1545 nm) onto an iodine line near 514 nm. The link between IR and visible regions is realized by means of a frequency tripling process. Previous attempts are reported in literature to realize the frequency tripling of an IR radiation to reach the green spectral region either by direct third harmonic generation (THG) [8] or by second harmonic generation (SHG) and sum frequency generation (SHG) within a single crystal [9]. In both cases, the tripling process was not efficient enough to give the possibility

to detect iodine transitions. The harmonic powers thus achieved in the nanowatts range, were not sufficient to realize iodine vapor saturation for the frequency stabilization purpose. Our scheme for THG is based on two cascaded non linear crystals, one for the SHG and one for the SFG from radiations emerging from the first one. We obtain by this way 1.5 mW of green radiation, a sufficient power for detecting iodine lines in a 20 cm long cell.

II. Frequency Tripling at 1545 nm

The experimental setup is depicted in Fig. 2. The IR source is an extended cavity laser diode (ECLD) operating over 100 nm from 1500 to 1600 nm emitting an output power of 20 mW. An Er doped fibre amplifier (EDFA) permits to reach an IR power more than 600 mW, incident onto the first non linear crystal involved in this experiment. The THG is operated in two steps by cascading two temperature controlled MgO: PPLN crystals (Fig. 2). The first one realizes the SHG at 772.5 nm from the IR radiation at 1545 nm produced by the amplified ECLD laser. The second one realizes the SFG between both radiations obtained at the output of the first crystal, i.e. the red beam at 772.5 nm and the residual IR beam at 1545 nm.

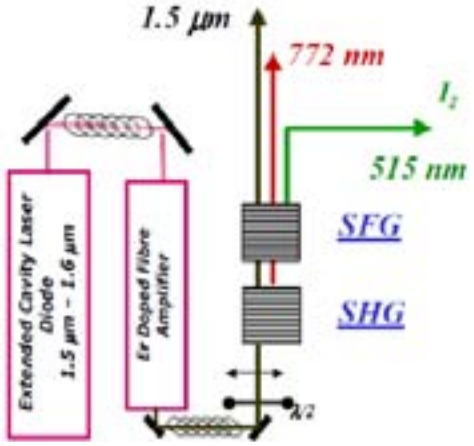

Figure 2. Experimental setup for third harmonic generation.

The dimensions of the fist crystal for SHG are 50 mm length, 1 mm width and 0.5 mm height. Its poling period is 18.2 µm. The quasi phase matching (QPM) is obtained around 50°C. The dimensions of the second crystal for SFG are 50 mm length, 2 mm width and 0.5 mm height. Its poling period is 6.92 µm. The quasi phase matching (QPM) is obtained around 19°C. The SH power measured at the output of the first crystal versus the IR power injected is plotted in Fig. 3. The conversion efficiency is found to be 0.9 %.W^{-1}.cm^{-1} and a maximum power of 12 mW of red radiation is obtained at 772.5 nm for 630 mW of IR power. Fig. 3 also shows the third harmonic (TH) power measured at the output of the second crystal producing the SFG between both radiations emerging from the output of the first crystal. A maximum output power of 1.5 mW at 514 nm is obtained (the conversion efficiency is estimated as 4.5 %.W^{-1}.cm^{-1}). This power is sufficient to detect hyperfine components of molecular iodine in a cell in saturation spectroscopy by means of the setup described in next section.

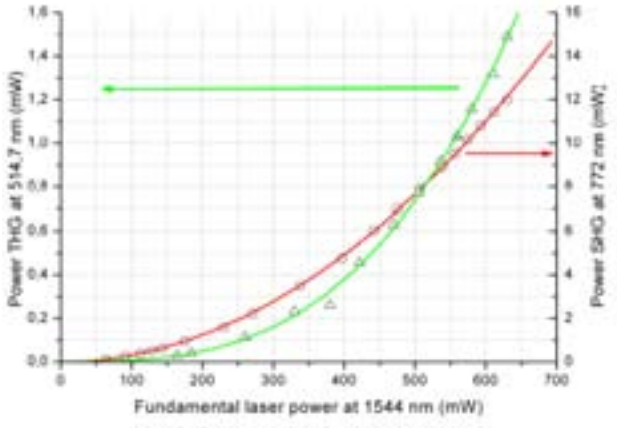

Figure 3. SHG and THG power versus the input IR power.

III. Spectroscopy of Molecular Iodine

A. *Iodine cell in multipass configuration*

We have developed a compact system for molecular iodine spectroscopy based on a multipass iodine cell (Fig. 4). The detail of this setup is in Fig. 5.

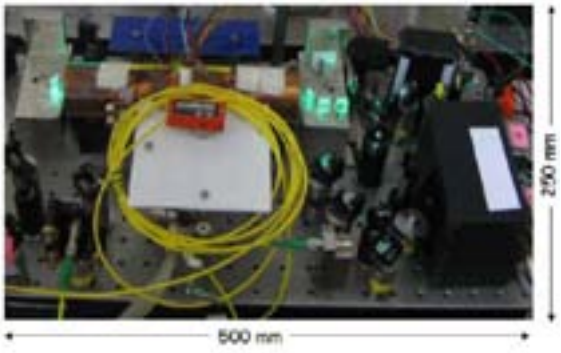

Figure 4. Photography of the experimental setup for saturation spectroscopy of iodine near 514 nm.

Hyperfine components at 514 nm are detected by saturation spectroscopy in a sealed cell (length 10 cm, diameter 2 cm) located in a thermal shield. The iodine pressure in the cell of about 0.8 Pa (6 mTorr) is controlled by thermo stabilization of a cold finger (-15°C). Probe and pump beams are counter propagating and pass four times through the cell. Input pump power of about 500 µW is sufficient to detect narrow hyperfine lines with excellent signal to noise ratio.

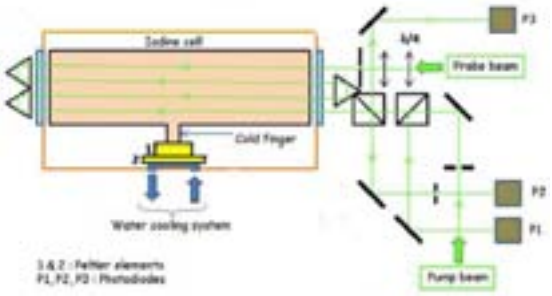

Figure 5. Experimental setup for saturation spectroscopy of iodine near 514 nm based on a multipass cell configuration.

B. Detected lineshapes

A typical spectrum showing the hyperfine splitting of a rovibrational transition near 514 nm detected with this setup is shown in Fig. 6, corresponding to the P46 (44-0) transition at 514.581 nm. The selection rules of hyperfine interaction in iodine lead to find 15 hyperfine components for an even rotational quantum number in the ground state ($J = 46$).

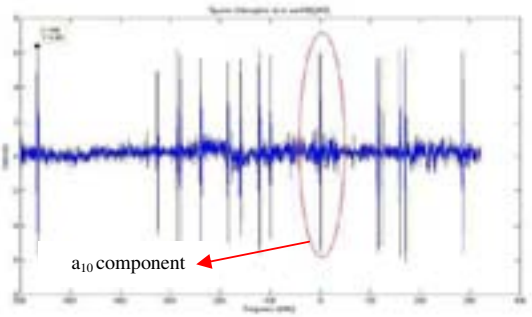

Figure 6. The complete spectrum of trasition P46(44-0) at 514.743 nm.

Fig. 7(a) shows the a_{10} component of this transition detected with the third harmonic and with a time constant of 300 µs. One can note the high signal to noise ratio of this signal and the good symmetry of the line shape. The peak-to-peak linewidth is close to 300 kHz.

We have identified a large number of rovibrational transitions with intense and narrow hyperfine components in the spectral region near 514 nm. Fig. 7(b) shows for instance the doublet a_3-a_4 belonging to transition R48 (44-0) at 514.585 nm.

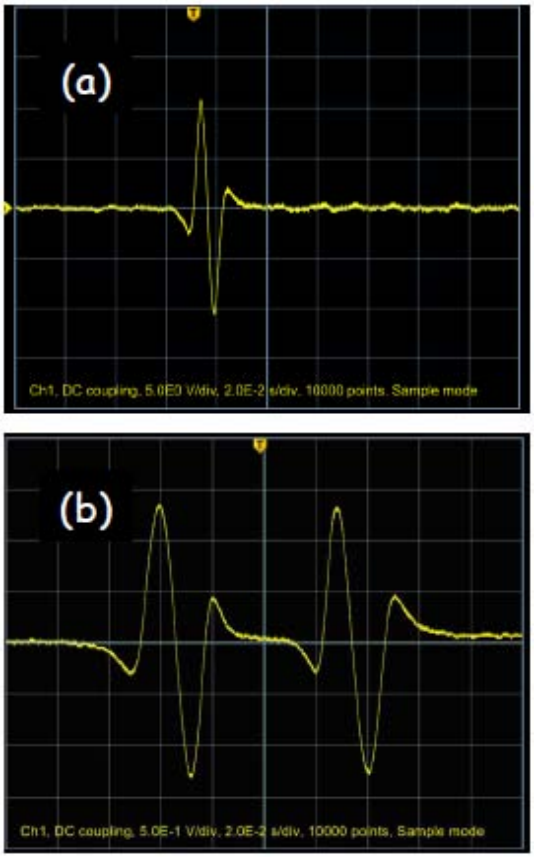

Figure 7. Third harmonic detection of hyperfine components near 514 nm.
(a) a_{10} component of the P46(44-0) line at 514.581 nm;
time constant is 300 µs;

(b) a_3-a_4 doublet of the R48(44-0) line at 514.585 nm;
time constant is 300 µs.

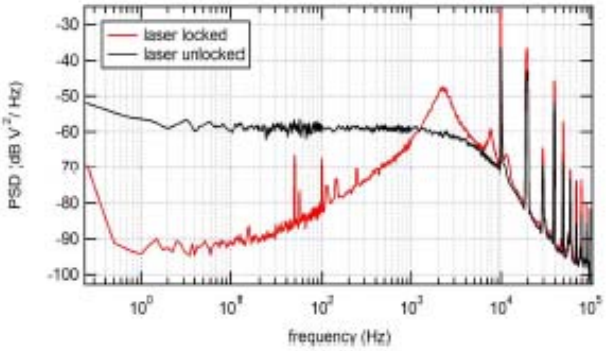

Figure 8. Noise spectrum of the error signal of the frequency stabilized IR source (inloop signal).

C. *Frequency stabilization of the source*

Such narrow lines are of first interest for the frequency stabilization of the IR source. We have locked the IR laser to the center of a_{10} component of transition P46 (44-0). Fig. 8 shows the noise spectrum of the error signal. A rejection of frequency noise more than 30 dB is reached up to 100 Hz. In this case, our laser can stay locked during several hours. The next step of this work consists on the metrological performances characterization by comparison with the cold atoms optical clocks of the SYRTE lab, located in an other building. This part is under development and the results will be reported subsequently.

IV. CONCLUSION

We have presented our first results concerning the frequency stabilization of an IR laser at 1.5 µm onto hyperfine components of molecular iodine near 514 nm. The IR emission is linked to the green region by means of a THG process achieved by cascading two PPLN crystals (SHG and SFG).

We have also developed a compact experimental setup based on a multi-pass iodine cell in which we have detected narrow hyperfine iodine lines (FWHM ~300 kHz) corresponding to a quality factor $Q > 10^9$.

Finally, we have locked the IR source onto those lines in order to stabilize the IR source frequency.

ACKNOWLEDGMENT

This work is supported by CNES (Contract R-S13/SU-0001-026) and DGA-ANR (Contract 11-ASTR 001-01).

V. REFERENCES

[1] B. Argence, E. Prevost, T. Lévèque, R. Le Goff, S. Bize, P. Lemonde, and G. Santarelli, "Prototype of an ultra-stable optical cavity for space applications", Optics express Vol. 20, N° 23, Nov. 2012, and references therein.

[2] J. Hald, L. Nielsen, J-C. Petersen, P. Varming and J-E. Pedersen, "Fiber laser optical frequency standard at 1.54 µm" , Opt. Express Vol. 19, N°3, January 2011 and references therein.

[3] A. Bruner, A. Arie, M. A Arbore and M. Fejer, "Frequency stabilization of a diode laser at 1540 nm by locking to sub_Doppler lines of potassium at 770 nm", Appl. Optics Vol. 37, N°6, February 1998.

[4] F. Ducos, J. Honthaas and O. Acef, "Development of optical frequency comb around 1556 nm referenced to a Rb frequency standard at 778 nm", Eur. Phys. Journal , Vol. 20, December 2002.

[5] S. Gerstenkorm, P. Luc, "Altas du spectre d'absorption de la molécule d'iode", Laboratoire Aimé Cotton, Ed. CNRS, Paris 1985.

[6] E. J. Zang et al., "Realization of four-pass I2 absortion cell in 532 nm optical frequency standard", IEEE Trans. Instrum. and Meas. Vol. 56, N°2, April 2007.

[7] O. Turazza, M. Lours, D. Holleville, G. Auger, A. Brillet, F. Du Burck, A. Clairon and O. Acef, "Progress on the development of Nd: YAG laser frequency stabilized on iodine transition around 532 nm", EFTF'2010 Proceedings, Noordwijk, Netherlands, April 2010.

[8] M. Marangoni, M. Lobino, R. Ramponi, "Simultaneously phase-matched second- and third-harmonic generation from 1.55 µm radiation in annealed proton-exchanged periodically poled lithium niobate waveguides", Opt. Lett. Vol. 31, N°18, 2006.

[9] R. Klein, A. Arie, "Observation of iodine transitions using the second and third harmonics of a 1.5 µm laser", Appl. Phys. B 75, 79-83, 2002.

Towards Large Scale Metrological Fibre Network

Anthony Bercy, Olivier Lopez, Fabio Stefani,
Christian Chardonnet and Anne Amy-Klein
Laboratoire de Physique des Lasers
CNRS, Université Paris 13
Villetaneuse, France
anthony.bercy@univ-paris13.fr

Paul-Eric Pottie
LNE-SYRTE
Observatoire de Paris, CNRS, UPMC
Paris, France

Giorgio Santarelli
Laboratoire Photonique, Numérique et Nanosciences
Université de Bordeaux 1, Institut
d'Optique and CNRS
Talence, France

***Abstract*—In the frame of the REFIMEVE+ project, aiming at disseminating an optical frequency standard to more than 20 laboratories in France, we present the progress made towards a metrological fibre wide-area network.**

Keywords—Optical link; frequency transfert; ultrastable laser;

I. INTRODUCTION

Today, the transfer of ultrastable frequency is mainly provided through by GPS system. But its resolution is one order of magnitude too low for the best microwave clocks cold atoms. To anticipate the transfer of a reference signal from an optical clock whose performances are approaching at least an order of magnitude better than the microwave clocks, it is important to develop new and better transfer methods.

Since a decade, many institutes and laboratories around the world work on fibre optical links. Stabilities obtained for links of hundreds of kilometers are reaching some 10^{-15} at 1 s and 10^{-18} at 10 000 s [1-2-3].

So far the work has been to transfer the frequency between two points A and B. But it is not feasible to design a point-to-point distribution network which needs a lot of fibres. It is more efficient to have a single optical fibre, for the ultrastable signal with distribution along the fibre (see fig. 1). The first part of this work will present the issue of multiple user distribution and the second part will present the solution to build long-haul links using the internet academic network.

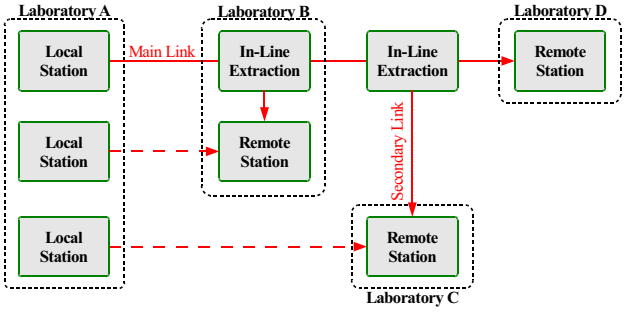

Fig. 1: Metropolitan network with a main link between Lab. A and Lab. D to transfer an optical frequency ultrastable and an In-line Extraction either directly distributed to Lab B or fed to another secondary link.

II. IN-LINE EXTRACTION

In-line extraction, as first proposed 3 years ago by G. Grosche [4], enables a very flexible distribution for several labs spread in the same metropolitan, area: the signal is extracted from the main link and either directly distributed to a lab or fed to another secondary link (see fig. 1).

A. Principle

A main link consists of copying the ultrastable signal from one end (Local Station) to the other end of the link (Remote Station). On the path of the optical fibre, the signal phase is disturbed by temperature fluctuation of the fibre and mechanical vibrations. The challenge is therefore to compensate these disturbances.

The principle of the phase correction is shown in Fig. 2. After a round trip in optical link, the signal has accumulated a phase noise $\varphi_A + \varphi_B$ and it is compared to the reference signal of the local station. Heterodyne detection allows discriminating the round-trip signal from stray reflections. The phase noise is corrected with a phase-locked loop (PLL) via an acousto-optic modulator (AOM).

The objective of the in-line extraction is to extract the reference signal along the optical fibre, at any distance from the ends of the link, and to compensate the phase noise accumulated between the starting end of the link and the extraction point. This setup must be inserted on the main link with the minimum of induced loss. Both forward and backward signals are extracted with a simple coupler and combined to detect the beatnote, which contains the fibre noise after the extraction. This provides a new phase correction applied to an

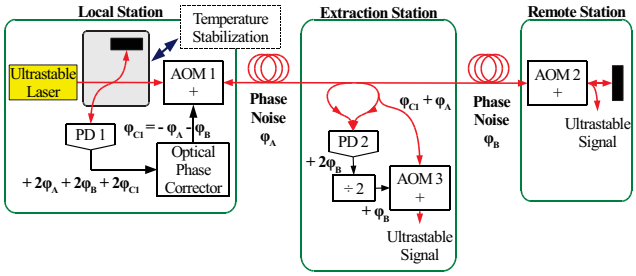

Fig. 2: The principle of a main link with phase noise correction at Local Station and the in-line extraction inserted on the link.

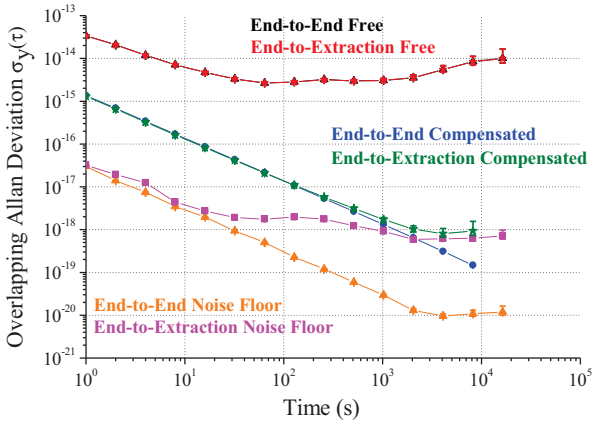

Fig. 3: Frequency Allan deviation for the end-to-end and extracted-to-end signals, in open and closed loop, and associated noise floors.

AOM. We can thus compensate for the over-correction of the phase noise at to the extraction point

B. Results

We tested this setup with an installed fibre link of 92 km in Paris area. The in-line extraction was inserted in this main link after 86th km. The relative frequency stability of σ_y (t) obtained with the main link is 1.5×10^{-15} at 1 s and some 10^{-19} after 10000 s, in accordance with the state of art. Concerning the in-line extraction signal, the results are consistent with those of the main link up to 1000 seconds of integration. Disturbances observed for longer integration time are due to thermal effect on the fibres used in the extraction setup.

III. LONG-HAUL LINKS

A link of 540 km of length has already been demonstrated from Laboratoire de Physique des Lasers (LPL) to Reims and back to LPL. An extension to Strasbourg is under progress which will leads to a link Paris-Strasbourg-Paris of around 1500 km.

This link is operated in parallel with data traffic and uses the academic internet network of RENATER (French Network for Technologies, Education and Research). For the data transmission, the telecom fibre is operated in one direction and mono-directional amplifiers are regularly placed in shelters. For the ultrastable signal transfer, the signal must flow in both directions. The fig. 4 presents the equipment to drop and add

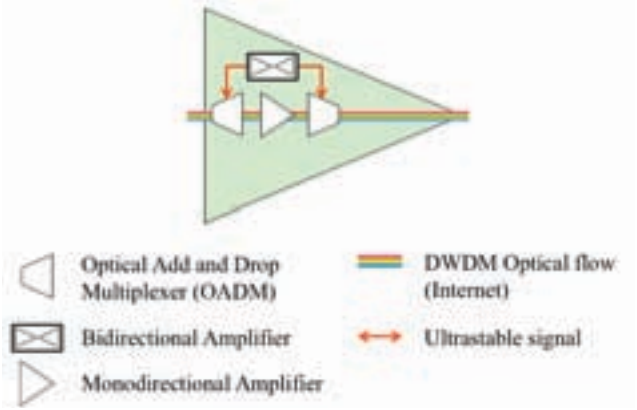

Fig. 4: Shelter with telecommunication mono-directional amplifier by-passed by two OADM and one bi-directional amplifier.

the ultrastable signal from the internet flow respectively before and after the mono-directional amplifier. For that purpose, we use two Optical Add and Drop Multiplexer (OADM) and the equipment includes also a bi-directional amplifier.

The Paris-Strasbourg-Paris optical link will be split in three cascaded link, which enables for a higher correction bandwidth and a better noise correction. Repeater stations will connect each segments, as already demonstrated in [5], and will achieve three functions, to send back part of the received signal to the previous station, to amplify and filter the received signal and to compensate the phase noise induced by the following segment. The amplification gain can reach more than 60 dB.

ACKNOWLEDGMENT

This work would not have been possible without the support of the GIP RENATER. The authors are deeply grateful to L. Gydé, T. Bono and E. Camisard from GIP RENATER for technical support. We also acknowledge S. Guellati-Khelifa and F. Biraben from LKB-Jussieu for encouraging part of this work and using the dedicated link between LKB and LNE-SYRTE. We acknowledge funding support from the Agence Nationale de la Recherche (ANR BLANC 2011-BS04-009-01), Université Paris 13 and IFRAF-Conseil Régional Ile-de-France.

REFERENCES

[1] H. Jiang et al., "Long-distance frequency transfer over an urban fiber link using optical phase stabilization," Optics Letters, vol. 25, pp. 2029-2031, 2008.

[2] K. Predehl et al., "A 920-kilometer optical fiber link for frequency metrology at the 19th decimal place," Science, vol. 336, pp. 441-444, 2012.

[3] O. Lopez et al., "Ultra-stable long distance optical frequency distribution using the Internet fiber network", Optics Express, 20, 23518, 2012.

[4] G. Grosche, "Method for making available a reference frequency" Physikalisch-Technische Bundesanstalt, Braunschweig, Germany, DE 10.2008.062.139, 2010.

[5] O. Lopez et al., "Cascaded multiplexed optical link on a telecommunication network for frequency dissemination", Optics Express 18, 16849, 2010.

We Know that MEMS is Replacing Quartz. But Why? And Why Now?

Aaron Partridge, Hae-Chang Lee, Paul Hagelin, Vinod Menon
SiTime Corp.
Sunnyvale CA, USA

***Abstract*—MEMS (Microelectromechanical) oscillators were first introduced commercially six years ago. Now MEMS is making significant incursions into what was once the exclusive territory of quartz oscillators. Why is this transition happening now, rather than ten years ago or ten years from now? The transition has been paced by the MEMS community developing the necessary high stability, high frequency, high Q, and high output resonators. Also, MEMS oscillators rely on advanced circuit architectures, particularly leveraging fractional-PLLs and precision temperature sensors. These specialized circuits have only recently become sufficiently small, low noise, power efficient, and accurate.**

Keywords-MEMS, MEMS oscillators, MEMS resonators, oscillators, resonators, frequency, frequency stabilility, encapsulation, temperature compensation, phase noise, jitter.

I. INTRODUCTION

MEMS-based oscillators were first produced commercially six years ago. Now MEMS is making significant incursions into what was once the exclusive territory of quartz. At the time of this paper's publication, over 200M MEMS oscillators have been shipped, with over 100M units expected to ship in 2013, at a growth rate of about 70% per year [1].

There are five fundamental drivers for the transition from quartz to MEMS: (1) Basic MEMS oscillators are maturing with decreasing phase-noise and decreasing power consumption in smaller packages, and with these improvements they are reaching further into common quartz applications. (2) Specialized MEMS oscillators are transitioning new markets, for example in applications requiring ultra-low power, sub-ppm precision, high frequency differential signaling, sub-picosecond integrated jitter, voltage control, digital control, spread, and output edge-rate control. (3) MEMS oscillators have shown higher reliability and lower failure rates than quartz oscillators. (4) MEMS oscillators have demonstrated lower electromagnetic, vibration, and acceleration sensitivity than quartz oscillators. (5) MEMS oscillators sell at lower price points than the quartz parts they replace.

Why is this transition happening now, rather than ten years ago or ten years from now? One answer is that the transition has been paced by the MEMS community developing the necessary high stability, high frequency, high Q, and high output resonators. A second answer is that MEMS oscillators rely on advanced circuit architectures, particularly leveraging fractional-PLLs (fractional Phase Lock Loops, or frac-N) and precision temperature sensors. And these specialized circuits have only recently become sufficiently small, low noise, power efficient, and accurate.

Looking forward, the depth and breadth of the applications served by MEMS oscillators will continue to expand, while the drivers favoring MEMS oscillators will further accelerate their adoption.

This paper focuses on the present technical status of the MEMS oscillators built by the author's company. The second section presents the resonators and encapsulation, the third section the oscillator circuitry, the fourth section a look ahead at MEMS OCXOs.

II. MEMS RESONATORS AND ENCAPSULATION

Development of MEMS resonators dates to the mid-1960, with the first published results by Nathanson 1967 [2]. These early resonators were intended to be audio filters, and were not suitable for references. Their stability was limited by the metallic resonator material and the packaging cleanliness.

Work at Berkeley in the 1990's developed polysilicon [3] as a resonator material, and further work at Stanford and elsewhere [4] in the 1990's and early 2000's extended this to single crystal silicon. Presently both single crystal and polycrystalline silicon are used in commercial MEMS resonators. Other silicon-centric materials, including Aluminum Nitride are in development and early deployment [5]. Research on more exotic materials such as polycrystalline diamond is in progress [6].

The resonators described here are based on electrostatically transduced lateral motion in single crystal silicon.

Figure 1 shows an isometric view of a 48MHz resonator. The arrows indicate the in-phase resonant mechanical motion of each ring. There are drive and sense electrodes inside and outside of each ring. The rings are anchored beside the midpoint crosses of the support beams. The resonator Q is nominally 147k at room temperature. Further detail may be found in [7].

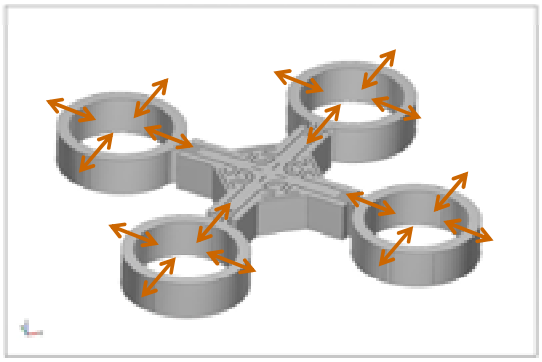

Figure 1. Low phase noise 48MHz resonator isometric diagram.

Figure 2 shows a 524kHz resonator that operates at very low power for sub-microamp timekeeping oscillators in applications now served by 32kHz quartz tuning fork crystals. In this application the output frequency is divided to 32kHz or drives a Real Time Clock (RTC) counter.

Figure 2. Low power 524kHz resonator isometric view.

As resonators are reduced in size their volume to surface ratio decreases, and consequentially their sensitivity to surface contamination increases. To maintain stabilities in the ppm (parts per million) to ppb (parts per billion) range expected of frequency references, it is necessary to minimize contamination mass-loading the resonators. Even a monolayer of surface contamination can shift a resonator's frequency out of specification. This drives a requirement for very clean packaging. Bonded covers have shown sufficiently clean vacuums to support commercial resonators with XO-type accuracy, while epitaxially encapsulation used for the parts in this paper enables tighter TCXO to OCXO-level stability.

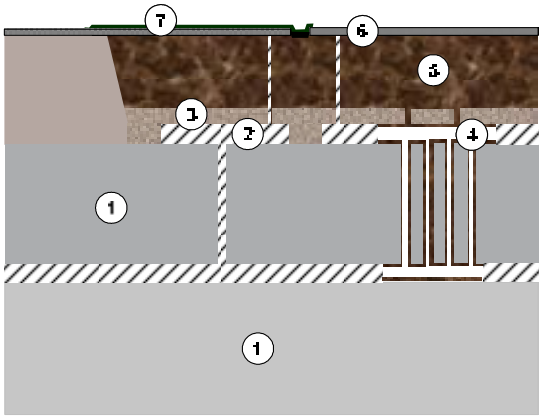

Figure 3. MEMS encapsulation process cross section.

Figure 3 shows a cross-section of the resonator and encapsulation fabrication. The resonators and encapsulation are built as follows: (1) an SOI wafer is trenched to define the resonator, (2) protective oxide is deposited and patterned, (3) silicon is deposited and patterned with vents, (4) the resonator is released, (5) the vents are closed and thick encapsulation is deposited, (6) contact isolation trenches are etched and oxide filled, and (7) metal traces are fabricated and passivated in the usual way.

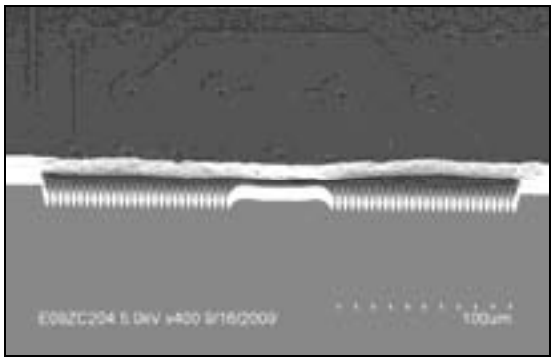

Figure 4. Cross section SEM of cleaved 524kHz resonator.

Figure 4 shows a cleaved wafer bisecting a 524kHz resonator. Aluminum interconnects are visible on the top surface, while the encapsulation is visible on the edge. The protruding serrated structure is one edge of a resonator.

MEMS thermistors for temperature sensing and frequency compensation can be built into the encapsulation beside the resonators. Like the resonators, they are fully vacuum encapsulated and released. Because they are encapsulated with the resonator, they are protected from environmental contamination and therefore highly stable [7].

The fully encapsulated resonators are singulated, paired with CMOS oscillators ICs, and molded into plastic QFN (Quad Flat No-lead) packages. These packages provide standard oscillator footprints for easy substitution into legacy quartz applications. Figure 5 shows a diagram of this package.

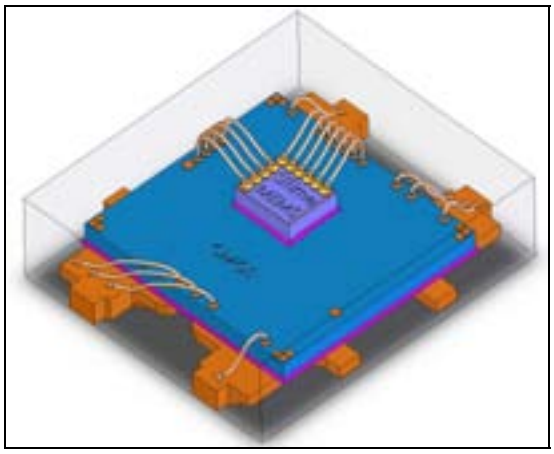

Figure 5. Package diagram showing leadframe, CMOS, and MEMS die.

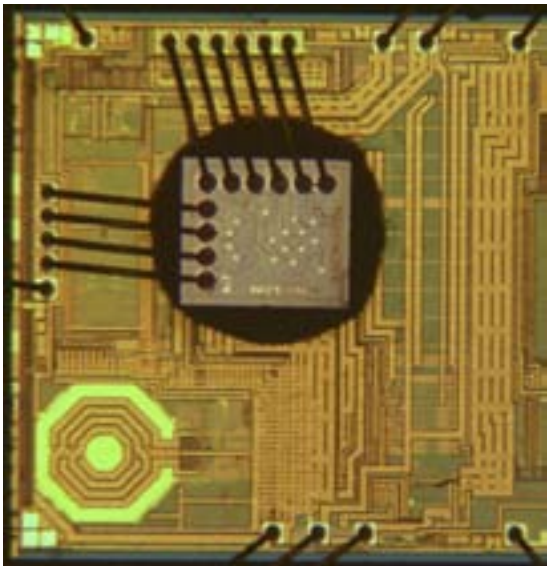

Figure 6. Die photo. The CMOS die size is 2.0x1.9mm^2, and the MEMS (bonded on top) die size is 0.55x0.48mm^2.

Figure 6 shows a photo of a MEMS die mounted on a CMOS die in a de-lidded package in which the plastic has been removed to expose the die and bondwires.

III. Circuit Architecture

There are two application drivers that quartz addresses with mechanical processes that MEMS addresses electronically: providing a wide range of application frequencies, and trimming the resonator frequency over production tolerances. In TCXOs, electronics also compensates the resonator frequency over temperature.

For MHz oscillators, applications require hundreds of different frequencies. For quartz, the resonators must normally be manufactured precisely to these frequencies, necessitating that the crystals be cut and ground to hundreds of different thicknesses. Second order effects often require the lateral dimensions of the crystals to be optimized for each frequency.

Building MEMS resonators across wide frequencies would be time consuming and expensive. Commercial MEMS resonators require years of individual development. For resonators with lateral modes, the dimensions or shapes are specific for each frequency, which implies dedicated mask sets for each frequency. For resonators with vertical modes, multiple material thicknesses must usually be optimized for each frequency, which implies process variants for each frequency. For MEMS oscillators, supplying dozens or even hundreds of frequencies could be commercially unviable.

Quartz crystals are individually trimmed to their specified frequencies, or in the case of TCXOs are trimmed to within the pull range of their specified frequencies. This mechanical trimming is usually done by ion milling or laser ablating the quartz or metallization. MEMS resonators can also be trimmed this way; however mechanical trimming can complicate the already difficult MEMS design and fabrication.

For most MEMS XO's and all TCXO's, the resonator temperature is measured and the resonator frequency is compensated across temperature. Unlike quartz TCXOs, MEMS oscillators are generally not compensated by resonator pulling, but instead with finely controlled multiplication in frac-N PLL's.

Frac-N PLL technology was not available for early quartz oscillators. The designers therefore had no alternative than to develop resonators that could be built in a range of frequencies, could be trimmed, and in some cases adjusted or pulled over temperature. On the other hand, we now have the circuit technology to translate MEMS resonator frequencies to their oscillator application requirements, trim them over production, and compensate them over temperature.

Using a circuit-centric approach also provides commercial benefits. For instance, inventories of oscillators with various pre-defined frequencies are not needed because the completed product can be quickly programmed. Further, custom frequencies can be readily supplied in large quantities.

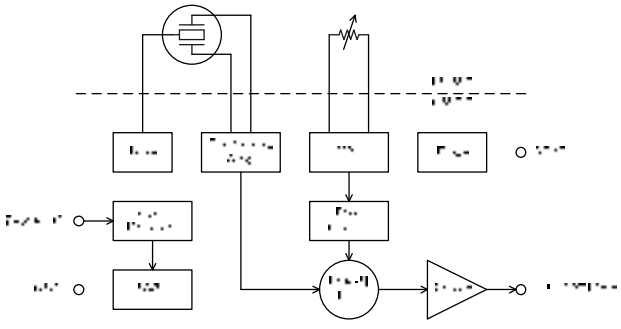

Figure 7. Oscillator topology.

Figure 7 shows the circuit-centric MEMS oscillator topology. The architecture includes a PLL to translate the resonator frequency to the application requirements. The PLL is fractional in order to trim the resonator across production tolerances, and its multiplication value is often variable in order to compensate for temperature. A state machine controls the PLL, drawing its parameters from non-volatile memory.

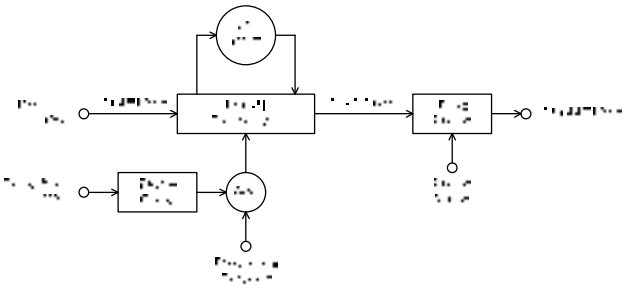

Figure 8. Frac-N PLL.

Figure 8 shows a block diagram of a frac-N PLL used in low-jitter oscillators. To provide low phase noise, and hence low integrated jitter, the PLLs use on-chip LC (inductor-capacitor) VCOs (Voltage Controlled Oscillators).

The frac-N PLL described here provides an output frequency programmable from 1MHz to 220MHz (after a final divide by 2) in sub-ppb increments. Details of the PLL have been published by F. Lee [8].

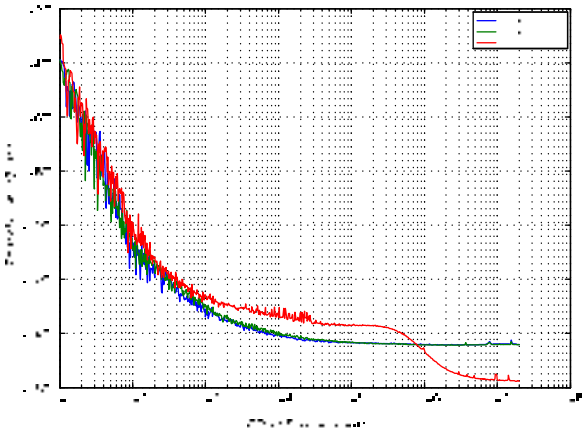

Figure 9. MEMS and PLL phase noise, reference frequency is 48MHz.

A PLL normally is thought of as a frequency translation circuit, and for that function it consumes power. It is sometimes thought that this is a "waste" of power because if the resonator had been at the output frequency then the PLL would not have been needed. However, a well-designed PLL like this one provides lower phase noise than its reference outside its filter bandwidth, and this is a significant advantage.

In Figure 9 one can see that outside of 1MHz offset the phase noise after the PLL (in red) is lower than the phase noise from of the MEMS sustaining amp (in blue and green). Phase noise is plotted on a log-log scale. In this case the phase noise outside of 1MHz dominates the integrated jitter because that integration is done on a linear scale. For that reason the decreased phase noise out of the oscillator is highly significant.

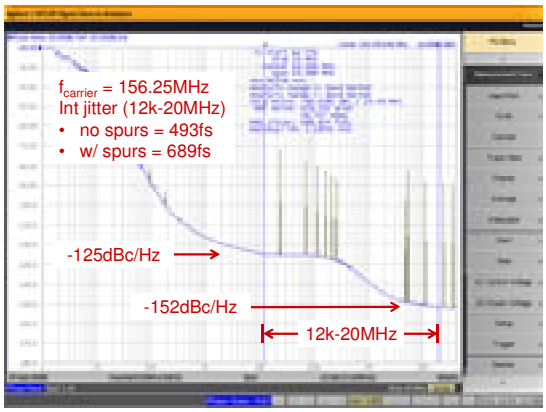

Figure 10. Output phase noise at 156.25MHz. Measured on Agilent 5052B.

Figure 10 shows the phase noise at 156.25MHz, a common reference frequency for high speed serial links. The integrated jitter from 12KHz to 20MHz in this case is 493fs not including spurs, and 689fs including spurs. Generally the telecom applications at this frequency account for spurs elsewhere and specify the integrated jitter without spurs to be under 1000fs.

The TDC (Temperature to Digital Converter) is need when resonator frequency is compensated over temperature. The TDC in the oscillator detailed here is optimized for low readout noise because noise in the temperature data becomes near phase noise in the output frequency.

One has many options when designing temperature sensors. Delta-VBE circuits using bipolar transistors in the CMOS die are ideal for consumer applications. These sensors have many favorable characteristics: they are linear, easy to calibrate, well understood, highly evolved, use moderate die area, and are low power. In addition they are purely circuit-based.

However, in these low jitter oscillators, we have chosen to use thermistors as the detection elements because they offer improved signal to noise.

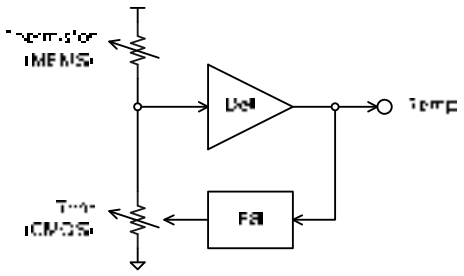

Figure 11. Balanced Bridge TDC.

Figure 11 shows a balanced bridge topology for digitizing thermistor resistance. A feedback loop keeps the node between the Thermistor and the Trim reference resistor at mid value. The variable resistance is implemented with switched capacitors and the feedback with a sigma-delta topology. The output of the feedback circuit is a high resolution digitized temperature value. A detailed description of the TDC is given in [9].

Note that there is never a voltage or current from the Thermistor to an ADC (Analog to Digital Converter). The Thermistor and TDC work in a feedback system to derive the temperature data, there is never an analog temperature value that is digitized.

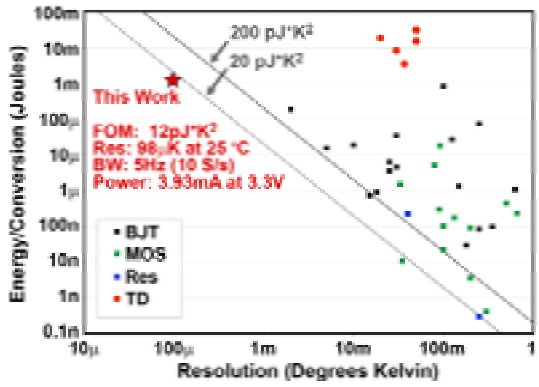

Figure 12. Figure of merit comparing conversion energy and resolution. Comparison data compiled by K. Makinwa [10].

The TDC delivers a resolution of 98uK at 5Hz bandwidth while consuming 3.9mA at 1.5V. Figure 12 compares its energy efficiency and resolution against other integrated TDCs. This TDC provides over an order of magnitude lower noise than others in the comparison population and does so at under 20pJK^2. The comparison data in this plot is compiled by K. Makinwa [10].

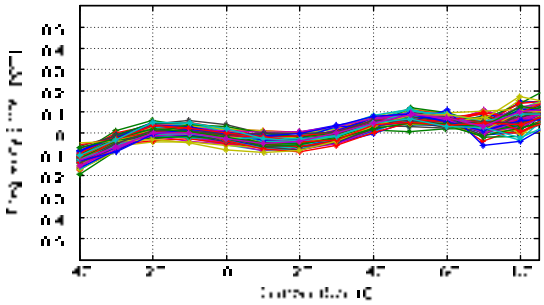

Figure 13. MEMS TCXO Compensated output frequency v. temperature.

Figure 13 shows the frequency over temperature of 68 MEMS TCXO's compensated to approximately 0.2ppm of their specified frequency from -40C to +85C.

IV. A MEMS OCXO

When an oscillator is maintained at an elevated temperature it delivers better frequency stability than when its temperature is allowed to vary with the ambient. This principle works as well in MEMS as it does in quartz.

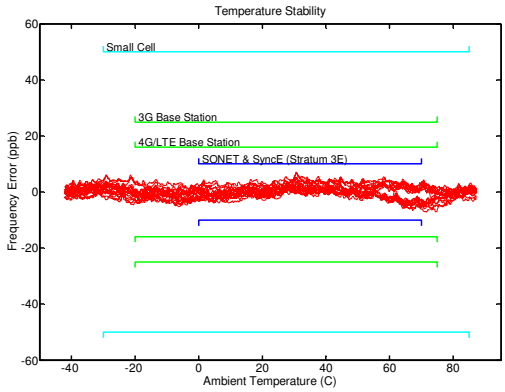

Figure 14. Oven controlled output frequency vs. ambient temperature.

Figure 14 shows the frequency vs. temperature of a MEMS oscillator built into an oven module. This is a single unit ramped over -45C to +90C at 0.5C/min bidirectionally for five days. The brackets in Figure 14 show the primary application temperature and accuracy requirements, including cell base stations and Stratum-3E oscillators for telecom networking. Accuracies better than 100ppb are normally provided by quartz OCXOs today.

Note that the results shown in this paper are from production material, except for the data in Figure 14 which is from a single part on a bench. Nonetheless, it is important to understand that MEMS oscillators will likely support OCXO applications.

V. CONCLUSIONS

Looking forward we believe that MEMS oscillators will replace quartz oscillators in consumer, telecommunication, and industrial applications.

Not discussed in this paper but still quite relevant are the higher quality levels and greater mechanical durability of MEMS oscillators. These features, combined with the performance described above, are driving MEMS oscillators into high reliability applications such as automotive and aerospace.

Presently over 200 million MEMS oscillators have been produced. The growth rate of this segment is strong, at about 70% per year. SiTime has been listed by Deloitte LLP in their Fast 500™ rankings as the fastest growing semiconductor company in North America [11]. This contrasts to modest or negative growth for the consumer quartz suppliers that are not adopting MEMS products.

ACKNOWLEDGMENTS

The authors would like to thank Mike Perrott, Jim Salvia and Renata Melamud for their contributions to the technology and data presented in this paper, and to Kofi Makinwa for guidance in temperature sensor development.

REFERENCES

[1] SiTime internal data and private conversatins with others in the industry.

[2] H.C. Nathanson, W.E. Newell, R.A. Wickstrom, J.R. Davis Jr., "The Resonant Gate Transistor," IEEE Trans. Electron Devices, Vol.ED14, pp.117133, 1967.

[3] C.T.-C Nguyen, R.T. Howe, "An Integrated CMOS Micromechanical Resonator high-Q oscillator," IEEE J. of Solid-State Circuits, v.34, n.4, pp.440-445, 1999.

[4] A. Partridge, A.E. Rice, T.W. Kenny, M. Lutz, "New Thin Film Epitaxial Polysilicon Encapsulation for Piezoresistive Accelerometers," 14th IEEE International Conference on Micro Electro Mechanical Systems, MEMS'01, pp.54-59, 2001.

[5] R. Ruby, P. Merchant, "Micromachined thin film bulk acoustic resonators," Proc. 1994 IEEE Int. Frequency Control Sym., pp.135-138, 1994.

[6] J. Wang, J. E. Butler, T. Feygelson, and C. T.-C. Nguyen, "1.51-GHz polydiamond micromechanical disk resonator with impedance mismatched isolating support," Proceedings, 17th Int. IEEE Micro Electro Mechanical Systems Conf., Maastricht, The Netherlands, Jan. 25-29, pp. 641-644, 2004.

[7] R. Melamud, P.M. Hagelin, C.M. Arft, C. Grosjean, N. Arumugam, P. Gupta, G. Hill, M. Lutz, A. Partridge, F. Assaderaghi, "MEMS enables oscillators with sub-PPM frequency stability," 2012 Hilton Head Workshop, Transducers Research Foundation 2012.

[8] F.S. Lee, J. Salvia, C. Lee, S. Mukherjee, R. Melamud, N. Arumugam, S. Pamarti, C. Arft, P. Gupta, S. Tabatabaei, B. Garlepp, H.-C. Lee, A. Partridge, M. Perrott, and F. Assaderaghi, "A programmable MEMS-based clock generator with sub-ps jitter performance," in Proc. Symp. VLSI Circuits, pp. 158–159, 2011.

[9] M. Perrott, J.C. Salvia, F.S. Lee, A. Partridge, S. Mukherjee, C. Arft, J. Jim, N. Arumugam, P. Gupta, S. Tabatabaei, S. Pamarti, H.C. Lee, F. Assaderaghi, "A temperature-to-digital converter for a MEMS-based programmable oscillator with frequency stability and <1ps integrated jitter", IEEE J. of Solid-State Circuits, v.48, i.1, pp.276-291, 2013.

[10] K.A.A. Makinwa, "Smart Temperature Sensor Survey", http://ei.ewi.tudelft.nl/docs/TSensor_survey.xls.

[11] Deloitte LLP, "Deloitte's 2012 Technology Fast 500TM Ranking," http://www.deloitte.com/assets/Dcom-UnitedStates/Local%20Assets/Documents/TMT_us_tmt/us_tmt_fast500_rankings_020713.pdf

Ion-Sliced Lithium Niobate on Silicon Dioxide for Engineering the Temperature Coefficient of Frequency of Laterally Vibrating Resonators

Lisha Shi
Department of Electrical and Computer Engineering
Carnegie Mellon University
Pittsburgh, PA
lishashi@andrew.cmu.edu

Gianluca Piazza
Department of Electrical and Computer Engineering
Carnegie Mellon University
Pittsburgh, PA
piazza@ece.cmu.edu

***Abstract*— This paper presents a new Laterally Vibrating Resonator (LVR) based on Y-cut ion-sliced Lithium Niobate (LN) thin films on silicon dioxide (SiO_2). In this work, the LN LVR is built on top of a SiO_2 layer and released from the underlying silicon wafer by dry etching in XeF_2. For a given sample having a LN layer thickness of 420 nm and SiO_2 thickness of 1600 nm, this first demonstration yielded resonators with temperature coefficient of frequency (TCF) of + 17 ppm/°C, and + 18 ppm/°C for devices vibrating at 500 MHz, respectively oriented at 10° and 30° to the x-axis, and TCF of +24.1 ppm/°C, and +27.7 ppm/°C for devices vibrating at 750 MHz, respectively oriented at 40° and 50° to the x-axis. The positive TCF clearly indicates the effect of the SiO_2, matches with finite element method simulations and non-linear analysis, and offers evidence that TCF engineering is possible. Most importantly, these LN LVRs still exhibited high values of electromechanical coupling, k_t^2, around 9% at 723.7 MHz , and Q in excess of 1,320 in air at 419.3 MHz. By optimizing the relative values of the LN and SiO_2 thickness it is ultimately possible to attain devices with zero first order TCF.**

Keywords*— Temperature coefficient of frequency (TCF), Lithium niobate ($LiNbO_3$) high coupling resonator, RF MEMS resonator, passive temperature compensation.

I. INTRODUCTION

Frequency references with low phase noise and drift, and temperature stable are key components of commercial and military wireless communication devices. Most of these communication systems also use many filters having relative bandwidths > 3%. Acoustic resonators and filters, such as surface acoustic wave (SAW) devices and thin film bulk acoustic resonators (FBARs), are primarily used in these systems. Nonetheless, these components are static and do not yet permit the synthesis of reconfigurable receivers capable of adapting their frequencies and bandwidths to variations in the spectrum. The development of high Q and temperature stable mechanical resonators having a high electromechanical coupling coefficient and capable of operating over a broad range of frequencies on a single chip would enable a new generation of reconfigurable communication systems.

The AlN Contour-Mode Resonators (CMRs) [1] previously demonstrated by our group have shown applicability up to 10 GHz and have introduced a paradigm shift over prior resonator technology because of the ability to devise multi-frequency filters on the same substrate. However, they are limited by the moderate material k_t^2 (~ 2% in AlN) to operate in systems that require BWs < 3 %. These devices also exhibit an uncompensated first order TCF of about - 25 ppm/°C, which is not adequate for accurate timing or frequency reference applications. The use of SiO_2 in the AlN CMR stack [2] [3] has achieved a low first-order TCF, but the moderate k_t^2 limits the applicability of these devices to wideband reconfigurable systems. Recently, LN laterally vibrating resonators (LVRs) have been demonstrated with both high k_t^2 and Q. The MEMS LN LVRs[4][5] have attained coupling larger than 20% and Q of about 1,000, but exhibited a rather large and negative TCF of about - 80ppm/°C. Furthermore, they were built on a LN substrate with either BCB or SiO_2 as sacrificial layers, which required a wet etch step for the release of the resonator.

In this paper, we present a new LVR technology based on Y-cut ion-sliced LN thin films on SiO_2 to intrinsically compensate the large negative TCF of LN films (see Fig.1). Additionally, dry etching in XeF_2 has been adopted to release the LN built on top of a SiO_2 layer from the underlying silicon wafer

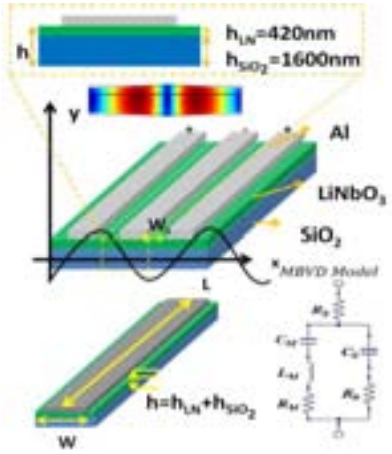

Fig. 1. Mock-up view of the LN on SiO_2 LVR. At the top, a zoomed in view of the cross section of one finger and the S0 mode of vibration of a full wavelenght (2 fingers) are shown. At the bottom, a 3D representation of a single finger with its characteristic geometrical parameters is also shown. The equivalent MBVD model of the resonator is displayed in the lower right corner.

II. ION-SLICE Y-CUT LN RESONATORS

A. Device Operation and Modeling

The LN LVR of this work consists of metal interdigital fingers (IDT) on top of a mechanically suspended LN/SiO_2 thin film. The electric field induced by the IDTs, which are alternatively connected to ground and signal, excites lateral expansion and compression in adjacent fingers (mode known as S0 lamb wave). The mechanical resonance is a function of the lateral dimension of the excitation electrode and is given by:

The author would like to thank NSF for funding.

$$f = \frac{1}{\lambda}\sqrt{\frac{E_p}{\rho}} = \frac{1}{2w}\sqrt{\frac{E_p}{\rho}} \quad (1)$$

Where w *is* the pitch of the IDTs, E_p the equivalent Young's modulus, and ρ the equivalent density of the resonator stack.

The resonator equivalent electrical circuit is described by the Modified Butterworth-Van Dyke (MBVD) model (Fig.1). The values of the motional parameters of the MBVD model are given by the following expressions [1]:

$$R_m = \frac{\pi^2}{8}\frac{1}{\omega_s C_0}\frac{1}{k_t^2 Q} \quad (2)$$

$$L_m = \frac{\pi^2}{8}\frac{1}{\omega_s^2 C_0}\frac{1}{k_t^2} \quad (3)$$

$$C_m = \frac{8}{\pi^2} C_0 k_t^2 \quad (4)$$

Where C_0 (static capacitance) is a function of finger pitch (w), length (L), and spacing between electrodes (w_s). k_t^2 refers to the effective electromechanical coupling, and Q is the quality factor of the series resonance frequency.

In this very first demonstration of LN/SiO_2 LVRs, the LN and SiO_2 thicknesses were set to 420 nm and 1600 nm because of sample availability from a third party vendor (Partow Technologies LLC). Nonetheless, as it will be shown in the next section, their relative values were appropriate to prove the concept of TCF engineering. The pitch of the electrode was set to 4 μm to ensure operation around 750 MHz for the fundamental S0 mode.

B. TCF Modeling of $LiNbO_3$ based Lamb Wave Resonator

The frequency shift of resonators under temperature variations is mainly caused by material softening. The resonator TCF is primarily related to the change of the stiffness coefficients with respect to temperature. Additionally, thermal expansion, which affects the resonator dimensions and material density, plays a secondary role.

In general, the TCF of a resonator is expressed in ppm/˚C and is defined as:

$$TCF = \frac{1}{f}\frac{\partial f}{\partial T} \quad (5)$$

$$TCF = -\frac{1}{w}\frac{\partial w}{\partial T} + \frac{1}{2}\frac{1}{E}\frac{\partial E}{\partial T} - \frac{1}{2}\frac{1}{\rho}\frac{\partial \rho}{\partial T} \quad (6)$$

Eq. (6) can be applied to the specific characteristics of the LN LVRs and results in [1]:

$$TCF = \frac{1}{2}(TC_{ij} + (\alpha_{11} + \alpha_{22} + \alpha_{33})] - \alpha_z \quad (7)$$

Where TC_{ij} refers to the relative temperature dependence of the stiffness constant C_{ij}; α_{11}, α_{22} and α_{33} are the thermal expansion coefficients along the x, y and z direction, respectively.

Given that LN becomes mechanically soft with an increasing temperature due to its negative TC_{ij}, uncompensated resonators based purely on Y-cut LN theoretically display a rather large and negative TCF of about - 80 ppm/°C. As SiO_2 exhibits positive TC_{ij}, it can be used in the device stack to enable temperature compensation of the LN LVR piezoelectric resonator.

In this work, the TCF characteristic of the S0 mode in a LN/SiO_2 composite plate has been modeled by COMSOL multiphysics finite element analysis (FEA). Both piezoelectric and thermal expansion moduli were used to describe the behavior of the device. The rotated stiffness and piezoelectric coupling matrix for each orientation in the Y-cut plane are derived from the Z-cut LN matrix [6] using the transformation matrix and bond matrix [7]. The obtained matrices are then input into the device model and used to predict the resonator frequency dependence on temperature. The simulated TCF for the S0 mode at various orientations are listed in Table I. Additionally, TCF FEA revealed that, for example, for 420 nm thick LN film, the ideal SiO_2 thickness for 0 TCF at 500MHz is 1.14μm. This value is definitely compatible with the manufacturing process of the sample and will be explored in future implementations.

C. Modeling of the electromechanical coupling of $LiNbO_3$ LVRs

Finite element method (FEM) was used to derive the electromechanical coupling factor for specific modes of vibrations as a function of the LN/SiO_2 composite plate thickness over acoustic wavelength ratio (h/λ) and in plane orientation. The coupling coefficient of the laterally vibrating devices is derived by comparing the phase velocity, v_m, of the thin film stack having electrodes patterned on the top surface with the phase velocity, v_0, of an unmetalized surface. The 2D FEA of the film stack is performed by imposing periodic boundary conditions at the two ends of the cross section having a width equal to the wavelength [8]. The k_t^2 can then be expressed as:

$$k^2 \approx \frac{v_0^2 - v_m^2}{v_0^2} \quad (8)$$

$$k_t^2 = \frac{k^2}{1 + k^2} \quad (9)$$

Where k^2 is the intrinsic electromechanical coupling. This technique permits us to rapidly evaluate different material orientations.

The FEM data suggested that, as expected, the introduction of a layer of SiO_2 in the resonator stack decreases the k_t^2 of the resonator. Nonetheless, for our sample, a maximum coupling for the S0 mode that exceeds 10 % is found for an in-plane rotation of 70° with respect to the x axis (see Fig.3). Additionally, the k_t^2 exhibits a slight dependence on wavelength (different h/λ ratio). The theoretically 0 TCF LN/SiO_2 device at 500MHz would yield a k_t^2 of 9.7%.

III. FABRICATION METHOD

As shown in Fig.2, a two mask fabrication process was adopted for the making of LN thin film on SiO_2 LVRs. In this work, a LN RIE recipe based on Cl_2/BCl_3 chemistry was developed for etching the Y-cut LN. SiO_2 is chosen to be the RIE mask for LN etching.

Devices having orientations varying from 0˚ to 90˚ in increments of 10˚ were fabricated on the same die to verify the k_t^2 and TCF dependency on orientation. The designed devices had pitch of 4 μm formed by 2 μm electrode and 2 μm spacing. The number of fingers was set to 10. Finger lengths of 40 and 80 μm were fabricated.

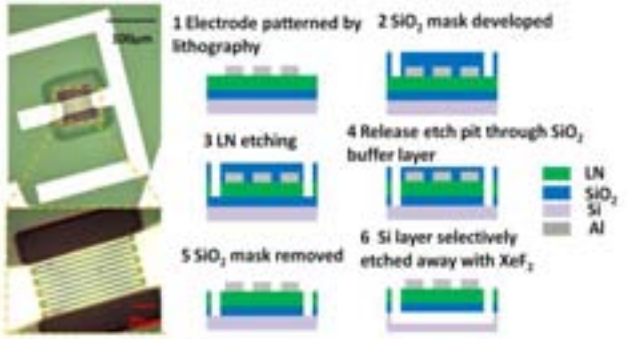

Fig. 2. Optical image of a fabricated LN LVR. The period of the interdigitated finger is 4 μm with each metal line having a width of 2μm , the length of each finger is 80 μm.On the right, a flow chart for the fabrication process of Y-cut ion-sliced LN thin film on SiO_2 MEMS resonators is shown.

IV. Experimental Results and Analysis

The first prototypes of LN on SiO_2 devices were tested in a Cascade RF probe station via an Agilent (N5230A) Network Analyzer. Q was extracted from the admittance plot by measuring the 3dB bandwidth of the resonance peak. The six equivalent circuit parameters were determined by fitting the measured results with the MBVD equivalent circuit model. A feedback controlled heating unit was employed to provide a control of the sample temperature during the measurements.

A. Characterization of k_t^2 and Q

The designed S0 mode is present in the admittance response of devices placed at all orientations, and is dominant (highest Q from 160 to 420) when the devices are placed at 40˚, 60˚, and 80˚ to x axis. As shown in Fig. 4(a), a maximum k_t^2 of 9.1% was measured for a resonator with center frequency of 730MHz and placed 60˚ to the x axis. The average value of the measured k_t^2 (Fig.4) displayed the same trend of the simulated results, but showed a value that is approximately 3/5 of the predicted one. The reason of this discrepancy is still under investigation.

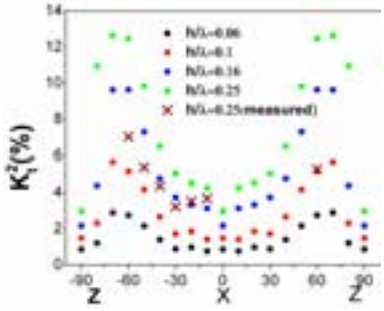

Fig. 3. The comparison of the averaged measured and simulated k_t^2 for LN on SiO_2 LVRs for various orientations.

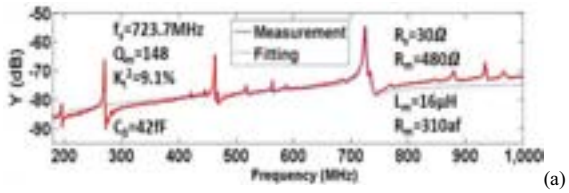

(a)

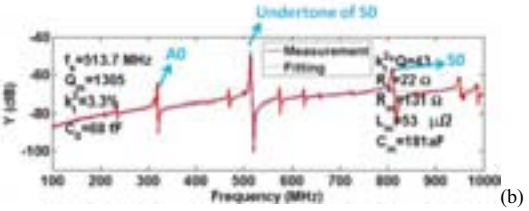

(b)

Fig. 4. (a) The measured and fitted admittance response of a LN on SiO_2 LVR with k_t^2 in excess of 9%. (b) The measured and fitted admittance response of LN on SiO_2 LVR with FOM(Figure of Merit = $k_t^2 \bullet Q$) of 43.

Devices oriented from 10˚ to 60˚ to the x axis also exhibited a resonance around 500 MHz. This resonance can be classified as an undertone of the main S0 mode. In particular, resonators oriented from 10˚ to 30˚ with respect to x axis displayed S0 undertone vibrations with high Q, and k_t^2. A Q higher than 1320 was observed on a LVR with a center frequency of 419.3MHz. A maximum k_t^2 of 6.2% was measured for a resonator with center frequency of 511.8MHz placed at 20˚ to the x axis. Hence, a FOM as high as 43 was obtained for a LVR having a 20˚ orientation to x axis (Fig.4 (b)). A0 mode vibrations were also seen in the spectrum of all resonators. The A0 mode has a lower phase velocity and lower coupling strength than the S0 mode and appears as a low frequency spurious mode (Fig.4 (b)).

B. Measurement of TCF

Resonators were measured in the temperature range of 25 to 115 °C in 10 °C increments. The TCF of devices exhibiting the main S0 mode at 750 MHz and an undertone of the S0 mode around 500 MHz were measured for various angles of orientation with respect to the x-axis (see Table I).

TABLE I. Comparison of TCF (ppm/°C) of LN LVRs at various orientations. TCF of the main S0 mode and undertone are shown. TCF is directly measured and extracted from non-linear analysis. For the main S0 mode the TCF was also calculated by FEM in COMSOL.

(a) Undertone of S0 mode, pitch of 4 μm formed by 2 μm electrode and 2 μm spacing

Orientation to X axis	TCF Direct Measurement	TCF Extracted from Non-Linear Analysis
20˚	20.4	18.8
-10˚	17	-
-20˚	15.3	17.1
-30˚	18	17.9
-40˚	15.4	15.5

(b) Main S0 mode, pitch of 4 μm formed by 2 μm electrode and 2 μm spacing

Orientation to X axis	TCF Direct Measurement	TCF Extracted from Non-Linear Analysis	TCF from COMSOL FEM
-20˚		32.2	27.7
-30˚		35	27.6
-40˚	24.1	-	27
-50˚	27.7	31.8	28
-60˚	32.5	-	28.4

C. TCF Extraction from Non-Linear Analysis

The nonlinear behavior and power handling capability of the LN on SiO_2 LVRs were experimentally investigated by measuring the admittance response at various power input

levels. As previously demonstrated for AlN CMRs [9], we hypothesize that self-heating is the main source of non-linearity in this kind of laterally vibrating micromechanical resonators. Self-heating can be used to extract the device TCF by monitoring the shift of the resonance peak as a function of the applied input power.

Self heating experiments were conducted on the LN LVRs reported in this paper. The input power was swept from -10 to +10 dBm in increments of 2 dBm. A characteristic Amplitude-frequency (*A-f*) response evolution for a resonator oriented at 50° to +x axis is shown in Fig. 3. The nature of the nonlinearities, which shows bending of the resonator admittance peak towards higher frequencies (stiffening of the resonator), is a clear evidence of a positive TCF. This supports our hypothesis that self-heating is the source of non-linearity.

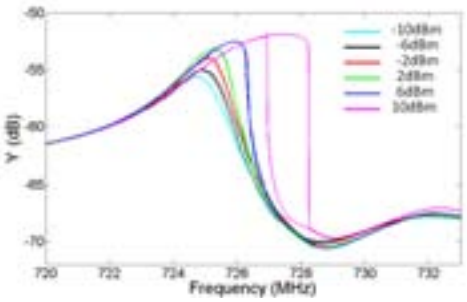

Fig. 5. A–f curves of a 724.1MHz resonator (VNA forward and backward frequency sweep, 1601 points, IF BW = 1 kHz) for P_{rf} from −10 to +10 dBm.

Applying the same analysis developed in [10] for AlN CMRs to LN LVRs, it is possible to model the thermal non-linearity in the resonator and use it to extract the resonator TCF.

Based on this model, the resonator temperature is described by the following equation:

$$T = \frac{(R_m + R_s)\omega_0^2 {q_{RMS}}^2 L_t}{2\sum \kappa_i T_{Ri} W_t} + T_{out} \tag{10}$$

Where κ_i is the material stack thermal conductivity, and L_t, W_t, and $T_{R,i}$ represent the geometrical dimensions of the structure through which the heat escapes (the anchors of the resonator). T_{out} refers to the reference temperature of the ambient environment and T, the effective temperature of the resonator undergoing vibration. q, is the charge flowing through the resonator, and ω is the input frequency. The effective TCF can then be derived as:

$$TCF = \frac{\Delta f}{T - T_{out}} = \frac{2\Delta f \sum \kappa_i T_{Ri} W_t}{(R_m + R_s)\omega_0^2 {q_{RMS}}^2 L_t} \tag{11}$$

Where Δf is the relative frequency shift recorded experimentally.

Using the geometrical parameters of the resonators and material properties from [11], [12], and [13], the TCF of LN LVRs was extracted from the self-heating measurements. Table I lists the TCF values and compares them to the direct measurements and prediction from COMSOL FEA. The agreement between these data further confirms our hypothesis that self-heating is the source of non-linearity in these devices.

V. Conclusion

This paper presented the first demonstration of LVRs based on Y-cut ion-sliced LN thin films on SiO_2. With 1.6 µm SiO_2 added to 420 nm LN, the micromechanical resonators exhibited $k_t^2 > 9\%$, *Qs* in excess of 1,320 in air at 419.3 MHz and FOM up to 43 at 513.7MHz. Moreover, the positive TCF measured from the manufactured devices clearly indicates the effect of SiO_2 and agrees well with FEM simulations and non-linear analysis results. By selecting an appropriate thickness ratio of SiO_2 to LN, a zero first-order TCF could be achieved.

Future work will mainly focus on attaining devices with zero first order TCF and simultaneously improving the performance of the resonators.

References

[1] G. Piazza, P. Stephanou, and A. Pisano, "Piezoelectric aluminum nitride vibrating Contour-Mode MEMS resonators," J. Microelectromech. Syst.,vol. 15, no. 6, pp. 1406 –1418, Dec. 2006.

[2] C.-M. Lin, T.-T. Yen, V. V. Felmetsger, M. A. Hopcroft, J. H. Kuypers, and A. P. Pisano, "Thermal compensation for aluminum nitride Lamb wave resonators operating at high temperature," in Proc. IEEE IFCS, 2010, pp.14–18.

[3] M. Rinaldi, A. Tazzoli, J. Segovia-Fernandez, V. Felmetsger, and G. Piazza, "High power and low temperature coefficient of frequency oscillator based on a fully anchored and oxide compensated AlN contour-mode MEMS resonator," in MEMS 2012, pp. 696–699.

[4] R.Wang, S. Bhave, and K. Bhattacharjee "High Kt2×Q, Multi-frequency Lithium Niobate Resonators" MEMS 2013(2013).

[5] S. Gong, L. Shi, and G. Piazza, "High electromechanical coupling resonators using ion sliced X-cut LiNbO3 thin film," in 2012 IEEE MTT-S, pp. 1-3, 17-22, June, 2012.

[6] R. T. Smith and F. S. Welsh, "Temperature dependence of the elastic, piezoelectric, and dielectric constants of lithium tantalate and lithium niobate," Journal of Applied Physics, vol. 42, no. 6, pp. 2219 –2230, May 1971.

[7] B. A. Auld, Acoustic Fields and Waves in Solids. Krieger Publishing Company, 1990

[8] J.J.Campbell, W.R.Jones "A method for estimating optimal crystal cuts and propagation directions for excitation of piezoelectric surface waves" IEEE Transactions on Sonics and Ultrasonics, vol. su-15, no. 4, OCT. 1968

[9] A. Tazzoli, M. Rinaldi, and G. Piazza, "Experimental Investigation of Thermally Induces Nonlinearities in Aluminum Nitride Contour-Mode MEMS Resonators", IEEE Electron Device Letters, vol. 33, no. 5, May 2012.

[10] Segovia-Fernandez, J.; Piazza, G., "Thermal Nonlinearities in Contour Mode AlN Resonators," J.Microelectromechanical Systems, vol.no.99, pp.1,1,0 doi:10.1109/JMEMS.2013.2252422

[11] T. Yamane, N. Nagai, S.-I. Katayama, and M. Todoki,"Measurementof thermal conductivity of silicon dioxide thin films using a 3ωmethod,"J. Applied Phys., vol. 91, pp. 9772–9776, 2002.

[12] K.K. Wong , properties of Lithium Niobate, INSPEC, The Institution of Electrical Engineers,London, United Kingdom, 2002

[13] Parker, *et al.,* "Flash Method of Determining Thermal Diffusivity, Heat Capacity, and Thermat Conductivity," Journal of Applied Physics, Vol. 32, 1961, pp. 1679

Experimental Determination of the Temperature Dependency of the Elastic Constants of Degenerately Doped Silicon

Antti Jaakkola, Mika Prunnila, Tuomas Pensala, James Dekker and Panu Pekko
VTT Technical Research Centre of Finland
Espoo, Finland
antti.jaakkola@vtt.fi

***Abstract*— We study experimentally the temperature dependence of the elastic constants of degenerately doped silicon as a function of the doping level. First and second order thermal coefficients of the elastic constants are extracted from the temperature dependent resonance frequencies of a set of MEMS resonators fabricated on phosphorus, arsenic and boron doped wafers having maximum doping levels of 7.5 x 10^{19}cm $^{-3}$, 2.5 x 10^{19}cm $^{-3}$ and 3 x 10^{19}cm $^{-3}$, respectively. Trends in the behavior of the thermal coefficients as a function of doping are identified and discussed.**

I. Introduction

Single-crystal silicon MEMS resonators are challenging quartz devices in the timing and frequency control market. The main disadvantage of silicon is the high thermal drift of about -30 ppm/K, which needs to be compensated to make a stable reference. Heavy doping of silicon has recently been found as an attractive way to achieve passive temperature compensation.

First experiments showing reduced temperature drift were achieved with p-type doping [1], but n-type doping soon appeared as a viable alternative [2]. Our work with bulk mode resonators has shown that n-type doping is an effective and versatile way of tailoring the temperature behavior of silicon resonators; we have demonstrated resonators with their f vs. T turnover point near room temperature, overcompensated devices (+18 ppm/K) [3], and shown that n-type doping is applicable to virtually all resonance modes of practical importance [4]. Recently, piezoelectrically driven temperature compensated devices [5] and resonators made of strongly n-type doped epitaxially grown silicon [6] have been reported.

In order to minimize the thermal drift of a MEMS resonator, a designer needs to know the temperature behavior of the elastic parameters of silicon; in particular the first and second order thermal derivatives of the elastic constants are of interest. However, experimental data of the thermal dependency of the elastic parameters of heavily doped silicon is limited; most usable results of n-type doped silicon have been published by Hall [7] for carrier concentration of 2×10^{19}cm $^{-3}$. In this work we study experimentally the temperature dependence of silicon elastic constants when doping is varied. Test wafers were phosphorus doped (carrier concentration 4.1 , 4.7 and 7.5×10^{19}cm $^{-3}$), arsenic doped (1.7 and 2.5×10^{19}cm $^{-3}$), and boron doped (0.6 and 3×10^{19}cm $^{-3}$). Elastic parameters are extracted from the temperature dependent resonance frequencies of a set of MEMS resonators.

II. Theory and Methods

The frequency of an acoustic resonator is given by

$$f = 1/L \times \sqrt{c/\rho}, \tag{1}$$

where ρ, c and L are the resonator material density, characteristic stiffness and characteristic length, respectively. Characteristic stiffness depends on elastic constants c_{11}, c_{12} and c_{44} that can be solved from a set of measured resonance frequencies of different resonators when their functional dependence on constants c_{ij} varies among the modes, and when there are three or more modes within the set. In our case, the set of two Lamé mode resonators and five length extensional (LE) modes in different orientations fulfill these conditions. Resonators are illustrated Fig. 1. Our approach is similar to that of Bourgeois et al. [8], [9], but we use a larger number of modes (7) for solving the three unknowns, and hence we are also able to assess the reliability of the results.

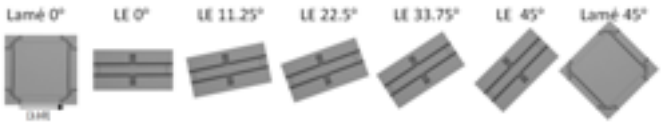

Figure 1. The set of resonators for determination of the elastic constants c_{11}, c_{12} and c_{44} consists of seven different resonators, each having different dependency on the c_{ij} parameters. Plate resonators operating in the Lamé resonance mode were fabricated in two different directions (either aligned with 100 or 110 directions). Beam resonators operating in the length extensional resonance were orientated at five different equispaced in-plane angles from 110 to 100.

The experimental data consists of measured resonance frequencies at different temperatures for all seven resonance modes $f_k^{\text{exp}}(T)$ ($k = 1, \ldots, 7$). Let us denote the corresponding theoretical estimates containing the c_{ij} dependencies – obtained through FEM modelling in our case – as $f_k^{\text{th}}(c_{11}, c_{12}, c_{44})$. We use an approach of first matching f_k^{exp} and f_k^{th} at $T_0 = 20$°C by numerical optimization to find elastic parameters $c_{ij}(T_0)$, and then linearize Eq. (1) to obtain the

relation

$$\frac{\delta f_k^{\text{exp}}(T)}{f_{k0}^{\text{exp}}} = \frac{1}{f_{k0}^{\text{th}}} \sum_{ij} \frac{\partial f_k^{\text{th}}}{\partial c_{ij}} \delta c_{ij}(T) + \frac{1}{2} \frac{\delta L}{L}(T). \quad (2)$$

Here $\delta c_{ij}(T)$ are the unknown changes in elastic parameters, $\delta f_k^{\text{exp}}(T)$ are the measured frequency differentials, while f_{k0}^{exp} and f_{k0}^{th} are shorthands for $f_k^{\text{exp}}(T_0)$ and $f_k^{\text{th}}(c_{ij}(T_0))$. Sensitivities $\partial f_k^{\text{th}}/\partial c_{ij}$ are calculated from the theoretical estimates. The last term accounts for thermal expansion $\beta(T)$. In matrix form Eq. (2) can be denoted as

$$\delta \mathbf{f}^{\text{exp}}(T) = A \cdot \delta \mathbf{c}(T) + \beta(T). \quad (3)$$

where $\delta \mathbf{f}^{\text{exp}}$ contains the relative frequency changes, and elements of the sensitivity matrix A are defined as

$$a_{kn} = \frac{1}{f_{k0}^{\text{th}}} \frac{\partial f_k^{\text{th}}}{\partial c_{ij}},\ n = 11, 12, 44;\ k = 1, ..., 7. \quad (4)$$

The changes in elastic parameters $\delta \mathbf{c}(T)$ can be solved as a least squares fit from Eq. (3):

$$\delta \mathbf{c}(T) = (A^T A)^{-1} A^T [\delta \mathbf{f}^{\text{exp}}(T) - \beta(T)]. \quad (5)$$

We assume that the thermal expansion has a form

$$\beta(T) = (\alpha_1 \Delta T + \alpha_2 \Delta T^2 + \alpha_3 \Delta T^3)/2, \quad (6)$$

and use the values reported for undoped silicon by Lyon et. al [10]; a similar choice was made in Ref. [9] by Bourgeois et al.

III. Experimental

Table I
DETAILS OF THE WAFERS. CARRIER CONCENTRATIONS ARE CALCULATED FROM THE RESISTIVITY SPECIFICATION USING REF. [11]. CARRIER CONCENTRATION RANGES ARE INCLUDED AS ERROR BARS IN FIG. 3A.

		specified resistivity [mOhm cm]		calculated carrier concentration n [10^{19} cm^{-3}]		
wafer id	dopant	min	max	min	max	avg
B3	B	3.48	3.66	2.88	3.04	2.96
B0.6	B	10	20	0.33	0.86	0.60
As1.7	As	3.98	4.36	1.55	1.77	1.66
As2.5	As	2.94	3.08	2.39	2.52	2.46
P4.1	P	1.67	1.76	3.98	4.22	4.10
P4.7	P	1.47	1.59	4.45	4.86	4.66
P7.5	P	0.95	1.05	7.05	7.89	7.47

Test resonators were fabricated on seven different Silicon-On-Insulator wafers with 15-μm-thick Czochralski grown device wafers. Dopants (B, P, and As) and their concentrations were varied according to Table I. Carrier concentration range for each wafer was calculated from the specified resistivity range using conversion method of Ref. [11]. Measured devices were located near the wafer center. As the wafers featured pre-etched cavities, it was possible to fabricate monolithic resonators without a grid of release etch holes within the devices, and thus the elastic properties of the resonators could be accurately modelled. Existence of release etch holes was a source of uncertainty in our previous studies [3]. The resonators (Fig. 1) were fabricated by a process including Al contact metallization and patterning followed by DRIE etching of vertical gaps (width $0.5\,\mu$m).

The resonators were measured in atmospheric pressure on wafer level with an impedance analyzer while applying a DC bias of 40 V over the gaps. Quality factors of $\sim 10,000$ were measured for all resonance modes, and thus the resonance frequencies could be detected with good accuracy. The wafer was held on a temperature controlled chuck, whose temperature was varied from -40°C to 85°C with seven steps. The accuracy of the chuck temperature was ± 0.5°C. Resonances of interest were identified and their frequencies were tracked over temperature.

IV. Results

Measured temperature dependent relative frequency changes are plotted and tabulated in Fig. 2(a)–(g) for each of the wafers. The elastic parameters $c_{ij}(T)$ were extracted from the frequency data using the least squares method described in Section II. We used Comsol Multiphysics for calculating numerical estimates for the modal frequencies f_k^{th}. Angular misalignment of the wafers was taken into account in the FEM simulations. Second-order polynomials centered at $T_0 = 25$°C were fitted to the elastic parameter data as

$$c_{ij}(T) = c_{ij}^0 [1 + a_{ij}(T - T_0) + b_{ij}(T - T_0)^2], \quad (7)$$

where a_{ij} and b_{ij} are the first-order and second-order temperature coefficients, respectively, and c_{ij}^0 is the constant term. A second-order expansion was found to be valid to within ± 20 ppm for all $c_{ij}(T, n)$. The results are summarized in Fig. 3(a)–(l). Fig. 2(e) shows an overlay of measured data and corresponding numerical estimates which use the solved parameters $c_{ij}(T)$ as an input.

V. Discussion

Following observations concerning the temperature coefficients of Fig. 3 can be made: i) Fig. 3(k) shows that the linear temperature coefficient a_{11-12} goes to zero at approximately $n = 2 \times 10^{19}$cm^{-3} , and it obtains values of more than $+40$ ppm/K with highest n-type doping. This is the key effect of n-type doping for MEMS applications [4]. The effect appears to saturate at highest carrier concentrations. ii) Fig. 3(l) reveals an attractive trend of the second order temperature coefficient b_{11-12}: it appears to approach zero with increasing carrier concentration. This suggests a possibility of a flat or positive second order response at high enough doping. iii) Arsenic and phosphorus as dopants do not stand out from the plots as separate groups. iv) Fig. 3(h) shows that the linear temperature coefficient a_{44} decreases in magnitude with increasing p-type dopant concentration.

Temperature coefficients measured in this work are compared to values found in literature in Fig. 3. Values for weakly n- or p-doped silicon, reported by Bourgeois et al. [9], appear to be in satisfactory agreement with our data; the data points near zero carrier concentration follow the trends observable from our data points. However, there is more

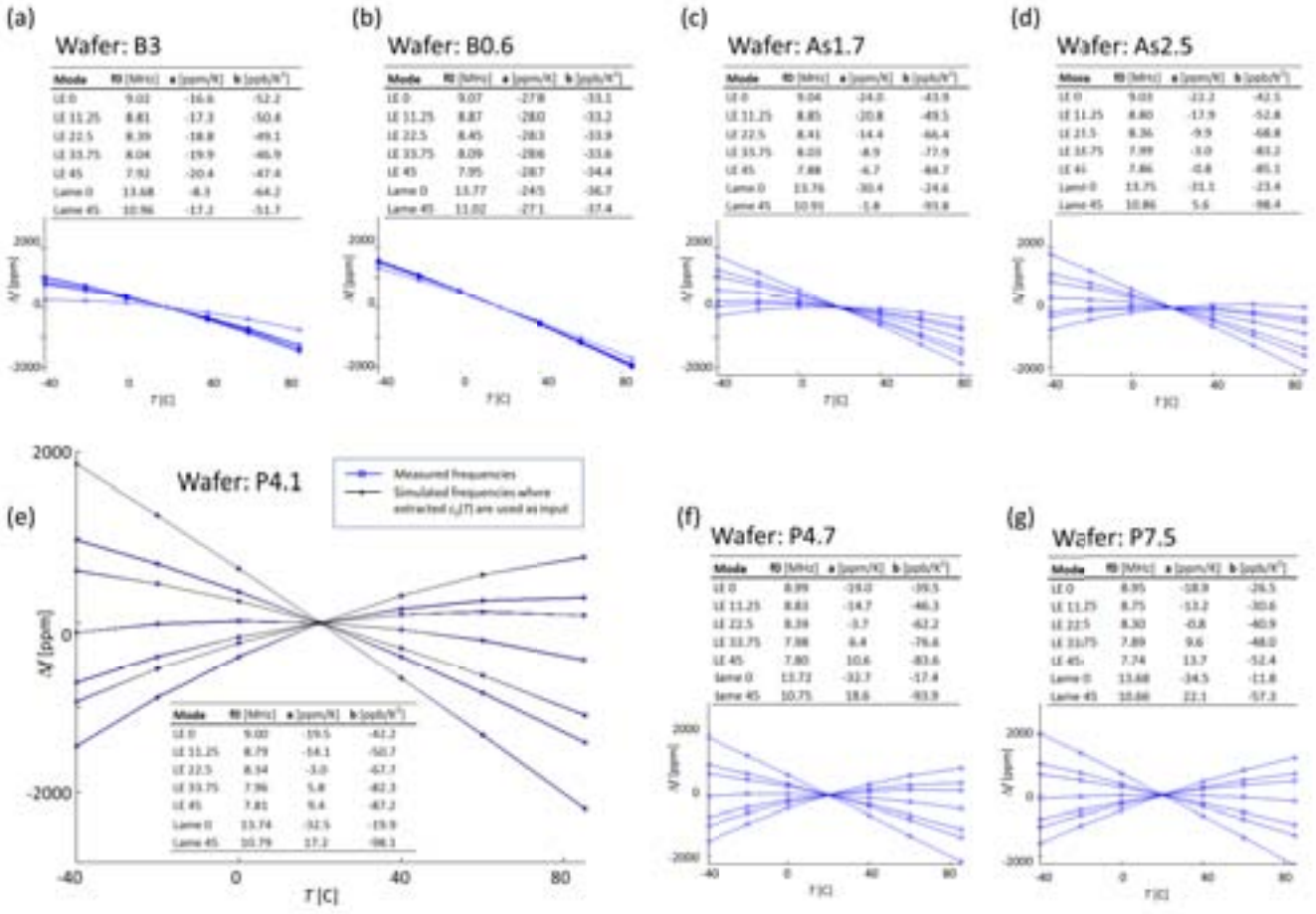

Figure 2. (a)–(g): temperature dependent relative frequency changes for each measured wafer. Temperature coefficients for resonance modes were calculated and they are shown in the tables. (e): measured data (blue line with hollow circles) from wafer P4.1 overlaid with corresponding numerical estimates $f_k^{\text{th}}(T)$ which use the solved parameters $c_{ij}(T)$ as an input (black lines with dots).

disagreement when our results are compared to data by Hall [7]. In particular, the second order temperature coefficients are not in line with the other data points. This could be explained by the fact that the values were extracted directly from the published plots of Ref. [7].

Quality of the least squares fit can be assessed by comparing the measured frequency data $f_k^{\text{exp}}(T)$ to the corresponding numerical estimates $f_k^{\text{th}}(T)$ obtained from FEM simulations which use the solved parameters $c_{ij}(T)$ as an input. Fig. 1(e) shows an example of the overlap between experimental and simulated data. Maximum deviation between the measured and simulated data points was below 30 ppm for all seven resonance modes under investigation for all of the wafers, which speaks for the reliability of the extraction method. We expect that the thermal drift of any resonance mode on a wafer with similar carrier concentration could be predicted with similar accuracy, when calculated using $c_{ij}(T)$ as an input.

VI. Conclusions

Elastic parameters of degenerately doped silicon were extracted from temperature drift measurements of a set of MEMS resonators fabricated on seven wafers with varied dopants (As, P, B) and doping concentrations. It was observed that the linear thermal coefficient of $c_{11} - c_{12}$ is zeroed at approximately $n = 2 \times 10^{19}\text{cm}^{-3}$, and that it appears to saturate to ~ 40 ppm/K with increasing n-type doping. The second order thermal coefficient of $c_{11} - c_{12}$ was found to decrease in magnitude when n-type doping was increased. Linear thermal coefficient of c_{44} was found to approach zero with increasing p-type doping.

VII. Acknowledgements

Authors would like to acknowledge the Finnish Funding Agency for Technology and Innovation (Tekes), Okmetic Oyj, Murata Electronics and Micro Analog Systems for funding. Okmetic Oyj is acknowledged for providing the silicon wafers.

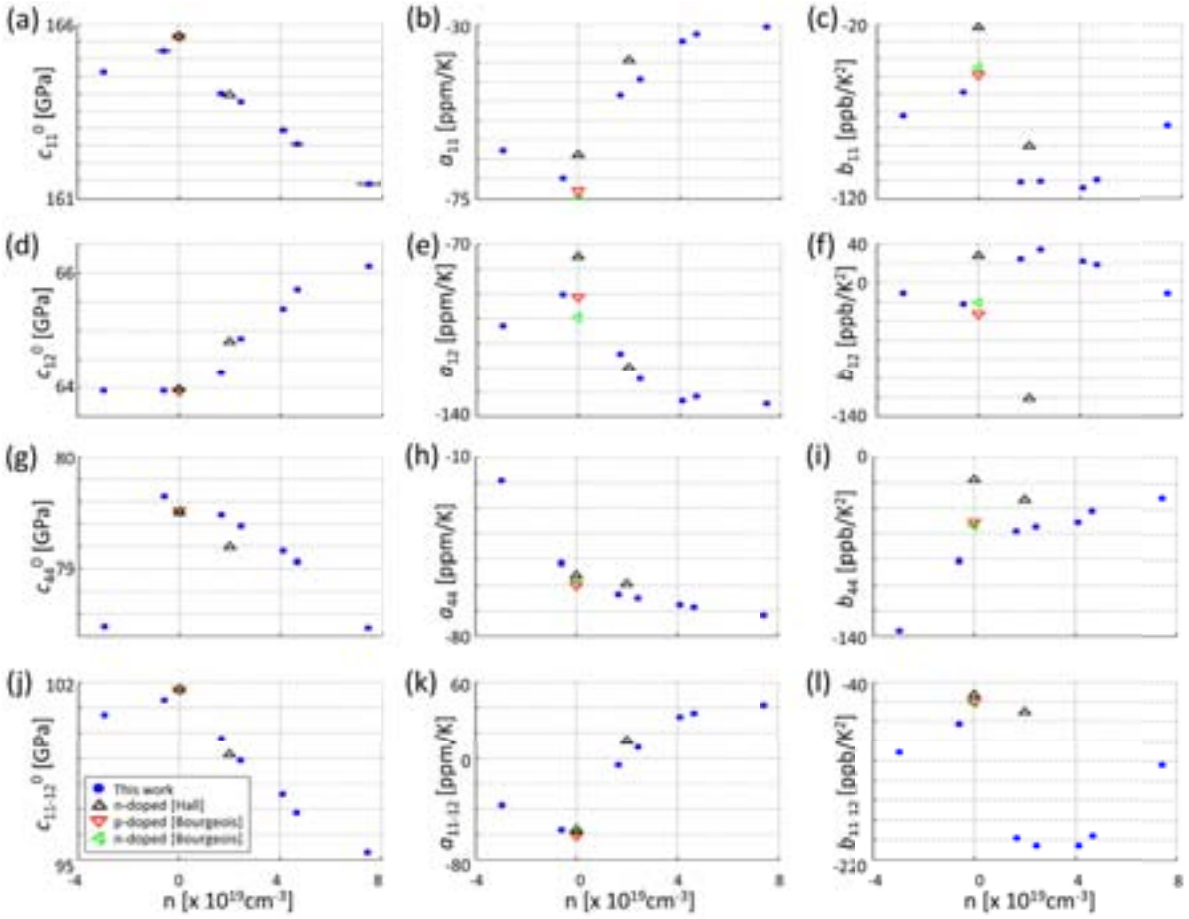

Figure 3. Temperature coefficients of the elastic parameters c_{ij} as a function of carrier concentration n. Data from p-type doped wafers is represented with negative carrier concentratios. First, second and third column represent the constant terms c_{ij}^0, linear coefficients (a_{ij}), and second-order coeffients (b_{ij}), respectively (see Eq. (7)). c_{11-12}^0, a_{11-12} and b_{11-12} are shorthands for the coefficients of $c_{11} - c_{12}$. Blue dots are the experimentally determined values of this work. Values reported in [9] are shown as red triangles pointing down (weak p-type doping) and as green triangles pointing left (weak n-type doping). Data reported by Hall in Ref. [7] was used for calculating data points shown as black triangles pointing up. The error bars of figure (a) indicate the carrier concentration ranges calculated from the resistivity specification for each wafer (see Table I).

A.J. acknowledges funding from the Academy of Finland, and wishes to thank Arto Nurmela for help in the measurements.

REFERENCES

[1] A. K. Samarao, G. Casinovi, and F. Ayazi, "Passive TCF compensation in high q silicon micromechanical resonators," in *IEEE International Conference on Micro Electro Mechanical Systems (MEMS 2010)*, Hong Kong, Jan. 2010, pp. 116–119.

[2] A. Hajjam, A. Rahafrooz, and S. Pourkamali, "Sub-100ppb/C temperature stability in thermally actuated high frequency silicon resonators via degenerate phosphorous doping and bias current optimization," in *Proc. IEEE International Electron Device Meeting (IEDM)*, 2010, pp. 7.5.1 – 7.5.4.

[3] T. Pensala, A. Jaakkola, M. Prunnila, and J. Dekker, "Temperature compensation of silicon MEMS resonators by heavy doping," in *Proc. IEEE International Ultrasonics Symposium*, 2011, pp. 1952–1955.

[4] A. Jaakkola, M. Prunnila, and T. Pensala, "Temperature compensated resonance modes of degenerately n-doped silicon MEMS resonators," in *Frequency Control Symposium (FCS), 2012 IEEE International*, May 2012, pp. 1 –5.

[5] M. Shahmohammadi, B. Harrington, and R. Abdolvand, "Zero temperature coefficient of frequency in extensional-mode highly doped silicon microresonators," in *Frequency Control Symposium (FCS), 2012 IEEE International*, May 2012, pp. 1 –4.

[6] E. J. Ng, C. H. Ahn, Y. Yang, V. A. Hong, C.-F. Chiang, E. Ahadi, M. W. Ward, and T. W. Kenny, "Localized, degenerately doped epitaxial silicon for temperature compensation of resonant MEMS systems," in *Transducers 2013*, Barcelona, Spain, 2013, pp. 2419—2422.

[7] J. J. Hall, "Electronic effects in the elastic constants of n-type silicon," *Physical Review*, vol. 161, no. 3, p. 756, 1967. [Online]. Available: http://link.aps.org/doi/10.1103/PhysRev.161.756

[8] C. Bourgeois, J. Hermann, N. Blanc, N. de Rooij, and F. Rudolf, "Determination of the elastic temperature coefficients of monocrystalline silicon," in *The 8th International Conference on Solid-State Sensors and Actuators, 1995 and Eurosensors IX.. Transducers '95*, vol. 2, June 1995, pp. 92 –95.

[9] C. Bourgeois, E. Steinsland, N. Blanc, and N. F. de Rooij, "Design of resonators for the determination of the temperature coefficients of elastic constants of monocrystalline silicon," in *IEEE International Frequency Control Symposium*, 1997, pp. 791–799.

[10] K. G. Lyon, G. L. Salinger, C. A. Swenson, and G. K. White, "Linear thermal expansion measurements on silicon from 6 to 340 k," *Journal of Applied Physics*, vol. 48, no. 3, pp. 865–868, Mar. 1977.

[11] "Standard practice for conversion between resistivity and dopant density for boron-doped, phosphorus-doped, and arsenic-doped silicon," in *Annual Book of ASTM Standards, F 723-99*. West Conshohocken, PA: American Society for Testing and Materials, 2000, pp. 275—291.

A Piezoresistive CMOS-MEMS Resonator with High Q and Low TC_f

Cheng-Syun Li, Ming-Huang Li, Chi-Hang Chin, Chao-Yu Chen, and Sheng-Shian Li
Institute of NanoEngineering and MicroSystems
National Tsing Hua University
Hsinchu, Taiwan

Philip X.-L. Feng
Department of Electrical Engineering and Computer Science
Case Western Reserve University
Cleveland, OH, USA

***Abstract*—A high-frequency CMOS-MEMS bulk-mode resonator via a differentially piezoresistive transduction was proposed in this work, demonstrating quality factor (Q) greater than 15,000, temperature coefficient of frequency (TC_f) around -12.5ppm/°C, and operating power lower than 400μW, all in a single device. To attain the highest Q among reported CMOS-MEMS resonators to date, a dog-bone design was adopted with its two oxide-rich longitudinally vibrating beams which consist of only low-loss materials (i.e., poly-Si and SiO_2) from a standard 0.35μm 2-poly-4-metal (2P4M) CMOS technology. To achieve such decent temperature stability, a constant-resistance control approach was implemented to enable an ovenized element where the poly-Si heater and thermometer are both embedded inside the resonator structure, hence providing excellent thermal isolation, localized heating capability, and on-site/real-time temperature measurement.**

Keywords*— *High Q, Thermal Stability, CMOS-MEMS, Piezoresistive, Resonator, Temperature Compensation, Oven

I. Introduction

Ubiquitous electronics are widely used in our daily life and most of them necessitate the timing reference devices for the signal processing. Demanded by the portable and wearable purpose, the device volume must be miniaturized and integrated with circuits. Discrete components, such as quartz and SAW resonators, are against the trend of miniaturization and integration due to their bulky size and non-silicon-based substrate. In the past decade, MEMS technology played an important role to address this issue due to the small form factor and batch production of the mature micromachining processes. However the effective solutions to MEMS/IC integration are still under development.

To integrate the circuits and mechanical structures, the prior literature has reported on the MEMS-first and MEMS-last processes [1]. However, those processes are complicated and have limited thermal budget. In contrast, micro structures formed by the CMOS back-end-of-line (BEOL) materials are simple to be implemented as micromechanical devices. For example, the CMOS-MEMS resonators can be released by two major post-CMOS processes, including the dry release [2] and wet release [3] processes. To construct the device, the metal, oxide, and polysilicon layers are used to form the resonator structure. However, pure metal or polysilicon capacitive transducers have to be designed by a very thin layer in this case, which would significantly limit the capacitive transduction areas. Furthermore, their gap spacing is also constrained by the foundry process rules; therefore, the electromechanical coupling coefficient becomes quite low, leading to much-larger-than-50Ω motional impedance. In addition to the high motional impedance, the CMOS-MEMS resonators often suffer poor thermal stability due to their structural materials. To enhance their thermal stability, the metal/oxide composite structures can be designed to take advantage of the balance of the negative TC_f from the metal and positive TC_f from the SiO_2. However, the metal layer of the CMOS BEOL process is not a low-loss material [4]. The more metal used to construct the structure, the lower quality factor of the resonator.

To solve the abovementioned issues on both Q and thermal stability, a bulk-mode resonator with an oxide-rich structure was previously developed in our group, demonstrating Q > 10,000 [5] which is more than sufficient for high-performance oscillator implementation. However, its electromechanical coupling coefficient is still limited by purely capacitive transduction caused by its relatively large transducer's gap. To enhance the coupling coefficient, a piezoresistive sensing was

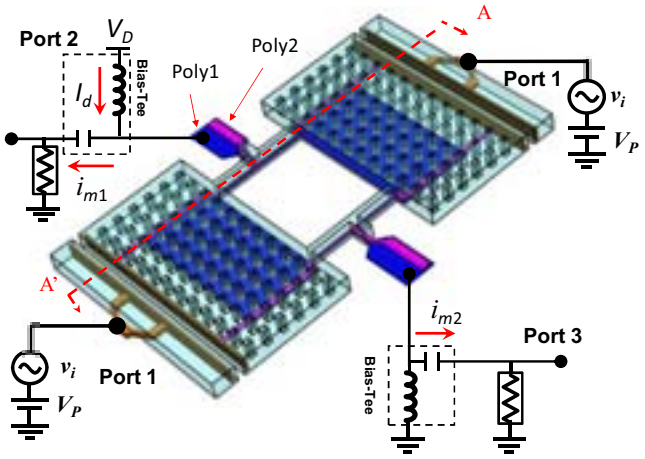

Fig. 1: Perspective-view schematic of a bulk-mode CMOS-MEMS resonator driven (common mode) by the electrostatic force and sensed (differential mode) by the piezoresistive transduction.

This work was supported by the National Science Council (NSC) of Taiwan and partial travel expense was generously supported by IEEE UFFC Society.

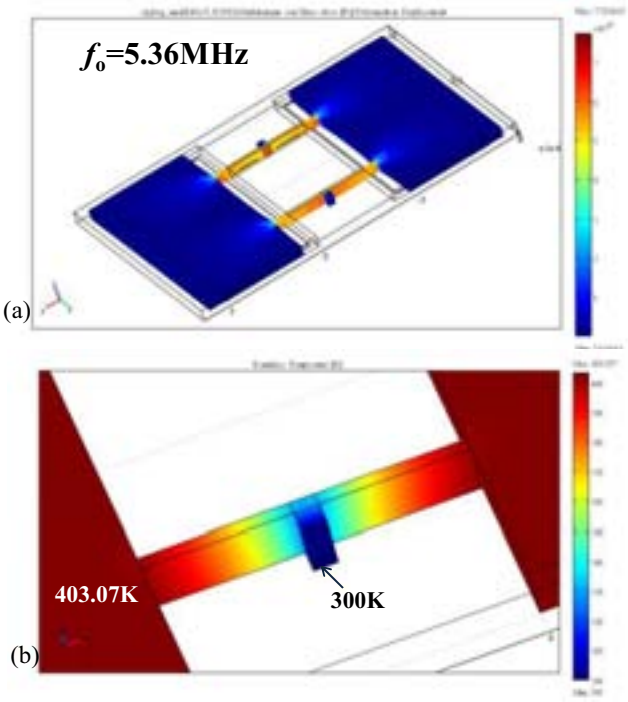

Fig. 2: (a) Finite-element simulated mode shape and stress distribution plot during vibration. (b) Simulated temperature distribution plot under resistive heating.

utilized by implementing the polysilicon layer of the CMOS process, previously showing the piezoresistive transduction is less sensitive to the gap spacing as compared to the purely capacitive transduction [6]. With that, the piezoresistive transduction has been proved as an alternative once the foundry process rules of the CMOS technology nodes are limited. Furthermore, the polysilicon layer not only serves as a piezoresistor, but a heater and a temperature sensor embedded inside the resonator. Therefore, a constant-resistance control [7] for the active temperature compensation can be easily applied into the CMOS-MEMS-based resonators.

In this work, the proposed CMOS-MEMS resonators were fabricated by a TSMC 0.35μm 2P4M CMOS process. The structure was designed as a dog-bone like resonator [8] which enables a large capacitive driving area from its wide proofmasses. Furthermore, the longitudinal beam structures of the resonator were designed using low-loss materials, such as silicon dioxide and polysilicon to attain high-Q performance. To enhance the overall transduction of the device, a differentially piezoresistive sensing was adopted, and at the same time alleviates the parasitic feedthrough effect. Due to the configuration of the CMOS process, two individual polysilicon layers can be used to serve as a piezoresistive sensor and a heater (i.e., ovenized element), separately. Unlike the silicon-based piezoresistive resonators, the piezoresistor and the heater of the proposed CMOS-MEMS resonator can be physically (or electrically) isolated by the oxide structure of the resonator. Therefore, the piezoresistive transduction can be decoupled from the power control of the ovenized functionality. The resonators finally exhibits high Q (>15,000) and enhanced thermal stability with the TC_f around -12.5ppm/°C, leading to an alternative single-chip solution for timing applications. It is worth mentioning that the demonstrated TC_f in this work shows the best temperature stability among any CMOS-MEMS resonators to date.

II. Device Design and Operation

The proposed resonator implemented two longitudinally vibrating beams consist of only low-loss materials, including poly-Si and SiO_2 from the standard CMOS BEOL process to attain high Q. Fig. 1 presents the drive and sense configurations of the CMOS-MEMS bulk-mode resonator. Both driving electrodes and embedded electrodes (yellow) of the resonator are stacked from poly-1 (original gate poly-Si) to metal-3 layer for the capacitive driving. The dog-bone like resonator is horizontally driven by the electrostatic force from the input electrodes. Then, the poly-1 and poly-2 (original resistor poly-Si) layers embedded in the beam serve as the piezoresistor (blue) and heater (pink), respectively. At the same time, poly-2 is also connected to the embedded electrode of the proofmasses to setup their bias voltage. To operate this device, an ac signal v_i (port-1) together with a dc-bias V_P generates an electrostatic force to drive the resonator into resonance with a mode shape shown in Fig. 2(a). The mechanical resonance frequency of the corresponding mode shape can be determined from the equivalent spring-mass-damper mechanical model with an effective spring constant k_{eff} and an effective mass m_{eff}.

When using the capacitive detection, the motional current becomes very weak due to the limited equivalent gap spacing g_o. To enhance the motional signal, the piezoresistor embedded inside the beam structure can be utilized to perform the piezoresistive transduction. As the resonator starts to vibrate, the displacement will be amplified by Q times. The displacement x is expressed as

$$x = \frac{Q \cdot F_e}{k_{eff}} = \frac{Q}{k_{eff}} \frac{\varepsilon W_e h_e}{g_o^2} \qquad (2)$$

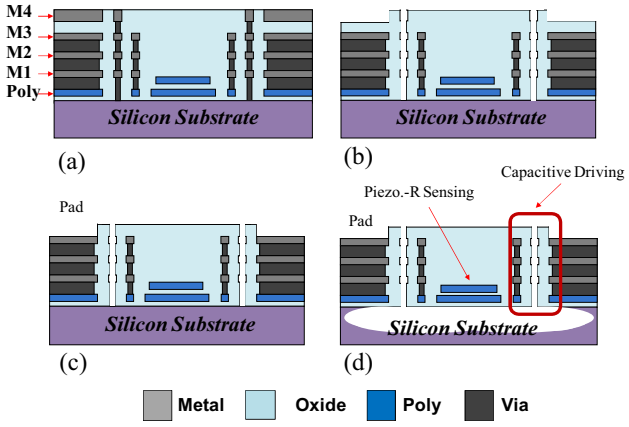

Fig. 3: Fabrication process flow, showing (a) the chip received from the CMOS foundry, (b) wet etching to remove the sacrificial metals, forming the air gaps and resonator geometry, (c) RIE to open bond pads, and (d) XeF_2 dry etching to finally release the resonator structures.

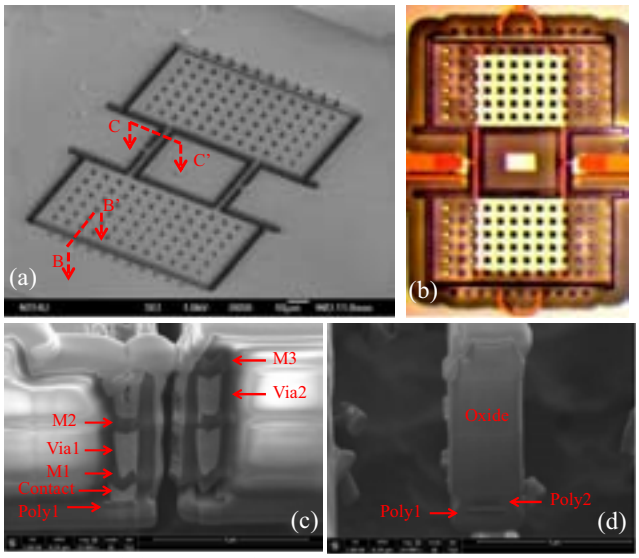

Fig. 4: (a) Global SEM view, (b) OM view, and (c) FIB cross-sectional view for a fabricated CMOS-MEMS resonator. (d) Close-up photo of the resonator beam structure consisting of two polysilicon layers from the CMOS BEOL configuration.

where F_e is the electrostatic force; W_e is the width of the capacitive driving electrode (about 99μm); h_e is the thickness of the driving electrode (about 4.865μm). When a dc current I_D is applied through the piezoresistor, variations of stress/strain caused by the beam vibration would induce a resistance change, resulting in output motional signals i_{m1} and $_{im2}$ which could be detected on port-2 or port-3, respectively, in Fig. 1 where both poly-1 and poly-2 resistors were measured in this work to evaluate their sensing capability. The feedthrough will be cancelled by the use of the differential readout, hence producing a symmetric frequency spectrum. As the dc current I_D is applied on the resistor, the resonator will also be heated. Fig. 2(b) presents the finite-element simulation of the temperature gradient. When the heating power is 0.895mW, the maximum temperature of 403.07K occurs on the proofmass.

III. Device Fabrication

To realize the high-Q structure, the composition of the metal materials should be as low as possible. In order to increase the ratio of the oxide inside the resonator, the metal wet release process was adopted [9]. In this work, the devices were manufactured using a TSMC 0.35μm 2P4M process. The bare chips were received from the foundry as shown in Fig. 3(a) which depicts the A-A' cross-sectional view of Fig. 1. Then a metal wet etching solution containing H_2SO_4 and H_2O_2 with very high selectivity between oxide and metal layers was utilized to remove both sacrificial metal and tungsten-via layers as shown in Fig. 3(b). The electrode-to-resonator gap spacing is defined by the width of the sacrificial metal stack while the transistor circuits were protected by the passivation layer. This maskless etching technique leaves the driving electrodes, piezoresistors, heaters, and oxide structures intact. Next, an RIE process was used to remove passivation and oxide layers to open the bond pads for later wire bonding as shown in Fig. 3(c). Finally, the underneath silicon substrate was isotropically etched away by XeF_2 to suspend the resonator structure as shown in Fig. 3(d).

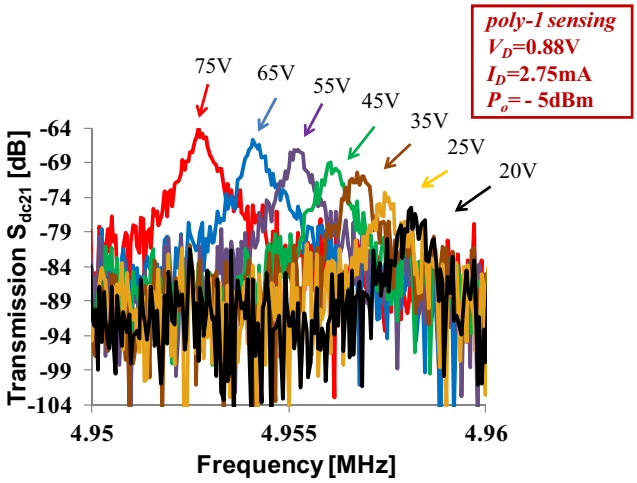

Fig. 5: Measured frequency transmission (Sds21) characteristics (in vacuum) under different bias voltages V_P using the piezoresistive detection (poly-1) for a fabricated CMOS-MEMS bulk-mode resonator.

Fig. 4(a) presents the global SEM view of a fabricated oxide-rich resonator. To clearly observe the inner of the fabricated resonator, Fig. 4(b) presents the optical photo view of the resonator structure since the high-Q structural material (SiO_2) is transparent to the visible light, showing the embedded electrodes and polysilicon layout. Fig. 4(c) presents an FIB-cut cross-sectional view of the embedded electrodes for the capacitive driving. The electrodes consist of the metal, tungsten via, and polysilicon layers stacked to form the capacitive transducer. Fig. 4(d) presents an FIB-cut cross-sectional view of the oxide-rich beam structure where two polysilicon layers are clearly seen.

IV. Measurement Results

The measurement scheme is shown in Fig. 1 where a three-port test setup was used to characterize the piezoresistive transduction of the CMOS-MEMS bulk-mode resonator. Since the resonator is driven by the electrostatic force, Fig. 5 presents

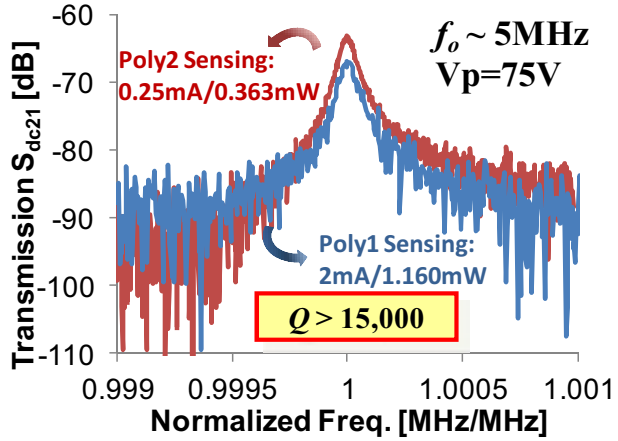

Fig. 6: Comparison of the measured frequency characteristics under poly-1 and poly-2 piezoresistive detections.

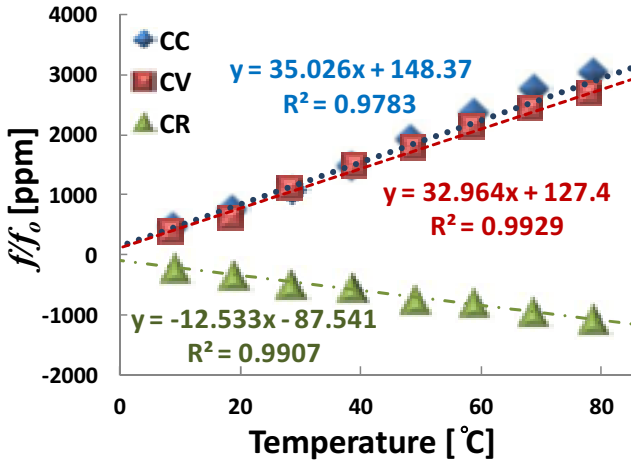

Fig. 7: Measured thermal stability of the CMOS-MEMS resonator under the constant-current (CC), constant-voltage (CV), and constant-resistance (CR) controls of the piezoresistor (poly-1).

the transmission amplitude, showing the resonance frequency can be tuned using the dc-bias voltage V_P through the electrical stiffness effect. Even the gap spacing is about 1μm, the piezoresistive output signal could still be measured under a low bias voltage of 20V. The frequency tuning range is around 1200ppm from 20V to 75V. Due to the large electrode-to-resonator gap spacing, we cannot find motional signal using the traditional capacitive sensing readout. As a result, the piezoresistive transduction not only brings signal enhancement but helps to ease the dc bias voltage which becomes more amenable to the CMOS charge pump designs.

Fig. 6 presents the measured frequency characteristics with clear resonance behavior under poly-1 and poly-2 piezoresistive detections, respectively. Both configurations were carried out by V_P of 75V, showing resonator Q > 15,000 and more than 20dB stopband rejection. It is worth noting that the poly-2 sensing scheme exhibits a low-power operation mode (only 363μW) and attains a high electromechanical coupling coefficient due to its larger gauge factor than that of the poly-1 scheme. The measured single-ended transconductance g_m from the poly-1 and poly-2 schemes are 3.144μS and 4.9μS, corresponding to the extracted gauge factors of 7.8 and 16, respectively.

Though the poly-1 resistor has a lower gauge factor, it allows a higher dc current to pass through (i.e., higher current density), making poly-1 a suitable heater candidate for the temperature compensation. TC_f of 76ppm/°C of the uncompensated resonator was simulated using COMSOL Multiphysics. As the power was applied on the poly-resistor, Fig. 7 presents the measured thermal stability of the resonator by using the constant-current (CC), constant-voltage (CV), and constant-resistance (CR) controls of the poly-resistor (poly-1), demonstrating the lowest TC_f (-12.53ppm/°C) to date in CMOS-MEMS resonators.

V. Conclusions

A CMOS-MEMS bulk-mode oxide-rich resonator was proposed in this work. These resonators were fabricated by a standard foundry CMOS technology together with maskless metal and silicon etching processes to accomplish high-Q oxide-rich structures. We utilized embedded metal electrodes and piezoresistor for capacitive driving and piezoresistive sensing configuration to enhance motional signals. To attain high Q, the longitudinally vibrating beams of the resonator consist of low-loss materials from the CMOS BEOL process. The measured Q of the proposed CMOS-MEMS resonator is greater than 15,000, a record-high value among CMOS-MEMS resonators, and also comparable to silicon-based resonators, thus benefiting phase noise of their oscillator implementation. To improve the thermal stability, the resonator takes advantage of the poly-resistor which serves as an ovenized element to perform active temperature compensation. A constant-resistance (CR) control was utilized, finally demonstrating the lowest TC_f feature among CMOS-MEMS resonators to date under a low-power operation mode. This work offers an alternative way for the future timing reference and time-keeping applications in a single-chip format.

Acknowledgment

This research was sponsored in part by the National Science Council of Taiwan under grant of NSC-101-2628-E-007-008-MY2. The authors wish to appreciate the TSMC and the National Chip Implementation Center (CIC), Taiwan, for the supporting of CMOS chip manufacturing. The authors would like to thank the Center for Nanotechnology, Materials Science and Microsystems (CNMM) of National Tsing Hua University for the use of fabrication and measurement facilities.

References

[1] G. K. Fedder, R. T. Howe, T.-J. K. Liu, and E. P. Que´vy, "Technologies for cofabricating MEMS and electronics," *Proc. IEEE*, vol. 96, no. 2, pp. 306-322, Feb. 2008.

[2] F. Chen, J. Brotz, U. Arslan, C. C. Lo, T. Mukhejcc, and G. K. Fedder, "CMOS-MEMS resonant RF mixer-filters," *Proceedings*, the 18th Int. IEEE Micro Electro Mechanical Systems Conf. (MEMS'05), Miami, Florida, Jan. 30 - Feb. 3, 2005, pp. 24-27.

[3] J. L. Lopez, J. Verd, J. Teva, G. Murillo, J. Giner, F. Torres, A. Uranga, G. Abadal, and N. Barniol, "Integration of RF-MEMS resonators on sub-micrometric commercial CMOS technologies," *J. Micromech. Microeng.*, vol. 19, no. 1, pp. 13-22, Jan. 2009.

[4] C.-C. Lo, "CMOS-MEMS resonators for mixer-filter application," Ph.D. Dissertation, Carnegie Mellon University, July, 2008.

[5] W.-C. Chen, W. Fang, and S.-S. Li, "VHF CMOS-MEMS oxide resonators with Q > 10,000," *Proceedings*, IEEE Int. Frequency Control Symp., Baltimore, Maryland, May 21-24, 2012, pp. 1-4.

[6] C.-S. Li, M.-H. Li, C.-H. Chin, and S.-S. Li, "Differentially piezoresistive sensing for CMOS-MEMS resonators," *IEEE/ASME J. Microelectromech. Syst.* (in press).

[7] C.-C. Chen, H.-T. Yu, K.-H. Lee, and S.-S. Li, "Enhancement of temperature stability via constant structural-resistance control for MEMS resonators," *Proceedings*, the 26th IEEE Int. Micro Electro Mechanical Systems Conf. (MEMS'13), Taipei, Taiwan, Jan. 20-24, 2013, pp. 765-768.

[8] J. T. M. van Beek, P. G. Steeneken, and B. Giesbers, "A 10MHz piezoresistive MEMS resonator with high Q," *Proceedings*, IEEE Int. Frequency Control Symp., Miami, Florida, USA, June 4-7, 2006, pp. 475-480.

[9] M.-H. Tsai, C.-M. Sun, Y.-C. Liu, C. Wang and W. Fang, "Design and application of a metal wet-etching post-process for the improvement of CMOS-MEMS capacitive sensors," *J. Micromech. Microeng.*, vol. 19, no. 10, Sept. 2009, pp. 105017.

Generalized Phase Measurement and Processing with Application in the Time-Frequency Measurement Control and Link

Wei Zhou, Zhiqi Li, Lina Bai, Huimin Song, Qianqian Du, Na Li, Wanying Li,Ying Zhang
Department of Measurement and Instrument Xidian University
Xi'an, P.R. China
wzhou@ xidian.edu.cn

Abstract—**Traditional phase measurement is limited by the identical nominal frequencies of two compared signals. In a lot of applications, there are higher requirements not only on measurement accuracy, but also on the frequency range of compared signals. After years of exploration and efforts, we have discovered some concepts and characteristics which can reflect mutual phase relationship among different frequency signals, such as Least Common Multiple Period, Phase Difference Quantization Step, Equivalent Phase Comparison Frequency, and the continuous phase group characteristics with the least common multiple period (as the time interval and the quantization step phenomenon that the phase difference of the two different frequency signals will change according to a specific value in one least common multiple period). In the process of experiments, we have discovered ambiguity zone edge effects and measurement method of periodic signal parameter quantization error elimination. We achieved precise frequency source synchronization and link, phase processing and measurement between completely different frequency signals with complex relationship. Through updating concepts, we move phase comparison and processing beyond identical frequency signals and extend to arbitrary frequency signals. Major applications include measurement of transient stability, phase noise measurement, edge effects for accurate frequency measurement method of Serial and Parallel. These breakthroughs promote rapid development in the area of measurement and instrument, and some difficult research problems have been solved.**

Keywords-frequency measurement; frequency link; edge effect

I. INTRODUCTION

Phase measurement and processing has the highest resolution in time-frequency measurement and processing area and even on generalized precision measurement area[1]. However, traditional phase measurement is limited by identical nominal frequencies of two compared signals [2]. Fig.1 shows phase detection between same nominal frequency signals.

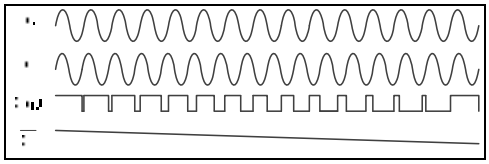

Figure 1. The work waveform of phase detector

In order to get wider frequency range in phase processing, assistive technologies such as frequency transformation and synthesis are applied [3]. These measuring methods increase the complexity of equipment and limit the further improvement of the measurement accuracy. Especially in recent years, in the industry and research applications, there are higher requirements on not only measurement accuracy, but also the frequency range of comparison signals [4]. In the area of precise frequency source synchronization and link, phase processing, comparing and measurement between completely different frequency signals are required in the accuracy and stability transmission of frequency signals with complex relationship [5]. Traditional limits must be broken from concepts and methods according to updating work.

II. THE BASIS OF GENERALIZED PHASE PROCESSING

From the basic consideration, an arbitrary periodic phenomenon has phase relation. Arbitrary periodic phenomenon should show their mutual phase difference changes, which means the research of phase relation does not depend on whether nominal frequencies of two signals are identical or not, but depend on whether they are stable periodic signals or not. What's more, a series of applications and purposes based on phase relation will be achieved, such as frequency measurement, phase noise measurement, frequency link, etc.

Generalized phase processing breaks the limit of traditional phase comparison method which can only compare identical frequency signals. This new technology can perform comparing and processing between any frequency signals. Through the research on phase variation of periodic signals, we analyzed characteristics of the greatest common factor frequency $f_{\max c}$ and the least common multiple period $T_{\min c}$ which exist between signals, and discovered the physics law of quantization step that is counted by equation (1), and equivalent phase detecting frequency that is counted by equation (2) of quantized phase difference of periodic signals [6].

The phase difference between different frequency signals is not necessarily continuous in $T_{\min c}$. It is often discrete. Fig.2 shows phase group synchronization phenomenon.

The work was supported by the National Natural Science Foundation of China (Grant Nos. 10978017 and 61201288)

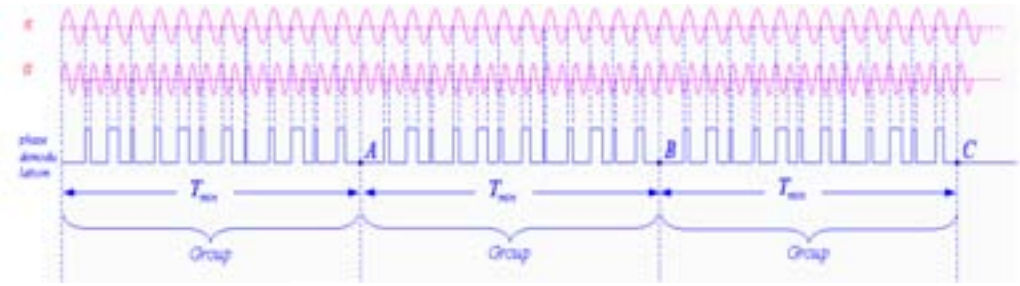

Figure 2. Phase group synchronization

$$\Delta T = \frac{f_{\max c}}{f_1 f_2} \tag{1}$$

$$f_{equ} = \frac{1}{\Delta T} = ABf_{\max c} \tag{2}$$

However, if we rearrange the phase differences according to the order or size, the quantum characteristics are displayed, which means the difference between two adjacent phase differences is constant[6]. The phase differences between $T_{\min c}$ present the continuity of group status. In addition to the inherent signal frequency relationship, if there are additional frequency differences, the changes in the phase difference between signals possess characteristics of synchronized increases and decreases. The follow fig.3 and fig.4 show the phase differences which have been converted into $V(t)$ between two frequency signals with simple or complex relationship. This phenomenon shows the quantization step feature of phase relationship.

Figure 3. Phase difference between two frequency signals with simple relationship

Figure 4. Phase difference between two frequency signals with complex relationship

Therefore, any periodic signal must have the phase comparability and a high processing resolution can be obtained in many situations. This result can produce a key foundation for the analysis and processing of comparison relationship in other periodic signals. Therefore, the research in this area has important significance.

Especially the variation characteristics of the regularity of phase differences shown by periodic signals are in response to the periodicity of mutual phase relationship between two signals[7]. It is not depending on the type of signal and the frequency value. So the periodicity phenomenon and variation regularity of phase difference is widespread applied [12].

III. Generalization Of Phase Processing

According to the research of basic signal characteristics, the limit of traditional phase processing method which can only process identical frequency signals is broken. Through updating concepts, we move phase comparison and processing beyond identical frequency signals and extend to arbitrary frequency signals. The repetition period of phase comparison is equal to the least common multiple period between frequency signals. The full period of phase comparison is equal to ΔT. Because ΔT is much smaller than the periods of two compared signals, so the processing resolution based on generalized phase processing is related to ΔT or equal to part of ΔT according to different situations. ΔT represents a time mark which reflects mutual periodic phase changes between completely different frequency signals. But ΔT absolutely is not the smallest in time.

Because frequency relationship between signals can be selected as adjusted, ΔT may be much smaller than period of radio frequency signed by equation (1). The signal processing accuracy is improved greatly, in which Picosecond, even Femtosecond resolution is reached[17].

In the application, there are significant differences among processing accuracy, ease of implementation, special performance of typical mutual frequency relationship in different phase processing methods [10]. Exploration about this aspect which makes phase processing in different applications has a significant advantage. The implementation of the phase processing problems becomes more flexible. The application will be broader and have more engineering application selection. The frequency range of the signal processing is overall expanded, the measurement accuracy is improved, and the equipment structure is simplified.

IV. The Improvement In Measurement Aspect Based On Generalized Phase Processing

Repeated capture and use of the special phase phenomenon between signals can be effectively used for eliminating the quantization error in the presence of the digital measurement [15], which can greatly improve measurement accuracy about 3-5 orders of magnitude, even higher.

TABLE I THE FREQUENCY MEASUREMENT RESULTS

f_x	Measured （Hz）	Frequency stability σ(/s)	Frequency stability σ(/10s)
10MHz Rubidium atomic frequency standard of X72	10 000 000.0001±1	7.3×10^{-12}	8.7×10^{-13}
5MHz signal of Austron 1250A	5 000 000.4731±1	6.2×10^{-12}	3.1×10^{-12}
12 800 000Hz signal of HP8662A	12 800 000.5379±1	6.7×10^{-12}	3.5×10^{-12}
16 384 000Hz signal of HP8662A	16 384 000.5584±1	6.6×10^{-12}	3.4×10^{-12}
20 971 523Hz signal of HP8662A	20 971 523.5796±1	6.3×10^{-12}	3.2×10^{-12}

We make captured "Phase coincidence" to be on signal and off signal of measurement gate[3], which can effectively eliminate a ± 1 count error. Fig.5 is the principle diagram of a frequency measurement instrument by means of phase coincidence capture and DDS-assisted measurement. This frequency measurement instrument can achieve broader frequency range, high-resolution, normal measurement gate time. Table Ⅰ shows the measurement results.

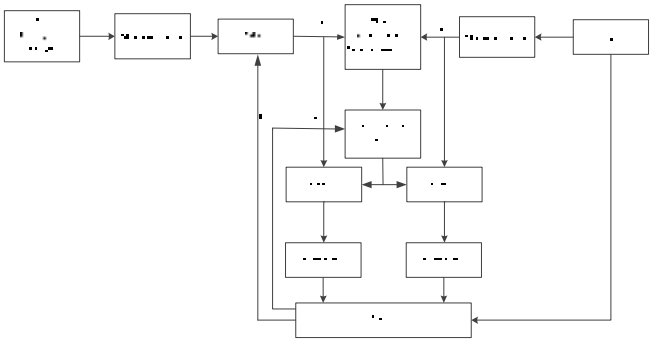

Figure 5. The principle diagram of frequency measurement

Usually the method of making phase coincidence detection to be measuring gate has low response time[17]. When the signals are in the phase "coincidence" detection edge, the phenomenon that coincidence detected signals appear in "0" or "1"(here"1" represents there is a signal pulse, "0" represents not), which results from signal phase noise, can reflect the fastest stability which is equivalent to the corresponding sampling time of the cycle of the compared signal[16] [8]. Using ΔT as small as possible makes the phase difference step values stable in the detected "phase coincidence cluster". The signal background noise, which makes the phase variation obvious, causes phase jitter and lose some "coincidences". So it has provided the basis for us to analyze the phase noise specification.

According to sampling interval of the coincidence information, the phase difference of the signals is increasing or decreasing by step ΔT. The "0" after coincidence detection "1" in different position represents amplitude change of the phase difference variation caused by noise. But when there appears some associate "0" in a certain position, the reflected amplitude changes need special treatment including the phase change value and duration time on the corresponding numbers of "0".

$$\sigma_y(\tau)=\frac{1}{\tau}\sqrt{\sum_{i=1}^{m}\frac{(\Delta\Phi_{i+1}-\Delta\Phi_i)^2}{2m}} \tag{3}$$

In equation(3), the parameters include the information of phase difference changes $\Delta\Phi$ and corresponding duration time τ[9]. This equation was used to calculate stability in the measurement results of the same nominal frequency by using phase comparison method. In fact, its inference and change has provided an important basis on frequency stability with the information processing of coincidence detection area. The duration detection of coincidence conditions can obtain whether $\Delta\Phi$ is changing or not. According these methods, the transient state stability measurement of an ordinary 10MHz crystal oscillator can be achieved by 10MHz higher stability. Table Ⅱ shows frequency stability calculation results by equation(3).

TABLE II FREQUENCY STABILITY MEASUREMENT RESULTS

group	**1**	**2**	**3**	**4**
Frequency stability（100ns）	7.23×10^{-4}	7.19×10^{-4}	7.19×10^{-4}	7.16×10^{-4}
group	**5**	**6**	**7**	**8**
Frequency stability（100ns）	7.02×10^{-4}	6.92×10^{-4}	6.67×10^{-4}	6.56×10^{-4}

V. FREQUENCY LINK AND ATOMIC CLOCK PERFORMANCE IMPROVEMENT BASED ON GENERALIZED PHASE PROCESSING

The frequency signals with large frequency difference can be linked through phase processing method, which performs the transfer of the accuracy and stability. The concept will bring new opportunities for the development of quantum frequency standard technology, such as the link between the signals with above 5 orders of magnitude frequency difference, and the phase group synchronization, different frequency optimization of phase-locked loop frequency standard of cesium and rubidium atomic clock circuits[16]. The detailed experiment about phase processing on

a large frequency ratio condition shows in reference [4]. On the basis of which the phase lock of large frequency ratio has been achieved.

At present, frequency link has played a significant role in atomic clock performance improvement [7]. Whether active atomic clock or passive atomic clock, the generalized phase processing frequency link method can modify the clock system structure and improve its performance. In the active atomic clock such as the hydrogen atomic clock, because of the directly high precision phase detection of different frequency signals, the hydrogen maser frequency from atomic energy level transition through simple transformation and the signal from the crystal oscillator will be able to realize different frequency detection and phase-locked [4]. In passive atomic clock, the crystal oscillator which is more easily to energize clock transition signal is been chosen to produce drive signal, thus, the output signal produced by phase-locked based on phase group synchronous between selected oscillator outputs and the 10 MHz oscillator not only has high accuracy and long-term stability, but also ensures a better short-term stability and phase noise specification. As in the corresponding cesium atomic clock, in order to simplify the system frequency transformation circuit, the 14,591,479Hz voltage-controlled crystal oscillator is used as source to produce drive signal of the physical package. Its 630 times can get the incentive signal of cesium atomic clock 9,192,631,770 Hz. The final output of the cesium atomic clock is 10MHz, we use more convenient and high quality 10MHz oscillator signal, by directly phase processing and control – using the method of the phase group synchronization of two signals, to achieve the link control of 14,591,479Hz signal to the oscillator signal 10MHz. Fig.6 shows the achievement process of phase group synchronization, the key is to use the equation $\frac{\Delta f}{f} = \frac{\Delta \Phi}{\tau}$. τ is effective comparing time, which should be the integer multiples of 1s; $\Delta\Phi$ is a selected fixed phase difference of the start signal - the corresponding change of the measuring interval time. The Comparison of the phase noise curve in Fig.7 and Fig.8 can fully show the advantage of frequency link based on generalized phase processing.

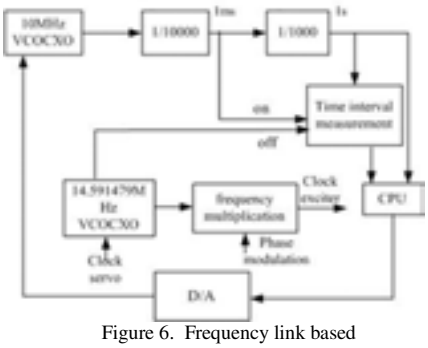

Figure 6. Frequency link based on phase group synchronization

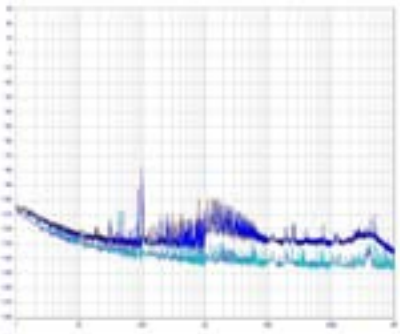

Figure 7. The phase noise of the DDS10MHz output when the clock is14.591479MHz

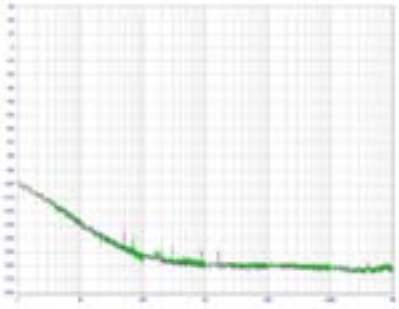

Figure 8. The phase noise of the10MHz output on the condition of group synchronization

VI. The Basis Performance Of Generalize Phase Processing In Broader Periodical Phenomenon And The Mutual Relationship

The basis application of generalize phase processing is mainly applied in the field of engineering. Fig.9 shows the various application of phase measurement based on generalized phase processing.

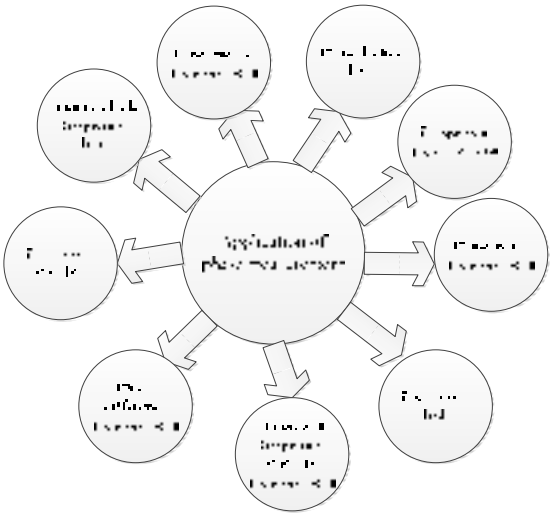

Figure 9. Various applications of phase measurement based on generalized phase processing

Furthermore, a periodic phenomenon is common one in nature [1]. The research of its change and mutual influence, especially the performance in high-accuracy has important significance[11].The technology can better explain the performance of different phase characteristics between the periodic movements, and the causes of the abnormal phenomenon. In the broader natural environment, this research can become the basis of exploring, analyzing, and predicting a variety of periodic relevant factors.

VII. CONCLUSION

Briefly, the exploring of the generalized phase relationship between the periodic signals and processing technology helps us to understand deeply the various relationships existing between the various cyclical movements. Now this thought and method have more application prospects on precise frequency and phase difference measurement and processing, high-precise frequency link, phase-locked loop devices, and system transformation of quantum frequency standard. We believe this method and corresponding technology can achieve extensive application in time-frequency measurement, control, process of periodic signals and periodic phenomenon which exist in a lot of corresponding subjects.

REFERENCES

[1] Wei Zhou, "Systematic Research on High Accuracy Frequency Measurements and Control," Shizuoka University,Japan, Doctor dissertation, 2000,pp.31-39.

[2] Wei Zhou, "The Greatest Common Factor Frequency and Its Application in the Accurate Measurement of Periodic Signals," Proceedings of the 1992 IEEE Frequency Control Symposium, May 1992, pp.354-359.

[3] Wei Zhou, "Equivalent Phase Comparison Frequency and Its Characteristics," Proceedings of the 2008 IEEE Frequency Control Symposium.2008, pp.468-470.

[4] Wei Zhou, Zong-Qiang Xuan, Jian Guo YU, "A Novel Frequency Measurement Method Suitable for a Large Frequency Ratio" Chinese Physics Letters.2004. pp.786-788.

[5] Zhiqi Li, Wei Zhou, "A Super-High Resolution Frequency Standard Measuring Approach Based on Phase Coincidence Characteristics Between Signals," Chin. Phys B. 2010, 19(9).

[6] Wei Zhou, Xiaojuan Ou, Hui Zhou, "The Time-frequency Measurement and Control Technology," 2006.7. Shan'xi, Xidian University Press,2006,pp.138-143.

[7] Ma Mingxiao, Wang Hao, Li Zhijun, "Phase-locked frequency source in the S-band transceiver system Frequency Source in the S-band Transceiver System.," Proceedings of 2012 IEEE 14th International Conference on Communication Technology 2012.

[8] Hu Xiao,Xiaolin Wang,Yanxing Ma,Pu Zhou,XiaojunXu,BingHe,Jun Zhou, "Phase noise measurement of high-power fiber amplifiers.," Chinese Optics Letters.2011 ,041404.

[9] David D.Lynch, "Random Drift in Terms of Allan Variance Coefficients,"Proceedings of 2010 International Symposium on Inertial Technology and Navigation 2010.

[10] Lin Dejiao, Yan Juqun, Wu Jian, Chao Zhixia, Yin ChunyongState, "Differential Phase Measurement with External Trigger" Proceedings of the Second International Symposium on Instrumentation Science and Technology ,2002.

[11] KANG Zhong-wei, PAN Meng-chun, LUO Fei-lu, CHEN Di-xiang, ZHANG Yu-hua, "Application of Frequency Sweeping Method in Alternative Current Field Measurement," 2004.

[12] Tian Guangming, Chen Guangju. "Time-Frequency Measurement for Sine Sweep Vibration Tests," 2005.

[13] R. Pelka. "A daptive calibration of time interval digitizer with picosecond resolution". IEEE Transactions on Instrumentation and Measurement," Vol.40, pp.502–504, 1991.

[14] T. W. Hansch, "Optical Clockwork and the Measurement of Laser Frequencies with a Mode-locked Frequency Come," IEEE J. Quantum Electron, Vol. 37, pp. 1493-1501, Dec. 2001.

[15] G. Paul Landis, Ivan Galysh, and Thomas Petsopolous. "A new Digital Phase Measurement System," Proceedings of the 33rd Annual Precise Time and Time Interval Meeting, 2001, pp 543-552.

[16] Hui Zhou, Wei Zhou, A Super High Resolution Phase Difference Measurement Method. Proceedings of 2007 IEEE International Frequency Control Symposium, 2007.

[17] Hui Zhou, Wei Zhou, "A High-resolution Frequency Standard Comparator Based on A Special Phase Comparison Approach," Proceedings of 2004 IEEE Frequency Control Symposium.

[18] Wei Zhou, et al, High- precise Frequency Measurement and Link Based on Phase Group Synchronization. 2012 IEEE Frequency Control Symposium.

[19] Jian-Guo Yu, Wei Zhou, A Novel Super-High Resolution Phase Comparison Approach. CHIN. PHYS. LETT. Vol. 29, No. 7 (2012) 070601.

Source Impedance Influence on Cross-Correlation Phase Noise Measurements

Jason Breitbarth, Ph.D.
Holzworth Instrumentation Inc.
Boulder, CO, USA
jason@holzworth.com

***Abstract*—The phase noise floor of an oscillator has been shown both theoretically and experimentally to be the ratio of the source noise power divided by the delivered power. In a 50Ω system this is determined by –177dBm - P_{OUT} in dBc/Hz. Recent measurements have shown what appears to be better than theoretical noise floors in some oscillators, assuming a 50Ω environment. However, oscillators rarely exhibit an output impedance of exactly 50Ω and vary significantly farther from the carrier. While the input impedance of a modern cross correlation analyzer may be 50Ω, the assumption the analyzer introduces 50Ω common mode noise can be erroneous. This paper presents theory and measurements that demonstrate the extremely low phase noise measured on some oscillators is real and not in violation of theoretical limits by isolating the noise sources in a series of additive phase noise measurements.**

Keywords—phase noise; additive; residual; noise; noise-floor cross-correlation.

I. Introduction

Leeson's model of an oscillator includes a term for the impedance of the system, usually set to 50Ω, and based on the assumed architecture of the oscillator, is often very accurate for predicting the performance of an oscillator [1]. This model assumes the output power of an oscillator is delivered from the output of the amplifier in the system and includes the noise due to the amplifier and the loop impedance. An alternative to this architecture is the block diagram of an oscillator in Fig 1. The output power is pulled prior to the amplifier and after the resonator. In an inductively coupled parallel resonator, such as a cavity, the impedance of the resonator far from the -3dB bandwidth can be a very low impedance. Regardless of the input impedance of the amplifier, the output noise source impedance far from the arrier will dominated by the resonator impedance past the -3dB point.

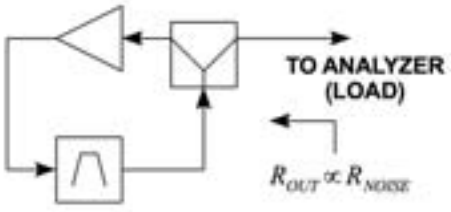

Fig. 1. Oscillator digram where output impedance and noise is dominated by the output impedance of the resonator, assuming the resonator has a low impedance.

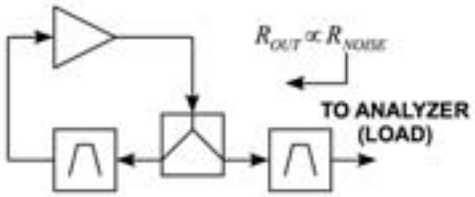

Fig. 2. Oscillator digram where output impedance and noise is dominated by a resonator clean-up loop.

A second architecture that Leeson's formula does not account for is shown in Fig. 2. This architecture adds a clean-up loop to a traditional oscillator. Again, the cleanup loop can be a resonator with a near short circuit far from the -3dB point. Since an oscillator is fundamentally just filtered noise from a positive feedback circuit, this additional loop will filter the noise induced by the amplifier in feedback. The source impedance of Fig. 2 is similar to Fig. 1 where far from the -3dB point it may be a very low impedance. In both of these systems, the measurement of delivered power is still in a 50Ω environment while far from the carrier the noise power is in an entirely different impedance. This discrepancy will result in phase noise levels, far from the carrier, that will be lower than what is possible in a theoretical 50Ω environment.

The fundamental question if the above is true is two-fold. First, can a cross correlation phase noise measurement truly differentiate between different sources of noise, itself and the source. Second, can a cross correlation system measure phase noise far from the carrier in which the noise source impedance is something other than 50Ω. Presented below are two measurement setups. First at baseband to demonstrate the ability of the baseband portion of measurement system to identify only noise that is common, regardless of impedance. Cross-correlation systems have shown to measure far below that of either individual channel [2-4]. Second, three additive phase noise measurements are shown in which the noise source is common to all three inputs at two different impedances and one where a 50Ω noise source is added to the common path as a verification. This verification is to provide a reference from [5] in which -177dBm has been determined to be thermal noise floor in a 50Ω environment.

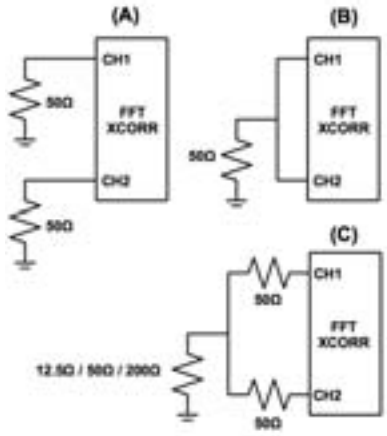

Fig. 3. Measurement setups for demonstrating the ability of a cross correlation system to identify only common noise, regardless of impedance.

II. Baseband Cross-Correlation

To demonstrate the cross correlation measurement and the ability to cancel noise that is common only between the two channels, regardless of the impedance of either channel, a simple test setup is shown in Fig 3.

The first test identifies the capability of the cross correlation system to show truly independent noise paths. In Fig. 4, the first (blue) and second trace (red) shows the measurement from Fig. 3c and Fig. 3b, respectively, as a single channel. The third trace (red) and fourth traces (black) are the cross correlation results from Fig 3c and Fig 3b, respectively. This measurement demonstrates that any noise introduced in either channel uniquely, but not common, will be correlated out of the measurement. The fourth trace (black) in Fig. 4 is from the setup in Fig 3a, demonstrating the isolation of the measurement. A setup similar to this was originally used to calibrate the cross correlation measurement system in [6].

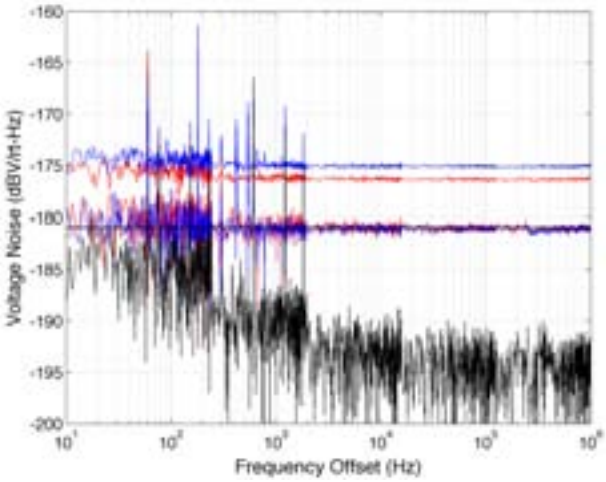

Fig. 4. Measurements from Fig. 3. The top trace (blue) is setup 3c with 50Ω in common to each port taken as a single channel measurement. The second trace down (red) is setup 3b with only 50Ω in common taken as a single channel measurement. The third and four traces down (nearly identical) are a cross correlation measurement of setups 3b and 3c, demonstrating the 50Ω in series adds no common noise. The fifth trace down is setup 3a where no noise is common. The measurement demonstrates the channels are independent. The rise in the noise at low frequencies is due to a different number of correlations per measurement band to optimize measurement speed. Low frequencies have fewer overall correlations.

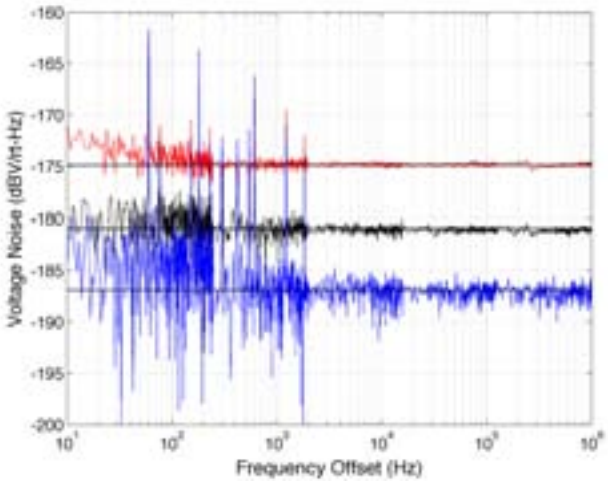

Fig. 5. Measurements from Fig. 3c. The top trace (red) is for a 200Ω impedance. The second trace (black) is for 50Ω. The bottom trace (blue) is for a 12.5Ω resistor. In all three cases, the measurements demonstrate results within ~0.1dB of theoretical noise for a resistor at 293K (temperature of measurement). The sold lines are the theoretical values.

The second test results are shown in Fig. 5 using the setup in Fig3c. The series 50Ω resistor into each path emulate a resistive splitter that can be used to split a signal without introducing common mode noise. The measurements in Fig. 5 demonstrate the near theoretical results for each resistor value inserted. In each case, the results are within 0.1dB of the theoretical noise values.

III. Cross-Correlation at RF Frequencies

A. Measurement Setup

Cross-correlation at RF frequencies accomplished two identical discriminators, each with their own unique noise source. A Holzworth HA7402B cross-correlation engine was used for these measurements. The input circuits were optimized for 0-5dBm levels to ease the measurement time. The important aspect of the HA7402B is the >100dB port-port isolation of each of the three ports at 100MHz. Port match is better than -30dB. A good cross-correlation measurement system is designed to not introduce any common mode noise into the DUT path while maintaining very high port to port isolation. In mixer only systems port isolation may only be 20-40dB, causing feedthrough and corrupting the measurements at these levels.

The source is a Wenzel Onyx series 100MHz OCXO with very good close to the carrier phase noise and a -175dBc/Hz floor. The output of the OCXO was buffered by attenuators and a Holzworth HX2400 amplifier. Careful attention was paid to isolate the OCXO from the measurements so as not to introduce any potential injection locking or pulling.

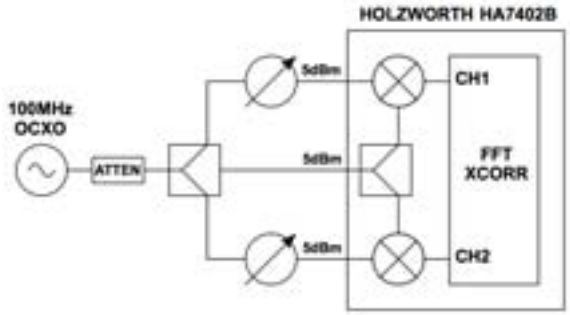

Fig. 6. Setup for measuring the floor of the cross-correlation system. Two different splitters were used, a resistive splitter with 12.5Ω resistance and a wilkinson three-way splitter with 50Ω port match and 20dB isolation. The splitters are shown in more detail in Fig. 10.

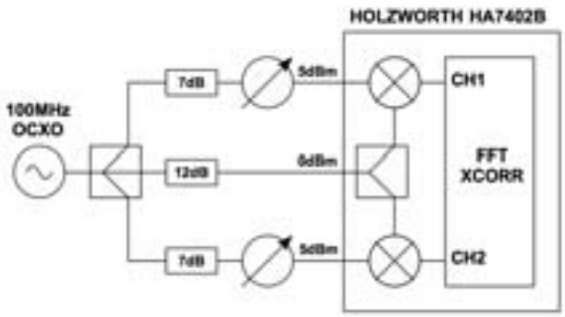

Fig. 8. Setup for proving the -177dBm/Hz floor in a 50Ω environment. The setup from Fig 6 was modified to introduce a 12dB attenuator in the common path, providing a 50Ω noise source that is unique only to the common path. The wilkinson power splitter from Fig. 7 was used.

To identify that the cross correlation system only measures noise unique to the common path, regardless of output impedance of the source, a setup was built shown in Fig. 6 using two different types of power dividers. One divider is resistive only at the input, providing a low impedance direct connection to all three paths while providing a 50Ω port match at the input. The output impedance is 12.5Ω. The second is a more traditional three-way wilkinson power divider. The schematic level of these dividers is shown in Fig. 10. This experiment identifies whether the cross-correlation engine with two discriminator paths can cancel noise due to the source, regardless of impedance. It adds a secondary result on whether a divider introduces a unique noise component to each path or is common to all and therefore cancelled.

B. Measurement Results

The measurement results of the two splitters are shown in Fig. 7. The measurements were stopped at 200 correlations for reasons of measurement time. After 200 correlations the measured floor was -186dBc/Hz for both power dividers and still relatively uncorrelated. At 5dBm input power and a 50Ω noise source system, the measurement noise floor would be -182dBc/Hz. What this measurement demonstrated was the noise was common between all three ports. This is easy to see for the resistive splitter but more difficult for the wilkinson, both shown schematically in Fig. 10. Two different source impedances were used to show that the source noise is cancelled out (similar to the noise around the carrier) regardless of impedance. The additive measurement will only measure noise added by the common path, regardless of impedance.

The verify that the correct floor is measured, assuming a 50Ω noise source environment unqiue to the DUT path, the setup in Fig. 8. was built to provide 0dBm into the HA7402B while maintaining 5dBm LO drive levels. To introduce 50Ω noise that is common only to the DUT path, a 12dB attenuator was used. The pi-attenuator topology introduces near 50Ω noise, incoherent with the other two channels. The measurement results are shown in Fig. 9. A level of -177dBc/Hz was measured, as predicted by theory.

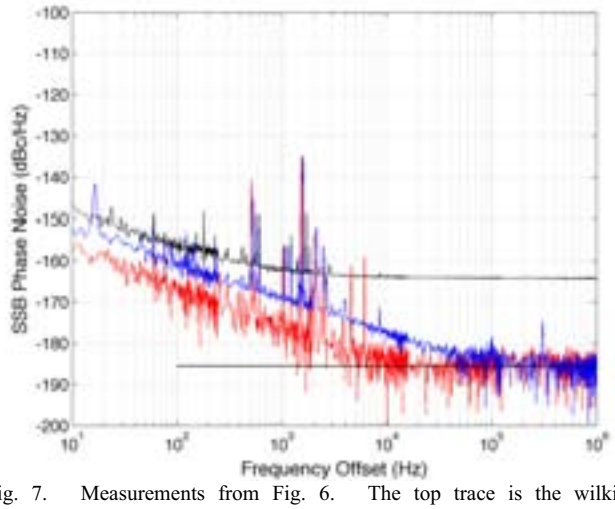

Fig. 7. Measurements from Fig. 6. The top trace is the wilkinson measurement from a single channel. The middle trace (blue) is from the resistive splitter and the bottom trace (red) is from the wilkinson using 200 cross-correlations. At that measurement level, there is no performance difference far from the carrier at -186dBc/Hz.

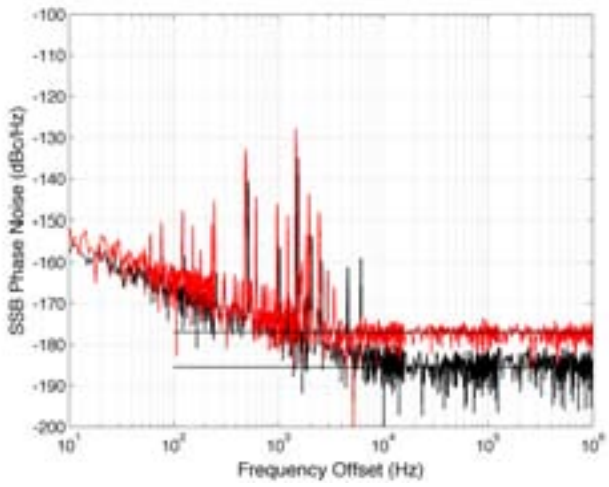

Fig. 9. Measurement of the setup from Fig. 8. demonstrates the -177dBc/Hz (or -177dBm/Hz at 0dBm) theoretical limit by introducing a 50Ω noise source common to both channels. This was taken using the wilkinson 50Ω power divider. The bottom plot is from Fig. 7 of the floor without the attenuator. The attenuator adds unique 50Ω noise to the system, matching theory.

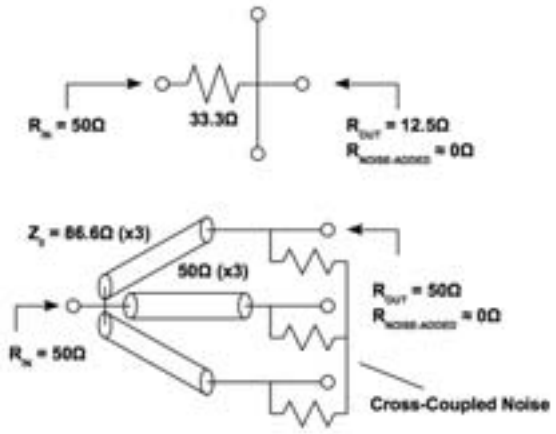

Fig. 10. Schematic representations of the two power dividers used in the cross-correlation measurements. Both split the signal equally with the resistive splitter port matched at the input with low output impedance. The wilkinson is band limited but provides additional isolation. The noise in both cases is entirely common to all three paths, being cancelled out in the discriminator. The resistors in the star-topology wilkinson add noise, but add it in common to all three channels.

C. Power Dividers as Noise Sources

Two drastically different power dividers were chosen. The first is resistive only. This changes the output impedance of the splitter to be 12.5Ω with the noise component being common by a direct connection. This was done deliberately to isolate the power divider from the noise source. The results are conclusive in that the cross-correlation engine, far from the carrier, is not adding 50Ω noise to the system.

The second splitter is the wilkinson. Given it's output impedance is 50Ω, it is not immediately clear that the noise source is common between all ports. Measurement results indicate that the noise component is transposed back to the input of the divider, becoming common mode. The cross-coupled nature of the resistors in the wilkinson also cross-couple the noise. This results in the noise becoming common and is input referred. This also demonstrates that a wilkinson divider, as the front end of a cross-correlation measurement setup, may actually introduce 50Ω noise, as it could input refer the resistor noise, which would be common in the DUT path

This is a significant result as potentially not all cross-correlation engines will have a similar front end as HA7402B and some may actually introduce noise in that path, limiting the dynamic range of the measurement. The HA7402B uses a broadband resistive splitter shown to not introduce common mode noise in the first series of baseband measurements.

IV. Conclusions

The impetus behind these series of measurements were to try to prove that source phase noise can be below that of the theoretical -177dBm/Hz - P_{OUT} levels of a 50Ω system, provided the output impedance is sufficiently low. The question is whether a cross correlation system could correctly measure a signal source noise that is below the 50Ω input impedance of the analyzer.

Based on the measurement results it can be concluded that the cross correlation measurement system has the ability to measure signals with a source noise impedance lower than 50Ω. A measurement can be taken (assuming enough correlations and time) that would show an oscillator could have better than the 50Ω assumed -177dBm/Hz - P_{OUT} provided the source impedance of the oscillator was sufficiently low and no other significant noise source was introduced after the oscillator. The power dividers at the input of the HA7402B analyzer do an effective job of isolating the noise channel to channel while not introducing 50Ω noise but maintaining a matched port impedance.

As a side note, modern simulators often include all noise sources in the system, including the noise due to a 50Ω termination. It may be unclear how this may affect the predicted noise floor. The cross-correlation engine is designed specifically to isolate only the oscillator and not include the presence of this noise. Therefore, simulator predicted noise floors may be different than actual measurements due to the uncertainty in the simulated noise sources.

The additive cross-correlation phase noise measurement technique was applied to test this theory to help isolate any form of injection locking or inadvertent non-linearity when using multiple oscillators. To add more proof to the basis of this work an additional measurement may be taken in which a very low noise oscillator is followed by a very high-Q cavity filter with an effective short circuit beyond the -3dB point. The author expects that a measurement floor below -177dBm - P_{OUT} will be observed based on the measurements provided in this paper.

Acknowledgment

I thank Wenzel Associates, Inc. for providing oscillators for testing and to Charles Wenzel for discussions regarding theoretical phase noise floors.

References

[1] D. B. Leeson, "A Simple Model of Feedback Oscillator Noise Spectrum", Proceedings Letters, pp. 329-330, February 1966.

[2] Warren F. Walls, "Cross-Correlation Phase Noise Measurements", IEEE Frequency Control Symposium, pp. 257-261, 1992

[3] Jason Breitbarth, “Cross Correlation in Phase Noise Analysis”, Microwave Journal, pp 78-85, February, 2011.

[4] Eugene N. Ivanov and Fred L. Walls, "Interpreting Anonalously Low Voltage Noise in Two-Channel Measurement Systems", IEEE Transactions on Ultrasonics, Ferroelectrics, and Frequency Control, Vol. 49, No 1. pp 11-19, January 2002.

[5] A. Hati and D. A. Howe and F. L. Walls and D. Walker, "Noise Figure vs PM Noise Measurements: A Study at Microwave Frequencies", IEEE Frequency Control Symposium, pp. 516-520, 2003

[6] Jason Breitbarth, “Design and Characterization of Low-Phase Noise Microwave Circuits”, University of Colorado Ph.D. Thesis, 2006.

Phase Noise Measurement Techniques, Associated Uncertainty, and Limtations

[1,2,3]Ulrich L. Rohde
[1]Cottbus University, BTU Cottbus, Germany
[2]Technical University Munich (TUM), Germany
[3]Synergy Microwave Corp, NJ, USA

[1,2]Ajay K. Poddar
[1]Synergy Microwave Corp, NJ, USA
[2]Technical University Munich (TUM), Germany
Email:akpodar@synergymwave.com

***Abstract*—This paper focuses on key phase noise measurement techniques for oscillators and reviews their advantages and disadvantages. Several test methods and test instruments are investigated. There's no "one size fits all" solution, for e.g., measuring a phase noise value of -130dBc/Hz at 1Hz offset from the carrier, and achieving a measurement noise floor better than -200dBm is challenge, using existing test equipment and methods.**

Keywords- Oscillator, AM, PM, Phase Noise, Cross-Correlation

I. INTRODUCTION

Noise is associated with all the components of the oscillator circuit; however the major contribution of the noise in an oscillator is from the active device, which introduces AM (amplitude modulation) noise and PM (phase modulation) noise [1]. The conventional wisdom is to ignore AM component of the noise because the gain limiting effects of the active device operating under saturation allow little variation in the amplitude noise in comparison to PM noise component, may directly affects the frequency stability of the oscillator and creates noise sidebands [2]. But in reality, many oscillator topologies create significant AM noise, therefore effective noise contribution is the combination of 1/f spectrum with the $1/f^2$ effect in all phase modulation, makes the low-frequency noise much greater, and that's where the information in most modulated signals resides [3]-[6].

In the order of increasing complexity, noise models are grouped into one of the three categories as: linear time invariant (LTIV), linear time variant (LTV), and nonlinear time variant (NLTV). Leeson's model [1] is based on LTIV (Linear-time-invariant) properties of the oscillator, such as resonator Q, feedback gain, output power, and noise figure; a second model is proposed by Lee and Hajimiri [7, 8], based on time-varying properties of the oscillator RF current waveform (LTV); and a third is proposed by Kaertner and Demir using a perturbation model based on numerical techniques (NLTV) [9]-[11]. Nallatamby et al. [2] revisited the Lesson's noise model, providing a detailed and enlightening analysis, demonstrating its applicability to several oscillator circuits. The theories proposed by Hajimiri and Lee, and from Kaertner and Demir are based on time-domain approaches for harmonic oscillator circuits (like LC resonator). The approach from Hajimiri and Lee can be seen as a particular case of the theory of Kaertner and Demir, as it can be shown in the analytical comparison between time and frequency-domain techniques for phase noise analysis, carried out by Suárez et al. [12]. The Impulse Sensitivity Function (ISF) proposed by Hajimiri and Lee can be employed to optimize the phase noise performances of a given oscillator and ISF can be obtained from Harmonic Balance (HB) as shown by Ver Hoeye et al. [13]. More insight about phase noise analysis can be found in the paper of Rizzoli [14], and Sancho et al, [15].

Table 1 shows the comparative analysis of 3-most cited phase noise models, their relative strength and weakness for the characterization of oscillator phase noise. All the three models discussed in Table 1 explain and predict the phase noise of autonomous circuits (oscillators), and one can argue the superiority of any of the three models based on accuracy, reliability, simulation time, and convergence for a given oscillator circuit topology. Comparing the noise models discussed above, it is up to the designers to choose noise models for predicting the phase noise because none of the 3-models allow closed form solution for both harmonic and non-harmonic oscillator circuits. Similarly, oscillator phase noise measurement is one of the most difficult measurements in all of electrical engineering. The biggest challenge is the huge dynamic range required in phase noise measurements. There are several methods to measure phase noise and the right one must be chosen to make the necessary measurements. To properly select among the various methods it is necessary to know and appreciate the weaknesses and strengths of each of the different measurement techniques, because none of these methods is perfect for every situation.

Table 1: Describes the strengths and weaknesses of the noise models

Model	Leeson	Lee and Hajimiri	Kaertner and Demir
Assumptions	LTIV	LTV	NLTV
Perturbing noise Source	Constant white noise (KTB)	Cyclostationary $1/f^k$ for any $k \in N$	Modulated $1/f^k$ for any $k \in N$
Accuracy	Reasonable	Good	Exact
Simplicity	Simple	Moderate	Involved
Computer dependence	Independent (Calculation by hand)	Computer to evaluate ISF	Computer dependent (no closed form solutions)
Predicts close-in phase noise	No	Yes	Yes
Retained circuit parameters	Loaded Q-factor (Q_L), output power (P_s)	Γ_{rms}	None

II. PHASE NOISE MEASUREMENT

In general, measuring phase noise is more difficult than measuring amplitude or frequency related properties. Different signal sources, whether it is an oscillator alone or within a synthesizer, have widely varying phase noise performances. Higher noise sources do not work well with phase noise measurement equipment optimized to measure very low noise

levels. An ability to measure the phase noise performance of ultra-low phase noise oscillators drives the specifications of the best performing phase noise analyzers.

Phase noise is usually expressed in units of dBc/Hz at some specific offset frequency f, from the carrier, the value of the noise level relative to the carrier level calculated in 1Hz bandwidth. Most often only single sideband (SSB) noise is considered. Some measurement set-ups measure both noise sidebands and a conversion factor is required to report SSB noise. The pioneer in Phase Noise measurement unquestionably was Hewlett Packard [17]. Once adequate for advanced designs, a noise floor dictated by SSB thermal noise (Johnson Noise at kT of -174 dBm) for zero dBm output power is not enough anymore for some special requirements and also marketing of these reference frequency sources. Any type of amplifier in the test signal chain will also serve as a source of noise. While the main purpose of the amplifier is to increase the power level of a weak carrier signal, it also adds its own noise to the signal and boosts any input noise. The net result is that the amplifier, thermal noise, and flicker noise continue to give any PN plot a characteristic shape and, more significantly, reduce the theoretical lower limit of sensitivity for any phase-noise measurement. The noise correlation technique allows us to look below kT level (< -174 dBm). But the usefulness of the noise contribution below kT is debatable in the perspective of overall system performance. To achieve a very low noise floor, modern phase noise measurement instruments use the cross-correlation principle [18]-[20].

A. Phase Noise Mesaurement Techniques

The usual goal for measuring phase noise in an R&D environment is to achieve the lowest measurement noise floor possible. As we shall see, this is not necessarily the best choice, depending on the signal source being measured. In a production environment, the objective is fast throughput for product phase noise performance testing. Again, this is best achieved by using a method that is appropriate for the source being measured. There are some very capable general purpose phase noise measurement instruments available on the market, including the Agilent-E5052B, Rhode & Schwarz-FSUP, Holzworth-HA7402A, Noise XT-DCNTS, Anapico-APPH6000-IS, and OE Wave-PHENOM™. With the growing demand for improved dynamic range and lower noise floor, equipment companies are introducing general purpose phase noise analysis software driven tools for extracting far out (offset frequency > 1MHz) noise below the kT floor even though claims of -200dBm or lower lack the practical utility. Modern phase noise test equipment addresses these issues, following primary phase noise measurement techniques, listed in the order of increasing precision [21]-[25] :

(a) Direct Spectrum Technique

(b) Frequency discriminator method

- Heterodyne (digital) discriminator method

(c) Phase detector techniques

- (Reference source/PLL method)

(d) Residual Method

(e) Two-channel cross-correlation technique

The Direct Spectrum Method, PLL method, delay line discriminator method, and cross-correlation method are frequently used to measure the oscillator phase noise. The first one is the simplest and has the biggest limitation. The last one requires the most complex measurement system but it is a most versatile, can measure phase noise performance better than that of its reference oscillator. Figure 1 shows the typical block diagram of the 2-channel cross-correlation technique [17]. As shown in Figure 1, there are two reference oscillators, one power splitter, two mixer/amplifier/PLL circuits and a cross-correlation FFT analyzer. The cross-correlation technique is used to minimize the noise contribution from mixer, filter and LNA from the measurement results. The noise from output of each mixer can be modeled using two noisy signals [18]-[27]:

$$x(t) = a(t) + c(t) \overleftrightarrow{FFT} X(f) = A(f) + C(f) \quad (1)$$

$$y(t) = b(t) + c(t) \overleftrightarrow{FFT} Y(f) = B(f) + C(f) \quad (2)$$

Where *a(t)* and *b(t)* are uncorrelated equipment noise present in each channel and *c(t)* represents the correlated DUT noise. The cross-spectrum of these two signals after averaging over *M* samples is described by

$$\overline{S_{XY}} = \frac{1}{M}\sum_{m=1}^{m=M}[X_m \times Y_M^*] \quad (3)$$

Where '*m*' represents the sample index and (*) implies the conjugate function. From (1)-(3),

$$\overline{S_{XY}} = \frac{1}{M}\sum_{m=1}^{m=M}[(A_m + C_m) \times (B_m + C_m)^*] \quad (4)$$

$$\overline{S_{XY}} = \frac{1}{M}\sum_{m=1}^{m=M}[(A_m B_m^*) + (A_m C_m^*) + (C_m B_m^*) + (C_m C_m^*)] \quad (5)$$

From (5) the DUT noise through each channel is coherent and is therefore not affected by the cross-correlation, whereas, the internal noises generated by each channel are incoherent and diminish through the cross-correlation operation at the rate of $\sqrt{M}$ (M=number of correlations):

$$[Noise]_{meas} = [Noise]_{DUT} + \left(\frac{[Noise]_{chanel\#1} + [Noise]_{chanel\#2}}{\sqrt{M}}\right) \quad (6)$$

Where $[Noise]_{meas}$ is the total measured noise at the display; $[Noise]_{DUT}$ the DUT noise; $[Noise]_{chanel\#1}$ and $[Noise]_{chanel\#2}$ are the internal noise from channels 1 and 2, respectively; and M the number of correlations. From (6), the 2-channel cross-correlation technique achieves superior phase noise measurement capability but the measurement speed suffers when increasing the number of correlations.

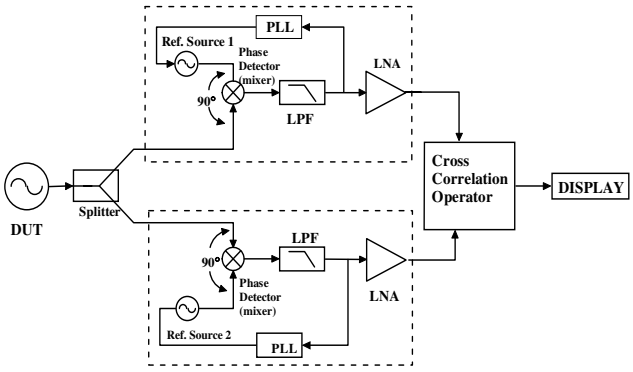

Fig.1: The block diagram of 2-channel cross-correlation technique

This method offers 15 to 20 dB improved phase noise measurement sensitivity when compared to the Reference source/PLL method, therefore, it is possible to measure oscillators with better noise performance than the reference oscillators, because phase noises from the reference oscillators are suppressed considerably [21]. The improved dynamic range and noise floor of the cross-correlation phase noise measurement technique comes at price; large samples are required for averaging out the uncorrelated noise. The practical value of the noise floor is given by [28]:

$$[L(f)_{SSB}] = -177 + N_a - P_i \quad (7)$$

Where N_a is the noise figure and P_i is the power available.

B. Phase Noise Measurement and Verification of 100 MHz Crystal Oscillator Using PN Measurement Equipments

Figures 2, 3, and 4 show the schematic and simulated plots of phase noise output power of 100 MHz oscillator circuit. For validation of the CAD simulated and theoretical phase noise plots shown in Figures (2) and (5), 100 MHz Crystal oscillator was built. The theoretical (Fig.5) and simulated (Fig.2) phase noise data agrees within 1-2dB of accuracy.

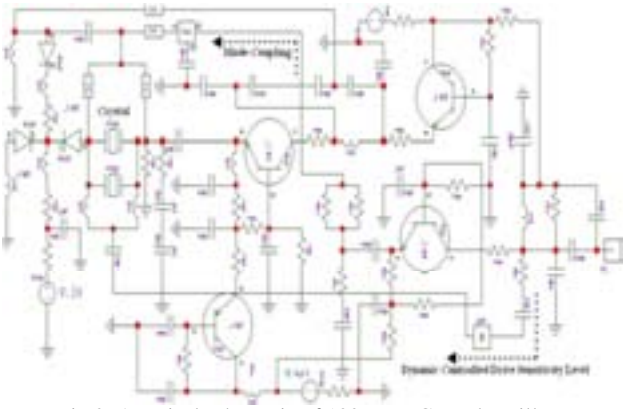

Fig.2: A typical schematic of 100 MHz Crystal oscillator

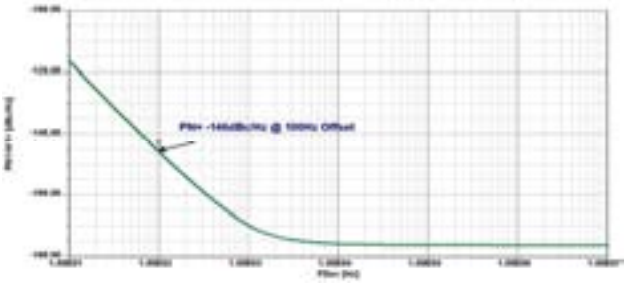

Fig.3: Simulated (Ansoft) PN plot of 100MHz Crystal oscillator

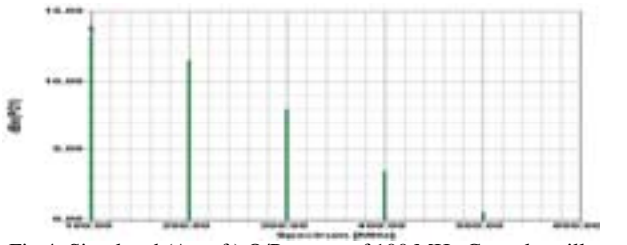

Fig.4: Simulated (Ansoft) O/P power of 100 MHz Crystal oscillator

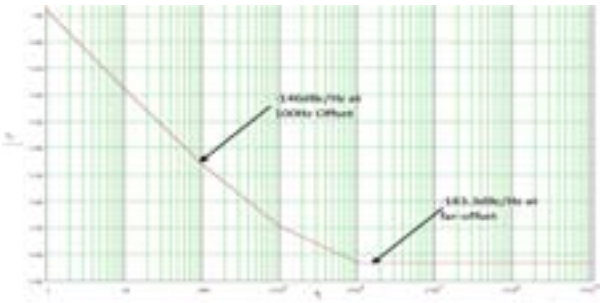

Fig.5: Theoretically calculated Phase noise plot of 100MHz OCXO

The rigorous measurements were conducted on 100 MHz Crystal oscillator using different Phase Noise Measurement Equipments (Agilent E5052B, R&S FSUP, Holzworth HA7402-A, Noise XT DCNTS, and Anapico APPH6000-IS) available on the market. The PHENOM™ (OEwaves) is high performance automated PN measurement system, this equipment was not made available for the validation in our Faraday Cage (Figure 6); nevertheless authors are keen to validate the PN measurement in future using PHENOM™ for broader acceptance of the fact and myth linked with variation in measurement phase noise data below the kT. Table 2 shows the measured phase noise of commercial available 100MHz OCXOs (Pascal, Synergy) on different test equipments for comparative analysis of the measured data under similar test conditions.

As shown in Table 2, it can be seen that there is a variation in PN measurement using identical DUT on different equipments. The consequences are the reliability and repeatability of the measured data below kT. If the equipment in use, after many correlations gives out a better number, it violates the laws of physics and if it gives a worse number, then either the correlations settings needs to corrected or the dynamic range of the equipment is insufficient.

Table 2: Comparative PN data measured on different Equipments

100 MHz OCXO O/P=14dBm, NF=7dB	Theoretical Model	Agilent E5052 B	R & S FSUP 26	Anapico APPH 6000-IS	Holzworth HA7402-A	Noise XT DCNTS
@ 100 Hz offset	-146 dBc/Hz	-143 dBc/Hz	-143 dBc/Hz	-141 dBc/Hz	-147 dBc/Hz	-140 dBc/Hz
@ 1 kHz offset	-170 dBc/Hz	-167 dBc/Hz	-163 dBc/Hz	-170 dBc/Hz	-170 dBc/Hz	-170 dBc/Hz
@ 10kHz offset	-182 dBc/Hz	-173 dBc/Hz	-174 dBc/Hz	-172 dBc/Hz	-178 dBc/Hz	-181 dBc/Hz
@ 100KHz offset	-183 dBc/Hz	-174 dBc/Hz	-183 dBc/Hz	-181 dBc/Hz	-179 dBc/Hz	-183 dBc/Hz
@ 1 MHz offset	-184 dBc/Hz	-174 dBc/Hz	-184 dBc/Hz	-182 dBc/Hz	-179 dBc/Hz	-186 dBc/Hz
@ 10MHz offset	-184 dBc/Hz	-174 dBc/Hz	-185 dBc/Hz	-188 dBc/Hz	-178 dBc/Hz	-196 dBc/Hz

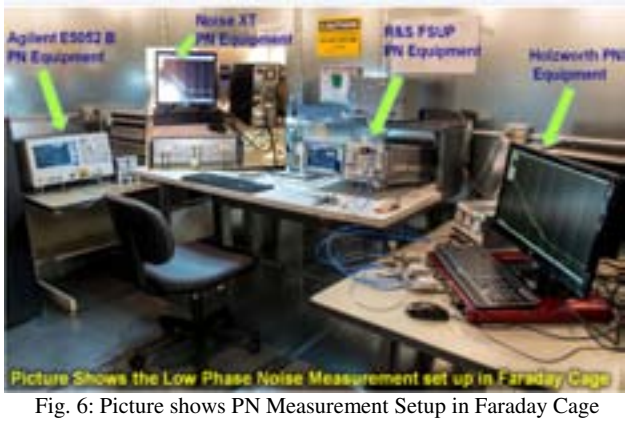

Fig. 6: Picture shows PN Measurement Setup in Faraday Cage

C. Phase Noise Mesaurement Issues

There are important measurement issues that, if not well understood, can lead to erroneous results and interpretations [24]. They involve measurement bandwidth masking of, and accurate distinction between, true discrete spurious signals and narrowband noise peaks (typically encountered under vibration). Although the phase noise data displayed by phase noise equipment is usually normalized to 1Hz measurement bandwidth, most automated phase noise measurement equipment actually measures the phase noise in measurement bandwidths that increase with increasing carrier offset frequency. This is done for two reasons: (1) it results in shorter, overall measurement time, and (2) at high carrier offset frequency (i.e., > 100 kHz), many measurement systems employ analog spectrum analyzers that are not capable of 1Hz resolution. Noise measured in a 1kHz bandwidth, for example, is 30dB higher than that displayed in a 1Hz bandwidth. That means that low level discrete spurious signals (and narrowband noise peaks typically encountered under vibration as a result of high Q mechanical resonances) may not be detected. The second problem involves the software employed by the noise measurement system vendor used to discriminate between random noise and discrete spurious signals. Usually, when a reasonably sharp increase in noise level is detected, the system software assumes the increase marks the presence of a "zero bandwidth" discrete signal. It therefore (when displaying the phase noise on a 1Hz bandwidth basis) applies a bandwidth correction factor to the random noise, but does not make a correction to what was interpreted as a discrete signal. This results in an erroneous plot if/when the detected "discrete" is really a narrowband noise peak [24].

Another problem is the physical length of the crystal oscillator connection cable to the measurement system. If the length provides something like "quarter-wave-resonance", incorrect measurements are possible. The uncertainty in PN measurement due to output load mismatch, output phase mismatch, cable length, equipment dynamic range, etc creates certain ambiguity whether or not to trust these measurements or can they be repeated on different PN equipments for a given DUT and test & measurement conditions.

III. CONCLUSION

There are many areas in which design engineers can be tricked into false readings or frustrated with the process of trying to achieve a good measurement. Characterizing the phase noise of a system or component is not necessarily very easy. Many different approaches are possible, but the key is to find the best approach for the measurement requirements at hand based on (1) accuracy, (2) repeatability, (3) speed, (4) operating range, (5) cost, and (6) ease of data retrieval.

REFERENCES

[1] D. B. Leeson, "A Simple Model of Feedback Oscillator Noise Spectrum, " *IEEE, Proc.* pp. 329-332, 1966.

[2] J.C. Nallatamby, M. Prigent, M. Camiade, and J. Obregon, "Phase noise in oscillators – Leeson formula revisited". IEEE Trans. on MTT, Vol. 51, No. 4, April 2003, pp. 1386-1394.

[3] A. Suárez, S. Sancho, S. Ver Hoeye, and J. Portilla, "Analytical comparison between time- and frequency-domain techniques for phase-noise analysis". IEEE Trans. on MTT, Vol. 50, No. 10, October 2002, pp. 2353-2361.

[4] S. Ver Hoeye, A. Suárez, and J. Portilla, "Techniques for oscillator nonlinear optimization and phase-noise analysis using commercial Harmonic-Balance software". 2000 IEEE MTT-S Digest, pp. 95-98.

[5] V. Rizzoli, F. Mastri, and D. Masotti, "General noise analysis of nonlinear microwave circuits by the piecewise Harmonic Balance technique". IEEE Trans. on MTT, Vol. 42, No. 5, May 1994, pp. 807-819.

[6] S. Sancho, A. Suárez, J. Domínguez, and F. Ramírez, "Analysis of near-carrier phase-noise spectrum in free-running oscillators in the presence of White and colored noise sources". IEEE Transactions on Microwave Theory and Techniques, Vol. 58, No. 3, March 2010, pp. 587-601.

[7] T. H. Lee, A. Hajimiri, "Oscillatator phase-noise: a tutorial," *IEEE J. Solid-State Circuits*, vol. 35, no. 3, pp. 326-336, March 2000.

[8] A. Hajimiri and T. H. Lee, "A general theory of phase noise in electrical oscillators," *IEEE J. SSC*, vol. 33, no. 2, pp. 179-194, Feb. 1998.

[9] A. Demir, A. Mehrotra, and J.Roychowdhury, "Phase noise in oscillators: a unifying theory and numerical methods for characterization," *IEEE Trans. CS-I*, vol. 47, no. 5, pp. 655 – 674, 2000.

[10] Kaertner F X, "Analysis of White and _übNoise in Oscillators", *Int Journal of Circuit Theory and Application*, 18:485.519, 1990.

[11] Demir A., "Phase Noise and Timing Jitter in Oscillators with Colored-Noise Sources", *IEEE Trans. on CS-I*, 49(12):1782.1791, Dec 2002.

[12] A. Suárez, S. Sancho, S. Ver Hoeye, and J. Portilla, "Analytical comparison between time- and frequency-domain techniques for phase-noise analysis". IEEE Trans. on MTT, Vol. 50, No. 10, October 2002, pp. 2353-2361.

[13] S. Ver Hoeye, A. Suárez, and J. Portilla, "Techniques for oscillator nonlinear optimization and phase-noise analysis using commercial Harmonic-Balance software". 2000 IEEE MTT-S Digest, pp. 95-98.

[14] V. Rizzoli, F. Mastri, and D. Masotti, "General noise analysis of nonlinear microwave circuits by the piecewise Harmonic Balance technique". IEEE Trans. on Microwave Theory and Techniques, Vol. 42, No. 5, May 1994, pp. 807-819.

[15] S. Sancho, A. Suárez, J. Domínguez, and F. Ramírez, "Analysis of near-carrier phase-noise spectrum in free-running oscillators in the presence of White and colored noise sources". IEEE Transactions on Microwave Theory and Techniques, Vol. 58, No. 3, March 2010, pp. 587-601.

[16] A. Abidi, "How phase noise appears in oscillators", http://www.rfdh.com/ez/system/db/pds_tn/upload/271/phase_noise.pdf, Nov 1997

[17] Agilent Phase Noise Measurement Solution, May 2013 (www.home.agilent.com/agilent/application).

[18] Samuel J. Bale, David Adamson, Brett Wakley, Jeremy Everard, " Cross Correlation Residual Phase Noise Measurements using Two HP3048A Systems and a PC Based Dual Channel FFT Spectrum Analyzer", 24th European Frequency and Time Forum, (April 13-16, 2010)

[19] Jeremy Everard, Min Xu, Simon Bale, "Simplified Phase Noise Model for Negative-Resistance Oscillators and a Comparison With Feedback Oscillator Models", IEEE Trans on UFFC, Vol. 59, No. 3, March 2012

[20] Jeremy Everard, Min Xi, "Simplified Phase Noise Model for Negative-Resistance Oscillators", IEEE Frequency Control Symposium, 2009 Joint with the 22nd EFTF, pp. 338-343, April 2009

[21] E. Rubiola and F. Vernotte. (2010, Feb 27). *The cross-spectrum experimental method* [online]. Available: http://arxiv.org/, document arXiv:1003.0113v1 [physics.ins-det].

[22] M. Sampietro, L. Fasoli, and G. Ferrari, "Spectrum analyzer with noise reduction by cross-correlation technique on two channels," *Rev. Sci. Instrum.*, vol. 70, no. 5, May 1999.

[23] U.L. Rohde, A.K. Poddar, and G. Boeck, 'The Design of Modern Microwave Oscillators for Wireless App: Theory and Optimization', Wiley, New York, 2005

[24] M. M. Driscoll, "Modeling phase noise in multifunction subassemblies," IEEE Trans. Ultrason. Ferroelectr. Freq. Control, vol. 59, no. 3, pp. 373–381, Mar. 2012.

[25] A. L. Lance, W. D. Seal, F. G. Mendozo and N. W. Hudson, "Automating Phase Noise Measurements in the Frequency Domain," *Proceedings of the 31st Annual Symposium on Frequency Control*, 1977

[26] W. F. Walls, "Cross-Correlation Phase Noise Measurements", 1992 IEEE FCS, pp. 257-261

[27] Frequency Extension for Phase Noise Measurements with FSUP26/50 and Option B60 (Cross-Correlation)", Rhode & Schwarz Application Note 1EF56, p. 3

[28] E. Rubiola, "Phase Noise and Frequency Stability in oscillators", Cambridge Univ. Press, Nov. 2008, ISBN 978-0-521-15328-7 (paperback)

ULISS Project: 2013 Progress Report

Vincent Giordano, Jean-Louis Masson, Gonzalo Cabodevila,
Enrico Rubiola, Yann Kersalé, Pierre-Yves Bourgeois and Gregory Haye.
FEMTO-ST Institute - Time and Frequency Dpt.
UMR 6174
CNRS - U. Franche-Comté - ENSMM-UTBM
ENSMM 26 Chemin de l'Epitaphe
25000 Besançon, France.
Email: *vincent.giordano@femto-st.fr*

Serge Grop, Benoît Dubois,
ULISS® Business Unit
FEMTO-ST/UFC
32 Av. de l'Observatoire
25044 Besançon cedex, France

***Abstract*—The ULISS Cryogenic Sapphire Oscillator (CSO) offers unprecedented short-term frequency performances. It was specially designed to be transportable by car in order to test this new technology in different European sites. During the last 18 months, it was used to qualify with success several high stability frequency sources. In February 2013, a new measurement campaign was lead at CNES, Toulouse (France) to qualify the flight model of the frequency synthesis of the PHARAO clock. During the same period we built a second CSO unit based on the same design and conducted new characterisations of frequency stability and environmental sensitivity. Optimisation of the system has led to an improved frequency stability reaching currently better than 1×10^{-15} at 10,000 s integration times. Eventually we developed a new low phase noise and high-resolution frequency synthesis delivering 10 GHz, 100 MHz and 9.192 GHz ultra stable signals. In this paper we draw a progress report on the ULISS project, updating performances and describing the latest experiments conducted with our CSO in different sites in Europe.**

I. Introduction

The ULISS project aimes to promotte the Cryogenic Sapphire Oscillator (CSO) technology, which today has reach enough maturity to be used outside a well equiped metrological lab [1]. The CSO offers unprecedented short term frequency stability currently reaching better than 1×10^{-15} for integration times ranging from few seconds to 3 hours. Some units have demonstrated a relative frequency stability of 5×10^{-15} over 1 day without any clear drift identified [2]. A specialy designed CSO was build to be transportable by road, and during the last year ULISS was tested in different european sites. Experience feedback allowed to make the prototype progress. In this paper we present the last results obtained by comparing directly two identical CSOs operating at 9.99 GHz.

II. FEMTO-ST CSO Technology

The CSO is based on a microwave whispering gallery mode sapphire resonator made of a 54 mm diamter and 30 mm hight high purity sapphire cylinder. This resonator was designed to present a high-Q quasi-TM mode, i.e. $WGH_{15,0,0}$ at 9.99 GHz ± 5 MHz. The difference to the 10 GHz round frequency allows the use of a low noise Direct Digital Synthesizer (DDS) to compensate for the sapphire resonator machining tolerances [3], [4]. At the liquid helium temperature, the Q-factor approches 1 billion and the temperature-frequency senstivity presents a null near 6K. We developped in the frame of an ESA project a CSO (nicknamed ELISA) incorporating a cryocooler as cold source, which can be operated during two years without any maintenance. This first prototype was eventually installed in the ESA ground station in Malargua (Argentina) in May 2012. ULISS a mobile version of the same instrument was build at the end of 2011. Before the implentation of the fisrt prototype in Argentina, the two CSOs was comparated and the results were presented in [5] demonstrating a relative frequency stabilty better than 1×10^{-15} at short term with a flicker floor of 4×10^{-16}. At long term, the Allan standard deviation was limited by the CSO residual temperature sensitivity. ADEV reaches 1×10^{-14} at one day. The figure 1 shows the interior of the CSO cryostat. We can see the two stages of the cryocooler with the copper braids used to transfert the cooling power to the resonator whithout transmitting the Pulse-Tube mechanical vibrations. The figure 2 shows the cryostat and rack containing the electronic controls and the frequency synthesis.

Fig. 1: *ULISS cryostat interior.*

Fig. 2: *ULISS CSO with electronic controls rack.*

The sustaining loop is placed at room temperature in a thermaly stabilized aluminium box (see Fig. 2). ULISS incor-

porates a Pound and a power servo controls to correct phase and power fluctuations along the sustaining loop.

III. ULISS's Odyssey continues

The objectif of the ULISS project is to propose to european potential users to test directly in their applications an ultrastable cryocooled sapphire oscillator. During the past 18 months, Uliss visited several sites by making approximately 9000 km by the road in a van:

- LTF Neuchâtel, Switzerland, January 2012. ULISS was used to qualify an ultrastable laser source looked on an ULE cavity and to measure the frequency stability of quartz Xtal oscillator industrial prototypes.
- CNES Toulouse, France, March 2012. First validation of the PHARAO clock synthesis.
- Exhibition of the EFTF 2012, Göteborg, April 2012.
- CNES, Toulouse, France, February 2013. Second run in the validation of the PHARAO instruments.
- UTINAM Institute, Besançon, France, April, 2013. Validation of the composite clock.
- SYRTE Paris, France, june, 2013. First tests with SYRTE metrological equipments.
- Exhibition of IFCS-EFTF joint meeting 2013, Prague, July 2013.
- Wettzel VLBI station, Germany, measurements with the ring laser, August 2013.

Between these differents measurement compaigns, ULISS came back to Besançon and was continously improved/adapted to fulfil the users requirements and to solve some encountered issues. The Pound servo was optimized: one integrator was added to provide enough gain at low frequencies. Preliminary tests using digital electronic controls have been realized during the past year, but due to the lack of time have not been integrated in the systems that we describe here. After the stay in SYRTE last June, where preliminary tests have been conducted with the higest resolution, a wide effort was recently dedicated to solve some EMC issues: replacement of bad switching power supplies, improvement of the earth and ground loops...

Initally ULISS was equiped with the same frequency synthesis than ELISA developped by TimeTech [6]. This frequency synthesis has three frequency outputs: 5 MHz, 100 MHz and 10 GHz. As several users need other frequencies, we designed our own frequency synthesis to get 500 MHz, 1 GHz and 9.192 GHz outputs. The CSO frequency stability is totally transfered at the microwave outputs. For the VHF and RF outputs, we observe as expected a small degradation due to the intrinsic noise of electronic components operating these frequency bands.

IV. Building of a new unit

The building of a new CSO was finalised at the end of 2012. In its design this CSO is identical to ULISS. Nevertheless some differences exist:

- The mechanical tolerances of sapphire resonator geometry were relaxed to decrease the cost of this key component. It results a frequency difference between the two CSOs of about 7 MHz.
- As the ULISS Odyssey focus a large part of our efforts, the second CSO is not totally optimized. It suffers from some technical problems that can be solved in a next step: i.e. i) the compressor He pressure is not optimized for 50 Hz supply, ii) due to some still non well identified leaks, the residual pressure inside the cryostat is 1×10^{-6} mbar, one order of magnitude higher than those obtained in the first system , iii) we suspect a possibly bad thermal contact in the resonator set-up. It results the cryocooler is less efficient than those of ULISS. The lower temperature currently achievable is 5 K (instead of 3.8 K), not far from the resonator turnover temperature, which is 5.8 K . In these conditions, the temperature control was found difficult to get optimized.

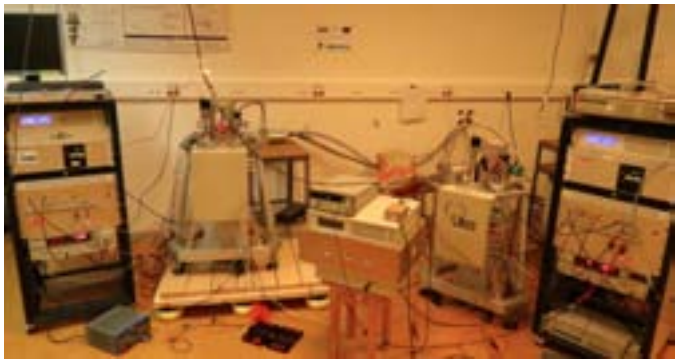

Fig. 3: The two CSOs during the last characterisation campaign (July 2013).

V. Improvements and comparison of the two CSOs

The ULISS travels requires a big effort of logistics and takes away our best reference for several weeks. Thus, since the first operation of the second CSO, we had only the possibility to make three short comparison campaigns in order to optimize its parameters. Nevertheless we made some progress in the electronic control loops (Pound and Power servos), improving the signal to noise ratio of the error signal detection and adding gain at low frequencies. We also modified the thermal filtering imrpoving the rejection of slow temperature variations of the Pulse-Tube.

The figure 4 shows multiple ADEV characterisations obtained by counting directly the 7 MHz beat-note during approximatly 15 hours. As usual we present the ADEV without any post-traitment. It clearly shows the reproductibity of the measurements and the exceptionnal flicker floor of 5×10^{-16}. At 1s the measurement is limited by the counter contribution due to the high value of the beat-nore frequency. The bump

at 20 s is due to a residual thermostat oscillation in the newly built CSO.

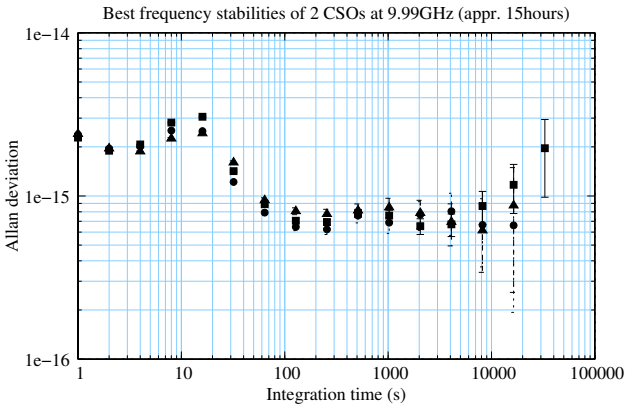

Fig. 4: 2 CSOs Short term frequency stability (July 2013).

The figure 5 shows the ADEV calculated after 5 days integration compared to the 2012 results [7]and to a state-of-the-art hydrogen Maser.

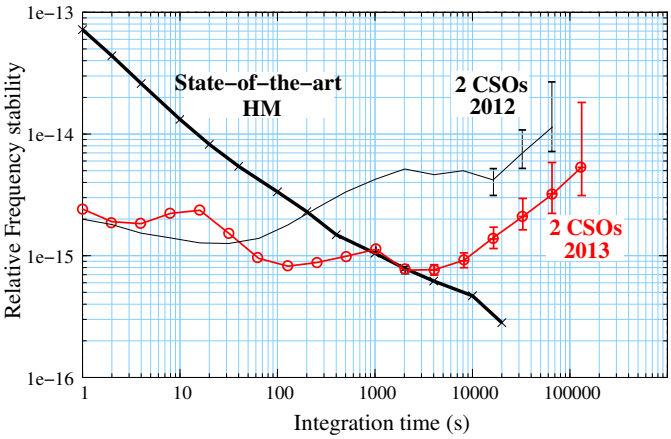

Fig. 5: CSO frequency stability.

ACKNOWLEDGMENT

The ULISS team wish to express acknowledgements to the *Fond Européen de développement Régional* (FEDER), *le Conseil Général de Franche-Comté* and OSEO for their support to the ULISS project.

The second CSO is founded by the ANR Oscillator IMP project and FIRST-TF network.

REFERENCES

[1] `http://www.uliss-st.com/`.

[2] S. Grop, W. Schafer, P.-Y. Bourgeois, Y. Kersalé, M. Oxborrow, E. Rubiola, and V. Giordano, "Unprecedented high long term frequency stability with a microwave resonator oscillator," *IEEE Transactions on Ultrasonics, Ferroelectrics and Frequency Control*, vol. 58, May 24, 2011.

[3] S. Grop, P.-Y. Bourgeois, N. Bazin, Y. Kersalé, E. Rubiola, C. Langham, M. Oxborrow, D. Clapton, S. Walker, J. D. Vicente, and V. Giordano, "A crycooled 10 GHz oscillator with 10^{-15} frequency stability," *Review of Scientific Instruments*, vol. 81, pp. 025102–1–7, 2010.

[4] S. Grop, P.-Y. Bourgeois, E. Rubiola, W. Schäfer, J. De Vicente, Y. Kersalé, and V. Giordano, "Frequency synthesis chain for the ESA deep space network," *Electronics Letters*, vol. 47, pp. 386–388, Mar. 17, 2011.

[5] S. Grop, B. Dubois, J.L. Masson, G. Haye, P.Y. Bourgeois, Y. Kersalé, E. Rubiola, and V. Giordano. Proceedings of the 2012 IEEE International Frequency Control , (Baltimore, US), 22-24 May 2012.

[6] S. Grop, P.-Y. Bourgeois, E. Rubiola, W. Schafer, J. DeVicente, Y. Kersalé and V. Giordano, Frequency Synthesis Chain For The ESA Deep Space Network, Electronics Letters, 47, 6, 386-388, 2011.

[7] V. Giordano, S. Grop, B. Dubois, P.Y. Bourgeois, Y. Kersalé, G. Haye, V. Dolgovskiy, N. Bucalovic,G. Di Domenico, S. Schilt, J. Chauvin, D. Valat, and E. Rubiola, "New-generation of cryogenic sapphire microwave oscillators for space, metrology, and scientific applications", *Review of Scientific Instruments*, 83, 085113 (2012);

Cancellation of Doppler Shifts in a Cold-Atom CPT Clock

E. A. Donley, F.-X. Esnault*, E. Blanshan, and J. Kitching
Time and Frequency Division
NIST,
Boulder, CO, USA
elizabeth.donley@nist.gov

***Abstract*— A compact cold-atom clock based on coherent population trapping (CPT) is being developed. Long-term goals for the clock include achieving a fractional frequency accuracy of 1×10^{-13} in a package of less than 10 cm^3 in volume. Here we present an overview of a prototype clock design, and a systematic evaluation of the first-order Doppler shift. We also introduce our second-generation physics package.**

Keywords- Atomic Clocks; Coherent Population Trapping; Doppler Shift; Laser Cooling; Ramsey Spectroscopy.

I. INTRODUCTION

A compact, cold-atom clock is under development. The clock is interrogated with light by use of coherent population trapping (CPT) in a lin ∥ lin polarization configuration [1]. This technique allows for excellent control of the phase of the interrogation fields on size scales much smaller than that of a microwave cavity, which is desirable for a small system. The use of cold atoms allows the system to achieve relatively long interrogation periods without requiring buffer gases, which introduce large, temperature-dependent shifts in clocks based on vapor cells.

The use of laser-cooled atoms eliminates the buffer-gas shift present in vapor-cell CPT clocks but in general introduces a 1st-order Doppler shift, since the atom cloud expands and falls during interrogation and the atoms are therefore not in the Lamb-Dicke regime [2]. Atomic fountains also operate outside of the Lamb-Dicke regime, and the distributed-cavity phase shift is equivalent to the Doppler shift in fountain clocks. In fountains, this shift is made to be small by use of interrogation with a standing wave in a high-Q microwave cavity [3], but the shift can nevertheless contribute to the overall clock uncertainty at the 1×10^{-16} level [4].

The atoms are interrogated by use of a combination of CPT and Ramsey absorption spectroscopy in a scheme similar to the approach taken by Hemmer and colleagues [5], who used Ramsey CPT spectroscopy to interrogate Na atoms in an atomic beam. Our system differs from theirs in that it is based on laser-cooled ^{87}Rb atoms, so the Ramsey pulses are time-separated instead of spatially separated. The use of Ramsey spectroscopy reduces the light shift [6-8] and eliminates power broadening [9].

The CPT scheme used here is a double-Lambda lin ∥ lin configuration [1], in which a higher contrast is achieved over conventional CPT spectroscopy owing to the elimination of trap states (for a review, see [10]). The linear polarization of the CPT light can be represented as a sum of σ^+ and σ^- circularly polarized light components, which results in probing the atoms with a superposition of two Lambda systems. The energy-level diagram for ^{87}Rb with the two clock Lambda systems is shown in Fig. 1. The frequencies of both of the resonances are sensitive to magnetic fields in first order, but the size of the first-order shift is equal and opposite. As long as the two Lambda systems have the same signal strength, the linear Zeeman shift will cause no net shift on the clock's frequency.

With the goal of making an atomic clock with a size of less than the microwave wavelength (44 mm for ^{87}Rb), we chose to use CPT interrogation with balanced counterpropagating beams to maintain good control of the CPT phase versus position in volumes that are much smaller than a microwave cavity. Early CPT clock work by Ezekiel and colleagues also pointed out that the CPT phase could be made uniform by use of counterpropagating beams [11].

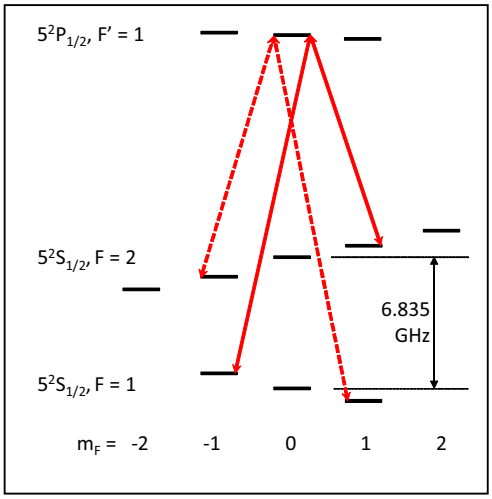

Figure 1. The energy-levels of ^{87}Rb probed with the double- Lambda lin ∥ lin technique. The two Lambda systems are shown. We use light resonant with the D1 transition at 795 nm.

* Current Address: Centre National d'Etudes Spatiales, 18 Avenue Edouard Belin, 31400 Toulouse, France.

II. EXPERIMENT

The apparatus has been described in detail previously [12], and will be briefly reviewed here. The system is based on a compact vacuum system that has a two-chambered design, with 2D and 3D magneto-optical traps (MOTs).

The CPT light is generated by use of an optical phase-lock loop built from two megahertz-broad DFB and DBR laser diodes, which produces a relatively clean, two-component spectrum that is free from zero- and higher-order modulation sidebands that cause light shifts without contributing to the CPT signal. The master laser is locked to the $F = 2 \rightarrow F' = 1$ transition on the D1 line at 795 nm via saturated absorption, and the slave laser is locked to a frequency near the $F = 1 \rightarrow F' = 1$ transition by locking the beat-note frequency between the master and slave lasers to an accurate reference, which enables accurate absolute frequency measurements for the evaluation of systematic shifts. So far, about 75 % of the power is in the coherent carrier. Work is in progress to increase this percentage.

The Ramsey spectroscopy performed here is different from traditional Ramsey spectroscopy in that the pulses are not $\pi/2$ pulses. Instead, the first pulse, which is typically 400 µs long and has an intensity of 20 µW/cm^2 for each frequency component, prepares the atoms in the dark quantum superposition state. Then the quantum superposition state evolves during the Ramsey period. The second pulse, which is typically 50 µs long, probes the relative phase of the quantum superposition state with respect to the light after the dark state has evolved during the Ramsey period. The clock signals are derived from the ratio of the transmission of the second Ramsey pulse to that of the first Ramsey pulse.

The Ramsey period, T_R, is typically less than 10 ms. The short interrogation periods allow for efficient recapture of atoms from cycle to cycle with 3 mm MOT beams, enabling a typical laser cooling-stage duration of 45 ms for loading about 10^6 atoms. For longer Ramsey periods, the fringes also begin to wash out because of magnetic-field gradients in the unshielded system combined with thermal expansion of the atomic cloud.

We observe Fourier-limited Ramsey resonances with a transmission contrast of 55 % and a typical absorption of 7 %. To lock the clock to the hyperfine ground-state splitting, we alternately probe the central fringe on opposite sides of the line and steer the clock to the central fringe. The short-term fractional frequency stability is currently limited to $4\times10^{-11}\tau^{-1/2}$. The atom shot noise contribution is $1\times10^{-12}\tau^{-1/2}$. The long-term fractional frequency stability is limited by magnetic field drift in our unshielded system to 2×10^{-12} for a 1000 second averaging period.

III. DOPPLER SHIFT MEASUREMENT

When the atoms are illuminated by a CPT light field from a single direction, a Doppler shift arises from motion of the atoms along the direction of the CPT beams during the Ramsey period. The phase of the CPT interrogation field varies linearly with position, and the moving atoms are pumped into the dark state and probed in different positions. The resulting frequency shift is given by

$$2\pi\Delta\nu_D = \Delta\phi/T_R = k_{HF}\cdot dz/T_R\,, \qquad (1)$$

where dz is the change in position of the atom along the propagation axis during the Ramsey period and $k_{HF} = k_2 - k_1 = 2\pi/\lambda_{HF}$, where $k_i = 2\pi/\lambda_i$ are the wavenumbers for the two CPT frequencies, and λ_{HF} is the microwave wavelength. When the atoms are probed with travelling-wave CPT beams along the direction of gravity, the fractional frequency Doppler shift from free fall from Eq. (1) is 1×10^{-10} for a 10 ms Ramsey period. To substantially reduce the shift, the atoms are probed with standing waves by applying CPT beams symmetrically from above and below.

When counterpropagating fields are applied to the atoms, the phase of the dark state created from the up and down CPT interrogation fields varies linearly with position as $\pm k_{HF}\cdot z$ [13, 14]. The slopes are opposite for the up and down beams. The dark-state phase versus position is visualized in Fig. 2. When the beams have equal intensity, the dark state phase is the average of the phases created by the up and down beams and is constant versus position and equal to the phase at the point where dark states created by the up and down beams have equal phase – the "equiphase point". The dark-state amplitude is modulated due to interference of the dark states created from the up and down beams, with maximum amplitude at the equiphase point.

Having balanced beams minimizes Doppler shifts when the signals from both the up and down beams are averaged during detection. In the experimental configuration described here, the absorption signals are detected independently and averaged. In a more elegant retroreflected configuration that we are currently using, the averaging is done automatically and only one signal is measured.

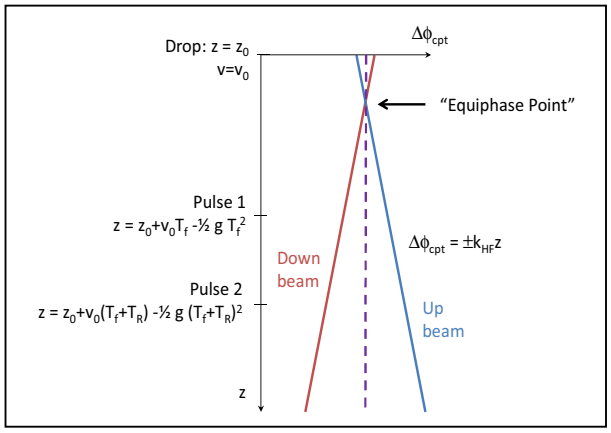

Figure 2. Phase versus height for dark states created by the up and down beams. The average phase for balanced up/down interrogation is shown as the dashed line. The atom position versus time after the drop is marked on the vertical axis. z_0 and v_0 are the atoms' mean initial position with respect to the "equiphase point" and the atoms' initial average velocity. The Doppler shift resulting from measuring the absorption signal on only one of the beams can be found from Eq. 1 and the position of the atoms during the second CPT pulse.

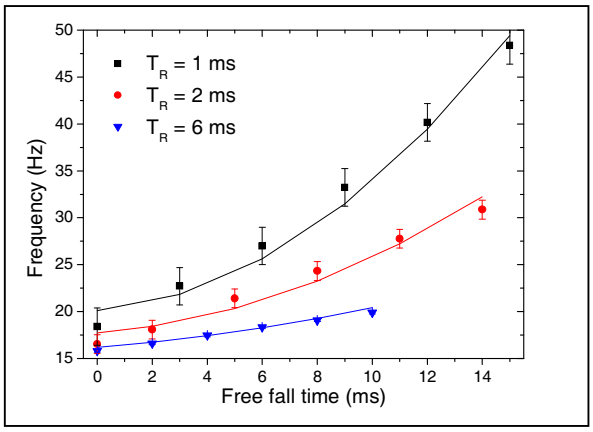

Figure 3. Clock frequency versus extra free-fall period for different Ramsey periods compared to the basic kinematic model for the Doppler shift. Only the signal from the downward beam was used to lock the clock, which maximizes the shift. The offset frequency is the only fit parameter. The three curves are slightly offset from each other because the Zeeman and light shifts were slightly different for the measurements with different Ramsey periods. The full scale (35 Hz) corresponds to a fractional frequency shift of 5×10^{-9}.

For our evaluation of the Doppler shift, independent up and down beams are simultaneously applied to the atoms, and absorption signals are measured for the up and down beams individually. The individual signals are then used to lock the clock to either the up beam signal only, the down beam signal only, or the average of the up and down signals. A variable extra period of free fall, T_f, is also inserted before the first Ramsey pulse to enlarge the shift so that it can be easily compared to a basic model.

Measurements of frequency shift versus free-fall period, Ramsey period, and probe direction show very good agreement with a simple kinematic model for the atoms' average position and velocity. Measurements of frequency shift versus free-fall period are shown in Fig. 3 for three different Ramsey periods when only the down beam signal was used to lock the clock. Detailed results from these studies are presented in a separate publication [15]. When the atoms are probed symmetrically along the direction of gravity, the total shift for the clock's typical Ramsey period of 6 ms is consistent with zero and has a current fractional frequency uncertainty of 1×10^{-11}. The shift magnitude should be more than an order of magnitude smaller when the probe direction is within 5° of a direction perpendicular to gravity.

ACKNOWLEDGMENT

S. Riedl, G. Hoth, R. Scholten and E. Ivanov are gratefully acknowledged for technical help and discussions. This work is funded by NIST and DARPA. NIST is an agency of the U.S. government, and this work is not subject to copyright. The views, opinions, and/or findings contained in this article are those of the authors and should not be interpreted as representing the official views or policies, either expressed or implied, of the Defense Advanced Research Projects Agency or the Department of Defense. (Approved for Public Release, Distribution Unlimited.)

[1] A. V. Taichenachev, V. I. Yudin, V. L. Velichansky, and S. A. Zibrov, "On the unique possibility of significantly increasing the contrast of dark resonances on the D1 line of ^{87}Rb," *JETP Lett.,* vol. 82, pp. 398-403, 2005.

[2] R. H. Dicke, "The effect of collisions upon the Doppler width of spectral lines," *Phys. Rev.,* vol. 89, pp. 472-473, 1953.

[3] G. Vecchi and A. De Marchi, "Spatial phase variations in a TE_{011} microwave cavity for use in a cesium fountain primary frequency standard," *IEEE Trans. Instrum. Meas.,* vol. 42, pp. 434-438, 1993.

[4] J. Guena, *et al.*, "Progress in atomic fountains at LNE-SYRTE," *IEEE Trans. Ultrason., Ferroelectr., Freq. Control,* vol. 59, pp. 391-409, 2012.

[5] P. R. Hemmer, S. Ezekiel, and J. C. C. Leiby, "Stabilization of a microwave oscillator using a resonance Raman transition in a sodium beam," *Opt. Lett.,* vol. 8, pp. 440-442, 1983.

[6] P. R. Hemmer, M. S. Shahriar, V. D. Natoli, and S. Ezekiel, "AC Stark shifts in a two-zone Raman interaction," *J. Opt. Soc. Am. B,* vol. 6, pp. 1519-1528, 1989.

[7] M. Zhu and L. S. Cutler, "Theoretical and experimental study of light shift in a CPT-based Rb vapor cell frequency standard," in *Proc. 2000 PTTI Mtg.*, Reston, VA, 2000, pp. 311-323.

[8] T. Zanon-Willette, E. de Clercq, and E. Arimondo, "Ultrahigh-resolution spectroscopy with atomic or molecular dark resonances: Exact steady-state line shapes and asymptotic profiles in the adiabatic pulsed regime," *Phys. Rev. A,* vol. 84, p. 062502, 2011.

[9] T. Zanon, *et al.*, "Observation of Raman-Ramsey fringes with optical CPT pulses," *IEEE Trans. Instrum. Meas.,* vol. 54, pp. 776-779, 2005.

[10] J. Vanier, "Atomic clocks based on coherent population trapping: a review," *App. Phys. B,* vol. 81, pp. 421-442, 2005.

[11] S. Ezekiel, P. R. Hemmer, and C. C. Leiby, Jr., "Ezekiel, Hemmer, and Leiby respond," *Phys. Rev. Lett.,* vol. 50, pp. 549-549, 1983.

[12] E. A. Donley, F.-X. Esnault, E. Blanshan, and J. Kitching, "A cold-atom clock based on coherent population trapping," in *Proc. 2012 PTTI Mtg.*, Reston, VA, 2012, pp. 327-334.

[13] C. Affolderbach, S. Knappe, R. Wynands, A. V. Taïchenachev, and V. I. Yudin, "Electromagnetically induced transparency and absorption in a standing wave," *Phys. Rev. A,* vol. 65, p. 043810, 2002.

[14] S. V. Kargapoltsev, *et al.*, "High-contrast dark resonance in $\sigma^+ - \sigma^-$ optical field," *Laser Phys. Lett.,* vol. 1, pp. 495-499, 2004.

[15] F.-X. Esnault, *et al.*, "A cold-atom double-lambda CPT clock," *Unpublished,* 2013.

MiniAtom: Realization of an Absolute Compact Atomic Gravimeter

Jean Lautier, Arnaud landragin
SYRTE, Observatoire de Paris
CNRS, UPMC and LNE
61 avenue de l'Observatoire
75014Paris, France
jean.lautier@obspm.fr

Baptiste Battelier, Philippe Bouyer
LP2N, UMR5298 - IOGS - CNRS - Université Bordeaux 1,
Bâtiment A30, 351 cours de la Libération, 33405
TALENCE Cedex

***Abstract*— We present the realization of a highly compact absolute atomic gravimeter. The main purpose is to prove that atomic interferometers can overtake the current limitations of inertial sensors based on "classical" technologies for field and on-board applications. We show that the complexity and the volume of cold-atom experimental set-ups can be drastically reduced while keeping the performances close to the state-of-the-art, enabling such atomic sensors to perform precision measurements outside of the laboratory.**

Atomic interferometry, compact quantum sensor, atomic gravimeter, field gravimetry

I. THE MINIATOM PROJECT

The MiniAtom project is a feasibility study meant to improve concepts and technologies to support the operation of inertial sensors relying on atom interferometry outside of the laboratory. As a prototype we chose to realize an absolute gravimeter to measure the acceleration of the Earth's gravity. It is a collaboration that gathers two laboratories and four companies Iksea, Kloé, Thalès and III-V Lab. The work on the reduction of size concerns the gravimeter head, the laser and electronic system and the filtering of the ground vibrations.

II. SINGLE LASER BEAM ATOMIC GRAVIMETER

A. Atom interferometry to measure accelerations

The measurement of the acceleration of gravity (g) is performed with a Mach-Zender type $\pi/2$ - π - $\pi/2$ interferometer using stimulated Raman transitions to couple $|F=1, mf=0\rangle$ and $|F=2, mf=0\rangle$ hyperfine states of free-falling ^{87}Rb atoms [1]. After the loading of a 3D Magneto-Optical Trap (MOT) and an optical molasses stage, a micro-wave pulse is used to select the internal quantum state $|F=1, mf=0\rangle$. The interferometer is then performed during the free fall of the atoms. The maximum achievable duration is on the order of 100 ms. The readout of the output ports of the interferometer then simply consists in determining the population of the two states. This is carried out by fluorescence measurements and gives access to the interferometer phase shift [2].

In the free-fall referential frame of the atoms, the Raman laser frequencies are linearly Doppler shifted. We apply a frequency chirp to the laser in order to stay at resonance and exactly compensate for the Doppler effect. It is the measurement of the slope of this chirp that results in the determination of g.

B. Sensor head

The use of an innovative hollow pyramid as the usual retro-reflecting mirror of quantum inertial sensors enables to perform all the steps of the atomic measurement (trapping and cooling the atoms, performing the interferometer and reading out its outputs) with only one single laser beam instead of 6 or more usually [3]. We use a magnetically shielded two liter titanium vacuum chamber whose windows are indium sealed. The length of the interferometer (~ 10 cm) and the dimensions of the pyramid (2 cm) scale the size of the sensor head. This design allows for a loading of a few 10^7 atoms in 400 ms and a maximum interrogation time for the interferometer of 100 ms. The reduction of number of optical beams results in a drastic dicrease of the volume of the sensor head which fits in a cylinder 40 cm high and 20 cm in diameter. By comparison the transportable absolute gravimeter developed in SYRTE has a sensor head size of a 80 cm high 50 cm wide cylinder [4].

C. A highly compact laser system

The laser system is based on a single telecom laser diode, frequency doubled to achieve 780 nm for manipulation of the Rb atoms [5]. Low noise phase modulation with EOMs creates sidebands to perform Raman transitions. The laser is stabilized thanks to a saturated absorption set-up. The laser system provides about 180 mW of output optical power with a polarization quality of 4.10^{-3}. The use of off-the-shelf fiber coupled optical telecom components enables a tremendous reduction of the complexity and the size of the laser system down to a 70 cm^3 physics package. In the future even greater integration of this module is envisioned. Most of these components are Telcordia certified, which is of great interest for the reliability needed for a field operation of the apparatus.

Particular efforts have been made to push on the integration of the micro-wave frequency reference chain used to drive both the frequency reference at 6.835 GHz for the Raman transitions and to deliver microwave pulse for the quantum state selection. The Raman output has an agility of 500 MHz and delivers an output power of 25 dBm. The overall size is 14x14x23 cm and with a 30 W electrical power. Our chain features a phase noise that will only limit our relative sensitivity to gravity at the level

of 10^{-7} m.s^{-2}, as seen in Fig 1. We thus reach a trade-off between the integration in a two-litter package and the required phase noise level.

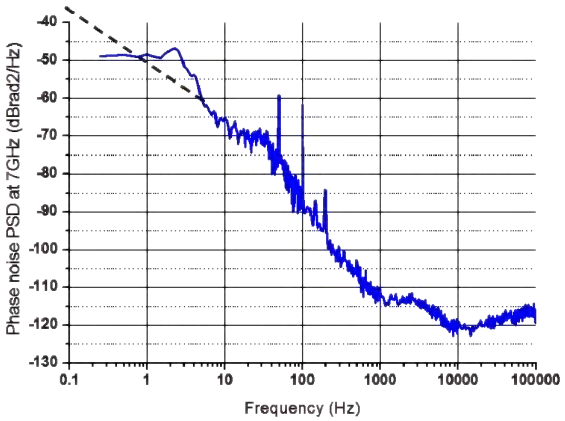

Figure 1. (Blue) Phase noise PSD of the compact frequency chain. (doted black line) Low frequency behaviour of the phase noise PSD measured separetly. The computation of the sensitivity function with this spectrum results in an atomic phase noise of 6 mrad, which corresponds to a limitation of the sensitivity in the 10^{-7} m/s2 level [6].

III. COMPACT QUANTUM SENSOR AND VIBRATIONS

An atomic accelerometer is sensitive to the motion of the referential frame of the laboratory with respect to the referential frame of the atoms. The phase shift at the output of the interferometer is a measurement of the relative acceleration between the atoms and the equiphase planes of the Raman lasers, which are referenced to the retro-reflecting mirror. As a result, any spurious motion of the mirror happening during the interferometer is recorded with the useful signal. In particular, ground vibrations with human or natural origins leads to a great limitation of the relative sensitivity of our measurement at a few 10^{-5} m/s^2 level. Previous works have addressed this issue by the use of active or passive isolation platform [1] or post signal processing [7]. However, these anti-vibration platforms are not convenient for field operation.

Within MiniAtom, we develop a method to perform a real time vibration compensation based on the post-processing signal method and without any platform. In this method, the atomic phase shift due to vibrations is compensated by a estimated phase shift applied on the Raman reference. In such method, one can site on the center of the fringe, where the sensitivity is the best. An auxiliary DC-coupled low noise mechanical accelerometer continuously monitors the motion of the retro-reflecting mirror. At each cycle, a 24-bits Analog-to-Digital Converter (ADC) acquires this signal during the interrogation in a synchronous manner. The sampled values are real-time processed with the sensitivity function of our instrument [7] by an FPGA board and a resulting atomic phase shift is calculated. This value is then sent to the DDS responsible for producing the frequency chirp of the laser line so that the pre-compensating phase jump is effective just before the third pulse closing the interferometer (less than 1 ms). This method enables to greatly improve the sensitivity of our measurement without any anti-vibration platform (see Fig. 2).

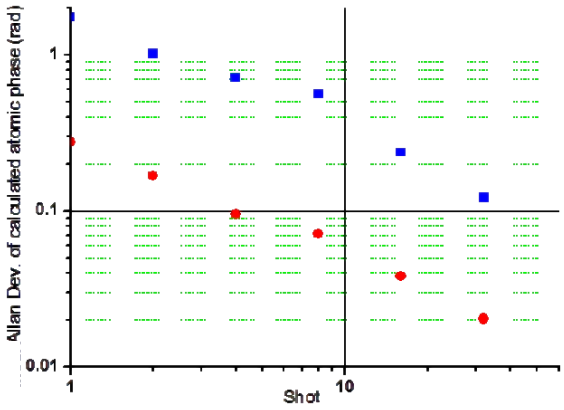

Figure 2. Allan deviation of the atomic phase at the output of the interferometer operating without anti-vibration platform during day-time:
(Blue squares) without real time compensation
(Red dots) with real time correction
Thanks to our method after 15 seconds (30 shots) of integration, the stability goes below the 40 mrad level, which corresponds to a 10^{-6} m/s^2 sensitivity.

IV. CONCLUSION

We target a relative sensitivity to acceleration of gravity below 10^{-7} m/s^2 at one shot in noisy environment like inside a big city [8]. This will allow to monitor time variation of g due to tides and to detect significant mass anomalies and mass displacements. We have shown promising long-term stability with a flicker floor on the 10^{-9} range and up to two day long measurements have been recorded with such architecture [3].

ACKNOWLEDGMENT

We would like to thank Franck Pereira Dos Santos for fruitful discussions and Michel Lours and Laurent Volodimer for the development of the real time vibration compensation module. We also would like to thank the French ANR agency and Région île de France (IFRAF) for funding.

REFERENCES

[1] A. Peters, K. Y. Chung, S. Chu, Metrologia **38**, 25, 2001

[2] C. J. Bordé, "Atomic interferometry with internal state labelling" Physics Letters, A**140**, 10-12, 1989

[3] Q. Bodart et al., "A cold atom pyramidal gravimeter with a single laser beam" APL **96**, 134101, 2010

[4] A. Louchet-Chauvet et al., "The influence of transverse motion within an atomic gravimeter" NJP **13**, 065025, 2011

[5] G. Stern et al., "Light-pulse interferometry in micro-gravity" EPJD **53**, 353-357, 2009

[6] P. Cheinet, et al., "Measurement of the sensitivity function in time-domain atomic interferometer", IEEE Trans. on Instrum. Meas. **57**, 1141, 2008

[7] J. Le Gouët, et al., "Limits in the sensitivity of a compact atomic interferometer", Appl. Phys. B **92**, 133–144, 2008

[8] S. Merlet, et al., "Operating an atom interferometer beyond its linear range", Metrologia 46, 87–94, 2009

An Integrated SAW Sensor with Direct Write Antenna

M.W. Gallagher*, W. C. Smith†, D.C. Malocha*
*Electrical Engineering and Computer Science Department
University of Central Florida
Orlando, FL 32816-2450
†MesoScribe Technologies, Inc.
St. James, New York 11780

***Abstract*—This paper presents a wafer-level integrated SAW sensor that uses conventional thin-film fabrication for the SAW, and the direct write of a thicker dissimilar metal for the antenna. An automated thermal spray process deposits the antenna conductor onto the SAW substrate, providing ease of fabrication, optimal film thickness, superior adhesion, and application specific materials. Results will highlight the direct printing of thick copper traces onto whole $LiNbO_3$ wafers. The design of a 915 MHz meandered dipole antenna with low mismatch loss and maximized radiation efficiency over a 7 % SAW fractional bandwidth is demonstrated. Experimental performance results of antennas fabricated on standard FR4 and on-wafer by the direct write process are contrasted. Temperature sensors are fabricated on YZ-$LiNbO_3$ and their wireless performance is evaluated.**

I. Introduction

For certain SAW sensor applications the challenge is building a wirelessly interrogatable device with the same lifetime as the SAW substrate. The design of these application intensive sensors is complicated by the degradation of device bond wires, adhesive, and antenna substrate. Previous results demonstrated the feasibility of fabricating an antenna directly onto a SAW substrate, but had a limited interrogation range [1]. For the first time, a direct write process is used to deposit the antenna conductor onto the SAW substrate, eliminating external interconnects. This plasma spray process has the advantage of rapid conformal fabrication without the need for a mask, leaves little waste material, and is automated with a high throughput. The combination of SAW and direct write technology offers a multitude of opportunities for new sensor and communication system embodiments.

The purpose of this paper is to demonstrate the effectiveness of the direct write process in fabricating integrated SAW sensors. A process was developed for writing thick-film copper to lithium niobate wafers that exhibits higher yield and superior adhesion, compared to traditional physical deposition methods. This process uses no adhesion layers and can be adapted to different substrates and metals depending on the application. A meander dipole antenna has been designed for use in conjunction with a 915 MHz RFID SAW sensor on YZ-$LiNbO_3$. Experimental performance results will contrast antennas fabricated using the direct write process to those made traditionally on FR4. Results presented will show an increase in range, compared to previous work, through an improved low loss design and the ability to deposit stable thick antenna traces. Proof of concept temperature sensors show comparable loss and bandwidth to traditionally packaged devices.

This work is partially supported by NASA SBIR contract #NNX11CB86C.

II. Direct Write Fabrication Overview

Several techniques are available for the direct write of patterns onto materials, including ink jet, laser assisted, and plasma spray; each process has its own drawbacks and merits. In this paper a proprietary high-definition plasma spray process is used that is being commercialized and developed by Mesoscribe Technologies. The spray system deposits by injecting material in powder form into a plasma flame and directing the molten material toward the substrate [2]. Dynamic collimation technology allows the line width to be controlled and other process parameters, gas flow and power level, control the density and structure of the deposited film.

A strength of the Mesoscribe process is the ability to conform onto non-planar surfaces while maintaining high throughput production for research or commercial products. A variety of materials can be deposited including dielectrics, metals, or sensor alloys. Materials can be stacked for integrated packaging and electrical isolation, eliminating adhesives. Films are robust and high temperature tolerant. Traces

(a) (b)

Fig. 1. (a) The automated 6-axis direct write robot writing material to a part. (b) An example of copper directly written onto a SAW delay line on lithium niobate. The diced SAW device is attached to a printed circuit board by adhesive and connections are made by directly writing copper traces up and onto the thin-film aluminum device.

are typically ≥25 µm in thickness and trace widths are actively controlled at ≥250 µm. The width can also be laser scribed after deposition to a width of 25 µm. Deposition is fully automated and performed by a 6-axis robotic control spray head, as shown in Fig. 1a.

A. Direct Write to SAW Substrate

Using these direct write techniques for SAW sensors, or general microelectronic fabrication, has several unique advantages. Traces are able to write up and over a variety of surfaces and at varying angles; Fig. 1b shows a copper trace written from a circuit board, up the die adhesive, and connecting to a SAW delay line. These films adhere well to substantially thinner dissimilar metals, aluminum in this example. For SAW sensor applications this eliminates bond wires and is a cost effective way to realize high temperature antenna traces and interconnects. The process can also be used to stack traces inside of direct write dielectric layers or inside a trench of the substrate material.

A process has been developed that successfully deposits high quality copper traces onto $LiNbO_3$. Fig. 2a shows an example of a 1 mm wide copper trace written onto a 3 inch diameter wafer. No surface preparation or trenching is required prior to deposition. Copper adheres well without an adhesion layer, passing a simple tape test. The copper is nominally 20 µm thick. Measurement of film thickness by contact profilometer yields an average surface roughness of 2.1 µm, shown in Fig. 2b, which is also evident in the optical image of the copper. These thick copper lines successfully bond to the 80 nm electron beam evaporated aluminum pad. The copper trace has been laser trimmed to provide a taper to the 0.5 mm wide aluminum probe pads of a SAW transducer. Measured sheet resistance is approximately 1.2 mΩ/□. These thick conductors are important in reducing resistive losses of microwave transmission lines because of skin depth effects [3]. A thin conductor, closer to the skin depth, will exhibit higher losses. For the frequency of 915 MHz used throughout this paper, the skin depth is 2.2 µm or 10 % of the total thickness.

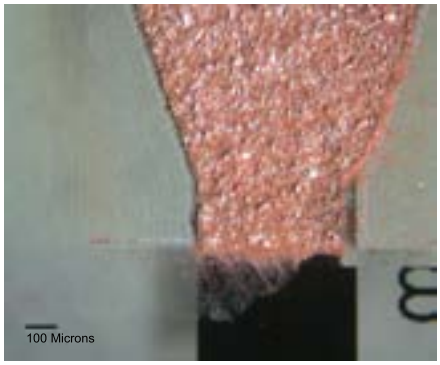

(a)

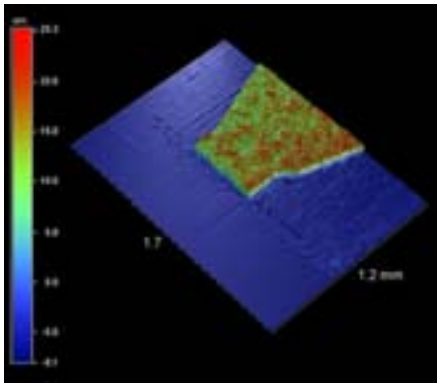

(b)

Fig. 2. (a) Optical image of a 1 mm wide copper trace directly written onto a 3 inch diameter $LiNbO_3$ wafer. The line has been laser trimmed to interface with an 80 nm aluminum probe pad. (b) A surface scan of the Cu/Al junction on $LiNbO_3$ performed by contact profilometer showing the relative surface heights and roughness. Average step height is approximately 20 µm for the copper and 80 nm for the aluminum.

III. Antenna Design

With a process available for depositing copper onto lithium niobate, an antenna design is required that solves the high loss from previous iterations and exploits the stability of the new metallization. The main considerations when designing an antenna for a SAW sensor is matching the transducer bandwidth, which is a function of device coding and expected temperature variation, and being an efficient radiator. A SAW substrate is not ideal for meeting these requirements due to its high relative permittivity and also the uniaxial anisotropy between the crystal axes.

This work used lithium niobate because of the availability of large wafer sizes, high SAW coupling, and previous delay line SAW design experience. There is a 2:1 difference in permittivity between the X or Y ($\epsilon_{11} = 45.6$) and Z ($\epsilon_{33} = 26.3$) cuts [4]. These properties make the use of a patch antenna difficult due to the high permittivity and thin substrate giving a narrow bandwidth and low efficiency. A loop antenna would be a natural choice for its inductive input impedance; however, for a single loop the efficiency is poor. Therefore, for proof-of-concept a dipole was chosen for an antenna embodiment.

Standard YZ-$LiNbO_3$ wafers come in sizes up to 100 mm, which is too small for a half-wave dipole at the target center frequency of 915 MHz. Typically electrically small antennas are narrowband and the radiation resistance is small, making them inefficient. A meander-line dipole was chosen for miniaturization as the radiation efficiency is acceptable for a small antenna [5] . The example antenna used in this paper is shown schematically in Fig. 3. A fixed straight dipole length is initially chosen and the impedance is determined using Ansys HFSS full-wave simulator. Meander sections are then added, effectively adding shunt capacitive elements to the dipole, to detune the large capactive reactance of the antenna. By increasing the height, h/2, and decreasing the width, w, of each meander will the antenna resonant frequency will decrease [6].

Final design optimizations were then carried out using HFSS with the goal of minimizing the mismatch loss at the SAW/Antenna interface. HFSS allows uniaxial dielectric anisotropy to be incorporated into the simulation. Simulated gain for initial antenna designs had a maximum gain of 1 dBi

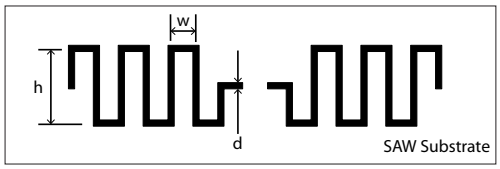

Fig. 3. Schematic representation of the meander line dipole used for this paper.

in a 50 Ω system. In spite of that gain the SAW tag will not be a 50 Ω system and the mismatch loss will need to be determined between the antenna and capacitive transducer impedance. The reflection coefficient at this interface is calculated by

$$\Gamma = \frac{Z_S - Z_A^*}{Z_S + Z_A}, \tag{1}$$

where Z_A is the antenna input impedance given by simulation and Z_S is the input impedance of the SAW found by RF probing. By properly choosing the inductive antenna reactance, the impedance of the antenna at the SAW interface will be purely resistive. Fig. 4 plots the response of the probed SAW transducer of interest and the designed antenna layout onto a Smith chart. The SAW device utilized has a 9 pair transducer, quarter wavelength electrodes, and 100 λ beamwidth. Impedance is adjustable for different transducer configurations and center frequency.

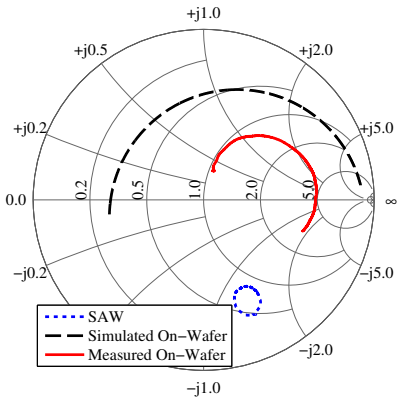

Fig. 4. Impedance Smith chart comparison of the response from an RF probed SAW device, simulated meander dipole antenna, and measured on-wafer antenna.

The calculated mismatch loss of the designed antenna is shown in Fig. 5. The loss at device f_0 is 1.5 dB. Predicted radiation efficiency is 82 %. The final antenna design has a d of 1 mm, h of 11 mm, w of 4 mm, and 10 total bends. The overall length of the antenna is 60 mm, which is short enough to fit 3 antennas onto a 3 inch wafer.

IV. Experimental Results

Several experimental devices were fabricated for testing as integrated sensors and also for experimental verification of the stand-alone antenna. Standard contact photolithography was utilized to define SAW reflective delay line sensors. Minimum

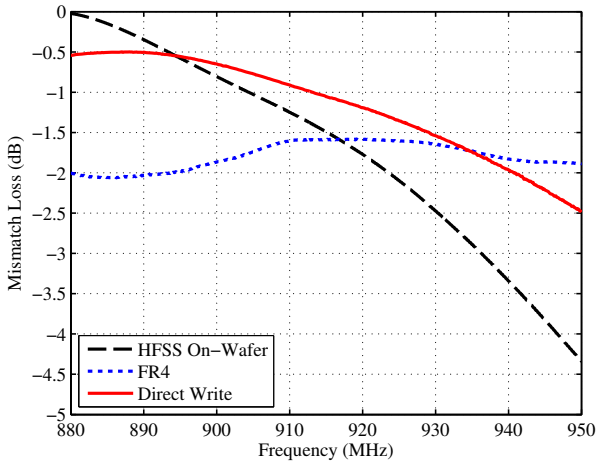

Fig. 5. The predicted and extracted mismatch loss at the SAW/antenna interface found by HFSS simulation and measurement of both a traditionally packaged FR4 device and on-wafer direct write device.

feature size of the SAW device is 0.9 µm, and in order to achieve strong mask contact, fabrication is required prior to antenna deposition. SAW metallization is Ti/Al deposited by electron beam evaporation. A photoresist mask is applied to protect the SAW propagation path from debris generated when depositing and trimming the antenna. Antennas have been written at various thicknesses and levels of corner trimming. However, antennas shown in this paper are only trimmed to taper to the SAW pads and for any over spray on either end, allowing higher throughput. All copper shown is approximately 20 µm in thickness. An example diced SAW/Antenna device is shown in Fig. 6, and compromises the middle third of a 3 inch diameter $LiNbO_3$ wafer.

A. Antenna Characterization

After fabrication, the SAW transducer was removed for stand-alone antenna characterization. Impedance was measured at the input to the antenna, and Fig. 4 shows the results. Measurements obtained follow a similar trend as the simulation.

The measured antenna impedance was used to calculate the mismatch loss at the SAW/Antenna interface. The SAW impedance is determined from RF probed results taken prior to antenna fabrication. Fig. 5 compares the mismatch of the on-wafer antenna to that of a simple dipole fabricated on a traditional FR4 substrate. These results do not consider added

Fig. 6. An example of a 915 MHz SAW sensor and direct write antenna integrated onto a 3 inch diameter, Y-cut lithium niobate wafer.

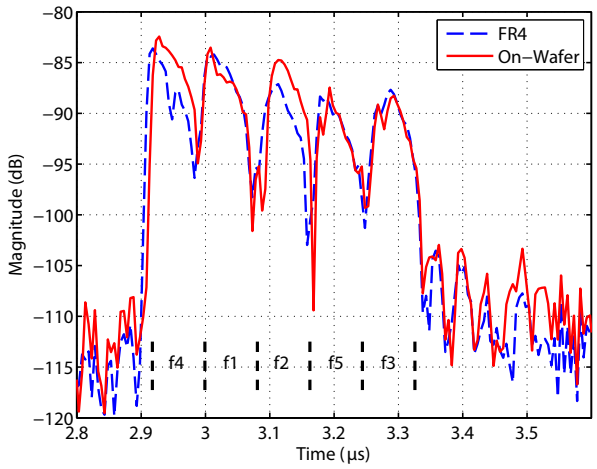

Fig. 7. A time domain comparison of the separate measurement of two SAW sensor configurations, interrogated wirelessly at 20 cm by a vector network analyzer. Each device has approximately 7% fractional bandwidth and the relative center frequencies of each coded reflector is shown.

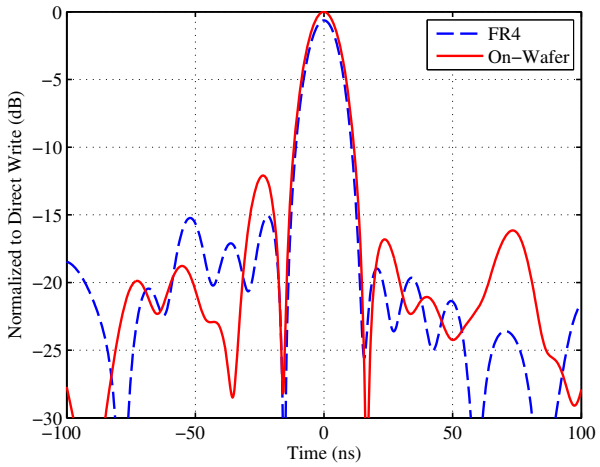

Fig. 8. Matched filter correlation of an integrated on-wafer device and a standard packaged device. Both responses are normalized to the integrated device for comparison. Measurements were taken wirelessly at 20 cm by a vector network analyzer.

parasitics from the device packaging required when mounting to the FR4 antenna.

B. Wireless Sensor Measurements

Fig. 7 compares the wireless measurement of similar wide-band reflective delay line temperature sensors connected to direct write and FR4 antennas. A vector network analyzer was used to wirelessly interrogate each device at a distance of 20 cm. Each device has a coded reflector bank with relative orthogonal reflector frequencies shown. Devices are designed to have 7% fractional bandwidth and a center frequency of 915 MHz [7]. The distributed frequency reflector bank of these devices illustrate the relative bandwidth of each SAW/Antenna combination. Device designs are identical and minimal SAW fabrication differences are assumed. Loss is comparable between the FR4 and integrated devices throughout the band of interest.

An ideal matched filter was generated for the two measured devices. Fig. 8 compares the relative correlation of the matched filter to the data obtained wirelessly at 20 cm. As expected the width of the two correlation peaks are the same. There is a 0.5 dB decrease in correlation amplitude between the FR4 and direct write because of decreased returned SAW signal level because of fabrication differences. Compared to previous published results in [1] loss has decreased approximately 25 dB. These results highlight the ability of the on-wafer antenna to operate in a coded multi-sensor environment without added attenuation.

V. Conclusion

This paper demonstrated a novel SAW sensor structure that integrated a traditional thin-film SAW device and a direct write antenna onto a SAW substrate. For example devices, copper was used for the antenna conductor and lithium niobate for the substrate. A process has been developed that produced reliable, stress free thick film traces that adhere well to the SAW substrate. A meander dipole antenna was designed for use in conjunction with a 915 MHz SAW sensor. Results shown highlight the low antenna loss and also compare well to results from a traditionally packaged and interrogated device. The Mesoscribe direct write process presented is adaptable to different substrates, conductors, and implementations. Direct write technology has many SAW sensor applications, such as high temperature antenna integration and package free strain sensors.

Acknowledgment

The authors wish to thank NASA for continued support, and especially William Cy Wilson of the Langley Research Center.

References

[1] M. Gallagher, B. Santos, and D. Malocha, "Wireless wideband SAW sensor - antenna design," in *IEEE Int. Frequency Control Symp.*, 2010, pp. 291–296.

[2] J. Gutleber, J. Brogan, R. Gambino, C. Gouldstone, R. Greenlaw, S. Sampath, J. Longtin, and D. Zhu, "Embedded temperature and heat flux sensors for advanced health monitoring of turbine engine components," in *IEEE Aerospace Conference*, 2006.

[3] D. M. Pozar, *Microwave Engineering*, 3rd ed. Wiley, 2005.

[4] G. Kovacs, M. Anhorn, H. Engan, G. Visintini, and C. Ruppel, "Improved material constants for $LiNbO_3$ and $LiTaO_3$," in *IEEE Ultrasonics Symp.*, 1990, pp. 435–438 vol.1.

[5] T. Endo, Y. Sunahara, S. Satoh, and T. Katagi, "Resonant frequency and radiation efficiency of meander line antennas," *Electron. Comm. Jpn. Pt. II*, vol. 83, no. 1, pp. 52–58, 2000.

[6] O. Olaode, W. Palmer, and W. Joines, "Characterization of meander dipole antennas with a geometry-based, frequency-independent lumped element model," *IEEE Antennas and Wireless Propagation Letters*, vol. 11, pp. 346–349, 2012.

[7] M. Gallagher and D. Malocha, "Mixed orthogonal frequency coded SAW RFID tags," *IEEE Trans. on Ultrasonics, Ferroelectrics, and Frequency Control*, vol. 60, no. 3, pp. 596–602, 2013.

Ultra-Wide-Band SAW Sensors and Tags

Marc Lamothe*, Victor Plessky†, Thomas Ostertag‡, Jean-Michel Friedt§ and Sylvain Ballandras
*FEMTO-ST/Time & Frequency, CNRS UMR 6174 - Besançon, France - Email: marc.lamothe@femto-st.fr
†GVR Trade S.A. - Chez-Le-Bart, Switzerland - Email: victor.plessky@gmail.com
‡RSSI GmbH - Geretsried / Gelting, Germany - Email: thomas.ostertag@rssi.de
§SENSeOR SAS, c/o FEMTO-ST/Time & Frequency - Besançon, France - Email: jmfriedt@femto-st.fr
frec'n'sys SASU - Besançon, France - Email: sylvain.ballandras@frecnsys.fr

***Abstract*—SAW tags and sensors often operate in 2.45 GHz ISM band using relatively narrow frequency Band = 82.5 MHz available there. The characteristics of these devices can be improved using the ultra wide band (UWB) technology. We have developed prototype devices operating in 200 MHz-400 MHz and 2000 MHz - 2500 MHz UWB frequency ranges. The UWB reader operating in continuous wave radar mode for 2 GHz range was developed and manufactured. The first remote measurements have shown that we get compressed RF pulses of about 2 ns duration, which include unique RF filing of a few sinusoids with amplitude modulation. The precise measurement of the pulse position is possible by correlation methods, avoiding the phase ambiguity problem.The temperature is measured with a precisions of about $0.1\,^{\circ}\mathrm{C}$ degree Celsius. Only 2 reflectors are necessary for such a sensor. The correlation method works even in multi-path environment with strong reflections form metal objects. The short compressed pulses allow measuring a number of sensors simultaneously just separating them in time. For tag application, we measure and identify three different tags at the same time without collision problem, this number can easily be increased. For such limited number of tags there is no "collision" problem.**

I. Introduction

Surface Acoustic Wave (SAW) tags operate on the basis of converting incoming electromagnetic energy into an acoustic propagating wave through piezoelectric effect. As such, they act as truly passive sensors since the acoustic velocity is dependent on the physical environment of the tag. Furthermore, they can be remotely interrogated over large distances ranging up to 10 m thanks to an interrogation reader operating through principles similar to RADAR, radiating less than 100 mW in order to comply with radiofrequency emission regulations [1].

Most sensing applications require that a single reader probes the response of multiple sensors with identification capability. The classical issue of collision lies in the multiple responses recovered simultaneously by the reader as a single interrogation pulse has been emitted [2]: various multiplexing strategies have been implemented including time domain multiplexing (TDMA [3]), spatial domain multiplexing (SDMA [2]), and even spatially separated tags [4]. and frequency domain multiplexing (FDMA [5]). SAW delay lines being intrinsically wideband devices, only the $B = 82.5\ MHz$-wide 2.45 GHz unregulated Industrial, Scientific and Medical (ISM) complies with the required bandwidth. Because of the rather high acoustic propagation loss in this frequency range, about 6 $dB/\mu s$, the possible code signal duration is limited to $T < 3\mu s$. Although the theoretical informative capacity, proportional to $B \cdot T$, is 200 bits, recent practical implementations use 30 bit [6]and the measured devices with 64 Data Bits, and 16 Bit Error Detection were demonstrated [7]. The collision problem is not addressed in these considerations and only allow for a fraction of this information capacity to be used by any single sensor at a given time. An alternative approach consists in using the Ultra-Wide-Band (UWB) strategy [8] is well suitable for SAW-tags and sensor applications [9]. The extended frequency band, ranging up to $B = 500$ MHz around 2.25 GHz, yields significantly increased informative capacity, provinding the entropy needed to prevent collision and allow for tag identification. It will be experimentally shown in this paper that thanks to short compressed signals, $1/B \simeq 2\ ns$, hence including only a few RF signal periods, the phase ambiguity is avoided [10], allowing for precise measuring delay between 2 pulses. The narrow compressed pulse is compatible with an increased number of sensors operating simultaneously, and measurements in an environment with strong reflections and multipath propagation.

II. Low frequency prototype

Due to techological constraints, initial sensor developments were performed in order to operate in the lower frequency range 200 MHz-400 MHz [6] and are discussed here to demonstrate basic principles of UWB readout. A single crystal (YXl)/128° $LiNbO_3$ substrate is patterned with Interdigitated Transducer (IDT) AlCu electrodes along a geometry allowing for Linear Frequency Modulated (LFM) chirp generation (Fig. 1). A bandwidth B close to 200MHz is covered during a dispersive delay $T = 0.5\ \mu$s with a negative rate of the frequency change in order to prevent high frequencies from being scattered by electrodes generating the low frequency signal and bulk wave conversion.

The selected interrogation scheme is based on recording the frequency dependent reflection coefficient S_{11} with a network analyzer. Digital signal post-processing involves multiplying the frequency domain response with the spectrum of the emitted pulse, matched to the electrode pattern, in order to perform pulse-compression. Then, an inverse Fourier transform yields

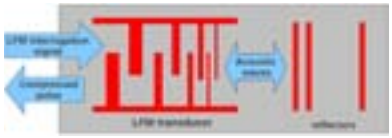

Fig. 1. Sensor layout including a chirped IDT and 3 reflectors.

the time domain response of the resulting dataset, followed by an auto-correlation in order to extract the time duration between successive echoes. In this case the reflected pulses are compressed (Fig. 2) to a duration of about $1/B \simeq 5$ ns associated with a pulse amplitude increase of $B \cdot T = 20$ dB.

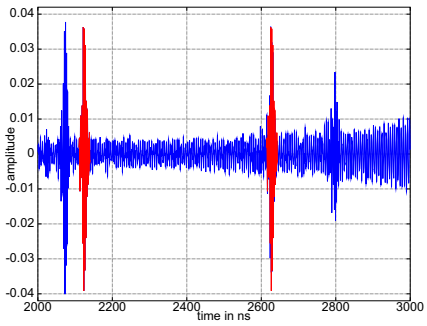

Fig. 2. Compressed responses.

Signal coding by the tag as a chirped returned response provides efficient means of getting rid of enviornmental clutter. The pulse compression gain of 20 dB only affects the signal returned from the sensor and not from reflections on passive reflectors, hence reducing the 1 μs delay usually included in the beginning of the interrogation to allow for clutter to fade out. This signal to noise ratio gain is significant since averaging does not allow to get rid of the passive reflector echoes which are recorded coherently with the emitted pulse in addition to the sensor response.

III. Correlation Measurement of Delays

UWB tags are characterized by the short duration of compressed pulses. As opposed to ISM band SAW-tags with $B = 80$ MHz whose interrogation pulse is at least 30 RF period long, the compressed pulse under investigation here only includes a few oscillations (Fig. 3). All echoes exhibit similar shapes and are well suited for a cross-correlation delay measurement [9], while we observe the lack of phase ambiguity thanks to the few periods included in the compressed pulses.

IV. Temperature Sensor

Acoustic velocity and hence delays between reflections are changed with temperature. The above described low frequency device with reflective delay line has been used for wired temperature measurements. The described signal processing schemes is applied to a sensor located in a temperature controlled oven and cycled from -5°C to +130°C (Fig. 4).

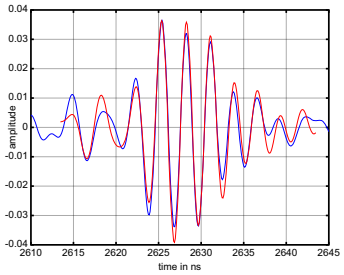

Fig. 3. 2^{nd} (red) and 3^{rd} (blue) pulses from Fig. 2 superimposed.

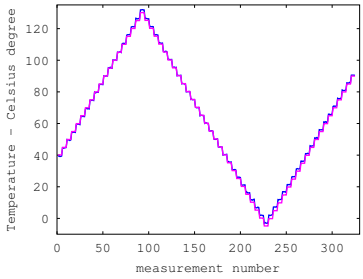

Fig. 4. Temperature calibration: SAW sensor (blue) and Pt100 reference temperature probe (red).

The temperature measurement resolution is estimated $< 0.3\,°C$ by comparing records with a reference Pt100 probe. Hysteresis behaviour attributed to the hard glue used for bond the SAW chip into a ceramic package is also observed.

V. 2.0 GHz - 2.5 GHz Devices

The 2.0 to 2.5 GHz frequency range is attractive for two main reasons: the band is low enough to allow for SAW devices to be mass-produced using optical lithography, and recently introduced US standards allow for increased emission power by the reader associated with increased interrogation range. Therefore, SAW sensors operating in this range were developed and manufactured as discussed here. One such device includes an original design scheme in which 6 transducers with 100 MHz passband are electrically connected in parallel are patterned allong different tracks (Fig. 5).

Fig. 5. Layout of the parallel track architecture.

Such a design was selected since reflectors are adapted to each sub- channel frequency and designed to strongly reflect the acoustic wave, hence providing low losses with a gain of up to 20 dB with respect to the LFM geometry. Simulation of the interrogation strategy is performed by probing (convolution) the sensor with a time-reversed version of its impulse response. The generated compressed signal is about

2 ns long and -11 dB losses are observed by comparing the amplitude of the compressed peak with the amplitude of the interrogation signal. However, strong sidelobes (Fig. 6) around the compressed pulse are a significant hindrance for practical use as they might be misidentified with weaker responses of other devices.

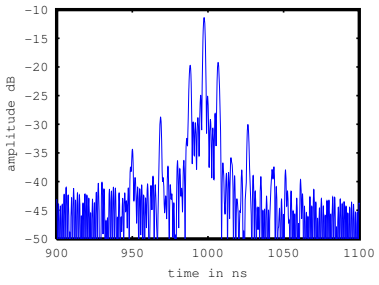

Fig. 6. Compressed pulse - 6 track device interrogated with matched signal

Chirped sensors including LFM transducer have been designed (center frequency 2250 MHz, $B = 500$ MHz, $T = 0.1$ μs). For such devices the efficient number of finger pairs synchronously operating at each given frequency is about $f_c \cdot T/\sqrt{(B \cdot T)} \simeq 32$ is too big for 128 ° $LiNbO_3$ substrate. As a result the waves are very intensively generated at the end of the structure and the generated signal exhibits strongly non-uniform amplitude. Furthermore, its phase deviates too much from the ideal quadratic dependence on time. To reduce these effects, additional electrodes with weighted aperture were added at the beginning and at the end of the chirp transducer (Fig. 7). The transducer is used in both directions, which helps to balance the level between the differents echoes.

Fig. 7. LFM weighted operating in both directions.

Although the response is not uniform, considering SAW-tag as a filter and simulating its interrogation by recording each packaged device transfer function and probing it using ideally matched signal (the time reversed impulse response, but with normalized unit amplitude) we observed compressed pulses with durations of about 2 ns.

Such procedures simulate a wireless reader operation and gives accurate loss levels in compressed pulses with respect to unit amplitude of the interrogation signal at the input of the tag.

VI. Wireless reader

We have used a newly developed interrogation device ("reader") which operates as following the principles of a frequency stepped continuous wave (FSCW) RADAR. For measuring reflected signals at each frequency step, the reader sends a fixed frequency signal during 7 μs.

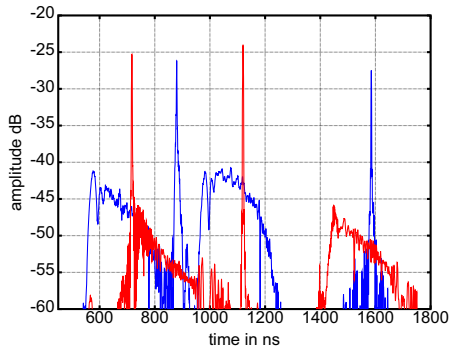

Fig. 8. Compressed pulses for LFM tag, blue curve for transducer operating for low to high frequencies, in red the same transducer in the opposite direction

UWB measuring systems are allowed to radiate power of -41.3 dBm/MHz [8], or about 0.07 μW/MHz, but measured within 1 ms averaging durations. If we measure 1 frequency point every 1 ms, the allowed instantaneous power of the interrogation signal is about $1000/7$ times higher, that is 10 μW or -20 dBm. Datasets provided by the reader are similar to the reflection coefficient S_{11} recorded by a network analyzer but compatible with a wireless readout scheme thanks to the switched emission/reception sequence.

VII. Remote measurements of the UWB sensors

Fig. 9 illustrates the simultaneous wireless measurement of 3 sensors designed along patterns similar to those shown in Fig. 7, with all reflectors on the same side of the transducer.

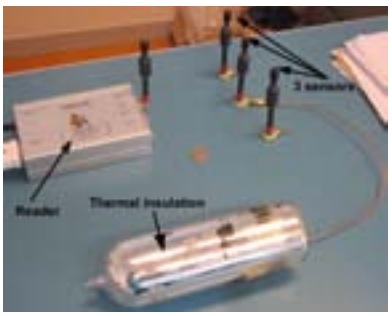

Fig. 9. Remote reading of 3 sensors: one sensor is shielded from room temperature fluctuations in a Dewar bottle.

These 3 acoustic tags are used as sensors for monitoring ambient temperature (Fig. 9). Anticollision is achieved by time multiplexing since all 3 echoes from the 3 sensors are time shifted (Fig. 10).

The temperature is extracted from the delay variations between echoes 1 and 2. No special calibration procedure was applied: the reference temperature point was taken from calibration measurements and assuming a linear delay variation with temperature, using the tabulated CTF_1 coefficient of (YXl)/128 ° $LiNbO_3$ (Fig. 11). The resulting temperature resolution is better than 0.1 ° C, while bias is attributed to the basic processing scheme which does not involve CTF_2.

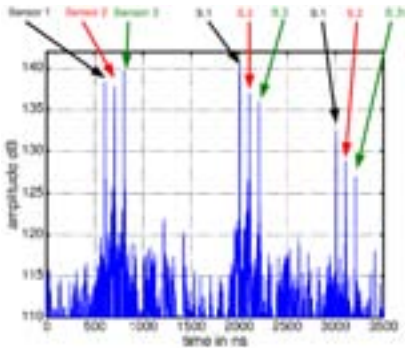

Fig. 10. Remote reading of 3 sensors

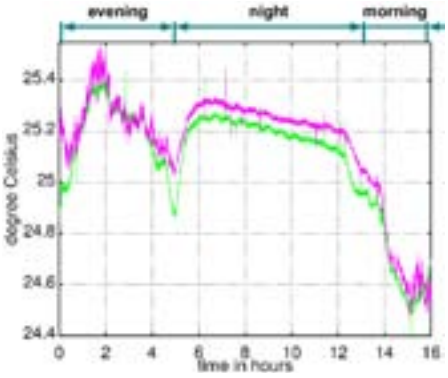

Fig. 11. 16-hour long remote reading of 3 sensors along the setup shown in Fig. 10.

The wireless interrogation range in a free space environment ranges from 1 m for the LFM chirped sensors to 3 m for the parallel track design.

The presence of reflections, possibly stronger than the SAW echoes, typical in industrial applications of SAW tags and sensors, complicates the operation of SAW-tag and SAW-sensor systems. Furthermore, due to multipath propagation, the sensor antenna receives multiple copies of the interrogation signal with different delays. The sensor, being a linear device, processes all of them and the signals returning by different paths to the reader antenna are further spread in time. As a result, instead of one compressed signal of duration $1/B$, a mixture of interfering signals of much longer duration is recorded.

Using the processing techniques discussed above, simultaneous remote temperature measurement of 3 sensors located in a closed oven was performed in the 0 °C to 40 °C range (Fig. 12).

VIII. Conclusion

The main advantage of using the UWB signals for SAW-tags-sensors is the available wide frequency band resulting in a possibility to use very short pulses either directly, or, preferably, after corresponding signal processing procedure. The large informative capacitance $B \cdot T$ can be partly used directly in SAW-tag/sensor and the processing gain of the order of 20 dB can be obtained. The time delay between

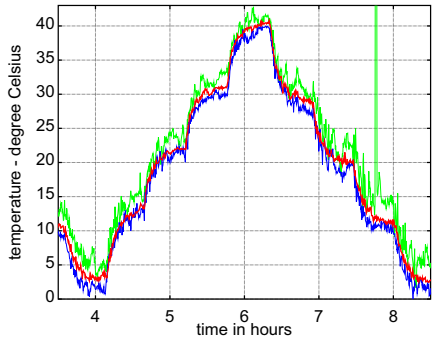

Fig. 12. Temperature recorded from 3 sensors located simultaneously in a closed oven.

the compressed pulses is measured by correlation methods, with the same precision as given by phase measurements, providing a temperature measurement resolution of 0.1 °C. The wideband signals allow measuring responses in strongly reflecting environment, such as inside a metal box.

The perspectives of using UWB technology in truly passive SAW-tag/sensors has been demonstrated, with a proposed solution to anticollision by a time domain multiplexing approach applied to 3 sensors.

Acknowledgment

Funding was provided by the French Agence Nationale de la Recherche (ANR), through the "Chaîre d'Excellence" SAWTAG project. The MIMENTO technological facility of FEMTO-ST, part of the RENATECH network, provided clean-room and packaging capabilities.

References

[1] V. Plessky and L. Reindl, "Review on saw rfid tags," *Ultrasonics, Ferroelectrics and Frequency Control, IEEE Transactions on*, vol. 57, no. 3, pp. 654–668, 2010.

[2] C. Hartmann, P. Hartmann, P. Brown, J. Bellamy, L. Claiborne, and W. Bonner, "Anti-collision methods for global saw rfid tag systems," in *Ultrasonics Symposium, 2004 IEEE*, vol. 2. IEEE, 2004, pp. 805–808.

[3] V. P. PLESSKY and S. N. KONDRATYEV, "Mobile transponder remote identification process," May 18 1996, wO Patent 1,996,014,589.

[4] A. Stelzer, S. Scheiblhofer, S. Schuster, and M. Brandl, "Multi reader/multi-tag saw rfid systems combining tagging, sensing, and ranging for industrial applications," in *Frequency Control Symposium, 2008 IEEE International*. IEEE, 2008, pp. 263–272.

[5] D. R. Gallagher, D. C. Malocha, D. Puccio, and N. Saldanha, "Orthogonal frequency coded filters for use in ultra-wideband communication systems," *Ultrasonics, Ferroelectrics and Frequency Control, IEEE Transactions on*, vol. 55, no. 3, pp. 696–703, 2008.

[6] V. Plessky, T. Ostertag, V. Kalinin, and B. Lyulin, "Saw-tag system with an increased reading range," in *Ultrasonics Symposium (IUS), 2010 IEEE*. IEEE, 2010, pp. 531–534.

[7] C. Hartmann, P. Brown, and J. Bellamy, "Design of global saw rfid tag devices," in *Proc. Second Int. Symp. on Acoustic Wave Devices for Future Mobile Commun. Syst., Chinba*, 2004, pp. 15–19.

[8] S. Harma, V. P. Plessky, and X. Li, "Feasibility of ultra-wideband saw tags," in *Ultrasonics Symposium, 2008. IUS 2008. IEEE*. IEEE, 2008, pp. 1944–1947.

[9] M. Lamothe and V. Plessky, "Temperature measurements with ultra-wideband saw sensors," 2012.

[10] L. Reindl, C. C. Ruppel, S. Berek, U. Knauer, M. Vossiek, P. Heide, and L. Oréans, "Design, fabrication, and application of precise saw delay lines used in an fmcw radar system," *Microwave Theory and Techniques, IEEE Transactions on*, vol. 49, no. 4, pp. 787–794, 2001.

A Wireless Electric Field Sensor Based on a Langasite Resonator

Tinghui Fan[a] and Haifeng Zhang[b]
[a]Department of Electrical Engineering, University of North Texas, Denton, TX, 76207
[b]Department of Engineering Technology, University of North Texas, Denton, TX, 76207

***Abstract*- Electric field measurement is not only important for the lift-off of guided missiles, rockets or spacecraft, but is also widely used for safety in urban environments (preventing pollution), super clean labs, oil refineries, bunker stations, explosive plants, wallpaper factories, mining, and in forest fire prevention Various electric field sensors have been developed to monitor electric field intensity on the ground or in the air, to implement effective survey and analysis, to provide reliable methods and basis for meteorological support, and to avoid the destructive effect of a high electric field. This article presents a wireless field sensor system based on a langasite resonator. By using frequency conversion techniques, the system converts the ultrasonic signal of the sensor to a microwave signal, so that it can transmit the signal wirelessly without digitization. The sensor uses passive components which modulate and transmit the full wave form of the ultrasound signal. A high voltage circuit is constructed in order to measure the frequency shifts of the langasite resonator caused by the applied high voltage. A doubly-rotated plano-plano *langasite resonator (YXlw)θ/Φ 45°/85°operating on* its third overtone (6.304844 MHz) was used as the sensor core in the test of wireless transmission system. A network analyzer was used to test wireless system data and compare it with similar wired system data. The comparison shows a good agreement This system has many potential applications and can also be transformed to other types of sensors.**

I. INTRODUCTION

Electric field measurement is critical in many areas of scientific research and engineering technology, especially in electric power systems. Measurements may be performed using an in-situ electric field sensor in the high voltage power system. In the past, many types of electric field sensors have been proposed. Li designed multi-channel fringing electric field sensors for imaging [1]. Vasa has developed an electric field sensor based on the second harmonic generation with electro-optic materials [2]. Roncin proposed an electric field sensor using electrostatic force deflection of a micro-spring supported membrane [3]. Kaplan performed a theoretical analysis for a low-cost DC electric field sensor [4]. Passard used Pockels effect to design and optimize a Low-Frequency electric field Sensor [5]. Bahreyni has analyzed and designed an electric-field sensor that is micromachined [6]. Moreover, Lee integrated an electric field sensor by combining a segmented modulator electrode and a reflective type $LiNbO_3$ Mach-Zehnder modulator [7]. Electric field measurement provides reliable methods and a basis for meteorological support , mitigation of the destructive effect of a high field, and lift-off of spacecraft [8-11].

Langasite is a promising kind of new piezoelectric material combining many advantages of quartz, barium titanate and lithium niobate in having high electromechanical coupling and good frequency-temperature characteristics. In this paper, we use a langasite bulk acoustic wave resonator to make an electric field sensor. A frequency conversion technique which is similar to a recent work [12] is used to convert the ultrasonic signal to a microwave signal so that the signal can be transmitted wirelessly. The sensor uses passive components which modulate and transmit the full waveform to transmit the ultrasound signal. In order to test the sensor's performance, a high voltage circuit is constructed to isolate the destructive effect of a high electrical field. A doubly rotated plano-plano langasite resonator (YXlw)θ/Φ 45°/85°operating on its third overtone (6.304844 MHz) was used as the sensor core in testing the wireless transmission system. A Bode 100 network analyzer was used to test wireless system data and compare it with similar wired system data. The wired and wireless test results both exhibit a good agreement. Many aspects of possible applications and other types of sensors can be achieved by using the wireless langasite resonator electric field sensing system.

II. PRINCIPLE OF OPERATION

A. Electroelastic Effect

The fundamental mechanism for the langasite electric field sensor is based on the electroelastic effect for resonators with circular shape. The electroelastic effect is defined as $\frac{df}{f \cdot E}$, where df is the frequency shift, f is the resonant frequency, and E is the applied DC electric field. A measurement of this effect for several doubly rotated langasite resonators can be found in [13].

B. Design of the langasite Resonator

978-1-4799-0342-9/13/$31.00 ©2013 IEEE

The core of the force sensor is a doubly rotated langasite resonator with gold keyhole electrodes. Table I lists the design parameters for this resonator.

Table I. Design parameters of the langasite resonator.

Cut angle	Diameter (mm)	Thickness (mm)	Fundamental frequency (Hz)	Configuration
YXlw θ/Φ 45°/85°	13.00±0.075	0.65±0.075	2101554±6	Plano-plano

C. The sensing system

Figure 1 shows a diagram of the sensing system. The langasite resonator is clamped in a standard HC-50 resonator holder. A Gamma ES20P-5w high voltage power supply is used to apply the high DC voltage (0-2.5kV) to the resonator. To avoid having the HF oscillations short-circuited by the power supply, a 3.3 MΩ resistor is connected between the sample and the high voltage DC source. Additional resistors are placed to provide a controlled path to ground in the event of a high-voltage DC discharge. A 0.001 μF blocking capacitor is connected between the sample and the network analyzer to isolate the high voltage supply from the frequency measurement system. The electronic circuit and the resonator sample are placed in a plastic electronics enclosure, and the enclosure is covered by a thick insulating glass layer. A Bode 100 network analyzer is used to transmit the excitation signal through a wire and to the langasite resonator and receive the signal from the langasite resonator wirelessly. The wireless transmission system is described in detail in [14].

III. EXPERIMENTAL MEASUREMENT

A. Measurement Procedure

The frequency sweep is generated by using the Bode 100 Network Analyzer whose experimental settings are the same to maintain comparable data in every experimental measurement. The antennas of SDS are mounted to make the receiver transmitter pairs lined up with identical orientations. The distance between the two antennas is 1.98 M. The start and stop frequencies are set to 6.300000 MHz and 6.310000 MHz with a center frequency of 6.305000 MHz and a span of 10 KHz. The sweep mode is set to linear with 1601 data points. The output signal level is set to 13.00 dBm. The attenuator is set to 20 dB for CH1 and 30 dB for CH2 with a receiver bandwidth of 30 Hz. The reference resistance is set to 50.00 Ω. The Gamma ES20P-5w high voltage supply is set from 0 to 1000 V in 100 V increments. The Bode 100 Network Analyzer begins to take measurements once the high voltage device starts to apply the voltage load. The frequency spectrum at each voltage step is recorded and the resonance frequencies are measured. Both wireless and wired transmission tests are performed and compared.

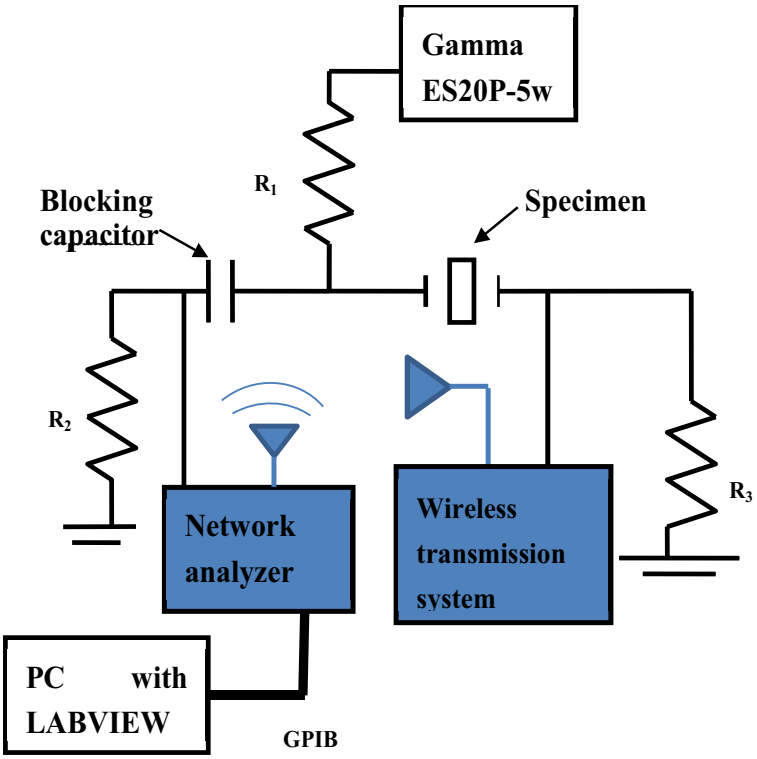

Fig. 1. Schematic diagram of the sensing system. The resistor R_1 is used to prevent an RF short-circuit across the resonator, while resistors R_2 and R_3 act to limit any damage in the event of a high-volatge DC discharge. The blocking capacitor is used to block the DC voltage applied to the specimen from the network analyzer used for the frequency measurements. The network analyzer is used to excite the langasite resonator through a wire and receive the signal from the langasite resonator wirelessly.

B.Experiment Result

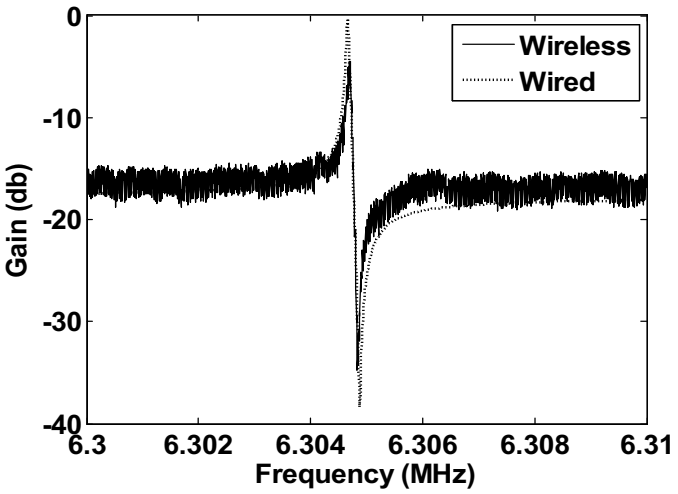

Fig. 2. A comparison between the wired and wireless frequency spectrum at zero voltage.

A comparison between the wired and wireless frequency spectra of the resonator at zero voltage is shown in Figure 2. Figs. 3-4 show the results of voltage-frequency relation. The compared data shows that the frequency spectrum is in good agreement and relationship between a voltage and the resonant frequency is linear as expected. We also found that there is a constant frequency offset of 20~40 Hz in resonant frequencies between wired and wireless data which is most likely arising from electrical loading effects on the crystal by the circuits. This frequency offset can easily be corrected for by a simple calibration, as the data is simply offset by a constant frequency. It is shown in Table II that the sensitivity (frequency vs. voltage slope) for wired and wireless operation is in good agreement.

IV. CONCLUSION

A prototype wireless langasite BAW electric field/voltage sensor was demonstrated experimentally using frequency conversion techniques. Good agreement between wired and wireless measurements can be achieved using a simple frequency offset calibration. The wireless transmission of a signal used in the experiment has the potential to be used in many other applications as well. Future work will be focused on making the system completely wireless and minimizing the components size.

Table II. Sensitivity of the sensor (Wired and wireless).

	SENSITIVITY
WIRED (HZ/N)	1.077
WIRELESS (HZ/N)	1.095
DIFFERENCE (%)	1.6

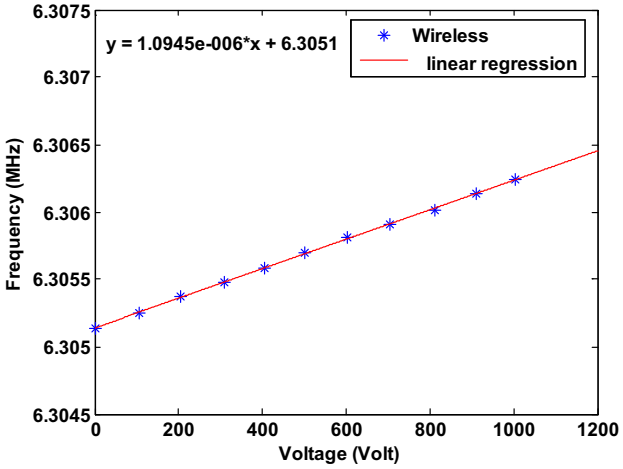

Fig. 3. Voltage-frequency relation for wireless data.

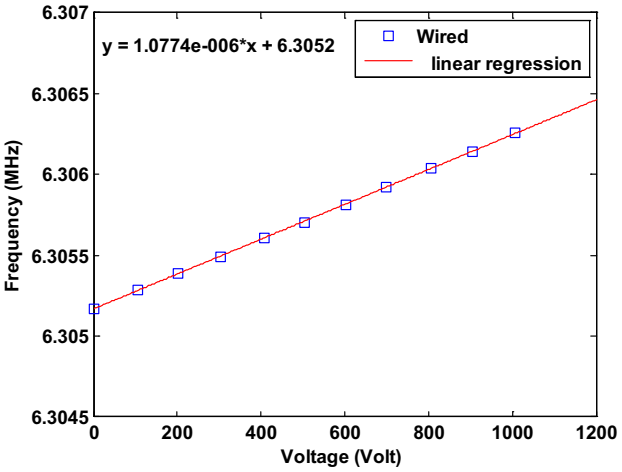

Fig. 4. Voltage-frequency relation for wired data.

REFERENCES

[1] X. B. Li, S. D. Larson, A. S. Zyuzin, and A. V. Mamishev, "Design of Multi-channel Fringing Electric Field Sensors for Imaging -- Part I: General Design Principles," in *IEEE ISEI Conference,* Indianapolis, IN, 2004.

[2] N.J. Vasa, Y. Kawata, R. Tanaka, S. Yokoyama, "Development of an electric field sensor based on second harmonic generation with electro-optic materials," *J. Mater. Process. Technol.,*. vol. 185, no. 1, pp. 173-178, 2007.

[3] A. Roncin, C. Shafai, D. R. Swatek, "Electric field sensor using electrostatic force deflection of a micro-spring supported membrane," *Sens. Actuators, A, Physical.* vol. 123, pp. 179-185, 2005.

[4] B. Z. Kaplan, V. Boroda, U. Suissa, "Low-cost DC electric field sensor," *Sens. Actuators, A. Physical,* vol. 134, no. 2, pp. 396-399, 2007.

[5] M. Passard, C. Barthod, M. Fortin, C. Galez, J. Bouillot, "Design and optimization of a low-frequency electric field sensor using pockels effect*," IEEE Trans. Instrum. Meas,* vol. 50, no. 5, pp. 1053-1059, 2001.

[6] B. Bahreyni, G. Wijeweera, C. Shafai, A. Rajapakse, "Analysis and design of a micromachined electric-field sensor," *J. Microelectromech. Syst.,* vol. 17, no. 1, pp. 31-37, 2008.

[7] H. Y. Lee, T. H. Lee, W. T. Shay, C. T. Lee, "Reflective type segmented electrooptical electric field sensor," *Sens. Actuators, A. Physical,* vol. 148, no. 2, pp. 355-359, 2008.

[8] C. S. Li and C. Xiang, "Summary of optical electric field sensor," *Electrotechnical Application,* vol. 27, no. 16, pp. 8-13, 2008.
[9] A Ferrero, "Measuring electric power quality Problems and perspectives," *Measurement,* vol. 41, pp. 121-129, 2008.
[10] X. Zhang, Q. Bai, S. Xia, "A tiny three-dimensional electric field sensor,"*Chinese J. of Sci. Instrum.,* vol. 27, no. 11, pp. 1433-1436, 2006.
[11] Y. Xu, Z. Fang, T. T. Chen, "Development of parallel plate structure three-dimensonal pulsed electric field sensor," *High Voltage Engineering,* vol. 34, no. 3, pp. 471-475, 2008.
[12] H. Huang, D. Paramo and S. Deshmukh, "Unpowered wireless transmission of ultrasound signals," *Smart Mater. Struct*., vo. 20, pp. 1-7, 2011.
[13] H. F. Zhang, J. A. Turner, J. S. Yang, J. A. Kosinski, and B. Y. Ye, "Experimental measurement of the electroelastic effect in thickness-mode langasite resonators, "*IEEE Trans. Ultrason. Ferroelectr. Freq. Control.* vol. 54, no. 10, pp. 2120-2128, 2007.
[14] H. F. Zhang, Benjamin D. Montz, Tinghui Fan and John A. Kosinski, "Wireless langasite resonator as a force sensor," in *Proc. of IEEE Int. Freq. Control Symp.*, pp. 1-6, 2012.

Resonant SAW Torque Sensor for Wind Turbines

V. Kalinin, A. Leigh, A. Stopps
Transense Technologies plc
Bicester, Oxfordshire, UK
victor.kalinin@transense.co.uk

E. Artigao
Brunel Innovation Center
Brunel University
Cambridge, UK

***Abstract*—A novel plate torque transducer based on UHF SAW resonant sensing elements has been developed allowing an easy aftermarket installation of passive wireless torque sensors on large diameter shafts by means of clamping. A design of a large diameter RF rotary coupler for wireless interrogation of the transducer was proposed that had a gap of 20 mm between the stator and the rotor and was insensitive to axial and radial misalignment as well as the rotation angle. The two plate transducers and the RF coupler were installed on a high-speed shaft of a wind turbine gearbox. The torque sensor accuracy achieved after calibration on a test shaft was better than 1% full range within the temperature range from +20°C to +80°C.**

Keywords-torque sensor; SAW resonator; torque transducer; RF rotary coupler; wind turbine gearbox

I. INTRODUCTION

Wind farms are at the moment one of the fastest growing sources of renewable energy. However, the cost of electricity generated by offshore wind turbines is still noticeably higher than that for fossil fuel power plants, and maintenance cost is an important contribution to it. Up to 80% of this cost is associated with unexpected failures of rotating components that could be prevented by predictive and corrective maintenance based on adequate condition monitoring systems. Currently they mainly include vibration, temperature and oil debris sensors [1] but there is also a clear demand for sensing torque. This would allow a more accurate estimation of load on rotating parts, correlation of this load with the data obtained from other sensors and overload protection.

At the moment torque sensors used on wind turbines are mostly realized with strain gauges but the latter are difficult to apply, require a telemetry system for signal transmission and a non-contact power supply, they are expensive and used mainly at the development stage rather than for continuous load monitoring. The aim of this paper is to present a batteryless non-contact SAW torque sensor suitable for easy aftermarket installation on high-speed shafts of wind turbine drivetrains.

Resonant wireless SAW torque sensors have been developed for automotive industry [2] but in this case the SAW die is attached by an adhesive directly to the surface of a relatively small part (shaft or flexplate) that can be cured in an oven. Dimensions of the wind turbine drivetrain high-speed shafts are too large (diameter is up to 200 mm) for curing them in ovens and subsequent calibration within a wide temperature range. At the same time, most gearbox manufacturers prefer not to install any bolt-on transducers on the shafts. This is the main motivation behind development of a novel clamp-on plate transducer with the SAW sensing elements that can be calibrated on a relatively short and light test shaft and then installed on the real large diameter wind turbine shaft. The design of this transducer is presented in Section II. Another issue is a design of the RF rotary coupler with a large gap between the rotor (sensor antenna) and the stator (reader antenna) that would tolerate strong vibrations of the shaft and provide wireless resonant frequency measurements insensitive to the angular position of the shaft and its radial and axial movement. Such a coupler is described in Section III. Results of calibration, testing of the torque sensor and its installation on a wind turbine are presented in Section IV.

II. THE SAW TORQUE TRANSDUCER DESIGN

A. SAW sensing elements

The torque applied to a shaft is measured by measuring strain on the surface of the plate clamped to the shaft. A clamp-on SAW torque transducer was theoretically studied in [3]. It had a beam connected between two clamp rings at an angle of 45° to the shaft axis that converted the torque into a uniaxial strain field on the beam surface. Our design of the transducer is different – it contains a relatively wide thin plate held by the two clamps and oriented along the shaft axis. It converts the applied torque into a biaxial shear strain field on the plate surface. This allows using the same SAW sensing elements as those developed for direct attachment to the shaft surface [4].

One of the sensing elements, HFSAW, contains three one-port SAW resonators connected in parallel, M1SAW, M2SAW and TSAW with the resonant frequencies $f_1 \approx 437$ MHz, $f_2 \approx 435$ MHz and $f_3 \approx 433$ MHz fabricated on Y+34° cut quartz substrate. All of them have unloaded $Q \approx 10000$ and the series resonant impedance close to 50 Ω. M1SAW and M2SAW are oriented at ±45° to the X axis of the substrate and the shaft axis so that $F_{m1} = f_1 - f_2$ linearly depends on the applied torque M. TSAW oriented at 30° to the X axis is used for temperature compensation since $F_t = f_2 - f_3$ depends differently on T than F_{m1}. The biaxial strain field on the plate surface gives a chance to perform differential frequency measurement of F_{m1} that reduced the influence of the variable impedance of the RF rotor couple, the bending moment normal to the plate surface and also doubles the torque sensitivity.

The HFSAW sensing element is bonded to the surface of the first plate transducer. There is also the second plate transducer with the sensing element LFSAW bonded to it.

The work has been supported by the European Commission FP7-SME-2011 INTELWIND project, Grant No. 283277.

LFSAW contains only two SAW resonators connected in parallel, M3SAW and M4SAW, similar to M1SAW and M2 SAW but with the resonant frequencies $f_4 \approx 431$ MHz and $f_5 \approx 429$ MHz. $F_{m2} = f_4 - f_5$ also linearly depend on M. Installing the two plate transducers on the shaft diametrically opposite to each other and calculating $F_m = (F_{m1} + F_{m2})/2$ reduces the influence of the bending moment parallel to the plate surface on the torque measurement result.

B. Mechanical design of the plate transducer

The plate transducers are designed for installation on the coupling shaft with the diameter of 120 mm and the thickness of 5 mm that connects the gearbox of the wind turbine to the generator. There are two main goals in the mechanical design of the transducers: (a) achieve a principal strain of at least 100-200 με on the plate surface at the maximum measurable torque of 5 kNm without yielding and (b) ensure a good repeatability of the measurement result and a low mechanical hysteresis.

Two of the designed transducers belonging to the first generation are shown in Fig. 1 before installation of the SAW sensing elements. They are made of stainless steel 316 cold finished and annealed. Both of them have a thin plate attached to the two relatively thick shoulders that are supposed to be clamped to the shaft by means of high-torque steel clamps. The transducer in Fig. 1a has four pins made of high carbon bright steel pressed into the back side of each of the shoulders. Their aim is to provide a repeatable strain transfer from the shaft surface to the plate. The second transducer does not have the pins but its shoulders have a cylindrical surface matching the curvature of the shaft. The shape and the dimensions of the plates are designed to ensure the principal strain of ≈130 με in the plate center at 5 kNm applied to the coupling shaft. Results of the finite element analysis (FEA) for the two plates installed on the coupling shaft are shown in Fig. 2 (a perfect mechanical contact is assumed).

The first generation of the transducers has been developed mainly for testing performance of different types of plate-shaft interfaces at a reduced amount of torque up to 800 Nm available from one of the Transense torque rigs. To withstand higher values of torque and stress associated with it, the second generation of the plate transducers has been manufactured using a higher specification stainless steel, PH17-4 SS. The two transducers with HFSAW and LFSAW bonded to

(a) (b)

Figure 1. The first generation of the plate transducers: (a) with pins and (b) without pins.

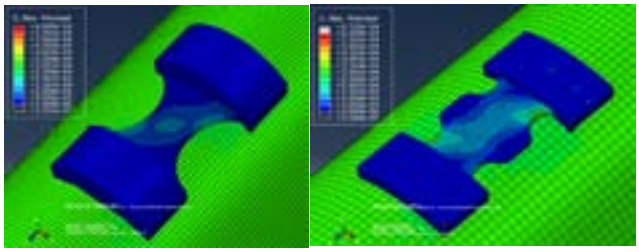

(a) (b)

Figure 2. FEA results: (a) 130 με and (b) 127 με at the plate center at 5 kNm applied to the coupling shaft.

them are shown in Fig. 3. The back side of the shoulders also have a cylindrical surface matching the coupling shaft and the geometry of the plates ensures the principal strain of 216 με at 5 kNm applied to the coupling shaft. The maximum shear stress for the transducer is 80 MPa at 10 kNm that is considerably lower than the material shear yield strength.

III. LARGE DIAMETER RF COUPLER DESIGN

A number of the RF rotary couplers for passive SAW sensors have been studied theoretically and experimentally in [5]. However, most of them are aimed at relatively small diameters of the shafts and 1-5 mm gaps between the rotor and the stator. They are not suitable for the application under consideration that require the rotor-stator gap to be at least 20 mm because of large vibration amplitude of the coupling shaft. At the same time, radiation from the coupler has to be minimal for EMC so the coupler design based on radiating antennas like the one suggested in [6] is also not acceptable.

The proposed coupler design is based on the microstrips coupled back-to-back as in [5]. However, instead of FR4 PCB material, the substrate is made of the Rochacell® WF foam with the dielectric constant close to unity in order to scale up the coupler cross-section and reduce the electrical length of the microstrips. The coupler with the 20 mm gap is shown in Fig. 4 together with the torque transducer installed on the test shaft. The microstrip width is 23 mm and its height ensured the characteristic impedance close to 50 Ω. The annular stator microstrip is terminated by the matched load and the rotor

Figure 3. The second generation of the plate transducers with the SAW sensing elements installed.

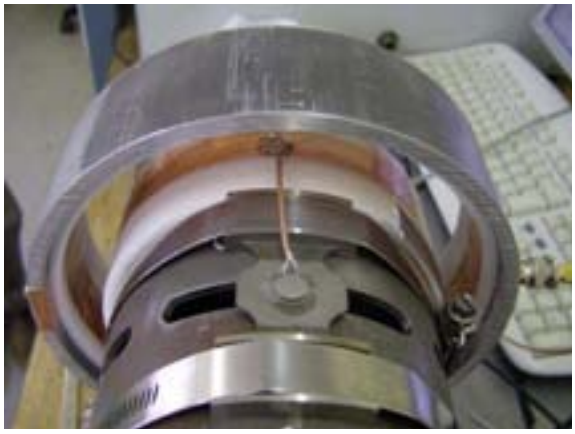

Figure 4. The RF rotary coupler with the SAW sensing element connected to it.

microstrip has two diametrically opposite gaps with one side grounded and another one connected to the sensing elements.

The angular variations of the measured frequency differences F_t, F_m and $F_{m1,2}$ as well as the standard deviation of the measured resonant frequencies are shown in Fig. 5. The pulsed SAW interrogator connected to the stator input (it is described in [7]) accumulates coherently 10 SAW responses and the PC logging software average 400 samples to reduce

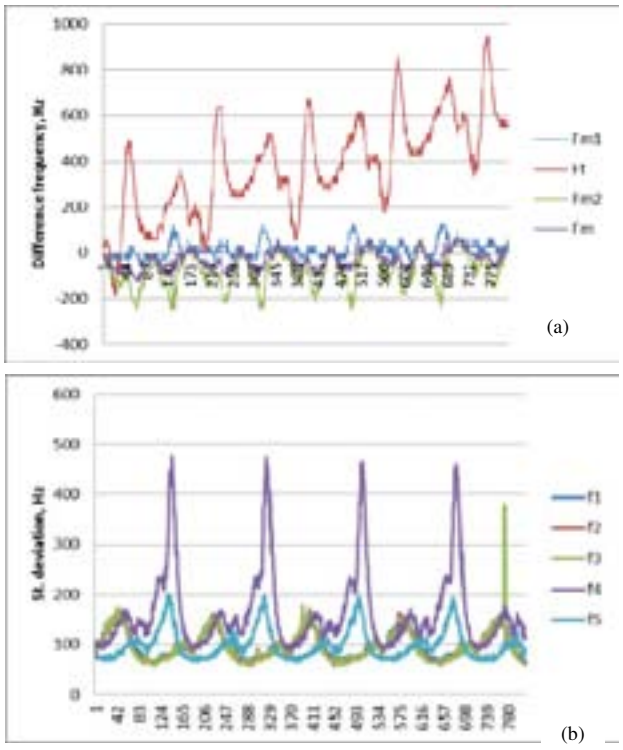

Figure 5. Angular variation of the measured (a) difference frequencies and (b) standard deviations of the resonant frequencies. Sample numbers are shown along the abscissa.

the noise in the frequency readings. The peak variation of F_m is below 100 Hz which is only 0.0083% of the estimated full range of the difference frequency variation due to ±5 kNm torque for the second generation plate transducer. The peak variation of F_t is 300 Hz (its drift is due to slowly changing temperature) that corresponds to the temperature reading variation of only ±0.1°C. The maximum standard deviation of F_m does not exceed 290 Hz that gives the estimated torque sensor resolution of 0.073% full range.

The coaxial cylindrical design of the RF rotary coupler with the wide microstrip is practically insensitive to the axial and radial displacement of the stator relative to the rotor by ±10 mm. Variation of F_m caused by the displacement does not exceed 1 kHz.

IV. Sensor Testing and Calibration

The first generation of the torque plate transducers has been tested on the 0.8 kNm torque rig after installation on the test shaft with the slots shown in Fig. 4. The slots in the shaft were made to increase the strain on the plate surface by the gain factor of $G_1 = 3$ compared to that for the real coupling shaft at the same value of torque. The room-temperature sensor characteristic achieved for the plate with the pins after 20 cycles of ±750 Nm exercising is shown in Fig. 6. The amount of hysteresis is quite large, 4.3 kHz which is 1.4% full range. Further exercising of the shaft slightly increased the hysteresis most likely because of the wearing-out of the pins.

A better result has been obtained for the plate transducer without the pins as shown in Fig. 7. The amount of hysteresis is 2 kHz or 0.9% full range and does not change with further exercising. The achieved torque sensitivity is 171 Hz/Nm while the theoretical value for the slotted test shaft is 213 Hz/Nm.

Since the linearity and the hysteresis obtained for the second plate are at the acceptable level, the next series of tests on a larger, 2 kNm torque rig have been performed for the second generation of the plate transducers also not having the pins (see Fig. 3). The two transducers were installed on a test shaft without slots but with thinner walls than those of the real

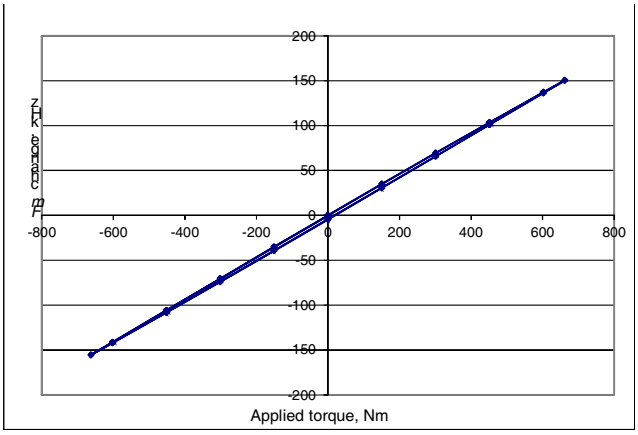

Figure 6. Variation of F_m with torque for the first generation of the plate transducer with pins on the slotted test shaft.

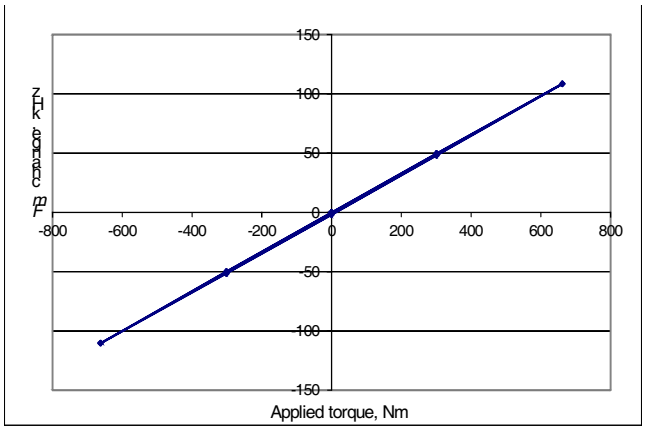

Figure 7. Variation of F_m with torque for the first generation of the plate transducer without pins on the slotted test shaft.

coupling shaft so that the gain factor for the strain was G_2 = 1.55. The set of calibration characteristics of the torque sensor measured at different temperatures is shown in Fig. 8. Special treatment of the plate-shaft interface helps achieve a low hysteresis of only 1.8 kHz at 77°C that is 0.34% full range. The torque sensitivity is 167 Hz/Nm for the test shaft and expected experimental value for the real coupling shaft is 108 Hz/Nm (the theoretical value is 121 Hz/Nm). After calibration, the torque measurement errors do not exceed ±11 Nm (±0.34% full range) on the test shaft within the entire temperature range. The torque sampling period is 1 ms.

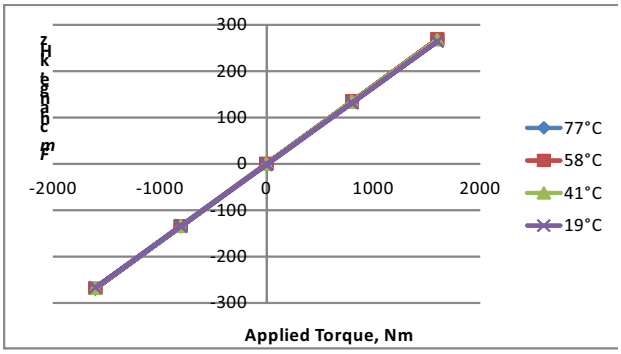

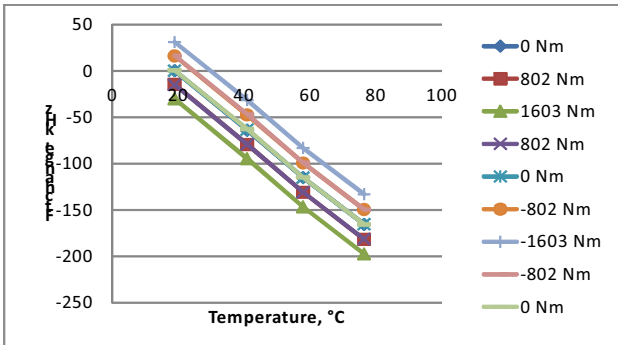

Figure 8. Calibration characteristics of the 2nd generation plate transducers installed on the test shaft without slots.

The calibrated torque sensor has been installed on the 750 kW NEG-MICON wind turbine at the Centre for Renewable Energy Sources & Saving (CRES) in Greece. After re-zeroing, the ambient temperature calibration was repeated on site. The torque readings of the SAW sensor turned out to be 22% lower than the applied torque indicated by a load cell. This could be due to the fact that the gain factor $G_{1,2}$ for the test shafts was found not experimentally but theoretically, by means of FEA. This introduced an uncertainty due to finite accuracy of FEA, unknown elastic constants of the coupling shaft material and imperfect mechanical contact at the shaft-plate interface. After introducing the correction factor, the SAW torque sensor has been integrated into a condition monitoring system of the wind turbine that is currently being tested.

V. Conclusions

A torque plate transducer based on passive wireless SAW strain sensing elements has been developed for installation on large diameter shafts by using heavy duty high torque clamps. The non-contact torque sensor employing the two plate transducers was calibrated on the test shaft and showed the torque measurement errors below 1% full range within the temperature range from 20°C to 80°C. A large diameter RF rotary coupler with the stator-rotor gap of 20 mm and small rotational error was also developed. Both the torque transducers and the RF coupler are suitable for aftermarket installation on large diameter shafts for wind turbines and other industrial and marine applications.

Acknowledgment

The authors are grateful to Dr. D. Lekou and Dr. F. Mouzakis from CRES, Greece, for the help in development of the sensor specification and its installation on the wind turbine.

References

[1] P. Caselitz, J. Giebhardt, M. Mevenkamp, "Application of condition monitoring systems in wind energy converters", Proc. EWEC 1997, Dublin, pp. 579-582.

[2] V. Kalinin. "Wireless physical SAW sensors for automotive applications", Proc. 2011 IEEE Int. Ultrason. Symp., pp. 212 – 221, 18-21 October 2011.

[3] E Zhukowski, T. Fellner, J. Wilde, M. Berndt, "Parameter Optimization of Torque Wireless Sensors Based on Surface Acoustic Waves (SAW)", Proc. 2012 13th Int. Conf. on Termal, Mechanical and Multi-Physics Simulation and Experiments in Microelectronics and Microsystems, 16-18 April 2012.

[4] V. Kalinin, G. Bown, A. Leigh, "Contactless Torque and Temperature Sensor Based on SAW Resonators", Proc. 2006 IEEE Int. Ultrason. Symp., p. 1490-1493, 2006.

[5] V. Kalinin, "RF Rotary Couplers for Contactless Torque Sensors Based on SAW Resonators", Proc. Europ. Freq. and Time Forum, Toulouse, France, 22-25 April, 2008.

[6] J.-M. Boccard, L. M. Reindl, "Ceramic and magnetic loop antennas for wireless interrogation of SAW resonators on rotating machinery", Proc. 2012 IEEE Int. Workshop on Antenna Technology: Small Antennas and Unconventional Applications, 5-7 March 2012.

[7] 2. V. Kalinin, R. Lohr, A. Leigh, G. Bown, "Application of passive SAW resonant sensors to contactless measurement of the output engine torque", Proc. IEEE Freq. Control Symp., pp. 499-504, 2007.

High-Overtone Bulk Acoustic Resonator as Passive Sensor Acting as Buried Cooperative Target Interrogated by Ground Penetrating RADAR

J.-M Friedt*, A. Saintenoy†, T. Baron‡, É. Lebrasseur‡, T. Laroche‡, S. Ballandras‡, M. Griselin§
*SENSeOR, Besançon, France, Email: jmfriedt@femto-st.fr
†IDES, UMR CNRS 8148, Université Paris Sud, France
‡FEMTO-ST Time & Frequency department, UMR CNRS 6174, Besançon, France
§ThéMA, UMR CNRS 6049, Université de Franche Comté, Besançon, France

***Abstract*—We consider a broadband bulk acoustic resonator architecture – the so called High-overtone Bulk Acoustic Resonator (HBAR) – as a transducer acting as cooperative target to a RADAR interrogation unit. Specifically, we consider the compatibility of such an acoustic device as a passive buried sensor interrogated through a wireless link by an unmodified Ground-Penetrating RADAR (GPR). While the comb of modes is detected as a series of echoes well within the typical interrogation duration of GPRs, with a spacing between adjacent echoes representative of the acoustic velocity and hence the physical quantity under investigation, the poor coupling coefficient of each individual mode due to the spreading of the piezoelectric transducer coefficient over many modes reduces the interrogation range with respect to the acoustic delay line approach. A sensor identification scheme within the clutter of reflections from dielectric buried interfaces is proposed.**

I. Introduction

The High-overtone Bulk Acoustic Resonator (HBAR) design, based on a stack of materials [1], was originally considered as a solution for increasing the operating frequency of resonators while keeping a robust mechanical setup and high quality factor while removing the lithography constraint associated with patterning electrodes in a surface acoustic wave approach. Based on a stack of a thin piezoelectric active layer on top of a low-loss thick substrate, the transfer function of such a device is intrinsically broadband and characterized by a comb of modes. The mode spacing is given by the low-loss substrate thickness, while the envelope is given by the transfer function of the thin piezoelectric film and characterized by the overtones which are odd multiples of the fundamental frequency.

Using HBAR transducers as sensors has been considered early after the initial design considerations, whether for sensing physical properties [2], [3] or for gravimetric sensing [4].

II. HBAR as passive wireless sensors

The use of an HBAR as a wireless sensor is less common [5] than frequency source applications, and requires different design considerations: rather than focusing on a high quality factor which must only be high enough for the resonator discharge to last longer than the clutter, loading the resonator requires a significant electro-mechanical coupling. Defined as the ratio of the acoustic to electrical energy, a high enough coupling coefficient is needed to load the transducer during a wireless interrogation following a strategy similar to pulsed-RADAR probing [6].

Since an HBAR operates by transferring the acoustic energy from the piezoelectric layer to the thick substrate, the coupling coefficient of the piezoelectric substrate is transferred more or less efficiently to the HBAR modes and opens a design consideration for yielding HBAR transducers most suitable for wireless probing. The multiple modes of the HBAR under investigation here (Fig. 1, modes spaced by 4.6 MHz) distribute the thin film coupling coefficient to all the modes. Even though 163^o-lithium niobate exhibits a strong coupling of up to $K^2 = 50$ %, distributing this value to all the modes yields a low coupling for individual modes, explaining the poor interrogation range [7] with respect to a delay line [8] designed on a strongly coupled material. Interestingly, in the particular case of the device characterized in Fig. 1, the sum of all coupling coefficients defined as $K^2 \simeq \frac{\pi^2}{4} \times \frac{f_a - f_r}{f_r}$ with f_r and f_a the resonance and anti-resonance respectively [9] reaches 50%, or the material coupling coefficient of the active piezoelectric layer.

We thus consider two contributions to a figure of merit of the suitability of an HBAR as passive wireless sensor. On the one hand the coupling coefficient K defines the efficiency of the electromagnetic to mechanical conversion – or the ratio of the incoming electromagnetic energy to the stored mechanical energy – and should be maximized to improve the returned power level. The interrogation range is directly related to this quantity since in the RADAR equation, the equivalent cross section of the cooperative target is replaced with K^2 since the wave is converted from electromagnetic to mechanical and back to electromagnetic, multiplied by the internal acoustic losses of the transducer: a drop by a factor of 10 of the coupling coefficient yields an interrogation range drop of 3 since the cross section appears as the fourth-root power in the RADAR equation. On the other hand the quality factor Q defines the ability of the device to store energy through the ratio of the energy lost for each oscillation period to the stored energy. The quality factor of each individual mode should be high enough to clearly separate each mode contribution and thus prevent the comb of modes to blur in a continuous envelope in which individual echoes would no longer be detectable. Hence, the considered figure of merit is

$K^2 \times Q$ (no unit). [10]

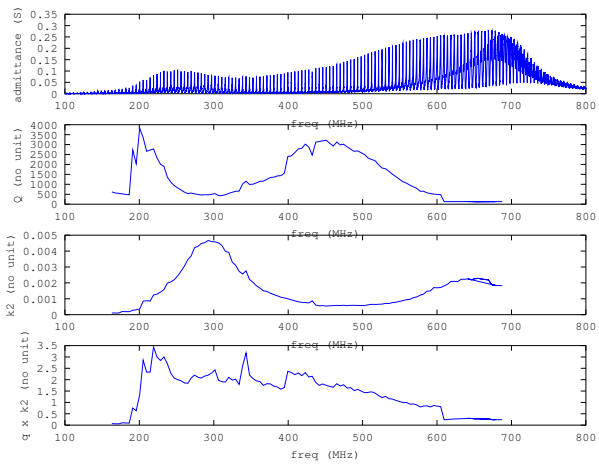

Fig. 1. Top to bottom: experimental admittance of the HBAR (lithium niobate on quartz) used in this report, quality factor and coupling coefficient. A figure of merit $K^2 \times Q$ is deduced, decreasing with frequency within the frequency range under investigation.

This observation yields some consideration as to the design of HBARs for use as passive wireless sensor. High quality factor, as required for frequency source applications, is no longer the most significant design factor: for wireless sensing, the incoming electromagnetic energy must be efficiently converted to a mechanical wave which itself is radiated back to the interrogation hardware. This electro-mechanical conversion coefficient K is unequally distributed over the modes as shown by modelling a lithium niobate (YXl/163^o-rotated cut) atop corindon (sapphire) stack (Fig. 2. Two cases are investigated: multitude of closely spaced modes when the low-loss substrate is thick (800 μm) or a few widely spaced (in the frequency domain) modes due to a thin substrate (100 μm). In the latter case, the distribution of the piezoelectric material K^2 over a few modes yields individual mode electro-mechanical coupling coefficients of a few percents, dropping by a factor of 10 in the case of a dense comb of modes. We hence conclude with a design tradeoff when manufacturing HBAR transducers dedicated to wireless sensing: the mode spacing must be low enough for the time domain echoes (separated by a delay equal to the inverse of the frequency spacing) to be well separated, while being large enough to minimize the number of modes in the piezoelectric layer envelope and hence maximize the coupling coefficient of each individual mode. We observe in both cases that the sum of the individual mode electro-mechanical coefficients yields a value of 47.5%$\pm$0.5%, in good agreement with the electro-mechanical coupling coefficient of the piezoelectric layer.

Furthermore, operating within the envelope of the fundamental mode of the thin piezoelectric layer is best suited since the piezoelectric thin film coupling coefficient K of the overtones drops as the overtone number N itself (*i.e.* K^2 drops as N^2, or a 9 to 14 dB drop when operating on $N = 3$ or $N = 5$ respectively with respect to the fundamental mode [11]). Hence, rather than operating at high frequency by using an overtone of the thin piezoelectric layer, the HBAR is best designed for operating as a wireless transducer by using a thinner piezoelectric layer so that the investigated modes remain in the fundamental mode of the active layer (Fig. 3).

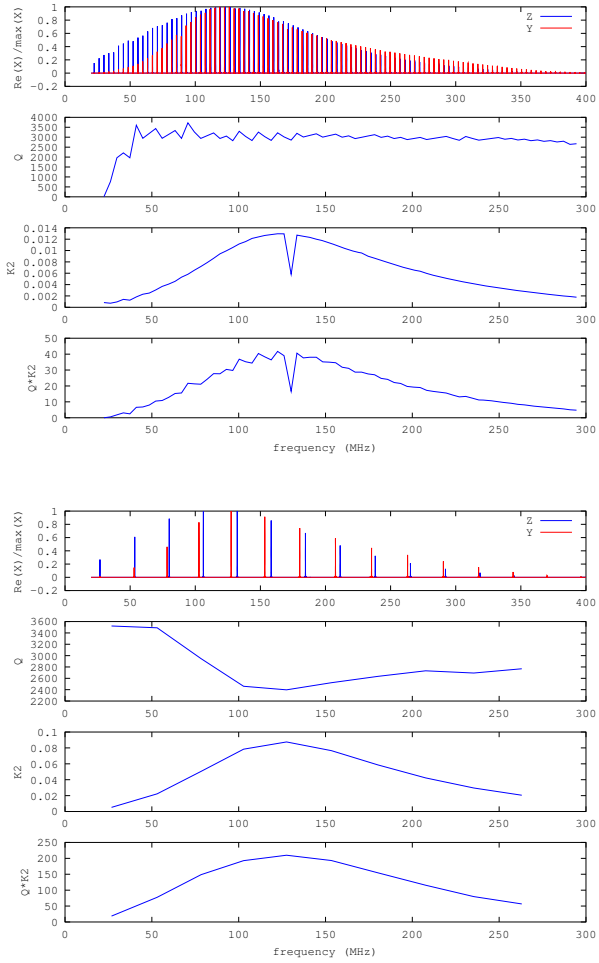

Fig. 2. Simulation of two configurations of HBARs in which a YXl/163^o lithium niobate layer is located atop a corindon substrate either 800 μm thick (top) or 100 μm thick (bottom). The thin piezoelectric film thickness defines the mode envelope while the substrate thickness defines the mode spacing. Top displays the normalized impedance (Z in blue) and admittance (Y in red), from which the quality factor (width at half height of the real part of the admittance) and the electro-mechanical coefficient K^2 – proportional to the distance of the admittance to impedance real parts maxima position. Finally, a figure of merit $Q \times K^2$ is computed.

Using the simulated data displayed on this figure, we have verified that the sum of the coupling coefficients of the modes within the envelope of the fundamental mode is 49.9% (close to the expected 50% of the lithium niobate layer), the sum of the coupling coefficients of the modes lying within the third overtone envelope is 3%, close to 49.9/9=5.5%, and the sum of the coupling coefficients of the modes lying under the fifth overtone is 0.8%, close to the expected 49.9/25=2%.

III. GPR FOR PROBING PASSIVE COOPERATIVE TARGETS

An alternative to the spectral approach of identifying a resonance frequency using a reflective frequency-sweep network analyzer to track the operating frequency of a single mode (FMCW based RADAR strategy) is to operate in the time domain. A HBAR is best suited for a time domain analysis since the Fourier transform of a comb of modes in the frequency domain is a comb of echoes in the time domain.

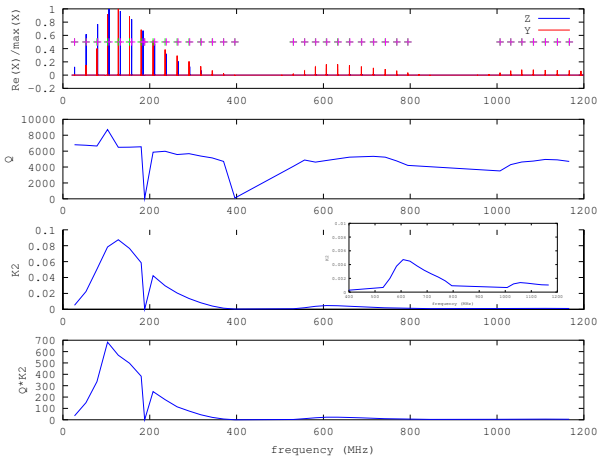

Fig. 3. Simulation of the S_{11} transfer function of an HBAR computed over a frequency range including the fundamental (0-500 MHz), third (500-900 MHz) and fifth overtone – on the top graph, the crosses indicate the position of the modes identified and automatically processed for computing the quality factor and the coupling coefficient. The fundamental mode of the piezoelectric layer extends from 0-500 MHz, the third overtone from 500 to 900, and the fifth overtone is above 900 MHz. The quality factor Q and electromechanical coupling coefficient K^2 are computed as well as the figure of merit $K^2 \times Q$, indicating that the only the fundamental mode of the piezoelectric layer should be considered. Inset of the third-from-top graph: zoom on the coupling coefficient of the third and fifth overtone of the piezoelectric layer.

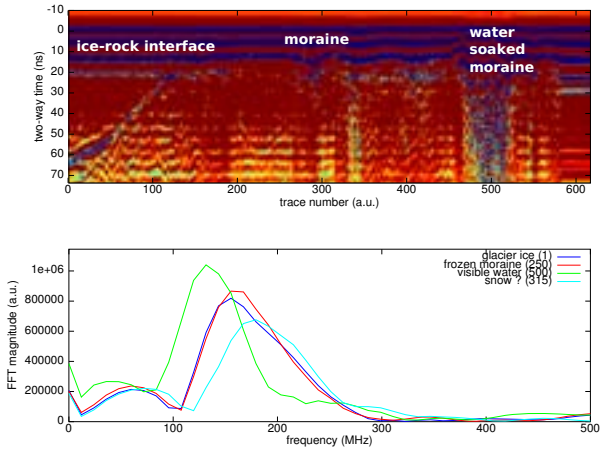

Fig. 4. Top: experimental B-scan GPR measurement over an area ranging from glacier ice (traces 0–100, with a clear interface from the bedrock visible for echoes delayed from 60 to 0 ns), to the moraine and surface-soaked water areas around trace 500, yielding the largest permittivity region and hence lowest operating frequency. Bottom: Fourier transform of the emitted pulse depending on the monitored region – the number next to the legend refers to the trace number as observed on the abscissa of the B-scan.

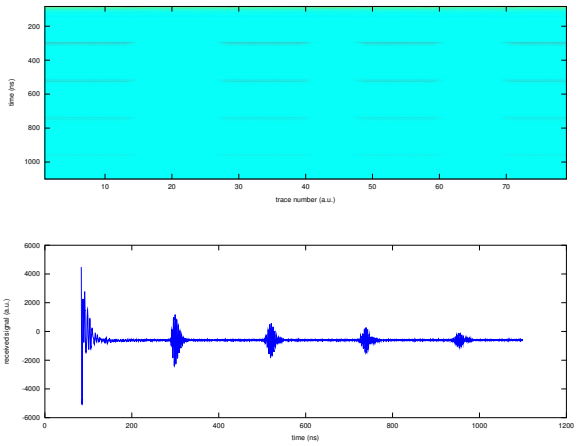

Fig. 5. Top: experimental B-scan of the HBAR sensor probed using a 200 MHz unshielded antenna, with-without-with... sequences of the HBAR located under the GPR. Bottom: experimental A-scan time domain reflections of the HBAR echoes recorded by the GPR.

A pulsed mode RADAR emitter as used in Ground Penetrating RADAR (GPR [12]) application is based on unloading a capacitor polarized by a high voltage (350 V in a Malå RAMAC unshielded-antenna emitter unit) in an avalanche transistor: the time constant of the resulting pulse is defined by the antenna reflection coefficient (S_{11}) minimum. This S_{11} minimum is given by the physical antenna dimensions and the surrounding medium permittivity. Practical use of a GPR in an environment ranging from ice to snow and water filled areas induces significant variation in the central frequency of the pulse spectrum (Fig. 4). In the classical patch-antenna equivalent permittivity approach, the GPR dipole antenna of length d operating frequency $f = \frac{c_0}{2d\sqrt{\varepsilon_r(eff)}}$ depends on the ground permittivity ε_r through $\varepsilon_r(eff) = 1/2 \times (\varepsilon_r + 1)$ with c_0 the electromagnetic velocity in vacuum [13, p.817]. Considering that $\varepsilon_r \in [3..15]$, the operating range might vary by up to a factor of 2.

This variable operating frequency is a strong incentive towards the HBAR thanks to the availability of modes in nearly one decade of frequency span. The dependence of these modes with the physical quantity under investigation is still an open question since the distribution of energy in the various materials of the stack is dependent on the overtone index. In order to illustrate this issue, the HBAR presented in Fig. 1 was probed using a GPR fitted with unshielded 200 MHz antenna (best suited for glacier investigation in this case) and then 500 MHz antenna (best suited for civil engineering investigations).

Due to the multitude of modes and hence of the echoes generated by the HBAR, identifying which echo is due to the sensor and which echo is due to passive buried interfaces is mandatory to apply a cross-correlation algorithm and identify the time delay in order to extract the monitored physical quantity. The classical Kirchhoff migration converts the hyperbolas observed in the (time, position) B-scans when a point-like reflector is detected by a scanning GPR: the hyperbola curvature is solely defined by the medium permittivity and the depth at which the target is located. As seen on Fig. 6, the HBAR delays by the time associated with the propagation duration in the acoustic transducer, hence shifting the hyperbola later in the B-scan. The deep hyperbolas are inconsistent with passive reflectors buried deep underground (in this example multiples of 200 ns or 26 m assuming a ground relative permittivity of 5) or would require inconsistent permittivities with respect to the surrounding environments. Hence, the shape of the hyperbola is a unique indicator of a HBAR response. Indeed, since the equation of the reflector depth t as the GPR scans along a line of abscissa x is $c^2t^2 = x^2 + d^2$ when probing a reflector located at depth d in a medium exhibiting an electromagnetic velocity c, the curvature of the hyperbolas at position $x = 0$

(hyperbola summit) is

$$\left.\frac{\partial^2 t}{\partial x^2}\right|_{x=0} = \frac{2}{cd} = \frac{2\sqrt{\varepsilon_r}}{c_0 d}$$

so that erroneously identifying a time-delayed echo of the HBAR would yield an unacceptable estimate of the permittivity, especially so if multiple echoes separated by constant time delays are observed.

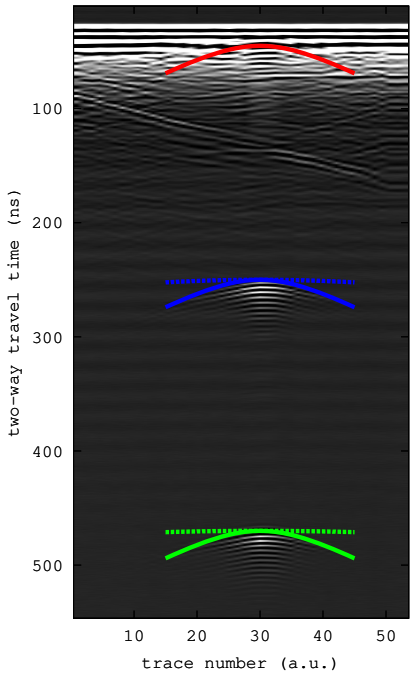

Fig. 6. Experimental B-scan recorded as the GPR is moved over the HBAR-sensor located 20 cm in ice. The top-most (red) hyperbola is due to the reflection on the antenna connected to the transducer. Two echoes, delayed by 200 ns (for a frequency comb spaced by 5 MHz steps), are identified as blue and green hyperbolas with the same shape as the initial reflection. Dashed line: the hyperbola shape if the passive dielectric interface were located at the indicated depth. Solid line: time translated electromagnetic reflection due to the acoustic delay: identifying the sensor reflection from passive interfaces is well defined.

One last unresolved issue is the dependence of the successive echo time delays with the physical quantity under investigation: since the acoustic velocity in the HBAR is a combination of the acoustic velocity in the piezoelectric transducer and the low loss substrate, the observed acoustic velocity depends on the energy distribution in these two layers. The relative energy distribution in each of these layers is dependent on the mode number, so that widely different overtone numbers might exhibit significant different dependence to a given physical effect. Hence, the preliminary calibration between the echo (time) separation and the physical quantity might be no longer valid if the probing frequency significantly differs from the frequency of the calibrated modes, a significant hindrance if the GPR operating frequency varies due to soil moisture content evolution over time and space.

IV. Conclusion

Having demonstrated the use of High-overtone Bulk Acoustic Resonators as passive cooperative targets suitable for applications in which the sensor is buried and hence no longer accessible for maintenance once installed, probed by a commercially available and unmodified Ground Penetrating RADAR, we describe design rules for optimizing the HBAR architecture to increase the interrogation range while keeping the sensing capability provided by the time delay between successive echoes. Maximizing the coupling coefficient requires operating on the thin piezoelectric film fundamental mode, while the low-acoustic loss substrate thickness is tuned to maximize individual mode coupling while keeping the returned echoes well separated. Identifying the echoes associated with the buried sensor as opposed to passive reflectors is achieved through time-domain separation and hyperbola curvature analysis.

Acknowledgments

This research was partly funded by the French National Research Agency (ANR) under the CryoSensors grant, the Université de Franche Comté BQR grant, and supported by the French RENATECH network and its FEMTO-ST technological facility. We acknowledge fruitful discussions with A. Reinhardt (CEA-LETI, Grenoble, France) and E. Lefeuvre (IEF, Orsay, France) concerning the figure of merit of HBAR used as passive sensors.

References

[1] H. Huang, J. Knox, Z. Turski, R. Wargo, and J. Hanak, "Fabrication of submicron $LiNbO_3$ transducers for microwave acoustic (bulk) delay lines," *Applied Physics Letters*, vol. 24, pp. 109–111, 1974.

[2] S. Alekseev, G. D. Mansfeld, I. Kotelanskii, and V. Veretin, "BAW microwave temperature sensor," in *18th European Frequency and Time Forum (EFTF)*, 2004, p. 569.

[3] T. Baron, D. Gachon, J.-P. Romand, S. Alzuaga, S. Ballandras, J. Masson, L. Cahterinot, and M. Chatras, "A pressure sensor based on a HBAR micromachined structure," in *IEEE International Frequency Control Symposium (IFCS)*, 2010, pp. 361–364.

[4] G. D. Mansfeld, "Theory of high overtone bulk acoustic wave resonator as a gas sensor," in *13th International Conference on Microwaves, Radar and wireless communications (MIKON)*, Wrolaw, Poland, 2000, pp. 469–472.

[5] J. Masson, W. Steichen, L. Fagot-Revurat, A. Artieda, P. Muralt, and S. Ballandras, "Hybrid resonant structures for wireless sensor applications," in *23rd European Frequency and Time Forum/IEEE International Frequency Control Symposium*, France, 2009, pp. 85–89.

[6] M. Pijolat, D. Mercier, A. Reihardt, E. Defaÿ, C. Deguet, M. Aïd, J. Moulet, B. Ghyselen, and S. Ballandras, "Mode conversion in high overtone bulk acoustic wave resonators," in *22nd European Frequency and Time Forum/IEEE International Frequency Control Symposium*, Besançon, France, 2009, pp. 290–294.

[7] J.-M. Friedt, A. Saintenoy, S. Chrétien, T. Baron, E. Lebrasseur, T. Laroche, S. Ballandras, and M. Griselin, "High-overtone bulk acoustic resonator as passive ground penetrating radar coopertive targets," *Journal of Applied Physics*, vol. 113, no. 13, p. 134904, 2013.

[8] J.-M. Friedt, T. Rétornaz, S. Alzuaga, T. Baron, G. Martin, T. Laroche, S. Ballandras, M. Griselin, and J.-P. Simonnet, "Surface acoustic wave devices as passive buried sensors," *Journal of Applied Physics*, vol. 109, no. 3, p. 034905, 2011.

[9] S.-Y. Pao, M.-C. Chao, Z. Wang, C.-H. Chiu, K.-C. Lan, Z.-N. Huang, L.-R. Shih, and C.-L. Wang, "Analysis and experiment of HBAR frequency spectra and applications to characterize the piezoelectric thin film and to HBAR design," in *IEEE International Frequency Control Symposium and PDA Exhibition*, 2002.

[10] V. Kaajakari, "Modeling of MEMS resonators: physics metts appliation requirements," in *Joint IEEE International Frequency Control Symposium and European Frequency and Time Forum*, San Francisco, USA, 2011, p. tutorial.

[11] J. Vig, "Quartz crystal resonators and oscillators – a tutorial for frequency and timing applications," 2000.

[12] V. Bogorodsky, C. Bentley, and P. Gudmandsen, *Radioglaciology*. D. Reidel Publishing Company, 1985.

[13] C. Balanis, *Antenna Theory, Analysis and Design, 3rd Ed.* J. Wiley & Sons, 2005.

Passive Wireless Surface Acoustic Wave CO_2 Sensor for Geological Sequestration Sites Monitoring

Yizhong Wang, Minking K. Chyu, Qing-Ming Wang*
Department of Mechanical Engineering and Materials Sciences, University of Pittsburgh, Pittsburgh, PA, USA
*Email: qiw4@pitt.edu

***Abstract*—A passive wireless CO_2 sensing system based on surface acoustic wave technology and carbon nanotube nanocomposite was developed. The gas response of the nanocomposite was about 10% resistance increase under pure CO_2. The sensor frequency change was around 0.03% for pure CO_2. With paralyne packaging, the sensor frequency change from relative humidity of 0% to 100% at room temperature decreased from over 0.1% to less than 0.01%. The lowest detection limit of the sensor is 1% gas concentration, with 0.0036% frequency change. Wireless module was tested and showed over one foot transmission distance at preferred parallel orientation.**

Keywords—CO_2;SAW; Sensor; CNT ;Composite; Humidity

I. INTRODUCTION

One of the most feasible ways of carbon emission control is geological carbon dioxide sequestration [1, 2]. Monitoring of CO_2 leakage on the ground around the sites is vital for the safety of human beings and animals nearby. Due to limited power supply in the remote location of these sequestration sites, a type of wireless operated passive CO_2 sensor is needed.

Commercially available non dispersive infrared (NDIR) CO_2 sensor[3] operated based on laser detection is one of the most widely used CO_2 sensor in mining industry and building monitoring. However, the high power consumption makes it unsuitable for sequestration site monitoring.

The other major CO_2 sensors are mostly based on chemical reaction. The major functions in these sensor are recognition of the CO_2 gas molecule and transduction of that recognition into a useful signal, such as pH, resistance, conductivity, or capacitance. Among them, CO_2 sensor based on surface acoustic wave (SAW) shows great potential.

Equipped with a comb-shape transmitting inter digit transducer (IDT) and a receiving IDT on a piezoelectric substrate, the SAW sensor generates SAW after receiving agitation signal either through wireless antenna or from direct connected power source. The SAW signal then travels along the substrate surface and is intercepted by the receiving IDT and then transferred to the measuring instrument or sent over the wireless antenna. The physical change on the SAW travelling path, such as change in mass or conductivity, will cause the change in SAW velocity and amplitude, thus the change of sensor resonant frequency and attenuation.

There are a lot of SAW sensor on different gases, such as H_2[4, 5], H_2S[6] or VOC[7]. Most of the SAW gas sensor utilizes a sensitive film between the transmitting IDT and receiving IDT, and the sensor response changes accordingly when the sensitive film reacts with target gases. For CO_2 detection, many of the SAW sensor uses gas absorption thin films and measures the resonant frequency change due to the mass change of the film. For example, SAW sensor with ZnO film will have 0.03% frequency change with 10ppm CO_2 [8]. SAW sensor with PVA film[9], PAPP/PAPO film[10], SiO_x and Teflon film[11], Teflon film[12, 13], polyimide film[14], and many other types of films are reported. These SAW CO_2 sensors have different sensitivities, depending on the choice of resonant frequency and sensitive film. They are mostly compact and have low power consumption. However, the mass loading type of sensor suffers from long term drift and false alarm caused by absorption of unwanted gases.

Since SAW signal changes not only with the change of mass loading, but also with the change of the conductivity, permittivity, mobility of the charge carrier and other parameters of the sensitive film[15], there are also SAW gas sensors that respond to the change of conductivity change of the sensing film. For example, PbPc[16] film changes conductivity after reaction with CO_2 and causes considerable amount of frequency change of SAW sensor. Among the SAW CO_2 sensors that make use of conductivity changes of the sensing film, nanotube and insulator (such as polymer) composite attracts more attention due to the large surface to volume ratio of nanotubes, thus higher possible sensitivities. These nanotube composites include SnO_2 [17] and carbon nanotube (CNT)-SiO_2 [18] and many other compositions. By far CNT and polyethyleneimine (PEI) composite proves to be one of the most promising combinations due to its ease of fabrication and low cost. There are some researches on CNT-PEI CO_2 sensing from industry (Honeywell [19] and Nanomix [20]) and academic institutions [21]. Due to the nature of CNT-PEI composite, the CO_2 sensor performance will be greatly influenced by humidity. However, most of the past researches omitted to address the impact of humidity on sensor performance. Some built a reference sensor for humidity sensing so as to compensate the humidity effect. Since the response to humidity change is normally much greater than the response to CO_2 concentration change, such sensor will suffer from unstable sensing performance in real applications.

It's thus vital to find a suitable packaging method for SAW CO_2 sensor based on conductivity change. Parylene, a material long been used in electronic packaging industry, proved to be good candidate for humidity resistant [22]. Parylene film is water vapor repelling and gas permeable when the film is thin enough. So a thin parylene layer will allow CO_2 molecules to

Sponsored by US DOE Grant# DE-FE0002138

go through while stopping water vapor from getting contact with sensing film.

II. THEORETICAL ANALYSIS AND PERFORMANCE EVALUATION OF SAW CO_2 SENSOR

A. SAW Dependence on sensing film conductivity

A SAW propagating in X direction (in the case of ST cut Quartz) has a surface electrical potential which can be expressed as [16]:

$$\phi(x,t) = \phi_0 e^{j(\omega t - kx)} \tag{1}$$

where ω is the angular frequency of the SAW and k is the wave number (For ST cut quartz with a period of 60μm, the wave number is 52.35E+3).

And considering the relationship between the current density J_x in the conductive sensing film and the surface potential through the continuity equation [16]:

$$\frac{\partial J_x}{\partial x} = -\frac{\partial}{\partial t}\left(\frac{\rho_s}{d}\right) \tag{2}$$

where d is the thickness of the film.

When neglecting the diffusion current and considering only the anisotropic SAW substrate, the complex power flow into carrier can be calculated. The fractional velocity perturbation and the attenuation per wave number can be finally calculated as [16]:

$$\frac{\Delta v}{v_0} \cong -\frac{\beta}{k} = -\frac{K^2}{2}\frac{(\sigma d)^2}{(\sigma d)^2 + v_0^2(\varepsilon_0 + \varepsilon_1)^2} \tag{3}$$

$$\frac{\alpha}{k} \cong \frac{K^2}{2}\frac{v_0(\varepsilon_0 + \varepsilon_1)\sigma d}{(\sigma d)^2 + v_0^2(\varepsilon_0 + \varepsilon_1)^2} \tag{4}$$

Here β is the imaginary part of the propagation factor $\gamma = \alpha + j\beta$, k is the wave number, σ is the film conductivity, K^2 is the electromechanical coupling factor, $v_0 = \omega / k$ is the unperturbed SAW velocity (3158m/s for ST cut quartz and 4000m/s for $LiNbO_3$), ε_0 is the permittivity of the region above the substrate and ε_1 is that of the substrate, d is the thickness of the film.

Equation (3) and (4) describe the velocity and acousto-electric attenuation change due to the change of the film conductivity on SAW propagation path. When considering the total surface wave velocity, from perturbation theory [16]:

$$\frac{\Delta v}{v_0} = \frac{1}{v_0}\left(\frac{\partial v}{\partial m}\Delta m + \frac{\partial v}{\partial c}\Delta c + \frac{\partial v}{\partial \sigma}\Delta \sigma + \frac{\partial v}{\partial \varepsilon}\Delta \varepsilon + \frac{\partial v}{\partial T}\Delta T + \frac{\partial v}{\partial p}\Delta p\right) \tag{5}$$

Here m is the variables mass, c is the stiffness, T is the temperature and p is the pressure. Together with unperturbed wave velocity v_0, conductivity σ and dielectric coefficient ε, these are the major components that can cause SAW velocity change, thus frequency shift.

Equation (5) can be exploited to design high efficient SAW gas sensor based on parameters other than mass loading and conductivity change for future research.

Based on (3), the relationship between the sensing film conductivity and SAW sensor performance can be plotted as shown in Fig. 1. From the figure, it can be seen that the best combination of SAW substrate and sensing film is $LiNbO_3$ and composite with 1.6S/m sheet conductivity.

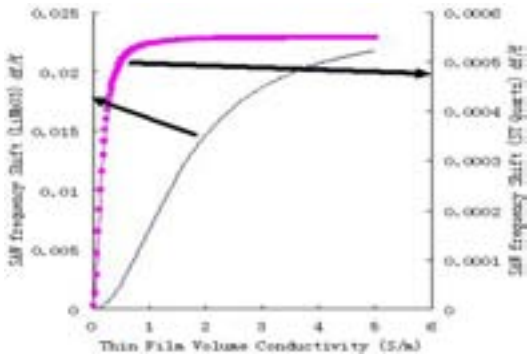

Fig. 1. SAW frequency shift corresponding to the thin film conductivity

B. SAW CO_2 Sensor Performance Evaluation

Based on preliminary test of the composite and the relationship from (3), the sensor performance can be estimated. A maximum of 0.1% frequency change is expected.

III. SURFACE ACOUSTIC WAVE SENSOR DESIGN, FABRICATION AND TEST SETUP

A. Piezoelectric Substrate Material Selection

The properties of common used piezoelectric materials are considered. $LiNbO_3$ is the best candidate for wireless communication. The conductivity dependence analysis above also shows that $LiNbO_3$ works best with sensing film of 1.6S/m sheet conductivity.

B. CNT-PEI Composite Fabrication

The CNTs are commercially available through Aldrich® (2g, St. Louis, Mo, USA) with 1-2nm outer diameter and 5-30um length. Dimethylformamide (DMF) is used to disperse CNT. CNT is mixed with DMF with 1:1000 weight ratio. The mixture is then agitated by ultrasonic convertor (Misonix® ultrasound liquid processors). The CNTs are well dispersed in the DMF solution after 90 minutes ultrasound at 70W. PEI is purchased from Aldrich with mean molecular weight of 25000. Starches are mixed with water using magnetic stir bar at elevated temperature around 100℃. The solution is then mixed with PEI.

The CNTs solution is drop coated on the sensing film region of the SAW sensor using pipette and let dry. The PEI-Starch solution is then applied onto the CNT film area and then washes away using deionized (DI) water so the CNTs will be surrounded by a thin layer of PEI and starch. The calculated volume conductivity of the resulted composite thin film based on resistance measurement proves to be within the optimum working zone of the SAW sensor, i.e. around 1.6S/m.

C. Design and fabrication of SAW Sensor

Two methods are adopted in sensor fabrication: photo lithography and shadow mask technology. 128°YX cut $LiNbO_3$ are selected for its excellent coupling coefficient (5.5% compared to 0.16% of ST cut quartz) and low transmission loss (0.26dB/cm compared to 0.95dB/cm of ST cut quartz). Surface acoustic wave velocity on $LiNbO_3$ is 4000m/s.

With IDT finger width and spacing of 15μm, the synchronous frequency of the SAW sensor from photolithography process is about 60 MHz, which limits the highest frequency of operation of SAW devices to a few GHz.

The IDT of the fabricated SAW sensor from shadow mask process has finger width of about 160um and spacing of about 150μm. The estimated resonant frequency of the sensor is 6.45MHz.

D. SAW Gas Testing System Setup

The gas testing system comprises of gas sources (Compressed Air gas tank and compressed CO_2 gas tank), flow controllers, one quartz gas testing flow chamber with oven, one sink connected with exhaust gas pipe, one current source measurement unit for thin film conductivity measurement (can be replaced by network analyzer in later characterization process), one computer connected to the current source unit for automatic data collection.

E. SAW Sensor Humidity Test Setup

The sensor is tested at several fixed humidity level. It's a common practice that in enclosed container with certain chemical solution, if the solution is over saturated at room temperature, the humidity level of the atmosphere above the solution will remain constant.

As shown in Tab. 1, the relative humidity of each saturated solution depends on the temperature of the solution. The testing environment can be assumed to have constant relative humidity.

TABLE I. RELATIVE HUMIDITY ABOVE SATURATED SOLUTIONS IN DIFFERENT TEMPERATURES (FROM OMEGA).

Relative Humidity (RH%)	***LiCl***	***$MgCl_2$***	***NaBr***	***$CaCl_2$***	***NaCl***	***KCl***	***K_2SO_4***
20℃	11.31	33.07	59.14	32.3	75.47	85.11	97.59
25℃	11.30	32.78	57.6	31	75.29	84.34	97.30
30℃	11.28	32.44	56.0		75.09	83.62	97.00

IV. EXPERIMENT RESULTS AND DISCUSSION

A. SAW Gas Sensor Performance

The fabricated SAW sensor with sensitive thin film is tested with network analyzer as measurement instrument. The SAW sensor performance is shown in Fig. 2.

After comparing test results from Fig. 2 with prediction, it can be seen that test results basically agree with prediction under 20% CO_2 concentration, while the predicted response based on resistance measurement is slightly higher than the real frequency measurement results, with over twice difference under pure CO_2. This might be caused by the slight difference in the fabrication process.

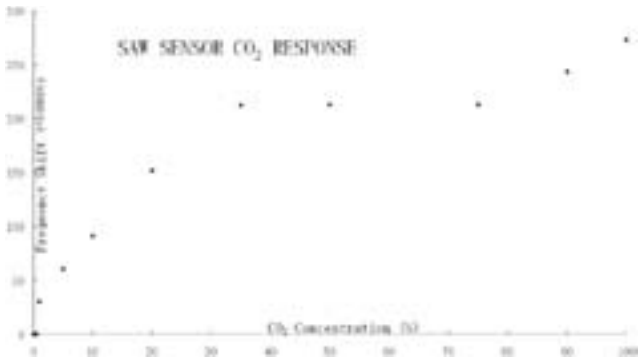

Fig. 2. SAW gas sensor performance.

Even the sensor response to CO_2 concentration higher than 20% is not as high as predicted, the fabricated sensor still shows reasonable response, with 0.003% frequency change under 1% CO_2. Since the CO_2 concentration in the air is around 400ppm, and occasional wild fire and other natural activities might further increase this concentration, 1% is safe for not to trigger false alarm and good enough for leakage monitoring.

B. SAW Sensor Humidity Response

The SAW sensor is then placed in the enclosed container above the saturated salt solution for testing. Test results from the top dotted points in Fig. 3 shows over 0.1% frequency change, which is over 3 times higher than the possible gas response.

C. Packaging Impact on SAW Sensor Humidity Response and Gas Sensing Performance

Parylene layer is coated by Specialty Coating Systems® PDS 2010. As seen in Fig. 3, coated SAW sensor shows an order of magnitude smaller frequency shift compared with uncoated SAW sensor, with less than 0.01% frequency change under saturated water vapor condition.

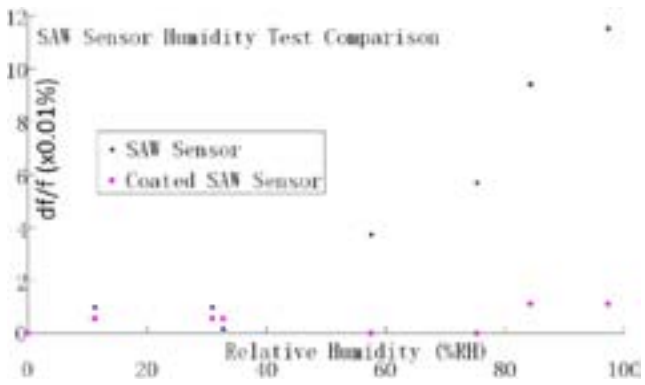

Fig. 3. SAW Sensor Humidity Response comparison after Parylene Coating.

The sensing performance between uncoated and coated sensors only have slight changes, which proves that the coating is gas permeable.

V. WIRELESS MODULE DESIGN, CONSTRUCTION AND TESTING

Due to fabrication limit, the maximum resonant frequency in current sensor design is below 100MHz, which means planar antenna is not the best choice so small scale macro size antenna is used. The inductor used in the project is 132-20SM_LB from Coilcraft®. For gas sensor with IDT from shadow mask, the design frequency is 6.45MHz. It can be calculated that for the design frequency, the desired capacitance is 1131.7μF.

Test results show that for a sensor with 23.633dB insertion loss, as observed for the fabricated SAW gas sensor, the maximum loss the antenna can have is about 68dB. In another word, the antenna range can be over one foot.

VI. CONCLUSION

A SAW CO_2 sensor was developed based on conductivity change upon gas concentration change. Gas test of sensor shows 0.03% frequency change under pure CO_2. Sensor test results basically agree with theoretical prediction of sensor performance. The impact of humidity, however, is more than two times larger than the gas response. After application of paralene coating, the humidity response is reduced to be less than 0.01% for saturated water vapor, while the gas sensing performance is not compromised. Wireless module is also built on coil and variable capacitor and the prelim results show the sensor capable of sensing over one foot distance. Overall, the sensor performance meets the requirement of wireless CO_2 leakage monitoring on geological sequestration sites.

REFERENCES

[1] S. Bachu, Screening and ranking of sedimentary basins for sequestration of CO_2 in geological media in response to climate change, Environmental Geology 44 (2003) 277-289.

[2] C.M. White, B.R. Strazisar, E.J. Granite, J.S. Hoffman, H.W. Pennline, Separation and Capture of CO_2 from Large Stationary Sources and Sequestration in Geological Formations—Coalbeds and Deep Saline Aquifers, Journal of the Air & Waste Management Association, 53 (2003) 645-715.

[3] Y. Wang, M. Nakayama, M. Yagi, M. Nishikawa, M. Fukunaga, K. Watanabe, The NDIR CO_2 monitor with smart interface for global networking, IEEE Transactions on Instrumentation and Measurement, 54 (2005) 1634-1639.

[4] K. Srinivasan, S. Cular, V.R. Bhethanabotla, S.Y. Lee, M.T. Harris, J.N. Culver, Nanomaterial Sensing Layer Based Surface Acoustic Wave Hydrogen Sensors, in: 2005 IEEE Ultrasonics Symposium, Rotterdam, The Netherlands, 2005, pp. 645-648.

[5] K.J. Singh, N. Nakaso, S. Akao, D. Sim, T. Fukiura, T. Tsuji, K. Ymanaka, Frequency-dependent surface acoustic wave behavior of hydrogen-sensitive nanoscale PdNi thin films, Nanotechnology, 18 (2007) 1-6.

[6] J.D. Galipeau, L.J. LeGore, K. Snow, J.J. Caron, J.F. Vetelino, J.C. Andle, The integration of a chemiresistive film overlay with a surface acoustic wave microsensor, Sensors and Actuators B: Chemical, 35 (1996) 158-163.

[7] C. Viespe, C. Grigoriu, Surface acoustic wave sensors with carbon nanotubes and SiO_2/Si nanoparticles based nanocomposites for VOC detection, Sensors and Actuators B: Chemical, 147 (2010) 43-47.

[8] C. Wen, Y. Ju, W. Li, W. Sun, X. Xu, Y. Shao, Y. Li, L. Wen, Carbon Dioxide Gas Sensor Using SAW Device Based on ZnO Film, Applied Mechanics and Materials, 135-136 (2012) 347-352.

[9] A. Buvailo, Y. Xing, J. Hines, E. Borguet, Thin polymer film based rapid surface acoustic wave humidity sensors, Sensors and Actuators B: Chemical, 156 (2011) 444-449.

[10] R. Zhou, S. Vaihinger, K.E. Geckeler, W. Gopel, Reliable CO_2 sensors with silicon-based polymers on quartz microbalance transducers, Sensors and Actuators B: Chemical, 19 (1994) 415-420.

[11] J.H. Choi, S.J. Kim, M.S. Jung, S.J. Kim, Development of a polymer-coated SAW sensor for detection of CO_2 gas, in: 3rd International Conference on Electrical, Electronics and Civil Engineering (ICEECE'2013), Bali, Indonesia, 2013, pp. 38-41.

[12] C. Lim, W. Wang, S. Yang, K. Lee, Development of SAW-based multi-gas sensor for simultaneous detection of CO_2 and NO_2, Sensors and Actuators B: Chemical, 154 (2010) 9-16.

[13] W. Wang, C. Lim, K. Lee, S. Yang, Wireless surface acoustic wave chemical sensor for simultaneous measurement of CO_2 and humidity, J. Micro/Nanolith. MEMS MOEMS, 8 (2009) 031306.

[14] A.E. Hoyt, A.J. Ricco, J.W. Bartholomew, G.C. Osbourn, SAW Sensor for the Room-Temperature Measurement of CO_2 and Relative Humidity, Analytical Chemistry, 70 (1998) 2137-2145.

[15] W.P. Jakubik, Surface acoustic wave-based gas sensors, Thin Solid Films, 520 (2011) 986-993.

[16] A.J. Ricco, S.J. Martin, T.E. Zipperian, Surface acoustic wave gas sensor based on film conductivity changes, Sensors and Actuators B: Chemical, 8 (1985) 319-333.

[17] S.A. Koyilothu, R.A. Raghurama, SAW based CO_2 Sensors using Carbon Nanotubes as the Sensitive Layer, in, Honeywell International, U.S.A., 2008.

[18] K.G. Ong, K. Zeng, C. Grimes, A Wireless, Passive Carbon Nanotube-Based Gas Sensor, IEEE Sensors Journal, 2 (2002) 82-88.

[19] B. Serban, A.K.S. Kumar, S. Costea, M. Mihaila, O. Buiu, M. Brezeanu, etc, Surface Acoustic Wave CO_2 Sensing with Polymer-Amino Carbon Nanotube Composites, in: 2008 International Semiconductor Conference (CAS 2008), Sinaia, Romania 2008, pp. 73-76.

[20] A. Star, T.-R. Han, V. Joshi, J.-C.P. Gabriel, G. Gruner, Nanoelectronic Carbon Dioxide Sensors, Advanced Materials, 16 (2004) 2049-2052.

[21] S. Sivaramakrishnan, R. Rajamani, C.S. Smith, K.A. McGee, K.R. Mann, N. Yamashita, Carbon Nanotube-Coated Surface Acoustic Wave Sensor for Carbon Dioxide Sensing, Sensors and Actuators B: Chemical, 132 (2008) 296-304.

[22] H.-w. Lo, Y.-C. Tai, Characterization of Parylene as a Water Barrier via Buried-in Pentacene Moisture Sensors for Soaking Tests, in: 2007 2nd IEEE International Conference on Nano/Micro Engineered and Molecular Systems (NEMS '07), Bangkok, Thailand, 2007

Simultaneous Remote Transfer of Accurate Timing and Optical Frequency Over a Public Fiber Network

Olivier Lopez, Christian Chardonnet, Anne Amy-Klein
Laboratoire de Physique des Lasers,
Université Paris 13, Sorbonne Paris Cité, CNRS,
Villetaneuse, France

Amale Kanj, Paul-Eric Pottie, Daniele Rovera, Joseph Achkar
LNE-SYRTE,
Observatoire de Paris, CNRS, UPMC,
Paris, France
paul-eric.pottie@obspm.fr

And Giorgio Santarelli
Laboratoire Photonique, Numérique et Nanosciences,
Université de Bordeaux 1, Institut d'Optique and CNRS,
Talence, France

***Abstract*— A two-way method to simultaneously transfer an ultra-stable optical frequency and an accurate timing over a fiber links is presented. The ultra-stable laser acts as frequency standard and as carrier for timestamps. Timestamps signals are encode by phase modulation with a spread spectrum pseudorandom modulation at 20 Mchip/s, provided by a pair of two-way satellite time transfer modems, one for each direction.**

Keywords— Time and frequency metrology, fiber links

I. Introduction

Ultra-stable optical fiber links have been successfully developed for 5 years enabling precise and accurate frequency transfer. The fractional frequency stability experimentally demonstrated is in the range of 10^{-18} after only 3 hours of measurement and frequency accuracy of a few 10^{-19}. Last year ground-breaking frequency transfer has been demonstrated on a record distance of 920 km on dedicated fiber [1]. Fiber links techniques were extended in our joined group to public fiber networks with simultaneous data traffic, providing a scalable technique at the continental level [2,3]. Fiber links with active noise compensation after a round trip demonstrated much more stable and accurate frequency comparisons than satellite-based frequency comparisons, achieved after a much shorter averaging time. This gives a tool for accurate remote clock comparisons, as modern atomic clocks having already demonstrated accuracy in the range of 10^{-16} or below [4-8]. This technique can also play a key-role in advanced time-frequency metrology and for advanced tests of fundamental physics [9]. Accurate frequency comparisons are essential for modern geodesy, high resolution radio-astronomy, and particle physics.

Not only frequency transfer but also accurate timing is important as it gives the ability to precisely synchronize distant experiments or distant detectors. A salient case is the neutrinos speed measurement from CERN to Gran Sasso. Fiber-optical two-way time transfer methods have been demonstrated on dedicated links with an accuracy of the order of one hundred of ps or better [10,11]. Long distance accurate time dissemination is usually based on GNSS signals, or geostationary telecommunication satellites, with timing accuracy of the order of 1 ns in the best case [12,13]. In this work we present a novel method based on two-way transfer method, to simultaneously disseminate an ultra-stable optical frequency and accurate timing over a public telecommunication network. The link is 540 km long, and carry simultaneously our signals on a dedicated "dark" channel and Internet data traffic on the other channels.

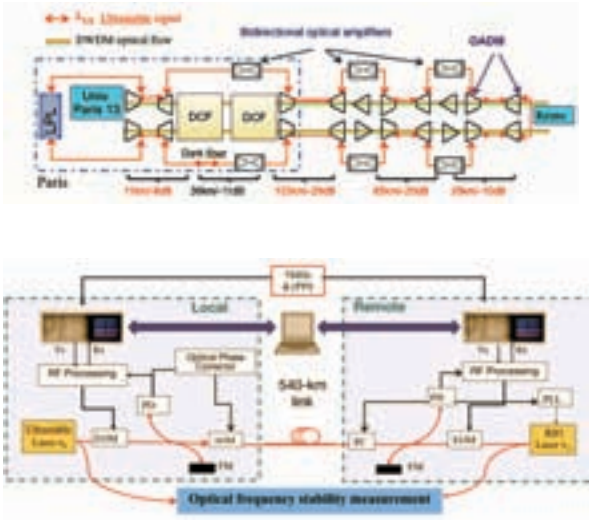

Fig. 1 : (a) 540-km link architecture. OADM (Optical Add-Drop Module), DWDM (Dense Wavelength Division Multiplexing), DCF (Data Center facility) (b) Sketch of the experimental set-up; FM : Faraday mirror, PD : photodiode, AOM : acousto-optic modulator, EOM : electro-optic modulator, OPC : Optical Phase Stabilization Correction, PLL : Phase-Locked Loop.

II. Experimental set up

A. Link architecture

At start our method exploits an ultra-stable laser at 1542 nm to carry both the frequency information as shown in

Ref [3] and the time stamps. The 540 km-long optical link (LPL-Reims-LPL) depicted in Fig. 1a is identical to the one reported in [3]. The timing signal is encoded through optical phase modulation. The scheme of the experiment is shown Figure 1b. Both ends of the links are located at the laboratory (Laboratoire de Physique des Lasers (LPL)). The French National Research and Education Network (NREN) RENATER give us access to the fibers of their network and allow us to set up our own equipment on the lines. The optical link is composed of five different fiber spans. Each span consists of two identical parallel fibers. The third, fourth and fifth spans are long-haul intercity links simultaneously carrying internet data traffic. Optical Add-Drop Multiplexers (OADMs) enable to add and drop the science signal in or from the telecommunication fibers. Total end-to-end attenuation for the 540 km link is 165 dB. 6 bi-directional amplifiers amplify the science signal by about 100 dB, so that the net optical losses exceed 65 dB. Figure 1b shows the hybrid time comparison and ultra-stable optical frequency distribution system. The detailed description of the ultra-stable optical frequency dissemination is given in [3].

B. Frequency transfer

As it was largely described elsewhere [2,3], we briefly remind the reader about the operation of the optical ultra-stable frequency transfer: The frequency signal consists of the frequency of an ultra-stable cavity-stabilised laser, which is partially coupled into the optical fiber. After a round trip propagation through the optical link, the fiber propagation noise is detected with an unbalanced Michelson interferometer where the returning back signal beats with the input signal. The phase noise is compensated by applying corrections with an Acousto-Optical Modulator (AOM) operated around 40 MHz. For the sake of simplicity we gather all error signal processing functions into a symbolic box called Optical Phase Correction (OPC). At the far end of the link the optical signal is regenerated by a narrow linewidth laser (3 kHz), phase-locked on the incoming light, and frequency-offset by 79 MHz. The optical frequency transfer stability is obtained by measuring the optical beat-note between the ultra-stable laser from the LOCAL subpart and the phase locked laser in the REMOTE subpart.

C. Accurate Timing transfer

Concerning time transfer, signals are provided by a pair of two-way satellite time transfer modems [15]. The transfer modems generate a pseudorandom noise modulation code at 20 Mchip/s carried on a radio frequency carrier around 70 MHz, that is related to the one-pulse-per-second (1 pps) and 5 MHz reference signals from a common clock. Orthogonal specific pseudo-random codes are allocated to each modem device. These equipments correlate the received signal with a local replica of the signal expected from the transmitting site and measures the time of arrival of the received signal with respect to the local clock. The time of arrival of both modems are collected by a computer. The data are then processed to compute the differential time delays.

We choose a low-index phase-modulation on the optical carrier to encode the time signal, so that enough energy is kept on the carrier and the signal-to-noise ratio is preserved for frequency transfer. Phase modulation is done at each link end with fiber pigtailed electro-optical modulator (EOM) exhibiting 4 dB insertion loss. The RF carrier frequencies are shifted shifted by 300 MHz, in order to avoid interference between optical signals and to enable efficient filtering of the time comparison signals. The low modulation depth (~1%) and the spread spectrum nature of the modulating time signals lead to a very pure optical spectrums, so that the optical frequency is transferred almost without degradation. The time signals are extracted by a second optical heterodyne beat-note of the local laser with the incoming signal at each link end, shifted in frequency. After successive frequency mixing and filtering the spread spectrum time signals are processed by the modems. Considering the frequency width of the pseudo-random codes (~20 MHz) and the large dynamic range of the signals in the detection system where parasitic signals are 40 dB larger than the useful signal, the RF processing of the signal is not trivial and require high performance filters and cautious operation.

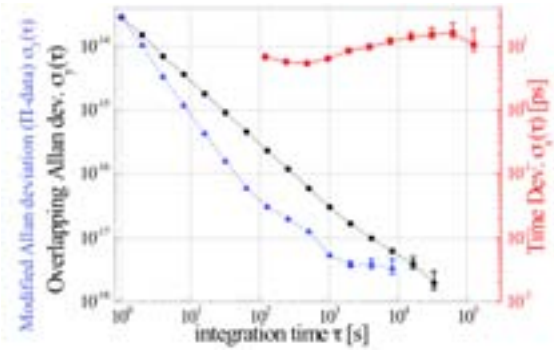

Fig. 2 : Left axis : Overlapping Allan deviation and modified Allan deviation of the frequency transfer as function of the integration time, while transferring an accurate timing. Right axis : Time deviation of the differential delay as a function of the integration time, while transferring an optical frequency.

III. RESULTS

The frequency transfer stability and the timing stability/ jitter were simultaneously measured and are plotted in Fig. 2. The frequency stability of the link reaches a resolution of $2x10^{-18}$ at 30 000 s averaging time, which is almost identical to the one reported in [3]. The accuracy of the frequency transfer is about $2x10^{-18}$. The time stability exhibits a noise smaller than 20 ps over the whole measurement time period.

We proceed standard calibration techniques to estimate the contribution of the varying delay of propagation to the uncertainty budget [15]. As the fiber optical length is unknown and fluctuates over time, a rigorous calibration test is indeed needed to guarantee the independence of the system from the optical fiber length. The propagation length was changed by short-cutting the links in the accessible places. We vary the link length from 10 m to 94 km, 400 km and the total length of 540 km. We measure that the differential time delay variation versus distance is at most 50 ps. We also performed several tests of disconnection/connection, power shutdown and restart without measuring appreciable time delay variation. Tests on fiber spools of 25 km, 50 km, 75 km and 100 km are consistent with the above reported results.

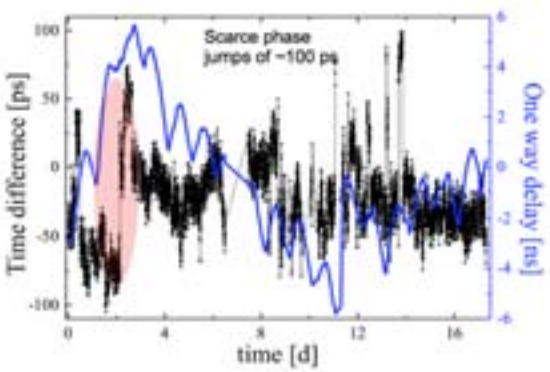

Fig. 3 : One-way time delay (blue plot, right axis) and differential delay (black plot, left axis) versus time for the 540-km fiber link (constant calibration time offset removed on both plots)

A variable optical attenuator was inserted into the common fiber path in order to keep the overall link attenuation approximately constant within ±2 dB. The delay variations in the modems depending on the variation of the received power were thus reduced. We checked experimentally the system sensitivity by changing the power of the signals from the optical detection up to the modem input. As long as the modems are operated in their optimal conditions (i.e. low input power level), the system shows a coefficient dependencies below 15ps/dB.

Fiber chromatic dispersion (FCD) play here a very little role as the frequency difference between the two counter-propagating time signals is very small. For instance FCD contribution for 300 MHz frequency difference between the 2 ways and for the 540-km link is below 25 ps. Polarisation Mode Dispersion (PMD) contributes also to the uncertainty budget. Derived from previous telecommunication fiber network characterization we estimates the timing fluctuations due to PMD well below 20 ps. This was confirmed by experiment by varying the input polarization state with Lefevre's three-loop rotating wave plate. We did not observe any significant variation within a measurement resolution of 50 ps. As both time measurements are collocated in this experiment, the set-up is not sensitive to the Sagnac effect and its contribution is therefore void.

The preliminary conservative accuracy budget we achieve with this experiment is 250 ps. The results is mainly dominated by scarce phase jumps of about 50-80 ps we observed on the datas. They can be related related to the propagation in the long-haul Internet fiber link, dysfunction of the SATRE modems, or uncontrolled effects within the RF processing chain. Additional tests performed by replacing the long-haul link with fiber spools did not reveal any phase jumps over several days of measurements. Despite efforts on the analysis and several trials to fix it, and due to their random and rare statistics, the cause of such behavior is not yet understood. The system is nonetheless quite robust : in addition to the results presented in Figure 3, we have several runs of about one week for which the peak-to-peak time fluctuations are below 200 ps while one-way fluctuations are in excess of 10 ns. The results in terms of timing stability and accuracy clearly outperform the satellite techniques [12].

Such technique can be extended to a wider range, in the case of slightly lower fiber losses and better distribution of the optical amplification. We believe that this method of accurate time transfer can be also extended to segmented optical links by the use of intermediate optical regeneration stations [2,3] which include RF signal processing techniques and station delay calibration procedures. Our method can be improved for example by developing new modems with wider pseudo-random codes. For a solely time transfer, the ultra-stable laser is not needed and the scheme proposed here can be drastically simplified. We point out finally that the use of heterodyne detection allows operation with very large optical losses, for which classical Intensity Modulation (IM) techniques are ineffective. This method has been proven to be applicable to non-dedicated fiber and installed long-haul fiber links carrying Internet data, opening the way to frequency and time dissemination on a continental scale via NRENs and european counter-part that could be used for that purpose.

The authors gratefully acknowledge fundings from Laboratoire National d'Essai, Agence Nationale pour la Recherche (contract ANR BLANC 2011-BS04-009-01), Université Paris 13 and IFRAF-Conseil Régional Ile-de-France.

REFERENCES

[1] K. Predehl, G. Grosche, S. M. F. Raupach, S. Droste, O. Terra, J. Alnis, Th. Legero, T. W. Hänsch, Th. Udem, R. Holzwarth, and H. Schnatz, Science 336, 441 (2012).

[2] O. Lopez, A. Haboucha, F. Kéfélian, H. Jiang, B. Chanteau, V. Roncin, C. Chardonnet, A. Amy-Klein, and G. Santarelli, Opt. Express 18 16849 (2010).

[3] O. Lopez, A. Haboucha, B. Chanteau, C. Chardonnet, A. Amy-Klein, and G. Santarelli, arXiv:1206.5591 (2012).

[4] J. Guena, M. Abgrall, D. Rovera, P. Laurent, B. Chupin, M. Lours, G. Santarelli, P. Rosenbusch, M.E. Tobar, R. Li, K. Gibble, A. Clairon and S. Bize, IEEE Trans. on Ultras., Ferro. and Frequ. Contr. 59, 391 (2012).

[5] S. Weyers, V. Gerginov, N. Nemitz, R. Li and K. Gibble, Metrologia 49, 82 (2012)

[6] H. Katori, Nature Photon. 5, 203 (2011) and references therein

[7] M. D. Swallows, M. Bishof, Y. Lin, S. Blatt, M. J. Martin, A. M. Rey, J. Ye, Science 331, 1043 (2011).

[8] N. Huntemann, M. Okhapkin, B. Lipphardt, S. Weyers, Chr. Tamm, E. Peik, Phys. Rev. Lett., 108, 090801 (2012)

[9] T C. W. Chou, D. B. Hume, T. Rosenband, and D. J. Wineland, Science 329, 1630 (2010)

[10] Ł. Śliwczyński, P. Krehlik, A. Czubla, Ł. Buczek and M. Lipiński, Metrologia **50** (2013) 133–145.

[11] M. Rost, D. Piester, W. Yang, T. Feldmann, T. Wübbena, A. Bauch, Metrologia **49**, 6, 772-778, (2012).

[12] M. Young, The Technical Writer's Handbook. Mill Valley, CA: University Science, 1989.

[13] D. Piester, A. Bauch, L. Breakiron, D. Matsakis, B. Blanzano and O. Koudelka, Metrologia 45,185, (2008).

[14] SATRE (Satellite Time and Ranging Equipment) TWSTFT (Two-Way Satellite Time and Frequency Transfer) TimeTech GmbH, www.Timetech.de.

[15] A. Bauch, D. Piester, M. Fujieda, and W. Lewandowski, Rapport BIPM2011/01, (2011)

LIFT-the Italian Link for Time and Frequency

F. Levi, D. Calonico, A. Mura, M. Frittelli,
C.E. Calosso and M. Zucco
INRIM, Torino, Italy.

C. Clivati and G. A. Costanzo.
Politecnico di Torino and INRIM, Torino, Italy.

R. Ambrosini.
INAF - Istituto di Radioastronomia, Bologna, Italy.

G. Galzerano,
CNR-IFN, Milano, Italy.

P. De Natale and D. Mazzotti
CNR-INO, Firenze and Sesto Fiorentino (FI), Italy.

N. Poli D. V. Sutyrin, and G. M. Tino
Università di Firenze, LENS and INFN, Sesto Fiorentino (FI), Italy

***Abstract*—We report on the realization of the coherent optical link for time and frequency dissemination developed in Italy. The fiber backbone connects scientific laboratories that need accurate time and frequency measurements located in Torino, Milano, Bologna and Firenze. We briefly describe the technique, and report the status of installation and preliminary characterization.**

Keywords—Fiber link, Time and Frequency transfer

I. INTRODUCTION

Optical fiber links are a key enabling technology for science and metrology. They are suitable for the remote comparison of very accurate clocks, such as Cs fountains or optical clocks [1-3] and their resolution exceeds the state-of-the-art satellite techniques by several orders of magnitude. The coherent optical link allows to exploit the accuracy of an optical clock in few hundred seconds over hauls up to hundreds of km, a performance otherwise impossible. This is an outstanding issue, as optical frequency standards are recommended by the BIPM for the secondary representation of the second in the International System (SI) of units, and are the most promising candidates for its future redefinition [4]. It is possible to achieve frequency dissemination (and comparisons) at the 10^{-16} level of stability [2,3] and time dissemination at the 100 ps level [5] over hauls of 1000 km. This level of resolution needs for the compensation of the phase noise introduced by the fiber due to mechanical stresses and temperature variations, using a bidirectional Doppler cancellation technique [6].

The National Institute of Metrology (INRIM) realizes in Italy accurate T&F signals and disseminates them to a variety of scientific laboratories and industries. Presently, INRIM maintains two Cs fountain primary frequency standards, with an accuracy at the 10^{-16} level [7], and is developing an optical clock based on Yb atoms [8]. To improve the quality of T&F dissemination, INRIM started together with other major National Institutions, the LIFT project (the Italian Link for Frequency and Time, funded within Progetti Premiali 2012), to realize an optical link along a 642 km fiber that connects Torino to Milano, Bologna, and Firenze.

The aim of the project is the distribution of the INRIM reference T&F signals to a variety of scientific laboratories via optical fiber, with a target relative instability of 10^{-14} at 1 s and 10^{-18} at one day measurement time. Those laboratories represent national centers of excellence in their fields; this facility will further improve their scientific capabilities, allowing them to better exploit existing experiments and to establish new ones in the future.

Present partners of the project are the National Institute of Nuclear Physics in Firenze (INFN), in collaboration with the European Laboratory for Non-linear Spectroscopy (LENS) and Department of Physics and Astronomy of University of Firenze; the National Institute of Astrophysics (INAF) in Medicina, near Bologna, and the National Council of Research (CNR) through the National Institute of Optics (INO) in Firenze and the Institute of Photonics and Nanotechnologies (IFN) in Milano.

Both INFN and CNR are involved in high resolution spectroscopic measurements, and will benefit from T&F dissemination via optical fiber. In particular, at LENS a Sr optical clock is under evaluation [9], and its frequency comparison to the frequency standards of INRIM could allow a number of new fundamental physics experiments. The INAF radiotelescope can be both an high demanding user of the external T&F standards as well as a source for their close inter comparison with Pulsar-derived time scales or with the Celestial Reference Frame defined via Very Long Baseline Interferometry (VLBI). Closing the loop between sky observations and the new atomic frequency standards, even spread in different Italian locations, could lead to detect subtle systematic effects or in any case improve both sides of science.

T&F measurements with improved resolution are expected to be performed from 2014, in the second stage of the project, whilst in the first start-up stage the fiber backbone will be fully characterized and preliminary tests and checks will be completed.

II. Coherent Time and Frequency Dissemination through Optical Fiber

A key point of the project is to use the same infrastructure to disseminate both time and frequency. When performing frequency dissemination, an ultrastable laser (1542 nm) is sent to the user, and its frequency is simultaneously measured in the two laboratories, with the aid of optical frequency combs. The frequency of the delivered laser is perturbed by environmental noise in the fiber. However, it is possible to compensate this noise with an optoacoustic actuator; this technique requires that the end laboratory redirects the incoming signal to the start laboratory, where the delivered signal is compared with the received one, and the added noise is cancelled in real time. For the noise cancellation to be effective, there must be a fully-optical backbone with no optical/electrical conversions, and the light has to travel exactly the same path in both directions. This is quite different from typical fiber transmission techniques, and poses several requirements on the optical instrumentation.

To disseminate time signals, a pseudorandom noise will be encoded on the optical carrier, similarly to the two way satellite time and frequency transfer: instead of cancelling the phase noise of the carrier itself, the measured transmission delay will be calibrated and stabilized, with a resolution of 100 ps.

The optical fiber used in our project is a ~ 640 km dedicated fiber, with a total loss of ~180 dB, due to hauls and connectors losses. To adequately compensate for optical losses, we installed dedicated, fully bidirectional Erbium-Doped Fiber Amplifiers (EDFAs) along the path, that use the same active fiber in both directions (Figure 1).

Fig. 1. The map shows the optical path and amplification sites.

III. Link Implementation and Characterization

One of the demanding steps of the link implementation is to compensate for the optical losses in such a bidirectional transmission scheme: the gain of our dedicated EDFAs could be set only with the whole link operating, as the gain and optical signal-to-noise ratio (OSNR) of each stage is affected by the others. Setting the gain below ~22 dB, we prevent oscillation lasing effects and OSNR degradation due to backscattering and Amplified Spontaneous Emission (ASE) [10]. Currently, 9 amplifiers have been installed, and optical filters have been used to keep the OSNR at an adequate level. In Figure 1, the optical path is shown with the location of the amplification sites; Table 1 reports for each station the distance from Torino and the optical losses of the haul. Measurements of the phase noise added by the fiber was performed during EDFA installation on several amplification sites, by reflecting the signal back towards INRIM. These measurements allowed us to check the noise contribution from each haul and the phase-compensation capabilities of the control loop.

Figure 2 shows the phase noise power spectral density of the back-reflected signal without the Doppler cancellation (free running fiber link). It represents the phase noise of the fiber up to three different intermediate stations. It is worth noting that the phase noise accumulated in the Bologna-Firenze track (100 km) is comparable to the remaining part of the link (450 km) and exceeds the expected figure by several dB. The reason for this excess of noise are under investigation with the fiber provider.

Figure 3 shows the phase noise power spectral density of the correction signal applied to the actuator when the compensation loop was activated on the full 642 km optical fiber link.

Location	Length	Losses
To-Lancia	25 km	9 dB
Santhia	67 km	18 dB
Novara	77 km	18 dB
Lainate	50 km	15 dB
Milano	60 km	18 dB
Piacenza	67 km	16 dB
Reggio Emilia	94 km	23 dB
Bologna	74 km	19 dB
Rioveggio	38 km	10 dB
Firenze	72 km	18 dB
LENS laboratories	18 km	7 dB

Table 1.Lenghts and losses of the various link hauls.

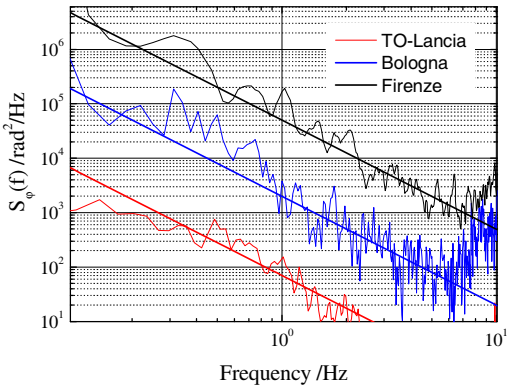

Fig. 2. Phase noise of several fiber link hauls: from INRIM to To-Lancia (25 km), to Bologna (+490 km) and to Firenze (+128 km). It is evident that anomaluos noise is present in the track between Firenze and Bologna.

Based on these measurements we can estimate the ultimate achievable stability of the transferred signal at Milano, Bologna and Firenze. The value obtained for the Torino Firenze link in terms of Allan deviation in 1 Hz bandwidth is

3×10^{-15}. This estimate is based on the assumption that the phase noise cancellation bandwidth is limited by the time (~ 6 ms) it takes the light to travel to the far fiber end and back [5].

Presently, we have completed and operated the link to Firenze but we have not yet extracted the signal for the intermediate users in Bologna and Milano. The laser transmitted from INRIM and delivered to LENS in Firenze is used as a reference to phase lock a 1542 nm diode laser. This laser is then frequency doubled and sent to a local Ti:Sa based optical frequency comb, to be compared with the local ultrastable laser at 698 nm used in the Sr clock experiment . In Figure 4 we report the frequency stability of the delivered laser measured against the local ultrastable laser in Firenze. There are also shown the stability of the free running fiber link (i.e. without noise compensation) and the stability of the 1542 nm laser at INRIM. The compensated link contribution is assessed to be $<1.5\times10^{-14}$ and does not degrade the stability performances of the delivered laser at 10 s. The Allan deviation of the delivered laser was measured in Torino using a twin stabilized laser as reference.

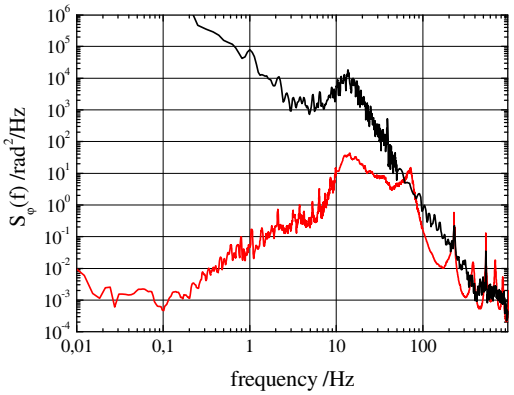

Fig. 3. Phase noise of the fiber link at Firenze (642 km), free running (black curve) and with Doppler compensation (red curve).

For an ultimate characterization, during next year, a second fiber link in an antiparallel configuration [2] is planned. This will allow us to determine the contribution of the non-compensated phase noise of the fiber itself, to detect possible sources of frequency inaccuracies, like cycle slips etc. and to state the ultimate stability performance of the optical link. Nevertheless, according to the preliminary characterization, the present optical link can already be used for frequency dissemination with high stability and accuracy.

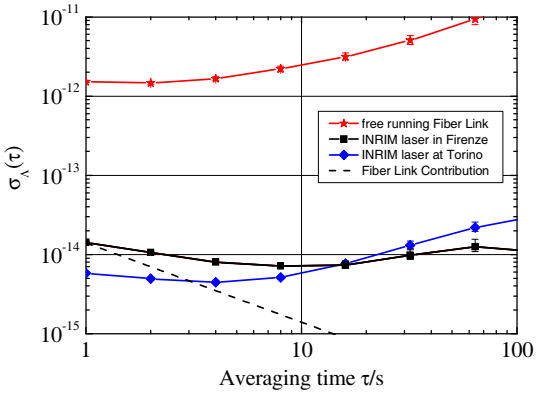

Fig. 4. Stability of the link: stablity of the free running link (red stars); stability of the INRIM 1542 nm laser measured at LENS vs the 698 nm Sr clock laser in closed loop (black squares); stability of 1542nm laser measured at INRIM (blu diamonds) and the deduced contribution of the compensated link (dashed line). Note that the measurement of the laser stability at INRIM is not taken contemporarely to the one in Firenze, hence the fluctuation of the noise around 100 s.

IV. Conclusions

We report on the implementation and preliminary characterization of the 642 km fiber link connecting Torino to Milano, Bologna and Firenze within the LIFT project. At present, the fiber backbone has been implemented and preliminary characterization is being carried on. The amount of phase noise added by the optical fiber that cannot be compensated is not a limitation, and we estimated that frequency dissemination at the 10^{-16} level of stability in few minutes of averaging time can be obtained. Experiments related to time distribution will also be performed in the next months.

Fiber frequency dissemination represents a dramatic improvement with respect to satellite techniques, and enables frequency comparisons and calibrations at unprecedented levels of uncertainty, paving the way for a number of scientific experiments in the fields of high resolution spectroscopy, radio-astronomy, fundamental physics.

The development of this National network is of major interest also for high–tech industries, making available high quality T&F signals in real time, without need of routine calibration. This infrastructure will be easily adapted to perform widespread dissemination towards a larger variety of users, with reduced costs. This secondary dissemination will use optical fibers as well, but instead of optical carrier it will distribute an amplitude modulated signal, much easier to be detected and used.

V. Acknowledgments

The authors thank G. Santarelli, H. Schnatz, G. Grosche and P. E. Pottie for their help and advice.

University of Florence thanks PTB for providing the 698 nm laser used in the characterization of the link.

University of Firenze, Politecnico of Torino and INRIM acknowledge the Italian Ministry of Education, University and Research (PRIN09-2009ZJJBLX) for funding the optical link.

INRIM acknowledges Compagnia di S. Paolo, the Italian Ministry of Education, University and Research (Progetti Premiali 2012), and the EMRP program (Project SIB02-NEAT-FT) for funding. The EMRP is jointly funded by the EMRP participating countries within EURAMET and the European Union.

University of Firenze acknowledges Ente Cassa di Risparmio di Firenze for funding.

The authors acknowledge GARR for the technical help with the fiber.

REFERENCES

[1] C. W. Chou, D. B. Hume, J. C. J. Koelemeij, D. J. Wineland, and T. Rosenband, "Frequency Comparison of Two High-Accuracy Al+ Optical Clocks," Phys. Rev. Lett. 104, 070802 (2010).

[2] O. Lopez, A. Haboucha, F. Kéfélian, H. Jiang, B. Chanteau, V. Roncin, C. Chardonnet, A. Amy-Klein, G. Santarelli, "Cascaded multiplexed optical link on a telecommunication network for frequency dissemination," Opt. Express 18, 16849-16857 (2010).

[3] K. Predehl, G. Grosche, S. M. F. Raupach, S. Droste, O. Terra, J. Alnis, Th. Legero,T. W. Hänsch, Th. Udem, R. Holzwarth, H. Schnatz, "A 920-Kilometer Optical Fiber Link for Frequency Metrology at the 19th decimal place," Science 336, 441-444 (2012).

[4] Bureau International Des Poids et des Mesures, Consultative Committee for Time and Frequency (CCTF), Report of the 19th meeting (13–14 September 2012) to the International Committee for Weights and Measures, http://www.bipm.org/utils/common/pdf/CCTF19.pdf

[5] O. Lopez, A. Kanj, P. Pottie, D. Rovera, J. Achkar, C. Chardonnet, A. Amy-Klein, G. Santarelli "Simultaneous remote transfer of accurate timing and optical frequency over a public fiber network" Appl. Phys. B 110, 3–6 (2013).

[6] P. A. Williams, W. C. Swann, and N. R. Newbury, "High-stability transfer of an optical frequency over long fiber optic links," J. Opt. Soc. Am. B 25, 1284-1293 (2008).

[7] F. Levi, C. Calosso, D. Calonico, L. Lorini, E. K. Bertacco, A. Godone, G. A. Costanzo, B. Mongino, S. Jefferts, T. P. Heavner, E. A. Donley "Cryogenic Fountain Development at NIST and INRIM: Preliminary Characterization", IEEE Trans. Ultrason. Ferroelectr. Freq. Control 57, 600-605, (2010).

[8] M. Pizzocaro, G. A. Costanzo, A. Godone, F. Levi, A. Mura, M. Zoppi, D. Calonico, "Realization of an Ultrastable 578 nm Laser for an Yb Lattice Clock", IEEE Trans. Ultrason. Ferroelectr. Freq. Contr. 59, 3, 426431 (2012).

[9] N. Poli, M. G. Tarallo, M. Schioppo, C. W. Oates and G. M. Tino "A simplified optical lattice clock", Appl. Phys. B 97, 27-33 (2009).

[10] L. Sliwczynski and J. Kolodziej, "Bidirectional Optical Amplification in Long-Distance Two-Way Fiber-Optic Time and Frequency Transfer Systems", IEEE Trans. Instrum. Meas. 62, 1, (2013).

Optical Infrastructure for Time and Frequency Transfer

Vladimir Smotlacha and Josef Vojtěch
Research Department
CESNET z.s.p.o
Prague, Czech Republic
Email: vs@cesnet.cz, vojtech@cesnet.cz

Alexander Kuna
Time and Frequency Department
Institute of Photonics and Electronics AS CR, v.v.i.
Prague, Czech Republic
Email: kuna@ufe.cz

***Abstract*—The paper describes optical infrastructure for time and frequency transfer in the Czech republic. The infrastructure is heterogeneous and utilises resources of the Czech academic optical network. It allows to interconnect Cesium standards in distant sites with the national time and frequency laboratory and to distribute accurate time and stable frequency. We also present results and compare them with other methods of time transfer.**

I. Introduction

The request for accurate time and stable frequency transfer has significantly increased in recent years. As the standard methods using satellite navigation system like GPS are reaching their limits, the most challenging technology is based on optical fibers. There were developed techniques utilizing one-way transfer or two-way transfer in either single fiber or pair of fibers. We can observe increased number of both theoretical studies and practical field implementations. This paper describes design of dedicated optical infrastructure for time and frequency transfer (TF-infrastructure) in the Czech Republic. We also present our experience and first results.

The TF-infrastructure uses resources provided by existing Czech National Research and Educational Network (NREN) that is based on DWDM (Dense Wavelength-Division Multiplexing) technology. The network is operated by CESNET which is for several years involved in time and frequency metrology applications that use optical links and cooperates with the National Time and Frequency Standard in Institute of Photonics and Electronics (UFE). Both organizations are also participants of European research project NEAT-FT [5].

Present networks are designed for simultaneous transmission of data streams. Data are typically packetized and are processed in electronic devices, e.g. routers and switches. This involves necessity of repeated conversions from optical to electrical domain and vice versa - OEO. Statistical multiplexing of packets, digital signal processing and repeated OEO causes that precise timing of data in packet networks is not guaranteed at the link layer. Time and frequency transfer shall be implemented at physical layer that provides dedicated optical channels isolated each to other.

II. Project Goals

The design of TF-infrastructure is based on our preliminary experience with time transfer between Czech and Austrian national time and frequency laboratories UFE and BEV [4], whose regular operation started in August 2011. The topology is determined be existing DWDM network extended by dedicated dark fiber links.

TF-infrastructure is heterogeneous platform that covers many current and near future tasks of involved organizations. The goals include:

- Transfer time from several deployed Cesium primary standards and Hydrogen masers to LNTFS in UFE. Higher number of these interconnected clocks will improve accuracy and stability of UTC(TP) - the national approximation of UTC time scale.
- Compare national approximation of UTC with that one in neighboring countries.
- Check accuracy and stability of other connected atomic clocks.
- Distribute accurate time and stable frequency to demanding users.
- Obtain experience with the coherent frequency transfer as a preliminary activity aimed at intended building of optical clock.

Fig.1 shows the actual state of the TF-infrastructure: it joins four organization that operate atomic clocks and another two organizations that are provided by atomic time scale or frequency. The TF-infrastructure includes also links to neighboring countries Austria and Poland. The link to BEV in Vienna is in use and connectivity to Polish network is ready and we are able to set up time transfer channel to Polish laboratories GUM (Warsaw) or AOS (Borowiec).

III. Technology

The TF-infrastructure physical topology is a star with center in CESNET, while the transport layer topology is a star having center in Institute of Photonics and Electronics (UFE). The dark fiber between these two localities is currently used for time transport UFE – BEV but we are going to install there a DWDM system providing at least 16 bidirectional channels. Links between CESNET and involved organizations utilize available technology, in most cases it is a combination of commercial and open DWDM transmission systems:

- pair of channels (with the same wavelength in both directions) in a production DWDM optical network,

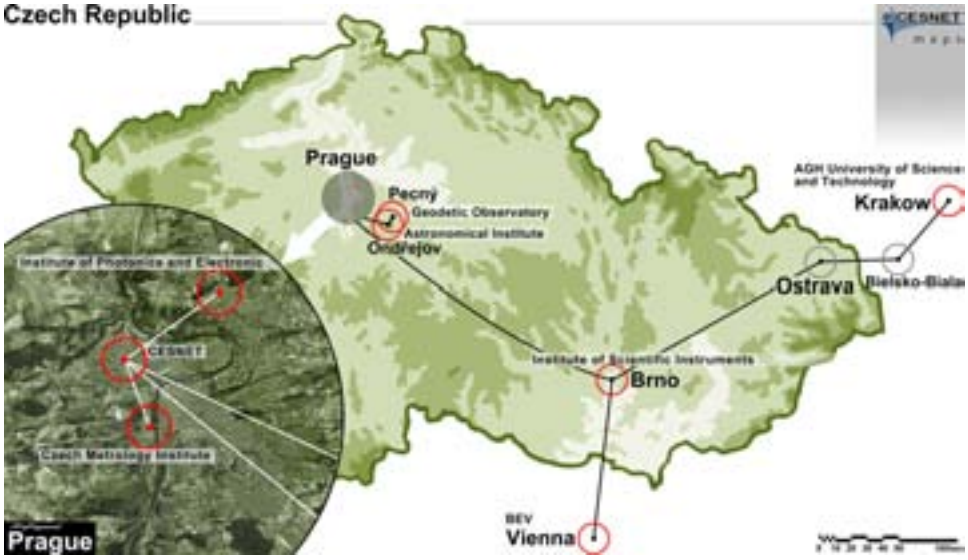

Figure 1. Map of TF-infrastructure

- pair of DWDM channels with different wavelengths in single fiber bidirectional transmission system,
- pair of DWDM channels (both uni- and bi-directional) in experimental links,
- dark fiber – usually the last mile in the urban area.

Despite this heterogeneous physical layer, the transport layer provides parameters required for accurate time transfer. Currently, channels for time transport are amplified by the same unidirectional amplifiers that are used for standard data channels but we already developed own bidirectional amplifiers in scope the project CzechLight [6]. Once deployed, these amplifiers will be dedicated for time (resp. frequency) transfer only. In future, we plan to install these new amplifiers even in the CESNET backbone links.

Typical example of TF-infrastructure is a fiber shared for both time transfer and standard data service (2x 10Gb/s) between CESNET and VUGTK (Geodetic Observatory in Pecny) as is depicted in Fig. 2. The geographical distance between both sites is 35.2 km. The main part of the line is represented by a 78 km long single fibre which has attenuation of about 21.2 dB. The link setup reserves four unamplified wavelengths in ITU grid for time transfer and supports up to 16 amplified DWDM wavelengths for standard 10Gbit/s Ethernet data channels. Time transfer wavelengths are available at connectors of ADD/DROP filters (see Fig.2). The direction CESNET to VUGTK uses channel #38 (1546.92 nm) of the ITU grid, the opposite direction uses channel #39 (1546.12 nm).

The link CESNET – VUGTK is considered a pilot implementation of the TF-infrastructure. Another part of it is the link to Vienna which is used for continuous time transfer between UFE and BEV for already two years [4]. Table I summarizes features of both links.

Table I. PAMETER OF TIME TRANSFER SETUP

	UFE – BEV	CESNET – VUGTK
Fiber	pair of unidirectional fiber	single bidirectional fiber
ITU channel (wavelength)	#32 (1551.72 nm) in both direction	#38 (1546.92 nm) and #39 (1546.12 nm)
Fiber length	550 km	78 km
Amplifiers	7x EDFA	no
Counters	SR-620 and CNT-91	interpolatin counter in FPGA

IV. RESULTS

Time transport between CESNET and VUGTK utilizes single bidirectional fiber, therefore symmetrical change of propagation delay, e.g. temperature dependence of chromatic dispersion, cancels in the first order. Similarly cancels influence of possible change of the fiber physical length, for example when the provider replaces a patch cord in the switch board. Possible exception of optical paths symmetry represents the fiber inside ITU grid filters (see the ADD/DROP elements in Fig.2) - length of that fiber 'pigtails' must be measured and the difference of propagation delay $T_{\Delta L}$ calculated.

As different wavelength is used in both directions, the corresponding propagation delay diference is done by formula:

$$T_{\Delta\lambda} = D_{fiber} \cdot \Delta\lambda \cdot L + D_{filter} \cdot \Delta\lambda \qquad (1)$$

Paper [3] discusses influence of other effects - Sagnac effect and birefringence of the fiber. However, these values are negligible for our link length compared with chromatic dispersion contribution.

The total difference of fiber propagation delay is:

$$\Delta T = T_{\Delta\lambda} + T_{\Delta L} \qquad (2)$$

Both terms in (2) can be calculated, therefore we can perform the calibration without using any other time transport system. In our case, $T_{\Delta L} = 0$ as fiber 'pigtails' length inside both filters match. Substituting wavelength difference 0.8 nm,

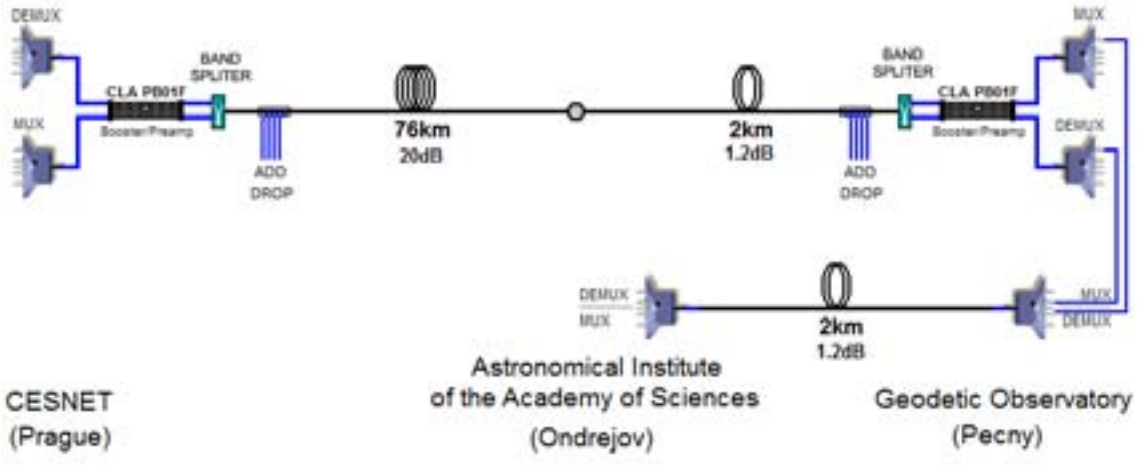

Figure 2. Link CESNET – VUGTK

filter chromatic dispersion 120 ps/nm, total fiber length 78 km, and 17 ps/nm/km as the chromatic dispersion coefficient for fiber type G.652 into (1), we evaluate propagation delay difference $\Delta T = 1.16$ ns.

The uncertainty of time transfer also depends on several physical effects, e.g. polarization mode dispersion, thermal dependency of refractive index of directionally disjoint paths (patchcords and filters), thermal dependency of fiber chromatic dispersion coefficient, and filters central wavelength thermal dependency. According to detailed analyzes in [3], uncertainty of any of these effects is up to few picoseconds and the sum does not exceed 10 ps for our setup. The common contribution to time transfer uncertainty is half of propagation delay uncertainty, i.e. no more than 5 ps. Similar contribution provides the uncertainty of 'pigtails' length measurement – error of 1 mm represents time difference of 5 ps. All these values are below main source of uncertainty, the error of utilized time interval counters. In former setup we used universal time interval counters SR-620 and Pendulum CNT-91, having random error 20 ps, resp. 50 ps. Recently, we developed own time interval counters based on interpolation delay line implemented in the FPGA chip having resolution about 20 ps. Detailed counter evaluation was not yet done but the estimated accuracy is 40 ps.

Fig. 3 and Fig. 4 provide comparison of optical time transfer with GPS based methods in term of TDEV for both UFE – BEV and CESNET – VUGTK. Graphs confirm that optical time transfer has smaller noise then both PPP method for both links. Noticable white phase noise is about 3 times lower in case of CESNET – VUGTK time transfer. The reason is probably the symmetry of the optical path due to single fiber without any optical amplifiers.

Evaluated difference (in 300 s intervals) between PPP and optical time transfer is shown in Fig. 5 and Fig. 6, respectively. Standard deviation of the difference between both measurements is 62 ps for link CESNET – VUGTK and 95 ps for UFE – BEV.

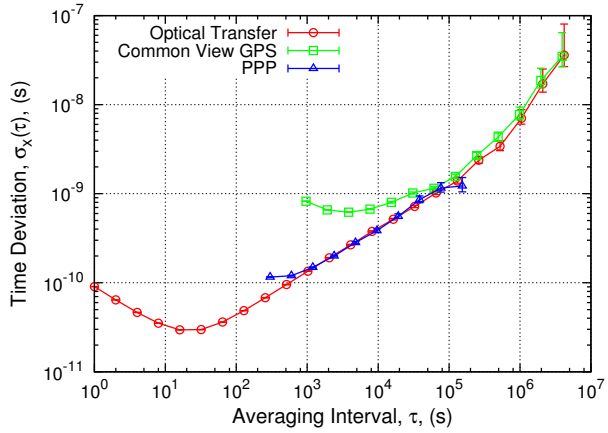

Figure 3. UFE – BEV time transfer stability

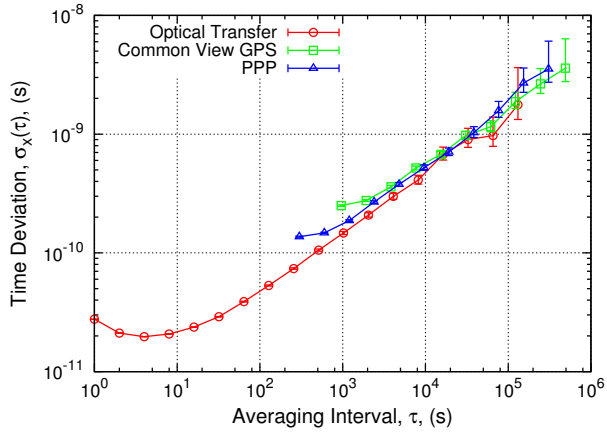

Figure 4. CESNET – VUGTK time transfer stability

ACKNOWLEDGMENT

This work was supported by the Ministry of Education, Youth and Sport of the Czech Republic as part of the CESNET Large Infrastructure project LM2010005 and by Technology Agency of the Czech Republic grant TA01011105.

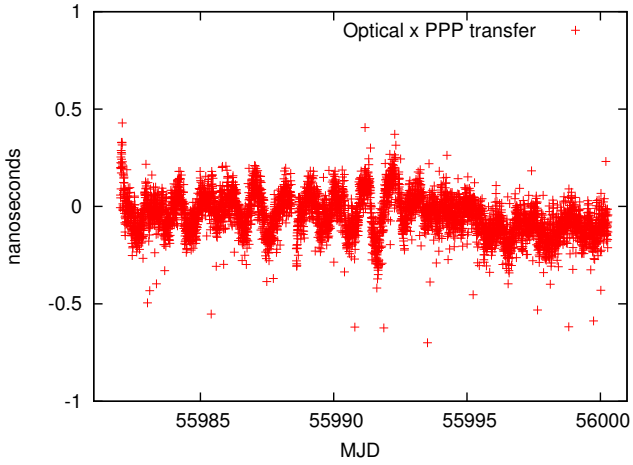

Figure 5. UFE – BEV diference between optical and PPP time transfer

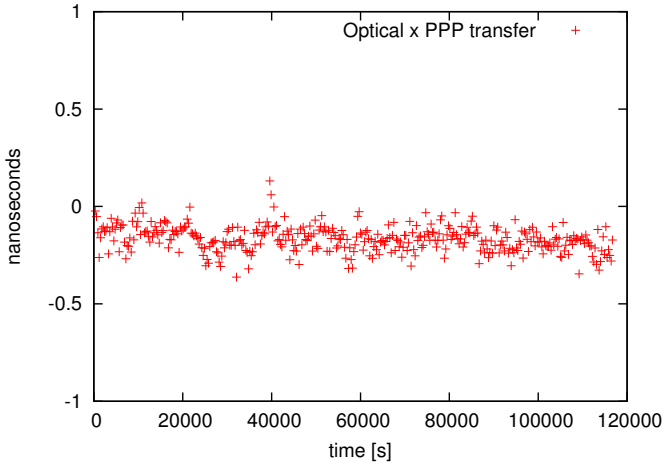

Figure 6. CESNET – VUGTK diference between optical and PPP time transfer

REFERENCES

[1] V. Smotlacha, A. Kuna, and W. Mache, 2010, *Time Transfer in Optical Network*, in Proceedings of the 42nd Annual Precise Time and Time Interval (PTTI) Systems and Applications Meeting, 15–18 November 2010, Reston, Virginia, USA, (U.S. Naval Observatory, Washington D.C.), pp. 427–436.

[2] G. P. Agrawal, *Fiber-Optic Communications Systems*, third edition, John Wiley & Sons, Inc., 2002.

[3] L. Sliwczyzski, P. Krehlik, A. Czubla, L. Buczek, M. Lipinski, *Dissemination of time and RF frequency via a stabilized fibre optic link over a distance of 420 km*, Metrologia, vol. 50, no. 2, pp. 133–145, 2013.

[4] V. Smotlacha, A. Kuna, *Two-way optical time and frequency transfer between IPE and BEV*, European Frequency and Time Forum (EFTF), 23–27 April 2012, Gothenburg, pp. 375–378, 2012.

[5] *Project NEAT-FT*, http://www.ptb.de/emrp/neatft_home.html.

[6] *Project CzechLight*, http://czechlight.cesnet.cz/en.

TWSTFT Calibration Involving Four Sites Using a Mobile Sation on a Trailer

Thorsten Feldmann, Arvind Balu, Shuo Liu, Wolfgang Schäfer
TimeTech GmbH
Stuttgart, Germany
Thorsten.Feldmann@timetech.de

Andreas Bauch, Jürgen Becker, Dirk Piester
Physikalisch-Technische Bundesanstalt (PTB)
Bundesallee 100
38116 Braunschweig, Germany

Joseph Achkar, Amale Kanj*
Observatoire de Paris (OP/LNE-SYRTE)
Paris, France

Christian Schlunegger, Jacques Morel
Federal Institute of Metrology (METAS)
Bern-Wabern, Switzerland

***Abstract*— In November 2012 the time transfer links between Physikalisch-Technische Bundesanstalt (PTB), Observatoire de Paris (OP/LNE-SYRTE), Swiss Federal Institute of Metrology (METAS), and TimeTech GmbH were calibrated using TimeTech's mobile TWSTFT calibration station for the first time.**

Keywords: TWSTFT; link calibration; mobile station

I. INTRODUCTION

Calibrated time transfer between two remote locations using the Two-Way Satellite Time and Frequency Transfer (TWSTFT) technique with telecommunication satellites requires the accurate knowledge of the internal delays of the equipment involved, the asymmetry between signal paths, and the delays of the connections of the equipment to local time scales. In case of a single satellite transponder used for both signal paths, these delays depend only on the ground equipment, because free space and atmospheric induced delays cancel out in the two-way combination. A single transponder also enables time transfer between two stations located at the same site. The traveling station is operated together with the fixed equipment at each site in a common-clock setup for some days. For each pair of ground sites the differences between the common-clock data reflect the delays of the fixed stations, while ideally the delays associated with the traveling equipment cancel out.

In November 2012 the time transfer links between Physikalisch-Technische Bundesanstalt (PTB), Observatoire de Paris (OP/LNE-SYRTE), Swiss Federal Institute of Metrology (METAS), and TimeTech GmbH (TIM) were calibrated using TimeTech's mobile TWSTFT calibration station assembled on a trailer.

The calibration trailer was firstly introduced at EFTF 2012 [1]. Its stability during the initial calibration campaign was verified by taking common-clock data at TimeTech before and after the trip to the metrology laboratories, and by triangle closures, which are based on the principle that the sum of calibrated links between three sites should be zero within the combined uncertainty.

We report on the current status of the calibration station and present the results of the calibration campaign, the uncertainty estimation, and comparisons to previous calibrations. Since the mobile station allows for a standardized and easily executable procedure at each laboratory, the systematic uncertainties are significantly below one nanosecond for the links contributing to TAI and UTC.

II. BRIEF DESCRIPTION OF CALIBRATION METHOD

TWSTFT between two remote laboratories 1 and 2 is based on the exchange of modulated radio signals via a communication satellite, which are coherent to the respective timescales UTC(1) and UTC(2). At both sites the signal of the remote site is compared to the local UTC(k). The difference between the measurements at laboratory 1 and 2 reflects the difference UTC(1) − UTC(2) plus the delays due to the ground station equipment, asymmetries of the signal path, and the Sagnac effect [2]

In mathematical term the two remote measurements are given by [3]

$$\begin{aligned} TW(k) = {} & UTC(k) - UTC(j) - 1PPSREF(k) + 1PPSREF(j) \\ & + TX(j) + SP(j) + RX(k) + SCD(k) - SCD(j), \end{aligned} \quad (1)$$

with k,j = 1 or 2, and k ≠ j. 1PPSREF(i) is the delay between the 1 PPS signal connected to the TWSTFT modem and the local representation of UTC, adjusted by the laboratory. TX(k) and RX(k) are the signal delays of the transmission and reception part of the respective ground station, SP(j) is the signal path delay from site j to site k, and SCD(k) and SCD(j) are the Sagnac delays for the two sides of the link. According to [3] the Sagnac effect is corrected with sufficient precision by applying fixed values calculated from the station positions

* Present address: Bureau International des Poids et Mesures (BIPM), Pavillon de Breteuil, F-92312 Sèvres Cedex, France

and the nominal position of the satllite.. The other delays are a priori unknown and have to be determined by calibrations.

In single transponder setup, where the same satellite antenna covers both stations 1 and 2, the signal path delays are equal: SP(1) = SP(2). Since the link is bi-directional, the delays through the Earth atmosphere cancel to first order. The timescale comparison is performed by exchanging the measurement data and reads

$$\begin{aligned} \mathrm{UTC}(1)-\mathrm{UTC}(2) &= \tfrac{1}{2}\left[\mathrm{TW}(1)-\mathrm{TW}(2)\right] \\ &+ \tfrac{1}{2}\left[\mathrm{DLD}(1)-\mathrm{DLD}(2)\right]+\left[\mathrm{SCD}(2)-\mathrm{SCD}(1)\right] \\ &+ \left[1\mathrm{PPSREF}(1)-1\mathrm{PPSREF}(2)\right] \end{aligned} \quad (2)$$

where DLD(k) denotes the station dependent delay difference defined by DLD(k) = TX(k) − RX(k).

The task of a link calibration is to determine the difference of station dependent delays [DLD(1) − DLD(2)] by operating a mobile station at site 1 in parallel with the fixed TWSTFT equipment in common-clock mode and then repeating the common-clock measurement at site 2. Common-clock mode means that the mobile station is operated close to the fixed stations and connected to the same reference signals. More details are in [1]. At both sites we define the common-clock difference (CCD) between mobile and fixed station as

$$\begin{aligned} \mathrm{CCD}(k) &= \tfrac{1}{2}\langle \mathrm{TW}_M - \mathrm{TW}(k)\rangle \\ &= \tfrac{1}{2}\left[\mathrm{DLD}(k)-\mathrm{DLD}_M\right]+\left[1\mathrm{PPSREF}(k)-1\mathrm{PPSREF}_M(k)\right], \end{aligned} \quad (3)$$

where <…> denotes the average over several measurements. DLD_M and $1\mathrm{PPSREF}_m(k)$ are the mobile station delay difference and the delay of the local UTC(k) with respect to the 1 PPS reference connector of the mobile station, respectively. There is no local UTC and SCD contribution in (3), because these contributions are the same for mobile and fixed station. The difference between the two CCD measurements yields

$$\begin{aligned} \mathrm{CCD}(2)-\mathrm{CCD}(1) &= \tfrac{1}{2}\left[\mathrm{DLD}(2)-\mathrm{DLD}(1)\right] \\ &+ \left[1\mathrm{PPSREF}(2)-1\mathrm{PPSREF}_M(2)\right] \\ &- \left[1\mathrm{PPSREF}(1)-1\mathrm{PPSREF}_M(1)\right]. \end{aligned} \quad (4)$$

The mobile station delay difference DLD_M cancels out, because it is the same at both laboratories (if the mobile station is not changed during the travel). The values for $1\mathrm{PPSREF}_m(k)$ have to be determined by local measurements at both sites. The calibration value for the link between site 1 and 2, CALR(1,2), is defined as

$$\mathrm{CALR}(1,2) = \left[\mathrm{CCD}(2)-\mathrm{CCD}(1)\right]+\left[\mathrm{SCD}(2)-\mathrm{SCD}(1)\right]. \quad (5)$$

The SCD contributions are calculated as recommended in [4]. After adding (5) to (2), the link performs calibrated time transfer between the UTC(1) and UTC(2). CALR(1,2) is stored in the ITU files of station 1 and with opposite sign in the respective files of station 2 [4].

III. MOBILE STATION

The mobile station consists of two parts: A small indoor rack with time and frequency distribution equipment and an outside trailer with on top antenna dish. Both parts are interconnected by a bi-directional optical fiber link in master-slave configuration. An overview scheme of the main components, the setup at a timing laboratory, and the connection to the laboratory's reference signals is shown in Fig. 1. The inside rack comprises a Pulse Distribution Amplifier (PDA) and the master reference generator for the optical link with integrated Time Interval Counter (TIC). The outdoor trailer hosts the slave reference generator, the TWSTFT modem, and all other equipment necessary for satellite communication, e.g. up- and downconverters. The antenna dish is motor-controlled and automatically points to the communication satellite using station and satellite position information. Computers and equipment for data storage and remote commanding is implemented in both indoor rack and outdoor trailer. The data communication is also realized via optical fiber.

The inside rack is connected to 5/10 MHz reference frequency and 1 PPS Ref signal coherent to the local UTC. The delay of the 1 PPS Ref signal with respect to local UTC however does not need to be known. Instead, it is split into two signals by a Pulse Distribution Amplifier (PDA). One of the pulses is used as input for the master reference generator, the second is connected to the stop channel of the inbuilt Time Interval Counter (TIC). The TIC start channel is connected to the local 1 PPS UTC(k) signal or a signal with known delay to UTC(k), provided by the laboratory. The TIC start channel is thus the calibration reference point, because the PDA, the internal cables in inside rack and outside trailer, and the optical link are the same during the complete calibration campaign and the delays cancel out in the calibration value (5).

A detailed description of the components of the mobile station is provided in [1].

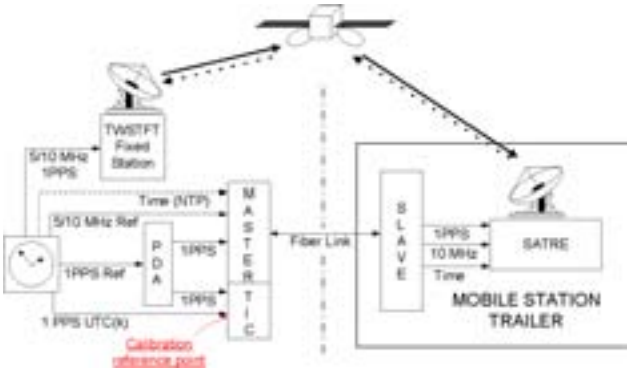

Figure 1. Scheme of main components of mobile station, setup at timing laboratory, and connection to laboratory reference signals.

IV. CALIBRATION WORKFLOW

Table I shows the designations of the local timescales at the participating laboratories and the identification of the fixed stations which are subject of the calibration. The timescale at TIM is denoted as TA(TIM), because it is not an official UTC realization. At OP the TWSTFT equipment is not directly connected to UTC(OP), but to a hydrogen maser (HM) which is measured externally with respect to UTC(OP).

TABLE I. LOCAL TIMESCALE AND STATION DESIGNATION.

Lab	Local timescale	Fixed station
TIM	TA(TIM)	TIM01
PTB	UTC(PTB)	PTB01
OP	UTC(OP)	OP01
METAS	UTC(CH)	CH01

The differential earth station delays between the fixed TWSTFT stations with respect to the mobile station TIM02 co-located at each site had to be determined. The first measurement at TIM at the beginning of the campaign was repeated at the end of the campaign to verify that the mobile station's internal delays have not significantly changed during the travel. The time schedule for the calibration campaign is shown in Table II.

TABLE II. CALIBRATION CAMPAIGN TIME SCHEDULE.

Day	Date	MJD	Activity
1	08.11.2012	56239	Start measurement at TIM
5	12.11.2012	56243	Travel to PTB
6	13.11.2012	56244	Start measurement at PTB
9	16.11.2012	56247	Travel to OP
12	19.11.2012	56250	Start measurement at OP
17	24.11.2012	56255	Travel to METAS
18	25.11.2012	56256	Start measurement at METAS
22	29.11.2012	56260	Travel to TIM
23	30.11.2012	56261	Start measurement at TIM
26	03.12.2012	56264	End of campaign

At each laboratory the trailer was placed outside at a location with good visibility to the communication satellite. The inside reference signals provided to the optical master reference generator (1 PPS, 10 MHz) are reproduced by the optical slave. Exemplarily, the placement of the trailer at OP is shown in Fig. 2.

Figure 2. Placement of the trailer at OP.

The communication satellite is Telstar 11N at longitude 37.5 ° W using a Ku band transponder. The nominal up- and downlink frequencies are 14.26 GHz and 10.96 GHz, respectively.

Since a standardized definition for a laboratory UTC reference point does not yet exist and access to signals in general depends on the local conditions, the connector for 1 PPS Ref and the calibration reference point at inbuilt TIC (see Fig. 1) were connected to dedicated long cables with BNC connectors in order to increase flexibility and avoid additional local cable length measurements. In the calibration values (5) the delay of the cable connected to the reference point cancels, because it is the same at all sites. In fact, the endpoint of the cable has turned into the reference point

The connection of the mobile station indoor equipment to the local 1 PPS signals is depicted in Fig. 3. At TIM and OP both cables were connected to fixed outputs of the distribution system. At PTB the signals were provided by laboratory cables and the interconnection was established by adapters. At METAS the 1 PPS Ref was taken from a fixed output, while the UTC signal was provided by a cable.

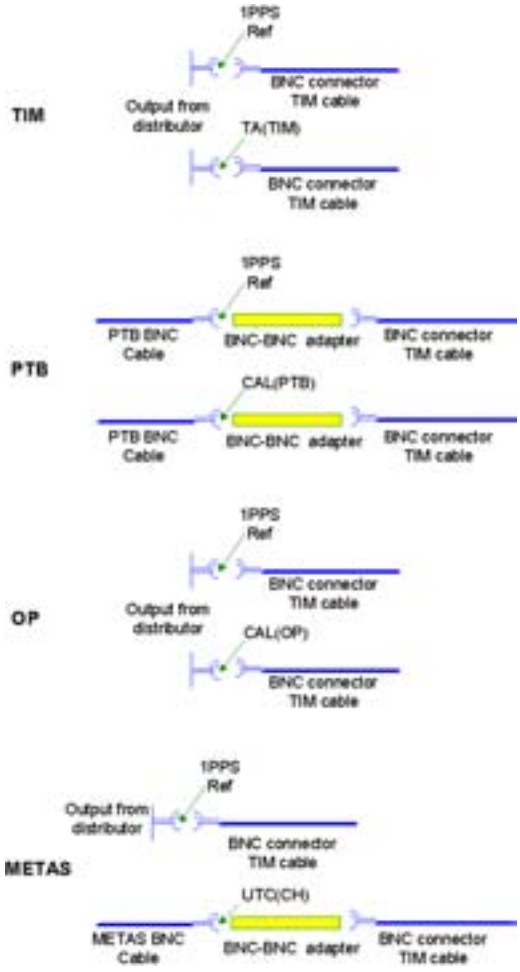

Figure 3. Connection of mobile station to local 1 PPS signals.

At TIM and METAS the distributor output and the endpoint of the cable were directly representing the local timescale, respectively. In contrast, at PTB and OP the signals had a delay with respect to the laboratories' UTC and HM reference points and are thus referred to as CAL(PTB) and CAL(OP) in Fig. 3, respectively. The delays with respect to local UTC were determined by additional local measurements.

The calibration values are calculated using averages of several samples generated from measurement sessions with 2 min duration, performed each 2 hours. The number of common-clock samples recorded at each laboratory are given in Table III. TIM-1 and TIM-2 denote the measurements at TIM at beginning and end of the campaign, respectively.

TABLE III. NUMBER OF CCD SAMPLES RECORDED AT EACH SITE.

TIM-1	PTB	OP	METAS	TIM-2
36	35	34	39	36

V. UNCERTAINTY ESTIMATION

The total calibration uncertainty is given by

$$U_{\mathrm{CALR}} = \sqrt{U_{a,k}{}^2 + U_{a,j}{}^2 + U_{b,1}{}^2 + U_{b,2}{}^2 + U_{b,3}{}^2}. \qquad (6)$$

$U_{a,k}$ and $U_{a,j}$ are the statistical uncertainties at lab k and lab j, respectively. Due to the relatively low number of samples (Table III), e.g. compared to GPS based calibrations [5], they are simply represented by the standard deviation (SD) of the common-clock (CCD) samples. They include the noise of the fixed and mobile TWSTFT equipment, the noise of the link itself, and the noise of the optical link between laboratory and outside trailer.

$U_{b,1}$, $U_{b,2}$, and $U_{b,3}$ are systematic uncertainty contributions: $U_{b,1}$ represents the delay stability of the mobile equipment [3]. An upper limit is estimated by the absolute value of the difference between the first CCD measurement at TIM and the verification measurement at the end of the campaign.

$U_{b,2}$ accounts for the uncertainty of the connection of the TWSTFT equipment to local UTC or reference signal. It consists of the uncertainty of the measurement of the 1 PPS signal from the internal PDA with respect to the reference signal using the internal TIC in the indoor rack ($1\mathrm{PPSREF_M(k)}$ measurement, see Fig. 1) and the uncertainty of the 1 PPS connected to the reference point, if this signal is not directly representing local UTC and the delay is determined by an external local measurement. Since the TIC inside the indoor rack is the same at both sites, only the measurement jitter contributes, while systematic errors are common and cancel out in (4). Although the jitter is the statistical uncertainty of the TIC measurement, it turns into systematic uncertainty of the CCD measurement, because the TIC mean value affects all TWSTFT data in the same way. If the 1 PPS signal connected to the fixed TWSTFT modem is monitored against the internal 1 PPS generated from the 5/10 MHz reference frequency, the jitter of these measurement also contributes to $U_{b,2}$. All contributions are added geometrically.

$U_{b,3}$ is related to all other suspected possible systematic effects. One of these effects is the stability of the local 1 PPS signal distribution. It can be accounted for by 0.1 ns, deduced from long-term laboratory experience [3], [5]. A second effect is accounted for by 0.2 ns related to changes in transmitter power and receiver signal-to-noise density ratio (C/N_0) changes, and the use of different pseudonoise (PN) codes for the CCD measurements compared to the operational links [3]. A third 0.25 ns uncertainty takes into account the group delay difference occurring due to different pulse rising times at different laboratories in the long cable connected to the reference point. The fourth contribution of 0.25 ns is due to the uncertainty of the 1 PPS generated by the optical slave generator. The last contribution of 0.01 ns uncertainty takes into account that adapters were used at PTB and METAS, but not at TIM and OP. The total contribution $U_{b,3}$ is set to 0.42 ns for all calibration values.

VI. RESULTS

The TWSTFT modem generated its internal 1 PPS signal (1 PPS TX) from the 5/10 MHz reference frequency. This pulse is initially triggered by the external 1 PPS when the modem is started. Additionally the 1 PPS TX can be measured continuously with respect to the external 1 PPS by an inbuilt TIC (IOTIC). This is very useful in the case that the 1 PPS and 5/10 MHz are not generated by the same clock. In the laboratories participating in this calibration campaign the external 1 PPS and the 5/10 MHz reference frequency are however coherently generated by the same source.

At TIM and METAS the IOTIC measurement is used for continuously monitoring the external 1 PPS against the internal 1 PPS TX. Thus, the 1PPSREF delay consists of a constant part due to the delay to local reference time signal and the IOTIC measurement, which is affected by jitter. At PTB, in contrast, the IOTIC measurement is not used and only the constant delay of external 1 PPS with respect to UTC(PTB) is taken into account. If the delay setting is not changed, it is completely absorbed by the calibration values (5) and no additional measurement noise increases the uncertainty. OP operates an old version of the TWSTFT modem without IOTIC. The 1 PPS TX is measured against external 1 PPS by an external SR620 TIC [6]. However, as in PTB a constant value for the delay of 1 PPS with respect to hydrogen maser reference point is set.

The 5/10 MHz and the 1 PPS signals connected to the mobile station's indoor rack were coherently generated from the same source in all four laboratories. Thus, the only relevant delay measurement for determining $1\mathrm{PPSREF_M}$ is that of the TIC in the optical link maser generator (cf. Fig. 1). During this campaign, the signal provided to the calibration reference point was continuously connected in all labs for the complete measurement period and thus continuously measured. As already mentioned, the delays of the mobile equipment parts were the same in all labs and are thus completely absorbed by the calibration values.

The 1PPSREF delay for each ground station and the related measurement uncertainty u_{F} are listed in Table IV, along with the $1\mathrm{PPSREF_M}$ measurement and its uncertainty u_{M} in the

respective lab (TIM-1 and TIM-2 denote the beginning and end measurement, respectively). The u_F uncertainty is the standard deviation (SD) of the fixed station IOTIC measurement. u_M consists of the SD of the measurement of the TIC in the optical link master generator and, at PTB and OP, an additional contribution given by the uncertainty of the local measurement, which was performed to determine the delay of the signal connected to the mobile station's calibration reference point with respect to the local reference point. For example, at PTB an SR620 counter was used for this task, and the systematic uncertainty of this device is specified as 0.5 ns by the manufacturer [6].

dREF is the delay difference 1PPSREF(k) – 1PPSREF$_m$(k) (last term in (3)). The uncertainty U_{Ref} is the geometrical sum of the two uncertainties u_F and u_M and an additional 0.02 ns contribution. The 0.02 ns account for the fact that the relation of 5/10 MHz zero-crossing and external 1 PPS is different at each lab. Thus, the initial triggering of the 1 PPS TX has an uncertainty, which was found to be at 0.02 ns level using the mobile TWSTFT modem's IOTIC.

TABLE IV. DETERMINATION OF REFERENCE AND DELAY DIFFERENCE BETWEEN FIXED AND MOBILE STATION .

Lab	1PPSREF [ns]	u_F [ns]	1PPSREF$_M$ [ns]	u_M [ns]	dREF [ns]	U_{Ref} [ns]
TIM-1	662.14	0.01	8.89	0.02	653.25	0.03
PTB	40.87	---	72.19	0.50	-31.32	0.50
OP	687.60	---	-46.56	0.14	734.12	0.14
METAS	753.03	0.02	-2.04	0.01	755.07	0.03
TIM-2	662.27	0.03	8.85	0.03	653.42	0.05

The TWSTFT measurements between fixed station and mobile station without reference delay difference applied are graphically depicted in Fig. 4, representing the ½ [DLD(k) - DLD$_m$] part in (3).

The CCD results, including all contributions of (3) are listed in Table V. For TIM station the average of beginning and end measurement is used. The uncertainty $u_{a,TIM}$ is the higher SD of the end measurement. The table also gives the Sagnac delay, which has to be used for calculating the calibration values (5).

TABLE V. COMMON-CLOCK DIFFERENCE AND SAGNAC DELAY FOR EACH PARTICIPATING GROUND STATION.

Lab	Start [MJD]	End [MJD]	CCD [ns]	$U_{a,Lab}$ [ns]	SCD [ns]
TIM	56239 56261	56243 56264	651.39	0.72	104.59
PTB	56244	56247	-31.48	0.30	99.11
OP	56250	56253	7791.39	0.23	92.00
METAS	56256	56260	675.67	0.59	105.32

The final calibration values and the related uncertainties are given in Table VI. The uncertainties $U_{b,2}$ are the geometrical sum of the U_{Ref} contributions of the respective Lab (Table IV). The combined uncertainty of all links contributing their data to BIPM for UTC generation are well below 1 ns.

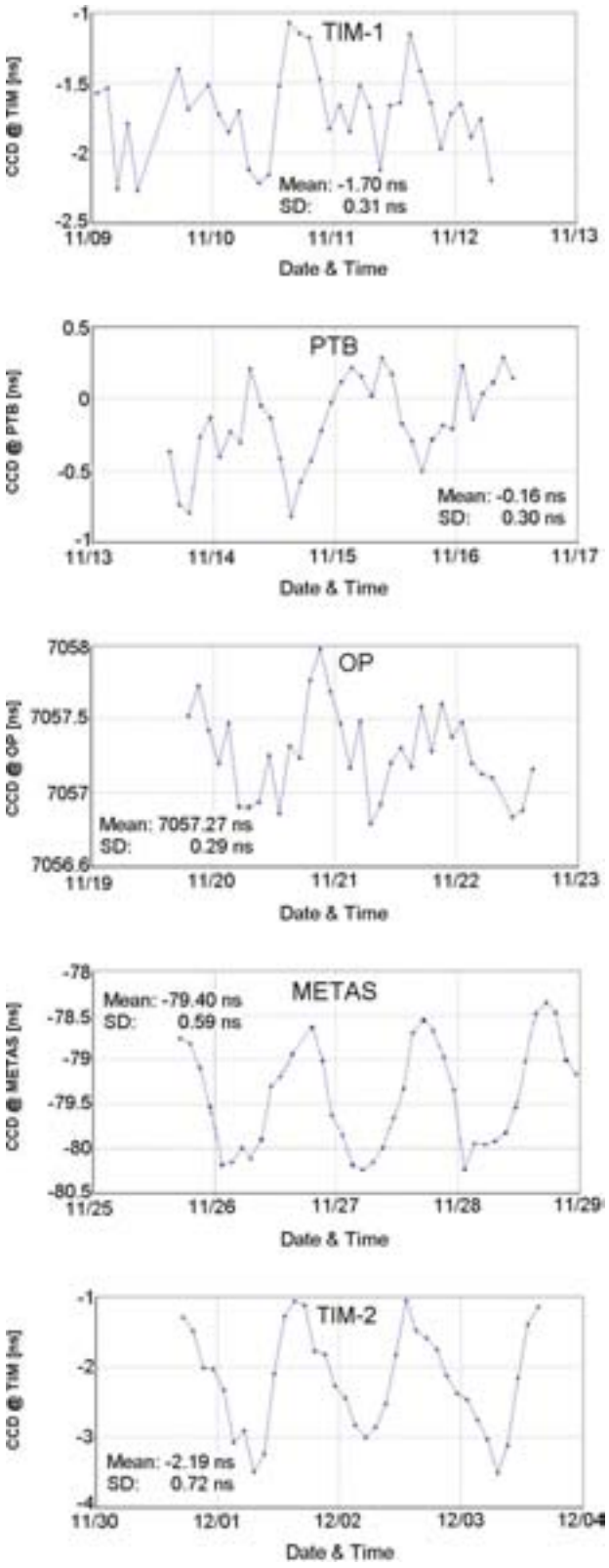

Figure 4. Common-clock differences without 1PPSREF-delay applied.

TABLE VI. CALIBRATION VALUES AND RELATED UNCERTAINTIES .

Link k-j	CALR(j,k) [ns]	$U_{a,k}$ [ns]	$U_{a,j}$ [ns]	$U_{b,1}$ [ns]	$U_{b,2}$ [ns]	$U_{b,3}$ [ns]	U [ns]
TIM-PTB	-688.35	0.72	0.30	0.32	0.50	0,42	1,07
TIM-OP	7127.41	0.72	0.23	0.32	0.14	0,42	0,93
TIM-CH	25.01	0.72	0.59	0.32	0.04	0,42	1,07
PTB-OP	7815,77	0.30	0.23	0.32	0.52	0,42	0,83
PTB-CH	713.36	0.30	0.59	0.32	0.50	0,42	0,98
OP-CH	-7102.40	0.23	0.59	0.32	0.14	0,42	0,84

VII. CLOSURE VERIFICATION

A verification of the calibration results can be done by the so-called triangle closure method. It is based on the principle that for 3 calibrated stations the sum

$$[\text{Lab}(1)-\text{Lab}(2)]+[\text{Lab}(2)-\text{Lab}(3)]+[\text{Lab}(3)-\text{Lab}(1)] \quad (7)$$

is zero, neglecting measurement noise and errors. (7) can be denoted as closure Lab(1)-Lab(2)-Lab(3).

In the calibration campaign 4 stations were participating. Thus, a total number of 4 triangle closures are enabled, as indicated in Fig. 5.

For the calculation of the closures, TWSTFT data of the complete period of the calibration campaign, from beginning to end (see Table II) are used. The newly calculated calibration values (Table VI) are applied to the respective links. The results are listed in Table VII. The data are distributed within a range of less than 2 ns around zero for all closures. The mean values are very close to zero within the 1-σ standard deviation (SD), showing that during the calibration campaign no unexpected systematic errors were occurring.

TABLE VII. RESULTS OF TRIANGLE CLOSURE VERIFICATION .

Closure	Min [ns]	Max [ns]	Mean [ns]	SD [ns]
TIM-PTB-OP	-0.82	0.81	0.01	0.29
PTB-CH-OP	-0.85	0.81	0.04	0.28
TIM-PTB-CH	-0.38	0.89	0.23	0.25
TIM-CH-OP	-0.89	0.50	-0.17	0.29

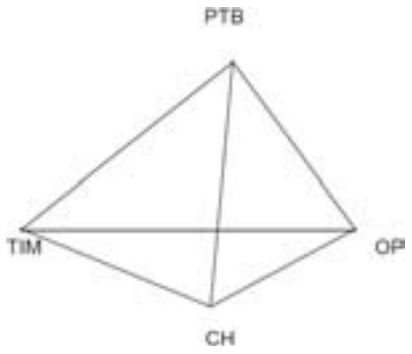

Figure 5. Scheme indicating the possible triangle closures.

VIII. COMPARISON TO PREVIOUS CALIBRATION

A second method to verify the calibration and to detect the long-term delay stability of the participating stations is the comparison to previous calibration campaigns. The difference is calculated by

$$\text{CALR\_dev} = \text{CALR}_{\text{Tt}} - \tfrac{1}{2}\left(\text{ESDVAR}_j - \text{ESDVAR}_k\right) - \text{CALR}_{\text{TM198}}. \quad (8)$$

CALR_{Tt} is the new calibration constant of the TimeTech calibration from Table VI, U_{tt} is the uncertainty from Table VI, ESDVAR_k and ESDVAR_j are the Earth station delay variations of station k and j, respectively, since the previous calibration, stored in the ITU files. ESIG_k and ESIG_j are the uncertainties of ESDVAR values. $\text{CALR}_{\text{TM198}}$ is the calibration value according to the BIPM calibration using GPS for bridging after a change of the satellite frequencies (Identification number TM198) [7] and U_{TM198} is the uncertainty. The combined uncertainty is calculated according to

$$U(\text{CALR\_dev}) = \sqrt{U_{\text{Tt}}^2 + \left(\frac{\text{ESIG}_j}{2}\right)^2 + \left(\frac{\text{ESIG}_k}{2}\right)^2 + U_{TM198}^2}. \quad (9)$$

The results of the calculations (8) and (9) and the used values are given in Table VIII. The deviation between old and current calibration value are very small (maximum –3.18 ns for PTB-CH link). This provides an indication for the success of the current calibration campaign.

TABLE VIII. CALIBRATION DEVIATION TABLE .

Link k-j	PTB-CH	PTB-OP	OP-CH
CALR_{tt} [ns]	713.36	7815.77	-7102.40
U_{tt} [ns]	0.92	0.76	0.77
ESDVAR_k	1035	1035	0.00
ESIG_k	2.80	2.80	0.00
ESDVAR_j	21.68	0.00	13.34
ESIG_j	2.00	0.00	2.00
$\text{CALR}_{\text{TM198}}$	209.88	7300.70	-7094.59
U_{TM198} [ns]	1.20	1.20	2.00
CALR_dev	-3,18	-2,43	-1,14
U(CALR_dev)	2.29	1.99	2.36

However, for both PTB-CH and PTB-OP link the deviations are slightly above the combined uncertainties, due to the long time period between current and previous calibration. This emphasizes that a frequent repetition of link calibrations shall be conducted, in order to ensure that the time transfer uncertainties of the operational links remain at low levels.

Previous link calibrations have been conducted with a portable station provided by Technical University Graz, Austria (see e.g. [8]). The setup of this station was very complicated labor extensive, because it required the manual installation and adjustment of the antenna dish and outside RF equipment at an adequate location. Due to the mobile station

based on a trailer the calibration process has now been simplified, because it requires only the installation of the small indoor rack. Thus, calibrations can be repeated periodically (or after major events like satellite changes) easily without time consuming preparations at the participating laboratories.

IX. CONCLUSION

In November 2012 the time transfer links between PTB, OP, METAS, and TimeTech GmbH were calibrated using TimeTech's mobile TWSTFT calibration station based on a trailer. The combined uncertainty of the calibration values for the links participating in the generation of UTC is at 1 ns level. The triangle closure sums are very close to zero, indicating that the calibration is not affected by unexpected systematic effects. The comparison to previous calibration results shows a maximum deviation of about –3 ns. Since the calibration procedure has been extremely simplified due to the mobile station on a trailer, frequent repetitions of the calibrations can now be aspired.

REFERENCES

[1] T. Feldmann, A. Balu, C. Molard, W. Schäfer, D. Piester, "State-of-the-Art Time Link calibration with a mobile TWSTFT Station," Proc. EFTF, Gothenburg, Sweden, April 24-26, 2012.

[2] E.J. Post, "Sagnac Effect," Rev. Mod. Phys., vol. 39, no. 2, pp. 475-493, April 1967.

[3] D. Piester, A. Bauch, L. Breakiron, D. Matsakis, B. Blanzano, and O. Koudelka, "Time transfer with nanosecond accuracy for the realization of International Atomic Time," Metrologia, vol. 42, no. 2, pp. 185-198, 2008.

[4] A. Bauch, D. Piester, M. Fujieda, W. Lewandowski, "Directive gfor operational use and data handling in two-way satellite time and frequency transfer (TWSTFT)," Rapport BIPM-2011/01.

[5] T. Feldmann, A. Bauch, D. Piester, M. Rost, E. Goldberg, S. Mitchell, and B. Fonville, "Advanced GPS Based Time Link Calibration with PTB´s New Calibration Set-Up," Proc. 42nd PTTI, Reston VA, USA, pp. 509-526, November 15-18, 2010.

[6] "SR620 Operating Manual and Programming Reference," SRS.

[7] Z. Jiang, D. Piester, K. Liang, "Restoring a TWSTFT Calibration with a GPS Bridge – A standard procedure for UTC time transfer," Proc. EFTF, Noordwijk, Netherlands, April 13-16, 2010.

[8] A. Bauch, D. Piester, B. Blanzano, O. Koudelka, E. Kroon, E. Dierikx, P. Wibberly, J. Achkar, D. Rovera, L. Lorini, F. Cordara, and C. Schlunegger, "Results of the 2008 TWSTFT Calibration of Seven European Stations," Proc. EFTF – IEEE FCS Joint Conference, Besançon, France, pp. 1209-1215, April 20-24, 2009.

Simulation Study for Commercial Time Transfer Service over Geostationary Satellite

Jacqueline Walker
Department of Electronic and Computer Engineering
University of Limerick
Limerick, Ireland
jacqueline.walker@ul.ie

Marco Genova
Mixed Processing Ltd.
Office 301, Shannon Airport House
Shannon, Ireland
marco.genova@mixed-processing.ie

***Abstract*— Over the last twenty years, many technologies and services have come to rely on the GPS for precise timing. Concern is increasing about the wisdom of being reliant on a single timing solution provided by a single country and because of the susceptibility of the GPS signal to unintentional interference, jamming and spoofing. In this paper, we report on further development of our system for timing signal transfer from a precision reference clock using commercial satellite links. The system will have master stations tracking the satellite position and using TWSTFT measurements to synchronize their clocks, transmitting data with the reference timing signal to allow slave stations to adjust the PPS timing signal, compensating for the satellite motion and other uncertainties in the path delay. We will report on a simulation of the full system, including models for the master station clocks and TWTT measurements, using a Kalman filter to track the satellite position.**

Keywords—time transfer; satellite; TWSTFT; TWTT; timing; synchronization

I. INTRODUCTION

Over the last twenty years, many technologies and services have come to rely on the GPS for precise timing. However, concern is increasing about the wisdom of being reliant on a single timing solution [1] provided by a single country because of the susceptibility of the GPS signal to unintentional interference, jamming and spoofing [2]. There are several projects underway to develop similar systems or upgrade existing ones, e.g. Galileo, GLONASS. Only one of these systems (GLONASS) is currently fully available as an alternative, with the other systems projected to become operational progressively during the next decade. In the current situation, if the quality of the GPS signal deteriorates, some of the main information and communications channels would not be usable in many countries, causing a wide range of problems [1], [2]. Other approaches to timing transfer exist and are being developed: over optical media [3] or using high power LF signals [4] and over satellite links [5],[6],[7],[8]. Timing transfer over optical media shows promising performance but requires the installation of a dedicated network infrastructure. High power, low frequency radio signals are an established solution but cannot easily cover such a wide geographical area as a satellite solution.

In this paper, we report on further development of our system for timing signal transfer from a precision reference clock using commercial geostationary satellite links [7],[8]. The system will have a set of master stations tracking the satellite position and using TWSTFT measurements to synchronize their clocks. Data transmitted with the reference timing signal will allow slave stations to adjust the timing signal, compensating for the satellite motion and other uncertainties in the path delay. Using projected ephemeris data and comparing that data in real time with measurements, which themselves are affected by other sources of delay, is a challenging task when the goal is timing signal transfer with no more than 100 ns of jitter peak-to-peak at the receiving stations and motivates study of the system using simulations. The paper is structured as follows: in Section II, we briefly review the structure of the time transfer system and previous experimental and simulation findings. In Section III, a new simulation of the system is presented. Results from the simulations are presented in Section IV. Finally, in Section V we present our conclusions.

II. ONE-WAY SATELLITE TIME TRANSFER SYSTEM

The time transfer system under development by Mixed Processing Ltd and University of Limerick researchers will provide a complete off-the-shelf system for precision time transfer over geostationary satellite. The full system will consist of three master stations to fix the satellite position. The master stations communicate with each other and with the receive-only slave stations using bandwidth rented from a commercial satellite provider. One master station will have a high precision clock such as a Cesium atomic clock and two sub-master stations will have precision clocks with a high holdover capability e.g. Rubidium clocks. Each of the master stations, whether master or sub-master, will have a bi-directional link to the satellite. Finally, there are slave or receive-only stations which have a uni-directional (receive) link with the satellite. The slave stations will be sent a pulse-per-second (PPS) time signal and data that allows them to compensate for the timing uncertainty arising from the satellite motion and other sources. The master stations will exchange satellite ranging data to track the satellite position and align their clocks using TWSTFT. In order to determine accurately the propagation time of signals between the master station and the slave stations it will be necessary to consider and correct

for errors in the path delay determination arising from: satellite ephemeris errors, satellite motion, atmospheric effects, temperature induced delay variation in cables and outdoor equipment, the Sagnac effect and general measurement errors.

A. *Proof of Concept Experiment and Simulations*

A previous proof of concept experiment was successfully conducted with a single master station broadcasting a PPS timing signal to three slave stations with an accuracy of at worst 1 μs when compared to a GPS PPS reference, was reported on in detail in [7],[8]. In a three master station system, the stations measure their own range to the satellite and the three measurements may be used to calculate the satellite position by trilateration. However, the range measurements contain extraneous delays, not all of which can be known exactly, e.g. the delay through the satellite transponder or the exact value of the atmospheric delay. Furthermore, with three master stations, each with their own independent clock, two of the measurements contain an error with respect to the measurement taken by the primary master station, due to the clock difference between stations. One approach is to measure and estimate the extraneous delays as accurately as possible. Clearly equipment and cabling delays at each station can be measured while an estimate for the troposphere delay can be predicted using an atmospheric model [9]. At the Ku-band transmission frequencies, the effect of the ionosphere can be neglected [10]. Then, using the satellite ephemeris, the master stations can find a correction factor to account for the remaining unknown and variable extraneous delay. The primary master station calculates the satellite position using trilateration, using two-way time and frequency transfer to correct for the clock phase difference. However, a simulation of this approach demonstrated the sensitivity of the satellite position calculation to unknown variation in the extraneous delays [7].

III. An Approach Using a Kalman Filter

To test an alternative approach, a simulation for a three station system where the primary master station uses an extended Kalman filter to predict the satellite position, thus integrating its own measurements with those of the other two master stations, has been developed.

As is well known [11], a discrete-time Kalman filter uses a two stage procedure to first predict the next state x_k of a discrete-time system which may be described by a linear stochastic difference equation,

$$x_k = Ax_{k-1} + Bu_{k-1} + w_k \tag{1}$$

where A is the state transition matrix, u_{k-1} is an optional control input, B is an optional control matrix and w_k is an independent white noise process. A measurement z_k, which is related to the state of the system by a linear measurement matrix H as:

$$z_k = Hx_k + v_k \tag{2}$$

where v_k is an independent white noise process, must also be available. In a linear discrete-time Kalman filter, where there is no control input, the next state of the process is estimated using:

$$\begin{aligned} \hat{x}_k^- &= A\hat{x}_{k-1} \\ P_k^- &= AP_{k-1}A^T + Q \end{aligned} \tag{3}$$

where $\hat{x}_{k-1}$ is the a posteriori state estimate, $\hat{x}_k^-$ is the a priori state estimate, P_k is the estimate error covariance matrix, where the superscript minus denotes the a priori estimate, and Q is the process noise covariance matrix, which is used to include an estimate of our uncertain knowledge of the underlying process [12]. In the second stage of the Kalman filter, the Kalman gain matrix, K_k, is updated using the measurement matrix H, the a priori estimate error covariance P_k^- matrix and R the measurement noise covariance matrix. The noisy measurement is compared with the predicted measurement made using the a priori state estimate, and the error, adjusted by the Kalman gain is used to update the state prediction to produce the a posteriori state estimate and the updated error estimate covariance predictions.

$$\begin{aligned} K_k &= P_k^- H^T \left(HP_k^- H^T + R\right)^{-1} \\ \hat{x}_k &= \hat{x}_k^- + K_k\left(z_k - H\hat{x}_k^-\right) \\ P_k &= \left(I - K_k H\right)P_k^- \end{aligned} \tag{4}$$

A. *Kalman Filter System Model*

The Kalman filter approach used for the simulation was originally developed based on that described in [13], where a Kalman filter was used to track the position of a geostationary satellite using GPS satellites. In [13], the satellite path is described by the simple circular motion continuous-time dynamics model:

$$\dot{x} = Fx \tag{5}$$

where the first three rows of $x = \begin{bmatrix} X & Y & Z & \dot{X} & \dot{Y} & \dot{Z} \end{bmatrix}^T$ are the position vector of the satellite, the bottom three rows are its velocity vector, and the dynamics matrix $F = \begin{bmatrix} 0 & 0 & 0 & 1 & 0 & 0 \\ 0 & 0 & 0 & 0 & 1 & 0 \\ 0 & 0 & 0 & 0 & 0 & 1 \\ -\mu/r^3 & 0 & 0 & 0 & 0 & 0 \\ 0 & -\mu/r^3 & 0 & 0 & 0 & 0 \\ 0 & 0 & -\mu/r^3 & 0 & 0 & 0 \end{bmatrix}$ where $\mu = 398600.4418 \pm 0.0008\ \text{km}^3/\text{s}^2$ is the gravitational constant and $r = \sqrt{X^2 + Y^2 + Z^2}$. In the simulation reported upon here,

as the equations of motion are non-linear, a linearized system dynamics matrix is used to develop the Kalman filter equations

$$\Delta\dot{x} = dF\Delta x \tag{6}$$

where dF is the Jacobian of the continuous-time dynamics matrix. The linearized continuous-time dynamics matrix is then discretized to produce the discrete-time state transition matrix using a first-order approximation [12].

In [13], the simulation used ECI (Earth-Centred Inertial) co-ordinates and the results were converted to the ECEF (Earth-Centred Earth Fixed) system for analysis and display. The ECI frame has its origin fixed at the centre of the earth and may be considered a fixed frame of reference (neglecting the much longer period motions of the earth in space [14]) so that the equations of motion of the satellite are simpler to express in this frame. However, as the ground truth for the simulation will be satellite ephemeris data in ECEF co-ordinates, the system dynamics matrix was transformed into that co-ordinate system. Another reason for formulating the satellite motion model in the ECEF frame is that the earth rotates with respect to the ECI frame and using it requires finding the position of the vernal equinox at a particular time [15]. Such a requirement is to be avoided in an application whose purpose is to transfer a precise and accurate determination of time, as it will add additional uncertainty to the path tracking. Hence, the system dynamics matrix was converted into its equivalent in ECEF co-ordinates.

The measurements available to the Kalman filter are the range measurements between each master station and the satellite position given by:

$$\rho = \sqrt{(x_s - x_{mi})^2 + (y_s - y_{mi})^2 + (z_s - z_{mi})^2} \tag{7}$$

where (x_s, y_s, z_s) is the satellite position at the given time instant and (x_{mi}, y_{mi}, z_{mi}) is the position of the ith master station. Since these measurements are nonlinear, an Extended Kalman filter is used where the measurement matrix is replaced by the observational partial derivative matrix [13].

An important aspect of the system is that the clocks in the master stations, being independent and geographically separated, will not be synchronous. In the present simulation, the error due to the difference between the clocks and two-way time transfer (TWTT) is easily incorporated by using a discrete-time random process to model the bias, drift and drift rate in the clocks at each master station in a similar approach to that used in [13]. Using the clock bias output of the clock model (in seconds) and multiplying the difference between two clocks' bias by the speed of light c the resulting measurement error due to the phase difference may be modeled by in meters and added to the measurements.

$$\rho_k = \sqrt{(x_s - x_{mi})^2 + (y_s - y_{mi})^2 + (z_s - z_{mi})^2} + cb_{mi} - cb_{mj} + v_k \tag{8}$$

where b_{mi} is the bias on the ith master station clock and v_k is the measurement noise. The two-way time transfer measurement between the primary master clock and the ith clock at the ith master station can be modelled as [13]:

$$\Delta T_{ij} = cb_{mi} - cb_{mj} + \upsilon_{ij} \tag{9}$$

where υ_{ij} is the error in the TWTT measurement.

B. Kalman Filter Simulation Procedure

The simulation uses as ground truth archived satellite path data for E33A from November 2010 as was used in the original experiment [7] interpolated to provide the ground truth satellite path. Given the master station positions, the measurements to be used by the simulation can then be created offline using equation (8). In the simulation the procedure assumed is that communication between the master stations permits the primary master station to collate the range measurements from the two other stations as well as the phase difference between its own clock and those of the two other master stations. The Kalman filter for tracking the satellite position is then run at the primary master station. The primary master station will send the PPS timing signal to the slave stations with the estimated satellite position and its own range to the satellite. At the slave station, the slave uses the satellite position to calculate its own range to the satellite and it can then calculate the expected time of arrival of the PPS signal. To measure the performance of the simulation, the expected time of arrival is compared with the simulated real travel time of the signal to determine the residual time variation on the received PPS signal after adjustment in a procedure which simulates that in the original experiment [7], [8].

IV. Results

To verify the tracking capability of the Kalman filter, it was run without perturbations, apart from the satellite motion. The standard deviation of the tracking error, the difference between the ground truth satellite co-ordinates and the filter's estimate is 0.3m to 0.6m and the standard deviation of the adjusted PPS signal at the slave is 2ns. To make the simulation more realistic, perturbations are then added back to the simulation. Fixed extraneous delay quantities such as equipment delay, mean troposphere delay or the Sagnac effect are not included as within a simulation it is pointless to add them in and then subtract them again. Instead, the approach is to use normally distributed noise to simulate the variable and unknown part of the extraneous delays. Thus, a variable component to represent the unknown and varying atmospheric delays is added to the time of travel of the PPS sent from primary master to slave station. This quantity is also added to the range measurements. As shown in (8), the clock phase differences are added to the range measurements along with a measurement noise which represents all the other uncertainties such as those to do with the resolution and noise within the transmitter and receiver systems.

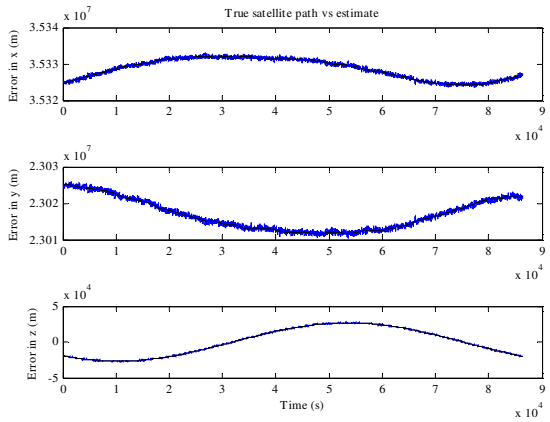

Fig. 1. Kalman filter tracking performance with perturbations.

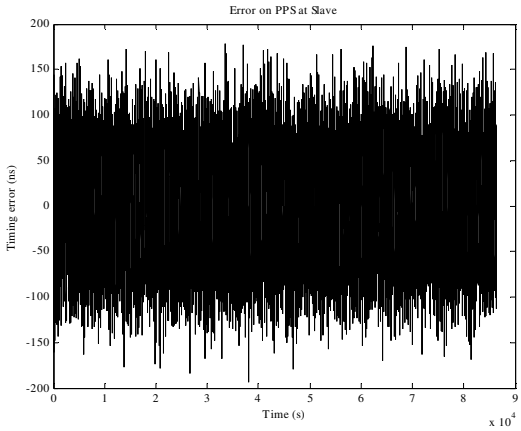

Fig. 2. Timing error after adjustment at slave.

Examples of typical simulated tracking and time transfer results obtained so far from the simulation are shown in Fig. 1 and Fig. 2. The standard deviation of the measurement noise was 15m, the variable component of the delay due to atmosphere was typically < 10m and the effect of noise on the TWTT measurements was modeled as < 1m. The measurement residual with these settings was typically 10-50m, resulting in a tracking error standard deviation of 200-400m. The simulated time transfer performance was within ± 150 ns as shown in Fig. 2.

V. CONCLUSION

In this paper we have described the proposal by Mixed Processing Ltd for an off-the-shelf system for timing signal transfer over geostationary satellite. The proposal for the full system with three master stations tracking the satellite position and broadcasting a timing signal to slave stations has now been simulated implementing a Kalman filter approach to the satellite tracking with some encouraging preliminary results. The simulation will now be used to explore the effect of variable extraneous delays on tracking and time transfer performance.

REFERENCES

[1] M.A. Lombardi, "Microsecond accuracy at multiple sites: is it possible without GPS?" IEEE. Instrum. Meas. Mag., vol. 15, no. 5, pp. 14-21, October 2012.

[2] C. Evans-Pughe, "GPS vulnerability to hacking", Engineering and Technology Magazine, vol. 6, no. 4, pp. 78-81,15 April 2011.

[3] S.-C. Ebenhag, "Frequency transfer techniques and applications in fiber optic communication systems," Ph.D. dissertation., Dept. Microtech. Nanosci., Chalmers Univ. Tech., Gothenburg, Sweden, 2013.

[4] Gibbons Media and Research LLC. (2012, Mar. 26). UrsaNav Tests eLoran LF Timing Potential [Online]. Available: http://www.insidegnss.com/node/2992.

[5] A. Sen Gupta and B. Mathur, "Standard time and frequency signal broadcast via INSAT- accuracy improvements using differential mode," IEEE Trans. Instrum. Meas., vol. 46, pp. 212-215, April 1997.

[6] J.-C. Yoon et al., "Geostationary orbit determination for time synchronization using analytical dynamic models," IEEE Trans. Aerosp. Electron. Sys., vol. 40, pp. 1132-1146, October 2004.

[7] J. Walker and M. Genova, "Experimental and Simulation Study for Commercial Time Transfer Service over Geostationary Satellite," in Proc. 44th Ann. Precise Time and Time Interval Meeting, Reston, Va., 2012, pp. 221-237.

[8] J. Walker and M. Genova, "Experimental and Simulation Study for Commercial Time Transfer Service over Geostationary Satellite," NCSLI Measure, vol. 8, no. 2, pp. 62-69, June 2013.

[9] J. Saastamoinen, "Atmospheric correction for the troposphere and stratosphere in radio ranging satellites," in The Use of Artificial Satellites for Geodesy, Geophys. Monogr. Ser., vol. 15, S. W. Henriksen, A. Mancini, and B. H. Chovitz, Eds. Washington D.C.: AGU, 1972, pp. 247–251.

[10] K. Davies and E.K. Smith, "Ionospheric effects on satellite land mobile systems," IEEE Antennas Propag. Mag., vol. 44, no. 6, pp. 24-31, December 2002.

[11] G. Welch and G. Bishop, "An Introduction to the Kalman filter," Dept. Comp. Sci., Univ. N. Carolina, Chapel Hill, N.C., Tech. Rep. TR 95-04124, 2006.

[12] P. Zarchan and H. Musoff, Fundamentals of Kalman Filtering: A Practical Approach, 3rd ed., Progress in Astronautics and Aeronautics, vol. 232, F.K. Lu, Ed. Reston: American Institute of Aeronautics and Astronautics, Inc., 2009.

[13] B. Dainty, J. Raquet, and R. Beckman, "Improving geostationary satellite GPS positioning error using dynamic two-way time transfer measurements," in Proc. 39th Ann. Precise Time and Time Interval Meeting, Long Beach CA, 2007, pp. 511-530.

[14] D. Woodfork, "The use of X-ray pulsars for aiding GPS satellite orbit determination," Masters Thesis, Air Force Inst. Tech., Wright Ptrsn AFB, OH, 2005.

[15] "Orbital mechanics with Numerit", Coordinate Conversion Utility Technical Report [Online]. Available: http://www.cdeagle.com/omnum/pdf/csystems.

Time Service Through BD GEO Satellites

YUAN Haibo
National Time Service Center/ Key Lab of Time-frequency Standard of the Chinese Academy of Science
Xi'an, China
yuanhb@ntsc.ac.cn

GUANG Wei， YANG Fan
National Time Service Center, Chinese Academy of Science
Graduate University of Chinese academy of Science
Xi'an, China
guangwei@ntsc.ac.cn

***Abstract*—The Space segment of BeiDou(Compass) global navigation satellite system consists of the 5 Geostationary Earth Orbit (GEO) satellites and 30 Non-GEO satellites (Medium Earth Orbit (MEO) satellites and Inclined Geo Stationary Earth Orbit (IGSO) satellites). At present the Beidou system（BDS） has begun to regional services based on the GEO satellites and the IGSO satellites. The range of services is covering China and neighboring countries and area. There are 5 GEO satellites on orbit. Users can receive the BeiDou system time which is steered to the UTC through the UTC(NTSC) by GNSS CV and TWSTFT. The time service performance of the BeiDou system is concerned by the time users. In this paper, the BeiDou system is introduced firstly, then the satellite time service and the data processing methods are analyzed, based on the analysis, the time service performance of the 5 GEO satellites is discussed, and the results show that eliminating the ionospheric delay and reducing the impact of the troposphere and relativistic effects, the time service performance of the 5 GEO satellites are all stable and their accuracy is quite close to 10ns which can meet the needs of the vast majority of high-precision time users.**

I. INTRODUCTION

The GNSS is a Global Navigation Satellite System that is used to pinpoint the geographic location and velocity of a user's receiver anywhere in the world, and transfer the system time to the user if necessary. With the development of GNSS, the four systems will provide Position, Navigation and Timing (PNT) to users, which are GPS, GLONASS, GALILEO and COMPASS (BEIDOU, BDS), among the four global navigation systems, the GPS and GLONASS have been operating for decades, and have been updated several times. The GALILEO and BDS are still under constructing, so time transfer technologies based on the two systems are being developed and tested.

The space segment of GPS and GLONASS consist of MEO satellites, however that of GALILEO includes MEO and GEO satellites, BDS includes MEO, GEO and IGSO satellites[1]. So far, 5 GEO satellites and 5 IGSO satellites and 4 MEO satellites have been launched, and they all are running normally. The 5+5+4 satellite system can provide stable regional service of PNT. The service range of BDS is now covering China and neighboring countries and area. With the construction of BDS, the application study is quickly developing. In this paper, the character of the five GEO satellites is analyzed; the method and data processing of time service based on the 5 GEO satellites are discussed in detail. Then the time service test is done by using the BDS receiver which is placed in the time keeping laboratory of National Time Service Center (NTSC).

This work is supported by a grant from the National Nature Science Foundation of China (No. 10873013)

II. THEORY OF BDS TIME SERVICE AND DATA PROCESSING

A. Theory of BDS Time Service

In this paper, the time service is that users can directly receive system time information through BDS receiver. In fact it is one-way time service based on BDS. Because the GEO satellite of BDS are more stable in orbit (satellite position) than that of IGSO and MEO satellite, and all of them are running well, in order to obtain precise BD time, it is necessary to study the time service through BD GEO satellite.

The method of how to obtain the BD time (BDT) is by calculating the deviation between local reference time and BD system time through receiver. In this paper, the reference time is UTC(NTSC) which is kept by NTSC. Figure 1 shows the process of one-way time service[2,3].

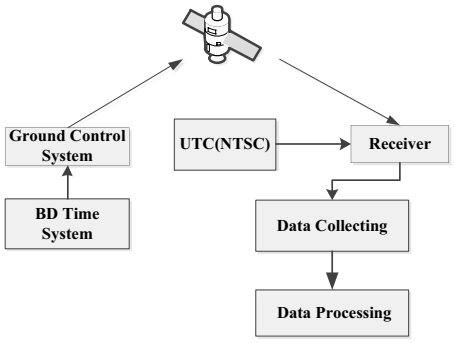

Figure 1 Process of One-Way Time Service

To introduce the one-way time service, a BD satellite (GEO or IGSO, No. i) is taken for an example. The satellite sends pseudo-code signal at the moment of t_0 (referring to satellite clock). Receiver receives this signal at the moment of

t_r (referring to local clock), and the launch time of satellite signal can be calculated by:

$$t_0 = t_r - \delta t_{iA} \quad (1)$$

The distance between satellite clock i and antenna receiver A can be expressed by

$$\rho_{i,A} = P_{i,A} + d_{trop} + d_{ion} + d_{Sagnac} + c\Delta t_{i,A} \quad (2)$$

Where, $\rho_{i,A}$ indicates pseudo-range on L_i frequency channel; $P_{i,A}$ is an indication of the geometry distance between satellite and receiver; d_{trop} is the correction of troposphere delay; d_{ion} is the correction of ionosphere delay; d_{Sagnac} indicates the correction of Sagnac effect, it means earth auto-rotation correction; c is light speed in vacuum 299792458m/s; $\Delta t_{i,A}$ the deviation between local clock A and satellite clock i is the only unknown parameter.

In formula (2), $\rho_{i,A}$ can be obtained from receiver directly, and the accurate coordinates of receiver antenna center are known data which are determined before antenna installation, the position of the satellite is transferred to the receiver through broadcast ephemeris. By using those data, the geometry distance $P_{i,A}$ between satellite and antenna can be calculated. Furthermore, d_{ion} , d_{trop} and d_{Sagnac} can also be calculated . So far, all the parameter but $\Delta t_{i,A}$ in formula (2) have been obtained, so the deviation between local clock A and satellite clock i $\Delta t_{i,A}$ can be worked out easily.

Based on the original observe data and the corrections of the satellite atomic clock obtained through ephemeris file, the deviation between satellite i and BDS time can be calculated, i.e. $\Delta t_{BD,i}$,

$$\Delta t_{BD,i} = a_0 + a_1\Delta t + a_2\Delta t^2 \quad (3)$$

Combining $\Delta t_{i,A}$ with $\Delta t_{BD,i}$, the deviation between local clock A and BDS time can be calculated , i.e. $\Delta t_{BD,A}$

$$\Delta t_{BD,A} = \Delta t_{i,A} + \Delta t_{BD,i} \quad (4)$$

As described above, after the deviation between local time and BDS time is got, the one-way time service through BDS has been accomplished.

B. Timing Data Processing

✧ Data Collecting and Data Processing Platform

The data collecting platform consists of a BDS receiver, a data collecting computer and a data processing computer, the input signal to BDS receiver includes a 1pps and a 10MHz frequency signal which are provided by UTC(NTSC). Data collecting computer receives and save the pseudo-rang and broadcast ephemeris information from the receiver in real time. Data processing computer calculates the deviation between the BDS time and the reference signal (UTC(NTSC)) $\Delta t_{BD,A}$. Figure 2 is the platform.

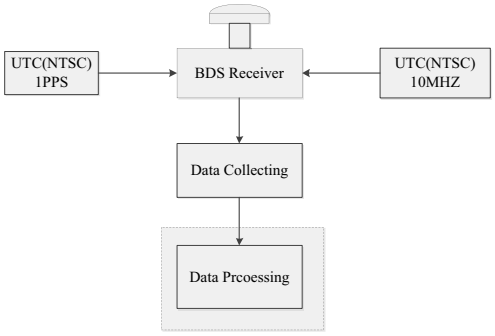

Figure 2 Data collecting and data processing platform

✧ Algorithm of Time Delay Corrections[]

The data processing of Beidou GEO satellite one-way time service is shown as figure 3. There mainly are three types of corrections in the algorithm, which are ionosphere delay, troposphere delay and Sagnac effect. The specific algorithms to correct the three types of error are described as follows.

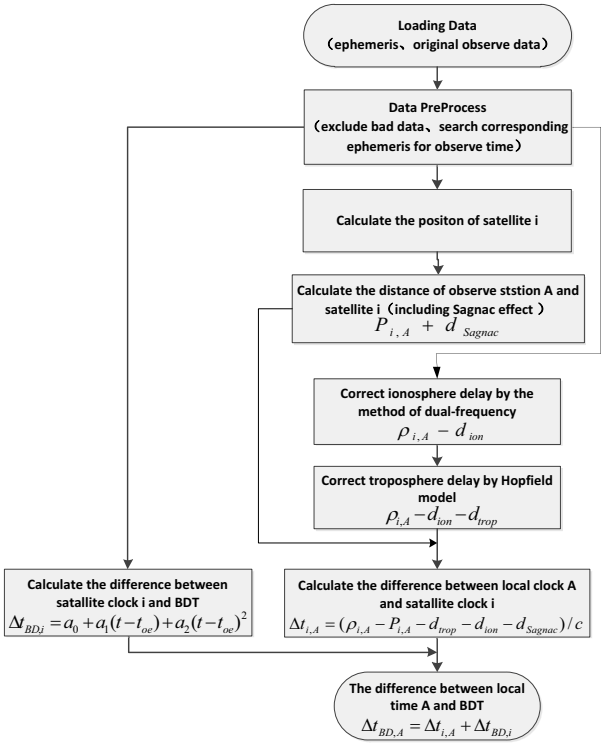

Figure 3 Data processing of Beidou GEO satellite one-way time service

Ionosphere Delay

Here, the correction method of ionosphere delay is dual-frequency correction algorithm, combined the observations of L_1 with that of L_2 , the formula (5) shows the pseudo-range eliminated ionosphere delay.

$$\rho = \frac{f_1^2 \rho_1 - f_2^2 \rho_2}{f_1^2 - f_2^2} \quad (5)$$

In formula (5), ρ is the pseudo-range without ionosphere delay; ρ_1 and ρ_2 are the pseudo-range with ionosphere delay on frequency range L_1 and L_2 respectively; f_1 and f_2 are the value of frequency on frequency range L_1 are L_2 respectively.

Troposphere Delay

Hopfield model is one of the widely used methods to correct the troposphere delay. It was developed an empirical tropospheric delay model by using data form different parts of the world, and it was based on the dry refractivity components as a function of station height. When the atmospheric temperature T, atmospheric pressure P and vapor pressure e_0 are of an observation station ground. The modified Hopfield model is expressed as:

$$\left.\begin{aligned} \Delta D_{trop} &= \Delta D_{dry}(E) + \Delta D_{wet}(E) \\ \Delta D_i(E) &= 10^{-12} N_i \sum_{k=1}^{9} \frac{\alpha_{k,i}}{k} r_i^k \end{aligned}\right\} \quad (6)$$

Where, $N_{dry} = \frac{77.6241P}{T}$, $N_{wet} = 371900\frac{e_0}{T^2} - 12.96\frac{e_0}{T}$, r_i can be calculated through equation (7):

$$\left.\begin{aligned} r_i &= \sqrt{(r_0 + h_i)^2 + (r_0 \cos E)^2} - r_0 \sin E \\ h_d &= 40136 + 148.72(T - 273.16) \\ h_w &= 1100 \\ r_0 &= 6378137m \end{aligned}\right\} \quad (7)$$

$\alpha_{j,i}$ can be expressed by formula (8).

$$\left.\begin{aligned} a_i &= -\frac{\sin E}{h_i}, b_i = \frac{\cos^2 E}{2h_i r_0} \\ \alpha_{k,i} &= [1, 4a_i, 6a_i^2 + 4b_i, 4a_i(a_i^2 + 3b_i), a_i^4 + 12a_i^2 b_i + 6b_i^2 \\ &\quad 4a_i b_i(a_i^2 + 3b_i), b_i^2(6a_i^2 + 4b_i), 4a_i b_i^3, b_i^4] \end{aligned}\right\} \quad (8)$$

In expressions above, $i = wet, dry$, E is the elevation of satellites.

Sagnac Effect

The error by Sagnac effect can be corrected in the calculating process of satellite position.

$$\begin{bmatrix} x' \\ y' \\ z' \end{bmatrix} = \begin{bmatrix} \cos(\omega\tau) & \sin(\omega\tau) & 0 \\ -\sin(\omega\tau) & \cos(\omega\tau) & 0 \\ 0 & 0 & 1 \end{bmatrix} \begin{bmatrix} x_{sat} \\ y_{sat} \\ z_{sat} \end{bmatrix} \quad (9)$$

$(x'\ y'\ z')$ stands for the corrected satellite position, ω is the earth auto-rotation speed, here ω =7.2921151467E-5 rad/s, τ is the transmission time of satellite semaphore. The calculation of τ need to use recursive calculation to correct satellite position with the initial value, which can be obtained using the pseudo-range divided by the light speed c, then the new τ can be gotten by the new pseudo-range to compute the new sent time of satellite semaphore. As described above, the satellite position is corrected. GEO satellites compared to other types of satellite, its position changes little, so in this paper, the emphasis is time service based on the GEO satellite of BDS. The time delay caused by the Sagnac effect can be expressed as:

$$T_{Sagnac} = 218.1976 \sin(Long_{Sat} - Long_{pos}) \cos(Lat_{pos}) \cos(Lat_{Sat}) \quad (10)$$

For a GEO satellite, the $\cos(Lat_{Sat})$ is 1, then the formula (10) can be written as formula (11):

$$T_{Sagnac} = 218.1976 \sin(Long_{Sat} - Long_{pos}) \cos(Lat_{pos}) \quad (11)$$

III. TEST AND RESULTS ANALYSIS

The test of BD GEO satellite time transfer began at January 1 2013, and end at January 31 2013. The data is from a BeiDou dual-frequency multichannel receiver of time keeping laboratory of NTSC. The input reference signal of BeiDou receiver includes a 1pps and a 10MHz from UTC(NTSC). The receiver has been adjusted by using two GPS CV receivers which are put in the time center of BDS and NTSC separately.

Figure 4 shows the result of UTC(NTSC)-GEO k (k=1 TO 5) from MJD 56239 to 56323.

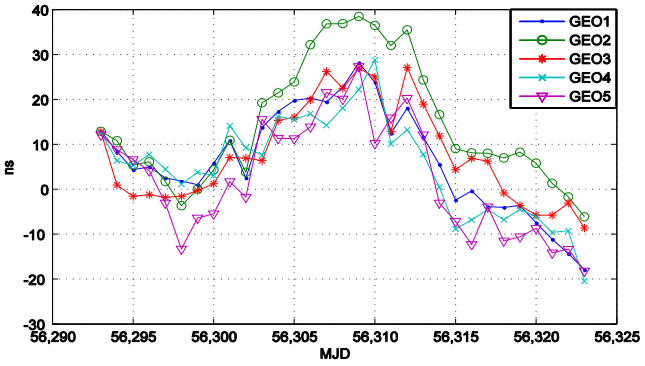

Figure 4 UTC(NTSC)-BDT by GEO k (k=1 to 5)

From Figure4, it is obvious that the fluctuation of time service by GEO 2 is much bigger than that of the other satellites. The reason we think is that GEO 2 was lunched at the end of last year, its state is not stable, the satellite clock is still in the term of test. The other line GEO1, GEO 3, GEO4 and GEO5 show good consistency.

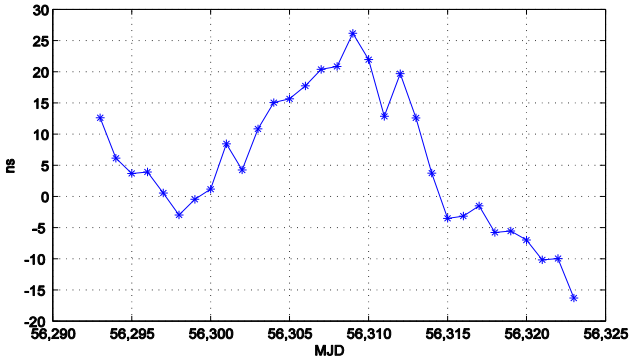

Figure 5 Average of UTC(NTSC)-BDT of GEO 1,3,4,5

In order to research the performance of time service by the five GEO satellites, the four stable data of GEO satellite are averaged with equal weight. Figure 5 is the average of the four groups of data. The table 1 shows the statistic result of different GEO satellite.

Table1. Performance time service by GEO 1~5

Item	G1	G 2	G 3	G 4	G 5	AVE*
MEA	6.56	14.39	7.79	5.24	2.59	5.55
STD	11.65	13.69	10.86	11.03	12.67	10.99
RMS	2.63	3.92	2.63	2.40	2.53	2.62

*AVE is the average of UTC(NTSC)-BDT by GEO 1, GEO3, GEO4 and GEO5. MEA is mean value, STD is standard deviation.

From the table 1, the same conclusion can be gotten that the fluctuation of GEO2 is bigger than that of the other satellites. Compared with UTC(NTSC), the highest precision time service is 10.86ns, the worst is 13.96ns.Figure 6 shows the time residual compare with AVE, which can be calculated by formula 12.

$$\mathrm{UTC(NTSC)} - \mathrm{AVE}\text{-}[\mathrm{UTC(NTSC)}\text{-}\mathrm{BDT(\ GEO\ k)}] = \mathrm{BDT(\ GEO\ k)}\text{-}\mathrm{AVE} \quad (12)$$

Where, k=1, 2, 3, 4,5.

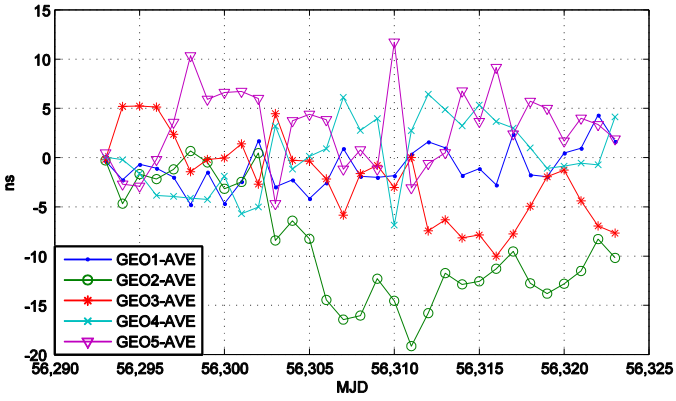

Figure 6 Residuals compared with average of GEO k

Table 2 Performance BDT(GEO k)-AVE

Item	G 1	G 2	G 3	G 4	G 5
AVE	-1.02	-8.85	-2.25	0.31	2.95
STD	2.12	5.83	4.29	3.66	4.03
RMS	0.46	2.10	0.95	0.72	0.98

Table 2 shows that the maximum AVE is 8.25 (GEO2), the minimum is 0.31 (GEO4); the maximum STD is 5.83 (GEO2), the minimum is 2.12 (GEO1); the maximum RMS is 2.10 (GEO2). To analyze the frequency stability of time service of every GEO satellite, the Allan deviation of the UTC(NTSC)-BDT(GEO k) is calculated by stable32. Figure 7 shows the Allan deviation of them. Form figure1, we could find except GEO2 the time service by the other GEO satellites expresses evident consistency.

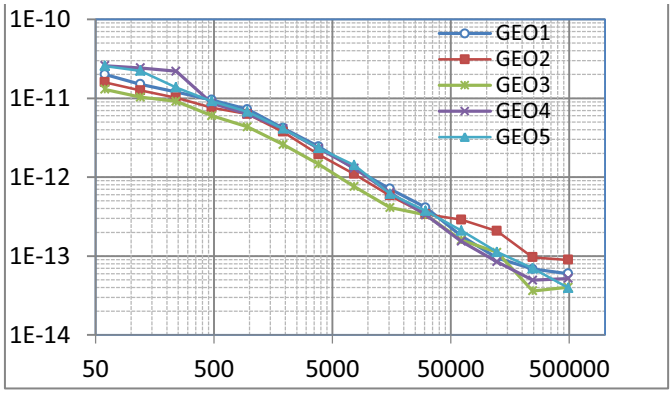

Figure 7 Stability of the UTC(NTSC)-BDT by GEO k

Analyzing the Figure 7, we find that the short term stability and long term stability of UTC(NTSC)-BDT by GEO 3 are all better than that of the others. The reason is that the observation condition is better than that of the others. the elevation at NTSC is about 50° , and the position of GEO 3 is at longitude 115°on the equatorial orbit. The longitude of the observation site is 107°, so GEO 3 is easy to be observed under the same condition. Figure 8 shows the Allan deviation of of UTC(NTSC)-BDT by GEO 3.

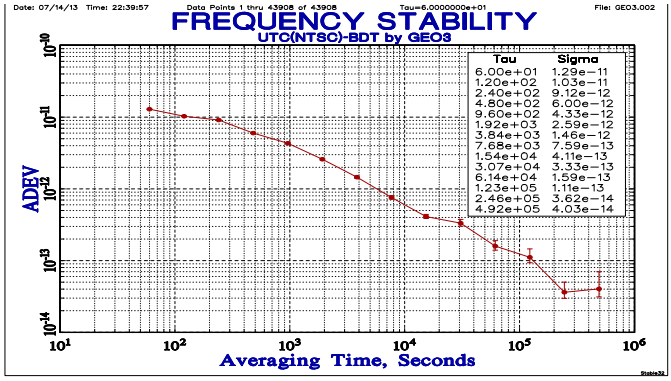

Figure 8 Stability of the UTC(NTSC)-BDT by GEO 3

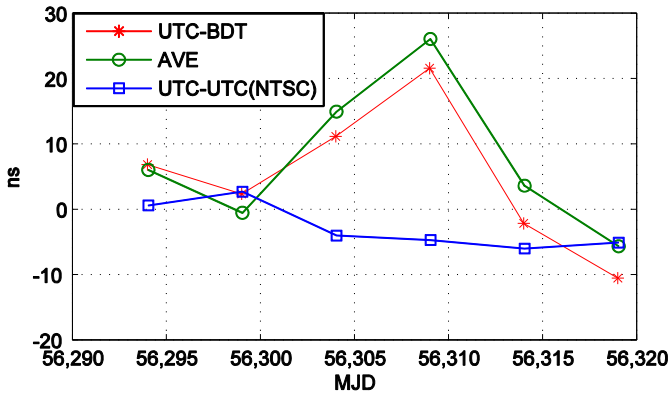

Figure 9 Deviation of BDT compared with UTC

Figure 9 shows the the deviation of BDT compared with UTC through UTC(NTSC)[5]. AVE in Figure 9 is an indication of the average of UTC(NTSC)-BDT by GEO k, k=1,3,4,5. Analyze the three lines, we could find that the fluctuations of lines are caused by BDS time and GEO satellite. The standard deviation of UTC-BDT is 11.1 in the period of test.

IV. SUMMARY

From the test and analysis, it is apparent that the deviation between BDT and UTC(NTSC) keeps in tens of nanoseconds in the period of experiment. Based on the different GEO satellites, though the deviation compared with UTC(NTSC) and UTC shows good consistency , there is still some diversity. The worst result is from GEO 2, and the best from GEO3. For GEO 2, it still in testing, the operation is unstable, however for GEO 3, its operation is stable and its observation condition is the best one of the five GEO satellites. Because the one-way time service by GEO satellites is the best in the three types of satellites [6], the result of the test shows that BD time service is about tens of nanoseconds at present. However, along with Beidou navigation system's gradually maturing and the orbit determination technology's improvement, the precision of Beidou one-way time service will be improved continuously.

REFERENCES

[1] BDS Iterface Control Document Verification.

[2] YUAN Haibo, GUANG Wei, Experiment and Analysis of Beidou Satellite Common—view Time Transfer, The 3rd China Satellite Navigation Conference,

[3] CHEN Xiao-yu,QI Jian-zhong, SONG Peng, Research and Implementation of A Method of Precise Time Transfer with GPS, The 3rd China Satellite Navigation Conference

[4] Thomas E.Parker and Denetrios Matsakis, Time and Frequency Dissemination Advances in GPS Transfer Techniques, GPS World, 2004,11

[5] BIPM Circlur T, 2013.1

[6] Yang Fan, Yuan Haibo, nalysis and Evaluation of One-Way Time Service by Beidou Dual-Frequency Multichannel Receiver, proceeding of Advanced Measurement and Test (AMT) 2013.

Review and Preview of Two-way Time Transfer for UTC generation – from TW*S*TFT to TW*O*TFT

Z. Jiang, H. Konaté and W. Lewandowski
Time Department, Bureau International des Poids et Mesures (BIPM)
Pavillon de Breteuil F-92312, SÈVRES CEDEX, France
zjiang@bipm.org

***Abstract*—Bi-directional methods are widely used in scientific and productive measurements. By the symmetric principle, systematic errors are largely cancelled. The technique of Two-Way *Satellite* Time and Frequency Transfer (TWSTFT) is a typical example. Using the reciprocated radio signals emitted at two Earth laboratories and exchanged through a geostationary telecommunication satellite, the atmosphere delay effects are greatly reduced in the combination of the up and down signals. Applications to time transfer of the optical fibre technique, here under the acronym TWOTFT (Two-Way *Optical fiber* Time and Frequency Transfer) developed rapidly. The reciprocity of the signal in both the directions allows balancing the propagation path delays in the fibre since they average out almost entirely by employing the two-way method. Based on historical documents and the latest developments and in view of metrology, we briefly review and preview the two-way techniques for application in accurate time transfer for UTC.**

Keywords- UTC, TWSTFT, TWOTFT

I. TWO-WAY SATELLITE TIME AND FREQUENCY TRANSFER (TWSTFT)

A. Initiation 1960-1986 [1]

As a promising tool for accurate time and frequency transfer, the technique of Two-Way Satellite Time and Frequency Transfer (TWSTFT, in the earlier documents, the term TWSTT, Two-Way Satellite Time Transfer, was used) started its experimental steps earlier than GNSS. Long before the GPS time transfer became popular in the 1980s', attempts to use the geostationary telecommunication satellites to compare clocks can be dated back to August 1960. Then Echo 1 the large silvered Mylar balloon was used for one-way time transfer attempts. The result was not ideal due to the unknown propagation delays in the atmosphere. In 1962, the USNO and the NPL used the first active-mode communication satellite, Telstar, to perform the very first transatlantic two-way clock comparisons. In 1965, the first transpacific clock comparisons through the communication satellite Relay II were carried out between the USNO and the Radio Research Laboratory in Japan (Figure 1).

In most of these early experiments, a one-pps signal was modulated onto the carrier wave of a video signal for transmission. Oscilloscopes, Polaroid cameras and other primitive methods of measurement were employed. The type A (u_A) and type B (u_B) uncertainties reached during the Telstar and Relay experiments were about 10~100 ns and 100~1000 ns levels respectively. Ten years later, by using the ATS-1 satellite, the u_A and u_B were reduced to 1 ns and 10 ns respectively. In the end of 1970s, experiments proved that u_A could be further improved to around 0.2 ns. An experiment in Europe in 1983 attained a similar result using the Intelsat-V satellite and MITREX modem.

Left- ECHO 1, first Passive Communication Satellite
Middle- TELSTAR, first Active Communication Satellite
Right- RELAY Communication Satellite

Figure 1. The early communication satellites (NASA images)

B. Development 1987-1997 [2]

Hardware technology has been quickly developed. The costs and the dimensions of the devices became smaller. Timing laboratories could invest in the required equipment with a more automated and operational timing transfer system.

In 1987, routine experiments began to use commercial Ku-band satellites. The NIST, the USNO and the NRC, joined later by the European laboratories TUG, NPL, NMi, VSL DTAG, PTB and OCA, started routine continuous observations (three measurements per week).

In the 1980s, the GPS had been used for accurate time transfer, and the GPS common-view was at that epoch the most advanced technique giving an accuracy of a few nanoseconds between European laboratories and 10 nanoseconds between continents. Unfortunately it was declared by the US military that in the near future the GPS system would be degraded for civilian users (Selective Availability). In addition the increasing of the altitudes of GPS satellites orbits was considered.

Meanwhile, significant improvement of atomic clock performances was expected in the years to come. So the timing community did not have simply to replace the GPS, but to find a new and more accurate technique. This was the 2-way time transfer. The importance of the clock comparisons has been emphasized in Resolutions and Recommendations by the General Conference on Weights and Measures (CGPM, Resolution 4 of the 18th CGPM, 1987) and the International Radio Consultative Committee – (CCIR, presently

Radiocommunication Sector of the International Telecommunication Union, ITU-R), calling for an international effort to establish the geo-satellite links on a permanent basis.

The 11th CCDS (Consultative Committee for the Definition of the Second, now the Consultative Committee for Time and Frequency, CCTF) in its declaration S1 (1989) encouraged the use of two-way time transfer and suggested the creation at the BIPM of an ad-hoc working group on the TWSTFT. The task of the Working Group was to specify the operational system, e.g.: satellites and frequency bands; specifications of Earth stations; station calibration; measuring procedures and schedules; data exchange and processing, etc. The first ad-hoc Group meeting was held at the VSL, in Delft, the Netherlands, on 15 June 1989.

The second meeting was held at Graz, Austria on 27-28 Oct. 1992 and was devoted to the exchange of information on the state-of-the-art of the method, available satellites and equipment, administrative issues, and reflections on possible operational links or experiments.

Ten laboratories actively intended to joint in the experimental plan. They were TUG, IEN(IT), PTB, FTZ(DTAG), NIST, USNO, NPL, VSL, LPTF(OP) and OCA. The modems available were of MITREX, SATRE, ATLANTIS and NIST. There were about 20 modems operational in different laboratories.

In 1992, several commercial satellite systems were available, and modems adapted for the technique were commercialized. Some ten UTC laboratories were equipped with different types of modems and other facilities for the clock comparisons with TWSTFT.

In March 1993, the BIPM ad-hoc Working Group was transformed to the permanent CCDS/CCTF Working Group on TWSTFT. Its first meeting was held in October 1993 at NPL, UK. The result of the European line-up campaign was reported. Stability in TDEV of hundred ps was reachable, cf. Figure 2.

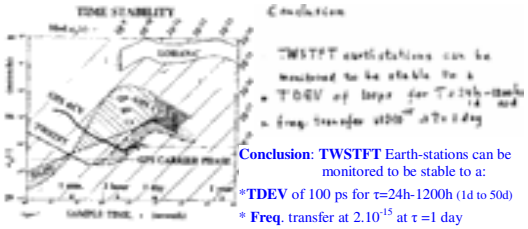

Figure 2. Report to the 5th TW WG in 1997 (hand writing transparent slides probably from PTB) [2]

C. *Application in UTC 1999-present [2]*

The International Telecommunication Union (ITU) approved in 1995 a recommendation fixing the standard data format for the TWSTFT operations.

The first TWSTT link officially introduced in the UTC computation was TUG-PTB in *Circular T* 139 published on 17 August 1999. GPS therefore lost its solo role as the tool for clock comparison in UTC for more than a decade. In 2000, there were four TW time links fully operational: TUG-PTB, VSL-PTB, NPL-PTB and USNO-NPL, as shown in the Figure 3 although at least 10 laboratories were operating TW stations.

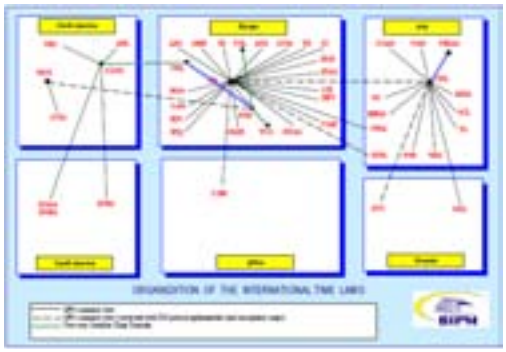

Figure 3. Configuration of the international UTC time link network in 2000

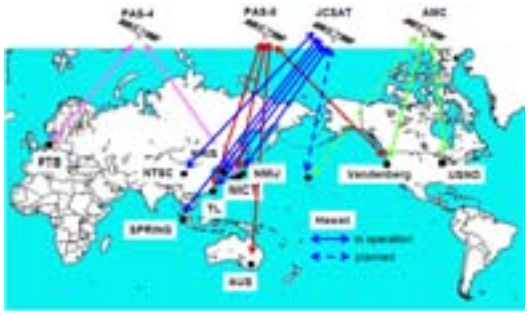

Figure 4. TWSTFT links in/between Asia, Europe and America in 2005 [2]

Figure 5. Setups of the Asia-Europe TWSTFT link between PTB-NICT [2]

The Asian-Pacific laboratories actively participated in the TWSTFT. In 2005, the high accurate Europe-Asia transcontinental link between NICT and PTB was established, Figures 4 and 5.

To contribute to UTC, the TWSTFT links must be calibrated, either indirectly through GPS links or through a mobile TW calibrator (Figure 6). Several calibration campaigns were organized in and between Europe (Table I), America and

Asia.

Figure 6. The TWSTFT mobile calibrators of TimeTech, USNO and VNIIFTRI [2]

TABLE I. CALIBRATION CAMPAIGNS IN EUROPE [2]

Calibration Period	Laboratories/campaigns
May-June 2003	IT-PTB-IT
July 2004	PTB-OP-NPL-VSL-PTB
Oct.-Nov. 2005	PTB-SP-VSL-NPL-OP-IT-PTB
May-June 2006	TUG-PTB-CH-TUG
Sept.-Oct. 2008	PTB-NPL-OP-IT-VSL-CH-TUG
2012-2013	PTB, CH, OP, VSL, ESTEC, AOS …

Meanwhile, in the passed years, the u_A in the GPS links dramatically decreased thanks to GPSPPP. From 2011 the combination of TWSTFT and GPSPPP is used to compute the UTC time links so as to take the advantages of the both techniques (Figure 7).

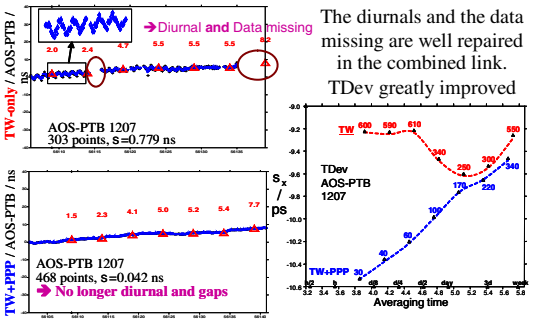

Figure 7. Combination of TWSTFT and GPSPPP

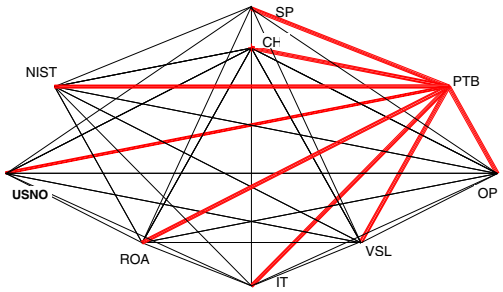

Figure 8. European-America TWSTFT network. Red lines are the UTC links

More than two third of the clocks in UTC and almost all the primary frequency standards are compared using TWSTFT. However, the TWSTFT is measured as a network but used as a single-link. The TW data are highly redundant. In general, for a N-point network, there are N(N-1)/2 independently measured links. Among them, only N-1 are used (red links in Figure 8). We have then (N²-3N+2)/2 redundant links. Full use of the high redundancy could be an effective way to improve UTC.

The concept of the TWSTFT network time transfer provokes several approaches in (quasi) real-time clock comparison and UTC dissemination with the TW network [2].

Figure 9 is the transcontinental TWSTFT network maintained at TL, NICT and USNO etc.

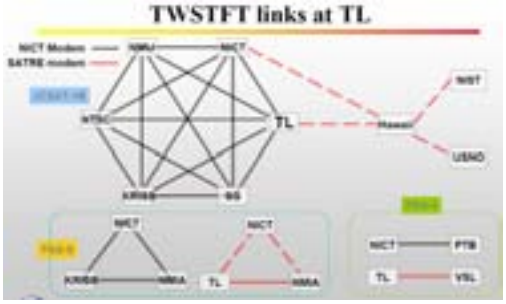

Figure 9. Asia-America TWSTFT network [2]

In addition to its direct contribution to UTC, TWSTFT has also served to test and validate the *new* GNSS techniques and methods incorporated to time transfer for UTC in the past 15 years, such as the GPS all in view, the GPSP3, the GPSPPP and GLONASS.

II. ONCOMING DEVELOPMENT

A. *Use of Carrier phase and DPN [2]*

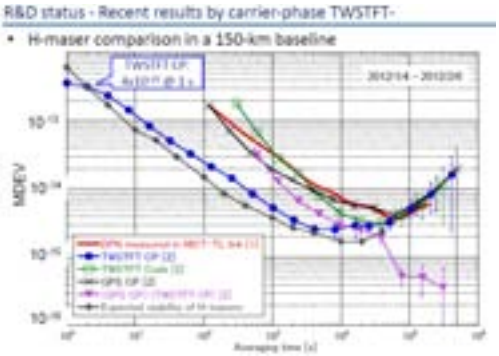

Figure 10. The MDev of the different techniques: DPN, TW CP, TW code, GPS CP vs. HM [2]

The current TWSTFT observable is only the code, which, affected of measurement noise and diurnals, is at its limits in accuracy. Further improvements should come from the uses of other observables, such as the DPN (dual pseudo-random noise) and carrier phase information. The DPN allows doubly reducing the measurement uncertainty, in particular that originated by the diurnals. Because the resolution of the carrier phase is 100 to 1000 times more precise than that of the code, TWSTFT carrier phase transfers may attain theoretically a stability of 0.1 ps in time and 10^{-12}@1s or 10^{-16}@1-day in frequency.

Figure 10 shows the MDev of the different techniques: DPN, TW CP, TW code, GPS CP with respect to the expected stability of a hydrogen maser.

B. *Two-way Optical Fibre Time and Frequency Transfer (TWOTFT) [3,4]*

The recent developments in the application of the optical fibre allow time transfer with a combined uncertainty (u_A and u_B) at the level of hundred ps. As same as TWSTFT, TWOTFT is based on telecommunication facilities, but this time, the optical fibre networks.

Optical clocks reach a fractional frequency uncertainty of order 10^{-17} and outperform the best cesium-based atomic standards in both accuracy and stability [4]. This outstanding performance makes them the most promising tool for the redefinition of the SI unit of time, the second, and an ideal tool for various tests of fundamental physics. Scientific programs or European space missions like the development of the GNSS Galileo, the Cosmic Vision program of ESA, or the ACES mission rely on the availability of highly accurate and ultra-stable frequencies or timing signals. However, today's conventional satellite based techniques lack the required performance for clock comparisons with relative frequency instability below 10^{-17} at one day measurement time.

Although the goal of fibre link is orientated to the next generation of optical clocks, some of its present outputs can be used immediately for improving the UTC generation, such as supporting time link calibrations and validations of high accurate GNSS time transfer methods.

The principle of the two-way transfer is the symmetry of the go and back signals whatever they go through the atmosphere or optical fibre or other media. Both TWSTFT and TWOTFT work with the same principle.

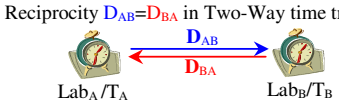

Figure 11. The symmetry in the two-way transfer signals go through atmosphere or optical fiber[5]

There are some 14 UTC laboratories that actively work on the optical fiber time and frequency transfers [5].

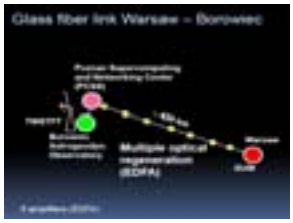

420 km – the distance along optical fiber
Combined uncertainty is estimated to be 112.3 ps

Figure 12. The characterization of the optical fiber link between UTC(AOS)-UTC(PL) [2]

AGH, GUM and AOS developed glass fibre time and frequency transfer facilities between two UTC laboratories and maintain a permanent, real-time time and frequency transfer link between UTC(AOS) and UTC(PL) (Figure 12) available at www.optime.org.pl/node/47. Meanwhile, AOS-PL started from May 2013 (1305) sending the fibre link data to the BIPM. Figure 13 illustrates the Tdev obtained from the TL 25 km fibre experiment.

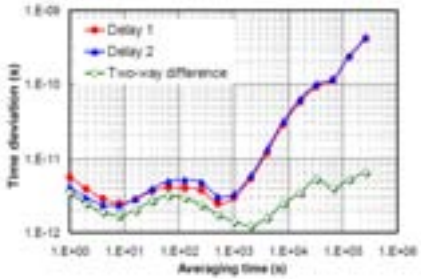

Figure 13. TL 25 km fiber time link experiment [5]

TWOTFT could fundamentally change the UTC generation. One application could be in the calibration of time links. TWOTT can reach hundred ps stability in a few minutes and therefore is an effective new tool for UTC link calibration vs. satellite methods with several days' measurements.

We suggest adapting the ITU TWSTFT data format for TWOTFT. Hence all the data exchanges, calibrations and processing as well as the related methodology could be kept with only slight modifications. This will speed up its applications. TWOTFT, with a potential uncertainty of hundred ps, could introduce fundamental changes in the UTC construction, such as the time link strategy and even the configuration of the international UTC time transfer network.

Since more than three decades, the UTC generation has been using the space-techniques. A new era of the ground based techniques (e.g. moving clock in the past) is back …

ACKNOWLEDGEMENTS

We thank the pioneers of the TWSTFT: B Guinot, G de Jong, F Cordara, P Hetzel, D Kirchner, D Knight, A Soering, W Klepczynski, W Hanson and T J Quinn. We thank also all the TWSTFT laboratories for their contributions to UTC and to the reference [2] based on which this paper is written.

REFERENCES

[1] http://tycho.usno.navy.mil/twstt_hi.html, history of TWSTFT

[2] http://www.bipm.org/wg/AllowedDocuments.jsp, documents of CCTF WG on TWSTFT back to 1989

[3] Z. Jiang, H. Konaté and W. Lewandowski 2013 TM220, Review and Preview of Two-Way Time and Frequency Transfer for UTC generation -history, present and future

[4] http://www.ptb.de/emrp/neatft_home.html, JRP NEAT-FT

[5] Z. Jiang, W. Lewandowski, L. Robertss, J. Nawrocki, A. Czubla and W.H. Tseng 2013 TM219, Evaluation of the first optical fiber time link between the UTC laboratories AOS and PL - TWOTFT and consideration for the Mis En Practique in UTC

Dual-Frequency Time Transfer Unit for Comparisons of the Remote Clocks Using GLONASS and GPS Signals

P. Bogdanov, A. Bandura, M. German, K. Kol'chenko, O. Nechaeva
"Russian Institute of Radionavigation and Time" JSC
St.Petersburg, Russia

Abstract— **Dual-frequency Time Transfer Unit (TTU) using GLONASS and GPS signals developed at "Russian Institute of Radionavigation and Time" JSC (RIRT) is intended for determining the offset between local clocks and GLONASS-time and GPS-time with the purpose of subsequent determining the mutual time and frequency offset between remote clocks, as well as for generating time scale signals synchronized to Russian National Universal Time Coordinated UTC(SU). The results of tests showed that the accuracy characteristics of the new Time Transfer Unit are higher than the same characteristics of the previous TTU model developed at RIRT as well as of TTS-3 and TTS-4 receivers, mostly when operating by GLONASS signals.**

Keywords- Time Transfer Unit, remote clock, GLONASS-time, GPS-time, accuracy estimate

I. INTRODUCTION

The method of using GLONASS and GPS signals is still being used for accurate comparisons of the remote clocks [1].

Time Transfer Unit (TTU) using GLONASS and GPS signals was developed at Russian Institute of Radionavigation and Time (RIRT) in 2002 and became the first Russian device to realize this method [2]. However, its abilities were considerably limited as it was made on the base of 16-channel single-frequency GLONASS/GPS receiver.

In this connection, the new Time Transfer Unit (TTU-1) based on 36-channel dual-frequency GLONASS/GPS receiver was developed in 2011. TTU-1 is intended for determining the offset between local clocks and GLONASS-time and GPS-time with the purpose of subsequent determining the mutual time and frequency offset between remote clocks, as well as for generating time scale signals synchronized to Russian National Universal Time Coordinated UTC(SU).

II. FUNCTIONALITY, MAIN CHARACTERISTICS AND COMPOSITION OF TTU-1

TTU-1 has the following main technical characteristics:

- determining the offset between a local clock and GLONASS-time and GPS-time with the error no more than 35 ns (rms) using GLONASS signals and no more than 20 ns (rms) using GPS signals over 13-min measurement interval;

- determining the mutual offset between two remote clocks using GLONASS or GPS signals with the error no more than 5 ns (rms) for the distances between clocks up to 100 km and no more than 10 ns (rms) for the distances up to 8000 km over 13-min measurement interval;

- determining the mutual frequency offset between two remote clocks at the distances up to 100 km using GLONASS or GPS signals with the error no more than $5 \cdot 10^{-14}$ over 1-day observation interval and no more than $1 \cdot 10^{-14}$ over 10-days observation interval;

- synchronizing the output signals 1 Hz, 1/60 Hz and 1/300 Hz to UTC(SU) or GLONASS-time with the error no more than 50 ns (rms).

The new Time Transfer Unit is presented in Fig. 1.

TTU-1 consists of the following components:

- an antenna box with built-in amplifier;

- a comparison unit including a receiver, a synchronizing device, an indication device and a power supply unit;

- a personal computer with special software which realizes the algorithms for TTU-1 functioning;

- a mounting kit.

The antenna box and the receiver are calibrated during their manufacturing process. The calculated signal delays for GLONASS and GPS signals are accounted for during the measurements processing. The special testing equipment with GPS/GLONASS signal simulator is used to calibrate the devices. Now the total error of the determined absolute signal delays is about 5 ns. Besides, the delay corrections are measured for each GLONASS frequency with the error no more than 1 ns.

TTU-1 provides the following output data:

- time measurement results in the standard international format "cggtts_format_v2" [3] including:

L1C - L1 code measurements;

L2C - L2 code measurements;

Figure 1. The new Time Transfer Unit

L3C - ionosphere-free combination of dual-frequency code measurements;

CL3 - ionosphere-free combination of dual-frequency code measurements;

- radionavigation parameters and digital information included into navigation message from SV in the standard international format RINEX.

III. TTU-1 TEST RESULTS

The accuracy of time scale comparisons (rms) was estimated for three sets of TTU-1 (6RRT, 10RRT, 2RRT) installed at RIRT and one set supplied to "Rostest-Moskva" company (ROST).

The value of the root mean squared of linear fit residuals for all measurements over 1 day was used as an accuracy estimate.

The results of the accuracy estimates for time comparisons between local clock and GLONASS/GPS-time, the instrumental accuracy estimates for the mutual time offset and frequency offset of local clocks (τ = 1 day) and the accuracy estimates for mutual time comparisons between local clocks at RIRT and "Rostest-Moskva" are presented in Tables I - IV.

The results show that TTU-1 accuracy characteristics satisfy technical requirements. At the same time, the results show that for the distances up to 100 km the required accuracy of comparisons between remote clocks can be provided only by single-frequency measurements.

TABLE I. ACCURACY ESTIMATES FOR TIME COMPARISONS BETWEEN LOCAL CLOCK AND GLONASS/GPS-TIME

Set	Comparison error (rms), ns					
	GLONASS			*GPS*		
	L1C	*L3C*	*CL3*	*L1C*	*L3C*	*CL3*
6RRT	8.7-10.8	6.3-8.0	6.3-7.6	6.2-6.7	4.5-4.8	2.7-3.1
10RRT	9.3-11.0	6.8-8.6	6.3-8.4	6.3-6.8	4.9-5.1	2.5-3.7
2RRT	9.6-10.5	6.9-8.7	6.7-8.6	6.1-6.6	4.4-4.8	3.2-4.0
ROST	8.9-10.6	6.7-8.9	7.2-8.4	6.0-6.4	4.1-5.2	2.8-3.8

TABLE II. INSTRUMENTAL ACCURACY ESTIMATES FOR THE MUTUAL TIME OFFSET BETWEEN LOCAL CLOCKS

Sets	Comparison error (rms), ns					
	GLONASS			*GPS*		
	L1C	*L3C*	*CL3*	*L1C*	*L3C*	*CL3*
6RRT – 10RRT	2.2-2.4	6.0-6.5	4.9-5.4	2.1-2.2	6.0-6.4	4.6-5.0
6RRT – 2RRT	2.4-2.6	9.3-9.6	8.0-9.0	2.1-2.4	5.0-5.1	3.3-3.9
10RRT – 2RRT	2.5-2.8	8.4-9.0	8.0-8.8	2.1-2.2	5.1-5.7	3.8-4.2

TABLE III. INSTRUMENTAL ACCURACY ESTIMATES FOR THE MUTUAL FREQUENCY OFFSET BETWEEN LOCAL CLOCKS (τ = 1 DAY)

Sets	Error, 10^{-14}					
	GLONASS			*GPS*		
	L1C	*L3C*	*CL3*	*L1C*	*L3C*	*CL3*
6RRT – 10RRT	≤ 0.8	≤ 1.2	≤0.9	≤ 0.6	≤ 1.1	≤ 0.8
6RRT – 2RRT	≤ 0.5	≤ 1.4	≤ 1.3	≤ 0.3	≤ 1.3	≤ 0.6
10RRT – 2RRT	≤ 0.6	≤ 1.5	≤ 1.3	≤ 0.4	≤ 1.2	≤ 0.5

TABLE IV. ACCURACY ESTIMATES FOR THE MUTUAL TIME COMPARISONS BETWEEN LOCAL CLOCKS AT RIRT AND "ROSTEST-MOSKVA"

Sets	Comparison error (rms), ns					
	GLONASS			*GPS*		
	L1C	*L3C*	*CL3*	*L1C*	*L3C*	*CL3*
6RRT – ROST	3.0-3.1	7.7-7.9	6.3-6.4	2.7-2.8	5.1-5.3	2.3-2.5
10RRT – ROST	2.7-2.9	6.7-7.4	6.1-6.6	2.9-3.1	5.3-5.5	2.7-2.8
2RRT – ROST	3.1-3.2	7.9-8.2	6.5-6.6	2.6-2.9	4.7-5.0	2.4-2.6

The results of the accuracy estimates for time comparisons between local clock and GLONASS/GPS-time and between remote clocks with using TTU and TTS-3 and TTS-4 receivers are presented in the Tables V - VIII.

TTUs are installed at RIRT (3RRT, 7RRT) and Main and Reserved Central Synchronizers of GLONASS (CSm and CSr).

TTS-3 and TTS-4 receivers produced by PIK Time Systems are installed at Russian Time and Frequency Service sites Mendeleevo (SU), Irkutsk (Im), Khabarovsk (Km) and Novosibirsk (Nm).

TABLE V. ACCURACY ESTIMATES FOR TIME COMPARISONS BETWEEN LOCAL CLOCK AND GLONASS/GPS-TIME USING TTU

Site	Comparison error (rms), ns	
	GLONASS (L1C)	*GPS (L1C)*
3RRT	7.8-13.3	5.9-6.6
7RRT	6.7-12.8	5.9-6.7
CSm	8.4-13.8	6.2-7.1
CSr	6.7-12.1	6.4-8.7

TABLE VI. ACCURACY ESTIMATES FOR THE MUTUAL TIME OFFSET BETWEEN LOCAL CLOCKS USING TTU

Sites	Comparison error (rms), ns	
	GLONASS (L1C)	*GPS (L1C)*
3RRT - 7RRT	3.7-4.7	2.8-3.8
3RRT – CSm	5.8-7.1	4.4-5.4
3RRT – CSr	6.5-8.8	6.6-8.0
CSm – CSr	6.8-9.8	7.7-9.7

TABLE VII. ACCURACY ESTIMATES FOR COMPARISONS BETWEEN LOCAL CLOCK AND GLONASS/GPS-TIME USING TTS-3/TTS-4

Sites	Comparison error (rms), ns			
	GLONASS		*GPS*	
	L1C	*L3C*	*L1C*	*L3C*
SU (TTS-3)	14.3-17.7	-	5.4-7.2	-
Im (TTS-3)	17.5-19.7	-	5.4-7.4	-
Km (TTS-4)	15.7-22.1	16.1-18.4	5.2-8.4	2.4-3.0
Nm (TTS-4)	15.7-18.4	14.7-17.4	5.5-7.8	2.6-3.0

TABLE VIII. THE ACCURACY ESTIMATES FOR THE MUTUAL TIME OFFSET BETWEEN LOCAL CLOCKS USING TTS-3/TTS-4

Sites	Comparison error (rms), ns			
	GLONASS		*GPS*	
	L1C	*L3C*	*L1C*	*L3C*
SU(TTS-3)–Im(TTS-3)	13.0-15.8	-	5.3-7.8	-
SU(TTS-3)–Km(TTS-4)	17.4-20.6	-	6.4-9.8	-
SU(TTS-3)–Nm(TTS-4)	9.3-12.5	-	5.9-8.5	-
Im(TTS-3)-Km(TTS-4)	6.8-11.8	-	4.6-6.9	-
Im(TTS-3)-Nm(TTS-3)	6.0-8.9	-	5.9-8.3	-
Km(TTS-4)-Nm(TTS-4)	10.0-14.4	9.3-10.7	5.2-8.5	2.3-2.6

The results presented in Tables I – IV and V - VIII show that the accuracy characteristics of the new TTU-1 are higher than the same characteristics of TTU equipment as well as of TTS-3 and TTS-4 receivers, mostly when operating by GLONASS signals.

IV. NOTATION OF MEASUREMENT TYPE FOR TIME SCALE COMPARISONS BY GNSS SIGNALS

According to CGGTTS GPS/GLONASS Data Format Version 02 the following frequency and code types are used for pseudo-range measurements:

L1C – L1 C code;

L1P – L1 P code;

L2C – L2 C code;

L2P – L2 P code.

The type L3C and L3P for ionosphere-free combination can also be used according to "Proposals to use geodetic-type receivers for time transfer using the CGGTTS format" [4].

But now the new "Glonass-K" SV also transmits signals with code division at L3 frequency band and, as a result, L3C type is supposed to be used.

So, there is a contradiction because according to the existing notation L3C should be used for both ionosphere-free combination and observations at L3 frequency band.

To sum up, we find reasonable to develop a new version of the data format for GPS/GLONASS and future GPS/GLONASS/Galileo time receivers and all existing and planned signals and methods of their processing.

V. CONCLUSION

The results of tests and experimental operation showed that the accuracy characteristics of the new Time Transfer Unit meet specified requirements and are higher than the same characteristics of the previous TTU model as well as of TTS-3 and TTS-4 receivers, mostly when operating by GLONASS signals.

The improvement of time comparison accuracy is possible in the mode of post-processing with using a *posteriori* ephemeris and other data presented by GNSS information processing centers, for example, by Information and Analysis Center (IAC) of “TSNIIMASH” Federal State Unitary Enterprise.

ACKNOWLEDGMENT

Authors thank the colleagues from RIRT and “Rostest-Moskva” for their assistance in testing the equipment and processing and analyzing the results obtained.

REFERENCES

[1] BIPM Annual Report on Time Activities, Volume 6, 2011.

[2] P. Bogdanov, V. Moskvin, N. Novikov, I. Galichina, M. Soshin, A. Feoktistov, "Time Transfer Unit on the base of the 16-channel GPS/GLONASS Receiver," in Proceedings of the 16th European Frequency and Time Forum, 2002.

[3] D. Allan, C. Thomas., "Technical Directives for Standardization of GPS Time Receiver Software", Metrologia, 31, 1994.

[4] BIPM Time Section Technical Memorandum TM.110.21, November 2001, section 2.3.

Advances in Multi-GNSS Time Transfer

P. Defraigne, W. Aerts
Royal Observatory of Belgium
Brussels, Belgium

A.Harmegnies, G. Petit
Bureau International
des Poids et Mesures
Sèvres, France

D. Rovera, P. Uhrich
LNE-SYRTE-Observatoire de Paris
Paris, France

***Abstract*—This paper proposes a method to combine GPS and GLONASS measurements for time transfer in All-in-View, using calibration data for both GPS and GLONASS. GLONASS has to date a complete constellation, but its use for time transfer is made difficult by the existence of biases for each satellite-receiver pair. These biases contain both a receiver contribution, due to the different frequencies emitted by the different GLONASS satellites, and a satellite contribution, varying with time, and coming from the satellite clock products. Up to recently, these biases were determined with respect to the calibrated GPS solution. We propose here to determine these biases for the two stations of a time link, in a constrained least square analysis, where the constraint is given by the GLONASS calibration data obtained from a link calibration with these two stations. With these biases, it is then possible to obtain an All-in View solution combining GPS and GLONASS measurements and calibrated for the GPS as well as GLONASS signals. The method was tested on the link Brussels-Paris for which a calibration was performed for GPS and GLONASS. Using one month of data, the impact of using or not the GLONASS calibration results is in that case smaller than 2.5 ns peak to peak.**

Keywords—GPS, GLONASS, Time Transfer

I. INTRODUCTION

GPS signals are used since the eighties [1] to perform precise and accurate Time and Frequency Transfer (TFT). In its classical version, the GPS time transfer is performed using clock offsets collected in a fixed format, called CGGTTS (Common GPS GLONASS Time Transfer Standard), as described in [2,3]. These clock offsets represent the differences between the ground clock (UTC(k) in most cases) and the reference timescale of the GNSS. They are obtained from the pseudorange measurements, corrected for the signal travel time (satellite-station), for the troposphere and ionosphere delays, and for the relativistic effects. A smoothing is then performed over 13 minute observation tracks. Originally developed for C/A code receivers, the method was then upgraded to take advantage of the dual-frequency receivers: combining codes carried by the L1 and L2 frequencies allows removing the ionosphere delays at the first order (i.e. 99.9 percent of the effect), thanks to the ionosphere-free dual-frequency combination. This led to a factor 2 improvement in the stability of the intercontinental time links up to averaging times of 10 days (e.g. [4]). Initially, the time transfer solution was based on the Common View (CV hereafter) [1], i.e. the clock comparison is computed as a weighted average of the differences between the CGGTTS results obtained in both stations for each satellite separately. In that case the weighting coefficient can be a function of the elevation since low elevation observation is more affected by noise and multipath. In order to improve the long distance clock comparisons, it was proposed to replace the CV approach by the All in View (AV hereafter) approach [5]. This consists in computing separately for each station the weighted average of the CGGTTS results and thereafter to compute the difference between the solutions obtained in the two stations.

In parallel, the time-transfer technique based on Precise Point Positioning (PPP) has proven to be a very effective technique allowing the comparison of atomic clocks with a statistical uncertainty of 0.1 ns, and a frequency stability reaching 10^{-15} at an averaging time of one day [6-8]. PPP [9,10] is based on a consistent modeling and analysis of GPS (and possibly GLONASS) dual-frequency code and carrier-phase measurements. The present paper however will concentrate only on CGGTTS results, i.e. code-only analysis; nevertheless the approach can be applied as well to PPP.

The next section reviews the state of the art of time transfer using GLONASS data, then Section III presents the calibration of the link Brussels-Paris set up in order to validate the method developed in Section IV to produce a fully calibrated combined GPS+GLONASS time transfer solution. The conclusions and perspectives of the paper are proposed in Section V.

II. GLONASS TIME TRANSFER: STATE OF THE ART

The main difference between GPS and GLONASS is that all GPS satellites share the same two carrier frequencies L1 and L2, while each GLONASS satellite transmits on a different frequency using a 15-channel frequency division multiple access (FDMA) technique spanning either side from 1602.0 MHz, known as the L1 band and either side of 1246.0 known as the L2 band. Due to the frequency-dependent nature of the hardware delays in the receiver and in the antenna, these are different for each satellite group emitting a given pair of frequencies L1, L2, inducing inter-frequency biases (ISB) up to 25 ns in the code measurements and hence in the CGGTTS data. These ISB in the CGGTTS data must be removed before these data can be used in either CV or AV.

Using GLONASS and GPS for time and frequency transfer in a combined analysis (for the AV and PPP approaches) requires a single common reference for all the satellite clock products used in the analysis. This is not the case with the broadcast satellite clocks, and also not the case with the IGS rapid or final satellite clock products. GLONASS satellite clocks are indeed provided in the navigation message with respect to the GLONASS system time, while GPS satellite clocks are referred to GPS time. GLONASS clocks are not yet

provided in the IGS products. However since 2008, the IGS analysis centre ESOC provides combined GPS and GLONASS products in which the satellite clocks from both constellations are given with respect to the same reference time scale [11]. These products can therefore be used for the combination of GPS and GLONASS data for time transfer. ESOC operates daily computations, and for each day they determine a bias for each receiver-satellite pair. As only differences between receiver and satellite clock parameters appear, it is only possible to solve for the GLONASS clock parameters in a relative sense. ESOC therefore fixes one bias for one given station-satellite pair, but this bias can change from day to day so that all biases change accordingly. As a consequence, using GLONASS measurements with ESOC or equivalent products for time transfer requires the estimation of inter-satellite biases (ISB) in addition to the clock solution for each satellite and on a daily basis. Indeed we have for GPS satellites:

$$(t_{rec} - ref) = meas\_GPS - (t_{sat} - ref) - CAL(rec)$$

and for GLONASS satellites: (1)

$$(t_{rec} - ref) = meas\_GLO - (t_{sat} - ref) - ISB\,(rec, sat, day)$$

where (t_{rec}-*ref*) is the synchronization error between the local clock and the reference of the satellite clock products, *meas_* is the code measurement corrected for the geometric distance and atmospheric delays, *CAL(rec)* is the station hardware delay for GPS. $ISB\,(rec, sat, day)$ is a daily bias for the satellite-receiver pair and has a magnitude around 400 ns, because the ESOC GLONASS clock products are also biased in order to be roughly aligned with the broadcast satellite clocks.

The necessary tools for using of ionosphere-free codes of GLONASS in CGGTTS are presented in [12], and are complemented with the approach recommended for the combination of CGGTTS results from GPS and GLONASS in All in View. This approach is based on a first computation of GPS-only AV solution, followed by the determination of the ISBs with respect to the GPS AV solution, and finally by the computation of the new AV solution combining GPS data and GLONASS data corrected for the ISBs. The results presented in [12] for 25 time links showed that correcting the GLONASS solution for ISBs reduces strongly the noise of the GLONASS solution, with a reduction from 35 % to 90% for the time links investigated (see an example in Figure 1, top). The combination of GPS and GLONASS ionosphere-free combinations in AV solutions were also compared to the GPS-only AV solutions for a set of 25 time links (see one example Figure 1, bottom). For some links where one of the receivers has a quite large GPS code noise level, the noise of the combined solution is better than the noise of the GPS-only solution. For the other time links, the noise level of both solutions is equivalent. For all the links investigated in [12], the statistical uncertainty of the combined GPS+GLONASS (corrected for ISBs) AV solution was smaller than 0.95 ns.

As explained before, we are presently obliged to determine the ISBs daily and for each satellite, while physically these ISBs should be constant with time and the receiver biases should be equal for two satellites emitting the same frequencies. Furthermore, as the biases are determined with respect to the calibrated GPS AV solution, it does not account for any GLONASS receiver calibration data. This is the reason why we propose a new approach in the next sections.

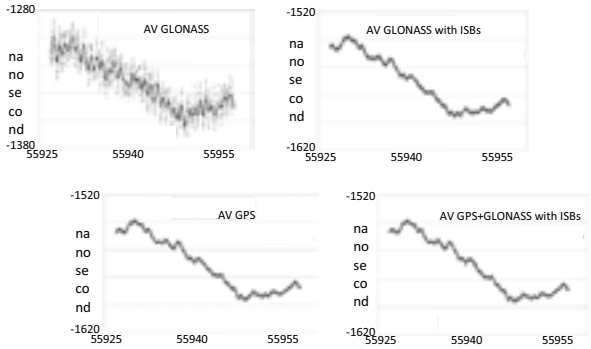

Fig. 1 (from [12]) : time transfer solution between AOS (Poland) and AUS (Australia); up: improvement of the GLONAS AV solution when correcting for the ISBs, bottom: comparison between the GPS AV solution and the GS+GLONASS AV solution when ISBs have been corrected for. Grey dots are the raw AV results, black dots are Vondraked smoothed (1D+5) results.

III. BRUX-OPM8 LINK CALIBRATION

An experimental GLONASS+GPS calibration has been realized in June 2013, using a traveling GNSS station, containing a Septentrio PolaRx4TR-PRO receiver, a 30 m antenna cable RG-8 (Belden 8214), and a Trimble Antenna Choke Ring 59800.00. The scheme of the calibration follows the procedure proposed in [13].The traveling station was first installed in common-clock at the Royal Observatory of Belgium (ORB), in colocation with the station BRUX, the reference station for participation of the ORB to the IGS and to the TAI. The traveling station was then installed in common-clock at the LNE-SYRTE, in colocation with the station OPM8. In both the OPM8 and BRUX stations the receiver is a Septentrio PolaRx4TR-PRO. After coming back, the traveling station was re-installed at ORB in order to have an additional set of measurements and to cross-check the calibration results.

Using 5 days of data of colocation with the traveling receiver for BRUX and for OPM8, we computed separately for C1, P1, C2 and P2 the pseudorange differences between the traveling receiver and the station receiver. We deduced the differential hardware delays (receiver+antenna) between the stations BRUX and OPM8 for GPS P1 and P2, as well as for each of the GLONASS frequencies. In a first time, the computation was done for each GLONASS satellite rather than for each GLONASS frequency in order to assure the hypothesis that satellite emitting the same frequencies have indeed the same receiver and antenna hardware delays. The differential hardware delays in the GLONASS P3 band for the link OMP8-BRUX are shown in Figure 2. Note that even if the calibration was done for P1 and P2 separately, in the following we only speak about P3 as it is the observable classically used for the computation of TAI. Furthermore, notice that no

uncertainty on these biases was estimated up to now. This paper is only devoted to the demonstration of the feasibility of the approach proposed in Section IV. The error budget is beyond the scope of the paper and will be one of the goals of future studies.

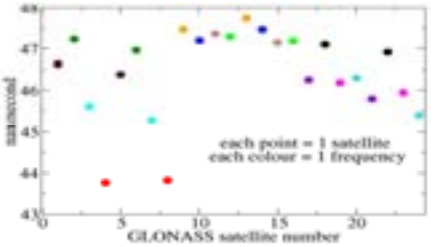

Fig 2. Differential GLONASS hardware delays of the P3 link OPM8-BRUX, computed for each satellite separately.

We can observe in Figure 2 that the satellite pairs corresponding to a given frequency channel have differential hardware delays with a difference smaller than half a nanosecond, except for satellites 20 and 24, which are on the frequency channel +2. This should be investigated in the future. We also observe that the dispersion of the differential delays between the frequencies remains within 4 nanosecond. This is quite small with respect to some other results found in the literature [e.g. 12] but can be explained by the fact that the two stations BRUX and OPM8 are equipped with the same receiver type.

IV. AV GPS+GLONASS FULLY CALIBRATED

Recall that AV can only be computed when the CGGTTS results are based on satellite clock products having the same reference for GPS and GLONASS, as for example the ESOC products. The results of a combined GPS+GLONASS AV proposed in [12] and summarized in Section II are calibrated only for the GPS part. The ISBs are then determined with respect to the calibrated GPS results. In this section we propose a new approach which allows providing a combined GPS+GLONASS AV calibrated for GPS as well as for GLONASS. The basic idea is that the ISBs appearing in equation (1) can be separated into two components: $D(rec, sat)$ the physical station (receiver+antenna) hardware delay for the frequencies of the GLONASS satellite, which is constant over time, and $B(day, sat)$ a satellite bias which varies from day to day, associated with the GLONASS satellite clocks, and which is the same for all the GNSS stations. This reads:

$$ISB(rec, sat, day) = B(day, sat) + D(rec, f_{sat}) \quad (2)$$

where f_{sat} is the satellite frequency. Therefore, the difference between the ISBs of two stations is equal to

$$\begin{aligned} ISB(rec1, sat, day) - ISB(rec2, sat, day) \\ = D(rec1, f_{sat}) - D(rec2, f_{sat}) \\ = \Delta_{12}(f_{sat}) \end{aligned} \quad (3)$$

and should be constant over time. The difference $\Delta_{12}(f_{sat})$ can furthermore be determined by relative calibration, as was done for the link BRUX-OPM8 and presented in the previous section.

Using these differential delays in CV is very simple: each of the differences between clock results made in the two stations on the satellite k should be corrected using $\Delta_{12}(f_k)$:

$$\begin{aligned} CV(sat, t) = REFGLO(rec1, sat, t) \\ - REFGLO(rec2, sat, t) - \Delta_{12}(f_{sat}) \end{aligned} \quad (4)$$

where *REFGLO(rec,sat,t)* is the clock solution from the CGGTTS computed with (or equivalently transformed from broadcast satellite orbits and clocks to) the ESOC products.

The differential delays can also be used for AV (and similarly in the future for PPP), but in that case the determination of the AV (or PPP) solution must be done at the same time for both stations. The reason is that for each station the biases $ISB(rec, sat, day)$ must be determined with respect to the GPS AV solution of the station, while verifying the relation

$$ISB(rec1, sat, day) - ISB(rec2, sat, day) = \Delta_{12}(f_{sat}) \quad (5)$$

We propose therefore, to first determine a GPS-only AV solution, and then to use a constrained least square approach to determine the ISBs of both stations. The constraints given by equation (4) are introduced as additional observations. The matrix system to be solved reads:

$$PAx = Py \quad (6)$$

where the vector x contains the unknown ISBs of the two stations, and the vector y contains all the differences between the GLONASS clock solutions and the GPS_AV solution, as well as the constraints, i.e. the calibration values $\Delta_{12}(f_k)$. The matrix A contains for each observation and constraint the derivative with respect to the ISBs, and the matrix P contains the weights attributed to the observations and constraints. The observations are weighted with the $sin^2(elevation)$. The constraints should receive a high weight, larger than the sum of the weights of all the observations. Finally, the biases of the two stations are determined as

$$x = (A^T P A)^{-1} A^T P y$$

These biases $ISB(rec, sat, day)$ can then be applied to the $REFGLO(rec, sat, t)$ in each of the stations, and the combined AV can then be computed using both the GPS and GLONASS (corrected for ISBs) clock solutions from the CGGTTS files.

This approach to compute a fully calibrated GPS+GLONASS AV time transfer was applied on BRUX and OPM8 data covering one month (June 6 to July 7, 2013). In a first step the CGGTTS results were computed for both stations using the ESOC products and the RINEX to CGGTTS software R2CGGTTS.V51 [12] slightly modified in order to use directly the ESOC products rather than the broadcast satellite orbits and clocks. In the second step the least square approach was used to determine the BRUX and OPM8 ISBs for each satellite and each day, constrained by the differential delays determined by calibration and presented in Figure 2. The differences between the ISBs so-obtained and the ISBs obtained without GLONASS calibration constraint are depicted in Figure 3 for BRUX and OPM8. These differences range between -2 and +2 nanosecond, and are not constant over the one month period analyzed. The large peaks for OPM8 at mjd 56456 are due to

an incomplete daily RINEX file, reducing the number of observations used to determine the ISBs.

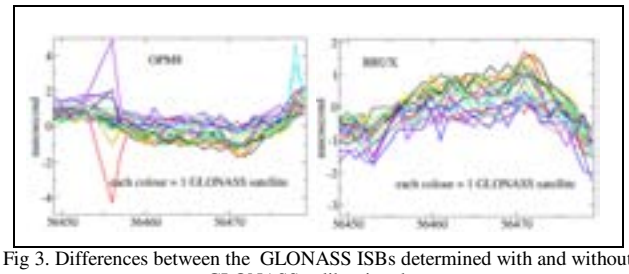

Fig 3. Differences between the GLONASS ISBs determined with and without GLONASS calibration data

Figure 4 presents the difference between the combined GPS+GLONASS solutions using or not the GLONASS calibration constraint to determine the ISBs of BRUX and OPM8. The global impact of using or not the GLONASS calibration constraint on the combined AV solution is, for this one month period and this particular baseline, between -1.2 and +1.2 nanosecond. Finally, Figure 5 shows the time transfer solution over one month for BRUX-OPM8, based on the AV solution using GPS-only, and using GPS+GLONASS with and without taking the GLONASS calibration into account.

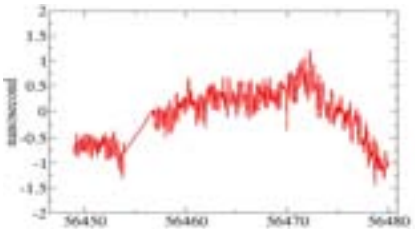

Fig 4. Differences between the time transfer solution OPM8-BRUX computed with AV in both stations determined with and without the calibration constraint.

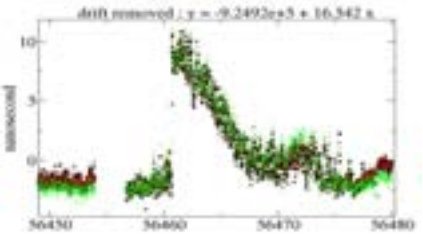

Fig 5. Comparisons between the time transfer solution for OPM8-BRUX computed with AV in both stations using GPS-only (black), GPS+GLONASS with (green) and without (red) the GLONASS calibration data.

V. CONCLUSONS

This paper proposed a method to combine GPS and GLONASS measurements for time transfer in All-in-View, using calibration data for both GPS and GLONASS. It is based on a three step approach:

1. Determining for each GLONASS frequency the differential hardware delay between the two stations of the time transfer link. This can be done by relative calibration using a traveling GNSS station;
2. Computing for each station the GPS-only AV solution;
3. Estimating for each receiver-satellite pair the biases between the GLONASS results from the CGGTTS and the GPS-only AV solutions. These biases should be estimated for both stations at the same time using a least square approach in which the differential hardware delays determined at item (1) are introduced as constraints on the biases estimated here;
4. Computing for each station the combined GPS+GLONASS solution in which the GLONASS results have been corrected for the ISBs determined in Item 3; and make the difference of the AV solutions of the two stations.

This procedure was tested successfully on a link between Brussels and Paris. The difference during one month between the time transfer solutions based on a combined GPS+GLONASS AV, obtained with and without GLONASS calibration results is in this case smaller than 2.5 ns peak to peak. This study will be extended to more baselines, and the uncertainty budget will be further evaluated. It will then be applied to Precise Point Positioning.

ACKNOWLEDGMENT

The authors thank Tim Springer and the ESOC for helpful discussions and availability of orbits and clock products.

REFERENCES

[1] D.W. Allan and M. Weiss, "Accurate time and frequency transfer during common-view of a GPS satellite," Proc. IEEE Freq. Contr. Symp., Philadelphia, PA, 1980, pp. 334-356.

[2] D.W. Allan and C. Thomas, "Technical directives for standardization of GPS time receiver software," Metrologia, 31, 1994, pp. 69-79.

[3] J. Azoubib and W. Lewandowski, "CGGTTS GPS/GLONASS data format Version 02," 7th CGGTTS meeting, 1998.

[4] P. Defraigne P and G. Petit, "Time transfer to TAI using geodetic receivers," Metrologia, 40, 2003, pp. 184-188.

[5] G. Petit and Z. Jiang, "GPS All in view time transfer for TAI computation," Metrologia**, 45,** 2008, pp. 35-45.

[6] Th. Schildknecht, G. Beutler, and M. Rotacher, "Towards sub-nanosecond GPS time transfer using geodetic processing technique," Proc. of the 4th EFTF, 1990, pp. 335-346.

[7] K. M. Larson, J. Levine, L. M. Nelson, and T. Parker, "Assessment of GPS carrier-phase stability for time- transfer applications," IEEE Trans. Ultrason., Ferroelect., Freq. Contr., vol. 47(2) , 2000, pp. 484-494.

[8] P. Defraigne, N. Guyennon, and C. Bruyninx, "GPS Time and Frequency Transfer: PPP and Phase-Only Analysis," Int. J. of Nav. and Obs., vol. 2008, Article ID 175468, 7 pages, doi: 10.1155/2008/175468, 2008.

[9] J. F. Zumberge, M. B. Heflin, D. C. Jefferson, M. M. Watkins, and F. H. Webb, "Precise point positioning for the efficient and robust analysis of GPS data from large networks," Journal of Geophysical Research, vol. 102(B3) , 1997, pp. 5005-5017.

[10] J. Kouba and P. Heroux, "GPS Precise Point Positioning using GPS orbit products," GPS solutions, vol. 5, pp. 12- 28, 2001.I.S. Jacobs and C.P. Bean, "Fine particles, thin films and exchange anisotropy," in Magnetism, vol. III, G.T. Rado and H. Suhl, Eds. New York: Academic, 1963, pp. 271-350.

[11] T. Springer, " NAPEOS mathematical models and algorithms, DOPSSYS-TN-0100-OPS-GN, 1.0, November 5, 2009.K.

[12] A. Harmegnies, P. Defraigne, G. Petit, "Combining GPS and GLONASS in all in view for time transfer", Metrologia 50, 2013, pp. 1–11.

[13] H. Esteban, J. Palacio, F. J. Galindo, T. Feldmann, A. Bauch, and D. Piester, 2010, "Improved GPS based time link calibration involving

ROA and PTB," IEEE Transactions on Ultrasonics, Ferroelectrics, and Frequency Control, UFFC-57, 714-720.

Time and Frequency Transfer Using Satellite Based Augmentation System GAGAN

Petr Pánek and Alexander Kuna
Institute of Photonics and Electronics AS CR, v.v.i.
Chaberská 57, 182 51 Prague, Czech Republic
Email: panek@ufe.cz, kuna@ufe.cz

***Abstract*—GAGAN (GPS – Aided Geo Augmented Navigation) is an Indian SBAS (Satellite Based Augmentation Systems). In contrast to the European EGNOS, this system already supports the navigation function and it transmits signals both in L1 and L5 frequency channels. We used the GAGAN signals for an experimental common-view time transfer between IPE Prague and PTB Braunschweig which is a distance of 370 km and we also tested the time transfer properties using a single clock common-view. The L1 and ionosphere-free code measurements have markedly lower accuracy compared to a GPS common-view because of rather narrow bandwidth of the SBAS signal in L1 frequency channel. L5 code measurement provides much better precision. It results from the single clock common-view that the observed fluctuations can be described as white noise with standard deviations of 6 ns, 1.3 ns and 14 ns for L1, L5 and ionosphere-free combination. The results obtained from the carrier phase measurements are promising. The single clock common-view precision was approximately 30 ps RMS even for the ionosphere-free combination. Interesting results followed from the comparison at the long distance where relatively fast fluctuations induced by ionosphere are obvious in the single frequency measurements. We believe that using GAGAN and other SBASs for permanent carrier phase frequency transfer could be an ideal solution for continuous comparisons of precise frequency sources.**

I. Introduction

GAGAN (GPS-Aided Geo Augmented Navigation) is an Indian satellite navigation system which augments GPS and makes it suitable for safety critical applications. It is one of the SBAS (Satellite Based Augmentation Systems). GAGAN uses geostationary satellites transmitting signals almost identical to the GPS signals thus it can be used for time and frequency transfer in similar way. In contrast to the European EGNOS, this system already supports the navigation function and it transmits signals both in L1 and L5 frequency channels. The signals are also available in good quality in Europe.

The GAGAN project involves establishment of 15 Reference Stations, 3 Navigation Land Uplink Stations, 3 Mission Control Centers and installation of all associated software and communication links. GAGAN is planned to get into full operation by the year 2014 and after its final operational phase completion will be compatible with other SBAS [1]–[3].

This work has been sponsored by the Czech Office for Standards, Metrology and Testing within the Project III/13/13 of the Program of Metrology Development in 2013.

The first GAGAN transmitter was integrated into the GSAT-4 geostationary satellite, and had a goal of being operational in 2008. Following a series of delays, GSAT-4 was launched on 15 April 2010, however it failed to reach its orbit. GSAT-8 (PRN 127) was successfully launched on 21 May 2011 and is positioned in geosynchronous orbit at 55° E. GSAT-10 (PRN 128) was successfully launched on 29 September 2012 and is positioned at 83° E. GSAT-15 is planned to be launched during 2014–15.

II. Using SBAS For Time Transfer

The SBAS satellites broadcast pseudo-random ranging signals of the same type as GPS together with data messages including ephemerides of the geostationary satellites (Message Type 9). When users are equipped with receivers capable to measure the delay between the received signal and an external time reference, it is possible to use this signal for comparison of time scales by the common-view technique.

SBAS makes use of geostationary satellites contrary to GPS. Therefore the variations in the relative position between the satellite and a receiver are small and very slow. The elevation and azimuth of the satellite can be considered nearly unchanging which has significant influence on the character of the multipath effect and the behavior of the ionospheric and tropospheric delay.

Multipath propagation is caused by signal reflection off objects in the vicinity of the receiver antenna. Multipath is then characterized locally. If the distance between the receivers is small, the overall error of comparison is given by the error from the multipath. Azimuth and elevation of a GPS satellite change dramatically during flyover. Therefore the variations in delay of reflected signals are fast and the measured delay fluctuates because of interference of the direct and reflected signals. Concerning a geostationary satellite, changes in azimuth and elevation are extremely slow and the error caused by multipath propagation fluctuates very slowly as well.

While going through the ionosphere and troposphere, the signal from a satellite is delayed up to some tens of nanoseconds. These delays are usually strongly reduced in the common view comparison, but even the residual error is proportional to the ionospheric and tropospheric delays at both sites and their variations still affect the comparison. Both atmospheric delays depend strongly on satellite elevation. This

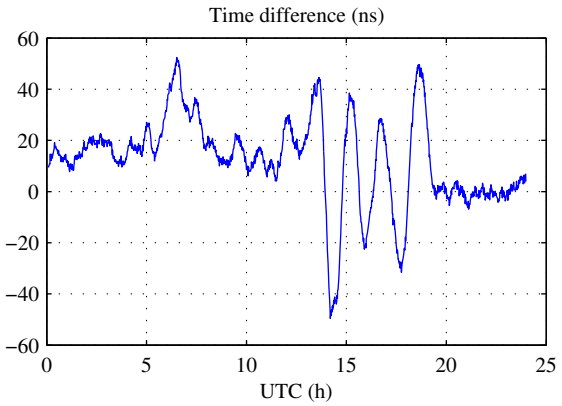

Figure 1. UTC(TP) − GAGAN, code measurements, ionosphere-free combination, $\sigma = 17$ ns.

dependence is extremely high in case of the tropospheric delay. It varies in the range of 6:1 for satellite elevation between 10° and 90°. The ionospheric delay varies in the range of 3:1 for the same range of elevation. Periodic daily changes in ionospheric delay are typically observed with minimum in early morning hours and maximum after the noon. Because the azimuth and elevation are nearly constant concerning geostationary satellite, the variations in the ionospheric delay are then small and slow compared to GPS. Possible variations in the tropospheric delay then respect only actual weather conditions.

It results from the above that the use of the SBAS signals for time transfer should provide much better time stability, but on the other side there cannot be expected a good chance to suppress the multipath effect on the basis of its averaging in time.

III. Experimental Measurements

In the experiments we used the GAGAN PRN 127 satellite signals in L1 and L5 frequency channels. A pair of GTR51 receivers capable to receive the SBAS signals in both frequency channels was used for the reception and measurement data processing. One of the receivers used the Novatel GPS-703-GGG antenna, the second receiver used the Novatel GPS-704X antenna with an external amplifier.

In the first experiment we directly compared the UTC(TP) time scale with the GAGAN system time. The comparison was based on all measurement data from MJD 56231. The resulting plots of the time difference UTC(TP) − GAGAN determined from L1, L5 and ionosphere-free code measurements are in Fig. 1. No ionospheric delay correction is applied on the plots. The ionosphere-free combination is noisiest, but it is best reflective of the properties of the GAGAN system time scale and the broadcast ephemerides. The standard deviation of this plot is 17 ns which corresponds to change of the radial distance between the satellite and the receiver antenna around 5 m RMS. This result indicates a good GAGAN system time and ephemerides quality.

In the second experiment we used the GAGAN signals for common-view between IPE Prague and PTB Braunschweig. The distance between these two sites is around 370 km. The goal of this experiment was to evaluate the time transfer using a SBAS geostationary satellite at a distance when the ionospheric and tropospheric delays play an important role together with the multipath and receiver noise.

As we compared two independent time scales, their difference naturally changed in time. For averaging intervals up to several hours the UTC(PTB) time scale provides significantly better stability than the UTC(TP). Therefore we can consider that the time difference stability is fully determined by UTC(TP) which has typical modified Allan deviation

$$\mathrm{MDEV}(\tau) = 6.4 \cdot 10^{-12}\sqrt{\tau}, \quad \tau > 10\,\mathrm{s}. \tag{1}$$

For characterization of the time transfer stability we will use the time deviation TDEV which is then

$$\mathrm{TDEV}(\tau) = 0.22\sqrt{\tau} \quad [\mathrm{ns},\ \mathrm{hour}]. \tag{2}$$

The time transfer instability substantially larger than the TDEV above has surely its origin in the time transfer. On the other side, instability of the time transfer smaller than the TDEV above will stay masked by the measured time difference instability and cannot be observed in the results of the experiment.

We processed all code and carrier phase measurements in L1 and L5 frequency channels from MJD 56231. The satellite elevation was 18° in Braunschweig and 21° in Prague. Changes in both azimuth and elevation were below 0.1°. The carrier-to-noise ratio was around 40 dBHz. The resulting time difference evaluated from the from L1, L5 and ionosphere-free code measurements is in Fig. 2. The results of the carrier phase measurements are in Fig. 3. The corresponding TDEV plots are in Fig. 4 and Fig. 5.

The L1 code measurement has markedly lower accuracy compared to a typical GPS common-view. This is caused by the rather narrow bandwidth of the SBAS signals in this frequency channel [4]. The observed fluctuations can be described as white noise with standard deviation of 7 ns. The L5 code measurement provides much better precision.

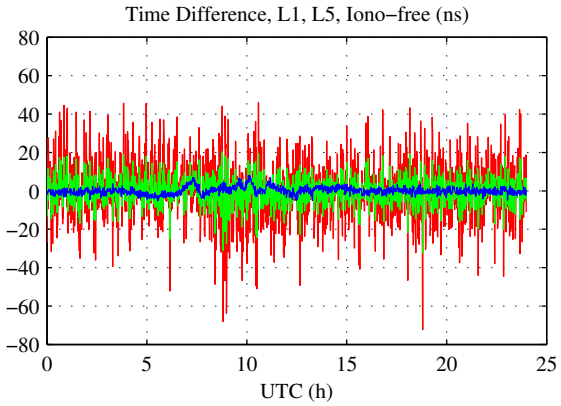

Figure 2. UTC(PTB)−UTC(TP) via GAGAN PRN 127, code measurements, L1 (green), L5 (blue) and ionosphere-free combination (red).

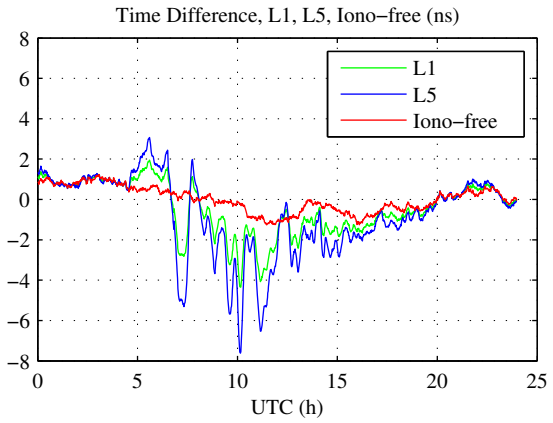

Figure 3. UTC(PTB) − UTC(TP) via GAGAN PRN 127, carrier phase measurements, L1, L5 and ionosphere-free combination. Fluctuations in L1 and L5 measurements are caused by ionosphere.

In this case we assessed the stability TDEV < 1.3 ns for averaging intervals from 1 min to several hours which is a behavior similar to a GPS common-view with no additional processing. Since the geostationary satellite moves just slightly towards the receivers, the observed variations caused by the multipath effect are very slow compared to GPS. The low L1 measurement precision was also projected into the L1/L5 ionosphere-free combination.

On the other side the results obtained from the carrier phase measurements are promising. The stability of the ionosphere free combination is TDEV($\tau = 1$min) < 40 ps. For longer averaging intervals it is masked by the expected instability of the measured time difference.

Interesting results followed from our comparison of the single frequency measurements and the ionosphere free combination where relatively fast fluctuations induced by ionosphere are obvious in the single frequency measurements. These fluctuations start at sunrise. During the daytime, the amplitude of these fluctuations reaches 5 ns in the L1 frequency channel and fully disappears before local midnight. This behavior is

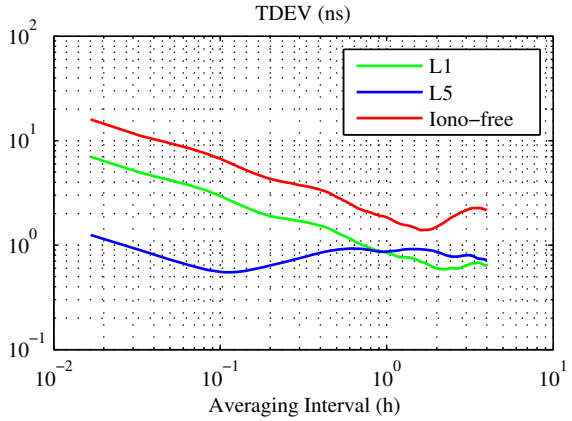

Figure 4. TDEV of UTC(PTB) − UTC(TP) via GAGAN PRN 127, code measurements, L1, L5 and ionosphere-free combination.

Table I
RESULTS OF SINGLE CLOCK COMMON-VIEW ON A SMALL BASELINE.

	Code (ns RMS)	Carrier phase (ps RMS)
L1	6.2	25
L5	1.3	29
Iono-free	14.1	33

quite far from simple ionospheric delay models. The slight imbalance of these fluctuations towards negative values is in a good agreement with the fact that the satellite elevation in Braunschweig is lower and thus the signal is more delayed in the ionosphere. These effects are fully suppressed in the ionosphere-free combination.

The third experiment took place in IPE Prague on MJD 56444. We used the GAGAN signals for a single clock common-view on a small baseline. In this situation the atmospheric delays are fully eliminated and we can evaluate the impact of the multipath and noise of the receivers. The receivers were denoted TPX and TPY. Both antennas were installed on the roof of the institute. The distance between the antennas was approximately 5 m. Both receivers were provided with the UTC(TP) time reference.

Code and carrier phase measurements in L1 and L5 frequency channels from the whole day were processed. All the data were sampled with the 10-s period. Fig. 6 and Fig. 7 show the comparison results. The displayed time differences are in fact equal to comparison error because both receivers were fed with the same reference. RMS of the comparison error in L1, L5 and ionosphere-free combination for code and carrier phase measurements are summarized in Tab. I. The corresponding TDEV plots are in Fig. 8 and Fig. 9.

The resulting code measurement precision in L5 is comparable with a GPS common-view. The L1 and ionosphere-free code measurements are significantly noisy because of the narrow bandwidth of the L1 signal. No substantial multipath effect was observed in the measurements. The carrier

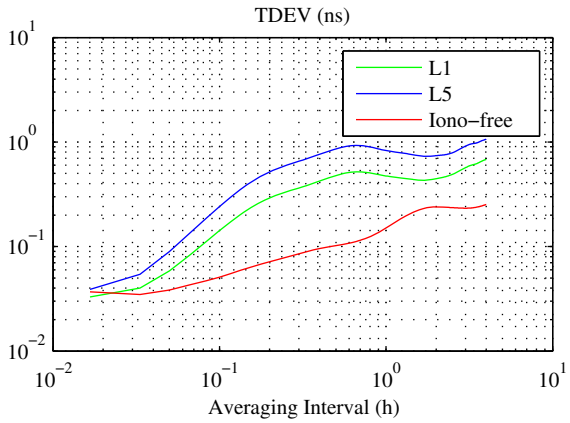

Figure 5. TDEV of UTC(PTB) − UTC(TP) via GAGAN PRN 127, carrier phase measurements, L1, L5 and ionosphere-free combination. TDEV of iono-free combination is covered by instability of UTC(PTB) − UTC(TP) difference.

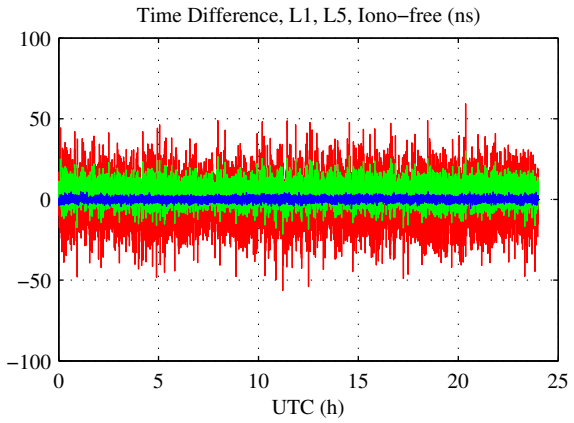

Figure 6. UTC(TPX) − UTC(TPY) via GAGAN PRN 127, code measurements, L1 (green), L5 (blue) and ionosphere-free combination (red).

phase measurements in both frequency channels as well as the ionosphere-free combination provide very good precision around 30 ps and better. This includes also very slow fluctuations which are probably related to temperature instabilities of the antenna cables and the reference time distribution.

IV. Conclusion

In contrast to the European SBAS EGNOS, the Indian GAGAN already provides both L1 and L5 signals thus it can be used for ionosphere-free time comparisons. Experimental measurements focused on the use of the GAGAN SBAS for the time transfer were done. The accuracy of ephemerides was estimated below 5 m and the system time seems to be stable and close to UTC. These results indicate that this system can be used for comparisons on relatively long baselines.

Unfortunately, the narrow L1 signal bandwidth degrades the L1 and ionosphere-free code measurements to 6 ns and 14 ns respectively. The precision of L5 code comparisons is near 1 ns which is similar to GPS. Some improvement of the code measurement could be probably achieved using a directional antenna.

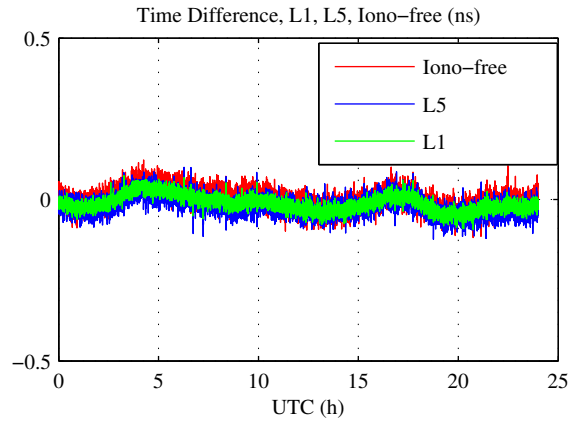

Figure 7. UTC(TPX) − UTC(TPY) via GAGAN PRN 127, carrier phase measurements, L1, L5 and ionosphere-free combination. Fluctuations in L1 and L5 measurements are caused by ionosphere.

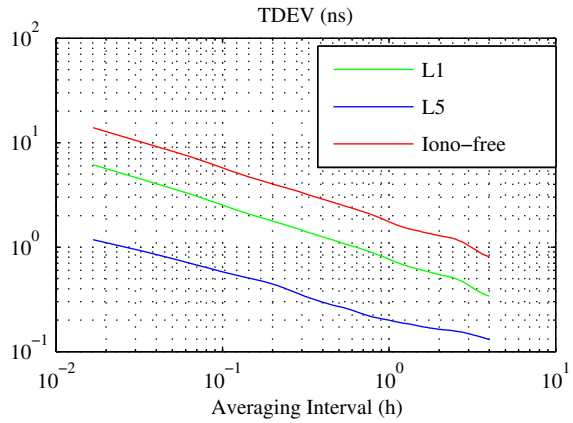

Figure 8. TDEV of UTC(TPX) − UTC(TPY) via GAGAN PRN 127, code measurements, L1, L5 and ionosphere-free combination.

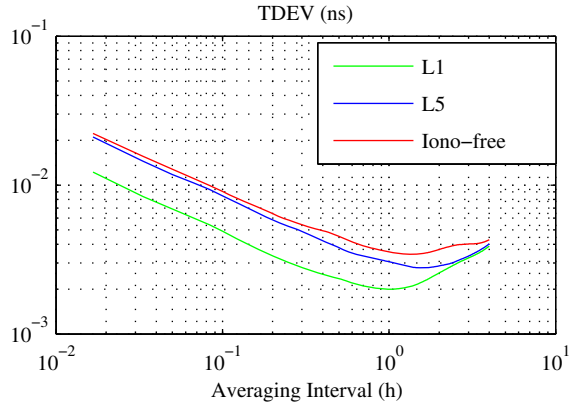

Figure 9. TDEV of UTC(TPX) − UTC(TPY) via GAGAN PRN 127, carrier phase measurements, L1, L5 and ionosphere-free combination. TDEV of iono-free combination is covered by instability of UTC(PTB) - UTC(TP) difference.

The carrier phase measurements are promising on the other hand. The standard deviation of fluctuations within one day was around 30 ps even for the ionosphere-free combination. Such phase measurement is available continuously which makes L1/L5 SBAS an ideal solution for comparisons of highly precise frequency sources at relatively long distances.

Acknowledgment

The authors would like to thank Dr. Andreas Bauch from PTB for his support and kind hospitality.

References

[1] K. N. Suryanarayana Rao, *GAGAN – The Indian satellite based augmentation system*, Indian J. Radio and Space Physics, Vol. 36, pp. 293–302, (August 2007).

[2] *Specification for the Wide Area Augmentation System (WAAS)*, DTFA01-96-C-00025, U.S. Department of Transportation.

[3] *EGNOS Service Definition Document – Open Service*, EGN-SDD OS V1.1 30/10/2009, European Commission.

[4] O. Razumovsky, C. Soddu, *Inmarsat's New Navigation Payload*, GPS World, Vol. 12, No. 11, pp. 23–32.

[5] P. Pánek, A. Kuna, *Time and Frequency Transfer Using EGNOS Satellite System*, in Proceedings of the 43rd Annual Precise Time and Time Interval (PTTI) Systems and Applications Meeting, 14–17 November 2011, Long Beach, pp. 301–310.

Preliminary Implementation of Time and Frequency Transfer by BDS

LIANG Kun, ZHANG Aimin
Division of Time and Frequency Metrology
National Institute of Metrology, NIM
Beijing, China
liangk@nim.ac.cn

PEI Chao, ZUO Fei,
School of Electronics and Information Engineering
Beijing JiaoTong University
Beijing, China

JIN Zhaofeng
Beijing Hoyateq Science&Technology Co., Ltd
Beijing, China

***Abstract*—Time and frequency transfer method using code and carrier phase by BDS has been developed by NIM. The CCD and long baseline results are comparable with GPS. The standard deviation of the BDS P3 code and carrier phase results in the CCD experiment could be better than 1 ns and 100 ps with one day measurement. The combination of BDS and GPS code measurement for time and frequency transfer led to the improved precision and robustness.**

Keywords- time and frequency transfer; GNSS; BDS

I. INTRODUCTION

Since 2003, the Beidou Navigation Satellite Demonstration System was officially brought into service. By the end of 2012, there are six GEO(Geostationary Earth Orbit), five MEO(Medium Earth Orbit) and five IGSO(Inclined Geosynchronous Satellite Orbit) satellites in orbit. Since 27th Dec 2012, BDS(BeiDou Navigation Satellite System) Signal in Space Interface Control Document-Open Service Signal B1I(Version 1.0)[1] has been released. The developing BDS system with the coverage of part of Asia-Pacific area at present has provided the official service and can be used for time and frequency transfer in this area.

II. TIME AND FREQUENCY TRANSFER BY BDS AND COMBINATION WITH GPS

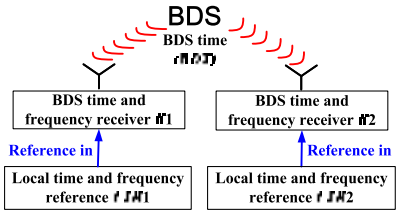

Figure 1. Time and frequency transfer by BDS

Time and frequency transfer methods by GPS(Global Positioning System) and GLONASS(GLObal Navigation Satellite System) are divided into three types that are C/A code, P3 code and carrier phase time and frequency transfer according to the measurement signals. The basic principles of time and frequency transfer by BDS are similar to those of them[2] as shown in Fig. 1.

Based on BDS OEM model with the first operation mode(mode 1)[2] with time and frequency directly synchronized to the local time and frequency reference by a internal phase lock loop, the original BDS observation can be acquired and the BDS code and carrier phase time and frequency transfer could be implemented preliminarily.

From the overall, BDS has more likeness with GPS. BDS has the similar communication mechanism to GPS, including the CDMA(Code Division Multiple Access) mode for all satellites. However, the GEO satellites that not are involved in the GPS space orbit generate one of the main differences in the error correction for BDS time and frequency transfer from GPS time and frequency transfer because of the difference of the calculation for satellite position between GEO and non-GEO satellites as shown in (1)-(5). In addition, the time difference from UTC is different from that of GPS.

$$\Omega_k = \Omega_0 + \dot{\Omega} t_k - \dot{\Omega}_e t_{oe} \tag{1}$$

$$\begin{cases} X_{GK} = x_k \cos\Omega_k - y_k \cos i_k \sin\Omega_k \\ Y_{GK} = x_k \sin\Omega_k + y_k \cos i_k \cos\Omega_k \\ Z_{GK=} y_k \sin i_k \end{cases} \tag{2}$$

$$\begin{bmatrix} X_k \\ Y_k \\ Z_k \end{bmatrix} = R_Z(\dot{\Omega}_e t_k) R_X(-5^\circ) \begin{bmatrix} X_{GK} \\ Y_{GK} \\ Z_{GK} \end{bmatrix} \tag{3}$$

$$R_X(\varphi) = \begin{bmatrix} 1 & 0 & 0 \\ 0 & \cos\varphi & \sin\varphi \\ 0 & -\sin\varphi & \cos\varphi \end{bmatrix} \tag{4}$$

$$R_Z(\varphi) = \begin{bmatrix} \cos\varphi & \sin\varphi & 0 \\ -\sin\varphi & \cos\varphi & 0 \\ 0 & 0 & 1 \end{bmatrix} \tag{5}$$

For the users of GNSS(including BDS) time and frequency transfer, the user position that should be known precisely in advance is not cared about in the solution in generally. The most important job is processing for error correction and the solution of the receiver clock bias. In terms of different measurement signals, measurement methods and models of the error correction, the different measurement precision and accuracy could be obtained. For code measurement, ionospheric error, tropospheric error, Sagnac effect, relativistic effect and satellite clock error[3] would be taken into consideration and enough information can be acquired from navigation ephemeris of GNSS in real-time. If one doesn't have to or is not eager for the real-time processing, IGS(International GNSS Service)-like products that refer to precise ephemeris will provide him the better precision with the much more complicated post-processing. For carrier phase time and frequency transfer solution, we'd better use these kind of precise products to get the corresponding precision of error correction or we use the differential method to have the most errors cancelled, and the solution of the integer ambiguity and the detection of the cycle jump are the most difficult parts for the whole processing of carrier phase time and frequency transfer. There is some near real time precise product for real-time carrier phase processing, however, the more and deeper try and tests to apply product in carrier phase time and frequency transfer need to be implemented.

For code based BDS time and frequency transfer, we use the combination of C1 code(civil code modulated in L1 carrier 1561.098 MHz(f_1)) and P2 code(some undocumented civil code modulated in L2 carrier 1207.140 MHz(f_2) that can be measured by BDS receiver we used) as shown in (6), and we can simply name the combination as P3 code.

$$P3 = \frac{f_1^2}{f_1^2 - f_2^2} C1 - \frac{f_2^2}{f_1^2 - f_2^2} P2 \tag{6}$$

III. Experiment Setup and Numric Results

To verify the performance and feasibility of BDS for time and frequency transfer, on the basis of Fig. 1, the CCD(Common Clock Difference) experiments, the zero baseline experiments with the different references and the long baseline(straight-line distance between two receivers) experiments with the different references have been implemented, using the two BDS OEM modules(BD01 and BD02, both involving GPS measurements) and the other GPS time and frequency transfer receivers including IMEU, and IMEN sites(NIMTFGNSS-1 receivers[2]), IMPR and BJNM sites(Septentrio PolaRx2eTR and PolaRx3eTR receivers respectively) of NIM located at NIM.

CCD experiment reflects the noise level of the time and frequency transfer link. Fig. 2 and 3 show CCD results of BDS code and carrier phase time and frequency transfer and the standard deviation of the data averaging one day are 639 ps and 17 ps separately. GPSTFP software[4] for GPS carrier phase time and frequency transfer was modified to be adapted for BDS. BDS has the comparable performance with GPS for time and frequency transfer in code and carrier phase.

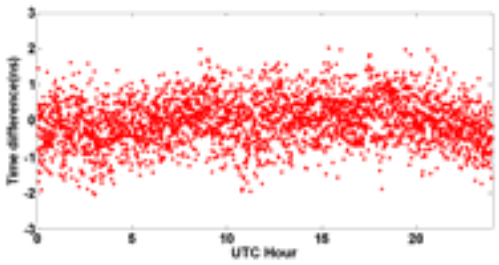

Figure 2. CCD by P3 code of BDS

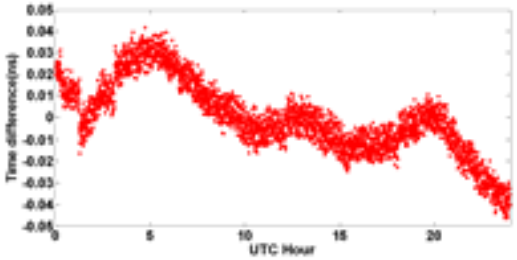

Figure 3. CCD by carrier phase of BDS

The development of multiple techniques for time and frequency transfer has generated the redundancy, so the combination of multiple techniques by data fusion principle that is one of the focuses by BIPM should be one good choice to convert the redundancy to the precision. We take the simple mean value *GBC* of GPS P3 code and BDS P3 code result by (7) as their combination. From the results of CCD experiments using BDS, GPS and the combined method at the same time, the standard deviations of them are 0.9 ns, 0.7 ns and 0.6 ns respectively. When we combine BDS with GPS to transfer time and frequency, the advantage of robustness over either of GPS and BDS thanks to the complementation of GPS and BDS and improvement in noise level have been acquired as shown in Fig. 4. Corresponding to these, we could get the better short term stability from the combined results. As well, we could get the weighted mean as (8) by figuring out the weights W_B for BDS and W_G for GPS using the noise level of each technique according to the basic principle of date fusion. The noise level would be thought as the standard deviation of the results for each type of link in the CCD experiments. However, from our CCD results, BDS has the quite comparable noise level with GPS, and we might get the quite negligent difference between using (7) and using (8).

$$GBC = \frac{1}{2}\left(P3_{GPS} + P3_{BDS}\right) \tag{7}$$

$$GBC = W_G \cdot P3_{GPS} + W_B \cdot P3_{BDS} \tag{8}$$

We compared the differences between NIMDO(UTC(NIM) disciplined oscillator) and UTC(NIM)hepingli(one Cesium clock with one micro-stepper steered by UTC at Hepingli campus of NIM) in the zero baseline experiments using the corresponding BDS, GPS and the combined links. From Fig. 5, the results are quite similar to those of GPS time and frequency transfer. GPS1 link consists of BD01 and BD02;

GPS2 link consists of IMPR and IMEN. As expected, these show that the combined GPS and BDS link is more stable than either of the single GNSS links. It is less noisy and robust maybe because the impacts of the atmosphere errors and the other effects have been reduced to some extent.

The results of BDS carrier phase show the good agreements with those of both BDS P3 code and GPS carrier phase got from NRCan_PPP software in Fig. 6.

The long baseline experiment characterizes the remote transfer performance of the transfer. Fig. 7 shows the comparison of five links between UTC(NIM)hepingli and UTC(NIM)(at Changing campus), including one BDS link, two GPS links and two combined links of GPS and BDS in about 40 km baseline. GPS1 link is between BD01 and BD02; GPS2 link is between IMPR and BJNM. The BDS link has the similar trend with the GPS links and the combination had the effect on the improvement on noise level of the transfer. All results are normalized for better view; link calibration was not implemented, so the results are meaningful for frequency transfer indeed.

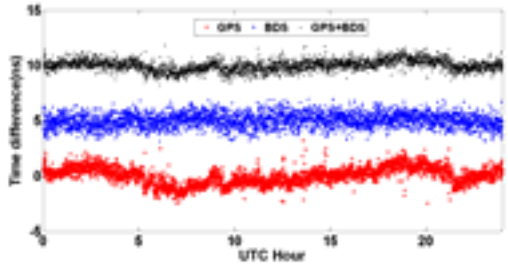

Figure 4. Comparison 1 among BDS, GPS and the combination

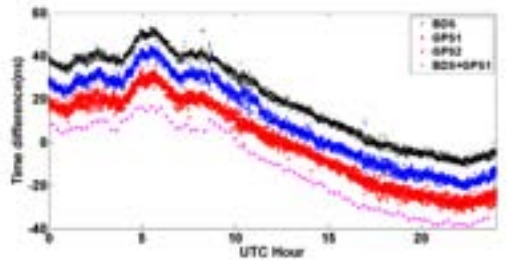

Figure 5. Comparison 2 among BDS, GPS and the combination

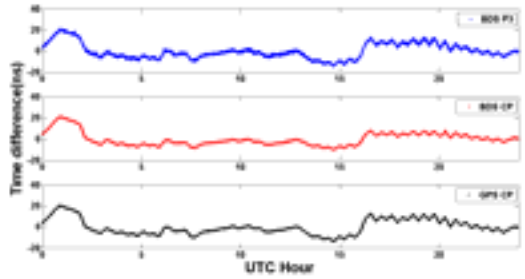

Figure 6. Comparison among BDS and GPS methods

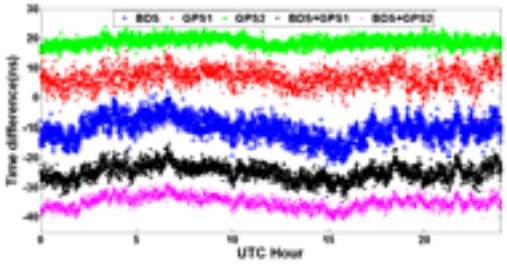

Figure 7. Comparison 3 among BDS, GPS and the combination

IV. Uncertainty Analysis

The uncertainty for time and frequency transfer usually includes the uncertainty evaluation of type A and type B. For type A, the only one item is the measurement jitter of the results for the time transfer link in the CCD experiment. For type B, uncertainty for calibration of GNSS time transfer link is the main part, which is usually better than 5.5 ns; the standard uncertainty components due to ionospheric and tropospheric errors are 0.3 ns and 0.7 ns respectively valid for baselines up to 5000 km[5]; due to the cables and the converters calibrated by VNA(Vector Network Analyzer), the standard uncertainty component is less than 0.1 ns. Thus we can get the combined uncertainty u_c by (9) as 5.7 ns, 5.7 ns and 5.6 ns respectively for GPS, BDS and the combination in our experiments.

$$u_c = \sqrt{u_A^2 + u_B^2} \tag{9}$$

V. Conclusion and Prospect

From the results of our experiments, the performance of BDS by code and carrier phase can match those of GPS for time and frequency transfer. Anyway, more experiments especially in the longer baseline are needed for verification. With the development of the near real-time or real-time precise ephemeris products, near real-time BDS carrier phase time and frequency transfer will be studied and tested at NIM. The combination of two systems(GPS and GLONASS[6] or BDS and GPS) would improve the robustness and noise level of time and frequency transfer, the combination of GPS, GLONASS and BDS would be more interesting in the future with the completeness of the BDS global constellation.

Acknowledgements

The authors thank Beijing Unicore Communications incorporation for the free loan of BDS OEM modules.

References

[1]. China Satellite Navigation Office, “BeiDou Navigation Satellite System Signal In Space Interface Control Document Open Service Signal B1I (Version 1.0),” 2012

[2]. LIANG Kun, ZHANG Side, ZHANG Aimin, GAO Xiaoxun, WANG Weibo, NING Dayu, “Study and Development of a New GNSS Receiver for Time and Frequency Transfer,” Proc. of EFTF 2012, pp. 529-536, 2012.

[3]. LIANG Kun, ZHANG Aimin, “Study on Time and Frequency Dissemination by GLONASS,” Acta Metrologica Sinica, 2011(2),172-177, 2011.

[4]. LIANG Kun, LI Tianchu, WANG Tianyi, WANG Weibo, NING Dayu,

ZHANG Aimin, FANG Fang, “GPS Carrier Phase Time Transfer Using a Modified Solution Model,” Proc. of IFCS 2012, 2012

[5]. Lewandowski, W. & Thomas, C., “GPS Time Transfer,” Proc. IEEE 79(7), pp991-1000, 1991

[6]. Jiang Z., Lewandowski W., “Use of GLONASS for UTC time transfer”, Metrologia, 2012, 49(1), 57-61

Control of the Systematic Shifts of the Strontium Ion Optical Frequency Standard at the 10 mHz Level

Pierre Dubé, Alan A. Madej, Maria Tibbo, and John E. Bernard
Measurement Science and Standards Portfolio
National Research Council of Canada
Ottawa, Canada K1A 0R6
Email: pierre.dube@nrc-cnrc.gc.ca

***Abstract*—An overview of the key methods used to reduce the uncertainty of the systematic shifts of the strontium ion optical frequency standard is presented. An uncertainty of 10 mHz at a clock frequency of 445 THz is obtained, limited by the uncertainty of the blackbody radiation shift. The uncertainty estimates of other shifts such as micromotion and electric quadrupole shifts are on the order of 1 mHz or less. The effectiveness of the methods used to reduce or cancel the shifts is illustrated with experiments comparing two ion traps. One has strong micromotion levels while the other, the reference trap, provides good control over the shifts. Despite nominal shifts of 70 Hz in the trap with large micromotion levels, the agreement with the reference trap is at the sub-Hz level.**

I. Introduction

A number of optical frequency standards have delivered record-breaking performance largely surpassing that of the best cesium fountain clocks which realize the SI second [1]. The lowest uncertainty evaluations are obtained with trapped and laser cooled single-ion systems [2]–[9], while the highest stabilities are obtained with optical lattice clocks [10]–[15].

This paper gives an overview of the recent improvements made to reduce the uncertainty of the systematic shifts of the $^{88}Sr^{+}$ ion optical frequency standard developed at the National Research Council of Canada (NRC). The reference frequency is realized with the 0.4-Hz-wide $5s\,^2S_{1/2} - 4d\,^2D_{5/2}$ transition at 445 THz. The most important systematic shifts for this transition are the micromotion and the electric quadrupole shifts. Typically, the electric quadrupole shift is on the order of a few Hz while the micromotion-related shifts can be several 10's of Hz in magnitude when no measures are taken to minimize them.

In the following sections, these shifts will be discussed with emphasis on the performance obtained in controlling their uncertainties. Since the cancellation and reduction methods implemented are very effective, the blackbody radiation shift has become the most important source of uncertainty in the realization of the unperturbed $^{88}Sr^{+}$ ion clock frequency. This shift will also be discussed briefly to show how its uncertainty was decreased by more than one order of magnitude compared to previously published work [16] and what are the limiting factors in its evaluation. The effectiveness of the cancellation methods is illustrated with a frequency comparison of two ion traps; one is a Paul trap with large micromotion levels which cannot be completely minimized in the current design [17], while the other, used as a reference trap, is a recently-built endcap trap with micromotion measurement and control along three orthogonal axes.

The methods developed for the control and evaluation of the shifts reduce the total uncertainty to a level of 10 mHz at 445 THz, a fractional frequency uncertainty of 2.3×10^{-17}. For comparison, the fractional uncertainty obtained previously with our Paul trap ranged from 1×10^{-13} [16] to 3×10^{-14} [17]. For a detailed description of the NRC endcap trap system and the methods discussed in this paper, the reader is referred to [8] and [9].

II. Electric Quadrupole Shift

The electric quadrupole shift (EQS) is caused by the interaction between an electric field gradient at the ion and the quadrupole moment of the upper state of the clock transition. The field gradient results from a trap potential modified by electric charge buildup and patch potentials on the trap structure. It varies slightly each time strontium metal is deposited on the electrodes during loading. Just a few years ago, the EQS was considered to be the largest source of uncertainty in single-ion systems based on an electric quadrupole transition [16], [18]–[21].

Unlike micromotion shifts which can be minimized as discussed in Sec. III, there is no simple method of controlling the field gradient at the ion and minimize the EQS. Instead, the shift is canceled by using the fundamental properties of the quadrupole interaction. To first order in perturbation theory, the electric quadrupole shift in Hz units, Δf_Q, of a magnetic sublevel $m_{J'}$ of the upper state of the clock transition is given by [17], [18], [22]

$$\Delta f_Q = \frac{1}{4}\,\nu_Q\,\left(3\cos^2\theta - 1\right)\left[m_{J'}^2 - \frac{J'(J'+1)}{3}\right], \quad (1)$$

where ν_Q is a characteristic frequency proportional to the electric field gradient and the electric quadrupole moment [23]. θ is the angle between the field gradient principal axis and the quantization axis defined by the ambient magnetic field. For the clock transition of $^{88}Sr^{+}$, $J' = 5/2$.

We have proposed a method which uses a property of (1) associated with the magnetic quantum numbers [9], [17], [24]. It can be implemented in two ways. In the first one, we note that the term in square brackets in (1) is zero when summed over $m_{J'}$:

$$\sum_{m_{J'}=-J'}^{J'} \left[m_{J'}^2 - \frac{J'(J'+1)}{3} \right] = 0. \tag{2}$$

This property is a consequence of the traceless nature of the electric quadrupole interaction energy. Experimentally, the averaging over the $^2D_{5/2}$ magnetic sublevel energies is realized by measuring three pairs of Zeeman components that connect to all of the possible $m_{J'}$ sublevels. One can view this method as an extension of method used to cancel the linear Zeeman shift which is realized by averaging the frequencies of a symmetric pair of components [25].

Alternatively, we use the intercept method which simply states that $\Delta f_Q = 0$ in (1) when $m_{J'}^2 = J'(J'+1)/3$. It is implemented by measuring the frequencies of two symmetric pairs of Zeeman components with different $m_{J'}^2$ sublevels, from which the quadrupole-shift-free clock frequency at the virtual value of $m_{J'}^2 = J'(J'+1)/3$ is calculated. For the $^{88}Sr^+$ ion, the intercept occurs at $m_{J'}^2 = 35/12$. An advantage of the intercept method is that only two pairs of components need to be measured to cancel the EQS. Both methods were used in the results reported in this paper.

These methods yield extremely high EQS cancellation levels. Experimentally, the cancellation is continuous as the lock program cycles through the selected Zeeman components when determining the S–D transition linecenter. We recently estimated that the fractional uncertainty on the canceled EQS shift is $< 3 \times 10^{-19}$, a cancellation level of more than four orders of magnitude [9].

The EQS cancellation methods described above simplify the uncertainty analysis of all the shifts that have a magnetic sublevel dependence. A welcome consequence is the cancellation of the tensor Stark shift [9] which can be rather large when the micromotion is not minimized, as in our Paul trap.

III. Micromotion Shifts

The interaction of the trap rf fields with the ion causes Stark and second-order Doppler shifts. For the most part, these so-called micromotion shifts result from ion displacement caused by stray electric fields. Micromotion shifts can also be caused by a phase difference between the voltages applied to the endcap electrodes and by thermal motion [26]. For the present discussion, we will ignore these smaller contributions [9].

Remembering that the tensor part of the Stark shift is canceled along with the EQS as mentioned in Sec. II, only the scalar part, $\Delta\nu_{\text{scalar}}$, needs to be considered. It is given by

$$\Delta\nu_{\text{scalar}} = -\frac{\Delta\alpha_0}{2h} \left\langle E^2 \right\rangle, \tag{3}$$

where h is Planck's constant, E the electric field at the ion, and $\Delta\alpha_0 = \alpha_0(D_{5/2}) - \alpha_0(S_{1/2})$ is the static differential scalar polarizability of the clock transition. $\Delta\alpha_0 = -4.83(17) \times 10^{-40}$ J m^2/V^2 for the $^{88}Sr^+$ ion [27].

The recently-built endcap trap was designed with three mutually orthogonal laser beam access ports for measurement of the micromotion levels and with three mutually orthogonal trim electrodes for control of the ion position. The mean-squared velocity of the ion at the trap frequency Ω is minimized and precisely measured using the carrier-normalized micromotion sideband intensities [9]. After minimization, the sum of the intensity ratios along the three orthogonal directions is $0.021(7)$, which translates into a scalar Stark shift of $\Delta\nu_{\text{scalar}}/\nu_0 = 2.2(7) \times 10^{-17}$.

The second-order Doppler shift is given by

$$\Delta\nu_{\text{D2}} = -\frac{\nu_0}{2} \frac{\left\langle v^2 \right\rangle}{c^2}, \tag{4}$$

where ν_0 is the clock transition frequency, c the speed of light, and $\left\langle v^2 \right\rangle$ the mean-squared velocity of the ion. The micromotion sideband intensity measurements provide the component of $\left\langle v^2 \right\rangle$ resulting from ion movement at the trap frequency [9]. The mean-squared velocities at other frequencies must be considered separately. For a trap frequency of $\Omega/2\pi = 14.4$ MHz and the sideband intensity measurements reported above, $\Delta\nu_{\text{D2}}/\nu_0 = -2.2(7) \times 10^{-17}$.

It is no coincidence that the Stark and second-order Doppler shifts caused by micromotion are equal in magnitude but opposite in sign as we have purposely set the trap frequency to obtain that result. The following discussion gives the relations that describe the optimum trap frequency to cancel the micromotion shifts in the pseudo-potential approximation.

The classical equations of motion for a charged particle in an rf electric field provide the relation between $\left\langle v^2 \right\rangle$ and $\left\langle E^2 \right\rangle$. After replacement of the result in (4), one obtains

$$\Delta\nu_{\text{D2}} = -\frac{\nu_0}{2} \left(\frac{e}{m\,\Omega\,c} \right)^2 \left\langle E^2 \right\rangle, \tag{5}$$

where m is the ion mass and e the elementary charge. The net micromotion shift, $\Delta\nu_\mu$, is simply the sum of (3) and (5):

$$\Delta\nu_\mu = -\frac{1}{2} \left[\frac{\Delta\alpha_0}{h} + \nu_0 \left(\frac{e}{m\,\Omega\,c} \right)^2 \right] \left\langle E^2 \right\rangle. \tag{6}$$

The term in square brackets can be nulled by adjusting the trap frequency provided $\Delta\alpha_0$ is negative. The trap frequency for $\Delta\nu_\mu = 0$ is given by

$$\Omega_0 = \frac{e}{m\,c} \sqrt{-\frac{h\,\nu_0}{\Delta\alpha_0}}. \tag{7}$$

For $^{88}Sr^+$, $\Omega_0/2\pi = (14.4 \pm 0.3)$ MHz. The uncertainty of 3.5% on $\Delta\alpha_0$ yields a micromotion suppression factor of 28. Therefore, the micromotion shifts of $\pm 2.2 \times 10^{-17}$ are reduced to 1×10^{-18} when combined. This is the uncertainty estimate of the net micromotion shift.

IV. Blackbody radiation shift

The blackbody radiation (BBR) field causes a scalar Stark shift of the clock transition given by (3), where $\Delta\alpha_0$ is replaced by $\Delta\alpha_0'$ to take into account a small dynamic correction that arises from the frequency distribution. The main source of uncertainty for the $^{88}Sr^+$ BBR shift is the uncertainty of $\Delta\alpha_0'$. Fortunately, an order of magnitude improvement over previous estimates [16] was recently reported in [27].

TABLE I. $^{88}Sr^{+}$ UNCERTAINTY BUDGET

Source	Shift	Uncertainty
Blackbody radiation shift	5.62×10^{-16}	2.2×10^{-17}
1092-nm ac Stark shift	-4×10^{-18}	2×10^{-18}
Collisional shift	0×10^{-18}	2×10^{-18}
Net micromotion shift	0×10^{-18}	1×10^{-18}
Second-order Doppler (thermal)	-3×10^{-18}	1×10^{-18}
Electric quadrupole shift	0×10^{-19}	3×10^{-19}
674-nm ac Stark shift	4×10^{-20}	2×10^{-20}
422-nm ac Stark shift	7×10^{-21}	7×10^{-21}
Quadratic Zeeman shift	8.3×10^{-20}	2×10^{-21}
Tensor Stark shift	0×10^{-22}	4×10^{-22}
Total shift	5.54×10^{-16}	2.3×10^{-17}

A model of the BBR field was developed to estimate $\langle E^2 \rangle$ and its uncertainty [9]. The model takes into account the trap components temperatures, the emissivities of the materials, the trap geometry, and multiple reflections. The temperatures were measured on a test trap, similar to the frequency standard endcap trap, using a small glass thermistor. The temperatures increased by about (33 ± 10)°C for an applied rf voltage amplitude of 212 V. The effect of electrode heating on the BBR field is mitigated by the low emissivity of the endcap electrodes; the shift increases by only 0.013 Hz from 0.237 Hz with rf heating. With modest accuracy in the BBR model, the contribution of $\langle E^2 \rangle$ to the uncertainty is only 0.005 Hz.

The total uncertainty on the BBR shift is 2.2×10^{-17}, still limited by the uncertainty on $\Delta\alpha_0'$. The current radiation model will begin to contribute significantly to the uncertainty budget of the BBR shift when the uncertainty on $\Delta\alpha_0'$ is reduced by a factor of two or more.

V. UNCERTAINTY BUDGET

The fractional uncertainty estimates for the clock transition frequency of the $^{88}Sr^{+}$ ion are summarized in Table I. In addition to the shifts discussed in the previous sections, several others are included for completeness [9]. The total fractional uncertainty obtained by adding in quadrature is 2.3×10^{-17}.

Table I shows that the BBR shift completely dominates the $^{88}Sr^{+}$ ion uncertainty budget, and that important gains can be made by improving on both the value of $\Delta\alpha_0'$ and the evaluation of the BBR field at the ion. An order of magnitude decrease in the uncertainty of these parameters is experimentally feasible. Moreover, the 1092-nm ac Stark shift can be drastically reduced by using a mechanical chopper instead of relying on an acousto-optic modulator for light shuttering [9]. With these potential improvements, the total uncertainty on the shifts could reach a level of 3×10^{-18} according to our current understanding of the shifts.

VI. COMPARISON OF TWO TRAPS

Two $^{88}Sr^{+}$ ion traps were compared to show the effectiveness of the methods discussed in Sections II and III to cancel or reduce the uncertainty of the systematic shifts. The first is the endcap trap with systematic shifts evaluated at 2.3×10^{-17}. It is used as a reference. All the currently known methods to reduce and cancel the shifts are implemented in that system: EQS cancellation, optimum trap frequency to suppress the micromotion shifts, and micromotion minimization. The second is the Paul trap which implements the same methods except for incompletely minimized micromotion. As a consequence, there is a large rms electric field at the ion estimated at 136 V/cm. It was determined by detuning the Paul trap frequency from the optimum value of 14.4 MHz and by observing the changes in the net micromotion shift.

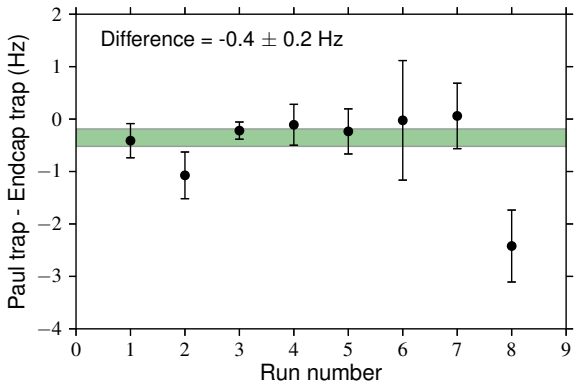

Fig. 1. Difference in the $^{88}Sr^{+}$ ion S–D frequency as realized by the Paul and endcap traps. For each measurement run, the uncertainty was determined from the Allan deviation of the frequency difference. The horizontal band is centered on the mean and it extends by $\pm 1\sigma$. Although it could easily be tagged as an outlier, the last point was included in the present analysis. If it is removed, the frequency difference becomes -0.3 ± 0.1 Hz.

The comparison data are reported in Fig. 1. The mean difference observed is $f_{\text{Paul}} - f_{\text{Endcap}} = -0.4 \pm 0.2$ Hz. The sub-Hz frequency difference is small compared to the actual shifts in the Paul trap. The scalar Stark and the second-order Doppler shifts are, respectively, $+70$ Hz and -70 Hz, the magnitude of the tensor Stark shift on the inner Zeeman components is ≈ 90 Hz, and the EQS is a few Hz. As reported in Sec. II, the EQS and tensor Stark shift are negligible after the application of the EQS cancellation method.

The uncertainty evaluation of the Paul trap indicates that most shifts are controlled with good accuracy except for the micromotion shifts and the BBR shift. The latter has not been evaluated in the Paul trap, but its contribution to the difference is expected to be below ≈ 0.1 Hz. We thus expect that the difference observed is mostly from micromotion. The preliminary data shown in Fig. 1 indicate that the micromotion shifts are reduced by a factor of 28 in the worst case, and by more than two orders of magnitude for the mean. This result validates the current value attributed to $\Delta\alpha_0$ and illustrates clearly the benefits of tuning the trap frequency to suppress the net micromotion shift.

VII. CONCLUSION

Significant progress was made during the last few years on the evaluation of the NRC $^{88}Sr^{+}$ ion systematic shifts. The total uncertainty evaluation has decreased by more than three orders of magnitude since 2005.

The main improvement came from the construction of an endcap trap designed with optical access ports for minimization of micromotion along three orthogonal axes. Further reduction in the micromotion uncertainty is obtained by selecting a trap frequency that purposely makes the scalar Stark and

second-order Doppler shifts cancel each other. The level of suppression is limited by the uncertainty on the differential scalar polarizability of the clock transition, $\Delta\alpha_0$. Also, the EQS cancellation method provides extremely efficient reduction of the electric-quadrupole and tensor Stark shifts, to levels much smaller than the total uncertainty on the clock transition frequency. With these improvements, the BBR shift has become the dominant source of uncertainty. Nevertheless, its contribution has been reduced by an order of magnitude with a recent evaluation of the differential scalar polarizability and a model of the BBR field that takes into account heating of the trap electrodes. The final fractional frequency uncertainty on the clock transition is 2.3×10^{-17}, mostly from the BBR shift.

The effectiveness of the methods used to cancel the shifts was demonstrated by comparing two ion traps; one of them had 70 Hz micromotion shifts while the other had its shifts controlled at the 10 mHz level. The sub-Hz agreement obtained validates the methods used, especially the value of $\Delta\alpha_0$ which determines the level of suppression of the net micromotion shift.

ACKNOWLEDGMENT

The authors would like to thank Bill Hoger and Wojciech Pakulski for the construction and maintenance of a number of custom-made electronic devices used to operate the ion trap systems.

REFERENCES

[1] J. Guéna, M. Abgrall, D. Rovera, P. Laurent, B. Chupin, M. Lours, G. Santarelli, P. Rosenbusch, M. E. Tobar, R. Li, K. Gibble, A. Clairon, and S. Bize, "Progress in atomic fountains at LNE-SYRTE," *IEEE Transactions on Ultrasonics, Ferroelectrics and Frequency Control*, vol. 59, no. 3, pp. 391–409, March 2012, and references therein.

[2] W. H. Oskay, S. A. Diddams, E. A. Donley, T. M. Fortier, T. P. Heavner, L. Hollberg, W. M. Itano, S. R. Jefferts, M. J. Delaney, K. Kim, F. Levi, T. E. Parker, and J. C. Bergquist, "Single-Atom Optical Clock with High Accuracy," *Phys. Rev. Lett.*, vol. 97, p. 020801, Jul 2006.

[3] T. Rosenband, P. O. Schmidt, D. B. Hume, W. M. Itano, T. M. Fortier, J. E. Stalnaker, K. Kim, S. A. Diddams, J. C. J. Koelemeij, J. C. Bergquist, and D. J. Wineland, "Observation of the $^1S_0 \longrightarrow {}^3P_0$ Clock Transition in $^{27}Al^+$," *Phys. Rev. Lett.*, vol. 98, no. 22, p. 220801, 2007.

[4] J. E. Stalnaker, S. A. Diddams, T. M. Fortier, K. Kim, L. Hollberg, J. C. Bergquist, W. M. Itano, M. J. Delany, L. Lorini, W. H. Oskay, T. P. Heavner, S. R. Jefferts, F. Levi, T. E. Parker, and J. Shirley, "Optical-to-microwave frequency comparison with fractional uncertainty of 10^{-15}," *Applied Physics B: Lasers and Optics*, vol. 89, pp. 167–176, 2007.

[5] T. Rosenband, D. B. Hume, P. O. Schmidt, C. W. Chou, A. Brusch, L. Lorini, W. H. Oskay, R. E. Drullinger, T. M. Fortier, J. E. Stalnaker, S. A. Diddams, W. C. Swann, N. R. Newbury, W. M. Itano, D. J. Wineland, and J. C. Bergquist, "Frequency Ratio of Al^+ and Hg^+ Single-Ion Optical Clocks; Metrology at the 17^{th} Decimal Place," *Science*, vol. 319, no. 5871, pp. 1808–1812, 2008.

[6] C. W. Chou, D. B. Hume, J. C. J. Koelemeij, D. J. Wineland, and T. Rosenband, "Frequency Comparison of Two High-Accuracy Al^+ Optical Clocks," *Phys. Rev. Lett.*, vol. 104, no. 7, p. 070802, 2010.

[7] N. Huntemann, M. Okhapkin, B. Lipphardt, S. Weyers, Chr. Tamm, and E. Peik, "High-Accuracy Optical Clock Based on the Octupole Transition in $^{171}Yb^+$," *Phys. Rev. Lett.*, vol. 108, p. 090801, Feb 2012.

[8] A. A. Madej, P. Dubé, Z. Zhou, J. E. Bernard, and M. Gertsvolf, "$^{88}Sr^+$ 445-THz Single-Ion Reference at the 10^{-17} Level via Control and Cancellation of Systematic Uncertainties and Its Measurement against the SI Second," *Phys. Rev. Lett.*, vol. 109, p. 203002, Nov 2012.

[9] P. Dubé, A. A. Madej, Z. Zhou, and J. E. Bernard, "Evaluation of systematic shifts of the $^{88}Sr^+$ single-ion optical frequency standard at the 10^{-17} level," *Phys. Rev. A*, vol. 87, p. 023806, Feb 2013.

[10] A. D. Ludlow, T. Zelevinsky, G. K. Campbell, S. Blatt, M. M. Boyd, M. H. G. de Miranda, M. J. Martin, J. W. Thomsen, S. M. Foreman, J. Ye, T. M. Fortier, J. E. Stalnaker, S. A. Diddams, Y. L. Coq, Z. W. Barber, N. Poli, N. D. Lemke, K. M. Beck, and C. W. Oates, "Sr Lattice Clock at 1×10^{-16} Fractional Uncertainty by Remote Optical Evaluation with a Ca Clock," *Science*, vol. 319, no. 5871, pp. 1805–1808, 2008.

[11] G. K. Campbell, A. D. Ludlow, S. Blatt, J. W. Thomsen, M. J. Martin, M. H. G. de Miranda, T. Zelevinsky, M. M. Boyd, J. Ye, S. A. Diddams, T. P. Heavner, T. E. Parker, and S. R. Jefferts, "The absolute frequency of the ^{87}Sr optical clock transition," *Metrologia*, vol. 45, no. 5, p. 539, 2008.

[12] N. D. Lemke, A. D. Ludlow, Z. W. Barber, T. M. Fortier, S. A. Diddams, Y. Jiang, S. R. Jefferts, T. P. Heavner, T. E. Parker, and C. W. Oates, "Spin-$1/2$ Optical Lattice Clock," *Phys. Rev. Lett.*, vol. 103, p. 063001, Aug 2009.

[13] A. Yamaguchi, M. Fujieda, M. Kumagai, H. Hachisu, S. Nagano, Y. Li, T. Ido, T. Takano, M. Takamoto, and H. Katori, "Direct Comparison of Distant Optical Lattice Clocks at the 10^{-16} Uncertainty," *Applied Physics Express*, vol. 4, no. 8, p. 082203, 2011.

[14] H. Katori, "Optical lattice clocks and quantum metrology," *Nat Photon*, vol. 5, no. 4, pp. 203–210, Apr 2011, and references therein.

[15] N. Hinkley, J. A. Sherman, N. B. Phillips, M. Schioppo, N. D. Lemke, K. Beloy, M. Pizzocaro, C. W. Oates, and A. D. Ludlow, "An atomic clock with 10^{-18} instability," *arXiv:1305.5869*, 2013.

[16] A. A. Madej, J. E. Bernard, P. Dubé, L. Marmet, and R. S. Windeler, "Absolute frequency of the $^{88}Sr^+$ $5s\,^2S_{1/2}$ – $4d\,^2D_{5/2}$ reference transition at 445 THz and evaluation of systematic shifts," *Phys. Rev. A*, vol. 70, p. 012507, 2004.

[17] P. Dubé, A. A. Madej, J. E. Bernard, L. Marmet, J.-S. Boulanger, and S. Cundy, "Electric quadrupole shift cancellation in single-ion optical frequency standards," *Phys. Rev. Lett.*, vol. 95, p. 033001, 2005.

[18] W. M. Itano, "External-field shifts of the $^{199}Hg^+$ optical frequency standard," *J. Res. Natl. Inst. Stand. Technol.*, vol. 105, pp. 829–837, 2000.

[19] Th. Udem, S. A. Diddams, K. R. Vogel, C. W. Oates, E. A. Curtis, W. D. Lee, W. M. Itano, R. E. Drullinger, J. C. Bergquist, and L. Hollberg, "Absolute frequency measurement of the Hg^+ and Ca optical clock transitions with a femtosecond laser," *Phys. Rev. Lett.*, vol. 86, pp. 4996–4999, 2001.

[20] H. S. Margolis, G. P. Barwood, G. Huang, H. A. Klein, S. N. Lea, K. Szymaniec, and P. Gill, "Hertz-level measurement of the optical clock frequency in a single $^{88}Sr^+$ ion," *Science*, vol. 306, pp. 1355–1358, 2004.

[21] W. H. Oskay, W. M. Itano, and J. C. Bergquist, "Measurement of the $^{199}Hg^+$ $5d^9\,6s^2\,{}^2D_{5/2}$ electric quadrupole moment and a constraint on the quadrupole shift," *Phys. Rev. Lett.*, vol. 94, p. 163001, 2005.

[22] A. Abragam, *The Principles of Nuclear Magnetism*, ser. International series of monographs on physics. New York: Oxford University Press, 1978.

[23] G. P. Barwood, H. S. Margolis, G. Huang, P. Gill, and H. A. Klein, "Measurement of the electric quadrupole moment of the $4d\,^2D_{5/2}$ level in $^{88}Sr^+$," *Phys. Rev. Lett.*, vol. 93, p. 133001, 2004.

[24] P. Dubé, A. A. Madej, J. E. Bernard, and A. D. Shiner, "$^{88}Sr^+$ single-ion optical frequency standard," in *Proceedings of the IEEE International Frequency Control Symposium and Exposition*. New York: IEEE, June 2006, pp. 409–414.

[25] J. E. Bernard, L. Marmet, and A. A. Madej, "A laser frequency lock referenced to a single trapped ion," *Opt. Commun.*, vol. 150, pp. 170–174, 1998.

[26] D. J. Berkeland, J. D. Miller, J. C. Bergquist, W. M. Itano, and D. J. Wineland, "Minimization of ion micromotion in a Paul trap," *J. Appl. Phys.*, vol. 83, pp. 5025–5033, 1998.

[27] D. Jiang, B. Arora, M. S. Safronova, and C. W. Clark, "Blackbody-radiation shift in a $^{88}Sr^+$ ion optical frequency standard," *J. Phys. B: At. Mol. Opt. Phys.*, vol. 42, no. 15, p. 154020, 2009.

Direct Frequency Comparison between a Single Ca^+ Clock and a Sr Lattice Clock

Kensuke Matsubara[1], Hidekazu Hachisu[1], Shigeo Nagano[1], Ying Li[1], Asahiko Nogami[1], Clayton Locke[1], Kazuhiro Hayasaka[1], Mizuhiko Hosokawa[1], Tetsuya Ido[1,2]

[1]Space-Time Standards Group, National Institute of Information and Communications Technology

[2]Japan Science and Technology Agency, CREST

[1,2]Tokyo, Japan

***Abstract*— Direct comparison between a single $^{40}Ca^+$ clock and an ^{87}Sr lattice clock has resulted in a frequency ratio of 0.957 631 202 358 049 9(2 3). The rapid nature of optical comparison allowed the statistical uncertainty of the frequency ratio Ca^+/Sr to be 1×10^{-15} in 1000 s and the value is consistent with that calculated from separate frequency measurements of $^{40}Ca^+$ using the International Atomic Time (TAI) link. The total uncertainty of the measured ratio is smaller than that obtained at the absolute frequency measurement. The absolute frequency of $^{40}Ca^+$ we measured deviates from other published values by more than three times our measurement uncertainty.**

***Keywords*— Single Ca^+ ion trap, Sr lattice clock**

I. INTRODUCTION

Comparison between independent frequency standards is the most reliable means to fully evaluate their reproducibility and stability. Comparison also enables the evaluation of the systematic shift by measuring dependence of the frequency on various experimental parameters. Optical frequency standards have a strong advantage in the speed of this comparison process, requiring less than 1,000 seconds evaluating a fractional frequency difference at the 10^{-16} level uncertainty. In contrast, state-of-the-art Cs fountain clocks operating in the microwave regime require more than six hours of integration time. Optical frequency combs can be employed as a bridge enabling the measurement of the relative instabilities of standards based on different atomic transitions. Such frequency ratio measurement can yield information on possible temporal variations of fundamental constants [1].

In this paper, we report a frequency comparison of a $^{40}Ca^+$ $^2S_{1/2}$-$^2D_{5/2}$ single-ion clock transition against the ^{87}Sr $^1S_0$-$^3P_0$ lattice clock transition [2]. The $^{40}Ca^+$ clock in this work has exceptional fractional frequency instability of parts in 10^{-16}. Neutral strontium and calcium ions are popular as quantum absorbers in the realization of optical clocks; worldwide five neutral strontium lattice clocks are already in operation [3–7], and calcium ions are ideal for portable optical clocks because of the availability of laser-diodes at all required wavelengths. $^{40}Ca^+$ clocks are being developed at NICT [8], Univ. of Innsbruck [9], and WIPM [10]. With such interest and development in these two optical standards around world it is imperative that we establish a benchmark frequency ratio with high precision.

II. SINGLE CA^+ OPTICAL CLOCK

The experimental setup for the Ca^+ clock was reported in [8]. An increase in production efficiency of $^{40}Ca^+$ ions was achieved by a photoionization process. A magnetic shield was installed on the vacuum chamber that reduced by more than 20 times stray ac magnetic fields. Mechanical shutters and acousto-optic modulator (AOM) shutters were installed to avoid coupling of cooling laser during the interrogation period. Further optimization of the clock laser [11] reduced its spectral width to less than 5 Hz, and a noise cancellation technique [12] implemented on the 40 m of optical fiber between it and the ion trap. These improvements resulted in an observed line width of the clock transition of about 25 Hz.

TABLE I. SYSTEMATIC SHIFTS OF THE $^{40}CA^+$ CLOCK

	***Shift* (Hz)**	***Uncertainty* (Hz)**
Gravitational	3.42	< 0.1
Blackbody radiation	0.39	0.05
Ac Stark due to 397 nm	0.27	0.54
Ac Stark due to 397 nm	0	0.20
Ac Stark due to 397 nm	0	0.30
Erectric quadrupole ($^2D_{5/2}$ M_J=3/2)	0.1	0.34
Quadratic Doppler	0	< 0.1
Second-order Zeeman	0	< 0.1
Stark due to secular motion	0	< 0.01
Stark due to micromotion	0	<0.1
Servo error	0	0.5
Total	4.2	0.89

The systematic shifts and the respective uncertainties to determine the Ca^+ clock transition frequency are shown in Table 1. In this table, the black body radiation frequency shift [13] was evaluated from measurements of temperature by constructing an identical ion-trap equipped with platinum resistance thermometers. A GPS based elevation measurement yields an estimation of the gravitational shift. From the magnetic field bias of 3 μT we estimate the quadratic Zeeman shift. In order to evaluate the electric quadrupole shift the dependence of the resonant frequencies on the upper magnetic sublevels was investigated [14]. Ac Stark shift due to cooling lasers was estimated from linear fitting of the clock frequency to the intensity of 397-nm light. Ac Stark shift due to the 854-nm light used for quenching the ion from the $^2D_{5/2}$ levels was estimated from the comparison between frequencies measured

This research was supported in part by the Japan Society for the Promotion of Science through its FIRST program.

with and without use of 854-nm light. We also measured frequency shifts by changing the power of the clock laser. The servo error was estimated from the analysis of the residual error.

III. Sr Lattice Clock

The optical lattice clock utilized as a stable frequency reference in this work is based on the $^1S_0$-$^3P_0$ transition (λ = 698 nm) of optically trapped spin-polarized fermionic ^{87}Sr atoms [3]. The clock is in a different room, 10 m from the Ca^+ clock. The absolute frequency of the ^{87}Sr lattice clock at NICT agrees with other clocks in various institutes within the so-called Cs-limit [7]. The systematic uncertainty has been evaluated to be 5×10^{-16}. Using a 60 km fiber link [15] we confirmed the agreement of the clock frequencies at the 10^{-16} level with another ^{87}Sr lattice clock in The University of Tokyo. This experiment also demonstrated that the instability of the clock at NICT reached 5×10^{-16} in 1000 s [16]. Since then the instability of the clock laser was improved by implementing optical compensation against vibration-induced phase noise. By this technique the short term stability is $< 2 \times 10^{-15}$ at 1 s. Systematic shifts and their uncertainties have been recently evaluated after some minor renovations which has resulted in a systematic correction of −1.25(22) Hz. In this paper we report on the use of our lattice clock as an independent optical frequency reference for the evaluation of the Ca^+ clock.

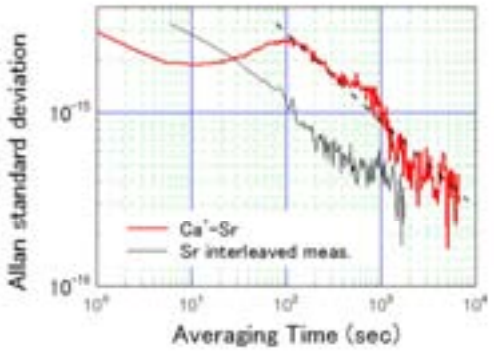

Figure 1. Instability of the frequency ratio (red) determined by the instability of Ca+ clock. An interleaved measurement of the Sr lattice clock has resulted in lower instability as shown in black.

IV. Frequency Comparison

A Ti:Sapphire-based optical frequency comb [17] bridges the two clocks and the frequency ratio ν_{Ca}/ν_{Sr} is measured as follows. The beat signal between the clock laser for the Sr lattice clock and the nearest comb component is first phase locked to a stable RF frequency f_{PLL} which is generated by a direct digital synthesizer with reference to a hydrogen maser. In this case, the repetition frequency f_{rep} is expressed as follows,

$$f_{rep} = (\nu_{Sr} - f_{ceo} - f_{PLL}) / N_1. \quad (1)$$

where N_1 and f_{ceo} are the mode number of the comb component and the carrier-envelope offset frequency of the comb. Measurement of the beat frequency f_b between the Ca^+ clock frequency and the nearest comb component (mode number N_2) yields the transition frequency ν_{Ca} according to

$$\nu_{Ca} = f_{ceo} + N_2 f_{rep} + f_b. \quad (2)$$

The frequency ratio ν_{Ca}/ν_{Sr} can be calculated as

$$\nu_{Ca}/\nu_{Sr} = n + \{(1-n) f_{ceo} - n f_{PLL} + f_b\} / \nu_{Sr}, \; n = N_2/N_1. \quad (3)$$

The instability of ν_{Ca}/ν_{Sr} is shown in Fig. 1. It slowly decreases with increasing integration time over 1-10 s, showing our clock laser is slightly above the thermal noise limit. The long term instability is $2.4 \times 10^{-14}/\tau^{1/2}$, where τ is the integration time, which is limited by the Ca^+ clock. The instability of the Sr lattice clock is $1 \times 10^{-14}/\tau^{1/2}$ according to an interleaved stabilizing operation. This is shown as the thin black trace in Fig. 1.

The Ca^+ frequency is estimated by forty quantum projection measurements in a cycle time of 17 seconds with a Fourier-limited linewidth of about 25 Hz. Random initial preparation of Zeeman substates ($m_J = \pm 1/2$) halves the number of effective measurements. The quantum projection limit estimated using these parameters is $2 \times 10^{-14}/\tau^{1/2}$, and is consistent with the observed long term stability shown as a broken line in Fig. 1.

The frequency ratio ν_{Ca}/ν_{Sr} measured for a half year is summarized in Fig. 2. The results indicate that both optical clocks have a day-to-day reproducibility better than 1×10^{-15}. Taking into account a statistical uncertainty of 1.8×10^{-16} and systematic uncertainties of Ca^+ clock and Sr clock ($2.2 \times 10^{-15}$and 5×10^{-16} respectively), we conclude the frequency ratio ν_{Ca}/ν_{Sr} is 0.957 631 202 358 049 9 with a fractional uncertainty of 2.3×10^{-15}.

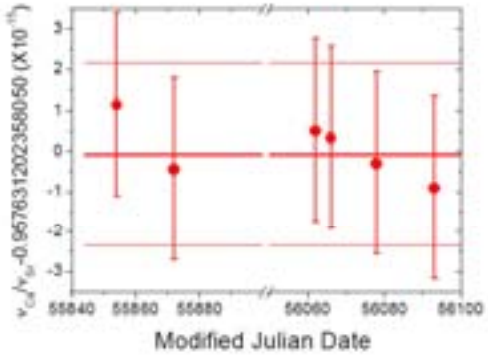

Figure 2. Frequency ratio obtained for half a year. The reproducibility of less than 10^{-15} is consistent with the systematic uncertainties of two clocks. The thick and thin lines indicate the weighted average and the uncertainty, respectively.

V. Absolute Frequency of $^{40}Ca^+$

The frequency of the Ca^+ clock transition was also evaluated by a microwave link to International Atomic Time (TAI). We measured a beat frequency between the clock laser and the nearest comb component of a frequency comb stabilized to a hydrogen maser. The maser was calibrated to

UTC(NICT). The link uncertainties consist of those in the UTC(NICT)-TAI link and TAI-TT link. We estimate that UTC(NICT) during the Ca^+ frequency measurement could be different from the five-day average calculated using the BIPM Circular T by the amount of the instability of UTC(NICT) over those five days. Forty-five days of our signal integration resulted in an instability of TAI-UTC(NICT) of 1.9×10^{-15}. Thus, the uncertainty due to the TAI link is evaluated to be 1.9×10^{-15} including minor contributions from the calibration of TAI to the SI second (3×10^{-16}). With considerations of the systematic uncertainty of the Ca^+ clock shown in Table 1 and the statistical uncertainty, the total fractional uncertainty of the absolute frequency measurement is 3.0×10^{-15}. We therefore determine that the absolute frequency for our measurement is 411 042 129 776 398.4(1.2) Hz. Combining the measured frequency ratio ν_{Ca}/ν_{Sr} with the absolute frequency of our Ca^+ clock we evaluate the absolute frequency of the Sr lattice clock to be 429 228 004 229 871.9 (1.2) Hz. This frequency is consistent with our previous measurement [7].

While our Ca^+ clock has a day-to-day reproducibility at the 10^{-16} level, the frequency is disparate by more than three times the measurement uncertainty when compared to two other published results [9, 10]. To address this discrepancy we are planning further experiments; firstly satellite-based inter-continental comparisons directly to other clocks, and secondly we will repeat the frequency measurement using an In^+-Ca^+ clock currently under development in our laboratory [18].

VI. Summary and Future Plan

We have measured the frequency ratio between the $^{40}Ca^+$ $^2S_{1/2}$-$^2D_{5/2}$ transition and the ^{87}Sr $^1S_0$-$^3P_0$ transitions with an uncertainty of 2.3×10^{-15}. The frequency ratio measurement demonstrated for the first time that the Ca^+ clock is able to reach the 10^{-16} level of instability. All optical comparison has also enabled quick and rigorous evaluation of the systematic shifts of the Ca^+ ion clock. The frequency ratio ν_{Ca}/ν_{Sr} was consistent with the absolute frequency measurement of the Ca^+ clock.

The Ca^+ and Sr optical clocks investigated here are two of the most popular in ion-based and lattice-based systems. The systematic uncertainty of the Ca^+ clock in this work is at the 10^{-15} level. The systematic uncertainties of both clocks are currently projected to be smaller than current state-of-the-art cesium fountain clocks and therefore further improved measurement of the ratio ν_{Ca}/ν_{Sr} may become an infrastructure of frequency metrology, enabling frequency comparison of two physically separated optical clocks more precisely than that of comparisons via SI second.

Furthermore, an In^+-Ca^+ clock is also under development in our laboratory [18-20]. Natural linewidth of the $^1S_0$-$^3P_0$ clock transition (λ = 237 nm) of In^+ ion is 0.8 Hz. Its BBR shift and electric quadrupole shift are estimated extremely small. We can therefore expect to reach the 10^{-18} level of uncertainty using this transition. It is presently difficult to generate 159-nm radiation for direct laser cooling of In^+ ions. Sympathetic cooling of In^+ with Ca^+ followed by the sideband cooling using the $^1S_0$-$^3P_1$ transition (λ = 230 nm) is therefore useful to reduce temperature of In^+ ions efficiently [21]. Ionic chains consisting of a single In^+ ion and a few Ca^+ ions have been observed in a linear trap. We are now constructing a setup for observing the $^1S_0$-$^3P_0$ clock transition.

References

[1] T. Rosenband, D. B. Hume, P. O. Schmidt, C. W. Chou, A. Brusch, L. Lorini, W. H. Oskay, R. E. Drullinger, T. M. Fortier, J. E. Stalnaker, S. A. Diddams, W. C. Swann, N. R. Newbury, W. M. Itano, D. J. Wineland, and J. C. Bergquist, "Frequency ratio of Al^+ and Hg^+ single-ion optical clocks; Metrology at the 17th decimal place," Science, Vol. 319(5871), pp. 1808–1812, 2008.

[2] K. Matsubara, H. Hachisu, Y. Li, S. Nagano, C. Locke, A. Nogami, M. Kajita, K. Hayasaka, T. Ido, and M. Hosokawa, "Direct comparison of a Ca^+ single-ion clock against a Sr lattice clock to verify the absolute frequency measurement," Opt. Express, Vol. 20, pp. 22034-22041, 2012.

[3] M. Takamoto, F.-L. Hong, R. Higashi, and H. Katori, "An optical lattice clock," Nature, Vol. 435(7040), pp. 321–324, 2005.

[4] G. K. Campbell, A. D. Ludlow, S. Blatt, J. W. Thomsen, M. J. Martin, M. H. G. de Miranda, T. Zelevinsky, M. M. Boyd, J. Ye, S. A. Diddams, T. P. Heavner, T. E. Parker, and S. R. Jefferts, "The absolute frequency of the ^{87}Sr optical clock transition," Metrologia, Vol. 45(5), pp. 539–548, 2008.

[5] X. Baillard, M. Fouche, R. Le Targat, P. G. Westergaard, A. Lecallier, F. Chapelet, M. Abgrall, G. D. Rovera, P. Laurent, P. Rosenbusch, S. Bize, G. Santarelli, A. Clairon, P. Lemonde, G. Grosche, B. Lipphardt, and H. Schnatz, "An optical lattice clock with spin-polarized ^{87}Sr atoms," Eur. Phys. J., Vol. D 48(1), pp. 11–17, 2008.

[6] St. Falke, H. Schnatz, J. S. R. V. Winfred, T. Middelmann, S. Vogt, S. Weyers, B. Lipphardt, G. Grosche, F. Riehle, U. Sterr, and C. Lisdat, "The ^{87}Sr optical frequency standard at PTB," Metrologia, Vol. 48(5), pp. 399–407, 2011.

[7] A. Yamaguchi, N. Shiga, S. Nagano, Y. Li, H. Ishijima, H. Hachisu, M. Kumagai, and T. Ido, "Stability transfer between two clock lasers operating at different wavelengths for absolute frequency measurement of clock transition in ^{87}Sr," Appl. Phys. Express, Vol. 5(2), 022701, 2012.

[8] K. Matsubara, K. Hayasaka, Y. Li, H. Ito, S. Nagano, M. Kajita, and M. Hosokawa, "Frequency measurement of the optical clock transition of $^{40}Ca^+$ ions with an uncertainty of 10^{-14} level," Appl. Phys. Express, Vol. 1, 067011, 2008.

[9] M. Chwalla, J. Benhelm, K. Kim, G. Kirchmair, T. Monz, M. Riebe, P. Schindler, A. S. Villar, W. Hänsel, C. F. Roos, R. Blatt, M. Abgrall, G. Santarelli, G. D. Rovera, and Ph. Laurent, "Absolute frequency measurement of the $^{40}Ca^+$ $4s^2S_{1/2}$-$3d^2D_{5/2}$ clock transition," Phys. Rev. Lett., Vol. 102(2), 023002, 2009.

[10] Y. Huang, J. Cao, P. Liu, K. Liang, B. Ou, H. Guan, X. Huang, T. Li, and K. Gao, "Hertz-level measurement of the $^{40}Ca^+$ 4s $^2S_{1/2}$–3d $^2D_{5/2}$ clock transition frequency with respect to the SI second through the Global Positioning System," Phys. Rev., Vol. A 85(3), 030503, 2012.

[11] Y. Li, S. Nagano, K. Matsubara, H. Ito, M. Kajita, and M. Hosokawa, "Narrow-line and frequency tunable diode laser system for S–D transition of Ca^+ ions," Jpn. J. Appl. Phys., Vol. 47(8), pp. 6327–6332, 2008.

[12] L.-S. Ma, P. Jungner, J. Ye, and J. L. Hall, "Delivering the same optical frequency at two places: accurate cancellation of phase noise introduced by an optical fiber or other time-varying path," Opt. Lett., Vol. 19(21), pp. 1777–1779, 1994.

[13] B. Arora, M. S. Safronova, and C. W. Clark, "Blackbody-radiation shift in a $^{43}Ca^+$ ion optical frequency standard," Phys. Rev., Vol. A 76(6), 064501, 2007.

[14] G. P. Barwood, H. S. Margolis, G. Huang, P. Gill, and H. A. Klein, "Measurement of the electric quadrupole moment of the 4d2D5/2 level in $^{88}Sr^+$.," Phys. Rev. Lett., Vol. 93(13), 133001, 2004.

[15] M. Fujieda, M. Kumagai, S. Nagano, A. Yamaguchi, H. Hachisu, and T. Ido, "All-optical link for direct comparison of distant optical clocks," Opt. Express, Vol. 19(17), pp. 16498–16507, 2011.

[16] A. Yamaguchi, M. Fujieda, M. Kumagai, H. Hachisu, S. Nagano, Y. Li, T. Ido, T. Takano, M. Takamoto, and H. Katori, "Direct comparison of

distant optical lattice clocks at the 10^{-16} uncertainty," Appl. Phys. Express, Vol. 4(8), 082203, 2011.

[17] S. Nagano, H. Ito, Y. Li, K. Matsubara, and M. Hosokawa, "Stable operation of femtosecond laser frequency combs with uncertainty at the 10^{-17} level toward optical frequency standards," Jpn. J. Appl. Phys., Vol. 48(4), 042301, 2009.

[18] K. Hayasaka, "Synthesis of two-species ion chains for a new optical frequency standard with an indium ion," Appl. Phys. B Vol. 107(4), pp. 965–970, 2012.

[19] J. von Zanthier, Th. Becker, M. Eichenseer, A.Yu. Nevsky,Ch. Schwedes, E. Peik, H. Walther, R. Holzwarth, J. Reichert, Th. Udem, T.W. Hänsch, P.V. Pokasov, M.N. Skvortsov, and S.N. Bagayev, "Absolute frequency measurement of the In^+ clock with a mode-locked laser," Opt. Lett. Vol. 25, pp. 1729-1731, 2000.

[20] Y.H. Wang, R. Dumke, T. Liu, A. Stejskal, Y.N. Zhao, J. Zhang, Z.H. Lu, L.J. Wang, Th. Becker, and H. Walther, "Absolute frequency measurement and high resolution spectroscopy of $^{115}In^+$ $5s^2\,^1S_0$–$5s5p\,^3P_0$ narrowline transition," Opt. Commun. Vol. 273, pp. 526-531, 2007.

[21] E. Peik, J. Abel, Th. Becker, J. von Zanthier, and H. Walther, "Sideband cooling of ions in radio-frequency traps," Phys. Rev. Vol. A 60, pp. 439-449, 1999.

RF Solid-State Vibrating Transistors

Wentao Wang, Radhika Marathe, Bichoy Bahr, Laura C. Popa, Dana Weinstein
Department of Electrical Engineering and Computer Science
Massachusetts Institute of Technology
Cambridge, MA, USA
Email: dana@mtl.mit.edu

Abstract— **This paper reviews our work on CMOS-integrated active MEMS resonators. Design, analysis and results are presented on CMOS-MEMS resonators fabricated at the Front-End-of-Line (FEOL) of a standard CMOS technology, realized without the need for any post-processing or packaging. Unreleased Resonant Body Transistors (RBTs) are driven capacitively to form longitudinal resonance confined by Acoustic Bragg Reflectors (ABRs), and sensed piezoresistively using an n-channel Field Effect Transistor (nFET). This first generation hybrid CMOS-MEMS RBTs consume footprints of 5µm×3µm, and operate above 11 GHz with quality factors (*Q*) of 24-30 and temperature stability <3 ppm/K, matching well with theory. In addition, acoustic mode localization using features of standard CMOS technology is discussed. The active transduction mechanisms developed for CMOS-MEMS resonators can be extended to piezoelectric III-V semiconductors available in mm-wave ICs (MMICs). Our recent work on switchable MEMS–HEMT resonators in AlGaN/GaN is presented using a standard GaN MMIC platform, providing a means of realizing configurable high-*Q* MEMS resonators in MMICs for high frequency, high power applications.**

Keywords-RF MEMS; resonator; CMOS-MEMS; GaN; HEMT; Resonant Body Transistor

I. INTRODUCTION

RF micro-electromechanical (MEM) resonators, with frequency-quality factor products ($f \cdot Q$) often exceeding 10^{13}, can provide a high performance, low-power, compact IC-compatible alternative to traditional LC tanks, off-chip Quartz crystals and SAW devices in clocking, communication, and sensing applications. Key challenges to wide-spread implementation of these devices include frequency scaling, incompatible fabrication with ICs and complex packaging. The work presented here focuses on new transduction mechanisms and new resonant structures that enable intimate integration with ICs at multi-GHz frequencies.

A. Frequency Scaling to Multi-GHz

The past decade has seen a continuous push towards multi-GHz frequencies for applications including personal navigation (94 GHz) and short distance local area networks (LAN) (60 GHz), imaging, and high-definition video links. A majority of MEMS resonators rely on passive transduction mechanisms such as electrostatic and piezoelectric transduction to sense acoustic resonance. However, in such passive systems, parasitic feed-through increasingly becomes dominant over the resonance signal at higher frequencies, reducing the dynamic range or out-of-band rejection of the signal. In-line amplifiers are ineffective at amplifying the signal over the parasitic feedthrough, necessitating the exploration of different sensing mechanisms.

The concept of Field Effect Transistor (FET) sensing in MEMS devices has been around since Nathanson's Resonant Gate Transistor in 1967 [1]. In Si-based resonators, FET sensing has been demonstrated up to 113 MHz [2] and in piezoelectric GaN-based resonators, up to 2 MHz [3]. Active sensing with piezoresistive elements has also been demonstrated up to 61 MHz [4]. The authors have previously demonstrated Resonant Body Transistors (RBTs) [5, 6] with internal dielectric drive and FET sensing up to 37 GHz. FET sensing has thus been shown to reach order of magnitude higher frequencies than possible with passive resonators due to the active amplification of the resonance signal before the presence of parasitics. The authors have demonstrated the first CMOS integration of RF RBTs with no post-processing or special packaging, taking advantage of high gain, high yield transistors in an all-access technology.

B. CMOS integration of MEMS resonators

The intimate integration of CMOS and MEMS is advantageous primarily because of reduced parasitics from on-chip and off-chip routing for high frequency operation, smaller size and weight, and decreased power consumption due to constraints on impedance matching networks. Typical methods for CMOS-MEMS co-fabrication include modular MEMS-first or MEMS-last processes, in which the circuit is independently fabricated before or after the mechanical structure is formed. This leads to increased mask count, reduced yield, process constraints, and performance compromise due to thermal budget [7]. Non-modular CMOS-MEMS co-fabrication has been demonstrated using the Back-End-of-Line (BEOL) CMOS stack, reducing mask count but limiting the structure to large feature sizes and materials to metals and low-quality dielectrics [8, 9]. Furthermore, as with most MEMS devices, these BEOL MEMS require a release step to freely suspend the moving structures. This necessitates costly, complex encapsulation methods and costly hermetic seal packaging [10, 11], and may impact the yield of the technology.

To address these challenges, the authors present the development of *unreleased* Si-based MEMS resonators in CMOS (Fig. 1). This solid-state solution allows seamless integration into Front End of Line (FEOL) processing with no post-processing or packaging. The unreleased nature of these resonators eliminates the release etch step and packaging, with the added benefit of increased robustness in harsh environments. Implemented with FET-sensing, these devices take advantage of high performance transistors, pushing operation frequencies to the multi-GHz domain. As a proof of

This work is sponsored in part by the FCRP IFC, FCRP MSD, NSF CAREER Award and DARPA Young Faculty Award.

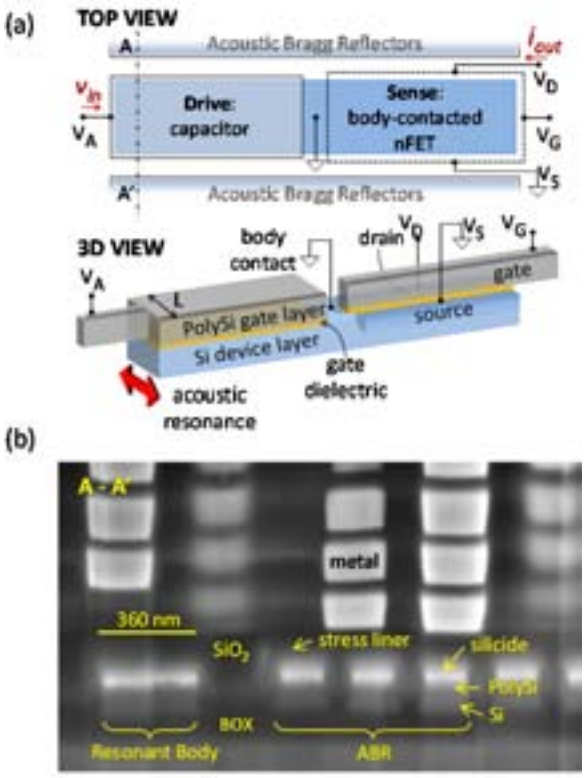

Figure 1. (a) Top and 3D views of Si-based CMOS-MEMS resonator excluding Acoustic Bragg Reflectors (ABRs). The resonator is driven capacitively on the left, and sensed through piezoresistive modulation of the nFET drain current on the right. Details of FET layout and doping layers are not shown. (b) SEM of CMOS stack obtained using FIB. The resonant cavity comprised of the single crystalline silicon (SCS) device layer and ABRs is seen fully buried under the metal layers.

concept, IBM's 32nm SOI process was chosen for its high f_T transistors, the small feature sizes down to <60 nm and the presence of a buried oxide (BOX) layer for acoustic localization of vibrations in the Si device layer.

On the mechanical side, the challenge for building unreleased MEMS resonator lies in maintaining its high quality factor (Q) inside a solid medium. The energy loss of elastic wave radiation into the surrounding medium can be mitigated by adding "acoustic mirrors" such as acoustic Bragg reflectors (ABRs) or phononic crystals (PnC). Both of these are periodic structures composed of two or more materials that can reflect waves coherently over a band of frequencies, acting as near-perfect acoustic mirrors at the resonance frequency. Out of the reflection frequency band, these reflectors act as leakage paths, damping undesired modes and giving unreleased resonators unique trait of spurious mode suppression.

ABRs have been employed to thickness mode piezoelectric resonators for wireless applications in high frequency integrated circuits [12, 13], which are composed of multiple depositions of alternating materials, resulting in acoustic isolation in one dimension for a single frequency per wafer. In-plane isolation can be achieved using lithographically defined ABRs, as demonstrated in a suspended plate [14]. This configuration enables resonators of multiple frequencies to be fabricated side by side on the same chip. In contrast to the 1D

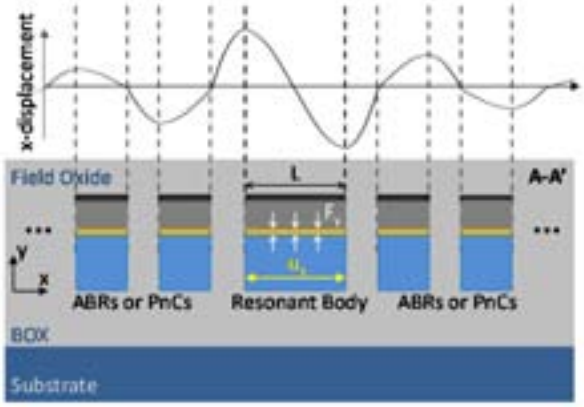

Figure 2. Cross-section of unreleased resonator with surrounding ABRs or PnC. The ABRs or PnC have solid inclusions (e.g. SiO_2 in the STI). The entire structure is sandwiched between capping materials (e.g. field oxide and buried oxide). The mode shape of an RBT in IBM 32nm SOI, corresponding to the A-A' line cut in Fig. 1, is shown.. Capacitive force is applied along the y-axis across the gate dielectric on the drive side of the resonator. Acoustic vibrations are excited in the resonant cavity along the x-direction through the Poisson effect and decay exponentially as a function of length along the ABRs.

mode confinement of ABRs, PnCs provide 2D or 3D lithographically-defined acoustic isolation. They have been explored by several groups for microscale applications, including acoustic mirrors for resonators in suspended plates [15], acoustic waveguides, and filters [16]. Most of these previous demonstrations of ABRs and PnCs are based on suspended released structures, with PnCs most commonly seen as air-filled perforations in a single material. However, the same principle can be implemented for an unreleased structure, where the in-plane resonance is confined by ABRs or PnCs and sandwiched between uniform materials on top and bottom, with PnCs designed as solid inclusions (Fig. 2). In addition, other reflection mechanisms such as high contrast grating can also in principle be borrowed for lithographically defined in-plane mode isolation [17].

In our demonstration, ABRs are built lithographically in FEOL processing in CMOS, defined in the same set of masks as the unreleased RBT. PnCs can be built in the BEOL metal stack, acting as 3D acoustic isolation for improved Q.

C. From Silicon to III-V semiconductors

One limitation of building CMOS-MEMS resonators in standard Si technology is that the driving mechanism is limited primarily to electrostatic transduction. Thermal actuation is also possible using CMOS materials, but it has much larger power consumption [4]. Electrostatic transduction exhibits low electromechanical coupling coefficient ${k_T}^2$ (.00001-.01%), resulting in high motional impedance R_m (up to MΩs). This can be dealt with by utilizing matching networks for these on-chip CMOS-MEMS devices [18]. However, for applications requiring low insertion loss and high bandwidth, high ${k_T}^2$ transduction mechanisms such as piezoelectric transduction are preferred. Piezoelectrically transduced resonators have dominated the market with successful products including the SAW and FBAR [19, 20].

Resonators composed of III-V materials, particularly wide band gap materials such as GaN, offer high transduction efficiency and device configurability through piezoelectric properties, large power handling, high frequency operation, and direct integration with III-V electron devices and circuits. GaN technology provides high electron velocities, charge densities (1×10^{13} cm^{-2} in AlGaN/GaN), and critical electric fields (>3 MV/cm), ideal for high power (>10W/mm), high frequency (>100 GHz) ICs. Moreover, GaN exhibits high piezoelectric coefficients ($k_T{}^2$ up to 2%) and low mechanical damping ($f \cdot Q > 10^{12}$). This technology platform therefore enables the integration of low loss, high-Q MEMS resonators with millimeter-wave ICs (MMICs) and high power electronics.

The same concept of FET sensing of acoustic resonance discussed for CMOS can be implemented in GaN using High Electron Mobility Transistors (HEMTs). Similarly, acoustic localization of unreleased resonators can be achieved by patterning the GaN and surrounding materials to form acoustic reflectors. In thsis review, we present our first results on switchable multi-GHz MEMS-HEMT resonators in GaN and their implications for channel-select radio design.

II. Active Sensing for GHz-Frequency Resonators

A. The Need for Active Sensing in CMOS

Passive schemes such as electrostatic or piezoelectric transduction have traditionally been used in the majority of MEMS resonators. The equivalent circuit model of such passive transduction, either electrostatic or piezoelectric, can be represented by a simple Butterworth-Van-Dyke (BVD) model (Fig. 3 (a)). The drive and sense capacitors are represented by C_0, and the mechanical resonance is represented by an RLC branch, with electrical feedthrough represented as C_f. For such passive schemes, as resonators scale to higher frequencies, the out-of-band rejection of the signal can be severely compromised by feedthrough, and cannot simply be mitigated by subsequent amplifier stages. To illustrate this effect, we take electrostatic sensing as an example, and consider a dielectrically driven and sensed resonator with a resonant length L whose geometry can be realized using FEOL fabrication in an SOI CMOS process (Fig. 3(a)). The electrostatic squeezing force from the top can translate to resonant mode in plane through the Poisson effect [21].

For simplicity, we assume that all dimensions, materials, Q, and the feedthrough capacitance C_f of such a device remain constant while only the length of the resonant cavity L changes as 1/f where f is the resonance frequency. Thus the shunt capacitor C_0 also reduces as 1/f since the non-resonant dimension is held constant. The motional impedance R_m scales as $W/C_0^2 f^2$ where W is the non-resonant dimension and hence remains constant with frequency in this configuration. Meanwhile the impedances of C_m and L_m cancel at resonance. Under these assumptions, the expected out-of-band rejection of the voltage gain from input to output reduces from >10dB at 100 MHz and to less than 0.1dB at 10 GHz. For such resonators, an in-line amplifier stage would indiscriminately amplify the resonance signal along with the feedthrough, thus providing no improvement in the out-of-band rejection.

Active sensing provides one solution to overcome the limits of out-of-band rejection by amplifying the mechanical signal

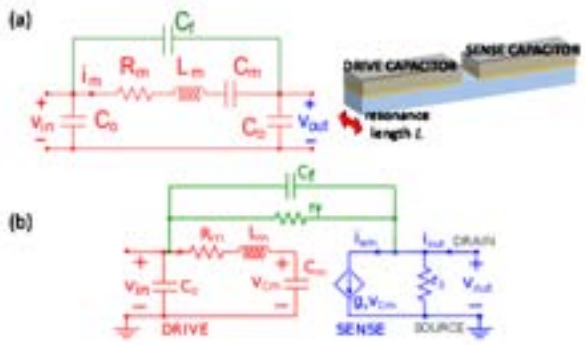

Figure 3. (a) Small signal model and schematic of passive electrostatic MEMS resonator. (b) Small signal model of the RBT consisting of an RLC branch modeling the mechanical resonant system (red) and a modified transistor small signal model (blue). Lumped feedthrough parasitics (green) are modeled by C_f and r_f.

before the presence of parasitics. The small signal equivalent circuit of a capacitively driven, piezoresistively sensed resonator is provided in Fig. 3 (b), consisting of a 1-port passive BVD model and a modified transistor π-model. The drive capacitor is represented by C_0 while the RLC components model the mechanical mass-spring-damper system of the resonator. The piezoresistive sensing is represented by a transconductance g_α. The integration of such an electromechanical amplification element into the resonant cavity enables improvement in the out-of-band rejection of the signal before the contribution of feedthrough parasitics modeled by the C_f and r_f.

B. Active Sensing: Resistive vs. FET Sensing

With the integration of the MEMS resonator into the FEOL IBM CMOS technology, FETs inherent to the process can be used to sense of acoustic vibrations. FET sensing relies on piezoresistivity as the dominant effect to modulate the mobility of carriers along the channel and result in a small signal output current. Secondary contributions to the current modulation include modulation in channel length, threshold voltage, gate capacitance and electrostriction. For simplicity these secondary effects are omitted from the small signal model presented in Fig. 3 (b).

Consider a resonator with the same geometry as that of the capacitively sensed resonator of the previous section, with the only variation being that of sense transducer. A schematic of this device is shown in Fig. 1 (a). In this device, strain induced at resonance is related to the input voltage in the same manner. Assuming the FET is biased in saturation, the change of the output current in terms of the drain bias current I, the mobility μ and the channel resistivity ρ is given by:

$$\frac{\Delta I}{I} = \frac{\Delta\mu}{\mu} = -\frac{\Delta\rho}{\rho} = -g_R v_{in} \quad (1)$$

where g_R is a coefficient with units V^{-1} that models the piezoresistive modulation in terms of the v_{in}. The small signal output voltage from the sensing FET is given in terms of its output resistance r_0 by $v_{out} = -Ir_0 g_R v_{in}$ with voltage gain of $A_v = -Ir_o g_R$. Given the large output resistance of the FET, the gain A_v can attain high values relative to simpler resistive sensing, in which a current is driven through a resistor R embedded in the resonant body. For the same mechanical structure and the same bias current, FET sensing thus has a

voltage gain that is r_o/R higher than its resistive counterpart. For a typical FET, this gain can be orders of magnitude higher than the resistive one. For the devices considered in this work, this ratio is as high as 200.

To assess the noise performance of FET sensing, the drain noise current PSD is first evaluated. For a FET in saturation this is given in terms of the thermal noise coefficient γ and the transconductance g_{mFET}:

$$i_{dn}^2 = 4k_B T \gamma g_{mFET} \quad (2)$$

For short channel devices γ is close to unity. Comparing the input referred noise PSD of both FET and resistive sensing, we have:

$$\frac{\overline{v_{in}^2}\big|_{FET}}{\overline{v_{in}^2}\big|_{Res}} = \gamma g_{mFET} R \quad (3)$$

For typical designs, g_{mFET} is a fraction of mS, such that the input referred noise of FET sensing is much lower than that of resistive sensing. For the devices considered in this work, g_{mFET} is of the order of 500μS, resulting in an input referred noise for the FET of only 5% that of its resistive counterpart. Moreover, FET output resistance remains sufficiently large regardless of the small dimensions necessary for frequency scaling, allowing both for voltage and current sensing.

The downside of FET sensing comes from its higher power dissipation. When biased in saturation, the sensor FET consumes more DC power than the resistive sensor. For the RBTs described in this work, designed for I_D of 60μA and V_D of 500mV, the FET sensing power dissipation is more than 80 times larger than the resistive sensing.

III. Energy Localization for CMOS-MEMS

One of the challenges for building unreleased resonator fully embedded in the CMOS stack lies in the generation of acoustic reflectors in the solid medium surrounding medium surrounding the resonant cavity and localizing the resonance. This can be achieved with frequency bandgap structures including ABRs and PnCs. Both of these are periodic structures composed of multiple materials, which can be conveniently found in the CMOS stack. For example, dummy transistors can be implemented in the FEOL as ABRs, consisting of Si and low-k dielectric; while dummy CMP fill in the metal layers and vias in the BEOL can be engineered to form ABRs or PnCs at the targeted frequency range. These concepts are elaborated as the following sections.

A. Acoustic Bragg Reflectors in FEOL

ABRs are the acoustic analogue of the optical distributed Bragg reflectors used in optical fibers. Typical ABRs consist of alternating materials of quarter wavelength with mismatched acoustic impedance, Z_{ac}, which is defined in terms of the elastic compliance c_{11}, the acoustic velocity c_l, the effective Young's modulus of the cavity *E*, the Poisson ratio ν and mass density ρ as

$$Z_{ac} = \frac{c_{11}}{c_l} = \sqrt{\frac{(1-\nu)\rho E}{(1+\nu)(1-2\nu)}} \quad (4)$$

The reflection coefficient at an interface between two materials is commonly known as

$$R = \frac{(Z_1 - Z_2)}{(Z_1 + Z_2)} \quad (5)$$

The reflectivity off multiple layers can be calculated through an iterative method [22]. The net reflectivity increases and converges to 1 with the number of reflecting surfaces. The converging rate differs for different material pairs, as illustrated by a comparison of material pairs in CMOS (Fig. 4). Similarly to other bandgap structures, this convergence rate can be equivalently represented as the frequency bandgap. Larger acoustic impedance contrast results in larger bandgap, translating to a faster converging rate.

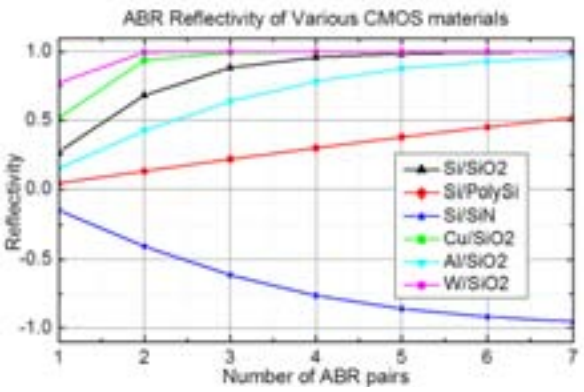

Figure 4. Comparison of the acoustic reflectivity of various ABR material pairs. For finite number of ABR pairs, the reflectivity increases with the number of pairs and converges to 1 or -1 rapidly for materials commonly found in CMOS.

In our FEOL ABR design, Si/SiO_2 was chosen as the material combination for ABRs as these materials occur in transistors and low-k dielectrics in Shallow Trench Isolations (STI). The acoustic impedance mismatch between Si and SiO_2 is $Z_{rel} = Z_{Si}/Z_{SiO_2}$~1.65 and the resultant reflectivity achieved using only 7 pairs of ABRs is *R*~ 99.4% based on 1D analysis [22]. A 2D correction result in a lower reflectivity depending

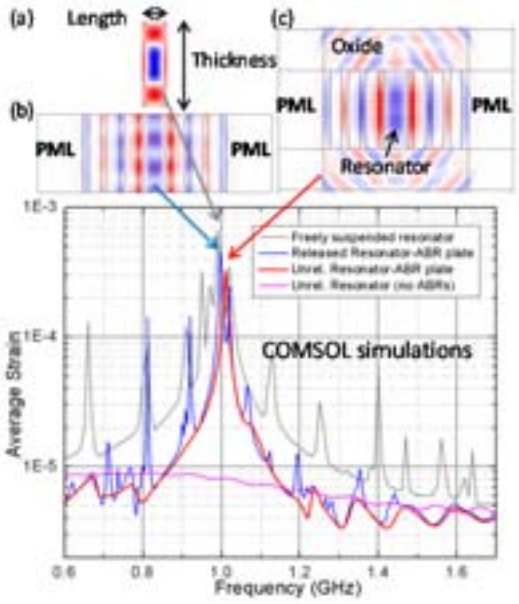

Figure 5. Frequency sweep in COMSOL for sideviews of free bar (a), released resonator-ABR plate (b), unreleased resonator-ABR structure embedded in oxide (c), and simple unreleased resonator embedded in oxide. Frequency response is for resonators of thickness-length ratio of 6.5 and ABR number of 7. Characteristic x-strain contour plots are given at an aspect ratio of 3.5 and ABR number of 3.

on the aspect ratio and resultant solid angle subtended by the reflector. This drop in reflectivity leads to the drop of Q from ~7500 in the 1D model to ~100 in the 2D model for 7 ABRs.

As illustrated in Fig. 2 & 4. The ABR serves as a near-perfect boundary, with reflectivity of 1 or -1 (1 for the Si/SiO_2 combination), in which the wave penetrates, but in an evanescent form. The portion of the wave in the ABR carries little energy propagation at resonance, and is part of the standing wave. Because the typical ABR has reflectivity of ±1 at resonance, it can be equivalently analyzed as a free or fixed boundary condition at the resonance frequency.

Fig. 5 shows frequency domain simulation in COMSOL comparing the performance of unreleased resonator with its released counterparts. The unreleased resonator has the Perfectly Matched Layer (PML) as boundary, and the released ones have simply free boundaries. The simulation shows that released bars have high Q peaks, but many spurious modes. On the other hand, the unreleased resonator with ABRs exhibits amplitude of vibration only 20% less than the released structure, with complete spurious mode suppression. More design variations and analysis on ABRs can be found in [22, 23].

B. Acoustic Bragg Reflectors as Deep Trenches

In real design environment in FEOL CMOS, the aspect ratio of the unreleased resonator is limited to <1 due to constraints of lithographic design rules and thickness of the device layer. To achieve higher aspect ratio for better Q in the ABR framework, other structures in CMOS are investigated. Some CMOS processes (e.g. IBM 45nm and below) have a high aspect ratio structure called Deep Trench (DT) used in high density DRAM capacitors or electrical isolation [24]. With aspect ratio exceeding 5:1, these DTs can be repurposed as structural elements for acoustic energy localization.

To demonstrate the feasibility of this concept, we have fabricated resonators defined using Deep Trench Capacitors in the Microsystems Technology Laboratories (MTL) at MIT (Fig. 6) [23]. Analogous to CMOS DTs, these devices use DT structures that are etched into single crystalline silicon (SCS) and filled with conformal dielectric and poly-Si. Identical DTs are spaced into a single array forming an ABR structure. A resonance cavity is sandwiched between two such arrays, with two transducer DT capacitors inserted into the cavity acting as internal dielectric transducers. [25]. Both the mechanical DTs and transducer DTs are defined in the same mask and are therefore self-aligned. These DT resonators exhibit Q >2000 operating at 3.3 GHz with no spurious modes in a multi-GHz range, with motional impedance R_X of only 1.23kΩ.

While this marks the best result to date in unreleased resonator performance, there are certain limitations to the DT resonator. (1) The DT structure is available in limited CMOS technologies, and can therefore not be applied to a generic solution for CMOS-MEMS integration. (2) Because the DTs are filled with doped poly-Si, the resistivity is at the range of 10^{-3} Ω·cm, and the RC delay becomes prohibitive for multi-GHz operation. (3) The CMOS foundry parameters are not optimized for mechanical applications for such DTs, so these DTs commonly contain voids, which can cut the wave paths and destroy its design purpose as ABRs.

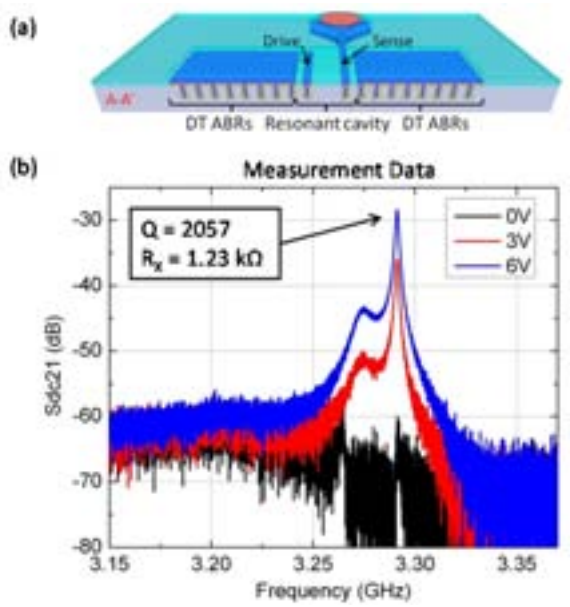

Figure 6. (a) Schematic of unreleased Deep Trench (DT) MEMS resonator. Acoustic Bragg reflectors (ABRs) formed from periodically spaced DTs define a high-Q resonant cavity in the center of the device. DT capacitors inside the resonant cavity form electrostatic drive and sense transducers. (b) Measured frequency response of DT resonators with 7.2 µm long resonant cavity, DT length of 950nm, and 1.7µm DT pitch in the ABRs. Devices with 50 ABRs are shown, with Q of 2057 and Rx of 1.23kΩ. Wide frequency sweeps show no spurious modes in a multi-GHz range.

C. Phononic Crystals in BEOL

While high aspect ratio for high Q unreleased resonators in CMOS is not always possible using the 1D ABR framework, there are a variety of structures in the CMOS stack that allow for 2D and 3D confinement of acoustic energy. In addition to patterning of surrounding Si and STI in FEOL, metal layers and vias in the BEOL can be patterned into a phononic crystal (PnC). Additionally, contacts connecting the first metal layer and the transistors and larger contacts to the substrate can be patterned into periodic arrays to enhance energy localization.

The PnC is the acoustic analogue of the photonic crystal, which is used extensively in optical waveguides and resonators [26, 27]. In contrast to the ABR that creates bandgap only in one dimension, the PnC relies on periodicity in 2D or 3D to create a frequency bandgap in all directions.

One example of a bulk CMOS resonator confined by a 2D PnC is shown in Fig. 7. Here we see a COMSOL simulation of the resonant mode of such a design, based on parameters and material properties of TSMC's 0.18um CMOS process. The resonant cavity consists of 5 transistors side by side on the same Si island (targeting a 5th harmonic bulk mode), sandwiched by contacts on either side, and capped by a PnC structure defined in the first 6 metal layers. Through a geometric parameter sweep, the PnC can be optimized for a center bandgap frequency around 2 GHz. In this complex geometry, both BEOL PnC and in-plane contact spacing should be adjusted together for optimized mode shape. A Q of 500 at 2.07 GHz is obtained in simulation, with a shear wave mode localized inside the resonant cavity.

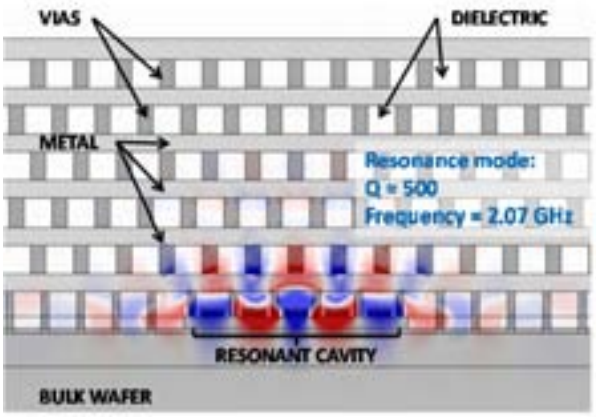

Figure 7. FEA simulation of resonant mode obtained using metal PnCs in the BEOL and vias between 1st metal layers and the transistor (CA bars). A 5th harmonic shear wave mode can be obtained from geometric optimization, with the blue and red indicating strain-x intensity.

IV. RBTs IN IBM'S 32SOI TECHNOLOGY

A. Design and Simulation

Based on the previous discussions, two constituent building blocks are essential for the development of multi-GHz CMOS-MEMS resonators: 1) FET sensing of acoustic vibrations due to its amplification of the mechanical signal before parasitics at high frequencies, and 2) ABRs or PnCs formed with structures inherent to the CMOS stack for energy localization. These concepts are demonstrated using the IBM's 32nm SOI technology to form unreleased resonators above 10 GHz [28]. Due to material restrictions in CMOS, electrostatic transduction is implemented to drive the resonator.

1) Design of Unreleased Resonator

As illustrated in Fig. 1, the unreleased RBT is created by modifying a standard CMOS body-contacted nFET, integrating a MOS capacitor on the same Si island as the nFET. On either side of this active device, an array of seven Si dummy features, composed of Si device layer/gate dielectric/poly-Si stack and separated by Shallow Trench Isolation (STI), form acoustic Bragg reflectors for mode confinement. This solid-state vibrating structure is sandwiched by the buried oxide (BOX) below and intermetal dielectric above.

In operation, superimposed DC and RF voltage $V_A + v_{in}$ is applied across the driving capacitor, generating an electrostatic force that excites acoustic wave in the plane of the wafer through the Poisson effect. On the sensing side, the FET is biased into saturation with DC gate and drain voltages, V_G and V_D, respectively. At resonance, strain modulates the carrier mobility inside the channel piezoresistively, and generates the drain current as $i_D = I_D + i_{out}e^{j\omega_0 t}$.

The mode shape and amplitude of vibrations U_0 of this unreleased resonator can be calculated using the model for damped vibrations in dielectrically driven released bar resonators [29]. This analogy is based on two assumptions: 1) each of the ABR layers is at an odd multiple of a quarter wavelength, ensuring no phase change at the ABR boundary so that it can be treated as a free or fixed boundary. 2) The aspect ratio of the structure is large, so that it can be approximated using a one-dimensional model, i.e. the wave leakage through the top and bottom is negligible.

In the course of design of the resonators, several structural aspects of the foundry-provided nFETs were modified. Standard FET doping layers which define the source/drain and body doping were changed to allow ABRs to be designed as close to the devices as possible. The shapes of the active device region of the SOI process and Poly gate regions were modified to create longitudinal bar like structures for definition of the resonant cavity. The number of metal contacts was reduced to reduce distortion of the resonant mode of vibrations. A summary of the resonator design parameters is provided in Table I.

TABLE I. DESIGN PARAMETERS OF CMOS-MEMS RBTS FABRICATED IN THE IBM 32NM SOI CMOS PROCESS.

Parameter	Value
Length (resonance dimension)	360 nm
Width	2.5 µm
# ABR pairs	7
Device footprint	5 µm × 3 µm
Capacitor doping	p or n-type
FET type	Body contacted nFET
FET W/L	10.3

2) Finite Element Analysis

As a result of limitations of simple 1D analysis, 3D finite element analysis (FEA) of the acoustic mode shape is necessary for Q analysis and design optimization. Here, the 3D model is constructed of half the resonant cavity, cut across the axis of symmetry. To correctly reflect the actual structures in the IBM 32nm SOI process, the 3D model is constructed consisting of the handle wafer, buried oxide layer (BOX), the resonant structure capped by the stress liner and the pre-metal dielectric. It also includes the sensing FET with source/drain contacts and contacts to the resonator body and drive capacitor. This geometry is shown in Fig. 8(a).

The top of the structure (above the FET and ABRs) was selected to be a free boundary condition. This is due to the fact that the subsequent layers are made of the low-κ dielectric (SiCOH) [30], which has very low acoustic impedance as compared to the materials in the acoustic cavity: Si ($Z_{Si}/Z_{SiCOH} \cong 10.5$) and SiO2 ($Z_{SiO2}/Z_{SiCOH} \cong 6$). The boundary terminating the handle wafer at the bottom was selected to be a low reflection boundary condition, to account for wave radiation loss into the substrate. This low reflection boundary condition is similar in function to Perfectly Matched Layers (PMLs), more commonly used for impedance matched boundary conditions in 2D simulations.

A frequency sweep of the structure is carried out by applying a squeezing force on the dielectric between the capacitor plates. Fig. 8(b) shows the resulting mode shape and stress plot in the longitudinal direction. The predicted resonance frequency is around 11.5 GHz for a longitudinal mode contained in the resonator and ABRs.

B. Small Signal Model

A small signal model for the CMOS-integrated RBT has been introduced in §II.A (Fig. 3(b)). The amplitude of vibrations U_0 is obtained from the electromechanical force convolved with the acoustic mode shape of the composite

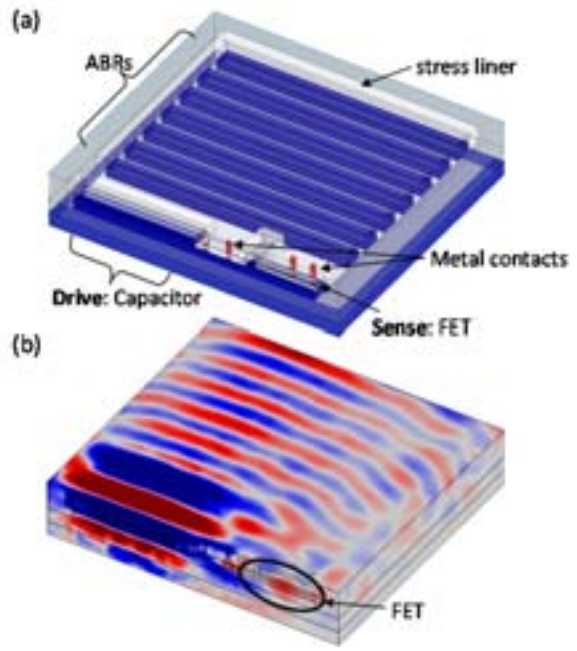

Figure 8. 3D Finite element analysis of unreleased RBT showing (a) Symmetric half-plane of the 3D geometry of resonant cavity and ABRs, including the full FEOL stack materials starting with the handle wafer up to the first metal layer. (b) stress plot along the resonance direction. The mode has a *Q*~110 at frequency of 11.6 GHz.

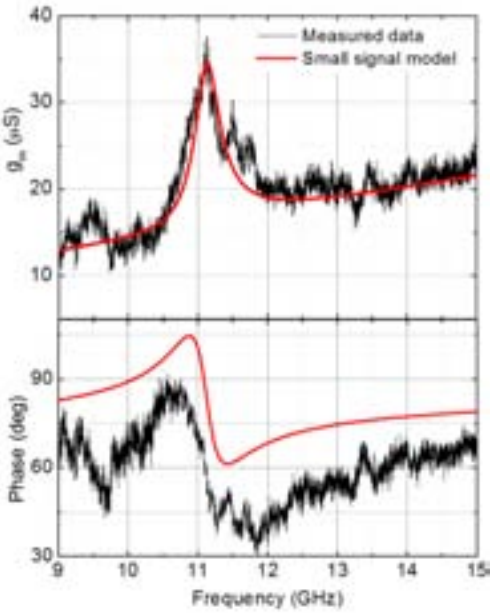

Figure 9. Measured response of nFET-ncap resonator at V_G= 0.4 V, V_A = 0.5 V (black) in close agreement with the equivalent small signal model (red) (Fig. 4). Extracted model parameters are included in Table II. The model shows a good response for the primary mode, but additional spurious modes are not captured by the single LC branch. The systematic offset in the phase is the result of imperfect open/short de-embedding.

structure with a resonance frequency of ω_0 and resonance length L. The motional current i_m, which is the electrical equivalent of the acoustic velocity, arises from the changing dimensions of the drive capacitance C_0, and its value at resonance is given by:

$$i_m = V_A \frac{dC_0}{dt} = \frac{2j\omega_0 V_A C_0 U_0}{L} \tag{6}$$

Thus the input current is proportional to and in phase with the velocity of acoustic vibrations. The motional RLC values may be calculated from the following equations.

$$R_m = \frac{v_{in}}{i_m} \tag{7}$$

$$L_m = Q\frac{R_m}{\omega_0} \tag{8}$$

$$C_m = \frac{1}{Q\,R_m\,\omega_0} \tag{9}$$

On the sensing side, the electromechanical trans-conductance g_α represents the piezoresistive modulation of the drain current I_D at resonance. The electromechanical output current i_{em} is proportional to the piezoresistive coefficient Π_{Si} and the Young's modulus of Si, E_{Si}:

$$i_{em} = \frac{\Delta\mu}{\mu} I_D = \frac{\pi(-\Pi_{Si})E_{Si}U_0 I_D}{L} \tag{10}$$

At resonance, this is used to calculate g_α in terms of i_{em} as:

$$g_\alpha = \frac{i_{em}}{V_{Cm}} = \frac{i_{em}}{v_{in}} j\omega_0 R_m C_m \tag{11}$$

In a well-designed structure, the feedthrough capacitance C_{fg} and body-contact feedthrough capacitance C_{fb} are both much smaller than the total gate capacitance C_{gg}, and the resonance frequency of the RBT ω_0 is much smaller than the cut-off frequency of the sensing FET ($\omega_0 \ll \omega_T$). Under these conditions, the overall transconductance g_m is:

$$g_m = \frac{i_{out}}{v_{in}} = \frac{g_\alpha}{s^2 L_m C_m + sR_m C_m + 1} + \frac{1}{r_f} + sC_f \tag{12}$$

This simplified small signal model can be used in circuit simulators to model the RBT behavior for the purpose of CMOS-MEMS co-design.

C. Experimental Results

Resonators were tested in a two-port configuration in a Cascade PMC200 RF probe system. Open and short structures on the die were used to de-embed routing parasitics down to the first metal level. RF measurements were carried out at 300K with -21.9 dBm input power and 30Hz IF BW using an Agilent PNA-X N5245A. The overall input-to-output transconductance as per the definition for a MOSFET were extracted as $g_m = \frac{i_{out}}{v_{in}} = Y_{21} - Y_{12}$.

1) RF measurements

Under the biasing conditions described in §IV.A, the nFET-ncap RBT exhibits frequency response of the input-to-output transconductance g_m shown in Fig. 9. A measured resonance peak of *Q*~30 at 11.1 GHz can be seen, matching closely with the predicted resonance frequency from the 3D simulation in Fig. 8.

This RF response can be fitted with the small signal model in Fig. 3(b). The driving capacitor C_0 was obtained from layout. The parameter values for R_m, L_m and C_m were extracted following (7-9) using measured value of Q and f_0. With these values, g_α was calculated based on (10) and (11), and r_0 was determined from the early voltage extracted from the FET DC. The value of C_f and r_f were extracted from the

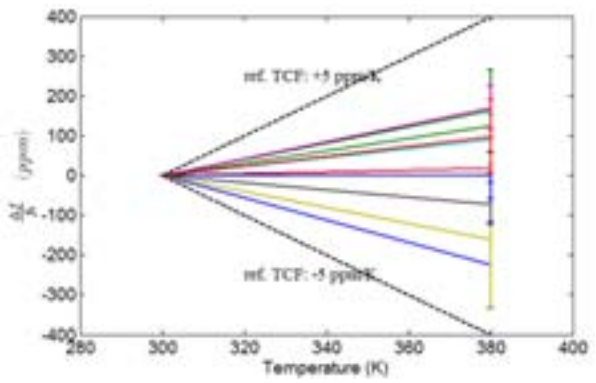

Figure 10. Extracted TCFs for multiple spurious modes on a single device. All the TCFs lie within ±3 ppm/K range. This result is consistant for all the devices.

broadband floor of the RF measurement. Fig. 9 plots the fitted data alongside the measurement data. It is important to note both from the fitted curve and experiment that the output current is 90° out of phase from the input voltage. Detailed values of the small signal model are listed in Table II.

TABLE II. EXTRACTED PARAMETERS OF 11.1 GHZ RESONATOR.

Parameter	Value
C_0	14 fF
R_m	1.1 MΩ
L_m	0.49 mH
C_m	4.2e-19 F
g_α	-0.62 µS
C_f	0.22 fF
r_f	290 kΩ
r_0	20 kΩ

2) Temperature Stability

Thermal stability is an important characteristic of any resonator required for reliable operation in oscillators, filters, sensors, and other communication and navigation systems. Si resonators typically exhibit temperature coefficient of frequency (TCF) of -20 to -30 ppm/K, but use of materials with positive temperature coefficient of Young's modulus (TCE) such as SiO_2 has been demonstrated for thermal compensation [31]. The CMOS-integrated resonators presented here are inherently surrounded by SiO_2 in the BOX and STI fill used to define ABRs, and are expected to show TCF compensation from the complimentary Si/SiO_2 pairing.

The temperature stability of the CMOS-MEMS resonators are characterized at room temperature (298K), 340K and 380K. Two different families of TCF are observed. Those showing positive TCF indicate oxide-dominated modes, and those with negative TCF show Si-dominated modes. All TCF data are observed to lie between ±3 ppm/K which agrees well with analysis and simulation (Fig. 10). Some modes are observed with sub-ppm TCF which demonstrates almost complete thermal compensation.

V. ALGAN/GAN MEMS RESONATORS

The concept of active transistor sensing in multi-GHz resonators can be extended from Si to other materials including III-V materials, used extensively for mm-wave ICs (MMICs). Specifically, wide band-gap compound semiconductors such as GaN are used increasingly for high power (>10W/mm), high frequency (>100 GHz) applications due to high electron velocity, charge density (1×10^{13} cm^{-2} in AlGaN/GaN), and critical electric field >3 MV/cm. In its Wurtzite crystal structure, GaN also exhibits high piezoelectric coefficients (k_T^2 up to 2%) necessary for low insertion loss, large bandwidth MEMS filters [32, 33].

A. Active HEMT sensing in GaN resonators

To achieve high frequency operation, AlGaN/GaN MEMS resonators in this work are driven piezoelectrically and sensed with a High Electron Mobility Transistor (HEMT). This type of device implements 2D electron gas (2DEG) electrodes, inherent to the AlGaN/GaN heterostructure (Fig. 11(a)). Large spontaneous and piezoelectric polarizations form a sharp potential well confining electrons in a 2D plane just below the interface between AlGaN and GaN [34]. Typical electron densities of the 2DEG are as high as $n_s \sim 1\times10^{13} cm^{-2}$ and the mobility can reach $1500\ cm^2/Vs$. This makes the 2DEG conductive enough to serve as an electrode for piezoelectric transduction, or as the channel for the HEMT (Fig. 11(a),(b)).

These AlGaN/GaN MEMS resonators are driven through the piezoelectric effect by applying an AC voltage between the Schottky metal contact and the 2DEG electrode. When driven into mechanical resonance, the resonance strain affects the charge polarization in AlGaN and GaN, which turns into a change of charge density inside the HEMT channel, translating to an AC modulation of the HEMT drain current. The AlGaN/GaN heterostructure has a unique feature of switchable piezoelectric transduction [35]. A negative DC bias can be used to deplete away the 2DEG. This negative voltage bias can be used to shut off both the driving and sensing transducers, ideal for applications requiring configurable frequency response such as cognitive radio.

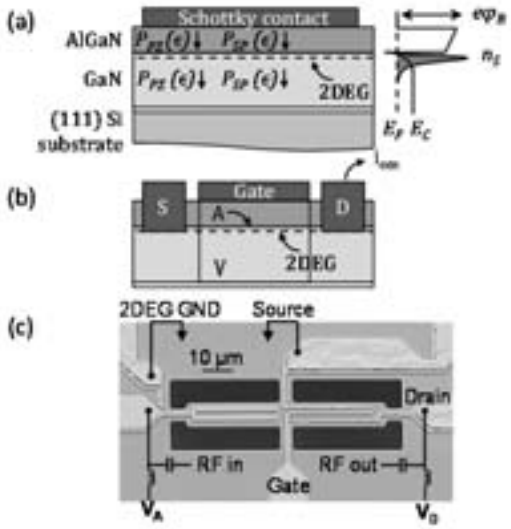

Figure 11. (a) 2DEG confined in conduction band potential well at the interface between AlGaN and GaN. (b) HEMT structure, with Ohmic metal S/D contacts to the 2DEG channel and Schottky metal gate. (c) SEM of piezoelectric-drive, HEMT-sensed 8.7×70 µm resonator. The HEMT has gate length of 1 µm.

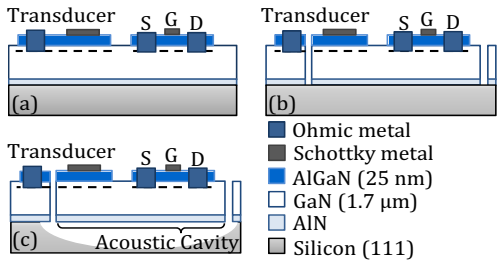

Figure 12. Fabrication involves two additional steps to (a) existing GaN MMIC technology, including (b) adeep GaN etch, and (c) a release step.

Combined with the high power, high frequency capabilities of GaN technology, this AlGaN/GaN MEMS resonator design could enable the integration of high-Q MEMS resonators with millimeter-wave ICs (MMICs) and high power electronics.

B. Small Signal Model

The piezoelectric-drive, HEMT-sensed GaN resonator has the small signal model identical to Fig. 3(b). However, a new expression for mechanical transconductance g_α must be considered due to the different physics contributing to drain current modulation. When driven into acoustic resonance, strain fields defined by the mode shape induce a polarization field through the direct piezoelectric effect in both GaN and AlGaN. The divergence of such polarization generates volume charge ρ throughout the heterostructure. In addition, an interface charge σ is generated by a discontinuity in the polarization at the AlGaN/GaN interface. These charges can be integrated in the region under the gate:

$$Q_{mech} = \iiint \rho dV + \iint \sigma dA \tag{13}$$

This translates into an AC modulation of the drain current:

$$i_{em} = \frac{Q_{mech}}{Q_{channel}} I_D \tag{14}$$

in which I_D and $Q_{channel}$ are the DC drain current and channel charge, respectively. With this expression, the g_α can be calculated through the same expression as (11).

C. Experimental Results

Fabrication of these devices requires only 2 modifications to a standard GaN technology This begins with an AlGaN(25nm)/GaN(1.7μm) stack gown by Molecular Beam Eptaxy on a (111) silicon substrate, using a thin AlN nucleation layer. The growth for the stack was performed at Raytheon and subsequent fabrication was completed at MIT. After steps creating the HEMT and the Schottky contact which are standard in GaN MMIC fabrication [36], two additional steps including a deep GaN etch to define the resonator and a XeF_2 release etch are performed to complete the devices (Fig. 12).

An SEM of the piezoelectric-drive, HEMT-sensed resonator is shown in Fig. 11(c). Fig. 13(a) shows the measured DC behavior of the HEMT embedded in the resonant structure after the XeF_2 release step, with $V_T = -5.75V$.

Using HEMT sensing, resonators up to 3.5 GHz were realized and detected with standard 2-port measurements as shown in Fig. 13(b). The active device is measured in air with 50Ω termination. A resonance at 2.67 GHz is obtained with a Q of 650 in air, with $f{\cdot}Q$ of $1.7{\times}10^{12}$. A COMSOL simulation of the stress distribution of this resonance is shown as an inset in Fig. 13(b), with maximum stress under the gate of the transistor. This translates into an efficient modulation of the

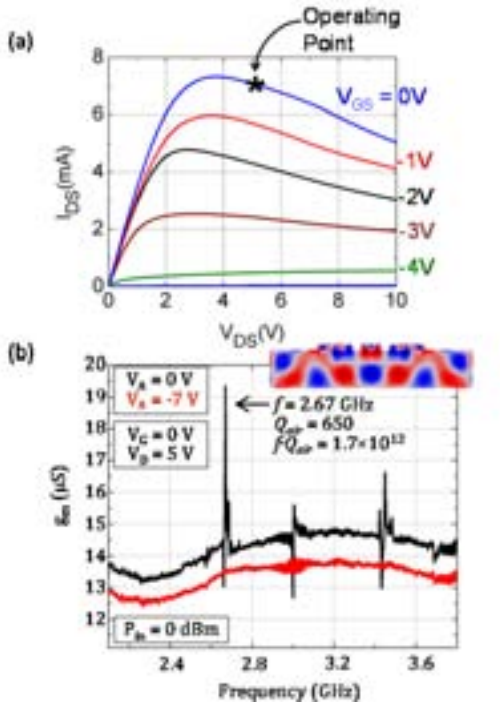

Figure 13. (a) Measured IV curves of the HEMT embedded in resonator after release step. (b) Measured frequency response of PE drive-HEMT sense AlGaN/GaN resonator, in air. The transconductance, $g_m = Y_{21} - Y_{12}$, is suppressed when the 2 DEG under the drive electrode is depleted.

charge density in the channel of the HEMT. The resonance can be suppressed by applying a negative voltage to the drive electrode, depleting the 2DEG and suppressing C_0 by 13×.

VI. Conclusion

The first CMOS-based unreleased RBTs are demonstrated in IBM's 32SOI process with resonance frequencies above 11 GHz, Qs of 24-30 and footprint of less than 5μm×3μm. These devices are fabricated at the transistor level of the CMOS stack and are realized without the need for any post-processing or packaging. CMOS-integrated RBTs are the first step towards realizing on-chip acoustic frequency sources with reduced size, power consumption, and parasitics in wireless communication, navigation and sensing systems.

Comparative analysis and experimental results from multiple resonator designs show the merits of active transduction mechanisms for scaling of resonators to multi-GHz frequencies. Device performance can be further enhanced by characterizing material properties of the CMOS stack and performing 3D geometric optimization. Furthermore, CMOS resonators demonstrate thermal stability under ±3ppm/K due to the complimentary nature of TCE of Si and SiO2. This poses the possibility for TCF manipulation for design of temperature sensors with high TCF or oscillators with sub-ppm/K sensitivity.

Seamless integration into a standard CMOS process obviates the need for complex and costly custom processes for MEMS fabrication. The demonstration of resonators fabricated side-by-side with CMOS circuitry greatly reduces parasitics of off-chip access, constraints of limited IO, and power

consumption associated with impedance matching networks. Such benefits can provide increased system speed and dynamic range, particularly at RF and mm-wave frequencies of operation.

Finally, to meet requirements of high power handling and high transduction efficiency, III-V semiconductors can be selected as an alternative to silicon, still taking advantage of active sensing mechanisms for high frequency. GaN-based MEMS resonators are demonstrated up to 3.5 GHz with a Q of 650 in air, and $f \cdot Q$ of 1.7×10^{12}, potentially enabling the integration of high-Q MEMS resonators with MMICs and high power electronics.

ACKNOWLEDGMENT

CMOS fabrication was made possible by TAPO, DARPA LEAP, and IBM. The authors thank William Hoke and Thomas Kazior at Raytheon for GaN growth. Fabrication of GaN took place at MIT's Microsystems Technology Laboratories and Harvard's Center for Nanoscale Systems.

REFERENCES

[1] H. C. Nathanson, W. E. Newell, R. A. Wickstrom, and J. R. Davis Jr, "The resonant gate transistor," IEEE Transactions on Electron Devices, vol. 14, pp. 117-133, 1967.

[2] S. Bartsch, D. Grogg, A. Lovera, D. Tsamados, and A. Ionescu, "Very high frequency double-ended tuning fork nano-mechanical Fin-FET resonator," Transducers 2011, pp. 938-941.

[3] M. Faucher, *et al.*, "GaN: A multifunctional material enabling MEMS resonators based on amplified piezoelectric detection," FCS 2011, pp. 1-5.

[4] A. Rahafrooz and S. Pourkamali, "High-frequency thermally actuated electromechanical resonators with piezoresistive readout," IEEE Transactions on Electron Devices, vol. 58, pp. 1205-1214, 2011.

[5] D. Weinstein and S. A. Bhave, "The resonant body transistor," Nano letters, vol. 10, pp. 1234-1237, 2010.

[6] D. Weinstein and S. A. Bhave, "Acoustic resonance in an independent-gate FinFET," Hilton Head 2010, pp. 459-462.

[7] G. K. Fedder, R. T. Howe, T.-J. K. Liu, and E. P. Quevy, "Technologies for cofabricating MEMS and electronics," Proceedings of the IEEE, vol. 96, pp. 306-322, 2008.

[8] H. Xie, L. Erdmann, X. Zhu, K. J. Gabriel, and G. K. Fedder, "Post-CMOS processing for high-aspect-ratio integrated silicon microstructures," JMEMS, vol. 11, pp. 93-101, 2002.

[9] W.-C. Chen, *et al.*, "A generalized foundry CMOS platform for capacitively-transduced resonators monolithically integrated with amplifiers," MEMS 2010, pp. 204-207.

[10] M. Lutz, *et al.*, "MEMS oscillators for high volume commercial applications," Transducers 2007, pp. 49-52.

[11] M. Small, *et al.*, "Wafer-scale packaging for FBAR-based oscillators," FCS 2011, pp. 1-4.

[12] W. Newell, "Face-mounted piezoelectric resonators," Proceedings of the IEEE, vol. 53, pp. 575-581, 1965.

[13] K. Lakin, "Thin film resonators and filters," Ultrasonics Symposium 1999, pp. 895-906.

[14] R. H. Olsson, J. G. Fleming, and M. R. Tuck, "Contour mode resonators with acoustic reflectors," ed: Google Patents, 2008.

[15] S. Mohammadi, A. A. Eftekhar, W. D. Hunt, and A. Adibi, "High-Q micromechanical resonators in a two-dimensional phononic crystal slab," Applied Physics Letters, vol. 94, pp. 051906-051906-3, 2009.

[16] R. Olsson Iii and I. El-Kady, "Microfabricated phononic crystal devices and applications," Measurement Science and Technology, vol. 20, p. 012002, 2009.

[17] V. Karagodsky, F. G. Sedgwick, and C. J. Chang-Hasnain, "Theoretical analysis of subwavelength high contrast grating reflectors," Optics Express, vol. 18, pp. 16973-16988, 2010.

[18] C.-C. Nguyen, "MEMS-based RF channel selection for true software-defined cognitive radio and low-power sensor communications," IEEE Communications Magazine, vol. 51, pp. 110-119, 2013.

[19] H. Saito, T. Noguchi, and K. Inoue, "Film bulk acoustic wave resonator," ed: Google Patents, 2007.

[20] Y. Ebata, "Surface acoustic wave resonator," ed: Google Patents, 1987.

[21] S. A. Bhave and R. T. Howe, "Silicon nitride-on-silicon bar resonator using internal electrostatic transduction," Transducers 2005, pp. 2139-2142.

[22] W. Wang and D. Weinstein, "Acoustic Bragg reflectors for Q-enhancement of unreleased MEMS resonators," FCS 2011, pp. 1-6.

[23] W. Wang and D. Weinstein, "Deep Trench capacitor drive of a 3.3 GHz unreleased Si MEMS resonator," IEDM 2012, pp. 15.1. 1-15.1. 4.

[24] G. Wang, *et al.*, "Scaling deep trench based eDRAM on SOI to 32nm and Beyond," IEDM 2009, pp. 1-4.

[25] D. Weinstein and S. A. Bhave, "Internal dielectric transduction in bulk-mode resonators," JMEMS, vol. 18, pp. 1401-1408, 2009.

[26] P. S. J. Russell, "Photonic-crystal fibers," Journal of lightwave technology, vol. 24, pp. 4729-4749, 2006.

[27] K. Vahala, Optical microcavities: World Scientific, 2004.

[28] R. Marathe, W. Wang, and D. Weinstein, "Si-based unreleased hybrid MEMS-CMOS resonators in 32nm technology," MEMS 2012, pp. 729-732.

[29] V. Kaajakari, A. T. Alastalo, and T. Mattila, "Electrostatic transducers for micromechanical resonators: Free space and solid dielectric," IEEE Transactions on Ultrasonics, Ferroelectrics and Frequency Control, vol. 53, pp. 2484-2489, 2006.

[30] A. Grill, "Porous pSiCOH ultralow-k dielectrics for chip interconnects prepared by PECVD," Annual Review of Materials Research, vol. 39, pp. 49-69, 2009.

[31] R. Melamud, *et al.*, "Temperature-insensitive composite micromechanical resonators," JMEMS, vol. 18, pp. 1409-1419, 2009.

[32] A. Ansari, V. J. Gokhale, J. Roberts, and M. Rais-Zadeh, "Monolithic integration of GaN-based micromechanical resonators and HEMTs for timing applications," IEDM 2012, pp. 15.5. 1-15.5. 4.

[33] M. Faucher, *et al.*, "Amplified piezoelectric transduction of nanoscale motion in gallium nitride electromechanical resonators," Applied Physics Letters, vol. 94, pp. 233506-233506-3, 2009.

[34] O. Ambacher, *et al.*, "Two-dimensional electron gases induced by spontaneous and piezoelectric polarization charges in N-and Ga-face AlGaN/GaN heterostructures," J Appl Phys, vol. 85, pp. 3222-3233, 1999.

[35] L. C. Popa and D. Weinstein, "Switchable Piezoelectric Transduction in AlGaN/GaN MEMS Resonators," Transducers 2013, pp. 2461-2464.

[36] T. Kazior, *et al.*, "High performance mixed signal and RF circuits enabled by the direct monolithic heterogeneous integration of GaN HEMTs and Si CMOS on a silicon substrate," 2011 IEEE Compound Semiconductor Integrated Circuit Symposium (CSICS), pp. 1-4.

Enhanced Temperature Sensitivity of a Single CMOS-MEMS Resonator via Resonant Modes in Orthogonal Axes

Ming-Huang Li[1], Chao-Yu Chen[1], Cheng-Syun Li[1], Chi-Hang Chin[1], and Sheng-Shian Li[1,2]
[1]Institute of NanoEngineering and MicroSystems, [2]Department of Power Mechanical Engineering
National Tsing Hua University
Hsinchu 30013, Taiwan
Email: ssli@mx.nthu.edu.tw

***Abstract*—A novel CMOS-MEMS composite ring resonator capable of a dual-mode operation has been proposed to enable self-temperature sensing in a single device. To maximize the temperature sensitivity between the dual modes, two resonant modes of a single resonator vibrating in orthogonal axes (i.e., in-plane and out-of-plane) are chosen due to the large difference of their temperature coefficients of frequency (TC_f's). By adjusting the constituent ratio and the position of metals and dielectrics through CAD layouts, different TC_f's have been successfully demonstrated in a single CMOS-MEMS resonator. By measuring the TC_f's of the in-plane (INP) and out-of-plane (OOP) mode concurrently, a beat frequency with a temperature coefficient of 72 ppm/°C was characterized. By employing a divider-based scaling concept, an estimated maximum beat frequency sensitivity of 3,244 ppm/°C can be obtained under proper scaling numbers.**

Keywords—CMOS-MEMS, dual-mode, beat frequency, resonators, back-end of line (BEOL)

I. Introduction

Temperature sensors are critical building blocks in modern electronic circuits for SOC power management [1] or environmental temperature monitoring [2] applications. Conventional CMOS-based temperature sensors are based on many different sensing schemes, including BJT-based PTAT [2], thermal diffusivity [3], and temperature dependent inverter-delay [4]. However, these complex circuits suffer the process variations in advanced technology nodes, leading to a large sensing inaccuracy. Individual calibration and trimming process can improve their sensing accuracy but would introduce extra cost. On the other hand, MEMS resonator has a strong potential to deliver better sensing accuracy due to its large temperature coefficient of frequency (TC_f), hence offering an alternative way for temperature sensing. In addition, advanced CMOS technology nodes provide more precise line width control in lithography and etching processes, hence reducing the process variation for CMOS-MEMS resonant type temperature sensors [5].

To address the aforementioned issue, many integrated MEMS resonator systems with large TC_f's were developed in standard CMOS technologies [6][7]. The metal-alloy (AlCu) and oxide (SiO_2) layers in the CMOS back-end-of-line (BEOL) process have negative and positive temperature coefficient of elastic modulus (TC_E), respectively, that provides an advantageous feature for designing the proper TC_f. By engineering the constituent ratio of these materials, various resonators with different temperature coefficients of frequency can be implemented on a single chip.

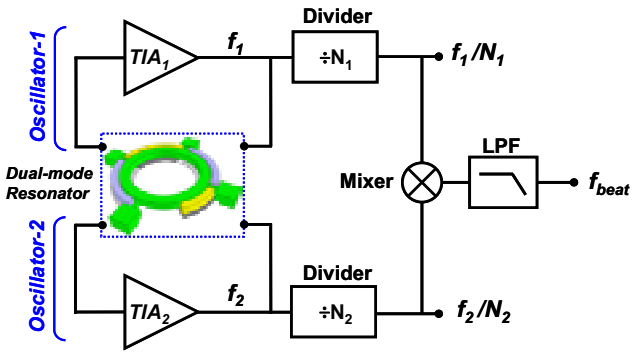

Fig. 1: Conceptual figure of a CMOS-MEMS temperature sensor when dual-mode MEMS resonator is employed.

In this work, we proposed a ring-shaped dual-mode CMOS-MEMS resonator which offers different TC_f's in a single device suited for temperature sensing. To generate the beat frequency that is sensitive to the environmental temperature change [8], a potential system configuration was proposed in Fig. 1 where two transimpedance amplifiers are connected to the corresponding electrodes to enable dual-mode oscillation. Two frequency dividers follow each oscillator loop to allow frequency scaling that provides a great flexibility for beat frequency generation. The temperature information can be deduced from the beat frequency, which is defined by

$$f_{beat} = \frac{f_1}{N_1} - \frac{f_2}{N_2} \quad (1)$$

where f_1 and f_2 are the oscillation frequencies, and N_1 and N_2 are the divider ratios, respectively. Notably, the proof-concept device was designed in a TSMC 0.35μm CMOS platform, but the design concepts and fabrication methods are compatible to advanced technology nodes, such as 90nm or 65nm process.

This work was supported by the National Science Council (NSC) of Taiwan.

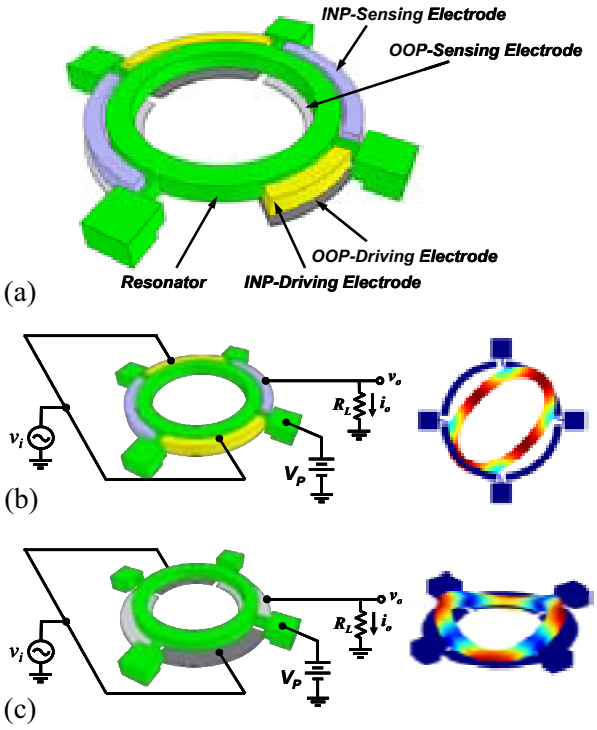

Fig. 2: Perspective-view schematics and mode shapes of a dual-mode CMOS-MEMS ring resonator. (a) Electrode configurations of the resonator that can be used to excite the (b) in-plane mode and (c) out-of-plane mode simultaneously.

II. Dual-mode Resonator Design

The perspective-view of the proposed resonator is shown in Fig. 2(a). The resonator is supported by four supporting tethers at shared in-plane and out-of-plane vibrating nodal points to enable high *Q* and eliminate the effects of thermal stress. To feature dual-mode operation, the resonator is surrounded by its in-plane and out-of-plane electrodes. Fig. 2(b) and (c) provide the electrical configurations for exciting the in-plane mode (INP) and out-of-plane mode (OOP), respectively. The vibrating mode shapes of the INP and OOP mode are also shown in Fig. 2(b) and (c).

To design the corresponding TC_f of each mode (INP and OOP), the vibration frequency of the composite MEMS resonator with laminated structural materials can be expresses as

$$f_{INP}(T) = \frac{2.683}{2\pi R^2}\sqrt{\frac{\sum E_i I_i(T)}{\sum \rho_i A_i(T)}} \tag{2}$$

$$f_{OOP}(T) = \frac{6}{2\pi R^2}\sqrt{\frac{\sum E_i I_i(T)}{\sum \rho_i A_i(T)\left(4+\frac{\sum E_i I_i(T)}{G_{eq}C(T)}\right)}} \tag{3}$$

where *R* is the radius of the ring; *C* is the torsion constant; G_{eq} is the equivalent shear modulus; and E_iI_i and ρ_iA_i are the bending stiffness and unit mass per area of the *i*-th material of the resonator, respectively [9]. The AlCu metal layers have a negative TC_E of -620 ppm/°C [10] while the oxide layers have a positive TC_E of +180 ppm/°C [11]. The interconnects between metals (i.e., VIAs) are made by tungsten (W), providing a negative TC_E of only -6 ppm/°C [12]. By adjusting the constituent ratio and the position of metals and dielectrics through the CAD layouts, different TC_f's have been successfully demonstrated in a single CMOS-MEMS resonator. The linear TC_f of each mode can be obtained by taking a derivative of equation (2) and (3) at a specific temperature point, given by

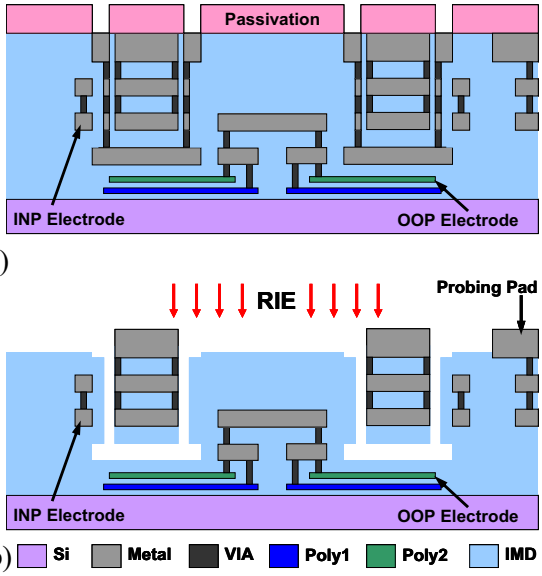

Fig. 3: Post-CMOS process. (a) Unreleased CMOS chip prepared by the foundry. (b) Metal etching and RIE pad opening.

$$TC_f = \frac{1}{f(T_o)}\left(\frac{\partial f(T)}{\partial T}\right)_{T_o} \tag{4}$$

where *f(T)* is a general frequency equation. From (2)-(4), the estimated TC_f's of the INP and OOP mode of the dual-mode resonator is -51ppm/°C and -92ppm/°C, respectively.

III. Post-CMOS Fabrication Process

To fabricate the proposed MEMS resonator, a previous-developed metal wet-etching process was adopted to release the resonator [7] due to its excellent selectivity between metal and oxide. Fig. 3(a) shows the cross-sectional view of a CMOS chip prepared by the foundry. Part of the passivation layers are removed from the top to define the resonator shape where the sacrificial metals are exposed to the environment. The metal etchant composed of sulfuric acid (H_2SO_4) and hydrogen peroxide (H_2O_2) was utilized to remove the sacrificial metals (AlCu and W-VIA), where the sulfuric acid is the etchant and hydrogen peroxide is the catalyst. An additional reactive ion etching (RIE) process was applied for opening the bond-pad areas, as shown in Fig. 3(b).

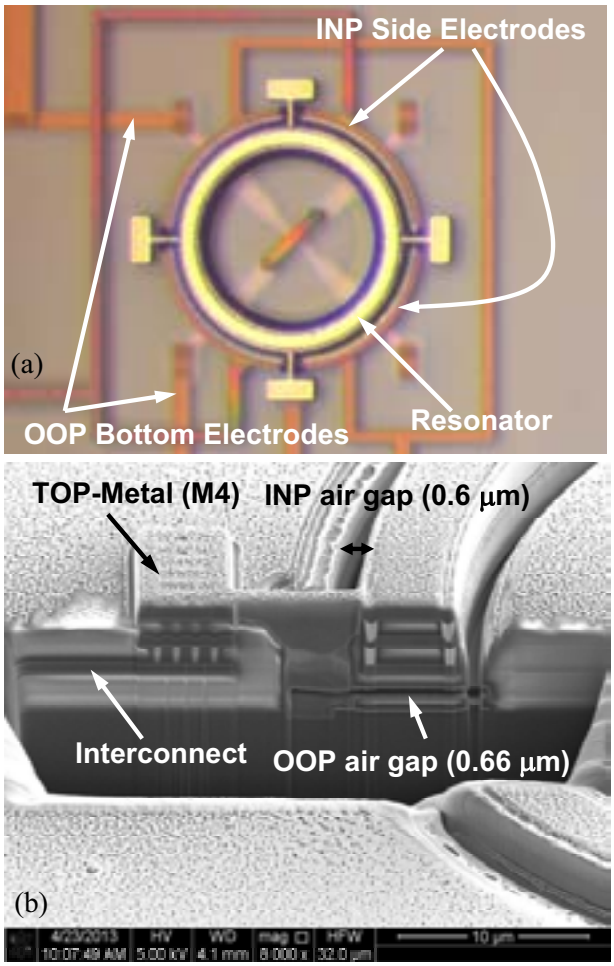

Fig. 4: (a) Optical image of the ring resonator. Electrical routings are identified. (b) SEM image of a focused-ion-beam (FIB) cut view of the resonator.

Fig. 4(a) is the optical view of the fabricated CMOS-MEMS resonator where the detailed electrical routings are identified. Fig. 4(b) is the FIB-cut cross-sectional view of the fabricated resonator, showing the laminated structural layers. The tungsten-VIAs were laid out at the edge of the ring to increase the in-plane driving and sensing transducer areas. The in-plane and out-of-plane gap spacing are around 0.6μm and 0.66μm, respectively.

IV. Characterization Results

The CMOS-MEMS resonator was placed in a cryogenic vacuum probe station and the resonance response was characterized by a vector network analyzer. The resonator is electrostatically actuated and capacitively sensed in a typical two-port configuration. By arranging the probes, the resonance spectra of both INP and OOP modes can be characterized. The output sensing electrode was connected to a transimpedance amplifier (TIA) ASIC to convert the output current into voltage for improving the signal-to-noise ratio. Fig. 5 presents the

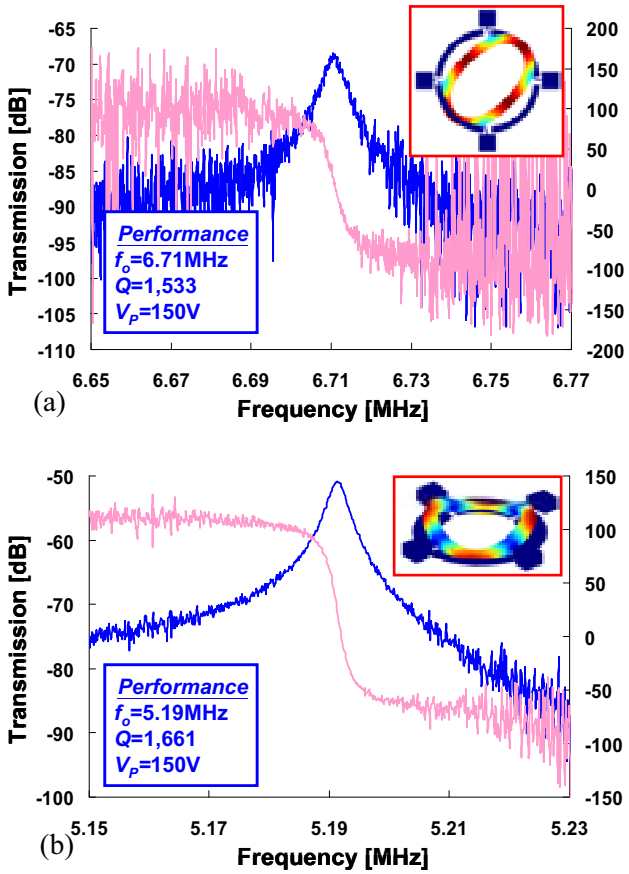

Fig. 5: Measured frequency spectra of the (a) in-plane vibration mode and (b) out-of-plane vibration mode for the dual-mode CMOS-MEMS resonator.

measured frequency responses for the dual-mode resonator. The INP mode of the resonator has a resonance frequency of 6.71MHz with a quality factor Q of 1,533 (cf. Fig. 5(a)) while the OOP mode of the resonator has a resonance frequency of 5.19MHz with a quality factor Q of 1,661 (cf. Fig. 5(b)]. The frequency responses were characterized at room temperature.

To understand the temperature sensitivity and cross-axis interference of the dual-mode operation, one pair of the side electrodes and bottom electrodes are connected together to drive the resonator into their INP and OOP modes simultaneously. Under such a experimental setup, the measured thermal responses are shown in Fig. 6(a). The TC_f of the INP mode is -57ppm/°C and that of the OOP mode is -95ppm/°C, respectively. The measured TC_f's are in good agreement with the calculated values. By adapting (1) with N_1=N_2=1 (i.e., no divider is used), an estimated beat frequency (f_{beat}) of 1.524MHz with a TC_{fb} of +72ppm/°C was obtained. However, by properly choosing N_1=N_{OOP}=50 and N_2=N_{INP}=64, an estimated maximum beat frequency sensitivity of +3,244ppm/°C can be obtained by a liner curve fit (f_{beat} = 1.192kHz @-23°C), as shown in Fig. 6(b). In a sense, the temperature sensitivity of the beat frequency could be flexibly tuned by the divider ratio.

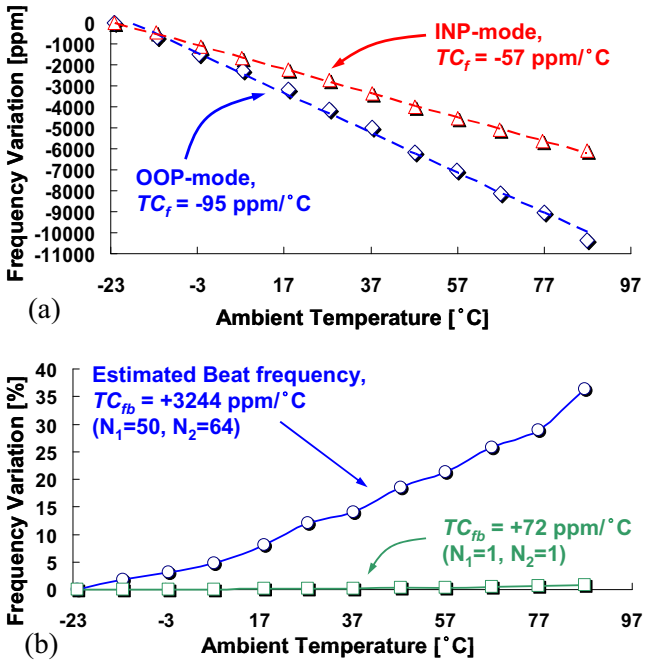

Fig. 6: (a) Measured TC_f's of the dual-mode resonator. (b) Estimated raw TC_{fb} (N_1=N_2=1) and best-case TC_{fb} (N_1=N_{OOP}=50, N_2=N_{INP}=64) with proper scaling numbers

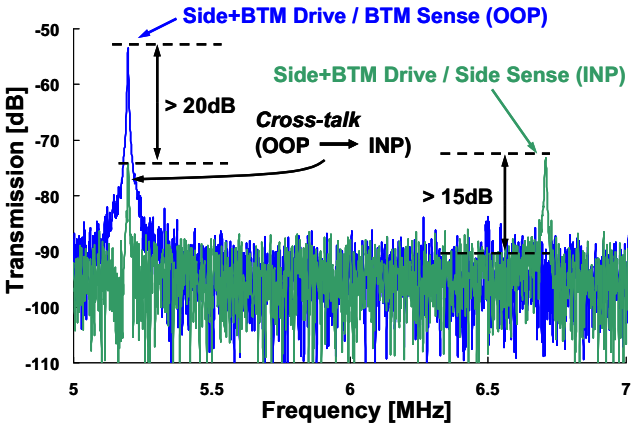

Fig. 7: Measured cross-axis sensitivity of the dual-mode CMOS-MEMS resonator.

Finally, the cross-axis sensitivity was characterized. For a dual-mode resonator via its vibration modes in orthogonal axes, the signal isolation from one axis to the other should be maximized. To characterize this sensitivity, the driving signal was applied on the side (in-plane) and bottom (out-of-plane) excitation electrodes simultaneously and the sensing signal was picked up from the side or the bottom electrodes separately. The measurement result is shown in Fig. 7, where the blue curve (5.2MHz, -53dB) was picked up from the bottom electrode and the green curve (6.7MHz, -73dB) was observed from the side electrode. In conclusion, the measured cross-axis sensitivity at least -15dB (i.e., the cross-talk signal is attenuated by 15dB) was characterized in this prototype device.

V. Conclusion

In this work, a prototype CMOS-MEMS dual-mode ring resonator was designed, fabricated, and fully characterized using a 0.35μm CMOS process. The design concept and fabrication process is compatible with advanced CMOS technology nodes. A TC_f difference of 38 ppm/°C between modes was achieved in this prototype, which is the largest difference compared to other MEMS dual-mode resonators to date. To enhance the temperature sensitivity, a potential system configuration was also proposed in this work based on a divider-based circuit. Although the dual-mode CMOS-MEMS resonator was characterized under a open-loop condition, the practical system implementation will be carried out in future.

Acknowledgment

This research was sponsored by the National Science Council of Taiwan (NSC-101-2221-E-007-100-MY3). The authors appreciate the TSMC and the Chip Implementation Center (CIC), Taiwan, for supporting IC fabrication and CAD tools. The authors would like to thank the Center for Nanotechnology, Materials Science and Microsystems (CNMM) of National Tsing Hua University for the use of fabrication and measurement facilities.

References

[1] H. Lakdawala, *et al.*, "A 1.05V 1.6mW, 0.45°C 3σ Resolution ΣΔ Based Temperature Sensor with Parasitic Resistance Compensation in 32nm Digital CMOS Process," *IEEE J. Solid-State Circuits*, vol. 44, no. 12, pp. 3621–3630, Dec. 2009.

[2] K. Souri, *et al.*, "A 0.12mm^2 7.4μW Micropower Temperature Sensor With an Inaccuracy of ±0.2°C (3σ) From -30°C to 125°C," *IEEE J. Solid-State Circuits*, vol. 46, no. 7, pp. 1693–1700, July 2011.

[3] C. P. L. von Vroonhoven, *et al.*, "An SOI thermal-diffusivity-based temperature sensor with ±0.6°C (3σ) untrimmed inaccuracy from −70°C to 170°C," *Dig. Transducers 2011*, pp. 2887-2890, June 2011.

[4] P. Chen, *et al.*, "A time-to-digital-converter-based CMOS smart temperature sensor," *IEEE J. Solid-State Circuits*, vol. 40, no. 8, pp. 1642–1648, Aug. 2005.

[5] R. Mahameed, *et al.*, "Fully Monolithic MEMS Based Thermal Sensor in 22nm CMOS Technology for SOC Thermal Management," *Dig. Transducers 2013*, pp. 734-737, June 2011.

[6] C.-S. Li, *et al.*, "Advanced CMOS-MEMS resonator platform," *IEEE Electron Device Lett.*, vol. 33, no. 2, pp. 272-274, Feb. 2012.

[7] W.-C. Chen, *et al.*, "A fully-differential CMOS-MEMS DETF oxide resonator with Q > 4,800 and Positive TCF," *IEEE Electron Device Lett.*, vol. 33, no. 5, pp. 721-723, May 2012.

[8] C. M. Jha, *et al.*, "High Resolution Microresonator-based Digital Temperature Sensor," *Appl. Phys. Lett.,* 91, 074101 (2007).

[9] S. S. Rao, Vibration of Continuous Systems, Hoboken, NJ: John Wiley & Sons, 2007.

[10] C.-C. Lo, "CMOS-MEMS Resonators for Mixer-Filter Applications," *Ph.D. Dissertation*, Carnegie Mellon University, 2008.

[11] R. Melamud, *et al.*, "Temperature-InsensistiveComposite Micromechanical Resonators," *IEEE/ASME J. Microelectromech. Syst.*, vol. 18, no. 6, pp. 1409-1419, Dec. 2008.

[12] G. P. Škoro, *et al.*, "Dynamic Young's moduli of tungsten and tantalum at high temperature and stress," *Journal of Nuclear Materials*, 409, 40 (2011).

Stress-Enhanced Chemical Vapor Deposited Graphene NEMS RF Resonators

Michael Lekas*, Sunwoo Lee*, Changyao Chen†,Wu-Joon Cha†, Karthik Ayyagari†,
James Hone†, and Kenneth Shepard*
*Department of Electrical Engineering, Columbia University in the city of New York, USA
†Department of Mechanical Engineering, Columbia University in the city of New York, USA

***Abstract*—In this work we present room-temperature measurements of graphene nanoelectromechanical resonators (GNERs) demonstrating quality factors (Qs) greater than 200 at resonance. A nominal resonant frequency (f_o) of 200 MHz is attained by applying strain to the suspended graphene using an SU-8 polymer clamp. Additionally, the device f_o can be tuned by more than 5% by application of a DC gate bias on the order of 5V. Chemical vapor deposited (CVD) graphene is used to demonstrate the scalability of the process.**

I. Introduction

Graphene has received much attention owing to its exceptional electrical and mechanical properties [1], [2]. For electronic applications, graphene has been considered as a potential channel material for RF field-effect transistors (FETs) due to its high carrier mobility, saturation velocity, and current carrying capacity [3], [4]. In nano-mechanics research, graphene has been used to construct RF mechanical resonators [5], [6], [7], which take advantage of its high tensile strength,high stiffness, and low mass.

It was recently demonstrated that a graphene nanoelectromechanical resonators (GNER) can be operated as a mechanically resonant FETs to improve transduction [6], [7]. In this configuration, shown in Fig. 1, a sheet of graphene is suspended over a local metal gate electrode, and a drain-source bias (V_{ds}) is applied across the graphene. By applying both a DC voltage and an RF signal to the gate, mechanical vibrations are actuated in the graphene. Motion of the graphene relative to the gate induces a capacitive displacement current in the device (similar to that seen passive MEMS devices), as well as a current due to the field-effect modulation of channel charge. By means of this second current component, the mechanical resonance signal is sensed and amplified by the transconductance (g_m) of the graphene FET structure.

This active sensing technique creates the possibility of using graphene NEMS resonators in RF circuits such as filters and oscillators [8]. Active sensing may be especially beneficial in filtering applications since it may be used to reduce insertion loss (IL), a parameter that is especially important for maintaining an acceptable receiver noise figure.

Nonetheless, there are still obstacles to implementing GNERs in these applications, including process scalability concerns, low quality factors (Q) at room temperature, and low resonance frequencies (f_o). In this work we present measurements on GNERs that address these problems by employing a stress-enhanced design to boost f_o, and chemical vapor deposited (CVD) graphene to demonstrate the potential for wafer-level fabrication.

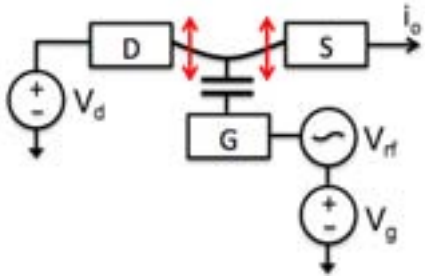

Fig. 1. Diagram showing operation of GNER.

II. Experiment

The process used to fabricate GNERs is described in detail elsewhere [9], but will be briefly outlined here. To begin, metal gates are patterned on fused silica substrates using deep-UV lithography. A layer of silicon dioxide (SiO_2) is deposited on top of the gates using plasma-enhanced chemical vapor deposition (PECVD). To improve adhesion and reduce potential wrinkling of the graphene, the oxide is chemical-mechanical polished (CMP) to reduce its roughness below 0.5 nm. CVD grown graphene is then transferred to the substrate using the technique outlined in [9].

Device channels are patterned in the graphene using electron beam lithography (EBL) and an oxygen plasma etch. Source and drain electrodes (1/15/50 nm of Ti/Pd/Au) are then patterned using EBL, and an SU-8 polymer clamp is patterned on top of the graphene in order to clamp the graphene in the shape of a drum. The sample is then hardbaked at 170C, causing the SU-8 clamp to contract and apply strain to the graphene. The devices in this work employ clamps with a circular geometry rather than a doubly-clamped structure. We find that this improves the uniformity of the strain applied to the graphene, and also serves to suppress higher-order modes that often arise in doubly clamped structures, which may adversely affect Q.

In the final fabrication step, the device is immersed in buffered oxide etchant and dried in a critical point dryer to remove the sacrificial oxide under the graphene channel and suspend the device. A scanning electron microscope (SEM) image of a finished device is shown in Fig. 2.

All measurements are conducted at room temperature in a

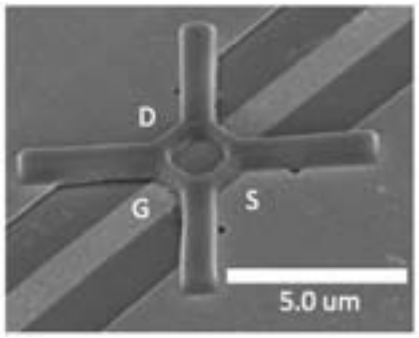

Fig. 2. SEM image of GNER.

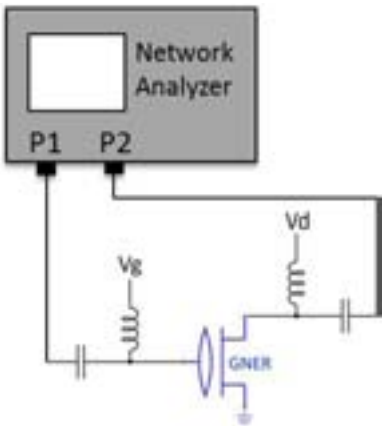

Fig. 3. RF measurement setup: gate and drain DC biases are applied through bias-T's. The input and output ports art P1 and P2, respectively.

Desert Cryogenics probe station at pressures lower than 10^{-6} torr. DC measurements are performed using an Agilent 4155c Semiconductor Parameter Analyzer. RF measurements were performed with the setup shown in Fig. 3, using an Agilent N5230A Network Analyzer.

III. Results and Discussion

Fig. 4 shows a measurement of drain current (I_{ds}) as a function of the DC gate-to-source bias (V_{gs}) for a GNER measured with a constant V_{ds}. The clamp geometry for this device is a 1.5-μm-diameter circular drum, and the graphene channel width and length underneath the clamp are 3-μm and 1.5-μm, respectively. The gate-to-channel spacing for this device is approximately 70 nm. A field-effect mobility (μ_{fe}) of 300 cm^2/V-s is calculated from these current-voltage measurements, which while lower than other data on CVD graphene samples which show mobilities as high as 40,000 cm^2/V-s [10], is sufficient to achieve g_m in excess of 15 μS. The lower mobility achieved here is most likely due to contamination of the graphene channel material during the more involved fabrication process to achieve these structures.

Fig. 5(a) shows a plot of the S_{21} magnitude for the same GNER as a function V_{gs} and frequency. Increasing V_{gs} increases the electrostatic force on the graphene, which induces additional strain in the membrane, causing f_o of the device to shift from approximately 201 MHz at 0 V to 198 MHz at 4 V. The reduction in f_o at higher V_{gs} is due to a spring softening effect that has been observed in many nanomechanical devices

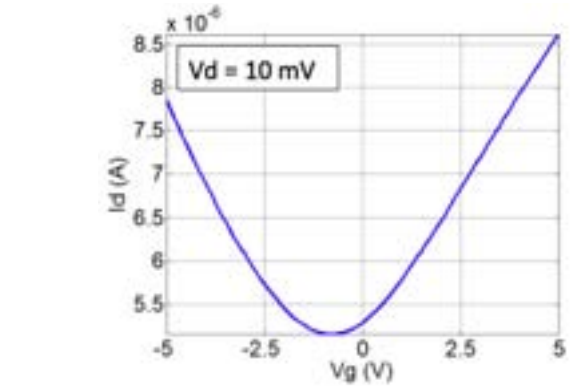

Fig. 4. Low-field transport measurement.

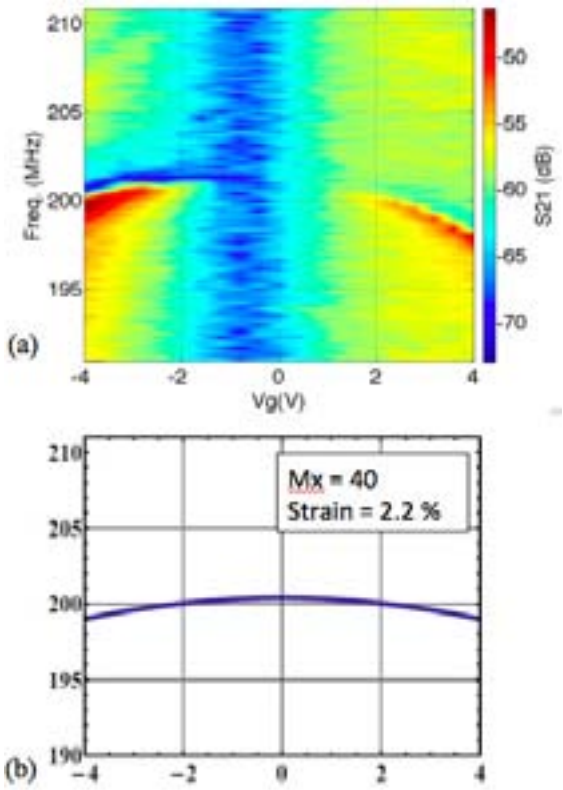

Fig. 5. (a) S_{21} magnitude as a function of frequency and V_{gs}. (b) Fitting of the resonant frequency tuning characteristic, used to extract resonator mass and strain.

[11]. Using the mechanical model for a circular membrane resonator given in [12], the tuning characteristic of fo can be modelled, as shown in Fig. 5(b), and the mass and built-in strain of the graphene can be determined. These models yield a mass of approximately 40 times that of intrinsic graphene, and a strain of 2.2%. This mass enhancement is attributed to the same contamination to which we ascribe the mobility reduction.

The small signal electrical model for the device is shown

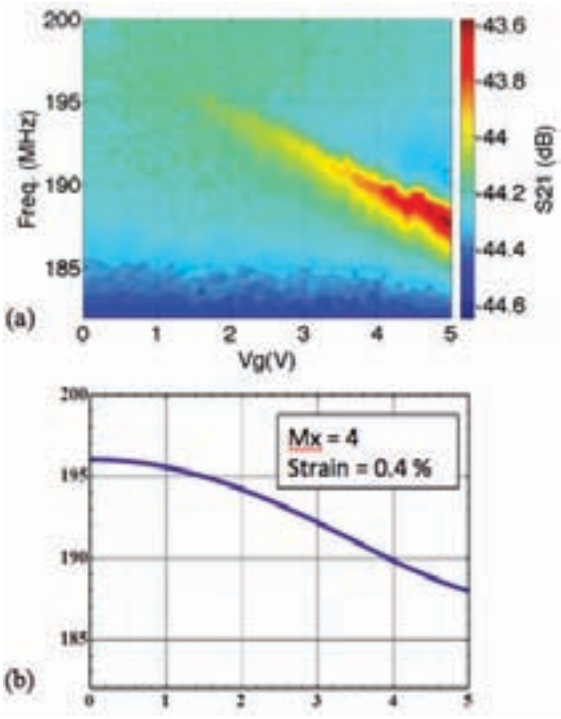

Fig. 6. S_{21} magnitude as a function of frequency and V_{gs}, which demonstrates a greater tuning range due to lower built-in stress from the SU-8 clamp.

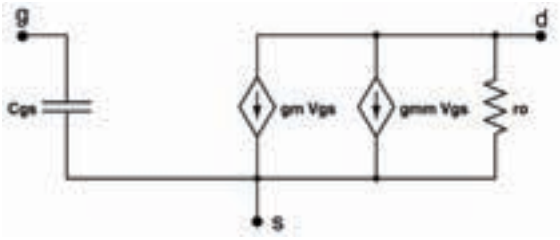

Fig. 7. Small signal electrical model for a GNER.

in Fig. 7. The small signal output current is given by

$$I_d = j\omega C_{tot}\tilde{V}_{gs} - j\omega\frac{\tilde{z}}{z_0}C_g V_{gs} + V_{ds}\frac{dG}{dV_{gs}}\tilde{V}_{gs} - V_{ds}\frac{dG}{dV_{gs}}\frac{\tilde{z}}{z_0}V_{gs} \quad (1)$$

$$\tilde{z} = -\frac{1}{m}\frac{C_g}{z_0}V_g\frac{1}{\omega_0^2 - \omega^2 + \frac{j\omega_0\omega}{Q}}\tilde{V_{gs}} \quad (2)$$

$$g_m = V_{ds}\frac{dG}{dV_{gs}} \quad (3)$$

where C_{tot} is the total capacitance of the device, $\tilde{V}_{gs}$ is the RF voltage amplitude, $\tilde{z}$ is the resonator displacement amplitude, $\tilde{z_0}$ is the average gate to channel distance, C_g is the gate capacitance, m is the resonator mass, and G is the graphene conductance.

The first two terms in this equation are the feedthrough current and the mechanical displacement current seen in traditional passive MEMS devices [7]. The third term is identical

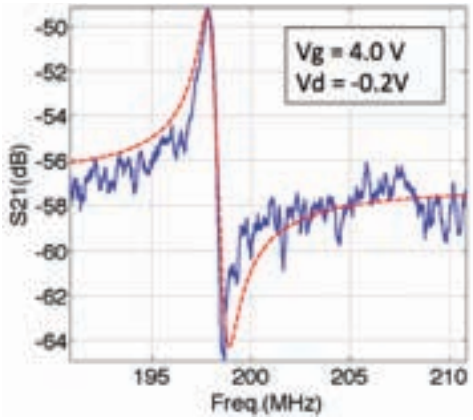

Fig. 8. S_{21} with model fit for a single bias point.

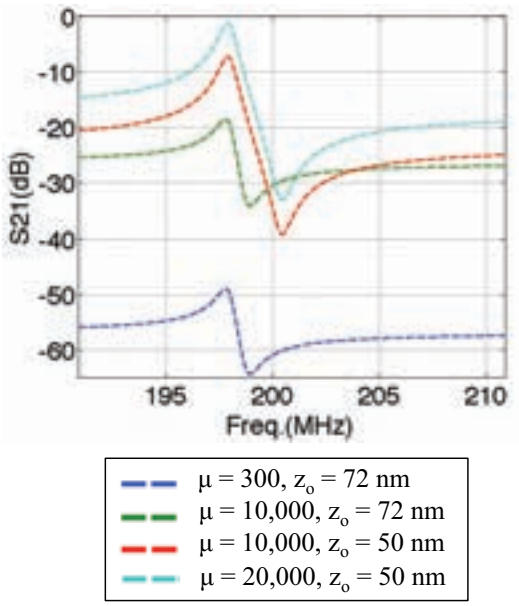

Fig. 9. Projected improvement of GNERs. The bottom trace is identical to the fit in Fig. 8. The other traces are for devices with identical lateral dimensions, but with improved mobility and lower z_0.

to the output current of a typical FET. The fourth term is due to the mechanical motion of the membrane being amplified by the device g_m. Using the extracted mass of the device from Fig 5, and the output current terms given in (4), the S_{21} of the device can be modelled as shown in Fig. 8. This device has a Q of 250 at an f_o of 197.8 MHz. The discrepancy in the model is probably due to capacitive parasitics not accounted for in the model, and spatial nonuniformity in the strain being applied to the graphene.

Fig. 9 shows projections for improved GNER transduction with decreasing z_0, and higher material quality which is reflected in increased μ_{fe}. The bottom trace in the figure is the same fit from Fig. 8. The additional traces are model simulations showing that as mobility is increased to 20,000 cm^2/V-s and z_0 is decreased to 50 nm, the same device may exhibit an IL approaching 0 dB. This IL would make GNERs competitive with existing resonator technologies such as film bulk acoustic resonators (FBARs).

IV. Conclusion

In this work we have shown that the room-temperature Q and f_o of GNERs can be improved by applying additional strain to the graphene membrane using an SU-8 clamp. A small-signal model is presented based on both the electrical and mechanical parameters of the device which shows good agreement with measured data. Although the electrical transport of the graphene used in this study is reduced due to contamination in the fabrication process, projections of resonator performance with improved material quality for a device with similar geometry indicate that GNERs may have IL values that are very comparable with other resonator technologies such as FBARs.

Acknowledgment

The authors like to thank Arend M. van der Zande, Nicholas Petrone, Victor Abramsky, Eugene Hwang, and Changhyuk Lee for critical discussions. Fabrication was performed at the Cornell Nano-Scale Facility, a member of the National Nanotechnology Infrastructure Network, which is supported by the National Science Foundation (Grant ECS-0335765), and Center for Engineering and Physical Science Research (CEPSR) Clean Room at Columba University. The authors acknowledge the support by Qualcomm Innovation Fellowship (QInF) 2012 and AFOSR MURI FA9550-09-1-0705.

References

[1] K. S. Novoselov, A. K. Geim, S. V. Morozov, D. Jiang, Y. Zhang, S. V. Dubonos, I. V. Grigorieva, and A. A. Firsov, "Electric field effect in atomically thin carbon films," *Science*, vol. 306, no. 5696, pp. 666–669, 2004.

[2] C. Lee, X. Wei, J. W. Kysar, and J. Hone, "Measurement of the elastic properties and intrinsic strength of monolayer graphene," *Science*, vol. 321, no. 5887, pp. 385–388, 2008.

[3] I. Meric, M. Y. Han, A. F. Young, B. Ozyilmaz, P. Kim, and K. L. Shepard, "Current saturation in zero-bandgap, top-gated graphene field-effect transistors," *Nature Nanotech.*, vol. 3, no. 11, pp. 654–659, 2008.

[4] C. R. Dean, A. F. Young, I. Meric, C. Lee, L. Wang, S. Sorgenfrei, K. Watanabe, T. Taniguchi, P. Kim, K. L. Shepard, and J. Hone, "Boron nitride substrates for high-quality graphene electronics," *Nature Nanotechnology*, vol. 5, no. 10, pp. 722–726, 2010.

[5] J. S. Bunch, A. M. van der Zande, S. S. Verbridge, I. W. Frank, D. M. Tanenbaum, J. M. Parpia, H. G. Craighead, and P. L. McEuen, "Electromechanical resonators from graphene sheets," *Science*, vol. 315, no. 5811, pp. 490–493, 2007.

[6] C. Chen, S. Rosenblatt, K. I. Bolotin, W. Kalb, P. Kim, I. Kymissis, H. L. Stormer, T. F. Heinz, and J. Hone, "Performance of monolayer graphene nanomechanical resonators with electrical readout," *Nature Nanotechnol.*, vol. 4, pp. 861–867, Dec. 2009.

[7] Y. Xu, C. Chen, V. V. Deshpande, F. A. DiRenno, A. Gondarenko, D. B. Heinz, S. Liu, P. Kim, and J. Hone, "Radio frequency electrical transduction of graphene mechanical resonators," *Applied Physics Letters*, vol. 97, no. 24, p. 243111, 2010.

[8] D. Weinstein and S. A. Bhave, "The resonant body transistor," *Nano Lett.*, vol. 10, no. 4, pp. 1234–1237, 2010.

[9] S. Lee, C. Chen, V. V. Deshpande, G.-H. Lee, I. Lee, M. Lekas, A. Gondarenko, Y.-J. Yu, K. Shepard, P. Kim, and J. Hone, "Electrically integrated su-8 clamped graphene drum resonators for strain engineering," *Applied Physics Letters*, vol. 102, no. 15, p. 153101, 2013.

[10] N. Petrone, C. R. Dean, I. Meric, A. M. van der Zande, P. Y. Huang, L. Wang, D. Muller, K. L. Shepard, and J. Hone, "Chemical vapor deposition-derived graphene with electrical performance of exfoliated graphene," *Nano Lett.*, vol. 12, pp. 2751–2756, June 2012.

[11] H. S. Solanki, S. Sengupta, S. Dhara, V. Singh, S. Patil, R. Dhall, J. Parpia, A. Bhattacharya, and M. M. Deshmukh, "Tuning mechanical modes and influence of charge screening in nanowire resonators," *Phys. Rev. B*, vol. 81, p. 115459, Mar 2010.

[12] W. W. S. Timoshenko, D. H. Young, *Vibration Problems in Engineering*. New York, Wiley, 1974.

Micromechanical Disk Array for Enhanced Frequency Stability Against Bias Voltage Fluctuations

Lingqi Wu, Mehmet Akgul, Wei-Chang Li, Yang Lin, Zeying Ren, Tristan Rocheleau, and Clark T.-C. Nguyen
Department of EECS, University of California, Berkeley, CA, USA, Email: wulingqi@berkeley.edu

***Abstract*—A 215-MHz polysilicon capacitive-gap transduced micromechanical resonator array employing 50 mechanically coupled radial-contour mode disks—the largest such array yet fabricated and measured—has achieved 3.5× better frequency stability than single stand-alone disks against fluctuations in the dc bias voltage (V_P) normally applied across electrode-to-resonator gaps during device operation. The key to enhanced frequency stability is the electrode-to-resonator capacitance (C_o) generated by the parallel combination of input/output electrodes overlapping each resonator in the array that in turn reduces the efficacy of the bias voltage-controlled electrical stiffness. Here, a new equivalent circuit based on negative capacitance provides improved visualization that helps to identify methods to suppress electrical stiffness induced frequency variation. The circuit model indicates that the more resonators in an array, the smaller the frequency shift imposed by a given bias voltage change. Both modeling and measurement suggest that the most stable MEMS-based oscillators (e.g., against supply noise and acceleration) are ones that utilize mechanically-coupled arrays of resonators.**

***Keywords*—array, negative capacitance, electrical stiffness, micromechanical resonator, frequency stability, capacitive-gap transducer.**

I. Introduction

High-Q capacitive-gap transduced micromechanical resonators constructed via MEMS technology have recently taken center-stage among potential next generation timing and frequency reference devices that might satisfy present and future applications. Notably, oscillators referenced to very high Q capacitively transduced MEMS resonators have already made inroads into the low-end timing market, and research devices have been reported to satisfy GSM phase noise requirements [1] [2]. Meanwhile, such devices have also posted some impressively low acceleration sensitivities, with measured sensitivity vectors less than 0.5ppb/g [3].

Interestingly, theory predicts that the acceleration sensitivity of these devices should be even better than this, if not for frequency instability due to electrical stiffness [3]. Indeed, electrical stiffness is predicted to set lower limits on not only short-term stability, but long-term as well, especially when one considers frequency variations due to charging or temperature-induced geometric shifts [4].

Pursuant to circumventing electrical stiffness-based instability, this work introduces a more circuit design-friendly model that uses negative capacitance to capture the influence of electrical stiffness on device and circuit behavior. This new circuit model reveals that capacitive-gap transduced micromechanical resonators can offer better stability against electrical-stiffness-based frequency instability when used in large mechanically-coupled arrays. Measurements confirm that a 215-MHz 50-resonator disk array achieves a 3.5× enhancement in frequency stability against dc-bias voltage variation over a stand-alone single disk counterpart. The new equivalent circuit predicts the measurement data and its trends quite well, creating good confidence for using this circuit to guide new oscillator and filter designs that, depending on the application, can enhance or suppress electrical stiffness.

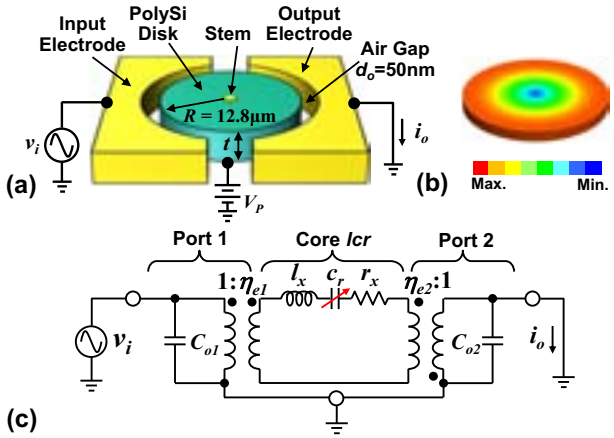

Fig. 1. (a) Schematic of a 215-MHz radial-contour mode polysilicon disk resonator in a two-port excitation and sensing configuration. (b) Radial-contour mode shape. (c) Classic equivalent electrical circuit for a capacitive gap micromechanical disk resonator with electrical stiffness lumped into the variable capacitance c_r.

II. Contour Mode Disk Resonator

Fig. 1(a) depicts a capacitive gap polysilicon contour mode disk resonator in a typical bias, excitation, and detection scheme. This device comprises a 2μm-thick (t=2μm) polysilicon disk supported by an anchored stem attached at the center of the disk and surrounded by two electrodes separated by a tiny 50nm air gap (d_o=50nm). The device is excited into resonance via a combination of a dc-bias voltage V_P applied to the conductive polysilicon resonant structure and an ac signal applied to the input electrode, which together induce a force at the frequency of v_i that drives the disk into a contour mode resonance with equal radial expansion and contraction around its perimeter, as shown in Fig. 1(b), when the frequency of v_i matches the resonance frequency. Once vibrating, the V_P-biased time varying capacitance between the disk and its output electrode generates an output current.

To conveniently model and simulate the behavior of this micromechanical disk resonator, [5] provided expressions for the element values of the electrical equivalent circuit shown in Fig. 1(c), which take the form

$$l_x = m_m,\ r_x = c_m,\ c_r = \frac{1}{k_m - k_e},\ \eta_{en} = \frac{V_P C_{on}}{d_o} \qquad (1)$$

where m_m, k_m, c_m, η_{en}, and C_{on} are the equivalent dynamic mass, mechanical stiffness, damping, electromechanical coupling factor, and electrode-to-resonator capacitance at corresponding ports, respectively. The electrical stiffness k_e models the frequency pulling effect of the force generated by time-varying changes in electric field strength as vibration changes the parallel-plate capacitive electrode-to-resonator gap and can be expressed as [6]

$$k_e = \frac{V_P^2 (C_{o1} + C_{o2})}{d_o^2} = \frac{V_P^2 \epsilon A}{d_o^3} \qquad (2)$$

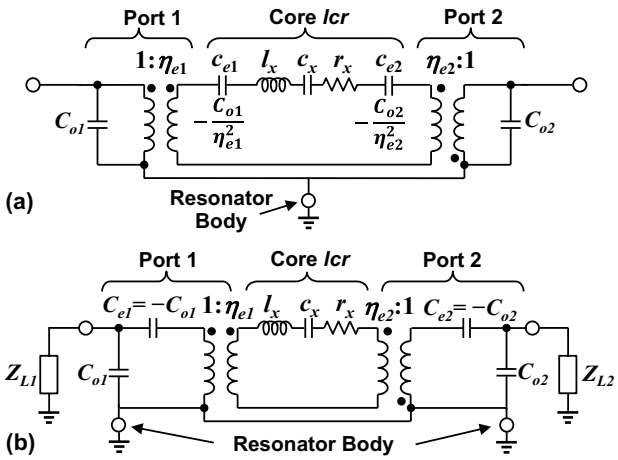

Fig. 2. Negative capacitance small-signal equivalent circuits for a two-port capacitive-gap micromechanical contour mode disk resonator: (a) Negative capacitance equivalent circuit with electrical stiffness separated from mechanical stiffness. (b) Negative capacitance equivalent circuit with electrical stiffness reflected through transformers to outside the core *lcr* loop.

where ϵ is the permittivity of the gap material (i.e., vacuum in this case) and A is the total overlap area between the resonator and its electrodes. Since the force generated by k_e is in phase with displacement and acts to accentuate motion, it acts against the mechanical spring restoring force, so subtracts from the mechanical stiffness, yielding a total resonator stiffness of $(k_m - k_e)$. Changes of any variables in k_e, such as dc-bias voltage noise, capacitance variation due to mechanical vibration, or charging induced bias voltage drift, can cause frequency stability issues for capacitive-gap MEMS resonators [7] [8].

The classic equivalent circuit in Fig. 1(c) models the influence of electrical stiffness on resonance frequency via the arrow through capacitor c_r (that indicates this capacitor is tunable) and by setting the value of c_r equal to $1/(k_m - k_e)$. Although this method for capturing electrical stiffness adequately predicts the resonance frequency, it does not convey clearly to a circuit designer the impact of electrical stiffness on the overall circuit performance. Modeling the electrical stiffness in this way in fact hides some very important capacitive-gap resonator behaviors when emplaced into certain circuits. This model also encourages designers to dismiss the impact of electrical stiffness, since many designers just neglect the k_e part in the value of c_r when drawing up equivalent circuits.

III. Negative Capacitance Equivalent Circuit

To remedy the above deficiencies, the circuit of Fig. 2(a) explicitly models the electrical stiffness contributed by each electrode-to-resonator gap as separate negative capacitors c_{en}, where *n* denotes the port. Using (1) and (2), c_{en} becomes

$$c_{en} = -\frac{1}{k_{en}} = -\frac{d_o^2}{V_P^2 C_{on}} = -\frac{C_{on}}{\eta_{en}^2} \tag{3}$$

Here, c_{en} entirely captures the electrical stiffness, allowing c_x in Fig. 2(a) to represent the pure mechanical stiffness. Further reflecting the negative capacitors c_{en} through the transformers on both sides to outside the core *lcr* loop yields C_{en} in the circuit of Fig. 2(b) as follows:

$$C_{en} = \eta_{en}^2 c_{en} = -C_{on} \tag{4}$$

where the physical shunt electrode-to-resonator capacitors C_{on} are now matched by negative capacitors with identical values. This new circuit reveals the potential for cancellation of the C_{on}'s in certain circuit configurations, which where possible, would remove entirely frequency changes induced by electrical stiffness, thereby stabilizing the frequency against all variables in (2)—something highly desirable for oscillator applications that require very high frequency stability.

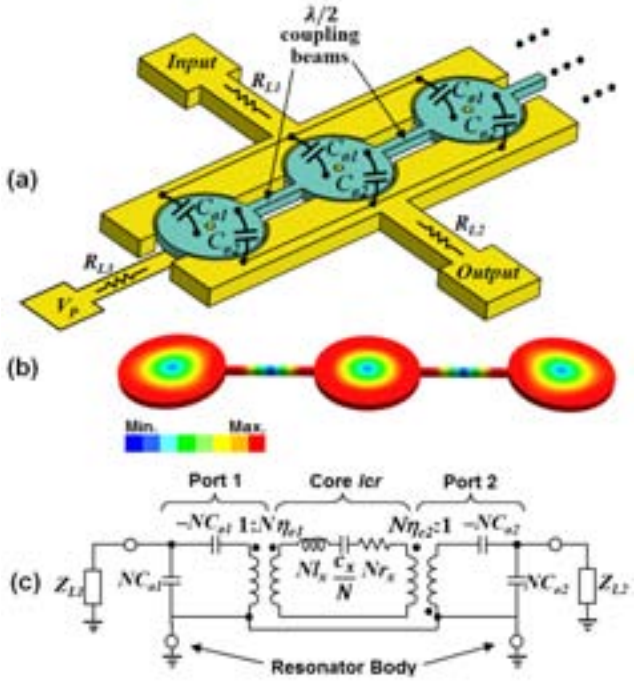

Fig. 3. (a) Schematic of a disk array-composite resonator with disks linked by λ/2 coupling beams to enforce in phase vibration of each individual resonator. (b) Simulated modal depiction of a 3-resonator disk array with all disks vibrating in phase in radial-contour shapes. (c) Negative capacitance equivalent circuit of a disk array-composite with *N* resonators based on element values of the single resonator equivalent circuit in Fig. 2(b)

Pursuant to determining which circuit configurations best promote k_e cancellation, Fig. 2(b) adds load impedances Z_{Ln}. In order for C_{on} to negate the electrical stiffness represented by $-C_{on}$, approximately same amount of current should flow through C_{on} and $-C_{on}$, which indicates that C_{on} should pass most of the current flowing into the parallel combination of C_{on} and Z_{Ln}. In other words, the impedance of Z_{Ln} should be much larger than that of C_{on}, or

$$|Z_{Ln}| \gg \frac{1}{\omega_o C_{on}} \tag{5}$$

From (5), to reduce electrical stiffness, both Z_{Ln} and C_{on} should be large. If Z_{Ln} has no reactive component, operation at high frequency also suppresses electrical stiffness. To address cases where a resonator might be used with reconfigurable drive and sense circuits that present non-constant loads, and to reap the motional resistance and power handling advantages of arrays, this work focuses on coupled-array-based methods to increase C_{on} towards better frequency stability against changes in electrical stiffness.

IV. Micromechanical Disk Array

Fig. 3(a) presents a micromechanical disk array-composite constructed by mechanically linking individual disk resonators via half-wavelength coupling beams. Here, coupling of resonators yields a coupled multi-mode system, where at each mode, all resonators vibrate at precisely the same frequency [9], allowing their outputs to be combined to boost input and output currents, thereby decreasing the motional resistance and increasing power handling. As first demonstrated in [1], the use of half-wavelength couplers both insures that all resonators vibrate in phase, as shown in Fig. 3(b); and spreads the mode

TABLE I. COMPARISON OF EQUIVALENT CIRCUIT ELEMENT VALUES FOR A 50-RESONATOR DISK ARRAY AND A SINGLE DISK RESONATOR

Parameters	Single Disk Resonator	Disk Array with N=50
C_{on} (fF)	9	451
η_{en}	1.58×10^{-6}	7.91×10^{-5}
l_x (H)	1.81×10^{-12}	9.03×10^{-11}
r_x (Ω)	1.17×10^{-7}	5.85×10^{-6}
c_x (F)	3.29×10^{-7}	6.59×10^{-9}

frequencies apart, making it easier to select a specific mode (when only one is wanted, e.g., in an oscillator application) by proper electrode phasing. Of course, this coupled array strategy not only produces a larger total output current and smaller motional resistance [10], but also attains much larger electrode-to-resonator overlap capacitors C_{on}, and thus reduces the electrical stiffness and its associated instability, according to (5).

For a disk array with N mechanically coupled disk resonators, the stiffness k_m, mass m_m, damping c_m, electromechanical coupling factor η_{en}, and electrode-to-resonator overlap capacitance C_{on} are all N times larger than for a single disk resonator. Thus, simple multiplication or division by N is all that is needed to derive coupled array equivalent circuit element values from those of a single disk resonator, as shown in Fig. 3(c). Note that although the electrical stiffness goes up by N according to (2), so does the mechanical stiffness, so their ratio k_e/k_m remains the same and the fundamental efficacy by which k_e pulls the frequency, as governed by

$$f_o = f_{nom}\sqrt{1-\frac{k_e}{k_m}} \qquad (6)$$

does not increase (where f_o is the resonance frequency and f_{nom} is the nominal resonance frequency with no electrical stiffness). Instead, with C_{on} presenting a much smaller impedance, more current flows through C_{on} than Z_{Ln}, allowing it to cancel more of C_{en}, thereby negating the electrical stiffness induced frequency instability via circuit interaction.

TABLE I summarizes the equivalent circuit element values for a 215-MHz 50-nm-gap disk array using 50 resonators (with Q=20,000 and V_P=10V) and compares them with that of a stand-alone single disk resonator. With a 451fF electrode-to-resonator overlap capacitance much larger than the 9fF of a single disk, the 50-resonator array should greatly suppress electrical stiffness induced frequency instability.

V. FABRICATION PROCESS

The fabrication process for the all-polysilicon contour mode disk resonator arrays of this work deviates from previous ones, such as that of [11], in that it does not use self-aligned peg-stem anchors and it employs chemical mechanical polishing (CMP) to remove electrode overhangs. The process begins with film depositions and etches identical to those of [11] to achieve the substrate isolation layer, polysilicon interconnects, and the bottom sacrificial layer. At this point, unlike previous self-aligned processes, a mask is used to define, pattern, and etch stem anchor holes into the bottom sacrificial oxide, followed by a 2-μm LPCVD in-situ doped polysilicon film that fills the holes to form the stems and serves as the resonator structural material. Here, an AMSL300 DUV Stepper is used to realize very precise alignment, with less than 100nm error—good enough to achieve Q's comparable to those of devices with self-aligned stems.

After depositing an oxide hard mask over the structural polysilicon, disk devices and coupling links are patterned and

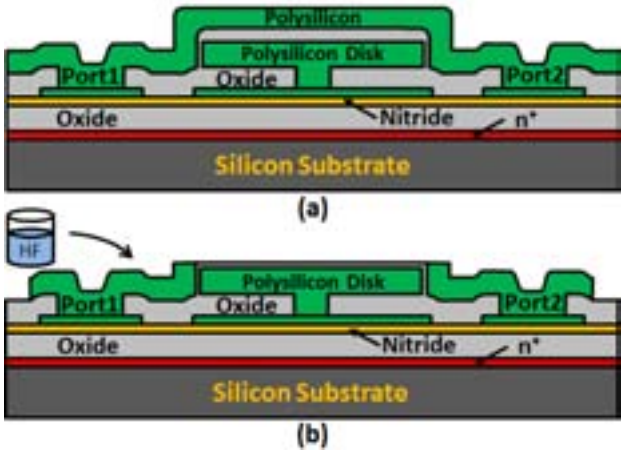

Fig. 4. Cross-sections showing the last few steps in the fabrication process for a 215-MHz all-polysilicon disk resonators with CMPed electrodes.

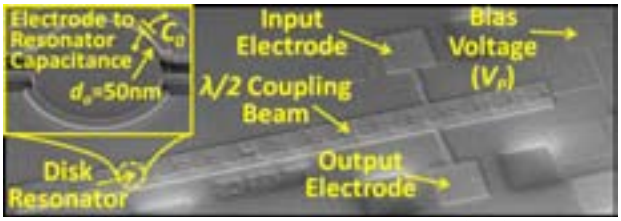

Fig. 5. SEM of a 215-MHZ 50nm capacitive-gap transduced contour mode disk array employing 16 mechanically coupled resonators.

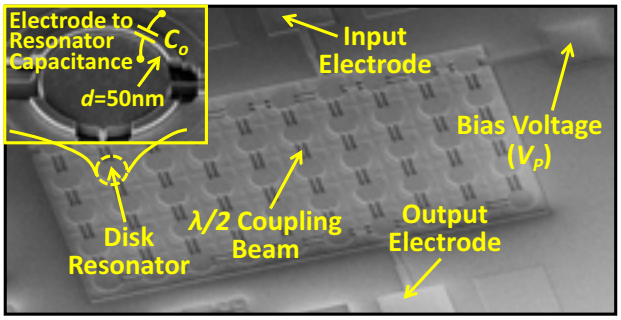

Fig. 6. SEM of a 215-MHZ 50nm capacitive-gap transduced contour mode disk array employing 50 mechanically coupled resonators.

etched as before, the gap-defining sacrificial sidewall oxide spacer is deposited, electrode to interconnect contact vias are etched, and the polysilicon electrode material LPCVD'ed 3-μm thick, all to yield the cross-section of Fig. 4(a). At this point, the process again deviates from that of [11] in that before patterning and etching the electrodes, the top polysilicon is first CMP'ed down to the hard mask. This step removes the electrode overhangs of Fig. 4(a), achieving the cross section of Fig. 4(b), and in the process greatly increasing the pull-in voltage of these devices, where contact between the disk and the electrode overhang is often the first to occur when dc-bias voltages increase. As before, devices are released in 49 wt. % hydrofluoric acid for ~40min.

Fig. 5 and Fig. 6 present SEMs of fabricated 215-MHz 50-nm capacitive-gap transduced half-wavelength-coupled disk arrays employing 16 and 50 resonators, respectively, in straight line and rectangular placement configurations.

VI. EXPERIMENTAL RESULTS

To gauge the degree to which arraying enhances frequency stability against dc-bias voltage changes, measured plots of frequency versus dc-bias voltage are in order, for both mechanically coupled disk array-composite resonators using various numbers of resonators, as well as for a single stand-alone disk for comparison. To this end, measurements were made under a

2μtorr vacuum environment in a Lakeshore FWPX vacuum probe station and using an Agilent E5071C network analyzer in the direct two-port excitation and sensing scheme depicted in Fig. 1(a). Fig. 7 presents measured curves that clearly show a shrinking frequency dependence on dc-bias voltage as the number of resonators used in an array increases. In particular, the 50-resonator 215-MHz disk array experiences a 20ppm frequency change when V_P varies over a 7V span, from 2V to 9V, 3.5× smaller than the 70ppm of a stand-alone device.

To confirm the validity of the negative capacitance equivalent circuit of Fig. 3(c), simulated plots using this circuit are also included in Fig. 7, showing very good agreement between theory and measurement. These simulations assume the load impedance Z_{Ln} derives from a combination of series trace resistance R_{L1} and R_{L2} from input/output electrode leads, as well as similar lead resistance R_{L3} from the V_P port, all shown in Fig. 3(a). Since probe coax and bond pad capacitance are nulled by calibration, the Z_{Ln} in these measurements is mainly resistive. It should be noted that the total equivalent load resistance $R_{Ln,tot}$ of a disk array in this work is generally larger than that of a single resonator and actually increases with the number of disks in the array. This comes about because, at least in the current layout, the distance between the V_P pad and the furthest resonator increases as the number of resonators increases, as seen from Fig. 5, resulting in a corresponding increase in series resistance R_{L3}. TABLE II summarizes overlap capacitance and equivalent load resistance values for disk arrays with N=1, 8, 16, and 50, clearly showing larger values as the number of resonators increases, at least for straight line arrays with N=8 and N=16, like that of Fig. 5. The series resistance of the 50-resonator array depicted in TABLE II is actually smaller than those of the 8- and 16-resonator ones, since its layout uses a rectangular or matrix topology, rather than a straight line, so the average distance of its resonators from its V_P pad ends up being smaller.

According to (5), increases in load resistance like those in TABLE II should also contribute to an overall nulling of the electrical stiffness, and thereby enhance frequency stability against dc-bias voltage fluctuations. Indeed, as the number of array resonators increases, electrical stiffness erodes due to increases in both electrode-to-resonator overlap capacitance and load resistance—a double whammy effect perfectly predicted by the negative capacitance equivalent circuit.

VII. Conclusions

The 50-resonator capacitive-gap transduced micromechanical disk array demonstrated here is the largest such array yet fabricated and measured and enables a mere 20ppm frequency change over a 7V dc-bias voltage variation−−a 3.5× reduction over a single stand-alone disk resonator counterpart. That the new negative capacitance equivalent circuit model introduced perfectly predicts this phenomenon, while also aiding circuit visualization, bodes well for its continued use in future resonator circuits for which tailored electrical stiffness strengths are desired. Indeed, the demonstrated stability enhancing attributes of mechanically-coupled arrays that make them less vulnerable to dc-bias voltage noise, dielectric charging, and external vibrations, together with already demonstrated array-derived reductions in the standard deviation of array resonance frequency [12], present strong cases for a more prevalent use of arrays in next generation MEMS-based frequency reference devices.

Acknowledgment: This work was supported by the DARPA CSSA program.

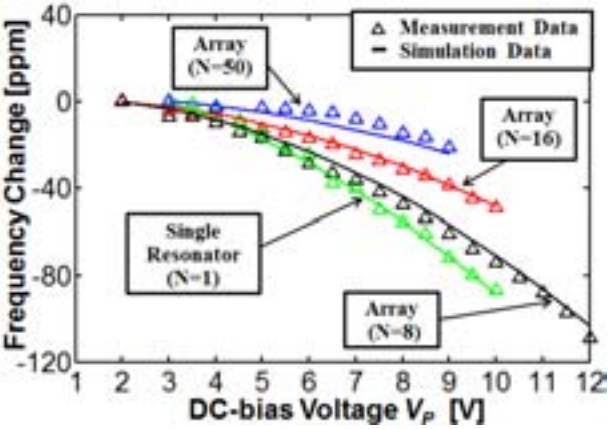

Fig. 7. Measured curves of resonance frequency versus dc-bias voltage V_P plotted against simulation using negative capacitance equivalent circuit models for disk arrays with N=1, N=8, N=16, and N=50.

TABLE II. *N*-Resonator Disk Array Parameters

Resonator Number (N)	Overlap Capacitance C_{on} [fF]	$R_{Ln,tot}$ [kΩ]
1	9	1.56
8	72	4.04
16	144	5.24
50	451	2.92

References

[1] Y.-W. Lin, S.-S. Li, Z. Ren and C. T.-C. Nguyen, "Low phase noise array-composite micromechanical wine-glass disk oscillator," in *Technical Digest, IEEE, Int. Electron Device Mtg.*, Washington, DC, Dec. 5-7, 2005.

[2] V. Kaajakari *et al.*, "Square-extensional mode single-crystal silicon micromechanical resonator for low-phase-noise oscillator application," *IEEE Electron Device Letters,* vol. 25, no. 4, pp. 173-175, 2004.

[3] T. L. Naing *et al.*, "vibration-insensitive 61-MHz micromechanical disk reference oscillator," in *IEEE Int. Frequency Control Symposium*, Baltimore, Maryland, May 22-24, 2012.

[4] V. Kaajakari, J. K. Koskinen and T. Mattila, "Phase noise in capacitively coupled micromechanical oscillators," *IEEE Transactions on Ultrasonics, Ferroelectric, and Frequency Control,* vol. 52, no. 12, pp. 2322-2331, 2005.

[5] F. D. Bannon, J. R. Clark and C. T.-C. Nguyen, "High-Q HF micromechanical filters," *IEEE Journal of Solid-State Circuits,* vol. 35, no. 4, pp. 512-526, 2000.

[6] H. C. Nathanson, W. E. Newell, R. A. Wickstrom and J. R. Davis JR., "The resonant gate transistor," *IEEE Transactions on Electron Devices,* vol. 14, no. 3, pp. 117-133, Mar. 1967.

[7] M. Agarwal *et al.*, "Effects of mechanical vibrations and bias voltage noise on phase noise of MEMS resonator based oscillators," in *19th IEEE Int. Micro Electro Mechanical System Conf.*, Istanbul, Turkey,, Jan. 22-26, 2006.

[8] G. Bahl *et al.*, "Model and observations of dielectric charge in thermally oxidized silicon resonators," *Journal of Microelectromechanical Systems,* vol. 19, no. 1, pp. 162-174, 2010.

[9] R. A. Johnson, Mechanical Filters in Electronics, New York: Wiley, 1983.

[10] M. U. Demirci and C. T.-C. Nguyen, "Mechanically corner-coupled square microresonator array for reduced series motional resistance," *Journal of Microelectromechanical Systems,* vol. 15, no. 6, Dec. 2006.

[11] J. Wang, Z. Ren and C. T.-C. Nguyen, "1.156-GHz self-aligned vibrating micromechanical disk resonator," *IEEE Transactions on Ultrasonics, Ferroelectrics, and Frequency Control,* vol. 51, no. 12, pp. 1607-1628, Dec. 2004.

[12] Y. Lin *et al.*, "Enhancement of micromechanical resonator manufacturing precision via mechanically-coupled arraying," in *IEEE Int. Frequency Control Symp.*, Besancon, France, Apr. 20-24, 2009.

Exploiting Irregular MoS_2 Nanostructures for Very High Frequency (VHF) Nanomechanical Resonators with Mode Shape Engineering and Frequency Control

Zenghui Wang*, Jaesung Lee, and Philip X.-L. Feng*
Department of Electrical Engineering & Computer Science, Case School of Engineering
Case Western Reserve University, Cleveland, OH 44106, USA
*Email: zenghui.wang@case.edu, philip.feng@case.edu

***Abstract*—Vibrating nanoelectromechanical systems (NEMS) made of atomically-thin two-dimensional (2D) crystalline nanostructures have demonstrated attractive potential for making new actuators and sensors. Nanoscale devices in new types of 2D materials are generally first obtained by mechanical exfoliation, which can often lead to irregular and asymmetric geometries. Here we investigate irregular molybdenum disulfide (MoS_2) nanoflakes and ultrathin 2D nanomechanical resonators at high & very high frequencies (HF/VHF). We explore the effects of irregularities and imperfections, such as incomplete drumhead structures partially covering microtrenches, upon the device characteristics. We observe that such irregular and seemingly nonideal boundary conditions with free edges do not compromise device performance. Instead, they provide an additional geometrical degree of freedom which allows novel engineering of the device vibrations, such as controlling the mode shape and mode index, and tuning the frequency ratios between different resonant modes. This capability may be interesting for designing multimode resonators in nanomechanical circuits.**

Keywords—molybdenum disulfide (MoS_2); two-dimensional (2D) crystal; nanoelectromechanical systems (NEMS); resonator; boundary condition; mode shape; multimode resonance

I. Introduction

Two-dimensional (2D) layered materials have attracted significant research interests for their unique properties and technological potential for novel nanodevice applications [1–4]. Started with graphene, new 2D materials continue to be isolated and explored. Early explorations into these 2D materials and devices have been mostly based on samples obtained by mechanical exfoliation [5–7]. This technique allows researchers to quickly access nanostructures isolated from the new layered materials and study their properties. Practical exfoliation processes of today (*e.g.*, the 'Scotch tape' method), however, can often lead to random sizes and shapes for the structures of interest. Such structural irregularities may be particularly relevant in 2D nanoelectromechanical systems (NEMS) made of suspended ultrathin crystals. Specifically, in drumhead-structured NEMS resonators made by exfoliated 2D crystals covering microtrenches [8], what would be the effects of incomplete coverage and hence a new configuration of the boundary condition? This irregularity has not yet been studied systematically. Often devices with such structures are deemed nonideal, defective, and may be simply discarded and never studied. In this work, we carefully assess the impact of the incomplete coverage boundary condition on exfoliated MoS_2 drumhead HF/VHF nanomechanical resonators. We show that the incomplete clamping does not compromise device performance; rather, it leads to interesting mode crossing and controllable spacing between multimode resonances.

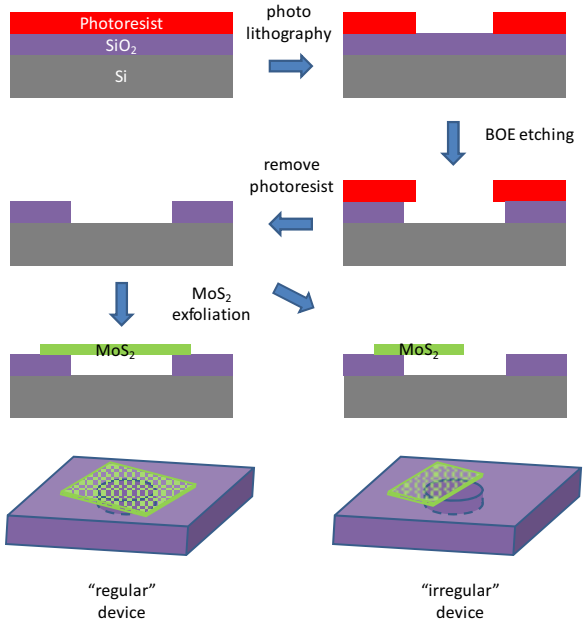

Fig. 1. Illustration of fabrication process for making MoS_2 nanomechanical resonators: spinning coating of photoresist on the SiO_2/Si wafer; defining pattern with photo lithography; BOE etching of SiO_2; removing photo resist; mechanical exfoliation of MoS_2. The schematics of both "regular" (MoS_2 flake fully covering the microtrench) and "irregular" (MoS_2 flake partially covering the microtrench) devices are shown at the bottom.

II. Experimental Techniques

A. Device Fabrication

The devices are prepared by mechanically exfoliating MoS_2 so that MoS_2 flakes are suspend on microtrenches in a 290nm-thick SiO_2 thermally grown on Si substrate. The microtrenches are predefined by photo lithography, followed by a buffered

oxide etch (BOE) to remove the exposed SiO_2. The etch time is controlled such that the entire depth (290nm) of SiO_2 is removed, exposing the flat Si surface underneath [8]. The resulting wafer has arrays of flat-bottom microtrenches. MoS_2 flakes covering the microtrenches make drumhead-structured nanomechanical resonators. Mechanical exfoliation of MoS_2 is more challenging than that of graphene, generally resulting in lower yields and smaller flakes, especially for suspended devices. Small flakes sometimes do not completely cover the microtrenches, enabling partially clamped drumhead structures. Figure 1 shows schematics of the device fabrication process and the resulting fully and partially clamped structures.

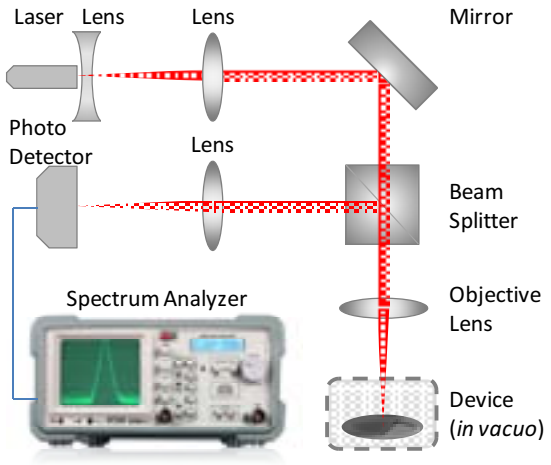

Fig. 2. Simplified schematic of the laser interferometry system for detection of MoS_2 nanomechanical resonance. The laser spot is focused onto the device surface, and reflected light is directed towards the photo detector by the beam splitter. The signal from the photo detector is fed to a spectrum analyzer.

B. Measurement Apparatus and Techniques

Nanomechanical resonances of the MoS_2 drumhead devices are measured using an optical readout technique. A simplified schematic of the measurement system is illustrated in Fig. 2. In our custom-built interferometry setup, the laser beam from a 633nm He-Ne laser first goes through a beam expander followed by a 50× microscope objective lens with optical window correction (NA=0.5). The laser is focused on the MoS_2 nanosheet and the spot size is ~1μm. The interference between light waves reflected from the MoS_2 nanosheet and the underneath reflecting Si surface determines the intensity of the optical signal from the device. Out-of-plane motion of the MoS_2 nanosheet modulates the interferometric output signal and can be analyzed in frequency domain. The interferometric signal is detected by a low-noise photodetector (PD), and fed into a spectrum analyzer. The ultrahigh motion sensitivity of the measurement system allows us to detect the minimal motions of the MoS_2 nanosheets arising from intrinsic thermomechanical fluctuations and thus find their thermo-mechanical resonances without external driving. We adjust on-device laser power to be ≤500μW, so that heating effect is negligible (no heating-induced frequency change within the range of applied power), while maintaining a good signal-to-noise ratio. All our measurements are conducted in moderate vacuum (p~6mTorr) at room temperature (T~300K).

III. Results and Discussions

Figure 3 demonstrates measured resonance response from a typical device with geometrical irregularity of partial coverage and incomplete clamping boundary condition. As shown by the wide-range frequency response and individual resonance curves, such devices often exhibit multiple resonances in the HF/VHF bands. The dashed red lines in these plots show the fit to the model of damped harmonic resonator with finite quality (Q) factors, demonstrating excellent agreement.

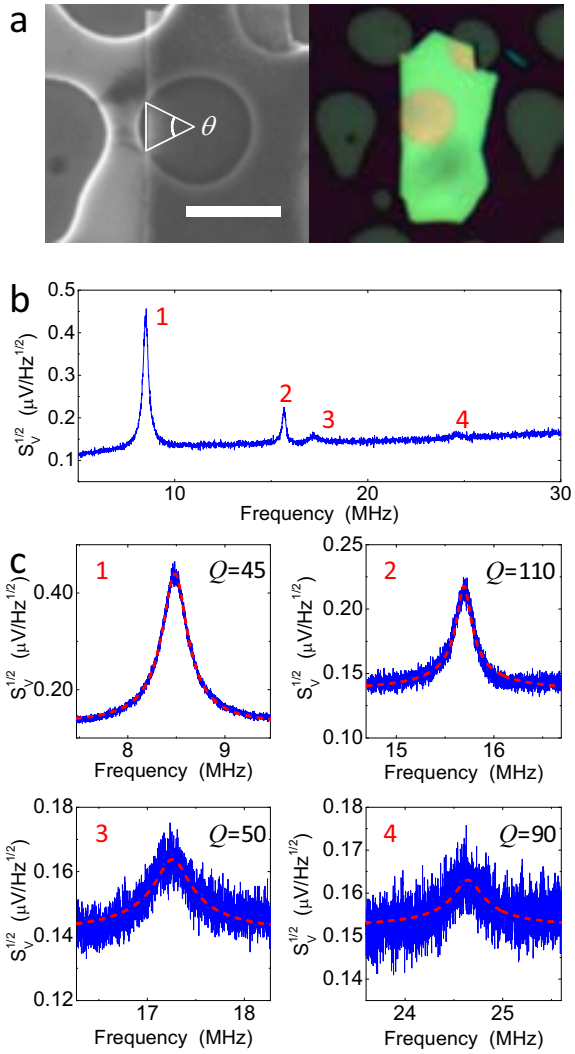

Fig. 3. Measured resonance response from a typical device based on a MoS_2 nanoflake partially covering the microtrench. **a**. SEM and optical image of the device. Scale bar (SEM only): 5μm. The definition of 'open angle' θ is shown in the SEM image. **b**. Measured thermomechanical noise spectrum, showing multiple resonances. **c**. High-resolution frequency scans centered around each of the individual thermomechanical resonances.

We have measured multiple devices with and without this type of geometric irregularity (*i.e.*, both partially covered and fully covered), and observe robust resonance behavior in both categories, with resonance frequencies and Q factors in similar ranges. Table 1 lists the measured devices. The devices with MoS_2 flakes completely covering the microtrench (and thus do

not have this type of geometric irregularity) are shown in bold font (*i.e.*, devices #5 and #6).

TABLE I. PARAMETERS OF MEASURED VHF MoS_2 RESONATORS

Device ID #	Device SEM Image	Micro-Trench Diameter d (μm)	MoS_2 Thickness t (nm)	1st Mode Resonance Frequency f_1 (MHz)	Quality Factor Q
1	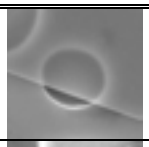	2.69	62.2±0.7	48.1	200
2	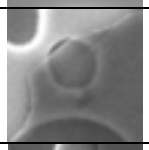	2.41	57.5±2.1	43.77	160
3	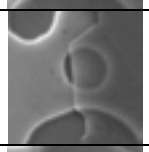	2.53	43.0±1.4	53.72	370
4	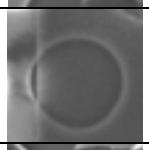	5.99	30.3±0.3	48.10	70
5	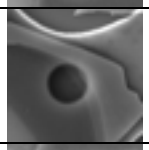	**1.90**	**6.1±0.7**	**49.70**	**80**
6	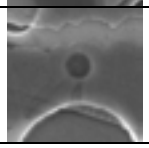	**1.51**	**27.2±0.5**	**57.89**	**80**

To quantify the degree of geometric irregularity in the incompletely clamped devices, we define the 'open angle' θ, as shown in Fig. 3a. It corresponds to the center angle of the open arc where the portion of the flake is not clamped and has a free edge. To fully understand how mode shape and resonance frequency of each mode varies with this geometric irregularity, we perform finite element modeling (FEM, using COMSOL) for the first three resonance modes of MoS_2 resonators (see Fig. 4, *dashed lines*: d=1μm and t=100nm; *symbols*: d=10μm and t=10nm) with varying θ values between 0º and 180º.

We make a few observations from the simulation results, as shown in Fig. 4. First, the effect of partial coverage on the resonance frequency (f_i, i being the mode number/index) is not monotonic. Take the lowest mode f_1 for example: as θ increases, f_1 first decreases and then increases. The other two modes (f_2 & f_3) also show similar dependence on θ. Second, the detailed shapes of the $f_i(\theta)$ curves, such as the position of the minimum, depend on the individual mode. Mode crossing between the second and the third lowest mode is observed at θ≈137º. Third, the $f_i(\theta)$ tendency does not depend on the dimensions of the device. Varying the thickness and the lateral size of the resonator structure does not affect the shapes of the $f_i(\theta)$ curves. For a larger thin device (d=10μm, t=10nm) and a smaller thick device (d=1μm, t=100 nm), the simulation results completely overlap each other after rescaling in frequency, despite the 100 fold difference in aspect ratio (d/t).

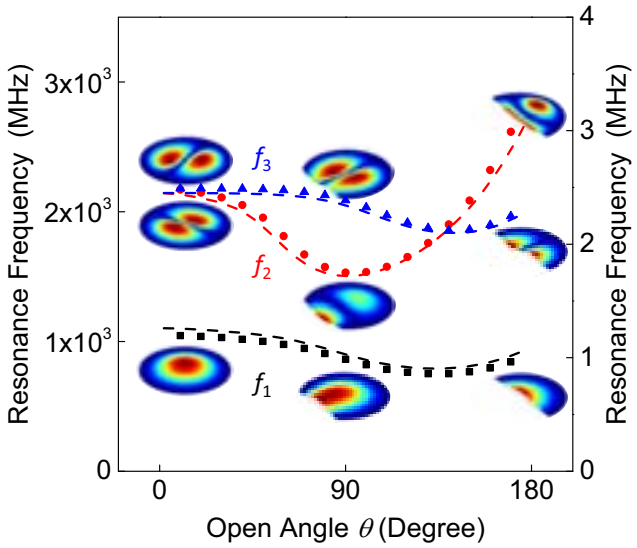

Fig. 4. Computed resonance frequencies and mode shapes for the three lowest modes for MoS_2 resonators with open angle $0<\theta<180$º. The three different colors denote the three modes. Calculations are shown for a small/thick device (*dashed lines*: d=1μm, t=100nm, left y axis) and a large/thin device (*symbols*: d=10μm, t=10nm, right y axis). The θ=0 case corresponds to the fully covered geometry.

These observations on the $f_i(\theta)$ curves clearly suggest a possibility of mode shape engineering and frequency control by designing and tuning the device's θ value. For fully covered devices (θ=0 only), one is limited with the frequency ratios between the modes, and with some degenerate mode pairs (usually appear as pairs with random, uncontrollable frequency splitting). With $\theta\neq$0, one can adjust the θ value and choose many possible frequency ratios between different modes within the allowed range, and the sequence of mode shapes can also be changed by choosing the proper θ values.

The observed behavior can be qualitatively understood by examining the interplay between two effects that depend on θ: (i) the change in the clamping boundary condition with varying θ, and (ii) the decrease in resonator size and mass as θ increases. Resonators with more clamped ends or boundaries can have higher resonance frequencies than their counterparts with free ends/edges, as more clamped edge provides more restoring force and thus a larger effective spring constant. In the range of small θ values, the effect of decreasing drumhead coverage is mostly reducing the clamping edge. This effect can be visualized in the mode shape. At θ=90º, the larger-displacement region in the center of the disk clearly 'diffuses' towards the free edge where the clamping condition is eased due to the missing coverage and lack of clamping. The resulting softening of the overall spring constant leads to lower resonance frequency. As θ continues to increase, the effect of decrease in resonator size (and hence the device mass) becomes dominant, and the frequency increases again.

Similarly, the behavior of the higher modes in Fig. 4 can be understood. For convenience, here we call each continuous area enclosed by nodal lines a 'motional region'. For the second mode f_2 whose nodal line in the mode shape is parallel to the free edge (the second lowest mode at low θ values), it has two motional regions. As the free edge starts to move inward, the outer motional region (the one closer to the free edge) quickly loses its clamped length at boundary as θ increases, while losing its device area at a slower pace. This effect takes place on f_2 faster than on the first mode f_1, because for each value of θ a larger fraction of the outer motional region in the f_2 mode is being removed compared with the motional region in the f_1 mode. This results in the initial faster decrease in f_2. As θ continue to increase, in this f_2 mode the nodal line start to move away from the free edge, which effectively decrease the size of the inner motional region (the one away from the free edge) and thus increases f_2. This effect is more pronounced as θ approaches 180º, when the outer motional region is most gone and effect is almost entirely on downsizing the inner motional region, which results in the fast increase in f_2 and mode crossing of f_2 becoming larger than f_3.

In the third mode f_3, where the nodal line is perpendicular to the free edge, the drumhead is divided into two motional regions that are equally affected by the advancing of the open arc and free edge. For both of the two motional regions, the ratio between clamping and surface area changes at roughly the same rate as that for the single motional region in the lowest resonance mode f_1. Therefore, the change in its resonance frequency f_3 follows a similar tendency as the lowest mode f_1, and at higher θ values, f_3 is surpassed by the second mode f_2.

We can also use a simple analytical model to qualitatively describe this behavior. We start with θ=0 (a fully covered, fully clamped device), as illustrated in Fig. 5a. For the lowest mode with full azimuthal symmetry, the potential energy of such a device with out-of-plane flexural deflection $w(r,\theta)$ is

$$U = \frac{D}{2}\int_0^{2\pi} d\varphi \int_0^R \left(\frac{\partial^2 w}{\partial r^2} + \frac{1}{r}\frac{dw}{dr}\right)^2 r dr, \qquad (1)$$

where $D=E_Y t^3/[12(1-\nu^2)]$ is the bending rigidity (E_Y is Young's modulus, t is thickness, and ν is Poisson's ratio). Its effective spring constant can be estimated accordingly, by

$$k_{eff} = \frac{d^2}{dw_{eff}^{\ 2}} U = \int_0^{2\pi} d\varphi \times \frac{D}{2}\frac{d^2}{dw_{eff}^{\ 2}} \int_0^R \left(\frac{\partial^2 w}{\partial r^2} + \frac{1}{r}\frac{dw}{dr}\right)^2 r dr \cdot \qquad (2)$$

For situations with $\theta \neq 0$ (Fig. 5b), assuming all the restoring force comes from the clamped edge, the effective spring constant can be written as

$$k_{eff} = \frac{d^2}{dw_{eff}^{\ 2}} U = \int_0^{2\pi-\theta} d\varphi \times \frac{D}{2}\frac{d^2}{dw_{eff}^{\ 2}} \int_0^R \left(\frac{\partial^2 w}{\partial r^2} + \frac{1}{r}\frac{dw}{dr}\right)^2 r dr, \qquad (3)$$

by extending the assumption of azimuthal symmetry for first order approximation. Therefore

$$k_{eff} \propto (2\pi - \theta). \qquad (4)$$

With similar assumptions and approximations the effective mass of the resonator is found to be proportional to the surface area of the resonator,

$$m_{eff} \propto \left[(2\pi - \theta) + \sin(\theta/2)\cos(\theta/2)\right]. \qquad (5)$$

In Fig. 5c we plot the normalized resonance frequency $f_1(\theta)/f_1(\theta=0)$, using Eqs. (4) and (5). It clearly captures the main features of the f_1 mode shown in Fig. 4, *i.e.*, f_1 first decreases then increases, between θ=0º and θ=180º.

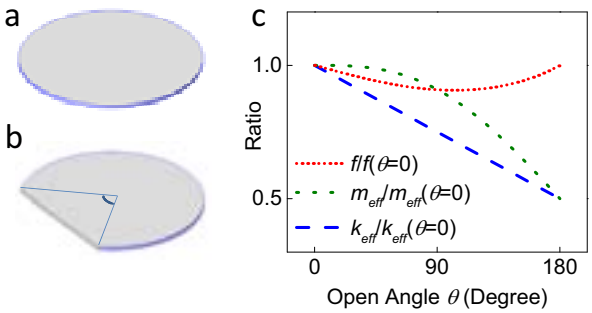

Fig. 5. Simple model demonstrating the effects of unclamped open edges on the resonance frequency, stiffness, and effective mass. **a**. & **b**. Schematics of the clamping conditions for completely and incompletely covered devices. **c**. Calculated ratios (normalized quantities) using Eqs. (4) & (5).

IV. Conclusions

In summary, we have demonstrated using irregular MoS_2 nanoflakes for making HF/VHF nanomechanical resonators with robust performance and interesting multimode characteristics that are comparable to or even better than in their counterpart ideal structures. In combination with FEM and intuitive modeling, we show the possibility of mode shape engineering and frequency control by exploiting this additional geometric degree of freedom, *i.e.*, the open angle θ, degree of coverage in incompletely clamped drumhead structures.

References

[1] A. K. Geim and K. S. Novoselov, "The rise of graphene," *Nat. Mater.*, vol. 6, pp. 183–191, Mar. 2007.

[2] A. K. Geim, "Graphene: status and prospects," *Science*, vol. 324, pp. 1530–1534, Jun. 2009.

[3] K. S. Novoselov, "Nobel lecture – graphene: materials in the flatland," *Rev. Mod. Phys.*, vol. 83, pp. 837–849, Aug. 2011.

[4] Q. H. Wang, K. Kalantar-Zadeh, A. Kis, J. N. Coleman, and M. S. Strano, "Electronics and optoelectronics of two-dimensional transition metal dichalcogenides," *Nat. Nanotechnol.*, vol. 7, pp. 699–712, Nov. 2012.

[5] K. S. Novoselov, A. K. Geim, S. V. Morozov, D. Jiang, Y. Zhang, S. V. Dubonos, I. V. Grigorieva, and A. A. Firsov, "Electric field effect in atomically thin carbon films," *Science*, vol. 306, pp. 666–669, Oct. 2004.

[6] K. S. Novoselov, D. Jiang, F. Schedin, T. J. Booth, V. V. Khotkevich, S. V. Morozov, and A. K. Geim, "Two-dimensional atomic crystals," *Proc. Nat. Acad. Sci. USA*, vol. 102, pp. 10451–10453, Jul. 2005.

[7] R. F. Frindt, "Single crystals of MoS_2 several molecular layers thick," *J. Appl. Phys.*, vol. 37, pp. 1928–1929, Mar. 1966.

[8] J. Lee, Z. Wang, K. He, J. Shan, and P. X.-L. Feng, "High frequency MoS_2 nanomechanical resonators," *ACS Nano*, vol. 7, pp. 6086–6091, Jun. 2013.

Dynamics of Microscale Thin Film AlN Piezoelectric Resonators Enables Low Phase Noise UHF Frequency Sources

Gianluca Piazza, Augusto Tazzoli, Nicholas Miller,
Jeronimo Segovia, Cristian Cassella
Department of Electrical and Computer Engineering
Carnegie Mellon University
Pittsburgh, PA, USA

Jabeom Koo, Brian Otis
Department of Electrical and Computer Engineering
University of Washington
Seattle, WA, USA

Kamala McNaul, Brian Gibson, Kimberly Turner
Department of Mechanical Engineering
University of California Santa Barbara
Santa Barbara, CA, USA

Todd Palmer
Vectron International
Mount Holly, PA, USA

Abstract— **Miniaturized, multi-band and high frequency oscillators that are compatible with CMOS processes are highly desirable for the synthesis of compact, stable, and low power frequency sources for reconfigurable radio frequency communication systems and cognitive radios. Aluminum nitride (AlN) contour mode MEMS resonators (CMR) are emerging devices capable of high *Q*, low impedance, and multi-frequency operation on a single chip. The frequency stability of these AlN MEMS devices is of primary importance in delivering oscillators that exhibit low phase noise, and low sensitivity to temperature and acceleration. In this article we describe how the resonator dynamics impacts oscillator performance and present some preliminary demonstrations of ultra-high-frequency (UHF) oscillators. An example of an oscillator prototype we synthesized with a 586 MHz AlN CMR exhibited phase noise < - 91 dBc/Hz and – 160 dBc/Hz at 1 kHz and 10 MHz offsets, temperature stability of 2 ppm from - 20 to + 85 ºC, and acceleration sensitivity < 30 ppb/G.**

Oscillator; aluminum nitride; piezoelectric resonator; non-linear dynamics; non-linear oscillator; phase nosie.

I. INTRODUCTION

Low phase noise (PN) frequency sources from 100 MHz to 1.5 GHz rely on mechanical resonators such as quartz crystals and surface acoustic wave devices to form stable references. Despite the impressive performance, these components cannot be directly integrated with CMOS electronics, are relatively bulky and are far from attaining the ultimate size, weight and power consumption that would be desirable for high-end commercial, industrial, and especially military applications. Furthermore, the synthesis of next generation highly reconfigurable radio frequency (RF) systems and cognitive radios hinges upon the deployment of new components that are smaller in size, are CMOS integrable, and can be dynamically reconfigured.

Thin film micro and nanoscale resonators have emerged as a promising class of devices to address these needs and synthesize stable frequency sources [1-6]. Thin film piezoelectrics have shown to be the only viable transduction mechanism to demonstrate Ultra High Frequency (UHF) references. Aluminum nitride (AlN) contour-mode resonators (CMR) [5, 6] can provide high *Q* and low motional impedance and are especially suited for the implementation of CMOS-integrable multi-frequency sources on a single chip.

Nonetheless, the ultimate performance of these devices is hindered by their miniaturized dimensions, their complex dynamics and the unknown noise mechanisms associated with it. In this summary paper we explain how the non-linear dynamics of the AlN resonators are due to self-heating. Furthermore, we experimentally show how the dynamics of the resonator can be exploited to evade amplifier noise and reduce the close-in PN of the oscillator. We also present measurement results of the intrinsic noise of these resonators in an open-loop configuration, a particularly challenging task at high frequencies, but of paramount importance in order to fully understand the limiting mechanisms of phase noise.

With the aim of delivering temperature stable oscillators, we introduce geometrical variations in the resonator layout to enable low power ovenization. Preliminary demonstration of UHF sources have yielded oscillators with PN < -91 dBc/Hz and – 160 dBc/Hz at 1 kHz and 10 MHz offsets for a 586 MHz carrier, temperature stability of 2 ppm from - 20 to + 85 ºC, and acceleration sensitivity < 30 ppb/G.

II. DYNAMICS OF MICROSCALE ALN MEMS RESONATORS

A. Principle of Operation of AlN MEMS Resonators

AlN CMRs (Fig. 1) are devices formed by a c-axis oriented thin film of AlN sandwiched between metal electrodes. The top electrode is generally patterned into interdigitated electrodes in a manner similar to what is done with surface acoustic wave (SAW) devices. The bottom electrode is used to confine the electric field and excite what is known as a symmetric lamb wave mode. The electrode configuration ensures that the CMR has a high electromechanical coupling (generally 1 % < k_t^2 < 2.5 %). The sound velocity of CMRs is about twice the one of a SAW device built with the same

The project was funded by the DARPA MTO through the MESO/DEFYS program. Award n. FA86501217264

material set. Hence the period of the interdigitated electrodes, which is used to define the center frequency of the CMR, is about twice the size of a SAW resonator. The CMR, being formed by a suspended membrane, can attain a higher Q than a thin film SAW device. Qs ranging from 2,000 to 4,000 in air have been recorded from 20 MHz to 1 GHz. Recent studies have shown that damping in the CMR is mostly affected by anchor loss [7] below 500 MHz, whereas interfacial dissipation dominates above 500 MHz. The device geometry has been optimized to mitigate anchor losses [8], improve k_t^2 [9], and minimize spurious modes [10]. The resonator k_t^2 and Q have a direct impact on the performance of an oscillator. A high k_t^2 helps reducing the power required to sustain oscillations, and ultimately improves the oscillator phase noise (PN) floor as the resonator has a lower motional resistance. In general, a high Q reduces the power required to attain a certain PN value.

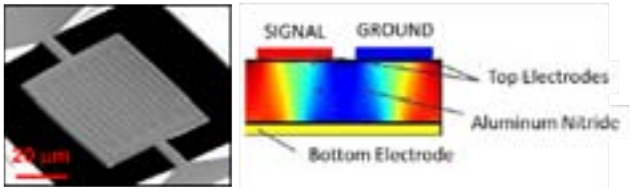

Figure 1. Scanning electron micrograph of a high frequency AlN CMR and schematic image of the mode of vibration of an electrode pair.

B. Fabrication of AlN MEMS Resonators

The AlN CMRs are fabricated by using standard processes that are common to the seminconductor industry for the making of integrated circuits [6]. The repeatable synthesis of these devices has been enabled by the development of low temperature sputtering processes for the deposition of highly oriented AlN thin films [11]. Being the device formed by a dielectric and two metal electrodes, the methods for deposition of the main materials and their patterning are compatible with complementary metal oxide semiconductor (CMOS) devices. Demonstration of direct integration of AlN CMRs with CMOS processes has been reported in the literature [12]. Additionally, efforts for large scale 3D heterogeneous integration of these devices with CMOS are ongoing.

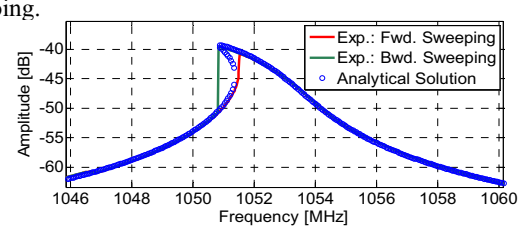

Figure 2. Characteristic non-linear admittance response (amplitude only) of a 1 GHz AlN CMR at high power. Experiments were fit by a duffing-like system of non-linear equations.

C. Non-Linear Dynamics of AlN MEMS Resonators

When driven by high power levels, the AlN CMRs exhibit Duffing-like non-linearity. Our studies on amplitude-frequency (A-f) response and intermodulation distortion have revealed that the source of this non-linearity is the self-heating of the resonator [13, 14]. We have labeled this non-linearity as thermal, as it is highly dependent upon the temperature coefficient of frequency of the CMR and its thermal time constant (Fig. 2). The resonator non-linearity has a direct impact on the performance of an electronic oscillator. The A-f effect converts the resonator amplitude noise into phase noise modulation, hence worsening the oscillator performance. On the contrary, non-linearity could be advantageously exploited to improve PN. A proper design of the oscillator operating point could ensure noise cancellation [15, 16]. As SAW devices resort to temperature compensated substrates, in most cases they do not exhibit this kind of non-linearity.

III. ALN MEMS BASED OSCILLATORS

A. Oscillator Design

Being the motional impedance of the CMR similar in value to the one of a SAW device, the same design techniques used for the synthesis of SAW oscillators can be adopted for CMRs. In most cases, a single transistor (or a coupled pair in the case of a differential solution) is used to sustain oscillations. Pierce and Colpitts oscillators are the most common configurations (Fig. 3). Either discrete or on-chip amplifiers have been used to sustain oscillations. In either case, the resonator is connected to the amplifier through wirebonds to traces designed on a printed circuit board (PCB). Si, SiGe and GaAs transistors have all been tested for the synthesis of AlN CMR oscillators.

Given the motional impedance of the resonator, the Barkhausen criterion is readily met by various values of the coupling capacitors (C_g and C_d in Fig. 4). Their value is generally set so as to minimize power consumption in the oscillator and eliminate any parasitic oscillation at high frequency. For a given motional impedance, power consumption in an oscillator tends to increase with the square of the frequency. This aspect needs to be taken into account when evaluating the performance of an oscillator. The figure of merit (FoM) of an oscillator takes this into account by scaling the PN performance by the amount of power consumption required to achieve such value.

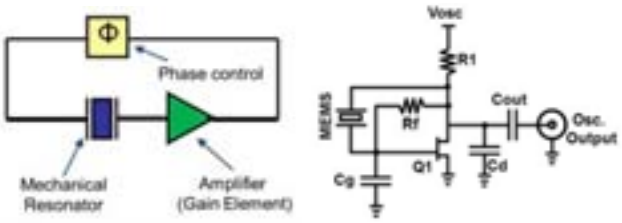

Figure 3. (left) Schematic representation of a closed loop oscillator. The resonator is the frequency setting element, whereas the amplifer is used to adjust the gain vs. frequency. Phase is separately adjusted to control the resonator operating point in a closed-loop system. (right) Schematic circuit of a simple Pierce oscillator used to demonstrate UHF oscillators. Transistor Q1 is used to sustain oscillations. A proper operating point, set by change the phase in the feedback loop, can ensure phase noisce canceling.

More details on the specific design of the oscillator circuit can be found in [17, 18].

B. Noise Sources and Methods to Attain Minimum Phase Noise

The main noise sources in an oscillator are either white phase fluctuations (generally encountered in any device due to Brownian motion) or flicker phase and frequency fluctuations, respectively in the sustaining amplifier or the resonator. The latter are known as parametric noise sources and do not scale

with the output power. Additional phase noise can also be generated by amplitude-frequency conversion due to non-linearity in the resonator.

The oscillator floor is generally set by the amplifier noise figure and the amount of power handling in the resonator. A lower noise figure and higher power handling will linearly improve the PN floor of the oscillator. These improvements occur for offset frequencies above the resonator mechanical time constant, known as the Lesson's frequency ($f_o/2Q_{loaded}$, where f_o is the resonator center frequency and Q_{loaded} is the loaded Q of the resonator in the circuit).

The phase diffusion of the amplifier (either white or flicker) is processed by the resonator dynamics. The resonator acts as an integrator and divides the power spectral density of the noise by f^2 for offset frequencies below the Lesson's frequency. This means that, in the case of additive white noise, a higher Q will reduce the amplifier and resonator noise, for a given oscillator output power. In the case of amplifier parametric noise, the output power will not scale the overall PN, but the Q would set the corner frequency at which the noise spectrum will change from $1/f$ to $1/f^3$ (or $1/f^2$ to $1/f^3$ depending on the location of the flicker corner frequency). Resonator non-linearity can worsen the oscillator PN by converting amplitude noise to frequency noise. Nonetheless, this non-linear phenomenon can also be exploited for evading amplifier phase fluctuations [15, 16]. In fact, a non-linear resonator exhibits specific phase/frequency relationship for which the oscillator dynamics can be substantially modified. Intuitively, as described in [19], the resonator time constant can be made infinite at special operating points generated by the resonator non-linearity. When the resonator is locked in that particular state in a closed-loop oscillator, then the amplifier phase fluctuations can be eliminated. An example of this demonstration is shown in Fig. 4.

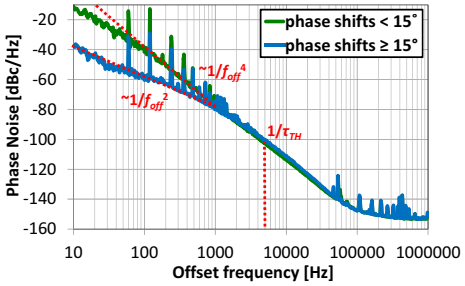

Figure 4. PN plot for a non-linearly driven AlN 220 MHz CMR in a close loop oscillator. For specific phases of the closed loop configuration, the oscillator exhibits clear PN cancellation. τ_{th} is the resonator thermal time constant.

It is important to note that this cancellation works only for noise sources external to the resonator. Hence, the ultimate noise will be set by the resonator intrinsic phase and frequency fluctuations. Therefore, it is of paramount importance to measure the intrinsic phase noise of the AlN CMR. We have performed this task in [20], where we have shown evidence that the oscillator phase noise is limited by the resonator flicker frequency fluctuations. These fluctuations cause a $1/f^3$ slope in the power spectral density of PN, which is a characteristic of many AlN CMR-based oscillators. The physical origin of these frequency fluctuations is still unknown (metal electrodes, AlN thin films defects or dielectric relaxation, substrate effects, piezoelectric coefficient modulation, *etc.*) and is under investigation.

C. Oscillator Ovenization

The oscillator temperature stability is of paramount importance in ensuring device operation over commercial or industrial temperature standards. Frequency stability in the order of few part per million (ppm) over a temperature range of about 125 °C is generally required. Since the AlN CMR intrinsic temperature coefficient of frequency (TCF) is about - 27 ppm/K, an uncompensated device cannot meet these stringent specifications. For this reasons methods to reduce the resonator TCF by introducing an external compensating material such as SiO_2 have been implemented [21]. This technique is successful in reducing the TCF to a fraction of few ppm/K, but it is frequency dependent and requires the introduction of an additional material in the resonator stack. This step also comes with drawbacks in terms of fabrication complexity and reduction in k_t^2. To obviate to these issues, we have decided to take advantage of the miniaturized dimension of the resonator and use heaters integrated in the body of the resonator to readily ovenize the device with just few mW of power (Fig. 5). In this implementation a serpentine heater embedded in the AlN CMR body is used simultaneously as the heater and temperature sensor. When inserted in a simple analog feedback circuit [22], the resonator temperature is maintained constant at the desired value set by the initial calibration of a Wheatstone bridge. It is important to note that any temperature fluctuations external to the resonator is not compensated by this approach.

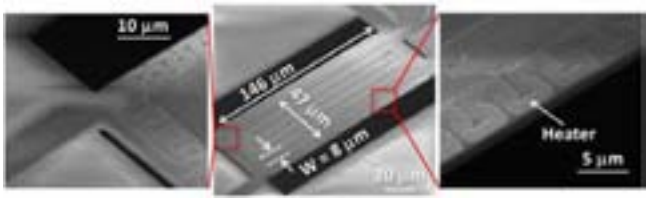

Figure 5. Scanning electron micrograph of an ovenized AlN CMR resonator.In this implementation, the heater is placed on the perimeter of the resonator body.

D. Oscillator Acceleration Sensitivity

The acceleration sensitivity of an oscillator can ultimately impact its use in the field. The presence of an external, low frequency vibration that couples into the resonator is up-converted to the carrier frequency and manifests itself as an increase of the oscillator PN at a specific offset [23]. The acceleration sensitivity is affected by many aspects of the oscillator including primarily the resonator mechanical supports, the way the resonator is bonded to the PCB, and the length of the wirebonds. Assuming a proper device assembly, though, the ultimate limit will be set by the resonator geometry. In the case of AlN CMRs, the structure is particularly subject to vibration in the vertical direction. In fact, the resonator is formed by a thin membrane; hence it has the lowest stiffness in the vertical direction. Finite element analysis of the resonator acceleration sensitivity has yielded $\Gamma < 0.05$ ppb/G. This value is about 10X better than the best commercially available quartz crystals.

E. Prototype Oscillator

A prototype oscillator was assembled by connecting a 586 MHz ovenized AlN CMR to a GaAs sustaining amplifier. Temperature stability was ensured by inserting the resonator in a Wheatstone bridge and controlling its temperature set point through an external analog feedback circuit. The oscillator was simultaneously tested for PN, temperature stability and acceleration sensitivity. The results of these tests are reported in Fig. 6. The oscillator exhibited phase noise < - 91 dBc/Hz and – 160 dBc/Hz at 1 kHz and 10 MHz offsets, temperature stability of 2 ppm (when manually tuned) from - 20 to + 85 ºC, and acceleration sensitivity < 30 ppb/G (limited by resonator to PCB mounting). Overall, the oscillator performance is on par or better than commercially available SAW oscillators.

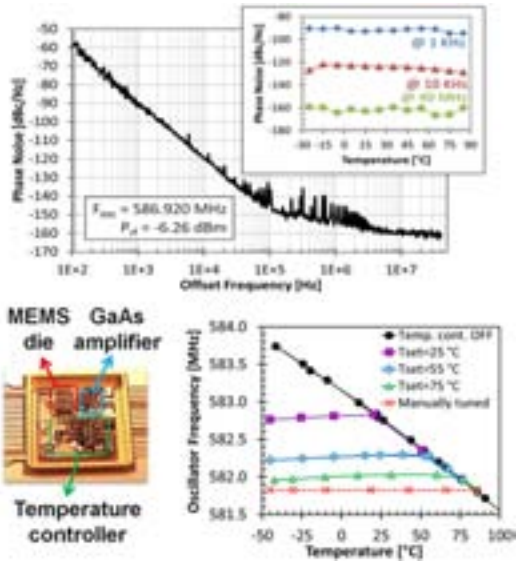

Figure 6. Photograph of a packaged 586 MHz oscillator based on an AlN CMR, its phase noise, and temperature stability.

IV. Conclusion

This paper provided an overview of the latest developments on the use of AlN CMRs for the synthesis of high frequency oscillators. Device operation and oscillator design were reviewed. Fundamental noise mechanisms and methods of evading phase noise were presented. Temperature and acceleration sensitivity were also discussed. Preliminary UHF prototypes have shown performance that are on par with existing commercial devices, but take on a fraction of their volume and, most importantly, can be directly integrated with electronics. Further developments and concerted effort from many research groups will help elucidate the fundamental limits of this technology and continue fueling the timing market revolution made possible by MEMS.

References

1. Chang, D.T., H.P. Moyer, R.G. Nagele, R.L. Kubena, R.J. Joyce, D.J. Kirby, P.D. Brewer, H.D. Nguyen, and F.P. Stratton, "Nonlinear UHF quartz MEMS oscillator with phase noise reduction", *2013 IEEE 26th International Conference on Micro Electro Mechanical Systems (MEMS), 20-24 Jan. 2013*, p. 781-4.
2. Nguyen, C.T.C., "MEMS technology for timing and frequency control", *IEEE Transactions on Ultrasonics, Ferroelectrics and Frequency Control*, 2007, **54**(2), p. 251-70.
3. Ayazi, F., "MEMS for integrated timing and spectral processing", *2009 IEEE Custom Integrated Circuits Conference (CICC), 13-16 Sept. 2009*, p. 65-72.
4. Weinstein, D. and S.A. Bhave, "Internal dielectric transduction of a 4.5 GHz silicon bar resonator", *2007 IEEE International Electron Devices Meeting - IEDM '07, 10-12 Dec. 2007*, p. 415-18.
5. Piazza, G., "Integrated aluminum nitride piezoelectric microelectromechanical system for radio front ends", *Journal of Vacuum Science & Technology A (Vacuum, Surfaces, and Films)*, 2009, **27**(4), p. 776-84.
6. Piazza, G., P.J. Stephanou, and A.P. Pisano, "Piezoelectric aluminum nitride vibrating contour-mode MEMS resonators", *Journal of Microelectromechanical Systems*, 2006, **15**(6), p. 1406-18.
7. Segovia-Fernandez, J., M. Cremonesi, C. Cassella, A. Frangi, and G. Piazza, *Experimental Study on the Impact of Anchor Losses on the Qualty Factor of Contour Mode AlN Resonators*, in *IEEE Transducers 2013, in print,* 2013.
8. C. Cassella, J. Segovia-Fernandez, M. Cremonesi, A. Frangi, and G. Piazza, *Reduction of Anchor Losses by Etched Slots in Aluminum Nitride Contour Mode Resonators*, in *to be presented at IEEE IFCS 2013*.
9. C. Cassella, J. Segovia-Fernandez, and G. Piazza, *Segmented Electode Excitation of Aluminum Nitride Contour Mode Resonators to Optimize the Device Figure of Merit* in *IEEE Transducers 2013, in print,* 2013.
10. Giovannini, M., S. Yazici, K. Nai-Kuei, and G. Piazza, "Spurious mode suppression via apodization for 1 GHz AlN contour-mode resonators", *2012 IEEE International Frequency Control Symposium (FCS), 21-24 May 2012*, p. 5 pp.
11. Piazza, G., V. Felmetsger, P. Muralt, R.H. Olsson III, and R. Ruby, "Piezoelectric aluminum nitride thin films for microelectromechanical systems", *MRS bulletin*, 2012, **37**(11), p. 1051-1061.
12. Wojciechowski, K., R. Olsson, M. Tuck, E. Roherty-Osmun, and T. Hill, "Single-chip precision oscillators based on multi-frequency, high-Q aluminum nitride MEMS resonators", *Solid-State Sensors, Actuators and Microsystems Conference, 2009. TRANSDUCERS 2009. International*, p. 2126-2130.
13. Segovia-Fernandez, J. and G. Piazza, "Thermal Nonlinearities in Contour Mode AlN Resonators", *Microelectromechanical Systems, Journal of*, 2013, **PP**(99), p. 1-1.
14. Tazzoli, A., M. Rinaldi, and G. Piazza, "Experimental Investigation of Thermally Induced Nonlinearities in Aluminum Nitride Contour-Mode MEMS Resonators", *IEEE Electron Device Letters*, 2012, **33**(5), p. 724-6.
15. Greywall, D.S., B. Yurke, P.A. Busch, A.N. Pargellis, and R.L. Willett, "Evading amplifier noise in nonlinear oscillators", *Physical Review Letters*, 1994, **72**(19), p. 2992-5.
16. Yurke, B., D.S. Greywall, A.N. Pargellis, and P.A. Busch, "Theory of amplifier-noise evasion in an oscillator employing a nonlinear resonator", *Physical Review A (Atomic, Molecular, and Optical Physics)*, 1995, **51**(5), p. 4211-29.
17. Chengjie, Z., N. Sinha, J. Van der Spiegel, and G. Piazza, "Multifrequency Pierce Oscillators Based on Piezoelectric AlN Contour-Mode MEMS Technology", *Journal of Microelectromechanical Systems*, 2010, **19**(3), p. 570-80.
18. Rinaldi, M., Z. Chengjie, J. Van der Spiegel, and G. Piazza, "Reconfigurable CMOS Oscillator Based on Multifrequency AlN Contour-Mode MEMS Resonators", *IEEE Transactions on Electron Devices*, 2011, **58**(5), p. 1281-6.
19. J. Segovia-Fernandez, C. Cassella, and G. Piazza, "Close-in Phase Noise Reduction in an Oscillator based on 222 MHz Non-linear Contour Mode AlN Resonators", *to be presented at IEEE IFCS 2013*
20. Nicholas Miller and G. Piazza, *Vector Network Analyzer Measurements of Frequency Fluctuations in Aluminum Nitride Contour-Mode Resonators*, in *to be presented at IEEE IFCS 2013*.
21. Rinaldi, M., A. Tazzoli, J. Segovia-Fernandez, V. Felmetsger, and G. Piazza, "High power and low temperature coefficient of frequency oscillator based on a fully anchored and oxide compensated AlN contour-mode MEMS resonator", *2012 IEEE 25th International Conference on Micro Electro Mechanical Systems (MEMS), 29 Jan.-2 Feb. 2012*, p. 696-9.
22. Tazzoli, A., M. Rinaldi, and G. Piazza, "Ovenized high frequency oscillators based on aluminum nitride contour-mode MEMS resonators", *2011 IEEE International Electron Devices Meeting (IEDM 2011), 5-7 Dec. 2011*, p. 20-2.
23. Filler, R.L., "The acceleration sensitivity of quartz crystal oscillators: a review", *IEEE Transactions on Ultrasonics, Ferroelectrics and Frequency Control*, 1988, **35**(3), p. 297-305.

Single Transistor Oscillator Based on a Graphene-Aluminum Nitride Nano Plate Resonator

Zhenyun Qian, Yu Hui, Matteo Rinaldi
Department of Electrical and Computer Engineering
Northeastern University
Boston, MA, USA
qian.z@husky.neu.edu
hui.y@husky.neu.edu
rinaldi@ece.neu.edu

Fangze Liu, Swastik Kar
Department of Physics
Northeastern University
Boston, MA, USA
liu.fang@husky.neu.edu
s.kar@neu.edu

***Abstract*—This paper reports on the first demonstration of a high frequency (245 MHz) single transistor oscillator based on Graphene-Aluminum Nitride (G-AlN) nano-plate resonator (NPR). For the first time, a 2-dimensional (2D) electrically conductive graphene layer was integrated on top of an ultra-thin (500 nm) AlN nano-plate and excited into a high frequency contour-extensional mode of vibration by piezoelectric transduction. The resulting ultra-thin, low mass and high frequency G-AlN nanomechanical resonator showed high values of electromechanical coupling coefficient (k_t^2≈1.8%) and quality factor (Q_m≈1000) which enabled the implementation of a low phase noise (-87 dBc/Hz @ 1kHz offset and -125 dBc/Hz floor) single transistor oscillator. The experimental results also demonstrate the great potential of the proposed technology for the implementation of a new class of ultra-sensitive and low noise G-AlN resonant sensors.**

Keywords—Graphene; Aluminum Nitride (AlN); MEMS; NEMS; Oscillators; Nano Plate Resonator

I. INTRODUCTION

Micro and Nano Electro Mechanical Systems (MEMS/NEMS) resonators have shown great potential for multiple sensing applications thanks to the unique combination of extremely high sensitivity to external perturbations (due to their very reduced dimensions) and ultra-low noise performance (due to the intrinsically high quality factor, *Q*, of such resonant systems). Among different MEMS/NEMS resonant sensors, the AlN nano plate resonant sensor (NPR-S) technology [1], which involves exciting high frequency (100 MHz to 10 GHz) bulk acoustic waves in piezoelectric nano plates (thickness < 1 μm) made out of AlN, has emerged as one of the most promising solutions for the realization of extremely sensitive, miniaturized and low power sensors due to their high *Q* factor values and power handling capabilities [2].

The performance of AlN NPR-S in terms of sensitivity, limit of detection and detection speed can be further improved by scaling thickness and decreasing the equivalent density of the AlN NPR maintaining, at the same time, high values of *Q* factor and transduction efficiency [3]. The physical and electrical properties of the metal electrodes fundamentally limit volume and frequency scaling of conventional MEMS/NEMS piezoelectric resonators [4]. Furthermore, it has been recently shown that metal electrode damping and interface strain are responsible for the *Q* limits in conventional AlN Lamb wave resonators [5].

In this work, a stepping stone towards the development of ultra-high resolution and fast resonant sensors is set by integrating a 2D graphene electrode on top of an AlN resonant nano plate [6] and using such G-AlN resonator to implement a low phase noise single transistor oscillator. Graphene is a one-atom thick layer of the mineral graphite with excellent electrical conductivity and extremely light weight. The ultra-low mass 2D graphene layer is employed, in lieu of a relatively thicker and heavier metal film, as top electrically floating electrode in the lateral field scheme [3] used to excite vibration in the piezoelectric nano plate. Such 2D graphene top layer not only represents the thinnest and lightest conductive electrode ever used to excite vibration in a piezoelectric NEMS resonator but it also has the potential to be used as an effective chemical interactive material with the largest possible surface to volume ratio [7].

II. GRAPHENE-ALUMINUM NITRIDE NANO PLATE RESONATOR

The three-dimensional schematic representation of the G-AlN NPR is shown in Fig. 1. The high frequency bulk acoustic mode of vibration is excited into the AlN nano plate by means of an interdigital bottom electrode and an electrically floating top electrode which acts to confine the excitation field across the thickness of the piezoelectric layer [8].

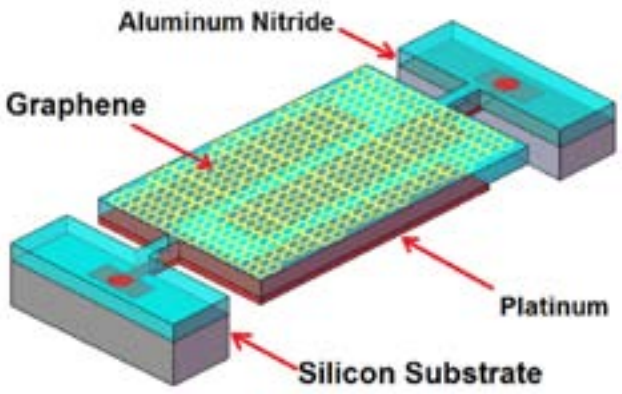

Fig. 1: Schematic representation of the G-AlN NPR

This work was partially supported by DARPA Young Faculty Award contract number: N66001-12-1-4221

Given the equivalent mass density, ρ_{eq} , and Young's modulus, E_{eq}, of the material stack (AlN and electrodes) that forms the resonator, the center frequency, f_0, of this laterally vibrating mechanical structure, is univocally set by the pitch, W_0, of the interdigital bottom electrode. The resonance frequency of the device can be expressed as (1) [9]

$$f_0 = \frac{1}{2W_0}\sqrt{\frac{E_{eq}}{\rho_{eq}}} \quad (1)$$

A fundamental parameter for gravimetric sensing applications is the resonator sensitivity, S, to mass per unit area, which, for a NPR-S loaded on its top surface, can be expressed as in (2) [10]

$$S = -\frac{f_0}{2\rho_{eq}T} \quad (2)$$

Table 1 compares the expected sensitivity, S, of the G-AlN NPR with one of the conventional AlN NPRs, based on the same core design but employing a 150 nm thick gold top electrode instead of the 2D graphene top electrode (gold is typically used as top metal electrode in NEMS resonant sensors since it can be easily functionalized with thiolated ligands). 3 fold improvement in sensitivity is expected with this first prototype of G-AlN NPR-S.

TABLE 1: COMPARISON OF SENSITIVITIES

	ρ_{eq}(kg·m^{-3})	E_{eq}(GPa)	T(μm)	S (kHz·μm^2/fg)
AlN	7022	348	0.70	18.1
G-AlN	4192	396	0.55	53.1

T is the equivalent thickness of the material stack

A combination of top-down microfabrication techniques (6 masks) and bottom-up growth for graphene was employed to fabricate the G-AlN NPR of this work (Fig. 2). A macroscopic sheet of graphene (1.5x1.5 cm limited by furnace dimensions) was grown directly on a copper (Cu) foil using a chemical vapor deposition (CVD) method and then transferred onto the pre-fabricated NEMS die. High quality graphene was maintained throughout the fabrication process (Fig. 3). [6]

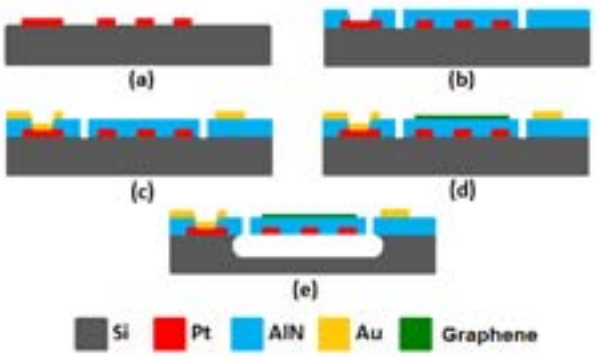

Fig. 2: Microfabrication process: (a) sputter deposition and lift-off of Pt bottom electrode; (b)Sputter deposition of AlN, wet etch to open vias and dry etch to define device lateral dimensions; (c) sputter deposition and lift-off of top Au probing pads; (d) graphene transfer and patterning; (e) graphene protection and XeF_2 dry release of the G-AlN NPR. Steps (a) to (c) were processed at wafer level, while (d) and (e) at the die level.

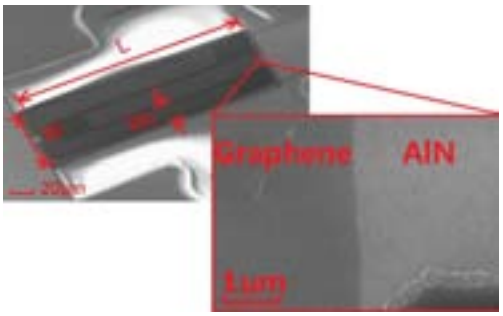

Fig. 3: SEM image of the fabricated G-AlN NPR and high magnification view of the anchor part which shows the boundary of the graphene plate. (W=60μm, L=200μm, W_0=20μm)

III. EXPERIMENTAL RESULTS

The fabricated G-AlN NPR was tested at room temperature and atmospheric pressure in a RF probe station and its electrical response was measured by an Agilent E5071C network analyzer after performing a short–open–load calibration on a reference substrate. The electromechanical performance of the device was extracted by Butterworth-Van Dyke (BVD) model fitting and compared to one of the conventional AlN NPRs, fabricated on the same substrate and based on the same core design but employing a 150 nm thick gold top electrode instead of the 2D graphene top electrode (Fig. 4 and Table 2).

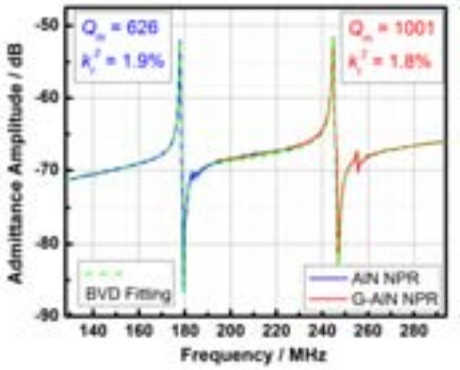

Fig. 4: Measured admittances and BVD fitting of the fabricated G-AlN NPR and the conventional AlN NPR.

Table 2 shows the comparison between the BVD model fitting parameters of the fabricated G-AlN NPR and the conventional AlN NPR. Higher operating frequency and comparable $k_t^2 \cdot Q_{load}$ was achieved with the G-AlN NPR. Despite the relatively high sheet resistance (~1.5kΩ/□) of the in-house synthesized graphene layer, the 2D graphene electrode introduced only a relatively small and tolerable value of electrical resistance, R_s, compared to the 250 times thicker and 3750 times heavier gold electrode. It is worth noting that much lower sheet resistance (~60 Ω/□) can be achieved in commercially available graphene [11] which would further reduce the electrical loading of the graphene electrode to < *2%* of the total loss of the system.

TABLE 2: COMPARISON OF BVD FITTING

	f_0	Q_{load}	k_t^2	C_0	R_m	R_s
AlN	178MHz	432	1.90%	324fF	285Ω	128Ω
G-AlN	245MHz	408	1.81%	282fF	157Ω	228Ω

Both the G-AlN NPR prototype and the conventional AlN NPR were directly wire-bonded to Pierce oscillator circuits implemented with an ATF-551M4 E-pHEMT GaAs transistor. (Fig. 5)

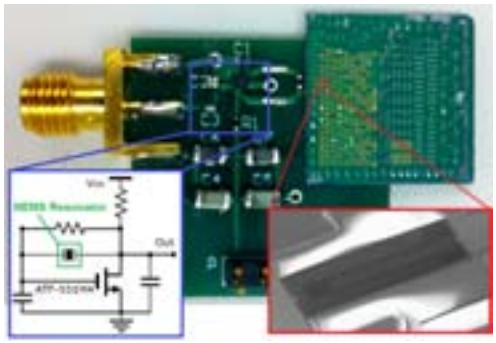

Fig. 5 Oscillator circuit

The phase noise was measured for best bias conditions using an Agilent N9010A EXA signal analyzer. Despite the 250 fold smaller volume of the top electrode and the 38% higher operating frequency, improved phase noise performance was recorded for the G-AlN device due to its higher mechanical Q ($Q_m \approx 1000$). (Fig. 6)

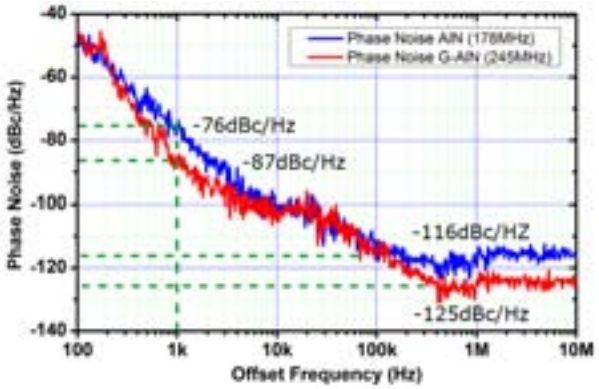

Fig. 6 Measured phase noise of the two oscillators

This experimental result demonstrates that the introduction of the graphene electrode not only enables the fabrication of AlN NPRs with lower volume and mass and improved sensitivity to mass loading but also, despite the volume scaling, allows the achievement of high values of Q_m, which guarantees ultra-low noise performance of the oscillator. The reduced mass and volume, and the increased frequency of operation of such G-AlN NPRs combined with their high Q factor values demonstrate the great potential of the proposed technology for the implementation of a new class of resonant sensors capable of achieving unprecedented values of limit of detection and detection speed.

IV. CONCLUSIONS

In this paper, a high frequency (*245 MHz*) Graphene-Aluminum Nitride (G-AlN) nano plate resonator (NPR) was designed, fabricated and tested. For the first time, a 2-dimensional electrically conductive graphene layer was integrated on top of an ultra-thin (*500 nm*) AlN nano plate and excited into a high frequency contour-extensional mode of vibration by piezoelectric transduction. Despite a bottom metal interdigital electrode is still employed in this first prototype, the fabricated G-AlN resonator is characterized by reduced mass (~53%) and volume (~20%), increased sound velocity, hence resonant frequency (~38%), and unchanged device figure of merit ($k_t^2 \cdot Q_{load}$) compared to one of the conventional AlN NPRs, fabricated on the same substrate and based on the same core design but employing a 150 nm thick gold top electrode instead of the 2D graphene top electrode. The achieved high electromechanical performance of the ultra-thin, low mass and high frequency G-AlN nanomechanical resonator enabled the implementation of a low phase noise (-87 dBc/Hz @ 1kHz offset and -125 dBc/Hz floor) single transistor oscillator.

These experimental results demonstrate that reliable electrical transduction of high frequency mechanical vibration in an ultra-thin and low-mass G-AlN nano plate is possible and can be employed for the making of a new class of resonant sensors with improved sensitivity (Table 1) and noise performance (Fig. 6), hence with unprecedented detection capabilities.

ACKNOWLEDGMENT

The authors wish to thank the staff of the George J. Kostas Nanoscale Technology and Manufacturing Research Center at Northeastern University where the devices were fabricated. This work was partially supported by DARPA Young Faculty Award contract number: N66001-12-1-4221 and NSF Award: ECCS-1202376.

REFERENCES

[1] M. Rinaldi, C. Zuniga and G. Piazza, "Ultra-Thin-Film AlN Contour-Mode Resonators for Sensing Applications", *Proceedings of the IEEE IUS 2009*, pp. 714-717.

[2] C. Zuo, M. Rinaldi and G. Piazza, "Power Handling and Related Frequency Scaling Advantages in Piezoelectric AlN Contour-Mode MEMS Resonators", *Proceedings of the IEEE IUS 2009*, pg. 1187-1190.

[3] M. Rinaldi and G. Piazza, "Effects of Volume and Frequency Scaling in AlN Contour Mode NEMS Resonators on Oscillator Phase Noise", *Proceedings of the IEEE IFCS 2011*, pp. 1-5.

[4] M. Rinaldi, C. Zuniga, C. Zuo, and G. Piazza, "Super High Frequency Two-Port AlN Contour-Mode Resonators for RF Applications", *IEEE Transactions on Ultrasonics, Ferroelectrics, and Frequency Control*, vol. 57, n. 1, pg. 38-45, 2010.

[5] T. Yen, A. P. Pisano and C. T.-C. Nguyen, "High-Q capacitive-piezoelectric AlN Lamb wave resonators", *Proceedings of the IEEE MEMS 2013* pg. 114-117.

[6] Z. Qian, Y. Hui, F. Liu, S. Kar and M. Rinaldi, "245 MHz Graphene-Aluminum Nitride Nano Plate Resonator", *Proceedings of the Transducers 2013*, pg 2005-2008.

[7] Y. Lu, B. R. Goldsmith, N. J. Kybert, and A. T. C. Johnson, "DNA-decorated graphene chemical sensors", *Appl. Phys. Lett.*, vol. 97, pp. 083107, 2010.

[8] G. Piazza, P. J. Stephanou and A. P. Pisano, "Piezoelectric Aluminum Nitride Vibrating Contour-Mode MEMS Resonators", *Journal of Microelectromechanical Systems*, vol. 15, pp. 1406-1418, 2006.

[9] M. Rinaldi, C. Zuniga, and G. Piazza,"5-10 GHz AlN Contour-Mode Nanoelectromechanical Resonators", *Proceedings of IEEE MEMS 2009*, pp. 916-919.

[10] C. Zuniga, M. Rinaldi, S. M. Khamis, A. T. Johnson and G. Piazza,"Nanoenabled Microelectromechanical Sensor for Volatile Organic Chemical Detection", *Appl. Phys. Lett.*, vol. 94, pp. 223122, 2009.

[11] Bluestone Global Tech, http://bluestonegt.com/products/grat-filmtm/

A 78-Microwatt GSM Phase Noise-Compliant Pierce Oscillator Referenced to a 61-MHz Wine-Glass Disk Resonator

Thura Lin Naing, Tristan O. Rocheleau, Elad Alon, and Clark T.-C. Nguyen
Dept. of Electrical Engineering and Computer Sciences
University of California at Berkeley
Berkeley, CA 94720 USA
E-mail: thura@eecs.berkeley.edu

***Abstract*— A 61-MHz Pierce oscillator referenced to a single polysilicon surface-micromachined wine-glass disk resonator has achieved phase noise marks of -119dBc/Hz at a 1-kHz offset and -139dBc/Hz at far-from-carrier offsets. When divided down to GSM's 13MHz, this corresponds to -132dBc/Hz at 1-kHz and -152dBc/Hz at far-from-carrier offsets, both of which satisfy GSM reference oscillator phase noise requirements. This Pierce oscillator achieves such performance using a single disk, not an array, while only consuming 78 microwatts of power, a reduction by a factor of ~4.5 compared with previous work. When power consumption is considered, this performance marks the best figure of merit at 1-kHz carrier offset among published on-chip oscillators to date. Such low phase noise and power consumption posted by a tiny MEMS device may soon become key enablers for low power "set-and-forget" autonomous sensor networks with substantial communication capability.**

Keywords*— *MEMS, oscillator, micromechanical, wine-glass disk, low phase noise, low power, resonator, RF MEMS.

I. Introduction

Reference oscillators based on high-Q MEMS resonators have recently become viable alternatives to traditional quartz versions. With resonator Q's exceeding 100,000, such oscillators have posted impressive phase noise performance, even achieving marks that meet the challenging GSM specification using a mechanically-coupled resonator array-composites occupying only 0.1mm^2 of area and consuming only 350μW of power [1]. While such devices offer compelling savings in power and space compared to quartz for cell phone applications, further reductions in these attributes are still desired for future autonomous wireless sensor networks [2], where nodes would be expected to operate and communicate for long periods without the luxury of replacing their power sources.

Pursuant to further reducing power and area consumption, this work introduces a 61-MHz Pierce oscillator referenced to a single polysilicon wine-glass disk resonator, cf. Fig. 1, reducing die area from 0.1mm^2 to 0.01mm^2, a factor of 10, compared with previous arrayed devices. Furthermore, even with this size reduction, the low noise figure of the improved amplifier design used here yields an oscillator with no degradation in phase noise performance even while total power consumption is lowered drastically. This Pierce oscillator design achieves measured marks of -119dBc/Hz at 1-kHz offset and -139dBc/Hz at far-from-carrier offsets, both of which satisfy GSM specifications (i.e., divided down to GSM's 13MHz, these correspond to -132 dBc/Hz at 1-kHz and -152dBc/Hz at far-from-carrier offsets) while consuming only 78μW power.

Much of the described work was supported by DARPA.

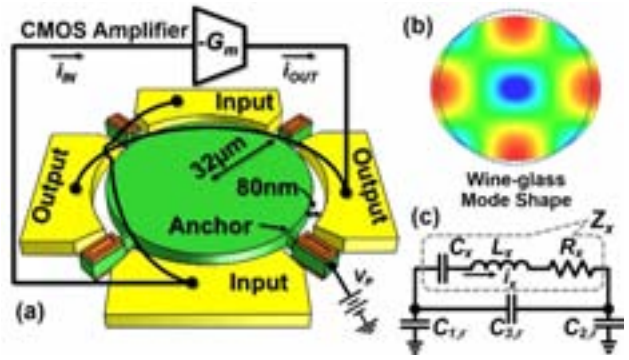

Fig. 1. Perspective-view schematic of (a) a micromechanical wine-glass disk resonator combined with a sustaining transconductance amplifier to form a Pierce oscillator, (b) resonator mode shape, and (c) equivalent electrical circuit.

II. Resonator Operation and Modelling

The wine-glass disk resonator used in this work, depicted in Fig. 1(a), comprises a 3μm-thick, 32μm-radius polysilicon disk supported at quasi nodal points by four beams and surrounded by electrodes spaced only 80nm from its edges. To excite the resonator into motion, a bias voltage V_P is applied to the disk and an ac drive voltage to the input electrode. These voltages combine to produce a force across the input electrode-to-resonator gap that at resonance can excite the wine-glass (i.e., compound (2, 1)) mode shape, shown in Fig. 1(b), which comprises expansion and contraction of the disk along orthogonal axes. The frequency of resonance is defined [3]

$$f_{nom} = \frac{K}{R}\sqrt{\frac{E}{\rho(2+2\sigma)}} \qquad (1)$$

where R is the disk radius, $K = 0.373$ for polysilicon structural material, and E, σ, and ρ are the Young's modulus, Poisson ratio, and density of the structural material, respectively.

In the electrical domain, the resonator behaves as the equivalent LCR tank shown in Fig. 1(c), where $C_{1,r}$, $C_{2,r}$, and $C_{3,r}$ are intrinsic and parasitic capacitors seen at the input and output nodes of the resonator. The dc-biased (V_P) vibrating electrode-

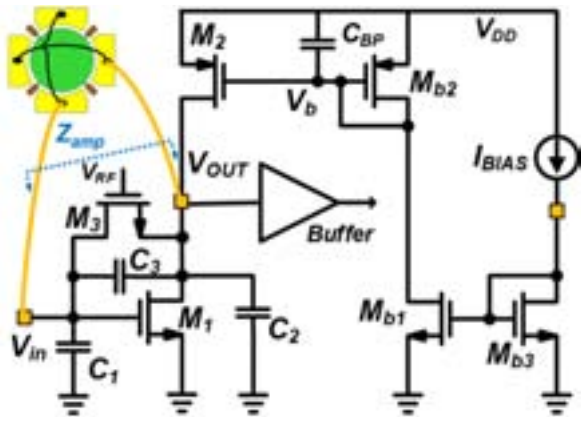

Fig. 2. Schematic of the CMOS amplifier used in the Pierce oscillator, including bias network and parasitic capacitance at input and output nodes.

to-resonator capacitors generate motional currents at each electrode proportional to the disk velocity. If the electrodes are placed as shown in Fig. 1, with the current directions indicated, the input and output currents are in-phase, and current flow can be modeled by a single motional current i_x through the *LCR* tank. The elements R_x, L_x, and C_x link to the mechanical properties of the resonator as follows [4]:

$$R_x = \frac{c_r}{Q\eta^2}, \quad L_x = \frac{m_r}{\eta^2}, \quad C_x = \frac{\eta^2}{k_r}, \quad \eta = V_P \frac{\partial C}{\partial r} \qquad (2)$$

where c_r, m_r, and k_r are the damping, mass, and stiffness of the resonator, respectively, determined via equations given in [5], $\partial C/\partial r$ is the change in resonator-to-electrode capacitance per unit radial displacement.

III. Oscillator Design

As shown in Fig. 2, the Pierce oscillator topology used in this work combines a frequency selective resonator with a single trans-conducting gain device: in this case, the MOS transistor M_1. M_2 serves as a load transistor, while M_3 provides feedback to properly dc-bias transistor M_1. For oscillation to occur, two conditions must hold: 1) the gain around the loop must be larger than unity; and 2) the phase shift around the loop must be zero. Focusing first on the latter, transistor M_1 introduces 180° of phase shift between the input and output voltages. However, at resonance the phase shift across the wine-glass mode disk resonator is 0°, so an additional 180° is needed to satisfy criterion 2. To supply this, the resonator must operate in the inductive region and resonate with C_1, C_2, and C_3, which comprise the total parasitic capacitors from the resonator, the amplifier, and surrounding structures, e.g., bond pads, at the input and output nodes, as shown in Fig. 2.

A. Linear Analysis

At start-up the amplitude of oscillation is small, the whole circuit stays linear, and the impedance looking into the gate and drain of M_1 can be modeled using small signal equivalent circuits, c.f. Fig. 3. Here, impedances Z_1, Z_2, and Z_3 include all resistive and reactive components of devices M_1 (except its transconductance g_{m1}), M_2, and M_3, plus the resonator's parasitic capacitors.

The critical condition for oscillation occurs when Z_{amp} and Z_x sum to zero. For oscillation to start, $|\mathrm{Re}(Z_{amp})|$ must be larger

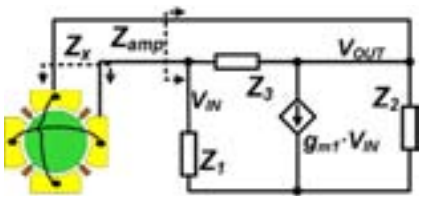

Fig. 3. The small signal equivalent circuits of the oscillator with impedances Z_1, Z_2, and Z_3, which include all the components of the transistors M_1 (except its transconduance g_{m1}), M_2, M_3, and the resonator's parasitic capacitance.

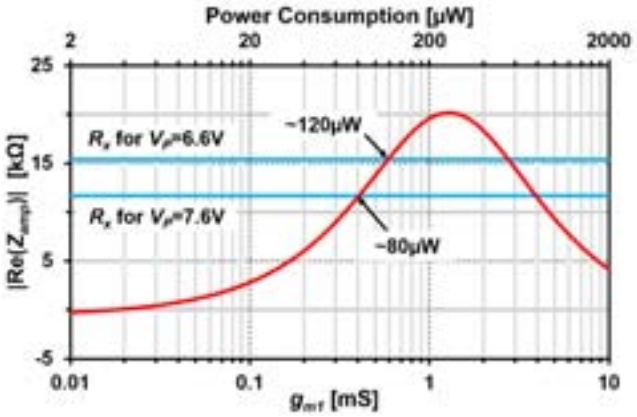

Fig. 4. Theoretical plot of $|\mathrm{Re}(Z_{amp})|$ vs. transconductance, g_{m1}, of the M_1 transistor and the required power consumption to achieve this g_{m1} with V_{DD}=2V. The blue lines correspond to calculated motional resistances of the resonator for different V_P's and indicate theoretical minimum powers required for oscillation.

than R_x. However, Z_1-Z_3 constrain the achievable $|\mathrm{Re}(Z_{amp})|$ to a maximum value as depicted by the red curve in Fig. 4, which is the theoretical plot of $|\mathrm{Re}(Z_{amp})|$ versus g_{m1} (bottom *x*-axis) and the required power consumption for V_{DD} of 2V (top *x*-axis). If the real part (resistances) of Z_1-Z_3 are large, then only the capacitors C_1, C_2, and C_3 remain, in which case the maximum value of $|\mathrm{Re}(Z_{amp})|$ becomes [6]:

$$\left|\mathrm{Re}\left(Z_{amp}\right)\right|_{\max} = \frac{1}{2\omega C_3\left(1 + C_3\left(\frac{1}{C_1} + \frac{1}{C_2}\right)\right)} \qquad (3)$$

If this value is smaller than R_x, no oscillation ensues, even if g_{m1} increases. From (3), there are two ways to increase $|\mathrm{Re}(Z_{amp})|_{\max}$: 1) raise the values of C_1 and C_2 at the cost of burning more power; and 2) reduce the input-to-output feedthrough capacitance C_3. The last of these reveals why self-sustained oscillation of a micromechanical resonator is possible using a Pierce circuit, despite its large motional resistance R_x. Indeed, the C_3 of a 61-MHz wine-glass disk resonator is on the order of 40-50fF, many times smaller than the 6pF in a typical 60-MHz quartz crystal, allowing $|\mathrm{Re}(Z_{amp})|_{\max}$ to exceed the disks R_x of 15kΩ. Interestingly, the C_3 of a wine-glass disk resonator is so small, and it allows a $|\mathrm{Re}(Z_{amp})|_{\max}$ greater than 20kΩ without the need to increase C_1 and C_2. In comparison, with C_3 =6pF, a typical quartz crystal cannot muster a $|\mathrm{Re}(Z_{amp})|_{\max}$ more than 118Ω, even with C_1 and C_2 as large as 14pF. Of course, the much smaller R_x =70Ω of a typical 60-MHz quartz crystal does not require that $|\mathrm{Re}(Z_{amp})|_{\max}$ be so large, but the needed C_1 and C_2 values are still on the order of 10pF. Since larger C_1 and C_2 demand higher transistor drive power, a MEMS-based Pierce oscillator circuit with a relatively small C_3 that in turn allows small

C_1 and C_2 should permit much lower power consumption. If the resonator R_x can be further lowered, e.g., by increasing its dc-bias voltage V_P, as illustrated in Fig. 4, the power consumption of a MEMS-based Pierce oscillator should shrink even more. Fig. 4 in fact shows that an increase in V_P by 1V decreases the oscillation power requirement by 33% (from 120μW to 80μW).

Once oscillation starts, the amplitude builds up exponentially from initial thermal noise with a time constant [7]

$$\tau = -\frac{2L_x}{\mathrm{Re}\{Z_{amp}\} + R_x} \qquad (4)$$

The total time required to reach steady-state oscillation depends on the time constant (4), the amount of noise in the system, and the initial energy impulse, the last of which can be tailored by an appropriate switch-on procedure at start-up.

B. Pierce vs. Transimpedance Amplifier (TIA)

The TIA used to instigate and sustain oscillation in previous work [1][5] comprised a fully differential CMOS amplifier biased by a common-mode feedback circuit that effectively canceled common-mode noise, especially low-frequency noise caused by vibration [8]. The Pierce oscillator presented here, however, with its single-ended Pierce topology, sacrifices this common-mode feedback to achieve lower noise-figure, hence lower phase noise, than previous TIA-based oscillators. This is made possible by 1) using only two active transistors compared to a minimum of four in the TIA; 2) using a very large shunt-shunt feedback MOS resistor, M_3, for biasing compared to the much smaller gain-setting resistor required by the TIA, where the larger the resistance, the smaller the current noise; and 3) using C_{BP}, at the cost of some area increase, between the gate of M_2 and V_{DD}, as shown in Fig. 2, to filter noise from bias transistors M_{b1}-M_{b3} and from V_{DD}. Per the last item, recall that the TIA of [5] relied on common-mode feedback to reject bias-derived noise, but note that the efficacy of this approach is only as good as the matching of its transistors.

Finally, the smaller transistor stack of the Pierce oscillator circuit allows it to operate at lower V_{DD}, hence lower power, without driving the two transistors into their triode regions.

IV. Experimental Verification

The wine-glass disk resonators used for testing were fabricated via a previously described three-polysilicon self-aligned stem small lateral-gap process [9]. Fig. 5 presents the scanning electron micrograph (SEM) of a fabricated 61-MHz wine-glass disk resonator along with a typical measured frequency response, where Q's of 130,000 in vacuum and motional impedances of 14kΩ with V_P=7V were common among devices.

The amplifier IC was fabricated in a 0.35μm CMOS technology. Although the entire die, shown in Fig. 6(a), occupies an area of 900μm×500μm, the actual sustaining amplifier with its biasing circuits only consumes about 60μm×45μm while the 44pF C_{BP} occupies about 200μm×100μm. The attenuation of noise at node V_b in Fig. 2—52dB in this case—depends on the pole, $g_{m,b2}/C_{BP}$, where $g_{m,b2}$ is the transconductance of diode-connected transistor M_{b2} in Fig. 2 and $1/g_{m,b2}$ is the resistance looking into M_{b2}. Therefore, for the same attenuation, the area of C_{BP} can be reduced easily by 2 to 4 times by simply decreasing $g_{m,b2}$. The rest of the IC area is consumed by 1) an on-chip buffer used to drive 50-Ω measurement systems; 2) by-pass capacitors that further reduce noise on DC supply lines that would normally be distributed among other on-chip integrated circuits; and 3) multiple bond pads.

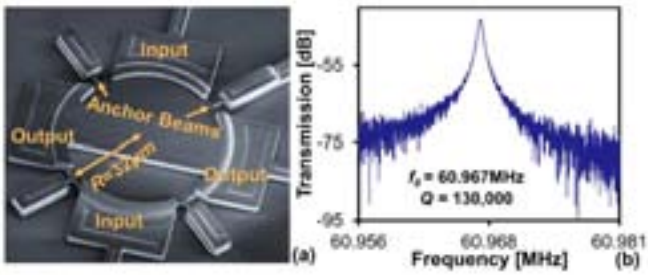

Fig. 5. (a) SEM of a fabricated wine-glass disk resonator and (b) the measured frequency response of the resonator used in this work.

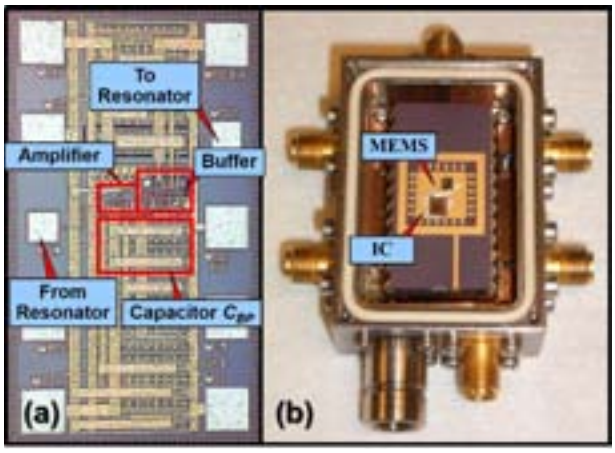

Fig. 6. (a) Die photo of custom-made IC. (b) Photo of the packaged oscillator in a custom-designed vacuum box.

The amplifier die was bond-wired to the resonator and package, as shown in Fig. 6(b), to yield the oscillator under test. To maintain high (i.e., over 50,000) resonator Q, and thereby minimize phase noise [10], the MEMS-based oscillator must operate in a stable vacuum environment, provided via the custom-made miniature vacuum chamber, depicted in Fig. 6(b), that encloses a printed circuit board (PCB) board housing the MEMS/CMOS device package and provides electrical feedthroughs to allow connection to outside instrumentation. Power and bias voltages for the oscillator were provided by a custom low-noise analog supply board. The output of the oscillator was measured using an Agilent E5500 phase noise test setup configured to use a low-noise PLL.

When biased with sufficient V_P to provide positive loop gain, the inset of Fig. 7 shows the output waveform of the packaged MEMS oscillator operating in vacuum. Fig. 7 additionally presents measured phase noise data for the Pierce oscillator alongside data for a TIA oscillator employing the same MEMS resonator design. Here, the Pierce oscillator achieves -119dBc/Hz at 1-kHz offset and -139dBc/Hz at far-from-carrier offsets from its 61-MHz oscillation frequency. When divided down to GSM's 13MHz, this corresponds to -132dBc/Hz at 1-kHz and -152 dBc/Hz far-from-carrier, both of which satisfy GSM reference

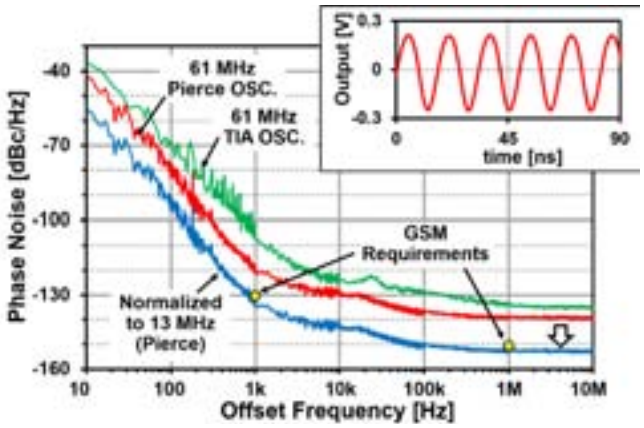

Fig. 7. Measured phase noise of 61-MHz oscillators comparing the new Pierce topology and an older TIA topology similar to [5], as well as the Pierce oscillator phase noise divided down to 13MHz for comparison to the GSM spec. Inset: the measured output waveform of the Pierce oscillator.

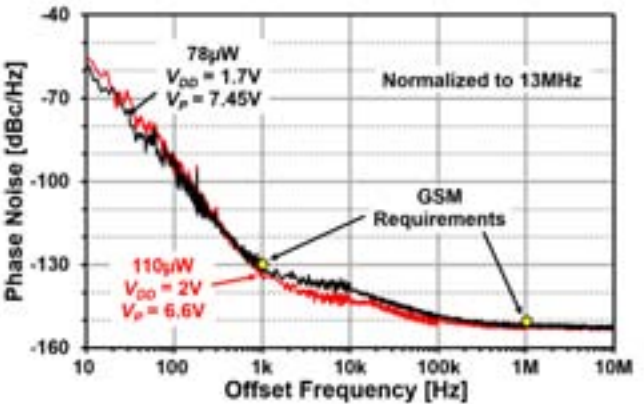

Fig. 8. Measured phase noise of the oscillator operating at two V_{DD} values. A reduction in V_{DD} and I_{BIAS} can be seen to decrease power consumption by 29% with only a modest decrease in phase noise performance.

oscillator phase noise requirements. This Pierce oscillator not only provides phase noise improvements of 9dB at 1-kHz offset and 7dB far-from carrier versus the TIA version of [5] using a similar single disk; it also reduces power consumption down to 78μW, which is ~4.5 times smaller.

Fig. 8 presents phase noise measurements for the Pierce oscillator that investigate the degree to which increases in resonator dc-bias V_P allow lower supply voltages, hence, lower power consumption. Here, a 0.85V increase in V_P allows V_{DD} and I_{BIAS} reductions that decrease overall power consumption from 110μW to 78μW, with very little degradation of phase noise.

For fair comparison of this work to other oscillators, a figure of merit (*FOM*) that accounts for the total power consumption required to achieve a given phase noise can be used:

$$FOM = 10\log\left(\mathcal{L}(\Delta f).\frac{P_{diss}}{1mW}.\left(\frac{\Delta f}{f_0}\right)^2\right) \qquad (5)$$

where $\mathcal{L}(\Delta f)$ is the oscillator phase-noise at Δf offset frequency and P_{diss} is its total power consumption. Use of (5) yields Table I, where the present Pierce oscillator achieves the best *FOM* at 1kHz amongst any published on-chip oscillator to date.

TABLE I. PERFORMANCE COMPARISON

Device Type	**This work**	Wine-Glass array [1]	AlN [11]	FBAR [12]	Quartz [13]
f_{osc} [MHz]	**61**	61	4.9	2000	10
Power [μW]	**78**	350	120	22	~1500
Normalized (13MHz) Phase Noise @ 1 kHz [dBc/Hz]	**-132**	-136	-130	-122	-135
FOM@1kHz [dB]	**-225**	-223	-221	-220	-211

V. CONCLUSIONS

The demonstration by this work of a 61-MHz capacitive-gap transduced wine-glass disk Pierce oscillator capable of meeting GSM specifications while using only 78μW of power marks a milestone for MEMS-based frequency control technology. Compared with previous TIA-based renditions, this oscillator reduces power and area consumption by 4.5 times and 10 times, respectively, and, to best of the author's knowledge, now posts the highest *FOM* of any published on-chip oscillator to date. That the small port-to-port feedthrough capacitance of the MEMS resonator is largely responsible for the *FOM* improvement is quite intriguing and suggestive of design approaches that might lead to further *FOM* increases. Whether or not such increases are achieved, the power reduction already achieved by the demonstrated oscillator while maintaining GSM-compliant phase noise performance already makes a very compelling case for application to future autonomous wireless sensor networks.

REFERENCES

[1] Y.-W. Lin, S.-S. Li, Z. Ren, and C. T.-C. Nguyen, "Low phase noise array-composite …," *Technical Digest, IEEE Int. Electron Devices Mtg*., Washington, DC, Dec. 5-7, 2005, pp. 287-290.

[2] J. M. Rabaey, *et al.*, "PicoRadios for wireless sensor networks: …," in *Digest of Tech. Papers. ISSCC. 2002 IEEE Int.*, 2002, pp. 200-201 vol.1.

[3] M. Onoe, "Contour vibrations of isotropic circular plates," *J. Acoust. Soc. Amer*., vol. 28, no. 6, pp. 1158–1162, Nov. 1956.

[4] F. D. Bannon III, J. R. Clark, and C. T.-C. Nguyen, "High-Q HF microelectromechanical filters," *Solid-State Circuits, IEEE Journal of*, vol. 35, pp. 512–526, Apr. 2000.

[5] Y.-W. Lin, S. Lee, S-S Li, Y. Xie, Z. Ren, and C.T.-C. Nguyen, "Series-resonant VHF micromechanical resonator reference oscillators," *Solid-State Circuits, IEEE Journal of*, vol.39, no.12, pp. 2477- 2491, Dec. 2004.

[6] E.A. Vittoz, M.G.R. Degrauwe, and S. Bitz, "High-performance crystal oscillator circuits: theory and application," *Solid-State Circuits, IEEE Journal of* , vol.23, no.3, pp. 774- 783, Jun. 1988.

[7] A. Rusznyak, "Start-up time of CMOS oscillators," *Circuits and Systems, IEEE Transactions on* , vol. 34, no. 3, pp. 259-268, Mar. 1987.

[8] T.L. Naing, T. O. Rocheleau, Z. Ren, E. Alon, and C. T.-C. Nguyen, "Vibration-Insensitive 61-MHz Micromechanical …," in *Proc. 2012 IEEE Int. FCS*, Baltimore, Maryland, May 22-24, 2012, pp. 276-281.

[9] M. A. Abdelmoneum, M. U. Demirci, and C. T.-C. Nguyen, "Stemless wine-glass-mode disk micromechanical resonators," in *MEMS, IEEE The Sixteenth Annual Int. Conf. on*, Kyoto, Japan, 2003, pp. 698 – 701.

[10] D. B. Leeson, "A simple model of feedback oscillator noise spectrum," *Proceedings of the IEEE*, vol. 54, no. 2, pp. 329 – 330, Feb. 1966.

[11] Z. Z. Wu, V. A. Thakar, A. Peczalski, and M. Rais-Zadeh, "A low phase-noise Pierce oscilator using ...," in *Proc. Solid-State Sensors, Actuators, IEEE Int. Conf. on,* Barcelona, Spain, Jum. 16-20, 2013, pp. 490-493.

[12] A. Nelson, J. Hu, J. Kaitila, R. Ruby, and B. Otis, "A 22μW, 2.0GHz FBAR oscillator," in *RFIC, 2011 IEEE*, 2011, pp. 1 –4.

[13] J.T.M. van Beek and R. Puers, "A review of MEMS oscillators for frequency reference and timing applications," *Journal Micromech. Microeng.,* vol. 22, no. 1, p. 013001, Jan. 2012.

A 995MHz Fundamental Nonlinear Quartz MEMS Oscillator

R.G. Nagele, H.P. Moyer, D.J. Kirby, Y. Yoon, R.L. Kubena, R.J. Joyce, P.D. Brewer and D.T.Chang

HRL Laboratories, LLC, Malibu, CA 90265 USA

Email: rgnagele@hrl.com

***Abstract*—A quartz resonator operating at 995 MHz in the fundamental mode has been characterized in a closed loop oscillating system under different drive levels to determine its nonlinear behavior and optimum phase noise performance. The best phase noise achieved was -106dBc/Hz at a 1 kHz offset frequency. The same quartz technology was used to build VCXOs in both the Colpitts and Pierce configurations at several frequencies above 650 MHz. The lowest phase noise level achieved in the Colpitts configuration operating at 705 MHz is –111dBc/Hz at a 1 kHz offset frequency while a Pierce Oscillator operating at 662 MHz achieved a phase noise of –112.8dBc/Hz at the same offset. Power consumption in these VCOs is typically on the order of 30-90mW.**

***Index Terms* -- Quartz, MEMS, oscillators, resonator, nonlinear dynamics, drive level dependency, DLD, phase noise, Duffing**

I. Introduction

Quartz resonators are often used for high performance navigation, radar systems, and communications systems, both commercial and military. In addition to exhibiting low phase noise, these resonators offer high stability over temperature and vibration. Typically these resonators operate at frequencies < 100MHz and need to be multiplied up to UHF frequencies or are used as the reference for phase locked loops. In this work, we propose fundamental mode quartz oscillators operating at UHF frequencies (> 500MHz) as a method of reducing the size, weight, and power (SWAP) of these systems and for improving the performance of phase locked loops operating at microwave frequencies. Due to their small size, UHF quartz resonators are naturally less susceptible to vibration than lower frequency quartz.

Competing technologies in the UHF region, such as surface acoustic wave (SAW) resonators and bulk acoustic wave resonators (BAW) can have low phase noise but temperature stabilities approximately an order of magnitude higher than quartz while dielectric resonators are large and have too high loss rendering them impractical at these frequencies. In order to achieve stable operation over temperature at these frequencies, designers typically use either a stable quartz reference oscillator multiplied up to the desired frequency or a higher overtone device. Multiplication processes add noise in addition to the 6dB associated with the multiplication process. Additionally, the circuitry required for the multiplication increases the size and power consumption of the system according to the number of multiplication stages. In phased lock loop applications, the lower the reference frequency the larger the required multiplication which leads to higher added noise levels. Quartz oscillators are commonly designed for higher overtones (typically 3rd and 5th) but assuming a fundamental frequency of 100MHz, this does not allow for operation close to 1 GHz. Higher overtones generally have higher motional resistance R_1, making sustained oscillation difficult and they are also plagued with problematic spurious modes [1].

Traditionally, engineers attempted to avoid nonlinear operation because it was usually associated with unstable oscillations and poor phase noise performance. Quartz resonators operating at UHF are smaller in size than lower frequency crystals which makes them more susceptible to nonlinear behavior under lower drive levels (~ 0dBm) Thus, understanding how UHF resonators behave under different drive levels is an important part of designing oscillators at these frequencies. Pioneering research on this topic was done in the 1990s by Greywall and Yurke in which they proposed taking advantage of the nonlinearity in a mechanical resonator to improve phase noise in a magnetically driven oscillator system [2, 3].

Recently, Lee et al demonstrated stable oscillation at ~ 1MHz of an electrostatic silicon MEMS resonator driven beyond the critical bifurcation point and they were able to characterize the resonator nonlinearity by measuring the admittance under various drive levels [4]. Efforts at HRL have focused on extending this characterization up to UHF (>500MHz) and the methodology and results have been documented [5, 6]. HRL's work uses the same process to characterize the fundamental mode operation of a 995MHz resonator.

Because many navigation and radar applications require temperature stability beyond the natural stability of the resonator, we have developed a number of Colpitts and Pierce VCXOs operating at frequencies >600MHz to allow for external temperature stabilization.

II. Quartz Technology

The basic equation used to describe the nonlinearity in the quartz as well as other flexural beam type resonator is the well known Duffing equation [7]:

$$m\frac{d^2x}{dt^2} + \gamma\frac{dx}{dt} + k_1 x + k_3 x^3 = A\sin(\omega t + \varphi) \quad (1)$$

This equation describes a mass and spring system with a cubic nonlinearity, k_3x^3, resulting in nonlinearities in the spring constant with a periodic driving force. This is a good representation for characterizing the resonator in an open loop configuration. Fig. 1 shows a Van Dyke model representation of a resonator. C_0 corresponds to the static parasitic capacitance of the resonator. Motional inductance, L_1, and motional resistance, R_1, correspond to the effective modal mass, m, and damping, γ, respectively in the Duffing equation. For the typical linear case,

motional capacitance, C_1, is analogous to model stiffness k_1 but is represented by the combination of k_1 and k_3 when nonlinearities are present.

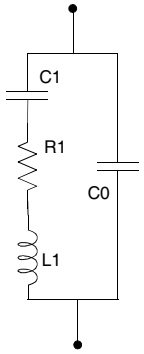

Figure 1. The Van Dyke circuit model of a quartz resonator.

The 995 MHz fundamental AT-cut quartz (35º15') thickness shear mode resonator, fabricated at HRL, consists of a blank of AT-cut quartz with a cut angle of 35º15'. The resonator has top and bottom side circular shaped aluminum electrodes that are 100 µm in diameter and 0.08 µm thick. The active region of the quartz plate is 290µm x 320 µm and 1.6 µm thick. The quartz resonator is vacuum sealed with a silicon cap for protection before dicing. The fabrication process is described in [8]. The physical layout of the resonator and a picture of the fabricated device are shown in Fig. 2.

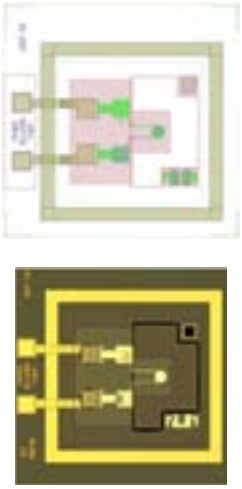

Figure 2. Physical layout of the resonator and photograph of fabricated device.

The device was first measured in an open loop configuration and the Van Dyke model fitted parameters are shown in Table I.

R_1	66.618 Ω
C_1	0.177 fF
L_1	145 µH
C_0	0.482 pF
Series f_o	995 MHz
Q	13600
f x Q product	1.35×10^{13}

Table I. Van Dyke model fitted parameters for the HRL AT-cut quartz resonator.

The 995MHz resonator was characterized with the Agilent E4991A RF Impedance Analyzer by directly probing resonator's contacts. Fig. 3 shows the magnitude of the measured admittance values for the resonator versus drive level in the open loop configuration. The results indicate that at a 100mVrms drive level, the resonator is well within the linear operating region. By a 300mV drive level, the admittance curve is bent over, indicating strong nonlinear effect (Duffing). The slight frequency shift of the peak is believed to be due to heating effects of the quartz.

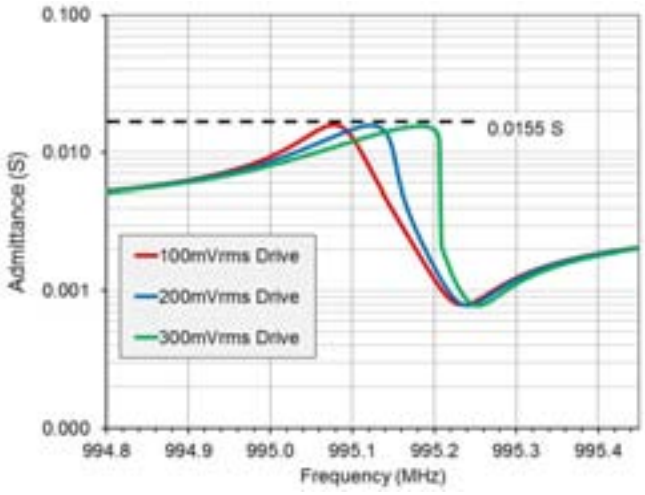

Figure 3. Magnitude of measured admittance for the resonator in an open loop configuration.

III. Nonlinear Characterization

A block diagram for the nonlinear characterization of the resonator is presented Fig. 4. The main components for the sustaining circuit in our test loop oscillator are a low noise amplifier, voltage controlled phase shifter, voltage controlled attenuator, and power splitter.

The low noise amplifier must exhibit high gain to ensure that the system will oscillate under a variety of amplitude and phase conditions on the resonator. The ZX60 is a GaAs FET amplifier

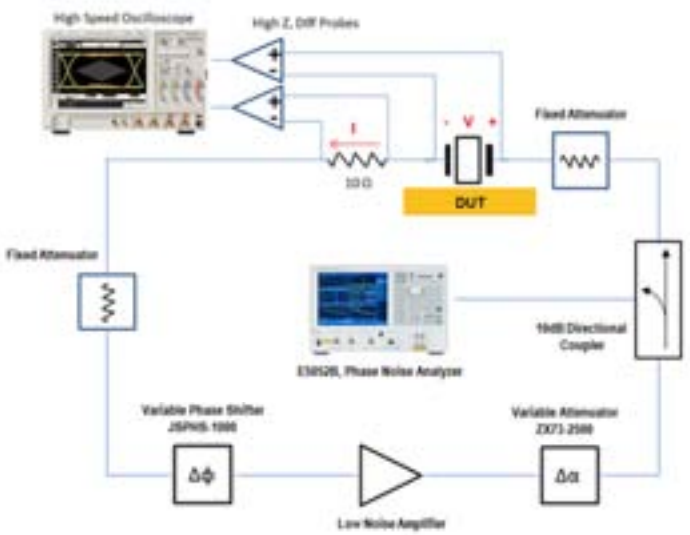

Figure 4. Block diagram of the measurement setup for the nonlinear characterization of the resonator.

which has 25dB gain and a noise figure of 0.5dB. Under lower drive levels the amplifier is well matched, but under higher drive levels reflections from the amplifier can distort the voltage and current measurements of the resonator and thus, alter the admittance curve. The JSPHS-1000 phase shifter provides 180º of phase shift from 700 to 1000 MHz, and the ZX73-2500 has approximately 40dB of attenuation range. A number of fixed coaxial attenuators are surrounding the amplifier to mollify the effects of reflections from the amplifier.

The resonator circuit is mounted on FR4 circuit board as shown in Fig. 5. A 10Ω resistor mounted in series acts to sense current. This value was chosen as a compromise between loading the resonator and reading a detectable voltage. Too high of a series resistance may lower the Q to the point that nonlinear behavior is affected while too low of resistance will yield undetectable voltages. A 10Ω resistor is ~15% of the resonator R_1 and does not load the Q down to a point where linear oscillator performance is seriously degraded.

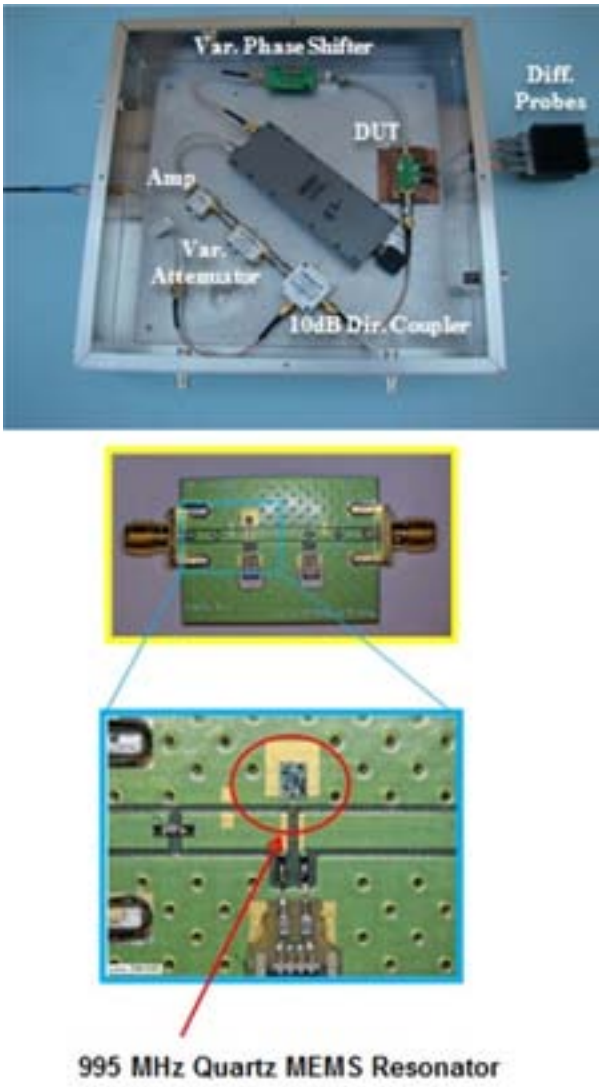

Figure 5. Picture of the experimental setup and mounted resonator.

Zero Insertion Force (ZIF) probe connections are used to interface to differential active probes (Agilent Infiniimax 5 GHz Probe System, model 1132A). Voltage across the resonator is measured directly by one probe and the current is derived from the probed voltage across the 10Ω resistor. An Agilent 5052B phase noise analyzer measures the oscillator output.

Upon establishing an oscillation condition, a LABVIEW computer program reads the voltage from the oscilloscope and adjusts the variable attenuator to achieve the desired voltage across the resonator. Our measurements focused on resonator drive levels that were determined to yield a strong nonlinear behavior as indicated by the open loop characterization. The voltage and corresponding current, frequency of operation, and phase noise are measured. The phase shifter is adjusted in 5° increments and the process is repeated until the phase shifter reaches a state where the oscillation condition is not satisfied. For each data point, the admittance is calculated via the ratio of the peak values for the current and voltage (I/V).

Fig. 6 depicts the results of the magnitude of the admittance vs. the frequency of oscillation which is observed to be linear at 125mV drive and nonlinear for drive voltages greater than 175mV. The low noise amplifier was not capable of driving the resonator greater than 200mV at these high frequencies. The main focus of our work is to compare the phase noise levels at 1 kHz offset at different points on the admittance curve shown in Fig. 7. The phase noise at the 1 kHz offset is usually specified for benchmarking UHF oscillators.

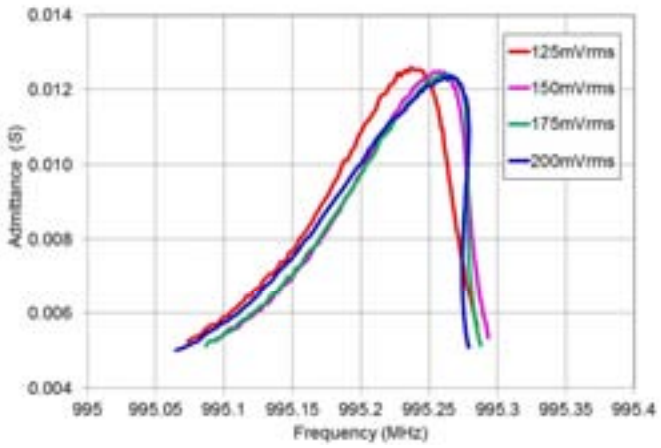

Figure 6. Admittance plot for the resonator in a closed loop configuration.

From Fig. 6, one can see that the admittance curves follow a pattern similar to that measured in the open loop case of Fig. 3. Consistent with earlier work, the peak of the admittance curve is slightly shifted in the closed loop case. In addition, the closed loop case exhibits higher bi-stability than the open loop case providing the potential for two different oscillation conditions at the same frequency. For our setup the attenuation of the voltage variable attenuator and the phase of the voltage variable phase shifter are altered interchangeably to 1) maintain the proper voltage across the resonator and 2) maintain the oscillation condition. The addition of these two variables in the loop allows for oscillations to be achieved at two different frequencies because the admittance of the resonator is different for each state.

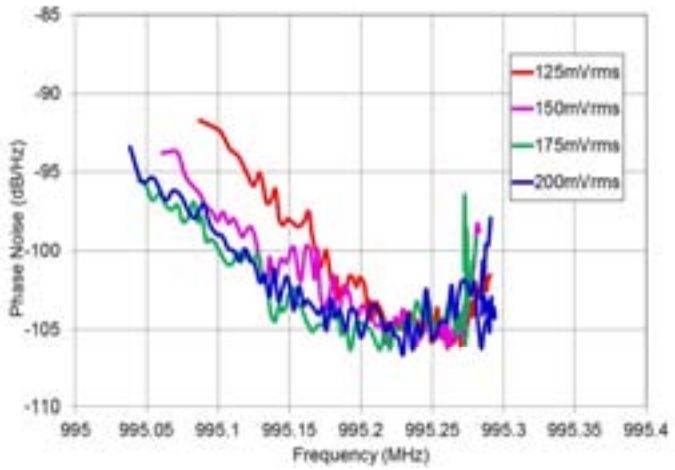

Figure 7. Plot of the phase noise of the 995 MHz oscillator at a 1 kHz offset.

As shown in Fig. 7, the best achieved phase noise at a 1 kHz offset is approximately -106dBc/Hz. From the plot it is apparent that driving the resonator into a nonlinear regime improves the bandwidth of the low phase noise region. At the low frequency end of the operating range, a larger phase noise improvement is exhibited. As the frequency increases, we approach bi-stability.

IV. VCXO Performance

Having demonstrated that the quartz technology allows for 1 GHz operation, the next step is to build discrete oscillators to further characterize the UHF resonators. VCXO circuits were chosen to test the frequency pull characteristics of the resonator and to allow for the integration of future temperature compensation circuitry. Although most of the initial designs used a Pierce topology, a Colpitts topology was also used to provide a phase noise and frequency tuning comparison.

The schematics for both topologies are shown in Fig. 8. Both circuits use one tuning element. The active transistor in the Pierce oscillator is the NEC68033 bipolar transistor in an SOT-23 package and the tuning element is an Aeroflex-Metelics varactor, model MTV4030-09. The MTV4030 series has an abrupt junction and the -09 has a capacitive tuning range between 6.3 (0V) and 1.73pF over a 15V bias range. The Colpitts oscillator uses the same NEC68033 device with the corresponding tuning element being an Aeroflex-Metelics model MTV4030-11 varactor in the same package. The -11 varactor has a capacitance varying between 9.61 (0V) and 2.36pF over the same voltage range.

Fig. 9 shows the phase noise performance of the VCXO using the Pierce topology. At zero varactor bias, the free running frequency of oscillation is 662 MHz and the collector voltage is 3.5V with a collector current of 9.5mA. The phase noise at a 1 kHz offset is -112.8dBc/Hz and the phase noise profile follows the expected $1/f^3$ slope until ~10 kHz when it changes over to 1/f. A noise floor of ~ -155dBc/Hz is finally achieved close to 1 MHz.

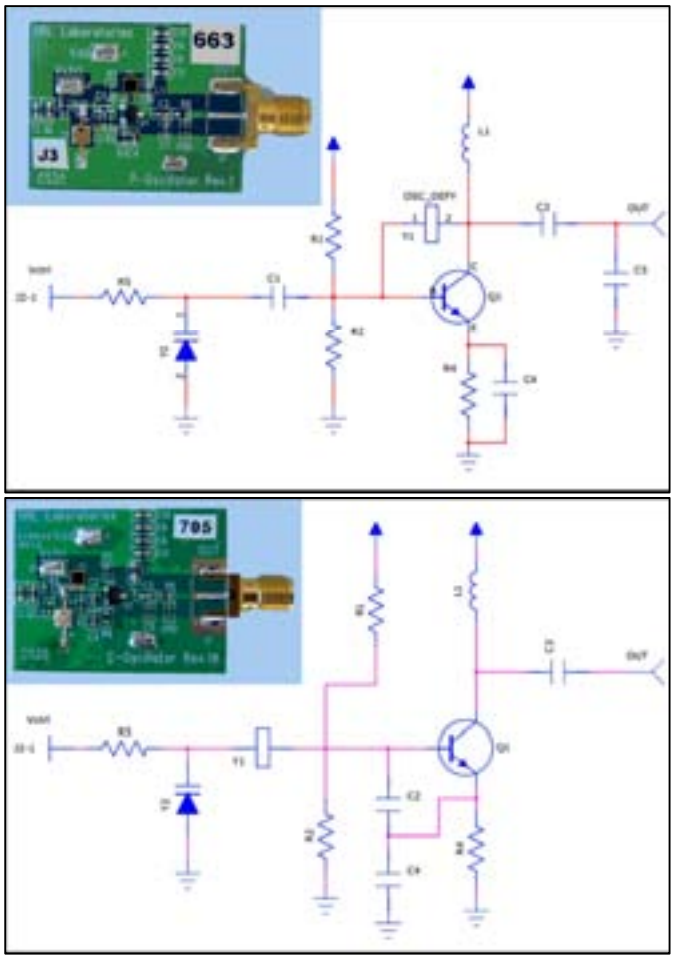

Figure 8. Schematic and photograph of a voltage controlled Pierce oscillator (top) and Clapp oscillator (bottom).

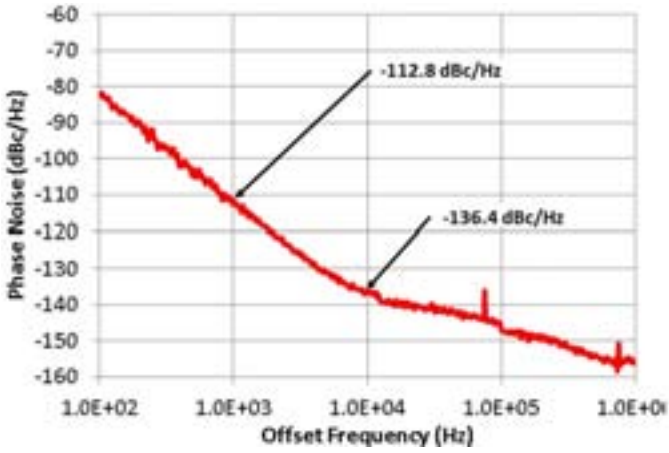

Figure 9. Phase noise measurement of the 663 MHz Pierce oscillator at a 1 kHz offset.

The output of the Colpitts oscillator is shown in Fig. 10. With a collector bias voltage of 6V and a collector current of 14mA, the free running frequency at zero varactor bias is 705 MHz. The measured phase noise at a 1 kHz offset is ~ -111.2dBc/Hz. From the plot, one can observe a slope of $1/f^3$ until a 10 kHz offset which transitions into the expected 1/f slope.

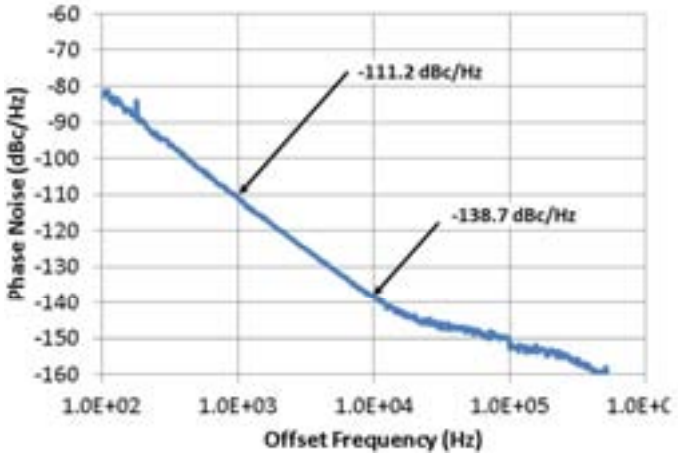

Figure 10. Phase noise measurement of the 705 MHz Colpitts oscillator at a 1 kHz offset.

The VCXO tuning range is lower than what is theoretically possible for both cases. For the Pierce oscillator, the stiffness factor, C_0/C_1 (see Table I above), predicts a pulling range of 140 kHz which translates to 140ppm for our operating frequency. The resulting tuning range is closer to 25ppm which is substantially lower. Similarly, the theoretical tuning range for the Colpitts oscillator is 140ppm and the actual tuning range is 30ppm. Reasons for these discrepancies include extra loading capacitances which limit the tuning range in all VCXOs and the choice of varactor which has less than a 5:1 tuning range. A varactor with a higher capacitance ratio should increase the tuning range.

V. Summary

A 995 MHz quartz resonator has been made to oscillate in the fundamental mode. Characterization of the phase noise under different drive levels and loop phase was completed to determine the optimum operating point for phase noise performance. In order to further characterize the resonator technology, VCXOs were constructed in the 650-750 MHz range. Phase noise results on the order of -112dBc/Hz are an improvement over our previous results. Upcoming efforts in nonlinear characterization will involve comparing the phase noise using different amplifiers to determine their effect on oscillator performance. Future work with VCXOs will involve using higher frequency resonators and integrating microprocessor controlled temperature compensation circuitry to develop an UHF TCXO.

Acknowledgment

The authors would like to thank Jeffrey Rogers of DARPA MTO, David Howe of NIST Boulder, and John Vig for program management and guidance. This material is based upon work supported by the Defense Advanced Research Projects Agency under Contract No. HR0011-10-C-0109. Any opinions, findings and conclusions or recommendations expressed in this material are those of the author(s) and do not necessarily reflect the views of the Defense Advanced Research Projects Agency.

References

[1] M.E. Frerking,"Crystal Oscillator Design and Temperature Compensation," New York: Van Nostrand Reinhold Company, 1978, p.30.

[2] D.S. Greywall, B. Yurke, P.A. Busch, A.N. Pargellis, and R.L. Willett," Evading amplifier noise in nonlinear oscillators," *Phys. Rev. Lett. 72*, 2992-2995 (1994).

[3] B. Yurke, D.S. Greywall, A.N. Pargellis, and P.A Busch, "Theory of amplifier-noise evasion in an oscillator employing a nonlinear resonator," *Phys. Rev. A51*, 4211-4229 (1995).

[4] H.K. Lee, R. Melamud, S. Chandorkar, Y.Q. Qu, J. Salvia, and T.W. Kenney," Motional Impedance of Resonators in the Nonlinear Regime," *Proc. Joint Conference of the IEEE International Frequency Control and the European Frequency and Time Forum*, 1-6 (2011).

[5] D.T. Chang et al., "Nonlinear UHF Quartz MEMS Oscillator with Phase Noise Reduction," *Proc. of the 26th IEEE International Conference on Micro Elector Mechanical Systems (MEMS),* pp. 781-784 (2013).

[6] H.P. Moyer et al," Nonlinear Behavior of an UHF Quartz Resonator in an Oscillating System," *Proc. of the 2012 IEEE International Frequency Control Symposium*, pp. 1-5 (2012).

[7] S.H. Strogatz," Nonlinear Dynamics and Chaos," Reading, MA: Addison-Wesley, 1994, p.215.

[8] F.P. Stratton, D.T. Chang, D.J. Kirby, R.J. Joyce, T.Y. Hsu, R.L. Kubena and Y.-K. Yong," A MEMS-Based Quartz Resonator Technology for GHz Applications," *Proc. of the IEEE International Frequency Control Symposium,* pp. 27-34 (2004).

Special Considerations for Specifying Oscillator Components with Resonators on the Micro/Nanoscale

Jon Lovseth, Ted Hoffmann, Vadim Olen, Jennet Volden and Paul Opsahl
Advanced Technology Center
Rockwell Collins
Cedar Rapids, Iowa USA
jalovset@rockwellcollins.com

***Abstract*— Some micro/nanoscale resonator oscillators' phase noise and temperature stability performance is inferior to traditional quartz crystal oscillators. But, does that matter? In other areas, micro/nanoscale resonator oscillators have demonstrated one or two orders of magnitude better performance. Measured devices have demonstrated frequency stability under vibration and a resiliency to shock not possible in traditional-sized quartz. Certain applications may have component specifications which can be derived differently by keeping in mind how a micro/nanoscale component will respond differently under these environmental conditions.**

A comparison of most important requirements for oscillator components in communication, navigation, and radar radio applications is presented. Areas of specification relief are identified related to measured performance of micro/nanoscale oscillators. Rockwell Collins has measured developmental and Commercial-off-the-shelf (COTS) Microelectromechanical systems (MEMS) / Nanoelectromechanical systems (NEMS) resonator oscillators as part of the DARPA Mesodynamics Architectures (Meso) program. This includes piezoelectric, piezoresistive, and electrostatic devices. Rockwell Collins has used these devices to demonstrate improved performance to existing radio hardware.

Keywords*— *MEMS; vibration; oscillator; phase noise; radio application

I. Current Oscillator Applications

A. *Traditional SATCOM*

Traditional satellite communication (SATCOM) terminals are typically land or ship-based and operate over relatively benign temperature ranges and vibration environments. Historically a Low Noise Block downconverter (LNB) is placed near the antenna to convert the SATCOM carrier frequency down to a lower Intermediate Frequency (IF) to reduce cable losses. At the other end of the cable is a modem that processes and demodulates the IF signal to data. The LNB and modem often have independent reference oscillator circuits (Fig. 1).

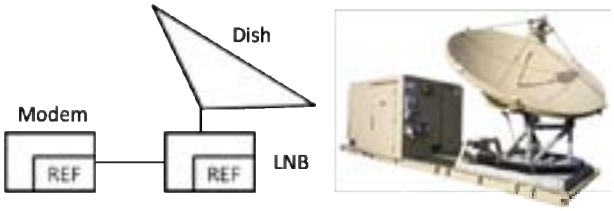

Fig. 1 Traditional SATCOM Terminal Architecture

B. *Airborne SATCOM Terminals*

To meet the need for continuous data connectivity, SATCOM terminals are increasingly being deployed on commercial and military aircraft. The antenna and LNB that are deployed near the skin of the aircraft face extreme temperature and vibration environmental requirements. The SATCOM antennas are typically mounted at the top, centerline, mid-fuselage or at the top of the tail. These mounting locations provide the optimal view of satellites. Equipment in the platform's avionics bay enjoy a temperature-controlled environment. Avionics bay equipment vibration requirements are tougher than terrestrial and maritime terminals but not as harsh as the environment near the skin of the aircraft.

The Radio Technical Commission for Aeronautics (RTCA) is a volunteer group comprised of avionics and aviation experts that develop technical guidance for government regulatory agencies and industry. DO-160F published by the RTCA defines a series of minimum standard environmental test conditions and procedures for airborne equipment. Airframe manufacturers and airlines may elect to specify more stringent standards. Chapter 8 of DO-160F specifies the minimum vibration conditions for avionics. These are further broken down by platform type (fixed wing, helicopter, etc.) and mounting location (fuselage, equipment rack, etc.). The most difficult vibration profile for the SATCOM antenna is the tail mount location defined by Curve E – Empennage & Fin Tip [1] (Fig. 2). In contrast, the vibration profile for equipment mounted in the avionics bay is much less, Curve B2 – Instrument Panel, Console, & Equipment Rack [1].

This work was sponsored by the Defense Advanced Research Projects Agency (DARPA) Mesodynamics Architectures Dynamics Enabled Frequency Sources (DEFYS) program and administrated through the Air Force Research Laboratories (AFRL) under contract number FA8650-10-C-7035.

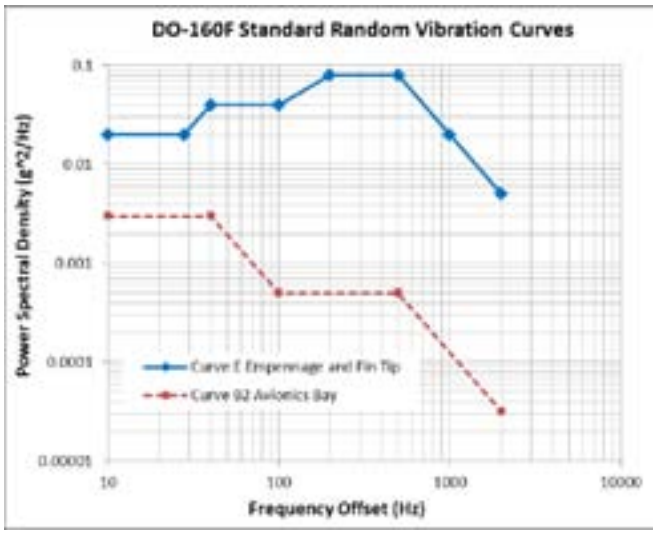

Fig. 2 DO-160F Standard Random Vibration Curves

As a reference oscillator for this application, consider the Wenzel 100MHz Rugged Oven Controlled Crystal Oscillator (Part Number 501-24760-01). This oscillator is a Commercial-Off-The-Shelf (COTS), macroscale quartz crystal oscillator with good phase noise performance and minimal sensitivity to vibration (0.5 ppb/g) [2]. But the vibration environment for mounting near the skin of the aircraft (Curve E Empennage and Fin Tip) is so difficult that the phase noise degradation is significant (Fig 3).

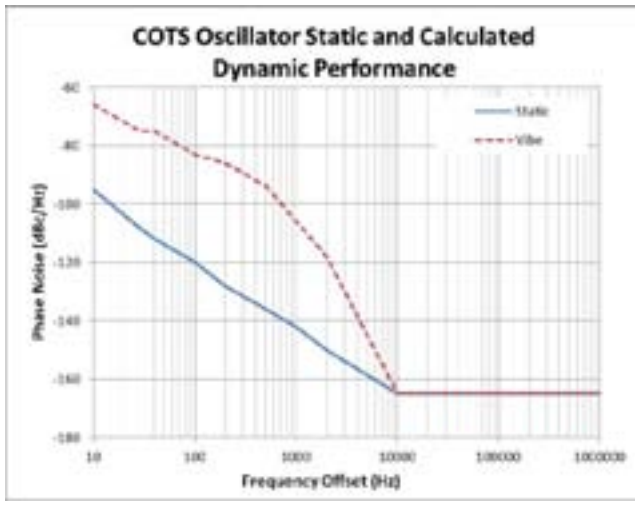

Fig. 3 COT Oscillator Static and Dynamic Phase Noise Performance

Aircraft use an adapted architecture to overcome this performance degradation. The LNB imports the reference signal from the modem where the vibration is less harsh (Curve B2 Avionics Bay). The phase-locked loop (PLL) for the LNB local oscillator has a loop bandwidth larger (typically greater than 10kHz) than the vibration frequencies (typically less than 2kHz) to suppress vibration induced phase noise in the voltage-controlled oscillator (VCO) and the phase noise degradation due to the less severe vibration in the avionics bay is minimal. Similar schemes are often employed in radar systems as well (Fig. 4).

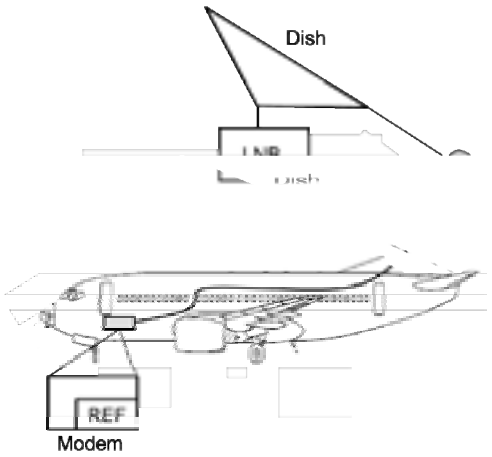

Fig. 4 Airborne SATCOM Architecture

II. TEST RESULTS

Rockwell Collins tested a 698 MHz fixed frequency oscillator, developed by HRL Laboratories under the DARPA Meso program. The Pierce oscillator (Fig. 5) was built using a wafer-scale packaged microscale quartz resonator and a transistor with positive feedback [3].

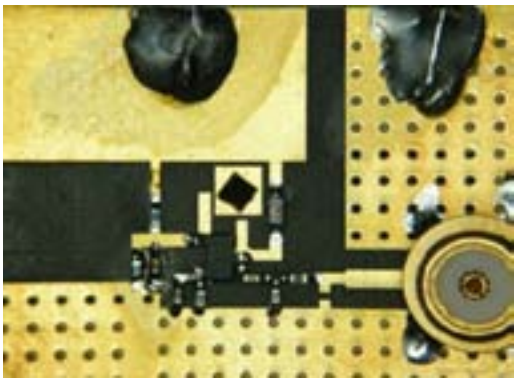

Fig. 5 HRL Microscale Quartz Oscillator at 698MHz

Rockwell Collins performed sinusoidal vibration testing of HRL oscillators. The evaluation board was tested in the X, Y, and Z axes. In the test set up (Fig. 6), sinusoidal vibration frequency is controlled from the waveform generator and amplitude is controlled by the amplifier. An accelerometer was placed near the resonator to confirm stimulus. Cables were clamped in various ways to prove that cable resonance was not distorting the measurement (Fig.7). Sideband modulation power was measured on an E4440A spectrum analyzer and compared to an E5052 phase noise analyzer. The device under test (DUT) sensitivity was calculated using the following equation:

$$\mathcal{L}\left(f_{vibe}\right) = 20\log\left(\frac{\overline{\Gamma} \bullet \overline{A} f_0}{2 f_{vibe}}\right) \qquad (1)$$

where f_{vibe} represents the frequency of the sinusoidal vibration in Hz, $\bar{A}$ represents the vibration intensity in g-rms, f_0 represents the fundamental oscillator frequency in Hz, and $\mathcal{L}$ represents the power of the vibration-induced sideband in dBc relative to the carrier power.

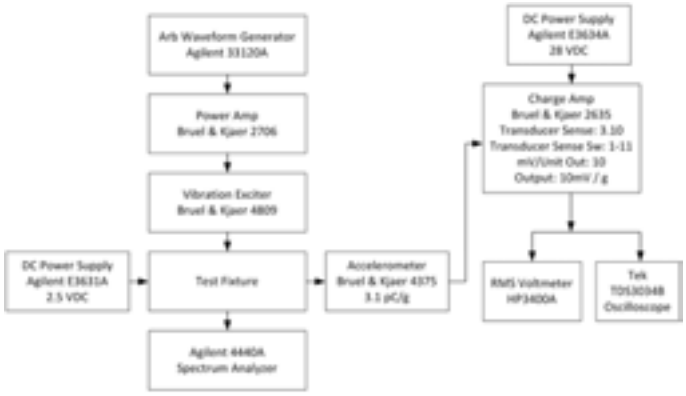

Fig. 6 Test Setup for Vibration Measurements

Fig.7 Vibration Table with Cables Clamped (left) Z-axis Setup with Accelerometer Placed Near Resonator (right)

Fig.8 shows the results of the HRL oscillator. Multiple points represent calculated Γ for varied vibration intensity. The HRL oscillator has several measurements better than 0.1 ppb/g.

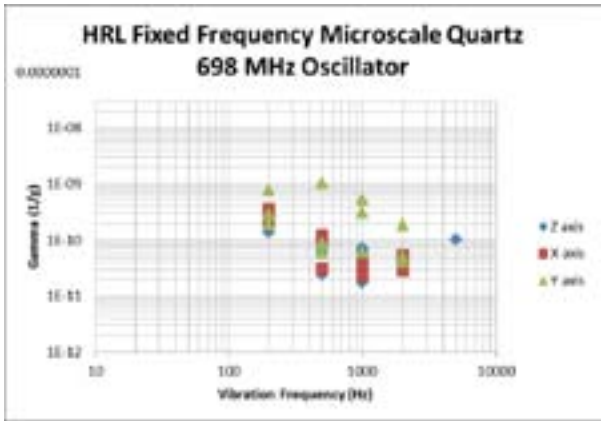

Fig.8 Vibration Sensitivity of HRL 698MHz Oscillator

III. FUTURE APPLICATIONS

Future systems for airborne systems desire less restrictive architectures. For example, modular or removable terminals that encompass the entire system (antenna, LNB, modem, etc.) could be mounted on the aircraft skin with only power and ethernet connections in addition to structural mounting. This would allow mission tailoring for military aircraft (select L, Ku, or Ka-band SATCOM) or optimization of commercial aircraft (installed for oceanic flights but removed for short flights to reduce weight and fuel expenditures). Unmanned Air Systems (UAS) are also becoming increasingly reliant on SATCOM systems. These platforms face extreme temperature ranges since constant temperature does not need to be maintained without people on board. UAS platform vibration profiles are even harsher since many of the platforms are quite small with a relatively small mass that is easily disturbed compared to manned aircraft. In these new applications, the reference oscillator must endure the harshest vibration profiles.

Microscale and nanoscale oscillators are a promising new technology that may be able to address these applications. Their relatively small mass compared to traditional oscillators makes them less sensitive to vibration. The vibration sensitivity of the HRL oscillator was measured and the average of the z-axis measurements is shown below (Table 1).

Table 1 - HRL Oscillator Z-Axis Vibration Sensitivity

Vibration Frequency (Hz)	G-sense (g^2/Hz)
200	0.16
500	0.06
1000	0.05
2000	0.05

The phase noise of a COTS oscillator and the 698MHz microscale oscillator developed by HRL are compared in Fig. 9. The native frequency of the Wenzel oscillator is 100MHz and the HRL oscillator is 698MHz. Both oscillators have been scaled to 1GHz for comparison.

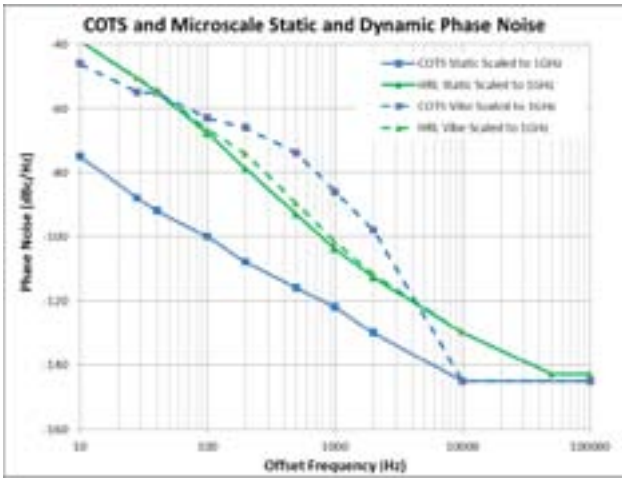

Fig. 9 COTS and Microscale Oscillator Static and Dynamic Phase Noise

Under static conditions, the COTS oscillator has superior phase noise performance compared to the HRL oscillator. At vibration frequencies less than 2 kHz under the harsh vibration conditions of DO-160F Profile E, the phase noise of the COTS oscillator degrades significantly. As a qualitative comparison, the single sideband phase noise was integrated from 10-2000Hz. The COTS oscillator degrades almost 30dB while the HRL oscillator increases less than 1dB (Table 2). Degraded phase noise performance can lead to reduced communication range [4].

Table 2 Single Sideband Jitter Integrated over 10-2000Hz

	COTS (dB)	HRL (dB)
Static	-67.5	-31.2
Dynamic	-34.6	-31.0

While the static phase noise performance of the HRL oscillator is not as good as the COTS oscillator, its dynamic performance under the same vibration profile is superior from 40-2000Hz offset frequency. This is an advantage for small mobile platforms facing harsh vibration environments such as UAVs, and larger platforms with installations near the skin of the aircraft.

IV. COTS AND HRL OSCILLATOR COMPARISON

A comparison of relevant parameters for the COTS and microscale oscillators is listed in Table 3. Some of the most promising aspects of microscale oscillators are their relatively small size and low power. The HRL oscillator is about one hundredth of the volume and about one thousandth of the power consumption of the COTS oscillator. Frequency stability of current microscale oscillators is not adequate for most applications. Most COTS oscillators have a frequency stability better than 100ppm. Research efforts are underway investigating ovenization techniques to improve frequency stability in microscale oscillators. Under static conditions, the COTS oscillator has superior phase noise performance at a 1kHz offset compared to the HRL oscillator. Applying the DO-160F Curve E vibration conditions, the microscale oscillator phase noise suffers minimal degradation while the COTS oscillator phase noise has increased significantly and surpasses the microscale oscillator phase noise.

Table 3 - Comparison of COTS and HRL Oscillator

Parameter	COTS	HRL

V. CONCLUSION

Microscale quartz crystal oscillators offer superior vibration performance to COTS quartz crystal oscillators in 100x smaller size. While their static phase noise is inferior to macroscale COTS quartz oscillators, they can achieve the same or better phase noise performance as COTS oscillators in high vibration scenarios. The microscale oscillator will require better frequency stability versus temperatures for most communication and navigation applications. Many radar systems measure frequency returns relative to themselves. Therefore, their frequency drift requirements may be more tolerant.

REFERENCES

[1] RTCA DO-160F Environmental Conditions and Test Procedures for Airborne Equipment, Dec 6,2007, RTCA

[2] ONYX Series Rugged Oven Controlled Crystal Oscillator Datasheet, Wenzel Associates, Inc.

[3] D. Chang, H. Moyer, R. Kubena, R. Joyce, D. Kirby, P. Brewer, H. Nguyen, R. Nagele, and F. Stratton, "Dynamics-enabled quartz reference oscillators," SPIE Proceedings, vol. 8373, May 2012

[4] J. Lovseth, T. Hoffmann, S. Kalyanaraman, A. Reichenauer, V. Olen, and D. Hrncirik "Communication and navigation applications of nonlinear micro/nanoscale resonator oscillators," SPIE Proceedings, vol. 8373, May 2012

Spatially Resolved Measurement of Relaxation Times in a Microfabricated Vapor Cell

Andrew Horsley
Guan-Xiang Du
and Philipp Treutlein
Departement Physik
Universität Basel, Switzerland
Email: andrew.horsley@unibas.ch

Matthieu Pellaton
Christoph Affolderbach
and Gaetano Mileti
Laboratoire Temps-Fréquence, Institut de Physique
Université de Neuchâtel, Switzerland

***Abstract*—We present a new characterisation technique for atomic vapor cells, combining time-domain measurements with absorption imaging to obtain spatially resolved information on decay times, atomic diffusion and coherent dynamics. The technique is used to characterise a microfabricated Rb vapor cell, with N_2 buffer gas, placed inside a microwave cavity. High-resolution images of the population (T_1) and coherence (T_2) lifetimes in the cell are presented. Atom-wall collisions and atomic diffusion result in a 'skin' of reduced T_1 and T_2 times around the edge of the cell. The technique also allows polarisation-resolved imaging of the microwave magnetic field inside the cell. Our technique is useful for vapor cell characterisation in atomic clocks, atomic sensors, and quantum information experiments.**

I. Introduction

The use of alkali vapor cells in atomic physics has a history extending back several decades [1], and has led to important applications in precision measurement [2] and quantum information [3]. Recent years have seen great interest in newly developed miniaturised and microfabricated vapor cells, with sizes on the order of a few millimeters or smaller. Applications include miniaturised atomic clocks [4], and magnetometers measuring both DC [5] and radio-frequency [6] fields. As new applications, one of our groups has recently demonstrated imaging of microwave magnetic fields using a vapor cell [7], and detection of microwave electric fields has been reported in Ref. [8]. Thanks to microfabrication, vapor cells have been miniaturised to a point where spatially resolved information on their properties, and on the external fields applied to them, is essential to their characterisation and performance.

In this paper, we describe a new characterisation technique, applying time-domain Ramsey, and Rabi measurements and absorption imaging [9] to a microcell. Time-domain measurements in vapor cells are currently experiencing a renaissance in interest [10]. Absorption imaging is well established in use with ultracold atoms, however its use with room-temperature atoms is a relatively unexplored area. We use these tools to characterise a microfabricated vapor cell [4] and a microwave cavity designed for compact vapor cell atomic clocks [11], obtaining spatially resolved images of decay times in the cell and images of the microwave field applied to the cell.

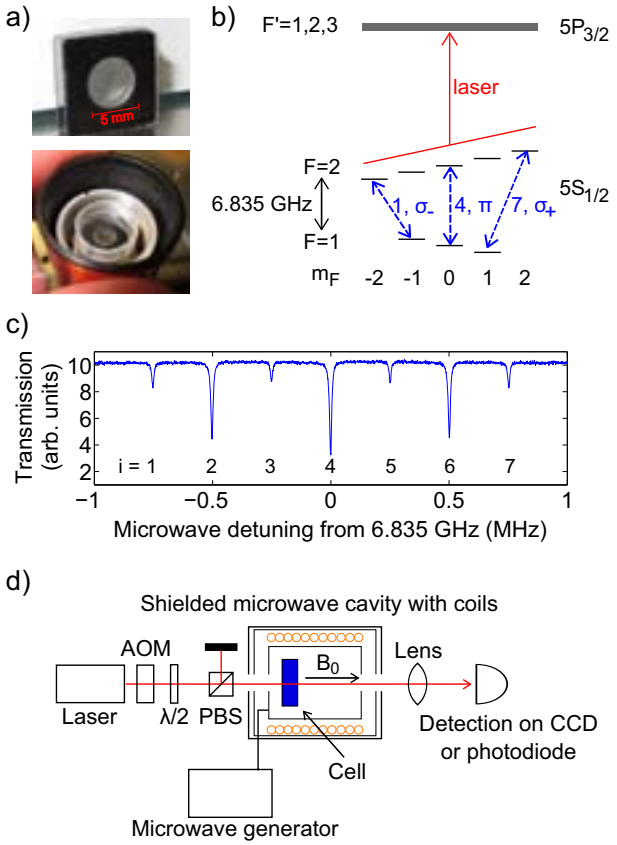

Fig. 1. a) Top: the microfabricated vapor cell used in this paper; Bottom: the cell inside the microwave cavity and coils; b) The ^{87}Rb D2 line. Due to Doppler and collisional broadening on the optical transitions, the excited state hyperfine levels F' are not resolved. Transitions between the Zeeman-split m_F levels of the ground state hyperfine structure can be individually addressed by the microwave field. The three hyperfine transitions used in this work ($i = 1, 4, 7$) are shown in dotted blue; c) A double resonance spectrum, showing laser transmission through the cell as the microwave frequency is scanned. Transmission is reduced whenever the microwave comes on resonance with a hyperfine transition; d) The experimental setup.

Readers are directed to Ref. [12] for a more in-depth coverage of this work.

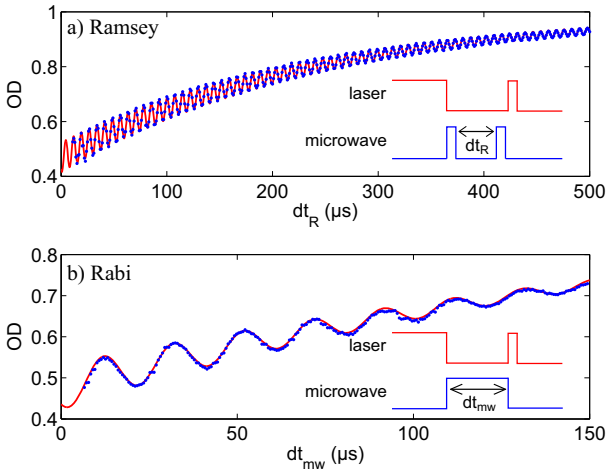

Fig. 2. Cell OD response to a) Ramsey, and b) Rabi sequences, recorded using a photodiode. Data is shown as blue dots, while the fitting curves (described in the text) are in red. Note the different scales. The insets show the laser and microwave sequences used. The OD increases with laser dark time, as the hyperfine population difference relaxes.

II. Equipment and Setup

We use the microfabricated cell shown in Figure 1a. The cell has a $5\,\mathrm{mm} \times 2\,\mathrm{mm}$ internal diameter and thickness, and contains natural abundance Rb and $63 \pm 2\,\mathrm{mbar}$ of N_2 buffer gas [4]. The cell is inserted into a microwave cavity [11], which is surrounded by a solenoid coil providing a static magnetic field (see Figure 1d). The resulting Zeeman splitting allows all seven ^{87}Rb hyperfine transitions to be individually addressed, as shown in the double-resonance spectrum of Figure 1c. We label the transitions $i = 1 \ldots 7$, in order of increasing frequency [12]. The cell temperature was set to 90°C for all data presented in this paper.

We use a laser frequency stabilised on the ^{87}Rb D2 line, pulsed using an acousto-optical modulator (AOM) to perform optical pumping [13] and absorption measurements using the single laser beam. Microwave signals near 6.835 GHz are produced by a frequency generator, and coupled into the cavity.

III. Experiment Sequences

We use pulsed Ramsey and Rabi sequences to characterize the vapor cell. Ramsey sequences provide both T_1 and T_2 times, where the T_1 times refer to population relaxation between all $F = 1$ and $F = 2$ sublevels, whilst the T_2 times are specific for the particular hyperfine m_F transition probed. Rabi sequences provide the microwave magnetic fields strengths applied to the cell.

In a typical sequence, we first apply an optical pumping pulse to the vapor that depopulates the $F = 2$ state. It is followed by microwave pulses that coherently manipulate the atomic hyperfine state. Finally, we measure the optical density (OD) in the $F = 2$ state with a probe pulse. Detection is performed using either a photodiode, or absorption imaging on a CCD camera.

We performed a first characterisation of the cell using a photodiode as the detector, described in the next two sections, III-A and III-B. An approximate laser intensity of $5\,\mathrm{mW/cm^2}$ was used.

A. Ramsey Measurements

In Ramsey sequences, we introduce two microwave pulses between the pump and probe laser pulses, separated by an evolution time dt_R (see Figure 2a). These result in coherent oscillations between the two coupled hyperfine m_F states, which we can record by scanning dt_R over multiple runs of the experiment. The oscillation frequency is given by the microwave detuning. Ramsey sequences are robust to laser and microwave field induced decoherence, as the majority of the atomic evolution occurs in the dark, with the microwave and optical fields off. As such, they provide a good measure of the T_2 time of the cell.

Figure 2a shows an example Ramsey sequence. A large-diameter laser beam was used, illuminating the entire cell, and the microwave was slightly detuned by δ from the $i = 4$ transition. The data is fit with the equation

$$\begin{aligned} \mathrm{OD} &= A - B\exp(-dt_R/T_1) \\ &\quad + C\exp(-dt_R/T_2)\sin(\delta\, dt_R + \phi) \end{aligned} \tag{1}$$

Where A, B, C, ϕ, T_1, T_2, and δ are fitting parameters. The fit gives the two relaxation times as $T_1 = (245 \pm 0.5)\,\mu$s and $T_2 = (322 \pm 4)\,\mu$s. The exact detuning of the microwave from resonance is given by the Ramsey oscillation frequency, $\delta = 2\pi \times (135.764 \pm 0.006)$ kHz.

B. Rabi Measurements

A Rabi sequence consists of a single microwave pulse applied during the dark time between the laser pumping and probe pulses. The microwave pulse drives Rabi oscillations between the two coupled hyperfine states, at a frequency proportional to the microwave magnetic field strength. By tuning the microwave frequency to transitions $i = 1$, 4, and 7, we are sensitive to the σ_-, π, and σ_+ components of the microwave magnetic field, respectively. This allows us to measure each vector component of the microwave magnetic field [7], [12].

An example Rabi sequence is shown in Figure 2b. A 1 mm diameter laser was used, and the microwave frequency was tuned exactly to the $i = 4$ transition, having been calibrated using a Ramsey sequence. Defining τ_1, the population difference lifetime, and τ_2, the Rabi oscillation lifetime, the data is fit with the equation

$$\begin{aligned} \mathrm{OD} &= A - B\exp(-dt_{mw}/\tau_1) \\ &\quad + C\exp(-dt_{mw}/\tau_2)\sin(\Omega\, dt_{mw} + \phi), \end{aligned} \tag{2}$$

where A, B, C, ϕ, τ_1, τ_2, and Ω are fitting parameters. We obtain $\tau_1 = (231 \pm 9)\,\mu$s and $\tau_2 = (94 \pm 3)\,\mu$s. On the $i = 4$ transition, we are sensitive to the π component of the microwave magnetic field, and so $\Omega_4 = 2\pi \times 50.39 \pm 0.05$ kHz corresponds to $B_\pi = 3.600 \pm 0.003$ μT at the point interrogated by the laser [12].

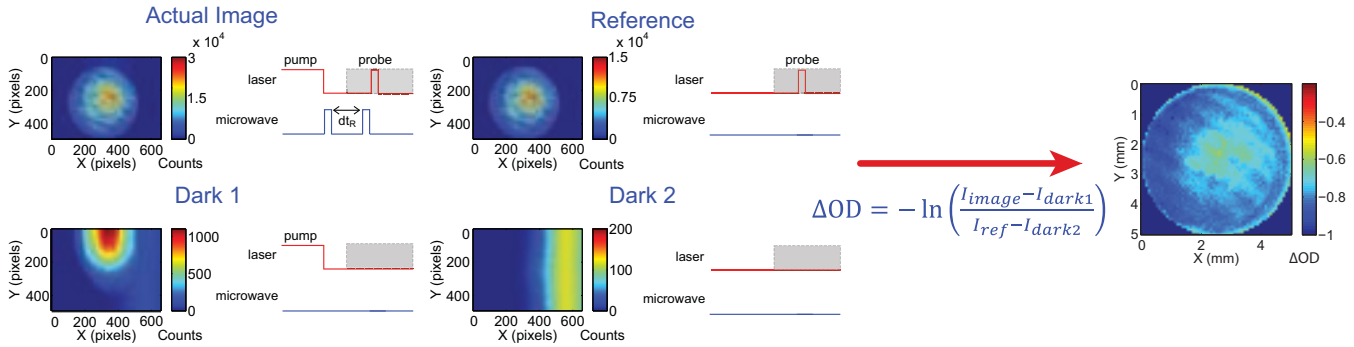

Fig. 3. Absorption imaging. Left: four images are used to create an image of the relative OD (ΔOD). These are the actual image (I_{image}), with the full experimental sequence of pumping, microwave pulses (in this example a Ramsey sequence), and probe pulse; a reference image (I_{ref}), consisting of a probe pulse, without optical pumping or microwave pulses; a dark image for the actual image (I_{dark1}), taken with pump pulse but no microwave or probe pulses; and a dark image for the reference image (I_{dark2}), taken with both the laser and microwave off. Grey boxes indicate when the camera electronic shutter is open. Right: These four images are then used to calculate ΔOD.

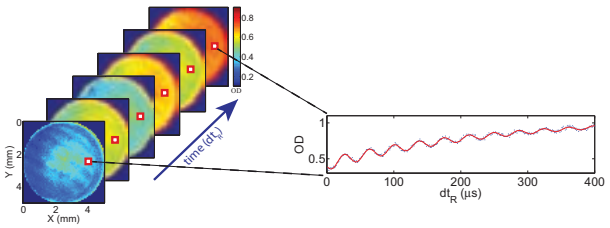

Fig. 4. Left: Images of the cell OD during a Ramsey sequence, at $dt_R = 5, 25, \ldots 105\,\mu$s. An experiment run results in an image of the optical depth for each dt timestep. Right: Examining a single pixel, we see oscillations in the OD in time, which we can fit using Eq. (1) to obtain T_1 and T_2 at that location.

IV. Spatially Resolved Imaging of Relaxation Times and Microwave Field Strength

We now turn our attention to measurements using the CCD camera. We use the technique of absorption imaging, which was developed in experiments with ultracold atoms to obtain accurate images of atomic density distributions in a given hyperfine state [9]. We record four images to create an image of the observed variation in optical density ΔOD, as described in Figure 3 and Ref. [12]. As a consequence of adapting the technique to hot atoms, we cannot directly obtain the OD from the four images [12], however this can in turn be obtained by normalising ΔOD to the OD measured with no optical pumping. The use of reference and dark images significantly reduces our sensitivity to short and long term drifts in the imaging system and to spatial variations in the laser intensity profile.

An image of the cell OD is produced for each dt timestep of an experimental sequence, as shown in the left-hand side of Figure 4. Each pixel has a time-varying signal (Figure 4, right-hand side), which is fit with either Eq. (1), for Ramsey sequences, or Eq. (2), for Rabi sequences.

In order to obtain a strong signal, the laser intensity averaged over the 5 mm cell diameter was set to $30\,\mathrm{mW/cm^2}$ for the data presented in the following sections, IV-A and IV-B.

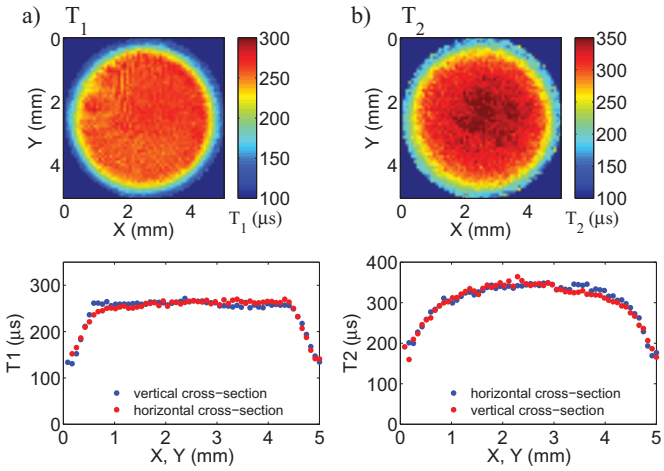

Fig. 5. Measured T_1 and T_2 times across the cell. The top panels show a) T_1 times obtained from fitting a Ramsey sequence; and b) T_2 times obtained from the same Ramsey sequence. The bottom panels show cross-sections of each image, averaged along 3 pixel wide lines passing horizontally and vertically through the image centres. Close to the walls, there is a significant decrease in T_1 and T_2 due to Rb-wall collisions.

A. Imaging Relaxation

Figure 5 shows images of the T_1 and T_2 times across the cell, produced using a Ramsey sequence with the microwave frequency set slightly detuned from the $i = 4$ (clock) transition, and the microwave input power to the cavity set to 21.8 dBm,. Each pixel of the Ramsey data was fit using Eq. (1), yielding T_1 and T_2 times with $\pm 1\%$ and $\pm 4\%$ fitting uncertainties, respectively.

The bottom panels of Figure 5 show cross-sections of the T_1 and T_2 images. The relaxation rate is uniform across the centre of the cell, with T_1 times around 265 μs, and dropping away to 150 μs at the cell edge, due to the depolarisation of Rb atoms after collisions with the cell walls [12]. This 'skin' of reduced atomic lifetimes near the cell edge is reproduced in a model of the T_1 time presented in Ref. [12]. The T_1

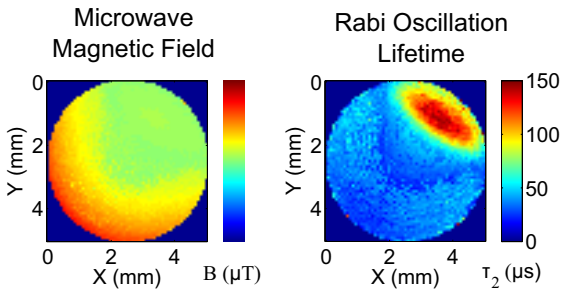

Fig. 6. Left: Image of the π component of the microwave magnetic field, obtained using a Rabi sequence on the clock transition. Right: Images of the corresponding Rabi oscillation lifetime, τ_2.

times obtained in the centre of the cell are larger than the values obtained using the photodiode in section III-A, as the photodiode measurements averaged the relaxation time over the entire cell, including the regions near the cell walls.

The T_2 time across the cell, shown in the right-hand panels of Figure 5, has a much smoother profile than the flat-top profile of the T_1 images, with the influence of the cell walls extending to the cell centre. T_2 values in the centre of the cell peak at around $350\,\mu$s.

B. Imaging the Microwave Magnetic Field

Figure 6 shows the π component of the microwave magnetic field, obtained using a Rabi measurement on the clock transition, $i = 4$. The right panel shows the corresponding decay time of the Rabi oscillations (τ_2). The microwave frequency was calibrated using a Ramsey sequence, and tuned exactly to resonance, and the microwave power at the input to the cavity was 26.8 dBm. Each pixel was fit using Eq. (2), and the microwave magnetic field strength was then calculated as described in Ref. [12]. The σ_- and σ_+ components were also imaged [12], with measured field strengths below $1.5\,\mu$T. The π component, whose dominance follows from the cavity design [11], is more than 3 times stronger, with field strengths up to $5\,\mu$T.

The lifetime, τ_2, of the Rabi oscillations is significantly shorter than the T_2 time, principally due to inhomogeneities in the microwave magnetic field [1]. This can be seen in Figure 6, where the τ_2 time is inversely correlated with the magnitude of the microwave magnetic field inhomogeneity, which in turn is linked to the field strength. The strong spatial variation in τ_2 highlights the importance of our technique for cell and cavity characterisation, in particular for high precision devices such as vapor cell atomic clocks.

V. Conclusions

We have used time-domain spatially resolved optical and microwave measurements to image atomic relaxation and the polarisation-resolved microwave magnetic field strength in a microfabricated Rb vapor cell placed inside a microwave cavity. The population and coherence relaxation times were measured to be uniform across the cell centre, with values at 90°C of $T_1 = 265\,\mu$s and $T_2 = 350\,\mu$s, respectively. Depolarising collisions between Rb atoms and the cell walls resulted in T_1 and T_2 times around $150\,\mu$s near the cell edge, and diffusion of these atoms lowered relaxation times within $0.7\,$mm of the cell wall. Images of the cavity microwave magnetic field show significant spatial inhomogeneity, due to perturbations to the cavity introduced by the dielectric cell material. For a given hyperfine transition, we can identify the cell region maximising the number of Rabi oscillations, and hence the region of optimal coherent manipulation.

Our measurement technique is fast, simple, and produces high resolution images for vapor cell and microwave-device characterisation. It is of particular interest for characterising cells in miniaturised atomic clocks and sensing applications. It is also of interest for characterising the cell and cavity properties in larger and high-performance vapor cell atomic clocks.

Acknowledgment

This work was supported by the Swiss National Science Foundation (SNFS) and the European Space Agency (ESA). We thank Y. Pétremand for filling the cell, and R. Schmied for discussions on the modelling of relaxation in the cell.

References

[1] M. Arditi and T. R. Carver, "Hyperfine Relaxation of Optically Pumped Rb^{87} Atoms in Buffer Gases," *Physical Review*, vol. 136, no. 3A, p. A643, 1964.

[2] D. Budker and M. Romalis, "Optical magnetometry," *Nature Physics*, vol. 3, pp. 227–234, 2007.

[3] B. Julsgaard, A. Kozhekin, and E. S. Polzik, "Experimental long-lived entanglement of two macroscopic objects." *Nature*, vol. 413, no. 6854, pp. 400–3, Sep. 2001.

[4] M. Pellaton, C. Affolderbach, Y. Pétremand, N. de Rooij, and G. Mileti, "Study of laser-pumped double-resonance clock signals using a microfabricated cell," *Physica Scripta*, vol. T149, p. 014013, May 2012.

[5] V. Shah, S. Knappe, P. D. D. Schwindt, and J. Kitching, "Subpicotesla atomic magnetometry with a microfabricated vapour cell," *Nature Photonics*, vol. 1, no. 11, pp. 649–652, Nov. 2007.

[6] I. Savukov, S. Seltzer, M. Romalis, and K. Sauer, "Tunable Atomic Magnetometer for Detection of Radio-Frequency Magnetic Fields," *Phys. Rev. Lett.*, vol. 95, no. 6, p. 063004, Aug. 2005.

[7] P. Böhi and P. Treutlein, "Simple microwave field imaging technique using hot atomic vapor cells," *Appl. Phys. Lett.*, vol. 101, no. 18, p. 181107, 2012.

[8] J. A. Sedlacek, A. Schwettmann, H. Kübler, R. Löw, T. Pfau, and J. P. Shaffer, "Microwave electrometry with Rydberg atoms in a vapour cell using bright atomic resonances," *Nature Physics*, vol. 8, no. 11, pp. 819–824, Sep. 2012.

[9] W. Ketterle, D. Durfee, and D. Stamper-Kurn, *Making, probing and understanding Bose-Einstein condensates...*, M. Inguscio, S. Stringari, and C. E. Wieman, Eds. IOS Press, Amsterdam, 1996.

[10] S. Micalizio, C. E. Calosso, A. Godone, and F. Levi, "Metrological characterization of the pulsed Rb clock with optical detection," *Metrologia*, vol. 49, no. 4, pp. 425–436, Aug. 2012.

[11] G. Mileti, I. Ruedi, and H. Schweda, *Proc. 6th European Frequency and Time Forum*, pp. 515–519, 1992.

[12] A. Horsley, G.-X. Du, M. Pellaton, C. Affolderbach, G. Mileti, and P. Treutlein, "Imaging of Relaxation Times and Microwave Field Strength in a Microfabricated Vapor Cell," *preprint arXiv:1306.1387*, 2013.

[13] W. Happer, "Optical pumping," *Reviews of Modern Physics*, vol. 44, no. 2, pp. 169–249, 1972.

The Integrated Swiss Miniature Atomic Clock

Jacques Haesler, Laurent Balet, Jacques-André Porchet, Thomas Overstolz,
Jörg Pierer, Rony Jose James, Sylvain Grossmann, David Ruffieux, Steve Lecomte

Centre Suisse d'Électronique et de Microtechnique (CSEM) SA
CH-2002 Neuchâtel, Switzerland
jacques.haesler@csem.ch

***Abstract* — The detailed design of the Swiss Miniature Atomic Clock (Swiss–MAC) was presented by CSEM in 2012. This paper describes the progress made in the meantime towards the realization of the integrated Swiss–MAC, by presenting a first prototype showing preliminary but very promising performances.**

I. INTRODUCTION

Miniature atomic clocks (MACs), typically based on the coherent population trapping scheme (CPT) [1], show the promise of having miniature (< 1 cm^3) and low-power (< 100 mW) portable microwave frequency standards [2]. The Swiss–MAC was designed to target such state of the art specifications. The current prototype integrates most of the desired functionalities, except the vacuum encapsulation of the physics package and the integrated temperature regulation of the atomic vapor cell. The prototype (Fig. 1) is powered by a separate PCB equipped with a battery pack and different monitoring and debugging inputs/outputs. The main PCB has a dimension of 50 x 100 mm^2 with 1/3rd of its surface populated by jumpers and connectors.

Fig. 1. Picture of the full Swiss–MAC prototype (caps removed).

II. SWISS–MAC DESIGN

The core physics package, as designed and presented in 2012 (Fig. 2) [3], is realized by a stacking of standard functionalized PCB layers (Fig. 3). It has dimensions down to 11 x 11 x 8.5 mm^3 (1 cm^3), including the functionalized atomic vapor cell with dimensions downsized to 4 x 4 x 1.6 mm^3 (26 mm^3). The cell is surrounded by a flex circuit for electrical connection (heater, Tsensor and C-coils) and by an internal magnetic shielding.

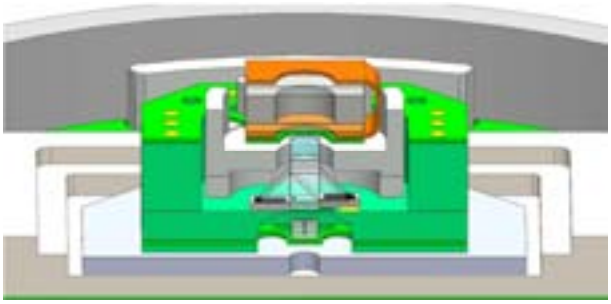

Fig. 2. Design of the physics package (sectional view).

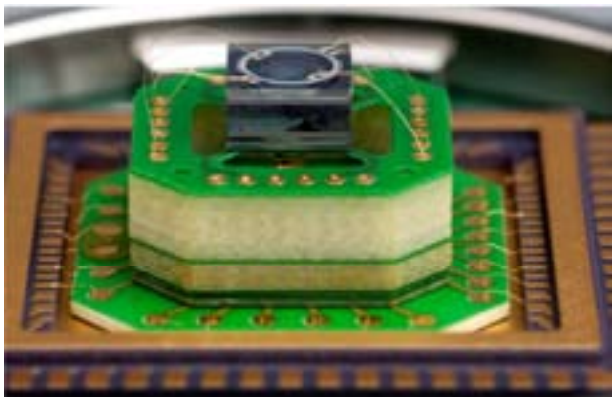

Fig. 3. Picture of the current physics package with stacked PCB layers. Internal magnetic shielding is not shown.

The core physics package is mounted in a commercial ceramic package for vacuum encapsulation. The resulting assembly (Fig. 4) is surrounded by an external Ø 42 mm magnetic shielding, the overall volume of the physics package reaching 22 cm^3. The SMAC prototype is controlled by means of a LabVIEW® interface communicating with an MSP430 microcontroller. The latter drives the 3rd generation of a dedicated proprietary ASIC, with built-in RF lock loop and laser lock loop, and with integrated laser bias current source, three temperature sensors, and four additional current sources.

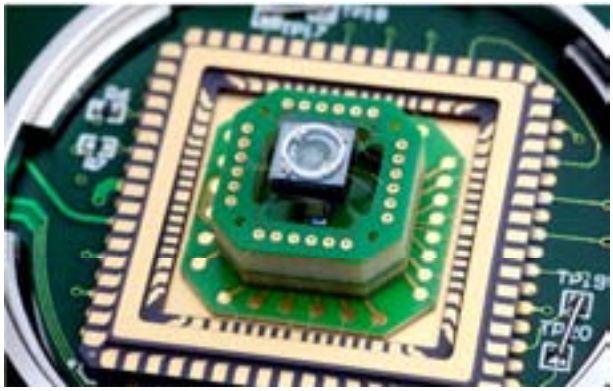

Fig. 4. Picture of the physics package with ceramic package and external magnetic shielding ring (caps not shown).

III. LOW-POWER INTEGRATED ELECTRONICS

Lowering the overall power consumption of the miniature atomic clock is partially done by integrating most of the electronics in an application-specific integrated circuit (ASIC). Version 3.0 of the RF chip integrates the RF frequency and the laser frequency lock loops (v2.0) [4], as well as four additional current sources for heating the laser and the atomic cell and for driving the Helmholtz coils (v3.0). Fig. 5 shows a graphical representation of the functionalities integrated in the different versions of the ASIC.

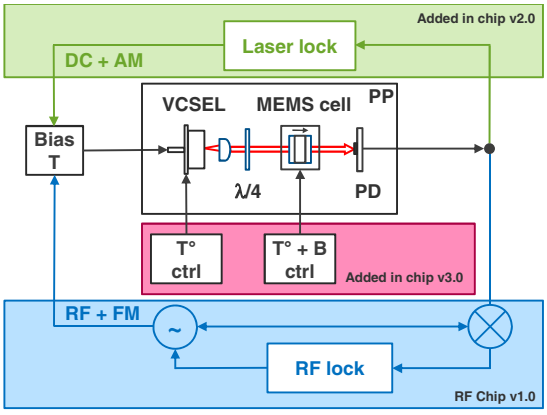

Fig. 5. Graphical representation of the 3 different chip versions.

Fig. 6 shows the layout and a picture of the chip version 3.0 that has been integrated into the Swiss–MAC prototype. The battery operated chip could successfully drive a laboratory CPT atomic clock (laser and RF frequencies lock loops) with 26 mW of power consumption [4].

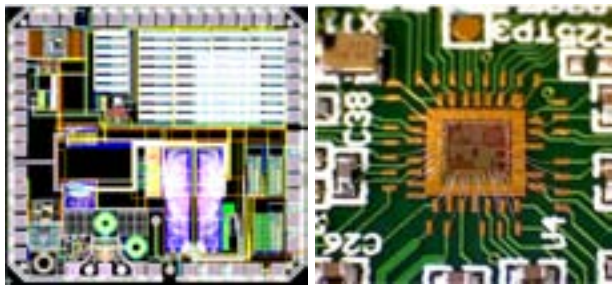

Fig. 6. Chip layout (left) and chip bonded on the Swiss–MAC PCB (right).

Ongoing work allowed to successfully temperature stabilize the laser and to lock its optical frequency on one Rubidium-87 absorption line with 42 mW of total power consumption, the physics package being exposed to room temperature air without vacuum encapsulation.

IV. MINIATURE ATOMIC VAPOR CELLS

Fabricating small leak free atomic cavities with reproducible filling is still challenging. An important effort has been done to develop wafer level fabrication of millimeter size atomic MEMS cells made of silicon and glass by using an alkali azide solution to fill the cell cavities.

After full evaporation of the solvent, the cavities are sealed by anodic bonding under controlled atmosphere. Metallic rubidium and nitrogen are obtained by UV decomposition of the crystallized rubidium azide.

The first cells (10 x 10 mm^2) fabricated in this way showed promising performances for a CPT miniature atomic clock and optimization of the buffer gas mixture is still ongoing.

The cells were miniaturized down to 1 x 1 mm^2 but much of the work has nevertheless been pursued on 4 x 4 mm^2 cells in order to add functionalities to the glass windows (Fig. 7). Both faces have integrated heaters, temperature sensors and Helmholtz coils.

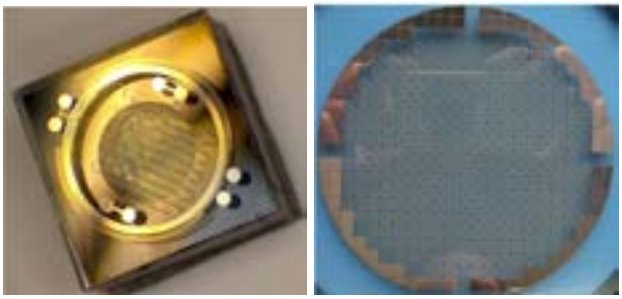

Fig. 7. Functionalized 4 x 4 x 1.6 mm^3 atomic MEMS cell (left) and 4 inch functionalized glass wafer (right).

The functionalized cells are currently characterized. Heating the cells up to 100°C has been achieved without problems and ^{87}Rb 0-0 CPT signals have been measured in a laboratory setup. Integrating the functionalized cells in the prototype is still ongoing.

V. RESULTS

The SMAC prototype is currently in its integration and test phase. The main lock loops could already be closed and preliminary frequency stability measurements could successfully be realized by using an external ^{87}Rb miniature glass atomic vapor cell (100 mm^3). The preliminary performances (Fig. 8) demonstrate a frequency stability of $\sigma_y = 3 \cdot 10^{-11}$ at one day integration time (no drift removal), while being at $\sigma_y = 6 \cdot 10^{-11}$ at 1 s, showing that our integrated electronics supports sub 10^{-10} short term frequency stability. The ^{87}Rb MEMS atomic vapor cells are being integrated in the Swiss–MAC prototype and further improvements and tests are ongoing. The complete prototype will be functional and fully characterized by the end of 2013.

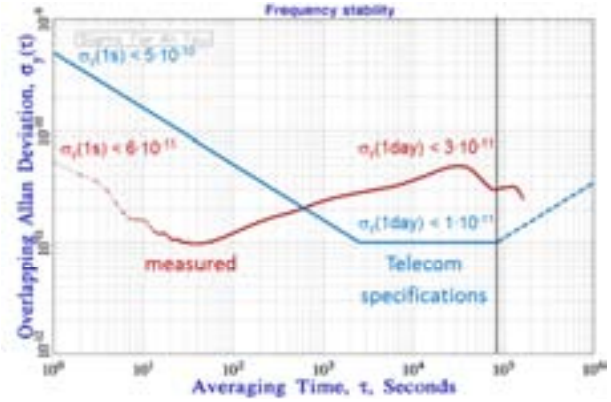

Fig. 8. Preliminary performances obtained with the Swiss–MAC prototype using an external ^{87}Rb miniature glass cell.

ACKNOWLEDGMENT

This research activity is performed in the frame of a multidivisional research program and CSEM would like to thank the Swiss Confederation, the Canton of Neuchâtel, the Canton of Basel and the Cantons of Central Switzerland for their financial support. Fruitful discussions and contributions from J.-F. Léchenne, M. Toimil, P. Pilloud, R. Rusconi, T. Le, S. Bitterli and J. Kaufmann are acknowledged.

REFERENCES

[1] R. Lutwak, D. Emmons, W. Riley, R. M Garvey, "The chip-scale atomic clock – coherent population trapping vs. conventional interrogation", 34th Annual Precise Time and Time Interval (PPTI) Meeting, pp. 539-550, December 2002.

[2] J. Kitching, S. Knappe, L. Liew, P. Schwindt, K. Shah, J. Moreland, L. Hollberg, "Microfabricated atomic clocks", IEEE International Conference on Micro Electro Mechanical Systems IEEE, pp. 1-7, February 2005.

[3] J. Haesler et al., "Swiss Miniature Atomic Clock: first prototype and preliminary results", European Time and Frequency Forum (EFTF), Gothenburg, April 2012.

[4] J. Haesler, T. Overstolz, R. Jose James, J. Pierer, M. Contaldo, D. Ruffieux and S. Lecomte, "Driving an extra small atomic resonator with low-power integrated RF frequency and laser locked loops", IFCS-EFTF, San Francisco (USA), May 2011.

Double Resonance Spectroscopic Studies Using a New Generation of Microfabricated Microwave Cavity

M. Pellaton, C. Affolderbach, G. Mileti
Laboratory of Time & Frequency (LTF),
University of Neuchâtel,
Neuchâtel, Switzerland
Email: matthieu.pellaton@unine.ch
gaetano.mileti@unine.ch

M. Violetti, J.-F. Zürcher, A. K. Skrivervik
Laboratory of Electromagnetics and Acoustics (LEMA),
École Polytechnique Fédérale de Lausanne (EPFL),
Lausanne, Switzerland

***Abstract*—We evaluate the potential of a new generation microwave cavity by double resonance spectroscopic studies. Both, the cell and the microwave cavity are microfabricated. This allows a substantial size reduction for the physics package, without compromising the RF field geometry and the optical quality of the cell windows. We demonstrate short term stability of $5 \times 10^{-12}\tau^{-1/2}$ (1-100 s), and below 1×10^{-12} up to 10^3 s. Finally, we report on the AC stark shift effect, one of the main limiting factors for long term clock stabilities.**

I. Introduction

Numbers of compact commercial double resonance (DR) clocks are using Loop-Gap Resonators (LGR) having the size of half the wavelength. Different names have been given to these resonators, magnetron-type resonator [1] or slotted-tube cavity [2], but still, loops and gaps define the field geometry. Reducing the size of this type of resonator is a challenging task which requires a complete redesign, and some successful alternatives have been presented in the past. One can cite, among others, Deng who proposed a "modified coaxial cavity" [3] and Braun et al. with two parallel non radiating RF feed loops [4]. This paper reports on a novel type of microwave resonator, the μ-LGR [5], [6], and its spectroscopic evaluation. Such a study aims towards a miniature atomic clock having similar stability performances to a compact commercial atomic DR clock but with a significant size and power consumption reduction.

II. Double Resonance (DR) and Experimental Setup

We use the DR interrogation technique [7]. Its principle consists in creating an inversion of the populations within the hyperfine ground states of a rubidium vapour by optical pumping, while the applied microwave, when at resonance, tends to equilibrate these populations. The DR spectrum is obtained by sweeping the frequency of the microwave frequency while the transmission of the cell is recorded (see Figure 2). In the clock operation, the clock signal, or $|F_g = 1, m_F = 0\rangle \leftrightarrow |F_g = 2, m_F = 0\rangle$ transition, is used as a reference to steer and stabilize the quartz oscillator at the basis of the microwave generation chain. In our setup, the pumping light is produced by an in-house made laser head [8] using a DFB laser of which light is resonant with the D2 line of the rubidium (780 nm). The laser head inbuilt sub-Doppler spectroscopic setup allows four different optical frequency references that can be used to lock the laser frequency. At the output of the laser head, the laser beam is split into two. One part is sent to a wavelength meter (HighFinesse WSU/30), the other part, before interacting with the Rubidium atoms, passes through different optics elements in order to control its polarization and power, and spatially homogenize its intensity. The enriched ^{87}Rb vapour is confined in a thick micro-fabricated cell [9], designed in parallel with the μ-LGR. The cell's internal volume has a cylindrical shape with dimensions of 4.05 mm height and 4 mm diameter. It is also filled with a buffer gas (BG) mixture of Argon and Nitrogen in order to reduce the collisions of the rubidium atoms with the cell's wall, as well as to diminish the sensitivity to temperature fluctuations [10]. The 6.834 GHz microwave radiation is produced from the 2.278 GHz output of a commercial synthesizer, via a frequency tripler. A similar DR setup is described in [11].

A. μ-LGR details

The μ-LGR was already presented at previous conferences [5], [12]; it consists of a multiple stack of printed planar loop-gap structures (see Figure 1) inductively coupled to a coaxial fed printed loop. The total cavity volume is < 0.9 cm^3. The development was done through software simulations in order to optimize the field orientation factor (FOF) [13], and study the influence of relevant geometrical features [5]. The advantages of such a cavity are:

- an excellent field geometry favouring the π-transitions, therefore the clock transition (see Figure 2). The FOF is measured to be 0.7; in other words, within the cell volume, 70% of the RF magnetic field power is parallel to the symmetry axis of the cell.
- a low RF power need, less than -20 dBm are required.
- an easy and low cost fabrication with an excellent reproducibility, thanks to the micro-fabrication process.

III. Experimental results

The clock transition resonance signal was recorded in many different experimental configurations; laser intensity and frequency as well as RF power and cell temperature were varied. Optimization of the clock signal, extraction of its intrinsic properties, as well as characterization of its environmental sensitivity were carried out.

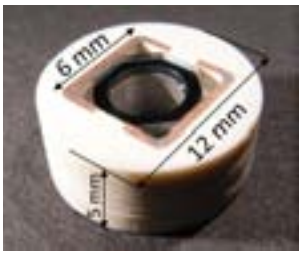

Fig. 1. μ-LGR containing the microfabricated cell.

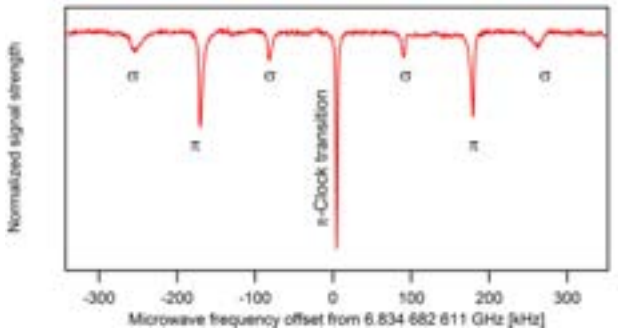

Fig. 2. Zeeman's spectrum at low RF power showing the π-transitions strongly favoured, sign of an excellent field geometry.

A. Clock signal lineshape

Figure 3 shows an optimized clock signal and its lorentzian fit. It has a contrast $> 7\%$ with a discriminator slope of 12 pA/Hz. Such a signal has a potential shot-noise limit of $2.5 \times 10^{-12}\tau^{-1/2}$. Contrasts up to 30% with similar shot-noise limit have also been measured, but the optimization was performed with the constrain to keep the light intensity as low as possible (less than 1 $\mu\mathrm{W/mm^2}$) in order to minimize the light shift effects (see discussion below). The total shift of 5 kHz matches well with the theoretical BG induced pressure shift.

Linear extrapolation of the linewidth to zero light intensity at low RF power gives an intrinsic value of less than 590 Hz; which is in excellent agreement with the 585 Hz theoretically predicted by the diffusion model in a cylindrical cell [14].

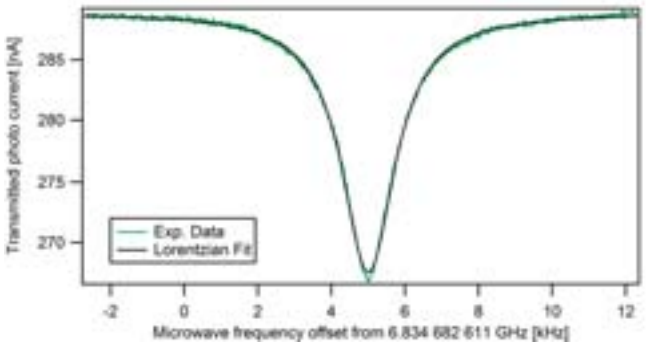

Fig. 3. Optimized DR signal and its lorentzian fit. the Linewidth is < 1.8 kHz for a contrast of $> 7\%$.

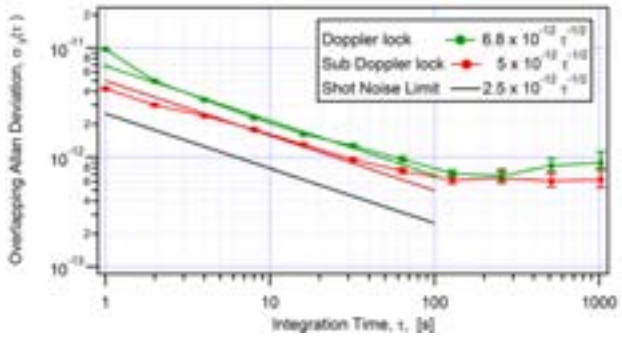

Fig. 4. Clock stability obtained with two different laser configurations: (red) laser frequency locked to CO23-21 dip of an external cell sub-Doppler spectrum; (green) laser frequency locked to the BG broadened peak of the clock cell ($|F_g = 2\rangle \rightarrow |F_e\rangle$). The shot-noise limit is draw in black.

B. Clock short-term stability

The short to medium term stabilities (see Figure 4) were measured using the optimized signal shown on Figure 3. Two different laser locking schemes were used. For the laser frequency locked to the sub-Doppler dip of the spectrum of the reference cell of the laser head (crossover between $|F_g = 2\rangle \rightarrow |F_e = 3\rangle$ and $|F_g = 2\rangle \rightarrow |F_e = 1\rangle$ transitions, or CO23-21), we obtained a short-term stability below $5 \times 10^{-12}\tau^{-1/2}$. A similar stability, $6.8 \times 10^{-12}\tau^{-1/2}$, is obtained when the frequency of the laser is referenced to the buffer gas broadened peak ($|F_g = 2\rangle \rightarrow |F_e\rangle$) of the clock cell itself. These obtained stabilities show a strong potential for a miniature atomic clock with the short to mid-term performances of a compact one.

C. Light-shift studies

Light shift effect, or AC Stark shift, is a well known process, and is also one of the main sources of instability in the different types of atomic frequency standards [15]. It is a direct consequence of the coupling between two states through an optical field, and can be calculated by the perturbation theory [16]. Since in the case of a real atom, many levels are coupled to the ground state levels, the contribution of each has to be taken into account [17]. The total light induced shift can be expressed as follows:

$$\Delta\nu_{LS} = \left(\frac{\Omega_L}{4\pi}\right)^2 \sum_{F_e=0}^{4} \left(\frac{\eta'_{F_e}\delta\nu'_{L_{F_e}}}{(\frac{\Gamma^*}{4\pi})^2 + (\delta\nu'_{L_{F_e}})^2} - \frac{\eta_{F_e}\delta\nu_{L_{F_e}}}{(\frac{\Gamma^*}{4\pi})^2 + (\delta\nu_{L_{F_e}})^2} \right). \quad (1)$$

where Ω_L is the optical Rabi frequency, $\delta\nu_{L_{F_e}}$ and η_{F_e} the frequency detuning and transition strength for the transition $|F_g = 1\rangle \rightarrow |F_e\rangle$ (the ' denotes for the transitions from the state $|F_g = 2\rangle$). Γ^* relates to the lifetime of the excited states. The frequency detunings are given by:

$$\delta\nu_{L_{F_e}} = \nu_L - \nu_{F_e} \quad (2)$$

for which ν_L is the laser frequency, and ν_{F_e} is the optical frequency for the atomic transition $|F_g = 1\rangle \rightarrow |F_e\rangle$, taking into account the induced BG collisional shift. The total pressure as well as the gas ratio are considered and the optical pressure shift coefficients taken from Rotondaro et al. [18].

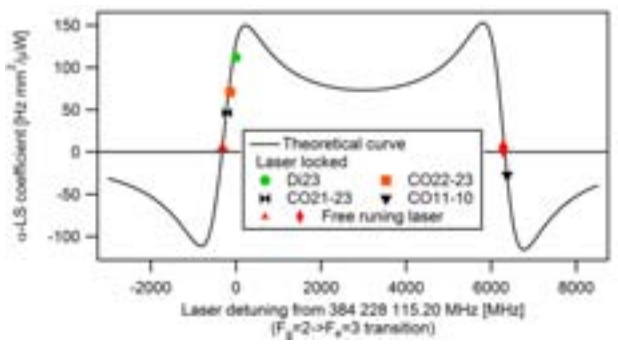

Fig. 5. Experimental (markers) and theoretical (line) light shift coefficients as a function of the laser frequency.

Figure 5 shows the theoretical and experimental intensity light shift coefficients (α-LS$= \frac{\partial \Delta\nu}{\partial I}$) as a function of the laser frequency. The experimental α-LS coefficients are measured by extracting the slope of the total shift of the clock signal as a function of the laser intensity at a given optical frequency. The abscissa zero detuning point corresponds to the direct transition $|F_g = 2\rangle \rightarrow |F_e = 3\rangle$, called Di23, of the unperturbed ^{87}Rb atom. A laser locked to this transition was used as a calibration reference for the wavelength meter. After the calibration, the optical frequencies were measured when the laser was locked to the other patterns of the sub-Doppler spectrum (crossover dips) of the reference cell. These experimental frequencies match within 1 MHz the theoretical values, validating the calibration over the full spectrum range. For the laser in free running mode, its frequency fluctuations during the measurement time imposes abscissa error bars of the order of ± 5 MHz. Both modes were tested at the four lockable frequencies in order to validate the α-LS coefficients obtained with the laser in free running mode. Similar coefficients are obtained with only 4% difference.

Equation (1) predicts two laser frequencies at which the α-LS coefficient is zero. These are offset from the Di23 transition of -327 MHz and 6321 MHz. The experimental α-LS coefficients measured at the -327 MHz offset is < 1.5 Hz mm$^2/\mu$W or $2.2 \times 10^{-12}/\%$ at 1 μW/mm^2. With a relative laser intensity fluctuation $< 10^{-3}$ at 10^4 s (in terms of Allan deviation), the α-LS coefficient contribution to the clock instability is $< 2.2 \times 10^{-13}$. The α-LS coefficient being laser frequency dependant, another coefficient has to be considered. Locally, the clock sensitivity to the laser frequency, $\frac{\partial \nu_{clock}}{\partial \nu_{laser}}$, is called β light shift [19], or β-LS coefficient. Since this coefficient scales linearly with the laser intensity (see (1)), a smaller intensity will therefore minimize its influence on the clock frequency. For a laser intensity of 1 μW/mm^2, at the -327 MHz offset, the relative β-LS coefficient is calculated to be 5.1×10^{-17} /Hz. Locked to a sub-Doppler atomic transition, our DFB-laser has a relative frequency stability $< 2 \times 10^{-11}$ at 10^4 s [8]. These frequency fluctuations results in a potential clock instability contribution of $\sim 4 \times 10^{-13}$. Table I summarizes the potential clock instabilities induced by the laser fluctuations in the two different lock schemes mentioned in section III-B. These results show a potential instability limit for the light shift clearly below 1×10^{-12} at 10^4 seconds.

TABLE I. α- AND β-LIGHT SHIFT COEFFICIENTS AND THEIR CORRESPONDING INDUCED CLOCK INSTABILITIES FOR A LASER INTENSITY OF 1 μW/mm^2.

	Coefficients	Parameter variations 10^4 s	Clock instability contribution
α-LS	$< 2.2 \times 10^{-12}/\%$	$< 10^{-3}$ rel.	$< 2.2 \times 10^{-13}$
	Doppler Lock strength		
β-LS	5.1×10^{-17}/Hz	$< 2 \times 10^5$ Hz [20]	$\sim 1 \times 10^{-11}$
	Sub-Doppler Lock strength		
β-LS	5.1×10^{-17}/Hz	$\sim 8 \times 10^3$ Hz	$\sim 4 \times 10^{-13}$

IV. Conclusion & Next steps

We have presented our spectroscopic studies using a new generation of physics package. The setup was also used as a clock demonstrator; two laser frequency locking scheme were used. Both allow excellent short term stabilities below $7 \times 10^{-12}\tau^{-1/2}$, and staying below 1×10^{-12} up to 10^3 seconds. Experimental and theoretical AC Stark shift were also presented, and an excellent agreement between them is observed. Though AC Stark shift remains one of the most limiting factor in terms of medium to long term stabilities, its limitation can be potentially reduced down to 4.6×10^{-13} at 10^4 s. Further spectroscopic studies still remain to be done, especially in term of temperature shift, power shift and the use of other light sources such as a microfabricated lamp [21], or other laser sources. Nevertheless, this study demonstrates a strong potential of the μ-LGR as part of a miniature atomic clock with highly competitive performances.

Acknowledgment

This work was supported by the SNSF (grant numbers 122693 and 140681) and the European Space Agency (ESA). We thank Y. Pétremand for the cell fabrication, F. Gruet, P. Scherler, and M. Durrenberger for their technical contributions.

References

[1] G. Mileti, I. Ruedi, and H. Schweda, "Line inhomogeneity effects and power shift in miniaturized rubidium frequency standard," in *Proc. EFTF 1992*, 1992.

[2] D. Zhong, B. Xia, S. An, H. Wu, Q. Wang, F. Zhao, F. Qi, F. Wang, and G. Mei, "Investigation on physics package with slotted-tube microwave cavity for rubidium atomic frequency standard," in *proc. joint IEEE FCS & EFTF 2009*, 2009, pp. 1019–1022.

[3] J. Deng, "Subminiature microwave cavity for atomic frequency standards," in *Proc. IEEE IFCS & PDA Exhibition 2001*, 2001, pp. 85 –88.

[4] A. M. Braun, T. J. Davis, M. H. Kwakernaak, J. J. Michalchuk, A. Ulmer, W. K. Chan, J. H. Abeles, Z. A. Shellenbarger, Y.-Y. Jau, W. Happer, T. McClelland, H. Fruehauf, R. Drap, W. Weidemann, and M. Variakojis, "RF-interrogated end-state chip-scale atomic clock," in *proc. PTTI 2007*, 2007.

[5] M. Violetti, F. Merli, J.-F. Zürcher, A. Skrivervik, M. Pellaton, C. Affolderbach, and G. Mileti, "New Miniaturized Microwave Cavity for Rubidium Atomic Clocks," in *proc. IEEE Sensors 2012*, 2012.

[6] M. Violetti, C. Affolderbach, F. Merli, G. Mileti, and A. K. Skrivervik, "Microwave resonator, quantum sensor, and atomic clock," *European Patent Application No. 12155696*, February 16, 2012.

[7] J. Vanier and C. Mandache, "The passive optically pumped Rb frequency standard: the laser approach," *Appl. Phys. B*, vol. 87, pp. 565–593, 2007.

[8] F. Gruet, C. Affolderbach, M. Pellaton, T. Bandi, R. Matthey, and G. Mileti, "Compact and frequency stabilised laser heads for rubidium atomic clocks," in *proc. ICSO 2012*, October 2012.

[9] Y. Pétremand, C. Affolderbach, R. Straessle, M. Pellaton, D. Briand, G. Mileti, and N. F. de Rooij, "Microfabricated rubidium vapour cell with a thick glass core for small-scale atomic clock applications," *J. Micromech. Microeng.*, vol. 22, no. 2, p. 025013, 2012.

[10] J. Vanier, R. Kunski, N. Cyr, J. Y. Savard, and M.Têtu, "On hyperfine frequency shifts caused by buffer gases: Application to the optically pumped passive rubidium frequency standard," *J. Appl. Phys.*, vol. 53, no. 8, pp. 5387–5391, August 1982.

[11] M. Pellaton, C. Affolderbach, Y. Pétremand, N. de Rooij, and G. Mileti, "Study of laser-pumped double-resonance clock signals using a microfabricated cell," *Phys. Scr.*, vol. 2012, no. T149, p. 014013, 2012.

[12] T. Bandi, M. Pellaton, D. Miletic, C. Affolderbach, F. Gruet, R. Matthey, and G. Mileti, "Double resonance in alkali vapor cells for high performance and miniature atomic clocks," in *proc. IEEE IFCS 2012*, May 2012.

[13] C. Stefanucci, T. Bandi, F. Merli, M. Pellaton, C. Affolderbach, G. Mileti, and A. K. Skrivervik, "Compact microwave cavity for high performance rubidium frequency standards," *Rev. Sci. Instrum.*, vol. 83, no. 10, p. 104706, 2012.

[14] J. Vanier and C. Audoin, *The Quantum Physics of Atomic Frequency Standards*. Adam Hilger, 1989.

[15] C. Affolderbach, C. Andreeva, S. Cartaleva, T. Karaulanov, G. Mileti, and D. Slavov, "Light-shift suppression in laser optically pumped vapour-cell atomic frequency standards," *Appl. Phys. B*, vol. 80, pp. 841–848, 2005.

[16] J. Bjorkholm and P. Liao, "Optically induced atomic energy level shifts and two-photon spectroscopy," in *Laser Spectroscopy*, ser. Lecture Notes in Physics, S. Haroche, J. Pebay-Peyroula, T. Hänsch, and S. Harris, Eds. Springer, 1975, vol. 43, pp. 176–185.

[17] M. Arditi and J. L. Picque, "Precision measurements of light shifts induced by a narrow-band gaas laser in the 0-0 133 cs hyperfine transition," *J. Phys. B: At., Mol. Opt. Phys.*, vol. 8, no. 14, p. L331, 1975.

[18] M. D. Rotondaro and G. P. Perram, "Collisional broadening and shift of the Rubidium D1 and D2 lines (52S1/2 $\rightarrow$ 52P1/2, 52P3/2) by rare gases, H2, D2, N2, CH4 and CF4," *J. Quant. Spectrosc. Radiat. Transfer*, vol. 57, pp. 497–507, 1997.

[19] D. Miletic, T. Bandi, C. Affolderbach, and G. Mileti, "Ac stark shift in double resonance and coherent population trapping in a wall-coated cell for compact rb atomic clocks," *Phys. Scr.*, vol. 2012, no. T149, p. 014012, 2012.

[20] F. Gruet, F. Vecchio, C. Affolderbach, Y. Pétremand, N. F. de Rooij, T. Maeder, and G. Mileti, "A miniature frequency-stabilized VCSEL system emitting at 795nm based on LTCC modules," *Opt .Lasers Eng.*, vol. 51, no. 8, pp. 1023–1027, 2013.

[21] V. Venkatraman, Y. Petremand, C. Affolderbach, G. Mileti, N.-F. de Rooij, and H. Shea, "Microfabricated chip-scale rubidium plasma light source for miniature atomic clocks," *IEEE Trans. Ultrason., Ferroelectr., Freq. Control*, vol. 59, no. 3, pp. 448–456, 2012.

Frequency Instability Investigations on a Cs Cell Clock Based on Pulsed Coherent Population Trapping

Jean-Marie Danet, Michel Lours, Peter Yun, Stéphane Guérandel, Emeric de Clercq
LNE SYRTE, CNRS-UMR 8630, UPMC, Observatoire de Paris
61 Avenue de l'Observatoire, 75014 Paris, France
jean-marie.danet@obspm.fr

***Abstract*— Recent progress are reported on a compact cesium cell atomic frequency standard based on pulsed coherent population trapping. The Dick effect has been modelized and measured. The short term frequency stability has been improved to $3.2\times10^{-13}\ \tau^{-1/2}$. Important steps have been taken toward the understanding of the impact of laser power fluctuations on the mid-term stability, currently limited at 3.10^{-14} at 200s.**

Keywords—atomic clock, coherent population trapping, vapor cell clock, Dick effect, line pulling

I. INTRODUCTION

Compact and stable frequency standards are needed in many applications such as GPS or Galileo, the European GNSS. Double resonance (microwave and optical) alkali-metal vapor-cell atomic clocks are currently used for this purpose. However the next generation of space clocks could be based on the coherent population trapping (CPT) phenomenon [1]. In such clocks the microwave interrogation, and the microwave cavity, are suppressed. The atomic vapor in the cell is pumped and probed, in the same time, by two laser beams whose frequencies are separated by the microwave clock frequency. Because of their scheme simplicity and potential high performances, CPT clocks are promising candidates for on-board applications.

In this paper we report investigations on some frequency stability limitations of a CPT clock prototype. In order to maximize the short-term stability our prototype tries to combine a high signal amplitude and a narrow resonance width by using a so-called double Λ scheme and a Ramsey interrogation technique [2, 3]. The experimental set-up is described in Section II. The short-term stability was previously limited to $7\times10^{-13}\ \tau^{-1/2}$ [4]. After a careful investigation we shown that the stability was not limited by the signal-to-noise ratio but by the Dick effect [5]. Dick effect leads to a limitation of the stability of a frequency standard due to the sampling process of the atomic interrogation. The high frequency noise of the local oscillator (LO) is down converted by an aliasing effect [5, 6, 7]. This is addressed in Section III. The choice of a more suited LO allowed an improvement of the frequency stability to $3.2\times10^{-13}\ \tau^{-1/2}$, still limited by the LO noise. Section IV addresses the mid-long term limitation of the frequency stability. A new effect is explored, line pulling by neighboring transitions induced by the double Λ scheme.

II. EXPERIMENTAL SETUP

The lasers are tuned to the Cs- D_1 line at 895 nm, the inset in Fig.1 shows a scheme of the involved energy levels. In order to build a double Λ scheme (simultaneous σ^+ and σ^- optical transitions, see inset), the laser beams are orthogonally linearly polarized. As shown in Fig. 1, the superimposed beams of two phase-locked extended cavity diode lasers (ECDL), 9 GHz apart, are switched on and off by an acousto-optic modulator (AOM) before crossing the Cs-buffer gas cell. Compared to conventional CPT clocks, the pulsed interaction provides a Raman-Ramsey signal which allows a good frequency discriminator, whose slope is limited by the atomic relaxation in the cell (a few milliseconds), avoiding the power broadening of the resonance.

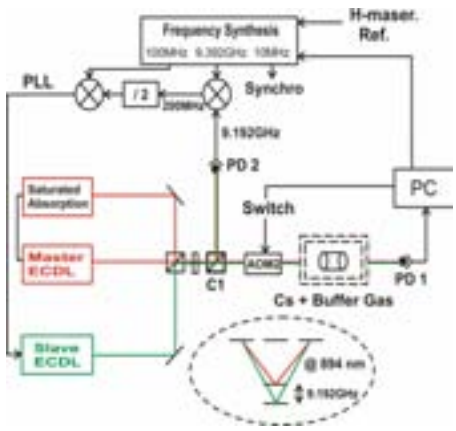

Fig. 1. Experimental setup. Red: Master extended cavity diode laser (ECDL). Green: Slave ECDL, locked at 9GHz from the master frequency using a phase locked loop (PLL). Clock evaluation is made by comparison with an H-maser. Inset: D1 Cs energy levels, red: master laser, green: slave laser. Cell : Ar/N2 mixture, P=21torr, P_{Ar}/P_{N2}=0.6, T=29°C.

The cell is enclosed in magnetic shields and temperature regulated. The transmitted laser intensity is measured by the photodiode PD1, linked to the computer (PC), which drives the time sequence of the AOM and lock the frequency synthesizer on resonance (the frequency splitting between the lasers). The clock frequency is measured versus an H maser of the laboratory.

III. Impact of Local Oscillator Noise on Short-Term Frequency Stability

In a sequentially operated clock, the effect of the LO frequency noise can been characterized by the sensitivity function $g(t)$ [5, 6, 7]. $g(t)$ is the sensitivity of the response of the atomic system, the signal S, to a phase step $\Delta\varphi$ of the interrogation oscillator at time t.

$$g(t) = \lim_{\Delta\varphi \to 0} \delta S(t, \Delta\varphi) / \Delta\varphi \qquad (1)$$

Its shape depends on the atomic system and on the kind of interrogation used. For our CPT pulsed clock, $g(t)$ has been measured and numerically calculated from the evolution equation of the density matrix ρ [8, 9], see Fig 2.

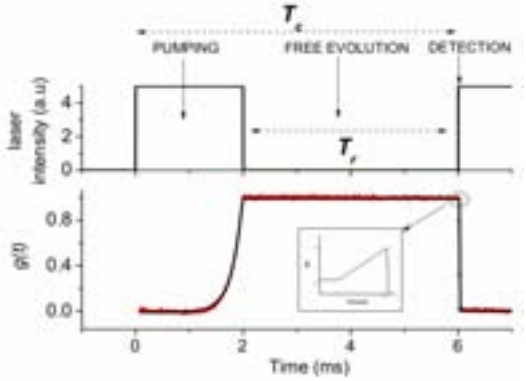

Fig. 2. Up : Sequence used, Pumping time: 2ms, Ramsey time: 4ms, detection 10µs after turn on of lasers, detection duration : 25µs. Laser intensity: 200µW/cm²/laser. Down : sensitivity function for CPT system Black : Numerical calculation, Red: measurements.

As $g(t)$ is zero during almost all the pumping period, the frequency noise of the local oscillator (LO) will only be detected during the Ramsey time Tr, leading to the generation of an imperfect correction signal. To fix the ideas, one can say that the larger the pumping time, the worse the frequency lock loop of the OL frequency on the atom will work. T_c is the length of an interrogation cycle, the duty cycle defined as Tr/Tc is 0.7 which is a favorable case compared to 0.3 in a cold atom setup [10]. The limitation to the fractional Allan deviation is [5, 6, 7]:

$$\sigma_y^2(\tau) = \frac{1}{\tau g_0^2} \sum_{m=1}^{\infty} |g_m|^2 S_y(m/T_c), \qquad (2)$$

Where $S_y(m/Tc)$ is the one-sided power spectral density (PSD) of the relative frequency fluctuations of the free running interrogation oscillator at Fourier frequency m/T_c, i.e. the harmonic frequencies of the operation frequency. The Fourier coefficient of $g(t)$ are given by :

$$g_m = \frac{1}{T_c} \int_0^{T_a} g(t) e^{-2\pi i m t / T_a} dt. \qquad (3)$$

As in the fractional Allan deviation expression (2) S_y is weighted by the Fourier coefficients of $g(t)$, its shape is of prime importance. Fig 3 compares three sensitivity functions corresponding to a squared (red), a 2 level system kind (blue) and a CPT system kind (black). The value of pumping and Ramsey time for the 2 level system kind are taken has typical one [11]. The starting point of the slope -40 dB/dec limits the bandwidth where the noise is still seen by the clock. After this point S_y will be weighted as $1/f^4$ in the Allan deviation calculation, meaning that the clock will no longer be sensitive to the LO frequency noise. For our clock, this point happens for harmonics three times higher than for a two level system. Such a behavior is due to the sharp decrease of $g(t)$ at the detection.

$$\alpha + \beta = \gamma \qquad (1) \qquad (1)$$

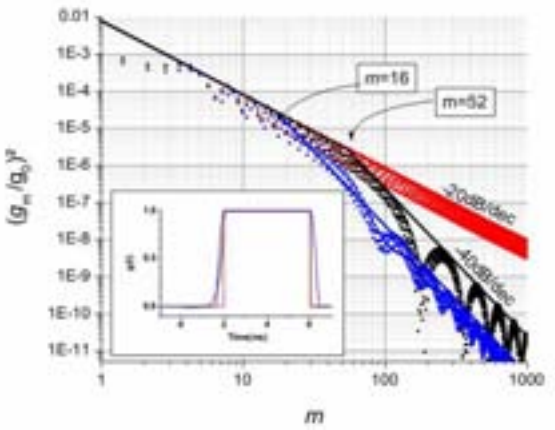

Fig. 3. Fourier coefficient of $g(t)$ for different $g(t)$ shapes : Squared type (red), CPT type (black) , 2 level type (blue). Inset: $g(t)$ shapes.

Our model has been successfully tested by injecting noise in the frequency multiplication chain, measuring it and comparing the corresponding measured and calculated frequency stability, see Fig 4.

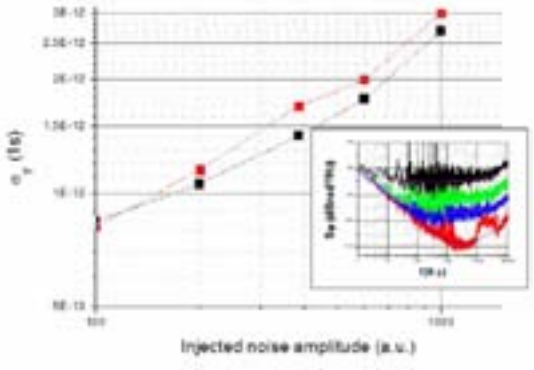

Fig. 4. Fractional Allan deviation at 1s, black: calculated value using the noised phase noise PSD. Red: measured. Inset : PSD of phase noise of the multiplication chain, for different injected noise amplitudes.

The understanding of the conversion phenomenon of LO frequency noise in our pulsed CPT clock led us to install a new 100 MHz quartz oscillator (Rakon, LNO100) to feed the multiplication chain. As shown in Fig. 5 it allowed reducing the S_y components at the first harmonics of the frequency interrogation, i. e. in the most critical domain where the weighting function g_n/g_0 is maximum. The noise contribution

of the 100MHz oscillator (green in Fig. 5) to the total microwave noise is now below the noise contribution of the multiplication chain, in almost all the sensitivity bandwidth.

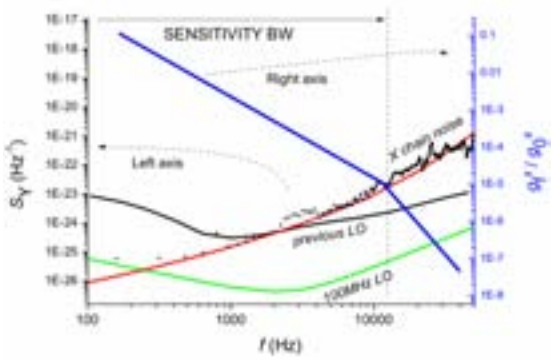

Fig. 5. Left axis: one-sided power spectral density (PSD) of the relative frequency fluctuations of the free running interrogation oscillator at Fourier frequency m/T_c : Black: Contribution of the prvious LO, Green: Contribution of LN0 100 oscillator. Red: Noise contribution of the multiplication chain Black dots: Setup with LN0 100 oscillator Right axis: Fourier coefficient of $g(t)$.

Following the LO change, the frequency stability have been measured, improving our short term stability from 7×10^{-13} to 3.2×10^{-13} at 1 second, see Fig 6.

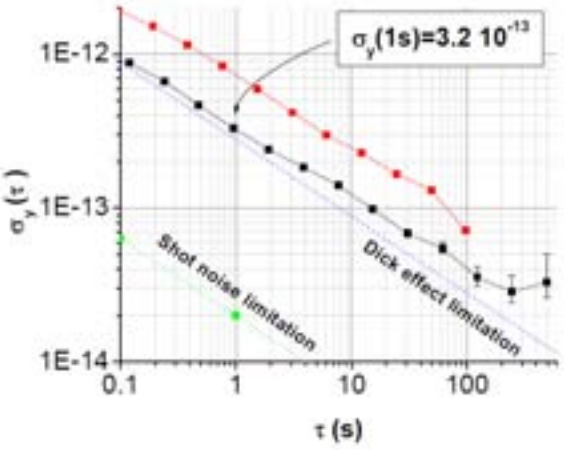

Fig. 6. Short term frequency stability. Black: previous stability. Red: Measurement after LO change. Green: calculation in case of the actual signal and shot noise limitation.

IV. Toward the Understanding of Long-Term Stability Limiting Effects

Vapor cell frequency standards are known for their relative high short-term frequency stability, and a frequency drift limiting the mid-long term stability. Until now our setup have always shown a stability degradation before 2000 s of integration time. Our last noise budget evaluation pointed out that the sensitivity of the clock to laser power fluctuations would limit the clock stability between 5×10^{-14} and 0.8×10^{-14} according as the noises are uncorrelated or fully correlated [12], respectively. Usual AC Stark shift models do not explain the measured shifts. Different hypotheses have then been made [13], and among them, the dissymmetry variation with the laser power seems to explain well the frequency shifts. The dissymmetry of the fringe system was measured for different powers, and the corresponding calculated frequency shifts have been plotted next to the measured ones, see Fig 7.

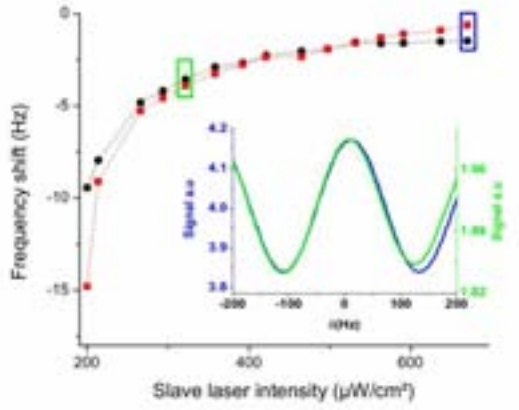

Fig. 7. Frequency shift as a function of slave laser power, master laser power unchanged Black: Calculated frequency shift due to dissymetry Red: measured frequency shift. Inset: Fringe system for slave laser intensity 150μW/cm² (green) and 500μW/cm² (blue), master laser intensity: 400μW/cm².

A main dissymmetry source arises from the double Λ scheme which allows $\Delta m_F = 2$ transitions, see dashed grey lines in Fig. 7, left. They are close (245Hz) to the clock resonance, and of pretty high amplitude (20% of 0-0 amplitude) for typical operating parameters, so that the detected signal is the sum of the three resonances.

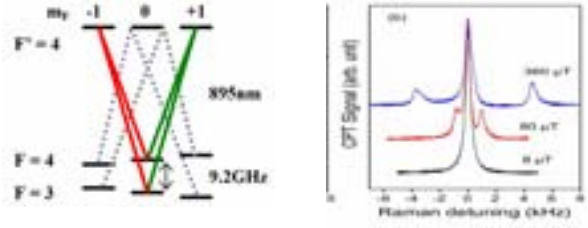

Fig. 8. Left: Optical transitions induced in the double Λ scheme. Only the clock levels ($m_F = 0$), and the nearest Zeeman sublevels are shown. $F = 3$ and $F = 4$ are the hyperfine levels of the ground state, F' is one excited level of the D_1 line. The clock transition is induced by the transitions shown in solid lines. The transitions in dashed lines induce hyperfine transitions with $\Delta m_F = 2$. Right: microwave spectrum around the clock transition at different values of the magnetic field.

The neighboring resonances split of the clock resonance with frequencies is given by the Breit-Rabi formula [14]:

$$\upsilon_{z,\pm} = \pm 11.1649B + 0.002672B^2 \quad (4)$$

where $\nu_{z,\pm}$ (Hz) refers to the transitions ($F = 3$, $m_F = +1$) - ($F = 4$, $m_F = -1$) and ($F = 3$, $m_F = -1$) - ($F = 4$, $m_F = +1$), respectively; B is in μT. It is worth to note that the frequencies $\nu_{z,\pm}$ are the frequency differences between these transitions and the clock transition, and that they are not symmetrically

spaced from the clock transition. Their effect can be seen directly in Fig. 9, which shows the measured clock frequency as a function of the magnetic field. The pulling by the neighboring transitions induces an oscillation around the classical quadratic Zeeman shift. This effect increases for larger imbalance of the neighboring peak amplitudes. For laser beams polarized perfectly linearly and orthogonally the amplitudes are equals. However a weak ellipticity of one beam polarization is enough to impact the equilibrium, increasing the shift. Fig. 9a shows the CW CPT signal for different elliptical polarization of the laser beams achieved by setting a retardation plate. The measured and calculated resulting shifts are shown in Fig. 9b as a function of the magnetic field in the case of the largest unbalance of Fig. 9a.

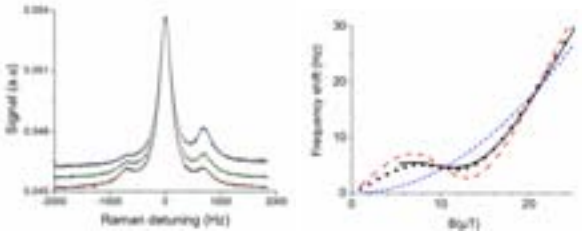

Fig. 9. CPT signal with a CW interrogation for three different polarisation states. B = 60 µT. b). Shift of the observed clock frequency as a function of the applied magnetic field. Dashed blue line: theoretical shift of the 0-0 transition, solid black line: experimental data, dashed red line: shift calculated with amplitudes of the blue curve on the left, dotted black line: shift calculated with a fit of the peak amplitudes.

Using laser beams with parallel polarizations it is possible to observe the two $\Delta m_F = 2$ transitions only without the clock transition. We have measured a frequency sensitivity to laser power 4 to 10 times higher than for the double Λ scheme. This shows that those $\Delta m_F = 2$ transitions are very sensitive to a laser power variation. Finally the power sensitivity of the clock frequency in the usual double Λ scheme has been measured as a function of the magnetic field, see Fig 10. A zero sensitivity point is shown. This point is of a great interest. By operating the clock with this specific magnetic field value the sensitivity of the frequency to any power fluctuation would be drastically reduced. A full explanation of this effect is under investigation.

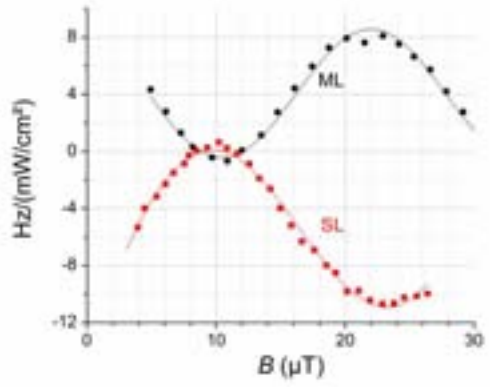

Fig. 10. Measured power shift rate of the clock frequency versus the magnetic field value. Dark dots : the master laser (4-3' transition) intensity is modulated. Red dots: the slave laser (3-3' transition) intensity is modulated.

V. Discussion

In summary we have described how a pulsed CPT clock is sensitive to frequency noise of the LO by Dick effect. This study allowed lowering the clock frequency instability down to 3.2×10^{-13} at 1s. The long term stability is still limited after 200s integration around $2\text{-}3\times10^{-14}$. We have shown that laser power fluctuations could lead to a signal distortion through line pulling effect of neighboring transitions. This line pulling effect varies with the static magnetic field value. For a specific value, a cancellation of power sensitivity of the clock frequency has been shown. Using this value as operating point could lead to a drastic reduction of power sensitivity of the clock. Further studies are needed to explain and experimentally confirm the interest of such a working point.

Acknowledgment

We are grateful to José Pinto and Laurent Volodimer of the SYRTE electronic team for their helpful assistance.

References

[1] J. Vanier, "Atomic clocks based on coherent population trapping: a review", *Applied Physics B*, vol. 81, pp. 421-442, 2005.

[2] T. Zanon., S. Guérandel, E. de Clercq, D. Holleville, N. Dimarcq, and A. Clairon, "High Contrast Ramsey Fringes with Coherent Population Trapping Pulses in a Double Lambda Atomic System", *Phys. Rev. Lett.*, vol. 94, 193002, 2005.

[3] T. Zanon., S. Trémine, S. Guérandel, E. de Clercq, D. Holleville, N. Dimarcq, and A. Clairon, "Observation of Raman-Ramsey Fringes with optical CPT pulses", *IEEE Trans. Instrum. Meas.*, vol. 54, pp. 776-779, 2005.

[4] R. Boudot, S. Guérandel, E. de Clercq, N. Dimarcq, and A. Clairon, "Current status of a pulsed CPT Cs cell clock", *IEEE Trans. Instrum. Meas.*, vol. 58, pp. 1217-1222, 2009.

[5] G. J Dick, "Local oscillator induced instabilities in trapped ion frequency standards", in *Proc. 19th Precise Time and Time Interval (PTTI) Applications and Planning Meeting,* Redondo Beach, CA, USA, pp. 133-147, 1987.

[6] C. Audoin, G. Santarelli, Ala'a Makdissi, and André Clairon, "Properties of an oscillator slaved to a periodically interrogated atomic resonator", *IEEE Trans. Ultrason., Ferroelect., Freq. Contr.,* vol. 45, pp. 877-886, 1998.

[7] G. Santarelli, C. Audoin, Ala'a Makdissi, P. Laurent, G. J. Dick, and André Clairon, "Frequency stability degradation of an oscillator slaved to a periodically interrogated atomic resonator", *IEEE Trans. Ultrason., Ferroelect., Freq. Contr.,* vol. 45, pp. 887-894, 1998.

[8] G. Orriols, "Nonabsorption resonances by nonlinear coherent effects in a three-level system", *Il Nuovo Cimento,* 53B, pp. 1-24, 1979.

[9] E. Arimondo, "Coherent Population Trapping in Laser Spectroscopy", *Progress in Optics*, vol. XXXV, pp. 257-353, 1996.

[10] F.-X. Esnault, D. Holleville, N. Rosseto, S. Guerandel, and N. Dimarcq, "High-stability compact atomic clock based on isotropic laser cooling", *Phys. Rev. A,* vol. 82, pp. 033436-1-5, 2010.

[11] S. Micalizio, C. E. Calosso, A. Godone and F. Levi, "Metrological characterization of the pulsed Rb clock with optical detection", *Metrologia*, vol. 49, 425, 2012.

[12] O. Kozlova, unpublished.

[13] O. Kozlova, PhD Thesis, Université Pierre et Marie Curie, Paris, France, 2012.

[14] N. Ramsey, *Molecular Beams*, Oxford Univ. Press, New York, 1956.

A Digitized Atomic Clock Based on Transient Oscillation of Detuned Coherent Population Trapping

Zhong Wang*, Jianye Zhao, Wan Mingyu, Yeqing Li,
Daiting Shi, Dong Hou, Shuangyou Zhang and Dawei Li

School of Electronics Engineering & Computer Science,
Peking University, Beijing, 100871, P. R. China
*Email: zw@pku.edu.cn

***Abstract* - We demonstrated a digitized atomic clock which is based on the transient oscillation of detuned coherent population trapping (DCPT). In the Λ structure atomic states system, the DCPT oscillation frequency exactly equals the absolute value of the frequency difference between the two pump laser fields minus the two ground states hyperfine splitting frequency. This DCPT atomic clock obtains the standard frequency by adding/subtracting the DCPT frequency from the laser modulation RF frequency. And it does not require a phase locking loop circuit to lock the standard frequency to the atomic transition. In addition, its data processing section can be easily digitized with high accuracy. The frequency instability of $1X10^{-11}/\tau^{1/2}$ (τ=1000s) has been achieved.**

Atomic clocks have been developed for over half a century [1]. From microwave clocks to optical clocks; from atomic fountain clocks [2] to chip scale atomic clocks [3,4], they have varying sizes and properties. However, to achieve a stable standard frequency, they all require an analog phase locking loop circuit to lock the output frequency to the atomic transition frequency. The stability of these clocks depend directly on the behavior of the phase locking loop; and the analog phase locking loop performance is limited by the hardware, which makes it difficult to actively control and adjust for better frequency identification accuracy.

We proposed and demonstrated an atomic clock based on the detuned coherent population trapping (DCPT) transient oscillation phenomenon [5, 6]. This DCPT atomic clock does not require a phase locking loop to stabilize the standard microwave frequency. We have theoretically proven [7] that when two laser fields transmit through a typical Λ system alkali atomic cell, and the two laser frequency difference is detuned from the CPT resonance by a few KHz, laser intensity will have a damping oscillation as it passes through the atomic cell. Also, the oscillation frequency exactly equals the absolute value of the frequency difference between the two pump optical fields minus the two ground states' hyperfine splitting frequency. Usually the two pumping optical fields are generated through a VCSEL which is modulated by a microwave oscillator, and the frequency difference of the two laser bands is equal to the microwave frequency. Therefore, we can directly measure the frequency detuning, which equals the DCPT oscillation frequency, and then add (or subtract) the value to the output frequency of the microwave oscillator to achieve the standard frequency. By this method, we can further simplify the structure of the CPT atomic clock, and make it easier to be digitized and miniaturized. Since the DCPT oscillation frequency is usually only a few KHz and very easy for AD conversion with enough accuracy, we can actively process the data to obtain higher frequency accuracy.

In 2009, we proposed the DCPT scheme to implement the atomic clock and have theoretically proven the detuning coherent population trapping transient oscillation phenomenon [6,7]. According to the semi-classic theory, the evolution of the density matrix operator $\hat{\rho}$ can be described by the quantum Liouville equation. Here, we mainly consider the matrix element ρ_{33}, the population of the excited state, which directly related to the transmitted laser intensity. Considering certain approximations and assumptions, we derived the analytical solution to ρ_{33}, which can be described as Eq. (1) [6, 7].

$$\rho_{33} = \mathrm{Re}\left\{ A\exp\left[-\left(\gamma_2 + \frac{\Omega^2}{\Gamma} \right) + i\Delta \right] t \right\} + \frac{2\kappa_3 \lambda}{\Gamma} \qquad (1)$$

In the equation (1), the first term damps to zero at the rate of $\gamma_2+\Omega^2/\Gamma$, which is equal to the line width of the CPT resonance. Therefore it creates a small damping in the oscillation signal, characterized as a damping oscillation with frequency exactly equals to the detuning frequency Δ. So we refer to it as "Transient Oscillation".

Based on the theoretical result, we have implemented and experimentally verified the digitized atomic clock based on

transient oscillation of detuned coherent population trapping (DCPT). In this design, the output standard frequency was achieved by directly adding/subtracting the transient oscillation frequency of DCPT to/from the RF frequency, which is used for the VCSEL modulation. We modulated the RF frequency with a 100 Hz square wave, and the RF frequency was set to alternate between the ground state hyperfine splitting frequency and the detuned frequency (a few kHz higher/lower). After the laser beam passes through the rubidium atom cell, a series of laser intensity oscillations (Fig.1.) was detected when the RF frequency was detuned. This is the DCPT transient oscillation signal, and the frequency is equal to the detuning frequency.

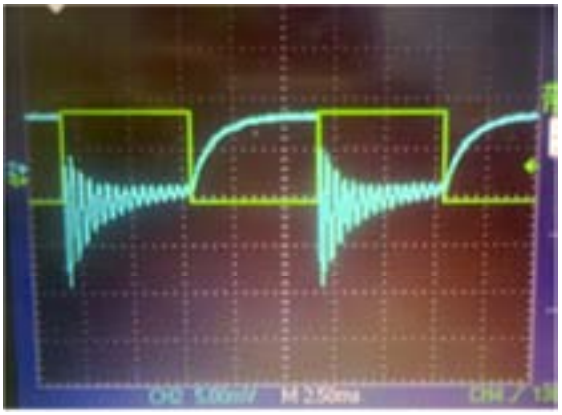

Fig.1. The DCPT oscillation signal. The RF frequency modulated by a 80Hz square wave and RF frequency is set to alternate between the ground state hyperfine splitting frequency and the detuned frequency which is 2KHz.higher than the hyperfine splitting.

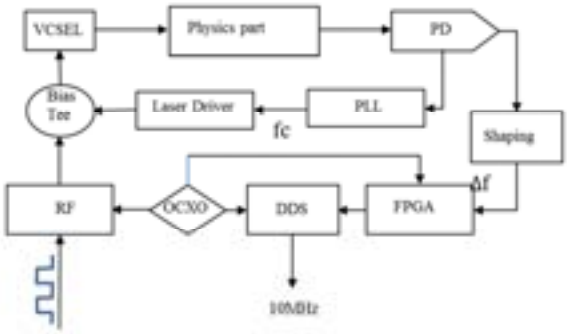

Fig.2. experimental setup

Our experiment setup is shown in Fig.2. The injection current of VCSEL is modulated by a RF signal to generate a series of sidebands; the baseband and one of the nearest sidebands will be used [8] to excite the DCPT transient oscillation. The RF frequency is modulated by a 80Hz square wave signal between the CPT resonance central frequency and few kHz detuned from it. The two laser bands' frequency difference will be switched between the two, and the two prepared laser fields will go through the ^{85}Rb cell. Then, periodically damping oscillations of the transmitted laser power at the detuning frequency are detected by the photon detector. The oscillations will be amplified to create a corresponding electronic signal, which would then be shaped into a square wave signal. From this, the frequency of detuning can be directly calculated by digital methods. At the same time, the OCXO 10 MHz reference signal of the RF oscillator will also be sent to the direct digital synthesizer (DDS) as its reference signal. Therefore, the DDS output frequency will shift with the reference signal shift and be proportional to the RF frequency shift. The DCPT oscillation frequency will be calculated by the FPGA, and will generate a delta-frequency word for the DDS to precisely compensate the detuning and shift. Subsequently, the 10 MHz standard frequency signal will be generated by the DDS, and will be proportional to the hyperfine splitting of the two ground states, working as an atomic frequency standard

In our DCPT atomic clock, the oscillation signal is detected, amplified, and reshaped, in order to facilitate digital processing. A typical digital method (Equal precision frequency measurement) is used to measure the DCPT oscillation frequency. As illustrated by Fig.3. We use a 3MHz signal to compare with the reshaped square wave whose frequency is equal to the DCPT oscillation and obtain the DCPT oscillation frequency. Since the detuning frequency is 10^3 Hz, using this typical digital processing with instability higher than 10^{-6}, we can extract the oscillation frequency with 10^{-3} Hz accuracy, which allows us to expect that the DCPT atomic clock will achieve very good frequency stability.

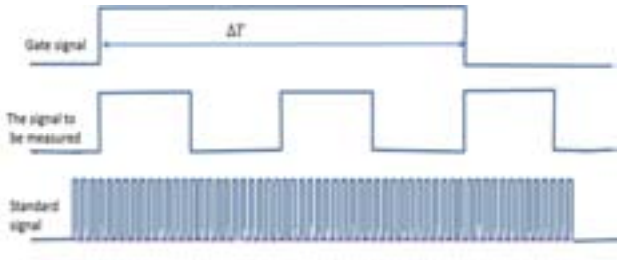

Fig.3. DCPT oscillation frequency measuring method. Using the DCPT reshaped square wave signals' (typically 3KHz) rising edge to open and close the gate, and compare the ΔT with the standard signal (3MHz)

When the detuning frequency is obtained, it will be calculated to generate a delta-frequency word for the DDS to correct the 10MHz output frequency. Since the DDS and the

RF oscillator have the same reference crystal oscillator, the RF and the DDS 10MHz will always maintain a fixed ratio. When the RF shifts, the DDS output also shifts with this constant ratio. From the changes of the detected DCPT oscillation frequency, we will be able to know how much the RF shifted, as well as the DDS output frequency shift. Then we can compensate for the shift by modifying the delta-frequency word, which has $1/2^{48}$ accuracy, and is accurate enough for the standard frequency generation.

We also used another method to get the DCPT oscillation frequency. In this data processing part, the DCPT oscillation frequency is extracted by a filter which is a simulation filter generated by MATLAB tools. As there exists a picket fence effect in the Fourier transform from the time domain to the frequency domain, we use the narrow-band simulation filter to scan the period of the square wave simultaneously. When 1/2 of the period is equal to integer multiple of the DCPT oscillation period, the spectral line intensity of oscillation frequency will be at a maximum. Using this method, the spectrum leakage can be decreased and the oscillation frequency can be extracted accurately. In both processing methods, the frequency reading accuracy is only related to the detuning frequency and the reference signal stability, but not related to the atomic transition frequency. Therefore we may extend this method to optical frequency and produce optical clocks and optical frequency combs.

When we use the RF oscillator signal as the reference frequency, and use the detected oscillation frequency to compensate for the RF frequency detuning as well as its shift with time, we will be able to obtain the DCPT atomic clocks standard frequency, which equals the two ground states hyperfine splitting frequency. In our preliminary experiments, the frequency instability of $1\times10^{-11}/\tau^{1/2}$ (τ=1000s) has been achieved (Fig.4.).

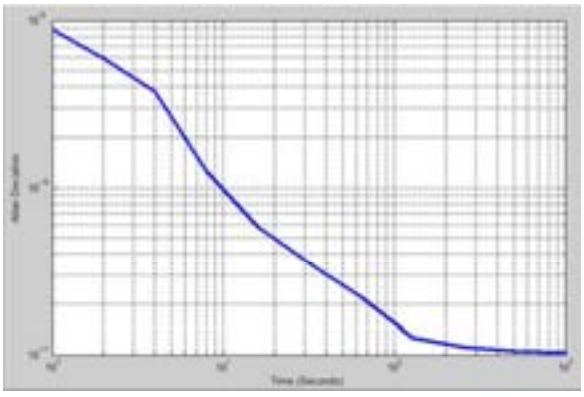

Fig.4. Measured Allan deviation for the ^{85}Rb DCPT atomic clock

Comparing with traditional atomic clocks, this DCPT atomic clock does not require a phase locking loop circuit to lock the microwave frequency. This eliminates the instability and loose locking probability brought on by the phase locking loop, which makes the DCPT atomic clock more stable and more reliable, especially when used in harsh environments. In addition, the DCPT oscillation signals have amplitude 3 to 4 times that of the CPT signals, which further benefits signal reshaping, AD conversion, and analysis. Its digital data processing is convenient for active analysis to increase the frequency reading accuracy, which gives the potential for achieving better frequency stability. In addition, the electrical component also can be easily integrated. As a result, this scheme has great potential in the design and manufacture of miniature atomic clocks. Finally, since the DCPT oscillation frequency reading accuracy is only related to the detuning frequency and the reference signal stability, but not related to the atomic transition frequency, we may extend this method to optical frequency for optical clock and optical frequency comb.

This work was supported by the National Natural Science Foundation of China under Grant No.11074012. We would like to thank Tao Guo and Ke Deng for their informative discussion, to thank Xin Wang for her constructive suggestions during the writing of this text.

References

[1]. Essen L and Parry V I 1955 Nature 176 280–4
[2]. Clairon, C. Salomon, S. Guellatt， W.D.Phillips. Ramsey resonance in a Zachaias fountain[J]. Europhys Lett. 1991, 16:165
[3]. S. Knappe, P.D.D. Schwindt, V. Shah†, L. Hollberg, and J. Kitching, Vol. 13, No. 4 / OPTICS EXPRESS 1249, 2005
[4]. Robert Lutwak, IEEE Frequency Control Symposium, 2009
[5]. S. J. Park and H. Cho, Phys. Rev. A 69, 023806 2004
[6]. Tao Guo, Ke Deng, Xuzong Chen, and Zhong Wang, Appl. Phys. Lett. 94, 151108 2009
[7]. Zhong Wang, Tao Guo, Ke Deng, and Xuzong Chen, IEEE Frequency Control Symposium, 2010
[8]. Ke Deng, Tao Guo, Juan Su, Dengzhu Guo, Xinyuan Liu, Lu Liu, Xuzong Chen, Zhong Wang, Physics Letters A 373 (2009) 1130–1132

Precision Measurement of the Gravitational Constant with Atom Interferometry

Guglielmo Maria Tino, Gabriele Rosi, Fiodor Sorrentino
Dipartimento di Fisica e Astronomia & LENS
Università di Firenze, INFN Sezione di Firenze
via Sansone 1, I-50019 Sesto Fiorentino (FI), Italy
Email: guglielmo.tino@fi.infn.it

Marco Prevedelli
Dipartimento di Fisica dell'Università di Bologna
Via Irnerio 46, I-40126, Bologna, Italy

Luigi Cacciapuoti
European Space Agency
Research and Scientific Support Department
Keplerlaan 1, 2200 AG Noordwijk, The Netherlands

***Abstract*—We report on the current performance of our atom interferometry gravity gradiometer. After careful elimination of the main sources of fluctuations and biases in the atom interferometer, we achieve a sensitivity of 3×10^{-9} g per second to differential gravity; by modulating the position of a set of source masses, we achieve a relative statistical uncertainty of 1.1×10^{-4} to the gravitational constant G.**

I. Introduction

In recent years, atom interferometry provided new techniques for the measurement of inertial forces, with important implications both in fundamental physics and applied research. The remarkable stability and accuracy that atom interferometers have reached for acceleration measurements can play a crucial role for science and technology. Quantum sensors based on atom interferometry [1] had a rapid development during the last two decades, and different schemes were demonstrated and implemented.

Atom interferometry has been demonstrated for precise measurements of gravity acceleration [2], [3], [4], [5], Earth's gravity gradient [6], [7], [8], and rotations [9], [10], [11], [12]. Currently, experiments based on atom interferometry are in progress to test Einstein's Equivalence Principle [13], [14] and to measure the Newtonian gravitational constant G [8], [15], [16], while experiments to test general relativity [14], [17] and the $1/r^2$ Newton 's law [18], [19], [20], [21], searching for quantum gravity effects [22] and gravitational waves detection [23], [24] have been proposed. Accelerometers based on atom interferometry have been developed for many practical applications including metrology, geodesy, geophysics, engineering prospecting and inertial navigation [7], [25], [26], [27], [28]. Further advances in atom optics are expected to improve the current performances of such sensors by orders of magnitude.

Operating an atom interferometer at its full performance requires a precise control over a number of experimental parameters. In this paper we describe an atom interferometer for precision measurement of gravity gradients. In particular, we focus on a specific experimental configuration for the measurement of the gravitational field produced by local source masses, presently being used for the measurement of the gravitational constant G. We show that our current sensitivity and long term stability are compatible with the measurement of G with a precision of 10^{-4} by controlling a limited number of parameters. A challenge in order to attain such extreme performances is to carefully control the external degrees of freedom of the atomic probe. We then analyze the influence of the position and velocity of the atoms in a fountain on the precision of gravity gradient measurement by atom interferometry.

II. Apparatus

Our apparatus consists of a double atom interferometer performing a simultaneous measurement of the differential acceleration experienced by two clouds of cold rubidium atoms with vertical separation [36], [16], [32]. The instrument is used to measure the gravitational field generated a well characterized set of source masses [29].

The atom interferometer is based on the scheme of the Kasevich-Chu light-pulse gravimeter [2]. Three Raman pulses separated by the time interval T in a $\pi/2-\pi-\pi/2$ sequence realizes an atom interferometer with a Mach-Zender-type geometry. At the output of the interferometer, the probability of detecting the atoms in one of the two hyperfine levels of the Rb ground state is given by $P=(1-\cos\phi)/2$, where ϕ represents the phase difference accumulated by the wave packets along the two interferometer arms. In the presence of a gravity field, atoms experience a phase shift

$$\phi = k_{eff} g T^2 \tag{1}$$

depending on the local gravitational acceleration g and on the time interval T between the Raman pulses [2]. The gravity gradiometer consists of two absolute accelerometers operated in differential mode. Two spatially separated atomic clouds in free fall along the same vertical axis are simultaneously interrogated by the same Raman beams to provide a measurement of the differential acceleration induced by gravity on the two samples. A Lissajous figure results from the composition of the trace of the upper accelerometer versus the lower one. The differential phase shift $\Phi=\phi_u-\phi_l$, which is proportional to

the gravity gradient, is obtained from the eccentricity and the rotation angle of the ellipse best fitting the experimental data [31].

The scheme of our interferometer is shown in Fig. 1 for two different configurations of the source masses (C_1 and C_2), together with a picture of the apparatus. A magneto-optical trap (MOT) with beams oriented in a 1-1-1 configuration collects ^{87}Rb atoms and launches them vertically at a temperature of about $2.5\,\mu$K. After juggling the atoms loaded in the MOT [30], two atomic clouds are launched with a constant vertical separation of $\sim 30\,$cm. Shortly after launch, the two atomic samples are velocity selected and prepared in the $(F = 1, m_F = 0)$ state using a combination of Raman π pulses and resonant blow-away laser pulses. The interferometers take place around the center of the vertical tube shown in Fig. 1. In this region, surrounded by two μ-metal shields (76 dB attenuation factor of the magnetic field in the axial direction), a uniform magnetic field of $25\,\mu$T along the vertical direction defines the quantization axis. The field gradient along this axis is lower than $5\,$nT/mm. After the Raman interferometry sequence, the normalized population of the ground state is measured in a chamber placed just above the MOT by selectively exciting the atoms on the $F = 1, 2$ hyperfine levels and detecting the resulting fluorescence.

The gravity gradient can be measured in two different configurations of source masses, in order to isolate the effect of source masses from other biases of acceleration difference between the two clouds (Earth's gravity gradient, Coriolis forces, etc.). The position of source masses is modulated between the two configurations shown in figure 1 with a period $T_{mod} \simeq 55\,$min. Such scheme is suited for the determination of the gravitational constant G.

III. Methods

The theoretical, shot-noise limited acceleration sensitivity of the atom interferometer can be deduced from equation 1 assuming a phase error per shot $\sim \sqrt{N}$, where N is the number of detected atoms. With $N \sim 10^6$ and $T \sim 0.15\,$s, the shot-noise limit is in the range of $10^{-9}\,$g per shot. In order to reach this sensitivity level we investigated main sources of instability in ellipse contrast, bias and phase angle. The most critical sources of noise instabilities are fluctuations in the main experimental parameters (laser frequencies and intensities, magnetic coils atc.) and in the atomic trajectories. The two issues are discussed in the following sections.

A. Influence of experimental parameters

As shown in [32] it is possible to obtain a reliable value for Φ with an ellipse containing a few tens of points. We typically use 720 points per ellipse, corresponding to a measurement time $t_{ell} \sim 1400\,$s. Thus the slow changes in bias and contrast, occurring on a time scale longer than t_{ell}, are efficiently rejected. The short term sensitivity will be mainly determined by detection noise, and possibly by fast fluctuations of ellipse contrast and position, such as those caused by changes in the detection efficiency or in the Raman laser power.

Noise sources which equally affect the upper and lower atom interferometer (i.e. vibrations, tidal effects, relative phase noise of Raman lasers, etc.) are rejected as common mode in the gravity gradient measurement. We have then investigated those experimental parameters which affect the two atom interferometers differently; such parameters can in principle limit the sensitivity and long term stability of gravity gradient measurements. The double differential scheme used for the G measurement further cancels additional noise sources. Indeed, in this configuration the G measurement can only be perturbed by effects which either depend on the position of source masses, or change on a time scale shorter than the cycling

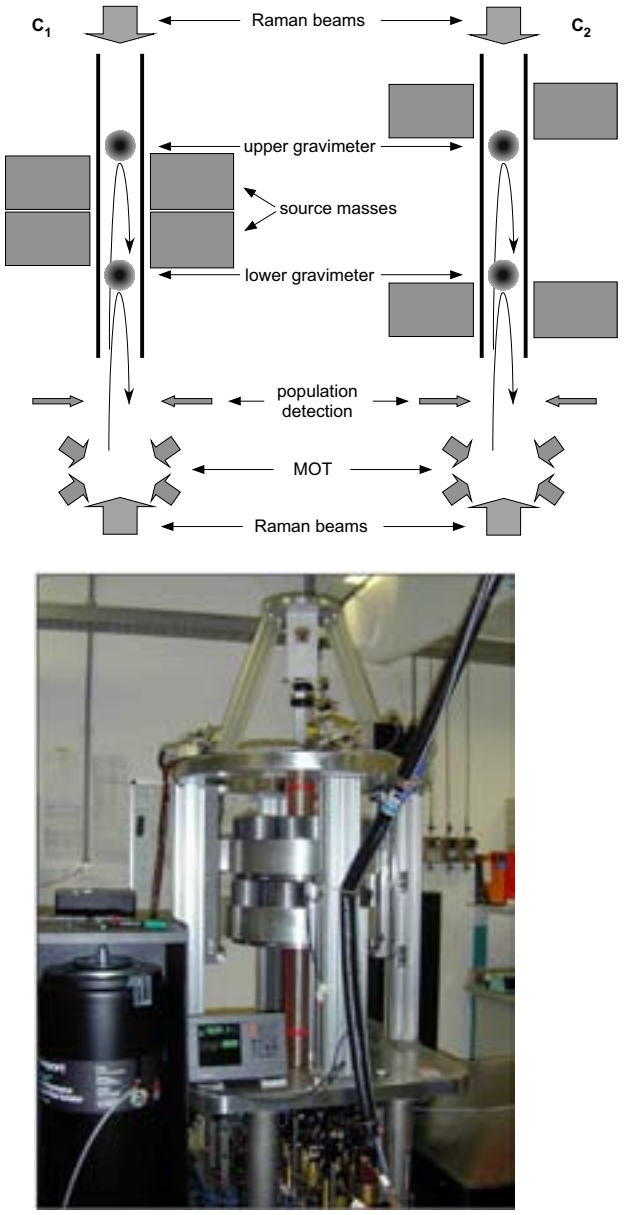

Fig. 1. Above: scheme of the gravity gradiometer (from [32]). ^{87}Rb atoms, trapped and cooled in a magneto-optical trap (MOT), are launched upwards in a vertical vacuum tube with a moving optical molasses scheme, producing an atomic fountain. Near the apogees of the atomic trajectories, a measurement of their vertical acceleration is performed by a Raman interferometry scheme. External source masses are positioned in two different configurations (C_1 and C_2) and the induced phase shift is measured as a function of masses positions. Below, a picture of the apparatus for the atomic fountain, including the source masses for G measurement.

time T_{mod} of masses positions.

We separately investigated the effect of various parameters. We recorded the ellipse phase angle in the two configurations of source masses, Φ_{C1} and Φ_{C2}, for different values of each parameter α; for each value of the parameter, we calculated the average ellipse angle $\bar{\Phi} = (\Phi_{C1} + \Phi_{C1})/2$ and the difference $\Delta\Phi = \Phi_{C1} - \Phi_{C2}$ of ellipse angle between the two different masses positions. From $\bar{\Phi}(\alpha)$ we can deduce requirements on the long term stability of the parameter α for gradient measurements, as well as on the stability of α on time scales shorter than T_{mod} for G measurements; from $\Delta\Phi$ we can deduce requirements on the long term stability of α for G measurements.

B. Influence of atomic motion

Both the accuracy and sensitivity of atom interferometry inertial measurements are affected by atomic motion [33]. The differential interferometric phase depends on the position and velocity of the two atomic clouds mainly through gravitational and magnetic gradients, rotations, and wavefront curvature of Raman beams.

Our atomic samples are vertically separated by ad distance Δh. Therefore in presence of a gravity gradient γ we have

$$\phi = k_{eff}\left(g_{up} - g_{dw}\right)T^2 = k_{eff}\gamma\Delta h T^2 \qquad (2)$$

For $T = 160$ms and $\Delta h = 30$ cm the induced phase shift is 0.336 rad corresponding to a differential acceleration of $\sim 10^{-7}$g. Fluctuations in the initial position or velocity of the atomic samples will convert into noise of the atom interferometry measurement through the gravity gradient. Something similar occurs due to magnetic gradients in the atom interferometer, due to second-order Zeeman effect.

In order to mitigate the effect of gravity gradients, we choose two configurations of the source masses which compensate the Earth gravity gradient at the location of the atomic samples during the atom interferometry sequence (see figure 2). Cancellation of the Earth gravity gradient in our apparatus is possible due to the high density of tungsten used for our source masses.

As long as the atoms are launched with some residual horizontal velocity along the East-West direction, the Coriolis force yields a phase shift on the atom interferometer output. The ellipse phase shift ϕ_{Coriol} due to Coriolis effect is proportional to the velocity difference Δv_{E-W} between the two clouds along the East-West direction:

$$\phi_{Coriol} = -2\Omega k_{eff} T^2 \cos\theta_l \Delta v_{E-W} \qquad (3)$$

where Ω is the angular velocity of Earth's rotation and θ_l is the latitude angle. With our numbers (i.e. $T = 160$ ms and $\theta_l \simeq 43°$) this reads ϕ_{Coriol}[mrad]$\simeq -43\,\Delta v_{E-W}$[mm/s].

In our experiment the two clouds are launched to about 60 and 90 cm above the MOT position, and the launching velocities are $v_l \simeq 3.5$ m/s and $v_u \simeq 4.3$ m/s for the lower and upper cloud respectively. If both clouds are launched with the same tilt angle θ_{tilt} along the E-W direction, their horizontal E-W velocities will differ by about 25% from each other, and the resulting Coriolis shift will be

$$\phi_{Coriol} = -2\Omega k_{eff} T^2 \cos\theta_l (v_u - v_l)\sin\theta_{tilt} \qquad (4)$$

On the other hand, the horizontal velocity spread corresponding to the $\sim 3\,\mu$K transverse atomic temperature is expected to contribute to the noise on the ellipse phase angle via the Coriolis effect. In order to compensate for this, we apply a uniform rotation rate to the retro-reflecting Raman mirror during the atom interferometry sequence by means of PZT actuators, as suggested in [34], [35].

Wave-front distortions of Raman beams depend essentially on the details of the front-wave distorsions introduced by the retro-reflecting optics, which are not in common between the upwards and downwards Raman beam. During the interferometer sequence distorsions are translated into an additional phase shift that affects atoms with a nonzero radial velocity. In principle, such offset can be numerically evaluated by studing the surface conformation of the interested optics. *In situ* analysis are not feasible, and extrapolation at zero atomic temperature is not obvious [33].

Nearly all of such effects cancel out in the doubly differential measurement for G, provided that the atomic trajectories are the same in the two configurations of source masses. This might not be the case if either

- fluctuations in atomic trajectories occur on a time scale faster than the period of modulation of source masses positions
- the movement of source masses induces changes in the atomic trajectories, either due to any deformation of the mechanical structure holding the vacuum system and attached optics/coils, or due to changes in magnetic fields

The former would limit the reproducibility of G measurement, while the latter would cause a systematic shift on the G measured value.

For instance, if the mass movement induces a change of E-W tilt $\Delta\theta$, the corresponding systematic shift of ellipse phase is $\Delta\phi_{Coriol} \simeq -34\,\Delta\theta_{tilt}$. Thus in order to keep the systematic effect on G measurement within ~ 50 ppm, i.e. $\Delta\phi_{Coriol} < 30\,\mu$rad, then it is necessary to measure $\Delta\theta$ within one μrad, i.e. to control the shift in the center of atomic distribution, induced by the masses movement, with micrometer precision.

Similar considerations apply to the effect of wavefront curvature of Raman laser beams as well as to magnetic and gravity gradients.

Besides the effects of trajectory fluctuations, other possible sources of systematic shift in the G measurement are those which are not canceled at all in the doubly differential measurement. This is the case of the gravity gradient induced by the source masses themselves. In fact, in our setup the geometry of source masses is chosen in such a way that the gravitational potential is stationary in the region of the atom interferometry measurement, i.e. at the apogees of atomic trajectories [36]. The curvature of gravitational potential is

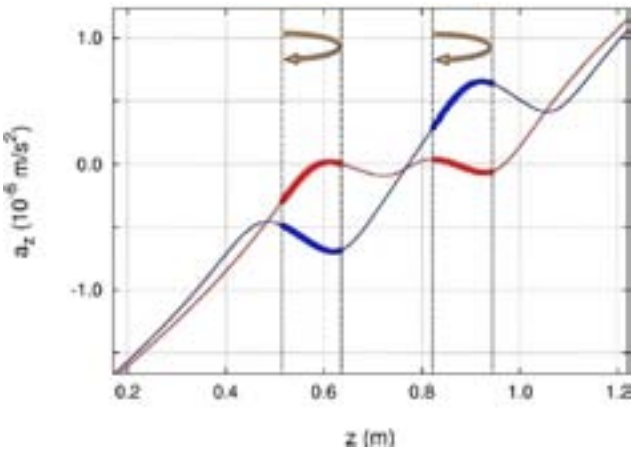

Fig. 2. Calculated relative acceleration along the axis of source masses for the two configurations (red: close masses; blue: far masses). The highlighted areas correspond to the atom trajectories during the atom interferometry sequence.

larger in the horizontal plane than in the vertical direction. In the case of point-like atomic clouds with a common traverse displacement from the symmetry axis of source masses, the differential interferometric phase varies by $42\,\mu$rad/mm^2 around the axis. Thus, in order to keep the systematic shift on G well below 10^{-4}, the atoms must stay within 1 mm from the symmetry axis. In the more physical situation of atomic clouds with finite size, the gravity gradient produces a systematic shift in the G measurement which is proportional to the square of the cloud size. In order to keep the systematic shift on G well below 10^{-4}, the width of atomic cloud should be smaller than 1 mm. For clouds with larger size, it is necessary to compute the phase shift to correct the measured data. This requires a precise knowledge of the density distribution in the atom clouds; i.e. the centers and widths must be measured with sub-mm precision in the region of the atom interferometry interrogation.

Similar considerations apply for vertical size and vertical displacement from the stationary point of the gravitational potential. We thus characterized the atomic density distribution in our fountain. In the following we will separately describe the measurement of vertical and horizontal degrees of freedom.

For the knowledge of vertical positions and velocities we employed time of flight (TOF) measurements. We determined the istant t_a at which the velocity selected atoms reach the trajectory apogee, i.e. when $v_z = 0$. Such condition can be easily identified using a Raman π transition: if atoms are at rest roughly half of them, performing the transition, will acquire a momentum recoil of $+\hbar k_{eff}$ while the remaining fraction $-\hbar k_{eff}$. As a consequence the detected signal shows two distinguishable and symmetrical peaks. Afterwards we measured the istant t_d at which the sample cross the detection region. Knowing the vertical position z_0 of the detection light sheet we can derive the apogee vertical coordinate z. This can be done independentely on both the clouds. An accuracy of ± 0.1 mm in vertical position has been reached, which leads to a systematic error on G of 2 ppm if atoms are properly placed on the stationary point of the gravitational potential.

We measured the position of MOT and tilt angles of the two clouds in the atomic fountain. To correctly evaluate systematic effects on G, all these measurements shall be performed with respect to the symmetry axis defined by the source masses and the gravity. To this purpose, we carefully aligned the Ramam beams along such axis and we used them to probe the atomic samples. We aim to reach a level of verticality better than 100 μrad.

We measured the horizontal distribution of atomic clouds at different heights in the ballistic flight of the fountain. We employed the Raman laser beams to define a reference frame for the atomic positions. A portion of radius $r \simeq 4$ mm of the downward-propagating Raman beam was selected with a diaphragm mounted on a 2D translation stage. We addressed the atoms with three Raman pulses in rapid sequence, and finally detected the number of atoms in $F = 1$. The horizontal distribution of atomic density was then probed in both clouds simultaneously by scanning the position of the diaphragm.

The number of detected atoms is proportional to the atomic density in the column selected by the diaphragm and to the transition probability of Raman beams. We deduced the distribution of transition probability from the intensity profile of Raman beams and from the direct measurement of transition probability versus Raman power. Performing this kind of measurement along two orthogonal directions provides a complete 2D picture of both the samples.

IV. Results

A. Sensitivity and long term stability

The dependence of the instrument sensitivity to differential gravity measurements as a function of the relevant experimental parameters allows to identify the main limits to the stability of Φ, once the typical fluctuations of the parameters are known. We constantly monitor the value of most relevant experimental parameters (i.e. the power of MOT, probe, repumper and Raman laser beams, the current in MOT compensation coils, in pulse coil and in bias solenoid, the tilt of Raman mirror) as well as the temperature in different points of the apparatus. We deduce that the main contributions arise from the instability of MOT laser beams intensity ratio, current in the bias solenoid and MOT compensation coils, and tilt of the Raman mirror. However, noise in the coils current is fairly white, and would not entail the long term stability, while fluctuations in laser powers and mirror tilt exhibit a low frequency flickering.

In order to improve the long-term stability, we actively stabilize the main experimental parameters, i.e. the optical intensity of cooling, Raman and probe laser beams, acting on the RF power driving acousto-optical modulators, and the Raman mirror tilt, acting on the piezo tip/tilt system.

The servo on cooling and Raman lasers intensity is done by means of a slow digital loop, sampling the four powers (up and down cooling beams, master and slave Raman beams) every 72 experimental cycles (i.e. ~ 2 min) and driving the RF power corresponding AOMs through a numerical loop filter. Residual fluctuations are below $0.3\,\%$.

The active control of cooling, Raman and probe laser intensities, together with Coriolis compensation, improves the long term stability of differential gravity measurements considerably. We reach a resolution of ~ 0.2 mrad on the

ellipse phase angle, corresponding to $\sim 5 \times 10^{-11}$ g after an integration time of about two hours.

We tested the long term stability of the measurement of the gravitational field of local masses by modulating the position of the source masses as shown in fig. 1. Typical elliptical plots in the two configurations of source masses are shown in fig. 3. We move the masses from the close (C_1) to the far (C_2) configuration and viceversa every ~ 27 minutes, corresponding to 720 measurement cycles of 1.9 s each plus a dead time of ~ 5 minutes to translate the masses. We reverse the direction of the Raman effective $k-$vector after each launch, in order to cancel possible k_{eff}-independent systematic errors, such as those arising from II order Zeeman shift and I order light shift [33]. We thus obtain two ellipses of 360 points each, corresponding to direct and reverse $k-$vector. We fit each set of 360 points to an ellipse, and from each pair of ellipses we determine the angle $\Phi_n(i) = \Phi_n^{dir}(i) - \Phi_n^{rev}(i)$ as the difference between direct and reverse angles, and the standard error $\delta\Phi_n(i) = \sqrt{\delta\Phi_n^{dir}(i)^2 + \delta\Phi_n^{rev}(i)^2}$. Here $n = 1, 2$ corresponding to the two configurations of source masses. From each couple $\{\Phi_1(i), \Phi_2(i)\}$ a value for the rotation angle $\Delta\Phi(i) = \Phi_1(i) - \Phi_2(i)$ due to the position of the source masses can be obtained.

Fig. 4 shows the Allan deviation of the experimental data up to an integration time of 50 hours, for a fixed configuration of source masses and for the difference of measurements in the two configurations. In the first case (gravity gradient measurement) the short-term stability is 3×10^{-9} g/$\sqrt{\text{Hz}}$, and we achieve a statistical uncertainty of 5×10^{-11} g after about two hours. In the second case (G measurement) we achieve a statistical uncertainty of 10^{-4} after an integration time of ~ 100 hours.

B. Atomic trajectories

The Coriolis compensation helps to improve the noise in the atom interferometry measurement. When plotting the rms error of ellipse phase angle versus the mirror rotation rate, we find that the optimal rotation rate, corresponding to the maximum contrast, is equivalent to the opposite of the local projection of the Earth rotation rate. In such conditions, the rms noise on ellipse fitting is minimum. The compensated error on ellipse angle is ~ 50 % lower than without compensation, while the contrast increases by ~ 4 % only.

We measured the density distribution map of the two atomic clouds at different heights with the method described in section III-B. We compared similar measurements in both source masses configurations in order to investigate possible effects related to the mass movement. The method provides a good spatial resolution ($\sim 100\mu$m), however it is not sensitive enough to measure accurately small changes (< 0.2 mm/s) in the transversal velocity. The launching direction of the atomic clouds turns out to be extremely stable.

From numerical computation we deduce that a cloud of radius $\sigma = 5$ mm and offset 5.0 ± 0.1 mm yields an angular correction of 1.450 ± 0.030 mrad on Φ, corresponding to an error on G of ~ 60 ppm.

We probe the atomic density distribution in-situ at the MOT location by tuning the frequency of one Raman laser

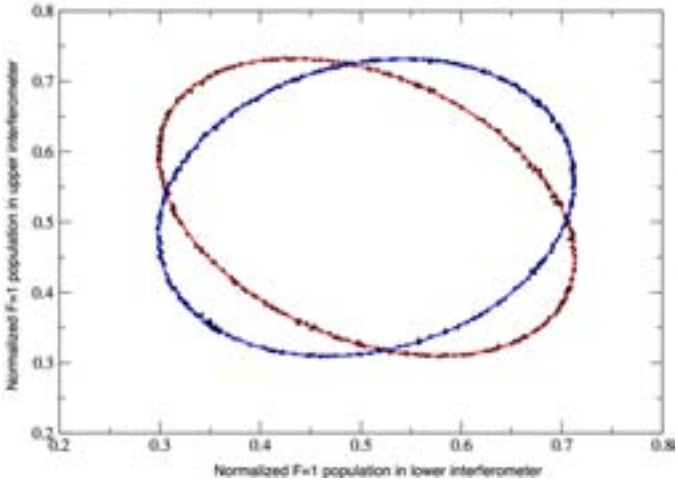

Fig. 3. Two experimental ellipses obtained with 360 experimental points each, for two different configuration of the source masses.

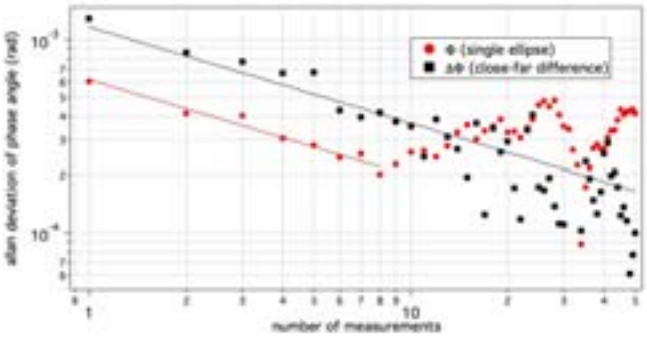

Fig. 4. Allan deviation of the atom interferometry phase; red circles represent the measurement of gravity gradient for a given position of the source masses: each measurement contains 360 points, corresponding to a measurement time of ~ 12 minutes; black squares represent the differential phase measurement for two configurations of source masses: each measurement contains 1440 points, corresponding to a measurement time of ~ 56 minutes (including the dead time for source masses translation). One-parameter fit with $A \times \sqrt{N}$ is shown with solid lines.

to the $F = 2 \rightarrow F' = 3$ transition. Using a diaphragm we select a thin portion (radius 0.5 mm) of the resonant upwards-propagating beam, to push the atoms away from the trap region. We measured the MOT position versus some relevant parameters such as total cooling power, up-down beams power ratio, compensation and MOT coils current. We conservatively conclude that the MOT center is stable within $\pm 100\mu$m on a time scale of few days.

V. Conclusion

We studied the sensitivity and long term stability of a gravity gradiometer based on Raman atom interferometry. We discussed the influence of the most relevant experimental parameters, in particular for a measurement of the Newtonian gravitational constant.

A serious issue in precision gravity measurements by atom interferometry is the control of atomic trajectories. We determined the center and width of the atomic clouds with sub-millimeter precision, both in the interferometric region and at the MOT location.

Our experiment can run continuously for several days, showing a reproducibility of the gravity gradient measurement compatible with the stated sensitivity on the time scale of a few weeks. Our measurement of the differential gravity signal of source masses reaches a statistical uncertainty of 1.1×10^{-4} after ~ 100 hours of integration time. A measurement of G by atom interferometry at the level of 100 ppm is within reach.

ACKNOWLEDGMENT

This work was supported by INFN (MAGIA experiment), EU (FINAQS STREP/NEST project Contract No. 012986) and ESA (SAI project Contract No. 20578/07/NL/VJ). The authors acknowledge M. Depas, M. Giuntini, A. Montori, R. Ballerini, M. Falorsi for technical support.

REFERENCES

[1] A. D. Cronin, J. Schmiedmayer, and D. E. Pritchard, "Optics and interferometry with atoms and molecules," *Rev. Mod. Phys.*, vol. 81, pp. 1051–1129, 2009.

[2] M. Kasevich and S. Chu, "Measurement of the Gravitational Acceleration of an Atom with a Light-Pulse Atom Interferometer," *Appl. Phys. B*, vol. 54, p. 321, 1992.

[3] A. Peters, K. Y. Chung, and S. Chu, "Measurement of gravitational acceleration by dropping atoms," *Nature*, vol. 400, p. 849, 1999.

[4] H. Müller, S.-W. Chiow, S. Herrmann, S. Chu, and K.-Y. Chung, "Atom-Interferometry Tests of the Isotropy of Post-Newtonian Gravity," *Phys. Rev. Lett.*, vol. 100, no. 3, p. 031101, Jan 2008.

[5] J. L. Gouët, T. Mehlstäubler, J. Kim, S. Melet, A. Clairon, A. Landragin, and F. P. D. Santos, "Limits to the sensitivity of a low noise compact atomic gravimeter," *Appl. Phys. B*, vol. 92, pp. 133–144, 2008.

[6] M. J. Snadden, J. M. McGuirk, P. Bouyer, K. G. Haritos, and M. A. Kasevich, "Measurement of Earth's Gravity Gradient with an Atom Interferometer-Based Gravity Gradiometer," *Phys. Rev. Lett.*, vol. 81, p. 971, 1998.

[7] J. M. McGuirk, G. T. Foster, J. B. Fixler, M. J. Snadden, and M. A. Kasevich, "Sensitive absolute-gravity gradiometry using atom interferometry," *Phys. Rev. A*, vol. 65, p. 033608, 2002.

[8] A. Bertoldi, G. Lamporesi, L. Cacciapuoti, M. D. Angelis, M. Fattori, T. Petelski, A. Peters, M. Prevedelli, J. Stuhler, and G. M. Tino, "Atom interferometry gravity-gradiometer for the determination of the Newtonian gravitational constant G," *Eur. Phys. J. D*, vol. 40, p. 271, 2006.

[9] T. L. Gustavson, P. Bouyer, and M. Kasevich, "Precision Rotation Measurements with an Atom Interferometer Gyroscope," *Phys. Rev. Lett.*, vol. 78, p. 2046, 1997.

[10] T. L. Gustavson, A. Landragin, and M. Kasevich, "Rotation sensing with a dual atom-interferometer Sagnac gyroscope," *Class. Quantum Grav.*, vol. 17, p. 2385, 2000.

[11] B. Canuel, F. Leduc, D. Holleville, A. Gauguet, J. Fils, A. Virdis, A. Clairon, N. Dimarcq, C. J. Bordé, A. Landragin, and P. Bouyer, "Six-axis inertial sensor using cold-atom interferometry," *Phys. Rev. Lett.*, vol. 97, p. 010402, 2006.

[12] A. Gauguet, B. Canuel, T. Lévèque, W. Chaibi, A. L. A. Gauguet, B. Canuel, T. Lévèque, W. Chaibi, and A. Landragin, "Characterization and limits of a cold atom sagnac interferometer," *Phys. Rev. A*, vol. 80, p. 063604, 2009.

[13] S. Fray, C. A. Diez, T. W. Hänsch, and M. Weitz, "Atomic Interferometer with Amplitude Gratings of Light and Its Applications to Atom Based Tests of the Equivalence Principles," *Phys. Rev. Lett.*, vol. 93, p. 240404, 2004.

[14] S. Dimopoulos, P. Graham, J. Hogan, M. Kasevich, and S. Rajendran, "Atomic gravitational wave interferometric sensor," *Phys. Rev. D*, vol. 78, p. 122002, 2008.

[15] J. B. Fixler, G. T. Foster, J. M. McGuirk, and M. Kasevich, "Atom Interferometer Measurement of the Newtonian Constant of Gravity," *Science*, vol. 315, p. 74, 2007.

[16] G. Lamporesi, A. Bertoldi, L. Cacciapuoti, M. Prevedelli, and G. M. Tino, "Determination of the Newtonian Gravitational Constant Using Atom Interferometry," *Phys. Rev. Lett.*, vol. 100, p. 050801, 2008.

[17] H. Müller, A. Peters, and S. Chu, "A precision measurement of the gravitational redshift by the interference of matter waves," *Nature*, vol. 463, pp. 926–929, 2010.

[18] G. Tino, "Cold atoms physics in space," *Nuclear Physics B-Proceedings Supplements*, vol. 113, no. 1-3, pp. 289–296, 2002.

[19] P. Wolf, P. Lemonde, A. Lambrecht, S. Bize, A. Landragin, and A. Clairon, "From optical lattice clocks to the measurement of forces in the casimir regime," *Phys. Rev. A*, vol. 75, no. 6, p. 063608, Jun 2007.

[20] G. Ferrari, N. Poli, F. Sorrentino, and G. M. Tino, "Long-lived bloch oscillations with bosonic sr atoms and application to gravity measurement at the micrometer scale," *Phys. Rev. Lett.*, vol. 97, p. 060402, 2006.

[21] F. Sorrentino, A. Alberti, G. Ferrari, V. V. Ivanov, N. Poli, M. Schioppo, and G. M. Tino, "Quantum sensor for atom-surface interactions below 10 μm," *Phys. Rev. A*, vol. 79, p. 013409, 2009.

[22] G. Amelino-Camelia, C. Laemmerzahl, F. Mercati, and G. M. Tino, "Constraining the Energy-Momentum Dispersion Relation with Planck-Scale Sensitivity Using Cold Atoms," *Phys. Rev. Lett.*, vol. 103, p. 171302, 2009.

[23] G. M. Tino and F. Vetrano, "Is it possible to detect gravitational waves with atom interferometers?" *Class. Quantum Grav.*, vol. 24, pp. 2167–2177, 2007.

[24] S. Dimopoulos, P. Graham, J. Hogan, M. Kasevich, and S. Rajendran, "Gravitational wave detection with atom interferometry," *Physics Letters B*, 2009.

[25] A. Peters, K. Y. Chung, and S. Chu, "High-precision gravity measurements using atom interferometry," *Metrologia*, vol. 38, p. 25, 2001.

[26] A. Bresson, Y. Bidel, P. Bouyer, B. Leone, E. Murphy, and P. Silvestrin, "Quantum mechanics for space applications," *Appl. Phys. B*, vol. 84, pp. 545–550, 2006.

[27] M. de Angelis, A. Bertoldi, L. Cacciapuoti, A. Giorgini, G. Lamporesi, M. Prevedelli, G. Saccorotti, F. Sorrentino, and G. M. Tino, "Precision gravimetry with atomic sensors," *Meas. Sci. Technol.*, vol. 20, p. 022001, 2009.

[28] G. Geneves, "The BNM Watt balance project," *IEEE Trans. on Instrum. and Meas.*, vol. 54, p. 850, 2005.

[29] G. Lamporesi, A. Bertoldi, A. Cecchetti, B. Dulach, M. Fattori, A. Malengo, S. Pettorruso, M. Prevedelli, and G. M. Tino, "Source mass and positioning system for an accurate measurement of G," *Rev. Sci. Instrum.*, vol. 78, p. 075109, 2007.

[30] R. Legere and K. Gibble, "Quantum Scattering in a Juggling Atomic Fountain," *Phys. Rev. Lett.*, vol. 81, p. 5780, 1998.

[31] G. T. Foster, J. B. Fixler, J. M. McGuirk, and M. A. Kasevich, "Novel method of phase extraction between coupled atom interferometers using ellipse-specific fitting," *Opt. Lett.*, vol. 27, 2002.

[32] F. Sorrentino, Y.-H. Lien, G. Rosi, G. M. Tino, L. Cacciapuoti, and M. Prevedelli, "Sensitive gravity-gradiometry with atom interferometry: progress towards an improved determination of the gravitational constant," *New J. Phys.*, vol. 12, p. 095009, 2010.

[33] A. Louchet-Chauvet, T. Farah, Q. Bodart, A. Clairon, A. Landragin, S. Merlet, and F. P. Dos Santos, "The influence of transverse motion within an atomic gravimeter," *New Journal of Physics*, vol. 13, no. 6, p. 065025, 2011.

[34] J. M. Hogan, D. M. S. Johnson, and M. A. Kasevich, "Light-pulse atom interferometry," in *Atom Optics and Space Physics, Proceedings of the International School of Physics "Enrico Fermi" ; course 168*, E. Arimondo, W. Ertmer, W. P. Schleich, and E. Rasel, Eds. Washington, DC: IOS Press Amsterdam, 2009, p. 411.

[35] S.-Y. Lan, P.-C. Kuan, B. Estey, P. Haslinger, and H. Müller, "Influence of the coriolis force in atom interferometry," *Phys. Rev. Lett.*, vol. 108, p. 090402, 2012.

[36] M. Fattori, G. Lamporesi, T. Petelski, J. Stuhler, and G. M. Tino, "Towards an Atom Interferometric Determination of the Newtonian Gravitational Constant," *Phys. Lett. A*, vol. 318, p. 184, 2003.

Pulsed Optically Pumped Rb Clock: a High Stability Vapor Cell Frequency Standard

F. Levi, C. E. Calosso, A. Godone and S. Micalizio
Optics Division
Istituto Nazionale di Ricerca Metrologica, INRIM
Torino, Italy
e-mail: f.levi@inrim.it

***Abstract*-. In this paper we report the results we obtained with a prototype of pulsed optically pumped (POP) Rb clock. In terms of frequency stability, an Allan deviation $\sigma_y(\tau)=1.7\times10^{-13}\tau^{-1/2}$ has been measured, where τ is the integration time. In addition, the long term frequency drift results below 10^{-14}/day. In the paper we also describe a technique to stabilize the amplitude of the microwave signal using the atoms themselves as discriminator. Moreover, an anomalously large temperature sensitivity of the clock frequency and a technique to keep it under control are also reported. Finally, we describe some non linear effects that modify the shape of the clock signal represented by the Ramsey central fringe.**

I. Introduction

In the pulsed optical pumping (POP) scheme the three phases of optical pumping, microwave excitation and detection of the transition signal are separated in time [1]. Besides suppressing the laser induced light shift, the pulsed operation allows a full optimization of the laser parameters both in the pumping and in the detection stages, where different power level are required. A Rb clock adopting this scheme has been implemented at INRIM and a short term frequency instability of $1.7\times10^{-13}\tau^{-1/2}$ was measured [2], together with a long term frequency drift below 10^{-14}/day [3]. The drift is thought to be due to a residual sensitivity to environmental parameters like temperature, atmospheric pressure and humidity.

These results represent a record achievement for a vapor-cell frequency standard and make the POP clock potentially very attractive for a variety of applications, including telecommunication and space radio-navigation .

Besides reporting these outstanding results, in this work we discuss some key techniques we exploited in order to obtain them and to make them repeatable.

First, we describe the technique to stabilize the amplitude of the microwave signal used to interrogate the Rb atoms; specifically, the microwave amplitude is locked using the atomic sample itself as discriminator.

Moreover, we report on the observation of an enhanced temperature sensitivity (ETS) of the clock frequency [4]. Specifically, despite we used in our cell a temperature compensated mixture of buffer gases, the observed temperature sensitivity is $\approx 1\times10^{-10}$/°C, more than one order of magnitude larger than the expected value. Yet, this phenomenon cannot be ascribed to cavity pulling and/or to spin exchange that are in fact negligible in our setup. We explain this effect in terms of a simple model based on the on the ideal gas law and we also describe a technique to keep it under control.

Finally, we describe a few phenomena that may affect the Ramsey fringes observed in our system. Specifically, cycle memory and atomic density effects can deviate the shape of the Ramsey central fringe from the common sinusoidal behavior. A simple three-level model well reproduces the experimental observations [5].

The paper is organized as follows.

In Section II we describe the set-up of the POP clock, its main operation phases, the Ramsey fringes and the stability performances.

In Section III we report on the microwave amplitude locking technique while the ETS is described in Section IV. Section V is devoted to the characterization of the Ramsey central fringe lineshape.

Conclusions are in Section VI.

II. The POP Rb clock

The prototype is based on a pulsed approach in which the clock transition is detected by observing Ramsey fringes on a laser absorption signal.

The experimental set-up is represented in Fig. 1.

It is composed of three main parts:

1) physics package;

2) optics;

3) electronics.

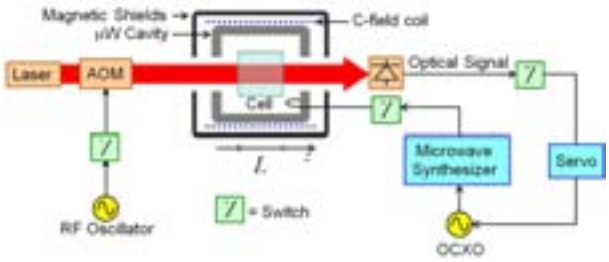

Fig. 1. Experimental setup of the POP clock.

The physics package is layer structure and several components can be identified (Fig. 2).

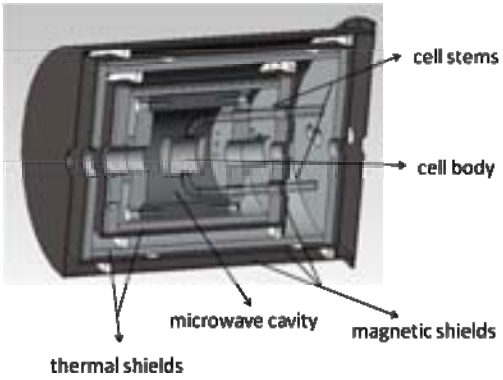

Fig. 2. Physics package of the POP clock.

The quartz cell contains the ^{87}Rb atoms and a buffer gas mixture N_2+Ar, at the total pressure P_s = 25 Torr. As shown in Fig. 2, the cell exhibits two large stems required to have a cold point in the cell; in this way, the condensation of Rb atoms inside the main body of the cell is in principle avoided.

The cell is placed in a Mo cavity resonating at 6.834 GHz. A quantization magnetic field along the cavity axis is applied (B_0 = 1.5 μT). Moreover, three mu-metal magnetic shields complete the physics package for an overall shielding factor of 1000.

Two thermal ovens working at different temperatures were implemented. The internal one works at 65.5 °C and is devoted the cell body-cavity system and the external one at 63.5 °C for the stems. The thermal stability for both the oven is of the order 1 mK for integration times up to 10000 s.

All the physics package is placed in vacuum structure in order to isolate the system from environmental fluctuations.

The optics is composed of a DFB laser at 780 nm (D_2 line) and delivers a full power of 15 mW. An AOM is used to switch on and off the laser during the pulsed operation.

The electronics is composed of a low phase noise synthesis chain delivering a signal at 6.834 GHz starting from a 10 MHz OCXO.

The synthesis chain (SC) is based on non-linear transmission lines (NLTL) [6]; a direct multiplication stage converts the signal from the 10 MHz of the OCXO to about 7GHz. The phase noise of the OCXO plus the SC is shown in Fig. 3; it has been obtained by the beat note of two nominally identical devices. The Dick effect turns out 7×10^{-14} at 1s.

A digital electronics was also implemented on FPGA to drive all the clock operation phases.

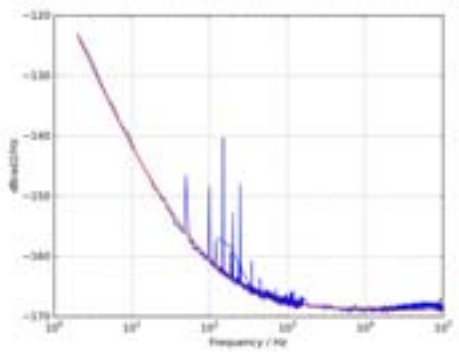

Fig. 3. Phase noise of the SC.

The clock operation is based on a pulsed optical pumping, followed by a microwave interrogation according to a Ramsey scheme, and a laser pulse for optical detection, as represented in Fig. 4. A typical timing sequence is also shown in the figure.

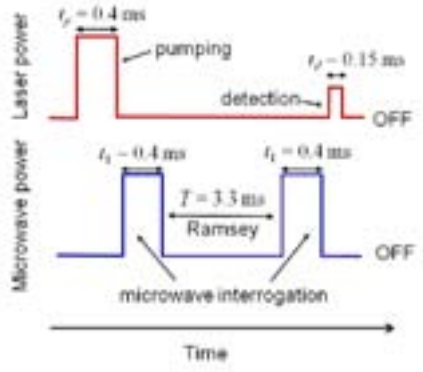

Fig. 4. Timing of the different operation phases of the POP clock

Fig. 5 shows the observed Ramsey fringes using a DFB laser locked to the D_2 line.

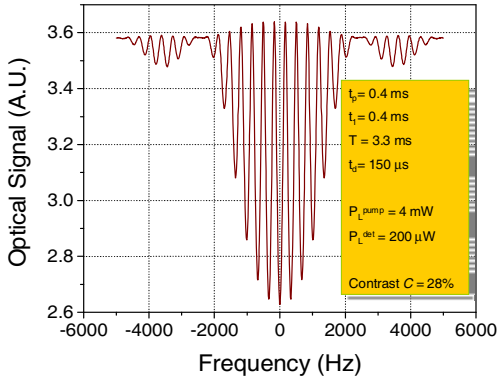

Fig. 5. Ramsey fringes observed with D2 line for a cell temperature 65.5 °C. The timing and the adopted laser powers are indicated in the figure.

A contrast of the 28 % for the central fringe is achieved. The corresponding frequency stability is reported in the following Fig. 6 and in terms of Allan deviation we have 1.7×10^{-13} at 1s; the white frequency region reaches the level of 5×10^{-15} at 10000s.

The drift has not been removed from the data and turns out -3×10^{-15}/day.

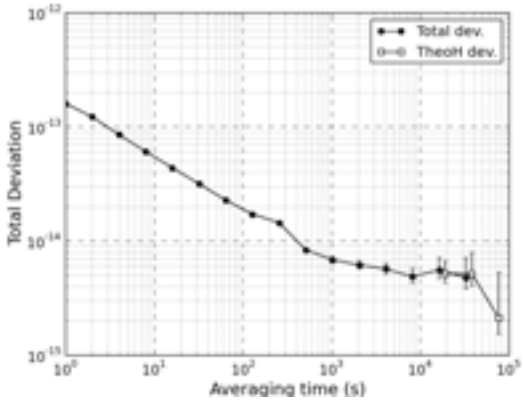

Fig. 6. Allan deviation of the POP clock with optical detection using D2 line as optical pumping.

III. Microwave Locking Technique

In order to obtain good frequency stability performances in the medium-long term period, it is often necessary to implement an active control of some parameters such as microwave and/or laser power.

Specifically, in the case of the POP clock, the microwave power is a particularly critical quantity since it may induce frequency fluctuations and or frequency drift through the cavity pulling effect. Moreover, since the cavity Q may degrade, the entity of the drift may change. It is then necessary a technique to lock the microwave amplitude to a signal coming from the atoms themselves.

To do that, we recall that the atomic signal P is essentially related to the population inversion Δ at the end of the second microwave pulse. It is easy to see that P can be written as [1]:

$$P \propto \frac{1 - e^{-\gamma_2 T} \sin^2 \theta \cos \Omega_\mu T}{2} \qquad (1)$$

where $\theta = b\, t_1$ is the microwave pulse area defined by the microwave Rabi frequency b and the duration t_1; Ω_μ is the microwave detuning between the interrogating frequency ω and the atomic frequency ω_{hfs}; γ_2 is the atomic coherence relaxation rate. Equation (1) then provides not only a frequency discriminator signal (proportional to cos $\Omega_\mu T$) but also an amplitude discriminator signal (proportional to $\sin^2\theta$).

In terms of the two locking variables Ω_μ and θ, the signal may be represented as a paraboloid around the two locking points, $\Omega_\mu = 0$ and $\theta = \pi/2$ (see Fig. 7).

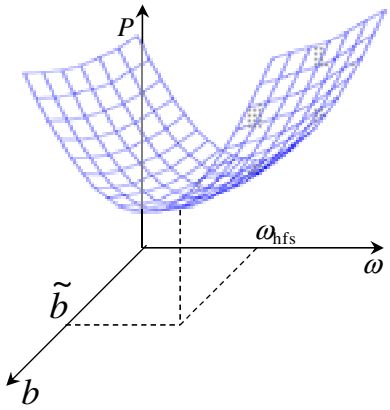

Fig. 7. Paraboloid which represents the signal (1). We call $\tilde{b}$ the microwave amplitude value which realizes the $\pi/2$ pulses.

We recall that the technique to lock the microwave signal frequency to the atomic frequency is similar to that adopted in an atomic fountain: two successive interrogations at frequencies $\omega \pm \Delta\omega$ are done and the corresponding signals are compared; specifically the difference between those signals has the meaning of error signal. The process is indefinitely repeated so that the LO frequency is continuously corrected and referenced to the ^{87}Rb atomic frequency.

To implement also the locking of the microwave amplitude we extended the algorithm previously described, so that the locking technique exploits four points, two for the microwave frequency and two for the microwave amplitude.

From a block scheme point of view, the locking of the microwave amplitude can be represented as in Fig. 8.

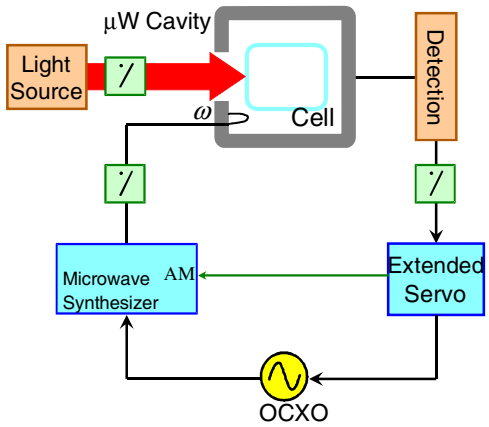

Fig. 8. Block scheme showing the technique adopted to actively stabilize the amplitude of the microwave signal to the atoms.

To show the importance of the microwave amplitude locking, we refer to Fig. 9 in which the clock frequency stability is reported. Figure 9 reports the clock stability with and without the servo of the microwave amplitude. It is possible to see a drift of the frequency of the order of -3×10^{-14}/day when the servo is not implemented. After the implementation of the servo system the frequency drift is reduced to -7×10^{-15}/day, also a benefit is observable on the short term behavior.

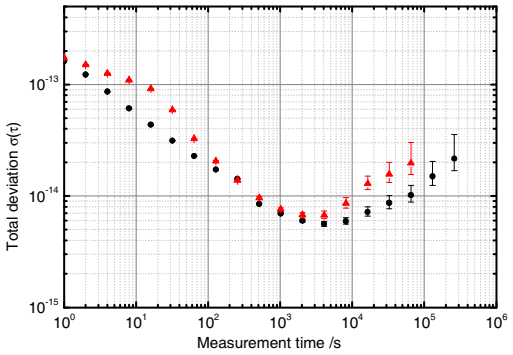

Fig. 9 Stability of the POP with (black circles) and without (red triangles) the microwave stabilization loop.

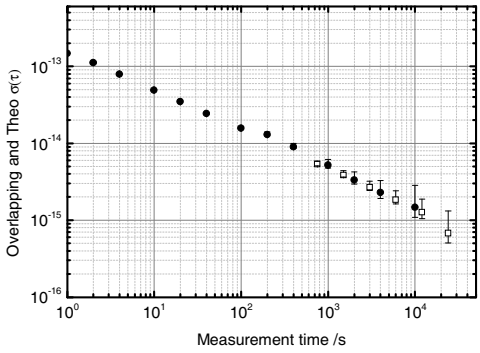

Fig. 10 Stability of a subset of data taken from the main set of fig. 9.

In Fig. 10 a subset of the data with the amplitude servo is analyzed, taken in a quieter environmental period of time. No significant drift appears, indicating the possible ultimate stability of the POP approach on the medium term, once the thermal criticalities should be resolved.

IV. Enhanced Temperature Sensitivity of the Clock Frequency

It is well established that the unperturbed ground state hyperfine frequency ν_0 of alkali-metal atoms is shifted by the interaction with buffer gas atoms/molecules [7]. This shift versus the cell temperature is a parabola: working around the maximum of the parabola it is in principle possible to reduce the temperature sensitivity of the clock frequency vs temperature (Fig. 11). Referring the coefficients of the curve to the inversion temperature T_i and fitting the experimental points with a parabola, the clock frequency can be written as:

$$\nu(T) = \nu_0 + P_S\left[\beta_i' + \gamma_i'(T - T_i)^2\right] \quad (2)$$

where β'_i=174 Hz/Torr and γ'_i = -0.00071Hz/K^2 Torr.

Supposing to work at a temperature T so that $|T\text{-}T_i|$<0.2 K, the temperature stability of the clock frequency is expected to be 4×10^{-12}/K.

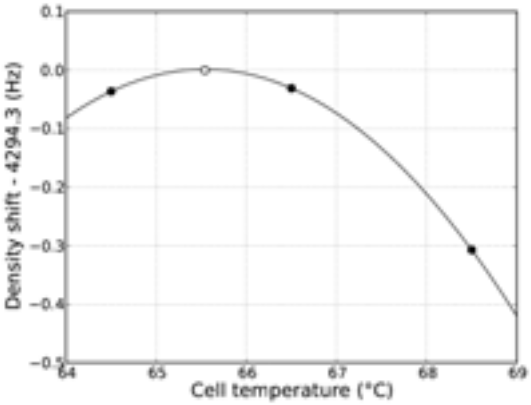

Fig. 11. Clock frequency shift versus temperature.

However, despite the use in the cell of a compensated mixture of buffer gases and the cell working temperature is set on the maximum of the parabola, a high sensitivity of the clock frequency vs temperature is observed.

In particular, the measured coefficient is of the order of 1×10^{-10}/K. To understand the origin of this phenomenon, we consider that a high unexpected correlation between the clock frequency and the stem temperature is observed (Fig. 12).

The effect is explained according to a model based on the ideal gas law.

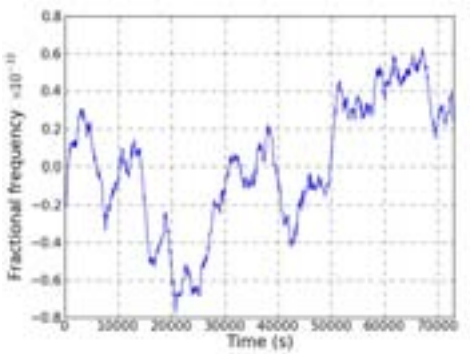

(a)

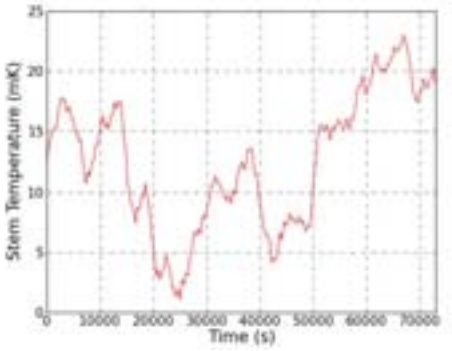

(b)

Fig. 12. Correlation between the clock frequency (a) and the stem temperature (b).

A. The model

We consider the model represented in Fig. 13. The cell is divided in two parts: part A (volume V_a) is the clock cell placed inside the microwave cavity and thermally coupled to

the internal oven at the temperature T_a; part B is defined by the two stems (volume V_b) that are outside the microwave cavity; they are thermally coupled to the external oven at the temperature T_b.

It is easy to see that thanks to the ideal gas law, the atomic density n_a of buffer gas particles taking part to the interaction is given by:

$$n_a \approx n_s\left(1-\frac{T_a-T_b}{T_b}\mathrm{v}_b\right) \tag{3}$$

where n_s is the buffer gas density in the entire cell and $\mathrm{v}_b = V_b/(V_a+V_b)$.

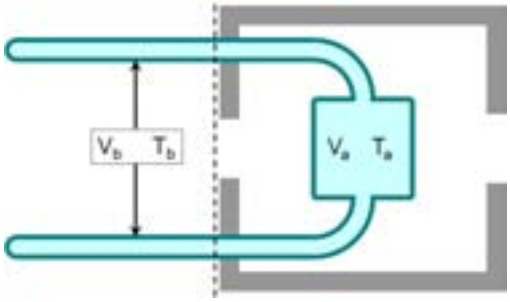

Fig. 13. Model used to explain the observed large temperature sensitivity.

From Eq. (3) it is easy to see the density of buffer gas atoms really involved in the interaction with Rb atoms depends on T_a and T_b, and for consequence may fluctuate due to variations of T_a and T_b. Conversely, n_s is fixed at the cell sealing time and is related to P_s by the ideal gas law (in our case $n_s \approx 8\times10^{17}$ cm^{-3}.

In a form totally equivalent to (2), the buffer gas shift can be written in terms of n_a:

$$\nu(T_a,T_b)=\nu_0+n_a\left[a'_{0i}+a'_{2i}(T_a-T_i)^2\right]\approx \nu_0+n_s\left(1-\frac{T_a-T_b}{T_b}\mathbf{v}_b\right)\left[a'_{0i}+a'_{2i}(T_a-T_i)^2\right] \tag{4}$$

with $a'_{0i} \approx 5.5\times10^{-15}$ Hz cm^{-3}, $a'_{2i} \approx -2.2\times10^{-20}$ Hz K^{2}cm^{-3} for our buffer gas composition. Deriving Eq. (4) with respect to and T_b (T_a) keeping constant T_a (T_b) we have:

$$\left.\frac{\partial\nu}{\partial T_b}\right|_{T_a=const} \approx n_s\, a'_{0i}\frac{\mathrm{v}_b}{T_b} \Rightarrow \frac{\partial\nu/\nu_0}{\partial T_b}\approx\frac{P_s\beta'_i\mathrm{v}_b}{\nu_0 T_b}=1.4\times10^{-10}/\mathrm{K} \tag{5}$$

that is of the same order of magnitude of the observed effect.

Similarly, we have:

$$\left.\frac{\partial\nu}{\partial T_a}\right|_{T_b=const} \approx n_s\, a'_{0i}\left[-\frac{\mathrm{v}_b}{T_b}+2\frac{a'_{2i}}{a'_{0i}}(T_a-T_i)\right] \tag{6}$$

From (5) it turns out that a new point where the clock frequency is insensitive to temperature fluctuations of the cell is found. In fact, Eq. (6) is null when:

$$T_a = T_i+\frac{a'_{0i}}{2a'_{2i}}\frac{\mathrm{v}_b}{T_b} \tag{7}$$

On the other hand, from (5) and (6) it is observed that $\left.\frac{\partial\nu}{\partial T_b}\right|_{T_a=const} = -\left.\frac{\partial\nu}{\partial T_a}\right|_{T_b=const}$ when the cell temperature is set to the inversion temperature T_i. This means that designing the physics package so that T_a and T_b are correlated the two temperature coefficients compensate each other.

According to previous equations, several solutions can be applied to reduce this anomalously large temperature sensitivity of the clock frequency:

- to make the cell with v_b negligible;
- good control of the temperature not only of the cell but also of the stems;
- adopt a mixture of three buffer gas to reduce not only the linear term but also the pressure coefficient β_i'.

In our system we used essentially the second technique, implementing an active temperature control devoted to the stems only. Moreover, to limit thermal bridges from the environment to the physics package, the vacuum structure was wrapped with highly insulating material.

In this way, the clock frequency stability in the medium long term remains at the level of 1×10^{-14} or better for integration times of the order of 1 day.

V. Lineshape of the Central Ramey Fringe

According to Eq. (1), it is expected that the shape of the Ramsey central fringe (RCF) is a pure cosine (in the following we assume $\theta = \pi/2$). Actually, in this section we discuss a couple of non-linear effects that contribute to the shape of the RCF. In a more detail, high-order harmonics appear in the Ramsey pattern and RCF is no more a pure cosine function of Ω_μ. This non-linear behavior may be attributed to two different physical causes. The first one is related to the incomplete extinction of the atomic coherence in the ground state between one operation cycle and the following one. This "phase memory" is responsible of the residual light-shift in a pulsed optically pumped (POP) clock and has been extensively discussed elsewhere [8, 9]. Here we show that a not complete separation among the different operation phases of the POP clock leads to a not elementary shape of the RCF.

The second effect is related to the optical thickness of the atomic sample. We observed in fact that the amplitude of high-order harmonics depends on the temperature (and then on the atomic density).

B. A. Cycle Memory Effect

Figure 14 shows the RCF as observed in a low temperature regime (45.5 °C) for a pumping time of 0.4 ms.

It is evident that the minimum appears flattened and the RCF is not well described by Eq. (1); that is, the shape is not a pure cosine function.

It can be demonstrated [5] that this phenomenon is related to a not complete extinction of the memory between one cycle and the successive one and as a consequence high-order harmonics appear on the signal. Specifically, the signal can be written as [5]:

$$\Gamma_p'(L) = \Gamma_p'(0)\left\{1 - \zeta\left[1 + \overline{\Delta}_{Ramsey}(\Omega_\mu)\right]\right\} \quad (8)$$

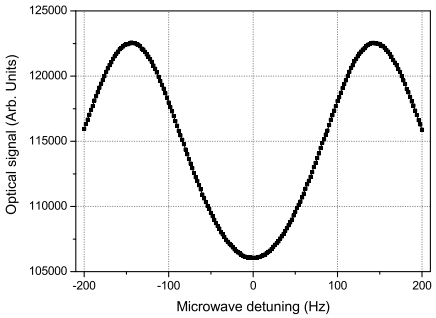

Fig. 14. RCF detected for the following values of the parameters: t_p = 0.4 ms, t_d =150 µs, T = 3 ms, t_1=0.4 ms.

where $\Gamma_p'(L)$ and $\Gamma_p'(0)$ are the laser pumping rates during the detection phase and the exit and at the entrance of the cell (of length L) respectively; ζ is the optical thickness of the medium and $\overline{\Delta}_{Ramsey}(\Omega_\mu)$ is the average over r cycles of the population inversion at the end of the Ramsey interaction phases:

$$\overline{\Delta}_{Ramsey}(\Omega_\mu) = \frac{1}{r}\sum_{k=1}^{r}\Delta^{(k)}_{Ramsey}(\Omega_\mu) \quad (9)$$

where each $\Delta^{(k)}_{Ramsey}(\Omega_\mu)$ is proportional to $\cos^k(\Omega_\mu T)$.

In particular, for the curve of Fig. 14 the ratio between the second order harmonic amplitude and the first order one turns out as large as 8.5 %.

In Fig. 15 we report the $\Gamma_p'(L)$ for three values of the pumping rate time as calculated according the model developed in [5].

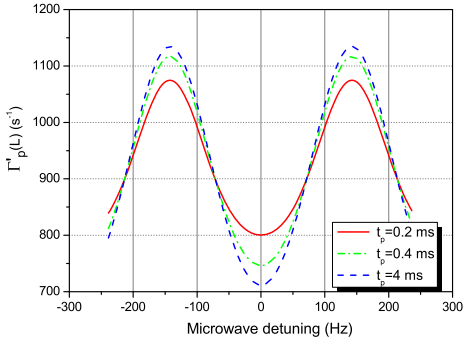

Fig. 15. RCF calculated for T= 3 ms, t_1 = 0.4 ms, $\Gamma_p(0)$= 20000 s^{-1}; $\Gamma'_p(0)$= 2000 s^{-1}; dash line t_p= 4 ms; dash dot line: t_p = 0.4 ms; continuous line: t_p= 0.2 ms.

As the pumping time increases, the laser pulse area $\Gamma_p t_p$ is able to suppress the memory between consecutive cycles and no high order harmonics are observed. To avoid this memory effect it is then required that the laser pulse area during the pumping phase satisfies the relation:

$$\Gamma_p t_p >> 1 \quad (10)$$

C. *High density case*

In this subsection we will investigate the effects related to the thickness of the atomic sample. Fig. 16 in particular refers to a RCF as detected at a temperature of 65.5 °C. To assure that the operation cycles are well separated and to exclude that any modification of the line shape may be attributed to the memory effect, a pumping time of 4 ms and a laser pumping rate of 20000 s^{-1} have been used, so that condition (10) is satisfied.

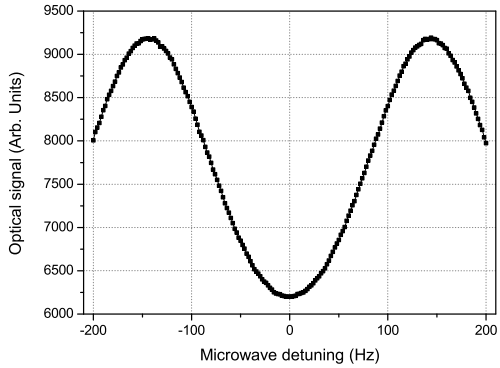

Fig. 16. RCF as observed in the high density regime (65.5 °C); T= 3 ms, t_1 = 0.4 ms, t_p= 4 ms; t_d = 0.15 ms.

It is observed that the curve is not a pure cosine function but the minimum appears flattened with respect the two side maxima, highlighting the presence of a second harmonic component in the Ramsey signal.

Since this effect cannot be due to the cycle memory, another mechanism should be responsible of it. To gain in physical insight, we observed the RCF for different atomic densities and through a non linear fit of the experimental curves we inferred the amplitude of the second harmonic component present on the signal. At the same time, we compared the experimental observations with the theoretical behavior obtained through the simple model used to interpret the results of subsection V*A*. The results are shown in Fig. 17.

From a theoretical point of view, it is found that the laser pumping rate at the detection stage is given by:

$$\Gamma_p'(L) = \Gamma_p'(0)e^{-\zeta}\left\{I_0(\chi) + 2\sum_{k=1}^{\infty} I_k(-\chi)\cos(k\,\Omega_\mu T)\right\} \quad (11)$$

where $I_k(x)$ are the modified Bessel functions of the first type with k integer ≥ 0 [10]. The argument χ is defined as χ=

$\zeta\ \Delta_{pump}\ e^{-\gamma_2 T}$; in this relation Δ_{pump} is the population inversion generated by the pumping light.

Since the $I_k(x)$ are monotone functions of the argument, the amplitude of the high-order harmonics increases with the product $\zeta\ \Delta_{pump}$; then, this effect is proportional to the optical length of the cell and to the population inversion generated by the pumping light. We note, however, that also γ_2 increases with the atomic density due to spin-exchange contribution [ref], leading to a suppression of the effect above a certain density value and explaining the two different regimes observed in Fig. 17. In other words, up to about 65 °C the second harmonic component amplitude increases due to the enhancement of the optical thickness of the medium ζ with temperature. Above that value, spin-exchange prevails and overcomes the pure density effect through the increasing of γ_2.

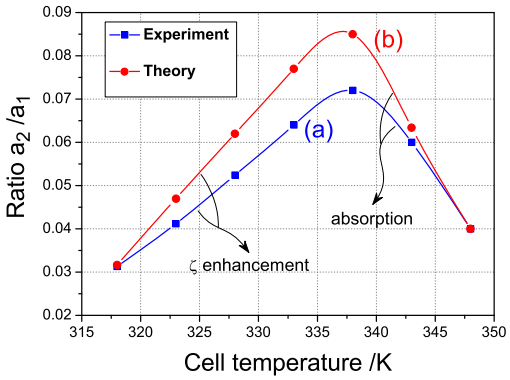

Fig. 17. Ratio between the coefficients a_2 and a_1 representing the amplitudes of the second and first-harmonic respectively versus the cell temperature; (a) experiment; (b) theory.

VI. Conclusions

In conclusion, we have implemented and characterized a Pulsed Optically Pumped frequency standard with optical detection. The frequency stability performances we achieved are among the best in the field of vapor cell clocks, both in the short and in the medium long term period.

We discussed also a technique to stabilize the microwave signal amplitude to the atomic signal. This technique is needed to control the drift of the clock frequency.

We also showed that due to the presence in our cell of large stems and because of a temperature gradient between the stems and the cell body, the clock frequency suffers of an unexpected large temperature sensitivity. To reduce it a tight control of the temperature stems has been implemented.

Finally, we discussed two phenomena that modify the shape of the Ramsey central fringe which results no more given by a simple cosine function of the microwave detuning but high-order harmonics may be present on the signal.

Acknowledgment

We thank E. Bertacco for his invaluable help.

References

[1] A. Godone, S. Micalizio, and F. Levi, "Pulsed optically pumped frequency standard", Phys. Rev. A vol. 70, p. 023409 (1-11), 2004.

[2] S. Micalizio, A. Godone, C. Calosso, F. Levi, C. Affolderbach and F. Gruet "Pulsed optically pumped Rubidium clock with high frequency - stability performance", IEEE Trans. Ultrason. Ferroelect. Freq. Control vol. 59, p. 457-462, 2012.

[3] S. Micalizio, C. E. Calosso, A. Godone, F. Levi, "Metrological characterization of the pulsed Rb clock with optical detection", Metrologia vol. 49, p. 425-436, 2012.

[4] C. E. Calosso, A. Godone, F. Levi, and S. Micalizio, "Enhanced temperature sensitivity in vapor-cell frequency standards", IEEE Trans. Ultrason. Ferroelect. Freq. Control vol. 59, p. 2646-2654, 2012.

[5] S. Micalizio, A. Godone, F. Levi, and C. Calosso, "Ramsey fringes shape in an alklai-metal vapor cell with buffer gas", unpublished

[6] R. Boudot, S. Guerandel, E. de Clercq, "Simple-Design Low-Noise NLTL-Based Frequency Synthesizers for a CPT Cs Clock", IEEE Trans. Instrum. Meas. vol. 58, p. 3659-3665, 2009.

[7] J. Vanier and C. Audoin, *The Quantum Physics of Atomic Frequency Standards*, Bristol, England: Adam-Hilger, 1989, pp. 1308-1310.

[8] E. I. Alekseyev, Y. N. Bazarov, and G. I. Telegin, Radio Eng. Electron. Phys. Vol. 20, p. 73, 1975.

[9] E. I. Alekseyev, Y. N. Bazarov, and A. E. Levishin, Radio Eng. Electron. Phys. Vol.19, p. 77, 1974.

[10] M. Abramowitz, *Handbook of Mathematical Functions With Formulas, Graphs, and Mathematical Tables*, Edited by M. Abramowitz and I. A. Stegun, National Bureau of Standards, Applied Math.55,1972.

Study of an Observation Method Based on Crossed Polarizers for High-contrast Coherent Population Trapping

Yuichiro Yano, Shigeyoshi Goka
Tokyo Metropolitan University
Hachioji, Tokyo, Japan
Email: yano-yuichiro@ed.tmu.ac.jp

***Abstract*—In this paper, we propose an observation method based on crossed polarizers to obtain high-contrast coherent population trapping (CPT) resonance with parallel linearly polarized light (lin‖lin field). Experimental results show that a high resonance contrast of 88.4 % can be observed using a ^{133}Cs gas cell and D_1-line vertical-cavity surface-emitting laser (VCSEL).**

I. Introduction

Atomic clocks based on coherent population trapping (CPT) resonance with a vertical-cavity surface-emitting laser (VCSEL) have attracted much attention for very small atomic references[1]. CPT atomic clocks are in great demand for many applications, such as, telecommunications, navigation systems, and synchronization of networks[2]. Atomic clocks are generally demanded for high frequency stability. In particular, short-term frequency stability is an important parameter for base stations of telecommunication systems. The short-term frequency stability, described as the Allan standard deviation $\sigma_y(\tau)$, is estimated as

$$\sigma_y(\tau) \propto \frac{\Delta f}{f_0}\frac{1}{SNR}\tau^{-1/2} \quad (1)$$

where Δf is the resonance linewidth, f_0 is the resonance frequency, and *SNR* is the signal-to-noise ratio. Contrast, which is generally used as a measure of *SNR*, is defined as the amplitude of CPT resonance over the background signal level[3]. Since short-term stability is determined from contrast and linewidth, both narrower linewidth and higher contrast are required to enhance short-term stability. A high-contrast CPT resonance can easily be observed in a high intensity laser field; however, the resonance linewidth broadened due to the power broadening effect[4]. It is difficult to enhance contrast together with linewidth. To solve this technical issue, a number of methods have been developed in the last decade (e.g., D_1 enhancement[5], pulsed CPT[6] , push-pull pumping[7],and polarization selective detection[8]).

In this paper, we focus on the Faraday effect in CPT and propose a method based on crossed polarizers for observing high-contrast CPT. The contrast and linewidth were measured using our proposed method and were compared with the results of the conventional observation method under the same experimental conditions using a ^{133}Cs gas cell and the D_1-line VCSEL. Since the Faraday effect is a magneto-optical phenomenon, we measured the dependence of resonance characteristics on transmission angle and magnetic field. The results show that transmission angle and magnetic field exist to maximize short-term stability. From these results, we conclude that our method has the potential to enhance the short-term stability of CPT atomic clocks.

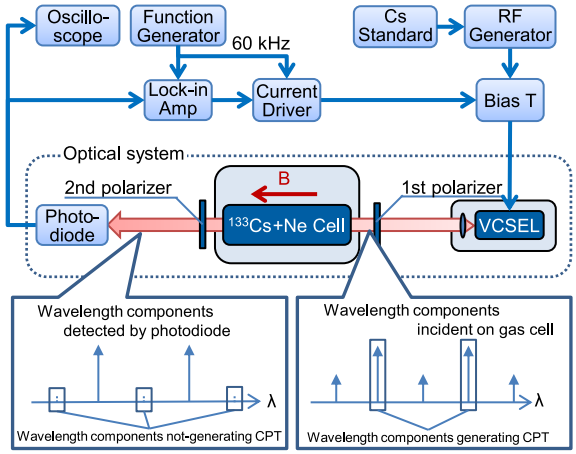

Fig. 1. Schematic of experimental setup

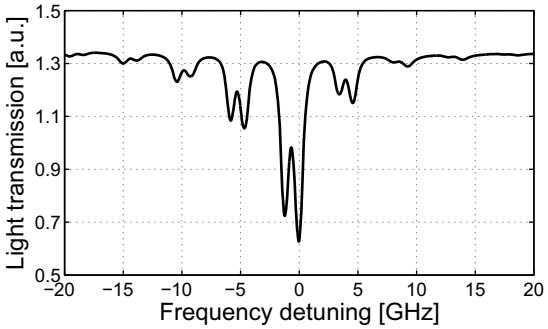

Fig. 2. Absorption profile of ^{133}Cs-D_1 line using VCSEL

II. Experimental Setup

Figure 1 shows the experimental setup of the proposed observation method. The two polarizers used near-infrared sheet polarizer. These polarizers were placed on both sides of the gas cell, and the transmission axes were set nearly

orthogonal to each other. Due to effect of the first polarizer, a parallel linear beam (lin$\|$lin field) was incident on the gas cell. The second polarizer selected the optical polarization of wavelength components incident on the photodiode. The light intensity signal transmitted through the second polarizer was detected by a photodiode, and the detected photodiode signal was connected to the oscilloscope.

The polarization of wavelength components that excited CPT was rotated by the Faraday effect while passing through the cell[10]. On the other hand, the polarization of wavelength components that did not excite CPT was not rotated. Therefore, the incidence of the non-exciting CPT wavelength components on the photodiode was suppressed by the second polarizer. As a result, the photodiode DC current could be reduced because the unwanted wavelength components incident on the photodiode decreased; thus, high-contrast CPT resonance could be obtained.

To excite CPT, we used a single-mode VCSEL fabricated by Ricoh Company, Ltd. The wavelength of the VCSEL is 895 nm to excite ^{133}Cs at the D_1-line. The VCSEL was driven by a DC injection current using a bias T and was modulated at 4.6 GHz using an analog signal generator to generate the first-order sidebands around the laser carrier. The absorption profile of the ^{133}Cs-D_1 line using VCSEL is shown in Fig.2. There were two absorption peaks in the transmitted light around a minimum, corresponding to two excited levels: $|F' = 3\rangle$ and $|F' = 4\rangle$. The frequency diffrence of the two excited states ($|F' = 3\rangle$ and $|F' = 4\rangle$) is sufficiently separated, that we can select excite state $|F' = 3\rangle$ or $|F' = 4\rangle$ as the absorption line. In this experiment, we selected $|F' = 3\rangle$ as an excited state to stabilize the wavelength of the VCSEL, since clock transition amplitude locking $|F' = 3\rangle$ is better than that of locking $|F' = 4\rangle$ under lin$\|$lin excitation [9].

A Pyrex gas cell containing a mixture of ^{133}Cs atoms and Ne buffer gas at a pressure of 2.0 kPa was used. The gas cell was cylindrical, it had a diameter of 20 mm and optical length of 22.5 mm. The gas cell temperature was maintained at 42.0 °C. The gas cell and Helmholz coil were covered with a magnetic shield to prevent an external magnetic field from affecting the magnetic field inside the cell. The internal magnetic field of the gas cell was created by Helmholz coil. The internal magnetic field was calibrated using the frequency diffrence between magnetic field insensitive transition and magnetic field sensitive transition by using σ-σ excitation. The axis of the magnetic field was set to be parallel to the direction of the laser light (C-axis direction). The frequency reference of the analog signal generator was connected to the Cs standard (Symmetricom 5071A High-performance tube).

III. Experimental results and Discussion

A. Line shape of CPT resonance with proposed method

Figure 3 shows the observed CPT resonance with the proposed method. When the transmission axis of the second polarizer was optimized, good reduction of background signal level (DC level) was achieved. Since the signal was greater than the DC level, the conventional contrast which was simply defined as sinal over DC level exceeded 100 %. In this paper, contrast is defined so as not to exceed 100% as follows.

$$\text{Contrast} := \frac{\text{Signal}}{\text{Signal} + \text{DC level}} \tag{2}$$

Although the DC level was suppressed by proposed method, weak light leakage occuerred and this light was received by the photo detector. The light leakage was caused by the lowness of the extinction ratio of the polarizers. Thus, if polarizers with higher extinction rate were used, the DC level could be suppressed. Owing to DC level reduction, the contrast reached 88.4 % with the proposed method. Since the contrast with the conventional lin$\|$lin observation method was 3.3 %, the contrast with our method was about 25 times better than that with the conventional method. And, a linewidth of 1.15 kHz is obtained with the proposed method. The linewidth was about twice as narrower as the conventional one of 2.15 kHz. This result means that the resonance with the proposed method has not only higher contrast but also narrower linewidth.

B. Contrast dependence on transmission angle of second polarizer

Figure 4 and 5 show the DC level and signal as a function of the transmission axis of the second polarizer. The magnetic field was set to 93 μT. The DC level was obtained as a quadratic function of the transmission angle of the second polarizer. The extinction rate of the polarizers was estimated to be about 10^4 from this result. The extinction rate was higher than that of a standard quarter-wave plate by several orders of magnitude. Since higher contrast was obtained with a higher extinction rate, the proposed method has an advantage over the polarization-selective method [8] using a quarter-wave plate.

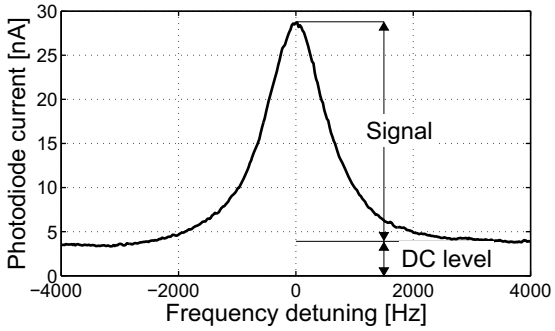

Fig. 3. Line shape of CPT resonance with crossed polarizers method

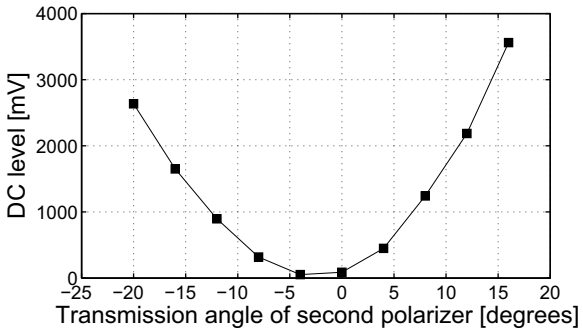

Fig. 4. DC level as a function of trasmission angle of second polarizer

By comparing the signal and DC level,it can be seen that the behavior of signal was different from that of the DC level. Therefore, this indicates that the polarization of wavelength components contributing to CPT was rotated. Figure 6 shows the contrast estimated from the signal and DC level. Since the signal has a high value despite DC level reduction, the contrast dramatically increased near 0°. In this experiment, a resonance contrast over 10 % was obtained in the range from -15 to 5°. Since the signal increased with increasing absolute value of transmission angle, even if the polarization rotation was small, it is expected that high contrast resonance can be obtained by appropriate adjustment of the transmission axis.

C. Characteristics dependence of magnetic field

Figure 7 shows the signal and DC level as a function of magnetic field in the range from 15 to 93 μT. The transmission angle of the second polarizer was optimized so as to maximize contrast. In weak magnetic fields ($<$ 15 μT), the signal was so small that we could not observe CPT resonance, and the maximum value of magnetic field of 93 μT was limited by the current source output supplying the Helmholz coil. The signal linearly increased with increasing magnetic field. On the other hand, the DC level was costant regardless of changes in the magnetic field. It is clearly shown that the Faraday rotation affected only the wavelength components contributing CPT. Figure 8 shows the contrast estimated from measured results. The contrast increased with increasing magnetic field. We assume that nearly 100 % contrast can be obtaiend in the strong magnetic field.

Next, we show the linewidth dependence of the magnetic field in Fig.9. The linewidth broadened with increasing magnetic field and approximately proportional to the magnetic field. However, the linewidth obtained with the proposed method is less than 2.15kHz of linewidth with the conventional excitation method in this range of magnetic field. The narrowest linewidth obtained was 760 Hz, which is about three

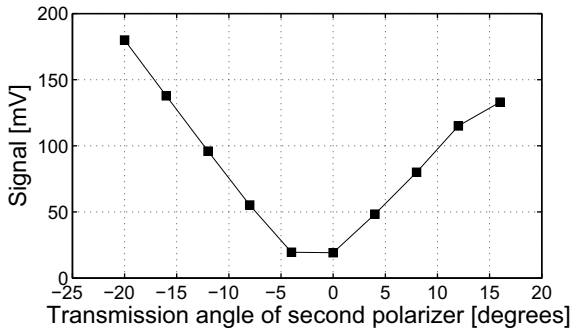

Fig. 5. Signal as a function of trasmission angle of second polarizer

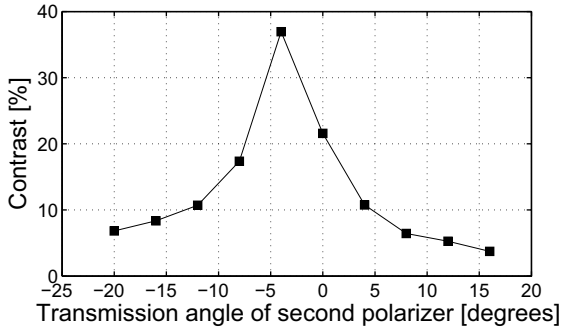

Fig. 6. Contrast as a function of trasmission angle of second polarizer

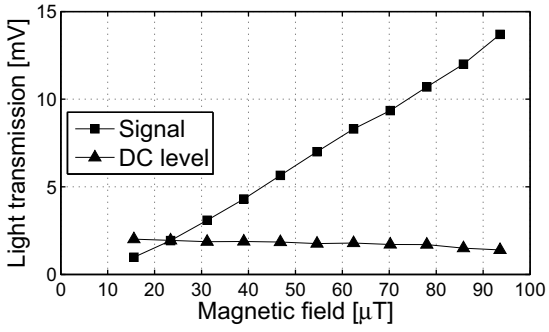

Fig. 7. Signal and DC level as a function of magnetic field

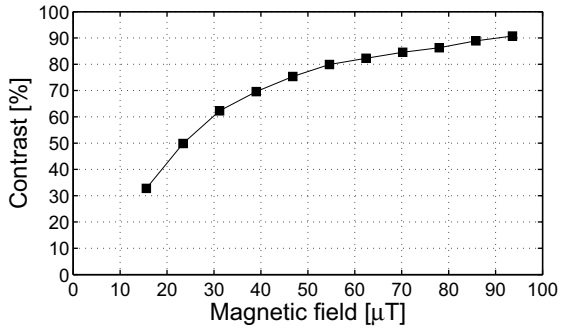

Fig. 8. Contrast as a function of magnetic field

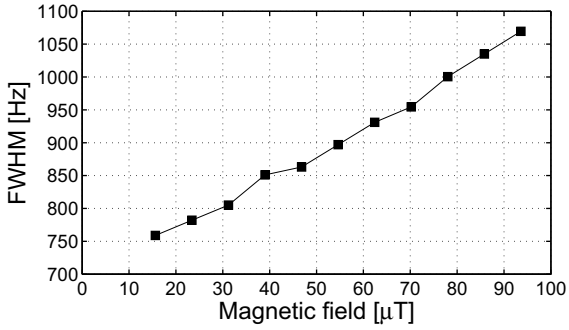

Fig. 9. Linewidth as a function of magnetic field

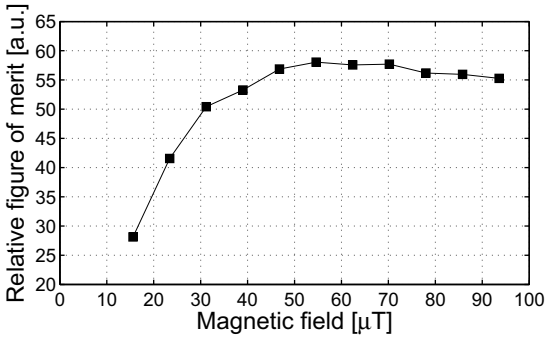

Fig. 10. Figure of merit as a function of magnetic field

times narrower than conventional one at a magnetic field of 5 μT.

Figure 10 shows the relative figure of merit (FoM) gainst changes in magnetic field. Since from Eq.(1) short-term stability is determined by contrast and linewidth, FoM is defined as follows.

$$\text{FoM} := \frac{f_0}{\Delta f} \cdot \text{Contrast} \tag{3}$$

In small magnetic fields ($< 40\mu$T), the FoM increased because the increase in contrast was dominant. However, in large magnetic fields ($> 60\mu$T), the FoM decreased with broadenning linewidth. Therefore, it is identified that magnetic strength exists so as to maximize the FoM of CPT resonance. In this experiment, the maximum value of FoM was obtained at 54.6 μT, and this value is 58 times better than the conventional one.

IV. Conclusion

We propose a new observation method based on crossed polarizers for observing high-contrast CPT resonance. When the transmission axis of second polarizer and magnetic field were optimized, the observed resonance had a contrast of 88.4% and linewidth of 1.15 kHz. Taking into account the 3.3% conventional contrast with lin$\|$lin excitation, the contrast with our method was about 25 times better than that with the conventional method. In addition to increasing the contrast, the linewidth with the proposed method was also two times narrower than the conventional one. We indicate that the resonance contrast and linewidth is dependent on the transmission angle of second polarizerand magnetic field. By optimizing the transmission angle of the second polarizer and magnetic field, the figure of merit was 58 times better than the conventional one. Therefore, this method has the potential to enhance the frequency stability of CPT atomic clocks.

Acknowledgment

The authors are grateful to RICOH Company, Ltd. for providing us with the Cs-D_1VCSEL.

References

[1] S. Knappe, V. Shah, P. D. Schwindt, L. Hollberg, and J. Kitching,"A microfabricated atomic clock" Appl. Phys. Lett. Vol. 85 (2004) p.1460.

[2] J. Vig, "Military Applications of High Accuracy Frequency Standards and Clocks", IEEE Trans. Ultrason. Ferroelectr. Freq. Control, Vol.40, No.5 (1993) p.522.

[3] R. Lutwak, D. Emmons, T. English, W. Riley,"THE CHIP-SCALE ATOMIC CLOCK - RECENT DEVELOPMENT PROGRESS" 35th PTTI Meeting pp.467-478.

[4] S. Knappe, R. Wynands, J. Kitching, H. G. Robinson, and L. Hollberg: J. Opt. Soc. Am. B **18** (2001) p.1545.

[5] M. Stähler, R. Wynands, S. Knappe, J. Kitching, L. Hollberg, A. Taichenachev, and V. Yudin, "Coherent population trapping resonances in thermal ^{85}Rb vapor: D_1 versus D_2 line excitation" Optics. Lett. Vol. 27, No. 16 (2002) pp.1472-1474.

[6] T. Zanon, S. Guerandel, E. de Clercq, D. Holleville, N. Dimarcq, and A. Clairong, "High Contrast Ramsey Fringes with Coherent-Population-Trapping Pulses in a Double Lambda Atomic System", Phys. Rev. Lett, **94**, 193002 (2005).

[7] Y.-Y. Jau, E. Miron, A. B. Post, N. N. Kuzma, and W. Happer, "Push-Pull Optical Pumping of Pure Superposition States", Phys. Rev. Lett, **93**, 160802 (2004).

[8] M. Zhu, "HIGH CONTRAST SIGNAL IN A COHERENT POPULATION TRAPPING BASED ATOMIC FREQUENCY STANDARD APPLICATION", IEEE FCS Proceeding 2003 pp.16-21.

[9] K. Watabe, T. Ikegami, A. Takamizawa, S Yanagimachi, S Ohshima, and S. Knappe, "High-contrast dark resonances with linearly polarized light on the D_1 line of alkali atoms with large nuclear spin", Applied Optics Vol. 48, No. 6 (2009).

[10] P. M. Anisimov, R. A. Akhmedzhanov, I. V. Zelensky, and E. A. Kuznetsova, "Influence of Transverse Magnetic Fields and Depletion of Working Levels on the Nonlinear Resonance Faraday Effect",Journal of Experimental and Theoretical Physics, Vol. 97, No. 5, 2003, pp. 868-874.

Frequency Stability Performance of a Laser Pumped Rubidium Vapor Cell Atomic Frequency Standard

M. Zhu
Agilent Laboratories
Agilent Technologies, Inc.
Santa Clara, CA, USA
miao_zhu@agilent.com

***Abstract*—The AC Stark shift (the light shift) is very important in the performance of laser-pumped vapor cell atomic frequency standards. The frequency stability of a compact rubidium vapor cell atomic frequency standard with an AC Stark shift suppression laser pumping method was evaluated. The applications of such a device include serving as primary reference clocks in communication systems such as Stratum 1 reference clocks.**

Keywords—AC Stark shift; light shift; vapor cell atomic frequency standard; frequency stability; optical pumping

I. INTRODUCTION

It is known that the AC Stark shift (the light shift), which is caused by the interaction between the atom and the applied optical field, plays an important role in the performance of laser-pumped vapor cell atomic frequency standards [1]. Methods have been developed to suppress/eliminate the negative impact of the AC Stark shift on vapor cell atomic frequency standards, both in the coherent-population-trapping (CPT) configuration [2–5] and in the population-altering-pumping (PAP) configuration [6–8]. For example, using a pulsed light source to pump a rubidium vapor cell eliminates the AC Stark shift because the rubidium atoms do not interact with the optical field when they are interrogated by the microwave field [6].

For a compact vapor cell atomic frequency standard, it is not trivial to implement a pulsed light source for optical pumping because of the need of an optical switch with a high extinction ratio such as an acousto-optic modulator and a separate vapor cell for laser frequency stabilization. Thus, a continuous wave optical pumping scheme in the PAP configuration was developed [7]. This method takes advantage of excited state hyperfine splitting in atoms to suppress the total AC Stark shift by adjusting the Rabi frequencies of the transitions between the clock transition energy levels and various hyperfine energy levels in the excited states of the atoms. Furthermore, the buffer gas pressure in the vapor cell is optimized to reduce the slope of the AC Stark shift with respect to the laser frequency detuning in the vicinity where the laser frequency is stabilized. The proof of concept results were reported using a large glass rubidium cell [7] and a micro-machined rubidium cell [8].

II. EXPERIMENT SETUP

Figure 1 depicts the experiment setup. A glass rubidium cell with an inner diameter of 8.5 mm and an inner length of 13.5 mm was embedded inside a microwave cavity/oven assembly. The rubidium D_1-line (λ = 795 nm) was used for optical pumping. The frequency of a diode laser was stabilized to the average frequency of the transitions of $|F = 2\rangle \rightarrow |F' = 1\rangle$ and $|F = 2\rangle \rightarrow |F' = 2\rangle$ by adjusting the injection current. The slow change of the laser power was corrected using the laser temperature. A neutral density (ND) filter attenuated the laser beam intensity while a half waveplate and polarizer set the laser beam polarization with respect to the direction of the bias magnetic field. The strength of the bias magnetic field was adjusted according to the measured frequency of the magnetic field sensitive transition $|F = 1, m_F = 1\rangle \rightarrow |F = 2, m_F = 1\rangle$.

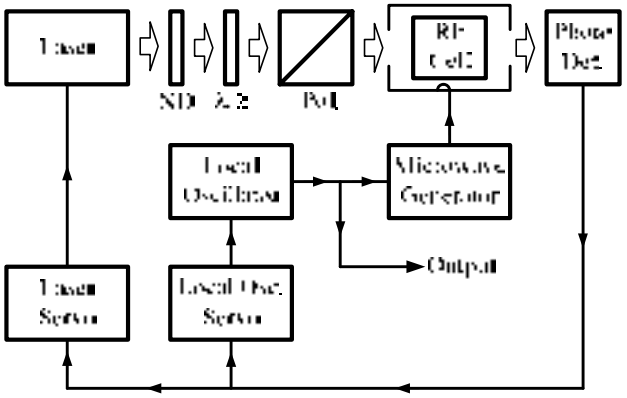

Fig. 1. Experiment setup. ND: neutral density filter. λ/2: half waveplate. Pol.: linear polarizer. The bias magnetic field and its adjustment are not shown in the figure (see text).

Figure 2 shows one of the initial measurements. Here the relative frequencies of the clock transition were measured with various total laser powers at three different linear polarization orientations. The measurement shows that indeed the AC Stark shift has been suppressed if the laser beam polarization is chosen correctly.

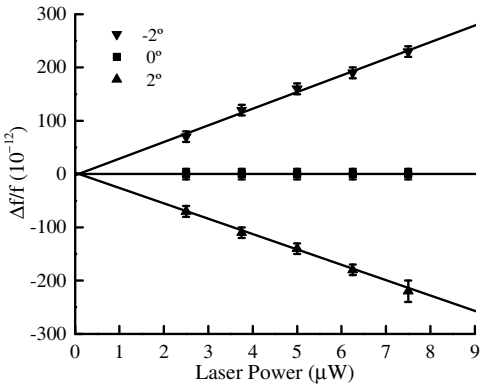

Fig. 2. Relative frequencies of the clock transition measured at various total laser powers and different linear polarization orientations. The reference direction (0°) was chosen to be the linear polarization direction that suppressed the total AC Stark shift.

III. Experiment Results

Several test runs were performed with the setup initially. After the various operating parameters were adjusted, the output frequency of the setup was measured continuously for more than 426 days. Figure 3 shows the measured short term frequency stability [9]. The expected performance of the reference system is also plotted in Fig. 3. It is seen that the measured Allan deviation is probably limited by the reference system in the averaging time between ~20 s and 10^5 s. Figure 4 shows that the relative frequency (averaging time = 1000 s) was bounded within $\pm 2.5\times10^{-12}$ during the entire measurement period.

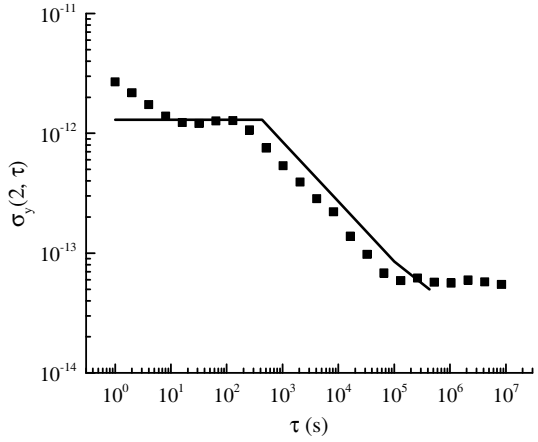

Fig. 3. Short term frequency stability. The squares represent experimental data. The solid line represents the expected performance of the reference system.

IV. Summary

A continuous wave population-altering-pumping method was implemented in a compact rubidium vapor cell atomic frequency standard to suppress the AC Stark shift. A short term frequency stability of $\sigma_y(\tau) < 3\times10^{-12}\ \tau^{-1/2}$ (τ in s) was obtained while the flicker frequency noise limited the longer term frequency stability to $\sigma_y(\tau) \approx 6\times10^{-14}$ for $10^5\ \text{s} < \tau < 10^7$ s. The absolute value of the relative frequency (averaging time = 1000 s) was measured as $<2.5\times10^{-12}$ during a measurement period of 426 days. The possible applications include serving as primary reference clocks in communication systems.

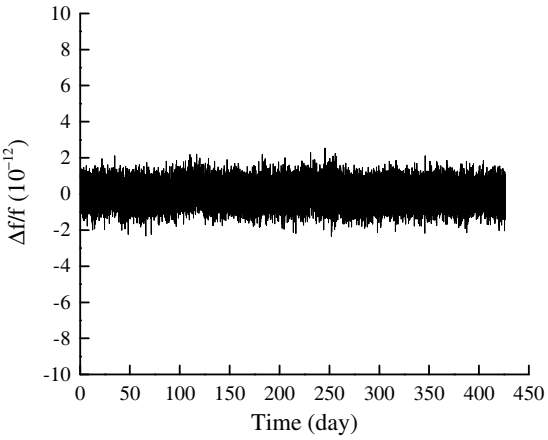

Fig. 4. Relative frequency (averaging time = 1000 s) vs. time.

Acknowledgment

The author thanks Frank Lucia for making various mechanical and electronic parts for this experiment. The author is grateful to Curt Flory, Jim Johnson, and Tad Weems for reading this manuscript carefully and providing many suggestions. The author is greatly indebted to Agilent Laboratories' management for supporting this work.

References

[1] See, for example, J. Vanier and C. Audoin, The Quantum Physics of Atomic Frequency Standards, Adam Hilger, (1989).

[2] M. Zhu and L. S. Cutler, Proceedings of the 32nd Annual Precise Time and Time Interval Systems and Applications Meeting, p. 311, (2000).

[3] M. Zhu and L. S. Cutler, US Patent 6,201,821 (2001).

[4] M. Zhu and L. S. Cutler, US Patent 6,363,091 (2002).

[5] See, for example, V. Shah, V. Gerginov, P. D. D. Schwindt, S. Knappe, L. Hollberg, J. Kitching, Appl. Phys. Lett., **89**, 151124 (2006).

[6] A. Godone, F. Levi, S. Micalizio, E. K. Bertacco, and C. E. Calosso, IEEE Trans. Instrum. Meas., **56**, 378, (2007).

[7] M. Zhu, Proceedings of IEEE International Frequency Control Symposium, 2007 Joint with the 22st European Frequency and Time Forum, p 1334 (2007).

[8] M. Zhu and J. DeNatale, Proceedings of IEEE International Frequency Control Symposium, 2009 Joint with the 22nd European Frequency and Time Forum, p 1183 (2009).

[9] D. Howe, *Proceedings of 1995 IEEE International Frequency Control Symposium*, p 337 (1995).

The Influence of Laser Polarization Noise on the Short-Term Stability of CPT Atomic Clocks

James Camparo, Michael Huang, and Travis Driskell
Physical Sciences Laboratories
The Aerospace Corporation, 2310 E. El Segundo Blvd.
El Segundo, CA 90245, USA
james.c.camparo@aero.org

***Abstract*— We have completed a series of experiments examining the effect of laser polarization noise on the short-term stability of a CPT atomic clock, when the CPT signal is generated in the "standard" fashion. Specifically, we have examined CPT signal amplitudes, CPT-signal noise, and CPT linewidths for various levels of randomly fluctuating circular polarization. We find that CPT signal amplitudes increase in the presence of polarization noise due to a decreasing efficiency of trapping states. However, we also find that CPT linewidths increase, since polarization fluctuations add to atomic dephasing, and that CPT-signal noise increases. This latter effect is due to bulk population movement between trapping states when the laser polarization changes. Consequently, more sophisticated CPT signal generation schemes that eliminate the trapping of atomic population might be more resilient to laser polarization noise.**

Keywords—atomic clocks, CPT, coherent population trapping, chip-scale clock, stochastic fields, polarization noise

I. Introduction

In the coherent-population-trapping (CPT) atomic clock, the microwave atomic signal is generated in an all optical fashion [1]. Briefly, sidebands are placed on the optical carrier at one-half the frequency of the ground state hyperfine splitting, ν_{hfs}, (i.e., 6.8 GHz for ^{87}Rb), and when the separation between the two sidebands, $2\Delta_s$, matches the ground state hyperfine splitting both levels are simultaneously coupled to the same excited state. Given that atomic excitation pathways interfere, when the two hyperfine states are coupled to the same excited state the pathways interfere destructively (i.e., the atom cannot make a real transition to the excited state). If the atoms cannot be excited, then there is no absorption of the laser light, and consequently the intensity of light transmitted by the vapor *increases*. The transmitted light thereby acts as a monitor of the atoms' interaction with a microwave signal (i.e., the laser sideband separation), and this can be used to lock the frequency of a quartz crystal oscillator to ν_{hfs}.

One obvious advantage to this design is that the microwave cavity of the traditional vapor-cell clock is eliminated. In addition to allowing for "chip-scale" atomic clocks [2], elimination of the microwave cavity removes many of the microwave power shifts that can give rise to frequency instability [3]. In particular, effects like alkali surface migration on the resonance cell's glass walls [4], which affect the microwave cavity Q, are eliminated. Nevertheless, though the CPT clock has real advantages over the conventional laser-pumped atomic clock [5], its novel nature suggests that it may be subject to new adverse processes that play little, if any, role in the conventional laser-pumped clock. One of these processes concerns the effect of laser polarization fluctuations on the CPT clock signal [6], which the present work investigates.

This work was funded by U.S. Air Force Space and Missile Systems Center under Contract No. FA8802-04-C-0001.

II. The Problem

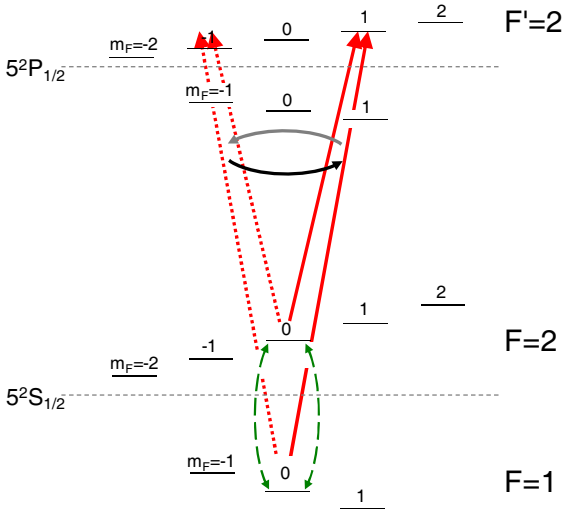

Fig. 1. In the typical CPT clock, two modes of a laser couple an atom's two $m_F = 0$ ground-state sublevels to the same excited state; here, the common excited sate is F' = 2, $m_F = +1$. The simultaneous coupling creates a coherence in the ground-state, indicated by the dashed green lines, and it this coherence that is at the heart of the CPT phenomenon. If the laser polarization fluctuates, then the common excited state will momentarily change to F' = 2, $m_F = -1$, and this will affect the ground-state coherence.

In the "standard" realization of the rubidium (Rb) CPT clock, the laser light is circularly polarized and connects the (F = 2, $m_F = 0$) and (F = 1, $m_F = 0$) ground state Zeeman sublevels to the (F' = 2, $m_F = +1$) Zeeman sublevel of the $5^2P_{1/2}$ excited state; this is illustrated in Fig. 1. As is well-known, this "lambda-system" coupling creates a coherence between the two $m_F = 0$ ground state sublevels, and it is this coherence that is at the heart of the CPT signal. If the circular polarization switches from right-circularly polarized light to left-circularly polarized and back again, then a transient will be introduced into the CPT signal since the common excited state changes:

(F' = 2, $m_F = +1$) → (F' = 2, $m_F = -1$) → (F' = 2, $m_F = +1$). If the polarization variations are stochastic [7], then the time series of these CPT transients will appear as noise on the CPT signal.

III. The Experiment

Figure 2 shows a block diagram of our experimental arrangement. We start with a cleaved-facet Fabry-Perot diode laser, which does not suffer intrinsic polarization fluctuations [8]. Though not shown in the figure, the laser light passes through an electro-optic modulator (EOM) that places sidebands on the laser at 3.4 GHz, and a neutral density filter. The modulated and linearly polarized field then passes through a ferroelectric liquid crystal (FLC) polarization rotator that has a bandwidth of 10 kHz. This polarization rotator changes the field's polarization by ninety degrees depending on an applied voltage supplied by a function generator. The field then passes through a quarter-wave plate, creating right or left circularly polarized light depending on the sense of linear polarization transmitted by the FLC polarization rotator.

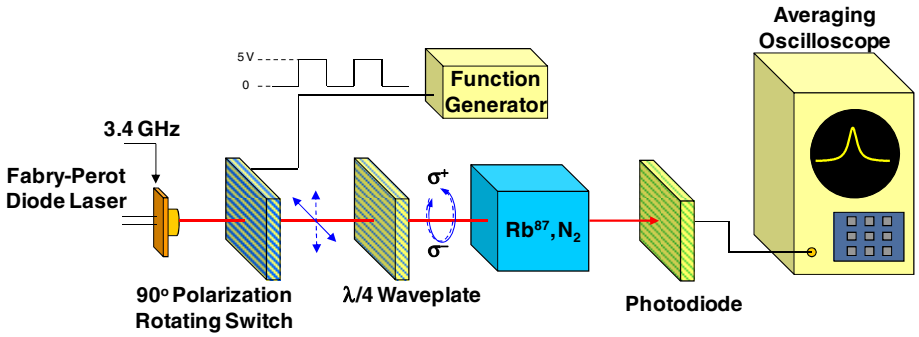

Fig. 2. Block diagram of our experimental arrangement. The Rb cell is maintained at 48 °C, corresponding to an alkali density of ~ 10^{11} cm^{-3}, and the Rb atoms are contained with a 50 torr N_2 buffer gas. The laser light passes through an electro-optic modulator (not shown) that places sidebands on the laser at ~ 3.4 GHz. In our experiments the sideband-to-carrier power ratio is 0.18, and we sweep the sidband spacing through the CPT resonance to generate the CPT lineshape. The sweep rate is relatively slow (i.e., 2.9 kHz/sec).

Our Pyrex resonance cell is 3.9 cm long with a 2.2 cm diameter, and for these experiments was maintained at 48 °C with braided heating wire wrapped around the cell body. The absorbance of the vapor, κ_o, was measured as 0.57: $I(L) = I_o e^{-\kappa_o}$ with I_o defined as $I_s 10^{-ND}$ (i.e., the sideband intensity after passing through the neutral density filter). The resonance cell was located in a set of three mutually perpendicular Helmholtz coils with a diameter of 66 cm: two pairs cancelled out the Earth's magnetic field, while the third provided a quantization axis for the atoms along the laser beam's propagation direction (i.e., B_z = 0.5 gauss). Our vapor of isotopically enriched ^{87}Rb vapor was contained with 50 torr of N_2, so that the dominant relaxation mechanism in our experiments was electron-spin randomization (also known as S-damping) [9].

In previous experiments, we investigated the response of the ^{87}Rb lambda system to a step-change in laser polarization [10]. We found that the *simplest* model capable of capturing the dynamics was an 8-parameter model, which indicates the complicated nature of CPT in the presence of polarization variations. Briefly, four parameters are needed to describe the re-establishment of electron-spin polarization following the laser's polarization change (i.e., movement of population from one "trapping state" to another), and four parameters are needed to describe the transient nutation that occurs in the CPT signal as the 0-0 coherence reestablishes equilibrium: a nutational amplitude, A_2, the dephasing rate, γ_2, a nutational frequency, $2\delta = 2\Delta\nu_s - \nu_{hfs}$, and a nutational phase, ϕ.

In separate experiments we also exposed the ^{87}Rb lambda system to squarewave laser-polarization modulation, and discovered that when the modulation frequency is greater than γ_2 the CPT resonance will split into a doublet [11]. This has implications for the short-term stability of CPT atomic clocks, since at a minimum it suggests that broadband polarization noise will degrade the CPT atomic-Q. Recently, we verified this prediction, and developed an Independent-Modulator Approximation theory to describe CPT signal amplitudes and linewidths in the presence of laser-polarization noise [12].

Here, we continue with this theme by considering not only the amplitude and linewidth of CPT signals in the presence of laser-polarization fluctuations, but also CPT-signal noise. To generate random laser polarization fluctuations, we first divide our sweep time across the CPT resonance, T = 1 sec, into subintervals δt, with $\delta t = 10^{-3}$ sec; and for each of these subintervals we define a Bernoulli distributed random variable, x(t), that can be either zero or one. Every time a one appears in the Bernoulli process, the function generator controlling the FLC changes: 0 → 5 V or 5 → 0 V. Thus, a zero in the Bernoulli process means that the laser-field's polarization remains constant, while a one implies that the polarization changes. Consequently, the number of polarization changes that occur over the entire time period of the sideband frequency sweep across the CPT resonance is equal to the number of ones that appear in the Bernoulli process over this period. If we define p as the probability for a one to appear in the Bernoulli process, then the mean number of polarization changes during a sweep, $\langle n \rangle$, will be given by $pT/\delta t$, and therefore the average polarization changing rate, R_p, is just $2\pi\langle n \rangle/T = 2\pi p/\delta t$. The fastest polarization-changing rate we can access in our experiment is $2\pi/\delta t = 6283$ s^{-1}, which is much faster than γ_2. In what follows, we characterize the stochastic polarization fluctuations by their correlation time, $1/\gamma_p \equiv -\delta t/\mathrm{Ln}[1-2p]$, which is derived in the Appendix.

Figure 3a shows an example of our CPT lineshape in the *absence* of stochastic polarization fluctuations for a relative

light intensity, I_o/I_s, of 6.3×10^{-2}, which is the light intensity that maximized the CPT contrast. The solid line through the data is a Lorentzian fit, which has a half-width half-maximum, $\Delta\nu_{1/2}$, of 580 s^{-1} (i.e., 92 Hz). Figure 3b shows an example of a CPT lineshape in the *presence* of stochastic polarization fluctuations; for this particular case p = 0.3. Comparison with Fig. 3a shows that the stochastic polarization fluctuations have led to a decrease in the CPT amplitude (i.e., $\Delta I_{CPT}/I_T = 0.22\%$), and a significant broadening of the CPT lineshape (i.e., $\Delta\nu_{1/2}$ = 1480 s^{-1}). Nevertheless, the CPT lineshape is still Lorentzian.

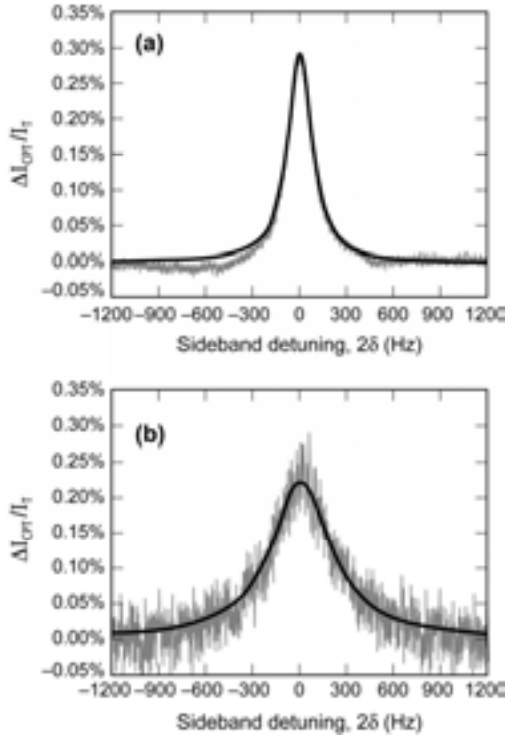

Fig. 3. (a) An example of our CPT lineshapes in the absence of stochastic polarization variations (i.e., p = 0); the data was taken with a relative light intensity, I_o/I_s, of 0.06, and the solid line through the data is a Lorentzian least-squares fit: Amplitude = 0.28% and $\Delta\nu_{1/2}$ = 580 s^{-1}. (b) An example of our CPT lineshape in the presence of stochastic polarization variations (i.e., p = 0.3); the data was taken with a relative light intensity, I_o/I_s, of 0.06, and the solid line through the data is a Lorentzian least-squares fit: Amplitude = 0.22% and $\Delta\nu_{1/2}$ = 1480 s^{-1}.

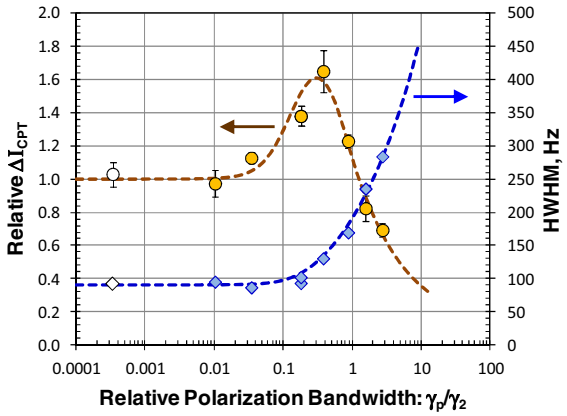

Fig. 4. Relative CPT signal amplitude and linewidth as a function of the polarization bandwidth. The points in white, furthest to the left, actually correspond to p = 0, and the dashed curves are simply aids to guide the eye.

Figures 4 and 5 show our principal results. In Fig. 4 we present the relative CPT amplitude and linewidth as a function of γ_p/γ_2. Note that as the polarization bandwidth, γ_p, increases there is an initial increase in the CPT amplitude as the trapping of atomic population is reduced. For large polarization noise bandwidths, however, this beneficial effect of polarization noise is lost [12]. Figure 5 shows the relative intensity noise (RIN), in a one hertz bandwidth and at a Fourier frequency of 327 Hz, as a function of γ_p/γ_2. The large increase in RIN with γ_p is due to the fact that large transmitted-light transients are induced in the signal following a polarization change as atomic population moves from one trapping state to another (i.e., $\langle S_z\rangle \Rightarrow -\langle S_z\rangle$) [12]. (The increase in RIN with γ_p for the laser tuned off resonance is due to the fact that the transmission of the FLC is not exactly balanced for its two polarization states.)

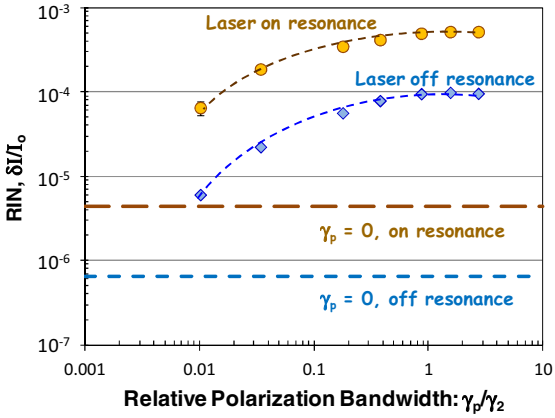

Fig. 5. Relative intensity noise (RIN) of the CPT signal as a function of the polarization bandwidth. The dashed lines through the data are simply meant as aids to guide the eye. Laser on/off resonance refers to the laser tuned on or off the Doppler-broadened absorption profile.

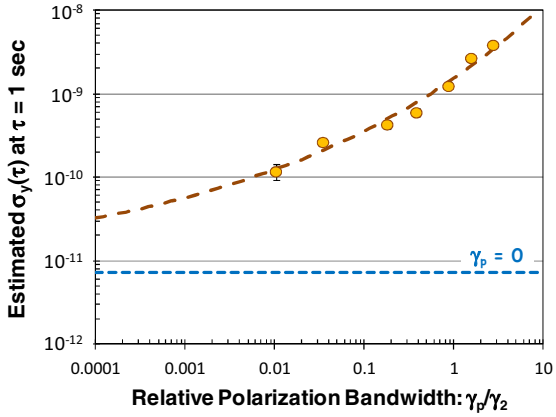

Fig. 6. Estimated performance of a CPT atomic clock as a function of polarization noise bandwidth. The dashed curve is a fit to the data.

Taking the short-term Allan deviation, $\sigma_y(\tau)$, as [13]

$$\sigma_y(\tau) = \frac{0.4\Delta\nu_{1/2}\times RIN}{\nu_{hfa}\left(\Delta I_{CPT}/I_o\right)}, \qquad (1)$$

Fig. 6 puts all of our data together to show the estimated short-term stability of a CPT clock as a function of the relative

polarization-noise bandwidth. Fitting the data to an empirical form, we get

$$\sigma_y(\tau) = \sigma_{y,o}(\tau)\,\mathrm{Exp}\left[A\left(\gamma_p/\gamma_2\right)^{\beta}\right], \qquad (2)$$

with $\sigma_{y,o}(\tau) = 8\times10^{-12}/\tau^{1/2}$, A = 5.36, and β = 0.138. Clearly, even for very low levels of laser polarization noise, there can be a dramatic loss of short-term frequency stability.

IV. Summary

We have completed experiments examining the effect of laser polarization noise on the short-term stability of a CPT atomic clock. For "moderate" polarization noise levels, we find that the CPT amplitudes increase due to a loss in the efficiency of trapping states when the laser polarization varies rapidly; this beneficial effect of polarization noise, however, cannot overcome the detrimental effects of polarization noise. In particular, at all levels of polarization noise there is an increase in the CPT signal's dephasing rate, and due to bulk population movement between trapping states there is a very large increase in the transmitted light's RIN.

Given the importance of population movement between trapping states under laser-polarization noise conditions, one must ask if more sophisticated CPT-signal generation techniques that reduce population trapping might not prove more resilient to laser polarization noise. In future work we plan to repeat our experiments using one or more of these sophisticated techniques (e.g., push-pull optical pumping [14]) in order to test this hypothesis.

Appendix

Let $\zeta(t)$ be a random process describing the polarization state of the laser: $\zeta = +1 \Rightarrow$ right-circularly-polarized light and $\zeta = -1 \Rightarrow$ left-circularly-polarized light, and constrain the polarization changes so that $\zeta(0) = +1$ (i.e., the random process always begins with the laser right-circularly-polarized). Then the polarization state of the field at some time t is just

$$\zeta(t) = (-1)^{k(t)} = \cos[k(t)\pi]\,. \qquad (A.1)$$

Here, k(t) is a binomial random process given by

$$k(t) = \sum_{i=1}^{n} x(t_i)\,, \qquad (A.2)$$

where $n \equiv t/\delta t$ = the number of "draws" of the Bernoulli random variable, x(t). The average value of $\zeta(t)$, $\langle\zeta(t)\rangle$, is then

$$\langle\zeta(t)\rangle = \sum_{k=1}^{n}\cos(k\pi)\binom{n}{k}p^k(1-p)^{n-k} = (1-2p)^{t/\delta t}, \qquad (A.3)$$

where $\binom{n}{k}$ is a binomial coefficient.

To compute the power spectrum, we first compute the correlation function of $\zeta(t)$:

$$\zeta(t)\zeta(t\pm\tau) = (-1)^{2k\pm m} = \cos(m\pi), \qquad (A.4)$$

where m is the number of polarization changes in the time interval τ. This, however, is just given by Eq. (A.3) with n replaced by $m = |\tau|/\delta t$. To obtain the power spectrum, we take advantage of the Wiener-Khintchine relations:

$$L(\omega) = \int_{-\infty}^{\infty} e^{-i\omega\tau}\langle\zeta(t)\zeta(t\pm\tau)\rangle d\tau = \int_{-\infty}^{\infty} e^{-i\omega\tau}(1-2p)^{|\tau|/\delta t}\,d\tau\,. \qquad (A.5)$$

Equation (A.5) yields a Lorentzian spectrum with a correlation time, γ_p^{-1}, equal to $-\delta t/\mathrm{Ln}[1-2p]$:

$$\frac{L(\omega)}{N} = -\frac{1}{\pi}\frac{\delta t\,\mathrm{Ln}[1-2p]}{(\mathrm{Ln}[1-2p])^2 + (\omega\,\delta t)^2}, \qquad (A.6)$$

where N is a normalization constant.

References

[1] J. Vanier, "Atomic clocks based on coherent populatin trapping: A review," Appl. Phys. B, vol. 81(4), pp. 421-442, 2005.

[2] S. Knappe, V. Shah, P. D. D. Schwindt, L. Hollberg, and J. Kitching, "A microfabricated atomic clock," Appl. Phys. Lett., vol. 85(9), 1460-1462, 2004; R. Lutwak, J. Deng, W. Riley, M. Varghese, J. Leblanc, G. Tepolt, M. Mescher, D. K. Serkland, K. M. Geib, and G. M. Peake, "The chip-scale atomic clock – low-power physics package," in Proc 36th Annual Precise Time and Time Interval (PTTI) Meeting. Washington, DC: US Naval Observatory, 2004, pp. 339-354.

[3] A. Risley, S. Jarvis, Jr., J. Vanier, "The dependence of frequency upon microwave power of wall-coated and buffer-gas-filled gas cell Rb^{87} frequency standards," J. Appl. Phys., vol. 51(9), pp. 4571-4576, 1980.

[4] J. G. Coffer, B. Sickmiller, and J. C. Camparo, "Cavity-Q aging observed via an atomic-candle signal," IEEE Trans. Ultrason. Ferroelec. & Freq. Control, vol. 51(1), pp. 139-145, 2004.

[5] J. Vanier, M. W. Levine, D. Janssen, and M. J. Delaney, "On the use of intensity optical pumping and coherent population trapping techniques in the implimentation of atomic frequency standards," IEEE Trans. Instrum. Meas., vol. 52(3), pp. 822-831, 2003.

[6] M. Huang, J. G. Coffer, and J. C. Camparo, "CPT transients induced by rapid changes in laser polarization: Validation of a semi-empirical model," J. Phys. B: At. Mol. Opt. Phys., vol. 43, 135001, 2010.

[7] J. Kaiser, C. Degen, W. Elsässer, "Polarization-switching influence on the intensity noise of vertical-cavity surface-emitting lasers," J. Opt. Soc. Am. B, vol. 19(4), pp. 672-677, 2002.

[8] J. C. Camparo, "The diode laser in atomic physics," Contemp. Phys., vol. 26(5), pp. 443-477, 1985.

[9] F. A. Franz, "Relaxation mechanisms in optical pumping," Phys. Rev., vol. 141(1), pp. 105-112, 1966.

[10] M. Huang, J. Coffer, and J. Camparo, "CPT transieints induced by rapid changes in laser polarizaiton: Validation of a semi-empirical model," J. Phys. B: At. Mol. Opt. Phys. 43, 135001 (2010).

[11] M. Huang and J. Camparo, "Coherent population trapping under periodic polarization modulation: Appearance of the CPT doublet," Phys. Rev. A 85, 012509 (2012).

[12] M. Huang, T. Driskell, and J. Camparo, "Coherent population trapping and polarization fluctuations: The independent-modulator approximation for coherent-population-trapping line shapes," Phys. Rev. A 87, 053419 (2013).

[13] J. Vanier and L.-G. Bernier, "On the signal-to-noise ratio and short-term stability of passive rubidium frequency standards," IEEE Trans. Instrum. and Meas. 30, 277-282 (1981).

[14] Y.-Y. Jau, E. Miron, A. Post, N. Kuzma, and W. Happer, "Push-pull optical pumping of pure superposition states," Phys. Rev. Lett. 93, 160802 (2004).

Sensor Design and Characterization Method for New Multimode Downhole Sonic Measurements

Hiroshi Hori, Yuichiro Wada, Hiroshi Nomura, Atsushi Oshima,
Tadashi Tajima, Junko Fujikawa, Takeshi Fukushima
Sonic Product Line,
Schlumberger K.K.
Kanagawa, Japan
hori1@slb.com

***Abstract*—Downhole sonic measurements provide compressional and shear wave propagation speeds of formations for hydrocarbon exploration purposes. We developed a new logging-while-drilling (LWD) tool that provides shear speed measurements in oil wells that are drilled in slow formations, where shear head waves are not excited using the conventional monopole source. To provide quality multimode measurements, azimuthally distributed transmitter and receiver elements of good output or sensitivity matching are required. We designed such devices, characterized them in-house, and tested them in the oil wells. This paper introduces our downhole sonic tool development method, focusing on receiver characterization and results.**

Keywords—downhole multimodes measurements, logging-while-drilling sonic tool, receiver sensitivity matching

I. INTRODUCTION

Tools for downhole sonic measurement were developed about half a century ago as a part of a suite of geophysical survey tools used to explore for hydrocarbons. By the 1990s, with the development of digital electronics, downhole sonic tools provided the measurements using array receivers and multiple transmitters, with computer-controlled data acquisition and a digital signal processing system [1]. Compressional- and shear- (or P- and S-) wave propagation velocities are inverted from full waveforms using semblance methods [2]. Combined with body wave velocity and density from nuclear measurements, sonic measurements are used to characterize a formation in terms of its mechanical properties.

The conventional measurements are limited for fully characterizing formation rock, especially in a "slow formation," a formation that has a slower shear wave propagation speed than that of well fluid. Shear refracted waves cease to be present under such a condition. An alternative measurement—shear slowness inversion from borehole modes—has been invented for such a case. The first multimode sonic measurements were developed for the wireline tool using a dipole source [3]. Shear velocities are inverted from borehole flexural signals utilizing model-based inversion techniques. Dispersion curves are sensitive to radial and azimuthal velocity variation in the formation near the wellbore surface location. Borehole stresses, induced by drilling and/or tectonic stresses, are one of the causes of such velocity variations, and advanced sonic measurements are useful not only to provide shear slowness in slow formation, but also for better understanding of the borehole stress state [4]. Such information is valuable when provided during the early stage of well drilling for safe and effective well placement. For this reason, the demand for logging-while-drilling (LWD) measurements is increasing.

We developed a new multimode sonic tool using a borehole quadrupole mode for LWD application. This paper introduces the sonic tool development process and the characterization methods, using the latest tool as an example.

II. SONIC TOOL DEVELOPMENT PROCESS

Development of a downhole sonic tool includes designing an acoustic measurement system. Fig. 1 shows the acoustic tool development process. Items in blue boxes are the key building blocks of both the base technologies and the human resources, whose areas of expertise are acoustics/physics, sensors, experiments, mechanics, electronics, embedded and acquisition software, signal processing, data evaluation and interpretation, and field operation. For sonic tool development, we start from numerical modeling to understand borehole acoustics under the presence of the tool structure. Hardware prototypes are built using technologies that enable measurement under harsh drilling conditions of high temperature (150 ^{o}C) and pressure (170 MPa), and mechanical shocks while deploying the tool kilometers below the surface. After building prototype parts, we integrate them into the tool and characterize the tool using in-house test facilities. The characterized tool is sent to the field to acquire data, and we then validate new measurements by comparing them with existing available measurements.

We apply and iterate the development process to design our acoustic measurements through the entire development cycle.

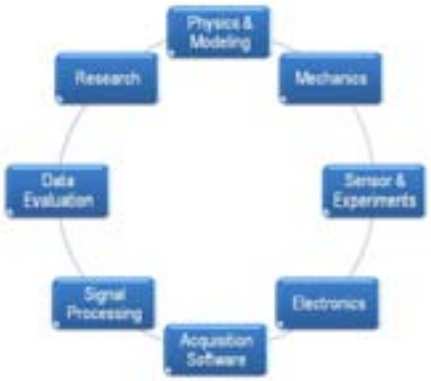

Fig. 1. Acoustic tool development process.

III. SONIC TOOL STRUCTURE OVERVIEW

LWD tools are mechanically designed as a part of rigid drill pipes. Fig. 2 shows a schematic view of the latest LWD multimode sonic tool. The nominal diameter and length of the tool are 0.12 and 9 m, respectively. The transmitter and receivers are mounted on the outer surface of the collar. The attenuator is a set of grooves that are machined on the inner surface of the collar to attenuate and delay direct tool arrivals. In monopole mode, the grooved section effectively attenuates and delays the pipe extensional mode signal. Details of the groove design methodology are introduced separately from this paper [5]. For slow shear inversion, we utilize borehole quadrupole mode. Unlike the wireline dipole sonic tool, a rigid LWD collar is not suitable for dipole measurements. The collar dipole mode is strongly coupled with the borehole flexural mode, and makes shear inversion challenging. On the other hand, the collar quadrupole mode is less coupled to the borehole mode in the range of borehole modes of interest.

The transmitter consists of four identical units positioned on the collar every 90°. Fig. 3 presents the schematic view of four units on the left as red and blue circles, particle displacement of fluid in the middle, and the azimuthal profile in the right. Monopole and quadrupole pressure fields are excited, respectively, when two diagonally paired units are operated in the same and opposite polarities. Drive circuits excite the transmitter in the wide frequency band from about 1 kHz to 20 kHz.

Four receiver arrays are mounted on the collar every 90° at a position in line with the transmitter units to receive the borehole quadrupole mode at the most efficient direction. The piezoceramic receiver element converts acoustic pressure into an electrical signal. Four azimuthal receiver positions relative to the borehole quadrupole are illustrated in Fig. 4. The black curve and blue circles, respectively, show the azimuthal pressure profile and four receiver element positions. Receiver elements are connected to amplifiers and digitization circuits near the elements. The time series of signals undergo digital modal decomposition before recording. Modal pressure is the sum of cosine-weighted azimuthal signals, as shown in Eq. 1, where $p_i(t)$ and $pn(t)$ are, respectively, the time series of acoustic signals recorded at i th (i=1,2,3,4) receiver and the resulting modal signal, θi, is the azimuth of the receiver, and n is the borehole mode order. Monopole and quadrupole mode numbers are 0 and 2, respectively.

One receiver array has 12 channels or elements, which are spaced at 100 mm, as illustrated in Fig. 5. Twelve modal pressure waveforms are computed using four receivers at the same transmitter-receiver spacing. When the transmitter is fired in monopole and quadrupole mode, 12 modal signals are recorded and used for slowness computation. Raw waveforms are intermittently stored for quality control.

Fig. 2. LWD sonic tool.

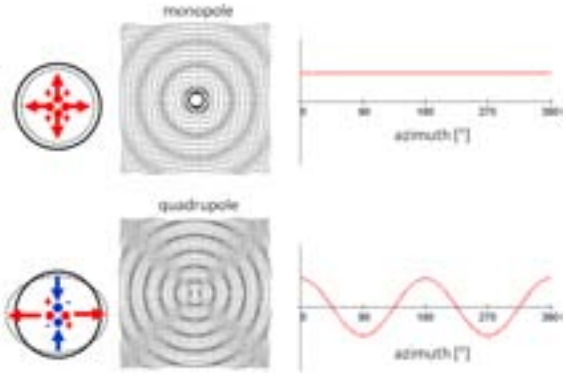

Fig. 3. Monopole and quadrupole mode excitation.

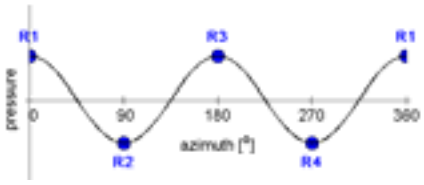

Fig. 4. Quadrupole azimuthal pressure profile and four receivers.

$$pn(t) = \frac{\sum_i p_i(t) \cdot \cos(n \cdot \theta_i)}{\sum_i \cos^2(n \cdot \theta_i)} \qquad \text{(Eq. 1)}$$

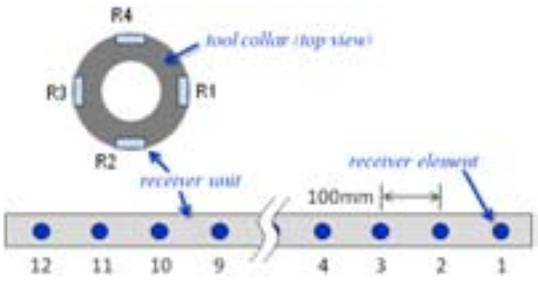

Fig. 5. Receiver array unit.

During drilling, sonic tools may be eccentered in the borehole and, with excitation, may record undesired signals because of this eccentering. In this situation, borehole excitation and received signals are no longer pure modal pressure, even using perfectly matched transmitter units and receiver elements. To minimize tool eccentering, stabilizers are added at the top and bottom of the tool. Transmitter output and receiver sensitivity matching help minimize modal signal contamination by unwanted modes. Below we discuss receiver characterization and evaluation methods using in-house test facilities.

IV. RECEIVER SENSITIVITY MATCHING EVALUATION

Multiple hydrophone and sonar calibration methods have been discussed in the past [6, 7]. Such methods are useful for receiver element characterization but are not always applicable to receivers assembled together with electronics. When elements are mounted on a structure, the sensitivity might vary because of surrounding structures, such as packaging and tool collar. For the multimode sonic tool, relative sensitivity of receivers was evaluated as a receiver array unit assembly, before and after integrating into the tool.

We characterized the sonic tools and receiver unit assemblies in a water pit, a part of the in-house test facilities. The water pit is a 9-m^3 tank that is useful for acoustically characterizing their free-field responses above the frequency of 1 kHz, under ambient pressure and temperature conditions.

A downhole tool is mainly operated under higher pressure and temperature, so environmental tests are important to finalize the design. Sensitivity measurements in such an environment are not trivial because there is no commercially available reference sound source or reference hydrophone for these measurements. Moreover, the electrical connections inside and outside a pressure vessel require special pressure-tight feedthrough with long cables. On the other hand, for the downhole sonic measurements, relative sensitivity matching has always been of primary interest, and methods for calibration or receiver sensitivity equalization have already been developed for the wireline sonic tools [8].

To evaluate sentivity matching, we assemble receiver and transmitter units on the tool and record pipe extensional mode signals in a high pressure and temperature vessel. The transmitter is operated in monopole mode. Pipe extensional mode propagates as the dominant and fastest arrivals at the receiver and is followed by other unwanted modes, including the direct collar arrivals, so that the signal amplitude of this extensional mode is representative of receiver sensitivity compared with other later arrivals. Fig. 6 presents a schematic view of receivers in the pipe and the photo of the vessel. Signals are acquired at six different combinations of pressure and temperature.

Fig. 7 presents recorded pipe-mode signal amplitude versus receiver channels. The horizontal and vertical axes are channel numbers and amplitude in arbitrary units. Curves in four different colors are signals from four azimuthal receiver arrays. From the left to right, we present amplitude recorded at three different pressures of 170, 135, and 100 MPa. Temperature was 150 ^{o}C. From four azimuthal signal amplitudes at the same channel number, we compute their average and azimuthal amplitude deviation from the average. Fig. 8 presents the devitation normalized by the average. We consider this deviation as representative of the sensitivity matching error. This method is not useful for absolute sensitivity measurements, but for characterizing relative azimuthal sensitivity matching.

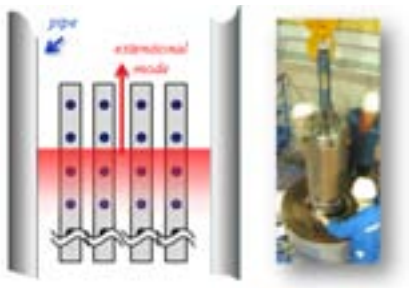

Fig. 6. Sensitivity test at high pressure and temperature.

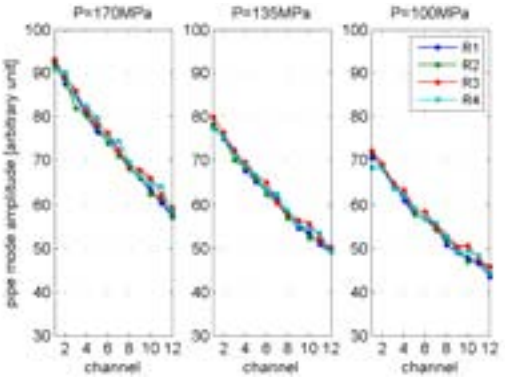

Fig. 7. *Pipe mode amplitude trend of four receiver arrays.*

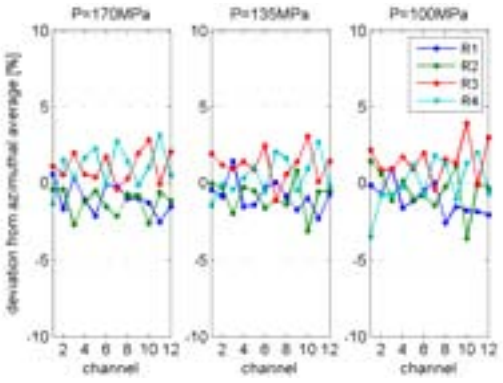

Fig. 8. Normalized amplitude deviation from azimuthal average.

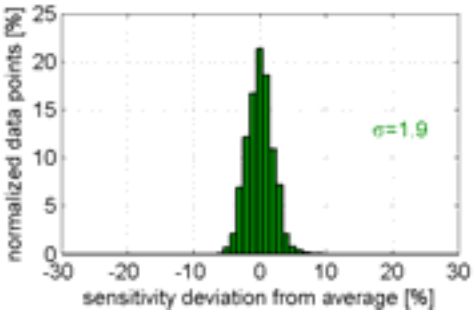

Fig. 9. Relative sensitivity distribution of LWD downhole receivers.

The results may include systematic error, such as submillimeters of tool eccentering in the pipe; however, thanks to the rigid LWD tool structure, mechanical alignment is nearly at the limit of precise tool position control, which is relatively easier than with the wireline tool. We evaluated the sensitivity deviation of the new LWD sonic receivers using 12 different tools at six different pressure and temperature conditions, for a total of 3,456 data points.

Fig. 9 presents the histogram of relative sensitivity distribution of downhole receivers obtained as the result of high pressure and temperature tests. The horizontal and vertical axes are sensitivity deviation from the average and quantity of data points in percentage values, after normalizing them respectively by the average and total data points. Relative sensitivity is distributed smoothly with the standard deviation of 1.9%. This number is satisfactory for sonic slowness computation purposes.

In the past, we applied a sensitivity correction or equalization to some downhole tools, compensating for receiver element sensitivity variation. For the newly developed LWD downhole receivers, we do not require a sensitivity correction.

The tool has been characterized in oil wells while drilling and has been proven to deliver a quality multimode waveform recording and a successful slowness inversion [9].

V. CONCLUSIONS

We successfully developed the latest LWD sonic tool that provides formation slowness from the conventional monopole and the newly developed quadrupole measurements, following our acoustic tool development process. One of the key design elements for quality multimode measurements is receiver sensitivity matching. We designed a new receiver array, developed a methodology for evaluating sensitivity matching at high pressure and temperature conditions, and demonstrated good sensitivity matching using more than 500 receiver elements.

ACKNOWLEDGMENT

We thank Fernando Garcia-Osuna, Alain Dumont, and Tetsuya Tanaka, who initiated new sensor designs and provided valuable advice through development cycle.

REFERENCES

[1] J. Aron, S. K. Chang, R. Dworak, K. Hsu, T. Lau, J-P. Masson, J. Mayes, G. McDaniel, C. Randall, C. Kostek, and T. J. Plona, "Sonic compressional measurements while drilling," SPWLA 35th Annual Logging Symposium, 19–22 June 1994.

[2] C. V. Kimball and T. L. Marzetta, "Semblance processing of borehole acoustic array data," Geophysics, vol. 49, no. 3, pp. 274-281, March 1984.

[3] V. Pistre, T. Kinoshita, T.Endo, K.Schilling, J.Pabon, B.Sinha, T.Plona, T.Ikagami, and D.Johnson, "Modular wireline sonic tool for measurements of 3D (azimuthal and axial) formation acoustic properties," SPWLA 46th Annual Logging Symposium, 26–29 June 2005.

[4] T. Plona, B. Sinha, M. Kane, R. Shenoy, S. Bose, J. Walsh, T. Endo, T. Ikegami, and O. Skelton, "Mechanical damage detection and anisotropy evaluation using dipole sonic dispersion analysis," SPWLA 43rd Annual Logging Symposium, 2–5 June 2002.

[5] T. Kinoshita, A. Dumont, H. Hori, N. Sakiyama, J. Morley, and F. Garcia-Osuna, "LWD sonic tool design for high-quality logs," SEG Annual Meeting, 17–22 October, 2010.

[6] L. G. Beatty, R. J. Bobber, and D. L. Phillipes, "Sonar transducer calibration in a high-pressure tube," J. Acoustictics Society of America, vol. 39, no. 1, pp.48-54, 1966.

[7] Bobber, R. J. Underwater Electroacoustic Measurements, 2nd ed. Los Altos: Peninsula, Los Altos, 1988, pp. 1–16.

[8] F. Garcia-Osuna and T. Ikegami, ,"Methods and systems for calibrating acoustic receivers," U. S. Patent 7,085,194 B2, 2006.

[9] D. Scheibner, S. Yoneshima, Z. Zhang, W. Izuhara, Y. Wada, P.Wu,, F. Pampuri, and M.Pelerosso, "Slow formation shear from an LWD tool: quadrupole inversion with a Gulf of Mexico example," SPWLA 51st Annual Logging Symposium, 19–23 June 2010.

Analysis of the Detection of Organophosphate Pesticides in Aqueous Solutions Using Polymer-Coated SH-SAW Sensor Arrays

Tian Newman, Fabien Josse, Arnold Mensah-Brown, Florian Bender
Dept. of Electrical and Computer Engineering
Marquette University
Milwaukee, WI, USA
fabien.josse@mu.edu

***Abstract*—There is a need for on-site and real time detection of organophosphate pesticides in aqueous environments. This work proposes the use of polymer coated shear horizontal surface acoustic wave (SH-SAW) sensors as a sensing platform for detection of organophosphate pesticides in aqueous environments. The chemically sensitive polymer coatings BPA-HMTS and BPA-PDMS, synthesized in-house, and the commercially available polymer PECH, were chosen as sensor coatings for organophosphate detection. The polymers are characterized at various thicknesses (0.25µm and 0.50µm) for their selectivity and sensitivity towards parathion, parathion-methyl, and paraoxon. A sensor array is designed for analyte identification and quantification using both steady-state and transient response information. Analyte identification is performed using a visual pattern recognition technique based on radial plots for the analytes at concentrations from 0.5mg/L to 3.0mg/L. It is shown that using the absorption time constant, which is unique to a given analyte-coating pair, in conjunction with steady-state frequency shifts permits direct identification and quantification of organophosphate pesticides in liquid-phase at low-ppm and sub-ppm concentrations.**

Keywords—shear horizontal surface acoustic wave (SH-SAW), liquid-phase detection, organophosphate pesticides, sensor array, pattern recognition, transient response information

I. INTRODUCTION

Hazardous contaminants in groundwater and surface water can have a serious effect on public health. One of the most common types of contaminants is pesticides, including organophosphate pesticides, which are used by the agro-industry due to their potency and effectiveness to kill insects. Although this class of contaminants is highly efficient as pesticides, they can reside in the environment and seep through the soil, and enter groundwater. Because of their solubility in water, they can easily be absorbed into the human body [1, 2]. Organophosphates have toxic effects on the human body, in particular the brain and nervous system [3]. Due to their high toxicity level, the US Environmental Protection Agency banned the use of organophosphates indoors and continues to monitor their output in industrial and agricultural settings. Current means of detection for organic compounds are time consuming, costly, and require samples to be collected and taken to the lab for analysis [4]. This procedure may also be inadequate because of loss of information during transportation. Therefore, there is a critical need for a portable, low cost sensor for on-site, real time detection of organophosphate pesticides in groundwater and surface water.

In this work, an array of polymer coated shear horizontal surface acoustic wave (SH-SAW) devices is used as sensing platform for identification and quantification of organophosphates in water. SH-SAW is the most promising and sensitive type of acoustic waves for liquid-phase sensing [5]. The polymers used as partially chemically selective coatings on the SH-SAW devices are 2,2'-diallylbisphenol A - 1,1,3,3,5,5-hexamethyltrisiloxane (BPA-HMTS), 2,2'-diallylbisphenol A- polydimethylsiloxane (BPA-PDMS), and polyepichlorohydrin (PECH). These polymers were chosen as effective sorbents for the target analytes, with desirable properties including high sensitivity, short response time, as well as reversible and reproducible response [6, 7]. The chemical contaminants tested are organophosphate-based compounds (parathion, parathion-methyl, and paraoxon).

The most important characteristics of a sensor are its sensitivity and selectivity. A chemical sensor array is used to increase selectivity and allow single analyte identification in multicomponent samples. An array of sensors was designed consisting of devices with different coatings and coating thicknesses (0.25µm and 0.50µm) to identify a target analyte and estimate its concentration. The time responses and steady-state frequency shifts were extracted from the response curves and used as input parameters for data processing to achieve both analyte identification and quantification. The analyte identification was performed using visual pattern recognition techniques and analyte quantification was achieved using the same approach as in Ref. 8.

II. EXPERIMENTS

A. Sensor Design

Fig. 1 shows the SH-SAW device used as a sensing platform in this work [9, 10]. This configuration uses a three-layer geometry: the liquid layer, polymer layer, and substrate. The device is fabricated on 36° rotated Y-cut, X-propagating

This work was supported in part by the NSF/IUCRC Program.

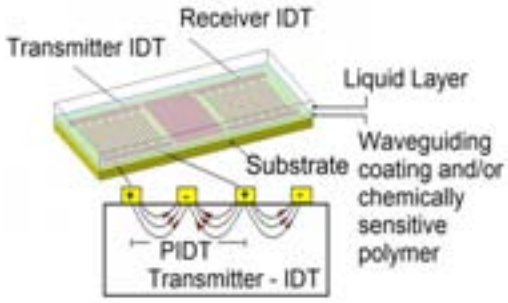

Fig. 1. Three layer acoustic wave sensor geometry

lithium tantalate ($LiTaO_3$) with 10/80nm thick Cr/Au interdigital transducers (IDTs) with a wavelength of 40 μm, giving an operating frequency of 103 MHz. The polymer acts both as a sensing layer and waveguiding layer, trapping the acoustic energy of the SH-SAW to the surface of the device, thus making it more sensitive to surface perturbations. The liquid layer is considered to be a Newtonian fluid and contains the analyte. The particle displacement of a SH-SAW is parallel to the surface and perpendicular to the direction of propagation to avoid acoustic attenuation due to coupling to compressional waves in the adjacent liquid.

B. Materials

Chloroform (99.8%), acetone (99%), methanol (99%), anhydrous toluene (99.8%), 2-propanol, monobasic dihydrogen phosphate, 1,1,3,3,5,5 hexamethyltrisiloxane (HMTS), Platinum(0)-1,3- divinyl-1,1,3,3-tetramethyldisiloxane (Pt-DVTMDS) complex solution in xylene (Pt ~2 %), 2,2'-diallylbisphenol A (BPA), poly(dimethylsiloxane), hydride terminated (PDMS), dibasic monohydrogen phosphate, parathion, parathion-methyl, and paraoxon were purchased from Sigma-Aldrich and used as supplied.

C. Polymer Synthesis

Hybrid organic/inorganic chemically sensitive layers BPA-HMTS and BPA-PDMS were synthesized using a hydrosilyation reaction [6, 7] and making modifications to a procedure reported by Grate et al [7]. BPA is an organic chemical that serves as the functional group for analyte/coating interaction [6]. HMTS and PDMS are inorganic chemicals that provide a porous polymer matrix for rapid analyte absorption [6].

D. Measurement Procedure

Before depositing the film, the devices are first cleaned for 3 min in ultrasonic baths of chloroform, acetone, and 2-propanol, respectively. The devices are then rinsed with Milli-Q de-ionized (DI) water and dried with nitrogen. Afterwards, BPA-HMTS, BPA-PDMS, and PECH solutions were prepared in chloroform and spin coated at using a P6708D spin coater (Specialty Coating Systems) to obtain 0.25 μm and 0.5 μm-thick layers. The coated device was allowed to dry at room temperature 21.7 – 22.5 °C in a dessicator for at least 15 hours. The film thickness was calibrated using an ellipsometer (Gaertner Scientific L2WLSE544). Ellipsometer measurements were performed directly on the sensor device.

A reference solution was created by mixing phosphate buffer solution (PBS) with methanol. Afterwards, a concentrated solution of parathion, parathion-methyl, and paraoxon was prepared and diluted with the reference solution to obtain desired concentrations.

A typical experimental run is started by exposing the coated device to the reference solution at a flow rate of 0.70 mL/min until a stable baseline is obtained. The coated device is then exposed to various analyte concentrations. Between analyte exposures, the sensor response was returned to its initial value by flushing the flow-cell with the reference solution. The differential measurement thus reflects the sensor response due to perturbations caused by only analyte absorption.

III. Data Processing

The response curve (frequency shift) for each sample was modeled using an exponential fit, and the steady-state frequency shift and the response time were extracted [7, 10]. The steady state frequency shift is plotted against analyte concentration and modeled with a linear fit. The slope of the fit represents the sensitivity of the polymer to the analyte. The response times are specific to the polymer/analyte interaction.

For each sample, steady-state frequency shift and response time were extracted for each sensor analyte/coating pair, and the resulting data set was processed using pattern recognition techniques [11]. A sensor array can be created by combining multiple sensors coated with different chemically sensitive polymers on the same wafer. In this case, there are only a limited amount of coatings. Therefore, the coatings available were used at different coating thicknesses (0.25μm and 0.5μm) to provide additional information.

Analyte identification is performed using a visual pattern recognition technique based on radial plots for the analytes, parathion, paraoxon, and parathion-methyl, at concentrations from 0.5mg/L to 3.0mg/L. These specific radial plots are made using the steady-state frequency shifts and time responses of BPA-HMTS, BPA-PDMS, and PECH at a thickness of 0.5μm as the axes, providing a total of six parameters for analyte recognition.

Once the analyte is identified, a level-of-confidence algorithm is calculated to estimate the concentration of an unknown sample by quantifying the similarity between known response patterns and the response pattern of the unknown sample [11]. First, the distance in the six-dimensional space of sensor response parameters is calculated between the known sample and the unknown sample using

$$d(\bar{y},\bar{z}) = \left[\sum_{j=1}^{3}(y_j - z_j)^2\right]^{1/2} \quad (1)$$

If the unknown sample shows a response pattern similar to that of the known sample, the distance between the two samples should be minimal. The certainty of the unknown pattern being identical to the known pattern can be quantified by a level of confidence parameter [11]

$$C_i = \frac{1}{d(\bar{y},\bar{z_i})} \quad (2)$$

The level of confidence is normalized and defined between the values of 0 and 1, corresponding to least certain and most certain, respectively.

IV. Results and Discussion

Fig. 2 shows an example of the frequency response when BPA-HMTS 0.5µm is exposed to various concentrations of parathion-methyl. Data were collected for all three polymers at both thicknesses, exposed to all three analytes. The sensitivities were calculated and recorded in Table I, and the following trends can be observed. The order in the sensitivities of the polymers to the analytes (from highest to lowest) is BPA-HMTS, BPA-PDMS, and PECH; for the analytes, the order is parathion, parathion-methyl, and paraoxon, respectively. In Table I, the sensitivities for PECH follow the (inverse) trend of analytes solubilities [7] as expected. However, for BPA-HMTS, parathion-methyl and paraoxon give similar sensitivities despite their very different solubilities [7]. This can be attributed to the hydrogen-bond interaction between paraoxon and BPA [7]. Such specific interactions between a coating and certain analytes will strongly contribute to the selectivity of the sensor array.

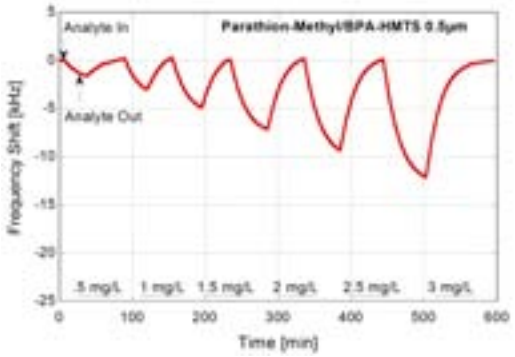

Fig. 2. Measured change in frequency shift upon exposure of the BPA-HMTS 0.5µm coated device to the indicated concentartions of parathion-methyl.

TABLE I. The sensitivities for 0.25µm and 0.5µm thick BPA-HMTS, BPA-PDMS, and PECH when exposed to parathion, parathion-methyl, and paraoxon.

	Sensitivity $\left({}^{kHz}/_{mg/L}\right)$					
polymer / analyte	*BPA-HMTS 0.25µm*	*BPA-PDMS 0.25µm*	*PECH 0.25µm*	*BPA-HMTS 0.5µm*	*BPA-PDMS 0.5µm*	*PECH 0.5µm*
parathion	2.449	1.073	1.491	20.791	9.002	9.093
parathion-methyl	0.572	0.196	0.512	4.246	0.725	2.278
paraoxon	0.450	0.049	0.026	4.413	0.489	0.175

Fig. 3 shows the radial plots for detection of paraoxon at concentrations of 0.5mg/L, 1.0mg/L, 1.5mg/L and 2.0mg/L. The six axes in each plot are the steady state frequency shifts and time responses of BPA-HMTS, BPA-PDMS, and PECH at 0.5µm thickness to paraoxon. When evaluating Fig. 3 it is possible to see the distinct arrow shape pattern with the arrow's point positioned on the BPA-HMTS 0.5µm time response axis. Minor fluctuations in the lower concentration range are due to the error in manually prepared analyte samples. This pattern is specific to paraoxon and it was observed that parathion and parathion-methyl have their own distinct patterns. It is

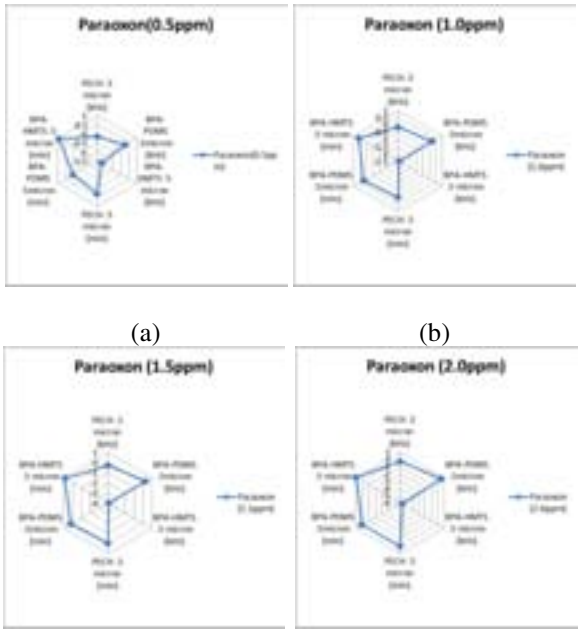

Fig. 3. Radial plots showing the detection of paraoxon at concentrations of (a) 0.5mg/L, (b) 1.0mg/L, (c) 1.5mg/L, and(d) 2.0mg/L using BPA-HMTS, BPA-PDMS, and PECH at a thickness of 0.5µm in an array. The frequency shift and time response serve as the input parameters.

demonstrated that single analyte identification is possible within the above concentration range using this approach.

Fig. 4 shows the level of confidence for the measured test sample 2. It is apparent that the level of confidence for the test sample is maximum for 2.0mg/L of paraoxon, in agreement with its actual concentration and type of analyte. Fig. 5 shows the level of confidence for test sample 5 whose concentration was not measured and recorded within the test database. It was noted that the highest levels of confidence for the latter test sample were found for 1.5mg/L and 2.0mg/L, giving identical level-of-confidence values for these concentrations, thus correctly identifying the test sample as 1.75mg/L of parathion. The accuracy can be improved if more information is added to the data set. Additional tests were conducted, and in all cases the sample analyte concentrations were successfully quantified.

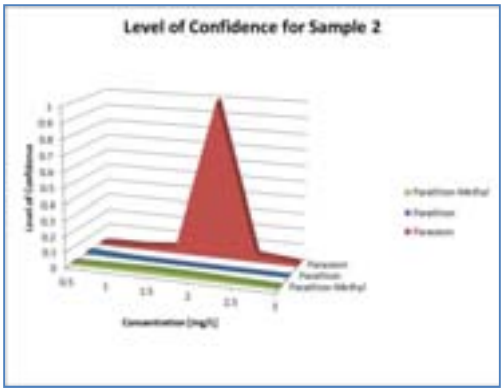

Fig. 4 The level of confidence for test sample 2, points towards 2.0mg/L of paraoxon as predicted by a pattern recognition technique based on an algorithm which computes the distance between the test sample and the known patterns in the 6-dimensional response data space.

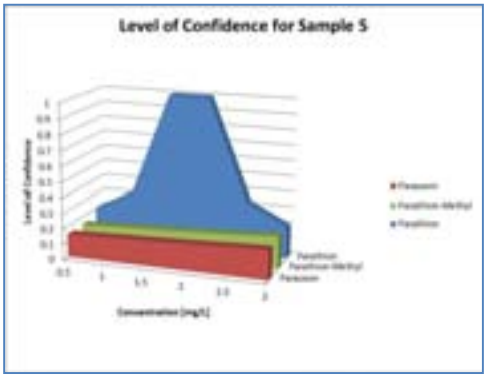

Fig. 5. The level of confidence for test sample 5, points towards 1.75mg/L of parathion as predicted by a pattern recognition technique based on an algorithm which computes the distance between the test sample and the knownpatterns in the 6-dimensional response data space.

V. Conclusion

A chemical sensor array has been designed, using the partially selective coatings BPA-HMTS, BPA-PDMS, and PECH, for the successful rapid identification and quantification of organophosphates in aqueous solutions. These coatings, exhibited very different sensitivity levels, with parathion generally giving the highest sensitivity and paraoxon the lowest. This trend largely reflects the different solubilities of the analytes in water. However, despite the very different solubilities of the analytes parathion-methyl and paraoxon, their sensitivities are very similar for the coatings containing BPA. This is due to the strong hydrogen bond that occurs between the oxygen atom from the paraoxon with the hydroxide groups in BPA, while the sulfur atom in parathion and parathion-methyl does not show particularly strong interaction with BPA.

The polymers at a thickness of 0.5µm exhibited a higher sensitivity and therefore were chosen over the 0.25µm-thick polymers for the radial plots and level of confidence algorithm. The radial plots successfully indicated three different patterns for the three analytes and the level of confidence algorithm successfully estimated the concentrations of measured test samples (e.g. 2.0mg/L of paraoxon) and extrapolated response patterns for sample concentrations that were not included in the pattern recognition design database (e.g. 1.75mg/L of parathion).

These findings have important implications for the in-situ, real-time detection of organophosphate pesticides in groundwater. The described chemical sensor array can form the basis for a sensor system for the monitoring of groundwater and surface water for harmful chemicals and thus make a significant contribution to the protection of public health.

References

[1] Environmental Protection Agency (2012, September 25). *Pesticides: Regulating Pesticides.* Retrieved July 7, 2013, from U.S. Environmental Protection Agency : http://www.epa.gov/pesticides/regulating/index.htm

[2] Yurumez, Y., Durukan, P., Yavuz, Y., Ikizceli, I., Avsarogullari, L., & Ozkan, S. (2007). Acute Organophosphate Poisoning in University. *Internal Medicine*, 965-969.

[3] P. Quinn, "Organophosphates," Illinois Department of Public Health, [Online].Available:http://www.idph.state.il.us/Bioterrorism/factsheets/organophosphate.htm. [Accessed 8 July 2013].

[4] M. Tankiewicz, J. Fenik and M. Biziuk, "Determination of organophosphorus and organonitrogen pesticides in water samples," *Trends in Analytical Chemistry*, vol. 29, no. 9, pp. 1050-1063, 2010.

[5] B. Drafts, "Acoustic Wave Technology Sensors*," IEEE Transactions on Microwave Theory and Techniques*, vol. 49, no. 4, pp. 795-802, 2001.

[6] J. W. Grate and D. A. Nelson, "A. Polymers for Chemical Sensors UsingHydrosilylation Chemistry," Pacific Northwest National Laboratory, Richland, 2001.

[7] A. K. Mensah-Brown, "Analysis of the Detection of Organophosphate Pesticides in Aqueous Solutions Using Polymer-Coated SH-SAW Devices [Dissertation]," Marquette University, Milwaukee, 2010.

[8] R. Dahint, Z. A. Shana, F. Josse, S. A. Riedel and M. Grunze, "Identification of Metal Ion Solutions Using Acoustic Plate Mode Devices and Pattern Recognition," in *IEEE Transactions on Ultrasonics, Ferroelectrics, and Frequency Control*, 1993.

[9] F. Josse, F. Bender and R. W. Cernosek, "Guided shear horizontal surface acoustic wave sensors for chemical and biochemical detection in liquids," *Anal. Chem.*, vol. 73, pp. 5937-5944, 2001.

[10] A. K. Mensah-Brown, M. J. Wenzel, F. J. Josse and E. E. Yaz, "Near Real-Time Monitoring of Organophosphate Pesticides in the Aqueous-Phase Using SH-SAW Sensors Including Estimation-Based Signal Analysis," *IEEE Sensors Journal*, vol. 9, no. 12, pp. 1817-1824, 2009.

[11] F. Bender, A. Skrypnik, A. Voigt, J. Marcoll and M. Rapp, "Selective Detection of HFC and HCFC Refrigerants Using a Surface Acoustic Wave Sensor System," *Anal. Chem.*, vol. 75, pp. 5262-5266, 2003.

Resonant Characteristics of Rectangular Hammerhead Microcantilevers Vibrating Laterally in Viscous Liquid Media

Jinjin Zhang[1], Fabien Josse[1], Stephen Heinrich[2], Nicholas Nigro[3]
[1]Electrical and Computer Engineering
[2]Civil, Construction and Environmental Engineering
[3]Mechanical Engineering
Marquette University, Milwaukee, USA
Fabien.Josse@marquette.edu

Isabelle Dufour[4], Oliver Brand[5]
[4]IMS Laboratory,
Université de Bordeaux CNRS,
Talence, France
[5]School of Electrical and Computer Engineering
Georgia Institute of Technology,
Atlanta, USA

***Abstract*—The resonant characteristics of laterally vibrating rectangular hammerhead microcantilevers in viscous liquid media are investigated. The rectangular hammerhead microcantilever is modeled as an Euler-Bernoulli beam (stem) and a rigid body (head). A modified semi-analytical expression for the hydrodynamic function in terms of the Reynolds number, *Re*, and aspect ratio, *h*/*b*, is proposed to rapidly evaluate the sensing characteristics. Using this expression, the resonance frequency, quality factor and normalized surface mass sensitivity are investigated as a function of the dimensions of the microcantilever and liquid properties. Guidelines for design of hammerhead microcantilever geometry are proposed to achieve efficient sensing platforms for liquid-phase operation. The improvement in the sensing area and characteristics are expected to yield higher sensitivity of detection and improved signal-to-noise ratio in liquid-phase chemical sensing applications.**

I. Introduction

Dynamically driven rectangular prismatic microcantilevers excited in the in-plane direction have been investigated and used in liquid-phase sensing applications due to their relatively high frequency stability and mass sensitivity [1-2]. However, in bio-chemical sensing applications, the performance of rectangular prismatic microcantilever-based sensors is restricted due to their limited surface sensing area. Thus, to increase the surface sensing area and improve sensing characteristics, it is proposed to investigate rectangular hammerhead microcantilevers driven in the in-plane flexural vibration mode in viscous liquid media.

For a rectangular hammerhead microcantilever laterally vibrating in a vacuum, the resonance frequency has been obtained in a close-form analytical expression by assuming the head as a point mass at the tip of the stem [3-4]. However, when the vibrating microcantilevers are immersed in viscous liquids, the liquid will impose hydrodynamic forces on the stem and head, which are not accounted for. Thus, it is no longer appropriate to model the head as a point mass. In this work, the stem and head are modeled as an Euler-Bernoulli beam and a rigid body, respectively. As a result, both translational and rotational motions of the head must be taken into account. In viscous liquids, the hydrodynamic forces exerted on the stem and head must be evaluated separately due to the difference in dimensions. Since the cross-section of either part is still rectangular, the semi-analytical expression for the hydrodynamic function in [1] can still be applied. However, in Ref. 1, the discrepancy between analytical and numerical results is relatively large for small thicknesses and high *Re*. As a result, it is necessary to obtain a new analytical expression for the hydrodynamic function to accurately determine the sensing characteristics.

In this work, a theoretical model of laterally vibrating rectangular hammerhead microcantilevers in viscous liquids is presented. A modified semi-analytical expression for the hydrodynamic function in terms of *Re* and *h*/*b* is proposed and compared with the numerical results. The sensing characteristics are investigated as a function of the geometrical parameters of the rectangular hammerhead microcantilevers and liquid properties, and compared with those of the rectangular prismatic beams. Guidelines for the design of hammerhead microcantilevers for sensor applications are proposed.

II. Theoretical Analysis

A. Equation of Motion

The geometry of a rectangular hammerhead microcantilever, with dimensions on the order of microns, is shown in Fig. 1. To model the stem as an Euler-Bernoulli beam, it is generally assumed that its length is much larger than its width (L_1>>b_1). The equation of motion for a laterally vibrating stem in viscous liquids is given by

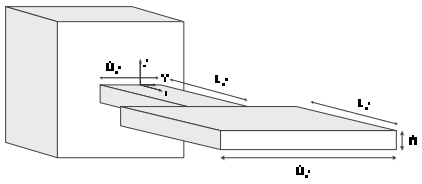

Figure 1: A rectangular hammerhead microcantilever with length and width of the stem being L_1, b_1, respectively; length and width of the head being L_2, b_2, respectively and thickness being h.

This work is supported in part by NSF Grant No. ECCS-1128992 and NSF Grant No. ECCS-1128554.

$$EI_{stem}\frac{\partial^4 v_{stem}(x,t)}{\partial x^4}+\rho_b b_1 h\frac{\partial^2 v_{stem}(x,t)}{\partial t^2}=F_{stem,liquid}(x,t), \quad (1)$$

where E is the Young's modulus, I_{stem} the second moment of area of the cross-section of the stem, ρ_{b} the mass density of the microcantilever; v_{stem} is the displacement in the y-direction. The hydrodynamic force on the stem, $F_{stem.liquid}$, is force per unit length, and is given by

$$F_{stem,liquid}(x,t)=-g_{1,stem}\frac{\partial v_{stem}(x,t)}{\partial t}-g_{2,stem}\frac{\partial^2 v_{stem}(x,t)}{\partial t^2}, \quad (2)$$

In equation (2), $g_{1,stem}$ and $g_{2,stem}$ are coefficients associated with the viscous damping and the effective mass coming from the liquid, respectively [1].

B. Boundary Conditions

In order to solve equation (1), four boundary conditions are needed. Two boundary conditions are defined at the fixed end. One of them states that the stem is perfectly fixed at the support end, and is given by

$$v_{stem}(0,t)=0 \quad , \quad (3)$$

The exciting force is assumed and modeled by an equivalent, harmonic support rotation [5]. The bending slope at the support end of the hammerhead microcantilever is given by

$$\frac{\partial v_{stem}(x,t)}{\partial x}\Big|_{x=0}=\theta_0 e^{j\omega t} \quad , \quad (4)$$

In equation (4), θ_0 and ω are the amplitude and angular frequency of the effective support rotation. The remaining two boundary conditions represent the moment and force balances at the junction between the stem and head (x=L_1). The width of the head is assumed to be much larger than that of the stem, i.e., b_2>>b_1. Thus, the head is modeled as a rigid body, and translational motion and rotational motion of the head are taken into account. In viscous liquids, the inertial and damping forces contribute in the moment and force balance equations, which are given by

$$\sum M_{moment}\Big|_{x=L_1}=0, \quad (5)$$

$$\sum S_{force}\Big|_{x=L_1}=0. \quad (6)$$

C. Hydrodynamic Function

The hydrodynamic function (Γ= Γ_R+jΓ_I) is defined as a normalized hydrodynamic force per unit length [1]. It consists of two components: the viscous damping force, which is associated with Γ_I, and the inertial force, which is associated with Γ_R:

$$g_1\left[\mathrm{Re}(x),h/b(x)\right]=\frac{\pi}{4}\rho_f b^2(x)\Gamma_I\left[\mathrm{Re}(x),h/b(x)\right]\omega, \quad (7)$$

$$g_2\left[\mathrm{Re}(x),h/b(x)\right]=\frac{\pi}{4}\rho_f b^2(x)\Gamma_R\left[\mathrm{Re}(x),h/b(x)\right], \quad (8)$$

Modified analytical expressions for Γ_R and Γ_I are developed to minimize the discrepancy between numerical and analytical results. The mathematical forms of Γ_R and Γ_I are proposed as shown in equation (9a-b).

$$\Gamma_R\left(\mathrm{Re},\frac{h}{b}\right)=\Gamma_{R1}(\mathrm{Re})\Gamma_{R2}\left(\frac{h}{b}\right), \quad (9a)$$

$$\Gamma_I\left(\mathrm{Re},\frac{h}{b}\right)=\Gamma_{I1}(\mathrm{Re})\Gamma_{I2}\left(\frac{h}{b}\right), \quad (9b)$$

In equation (9a-b), $\Gamma_{R1}(Re)$ are $\Gamma_{I1}(Re)$ are expected to depend on the boundary layer thickness, and are functions of $Re^{-0.5}$ [6]. $\Gamma_{R2}(h/b)$ and $\Gamma_{I2}(h/b)$ can be expanded into a summation of multiple h/b terms (similar to Taylor series expansion). The proposed real and imaginary parts of the hydrodynamic function are as follows:

$$\Gamma_R\left(\mathrm{Re},\frac{h}{b}\right)=\left[\frac{1}{\sqrt{\mathrm{Re}}}\sum_{m=0}^{m_{\max}}C_m\left(\frac{h}{b}\right)^{\frac{m}{2}}\right]+\left[\sum_{n=0}^{n_{\max}}D_n\left(\frac{h}{b}\right)^{\frac{n}{2}}\right] \quad (10a)$$

$$\Gamma_I\left(\mathrm{Re},\frac{h}{b}\right)=\left[\frac{1}{\mathrm{Re}}\sum_{p=0}^{p_{\max}}E_p\left(\frac{h}{b}\right)^{\frac{p}{2}}\right]+\left[\frac{1}{\sqrt{\mathrm{Re}}}\sum_{q=0}^{q_{\max}}F_q\left(\frac{h}{b}\right)^{\frac{q}{2}}\right] \quad (10b)$$

Using the surface fitting tool in Matlab, each coefficient and power index in equation (10a-b) is determined simultaneously to obtain the optimum fitting results. The coefficients (C_m, D_n, E_p, F_q) and power indices (m_{max}, n_{max}, p_{max}, q_{max}) are determined to minimize the differences between the numerical data and the proposed analytical expression. The power indices and coefficients are determined as m_{max}=2, n_{max}=4, p_{max}=1, q_{max}=4, C_0=0.9003, C_1=0.6105, C_2=2.1722, D_0=0, D_1= -0.0021, D_2= -0.1459, D_3=0.8255, D_4= -1.3388, E_0=2.5758, E_1= -1.3388, F_0=0.9003, F_1= -0.7121, F_2=1.6845, F_3=0.8236 and F_4=0.4178.

D. Frequency Response

Based on the boundary conditions, the equation of motion can be solved and the normalized frequency response at the tip of the stem is obtained as

$$\left|\frac{X(L_1)}{L_1\theta_0}\right|= \left|\frac{A_1(\cosh KL_1-\cos KL_1)+A_2(\sinh KL_1-\sin KL_1)+\frac{\theta_0}{K}\sin KL_1}{L_1\theta_0}\right|. \quad (11)$$

In equation (11), K, A_1 and A_2 are functions of the properties of the hammerhead microcantilever and surrounding liquid medium. A_1 and A_2 also depend on θ_0. Using equation (11), the resonance frequency and quality factor can be extracted from the frequency spectrum.

III. RESULTS AND DISCUSSIONS

A. Results of the Semi-analytical Expression

Real and imaginary parts of the hydrodynamic function obtained analytically and numerically are compared. The ranges of the percent differences between the analytical and numerical results of the real and imaginary parts are [-3.8%,

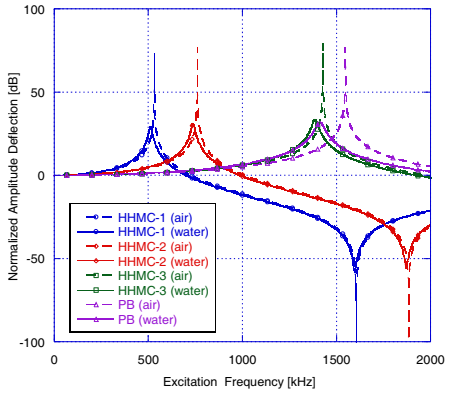

Figure 2: Calculated frequency spectra of three hammerhead microcantilevers (HHMC) of dimensions [(200×45×12) + (50×200×12)] µm^3 (HHMC-1), [(150×45×12) + (50×200×12)] µm^3 (HHMC-2), [(200×90×12) + (50×200×12)] µm^3 (HHMC-3) and a rectangular prismatic beam (PB) of dimensions (200×45×12) µm^3 laterally vibrating in air and water.

6.1%] and [-2.0%, 2.8%], respectively, for Re ~ [10, 10000] and h/b ~ [1/56, 1].

B. *Frequency Spectrum*

Using equation (11), the simulated frequency spectra of four microcantilevers of different dimensions vibrating laterally are shown in Fig. 2. For the investigated geometries, the resonance frequency is highest for the prismatic rectangular beam, because no additional mass is attached at the end of the beam. Percent change of the resonance frequency from air to water for the prismatic beam, 8.8%, is larger than those of rectangular hammerhead microcantilevers, 1.8%~4.9%. It is also found that the 3-dB bandwidths for the hammerhead microcantilevers are narrower than that of the prismatic beam.

C. *Resonance Frequency*

The resonance frequency is investigated as a function of liquid properties and dimensions of the rectangular hammerhead microcantilevers. Fig. 3 (top) shows the resonance frequency as a function of glycerol concentration in water. As viscosity increases, the resonance frequency will decrease. Fig. 3 (bottom) shows the resonance frequency with respect to length (L_2) and width (b_2) of the head for three different stems at a thickness of 12µm. As the length or width of the head increases, the resonance frequency decreases for hammerhead microcantilevers, and it is due to the increase in the mass of the head. For hammerhead microcantilevers with stiffer stems (smaller L_1/b_1), the resonance frequency is higher.

D. *Quality Factor*

The quality factor is investigated as a function of liquid properties and dimensions of the rectangular hammerhead microcantilever. Fig. 4 (top) shows the quality factor as a function of glycerol concentration in water. As viscosity increases, the quality factor will decrease. Fig. 4 (bottom) shows the quality factor with respect to the length (L_2) and width (b_2) of the head for three different stems at a thickness of 12µm. As the length of the head increases, the quality factor decreases (because the increase in damping exceeds the increase in mechanical energy), and the mass center of the head moves away from the tip of the stem. As the width of the head increases, for shorter heads, the quality factor increases because the increase in mechanical energy exceeds the increase in damping. Note that the distance between the mass center of the head and the tip of the stem remains fixed at $L_1+L_2/2$.

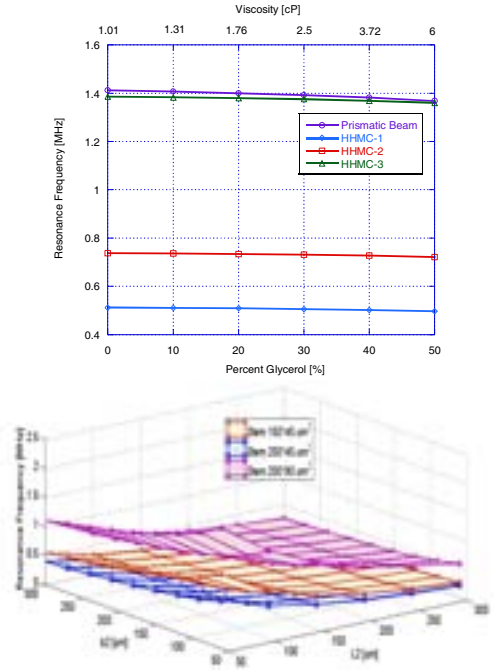

Figure 3: Calculated resonance frequency as a functions of glycerol concentration in water (top: microcantilever dimensions as in Fig. 2) and of the dimensions of the head (bottom).

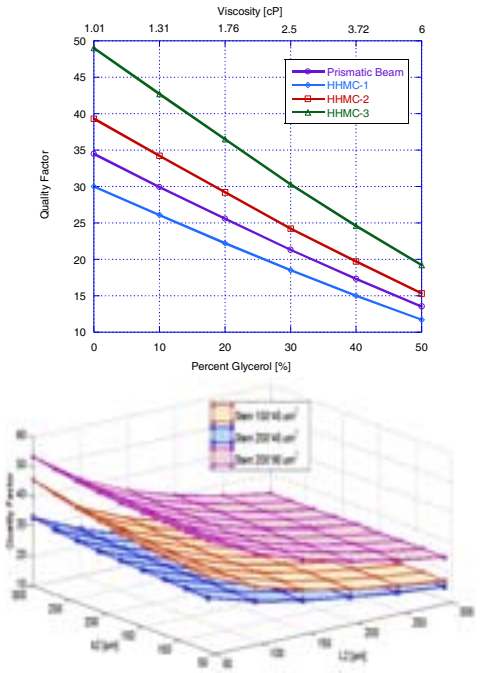

Figure 4: Calculated quality factor as a functions of glycerol concentration in water (top: microcantilever dimensions as in Fig. 2) and of the dimensions of the head (bottom).

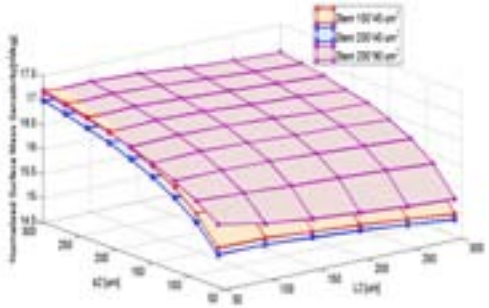

Figure 5: Calculated normalized surface mass sensitivity as a function of the dimensions of the head.

E. Normalized Surface Mass Sensitivity

Normalized surface mass sensitivity is defined and used for comparison between the microcantilevers with different resonance frequency and surface sensing area, and is given by

$$S_n = \frac{\Delta f_{res} / f_{res}}{\Delta m / A}. \qquad (12)$$

In equation (12), Δf_{res} is the shift of the resonance frequency due to added mass, Δm (sorption of target molecules), on the microcantilever surface; A is the surface sensing area of the microcantilever. It is assumed that Δm is dominated by the change in the effective density.

The normalized surface mass sensitivity, S_n, is investigated as a function of the dimensions of the rectangular hammerhead microcantilever. Fig. 5 shows S_n as a function of the length (L_2) and width (b_2) of the head for three different stems at a thickness of 12μm. As the width of the head increases, S_n increases, because the decrease in Δf_{res} is smaller than that of the resonance frequency.

F. Comparison between the Prismatic Beam and Hammerhead Microcantilever

The sensing characteristics of rectangular and prismatic microcantilevers are analyzed and compared in Table I. It is found that the decrease in the resonance frequency from air to water is smaller for the hammerhead microcantilevers. It indicates that a laterally vibrating hammerhead microcantilever will have high chemical sensitivity in both air and viscous liquids. The resonance frequency and quality factor of prismatic beams are larger than those of the hammerhead microcantilevers with the dimensions of the stem being identical to those of the prismatic beams. Although the resonance frequency for a hammerhead microcantilever of dimensions $L_1 \times b_1 \times h + L_2 \times b_2 \times h$ with a wider and shorter head is lower compared to a prismatic beam of dimensions $(L_1+L_2) \times b_1 \times h$, the quality factor for the hammerhead microcantilever is higher. It indicates that a microcantilever with a lower resonance frequency may yield higher quality factor due to geometrical effects.

TABLE I. SENSOR CHARACTERISTICS PREDICTED FOR TWO PRISMATIC BEAMS AND THREE HAMMERHEAD MICROCANTILEVERS

Geometry $[\mu m^3]$	f_{air} [MHz]	f_{water} [MHz]	**Percent Change**	Q_{water}	$S_{n,water}$ [$\mu m^2/ng$]
200×45×12	1.548	1.412	8.8%	36	14.9
200×90×12	3.095	2.944	4.9%	59	15.8
200×90×12+ 50×200×12	1.428	1.386	2.9%	49	15.5
150×45×12+ 50×200×12	0.761	0.738	3.0%	40	16.8
150×45×12+ 50×300×12	0.564	0.554	1.8%	46	17.2

IV. CONCLUSIONS

The sensing characteristics of laterally vibrating rectangular hammerhead microcantilevers in a viscous liquid were analyzed in terms of the microcantilever geometry and the properties of the liquid and compared to those of laterally vibrating prismatic beams. A modified analytical expression for the hydrodynamic function was presented for the purpose of rapid evaluation of the sensing characteristics.

For the range of dimensions investigated, if only the length of the head increases, the mass center of the head will move away from the tip of the stem and the resonance frequency and quality factor will decrease due to the increase in the mass attached at the end of the stem. In contrast, if only the width of the head increases, the mass center of the head will not move and the resonance frequency will decrease, but the normalized surface mass sensitivity will increase; the quality factor will increase rapidly for shorter heads. This is because the increase in mechanical energy exceeds the increase in damping. Such trends can be used to optimize device geometry and maximize the frequency stability in sensing applications. In general, to obtain an efficient hammerhead microcantilever-based sensor platform, the stem of the microcantilever can be designed stiffer and the head can be made wider and shorter. For appropriately designed hammerhead microcantilevers, the improvement in the sensing area and quality factor are expected to yield much lower limits of detection in (bio) chemical sensing applications.

REFERENCES

[1] Russell Cox, Fabien Josse, Stephen M. Heinrich, Oliver Brand, Isabelle Dufour, "Characteristics of laterally vibrating resonant microcantilevers in viscous liquid media", Journal of Applied Physics, 111, 014907, 2012.

[2] D. Brumley, M. Willcox, and J. Sader, "Oscillation of Cylinders of Rectangular Cross section Immersed in Fluid," Physics of Fluids vol. 22, no. 052001, 2010

[3] Wen-Hsien Chuang, Thomas Luger, Rainer K. Fettig, R, Ghodssi, "Mechanical Property Characterization of LPCVD Silicon Nitride Thin Films at Cryogenic Temperatures", Journal of Microelectromechanical Systems, vol. 13, pp. 870–879, Oct 2004.

[4] Narducci, M., Figueras, E., Garcia, I., Fonseca, L., Santander, J., Cane, C., "Modeling of T-shaped Microcantilever Resonators" IEEE SENSOR Conference, pp. 1127-1130, 2008.

[5] S.M. Heinrich, R. Maharjan, I. Dufour, F. Josse, L. Beardslee, and O. Brand, "An analytical model of a thermally excited microcantilever vibrating laterally in a viscous fluid", Journal of Microelectromechanical Systems, 19(4), pp. 1399-1404, 2010.

[6] A. Maali, C. Hurth, R. Boisgard, C. Jai, T. C-B. Touria and J-P. Aime, "Hydrodynamics of Oscillating Atomic Force Microscopy Cantilevers in Visouc Fluids", Journal of Applied Physics, 97(7), 074907, 2005.

Design of SH-Surface Acoustic Wave Sensors for Detection of ppb Concentrations of BTEX in Water

Florian Bender and Fabien Josse
Department of EECE
Marquette University
Milwaukee, WI 53233
fabien.josse@mu.edu

Rachel E. Mohler
Chevron Energy Technology Co.
100 Chevron Way
Richmond, CA 94801

Antonio J. Ricco
Department of Electrical Engineering
Center for Integrated Systems
Stanford University
Stanford, CA 94305

***Abstract*—To address the need to protect public health from contamination of drinking water and water for recreational use, a compact sensor system for in-situ detection of fuel and oil components in water is being investigated. The system makes use of shear-horizontal surface acoustic wave (SH-SAW) sensors coated with thin chemically sensitive polymer films. For this work, the BTEX compounds (benzene, toluene, ethylbenzene, and xylenes) were selected as target analytes because they are good indicators of fuel and oil releases, but also because they include known carcinogens (benzene, ethylbenzene). Chemical selectivity is achieved by combining sensors with various polymer coatings into a sensor array, and by evaluating both steady-state and transient response information. This work focuses on the influence of interdigital transducer (IDT) design on signal distortion and rms (root-mean-square) noise level. It is demonstrated that for suitable IDT design and experimental approach, it is possible to detect all BTEX compounds at concentration levels of 100 ppb or below, and to quantify benzene concentration in binary analyte mixtures at concentrations well below 1 ppm.**

Keywords—groundwater, surface acoustic wave sensors, liquid-phase sensing, benzene, rms noise level, multi-electrode interdigital transducer design

I. INTRODUCTION

The processing, storage and transport of fuel and oil are often associated with potential environmental hazards. In particular, places where large amounts of fuel or oil are stored, such as gas stations, present significant potential threats to public health through unintentional releases into groundwater and surface water [1]–[4]. Timely detection of such releases can minimize the impact on public health and reduce clean-up costs. However, current monitoring practice is largely based on collection of samples in the field, transport and subsequent analysis in the laboratory [3], procedures which can become very time-consuming for high monitoring frequencies. To enable frequent or continuous, *in-situ* monitoring of groundwater and surface water at critical sites, a number of suitable sensor systems are under development [5].

Sensor systems based on SH-SAW (shear-horizontal surface acoustic wave) sensor platforms represent a promising approach for this application. SH-SAWs combine the advantages of high surface confinement of the acoustic energy (which facilitates high sensitivity to the analyte) and the ability to propagate along a solid-liquid interface without suffering excessive acoustic wave attenuation [6]. In our previous studies, the performance of the sensors and various coating materials was investigated under varying environmental conditions, including changes in temperature, acidity, and salinity [7]. It was demonstrated that by evaluating both steady-state and transient response information, this type of sensor can be used to quantify the concentration of benzene in binary analyte mixtures in the low ppm concentration range [8].

The BTEX compounds (benzene, toluene, ethylbenzene, and xylenes) were selected as target analytes for this study because they are good indicators of fuel and oil releases [3], [4], [9], but also because they include known carcinogens (benzene, ethylbenzene) [10]. Due to their hazard potential for public health, legal concentration limits for the BTEX compounds in drinking water are low, with MCL (maximum contaminant level) values in the US ranging from 5 ppb (µg/L) to 10 ppm (mg/L) [5], [11]. Detection of these contaminants at ppb levels is a challenging task, especially if the concentration of one BTEX compound has to be quantified in the presence of similar aromatic compounds.

The BTEX detection challenge is addressed in our work by evaluating both the steady-state frequency shift and the time-dependent behavior of the sensor response. We investigated various polymer materials (≤ 1 µm thick) as sensor coatings based on their partial selectivities for the analytes of interest [8]. In order to achieve detection limits for BTEX compounds in the ppb range, every aspect of the sensor design has to be evaluated for its potential to minimize rms (root-mean-square) noise and signal distortion. For this study, 36°-rotated YX-$LiTaO_3$ was selected as piezoelectric substrate because of its high dielectric constants [12], permitting immersion of the entire device surface—including the polymer-coated interdigital transducers (IDTs)—in water, thus obviating the need for a gasket on the acoustic delay line, which could lead to signal distortion. $LiTaO_3$ also has high piezoelectric constants [12], restricting the number of electrode fingers per

IDT if overcoupling (and consequent signal distortion) is to be avoided. One solution would be to use a wideband IDT, but this could lead to overlap between the SH-SAW and neighboring bulk modes with further adverse consequences for signal distortion. Therefore, another approach is investigated here, based on the use of multi-electrode IDTs [13]. In this way, overcoupling can be avoided by placing many electrode fingers in antiphase with the acoustic wave. It is demonstrated that a suitable multi-electrode IDT design leads not only to better bulk mode suppression and lower phase distortion, but also has a beneficial effect on rms noise, resulting in lower detection limits and higher accuracy in analyte quantification in binary mixtures. In addition, multi-electrode IDTs can be designed to generate multiple SH-SAWs at different frequencies in a single delay line, permitting investigation of frequency-dependent contributions in sensor responses.

II. Experimental

The first of the SH-SAW sensor platforms used in this work has been described previously [14], [15]. The sorbent polymers selected as sensor coatings are poly(ethyl acrylate) (PEA), poly(epichlorohydrin) (PECH), and poly(isobutylene) (PIB) (all from Sigma-Aldrich). Sorbent polymers were deposited from solution by spin coating and baked for 15 min at 55 °C, resulting in thicknesses ranging from 0.55 to 1.0 µm as indicated below. All sensor platforms utilize a dual-delay-line design, with the second line coated with poly(methyl methacrylate) (Scientific Polymer Products) and baked for 120 min at 180 °C, resulting in a glassy, non-sorbent coating. The purpose of this reference line is to compensate for the influence of temperature drifts and other secondary effects. All BTEX analytes had purities of 98.5% or higher.

The experimental set-up used a network analyzer (Agilent E5061B; the 16-fold data averaging function was activated) and a switch/control system (Agilent 34980A) to switch between the two SH-SAW delay lines. The sensor was placed inside a flow cell made in-house, and the peristaltic pump (Ismatec Reglo Digital MS-CA4/12-100) was set to a sample flow rate of 7 µL/s. Switching between different samples was accomplished without interruption of sample flow in order to avoid any resulting signal distortions. The flow cell and samples were set up inside a box, simulating an environment similar to a groundwater monitoring well, and measurements were conducted at room temperature (22.0 ± 0.1 °C). All data shown are corrected for linear baseline drift.

III. Results and Discussion

In previous studies, a 103-MHz SH-SAW sensor device has successfully been used to detect BTEX compounds in the ppm concentration range [7], [8], [14], [15]. This device used an IDT pattern with four electrode fingers per electrical period (S_e = 4), schematically illustrated in the inset of Fig. 1a. Two versions of this device were fabricated which differed in their bandwidths; one used an IDT length of 29 electrical periods (L_{IDT} = 29P), the other design used L_{IDT} = 44P. While the former shows relatively low phase distortion and good bulk mode and sidelobe rejection, the large bandwidth leads to larger overlap between the SH-SAW and adjacent bulk modes and results in a significant asymmetry of the SH-SAW passband. The latter design has a lower bandwidth, but the larger number of electrode fingers leads to stronger acoustic wave reflections and phase distortions, and the coupling of unwanted bulk modes is also enhanced. The mode spectrum of the L_{IDT} = 44P design is shown in Fig. 1a for a polymer-coated device. The highest peak (at 103 MHz) is the SH-SAW; it is followed by a series of bulk modes.

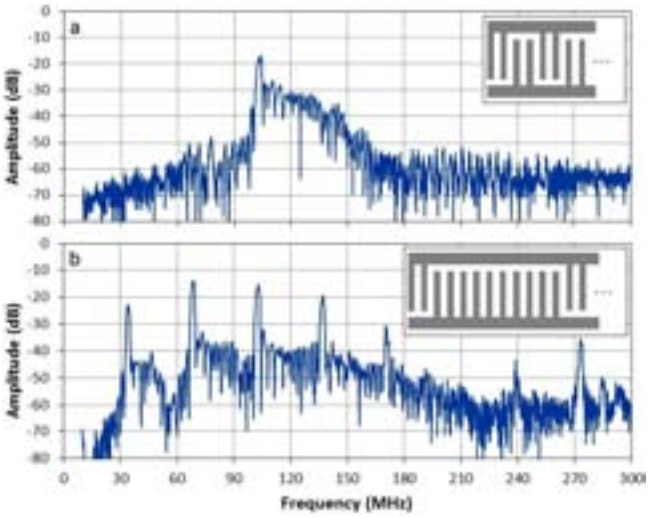

Fig. 1: Mode spectra (in air) for SH-SAW sensors with S_e = 4 (a) and S_e = 12 (b). Sensors were coated with 0.5 µm PMMA. Insets are schematics of the IDT electrode patterns (only part of the IDT is shown).

A solution of the above dilemma is offered by multi-electrode IDT designs [13] where a number of the electrode fingers are deliberately placed in anti-phase with the acoustic wave in order to reduce overall mode coupling. This allows the combination of a narrow IDT bandwidth with low bulk mode coupling and modest acoustic reflections. As an example, Fig. 1b shows the mode spectrum and IDT pattern for a SH-SAW device with S_e = 12. In this case, a series of SH-SAW modes is obtained with frequencies which are multiples of 34 MHz. This IDT design also leads to a lower wave reflection and better triple-transit echo suppression, a more symmetrical passband, and lower phase distortion. The latter is illustrated in Fig. 2.

While the relationship between phase linearity and rms noise level is not a straightforward one, it was experimentally observed that the IDT design giving the lowest phase distortion also gave the lowest rms noise level. This is shown in Fig. 3.

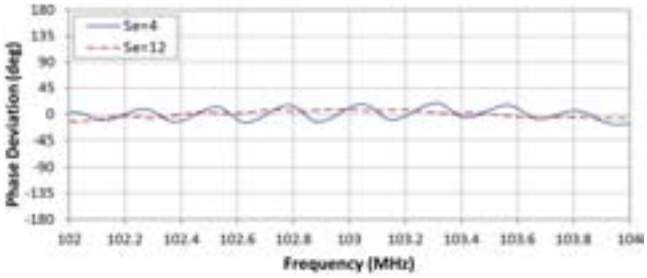

Fig. 2: Phase deviation (from linear phase) for SH-SAW sensors with S_e = 4 (—) and S_e = 12 (- -). Sensors were coated with 0.5 µm PMMA and immersed in water.

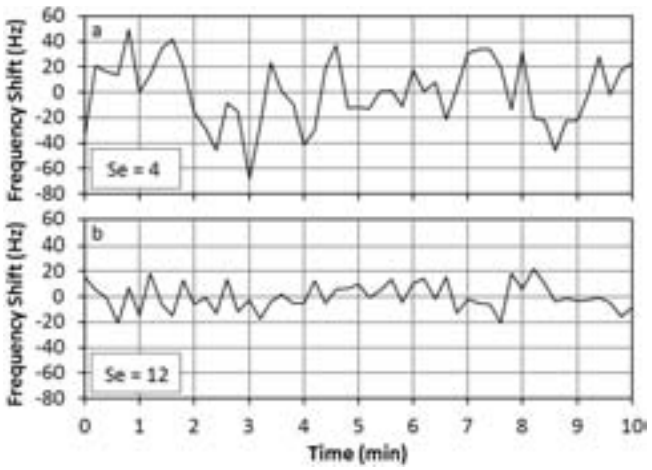

Fig. 3: Baseline noise levels for the 103-MHz SH-SAW mode for devices with S_e = 4 (a) and S_e = 12 (b). Sensors were coated with 1.0 µm PEA and immersed in water (flow rate: 7 µL/s).

For the S_e = 4 IDT design, a rms noise level of 25.9 Hz was calculated for a 1.0 µm PEA coating and the same flow rate used in BTEX detection. (Note that such a relatively thick coating of a rubbery polymer will slightly increase the rms noise level but also will enhance the quantity of BTEX sorbed). For the S_e = 12 IDT design, under the same conditions an rms noise level of only 10.7 Hz was found. For a 0.6 µm PECH coating and S_e = 12 IDT design, the rms noise level was further reduced to 7.1 Hz (data not shown).

In order to evaluate the performance of the improved SH-SAW sensor devices in BTEX detection, measurements were conducted on detection of single analytes and binary analyte mixtures in the concentration range of 100 ppb to 1 ppm. Sample data are shown in Fig. 4; it clearly demonstrates that benzene can be detected at a concentration as low as 200 ppb. From these measurements, the detection limits listed in Table I have been calculated using the relation: detection limit = 3 × rms noise / sensitivity. Note that xylene and ethylbenzene are chemical isomers and thus will give nearly identical sensitivities; therefore, only ethylbenzene is listed. As expected, the detection limits approximately follow the trend in analyte solubilities. In all cases, analytes can be detected at less than 10^{-4} of their saturation concentration in water.

Fig. 4 also shows several responses to binary mixtures. Assuming the sensor responses to multiple analytes in a sample

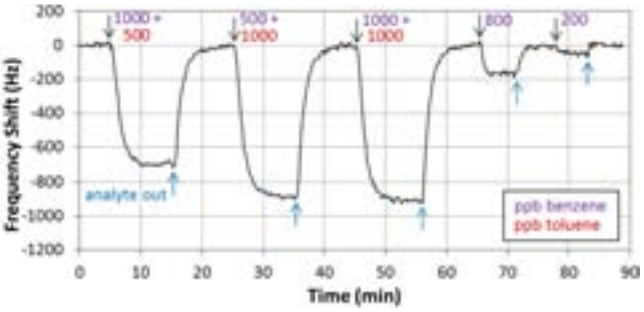

Fig. 4: Response of a SH-SAW device (103-MHz mode) with S_e = 4 and a 0.6 µm PECH coating to various benzene samples and binary mixtures. Analyte concentrations are given in the graph.

TABLE I. EXPERIMENTALLY DETERMINED DETECTION LIMITS (3 × RMS NOISE LEVEL / SENSITIVITY) FOR SH-SAW SENSORS WITH S_E = 12 FOR SIX COATING/ANALYTE COMBINATIONS.

Analyte	Solubility (ppm) [16]	Detection Limit (ppb)	
		1.0 µm PEA	*0.6 µm PECH*
Benzene	1780	100	100
Toluene	531	35	33
Ethylbenzene	161	11	9

are additive in the concentration ranges investigated [8] and that the transient response to a step change in analyte concentration is approximately exponential with time, the response to a binary mixture can be modeled using a dual-exponential fit, whereby the response times and sensitivities for the two analytes in the mixture can be taken from single-analyte measurements. This allows an estimation of the concentrations of two analytes in a mixture using a single sensor device simply by evaluating the transient response information. As an example, for the responses to binary mixtures in Fig. 4, analyte concentrations estimated using dual-exponential fits of the measured data are presented in Table II and compared to nominal (actual) concentrations. Note that the manual sample mixing procedure will introduce slight error in analyte concentrations. Nevertheless, there is a good agreement between nominal and estimated concentration for benzene. Even better agreement is observed for toluene (because of the higher sensitivity for this analyte).

The above results illustrate the detection limit in single-analyte detection and the accuracy in binary mixture analysis that can be achieved using the multi-electrode sensor platform designs. Another advantage of multi-electrode IDT designs is the presence of multiple SH-SAW passbands [13], which can be used for analysis of frequency-dependent effects in a single measurement with a single device. As an example, Fig. 5 shows the response of a SH-SAW device with S_e = 20 to 5 ppm benzene. The basic SH-SAW frequency for this device is 41 MHz; the responses of the 2nd to 4th SH-SAW harmonics to the same sample are shown at 82, 123, and 164 MHz.

To facilitate a more detailed analysis, the exact steady-state frequency shifts for this measurement are listed in Table III. The dependence of the observed frequency shifts on mode frequency contains a contribution from Sauerbrey-type mass loading [17]. Since all SH-SAW modes are propagating along the same delay line and will be exposed to the same amount of mass loading, this contribution is expected to give a $\Delta f \propto f^2$ dependence, where f is the device operating frequency. But the last column of Table III reveals significant additional contributions for the higher harmonics. This can be explained

TABLE II. NOMINAL ANALYTE CONCENTRATIONS FOR THE FIRST THREE SENSOR RESPONSES (TO BINARY MIXTURES) IN FIG. 4, AND CONCENTRATIONS ESTIMATED USING DUAL-EXPONENTIAL FITS.

Sample	Benzene Conc. (ppb)		Toluene Conc. (ppb)	
	nominal	*fit*	*nominal*	*fit*
# 1	1000	1200	500	690
# 2	500	810	1000	1110
# 3	1000	1280	1000	990

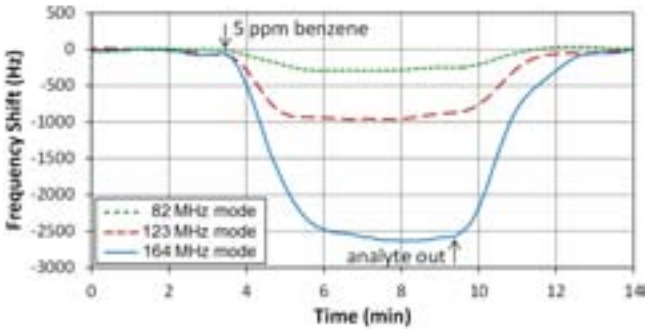

Fig. 5: Response of a SH-SAW device with S_e = 20 to 5 ppm benzene, shown for three different SH-SAW modes with frequencies indicated in the graph. The device was coated with 0.55 µm PEA.

by the higher ratio of waveguide thickness to wavelength for the higher modes, resulting in more efficient waveguiding and a corresponding increase in mass sensitivity for SH-SAW devices [15], [18]. Another contribution is from viscoelastic effects, which would also be expected to result in increased frequency shifts for higher ratios of waveguide thickness to wavelength [7], [14], [19].

IV. Conclusions

In chemical sensor applications, for a high-coupling piezoelectric material like $LiTaO_3$, use of the standard double-finger (S_e = 4) IDT leads to a dilemma: use of a wideband IDT will result in significant overlap of adjacent mode passbands; use of a narrowband IDT will lead to overcoupling and increased acoustic wave reflections. Thus, both alternatives will lead to significant signal distortions. It was demonstrated that the use of multi-electrode IDTs solves this issue, and narrowband SH-SAW modes can be obtained with high phase linearity, low acoustic wave reflection, and good sidelobe and bulk mode suppression.

It was observed that properly designed multi-electrode IDTs also result in significantly lower rms noise levels, with beneficial effects for BTEX detection in water including lower detection limits and higher accuracy in binary mixture analysis, as well as improved reproducibility. In addition, multi-electrode IDTs produce spectra of SH-SAW harmonics which permit investigation of frequency-dependent contributions in sensor responses using a single device in a single measurement. This option can also be useful in a sensor array since it permits collection of information from a larger number of input parameters using a compact sensor platform.

TABLE III. Steady-State Frequency Shifts, $-\Delta f$, for the Sensor Responses Shown in Fig. 5. A Frequency Dependence Stronger than $\Delta f \propto f^2$ is Observed.

Mode	$-\Delta f$ (Hz)	$(f/f_2)^2$	$\Delta f/\Delta f_2$
f_2 = 82 MHz	280	1	1
f_3 = 123 MHz	930	2.25	3.32
f_4 = 164 MHz	2600	4	9.29

Acknowledgment

The authors would like to thank Karen A. Synowiec and Urmas Kelmser for helpful discussion.

References

[1] U.S. Environmental Protection Agency, FY 2011 Annual Report On The Underground Storage Tank Program (2012); EPA-510-R-12-001.

[2] U.S. Environmental Protection Agency, Underground Storage Tank Flood Guide (2010); EPA-510-R-10-002.

[3] Z. Wang, S.A. Stout, and M. Fingas, "Forensic Fingerprinting of Biomarkers for Oil Spill Characterization and Source Identification", Environ. Forensics, vol. 7, pp. 105–146, 2006.

[4] R. Johnson, J. Pankow, D. Bender, C. Price, and J. Zogorski, "MTBE—To What Extent Will Past Releases Contaminate Community Water Supply Wells?" Environ. Sci. Technol., vol. 34, pp. 210A–217A, 2000.

[5] C.K. Ho, A. Robinson, D.R. Miller, and M.J. Davis, "Overview of Sensors and Needs for Environmental Monitoring", Sensors, vol. 5, pp. 4–37, 2005.

[6] E. Gizeli, "Design considerations for the acoustic waveguide biosensor", Smart Mater. Struct., vol. 6, pp. 700–706, 1997.

[7] F. Bender, F. Josse, and A.J. Ricco, "Influence of Ambient Parameters on the Response of Polymer-Coated SH-Surface Acoustic Wave Sensors to Aromatic Analytes in Liquid-Phase Detection", 2011 Joint Conference of the IEEE IFCS and the EFTF, pp. 422–427, 2011.

[8] F. Bender, R. Mohler, A.J. Ricco, and F. Josse, "Quantification of Benzene in Groundwater Using SH-Surface Acoustic Wave Sensors", IMCS 2012 Proc., pp. 473–476, 2012.

[9] J.S. Arey and P.M. Gschwend, "Estimating Partition Coefficients for Fuel-Water Systems: Developing Linear Solvation Energy Relationships Using Linear Solvent Strength Theory To Handle Mixtures", Environ. Sci. Technol., vol. 39, pp. 2702–2710, 2005.

[10] www.sigmaaldrich.com: material safety data sheets for benzene and ethylbenzene, accessed 7/9/2013.

[11] U.S. Environmental Protection Agency, National Primary Drinking Water Regulations (2009); EPA-816-F-09-004.

[12] G. Kovacs, M. Anhorn, H.E. Engan, G. Visintini, and C.C.W. Ruppel, "Improved Material Constants for $LiNbO_3$ and $LiTaO_3$" Proc. 1990 IEEE Ultrason. Symp., pp. 435–438, 1990.

[13] H. Engan, "Surface Acoustic Wave Multielectrode Transducers", IEEE Trans. Son. Ultrason., vol. 22, pp. 395–401, 1975.

[14] Z. Li, Y. Jones, J. Hossenlopp, R. Cernosek, and F. Josse, "Analysis of Liquid-Phase Chemical Detection Using Guided Shear Horizontal-Surface Acoustic Wave Sensors", Anal. Chem., vol. 77, pp. 4595–4603, 2005.

[15] F. Josse, F. Bender, and R.W. Cernosek, "Guided Shear Horizontal Surface Acoustic Wave Sensors for Chemical and Biochemical Detection in Liquids", Anal. Chem., vol. 73, pp. 5937–5944, 2001.

[16] D.L. Lide, Handbook of Chemistry and Physics, 82nd ed., CRC Press: Boca Raton, FL, 2001–2002, pp. 8–95.

[17] G. Sauerbrey, "Verwendung von Schwingquarzen zur Wägung dünner Schichten und zur Mikrowägung" (in German), Z. Phys., vol. 155, pp. 206–222, 1959.

[18] E. Gizeli, N.J. Goddard, C.R. Lowe, and A.C. Stevenson, "A Love plate biosensor utilising a polymer layer", Sens. Actuators, B, vol. 6, pp. 131–137, 1992.

[19] S.J. Martin, G.C. Frye, and S.D. Senturia, "Dynamics and Response of Polymer-Coated Surface Acoustic Wave Devices: Effect of Viscoelastic Properties and Film Resonance", Anal. Chem., vol. 66, pp. 2201–2219, 1994.

T2L2: Five Years in Space

P. Exertier, E. Samain, C. Courde, N. Martin, J.-M. Torre, J.-L.Oneto, M. Laas-Bourez
Geoazur, Université de Nice Sophia-Antipolis, Observatoire de la Côte d'Azur, CNRS (UMR 7329), 250 rue A. Einstein 06560 Valbonne, France
Pierre.Exertier@oca.eu

Ph. Guillemot, S. Léon
CNES, French Space Agency, 31401 Toulouse, France
Philippe.Guillemot@cnes.fr

***Abstract*— The Time Transfer by Laser Link (T2L2) experiment aims to synchronize remote ultra stable clocks over very long distances using the Satellite Laser Ranging (SLR) technique. T2L2 was launched in July 2008, on board the Jason2 satellite; from 5-6 stations ranging T2L2 during the first months of the mission, around 22 stations of the worldwide SLR network are now participating in the tracking. In addition to the permanent data acquisition and processing (accessible from our website https://t2l2.oca.eu/), several field experiments have been conducted to alternatively demonstrate the ultimate time transfer capability of T2L2, in terms of stability, exactness, comparison with the GPS and Two-Way microwave techniques.**

This paper synthetizes the best performances that T2L2 allows us to achieve, as a result of recent improvements made in the data reduction. The time stability of the T2L2 ground to space time transfer is established at 6-8 ps at 75 seconds, for SLR systems equipped with an H-maser as the reference clock. The ground to ground time transfer stability between 2 SLR stations (in Common View) is estimated at 11 ps rms (average) over one passage and better than 50 ps over several days. We present also the advantages and drawbacks of this unique time transfer technique based on an optical link.

Keywords—Space technique, time transfer, Laser ranging

I. INTRODUCTION

The Time Transfer by Laser Link (T2L2) instrument is passenger of the oceanographic space mission Jason2, that was launched in June 2008 at an altitude of 1335 Km. On board the Jason2 satellite, T2L2 consists of an optical system (detection) and an electronic device for the timing [1]. The principle of the experiment is based on the Satellite Laser Ranging (SLR) technique; thanks to the laser reflector array located on the satellite Jason2 in support of the precise orbitography, T2L2 benefits from the 2-way ranging, whose repeatability error and accuracy reach a few millimeters and less than 1 centimeter, respectively [2]. At ground level, T2L2 relies on the International Laser Ranging Service (ILRS) network [3], whose stations are tracking the satellite for 5 to 6 times per day maximum of 10 to 15 minutes each.

Actually, T2L2 is a technology demonstrator and also a platform permitting to realize some scientific experiments in metrology and fundamental physics. Its performances are in the range of 100 ps of accuracy, and in the range of a few ps at 1000 s. Apart from a few interruptions in 2009, 2010 and 2013 (a few days each time), the instrument is working properly and continuously since 2008.

Since 2009, we have conducted several field experiments, implementing very different configurations to: *i*) properly measure the performances of the time transfer by laser link (for short and long term stability), *ii*) progress in the measurement (method and hardware) of the ground links (delay, cables, etc.) including the time distribution of pulses between equipment such as clock, SLR system, and GPS and Two-way antennas (for exactness), *iii*) compare the T2L2 time transfer to existing microwave techniques such as GPS. In addition, we used the French mobile laser station (300 kg) [4] to conduct some field experiments at the Observatoire de Paris (2010), Tahiti (2011) and Grasse (2012) [5] [6] [7].

We present the most significant events and results of the T2L2 mission that have been obtained so far — ground and onboard characteristics, noise, available data — in Section II. The advantages and drawbacks of the T2L2 technique based on laser technology are discussed in Section III. Finally, some scientifical applications (current and future) are overviewed in Section IV.

II. THE CHARACTERISTICS OF T2L2

T2L2 receives an average of 100,000 optical events (t_B dates) per day. From 5 to 6 SLR participating stations in 2008, T2L2 implies today 22-24 stations (see Fig. 1).

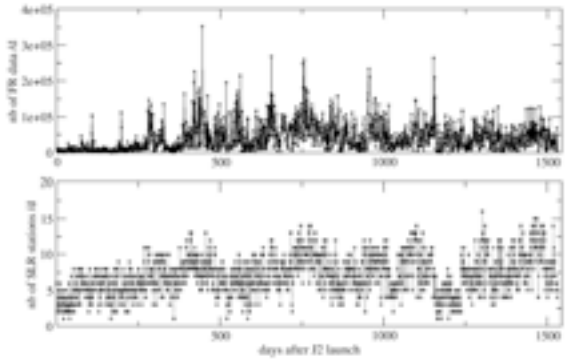

Fig. 1. Number of SLR Full Rate data, from 2008 to 2012, and number of SLR stations per day particiting in the T2L2/Jason2 tracking.

They send their data (t_e dates in UTC and 2-way distances dt_{2w}) regularly to the European Data Center (located in

Germany) and to the Crustal Dynamics Data Information System (US) that specialize in the geodetic space techniques.

Given the very high reliability of T2L2 over time (5 years in space), we developed a data reduction scheme that operates on a daily basis. In parallel, we have developed an interactive website (https://t2l2.oca.eu/) to describe the data over time: ground and board data and statistics. For the web user, it's possible to compute a given ground to space time transfer (from a selected set of SLR stations) or to obtain a history over several days. Actually, the website serves primarily to calculate the ground to ground time transfer ($\Delta t_{B\text{-}S}$ - $\Delta t_{B\text{-}S'}$) between the two reference clock systems of two selected SLR stations (S) and (S'). The basic equation that has been implemented corresponds to the following:

$$\Delta t_{B\text{-}S} = t_B + Corr_{\text{Instrum}} - [\, t_e + (dt_{2w} - Corr_{\text{Sagnac}})/2 \,] \qquad (1)$$

where:

$Corr_{\text{Instrum}}$: is the sum of the instrumental corrections; correction of time walk of the T2L2 non linear diode, and geometrical correction between the locations of the reflector array and the T2L2 optics (around 10 cm or 0.3 ns) on the platform.

$Corr_{\text{Sagnac}}$: Sagnac effect (due to both Earth's and satellite rotations) that is necessary to use when computing the equivalent time travel of the light between the station on the ground and the satellite, from the 2-way measurement (dt_{2w}).

Outside the expected performances mentioned earlier, we can establish a budget error of the ground to space time transfer (Eq. 1) according to Table I [8]. Here, the amounts shown are from recent analyzes from a SLR station equipped with an H-maser as reference clock.

Given the wide variety of clock systems and laser stations, we built a data reduction scheme based on the robust estimation (mathematical and numerical meaning). Statistically, we can say that the estimated noise at 1 s ranges from 45 to 65 ps. The average stability achieved in today's data processing is 4-8 ps at 75 s (see Fig. 2, the Time Variance obtained from many passages of ground to space time transfer for 2 laser stations).

TABLE I. A priori noise of the laser link for ground to space time transfer (in picosecondes).

Items	***Noise by type***		
	Ranging (dt_{2w})	***Board***	***$\Delta t_{B\text{-}S}$***
Timing at ground : t_e	5-10		
Return	5-10		
Laser pulse width	15-35		
Detector at ground	10-15		
Target signature	10-15		
Calibration	1-5		
Timing onboard : t_B		2-3	
Detector onboard		5-35	
Instrument Correct.		1-8	
Sub-total	20-45	5-35	
Total			20-55
Stability (σ_x)	1-5 / 15 s		4-8 / 75 s

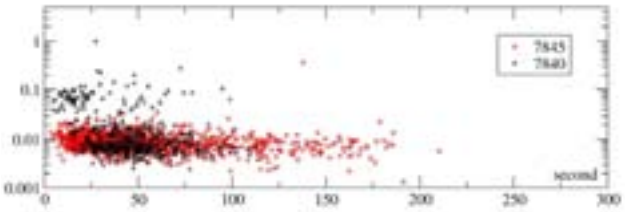

Fig. 2. Time Variance (in ns) of the ground to space time transfer, for each satellite passage, during 4 years; 7845: SLR Grasse, France; 7840: SLR Herstmonceux, UK.

The onboard timing of all optical events (laser pulses coming from ground stations) is referenced by an Ultra Stable Oscillator (USO, quartz) which is the heart of the Doppler tracking technique DORIS (Doppler Orbitography and Radiopositioning Integrated on Satellite) [9]. From recent improvements made in the data reduction, the estimate of the USO frequency from a T2L2 passage above a SLR station reaches 6-8.10^{-14} Hz at best. Thus, we are able to compare the USO frequency as estimated by the T2L2 time transfer and the one resulting from the DORIS orbit determination process. The a priori DORIS performance (in support of the orbitography) being of 0.3 mm/s it roughly corresponds to 3.10^{-12} Hz. As a matter of fact, the quality of the DORIS space technique partly depends on the ability to permanently monitor the USO frequency at least at that level. According to several T2L2 passages, we have established an empirical model describing the frequency variations of DORIS over 30 days; the residuals are in the range of 1-2.10^{-13} Hz. The next step will consist of introducing this model in the estimation process of the Jason2 orbit. Note that at this level of accuracy, we must take into account the relativity corrections: frequency "red shift" and second order Doppler.

Data processing for ground to ground time transfer consists of calculating the differences ($\Delta t_{B\text{-}S}$ - $\Delta t_{B\text{-}S'}$). As laser measurements between two (or more) stations are not synchronized on board (CV), we determine separately each synchronisation (Eq. 1); after filtering (white noise) an interpolation procedure permits to compute ($\Delta t_{B\text{-}S}$) for each second in the onboard time scale. Finally, the search for common seconds (between S and S') led us to calculate directly the difference between the ground clocks. The signal obtained depends essentially on the frequency difference between the two clocks; this difference of 1-3.10^{-13} Hz is due to the frequency error of each clock, and also to the altitude difference between the stations if any (the "red shift" is of ~1.10^{-13} Hz every 1,000 m). The resulting signal has a duration between 250 and 600 s, with an average 300 dots. After removing a linear fit, the ground to ground stability reach 11 ps over one passage (see examples Fig. 3). The time evolution of the mean value of the phase difference present a repeatibility error of ~50 ps.

Finally, great efforts have been made on the ground in order to: *i*) improve the measurement of the time delays in the cables (principle, methods and hardware), *ii*) determine the best point of reference of the time and frequency laboratory (PPS and its distribution to devices: GPS, laser, etc.) [10], *iii*) calibrate each time transfer technique, optical and microwaves.

Several have been conducted to this purpose, notably in Grasse (F), Herstmonceux (UK), and Wettzell (G).

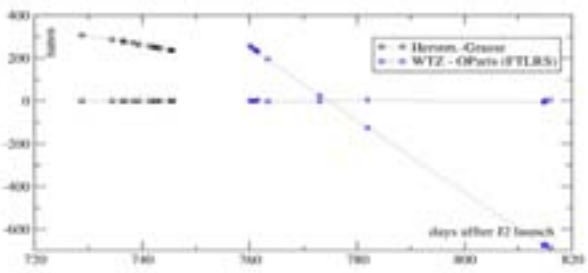

Fig. 3. Ground to ground time transfer (June to September 2010), signals and residuals after quadratic fit; 2 couples of SLR's (FTLRS is the French Transportable Laser Ranging Station, Herstm. in the UK, and WTZ in G).

III. THE POTENTIAL OF T2L2

The a priori potential of the T2L2 experiment is very important (see Table II). There is a good geographical coverage of the Jason2 satellite orbit from the ILRS network, the reliability of the onboard instrument for many years, the principle of the 2-way laser ranging is very simple and the quality of the measurements is very high. The satellite orbit has an altitude of 1335 km and the field of view of the optics of T2L2 being of ±55°, Common View (CV) passes are possible between remote ground stations at 6000 km. The acquisition of measurements on board is possible up to 5,000 Hz, the dead time of the electronic device being of 200 µs. This is more than enough since the SLR stations emit laser pulses usually in the green at 10 Hz. Finally, the onboard detector has been working on a multi-photon mode at 532 nm, this permits us to acquire data from all the SLR stations; heavy and complicated developments or tuning are then avoided.

On the other hand, the T2L2 experiment is constrained by several aspects. Since 2008, only some SLR stations are equipped with a highly stable clock (like a H-maser clock): 1 in China, 4+1 mobile in Europe, 1 in Japan, and 1 in the USA. The measurement dates (t_e) are provided at 1 ps resolution by these stations; other stations use less stable clock system and they provide data with a resolution of 100 ns sometimes. For its part, the onboard USO has a stability < 4 10^{-13} at 10 s but with a decreasing in terms of $t^{3/2}$ giving around 300-350 ps at 1000 s. Finally, the time-frequency laboratories (including those participating in the Atomic Time) are not close to laser stations and vice versa.

In summary, we can expect to "read" very accurately the onboard USO during Jason2 passes of 10 to 15 minutes, assuming that SLR stations use H-maser. For example, with favorable weather over Europe, it is possible to make ground to ground time transfers (CV) several times a day for several days. We must of course admit that with the orbital period of the satellite (almost 2 hours), the vagaries of weather, stops and breakdowns of the SLR stations, it is necessary to focus on a strict organization of field experiments; a planned organization and monitoring of operations on the ground; it has a lot of influence on the outcome.

TABLE II. Current status of T2L2 experiment: expected performances and results; the 2013-2014 follow-on mission shall allow to fulfill the remaining objectives (σ_x in picosecondes; tt: time transfer, gr.: ground).

Objectives		*Status*	
		Expected	***Current***
T2L2 gr. 2 space tt	(0.1 s)	65	55-65
	(1,000 s)	1	< 10
T2L2 gr. 2 gr. tt (CV)	(1000 s)	1.5	10
	(1 day)	5	< 50
T2L2 gr. 2 gr. tt (~~CV~~)	(300 s)	150	150
	(3,000 s)	2,000	-
T-F metrology: Comparison of remote clocks	(1 d)	10	20
	(100 d)	50	30
T-F metrology: Time scales, calibration of UTC		E = 1,000	E = 100
T-F metrology: Comparison to GPS-CP			
	(10,000 s)	15	20
	(1 d)	40	20
T-F metrology: Compar. to TWSTFT CP			
	(10,000 s)	15	20
	(1 d)	30	20
T-F metrology: Accuracy of RF links		E = 1,000	E = 100
Fundamental Physics	(1,000 s)	5	10
(anisotropy of *c*)	(> 100 d)	-	-
Jason2: Charcaterization of DORIS USO			
	(10 s)	2.5	10
	(300 s)	100	< 100
Jason2: One-way ranging (observation > 80° elvevation)	(15 s)	10	10
Optical link budget		Model validation	-

IV. APPLICATIONS AND PERSPECTIVES

T2L2 is an instrument available to the scientific community involved in the field of time-frequency, space geodesy and fundamental physics (Table II). Planned for two years at the start of the mission, it was extended for two years (2011-2012) in 2010, and again for two years (2013-2014) in 2012 by the Centre National d'Etudes Spatiales (CNES). We continue to propose field experiments, including synergy with GPS and the Two-way technique, with a view to studying the long-term stability and accuracy of links. Some important effects are also done to improve time stability and time accuracy of laser ranging stations involved.

The applications of the T2L2 time transfer that will be pursued are: *i*) a study of the Lorentz Invariance (the anisotropy of the speed of light should be estimated at 10^{-9} to 10^{-10} [11]), *ii*) a monitoring of the USO frequency at 1-2.10^{-13} Hz should improve the orbit of Jason2 and especially the ground positioning, *iii*) an ultimate validation of T2L2 at the best possible performance, *iv*) a synchronization at 5-10 ns of the reference clocks of the SLR stations permitting improve the orbit determination of several geodetic satellites (now, the dates of SLR measurements differ from a station to another station of a few microseconds, see Fig. 4), *v*) a very accurate

link budget based on the analysis of both energy received at ground and onboard.

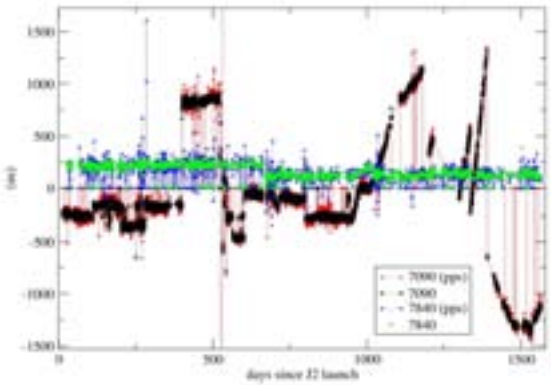

Fig. 4. Synchronisation of the reference clock systems of 2 SLR stations thanks to T2L2 on board Jason2 (7090: Yarragadee, AUS, and 7840: Herstmonceux, UK).

ACKNOWLEDGMENT

The authors wish to thank ILRS and SLR station that are participating to the T2L2 experiment. They wish to thank also the Centre National d'Etudes Spatiales for its support.

REFERENCES

[1] P. Fridelance, E. Samain and Ch. Veillet, "T2L2 – Time Transfer by Laser Link: A new Optical Time Transfer Generation", Experimental Astronomy, Vol. 7 (3), 191-207, 1997.

[2] P. Exertier, et al., "Contribution of Laser Ranging to Earth's sciences", CRAS Geoscience Serie, Vol. 338, 958-967, 2006.

[3] M. Pearlman, et al., "The International Laser Ranging Service", Adv. Space Res., Vol. 30 (2), 135-143, 2002.

[4] J. Nicolas, et al., "*French Transportable Laser Ranging Station: scientific objectives, technical features, and performances*", Applied Optics, Vol. 39 (3), 402-410, 2000.

[5] Ph. Guillemot, et al., "Improvement of comparisons between T2L2 & RF Links", Proceedings of the EFTF 2012, Gothenburg, Sweden, April 23-27 2012, pp 345-348.

[6] E. Samain, et al., "Time Transfer by Laser Link - T2L2: Current Status and Future Experiments", Proc. of the European Frequency and Time Forum, San Francisco, California USA, May 1-5 2011, pp. 378-383.

[7] E. Samain, et al., "T2L2: Ground to ground Time Transfer", Proc. 26th European Frequency and Time Forum, Gothenburg, Sweden, May 23-27 2012, pp. 36-40.

[8] P. Exertier, E. Samain, P. Bonnefond, and Ph. Ghillemot, "Status of the T2L2/Jason2 Experiment", Adv. Space Res., Vol. 46 (12), 1559-1565, 2010.

[9] Ph. Guillemot, et al., "First Application of the T2L2 Ground to Space Time Transfer: Characterisation of the DORIS USO", Proceedings of EFTF 2009, Besançon, France, April 19-25 2009, pp 711-714.

[10] M. Laas-Bourez et al., "Time and frequency distribution improvement in Calern/Geoazur laboratory for T2L2 campaigns", this EFTF Proceedings, 2013.

[11] P. Wolf, "Proposed satellite test of special relativity", Phys. Rev. A, Vol. 51 (6), 5016-5018, 1995.

Design of the Frequency and Timing Subsystem for ESA's Deep Space Antenna 3

Ainhoa Solana, Wolfgang Schäfer, Theo Schwall
TimeTech GmbH
Stuttgart, Germany
Ainhoa.Solana@timetech.de

Maria Antonia Ramos, Javier de Vicente
European Space Agency (ESA-ESOC)
Darmstadt, Germany

Sylvère Froidevaux
T4Science
Neuchâtel, Switzerland

Vincent Giordano
Femto-ST
Besançon, France

Serge Grop, Benoit Dubois
ULISS-ST, SAIC Université de Franche-Comté
Besançon, France

***Abstract*— In December 2012, ESA inaugurated their third Deep Space Antenna tracking station near Malargüe, Argentina. Due to the nature of the deep space operations, exigent requirements for stability of reference signals and low phase noise characteristics were necessary on the ground station equipment. In order to fulfill the requirements, new concepts and hardware development were carried out, resulting in an improvement of the performance of the frequency and timing reference system.**

Keywords: maser; cryogenic sapphire oscillator; deep space

I. INTRODUCTION

ESA's Deep Space Antenna 3, with its 35m dish antenna, was succesfully installed in a remote area near Malargüe in Argentina. This antenna follows the two previous Deep Space Antennas installed in New Norcia, Australia, in 2002 and Cebreros, Spain, in 2005. These three antennas are situated at about 120° with respect to each other making possible global coverage. This station profits, in addition, of minimum impact from the atmosphere as a consequence of its strategic location, which results in an enhancement of its performance [1].

New concepts and techniques to improve the overall performance of the Frequency and Timing (F&T) subsystems were developed and applied to ESA's third Deep Space Antenna. In contrast to previous stations, the clocks were not installed in the antenna, but in a distant building 100m away. Preservation of the performance along the long distribution path while maintaining the simplicity of the system as much as possible was not an easy task and was the main motivation during the design of the system. The performance achieved after adaptation and optimization of the key elements of the F&T subsystem and the reduction of the thermal sensitivity, allowed distribution to the antenna site, without degradation of the performance.

Figure 1. DSA3 antenna in Argentina – 35m dish

Independent and well environmentally-controlled clocks room, together with an improved short term stability and phase noise lead the way into the introduction of a 100 MHz frequency distribution system, in spite of the distance. Lower frequencies, such as 5 MHz and 10 MHz, were locally generated in each building out of the 100 MHz distributed signals. Timing signals, on the other hand, were regenerated and synchronized to the remote end.

Furthermore, the introduction of a cryogenic cooled sapphire oscillator (CSO) as a third source, in addition to the two redundant active hydrogen masers, accomplished to combine the CSO's good short term stability together with the better long term stability of the masers by locking the CSO to one of the available masers.

The system design, architecture, key aspects and the results of the tests carried out are presented on this paper.

II. Deep Space Antenna 3 applications

ESA's deep space antenna station incorporates a 35m dish equipped with a Cassegrain Beam Wave Guide feed RF system operated with dichroic mirrors and low noise amplifiers. Ka-band reception and X-band transmission and reception are already supported. Ka-band transmission, and K-band reception are planned to be supported in the near future [1].

The station is prepared to provide telemetry and telecommand functions, as well as serve for other purposes such as satellite tracking and ranging, Radio Science research, and support future scientific missions like LISA Pathfinder [9], Gaia [10] or BepiColombo [11]. ESA's deep space antennas already provide support to Venus express [12], Mars Express [13], Herschel [14] and Planck [15] missions.

While spacecraft tracking for orbit determination requires stable reference frequencies in the medium term and accurate time to obtain positions of satellites with sufficient precision (0.1mm/s). Some Radio Science missions impose, at the same time, high stability in the short term so that once per second events can be measured properly [2][6][7]. All these demanding requirements, added to the difficulty of having the clocks far away from the antenna made the design of the frequency and timing generation and distribution system a continuous challenge.

III. System design and Architecture

The F&T system for the Deep Space Antenna 3 station is distributed among three main locations; Clocks Room, Main Equipment Room (MER) and Antenna Equipment Room (AER). The clock room, is, in turn, subdivided into three smaller rooms, one room for the two Active Hydrogen Masers (Maser room), one room for the cryogenic sapphire oscillator (CSO room) and an Optical Clock room prepared for housing an optical clock in the future. Having the clocks so distant from the antenna results in a critical distribution, however, it has an advantage from the station level point of view. Ka-band transmission and K-band reception equipment, as well as future front-ends can be easier added, keeping the references in the main building and implementing a star topology to distribute the necessary signals to the different antennas. At the moment, reference frequency and timing signals from the clocks are distributed to the MER, and from the MER distributed to the AER, located 100m away from the Operations Building. A simplified block diagram with the different locations of the F&T system is presented in Fig. 2.

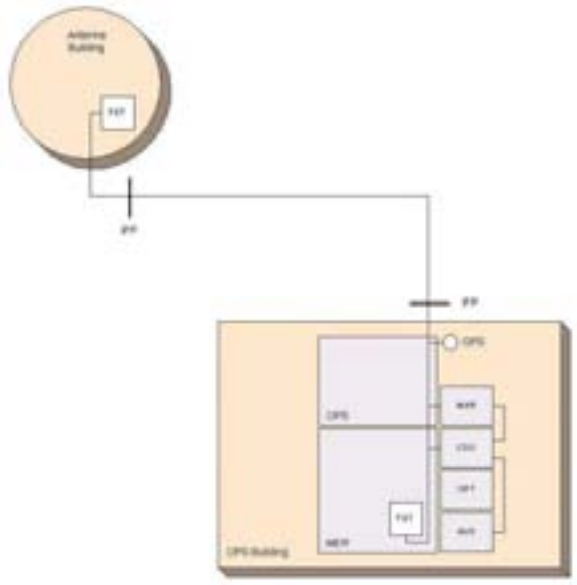

Figure 2. Simplified diagram of DSA3 locations with F&T equipment.

The system is prepared to store all data and measurements available from the system in order to provide long-term analysis of the frequency and timing signals' performance. Additionally, the system uses 3-corner hat ADEV post-processing software to determine the performance of each individual clock. Temperature and magnetic field in the maser room are continuously controlled. Undesired events are also logged for problem detection and troubleshooting activities.

A. Reference Clocks

Three high performing clocks are available at the station. The different rooms comprising the Clocks Room, are all environmentally controlled to avoid temperature variations of more than ± 0.5°C, assuring a stable thermal environment in which the clocks can perform at their best.

Figure 3. The two masers inside the Maser Room (MAR)

The two redundant Active Hydrogen Masers (AHM), see Fig. 3, manufactured by T4Science in Neuchâtel, Switzerland,

exhibit an improved thermal design and high performance. For DSA3, the masers were modified to improve the phase noise of the 100 MHz maser frequency signal at frequency offsets below 100 Hz from the carrier, eliminating the need of external clean-up oscillators and/or Phase Locked Loops (PLL) outside of the maser. To do so, an Oven Controlled Crystal Oscillator (OCXO) manufactured by Pascall, United Kingdom, with a performance at 100 MHz of –138 dBc/Hz at 100 Hz offset was used instead of the original Voltage Controlled Crystal Oscillator (VCXO). The Pascall oscillator is locked to a 5 MHz BVA-type Ultra Stable Oscillator (USO) model 8607 from Oscilloquartz, Neuchâtel, Switzerland, which provides the good phase noise at lower frequency offsets. The OCXO is located outside of the ovenised maser electronics compartment due to heat dissipation concerns and supplied with regulated stable power supply. In addition to these modifications, the number of available 100 MHz signal outputs in the PLL board of the maser was duplicated from two to four, and distributed from the Maser interface directly to the units in MER.

Fig.4 shows the phase noise performance of the modified maser at 100 MHz. The figure represents one maser against the other. Assuming that both perform similarly, 3 dB can be subtracted from the values shown in the plot. For frequency offsets very close to the carrier (until about 30 Hz) one can appreciate the performance of the BVA, whilst, for instance, at 100 Hz, the signal already benefits from the phase noise of the Pascall OCXO, as a result of the selected PLL bandwidth .

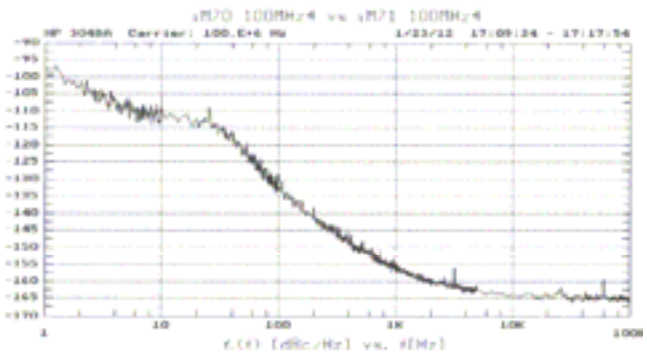

Figure 4. Maser 1 vs. Maser 2 – 100 MHz phase noise

Table 1 shows the improvement gained with respect to previous systems in terms of phase noise performance. Significant improvement can be seen at high frequency offsets.

TABLE I. MASER IMPROVEMENT WITH RESPECT TO PREVIOUS STATIONS

Phase Noise in dBc/Hz of the 100 MHz signal at the Maser interface		
Frequency Offset	***Previous Stations***	***DSA3***
1 Hz	-102	-102
10 Hz	-115	-115
100 Hz	-125	-136
1 kHz	-148	-160
10 kHz	-156	-164
100 kHz	-160	-165

In addition to the two AHM, ESA backed the design and implementation of a third clock to be used in DSA3. This clock is a Cryogenic Sapphire Oscillator prototype manufactured by Femto-ST in Besançon, France (See Fig. 5).

Figure 5. CSO in DSA3

The CSO consists of a high-Q sapphire whispering gallery mode resonator [5]. The resonator is thermally regulated by means of a cryocooler which sets the temperature close to 6K, so that any first order variation due to temperature cancels out. Electronics are comprised by amplifiers and filters belonging to the oscillator loop, and work at room temperature [5]. Finally, a synthesizer is needed in order to [6]:

- Perform the down-conversion from the CSO reference output frequency 9.989 GHz to 100MHz, 10 MHz and 5 MHz.
- Lock the CSO to the selected maser. The CSO counts with its own dedicated phase comparator which measures the phase difference between the masers and the CSO. By means of this phase comparator it is possible to lock the CSO to a maser with a long time constant (around 1000s). The result of this practice is an output frequency which profits from the good short term stability of the CSO and benefits from the good long term stability of the maser to which is locked to.

Fig. 6 shows the phase noise of the synthesizer measured during Factory Acceptance Tests. Two equal synthesizers were manufactured and measured against each other. As a result, and assuming that both units contribute the same amount to the measured phase noise, one can subtract 3 dB to obtain the real performance of one single synthesizer.

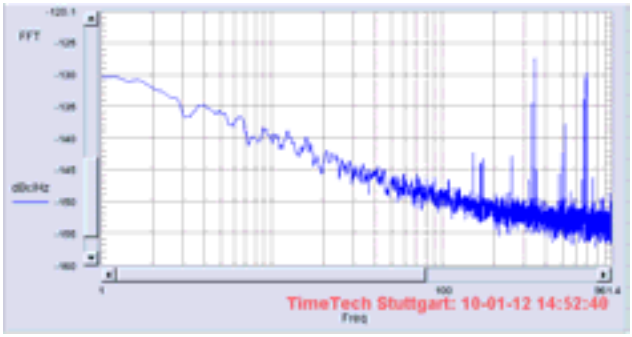

Figure 6. CSO synthesizer phase noise up to 1kHz at 100 MHz.

Moreover, having three clocks has further advantages. It is possible to measure the performance of each individual clock. Fig.7 shows the performance of the three clocks in DSA3 measured by means of the three-corner-hat method up to 1000s. One can see the better short-term performance of the CSO compared to that of the masers.

B. Frequency Distribution System

DSA3 F&T subsystem is based on a 100 MHz distribution system. Active distribution units to compensate for internal losses were equipped with low temperature coefficient (150 fs/K), standard high performance buffer amplifiers and low noise figure Monolithic Microwave Integrated Circuits (MMIC) set in parallel. 5 MHz and 10 MHz signals are also provided by the system, generated by division of the 100 MHz reference frequency signal. This state-of-the-art high performing low phase noise divider and distribution board shows improved phase noise characteristics (see Fig. 8) and was developed during the design of the F&T system for DSA3.

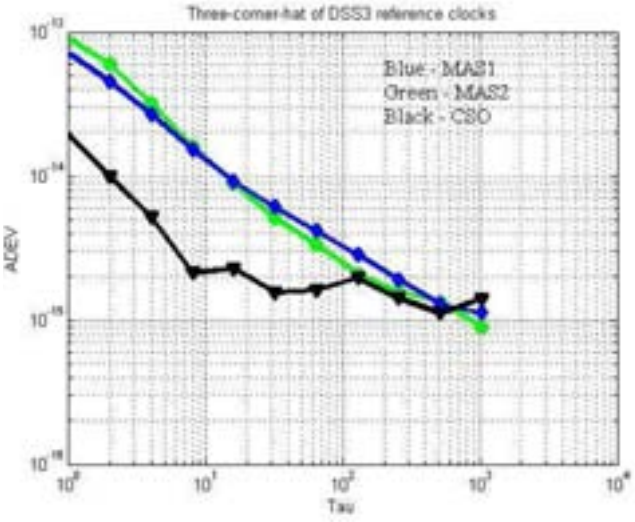

Figure 7. Individual Allan deviation performance of each clock

To assure a successful design, appropriate cables were selected to transmit the 100 MHz signals from the Clocks room to the MER and from the MER to the AER, without degrading the performance of the signal. In fact, implementing a long cross-site link, such as that between MER and AER, at frequencies below 100 MHz would have degraded the maser/CSO performance due to the very high thermal sensitivity of all coaxial cables at low frequencies [3]. Consequently, LDF4 50Ω cables with foam dielectric from Andrew, and presenting an extremely low thermal coefficient (0.6 ppm/K at 100 MHz), were selected for the cross-site link. In addition, cable ducts were buried 80 cm deep to attenuate the temperature variations as much as possible.

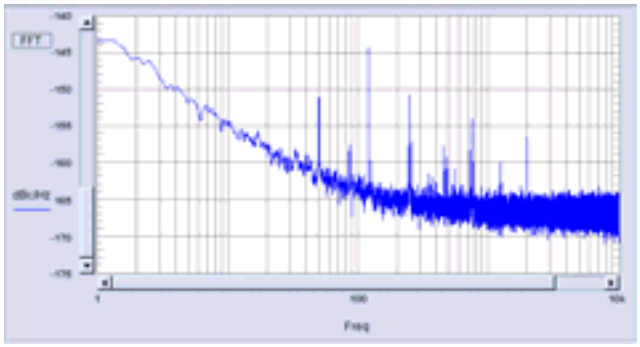

Figure 8. Divider phase noise at 100 MHz (*)

For the transmission of the 100 MHz from the Masers and CSO to the F&T rack inside the MER, and for the cables between the Maser room and the CSO room, FSJ-4 and FSJ-1 cables were used, respectively. These high quality cables have a greater thermal coefficient than LDF-4 50Ω, but, sufficient for adjacent rooms and short distances. A trade-off between thermal characteristics and cost had to be conducted.

Concerning performance at system level, Fig. 9 shows the performance achieved at the furthest point from the clocks (i.e. AER). The setup consisted of using one redundancy chain distributing the signals from one maser, against the second redundancy chain distributing the frequency of the second maser. (3 dB to be subtracted)

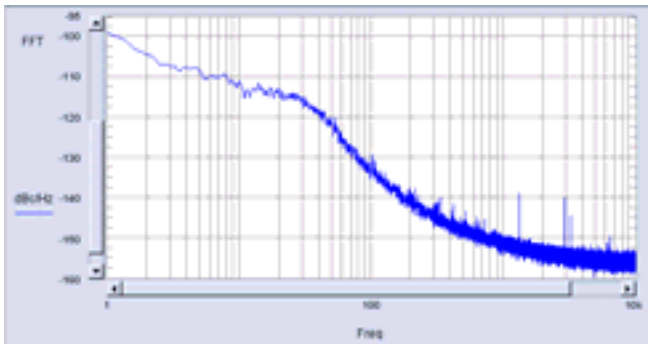

Figure 9. Phase Noise: Maser 1 through chain 1 vs Maser 2 through chain 2 at 100 MHz

* 3 dB to be subtracted to get phase noise of single unit

C. *Timing Distribution System*

Timing signals are generated using the derived 5 MHz signal from the masers (or CSO). The generated 1pps is constantly monitored against UTC (GPS) and maintained within 100ns. Moreover, the GPS comparison also allows long-term frequency accuracy analysis.

There is no distribution of timing signals as such, but regeneration of these signals on the remote side out of a 1pps two-way measurement. An optical link with active delay compensation assures that the remote 1pps signal is aligned to less than 1ns to the transmitted one [4]. IRIG-B timing signals also follow this 1pps and will therefore also appear aligned.

IV. Summary and Conclusions

Designing a well-performing F&T subsystem for DSA3 was a challenge. The requirement of locating the clocks at a substantial distance of 100 m from the antenna imposed applying new concepts to the F&T system design. In this paper, we have presented the motivation, architecture, design process, developments and results from the F&T system installed in DSA3, Argentina.

Main differences and new developments with respect to previous stations were, among others:

- Special configuration of the AHM with improved phase noise performance to avoid the use of external clean-ups.
- Design of a 100 MHz distribution system to profit from the reduced temperature coefficient at high frequencies.
- Selection of thermally stable cables running on deep cable ducts to decrease temperature variations.
- Low phase noise, high performing dividers to provide lower frequencies out of the 100 MHz distributed signal.
- Introduction of a third clock with excellent short term performance which could be locked to an AHM at integration times of around 1000 s.
- Improved optical link for time synchronization with active delay compensation and uncertainty below 1ns.

In this paper, we have presented the motivation, architecture, design process, developments and results from the F&T system installed in DSA3, Argentina.

References

[1] DSA3 Malargüe ground Station: http://www.esa.int/Our_Activities/Operations/Malarguee_-_DSA_3

[2] W.Schäfer, A.Jornod, J.de Vicente, "ESA's Deep Space Frequency and Time systems. An asset for Operations and Radio Science investigations," ATF Proceedings, NIM, Beijing, China, Oct 18-19, 2004.

[3] G.Hejc, W.Schäfer, A.Seidel, M.P.Hess, J.Kehrer, G.Santarelli, et al, "Frequency Dependency of Phase Stability of RF Cables," Proc. EFTF, Geneva, Switzerland, June 2007.

[4] C.Molard, W.Schäfer, M.Kufner, S.Durand, "Phase Stability of Two-Way Optical Fiber Frequency and Time Transfer," Proc. EFTF, San Francisco, United States, May 2-5, 2011.

[5] S.Grop, V.Giordano, P.-Y Bourgeois, Y.Kersalé, N.Bazin, et al, "ELISA : an ultra-stable frequency reference for space mission ground segment," ESTEC Noordwijk, May 6-8, 2008.

[6] W:Schäfer, G.Hejc, S.Grop, E.Rubiola, P.-Y Bourgeois, V.Giordano, Y.Kersalé, J. de Vicente, "Design and Performance of the RF Synthesizer for the ELISA cryo-cooled Sapphire Oscillator," Proc. EFTF, San Francisco, United States, May 2-5, 2011.

[7] E.Vassallo, R.Martin, R.Maddé, M.Lanucara, P.Besso, P.Droll, G.Galtié, J.de Vicente, "The European Space Agency's Deep-Space Antennas," Proc IEEE, Vol 95, Nov 2007.

[8] W.Schäfer, J. de Vicente, „ESA's Frequency and Timing Systems for Deep Space operations and Radio Science Investigations," ESA 4th International workshop on tracking, telemtery and command systems for space applications, TTC, Darmstadt, Germany, September 11-14, 2007.

[9] LISA Pathfinder Mission: http://www.esa.int/Our_Activities/Operations/Malarguee_-_DSA_3

[10] Gaia Mission: http://www.esa.int/Our_Activities/Space_Science/Gaia

[11] BepiColombo Mission: http://www.esa.int/Our_Activities/Space_Science/BepiColombo_overview2

[12] Venus Express Mission: http://www.esa.int/Our_Activities/Space_Science/Venus_Express

[13] Mars Express Mission: http://www.esa.int/Our_Activities/Space_Science/Mars_Express

[14] Herschell Mission: http://www.esa.int/Our_Activities/Space_Science/Herschel

[15] Planck Mission: http://www.esa.int/Our_Activities/Space_Science/Planck/Science_objectives

Clock Composition by Wiener Filtering Illustrated on Two Atomic Clocks

Marek Peca*, Vojtěch Michálek, Michael Vacek
Serenum, a. s., Beranových 130, Praha – Letňany, Czech Republic
České vysoké učení technické v Praze, Břehová 7, 115 19 Praha 1, Czech Republic
*e-mail: peca@vzlu.cz

***Abstract*— Estimation instead of feedback loops is recommended to obtain a composite clock. Wiener filtering approach to clock ensembling is introduced and demonstrated on the simplest case of two clocks. Design procedure dealing with clock system non-stationarity, non-observability and numerical issues, is given. Impact of causality to unexpected performance degradation is discussed.**

I. Introduction

Composite clock, or clock ensembling, i. e. calculation of best time estimate given readings from multiple clocks, is a must for state-of-art timekeeping. There are two distinct tools for clock ensembling: (i) feedback; (ii) estimation. Using (i), a phase- or frequency-locked loop or loops (PLL, FLL) are formed, containing clock and a controller. The controller corrects clock's time (by tuning, modulation, phase stepping, etc.), and the corrected signal is fed back into the controller. On the other hand, in case of (ii) an estimator senses clocks' reading without any modification, and produces estimate of clocks' state, applicable as a correction to time reading. The corrected signal is not fed back into the estimator.

Realizations of (i) are e. g. Network Time Protocol (NTP), and Atomic Clock Ensemble in Space (ACES [1]). Suppose the controller (i) is constrained to be linear (what is the common case). Then, following separation principle [2], even the optimal controller (minimum variance controller) will give worse or same performance, as an optimal linear estimator (ii); the limit case of the same performance requires zero control noise. Therefore, we claim that use of (i) is justified only when implementation of estimator is not feasible (e. g. in case of specific analogue circuitry). Otherwise, including ACES and NTP in our opinion, the estimator (ii) is the right way to choose.

II. Clock modelling

The essential prerequisite for design of ensembling is a clock model, describing statistical properties of phase evolution over time $x(t)$. A clock is described as a linear stochastic system, defined by phase spectrum $\mathcal{S}_{xx}(f)$. The system is marginally stable: it contains one or more integrators in cascade, corresponding to $f^{-n}, n = 2, 4, \ldots$ terms in $\mathcal{S}_{xx}(f)$. In addition, it may contain stable modes as well. Within estimation approach to ensembling, clocks are not disciplined, the system is purely stochastic, no deterministic input (tuning).

A discrete-time processing is assumed further. Estimates are calculated digitally from sequence of measurements. For convenience, these shall be acquired at equidistant time instants $t_k, t_k - t_{k-1} = T_s = const.$. This can be fulfilled only approximately, because T_s is perturbed by clock noise as well. Although considered by [3], we follow the conclusion of [4], that the effect is negligible for the purpose of ensembling.

Confinement to a class of linear discrete-time systems, containing stable and marginally stable modes, is sufficient for estimator design procedure (Sec. III). Assumption of clock process linearity implies that properly designed linear estimator is optimal in sense of mean squared error (MSE). It also implies, that spectrum $\mathcal{S}_{xx}(f)$ is sufficient description of the process – possibly different clocks with equal $\mathcal{S}_{xx}(f)$ are indistinguishable, regardless of their internal structure (Spectral factorization theorem [2], [5]).

Assumption of linearity works well for f^{-2}, f^{-4}, f^{-6} spectrum terms, which indeed origin from cascaded integration of error. A more peculiar component of the spectrum is $1/f$-noise (flicker), constituting f^{-3}, f^{-5} terms [6]. Works on deterministic chaos suggest an inherently non-linear behavior as a cause of $1/f$-noise [7]. The $1/f$-noise can not be generated by linear system of finite order. However, for a given frequency band of interest and required fidelity, the spectrum may be approximated by a linear system of some finite order. The interesting question follows, whether a linear estimator designed for such an approximate system may approach the optimal estimator even for a process, containing non-linear (chaotic) $1/f$-noise. The answer is not known to us, so we follow [3], approximating $1/f$-noise terms by finite-order, linear, discrete-time model.

A single-input, single-output (SISO) discrete-time linear system can be described by its transfer function $G(z)$: $x(t) = G(z)u(t)$ (input signal u transformed to output y; z is a forward shift operator). In our case of purely stochastic system (no control input) $u(t)$ is a unit variance white noise. For finite-order systems $G(z) = B(z)/A(z)$ where B, A are polynomials. A spectrum of x ($S_{xx}(z)$ or $\mathcal{S}_{xx}(f)$) is given by:

$$S_{xx}(z) = G^*(z)G(z)S_{uu} = \frac{B^*(z)B(z)}{A^*(z)A(z)}S_{uu}, \qquad (1)$$

$$\mathcal{S}_{xx}(f) = S_{xx}(e^{j\theta}), \quad \theta = 2\pi f T_s,$$

where $G^*(z) = \overline{G(1/z)}$. If x is real-valued, $S_{xx} = S^*_{xx}$. Given S_{xx} can be always factored as product of G, G^* (1) so that roots of B, A lie inside the unit disc. The step is called spectral factorization, denoted $G(z) = \mathrm{spf}(S_{xx}(z))$, producing stable, minimum-phase model G [2], [5]. $\mathrm{spf}(\cdot)$ allows to create clock model out of a given phase spectrum. A state-space clock model $\mathbf{x}(t+1) = \mathbf{\Phi x}(t) + \mathbf{u}(t)$ [4], [8], [3], [9], [10] can be converted to SISO $G(z)$ by standard means [2].

The model of single clock has been given. Ensemble is a set of N clocks (Fig. 1a). Using any meaningful physical means of time signal processing (counters, phase comparators, mixers, etc.), only time differences between the clocks may be measured. There is no clue about an "absolute" time offset. With any number of mutual measurements, we end up with only $N-1$ degrees of freedom in data: measurement matrix is singular.

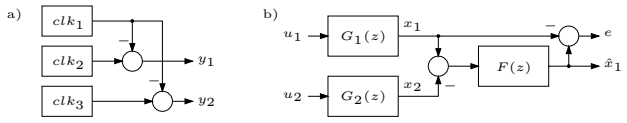

Fig. 1. (a) Clock ensemble (b) Composition of two clocks

Two important consequences follow, whose conjunction makes the estimation task non-trivial one: (i) time offset (error) of each individual clock grows without bounds; (ii) clock ensemble system is not completely observable. Therefore, any possible time estimator produces time estimate whose error grows without bounds as well. The goal is to achieve the lowest possible error within finite horizon. It is probably this specialty, why the topic of clock ensembling is still in active research [9], [10].

III. Estimator design

The most general form of MSE optimal linear estimator is Kalman filter (KF [2]). The mentioned clock ensemble's non-stationarity and non-observability cause difficulties to practical KF computation due to unbounded covariance growth. This problem gave rise to KF variants with specific covariance treatment [4], [8], [3], [10]. We have chosen another way, leading to a simple, closed-form estimator: Wiener filter (WF [5], [2]). The only limitation of WF for clock applications is that time-invariant processes are assumed, i. e. clock spectra supposed to be constant during estimation. In the simplest case of only two clocks [1], the WF becomes SISO, and the expressions are very simple.

The ensemble of $N = 2$ clocks $G_{1,2}(z)$ thus produces only one $(N-1)$ measurement y, Fig. 1b. $G_{1,2}$ are assumed SISO, i. e. $\mathrm{spf}(\cdot)$ performed if necessary. The time difference y is fed into estimator $F(z)$, which is designed to estimate output of one of the two clocks, $\hat{x}_1$. The $\hat{x}_1$ samples constitute corrections of x_1 signal, reducing effectively an uncertainty of composite time to that of residual signal e. The task is symmetrical, after exchanging $G_1 \leftrightarrow G_2$, the estimator becomes $F'(z) = 1 - F(z)$. Optional measurement noise may be incorporated into G_2 model.

The design of linear, MSE optimal estimator following Wiener formalism is based on two spectra: spectrum S_{yy} of the measured signal y, and cross-spectrum between y and signal to be estimated x, designated S_{xy}. In our case $y = x_1 + x_2$ and $x_{1,2}$ are uncorrelated ($x_1 \perp x_2$) therefore simply $S_{xy} = S_{xx}$.

There are three different variants of resulting estimators: non-causal $F_{nc}(z)$, causal $F(z)$ and finite-lag $F_T(z)$ WF. $F_{nc}(z)$ is best (lowest MSE), but requires to process future samples $y(t+1) \ldots y(+\infty)$. It can not be used in real-time, only offline in batch processing (smoothing). $F(z)$ is designed to deliver estimates without any lag, within the measurement cycle, possibly in real-time. Because of the lack of future y development information, its MSE is worse. A gap between $F_{nc}(z)$ and $F(z)$ is filled with $F_T(z)$, allowing to trade performance vs. filter lag T (number of future samples to wait for). The non-causal solution is simple [5], [2]: $F_{nc} = S_{xy}/S_{yy}$; in our specific case:

$$F_{nc} = \frac{S_{xx}}{S_{yy}} = \frac{S_{11}}{S_{11} + S_{22}},$$

where $S_{kk} = G^*_k G_k$ are clock spectra; the residual error is:

$$e = x_1 - \hat{x}_1 = \frac{1}{w_1 + w_2}(w_1 x_1 + w_2 x_2), w_k = \frac{1}{S_{kk}}.$$

Residual spectrum is easily plotted, or even sketched:

$$S_{ee} = \frac{S_{11} S_{22}}{S_{11} + S_{22}}$$

.

Considering $\mathcal{S}_{xx}(f) = \sigma^2_x(f)\mathrm{d}f$, we see that estimator averages input signals $x_{1,2}$ weighted by inverse of their respective variances at given frequency. If both clocks have a spectrum of the same shape $S_{11} \propto S_{22}$, estimator reduces to mere static weighted average $F_{nc}(z) = const.$, and it is also the only case when $F_{nc}(z) = F(z)$ is causal.

If both processes $x_{1,2}$ (or the output y), are filtered by common transfer function $G'_1(z) = G_c(z)G_1(z)$, $G'_2(z) = G_c(z)G_2(z)$, then $F_{nc}(z)$ remains unchanged. Thanks to this property, $F_{nc}(z)$ is equally optimal for estimation of time (phase), as for estimation of frequency.

$F(z)$ is not allowed to weight future data so its impulse response must be zero in negative time, $h(t<0) = 0$. Operation to truncate $H(z)$ to its causal part is denoted $[H(z)]_+$. A naïve approach to $F(z)$ might be to take $[F_{nc}(z)]_+$. This resembles a common practice of block data processing: samples outside of a dataset are expected to be zero. Despite of that, $[F_{nc}(z)]_+$ is not the MSE optimal $F(z)$. The right solution is derived with help of a notion of whitening filter $W(z)$ [5]:

$$W(z) = \mathrm{spf}(1/S_{yy}), \qquad F(z) = [S_{xy}W^*]_+ W.$$

Compare $F_{nc}(z) = (S_{xy}W^*)W$ – only a part of $F_{nc}(z)$ underwent the causal truncation. $F(z)$ is no longer invariant to multiplication by common factor G_c. Therefore, MSE

optimum for time generally differs from MSE optimum for frequency in case of causal estimator. $F_T(z)$ is similar to $F(z)$, only the $(S_{xy}W^*)$ is allowed to look T samples into the future: $F_T(z) = z^T[z^{-T}S_{xy}W^*]_+W$. The properties are similar to that of $F(z)$, performance compares as follows: var $e_{causal} \geq$ var $e_T \geq$ var e_{nc}.

Design procedure begins with clock models in form of polynomial fractions $G_1(z) = B_1(z)/A(z)$, $G_2(z) = B_2(z)/A(z)$, common denominator $A(z)$ is assumed. Models may be safely expanded to common $A(z)$ if required. Spectrum of measured signal is:

$$S_{yy} = (U_1^*G_1^* + U_2^*G_2^*)(G_1U_1 + G_2U_2)$$

Since $u_1 \perp u_2$, var $u_1 =$ var $u_2 = 1$, $U_1^*U_2 = 0, U_1^*U_1 = U_2^*U_2 = 1$:

$$S_{yy} = G_1^*G_1 + G_2^*G_2 = \frac{B_1^*B_1 + B_2^*B_2}{A^*A} = \frac{C^*C}{A^*A}$$
$$\text{where} \quad C = \mathrm{spf}(B_1^*B_1 + B_2^*B_2). \tag{2}$$

Note $C(z)$ is obtained by $\mathrm{spf}(\cdot)$ (2). Cross-spectrum of $x = x_1 \rightarrow y$ is:

$$S_{xy} = (U_1^*G_1^*)(G_1U_1 + G_2U_2) = G_1^*G_1 = \frac{B_1^*B_1}{A^*A}$$

.

Giving the non-causal WF:

$$F_{nc} = \frac{S_{xy}}{S_{yy}} = \frac{B_1^*B_1}{C^*C}.$$

Causal WF follows:

$$W = A/C, \text{ so that } S_{yy} = 1/(W^*W)$$
$$F = [S_{xy}W^*]_+W = \left[\frac{B_1^*B_1}{AC^*}\right]_+ \frac{A}{C} = \left[\frac{D_+}{A} + \frac{D_-}{C^*}\right]_+ \frac{A}{C}$$

$$B_1^*B_1 = D_+C^* + D_-A \tag{3}$$

$$F(z) = \frac{D_+(z)}{C(z)}. \tag{4}$$

The polynomials $D_{+,-}$ result from (3). Their orders should be constrained so that D_+/A is causal (and possibly containing absolute term $z^0 \equiv h(0)$), while D_-/C^* is strictly anti-causal, non-containing the absolute term. Such a constraint assures unique solution to (3) [11].

IV. Specific problems

The central problem of clock ensembling is the non-stationarity and non-observability of the system (Sec. II). The non-stationarity manifests itself as a marginally-stable $(z-1)^m$ factor: $A(z) = (z-1)^m\tilde{A}(z)$, where $\tilde{A}(z)$ are stable factors (possibly $\tilde{A}(z) = 1$ for pure integrator models). Some of the WF formulations disallow marginally stable factors at all; others [11] do allow them, but they require at least the residual error e variance to be bounded. In our case, this condition is not satisfied. To overcome problems caused by $(z-1)^m$ ($\mathcal{S}_{..}(f \rightarrow 0) \rightarrow \infty$), we employ following notional alteration $A(z) = (z-(1-\epsilon))^m\tilde{A}(z)$.

Integrators were substituted by 1^{st}-order low-pass filters with cutoff $f_c \rightarrow 0$ smaller than any interesting frequency in the system. An important feature of this workaround is that the infinitesimally displaced factor $(z-(1-\epsilon))$ is interchangeable with pure $(z-1)$ in actual computation: $A(z)$ does not enter (2) at all, and there are no roots close to $(z-1)$ in (3) except $A(z)$ itself. The only purpose of said alteration is to determine that $A(z)$ is a stable, or causal (4) polynomial, and $A^*(z)$ is an unstable, anti-causal one. Observe also that $A(z)$ cancels out of both $F_{nc}(z)$ as well as $F(z)$ result.

Another design difficulty is due to a huge range of interesting frequencies to be modelled in clock ensembles. E.g., in [1] two-clock ensemble, a key area of interest lies around band from 5×10^{-6} Hz to 1 Hz. Suppose system sampling frequency is $f_s = 10$ Hz. A filter requested to emphasize or suppress signal in given band needs to contain poles located near $z = 0.54$, $z = 0.999997$. This makes (2) hard or impossible to solve by means of root-finding in ordinary double-precision floating point arithmetics (64b FP). Therefore, we have switched to arbitrary-precision arithmetic software (Maple 9.5). The $\mathrm{spf}(\cdot)$ (2) has been solved by addition, multiplication, root-finding, and discarding all $|z| > 1$ roots.

The second step consists in solving (3), leading to a system of linear algebraic equations. We have not noticed numerical difficulties here using 64b FP, but anyway we continued to solve the linear system in arbitrary-precision domain as well. For the examples described below, a precision of hundred(s) of decimal digits always yielded plausible results.

The design procedure yields an estimator as a polynomial fraction such as $F(z) = D_+(z)/C(z)$ in the causal variant. It is an infinite impulse response (IIR) filter, whose modes correspond to roots of $C(z)$. The $C(z)$ should be stable by definition of $\mathrm{spf}(\cdot)$, unless (2) fails to compute due to insufficient arithmetic precision.

Filter coefficients come from (2,3) in overly large precision, unjustified for practical implementation. Implementation of the filter using chosen word length and calculation structure, stability and performance might be degraded by means of: (i) signal round-off error and its propagation; (ii) filter coefficient displacement. Respective countermeasures belong to field of DSP expertise [12]. Good tool to asses implementation performance shift due to (ii) is residual spectrum S_{ee}. In our examples, we have used 64b FP and direct form IIR structure.

It should be stressed that the stability of whole clock composition system lies in the estimator. Therefore, if the IIR filter implementation is stable on finite wordlength arithmetic level, the whole system is guaranteed to be stable. This is a remarkable difference from the ensembling systems relying on feedback loops (PLL, FLL, etc.), where an improper matching of system model to physical clocks or tight stability margin may cause instability.

V. Examples

First example is artificial; both clocks follow the same model $x_k(t) = (r_{k,1}/(z-1)^2)u_{k,1} + r_{k,2}u_{k,2}$, but different parameters. S_{11}, S_{22}, and S_{ee} for both $F(z)$, $F_{nc}(z)$ is shown in Fig. 2. $F(z)$ is apparently worse than $F_{nc}(z)$, interestingly, in small region it is worse than any of the two input clocks. Still, it remains optimal by means of S_{ee} integral over f.

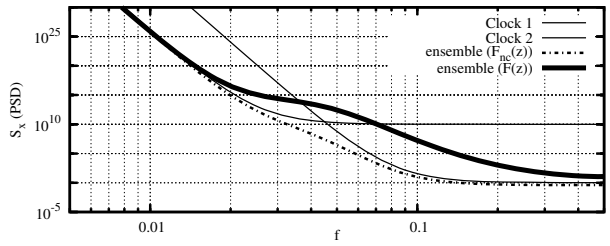

Fig. 2. Comparison of non-causal vs. causal WF for artificial clocks

Second, WF has been applied to two-clock (Cs clock "PHARAO", H-maser "SHM") ensemble model, as published [1]. $1/f$-noise of SHM has been approximated by 3^{rd}-order model, Fig. 3. While $F_{nc}(z)$ acts as expected, $F(z)$ is a real surprise: the time (phase) MSE-optimal causal estimator almost completely discards the SHM reading, weighting it up to $|F(z)|_{max} = 0.063$. S_{ee} is nearly identical to spectrum of PHARAO.

Is it correct? For MSE optimum in time ($\equiv$ phase), yes. By intuition, this probably is not the desired solution. We suppose, that the best way to get the most of the two clocks is to employ $F_T(z)$, in the graph plotted for chosen lag $T = 10^4\,\mathrm{s}$.

Recall, that any (linear) feedback system, as the present PLL&FLL solution [1], must be same or practically worse than even $F(z)$ by means of MSE. Performance of $F(z)$ and $F_{T=10^4\,\mathrm{s}}(z)$ is compared to PLL&FLL in Allan variance graph, Fig. 4. It is worth mentioning that PLL&FLL implementation is much more complex than that of IIR WF in this case.

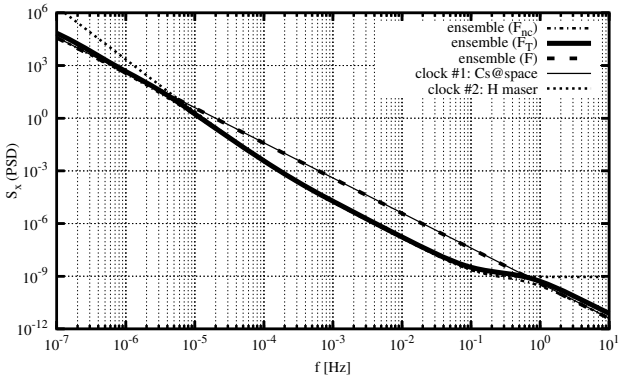

Fig. 3. Clock and residual phase spectra of ACES clocks and WF

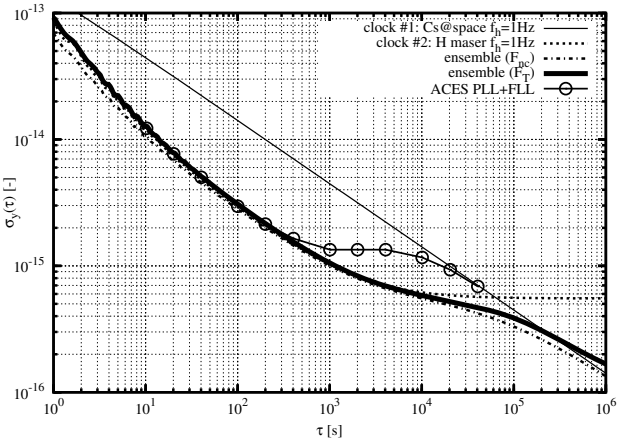

Fig. 4. Allan deviation of ACES clocks and WF residuals

VI. Conclusion

Use of estimation approach to clock composition instead of feedback loops is encouraged, wherever estimator implementation is possible. Design of WF for two-clock ensemble has been provided, dealing with non-observability of the system. Practical example of the ACES project model shows, how WF outperforms current PLL&FLL-based solution in performance as well as simplicity. Besides this, it shows how significant may be an advantage of finite-lag over causal WF.

References

[1] J. K. Dam, W. Schäfer *et al.*, "Simulation of Servo Loops in Atomic Clock Ensemble in Space (ACES)," in *EFTF 2010 – 24th European Time and Frequency Forum*, 2010.

[2] K. J. Åström and B. Wittenmark, *Computer Control Systems: Theory and Design*, 2nd ed. Prentice Hall, 1990.

[3] J. A. Davis, C. A. Greenhall, and P. W. Stacey, "A Kalman filter clock algorithm for use in the presence of flicker frequency modulation noise," *Metrologia*, vol. 42, no. 1, pp. 1–10, 2005.

[4] K. R. Brown, "The Theory of the GPS Composite Clock," in *Proceedings of ION GPS-91*, Albuquerque, New Mexico, September 1991, pp. 223–241.

[5] E. W. Kamen and J. K. Su, *Introduction to Optimal Estimation*. Springer London, 1999.

[6] J. A. Barnes, A. R. Chi *et al.*, "Characterization of Frequency Stability," *IEEE Transactions on Instrumentation and Measurement*, vol. IM-20, pp. 105–120, 1971.

[7] H. G. Schuster and W. Just, *Deterministic Chaos: An Introduction*, 4th ed. Wiley-VCH Verlag GmbH, 2005.

[8] C. A. Greenhall, "Forming stable timescales from the Jones-Tryon Kalman filter," *Metrologia*, vol. 40, no. 3, pp. 335–341, 2003.

[9] L. Galleani and P. Tavella, "Time and the Kalman Filter," *IEEE Control Systems*, vol. 30, no. 2, pp. 44–65, April 2010.

[10] C. A. Greenhall, "A Review of Reduced Kalman Filters for Clock Ensembles," *IEEE Transactions on Ultrasonics, Ferroelectrics and Frequency Control*, vol. 59, no. 3, pp. 491–496, March 2012.

[11] A. Ahlén and M. Sternad, *Polynomial Methods in Optimal Control and Filtering*, K. Hunt, Ed. Institution of Engineering and Technology, 1993, Chapter 5: Optimal Filtering Problems.

[12] B. W. Bomar, *The digital signal processing handbook*. CRC Press, 1998, ch. Finite wordlength effects.

Characterization of Atomic Clock Anomalies in the Dynamic Allan Variance Domain

Lorenzo Galleani
Politecnico di Torino
10129 Torino, Italy
Email: galleani@polito.it

Patrizia Tavella
INRIM
10135 Torino, Italy
Email: tavella@inrim.it

***Abstract*—The stability of an atomic clock changes with time due to several factors, such as mechanical vibrations, temperature, and radiations. To represent this time variation, we introduced the dynamic Allan variance (DAVAR). The DAVAR is a surface function of time and the observation interval. This surface is stationary with time when the clock follows the specifications, whereas it changes with time when an anomaly occurs. We derive the exact analytic DAVAR for a series of common anomalies, namely, a sinusoid, a phase jump, and a frequency jump. These anomalies are of fundamental interest in space clocks. Our results establish a clear connection between the nature and properties of the anomalies and the corresponding shape of the DAVAR.**

I. Introduction

Atomic clocks play a fundamental role in global navigation satellite systems (GNSSs), such as GPS, GLONASS, and the future European system Galileo. In GNSSs, atomic clocks are employed both onboard satellites and in ground stations. Monitoring the quality of the atomic clocks is an essential task, since an error in time generates an error in position. Although atomic clocks are ultra-stable oscillators, they do experience anomalous behaviors, especially onboard satellites. These anomalies are caused by several factors, such as temperature, radiations, and aging.

In this article we analyze the most common anomalies, namely, oscillations, phase jumps, and frequency jumps. These anomalies are deterministic variations in the trend of the clock time and frequency deviations. In a future work we will consider variations in the statistics of the clock noise. For each of the considered anomaly we obtain the exact analytic dynamic Allan variance (DAVAR). The DAVAR is a surface function of time and the observation interval, which represents the variation with time of the clock stability [1], [2]. When the clock follows the specifications, the DAVAR is stationary with time. When an anomaly occurs, the DAVAR changes with time, its shape being a function of the occurred anomaly. By observing the DAVAR surface we can better monitor the clock behavior [3], [4], and by setting detection surfaces we can also reveal anomalous behaviors automatically [5]. The obtained analytic results clarify how the clock stability changes when an anomaly occurs.

The article is organized as follows. In Sect. II we establish our notation for the key clock quantities, as well as for the Allan and dynamic Allan variance. Then, in Sect. III we obtain the analytic DAVAR for an oscillation, a phase jump, and a frequency jump.

II. Notation

We indicate by $x(t)$ the time deviation of the clock with respect to a reference time. The corresponding normalized frequency deviation is given by [6]

$$y(t) = \frac{dx(t)}{dt}. \tag{1}$$

The standard definition of clock stability is the Allan variance [7]-[10]

$$\sigma_y^2(\tau) = \frac{1}{2}\left\langle \Delta^2(t,\tau) \right\rangle, \tag{2}$$

where

$$\Delta(t,\tau) = \bar{y}(t+\tau) - \bar{y}(t), \tag{3}$$

and the average frequency deviation is defined as

$$\bar{y}(t) = \frac{1}{\tau}\int_{t-\tau}^{t} y(t')dt'. \tag{4}$$

Writing the time average explicitly,

$$\sigma_y^2(\tau) = \frac{1}{2}\lim_{T\to\infty}\frac{1}{T}\int_{-T/2}^{T/2}\Delta^2(t,\tau)dt. \tag{5}$$

It is convenient to rewrite $\Delta(t,\tau)$ through a convolution operation

$$\Delta(t,\tau) = h_\tau(t) * y(t), \tag{6}$$

where

$$h_\tau(t) = \frac{1}{\tau}[P_\tau(t+\tau/2) - P_\tau(t-\tau/2)] \tag{7}$$

and $P_\tau(t)$ is a rectangular window defined as

$$P_\tau(t) = \begin{cases} 1, & |t| < T/2, \\ 0, & |t| \geq T/2. \end{cases} \tag{8}$$

The DAVAR is defined as [1]

$$\sigma_y^2(t,\tau) = \frac{1}{2(T-2\tau)}\int_{t-T/2+\tau}^{t+T/2-\tau} E[\Delta^2(t,t',\tau)]dt', \tag{9}$$

where E is the expected value, T is the analysis window, the observation interval τ is subject to $0 < \tau < T/2$,

$$\Delta(t,t',\tau) = \bar{y}_T(t,t'+\tau) - \bar{y}_T(t,t'), \tag{10}$$

the average frequency deviation is defined by

$$\bar{y}_T(t,t') = \frac{1}{\tau}\int_{t'-\tau}^{t'} y_T(t,t'')dt'', \tag{11}$$

and

$$y_T(t,t') = y(t')P_T(t-t'). \tag{12}$$

We see that

$$\bar{y}_T(t,t') = \bar{y}(t'), \tag{13}$$

for $t-(T/2-\tau) \le t' \le t+T/2-\tau$. Replacing this result in (10),

$$\Delta(t,t',\tau) = \Delta(t',\tau), \tag{14}$$

for $t-(T/2-\tau) \le t' \le t+T/2-\tau$, and then in (9),

$$\sigma_y^2(t,\tau) = \frac{1}{2(T-2\tau)} \int_{t-T/2+\tau}^{t+T/2-\tau} E[\Delta^2(t',\tau)]dt'. \tag{15}$$

For a deterministic frequency deviation $y(t)$ it is

$$\sigma_y^2(t,\tau) = \frac{1}{2(T-2\tau)} \int_{t-T/2+\tau}^{t+T/2-\tau} \Delta^2(t',\tau)dt'. \tag{16}$$

This simplified form is extremely useful for the analytic evaluation of the DAVAR.

III. Analysis of Clock Anomalies

We have obtained the exact analytic DAVAR for an oscillation, a phase jump, and a frequency jump. We show the details of these calculations for the case of the oscillation, whereas the phase and frequency jumps will be discussed in a future publication.

A. Oscillation

We consider the sinusoid

$$y(t) = A\cos(2\pi f_0 t + \varphi). \tag{17}$$

We first obtain its Allan variance. From (4), it is

$$\bar{y}(t) = \frac{1}{\tau}\int_{t-\tau}^{t} A\cos(2\pi f_0 t + \varphi)dt, \tag{18}$$

which integrates to

$$\bar{y}(t) = A\frac{\sin \pi f_0 \tau \cos[\pi f_0 (2t-\tau)+\varphi]}{\pi f_0 \tau}. \tag{19}$$

Similarly,

$$\bar{y}(t+\tau) = A\frac{\sin \pi f_0 \tau \cos[\pi f_0 (2t+\tau)+\varphi]}{\pi f_0 \tau}. \tag{20}$$

Substituting in (6),

$$\Delta(t,\tau) = -2A\frac{\sin^2 \pi f_0 \tau}{\pi f_0 \tau}\sin(2\pi f_0 t + \varphi). \tag{21}$$

From (5),

$$\sigma_y^2(\tau) = 2A^2\frac{\sin^4 \pi f_0 \tau}{\pi^2 f_0^2 \tau^2}\lim_{T\to\infty}\frac{1}{T}\int_{-T/2}^{T/2}\sin^2(2\pi f_0 t+\varphi)dt, \tag{22}$$

which integrates to

$$\sigma_y^2(\tau) = A^2\frac{\sin^4 \pi f_0 \tau}{\pi^2 f_0^2 \tau^2}. \tag{23}$$

The corresponding Allan deviation is

$$\sigma_y(\tau) = A\frac{\sin^2 \pi f_0 \tau}{\pi f_0 \tau}. \tag{24}$$

From (16), the DAVAR is obtained by solving

$$\sigma_y^2(t,\tau) = \frac{1}{2(T-2\tau)}\int_{t-T/2+\tau}^{t+T/2-\tau}\Delta^2(t',\tau)dt'. \tag{25}$$

It is

$$\begin{aligned}\sigma_y^2(t,\tau) &= A^2\frac{\sin^4 \pi f_0 \tau}{\pi^2 f_0^2 \tau^2} \\ &\times\left[1-\frac{\sin 2\pi f_0(T-2\tau)}{2\pi f_0(T-2\tau)}\cos(4\pi f_0 t+2\varphi)\right].\end{aligned} \tag{26}$$

We see that the first term is (23), namely, the Allan variance of a sinusoid. Therefore, the DAVAR of a sinusoid can be written as

$$\sigma_y^2(t,\tau) = \sigma_y^2(\tau)\left[1-\frac{\sin 4\pi f_0(\tau-T/2)}{4\pi f_0(\tau-T/2)}\cos(4\pi f_0 t+2\varphi)\right], \tag{27}$$

and the corresponding dynamic Allan deviation (DADEV) is

$$\sigma_y(t,\tau) = \sigma_y(\tau)\sqrt{1-\frac{\sin 4\pi f_0(\tau-T/2)}{4\pi f_0(\tau-T/2)}\cos(4\pi f_0 t+2\varphi)}. \tag{28}$$

We rewrite the DADEV as

$$\sigma_y(t,\tau) = \sigma_y(\tau)\sqrt{1-\alpha(\tau)\cos(4\pi f_0 t+2\varphi)}, \tag{29}$$

where

$$\alpha(\tau) = \frac{\sin 4\pi f_0(\tau-T/2)}{4\pi f_0(\tau-T/2)}. \tag{30}$$

This function is a sine centered in $\tau = T/2$, and

$$\alpha(\tau) = \begin{cases} 1, & \tau = T/2, \\ 0, & \tau = T/2 - \frac{m}{4f_0},\ m = 1,2,\ldots \end{cases} \tag{31}$$

Therefore

$$\sigma_y(t,\tau) = \sigma_y(\tau), \tag{32}$$

when $\tau = T/2 - \frac{m}{4f_0}$, and m is a positive integer, provided that $\tau > 0$, namely, $m < 2f_0 T$. Moreover, for large values of f_0, the denominator $4\pi f_0(\tau - T/2)$ of $\alpha(\tau)$ decays rapidly, and, for small τ values, it is $\alpha(\tau) \approx 0$, and

$$\sigma_y(t,\tau) \approx \sigma_y(\tau). \tag{33}$$

In Fig. 1 we show the DADEV obtained when $f_0 = .2$, $\varphi = 0$, and $T = 100$. (We use dimensionless quantities for simplicity.) For this large f_0 value the approximation (33) holds, and the DADEV basically corresponds to the Allan deviation at any time t. Since f_0 is large, the oscillation period is small, and the main lobe of the DADEV is located at small τ values. Conversely, in Fig. 2 we show the DADEV obtained when $f_0 = .01$, with identical φ and T values. For this small f_0 value the denominator of $\alpha(\tau)$ decays slowly, and the oscillation in time due to the term $\cos(4\pi f_0 t + 2\varphi)$ is clearly visible.

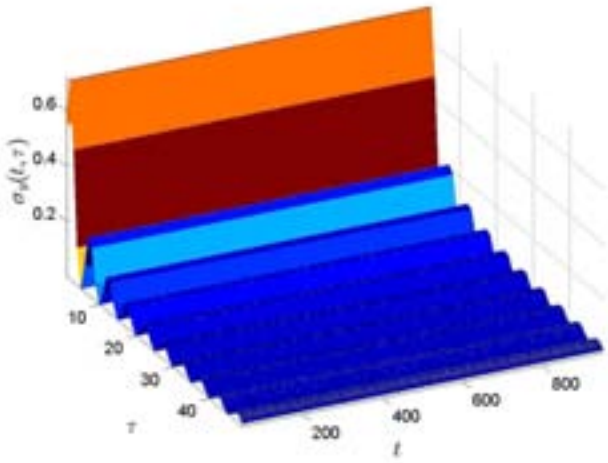

Fig. 1. DADEV of a sinusoid with large oscillation frequency. The plot shows the DADEV obtained when $f_0 = .2$. For this large f_0 value the DADEV is approximately equal to the Allan deviation of the sinusoid at any time interval.

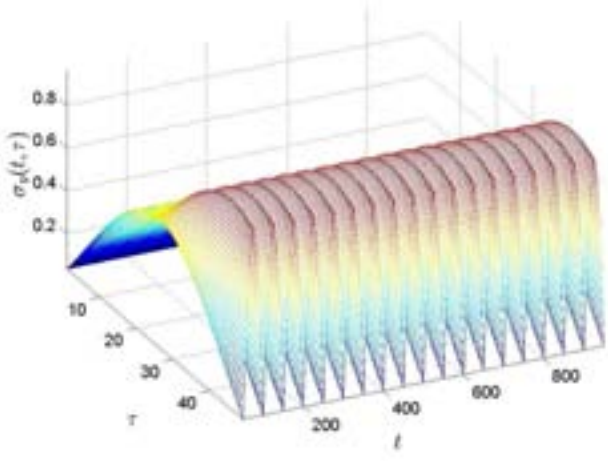

Fig. 2. DADEV of a sinusoid with small oscillation frequency. The plot shows the DADEV of a sinusoid whose oscillation frequency is $f_0 = .01$. For this small f_0 value the oscillation with respect to time is clearly visible. This oscillation is due to the term $\cos(4\pi f_0 t + 2\varphi)$ in (29).

B. Phase jump

We consider the phase jump

$$x(t) = u(t), \tag{34}$$

where $u(t)$ is the Heaviside step function, defined as

$$u(t) = \begin{cases} 1, & t \geq 0, \\ 0, & t < 0. \end{cases} \tag{35}$$

By using (1), we have

$$y(t) = \delta(t). \tag{36}$$

Consequently

$$\Delta(t,\tau) = h_\tau(t), \tag{37}$$

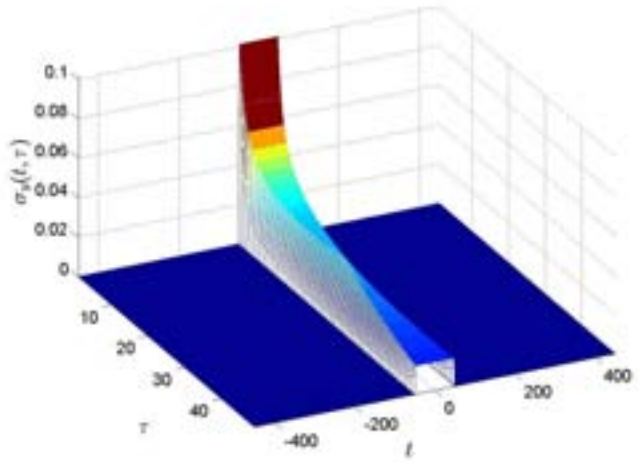

Fig. 3. DADEV of a phase jump. The plot shows the DADEV for a phase jump located at $t = 0$. This anomaly produces a local degradation of the clock stability concentrated in the interval $-T/2 \leq t \leq T/2$. The surface decreases with τ because the anomaly is averaged out at large τ values.

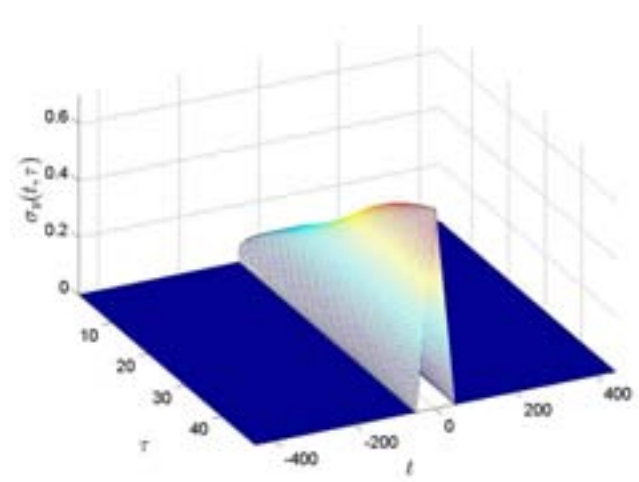

Fig. 4. DADEV of a frequency jump. The plot shows the DADEV of a step variation in the frequency deviation. This anomaly causes a degradation in the local clock stability concentrated in the interval $-T/2 \leq t \leq T/2$. In this interval, the DADEV increases with τ because the step change in the frequency deviation is tracked more often by the incremental average frequency deviation $\Delta(t,\tau)$.

and

$$\Delta^2(t,\tau) = \frac{1}{\tau^2} P_{2\tau}(t). \tag{38}$$

The corresponding analytic DAVAR, obtained by solving (16), can be computed exactly. In Fig. 3 we show the DADEV. Since the frequency deviation is a delta function, the instability is more visible at low observation interval values, whereas it is averaged out at large observation interval values. Consequently, the DADEV is a surface decreasing with τ. Moreover, it is concentrated about the $-T/2 \leq t \leq T/2$ interval. Therefore, as expected, a phase jump produces a local degradation of the clock stability.

C. Frequency jump

We consider the frequency jump

$$y(t) = u(t). \tag{39}$$

It is

$$\Delta(t,\tau) = \left(1 - \frac{|t|}{\tau}\right) P_{2\tau}(t). \tag{40}$$

Therefore

$$\Delta^2(t,\tau) = \left(1 - 2\frac{|t|}{\tau} + \frac{t^2}{\tau^2}\right) P_{2\tau}(t). \tag{41}$$

By solving (16) we can compute the exact analytic DAVAR. In Fig. 4 we show the corresponding DADEV. The frequency jump generates a local degradation in the clock stability, concentrated in the interval $-T/2 \leq t \leq T/2$. In this interval, the DADEV surface increases with τ. For small τ values, in fact, the incremental average frequency deviation $\Delta(t,\tau)$ is zero for most of the time values. Conversely, at large observation interval values $\Delta(t,\tau)$ captures the step variation in the frequency deviation more often, resulting in a larger instability.

IV. Conclusions

We have obtained the exact analytic DAVAR for an oscillation, a phase jump, and a frequency jump. These anomalies are common for space clocks in GNSSs, and cause a local degradation in the positioning error performances. Understanding their impact on the clock stability is hence of fundamental interest. The obtained results clarify the variation in stability produced by each of the considered anomaly.

References

[1] L. Galleani and P. Tavella, "The Dynamic Allan Variance," *IEEE Trans. Ultra. Ferro. Freq. Contr.*, vol. 56, no. 3, pp. 450-464, 2009.

[2] L. Galleani, "The Dynamic Allan Variance II: A Fast Computational Algorithm," *IEEE Trans. Ultra. Ferro. Freq. Contr.*, vol. 57, no. 1, pp. 182-188, 2010.

[3] I. Sesia, L. Galleani, and P. Tavella, "Application of the Dynamic Allan Variance for the Characterization of Space Clock Behavior," *IEEE Trans. Aero. Elect. Sys.*, vol. 47, no. 2, pp. 884-895, 2011.

[4] P. Tavella, "Statistical and mathematical tools for atomic clocks," *Metrologia*, vol. 45, no. 6, pp. S183-S192, 2008.

[5] L. Galleani, "The Dynamic Allan Variance III: Confidence and Detection Surfaces," *IEEE Trans. Ultra. Ferro. Freq. Contr.*, vol. 58, no. 8, pp. 1550-1558, 2011.

[6] P. Kartaschoff, *Frequency and time*, Academic Press, 1978.

[7] D. W. Allan, "Statistics of atomic frequency standards," *Proc. IEEE*, vol. 54, pp. 221-230, 1966.

[8] D. W. Allan, "Time and Frequency (Time-Domain) Characterization, Estimation, and Prediction of Precision Clocks and Oscillators," *IEEE Trans. Ultra. Ferro. Freq. Contr.*, vol. 34, no. 6, pp. 647-654, 1987.

[9] IEEE Standard Definitions of Physical Quantities for Fundamental Frequency and Time Metrology, IEEE Std. 1139-1999.

[10] ITU-R Recommendation TF 538-3, "Measures for random instabilities in frequency and time (phase)," *International Telecommunication Union – Radiocommunication ITU-R*, vol. 2000, TF Series, Geneva, 2001.

The New UTC(OP) Based on LNE-SYRTE Atomic Fountains

G. D. Rovera, M. Abgrall, S. Bize, B. Chupin, J. Guéna, Ph. Laurent, P. Rosenbusch, P. Uhrich
LNE-SYRTE, Observatoire de Paris - CNRS - UPMC, France
Email: daniele.rovera@obspm.fr

***Abstract*—The new realization of UTC(OP) is described. The steering algorithm and the prediction of UTC(OP) are presented in details. The results of the first semester of operation are reported.**

I. Introduction

The generation of a timescale by steering a H-maser signal to the average of all SYRTE commercial clocks has been tested for a few years [1]. After running this time scale in parallel with the official UTC(OP), which was based on one single commercial Cs clock, we concluded that the performances were not justifying the complexity of the system. Instead, we have developed a very new algorithm for the steering of a H-maser signal to the SYRTE atomic fountain ensemble [2] (comprising 3 Cs primary frequency standards and one Rb fountain). Preliminary tests of the new algorithm started in December 2011. For these tests we used a new 100 MHz phase micro stepper developed by SKK Electronics in collaboration with SYRTE [3]. The results were promising. Hence in October 2012 we implemented the new algorithm to generate the official realization of UTC(OP).

At SYRTE all fountains share the same cryogenic oscillator which is phase locked to a H-maser. This way, all fountains measure the frequency of the same H-maser. Automatic fountain data processing provides preliminary data corrected of all systematic frequency shifts, hourly. At the present stage, the daily steering to this data-stream is sufficient to drive the timescale with a stability in the low 10^{-16}.

Where previously a few tens of ns were observed, the difference between UTC(OP) and UTC has not exceeded 5 ns since the implementation of this new UTC(OP).

II. Scientific background

In common meaning a UTC(k) is the physical realization of a (independent) prediction of UTC. The word independent is often forgotten and a number of UTC(k) is realized by using as reference some other UTC(k) or GPStime with a short time constant phase lock.

Although not officially required, in order to guarantee the independence of a UTC(k), one can only use the *Circular T* to assess the position of his own UTC(k) with respect to UTC, and to estimate the adequate steering planning which is valid until the publication of the following *Circular T*. This is roughly equivalent to stating that a UTC(k) can only be phase locked to UTC with a time constant longer than 40 days (30 or 35 days of span of the circular plus a few days for the TAI data collection and calculation by the BIPM). It is evident that for times up to of forty days the stability of the local oscillator is the key element for the performances of an independent UTC(k).

The commercial Cs beam frequency standards traditionally used in the generation of UTC(k)'s have a flicker floor of about 10^{-14} or slightly better. Hydrogen masers have a short term stability that is two orders of magnitude better than a Cs beam standard, but the flicker floor is reached earlier and at 40 days one can expect a stability only in the low 10^{-15}. It is straightforward to infer that the frequency of the maser can be predicted only at the level of its expected stability. Therefore using a maser allows a gain of about one order of magnitude on the stability of a UTC(k). As rule of thumb an error of 10^{-15} over 40 days can lead to a time error of 4 ns.

Practically this error is only a component of the uncertainty of the prediction because the frequency stability of UTC itself and the link instabilities have to be considered also. If an atomic fountain is used as local reference oscillator this term can be reduced well below 1 ns, as the frequency stability of a fountain over such period is in the low 10^{-16}. In this case it is evident that the stability is no longer the limiting factor in the realization of a UTC(k).

Nevertheless a time scale requires an oscillator that is running uninterruptedly and this is not the case with atomic fountains. In some cases, as for the LNE-SYRTE, the fountains does not produce a continuous physical signal but they allow to calibrate (almost continuously) a free-running fly-well oscillator, typically a H maser. In this case the steering of the maser frequency is evaluated by adding two components, the bigger one, daily adjusted, is the opposite of the frequency error of the maser as measured from the atomic fountain. If only this correction is applied to the phase micro stepper used to steer the maser, the generated timescale will be a realization of the SI second by the fountain. To better predict UTC a second coefficient is introduced. This coefficient is evaluated monthly using the *Circular T*.

III. UTC(OP) implementation

A simplified schematic of the hardware used for the generation of UTC(OP) is shown in fig. 1. The figure represents the actual situation but we plan the replacement of some hardware components to fulfill the requirements for hosting a ground station for ACES space project. The flywheel clock is currently the H-maser 1400889 operated free-running. The 100 MHz output of the maser is used as reference for the frequency lock of the cryogenic oscillator that drives the three SYRTE atomic fountains. In near future the same output will also drive

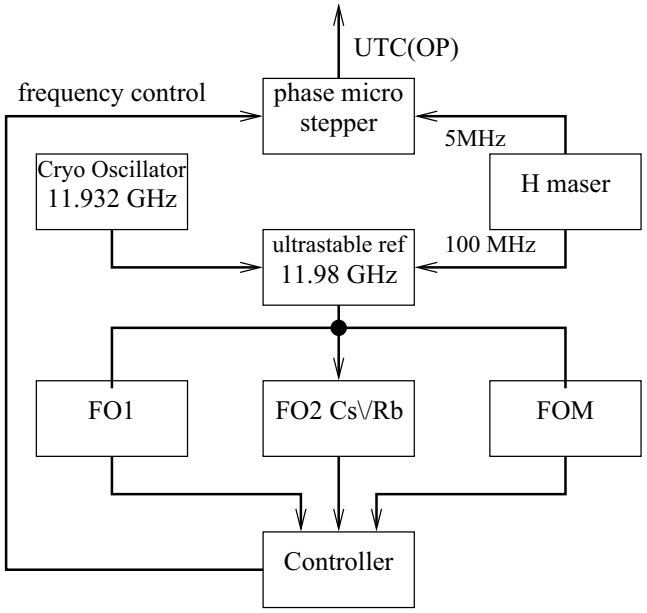

Fig. 1. Simplified block schematic.

the newly developed phase micro stepper [3], but at present the 5 MHz commercial phase micro stepper , historically used in time comparison is still in use. A detailed description of the maser frequency distribution, filtered by the cryogenic oscillator can be found in [2].

For the mobile fountain FOM, a post-processing of data has been running for many years in quasi real time. Cleaned and shifts corrected data are made available within about 1 hour latency. A similar but more sophisticated post-processing was also implemented a couple of years ago for FO2Cs FO2Rb and FO1 fountains. The quasi real time data have to be approved and eventually reprocessed before the generation of TAI reports, but they are largely sufficient to guarantee a stability at 10^{-16} level for the daily steering of the H maser.

The generation of a time scale by combining several low performances clocks is a complicate task that belongs to the art domain more than the basic science. In the case of UTC(OP), where at the starting point there are fountains with accuracy (not only stability) in the low 10^{-16}, there is no need of sophisticated statistic tools. The choice of the algorithm has been oriented to obtain robustness of the system instead of the ultimate optimization of performances. For instance, the frequency of the maser is measured simultaneously by all the available SYRTE fountains (at present FOM is in Toulouse), but only data of one fountain are used for the automated steering. The decision of which fountain is used depends on the operating planning. Typically we commute from one to another when a fountain is expected to interrupt regular operation for a few days for planned experiment or maintenance. We plan to use the data of the other fountains to rise a warning in case of non coherent measurement. We believe that setting up an automated switch in case of bad or missing data is too sophisticated for the purpose. Owing to the stability of the maser, a few days of missing fountain data have negligible impact on the realization of UTC(OP). In the normal data post-processing of SYRTE fountains all the systematic are corrected every one cycle. Nevertheless those files are too big and difficult to manipulate for the purpose of fountain comparison. For routine fountain comparison, and UTC(OP) generation, the original data files are converted (in quasi real time) to files with a reduced set of data averaged over 0.1 day. These "pack" files contain ten frequency values per day dated at pre-established times, notably 0.05 0.15 etc. Each point is obtained after filtering some period of the original file due to eventual problems in fibers link or in the lock of the cryogenic oscillator. A further cleaning is performed by fitting each 0.1 day period with a straight line and removing eventual outlier exceeding 5 sigma. The value of the fit at the middle of the interval is used to generate the pack file.

The steering software once a day predicts the maser frequency for the next day by extrapolating the linear fit of pack files covering the last 20 days. The correction to be applied at the phase micro stepper for the next day is the sum of the predicted maser frequency and the monthly coefficient that finely adjust the frequency of UTC(OP) to UTC. When the steering algorithm has been implemented in October 2012 the coefficient using the data in the last *Circular T* was calculated manually by adding 2 terms. The first one was the average of the frequency difference between UTC(OP) and UTC calculated over the *Circular T* period. The second term was calculated to compensate the last known time offset between UTC(OP) and UTC within 60 days. Since a few months this steering procedure has been implemented in quasi automated software. At that occasion the calculation of the frequency of the previous month has been modified to take into account the fact that the corrections of the previous month are applied with a delay of at least 10 days.

The same software is also used to generate a prediction of the difference of UTC(OP) and UTC for the next month. The quality of the prediction can be verified a posteriori when a new *Circular T* is published.

IV. Results

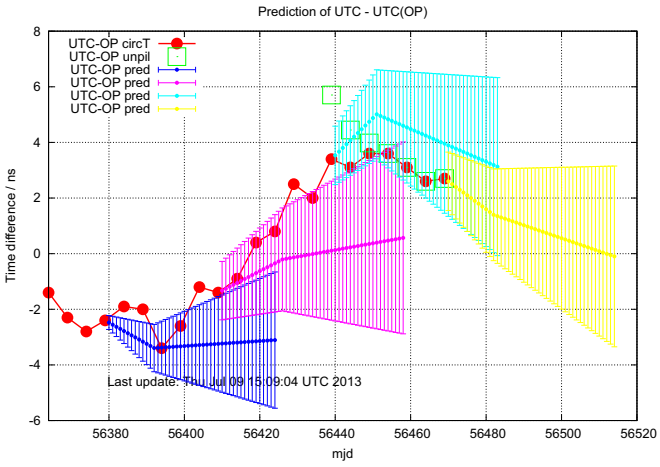

Fig. 2. The red line shows UTC-UTC(OP) using the new algorithm, the other data are explained in the text.

Since the beginning of operation of the new algorithm in Oct 2012, the difference between UTC and UTC(OP) did never reach the limit of 5 ns with an rms value of less than 3 ns.

In figure 2 the red line with circles shows the difference between UTC and UTC(OP) during the last four months, while the green big square are the point actually used to calculate the frequency of UTC(OP) over the period of *circular T306*. The differences between the green squares and the red dots at the beginning of the period are due to the fact that we have to take in account the impact of the previous applied steering in order to estimate the actual frequency difference between UTC and UTC(OP). Indeed the previous correction was applied at some time near the middle of the BIPM interval, corresponding to the date of publication of the *Circular T*. The same correction must be applied backward in order to estimate the actual frequency of UTC(OP), averaged over the entire interval. The points with error-bars in colors blue, lilac, cyan and yellow represents the predicted value with the associated uncertainty after publication of *Circular T303* to *T306*.

As we do not have long experience in this field we miss statistical data for the evaluation of error-bars. Therefore we have arbitrarily chosen a realistic (conservative) uncertainty of 10^{-15} on the frequency. The second component of the total uncertainty is due to the estimation of the starting point of the prediction. After the first month where this therm has been set at 0.3 ns, deduced by the statistical uncertainty published in *circular T*, we had the feeling that the term was too small and therefore it has been fixed arbitrarily at 1 ns, that is half way between the published uncertainties of type A and B of the dime difference between UTC and UTC(OP). The plot of the following months confirms that this choice is more realistic and eventually ask for a further increase. In fact the cyan data set has an evident offset of 1 ns, almost constant over the entire period.

ACKNOWLEDGMENT

The authors would like to thank the technical staff of Réferences Nationales de Temps of LNE SYRTE for the continuous support and monitoring. We also acknowledge the precious support of Service d'Electronique for improving the reliability of the frequency distribution and measurement systems.

REFERENCES

[1] M. Abgrall, P. Uhrich, and D. Valat, "Ongoing improvements of the time and frequency references at LNE-SYRTE," in *Proc. of the* 24^{th} *European Frequency and Time Forum Noordwijk, The Netherlands*, 2010.

[2] J. Guéna, M. Abgrall, D. Rovera, P. Laurent, B. Chupin, M. Lours, G. Santarelli, P. Rosenbusch, M. Tobar, R. Li, K. Gibble, A. Clairon, and S. Bize, "Progress in atomic fountains at LNE-SYRTE," *Ultrasonics, Ferroelectrics and Frequency Control, IEEE Transactions on*, vol. 59, pp. 391 –409, march 2012.

[3] D. Rovera, M. Abgrall, and M. Siccardi, "Characterization of an auxiliary offset generator for steering of H masers," in *Proc. of the* 26^{th} *European Frequency and Time Forum*, 2012.

A New Weighting Procedure for UTC

Gianna Panfilo, Aurélie Harmegnies
International Bureau of Weights and Measures (BIPM)
Pavillon de Breteuil, 92312, Sèvres, France
aharmeg@bipm.org

***Abstract*—This paper deals with the new weighting procedure studied and developed at the BIPM Time Department for the calculation of the Coordinated Universal Time (UTC). After the implementation of the quadratic prediction model in UTC algorithm, no effect has been observed on the clock weight distribution. To optimize the use of atomic clocks in order to improve the stability of UTC, a proposed review of the weighting algorithm is described.**

Time scale; UTC; TAI; weight; algorithm; frequency drift;

I. INTRODUCTION

To generate UTC, three main algorithms are used: the prediction and the weighting algorithms used to calculate the free atomic time scale (EAL) from about 400 free-running clocks spread worldwide, and the steering algorithm to steer the EAL frequency on the SI frequency provided by the Primary Frequency Standards.

The clock frequency prediction method has been reviewed and the clock prediction model has been changed from a linear to a quadratic model [1] adapted for clocks presenting frequency drift (case of H-masers and ageing caesium clocks). The new version of the prediction algorithm was implemented in September 2011 with significant effects in terms of improvement of the EAL stability. As aimed, the frequency drift of -1.3×10^{-17}/day affecting EAL has almost completely disappeared after the introduction of the new prediction algorithm and no additional steering has been applied to obtain the International Atomic Time (TAI) since last months of 2012.

II. CLOCK WEIGHTS STATUS

After the introduction of the new prediction algorithm in the UTC generation, the distribution between H-masers and caesium clocks on the total weight did not change because the frequency prediction does not influence the weighting procedure [2, 3] which considers the difference [EAL- clock] as the relevant weighting parameter. In particular in the current weighting algorithm the inverse of the variance of the frequency of [EAL – clock] over one year is used to estimate the performance of the atomic clocks and to assign a weight. The long term performance of the time scale is guaranteed by de-weighting those atomic clocks presenting a frequency drift (case of H-masers) or an ageing. One consequence of this procedure was the low impact of the contribution of the H-masers in the time scale ensemble: indeed, H-masers which represent about 100 out of the 400 clocks used in TAI computation, contribute only at about 10% of total weight and only few of them (less than 10) reach the maximum weight. Considering that to ensure its extreme reliability and its long-term frequency stability, UTC should rely on the largest possible number of atomic clocks of different types and spread worldwide then the need for a weighting procedure revision comes clear.

III. REVIEWED WEIGHTING PROCEDURE

The new version of the weighting algorithm is supported on the concept of weighting the clocks according to their predictabilities, instead of their frequency stability as in current version [2, 3]. In this new weighting procedure, the difference between the frequency of the atomic clocks y[EAL-clock] and its prediction $\hat{y}$[EAL-clock] is used. The main idea is that a clock with strong signature like frequency drift or ageing can be correctly used in the timescale ensemble if well predicted. In the new weighting algorithm the difference between the predicted and the real frequency of the atomic clocks is evaluated.

$$\epsilon_{i,I_k} = |\, y(i,I_k) - \hat{y}(i,I_k)| \qquad (1)$$

where the index i identifies the clock and I_k the calculation interval.

In time scale algorithm, a statistical quantity characterizing frequency stability of a clock is generally used to compute the corresponding clock weight. A filter over one year of these data is applied to evaluate the weights and to guarantee the long term stability of the clock ensemble. This filter gives a predominant role to the new measurements:

$$\sigma_i^2 = \frac{\sum_{j=1}^{M}\left(\frac{M+1-j}{M}\right)\epsilon_{i,j}^2}{\sum_{j=1}^{M}\left(\frac{M+1-j}{M}\right)} \quad (2)$$

and a temporary weight is calculated:

$$\omega_{i,TEMP} = \frac{1/\sigma_i^2(12,T)}{\sum_{i=1}^{N} 1/\sigma_i^2(12,T)} \quad (3)$$

The new weight ω_i of clock H_i is equal to $\omega_{i,TEMP}$ except in two cases:

1. Clock H_i satisfies the requirement set for the limitation of weight as for the current algorithm [2, 3].

2. Clock Hi shows abnormal behavior during the interval of computation so it cannot contribute. In this case the current value of the difference between the real frequency and the predicted one is checked. If the value is larger than a fixed threshold the clock is temporarily excluded from the ensemble.

IV. Effect of the new clock weighting

The effect of the new weighting model on the EAL stability seems to be satisfactory. A frequency stability improvement of the time scale at short and long term is observed. Moreover a better clock weight distribution is obtained which allows the H-masers to play a significant role on the time scale (about 30% of the total weight and 40 H-masers having the maximum weight) and limits the preponderance of caesium clocks in the EAL generation (from about 85% of the total weight in the current procedure to about 65% when using new weighting algorithm).

V. Conclusion

This new weighting algorithm is planned to be implemented in the procedure of TAI calculation before the end of 2013. Time laboratories contributing to the computation of the Rapid UTC at the BIPM [4] provide daily clock data; these data will serve for studying the impact of this new algorithm at shorter term stability.

References

[1] G. Panfilo , A. Harmegnies, L. Tisserand, "A new prediction algorithm for the generation of International Atomic Time", Metrologia, vol. 49, n°1, pp. 49-56, 2012.

[2] Azoubib J "A revised way of fixing an upper limit to clock weights in TAI computation" *Proc. 32nd Annual Precise Time and Time Interval (PTTI) Meeting, Reston (USA), 195-210,* (2000).

[3] Thomas C and Azoubib J "TAI computation: study of an alternative choice for implementing an upper limit of clock weights", *Metrologia, 33, 227-240,* (1996).

[4] G. Petit, E.F. Arias, A. Harmegnies, Z. Jiang, H. Konaté, W. Lewandowski, G. Panfilo, L. Tisserand, "UTCr : a rapid realization of UTC." *Proc. EFTF, Gothenburg (Sweden)* (2012).

Reconstruction of UTC (NIM)

Aimin Zhang, Yuan Gao, Kun Liang, Weibo Wang, Zhiqiang Yang, Dayu Ning, Zhanjun Fang
Time and Frequency Division, National Institute of Metrology
Beijing, China
Email: zhangam@nim.ac.cn

***Abstract*—NIM has reconstructed UTC (NIM) since 2010 at new campus, and the official UTC (NIM) was switched to the new campus in October 2012. The new clock ensemble includes 6 Hydrogen masers and 7 Cesium clocks, with 1 Hydrogen maser and 2 Cesium clocks placed at the old campus. The master clock is a Hydrogen maser at new campus, and UTC (NIM) is generated from a micro phase stepper steered by a new algorithm and UTC, the frequency of the Hydrogen maser is predicted and rapid UTC data is used to steer UTC (NIM). A dual mixer time difference measurement system is used to measure the time difference between the clocks and UTC (NIM) at new campus, the clocks at old campus are linked to UTC (NIM) by GPS. GPS and TWSTFT data are reported to BIPM everyday automatically. The GPS receivers at new campus are calibrated with reference to one GPS receiver calibrated by BIPM. The UTC (NIM) has been operated normally at new campus; the accuracy and stability are improved. In this paper the generation of new UTC (NIM) is described and the performance of UTC (NIM) is presented.**

***Key words*-- UTC, UTC(NIM), UTCr, GNSS, TWSTFT, algorithm**

I. INTRODUCTION

The Coordinated Universal Time (UTC) is the universal standard time and it is the paper time implemented by the definition of the atomic second, Local representations of UTC is commonly called UTC(k) time scales, where k is a acronym representing an organization or a country[1]. UTC (NIM) is one of the physical realization of UTC, and it is also the time and frequency primary standard in China, it plays a very important role in time and frequency system in China. National Institute of Metrology (NIM) is responsible to construct and maintain UTC (NIM).

In the year of 2008, NIM has realized an independent time scale TA(NIM) which is generated from a Hydrogen maser steered by the cesium fountain clock[2], and UTC(NIM) is generated from TA(NIM) steered by UTC.

In the year of 2009, NIM's new campus, a 56-hectare advanced experimental base was put in use, it is approximately 40 kilometers northwest of the old Campus and it can provide tightly controlled laboratory conditions to maintain the integrity of the measurements.

Since 2010, new UTC (NIM) was under construction at the new campus. The clock ensemble, internal measurement system and the international comparison system were reconstructed. A new algorithm was developed to generate UTC (NIM), we still use a stable Hydrogen maser as the master clock, its frequency is predicted, and UTC (NIM) is generated from a micro phase stepper steered by the UTC together with the predicted value. UTC（NIM）is traced to UTC based on GNSS (Global Navigation Satellite System) time and frequency transfer and TWSTFT (Two-way Satellite Time and Frequency Transfer) system. The GNSS receivers working at the new campus were calibrated by differential method with reference to the receiver calibrated by BIPM. The UTC (NIM) was switched to the new campus officially on October 14, 2012. Since then, UTC (NIM) works normally. The data from BIPM *Circular T* shows that the maximum time difference between UTC (NIM) and UTC is within ±10ns, the time stability is less than 0.6 ns/5d, and the frequency stability is less than 3×10^{-15}/5d.

II. GENERATION OF UTC(NIM)

A. Setup of UTC(NIM)

Fig. 1 shows the block diagram of the UTC (NIM). The whole system consists of atomic clock ensemble, internal measurement system, UTC (NIM) algorithm and international comparison system.

The new atomic clock ensemble consists of 6 hydrogen masers (MHM2010) and 7 Cesium clocks (HP5071A, high-performance cesium beam tube) including 1 Hydrogen maser and 2 Cesium clocks located at the old campus. All the atomic clocks run in the temperature controlled and shielding chambers at both campus, with dual AC power supplies and DC UPS power supplies for protection. The temperature variation of the clock chamber at the new campus is within ±0.5°C.

The internal comparison system is used to measure the time difference between the clocks, the reference time is UTC (NIM). The internal comparison system at the new campus contains a time difference measurement system (multi-channel switch 3499A and time interval counter SR 620) and a dual-mixer time difference (DMTD) measurement system (MMS). The DMTD system has much higher resolution than the counter.

The 1 PPS (Pulse per Second) output of UTC (NIM) is produced by a controlled phase micro stepper (HROG-5). The input reference signal of the micro phase stepper comes from the frequency output of a stable hydrogen maser which is chosen as the reference clock (master clock). And the frequency deviation adjustment of the controlled phase micro stepper is determined by the UTC (NIM) algorithm. A backup UTC (NIM) is also realized at the same time.

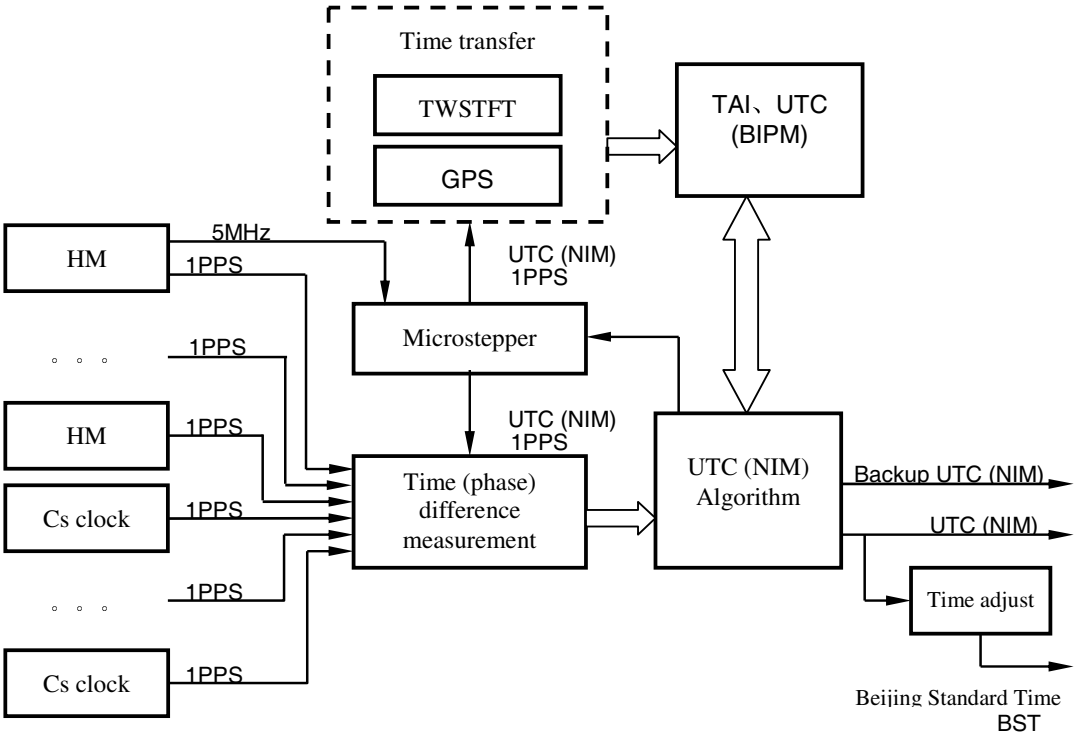

Figure 1. The block diagram of UTC (NIM)

B. Algorithm of UTC(NIM)

Each month the time differences between the UTC and the UTC (*k*) are reported at 5-day intervals together with the uncertainty u_A and u_B in BIPM *Circular T.*

In the generation of a time scale UTC (k), prediction of atomic clock behavior plays an important role and it is inserted in all time scale algorithms [3]. Based on the *Circular T*, extrapolation of values over 10 to 45 days based on prediction models is necessary to many applications.

A rapid realization of UTC named UTCr was realized by BIPM in January 2012; it is published every week and based on daily data reported daily by contributing laboratories. It is disseminated through daily values of [*UTC*r – *UTC* (*k*)] [4]. We can access UTC more frequently by the rapid UTC; UTCr data are used in Algorithm of UTC (NIM).

The UTC (NIM) algorithm has 3 functions, the first function is to make the UTC (NIM) and UTC remain in phase, and implementation steps are as follows.

(1) Get the [UTC - UTC (NIM)] time difference value from *Circular T*;
(2) Get the [UTC(NIM) – the master clock] time difference value from the internal measurement system;
(3) Calculate the [UTC- the master clock] time difference value by step(1) (2), then we will be able to calculate the frequency difference between TAI and the master clock $\Delta f_{TAI\text{-}masterclock}$;
(4) Predict the next $\Delta f_{TAI\text{-}masterclock}$ value through linear fitting and Kalman filtering;
(5) Obtain [UTCr- UTC(NIM)] time difference value;
(6) Work out [UTCr – the master clock] time difference value by the step (2) (5), then calculate the frequency difference between UTCr and the master clock $\Delta f_{UTCr\text{-}masterclock}$;
(7) Estimate the next $\Delta f_{UTCr\text{-}masterclock}$ by linear fitting;
(8) Combine the predicted $\Delta f_{UTCr\text{-}masterclock}$ and $\Delta f_{TAI\text{-}masterclock}$ and used it as the estimated hydrogen maser frequency deviation;
(9) Obtain the final frequency adjustment value by adding the estimated hydrogen maser frequency deviation and the frequency deviation adjustment derived from [UTC- UTC (NIM)] data in *Circular T*;
(10) The frequency of the master clock is steered with the final frequency adjustment value by the phase micro stepper to generate UTC (NIM).

In order to ensure the safety of the time scale, a backup UTC (NIM) is also realized at our new campus. A second Hydrogen maser is used as back up master clock; it is connected to another micro phase stepper which is steered by the UTC (NIM) algorithm.

Thus the second function of the algorithm is to generate the backup UTC (NIM). It is realized in two steps. The first step is to steer the hydrogen maser and make its frequency to be consistent with UTC, which is similar with above (1) to (8). The second step is to make its phase to be consistent with

UTC (NIM), which is similar with the above (9) and (10). At present, the time difference between backup UTC (NIM) and UTC (NIM) is less than 5 ns.

The third function of the algorithm is to monitor the phase and frequency hopping in the system. This function is achieved by measuring the time and frequency difference between the UTC (NIM) and every clock in the clock ensemble.

C. *Time and frequency transfer system*

UTC time transfer is based on two basic techniques: TWSTFT and GNSS [5]. Both GNSS and TWSTFT system were set up at the new campus. GNSS code-based and GPS carrier phase (GPSCP) methods are used to do the time and frequency transfer. At the old campus, GNSS method is used. The 2 Cesium clocks and 1 Hydrogen maser at old campus are linked to UTC (NIM) by GPS, the clock data are also reported to BIPM.

Before Oct.14, 2012, UTC (NIM) is generated at the old campus. One GNSS receiver (IMPR: Septentrio PolaRx2eTR) located at the old campus which contributed data to BIPM was calibrated in the end of 2009 by BIPM. Since then the uncertainty u_B of UTC-UTC (NIM) in *circular T* is approximately 5ns instead of 20ns.

In order to calibrate the GNSS receivers working at the new campus with the differential calibration method, IMPR is used as the reference receiver. A self-developed GPS receiver IMEU was first calibrated with the reference receiver IMPR at the old campus. Shortly After that, IMEU was used as a traveling receiver and moved to the new campus; two GNSS time and frequency transfer receivers including IMEJ (Dicom GTR50) and BJNM (Septentrio PolaRx3eTR) were calibrated reference to IMEU. The calibration setup is shown as in Fig. 2.

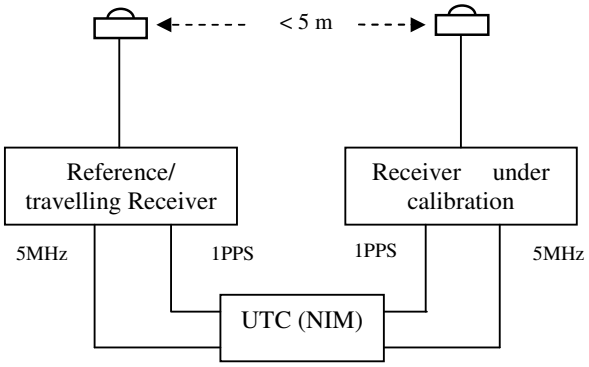

Fig. 2. Setup of receiver calibration

The calibration was finished in April 2012, and the results were reported to BIPM. After the switching, the uncertainty u_B of UTC-UTC (NIM) in *circular T* remains approximately 5ns, and in the same time the uncertainty u_A is reduced to (0.3-0.5) ns.

NIM established TWSTFT station at the new campus in the year 2008 and participated the Europe-Asia TWSTFT link, now the communication satellite is AM2 and the participant laboratories of Europe-Asia TWSTFT link include PTB, TL, NICT, NIM, NTSC, SU and NPLI. According to the measurement results, the 1-day frequency stability between NIM and PTB is less than 3×10^{-15}. The time transfer result between NIM and PTB during MJD56050-56200 by TWSTFF and GPSCP is shown as in Fig 3.The two time transfer results are consistent.

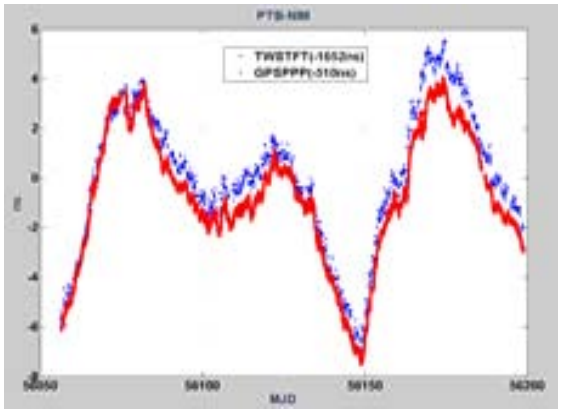

Fig. 3. TWSTFT and GPSCP comparison result between NIM and PTB

III. PERFORMANCE OF UTC(NIM)

The time scale at the new campus was put into test running in the end of 2010, and it was synchronized to the UTC (NIM) at the old campus in May of 2012. UTC (NIM) was switched to the new campus officially on October 14, 2012, since then, the clock data, GPS data and the TWSTFT data are reported to BIPM from the new campus every day.

Figure 4 shows the performance of the UTC (NIM) before and after the switching compared with other 7 UTC (k), including UTC (USNO), UTC (SU), UTC (PTB), UTC (IT), UTC (NIST), UTC (NICT) and UTC (UTSC). Before switching（2012.1.3-2012.10.13）, UTC(NIM) is generated from the old campus, the maximum variation from UTC is within ±15 ns, the time stability is 0.74ns/5d. After switching (2012.10.14-2013.6.26), the maximum variation from UTC is within ±10 ns, the time stability is 0.54ns/5d.

The 5-day time stability and frequency stability of these laboratories are listed in table 1.

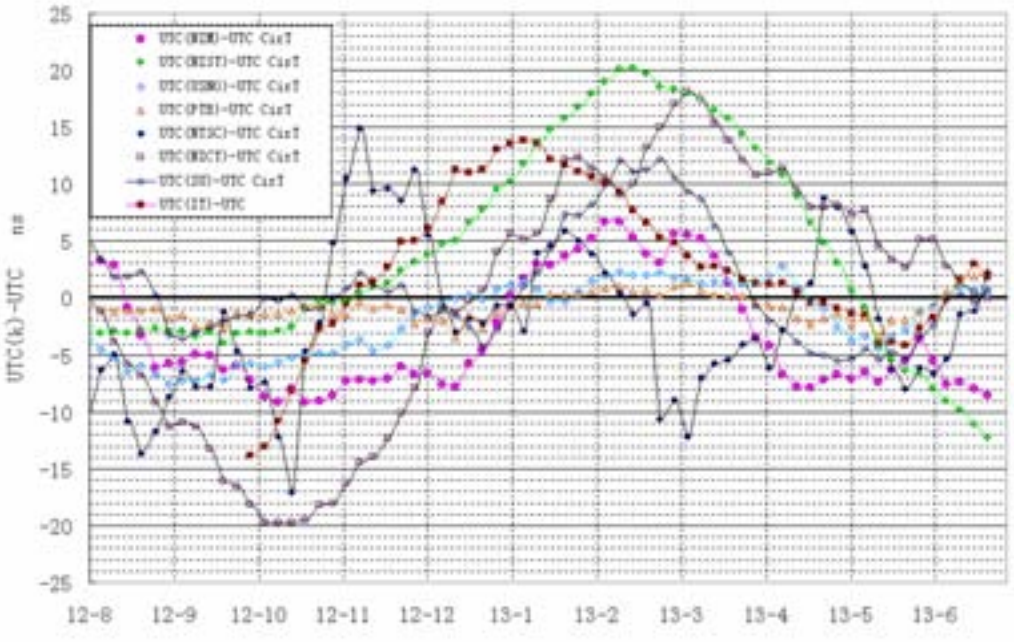

Fig. 3. Performance of UTC (NIM) compared with other 7 labs

Table1
Time and frequency stability comparison(2012.10.14-2013.6.26）

NMI	Time Deviation/5d	Allan Deviation/5d
NIST	0.29 ns	1.2e-15
USNO	0.34 ns	1.5e-15
PTB	0.46 ns	2.0e-15
IT	0.46 ns	1.9e-15
NIM	0.54 ns	2.2e-15
SU	0.61 ns	2.4e-15
NICT	0.68 ns	2.7e-15
NTSC	1.93 ns	7.9e-15

IV. CONCLUSION

UTC (NIM) has been reconstructed at NIM's new campus and the data has been reported to BIPM officially since Oct.14, 2012, a stable Hydrogen maser is selected as the master clock, and UTC (NIM) is generated from a micro phase stepper steered by a new algorithm and UTC, a backup UTC (NIM) is also realized. The data in BIPM Circular T shows that the time deviation of UTC (NIM) from UTC is within ±10 ns. In order to increase the reliability of UTC (NIM), at present an algorithm based on a Hydrogen maser ensemble is under development at NIM.

REFERENCES

[1] Peter b Whibberley, John A David and Setnam L Shemar, Local representations of UTC in national laboratories, Metrologia 48(2011) S154-S164

[2] Gao Yuan, Gao Xiaoxun, Zhang Aimin ,et al, The generation of new TA(NIM), which is steered by NIM4 caesium fountain clock, Metrologia 45(2008) S34-S37

[3] Gianna Panfilo, The new prediction algorithm for UTC: application and results, EFTF 2012,pp242-246.

[4] G. Petit, F. Arias, A. Harmegnies, Z. Jiang, H. Konaté,W. Lewandowski, G. Panfilo, L. Tisserand, UTCr: a rapid realization of UTC, EFTF2012,pp.24-27

[5] E F Arias1,2, G Panfilo1 and G Petit1Timescales at the BIPM, Metrologia 48 (2011) S145–S153

Predicting The Polish Timescale UTC(PL) Based On The Corrections Designated By The UTC And UTCr Scale

Łukasz Sobolewski
Institute of Electrical Metrology
University of Zielona Góra
Zielona Góra, Poland
e-mail: L.Sobolewski@weit.uz.zgora.pl

Abstract— **The article presents the results of research on the prediction of the Polish timescale UTC(PL) based on the corrections designated according to UTC and UTCr scale. In both cases for prediction the GMDH neural networks and time series analysis method were used. For predicting the UTC(PL) the influence of the input data preparation method for the GMDH neural network was examined. The obtained results were compared with the predictions designated using linear regression method. Better results of predicting the UTC(PL) were obtained using GMDH neural network. The most preferred results have been obtained for the input data containing only the corrections designated by the UTCr scale.**

Keywords-GMDH neural networks; Polish timescale UTC(PL); Rapid UTC; atomic clock

I. INTRODUCTION

In Poland, the organization responsible for maintaining the national time scale UTC(PL) is the Central Office of Measures (GUM, *pl.* Główny Urząd Miar). It uses a 5071 A cesium atomic clock and a device (Microstepper Austron 2055), which enables corrections to be made to ensure the maximum compatibility of the UTC(PL) with the UTC [3, 6].

The problem of maintaining the highest compliance of the UTC(PL) with the UTC is due to a delay in publication of the corrections designated for a given month with a five-day interval by the International Bureau of Weights and Measures (BIPM, *fr.* Bureau International des Poids et Mesures). These corrections defines the divergence of the national timescales in relation to the UTC and are generally published between the 8^{th} and 12^{th} day of the following month. Therefore, the problem of maintaining the highest compliance of the UTC(PL) with the UTC in the current month can be solved only by predicting the corrections.

The GUM uses the laborious procedure of predicting the corrections based on the analytical linear regression method, which requires a lot of metrological experience form the person who performs the analysis [3]. For predicting the corrections for the UTC(k) can also be used other analytical methods such as linear regression method with stochastic differential equations [11], an analytical method using Allan deviation [1], or a method based on Kalman filter [4].

Other approach for creating simulated time scale is shown in [7]. It involves the prediction of the simulated scale NRT (neural-fuzzy reference timescale), based on the 48 clocks of four laboratories (Japan, China, Korea, and Taiwan) compared with TWSTFT method, using ANFIS system (adaptive network-based fuzzy inference system). Results show that the difference between UTC and NRT do not exceed ±5 ns.

Institute of Electrical Metrology of the University of Zielona Góra, in collaboration with GUM has been running research on the application of neural networks in predicting the corrections for the UTC(PL). The obtained results of the research suggest the possibility of using the MLP and RBF networks [6, 8] for predicting the corrections for the UTC(PL). A disadvantage of this type of neural networks is the long duration in obtaining a result for the prediction. This stems from the need to match the appropriate network structure and number of neurons to the nature of the data provided on its entry in the training process.

In order to eliminate this problem in further research the GMDH neural network were used, which uses the group method of data handling and belong to the self-organizing networks. GMDH network structure is formed automatically on the basis of prepared training and testing data sets. In the course of the training process, the network expands and evolves until the enhanced efficiency of its operation has been achieved [5]. Until a new layer of neurons is attached to the current structure of the network, elements of the new layer are subjected to selection for accuracy of processing. Neurons that do not meet the criterion for assessing the condition imposed, i.e., the processing error is too large, are eliminated from the structure of the network.

The first obtained results shows that the corrections designated by the GMDH neural network provide better compatibility of the UTC(PL) with the UTC, than the corrections received in the GUM. The results of these research are presented in [9]. It decided to carry out further research on predicting the corrections for the UTC(PL) using GMDH neural network.

The results shown in the article concern on predicting the Polish timescale UTC(PL) based on the corrections designated by the UTC and UTCr scale. In both cases of predicting the corrections for the UTC(PL) the commercial tool GMDH Shell 2.2 and time series analysis method was used

II. Predicting The UTC(PL) Based On The Corrections Designated By The UTC Scale

The basis for preparation of the input data set for the GMDH neural network, as in the linear regression method used in the GUM, were the two groups of historical data available from 1 January 2006 (MJD 53736) to April 2010 (MJD 55299) (MJD - Modified Julian Date). The first of these were the results of measurements of phase time $x\_a(t)$ between the 1pps signals (pulse per second) of the UTC(PL) and atomic clock realizing the UTC(PL) scale [6], determined for each day according to relation

$$x\_a(t) = UTC(PL) - clock. \quad (1)$$

The second group of data were the corrections $x\_b(t)$ determined by the BIPM for the UTC(PL), which are designated on the MJD days ending with the digit "4" or "9", according to the relationship

$$x\_b(t) = UTC - UTC(PL). \quad (2)$$

Using MATLAB's polynomial interpolation function PCHIP (Piecewise Cubic Hermite Interpolating Polynomial) for the data set from the BIPM, a mathematical model was determined, which permitted an extension of the training data set by calculating the values of the corrections for the UTC(PL) relative to UTC for each day of the analysed period of time. This action made it possible to increase the number of data provided at the input of the GMDH neural network.

The final data set, which is the basis for determining at each day the input data for the GMDH neural network, was calculated according to the formula

$$x(t) = x\_a(t) + x\_b(t) = UTC - clock. \quad (3)$$

The data set calculated from relation (3), called time series (ts1), was the first set of data for which the training process of GMDH neural network and prediction of correction values for the UTC(PL) was performed. Time series ts1 contains a linear trend component $x_r(t)$ and a variable component. Therefore, for the training process of the GMDH neural network and predicting the corrections for the UTC(PL), also the second time series (ts2) was prepared. Such an approach was dictated by the small values of deviations from trend, which may cause that the neural network will adopt the trend as an important piece of information in the training process, and this may affect the deterioration of the prediction results of the UTC(PL). However inputting data represented by time series ts2 to the GMDH neural network will cause the network training process to adopt a model that describes the deviation from the trend. The final form of time series ts2 was obtained via elimination from the time series ts1 a long-term trend of the phase-time changes $x_r(t)$ described with the linear regression equation. The various components of time series ts2, formed by the values of the deviations from the trend, were calculated from the relation

$$xd(t) = x(t) - x_r(t). \quad (4)$$

A detailed description of the time series ts1 and ts2 preparation is shown in [8, 10].

Predicting the corrections for the UTC(PL) was made on the 15th day of the month for 28 consecutive months from January 2008 (MJD 54479) to April 2010 (MJD 55299). In course of the research at the input of the GMDH neural network the data vectors were given prepared on the basis of time series ts1 and ts2. At the output of the neural network a prediction was obtained, on the same day as in the GUM. In the predicting process the prediction value x_p for the time series ts1 was designated, and on this basis in the next step the correction value $(\text{UTC-UTC(PL)})_p$ was calculated. This prediction represents the value of correction needed to correct the UTC(PL) in order to ensure the best compatibility of the UTC(PL) with the UTC. In the case of time series ts2 the first step, using GMDH neural network, was to designate the prediction value of the deviation from the trend xd_p, which was next added to the prediction value of the trend calculated using a regression equation. The obtained result was the sought value of the prediction x_p. Further calculations aimed at achieving the value of predicted correction were carried out similarly as for the time series ts1 [10].

The research results shown in the article are presented as the prediction error (Δ_1), determined according to the relationship

$$\Delta_1 = (UTC - UTC(PL))_p - (UTC - UTC(PL))_{CIRT}. \quad (5)$$

It is the difference between the predicted value of the UTC(PL) correction relative to the UTC, and the value of the correction read from the "Circular T" bulletin for the day of determining the prediction.

For each of the predicting methods the parameters of the GMDH neural network were selected individually for each day of prediction, so that the obtained prediction error Δ_1 was as small as possible.

Fig. 1 shows the prediction errors obtained for time series sc1 and sc2, which were compared with the values of prediction errors obtained in the GUM using linear regression method.

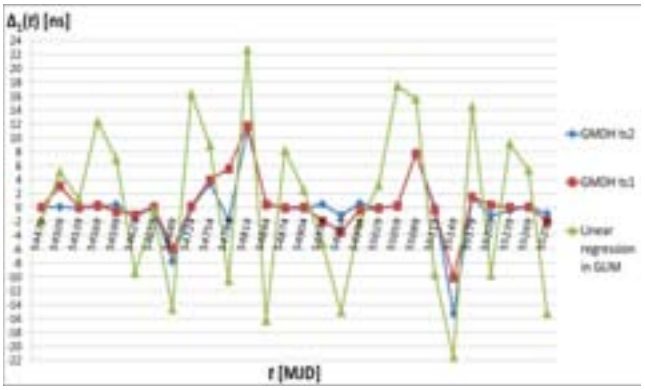

Fig. 1. Prediction errors in predicting the corrections for the UTC(PL).

In the case of determining the corrections for the UTC(PL) it can be noted that the method of preparation of both time series (ts1 and ts2) has little effect on the results of predicting. The obtained prediction errors in the analyzed period of 28 consecutive months are much smaller than the prediction errors obtained in the GUM. In the worst cases i.e., for the prediction day MJD 54814 for time series ts1 and MJD 55149 for time series ts2, the prediction error using time series analysis method, for times series ts1 was 11.73 ns, and for times series ts2 -15.23 ns. For the same days of prediction the prediction error obtained in the GUM using linear regression method, was also the highest and was respectively 22.7 ns and -21.5 ns.

Predicting the corrections for the UTC(PL) using GMDH neural network can also be performed using regression method. The results presented in [10] shows that using GMDH neural network and a regression method generates prediction errors of greater value than the time series analysis method.

III. Predicting The UTC(PL) Based On The Corrections Designated By The UTCr Scale

As already mentioned the problem of maintaining the best compliance of the UTC(PL) with the UTC is due to a delay in publication of the corrections designated by the BIPM. To remedy this situation on the 1st of January 2012 the BIPM has launched a pilot project called a Rapid UTC. The main idea is to expedite the transfer of information about the differences between national timescales, including UTC(PL) and UTC. Based on data transmitted daily from clocks and time transfer systems to the BIPM it is possible to designate a weekly sub-scale UTC Rapid (UTCr). Based on a designated scale UTCr every Wednesday on the BIPM ftp server the corrections for the last week defined for each day are published for each clock which realizes the UTC(k) scale [2]. Analysis of the published corrections for the Polish timescale UTC(PL) according to UTCr scale (UTCr-UTC(PL)) and UTC scale (UTC-UTC(PL)), showed little differences between received corrections, of a few ns. This meant a more accurate prediction of the corrections for the UTC(PL) and, consequently achieves better stability and compatibility of the UTC(PL) with the UTC. The advantage of this solution is also a smaller, three-day, delay in the publication of the corrections according to the UTCr scale. These facts were decisive in the initiation of research on predicting the corrections for the UTC(PL), using GMDH neural networks, based on previous known values of UTCr-UTC(PL) corrections.

In order to ensure the sufficient training data set for the GMDH neural network a basic set of data containing values of UTC-UTC(PL) corrections for the period from 1 February 2012 (MJD 55958) to 31 August 2012 (MJD 56170) was prepared. For the prepared data set, similarly as in predicting the UTC(PL) based on the corrections designated by the UTC scale, the PCHIP function was used to obtain the values of UTC-UTC(PL) corrections for each day of the analysed period of time. The rest of the training data for the GMDH neural network, attached to a basic set of data, were prepared in two ways. The first method of data preparation assumed adding to the basic set of data, after 31 August 2012, only the UTCr-UTC(PL) corrections. In the second case, added to the basic training data set of corrections were the UTC-UTC(PL) corrections for the last month, after the publication of the BIPM, and the UTCr-UTC(PL) corrections available in the month of determination of the correction for the UTC(PL). For the UTC-UTC(PL) corrections too, the PCHIP interpolation function was used to obtain the values of corrections for each day of the analysed period of time. Preparing two additional sets of data was aimed to examine how preferable will be the use of the UTC-UTC(PL) corrections in relation to the UTCr-UTC(PL) corrections.

At the input of the GMDH neural network, data vectors were given prepared according to the first or the second method. At the output of the neural network the $(UTCr-UTC(PL))_p$ predicted correction was obtained. However, presented results represent the prediction error determined according to the relationship

$$\Delta_2 = (UTCr - UTC(PL))_p - (UTC - UTC(PL))_{CIRT}. \quad (6)$$

This error is the difference between the predicted value of the (UTCr-UTC(PL))p correction, and a value of the UTC-UTC(PL) correction read from the "Circular T" bulletin.

BIPM designate the UTC-UTC(PL) corrections on the MJD days ending with the digit "4" or "9", so it was assumed that the predictions will be determined on the same days.

For comparison, there are also calculated the prediction errors designated according to the formula

$$\Delta_3 = (UTCr - UTC(PL)) - (UTC - UTC(PL))_{CIRT}. \quad (7)$$

They define the difference between the UTCr-UTC(PL) correction read from the BIPM's ftp server, with the value of the UTC-UTC(PL) correction read from the "Circular T" bulletin on the same day of the prediction.

On fig. 2 and fig. 3 are presented the obtained prediction errors (Δ_2 and Δ_3) for the first and the second method of input data preparation. Also the prediction errors (Δ_1) obtained in the GUM using linear regression method are presented.

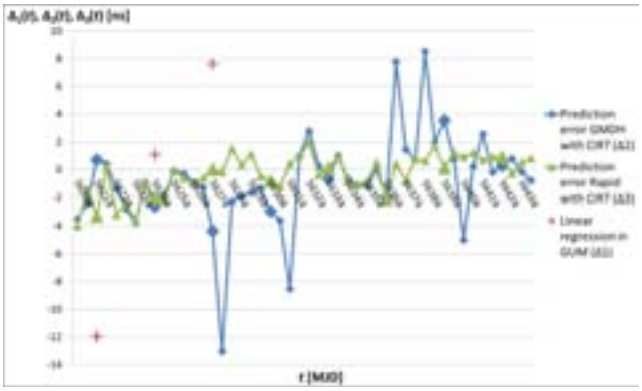

Fig. 2. Prediction errors in predicting the corrections for the UTC (PL) according to the first method of data preparation.

The obtained results (Fig. 2) indicate a correct prediction of the corrections by the GMDH neural network. The obtained prediction error values in the most cases are at the level of prediction error values Δ_3 calculated from the formula (7). The maximum prediction error obtained for the prediction day MJD 56279 is -13.03 ns. The value of this error results from a large

change in trend direction of the UTCr corrections. In other cases, the prediction errors are in the range of ±10 ns.

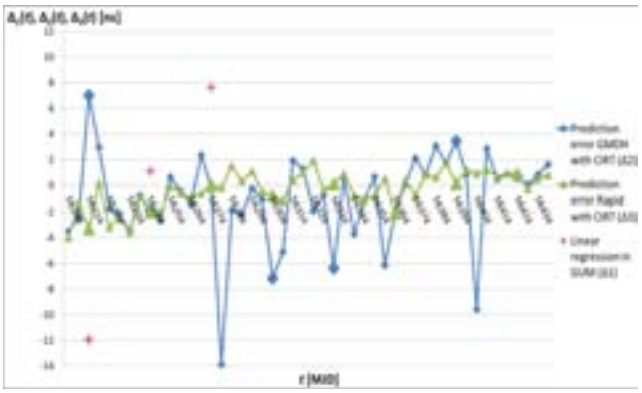

Fig. 3. Prediction errors in predicting the corrections for the UTC (PL) according to the second method of data preparation.

Fig. 3 presents the prediction errors (Δ_2) obtained for the second method of input data preparation for the GMDH neural network. In this case the obtained prediction error values cover a much greater range than the prediction error values Δ_3 obtained from the data from the BIPM. The highest value of the prediction error, equal to -13.9 ns, was also obtained at MJD 56279. The value of this error is also due to the large change in trend direction of the UTCr corrections.

On fig. 2 and fig. 3 shown with enlarged markers are presented the prediction errors occur on the 15th day of the month, so on the same day as the predictions obtained in the GUM using linear regression method. In the case of the first method of data preparation the prediction errors are in the range of ±5 ns, and for the second method ±8 ns.

IV. CONCLUSIONS

Carried out a series of first studies on the prediction of the Polish timescale UTC(PL) based on the corrections designated by the UTC and UTCr scale, indicates that the lower values of prediction error were obtained using the prediction based on the corrections designated by UTCr scale for the first method of input data preparation for the GMDH neural network. This is due to the fact that the publication of the UTCr corrections is delayed by up to three days, compared to the dozen days delay in publication of the corrections in the "Circular T" bulletin. This means the better quality of prediction of the Polish timescale UTC(PL) based on the corrections designated by the UTCr scale, because it is made for shorter period of time, than in the case of predicting the UTC(PL) based on the corrections designated by UTC scale. In the case of using UTCr scale the first prediction of the correction for the UTC(PL) in the following month could be designated between 1st and 10th day. Further predictions of the corrections for the UTC(PL) are designated based on new training data for the GMDH neural network. However, in the case of application of the UTC scale the first result of the prediction is available on the 15th day of the following month. Predictions of the corrections for the UTC(PL) for the consecutive days are designated based on the same training data set for the GMDH neural network.

In addition, an advantage of the Rapid UTC project is the fact that the UTCr corrections are calculated for each day. Thus there is no need to use the PCHIP functions to extend the data set for each day of the analysed period of time, as in the case of UTC-UTC(PL) corrections.

The obtained results showed that the GMDH neural networks can be used to predict the Polish timescale UTC(PL). The application of the commercial tools GMDH Shell version 2.2 allows to obtain lower values of prediction error, than when using linear regression method used in the GUM.

REFERENCES

[1] L. G. Bernier, Use of the Allan Deviation and Linear Prediction for the Determination of the Uncertainty on Time Calibrations Against Predicted Timescales, IEEE Transactions on Instrumentation and Measurement, Vol.52, No.2, 2003, pp. 483-486.

[2] BIPM Annual Report on Time Activities, Vol. 6, Sevres, BIPM 2011.

[3] A. Czubla, J. Konopka, J. Nawrocki, Realization of atomic SI second definition in context UTC(PL) and TA(PL), Metrology and Measurement Systems, No. 2, 2006, pp. 149-159.

[4] J. A. Davis, S. L. Shemar, P. B. Whibberley, A Kalman filter UTC(k) prediction and steering algorithm, NMS Physical Metrology Programme, United Kingdom, 2007.

[5] S. J Farlow, Self-organizing Methods in Modelling: GMDH-type Algorithms, Vol. 54, New York: Marcel Dekker Inc., 1984.

[6] J. Kaczmarek, W. Miczulski, M. Kozioł, A. Czubla, Integrated System for Monitoring and Control of the National Time and Frequency Standard, IEEE Transactions on Instrumentation and Measurement, 2013, Early Access.

[7] C. S. Liao, F. D. Chu, H. T. Lin, K. Y. Tu, Y. W. Chung, W. C. Hsu, Formation of a paper neural-fuzzy time scale in the Eastern Asia. Proc. 2011 Joint Conference of the IEEE International Frequency Control & European Frequency and Time Forum, San Fransisco, California, USA, May 1-5, 2011, pp. 292-295.

[8] W. Miczulski, M. Cepowski, Influence of type of neural network and selection of data pre-processing method on UTC-UTC(PL) prediction result; The Measurements, Automation and Monitoring, No. 11, 2010, pp. 1330-1332 (in polish).

[9] W. Miczulski, Ł. Sobolewski, Application of the GMDH neural networks in prediction of corrections of the national time scale; Electronics: Framework, Technologies, Applications, No. 6, 2011, pp. 45-47.

[10] W. Miczulski, Ł. Sobolewski, Influence of the GMDH neural network data preparation method on UTC(PL) correction prediction results, Metrology and Measurement Systems, Vol. XIX, No. 1, 2012, pp. 123-132.

[11] Panfilo G. and Tavella P., Atomic clock prediction based on stochastic differential equations, Metrologia, No 45, 2008, pp. 108-116.

Experimental and Theoretical Results on SC-Cut Quartz Resonators Collectively Realized on 4” Wafers

A. Clairet and L. Couteleau
RAKON France
2 rue Robert Keller
10150 Pont-Sainte-Marie, FRANCE
alexandre.clairet@rakon.com

T. Laroche
Frec’n sys SAS
18, rue Alain Savary
25000 Besançon, FRANCE

J-J. Boy
ENSMM/FEMTO-ST
Department TF
26 chemin de l’Epitaphe
25000 Besançon, FRANCE

Abstract—**In order to produce collective SC-cut quartz resonators on 4’’ wafers, we use a Finite Element Analysis software to model and simulate new resonator design. The modeling allowed us to optimize the geometrical and the physical parameters of the prototypes. These resonators are encapsulated under vacuum to not damage their performances. Knowing that a structure with radius of curvature is hardly compatible with collective fabrication, we have realized plano-plano structure working at 14 MHz.**

Keywords: Quartz, Piezoelectric resonator, Bulk Acoustic Wave, Finite Element Method, Quality factor

I. INTRODUCTION

In the light of modern computer modeling, innovative processes and a multidisciplinary approach of research and industry, our project (for more details, see [1]) has been proposed to revisit designing low-cost miniaturized quartz resonators without compromising on the performance characteristics. A lower cost of manufacturing induces collective processes. So, we achieved 4’’ wafers (standard of microelectronics) in which our prototypes will be cut. To insure the best of them, each of these resonators will be encapsulated under vacuum thanks to a procedure of wafer bonding (quartz on quartz). Our study focuses on a flat plate vibrating at 14 MHz on the 3rd overtone of the C-mode. Thanks to Finite Element Method (FEM) software, we are able to find optimal geometrical and physical parameters of the resonators, as well as their characteristics (motional parameters, Q factor …).

II. QUARTZ WAFER SPECIFICATION AND CHARACTERISATION

A. Required physical parameters

The cutting process of 4 inches quartz wafers, SC-cut oriented, requires very big blocks of quartz crystal. If we want to cut the wafers only in pure Z-zone (i.e. on each side of seed), we have to initiate the growth from seeds with its dimension along X-axis equal at least to 100 mm. In the contrary, we must settle for smaller seeds and some resonators defined partially in “+X” and “–X”-zones. But, in all cases, we must avoid the seed which crosses the middle of the wafer. So, we have worked on wafers extracted from blocks whose the dimensions are the following:

100, 120 and 86 mm along X, Y and Z respectively
(corresponding to the blue square on the Fig. 1).

The red rectangle, meanwhile, defines the seed whose the length should be greater than 180 mm if we do not want to obtain truncation on the parallelepiped.

Fig. 1: Quartz block for 4 inches wafer

So, in the first “blue” parallelepiped, we cut another quasi-cube defined by the first angle Phi with a rotation around the Z-axis (as indicated in the Fig. 2). Its dimensions are about: 85, 106 and 86 mm along X’, Y’ and Z respectively.

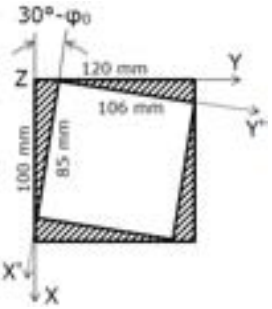

Fig. 2: First block set from the first cutting angle

Finally, a maximum of 20 to 25 slices are cut into the last block (see Fig. 3), and then cut circularly (with a diameter of 100 mm) without forgetting the orientation marks determining the directions of X’’ and Z’’.

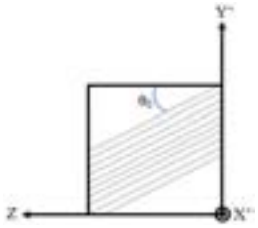

Fig. 3: Cutting process of the slices (second angle)

For these beveled wafers, we ask for physical parameters as:

- thickness of 380 µm +/- 10 µm
- TTV (Total Thickness Variation) better than 5 µm
- and surface roughness corresponding to a polish state (with Ra of the order of 10 nm).

B. Orientation checking and influence on the frequency curve temperature of the C-mode, 3rd overtone

The orientation of such a wafer is directly linked to the position of the turnover point (TOP) of the frequency temperature curve of the C-mode, 3rd overtone (i.e. the operating temperature of the oscillator). It is generally fixed to 75 +/- 5°C. So, we need the accuracy with which each area (corresponding to the vibrating zone of each resonator) is oriented, better than +/- 1'. Indeed, as shown in the following Fig. 4, a variation of 1' of the θ angle induces a variation of about 8°C (it means +/- 4°C around 75°C) of the first TOP of the frequency versus temperature curve.

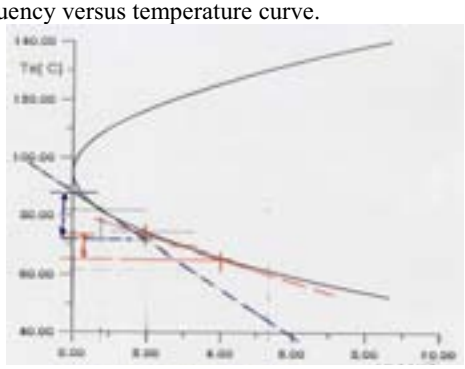

Fig. 4: Influence of the cutting angles on the TOP
1' of θ-angle corresponds to 8°C around 75°C

After cutting one wafer in 16 squared samples, we have checked the orientation of each small area. For the θ-angle, we obtain a range of measures of +/- 1'10'' around θ_0 and +/- 1' around φ. Such an angular deviation between 2 consecutive resonators corresponds to a deflection of about 5 µm. So, our requirements are achieved.

III. Finite Element Analysis

A. Physical description

The resonator is a plano-plano disc whose the vibrating part can be isolated from the dormant one by "bridges" (adequately oriented) or by a groove as shown in the Fig. 6a and 6b. Its dimensions are 15.75 x 15.75 mm and its thickness 1.14 mm (3 times 380 µm). The diameter of the active part is 13.55 mm.

The caps, dug in the center, are bonding around on each side of the resonant plate. The bonding processes are realized at different temperatures, the first one at the higher temperature (about 430 °C) while the second one is sealed at 350 °C. The applied pressure is estimated at about 150 N.

The following figure (Fig. 5a and 5b) are photographs of the glass frit deposition on one caps-wafer defining the 16 resonators and a detail of one resonator on which we see the drilling of the via and the digging of the cap.

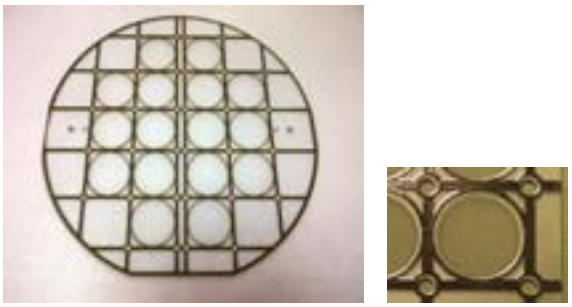

Fig. 5: 4'' caps-wafer and detail of one cell

Once the resonator encapsulated, it is clamped by 2 clips in opposite corners, corresponding to the metallization.

B. Modeling

The Finite Element Method software used is COMSOL Multiphysics®. Part of computations have been performed on the supercomputer facilities of the "Mésocentre de calcul de Franche-Comté". The squared resonator, as described in Fig. 6a, is meshed as shown below (Fig. 6b):

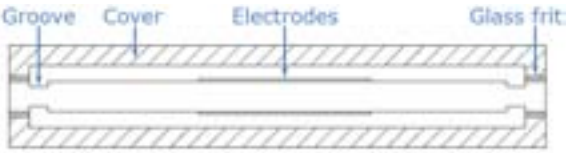

Fig. 6a: Schematic diagram of the resonator

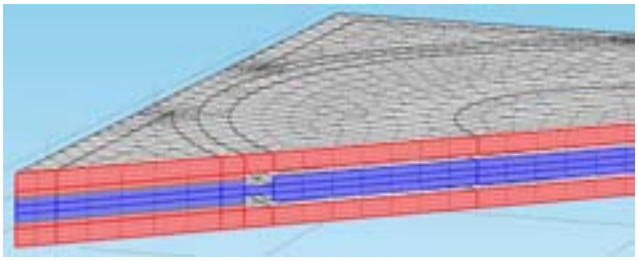

Fig. 6b: Mesh of the complete resonator with groove

The electrical potential is applied by the mean of circular gold electrodes with a diameter of 6.4 mm and a thickness of 185 nm. It is very small compared to that of the resonator. So, they are replaced by boundary load conditions in order to avoid a possible discontinuity of mesh. They are:

$$\sigma_i\ [N.m^{-2}] = \rho.h.\omega^2.u_i$$

where ρ is the density, h the thickness of the electrodes, ω the angular frequency and u_i the displacements.

We introduce the tensor of viscosity constants η_{ij} measured by Lamb and Richter [2] in the elasticity matrix of the blank to evaluate the acoustic losses.

$$C_{ij} + j\omega.\eta_{ij}$$

As for electrodes, the thin layers of glass frit between the central wafer and the 2 covers are not meshed. And so, the dissipation of energy through the glass frit and the covers is replaced by Rayleigh damping [3 - 4] in the caps, inducing imaginary part on the constitutive constants.

$$\xi = \frac{1}{2}\left(\frac{\alpha_{dM}}{2\pi f} + \beta_{dK} 2\pi f\right)$$

$$\alpha_{dM} = \omega/Q_R \text{ and } \beta_{dK} = 0$$

where ξ is the damping factor, α_{dM} and β_{dK} are the mass and stiffness damping parameters, respectively and Q_R is the estimated quality factor. Otherwise, we decide to neglect the clamping of the resonator in 2 opposite corners because they are far from the vibrating area.

IV. Determination of the Quality Factor

To visualize the electrical response of the system, an harmonic analysis is performed. The table 1 presents the frequency spectrum of the resonator in the range 14 to 14.5MHz, together with the motional resistance of each anharmonics.

	C300	C320	C302	C340	C322	C304
f [kHz]	14.233	14.263	14.271	14.321	-	14.330
Rm (Ω)	30	4,280	760	35,000		39,500

Table 1: Frequencies of the anharmonic modes

whereas the resonant frequency of the B300 (which is B-mode 3rd overtone) is 15,620 kHz with a motional resistance of 18 Ω. The C322 mode of vibration has been not found.

This modal spectrum allows us to observe the existence of several vibration modes at different resonant frequencies. We note the presence of modes, called anharmonic or sometimes spurious, after the "main" resonance. All of these modes depend on the geometry of the resonator and its orientation in the crystal frame. We note, at least, that the fastest thickness-shear mode (the B one) is 9.7% higher than the slowest one (named C), which is close to the experience (9-10%).

A. Method of calculation

The determination of the quality factor is performed by computing the electrical parameters of the resonator. This step is done with the method reported in [5]. To calculate the quality factor of a tuning fork resonator, the authors used the equivalent electrical model of quartz resonator (Fig. 7) and the complex admittance. The top electrode is set to 1 V while the bottom electrode is grounded. In this way, the value of the admittance of the system will be equal to the value of the current at the top electrode.

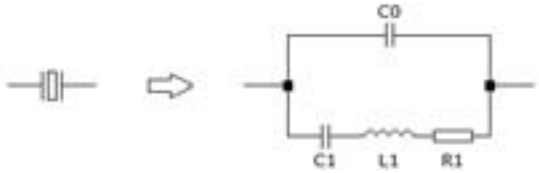

Fig. 7: Butterworth-Van Dyke model of quartz resonator

The conductance (noted G), is the real part of the admittance, while the imaginary part (noted B), is the susceptance.

$$Y = G + jB$$

The electrical parameters of the equivalent model are determined by solving the following equations:

$$B_1 = B - \omega C_0$$

$$R_1 = \frac{G}{G^2 + B_1^2} \quad ; \quad X_1 = \frac{-B_1}{G^2 + B_1^2}$$

$$\left[\frac{dX_1}{df}\right]_i = \frac{[X_1]_{i+1} - [X_1]_{i-1}}{f_{i+1} - f_{i-1}}$$

$$L_1 = \frac{1}{4\pi}\frac{dX_1}{df}\bigg|_{f=fs}$$

$$C_1 = \frac{1}{4(\pi f_s)^2 L_1} \quad ; \quad Q = \frac{1}{2\pi f_s C_1 R_1}$$

In these equations, B_1 is the susceptance of the motional branch and X_1 its reactance. The value of the static capacitance C_0 is obtained by performing an electrostatic analysis of the quartz plate.

As the parameters R_1, L_1, C_1 and Q slightly vary with the frequency, a large spectrum and small frequency increments are not necessary. So, the time and the quantity of memory used for the frequency response analysis are low.

B. Results

Firstly, we focus our study on the 3rd overtone of the C-mode, vibrating at about 14 MHz. The variations of Q and R_1 versus Q_R have presented in the following figure (Fig. 8) and compared to those of the B-mode (Fig. 9).

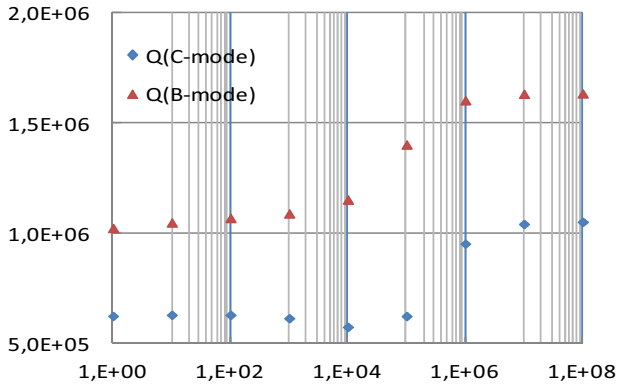

Figure 8: Variations of Q-factor vs. Q_R for B and C-modes

On each curve of the Fig. 8, we observe 2 levels at their 2 ends. For small values of Q_R (corresponding to the clamping infinitely rigid), the Q-values are the smallest. In contrast, it tends to the Q-value yet calculated without damping and equal to 1.05 million for the C-mode. In this case, the model based on the use of the Rayleigh damping is less than 1% of the calculated value without damping.

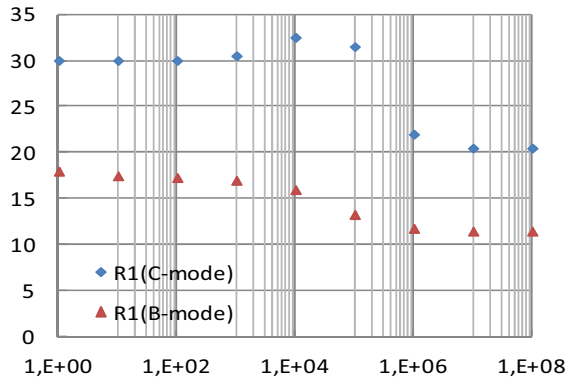

Fig. 9: Variations of R_1 (in Ω) vs. Q_R for B and C-modes

The mean values for L_1 and C_1 of the C- and B-modes are, respectively: L_1 = 220 mH, C_1 = 0.57 fF and L_1 = 190 mH, C_1 = 0.55 fF.

V. Comparison with Measures

Sixteen prototypes were realized on a 4" wafer (as shown in the Fig. 10). Only 6 of them have been sealed without defects or leaks due to the bonding process, not yet completely achieved. One, the number 2, has been broken. The measurements on the C-mode for the 5 others numbered as indicated below are summarized in the Table 2:

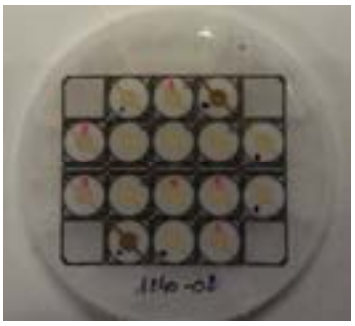

Fig. 10: Prototypes on 4" wafer

Piece	1	3	4	5	6
R_1 [Ω]	25.6	32.6	31.2	31.5	32.6
L_1 [mH]	196	225	200	197	197
Q [k]	686	622	576	559	541
C_1 [fF]	0.64	0.56	0.62	0.64	0.63

Table 2: Electrical parameters for C-mode

where C_1 is calculated with: $L_1.C_1\,\omega^2 = 1$

The same measurements were realized on the B-mode for the five prototypes. The results are summarized in the following table:

Piece	1	3	4	5	6
R_1 [Ω]	22	24.1	31.2	24.2	22.5
L_1 [mH]	174	170	200	185	175
C_1 [fF]	0.60	0.61	0.52	0.56	0.60
Q [k]	773	691	576	750	762

Table 3: Electrical parameters for B-mode

The number 1 is largely better than the others (Q-value close to 0.7 million for C-mode). With reference to the C-mode, the clamping is well modeled when Q_R is less than 10^{+5}. In contrary, the mean Q-value measured for the B-mode 3rd overtone is lower than the worst calculated value. We suppose that other damping cause can affect the B-mode, more than the C-mode, and particularly the damping due to the surface roughness under the electrodes.

At least, we can see that the experimental values of the inductance L_1 and the capacitance C_1 are very close to the computations: difference of 8% for C-mode (4% when Q_R is less than 10^{+5}) and 5% for B-mode.

VI. Conclusion

In the goal to realize collective SC-cut quartz resonators, Finite Element Method help us to find the optimal characteristics of the prototypes such as motional parameters, Q factor … After checking that the SC-cut 4 inches wafers are consistent with our requirements, we have implemented a manufacturing process that allowed us to get resonators whose the specifications are also consistent to our model. Indeed, on the C-mode, we have observed a good agreement between the experimental results and those obtain with FEM software (difference less than 10%). However, the results obtained for the B-mode show a discrepancy on the Q factor, probably due to parameter which is not taken into account in our model. The inclusion of other factor (like surface roughness) will allow us to improve our model, especially for the B-mode.

Acknowledgment

This work was funded by the "Agence Nationale de la Recherche" in the framework of a French research project entitled "FREQUENCE2009".

We thank KRYSTALY, a Czech company for delivery the SC-cut 4" wafers.

Reference

[1] A. Clairet, T. Laroche, L. Couteleau and J-J. Boy, "Modeling of BVA resonators for collective fabrication", Proceedings of the European Frequency and Time Forum, pp. 49-52, Gothenburg, 2012

[2] J. Lamb and J. Richter, "Anisotropic acoustic attenuation with new measurements for quartz at room temperatures", Proceedings of the Royal Society of London, Series A. Mathematical and Physical Sciences, vol. 293, no. 1435, pp. 479-492, 1966

[3] D. Puccio and E. EerNisse, "Attached particle effects on quartz thickness shear mode crystals", Proceedings of the COMSOL Conference, Boston, 2008

[4] COMSOL® User's Guide

[5] Yong YK, Patel MS and Tanaka M, "Theory and experimental verifications of the resonator Q and equivalent electrical parameters due to viscoelastic and mounting supports losses", IEEE Trans. Ultrasonics, Ferro. and Freq. Control, vol. 57, no. 8, pp. 1831-1839, 2010

Vector Network Analyzer Measurements of Frequency Fluctuations in Aluminum Nitride Contour-Mode Resonators

Nicholas Miller and Gianluca Piazza
Department of Electrical and Computer Engineering
Carnegie Mellon University
Pittsburgh, Pennsylvania, USA, 15213
Email: njmiller@andrew.cmu.edu

***Abstract*—As part of the current drive to engineer minitureized monolithic high performance microelectromechanical enabled oscillators there is a need for further study of frequency fluctuations in microelectromechanical resonators. To facilitate this we consider the measurement of frequency fluctuations using a vector network analyzer and demonstrate the utility of this approach using an aluminum nitride contour-mode resonator. We examine a generalized quasi-static model as well as a more detailed dynamic model and compare one- and two-port measurement setups.**

***Keywords*—Frequency fluctuation, phase noise, vector network analyzer, aluminum nitride contour-mode resonator.**

I. Introduction

In order to engineer high performance and low phase noise oscillators it is essential to understand the frequency fluctuations present in the resonator. These fluctuations contribute directly to the phase noise of the closed-loop oscillator and set the lower bound of achievable phase noise levels in any oscillator where the resonator serves as the frequency reference [1], [2]. Unlike phase noise arising in the amplifier, resonator frequency fluctuations cannot be evaded by employing bending in the frequency response found in Duffing and similar nonlinear resonators.

Frequency fluctuations in quartz acoustic resonators have been studied in great detail [3]. The stability of microelectromechanical (MEMS) resonators has also been studied [5], though to a lesser extent. As part of the present drive to engineer miniturized and monolithic high performance MEMS enabled oscillators there is a need for further study of frequency fluctuations in MEMS resonators. To facilitate this we consider the measurement of frequency fluctuations using a vector network analyzer (VNA) and demonstrate this method using an aluminum nitride contour-mode resonator.

Interferometric techniques for measuring resonator frequency fluctuations, such as the single and dual resonator bridges, have long been standard practice [2], [4]. High performance tools designed for this purpose (e.g. R&S FSUP OR NXA-26) are application specific and can be costly. The VNA, however, is a general purpose interferometric measurement tool that is commonly already a part of any RF laboratory's toolset. The VNA can be used in lieu of more specialized equipment provided it is equipped with continuous wave or time-domain measurement capability. The precision of the VNA measurement naturally depends on the instrument's noise floor. This can controlled to some extent by adjusting the bandwidth of the intermediate filter (IF). The tradeoff is that lowering the IF bandwidth decreases the measurement noise but also decreases the highest offset frequency that can be reached with the measurement.

The remainder of this paper is arranged as follows. In section II we discuss the principle of the measurement using a general quasi-static model. In section III we examine the measurement using a more detailed, but less general, dynamic model; an RLC series resonator. In section IV we demonstrate the measurement of frequency fluctuations in an aluminum nitride contour-mode resonator and follow up with conclusion in section V.

II. Quasi-Static Measurement Analysis

In this section we present a general, although simplistic, quasi-static analysis of frequency fluctuation measurement using the VNA. We consider the one-port measurement of a resonator with reflection coefficient Γ. This analysis can easily be generalized to a two-port measurement by replacing Γ with the s_{21} scattering parameter. The VNA port emits an outward traveling wave with complex amplitude a. The received wave will have complex amplitude b given by

$$b = \Gamma a. \tag{1}$$

When the device is driven near resonance we can expand the reflection coefficient in the frequency detuning

$$\Gamma = \Gamma_0 + \Gamma_1(\Omega - \omega_0), \tag{2}$$

where Ω is the drive frequency and ω_0 is the resonant frequency. The phase of the reflection coefficient is

$$\angle\Gamma = \tan^{-1}\left(\frac{\mathrm{Im}[\Gamma_0 + \Gamma_1(\Omega - \omega_0)]}{\mathrm{Re}[\Gamma_0 + \Gamma_1(\Omega - \omega_0)]}\right), \tag{3}$$

$$\approx \angle\Gamma_0 + \frac{\mathrm{Im}[\Gamma_0^*\Gamma_1]}{|\Gamma_0|^2}(\Omega - \omega_0), \tag{4}$$

This material is based on work supported by the Defense Advanced Research Project Agency under the MTO-DEFYS program, award # FA86501217264.

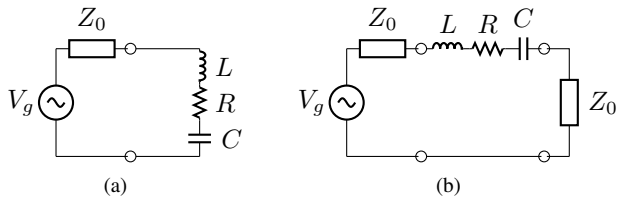

Fig. 1: One- (a) and two- (b) port RLC measurement models.

where we have expanded to leading order in $\Omega - \omega_0$. The sensitive of the phase to the frequency detuning $(\Omega - \omega_0)$ is

$$\frac{\mathrm{Im}[\Gamma_0^* \Gamma_1]}{|\Gamma_0|^2} = \frac{\partial \angle\Gamma}{\partial\Omega}\bigg|_{\omega_0}. \tag{5}$$

Now we suppose that both the drive frequency and the resonant frequency fluctuate in time. In addition, we assume that the fluctuations in the drive frequency and resonant frequency are uncorrelated. Using the VNA in continuous wave mode to drive the resonator at resonance ($\langle\Omega\rangle = \langle\omega_0\rangle$) and measure the reflection coefficient as function of time provides us with $\Gamma(t)$. Calculating the power spectral density of $\angle\Gamma(t)$ for small fluctuations in Ω and ω_0 gives

$$S_{\angle\Gamma}(\omega) = \left(\frac{\partial \angle\Gamma}{\partial\Omega}\bigg|_{\omega_0}\right)^2 \Big(S_\Omega(\omega) + S_{\omega_0}(\omega)\Big) + S_m(\omega), \tag{6}$$

where S_Ω is the power spectral density of the drive frequency fluctuations, S_{ω_0} is the power spectral density of the resonator frequency, and S_m is the measurement noise spectrum. Provided the measurement noise and the source frequency fluctuations are sufficiently small, the measurement of the reflection coefficient phase as a function of time will give the frequency fluctuations of the resonator.

III. Dynamic RLC Model

The analysis in the previous section captures the principle of the measurement. However, a more detailed analysis reveals some interesting points. Accordingly, in this section we consider the measurement using a more detailed model that includes additional noise sources and the resonator dynamics. The model we consider is series RLC resonator with additive and parametric noises. We consider this resonator model in both a one-port and a two-port configuration, see figure 1. In this analysis we assume that Z_0 is real. The series RLC model is a valid model of an aluminum nitride contour-mode resonator near resonance. The resonator equation is

$$L\ddot{q} + \big(R + 2L\zeta_r(t)\big)\dot{q} + \left(\frac{1}{C} - 2\sqrt{\frac{L}{C}}\zeta_i(t)\right) q = V_0\big(1+\alpha(t)\big)\cos\big(\Omega t + \theta(t)\big) + n(t), \tag{7}$$

where q is the charge in the capacitor, $\zeta_r(t)$ and $\zeta_i(t)$ are parametric noises that produce quality factor and resonant frequency fluctuations, $\alpha(t)$ and $\theta(t)$ are the amplitude and phase noise of the VNA drive signal, and $n(t)$ is addtive noise. The additive noise can be approximated as white since the resonator is sensitive only to the spectrum in a narrow band around the resonant frequency. Thus we assume $\langle n(t)n(t')\rangle = D\delta(t-t')$. When $n(t)$ is thermal noise $D = 2Rk_BT$ where k_B is Boltzmann's constant and T is the temperature. When the noise and damping are weak $q(t)$ follows a nearly harmonic orbit. Thus we make the change of coordinates

$$q = a_0 u(t) e^{i\Omega t + i\theta} + \text{c.c.}, \tag{8}$$

$$\dot{q} = i(\Omega + \dot{\theta}) a_0 u(t) e^{i\Omega t + i\theta} + \text{c.c.}, \tag{9}$$

where $u(t)$ is the complex amplitude of the resonator motion, $a_0 = V_0/4iL\Omega$ is the characteristic amplitude, and c.c. stands for the complex conjugate of the preceeding terms. The resonator admittance is conveniently expressed in terms of the resonator complex amplitude,

$$Y = \frac{2i\Omega a_0 u}{V_0(1+\alpha)}. \tag{10}$$

The reflection and transmission coefficients,

$$\Gamma_r = \frac{1 - Z_0 Y}{1 + Z_0 Y} = \frac{1 + \alpha - u\mu_r}{1 + \alpha + u\mu_r}, \tag{11}$$

$$\Gamma_t = \frac{2Z_0 Y}{1 + 2Z_0 Y} = \frac{2u\mu_t}{1 + \alpha + 2u\mu_t}, \tag{12}$$

where Γ_r is the reflection coefficient for a one-port measurement, Γ_t is the s_{21} scattering parameter for a two-port measurement, $\mu_r = Z_0/2L$, and $\mu_t = Z_0/L$.

Applying the method of averaging to the resonator equation in the new complex coordinate, u, gives the approximate resonator equation

$$\dot{u} \approx -\big(\Lambda + \xi(t)\big)u + 1 + \eta(t), \tag{13}$$

where $\Lambda = \lambda + i\sigma$, $\lambda = R/2L$, $\sigma = \Omega - (LC)^{-1/2}$, $\xi(t) = \zeta_r(t) + \ddot{\theta}/2\Omega + i\zeta_i(t) + i\dot{\theta}$, and $\eta(t) = \alpha(t) + 2e^{i\Omega t + i\theta} n(t)/V_0$. The complex parametric noise ξ is a combination of the resonator parametric noise and the source frequency noise. Through measuring the reflection coefficient we can extract the power spectra of the real and imaginary parts of ξ, but we will be able to measure the frequency fluctuations of the resonator, ζ_i, only if they are larger than the frequency fluctuations of the source. If this is not the case a dual resonator bridge measurement is required [2], [4]. Solving equation (13) in the weak noise limit gives

$$u = \int_{-\infty}^{t} dt_1 \exp\left[-\int_{t_1}^{t} dt_2 \big(\Lambda + \xi(t_2)\big)\right]\big(1 + \eta(t_1)\big), \tag{14}$$

$$\approx \int_{-\infty}^{t} dt_1 e^{\Lambda(t_1 - t)} \left(1 - \int_{t_1}^{t} dt_2 \xi(t_2) + \eta(t_1)\right). \tag{15}$$

From equation (15), the mean value of the resonator's complex amplitude and the reflection coefficient are

$$\langle u\rangle = \frac{1}{\Lambda}, \qquad \langle\Gamma_r\rangle = \frac{\Lambda - \mu_r}{\Lambda + \mu_r}, \qquad \langle\Gamma_t\rangle = \frac{\mu_t}{\Lambda + \mu_t}. \tag{16}$$

With the VNA in continuous wave mode we measure Γ_r or Γ_t as a function of time with a fixed driving frequency. We then consider the fluctuations in Γ,

$$\gamma \equiv \Gamma - \langle\Gamma\rangle \approx -\beta\Lambda^2(u - \langle u\rangle) + \beta\Lambda\alpha(t), \tag{17}$$

$$\beta = \begin{cases} \frac{2\mu_r}{(\lambda+\mu_r)^2} & \text{one-port reflection,} \\ -\frac{\mu_t}{(\lambda+\mu_t)^2} & \text{two-port transmission,} \end{cases} \tag{18}$$

where γ has been expanded in Taylor series to leading order in terms of $u - \langle u\rangle$ and α. For notational convenience the

subscripts have been dropped. It is understood that when considering a one-port or a two-port transmission measurement the appropriate definition of β, given in equation (18), is to be used.

It was shown in [6] that the complex power spectral density of $\langle\gamma(t)\gamma(t+t_1)\rangle$ can be used to average out the additive noise and extract the frequency fluctuations of the resonator. We emphasize that this is the Fourier transform of $\langle\gamma(t)\gamma(t+t_1)\rangle$ and not $\langle\gamma(t)\gamma^*(t+t_1)\rangle$. Indeed, this gives

$$S_\gamma(\omega) = \int_{-\infty}^{\infty} dt_1 \langle\gamma(t)\gamma(t+t_1)\rangle e^{-i\omega t_1}, \tag{19}$$

$$= \frac{\beta^2\Lambda^2\big(S_\xi(\omega)+\omega^2 S_\alpha(\omega)\big)}{(\Lambda^2+\omega^2)}, \tag{20}$$

where $S_\xi(\omega)$ is the complex power spectral density of ξ given by $S_\xi(\omega) = S_{\xi_r}(\omega) - S_{\xi_i}(\omega) + 2i\,\mathrm{Re}[S_{\xi_r,\xi_i}(\omega)]$ and S_{ξ_r}, S_{ξ_i}, and S_{ξ_r,ξ_i} are the power spectra and cross-sprectum of the real and imaginary parts of ξ. For small offset frequencies, ω, equation (20) gives the complex power spectral density of the parametric noise. Unfortunately there are two potential issues with this approach. The first is that the measurment of S_ξ is not sufficient to extract S_{ξ_r} and S_{ξ_i} separately. This approach is most useful when one knows, for example, that $S_{\xi_r} = 0$. The second issue is that even if $S_{\xi_r} = 0$, we will not measure zero because of the measurement noise. This can lead to erroneously large measured values for S_γ. If these issues cause a problem we must calculate the power spectral densities of $\mathrm{Re}[\gamma]$ and $\mathrm{Im}[\gamma]$ separately. These spectra are much more cumbersome to express analytically and so we will give only their expression at resonance, $\sigma = 0$,

$$S_{\mathrm{Re}[\gamma]}(\omega)\Big|_{\sigma=0} = \frac{\beta^2\lambda^2\big(S_{\xi_r}(\omega)+\omega^2 S_\alpha(\omega)+2\lambda^2\frac{D}{V_0^2}\big)}{\lambda^2+\omega^2}, \tag{21}$$

$$S_{\mathrm{Im}[\gamma]}(\omega)\Big|_{\sigma=0} = \frac{\beta^2\lambda^2\big(S_{\xi_i}(\omega)+2\lambda^2\frac{D}{V_0^2}\big)}{\lambda^2+\omega^2}, \tag{22}$$

$$S_{\mathrm{Re}[\gamma],\mathrm{Im}[\gamma]}(\omega)\Big|_{\sigma=0} = \frac{\beta^2\lambda^2 S_{\xi_r,\xi_i}(\omega)}{\lambda^2+\omega^2}, \tag{23}$$

If we fix R and L and vary Z_0 we find that β^2 is maximized when $Z_0 = R$ for a one-port reflection measurement and $2Z_0 = R$ for a two-port transmission measurement. The optimal values of β^2 are $\beta^2 = L^2/R^2 = Q^2/\omega_0^2$ for a one-port reflection measurement and $\beta^2 = L^2/4R^2 = Q^2/4\omega_0^2$ for a two-port transmission measurement. This result suggests that high frequency resonators with modest Q are more difficult to measure. Yet, we might consider that the spectrum of frequency fluctuations should scale with ω_0^2 if time-keeping ability is kept fixed. This should cancel the ω_0^2 in the denominator of β^2 and so the measurement sensitivity comes down to the unloaded Q of the resonator. In addition, it is interesting to note that the reflection measurement is four times more sensitive assuming ideal matching conditions in both cases and identical measurement noise.

IV. Contour-Mode Resonator Measurements

In this section we demonstrate the measurement outlined above. We consider a 473 MHz one-port aluminum nitride contour-mode resonator [7] measured by an Agilent N5230A vector network analyzer. The reflection coefficient of the resonator is shown in figure 3. The figure shows the measured reflection coefficient in blue and the least squares fit to the modified Butterworth Van Dyke (MBVD) model in red. The MBVD equivalent circuit is shown in figure 2 and the model parameters are shown in table I.

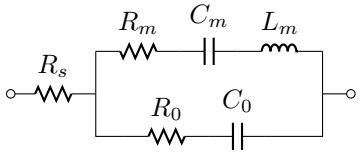

Fig. 2: Modified Butterworth Van Dyke (MBVD) circuit model.

$L_m = 81.666\ \mu\mathrm{H}$	$C_m = 1.3841$ fF	$R_m = 122.039\ \Omega$
$C_0 = 241.67$ fF	$R_0 = 168.49\ \Omega$	$R_s = 14.09\ \Omega$

TABLE I: MBVD resonator parameter values.

In order to measure the intrinsic frequency fluctuations of the resonator, the resonator was driven in continuous wave (CW) mode at resonance, 473.4125 MHz. The CW measurement point is shown as a black dot in figure 3. Linearizing the phase curve about this point, we find

$$\left.\frac{\partial\angle\Gamma}{\partial\Omega}\right|_{\omega_0} = 1.1279\times10^{-4}\ \text{rad/Hz}. \tag{24}$$

In order to characterize the VNA the VNA source phase noise was measured using the Agilent E5052B signal source analyzer. The phase noise spectrum is shown in figure 4 in green. In addition a passive attenuator was measured using the VNA. The attentuation was similar to the loss in the resonator reflection coefficient and so the phase fluctuations of the attenuator measurement should provide a valid measure of the VNA measurement noise floor. Moreover, if we compare the VNA measurement noise to the phase noise of the VNA source we find the VNA phase noise is much lower and thus negligible.

Next we measured the resonator, performing 9 CW sweeps of 16001 points with a sampling frequency and IF banwidth of 200 Hz. The power spectral density of the frequency fluctuations was then calculated using equation (6), ignoring

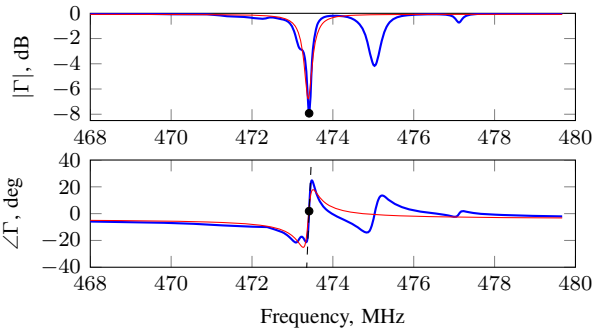

Fig. 3: Resonator reflection coefficient. The measured reflection coefficient is in blue and the MBVD model fit is in red. The MBVD coefficients were fit via least squares regression.

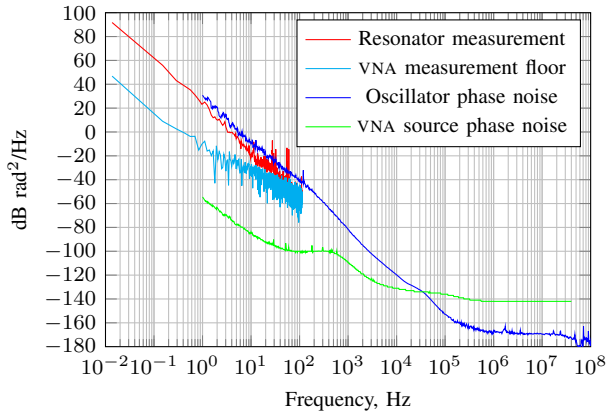

Fig. 4: Spectrum of phase noise for the oscillator, the resonator measured in open-loop, the VNA source, and a passive attenuator used to determine the measurement noise floor.

the source frequency fluctuations and the measurement noise, and averaging over the multiple CW sweeps. As a point of comparison, the same oscillator was placed into an oscillator and the phase noise of that oscillator was measured using the E5052B. The oscillator was constructed with a simple Pierce amplifier circuit on a printed circuit board and wirebonded to the resonator. In order to compare the oscillator phase noise and the measured frequency fluctuations it is necessary to divide the frequency fluctuations by ω^2. The reason is that frequency fluctuations in the resonator contribute directly to the frequency fluctuations of an oscillator because the resonator serves as the frequency selective component (*i.e.* frequency reference) of the oscillator. Figure 4 shows both the oscillator phase noise and the resonator frequency fluctuations, referred to phase by division by ω^2. The VNA measurement floor was also referred to the oscillator phase by dividing by ω^2. In figure 4 it is clear that the measurement noise floor (cyan) is well below the measured resonator noise (red). The resonator noise (red) is matched in slope and only 5-10dB below the closed-loop oscillator phase noise (blue). This comparison supports the validity of the proposed measurement technique.

V. Conclusion

In this work we have discussed the principles of measuring resonator frequency fluctuations with a vector network analyzer. By consider a simple RLC model we have discussed the issues invovled with measuring the frequency fluctuations via the complex spectrum of the reflection or transmission coefficient. This measurement averages out the additive noise, but has difficulty distinquishing frequency and damping fluctuations in the resonator. In addition, we have shown that the reflection measurement is four times more sensitive than the transmission measurement if the measurement noise is equal in both cases. Finally, we have demonstrated the measurement with a 473 MHz aluminum nitride contour-mode resonator. By comparing the measurement to a closed-loop phase noise measurement using the same resonator and to noise floor measurements we comfirmed the validity of the proposed measurement technique.

References

[1] T. E. Parker, "Characteristics and sources of phase noise in stable oscillators", *41st Annual Symposium on Frequency Control, 1987*, pp.99-110, 27-29 May 1987.

[2] G. S. Curtis, "The relationship between resonator and oscillator noise, and resonator noise measurement techniques", *41st Annual Symposium on Frequency Control. 1987*, pp.420-428, 27-29 May 1987.

[3] T. E. Parker, "1/f Frequency fluctuations in quaryz acoustic resonators", *Appl. Phys. Lett.* **46**:246-248, 1985.

[4] E. Rubiola, J. Groslambert, M. Brunet, and V. Giordano. "Flicker noise measurement of HF quartz fresonators", *IEEE Trans. Ultrason., Ferroelectr., Freq. Control*, **47**:361-368, 2000.

[5] J. R. Vig and Y. Kim, "Noise in microelectromechanical system resonators", *IEEE Tran. Ultrason., Ferroelectr., Freq. Control*, vol.**46**, no.6, pp.1558-1565, Nov. 1999.

[6] Z. A. Maizeliz, M. L. Roukes, and M. I. Dykman, "Detecting and characterizing frequency fluctuations of vibrational modes", *Phys. Rev. B*, **84**:144301, 2011.

[7] G. Piazza, P.J. Stephanou, and A.P. Pisano, "Piezoelectric aluminum nitride vibrating contour-mode mems resonators", *Journal of Microelectromechanical Systems*, **15**:14061418, 2006.

New Calibration Method for Experimental Study of Nonlinear Behavior of Bulk Acoustic Wave Resonator with Power

L Catherinot
TRONICO: Innovation dept.
Nantes, France
lcatherinot@tronico-alcen.com

M. Chatras, S. Bila, D. Cros
XLIM INSTITUTE: MINACOM dept.
Limoges University
Limoges, France
matthieu.chatras@xlim.fr

***Abstract*— This paper deals with experimental studies of nonlinear behavior of Bulk Acoustic Wave (BAW) devices, in a Solidly Mounted Resonator (SMR) structure. The purpose is to extend the Modified Butterworth Van Dyke model to a complete non-linear model of a BAW resonator, which takes into account all nonlinear effects. Frequency shifts were studied when high Radio Frequency (RF) power (up to 5W) is applied to the resonators. We have focused on the W-CDMA frequency standards, for resonators of emission filters of a front-end module in mobile phones. To stabilize the input power, we have developed a new calibration method, which is able to match the data correction between a high and small signal at any frequencies. With this method, we have access to the power waves, and we recalculate the S-parameters externally as a function of the frequency sweep.**

Keywords—Bulk Acoustic Wave; Calibration; VNA; High RF Power;Non Linearities.

I. INTRODUCTION

The race industry to improve the integration and performance of the components used today is fraught with more complex technological problems. It leads to the emergence of new structures such as acoustic wave devices, and more particularly to Bulk Acoustic Wave (BAW) [*1*] devices, which have the capacity to meet the needs of filtering and local oscillators.

Current solutions to meet these needs will be presented first, integrating in the current context of increasing speed of transmission of digital data. The different causes of nonlinearities in BAW devices will be presented and we quantify their preponderance. Finally, we show the tester in automated power has been achieved and we will describe the measurement results. Finally, we see that the full non-linear study of a piezoelectric device may require the study of the acoustic aspect of the phenomenon.

II. CONTEXT OF THE STUDY

A. Filters and oscillators in mobile phones

The filtering function is one of two main applications achieved by bulk acoustic wave devices in mobile devices (figure 1).

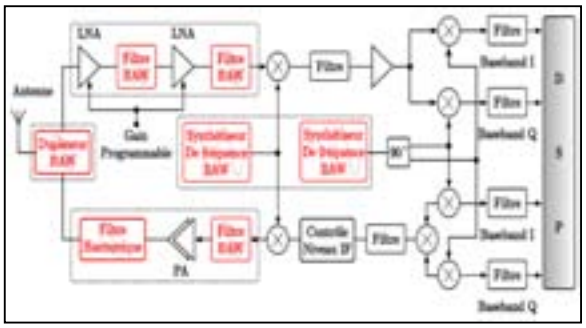

Fig. 1. Front-end multistandard architecture of mobile phones

RF filters used in the European Mobilis project are BAW narrow-band filters which may be used as filters or duplexers [*2*][*3*]. Mobilis project has been initiated by the IMS Laboratory [*4*].

They are further characterized by an input and output impedance level, input / output (single or differential) type, maximum acceptable level of input power (especially for Tx filters for signal transmission), a temperature range of operation which does not generate an excessive drift, characterization and quantification of non-linear effects due to the filter design and the critical parameter which is the integration of the component in a mobile phone [*5*] .

On of the aim is to develop a technology platform based on mobile applications for Ambient Intelligence, and improve performance to check the requirement of mobile telephony [*5*].

The aim is the following: study and model BAW filters subjected to a strong signal. The purpose is to identify the main effects that may impact the reliability of the component, including the effect of high power RF bandwidth on SMR BAW filter, ie the insertion losses, frequency shift and possible damage on different resonators (according to their position in the filter and the power distribution in the circuit).

By these criteria we performed measurements; results should enable the development of a nonlinear electrical model valid around the resonance. So we will first focus on different non-linear effects caused by high power RF in the following

section, before describing the test bench used and discuss the results.

B. High RF power main effects on BAW devices

The direct consequence of high power is the heating of the component. We must therefore take into account the effects of heat on the center frequency shift. Thermal effects have also consequences on the elastic stiffness. The electrostriction effect is also very important. The mechanical constraint is quadratic response of the electric field applied on the device. It is quite hard to analyze non linearities due to heating effects because these variations evolve simultaneously in time and space[*6*][*7*][*8*][*9*] [*10*] [*11*].

III. HIGH POWER MEASUREMENTS

S-parameters at high RF powers are difficult to measure and require a special test bench. Measurement results obtained with the reflection tester (figure 3) were supplemented with the tester in transmission (figure 5). This one has been built with conventional RF equipment, and has been carefully calibrated to determine precisely the power injected in the device at any frequency value, without any post-computation [*6*].

A. High Power Reflection Test Bench

The used test-bench in reflection is shown figure, it does not allow direct access to the value of the incident power. It is necessary to make a classic S parameter measurement, small signal, and discretize the frequency points.

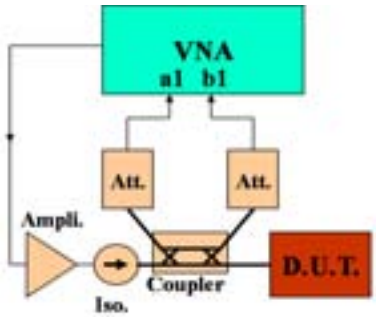

Fig. 2. High Power Reflection Test Bench

Value for each selected frequency, a measure of power is carried out. With a computation process one can obtain the value of the input impedance. Then the electrical response of the resonator is obtained, for small and high signals (figure 3).

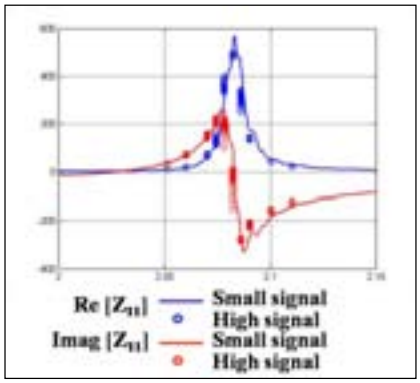

Fig. 3. Power parametrization of the input impedance

Due to variations of the amplifier and due to the attenuation, it is necessary to adapt for each point of the frequency shift of the impedance of the BAW resonator as a function of the input power Pe. The curve of variation of the impedance of the device is obtained after correction for a frequency band. It is then possible to evaluate an approximation of the BAW resonator impedance versus frequency for each value of input power Pe as shown figure 4.

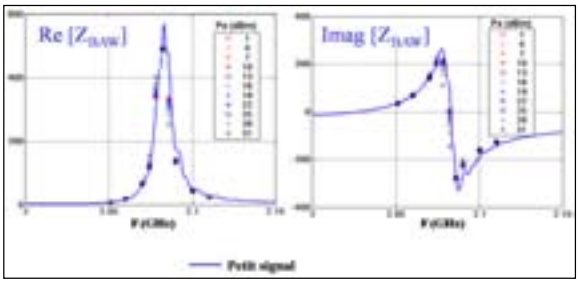

Fig. 4. Real and Imaginary parts of the impedance of the resonator for each input Power Pe

We have seen that it is possible to extract the values of the localized equivalent model MBVD around resonance. It can therefore highlight from the approximation made of these measurements the change in capacitor Cm and resistance Rm according to the power. The most significant results by this method are:

• A relative shift of Cm close to 0.2% (0.15% for loaded resonators) and a shift on the resistance Rm of 17% (27% for loaded resonators) have been observed.

• A relative shift of the resonant frequency close to 0.1% in both cases.

• A shift of the anti-resonance frequency close to 0.1% in both cases, and a resonant frequency shift lower than 0.3%.

The contribution of the effect of power on the value of the resonant frequency remains weak.

B. High Power Transmission Test Bench

A 4-port Vectorial Network Analyzer (VNA) is used both as measuring device and RF source. It delivers -20dBm power, swept around 2GHz. The signal is amplified by a Power

Amplifier (PA) (40dB gain) previously characterized as sufficiently linear for the used frequency range. All used devices for the test bench, including attenuators and couplers, have been chosen to be functional in the frequency band (figure 5).

Finally, the test bench is connected to a probe station to overcome various effects such as landslides, claw arks on the wafer or apparatus damage. In addition, the set up has a power sensor connected to the resonator's input, in order to manage the input power, which enables a power feedback loop. This is a particularly delicate step that requires the establishment of an original procedure of double calibration (frequency/power).

This calibration method simplifies the equipment and locates the input power measurement very close to the resonator. Initially, a calibration is performed on the power level output of the coupler, so that the VNA corrects the power supplied simultaneously: the power is well known in the DUT plane and it is fixed, and we also take into account losses in probe cables. In a second step, a standard S-parameters calibration is carried out under the probes (Short Open Load Thru), so low power and high power are enabled. The choice of the maximum power value was studied taking into account return wave limits of the measuring devices and power densities available on the resonators that are being evaluated for future use as the input stage of mobile phone emission filters.

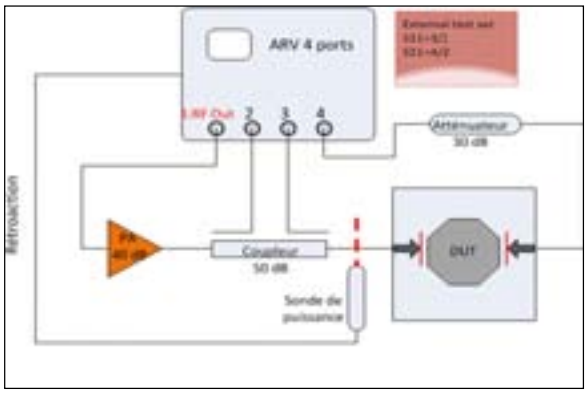

Fig. 5. High Rf Power Measurement Transmission Test Bench

C. Results

We performed measurements on small resonators ($100*100\mu m^2$ and $50*50\mu m^2$), with rectangular and apodized shape, wich have been designed by EPCOS [*12*] and XLIM [*13*]. The maximum input power value is 34 dBm, above which we observe device breakage (deterioration of the top electrode, undesirable resistive effects on the access pads). The power density varies between $36dB/mm^2$ and $60dB/mm^2$. In particular, a frequency shift is observed on the resonant frequency, which decreases by 5% from its initial value from 20 dBm to 34 dBm.

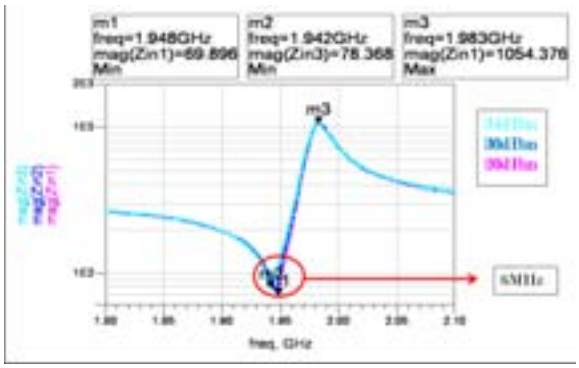

Fig. 6. Electric Response for the apodized resonators

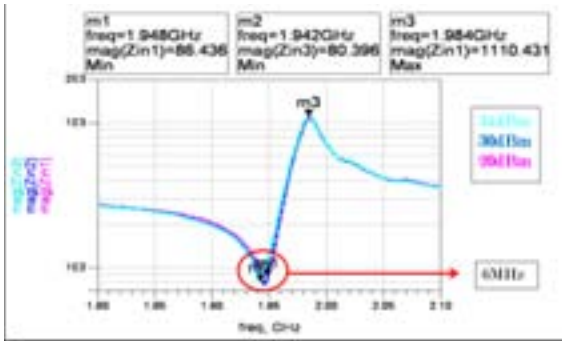

Fig. 7. Electric Response for the rectangular resonators

D. Discussion

When the incident power increases, the shifts in geometric parameters of the resonator is small compared to the variations of parameters in the piezoelectric material. To accurately model the nonlinear behavior of a BAW resonator, it is then necessary to consider elastic, dielectric and electro-acousticof the piezoelectric layer.

IV. CONCLUSION

The European Mobilis project aims to develop a filtering solution based on BAW SMR technology, suitable for mobile multistandard applications. This context creates a thorough study of the possibilities of these devices in terms of linearity and reliability when subjected to high power. Indeed, the BAW resonators are integrated in WCDMA duplexers, and should not be damaged by the signals of high power transmission.

It is therefore necessary to determine the possible causes of non-linearity in the BAW resonators, and identify phenomena related to nonlinear piezoelectricity. The electrostriction, the variation of the MIM capacitor and thermal effects appear to be the main causes of nonlinearities in BAW devices.

These preliminary studies allowed us to highlight the existence of localized elements shifts and propose parametric linear models. We performed several measurement campaigns on the power handling on transmission Tx resonators.

A bench of specific measurement was performed. This bench is used to find the input power fed into the device under

test and to monitor the frequencies of resonance and anti-resonance according to the power. For this, it was required to perform a double careful calibration to take into account simultaneously all the parameters. The results showed a weak shift of the resonant frequency. We then extracted the localized components potentially variables by comparing the results obtained in transmission and reflection.

The contribution of the power on the value of the resonant frequency is low, so this shows that the BAW devices are reliable and have good power handling [*14*].

Evolution of the test bench is being considered, specifically to further knowledge on mechanical and spectral aspects.

ACKNOWLEDGMENT

This work was carried out within the European project Mobilis with the support of the French National Scientific Research Center CNRS. All the measurements have been performed in XLIM Institute, Limoges, France.

REFERENCES

[1] S.Giraud, M.Chatras, S.Bila, D.Cros, T.Baron, S.Balandras, P.Monfraix, L.Estagerie L.Catherinot, "A general procedure for the design of BAW filters," *International Journal of RF and Microwave Computer-Aided Engineering*, vol. 21, no. 5, pp. 458-465, Sept 2011.

[2] E. Schmidhammer, F. Constantinescu M. Ylilammi, "Report on the basics about non-linearity and power durability," *Mixed SiP and SoC Integration of Power BAW Filters for Digital Wireless Transmissions*, February 2007, confidential report on MOBILIS project.

[3] Al.-G. Gheorghe, M. Nitescu F. Constantinescu, "Nonlinear circuit models of power BAW resonators," *Mobilis Meeting*, January 2007.

[4] Laboratoire d'Intégration du Matériau au Système Système. [Online]. http://www.ims-bordeaux.fr

[5] B.Stefanelli, A.Kaiser, A.Cathelin, S.Giraud, M.Chatras, S.Bila, D.Cros, J.B David, L.Leysenne, E.Kerhervé Flament, "A complete UMTS transmitter using BAW filters and duplexers, a 90 nm CMOS igital RF signal generator and a 0.25µm BiCMOS power amplifier," *International Journal of RF and Microwave Computer-Aided Engineering*, vol. 21, no. 5, pp. 466-476, Sept 2011.

[6] S.Hirose, "New method for measuring mechanical vibration loss and dielectric loss of piezoelectric transducer under high-power excitation," *Jpn. J. Appl. Phys*, pp. 329-332, 1994.

[7] E Schmidhammer, "Nonlinear effects in acousto-electric devices," *4th European Conference on Circuits and Systems for Communications*, pp. 221 – 226, 2008.

[8] A.Albareda et al., "Nonlinear direct and indirect third harmonic generation in piezoelectric resonators by the intermodulation method," *Rev. Sci. Instrum.*, vol. 72, no. 6, pp. 2742-2749, 2001.

[9] B.Kaltenbacher et al., "Identification of material nonlinearities in piezoelectric ceramics," *IEEE Ultrasonics Symp.*, pp. 358-361, 2003.

[10] R. Aigner et al., "Behavior of BAW devices at high power levels," *Intern. Ultrasonics Symp IEEE*, 2004.

[11] Jaroslav Nosek, "Drive Level Dependence of the Resonant Frequency in BAW Quartz Resonators and His Modeling," *IEEE transactions on ultrasonics, ferroelectrics, and frequency control*, vol. 46, no. 4, pp. 823-829, 1999.

[12] EPCOS. [Online]. http://wwww.epcos.com

[13] S.Bila, M.Chatras, D.Cros, M.Aubourg S.Giraud, "Bulk Acoustic Wave Filters Synthesis and Optimization for Multistandard Communications Terminals," *IEEE TUFFC*, pp. 52-58, Jan 2010.

[14] E.Lebrasseur,F.Bassignot, H.Wang, S.Balandras, J.Fan, L.Catherinot, M.Chatras, P.Monfraix, L.Estagerie T.Baron, "Wideband Lithium Niobate FBAR Filters," *Journal of Microwave Sceince and Technology*, no. 459767, Jan 2013.

Numerical Study of the Impact of Process Variations on the Motional Resistance of Weakly Coupled MEMS Resonators

Andreja Erbes*, Pradyumna Thiruvenkatanathan and Ashwin A. Seshia
Engineering Department
University of Cambridge, Cambridge, United Kingdom
Email*: ae279@eng.cam.ac.uk

***Abstract*—This paper presents a numerical study of the impact of process-induced variations on the achievable motional resistance R_x of one-dimensional, cyclic and cross-coupled architectures of electrostatically transduced MEMS resonators operating in the 250 kHz range. Monte Carlo numerical simulations which accounted for up to 0.75% variation in critical resonator feature sizes were initiated on 1, 2, 3, 4, 5 and 9 coupled MEMS resonators for three distinct coupling architectures. Improvements of 100X in the spread of R_x and 2.7X in mean achievable R_x are reported for the case of 9 resonators when implemented in the cross-coupled topology, as opposed to the traditional one-dimensional chain.**

I. Introduction

The demand for high performance and reduced size wireless communication devices has pushed research interests towards the design and development of low power, small footprint and single chip CMOS integrated wireless-transceiver solutions. The potential of Micro Electro Mechanical Systems (MEMS) technology to meet some of these requirements has led to the recent development and adoption of miniaturized, silicon micro-machined mechanical resonators for operation as timing references [1]. Such micro-resonators, unlike their traditional quartz crystal counterparts, are manufactured using silicon micro-fabrication techniques and offer considerably smaller form factor as well as shorter lead times. Electrostatically transduced silicon MEMS resonators have also been shown to provide a number of advantages including - high mechanical quality factors (Q), low static power dissipation and CMOS manufacturing compatibility making them attractive alternatives to quartz based timing references. However, such silicon micro-resonators are still limited by their high motional resistance (R_x) that consequently hinders direct deployment in RF front-end applications.

Although one-dimensional (1D-κ) mechanical coupling of micro-resonators (see discrete element model in Fig. 1) has been suggested as a potential route to help reduce the R_x of such devices [2]-[3], weakly coupled micro-mechanical devices are highly prone to structural asymmetries induced by manufacturing tolerances. The presence of small imperfections in an array of identically designed resonators leads to a distortion in the vibratory mode shape from the case of a structurally symmetric system [4]. The vibration energy becomes spatially localized and does not extend throughout the structures anymore. This effect often results in non-uniform reductions in R_x from the case of perfect symmetry [5]. While it is possible to tune the structural symmetry and consequently improve conformity in R_x reduction [3][5], this method still remains impractical for larger 1D-κ arrays.

Alternative design methodologies have been investigated to help improve the immunity of such coupled arrays to the impact of manufacturing tolerances in the context of their application to micro-electro-mechanical filters. More specifically, two-dimensional coupling [6] as well as cyclic coupling architectures [7] have been shown experimentally and numerically to provide improved insertion loss and ripple characteristics, indicating an enhancement in robustness to vibration localization effects relative to their 1D-κ counterparts.

In an attempt to obtain better scalability and more predictable R_x reduction of such weakly coupled arrays, this paper presents a numerical study of the impact of manufacturing tolerances on the achievable R_x for three classes of mechanical coupling topologies: one-dimensional coupling 1D-κ (Fig. 1a), cyclic-coupling C-κ (Fig. 1b) and cross-coupling X-κ (Fig. 1c). The numerical study is based on a flexural mode Si MEMS double-ended-tuning fork (DETF) resonator operating at 250 kHz (Fig. 2) where the normalized inter-resonator spring coupling is experimentally quantified as $\kappa = k_c/k = 5\text{x}10^{-3}$. In order to assess the robustness to process-induced variations, Monte Carlo numerical simulations, which accounted for up to $\pm$ 0.75% random variations in resonator beam widths (with nominal value of 6 μm), were initiated to produce R_x estimates of the three coupling schemes for N = 1, 2, 3, 4, 5 and 9 coupled resonators.

II. Theory

A. System modelling

The degree of vibration energy confinement in a mechanically coupled array depends on the magnitude of the structural perturbations as well as the strength of the internal coupling spring constant κ. One possible approach to improving device immunity to structural perturbations is to increase the number of paths for the vibration energy to flow within the system.

Three distinct coupling schemes with different degrees of internal coupling are investigated in this paper:

1) The traditional one dimensional chain 1D-κ (Fig. 1a) with adjacent coupling k_c and free-ends at the edges
2) Cyclic-coupling C-κ (Fig. 1b) with adjacent coupling k_c throughout the array

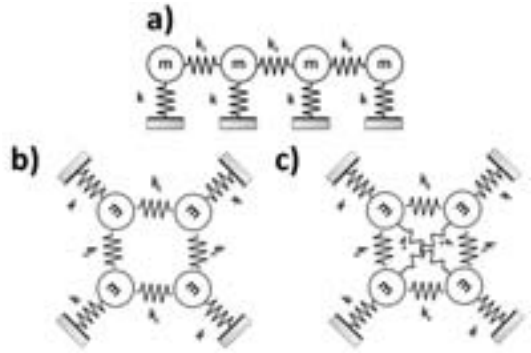

Fig. 1. Schematics of the equivalent mechanical models of the a) 1D-κ one dimensional coupled chain, b) C-κ cyclic-coupling and c) X-κ coupled confugration, respectively, for the special case of N = 4 resonators.

3) Cross-coupling X-κ (Fig. 1c) with adjacent coupling k_c and non adjacent coupling k_x

The N resonators composing a particular coupled-system are represented by a single-degree-of-freedom system with nominal mass m, stiffness k and damping coefficient c.

Combining the N equations of motion in matrix form with sinusoidal forcing yields to

$$\underline{M}\ \underline{\ddot{X}} + \underline{C}\ \underline{\dot{X}} + \underline{K}\ \underline{X} = \underline{F} \tag{1}$$

The three mechanical coupling schemes investigated in this paper differ from each other by their stiffness matrices $\underline{K}_{1D}$, $\underline{K}_{C-\kappa}$ and $\underline{K}_{X-\kappa}$ for the 1D-κ, C-κ and X-κ topology, respectively.

The complex valued amplitude response vector $\underline{X}$ of the system is computed as

$$\underline{X}(j\omega) = [-\omega^2\underline{M} + j\omega\underline{C} + \underline{K}]^{-1}\underline{F} \tag{2}$$

In the case of electrostatically transduced MEMS resonators, the driving force f_i is given by

$$f_i = \frac{\epsilon A_i}{g_i^2} v_{ac} V_{DC} \tag{3}$$

where ϵ, A_i, g_i are the vacuum permittivity, effective transduction area and nominal transduction gap, respectively, v_{ac} and V_{DC} are the small signal drive voltage and DC-polarization voltage, respectively.

The N-DOF spring-mass system yields to N fundamental modes of vibrations $\underline{u}_k$ at N distinct natural frequencies ω_k.

As the resonators vibrate at the kth mode of vibration ω_k, the sense electrodes of the N resonators generate a total motional current i_{out} expressed as

$$i_{out} = j\omega_k \epsilon V_{DC} \sum_{i=1}^{N} \frac{A_i}{g_i^2} \underline{X_i} \tag{4}$$

The overall R_x of the coupled-resonator device is then numerically computed as

$$R_x = \frac{v_{ac}}{max(|i_{out,\omega=\omega_k}|)} \tag{5}$$

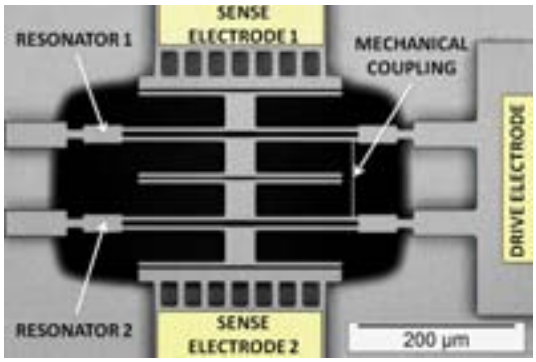

Fig. 2. Optical micrograph of two mechanically coupled double-ended tuning fork (DETF) silicon resonators.

TABLE I. DESIGN PARAMETERS

Beam width b_0	6 μm
Beam length l_0	300 μm
Device thickness t_0	25 μm
Gap g_0	2 μm
$Q = \sqrt{mk}/c$	30000
$\kappa = k_c/k$	5x10^{-3}

For the three topologies considered, we choose the fundamental mode $\underline{u}_1$ of vibration for comparison occurring at the lowest eigenfrequency ω_1 which is defined as

$$\underline{u}_1^T = \frac{1}{\sqrt{N}}[1 \ldots 1] \tag{6}$$

B. Robustness to process-induced variations

In order to quantify the robustness of the distinct coupling schemes in the face of process-induced variations, numerical simulations were based on DETF resonators shown in Fig. 2 operating at the fundamental in-phase tuning fork mode at 250 kHz. The tines of the DETFs are 300 μm long, 6 μm wide and 25 μm thick. The gap between individual tines is 6 μm while the coupling rod is 94 μm long. The electro-mechanical transduction is conducted through two parallel plate electrodes attached to each tine of the DETF with an air-gap spacing g_0 of 2 μm. The devices were manufactured using a standard Silicon-On-Insulator (SOI) process. These nominal values are summarized in Table I.

The value of the mechanical coupling spring κ is experimentally quantified using the coupled device of Fig. 2. This is done using the curve-veering phenomenon [8] by electrostatically tuning the mechanical stiffness of one of the resonators, while keeping all other structural parameters constant.

The negative spring constant k_e achieved with this tuning is given by

$$k_e(V_{DC}) = -\frac{\epsilon A}{g_0^3} V_{DC}^2 \tag{7}$$

Figure 3 shows the plot of the squared eigenfrequencies ω_i^2 as a function of the induced stiffness perturbations $\delta k \propto V_{DC}^2$.

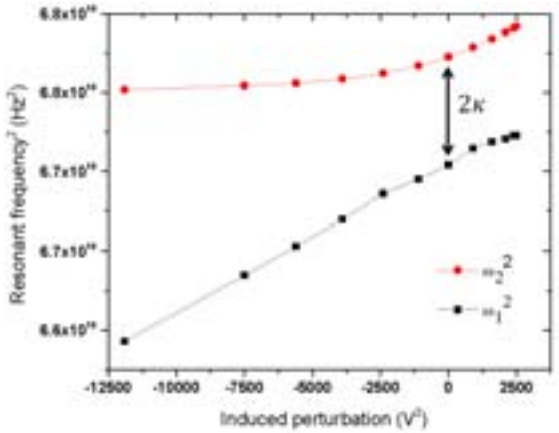

Fig. 3. Experimentally measured variations in the eigenvalues as a function of the induced stiffness perturbations on the DETF resonator.

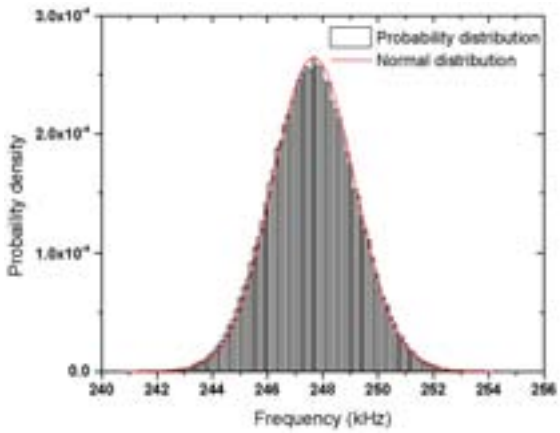

Fig. 4. Simulated probability density of the DETF frequency for random variations in the beam widths.

This enables us to quantify the spring coupling κ (Table I) between the two DETF resonators when the loci of the two eigenmodes achieve a minimum frequency separation.

C. Numerical simulations

Monte Carlo numerical simulations, which accounted for up to 0.75% random variations in resonator beam widths, were initiated to produce R_x estimates of the three coupling schemes for N = 1, 2, 3, 4, 5 and 9 resonators. These random variations were achieved numerically by setting the beam width b_i of the ith resonator as

$$b_i = b_0\left(1 + \mathcal{N}(0,\sigma)\right) \tag{8}$$

where b_0 is the nominal value of the beam width, $\mathcal{N}(0,\sigma)$ is the normal distribution with zero mean and standard deviation 3σ = 7.5x10^{-3} (i.e. 99.7% of the random beam widths generated are within 45 nm from their nominal value b_0 = 6 μm).

Choosing these values allows for 2.25% of random variations in the resonator stiffness k which can considerably affect the vibration dynamics of such high-Q, weakly coupled resonator systems. Randomly modifying the beam widths of the DETF tines allows us to simulate breaks in structural symmetry due to both mass and stiffness perturbations. The normalized distribution of the natural frequency for a single DETF with these parameters is shown in Fig. 4.

The distribution of the frequency follows approximately a normal distribution with a mean $\mu_0 = 247.6$ kHz and standard deviation σ_0 = 770 Hz.

D. Choosing the right eigenmode

Since there are N modes of vibrations, the recording of the amplitude of vibration vector $\underline{X}$ as a function of the input frequency, will yield to N distinct peaks corresponding to the N eigenmodes. To evaluate the R_x of the whole system, we would then have to specifically find the maximum amplitude corresponding to the particular vibration mode of interest (i.e. in our case the $\underline{u}_1$ mode). These random trials are then repeated until satisfactory convergence is achieved (in this case 2x10^5 experiments).

In order to correctly identify the frequency range for which we should perform the frequency sweep to record the vibration response of mode $\underline{u}_1$ around ω_1, we first consider the undamped eigenvalue problem, given the initial random distribution of the geometrical parameters.

This is done by solving

$$\underline{K}\ \underline{u}_i = \lambda_i \underline{M}\ \underline{u}_i \tag{9}$$

where $\underline{u}_i$ and λ_i are the ith eigenvector and corresponding normalized eigenvalue $\left(\lambda_i = \omega_i^2/\left(k/m\right)\right)$.

Once the N eigenvalues are identified, we choose the lowest eigenvalue which will always correspond to the $\underline{u}_1$ eigenmode. Using the solutions of the undamped eigenvalue problem to identify the correct frequency range of the damped system is used to speed up the simulation times and improve the accuracy of the measurements as a greater number of points can be taken around the particular frequency of interest. Furthermore, we can easily modify the algorithm to track another mode of vibration simply by adjusting the range of frequency sweep.

In order to return motional resistance values which we would expect from experimental measurements, we specify the small signal driving voltage v_{ac} = -20 dBm and polarization voltage as V_{DC} = 10 V.

III. Results

Fig. 5 and Fig. 6 are plots of the probability distribution (normalized to have unit area) of the R_x for the three coupling schemes when N = 4 and N = 9, respectively. The X-κ topology is chosen such that $\kappa = \kappa_x$. For the case N = 4, we see a clear improvement in the mean value as well as spread for higher order coupling. For N = 9, there is a clear advantage of the X-κ topology against the other two topologies as it achieves an improvement by one order of magnitude in σ as compared to the 1D-κ and C-κ schemes.

The results for the other array lengths N are summarized in Table II where the mean (μ) and standard deviation (σ)

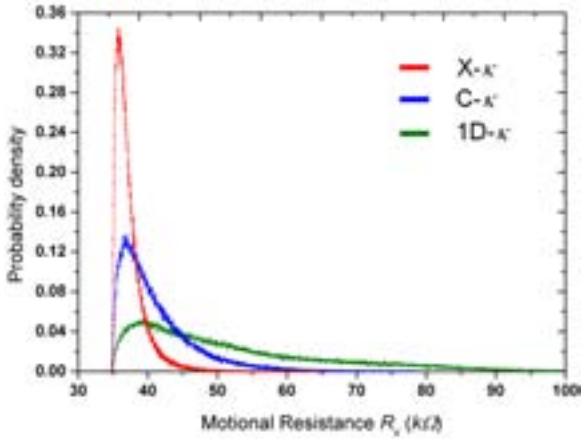

Fig. 5. Simulated probability distributions of the R_x for the 1D-κ, C-κ and X-κ configurations, respectively, for the case of N = 4 coupled resonators.

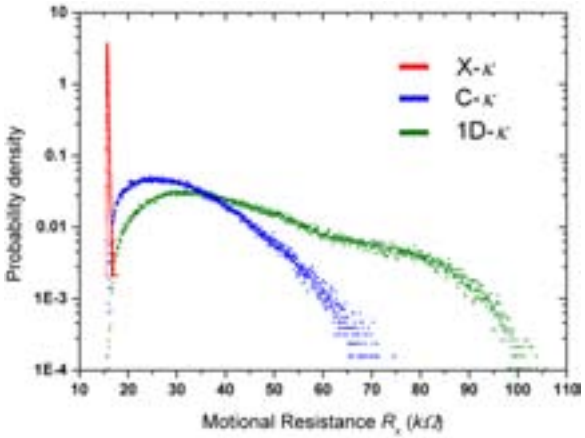

Fig. 6. Simulated probability distributions of the R_x for the 1D-κ, C-κ and X-κ configurations, respectively, for the case of N = 9 coupled resonators.

of the R_x distribution for the different coupling schemes are reported. From Table II we see that for the 1D-κ and C-κ configurations, the spread in R_x increases as N is increased. Using mechanically coupled topologies remains beneficial for an R_x reduction purpose as the achievable mean value of R_x drops with increasing N at the cost of a larger spread for the 1D-κ and C-κ schemes. However, for the case of the X-κ, increasing the number of resonators significantly decreases the spread in the R_x value from σ = 2.11 at N = 4 to σ = 0.14 at N = 9.

TABLE II. DISTRIBUTION OF THE MOTIONAL RESISTANCE R_x FOR THE DIFFERENT COUPLING SCHEMES AND ARRAY SIZE N

Array size N		1	2	3	4	5	9
1D-κ	μ (kΩ)	140	77.17	59.1	51.48	47.54	42.28
	σ (kΩ)	0.63	7.24	11.0	13.27	14.67	16.43
C-κ	μ (kΩ)	X	X	50.89	41.06	36.0	30.76
	σ (kΩ)	X	X	4.04	5.20	6.31	9.04
X-κ	μ (kΩ)	X	X	X	37.30	29.31	15.79
	σ (kΩ)	X	X	X	2.11	1.11	0.14

IV. CONCLUSION

This paper presents a numerical study of the impact of process variations on the motional resistance of three distinct mechanical coupling topologies of MEMS resonators. The numerical trends, based on Monte Carlo simulation methods, suggest an improvement in the mean and spread of R_x as the number of coupled resonators N is increased for the X-κ scheme as opposed to the traditional 1D-κ linear chain and the cyclic C-κ configuration. For the special case of N = 9, we expect a 2.7X improvement in mean R_x and more than 100X decrease in R_x spread as we go from the 1D-κ to the X-κ topology. A fully cross-coupled topology where $\kappa = \kappa_x$ can be challenging to achieve in practice. Further numerical studies are necessary to evaluate the optimal cross-coupling spring constant for a given resonator topology, manufacturing variability and number of coupled resonators N in order to achieve good performance. The numerical scheme presented in this paper is an efficient design procedure to evaluate the structural immunity to process variations of resonator performance metrics (in this case the R_x). These numerical results motivate in-depth studies of alternative coupling topologies, in the case of weakly coupled resonators, towards designing process tolerant, highly scalable resonator arrays.

ACKNOWLEDGMENT

The authors would like to gratefully acknowledge the Qualcomm European Research Studentships in Technology and the UK Engineering and Physical Sciences Research Council for financial support as well as the IEEE UFFC for the travel support.

REFERENCES

[1] C.-C. Nguyen, "MEMS technology for timing and frequency control," *Ultrasonics, Ferroelectrics and Frequency Control, IEEE Transactions on*, vol. 54, no. 2, pp. 251 –270, feb. 2007.

[2] M. Demirci and C.-C. Nguyen, "Mechanically corner-coupled square microresonator array for reduced series motional resistance," *Microelectromechanical Systems, Journal of*, vol. 15, no. 6, pp. 1419 –1436, dec. 2006.

[3] M. Akgul, Z. Ren, and C.-C. Nguyen, "Voltage-controlled tuning to optimize MEMS resonator array-composite output power," in *Frequency Control and the European Frequency and Time Forum (FCS), 2011 Joint Conference of the IEEE International*, may 2011, pp. 1 –6.

[4] C. Pierre, "Mode localization and eigenvalue loci veering phenomena in disordered structures," *Journal of Sound and Vibration*, vol. 126, no. 3, pp. 485 – 502, 1988.

[5] A. Erbes, P. Thiruvenkatanathan, and A. Seshia, "Impact of mode localization on the motional resistance of coupled MEMS resonators," in *Frequency Control Symposium (FCS), 2012 IEEE International*, 2012, pp. 1–6.

[6] D. Weinstein, S. Bhave, M. Tada, S. Mitarai, and S. Morita, "Mechanical coupling of 2D resonator arrays for MEMS filter applications," in *Frequency Control Symposium, 2007 Joint with the 21st European Frequency and Time Forum. IEEE International*, 2007, pp. 1362–1365.

[7] V. B. Chivukula and J. F. Rhoads, "Microelectromechanical bandpass filters based on cyclic coupling architectures," *Journal of Sound and Vibration*, vol. 329, no. 20, pp. 4313–4332, 2010.

[8] P. Thiruvenkatanathan, J. Yan, J. Woodhouse, and A. Seshia, "Enhancing parametric sensitivity in electrically coupled MEMS resonators," *Microelectromechanical Systems, Journal of*, vol. 18, no. 5, pp. 1077 –1086, oct. 2009.

Unwanted Transverse Modes in SAW Resonators Caused by Stitching Errors And Stripe Nonlinearities

Pierre Dufilie, Raymond Zeitler, Jim Jacobs, Merle Yoder
Phonon Corporation
Simsbury, CT, USA

Abstract — **High Q SAW and STW resonators utilize interdigital transducers with transverse weighting. This weighting is fit to the fundamental mode (M0) of the resonator cavity, so the transducer should not couple to the higher order transverse modes (M1, M2, ...). Errors in the actual resonator pattern caused by stitching errors in laser generated photomasks will introduce an asymmetry which can excite both higher order symmetric (M2, M4, ...) and antisymmetric (M1, M3, ...) transverse modes. Non-uniformities due to processing can also contribute to these higher order modes. Higher order modes in oscillators are undesirable because they degrade linearity or induce frequency popping.**

The majority of high resolution (0.5um or better) 1X photomasks are fabricated using laser mask-making machines. This approach is adequate for most SAW devices; however SAW resonators are very sensitive to small variations in linewidths and line positions -- variations that cannot be detected by normal optical examination. A typical resonator pattern (2mm x 2mm active area) is too large to be exposed in a single laser stripe.

The objective of this study is to determine the photomask fabrication method which can minimize the higher order transverse modes. A 695MHz STW resonator was designed and realized in an array of 26 rows and 16 columns on multiple 1x dark field quartz masks exposed with different photomask tools. The tools were Etec Alta 3500 and 3900 laser pattern generators, Micronic laser writer and an ASET 645 15" Image Repeater used with a 10x reticle.

Multiple wafers were contact-printed from each mask, and all dies on the wafers were RF-probed to acquire S11 over a span of 40MHz centered at 695MHz. The data was converted to admittance, and the main response was fitted to a lumped-element model, which was then removed. The residual data, which contained the extraneous modes, was then analyzed for correlation to: position in the array of dies; mask technology; wafer number.

Electrical measurements of STW resonators fabricated with different photomask tools do exhibit differences in transverse mode levels, the newer pattern generators having lower high order modes. Those fabricated with mask generated with the 10X stepper exhibited the best performances.

Keywords – SAW Resonator, photomask, fabrication

I. INTRODUCTION

Over the years, manufacturing methods for photomasks, used to pattern SAW devices, have dramatically evolved. In the 1960's photomasks were created by manually cutting Rubylith films and then reducing the pattern size using a large reduction copy camera. Rubylith was then replaced with a layer of photographic emulsion on a Mylar film patterned by an optical plotter.

With the development of optical pattern generators such as the GCA 3600, masks with features as small as 2um could be written directly. These patterns were composed of individual rectangles rotated at various angles.

Raster scanning led to additional advancements in photomask printing. Ebeam pattern generators using raster scanning were developed to obtain submicron features. Later, many ebeam systems were replaced with faster laser pattern generators where the stage moves at a constant speed while the laser beam scans perpendicular to the stage motion using either a rotating mirror or an acousto-optic modulator. The Micronic Laser writer is an example of a single beam system while the Alta systems use 32 parallel beams created by a beam splitter.

Even with the abovementioned advancements in photomask patterning, manufacturing masks for SAW resonators still presents a challenge. In most cases the size of the resonator is such that the critical features must be split up into two or more stripes. The resulting butting errors at the boundaries of adjacent stripes have a strong effect on device performance.

II. 1-PORT STW RESONATOR

For this study a 695MHz STW resonator was used. The resonator is shown in fig 1 (a). It consists of a transducer and two reflective gratings. The resonator is asynchronous with 55 transducer fingers that have a period of 3.57um and 1.86um linewidth and two 300-strip grating reflectors with 3.608um period and 1.88um linewidth. The acoustic aperture is 900um and the total resonator length is 2360um. The die size for the resonator is 3000um x 1900 um. The transducer is transversely weighted to excite only the fundamental transverse acoustic cavity mode 0.

Photomasks were made with a 16 x 26 array of resonator patterns. 38° yx quartz wafers were processed using the lift-off

process. The wafers were first coated with photoresist and then patterened using contact printing with each photomask. Then the patterned wafers were reactive ion etched [5] to a depth of 1500Å. Next, the wafers were metalized with 3000Å of 2% Cu doped aluminum. After liftoff wafer probe measurements were made on the resonators.

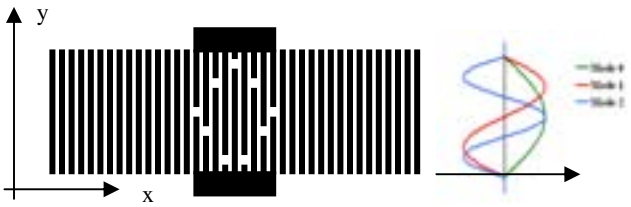

Fig 1 – (a) One-port STW resonator consisting of a transverse weighted transducer and two reflective gratings and (b) transverse mode profiles for modes 0, 1, and 2 .

The resonator has an effective cavity length of 895um and a nominal Q of 16500. The equivalent group delay τ of the resonator is related to the unloaded Q by equation 1, where f_R is the resonance frequency.

$$Q = \pi f_R \tau \qquad (1)$$

The nominal Q corresponds to a delay of 7.56us which corresponds to an effective acoustic path length L_{eff} of 38mm.

The transducer is transversely weighted to excite only mode 0 (M0). Seven transverse modes can exist with an acoustic aperture of 900um. Using the parabolic velocity approximation, the relative mode frequencies in table 1 are obtained for modes 0-5.

Mode	0	1	2	3	4	5
f-f_{R0} (kHz)	0.000	-0.044	-0.117	-0.219	-0.350	-0.510

Table 1 – Relative transverse mode frequencies for modes 0-5 computed using the parabolic velocity approximation.

The conductance of two measured resonators is plotted in fig 2. One resonator (blue) excites only the fundamental mode. This is the desired resonator characteristic. The resonator conductance in red is a defective resonator which excites all of the transverse modes. The parabolic approximation gives accurate results for the M1 and M2 mode frequencies and has reduced accuracy for the higher order modes.

III. TRANSVERSE MODES AND MASK ERRORS

Transverse modes in a single-mode resonator design can be excited when the acoustic velocity is not constant in the acoustic aperture (y-axis).

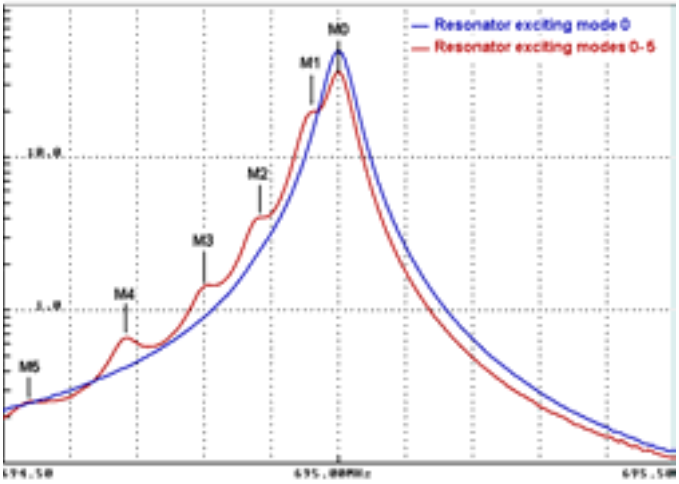

Fig 2 – Conductance plots of two measured resonators. The conductance in blue has only the fundamental mode M0. The conductance in red exhibits transverse modes M0-M5.

An example of the mode conversion mechanism is shown in fig 3. As the acoustic wave exits the transducer only the fundamental mode M0 exists. As the wave propagates over the effective path length some of the wave is converted into the antisymmetric mode M1.

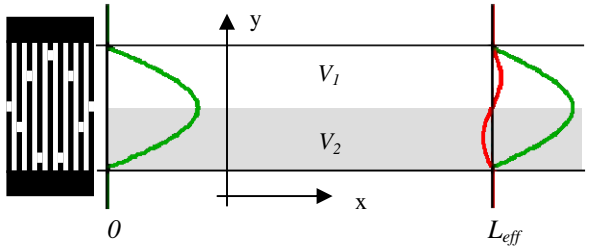

Fig 3 – Mode conversion due to a stepped velocity variation over the acoustic aperture of the transducer.

A second way in which unwanted transverse modes may be excited is when stripe butting errors (in x or y) exist in the resonator pattern.

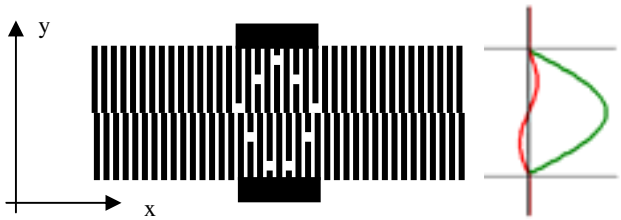

Fig 4 – Unwanted transverse mode generated due to stripe offset errors in the propagation direction (x-axis butting errors).

Both e-beam and laser mask generators write the mask patterns in a series of stripes. Linewidth differences between adjacent stripes will result in a difference in velocity. For the 695MHz resonator a 0.01um difference in linewidth results in a 28º phase difference at L_{eff} (fig 3). Butting errors at the stripe boundaries can also occur. An x-offset butting error of 0.01um corresponds to a 0.25° error and is large enough to affect the higher order modes M4, M5, …. These effects, along with nonlinearities within the stripes, will contribute to unwanted transverse modes in the resonator.

IV. PHOTOMASK TOOL EVALUATION

Photomasks were made using the Etec Alta 3500 and 3900 laser pattern generators, Micronic laser writer and an ASET 645 15" Image Repeater used with a 10x reticle. Note that the results which follow may not represent the optimum performances of the photomask tools. The x-axis of the resonator pattern is in the direction of stage motion and the y-axis is the direction of the raster scan. All but one of the Alta 3900 photomasks will have this orientation. The criteria for a useful resonator is that the mode 1 is suppressed. This will insure that, when used in an oscillator, frequency "popping" will not occur.

A photomask made using the Micronic laser writer was used to fabricate resonators. The conductance for the 16 resonators in row 6 are superimposed in fig 5. For this wafer the wafer yield is less than 8%.

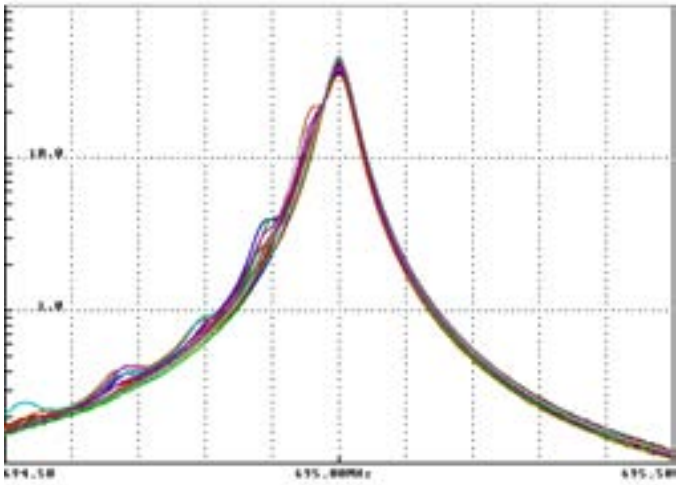

Fig 5 – Conductance plots for row 6 of wafer manufactured with a Micronic laser writer. Vertical scale in mS.

Two photomasks were made using the Alta 3500. One was made using 2-pass mode where the stripe is written twice. The second was made using 4-pass mode. Although using more passes increases the total write time, the stripe uniformity is improved. Measured conductances on a wafer manufactured with the 2-pass mode mask are shown in fig 6. In the figure there are 25 plots, one for each row on the wafer. The y-axis boundary positions of the stripes in the acoustic aperture are different for rows 1-5, however they repeat every 5 rows. These measurements demonstrate that stripe uniformity and butting errors can have a strong effect on resonator performance.

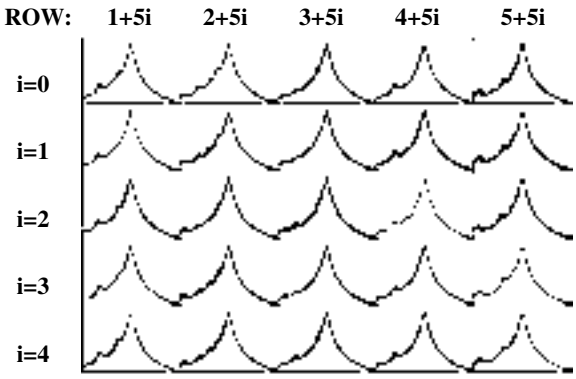

Fig 6 – Conductance plots of resonators in 25 rows on a quartz wafer manufactured with an Alta 3500 in 2-pass mode. Transverse mode patterns repeat every 5 rows.

The effect of going from a 2-pass mode to a 4-pass mode for mask generation is shown in fig 7. The extra passes suppress the high order transverse modes M3-M5 and reduce the M2 mode. The stitching errors do not appear to be effected.

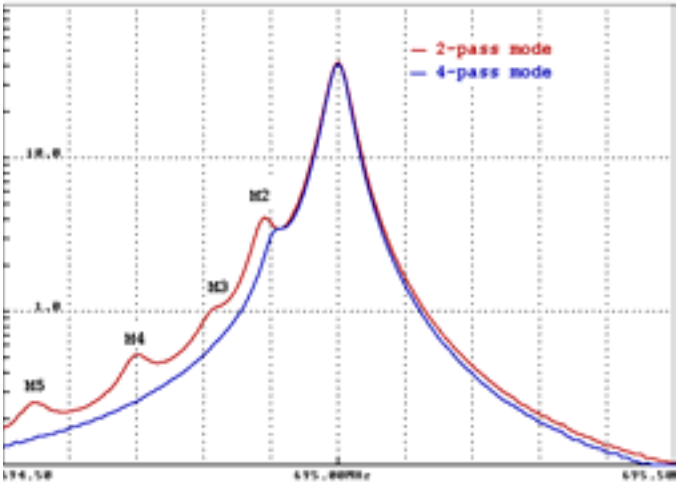

Fig 7 – Conductance plots of resonator in row 7, column 9 manufactured with an Alta 3500 in 2-pass mode (red) and 4-pass mode (blue). Vertical scale in mS.

Two photomasks were made using the Alta 3900, both in 2-pass mode. The first photomask has the standard pattern orientation (0° mask). For the second photomask (90° mask), the entire mask pattern was rotated 90° such that the acoustic aperture of each resonator is not split into stripes. A plot of 8 resonators fabricated with each photomask is given in fig 8.

The wafer yield is 28% for the wafer fabricated with the 0° mask. The yield increases to 45% with the 90° mask.

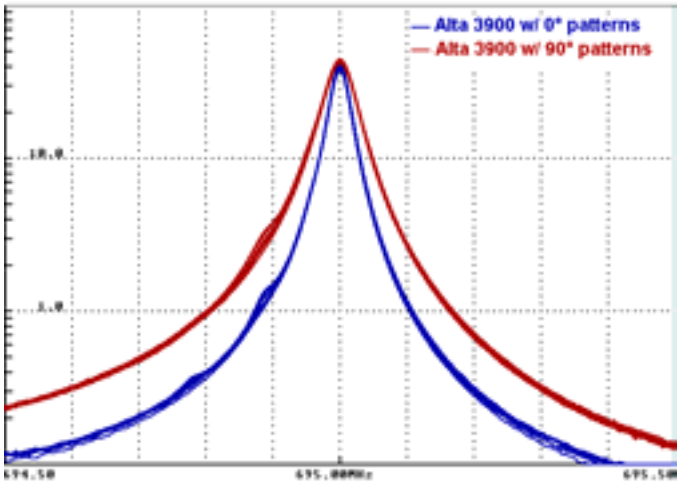

Fig 8 – Conductance plots of resonators in wafer row 17 manufactured with an Alta 3900 in 2-pass mode with a 0° pattern (blue) and with the 90° pattern (red). Vertical scale in mS.

The final photomask was made by first making a 10X reticle using an Alta 3900 and then stepping the pattern in a 16X26 array using a ASET 645 15" Image Repeater. This photomask will not have the types of errors which occur with laser pattern generators. Measurements of 44 resonators on a wafer are superimposed in the plot of fig 9, showing excellent repeatability.

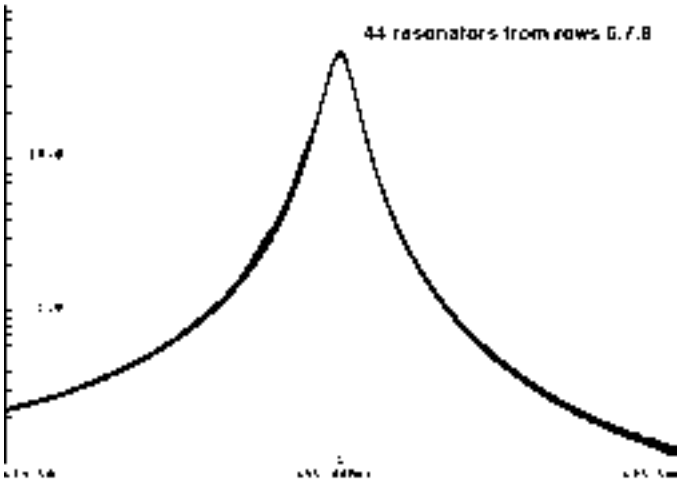

Fig 9 – Conductance plots of resonators wafer rows 6-8 fabricated with the ASET 645 15" Image Repeater. Vertical scale in mS.

An alternate method for testing for good resonators is to examine only a single parameter, motional resistance RM0 of mode M0 or 1/Gmax, where Gmax is the peak conductance of the resonator. When we compare two resonators (see fig 2) the resonator with unwanted modes will exhibit a smaller peak conductance or a larger value for RM0. By plotting the distribution of RM0 on a wafer we can estimate the wafer yield. The RM0 distributions for the six wafers are plotted in fig 10.

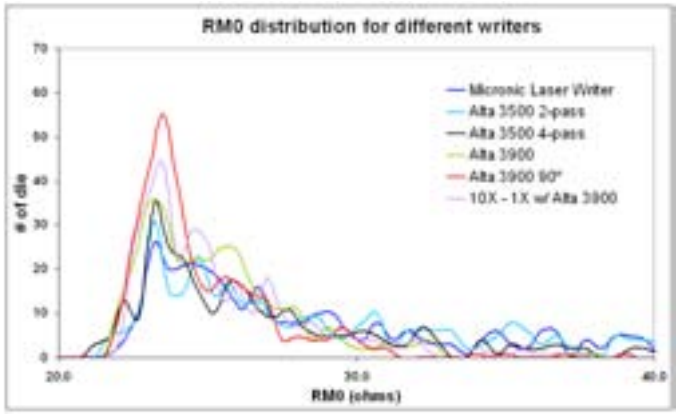

Fig 10 – Measured motional resistance distributions of mode 0 for 38° yx quartz with a 16 x 26 array of 1-port STW resonators fabricated with six different photomasks using 0.5Ω increments in RM0.

V. CONCLUSIONS

It has been shown that high order transverse modes in a STW resonator can be attributed to nonuniformities in the photomask. Variations in mask uniformity smaller than 0.01μm are detectable electrically using this method. This effect has been used to evaluate different photomask tools.

Tests have shown that newer generations of laser pattern generators are achieving better mask uniformity. Increasing the number of writing passes significantly reduces the higher order mode strengths.

The choice of pattern orientation (0º vs 90º) has an impact on the yield for resonators.

Finally, a photomask generated with a 10X stepper results in the best resonator performance.

REFERENCES

[1] A.G. Zanzal, Handbook of Photomask Manufacturing Technology, 2005 CRC Press, ISBN 082475347

[2] H. J. Levinson, Principles of Lithography, 2001 SPIE Press, isbn 0-8194-4045-0

[3] Ken-ya Hashimoto, Surface Acoustic Wave Devices in Telecommunications, Springer 2000, ISBN 3-540-67232-X

[4] M. Tanaka, T. Morita, K. Ono, and Y. Nakazawa, "Narrow Bandpass Filter Using Double-Mode SAW Resonators on Quartz", 1984 Frequency Control Symposium Proceedings, pp 286-293

[5] P. Ventura, P. Dufilie, and F. Hecht, "STW Devices with Buried Electrodes Based on a Mixed FEM/BEM Numerical Model", 2011 IEEE Ultrasonics Symposium Proceedings, 563-567

X-ray Imaging of the Surface Acoustic Wave Propagation in $La_3Ga_5SiO_{14}$ Crystal

Dmitry Roshchupkin
Institute of Microelectronics Technology and High-Purity Materials Russian Academy of Sciences
Chernogolovka, Moscow District, Russia
rochtch@iptm.ru

Luc Ortega
Laboratoire de Physique des Solides, Univ. Paris-Sud, CNRS, UMR 8502
Orsay, France

Anatolii Snigirev and Iraida Snigireva
European Synchrotron Radiational Facility
Grenoble, France

***Abstract*—Direct imaging of a 10 μm surface acoustic wave (SAW) propagation in a $La_3Ga_5SiO_{14}$ (LGS) crystal was obtained on the ESRF synchrotron radiation source in the saggital diffraction geometry using the Talbot effect. Imaging of the SAW wave field with the period 10 μm was observed at a distance corresponding to the Talbot distance. It is shown that the presence of the growth banding in the crystal does not influence on the propagation of acoustic wave-fields in the crystal nor does it cause a distortion of the SAW wave front.**

Keywords-surface acoustic waves; $La_3Ga_5SiO_{14}$ crystal; X-ray diffraction; ssynchrotron radiation; Talbot effect

I. INTRODUCTION

Recent progress in modern telecommunication systems and sensors based on SAW-devices urges the development of methods to study the SAW propagation in solids. Most interesting and promising for the analyses of acoustic wave field in solids are scanning electron microscopy (SEM) and X-ray diffraction and topography. Scanning electron microscopy in the mode of low-energy secondary electron registration permits the visualization of surface and bulk, traveling and standing acoustic waves and makes it possible to study diffraction phenomena in acoustic beams and interaction of acoustic waves with crystal structure defects [1-5]. However, this method is efficient for the investigation of acoustic wave propagation only in piezoelectric crystals. The method gives only qualitative information on the acoustic wave propagation and allows measuring the wavelength of acoustic waves. Unlike scanning electron microscopy, X-ray diffraction and topography are the methods of quantitative analysis and permit studying acoustic wave fields both in piezoelectric and non-piezoelectric materials. Using high-resolution X-ray diffraction, amplitudes and wavelengths of acoustic wave can be determined, acoustic waves attenuation in the crystal depth and along their propagation direction can be measured by the analysis of their X-ray diffraction spectra [6-10]. Stroboscopic X-ray topography, like SEM, permits direct imaging of an acoustic wave field in the real time mode [6, 11-14]. Direct imaging of traveling SAW by stroboscopic X-ray topography is based on focusing of X-ray radiation by the SAW minima. In this case the image of a traveling SAW can be observed in the focal plane at a distance D from an acoustically modulated crystal surface. Since a SAW length consists of one minimum and one maximum, the period of an observed image is equal to one wavelength. Distance D is determined from the expression [11]

$$D = \sin\Theta_B / 2hK^2 \left(\sin^2\Theta_B \sin^2\beta + \cos^2\beta\right), \qquad (1)$$

where Θ_B is the Bragg incidence angle of X-ray radiation onto the modulated crystal surface, h is the SAW amplitude, $K = 2\pi/\Lambda$, Λ is the SAW wavelength, and β is the angle between the projection of incident X-ray radiation onto the crystal surface and SAW propagation direction. As is seen from (1) the focal distance D is directly proportional to the square of the SAW wavelength Λ and inversely proportional to the SAW amplitude h. However, it should be noted that imaging of a traveling SAW by stroboscopic X-ray topography is only possible at temporal synchronization of SAW excitation and inherent temporal structure of the synchrotron radiation source, which considerably limits the application of the method for the investigation of acoustic wave fields.

As to X-ray topography, it has no limitations for the analysis of standing SAW fields where an acoustic wave image is formed through focusing of X-ray radiation by antinodes of a standing wave and the period of image observation is two times smaller than the SAW wavelength [15].

The aim of this work is to study the traveling SAW propagation in the $La_3Ga_5SiO_{14}$ crystal by X-ray topography on a synchrotron radiation source.

Russian Foundation for Basic Research

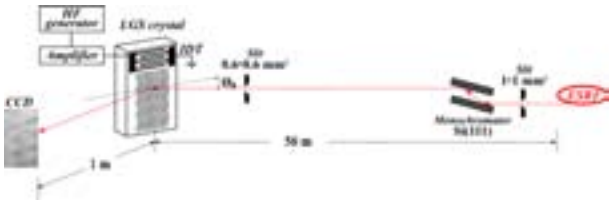

Figure 1. Experimental setup.

II. Experimental Setup

X-ray diffraction on the acoustically modulated $Y-$cut of the LGS crystal (reflecting planes (100) are parallel to the crystal surface) was studied in the saggital diffraction geometry in the scheme of a double-crystal X-ray diffractometer on the optical beamline ID06 of the ESRF synchrotron radiation source. The experimental scheme is shown in Fig. 1. The X-ray wavelength $\lambda = 1$ Å was selected with a Si(111) double-crystal monochromator which diffracts X-ray in vertical plane. The LGS crystal modulated with a $\Lambda = 10$ μm SAW was positioned at 56 m off the X-ray source. X-rays at the Bragg incidence angle Θ_B to the studied LGS crystal diffract on the SAW serving as diffraction grating for normal incidence. A CCD-camera was placed at 1 m from the acoustically modulated crystal to register a diffracted image of the crystal. The CCD-camera pixel was 0.645 μm.

III. SAW Device

LGS is a piezoelectric crystal of the 32 space group symmetry. The crystal lattice resembles the quartz crystal lattice with unit cell parameters $a = 8.170$ Å and $b = 5.128$ Å [9]. The LGS crystal was grown along the growth axis {11.0} by the Czochralski method in the "FOMOC Materials Co".

The $Y-$cut of the LGS crystal was used in the experiment. An interdigital transducer (IDT) was fabricated on the crystal surface by the photolithography method to excite the SAW. The IDT consists of 20 pairs of electrodes with a 5 μm period, which corresponds to a SAW with a wavelength of $\Lambda = 10$ μm. The velocity of SAW propagation in the $Y-$cut along axis X is $V = 2340$ m/s. This crystallographic orientation of SAW propagation in the LGS crystal obviates the power flow angle, which considerably simplifies the experiment. The resonance frequency of a $\Lambda = 10$ μm SAW excitation is $f_0 = V/\Lambda = 234$ MHz. The propagation of the traveling SAW leads to a strictly periodic sinusoidal deformation of a crystal lattice. The SAW amplitude can be varied from zero to several Å by varying the IDT high-frequency input signal.

IV. Experimental Results

Figure 2 presents an X-ray topograph of the $Y-$cut of the LGS crystal excited by the SAW. The image was registered at a distance of 1 m from the crystal. Reflection from the (100) planes at $\Theta_B = 4.175°$ was used. The topograph exhibits the growth banding which appear during the LGS crystal growth

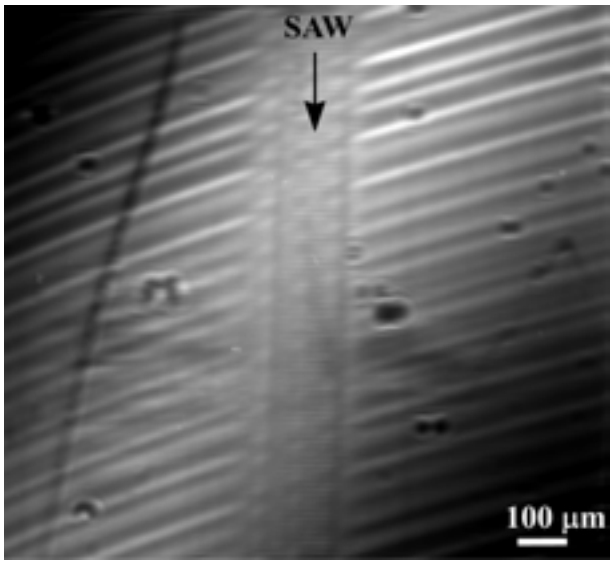

Figure 2. X-ray topograph of the $Y-$ cut of an LGS crystal excited by SAW. $\lambda = 1$ Å; $\Lambda = 10$ μm; $f_0 = 234$ MHz; reflection (100); $\Theta_B = 4.175°$.

by the Czochralski method. An image of the SAW acoustic wave field is clearly seen in the topograph center. It is also seen that no diffraction divergence occurs in the acoustic beam.

At higher magnification, the image of the acoustic wave fields appears as a periodic structure with a 10 μm period, which is equal to the $\Lambda = 10$ μm SAW wavelength (Fig. 3a). Figure 3b shows the corresponding distribution of the diffracted X-ray intensity in the SAW propagation direction along the X axis. The distribution of the diffracted X-ray intensity is a periodic structure with a 10 μm period.

The topographs in Figs. 2 and 3 show that the growth banding in the crystal do not influence the SAW propagation and do not cause a distortion of the acoustic wave front. Modulation of the diffracted X-ray intensity in the acoustic beam is a result of summation of the images of SAW and growth banding in the crystal. The distribution of the diffracted X-ray intensity (Fig. 3b) also exhibits modulation with a ~100 μm period, which corresponds to the period of growth banding in the crystal.

The possibility of SAW imaging is directly connected with the Talbot effect [16-17]. The effect consists in that the grating image is restored if the periodic grating is illuminated with a coherent radiation from a certain distance (the Talbot distance). A SAW can be regarded as a stationary diffraction grating because the velocity of SAW propagation is by five orders of magnitude slower than that of X-ray photons. In our case, SAW is stationary with respect to X-ray radiation. The synchrotron radiation at ESRF is, in part, coherent and this is one of the conditions for the realization of the Talbot effect. If an X-ray wavelength λ is much smaller than that of SAW, the Talbot distance is determined as [18-19]

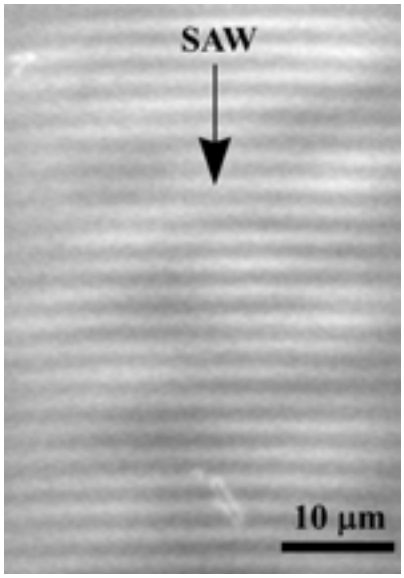

(a)

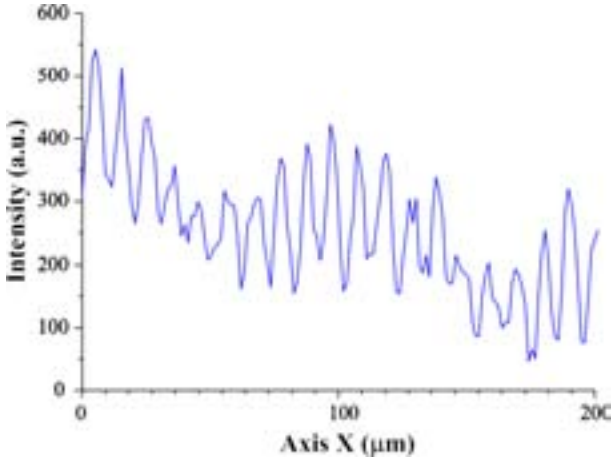

(b)

Figure 3. Acoustic wavefield in the Y – cut of an LGS crystal: (a) SAW image; (b) distribution of the diffracted X-ray radiation along direction of SAW propagation. $\lambda = 1$ Å; $\Lambda = 10$ μm; $f_0 = 234$ MHz; reflection (100); $\Theta_B = 4.175°$.

$$Z_T = \frac{2\Lambda^2}{\lambda}. \qquad (2)$$

In our experiments at $\lambda = 1$ Å and $\Lambda = 10$ μm, the Talbot distance is $Z_T = 2$ m. The X-ray topographs in Figs. 2 and 3 were registered at the distance 1 m, which is two times smaller than the Talbot distance. At this distance $(Z_T/2)$ as at the Talbot distance (Z_T), the period of an image observed should be equal to the SAW wavelength [18-19]. In our experiment, a periodic structure of acoustic wave field with a 10 μm period was observed, which is equal to the SAW wavelength $\Lambda = 10$ μm.

Any changes in the distance to the crystal (large or smaller deviation from $Z_T/2$ distance) cause the disappearance of acoustic wave field image on the LGS crystal surface. Note that changes in the amplitude of the IDT input signal (hence, in the SAW amplitude) do not cause changes in the acoustic wave field image on the crystal surface.

V. Conclusion

The possibility of direct imaging of an acoustic wave filed on the crystal surface in the real time mode was demonstrated on an acoustically modulated LGS crystal in the saggital geometry of X-ray diffraction. It is shown that the formation of an acoustic wave field image is connected with the Talbot effect that can be realized on a synchrotron radiation source under the conditions of a partially coherent X-ray radiation and strongly periodic modulation of the crystal lattice with a surface acoustic wave.

Note that this method is optimal for direct imaging of acoustic wave field on the crystal surface since it does not require synchronization of acoustic wave excitation and X-ray irradiation of the crystal surface.

The analysis of the acoustic filed image on the LGS crystal surface showed that presence of crystal growth banding formed during the crystal growth by the Czochralski method does not cause a distortion of the acoustic wave field even if the SAW wavelength is smaller than the growth banding width.

Thus, the Talbot effect is an ideal instrument for direct imaging of acoustic wave fields and for investigation of acoustic wave interaction with the crystal structure defects.

Acknowledgment

This work has been supported by the Russian Foundation for Basic Research (grant # 13-02-00459-a).

References

[1] W. J. Tanski and D. Wittels, "SEM observation of SAW resonators transverse mode," Appl. Phys. Lett., vol. 34, pp. 537-539, 1979.

[2] G. Eberharter and H. P. Feuerbaum, "Scanning-electron microscopy observation of propagating acoustic waves in surface acoustic wave devices," Appl. Phys. Lett., vol. 37, pp. 696-699, 1980.

[3] H. Bahadur and R. Parshad, "Scanning electron microscopy of vibrating quartz crystals," Scanning Electron Microscopy, vol. 1, pp. 509-522, 1980.

[4] D. V. Roshchupkin and M. Brunel, "Scanning electron microscopy observation of surface acoustic wave propagation in the $LiNbO_3$ crystals with regular domain structures," IEEE Transaction on Ultrasonics, Ferroelectrics, and Frequency Control, vol. 41, pp. 512-517, 1994.

[5] D. V. Roshchupkin, M. Brunel, R. Tucoulou, E. Bigler, and N. G. Sorokin, "Reflection of surface acoustic waves on domain walls in a $LiNbO_3$ crystal," Appl. Phys. Lett., vol. 64, pp. 164-165, 1994.

[6] W. Sauer, T. H. Metzger, A. G. C. Haubrich, S. Manus, A. Wixforth, J. Peisl, A. Mazuelas, J. Härtwig, and J. Baruchel, "X-ray imaging and diffraction from surface phonons on GaAs," Appl. Phys. Lett., vol. 75, pp. 1709-1711, 1999.

[7] R. Tucoulou, F. de Bergevin, O. Mathon, and D. Roshchupkin, "X-ray Bragg diffraction of $LiNbO_3$ crystals excited by surface acoustic waves," Phys. Rev. B, vol. 64, 134108(9), 2001.

[8] D. V. Roshchupkin, D. V. Irzhak, R. Tucoulou, and O. A. Buzanov, "X-ray Bragg diffraction from langasite crystal modulated by surface acoustic wave," J. Appl. Phys., vol. 94, pp. 6692-6696, 2003.

[9] I. A. Schelokov, D. V. Roshchupkin, D. V. Irzhak, and R. Tucoulou, "Dynamical theory for calculation of X-ray spectra from crystals modulated by surface acoustic waves," J. Appl. Cryst., vol. 37, pp. 52-61, 2004.

[10] D. V. Roshchupkin, A. I. Erko, L. Ortega, and D. V. Irzhak, "X-ray diffraction analysis of the surface acoustic wave propagation in langatate crystal," Appl. Phys. A, vol. 94, pp. 477-484, 2009.

[11] H. Cerva and W. Graeff, "Contrast investigation of surface acoustic waves by stroboscopic topography," Phys. Status Solidi (a), vol. 82, pp. 35-45, 1984.

[12] R. W. Whatmore, P. A. Goddard, B.K. Tanner, and G. F. Clark, "Direct imaging of traveling Rayleigh waves by stroboscopic X-ray topography," Nature, vol. 299, pp. 44-46, 1982.

[13] A. Zarka, B. Capelle, M. Pilard, J. Schwartzel, J. Detaint, and M. Solal, "An analysis of the S. A. W. displacement in quartz and lithium niobate by X-ray topography," in Proc. IEEE Int. Freq. Contr. Symp., 1994, pp. 315-322.

[14] E. Zolotoyabko, D. Shilo, W. Sauer, E. Pernot, and J. Baruchel, "Visualization of 10 μm surface acoustic waves by stroboscopiv X-ray topography," Appl. Phys. Lett., vol. 73, pp. 2278-2280, 1998.

[15] D. V. Roshchupkin, E. D. Roshchupkina, and D. V. Irzhak, "X-Ray topography analysis of acoustic wave fields in the SAW-resonators structures," IEEE Transaction on Ultrasonics, Ferroelectrics, and Frequency Control, vol. 52, pp. 2081-2087, 2005.

[16] H. F. Talbot, "Facts Relating to Optical Science," Philos. Mag., vol. 9, pp. 401–407, 1836.

[17] L. Rayleigh, "On Copying Diffraction-Gratings, and some Phenomena Connected Therewith," Philos. Mag., vol. 11, p. 196, 1881.

[18] D. S. Mehta, S. K. Dubey, C. Shakher, and M. Takeda, "Two-wavelength Talbot effect and its application for three-dimensional step-height measurement," Appl. Opt., vol. 45, pp. 7602-7609.

[19] A. Momose and S. Kawamoto, "X-ray Talbot Interferometry with Capillary Plates," Jap. J. Appl. Phys., vol. 45, pp. 314–316, 2006.

Investigation of Surface and Pseudo-Surface Acoustic Waves Excitation and Propagation in $La_3Ga_5SiO_{14}$ Crystal

Dmitry Roshchupkin, Dmitrii Irzhak, Olga Plotitcyna, Evgeny Emelin
Institute of Microelectronics Technology and High-Purity Materials Russian Academy of Sciences
Chernogolovka, Moscow District, Russia
rochtch@iptm.ru

Luc Ortega
Laboratoire de Physique des Solides, Univ. Paris-Sud, CNRS, UMR 8502
Orsay, France

Sergey Sakharov, Oleg Buzanov
FOMOS Materials
Moscow, Russia

***Abstract* — X-ray diffraction on the $La_3Ga_5SiO_{14}$ (LGS) crystal modulated by surface (SAW) and pseudo-surface acoustic waves (PSAW) with wavelength of Λ=6 μm was studied using a double axis X-ray diffractometer at the BESSY II synchrotron radiation source. The propagation of SAW and PSAW leads to sinusoidal modulation of the crystal lattice and gives rise to diffraction satellites on the rocking curve, with the intensity and angular divergence between the diffraction satellites depending on the wavelength and amplitude of the crystal lattice acoustic modulation. The analysis of diffraction spectra enables the determination of the amplitude and acoustic wavelengths, and power flow angles of acoustic energy propagation. The investigation of acoustic wave fields showed that PSAW is a flowing back wave.**

Keywords- surface acoustic wave; pseudo-surface acoustic wave; synchrotron radiation; X-ray diffraction

I. INTRODUCTION

Acoustoelectronic devices based on SAW are widely used in telecommunication systems for information processing and data transfer. Such devices are also efficient in sensor devices, wireless ones included. In recent years, novel piezoelectric materials promising for acoustoelectronics have been extensively searched. Much attention has been given to crystals of lanthanum-gallium silicate group which possess both good piezoelectric and thermal properties [1-4]. Note that SAW velocities in these crystals are small, which makes the crystals attractive for the fabrication of miniature acoustoelectronic devices.

Methods of X-ray topography and diffraction are of special interest in the studies of the crystal acoustic properties because they enable the visualization of acoustic wave fields in the crystals in the on-line mode. The X-ray topography method used in the region of Fresnel diffraction provides the visualization of acoustic wave fields on the crystal surface [5-8]. The acoustic wave fields were visualized in the main acoustic cuts of the langasite $La_3Ga_5SiO_{14}$ crystal, and power flow angles were measured by X-ray topography, because in this crystal the direction of the SAW wave vector does not coincide with the direction of the power flow vector [8]. The SAW propagation in the crystals can also be studied by X-ray diffraction which permits the SAW amplitude to be measured by the analysis of the diffraction spectra [9-12].

The aim of this work was to study the PSAW excitation and propagation in the LGS crystal. PSAWs are now an interesting object of investigation because PSAW, like SAW, can be excited using an IDT. SAW and PSAW have the same wavelength but different velocities and, consequently, are excited at different frequencies. In this work the double axis X-ray diffractometer was used to study SAW and PSAW excitation and propagation in the $Z-$cut of the LGS crystal.

II. EXPERIMENTAL SETUP

Figure 1 displays the schematic drawing of a double axis X-ray diffractometer setup on the KMC2 optical beamline at the BESSY II synchrotron radiation source. The energy of X-ray radiation near the $K-$edge of Ga was $E=12.5$ keV, which corresponds to kinematical diffraction. The energy was selected with a Si(111) double-crystal monochromator, and X-ray radiation was collimated with a 60×60 μm^2 entrance slit. The incident angle of X-ray radiation was the Bragg angle. Acoustic modulation of the crystal lattice gives rise to diffraction satellites on the rocking curve with the angular divergence between the satellites

$$\delta\Theta = d/\Lambda, \qquad (1)$$

where d is the interplanar spacing, and Λ is the acoustic wavelength. The angular divergence between the diffraction satellites is determined from expression (1) and the intensity of

Russian Foundation for Basic Research

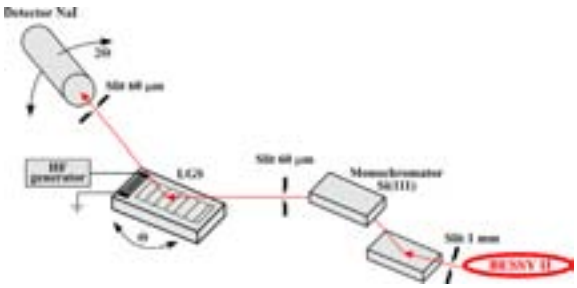

Figure 1. Experimental setup.

diffraction satellites depends on the amplitude of the crystal lattice acoustic vibrations [11-12]. A standard NaI scintillation detector with a 60 μm entrance slit was used to recorder the diffracted X-ray intensity.

III. SAW Device

LGS is a piezoelectric crystal of the point group symmetry 32. The crystal was grown along the {110} axis by the Czochralski method at the FOMOS Materials Co.

The $Z-$ cut of the LGS crystal (the (001) planes are parallel to the crystal surface) was used to study the SAW and PSAW propagation. On the crystal surface an interdigital transducer (IDT) was formed by e-beam lithography technique to excite the SAW and PSAW. The IDTs were formed on the crystal surface so that the wave vectors of the acoustic wave are along the $(X+30°)$ and $(X+60°)$ directions. The IDT consisted of 50 pairs of metallic electrodes with a 3 μm period, which corresponds to the SAW wavelength of $\Lambda = 6$ μm. The acoustic wave amplitude could be varied linearly from zero to several angstroms by changing the amplitude of the input high-frequency signal supplied to the IDT. The propagation of SAW and PSAW in the $Z-$cut of the LGS crystal is characterized by the power flow angle, i.e. the direction of power flow vector (PFV) does not coincide with the direction of the acoustic wave vector.

IV. Experimental Results

To study the SAW and PSAW propagation in the $Z-$cut of the LGS crystal along the $(X+30°)$ and $(X+60°)$ directions at various acoustic amplitudes, rocking curves were measured at X-ray energy $E=12.5$ keV (X-ray wavelength $\lambda = 1.03$ Å). The reflection from the (001) planes at the Bragg incidence angle $\Theta_B = 5.619°$ was used in the experiment.

Fig. 2 shows the maps of acoustic wave field distribution of SAW (a) and PSAW (b) on the $Z-$cut surface of LGS in the case of acoustic wave propagation along the $(X+30°)$ direction. The resonance frequency of $\Lambda = 6$ μm SAW excitation was $f = 416$ MHz, which corresponds to SAW velocity of $V = 2496$ m/s, while in the case of PSAW excitation the resonance excitation frequency is $f = 496$ MHz at the velocity of $V = 2976$ m/s. Thus SAW and PSAW have

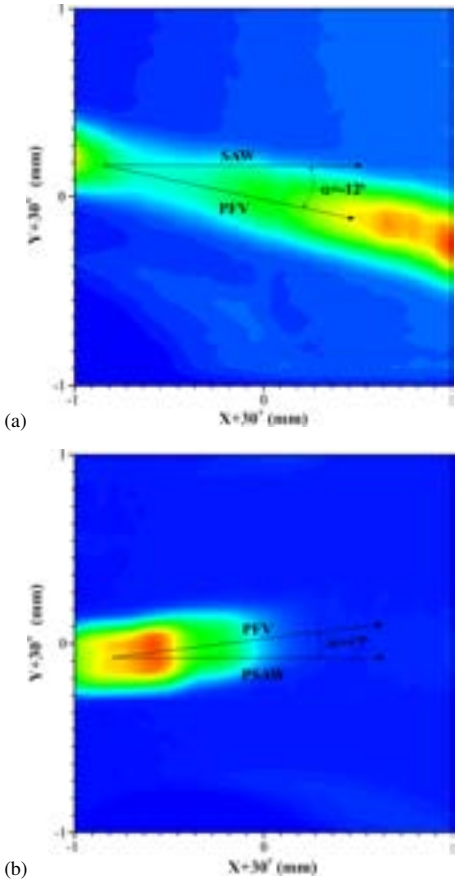

Figure 2. Maps of the diffracted X-ray intensity: (a) SAW, (b) PSAW. E=12.5 keV; reflection (001); Θ_B=5.619°; Λ=6 μm; SAW propagation along direction (X+30°).

the different velocities. The data in Fig. 2 were obtained at the amplitude of the input signal on an IDT $U = 15$ V and present the distribution of X-ray intensity on the crystal surface, which was diffracted to the first diffraction satellite. It is clearly seen from the maps that the direction of the SAW and PSAW wave vectors does not coincide with the PFV directions, i.e. the power flow angle occurs. Moreover, SAW and PSAW propagations differ by the direction and signs of the power flow angle. For SAW the power flow angle is $\alpha = -12°$, for PSAW it is $\alpha = +7°$. It is also seen in the figure that the PSAW acoustic wave field on the $Z-$cut surface of LGS can be observed only near the IDT, whereas the SAW acoustic wave field can be observed on the whole surface of the piezoelectric substrate. This means that PSAW is a flowing-back wave which propagates from the IDT into the crystal depth at an angle to the crystal surface. X-ray diffraction on the PSAW-modulated crystal can be observed only near the IDT.

Fig. 3 displays the rocking curves of the $Z-$cut of LGS crystal modulated by the SAW and PSAW with the wavelength $\Lambda = 6$ μm. The rocking curves were measured at the amplitude of the input signal on an IDT $U = 15$ V. The angular divergence between the diffraction satellites on the rocking curve is $\delta\Theta \approx 0.0051°$, which corresponds to the value

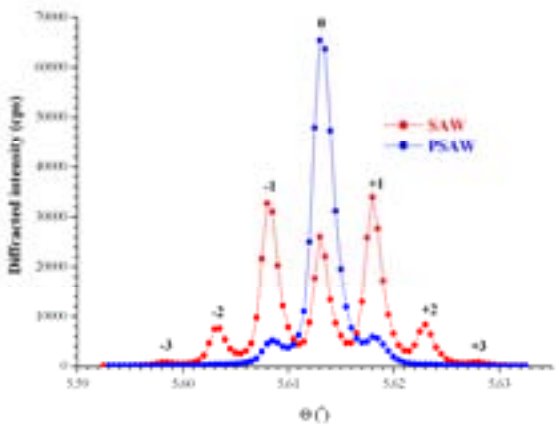

Figure 3. Rocking curves of the *Z*-cut of an LGS crystal modulated by SAW and PSAW propagating along (*X*+30°) direction. *E*=12.5 keV; reflection (001); Θ_B=5.619°; Λ=6 μm.

calculated from eq. (1) for the acoustic wavelength $\Lambda = 6$ μm. This similar divergence between diffraction satellites in the cases of SAW and PSAW suggests that these wave processes have similar wavelengths. As can be seen from Fig. 3, the rocking curves of the $Z-$cut of LGS crystal modulated by SAW and PSAW differ from each other. In the case of SAW modulation, the large number of the diffraction satellites can be seen on the rocking curve, which corresponds to more high acoustic amplitude than in the case of PSAW. In the case of diffraction on PSAW, the X-ray radiation first diffracts on the near-surface non-modulated crystal lattice and then diffracts on deeper PSAW-modulated layers of the crystal lattice. This results in that the intensity of the zero diffraction satellite exceeds the diffracted intensities of the rest orders.

Fig. 4 shows the maps of SAW (a) and PSAW (b) propagation along the $(X+60°)$ direction in the $Z-$cut of LGS crystal. It is seen that the power flow angle for SAW propagation is $\alpha = -6°$, while the power flow angle for PSAW is $\alpha = +5°$. Therefore the SAW and PSAW have the different excitation frequencies and velocities. The SAW with wavelength of $\Lambda = 6$ μm was excited at resonance frequency $f = 396$ MHz and propagated on the crystal surface with a velocity of $V = 2376$ m/s. The PSAW was excited at resonance excitation frequency $f = 516$ MHz and propagated with a velocity of $V = 3096$ m/s.

Fig. 5 presents the dependences of diffraction satellite intensities versus amplitude of the input signal supplied to the IDT for SAW (a) and PSAW (b). The character of the dependences is similar for SAW and PSAW. As the amplitudes of SAW and PSAW increase, the intensity of the zero diffraction satellite decreases. The intensities of the first diffraction satellites increase with increasing of the amplitude of acoustic wave. It is clearly seen in Fig. 5 that the diffraction satellites appear on the rocking curves at different amplitudes for SAW and PSAW. For SAW the first satellites appears on the rocking curve at $U = 1$ V, the second satellites appears at $U = 7$ V, while for the PSAW the first diffraction satellites appears at $U = 4$ V and the second satellites appears at $U = 14$

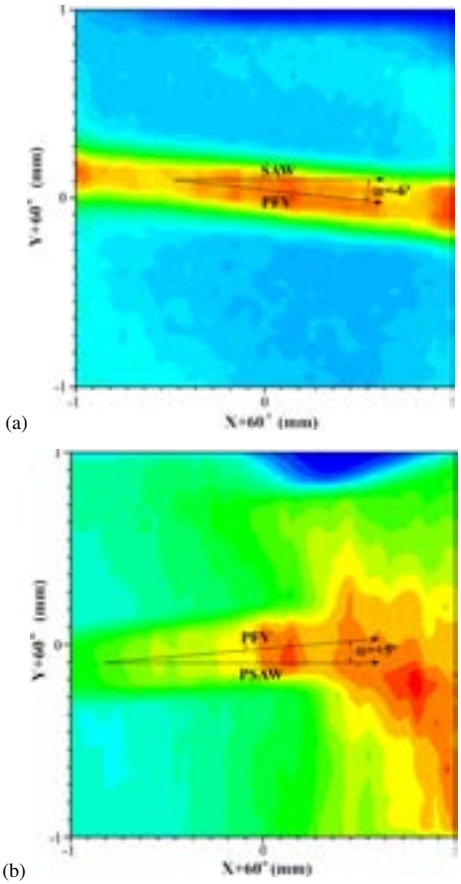

Figure 4. Maps of the diffracted X-ray intensity: (a) SAW, (b) PSAW. *E*=12.5 keV; reflection (001); Θ_B=5.619°; Λ=6 μm; SAW propagation along direction (*X*+60°).

V. Therefore in the case of PSAW in the LGS crystal the intensity of the zero diffraction satellite exceeds the intensity of the rest diffraction satellites because PSAW is excited by the IDT and tends to crystal depth at an angle to the surface.

V. Conclusion

X-ray diffraction on SAW and PSAW in the $Z-$cut of the LGS crystal was studied for the first time. The analysis of the diffraction spectra enabled the determination of the propagation velocities and power flow angles of the SAW and PSAW. It was shown that the velocity of PSAW exceeds that of SAW and the power flow angles of SAW and PSAW are of different values and signs. It was also found that SAW and PSAW are excited by the IDT although at different resonance frequencies. The Rayleigh SAW was found to propagate in the crystal subsurface whereas the PSAW propagates from the IDT towards the crystal depth at an angle to the crystal surface. Fig. 6 exhibits schematically the cross-section of the LGS crystal, the SAW (a) and PSAW (b) propagations, and X-ray diffraction on SAW and PSAW. In the case of PSAW, the X-ray radiation first diffracts on the crystal subsurface non-modulated by the acoustic wave and then part of the penetrated radiation diffracts deeper on the

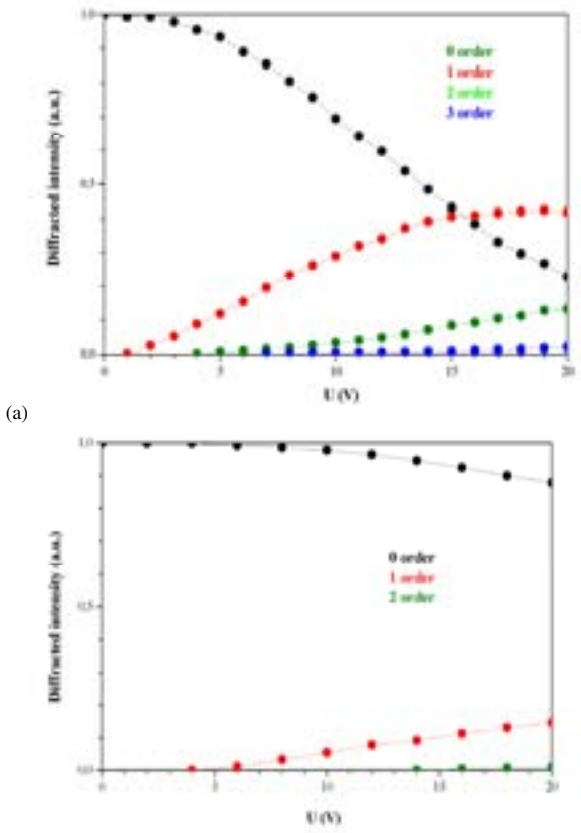

Figure 5. Intensities of the diffraction satellites in the *Z*-cut of an LGT vs. amplitude of the input signal supplied to the IDT *U*: (a) SAW; (b) PSAW. *E*=12.5 keV; reflection (001); Θ_B=5.619°; Λ=6 μm; SAW propagation along direction (*X*+60°).

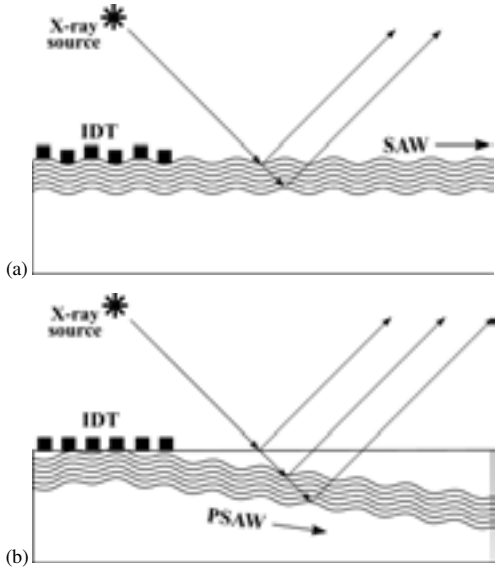

Figure 6. Schemes of SAW (a) and PSAW (b) propagation in the *Z*-cut of an LGS crystal.

crystal lattice modulated by PSAW (fig. 5b). This sequence of diffraction processes leads to a greater intensity of the zero diffraction satellite.

The difference in the power flow angles of SAW and PSAW looks promising from the viewpoint of creation of multifunctional multifrequency acoustoelectronic devices which can operate in various frequency ranges using one source of generation of various acoustic waves (e.g. an interdigital transducer).

Further development of the X-ray diffraction model and employment of the X-ray diffraction on a PSAW modulated crystal would enable the angle between the crystal surface and PSAW propagation direction to be determined.

ACKNOWLEDGMENT

This work has been supported by the Russian Foundation for Basic Research (grant # 13-02-00459-a).

REFERENCES

[1] M.P. du Cunda and S.A. Fagundes, "Investigation on recent quartz–like materials for SAW applications," IEEE Trans. Ultrason. Ferroelectr. Freq. Control, 1999, vol. 46, pp. 1583-1694.

[2] R.C. Smythe, R.C. Helmbold, G.E. Hague, and K.A. Snow, "Langasite, Langanite, and Langatate Bulk-Wave Y-Cut Resonators," IEEE Trans. Ultrason. Ferroelectr. Freq. Control, vol. 47, pp. 355-360.

[3] H. Fritze and H.L. Tuller, "Langasite for High-Temperature Bulk Acoustic Wave Applications," Appl. Phys. Lett, 2001, vol. 78, pp. 976-977.

[4] N. Naumenko, "Optimal cuts of langasite, $La_4Ga_5SiO_{14}$ for SAW devices," IEEE Trans. Ultrason. Ferroelectr. Freq. Control., 2001, vol. 48, pp. 530-537.

[5] H. Cerva and W. Graeff, "Contrast investigation of surface acoustic waves by stroboscopic topography," Phys. Status Solidi (a), vol. 82, pp. 35-45, 1984.

[6] R. W. Whatmore, P. A. Goddard, B.K. Tanner, and G. F. Clark, "Direct imaging of traveling Rayleigh waves by stroboscopic X-ray topography," Nature, vol. 299, pp. 44-46, 1982.

[7] E. Zolotoyabko, D. Shilo, W. Sauer, E. Pernot, and J. Baruchel, "Visualization of 10 μm surface acoustic waves by stroboscopic X-ray topography," Appl. Phys. Lett., vol. 73, pp. 2278-2280, 1998.

[8] D. V. Roshchupkin, E. D. Roshchupkina, and D. V. Irzhak, "X-Ray topography analysis of acoustic wave fields in the SAW-resonators structures," IEEE Transaction on Ultrasonics, Ferroelectrics, and Frequency Control, vol. 52, pp. 2081-2087, 2005.

[9] W. Sauer, T. H. Metzger, A. G. C. Haubrich, S. Manus, A. Wixforth, J. Peisl, A. Mazuelas, J. Härtwig, and J. Baruchel, "X-ray imaging and diffraction from surface phonons on GaAs," Appl. Phys. Lett., vol. 75, pp. 1709-1711, 1999.

[10] R. Tucoulou, F. de Bergevin, O. Mathon, and D. Roshchupkin, "X-ray Bragg diffraction of $LiNbO_3$ crystals excited by surface acoustic waves," Phys. Rev. B, vol. 64, 134108(9), 2001.

[11] D. V. Roshchupkin, D. V. Irzhak, R. Tucoulou, and O. A. Buzanov, "X-ray Bragg diffraction from langasite crystal modulated by surface acoustic wave," J. Appl. Phys., vol. 94, pp. 6692-6696, 2003.

[12] D. V. Roshchupkin, A. I. Erko, L. Ortega, and D. V. Irzhak, "X-ray diffraction analysis of the surface acoustic wave propagation in langatate crystal," Appl. Phys. A, vol. 94, pp. 477-484, 2009.

Double-Rotated Cut Quartz Resonator's Electrodes Optimisation

Lepetaev A.N.
OmSTU
Omsk, Russian federation
LAN@inbox.ru

Kosykh A.V.
OmSTU
Omsk, Russian federation
AVKosykh@omgtu.ru

Abstract— **The article observes the calculation technology of the surface specific gravity current in the contoured quartz resonators. And besides the authors of the article offer the construction of the electrodes optimized for the functional relation of the current distribution. Besides the article regards the calculation of the SC resonator's resistence- a SC - cut at various parameters of the surface's curves for optimized electrodes. The calculations' results are compared with the results for the electrodes of a standard construction.**

Keywords-component;quartz rezonator, calculation of the rezonator's resistance, rezonator's electrodes construction.

Double-rotated resonators of the SC-cut are widely spread in quartz generators because they possess robustness for the heat stress and changes. However they have a drawback- high activity of the temperature mode at a standard electrodes' construction. This work is aimed to calculate the optimized electrodes construction at which the activity of the temperature mode lowers and on the contrary the activity of the fundamental mode rises.

Practically, all data sources offer the following formula for the calculation of a surface electric current density in the sphere of electrode's covering:

$$Is = \omega \cdot \left(e_{22} \cdot Ay + e_{24} \cdot Az + e_{26} \cdot Ax\right) \cdot 2 / h, \quad (1)$$

where *Ax*, *Ay*, *Az* –are the components of the particle's displacement's phasor at vibrations, ω –angular rate of the present vibration mode, *h* –rezonator's thickness of a plate,

e_{2p} (p = 2, 4, 6) – the index of piezoelectric quartz rates in the system of coordinates of the resonator's plate. Besides, as it will be shown below, a formula (1) doesn't allow to optimize the electrodes' construction for the double- rotated cut resonators. Let's regard the processes of polarized currents' origin in quartz resonator electrodes more detailed than it is presented in classical literature. In this case let's take the following hypothesis:

- The gradients of displacements along the surface's plate are less than relevant gradients along the thikness.
- The distribution of amplitude's displacement obeys the sinusoidal manner.

Let's take the following identification marks for the coordinates: x z – coordinates along long and short sides of resonator, y – coordinate along the thickness of a plate (this is a standard system of coordinates for double-rotated cut resonators), the zero of coordinate system is in the centre of resonator; in some cases we will use indexes 1, 2 and 3 instead of letters to identify the coordinates (for coordinates x, y and z the indexes will be relevant), in this case the coordinates themselves will be marked as x_1, x_2 and x_3.

Let's write the data of the component's displacements:

$$U_i = A_i \cdot \sin\left(\frac{n \cdot \pi \cdot x_2}{h}\right) \cdot \sin\left(\frac{n \cdot \pi}{2}\right), \quad (2)$$

where i = 1 … 3. The components of the amplitudes' displacements A_i depends on the coordinates along the surface of the plate. (x_1 and x_3). Additional constant multiplier, depended on the number of a mode n, is inserted for the independence of the displacement mark on the surface of resonator from the number of a mode. Let's mark the components of deformations :

$$S_{ij} = \frac{1}{2}\left(\frac{\partial U_i}{\partial x_j} + \frac{\partial U_j}{\partial x_i}\right), \quad (3)$$

Let's pass to single-index identifications from double-indexe ones:

$$\begin{cases} S_p = r_{ij}, & i = j,\ p = i \\ S_q = 2S_{ij},\ i \neq j,\ q = 9 - i - j \end{cases} \quad (4)$$

Let's express the components of polarization through deformations:

$$D_i = e_{ip} S_p \quad (5)$$

Here and after Einstein's law will be used, according to which in the expressions the summation by repeated indexes is made.

The presence of gradients of polarization means the origin of the volume charges. Let's write the Poisson's equation (with account for correlation (5)):

$$\rho = div(\bar{D}) = \frac{\partial D_i}{\partial x_i} = \frac{e_{ip} \partial S_p}{\partial x_i} \quad (6)$$

Let's mark the normal component of the electric field:

$$E_2 = \frac{1}{\varepsilon_{22}} \int \rho dy + C1 = \frac{1}{\varepsilon_{22}} \int e_{ip} \frac{\partial S_p}{\partial x_i} dx_2 + C1 \quad (7)$$

According to (7) we can express the amount of current potential.

$$V = -\int E_2 dy + C2 = -\int\left(\frac{1}{\varepsilon_{22}}\int e_{ip}\frac{\partial S_p}{\partial x_i}dx_2 + C1\right)dx_2 + C2 \quad (8)$$

The amount of a constant $C1$ in (7) and $C2$ in (8) for the area under electrodes can be determined according to conditions:

$V(h/2) = 0$, $V(-h/2) = 0$. (9)

For calculation of constanta $C2$ let's write the expression for the sum of potentials on the upper and lower plate: $V(h/2) + V(-h/2) = 0$. If we put here (8) with regard to (2...7), than we will have: $2 \cdot C2 = 0$, whence it follows that $C2 = 0$.

For determination of the amount of $C1$ lets write the expression for the contrast of the potentials on the upper and lower sides of a plate: $V(h/2) - V(-h/2) = 0$. The substitution of expressions here (2...8) gives the following result:

$$C1 = \frac{2h}{\varepsilon_{22} n^2 \pi^2}\left(\frac{\partial^2\left(e_{11}Ax + e_{16}Ay + e_{15}Az\right)}{\partial x^2} + \frac{\partial^2\left(\left(e_{15}+e_{31}\right)Ax + \left(e_{14}+e_{36}\right)Ay + \left(e_{13}+e_{35}\right)Az\right)}{\partial x \partial z} + \frac{\partial^2\left(e_{35}Ax + e_{34}Ay + e_{33}Az\right)}{\partial z^2}\right) - \frac{e_{22}\cdot Ay + e_{24}\cdot Az + e_{26}\cdot Ax}{h\cdot\varepsilon_{22}} \quad (10)$$

The formula evaluation (2...8) due regard to (10) gives the following result:

$$Is = \omega \cdot e_{ip} K_{ip}, \quad (11)$$

where wheight multipliers K_{ip} are expressed through the components of the amlitude's changes according to the table 1.

Table 1.

p	***i* = 1**	***i* = 2**	***i* = 3**
1	$\frac{-2h}{n^2\pi^2}\cdot\frac{\partial^2 Ax}{\partial x^2}$	$-\frac{\partial Ax}{\partial x}$	$\frac{-2h}{n^2\pi^2}\cdot\frac{\partial^2 Ax}{\partial x \partial z}$
2	$-\frac{\partial Ay}{\partial x}$	$2\frac{Ay}{h}$	$-\frac{\partial Ay}{\partial z}$
3	$\frac{-2h}{n^2\pi^2}\cdot\frac{\partial^2 Az}{\partial x \partial z}$	$-\frac{\partial Az}{\partial z}$	$\frac{-2h}{n^2\pi^2}\cdot\frac{\partial^2 Az}{\partial z^2}$
4	$\frac{-2h}{n^2\pi^2}\cdot\frac{\partial^2 Ay}{\partial x \partial z} - \frac{\partial Az}{\partial x}$	$2\frac{Az}{h} - \frac{\partial Ay}{\partial z}$	$\frac{-2h}{n^2\pi^2}\cdot\frac{\partial^2 Ay}{\partial z^2} - \frac{\partial Az}{\partial z}$
5	$\frac{-2h}{n^2\pi^2}\cdot\left(\frac{\partial^2 Ax}{\partial x \partial z} + \frac{\partial^2 Az}{\partial x^2}\right)$	$-\left(\frac{\partial Az}{\partial x} + \frac{\partial Ax}{\partial z}\right)$	$\frac{-2h}{n^2\pi^2}\cdot\left(\frac{\partial^2 Az}{\partial x \partial z} + \frac{\partial^2 Ax}{\partial z^2}\right)$
6	$\frac{-2h}{n^2\pi^2}\cdot\frac{\partial^2 Ay}{\partial x^2} - \frac{\partial Ax}{\partial x}$	$2\frac{Ax}{h} - \frac{\partial Ay}{\partial x}$	$\frac{-2h}{n^2\pi^2}\cdot\frac{\partial^2 Ay}{\partial x \partial z} - \frac{\partial Ax}{\partial z}$

The parameters in the table 1 are given for that side of a resonator that corresponds to the positive y-direction (at $y = h/2$). For the other side of a resonator (at $y = -h/2$) the amount of the multiplying parameters are resulted from the relevant expressions of the table 1 through multiplication of every expression component by $(-1)^{n+1}$, where n – is the order of coordinate derivative.

It's easy to assure oneself, that the expression (11) turns to (1) if all derived amplitudes of vibrations with respect to coordinates of the surface plate are equal to zero.

The formula of the calculation of functions on the surface of a resonator is given in [1]. The realization of the calculation's program of these functions in a format of a descriptor file FlexPDE is given in [4] and the calculation of the current's surface density according to the formula of the table 1 is given in [5].

Fig. 1 shows the calculation's results of the current's surface density of the mode f_{300} according to formula of the Table 1 for the plane-convex contoured SC – cut resonator (*yxbl*/22°20'/34°06') with the frequency of 10 MHz with contour radius of 100 mm.

The results of the calculations show that there are areas with the opposite signs of the charge destiny on the surface of the SC-cut resonator. Optimal electrode's design must take into consideration this phenomenon. In [2] and [3] the constructions of the resonator electrodes are described, where only the attempt is made without calculations.

Schematic sketch of a resonator and the electrodes constructions with account for the surface distribution of a current density show at fig 2. At this drawing the borders 1 and 2 corespond the electrodes at upper side of resonator, the borders 3 and 4 – at the lower. Y' axis is directed away from the observer, so the visible side of the resonator - the bottom. Electrode 1 is connected with electrode 4, and electrode 3 is connected with electrode 2. So an electrode is divided on two segments of different amount on every side of a plate and also there is a gap between them. The gap spreads along the border division of the polarization area with different signs. The gap's parameter is an angle with the X-axis (φ), and the amount of a shift of its centre from the centre of a resonator (S).

Electrodes' diameter is equal to 5mm in all cases.

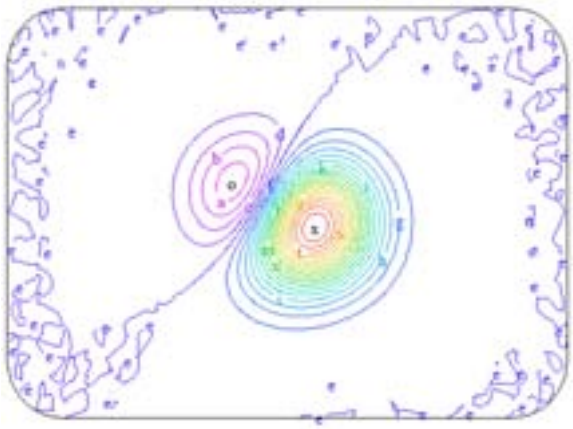

Fig.1. The distribution of a surface current density in the SC – cut resonator on top side (y=+h/2), view from bottom side through the plate.

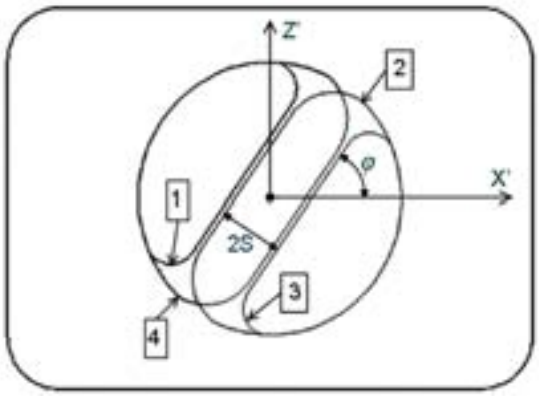

Fig.2. Scheme representation of a resonator and an electrodes

The results of calculations for resonator with the parameters mentioned above under exciting a mode C are given in the fig. 3 ... 5. Fig. 3 shows the lines of the vibration amplitude's level distribution for mode C. Picture 4 demonstrates the lines of the of a surface current density level (normalized in relation to the ordinary amplitude of vibration). It may be seen from the picture that the electrodes' construction is optimized for the distribution of surface charges. Picture 5 shows the same lines of the charges' distribution level but this time on the other side of resonator. (sight through resonator). Distributions shown on the pictures 4 and 5 are centrally symmetrical, so electrodes on the upper and lower sides must be mirror symmetrical. The same calculations for the mode B are given on the pictures 6 … 8. These pictures demonstrate that these electrodes are not more optimal for surface current of a mode so the resistance for this mode must rise essentially. The calculation results of the C and B's modes' resistance for different curve's values of resonator's surface are given in the Table 3.

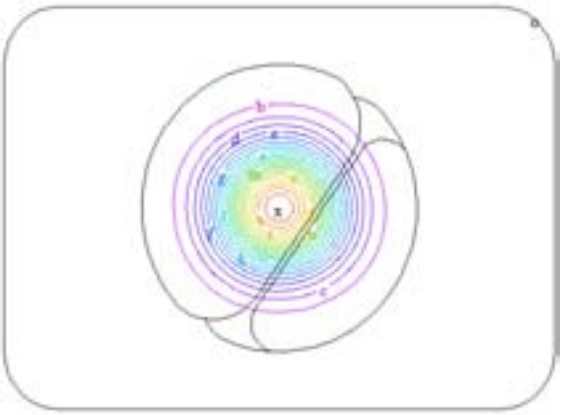
Fig.3. Lines of vibration amplitude's level distribution on the surface of a resonator for C-mode.

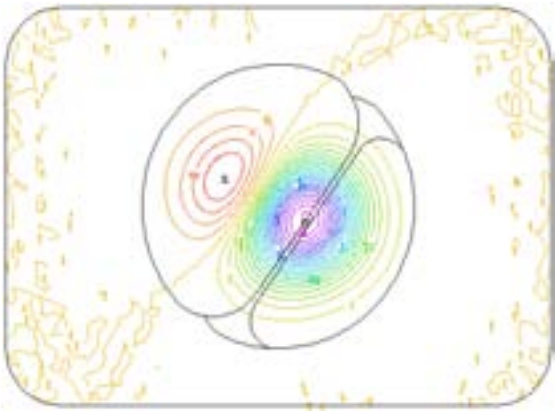
Fig.4. Lines of the current density level on the upper surface of a resonator for mode C (sight through the plate on the part of upper surface of a resonator)

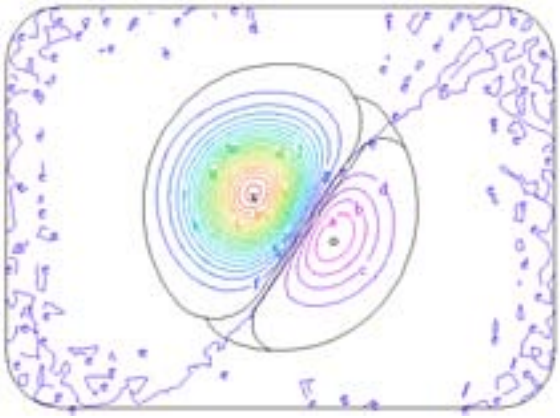
Fig.5. Lines of low surface-charge density level for mode C

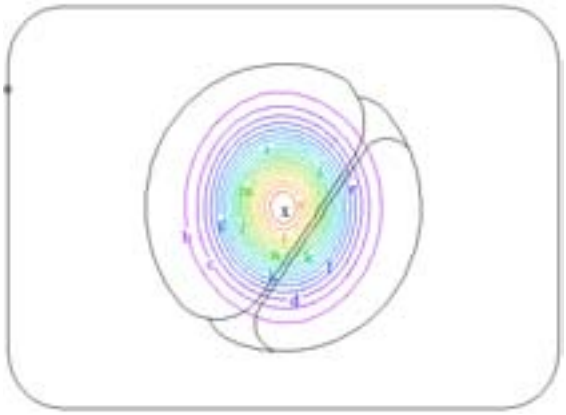
Fig.6. Lines of vibration amplitude's level distribution on the surface of a resonator for mode B.

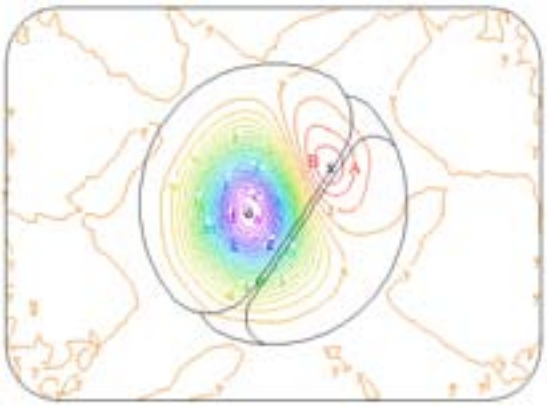

Fig.7. Lines of upper surface-charge density level of a resonator for mode B (sight through the plate on the part of resonator's upper surface)

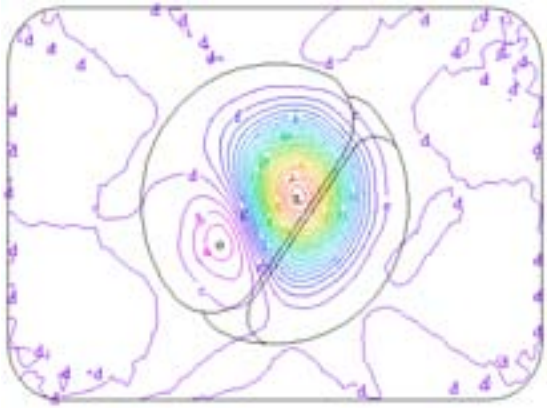

Fig.8.Lines of lower surface-charge density level for mode B

Table 3.

Contour radius, mm	300	200	150	100
Gap azimuth φ, degree	77	57	57	55
Gap shift S, mm	1	0.8	0.7	0.6
Mode C resistance (Rc), Ohm	68	70	72	76
Mode B resistance (Rb), Ohm	328	629	1007	1737
Rb/Rc	4.8	9.1	14.1	23.0

To compare the given results with the classical ones the Table 4 proposes the calculation results of a mode resistance for standard electrode's construction (entire electrodes) for the same resonator with the same electrode's diameter parameters.

Table 4.

Contour radius, mm	300	200	150	100
Mode C resistance (Rc), Ohm	91	107	120	144
Mode B resistance (Rb), Ohm	111	133	154	190
Rb/Rc	1.22	1.25	1.28	1.32

As it may be seen from the table above, for an standard electrode's construction the resistances Rb/Rc ratio lies within the range from 1.22 to 1.32, and for the offered construction within the range from 4.84 to 23.02. In a case of a standard construction it's quiet difficult to use a resonator in a generator because of the danger of a temperature mode excitement, so it's necessary to use special schemotechnical variants to reject an unwanted mode.

In case of electrodes' optimization, the correlation of resistances scales up till the parameter when it's possible to go without any additional instruments (as frequency-selective circuits). This method will allow to improve the stability of generator's frequency and to lessen its noises.

So, the presentation of electrodes improves the quality parameters of quartz resonator and leads to elevation of the safety of its functioning and also to reduction of the unwanted mode's vibration influence.

REFERENCES

[1] A. Lepetaev, I. Khomenko, A. Kosykh. Numerically-analytical calculation method for vibration amplitude distributions of inharmonic modes of double rotated cuts thickness-shear resonators. //Proceedings of 2007 IEEE Ultrasonics Symposium: New York, USA, 2007.- P. 1393 – 1396.

[2] Patent RU № RU 2276455 C1 «Quartz resonator». // Bezmaternykh G.V., Dikidji A.N., Terenko V.S. – Bul. № 13, 2006.

[3] Patent RU 2334352 C1 «Quartz resonator». // Bagayev S.P., Dikidji A.N. – Bul. № 23, 2007.

[4] Lepetaev A.N. Program for the calculation of quartz resonator's anharmonic oscillations parameters.// Certificate of State registration of a program for computers № 2013610342. Request № 2012619679 from 9th November 2012. Date of registration in a Catalogue for computer programs is 9th January 2013

[5] Lepetaev A.N. Program for quartz resonator mode's resistence at acentral electrodes' disposition. // Certificate of State registration of a program for computers № 2013610341. Request № 2012619678 from 9th November 2012. Date of Registration in a Catalogue for computer programs is 9th November 2013.

Correction Factors for the Mindlin Plate Equations for Thickness Vibrations of Crystal Plates with Thicker Electrodes

Dejin Huang[1], Guijia Chen[1], Rongxing Wu[1,2], Tingfeng Ma[1], Jianke Du[1], Ji Wang[1*]
[1]Piezoelectric Device Lab, School of Mech Eng & Mechanics, Ningbo Univ, 818 Fenghua Rd, Ningbo, Zhejiang 315211, CHINA
[2]Department of Architectural Eng, Ningbo Polytechnic, 1069 Xinda Rd, Beilun District, Ningbo, Zhejiang 315800, CHINA
[*]E-mail: wangji@nbu.edu.cn

Abstract—The Mindlin plate theory has been widely used for the study of high frequency vibrations of quartz crystal plates for resonator design and analysis. To improve the accuracy, the plate equations have to be corrected for the exact thickness-shear frequencies which in turn ensure the accurate results for other coupled modes. The correction procedure was suggested by Mindlin and the correction factors for the first-order equations have been available. Lately, a systematic procedure for the correction factors up to the fifth-order has been established and two correction schemes with different correction factors have been adopted for the higher-order vibrations. These results have expanded applications of the Mindlin plate equations to the overtone vibration analysis which is required for the overtone resonators. One critical issue concerning the applications of the Mindlin plate with correction factors are the effect of electrodes, which are essential part of resonators and complications are resulted. With this objective in mind, we start from the Mindlin plate equations with a full set of vibration modes for the consideration of electrode mass and stiffness effects as a continuation of our earlier studies which only considered the mass effect in terms of mass ratios. The analysis regarding to the AT-cut of quartz crystal plates show that the consideration of electrode stiffness and mass will change the correction factors, thus making the equations more accurate in the calculation of frequency spectra and mode shapes. For very thin electrodes, the correction factors should be the same as suggested by earlier studies. The procedure is implemented to the SC-cut quartz crystal plates which have more enhanced couplings of vibration modes due to the material anisotropy. Correction factors for both AT- and SC-cut quartz crystal plates with consideration of electrode stiffness are given in polynomials of mass ratios for different metals.

Keywords—Mindlin; plate; vibration; quartz; crystal; resonator

I. INTRODUCTION

The Mindlin plate theory was developed for analysis thickness-shear vibrations of quartz crystal resonators without considering complication factors in the beginning [1, 2]. Since electrodes are important parts of quartz crystal resonators with great influence on the frequency and other properties, they should not be neglected when analyzing vibrations for practical applications. Mass effect of electrodes as the dominant feature has always been taken into consideration through mass ratio [3, 4, 5, 6, 7, 8], because thicknesses of electrodes are much thinner but heavier compared with crystal plates. While crystal blanks in resonators are shrinking in size and the electrodes remaining constant, the relative increase of influence of electrodes on the performance of plate resonators should be considered. In this case, it is natural that both stiffness and mass effects of electrodes are taken into consideration simultaneously. The stiffness and mass effects of electrodes can be considered through the ratio of thickness, density, and elastic constants of electrodes to those of quartz crystal plates, as demonstrated in an earlier study [9].

For the analysis with the Mindlin plate theory, Wang [5, 10, 11] have the plate equations corrected without and with mass effect of electrodes considered. The inclusion of stiffness effect was demonstrated before and the calculation is carried out in this study as part of the continued refinement of plate equations for the analysis of quartz crystal resonator.

II. MINDLIN PLATE EQUATIONS WITH THE CONSIDERATION OF STIFFNESS AND MASS EFFECTS OF ELECTRODES

From the higher-order Mindlin plate equations, the two-dimensional stress equations of motion for electroded quartz crystal plates are [9]

$$\begin{Bmatrix} T_{1,1}^{(n)} \\ T_{6,1}^{(n)} \\ T_{5,1}^{(n)} \end{Bmatrix} + \begin{Bmatrix} T_{5,3}^{(n)} \\ T_{4,3}^{(n)} \\ T_{3,3}^{(n)} \end{Bmatrix} - n \begin{Bmatrix} T_{6}^{(n-1)} \\ T_{2}^{(n-1)} \\ T_{4}^{(n-1)} \end{Bmatrix} = \sum_{m=0}^{N} \rho B_{mn} \left[1 + (m+n+1) R \right] \begin{Bmatrix} \ddot{u}_1^{(m)} \\ \ddot{u}_2^{(m)} \\ \ddot{u}_3^{(m)} \end{Bmatrix}, \quad (1)$$

where

$$B_{mn} = \begin{cases} \dfrac{2b^{m+n+1}}{m+n+1}, & m+n = \text{even}, \\ 0, & m+n = \text{odd}, \end{cases} \quad (2)$$

and $T_p^{(n)}$, R and $u_j^{(n)}$ are the nth-order stresses, mass ratio of electrodes and crystal plate, and displacements. Further details on this and following equations can be found in references listed in this paper.

The two-dimensional strain components with higher-order displacements in the abbreviated notations [2] are

$$S_1^{(m)}=u_{1,1}^{(m)},S_2^{(m)}=(m+1)u_2^{(m+1)},S_3^{(m)}=u_{3,3}^{(m)},$$
$$S_4^{(m)}=u_{2,3}^{(m)}+(m+1)u_2^{(m+1)},S_5^{(m)}=u_{3,1}^{(m)}+u_{1,3}^{(m)},\quad(3)$$
$$S_6^{(m)}=u_{2,1}^{(m)}+(m+1)u_1^{(m+1)},m=0,1,2,3\cdots.$$

We consider the electrodes are symmetric, then [9]

$$T_p^{(n)}=\sum_{m=0}^{N}B_{mn}c_{pq}\left[1+(m+n+1)\frac{2b'}{b}\frac{c'_{pq}}{c_{pq}}\right]S_q^{(m)},\quad(4)$$

where c_{pq},c'_{pq} are constants of quartz crystal plate and electrodes.

The *n*th-order constitutive equations of symmetric correction are [10]

$$T_p^{(n)}=\sum_{m=0}^{N}B_{mn}c_{pq}\kappa_p^{(m)}\kappa_q^{(n)}S_q^{(n)}.\quad(5)$$

The correction factors are needed in maintaining the cut-off frequency of the thickness-shear and other important modes accurate in comparison with the three-dimensional solutions.

Substituting (3) into (4), with (5) we can obtain the full constitutive relation in terms of displacement components and electrode stiffness as

$$\begin{aligned}T_p^{(n)}=\sum_{m=0}^{N}B_{mn}\kappa_p^{(n)}\Bigg\{&c_{p1}\kappa_1^{(m)}\left[1+(m+n+1)\frac{2b'}{b}\frac{c'_{p1}}{c_{p1}}\right]u_{1,1}^{(m)}+\\&c_{p2}\kappa_2^{(m)}(m+1)\left[1+(m+n+1)\frac{2b'}{b}\frac{c'_{p2}}{c_{p2}}\right]u_2^{(m+1)}\\&c_{p3}\kappa_3^{(m)}\left[1+(m+n+1)\frac{2b'}{b}\frac{c'_{p3}}{c_{p3}}\right]u_{3,3}^{(m)}+\\&c_{p4}\kappa_4^{(m)}\left[1+(m+n+1)\frac{2b'}{b}\frac{c'_{p4}}{c_{p4}}\right]\left[u_{2,3}^{(m)}+(m+1)u_3^{(m+1)}\right]+\\&c_{p5}\kappa_5^{(m)}\left[1+(m+n+1)\frac{2b'}{b}\frac{c'_{p5}}{c_{p5}}\right]\left(u_{3,1}^{(m)}+u_{1,3}^{(m)}\right)\\&c_{p6}\kappa_6^{(m)}\left[1+(m+n+1)\frac{2b'}{b}\frac{c'_{p6}}{c_{p6}}\right]\left[u_{2,1}^{(m)}+(m+1)u_1^{(m+1)}\right]\Bigg\}.\end{aligned}\quad(6)$$

We focus on the cut-off frequency at zero wavenumber and assume straight-crested waves in crystal plates, then we can have (6) reduced to

$$\begin{aligned}T_p^{(n)}=\sum_{m=0}^{N}B_{mn}\kappa_p^{(n)}\Bigg\{&c_{p2}\kappa_2^{(m)}(m+1)\left[1+(m+n+1)\frac{2b'}{b}\frac{c'_{p2}}{c_{p2}}\right]u_2^{(m+1)}\\&+c_{p4}\kappa_4^{(m)}(m+1)\left[1+(m+n+1)\frac{2b'}{b}\frac{c'_{p4}}{c_{p4}}\right]u_3^{(m+1)}\\&+c_{p6}\kappa_6^{(m)}(m+1)\left[1+(m+n+1)\frac{2b'}{b}\frac{c'_{p6}}{c_{p6}}\right]u_1^{(m+1)}\Bigg\}.\end{aligned}\quad(7)$$

Similarly, the *n*th-order constitutive equations of natural correction, in comparison with (5), are

$$T_p^{(n)}=\sum_{m=0}^{N}B_{mn}c_{pq}\kappa_p^{(m)}\kappa_q^{(m)}S_q^{(m)}.\quad(8)$$

Substituting (3) into (4), with (8) we can obtain

$$\begin{aligned}T_p^{(n)}=\sum_{m=0}^{N}B_{mn}\kappa_p^{(m)}\Bigg\{&c_{p1}\kappa_1^{(m)}\left[1+(m+n+1)\frac{2b'}{b}\frac{c'_{p1}}{c_{p1}}\right]u_{1,1}^{(m)}+\\&c_{p2}\kappa_2^{(m)}(m+1)\left[1+(m+n+1)\frac{2b'}{b}\frac{c'_{p2}}{c_{p2}}\right]u_2^{(m+1)}+\\&c_{p3}\kappa_3^{(m)}\left[1+(m+n+1)\frac{2b'}{b}\frac{c'_{p3}}{c_{p3}}\right]u_{3,3}^{(m)}+\\&c_{p4}\kappa_4^{(m)}\left[1+(m+n+1)\frac{2b'}{b}\frac{c'_{p4}}{c_{p4}}\right]\left[u_{2,3}^{(m)}+(m+1)u_3^{(m+1)}\right]+\\&c_{p5}\kappa_5^{(m)}\left[1+(m+n+1)\frac{2b'}{b}\frac{c'_{p5}}{c_{p5}}\right]\left(u_{3,1}^{(m)}+u_{1,3}^{(m)}\right)+\\&c_{p6}\kappa_6^{(m)}\left[1+(m+n+1)\frac{2b'}{b}\frac{c'_{p6}}{c_{p6}}\right]\left[u_{2,1}^{(m)}+(m+1)u_1^{(m+1)}\right]\Bigg\}.\end{aligned}\quad(9)$$

We focus on the cut-off frequency at zero wavenumber and assume straight-crested waves. Since electrodes are always isotropic, $T_p^{(n)}$ can be reduced with the elastic constants to

$$\begin{aligned}T_p^{(n)}=\sum_{m=0}^{N}B_{mn}\kappa_p^{(m)}\Bigg\{&c_{p2}\kappa_2^{(m)}(m+1)\left[1+(m+n+1)\frac{2b'}{b}\frac{c'_{p2}}{c_{p2}}\right]u_2^{(m+1)}\\&+c_{p4}\kappa_4^{(m)}(m+1)\left[1+(m+n+1)\frac{2b'}{b}\frac{c'_{p4}}{c_{p4}}\right]u_3^{(m+1)}+\\&c_{p6}\kappa_6^{(m)}(m+1)\left[1+(m+n+1)\frac{2b'}{b}\frac{c'_{p6}}{c_{p6}}\right]u_1^{(m+1)}\Bigg\}.\end{aligned}\quad(10)$$

III. Correction Factors with the Consideration of Stiffness and Mass of Electrodes

With the known exact thickness-shear vibration frequency obtained in an electroded quartz crystal plate [7] and the approximate solutions from the Mindlin plate equations with the consideration of stiffness and mass effect in constitutive equations and stresses equations of motion above, we can determine the correction factors through numerical solutions of the algebraic equation.

A. Symmetric Correction of Plate Equations for AT-cut Quartz Crystal

A.1. Correction of the First-order Plate Equations

With the two-dimensional constitutive equations, we can obtain stress $T_p^{(n)}$, and substitute the zeroth-order stresses (7) into first-order equations of motion (1) with parameters

$$s_{22}=\frac{2b'}{b}\frac{c'_{22}}{c_{22}},\quad s_{44}=\frac{2b'}{b}\frac{c'_{44}}{c_{44}},\quad s_{66}=\frac{2b'}{b}\frac{c'_{66}}{c_{66}}.\quad(11)$$

then we have

$$\left[\kappa_6^{(0)}\kappa_6^{(0)}(1+s_{66})-\frac{\Omega^2}{3}(1+3R)\right]A_1^{(1)}=0,$$
$$\left[\frac{c_{22}}{c_{66}}\kappa_2^{(0)}\kappa_2^{(0)}(1+s_{22})-\frac{\Omega^2}{3}(1+3R)\right]A_2^{(1)}+\frac{c_{24}}{c_{66}}\kappa_2^{(0)}\kappa_4^{(0)}A_3^{(1)}=0,$$

$$\frac{c_{42}}{c_{66}}\kappa_4^{(0)}\kappa_2^{(0)}A_2^{(1)}+\left[\frac{c_{44}}{c_{66}}\kappa_4^{(0)}\kappa_4^{(0)}\left(1+s_{44}\right)-\frac{\Omega^2}{3}\left(1+3R\right)\right]A_3^{(1)}=0. \tag{12}$$

Substituting the exact cut-off frequencies into (12), for non-zero solutions, determinant mush vanish, we can obtain correction factors. After obtaining correction factors with different thickness and mass ratios, for practical applications we have an empirical formula for correction factors as function of the mass ratios

$$\begin{aligned}\kappa_2^{(0)}&=0.9069+0.9122R-1.3865R^2+1.2484R^3,\\ \kappa_4^{(0)}&=0.9069+0.9361R-1.3670R^2+1.2240R^3,\\ \kappa_6^{(0)}&=0.9070+0.3850R-1.2796R^2+1.7362R^3.\end{aligned} \tag{13}$$

A.2. Correction of the Third-order Plate Equations

Substituting the second-order stresses (7) into third-order equations of motion (1) we can obtain

$$\begin{aligned}&\left[\kappa_6^{(0)}\kappa_6^{(0)}\left(1+s_{66}\right)-\frac{\Omega^2}{3}\left(1+3R\right)\right]A_1^{(1)}+\\&\left[\kappa_6^{(0)}\kappa_6^{(2)}\left(1+3s_{66}\right)-\frac{\Omega^2}{5}\left(1+5R\right)\right]b^2A_1^{(3)}=0,\\&\left[\frac{c_{22}}{c_{66}}\kappa_2^{(0)}\kappa_2^{(0)}\left(1+s_{22}\right)-\frac{\Omega^2}{3}\left(1+3R\right)\right]A_2^{(1)}+\\&\frac{c_{24}}{c_{66}}\kappa_2^{(0)}\kappa_4^{(0)}A_3^{(1)}+\frac{c_{24}}{c_{66}}b^2\kappa_2^{(0)}\kappa_4^{(2)}A_3^{(3)}+\\&\left[\frac{c_{22}}{c_{66}}b^2\kappa_2^{(0)}\kappa_2^{(2)}\left(1+3s_{22}\right)-\frac{\Omega^2}{5}\left(1+5R\right)\right]A_2^{(3)}=0,\\&\left[\frac{c_{22}}{c_{66}}\kappa_2^{(0)}\kappa_2^{(0)}\left(1+s_{22}\right)-\frac{\Omega^2}{3}\left(1+3R\right)\right]A_2^{(1)}+\\&\frac{c_{24}}{c_{66}}\kappa_2^{(0)}\kappa_4^{(0)}A_3^{(1)}+\frac{c_{24}}{c_{66}}b^2\kappa_2^{(0)}\kappa_4^{(2)}A_3^{(3)}+\\&\left[\frac{c_{22}}{c_{66}}b^2\kappa_2^{(0)}\kappa_2^{(2)}\left(1+3s_{22}\right)-\frac{\Omega^2}{5}\left(1+5R\right)\right]A_2^{(3)}=0,\\&\left[\kappa_6^{(2)}\kappa_6^{(0)}\left(1+3s_{66}\right)-\frac{\Omega^2}{3}\left(1+5R\right)\right]A_1^{(1)}+\\&\left[\frac{9}{5}\kappa_6^{(2)}\kappa_6^{(2)}\left(1+5s_{66}\right)-\frac{\Omega^2}{5}\left(1+7R\right)\right]b^2A_1^{(3)}=0,\\&\left[\frac{c_{22}}{c_{66}}\kappa_2^{(2)}\kappa_2^{(0)}\left(1+3s_{22}\right)-\frac{\Omega^2}{5}\left(1+5R\right)\right]A_2^{(1)}+\\&\frac{c_{24}}{c_{66}}\kappa_2^{(2)}\kappa_4^{(0)}A_3^{(1)}+\frac{9}{5}\frac{c_{24}}{c_{66}}b^2\kappa_2^{(2)}\kappa_4^{(2)}A_3^{(3)}+\\&\left[\frac{9}{5}\frac{c_{22}}{c_{66}}b^2\kappa_2^{(2)}\kappa_2^{(2)}\left(1+5s_{22}\right)-\frac{\Omega^2}{7}\left(1+7R\right)\right]A_2^{(3)}=0,\\&\frac{c_{42}}{c_{66}}\kappa_4^{(2)}\kappa_2^{(0)}A_2^{(1)}+\frac{9}{5}\frac{c_{42}}{c_{66}}b^2\kappa_4^{(2)}\kappa_2^{(2)}A_2^{(3)}+\\&\left[\frac{c_{44}}{c_{66}}\kappa_4^{(2)}\kappa_4^{(0)}\left(1+3s_{44}\right)-\frac{\Omega^2}{5}\left(1+5R\right)\right]A_3^{(1)}+\\&\left[\frac{9}{5}\frac{c_{44}}{c_{66}}b^2\kappa_4^{(2)}\kappa_4^{(2)}\left(1+5s_{44}\right)-\frac{\Omega^2}{7}\left(1+7R\right)\right]A_3^{(3)}=0.\end{aligned} \tag{14}$$

Substituting the exact cut-off frequencies into (14), for non-zero solutions the determinant must vanish. After obtaining correction factors with different thickness and mass ratios, we have symmetric correction factors fitted into curves for different mass ratios as

$$\begin{aligned}\kappa_2^{(0)}&=0.9480+0.9164R-2.2725R^2+3.3899R^3,\\ \kappa_4^{(0)}&=0.9480+0.9415R-2.2689R^2+3.3868R^3,\\ \kappa_6^{(0)}&=0.9480+0.3632R-2.0880R^2+3.8494R^3,\\ \kappa_2^{(2)}&=0.7635+0.9104R-8.4394R^2+14.0294R^3,\\ \kappa_4^{(2)}&=0.7635+2.0148R-8.3618R^2+13.6602R^3,\\ \kappa_6^{(2)}&=0.7637+1.4842R-8.5784R^2+15.4158R^3.\end{aligned} \tag{15}$$

B. Natural Correction of Plate Equations for AT-cut Quartz Crystal

B.1. Correction of the First-order Plate Equations

Substituting the zeroth-order stresses (10) into the first-order equations of motion (1), we obtain the same equations as (12), and the results of correction factors are obtained as given in (13).

B.2. Correction of the Third-order Plate Equations

Substituting the second-order stresses (10) into the third-order equations of motion (1) we can obtain

$$\begin{aligned}&\left[\kappa_6^{(0)}\kappa_6^{(0)}\left(1+s_{66}\right)-\frac{\Omega^2}{3}\left(1+3R\right)\right]A_1^{(1)}+\\&\left[\kappa_6^{(2)}\kappa_6^{(2)}\left(1+3s_{66}\right)-\frac{\Omega^2}{5}\left(1+5R\right)\right]b^2A_1^{(3)}=0,\\&\left[\frac{c_{22}}{c_{66}}\kappa_2^{(0)}\kappa_2^{(0)}\left(1+s_{22}\right)-\frac{\Omega^2}{3}\left(1+3R\right)\right]A_2^{(1)}+\\&\frac{c_{24}}{c_{66}}\kappa_2^{(0)}\kappa_4^{(0)}A_3^{(1)}+\frac{c_{24}}{c_{66}}b^2\kappa_2^{(2)}\kappa_4^{(2)}A_3^{(3)}+\\&\left[\frac{c_{22}}{c_{66}}b^2\kappa_2^{(2)}\kappa_2^{(2)}\left(1+3s_{22}\right)-\frac{\Omega^2}{5}\left(1+5R\right)\right]A_2^{(3)}=0,\\&\frac{c_{42}}{c_{66}}\kappa_4^{(0)}\kappa_2^{(0)}A_2^{(1)}\frac{c_{42}}{c_{66}}b^2\kappa_4^{(2)}\kappa_2^{(2)}A_2^{(3)}+\\&\left[\frac{c_{44}}{c_{66}}\kappa_4^{(0)}\kappa_4^{(0)}\left(1+s_{44}\right)-\frac{\Omega^2}{3}\left(1+3R\right)\right]A_3^{(1)}+\\&\left[\frac{c_{44}}{c_{66}}b^2\kappa_4^{(2)}\kappa_4^{(2)}\left(1+3s_{44}\right)-\frac{\Omega^2}{5}\left(1+5R\right)\right]A_3^{(3)}=0,\\&\left[\kappa_6^{(0)}\kappa_6^{(0)}\left(1+3s_{66}\right)-\frac{\Omega^2}{3}\left(1+5R\right)\right]A_1^{(1)}+\\&\left[\frac{9}{5}\kappa_6^{(2)}\kappa_6^{(2)}\left(1+5s_{66}\right)-\frac{\Omega^2}{5}\left(1+7R\right)\right]b^2A_1^{(3)}=0,\\&\left[\frac{c_{22}}{c_{66}}\kappa_2^{(0)}\kappa_2^{(0)}\left(1+3s_{22}\right)-\frac{\Omega^2}{5}\left(1+5R\right)\right]A_2^{(1)}+\\&\frac{c_{24}}{c_{66}}\kappa_2^{(0)}\kappa_4^{(0)}A_3^{(1)}+\frac{9}{5}\frac{c_{24}}{c_{66}}b^2\kappa_2^{(2)}\kappa_4^{(2)}A_3^{(3)}+\\&\left[\frac{9}{5}\frac{c_{22}}{c_{66}}b^2\kappa_2^{(2)}\kappa_2^{(2)}\left(1+5s_{22}\right)-\frac{\Omega^2}{7}\left(1+7R\right)\right]A_2^{(3)}=0,\end{aligned}$$

$$\frac{c_{42}}{c_{66}}\kappa_4^{(0)}\kappa_2^{(0)}A_2^{(1)}+\frac{9}{5}\frac{c_{42}}{c_{66}}b^2\kappa_4^{(2)}\kappa_2^{(2)}A_2^{(3)}+$$
$$\left[\frac{c_{44}}{c_{66}}\kappa_4^{(0)}\kappa_4^{(0)}\left(1+3s_{22}\right)-\frac{\Omega^2}{5}\left(1+5R\right)\right]A_3^{(1)}+ \quad (16)$$
$$\left[\frac{9}{5}\frac{c_{44}}{c_{66}}b^2\kappa_4^{(2)}\kappa_4^{(2)}\left(1+5s_{22}\right)-\frac{\Omega^2}{7}\left(1+7R\right)\right]A_3^{(3)}=0.$$

Substituting the exact cut-off frequencies into (16), for non-zero solutions the determinant must vanish. Then we have natural correction factors fitted into curves for different mass ratios as

$$\begin{aligned}
\kappa_2^{(0)} &= 0.9408+1.0243R-3.2428R^2+5.4746R^3,\\
\kappa_4^{(0)} &= 0.9369+1.0603R-3.0354R^2+4.8909R^3,\\
\kappa_6^{(0)} &= 0.9370+0.4817R-2.8695R^2+5.4039R^3,\\
\kappa_2^{(2)} &= 0.7736+1.8259R-7.9338R^2+13.1607R^3,\\
\kappa_4^{(2)} &= 0.7725+1.9270R-7.8163R^2+12.6678R^3,\\
\kappa_6^{(2)} &= 0.7727+1.3951R-8.0023R^2+14.3097R^3.
\end{aligned} \quad (17)$$

IV. Conclusions

For practical applications, it is more convenient to have an empirical formula for correction factors as functions of mass ratios. Correction factors with stiffness and mass effects of electrodes considered are more useful in actual applications for the analysis of thickness-shear vibrations of miniaturized quartz crystal resonators with the Mindlin plate equations. While the correction factors with natural approach can be used in analytical solutions, the symmetric correction factors can also be implemented in the finite element analysis based on the Mindlin plate theory for numerical solutions. With the correction factors for thicker electrodes on the SC-cut quartz crystal substrates, we now have the full set of correction factors for both AT- and SC-cut quartz crystal blanks for vibration analysis needed in the design and optimization of quartz crystal resonators. Since accurate analysis can only be done with the finite element method, the new set of correction factors from this paper will enrich the capability and functions of our existing finite element software for quartz crystal resonator design.

Acknowledgments

This research is supported in part by the National Natural Science Foundation of China (Grant Nos. 10932004 & 11072116) and the Ministry of Education of China (Grant No. 20093305110003). Additional support is provided by the K. C. Wong Magna Fund administered by Ningbo University and the Young Doctoral Faculty Innovation Fund of Ningbo Polytechnic.

References

[1] R. D. Mindlin, "Thickness-shear and flexural vibrations of crystal plates," J. Appl. Phys., vol. 22, pp. 316-323, 1951.

[2] R. D. Mindlin, An Introduction to the Methematical Theory of Vibrations of Elastics Plates, J. S. Yang, Ed., NJ: World Scientific, 2006.

[3] P. C. Y. Lee, S. Syngellakis and J. P. Hou, "A two-dimensional theory for high-frequency vibrations of piezoelectric crystal plates with or without electrodes, " J. Appl. Phys., vol. 61, no. 4, pp. 1249-1262, 1987.

[4] H. F.Tiersten and T.-L. Sham, "Forecd vibration of fundmental family of modes in AT-cut quartz strip resonators, " J. Appl. Phys, vol. 89, no. 1, pp. 575-585, 2001.

[5] J. Wang, R. X. Wu, W. H Zhao, J. K. Du and D. J. Huang, "Correction factors for Mindlin high-order plate theory with the consideration of electrodes," Proc.of 2007 IEEE Int. Freq. Control Symp., pp. 203-207, 2007.

[6] J. S. Yang, H. G. Zhou, and W. P. Zhang, "Thickness-shear vibration of rotated Y-cut quartz plates with relatively thick electrodes of unequal thickness," IEEE Trans. Ultrason. Ferroelectr. Freq. Control, vol. 52, no. 5, pp. 918-922, 2005.

[7] J. Wang, L. J. Shen, "Exact thickness-shear resonance frequency of electroded piezoelectric crystal plates," J. Zhejiang Univ. Sci., vol. 6A, no. 9, pp. 980-985, 2005.

[8] J. L. Bleustein, H. F. Tiersten, "Forced thickness-shear vibrations of discontinuously plated piezoelectric plates, " J. Acoust. Soc. Am, vol.43, no. 6, pp. 1311-1318, 1968.

[9] J. Wang, "Consideration of stiffness and mass effects of relatively thicker electrodes with Mindlin plate theory," IEEE Trans. Ultrason. Ferroelectr. Freq. Control, vol. 53, no. 6, pp. 1218-1221, 2006.

[10] J. Wang, J.-D. Yu, and Y.-K. Yong, "On the correction of higher-order Mindlin plate theory," Int. J. Appl. Electromagn. Mech., vol. 22, pp. 83-96, 2005.

[11] J. Wang, J.-D. Yu, Y.-K. Yong, and T. Imai, "A Finite Element Analysis of Frequency-temperature Relations of AT-cut Quartz Crystal Resonators with Higher-order Mindlin Plate Theory," Acta Mechanica, vol. 199, no. 1-4, pp. 117-130, 2008.

Optimizing UHF Quartz MEMs Resonators for High Thermal Stability

D.J. Kirby, Y.K. Yong*, R.L. Kubena, R. Perahia, D.T. Chang, H. Nguyen, F.P. Stratton, R.J. Joyce, H.P. Moyer R.G. Nagele & P.D. Brewer

HRL Laboratories, Malibu California, USA, *Rutgers University, Piscataway, New Jersey, USA

Email: djkirby@hrl.com

***Abstract*— A 1 GHz AT-cut quartz thickness shear mode resonator is modeled for the first time with thermally induced bonding stresses and their effect on the device frequency-temperature (*f-T*) characteristic. Without the details of the bonding configuration, modeling indicates the *f-T* characteristic slightly rotates as a function of the change in stiffness of a simplified absorbing mount. However, if details of the bonding configuration are included, our modeling predicts the potential for a significant distortion in the *f-T* curve. High or varying stress over temperature in the device active region is found to lead to an undesirable increase in the *f-T* slope. The origin of the active region stress can be varied, but in practice it frequently originates from a temperature dependent bonding stress, or from fabrication steps such as metal depositions. In this paper we highlight the magnitude of the thermal stress effect on the *f-T* curve, and offer design methods that mitigate the thermally induced bonding stress by de-coupling the active resonator area from high stress regions of the quartz device.**

Keywords- Quartz MEMS, oscillators, resonators, frequency stability, stress, thickness shear mode.

I. Introduction

Frequency stability of oscillators used in timing applications is of paramount importance. It is well known that one dominant source of frequency instability in quartz oscillators relates to the mounting stresses incurred during wafer bonding[1]. A resonator bonded to a substrate at elevated temperature and subsequently cooled can experience significant residual stress in the device active region. As the operating temperature of the device varies, so does the magnitude of the residual stress. This stress acts to perturb the device resonant frequency thereby compromising frequency stability. Mounting stress relaxation over time can also lead to device hysteresis. As the need for higher frequency and smaller devices has developed for many new commercial applications, these effects are exacerbated in smaller packages. This paper discusses how ~1 GHz ultra-high-frequency (UHF) MEMs thickness-shear quartz resonator designs[2] can be optimized for improving thermal frequency stability via reduced residual stresses.

A newly developed 3-D FEA simulation technique which includes mounting stresses[3] is applied to optimize UHF device designs for high thermal stability. One of the effects of stress is to produce a rotation of the *f-T* characteristic. Very small stresses can produce significant frequency shifts, especially for fundamental mode UHF devices. This rotation can often mask the true quartz *f-T* characteristic and results in resonator thermal instability.

II. Mounting Stress Analysis

As an example of the effect of mounting stresses on device resonant frequency, Fig. 1 shows a simulation of frequency perturbation versus stress in the active region for a 770 MHz 2-µm-thick AT-cut quartz resonator. The inset of Fig. 1 shows a simulation of the thermally induced stress for a ΔT = +75°C of a single-thickness quartz resonator rigidly bonded to a silicon substrate with zero stress at T = 25°C. A mounting stress of 130 MPa near the mounts produces a stress of 1 MPa in the active region and a resulting resonator frequency shift of 21 ppm. We determine a sensitivity of 1 ppm/50 kPa stress in the active region which represents a significantly higher frequency sensitivity than for larger, thicker, lower frequency designs. In this paper, new UHF resonator designs are explored for mitigating this effect in sub-mm-size UHF quartz resonators.

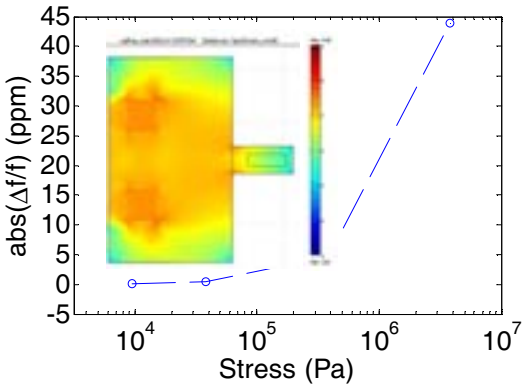

Figure 1. Frequency perturbation of a 2-µm-thick 770-MHz AT-cut resonator versus stress in the active electrode region.

At 1 GHz the effect of resonator frequency shift from residual stress becomes more pronounced. Here we explore the effect of varying mounting stiffness of a simplified resonator model. Fig. 2 presents a resonator model where

This material is based upon work supported by the Defense Advanced Research Projects Agency under Contract No. HR0011-10-C-0109. Any opinions, findings and conclusions or recommendations expressed in this material are those of the author(s) and do not necessarily reflect the views of the Defense Advanced Research Projects Agency.

the mounting condition is initially an absorbing soft rubber strip with Young's Modulus, E = 2 x 10^{-8} Pa, which is fixed in space along its back surface to represent the anchor of the device. The AT-cut quartz resonator has plate dimensions 235 x 1.5 x 105 µm, and aluminum electrodes 150 x 0.04 x 50 µm. A thermally induced stress profile is calculated in COMSOL for this simplified quartz resonator and mount geometry for a ΔT = 75°C. In this model, bonding stress is assumed to be zero at T = 25°C. When elevated to T = 100°C, the residual stress in the center of the resonator active region (under the electrodes) is found to have increased to 319 kPa. Fig. 3 presents a corresponding linear cross section of the stress in the device along the quartz crystal x-axis.

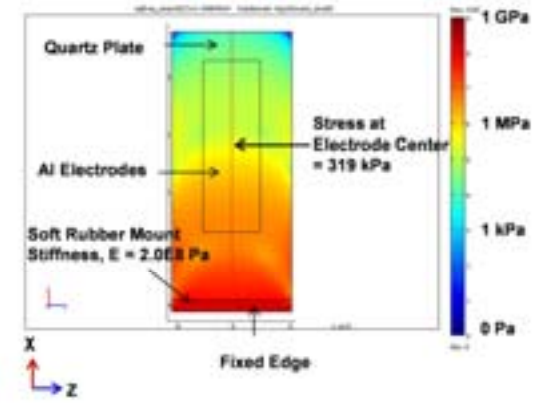

Figure 2. Simplified resonator design with ideal (soft) rubber mounts of Young's modulus E=2.0E8 Pa. Thermally induced stress at the mounts from a ΔT=75°C increase results in a Von Mises stress of 319 kPa in the active electrode region.

Consider the *f-T* characteristic of the simple resonator case as illustrated by the red curve in Fig. 4. This represents the unperturbed or unrotated *f-T* characteristic for soft mounts of stiffness E = 2 x 10^{-8} Pa. The absolute frequency shift for a temperature excursion from -40°C to 85°C corresponds to a 22 ppm change from the frequency observed at 25°C. Using COMSOL we calculate the device admittance parameters as f_0 = 1.05 GHz, R_1 =10.5Ω, L_1 = 2.1 x 10^{-5} H, C_1 = 1.1 fF, C_0 = 0.17 pF, and Q = 13.5K. The $f \times Q$ product for this design is $f \times Q$ = 1.42 x 10^{13}. As the stiffness of the fixed mount is stepped toward a more rigid condition (E = 2 x 10^{12} Pa), the corresponding *f-T* curves in Fig. 4 exhibit a slight counterclockwise rotation. While the absolute frequency at T = 25°C is maintained for all three stiffness cases, the frequency shifts to lower values

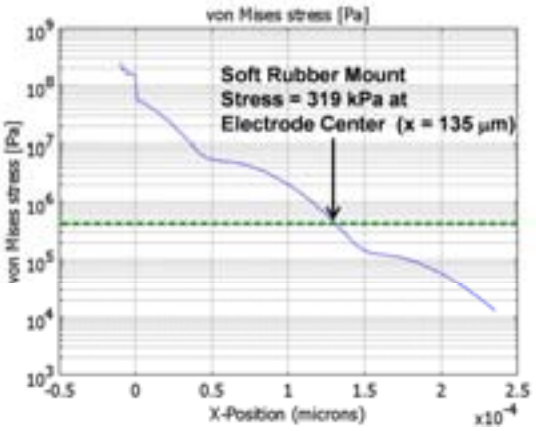

Figure 3. Plot of thermally induced Von Mises stress along the length of the resonator for a ΔT=75°C. The residual stress is 319 kPa at the center of the electrode.

below 25°C and higher values above this temperature as the mounts become more rigid. At 1GHz, this result is consistent with the theoretical analysis performed at 500 MHz by Y.K. Yong et al [3].

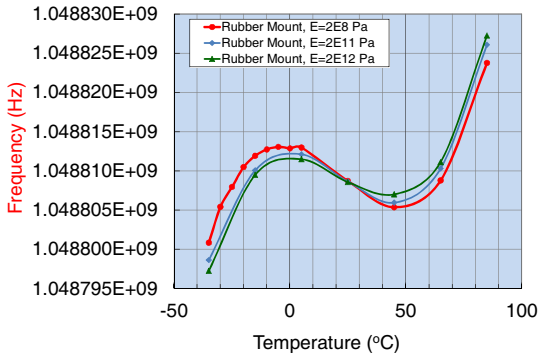

Figure 4. Variation of frequency over temperature for a simplified resonator design with zero mounting stress defined at T = 25°C.

For comparison, consider the case of a more detailed model that includes the mounting configuration with rigid (epoxy) bonds attaching the resonator to a silicon substrate as in Fig. 5. For a mount stiffness of E = 2.0 x 10^{11} Pa and the same ΔT = 75°C, the Von Mises stress is found to be significantly higher (σ = 731 kPa) in the active electrode region than for the simplified case (σ = 319 kPa). Fig. 6 shows the corresponding linear cross section of the stress along the x-axis of the crystal for this more detailed analysis.

The revised predicted *f-T* characteristic for varying stiffness of the bond regions (mounts) is presented in Fig. 7. For the rigid mount case where E = 2 x 10^{11} Pa, we calculate the admittance parameters of the device as f_0 = 1.05 GHz, R1 = 7Ω, L1 = 1.4x 10^{-5} H, C_1 = 1.6 fF, C_0 = 0.17 pF, and Q = 13.5K. The $f \times Q$ product remains high at $f \times Q$ = 1.42 x 10^{13}. If we replace the rigid mounts to the silicon substrate with a soft rubber like material of stiffness E = 2.0 x 10^{8} Pa, the *f-T* characteristic remains fairly unchanged from the simplified case. However, for stiffer mounts with a Young's

Modulus closer to that of quartz (E = 2.0 x 10^{11} Pa), the *f-T* characteristic becomes severely compromised. The *f-T* behavior takes on a more parabolic form, rapidly deviating in frequency above the simplified case as we depart from the zero bonding stress temperature of T = 25°C. This is consistent with empirical data for non-optimized devices which exhibit a high positive *f-T* slope above room temperature.

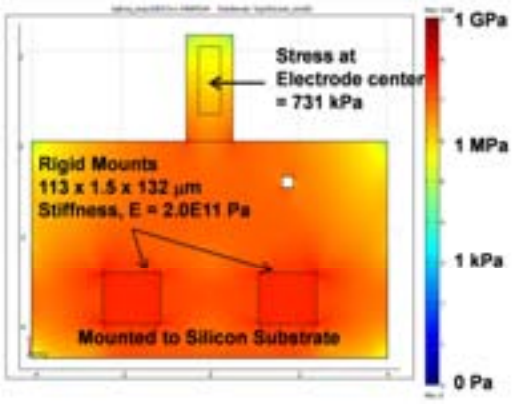

Figure 5. Von Mises stress of more detailed resonator design with mounts bonding the quartz to a silicon substrate. Stress is computed for ΔT = 75 °C.

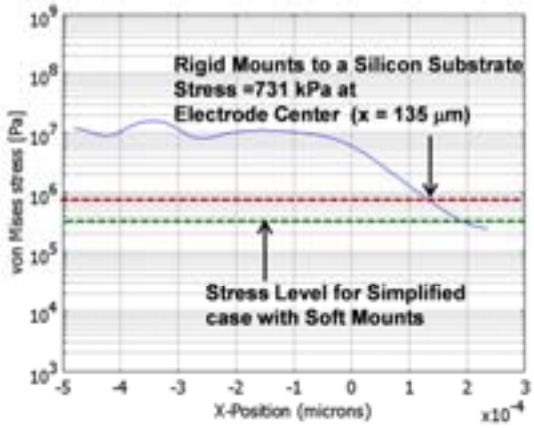

Figure 6. Plot of thermally induced Von Mises stress along the length of the resonator for a ΔT = 75°C. The resonator is bonded to a silicon substrate with rigid mounts. The residual stress magnitude is 731 kPa at the center of the electrode.

III. DESIGNS WITH IMPROVED FREQUENCY-TEMPERATURE CHARACTERISTIC

We determine that in order to correct the distorted *f-T* behavior of Fig. 7, one must de-couple the resonator mechanically from high stress regions. As an example, we incorporate stress relieving springs in the mounting configuration as shown in Fig. 8. The springs of width = 30µm efficiently relieve in-plane stress from the bonding sites (mounts) in both the x- and z-axes. The resonator is then effectively

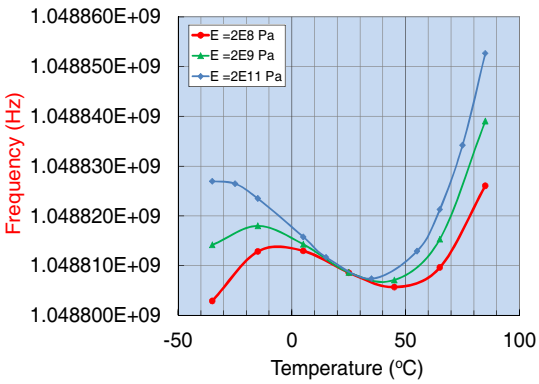

Figure 7. Variation in the f-T characteristic when residual stress from a more detailed mounting configuration is included. The f-T curve for soft mounts (red) is unrotated. High f-T distortion occurs as the stiffness of the mounts is increased to a rigid, epoxy like material (blue).

mechanically de-coupled from the high stress mounting areas. The calculated admittance parameters for this design are f_0 = 1.05 GHz, R_1 = 9.8Ω , L_1 = 2.0 x 10^{-5} H, C_1 = 1.2 fF, C_0 = 0.17 pF, and Q = 13.5K. For this design we maintain the $f \times Q$ product of 1.42 x 10^{13}.

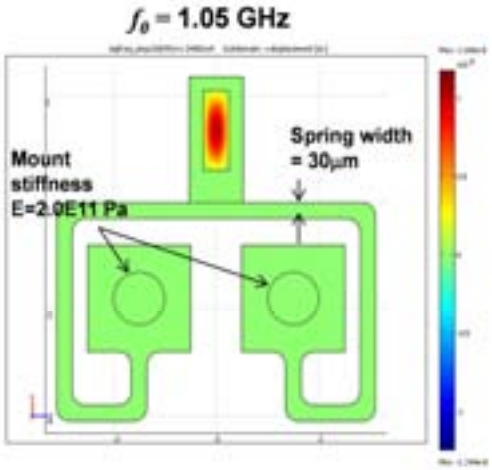

Figure 8. Schematic of improved 1GHz design with springs for stress relief in the active electrode region.

The resulting stress profile for a ΔT = 75°C is presented in Fig. 9 where we calculate a high stress in the mounting area but a low stress value of 21 kPa in the electrode region. The corresponding linear cross-section of stress across the resonator is presented in Fig. 10. Clearly, the spring mounting configuration predicts significantly lower stress in the electrode area over the simplified resonator case, therefore we anticipate an improved unrotated *f-T* characteristic.

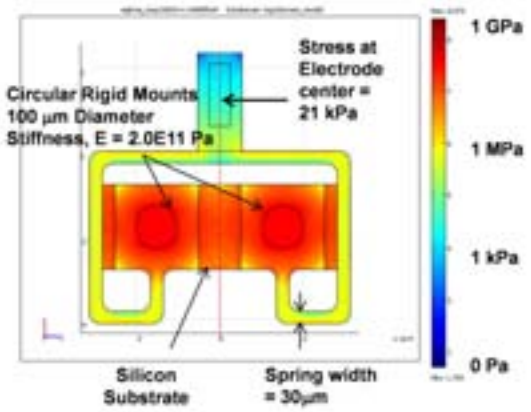

Figure 9. Springs provide stress isolation reducing the residual thermally induced stress in the active region to 21 kPa. ΔT=75°C.

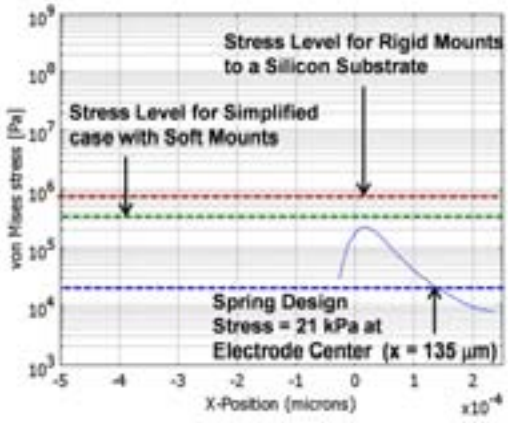

Figure 10. Stress isolation of the resonator from the bonding region significantly reduces residual stress in the active region to σ = 21 kPa.

The theoretical improvement in frequency stability over temperature is confirmed in the simulation result of Fig. 11. In this Figure, the *f-T* results are compared for (i) a resonator mounted via a quartz base to a silicon substrate (standard mount), and (ii) the same resonator mounted to the silicon substrate but isolated from the mounts by stress relieving springs (spring mount). The predicted *f-T* performance for soft versus rigid mounts is calculated for each case. Recall, for case (i) we observed a higher residual stress in the electrode region and rigid mounts showed the large frequency instability over temperature. However, implementation of stress isolation of the resonator with springs, e.g. case (ii), dramatically reduces frequency deviation from the soft mount case. The *f-T* characteristic maintains the classic S-shaped AT-cut quartz profile. The improvement in the *f-T* profile with springs corresponds to a 25 ppm improvement in thermal frequency stability for a ΔT = 50°C.

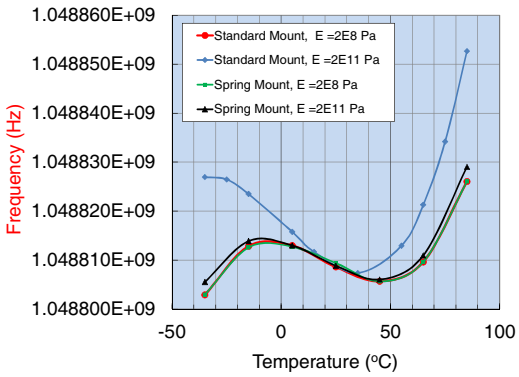

Figure 11. Distortion of the fT curve of the resonator with mounts bonded to a silicon substrate is significantly reduced for designs incorporating stress isolation in the form of spring elements.

CONCLUSIONS

Thermally induced mounting stresses in UHF quartz resonators has been modeled and its effect on frequency-temperature stability analyzed. The mounting condition plays an important role in the frequency stability of UHF devices over temperature. A detailed model shows that as the stiffness of mounts is increased from soft rubber to rigid mounts, the *f-T* curve rotates counterclockwise and can result in highly compromised frequency stability over temperature.

1GHz AT-cut quartz thickness shear mode resonators have been designed and analyzed offering significantly improved thermal frequency stability via a de-coupling of variable mounting stresses from the active electrode region. We have shown that implementation of stress relieving elements such as springs can greatly reduce the stress in the active electrode region and thereby eliminate the *f-T* instability caused by thermally and time varying mounting stress. We will apply this analysis method to future UHF oscillator designs for improved thermal frequency stability.

IV. ACKNOWLEDGMENTS

This material is based upon work supported by the Defense Advanced Research Projects Agency under Contract No. HR0011-10-C-0109. The authors would like to thank Jeffrey Rogers of DARPA MTO for his support of this program.

REFERENCES

[1] John R.Vig, "Quartz crystal resonators and oscillators for frequency control and timing applications - a tutorial", Rev.8.5.4.4, April 2012.

[2] D. Chang et al, "Nonlinear UHF quartz MEMs oscillator with phase noise reduction", Proceedings of IEEE MEMS 2013, Taipei, Taiwan, January 20 – 24, pp. 781, 2013

[3] Yook-Kong Yong et al, "Modeling approach to analyze bonding stress in UHF quartz resonators", IEEE FCS 2013

Modeling Approach to Analyze Bonding Stress in UHF Quartz Resonators

Yook-Kong Yong*, R.L. Kubena, D.J. Kirby, R. Perahia, and D.T. Chang
*Rutgers Univ., Piscataway, NJ
HRL Laboratories, LLC, Malibu, CA, 90265 USA
Email: yyong@rci.rutgers.edu

Abstract— **We have observed a phenomenon of high precision MEMS quartz resonators to change their frequency-temperature characteristics when they are mounted or bonded onto a substrate. This is due to the difference in thermal expansion coefficients between the quartz and substrate. When the temperature is changed, the mounting points between the quartz resonator and substrate become a source of mounting stress/strain in the resonator. We have defined a zero-stress temperature as the temperature at which the mounting stress is zero. We could determine the zero-stress temperature from the aging data of the resonator.**

We have derived a set of incremental equations for small vibrations superposed on mounting stress/strain that included the zero-stress temperature. The equations were employed in a COMSOL model of a UHF quartz resonator. The resonator frequency versus temperature profile was calculated by the change in eigenfrequency of the thickness shear mode as a function of the temperature. The eigenvalue problem of the resonator was modeled in COMSOL. The frequency-temperature curve of the resonator was shown to rotate counter-clockwise with the mounting stiffness and zero-stress temperature with respect to the frequency-temperature curve of the same resonator with no bonding stress. Furthermore the frequency-temperature curve of a bonded resonator will intersect the frequency-temperature curve of the same resonator without bonding stress at the zero-stress temperature.

Keywords- Quartz MEMS, frequency-temperature behavior, -zero-stress temperature, -bonding stress/strain, -COMSOL model.

I. INTRODUCTION

Bonding and mounting stress in quartz resonators is known to produce frequency shifts which can also modify the frequency-versus-temperature (f-T) profiles [1]. This stress/strain is produced by two events. First, when the quartz plate is initially bonded into the final package, the bonding process may require high temperature annealing or processing. When the package is cooled, the difference in thermal expansion coefficients between the quartz and the package produces stress that can partially relax to yield an initial stress condition at room temperature. Second, when the package is then varied over temperature during use, this initial stress is modified by the same thermal expansion coefficient differences. Depending on the thermal history of the device, the mounting stress can be minimized or reduced to zero at a particular temperature (T_{ref2}) as evidenced by a very low relaxation or aging rate. Previous numerical models for quartz f-T profiles [2] have not included this zero stress condition nor the variations in the stress and strain in the quartz due to the mounts in calculating the f-T profiles. In this paper, we describe a method within a COMSOL finite element analysis to include these effects for the first time.

II. GOVERNING EQUATIONS

A. *Definition of T_{ref2}, the zero-stress temperature*

It is necessary for our discussion of bonding stress to define the idea of a zero-stress-temperature T_{ref2}. Furthermore, it is also necessary for us to differentiate the zero-stress-temperature T_{ref2} from another reference temperature T_{ref} =25°C which is the reference temperature of the crystal material properties and the temperature at which the resonator is both stress and strain free.

The resonator is bonded to the substrate at some temperature above the reference temperature T_{ref}=25°C, and annealed at a higher temperature. At some point the mounts are "hardened". The wafer is brought back to room temperature and the mounting stress relaxes slowly over time. If the wafer sits at room temperature for several hours or days, the mounting stress/strain settles to some value. If the wafer is then increased in temperature to T_{ref2}, the mounting stress is found to be zero (based in aging data). We call T_{ref2} the zero-stress temperature. Note that while the resonator is stress-free at both T_{ref} and T_{ref2} it is strain free only at T_{ref}. While T_{ref} is equal to 25°C the value of T_{ref2} depends on the resonator bonding and processing

B. *Four states of the resonator*

For modeling the bonding stress and its effects on the frequency-temperature behavior of the resonator it is necessary to describe the resonator in four states in order to derive the governing equations.

Figure 1 shows the four states of the resonator and its respective material displacement vectors $\underline{\mathbf{U}}^{(a)}$, $\underline{\mathbf{U}}^{(b)}$, $\underline{\mathbf{U}}^{(c)}$, and $\underline{\mathbf{U}}^{(d)}$. State 0 is the initial reference frame at temperature T_{ref} = 25°C for the material properties, resonator geometry, and a stress-strain free state. The next state is State 1 when at temperature T_{ref2} the resonator is stress-free but *not* strain-free as explained in the previous section on the zero-stress

This work was sponsored in part by DARPA'S MTO office under the DEFYS program, issued by DARPA /CMO under contract No. HR0011-10-C-0109. The views and conclusions contained in this document are those of the authors and should not be interpreted as representing the official policies, either expressly or implied, of DARPA or the U.S. Government.

temperature T_{ref2}. State 2 of the resonator is at any operating temperature T wherein the resonator experiences both stress and strain due to bonding stress and thermal strain. Finally State 3 is when the resonator is excited and experiences small vibrations superposed on the previous State 2. In the next section, we derive the governing equations for small vibrations of the resonator superposed upon the strains and deformation of State 2.

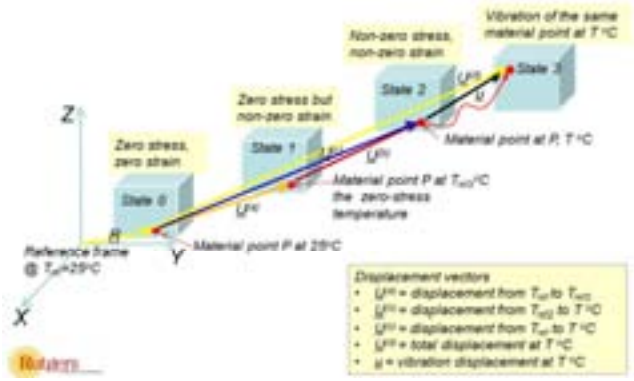

Figure 1. Four states of the resonator.

C. *Nonlinear Lagrangean governing equations for the resonator at State 2 and State 3*

The following are the governing nonlinear Lagrangean equations for the resonator at States 2 and 3.

Nonlinear strain-displacement relations:

$$E_{ij}^{(s)} = \tfrac{1}{2}\left(U_{i,j}^{(s)} + U_{j,i}^{(s)} + U_{k,i}^{(s)} U_{k,j}^{(s)}\right) \qquad \text{Eq(1)}$$

Nonlinear constitutive relations:

$$T_{ij}^{(s)} = C_{ijkl} S_{kl}^{(s)} + \frac{1}{2} C_{ijklmn} S_{kl}^{(s)} S_{mn}^{(s)} \qquad \text{Eq(2)}$$

Nonlinear stress equations of motion:

$$\begin{aligned} &(T_{ij}^{(s)} + T_{jk}^{(s)} U_{i,k}^{(s)})_{,j} = \rho \ddot{U}_i^{(s)} \quad \text{in V} \\ &\text{Specify } P_i^{(s)} = n_j (T_{ij}^{(s)} + T_{jk}^{(s)} U_{i,k}^{(s)}) \text{ or } U_i^{(s)} \text{ on S} \end{aligned} \qquad \text{Eq(3)}$$

$U_i^{(s)}$ is the displacement and the "s" superscript in parenthesis represents the state at which the displacement is defined, that is, s = c for State 2, and s = d for State 3. $E_{ij}^{(s)}$, $T_{ij}^{(s)}$, and $P_i^{(s)}$ are respectively the strain, stress and stress traction. C_{ijkl} and C_{ijklmn} are respectively the linear elastic constants and nonlinear elastic constants.

D. *Incremental equations for small vibrations superposed on thermal stress-strain in a resonator*

It is very difficult to solve computationally the set of nonlinear equations Eq(1), Eq(2) and Eq(3). However for small <u>*linear*</u> vibrations u_i superposed on State 2 we could derive a set of incremental equations that are linear if the displacements, stain and stress at State 2 are known a priori. We take the difference between the displacements, strain and stress at States 3 and 2, respectively, to obtain their incremental displacements, strain and stress:

$$\begin{aligned} u_i &= U_i^{(d)} - U_i^{(c)} \\ e_{ij} &= E_{ij}^{(d)} - E_{ij}^{(c)} \\ t_{ij} &= T_{ij}^{(d)} - T_{ij}^{(c)} \end{aligned} \qquad \text{Eq(4)}$$

We used the definition of incremental quantities in Eq(4), and a methodology similar to reference [3] to derive the incremental equations for small vibrations superposed on State 2:

Incremental strain-displacement relations:

$$e_{ij} = \frac{1}{2}(u_{j,i} + u_{i,j} + U_{k,i}^{(c)} u_{k,j} + U_{k,j}^{(c)} u_{k,i}) \qquad \text{Eq(5)}$$

Incremental stress-strain relations:

$$t_{ij} = (C_{ijkl} + C_{ijklmn} E_{mn}^{(c)}) e_{kl} \qquad \text{Eq(6)}$$

Incremental stress equations of motion:

$$\begin{aligned} &(t_{ij} + t_{jk} U_{i,k}^{(c)})_{,j} = \rho \ddot{u}_i \quad \text{in } V \\ &p_i = n_j (t_{ij} + t_{jk} U_{i,k}^{(c)}) \quad \text{in } S \end{aligned} \qquad \text{Eq(7)}$$

In the derivation of Eq(7) we have neglected the stress $T_{jk}^{(c)}$ because it was shown in reference [3] using variational analysis and Hamilton's equation that the initial stress $T_{jk}^{(c)}$ is a second order quantity that could be neglected in the incremental equations. Hence in Eq(5) to (7), only the deformation gradient and strain of State 2 are assumed known a priori in order for the governing incremental equations to *be linear*.

E. *Displacement and strain in the resonator at State 2*

It is necessary that we know the deformation gradient and strain at State 2 of the resonator in order to solve linearly the incremental governing equations (Eq(5) to (7)). From Fig. 1 we see that:

$$\begin{aligned} U_i^{(c)} &= U_i^{(a)} + U_i^{(b)} \\ E_{ij}^{(c)} &= E_{ij}^{(a)} + E_{ij}^{(b)} \end{aligned} \qquad \text{Eq(8)}$$

Hence, the displacement and strain in the resonator at State 2 are dependent on their respective quantities at State 1.

1) Thermal strains under stress-free and steady-state uniform temperature at T_{ref2}: State 1

The constitutive equations for an elastic material with thermal expansion are:

$$\sigma_{ij} = C_{ijkl}(E_{kl}^{(a)} - \alpha_{kl}\theta_a) \quad \text{Eq(9)}$$

where σ_{ij} is the stress tensor, C_{ijkl} elastic constants, $E_{kl}^{(a)}$ strain tensor at State 1, α_{kl} thermal expansion coefficients and $\theta_a = (T_{ref\,2} - T_{ref})$. The thermal expansion coefficients for quartz were measured by Bechmann, Ballato and Lukaszek [4]. Since at State 1 the resonator is stress-free, that is $\sigma_{ij} = 0$, Eq(9) implies that $E_{kl}^{(a)} = \alpha_{kl}\theta_a$. Therefore at State 1 the resonator has thermal strains:

$$E_{kl}^{(a)} = \alpha_{kl}\theta_a . \quad \text{Eq(10)}$$

2) Thermal strains at temperature T: State 2

Resonator not bonded: If the resonator is *not bonded* to any substrate it will have negligible stress at any temperature T. The resonator remains stress free, therefore the thermal strains will be like Eq(10) by a similar argument:

$$E_{kl}^{(c)} = \alpha_{kl}\theta \quad \text{where} \quad \theta = (T - T_{ref}) \quad \text{Eq(11)}$$

Eq(11) can also be written as $E_{kl}^{(c)} = \alpha_{kl}\theta_a + \alpha_{kl}\theta_b$

where $\theta_a = (T_{ref\,2} - T_{ref})$ and $\theta_b = (T - T_{ref\,2})$

Or

$$E_{kl}^{(c)} = E_{kl}^{(a)} + E_{kl}^{(b)} \quad \text{Eq(12a)}$$

$$\text{where} \quad E_{kl}^{(a)} = \alpha_{kl}\theta_a \quad \text{Eq(12b)}$$

$$\text{and} \quad E_{kl}^{(b)} = \alpha_{kl}\theta_b \quad \text{Eq(12c)}$$

$E_{kl}^{(a)}$ is the thermal strain at State 1 induced when the temperature changed from T_{ref} to T_{ref2} while $E_{kl}^{(b)}$ is the thermal strain induced in the stress-free resonator when the temperature changed from T_{ref2} to T.

Resonator bonded: If the resonator is *bonded* to a substrate the resonator will have stresses at temperature T, and Eq(12c) is then not valid because with the bonding stress $E_{kl}^{(b)} \neq \alpha_{kl}\theta_b$. It is necessary then to calculate $E_{kl}^{(b)}$ by a finite element software such as COMSOL. Eq(12c) must be amended for the bonded resonator to read:

$$E_{kl}^{(b)} = \text{thermal strains calculated by COMSOL} \quad \text{Eq(12d)}$$

Eq(12b) is still valid since by definition the resonator is stress-free at both temperatures T_{ref} and T_{ref2}.

III. Frequency-Temperature Curves of the Bonded Resonators

The resonator frequency versus temperature profile is calculated by the change in eigenfrequency of the thickness shear mode as a function of the temperature. The eigenvalue problem of the resonator is modeled in COMSOL where Eq(12a) to Eq(12d) are first solved, and followed by the solution of the eigenvalue problem of Eq(5) to (7). We show in Fig. 2 a COMSOL model of a 526 MHz, AT-cut quartz resonator. The resonator is bonded to a silicone strip at the bottom end, and the silicone strip is fixed. The resonator plate is hence mounted like a cantilever plate.

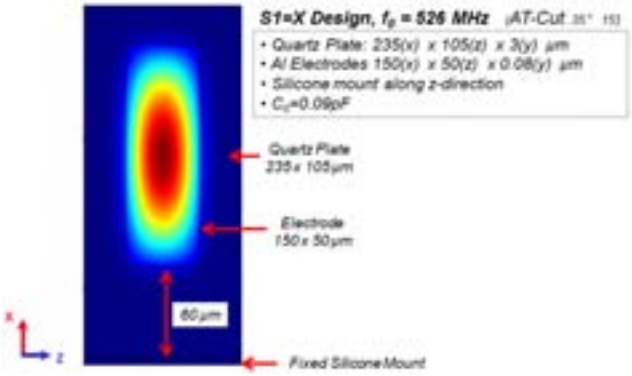

Figure 2. COMSOL of a 526 MHz, AT-cut quartz resonator.

A. *Effects of the mounting stiffness on the frequency-temperature curves.*

The effect of bonding stress on the frequency versus temperature profile (f-T curve) of the resonator is studied by changing the elastic stiffness constant of the silicone strip mount (mounting stiffness) from $2.0\text{x}10^8$ Pa to $2.0\text{x}10^{11}$ Pa and $2.0\text{x}10^{12}$ Pa, respectively. The bonding stress in the resonator depends on the mounting stiffness relative to the elastic stiffness constants of the quartz plate (quartz stiffness). Since the quartz stiffness are in the order of 10^{11} Pa, the bonding stress is negligible when the mounting stiffness is $2.0\text{x}10^8$ Pa. The bonding stress when the mounting stiffness is $2.0\text{x}10^{12}$ Pa will be greater than when the mounting stiffness is $2.0\text{x}10^{11}$ Pa. Figure 3 shows the effect of mounting stiffness on the f-T curves of the AT-cut resonator. The zero-stress temperature T_{ref2} was kept at 25°C. We observe that at higher bonding stress

(higher mounting stiffness), the f-T curves rotate counter clockwise about the 25°C reference temperature point. The f-T curve for mounting stiffness=2.0x10^{12} Pa does not quite cross the other curves at 25°C due to a spurious mode at about -5°C.

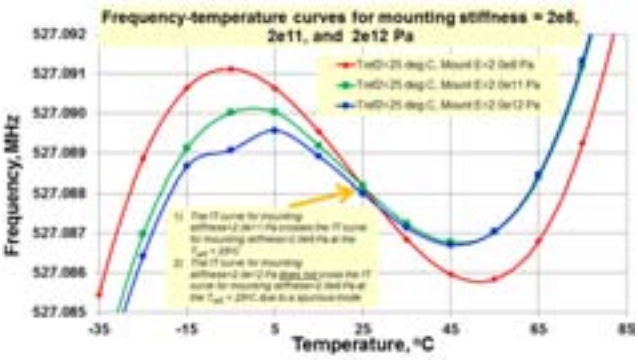

Figure 3. Effect of the bonding stress and mounting stiffness on the f-T curves of the AT-cut resonator.

B. *Effects of the zero-stress temperature T_{ref2} and mounting stiffness on the f-T curves.*

The effects of both the zero-stress temperature and mounting stiffness on the f-T curve of the AT-cut resonator are studied. Figure 4 shows the effect of the zero-stress temperatures 25, 35 and 45°C on the f-T curves when the mounting stiffness is set to 2.0x10^{8} Pa. We see that the three f-T curves mutually coincide. Since the mounting stiffness is about a thousand times smaller than the quartz stiffness there is negligible bonding stress in the resonator. Therefore, there is negligible effect from the change of the zero-stress temperature from 25 to 45°C

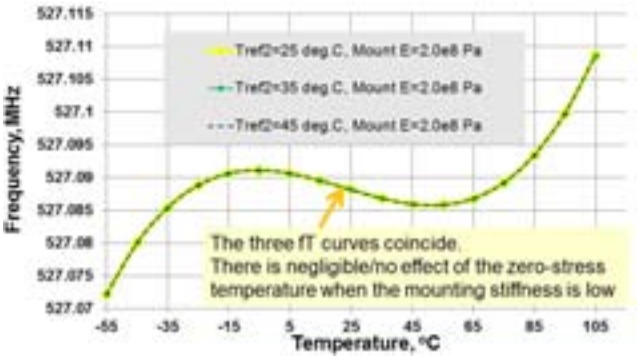

Figure 4. Effect of the zero-stress temperature on the f-T curves when the mounting stiffness = 2.0x10^{8} Pa.

When the mounting stiffness is increased to 2.0x10^{11} Pa we see the presence of bonding stress in the resonator. Figure 5 shows the counter clockwise rotation of the f-T curves for increasing zero-stress temperature when the mounting stiffness is set to 2.0x10^{11} Pa. Also we observe in the figure that the f-T curves for the zero-stress temperatures 25, 35 and 45°C cross the curve for mounting stiffness=2.0x10^{8} Pa at 25, 35 and 45°C, respectively. Since the f-T curve when the mounting stiffness = 2.0x10^{8} Pa represents a resonator without bonding stress, the temperature at which the other frequency-temperature curve intersects it would represent the zero-stress temperature of the resonator with bonding stress. This validates our concept and definition of the zero-stress temperature of a resonator.

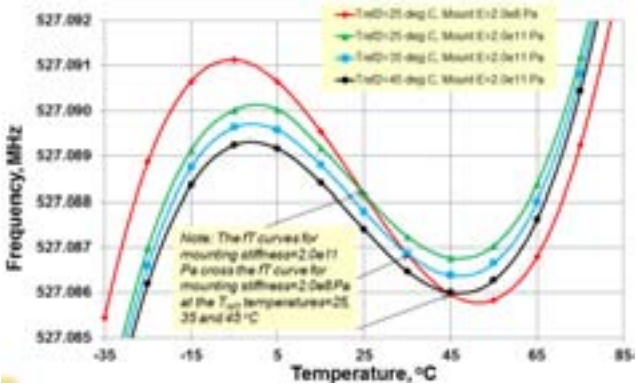

Figure 5. Effect of the zero-stress temperature on the f-T curves when the mounting stiffness = 2.0x10^{11} Pa.

When the mounting stiffness is increased to 2.0x10^{12} Pa the bonding stress is greater than when the mounting stiffness was 2.0x10^{11} Pa. Figure 6 shows the effect of this increased bonding stress on the f-T curves with zero-stress temperatures 25, 35, and 45°C, respectively. There are counter clockwise rotations of the f-T curves. In addition we observe that the increased bonding stress has induced an unwanted mode (spurious mode) at about -5°C which in turn has affected the f-T curves so that they do not cross the f-T curve with mounting stiffness=2.0x10^{8} Pa at their respective zero-stress temperatures. Instead, the f-T curves cross at higher temperatures than their respective zero-stress temperatures. For example the f-T curve of the resonator with mounting stiffness=2.0x10^{12} Pa and zero-stress temperature 45°C crosses the f-T curve with mounting stiffness=2.0x10^{8} Pa at about 50°C

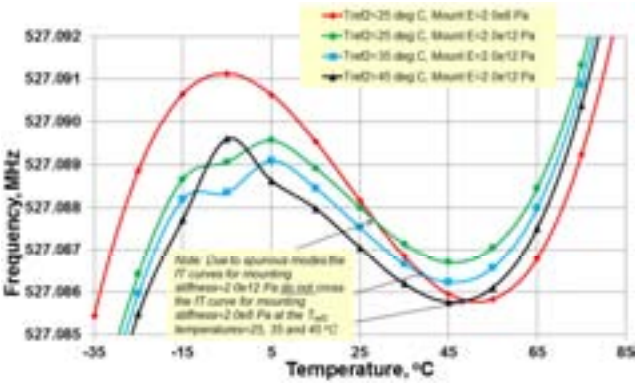

Figure 6. Effect of the zero-stress temperature on the f-T curves when the mounting stiffness = 2.0x10^{12} Pa.

IV. CONCLUSIONS

A set of incremental equations for small vibrations superposed on initial thermal strains, including the zero-stress temperature, was derived and employed to study the effects of mounting stiffness and zero-stress temperature on the frequency-temperature behavior of a UHF quartz resonator. The zero-stress temperature T_{ref2} is the temperature at which the plate resonator is stress-free but *not* strain-free. The zero stress point will be governed by the bonding of the plate, and relaxation after bonding. The mounting supports will create inhomogeneous thermal strains and stresses in the plate as the temperature is changed from T_{ref2}. These strains are a function of the stiffness of the mounting material, mounting geometry and resonator geometry.

The resonator frequency versus temperature profile was calculated by the change in eigenfrequency of the thickness shear mode as a function of the temperature. The eigenvalue problem of the resonator was modeled in COMSOL. With increasing mounting stiffness and zero-stress temperature the frequency-temperature curve of a quartz resonator was shown to rotate counter-clockwise with respect to the frequency-temperature curve of the same resonator with no bonding stress. Furthermore the frequency-temperature curve of a bonded resonator will intersect the frequency-temperature curve of the same resonator without bonding stress at the zero-stress temperature

Relaxation of the inhomogeneous stresses over time can create hysteresis if the resonator is not sufficiently isolated from the mounts. Compared to soft mounts such as rubber or epoxy, hard mounts can create larger rotations of the f-T profiles. Our general analysis can be applied to any resonator geometry and mounting design to optimize the predictability of the f-T curve and minimize hysteresis and aging. This is particularly important for UHF shear-mode device designs where micron-thick quartz plates are utilized.

REFERENCES

[1] John R.Vig “Quartz Crystal Resonators and Oscillators For Frequency Control and Timing Applications - A Tutorial”, April 2012,.

[2] Y-K Yong, M. Patel, M. Tanaka, “Effects of Thermal Stresses on the Frequency-Temperature Behavior of Piezoelectric Resonators”, Journal of Thermal Stresses, Vol. 30, No. 6, June 2007, pp. 639 -661.

[3] P.C.Y. Lee and M.S.H. Tang, "Thickness Vibrations of Doubly Rotated Crystal Plates under Initial Deformations," IEEE Trans. on Ultrasonics, Ferroelectrics, and Frequency Control, UFFC-34 (6) 659, 1987.

[4] R. Bechmann, A. D. Ballato, and T. J. Lukaszek, “Higher-order temperature coefficients of the elastic stiffnesses and compliances of the alpha-quartz”, USAELRDL Technical Report 2261, Sept. 1963.

Dynamic Range Vs Spectral Clarity Trade-off in All-Digital Frequency Synthesis via Single-Bit Sinewave Quantization

Paul P. Sotiriadis
Department of Electrical and Computer Engineering
National Technical University of Athens
Greece
pps@ieee.org

Nikos Stamatopoulos
Department of Electrical and Computer Engineering
National Technical University of Athens
Greece
nstam@ieee.org

***Abstract*—Single-bit Nyquist-rate quantization of sinewaves with amplitude dithering using a sequence of independent and uniformly distributed random variables has been proposed for all-digital RF frequency synthesis generation. This work demonstrates how we can improve the Dynamic Range using non-uniformly distributed dithering by selectively allowing some of the harmonics to be present in the spectrum (vs. the spurs-free output of the uniform distribution.). MATLAB simulation examples illustrate the results of the proposed approach.**

Keywords—Digital-to-frequency converter, direct digital synthesis, frequency spurs, quantization

I. INTRODUCTION

Over the past few years all-digital frequency synthesis has attracted the attention of the R.F.I.C. industry [1]-[3]. This was motivated by the increasing challenge in the design of R.F., analog and mixed-signal related circuit blocks, compared to alternative digital ones, as technologies downscale. Interestingly, efforts towards all-digital frequency synthesizers can be traced at least thirty years back [4]-[6].

Fully digital architectures have been proposed for generating synchronous single-bit digital outputs of sinewave-like spectrum which can be used as local-oscillator signals in RF chains and be amplified for transmission without distortion and with very high efficiency using a switching amplifier.

Here we consider a single-bit-output Nyquist-rate sinewave quantization scheme, discussed in [7]-[8], which is practically realized by a Direct Digital Synthesizer (DDS) with a 1-Bit output Nyquist-rate Digital to Analog Converter (DAC). Dithering is added to the output of the Look-Up-Table (LUT) before the single-bit quantization to alleviate the frequency spurs by breaking the periodicity of the truncation error.

It has been shown in [7]-[8] that uniform dithering of appropriate range completely eliminates the spurs. This paper illustrates that by selectively allowing some output harmonics we can reduce the noise floor level and improve the dynamic range of the output.

II. ABSTRACT ARCHITECTURE AND DEFINITIONS

It is a common practice to use random dithering to suppress the frequency spurs of quantization in DDS [9]-[10] and data converters [11]. Here we consider the extreme case of a DDS with Nyquist-rate single-bit output quantization and amplitude dithering as shown in Figure 1. Sequence $\cos(\Omega k)$ can be generated by a phase accumulator and a LUT. The Zero Order Hold (ZOH) provides the continuous-time single-bit digital waveform output and all blocks are clocked by a reference clock of frequency $f_S = 1/T_S$.

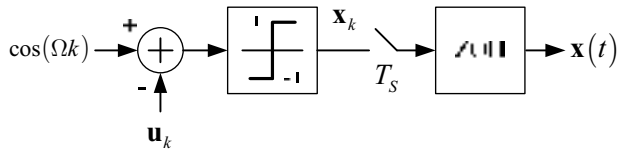

Figure 1: Dithered single-bit quantization of a sinewave

Let $\Omega = 2\pi w/q$ for some integers w and q such that $0 < w < q/2$. It is not necessary that q is a power of 2. Random dithering sequence $\{\mathbf{u}_k\}$ is subtracted from $\cos(\Omega k)$ resulting in the discrete-time single-bit (± 1) signal

$$\mathbf{x}_k = \operatorname{sgn}\left(\cos\left(2\pi wk/q\right) - \mathbf{u}_k\right). \tag{1}$$

We assume that $\{\mathbf{u}_k\}$ is composed of independent and identically distributed (IID) random variables of cumulative density function (CDF) $G:[-1,1]\to[0,1]$ with continuous second derivative. It is of course $\Pr(\mathbf{u}_k \le u) = G(u)$. Also, it is convenient for our analysis to express the CDF G as a series of Chebyshev polynomials of the first kind, i.e.,

$$G(u) = \frac{1}{2} + \frac{1}{2}\sum_{j=0}^{\infty} a_j T_j(u). \tag{2}$$

where the summand and multiplier $1/2$ are used to simplify the algebra. Coefficients a_j are derived according to [8], [12].

Inversely, CDF G can be defined using Eq. (2). Assuming the series in (2) converges appropriately and is term-by-term differentiable, G is a CDF if and only if $G(-1)=0$, $G(1)=1$ and $G'(u)\geq 0$ for every $u\in[-1,1]$. These three conditions can be expressed as

$$\sum_{j=0}^{\infty}(-1)^j a_j=-1 \quad , \quad \sum_{j=0}^{\infty}a_j=1 \tag{3}$$

and

$$\sum_{j=1}^{\infty} j a_j U_{j-1}(u)\geq 0 \qquad \forall u\in[-1,1] \tag{4}$$

using the fact that $T_j(\pm 1)=(\pm 1)^j$ for every $j=0,1,2,...$, and $T_j'(u)=j\cdot U_{j-1}(u)$, for $j=1,2,3,...$, where U_j is the j-th Chebyshev polynomial of the 2nd kind [12].

III. Output Spectrum

Under the assumption that the dithering sequence $\{\mathbf{u}_k\}$ is composed of IID random variables, the discrete-time sequence $\{\mathbf{x}_k\}$ is formed of independent but not identically distributed random variables. The distribution of $\mathbf{x}_k$ is a periodic function of $k\in\mathbb{Z}$ of period equal to q or a divisor of it. Therefore $\{\mathbf{x}_k\}$ is cyclostationary of period q. In this case it is common [13]-[14] to define the *period-average* autocorrelation function $\overline{r}_x(k)=\left(\sum_{m=0}^{q-1} r_x(k+m,m)\right)/q$, where $r_x(n,m)=E\{\mathbf{x}_n\mathbf{x}_m\}$; then, use $\overline{r}_x(k)$ to define the PSD of $\{\mathbf{x}_k\}$ as the discrete-time Fourier Transform of it, i.e., $s_x(\omega)=\sum_{k=-\infty}^{\infty}\overline{r}_x(k)e^{-ik\omega}$.

The ZOH in Figure 1 converts the discrete-time sequence $\{\mathbf{x}_k\}$ into the continuous-time signal

$$\mathbf{x}(t)=\sum_{k=-\infty}^{\infty}\mathbf{x}_k p(t/T_S-k) \tag{5}$$

where $T_S=1/f_S$ is the sampling period and $p(t)$ is the pulse equal to 1 for $t\in[0,1)$ and zero otherwise corresponding to ZOH's operation. The PSD of the continuous-time signal $\mathbf{x}(t)$ can be expressed [8] using $s_x(\omega)$ as

$$S_x(f)=T_S\cdot\mathrm{sinc}^2(f\cdot T_S)\cdot s_x(2\pi f T_S). \tag{6}$$

The following Theorem, [8], based on the above definitions provides the means to calculate analytically the PSD $S_x(f)$.

Theorem: Based on the aforementioned definitions and assumptions, if $\gcd(w,q)=1$ then the PSD of $\mathbf{x}(t)$ is

$$S_x(f)=\mathrm{sinc}^2\left(\frac{f}{f_S}\right)\cdot\left(\ S_{HA}(f)+S_N(f)+S_{DC}(f)\ \right) \tag{7}$$

where the HArmonics, Noise and DC components are

$$S_{HA}(f)=\frac{1}{4}\sum_{h=1}^{\infty}b_h\left(\delta\left(f-\frac{h}{q}f_S\right)+\delta\left(f+\frac{h}{q}f_S\right)\right), \tag{8}$$

$$S_N(f)=\frac{1}{f_S}\cdot\left(1-a_0^2-\frac{1}{2}\sum_{j=1}^{\infty}a_j^2\right), \tag{9}$$

and

$$S_{DC}(f)=\frac{b_0+3a_0^2}{4}\delta(f) \tag{10}$$

respectively. The power of the frequency components at $\pm(h/q)f_S$, $h=0,1,2,...$ in Eq. (8) is $b_h/4$ and

$$b_h\triangleq\sum_{r=-\infty}^{\infty}a_{I(h,r)}^2 \tag{11}$$

where $I(h,r)=|j_1 h+qr|$; constant j_1 (and k_1 which is not used in the expression) is derived solving the Diophantine equation $wj_1+qk_1=1$. Specifically, coefficient b_w of the frequency components at $\pm(w/q)f_S$ is $b_w=\sum_{r=-\infty}^{\infty}a_{|1+qr|}^2$. □

The application of the Theorem is illustrated in the following sections.

IV. DR and the Trade-Off With Spectral Clarity

In most practical cases the desirable frequency component is the one at $\pm(w/q)f_S$ with amplitude $\mathrm{sinc}^2(f/f_S)\cdot b_w/4$, captured by $S_{HA}(f)$ in Eq. (8). The output noise level has PSD $\mathrm{sinc}^2(f/f_S)\cdot S_N(f)$ captured by Eq. (9). We define the Dynamic Range (DR) as the ratio of the desirable signal's power to noise's PSD, $DR=10\log_{10}\left(\frac{\mathrm{sinc}^2(f/f_S)\cdot b_w/4}{\mathrm{sinc}^2(f/f_S)\cdot S_N(f)}\right)$, in (dB), which replacing the values of b_w and $S_N(f)$ becomes

$$DR=10\log_{10}\left(\frac{\sum_{r=-\infty}^{\infty}a_{|1+qr|}^2}{1-a_0^2-\sum_{j=1}^{\infty}\frac{a_j^2}{2}}\right)+10\log_{10}(f_S)-6.02 \quad \text{(dB)} \tag{12}$$

Note that the summand $10\log_{10}(f_S)$ in Eq. (12) should be expected because the power of the sinewave's quantization error is spread over the whole frequency bandwidth which is proportional to the sampling frequency.

A. Case 1: Uniformly Distributed CDF G

We consider first the case of dithering sequence $\{\mathbf{u}_k\}$ with *uniformly distributed* IID random variables, i.e. constant probability density $G'(u)=1/2$ in $[-1,1]$ and CDF given by $G(u)=(u+1)/2$. Observing Eq. (2) and using the fact that $T_1(u)=u$ we get $a_0=0$, $a_1=1$ and $a_k=0$ for $k=2,3,4,...$.

Now we apply the Theorem for a pair of integers w and q with $0 < w < q/2$ and $\gcd(w,q) = 1$. Since only $a_1 = 1$ is nonzero, for b_h, $h = 0,1,2,...$ to be nonzero there must exist an integer $r \in \mathbb{Z}$ such that

$$I(h,r) = |j_1 h + qr| = 1 \qquad (13)$$

Since (j_1, k_1) is a solution of the Diophantine equation $wj_1 + qk_1 = 1$ the general solution of Eq. (13) is

$$(h,r) = \pm(w,k_1) + \rho(q,-j_1),\ \rho \in \mathbb{Z} \qquad (14)$$

and since $0 \le w < q$, the nonnegative values of h are $h = w + \rho q$ for $\rho = 0,1,2,...$ and $h = -w + \rho q$ for $\rho = 1,2,...$. We conclude that the only nonzero coefficients b_h, $h = 0,1,2,...$ are b_w and $b_{\eta \cdot q \pm w}$ for $\eta = 1,2,3,...$ giving

$$S_{HA}(f) = \frac{1}{4} \sum_{\substack{h=w,\ \eta \cdot q \pm w \\ \eta = 1,2,3,...}} \left(\delta\left(f - \frac{h}{q} f_S \right) + \delta\left(f + \frac{h}{q} f_S \right) \right),$$

$S_N(f) = 1/(2f_S)$ and $S_{DC}(f) = 0$ respectively. So the only two frequency components in the frequency range $[0, f_S]$ are at $(w/q) f_S$ and its image at $(1 - w/q) f_S$. This is true in general for integers w and q satisfying our assumptions. Therefore uniform CDF G leads to spurs-free output.

For example if $w = 25$ and $q = 64$ then the only nonzero coefficients are b_{25} and $b_{\eta \cdot 64 \pm 25}$ for $\eta = 1,2,3,...$. Moreover $b_{25} = b_{\eta \cdot 64 \pm 25} = 1$, $\eta = 1,2,3,...$ .The results are confirmed by the PSD in Figure 2 derived using simulation, where the weighting factor $\text{sinc}^2(fT_S)$ is ignored.

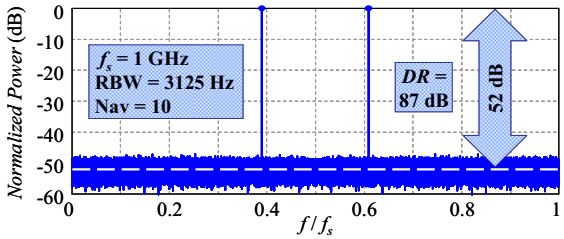

Figure 2: Spectrum of single-bit quantized sinewave with uniformly distributed dither when $w = 25$ and $q = 64$; the weighting factor $\text{sinc}^2(f/f_S)$ is ignored. $f_S = 1\,GHz$, Resolution BW = 3125 Hz and waveform averaging Nav=10 runs.

Two more cases of simulated PSD when $a_0 = 0$, $a_1 = 1$ and $a_k = 0$ for $k = 2,3,4,...$ are shown in Figures 3 and 4 for different values of w, q, f_s and waveform averaging runs Nav. As expected from the Theorem the spectra are spurs-free.

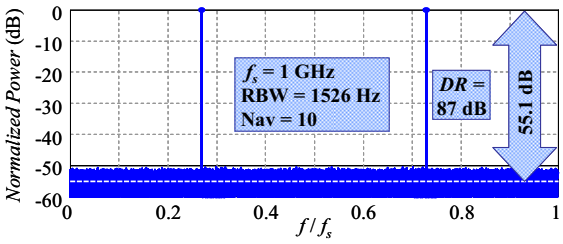

Figure 3: PSD of simulated random sequence $\{\mathbf{x}_k\}$ when $a_0 = 0$, $a_1 = 1$ and $a_k = 0$, $k = 2,3,4,...$; $w = 17723$, $q = 2^{16}$; $f_S = 1\,GHz$, Resolution BW = 1526 Hz and waveform averaging Nav=10 runs.

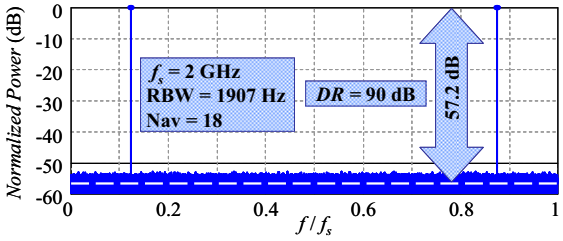

Figure 4: PSD of simulated random sequence $\{\mathbf{x}_k\}$ when $a_0 = 0$, $a_1 = 1$ and $a_k = 0$, $k = 2,3,4,...$; $w = 2^{16} - 1$, $q = 2^{19}$; $f_S = 2\,GHz$, Resolution BW = 1907 Hz and waveform averaging Nav=18 runs.

The dynamic range for the case of $a_0 = 0$, $a_1 = 1$ and $a_k = 0$ for $k = 2,3,4,...$, is derived from Eq. (12) to be

$$DR = 10\log_{10}(f_S) - 3.01 \text{ dB} \qquad (15)$$

In the PSD of the case $w = 25$ and $q = 64$ in Figure 2 the dashed white line indicates the averaged noise floor power. For $f_S = 1\,GHz$ we get $DR \cong 87$ dB. Subtracting $10\log_{10}(RBW)$ dB, where $RBW = 3125\,Hz$, to account for the resolution BW used for the simulation we get a very good match to the simulated 52 dB (Figure 2). Similarly for the case $w = 17723$ and $q = 2^{16}$ in Figure 3 where again Eq. (15) gives $DR \cong 87$ dB and after subtracting $10\log_{10}(RBW) \cong 32$ we get about 55 dB (Figure 3). Similarly in the case in Figure 4.

B. *Case 2: $a_1, a_3 \neq 0$ & All Other Coefficients a_k are Zero*

Suppose now that $a_1, a_3 \neq 0$ and all other coefficients a_k are zero then since $T_1(u) = u$ and $T_3(u) = 4u^3 - 3u$ we have $G(u) = \frac{1}{2} + \frac{a_1}{2}u + \frac{a_3}{2}(4u^3 - 3u)$ from Eq. (2). For G to be a CDF Eqs. (3) and (4) must hold implying $a_1 + a_3 = 1$ and $2G'(u) = a_1 + a_3(12u^2 - 3) \ge 0$ for every $u \in [-1,1]$.

Note that function $2G'(u)$ achieves its minimum either at $u = 0$ or at $u = \pm 1$ so $G'(u) \ge 0$ for every $u \in [-1,1]$ if and only if $a_1 - 3a_3 \ge 0$ and $a_1 + 9a_3 \ge 0$. Therefore G is a CDF if and only if $a_1 + a_3 = 1$, $a_1 + 9a_3 \ge 0$ and $a_1 - 3a_3 \ge 0$. The solution is $a_1 = (6 + 3\rho)/8$ and $a_3 = (2 - 3\rho)/8$, $\rho \in [0,1]$.

Assuming $q>4$ implies $\sum_{r=-\infty}^{\infty} a_{|1+qr|}^2 = a_1^2$ and Eq. (12) gives $DR = 10\log_{10}\left(\frac{2a_1^2}{2-\left(a_1^2+a_3^2\right)}\right)+10\log_{10}\left(f_S\right)-6.02$ dB. Using the expressions of a_1 and a_3 above, DR becomes a strictly increasing function of ρ with maximum value $DR = 10\log_{10}\left(f_S\right)-0.55$ (dB) for $\rho=1$, corresponding to $a_1 = 9/8$ and $a_3 = -1/8$. In this case the DR is about 2.5 dB higher than in Case I but the 3rd harmonic is present here as shown in the following.

For $w=25$ and $q=64$ the simulated PSD is shown in Figure 5. Applying the Theorem again we conclude that the only frequencies in the spectrum $(0, f_S)$ are at $(25/64)f_S$ and $(1-25/64)f_S$ corresponding to the fundamental and its image as well as $(-1+3\cdot 25/64)f_S$ and $(2-3\cdot 25/64)f_S$ corresponding to the 3rd harmonic and its image. Moreover for $h=0,1,2,...,63$ the only nonzero b_h are $b_{25}=(9/8)^2$, $b_{39}=(9/8)^2$, $b_{11}=(1/8)^2$ and $b_{53}=(1/8)^2$ corresponding to frequencies above. Results agree with simulation in Figure 5.

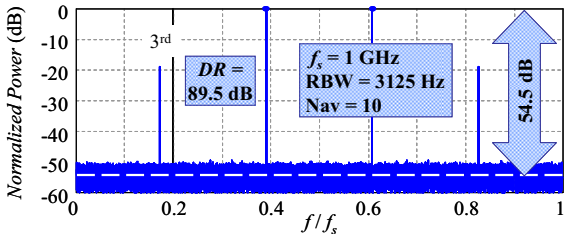

Figure 5: PSD of simulated random sequence $\{\mathbf{x}_k\}$ when $a_1 = 9/8$, $a_3 = -1/8$ and all other coefficients $a_k = 0$; $w=25$ and $q=64$

C. *Case 3: $a_1, a_3, a_5 \neq 0$ & All Other Coefficients a_k are Zero*

The case of $a_1, a_3, a_5 \neq 0$ with all other coefficients a_k zero implies $G(u) = \frac{1}{2}+\frac{a_1}{2}T_1(u)+\frac{a_3}{2}T_3(u)+\frac{a_5}{2}T_5(u)$ which is a CDF if and only if $a_1+a_3+a_5=1$ and $2G'(u) = 80a_5u^4+(12a_3-60a_5)u^2+a_1-3a_3+5a_5 \geq 0$ for all $u\in[-1,1]$.

The derivation of (a_1, a_3, a_5) maximizing DR is more involved than before. It turns out that the maximum is achieved for $a_1 = 1.1906$, $a_3 = -0.2375$, $a_5 = 0.0469$ and all other coefficients a_k zero; $DR = 10\log_{10}\left(f_S\right)+1.31$ (dB), i.e. about 4.3 dB higher than with uniformly distributed dither in Case I.

For $w=25$ and $q=64$ the simulated PSD is shown in Figure 6. The fundamental the 3rd and the 5th harmonics and their images are the only components in the spectrum, which can be shown using the Theorem as well.

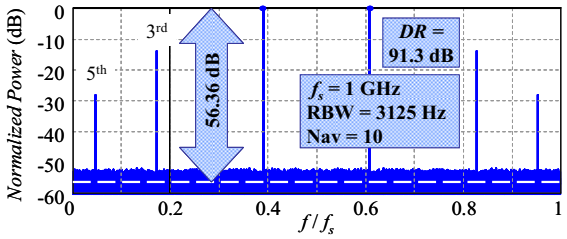

Figure 6: PSD of simulated random sequence $\{\mathbf{x}_k\}$ when $a_1 = 1.1906$, $a_3 = -0.2375$, $a_5 = 0.0469$, all other coefficients $a_k = 0$; $w=25$, $q=64$

V. CONCLUSIONS

Single-bit, Nyquist-rate quantization of sinewave with additive random dithering formed of independent and identically distributed random variables has been discussed as a means for all-digital frequency synthesis. Using the uniformly distributed dither, resulting in spurious free output, as a reference, other distributions have been considered in an effort to increase the dynamic range by trading-off the presence of selected harmonics in the output for lower output noise floor. An improvement of about 4.3 dB has been shown when the third and fifth harmonics are allowed to be present. Examples based on MATLAB simulation have been discussed illustrating the presented theory.

REFERENCES

[1] R.B. Staszewski, "State-of-the-art and future directions of high-performance all-digital frequency synthesis in nanometer CMOS", IEEE Trans. Cir. and Sys. I, Vol. 58, Iss. 7, 2011, pp. 1497-1510.

[2] H. Mair and L. Xiu, "An architecture of high-performance frequency and phase synthesis," IEEE J. Solid-State Circuits, vol. 35, no. 6, pp. 835–846, Jun. 2000.

[3] Paul P. Sotiriadis, Kostas Galanopoulos, "Direct All-Digital Frequency Synthesis techniques, Spurs Suppression and Deterministic Jitter Correction", IEEE Trans. on Circuits and Systems-I, Volume: 59 , Issue: 5, Pages: 958 – 968, May 2012.

[4] V.S. Reinhardt, "Direct digital synthesizers", Technical Report, Hughes Aircraft Co, Space and Communications Group, L.A., CA, Dec. 1985.

[5] C. E. Wheatley, III, "Digital frequency synthesizer with random jittering for reducing discrete spectral spurs," U.S. Patent 4410954, Oct. 1983.

[6] V. N. Kochemasov and A. N. Fadeev, "Digital-computer synthesizers of two-level signals with phase-error compensation," Telecommun. Radio Eng., vol. 36/37, pp. 55–59, Oct. 1982.

[7] P. Sotiriadis, N. Stamatopoulos, "All-Digital Frequency Synthesis based on Single-Bit Nyquist-Rate Sinewave Quantization with IID Random Dithering", to appear in the IEEE Int. Freq. Control Symp. 2013.

[8] P. Sotiriadis, N. Miliou, "Single-Bit Digital Frequency Synthesis via Dithered Nyquist-rate Sinewave Quantization", to appear in the IEEE Trans. on Circuits and Systems-I (TCAS-I 13452).

[9] J. Vankka and K. Halonen, *Direct Digital Synthesizers: Theory, Design and Applications,* New york, Springer 2006.

[10] U.L. Rohde, *Microwave and Wireless Synthesizers: Theory and Design*, 1st ed. Singapore: Wiley-Interscience, 1997.

[11] J.C. Candy (Ed.), G.C. Temes (Ed.), *Oversampling Delta-Sigma Data Converters: Theory, Design, and Simulation*, Wiley-IEEE Press, 1991.

[12] J.P. Boyd, *Chebyshev and Fourier Spectral Methods*, Dover Publications, 2nd Ed., 2001

[13] J.G. Proakis, M. Salehi, *Digital Communications*, 5th Ed., McGraw-Hill Companies,Inc. , 2007.

[14] R.M. Gray, "Quantization noise spectra", *IEEE Trans. Information Theory, Vol.* 36, Iss. 6, 1990, pp. 1220-1244.

Measuring an Optical Frequency Difference of Semiconductor Lasers Based on Coherent Detection and Frequency Dividers

Łukasz Buczek
AGH, University of Science and Technology
Krakow, Poland
lbuczek@agh.edu.pl

***Abstract*—Currently a number of electronic components capable of processing multi-GHz electrical signals are available on the market. This allows building a system for measuring the difference of optical frequencies of two semiconductor lasers, exploiting high-speed photodiode and frequency prescalers and based on coherent detection and down-conversion.**

Keywords—semiconductors laser; coherent detection; down-conversion; high-speed frequency prescalers

I. INTRODUCTION

There is a group of applications useing semiconductor lasers with optical frequencies separated by tens of GHz [1-5]. In these cases, we usually need a method for precise measurements of the difference of optical frequencies. Using of high-speed electronic components allow building a system for measuring the difference of optical carrier frequencies of two semiconductor lasers, exploiting photodiode and frequency prescalers and base on coherent detection and down-conversion. The proposed system may be used for measuring of difference of the optical frequency semiconductor laser in fiber optic time and frequency dissemination system exploiting two closely spaced laser transmitters [5,6]. This system may be useful also for characterizing ultra-dense WDM laser sources [2,3]. Analysis of the measurement results would be helpful to determine the difference of optical frequencies and its fluctuation.

II. THE MEASUREMENT SYSTEM

The block diagram of proposed system is presented in Fig. 1. Two optical signals from distributed feedback (DFB) semiconductor lasers are supplied to a high-speed photodiode. State of polarization (SOP) of the optical signal of one of them may be controlled. Resulting beat-note with the frequency equal to the difference of the laser carriers is further processed by a set of high-speed prescalers. They divide the frequency of signal to the value low enough for counting by the system based on a field programmable gate array (FPGA) and a microcontroller. In the first stage prescaler divides by 8 and operates up to 18GHz. Prescaler in the second stage may be slower than in the first stage and its division ratio may be programmable.

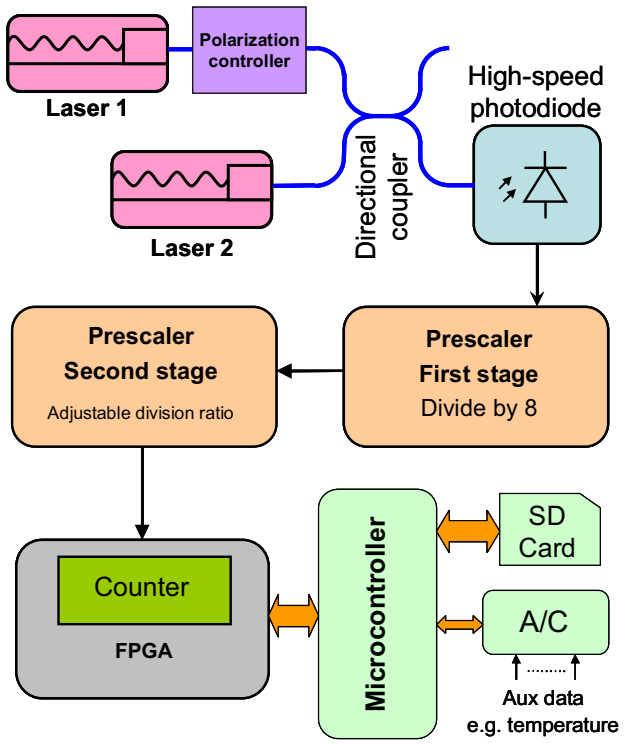

Fig1. Idea of measuring the difference of semiconductor lasers carrier frequencies using high-speed prescalers.

A frequency counter and communication interface with a microcontroller is implemented in FPGA circuit. Microcontroller supports typical SD memory card and multi-channel analog to digital converter. Measurements results of the difference of optical frequencies are recorded onto standard SD memory cards. At the same time it is possible record any analog signal, other parameters as laser current and ambient temperature and so on. Described measurement system allows taking up to some hundred measurements per second for a period determined by capacity of the memory card.

The efficiency of the beating process is directly affected by the state of polarization (SOP) of optical signals that beat in the photodiode. In the worst case of orthogonal polarization the output signal will disappear. Thus the SOP should be controlled to ensure the robust operation of the system.

The prototype system was designed to operate with the frequencies up to 18 GHz that corresponds to the wavelength difference of the lasers up to 0.14 nm. Using currently available technology this difference may be easily extended to 26 GHz (i.e. 0.2 nm).

III. Verification of the Presented System

A verification was performed by comparing results obtained using presented system with results from a real time spectrum analyzer. The block diagram of the verification method is presented in Fig. 2.

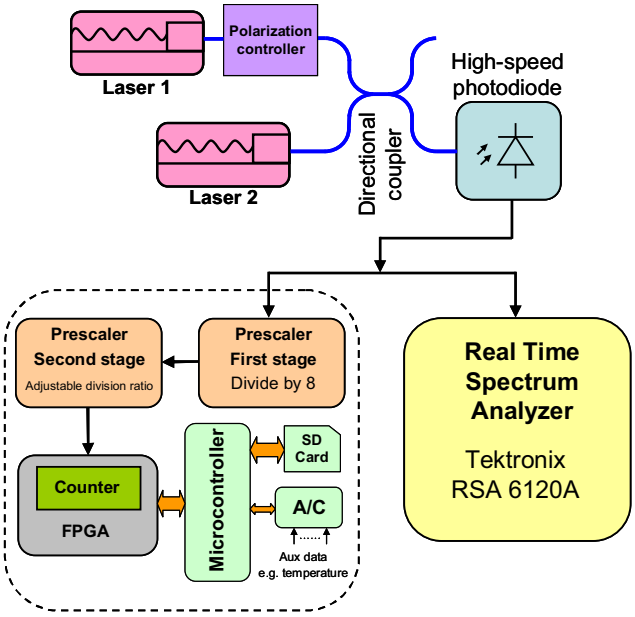

Fig2. Block diagram of the verification method of the presented system

In the presented method of verification, electrical signal from the photodiode is simultaneously supplied to system with prescaler and to the real time spectrum analyzer Tektronix RSA 6120A. Obtained result of measurement should by same on both measurement methods. During the verification lasers were stabilized using simple method based on internal thermistor. Measurement results obtained using real time spectrum analyzer is presented in Fig. 3. Measurement results obtained using described system is presented in Fig. 4. Comparison of the measurements results confirm usefulness of the described system for measuring difference of the optical frequencies of the semiconductor lasers.

This work was supported by Faculty of Computer Science, Electronics and Telecommunications under the decision 15.11.230.079

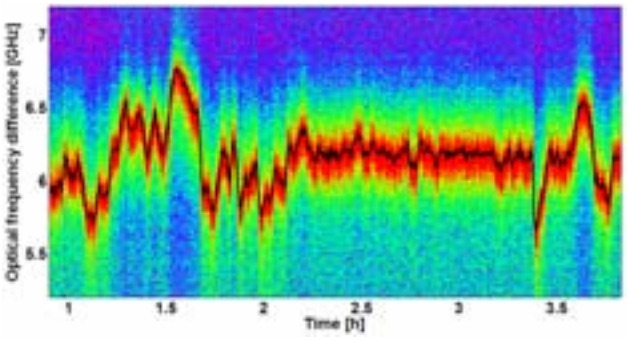

Fig3. Measurement results obtained using real time spectrum analyzer (black line is peak of spetrogram)

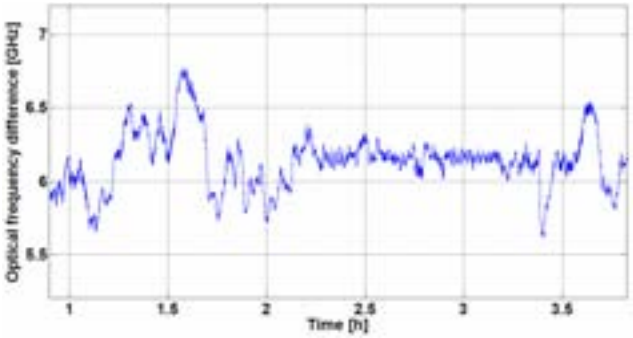

Fig4. Measurement results obtained using presented system based on prescaler and down-conversion

IV. Exmple Measurement

An example of 10-day record showing the relative stability of two telecommunication-grade DFB lasers stabilized using Fabry-Perot etalons and fluctuations of ambient temperature are presented in Fig. 5

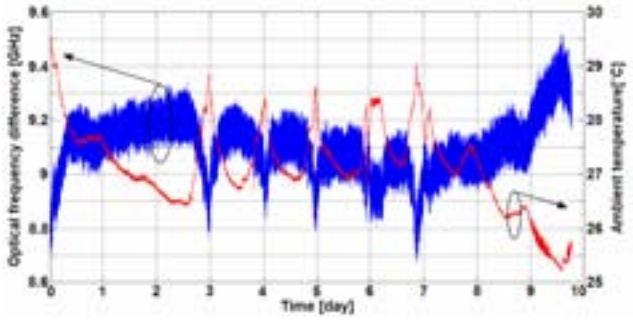

Fig5. The record of 10-days measurement of frequency difference of two DFB lasers stabilized using Fabry-Perot etalons.

In this measurement one can observe a strong correlation between difference of optical frequencies of the two semiconductor lasers and fluctuations of the ambient temperature.

V. CONCLUSION

Advantages of the presented system are simplicity, small size and relatively low cost. Small size allow to use the system as part of another system such as fiber optic time and frequency dissemination system. Comparison of the measurements method confirm usefulness of the described system for measuring the difference of the optical frequencies of the semiconductor lasers.

REFERENCES

[1] D. Piester, H. Schnatz, "Novel techniques for remote time and frequency comparisons", PTB-Mitteilungen, 2009 119 33–44

[2] Y.Yamada, SI.Nakagawa, K.Takashina, et al, "25 GHz spacing ultra-dense WDM transmission experiment of 1Tbit/s (100WDM x 10Gbit/s) over 7300km using non pre-chirped RZ format", ELECTRONICS LETTERS, 1999 Vol. 35 Iss. 25

[3] S. Kim, J. Lee, K. Ra, "Simultaneous beat-frequency locking of conventional and ultra-dense WDM channels using a modulated tunable-laser source", ELECTRONICS LETTERS, 2004 Vol. 40 Iss. 13

[4] O.Lopez, A.Amy-Klein, C.Daussy, C.Chardonnet, F.Narbonneau, M.Lours, G.Santarelli, "86-km optical link with a resolution of 2 × 10-18 for RF frequency transfer", THE EUROPEAN PHYSICAL JOURNAL D, 2008, 48 (1) 35-41

[5] Ł. Śliwczyński, P. Krehlik, A. Czubala, Ł. Buczek, M. Lipiński , „Dissemination of time and RF frequency via a stabilized fibre optic link over a distance of 420 km”, Metrologia , 2013 vol. 50 nr 2

[6] Ł. Śliwczyński, P. Krehlik, Ł. Buczek, M. Lipiński , „Frequency transfer in electronically stabilized fiber optic link exploiting bidirectional optical amplifiers” , IEEE Transactions on Instrumentation and Measurement , 2012 vol. 61 no. 9

A 15 mW, 4.6 GHz Frequency Synthesizer ASIC with -85 dBc/Hz at 2 kHz for Miniature Atomic Clocks

Yazhou Zhao, Steve Tanner and Pierre-André Farine
Electronics and Signal Processing Laboratory
Ecole Polytechnique Fédérale de Lausanne (EPFL)
2000 Neuchatel, Switzerland
yazhou.zhao@epfl.ch

Luc Schneller, Florian Gruet, Christoph Affolderbach, and Gaetano Mileti
Laboratoire Temps-Fréquence (LTF)
University of Neuchatel
2000 Neuchatel, Switzerland

***Abstract*—In this paper, we present the characterization results of an optimized 4.6 GHz frequency synthesizer ASIC targeted for miniature atomic clock applications. Fabricated into a 130 nm RF CMOS process, the circuit occupies an active area of 2 mm^2 and consumes 15 mW of power. The measured phase noise is about -85 dBc/Hz in the range of 2 kHz to 100 kHz frequency offset from the carrier. The circuit was used as RF synthesizer in an experimental cesium atomic clock setup. The obtained clock stability of 5×10^{-11} at $\tau = 1$ second corresponds to the stability obtained with a laboratory synthesizer on the same setup, and is limited by the signal-to-noise ratio of the detected CPT signal. The theoretical stability limit due to the ASIC phase noise is $2\times10^{-11}\,\tau^{-1/2}$, which is not limiting the measured clock stability.**

Keywords—microwave, synthesizer, ASIC, PLL, low power, low phase noise, atomic clock.

I. INTRODUCTION

We have previously reported on the preliminary development and evaluation of a 4.6 GHz frequency synthesizer CMOS ASIC for miniature atomic clocks based on Coherent Population Trapping (CPT) in micro-fabricated Cs vapor cells [1]. The circuit consumes around 15 mW and features a frequency resolution better than 10^{-13}.

For guaranteeing the lowest power consumption and the smallest dimension for miniature atomic clock systems [2], an application specific integrated circuit (ASIC) is the best choice for frequency synthesis, compared to commercial frequency synthesizers. In [1], the frequency synthesizer ASIC is built around a fractional-N phase-locked loop (PLL). It consists of a low power, low phase noise voltage-controlled oscillator (LC-VCO). The VCO is buffered by a high-efficiency power amplifier (PA) with programmable output power level. A programmable divider controlled by a 3rd-order, 40-bit MASH sigma-delta modulator (SDM) is used to provide sub-mHz frequency tuning steps at the 4.6 GHz carrier output.

A 20 MHz voltage-controlled quartz oscillator (VCXO) provides the PLL reference frequency. The PLL bandwidth is typically 300 kHz. The chip is implemented in a 130 nm RF CMOS process, and is powered at 1.2 Volt. Fig. 1 shows the block diagram of the PLL ASIC.

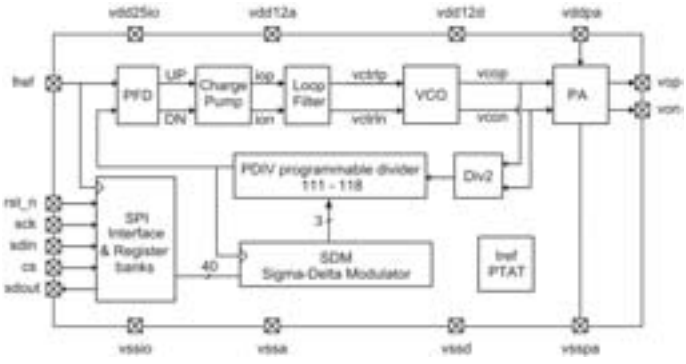

Figure 1. Schematic block diagram of the PLL ASIC [1].

II. DESIGN OPTIMIZATION

Compared to the initial design [1], the ASIC in this paper was optimized at the layout level. Since the on-chip digital switching noise was verified to be an important noise source in the initial design, resulting in degraded PLL phase noise by substrate coupling, efforts were made in this current circuit to reduce the effect of on-chip digital noise. Three techniques were applied:

1. Guard rings around all the digital blocks, including the SDM, programmable divider, phase/frequency detector and charge pump.

This work was funded by the EU 7th framework program FP7, under contract no. 224132 (MAC-TFC project www.mac-tfc.eu). Work at LTF was also supported by the Swiss National Science Foundation (grants no. 200020_140681 and Sinergia CRSI20_122693).

2. Increased decoupling capacitors on the digital power supply, to filter switching peaks.
3. Improved reference frequency input pad. In the first design, a digital input buffer was used, with a dynamic level shifter for conversion between IO voltage (2.5 Volt) and core voltage (1.2 Volt). This circuit showed poor noise performance, and was adding jitter on the reference clock signal. It was then replaced by an analog-wire pad with no level-shifter.

III. Phase Noise Measurement

The phase noise performance of the optimized ASIC synthesizer was measured using a phase noise measurement system (model NMS by Spectradynamics inc. [3]). A commercial laboratory-type frequency generator was used as a noise reference, showing a phase-noise performance of less than -100 dBc/Hz at 1 kHz offset from the 4.6 GHz carrier and down to -123 dBc/Hz in the frequency band of 10 kHz to 100 kHz, which is our frequency range of interest for atomic interrogation.

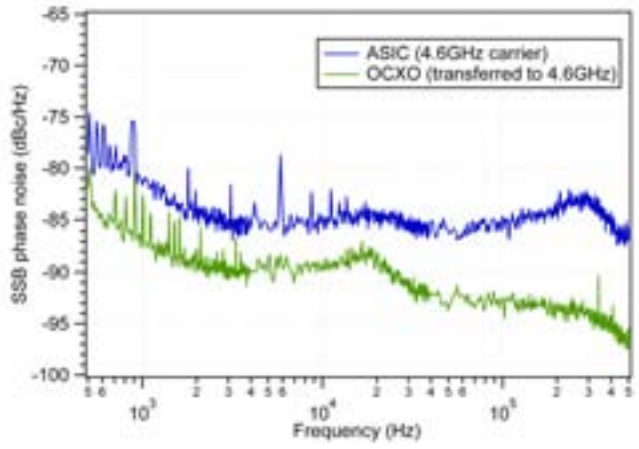

Figure 2. Measured phase noise of the ASIC at 4.6 GHz carrier (blue upper trace) and of the 20 MHz VCXO (transferred to 4.6 GHz, green lower trace).

Fig. 2 reports the measured single-sideband phase-noise of the ASIC synthesizer at 4.6 GHz, reaching ≈ -85 dBc/Hz in the band of interest from 2 kHz to 100 kHz (upper, blue trace). This phase-noise level is only slightly higher (4 to max 10 dB higher) than the phase-noise of the 20 MHz thermally-compensated quartz oscillator (TCVCXO) transferred to 4.6 GHz carrier (lower, green trace). This result proves the good phase-noise performance of the synthesizer ASIC, and especially the improvement compared to the initial circuit, which showed a phase noise of -77 dBc/Hz @ 2 kHz offset and -83 dBc/Hz @ 100 kHz offset from the carrier.

IV. Clock Stability Tests

The performance of the ASIC used as RF frequency synthesizer in an atomic clock was evaluated on an experimental atomic clock setup based on coherent population trapping (CPT) [4] as described in [5]. A distributed feed-back (DFB) laser diode was used, emitting laser radiation at 894.6 nm, in resonance with the Cs D1 optical transition. A fiber-coupled electro-optical modulator (EOM) driven at half of the Cs hyperfine splitting (i.e. at 4.6 GHz) was used to create modulation sidebands, of which the positive and negative first-order sidebands were used to induce the CPT effect in a thermal Cs vapor contained in a micro-fabricated cell [6]. The Cs cell was held in a physics package providing a stable temperature, and well-controlled magnetic field conditions. The signal from a photo-detector placed behind the physics package was demodulated at $f_m \approx 1$ kHz using a lock-in amplifier and subsequently used to steer the frequency of a 20 MHz TCVCXO that serves as frequency reference for the microwave synthesizer providing the 4.6 GHz frequency driving the EOM.

Two configurations of quartz oscillator and microwave synthesizer were used in this study. The reference configuration consists of a laboratory-type low-noise frequency synthesizer (spectradynamics inc., model CS-1) including both a 5 MHz quartz oscillator and the 4.6 GHz synthesizer itself [3]. This synthesizer shows a phase noise at 4.6 GHz carrier of -113 dBc/Hz at 1 kHz offset and -126 dBc/Hz at 10 kHz to 100 kHz offset, which is well below the phase-noise performance of the ASIC synthesizer. However, as a laboratory instrument this reference synthesizer has several orders of magnitude higher mass, volume, and power consumption than the ASIC synthesizer discussed here. The ASIC test configuration consists of a commercial 20 MHz quartz TCVCXO and the ASIC synthesizer chip. In the ASIC test configuration, an additional RF amplifier was connected to amplify the -5 dBm output power of the ASIC to the +3 dBm power level used to drive the EOM. Note that in a final miniature atomic clock realization using direct modulation of the VCSEL laser current, the -5 dBm output power of the ASIC synthesizer is in the power range required for appropriate clock operation [7, 8]. In both the reference and test configurations, an external frequency generator was used to produce the $f_m \approx 1$ kHz modulation frequency for the microwave signal, while the modulation depth was set in the respective microwave synthesizer used.

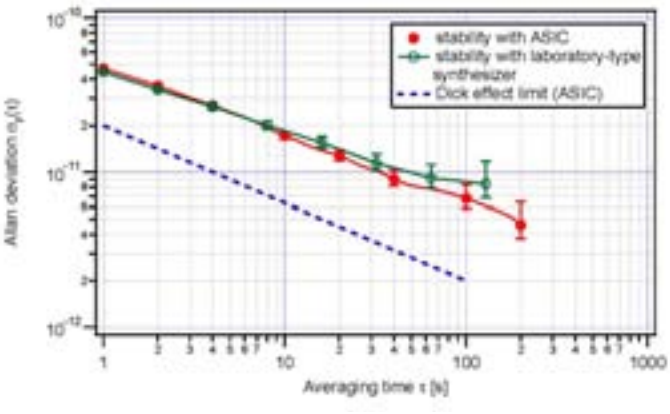

Figure 3. Clock stabilities recorded with the experimental clock setup, using the reference synthesizer (green, open symbols) and the ASIC synthesizer chip (red, filled symbols). The blue dashed line gives the Dick-effect stability limit due to the ASIC phase noise.

Fig. 3 shows the clock stabilities recorded with the two synthesizer configurations. Both the clock stability obtained with the laboratory-type reference synthesizer (green, open symbols) as well as the clock stability obtained with the ASIC synthesizer chip (red, filled symbols) show a stability of 5×10^{-11} at $\tau = 1$ s and down to $\approx 8\times10^{-12}$ at $\tau = 100$ s, in good agreement with the theoretical stability limit of $\approx 7\times10^{-11}\,\tau^{-1/2}$ calculated from the signal-to-noise ratio of the CPT signal on the photo detector. Small differences between the two stabilities measured are within the error bars and can also be attributed to slightly different loop settings. These results show that the performance of the ASIC synthesizer chip is well suited for realizing miniature atomic clocks with excellent frequency stabilities.

Fig. 3 shows also the theoretical stability limit of an atomic clock in which the ASIC phase noise would represent the highest contribution to clock stability limitation. Due to the Dick effect [9], the phase noise of a synthesizer at higher order harmonics of the modulation frequency f_m (applied to the microwave signal in order to obtain an error signal for stabilization of the microwave frequency to the center of the atomic reference line) results in a limit to the clock frequency stability given by:

$$\sigma_y(\tau) = \sqrt{\sum_{n=1}^{\infty} C_{2n} \cdot S_\varphi(2nf_m)} \cdot \tau^{-1/2} \qquad (1)$$

where n is the harmonic number, S_φ is the phase noise measured at even harmonics of the modulation frequency, and C_{2n} is the coefficient of sensitivity given by:

$$C_{2n} = \frac{2n}{(2n-1)(2n+1)} \frac{f_m}{\nu_{\mathrm{Cs}}} \qquad (2)$$

where $\nu_{Cs} = 4.6$ GHz is the synthesizer output frequency (half of the Cs hyperfine splitting). Using $f_m = 1$ kHz and the measured phase-noise of Fig. 2, we obtain a short-term stability limit due to the Dick effect of $\sigma(\tau) = 2\times10^{-11}\,\tau^{-1/2}$. This stability limit is well below the typical short-term stability specification of $6\times10^{-10}\,\tau^{-1/2}$ for miniature atomic clocks [2,10].

V. Conclusion

We have presented the characterization results of an optimized version of a microwave synthesizer ASIC chip capable of providing 4.6 GHz output frequency with full modulation capabilities required for interrogation of a miniature atomic clock. The optimized ASIC is fabricated in a 130 nm RF CMOS process, occupying an active area of 2 mm^2 and consuming about 15 mW. The measured phase noise of the ASIC is around -85 dBc/Hz in the 2 kHz to 100 kHz frequency band of relevance for atomic clock interrogation. This is only up to 10 dB higher than the phase noise of the 20 MHz VCXO reference used in our studies.

Measurement of the clock stability obtained with an experimental clock setup (using a micro-fabricated Cs cell) shows that using the ASIC synthesizer does not result in any degradation of clock stability compared to using a reference laboratory-type microwave synthesizer. Both clock stabilities obtained are limited to the same level of $\leq 7\times10^{-11}\,\tau^{-1/2}$, by the signal-to-noise ratio of the clock signal obtained from the micro-fabricated Cs cell, but not by the Dick-effect limit which is calculated to be $2\times10^{-11}\,\tau^{-1/2}$ for the ASIC synthesizer.

The obtained results prove that the realized ASIC design is well suited for the realization of state-of-the-art miniature atomic clocks, while having very attractive size and power consumption, and good perspectives for low-cost mass production.

Acknowledgment

We thank M. Haldimann for helpful discussions.

References

[1] Y. Zhao, S. Tanner, A. Casagrande and P.-A. Farine, "A 4.6-GHz, 15-mW frequency synthesizer CMOS ASIC with milli-Hertz frequency resolution for miniature atomic clocks", in *Proc. IEEE Int. Freq. Control Symp. Euro. Freq. Time Forum*, pp. 1 – 4, May, 2011.

[2] S. Knappe, "MEMS atomic clocks", in *Comprehensive Microsystems*, Elsevier B.V., 2010, vol. 3, pp. 571 – 612.

[3] www.spectradynamics.com/products

[4] J. Vanier, "Atomic clocks based on coherent population trapping: a review", *Appl. Phys. B*, vol. 81, no. 4, pp. 421 – 442, Aug. 2005.

[5] D. Miletic, C. Affolderbach, M. Hasegawa, R. Boudot, C. Gorecki, G. Mileti, "AC Stark-shift in CPT based Cs miniature atomic clocks", *Appl. Phys. B*, vol. 109, no. 1, pp. 89 – 97, Oct. 2012.

[6] M. Hasegawa, R. K. Chutani, C. Gorecki, R. Boudot, P. Dziuban, V. Giordano, S. Clatot, L. Mauri, "Microfabricated cesium vapor cells with buffer gas for long-term operation of atomic clocks", *Sensors and Actuators A*, vol. 167, pp. 594 – 601, 2011.

[7] S. Knappe, P. Schwindt, V. Shah, L. Hollberg, J. Kitching, L. Liew, J. Moreland, "Microfabricated Atomic Frequency References", in *Proc. IEEE Int. Freq. Control Symp., pp. 87 - 91* August 2004.

[8] F. Gruet, E. Kroemer, L. Bimboes, D. Miletic, C. Affolderbach, A. Al-Samaneh, D. Wahl, R. Boudot, G. Mileti, R. Michalzik, "Metrological Characterization of Custom-Designed 894.6 nm VCSELs for Miniature Atomic Clocks", *Optics Express* 21 (5), 5781-5792 (2013).

[9] C. Audoin, V. Candelier, and N. Dimarcq, "A limit to the frequency stability of passive frequency standards", *IEEE Trans. Instrum. Meas.*, vol. 40, no. 2, pp. 121 – 125, Apr. 1991.

[10] R. Lutwak, A. Rashed, M. Varghese, G. Tepold, J. LeBlanc, M. Mescher, D. K. Serkland, K. N. Geib, G. M. Peake, S. Römisch, "The Chip-Scale Atomic Clock – Prototype Evaluation", in: *Proc. 39th Annual Precise Time and Time Interval (PTTI) Meeting, pp. 269 – 290, December 2004.*

Reducing the Time Transfer Uncertainty In the Fiber Optic Time and Frequency Dissemination System

Wojciech Słowik
Department of Electronics
AGH University of Science and Technology
Krakow, Poland
wslowik@agh.edu.pl

***Abstract*—In this work we present a newly designed compensating module, which reduces the delay mismatch between two integrated delay lines used in time transfer system. In this work we show the measured results of the compensation efficiency, both in nominal temperature, and for ± 5°C temperature excursions. We find the remaining mismatch as no greater than 3 ps. After applying the compensation module, the problem of the delay lines mismatch go below other factors limiting the overall system performance.**

Keywords—fiber network, frequency distribution, optical fibers, time transfer, delay lines, mismatch compensation

I. INTRODUCTION

In last years our group is developing the fiber optic system for accurate time and frequency (T&F) dissemination [1][2][3]. The main idea is to actively stabilize the propagation delay of the link by organizing a delay locked loop (DLL) system, using the feedback signal from remote side of the system. The core element of the hardware is a set of two precisely matched electronic delay lines, fabricated as an application-specific integrated circuit (ASIC). Without the proposed compensation module the mismatch of the tuning characteristics of the delay lines may be as much as 150 ps, and it affects the overall T&F dissemination accuracy and stability [1][2].

In our system (see Fig. 1) the reference frequency signal after passing through one of the electronic delay lines and after reaching remote destination point is then returned. After passing through the second delay line, its phase is being compared with the phase of the primary reference signal. Then the error signal from the phase comparator controls the line's delay so as to minimize variations of the signal propagation time. Compensating module, which is the subject of discussion in this article is circled in Fig. 1. Its purpose is to minimize the impact of the mismatch of the two delay lines, caused by fabrication process impairments.

II. CONCEPT OF COMPENSATING MODULE

The block diagram of the presented solution is shown in Fig. 1. It is known that it is not possible to produce two delay lines which would have the same parameters even in the integrated circuit. Between the lines, there is always some very little mismatch. Without any actions undertaken to reduce it, the mismatch has magnitude up to about 150 ps (see Fig. 6). The main idea of the compensating module is to measure output voltage from phase comparator, make some modifications according to the relevant characteristics and add

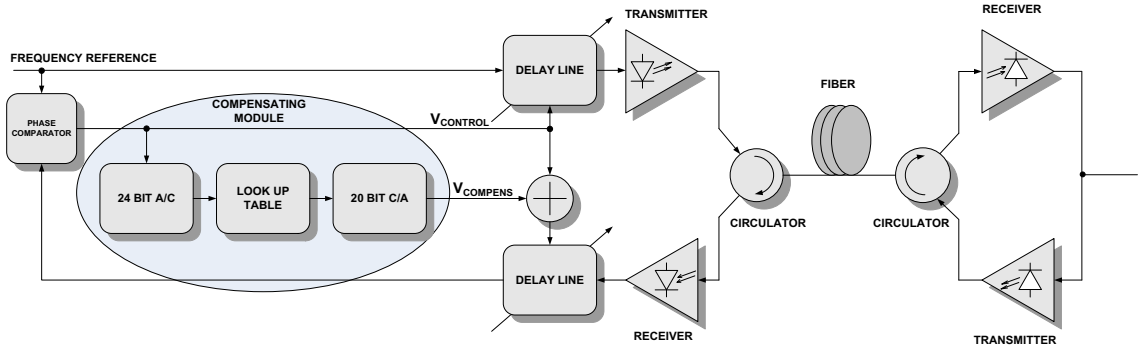

Fig. 1. General concept of compensating module applied in the active propagation delay stabilization system [1] using controlled electronic delay lines.

This work was partially supported by Polish National Science Centre under the decision DEC-2011/03/B/ST7/01833.
This work was partially supported by Faculty of Computer Science, Electronics and Telecommunications under the decision 15.11.230.078

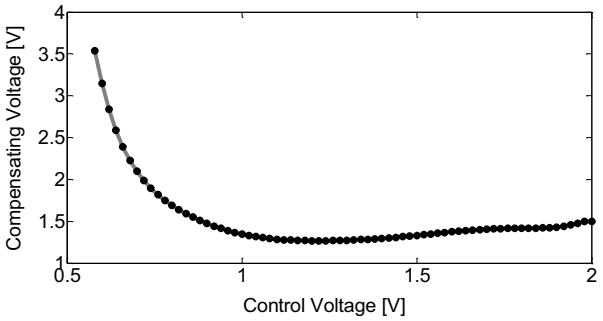

Fig. 2. Example characteristic of compensating voltage versus phase comparator output voltage.

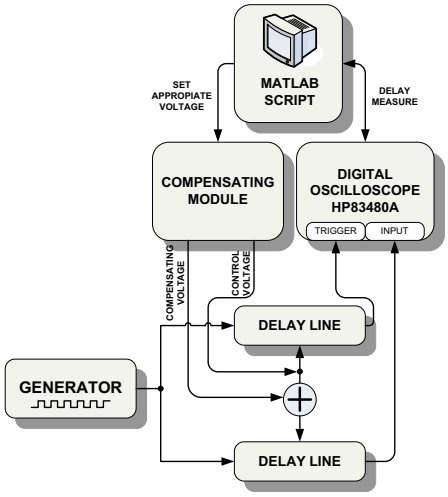

Fig. 3. Test bench to determine the LUT content.

compensating voltage to one of the delay lines. Unfortunately the mismatch is a non-linear function of the control voltage, and is different for each particular chip, therefore it is necessary to also develop algorithm for determining characteristics of compensating voltage. After that, data points are written to the LUT (*Look-Up-Table*). Because the module uses precise *a/d* and *d/a* converters, it is possible to apply the changes of a control voltage of the order of a few microvolts. The example characteristic of the compensating voltage (correction points stored in LUT table) is shown in Fig. 2.

Due to the LUT implemented in the microcontroller memory, there is an ability to save any characteristics of the compensating voltage against the control voltage. In the target system, the module continuously measures output voltage from phase comparator and corrects the control voltage of one of the lines thereby reducing the mismatch to acceptable level.

This is the main function of the module but not the only one. As mentioned before, each newly fabricated delay line will have slightly different characteristics of the mismatch. It is therefore reasonable to develop an algorithm which quickly and accurately allow as to determine the correction factors, thus filling up the LUT table with appropriate values.

Script running under Matlab environment sends commands and data to the presented module and also to the digital oscilloscope HP83480A. The scope measures the delay between trigger signal slope position and current signal slope position and return this value to Matlab script via GPIB. Block diagram of the hardware configuration to determine the LUT coefficients is shown in Fig. 3. The algorithm of the Matlab script is presented as a block diagram in Fig. 4.

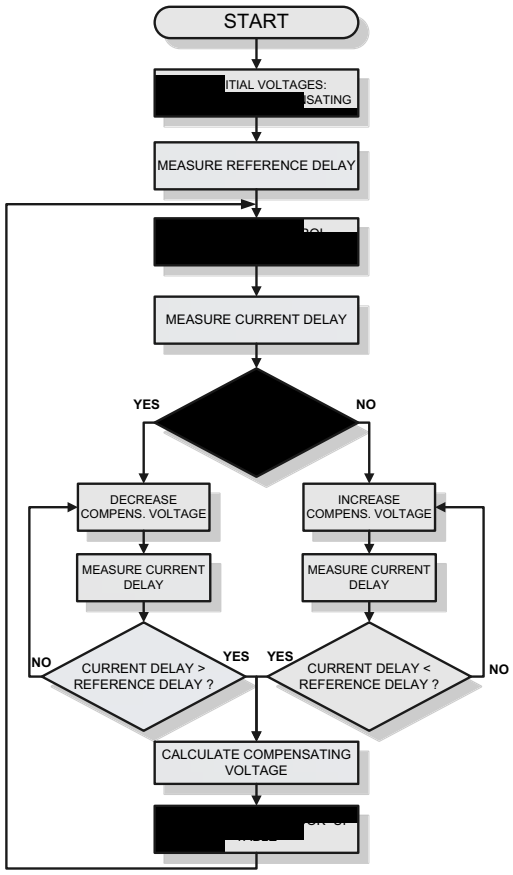

Fig. 4. Algorithm block diagram for determining LUT correction coefficients.

III. OBTAINED RESULTS

After fulfilling the LUT table with relevant correction coefficients the module was tested in the target system. Fig. 5 shows summary comparison between mismatch without active compensating module and with this solution. We can see that without any compensation, the mismatch would reach level of about 150 ps. Fig 6 shows measured mismatch for different temperatures. Curve for 28°C is a reference one as LUT coefficients were determined exactly in such temperature. We can see that residual mismatch do not exceed 3.1 ps peek-to-peek. It is less than other factors limiting overall accuracy. Despite the variations of the mismatch caused by temperature changes, we can see that for 32°C mismatch does not exceed

4 ps peek-to-peek which value is still acceptable. Only for lower ambient temperatures the mismatch is increasing, reaching 10 ps (Fig. 6, curve for 23°C).

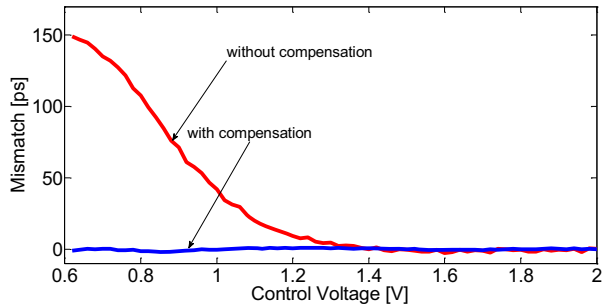

Fig. 5. Delay line mismatch with and without compensating module (measures at 28°C).

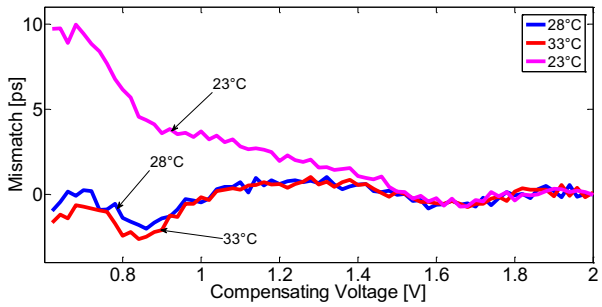

Fig. 6. Residual mismatch for different temperatures.

IV. Conclusion

In summary, the described circuit performed its main task. As a further improvement of the module it seems to be reasonable to determine and save in the module memory more LUT tables of the compensating voltages for some temperature range. Signal from the local temperature sensor would allow the module to change the characteristic of the compensating voltage on an ongoing basis.

References

[1] Ł. Śliwczyński, P. Krehlik, Ł. Buczek, and M. Lipiński, "Active propagation delay stabilization for fiber optic frequency distribution using controlled electronic delay lines," IEEE Trans. Instrum. Meas., vol. 60, no. 4, pp. 1480–1488, Apr. 2011.

[2] P. Krehlik , Ł. Śliwczyński , Ł. Buczek , M. Lipiński,: Fiber-optic joint time and frequency transfer with active stabilization of the propagation delay; IEEE Transactions on Instrumentation and Measurement.

[3] Ł. Śliwczyński, P. Krehlik, A. Czubla, Ł. Buczek and M. Lipiński, "Dissemination of time and RF frequency via a stabilized fiber optic link over a distance of 420 km", Metrologia 50, 133-145, 2013.

Research on Hybrid-Compensation Technology for Reducing Acceleration Sensitivity of TCXO

Liangpeng Chen[1]
College of Mechatronic Engineering and Automation,
National University of Defense Technology
Changsha, Hunan, P. R. China 410073

Qingxiao Shan[1]
College of Mechatronic Engineering and Automation,
National University of Defense Technology
Changsha, Hunan, P. R. China 410073
tsingxiao@163.com

***Abstract*—Temperature compensated crystal oscillator (TCXO) is widely used in GPS receiver for its small size and low cost, but the g sensitivity of TCXO decrease the frequency stability and deteriorate the performance of GPS receiver when suffering from serious vibration. To reduce the g sensitivity, the way used prevalently is mechanic cushion but it is not efficient at low frequency vibration. This paper proposed hybrid-compensation which is made up of electronic compensation and mechanic cushion. The electronic compensation aims at low frequency vibration while mechanic cushion aims at high frequency. The method proposed can reduce the g sensitivity and improve reliability of TCXO by adding extra devices to the original TCXO. Experiments show that, the using of hybrid-compensation technology can effectively reduce the phase noise of crystal oscillator and extend the applicability of TCXO, for maintained more than 15dB decay at 4g@1kHz vibration.**

Keywords—TCXO; acceleration effect; hybrid-compensation; electronic compensation; mechanic cushion

I. INTRODUCTION

TCXO is widely used as frequency source in aircraft, missile, navigation instruments and timing devices for its small size, high precision and low aging rate [1]. But both aircraft and missile suffer from serious vibration, because the stress frequency effect of crystal, the crystal oscillator's stability is extremely poor [2-4]. As frequency source, the frequency drift of crystal oscillator will directly lead to a decline in the whole system performance, such as poor missile hit rate, bad communication and not accurate of GPS vehicle positioning.

In order to improve the stability of TCXO and keep small size, reference [5] proposed a method, which using two crystal oscillators of same characteristics parallel connected can counteract acceleration sensitivity, to improve the crystal oscillator frequency stability. But it is hard to find matching crystal oscillators in practice. This paper presents a hybrid-compensation technology combined with electronic compensation technology and mechanic cushion. The electronic compensation technology to obtain the real time acceleration of TCXO through the MEMS sensor which has small size, and then compensate the frequency drift of TCXO by digital controller, while the mechanic cushion to reduce the phase noise by mechanical snubber. The combined hybrid-compensation technology will effectively reduce the TCXO acceleration sensitivity, and extend the applicability of TCXO.

II. VIBRATION & PHASE NOISE

The crystal oscillator is an oscillation circuit based on quartz crystal, so the performance of quartz crystal directly determines the performance of the oscillator. As quartz plate has stress relaxation effect [2], TCXO will produce frequency jitter due to the stress relaxation effect of wafer in vibration environment, commonly known as the acceleration effect of crystal oscillator. In the experimental study, usually use phase noise of crystal oscillator to measure the influence caused by the vibration. More details about the theory of phase noise please refer to classic reference wrote by the Filler [4].

A. *The acceleration effect of TCXO*

The relatively rigorous output signal of the TCXO model can be rewrite as

$$V(t)=[V_0+\varepsilon(t)]\cos[2\pi f_0 t+\upsilon(t)] \qquad (1)$$

Where V_0 is the nominal amplitude, f_0 is the nominal frequency, $\varepsilon(t)$ is the amplitude jitter, also call as the amplitude noise, $\upsilon(t)$ is phase drift, visibly, both $\varepsilon(t)$ and $\upsilon(t)$ closely related to vibration a. Rewrite the phase of equation (1) as a function of f as

$$S_f=\vec{\Gamma}\cdot\vec{a}=\frac{f(\vec{a})-f_0}{f_0}=\frac{\Delta f}{f_0} \qquad (2)$$

Where $\vec{\Gamma}$ means acceleration sensitivity vector of crystal oscillator, $\vec{a}$ means vibration vector, S_f represents frequency drift rate. From equation (2) can be seen, the vibration impact on the crystal oscillator is strict related to vibration direction. Fig.1 shows two kinds of frequency drift of crystal oscillator caused by vibration of different directions.

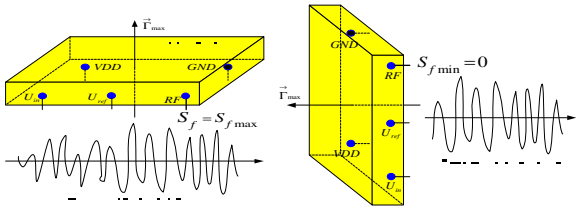

Fig. 1. Frequency drift caused by vibration of different directions

B. The phase noise of TCXO

When TCXO suffers from vibration of harmonic vibration, the output signal can be given by

$$V(t)=[V_0+\varepsilon(t)]\cos[2\pi f_0 t+\beta\sin(2\pi f_v t)] \quad (3)$$

Where $\beta=\frac{\Delta f}{f_v}$ is the modulation coefficient, f_v is the harmonic vibration frequency. So we can get

$$V(t)=[V_0+\varepsilon(t)]\sum_{n=-\infty}^{+\infty} J_n(\beta)\cos[2\pi(f_0+n\cdot f_v)t] \quad (4)$$

$$\varepsilon(t) << V_0$$

It is obvious that the energy on both sides of the sideband is equal. When the modulation index β<0.1 , then the modulation caused by vibration is mainly manifested in the first sideband, so we can get

$$L_v^1=20\log\frac{J_1(\beta)}{J_0(\beta)}=20\log\frac{(\vec{\Gamma}\cdot\vec{A})f_0}{2f_v} \quad (5)$$

When in experiments, in order to make a quantitative test of the influence caused by external vibration, the ratio with the first sideband energy and the baseband energy is calculated in general, viz. phase noise, show as Fig.2.

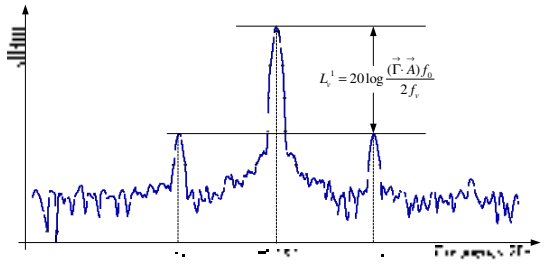

Fig. 2. The modulation effect of TCXO caused by external vibration

III. HYBRID-COMPENSATION TECHNOLOGY

To reduce the g sensitivity, the way used prevalently is mechanic cushion but it is not efficient at low frequency vibration. In fact the frequency drift in crystal oscillator caused by lower frequency vibration is still great, and it cannot be tolerated especially in precision equipments. The result of reference [6] shows that digital compensation technology can effectively reduce the influence of low-frequency vibration on the crystal oscillator. Therefore, the combination of mechanical cushion and electronic compensation technology can effectively improve the frequency stability of crystal oscillator.

A. Electronic compensation technology

With the piezoelectric effect of crystal plate, design an additional voltage control terminal for crystal oscillator circuit use the variable capacitance diode is meaningful. Then the signal frequency can be adjusted in a certain range through applying voltage to the voltage control terminal, so to achieve the precise compensation of crystal oscillator can use the method with an certain compensation algorithm.

Suppose the piezoelectric coefficient of crystal oscillator is k_v, there is

$$V_c(t)=\frac{[f(t)-f_0]\cdot k_v}{f_0}=k_v\cdot\vec{\Gamma}\cdot\vec{a} \quad (6)$$

Where $V_c(t)$ is compensation voltage, $f(t)$ is the instantaneous output frequency. $V_c(t)$ can be calculated by measuring the g sensitivity and the acceleration of crystal oscillator. The electronic compensation system is shown as Fig.3.

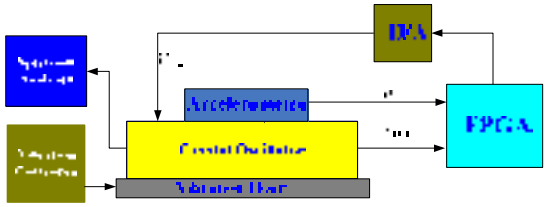

Fig. 3. Diagram of electronic compensation system

As there is only a small range of frequency through voltage compensation, and there still have compensate time delay [1]. So the electronic compensation technology applied at low frequency vibration environment is of better effect, but it is not efficient at high frequency vibration.

B. Mechanic cushion

In industrial applications usually adopts mechanic cushion to isolate external vibration, for mechanic cushion performs excellent in high frequency vibration environment [7,8]. In order to achieve the required spectrum of crystal oscillator output signal, a mechanic cushion device is designed, the simple structure model is shown as Fig.4.

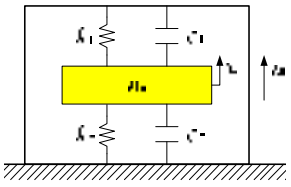

Fig. 4. Diagram of mechanical cushion structure

In Fig.4 *m* means the mass of crystal oscillator; *k1*, *k2* means the stiffness coefficient of each level; *c1*, *c2* means the

damping coefficient of each level. x means the vertical displacement of each level; u means the vertical displacement of the base.

Therefore the differential equations of mechanical motion can be obtained by the following

$$m\ddot{x}+(c_1+c_2)\dot{x}+(k_1+k_2)x=(k_1+k_2)u+(c_1+c_2)\dot{u} \quad (7)$$

Then transfer function can be rewritten from equation (7).

$$G_T=\sqrt{\frac{(c_1+c_2)^2w^2+(k_1+k_2)^2}{(k_1+k_2-mw^2)^2+(c_1+c_2)^2}} \quad (8)$$

Using MATLAB to make a simulation, here assuming that the damping coefficient of each level is c_1=c_2=0.01Ns/m, the stiffness coefficient of each level is k_1=k_2=200N/m, the mass of crystal oscillator is m=0.12kg. The simulation result is shown in Fig.5. It is obviously that when the vibration frequency is lower than 231.1Hz the mechanical cushion device cannot compensate effectively.

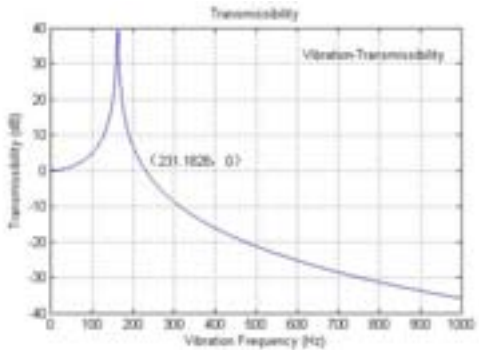

Fig. 5. The transfer function of mechanical cushion

IV. EXPERIMENTAL PERFORMANCE

Based on the theory analysis above, firstly experiment with voltage control terminal under static conditions. Result of the relationship between the control voltage and the output frequency of the crystal oscillator (V_c—f) is shown in Fig.6, it can be seen from the figure that the control voltage and the frequency of the crystal oscillator is a linear correlation. So it is doable to compensate the frequency drift of crystal oscillator by applying voltage to the voltage control terminal of crystal oscillator.

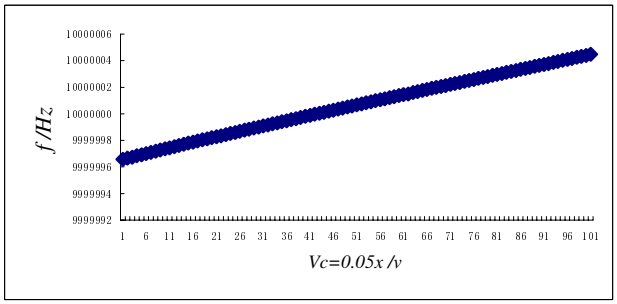

Fig. 6. The relationship between the control voltage and output frequency

The experimental platform is mainly composed of vibration controller, vibration platform, mechanical buffer, crystal oscillator, spectrum analyzers and DC power supply. During the experiment the crystal oscillator is fixed on the vibrating table, through advance setting the vibration environment, using the spectrum analyzer can observe the spectrum of crystal oscillator output signal real time.

Experiment makes crystal oscillator test in multi-frequency point for 4g in amplitude. Considering the electronic compensation technology functions more efficient than mechanic cushion in low frequency vibration, while mechanic cushion functions more efficient than electronic compensation technology in high frequency vibration, apply mechanic cushion at first and then add electronic compensation technology in low frequency vibration (f<300Hz) , and in turn in high frequency vibration environment (f>300Hz) . The test results as shown in Fig.7.

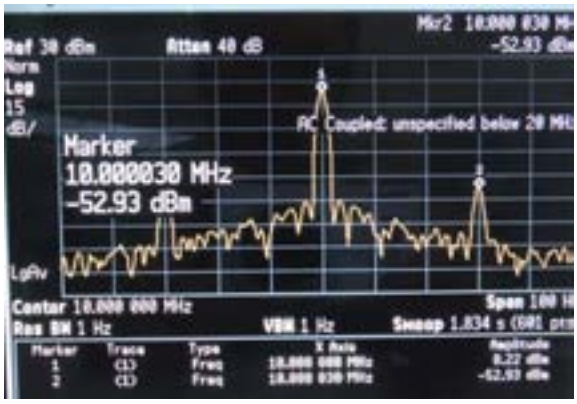

(a) With mechanical cushion no electronic compensation (4g, 30Hz)

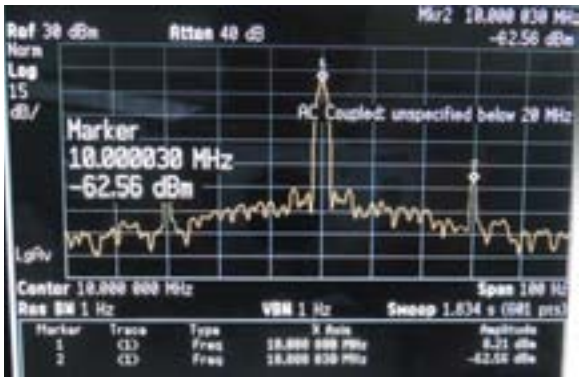

(b) With mechanical cushion and electronic compensation (4g, 30Hz)

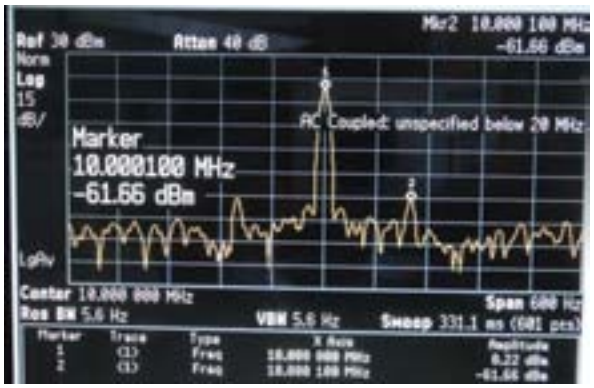

(c) With mechanical cushion no electronic compensation (4*g*, 100Hz)

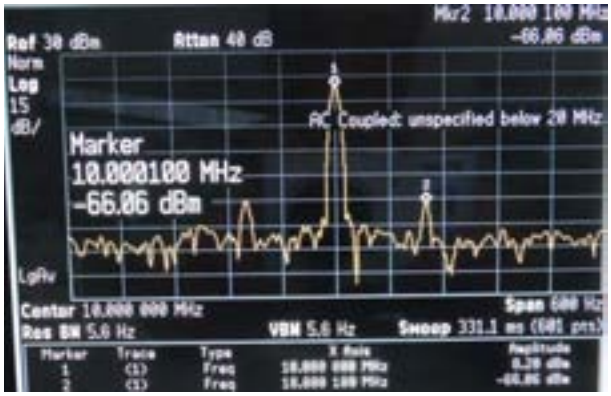

(d) With mechanical cushion and electronic compensation (4*g*, 100Hz)

(e) With electronic compensation no mechanical cushion (4*g*, 1kHz)

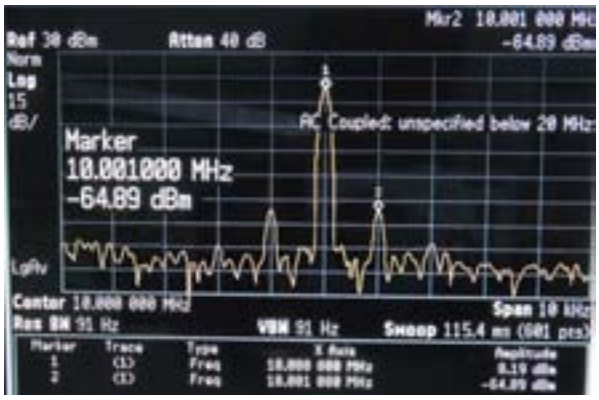

(f) With electronic compensation and mechanical buffer (4*g*, 1kHz)

Fig. 7. Experimental results in multi-frequency at 4*g*

Conclusion can be made from the experimental results is that the mechanic cushion makes negligible compensation on the crystal oscillator when at low frequency vibration, and the same to electronic compensation technology at high frequency vibration. Combine the different compensation characteristics of mechanic cushion and electronic compensation technology, the applying of hybrid-compensation technology performs excellent especially in high frequency vibration environment. So the using of hybrid-compensation technology which is based on electronic compensation technology and mechanic cushion has a very important significance.

V. CONCLUSION

The paper first analysis the relationship between vibration and phase noise, and briefly discusses the basic principle of digital compensation method and mechanic cushion. Then make a simulation of two-level mechanic cushion by MATLAB, the results show that the mechanic cushion performance excellent when the vibration frequency is higher than 231Hz, even the parameters of the isolate system is not rigorous, the results can prove the mechanical cushion is beneficial for high frequency vibration. On the basis of these works, then verified in experiments, the experimental results show that control voltage and the frequency of crystal oscillator is linear correlation. And electronic compensation technology only effective in low frequency vibration while the mechanic cushion effective in high frequency vibration. The combination of electronic compensation technology and mechanic cushion can effectively improve the phase noise of the crystal oscillator in wide frequency range. Experimental results show that the applying of hybrid-compensation technology can reach about 15dB improvement in 4g@1kHz. It is obvious that the research of hybrid-compensation technology has very important significance.

ACKNOWLEDGMENT

The authors thank the reliability lab provide simulation environment for them.

REFERENCE

[1] Shan Qingxiao,Yang Jun,Chen Jianyun.ect, Real-time digital compensation to reduce acceleration's sensitivity in quartz resonator, Review of scientific instruments,83(6),2012.06:1-7.

[2] Zhao Shengheng,Zhao ying.Crystal Oscillator[M].Beijing:Science Press.2008.05:120-122.

[3] John R. Vig, Fred L. Walls. Fundamental limits on the frequency instabilities of quartz crystal oscillators[C]. IEEE International Frequency Control Symposium,1994:50523.

[4] L.Filler.The Acceleration Sensitivity of Quartz Crystal Oscillators: A Review[J]. IEEE Transaction on Ultrasonics,Ferroelectrics and Frequency Control , 1988,35(3):297-305.

[5] Steven J.Fry, Gregory A.Burnett. Reducing the acceleration sensitivity of AT-strip quartz crystal oscillators.IEEE Frequency Control Symposium,2010.06:25-30.

[6] M.Bloch,O.Mancini,T.McClelland etc.Acceleration "G" compensated quartz crystal oscillator. EFTF-IFCS,2009 Joint Conference.Besancon,France,2009.04:175-180.

[7] VJoseph B.Donovan, Vibration isolation of acceleration sensitive devices.IEEE Frequency Control and the European Frequency and Time Forum,2011.05:1-6.

[8] J.B. Donovan and M.M. Driscoll, Vibration-induced phase noise in signal generation hardware, EFTF-IFCS 2009 Joint Conference,Besancon,France,2009.04:14-15.

Demonstration of Doubly Rotated X-Cut Quartz Plate Oscillators with a Slot Vibrating in Length Extensional Mode

Tomiharu Yamaguchi, Kiyoto Katakura, Yusuke Todo, and Hisashi Kanie
Department of Applied Electronics
Tokyo University of Science
Katsushika, Tokyo, Japan
t-yama@te.noda.tus.ac.jp

***Abstract*—This paper describes the finite element method analysis of (XY*lt*) −35°/−1° rotated X-cut quartz oscillators vibrating in the length-extensional mode and the experimental data of the sample processed monolithically by the wet etching. The oscillator consists of the resonator with a slot and an integral mounting system and has the first order temperature frequency coefficient $\alpha = -0.6 \times 10^{-6}$ /°C, the second order temperature frequency coefficient $\beta = -3.5 \times 10^{-8}$ /°C^2, and the parameters of the electrical equivalent circuit in the air: the series inductance L_1 = 2.70 H, the capacitance ratio r = 192, the series resistance R_1 = 1080 Ω, and Q = 19000.**

Keywords—quartz oscillator; X-cut; length extensional mode; slot structure; wet etching

I. INTRODUCTION

X-cut quartz rod oscillators vibrating in length extensional mode (LE) were fabricated for 1 MHz oscillators[1]. A singly rotated (XY*t*) −5° X-cut quartz plate was used for this type oscillator because it has a zero first order temperature frequency coefficient α when an aspect ratio $R_{ZY} = w/l$ (w: resonator width, l: resonator length) is less than 0.1[2]. To obtain a smaller series resistance R_1 and a smaller capacitance ratio r, the rectangular resonators with R_{zy} in a range from 0.3 to 0.5 using a singly rotated X-cut quartz plate with a rotation angle from (XY*t*) −5° to (XY*t*) −25° have been investigated[3-4]. The resonators, however, cannot be mounted on its sides because they have a node located in the center.

This paper describes theoretical analysis by a finite element method of a doubly rotated X-cut quartz oscillator composed of a resonator with a slot and a monolithical mounting system among rotation angles ranging from (XY*lt*) 0°/0° to (XY*lt*) −60°/−10°. The paper also describes the experimental data of the fabricated doubly rotated (XY*lt*) −35°/−1° X-cut resonator, such as frequency-temperature characteristics and electrical properties measured and comparison with the theoretical values.

II. STRUCTURE OF A X-CUT QUARTZ CRYSTAL RESONATOR WITH A SLOT

A designed doubly rotated X-cut oscillator consists of a resonator with a slot, a folk type mounting system and two supports. Figure 1 shows a schematic diagram of the designed LE mode X-cut oscillator. The overall size of the resonator is 2000 μm long and 920 μm wide. The mount with two arms connected to supports enables a cylinder type packaging of the fabricated oscillator. Metal electrodes Au(150 nm)/Cr (50 nm) were sputtered on both X″-surfaces. The (XY*lt*) 0°/−5° X-cut rectangular resonator has zero α for R_{ZY} ranging from 0 to 0.2 or from 0.28 to 0.60[2]. The gap occurred because when R_{ZY} = 0.23 the coupling of the second-order flexural mode of the X-cut rod couples the LE mode. Thus, we determined R_{ZY} for the single rod composing the resonator to be 0.2.

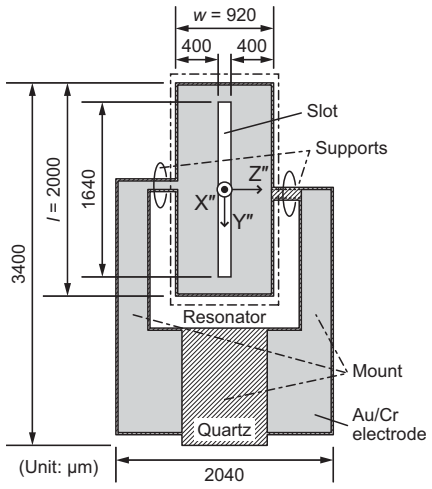

Figure 1. Schematic diagram of the designed quartz resonator. The X″, Y″, and Z″ axes means doubly rotated X, Y, and Z axes of a quartz crystal.

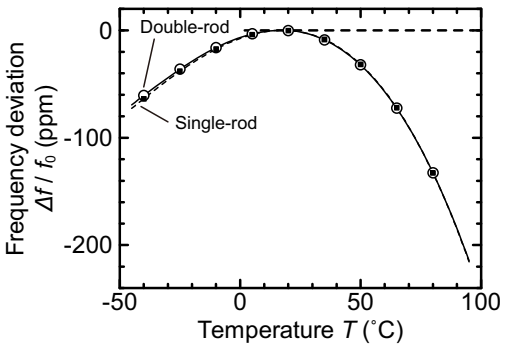

Figure 2. Temperature-frequency characteristics of the X-cut quartz resonators with a single rod and double rods with R_{ZY}= 0.20. The resonant frequencies of both resonators were f= 1.32 MHz at a reference temperature of 20°C

III. A X-CUT QUARTZ CRYSTAL OSCILLATORS WITH THE DOUBLE-ROD QUARTZ RESONATOR ANALIZED BY FEM

The frequency-temperature characteristics of a single-rod and a double-rod quartz resonators with R_{ZY} = 0.2 were calculated by the ANSYS (ANSYS Inc. PA, USA). The simulated resonant frequency f_0, α, and the second order frequency coefficient β of the double-rod resonator was 1.33 MHz, -1.59×10^{-7} /°C, and -2.73×10^{-8} /°C^2, respectively (Fig. 2). The simulated frequency f_0 agreed well with the one derived from the LE mode frequency equation, f_0 = 1.36 MHz. The frequency f_0 and temperature coefficients of the resonator hardly changed by mounting. These results indicate that the temperature character of the resonator with a slot is similar to that of the resonator which has two rods connected at both ends.

The conventional tuning-fork type quartz resonator is fabricated using Z-cut plate by the wet etching process. Z-cut quartz LE mode rod oscillators with sidewall electrodes on the X planes were also fabricated by wet etching[5]. Although the etching speed in the X-axis direction is rather slow, the rotation around the Y axis of the X-cut plate increases the etching speed normal to the surface and allows to process complex structure monolithically. To design a zero temperature coefficient double-rod resonator and a tuning-fork type mount, a doubly rotated X-cut (XY*lt*) φ_Y /θ_X quartz plate was analyzed by FEM. As shown in Fig. 3(a), α of the double-rod resonator became positive for $\varphi_Y < -35°$. We designed the LE mode double-rod resonator with $\varphi_Y = -35°$ where the wet etching speed is fast enough. With decreasing θ_X, α of the doubly rotated X-cut double-rod resonator increase (Fig. 3(b)), which allows to compensate the possible decrement of α by mounting the resonator[3].

As shown in Fig. 4, the root mean square displacement d of the element on the side along the +Z″-axis of the double-rod resonator was minimum at Y = 40 μm and the minimum d became smaller than that of the single rod resonator. When the aspect ratio R_{ZY} = 0.2 , d of the resonator on the side along the +Z″-axis became small enough for the double rod resonator to be supported not at the midpoint but the 40-μm offset point from the midpoint of side (Fig. 5). The height of the support was designed so that the vibration modes of the mount do not

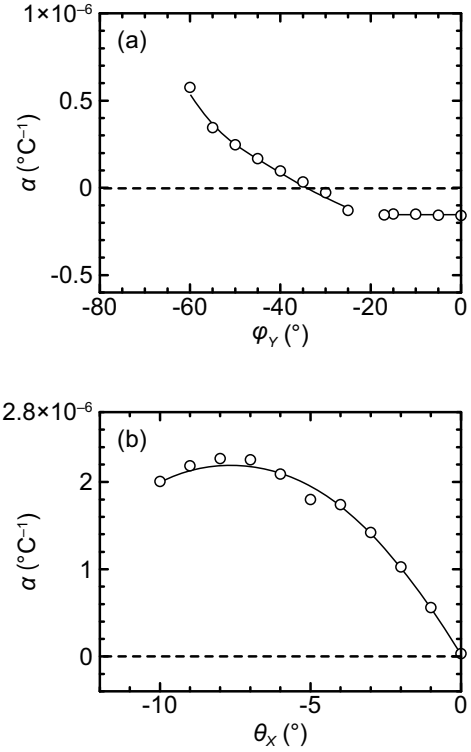

Figure 3. First order coefficient α of the doubly-rotated X-cut quartz resonator with a double-rod structure. (a) Rotation around the Y-axis. (b) Rotation around the X-axis.

couple with the LE mode shown in the displacement field images calculated by the FEM analysis. With increasing the support width W_1 from 60 μm to 320 μm, α decreased (Fig. 6). As there was a little change for W_1 < 180 μm, W_1 was determined at 120 μm to remain α almost zero and positive.

IV. FABRICATION OF THE DOUBLY ROTATED X-CUT QUARTZ OSCILLATOR BY THE WET ETCHING PROCESS

The (XY*lt*) −35°/−1° double-rod quartz resonator was fabricated by the wet etching process in 20% buffered HF (BHF) at 50°C for 14 h and 30% BHF at 50°C for 1 h. Table 1 shows the size of a fabricated sample. The sample has a temperature coefficient α of -0.6×10^{-6} /°C (Fig. 7). The little difference from the calculated α indicates the vibrating mode of the double-rod resonator in the oscillator did not coupled with the vibrating mode of the supports and the mount.

Because of the anisotropical etching of the quartz crystal, the sample with the etch residue and undercut had the longer length of the oscillator along the Y″-axis than the designed length and the narrower width along the Z″-axis than the design width. Substituting parameters in the FEM model with the measured size α was calculated to be -0.4×10^{-6} /°C, which agreed better with the measured value than the calculated value α of 0.2×10^{-6} /°C based on the design values did. A series resistance R_1, a series inductance L_1, a capacitance ratio r, and Q were 1080 Ω, 2.46 H, 187, and 19000, respectively.

TABLE I. DESIGNED AND MEASURED SIZES OF THE NEWLY FABRICATED X-CUT QUARTZ RESONATOR. DESINED AND MEASURED SIZES OF THE NEWLY FABRICATED X-CUT QUARTZ RESONATOR.

	Resonator size		Support width		Slot size	
	Length [μm]	Width [μm]	Left side [μm]	Right side [μm]	Length [μm]	Width [μm]
Designed value	2000	920	120	120	1640	120
Measured value	2045	904	153	154	1553	134

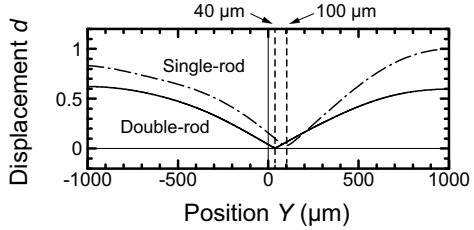

Figure 4. RMS displacement of the element on the +Z″-axis direction side of the (XY*lt*) −35°/−1° cut resonator. *Y* is the distance along the Y″-axis from the midpoint of the side.

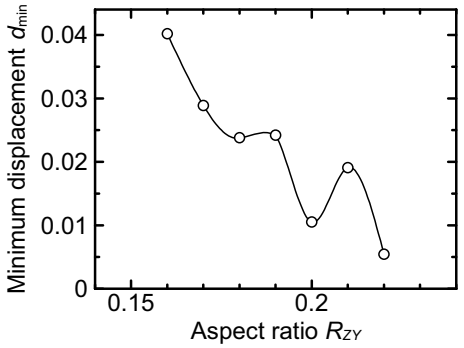

Figure 5. RMS minimum displacement of the element on the +Z″-axis direction side of the (XY*lt*) −35°/−1° cut resonator vs. R_{ZY}.

V. CONCLUSION

The LE mode X-cut quartz oscillator consists of the resonator with a slot and a fork type mount was analyzed by FEM to reduce the series resistance and capacitance ratio. The resonator structure is regarded as the double-rod resonator connected at both ends and mounted at effective nodes of the rod resonator. By using (XY*lt*) −35°/−1° cut quartz plate the oscillator fabricated had $\alpha = -0.6\times10^{-6}$ /°C, $R_1 = 1080\ \Omega$, $L_1 = 2.70$ H, $r = 192$, and $Q = 19000$ by the wet etching process.

REFERENCES

[1] R. J. Dinger, "A minuture quartz resonator vibrating at 1MHz," Proc. 35th Ann. Freq Control symposium, 144-148. 1981.

[2] W. Mason, "Physical Acoustics," vol. 1, pt. A, New York:Academic, 1964.Kawashima et al., Proc. of the 44th Annual Symposium on Frequency Control, 378-386, 1990.

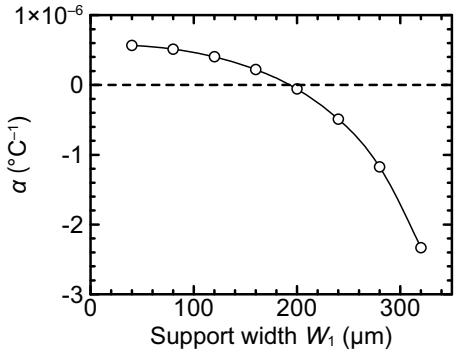

Figure 6. Supports width dependence of first order coefficient α of the designed (XY*lt*) −35°/−1° double-rod quartz resonator.

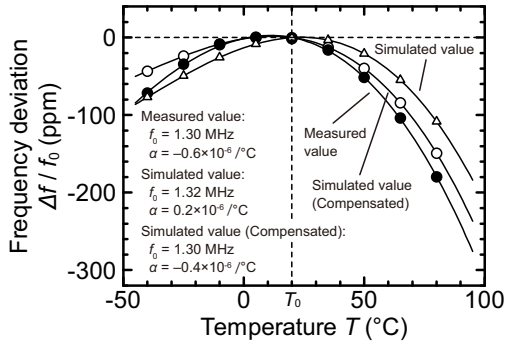

Figure 7. First-order coefficient of the doubly-rotated X-cut quartz plate resonator (XY*lt*) −35°/−1° with the slot structure consisting of the double-rod quartz resonator.

[3] Y. Yokoyama, H. Kawashima and H. Kanie, "Design and fabrication of a length-extensional mode rectangular X-cut quartz resonator," IEEE Trans. Ultrason., Vol. 53, No. 5, pp. 847-852, 2006.

[4] Y. Yokoyama, H. Kawashima and H. Kanie, "Analysis of Capacitance Ratio of a Rectangular X-Cut Length-Extensional Mode Quartz Crystal Resonator by Stresses with Zero Temperature Coefficient," IEEE Trans. Ultrason., , Vol. 53, No. 9, pp. 1551-1553, 2006.

[5] H. Kawashima and M. Nakazato, "Variational analysis of new shape length extensional mode quartz crystal resonator taking account of lateral motion" Proc. of the 44th Annual Symposium on Frequency Control, 378-386, 1990.

Investigation into Spectrum Shape Fluctuations of Oscillators and Signal Sources

Michael Underhill
Underhill Research Limited
Lingfield, UK
E-mail: mike@underhill.co.uk

***Abstract*—A standard SDR receiver with digital FFT type spectrum analysis software and a time waterfall display is used to investigate spectrum shape and 'spur' fluctuations in LC and crystal oscillators. Oscillator start-up spectra are found to narrow exponentially in time towards the expected Leeson model 'bell' shape, with a time constant inversely proportional to the resonator bandwidth. Spurs can be seen most prominent around the 3dB bandwidth frequencies of the oscillator resonator. The spur frequencies in general are a constant fixed offset from the carrier frequency and do not drift. Spur amplitude fluctuations appear to be random but with an average periodicity inversely proportional to spacing from the carrier. Some theory for the fluctuations is under development.**

Keywords—oscillator time spectra; digital FFT spectrum analyser; spectrum time waterfall; oscillator fluctuation theory.

I. INTRODUCTION

Spurious 'spikes' or 'spurs' can be observed in the spectra of oscillators and signal sources using both analogue and digital spectrum analyzers Some tentative explanations for the occurrence of such spurs and related phase and frequency jumps have been put forward [1-3]. The fluctuations of these in time need further investigation so that theory may be constructed. The RF Space ™ Software Defined Radio shown in Fig. 1 is the measurement equipment used for this investigation.

II. SOFTWARE DEFINED RADIO (SDR) AS DIGITAL SPECTRUM ANALYSER

Fig. 1. RF Space ™ Software Defined Radio, SDR-IQ, used as a FFT Spectrum Analyzer. ADC of 14 bits, clocked at 66.6 MHz. I and Q format data signals from a **direct** digital converter (DDC), with a bandwidth of 192 kHz anywhere within the range 0 to 30 MHz to 1 Hz precision. SpectraVue software provides SDR control and a selectable time waterfall display. Power is supplied via the USB port connection. Size is 3×10×12 cm.

Fig. 1 shows the RF Space ™ Software Defined Radio, SDR-IQ, used as a FFT Spectrum Analyzer. SpectraVue freeware is used for the time waterfall and other time plotted displays in the following figures.

Because of the parallel processing of the FFT the spectrum samples are available at a sampling rate that is typically more than a thousand times faster than is possible with a traditional swept frequency spectrum analyser.

Also the sideband noise dynamic range of a 14 bit DAC clocked at 66.6MHz as in the SDR-IQ is $14\times6 + \log 3.33\times10^7 = 84 + 75 = 159$dBC/Hz. This performance is well in excess of what can be achieved with the best swept frequency analogue spectrum analysers by about 40dB typically.

III. SOFTWARE SPECTRUM OF LC OSCILLATOR WITH SPURS

Fig. 2 shows the spectrum of a 9.728MHz LC oscillator in a Malden Electronics model 754 signal generator. A varactor has been placed across the LC tuned circuit to allow externally applied frequency modulation. Spurious 'spikes' or 'spurs' can be observed in the snapshot spectrum at the top. And amplitude fluctuations of the spectrum and spectrum spurs can be seen in the time waterfall at the bottom. Time markers are at the left of the waterfall. Colour amplitude calibration in dBs is to the left of the waterfall.

In Fig. 2 there are visible spurs at ±38kHz, ±19kHz, and –9.5kHz and +51kHz. Note that the periodicity of the ~2dB fluctuations are approximately inversely proportional to the spacing from the carrier. The reason for this needs further investigation. But it provides evidence that the coupling between the energy in different parts of the frequency spectrum is a function of sideband frequency, or level above thermal noise kT, or oscillator resonator bandwidth, or a combination of these.

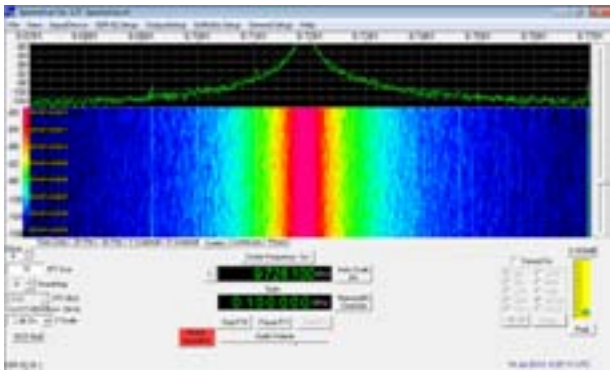

Fig. 2. Spectrum of LC Oscillator at ~9.728MHz over a 100kHz FFT analyser bandwidth, with LC Q ~120, and 3db bandwidth of ~80kHz. Vertical scale steps of 4dB. Plateau noise at ~-104dB and carrier at ~0db level. Waterfall time markers are at one second intervals.

IV. Spur Fluctuation over Time

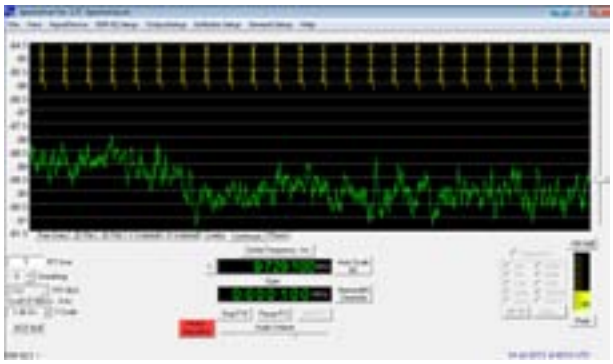

Fig. 3. Slow time variation of single spur at +2.3kHz from 9.728MHz carrier. Vertical scale steps of 0.5dB. Plateau noise at ~-104dB level and carrier at ~0db level. Horizontal time scale markers are at ten second intervals. .

Fig. 3 is a four minute duration right-to-left amplitude measurement of a single spur. Note that these slow fluctuations averaged over 5 sampling periods have a typical amplitude excursion of about 2dB.

V. Spur Fluctuations in 20MHz Crystal Oscillator

Fig. 4 shows the spectrum of a CMAC IQXO-22 20MHz crystal oscillator. The supply was a 3×1.4 = 4.2v NiMH rechargeable battery of three cells. Prominent 100Hz harmonic mains sidebands at −70 to −90dBC can be seen. The oscillator and supply were not sufficiently screened or decoupled from mains interference. However ~2db amplitude fluctuations can be seen on most of the interlaced 50Hz harmonics. It might have been supposed that injection locking by mains interference might have had the effect of suppressing these fluctuations.

In this case the 'Blackman-Harris' windowing function available in Spectra Vue gave the very good FFT adjacent signal selectivity performance needed to separate the weak 50Hz harmonic components from the relatively strong 100Hz components. This windowing function gives the best adjacent FFT bin selectivity at the cost of a peak response widened to two or three FFT bins.

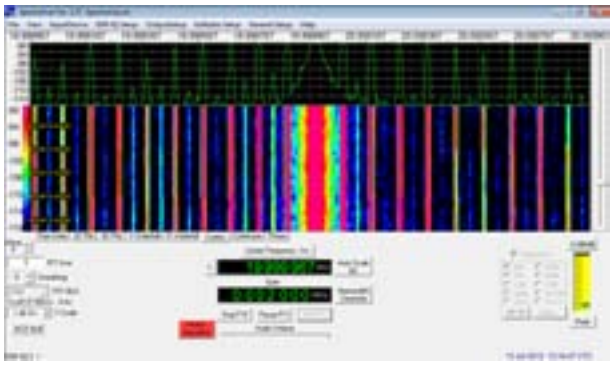

Fig. 4. Spectrum of 20MHz Crystal Oscillator with prominent 100Hz mains harmonic sidebands at about 70 to 90dBc. Time markers are at ten second intervals.

VI. Start-Up and Shock Spectrum Shape Transients of a 20MHz Crystal Oscillator.

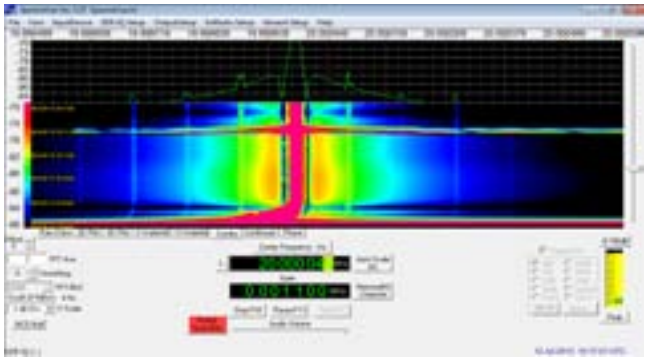

Fig. 5. Crystal mechanical shock spectrum shape transient at top of waterfall. Start-up transient at bottom of waterfall. 1.1kHz display bandwidth and 10sec spaced time markers. Blackman windowing was used.

Fig.5 compares the spectrum shape transient of a 20MHz crystal oscillator (CMAC IQXO-22) on start-up (at the bottom of the waterfall) with what occurs after a mechanical shock applied to the crystal. In both cases the spectrum shape narrows with a time constant that is inversely proportional to te resonator bandwidth. Start-up drift from a lower than final frequency is apparent. In the mechanical shock case the spurs can also be seen to be initially widened.

Here the Blackman windowing algorithm was used. It has less effective far-out selectivity but has two close-in nulls to improve close-in filter selectivity. These can be seen in Fig. 5 either side of the central carrier. However the orange and green 'blooming' of the spectrum seen between the two transients was found to be an unwanted artefact of the Blackman windowing algorithm. Long term variations (~20min) of up to 20dB were observed in this part of the spectrum. When Blackman-Harris windowing was applied better wide plateau selectivity was achieved, the close-in nulls disappeared and the long-term variations also disappeared. Thus the use of 'Blackman-Harris' windowing, rather than

'Blackman' windowing, appears to be essential in this application and this is used elsewhere in this paper.

VII. Strobe Measurement of LC Oscillator Switching Transients

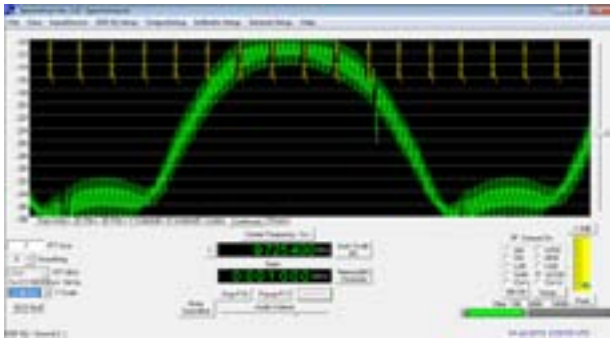

Fig. 6. Strobed time transients for 9.73MHz LC oscillator. Frequency jumpsTime markers at 1sec intervals. Strobe frequency of 18.51Hz. .

The 9.73MHz LC oscillator used for Fig. 6 and Fig. 7 has a resonator Q of ~120 and a bandwidth of ~800kHz. This means that the spectrum settling time constant is ~1.2µs. Depending on the 'RBW' bandwidth of the SpectraVue FFT the spectrum sampling rate will typically be no more than 2 to 4Hz. This is not sufficient for direct sampling of the spectrum transient in this case. However repetitive 'strobing' was found to be possible and to give a much expanded in time, albeit sampled, display of switching transients of this oscillator.

In Fig. 6 and Fig. 7 the oscillator frequency is being 'jumped' by a 18.51Hz square wave applied by a varactor across the tuned circuit. In Fig 6 the time scale has been expanded by the strobing from 1/18.51 to ~12s or ~200 times. In Fig. 7 the time expansion is ~40 times. The strobing expansion depends on there being a stable small fractional frequency offset from a whole number ratio between the FFT sampling frequency and the switching frequency stimulating the oscillator transient.

Fig. 6 is a right-to-left time display of the total lower sideband energy in response to the frequency switching at 18.51kHz. Fig. 7 shows the time decay of the lower sideband power as a spectrum.

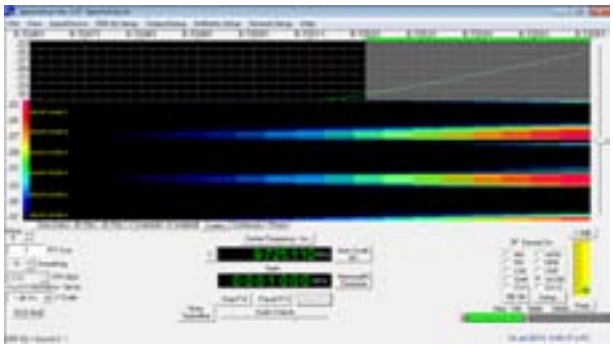

Fig. 7. Strobed Spectrum transients for 9.73MHz LC oscillator. Time markers at 1sec intervals. Strobe frequency of 18.51Hz.

VIII. Qualitative Theory of Spectrum Fluctuations

The Leeson model of an oscillator is as shown in Fig. 8 and its spectrum is shown in Fig. 9 [4]. The problem to be addressed is that the idealised 'bell-shaped' spectrum is only true as a long term time average. In practice we find that in the short term the spectrum shape is noisy and it fluctuates in amplitude and in the phase of its sideband components.

The fluctuations are found to be greatest when the sideband power density is comparable to the thermal noise and this occurs in the regions around the oscillator resonator 3dB bandwidth points.

We also find that the small amount of external discrete signal noise electromagnetically coupled into the oscillator resonator will cause 'spurs' which are constant in frequency but can fluctuate in amplitude. The process is one of partial injection locking [2] as indicated in Fig. 9.

Even if all external sources of interference can be filtered out then such low level spurs can still occur, but in this case their frequencies are less predictable and more random. It could then be regarded as a case of random self-injection locking. Such a concept needs further investigation.

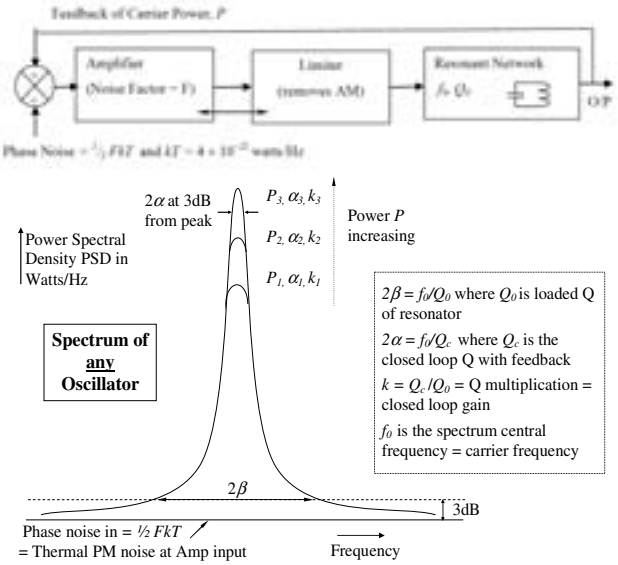

Fig. 8. Leeson Oscillator model at top with spectrum as a function of oscillator power below.

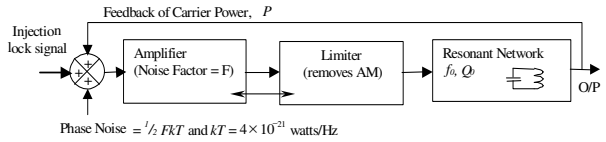

Fig. 9. Injection locking in the Leeson oscillator model.

The underlying assumption for spectrum fluctuations is that the total power of the oscillator remains constant, but power

can be temporarily transferred from one part of the spectrum to another to cause local spectrum fluctuations.

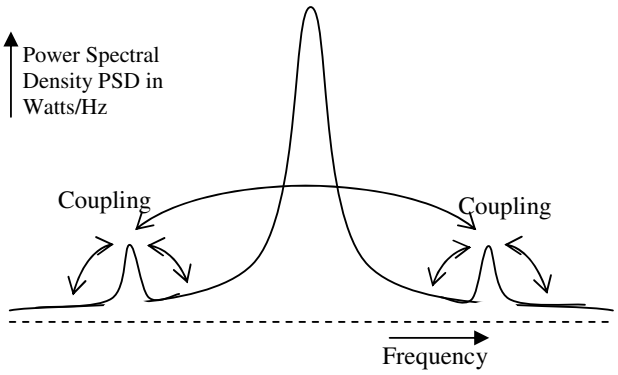

Fig. 10. A pair of oscillator spectrum noise components shown with exaggerated amplitude and coupling to other parts of the spectrum.

A more quantitative model of spectrum fluctuations can be envisaged on the basis that the power *coupling* factors for different parts of the spectrum determine the fluctuation periodicity and statistical time constants as shown in Fig. 10.

At present the coupling factors need to be observed and calibrated empirically. This is a step towards extracting a predictive theoretical model of oscillator fluctuations. However on the basis of the experiments and results so far we can deduce the following:

1. Coupling is strongest to adjacent parts of the surrounding spectrum and between opposite sideband pairs.

2. Coupling is strongest between components of almost the same spectral density. Otherwise the strongest component dominates and partially suppresses all weaker components.

3. The coupling factors are dependent on some inverse power of sideband frequency. The power could be $1/f^2$ or $1/f$ or $1/f^{½}$. More measurements are needed.

4. For stability when there are a multiple of coupled components the strongest component should exceed in power the sum of the powers of all the weaker components. When this is not the case the stronger component can be suppressed randomly by the ensemble of weaker components.

5. This is thought to be the main mechanism that can cause fluctuations in the shape of the spectrum, particularly around the 3dB resonator bandwidth points where the oscillator sidebands are not much stronger than the thermal noise.

IX. Conclusions

SDR Digital Spectrum Analyser techniques have made it possible to measure spectrum shape time fluctuations of crystal oscillators and LC oscillator signal sources for the first time with good accuracy.

Thus theory for oscillator spectrum shape fluctuations is being developed based on the measurements made so far. A second order Leeson model [4], with an energy constraint on the total spectrum power, is being considered. The coupling factor for transfer of energy between different parts of the spectrum appears to be inversely proportional to a (fractional) power of the frequency spacing. Further measurements are needed.

References

[1] M. J. Underhill, "Fundamental Phase Jumps in Oscillators?" Proc 20th EFTF, Braunschweig, Germany, 2006

[2] M. J. Underhill, "More fundamental instabilities in oscillators?", 15th EFTF'09: IEEE-IFCS'09, Besancon, France, 20-24 April 2009, pp 334-337.

[3] M. J. Underhill., "Time jitter and phase noise — Now and in the future?" IEEE International Frequency Control Symposium (FCS), p1-8, 2012.

[4] D. B. Leeson, "A simple model of feedback oscillator noise spectrum," Proc. IEEE, 54, No. 2, 1966, pp. 329-330.,

All-Digital Video RF Transmitter with Embedded Direct Frequency Synthesizer And an FPGA Implementation of It

Konstantinos Vasiliou
Electrical and Computer Engineering
National Technical University
Athens, Greece
costas290a@gmail.com

Kostas Galanopoulos
Electrical and Computer Engineering
National Technical University
Athens, Greece
galanopu@ieee.org

Paul P. Sotiriadis
Electrical and Computer Engineering
National Technical University
Athens, Greece
pps@ieee.org

***Abstract*— This paper presents a fully-digital analog-television RF transmitter realized on a small FPGA. Phase Alternating Line (PAL) encoding algorithms have been implemented along with digital filters and a Direct Digital frequency Synthesizer, for generating the carrier signal, achieving RF transmission of greyscale image captured from an onboard video camera.**

Keywords—Direct digital synthesis, frequency spurs, quantization, Digital-to-Analog converter

I. INTRODUCTION

Direct digital synthesizers (DDS) or numerically controlled oscillators are important in many digital communication systems [1], [2]. Quadrature synthesizers are used for constructing digital up and down converters, demodulators, and implementing various types of modulation schemes, including PSK (phase shift keying), FSK(frequency shift keying), and MSK (minimum shift keying) [3].

A common method for digitally generating a complex or real valued sinusoid employs the use of a phase accumulator and a sine/cosine lookup table. The lookup table stores samples of a sinusoid whereas the phase accumulator is used to generate a suitable phase argument that is mapped by the lookup table to the desirable output waveform. The average frequency of the DDS is defined by the frequency control word *w* and the system clock, $f_{clk.}$ The desirable frequency generated by the DDS is given by the following equation [4]:

$$f_{out} = \frac{W}{2^n} \cdot f_{clk}$$

Often a quantizer [5] is introduced between the phase accumulator and the LUT. The quantizer receives high precision phase angle and generates a lower precision representation of the angle in order to reduce the size of the LUT. This process decreases the size of the LUT from $2^n \cdot M$ to $2^t \cdot M$ but as an aftereffect introduces phase noise and unwanted spurious spectral components in the DDS output signal.

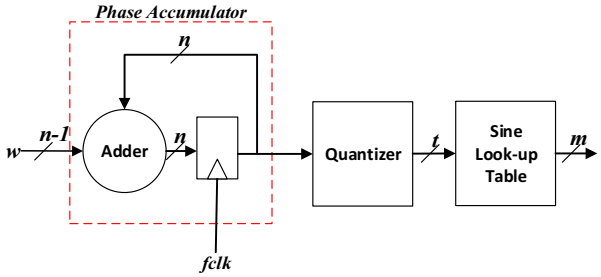

Figure. 1. Direct digital synthesizer core

Amplitude quantization is often employed in the output of the LUT, decreasing the world length of the amplitude to m bits. Amplitude quantization has an important effect on the spectral fidelity of the output signal introducing noise which decreases the signal-to-noise ratio. An approximation of the SNR in the output is given by [4]:

$$SNR = -6.02 \cdot m - 1.76\ dB$$

The maximum frequency output is given by the uniform sampling theorem $f_{outMAX} = \frac{Fs}{2}$ although a maximum frequency of $\frac{Fs}{4}$ is often preferred.

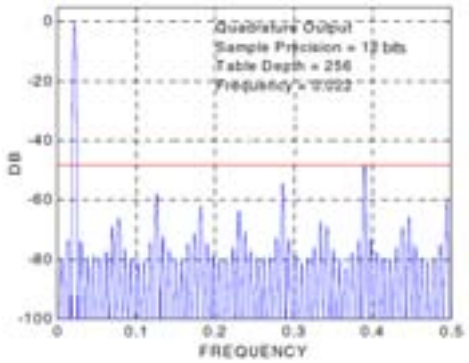

Figure. 2. Typical spectrum of the DDS core used with table depth = 256 and 12-bit precision samples [3]. Here it is $f_{out} = 0.022 \cdot f_{clk}$

The output of DDS is not perfectly periodic for most of the values of w resulting in an output signal with deterministic timing irregularities and a spectrum full of possibly strong and undesirable frequency spurs [6],[7]. Both phase and amplitude quantization techniques used in the process result in spectral artifacts. The depth of the look-up table affects the phase angle resolution and width affects the amplitude resolution of the signal. These resolution constraints are equivalent to time base jitter [8] and amplitude quantization of the signal and add spectral modulation lines and a broad-band noise floor to the signal's spectrum as shown in Fig. 2.

II. Phase Alternating Line (PAL) Analog Television Encoding System

A fully digital PAL television signal transmitter has been designed and implemented. PAL, short for Phase Alternating Line, is one of the three color encoding systems for analogue television and has been popular in most European countries. The other two analogue systems are NTSC and SECAM [9].

PAL encoding system has some advantages compared to the other two encoding systems. In contrast to NTSC, PAL does not require tint control circuit in order to perform color correction. In contrast to NTSC, the PAL standard automatically cancels hue errors by phase reversal, so tint control is unnecessary. This causes lower saturation, which is much less noticeable to the eye than NTSC hue errors. SECAM on the other hand uses Frequency Modulation with alternative transmission of the chrominance vectors. Although this technique solves the hue errors, the signal is more sensitive to cross-color intermodulation and a delay line is required at the receiver.

A frame in PAL encoding system (576i) consists of 625 lines, with 610 visible lines divided into two interlaced frames and 15 synchronizing lines.

Vertical synchronizing sequence for field 1, starts from scanline 623 and ends in scanline 5 inclusive. It consists of 6 pre-equalizing pulses, 5 long sync pulses and 5 post-equalizing pulses.

The synchronizing sequence for filed 2 starts from line 311 and ends in line 317 inclusive. It consists of 5 pre-equalizing pulses, 5 long sync pulses and 4 post-equalizing pulses. During the transmission of vertical sync pulses, teletext data can also be transmitted.

A typical PAL encoder consists of a complex system, where the chrominance components (U and V) are quadrature amplitude modulated and then added to the luminance signal (Y) in order to produce a complex baseband composite signal.

Then this signal is amplitude modulated to the desirable frequency and passed through a vestigial filter. Along with the visible components of the signal, horizontal and vertical synchronizing pulses and color subcarrier bursts are transmitted. The audio signal is Frequency Modulated and transmitted on a different carrier frequency in the same channel. The total bandwidth of the channel, including the picture and audio signal cannot extend more than 8 MHz as shown in fig. 5.

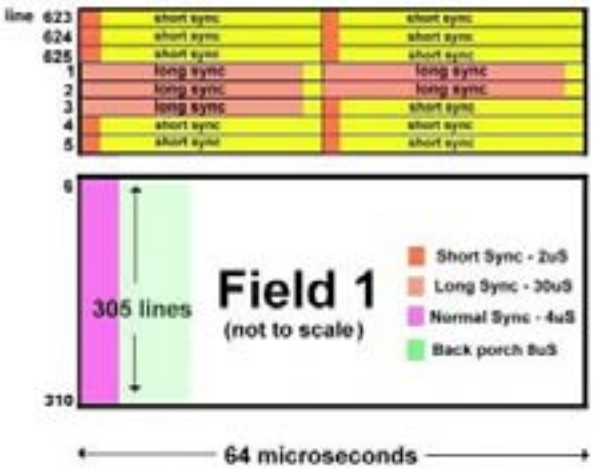

Figure. 3. Field 1 in PAL consisting of picture and synchronizing scanlines

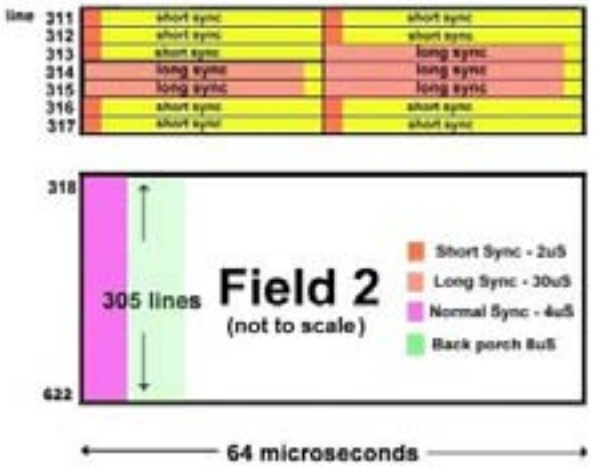

Figure. 4. Field 2 in PAL consisting of picture and synchronizing scanlines

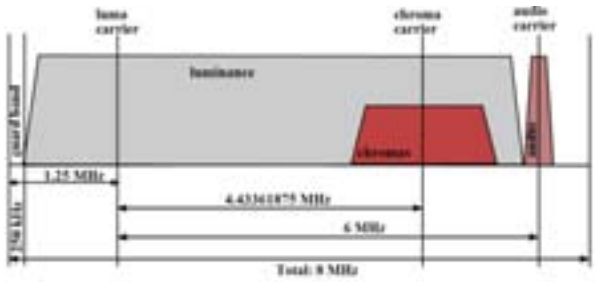

Figure. 5. Spectrum of a television channel with PAL

In order to implement a PAL encoder, a specially designed Finite State Machine and visual encoding algorithms have been created Fig.6. The image transmitted can be provided from another system, using a digital interface (ie. a PC using USB) or captured directly from a

video camera. For the purpose of the live demo we selected the second approach.

Image is live captured from an onboard inexpensive VGA camera module. Due to the different timings of VGA and PAL protocols, a RAM-based frame buffer is used to store the contents of a frame. The image is then encoded to the phase alternating line system and filtered in order to meet the bandwidth limitations. We have to note that due to limitations of RAM blocks on this entry level FPGA board, only a black and white picture is transmitted, whereas in a bigger FPGA board or an ASIC, a color transmitter can be implemented with minor modifications in the architecture.

In order to modulate the encoded baseband data stream, an n-bit wide Direct Digital Synthesizer is needed. Using multi-bit-output phase-dithered DDS we generate a 9-bit wide carrier sinusoid. The amplitude modulation is digitally implemented by directly multiplying the binary carrier and the DC-shifted composite data stream. Finally using digital amplitude dithering the multi-bit modulated signal is converted to 4-bit digital stream which is converted to analog trivial DAC realized with a resistor network.

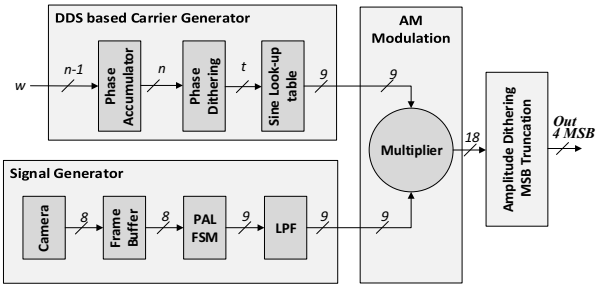

Figure. 6. DDS-based all-digital PAL video RF transmitter architecture using 4 bit random dithering DAC

III. Random Number Dithering And 4-Bit Quantization

Although many techniques are proposed in order to convert the multi-bit digital signal to a single-bit analog one, many of them require the use special or accurately matched analog components and detailed and time consuming analog design.

The proposed architecture requires the minimal use of analog components and can be easily implemented on any FPGA or ASIC integrated circuit. Instead of driving the multi-bit signal to the output DAC, amplitude dithering is employed and the most significant bits are driven to a low resolution DAC. This technique eliminates most of the unwanted spurs generated in all the stages of the signal path with the cost of the increased noise floor. The noise floor at the output is given in relationship to process gain and SNR by the following equation:

$$NF = 10 \cdot log_{10}\left(\frac{f_{clk}}{2}\right) + 6.02 \cdot log_2\left(\frac{output\ levels}{2}\right)\ dBc/Hz$$

Where the first term represents the process gain and the second term represents the gain due to the use of more than one output bits.

There are two techniques proposed for quantization of a fully digital multi-bit signal into an analog single-bit one. In both techniques a source of random a uniform noise is used [10], [11]. The multi-bit uniform noise generated by a random number generator is added to the AM modulated signal fig.7 and fig.8. and then the three or four most significant bits are kept.

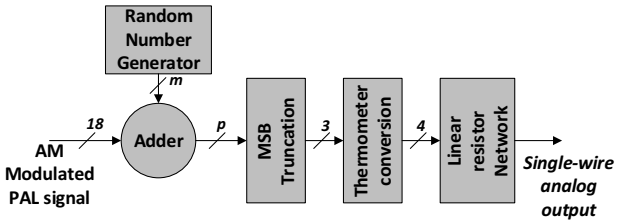

Figure. 7. Birary resistor network

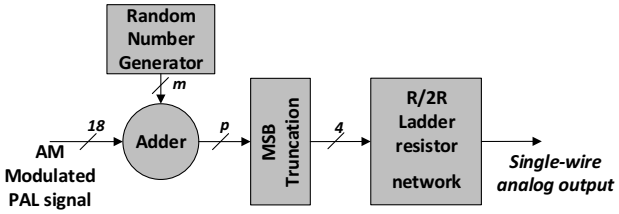

Figure. 8. R/2R Ladder resistor network

In the case we use a binary resistor network, the three MSBs are thermometer coded and then driven to a binary resistor network fig. 9a.

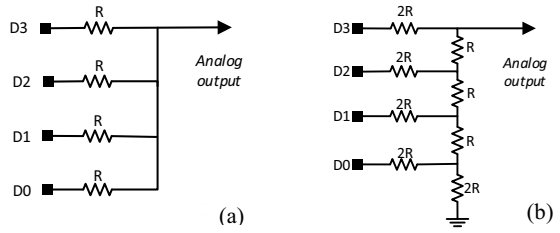

Figure. 9. (a) Birary resistor network,
(b) R/2R ladder resistor network

The second technique employs the use of an R/2R ladder resistor network. This technique improves the precision with the use or the same number of components fig. 9b.

IV. FPGA Implementation/Live Demo

Based on the proposed architecture in section II, and for the purpose of a live demonstration, the demo board in fig.10 was built. It is based on Papilio One [12], an entry level FPGA board, using Xilinx's Spartan 3E XC3S250E FPGA. This entry level FPGA has an equivalent of 250K gates and

only 216Kbits of Block RAM. A phase dithered DDS of n = 9 bits has been selected.

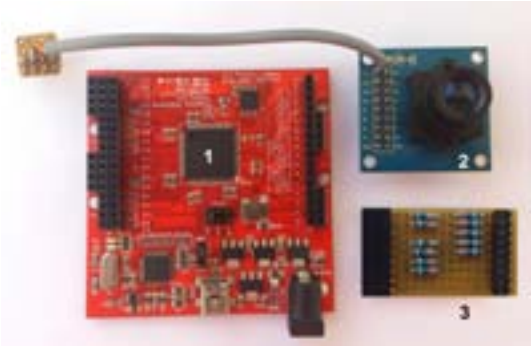

Figure. 10. Board built fot the purpose of the Live Demo

1. Papilio One/ Spartan 3E FPGA Board
2. OV7670 VGA Video Camera Module
3. R/2R ladder resistor network

For the analog-to-digital conversion, a random-dithering DAC was used. The only analog components are eight resistors, avoiding the use of active analog components.

The FPGA utilization of this implementation is presented in fig.11. Despite the use of a small FPGA chip, the whole project, including the camera module, PAL encoding algorithms, AM modulation and dithering module, occupies only 14% of the total chip resources.

The implementation operated at 200MHz achieving noise floor of about 88dBc/Hz (within the desirable frequency range) fig.13.

Device Utilization Summary			
Logic Utilization	Used	Available	Utilization
Number of Slice Flip Flops	352	4,896	7%
Number of 4 input LUTs	495	4,896	10%
Number of occupied Slices	365	2,448	14%
Number of bonded IOBs	20	66	30%

Figure. 11. Device utilization of the implemented Video RF transmitter

Figure. 12. Footage from the FPGA-based PAL Video RF transmitter

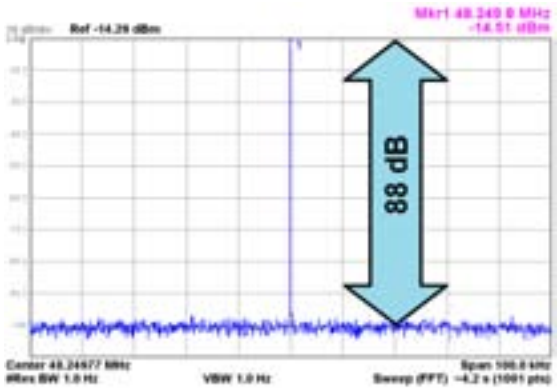

Figure. 13. FPGA Implementation (spectrum analyzer measurement of DDS output) using binary resistor network. Resolution BW = 1 Hz and waveform averaging Nav=10 runs

V. CONCLUSIONS

A versatile purely digital analog video transmitter architecture, that results in minimum chip-area, low-power and low-cost implementations, has been presented, including a nearly all-digital DAC. Measurements have demonstrated a dynamic range of over 88dBc/Hz. Random number dithering can reduce the size of the DAC, finally resulting in a single-bit output analog circuit. Through this work, it has been shown that the fabrication of traditionally analog circuits is possible, using only digital design techniques.

REFERENCES

[1] U.L. Rohde, Microwave and Wireless Synthesizers: Theory and Design, 1st ed. Singapore: Wiley-Interscience, 1997

[2] J. Vankka and K. Halonen, Direct Digital Synthesizers: Theory, Design and Applications, New york, Springer 2006

[3] K. Galanopoulos*, P. Sotiriadis, "Modulation Techniques for All-Digital Transmitters Based on Pulse Direct Digital Synthesizers", IEEE International Frequency Control Symposium 2012.

[4] Victor S. Reinhardt, "Spur Reduction Techniques in Direct Digital Synthesizers", Los Angeles: Hughes Space and Communications Company,1993

[5] "Xilinx DDS v5.0 Compiler Product Specification", DS246 April 28, 2005

[6] Lionel Cordesses, "Direct Digital Synthesis: A Tool For Periodic Wave Generation", Signal Processing Magazine, IEEE, July 2004

[7] P. Sotiriadis, K. Galanopoulos*, "Direct All-Digital Frequency Synthesis Techniques, Spurs Suppression, and Deterministic Jitter Correction", IEEE Trans. on Circuits and Systems-I, Vol. 59, No. 5, May 2012, pp. 958-968.

[8] O'Leary, P. ; Joanneum Res." A direct-digital synthesizer with improved spectral performance", July 1991

[9] ITU Radiocommunication Bureau (BR) "BT.470-5 - Conventional television systems", February 2005.

[10] K. Galanopoulos, P. Sotiriadis, "Optimal Dithering Sequences for Spurs Suppression in Pulse Direct Digital Synthesizers", IEEE International Frequency Control Symposium, 2012.

[11] P. Sotiriadis, N. Miliou, "Single-Bit Digital Frequency Synthesis via Dithered Nyquist-rate Sinewave Quantization", to appear in the IEEE Trans. on Circuits and Systems-I

[12] Papilio One FPGA Board Product Information, Available at: http://papilio.cc/index.php?n=Papilio.Hardware

Theoretical and Experimental Investigations of 1/*f* Noise in Quartz Crystal Resonators

S. Ghosh, F. Sthal, J. Imbaud, M. Devel, R. Bourquin, C. Vuillemin, A. Bakir, N. Cholley, P. Abbe, D. Vernier
FEMTO-ST Institute
UFC, CNRS, ENSMM, UTBM
Besançon, France
fsthal@ens2m.fr

G. Cibiel
Microwave and Time-Frequency
CNES
Toulouse, France

***Abstract*—Fluctuation dissipation theorem allows to recover a 1/*f* noise spectral density at low frequency. The level of this 1/f noise is governed by a single fitting parameter that can be connected to the onset frequency of this 1/*f* regime. It constitutes the fundamental intrinsic limit of quartz crystal. Some preliminary considerations on the physical origin of this parameter in terms of microscopic processes in the crystal are given. Experimentally, quartz crystal resonators have been cut from a quartz crystal block supplied specifically for this study on 1/f noise. The short-term stabilities of several resonators have been measured to be lower than $8{\cdot}10^{-14}$. A comparison of these resonators is given and the results are discussed according to the position of the resonators inside the crystal block.**

Keywords-1/f noise; quartz resonator; fluctuation-dissipation theorem; short-term stability.

I. INTRODUCTION

The Centre National d'Etudes Spatiales (CNES), Toulouse, France and the FEMTO-ST Institute, Besancon, France, have initiated investigations on the origins of noise in bulk acoustic wave resonators together with several European manufacturers [1]. Theoretical and experimental works are reported in this paper. We first improve on our previous study using fluctuation dissipation theorem (FDT) by adding a term for internal damping [2] to the classical wave equation already studied [3]. This allows us to recover a 1/*f* noise spectral density at low frequency. The level of this 1/*f* noise is governed by a single fitting parameter that can be connected to the onset frequency of this 1/*f* regime. It constitutes the fundamental intrinsic limit of quartz crystal. Some preliminary considerations on the physical origin of this parameter in terms of microscopic processes in the crystal are given.

Experimentally, quartz crystal resonators have been cut from a quartz crystal block supplied specifically for this study on 1/*f* noise. The reader is reminded of the description of the blank realization and the topology of the resonator prototype is exposed. The resulting resonators are SC-cut with a 5 MHz resonant frequency. Then, we report noise measurements made on these quartz crystal resonators using a passive phase noise measurement system. The short-term stabilities of several resonators have been measured to be lower than $8{\cdot}10^{-14}$. A comparison of these resonators is given and the results are discussed according to the position of the resonators inside the crystal block.

II. THEORETICAL APPROACH

A. Fluctuation-Dissipation Theorem

The fluctuation-dissipation theorem (FDT) as formulated in [4] and [5] is used to estimate the power spectral density of thermal noise coming from fluctuations in the thickness (2*h*) of quartz resonators (cf. Fig. 1).

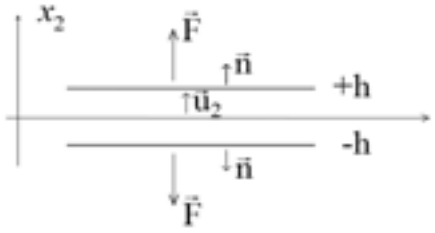

Figure 1 : Resonator design.

In a previous paper [3], we described these fluctuations by a 1D viscoelastic model of the longitudinal vibrations along the thickness of the quartz resonator (axis x_2). The level of white noise was found to be far below what is measured, meaning that viscoelastic damping of thickness fluctuations is not the dominant noise process. Here, an internal friction term, φ, is added in the formulation, in order to obtain a 1/*f* spectrum at low frequencies. Indeed, for this mode (characterized by the mechanical displacement inside the resonator $u_2(x_2,t)$), the strain S_2 and stress T_2 are then respectively given by:

$$S_2 = \frac{\partial u_2}{\partial x_2} \tag{1}$$

$$T_2 = c_{22}(1 + j\varphi)S_2 + \eta_{22}\frac{\partial S_2}{\partial t} \tag{2}$$

with c_{22} the elastic constant and η_{22} the viscoelastic damping constant of quartz crystal. φ is an internal friction coefficient [2], [5].

The fundamental principle of dynamics for continuum media can then be written as:

$$\rho \frac{\partial^2 u_2}{\partial t^2} = c_{22}(1 + j\varphi) \frac{\partial^2 u_2}{\partial x_2^2} + \eta_{22} \frac{\partial^3 u_2}{\partial x_2^2 \partial t} \quad (3)$$

with ρ the quartz mass per unit volume.

Searching for solutions of the type:

$$u_2(x_2, t) = [a \sin(kx_2) + b \cos(kx_2)]e^{j\omega t} \quad (4)$$

with limit condition given by:

$$T_2(\pm h, t) = F \cdot e^{j\omega t}/S \quad (5)$$

with F the modulus of the harmonic mechanical force applied to the surface S of the electrodes (perpendicular to x_2), gives:

$$k^2 = \frac{\rho\omega^2}{(c_{22}+j(c_{22}\varphi+\eta_{22}\omega))} \quad (6)$$

$$a = \frac{F/S}{(k\cos(kh)(c_{22}+j(c_{22}\varphi+\eta_{22}\omega))} \quad (7)$$

$$b = 0 \quad (8)$$

The complex mechanical admittance of the system is defined by:

$$\bar{Y}(\omega) \equiv \frac{\frac{\partial u_2(\pm h,t)}{\partial t}}{\pm F \cdot e^{j\omega t}} = \frac{j\omega a \sin(kh)}{F} \quad (9)$$

The FDT then states that the spectral power density of the thickness fluctuations can be computed by [4] and [5]:

$$u_2^2(\pm h, \omega) = \frac{4k_B T}{\omega^2} Re\left(\bar{Y}(\omega)\right) \quad (10)$$

with T the absolute temperature (in K) and k_B the Boltzmann constant (in J/K).

Inserting (7) into (9), then the result into (10) with the assumptions $\varphi \ll 1$ and $\omega \ll c_{22}/\eta_{22}$ gives:

$$u_2^2(\pm h, \omega) \approx \frac{4k_B T h}{S\omega c_{22}^2}(\eta_{22}\omega + c_{22}\varphi) \quad (11)$$

Moreover, we can consider that the circular frequency at resonance $\omega_r \sim 1/h$, thus:

$$S_y(\omega) = \frac{\langle(\partial\omega_r)^2\rangle_\omega}{\omega_r^2} = \frac{u_2^2}{(2h)^2} \quad (12)$$

then:

$$S_y(\omega) \approx \frac{1}{\omega} \times \frac{2k_B T}{V c_{22}} \left(\frac{\eta_{22}}{c_{22}}\omega + \varphi\right) \quad (13)$$

where V is the volume of the resonator. One can then see from the previous expression that for circular frequencies lower than $\varphi\, c_{22}/\eta_{22}$, the internal friction becomes dominant and gives a $1/f$ spectrum. Hence, φ could, in principle, be determined by the corner frequency between 1/*f* noise and white noise in the bare resonator (Fig. 2).

For 1/*f* (flicker) noise, the standard deviation of the difference of the average fractional frequencies measured for two consecutive samples is given by the expression [6]:

$$\sigma_{y\_flicker} = \sqrt{2\ln(2) S_y(1Hz)} \quad (14)$$

This is the square root of the Allan variance [7]. It is commonly used to compare the short-term stabilities of various resonators, since it is the noise at low frequencies floor in terms of relative frequency fluctuations.

Provided the corner frequency is bigger than 1 Hz, $\sigma_{y\_flicker}$ would be given by:

$$\sigma_{y\_flicker} = \sqrt{2\ln(2) \frac{2k_B T}{V c_{22}} \varphi} \quad (15)$$

We note that φ could depend upon the temperature and that no assumption where made about this possible dependence.

B. Numerical application

We consider here numerical values typical for a 5 MHz oscillator equipped with an SC-cut quartz crystal resonator. Due to the rotation of the axis, the 2 axis is not the usual one, so that the constants must be evaluated in the rotated basis: c_{22} = 115 GPa, η_{22} = 1.36·10^{-3} Pa·s, $T = 350$ K and $V = 0.104$ cm^3. This gives:

$$\sigma_{y\_flicker} \approx 1.06 \cdot 10^{-12} \sqrt{\varphi} \quad (16)$$

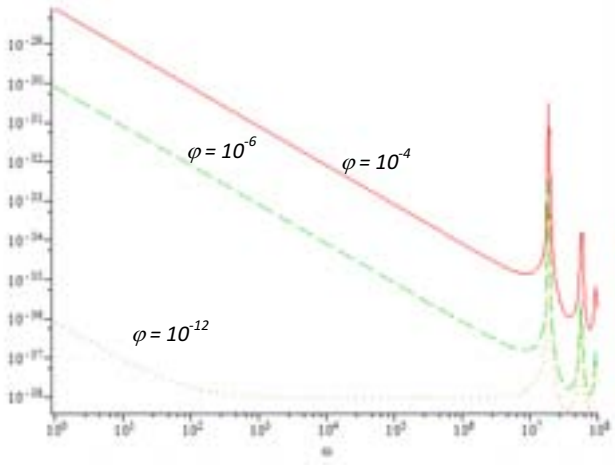

Figure 2 : Behavior of $S_y(\omega)$ for various values of φ. The transition frequency between the $1/\omega$ regime and the white noise regime is proportional to φ.

Unfortunately, in present measurements, the white noise of the amplifier is masking the white noise of the resonator, so that we cannot estimate the maximum possible value of φ from our measurements.

In order to recover measured values of $\sigma_{y\_flicker}$ with this expression, we would need to have φ between 10^{-2} and 10^{-4}, which would mean that even at resonance the internal damping would be dominant over viscoelastic damping…

III. EXPERIMENTAL RESULTS

A. Short term stability definition

The passive technique using carrier suppression is used to characterize the inherent phase stability of the ultra-stable resonators [6]. The noise results are usually measured in term of $\mathcal{L}(f)$, the one-sided power spectral density (PSD) of the phase fluctuations. If the two resonators can be considered reasonably identical, then, half of the total noise is attributed to each resonator. In that case, $\mathcal{L}(1Hz)$ is equal to $S_\phi(1Hz)$, which can be used to compute the PSD of relative frequency fluctuations $S_y(f)$, using [6]:

$$S_y(1Hz) = \left[\frac{F_L^2+1}{f_{res.}^2}\right] S_\phi(1Hz) \qquad (17)$$

with $f_{res.}$ the resonant frequency of the resonator. Finally, for $1/f$ (flicker) noise, the standard deviation of the difference of the average fractional frequencies measured for two consecutive samples is given by (14).

B. Resonator realization

The crystal block is presented in Fig. 3. This crystal block is obtained from a seed cut in a previous synthetic crystal which was grown using a natural seed. Its dimensions were approximately 220 mm along the Y-axis, 36 mm along the Z-axis and 110 mm along the X-axis. Two Y-cut slices have been cut before and after an oriented block used to achieve ten quartz bars. The Y-cut slices are used to obtain for dislocations evaluation by X-ray topographies. The red marks show how the crystal is cut in order to get SC-cut blanks from 14 initial bars. First, Fourteen quartz bars pre-oriented on the first rotation angle have been achieved. The length of the bars was about 70 mm. Taking into account the width of the cutting saw, about 24 resonators can be obtained in each bar.

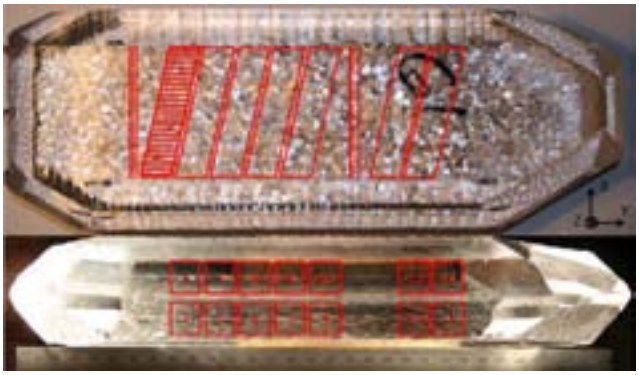

Figure 3 : Quartz crystal resonators according to their positions in the mother block.

The final prototype of the resonator is a typical 5 MHz SC-cut resonator. The diameter of the resonator is 14 mm for a thickness of 1.09 mm. A plano-convex shape allows the energy trapping for the 3rd overtone of the slowest thickness shear mode (C-mode). A radius of curvature of 130 mm has been chosen to optimize this energy trapping according to the Tiersten-Stevens model [8]. Electrodes diameter is 8 mm. The temperature turn over point of the resonator is chosen between 80 °C and 85 °C by adjusting the cutting angles.

C. Noise results

Fig. 4 and 5 give the short-term stability floors of resonators obtained in bars 12 and 14. They span approximately two orders of magnitude. The best resonators have a short-term stability (Flicker floor) below $8{\cdot}10^{-14}$, whereas the worst are above 10^{-12}. Although the positions of the blanks are known, no clear correlation between the noise results and the blanks positions (e.g. center or edges) can be found for these bars.

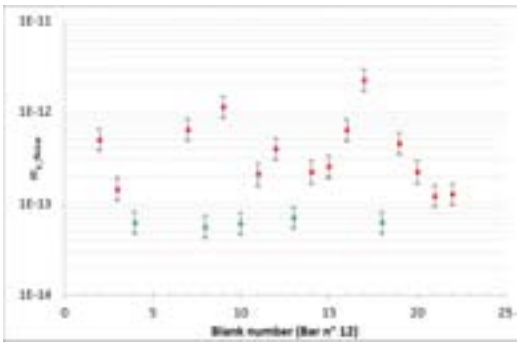

Figure 4 : Noise measurements from resonators cut in bar 12.

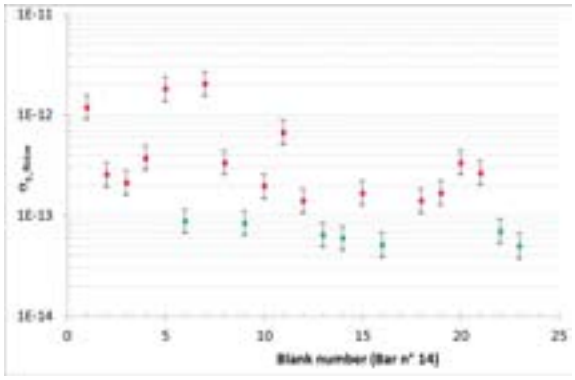

Figure 5 : Noise measurements from resonators cut in bar 14.

Fig. 6 presents the standard deviation of the noise floor of all the resonators measured so far, including those from bar 12 and 14. Resonators from bar 1 to 11 are not precisely localized along the bar. No clear effect of the bar position can be seen in these preliminary results. Other measurements are under way.

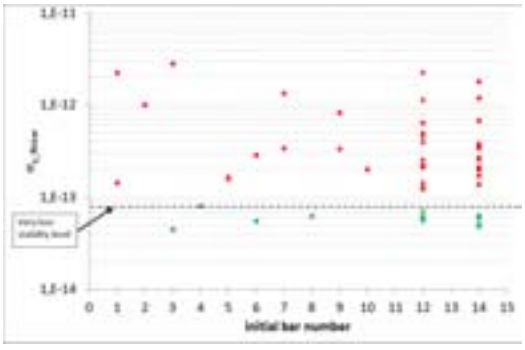

Figure 6 : Short-term stability of quartz crystal resonators according to the position in the mother block.

IV. Conclusion

Using a damping force proportional to strain and independent of frequency, naturally allows to get a $1/f$ noise spectrum at low frequencies. Indeed, we could get the noise limit of measured resonators, a few 10^{-14} [9-11], with $\varphi > 10^{-4}$. However, this would mean that the effective value of Q at the resonance would be dominated by internal damping (addition of losses: $1/Q_{eff} = (1/Q_{viscous} + \varphi)$ and lower than what is measured by at least 2 orders of magnitude. We therefore conclude that internal damping of thickness fluctuations by any force proportional to strain and independent of frequency, may not be the dominant noise mechanism for the best SC-cut quartz resonators.

The short-term stability of ultra-stable resonators has been studied according to the position of the blanks in the mother crystal. The short term stability of several resonators has been measured lower than $8 \cdot 10^{-14}$. No clear correlation between the blank position and the quality of the resonator can be seen in these preliminary data. Results coming from the other blanks are expected in a near future and may give some more indications.

Acknowledgment

The authors would like to thank the Centre National d'Etudes Spatiales for the project's financial support.

References

[1] F. Sthal, S. Galliou, J. Imbaud, X. Vacheret, P. Salzenstein, E. Rubiola, G. Cibiel, "About Quartz Crystal Resonator Noise: Recent Study," Proc. ICNF, Pisa, Italie, 15-19 June, pp. 607-610, 2009.

[2] G. I. Gonzalez and P. R. Saulson, "Brownian motion of torsion pendulum with internal friction," Phys. Lett. A, vol. 201, pp. 12-18, May 1995.

[3] M. Devel, R. Bourquin, S. Ghosh, J. Imbaud, G. Cibiel, F. Sthal, "Quartz crystal resonator noise and fluctuation-dissipation theorem considerations," Proc. IEEE Int. Freq. Cont. Symp., Baltimore, Maryland, 22-24 May, pp. 425-429, 2012.

[4] H. B. Callen and R. F. Greene, "On a theorem of irreversible thermodynamics," Phys Rev., vol. 86, no. 5, pp. 702–710, 1952.

[5] P. R. Saulson, "Thermal noise in mechanical experiments," Phys. Rev. D, vol. 42, no. 8, pp. 2437–2445, 1990.

[6] F. Sthal, J. Imbaud, X. Vacheret, P. Salzenstein, G. Cibiel, S. Galliou "Computation method for the short-term stability of quartz crystal resonators obtained from passive phase noise," IEEE Transactions on Ultrasonics, Ferroelectrics and Frequency Control, , vol. 60, no. 7, July, pp. 1530-1532, 2013.

[7] D. W. Allan, "Statistics of atomic frequency standards," Proc. IEEE, vol. 54, no. 2, Feb., pp. 136-154, 1966.

[8] D.S. Stevens, H.F. Tiersten, "An analysis of doubly rotated quartz resonators utilizing essentially thickness modes with transverse varation," J.A.S.A., vol. 79, no. 6, pp. 1811-1826, June 1986.

[9] J. R. Norton, "Performance of ultrastable quartz oscillators using BVA resonators," Proc. European Frequency and Time Forum, Weihenstephan, Germany, March, pp. 457-465, 1994.

[10] R. J. Besson, M. Mourey, S. Galliou, F. Marionnet, F. Gonzalez, P. Guillemot, R. Tjoelker, W. Diener, A. Kirk, "10 MHz Hyperstable quartz oscillators," Proc. Joint Meeting IEEE Ann. Freq. Cont. Symp. and European Frequency and Time Forum, Besançon, France, april, pp. 326-330, 1999.

[11] P. Salzenstein, A. Kuna, L. Sojdr and J. Chauvin, "Significant step in ultra high stability quartz crystal oscillators," Electron. Lett., vol. 46, no. 21, pp. 1433-1434, 2010.

Switching Down-Converting RF Mixer with Embedded Single-Bit-Output All-Digital Frequency Synthesizer

Nikos Stamatopoulos
Department of ECE
National Technical University of Athens
Greece
nstam@ieee.org

Kostas Galanopoulos
Department of ECE
National Technical University of Athens
Greece
galanopu@ieee.org

Paul P. Sotiriadis
Department of ECE
National Technical University of Athens
Greece
pps@ieee.org

***Abstract*—An RF switching down-converting mixer with an embedded single-bit-output all-digital frequency synthesizer is proposed. The output spectrum of the mixer is derived analytically based on that of the synthesizer as well as with simulation. A test setup using an FPGA implementation of the synthesizer and a discrete-component switching mixer has been built. Measurements are presented confirming the theoretical derivations.**

Keywords—switching mixer; frequency synthesizer;

I. INTRODUCTION

The interest in all-digital architectures has been intensified in the RFIC industry over the past few years due to the increasing challenge in the design and the extra cost of fabrication of RF analog and mixed-signal IC versus standard digital ones in modern nano-scale IC technologies. Digital circuit design has the advantage of portability, reconfigurability, automated checking and verification.

This paper proposes a switching RF down-converting mixer whose Local Oscillator (LO) input is driven by an embedded single-bit output all-digital frequency synthesizer, offering some of the aforementioned advantages compared to traditional analog mixer architectures.

Switching mixers are popular blocks in discrete-component designs and have been implemented in RFICs [1][1]. However, they are typically driven by classical PLLs or complex mixed-signal frequency synthesizers.

The proposed mixer architecture is shown in Fig. 1 below and is based on digital transmission gates which are driven directly by the single-bit output stream of the embedded all-digital frequency synthesizer. Certain dithering techniques are also used to make the synthesizer's spectrum sinewave-like and convert spurs to continuous noise floor.

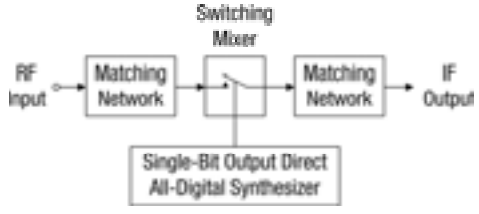

Fig. 1. Proposed switching mixer with embedded all-digital synthesizer.

First we discuss the embedded all-digital frequency synthesizer in Section II and state analytically its output spectrum. Then, the switching mixer architecture is described in Section III and its output spectrum is mathematically derived using that of the synthesizer. Finally the test setup is discussed and the measurements derived are presented and compared to the theoretical ones in Section IV.

II. EMBEDDED ALL-DIGITAL FREQUENCY SYNTHESIZER

The proposed mixer, shown in Fig. 1, comprises of a transmission gate which is digitally controlled by the all-digital frequency synthesizer. The synthesizer architecture and its output spectrum are described in the following sections.

A. Frequency Synthesizer's Architecture

The LO signal is provided by a Pulse Direct Digital Synthesizer (PDDS). It consists of a phase accumulator (n-bits wide), the Most Significant Bit of which is used as the output signal.

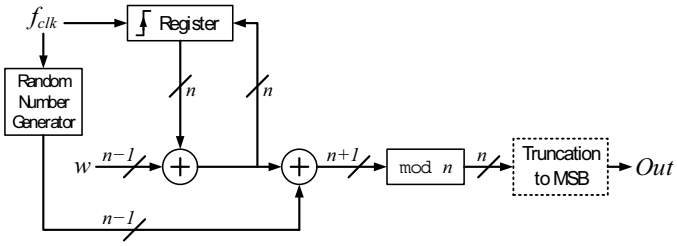

Fig. 2. Block diagram of single-bit output frequency synthesizer with phase dithering implementation.

PDDS is an extreme case of a single-bit DDS. Thus, especially when no oversampling is used, the output of the PDDS has deterministic timing irregularities and a spectrum full of strong and undesirable frequency spurs. Although the strongest frequency component is typically at the desirable average frequency, the spectral quality is unacceptable for analog and RF applications, unless a spurs-suppression technique is used.

Here we use phase dithering to randomize the synthesizer's output (otherwise) deterministic jitter and break any periodicity of it, spreading the power of the frequency spurs over the sampling bandwidth $[0, f_{clk}]$. As a drawback, a continuous noise floor is formed.

Dithering is implemented by generating a digital random sequence formed of independent and identically distributed random variables and adding it to the output of the Phase Accumulator (just before truncation) [2]. The cumulative distribution function of the random variables is of the form

$$F(u)=\left(1+\sin\left(\frac{\pi u}{2^{n-1}}-\frac{\pi}{2}\right)\right) \text{ with } u=0,1,2,\ldots,\left(2^{n-1}-1\right) \quad (1)$$

It has been demonstrated [1] that the PDDS in Fig. 1 with such a dithering sequence results in spurs-free output.

B. Frequency Synthesizer's Output Spectrum

The average output frequency of the synthesizer, based on the clock frequency f_{clk}, is equal to $f_{LO}=\left(w/2^n\right)f_{clk}$ where the Frequency Control Word w (n-1 bits wide) ranges within $0<w<2^{n-1}$ and so f_{LO} takes values within $\left[0, f_{clk}/2\right]$ with step $f_{clk}/2^n$.

It can be shown that the output of the considered PDDS is equivalent to that of the uniformly dithered single-bit Nyquist-rate quantized sinewave [3]. So the Power Spectral Density (PSD) of the synthesizer's output $v(t)$, considered as a ±1 signal (and *not* as a digital 0/1 one) is given by

$$S_v(f)=\operatorname{sinc}^2\left(\frac{f}{f_{clk}}\right)\left[\frac{1}{4}\delta\left(f\pm\frac{w}{2^n}f_{clk}\right)+\frac{1}{2f_{clk}}\right] \quad (2)$$

where $f\in\left[-f_{clk}, f_{clk}\right]$ and the spectrum is f_{clk} - periodic except the envelop function $\operatorname{sinc}^2\left(f/f_{clk}\right)$.

III. Mixer Architecture & Output Spectrum

The mixer, shown in Fig. 1, has a simple single-ended switching structure with passive networks on the RF input and IF output ports for impedance matching. The switch, controlled by the PDDS's output acts essentially as 0/1 multiplier.

A. Mixer Output Spectrum

In this section we derive expressions of the output spectrum of the mixer. We denote the RF input signal as $g(t)$. The output of the mixer is essentially the multiplication result $y(t)=g(t)x(t)$ where $x(t)$ is the 0/1 single-bit output of the frequency synthesizer. We write $x(t)=\left(v(t)+1\right)/2$ to relate it with the ±1 signaling used for the expression of the spectrum in Eq. (2).

To determine the power spectral density of the mixer output $y(t)$ we calculate the autocorrelation function of the output[1] which is given by

$$R_y(t,t+\tau)=\frac{1}{4}E\left\{\left[v(t)+1\right]g(t)\left[v(t+\tau)+1\right]g(t+\tau)\right\} \quad (3)$$

[1] Recall that the output of the mixer is a random signal due to the dithering.

Although $g(t)$ can be any signal, we consider it to be deterministic, e.g. a sinewave. The above equation becomes

$$\begin{aligned}R_y(t,t+\tau)&=\frac{g(t)g(t+\tau)}{4}E\left\{v(t)v(t+\tau)+v(t)+v(t+\tau)+1\right\}\\&=\frac{g(t)g(t+\tau)}{4}E\left\{v(t)v(t+\tau)+1\right\}\\&=\frac{g(t)g(t+\tau)}{4}\left[1+R_v(t,t+\tau)\right]\end{aligned}$$

where we used the fact $E\left\{v(t)\right\}=0$ for all values of t.

Since $y(t)$ is not a Wide-Sense Stationary (WSS) signal, instead of R_y we have to use the more general average-autocorrelation function defined as

$$\bar{R}_y(\tau)=\lim_{T\to\infty}\left[\frac{1}{2T}\int_{-T}^{T}R_y(t,t+\tau)\,\mathrm{d}t\right] \quad (4)$$

To simplify the algebra we assume that $g(t)=A\sin\left(2\pi f_g t\right)$, implying after a few steps that[2]

$$\bar{R}_y(\tau)=\frac{A^2}{8}\cos\left(2\pi f_g\tau\right)\left[1+\bar{R}_v(\tau)\right] \quad (5)$$

The power spectral density of $y(t)$ is the Fourier transform of $\bar{R}_y(\tau)$ [4], which is the convolution of the Fourier transforms of $\cos\left(2\pi f_g\tau\right)$ and $\left[1+\bar{R}_v(\tau)\right]$. The latter becomes $\left[\delta(f)+S_v(f)\right]$ where S_v is given by (2). Therefore,

$$\begin{aligned}S_y(f)&=\frac{A^2}{16}\left[\delta\left(f-f_g\right)+\delta\left(f+f_g\right)\right]\otimes\left[\delta(f)+S_v(f)\right]\\&=\frac{A^2}{16}\left[\delta\left(f-f_g\right)+\delta\left(f+f_g\right)+S_v\left(f-f_g\right)+S_v\left(f+f_g\right)\right]\end{aligned} \quad (6)$$

Combining it with Eq. (2) we derive

$$\begin{aligned}S_y(f)=&\frac{A^2}{16}\left[\delta\left(f-f_g\right)+\delta\left(f+f_g\right)\right]\\&+\frac{A^2}{16}\operatorname{sinc}^2\left(\frac{f-f_g}{f_{clk}}\right)\left[\frac{1}{4}\delta\left(f-f_g\pm\frac{w}{2^n}f_{clk}\right)+\frac{1}{2f_{clk}}\right]\\&+\frac{A^2}{16}\operatorname{sinc}^2\left(\frac{f+f_g}{f_{clk}}\right)\left[\frac{1}{4}\delta\left(f+f_g\pm\frac{w}{2^n}f_{clk}\right)+\frac{1}{2f_{clk}}\right]\end{aligned} \quad (7)$$

Since the mixer is used for down-conversion, the desirable component at the output is at frequency[3] $f=\left(w/2^n\right)f_{clk}-f_g$ and of amplitude $A^2\operatorname{sinc}^2\left(w/2^n\right)/64$ (see Eq. (7)). Again, from Eq. (7) the continuous noise power spectral density at the same frequency is given by

[2] Under some minor assumptions on the relationship between w, n and f_g.

[3] It is assumed that $f_{LO}\equiv\left(w/2^n\right)f_{clk}>f_g\equiv f_{RF}$.

$$\frac{A^2}{32 f_{clk}}\left[\operatorname{sinc}^2\left(\frac{w}{2^n}-\frac{2f_g}{f_{clk}}\right)+\operatorname{sinc}^2\left(\frac{w}{2^n}\right)\right].$$

Therefore, the noise level with respect to the carrier equals

$$NPower = 10\log_{10}\left(1+\frac{\operatorname{sinc}^2\left(\frac{w}{2^n}-\frac{2f_g}{f_{clk}}\right)}{\operatorname{sinc}^2\left(\frac{w}{2^n}\right)}\right)+3-10\log_{10}\left(f_{clk}\right)\ (\text{dBc})$$

If $w/2^n$ and f_g / f_{clk} are smaller than 0.3 or so then one can approximate the sinc functions with one and derive the simplified expression

$$NPower = 6-10\log_{10}\left(f_{clk}\right) \qquad (8)$$

IV. Measurements & Results

Our test setup consists of the mixer architecture in Fig. 1 with the all-digital frequency synthesizer implemented in a mini FPGA board (XuLA-50 / Xilinx Spartan-3A). Both the low-cost off-the-shelf transmission gate (with on/off switching time ~5ns) and the low-cost FPGA limit the frequency of operation of the mixer to a few tens of MHz.

Case 1: The clock frequency of the PDDS is $f_{clk} = 10\,\text{MHz}$ and its synthesized output frequency is set to $f_{LO} = 3$ MHz. The RF signal is a sinewave at $f_{RF} \cong 2.7$ MHz. The mixer's output spectrum centered at the desirable output frequency component $f_{LO} - f_{RF}$ is shown in Fig. 3.

From Eq. (8) we derive that the noise floor in this case is about $-64\,\text{dBc}$. This is exactly what the measurement in Fig. 3 below shows.

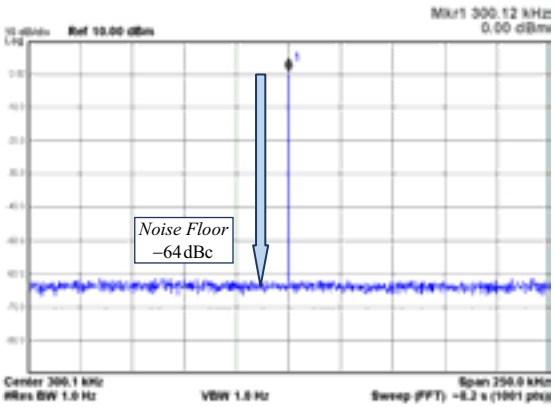

Fig. 3. Output of the switching mixer, with $f_{clk} = 10\,\text{MHz}$, $f_{RF} = 2.7$ MHz, $f_{LO} = 3$ MHz (centered at 300 kHz).

Case 2: The clock frequency of the PDDS is $f_{clk} = 200\,\text{MHz}$ and its synthesized output frequency is set to $f_{LO} = 21.2$ MHz. The RF signal is a sinewave at $f_{RF} \cong 20$ MHz. The mixer's output spectrum $0-50$ MHz is shown in Fig. 4 as well as in Fig. 5 which is centered at the desirable frequency component $f_{LO} - f_{RF}$. The gradient of the noise floor near zero frequency is probably due to the lack of calibration of the spectrum analyzer below 10MHz.

Again, using Eq. (8) we derive that the noise floor level should be about $-77\,\text{dBc}$. The estimate is confirmed by the measurement in Fig. 5 below.

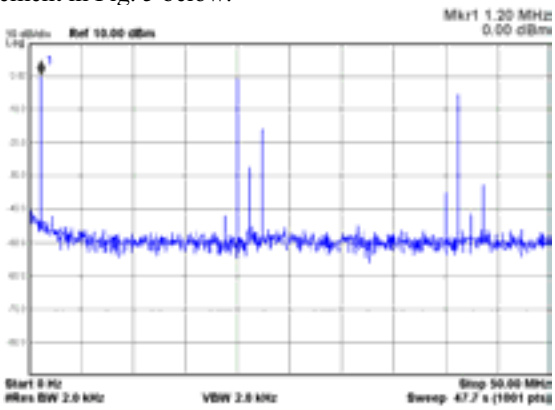

Fig. 4. Output (0-50 MHz) of the switching mixer, with $f_{clk} = 200\,\text{MHz}$, $f_{RF} = 20$ MHz, $f_{LO} = 21.2$ MHz.

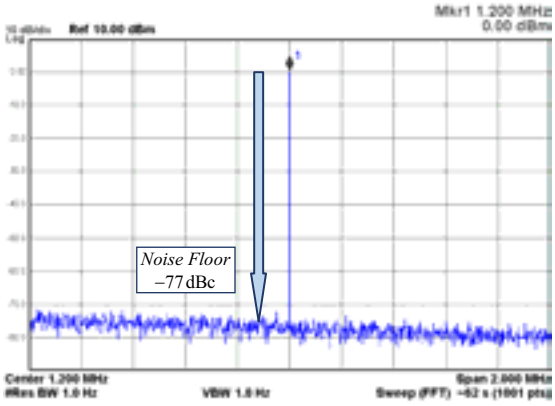

Fig. 5. Output of the switching mixer, with $f_{clk} = 200\,\text{MHz}$, $f_{RF} = 20$ MHz, $f_{LO} = 21.2$ MHz (centered at 1.2 MHz).

V. Conclusions

A switching RF down-converting mixer with an embedded all-digital frequency synthesizer has been proposed and its output spectrum has been derived mathematically. The measurements with our test setup agree with the theory. Future directions include balanced switching architectures and VLSI implementations of this approach in order to illustrate results in higher frequencies.

References

[1] George D. Vendelin, Anthony M. Pavio, Ulrich L. Rohde, "Microwave Circuit Design Using Linear and Nonlinear Techniques", 2nd edition, Wiley-Interscience, 2005.

[2] Kostas Galanopoulos, Paul P. Sotiriadis, "Optimal Dithering Sequences for Spurs Suppression in Pulse Direct Digital Synthesizers", IEEE International Frequency Control Symposium 2012.

[3] Paul P. Sotiriadis, Natalia Miliou, "Single-Bit Digital Frequency Synthesis via Dithered Nyquist-rate Sinewave Quantization", to appear in the IEEE Trans. on Circuits and Systems-I (TCAS-I 13452).

[4] J.G. Proakis, M. Salehi, Digital Communications, 5th Ed., McGraw-Hill Companies, Inc., 2007.

433 MHz Wide-tunable High Q SAW Oscillator

Tsubasa Yasuda*, Kohei Uchino, Shyoji Izumiya, and Takehiko Adachi
Faculty of Engineering
Yokohama National University
Yokohama, Japan
E-mail:ada@ynu.ac.jp

Shasika Shaminda Senanayaka
Engineering Dept. 3
NIHON DEMPA KOGYO CO. LTD.
Sayama, Japan
E-mail:shashika@ndk.com

Abstract— **In this paper, we have made a 433 MHz dual-T SAW oscillator. The oscillator is made of an amplifier, variable gain amplifiers, phase shifters and dual-T SAW resonator circuit. Oscillation frequency can be changed by controlling the gains of variable gain amplifiers. The effective quality factor of the oscillator is enhanced by adjusting phase shifts of phase shifters. Frequency tunable range is about 1,200 ppm, exceeding the limit restricted by used SAW resonators. The effective quality factor of the oscillator is about 30,000, about three times of the unloaded Q of SAW resonators. Phase noise of the oscillator is estimated from the measured spectrum. Above 6 dB improvement of phase noise is obtained at 1kHz offset frequency compared to that of a colpitts oscillator.**

Keywords—SAW resonator; SAW oscillator; VCSO; VCXO; crystal resonator; crystal oscillator; quality factor; dula-T circuit; resonator; oscillator;

I. INTRODUCTION

Quartz crystal and SAW resonators are widely used in high precision voltage controlled oscillators. Recently, demand for wide tunable range and reduction of phase noise has been increasing for VCOs. But the frequency tunable range is limited by the capacitance ration of a crystal resonator or SAW resonator within a few hundred ppm. And the phase noise is limited by the effective quality factor of a VCO. To overcome these restrictions, a variety of piezoelectric material resonators and oscillator circuits have been developed. But, reported results were not sufficient for recent demands. To attain the demand for wide tunable range, a dual-T quartz crystal resonator circuit was proposed [1]. The resonance frequency of a dual-T crystal resonator circuit can be changed a several thousand ppm exceeding the limit determined by the piezoelectric coupling factor of a crystal resonator. We have been studying the properties of the dual-T crystal resonator circuit[2]-[4]. Omori et al. proposed a widely tunable dual-T SAW band elimination filter and its application to wideband UHF VCO[5].

In this paper, we have investigated a dual-T SAW oscillator. At first, we explain the circuit of a dual-T SAW oscillator. Then we show the simulation and measurement results of a dual-T SAW resonator circuit. Finally, we show the characteristics of the dual-T SAW oscillator.

II. DUAL-T SAW OSCILLATOR CIRCUIT

Fig. 1 shows the schematic diagram of a dual-T SAW oscillator circuit. A dual-T SAW resonator circuit is composed of two T circuits. Each T circuit is composed of an inductor and a capacitor in a series arm and a SAW resonator in a shunt arm. Each SAW resonator has different resonance frequency. The inputs of two T circuits are connected to the output terminal of the amplifier via different variable gain amplifier VGA1 and VGA2. The output terminals of two T circuits are connected and fed back to the amplifier. In order to cancel out the parallel capacitance C_0 of a SAW resonator, the values of L_S and C_S are determined so that the resonance frequency of L_S and $C'_S=C_S+C_0$ is approximately equal to the resonance frequency of a SAW resonator. The same value C_S is used for C_{S1} and C_{S2} because the difference of the resonance frequencies of the two series arms is small. The values of L_{S1} and L_{S2} are set to equal value L_S by the same reason. A phase shifter is inserted in series with each T circuit to improve the effective quality factor.

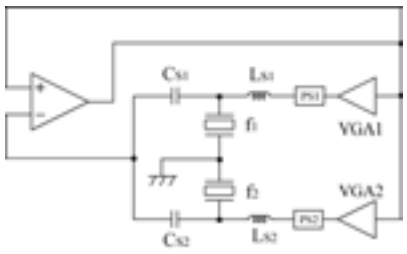

Figure 1 Dual-T SAW oscillator circuit.

III. FREQUENCY RESPONSE OF DUAL-T SAW RESONATOR CIRCUIT

We have made the simulation of frequency response of a dual-T resonator circuit. Table 1 shows the equivalent parameters of SAW resonators. Fig.2 shows the simulated frequency response. The solid line shows the frequency response for 10.6 degree phase shift and the dotted line for 0 degree phase shift. By insertion of phase shift, the notch depth and the slope of phase increase. This result suggests the increase of the effective Q of a dual-T resonator circuit. The notch at 433.59MHz represents the spurious response of lower

* He joined AISIN COMCRUISE Co., Ltd. on 1 April, 2013.

resonance frequency SAW resonator. This response is considered explaining the measured frequency response.

Tabel 1 Equivalent parameters of SAW resonators

Parameters	No.1	No.2
Resonance frequency [MHz]	433.42	433.92
R1 [Ohm]	26.1	16.0
L1 [uH]	101	61.6
C1 [fF]	1.32	2.18
C0 [pF]	2.3	2.2
Q	10600	10500

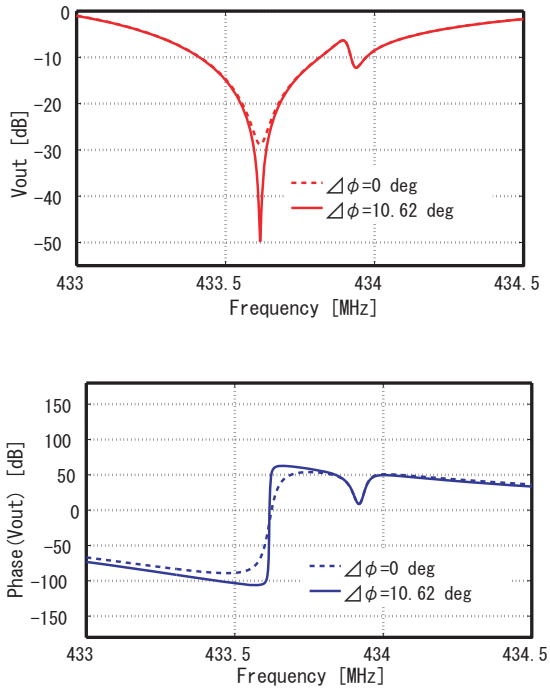

Figure 2. Frequency response of dual-T SAW resonator circuit. (simulation)

Fig.3 shows the measured frequency response. The solid line shows the frequency response for 10 degree phase shift and the dotted line for 0 degree phase shift. The measured result is similar to the simulation result.

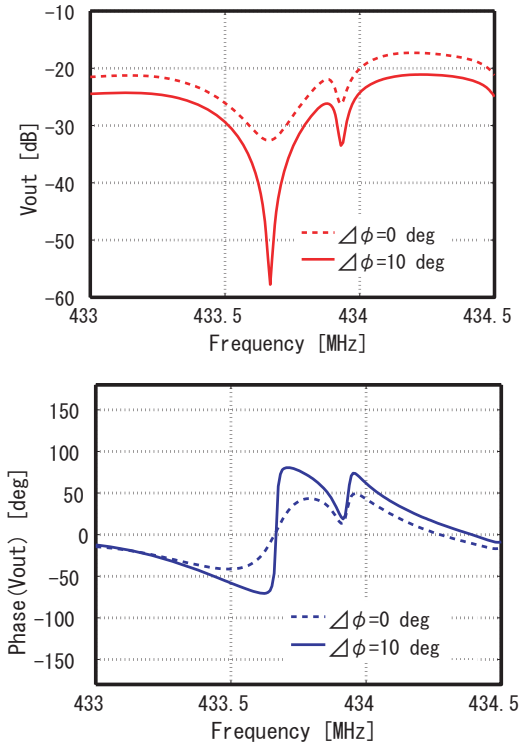

Figure3. Frequency response of Dual-T SAW resonator circuit. (measurement)

IV. OSCILLATOR CHARACTERISTICS

Fig. 4 shows the simulated relation between oscillation frequeny and control voltage of variable gain amplifier. This result suggests about 1200 ppm frequency variation range.

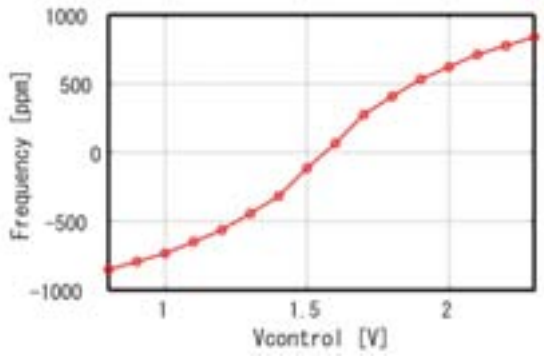

Figure 4. Relation between oscillation frequency and control voltage.

Then, we measured the characteristics of the oscillator. Fig. 5 shows the measured open loop gain of the oscillator when the oscillation frequency is set to be the center of tunable range. Effective Q values evaluated from both the voltage and phase transfer characteristics are about 33,000. These values are around three times of unloaded Q of SAW resonators.

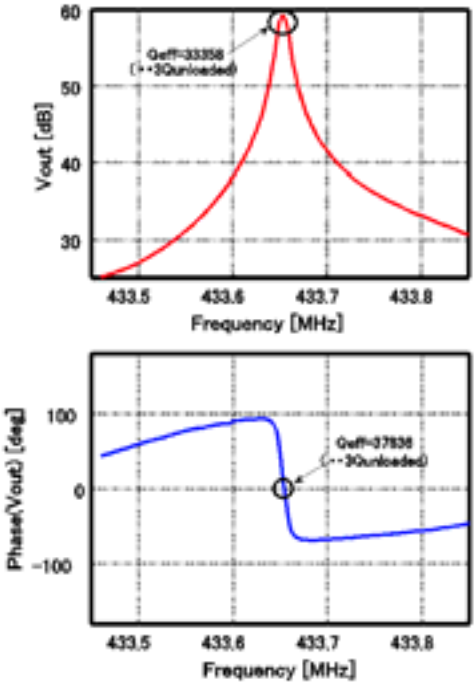

Figure 5. Open loop gain.

Fig. 6 shows the measured spectrum of the output voltage. We estimated the phase noise from the measured spectrum. Fig. 7 is the phase noise at 1kHz offset frequency. The phase noise at the frequency 600ppm higher from the center frequency is -92 [dBc/Hz] The phase noise at the center frequency is -97 [dBc/Hz]. About 6 dB improvement is observed. This value suggests that the effective Q of the oscillator becomes two times of the unloaded Q of a SAW resonator. From this result, we think the Q enhancement method is effective. The evaluated effective Q is small compared to that of the value evaluated from the measured open loop gain of the oscillator. The reason of this difference is the limit of our measurement system. In Fig.7, we shows the measured phase noise of the coplitts oscillator made using the same SAW resonator, for comparison. The phase noise of the colpitts oscillator is almost same with that of the dual-T oscillator at the upper end of frequency tunable range. This means that the effective Q of the dual-T oscillator is almost equal to that of the colpitts oscillator. This fact is reasonable because the dual-T resonator behaves as the single resonator at the upper or lower end of the frequency tunable range.

V. SUMMARY

In this paper, we investigated a dual-T SAW oscillator. It was shown that the frequency tunable range beyond the resonator limited value can be attained. Effective Q enhancement is observed from both the frequency response of the dual-T resonator circuit and the open loop gain of the oscillator. The phase noise estimated from measured spectrum supported the effective Q enhancement effect.

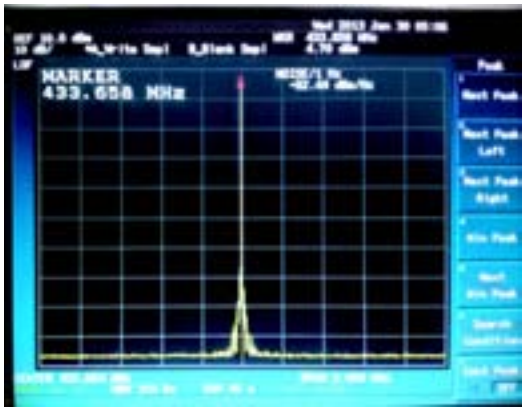

Figure 6. Measured spectrum of oscillator output.

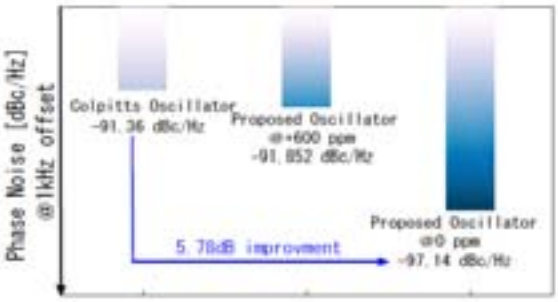

Figure 7. Phase noise estimated from measured spectrum.

REFERENCES

[1] K. Hirama, Y. Nakagawa, and T. Yanagisawa ; "Dual-Input Twin-T Quartz Circuit and its Null Frequency Control Behavior", IEICE Technical Report, US2006-29, pp.41-46, 2006-07.(in Japanese)

[2] T. Adachi and D. Akamatsu;"A Dual-T Quartz Crystal Resonator Circuit and its Application to 10MHz Oscillator", Proceedings of 2008 IEEE Frequency Control Symposium, pp.229-232, 2008-06.

[3] T. Adachi, D. Akamatsu, K. Hirama, Y. Nakagawa, and T. Yanagisawa;"Constancy on Quality Factor of Dual-T Quartz Crystal Resonator Circuit", Proceedings of 2008 IEEE International Ultrasonics Synposium, pp.437-438, 2008-10.

[4] S. Senanayaka, T. Haba, S. Yamamoto, S. Izumiya, and T. Adachi;"Realization of Ultra-High Quality Factor of Dual-T Quartz Crystal Resonator Circuit", Proceedings of 2012 IEEE International Ultrasonics Synposium, pp.2199-2201, 2012-10.

[5] T. Omori, N. Matsuoka, C.Ahn, M. Yamaguchi, and K. Hashimoto;"Dual-T SAW Tunable Band Elimination Filter and its Application to Wideband UHF VCSO", Proceedings of 2012 IEEE International Ultrasonics Synposium, pp.1778-178, 12012-10.

Tracking DDS in Time and Frequency Metrology

Claudio E. Calosso
Division of Optics
INRIM
Torino, Italy
e-mail: c.calosso@inrim.it

***Abstract*— It is possible to implement a real-time phasemeter/frequencymeter, by simply using a Direct Digital Synthesizer (DDS) in a Phase Locked Loop. Data written into the DDS to track the input is the output of this instrument. This scheme is compact, low noise, cheap, wide input range, real time and can be used in many applications both in RF and in Optical Frequency metrology.**

Keywords— aliasing; digital frequency divider; phase noise; white noise; flicker

I. INTRODUCTION

The Phase-Locked Loop (PLL) in electronics was introduced in early 1930s to surpass the superheterodyne technique in radio receiver [1]. Since then, its diffusion has been very wide: in telecommunication, in digital electronics, in motor controls… and also in time and frequency: indirect frequency synthesis, clean-up and tracking oscillators, phase noise measurement, but also comb stabilizations, laser locks or even fiber link compensation.

Here I will consider the case where the Voltage Controlled Oscillator (VCO) is replaced with a Direct Digital Synthesizer (DDS) [2] clocked by a good reference. Even if the equations that rule the new scheme and the classical one are the same, the meaning and the use of the tracking DDS is completely different.

II. ANALOG PLL VS TRACKING DDS

In a PLL the phase of the controlled oscillator is compared with the phase of the input and an error signal is generated and fed to a servo. When the loop is closed, the latter applies a correction to the controlled oscillator to null the phase error and consequently to align the output phase to the input one. In this condition, within the loop bandwidth, the output phase is equal to the input one (Fig. 1).

This is true for the analog implementation and for the tracking DDS. The difference is in the noise level of the controlled oscillator with respect to the input. In the classical analog PLL, the phase noise of input is better than the one of the VCO for low Fourier frequency. Usually, the loop bandwidth corresponds to the cross-point of the two spectrums, in order to get the best of both. At the output of the PLL we can find a filtered replica of the input. In this sense, the classical PLL is a filter.

In the Tracking DDS scheme, instead, the controlled oscillator is represented by a DDS clocked by a good quality oscillator i.e. an OCXO, a rubidium, an hydrogen maser… whose phase noise is better than the input one for the entire spectrum. In this case, by closing the loop, the output is degraded to the level of the input phase noise. To do this, within the bandwidth *D*, the servo writes into the DDS a sequence of data that is the digital representation of the input phase. So the Tracking DDS is a phase or frequency meter, depending on which one the loop is closed.

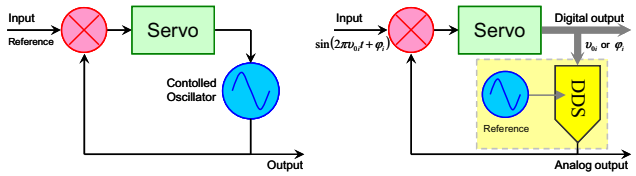

a) b)

Fig. 1. Fig. 1. Classical PLL (a) and Tracking DDS (b) block diagrams

III. IMPLEMENTATION

The implementation of a trancking DDS is very similar to the one of a digital PLL. The difference is that we have to drive a DDS instead of a VCO.

In general a VCO has an imprecise relation between the input voltage and the output frequency, due to the poor medium-long term stability of the oscillator, to the variability of the VCO constant, to the temperature sensitivity… With DDS, instead, the relation between the digital number at the input and the output is well defined. For this reason we can use the data written in the DDS and state that it is the digital representation of the output. In this manner, by putting the DDS in the loop, we can reverse its function and use it to implement an instrument instead of a generator.

In some particular applications, the same can be done with traditional PLL, but only for high Fourier frequency, where the VCO is better than the input. With DDS, this can be extended even for low Fourier frequency and, that is the same, for longer integration time.

Another big difference, is that the only accessible variable in VCO is the frequency. With DDS, we can write both the

phase and the frequency. In many cases, having a direct access to the phase has significant advantages.

An important point is the digital delay of the loop that limits the tracking bandwidth. This has to be considered according to the application requirements. The delay induced by the DDS is of the order of 100 ns that theoretically limits the bandwidth to 2.5 MHz. In addition, we have also to consider the delay induced by the Analog to Digital Converter (ADC) and to the servo. A 1 MHz bandwidth is an achievable goal.

If the application does not require such a bandwidth, it is possible to use serial components, with great reduction of the required PCB area.

The mixer usually does not represent a limit, being a low noise component. The same for the ADC, because it is preceded by an amplifier. The servo can be implemented into and FPGA, with no practical limitation about speed, resolution and functionalities.

IV. Applications

The tracking DDS has plenty of applications both in Radio Frquency (OF) metrology and in Optical Frequency (OF) metrology.

A. RF applications

In the first case, the noise in the input signals is low and the design is devoted to fully exploit the low residual phase noise of the DDS. To get the best, a direct clock is recommended, being not negligible the noise of the internal multiplier. On the opposite, the required tracking bandwidth is low. Infact, typical applications concern the measurement of frequency standards, where the information is for Fourier frequencies below 1 Hz.

By applying the tracking DDS scheme, we can implement high resolution phase/frequency meters with many channels. In this case, the information can be sent to a PC that stores them for further analysis.

By considering that tracking DDS works in real-time, it is possible to think to other applications where this information is used to close a loop. [3] describes an OCXO ensemble, where the measurement of several OCXOs with respect to a local one is processed to steer the local OCXO. This is done by driving a DAC. The same principle can be extended and used to generate a time scale in real-time.

B. OF applications

The optical frequency metrology is an emerging field. A common characteristic is the high noise level of the electronic signals.

The existing electronics was developed to deal with very low noise signals as the ones encountered in RF. It many cases there are problems when this kind of electronics is used in OF domain. By example, in the beat-note between two lasers, the noise power is higher than the signal and a classical frequency meter cannot be directly used, because the input trigger cannot "see" the signal. In this case, the use of a tracking DDS is advantageous, due to the fact that the out-of-bandwidth noise is filtered out the scheme. In this sense, it can be considered as a robust phase/frequency meter.

In case of high level coloured phase noise, the required tracking bandwidth has to be high, in order to be able to track the big amount of noise and to avoid cycle slips.

By considering the real-time facility, it is possible to approach many applications. Here I report two examples. The first one concerns phase data stream that fed to a DDS to drive an Acousto-Optic Modulator. In this case it is possible to implement the complete electronics for a coherent fiber link [4].

The second case is when phase data is sent to a DAC to drive a piezo. This can be used for comb and laser locking.

V. Results

I tested the tracking DDS by measuring a 161.000001 MHz signal generated by a second DDS that shares the same 10 MHz clock. For simplicity, I used the internal multiplier of the DDSs. In case of direct clock, the results are 10 time better.

The tracking bandwidth is 10 kHz, the measurement bandwidth is 100 Hz and the sample-rate after the decimator is 200 Hz.

Fig. 2 reports the overlapping Allan deviation of data saved into the monitoring PC.

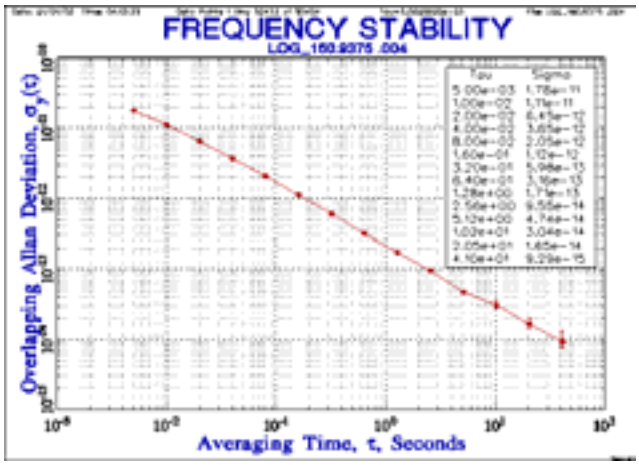

Fig. 2. Fig.2. Overlapping Allan deviation of the tracking DDS residual noise.

The plot is dominated by flicker phase noise. The stability is 2×10^{-13} at 1 s. Even if the goal of the experiment was to demonstrate the principle of the tracking DDS, the residual phase noise is low enough to be used to characterize and active hydrogen maser for measurement time longer than few seconds.

VI. Conclusions

I demonstrated that it is possible to implement a new type of phase/frequency meter by using a DDS in a PLL. The scheme is very flexible and can be used in a wide range of applications, thanks to the digital and real-time nature of the

scheme. The preliminary results are promising and demonstrates that this scheme is suitable to be used both in RF and in Optical Frequency Metrology.

ACKNOWLEDGMENTS

The author thanks Enrico Rubiola for useful discussions and Elio Bertacco for his invaluable help.

REFERENCES

[1] de Bellescize, Henri (June 1932), "La réception Synchrone", *L'Onde Electrique* **11**: 230–240.

[2] Calosso C. E., Gruson Y., Rubiola E. (2012). Phase noise in DDS. Proc. International Frequency Control Symposium (IFCS) p.777-782, Baltimore, MD, USA, 21-25 May 2012.

[3] Calosso C. E., Bertacco E. K., Micalizio S., Godone A., Calonico D., Costanzo G. A. (2012). OCXO Ensemble As Improved Local Oscillator For Atomic Fountains. In: The European Frequency and Time Forum (EFTF). Goteborg, 23-27 April 2012, pp. 271-274

[4] Calosso et al, "Tracking DDS for Coherent Optical Links ", these proceedings.

A Miniature Timing Microsystem Using Two Silicon Resonators

D. Ruffieux, J. Baborowski, N. Scolari, T. C. Le
CSEM
Neuchâtel, Switzerland
david.ruffieux@csem.ch

A. Jaakkola, T. Pensala, J. Dekker
VTT
Espoo, Finland

C. A. Manier, K. Zoschke, H. Oppermann
Fraunhofer IZM
Berlin, Germany

***Abstract*— This paper presents a miniature timing microsystem based on a pair of co-integrated low and high frequency silicon resonators -430kHz or 522kHz and 26MHz respectively- so as to implement a µW-level accurate, low power, temperature-compensated real time clock (RTC) and to generate low noise, low jitter clocks at any frequency between 1-50MHz in a reconfigurable way at less than 10mW power dissipation.**

Keywords - Silicon resonators, TCMO, hybrid integration, CMOS, timing, RTC, programmable clocks, TSV, 3-D integration

I. INTRODUCTION

Over recent years the several decades long quartz-dominated timing industry has been continuously challenged by the introduction of new products or demonstration of prototypes based on MEMS resonators (see [1] for a comprehensive survey). Temperature compensated MEMS oscillators (TCMO) are now rivaling in stability with XTALs despite their much larger temperature sensitivity which mandates accurate high resolution temperature sensors for efficient compensation [2]. On the other hand, they offer interesting miniaturization perspectives with eased packaging done at wafer or chip-scale level using silicon manufacturing lines [3]. This paper address such challenges with the demonstration of co-integrated AlN-actuated silicon resonators used to derive both a low power, low frequency clock to generate a real time clock (RTC) and low jitter programmable clocks between 1-50MHz in a reconfigurable way.

II. CONCEPT AND ARCHITECTURE

A. *Hybrid integration for more than Moore*

Fig. 1 shows a schematic cross-section illustrating the timing microsystem concept that is currently under development. Two packaging approaches are being pursued in parallel. In both, CMOS wafers are used as part of the package to reach extreme miniaturization. In a first scenario, light post-CMOS processing is applied on top of the active circuits to deposit an Al redistribution layer (RDL), Au/Sn electro-plated sealing rings and bumps and Au stoppers. Then, 150µm-thick co-integrated AlN-actuated silicon resonators know good dies (KGD) built over buried cavities in SOI, are soldered directly atop the CMOS wafer thinned down to 100µm using a die to

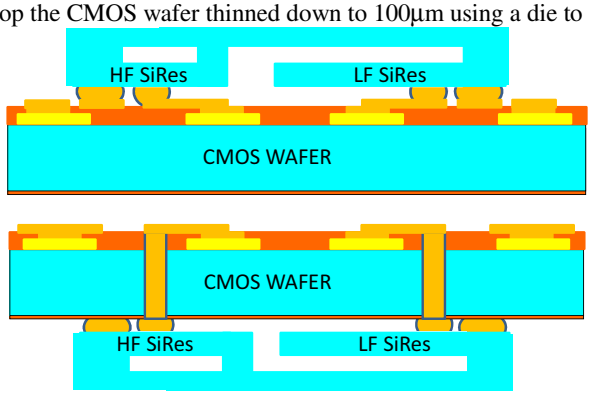

Figure 1. Schematic cross-section of the timing microsystem

wafer attach approach forming a vacuum sealed cavity around the resonators. The resulting housing that is immune to moisture and further nearly eliminates any temperature gradient between the resonator and active circuitry can then merely be wire-bonded on the application board or further overmolded in a DFN plastic package. In a more post-CMOS processing intensive approach, through silicon via (TSV) are first etched and Cu-filled within the CMOS wafer. The silicon resonators are then assembled at the backside of the CMOS wafer after deposition of the appropriate layers. Resulting chip-scale packaged components are then amenable for direct soldering on board using flip-chip bonding. Early validation of the combination of the sealing and TSV technologies applied to the packaging of miniature XTALs in a mostly similar way has been demonstrated in [4].

B. *System architecture*

Fig. 2 shows a detailed block diagram of the timing microsystem. A low frequency 430kHz or 522kHz silicon resonator-based oscillator combined intermittently to a temperature sensitive 10MHz RC oscillator is used to derive a temperature-compensated 32,768Hz clock after fractional

division (÷R) for coarse or long term frequency adjustment (~1ppm over 2s) in a fully digital manner without impacting the oscillator. Short term fine adjustment over a limited frequency range can be obtained using interpolation by switching part of the oscillator loading capacitance in an on/off way with a controllable duty cycle to reach sub-ppm resolution over 1s. Digitally controlling the oscillator between only two frequencies eliminates analog varactors, a DAC and most of the non-linearity inherent to pulling a MO over a large range. Both techniques can advantageously be combined to compensate the temperature sensitivity of the silicon resonator over an arbitrary large temperature range [5]. The 32,768Hz signal then merely drives the real time clock (RTC) sub-circuit implementing clock, calendar, timer and alarm functions. Any of the above clocks as well as 1024Hz and 1Hz ones obtained from the RTC division chain can be made available externally

Besides the RTC, HF clocks re-programmable between 1 to 50MHz via a serial interface can be generated on demand using a 26MHz silicon resonator-based oscillator combined to a fully integrated fractional PLL (divider N, Phase Frequency Detector, Charge Pump and Loop Filter). Up to two independent temperature compensated clocks with low noise and jitter performances, such as required for radio applications or high DR converters are obtained after integer (÷M) or fractional division (÷P) of the LO signal that is compensated by adjusting the N division ratio in a temperature dependent way. Two output pads are available to multiplex the HF clocks.

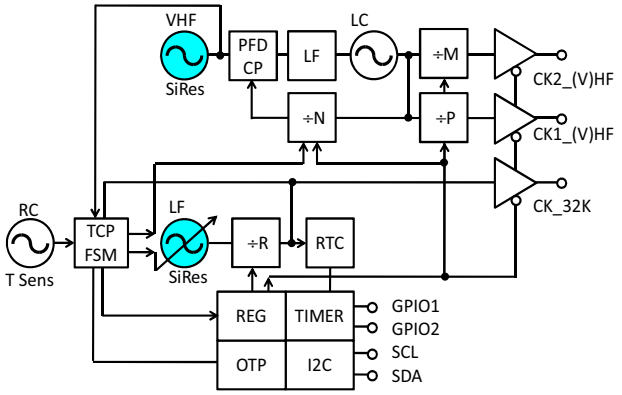

Figure 2. Block diagram of the timing microsystem

III. CHARATERIZATION

A. *Resonators performances*

Table 1 shows the co-integrated silicon resonators electro-mechanical parameters obtained from measurements on a vacuum prober. Moderate Q-factors of 11k and 18k are obtained at 26MHz and 500kHz respectively. The impedance levels of the HF and LF, AlN-actuated resonators reach 130 to 200Ω and 60 to 75kΩ respectively, much closer to the motional resistance of XTAL counterparts compared to that reached with parallel-plate actuated resonators. This is obtained owing to a better coupling coefficient (k^2). The measured resonator FOM (Q times coupling product) are however still worse than that of equivalent quartz XTALs lagging by a factor 5 when taking into account that the LF resonator one is degraded by half by the process dependent large pad capacitance. A further advantage of piezoelectric resonators is that no DC biasing is required allowing standard transconductance XO topologies, such as that presented in [6], to be reused in a straightforward way.

TABLE I. MEASURED CO-INTEGRARED RESONATORS PARAMETERS

High Frequency Resonators

	Rm	C0	f	Q	K2	FOM
HF01	214 Ohm	3,47 pF	27,0 MHz	5600	0,175%	9,8
HF02	134 Ohm	3,45 pF	26,3 MHz	10900	0,149%	16,2

Low Frequency Resonators

	Rm	C0	f	Q	K2	FOM
IN12	59 kOhm	1,64 pF	430,4 kHz	17.2k	0,028%	4,8
IN14	74 kOhm	1,45 pF	522,0 kHz	18.4k	0,024%	4,4

B. *Temperature compensation of the LF SiRes*

Fig. 3 shows a measurement of the uncompensated (blue and red curves spanning -3000ppm over -40 to 85°C) and temperature compensated (green, ±20ppm) LF silicon resonator using both frequency interpolation and variable division for fine (~50ppm range) and coarse adjustments respectively. Calibration was done at three temperature points by measuring the MO frequencies (f_H and f_L) at two loading capacitance values and reading via the serial interface the output of a counter clocked by the 10MHz highly temperature-sensitive, mostly linear RC oscillator and enabled during a given number of the MO periods. As the RC oscillator temperature sensitivity is 100x larger than that of the MO, a digital representation of the system temperature is obtained in a very simple way without requiring complex and energy/area consuming analog to digital conversion. Polynomial coefficients of the corresponding function $f_{MO}(f_{RC})$ are then stored in the non-volatile one time programmable (OTP) memory embedded on the ASIC. During operation, the on-chip temperature compensation state machine then periodically turns on the RC oscillator to get a new temperature measurement, calculates and updates the compensation to be applied to the MO and divider using the stored coefficients. The average current consumption in this mode is 1µA. The HF MO is temperature compensated through the frequency synthesizer by adjusting the N divider value. Up to 4^{th} order compensation using a 5 temperature trim can be applied to both the RTC and HF clocks.

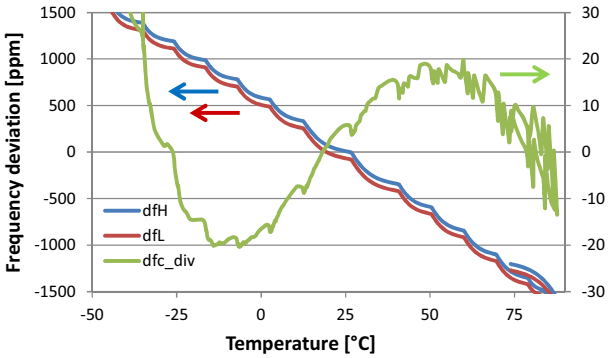

Figure 3. LF (TC)MO temperature stability measurements

C. *Clock generation with HF SiRes*

Fig.4 shows a measurement of the phase noise of the HF clock generation circuit. The 26.36MHz MO clock is plotted together with the LC VCO divided clock exhibiting the characteristic Δσ modulator induced quantization noise shaping towards higher frequencies. The LC PLL is locked via the fractional-N divider at 2.16GHz from which a low noise 48MHz clock is obtained by integer division by M=45. Apart in the vicinity of the loop filter bandwidth (200-300kHz), the generated clock phase noise tracks that of the reference with a scaling of 20 log(N/M) as expected.

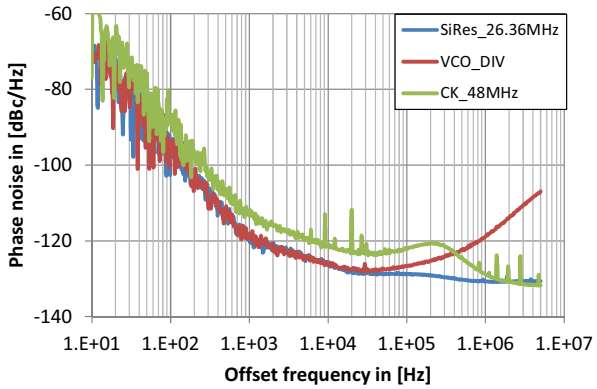

Figure 4. Phase noise plot of the HF clock generation circuit

Fig.5 shows a measurement of thepower consumption breakdown in the clock generation mode when a 48MHz clock is generated. The current consumption is 5.6mA at 1.6V (9mW) shared quite evenly between the 2.16GHz LO, the two N and M dividers including the PFD/CP, ΔΣ modulator and 26MHz MO reference and the on-chip buffer driving an on-board 50Ω driver.

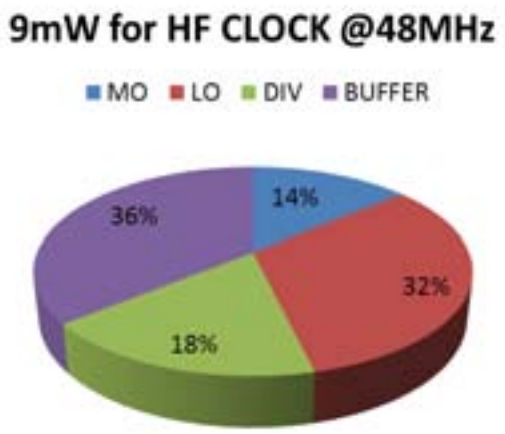

Figure 5. Power consumption breakdown of the HF clock generation circuit

D. *Components and die photograph*

Fig. 6 shows a picture of the LF and HF silicon resonators co-integrated on a die measuring 660x1480μm^2 together with an ASIC die photo highlighting its floor plan (size is 1100x1500μm^2). The ASIC has been integrated in a 180nm 1P6M CMOS generic technology first using MPW service and eventually using a MLM approach to allow post-CMOS processing. Resonators are also being packaged at wafer scale in a housing compliant with direct assembly on the ASIC using thermo-compression on Au stud-bumps. As such tasks are still ongoing, early system level characterization was performed using unpackaged HF resonators and more pressure sensitive LF resonators sealed in vacuum in standard ceramic packages.

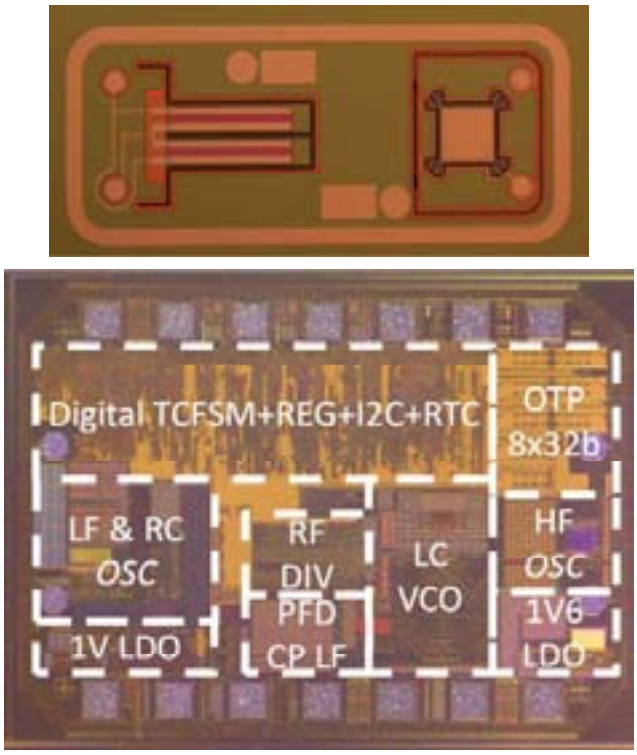

Figure 6. Die photographs at same scale

IV. Summary and Conclusions

A 1.5x1.1mm^2 timing microsystem relying on two co-integrated 430kHz and 26MHz AlN-actuated silicon resonators and capable of generating both a 1µW-level RTC with calendar and alarm functions and on-demand low jitter reprogrammable clocks between 1 to 50MHz at a power dissipation below 10mW was presented. A direct KGD to CMOS wafer packaging approach minimizing the overall microsystem thickness to 250µm but that is still under development was introduced and early system level measurements using standalone packaged resonators were given demonstrating ±20ppm accuracy after a trim at three temperatures. Better stability performances are expected using a 5-point trim and intimate contact between the resonators and the ASIC temperature sensor once the final system is implemented.

Acknowledgment

The authors thank R. Caseiro, C. Monneron, C. Henzelin and P.A. Beuchat for their contribution to the layouts and the realization of the PCB.

References

[1] J. Van Beek and R. Puers, "A Review of MEMS Oscillators for Frequency Reference and Timing Applications," in J. of Micromech. and Microeng. Vol. 22, No 1. 2012, pp. 1-35.

[2] M. Perrot et al, "A Temperature-to-Digital Converter for a MEMS-based Programmable Oscillator with < ±0.5ppm Frequency Stability and <1ps Integrated Jitter," in IEEE J. of Solid-State Circuits, Vol. 48, Iss. 1, pp. 276–291, Jan. 2013.

[3] R.N. Candler, W.-T. Park, H. Li, G. Qama, A. Partiridge, M. Lutz, and T.W. Kenny, "Single wafer encapsulation of MEMS devices," in IEEE Transactions on Advanced Packaging, Vol. 26, Aug. 2003, pp. 227-232.

[4] K. Zoschke, C.-A. Manier, M. Wilke, N. Jürgensen, H. Oppermann, D. Ruffieux, J. Dekker, H. Heikkinen, S. Dalla Piazza, G. Allegato and K.-D. Lang "Hermetic Wafer Level Packaging of MEMS Components using Through Silicon Via and Wafer to Wafer Bonding Technologies," in 63rd Electronic Components & Technology Conference, LasVegas, May 2013, pp. 1500-1507

[5] D. Ruffieux, F. Krummenacher, A. Pezous and G. Spinola Durante, "Silicon Resonator-Based 3.2uW Real Time Clock with +-10ppm Frequency Accuracy," *IEEE Journal of Solid-State Circuits, vol. 45, no. 1, Jan. 2010, pp. 224-234.*

[6] D. Ruffieux, "A high-stability, ultra-low power differential oscillator circuit for demanding radio applications," in Proc. European Solid-State Circuit Conference, Sep. 2002, pp. 85-88.

A Comparison of FBAR Oscillators with Standard Resonators and Stress Relieved Resonators

R. Ruby[1], S. Sridaran[1], S. Ortiz[1], K.G. Oppermann[2]
[1]Avago Technologies, San Jose, CA
[2]Avago Technologies, Munich, DE

Abstract— **One of the issues facing many types of oscillators is the transference of stress from the external world through the die to the resonator. Typically, resonators are clamped at more than one location. Integrated FBAR oscillators (referred to as FMOS[1,2]), uses a resonator that is clamped on all sides and integrated into an all-silicon, chip-scale package with integrated circuits. For filter applications, this is quite reasonable, but, for oscillators this may not be acceptable. Mounting FBAR oscillators (epoxy die attach, over-molding and soldering) onto a customer board exposes the FBAR oscillator to stresses that occur during the assembly, plus additional stresses that occur during the wear and tear (as well as temperature induced stresses) that the customer board experiences. Although intuitively, applied stress will change frequency of the resonator, this is hard to quantify. This paper does a first cut model of the stresses and then matches that to the changes in the measured frequency. Next, we discuss several designs that help mitigate the effect of external stresses on the resonator.**

I. INTRODUCTION

We are attempting to make production-worthy, commercially viable chip-scale oscillators and VCOs. The all-silicon packaged die uses wafer-level packaging techniques to create both a hermetic package for the resonator and circuit as well as hermetic vias connecting the resonator/circuit to outside pads. We refer to this integrated platform of circuit and resonator, FMOS (FBAR, Metal Oxide and Silicon). And if successful, will be one of the smallest commercially available products of their kind on the market.

The first generation all-silicon package consists of 6 pads on the top surface (Fig. 1) with 6 vias to a resonator (FBAR) located in the base wafer and a IC in the lid wafer as shown in Fig. 2.

One concern for this device as used for XO applications (precision timing) would be any change in frequency as a function of customer assembly. In crystal oscillators, the crystal is attached to the IC via conductive silicone connections that provide both electrical contact and compliance and isolation to any external stresses applied to the package housing the IC and crystal. In Fig. 2, it can be seen that the FBAR resonator is attached on all sides. For any external stress applied to the package (for example when it is soldered to a pcb during customer assembly into a module), the frequency will shift.

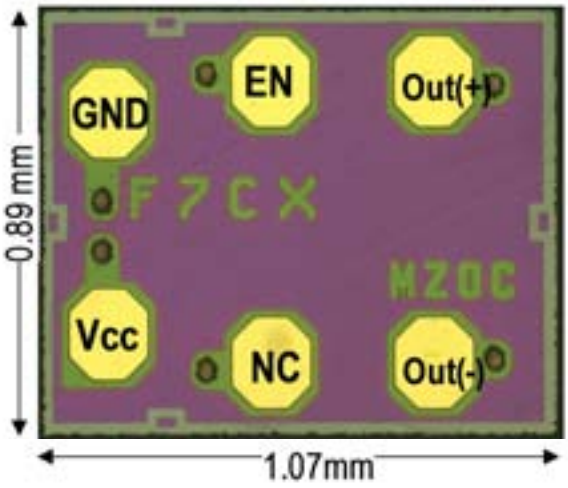

Fig.1; Optical micrograph of the top view of a FMOS die. The copper pads are labeled. Besides a differential output, the die has an enable pin, a Vcc pin and Ground pin. The sixth pin can be used in a VCO as a tuning pin.

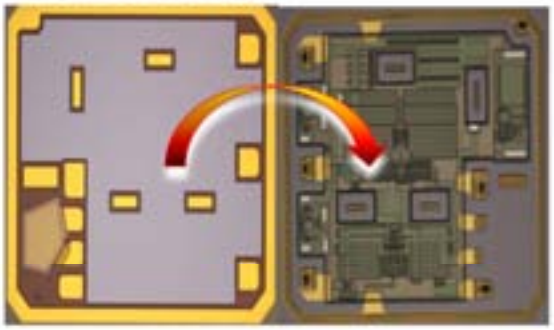

Fig.2; Optical micrograph of the base wafer containing the FBAR resonator and the lid wafer containing the circuitry.

Figure 3a shows a COMSOL model of our device. Typical values for the geometries, material constants were assumed. Figure 3b shows the simulated stresses across the resonator shown in Figure 2. The stresses shown in Figure 3b are created by simulating a net 125°C change in temperature of a FMOS die (as shown in Fig 1) attached to a pcb (via a standard solder mount). The die in this simulation assumes an

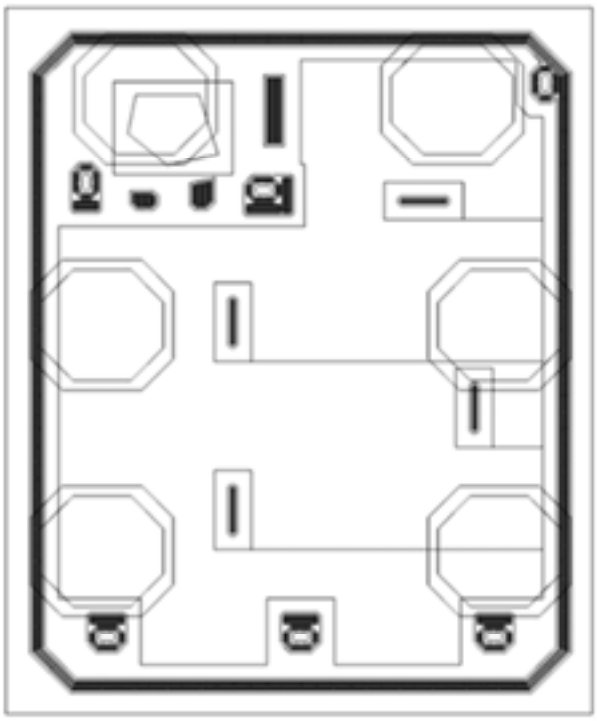

Fig.3a; COMSOL layout used to simulate in-plane forces on the resonator (upper right – apodized shape polygon)

over mold as well as an under fill. Although both over mold and under fill affect the values of the amount of stress, it is important to note that there is a stress. Associated with this stress, one can expect both a strain on the resonator and a frequency shift.

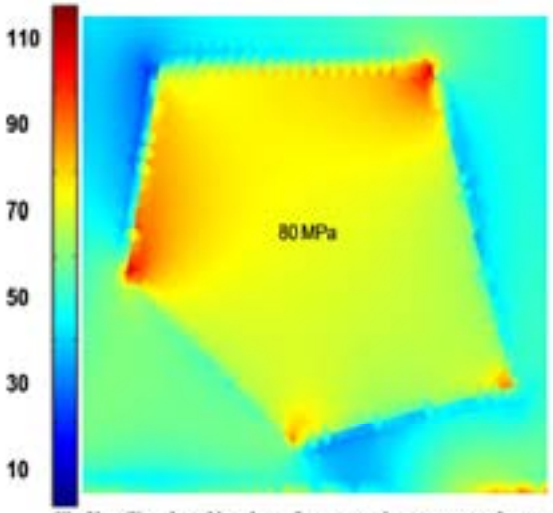

Fig.3b; Simulated in-plane forces on the resonator due to externally applied stresses when a die is soldered to a pcb.

II. DISCUSSIONS

To quantify the amount of frequency shift one might expect from externally applied in-plane stress, the following experiment was done. A wafer consisting of thousands of oscillators on a 6" wafer is mounted on a vacuum chuck and frequencies of individual oscillators are measured. The wafer is removed and then re-mounted on the vacuum chuck and the same dies are measured again. From this, we determine a base line of the spread and median of the ensemble of measured oscillators. Next, the wafer was removed and then placed on top of a thin (13 um) Mylar substrate 57 mm in diameter – all on the same vacuum chuck. The Mylar spacer lies inside the vacuum rings of the chuck and thus the wafer is pulled down under vacuum, the wafer is held fast to the chuck –with a slight bending of the wafer due to the Mylar spacer. This bending approximates real life stress applied by external forces.

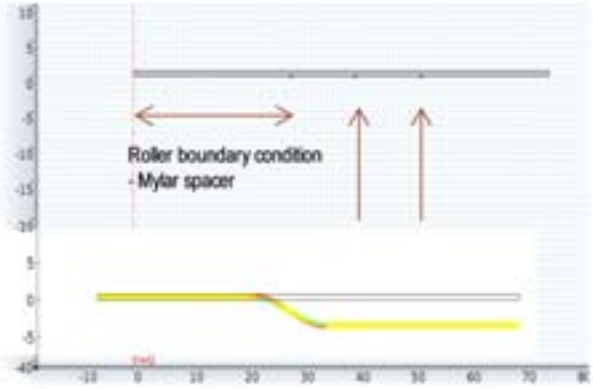

Fig.4; Drawing of the wafer (75 mm rad.), location of the edge of the Mylar spacer (27.5 mm rad.) and the location of the two vacuum rings on the vacuum chuck. Below is a COMSOL simulation of the bending moments.

Figure 4 shows the COMSOL model of the stresses on the silicon wafer as it bends due to the Mylar spacer. A simplifying assumption was made that the silicon was solid and that the resonator, ~600 to 680 um above the bottom edge and surrounded by an air gap is seeing a similar stress as the hypothetical device surrounded by silicon. Because the lid wafer is only 80 to 100 um thick, we believe that the neutral plane lies well below the resonator. Hence, as the wafer bends down at the Mylar edge, the resonator is seeing a tensile stress and when the wafer bends up at the contact point of the vacuum chuck, the resonator is in compression.

Figure 5a is a plot of the calculated in-plane stresses on individual resonators as a function of radius on a wafer. Figure 5b is a plot of the change in frequency (δ f) in ppm as a function of radius. From this, we conclude that we are getting about 0.8 ppm/MPa shift in frequency due to in-plane stresses. From COMSOL modeling of the stresses applied to the resonator in Fig. 3b, one can see that a 125 ^{o}C shift in temperature can cause up to about ~80 MPa of in-plane stress. This is due to the fact that the pcb will grow (shrink) faster than the silicon die.

When a die is soldered down to a pcb substrate, the part sits on a liquidus of solder (eutectic between 205 ^{o}C and 220 ^{o}C) at the ~230 ^{o}C maximum IR reflow temperature. As the die/board cool down, the solder passes its eutectic and solidifies. After which, further cooling down to room temperature will create stresses due to the larger pcb thermal coefficient of expansion (relative to the silicon). One can easily argue that the resonator modeled in Fig. 3a will see up to 125 MPa of external stress. Thus, one might expect frequency shifts on the order of 100 ppm. As a sanity check,

serialized oscillators whose frequencies were measured before and after bonding to a pcb showed a median 140 ppm shift.

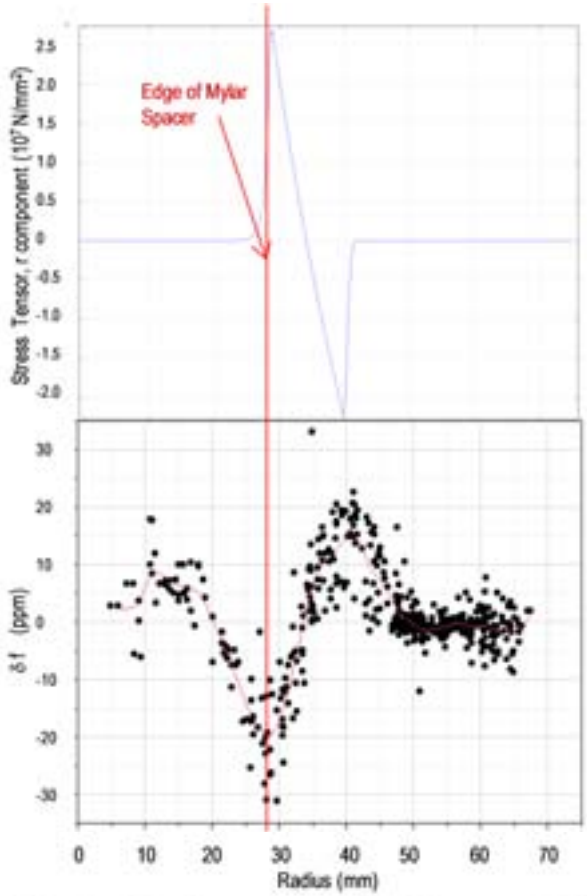

Fig.5a; The simulated stress across a wafer as it is traverses a Mylar spacer. Fig. 5b; The measured change in oscillators across the wafer as plotted on a radius (~1000 oscillators)

III. STRESS RELIEVED RESONATORS

Figure 6a is an SEM micrograph taken of a novel FBAR device on a pedestal [3]. The electrical leads to and from the resonator go under the resonator (in the cavity formed under the active area of the resonator) and up the sides of the pedestal. The actual resonator active area forms a disc around the pedestal and hence, no part of the acoustically active area 'sees' the pedestal. Figure 6b highlights an important modification of this device. With the pedestal centered with respect to the FBAR disc, lateral modes based on Bessel type eigen modes can and will create sub resonances. These resonances are problematic for both filters and oscillators. In the latter case, these modes can 'walk' thru the main resonance due to changes in temperature (the main, 'desired' mode having one temperature coefficient of frequency and the parasitic mode have a different coefficient). This issue is dealt with by apodizing the resonator [4]. In the case of a single mount with nominal radial symmetry, the resonator is laid out to be off-center with respect to the pedestal. Figure 7 shows two superimposed, measured Q-circles of the devices shown in Fig. 6a and 6b.

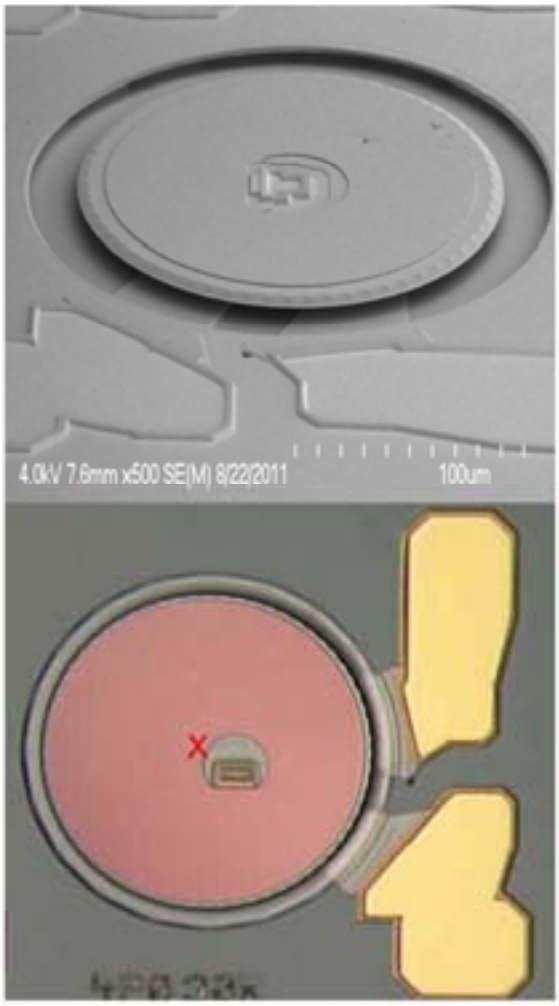

Fig.6a; SEM Micrograph of a center mounted resonator. Here the pedestal is in the center of the disk. Fig. 6b; an Optical micrograph of a similar resonator, but here, the pedestal is offset from the center (the center of the resonator is marked with an X).

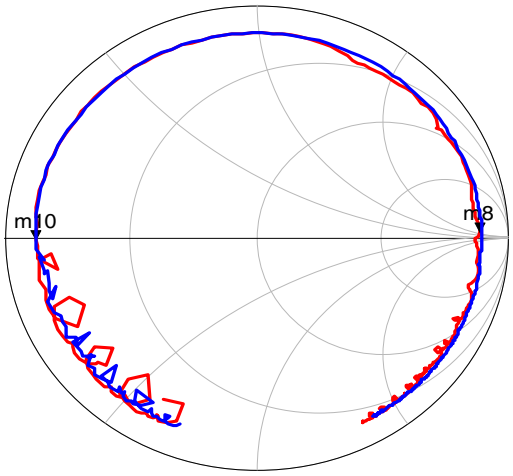

Fig.7; Measured Q-circles of the two kinds of resonators shown in Fig. 6. The Red curve highlights the issues of lateral modes when using a symmetrical device and the blue curve shows the effect of apodization by moving the pedestal off-center.

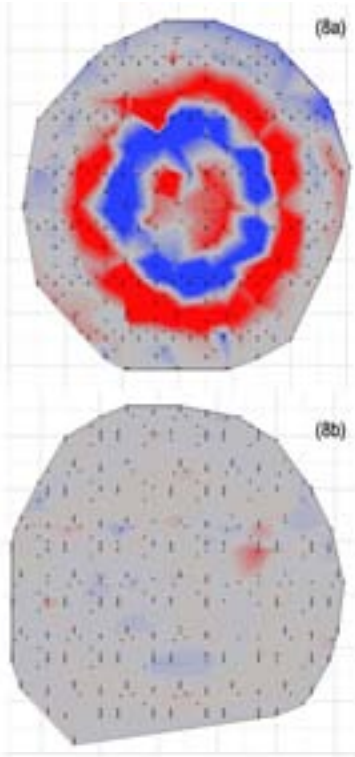

Fig.8; Wafer maps of the change in oscillator frequency as measured before and after a Mylar spacer is placed under the center of the wafer. There is roughly an equal distribution of non-stress relieved devices (8a), to stress relieved devices described in Fig. 6 (8b). The color coding matches Fig 5b, blue – -20 ppm, red – +20 ppm.

The major point of this new design for an FBAR resonator is that any external forces applied to the pedestal are not significantly applied to the resonator. Hence, there are no frequency offsets due to externally applied forces. Highlighting this point; Figure 8 shows wafer maps of the frequency change of two kinds of oscillators distributed over a wafer. Oscillators using the POR resonator shown in Fig 3b are plotted in Fig. 8a. Oscillator using stress released resonators shown in Fig. 6 are plotted in Fig 8b. Both oscillators use the same IC circuitry in the lid. In the former case, one can clearly see the effect of the Mylar spacing under those POR resonators, while in the latter case; there is no evidence of the Mylar spacer.

IV. Conclusion

One issue, the sign of the frequency change vs. applied external stress, remains unresolved. From simple 'string' theory (as in a violin string); it is intuitive that as one increases the tension of the string, the frequency goes up with the square root of the increased stress. Instead, we see that the frequency goes down with frequency and up with added compression. We are now investigating the root cause of this. Secondly, we see differing amounts of frequency shift as a function of a fixed stress. We attribute this to better die design and some confounding effects due to resonators that are bowed due to internal residual stress.

Acknowledgment

The Authors would like to Martha Small, Frank Bi, Don Lee, Steve Gilbert and Lori Callaghan for their invaluable discussions as well as the Engineers and Management teams of the Fort Collins Fab.

References

[1] R. Ruby et al., "Positioning FBAR Technology in the Frequency and Timing Domain", Trans. Ultrasonics. Ferroelectrics, and Freq. Control (TUFFC), v. 59 #3, March 2012, pp. 334-345

[2] R. Ruby, M. Small, "packaged device with acoustic resonator and electronic circuitry and method of making same", US Patent 8, 232,845, Issued July 2012

[3] R. Ruby, "Acoustic Resonator formed on a Pedestal", Patent Application #US 20130049888 A1, published Feb. 2013

[4] P. Bradley, J. Larson, R. Ruby, "Bulk Acoustic Wave Resonator with Improved Lateral Mode Suppression", US Patent **6,215,375**, Issued April 2001

An Accurate Measuring Method for the Transient Oscillation Frequency of Detuned Coherent Population Trapping Atomic Clock

Daiting Shi, Yeqing Li and Zhong Wang*
School of Electronics Engineering & Computer Science (EECS)
Peking University
Beijing, 100871, P. R. China
*Email: zw@pku.edu.cn

***Abstract*— We proposes a method for measuring the transient oscillation frequency observed when Coherent Population Trapping is excited by means of optical pumping radiation fields whose frequency difference is detuned slightly from the ground state hyperfine frequency of the atom used. Using narrow-band simulation filter and phase matching techniques this measuring method can provides a measurement precision of about 0.5Hz. Based on this reading accuracy the DCPT atomic clocks frequency instability can be better than 5e-11 (t=100s) and tend to more stable at longer integration time. According to our experimental results, we demonstrate that a DCPT atomic frequency standard could give good short and long term frequency stability.**

During the last decade, coherent population trapping (CPT) has been widely used in miniaturized atomic clocks. And in traditional CPT atomic clocks, a circuit loop is applied to lock the microwave frequency to the ground state hyperfine splitting. This servo circuit influences the volume and brings in instability to the clock system. In 2009, our team proposed an atomic clock based on the transient detuned CPT phenomenon, which does not require a phase-locking-loop to lock the microwave frequency to the hyperfine splitting frequency, and enables us to directly read the two ground states' transition frequency. In this design, CPT is excited by two optical pumping fields and their frequency difference is detuned slightly from the ground state hyperfine splitting of 85Rb. The pumping optical fields are created by modulating the frequency of a laser. After the laser passes through the rubidium atom cell, a oscillation signal will be detected whose frequency is equal to the detuning frequency, as is shown in Fig.1. We call it transient oscillation of detuned coherent population trapping (DCPT). The DCPT atomic clocks' output standard frequency can be achieved by directly adding/subtracting the transient oscillation frequency of DCPT to/from the microwave frequency used for modulating the pumping laser. Meanwhile, this scheme eliminates the PLL that locks the microwave frequency to the ground state hyperfine splitting in traditional atomic clocks. And in this scheme, the stability of the atomic clock is mainly limited by measurement precision of the detuning frequency.

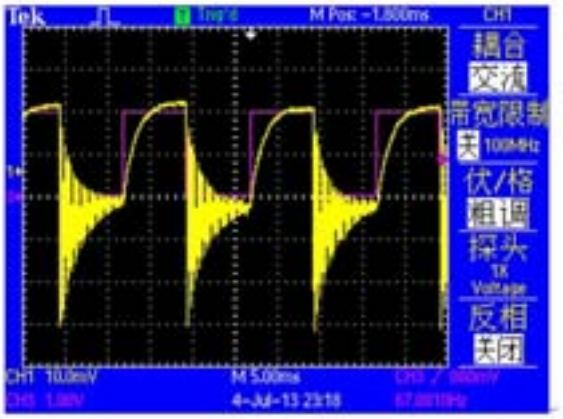

Fig. 1. The yellow line is the transient oscillation signal, and the blue line is the modulation signal of RF.

In this paper we proposed a method for measuring the transient oscillation frequency, as well as an improved design for the DCPT atomic clock. According to our experiment results, this method provided a measurement precision better than 1Hz, and the expected frequency instability will be in the order of 10-10-10-11. We have also experimentally proven the validity of the theoretical result using this more precise method. With its advantages in digits, signal analysis and system simplification, there are great potentials in its further integration and miniaturization as well.

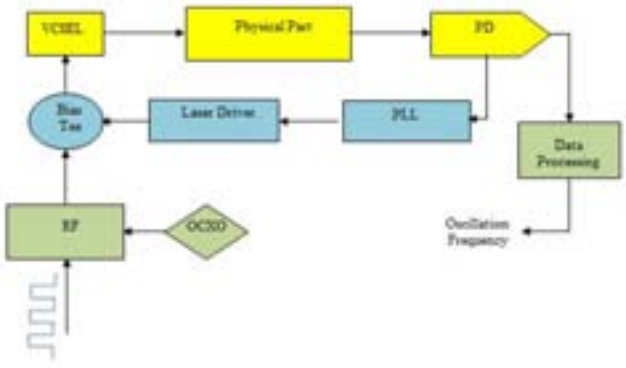

Fig. 2. Experimental setup of the scheme. The data processing module is used to extract the oscillation signal.

Fig.2 shows our experimental system of this atomic clock. The microwave signal was generated by a frequency synthesizer, and modulated by a 60Hz square wave with the lower and higher levels corresponding to the frequency of the dark resonance and a positive 1.3KHz detuning, respectively. According to the linewidth data in our experiment, the detuning can be set within the range of 1K Hz to 10K Hz. Fig.3 shows that the oscillation occurs at the edge of square wave, and it was observed in the oscilloscope that was connected to PD.

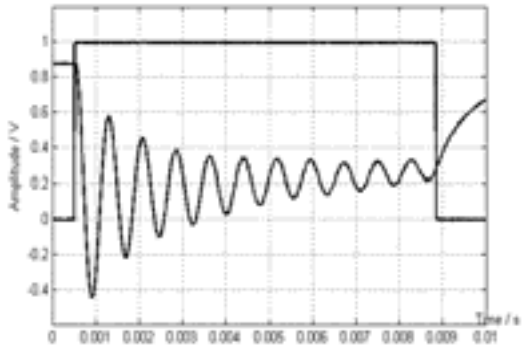

Fig. 3. Optical signal modulated by the square wave.

In the data processing part, the DCPT oscillation frequency is extracted by a filter which is a simulation filter generated by MATLAB tools. After the FFT transformation, we will get the spectrum of the oscillation signal, as is shown in Fig.4. As there exists a picket fence effect in the Fourier transform from the time domain to the frequency domain, we use the narrow-band simulation filter and scan the period of the square wave simultaneously, when 1/2 of the period is equal to integer multiple of the DCPT oscillation period, the spectral line intensity of oscillation frequency will be the maximum, as is shown in Fig.5.

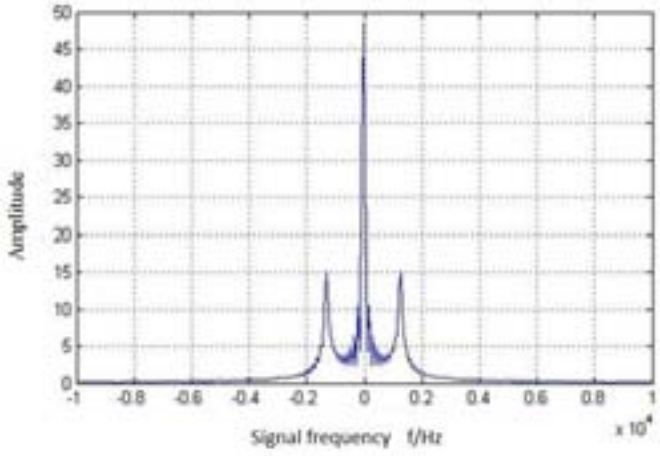

Fig. 4. The light spectrum of the transient oscillation

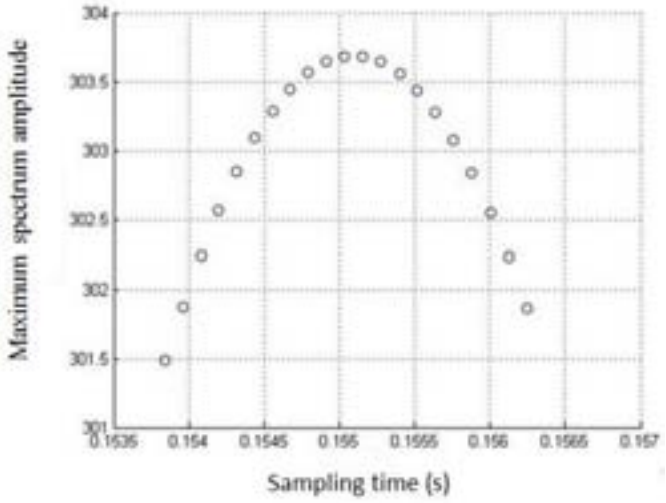

Fig. 5. We scan the period of the square wave to get the largest spectrum amplitude.

Using this method, the spectrum leakage can be decreased and the oscillation frequency can be extracted accurately.

Since the oscillating frequency equals the detuning frequency theoretically, we can obtain the output standard frequency by adding or subtracting the oscillation frequency and microwave frequency without an extra frequency-locking-loop.

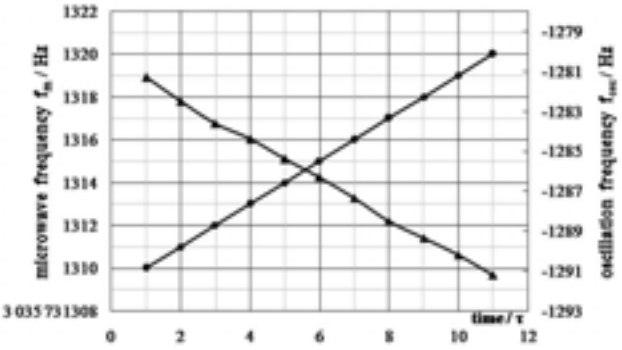

Fig. 6. Ascending microwave frequency at a sample rate of 1Hz/s is marked with dots, and correspondingly changing oscillating frequency is represented by a series of triangles. τ is the time interval of sampling, which was 20 seconds here. In our experiment, $f_m > f_h$, so we added a minus sign in front of f_{osc}.

Based on the theories and analysis demonstrated above, we used the experimental setup shown in Fig. 1 to measure the changing DCPT oscillating frequency, following the shift of fm. We manually changed the microwave frequency fm every 20 seconds, and measured corresponding DCPT oscillating frequency. The results are shown in Fig.6.

From Fig.6, it is observed that the DCPT oscillating frequency fosc and microwave frequency fm changed correspondingly by same magnitude, but in opposite directions. This result concurs with the theory that the oscillation frequency fosc changes as a consequence of the detuning frequency fd. Compared to the related prior research, the

Identify applicable sponsor/s here. If no sponsors, delete this text box (*sponsors*).

precision was greatly improved, which makes it more probable to achieve this atomic clock with an average stability(a standard stability). Using the fm and fosc data from Fig. 3, we can achieve a stable output frequency, as seen in Fig. 7.

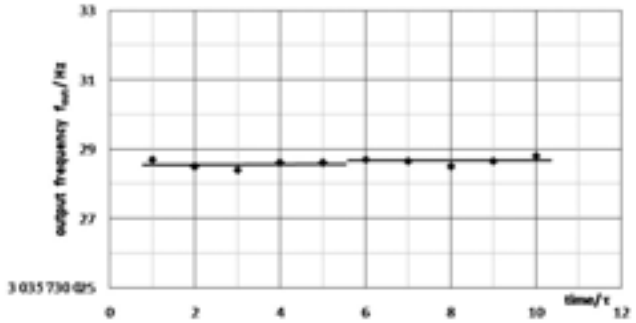

Fig.7. Output frequency results. Scattered dots and the black line jointed by three square dots indicate corresponding results before and after the averaging process, respectively.

In Fig. 6, the scattering data represent the output standard frequency fout derived by subtracting measured oscillation frequency fosc from microwave frequency fm,. The precision of the output frequency instability was about 0.5Hz, leading to a short-term instability of around 2×10-10.

Since the measurement error of fosc was mainly caused by random noise, in order to further improve the precision, we averaged every 5 data and increased the averaging time to 100 seconds. This averaging result is demonstrated by two lines in Fig. 6, which represent the numerical result of averaging the first 5 data and the following 5 data respectively. It is shown that the measurement precision was increased to about 0.2Hz, and the long term stability was about 5×10-11, which also suggest the possibility to be better. In addition, here the sampling rate was limited by the computing rate.

Therefore, if the performance index of data processing device is increased and the averaging method is implemented, the short-term and long-term stability will be further improved. In our experimental setup, the frequency synthesizer as the microwave source has a hundred-second-frequency instability better than 5×10-11, which makes our results reasonable. In addition, properly chosen relative facilities, such as a steadier square wave generator, can be used to optimize the precision and stability as well.

In comparison with traditional atomic clocks, this DCPT atomic clock makes it unnecessary to use the circuit for locking the microwave frequency, which eliminates the instability and loose locking probability brought in by the phase locking loop, especially when the scheme is used in harsh environments. And the transient signal has an amplitude 3 to 4 times that of the CPT signal, which further benefits observation and analysis. In addition, this data processing section can be easily digitalized and integrated. As a result, this scheme has great potential in the design and manufacture of miniature atomic clocks.

In conclusion, we have proposed and implemented a method which allows us to obtain the transient oscillating frequency with a relatively high stability for the DCPT atomic clock, and we have experimentally proven that the transient oscillation frequency is equal to the detuning frequency on the scale of 0.2Hz. We have supplemented our prior research with increased precision which further indicates the possibility to achieve a DCPT atomic clock with good short-term and long-term stability. This DCPT atomic clock also provides great advantages to both integration and miniaturization, which make it a potential scheme for CSACs in the future.

ACKNOWLEDGMENT

This work was supported by the National Natural Science Foundation of China under Grant No.11074012. We would like to thank Tao Guo and Ke Deng for their informative discussion, to thank Xin Wang for her constructive suggestions during the writing of this text.

REFERENCES

[1] Tao Guo, Ke Deng, Xuzong Chen, and Zhong Wang, Appl. Phys. Lett. 94, 151108 2009

[2] Zhong Wang, Tao Guo, Ke Deng, and Xuzong Chen, IEEE Frequency Control Symposium, 2010

[3] K. Deng, T. Guo, D. W. He, X. Y. Liu, D. Z. Guo, X. Z. Chen, and Z. Wang, Applied Physics Letters 92, 211104 (2008)

[4] Ke Deng, Tao Guo, Juan Su, Dengzhu Guo, Xinyuan Liu, Lu Liu, Xuzong Chen, and Zhong Wang, Physics Letters A 373, 1130 (2009)

[5] Ke Deng, Xuzong Chen, and Zhong Wang, Optics Letters, in press (2011).

Microwave Cavity Design for an Optically-Pumped Rubidium Atomic Beam Clock

Chang Liu, Yanhui Wang
Institute of Quantum Electronics,
School of Electronics Engineering and Computer Science, Peking University
Beijing, China
wangyanhui@pku.edu.cn

Abstract—**We design a microwave cavity for our developing compact optically-pumped rubidium beam frequency standard. For clock transition of ^{87}Rb (F=2, m_F=0 to F=1, m_F=0), the central frequency is 6.8347GHz. The cavity made of WR90 waveguide in previous cesium beam clocks no longer works. In our design, we follow the method of Ramsey-type cavity in cesium beam clocks but change the cross section of waveguide. Some related modifications have to be made such as the lengths of waveguide. Unfortunately one is not likely to obtain analytical results on these values. Finite element analysis software helps to numerically solve the electromagnetic field based on arbitrary boundary conditions. Therefore, the resonant frequency and other characters of a cavity are computable when its dimensions are given. As a result, suitable dimensions can be determined to get a resonant frequency of 6.8347GHz. Considering other effects, e.g. end-to-end phase difference, more optimizations and requirements are proposed.**

Keywords-rubidium beam clock; microwave cavity; resonant frequency; frequency stability

I. INTRODUCTION

A. Optically-pumped Beam Clocks

Manufactured atomic beam clocks, especially cesium clocks, free of collision frequency shift and first-order Doppler shift, have good performance on long-term stability. The restrictions of beam clock's short-term stability lie in the limited time period of atom-microwave interaction and the low utilization of atoms. The former is solved by the use of cold atoms, i.e. in fountain clocks, but the system becomes so complicate that the fountain clocks is more likely to operate in laboratories. On the other hand, optical pumping and detection, which increase prominently the utilization rate of atoms, are quite suitable for a beam device, where the pumping, microwave interrogation and detection are separate in space, making the disturbance between the interactions relatively small. However, unexpected effects, such as the light shift, still exist, of which extra care should be taken. Research on compact optically-pumped cesium and rubidium clocks are reported [1-3].

We are working on an optically-pumped rubidium beam clock, schematic of which is shown in Fig.1. One problem we are facing is the long-term working of laser diodes. A method using rubidium lamps instead of laser diodes was proposed [4]. The advantage of lamps is their stability while the shortcomings are the wide span in spectrum and weak intensity, which influence the pumping and detection rate. To make a comparison, we will test both laser diodes and lamps as light sources in experiment.

B. Microwave Cavity in Atomic Frequency Standards

A microwave cavity is a vacuum space surrounded by conducting boundaries. According to Maxwell equations, the modes of standing electromagnetic field inside are fixed when boundary condition is given. Most of the time, the fundamental mode is used. The characters of a cavity are described by its resonant frequency and quality value. Basic theories about microwave cavity can be found in many related materials such as [5].

The microwave cavity provides the environment for atom-microwave interaction, because in fundamental modes, direction, amplitude and phase of magnetic field are all uniform along particular lines in the cavity, which are just suitable trajectories for atoms to traverse the cavity.

In beam frequency standards, a long atom-microwave interaction time indicates a narrow line width, which improves the short-term stability. The atoms' velocity distribution is dependent on the oven temperature, whose variation's range is quite little, less than 10% during experiment. Hence, the line width is mainly determined by the length of the cavity, measured along the atoms' trajectory. However, the cavity is not as long as good, for the uniform of field is hard to ensure if the cavity is too large. Moreover, the total size of a commercial clock is usually limited.

The separated field method, proposed by N. F. Ramsey [6], adopts a U-shaped cavity, which is traversed twice, at the ends, by atoms, as seen in Fig.1. For atoms, there is a long drift distance between the two traversing. The Ramsey line width is inversely proportional to this microwave-free distance and independent on the traversing distance. The drift distance could be very long, from 10cm to several meters, depending on the design.

Sponsored by National Natural Science Foundation of China (Grant No. 11174015)

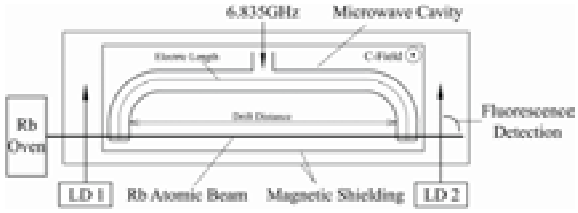

Figure 1. The schematic diagram of our rubidium beam tube.

Some methods and improvements on U-shape cavities in cesium beam clocks are given in [7-8].

II. METHODS

A. Simulation of Field in the Cavity

For a straight cavity, all characters can be given theoretically. But it is not so easy for a U-shape cavity, taking into account the bends, apertures that enable atoms to cross, T-junction for energy input and so on. Finite element analysis software, HFSS ANSYS in our design, which is able to numerically calculate the field inside a model, is used to calculate the resonant frequency, intrinsic quality value (quality value without regard to the energy input), and field pattern of a given cavity shape. Fig.2 is an example of the simulated magnetic field distribution in our U-shape cavity.

B. Requirements

The resonant frequency of the cavity, denoted by ν_c, is the peak location of the power-frequency line. That is to say, if the microwave is at the resonance frequency of the cavity, the power input is at maximum. As a result, to get sufficiently large microwave power, ν_c should be, in our device, close to 6.8347GHz, which is the frequency the microwave signal tends to be, i.e. the frequency of clock transition of ^{87}Rb. Besides, cavity pulling effect, as a cause of frequency shift, again requires ν_c to be close to the clock transition frequency. The corresponding frequency shift is [9]

$$\Delta\nu_c \propto \frac{T_c^2}{T_i^2}\cdot(\nu_c-\nu_0), \tag{1}$$

where T_c is equal to $Q_L/\pi\nu_0$, T_i is a characteristic time of flight during drift distance and ν_0 is the clock transition frequency. One can see that the frequency shift is proportional to the mistuning of the cavity. Consequently, instead of WR90 in cesium clocks, the type of waveguide is chosen to be WR112, whose cross section is $28.499\cdot12.624\text{mm}^2$, for it is applicable for the clock transition frequency, 6.8347GHz. On the other hand, the cavity pulling is also proportional to the square of loaded quality value Q_L (quality value considering energy input). If Q_L is sufficiently small, e.g. less than 1000, the cavity pulling effect may be negligible.

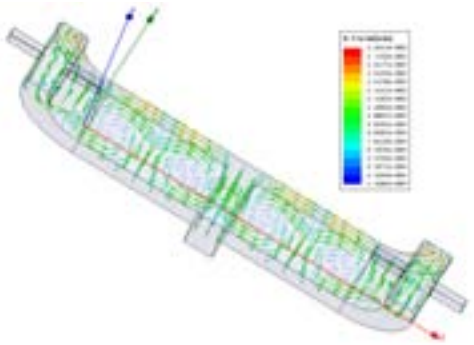

Figure 2. An example of simulated magnetic field (vector).

III. THEORIES AND NUMERICAL SIMULATIONS

A. Rectangular Cavity as an Approximation

Properties of isolated, straight cavities made of shorted rectangular waveguide are given [5]. Under TE_{10n} mode, the relation between resonant frequency and the electric length of a straight cavity, which is denoted by c, is

$$c = n\cdot[(\frac{2}{\lambda})^2-(\frac{1}{a})^2]^{-1/2} \tag{2}$$

where λ is the wavelength in vacuum and a is the long side of the cross section of waveguide. Note that c/n is the so-called waveguide wavelength, which is 68.67mm for waveguide WR112 and microwave frequency of 6.8347GHz. Considering the size of the clock, we use TE_{106} mode of the cavity, i.e. n=6, leading to the total length to be 206.02mm. If bends, apertures and energy input are added, the total length has to be slightly adjusted to meet the frequency. It is worth noting that theoretically the cavity's resonant frequency decreases linearly with the increase of the total electric length.

B. Field Simulation

An example of the simulation of magnetic field inside the U-shape cavity has been shown in Fig.2. With the simulation, we get the resonant frequency with different lengths of the cavity. By this means, the suitable lengths can be found, when the resonant frequency is equal to the clock transition frequency, as mentioned in Section II. The simulation result of the resonant frequency depending on drift length of the cavity is shown in Fig.3, where the variation tendency, as can be seen, is quite in accordance with the theory. The drift distance is thus determined to be 151.33mm, and the total electric length to be 207.26mm correspondingly, a little different with the theoretic result mentioned before. The other variable lengths are determined in the similar way.

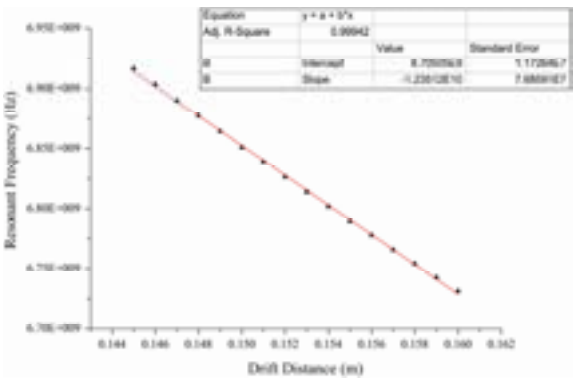

Figure 3. Simulation result of resonant frequency varying with drift distance.

IV. Results and Discussion

A. Configuration of the Cavity

The final configuration of the U-shape cavity is shown in Fig.4. The apertures that allow atoms to pass are $3.6 \cdot 6\text{mm}^2$ in size. Sections of cutoff waveguide are attached to the apertures where atoms traverse, preventing microwave leakage.

Beyond the U-shape cavity (not shown), the microwave signal is transferred by coaxial. A coaxial-to-waveguide transducer is used to couple the signal into the cavity. Posts of variable heights are on the transducer's wall, to tune the total resonant frequency and quality value. Besides, a ceramic window isolates the U-shape cavity from the transducer, which is the usual method for a sealed cavity. The total loaded quality value of the cavity is about 1000, which is also obtained from the simulation result.

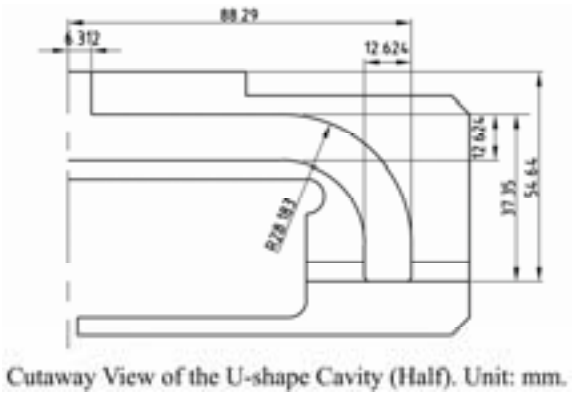

Figure 4. The final result of U-shape cavity.

B. Estimation on the Ramsey Line Width

In optically-pumped frequency standard, the Ramsey line width is calculated by [10]

$$\Delta\nu = \frac{\Delta_L}{2\pi T_i}. \tag{3}$$

Here $T_i=\alpha/L$, where α is the most probable velocity and L is the drift length. Δ_L is value which depends on the velocity distribution, 3.02 in the cycling transition detection scheme. Assuming the oven temperature is 400K, the most probable velocity is then 283m/s. Thus the Ramsey line width is estimated to be approximately 900Hz. This width is about two times larger than what we measured in our previous cesium clocks, because both the drift distance is shorter, and the most probable velocity is higher here than in cesium tube. Besides, actual operating conditions will influence this width.

V. Conclusion

A method based on field simulation of microwave cavity design for a compact rubidium beam clock is presented. The simulation result is quite in accordance with the theories. The final performance of the cavity is a resonant frequency of 6.8347GHz and a loaded quality value of 1000. The drift distance is 151.330mm and the total electric length of the cavity is 207.26mm. The Ramsey line width is a little larger than what we expect. Improvement on the drift length or atoms' velocity control may be proposed in the future.

References

[1] S. Lecomte, M. Haldimann, R. Ruffieux, P. Berthoud and P. Thomann, "Performance demonstration of a compact, single optical frequency Cesium beam clock for space applications," Proceedings of the Frequency Control Symposium 2007, pp. 1127–1131.

[2] C. Sallot, M. Baldy, D. Gin and R. Petit, "3.10-12. τ- 12 / On industrial prototype optically pumped cesium beam frequency standard," Proceedings of the Frequency Control Symposium 2003, pp. 100–104.

[3] A. Besedina, A. Gevorkyan and V. Zholnerov, "Two-frequency pumping in ^{87}Rb atomic beam frequency standard with laser pumping/detection for space application," Proceedings of Frequency Control Symposium, 2007, pp. 623–628.

[4] Y. H. Wang, J.Q. Huang, Y. Gu, S. Q. Liu, T. Q. Dong and Z.H. Lu, "Improved rubidium atomic beam clock based on lamp-pumping and fluoresence-detection scheme," Journal of the European Optical Society – Rapid Publication, vol. 6, p. 11005, 2011.

[5] R. E. Collin, Foundations for Microwave Engineering, New York: McGraw-Hill, 1966

[6] N. F. Ramsey, Molecular Beams, 1st ed., Oxford: Clarendon, 1956.

[7] A. G. Mungall and H. Daams, "Cesium Beam Frequency Standard Cavity Design," Metrologia, vol. 6(2), pp. 60–64, April 1970.

[8] A. De Marchi, J. Shirley, D. J. Glaze and R. Drullinger, "A new cavity configuration for cesium beam primary frequency standards," IEEE Trans. Instrum. Meas., vol. 37(2), pp. 185-190, June 1988.

[9] C. Audoin, N. Dimarcq, V. Giordano and J. Viennet, "Physical origin of the frequency shifts in cesium beam frequency standards-related environmental sensitivity," IEEE Trans. Ultrason. Ferroelectr. Freq. Control, vol. 39(3), p. 412, May 1992.

[10] J. Vanier and C. Audoin, The Quantum Physics of Atomic Frequency Standards, Bristol, Philadelphia: A. Hilger, 1989.

Distributed Cavity Phase Calculation for a Rectangular Ramsey Cavity in NRC-FCs1

Louis Marmet
Measurement Science and Standards
National Research Council
Ottawa, Ontario, Canada
Email: louis.marmet@nrc.ca

Nicolás Shtin
SMK Electronica S.A. de C.V.,
Aguila Azteca No. 19308,
Col. Baja Maq El Aguila,
22215 Tijuana, BC, México

Pierre Dubé
Measurement Science and Standards
National Research Council
Ottawa, Ontario, Canada

J. Mauricio López R.
Time and Frequency Division,
CENAM,
Queretaro, Qro. 76241, México

***Abstract*—A preliminary calculation of the frequency shifts resulting from the distributed phase of a rectangular cavity is used to model frequency measurements of the fountain clock NRC-FCs1. The calculation is based on a numerical evaluation of the cavity field made with a finite element EM solver. The frequency shift is obtained by solving the Bloch-equations numerically along the path of the atoms on the free-fall trajectories through the cavity. We study the frequency shifts as a function of the launch direction, the tilt of the physics package and offsets in the position of the MOT relative to the axis defined by the state-selection cavity and the Ramsey cavity.**

I. Introduction

The evaluation of frequency offsets arising in a Ramsey interrogation require a careful experimental evaluation of a fountain clock supported by numerical modeling of the electromagnetic field of the Ramsey cavity. The frequency of a fountain clock is dependent on phase variations in the rf-field and various geometrical factors. Phase variations arise from losses in the cavity walls and coupling to the antennas, all of which create traveling waves. The atomic motion through the phase variations produce first order Doppler shifts which are position dependent. As a result, distributed cavity phase (DCP) frequency shifts are often the leading contribution to the uncertainty of many fountain clocks [1]. Decades of work have resulted in a good understanding of DCP. However most atomic fountain clocks use TE_{011} cylindrical cavities while NRC-FCs1's design is based on a rectangular cavity and transversal C-field configuration borrowed from laboratory beam clocks. DCP calculations require three-dimensional solutions of the cavity field, a process which requires intensive computing resources. Simplifications to a two-dimensional problem exist for cylindrical cavities [2] but the symmetry of the system cannot be exploited advantageously for a rectangular cavity. However, decreasing costs of computer resources and improved performance of computers have reduced the time required to obtain results from a finite element model.

FCs1's Ramsey cavity is designed with conical below-cutoff waveguides in order to keep atoms away from the high fields near sharp edges and minimize phase shifts [3]. This configuration also gives a computational advantage since the atoms do not interact with the field where dense meshing calculations would be required. Our first partial numerical results show a behaviour consistent with the frequency shifts measured in NRC-FCs1 as a function of the launch direction, the tilt of the physics package and the choice of the antenna used to feed the Ramsey cavity. Measurements showed that a significant frequency difference exists between operation of the fountain clock with one antenna or the other. This difference may be a result of a misalignment of the MOT with respect to the axis defined by the state-selection and Ramsey cavities.

II. The physics package

The fountain clock NRC-FCs1 operates with a MOT loaded in $825\,\text{ms}$ and a launch cycle of $1575\,\text{ms}$ [4]. The atoms are trapped, accelerated and cooled with six $\sigma^+ - \sigma^-$ beams in the 110-configuration. They leave the MOT region in the $|F = 4, m_F\rangle$ states and are pumped to the $|F = 3, m_F = 0\rangle$ state by the state-selection cavity. The states remaining in the $|F = 4, m_F \neq 0\rangle$ are removed by a σ^+ polarized $4-5'$ pusher beam. Ramsey pulses are provided by a rectangular cavity

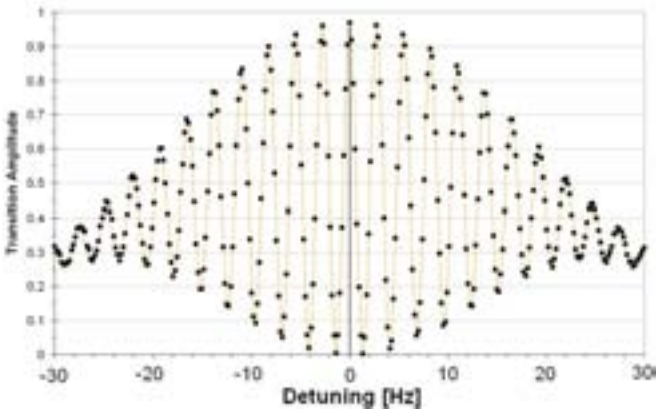

Fig. 1. Ramsey fringes for a 25cm fountain, one measurement per point.

operating in the TM_{210}-mode and fed with two magnetically-coupled antennas. A transversal C-field is generated by four linear electrodes. Because of a longer interaction between the atoms and the rf-field, the rectangular cavity produces a narrower Rabi pedestal than obtained with cylindrical cavities. In addition, it does not have field reversals in the neighborhood of the ends of the below-cutoff waveguides which could produce potentially large frequency shifts. Since the C-field is transversal the configuration takes advantage of a higher shielding from the inner cylindrical magnetic shield. The best short-term frequency stability is achieved at the optimal fountain height of 25 cm above the Ramsey cavity. The microwave signal is generated with a synthesizer chain synchronized with the NRC-SM1 maser which offered the best stability ($\sigma_y(\tau = 1s) < 2 \times 10^{-13}$). After Ramsey interrogation, the population in the $F = 4$ and $F = 3$ states is measured from the fluorescence signals obtained from four state-selecting beams: the $|F = 4\rangle$ detection beam, the pusher beam, the repumper beam, and another $|F = 4\rangle$ detection beam. Figure 1 shows the measured Ramsey fringes with a 96% contrast. An Allan deviation of $\sigma_y(\tau) = 3 \times 10^{-13}\,\tau^{-1/2}$ was obtained for $\tau < 10^5$ s. Changes to laser polarization in the detection system and the light shift contribute to the uncertainty by $< 10^{-15}$. The sample deviation of the frequency measurements show a repeatability $\sigma = 1.8 \times 10^{-15}$ over weeks of operation.

Six circular apertures can clip the atomic cloud during their free-flight. The lowest aperture, 162 mm above the MOT and 5.0 mm in diameter, is part of the lower light-shutter. The the cut-off waveguide of the state-selection cavity is located 186 mm above the MOT and has a diameter of 5.0 mm. A second light shutter has an aperture located 187 mm below the Ramsey cavity with a 10.5 mm diameter. The Ramsey cavity, located 768 mm above the MOT, has 10.5 mm diameter apertures at the ends of the cut-off waveguides each located 62 mm below and above the center of the cavity. The geometry of the system also includes detection beams having a 20 mm diameter. However, the intensity profile of these beams is not included in the current simulation.

III. Cavity field

The numerical evaluation of the field in the cavity is made using of a full-wave finite element EM solver (Ansoft HFSS finite element method solver). The precise shape of the cavity ($d_x = 39.2$ mm, $d_y = 26.67$ mm and $d_z = 18.0$ mm, and rounded internal corners) was reproduced in a CAD drawing in the solver. The dimension d_y was varied until the resonance frequency matched 9.192 GHz with $d_y = 26.84$ mm. The resonant frequencies of the model cavity are compared with the measured values in Table I. The RMS difference between theory and measurements for the remaining five modes is 45 MHz.

The Ramsey cavity is made of two identical copper halves held together symmetrically about the XZ-plane. The microwave signal is coupled into the cavity via two magnetic antennas (rectangular loops 2.6 mm $\times$0.5 mm) through 2.0 mm-wide slits located on the sides of the cavity (Fig. 2). The cutoff waveguides have cylindrical symmetry, with a conical shape near the cavity center in order to keep the atoms away from the high fields at the edges and minimize phase shifts. The cavity has a measured loaded $Q_{\text{measured}} = 4600$ and a numerically estimated unloaded $Q = 10000$.

TABLE I. Frequencies of the modes

Mode	Measured	Calculated
TM_{110}	7.036 GHz	6.999 GHz
TM_{210}	9.192 GHz	9.192* GHz
TE_{011}	9.262 GHz	9.280 GHz
TE_{111}	10.691 GHz	10.637 GHz
TM_{111}	11.019 GHz	10.967 GHz
TE_{211}	11.711 GHz	11.658 GHz

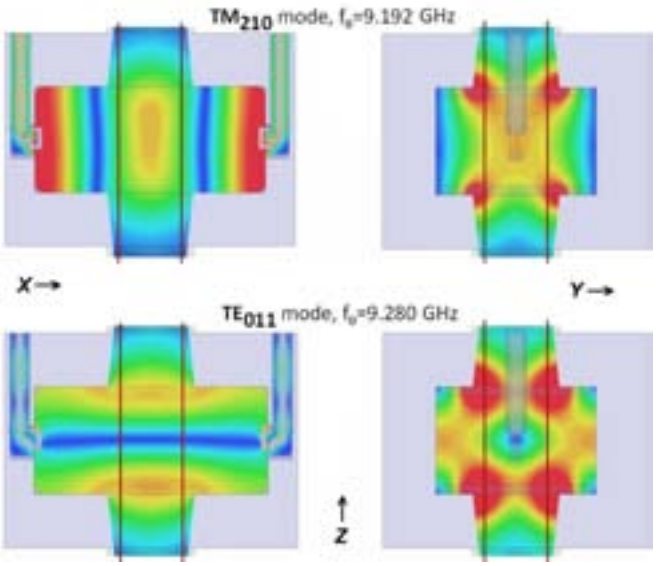

Fig. 2. Magnetic field amplitude for the TM_{210} and TE_{011} modes. The atoms are confined inside the space limited by the vertical lines.

The forward transmission plotted in Fig. 3 shows the resonances of the various modes. Two sharp dips occur at 9.2 GHz and 10.8 GHz. These are the result of destructive interference between three coupling fields (the two adjacent modes and the direct coupling from one antenna to the other) which occur when the first index l of the adjacent modes TM_{lmn} or TE_{lmn} have the same parity. The model gives a loaded $Q_{\text{model}} = 1000$. It is suspected that the exact position of the antennas is not modeled correctly which results in a larger coupling.

Although the finite element model includes in its solution every mode of the cavity, it is convenient to think of the field as the sum of many fields [1]. This could be useful to distinguish the small phase and amplitude variations generated by the solver from the errors generated by the calculations. Here we write the cavity field as the sum of a large amplitude standing wave $\mathbf{H}_0(\vec{r})$ representing the resonator's TM_{210} mode and other small amplitude fields representing an expansion of the non-resonant modes of the cavity and the field from the antennas:

$$\vec{H}(\vec{r}) = \vec{H}_0(\vec{r}) + \sum_k \left[\beta_k(\Delta\omega_k)\vec{h}_k(\vec{r})\right] + \vec{a}(\vec{r}),$$

where $\vec{H}_0(\vec{r})$ and $\vec{h}_k(\vec{r})$ are real and $\vec{a}(\vec{r})$ is the field from

the antennas. The fields $\vec{h}_k(\vec{r})$ are from other cavity modes and each factor $\beta_k(\Delta\omega_k)$ contains the phase and amplitude of the standing wave k relative to the phase and amplitude of the large standing wave at a detuning $\Delta\omega_k = \omega_{\mu\text{wave}} - \omega_k$. Using this expansion, it is possible to accurately evaluate the phase contributions of the non-resonant fields $\vec{h}_k(\vec{r})$ by calculating each one with the solver tuned on the resonant frequency of each mode k. The solutions for each field can be added differentially (with the factor $\beta_k(\Delta\omega_k)$) to the resonant solution for TM_{210} to study the effect on the phase.

IV. Frequency shift

The frequency shift is calculated by simulating the path of the atoms along the free-fall trajectories through the cavity while solving numerically the Bloch equations using the differential form:

$$\begin{aligned} \delta u &= +\Delta\, v\, \delta t \\ \delta v &= -\Delta\, u\, \delta t + \Omega\, w\, \delta t \\ \delta w &= -\Omega\, v\, \delta t \end{aligned}$$

where $\Delta = 2\pi(f_{\text{mw}} - f_0)$, Ω is the Rabi frequency, f_{mw} is the frequency of the microwave field and f_0 is the atomic resonance frequency [5]. For this work, the Rabi frequency is derived from the Y component (parallel to the C-field) of the cavity field.

The calculation proceeds as follows. Initial positions and launch velocities of an atom are used to generate a set of trajectories $\vec{r}(t)$ through the physics package. Only trajectories which do not stop on any of the apertures are kept in the set. For each position along the trajectory intersecting regularly spaced constant-z planes inside the Ramsey cavity, $\vec{r}(nz_0)$, the field H and its phase Φ are sampled from the results of the finite element solver. A bilinear interpolation along the X- and Y- axes is made to obtain a list of field values $H(nz_0)$ and $\Phi(nz_0)$ at the locations $\vec{r}(nz_0)$. The lists are converted to time dependent values and smoothed using a spline fitting function. Starting with the Bloch vector $(u = 0, v = 0, w = -1)$, the Bloch equations are integrated along the trajectory with time intervals $\delta t = t(nz_0) - t((n-1)z_0)$.

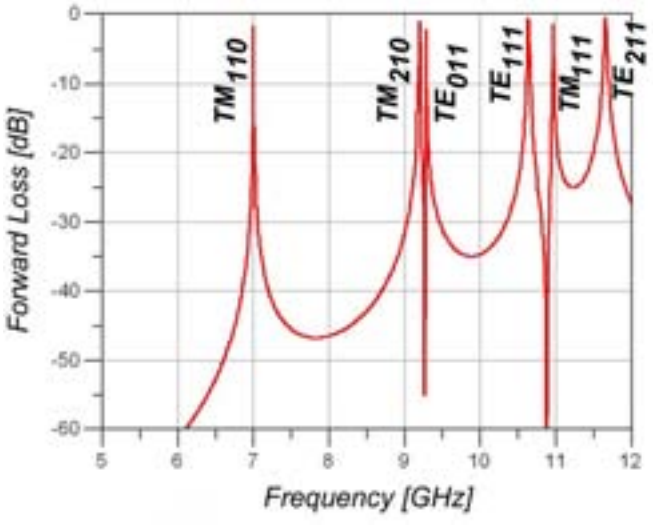

Fig. 3. Forward loss through Ramsey cavity. Canceling interference produces sharp dips between modes for which the parity of their first index is the same.

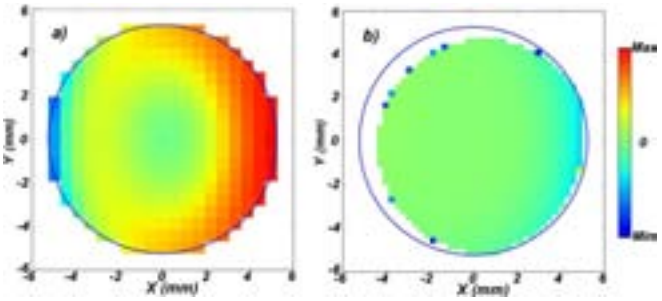

Fig. 4. Atomic population after Ramsey interrogation. The colour code represents the value w of the Bloch vector plotted as a function of the position of the atom at the exit of the Ramsey cavity. The antennas, located on the left- and right-hand side of the image, are labeled W and E respectively.

The initial launch velocities used for the calculation are selected according to a Gaussian velocity distribution representing the measured distributions along the three axes. Launching with a 110-configured MOT results in three different velocity distribution in the X-, Y- and Z-directions with equivalent temperatures $15.0\,\mu$K, $2.1\,\mu$K and $6.0\,\mu$K respectively [6]. For each trajectory a probability is assigned representing the probability of finding an atom within a velocity space element. A graph representing the population of the atoms (w component of the Bloch vector) as a function of the exit position after Ramsey interrogation is obtained from an average of the w values weighted by the probability of the trajectory. Two examples of the results are given in Fig. 4 for (a) two antennas and a tilted physics package and (b) one antenna and misaligned MOT. Atoms launched with a faster velocity are blocked at the edge of the apertures, resulting in a different excitation value seen as a dark pixel at the periphery of the disk. The frequency offset is found from the total population calculated at microwave frequencies $+f_m$ and $-f_m$ at half maximum on the Ramsey fringe.

V. Results and discussion

The experimental conditions were reproduced numerically, with the physics package tilted ± 1 mrad from the vertical along the x and y directions. A perfect alignment of the MOT along the axis defined by the center of the state-selection and Ramsey cavities was used as well as as a MOT offset by $x = -1.8$ mm and $y = 0.9$ mm. In all cases, antenna-E, antenna-W (see caption of Fig. 4) and both antennas were tested. In order to simulate the use of the antenna-W, the field from antenna-E was used with the geometry rotated by $180°$ about the z-axis. The results are shown in Table II. The table shows the offsets normalized by $\sqrt{Q_{\text{model}}/Q_{\text{measured}}} = 0.47$ to compensate for the weaker antenna coupling of the measurement system.

The first block in the table lists results obtained with one antenna and a perfectly centered MOT. The relative frequency shift dy of the clock as a function of tilt varies by $dy/d\theta_x = 2.7 \times 10^{-15}$/mrad while $dy/d\theta_y < 0.1 \times 10^{-15}$/mrad. The effect does not change significantly when the MOT is misaligned ($x_0 = -1.8$ mm and $y_0 = 0.9$ mm), as shown in the second block of Table II. In this case, the frequency shift as a function of tilt is $dy/d\theta_x = 2.1 \times 10^{-15}$/mrad

TABLE II. CALCULATED FREQUENCY SHIFTS

Number of Antennas	Initial position x_0, y_0[mm]	v_x, v_y [mm/s]	Tilt θ_X, θ_Y [mrad]	Frequency Offset $\left[10^{-15}\right]$
1	0, 0	0, 0	0, 0	-5.0
1	0, 0	0, 0	-1, 0	-8.0
1	0, 0	0, 0	$+1$, 0	-2.7
1	0, 0	0, 0	$0, -1$	-5.1
1	0, 0	0, 0	$0, +1$	-5.1
1	$-1.8, +0.9$	$+16, -8$	$-4, +2$	-5.6
1	$-1.8, +0.9$	$+16, -8$	$-5, +2$	-7.7
1	$-1.8, +0.9$	$+16, -8$	$-4, +1$	-5.8
1	$+1.8, -0.9$	$-16, +8$	$+4, -2$	-1.8
1	$+1.8, -0.9$	$-16, +8$	$+5, -2$	$+1.7$
1	$+1.8, -0.9$	$-16, +8$	$+4, -1$	-2.3
2	0, 0	0, 0	0, 0	-4.9
2	0, 0	0, 0	± 1, 0	-5.2
2	0, 0	0, 0	$0, \pm 1$	-5.0
2	$\mp 1.8, \pm 0.9$	$\pm 16, \mp 8$	$\mp 4, \pm 2$	-3.6
2	$-1.8, +0.9$	$+16, -8$	$-5, +2$	-3.0
2	$-1.8, +0.9$	$+16, -8$	$-4, +1$	-4.0

and $dy/d\theta_y = 0.2 \times 10^{-15}$/mrad. However, the misaligned MOT produces an asymmetry in the system and the frequency difference $\Delta f = 3.8 \times 10^{-15}$ arises when the other antenna is used. In the last case, when both antennas are used, the frequency offset has a weak dependence on tilt remaining $dy/d\theta < 0.2 \times 10^{-15}$/mrad for small angles (third block in Table II. However a constant offset is present due to a quadratic dependence of the DCP not canceled by the two antennas. A change in the launch direction does not cause a significant effect, mostly as a result of the velocity selection made by the apertures of the Ramsey cavity.

The measured frequency shifts as a function of tilt are: for antenna-E $dy/d\theta_x = 1 \times 10^{-15}$/mrad and $dy/d\theta_y = 5 \times 10^{-15}$/mrad; for antenna-W $dy/d\theta_x = 3 \times 10^{-15}$/mrad and $dy/d\theta_y = 3 \times 10^{-15}$/mrad. All measurements have an uncertainty of 1.8×10^{-15}/mrad. The measured frequency are comparable to the calculated values. However, the measured frequency shift between the two antennas is 18×10^{-15} which seems to indicate that the misalignment of the MOT is even greater than the numbers used in the model. This could also explain some of the variations in the measured $dy/d\theta$.

It is possible that the position of the MOT is shifted away from the symmetry axis due to the asymmetric construction of the electrostatic shutters [4]. The shutter enclosures are 20 cm diameter disks installed off-axis. When under vacuum, the compressed disks may flex in a way to produce a misalignment. Correction coils were added for the added possibility of centering the MOT (X and Y directions) and shift the launch location. The model helps in determining the direction the MOT has to be moved to correct the offset.

VI. CONCLUSIONS

The numerical method presented in this work produces consistent evaluations of the DCP frequency shifts in a rectangular Ramsey cavity and are consistent with the measured results obtained with NRC-FCs1. The model brings a better understanding of the causes of the frequency shifts. Two principal contributions arise from a misalignment of the MOT and a strong coupling of the antennas resulting in an important flux from antenna to the other.

Further work is required to complete this evaluation. A model with the correct $Q_{\text{loaded}} = 4600$ is necessary and the field of the state-selection cavity can be added to the simulation. Contributions from phase gradients of other modes should be calculated separately and added as a perturbation to the field. This would provide a good check of the results of the finite element solver. The coupling of the antennas can also be separated from the unloaded cavity modes by using the eigenmode solver. One can thus verify that the frequency offsets are mainly due to the coupling between the antennas. Finally, the intensity distribution of the laser beams can be accounted for, but this is not expected to change the results significantly.

ACKNOWLEDGMENT

L.M. would like to thank Ph. Laurent (Observatoire de Paris) and K. Szymaniec (NPL) for useful discussions and advice on the distributed cavity phase shift. The computations were made in the Python computing language with the Numpy, Scipy and Matplotlib extensions and IPython interactive computing [7].

REFERENCES

[1] R. Li, K. Gibble, "Evaluating and minimizing distributed cavity phase errors in atomic clocks," Metrologia 47, 534, 2010, and references therein

[2] R. Li, K. Gibble, "Phase variations in microwave cavities for atomic clocks," Metrologia 41, 376, 2004

[3] C. Fertig, R. Li, J.I. Rees, K. Gibble, "Distributed Cavity Phase Shifts & Microwave Photon Recoils," Proceedings of the 2002 IEEE International Frequency Control Symposium and PDA Exhibition, 469, 2002

[4] L. Marmet B. Hoger, P. Dubé, A.A. Madej, J.E. Bernard, "Detailed description of FCs1: NRCs cesium fountain primary standard," Proceedings of the 2008 IEEE International Frequency Control Symposium, 386, 2008

[5] L. Allen and J.H. Eberly, "Optical Resonance and Two-Level Atoms," Dover Publications, Inc., New York, N.Y. (1987)

[6] L. Marmet, "Update on the development of NRC-FCs1," Proceedings of the IEEE International Frequency Control Symposium Joint with the 22nd European Frequency and Time forum, Besan con France, 562, 2009

[7] F. Pérez and B.E. Granger, "IPython: a System for Interactive Scientific Computing," Comput. Sci. Eng., Vol. 9, No. 3, pp. 21–29, May 2007

Figure of Merit and Limit of Short-Term Stability in Passive Hydrogen Maser

V.I. Vasilyev, S.A. Kozlov
Institute of Electronic Measurements KVARZ, Nizhny Novgorod, Russia
Email: nnipi_kvarz@sinn.ru

Abstract — **Frequency stability of passive frequency standard is associated with the figure of merit of a quantum discriminator. The method of the discriminator figure of merit measuring and the lowest achievable short-term frequency stability in the passive hydrogen maser are presented. Results of theoretical and experimental research are compared. The result of investigation shows that with increase in a excitation signal power, spectral line shape can be considered as the sum of several lines.**

Keywords - passive hydrogen maser; figure of merit; stability; spectral line shape.

I. INTRODUCTION

Frequency stability of any passive frequency standard is associated with the figure of merit of a quantum discriminator (physics package), characterized by the ratio of signal/noise to the width of the atomic transition spectral line during indicating the atomic resonance. The larger this parameter, the higher is short-term frequency stability of the maser [1]:

$$\sigma(\tau) = \frac{\Delta f_l}{F_{\text{s-n}}} \times \frac{const}{f_l \sqrt{\tau}} \quad ,$$

where $F_{s\text{-}n}$ – signal-to-noise ratio (SNR), Δf_l – width of the atomic spectral line, f_l – frequency of the atomic transition, *const* – coefficient dependent on line detection method, τ – averaging time.

II. THEORETICAL ESTIMATION OF A PASSIVE HYDROGEN MASER STABILITY

Let us consider a passive hydrogen maser (PHM) with single frequency modulation [2]. Block diagram of PHM is given in Fig.1. Expression can be concretized for the quantum discriminator:

$$\sigma(\tau) = \sqrt{\frac{S_n(\Omega)}{2 f_l^2 S_d^2 \tau}},$$

where $S_n\ (\Omega)$ – noise spectral density at the output of the selective amplifier; S_d – the slope of discriminator curve at frequency offset excitation signal from spectral line centre by Δf.

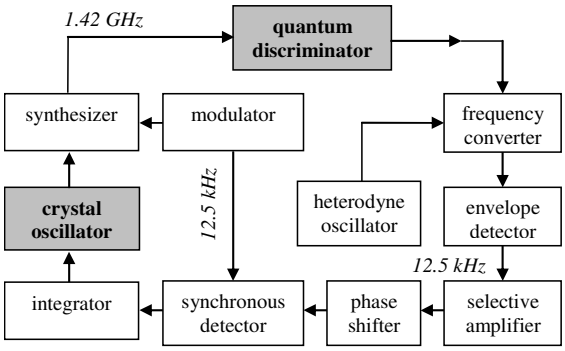

Fig. 1. Block diagram of Passive Hydrogen Maser.

If a selective voltmeter with a pass-band ΔB_{sel}, is used, S_d can be measured as the effective voltage U_{sel} of a first harmonic signal at the output of the selective amplifier, which appears as a result of detuning. U_{n} can be measured as effective noise voltage U_{n} when there is no signal at input. Frequency stability of passive frequency standard can be estimated from the following expression:

$$\sigma(\tau) = \frac{U_n \Delta f}{2\pi\ f_l U_{sel}} \frac{1}{\sqrt{\Delta B_{sel} \tau}} \quad .$$

Experimental dependence of PHM CH1-76A stability at time of averaging 100 sec upon the SNR during frequency offset $\Delta f = 0.1$ Hz is given in Fig. 2.

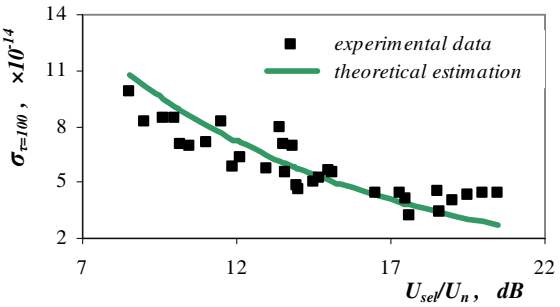

Fig. 2. Dependence of CH1-76A stability at time of averaging 100 sec upon the SNR during frequency offset $\Delta f = 0.1$ Hz.

The SNR was measured by means of the selective microvoltmeter with $\Delta B_{sel} = 300$ Hz. Also estimated value calculated by means of the given formula is shown in figure. The analysis of the figure plot shows close agreement of a theoretical estimation and experimental results up to signal/noise values equal to 19 dB, and then there comes limitation on stability improvement.

III. Investigation of Stability Limitation

For investigation of stability limitation we will refer to the slope of discriminator curve S_d. The expression received by us is based on the solution of the equation of PHM [3, 4] in a "steady-state" approximation:

$$S_\partial \approx \frac{2J_1(m)}{J_0(m)\sqrt{1+q}} \frac{\alpha S_0}{T_1 T_2 (1+S_0)}, \qquad (1)$$

where $q = \Omega/\gamma_c$; γ_c – the halfwidth band of the microwave cavity of the hydrogen discriminator; m, Ω – the index and the angular frequency of the phase modulation; $J_n(m)$ – the Bessel function of the first kind of the n order from the argument m; α и S_0 – the hydrogen discriminator excitation and saturation factor; T_1 и T_2 – longitudinal and transverse relaxation time of the atomic ensemble. The expression shows (Fig. 3) that at small saturation the slope of discriminator curve is proportional to S_0 (therefore, to an excitation signal power), and at $S_0 >> 1$ the slope of discriminator curve tends to a limit. But the results of the experiment given in Fig. 4 show that after achievement of a maximum reduction S_d begins at increase of a excitation signal power P_{ex}.

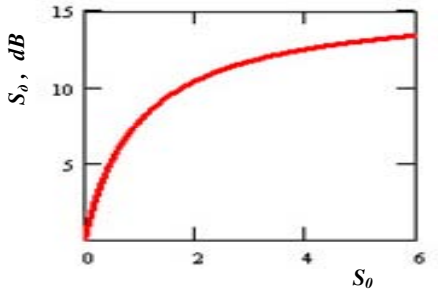

Fig. 3. Theoretical dependence of the slope of discriminator curve upon the hydrogen discriminator saturation factor.

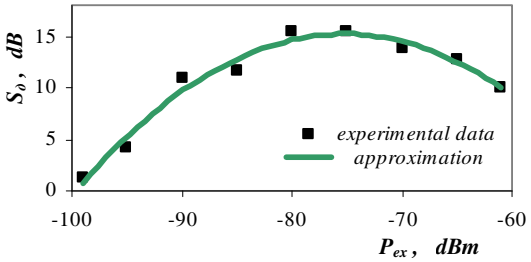

Fig. 4. Experimental dependence of the slope of discriminator curve upon the power of a excitation signal power during frequency offset $\Delta f = 0.1$ Hz.

Amplitude characteristics of the quantum hydrogen discriminator were experimentally investigated for verification of theoretical model. According to the conventional representations the atom spectral line has a Lorentz line shape. For example, such result is obtained due to the solution of the equation of a hydrogen maser in a "steady-state" approximation [3].

For verification the equipment with accumulation of data was used. It allowed to increase the accuracy of measurements. As a source of a signal the Anritsu MG3642A signal generator was used. As the receiver the spectrum analyzer E4402B-COM of Agilent Technologies was used. The generator and the spectrum analyzer were synchronized by a highly stable signal of 10 MHz from the active hydrogen standard of frequency CH1-75A. Between the generator and the quantum discriminator the ferrite isolator with the return losses more than 100 dB was placed, and between the discriminator and the receiver the variable attenuator was placed for improvement of wave impedance matching and reduction of signal distortion [5]. We increased attenuation at increase in a signal of the generator.

Experimental data in a form of the hydrogen line shape are given in Fig. 5. Parameter is the power of a excitation signal. The result of investigation shows that the spectral line shape corresponds to Lorentz line shape only at small ($\approx -90...-100$ dBm) excitation signal power. With increase in a excitation signal power it is observed not only broadening, but also strong distortion of the spectral line. The line shape can be considered as the sum of several (possibly three) spectral lines detuning from each other.

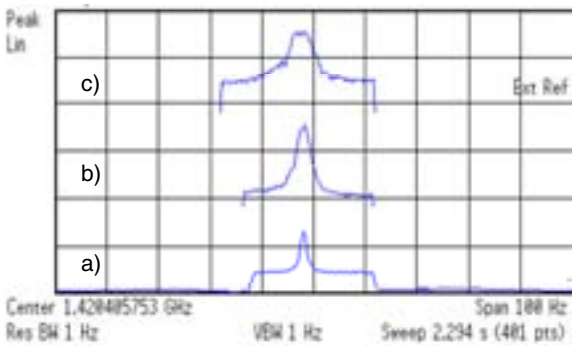

Fig. 5. The PHM spectral line shape at a different excitation signal power P_{ex}: a) – 94 dBm; b) – 74 dBm; c) – 67 dBm.

IV. Discussion

In a "steady-state" approximation it is considered that all atoms give quantum of energy and after that leave the microwave cavity. Actually the quantity of the atoms which have given quantum of energy is defined by induced atom transition rate. The transition rate depends on the power of a excitation signal power. Quantity of atoms which can give and again receive energy quantum grows at increase of signal power.

In these conditions Stark – Zeeman dynamic effect has to be apparent. It is the effect of splitting of the spectral line that

appears in strong alternating electromagnetic fields [6, 7]. Splitting of satellites is equally to the Rabi frequency:

$$b_R = \mu_{12}\mu_0 H/\hbar$$

where H – intensity of magnetic microwave field component, μ_{12} – magnetic dipole moment of transition, μ_0 –magnetic constant, $\hbar$ – Planck constant. According to our theoretical estimates at an excitation signal power equal to – 70 dBm we have $b_R/2\pi \approx 2$ Hz.

At a low excitation signal power the Rabi frequency is small and shift of satellites from the central peak is also small in comparison with line width. In this case satellites in Fig. 5 are not observed. Then summation of several lines leads to a flat top of the line. At further increase in Rabi frequency there is an observed splitting of the line.

The analysis shows that there are two main factors defining behavior of the slope of discriminator curve in Fig. 4. The first factor leads to increase in S_d. According to the expression 1 at the small saturation factor S_0 the slope of discriminator curve is proportional to excitation signal power. The second factor is associated with broadening and line splitting, it contributes to S_d reduction. The broadening and splitting leads at the beginning to emergence of a plateau on a discrimination curve near zero frequency offset. After that the general reduction of a tilt angle of the discrimination curve occurs.

V. Conclusion

- The larger figure of merit of a quantum discriminator, the higher is short-term frequency stability of the maser.
- At small ($\approx -80...-100$ dBm) excitation signal power the experimental slope of discriminator curve increases. At further increase of a excitation signal power S_d begins to decrease. The experimental spectral line shape can be considered as the sum of several spectral lines. We explain the spectral line splitting by Stark – Zeeman dynamic effect that appears in strong alternating electromagnetic fields.
- The discovered effect limits short-term stability of passive hydrogen maser.

References

[1] R.F. Lacey, A.L. Helgesson, J.H. Holloway. Short-term stability of passive atomic frequency standards.// Proc. of the IEEE, 1966, vol.54, issue 2, pp.170-176.

[2] N.A. Demidov, A.V. Pastukhov, A.A. Uljanov. Progress in the development of IEM Kvarz passive hydrogen masers.// Proc. 31 Annual Precise Time and Time Interval (PTTI) Applications and Planning Meeting, USA, 1999, pp. 579-588.

[3] C. Audoin, J. Vanier. The quantum physics of atomic frequency standards. – IOP Publishing, Bristol and Philadelphia. – 1989, vol. 2..

[4] S.A. Kozlov, V.A. Logachev. Influence of the various factors on the passive hydrogen maser frequency instability.// Proc. 51 Annual Frequency Control Symposium. – USA, Orlando. – 1997, pp. 286-294.

[5] N.A. Demidov, V.I. Vasilyev. The development and future of hydrogen maser clock technology.// Electronics: NTB, 2008, vol.4, pp.92-98.

[6] V. M. Kiselev, N. A. Gryaznov, L. I. Rodina. Dynamic Zeeman effect in the active medium of an iodine laser amplifier.// SOV J QUANTUM ELECTRON, 1989, 19(3), pp. 328–333.

[7] A. Hayat, C. Lange, L. A. Rozema, et al. Dynamic Stark Effect in Strongly Coupled Microcavity Exciton-Polaritons.// Phys. Rev. Lett., vol. 109, issue 3, 2012, pp. 033605 – 033609.

A Stroboscopic Approach To Surface Acoustic Wave Delay Line Interrogation

N. Chrétien, J.-M. Friedt
SENSeOR
BESANCON, France
Email: jmfriedt@femto-st.fr

G. Martin, S. Ballandras
FEMTO-ST, Time & frequency
UMR CNRS 6174, BESANCON, France
Email: ballandr@frecnsys.fr

***Abstract*—A pulsed RADAR approach is investigated to probe acoustic delay lines used as passive sensors. In order to comply with the requirements of compact, low power receiver electronics, a stroboscopic equivalent time sampling approach is demonstrated. A strategy for generating high resolution time delays while allowing for long interrogation durations (up to 5 μs) is implemented by combining an FPGA-based delay generator with commercially available programmable digital delay lines. The measurement sequence of generating interleaved combs is due to the long delay line reconfiguration duration (SPI communication) with respect to the coarse comb (FPGA based counter). The response of the sensor is recorded and processed to acquire the coarse acoustic velocity information through magnitude measurement, and an accurate physical quantity estimate is computed thanks to the phase information. We demonstrate an improved software measurement strategy which prevents the slow process associated with a stroboscopic approach and allows to reach refresh rates of up to 20 kHz when probing an acoustic tag for a physical property measurement, while keeping the hardware to a bare minimum.**

I. Introduction

Acoustic delay lines are well know transducers used as passive sensors interrogated through a wireless link. The inverse piezoelectric effect converts the energy of an incoming electromagnetic pulse, trough the interdigitated transducer (IDT) connected to the antenna, to an acoustic wave propagating on a piezoelectric substrate. Mirrors patterned on this substrate reflect a fraction of this wave back and the direct piezoelectric effect converts these acoustic pulses to electromagnetic signals detected by the receiver. The interrogation unit design is given by the characteristics of the sensor response. As part of this study, we will be interested in probing a commercially available acoustic delay line provided by the Carinthian Tech Research (CTR, Villach, Austria) whose spectral and time response is displayed in Fig. 1.

The delay line is probed with an excitation signal whose spectral characteristics lie in the 2.4 to 2.454 GHz range, hence complying with the industrial, scientific and medical (ISM) band regulations. The time-domain response of this line for a 54 MHz bandwidth excitation signal exhibits eight echoes between 994 ns and 2.19 μs. Two of these echoes partially overlap due to the reduced bandwidth, but are still separated by a gap exhibiting a 17 dB dynamic range.

Multiple electronic reader units have been presented in the literature, most of which are based on the Frequency Modulated Continuous Waves (FMCW) RADAR approach [1],

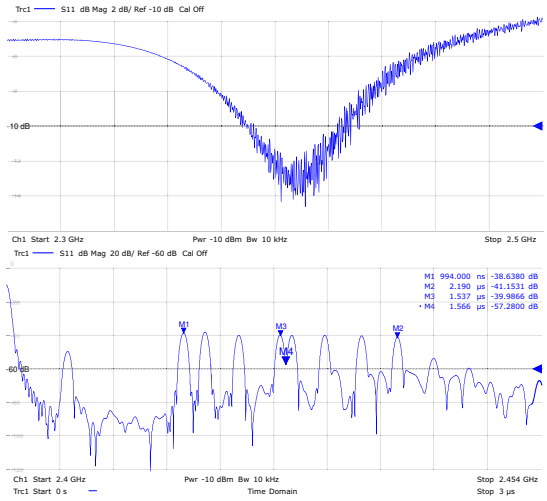

Fig. 1. Top: S_{11} spectral response of a CTR delay line between 2.3 GHz and 2.5 GHz. Bottom: 3 μs time response with an excitation signal of 2.427 GHz and a bandwidth of 54 MHz. The 8 echoes are visible, with insertion losses of 40 dB, due to mirror efficiency, with an additional parasitic echo due to the back edge of the device at 350 ns after the excitation signal.

[2] whose control of the spectrum use and radiofrequency synthesis circuit is most basic, although requiring significant computational power (periodic audio-frequency rate sampling and Fourier transform) to extract the electrical properties of the acoustic delay line acting as cooperative target. Furthermore, FMCW requires a well linearized voltage controlled oscillator or linear digital synthesis for the Fourier transform components to coherently sum throughout the frequency excursion over the transfer function of the transducer [3], [4].

Another complementary approach is the pulsed RADAR method in which the frequency band, rather than being continuously swept, is probed by a wideband pulse. Echoes in the time domain are returned by reflectors following a delay proportional to their distance. In such a configuration, the challenge no longer lies in the signal source but on the wideband receiver whose sampling rate must be high with respect to the occupied bandwidth. One well known solution, best suited in the case of RADAR in which the environment is probed by a signal generated by the instrument and acting as a trigger signal, is the stroboscopic method as used for example in Ground Penetrating RADARs (GPR). Such an instrument has been demonstrated to be compatible with recovering the time domain response of acoustic transducers acting as passive cooperative targets [5], [6].

Before discussing the operation of the proposed reader unit, we first explain the reasons for choosing a pulsed RADAR approach rather than the classical FMCW RADAR method. Secondly, we explain the principle of equivalent time sampling and our system requirements. Details and implementation of this method are then discussed. Finally, measurements and results are reported with a discussion of the reader improved sampling rate.

II. Pulsed Radar

We assess the use of a pulsed RADAR approach in which the instantaneous power reaching the target is greatly increased with respect to a continuous emission, even though the average power consumption (depending on pulse repetition rate) is of the same order of magnitude than those found in FMCW. We assume that the emitted power must comply with ISM band regulations [7, Annex 1H] – 10 dBm emitted power in the 2.4 to 2.483 GHz ISM band – since common acoustic sensors do not occupy wide enough bandwidths to be considered as ultra-wideband devices.

Both FMCW and pulsed RADAR propagation characteristics are governed by the RADAR equation which will be used to assess the maximum interrogation range of acoustic transducers acting as cooperative targets. The one-way propagation equation relates the received power P_r to the instantaneously transmitted power P_t through

$$P_r = \frac{P_t G^2 \lambda^2}{(4\pi R)^2} \tag{1}$$

assuming that both the transceiver and the sensor are fitted with an antenna exhibiting a gain (G) equal to 1. λ is the signal wavelength and R the range between the RADAR and the sensor.

Once the sensor is loaded, the reflected power P_r' must account for the insertion loss IL of the device. We thus estimate the interrogation range R of a sensor by considering that the returned signal power S is given following

$$R = \frac{G \cdot \lambda}{4\pi} \sqrt[4]{\frac{P_t}{S \cdot IL}} \tag{2}$$

Hence, the range limitation is given by the P_t to S ratio and we consider S_{min} the minimum detectable power on the receiver defined as the minimum acceptable signal to noise ratio $(S/N)_{min}$ multiplied by the thermal noise injected into the low noise amplifier (LNA) $k_B T_0 B F$ with k_B the Boltzmann constant, T_0 the antenna and LNA temperature, B the receiver bandwidth and F the amplifier noise factor.

The relationship providing an estimate of the acoustic device interrogation range as a function of the instantaneously transmitted power is:

$$R_{max} = \frac{G \cdot \lambda}{4\pi} \sqrt[4]{\frac{P_t}{S_{min} \cdot IL}} \tag{3}$$

The receiver bandwidth defines the thermal noise level on the receiver and hence the detection limit: in the case of FMCW, typical sweep rates of the frequency source spanning 50 MHz is in the 10 ms range, yielding beat frequencies when probing an acoustic delay line with echoes delayed by up to 5 μs of $50 \times 10^6 \times 5.10^{-6}/10^{-2} = 25$ kHz. We will thus consider and FMCW recording bandwidth of 30 kHz, much lower than the pulsed RADAR receiver bandwidth of a few hundred MHz.

Assuming an FMCW system continuously transmitting 10 dBm and fitted with a receiver with 30 kHz bandwidth characterized by a noise figure of 3 dB, a signal to noise ratio of 3 dB and 40 dB of insertion losses in the acoustic device, then the maximum interrogation range is about 1.5 m. Such an interrogation range is achieved by instantaneously emitting 43 dBm (20 W or 32 V in a 50 Ω load) pulses by a pulsed RADAR setup designed with a receiver bandwidth of 54 MHz. For such a device to comply with ISM regulation and emit the same average power, the 20 ns long pulses must be emitted no faster than once every 34 μs. In this context, the pulsed RADAR refresh rate can reach 29.4 kHz. A tradeoff aimed at reducing the time interval between pulse emission is achieved by lowering peak power, at the cost of reduced range. In the next part, we will assume a pulse repetition rate interval of 5 μs (with a peak power of 34 dBm providing an interrogation range of 93 cm following the previous calculation).

The general pulsed-RADAR system architecture is shown in Fig. 2. A carrier frequency generated by a continuous source centered around 2450 MHz is chopped by a fast (<30 ns rise time) switch to load energy in an acoustic delay line. The returned echoes are translated to baseband by a wideband I/Q demodulator, feeding the dual-channel acquisition system which will be the topic of the next section.

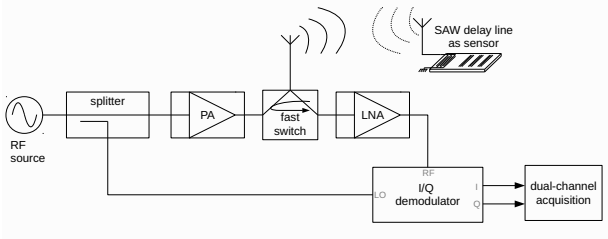

Fig. 2. Schematic of a passive wireless acoustic sensor interrogation unit

In order to comply with the requirements of compact, low power receiver electronics, a stroboscopic equivalent time sampling approach is used. The two values representative of the physical quantity detection by the transducer are the returned power magnitude and phase, as provided by an I/Q demodulator. This demodulator provides an output signal of up to 100 MHz bandwidth, which involves digitizing a signal at 200-1000 MSamples/s to obtain a sufficient number of points to extract magnitude and phase with the targeted resolution aimed at only being limited by the local oscillator phase noise. The equivalent-time sampling approach provides a trade-off between reducing the demand for fast electronics components and increasing the acquisition time.

III. Equivalent Time Sampling

Equivalent time sampling (ETS) is based on repeating the probe signal and recording at each iteration a single sample at various time delays with respect to the emitted pulse. This measurement strategy is best suited when actively probing the medium, as done in RADAR systems, since the emitted pulse

acts as a synchronization trigger to define the recording time delay.

Considering the time reference, common to all measurements, defined as T_0, then at each iteration the ETS system record a sample at $T_0+n\cdot\delta T$ with sample index $n \in [1:N]$, N being the number of samples in the reconstructed signal. The time step δT yields an equivalent sampling rate $f_s = 1/\delta T$. The two main disadvantages of this technique are the duration of the acquisition which depends on the number of samples and the repetition rate since N individual measurements are needed, and the need for a reproducible signal during the N measurements. These drawbacks are considered here to be overcome by the simple hardware setup made solely of a fast track and hold controlled by a programmable delay line while only low bandwidth analog to digital converter and memory access are needed otherwise.

In order to perform post-processing calculation on echoes characterization with at least 10 samples during each echo lasting about 10 ns, a sampling rate of at least 1 GS/s is targeted. Commercially available programmable delay lines suiting our needs exhibit delay resolutions between 1 ns and 100 ps. Acquisition of a time response between 500 ns and 5 μs at a rate of 1 GS/s involves 4,500 measurements. When acquiring one measurement point, it is necessary to wait 5 μs to avoid temporal aliasing and allowing for all returned signal from the acoustic sensor to fade out: hence yielding an incompressible measurement duration between 22.5 ms. Obtaining the same result while complying with ISM regulations requiring repetition rates no faster than 34 μs yields an acquisition time of at least 153 ms.

IV. Experimental setup

The challenge in using such commercially available delay lines is the range of accessible delays: an 8-bit programmable delay line such as Maxim DS1023-25 providing a resolution of 250 ps only generates a maximum delay of $2^8 \cdot 250$ ps $= 63.75$ ns, much below the targeted 5 μs. Two delay lines are thus cascaded, one for coarse delay generation and another for high resolution delay generation. The coarse delay line must exhibit low jitter (necessarily less than the accurate line delay, in this case 250 ps): in our case, the delay generator is provided by a Programmable Logic Device (PLD) clocked at 100 MHz which ensures a time resolution of 10 ns. This device also generates the trigger signal of the switch.

The duration for programming a Maxim DS1023-25 delay line through a SPI link is also taken into account for the total measurement time estimate. Although the fastest clock rate on the SPI bus is 10 MHz, we secure communication by clocking the bus at 1 MHz. For each measurement, the delay line must be programmed by an 8-bit word, so the programming duration 8 μs. In addition, some latencies is associated with the delay line programming, requiring an additional 530 ns, and measurements can only be repeated after the acoustic sensor response has faded out after 5 μs. Thus, the total duration for a 4,500 point dataset is $4500\times(8+0.53+5+0.02) = 60975$ μs $\simeq 61$ ms. Fortunately, thanks to an optimized scanning strategy of the response, it is possible to reduce the programming time.

Considering a 10 ns resolution coarse delay, and a 1 ns fine delay equal to 4-delay line steps, 10 measurements are needed between two coarse delays to achieve a 1 GS/s sampling rate. The programming time of a PLD is at most two periods of the core clock. Rather than continuously reprogramming the slow (SPI bus) fine delay, an optimized approach consists in setting the fine delay and sweeping the coarse delay over the whole acoustic sensor response range (0 to 5 μs). Having acquired this first dataset, the fine delay line is set again (requiring a 8.53 μs lag) and the system retrieves a second dataset. The operation is repeated 10 times to get the full response. This stroboscopic acquisition using interleaved coarse and fine delay combs (Fig. 3) allows a theoretical acquisition time of 22.7 ms in the same conditions of the previous calculation, or a threefold update rate improvement with respect to the basic strategy described above.

So far no assumption is made on the acoustic sensor echo position. However, once the measurement has been performed, a strong assumption is that the echoes will be located close to their last identified position. Hence, rather than scanning the whole acoustic sensor delay of 0.5 to 5 μs by 1 ns steps, we focus solely on a feedback loop approach requiring 3-measurements on each echo. The central delay is then computed using a parabolic fit and feeds the next measurement step. The total measurement duration is then reduced by limiting from 4,500 to $3 \times 8 = 24$ samples for an acoustic sensor encoding 8 bits. The associated measurement duration is $24\times(8+0.53+5+0.02) = 325.2$ μs. If furthermore only the central delay needs fine tuning and the two other measurements before and after the central delay only require reprogramming the coarse delay (10 ns steps), then the measurement duration is further reduced to $8\times(8+0.53+5+0.02)+16\times(5.02) = 189$ μs or a 5.3 kHz refresh rate.

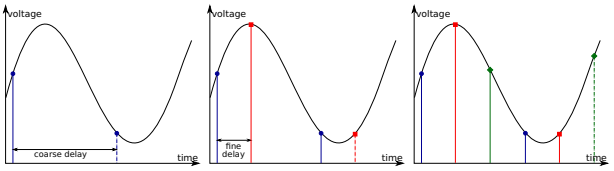

Fig. 3. Example of a sine-wave reconstruction with stroboscopic acquisition interleaving coarse and fine delay combs. Each case represents a coarse comb of recorded samples. The transition from one case to another requires setting the fine delay line.

V. Results

This acquisition system scans the output of the I/Q demodulator to calculate the physical quantity to be measured in a post-processing step. Fig. 4 shows the I and Q data recorded from 500 ns to 3 μs and the resulting $|I+iQ|$ magnitude, favorably compared to the measurement performed using a network analyzer (Fig. 1).

Beyond the acoustic tag identification based on the magnitude calculation, extracting a velocity information associated with a physical quantity measurement is achieved by computing $\arg(I+iQ)$. A differential measurement only requires the estimate of the phase difference between two echoes: only two acquisition points of both I and Q signals with a dual analog-to-digital converter are needed. Using the afore mentioned 3-point strategy for each echo, only 6 measurements are performed requiring a total measurement duration of $2\times(8+0.53+5+0.02)+4\times(5.02) = 47$ μs. Circles on Fig. 4 display the delay at which these 6 measurements are performed in order to characterize the first two echoes in the context of

a temperature measurement, thus providing a refresh rate of about 20 kHz. While such an update rate is still 10 times lower than the maximum achievable measurement speed of a 5 μs delay acoustic sensor, it optimizes an embedded electronics approach requiring only a few high-bandwidth components (track and hold, switch, I/Q demodulator).

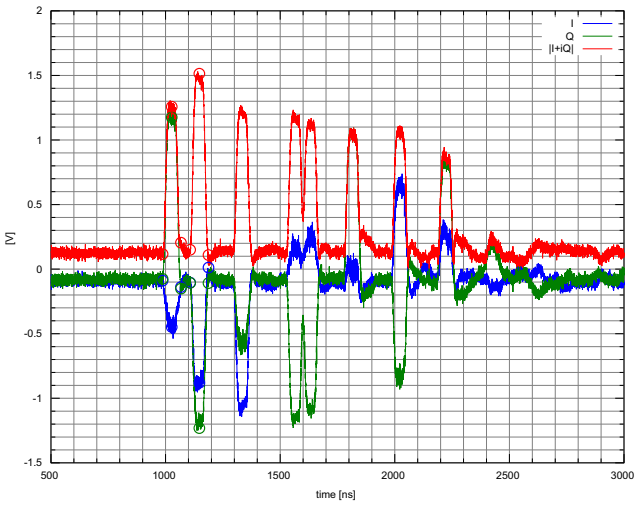

Fig. 4. Acoustic delay line response sampled by a stroboscopic interrogation unit. Six circles are highlighted on each trace over the first two echoes, representing the minimum number of samples recorded for a temperature measurement.

VI. Conclusion

A pulsed mode RADAR optimized for minimizing the number of high-bandwidth components and fast sampling rate is demonstrating for probing wideband acoustic transducers acting as passive wireless sensors. Compliance with ISM regulation and reaching the same range than an FMCW approach nevertheless allow a pulsed RADAR approach to improve at least 10-fold the refresh rate assuming a wideband receiver (fast radiofrequency analog to digital converter).

A stroboscopic strategy reducing the number of wideband components to a switch, a fast track and hold and I/Q demodulator associated with an optimized algorithm of interleaved coarse and fine time delays provides tag identification at 5.3 kHz refresh rate while measuring a physical quantity using acoustic phase computation on two echoes is performed at 20 kHz.

References

[1] A. Stelzer, S. Schuster, and S. Scheiblhofer, "Readout unit for wireless SAW sensors and ID-tags," in *International Workshop on SiP/SoC Integration of MEMS and Passive Components with RF-ICs*, 2004, pp. 37–43.

[2] S. Scheiblhofer, S. Schuster, and A. Stelzer, "Signal model and linearization for nonlinear chirps in FMCW radar SAW-ID tag request," *Microwave Theory and Techniques, IEEE Transactions on*, vol. 54, no. 4, pp. 1477–1483, 2006.

[3] J. Fuchs, K. D. Ward, M. P. Tulin, and R. A. York, "Simple techniques to correct for VCO nonlinearities in short range FMCW radars," in *Microwave Symposium Digest, 1996., IEEE MTT-S International*, vol. 2. IEEE, 1996, pp. 1175–1178.

[4] G. M. Brooker, "Understanding millimetre wave FMCW radars," in *1st International Conference on Sensing Technology*, 2005, pp. 152–157.

[5] J.-M. Friedt, T. Rétornaz, S. Alzuaga, T. Baron, G. Martin, T. Laroche, S. Ballandras, M. Griselin, and J.-P. Simonnet, "Surface acoustic wave devices as passive buried sensors," *Journal of Applied Physics*, vol. 109, no. 3, p. 034905, 2011.

[6] J.-M. Friedt, A. Saintenoy, S. Chrétien, T. Baron, É. Lebrasseur, T. Laroche, S. Ballandras, and M. Griselin, "High-overtone bulk acoustic resonator as passive ground penetrating radar cooperative targets," *Journal of Applied Physics*, vol. 113, no. 13, pp. 134 904–134 904, 2013.

[7] E. R. Committee *et al.*, "ERC recommendation 70-03 relating to the use of short range devices," 2013.

SAW Sensor Exploiting Palladium Layer Properties for Selective Detection of Hydrogen.

Meddy Vanotti, Virginie Blondeau-Patissier, Jean-Yves Rauch, David Rabus, Benjamin Mazal
FEMTO-ST Institute, Besançon, France
Email: meddy.vanotti@femto-st.fr , virginie.blondeau@femto-st.fr, jyves.rauch@femto-st.fr, david.rabus@femto-st.fr, benjamin.mazal@femto-st.fr

Sylvain Ballandras
frec|n|sys
Besançon, France
Email: sylvain.ballandras@frecnsys.fr

***Abstract*—For an increasing number of application (energy production, car industry, space, etc.), hydrogen appears as a solution of the future as it is the most common body in the Universe (and therefore on Earth). However, due to its unstable properties, a particular care must be dedicated to control possible gaseous leaks close to facilities using this resource. Here we propose surface acoustic wave sensors for detecting gaseous hydrogen in standard environmental conditions (atmospheric pressure and room temperature). The proposed SAW sensors consists in two Rayleigh-wave delay lines built on Quartz. One equipped with a Palladium overlay and the other exhibiting a free path between the two interdigitated transducers. A dedicated hermetical gas test cell has been developed to test the efficiency of the sensor when exposed to hydrogen-composed atmospheres. A particular care was paid to avoid hydrogen leakage in the working environment and to perform the regeneration of the gas absorbing layer. The developed SAW devices exploiting hydrogen absorption capabilities of palladium layers exhibiting different thicknesses have been here used to make the detection and the identification of hydrogen concentrations (in the 0.25-2% range) diluted in nitrogen and is also able to make detection in current atmosphere. The effect of the palladium thickness variations along with the influence of an Yttrium doping of the palladium layer on the sensor behavior will be studied here.**

I. Introduction

The raising shortage of fossil energy resources added to the increasing concern towards environmental issues have led to consider hydrogen as one of the most promising energy resource. This odorless and colorless gas being highly explosive over 4% concentration in air, the availability of a fast and accurate detection system close to storing facilities and equipping hydrogen-operated machines is mandatory for obvious security reasons. Such a system must exhibit a significant selectivity as it must detect the presence of gaseous hydrogen in air with concentrations smaller than the above-mentioned critical limit at standard conditions (room temperature and atmospheric pressure) as well as in harsher environment (very low or significantly high temperature). Besides some solutions have been proposed [1] [2] [3] [4] [5] [6] [7]. The current availability of such a detection system meeting modern specifications of hydrogen use and storage is still questionable. The mains improvements for such sensors are their sensitivity, their selectivity and their reliability together with sensor size, cost reduction, energetic needs and response time [8]. Many methods of detection of hydrogen and a comprehensive review can be found in the literature [9], providing a substantial material base to try and address the above challenges. Among the possibilities, SAW (Surface Acoustic Wave) sensors have been widely studied in the last decades because of their attractive capabilities. Indeed, SAW devices exhibit high sensitivity to surface perturbation since the quasi totality of the energy propagates in a region that thickness is a few times the wavelength of the propagating acoustic wave. It is also a mature technology, SAW device do exhibit limited size (less than 1 cm²) and they allow for wireless use [10]. Initial works were made by D'Amico et al. [11] using the properties of palladium layer to trap the targeted gas. Since this pioneer work, innovations concerning the selectivity and stability of sensitive layers versus external parameter have been proposed to improve hydrogen detection using SAW devices [12] [13] [14] [15] [16] [17] [18] [19]. In this paper, a SAW sensor is proposed for detecting gaseous hydrogen in standard environmental conditions (atmospheric pressure and room temperature). The proposed SAW sensor consists in two Rayleigh-wave delay lines built on Quartz, one covered with a Palladium (Pd) overlay and the other exhibiting a free path between the two interdigitated transducers (IDTs) used to excite and detect the acoustic wave. These IDTs are built using aluminum electrodes, as this metal is known to be inert versus gaseous hydrogen. An innovative aspect of the proposed sensing system consist in the open-loop strategy for phase changes monitoring [20]. Moreover, delay lines are monitored in parallel using a synchronous detection approach that provides high frequency measurement resolution and that permits a systematic characterization of the device before operated. Along this approach, the impact of changes of intrinsic properties of the devices such as working frequency drift with aging can be minimized. The developed device allows for identifying different concentrations of hydrogen diluted in N_2 and is also able to detect H_2 in current atmosphere. The SAW sensor as well as the exploited monitoring system will be first exposed. Experimental validation of H_2 detection then is reported, with a description of the chemical test bench and detection results for various palladium layer thicknesses. An analysis of the influence of that thickness on H_2 adsorption and its influence on SAW propagation is proposed to provide routes for the device optimization.

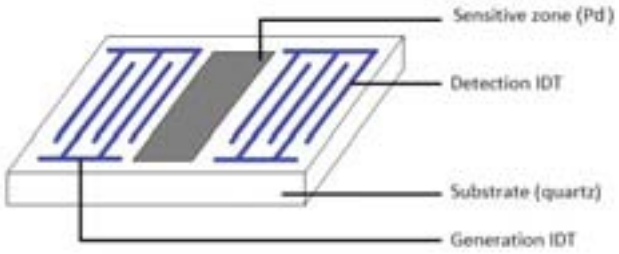

Fig. 1. Scheme of a SAW delay line using Rayleigh surface acoustic wave at 78MHz.

II. SAW SENSOR AND ASSOCIATED MONITORING SYSTEM

Selective detection of hydrogen at room temperature and pressure have been achieved using SAW delay lines exploiting Rayleigh waves on AT-cut Quartz, as the corresponding first order temperature coefficient of frequency (TCF) is close to zero, yielding frequency-temperature compensation for the above-mentioned operating conditions. The configuration of both generation and detection IDTs used for the sensor consist in 50 fingers pairs with a grating period of 10 μm and a center-to-center spacing of 5mm (the reactive surface). The wavelength is 40μm, yielding a frequency operation in the vicinity of 78MHz as the wave velocity approaches 3100m.s^{-1}. The Pd and Y-Pd alloy films were deposited by thermal evaporation on a single run and shaped by a lift-off technique. Its length along the propagation path was 3mm and its thickness varies from 15 nm to 300 nm. The device configuration is shown on Fig. 1.

Using a network analyzer, the transfer function of the device can be easily determine and hence the phase shift induced by gas absorption has been first monitored that way. However, the use of a dedicated electronics has been implemented and delivers similar information. That is represented on Fig. 2. This system includes two separated phase measurement schemes: a rough characterization stage using the AD8302 phase and magnitude detector, and a high sensitivity phase measurement using dedicated phase detectors and variable gain, low noise operational amplifiers as presented in another work [20]. The sensitivity of the set-up allows for some tens mill-degrees resolution and is easily transportable. The response of the bare device and the functionalized one are respectively measured. This configuration has been used so as to make a systematic characterization of each new device used for H_2 detection. Fig. 3 illustrates the way the phase shift measurement is achieved.

III. SIMULATION RESULTS

A crucial part of the developement of such a sensor consists in the improvement of its sensitivity and its response time. Simulation results are expected to provide informations on the way the sensing layer has to be designed in order to optimize its efficiency. In that purpose, a theoretical study of the influence of the palladium layer thickness on the sensor response upon the hydrogenation is here exposed.

Accurate calculations have been achieved, based on a set of programmes dedicated to the analysis of stratified structures

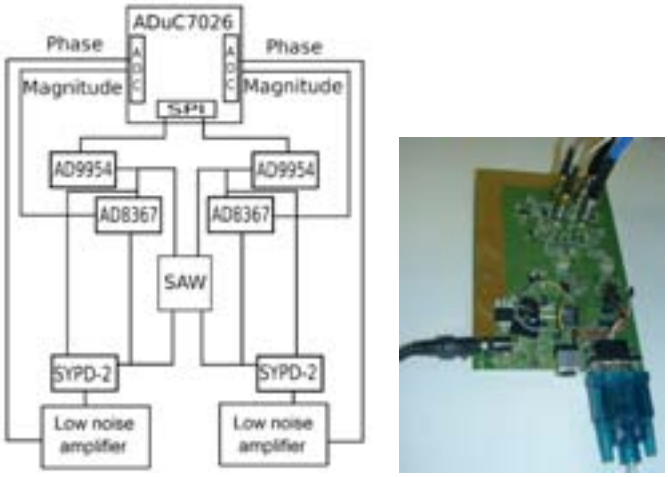

Fig. 2. Scheme and photograph of the SAW devices probing card.

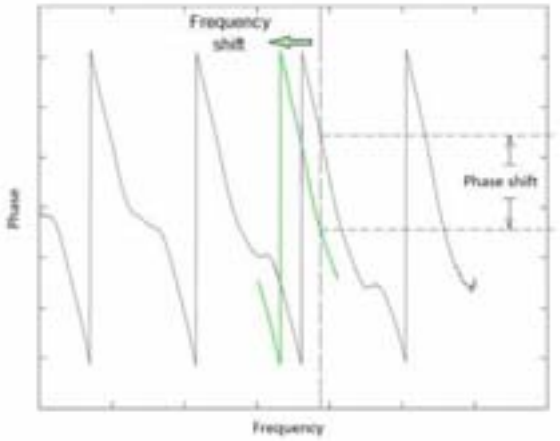

Fig. 3. Phase shift measurement principle using a dedicated instrumentation.

used as elastic wave guides. The fundaments of the corresponding developments have been presented in [21] [22]. The calculation principle is based on the derivation of a surface or interface effective permittivity yielding numerous information about the wave propagation characterictics such as the wave velocity, the mode coupling and possible propagation losses. The model accounts for all the known linear properties of the materials constitutive of the layered structure which directly condition the accuracy of the results as no assumption is made on the device operation (provided flat interfaces). Moreover, since only devices composed of Quartz substrates have been used here, changes in electrodes conductivity are not consider as a possible origin of the observed phase velocity drift and therefore were not taken in account in the proposed analysis. Electromechanical coupling of Rayleigh waves on Quartz substrates is actually small enough to consider conductivity changes negligible. As shown by Anisimkin and al in [23] the two main phenomena that influence the phase velocity change of elastic waves on Quartz are mass- and elastic-loading. This theoretical study takes into account the contribution of

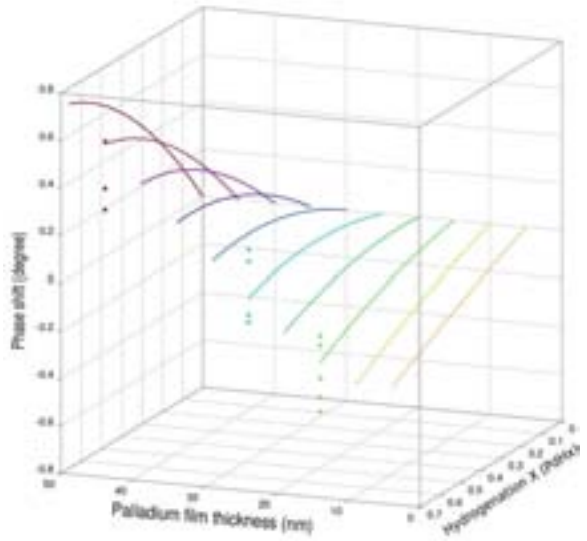

Fig. 4. Simulated phase shift of the Rayleigh wave that propagate through palladium films of different thicknesses upon its hydrogenation.

both phenomena provided some parametric adjustement. It is actually considered here that the finer the sensitive layer is the more important mass-loading effect becomes. Indeed, for Pd layer that thickness is less than 20nm, we consider an expansion of the layer close to zero because of the influence of the substrate. This assumption permits to explain the mass-loading observed for very thin films. Otherwise mass-loading is evidenced by the damping of the transfert function in magnitude which is characterictic of this phenomenon. On an other hand, the Rayleigh wave is more affected by elasticity modification of the Pd layer than mass-loading then the thickness of this one increases. One can see on Fig. 4 the theoretical phase shift upon hydrogenation for different film thicknesses. These calculation are in adequacy with experimental results symbolized by the points. One can notice a difference between the shape of simulation results and the experimental ones exposed in the next section. Actually, calculations don't take into account the absorption dynamics of the hydrogen through the palladium layer. The comparison with experimental data is so made for a total hydrogenation of the palladium layer that corresponds to an hydrogenation coefficient $X = 0.66$ on Fig. 4.

IV. Experimental results

Detection of hydrogen using SAW delay lines exhibiting different thicknesses of palladium as functionalizing films have been achieved at room conditions. Figs. 5 and 7 present experimental results when using nitrogen as carrier gas. The detection of about 2%vol of hydrogen in N_2 at 35% RH and 20°C can be achieved with a minimum response delay of 10 seconds for considering that the determination of the H_2 concentration in the melting gas is derived from the phase shift velocity during the exposure and not from the steady state.

As shown on Fig. 7, the functionalizing film thickness appears as a way of improving the reactivity of our sensor.

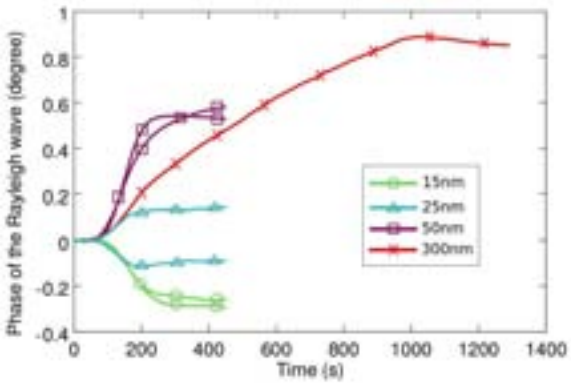

Fig. 5. Experimental Rayleigh wave's phase shift induced within palladium layers of different thicknesses during hydrogenation under 2%vol H_2.

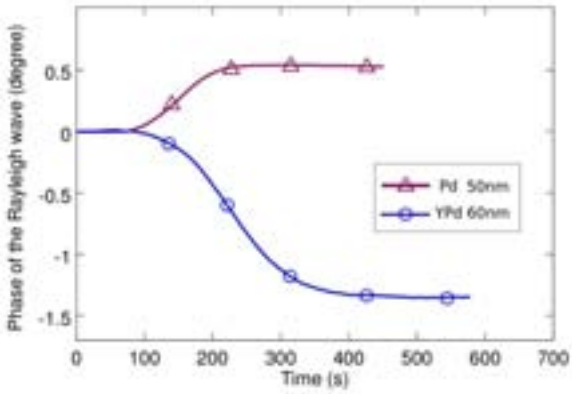

Fig. 6. Experimental Rayleigh wave's phase shift induced within Pd and Y-Pd alloy sensitive layers during hydrogenation under 2%vol H_2.

Indeed, a maximum phase shift velocity of 4±0.7 degree.s^{-1} has been observed for the 50nm palladium functionalized device. Contrary to the others for which the phase shift velocity modulus doesn't exceed 2 degree.s^{-1}. One will notice that the parameter to improve is the phase shift velocity modulus. Actually, depending on either mass- or elastic-loading is the largest effect occuring during the hydrogenation, an decrease or an increase of the phase will be observed. The aim of this work is to maximize the phase shift velocity irrespectively of the direction of change.

As the sensitivity and reactivity of our device depends on the capability of the functionalizing layer to trapp the surrounding hydrogen, a chemical doping of this layer has been made to investigate its influence on the sensor operation. Preliminary result concerning Yttrium doping can be seen on Fig. 6 and 7. It shows that the Yttrium doping allows for increasing the phase shift velocity during the hydrogenation. Indeed, this velocity is -7.62 milidegree.s^{-1} for an exposition to 2%vol H_2 in N_2 that is about twice the largest value reached this undoped palladium. In this case, mass-loading is the most efficient effect that impact the behavior of the wave. We note that this is an encouraging preliminary result that needs to be validated in terms of repeatability and reversibility.

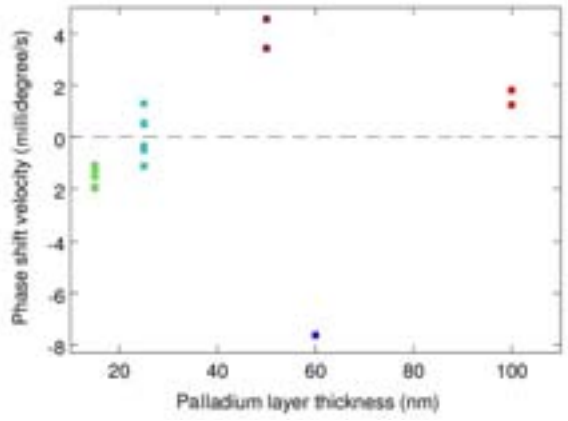

Fig. 7. Experimental phase shift velocity observed with different thicknesses of palladium and Y-Pd alloy under hydrogen 2%vol.

V. Conclusion and further works

Here has been evidenced the capability of our hydrogen sensor to operate in the 0.25-2% range in nitrogen. The influence of thickness variations of the palladium film together with the Yttrium doping of the sensing layer have been studied. It finally appears that the use of a certain sensing layer thickness allows for exploiting either mass- or elastic-loading that both occure during the hydrogenation. Considering the technological restraint, a few thicknesses have been investigated and it has been observed that the use of palladium layer that thickness are less than 300nm allows for minimizing the dependence on the adsorption dynamics of H_2 through Pd of the response time of the device.

Further works will consist in studing the absorbtion dynamics of hydrogen through palladium film and also the ways to promote a faster absorption so as to enhance the sensitivity and reactivity of our sensor. Physical analysis of sensitive layers during hydrogenation will be made in order to explain and improve the parametric adjustment used to simulate the comportment of our devices. The use of different thicknesses of Y-Pd alloy will also be studied in order to reinforce our knowledge concerning this promising way of trapping hydrogen.

Acknowledgment

This work was partly supported by the french RENATECH network and its FEMTO-ST technological facility.

References

[1] V. Katti, A. Debnath, S. Gadkari, S. Gupta, and V. Sahni, "Passivated thick lm catalytic type h2 sensor operating at low temperature," *Sens. Actuators B: Chem.*, vol. 84, pp. 219 – 225, 2002.

[2] C. Ramesh, N. Murugesan, M. Krishnaiah, V. Ganesan, and G. Periaswami, "Improved naon-based amperometric sensor for hydrogen in argon," *J. Solid State Electrochem.*, vol. 12, pp. 1109 – 1116, 2008.

[3] I. Simon and M. Arndt, "Thermal and gas-sensing properties of a micromachined thermal conductivity sensor for the detection of hydrogen in automotive applications," *Sens. Actuators B: Chem.*, no. 9798, pp. 104 – 108, 2002.

[4] T. Anderson, H. Wang, B. Kang, F. Ren, S. Pearton, A. Osinsky, A. Dabiran, and P. Chow, "Effect of bias voltage polarity on hydrogen sensing with algan/gan schottky diodes," *Appl. Surf. Sci.*, vol. 255, pp. 2524 – 2526, 2008.

[5] F. D. et al., "Mems-based hydrogen gas sensors," *Sens. Actuators B: Chem.*, vol. 117, pp. 10 – 16, 2006.

[6] T. Kiefer, A. Salette, L. Villanueva, and J. Brugger, "Large arrays of chemo-mechanical nanoswitches for ultralow-power hydrogen sensing," *J. Micromechn. Microeng.*, vol. 20, 2010.

[7] Z. Zhao, M. Carpenter, H. Xia, and D. Welch, "All-optical hydrogen sensor based on a high alloy content palladium thin lm," *Sens. Actuators B: Chem.*, vol. 113, pp. 532 – 538, 2006.

[8] L. Boon-Brett, J. Bousek, G. Black, P. Moretto, P. Castello, T. Hubert, and U. Banach, "Identifying performance gaps in hydrogen safety sensor technology for automotive and stationary applications," *International Journal of Hydrogen Energy*, vol. 35, no. 1, pp. 373 – 384, 2010.

[9] T. Hubert, L. Boon-Brett, G. Black, and U. Banach, "Hydrogen sensors a review," *Sensors and Actuators B: Chemical*, vol. 157, no. 2, pp. 329 – 352, 2011.

[10] T. Rétornaz, N. Chrétien, J.-M. Friedt, G. Martin, and S. Ballandras, "Time reversal: a flexible approach for identifying and measuring surface acoustic wave delay lines acting as wireless, passive sensors," *IFCS Proceeding*, 2012.

[11] A. D´Amico, A. Palma, and E. Verona, "Palladiumsurface acoustic wave interaction for hydrogen detection," *Appl. Phys. Lett.*, vol. 41, p. 300, 1982.

[12] W. P. Jakubik, M. W. Urbaczyk, S. Kochowski, and J. Bodzenta, "Bilayer structure for hydrogen detection in a surface acoustic wave sensor system," *Sensors and Actuators B: Chemical*, vol. 82, no. 23, pp. 265 – 271, 2002.

[13] W. P. Jakubik, "Hydrogen gas-sensing with bilayer structures of wo3 and pd in saw and electric systems," *Thin Solid Films*, vol. 517, no. 22, pp. 6188 – 6191, 2009.

[14] D. Phan and G. Chung, "Identifying performance gaps in hydrogen safety sensor technology for automotive and stationary applications," *Sensors and Actuators B: Chemical*, vol. 161, no. 1, pp. 341 – 348, 2012.

[15] S. Ippolito, S. Kandasamy, K. Kalantar-Zadeh, and W. Wlodarski, "Layered saw hydrogen sensor with modified tungsten trioxide selective layer," *Sensors and Actuators B: Chemical*, vol. 108, no. 12, pp. 553 – 557, 2005.

[16] A. Sadek, W. Wlodarski, K. Shin, R. Kaner, and K. Kalantar-zadeh, "A polyaniline/wo3 nanofiber composite-based zno/64 yx linbo3 saw hydrogen gas sensor," *Synthetic Metals*, vol. 158, no. 12, pp. 29 – 32, 2008.

[17] D.-T. Phan and G.-S. Chung, "Surface acoustic wave hydrogen sensors based on zno nanoparticles incorporated with a pt catalyst," *Sensors and Actuators B: Chemical*, vol. 161, no. 1, pp. 341 – 348, 2012.

[18] N. Dewan, S. Singh, K. Sreenivas, and V. Gupta, "Influence of temperature stability on the sensing properties of saw nox sensor," *Sensors and Actuators B: Chemical*, vol. 124, no. 2, pp. 329 – 335, 2007.

[19] S. Fardindoost, A. Zad, F. Rahimi, and R. Ghasempour, "Pd doped wo3 films prepared by solgel process for hydrogen sensing," *International Journal of Hydrogen Energy*, vol. 35, no. 2, pp. 854 – 860, 2010.

[20] D. Rabus, J. Friedt, S. Ballandras, G. Martin, E. Carry, and V. Blondeau-Patissier, "A high sensitivity open loop electronics for gravimetric acousticwave-based sensors," *EFTF Proceeding*, 2010.

[21] A. Reinhardt, T. Pastureaud, V. Laude, and S. Ballandras, "Scattering matrix method for acoustic waves in piezoelectric, fluid, and metallic multilayers," *J. Appl. Phys.*, vol. 94, pp. 6923 – 6931, 2003.

[22] T. Pastureaud, V. Laude, and S. Ballandras, "Stable scattering-matrix method for acoustic waves in piezoelectric multilayers," *Appl. Phys. Lett.*, vol. 80, pp. 2544 – 2546, 2002.

[23] V. Anisimkin, I. Kotelyanskii, P. Verardi, and E. Verona, "Elastic properties of thin-film palladium for surface acoustic wave (saw) sensors," *Sensors and Actuators B: Chemical*, vol. 23, no. 23, pp. 203 – 208, 1995.

Large Capacity SAW Tag

Xin Huang, Zhijun Chen, Mengyang Wang
College of Automation Engineering
Nanjing University of Aeronautics and Astronautics
Nanjing, China
Email: zjchen76@sina.com

Hailin Xu, Peidi Chen
No.55 Research Institute
China Electronics Technology Group Corporation
Nanjing, China

Abstract—**The research on surface acoustic wave (SAW) tag has lasted many years. However, the application and promotion are unsatisfactory due to the inherent defects of the manufacturing technology of the large capacity SAW tag. From the perspective of practical production, this paper proposes a novel design of SAW tag to reduce costs. The method is based on the correlation IDT and permutations and combinations theory. At the same time, some ideas about the reader structure for this SAW tag are given.**

Keywords- SAW Tag; large capacity; correlation IDT; anti-collision tag unit; SAW Tag reader.

I. INTRODUCTION

Compared with the integrated circuit (IC) tag, the SAW tag has many advantages, including wireless, passive operation, but the biggest disadvantage is that the capacity is too small especially in the case of the amplitude modulation SAW tag. The capacity of SAW tag based on the simultaneous time position and phase shifting is enough for global application.[1] But in order to ensure the consistent amplitude of reflector echoes and time domain resolution sensitivity, tags with different codes need to be designed and manufactured separately, leading to high manufacturing cost. The correlation SAW devices with phase-shift keying (PSK) method avoid the adverse effects of low SNR [2], and also get the characteristic of anti-collision. [3] This paper presents two types of SAW tag, one is the medium data capacity type consisting of the traditional interdigital transducer (IDT), and the other is the large data capacity type that contains correlation IDT coded by PSK method. Both of them use the pulse position modulation (PPM) and theory of permutations and combinations.

II. MEDIUM CAPACITY SAW TAG

A. Basic PPM SAW Tag

The SAW pulse propagates along the surface of the substrate, which is usually made of a material with strong piezoelectricity, such as lithium niobate (LiNbO3). The SAW pulse is partially reflected and partially transmitted by each of the code reflectors, placed at precisely determined positions on the chip. These reflectors usually consist of one or a few narrow aluminum strips. The reflected SAW pulse returning to the IDT carries a code based on the positions of the reflectors. In other words, this encoding method is based on the time delays of reflected pulses. It is known as time position encoding or pulse position modulation (PPM) in figure 1. When the echo pulses returns to the IDT, the acoustic signal is then reconverted into an electrical form and retransmitted by the tag antenna. The response signal is then detected and decoded by the reader. [4]

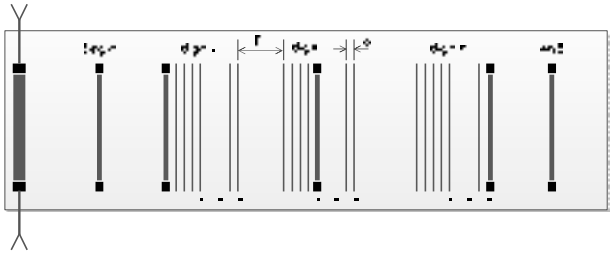

Figure 1. Structure of PPM SAW tag

The tag contains begin and end reflectors used for calibration and several digit areas. In each digit area there is one or more reflectors, and the number of the positions in every digit area is determined by time slots. D is the width of pulse exclusion region, and d is the width of a slot.

In figure 1, the number of the slots in each digit area is x and there is only one reflector in it. The number of digit area is n. So the capacity of this tag is x^n. When the length of the tag is constant value, the larger capacity means bigger x and n, then D and d are smaller, which are determined by the band width of IDT and the time resolution of the reader. The design will be much more difficult because the reader relies on the echoes amplitude and time delay to decode. The situation of each tag is different, so we need to design and manufacture each tag separately to ensure the consistent amplitude of reflector echoes and time domain resolution sensitivity, which is impossible.

B. Mediun Data Capacity SAW Tag

Compared with single acoustic channel, multi acoustic channels SAW tag partly reduced the multiple reflections. [4] Even if the loss is higher in every channel, but it is still a good idea to pre divide the energy of the integration pulse. So we come up with a new type of combined SAW tag. Assume that there are eight reflectors including two calibration reflectors and six digit area reflectors. First they are parity divided into

two tag units, and then in each unit the reflectors are equally distributed on two acoustic channels as shown in figure 2.

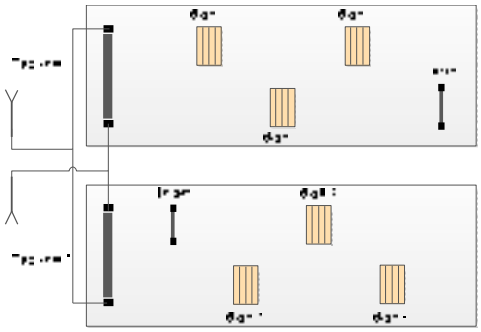

Figure 2. Multi acoustic channels and combination of PPM SAW tag

The two tag units access the antenna in parallel and form a combined tag. Figure 3 shows the Amplitude verse Time of echoes. The calibration reflectors in different units are used to calibrate the fabrication error. tag unit 1 uses the end reflector as reference while tag unit 2 uses the begin reflector as reference. The time delay between digit reflectors and calibration reflectors is used for distinguishing which tag unit an echo belongs to and for getting the code of each tag unit.

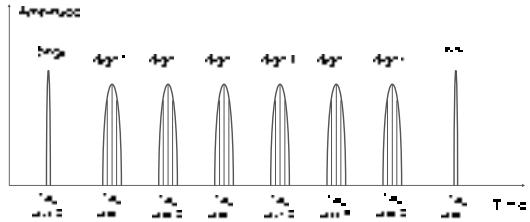

Figure 3. Amplitude verse Time of combined PPM SAW tag choes

The data capacity of this combined tag is the same as the traditional PPM tag, but the echo consistency is much better. The most significant point is that it can greatly reduce the number of photo masks, which are the most expensive during manufacturing. If the number of slots in each digit area is 4, the capacity is 4^6 equals to 2^{12}. To conventional PPM tag, it needs 4^6 photo masks; to this type of SAW tag it only needs $2*4^3$ photo masks. Because tag unit 1 and tag unit 2 can be combined freely. The cost is reduced to one tenth.

But this combined tag also has drawback; in this example, if the tag operates at 434MHz and IDT bandwidth is 20MHz, we must carefully choose the positions of the first and second reflectors so as to shift the round-trip interference of them to the pulse exclusion region or behind the last digit area. When expanding the data capacity of this type SAW tag, it's necessary to take the round-trip interference of more reflectors into consideration. So it is not suitable for large capacity applications.

III. LARGE CAPACITY SAW TAG

IDT modulated by PSK method can be called Correlation IDT (CIDT). It can only respond to the corresponding PSK modulated carrier pulse, namely the autocorrelation while to the wrong PSK modulated carrier pulse it wouldn't return any response, called cross-correlation. In the case of autocorrelation, the CIDT will generate a typical peak on the substrate while in cross-correlation it won't.

A. *Anti- collision CIDT*

The key of an anti-collision SAW tag unit is the CIDT. By using barker code sequence or Orthogonal Frequency Coding (OFC) method [5] etc., the CIDT obtains coding and anti-collision characteristics. For example, figure 4 shows the simulation result of the coding IDT output when a 7-bit barker code sequence [1110010] is used. Figure 4(a) shows the autocorrelation. Figure 4(b) is the output when input sequence is [1011000], which is the minimum cross-correlation peak value among 7-bit barker codes.

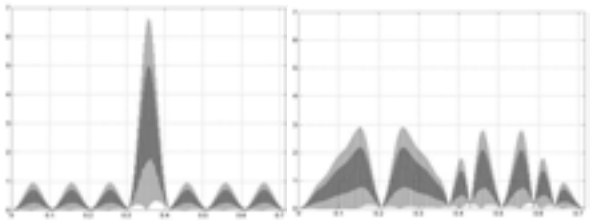

(a)7-bit barker code autocorrelation (b)[1011000] with [1110010] cross- correlation

Figure 4. Simulation result of CIDT output

B. *Structure of anti-collision SAW Tag units*

The structure of the anti-collision SAW tag unit (in figure 5) also contains multi acoustic channels and adapts on PPM. But the position of digit area in each tag unit doesn't have any relevance which is different from the medium capacity SAW tag. When a corresponding PSK carrier pulse loads on the CIDT, it will generate a typical peak that propagates along the substrate. After the peak meets the digit reflector and returns to the CIDT, it will be shifted to PSK code output from antenna.

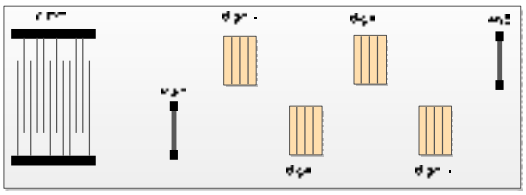

Figure 5. Structure of anti-collision SAW tag units

C. Structure and the capacity of conbined SAW tag

The combined SAW tag (in figure 6) is formed by a number of anti-collision SAW tag units which also access the antenna in parallel.

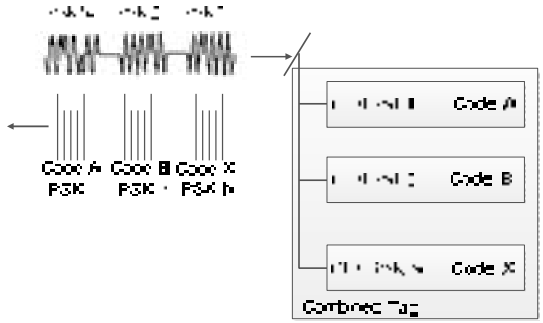

Figure 6. Structure of large capacity SAW tag

When the reader sends a sequence of PSK code modulation carrier pulses, the tag units with corresponding CIDT respond one by one according to the order of the inquire pulses.

The compatibility N is the number of anti-collision SAW tag units in a combined tag, which is determined by the PSK code group used on the CIDT. Thus, high compatibility of a non-periodic polar code group is necessary in large capacity applications.

Our team recently has found a 13-bit encoding group based on the communications coding theory, the compatibility of which reaches 8. If the number of the digit slots and digit areas in each unit is 6 and 4, the capacity of this combined SAW tag is $(6*6*6*6)^8$equals 2^{83}. It is enough for global applications, and only 6^4*8 photo masks are needed.

D. Some ideas about the reader structure

As the frequency of the carrier is very high (434MHz), how to generate a PSK modulated carrier pulse becomes a problem. The first solution presented in figure 7 (a) is to use a SAW en coding correlator.

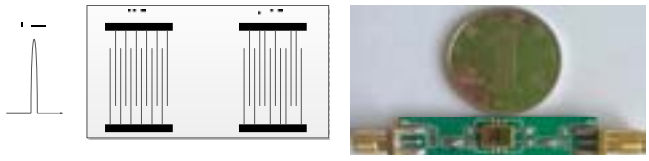

(a). Structure of correlator (b). instance of correlator

Figure 7. SAW encoding correlator

When a carrier pulse is loaded on the ordinary IDT, we can get a PSK code modulated signal from the CIDT which can be used as interrogation pulse for the combined tag.

We have built a 8 bit PSK code SAW encoding correlator (in figure 7(b)) for test. Every bit contains 28 carrier cycles and the code is [00101100], the width of the load pulse is 10ns, the result as shown in figure 8.

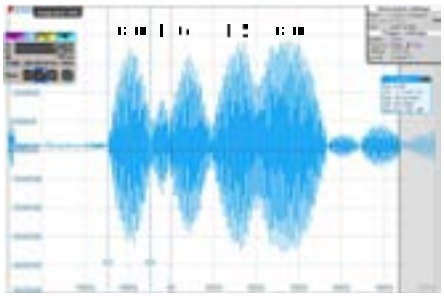

Figure 8. Output of SAW encoding correlator

The result agrees with our design well, every bit last 65ns,which equals 28*(1/434MHz). But there are two defects of this solution. First, the number of the encoding correlators in a reader is the same with the number of the anti-collision SAW tag units in a combined tag, which is very inconvenient for reader switching among encoding correlators when reading a combined tag. Second, when the reader and the tag are in different temperature areas, the reader may not get any response.

According to the definition of Software Defined Radio (SDR), the second solution uses fast switching single pole double throw (SPDT) to switch a differential carrier signal to generate a PSK modulated pulse. Figure 9 shows the structure of this solution and figure 10 shows the test result.

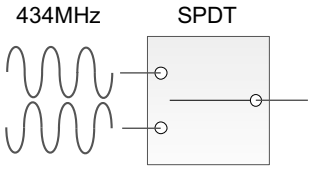

Figure 9. Structure of second solution

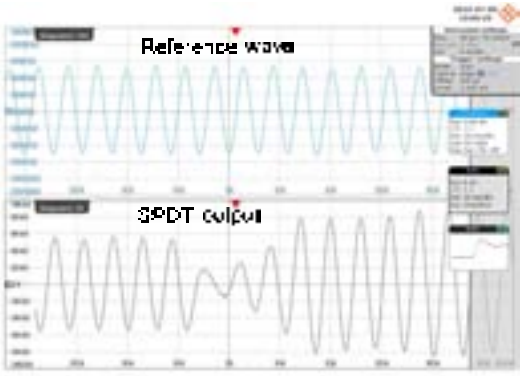

Figure 10. Output of SPDT

Contrast reference with output, the switch time of the SPDT is less than 5ns, which is very fast. The second solution overcomes the two defects mentioned above. By changing the control signal on the SPDT，the output can be any PSK code.

And by sweeping the frequency of the carrier, the center frequency of the combined tag can be found and the max echo amplitude can be obtained no matter what the temperature is.

IV. CONCLUSION

A novel large capacity SAW tag has been presented. The capacity can achieve 2^{83}, which is enough for global applications, and it is suitable for massive production by using correlation IDT and permutations and combinations theory. The reader structure is also discussed and the SPDT solution is much better.

The medium capacity SAW tag is very simple and the reader is easy to realize. It is suitable for some industrial application in a small area.

ACKNOWLEDGMENT (HEADING 5)

The authors would like to thank the No.55 Research Institute of China Electronics Technology Group Corporation, especially Prof. Chen, the National Natural Science Foundation of China (Grant No. 51005121) and the Key Technologies R& D Program of Jiangsu Province (Grant No. BE2011180) for their supports to this work.

REFERENCES

[1] C. S. Hartmann, “A Global SAW ID Tag with Large Data Capacity”, Proc. 2002 IEEE Ultrasonics Symposium, pp. 63-67.

[2] H. Hofinann, H. Stab, S. Komarov; “Design of SAW Correlation Devices With Evolutionary Strategy Methods (EVCOR)”, Proc. of the Cod: 1997 IEEE Ultrasonics Symposium. TorontoiCa- nada, pp. 17 1 - I74 .

[3] Buff, W.; Ehrenpfordt, J.; Klett, St; Rusko, M.; Goroll, M., "On-chip correlation-a new approach to narrow band SAW identification tags," *Ultrasonics Symposium, 1998. Proceedings., 1998 IEEE* , vol.1, no., pp.385,388 vol.1, 1998 doi: 10.1109/ULTSYM.1998.762171

[4] V. Plessky and L. Reindl, “Review on SAW RFID tags,” IEEE Transactions on Ultrasonics, Ferroelectrics and Frequency Control, vol. 57,no. 3, pp. 654 – 668, mar. 2010.

[5] Malocha, D.C.; Puccio, D.; Gallagher, D., "Orthogonal frequency coding for SAW device applications," Ultrasonics Symposium, 2004 IEEE , vol.2, no., pp.1082, 1085 Vol.2, 23-27 Aug. 2004doi:10.1109/ULTSYM. 2004.1417965

A Micro-Machined Tonpilz Hydrophone for Audible Frequency Sounds

Min Sung
Dept. of Mechanical Engineering
Pohang Univ. of Science and Technology (POSTECH)
Pohang, Kyungbuk, Republic of Korea

Hak Sue Lee
Underwater Acoustics Laboratory
Agency for Defense Development (ADD)
Changwon, Kyungnam, Republic of Korea

Won Kyu Moon
Dept. of Mechanical Engineering
Pohang Univ. of Science and Technology(POSTECH)
Pohang, Kyungbuk, Republic of Korea
wkmoon@postech.ac.kr

***Abstract*—We report a micro-machined Tonpilz hydrophone that uses the piezoelectric thickness mode and is suitable for the audible frequency range (i.e., 20Hz–20kHz). The structure of the sensor is based on the structure of a conventional Tonpilz transducer; however, two different design approaches were investigated to enhance sensitivity and to withstand the high-pressure underwater environment. To improve the sensitivity, the area ratio of the head mass to the piezoelectric body is several hundreds to one, which amplifies the acoustic pressure input of the transduction body. To improve the resistance to the hydrostatic pressure in the deep-water environment, the structure uses a castor oil backing to balance the hydrostatic pressure at the front surface of the acoustic sensing structure. We developed a lumped element model to investigate the design parameters for miniaturized hydrophones. The hydrophone was then fabricated using micromachining, and tested by comparing the device with a commercially available hydrophone in an anechoic bath to assess the feasibility of its use as an effective underwater sound receiver.**

Keywords-Piezoelectric MEMS; Underwater receiver; Acoustic sensor; SONAR

I. INTRODUCTION

Micromachined underwater acoustic sensors have numerous advantages including their small size, practicality, and low-cost due to batch fabrication [1-4]. Micromachined hydrophones may enable a number of new applications if they can be constructed with satisfactory specifications. For example, the hydrophones used as components of towed-array SONAR (TAS) for both civilian and military purposes require high sensitivity, stability to environmental noises, and robustness for deep-sea applications [5]. Low-cost miniaturized hydrophones with the required specifications may allow the realization of usable thin TAS, cost-effective sonobuoys, and compact arrays that can be used as a new type of vector sensor. Miniaturized hydrophones may also find uses in applications such as underwater unmanned vehicles (UUVs) [6].

Conventional hydrophones are typically fabricated using assembly processes with a number of specially designed parts. In recent years, various types of micromachined hydrophones have been reported, including condenser hydrophones and piezoresistive hydrophones [1-4]. These existing devices have shown feasibility for specific applications; however, it should be noted that the reported sensitivities were relatively low at frequencies below several kHz. In this paper, we describe the development of a micromachined Tonpilz hydrophone (hereafter referred to as a micro-Tonpilz hydrophone) for audible frequencies. The basic structure of the sensor, shown in Fig. 1, is based on the structure of a conventional Tonpilz transducer; however, two different design approaches were used to enhance the sensitivity and improve the resistance to the high hydrostatic pressure of the deep-sea environment.

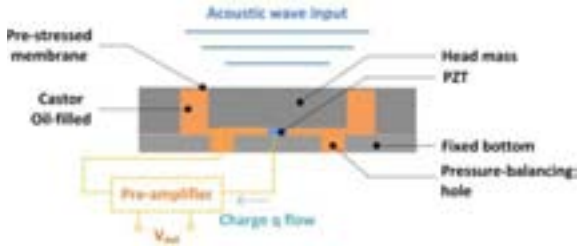

Figure 1. Cross-sectional schematic diagram of the micro-Tonpilz hydrophone. The device is circularly symmetric.

In contrast to conventional Tonpilz transducer, we designed our device with so that the area ratio of the head mass to the piezoelectric body was very large, up to several hundreds to one. This amplifies the input acoustic pressure to the transduction body, and the pressure amplification mechanism is expected to realize high sensitivity with a small device size if a properly designed pre-amplifier is used.

Additionally, the structure used a castor oil backing, which is effective in balancing the hydrostatic pressure of the deep-sea environment. To design the hydrophone for deep-sea applications, we developed a lumped element model to identify

This research was financially supported by a grant to MEMS Research Center for National Defense funded by DAPA/ADD, in the Republic of Korea.

the requirements for the pre-amplifier circuits and to design the miniaturized hydrophones appropriately.

II. Design of the Micro-Tonpilz Hydrophone

A. System model based on a 1-DOF lumped-element model

Figure 2 shows the 1-degree-of-freedom (DOF) lumped element model (LEM) of the micro-Tonpilz hydrophone. The model represents the mechanical impedances of the sensor, and comprises the impedance of the sensor itself Z_m, the radiation impedance applied by medium on the sensor Z_r, and the impedance at the back of the structure Z_b.

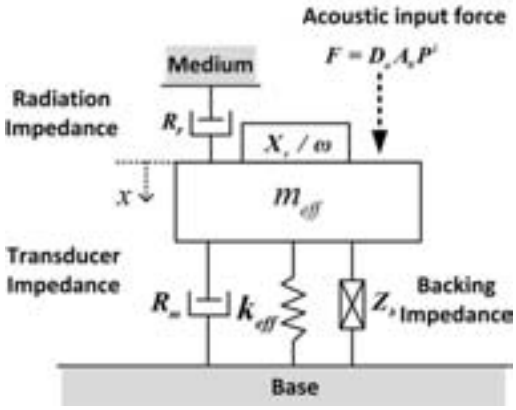

Figure 2. 1-DOF LEM of the micro-Tonpilz hydrophone

The modeling was performed assuming that the sensor is much smaller than the wavelength of the sound. The impedance of the sensor was analyzed as a function of the major parameters of the structure. The mass of the head attached to the central core on the membrane was considered the dominant effective mass. The stiffness was also analyzed by considering the compliance of the lead zirconate titanate (PZT) and the membrane separately. The PZT was assumed to be a bar with one DOF in the LEM; however, the electromechanical coupling was also considered to improve the accuracy of the modeling of the motion of the PZT.

Although the modal analysis of the proposed sensor structure calculates the fundamental mode (PZT thickness mode), the following points should be carefully considered. If the head mass is too large and the membrane is too compliant, an unwanted lateral fundamental mode of the structure can occur. In this case, we cannot expect that pressure amplification will be effective. Even though the membrane surrounding the head mass can be expected to lead the fundamental mode of the structure with motion in the axial direction, if the surrounding membrane is too stiff, which helps to avoid the lateral mode, this can reduce the sensitivity. This implies that membrane stiffness should be carefully chosen. The stiffness of the surrounding membrane was calculated assuming a circular membrane with an attached core. The impedance components are listed in Table I.

TABLE I. Impedance components

Impedance	Component	Description
$Z_m = R_m + j(\omega m_{eff} - k_{eff} / \omega)$	m_{eff}	Effective mass
	k_{eff}	Effective stiffness (PZT stiffness + membrane stiffness)
	R_m	$R_m = Q_m^{-1} \cdot (m_{eff} k_{eff})^{1/2}$, where Q_m is the mechanical quality factor at resonance in a vacuum.
$Z_r = R_r + jX_r$	R_r	Assuming that $kR \ll 1$, R_r can be approximated to $(1/2) \cdot \rho_0 c A_0 \cdot (kR)$, where ρ_0 is the density, c is the speed of sound, k is the wave vector; A_0 is the area and R the radius of a rigid circular piston.
	X_r	$\approx (8/3\pi) \cdot \rho_0 c A_0 \cdot (kR)$
$Z_b = R_b - jX_b / \omega$	R_b	The backing impedance was considered as a resistive element from the flow of the castor oil through backing hole R_b, and the backing stiffness can be determined from the backing chamber dimensions X_b.
	X_b	

Now we consider the open-circuit piezoelectric constitutive equation, i.e.,

$$\begin{pmatrix} F \\ e \end{pmatrix} = \begin{pmatrix} k_{eq} & -1/d_{eq} \\ -1/d_{eq} & 1/C_{eq} \end{pmatrix} \begin{pmatrix} \delta \\ q \end{pmatrix}, \tag{1}$$

where

$$k_{eq} = \left(\frac{1}{1-k_{33}^2} \right) \cdot \frac{A_1}{s_{33}^E t}, \quad \frac{1}{d_{eq}} = \frac{k_{33}^2}{1-k_{33}^2} \cdot \frac{1}{d_{33}}, \quad C_{eq} = (1-k_{33}^2) \cdot \frac{\varepsilon_{33}^T A_1}{t},$$

and

$$k_{33}^2 = \frac{(d_{33})^2}{\varepsilon_{33}^T s_{33}^E}$$

is the electromechanical coupling coefficient and A_1 is the area of the PZT transducer. Taking the mechanical impedances of the 1-DOF LEM, the constitutive equation for the PZT connected to a pre-amplifier that has an electrical input impedance of Z_{in}, we can derive the electromechanical system model and frequency response function by taking the Fourier transformation for the equation of motion.

B. Advantages of the pressure-amplification structure

Using the analytic system model for the micro-Tonpilz hydrophone, we can calculate both the frequency response of the structure and the pressure amplification. The frequency response was simulated using the material properties of PZT based on model C-6 from the Fuji Ceramics Corporation.

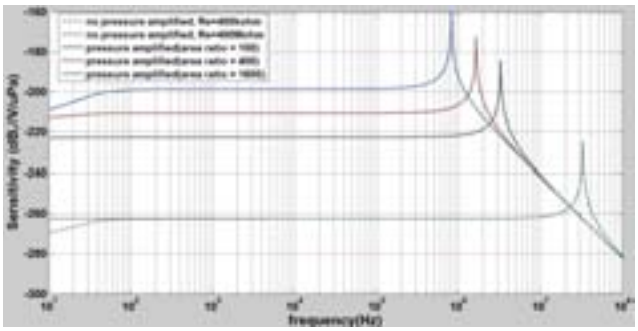

Figure 3. Simulated sensitivity as a function of frequency. The solid line is the amplified pressure, and the dashed line is without pressure amplification (i.e., with an area ratio of 1).

Simulated data are shown in Fig. 3 using a sensor with a diameter of 2 mm. The designation "without pressure amplification" refers to the area of the PZT similar to that of the head, which is typical in ultrasonic applications. "Pressure amplification" corresponds to a relatively small area of PZT compared with the area of the head. The PZT was 3 μm thick, which is consistent with the sol-gel PZT deposition process used in microelectromechanical systems (MEMS) fabrication. The open-circuit sensitivity in the flat-frequency response range is $V / p_i = g_{33} t$, where g_{33} is the piezoelectric constant, and t is the thickness of the PZT. This implies that the sensitivity in the flat-frequency response region of the micromachined hydrophone using the PZT thickness mode may be limited to relatively low sensitivities. This is reflected in the simulated data shown in Fig. 3; without pressure amplification, the sensitivity was relatively low in frequencies below the fundamental resonance, and only frequencies close to the resonant frequency showed acceptable sensitivities. This may explain why most previous applications of micromachined hydrophones using the piezoelectric thickness mode have focused on ultrasonic resonant applications.

Pressure amplification significantly increased the sensitivity in the flat-frequency response range, even with a thin PZT layer and small sensor size, which increased the bandwidth. Assuming a pre-amplifier input impedance of 400 MΩ, a good frequency response with a wide bandwidth is expected. The sensitivity was -200 dB (Ref. V/μPa) without pre-amplification, which is significantly higher than that of a commercially available miniature hydrophone.

III. Fabrication of the Micro-Tonpilz Hydrophone

The fabrication of a number of designs derived from the system model was carried out. The micromachining fabrication of the sensor includes two main elements: the fabrication of the pressure amplification structure (i.e., head mass and surrounding membrane) and the fabrication of the patterned PZT that is electrically connected to the output line. The final step is eutectic bonding to combine the fabricated parts. After bonding, the micro-sensor was diced, assembled, and packaged with a custom pre-amplifier.

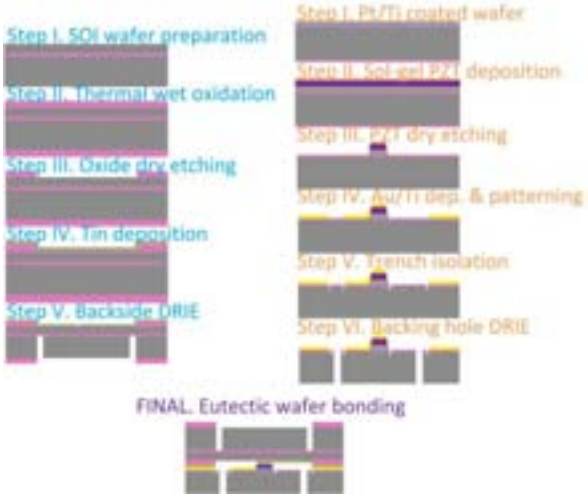

Figure 4. Micromachining process for the micro-Tonpilz hydrophone.

The fabrication process is shown schematically in Fig. 4. A 300-nm-thick layer of thermally grown oxide was prepared on a silicon wafer, and then the Pt/Ti bottom electrode layer was deposited. The PZT film was deposited using the sol-gel process. The Zr/Ti ratio of the PZT layer was 52/48. A Pt top electrode layer was deposited, and a thermal anneal was performed. The PZT layer was then patterned using photolithography and dry etched. To form the signal line, an Au/Ti layer was deposited using an electron-beam evaporator and patterned using photolithography. Shallow trench isolation was performed to suppress the leakage currents. Finally, the backside was etched away using deep reactive ion etching (DRIE) to form the backing hole.

The head-mass part was fabricated from a silicon-on-insulator (SOI) wafer to form a membrane structure. A high-resistivity SOI wafer (>10 kΩ·cm) was used to minimize the leakage current. The head-mass structure surrounded by the membrane was fabricated using DRIE. The final eutectic bonding was performed as a wafer-level process.

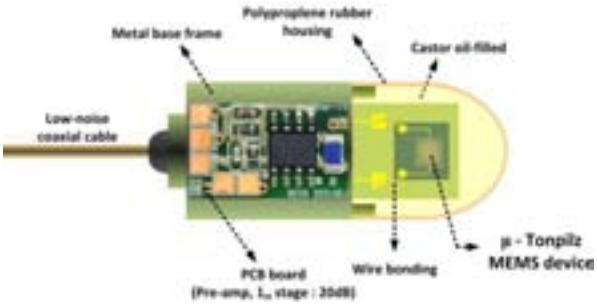

Figure 5. The assembly and packaging of the micro-Tonpilz hydrophone.

The completed micro-Tonpilz hydrophone was diced into chips and packaged as shown in Fig 5. The gain of the first stage pre-amplifier was 20 dB. The second stage pre-amplifier amplified the signal, which was transmitted using low-noise coaxial cable. A metal base frame made from stainless steel

and PCB housed the first stage pre-amplifier and was fixed to the frame. The micromachined sensor was attached on to the PCB and electrically connected using wire bonding. Finally, an acoustically transparent polypropylene rubber cap was placed on the structure, and the assembly was filled with castor oil.

IV. Results and Discussion

The hydrophone was characterized experimentally using small anechoic bath. Using a comparison method in which the micro-Tonpilz hydrophone and a reference hydrophone (B&K 8103) were fixed in similar positions and received the sound generated from an underwater loudspeaker, the micro-Tonpilz hydrophone was characterized. The underwater experimental set-up is shown in Fig. 6.

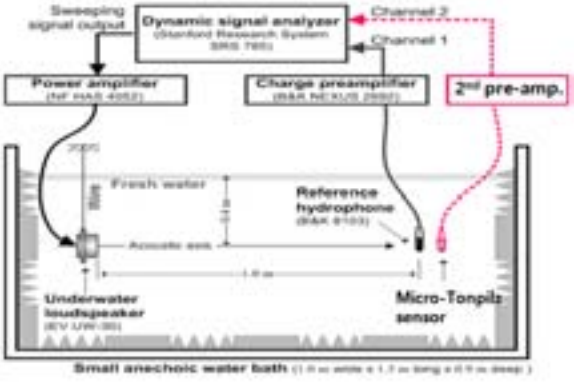

Figure 6. Underwater experimental set-up using a small anechoic bath.

Both the frequency response and the time-domain response were measured; the results are shown in Fig. 7. The sensitivity of the micro-Tonpilz hydrophone was approximately -200 dB (Ref. V/μPa, pre-amplified) in the range 700–4,000 Hz. At low frequencies, the underwater loudspeaker generated a relatively low sound-pressure level, and the measured signal-to-noise ratio was poor. This is attributed to roll-off noise and external electromagnetic interference. Although the fabrication of the micro-Tonpilz hydrophone was successful, some problems can be observed from the measured data. First, more effective shielding to block external electromagnetic noise is required. This seems to be critical, as both the sensor and the pre-amplifier had very high electrical impedance, making the device sensitive to the external noise sources. Second, the pre-amplifier design and sensor design should be optimized more. Although the sensitivity of the micro-hydrophone was not as great as expected, we have demonstrated feasibility for signal transduction at audible frequencies.

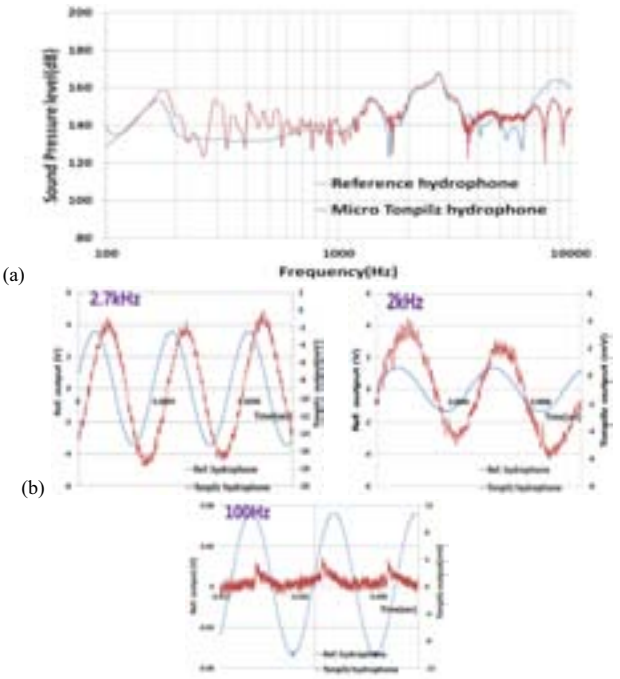

Figure 7. Underwater experiment results.
(a) Frequency response. (b) Time domain response.

Acknowledgment

This research was financially supported by a DAPA/ADD grant for the MEMS Research Center for National Defense in the Republic of Korea. We cooperated with MEMS-Solution and INOSTEK to fabricate the device in this work.

References

[1] J. Bernstein, "A micromachined condenser hydrophone," in Digest IEEE Solid-State Sensor and Actuator Workshop (1992), pp. 161–165. J. Clerk Maxwell, A Treatise on Electricity and Magnetism, 3rd ed., vol. 2. Oxford: Clarendon, 1892, pp.68–73.

[2] J. Bernstein, L. C. Niles, H. D. Chen, L. E. Cross, K. K. Li, and K.Udayakumar, "Micro-machined high frequency ferroelectric sonar transducers," IEEE Trans. Ultrason. Ferroelectr. Freq. Control 44, 960–969 (1997).

[3] H. Asanuma, S. Hashimoto, G. Suzuki, and H. Niitsum, "Optical interference type micro hydrophone fabricated by micro-machining," SEG Exp.Abstr. 1, 45–47 (2001).

[4] C. Xue, Z. Tong, B. Zhang, and W. Zhang, "A novel vector hydrophone based on the piezoresistive effect of resonant tunneling diode," IEEE Sens. J. 8, 401–402 (2008).

[5] M. Lasky, R. D. Doolittle, B. D. Simmons, and S. G. Lemon, "Recent progress in towed hydrophone array research," IEEE J. Ocean. Eng. 29, 374–387 (2004).

[6] J. W. Zehner and C. D. Loggins, "Selection criteria for UUV sonar systems," in Proceedings of the 6th International Symposium on Unmanned Untethered Submersible Technology, pp. 349–358 (1989).

Characterization of Parylene-C Using Quartz Thickness Shear Mode (TSM) Resonators

Huiyan Wu, Hongfei Zu, Xiaotian Li, and Qing-Ming Wang
Department of Mechanical Engineering & Materials Science
Swanson School of Engineering, University of Pittsburgh
Pittsburgh, Pennsylvania, USA
qiw4@pitt.edu

Abstract—**Due to its high sensitivity, repeatability and easy connection with electrical measurement systems, Quartz thickness-shear-mode (TSM) resonator is adopted to extract the complex shear modulus of Parylene-C films, which play an important role as both an effective wave-guiding layer and biocompatible interfacial layer in Shear-Horizontal Surface Acoustic Wave Device (SH-SAW, Love Mode). Parylene-C films of different thicknesses were deposited on the surface of AT-cut quartz TSM resonators, and admittance spectrums of these uncoated and coated TSM were measured by an impedance analyzer. Results indicated that the ideal thickness range for extraction was from 2.04 *μm* to 3.55 *μm*, effectively avoiding inadequate acoustic deformation as well as excessive electrical-response attenuation. The storage modulus *G′* and loss modulus *G″* of Parylene-C were 0.155±0.011 *GPa* and 4.78±0.44 *GPa*, respectively.**

Keywords-SH-SAW; TSM; TLM; Parylene-C; shear modulus

I. INTRODUCTION

Shear-Horizontal Surface Acoustic Wave Device (SH-SAW, Love Mode) is considered as one of the most promising probing methods in both fundamental biology and biomedical engineering, detecting behaviors of cells on their surface in a non-invasive, simple and quantitative manner [1-2]. Comparing with the traditional Bulk Acoustic Wave Sensors (BAW), Rayleigh waves excited by surface electrodes in SH-SAW perform extremely sensitivity to certain surface perturbations as well as favorable inertness to other surrounding factors, resulting in an extensive application prospect of SH-SAW in complicate liquid or multiphase circumstances [3-4]. As the key part of SH-SAW, acoustic-wave guiding layer on surface plays a crucial role in improving the device performance. Parylene-C (poly(2-chloro-*p*-xylylene)) has been proven as ideal acoustic-wave guiding layer owing to its good uniformity, compactness and adhesion to the substrate [5]. Meanwhile, of comparative cell compatibility, Parytlene-C films also have preferable effects on the bio-sensitivity interference on SH-SAW surface [6]. Presently, some relevant studies have been explored concerning SH-SAW with Parylene-C guiding layer [5,7]. However, most of them neglected the innovative applications of SH-SAW as cell-based sensors. Besides, based on experimental detail evidences, few researchers have provided further theoretical analysis accordingly. In order to establish a reliable theoretical analysis for Parylene-C-guiding SH-SAW biosensors, a series of physical and mechanical parameters are needed as the initial inputs in algorithm.

Due to its high sensitivity, simple structure, and easy interconnection with electronic measurement systems, quartz thickness-shear-mode (TSM) resonator is adopted to characterize the mechanical properties of Parylene-C [8]. As its surface loading condition varies, for example Parylene-C films deposited on the surface, the electrically-excited acoustic-wave propagation could change accordingly through entire quartz crystal. Two general types of equivalent-circuit models are proposed to describe the TSM resonator: the lumped-element model (Butterworth-Van Dyke, BVK) and the distributed model (Transmission Line Model, TLM), and the former could be derived from reduction of the later in near-resonant circumstances [4]. Because of the zero error between its assumptions and actual TSM electrical response, the distributed model TLM is chosen to provide a comprehensive description for TSM with viscoelastic films in this study [4, 9]. TLM is also widely used in SH-SAW devices studies, which would help optimize the parameter matching between TSM and SH-SAW model analysis in future research. Nevertheless, some problems of coating property extraction in TSM have not been solved completely, including approximately-theoretical measurement and calculation error control. It has also been found that viscoelastic coatings of various thicknesses could induce other resonance effects, leading to incompatible with calculation model [10].

In this study, uniform Parylene-C films of different thickness were prepared on TSM surface by thermal deposition, and admittance spectrums of both uncoated and coated TSM were measured through an impedance analyzer. Based on a modified TLM, corresponding storage shear modulus G' and loss shear modulus G'' of Parylene-C films were extracted. We reported the variation of G', G'' with increasing Parylene-C thickness, proposing the desirable thickness range for complex-shear-modulus extraction as from 2.04 μm to 3.55 μm. Referring to these accurate G', G'' values, reliable theoretical analysis could be established for SH-SAW with Parylene-C films as both an effective wave-guiding layer and biocompatible interfacial layer in future research.

II. THEORETICAL MODEL OF TSM RESONATOR

TLM for TSM has two acoustic ports and one electrical port, and via a transformer the acoustic variables, force F and linear velocity v, are coupled to an electrical port [11].

The acoustic-electrical analogy of TLM could be defined as that,

$$\begin{bmatrix} F_1 \\ F_2 \\ V \end{bmatrix} = -j \begin{bmatrix} Z_C \cot\alpha_q & Z_C(\sin\alpha_q)^{-1} & h/\omega \\ Z_C(\sin\alpha_q)^{-1} & Z_C \cot\alpha_q & h/\omega \\ h/\omega & h/\omega & 1/\omega C_0 \end{bmatrix} \begin{bmatrix} v_1 \\ v_2 \\ I \end{bmatrix} \tag{1}$$

where $F_{1,2}$ and $v_{1,2}$ are the external force and linear velocity at TSM resonator surfaces, respectively; and Z_C, α_q, h and C_0 are defined as follows, with relevant parameters shown in Table 1.

$$\begin{aligned} Z_C &= AZ_q = A\sqrt{\rho_q c_q} \\ \alpha_q &= \omega h_q \sqrt{\rho_q / c_q} \\ h &= e_q / \varepsilon_q \\ C_0 &= \varepsilon_q A / h_q \end{aligned} \tag{2}$$

Letting $Z_1=F_1/v_1$, $Z_2=F_2/v_2$ to represent the surface loading condition of TSM resonator, (1) is rewritten as [12],

$$\begin{bmatrix} V \\ I \end{bmatrix} = [B] \cdot \begin{bmatrix} F_1 \\ v_1 \end{bmatrix} = \frac{1}{\varphi H} \begin{bmatrix} 1 & \frac{j\varphi^2}{\omega C_0} \\ j\omega C_0 & 0 \end{bmatrix} \cdot \begin{bmatrix} \cos\alpha_q + j\frac{Z_2}{Z_C}\sin\alpha_q & Z_C(\frac{Z_2}{Z_C}\cos\alpha_q + j\sin\alpha_q) \\ \frac{j}{Z_C}\sin\alpha_q & 2(\cos\alpha_q - 1) + j\frac{Z_2}{Z_C}\sin\alpha_q \end{bmatrix} \cdot \begin{bmatrix} F_1 \\ v_1 \end{bmatrix} \tag{3}$$

where

$$H = \cos\alpha_q - 1 + j\frac{Z_1}{Z_q}\sin\alpha_q, \varphi = hC_0 \tag{4}$$

Defining $Z=V/I$, $Y=I/V$, then Z and Y are expressed as,

$$\begin{aligned} Z &= \frac{1}{j\omega C_0} - \frac{K^2}{j\omega C_0 \alpha_q} \frac{2\tan(\alpha_q/2) - j(Z_1+Z_2)/Z_C}{(1+Z_1Z_2/Z_C^2) - j(Z_1+Z_2)/Z_C \cot\alpha_q}) \\ Y &= j\omega C_0 + \frac{j\omega C_0(2\tan(\alpha_q/2) - j(Z_1+Z_2)/Z_C)}{\alpha_q / K^2((1+Z_1Z_2/Z_C^2) - j(Z_1+Z_2)/Z_C \cot\alpha_q) - 2\tan(\alpha_q/2) + j(Z_1+Z_2)/Z_C}) \end{aligned} \tag{5}$$

where

$$K^2 = e_q^2 / \varepsilon_q c_q \tag{6}$$

Generally, for uncoated TSM, both surfaces are stress free with two short-circuit acoustic terminations of $F_1=Z_1=F_2=Z_2=0$. However, when extra films (upper/lower electrodes and Parylene-C) are deposited directly on the surfaces, Z_1 and Z_2 are changed accordingly depending on these films' own physical and mechanical properties. For Au/Cr electrodes on both sides are very thin (~100 *nm*), their effects on surface loading Z_1 and Z_2 values are neglected, simplifying the original theoretical model effectively. Thus, Z_1 is only determined by Parylene-C's properties, and Z_2 is always zero. Assuming Parylene-C films as isotropic, homogeneous and uniform coating on Quartz, Z_1 could be calculated as follows, with relevant parameters shown in Table 1 also.

$$Z_1 = jZ_1^C A\tan\alpha_1 \tag{7}$$

where

$$\begin{aligned} Z_1^C &= \sqrt{\rho_1 G_1}, G_1 = G' + jG'' \\ \alpha_1 &= \omega h_1 \sqrt{\rho_1 / G_1} \end{aligned} \tag{8}$$

Substituting the Z_1 and Z_2 into (5) Y expression,

$$Y = j\omega C_0 + \frac{j\omega C_0(2Z_C\tan(\alpha_q/2) + Z_1^c A\tan\alpha_1)}{\alpha_q / K^2(Z_C + Z_1^c A\tan\alpha_1\cot\alpha_q) - 2Z_C\tan(\alpha_q/2) - Z_1^c A\tan\alpha_1} \tag{9}$$

Nevertheless, considering the excluded electrode effect of TSM, other non-uniformity influences and surrounding perturbations, modified TLM model is proposed as shown in Fig.1 (b). Taking these uncertainties into account, the total parallel capacitance C_0^* is defined as that [13],

$$C_0^* = C_0 + C_p \tag{10}$$

where C_0 is TSM static capacitance, and C_p is the external capacitance. With C_0^* as a desirable way of compensation for previous model, (7) (9) are respectively rewritten into (12) (13). This model establishes an explicit relationship between experimental observations (TSM electrical response) and relevant device parameters, which is of great significance in the following algorithm analysis.

$$Y = j\omega C_0^* + \frac{2j\omega C_0\tan(\alpha_q/2)}{\alpha_q / K^2 - 2\tan(\alpha_q/2)} \tag{11}$$

$$Y = j\omega C_0^* + \frac{j\omega C_0(2Z_C\tan(\alpha_q/2) + Z_1^c A\tan\alpha_1)}{\alpha_q / K^2(Z_C + Z_1^c A\tan\alpha_1\cot\alpha_q) - 2Z_C\tan(\alpha_q/2) - Z_1^c A\tan\alpha_1} \tag{12}$$

TABLE I. PARAMETERS OF TSM RESONATORS [14]

Density of Quartz	ρ_q	$2.651\times10^3\ kg\cdot m^{-3}$
Shear Stiffness of Quartz	$c_q = c_{66} + e_{26}^2/\varepsilon_{22} + j\omega\eta_q$	$2.970\times10^{10}\ N\cdot m^{-2} + j\omega\eta_q$
Piezoelectric Constant of Quartz	$e_q = e_{26}$	$9.657\times10^{-2}\ A\cdot s\cdot m^{-2}$
Dielectric Permittivity of Quartz	$\varepsilon_q = \varepsilon_{22}$	$3.982\times10^{-11}\ A^2\cdot s^4\cdot kg^{-1}\cdot m^{-3}$
Surface Area of TSM Resonator	A	$2.047\times10^{-5}\ m^2$
Thickness of TSM Resonator	h_q (theoretical)	165 μm
Density of Parylene-C	ρ_1	$1.289\times10^3\ kg\cdot m^{-3}$
Shear Modulus of Parylene-C	G_1	To be determined
Thickness of Parylene-C Films	h_1	To be determined

III. EXPERIMENTALLY DETAILS AND ANALYSIS METHODS

The admittances of uncoated 10-MHz TSM resonators (International Crystal Manufacturing Co., Oklahoma City, OK) were firstly measured by an Agilent 4294A Precision Impedance Analyzer (Agilent Technologies, Palo Alto, CA), which were recorded for the extraction of effective parameters of TSM. Subsequently, Parylene-C films were deposited on TSM surface by thermal deposition system (SCS PDS 2010 Labcoter 2, SCS Equipment, Dallas, TX). The thicknesses of as-deposited Parylene-C films were analyzed by a profilometer (Dektak3 ST surface profiler, Veeco Instruments

Inc., Woodbury, NY) and surface morphology was observed by Scanning Electron Microscopy (XL-30 FEG SEM, FEI/Philips, Japan). The admittances of TSM resonators with different Parylene-C thickness were recorded also. For getting precise results in succeeding fitting procedure, each sample with certain-thickness films was measured three times under the same conditions.

Based on TLM equivalent-circuit model presented in Section 2, a fitting procedure is introduced to obtain accurate values for both storage shear modulus G' and loss shear modulus G'' [15]. The total parallel capacitance $C_0^* = 6.0874$ pF, which is measured at double fundamental-resonance frequency based on the limiting relationship $Y = j\omega C_0^*$ [16].

IV. Results and Discussions

Fig.1 gives the admittance spectrums of TSM resonators with different Parylene-C thickness. The marked thickness of Parylene-C films is detected by Surface Profiler, and the inset morphology image for TSM with 1.6 μm Parylene-C is obtained by Scanning Electronic Microscopy. It is indicated that as-deposited Parylene-C films are smooth and compact, without any obvious bumps or pores across the surface. Based on the admittance spectrum of uncoated TSM resonator, effective parameters h_q, μ_q, C_0^* and C_p are extracted as Table 2 lists. The fitting process is well-acceptable with the error of 0.0430%, leading to affirmative calibrated parameters of TSM resonator.

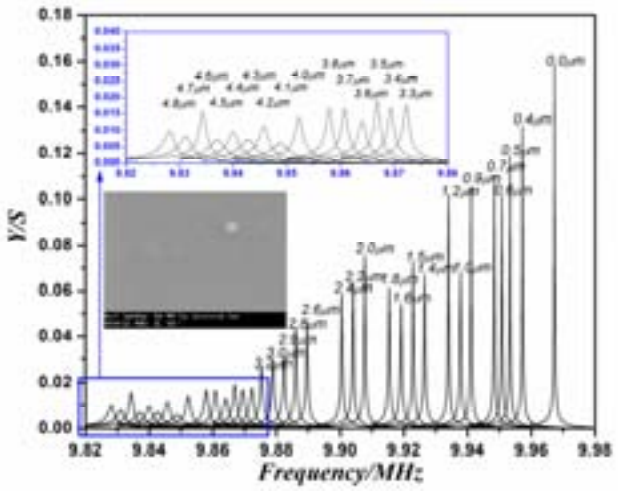

Figure 1. Admittance curves of TSM with different Parylene-C thickness

TABLE II. Calibrated Parameters of TSM Resonator

Effective Thickness of TSM	h_q	166.72 μm
Effective Viscosity of Quartz	μ_q	0.0053 $Pa{\cdot}s$
Effective Static Capacity of TSM	C_0	4.4280 pF
Effective External Capacity of TSM	C_p	1.6594 pF

Fig.2 shows the complex shear modulus (storage modulus G' and loss modulus G'') of Parylen-C films with different thickness. Fitting calculation provides the optimal solution set of G', G'' as well as the corresponding Parylene-C thickness, which are in good agreement with the Surface Profiler analysis. This figure illustrates that G′ and G″ have the similar variation tendency: In the beginning, the shear modulus increase with Parylene-C's thickness increasing from 0.34 μm to 2.04 μm (Range I), and then inclined to be constant relatively as the thickness ascending further (Range II and III). Meanwhile, with no obvious changes observed in Range II, the dispersion of shear modulus is increasing gradually from Range II to III. When the Parylene-C films are thin as in Range I, the entire Parylene-C films tend to move with TSM surface synchronously, and the displacement of films inclines to be uniform. The acoustic phase shift across viscoelastic films is relatively small, constraining the typical deviations of viscoelastic films' behavior from rigid films'. During this range considered as gravimetric region, the films thickness and density contributed mostly to TSM's electrical response other than the mechanical properties. With the thickness' further rising to non-gravimetric region, Parylen-C displacement is not synchronous with TSM surface, resulting in an appreciable acoustic phase shift through the films. Thus, considerable shear deformation is introduced into the films' behavior, causing the viscoelastic contribution in electrical response to be substantial and quantifiable [4]. From this perspective, an appropriate thickness range of Parylene-C films (2.04 μm - 3.55 μm) should be selected to get the accurate characterization of the viscoelastic properties.

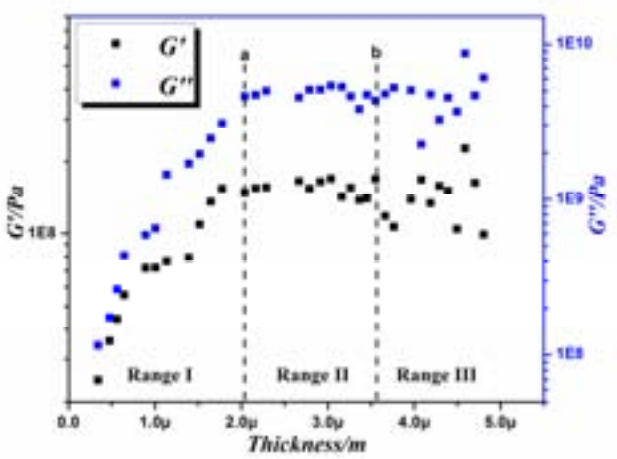

Figure 2. Shear modulus G′ and G″ of Parylene-C with different thickness

As a result, the shear modulus values in Range II (Parylene-C thickness from 2.04 μm to 3.55 μm) are adopted, and storage modulus G' and loss modulus G'' of Parylene-C are 0.155±0.011 GPa and 4.78±0.44 GPa, respectively. Fig. 3 exhibits the fitting-error analysis for Range II. The upper plot is fitting-error curve with the variation of Parylene-C thickness; the lower two are for TSM resonator with 2.91-μm Parylen-C, as the comparison of experimental and fitting curves of Y's real part G and image part B, respectively. The error upper limit is set as 1% in algorithm of shear-modulus

extraction. Much smaller than this setting point, the final fitting error for Range II keep stable under 0.100%, and even for most samples less than 0.050%. Besides, the fitting error for both the real part G and image part B of admittance Y is limited similarly, which proves high reliability and resolution of fitting process further.

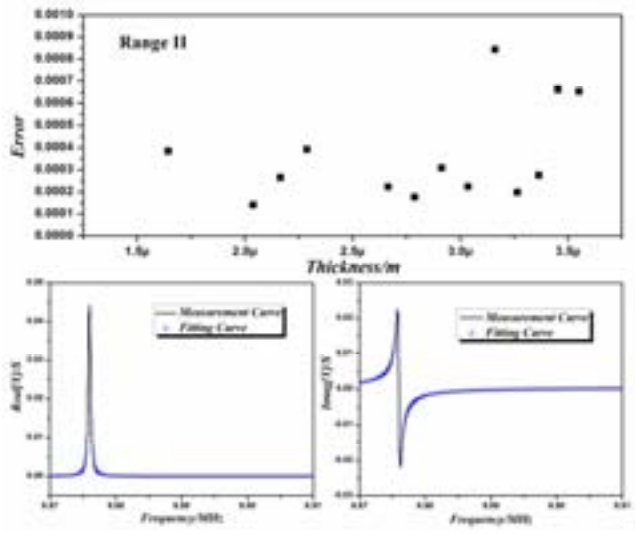

Figure 3. Fitting of TSM resonators with different Parylene-C thickness

V. CONCLUSIONS

In this study, quartz thickness-shear-mode (TSM) resonator is adopted to extract the complex shear modulus of Parylene-C films. Accordingly, with null error between its assumptions and actual TSM electrical response, the distributed model - Transmission Line Model (TLM), which is also widely used in SH-SAW devices analysis, is applied to provide a comprehensive description for TSM with viscoelastic films. Considering the electrode effect, surrounding perturbations and other kinds of non-uniformity, non-certainties influences, total parallel capacitance C_0^* is introduced to substitute static capacitance C_0 in modified TLM. In the meantime, preliminary calibration is conducted to determine the effective parameters of uncoated TSM before extraction of complex shear modulus. Additionally, a fitting procedure in algorithm also contributes to the accuracy of both storage shear modulus G' and loss shear modulus G''. The error threshold is set as 1% and the optimal solution set is chosen based on the minimum error function value.

Parylene-C films of different thicknesses were prepared on TSM surface by thermal deposition. In the beginning, G' and G'' increase with Parylene-C's thickness rising from 0.34 μm to 2.04 μm because of inadequate sensitivity of viscoelastic effect, and then inclined to be constant relatively; however, as the thickness ascending further, the dispersion of G' and G'' is increasing gradually due to the excessive electrical-response attenuation. As a result, the ideal thickness range for Parylene-C on TSM is from 2.04 μm to 3.55 μm, and the average G' and G'' are 0.155±0.011 GPa and 4.78±0.44 GPa, respectively. With total fitting error keeping stable below 0.100%, the high reliability and resolution of the whole extraction process is confirmed.

ACKNOWLEDGMENT

This research work was partially supported NSF awards No. CMMI 0653764, and No. ECCS 0925716; and DOE grant No. DE-FE0002138.

REFERENCES

[1] M. Saitakis, A. Tsortos, and E. Gizeli, "Probing the Interaction of a Membrane Receptor with a Surface-attached Ligand using Whole Cells on Acoustic Biosensors", Biosensors & Bioelectronics, vol. 25, pp.1688-1693, 2010.

[2] F. Li, Q. -M. Wang, and J. Wang, "Theoretical Analysis of Love Mode Surface Acoustic Wave Device as Cell-based Biosensor", IEEE Ultra. Sympo. 2007, pp. 2111-2114, 2007.

[3] R. M. White, "Surface Elastic Waves", Proc. IEEE, vol. 58 (8), pp.1238-1276, 1970.

[4] D. S. Ballantine, R. M. White, S. I. Martin, A. J. Ricco, E. T. Zellers, G. C. Frye, and H. Wohltjen, "Acoustic Wave Sensor: Theory, Design, and Physico-Chemical Applications", Academic Press, 1997.

[5] K. Lange, S. Grimm, and M. Rapp, "Chemical Modification of Parylene C Coatings for SAW Biosensors", Sensors & Actuators B, vol. 125, pp.441-446, 2007.

[6] T. Y. Chang, V. G. Yadav, S. D. Leo, A. Mohedas, B. Rajalingam, C. -L. Chen, S. Selvarasah, M. R. Dokmeci, and A. Khademhosseini, "Cell and Protein Compatibility of Parylene-C", Langmuir, vol. 23, pp.11718-11725, 2007.

[7] F. Bender, K. Lange, N. Barie, J. Kondoh, and M. Rapp, "On-line Monitoring of Polymer Deposition for Tailoring the Waveguide Characteristics of Love-Wave Biosensors", Langmuir, vol. 20, pp.2315-2319, 2004.

[8] J. Hossenlopp, L. Jiang, R. Cernosek, and F. Josse, "Characterization of Epoxy Resin (SU-8) Film Using Thickness-Shear Mode (TSM) Resonator Under Various Conditions", J. Polymer Sci. B: Polymer Physics, vol. 42, pp. 2373-2384., 2004

[9] Y. Jimenez, R. Fernandez, R. Torres, and A. Arnau, "A Contribution to Solve the Problem of Coating Properties Extraction in Quartz Crystal Microbalance Applications", IEEE Trans. Ultra. Ferro. & Freq. Contr., vol. 53, pp. 1057-1069, 2006.

[10] A. R. Hillman, A. Jackson, and S. J. Martin, "The Problem of Uniqueness of Fit for Viscoelastic Films on Thickness-Shear Mode Resonator Surfaces", Anal. Chem., vol. 73, pp. 540-549, 2001.

[11] G. S. Kino, "Acoustic Wave: Devices, Imaging & Analog Signal Processing", Prentice-Hall Inc, 1987.

[12] Q. M. Chen, and Q. M. Wang, "The Effective Electromechanical Coupling Coefficient of Piezoelectric Thin Film Resonators", Appl. Phys. Letter, vol. 86, pp.022904-1-3, 2005.

[13] R. Lucklum, C. Behling, R. W. Cernosek, and S. J. Martin, "Determination of Complex Shear Modulus with Thickness Shear Mode Resonators", J. Phys. D: Appl. Phys., vol. 30, pp. 346-356, 1997.

[14] D. Salt, "Hy-Q Handbook of Quartz Crystal Devices", Van Nostrand Reinhold (UK) Co. Ltd, 1987.

[15] L. Qin, H. Cheng, J. M. Li, and Q. -M. Wang, "Characterization of Polymer Nanocomposite Films Using Quartz Thickness Shear Mode (TSM) Acoustic Wave Sensor", Sensors & Actuators A, vol. 136, pp. 111-117, 2007.

[16] W. G. Cady, "Piezoelectricity: An Introduction to the Theory and Applications of Electromechanical Phenomena in Crystals", vol. II, New York: Dover, 1964.

A SH-APM Liquid Viscosity Sensor Based on PZT-5H

Zhijun Chen, Mengyang Wang, Peng Ruan, Xin Huang
College of Automation Engineering
Nanjing University of Aeronautics and Astronautics
Nanjing, China
Zjchen76@sina.com

Jingyong Liu
No.55 Research Institute
China Electronics Technology Group Corporation
Nanjing, China

***Abstract*—Viscosity is one of the characteristic parameters of liquid. The measurement of liquid viscosity is required in many applications. Compared with other acoustic wave device, the shear-horizontal acoustic plate mode wave (SH-APM) device is suitable for liquid sensing. In this paper, the theoretical model of SH-APM device loaded with viscous liquid is built using the propagation characteristics of acoustic wave in laminated mediums, the liquid viscosity is introduced by adding the imaginary part in liquid elastic tensor, and the condition of exciting SH-APM in the piezoelectric plate by inter-digital transducers is researched. Choosing PZT-5H piezoelectric ceramic as substrate material, the numerical calculation is implemented and the SH-APM device is fabricated accordingly. Using different ratios of pure water and glycerol as liquid samples, the validity of liquid viscosity sensing by SH-APM is proved by the experimental results.**

Keywords—shear horizontal acoustic plate mode wave; liquid viscosity; PZT-5H; propagation velocity; propagation attenuation

I. INTRODUCTION

As to the acoustic wave device, generally the excitation and detection of the acoustic wave are realized by the inter-digital transducers (IDT) deposited on the surface of the piezoelectric substrate. The changes of the acoustic wave propagation characteristics with external pressure, temperature, gas, and liquid, etc. could be used as sensing functions [1]. Compared with surface acoustic wave (SAW) device, the acoustic plate mode wave (APM) device has two interfaces. When one interface is deposited with IDTs as acoustic excitation, the other interface can be loaded with liquid sample. Furthermore, when the APM has only SH (shear-horizontal) particle displacement normal to the propagation direction and parallel to the plate surface, the attenuation because of the liquid sample is very small. So the SH-APM device is suitable for liquid sensing [2].

The characteristic parameters of liquid include density, viscosity, volume elastic modulus, permittivity, and conductivity, etc. Among these liquid parameters mentioned above, the former three belong to mechanical parameters, and the latter two are electrical parameters. Because of the variety of liquid's characteristic parameters and the complexity of APM's propagation characteristics, until now the researches in APM liquid sensing mainly focus on non-viscous liquid [3]. That is, the viscosity of the liquid is neglected; only the detection of the non-viscous liquid by APM is analyzed, which limits the development of the APM liquid sensors. In fact, the measurement of liquid viscosity is required and important in many applications.

In this paper, the liquid viscosity is introduced by adding the imaginary part in liquid elastic tensor, the condition of exciting SH-APM in the piezoelectric plate by inter-digital transducer is concluded, and the theoretical model of SH-APM device loaded with viscous liquid is built using the propagation characteristics of acoustic wave in laminated mediums. The piezoelectric ceramic PZT-5H is used as substrate material, by numerical calculation and experimental analyses, the validity of liquid viscosity sensing by SH-APM is proved, which provides guidance for the further research on APM liquid viscosity sensors.

II. THEORETICAL ANALYSIS

Strictly speaking, all the elastic mediums including piezoelectric materials could show viscosity to a certain extent [4]. Considering the viscosity of the medium, the extended Hooke's law is as follows [5].

$$T_{ij} = (c_{ijkl} + j\omega\eta_{ijkl})S_{kl}, \tag{1}$$

where T_{ij} and S_{ij} are the stress and strain tensor, respectively; c_{ijkl} and η_{ijkl} are the medium's elastic and viscous tensor, respectively, which have the same symmetry characters; the indices i, j, k and l are assumed to be 1, 2, 3; $\omega=2\pi f$ is the circular frequency, With the compressed matrix notation, the constants $\boldsymbol{c}_{ijkl}$ and η_{ijkl} can be represented by matrices $\boldsymbol{c}_{pq}$ and η_{pq} with the conventions p and q varying from 1 to 6.

Therefore the viscosity of the medium is shown by introducing the imaginary part in liquid elastic tensor. Generally, the viscosity of the piezoelectric material could be neglected. When the liquid's viscosity is above 0.0015Pa.s, the viscosity of the liquid must be considered. The liquid viscosity is marked as η_L, which denotes the shear viscous constant η_{44}.

The liquid's viscous constants are [6]:

$$\eta_{44} = \eta_L,\ \eta_{11} = \frac{4}{3}\eta_L,\ \eta_{12} = \eta_{11} - 2\eta_{44} = -\frac{2}{3}\eta_L. \tag{2}$$

After considering the liquid's viscosity, the elastic constants of the viscous liquid are:

$$c_{44} = j\omega\eta_L,\ c_{11} = c_L + \frac{4}{3}j\omega\eta_L,\ c_{12} = c_{11} - 2c_{44} = c_L - \frac{2}{3}j\omega\eta_L, \tag{3}$$

where c_L is the liquid's volume elastic modulus.

The APM device coordinates loaded with liquid is shown in Fig. 1. The APM is excited by the IDTs on the surface of the substrate. The liquid is in contact with the other interface of the substrate, and the region $x_3 < -d$ is the liquid medium.

When the APM device is loaded with viscous liquid, generally the energy leakage would happen, and the APM becomes the leaky plate wave. This leads to the attenuation

along the propagation direction x_1, and the acoustic field quantities have the following form:

$$\begin{cases} u_i = A_i \exp[-jk(\xi x_1 + \beta x_3 - vt)] \\ \phi = A_4 \exp[-jk(\xi x_1 + \beta x_3 - vt)] \end{cases}, \quad (4)$$

where u_i (i =1, 2, 3) is mechanical displacement; ϕ is electrical potential; v and A_i are the propagation velocity and wave amplitude, respectively; k is the wave vector along the propagation direction; ξ and β represent the attenuation factors along the propagation direction x_1 and the depth direction x_3, respectively.

$$\xi = 1 - j\gamma, \quad (5)$$

where γ is the propagation attenuation of the APM. When the APM hasn't energy leakage, γ =0.

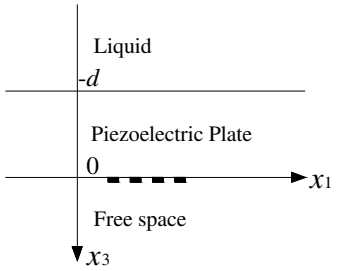

Fig. 1 The APM device coordinates loaded with liquid

The Christoffel equations in the piezoelectric medium have the following matrix form:

$$\begin{bmatrix} \Gamma_{11} & \Gamma_{12} & \Gamma_{13} & \Gamma_{14} \\ \Gamma_{21} & \Gamma_{22} & \Gamma_{23} & \Gamma_{24} \\ \Gamma_{31} & \Gamma_{32} & \Gamma_{33} & \Gamma_{34} \\ \Gamma_{41} & \Gamma_{42} & \Gamma_{43} & \Gamma_{44} \end{bmatrix} \begin{bmatrix} A_1 \\ A_2 \\ A_3 \\ A_4 \end{bmatrix} = 0. \quad (6)$$

Because of the material symmetry character, in some particular substrate cut orientation and acoustic wave propagation direction or the polarization direction, the Christoffel equations would become

$$\begin{bmatrix} \Gamma_{11} & 0 & \Gamma_{13} & 0 \\ 0 & \Gamma_{22} & 0 & \Gamma_{24} \\ \Gamma_{31} & 0 & \Gamma_{33} & 0 \\ 0 & \Gamma_{42} & 0 & \Gamma_{44} \end{bmatrix} \begin{bmatrix} A_1 \\ A_2 \\ A_3 \\ A_4 \end{bmatrix} = 0. \quad (7)$$

On the above conditions, (u_1, u_3) and (u_2, ϕ) decouple. The Christoffel equations turn to two independent sub-equations. One is the pure mechanical Rayleigh wave with u_1 and u_3 coupling without u_2 and ϕ.

$$\begin{bmatrix} \Gamma_{11} & \Gamma_{13} \\ \Gamma_{31} & \Gamma_{33} \end{bmatrix} \begin{bmatrix} A_1 \\ A_3 \end{bmatrix} = 0. \quad (8)$$

The other is the acoustic wave with u_2 and ϕ coupling without u_1 and u_3.

$$\begin{bmatrix} \Gamma_{22} & \Gamma_{24} \\ \Gamma_{42} & \Gamma_{44} \end{bmatrix} \begin{bmatrix} A_2 \\ A_4 \end{bmatrix} = 0. \quad (9)$$

As to the acoustic wave excited by IDTs on the piezoelectric substrate, the vibration displacement and electrical potential must couple. So the acoustic wave corresponding to the latter sub-equations has only the vibration displacement along x_2 direction, which is called the shear-horizontal (SH) APM.

Corresponding to the APM device coordinates as shown in Fig. 1, when the substrate's elastic constants and piezoelectric constants satisfy the following conditions, the SH-APM would be excited by IDTs.

$$\begin{cases} c_{14} = c_{16} = c_{34} = c_{36} = c_{45} = c_{56} = 0 \\ e_{11} = e_{13} = e_{15} = e_{31} = e_{33} = e_{35} = 0 \end{cases}. \quad (10)$$

When the propagation characteristics of the acoustic wave in laminated mediums are researched, the following principles should be followed [7]:

(1). At the interface between two mediums, the wave vectors along the propagation direction should be equal.

(2). When both the two mediums are solids, the stress and displacement at the interface between the two mediums should be continuous.

(3). When one medium or both the two mediums are liquids, the stress at the interface should be continuous. As to the continuity of the displacement, it differs depending on the viscous character of the liquid. When the liquid is non-viscous, the interface is allowed to generate surface glide, only the normal component of the displacement satisfies the continuity condition; when the liquid is viscous, the displacement components in the three directions must be continuous.

According to the above principles, the boundary conditions of the SH-APM loaded with viscous liquid could be expressed in the following matrix form:

$$[N][H] = 0, \quad (11)$$

where [H] is a vector, [N] is a 6×6 matrix.

The equation group (11) includes six boundary conditions: the continuity of the normal component of the stress T_{32} at x_3= 0 and x_3= -d; the electrical boundary conditions at x_3= 0 and x_3= -d; the continuity of the displacement u_2 at x_3= -d; the continuity of the electrical potential ϕ at x_3= -d.

The SH-APM's displacement u_3=0, and there is not the continuity of the stress T_{33} in (11), so the volume elastic modulus c_L of the liquid is not included in the boundary conditions. Furthermore, similar to the APM loaded with non-viscous liquid, the elimination of the influences of the liquid permittivity and conductivity to the SH-APM's propagation characteristics could be realized by sputtering a thin metal film at x_3= -d. When the electrical boundary condition is free at x_3= 0 and metalized at x_3= -d, only the liquid's density and viscosity influence SH-APM's propagation characteristics.

Based on the above boundary conditions, utilizing the partial wave theory and the surface effective permittivity method [8], the changes of SH-APM's propagation velocity and attenuation with liquid's density and viscosity could be numerically simulated and analyzed.

III. NUMERICAL SIMULATION

According to the theoretical analysis, when the electrical boundary condition is free at the interface deposited with IDTs and metalized at the interface loaded with liquid, the liquid sensing model of SH-APM can be formulated as follows:

$$\Delta v = \left(\frac{\partial v}{\partial \rho_L}\right)\rho_L + \left(\frac{\partial v}{\partial \eta_L}\right)\eta_L, \quad (12)$$

$$\Delta \gamma = \left(\frac{\partial \gamma}{\partial \rho_L}\right)\rho_L + \left(\frac{\partial \gamma}{\partial \eta_L}\right)\eta_L. \quad (13)$$

The piezoelectric ceramic belongs to polycrystalline material, which has the merits of large electro-mechanical coupling coefficient, isotropic in transverse orientation, unlimited in geometrical dimensions, high performance-to-price ratio, etc. The material constants of the piezoelectric ceramic PZT-5H satisfy the conditions of exciting SH-APM, at the same time the excitation efficiency is comparatively high. Therefore PZT-5H becomes the preferable material for the research of SH-APM. As to the PZT-5H piezoelectric substrate with the ratio of plate thickness to acoustic wavelength d/λ=0.15, the period of IDT P =1mm, when the electrical boundary condition is free at x_3= 0 and metalized at x_3= -d, the changes of SH-APM propagation velocity and attenuation with liquid density and viscosity are depicted in Figs. 2 and 3, respectively.

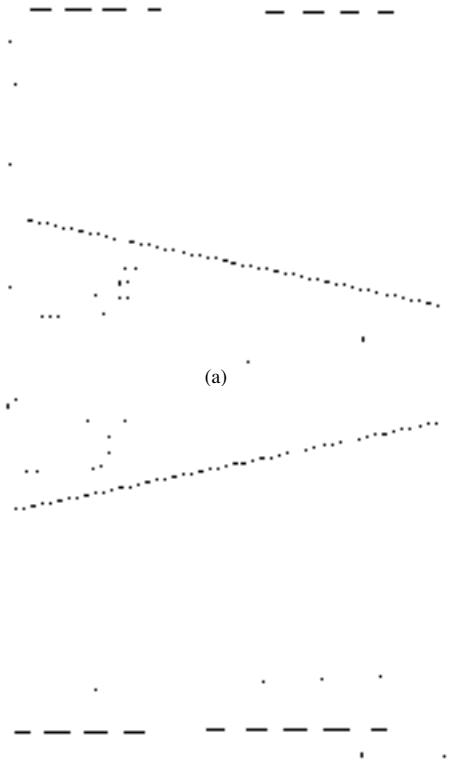

(a)

(b)

Fig. 2 The changes of SH-APM propagation characteristics of PZT-5H with liquid density: (a) propagation velocity; (b) propagation attenuation

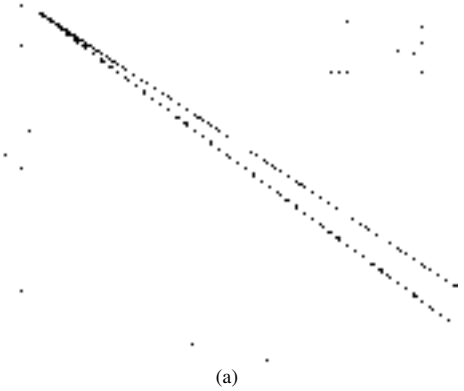

(a)

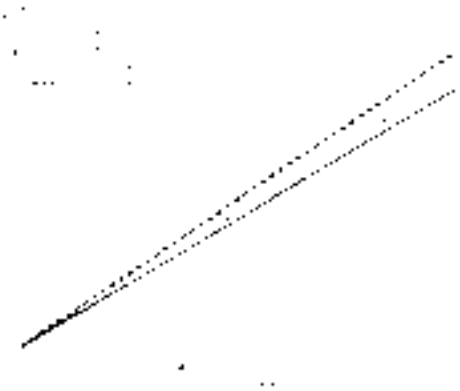

(b)

Fig. 3 The changes of SH-APM propagation characteristics of PZT-5H with liquid viscosity: (a) propagation velocity; (b) propagation attenuation

As can be seen, the propagation velocity v and propagation attenuation γ of SH-APM have linear relation with the square root of liquid density ρ_L and viscosity η_L. The velocity v decreases with the increases of ρ_L and η_L. On the contrary, the attenuation γ increases with the increases of ρ_L and η_L. By comparing Figs. 2 and 3, we find out that the changes of v and γ because of η_L are much larger than those because of ρ_L. It could be approximated that the changes of v and γ result only from liquid viscosity η_L, and the liquid sensing model of SH-APM can be further simplified as:

$$\Delta v = (\frac{\partial v}{\partial \eta_L})\eta_L, \tag{14}$$

$$\Delta \gamma = (\frac{\partial \gamma}{\partial \eta_L})\eta_L . \tag{15}$$

IV. Experimental Analysis

The SH-APM device is fabricated for the purpose of researching its liquid viscosity sensing characteristics. The piezoelectric material is PZT-5H whose polarization direction is normal to the sagittal plane. The geometrical dimensions of the device are listed in Table. 1. The encapsulation and photo of the SH-APM device are shown in Figs. 4 and 5, respectively.

Table.1 Geometrical dimensions of the SH-APM device

Substrate	length LL (mm)	25
	width W (mm)	10
	thickness d (mm)	0.15
IDT	pairs N	6
	period P (mm)	1
	width a (mm)	0.25
	distance b (mm)	0.25
	aperture w (mm)	5
	center distance l (mm)	12

The network analyzer is utilized as the measurement instrumentation. The resonant frequency f and insertion loss IL could be obtained by the amplitude-frequency characteristic curve.

The relation between resonant frequency f and propagation velocity v is:

$$f = v/\lambda = v/P . \tag{16}$$

The relation between loss L and propagation attenuation γ is:

$$L = -\frac{20}{\ln 10} k\gamma \cdot l = -54.575 \frac{l}{P} \cdot \gamma \cdot \quad (17)$$

In the experiment, the loss L is obtained by the insertion loss IL loaded with liquid subtracted from the insertion loss IL' in the free space. Therefore, after f and IL are measured by the network analyzer, the realistic v and γ of the fabricated SH-APM device could be calculated by equations (16) and (17).

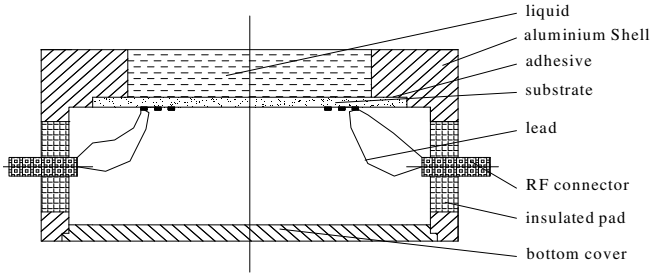

Fig. 4 The encapsulation of the SH-APM device

Fig. 5 The photo of the SH-APM device

Fig. 6 shows the amplitude-frequency curves of the SH-APM device in the free space, loaded with pure water and glycerol. As can be seen, because the pure water is non-viscous, there is almost no difference between the curve in the free space and that loaded with pure water. Because the glycerol is viscous, the SH-APM becomes the leaky plate wave, resulting in the increase of the propagation attenuation.

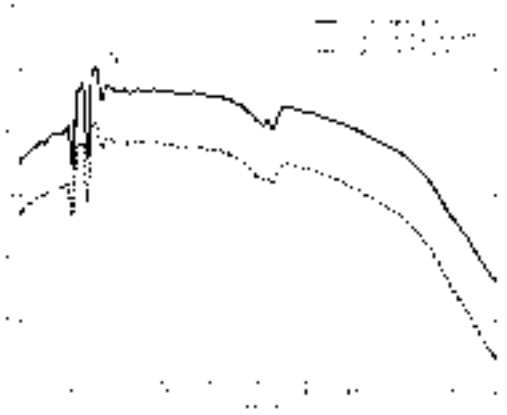

Fig. 6 The amplitude-frequency curves of the SH-APM device in the free space, loaded with pure water and glycerol

Using different ratios of pure water and glycerol as the liquid samples, the amplitude-frequency curves of the SH-APM device are shown in Fig. 7. The higher the glycerol's concentration is, the bigger the liquid's viscosity is. As can be seen, the insertion loss IL increases with the increase of liquid viscosity. At the same time, the increase of liquid viscosity leads to the corresponding decrease of resonant frequency f.

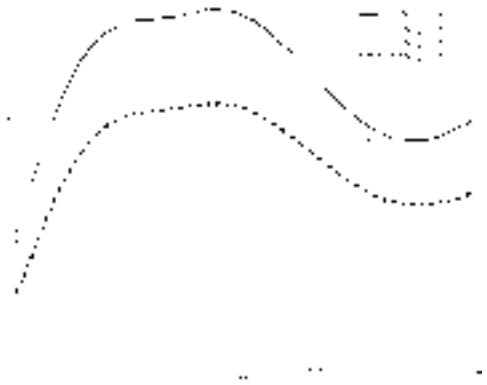

Fig. 7 The amplitude-frequency curves of the SH-APM device loaded with different ratios of pure water and glycerol

V. CONCLUSION

This paper describes the theoretical analysis, numerical simulation, and experimental analysis of the SH-APM device as liquid viscosity sensing. Choosing PZT-5H piezoelectric ceramic as substrate material, the SH-APM device is fabricated. Using different ratios of pure water and glycerol as the liquid samples, the experimental results are in agreement with the theoretical analyses.

ACKNOWLEDGMENT

The authors would like to thank the National Natural Science Foundation of China (Grant No. 51005121) and The Key Technologies R& D Program of Jiangsu Province (Grant No. BE2011180) for their supports to this work.

REFERENCES

[1] B. Drafts, "Acoustic wave technology sensors," IEEE Transactions on Microwave Theory and Technology, vol. 49, pp. 795-802, April 2001.

[2] F. Herrmann, B. Jakoby, J Rabe, "Microacoustic sensors for liquid monitoring," Sensors Update, vol. 9, pp. 105-160, January 2001.

[3] Z. J. Chen, L. E. Li, W. K. Shi, H.W. Guo, "Optimization design of a Lamb wave device for density sensing of nonviscous liquid," IEEE Transactions on Ultrasonics, Ferroelectrics, and Frequency Control, vol. 54, pp. 1949-1959, October 2007.

[4] J. Wang, W. H. Zhao, J. K. Du, "The effect of viscosity on thickness-shear and flexural vibrations of crystal plates," IEEE International Frequency Control Symposium, pp. 184-187, August 2005.

[5] D. Ballantine, S. Martin, A. Ricco, "Acoustic wave sensors: theory, design, and physico-chemical applications," San Diego, CA: Academic press, 1997.

[6] T. T. Wu, T. Y. Wu, "Surface waves in coated anisotropic medium loaded with viscous liquid," Journal of Applied Mechanics, vol. 67, pp. 262-266, February 2000.

[7] A. H. Nayfeh, "Wave propagation in layered anisotropic media," Amsterdam: North-Holland, 1995.

[8] Z. J. Chen, X. N. Zhang, J. Q. Xuan, "Optimum cut orientation of piezoelectric substrate and propagation direction of SAW for rotation rate sensor," Measurement, vol. 44, pp. 478-486, February 2011.

Absolute Control of the Scale Factor in GP2 Laser Gyroscope: Toward a Ground Based Detector of the Lense-Thirring Effect

J.Belfi, N.Beverini, M.Calamai, G.Carelli, E.Maccioni
Dept. of Physics, University of Pisa,
Pisa, Italy

A. Di Virgilio
INFN, Section of Pisa,
Pisa, Italy

R. Santagata
Dipartimento di Fisica, Università di Siena,
Siena, Italy

A. Porzio
CNR-SPIN and INFN sezione di Napoli
Napoli, Italy

D. Cuccato
Dept. of Information Engineering,
University of Padova,
Padova, Italy

A. Ortolan
INFN National Laboratories of Legnaro,
Legnaro, Padova, Italy

S. Solimeno
Dipartimento di Fisica, Univ. "Federico II",
and INFN sezione di Napoli ,
Napol, Italy

***Abstract*—The sensitivity achieved by large laser gyroscopes opens the perspective of observing in a ground laboratories very thin relativistic effect related to the Earth rotating mass (gravitomagnetic effect or Lense-Thirring effect). The required accuracy asks for a strict control of the ring cavity geometry. Here we present a control procedure that can be applied in order to solve this task.**

Keywords- Laser gyroscopes; Geodetic; Optical resonators; Gravitomagnetism; General relativity; Multiagent control, Derivative free minimization

I. INTRODUCTION

Ring lasers have achieved very high sensitivity for precise monitoring of the Earth rotation. The 16 m^2 square G gyrolaser, located in laser ranging station of Wettzell, Bavaria, has a resolution better than 10^{-12} rad/s, attained in approximately one hour of data taking (~$4 \cdot 10^3$ s) [1]. It is, actually, the most accurate ring-laser in the world. Thanks to its monolithic structure, where the mirrors are kept in position by optical contact on precisely tooled monolithic block of Zerodur, a glass with a "null" linear thermic expansion coefficient, G demonstrates a very high long-term stability that made possible the observation of very tiny geodetic effect, like polar motion and Chandler wobble [2]. A further increase in the angular resolution and a tri-axial gyro-system would, then, allow to reach 10^{-14} rad/s; the sensitivity requested for measuring the Lense-Thirring General Relativity effect (also known as frame dragging) [3]. Such a task requires a precise control of the gyros geometry as well as a full understanding of its dynamics. In the present communication we analyze the problem of the geometry control, while the problem of the control of the laser dynamics has been presented elsewhere [4].

.

II. GEOMETRY CONTROL

The rotational resolution necessary for an accurate measurement of the Lense-Thirring effect is about one order of magnitude better than the actual G performance. Gyro's sensitivity depends on its scale factor, *i.e.* A/λp the ratio between the area enclosed by the optical path and its length times the optical wavelength. So that the first action is to increase the dimension of the optical ring cavity. As a matter of fact, the longer is the optical cavity the larger is its quality factor for equal round-trip losses (this is a reasonable assumption, considering that the losses are essentially given by the mirrors). Then we should expect that the ultimate resolution of a ring laser gyroscope will increase proportionally at least to the second power of its linear dimension. Larger ring laser gyroscopes, named UG-1 and UG-2, with heterolithic structure enclosing an area respectively of 367.5 m^2 and 834.34 m^2, were built in Christchurch (New Zealand) [5], but, in spite of the increasing of the dimensions, they demonstrated a much lower performance with respect G; this is due to the lack of long term stability of their heterolithic structure (G in Wettzell has a monolithic structure in Zerodur). However, Zerodur blocks

The research is sponsored by INFN

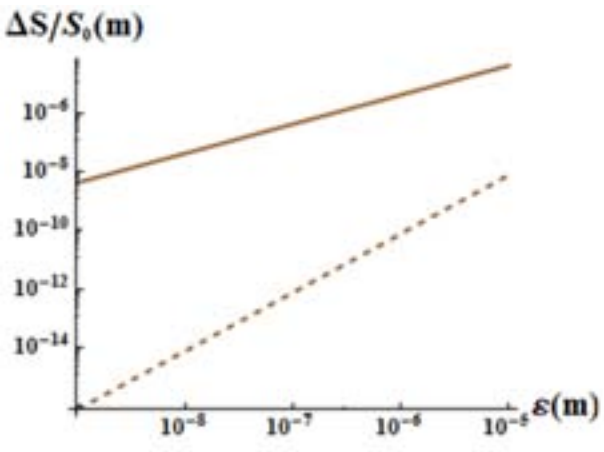

Figure 1. Relative variation of the scale factor of a gyroscope of 1 m in side, when the mirrors are moved from the "perfect square" geometry by a quantity ε for each degree of freedom. Continous line: movements in all the 6 degrees of freedom are considered. Dashed line: the diagonal lengths are locked to a fixed value.

larger than G are not available, and in any case it would be prohibitely costly.

So, to increase the long-term stability by suitable active controls on the ring geometry is a necessary step toward the realization of ring laser for General Relativity test.

Let us consider a ring optical cavity, defined by four identical spherical mirrors, very close to a "perfect" square. In principle, such a system has 12 degrees of freedom so that tri-axial linear actuators acting on the 4 mirrors would give a complete control of the optical cavity. However, the system rigid body movements reduce the actual degrees of freedom to 6. The stability problem can be further simplified by considering the symmetry of a perfect square. We, in addition, ask that the passive linear Fabry-Pérot cavities that are naturally installed along the square diagonal are optically accessible so that an external laser can be used for monitoring their configurations. The interferometric measure of the length of these diagonal cavity can be used for monitoring the geometry of the whole ring. Moreover, we note that, the stability of the ring cavity implies that also these Fabry-Pérot cavities are stable. The optical perimeter of the ring, as well as the linear FP lengths, can be accessed with high accuracy by comparing the laser emission wavelength with an optical reference standard (say, a I_2 stabilized He:Ne or a frequency comb locked to an atomic frequency standard).

It is easy to demonstrate that, by locking the two linear cavities to an equal constant value d, for small deviations ε_i of the mirrors coordinates from the perfect square, the deviation of the perimeter length from the exact value of $2d\sqrt{2}$ can be expressed as the sum of quadratic terms in ε_i. As we show in Fig. 1, we can achieve 10^{-10} accuracy on the scale factor with a 10^{-5} accuracy on the mirrors positions, provided that d is stabilized better that one part on 10^{10}.

Exploiting these geometrical properties, it will be possible to design a multivariable control algorithm that performs the initial calibration, starting from a generic geometry in order to reach a "near perfect" square shape. It will be as well possible to stabilize the desired geometry against drifts driven by changes in the environmental conditions. The procedure will be implemented by means of standard control techniques, by acting on a suitable linear combination of the residual degrees of freedom that diagonalizes the error matrix, using extremality conditions on the ring perimeter.

III. Experimental work

In the INFN laboratory in Pisa a laser gyroscope of relative small dimension (1.35 m of side) has been developed [6,7]. This apparatus is presently located in the Gran Sasso underground laboratories of INFN, in order to test whether the site is suitable to locate the GINGER (Gyroscopes IN General Relativity) experiment. At the same time, a new ring laser gyroscope, with optical access to linear cavities along the diagonals, has been designed aiming at testing the ring response to known geometrical distortion, and as well validating the control model. The gyroscope, named GP-2 is a square ring cavity, with 1.6 m side. The mirror holder is placed on a flat granite slab with a design accuracy of the order of a few hundreds of μm. A coarse horizontal adjustment of the mirrors position is available through manual micrometer stage, while 6 PZT linear stages allow finer control.

As explained above, of the original 12 degrees of freedom related to the mirrors' center of curvature, 6 can be traced out by considering rigid body translations and rotations of the whole apparatus. Then, acting on 6 linearly independent degrees of freedom by PZT is sufficient for realizing the full geometrical control. To this aim, one of the mirror holder will be equipped with a tri-axial PZT (x and y parallel to the granite table along the diagonal and orthogonally to it respectively, z perpendicular to the granite), while the other three mirrors are equipped with a 1-dimension stage in the direction of the respective diagonal. The granite will be mounted with the axis parallel to the Earth rotation axis (that is in the meridian plane with an inclination, at our latitude, with respect to the vertical of about 47°), in order to maximize the Sagnac signal thus minimizing the orientation errors on the scale factor. The requested control of the diagonal cavities length will be implemented by standard Pound-Drever-Hall (PDH) technique. Each cavity will be referenced to a stabilized laser source in order to retrieve its absolute length. The goal is to reach equal lengths in order to ensure that the corresponding ring cavity draws a prefect square. As a matter of fact, the cavity length L is related to the resonance frequency by :

$$\nu_n = \frac{c}{2L}(n+\varepsilon),$$

where $\varepsilon = \frac{1}{\pi}\arccos(1-L/R)$ and R is the mirrors radius of curvature. To remove the ambiguity on the mode number n, we measure the Fabry-Pérot free spectral range (FSR) by applying to the interrogating laser a second modulation at a frequency that is a multiple of the FSR itself.

To study, onto a test bench, the locking process we have built a linear cavity of 1.320 m of length. By scanning the laser

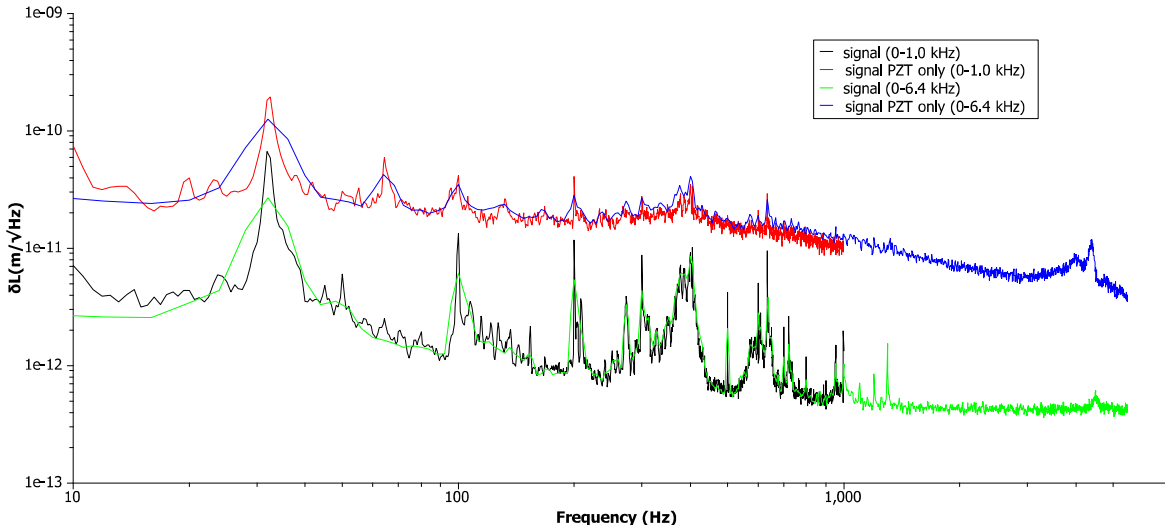

Figure 2 – Spectral density of the cavity length with the laser locked to the laser by slow (PZT only, upper trace) and by broad-band correction (lower trace)

frequency, we measured a finesse near to 470, consistent with the actual mirror reflectivity of 99.7%. In Fig. 2 we report preliminary PDH locking of the interrogating laser to such cavity, using a modulation frequency of 37 MHz.

ACKNOWLEDGMENT

We would like to acknowledge Filippo Bosi for its support on the mechanical design of GP2; we acknowledge also Gabriele Balestri, Giulio Petragnani. Antonino Ragonesi, and Francesco Francesconi for the technical support.

REFERENCES

[1] K. U. Schreiber, and Jon-Paul R. Wells, Large ring lasers for rotation sensing, Rev. Sci. Instr. 84, 041101 (2013)

[2] K. U. Schreiber, T. Klügel, J.-P. R. Wells, R. B. Hurst, and A. Gebauer , How to Detect the Chandler and the Annual Wobble of the Earth with a Large Ring Laser Gyroscope, PRL 107, 173904 (2011)

[3] F. Bosi, G. Cella, A. Di Virgilio, A. Ortolan, A. Porzio, S. Solimeno, M. Cerdonio, J.P. Zendri, M. Allegrini, J. Belfi, N. Beverini, B. Bouhadef, G. Carelli, I. Ferrante, E. Maccioni, R. Passaquieti, F. Stefani, M.L. Ruggiero, A. Tartaglia, K.U. Schreiber, A. Gebauer, and J-P. R. Wells, Measuring Gravito-magnetic Effects by Multi Ring-Laser Gyroscope, Phys. Rev. D 84, 122002 (2011)

[4] A. Beghi, J. Belfi, N. Beverini, B Bouhadef, D. Cuccato, A. Di Virgilio, A. Ortolan, Compensation of the laser parameters fluctuations in large ring laser gyros: a Kalman filter approach, Appl. Opt. **51**, 7518-7528 (2012)

[5] B. Pritsch, K. U. Schreiber, A. Velikoseltsev, J.-P. R. Wells Scale-factor corrections in large ring lasers, Appl. Phys. Lett. 91, 061115 (2007)

[6] A. Di Virgilio, M. Allegrini, J. Belfi, N. Beverini, F. Bosi, G. Carelli, E. Maccioni, M. Pizzocaro, A. Porzio, U. Schreiber, S. Solimeno, and F. Sorrentino, Performances of 'G-Pisa': a middle size gyrolaser, Class. Quantum Grav. **27**:084033 (2010);

[7] J. Belfi, N. Beverini, F. Bosi, G. Carelli, A. Di Virgilio, E. Maccioni, A. Ortolan, F. Stefani,: A 1.82 m^2 ring laser gyroscope for nano-rotational motion sensing, Appl Phys B **106**, 271–281 (2012)

A Heterodyne Frequency-Stabilization Method for Large Ring Laser Gyroscopes with Sub-nW Output Power

Fabio Stefani
Laboratoire de Physique des Lasers (LPL)
Paris 13 University
Villetaneuse, France
Email: fabio.stefani@univ-paris13.fr

Jacopo Belfi, Enrico Maccioni
Dept. of Physics
University of Pisa
Pisa, Italy

***Abstract*—We present the characteristics and the performances of a heterodyne detection scheme allowing a robust frequency lock of the G-Pisa ring laser [1,2] to a He-Ne Doppler shift stabilized reference laser. The system demonstrated a continuous unattended control of the laser frequency for several days of operation of the gyroscope with a single mode output power of about 500 pW.**

I. INTRODUCTION

Ring laser gyroscopes are presently one of the most important instrument in the field of precise rotation measurement [3]. They have high resolution, excellent stability and a wide dynamic range. The principle of operation of that sensor is based on the Sagnac effect, which states that two optical beams counter propagating inside the same ring complete the turn with a time difference proportional to the angular velocity of the local reference frame measured with respect to an inertial reference frame. Inside an optical cavity this difference becomes proportional to the frequency.

He-Ne ring lasers with cavity dimensions larger than 1 m can operate as ultra stable rotation rate sensors. For such systems, the two opposite beams generated inside the cavity are frequency split because of the Sagnac effect. The information about the rotation rate of the cavity is encoded in the optical beat between the counter propagating beams. If A is the laser area, P the perimeter, λ the wavelength, Ω the Earth rotation rate, and $\mathbf{n}$ the normal to the laser plane, this beat frequency is written as:

$$\Delta f_{Sagnac} = \frac{4A}{P\lambda}(\vec{\Omega} \cdot \vec{n})$$

In order to reduce the mutual coupling between the two opposite beams, a high Q-factor of the optical resonator is required and no intracavity elements can be used to select single mode operation. This implies, in general, a very low output power down to the level of some hundreds pW. Such a low power and the large acoustic phase jitter make the extraction of a clean measurement of the optical frequency of the gyroscope a not trivial operation.

II. FREQUENCY STABILIZATION

The experimental apparatus showing all the conditioning electronics is sketched in Fig.1.

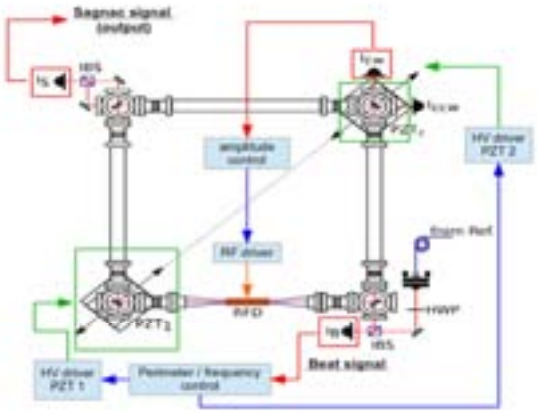

Fig. 1. G-Pisa experimental apparatus. ICW, ICCW: gyrolaser monobeams; IS: Sagnac signal (main system output); IBS: beam splitter; PZT1, PZT2: piezoelectric actuators; RFD: Radio Frequency Discharge; Amplitude Control: controller for the output power stabilization; RF Driver: power amplifier driving the discharge.

The beat note between the He-Ne reference laser [5] and the Gyro-laser (about 200 MHz) is detected by means of an Avalanche Photo-Diode (APD). After amplification, the

voltage signal is mixed with that coming from a local oscillator (Voltage Controlled Oscillator: VCO) operating at a carrier frequency of 130 MHZ. The mixed output is filtered around 70 MHZ with a bandwidth of 2 MHz, and an envelope detector determines the amplitude to frequency discrimination around the filter frequency pass band. Scanning the controlling voltage of the VCO and adding a sine wave modulation, it is possible to extract an error signal by using a lock-in amplifier. The lock-in filtered output signal is finally sent to the Gyro-laser piezo controls, to stabilize its length (i.e. frequency).

The beat note detection and the frequency stabilization schemes are shown in Fig.2 and Fig. 3 respectively.

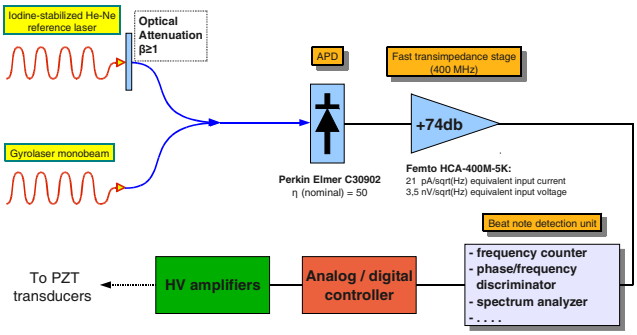

Fig. 2. Beat note detection scheme

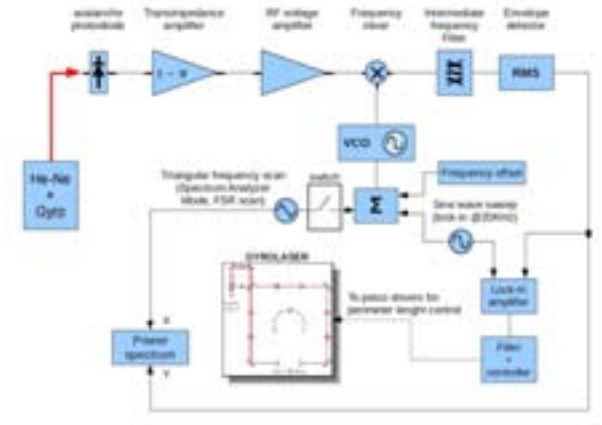

Fig. 3. Frequency stabilization scheme

The lock-in output (error signal) is shown in Fig. 4.

III. Results

The fractional frequency Allan deviation of the beatnote between the moonbeam gyrolaser output and the reference laser has been determined during a 10 days run, and the result is reported in Fig. 5 (black curve, left axis). The red curve represents the open loop fractional frequency instability of the system, and was obtained monitoring the signal sent to the piezoelectric actuators in order to close the loop.

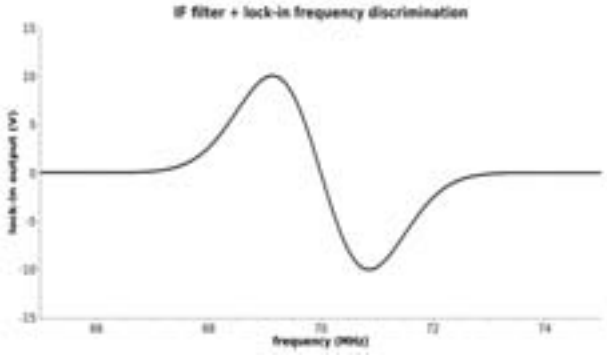

Fig. 4. The lock-in output (error signal)

On the right axis we provided a scale representing the equivalent length instability referred to the gyrolaser perimeter, that is 5.4 meters.

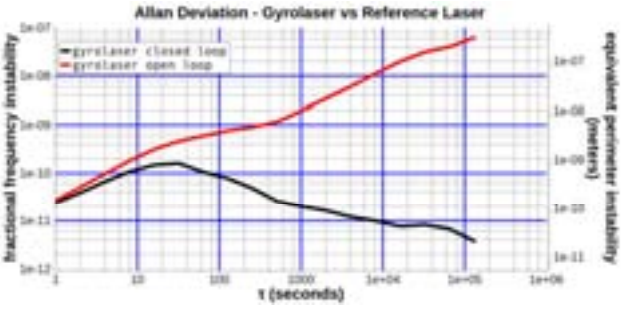

Fig. 5. Open loop and closed loop Allan deviation

IV. Conclusions

Such a scheme could be utilized to stabilize a gyrolaser frequency, and could also be employed to allow a phase lock in conjunction with a traditional PLL.

We can enumerate some peculiarities of a frequency stabilization system like that: it is cost effective, robust, and simple to implement. Moreover, it could be employed to allow the PLL phase lock of the system. Further improvements are possible employing a Iodine stabilized reference laser, increasing the bandwidth of the control.

References

[1] A 1.82 m2 ring laser gyroscope for nano-rotational motion sensing, J. Belfi, N. Beverini, F. Bosi, G. Carelli, A. di Virgilio, E. Maccioni, A. Ortolan, F. Stefani, Applied Physics B: Lasers And Optics, vol. 106, p. 271 (2012)

[2] Compensation of the laser parameters fluctuations in large ring laser gyros: a Kalman filter approach, A. Beghi, J. Belfi, N. Beverini, B. Bouhadef, D. Cuccato, A. Di Virgilio, A. Ortolan, submitted to Applied Optics

[3] Invited Review Article: Large ring lasers for rotation sensing , K. U. Schreiber and J.P.R. Wells, Review of Scientific Instruments 84, 041101 (2013)

[4] Performance of "G-Pisa" ring laser gyro at the Virgo site, J. Belfi, N. Beverini, F. Bosi, G. Carelli, A. Di Virgilio, D. Kolker, E. Maccioni, A.

Ortolan, R. Passaquieti, F Stefani, Journal of Seismology, October 2012, Volume 16, Issue 4, pp 757-766

[5] Frequency stability measurements on polarization-stabilized He-Ne lasers, T. M. Niebauer, James E. Faller, H. M. Godwin, John L. Hall, and R. L. Barger, Applied Optics, Vol. 27, Issue 7, pp. 1285-1289 (1988)

[6] L'ether lumineux demontré par l'effet du vent relatif d'éther dans un interfèromètre en rotation uniforme, G. Sagnac, Comptes Rendus Hebdomadaires des Seances de l'Academie des Sciences 157, 708–710 (1913)

High Stability Composite Clock Performances

F. Vernotte, N. Gautherot, H. Locatelli, P.M. Mbaye, E. Meyer, O. Pajot, C. Plantard and E. Tisserand
UTINAM, Observatory THETA (Besançon)
University of Franche-Comté & CNRS
Besanon, France
francois.vernotte@obs-besancon.fr

***Abstract*—The composite clock architecture we explored is composed of a VCO controlled by both a hydrogen maser and a cesium standard. We realized two composite clock prototypes: an industrial one (passive maser + commercial cesium) and another one suitable for metrological laboratories (active maser + high stability cesium).**

This paper describes the performances of both systems, from 0.01 s to 10 days.

I. Dual frequency locked loop principle

How to lock a VCO on a H-Maser for mid term stability and on a Cesium for long term stability (see fig. 1)?

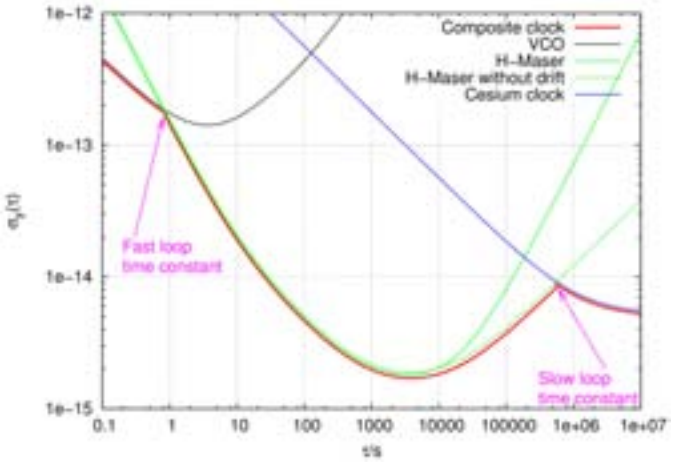

Fig. 1. Time stability of reference clocks.

By using both a fast ($\tau \sim 1$ s) and a slow loop ($\tau \sim 10$ d) as described in fig. 2.

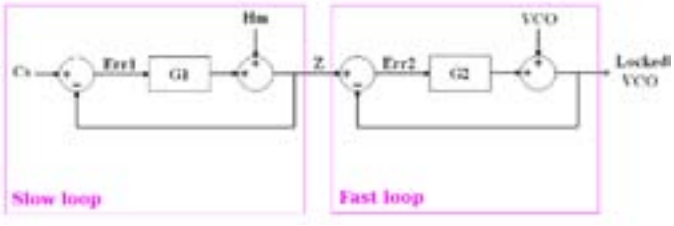

Fig. 2. Dual frequency locked loop principle.

II. Reference clocks and prototypes

A. Two prototypes

We decided to realize two composite clock protypes in order to compare them together.

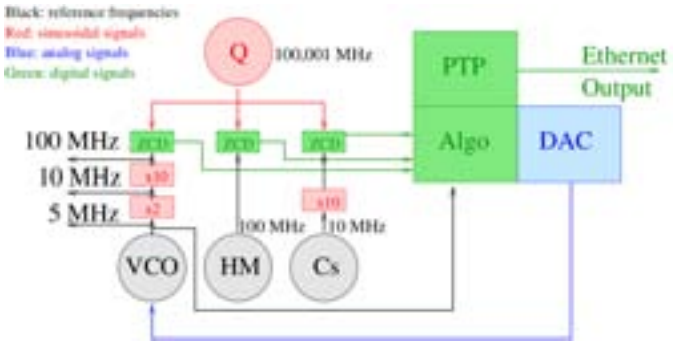

Fig. 3. Block diagram of the composite clock.

Composite clock	Short term reference	Mid term reference	Long term reference
CC 1	5 MHz BVA VCO	OSA 3705 passive H-Maser	OSA 3210 Cs clock
CC 2	10 MHz BVA VCO	Datum MHM 2010 act. H-Maser	5071A opt. 001 Cs clock

Each prototype (see fig. 4) is composed of [1], [2]:

- a DMTD block, where are connected the 100 MHz input from the reference clocks; the ZCD mixes the input frequencies with a 100.001 Mhz coming from a shifted VCO and provides beat frequencies of $\sim$ 1 kHz
- a ZCD block which converts the sine beat frequencies into square signals
- an FPGA where the algorithm [3] is implemented
- a Digital to Analog Converter for the VCO control.

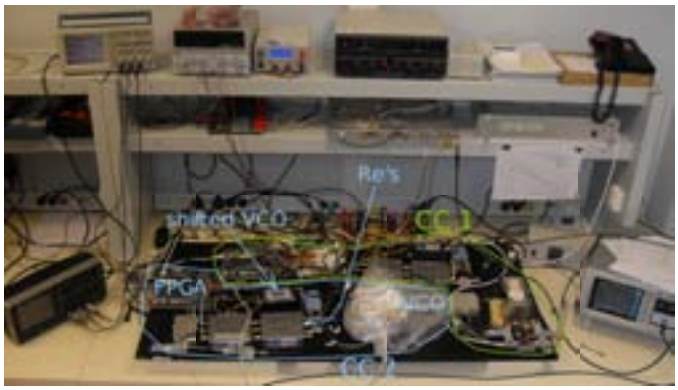

Fig. 4. The two Composite Clock prototypes.

B. Expected stability performances:

CC 1: $\sigma_y(1\text{ s}) < 3 \cdot 10^{-13}$, $\sigma_y(\tau) < 10^{-13}$ for 10 s $< \tau <$ 1000 s, $\sigma_y(1000\text{ s}) = 10^{-14}$, $\sigma_y(\tau) < 10^{-13}$ for $\tau >$ 1000 s

CC 2: $\sigma_y(1\text{ s}) = 10^{-13}$, $\sigma_y(\tau) < 10^{-13}$ for 1 s $< \tau <$ 100 s, $\sigma_y(\tau) < 10^{-14}$ for 100 s $< \tau <$ 1 day, $\sigma_y(\tau) = 10^{-14}$ for $\tau >$ 1 d.

III. Adjustment of the Control Parameters

The performances of the composite clocks are directly connected to the choice of the time constants (see fig. 5).

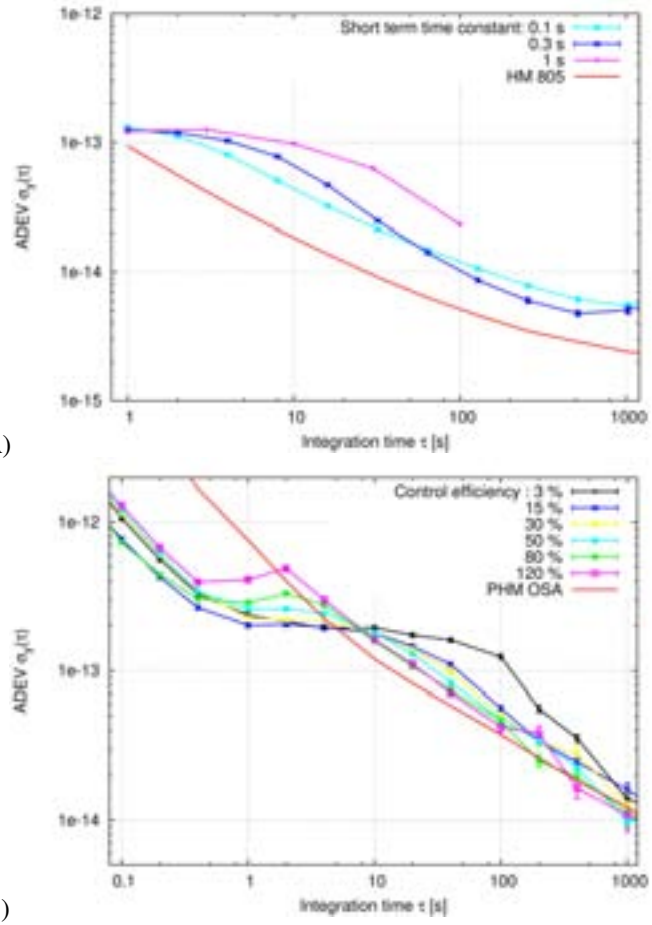

Fig. 5. Influence of the short term time constant (A) and long term time constant (B).

Beside the short and long term time constants, the control efficiency must also be chosen carefully (see fig. 6). It can be defined as the ratio of the command value sent to the VCO over the setpoint, i.e. the command value which should be used in order to totally cancel the error signal.

We selected the following parameters:

Composite clock	CC 1	CC 2
Control efficiency	30 %	30 %
Short term time constant	0.50 s	0.33 s
Long term time constant	10 d	3 d

IV. Initialization Phase and Steady State

During initialization phase ($\equiv$ short term time constant), CC is solely controlled by the Maser. Fig. 7 shows how the

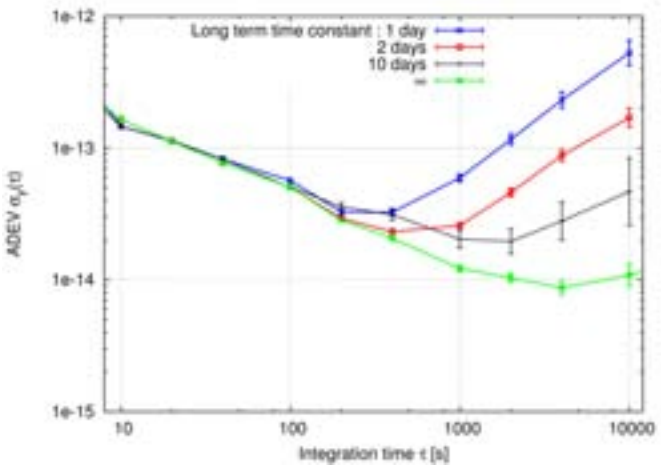

Fig. 6. Influence of the control efficiency for a given short term time constant (1 s).

composite clock frequency of the composite clock switches from the one of the Maser to the one of the Cesium clock.

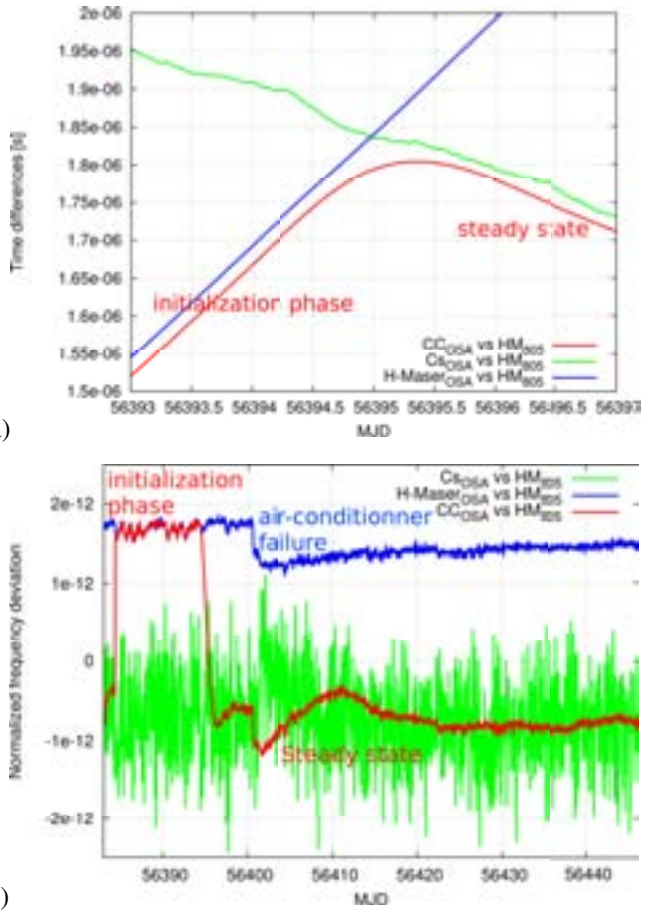

Fig. 7. Transition between the initialisation phase and the steady state of the composite clock seen from the time error data (A) and frequency deviation samples (B).

Fig. 7 shows also the effects of an air-cooler failure in the clock room (MJD 56402).

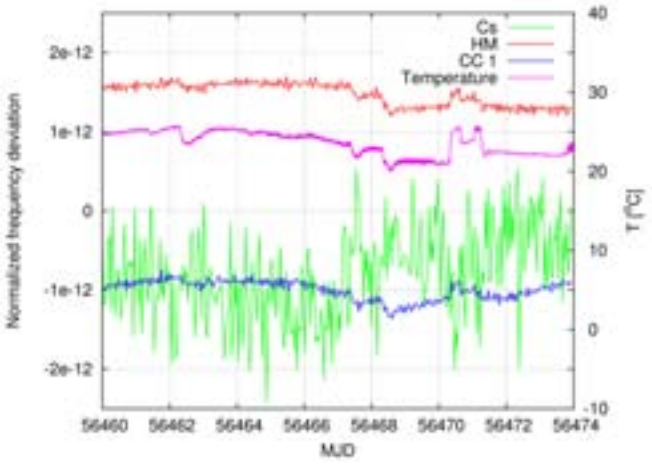

Fig. 8. Correlation between the clock room temperature and the frequencies of the clocks.

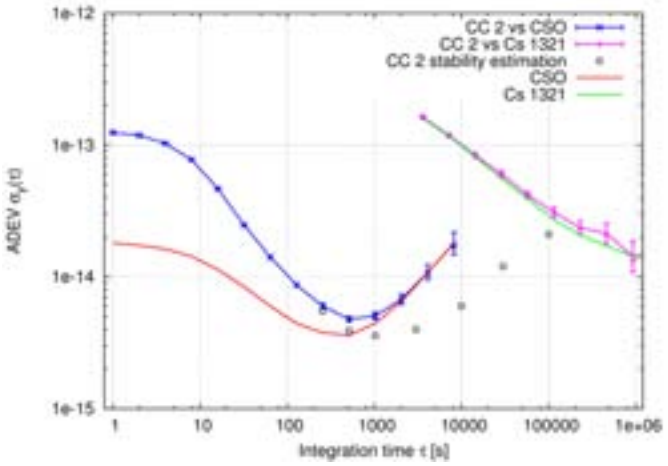

Fig. 10. Measurement of the short and long term stability of CC 2 and estimation of its mid term stability.

V. Temperature sensitivity

Fig. 8 exhibits clearly that the temperature sensitivity of the composite clocks is due to the temperature sensitivity of the reference clocks.

VI. Stability of CC 1

CC 1 stability was measured against the HM 2010 and a Cs 5071A which are more stable than the references of this composite clock. Fig. 9 shows that CC 1 meets partially the specifications.

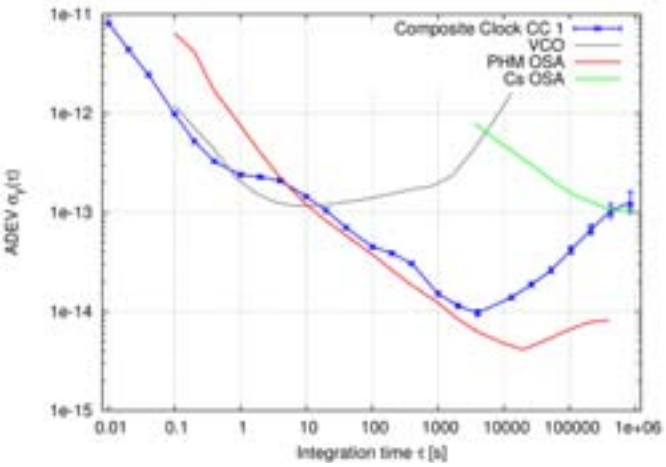

Fig. 9. Stability of CC 1.

VII. Stability assessment of CC 2

The stability of CC 2 was more difficult to measure because we only have one active H-Maser.

Its short term stability was measured thanks to a measurement campaign with the mobile Cryogenic Sapphire Oscillator "Uliss" of Femto-ST (April 2013). The long term stability was measured against another 5071A. However, the mid term stability of CC 2 may only be estimated (see fig. 10).

Fig. 11 shows that CC 1 meets partially the specifications.

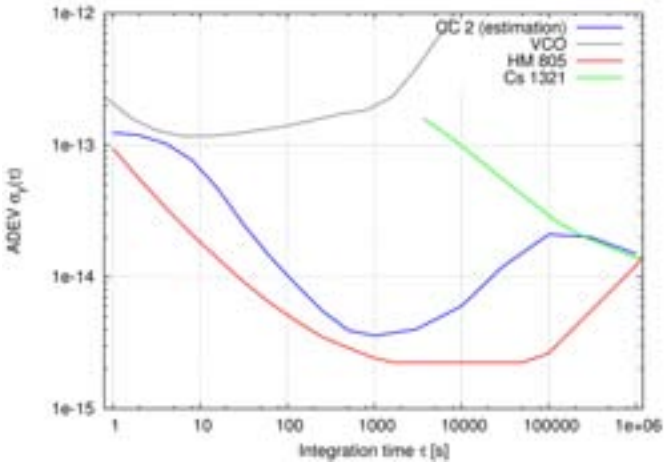

Fig. 11. Estimated stability of CC 2.

VIII. Expected improvements

We could obtain a better fit of the reference clocks by:

- optimizing the long term time constant
- reducing the control sensitivity to electromagnetic disturbances
- increasing the control acuteness.

IX. Acknowledgements

This work was partially funded by an Interreg contract. The authors whish to thank Oscilloquartz for their support and Femto-ST for the measurement campaign with Uliss.

References

[1] C. Plantard, P. Mbaye, and F. Vernotte, "Composite clock including a cs clock, a h-maser clock, and a vco," *IEEE Transactions on Ultrasonics, Ferroelectics and Frequency Control*, vol. 57, no. 3, pp. 707–713, 2010.

[2] O. Pajot, F. Vernotte, C. Plantard, and P. Mbaye, "First working prototype of composite clock," *Electronics Letters, 48(6), 329-330, 2012*, vol. 48, no. 6, pp. 329–330, 2012.

[3] P. Mbaye, A. Makdissi, C. Plantard, and F. Vernotte, "Composite clock: New algorithm for servoing vco firstly to hydrogen maser clock and then to ceasium clock," *Metrologia*, vol. 45, no. 6, pp. s74–s81, 2008.

Research on Timescale Algorithms in Database for TA(PL)

Michał Marszalec, Marzenna Lusawa
National Institute of Telecommunications
Warsaw, Poland
M.Marszalec@itl.waw.pl

Albin Czubla
Central Office of Measures
Electricity Department
Warsaw, Poland
a.czubla@gum.gov.pl

Włodzimierz Lewandowski
International Bureau of Weights and Measures, Time Department
Sevres
wlewandowski@bipm.org

***Abstract*—The group of Polish Time Laboratories has been cooperating closely from at least 15 years. From very beginning also Lithuania was participating in this group. The first common initiative was organizing independent Polish Atomic Timescale TA(PL) [8]. In 2004 has started a project to develop Database for Polish Atomic Timescale TA(PL) [5] to automate the process of time-standards comparison and calculate implemented group timescale ensembles algorithms (weighted average algorithm for a group of time-standards).**

Ensemble algorithms are supposed to be more stable than any of the standard within the group. This very useful feature makes an ensemble a very good stable reference to control and supervise behavior of every standard. In the future it could be also used to steer Polish official realization of international Universal Coordinated Time (UTC) the UTC(PL) maintained by Central Office of Measurement (GUM). The set of ensemble algorithms was primary implemented in Database: original algorithm of TA(PL) based on ALGOS [6], [7] (algorithm developed by International Bureau of Measurements –BIPM), one day-shifted ALGOS version and AT1 [2] (algorithm developed by National Institute of Standard and Technology -NIST).

During last years the Time-team of Institute of Telecommunications has implemented in Database a realization of AT2 algorithm developed on the basis of theorem published by NIST. Preliminary results shows that AT2 is more stable than others.

The last part of article shows analysis of results of new implemented algorithms and comparison to former implementations.

Keywords—time, timescalescale ensemble, database, Polish Atomic Timescale

I. DATABASE FOR POLISH ATOMIC TIMESCALE (TA(PL))

The National Institute of Telecommunications (NIT) cooperates within Group of polish Time Laboratories which are developing Polish Independent Atomic Timescale TA(PL). From the beginning Lithuanian Center for Physical Sciences and Technology (CPST) also has participated in calculations. Number of time standards which form our timescale have changed from 7 to about 20 during the time. All Laboratories are equipped with atomic standards which are held in special rooms equipped with precise air-condition, secure electricity supply and with appropriate time transfer systems satellite or optical fiber.

Complete list of Laboratories is shown below:

- Central Office of Measurements (GUM): 4 timestandards

  Astro-geodynamical Laboratory (AOS) of Polish Research Space Center: 4 timestandards
- National Institute of Telecommunications: 2 timestandards
- Military Metrology Laboratories: 3 locations (CWOM-B, CWOM-Z, SWOM), 4 timestandards
- Polish Telecommunication – Orange: former national telecommunication operator, 3 locations (CBR, ZGO, TP_Anin) – 3 timestandards (3 waiting for connection)
- Lithuania – Center for Physical Sciences and Technology (CPST) – 2 timestandards

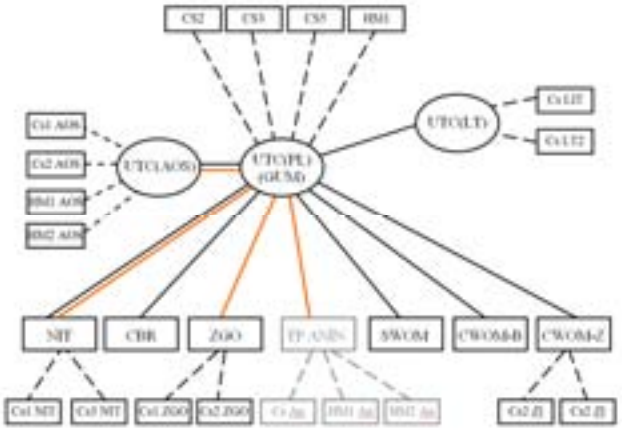

Fig. 1. Independent Polish Atomic Timescale (TA(PL)) timestandards comparision scheme

Presented results were obtained during realization of the project „Research and development of time and frequency ensembles on Database for TA(PL)" financed by polish National Science Centre.

The figure above (Fig.1.) shows actual TA(PL) comparisons scheme. Dashed lines represents internal comparisons of clocks within every laboratory. Black lines represents GPS CV satellite links and orange lines shows fiber-optics connections/comparisons [1].

The task for Time and Frequency Metrology Laboratory (of NIT) is to create timescale ensemble algorithms and implement it on Database for TA(PL) [3], [5]. The result was the automated system that allows almost real time control over compared time standards. The main participant of these works is polish Central Office of Measures (GUM) which is assigned by law as a distributor of official Polish Time UTC(PL) and other laboratories from the Group.

Main role of the Database was to reduce time of waiting for results of comparisons of clocks from BIPM which was necessary to control time and frequency. In the beginning the delay was about 1.5 month. Now the UTC Rapid test-service is available once a week. Database allows to get the needed corrections every day or even few times a day with appropriate ensemble timescale algorithm.

Database is organized in three major subsystems:

- Data acquisition unit – managing of data files
- Calculation unit – calculation of clocks comparisons and timescales algorithms
- Results presentation unit – presenting demanded results

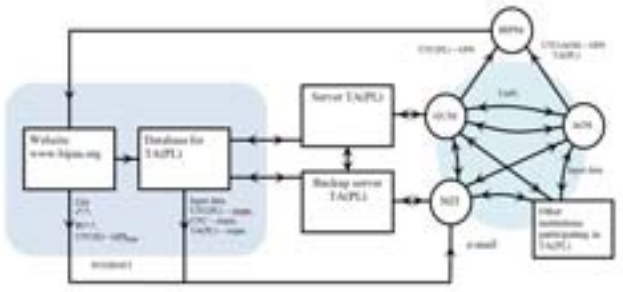

Fig. 2. Database workflow scheme

Database can handle wide range of comparison file types:

- Standard GPS/GLONASS data files – compatible with CGGTTS format
- Direct clock-clock data files (also via fiber-optic links)
- Correction files – with information about known phase and frequency steps

Database provides many useful functions such as comparisons clocks one to one, UTC and any of implemented algorithm, comparisons of any algorithm to UTC/TAI and also for advanced users it also allows to modify initial parameters of test timescales and proceed calculation (this function is very useful to tune up algorithms). It is possible to calculate standard analysis such as ADEV and TDEV or estimation of drift by using Discrete Model function.

Database presents also different useful information about localization of clocks and their types, information board to announce important declarations by users of Database, upload function of many types of files to share with other users and download function of original clocks comparison data files.

Fig. 3. Analytical functions of Database for TA(PL)

II. Database Timescale Ensemble Foundations

The main function of the Database is to automatically calculate implemented timescale ensemble algorithms and Polish Atomic Timescale algorithm among others. It makes possible to steer physical realization of Official Polish Time UTC(PL) by GUM, as close as possible to UTC.

Timescale ensemble algorithm [7], [10] is a special construction of weighted mean average of comparisons' results of atomic timestandards. Weights for individual timestandards are calculated from the results history.

The final result of calculation is a table of corrections for every clock within the group compared to timescale ensemble. The equation below presents a base definition of timescale ensemble $A(t)$:

$$A(t) = \frac{\sum_{k=1}^{N} w_k(t)\left[H_k(t) - \hat{H}_k(t)\right]}{\sum_{k=1}^{N} w_k} \quad (1)$$

where:

$w_k(t)$ – weight of the timestandard k
$H_k(t)$ – result of the timestandard k in moment t
$\hat{H}_k(t)$ – prognosis of the timestandard k in moment t from timescale A
t – time of calculation of the ensemble
N – number of timestandards.

III. ALGORITHMS IMPLEMENTED IN DATABASE FOR TA(PL)

At the beginning the number of standards in our Group was close to 10 rather than 20. So small number was very hard to overcome due to target we wanted to achieve. The purpose of implement new timescale algorithms was:

- Realization of timescale ensemble with good med-term stability and shortest access time possible
- Better control of timestandards beetween BIPM and GUM reports publication
- Possibilty of steering the physical time signals (eg. National realization of UTC)

In the course of the number of timestandards has increase making this tasks easier to complete.

At the beginning there were implemented three ensemble timescale algorithms original ALGOS based, day-shifted ALGOS and AT1. In the next part of this section, the main features of implemented algorithms will be listed.

ALGOS algorithm (the both versions) can be characterized as follows:

- Algorithm is calculating weights by analyzing frequency changes in set period of time
- Frequency deviations are calculated for period of a month
- The average value of frequency deviations is calculated for last 12 previous months and then compared with the last result

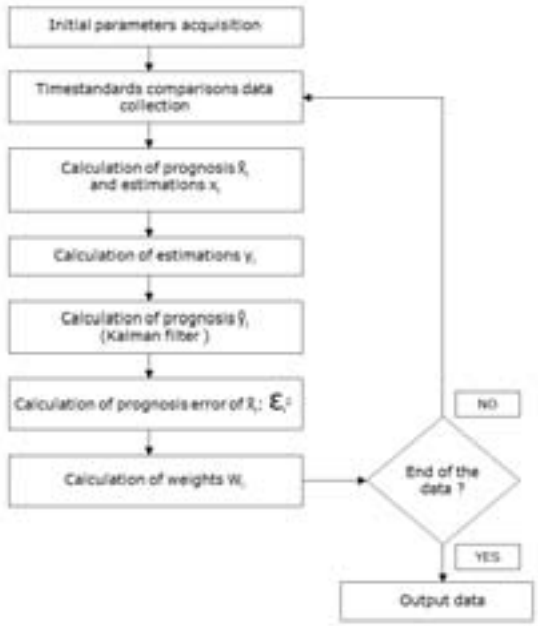

Fig. 4. AT2 algorithm scheme

The last activity was implementation a new timescale algorithm better suited for our Group AT2 developed and presented by NIST [2]. Fig. 3. shows the workflow scheme of this algorithm.

AT1 and AT2 algorithms are very similar. Basic differences:

- Noise model
- Prognosis calculation method for drift and frequency deviation

In the case of an AT1 algorithm, frequency prognosis is calculated as the mean average of results obtained in previous steps of algorithm. Weights are decreasing in geometric progression in time and drift is constant.

An AT2 algorithm is modification of AT1. It calculates frequency deviations and drift from Kalman filter.

Next figures show some results of research. Fig.5. presents the result of research on initial parameters of AT2 algorithm. All initial parameters was exactly thy same except matrix element in Kalman model responsible for the drift and frequency deviation estimation. Despite the fact tahat agorithm is higly adaptive, if goal woud be to reduce frequency deviation with reference to TAI [6], [7], [10], precise analysis shoud be done before starting the algorithm. Stability of compared results was very similar.

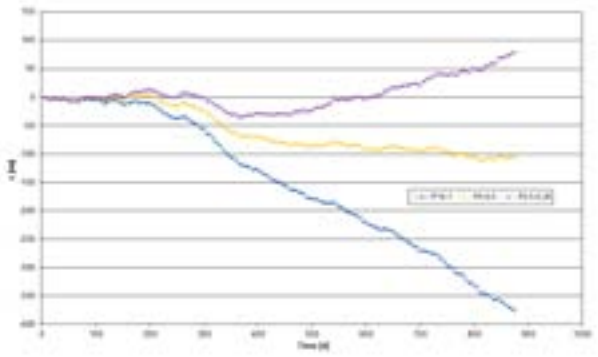

Fig. 5. Research on initial parameters dependencies of AT2 algorithm

Next two figures shows stability comparison between implemented in Database three ensemble algorithms.

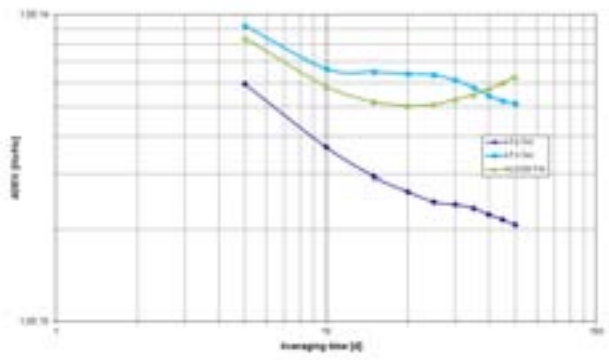

Fig. 6. ADEV comparison of implemented algorithms

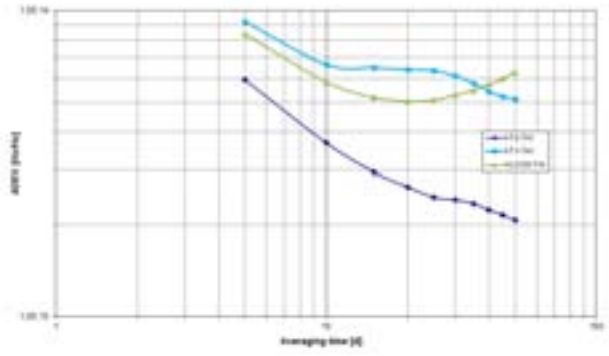

Fig. 7. TDEV comparison of implemented algorithms

Fig. 6. and Fig. 7. shows that AT2 algorithm implemented in Database seems to be more stable than others, at least in case of rather not so big number of clocks in our Group.

IV. FUTURE PLANS

Presented results shows, that implemented AT2 algorithm have a great potential to be very useful reference for steering UTC(PL), but research must be continued and new set of functions added to Database for TA(PL).

Our work concerns now on implementation new functions for fault detection problems (accidental phase or frequency shifts), advanced filtering of input data (Vondrak filtering), and functions for automatic steering of physical time signal (eg. UTC(PL)). Further development of Database should allow also real-time automatic comparison of different time transfer methods.

We are planning also implementations of new analytical functions and prepare daily automatic report sent by email to Database users.

REFERENCES

[1] A. Czubla, R.Osmyk, P.Szterk, M.Marszalec, W.Adamowicz, Ł.Śliwczyński „Optical Fiber Time and Frequency Transfer inside Urban Telecom Network in Warsaw – Results of Initial Tests", European Frequency and Time Forum (EFTF) 2012, Gothenburg, Sweden.

[2] M. Weiss and T. Weissert, „AT2, A New Time Scale Algorithm:AT1 Plus Frequency Variance", Metrologia, 1991, 28, pp. 65-74.

[3] M. Marszalec, D. Nerkowski, „Baza danych dla zespołowych atomowych skal czasu TA(PL) i UTC(PL)", Przegląd telekomunikacyjny i Wiadomości Telekomunikacyjne 10/2009.

[4] M. Marszalec, T. Kossek, M. Lusawa „Analiza wyników porównań atomowych wzorców czasu". Przegląd Telekomunikacyjny i Wiadomości Telekomunikacyjne 8-9.2009

[5] M. Marszalec, A. Czubla and D. Nerkowski,2008, "DataBase for TA(PL) and UTC(PL)," in Proceedings of the 40th Annual Precise Time and Time Interval (PTTI) Systems and Applications Meeting, 1-4 December 2008, Reston,Virginia, USA (U.S. Naval Observatory, Washington, D.C.), pp. 680-690.

[6] C. Thomas, P. Wolf, and P. Tavella, 1994, "Time scales," BIPM Monographie 94/1.

[7] ITU, 1997, "Time Scales – Handbook on the Selection and Use of Precise Frequency and Time Systems," ITU Radiocommunication Bureau, Sec. 6, pp. 119-149.

[8] J. Azoubib, J. Nawrocki, and W. Lewandowski, 2003, "Independent atomic time scale in Poland –organization and results," Metrologia, 40, S245-S248.

[9] P.Kartaschoff, „Czas i częstotliwość", WKŁ 1985, Warszawa

[10] W.Lewandowski, "International Atomic Time Scales and Related Time Transfer", special issue of MAPAN-JMSI, Metrology Society of India, based of guest talk at ATF'2006.

[11] F. Arias, W. Lewandowski, „Role of international time reference UTC in the definition of Galileo System Time", Symposium on Scientific and Fundamental Aspects of the Galileo Program, 1-4 October 2007, Toulouse.

Iterative Method for Signal Path Delay Difference Estimation of Two-way Satellite Time and Frequency Transfer

Wenke Yang, Jianwei Zhan, Hang Gong, Xiangwei Zhu, Guangfu Sun
College of Electronic Science and Engineering, National University of Defense Technology
Changsha, China
ywk@nudt.edu.cn

***Abstract*—The signal path delay difference due to satellite motion relative to the ground stations adds non-reciprocity to Two-way Satellite Time and Frequency Transfer (TWSTFT). For the availability of broadcast ephemeris for the geostationary satellite for TWSTFT in BeiDou navigation system, an iterative method for signal path delay difference estimation due to the satellite motion is proposed, which is compared with the ranging method. The one day TWSTFT experiment data with BeiDou GEO satellite at 140°E experiment between Beijing and Sanya has been analyzed, which show that the signal path delay difference is less than 0.14ns and the difference of the results using these two methods is less than 0.11ps. This implies that there is no need to conduct ranging when the broadcast ephemeris is available for the estimation signal path delay difference.**

Keywords—TWSTFT; iterative method; ranging; signal path delay difference; broadcast emphmeris

I. INTRODUCTION

Two-way Satellite Time and Frequency Transfer (TWSTFT) based on signal exchange via Geostationary Earth Orbit (GEO) Satellite has been conducted worldwide [1]. The non-reciprocity correction is important for TWSTFT, which includes Sagnac correction, ionospheric correction, tropospheric correction, earth station delay difference and signal path delay difference geometrically due to satellite motion relative to the earth [1]. In previous studies, the ranging data between the ground station and GEO satellite is used to estimate signal path delay difference [2-4]. In BeiDou Navigation System, TWSTFT via navigation GEO satellite is implemented [5]. The broadcast ephemeris is available as orbit data for the GEO satellite in BeiDou Navigation System, which gives a chance for a new method called iterative method to estimate signal path delay difference.

II. SYSTEM AND EXPERIMENT DESIGN

Since the distances of the satellite from the two sites are usually different, the signals transmitted by the two sites at the same time will reach the satellite at different time [6]. Due to the relative motion of GEO satellite to the ground stations, the signals will reach the satellite at different positions as demonstrated in Fig.1.

In TWSTFT, each ground station transmits a radio frequency signal modulated by pseudorandom noise (PRN) codes referring to its own clock to GEO satellite as the real lines upwards in Fig. 1. The GEO satellite retransmits the signals to the earth. Each ground station receives the transmitted signals from the other station demonstrated as the real lines downwards in Fig. 1 and its own (called round-trip ranging) demonstrated as dashed lines in Fig. 1.

If we define $\tau_{\mathrm{Ui|Sat}}$ as signal path delay geometrically from ground station i upward to GEO satellite, and $\tau_{\mathrm{Di|Sat}}$ as signal path delay geometrically from GEO satellite downward to ground station i, the non-reciprocity for TWSTFT due to signal path delay difference geometrically is as below:

$$\tau_{UD,Sat} = 0.5((\tau_{U1}|_{Sat} - \tau_{D1}|_{Sat}) - (\tau_{U2}|_{Sat} - \tau_{D2}|_{Sat})) \quad (1)$$

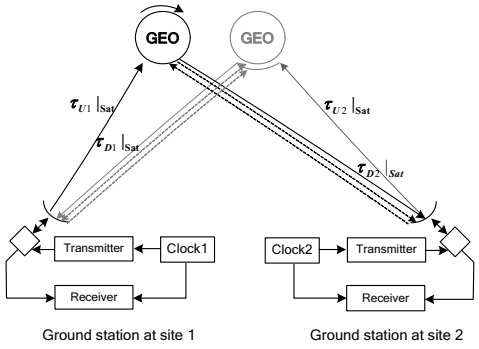

Fig. 1. Two-way Satellite Time and Frequency Transfer with satellite motion

III. ITERATIVE METHOD

As demonstrated in Fig.1, the positions of GEO satellite when it transmits signals for two-way links are important for signal path difference estimation. The iterative method is a way to estimate these GEO satellite positions when the receiving epoch is known and the broadcast ephemeris is available.

The proposed iterative method works as follows.

- Step 1: to estimate an initial signal transfer delay from GEO satellite to the ground station.
- Step 2: to estimate the epoch when GEO satellite transmits signal with the receiving epoch subtracted by the initial signal path delay.
- Step 3: to estimate the GEO satellite position at the transmitting epoch with the broadcast ephemeris.
- Step 4: to estimate the signal transfer delay between the estimated GEO satellite position and the position of ground station receiving signal with Sagnac correction by coordinate rotation [7], ionospheric correction [1], and tropospheric correction [8].
- Step 5: to repeat from Step 1 to Step 4 using the updated estimated signal transfer delay as the initial signal transfer delay in Step 1, until the error between the adjacent estimated signal path delays is below the defined threshold.

Then, the GEO satellite position at the transmitting epoch for two-way links can be estimated. Finally, signal path delay difference between two ground stations via GEO satellite can be obtained by the difference of geometry distances of two-way links after Sagnac correction.

IV. Experiment and Conclusions

The TWSTFT experiment data for one day with BeiDou GEO satellite at 140°E experiment between Beijing and Sanya has been analyzed. The signal path delay difference is estimated with ranging method described in [2] and the iterative method respectively.

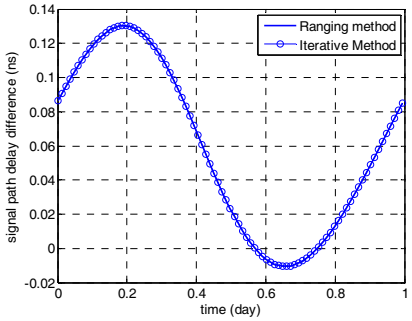

Fig. 2. Signal path delay difference estimated by ranging method and iteration method.

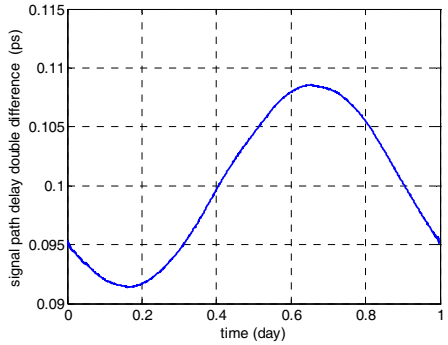

Fig. 3. Signal path delay double difference: the difference of the signal path delay estimated by ranging method and iterative method.

The experiment results show that the signal path delay difference is less than 0.14ns and the difference of the results using these two methods is less than 0.11ps.

This implies that there is no need to conduct ranging when the broadcast ephemeris is available for the estimation signal path delay difference.

References

[1] A. Bauch, D. Piester, M. Fujieda and W. Lewandowski, "Directive for operational use and data handling in two-way satellite time and frequency transfer (TWSTFT)," Bureau International des Poids et Mesures, Rapport BIPM-2011/01

[2] W.Yang, H. Gong, X. Zhu and G. Sun, "Non-reciprocity correction using broadcast ephemeris in Two-way Satellite Time and Frequency Transfer (TWSTFT)", the 4th China Satellite Navigation Conference, 2013, pp.407-417.

[3] D. Piester, A. Bauch, M. Fujieda, T. Gotoh, M. Aida, H. Maeno, M. Hosokawa and S.H.Yang, "Studies on instabilities in long-baseline two-way satellite time and frequency transfer (TWSTFT) including a troposphere delay model," 9th Annual Precise Time and Time Interval Systems and Applications Meeting, 2007, pp. 211-222.

[4] T.E.Parker and V.Zhang, "Sources of Instabilities in Two-Way Satellite Time Transfer," Frequency Control Symposium and Exposition,2005, pp. 745-751.

[5] C. Han, Y. Yang, Z. Chai, "BeiDou Navigation Satellite System and its time scales," Metrologia, Vol. 48, 2011:S213-S218.

[6] H. Sun, M.W.I. and G.T., "Impact of satellite motion on two-way satellite time and frequency transfer," Ele. Lett., vol. 39, No. 5, pp. 482-483.

[7] E.D.Kaplan, C.J. Hegarty, Undersatanding GPS Principles and Applications, 2nd ed., Artech House, 2006, pp. 308.

[8] J. Farrell, M. Barth, The Global Positioning System and Inertial Navigation, McGraw Hill, 1998, pp. 156.

Study and Application of Real-Time Frequency Deviation Adjustment Algorithm in Establishing a Time Scale

Yiwei Wu, Lei Chen, Xiangwei Zhu, Gang Ou
School of Electronic Science and Engineering, National University of Defense Technology
Changsha, China
Email: Yiwei_Wu_sh@126.com

***Abstract*—The time scale algorithm is the key of the establishment of a time scale. This paper proposes a real-time frequency deviation adjustment algorithm. This paper describes the idea and implementation of this algorithm. The algorithm utilize a Kalman filter to estimate the state between the master clock and the other clock, and then adjust the frequency deviation and predict the next time deviation between these two clocks and thus reconstruct the time deviation. The simulated experiments utilize two commercial cesium clocks (Symmetricom -5071A). The principle, idea and performance of the Kalman filter is studied and analyzed. The simulated results indicate that the frequency stability of this reconstructed time deviation is improved effectively when utilizing this algorithm. Since the reconstructed time deviation is the adjusted clock difference between the master clock and the other clock, the conclusion can be got that the frequency stability of the master clock's time scale is also improved effectively. The algorithm is real-time, and its implementation is with low cost and easy to realize and control, so the algorithm is of high engineering and application values.**

Keywords—Time scale algorithm; Frequency stability; Kalman filter; Real-time frequency deviation adjustment;

I. INTRODUCTION

Satellite navigation system is essentially a time synchronization system. It is necessary to establish a stable time scale of satellite navigation system. The time scale algorithm[1] is the key of the establishment of a time scale. Since satellite navigation system needs real-time forecasting the state of onboard atomic clocks, the time scale should be real-time and predictive. For high-precision positioning and timing, the requirement for the short-term stability of the time scale is relatively high.

This paper proposes a real-time frequency deviation adjustment algorithm. The principle, the essential idea and the implementation of the algorithm are described in this paper. Since this paper utilizes a Kalman filter to estimate the state of the atomic clocks, the principle, idea and performance of the Kalman filter are also studied in depth in this paper. In this paper, the observations are measured clock difference of PTB (Germany). The simulated results of the established time scale are analyzed. The appropriate conclusions are drawn in the end. The research will have impact on the establishment of a time scale.

II. BASIC PRINCIPLES AND ANALYSIS OF THE ALGORITHM

A. Basic principles and implement of the real-time frequency deviation adjustment algorithm

The main aim of a time scale algorithm is to improve the frequency stability of a time scale. This paper proposes a real-time frequency deviation adjustment algorithm which is different from the frequency steering algorithm and the weighted-average algorithms.

To illustrate the main idea more clearly, only two atomic clocks are used at first. The main steps of this algorithm are follows. Firstly, use a Kalman filter to estimate the state between the master clock and another clock. Secondly, adjust the frequency deviation and predict the next time deviation between these two clocks and thus reconstruct the time deviation.

$$x'(t+\tau) = x(t) + \hat{y}(t) \times \tau \qquad (1)$$

$\hat{y}(t)$ is the estimated frequency deviation. τ is the time interval. $x(t)$ is the first time deviation. $x'(t+\tau)$ is the reconstructed time deviation.

These two steps make up a whole cycle. In the next cycle, the time deviation at the next time can be predicted by the estimated frequency deviation and the reconstructed time deviation, and the next reconstructed time deviation can be obtained.

$$x'(t+2\tau) = x'(t+\tau) + \hat{y}(t+\tau) \times \tau \qquad (2)$$

Then continue the cycle. At last, a whole reconstructed time deviation can be obtained. The whole reconstructed time deviation is the adjusted clock difference between the master clock and the other clock. The observations of this algorithm are the first time deviation and each estimated frequency deviations.

If there exist N clocks, N-1 estimated frequency deviations between the master clock and other clocks can be obtained when running this algorithm. After that, a weighted-average algorithm will be designed to further improve the stability,

which is not the emphasis in this paper. This paper utilizes two clocks to illustrate the performance of the algorithm.

The common implementation is given below.

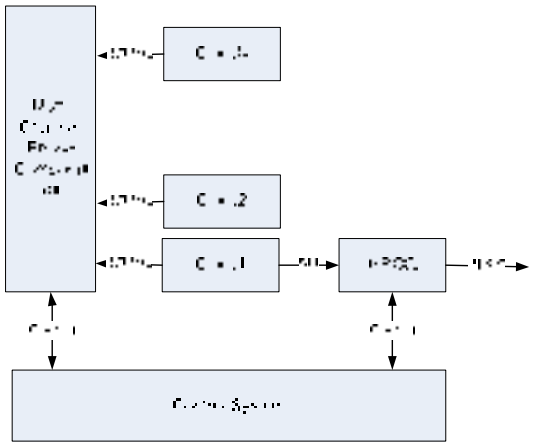

Figuer 1 Implementations of the algorithm

In the picture, HROG represents a high resolution phase and frequency offset generator. Clock represents an atomic clock, which can be a cesium clock or a hydrogen maser. Control System can be a PC.

The multi-channel phase comparator measures the clock differences between each clock. The PC obtains the clock differences in real time, and utilizes the Kalman filter to estimate the state between the master clock and the other clock. At the same time the PC sends command to the HROG to adjust the frequency deviation of the master clock according to equation (1) and (2). The output of the HROG is the time scale, which can be used as UTC(k). Thus, a time scale is established[1][2].

To conclude, the algorithm is real-time, and its implementation is with low cost and easy to realize and control, so the algorithm is of high engineering and application values.

In the following of this paper, since Kalman filter[2][3][4][6] plays important role in this algorithm, the idea, principle of the Kalman filter are described in detail.

B. Idea, principle of the Kalman filter

The stochastic differential equation of an atomic clock[2][6][7][8] can be described as follow.

$$\begin{cases} x(t) = x_1(t) + n_1(t) \\ \cdot \\ x_1(t) = x_2(t) + n_2(t) \\ \cdot \\ x_2(t) = x_3(t) + n_3(t) \\ \cdot \\ x_3(t) = 0 \end{cases} \quad (3)$$

$x_1(t)$, $x_2(t)$ and $x_3(t)$ represent the time deviation, a part of the clock frequency deviation and part of the so-called frequency drift of this clock respectively. $n_1(t)$、$n_2(t)$ and $n_3(t)$ are Gaussian processes, which represent the white phase noise, the white frequency noise and the walk random frequency noise whose variances are σ_1^2, σ_2^2 and σ_3^2 respectively.

The atomic clock state equation and observation equation[6][8][9][10] can be written as equation (4) and (5) respectively.

$$X[k+1] = \Phi X[k] + \eta[k] \quad (4)$$

$$Z(k) = H \bullet X(k) + V \quad (5)$$

X[k] represents the state of the atomic clocks. Φ represents the state transition matrix. $\eta[k]$ represents the innovation. *Z(k)* represents the observation which is usually the clock difference. *H=[1 0 0]* is the design matrix. *V* represents the measurement noise whose covariance matrix is *R*. *Q* is the covariance matrix of η [k] which can be written as follow.

$$Q = \begin{bmatrix} \tau\sigma_2^2 + \frac{1}{3}\tau^3\sigma_3^2 & \frac{1}{2}\tau^2\sigma_3^2 & 0 \\ \frac{1}{2}\tau^2\sigma_3^2 & \tau\sigma_3^2 & 0 \\ 0 & 0 & 0 \end{bmatrix} \quad (6)$$

Equations (3), (4) and (5) imply that the noise component of *Z(k)* are the linear sum of the phase white noise $n_1(t)$ and the measurement noise *V*[8].

The estimated atomic clock state can be obtained according to the following Kalman filter equations.

$$\begin{cases} \hat{\overline{X}}_{k,k-1} = \Phi_{k,k-1}\hat{\overline{X}}_{k-1,k-1} \\ P_{k,k-1} = \Phi_{k,k-1}P_{k-1,k-1}\Phi_{k,k-1}^T + Q_{k-1} \\ K_k = P_{k,k-1}H_k^T(H_kP_{k,k-1}H_k^T + R_k)^{-1} \\ P_{k,k} = (I - K_kH_k)P_{k,k-1} \\ \hat{\overline{X}}_{k,k} = \hat{\overline{X}}_{k,k-1} + K_k\left(\overline{Z}_k - H_k\hat{\overline{X}}_{k,k-1}\right) \end{cases} \quad (7)$$

The conclusion can be got that the essential idea of the Kalman algorithm is to estimate $x_1(t)$, $x_2(t)$ and $x_3(t)$ of an atomic clock respectively. At the same time, the phase white noise $n_1(t)$ and the measurement noise *V* in $x_1(t)$ are smoothed out compared to the original clock difference. Besides those noise components, the white frequency noise in $x_2(t)$ is also smoothed out compared to the original frequency deviation. Besides those noise components, the walk random frequency noise in $x_3(t)$ is further smoothed out compared to the original frequency drift. To conclude, the Kalman algorithm is a status estimation algorithm as well as a noise removing algorithm.

The above analysis implies the reference is an ideal time scale which contains no noise. But in fact the observation is the clock difference. The noise components of the time difference are the linear sum of those of the two clocks.

The Allan variances of these two atomic clocks can be written as follows.

$$\sigma_{y1}^2(\tau)=h_{-2}^1\frac{(2\pi)^2}{6}\tau+h_{-1}^1 2\ln 2+h_0^1\frac{1}{2\tau}+ h_1^1\frac{1}{(2\pi\tau)^2}\{3[2+\ln(2\pi f_h\tau)]-\ln 2\}+h_2^1\frac{3f_h}{(2\pi\tau)^2} \quad (8)$$

$$\sigma_{y2}^2(\tau)=h_{-2}^2\frac{(2\pi)^2}{6}\tau+h_{-1}^2 2\ln 2+h_0^2\frac{1}{2\tau}+ h_1^2\frac{1}{(2\pi\tau)^2}\{3[2+\ln(2\pi f_h\tau)]-\ln 2\}+h_2^2\frac{3f_h}{(2\pi\tau)^2} \quad (9)$$

$\sigma_{y1}^2(\tau)$ and $\sigma_{y2}^2(\tau)$ are the Allan variances of these two clocks. h_{-2} , h_{-1}, h_0, h_1 and h_2 represent noise coefficients. The superscript 1 and 2 of the noise coefficients represent the first and second atomic clocks respectively. f_h is the high cut-off frequency.

The Allan variance of the clock difference is follows.

$$\sigma_y^2(\tau)=(h_{-2}^1+h_{-2}^2)\frac{(2\pi)^2}{6}\tau+(h_{-1}^1+h_{-1}^2)2\ln 2+(h_0^1+h_0^2)\frac{1}{2\tau} +(h_1^1+h_1^2)\frac{1}{(2\pi\tau)^2}\{3[2+\ln(2\pi f_h\tau)]-\ln 2\}+(h_2^1+h_2^2)\frac{3f_h}{(2\pi\tau)^2} \quad (10)$$

The noise variances can be obtained as follows.

$$\begin{cases}\sigma_1^2=\sigma_{pw}^2=\dfrac{f_h}{(2\pi)^2}(h_2^1+h_2^2)=\sigma_{pw1}^2+\sigma_{pw2}^2\\ \sigma_2^2=\sigma_{fw}^2=\dfrac{1}{2}(h_0^1+h_0^2)=\sigma_{fw1}^2+\sigma_{fw2}^2\\ \sigma_3^2=\sigma_{rw}^2=\pi^2(h_{-2}^1+h^2{}_{-2})=\sigma_{rw1}^2+\sigma_{rw2}^2\end{cases} \quad (11)$$

So the each kind of noise variance of the clock difference is the linear sum of that of the two clocks.

Given the clock difference, the noise coefficients can be obtained by the inversion of the Allan variance, and then the noise variances and Q can be obtained.

Although Q contains noises of two clocks, the Kalman filter cannot distinguish them. We can suppose that the noises come from one clock and the other clock is an ideal time scale. Thus we can use the same method to remove the noise components of the clock difference as that to remove the noise components of an atomic clock.

III. Performance of the Algorithm

A. Performance of the Kalman filter

Using clock difference between two commercial cesium clocks (Symmetricom-5071A) C8-C3 as the observation, running the Kalman algorithm, the estimated state can be obtained.

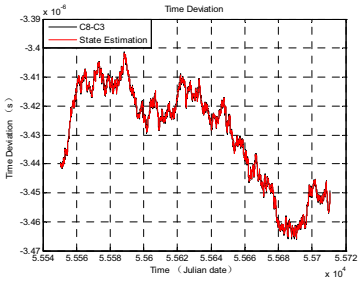

(a) The original time deviation and $x_1(t)$

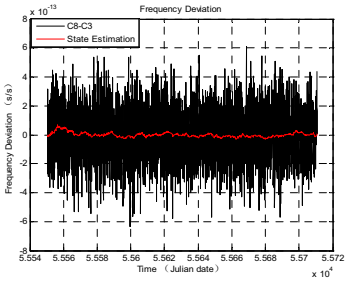

(b) The original frequency deviation and $x_2(t)$

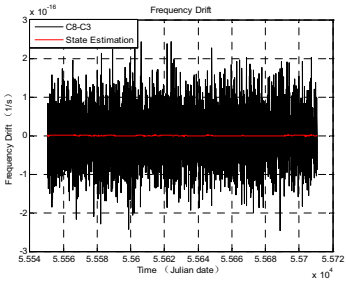

(c) the original frequency drift and x3(t)

Figuer 2 the original state and the estimated state

The simulation results indicate that the Kalman algorithm can estimate $x_1(t)$, $x_2(t)$ and $x_3(t)$ and smoothes out the noise components in $x_1(t)$, $x_2(t)$ and $x_3(t)$ from the original time deviation, frequency deviation, frequency drift respectively.

B. Performance of the Real-Time Frequency Deviation Adjustment Algorithm

Using clock difference C8-C3 as the observation, running the real-time frequency deviation adjustment algorithm to reconstruct the time deviation, the adjusted clock difference is obtained.

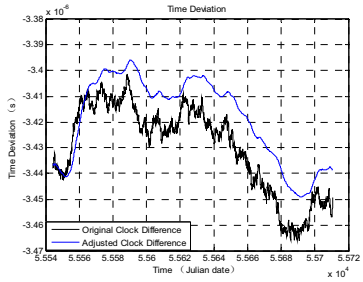

（a） The original clock difference and the adjusted clock difference.

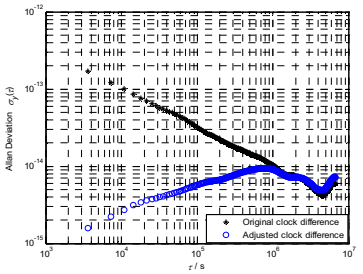

（b） The Allan Deviations of the original clock difference and the adjusted clock difference.

Figuer 3 Time Deviations and Allan Deviations of the Time Scale and the original clock difference

In the picture, the black curves represent the original C8-C3 clock difference and its Allan deviation, and the blue curves represent the adjusted clock difference and its Allan deviation. The stabilities of the original clock difference and the adjusted clock difference are shown in the following table.

Table 1 Frequency Stabilities of each Time Scales

Frequeny Stability (ADEV)	Original Clock Difference	Adjusted Clock Difference (Reconstructed Time Deviation)
1h	1.78×10^{-13}	8.38×10^{-16}
1d	3.53×10^{-14}	4.60×10^{-15}
5d	1.56×10^{-14}	8.50×10^{-15}
30d	6.63×10^{-15}	6.69×10^{-15}
60d	4.60×10^{-15}	5.58×10^{-15}

Conclusions can be got as follows. Since the Kalman filter smoothes out the noises from the frequency deviation effectively, the white frequency noise component of the adjusted clock difference is decreased. The stability at the average time less than 5 days is significantly improved. When $\tau = 3600s$, the stability of the adjusted clock difference is 8.37 $\times$ 10^{-16}, which is significantly better than that of an active hydrogen maser VCH-1003M. Since the adjusted clock difference contains noises of the master clock and the other clock, the conclusion can be got that the stability of the master clock's time scale is also improved effectively. The simulation results indicate that this real time frequency deviation adjustment algorithm is effective.

IV. CONCLUSION

This paper proposes a real-time frequency deviation adjustment algorithm, and gives its implementation. The idea and main steps of this algorithm are described in this paper. This paper proves that the Kalman filter can effectively estimate the state and smooth out noises. To illustrate the main idea more clearly, only two commercial cesium clocks (Symmetricom-5071A) are used in the simulation. The simulate results indicate that the amount of the white frequency noise of this time deviation is decreased and the stability of this time deviation at the average time less than 5 days is improved effectively. The stability at the average time of 1 hour of this time deviation is 8.37 × 10^{-16}, which is significantly better than the stability of an active hydrogen maser VCH-1003M. Since the time deviation is the adjusted clock difference between the master clock and the other clock, the conclusion can be got that the stability of the master clock's time scale is also improved effectively. The algorithm is real-time, and its implementation is with low cost and easy to realize and control, so the algorithm is of high engineering and application values.

ACKNOWLEDGMENT

To express my sincere appreciation to PTB who provides the experimental data.

REFERENCES

[1] DONG Shaowu, Study on Several Important Technical Issues in Time-keeping [D]. Graduate University of Chinese Academy of Sciences. 2007

[2] Ouinot B, Thomas C, Establishment of International Atomic Time[J], BIPM Annual Report of the time Section, l988, D1～D22

[3] M.Weiss, et al, A New Time Scale Algorithm: AT1 Plus Frequency Variance[C] , Proceedings of the Twenty-first Annual Precise Time and Time Interval (PTTI), 1989

[4] Weiss M A, et al, A Study of the NBS Time Scale Algorithm [J], IEEE Trans.Instrum.Meas. 38 631-5

[5] Cristina Zucca, Patrizia Tavella, The Clock Model and Its Relationship with the Allan and Related Variances[J], IEEE Transaction on ULTRASONICS, FERROELECTRICS, AND FREQUENCY CONTROL, VOL52, No.2, 2005.

[6] Richard H. Jones, Peter V. Tryon, Estimating Time from atomic clocks[J], Journal of Research of the National Bureau of Standards, Vol.88, No.1,1983.

[7] Lorenzo Galleani, A tutorial on the two-state model of the atomic clock noise [J], Metrologia 45 (2008) S175–S182

[8] Lorenzo Galleani, et al, Time and the Kalman Filter [J], IEEE Control System Magazine, April 2010.

[9] Charles A Greenhall, Forming stable timescales from the Jones–Tryon Kalman filter[J], Metrologia 40 (2003) , S335–S341

[10] S.R. Stein, Time Scales Demystified [C], Proceedings of the 2003 IEEE International Frequency Control Symposium and PDA Exhibition Jointly with the 17th European Frequency and Time Forum.

Precise Point Positioning Technique for Short and Long Baselines Time Transfer

P. Lejba, J. Nawrocki, D. Lemanski, P. Nogas, P. Dunst
Space Research Centre, Polish Academy of Sciences,
Astrogeodynamic Observatory, Borowiec
Drapalka 4, 62-035 Kornik, Poland

***Abstract*- In this work the clock parameters determination of several timing receivers TTS-4 (AOS, PL), ASHTECH-Z-XII3T (PTB, USNO) and SEPTENTRIO POLARX4TR (ORB,) by use of the Precise Point Positioning (PPP) technique were presented. The clock parameters were determined for several time links based on the data delivered by time and frequency laboratories mentioned above. The computations cover the period from June 1 2012 to May 31, 2013 and were performed in two modes with 7-day and one-month solution for all links. All RINEX data files which include phase and code GPS data were recorded in 30-second intervals. All calculations were performed by means of Natural Resource Canada's GPS Precise Point Positioning (GPS-PPP) software based on high-quality precise satellite coordinates and satellite clock delivered by IGS as the final products. The received results were compared with the results obtained by GPS CV and TWSTFT.**

The used independent PPP technique is a very powerful and simple method which allows for better control of antenna positions in AOS and a verification of other time transfer techniques like GPS CV, GLONASS CV and TWSTFT. The precision of the PPP technique is only comparable to the glass fiber link PL-AOS realized at present by PL and AOS time labs. Currently PPP technique is one of the main time transfer methods used at AOS considerably improving and strengthening the quality of the Polish time scales UTC(AOS), UTC(PL), and TA(PL).

I. INTRODUCTION

In this paper, the results of analysis of the GPS 30-seconds phase and code RINEX data by use of the Precise Point Positioning technique are presented. The PPP method is described in [1, 2]. All analyzed data were gathered by different timing receivers: two TTS-4 [3] receivers located at Astrogeodynamic Observatory Borowiec (AOS) and Central Office of Measures (GUM, PL), two ASHTECH Z-XII3T's working at Physikalisch-Technische Bundesanstalt (PTB) and U.S. Naval Observatory (USNO) and one SEPTENTRIO POLARX4TR situated at Observatoire Royal de Belgique (ORB). All laboratories are equipped with H-masers, excepting PL where the reference clock is a caesium standard. For the first time we presenting a one year comparison of UTC(AOS), UTC(PL), UTC(PTB), UTC(ORB) and UTC(USNO) atomic timescales supported by PPP technique. This work is a continuation and extension of the studies presented during 43th PTTI [4].

All PPP calculations were made in two modes: 7-day and 35-day solutions for the period from June 1, 2012 to May 31, 2013. In these modes the computations were done for four time links: AOS-PL and AOS-PTB (short baselines), AOS-ORB (medium baseline) and AOS-USNO (very long baseline). All computations were performed by means of the Natural Resource of Canada GPS Precise Point Positioning (GPS-PPP) software [5], release 052011; IGS's *sp3* precise orbits and *clk* final products were used.

Additionally the comparison of UTC(AOS)-UTC(PTB) and UTC(AOS)-UTC(USNO) using three time transfer techniques (GPS CV, TWSTFT and PPP) were accomplished in order to show what is the difference in precision for various time transfer techniques realized nowadays by most time labs in the world.

The obtained PPP results presented in this paper characterize a high precision of PPP method w.r.t. other time transfer techniques, which is essential for advanced future works with other GNSS systems of the new generation like Galileo, Beidou and IRNSS.

It is remarkable that today PPP method is only comparable to the glass-fiber link experiments [6].

II. PPP STRATEGY

The all RINEX data were downloaded directly from the receiver (AOS), from BIPM server (PL) and from CDDIS server (PTB, ORB and USNO). The 7-day solution means that seven 24-hour files of data were combined into one file. The same method was applied for 35-day mode. All RINEX data files contained phase and code GPS measurements. For PPP computations the NRCan PPP software were used. In Fig. 1 the basic options nad parameters of the software are shown. The software takes into account both code and phase observations. All processing was carried out for L3 in static mode, in reference to the ITRF2008 frame and was based on GPS 15-minute *sp3* and 30-second *clk* final files delivered by IGS, downloaded from the CDDIS data base.

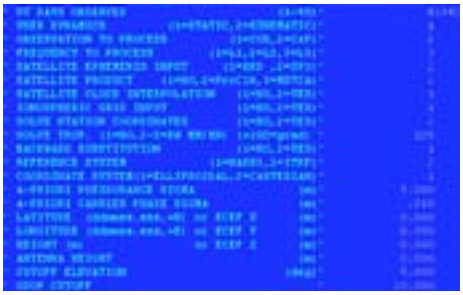

Fig. 1. Basic options and parameters of the NRCan PPP software (release 05211).

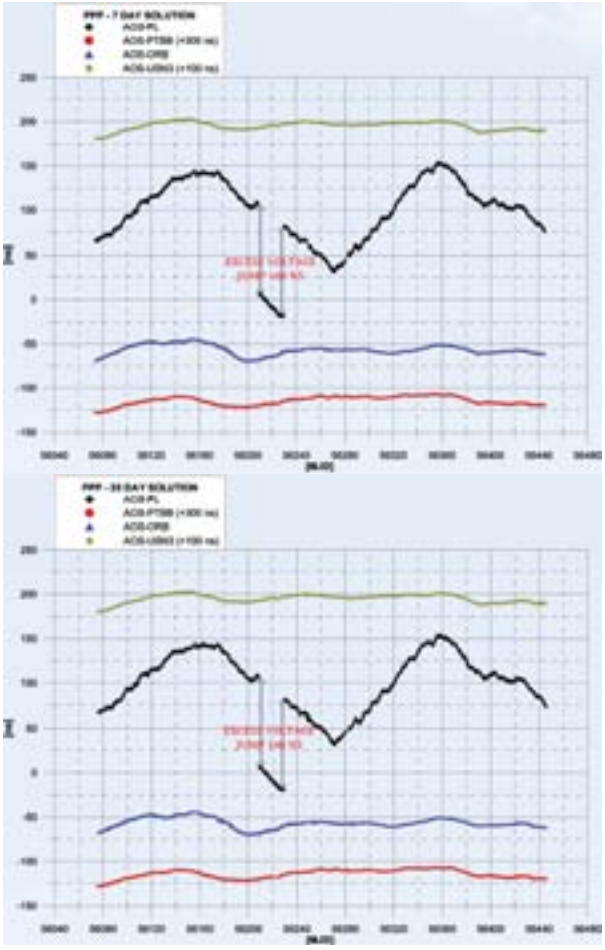

Fig. 2. PPP 7-day (top) and 35-day (bottom) solutions for AOS-PL (black), AOS-PTB (red), and AOS-ORB (blue) and AOS-USNO (brown).

In Fig. 2, the results of PPP computations of all discussed time links are presented. The results cover the period from June 1, 2012 (56079 MJD) to May 31, 2013 (56443 MJD). For better clarity of Fig. 2, the results are rescaled by +300 ns for AOS-PTB and +100 ns for AOS-USNO. In the case of AOS-PL time link a big jump about 100 ns is visible. This disturbance was appeared because of an excess voltage in GUM on October 8, 2012 (56208 MJD) and was eliminated 21 days later on October 29, 2012 (56229 MJD).

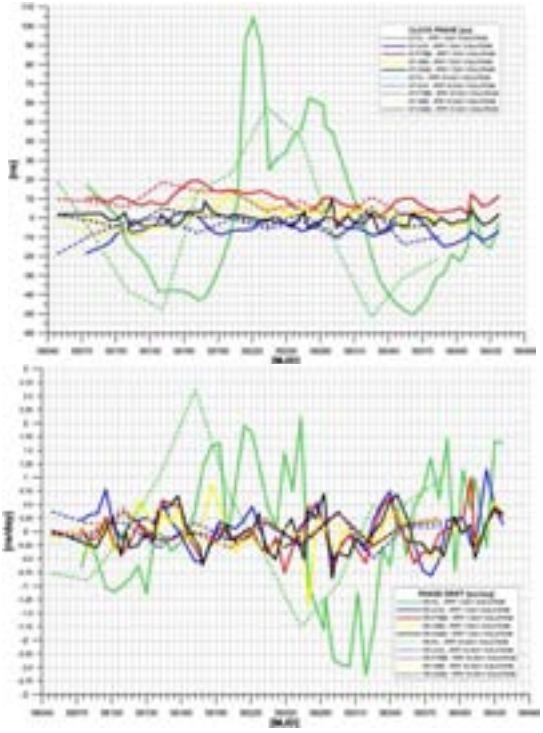

Fig. 3. Clock phase (top) in ns and phase drift (bottom) in ns/day for GUM (green), AOS (blue), PTB (red), ORB (yellow) and USNO (black) for 7-day (solid line) and 35-day (dashed line) PPP solutions.

In Fig. 3 the PPP results of clock phase (CP) and phase drift (PD) are displayed. The CP means receiver clock offset and the PD means receiver clock offset in the function of time. CP is expressed in ns and PD in ns/day. In Fig. 3 the results of CP and PD were presented for each time lab (receiver) separately. The 7-day mode gaved 53 points and 35-day mode gaved 12 points. All points were combined by means of solid and dashed lines, respectively.

Fig. 3 confirms that regulated UTClabs scales synchronized by 1 pps and frequency signal from H-maser reference standard characterized high stability of the realized time scale. In the case of PL (GUM) the big jump of CP and PD in the middle of Fig. 3 is clearly visible. It is connected to the excess voltage occured on October 2012 in GUM (see Fig. 2).

Other form of the results presentation is time deviation demonstration. In Fig. 4-7 the time deviation of all analyzed time links in 7-day and 35-day PPP modes are shown.

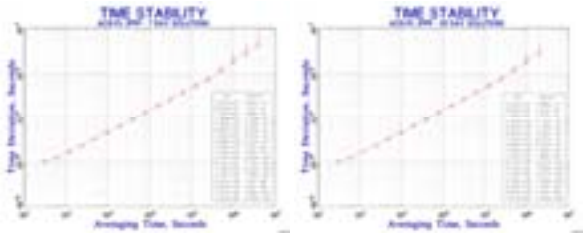

Fig. 4. Time deviation for AOS-PL time link in 7-day (left) and 35-day (right) solution.

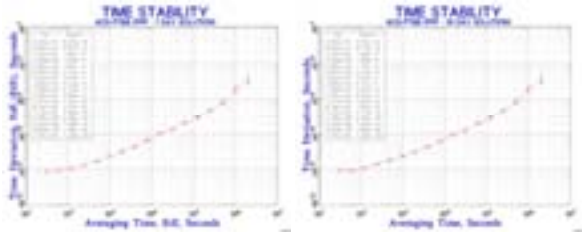

Fig. 5. Time deviation for AOS-PTB time link in 7-day (left) and 35-day (right) solution.

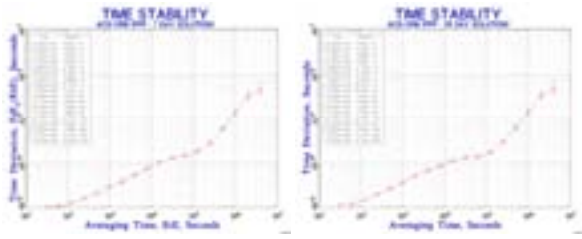

Fig. 6. Time deviation for AOS-ORB time link in 7-day (left) and 35-day (right) solution.

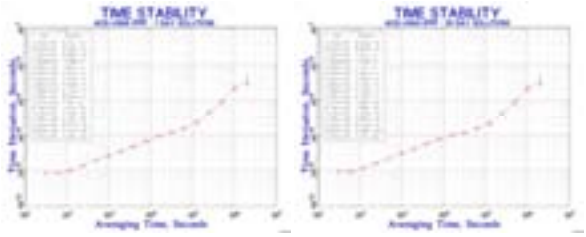

Fig. 7. Time deviation for AOS-USNO time link in 7-day (left) and 35-day (right) solution.

Table 1 shows the time deviation obtained for all PPP time links both for 7-day (7D) as well as 35-day (35D) modes. The best short-term time stability (σ) is for the AOS-PTB and AOS-USNO baselines. If τ is increasing into 24-hour direction then the best time stability are presented by AOS-ORB baseline.

The quality of the results of time transfer techniques, presented in this work is described by RMS as calculated from averaged 24-hour solutions by least squares estimation according to the following formula:

$$\mathrm{RMS} = \sqrt[2]{\frac{\sum_{i=1}^{n} r_i^2}{n}}. \qquad (1)$$

TABLE I
TIME DEVIATION FOR ALL ANALYZED PPP TIME LINKS

time link	AOS-PL		AOS-PTB	
tau [s]	7Dσ [s]	35Dσ [s]	7Dσ [s]	35Dσ [s]
3.00e+01	9.82e-11	9.88e-11	8.35e-12	9.16e-12
6.14e+04	3.75e-9	3.80e-9	2.01e-10	1.93e-10
1.23e+05	5.42e-9	5.47e-9	2.86e-10	2.75e-10
time link	AOS-ORB		AOS-USNO	
tau [s]	7Dσ [s]	35Dσ [s]	7Dσ [s]	35Dσ [s]
3.00e+01	1.02e-11	1.19e-11	8.11e-12	8.92e-12
6.14e+04	1.46e-10	1.35e-10	1.47e-10	1.48e-10
1.23e+05	1.80e-10	1.73e-10	2.19e-10	2.04e-10

Residuum *r* is defined as the difference between the actual value (time lab1 clock – time lab2 clock) and the value predicted by linear regression. The *n* is the number of residua. For 7-day PPP mode the RMS are from 0.08 to 0.98 ns for AOS-PL, from 0.01 to 0.26 ns for AOS-PTB, from 0.01 to 0.31 ns for AOS-ORB and from 0.01 to 0.53 ns for AOS-USNO. For 35-day PPP solution the RMS are from 0.05 to 0.87 ns for AOS-PL, from 0.01 to 0.26 ns for AOS-PTB, from 0.01 to 0.51 ns for AOS-ORB and from 0.01 to 0.53 ns for AOS-USNO. The results showed above mean that PPP results both for 7-day as well as 35-day solutions are comparable.

III. PPP vs. GPS CV and TWSTFT

The last step in these studies were to compare the PPP results with the results obtained from GPS CV (L3P) and TWSTFT techniques. The computations were performed for two time links, AOS-PTB and AOS-USNO and cover the period from September 20, 2012 (56190 MJD) to May 31, 2013 (56443 MJD). This period is shorter to period used for PPP strategy (see section 2) because of an accessibility of CGGTTS and TWSTFT data for PTB and USNO. The data were downloaded from BIPM where are available as of September 20, 2012. In Fig. 8 the PPP, GPS CV (L3P) and TWSTFT results were shown. For better view of Fig. 8 the PPP results for an appropriate time links were rescaled.

The comparison results were presented with time deviation expressed by σ in seconds.

Table 2 shows the time deviation obtained for all PPP time links both for 7-day (7D) as well as 35-day (35D) modes and for GPS CV (L3P) and TWSTFT computations.

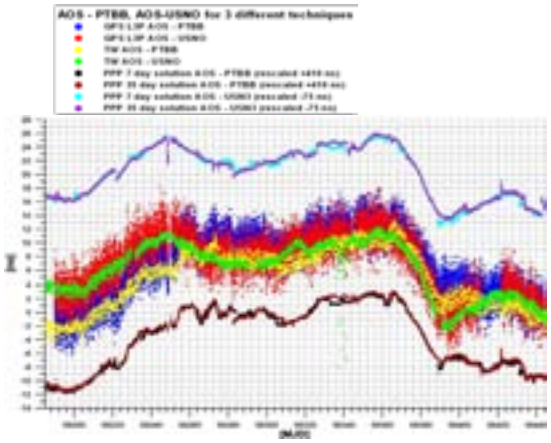

Fig. 8. The comparison of PPP, GPS CV(L3P) and TWSTFT results for AOS-PTB and AOS-USNO time links in the period from September 20, 2012 to May 31, 2013.

TABLE II
TIME DEVIATION FOR AOS-PTB AND AOS-USNO TIME LINKS OBTAINED FOR PPP, GPS CV (L3P) AND TWSTFT COMPUTATIONS IN THE PERIOD 56190-56443 MJD.

time link	AOS-PTB		AOS-USNO	
	PPP			
tau [s]	7Dσ	35Dσ	7Dσ	35Dσ
3.00e+01	6.51e-12	7.37e-12	6.19e-12	7.24e-12
6.14e+04	1.33e-10	1.23e-10	1.18e-10	1.17e-10
1.23e+05	2.08e-10	2.01e-10	1.53e-10	1.59e-10
tau [s]	GPS CV L3P			
9.60e+02	1.37e-09		1.69e-09	
6.14e+04	3.42e-10		5.98e-10	
1.23e+05	4.34e-10		5.94e-10	
tau [s]	TWSTFT			
7.20e+03	4.68e-10		2.75e-10	
5.76e+04	3.42e-10		1.86e-10	
1.15e+05	2.47e-10		1.64e-10	

The averaged RMS received for GPS CV calculations are from 1.15 to 1.85 ns for AOS-PTB and from 1.27 to 2.40 ns for AOS-USNO. The RMS for TWSTFT are from 0.05 to 1.05 ns for AOS-PTB and from 0.04 to 1.23 ns for AOS-USNO. The RMS obtained from PPP both 7-day as well as 35-day PPP solutions are the same and were estimated to be between 0.01 to 0.26 ns and 0.01 to 0.53 ns for AOS-PTB and AOS-USNO, respectively. The best precision is for PPP technique.

The foregoing results are comprehensible because code and phase GPS measurements used by PPP are recorded every 30 seconds. For GPS CV this interval is 16 minutes and for TWSTFT only 2 hours.

IV. SUMMARY AND CONCLUSIONS

This work covers the analysis of one year of data for several (short and long) time links AOS-PL, AOS-PTB, AOS-ORB and AOS-USNO. All calculations and analyses are based on the results obtained with Precise Point Positioning technique. All PPP results confirm the high quality of this technique in comparison to the other time transfer techniques presented in this study. It is noticeable that the all PPP results both for 7-day as well as 35-day solutions are comparable. The quality of the results of time transfer techniques, presented in this work is described by RMS calculated from averaged 24-hour solutions by least squares estimation. The RMS obtained for AOS-PTB, AOS-ORB and AOS-USNO time links vary from 0.04 to 0.05 ns. The PPP results obtained for AOS-PL time link are more or less 1 order of magnitude worse because of cesium atomic clock used by GUM. In this case the RMS is 0.27 ns both for 7-day as well as 35-day solutions. The short-term time stability (30 sec. interval) PPP results differ from 8.11e-12 s (USNO) to 9.82e-11 s (PL) for 7-day solution and from 8.92e-12 s (USNO) to 9.88e-11s (PL) for 35-day solution. More results for time deviation analysis are presented in the paper.

The PPP results obtained in two modes (7 and 35-days) were compared with the results obtained from GPS CV (L3P) and TWSTFT techniques. The computations were carried out for two time links, AOS-PTB and AOS-USNO. The RMS for GPS CV L3P results are 1.44 ns (AOS-PTB) and 1.77 ns (AOS-USNO). For TWSTFT the RMS results are 0.53 ns and 0.25 ns for AOS-PTB and AOS-USNO, respectively. As an independent method, the PPP allows the verification of other time transfer techniques like GPS CV and TWSTFT realized by AOS.

The PPP technique is currently the only time transfer technique comparable to the glass fiber link PL-AOS. The application of the PPP method improves and strengthens the quality of the Polish time scales UTC(AOS), UTC(PL), and TA(PL).

This work continues with calculations including GLONASS ephemeris products and GLONASS RINEX data.

REFERENCES

[1] J. Kouba and P. Héroux, 2001, „Precise point positioning using IGS orbits and clock products", GPS Solutions, Vol. 5, no. 2, 12–28.

[2] P. Tavella and D. Orgiazzi, 2004, „Timing-oriented Processing of Geodetic GPS Data using a Precise Point Positioning (PPP) Approach", in Proceedings of the 6th Meeting of Representatives of Laboratories Contributing to TAI, 31 March 2004, Sèvres, France.

[3] J. Nawrocki, P. Lejba, P. Nogaś and D. Lemański, 2010, „AOS studies on GNSS time transfer", 42th Annual Precise Time and Time Interval (PTTI) Meeting, 15-18 November 2010, Reston, Virginia, USA.

[4] P. Lejba, J. Nawrocki, D. Lemański and P. Nogaś, 2011, „AOS studies on use of PPP technique for time transfer", 43th Annual Precise Time and Time Interval (PTTI) Meeting, 14-17 November 2011, Long Beach, California, USA.

[5] F. Lahaye, D. Orgiazzi, P. Tavella, and G. Cerretto, 2006, „GPS time transfer: using precise point positioning for clock comparisons", GPS World, November 2006.

[6] J. Kołodziej, P. Krehlik, M. Lipiński, Ł. Śliwczyński, P. Dunst, D. Lemański, J. Nawrocki, P. Nogaś, A. Czubla, A. Binczewski, W. Bogacki, P. Ostapowicz, M. Stroiński, K. Turza, W. Adamowicz, J. Igalson, T. Pawszak, J. Pieczerak, „OPTIME – time and frequency dissemination system based on fiber optical network – PIONIER", 27th European Frequency and Time Forum, 21-25 July, 2013, Prague, Czech Republic.

The study of GPS Time Transfer Based on Extended Kalman Filter

Jian-feng Wu, Yong-hui Hu, Zai-min He
National Time Service Center,CAS/Key Laboratory of Time and Frequency Primary Standards, CAS
Xi'an,China
wujianf@126.com

Wen-fang Jing, Hong-chun Lv, Jin-lin Li
National Time Service Center,CAS/University of Chinese Academy of Sciences
BeiJing, China

Abstract—**GPS Time Transfer is a perfect combination of the advantages of GPS atomic clock group and the receiver crystal oscillator. But is now mostly just used code pseudorange observation equation solving user clock offset in GPS timing receiver, while ignoring the impact of the receiver clock drift. In order to improve the GPS receiver Timing precision, the single satellite timing method is discussed, and the extended Kalman filter algorithm is used to estimate and predict the clock offset and clock drift. The receiver clock model is constructed by the clock offset and clock drift. The clock offset and clock drift have integral relationship, and often used as Kalman filter state variables. The white noise spectral amplitudes of clock offset noise and clock drift noise can be related to the classical Allan variance parameters Based on relationship between Allan Variances and Power spectral density Parameters. The pseudorange-rate equation is derived according to pseudorange observation equation. The error source is analyzed and quantified with respect to the pseudorange and the pseudorange-rate. The EKF method is tested and verified based on IGS data, and the timing precision of the GPS single satellite can be improved through this method.**

Keywords-Kalman filter; The single satellite timing; Clock offse; Clock drift

I. GPS TIME TRANSFER PRINCIPLE

The Global Positioning system (GPS) is global satellite navigation system that provides three major functions of positioning, velocity measurement, and time transfer. The key of the precise time transfer is three types of time synchronization which are the time synchronization between Universal Time Coordinated (UTC), GPS Time (GPST), satellite clock and user clock. Synchronization of a satellite clock with UTC at nanosecond level is made possible by use of atomic frequency standards aboard the satellites and in the monitor stations of the Control Segment [1].

The receiver clock bias at epoch t(GPS time) can be modeled as

$$\delta t_u(t)=\frac{1}{c}(\rho^{(k)}(t)+c\delta t^{(k)}(t-\tau)-c\delta t_{rec}-r^{(k)}(t,t-\tau)-I^{(k)}(t)-T^{(k)}(t)-\varepsilon_\rho^{(k)}(t)) \quad (1)$$

Where $\rho^{(k)}(t)$ is the pseudorange measurement from the k-th satellite at epoch t; $r^{(k)}(t,t-\tau)$ is the actual distance between the receiver antenna at signal reception time t and the satellite antenna at signal transmission time(t- τ), and it is known if we can get the antenna position; $r^{(k)}(t,t-\tau)$ is the satellite clock offset relative to GPST which can be computed by formula (1); $I^{(k)}(t)$ and $T^{(k)}(t)$ are the ionospheric and tropospheric propagation delays, respectively; δt_{rec} includes signal delays due to the antenna, preamplifier, cable, and receiver hardware; $\varepsilon_\rho^{(k)}(t)$ accounts for modeling errors and unmodeled effects. It can be modeled by Gaussian noise which has zero mean and σ_ρ^2 variance .

II. GPS TIME TRANSFER METHOD BASED ON EKF

Substituting the antenna position (x_{R1}, y_{R1}, z_{R1}) at epoch t and satellite position $(x_{sat}, y_{sat}, z_{sat})$ at epoch $t-\tau$ into equation (1), the result is

$$\rho^{(k)}(t)=r^{(k)}(t,t-\tau)+I^{(k)}(t)+T^{(k)}(t)-c\delta t^{(k)}(t-\tau)+c\delta t_{rec}+c\delta t_u(t)+\varepsilon_\rho^{(k)}(t) \quad (2)$$

Where $r^{(k)}(t,t-\tau)=\sqrt{(x_{rec}-x_{sat})^2+(y_{rec}-y_{sat})^2+(z_{rec}-z_{sat})^2}$.

One obtains the receiver clock bias by equation (2). In order to get the receiver clock bias relatively accurately, the receiver clock drift should be considered. The clock offset and clock drift have integral relationship, and often used as Kalman filter state variables.

The receiver clock drift can be found by taking the derivative of $\rho^{(k)}(t)$ with respect to t. The result is:

$$\dot{\rho}^{(k)}(t)=\dot{r}^{(k)}(t,t-\tau)+\dot{I}^{(k)}(t)+\dot{T}^{(k)}(t)+c\delta f_u(t)-c\delta f^{(k)}(t-\tau)+c\delta \dot{t}_{rec}+\dot{\varepsilon}_\rho^{(k)}(t) \quad (3)$$

Where $\dot{I}^{(k)}(t)$ is the ionospheric propagation delay rate; $\dot{T}^{(k)}(t)$ is the tropospheric propagation delays rate; $\delta \dot{t}_{rec}$ is signal delay rate due to the antenna, preamplifier, cable, and receiver hardware ; These values can be ignored because of tiny variable in short time. The satellite clock drift can be obtained by

This paper is supported by West Light Foundation of The Chinese Academy of Sciences(No:2012YD04).

$$\delta f^{(k)}(t-\tau) = a_{f1} + 2a_{f2}(t_{GPS} - t_{oc}) + \Delta\dot{t}_r \quad ,$$
$$\Delta\dot{t}_r = Fe_s\sqrt{a_s}\dot{E}_k \cos E_k .$$

Actually, $\dot{r}^{(k)}(t, t-\tau)$ is the range rate between user and satellite, and can be written as a projection of the relative velocity vector on the satellite line-of-sight vector. The result is

$$\dot{r}^{(k)}(t, t-\tau) = (v^k - v)\cdot l^k \qquad (4)$$

Where, v^k is satellite velocity vector, known from the navigation message broadcast by the satellite; v is the user velocity, to be estimated; The user-to-satellite line-of-sight unit vector l^k can be given by

$$l^k = \frac{1}{\sqrt{(x_{sat}-x_{R1})^2 + (y_{sat}-y_{R1})^2 + (z_{sat}-z_{R1})^2}} \begin{bmatrix} x_{sat}-x_{R1} \\ y_{sat}-y_{R1} \\ z_{sat}-z_{R1} \end{bmatrix}.$$

If user is stationary, the user velocity v is zero. Since $\dot{I}^{(k)}(t)$, $\dot{T}^{(k)}(t)$ and $\delta\dot{t}_{rec}$ are very small, they can be approximated as zeros. Substituting $\dot{I}^{(k)}(t), \dot{T}^{(k)}(t)$, $\delta\dot{t}_{rec}$ and v into equation (4), the result is

$$\dot{\rho}^{(k)}(t) = v^k \cdot l^k + c\delta f_u(t) - c\delta f^{(k)}(t-\tau) + \varepsilon_{\dot{\rho}}^{(k)}(t) \qquad (5)$$

Since the carrier phase difference of the adjacent sampling time is more smoother than the pseudorange difference, the pseudorange-rate is represented by the carrier phase difference. $\varepsilon_{\dot{\rho}}^{(k)}(t)$ can be modeled by Gaussian noise which has zero mean and $\sigma_{\dot{\rho}}^2$ variance , and be independent of $\varepsilon_{\rho}^{(k)}(t)$.

As can be seen from above, the unknown timing errors δt_u and $\delta f_u(t)$ arising from user receiver clock and the GPS system time play a role in GPS time transfer. Two state components are used to model this offset, namely clock bias δt_u and clock drift $\delta f_u(t)$, which represent the phase and frequency errors of receiver clock respectively. Within the navigation algorithm, the two state models are employed commonly as Fig.2 shown.

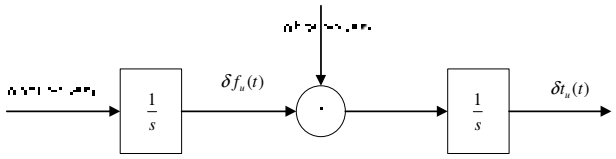

Figure 1. Receiver clock model

The equivalent discrete model can be modeled as

$$\begin{bmatrix} \delta t_{u,k} \\ \delta f_{u,k} \end{bmatrix} = \begin{bmatrix} 0 & T_s \\ 0 & 0 \end{bmatrix} \begin{bmatrix} \delta t_{u,k-1} \\ \delta f_{u,k-1} \end{bmatrix} + \begin{bmatrix} e_{t,k-1} \\ e_{f,k-1} \end{bmatrix} \qquad (6)$$

Where e_t is the clock bias white noise with mean value is zero; e_f is the clock drift white noise with mean value is zero. They are independent mutually and their power spectra are S_t and S_f respectively.

The process noise covariance matrix in discrete time is given by

$$Q_{k-1} = \begin{bmatrix} S_t T_s + S_f \frac{T_s^3}{3} & S_f \frac{T_s^2}{2} \\ S_f \frac{T_s^2}{2} & S_f T_s \end{bmatrix} \qquad (7)$$

III. Recursive Extended Kalman filtering algorithm

The Kalman filter estimates a process by using a form of feedback control: the filter estimates the process state at some time and then obtains feedback in the form of measurements. As such, the equations for the Kalman filter fall into two groups: time update equations and measurement update equations.

Assuming that the initial state-space is $\begin{bmatrix} \delta t_{u,0} \\ \delta f_{u,0} \end{bmatrix}$, and the initial posteriori estimate error covariance matrix is P_0, the recursive process is shown as following:

1) **Predict:** The time update equations are responsible for projecting forward the current state and error covariance estimates to obtain the a priori estimates for the next time step. The time update equations can also be thought of as predictor equations.

$$\begin{bmatrix} \delta\hat{t}_{u,k}^- \\ \delta\hat{f}_{u,k}^- \end{bmatrix} = A \begin{bmatrix} \delta\hat{t}_{u,k-1} \\ \delta\hat{f}_{u,k-1} \end{bmatrix} \qquad (8)$$

The state transition matrix is then

$$A = \begin{bmatrix} 1 & T_s \\ 0 & 1 \end{bmatrix}.$$

The a priori estimate error covariance is then

$$P_k^- = AP_{k-1}A^T + Q \qquad (9)$$

P_{k-1} is the a posteriori estimate error covariance, while Q is from equation (7).

The time update projects the current state estimate ahead in time.

2) **Correct:** The measurement update equations are responsible for the feedback—i.e. for incorporating a new measurement into the a priori estimate to obtain an improved a posteriori estimate. The measurement update equations can be thought of as corrector equations.

The first task during the measurement update is to compute the Kalman gain. The Kalman gain is given by

$$K_k = P_k^- C^T (CP_k^- C^T + R)^{-1} \qquad (10)$$

Where , R is the measurement noise covariance, $C = 3\times10^8 \times \begin{bmatrix} 1 & 0 \\ 0 & 1 \end{bmatrix}$.

The next step is to actually measure the process to obtain y_k, and then to generate an a posteriori state estimate by incorporating the measurement as in equation (11).

$$\begin{bmatrix} \delta\hat{t}_{u,k} \\ \delta\hat{f}_{u,k} \end{bmatrix} = \begin{bmatrix} \delta\hat{t}^-_{u,k} \\ \delta f^-_{u,k} \end{bmatrix} + K_k\left(y_k - C\begin{bmatrix} \delta\hat{t}^-_{u,k} \\ \delta f^-_{u,k} \end{bmatrix}\right) \qquad (11)$$

Where,

$$y_k = \begin{bmatrix} \rho^{(1)}(t) - \sqrt{(x_{sv} - x_u)^2 + (y_{sv} - y_u)^2 + (z_{sv} - z_u)^2} - I^{(1)}(t) - T^{(1)}(t) + c\delta t^{(1)}(t) - t) - c\delta t_{sv} \\ \dot{\rho}^{(1)}(t) - v^T \cdot I^1 + c\delta f^{(1)}(t - t) \end{bmatrix}$$

The final step is to obtain an a posteriori error covariance estimate. The a posteriori estimate error covariance is given by

$$P_k = (I - K_k C)P_k^- \qquad (12)$$

Where, I is the identity matrix.

The measurement update adjusts the projected estimate by an actual measurement at that time.

3) Repeat the procedure from 1) to 2).

After each time and measurement update pair, the process is repeated with the previous a posteriori estimates used to project or predict the new a priori estimates. This recursive nature is one of the very appealing features of the Kalman filter—it makes practical implementations much more feasible.

IV. THE DETERMINATION OF FILTER PARAMETERS

In the actual implementation of the filter, the measurement noise covariance R is usually measured prior to operation of the filter. The determination of the process noise covariance Q is generally more difficult, because we typically do not have the ability to directly observe the process [9].

The long-term stability of GPS timing receiver depends on GPS atomic clock group mostly. The short-term stability of GPS timing receiver is determined by the receiver crystal oscillator. The typical calculating cycle is 1s, namely T_s=1s, and the short-term stability is determined by the crystal oscillator's performance during the 1s. Most receivers use Quartz Crystal Oscillator which are relative cheap and have good stability in 0-10s. The white noise spectral amplitude S_t and S_f can be related to the classical Allan variance parameters [3].The approximate relation is $S_t = 2h_0$ and $S_f = 8\pi^2 h_{-2}$. Typical Allan Variances for various timing standards are shown in Table 1 [4,5]:

TABLE 1. TYPICAL ALLAN VARIANCES FOR VARIOUS TIMING STANDARDS

Clock Standard	h_0	h_{-1}	h_{-2}
TXCO, Temperature compensating crystal oscillator	2×10^{-19}	7×10^{-21}	2×10^{-20}
Temperature-controlled Crystal Oscillator	8×10^{-20}	2×10^{-21}	4×10^{-23}
Rubidium Clock	2×10^{-20}	7×10^{-24}	4×10^{-29}

Substituting T_s=1s, S_t and S_f into formula (7), the result is

$$Q = \begin{bmatrix} 2h_0 + \frac{8}{3}\pi^2 h_{-2} & 4\pi^2 h_{-2} \\ 4\pi^2 h_{-2} & 8\pi^2 h_{-2} \end{bmatrix} \qquad (13)$$

The measurement noise covariance R which is equal to $R = \begin{bmatrix} \sigma_\rho^2 & 0 \\ 0 & \sigma_{\dot\rho}^2 \end{bmatrix}$ is derived through formula (2) and (3). The equivalent measurement noise for the pseudorange and the pseudorange-rate is analyzed as following:

Through formula (1), such parameters as user position, satellite position, satellite clock offset, the receiver hardware delay, the ionospheric delay and the tropospheric delay are needed to calculate receiver clock bias. Parameters mentioned above are obtained from navigation messages, but have some errors. Errors are absorbed into the equivalent measurement noise, and are listed in table 2. They are assumed to be independent of each other, so the equivalent measurement noise of pseudorange is given $\sigma_\rho^2 = (16.3e-9\times3e8)^2 \approx 24m$.

TABLE 2. TYPICAL MEASUREMENT ERRORS OF PSEUDORANGE

Error source	Standard error(ns)
Satellite clock	6.7
Group delay	1
Broadcast ephemeris	6.7
the ionospheric delay	13
the tropospheric delay	1.67
Receiver noise and Resolution	0.03
Multipath	0.67
Receiver position	0.33
Receiver hardware delay	1
Total	16.3

Through formula (5), such parameters as user position, satellite position, satellite velocity, and satellite clock drift are needed to calculate the clock drift $\delta f_u(t)$. Such parameters are listed in table 3. Satellite clock drift is in the order of magnitude 1e-11, which is converted to about 0.01ns. They are assumed to be independent of each other, so the equivalent measurement noise of pseudo-range rate is given $\sigma_{\dot\rho}^2 = (6.71e-9\times3e8)^2 \approx 4m$.

TABLE 3. TYPICAL MEASUREMENT ERRORS OF PSEUDORANGE RATE

Error source	Standard error(ns)
Satellite clock drift	0.01
Broadcast ephemeris	6.7
Receiver noise and Resolution	0.03
Receiver position	0.33
Total	6.71

P_0 is the initial posteriori estimate error covariance matrix. A smaller initial value of P_0 means a greater weight factor given to the priori state estimate. If the output of filter mainly depends on the priori state estimate information, it can easily lead to filter diffusion[8]. In the actual implementation of the filter, considering the model error and the current measurement information, P_0 can be tune largely.

V. SIMULATION AND VERIFICATION

We can get the observation file and the GPS satellite ephemerides file of IGS tracking stations. We use the above

model and the traditional model to calculate the receiver clock offset using MATLAB.

At first, the smoothness of the pseudorange difference(the single difference and the double difference) and the carrier phase difference(the single difference and the double difference) is compared. The observation data is the GPS 20th satellite from IGS tracking stations. The simulation result is shown in Fig.2.

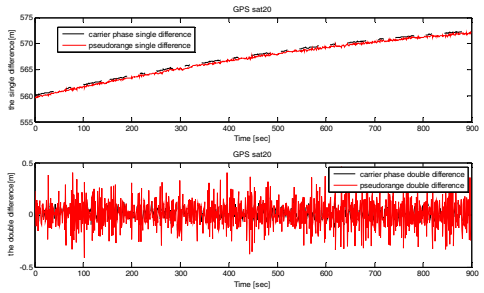

Figure 2. Smoothness comparison of Pseudorange-rate and carrier phase rate

The standard deviation of the pseudorange double difference is 0.14m, but the standard deviation of the carrier phase double difference is only 0.05m. Since the carrier phase difference of the adjacent sampling time is more smoother than the pseudorange difference, the pseudorange-rate is represented by the carrier phase difference.

Usually in the practical application, considering the model error and the current observation information, P_0 can be tune largely. In the article, $P_0 = \begin{bmatrix} 10 & 0 \\ 0 & 10 \end{bmatrix}$, $\begin{bmatrix} \delta t_{u,0} \\ \delta f_{u,0} \end{bmatrix} = \begin{bmatrix} 0.1 \\ 0.001 \end{bmatrix}$ simulation result is shown in Fig.3 .

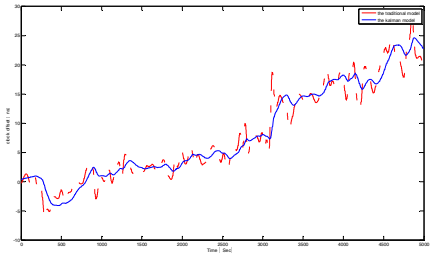

Figure 3. Simulation result

Fig.3 illustrates the clock offset of the Kalman model has the same tendency with the traditional model, but jumping range decreases greatly.

The standard deviation of the clock offset single difference based on kalman filter is 0.02ns, but the standard deviation of the clock offset single difference based on traditional model is 0.07ns. This can be seen in figure 4.

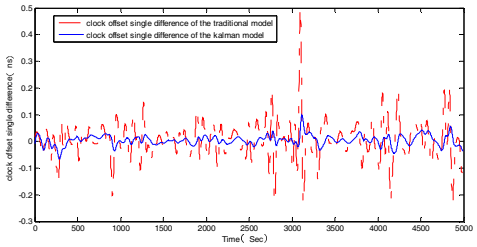

Figure 4. the clock offset single difference

This simulation proves that the kalman filter is effective and the accuracy of time transfer can be improved by the kalman model.

VI. CONCLUSION

This paper study the application of extended kalman filter in GPS time transfer. Two state models is used to estimate and predict the clock offset and clock drift. Based on relationship between Allan Variances and Power spectral density Parameters, process-noise covariance matrix is deduced. The error source is analyzed and quantified with respect to the pseudorange and the pseudorange-rate, and the measurement noise covariance matrix is presented. The EKF method is tested and verified based on IGS data, and the timing precision of the GPS single satellite can be improved through this method.

ACKNOWLEDGMENT

My deepest gratitude goes first and foremost to Professor Hu Yonghui, for his constant encouragement and guidance.

This paper is supported by West Light Foundation of The Chinese Academy of Sciences(No:2012YD04).

REFERENCES

[1] Pratap Misra, Per Enge. Global Positioning System:signals, Measurement,and performance(2th Edition), Ganga-Jamuna Press, 2006.

[2] Xie Gang. Principles of GPS and Receiver Design. Beijing:Publishing House of Electronics Industry, 2008.

[3] Parkinson B.,Spilker J.,Axelrad P.,Enge P. Global Positioning System: Theory and Applications, Amercian Institute of Aeronautics and Astronautics,1996.

[4] Brown,R.G.,and Hwang,P.Y.C.. Introduction to Random signals and Applied Kalman Filtering, second Edition. Wiley,New York,1992.

[5] Van Dierendonck,A.J.,McGraw,J.B.,and Brown,R.G.. Relationship between Allan Variances and Kalman Filter Parameters. Proceedings of the 16th Annual Precise Time and Time Interval (PTTI) applications and Planning Meeting, NASA Goddard Space Flight Center,Nov.,1984,pp:273-293.

[6] J. Furthner, A. Moudrak, A. Konovaltsev, J. Hammesfahr, and H. Denks. Time Dissemination and Common View Time Transfer with Galileo : How Accurate Will It Be? The 35th Annual Precise Time and Time Interval (PTTI) Meeting,2004.9.

[7] Kaplan, E. D., and C. J. Hegarty, eds., Understanding GPS: Principles and Applications (2th edition), Norwood, MA: Artech House, 2006.

[8] HE Zhengbin,WU Fumei,NIE Jianliang.Error Influences of Prior Covariance Matrices on Dynamic Kalman Fi ltering. Geomatics and Informat ion Science of Wuhan Univer sity, 36(1),34-38,2011.1.

[9] Greg Welch,and Gary Bishop. An Introduction to the Kalman Filter. UNC-Chapel Hill, TR 95-041, July 24, 2006.

A Method of High Precision Time Transfer Based on DVB-S

Xiang Yu
National Time Service Center, Chinese Academy of Sciences, Xi'an China
Key Laboratory of Precision Navigation and Timing Technology, NTSC,CAS, Xi'an , China
University of Chinese Academy of Sciences, Beijing China
xy@ntsc.ac.cn

Hua Yu
National Time Service Center, Chinese Academy of Sciences, Xi'an China
Key Laboratory of Precision Navigation and Timing Technology, NTSC,CAS, Xi'an , China
hy@ntsc.ac.cn

Xu Linsheng
National Time Service Center, Chinese Academy of Sciences, Xi'an China
Key Laboratory of Precision Navigation and Timing Technology, NTSC,CAS, Xi'an , China
xls@ntsc.ac.cn

Shi Shaohua
National Time Service Center, Chinese Academy of Sciences, Xi'an China
Key Laboratory of Precision Navigation and Timing Technology, NTSC,CAS, Xi'an , China
ssh@ntsc.ac.cn

***Abstract*—A method of transferring high precise time based on the satellite digital TV broadcasting system (DVB-S) is presented in this paper. PCR (Program Clock Reference) in the signal of TV is considered as the Time Synchronization Flag, precise timestamp captured by PCR is real-time recorded in both transmitting segment and user segment, so time in both sides will be synchronized roughly. Then the period of signal from transmitting segment to user segment is calculated by Precise Satellite Ephemeris, and the time will be synchronized precisely. The experimental result showed the method is feasible, and the RMS< 100ns.**

Keywords—DVB-S, satellite digital TV, PCR, time service, signal transmission delay

I. INTRODUCTION

The TV system is one of the modern radio broadcasting systems. It has the advantage of low prices and operating easily to the method of transmission and adjustment of time and frequency by TV signals. High precision can be achieved by this method in a short time. Furthermore, TV signal is strong and can be obtained easily. So this is a remote transmitting and adjusting time and frequency method which will be popularized easily.

The research of transmitting and adjusting time and frequency by TV system is? started in the 1960s of the last century, and some achievements have been achieved by analog TV standard. With the development of TV industry, the Analog TV will be replaced by the Digital TV gradually. Nowadays digitization is generally completed by the TV broadcast station all around China. So it is necessary to work out a new method of transmitting and adjusting time and frequency under new TV system standard.

All TV broadcast stations in China broadcast program by DVB-S. The main content of this paper is the method of transferring high precise time based on the satellite digital TV broadcasting system.

The work was supported by "Western Light Talents training program of CAS"(Y305YZ1301) and "Scientific Research Equipment Development Project of CAS"(YZ201218(Y307YR1301))

II. METHODS

The main idea of the method is broadcasting signals with standard time information to area which can be covered by the scope of satellite by using Satellite Digital TV broadcasting system. The users can compare the received signal from TV broadcasting system with standard time for high-precision time synchronization?. System block diagram is shown in Fig. 1.

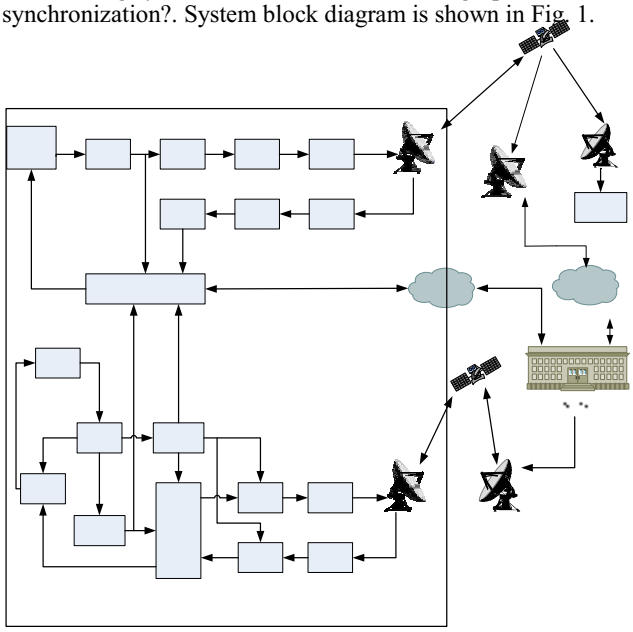

Figure 1. System block diagram of Satellite Digital TV Time Service System

The method is constituted of three parts described as follows:

A. Standard Time Source

There are many methods to obtain standard time in the Satellite Digital TV broadcasting stations, such as obtain UTC

time by using GNSS High-precision Time Service Receiver, trace local time to UTC reference laboratories by using cable and so on. In this test, UTC (NTSC) is used as the standard time reference, and TV broadcasting station is in Nanjing, China. It is about 1000 kilometers between them. That's why we use Two-way Satellite Time and Frequency Transfer (TWSTFT) for tracing time in TV broadcasting station to UTC (NTSC), and the precision of synchronization which will be maintained by atomic clock is 1ns.

B. Remote time synchronization based on the Satellite Digital TV Time Service System

Signals in Satellite Digital TV System are the platform of this method. PCR in TV system is regarded as the Synchronization Flag. The PCR is detected in the end of Multiplexer under broadcasting station on the floor, and timestamp will be captured by PCR. Meanwhile, the timestamp is broadcasted by private channel. After terminal users receiving the TV signals, timestamp can be captured by PCR. At the same time, the moment of broadcasting PCR can be obtain by receiving data in private channel. Finally, the time of broadcasting and receiving each PCR can be recorded by users, so the time synchronization can be achieved by the time interval between broadcasting and receiving one PCR.

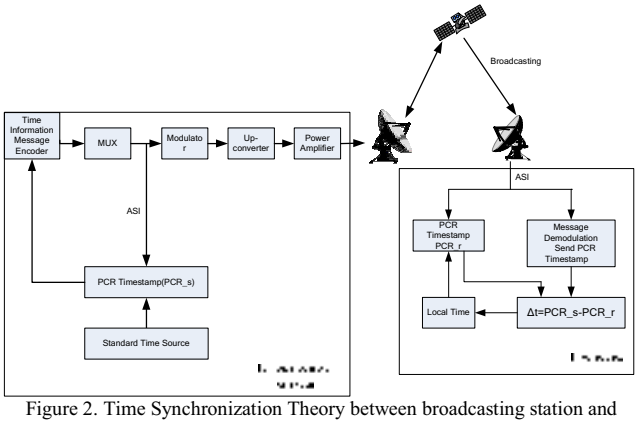

Figure 2. Time Synchronization Theory between broadcasting station and users

In the TV broadcasting station, PCR in TV signals is detected in the output of Multiplexer, and the moment PCR is transmitted will be recorded with reference to standard time source. Then the PCR data and the transmitting time information will be packed to timestamp which is PCR_s, and the timestamp will be broadcasting by private channel.

Under the user terminal, TV signals are received and PCR is detected. The receiving time of PCR in the signals is recorded with reference to of local time by receiver. Then the PCR data and the receiving time information will be packed to timestamp which is PCR_r. At the same time, the transmitting time information of this PCR can be obtained by demodulating data from private channel. Finally, Time Correction between the standard time in broadcasting station and the time in user receivers can be calculated by the transmitting and receiving time information of one same PCR.

$$\Delta t = PCR\_r - PCR\_s \tag{1}$$

C. Precise measurement of delay time in the channel

Rough time synchronization in user receiver to broadcasting station can be achieved by the method descried above. Precise time synchronization needs to measure the delay time in the channel from stations to users, and the receiving time also needs to be corrected.

The path of broadcasting is shown in Fig. 3.

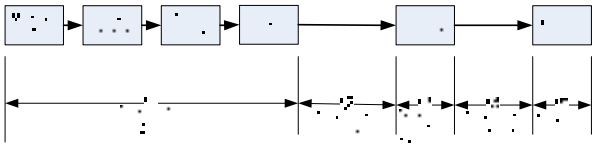

Figure 3. Path of broadcasting time service

As is shown in the Fig. 3, the whole delay time in the path includes: delay time of ground equipment, delay time in the up path, delay time of satellite transponder, delay time in the down path, and delay time of receiver, etc. The whole delay time is about 200ns~300ns in the entire path with experience. So the time in user receiver must be corrected by measuring delay time described above precisely in order to achieve high-precision time synchronization.

The TV system is a one-sided communication system. The positions in space of main nodes need to be known for precise measurement. The positions of antennas in the broadcasting station and user receiver can be measured precisely on the floor, and the satellite orbits can be measured and forecasted by the Ground Tracking and Orbit Determination Net of National Time Service Center (NTSC). So the whole path is divided into two parts: *t1+t2+t3* is the up path *dt1*, *t4+t5* is the down path *dt2*.

For *dt1*, signal loop delay time can be measured by receivers placed in the broadcasting station. The positions of satellites can be calculated by ephemeris, and the one-sided delay time can be calculated by the positions of broadcasting antennas. Then *dt1* is obtained by the loop delay time deducted one-sided delay time. It is shown in Fig. 4.

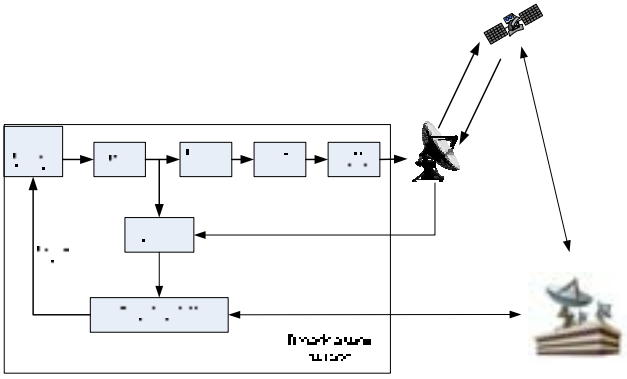

Figure 4. Difference method for measuring up path delay time

Down path delay time is mainly included of the space down path delay time dt_{down} and the receiver delay time *t5*. Space down path delay time dt_{down} can be calculated by using equation 2 below.

$$dt_{down} = \frac{\sqrt{(s_x - du_x)^2 + (s_y - du_y)^2 + (s_z - du_z)^2}}{c} \quad (2)$$

In this equation:

s_x, s_y, s_z is the three-dimensional coordinate of satellites;

du_x, du_y, du_z is the three-dimensional coordinate of ground broadcasting antennas;

c is the speed of light;

The real-time coordinate is calculated by satellite ephemeris in the navigation message. The positions of broadcasting antennas and the speed of light are known.

In the down path delay time, receiver delay time *t5* is as same as receiver down path delay time, so it will be offset after processing and be ignored afterwards. The up path delay time *dt1* is express by equation 3

$$dt1 = dt_{circle} - dt_{down} - t5 = dt_{circle} - \frac{\sqrt{(s_x - du_x)^2 + (s_y - du_y)^2 + (s_z - du_z)^2}}{c} - t5 \quad (3)$$

In this equation, dt_{circle} is obtained by difference receivers, and dt_{down} is obtained by equation 2.

For *dt2*, it is mainly include of space down path delay time dt_{down} and user receiver delay time *t5*. It can be obtained by equation 4.

$$dt2 = dt_{down} + t5 = \frac{\sqrt{(s_x - u_x)^2 + (s_y - u_y)^2 + (s_z - u_z)^2}}{c} + t5 \quad (4)$$

In this equation,

s_x, s_y, s_z is the three-dimensional coordinate of satellites;

u_x,u_y,u_z is the three-dimensional coordinate of user receiving antennas;

c is the speed of light;

The whole delay time *dt* in all path can be obtained:

$$dt = dt1 + dt2 = dt_{circle} - \frac{\sqrt{(s_x - u_x)^2 + (s_y - u_y)^2 + (s_z - u_z)^2} - \sqrt{(s_x - du_x)^2 + (s_y - du_y)^2 + (s_z - du_z)^2}}{c} \quad (5)$$

III. RESULT

The Satellite Digital TV Time Service Broadcasting System is established in Satellite Earth Station of Jiangsu Broadcasting Corparation in China based on the method described above. Function and performance of system is tested in five cities of China (Urumchi, Changchu, Xi'an, Nanjing, Haikou). The results demonstrate that the method is feasible, and the precision of synchronization < 100ns.

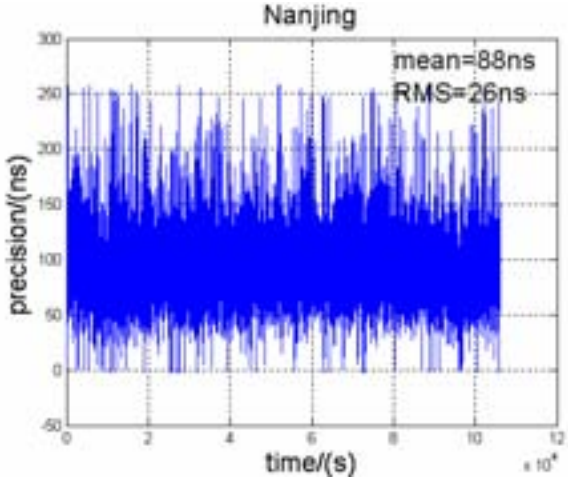

Figure 5. Test result in Nanjing

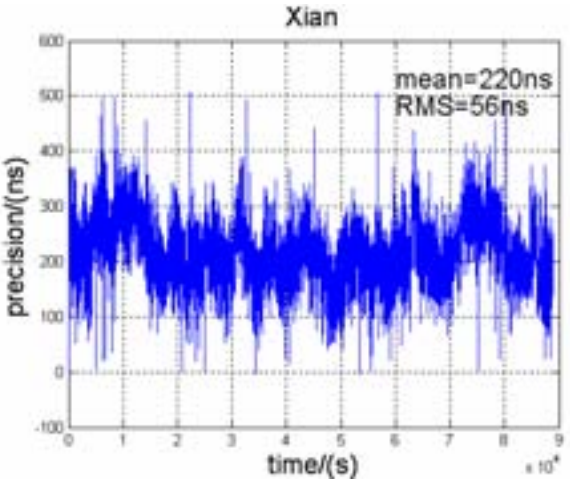

Figure 6. Test result in Xi'an

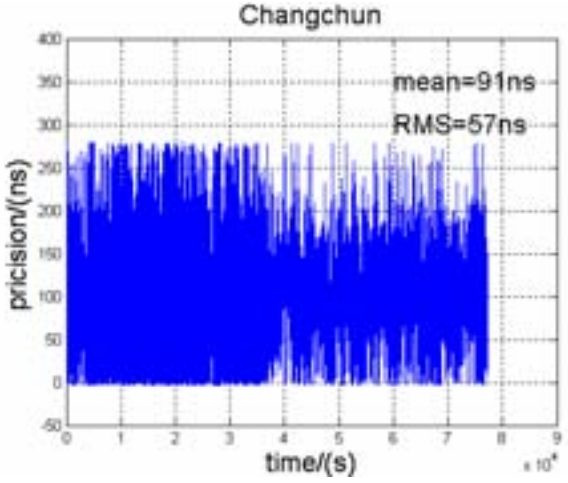

Figure 9. Test result in Changchun

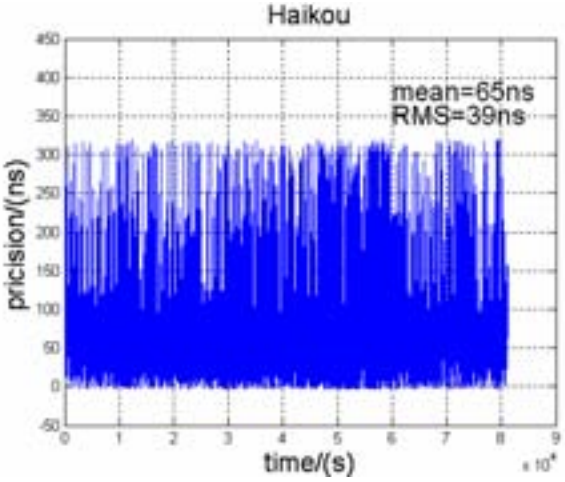

Figure 10. Test result in Haikou

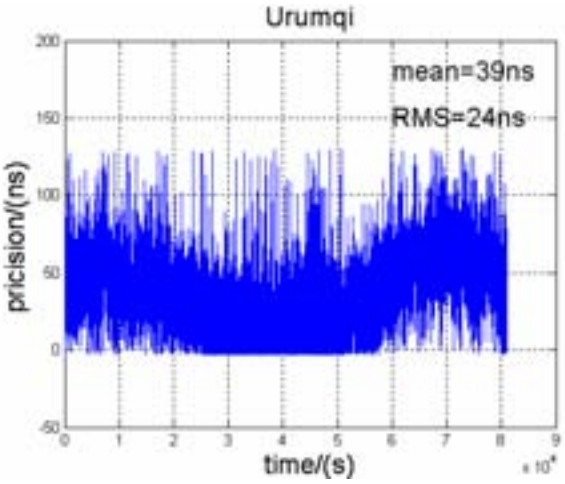

Figure 11. Test result in Urumchi

This system is only designed for checking correctness. The GPS time source is used as the time reference standard. So the time reference errors in broadcasting station and the errors in the test places is also included in the test result. In addition, device delay time, atmosphere errors, Sagnac effection, etc is not to taken into account in the test system. So there are many spaces to improve.

IV. CONCLUSION

The tested results demonstrate that it is feasible to precise synchronize time by Satellite Digital TV system. It is high-precision and strong anti-jamming of this method. Based on this test, delay time analysis and correction is need for improving time synchronization precision in subsequent work.

REFERENCES

[1] ISO/ICE-13818-1_2000. Information technology-Generic Coding of Moving Pictures and Associated Audio Information: Systems. ETSI.2000.12.

[2] EN50083-9. Cable networks for television signals, sound signals and interactive services(Part 9: Interfaces for CATV/SMATV headends and similar professional equipment for DVB/MPEG-2 transport streams). CENELEC.1998.

[3] William Bamford. Real-time Geostationary Orbit Determination Using The Navigator GPS Receiver.2004.06.

[4] Altera Corporation. Cyclone II Device Handbook, Volume 1 , November, 2004.

[5] Tropp J, Gilbert A, Signal recovery from random measurements via orthogonal matching pursuit, Transactions on Information Theory, 2007, 53(12).

[6] Digital Video Broadcasting(DVB) Implementation Guid Asynchronous Serial Interface Document A055, May,2000.

[7] Haskell, B.Puri, A.Netravali; An Introduction to MPEG-2. Chapman & Hall, New York.

A Simple Computation Technique for Improving the Short Term Stability and the Robustness of GPS TAIP3 Common-Views

G.D. Rovera, B. Chupin, M. Abgrall and P. Uhrich
LNE-SYRTE
Observatoire de Paris (OP), LNE, CNRS, UPMC
61 avenue de l'Observatoire
75014 Paris, France
daniele.rovera@obspm.fr

***Abstract*— We propose a new simple technique to improve the short term stability and the robustness of Common-Views (CV) of Global Positioning System (GPS) satellites. We use the ionosphere free linear combination of P-code data broadcast on both GPS carriers, called TAIP3, the data files being built according to the Common GNSS Time Transfer Standard (CGTTS) format. Instead of averaging the outliers out by using a given filter around a mean value computed for each CGTTS sampling epoch, we average the outliers out from a linear fit on daily CV files. We analyze the results over more than 200 d of data. Over a short baseline between remote stations, we see that the average number of satellites left by the daily filtering for the CV computation is almost twice as large as the number obtained from the epoch filtering, increasing that way the robustness of the time transfer. On the short term stability of the time transfer, the white phase noise modulation is improved by a factor larger than the square root of 2, above what was expected. Over a long baseline, the improved short term stability is about twice smaller between 10 000 s and 1 d, together with an average increase of more than 20 per cent on the number of satellites left after filtering for the CV computation. We study the singular event which causes the discrepancy between these two criteria, and conclude that the daily approach is providing the best results in all cases. This automated filtering technique might be useful for any GNSS time transfer based on code data.**

Keywords: GPS, Common-Views, time transfer.

I. INTRODUCTION

The LNE-SYRTE in Observatoire de Paris (OP), Paris, France, is the institute designated by the French National Metrology Institute (NMI) Laboratoire National de Métrologie et d'Essais (LNE) in the field of Time and Frequency metrology. In this frame, the laboratory has a long history in developing remote clock comparisons by using the well-known Common-View (CV) technique on signals broadcast by the Global Positioning System (GPS). In particular, OP has been using for more than ten years data files in the Common GNSS Time Transfer Standard (CGTTS) format [1] based on the ionosphere free linear combination of GPS P-Code pseudo-ranges collected on both carriers by geodetic receivers, namely the TAIP3 technique [2]. To improve the time transfer short term stability, OP had also developed a technique based on the filtering of CV around a mean value computed for each CGTTS epoch, which are sampled on 16 min periods, in order to average the outliers out [3]. Through the years, other teams had also proposed some averaging techniques like for instance in [4].

In this paper, we propose a new simple approach, aiming at improving the short term stability together with the robustness of GPS CV from TAIP3 data files. The technique is described in Section II. We analyze the results obtained over two different kinds of baselines: one short baseline between OP and the Physikalisch Technische Bundesanstalt (PTB), Braunschweig, Germany, in Section III; and one long baseline between OP and the United States Naval Observatory (USNO), Washington DC, USA, in Section IV. The conclusion is in Section V.

II. THE NEW AVERAGING TECHNIQUE

LNE-SYRTE is operating continuously two geodetic GPS receivers in a common-clock and common-antenna set-up. The receivers are called OPMT and OPM2, and this ensemble is for more than ten years the basis of the International GNSS Service (IGS) station located in OP called OPMT. When looking at the TAIP3 CV between both receivers, we noticed that there were epochs where some given satellite data were outside the global mainstream. Figure 1 shows a typical plot of raw TAIP3 CV data between OPMT and OPM2 over one month, for all GPS satellite vehicles (SV) tracked, with a different symbol for each satellite. For such outliers, the epoch filtering might sometimes lead to biased mean values, increasing that way the short term noise of the time transfer.

From there we decided to try to improve the computation of the CV mean values by averaging out the kind of satellite outliers we see in Figure 1 in a different way. We start from the CGTTS GPS TAIP3 files collected by two different receivers, and we compute CV daily files. We then compute a linear fit over one day of CV data, and we average out all 3 sigma outliers in an iterative process. We tested different cycles, but we finally concluded that the best results were obtained with an iterative process without any limitation. This allows to suppress

either “bad” CV due to some problems in the reception of a given satellite signal, or CV exhibiting abnormal high noise, or any unusual outliers from a biased satellite. Back to the CGTTS TAIP3 CV data files, we compute a mean value between the remaining CV for each common CGTTS epoch, leading to the time transfer results for the reference time scales. Figure 2 shows the processing results on the TAIP3 CV between OPMT and OPM2 over the same period of time as in Figure 1. The dispersion of the data after daily filtering appears limited to a little more than 3 ns peak to peak. Note that the quantified distribution of the filtered CV displayed here is only due to the limited resolution of 0.1 ns in the CGTTS data format.

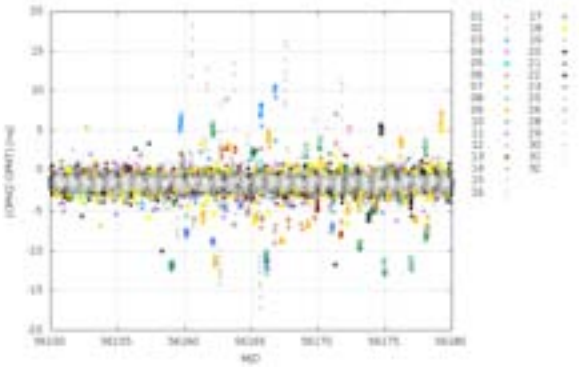

Fig. 1. Raw TAIP3 CV data between OPMT and OPM2 implemented in OP in a common-clock and common-antenna set-up. The corresponding GPS SV number symbols are given on the right of the figure.

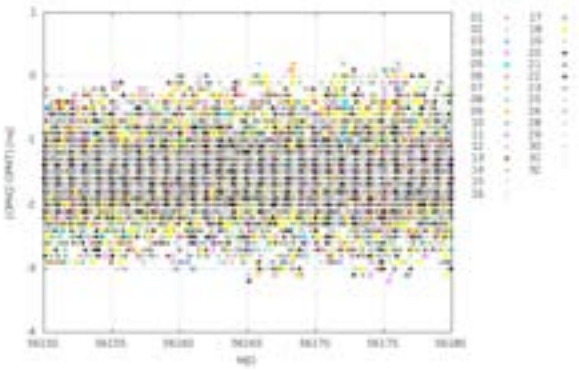

Fig. 2. TAIP3 CV between OPMT and OPM2, after application of the new filtering approach. The corresponding GPS SV number symbols are on the right of the figure.

The analysis of this new technique is based on two different criteria. First, we compare the average number of remaining satellites between the former OP epoch filtering and the new daily approach on time transfer data. In the case the new technique would average out less satellite CV compared to the former one, it would show an increase of robustness in the time transfer link. And second, we compute the Allan Time Deviation (TDEV) of the CV, obtained either from the former OP epoch filtering or with the new daily approach for the same period of time between two stations. We expect there should be some consistency between both criteria if the short term noise is white, as an average increase in the remaining CV by a factor n should lead to a decrease in the TDEV by a factor $\sqrt{n}$.

We have applied this technique on the TAIP3 CV between OPMT and OPM2. The remaining number of satellites left after filtering is about 82 % larger for the daily new approach compared to the former epoch filtering, increasing that way the robustness of the resulting CV. Figure 3 shows the TDEV of the OPM2 – OPMT CV for three different data sets over 200 d. In blue, the TDEV of raw data is plotted. A very small number of data have already been filtered out here, either because the figures were obviously not related to any measurement with GPS satellites, or because of some technical problems in OP for that given epoch. What appears as a large periodic effect in this TDEV is related to some regular and irregular outliers, which are precisely the outliers we wish to suppress. In red, the TDEV of the former epoch filtering developed by OP [3]. The outliers having been averaged out, the TDEV exhibits a white phase noise modulation (slope – ½) up to an averaging period of about 2 d, where the flicker floor of the common receivers’ noise is limiting the stability to between 20 and 30 ps [5]. And in green, the TDEV of the new daily approach shows from the sampling period on an improvement by a factor 1.37, which is in complete agreement with the increased number of CV after filtering, as we get $\sqrt{1.82} = 1.35$. It confirms the white phase noise modulation which dominates until the flicker floor of both receivers’ noise.

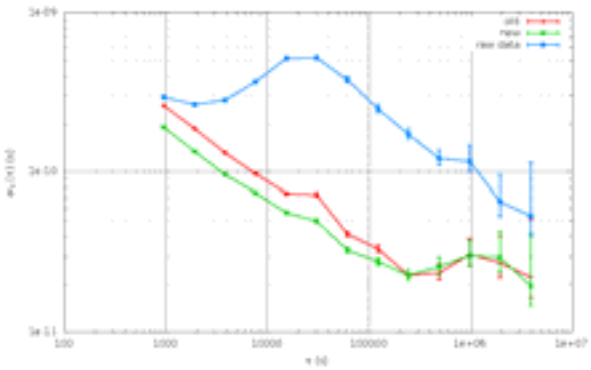

Fig. 3. Allan Time Deviation (TDEV) of the TAIP3 CV between OPMT and OPM2 in a common-clock and common antenna set-up. In blue, the original raw data. In red the former epoch filtering OP process. And in green the new daily approach.

To analyze what happens between remote UTC(k) time scales, we have applied this new daily filtering approach on two different links. In Section III, we show the results obtained over a short baseline of around 1000 km between OP and PTB. In Section IV, we show the results over a long baseline of more than 6000 km between OP and USNO.

III. THE OP – PTB LINK

This GPS link is of particular importance for LNE-SYRTE, because it may be used by the Bureau International des Poids et Mesures (BIPM) for its computation of the Temps Atomique

International (TAI), leading to the Key Comparison UTC – UTC(OP) [6]. We have used TAIP3 data collected in remote stations for more than 200 d. The average number of remaining satellite CV after filtering of the outliers through the new daily approach appears to be 80 % larger than the CV number obtained from the former OP epoch filtering technique.

Figure 4 shows the TDEV obtained from filtered CV between OP and PTB, either when using the former averaging software (in red) or with the new daily approach (in green). As expected over such a short baseline, because of numerous satellites available to compute the CV, the short term noise is very close to a white phase noise modulation, as can be seen in the – ½ slope, until the noise of the UTC(k) difference becomes higher. Therefore, the short term stability should be improved by a factor close to $\sqrt{1.80} = 1.34$. But we see here a gain of 1.49 on the TDEV from the sampling period on, which is slightly larger than expected. This does not question the consistency of both results: it only indicates that the filter quality was also improved, and this is discussed in more detail in the next Section. A noise below 0.2 ns can be reached just above an averaging period of 10 000 s, where the asymptotic behavior of the plot is limited by the remote time scale noise.

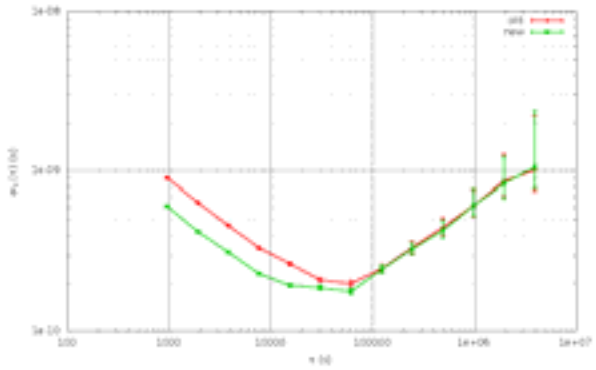

Fig. 4. Time Allan Deviation (TDEV) of the TAIP3 CV between OP and PTB: the former OP epoch filtering results are in red, the new daily approach results are in green.

These results are showing a clear improvement over short baselines when using the new daily filtering approach compared to the former OP epoch filtering. Next Section discusses the example of a long baseline.

IV. THE OP – USNO LINK

Here too, we have used TAIP3 data collected in remote stations for more than 200 d. The average number of remaining satellite CV after filtering of the outliers through the new approach appears to be 22 % larger compared to the CV number obtained from the former OP technique. But it has to be remembered that over such a large baseline, the total number of available CV is always lower compared to a continental link.

Figure 5 shows the TDEV obtained from filtered CV between OP and USNO, either when using the former epoch averaging OP software (in red) or with the new daily filtering approach (in green). In the case the phase noise modulation would be white, the improvement on the TDEV first points from sampling period on should be about 11 %. We see here a gain of a factor 1.38 on the first TDEV point at the sampling period, and 1.29 on the second TDEV point, both being much larger than expected. But before reaching an averaging period of 10 000 s, the noise of the data filtered by the former OP epoch processing seems affected by an unexpected modulation, leading to a difference close to a factor 2 between that TDEV and the new daily filtering approach up to an averaging period above 1 d. The noise of the UTC(k) difference becomes higher than the time transfer noise for an averaging period above 5 d.

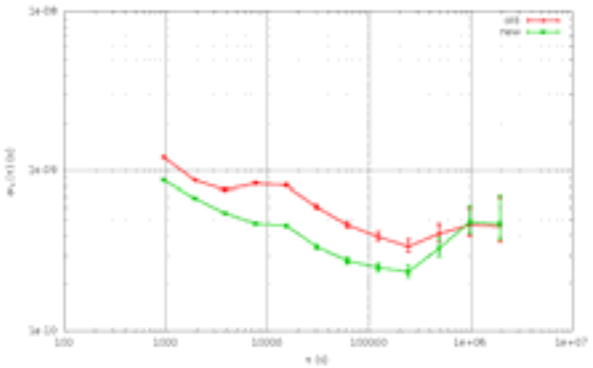

Fig. 5. Time Allan Deviation (TDEV) of the TAIP3 CV between OP and USNO: the former OP epoch filtering results are in red, the new daily approach results are in green.

After analysis, it appears that the large unexpected TDEV improvement between 10 000 s and 1 d is related to a singularity in the TAIP3 CV data. For some unknown reason, during a few consecutive CGTTS epochs, the TAIP3 CV raw data were biased on some satellite measurements which were not in line with the time transfer results obtained before and after that singularity. Figure 6 shows the event on the filtered results of CGTTS epoch sampled CV mean values.

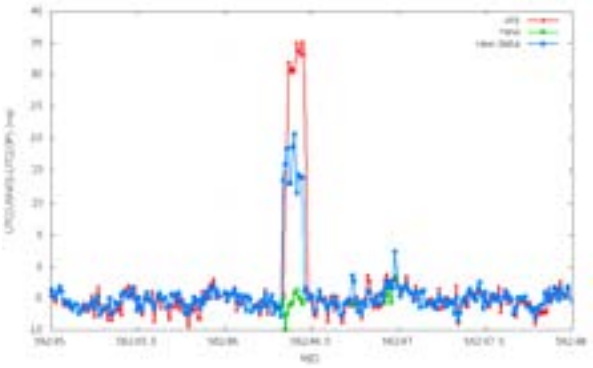

Fig. 6. Biased singularity in the OP-USNO CV. In blue, the mean value of the raw CV data including outliers to be averaged out. In red the results obtained from former OP epoch filtering. In green the results obtained after application of the new daily filtering approach.

In Figure 6, the mean values issued from an epoch averaging of the raw data are in blue. During the singularity event having appeared, the mean values are located between the mainstream data before and after the event and some large outliers which CV are far above 40 ns away. But because there were numerous satellites involved, the former OP epoch averaging technique provides as mean values the inconsistent results in red. The former OP epoch filtering gives too much credit to the outliers, rejecting the good data and computing a mean value based on unfiltered outliers: the CV averages are not in line anymore with the other CV mainstream results. In the contrary, the new daily approach in green consistently averages out the outliers, and provides the expected results in line with the CV mainstream results. We assume that this happens even for small outliers, and this explains why the improvements on the TDEV are larger than expected in the short term when comparing to the increase of CV numbers. Clearly, the new approach provides more stable and more robust results than the former OP processing.

V. CONCLUSION

In this paper, we propose a new simple averaging technique for TAIP3 GPS CV which improves both the stability and the robustness of time transfer between remote stations. Instead of averaging the outliers out by using a given filter around a mean value computed for each CGTTS sampling epoch, we average the outliers out from a linear fit on daily CV files. Between two GPS receivers in common-clock and common antenna set-up, the number of available CV left after filtering is 82 % larger than with the former epoch filtering developed by OP. The white phase noise improvement on a TDEV plot is consistently in line with that result, from the sampling period on until the averaging period where the flicker floor of the receivers' noise is the limit.

Over a short baseline of less than 1000 km between remote stations, we obtain a similar increase in the CV number after filtering, but the TDEV improvement is slightly larger than expected. Over a long baseline of more than 6000 km, the TDEV improvement is also much larger than expected. But this can be explained by the way the former OP epoch processing was giving too much credit to some outliers for the computation of the CV mean values compared to the global mainstream. The new daily approach gives more consistent results, improving that way both the short term stability and the robustness of time transfer in all cases.

This new processing approach has been implemented in OP in a completely automated way. As being a very simple filtering technique, we expect it might be useful in the future for any GNSS time transfer based on code data.

ACKNOWLEDGMENT

The authors are grateful to P. Defraigne from Observatoire Royal de Belgique (ORB) for having made her TAIP3 software freely available to the Time Metrology community.

REFERENCES

[1] http://www.bipm.org/wg/AllowedDocuments.jsp, BIPM open access website devoted to CGTTS format, June 2013.

[2] P. Defraigne and G. Petit, "Time transfer to TAI using geodetic receivers", *Metrologia* 40 (2003), 184-188.

[3] J. Achkar, P. Uhrich, Ph. Merck and D. Valat, "Recent Time and Frequency Transfer Activities at the Observatoire de Paris", Proc. of the 2005 IEEE Frequency Control Symposium and Annual Precise Time and Time Interval Meeting, Vancouver, Canada, 2005, 247-253.

[4] R. Costa, D. Orgiazzi, V. Pettiti, I. Sesia and P. Tavella, "Performance comparison and stability characterization of timing and geodetic GPS receivers at IEN, Proc. of the 18th European Frequency and Time Forum (EFTF), Guildford, United Kingdom, 2004, 279-286.

[5] P. Uhrich, D. Valat and A. Proia, "Comparisons between different types of GPS equipment by using TAIP3 processing", Proc. of the 22nd European Frequency and Time Forum (EFTF), Toulouse, 2008, France, CD-Rom.

[6] http://kcdb.bipm.org/, BIPM key Comparison database, June 2013.

Design and Implementation of Dual One-way Precise Ranging and Time Synchronization System

Hong-Jiao Ma[1,2,3], HuaBing Wu[1,2,3,4], JianFeng Wu[1,2,3], Meng Li[1,2,3,4], Kang Wang[1,2,3,4], ZaiMing He[1,2,3], DangLi Zhao[1,2,3]
(1. National Time Service Center, Chinese Academy of Sciences, Lintong, Xi'an, China;
2. Key Laboratory of Precise Navigation and Timing Technology, CAS, Lintong, Xi'an, China
3. Key Laboratory of Time and Frequency Primary Standard, CAS, Lintong, Xi'an, China;
4. University of Chinese Academy of Sciences, Beijing, China)
E-mail: mahj@ntsc.ac.cn

***Abstract*—With the development of science technique in aeronautic and astronautic testing navigation, communication, as well as electric power, etc, time synchronization has been needed in more and more engineers and sciences fields. Dual one-way ranging can get more veracity of measure precision than one-way due to eliminating the common measure error between two points. This article describes the use of dual one-way pseudo-code and carrier phase precise measurement for realizing time synchronization technique. The results of the experiment showed that DRTS system reached 0.15cm and 5ps in 1s time interval, the precision of this system reached 3.46ns and 9.43ps by using different and the same frequency reference of the order of e-10/d respectively. Dual one-way ranging and time synchronization can be applied in aeronautic and astronautic measurement and control system, and in achieving high precision time platform in message transfer field. It also can provide time service between satellite and satellite, satellite and ground station, aircrafts, stations and other patterns.**

Keywords—Precise Ranging; Time Synchronization; Dual One-way Ranging Measurement.

I. INTRODUCTION

With the rapid development of aerospace test, navigation, communications, electricity and other scientific technology, more and more engineering and scientific fields require precision time synchronization. Such as: the world time laboratory needs the precision time synchronization which is based on the order of a nanosecond or sub-nanosecond; Satellite launching, monitoring and control, test range atomic clocks need the Calibration; During communications between the navigation satellites, satellite and ground station, and ground stations, precision time synchronization is required; In addition, the Autonomous Formation flight AFF, networking aircraft, also need the precision baseline measurements and time synchronization. However, in our country, there is no mature commercial product of time synchronization terminal which is based on two-way precision ranging. Therefore, the users still have to import this kind of product from other countries.

II. THE PRINCIPLE OF DUAL ONE-WAY RANGING [1, 2]

In Dual one-way pseudo-range measurement, at least one transmitter and one receiver need to be installed in each of the two terminals. By means of dual one-way ranging, both of them can obtain a relative pseudo-range through pseudo-code and carrier phase measurements, which can eliminate the clock error and realize precision time synchronization between the two terminals. The Timing principle of DOWR is shown in figure 1.

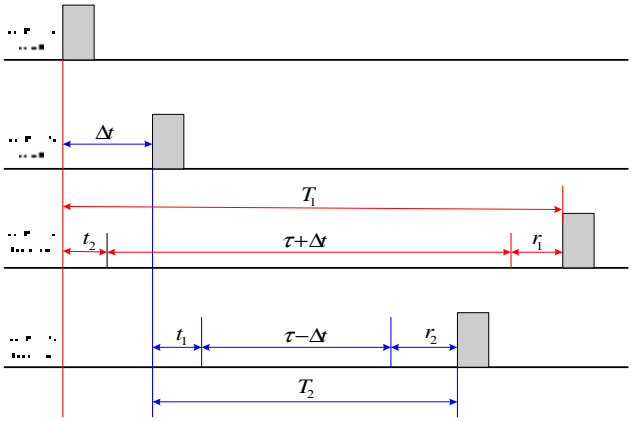

Fig. 1. Timing principle of DOWR.

Figure 1 shows that:

$$T_1 = t_2 + \tau + r_1 + \Delta t \quad (1)$$

$$T_2 = t_1 + \tau + r_2 - \Delta t \quad (2)$$

Δt is The clock difference between the two terminals A and B; T_1 and T_2 are the local pseudo-range respectively measured by terminal A and B; the transmitting device delay and the receiving device delay of terminal A are t_1 and r_1; similarly, the transmitting device delay and the receiving device of terminal B are t_2 and r_2; and the electromagnetic wave propagation delay between the antennas of the two terminals is τ. Through the Equations 1 and 2, the clock error and the real distance between terminal A and B can be obtained.

$$\Delta t = \frac{1}{2} \cdot [\,(T_1 - T_2) - (t_2 - t_1) - (r_1 - r_2)\,] \quad (3)$$

$$D = \frac{1}{2} \cdot [\,(T_1 + T_2) - (t_1 + t_2) - (r_1 + r_2)\,] \cdot c \quad (4)$$

Here, assume $t_{12} = t_1 + r_2$, $t_{21} = t_2 + r_1$:

Supported by West Light Foundation of The Chinese Academy of Sciences (Y211YR2601).

$$\Delta t = \frac{1}{2} \cdot [(T_1 - T_2) + (t_{12} - t_{21})] \quad (5)$$

$$D = \frac{1}{2} \cdot [(T_1 + T_2) - (t_{12} + t_{21})] \cdot c \quad (6)$$

In the process of measurement, T_1 and T_2 can be respectively extracted from the code tracking loop of terminal A and B, and then be embed into the data region of a transmission frame, which can be sent to each other through the data exchange link. Since the one-way propagation delay t_{12} and t_{21} can be obtained through the Calibration, therefore, by means of DOWR, the measurement value of time comparison and the precise distance can be obtained.

III. THE CONSTRUCTION FRAMEWORK OF DRTS

The DRTS system consists of six parts, which are receive channel, transmit path, frequency reference, IF signal processor, display and control computer and power distribution, as shown in figure 2. This system mainly consist of such device as rubidium, Doppler analog unit, the reference amplifier and splitter, frequency synthesizer, noise source, A/D sampling, baseband processing unit, BPSK modulator, equipment monitor unit and computer.

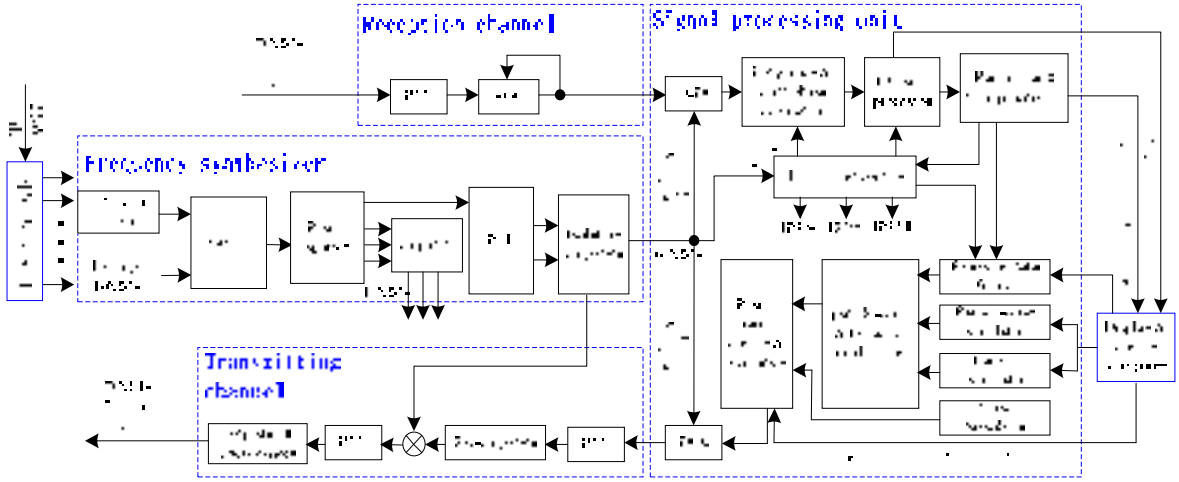

Fig. 2. Block diagram of the overall function of the device

IV. THE TECHNOLOGY USED IN DRTS SYSTEM

The principle of One-way pseudo-range measurement in DRTS system and pseudo-range measurement in GNSS are substantially the same. When the code tracking loop of Terminal A is locked, parameters like synchronous frame count, data bits count, spread code phase count and spread chip phase count will be output, so that the terminal A will get the time delay measurement between the synchronization timing of a local transmitting frame and the synchronization timing of a received frame transmitted by terminal B after a series of calculation. The distance we get is the distance between A and B at the time that the head of a frame is transmitted. For each received frame head sent by terminal B, the distance value will be updated correspondingly. Therefore, the output cycle of distance and the cycle of transmission frame are equal in value.

The main technologies of the system includes: the design, generation and transmission of ranging signal; the rapid capture of the ranging signal; Tracking and demodulation of the ranging signal; and the high-precision signal processing method. The accuracy of Time synchronization depends directly on the accuracy of the pseudo-range measurement, which can be greatly improved by the method of carrier phase smoothed pseudo-range. The detailed content could be found in reference [3]. Meanwhile, in order to adapt to the highly dynamic environment, an algorithm of second-order FLL assisted third-order PLL will be used in the tracking loop. Some of the indicators for the simulation environment of figure 2, 3 and 4 are: the velocity is 8000m/s, the acceleration is 20g and the accelerated acceleration (jerk) is 2g/s. As can be seen from the figures, about two seconds after the signal capture, the estimated carrier phase residual, carrier frequency residuals and pseudo-code phase residuals tend to be zero, which means the tracking loop of this system has the ability to adapt to the high dynamic environment.

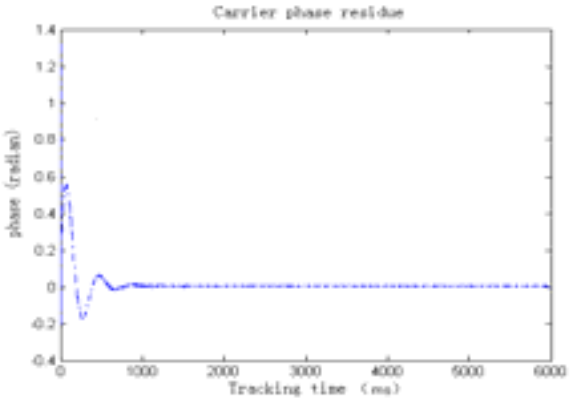

Fig. 3. Carrier phase residue

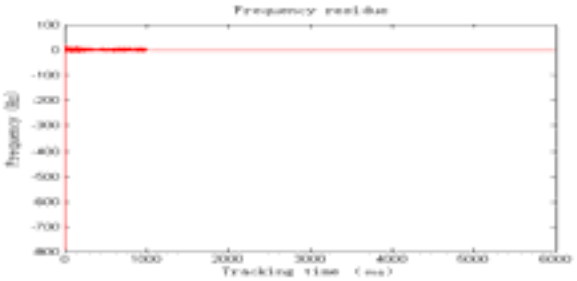

Fig. 4. Carrier frequency residue

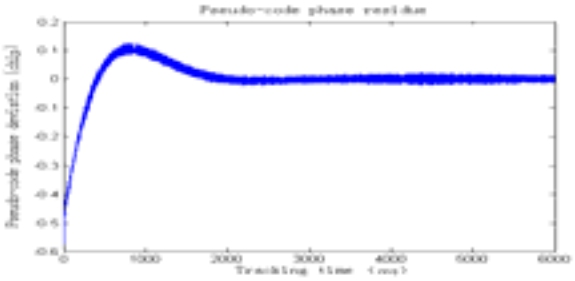

Fig. 5. Pseudo-code phase residue

V. SIMULATION AND EXPERIMENTAL RESULTS

A. *The prototype of DRTS system*

The prototype of DRTS Experimental system is shown in figure 6.

Fig. 6. The prototype of the experimental system

B. *The discrimination of signal tracking quality*

The oscilloscope display of the transmitting pseudo-code and the traced pseudo-code are shown in Figure 7, from which we can easily find that there is an obvious fixed delay between them.

The error output of DLL phase discriminator represents the tracing accuracy of the code loop; similarly, the error output of carrier phase loop discriminator represents the tracing accuracy of carrier loop. Inside the FPGA, the output of the code tracing loop filter is a 0.2ms-long data, and the per second acquisition of the tracking error of a data code phase std=0.00487chip, as shown in figure 8. The tracing error of carrier phase std=0.398 ° , as shown in figure 9.

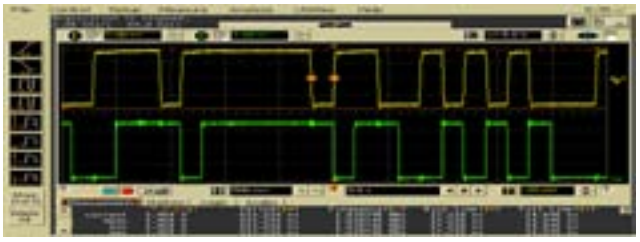

Fig. 7. The oscilloscope display of the transmitting pseudo-code and the traced pseudo-code

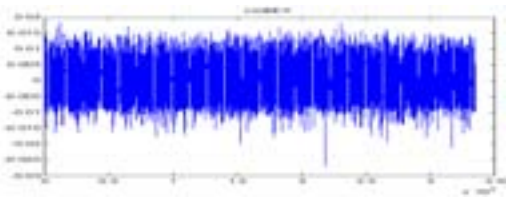

Fig. 8. Code phase tracking error

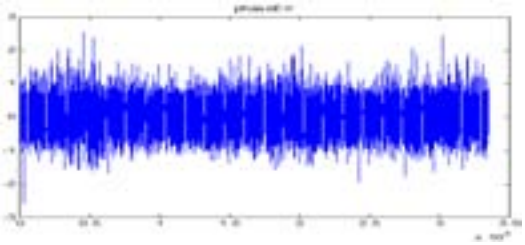

Fig. 9. Carrier phase tracking error

C. *Result figure of system test*

Use a 60-meter-long symmetrical cable to simulate the space link in the test. Assume that the delay of two-way symmetrical coaxial cable is T, which also means that T is equal to the product of the propagation velocity v (ns/m) of the signal in the cable and the length of the cable, plus the transmission delay t1 and the reception delay t2 of the system, which can be expressed by the equation 60*v+t1+t2=T. After several tests and calculations, we can get these results that the propagation velocity v of the obtained signals in the coaxial cable is about 5ns / m, and the sum of transmission and reception delay of the device at the time of boot is about 40.2ns.

Then, use the same source and different sources rubidium clock to do some tests, which can get the local pseudo-distance, pseudo-range of the opposite side, clock error and the true distance. The test results are shown in Figure 10 and Figure 11. After the indicators of the entire terminal system has been tested, the results show that the daily stability of different sources rubidium atomic frequency standard is e-10 and the daily accuracy is e-9, and the accuracy of ranging and time synchronization of the terminal ≤1.038m/3.46ns (STD), which has met the original design requirements and can be used in the

precision baseline measurement and time synchronization of the inter-satellite network, such as the Autonomous Formation aircraft.

If use the same source rubidium in the same order of magnitude, then the testing accuracy is 0.279cm/9.3ps (STD), which characterizes the measurement optimum in this certain environment. And the ranging and time synchronization resolution is up to 0.15cm and 5ps (@1s), one time higher than the similar foreign products [4]. Detailed comparison is shown in Table 1. Due to the lower stability and accuracy of the reference frequency resource used by foreign similar product, the ranging and time synchronization accuracy are not directly comparable. However, according to the data analysis, we know that if the frequency of the reference sources are in the same order of magnitude, this system will have a better performance than foreign similar products.

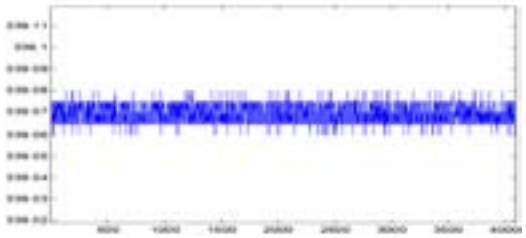

Fig. 10. 60m with the same resource

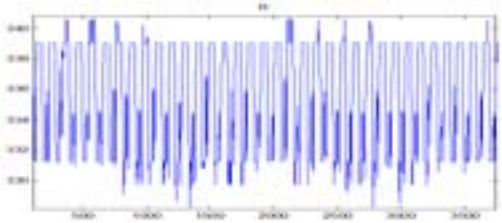

Fig. 11. 60m with different resource

TABLE I. COMPARISON OF DRTS AND SATRE

comparison	Dual Ranging Time Synchronization (DRTS)	Satellite Time and Ranging Equipment (SATRE)
Code rate	5M	0.5,1,2.5,5,10,20M
Center frequency	15MHz	70MHz
Resolution of Ranging and Time Synchronization	0.15cm、5ps(@1s)	0.3cm、10ps(@1s)
Accuracy of ranging and time synchronization	Different resource 3.46ns(reference frequency <e-10/d); The same resource 9.3ps(reference frequency <e-10/d)	<200ps(reference frequency-14/d)

D. Computer supporting software package

Computer supporting software function modules include:

- Parameter control of serial communication port, baud rate, data bits, stop bits, parity, etc.
- Numerical display and graphical interface display: including the respective pseudo-range measurement value, the clock difference and the true distance between the two stations.
- Data analysis and processing modules: data acquisition, display and storage of the results.

The new technology and method used in this software includes:

- Automatically adjust the size and location of character and control button on the software interface according to the resolution.
- This program can read the number of the existed logical serial port from the system registry form, and make it available to the users to choose, which avoid the occurrence of such problems as the blind display of the software and the blind serial selection of the users.
- Create a dedicated thread to ensure the timeliness and stability of communication.

VI. CONCLUSION

Due to the symmetry of the measurement path of DOWR principle, the common error between these two points is eliminated and higher measurement accuracy is obtained compared to one-way ranging. In this paper, on the basis of pseudo-code phase and carrier phase of the dual one-way precision ranging, a preliminary exploration of time synchronization between two points is conducted. Systematic errors are mainly caused by these two aspects, that is, the zero drift caused by the RF front-end and combination of zero drift caused by baseband circuit, and the RF phase delay caused by the temperature change [5]. In addition, when it comes to the versatility of device and its ability of the seamless connection with similar foreign product, the system needs to be further optimized. In brief, the Two-way ranging and time synchronization system can be applied to future earth integrated aerospace monitoring and control, high-precision time measurement and control platform of information transmission, and also can provide time service to the communication between the satellites, satellite and ground station, aircraft, ground stations, etc.

REFERENCES

[1] U. Ko, Analysis of the characteristics of the GRACE Dual One-Way Ranging system, Ph.D. Dissertation, Department of Aerospace Engineering and Engineering Mechanics, the University of Texas at Austin, May 2008.

[2] Thomas, J.B., "An Analysis of Gravity-Field Estimation Based on Intersatellite Dual-1-Way Biased Ranging", Jet Propulsion Laboratory, JPL Publication 98-15, Pasadena, California, May 1999.

[3] Meng Li, Hong-Jiao Ma, The application of carrier phase smoothed pseudo-range in two-way ranging and time synchronization. China Satellite Navigation Conference 2013, WuHan, China, 2013.5.

[4] SA-TIM-MA-1004, SATRE Modem Overview, SATRE Operation Manual, T. Kuhn, TimeTech, 2002.

[5] Wu Huabing, Hu Yonghui. Design and implementation of precise ranging and time synchronization system based on DOWR [C]. 2012 International Conference on Measurement, Information and Control, Harbin, China, IEEE Computer Society, 2012: 239-243.

Analysis on GNSS Space Clocks Performances

Alice Cernigliaro
Aizoon
Torino, Italy
alice.cernigliaro@aizoon.it

Stefano Valloreia, Gianluca Fantino and Lorenzo Galleani
Politecnico di Torino
Torino, Italy
galleani@polito.it

Patrizia Tavella
INRIM
Torino, Italy
p.tavella@inrim.it

Abstract— **In Global Navigation Satellite Systems (GNSS) the role of atomic clocks is essential for the determination of the user position. Nowadays, several satellite navigation systems are operating and different clock technologies have been employed on board satellites, taking benefit of the improvements reached during the last tens of years. The analysis of GNSS clock performance is thus crucial for ensuring the GNSS positioning and timing capabilities.**

We performed an analysis on the clock estimates generated by the Information-Analytical Centre [1] (IAC) of the Russian Federal Space Agency, which provides a service similar to the one of the International GNSS Service (IGS). Therefore, we collected and processed the RINEX for clock files containing satellite clock estimates for GPS and GLONASS constellations, from 2008 to 2013: with our statistical tools [2] we performed an analysis of the performances of the different space clock technologies employed on board different GNSSs. In particular, we focused the attention on the frequency behaviour and the frequency stability, evaluating also the stationarity of these characteristics, with the aim of classifying and analysing the clock anomalies.

In this paper, the attention is mostly focused on the change in clock noise variance.

Keywords—GNSS timing; atomic clocks; clock anomalies; change in noise variance

I. INTRODUCTION

Atomic clocks and time scales are fundamental in Global Navigation Satellite Systems (GNSSs). Each satellite of the constellation carries more than atomic clocks, as a reference for all the timing operations.

It is known that in GNSSs the position is determined from the time of flight of signals transmitted from satellites: hence, any error in the time measures generates an error in the positioning. This is the main reason why very stable and accurate atomic clocks are of extreme importance to guarantee small positioning errors.

In GNSS, different clock types are employed on board satellites: Rubidium Atomic Frequency Standards (RAFS) are used in GPS and Galileo, Caesium clocks are used in GPS and GLONASS, while Passive Hydrogen Masers (PHM), the best clocks ever realized for space applications, are flown on Galileo satellites.

Clocks can experience anomalies for several physical reasons [3,4]. Clock anomalies impact directly on the positioning error: in fact clock stability and predictability are dramatically corrupted in case of anomalous clock behaviour and the user ranging error is increased. It is therefore crucial to understand clock anomalies.

We are carrying out a thorough study of clock anomalies on GPS and GLONASS clocks. Our interest arises from the fact that we have been characterizing clock anomalies for Galileo and we aim to have a clear general picture on space atomic clock behaviour .

We start by classifying the main anomalies in GNSS clocks.

Main families of anomalies that we are observing on satellite clocks are:

- apparent deterministic oscillations
- frequency jumps
- change in the noise variance

Our final goal is to build a detailed statistics of all the anomalies affecting GNSS space clocks.

In this work we will focus on the changes in the clock noise variance.

II. EXPERIMENTAL ACTIVITY

A. Sources of Data

As input for our analysis, we collected the GPS and GLONASS RINEX for clock files from June 2008 to April 2013, from the Information-Analytical Centre (IAC) [1] of the Russian Federal Space Agency.

The IAC is an organization which provides accurate estimates of clocks and orbits of GPS and GLONASS satellites, in addition to information on the GNSS status.
The IAC estimates of satellite clocks and orbits are comparable with those evaluated by the International GNSS Service (IGS) [5], the leading processing centre in the world.
We collected also the first Galileo clock data from the Multi-GNSS Experiment (MGEX) of the IGS [6].
We processed the satellite clock data with the tools regularly employed at INRiM for clock characterization [7], to assess the performances of the different clock families.
We concentrated on the main anomalies present in the satellite clocks, namely apparent deterministic oscillations, frequency jumps, and changes in the noise variance.
Changes in the noise variance are addressed in this paper.

B. Changes in the noise variance

When a clock experiences a change in the variance the performances are degraded.
The change can be local, as in the example illustrated in Fig 1, where the noise variance, as estimated by the Allan deviation, is increased then returns to the original level.
We study the changes in the noise variance with the Dynamic Allan Deviation (DADEV) [8,9], which allows to observe also some phenomena which would not be visible with the classical Allan Deviation.
Fig 2 shows the dynamic Allan deviation of the data presented in Fig 1: the first two peaks are due to the two jumps in the clock phase offset illustrated in Fig 3, while the change in the noise variance is clearly visible in the increase of DADEV level between days 260 and 265.
Changes in the noise variance may indicate major problems in the clock behaviour.
As seen in Fig 4, showing the evolution of caesium clock on board GPS satellite G30, the noise variance started increasing progressively: on day 133 the clock was then declared not usable until further notice, before being definitely decommissioned on day 201 [10].
After this malfunctioning, satellite SVN 30 (labelled with PRN G30) was then substituted by the spare satellite SVN 35 on day 228, with a Rubidium clock. [11].

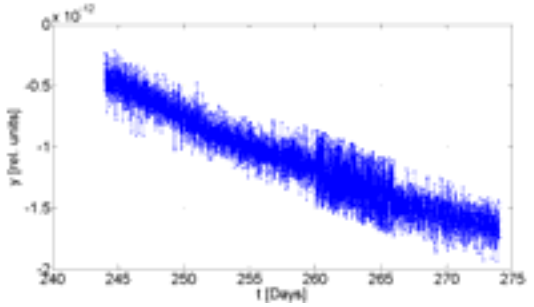

Fig 1: GPS G25 RAFS clock vs GPS Time Normalized Frequency Offset, September 2010

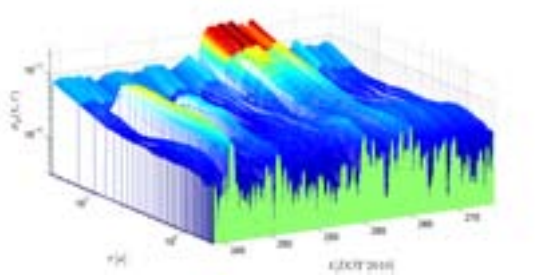
Fig 2: GPS G25 RAFS clock vs GPS Time Dynamic Allan Deviation, September 2010

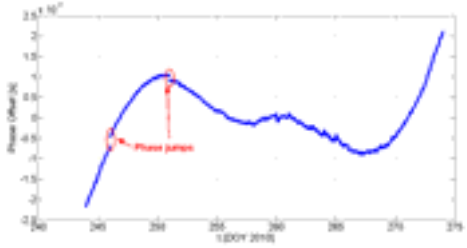

Fig 3: GPS G25 RAFS clock vs GPS Phase Offset, 2nd order drift removed, September 2010

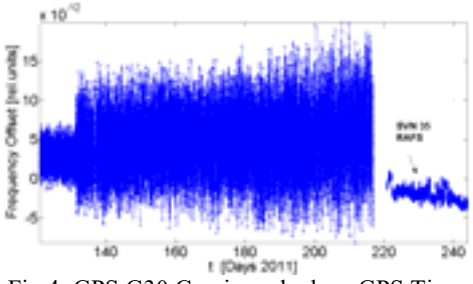

Fig 4: GPS G30 Caesium clock vs GPS Time Normalized Frequency Offset, May-June 2011

This is a clear example in which the change in noise variance indicates the status of clock health, which can be monitored by means of the Dynamic Allan Deviation.
Fig 5 reports the Dynamic Allan Deviation of satellite G30, including the period before and after the breakage: the higher level of the DADEV until day 220 represents the increase in the noise variance. The single peak before day 140 is generated by a jump in the clock phase offset.
After the satellite change, it can be observed that the level of DADEV is noticeably decreased.
In both the examples reported in this paper, the change in the noise variance is associated to an increase of the level of Dynamic Allan Deviation: a detection surface can be set [12]

in order to rise alarms for potential anomalies when the threshold is exceeded.

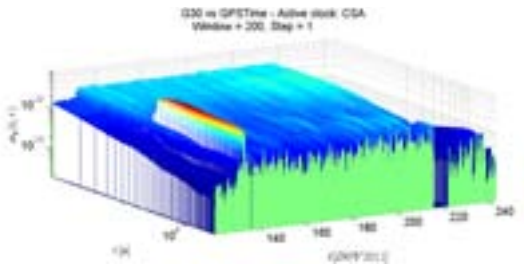

Fig 5: GPS G30 vs GPS Dynamic Allan Deviation, May-June 2011

III. CONCLUSIONS

The exam of the GNSS space clock behavior reveals some anomalies that can be significantly impacting the navigation performance. We have carried out an analysis over 4 years of GPS and GLONASSS space clock data and we have identified a few type of clock anomalies. Among them the increase of the clock noise variance can be a sign of the end of life f a clock and can therefore be a warning at system level. We have investigated the capacity of the Dynamic Allan variance to detect and interpret such situations, showing the potentiality of the tool and its valid application to GNSS clock management.

REFERENCES

[1] http://www.glonass-ianc.rsa.ru/en/

[2] A. Cernigliaro and I. Sesia, "Satellite Clocks Characterization and Monitoring for Global Navigation Satellite Systems," Proc. of the XXX URSI General Assembly and Scientific Symposium of International Union of Radio Science, 13-20 August 2011, Istanbul, Turkey

[3] K. L. Senior, J. R. Ray, and L. R. Beard, "Characterization of periodic variations in the GPS satellite clocks," GPS Solutions, Springer-Verlag 2008.

[4] M. Epstein, T. Dass, J. Rajan, and P. Gilmour, "Long Term Clock Behaviour of GPS IIR Satellites," Proc. of 39th Annual Precise Time and Time Interval (PTTI) Meeting, 26-29 November 2007, Long Beach, California (USA).

[5] IGS Tracking Network Web Site, IRKT Log, http://igs.org/network/site/irkt.html

[6] http://igs.org/mgex/

[7] A.Cernigliaro, I.Sesia, "Satellite Clocks Characterization and Monitoring for Global Navigation Satellite Systems", in Proc of the XXX URSI General Assembly and Scientific Symposium of International Union of Radio Science, August 13th-20th 2011, Istanbul, Turkey

[8] L. Galleani, P. Tavella, "Dynamic Allan variance" , IEEE Transactions on Ultrasonics, Ferroelectrics, and Frequency Control, UFFC, vol. 56, no. 3, March 2009, pp450-464

[9] L. Galleani, P. Tavella, " Interpretation of the Dynamic Allan Variance of Nonstationary Clock Data", " in proc Joint IEEE International Frequency Control Symposium and European Frequency and Time Forum, May 2007, Geneve, Switzerland, on CD.

[10] ftp://tycho.usno.navy.mil/pub/gps/

[11] http://www.insidegnss.com/node/2731

[12] L.Galleani, "The Dynamic Allan Variance III: Confidence and Detection Surfaces," IEEE Transactions On Ultrasonics Ferroelectrics And Frequency Control, vol. 58, no. 8, pp. 1550-1558, 2011.

A Method of GNSS System Time Offset Monitoring

Huijun Zhang,Lin Zhu, Xiaohui Li
National Time Service Center, Chinese Academy of Sciences，LinTong, Xi'an ,China
Key Laboratory of Precision Navigation and Timing Technology，National Time Service Center, Chinese Academy of Sciences，LinTong, Xi'an ,China
zhj@ntsc.ac.cn

Xue Zhang
National Time Service Center, Chinese Academy of Sciences, LinTong, Xi'an ,China
University of Chinese Academy of Sciences
Beijing, China

***Abstract*—With the progress of Global Navigation Satellite Systems(GNSSs),which mainly includes GPS, GLONASS, GALILEO as well as BeiDou, multi-system joint working mode has become research focus and application trend. But, Each satellite navigation system has its own independent system time, such as GPST, GLONASST, GST and BDT. The System time offset between the two satellite navigation systems is one of the most important aspects of their interoperability. It will cause combined navigation position solution bias and time solution. Therefore, it is necessary and significant to monitor and research system time offset.**

A method of GNSS System Time Offset monitoring which is called Signal- in-Space Reception method is put forward and its principle is described. In this method, UTC(NTSC) time scale is regarded as reference time scale on account of its status of standard time and frequency resources. Then, The time offset between each satellite navigation system time and UTC(NTSC) which include UTC(NTSC)-GPST, UTC(NTSC)-GLONASST, UTC(NTSC)-BDT,UTC(NTSC)-GST can be acquired. Thus, system time offset among satellite navigation systems, such as GPST-GLONASST, can be acquired with about 5ns (1 σ) precision.

On the basis of above described method, GNSS System time offset monitoring system has been set up since 2011 and it is gradually improved and perfected. A great deal of monitoring data has been collected. Addition to common error sources, some special error sources related to GNSS timing receiver such as receiver delay, inter-system hard delay bias, inter-frequency biases and so on are analyzed, as they can effectively affect monitoring results and precision. The monitoring data and IGS precision orbit as well as corresponding data published by BIPM Circular T Bulletin are combined together to determine above error values. The results of the error items and GNSS system time offset monitoring results are to be showed.

Keywords—GNSS; System time offset; Monitoring; Signal-in-Space Reception; Error sources

I. INTRODUCTION

At present, GNSSs (Global Navigation Satellite Systems) has got into a new era of vigorous development, which mainly includes GPS, GLONASS, Galileo and BDS[1,2,3,4,5].Each GNSS systems are based on time difference measurement that is why accurate and stable system time is one of the security conditions for the satellite navigation system working. Therefore, every GNSS system has its own time reference system, the system time of GPS is GPST, which is traceable to UTC (USNO); GLONASS system time is GLONASST, traceable to UTC (SU); Galileo system is GST (Galileo System Time), was controled to the TAI or UTC by the Time Service Provider (TSP). BDs system time is referred as BDT, BDT using a continuous time scale which is no leap second insertion, and it traces to international TAI or UTC through UTC (NTSC) [6, 7]. In the multi-mode navigation applications, the use of satellite clock correction broadcast by satellite navigation message, GPS pseudorange correction to GPST, GLONASS pseudoranges correction to GLONASST and BDs pseudorange correction to the BDT. Thus, the system time offset between different systems will cause the deviation of positioning[8], so that users encounter the bias of position information when they are calculating. For the above reasons, it is necessary to using a unified system time in user terminal for positioning. There are many ways to measure and determine the system time offset [4], this article focuses on the method of GNSS system time offset monitoring which is called Signal-in-Space Reception method.

II. METHOD OF GNSS SYSTEM TIME OFFSET MONITORING

A. *Review of monitoring methods*

GPS and Galileo have already reached agreements between the two systems, and the advance of GGTO monitoring is in processing. Due to the permission of where USA and Europe are located, GGTO monitoring technologies include two-way satellite time transfer and common view methods [9]. China's Beidou satellite navigation system, Galileo satellite navigation system and the Russian GLONASS systems also can use these two methods for monitoring the system time offset. However, these methods require both sides to negotiate firstly, and also including political factors as well as expensive fees, another important problem is the geographical constraints, because it needs to be observed with the same satellite whether it is two-way satellite time transfer method or common view method. Based on the above considerations, the best monitoring method of GNSS system time offset can turn to receive the Siganl-in-Space. The reasons are as follows: 1.every GNSS system is a high-precision timing system, each GNSS system not only has their own time system and traceable links, but also has ability for transferring the system time to users through the GNSS satellites.2. Currently, the performance of high-end commercial receiver is more and more remarkable for timing and positioning, moreover combined GPS / GLONASS /

Spported by"Western Light Talents training program of CAS" roject (Y109YR2701),2010

GALILEO / BDS, its precision can be further improved by accessing a high-precision external frequency reference .3. System time offset monitoring by Signal-in-Space Reception without geographical limitations and much cheaper. Nevertheless, using this method to monitoring system time offset needs to consider many error factors, these will be described in later chapters.

National Time Service Center(NTSC) of CAS is the specialized research institute for Chinese national standard time production, maintain and dissemination. Since 2005, the deviation between the Coordinated Universal Time (UTC (NTSC)) establishes and maintains in National Time Service Center and the international standards Coordinated Universal Time (UTC) is in remains within 20ns. Signal-in-space Receiption method for system time offset monitoring is based on the UTC (NTSC) standard time and frequency.

B. Signal-in-Space Reception method for GNSS system time offset monitoring

The system time offset monitoring principle by receiving space signals is as follows: we take the standard frequency signal of the National Time Service Center as a frequency reference, the standard time signal as the reference time scale, the differences between UTC (NTSC) and GNSST are measured (including UTC (NTSC)-GPST, UTC (NTSC)-GLONASST, UTC (NTSC)-BDT, UTC (NTSC)-GST, etc.), Figure 1 shows the measuring principle, take the GPS and GLONASS systems as an example, UTC (NTSC)-GPST and UTC (NTSC)-GLONASST can be measured at the NTSC ,then we can obtain the GPST-GLONASST directly.

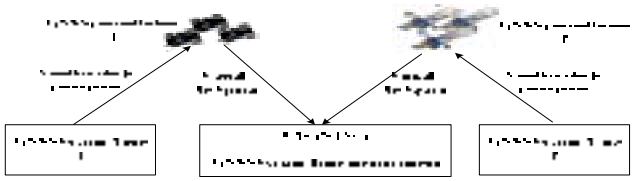

Figure1. Schematic diagram of system time offset monitoring by signal-in-space reception

Figure 2 describes the core equipment of this monitoring method is GNSS timing receiver and the time interval counter. In the precise known of GNSS receiver antenna phase center, each navigation system spatial navigation signals received by timing receiver, the receiver pseudo-range and high-precision time interval counter measurement value are used so as to calculate the difference between UTC (NTSC) and each GNSS system time.

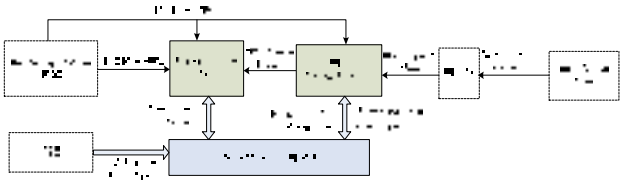

Figure2 Block diagram of receiving space signal to achieve the system time offset monitoring

Figure2 shows that the difference between UTC (NTSC) and GNSST (GPST, GLONASST,BDT, GST, etc.) can be calculated in Equation (1) below:

$$UTC(NTSC)-GNSST=\left(\rho-\mathrm{r}+dt-\mathrm{pd}-\mathrm{d}\left(\mathrm{ion}\right)-\mathrm{d}\left(\mathrm{trop}\right)-\mathrm{Ep}\right)/\mathrm{c}-TICValue-\Delta ChDelay+\Delta ISDB \quad (1)$$

Where GNSST is the GNSS system time, ρ indicates the pseudorange from receiver to the satellite, r represents the real geometric distance between satellite and ground, dt is the satellite clock bias, pd is the orbit error, d (ion) is the ionospheric delay, d (trop)is the tropospheric delay, Ep indicate other errors, c is the speed of light, TICValue is the measurement value of precision time interval counter, ΔChDelay indicates that the receiver relative channel delay bias, ΔISDB represents the inter-system hardware delay bias.

Since more than 5 satellites of every GNSS constellation can be received at a fixed position, at the NTSC, the average number of received GPS satellites and GLONASS satellites both over 8. In addition, the system time offset monitoring is done at one second interval, so we can use the following ways to further improve the monitoring precision: (1)Averaging the system time offset monitoring results for all visible satellite.(2)Smoothing monitoring data per minute.(3)Using IGS or other precise orbit to correct monitoring data, further eliminating the ephemeris error.

III. THE ERROR SOURCES OF SYSTEM TIME OFFSET MONITORING AND MEASUREMENT OF THE IMPORTANT PARAMETERS

A. Error budget for system time offset monitoring

The monitoring precision error budget of system time offset determination by Signal-in-Space reception is as follows[10,11]:

(1). Satellite orbit error is about 4.5ns;

(2). Satellite clock error is about 4.5ns;

(3).Transmission link error is about 3ns, including the ionosphere and troposphere, ionosphere using dual-frequency correction;

(4). Receiver error is about 3ns, including receiver noise error, the receiver delay error, inter-frequency bias, multipath errors, etc;

(5). The error of time interval counter measurement is about 0.5ns;

(6). The reference clock error of about 2ns;

(7). The inter-system hardware delay bias is about 2ns.

NO.1-NO.6 errors are caused by monitoring a single satellite, error No. 7 result from difference between the signal frequencies of multi-GNSS systems in receiver [12], the total error estimate as follows:

$$\sqrt{4.5^2+4.5^2+3^2+3^2+0.5^2+2^2+2^2}\approx 8.0ns \quad (2)$$

It has been described in 2.2, using multi-satellite system time offset monitoring value for the mean, and the average

values were further smoothed in a period of time, this will eliminate monitoring errors witch have characteristic of noise, such as receiver measurement noise. And part of the satellite clock error and signal propagation delay will be eliminated as well. Therefore, the monitoring result can be acquired with the 5ns (1σ) estimation precision.

B. Receiver delay measurement

In order to implement the function to monitor the GNSS system time offset, we use a simpler method for determining the receiver delay, which is that measurement of receiver time delay based on UTC (NTSC). As National Time Service Centre maintaining the standard time scale UTC (NTSC) is set by the internal atomic clock comparison, as well as international internal laboratory comparisons (TWSTFT and GPS) to maintain its precision, we can take advantages of its resources to the measurement of receiver relative delay. Reference[13] can explain the specific principle for receiver delay measurement.

The following table shows the 6 groups of receiver delay values which are calculated by the application of 27 days of monitoring data and the corresponding BIPM data(including $\Delta\tau_2$ = UTC-UTC(NTSC) and $\Delta\tau_3 = UTC - GPST$). Where $\Delta\tau_1$ represents monitoring value of UTC(NTSC)-GPST which contains τ_{rec} and τ_{rec} is the receiver delay to be measured, which contains an antenna and the cable delay. The results can be seen from the table that the receiver delays are about 186.86±0.85ns and fluctuation range is small. This receiver delay value is measured from the antenna phase center to 1PPS output of the timing receiver, which includes an antenna delay, antenna cable delay, the receiver internal delay and a cable delay τ_{cable} for connecting 1PPS of the timing receiver.

TABLE 1 RECEIVER RELATIVE DELAY MEASUREMENT RESULTS

Date	$\Delta\tau_1$	$\Delta\tau_2$	$\Delta\tau_3$	τ_{cable}	τ_{rec} **(ns)**
2013.2.21	185.0	0.5	-0.1	21.2	**185.7**
2013.2.26	173.4	10.6	-2.7	21.2	**186.8**
2013.3.3	174.9	8.9	-3.9	21.2	**187.8**
2013.3.8	173.5	12.2	0.0	21.2	**185.9**
2013.3.13	176.2	7.0	-3.9	21.2	**187.2**
2013.3.18	175.0	5.7	-7.0	21.2	**187.8**
Average	**176.3**	**7.5**	**-2.9**	**21.2**	**186.9**

C. Inter-frequency biases measurement

The receiver channel delay biases depend on the frequency of the satellite signal. For the GPS system, as the use of code division multiple access (CDMA) signal system, all the satellites using the same carrier frequencies (the inter-frequency bias which is caused by the same satellites transmitting signals at different carrier frequencies is outside the scope of this paper), the delay biases between each channel is very small, about sub-millimeter and can be neglected. However, the GLONASS system uses frequency division multiple access (FDMA) signal system, satellite signals of different frequencies generated the receiver channel delay different from each other, and there is a certain deviation, called the inter-frequency bias. In a single navigation system data processing, the delay of each channel does not be calibrated in general, because the biases will be absorbed by clock error parameters. But Observed in the case of multi-mode, in order to improve the monitoring precision of GNSS system time offset, it is necessary in advance to the GLONASS channel delay biases for precision measurements.

The use of GNSS simulator to test the GLONASS L1 carrier signal inter-frequency biases of Septentrio PolaRx4 receiver, take the receiver channel which receives the frequency number 0 GLONASS satellites as reference channel, the inter-frequency biases of other channels can be calculated relative to the reference channel, thus the results were compared to analyzed.

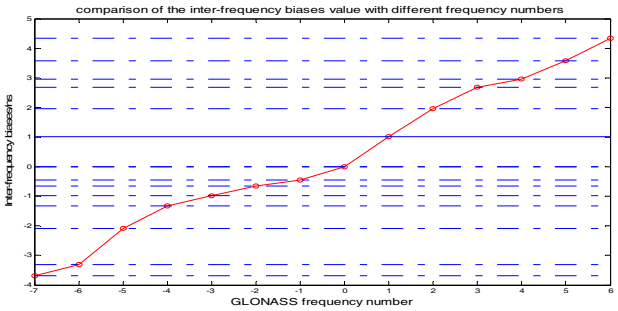

Figure3 Comparison of the inter-frequency biases value with different frequency number of GLONASS

Figure 3 shows the measurement results of GLONASS infer-frequency biases on different frequency number. It can be seen from figure above that for the Septentrio PolaRx4 receiver, the inter-frequency of GLONASS seems to vary with the frequency number. Although the magnitude of change is uncertain, the value exhibits linear increasing trend along with frequency number is increasing in general, and it is vary with respect to the frequency number 0 of GLONASS satellites in-4ns to +5 ns. Fortunately, for receiver of the same brand, the variation did not change with temperature change, it is the result of the carrier phase measurement in receiver DSP chain [14]. The GLONASS channel delay bias is found to have a wide range, hence it must be eliminated based on the received GLONASS frequency value in the system time offset monitoring.

IV. DATA ANALYSIS OF SYSTEM TIME OFFSET MONITORING

A. Monitoring data analysis

On the basis of the method of system time offset monitoring and the measurement results of some important parameters above described, UTC (NTSC)-GPST and UTC (NTSC)-GLONASST data between February 20 to March 29 in 2013 are analyzed in detail, the results are shown in Figure 4 and Figure 5.In order to analyze the monitoring precision, three kinds of time offset results were compared, one is monitoring result, another is calculated value with BIPM, the third one is data from GLONASS broadcast ephemeris. The

UTC (NTSC)-GPST data with BIPM shown in Figure 4 is calculated from UTC-UTC (NTSC) and UTC-GPST data as well as the GPST-GLONASST data with BIPM is calculated from UTC-GPST and UTC-GLONASST data shown in figure 5.However, the monitoring result, GPST-GLONASST is calculated by UTC (NTSC)-GPST and UTC (NTSC)-GLONASST. It is noteworthy that there is a inter-system hardware delay for 210ns between calculated GPST-GLONASST value by circular T and our monitoring data GPST-GLONASST, and the value was deducted during the drawing.

From figure 4 and figure 5 can be seen, the changing trends of both the UTC (NTSC)-GPST or GPST-GLONASST monitoring data are consistent with data from the broadcast ephemeris and value with BIPM.

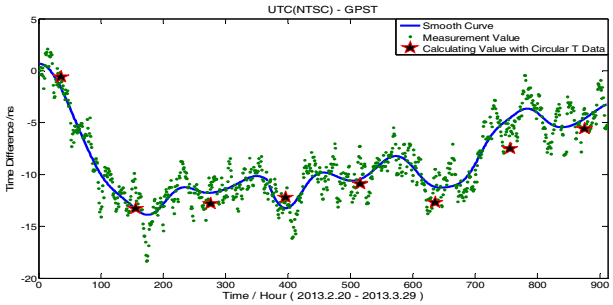

Figure 4 Comparison of measurement value and calculating value with circular T data for UTC (NTSC)-GPST

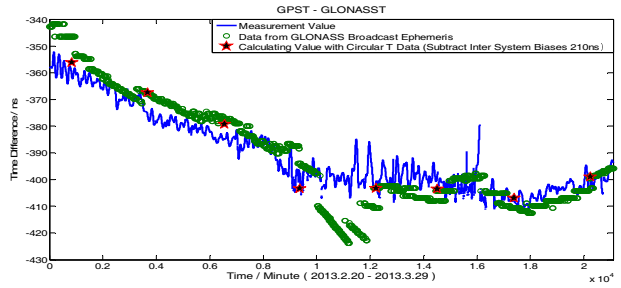

Figure 5 Comparison of three kinds of Results for GPST-GLONASST

B. Afterwards correction for monitoring results using IGS data

When monitoring the system time offset by receiving space signals, as the ephemeris error is one of the most important factors. Therefore,we have adopted the IGS rapid precise ephemeris data (delayed 17 hours) from March 1, 2013 to March 28, 2013,the corresponding monitoring data UTC (NTSC)-GPST were subsequently corrected. Modified result as shown in Figure 6:

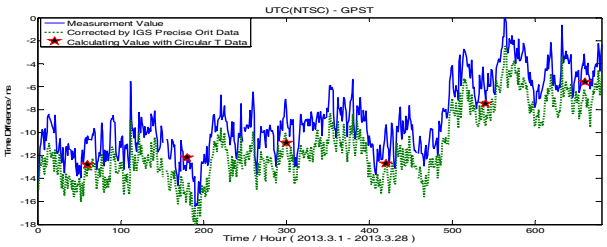

Figure6 Comparison of three kinds of Results for UTC (NTSC)-GPST

As can be seen from figure 6, there is a little difference between the monitoring result UTC (NTSC)-GPST after correction and calculated value with circular T, effect is not very obvious yet .in fact, we do not currently have an absolute standard reference to assess the monitoring value for the before and after correction. Nevertheless, it is certain that the IGS precise orbit products provide precise data [15].

V. CONCLUSIONS AND OUTLOOK

This paper mainly focus on the discussion of monitoring system time offset by means of Signal-in-Space Reception. GNSS system time offset monitoring system by Signal-in-Space Reception has begun trial operation at NTSC. We have been able to monitor UTC (NTSC)-GPST and UTC (NTSC)-GLONASST so far and expect to gradually improve the monitoring system in the future. We are planning to add UTC(NTSC)-BDT monitoring .

REFERENCES

[1] Chinese satellite navigation system management office. Beiyou satellite navigation system spatial signal Interface Control Document [S]. 2012.10.

[2] MOSCOW. GLONASS Interface Control Document[S]. 2008

[3] European Union. European GNSS Open Service Signal In Space Interface Control Document[S]. 2010.9.

[4] A.Moudrak, A. Konovaltsev, J.Furthner, J.hammesfahr, A.Bauch, P.Defraigne, S.Bedrich, 2004. timing aspects of GPS-Galileo interoperability: Challenges and solutions,[C] //Proceedings of the 36rd Annual Precise Time and Time Interval(PTTI) Metting, 279~292

[5] A. Moudrak, A. Konovaltsev, J. Furthner, J. Hammesfahr, and P. Defraigne, 2005, "GPS Galileo Time Offset: How it Affects Positioning Accuracy and How to Cope with It," Proc. in Proceedings of ION GNSS 2004, 21-24 September 2004, Long Beach, California, USA.

[6] Shaowu Dong, Haitao Wu,Xiaohui Li, The Compass and its time reference system[C]. Metrologla, 45(2008), S47-S50.

[7] Shaowu Dong, Xiaohui Li, and Haitao Wu, 2007. about compass time and its coordination with other GNSSs, [C]//Proceedings of the 39rd Annual Precise Time and Time Interval(PTTI) Metting, 21~24

[8] Vanschoenbeek, I., Bonhoure, B., Boschetti, M., et al. (2007).GNSS time offset: Effects on GPS-Galileo interoperability performance. Inside GNSS (pp.60-70).

[9] JH Hahn, ED Powers, 2007, "A report on GPS and Galileo time offset coordination efforts", Proc. IEEE Int Frequency Control symp. pp440-445.

[10] Liu Jiyu, 《 Principles and approach of GPS Satellite Navigation Positioning》 , Publishing House of Science.

[11] Hegarty C,Powers E and Fonville B 2004 ,"Accounting for timing biases between GPS,modernized GPS, and Galileo signals",Proc. 36th Annual Precise Time and Time Interval(PTTI) Systems and Applications Meeting(Washington,DC,7-9 December 2004)

[12] Xiao Pei, Junping Chen, Jiexian Wang, Yize Zhang and Haojun Li ,2012,"Application of Inter-system Hardware Delay Bias in GPS/GLONASS PPP",Chinese Third Navigation academic Symposium.

[13] Xiaohui Li，Yang Liu，Huijun Zhang，Shaohua shi. Measurement of Time delay of GPS Timing Receiver based on UTC (NTSC). [J]. Journal of Time and Frequency，2009，32（1）：18~21。

[14] Jean-Marie Sleewaegen, Andrew Simsky, Wim De Wilde, Frank BOON, Tom Willems,"Demystifying Glonass Inter-frequency Carrier Phase Biases", PP.57-61, May/June 2012.

[15] Jim Ray and Ken Senior, Geodetic techniques for time and frequency comparisons using GPS phase and code measurements[J], INSTITUTE OF PHYSICS PUBLISHING, Metrologia 42, 215–232(2005). DOI:10.1088/0026-1394/42/4/005.

Implementation of the Real-Time Multi-Channel ADEV, TDEV, and HDEV Computation Methods

Michal Kasznia
Chair of Telecommunication Systems and Optoelectronics
Poznan University of Technology
Poznan, Poland
mkasznia@et.put.poznan.pl

***Abstract*—In the paper the realization of the method enabling real-time computation of ADEV, TDEV, and HDEV performed in the real time for multi-channel time error measurement is described.**

Keywords-timing signal; time error; Allan deviation; time deviation; Hadamard deviation; real-time computation

I. INTRODUCTION

Allan deviaton ADEV, time deviation TDEV, and Hadamard deviation HDEV are the parameters used for describing the quality of timing signals generated by the clocks. Time deviation is commonly used for evaluation of the synchronization signals in the telecommunication network. The limit values of TDEV for the network interfaces are defined by the telecommunication standards [1, 2, 3]. These parameters allow the variations of time interval provided by the synchronization signal to be assessed and the type of phase noise affecting the signal to be recognized. Hadamard deviation is insensitive for the presence of the frequency drift and can be used for recognition of higher types of the phase noise. The estimates of the parameters are computed for a series of observation intervals using the sequence of time error samples previously measured at some network interface. The evaluation of the timing signal is commonly a two-stage process: calculation of a parameter follows the time error measurement. However, the real-time parameters' computation performed during the time error measurement process is also possible. The application of the real-time computation allows to simplify the analysis of the timing signals.

There are many situations, that more than one timing signal has to be analyzed in the same time. In the node of the telecommunication network, we have access to timing signals generated by several clocks installed in the node equipment (e.g. SSU, SEC, or central office's clock), as well as to the timing signals obtained from the data streams arriving from several directions. Such situation can be also considered when we want to perform the three cornered hat procedure in order to compare some clocks without the knowledge, which one is better. A multi-channel time error meter with computation algorithms applied could be suitable for this analysis.

The computation methods enabling assessment of the parameters in the real time were previously proposed and tested [6, 8]. The experimental tests have proved the ability of the computation of these parameters in the real time for a single data series as well as for multi-channel time error measurement [7].

In the paper the results of the implementation of the algorithms enabling joint real-time ADEV, TDEV, and HDEV assessment performed during multi-channel time error measurement are presented. To test these methods in a real measurement process, a special measuring system enabling multi-channel time error measurement was used.

II. ADEV, TDEV, AND HDEV ESTIMATORS

Allan deviation and time deviation are computed based on the averaging of second differences of the phase process $x(t)$ of the analyzed timing signal. We can assume for the telecommunication applications, in the case of negligible influence of frequency drift, that ADEV and TDEV are estimated based on the time error function measured between the analyzed timing signal and the reference one [4]. In the case of Hadamard deviation the third difference of the phase process $x(t)$ is averaged.

When computing in the real time, we do not have access to the time error samples indexed by $i+n$ or $i+2n$ (as in the common parameters' estimators) for the current time instant described by the index i, because these samples have not been measured yet. We have access to the sample currently measured (for the current sampling instant i) and the samples measured earlier (with indexes smaller than i) and stored in the equipment's memory. Therefore, the indexes in formulae for common ADEV, TDEV, and HDEV estimators should be changed in the case of real-time calculation.

The rearrangement of indexes for the parameters' estimators was performed in [5, 7]. As result of the conversion the estimators were obtained in the forms suitable for the real-time computation. The value of the parameter currently computed (for current sampling instant i) depends on the currently measured sample, small number of previously measured samples, and values of sums accumulated in the previous sampling instant. ADEV estimator's formula for a current instant i and selected measurement channel m is given in the form:

This work was supported by the National Science Centre in the frame of the project N N517 470540.

$$ {}_m\hat{ADEV}_i(n\tau_0)=\sqrt{\frac{1}{2n^2\tau_0^2(i-2n)}\left({}_mA_{i-1}(n)+\left({}_mx_i-2{}_mx_{i-n}+{}_mx_{i-2n}\right)^2\right)} \quad (1) $$

were ${}_mA_i(n)$ is the sum of squares of second differences of time error samples

$$ {}_mA_i(n)=\sum_{j=2n+1}^{i}\left({}_mx_j-2{}_mx_{j-n}+{}_mx_{j-2n}\right)^2, \quad i>2n $$

and ${}_mx_i$ denotes the time error sample measured at the sampling instant i in the m-th channel. The value of time deviation for the current sampling instant i is estimated using the formula:

$$ {}_m\hat{TDEV}_i(n\tau_0)=\sqrt{\frac{1}{6n^2(i-3n+1)}\left[{}_mS_{ov,i-1}(n)+\left({}_mS_{i-1}(n)+{}_m\Delta_i(n)\right)^2\right]} \quad (2) $$

where ${}_mS_{ov,i}(n)$ and ${}_mS_i(n)$ are the sums updated for each sample i, given in the form:

$$ {}_mS_{ov,i}(n)={}_mS_{ov,i-1}(n)+{}_mS_i^2(n) $$

$$ {}_mS_i(n)={}_mS_{i-1}(n)+{}_m\Delta_i(n), \quad i>3n $$

$$ {}_mS_{3n}(n)=\sum_{j=2n+1}^{3n}\left({}_mx_j-2{}_mx_{j-n}+{}_mx_{j-2n}\right), \quad j>2n $$

and ${}_m\Delta_i(n)$ is a third difference of the time error samples measured in the m-th channel:

$$ {}_m\Delta_i(n)=-{}_mx_{i-3n}+3{}_mx_{i-2n}-3{}_mx_{i-n}+{}_mx_i $$

The sum ${}_mS_{3n}(n)$ is the first element of the overall sum ${}_mS_{ov,i}(n)$. The conversion of the Hadamard deviation estimator brought the formula in the form dependent on the sum of squares of third differences computed for the preceding sampling instant $i-1$ and the current difference ${}_m\Delta_i(n)$

$$ {}_m\hat{HDEV}_i(n\tau_0)=\sqrt{\frac{1}{6n^2\tau_0^2(i-3n)}\left({}_mB_{i-1}(n)+\left({}_m\Delta_i(n)\right)^2\right)} \quad (3) $$

where ${}_mB_i(n)$ is the sum of squares of third differences of time error samples

$$ {}_mB_i(n)=\sum_{j=3n+1}^{i}\left({}_mx_j-3{}_mx_{j-n}+3{}_mx_{j-2n}-{}_mx_{j-3n}\right)^2, \quad i>3n $$

As a result of the conversion of the parameters' formulae, in order to compute ADEV, TDEV, and HDEV for a selected data sequence m (m-th measurement channel), current sampling instant i and given observation interval $\tau=n\tau_0$, we need the values of appropriate sums ${}_mA_{i-1}(n)$, ${}_mS_{ov,i-1}(n)$, ${}_mS_{i-1}(n)$, and ${}_mB_{i-1}(n)$, currently measured sample ${}_mx_i$, and previously measured samples ${}_mx_{i-n}$, ${}_mx_{i-2n}$, and ${}_mx_{i-3n}$ stored in the memory.

III. Multi-channel Computation of the Parameters

The idea of real-time computation for multi-channel time error measurement is presented in Fig. 1. The measurement of the time error is performed using a multi-channel measuring system consisting of M time error meters. We assume that the measurement is performed with the same sampling interval for each time error meters. The time error samples are collected from the time error meters, aggregated in one data stream, sent jointly to the computer and then stored in one data structure on the hard drive of the computer. Recently measured time error samples can be temporarily stored in the buffer placed in the memory. The organization of data structures can play important role in the real-time computation [6].

The real-time computation process of the parameters was designed as single-threaded process, i.e. all necessary operations are performed within one sampling interval, between the successive sampling instants. Therefore the algorithm must be time effective, in order to not exceed the sampling interval by the computation time.

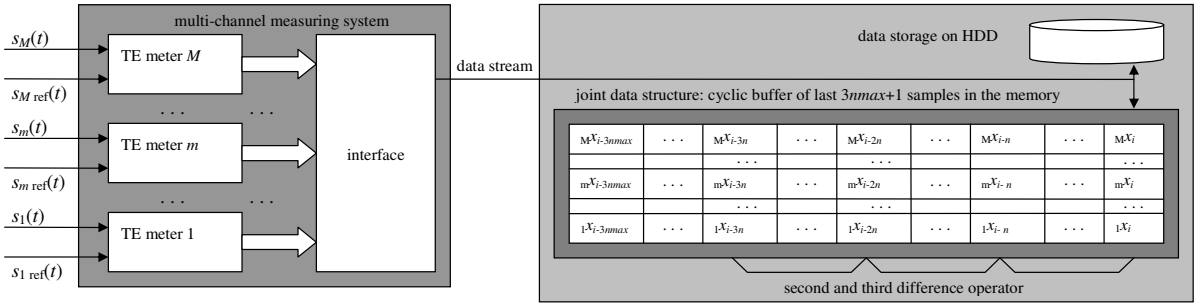

Figure 1. Idea of multi-channel TE measurement and data structures for real-time computation

The results of the experimental tests of the computation methods described in [7] proved the possibility of joint computation of the parameters in the real time. The computational experiments have shown better performance of joint data structure applied in the real-time multi-channel computation [6]. In order to minimize the time of data access, the cyclic buffer in the memory is created. The time error samples received from the time error meters are simultaneously stored on the hard drive and in the cyclic buffer in the computer memory. All computational operations according to (1), (2), and (3) will be performed on the samples stored in this buffer, which will reduce the time of data access. The buffer should have the length of $3n_{max}+1$ items (where $\tau_{max}=n_{max}\tau_0$ is the maximum observation interval considered), in order to store all samples necessary for the computation.

Detailed procedure of the operations performed within one sampling interval during multi-channel real-time computation for the data structure described above will be as follows:

1. Read TE samples from the TE meters and store them in the data file and in the buffer.
2. For a given observation interval $\tau = n\tau_0$ (given n) read TE samples measured n, $2n$, and $3n$ sampling intervals earlier for each channel from the buffer.
3. Compute the sums according to (1-3) successively for each channel.
4. Compute current averages and their square roots according to (1-3) successively for each channel.
5. Execute Steps 2-4 for successive greater observation intervals (greater n) from the range considered.
6. Go to the Step 1 (measure a new vector of TE samples).

The object of the computation performed using this procedure operating on joint data structure is M-dimensional vector. Therefore the computation performed for a given n requires only one execution of the data reading procedure within a single loop. As result the time of data access is reduced.

IV. Realization of Multi-Channel Computation

The algorithm described above was implemented using a modified version of the measuring system SP-4000 designed in the laboratories of Poznan University of Technology [8]. This system consists of two separate units: a measuring unit and an external computer controlling the measurement and computation process. The measuring unit contains four time error meters, build-in rubidium oscillator as a source of reference signal, and additional devices enabling synchronization to the GPS signals and communication with the external computer. This system enables independent time error measurement in four channels, recording of measured values, and *off-line* analysis using its usually software. The new algorithm proposed brings a new functionality to the timing signal evaluation process. The features of this software are following:

- 4-channel TE measurement in the same time with the same sampling interval;
- sampling interval range from 1/32 s till 1 s;
- real-time joint computation of ADEV, TDEV, and HDEV for all channels;
- graphic user interface enabling the presentation of measured TE values and computed parameters' values in the real time;
- range of observation intervals from 0.1 s till 1000 s;
- number of observation intervals considered within one decade:1, 2, 5, 10, or 20.

The time error meters are set for the measurement of timing signals used in the telecommunication network having the frequency of 2048 kHz, but the signals with different frequencies can be also measured.

The example screenshots showing the measurement and computation process are presented in Fig. 2 and 3. Time error is measured in four channels (timing signals generated by unsynchronized OCXO and rubidium oscillators were compared) with the sampling interval τ_0=1/32 s (Fig. 2) and τ_0=0.5 s (Fig. 3). The values of ADEV, TDEV, and HDEV are computed for 5 observation intervals per decade in the range from $3\tau_0$ (0.1 s and 1.5 s) till 1000 s. Successive points on the parameters' plots representing the values computed for successive observation intervals are added when the sufficient number of samples have been measured.

V. Conclusions

In the paper the realization of multi-channel real-time computation of ADEV, TDEV, and HDEV have been presented. The solutions that make possible the cooperation between multi-channel time error measuring unit and the real-time assessment of the parameters have been described. These methods can be applied in a measuring system controlled by usual personal computer, as well as in a system with build-in especially designed microprocessor system. The solution enabling multi-channel real-time analysis of timing signals can be very useful in the service and maintenance of the telecommunication networks as well as in the analysis of high quality oscillators.

Acknowledgment

Author wish to thank his students: Michal Krysciak, Pawel Malak, and Seweryn Grabski, for their help in software implementation.

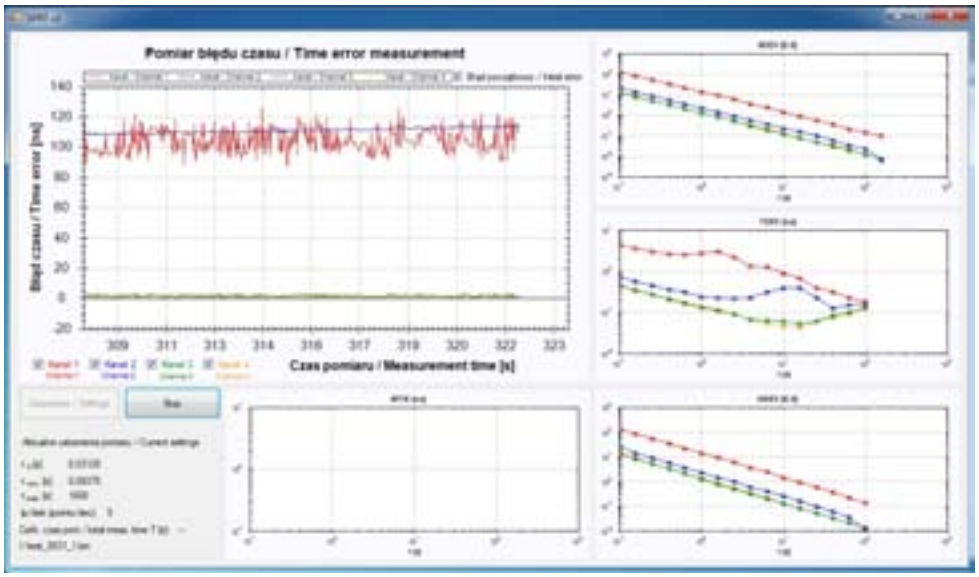

Figure 2. Time error measurement and parameters computation for 1/32 s sampling interval

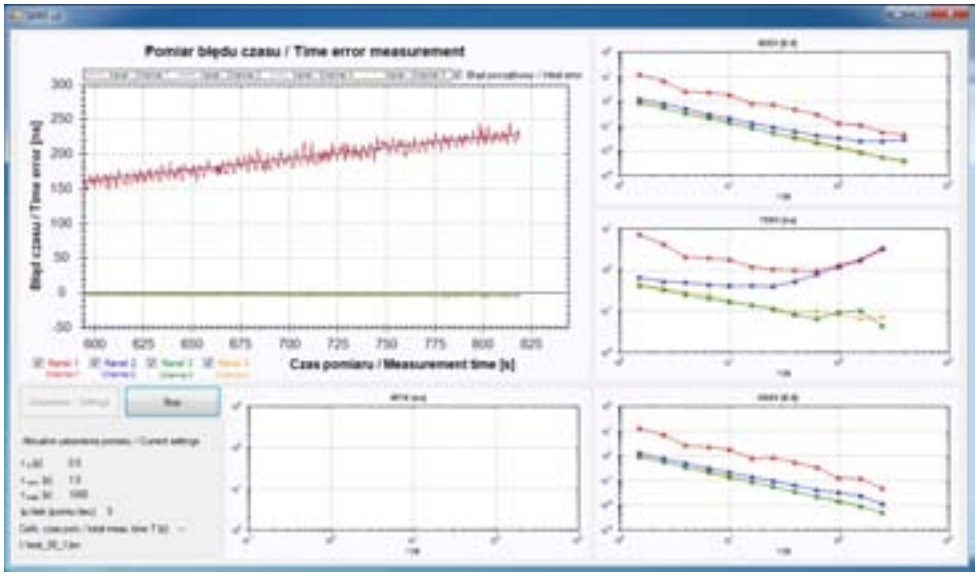

Figure 3. Time error measurement and parameters computation for 0.5 s sampling interval

REFERENCES

[1] ETSI EN 300 462, Generic requirements for synchronization networks

[2] ITU-T Rec. G.810, Considerations on timing and synchronization issues.

[3] ANSI T1.101-1999, Synchronization interface standard.

[4] S. Bregni, Synchronization of Digital Telecommunications Networks, J. Wiley & Sons, 2002.

[5] A. Dobrogowski, M. Kasznia, "Real-time assessment of Allan deviation and time deviation", Proc. of the 2007 IEEE International Frequency Control Symposium Jointly with the 21st European Frequency and Time Forum, pp. 887-882, Geneva, 29 May – 01 June 2007.

[6] M. Kasznia, "Multi-channel real-time computation of ADEV and TDEV," Proc. of 24th European Frequency and Time Forum, 13-16 April 2010, Noordwijk, Netherlands.

[7] A. Dobrogowski, M. Kasznia, "Joint real-time computation of Allan deviation, time deviation, and Hadamard deviation," Proc. of 24th European Frequency and Time Forum, 13-16 April 2010, Noordwijk, Netherlands.

[8] A. Dobrogowski, M. Kasznia, M. Jessa, K. Lange, M. Jaworski, "Hardware and software realization of time terror measurements with real-time assessment of ADEV, TDEV, and MTIE," Proc. of 24th European Frequency and Time Forum, 13-16 April 2010, Noordwijk, Netherlands.

Experimental Tests of the Real-Time MTIE Assessment Methods for Multi-Channel Time Error Measurement

Andrzej Dobrogowski, Michal Kasznia
Chair of Telecommunication Systems and Optoelectronics
Poznan University of Technology
Poznan, Poland
dobrog@et.put.poznan.pl, mkasznia@et.put.poznan.pl

***Abstract*—This paper deals with the problem of real-time computation of Maximum Time Interval Error for multi-channel time error measurement. The results of tests of the computation methods are presented and discussed.**

Keywords-timing signal, time error, maximum time interval error, real-time computation

I. INTRODUCTION

The effective diagnostics of the telecommunication network often requires an investigation into the quality of a timing signal at several interfaces of the network at the same time. This investigation involves in measurements of adequate time errors and computations of some standard parameters – point estimates of Maximum Time Interval Error (MTIE) among others [1, 2, 3]. Since MTIE should be watched at different network interfaces simultaneously and in real time, a multi-channel time error meter equipped with programs implementing appropriate algorithms could be applicable for such investigation.

Authors of this paper have proposed and described [10] two methods enabling MTIE assessment performed in the real time for multi-channel time error measurement. First solution is based on the time effective MTIE computation method with binary decomposition [4]. Second solution exploits the time effective extreme fix (EF) method [5] successfully applied earlier for single-channel real-time MTIE assessment [6, 8, 9]. In the paper the results of experimental tests of these methods are presented. The calculations were performed for several data sequences representing different behavior of time error taken with sampling interval τ_0=1/30 s, which is often used in the telecommunication applications. The results of calculation for various conditions using both methods are discussed.

II. MTIE POINT ESTIMATE

According to the international standards, the point estimate of the Maximum Time Interval Error is defined as the maximum peak-to-peak time error variation of a given timing signal, with respect to an ideal timing signal within a particular time period [1, 2, 3]. MTIE can be estimated from the formula

$$\hat{MTIE}(n\tau_0) = \max_{1\le k\le N-n}\left(\max_{k\le i\le k+n} x_i - \min_{k\le i\le k+n} x_i\right) \qquad (1)$$

where $\{x_i\}$ is a sequence of N samples of time error function $x(t)$ taken with sampling interval τ_0, $\tau=n\tau_0$ is an observation interval, and n can change from 1 till N–1 depending on the considered values of observation intervals.

III. MULTI-CHANNEL MTIE COMPUTATION

Real-time computation of the timing signal parameters for multi-channel time error measurement enables continuous observation of the quality of a series of timing signals simultaneously at the same time. The idea of the real-time multi-channel computation is presented in Fig. 1 [10]. The multi-channel measuring system consists of M time error meters. The time error samples are measured with the same sampling interval, collected from the time error meters, aggregated in one data stream, sent jointly to the computer and then stored in one data structure on the hard drive of the computer. Recently measured samples can be temporarily stored in the buffers placed in the memory. The organization of data structures can play important role in the real-time computation. It depends on the computation method applied.

IV. REAL-TIME COMPUTATION PARADIGM AND METHODS

The following computation paradigm is assumed: in order to compute the MTIE estimate simultaneously for several observation intervals and several data series (obtained from the measurement channels) in the real time, all necessary operations have to be done in the time interval between two successive time error samples, i.e. during the sampling interval τ_0; if some operation cannot be completed during prescribed time it is suspended until the end of measurement and then finished. The ability of real-time assessment depends on the several conditions: number and length of the observation intervals considered, number of measurement channels, data structures and organization, computation ability of the equipment, and time error data behavior.

This work was supported by the National Science Centre in the frame of the project N N517 470540.

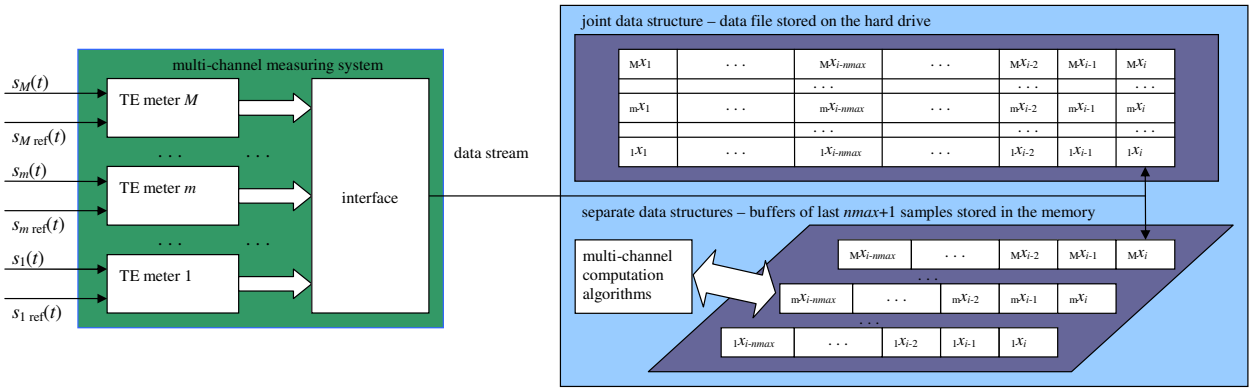

Figure 1. The idea of multi-channel time error measuring system with real-time MTIE computation

Two methods – extreme fix (EF) method [6] and binary decomposition method [4, 7] are used in presented test. Effectiveness of EF method depends on nature of data, in opposite to the effectiveness of binary decomposition method which is data independent.

The calculation process by means of the EF method runs independently for all observation intervals in all channels. The computations for current sampling instant are performed for particular observation intervals in order from shortest to longest interval. First, the observation intervals having the same length for each channel are analyzed. Next the longer observation intervals are considered. The idea of the real-time computation using the EF method for multi-channel measurement is presented in Fig. 2. Suspension of the analysis for particular observation interval can be performed in order to protect the measurement and computation process against exceeding the limit of the computation time (length of the sampling interval). Recently measured $n_{max}+1$ time error samples ($\tau_{max}=n_{max}\tau_0$ is the longest observation interval considered) for each channel can be stored in the buffers in the memory in order to reduce the data access time, which is the crucial issue in the real-time computation [6, 8]. Therefore all search operations will be performed using the data stored in the tables in the operational memory of the computer, which will reduce the computation time substantially.

The calculation process by means of the binary decomposition method runs independently for each channel. Application of joint data structure for the reduced samples – placed in the operational memory (if possible) or on the hard drive – is suggested in order to simplify the data access. Because of regularly running data reduction process, the samples with the same indexes are used for comparison for each channel. Single data reading procedure involving vector of samples will be more time effective than several independent procedures, especially for the data structures placed on the computer hard drive. The computations for current sampling instant are performed for particular observation intervals in order from shortest to longest interval. The idea of real-time computation using the binary decomposition method for multi-channel measurement is presented in Fig. 3.

V. Computation Experiment

The real-time multi-channel MTIE computation methods presented above were tested in the computational experiment. The calculations were performed *off-line* but the *on-line* real-time work was imitated. Three sets combining four time error sequences were used in the experiment. The first set (set A) consists of four sequences representing the realizations of one of typical noises of the timing signals – white phase modulation (WPM). The second set (set B) contains the results of comparison of unsynchronized oscillators: two sequences are obtained from the comparison of OCXO with rubidium oscillator, the other two from the comparison of two rubidium oscillators. These sequences show the effect of frequency difference, which is critical for the efficiency of the EF computation method. The last set of TE sequences (set C) represents various performance of timing signal. This set contains two WPM sequences, one OCXO versus rubidium sequence, and one rubidium versus rubidium sequence. The time error samples were taken with the sampling interval $\tau_0=1/30$ s.

Two different personal computers were used in the experimental tests: first computer with Core 2 Quad 2.83 GHz, and second one with I7 3.5 GHz microprocessor. The observed quantity was the maximum time spent for the calculation performed within one sampling interval. We have assumed that this time cannot exceed the length of sampling interval $\tau_0=1/30$ s = 33.3… ms.

In order to compare the time efficiency of both methods, the MTIE computations were performed for the same set of observation intervals. Because we cannot compute the MTIE using binary decomposition for arbitrary chosen observation intervals, the calculations were performed for observation intervals having the power of 2 samples. The starting (shortest) observation interval had 2 samples for binary decomposition and 4 samples for EF method (the computation for 2-samples interval is not necessary in this case). The maximal observation interval had 32 768 samples. Therefore MTIE was computed for 15 observation intervals by means of binary decomposition and for 14 observation intervals by means of the EF method. The results of the computations are presented in Table I.

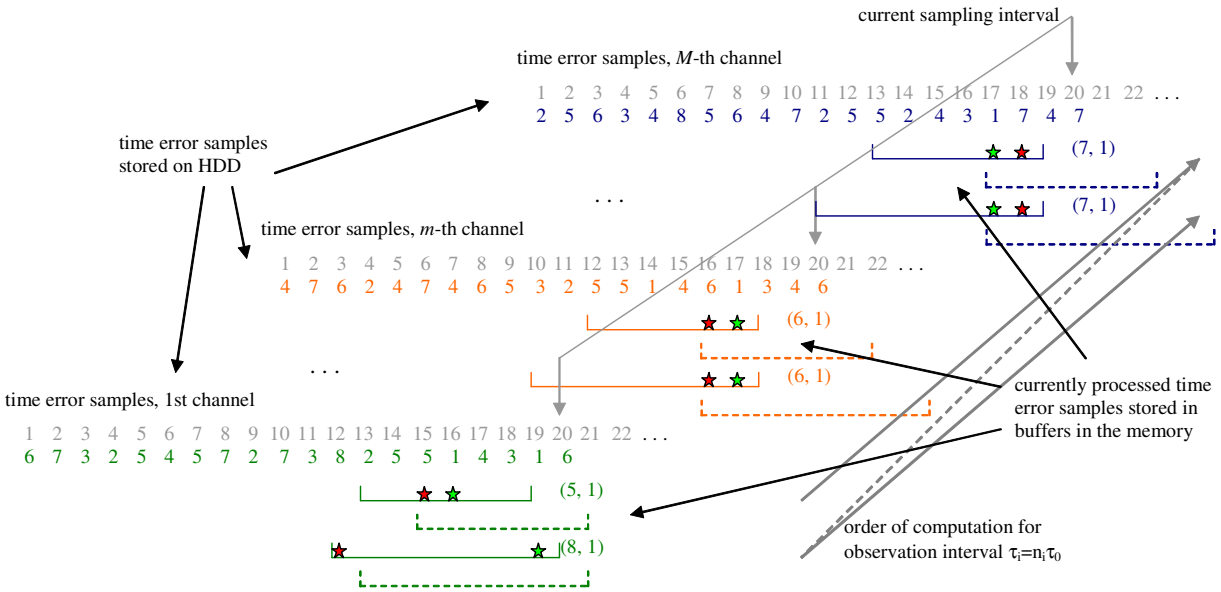

Figure 2. Real-time multi-channel MTIE computation using the EF method

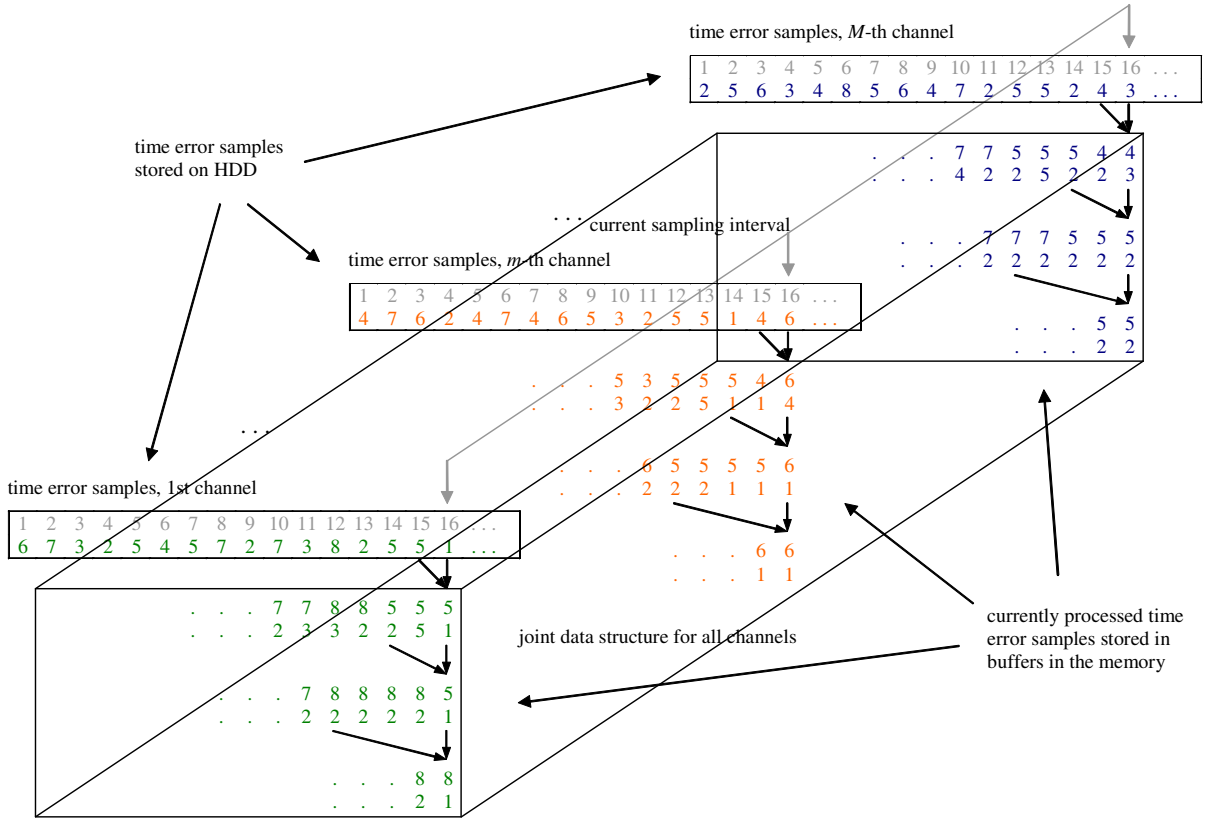

Figure 3. Real-time multi-channel MTIE computation using binary decomposition method

TABLE I. MAXIMUM TIME OF MTIE COMPUTATION USING EF AND BIN METHODS

computer	method	set of TE sequences		
		A	*B*	*C*
		t-max [ms]		
Core2Quad 2.83 GHz	EF	0.578	1.906	1.609
	BIN	0.017	0.017	0.017
I7 3.5 GHz	EF	0.250	0.920	0.702
	BIN	0.014	0.014	0.014

In order to examine the performance of the EF method for various configurations of observation intervals, another series of MTIE computations was performed. The computations were made for two set of 21 observation intervals from the range from 0.1 s till 1000 s. The first set consist the intervals having linear distribution of their values within one decade (i.e. 0.2 s, 0.4 s, 0.6 s, 0.8 s, and 1 s within the first decade, 2 s, 4 s, 6 s, 8 s, and 10 s in the second decade etc), the second set contains the values with logarithmic distribution. The results of computation are presented in Table II.

TABLE II. MAXIMUM TIME OF MTIE COMPUTATION USING EF METHOD

computer	set of intervals	set of TE sequences		
		A	*B*	*C*
		t-max [ms]		
Core2Quad 2.83 GHz	LOG	0.344	3.141	2.875
	LIN	0.297	3.219	2.859
I7 3.5 GHz	LOG	0.243	1.076	0.733
	LIN	0.218	1.232	0.764

The results presented in Table I show the supremacy of the binary decomposition methods applied for the real-time MTIE computation. The regular process of data reduction resulting in the operations performed on the pairs of samples caused very short time of computation observed within one sampling interval. The maximal time of computation observed for EF method was much longer, but still shorter than the length of sampling interval considered. The longest computation time (almost 2 ms for the computer with Core 2 Quad microprocessor) was obtained for the set of time error sequences showing the effect of the frequency difference. The same set have caused the longest computation time observed (more than 3 ms) for the calculations performed for other configurations of observation intervals (Table II). However, increasing of the number of intervals considered simultaneously (from 14 to 21) and changing their values has not changed the observed time dramatically. The suspension of computation is not necessary for the conditions considered.

The results of the tests show the possibility of extending the operations performed within one sampling interval. Short computation time observed allows to consider increasing the number of analyzed intervals within the same range or extending the range of observation intervals. A greater number of time error sequences analyzed (more measurement channels) could also be considered. At least, a shorter sampling interval or a slower computer could be applied.

VI. CONCLUSIONS

The methods presented allow to perform the MTIE computation in the real time for multi-channel time error measurement. The experimental tests proved the ability of real-time MTIE computation by means of both methods proposed for time error measurement performed in four or more channels with sampling interval 1/30 s. The methods can be applied in a measuring system controlled by usual personal computer, as well as in a system with build-in especially designed microprocessor system. The regular data reduction of binary decomposition method results in very short time of computation observed within one sampling interval. The EF method is more flexible in terms of length and range of the observation intervals considered than the binary decomposition method.

ACKNOWLEDGMENT

Authors wish to thank their student: Jakub Nikonowicz and Adam Grzelka for their help in software implementation.

REFERENCES

[1] ETSI EN 300 462, Generic requirements for synchronization networks.

[2] ITU-T Rec. G.810, Considerations on timing and synchronization issues.

[3] ANSI T1.101-1999, Synchronization interface standard.

[4] S. Bregni, S. Maccabruni, "Fast computation of Maximum Time Interval Error by binary decomposition," IEEE Trans. Instrum. Meas., vol. 49, No. 6, pp. 1240-1244, Dec. 2000.

[5] A. Dobrogowski, M. Kasznia, "Time effective methods of calculation of Maximum Time Interval Error," IEEE Trans. Instrum. Meas., vol. 50, No. 3, pp. 732-741, June 2001.

[6] A. Dobrogowski, M. Kasznia, "Testing of the methods of real-time MTIE calculation," Proc. of the 2005 Joint IEEE Frequency Control Symposium and Precise Time and Time Interval Systems Application Meeting, pp. 397-403, Vancouver, 29-31 August 2005.

[7] A. Dobrogowski, M. Kasznia, "On-line computation of MTIE using binary decomposition and direct search with sequential data reducing," Proc. of the 2007 IEEE International Frequency Control Symposium Jointly with the 21st European Frequency and Time Forum, pp. 877-882, Geneva, 29 May – 01 June 2007.

[8] A. Dobrogowski, M. Kasznia, "Real-time MTIE assessment with flexible control of computation process," Proc. of European Frequency and Time Forum and IEEE Frequency Control Symposium Joint Conference EFTF'09 IEEE-FCS'09, pp. 1102-1107, Besancon, France, 20-24 April 2009.

[9] A. Dobrogowski, M. Kasznia, "Implementation of real-time MTIE assessment method," Proc. of 2011 Joint Conference of the IEEE Frequency Control Symposium and European Frequency and Time Forum, pp. 304-309, San Francisco, California, USA, May 2-5, 2011.

[10] A. Dobrogowski, M. Kasznia, "Some concepts of the real-time MTIE assessment for multi-channel time error measurement," Proc. of 2012 IEEE Frequency Control Symposium, pp. 493-498, May 21-24, 2012, Baltimore, USA.

A Novel Timing-Delay Measuring Method Based On PN Code in Telephone Time Service

Dong Dao-peng
National Time Service Center of Chinese Academy of sciences.
Xi'an , China
Key Laboratory of Precision Navigation and
Timing Technology, National Time Service Center,
Chinese Academy of Sciences. Xi'an , China
University of Chinese Academy of Sciences.Beijing , China

ZengTing1,2
National Time Service Center of Chinese Academy of sciences.
Xi'an , China
Key Laboratory of Precision Navigation and
Timing Technology, National Time Service Center,
Chinese Academy of Sciences. Xi'an , China

Shi Shao-Hua1,2
National Time Service Center of Chinese Academy of sciences.
Xi'an , China
Key Laboratory of Precision Navigation and
Timing Technology, National Time Service Center,

***Abstract*—The key problem of telephone time service by PSTN is how to synchronize user time with standard time, in other words, measuring time delay of transmission is the important problem. Now, there are two methods of measuring time delay, the first way is by transmitting character signal; the second way is through phase-detecting. The precision of measuring time delay will have a directly influence on system synchronization time precision, also, The traditional analog modulation/demodulation will highly effect the precision, but the phase error is inevitably because of the effect caused by the noise and channel characteristic when using phase-detecting. A new method, using correlation of PN code will be presented in this paper. Testing shows it can obviously improve the precision of telephone timing service.**

Keywords—PSTN, NTSC, Telephone Time Servict

I. INTRODUCTION

The telephone time service is one of the method that transfer time information with the public switched telephone network (PSTN), whose accuracy is mainly affected by the precision of measurement of propagation time-delay. At the present time, the system is commonly shown in Figure 1, which is composed of the user device and the time server which synchronize with the standard time. An external standard time signal is received as a time reference to establish a standard digital clock in the telephone time service system, and then to build up the transmission time code format with it. Between the server and the user machines, it's through a modem connected to the PSTN for data exchange, that means the server transfers the standard time information to the users or the user machine inquires the server for the standard time information.

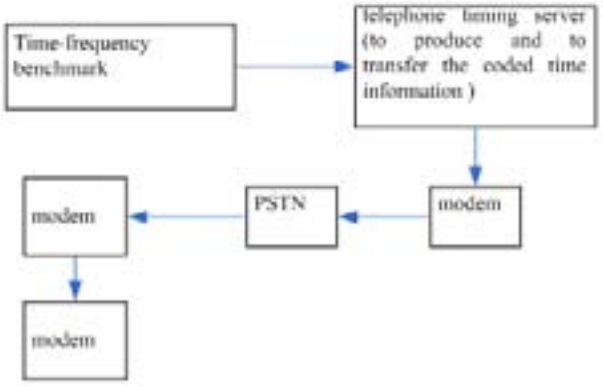

Fig 1 Telephone time service system

The primary problem of telephone time service which transfers the time information with PSTN is accurate measurement of the propagation time delay and encoding the time information. But the accurate measurement of the propagation time delay is more important, which directly affects the synchronization accuracy of the phone timing, therefore, the following introduces two existing methods, the character method and the single-carrier phase method, to measure the propagation time delay.

A. Character method

Due to the modulation and demodulation for the character signals in telephone timing system needing some time to setup which is accumulated and unsure, so that each transmitted character generates different time delay, with which a large error will be leaded. In other way, the volatility of the establish time needed in the process of MODEM modulating or demodulating signals is much greater than the channel

propagation time delay, which severely restricts the accuracy of telephone timing.

B. Single-Carrier Phase method

This method often appears larger deviations, after repeatedly measuring, which reveal channel time delay fluctuation small. The result of time synchronization between the client and the server is poor. It is because the UTP (unshielded twisted pair) from the user's machine to the telephone switching end office is easily induces the electromagnetic noise, industrial noise, day electrical interference, etc around. These kinds of noise impact easily on the phase signals, as well as its own characteristics of telephone channel and some unclear reasons, which will cause serious distortion of the phase signal. For the characteristics of telephone UTP easily induces the electromagnetic noise interference, it needs to further improve the delay detection signal's robustness. Further, the method based on zero-crossing detection has some errors, in the detection of phase point often causes false judgments, resulting in the precision of time detection is lower.

It shows the character and single-carrier phase methods both has some deficiencies from the above analysis, in order to improve the measurement accuracy, a new method which use pseudo-random code for PSTN channel propagation time delay measurement is especially presents.

II. A NOVEL TIME-DELAY MEASURING TECHNOLOGY BASED ON PN CODE

At present, the telephone time service systems have disadvantage in time-delay measuring in channel, for example the serious error occurred by environment, the weak anti-jamming time-delay detecting signal, the low time-delay detecting precision. Because the time-delay detecting precision affects the synchronization precision of the telephone time service system, we suggest a novel time-delay measuring method that the pseudo random code is used to measure propagation time-delay to improve the telephone time service system grant time precision.

Now, the pseudo random code is widely used in the communication area and the wireless range finding area and so on. This technology based on the research of the traditional single carrier wave, the transmitting character and the theory of the PSTN and the mode of the PSTN, uses the relativity of the pseudo random code to measure the time-delay. It has the character of anti-jamming and high time-delay detecting precision and secrecy of the pseudo random code. The pseudo random code cans also achieve a low Signal-to-Noise reception, CDMA communication and so on.

A. Designing of PN code in telephone channel

In the telephone time service system, the frequency of the pseudo random code is 1.023KHz, the list length is 1023-bit (cardinal code number). The cycle of the pseudo random list is 1023/1.023*1023 or 1s. The structure of the PN code generator is illustrated in Figure 2. G1 and g2 are two 10-bit shift registers which generate the pseudo random code with 1023-bit length. The register's state is united with XOR circuit and fed back to the front level. The character multinomial of g1 and g2 is:

$$\begin{cases} g_1(x) = 1 + x^3 + x^{10} \\ g_2(x) = 1 + x^2 + x^3 + x^6 + x^8 + x^9 + x^{10} \end{cases} \quad (1)$$

The band width value of the telephone channel ranges from 0.3KHZ to 3.4KHZ. To reduce the lost frequency of the transmitting signal in the phone channel, we use a frequency shift technology which is a modulation method to generate the PN code with 1.023Khz frequency value and 1023-bit length. The generated PN code is modulated with 2Khz sine wave and its frequency band width value ranged from 0.977Khz to 3.023Khz, whose frequency is suitable for the phone channel in theory.

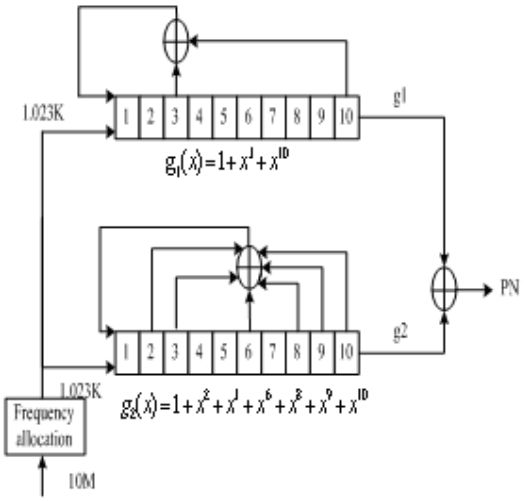

Fig 2 The frame of the PN code generator

In the telephone time service system the measurement technology of propagation time-delay which uses PN code is adopted. It takes a longer circuit specific pseudo random list which has better self-relativity to measure the propagation time-delay. The pseudo random code list has the character of self-relativity and mutual-relativity to ensure the system can capture the received pseudo random list reliably under the proper condition of Signal-to-Noise value. Because the frequency of the pseudo random code list has been expanded, the system has better anti-jamming character and is less disturbed to reduce the probability of miscarriage of justice. Once the connection is set up in the PSTN channel, the propagation time interval serial number is affirmed, that is to say the time-delay is invariable in one communication. The dissymmetrical channel is changed into the symmetrical channel to resolve the time-delay measure problem consisted in the dissymmetrical channel.

B. The self-relativity simulating of PN code in the phone channel

8KHZ sampling frequency is used to sample the pseudo random code signal modulated in the transmitting with 100s length and that transmitted to the receive end, and then sampled data is separately operated with the local pseudo random code signal in relativity by Matlab to get the relative peak value. The pseudo random code signal with the length 100s is generated by FPGA and modulated to transmit.

To analyze if the self-relativity character of the received pseudo random code signal passed through the phone channel is affected by the PSTN or not, we separately operate them in relativity in frequency field and get their relative peak value.

The relative peak value of the signal before transmitted through PSTN and the local pseudo random code showed as figure 3. The relative peak value of the signal transmitted through the PSTN and the local pseudo random code showed as figure 4. IT is shows that the relativity character changed in a small way in fig3 and fig4. The relativity character of the pseudo random code passed through the channel does not deteriorate evidently.

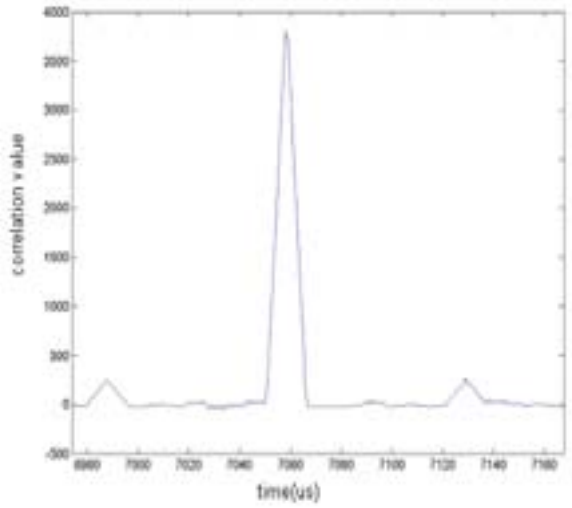

Fig 3 the relative peak value of the signal before transmitted through PSTN and the local pseudo random code in time field.

III. RESULT OF TESTING

In processing of testing, it is designed two steps to measure the propagation time-delay in PSTN channel. First, data on the end of receive is sampled, and then the method of software is used to analyse the tracking PN code. By this way, the fluctuation of propagation delay of PSTN channel is estimated, which is used to design the parameter of loop. After designing the parameter of loop, the counter is used to test the propagation delay. The following testing is realized between the telephone exchange end, the status of telephone link is better.

The fluctuation of propagation delay is estimated. In order to do this, the software of data sampling is used to sample the pseudo code signal which propagated in the PSTN channel. The sample rate is 200KHz and time is 20 seconds. The data sampled is operated to correlate with the pseudo code signal generated locally. It is because of the period of PN code which is 1 second, so, the peak value of correlation is obtained each second. The propagation delay is obtained from the position of sampling which is the peak value.

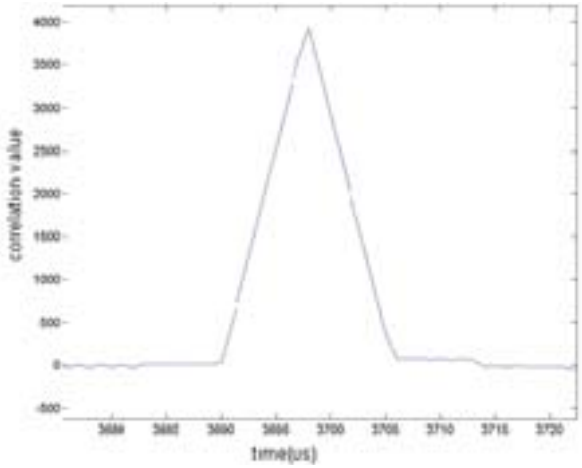

Fig 4 the relative peak value of the signal transmitted through the PSTN and the local pseudo random code in time field

Because of the 200KHz sampling rate, there is 200000 data. The position of each data denotes the 5 us time interval. The position of peak value of 20 seconds is in the same position. It shows the propagation delay measured by this way is under 5 us. So, the result that the measuring precision with the novel timing-delay measuring method based on the PN code in PSTN is better than 5 us is obtained.

IV. CONCLUSION

In this paper, the novel timing-delay measuring method based on the PN code in PSTN is presented, which can be used to improve the propagation delay measuring precision better than 5us. It can greatly improve the quality of the telephone time-service and it has a very better foreground in application in the future.

REFERENCES

[1] http://tf.nist.gov/service/acts.htm.

[2] Li Hui and Zhao Hui, Comparative Research Between PSTN and VOIP,Journal of UEST of China, Vol.33, No.2, Apr. 2004, pp.192-195.

[3] FENG Ping BAI Yan YUAN Ha-i Bo LI Bian, Study and Test on the Frequency Correcting for the User Receiver of the Telephone Service System, CSAO Publications,Vol.23, No.1,2000, pp53-57.

[4] M.A Lombardi. An lntroduction to frequency calibration, Cal Lab Int. J. Metrology, 1996, Jan.-Feb.pp:17—28.

[5] Haibo Yuan,Bai yan and Feng ping. Optical control time service system by using telephone line, Joint meeting of the 13th Furopean frequency and time forum And 1999 IEEE international frequency control symposium.

VLBI Receiver Chain Monitoring

Vojtěch Michálek*, Jan Kodet†, Karl Ulrich Schreiber†‡, Gerhard Kronschnabl‡, Christian Plötz‡,
Ivan Procházka*, and Petr Pánek§
*Czech Technical University in Prague, Břehová 7, 115 19 Prague 1, Czech Republic
†Technische Universität München, Wettzell Observatory, 93444 Bad Koetzting, Germany
Email: kodet@fs.wettzell.de
‡Bundesamt für Kartographie und Geodäsie, Geodätisches Observatorium Wettzell, Germany
§Institute of Photonics and Electronics AS CR, Chaberská 57, 182 51 Prague, Czech Republic

***Abstract*—The most demanding goal of the Global Geodetic Observing System initiative is the definition of station positions to an accuracy of 1 mm and the corresponding velocities to 0.1 mm/year. The main remaining sources of error are caused by systematics, leading to intra- and inter- technique biases. In this work, we have focused on Very Long Base Interferometry (VLBI) and phase calibration generator currently in operation. This unit is injecting calibration tones into the detection chain through an input coupler located near the input of the antenna. The tones propagate further through entire detection chain and are recorded with the observed signal. Then they are extracted in post processing. These tones are generated out of an atomic frequency standard. The supplied frequency is significantly influenced by temperature and mechanical changes since usually a long cable is employed to bring the frequency to the calibration unit. To monitor the electrical length of the cable, calibration with a picosecond precision is essential. We have redesigned a phase calibration unit so that it enables the implementation of the Two Way Time Transfer (TWTT) method on single coaxial cable using two event timers to monitor the electrical length of the critical cable. Such a system has been installed in parallel to the unit currently in operation. The comparison of the TWTT method with previous measurement method is presented.**

I. Introduction

The aim of this project is to check the system currently in use which measures the cable delay carrying 5 MHz from VLBI building to the receiver of the VLBI antenna at Geodetic Observatory Wettzell. A new phase calibration system based on Two Way Time Transfer (TWTT) is used for this purpose; and the results of both methods are compared. The VLBI technique is very critical to phase stability measurement with respect to the reference frequency, which is in many cases hydrogen maser. To fulfill extreme phase stability measurement of the astronomical radio sources in the receiving chain (local oscillators, filter, cables, etc.) there is an test signal injected near the VLBI input receiver. Use of such a signal allows monitoring of phase variations of the open loop detection system over the observation time by comparing received signals to a stable calibration tones locally generated in the detection bandwidth. For such a system the one of the most important thing is to monitor the cable delay carrying the reference frequency into the antenna.

The currently implemented pCal system is using cable delay measurement system, which is based on mixing the reference signal from H Maser with divided signal from the same source. Such signal is then sent up to the phase calibration unit, where the signal is reflected back. After the reflection, the signal carries the phase modulation which is proportional to the cable length. In the VLBI room, there is a high resolution phase comparator comparing phase of the reflected signal with H Maser reference. Thanks to time expansion in the phase comparator (2.5 ps of cable length is equal to 1 us phase difference) the phase can be measured using common counter, with high resolution [1].

The approach described in this paper is based on TWTT using two Event Timing (ET) devices [2].

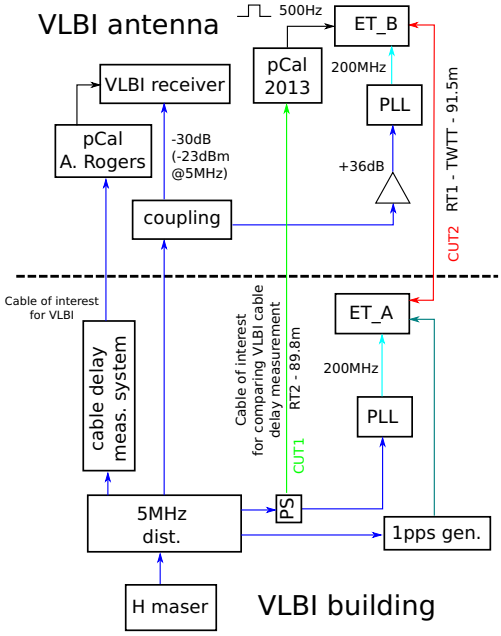

Fig. 1. Block diagram of the experiment setup. Delays of two RG-214 cables (indicated as CUT1 and CUT2) between VLBI antenna and VLBI building were monitored in addition to RG-214 cable used by original system. Event timing device NPET B along with a frequency multiplier and pCal were situated inside the antenna horn whereas identical event timer NPET A along with its frequency multiplier were situated at VLBI building.

II. Experiment

The experiment lasted several weeks and consists of cable delay measurements during several VLBI observing sessions

as well as during out of service periods.

A. Experiment topology

A new phase calibration system was installed in parallel to the system currently in use allowing delay measurements another cable of the same type (RG-214) and similar length during the experiment. Moreover, by employing the TWTT method, delay of third RG-214 cable is obtained as byproduct. All the three cables lie along each other on the same way from VLBI antenna horn to the VLBI building, thus all cables are affected by almost the same influences. Temperature variations and cable bending (during the azimuth and elevation transitions of the antenna) are the most significant influences affecting the cable delay.

The block diagram of the experiment is depicted in Fig. 1. Delays of two RG-214 cables were measured using two event timers with subpicosecond precision. A new pCal, the block diagram of which is in Fig. 2, was employed to generate calibration pulses synchronous with the frequency transmitting through the cable under test (CUT1). As opposed to current way of the cable delay measurements, the phase variations are measured directly by ET.

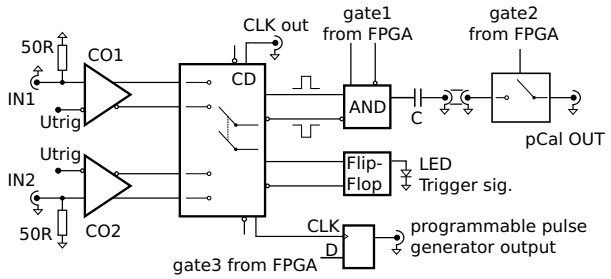

Fig. 2. Block diagram the new pCal.

Each cable delay measurement is performed as follows. At first, the difference of the two time scales are measured by means of TWTT. NPET A generates a pulse and measures the time of its generation (t_{A1}). After the pulse propagates through the measured cable, NPET B detect it and store the time of arrival (t_{B1}). Then the procedure is performed in reverse order: NPET B generates a pulse and measure its time of arrival (t_{B2}) as well as NPET A after the pulse propagation through cable under test (t_{A2}). The time scale difference may be computed as

$$\tau_s = \frac{(t_{B1} - t_{A1}) + (t_{B2} - t_{A2})}{2}.$$

Additionally, having these four values, the cable delay (of CUT2) is obtained as

$$\tau_c = \frac{(t_{B1} - t_{A1}) - (t_{B2} - t_{A2})}{2}.$$

Note that this byproduct can be used as a reference cable delay measurement.

Meanwhile the new pCal generates pulses synchronous with the reference frequency. After the difference of both ET time scales is obtained, the ET in the VLBI antenna switches to the second input and measures the times of arrival of these pulses. In this manner, the phase variations of the reference frequency (on CUT1) can be monitored, e.g., with the electrical elongation of the cable, the cable delay increases and, consequently, the pCal pulses are retarded. Opposite process is observed with shortening of the cable.

B. Results

The experiment lasted several weeks during which the delay of the two cables under test were monitored. Moreover, data from current method of cable delay measurement were gathered as well. The monitoring ran under different conditions, namely during standard VLBI observing session, during out of service periods, and also during deliberate out-of-session antenna movements. The first case is shown in Fig. 3.

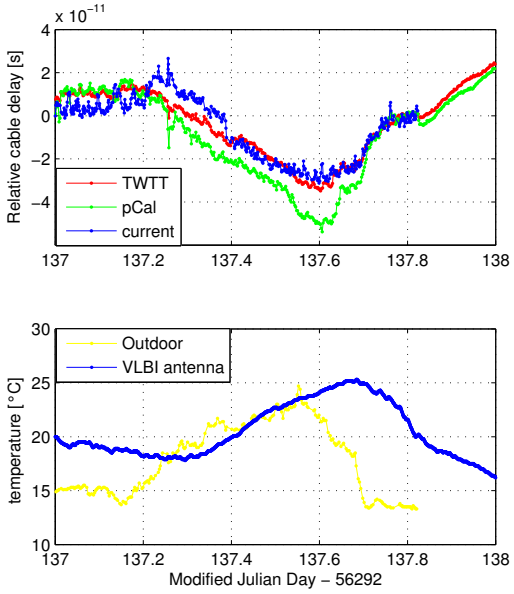

Fig. 3. Cable delay measurement during VLBI observing session. Blue, red, and green curves show cable delay variations measured by current method, TWTT method (CUT2), and by means of new pCal (CUT1) respectively. A clear dependency on outdoor temperature and temperature inside VLBI antenna (measured near pCal) is shown.

Dependency on outdoor (and consequently inside VLBI antenna) temperature is apparent. The cable leading to the pCal seems to be more dependent on outdoor temperature. The slightly different temperature dependency among the cables is probably due to different lengths of the cables. Subtracting the lengths of CUT1 and CUT2, cable length difference of 1.7 m is obtained. It is hard to determine the temperature distribution along the way of the cables; however, it may be roughly estimated from outdoor temperature and temperature inside the VLBI antenna. Considering temperature dependency of RG-214 of -0.5 $\mathrm{ps\,K^{-1}m^{-1}}$ (measured in temperature chamber), cable length difference of 1.7 m, and 10 K temperature

step, the cable delay difference will be of 8.5 ps. Along with temperature dependency of the new pCal (below 1 ps/K), this can explain different slopes of the cable delay changes seen on Fig. 3.

It is also worth to focus on the cable delay variations after the end of the VLBI session (day of year >137.82). These are significantly smoother due to absence of the VLBI antenna transitions among various attitudes (azimuth and elevation), thus constant strain imposed on cable.

Influence of azimuth and elevation changes on cable delay is illustrated in Fig. 4. During the test, the azimuth and subsequently elevation of the VLBI antenna was gradually increased. Dependence of cable delay on the antenna position is quite apparent. Note that unlike the temperature dependency which had the same sign for all the cables, the sign of antenna attitude dependency of one cable is opposite to the other two.

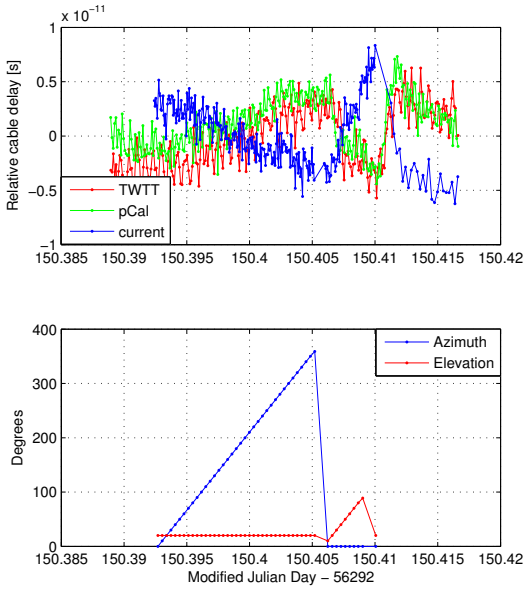

Fig. 4. Cable delay dependency on azimuth and elevation of the VLBI antenna. Position of the antenna was gradually changed and delays of all the three cables were measured. The test was performed in a quite short time in order to prevent the temperature influences from affecting the measurement results. Note the opposite dependency for one of the cables.

Each cable delay measurement with the new pCal is calculated from times of arrival of 500 pulses each two seconds. The precision of the pulse measurements is securely below 20 ps RMS, thus the precision of cable delay measurement is below 0.9 ps ($20/\sqrt{500}$ ps). Unlike the new concurrently installed system which measures the cable delay continuously notwithstanding VLBI measurements, the original system measures the cable delay once before each VLBI measurement (approximately once per one to three minutes) during the observing session. In order to estimate the precision of such a cable delay measurement, an out-of-session measurement with 1 second repetition rate (practical limit of the method) was performed. The precision calculated over 100 measurements is of 1 ps RMS.

III. Conclusion

The function and performance of the VLBI phase calibration system at Geodetic Observatory Wettzell was veryfied by newly designed pCal system with picosecond precision. Additionally, the results were confirmed by measurements of third cable delay obtained as a byproduct of the TWTT method. Both temperature and strain influences affecting the cable delay were identified. Results of all the three cables match each other to the level of few picoseconds. The differences of the results were explained by slightly different lenghts of the cables leading from VLBI building to the VLBI antenna resulting in slightly different sensitivity to external influences.

Acknowledgement

This research has been supported by DFG FOR1503.

References

[1] A. E. E. Rogers, *Phase and group delay calibration of a very long baseline interferometer by East Coast VLBI Group*, Radio Interferometry Techniques for Geodesy, NASA, July 1980, http://archive.org/details/nasa_techdoc_19800020297

[2] P. Panek, *Time-Interval Measurement Based on SAW Filter Excitation* Instrumentation and Measurement, IEEE Transactions on, Vol. 57, p. 2582-2588, 2008

[3] K. U. Schreiber et al.: *Improving VLBI Station Performance*, IVS 2012 General Meeting Proceedings, p.120-127, http://ivscc.gsfc.nasa.gov/publications/gm2012/schreiber.pdf

An Algorithm with Periodic Item for Steering UTC(NTSC) to UTC

REN Ye, LI Xiao-hui,Wu Hai-tao, ZHANG Hui-jun, XUE Yan-rong, LI Yu-wei
National Time Service Centre,Chinese academy of Sciences
Xi'an，China;
E-mail:renye@ntsc.ac.cn

REN Ye, LI Xiao-hui,Wu Hai-tao, ZHANG Hui-jun, XUE Yan-rong, LI Yu-wei
Key Laboratory of Precision Navigation and Timing ,
National Time Service Centre,Chinese academy of Sciences
Xi'an，China;

REN Ye, XUE Yan-rong
Graduate University of Chinese Academy of Sciences,
Beijing， China

***Abstract*—In order to steer master clock in timekeeping laboratory, it is necessary to identify a suitable algorithm for steering UTC(K) to UTC for a period of 45 days with 5-day latency. An algorithm is proposed to modify a traditional quadratic polynomial prediction model whose random error term is represented by a linear combination of periodic term. In the case of steering, the performance of the underlying algorithm is examined in depth, together with a comparison against simulated results of QP .**

Keywords- UTC-UTC(K) time offset; classic spectral Analysis; Quadratic Polynomial Model

I. INTRODUCTION

Coordinated Universal Time (UTC) is regarded as reference timescale for the time coordination around the world. UTC is equivalent to TAI, but with the addition of leap seconds, so that offset between UT and UTC is constrained within 0.9 s. It is computed and made available every middle month by BIPM through its Circular T which is represented by the values of the offsets UTC- UTC (K) in the last month with 5-day latency. In order to steer master clock in timekeeping laboratory, it is necessary to identify a suitable algorithm for steering UTC(K) to UTC for a period of 45 days with 5-day latency. In another word, the algorithm is developed to predict the time offset between UTC and UTC(K) for up to 45 days with 5-day latency.

One of the traditional prediction models for UTC-UCT(K) time offset is the quadratic polynomial model [1] which is represented as QP in this paper. Fig. 1 shows the random error of UTC-UCT(NTSC) time offset based on the QP with different historical data length, and the curves display a certain periodic. By describing as a linear combination of periodic term[2][3], the random error term in QP is able to be predicted in terms of spectral analysis as well as lease square. Therefore, an algorithm combining with quadratic polynomial model and random error is established. In the case of prediction, a brief introduction of the underlying algorithm is illustrated at the beginning. The performance of the algorithm is examined in depth, together with a comparison against the simulated results of .

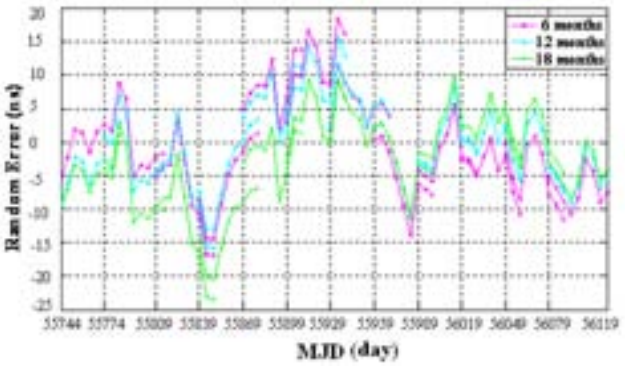

Figure 1 Random error of quadratic polynomial model for UTC-UTC(NTSC) with different fitting data length (July 2011-June,2012) (ns)

II. OVERVIEW OF THE ALGORITHM

A. The quadratic polynomial model with periodic item

As for the quadratic polynomial model, its random error can be divided into two parts, system error and residual. The system error is considered as linear combination of periodic term, while the residual term is regarded as white noise.The algorithm to predict the UTC-UCT(K) time offset is given by [4]:

$$x_i = a_0 + a_1\Delta t_i + a_2\Delta t_i^2 + \left[\sum_{j=1}^{m} A_j\cos(\omega_j\Delta t_i) + B_j\sin(\omega_j\Delta t_i)\right] + v_i \qquad (1)$$

Where $x_i = UTC_i - UTC(K)_i$, $i = 1,2,\mathrm{L}\ ,n$, n is data length, $\Delta t_i = t_i - t_0$, t_0 is initial time, ω_j is frequency, $j = 1,2,\mathrm{L}\ ,m$, m is order of the periodic term， v_i is residual term，and a_0, a_1, a_2, A, B are parameters. Before getting these

This paper is supported by Key Program of The National Nature Science Fundating of China (Grant No. 11033004).

parameters by least square, it is necessary to identify ω and m by means of wavelet and classical spectral analysis .

Represented by the periodic term, the random error term in equation (1) should get rid off noise first by the Daubechies wavelet with one order, which is able to convert the time series data into discrete data that is match Fourier transformation, and ,then,the low frequency parts remain.

The system error with low frequency part is the sum of periodic term under different frequencies which correspond to a certain power spectral density $P_x(\omega)$ respectively. The bigger the power spectral density , the more contribution of a signal corresponding to a certain frequency to the original data. Therefore, the classic spectral analysis is introduced to identify the frequency ω and the order m . The classic spectral analysis, is based on Fourier reformation and it mainly contains two methods, periodogram and correlogram.

The periodogram obtains the power spectral density $P_x(\omega)$ by processing data on time field by Fourier Transformation directly and multiplying frequency spectral by its conjugate , which is shown as (2) and (3):

$$X_N(\omega)=\sum_{n=0}^{N-1}x(n)e^{-jn\omega} \quad (2)$$

$$P_x(\omega)=\frac{1}{N}\left|X_N(\omega)\right|^2 \quad (3)$$

The correlogram, on the other hand, processes the time field data based on correlation function $\hat{R}_x(k)$ and, according to the Wiener-Khintchine theory, it obtain the power spectral $P_x(\omega)$ by Fourier Transformation from $\hat{R}_x(k)$. The procession is described as equation (4) and (5):

$$\hat{R}_x(k)=\frac{1}{N}\sum_{n=0}^{N-1}x(n+k)x^*(n),k=0,1,L\ ,M \quad (4)$$

$$P_x(\omega)=\sum_{K=-M}^{M}\hat{R}_x(k)e^{-jk\omega} \quad (5)$$

The result of either method provides the series of power spectral against their corresponding frequency and ω and m are identified by a reference value of the power spectral density. The frequency ω is selected by its corresponding power spectral density which is bigger than the reference value , while the order m is number of the power spectral density which is bigger than the reference value. In this paper, we implement periodogram and correlogram seperately and denote the algorithm based on periodogram as “ QP+MP ” and correlogram as “QP+MC”.

III. SIMULATION AND ANALYSIS

Based on the QP+MP and QP+MC, a simulation is implemented to predict UTC-UTC(NTSC) time offset for up to 45 days with 5-day latency. The steering is processed for 12 months since July 2011((MJD55744- MJD56119). In this case, UTC-UTC(NTSC) time offset data from Circular T of BIPM[7] is used and it is divided into two parts in which one is treated as historical data to fit the model and another is used to evaluate it. The evaluation is primarily justified by predicted residual Root Mean Square (RMS) which is the predicted residuals root mean square of the difference between simulated value and observed value of Circular T, which is given by equation (6).The smaller RMS, the better simulation performance.

$$RMS=\sqrt{\frac{\sum_{i=1}^{n}(\mu_i-x_i)^2}{n}} \quad (6)$$

Since the long time span of the historical data which data back to 1998, it is necessary to select a proper historical data length before the simulation. Besides, in order to evaluation convenience, RMS is the mean of the simulated results for 12 months.

A. *Identifying Historical Data Length*

The simulation of UTC-UTC(NTSC) time offset is processed based on QP+MP and QP+MC separately with up to three years of historical data , along with the corresponding results from quadratic polynomial model.

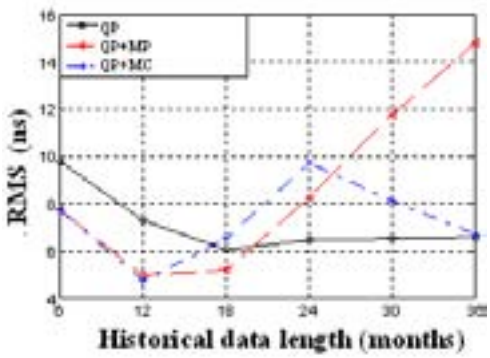

Figure 2 the mean of RMS (ns)of QP, QP+MP and QP+MC with difference historical data length（July,2011——June,2012）(ns)

As Fig. 2 shows, with 12 months length of historical data, both QP+MP and QP+MC shows competitive results against quadratic polynomial model. However, with the historical data increase up to three years, the simulation results of three models show different trend respectively, but neither of them show better prediction. Therefore, 12 months historical data length is proper to predict UTC-UTC(NTSC) time offset based on either QP+MP or QP+MC .

B. *Performance Evaluation*

Table 1 displays the statistical results of the simulated residual, such as mean and standard deviation as well as combined uncertainty ($\mathbf{U_c}$).Combined uncertainty comprises type a uncertainty（ $\mathbf{U_a}$ ） and type b uncertainty($\mathbf{U_b}$) and it is given by:

$$U_c=\sqrt{U_a^2+U_b^2}\ . \quad (7)$$

In this paper, $\mathbf{U}_a$ is random uncertainty and is represented by Allan variance in time filed, while $\mathbf{U}_b$ is system uncertainty and it is difference between mean of simulated data and mean of observed data. Fig 3 and Table 1 show that the simulated results of QP+MP or QP+MC are very close and both are better than the quadratic polynomial model.

TABLE I PERFORMANCE EVALUATIONS OF PREDICTION MODEL（NS）

Criterion / Model	SD	Mean	U_c
PQ	4.4	5.2	4.3
PQ+MP	3.5	4.2	3.2
PQ+MC	3.4	4.1	3.2

Besides, with the 12 months historical data length, the predicted residuals of UTC-UTC(NTSC) time offset based on QP+MP or QP+MC separately between July 2011 and June 2012, together with the observed UTC-UTC(NTSC) time offset from T-Circular in the same period, are shown in Fig. 3.

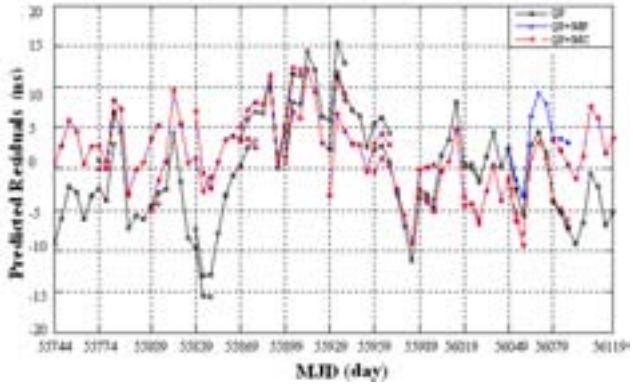

Figre 3 Predicted Residuals throughout 12 months based on three models （July,2011——June,2012）(ns)

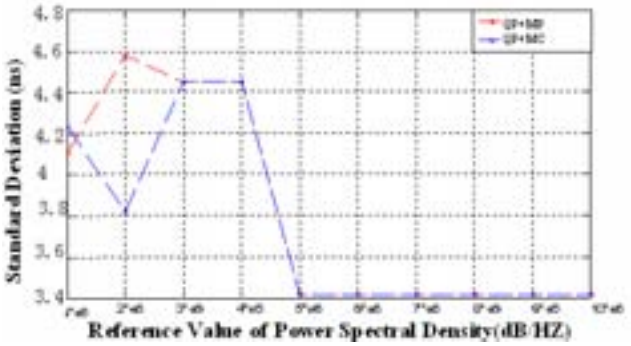

Figure 4 the SD of QP+MP or QP+MC with different reference value of power spectral（July,2011——June,2012）(ns)

It is worth to notice that Fig. 3 shows a very similar simulated results between QP+MP or QP+MC. Few difference become obvious since MJD56019. There are some possible reasons may contribute to this situation. On one hand, based on the theory of classic spectral analysis, the correlatgram differ from the poredicogram by an additional parameter —— maximum delay. The smaller maximum delay, the smoother of power spectral density. The simulation shows that the SD of QP+MC do not change until the maximum delay increase to 20。This paper defines maximum delay for QP+MP as 1. In particular, when the maximum delay m=N-1， QP+MP is equivalent to QP+MC [5]. On the other hand, the reference value of power spectral density is one of the key factors for the algorithm in that it identify the ω and m. However, in this paper, it is an experience value. Therefore, the definition of maximum delay and the reference value may contributes to the difference between QP+MP or QP+MC. Furthermore, Fig.4 displays the effect of selection of reference power spectral density against standard deviation(SD) and it displays that the same competitive performance of both methods turn up when the reference value increase. As it is the general feature including simulated results12 months, it can not avoid some special case which is shown in end of the curve in Fig. 3. Therefore, the selected reference value leads to the similar results of both methods. But it may differ at same special period. At last, the little difference of prediction between QP+MP or QP+MC may be caused by the selection of reference value of power spectral density.

IV. CONCLUSION

Steering UTC(K) to UTC is important to realize the evaluation between local master clock and other system timescale. In this paper, an algorithm with additional linear combination of periodic term is introduced so that the performance of quadratic polynomial model is improved. According to the discussion and analysis of the simulated results, the underlying algorithm based on 12 months historical data shows a plausible feature against the quadratic polynomial model. However, one of the shortcomings of this algorithm is that the prediction precision fails to improve with historical data increase. Besides, as for the spectral analysis for this algorithm, both reference value of power spectral density as well as maximum delay are considered as two factors that limit the performance of the algorithm.

REFERENCES

[1]G.Panfilo,P.Tavella, “Preliminary test on the steering algorithm for keeping a time scale synchronized to UTC, ”Proceedings of the 2003 IEEE International Frequency Control Symposium and PDA Jointly with the 17th European Frequency and Time Forum, 2003,pp.301-305 .

[2] Z.Y. Zheng, Y.M. Dang, X.S. Lu, W.M. Xu, “Prediction model with periodic item and its application to the prediction of GPS satellite clock bias,” Acta Astronomica Sinica, vol.51 , pp.95-102, January 2010,.

[3] B. Zhang, J.K. Ou, Y.B. Yuan, M. HAO, “Fitting method for GPS satellite clock errors using wavelet and spectral analysis,” Geomatics and Information Science of Wuhan University, vol.32, pp.715-718, August 2007.

[4] X.D. Zhang, “Modern Signal Processing”, 2nd ed., Beijing: Tsinghua University press2, 2002, pp.67.

[4] D.C. Jonathan, K. S. Chan, “Time series analysis with applications in R,” 2nd ed, H.Y Pan, Beijing: China Machine Press,2011, pp.230.

[5] P. Stoica, R. Moses, “Spectral analysis of signals,” R.B. Wu, Beijing: Publishing House of Electronics Industry,2007, pp.18-58.

[6] BIPM Web Site:ftp://ftp2.bipm.org/pub/tai/publication/utc-ntsc.

Progress in the Link Calibration for UTC Time Transfer

Z Jiang[1], G Petit[1], L Tisserand[1]
1 Time Department, Bureau International des Poids et Mesures (BIPM), Pavillon de Breteuil F-92312, SÈVRES CEDEX, France
zjiang@bipm.org

P Uhrich[2], G D Rovera[2] and S Y Lin[3]
2 Laboratoire National de Métrologie et d'Essais - Systèmes de Référence Temps-Espace, CNRS, UPMC, Observatoire de Paris (OP), France
3 National Standard Time and Frequency Laboratory, Telecommunication Laboratories (TL), Chunghwa Telecom

Abstract—**The dominant part of the total uncertainty budget in the [UTC-UTC(*k*)] is from the type B uncertainty (u_B) in time link calibration. In fact, 60% of the type A uncertainty (u_A) in UTC time links are < 1 ns while the 93% of $u_B \geq 5$ns. In 2011, the BIPM launched a pilot experiment to reduce the u_B from 5 ns at present to ≤ 2 ns and has developed a standard calibration scheme, namely METODE, associated with an integrated portable GNSS calibrator together with the reference receivers stationary at BIPM. Similar setups are made in TL. Using these systems, we performed a series experiments at BIPM, OP and TL to study the attainable uncertainty of METODE. The results are compared to that of the traditional differential receiver calibrations.**

Keywords : UTC, Time transfer, Calibration

I. THE UTC TIME LINK CALIBRATION

60% of the type A uncertainty (u_A) in the UTC time links are < 1 ns meanwhile 93% of type B uncertainty (u_B) are ≥ 5ns. The u_B in the time transfer calibration is the dominant part in the combined uncertainty budget (u) in the [UTC-UTC(*k*)] [12]. u_B < 2 ns suggests u < 2 ns. This is the target of the time link calibration experiment [7,8].

Time *link* calibration has a long history in the BIPM Circular T computations. The most often case is to transfer a more accurate time link calibration to a lower accurate or no calibrated one [6,14] between the TWSTFT (TW), GPS and GLONASS time links, termly the *alignment*. The relative *equipment* calibrations for UTC generation are in principle: the TW *link* calibration with a mobile TW station [19] and the GNSS *receiver* calibration with a traveling GPS receiver [15,16,20]. In Circular T, the u_B of the first case is about 1.0 ns that makes about 7% of the total UTC links and 5-10 ns for the second that make about 65%. The rest of 28% of UTC links have the u_B=20 ns, i.e., never calibrated [2]. Absolute calibrations are not considered in this paper.

Since 2007, the BIPM began to consider to unify the TW and GNSS calibrations and proposed a new calibration method, namely **METODE** (MEasurement of TOtal DElay) [1,6-9]. Unlike the *alignment*, the *equipment link* calibration requires a traveling calibrator which might be a mobile TW ground station [19] or a traveling GPS receiver [3,4]. Associated with METODE, BIPM developed a standard calibration scheme in which an integrated and pre-cabled portable calibrator (Std_B) is used. It is composed of a 10 MHz distributor, a PPS distributor and two GNSS geodetic setups each include a set of independent receiver, antenna and cables, as illustrated in Figure 1. The calibrator and the fixed reference receivers are like '*black*' boxes for which we do know and do not need to know their internal delays. All we require is their short-term stabilities during the calibration tours, typically 3 months. In this paper, we discuss the reachable uncertainty of the METODE through carefully designed experiments [7,9].

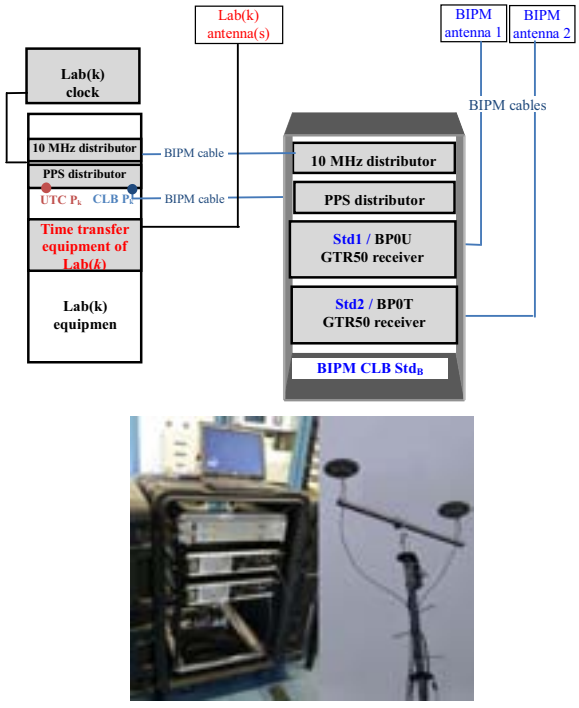

Figure 1. The 2013 setup of the BIPM travelling calibrator Std_B with two GTR50 GPS receiver-antenna systems

II. TOTAL DELAY AND TOTAL UNCERTAINTY IN THE UTC TIME LINK CALIBRATIONS

The *total delay of a GNSS receiver* (Dly_R) at Lab(*k*) is the total electronic delay between the phase center of the antenna and the UTC point $UTCP_k$, Figure 1. It is the sum of all the

sub-delays of all the pieces of equipments including the receiver, the splitter(s), the frequency and pps distributor(s), the amplifier(s), the phase micro stepper(s) etc. plus the cables/connectors between the antenna and the receiver as well as the cables between all the laboratory equipments. In short, Dly_R is the delay on the path of the satellite signal from the antenna to the $UTCP_k$.

However the Dly_R is not measurable and not need to be known in the BIPM link calibration scheme. The Dly_R serves only to define the Dly_L, the total delay of a time *link* between Lab(*i*) and Lab(*j*). The Dly_L is defined as $Dly_L(i\text{-}j)=Dly_R(i)-Dly_R(j)$. Correspondingly, the total uncertainty in Dly_L is that in the total delay of a link U_M. Taking Lab(*j*)=PTB, the pivot of the UTC time links, the difference: $D(i)=Dly_L(Std_B\text{-PTB})-Dly_L(i\text{-PTB})$ is the calibration correction for Lab(*i*).

III. Design of the Experiments to Evaluate the Total Uncertainty

We use different methods with respect to other studies, e.g. [3,4]. The basic idea is to measure a delay using completely different and independent methods and to compare the results. The RMS (the root of mean squares of the differences between the different and independent methods) will provide an estimate of the total uncertainty (u_M). This plus the instabilities of the reference and the travel receivers (by comparing the reference receivers and the closures) make the total uncertainty of the METODE link calibration: U_M (u_B).

Four independent methods are being used:

A) The METODE using the GPS P3 or PPP data;
B) A SR620 time interval counter (TIC), for which the measurement uncertainty is given by the manufacturer to be about 0.5 ns [13], actually smaller from our experience;
C) A portable Cs standard;
D) The comparison with the earlier calibration experiments between BIPM and OP [25,28]

The estimation takes the RMS as the U_M. The crucial issue is the instabilities of the stationary and traveling receiver-systems involved in the METODE, as seen the variations in the reference receiver-system. Figures 2 and 3 demonstrate the relative variations in CCD (common clock differences) of P3 and PPP between the two Z12T BIPM reference receivers (BP0C and BP0M) over two 10-day periods. Both are maintained in the air-conditioned time laboratory. The variations are up to 1 ns. This explains the necessity of the closure measurements and the use of the double receiver-cable-antenna systems for both the fix and travel equipments. In the discussion below, the mean value of the double system is used.

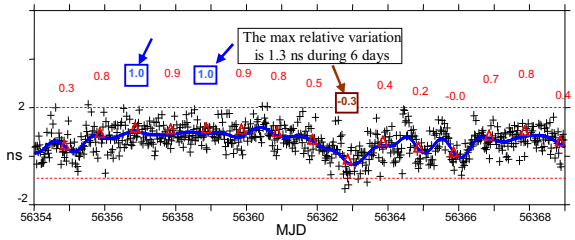

Figure 2. P3 CCD of BP0M-BP0C between 56354-56369

The GTR50 [5] is chosen in the calibrator Std_B thanks to its facility in application and the easier traveling condition. It requires only the PPS signal inputs and no additional latching determination with a TIC is needed at Lab(*k*). One assumption is that the trigger error of each reboot is near constant so as to be partially cancelled in the METODE differential setups. This is proven in our tests.

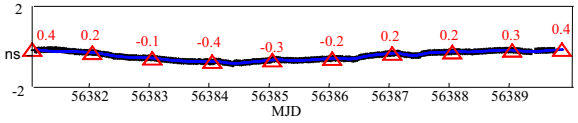

Figure 3. PPP CCD of BP0M between MJD 56381-56390

IV. Main Results

A. METODE vs. TIC SR620 over cables of different lengths

By adding and removing the cables of different lengths before the 1PPS input of the Std_B, we can artificially produce delays/offsets, as described in Figure 4. We then compare the delays measured by two methods: a TIC directly measuring the cable delays and the METODE. In the later, we compute the differences between the GPS data collected by the Std_B which are impacted by the added/removed cables and that of the non-impacted reference receivers. See Figure 4 for the 15.1 ns and 52.5 ns artificial offsets in the CCD.

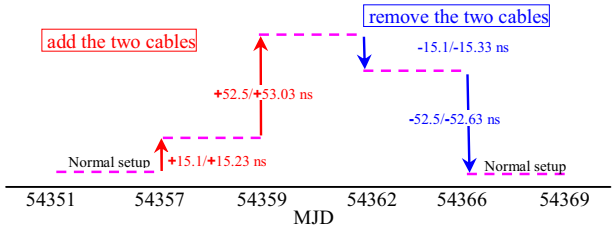

Figure 4. The 4 offsets in the total delays designed on different MJD measured by the TIC SR620 and the METODE calibrator StdB (P3)

Table I lists the results. The mean values of the differences between the METODE and the TIC SR620 are -0.032 ns for the cable of delay 15.1 ns and -0.291 ns for the cable of delay 52.5 ns. Take the bigger one 0.3 ns which can be considered as the u_M of the METODE and is smaller than the u_A of the P3 code (0.7 ns) and that of the total uncertainty of the TIC SR620 of about 0.5 ns [13]. GPS PPP and GLONASS data gives similar result. Note here that the u_M covers all the uncertainty sources due to the GPS's, the TIC's and all the cable delays.

TABLE I. Result of the Measured Delay/Offset Values by TIC and METODE by P3

MJD	Add(+) and Remove(-) Cables	TIC SR620 /ns	METODE GPSP3 GTR-Z12T/ns	Mean Dif. of TIC-METODE /ns
1	*2*	*3*	*4*	*5*
56357.4	+C158	15.1±0.5	15.228±0.053	0.228
56359.6	+C58+C83	52.5±0.5	53.029±0.096	-0.478
56362.6	-C158	15.1±0.5	15.325±0.045	-0.291
56366.5	-C58-C83	52.5±0.5	52.627±0.066	-0.107
		15.1±0.5	15.276±0.049	-0.031

	52.5±0.5	52.828±0.082	-0.292
Mean Dif. of TIC-METODE	15.1±0.5	-0.176	-0.032
	52.5±0.5	-0.328	-0.291

B. METODE vs. TIC SR620 or other method over short baselines

A 10 m CCD test was performed at TL in April 2013. The two clocks are compared with METODE calibrator (P3) and a TIC. The setup is shown in the Figure 5. The RMS of the differences of METODE and TIC is 0.7 ns.

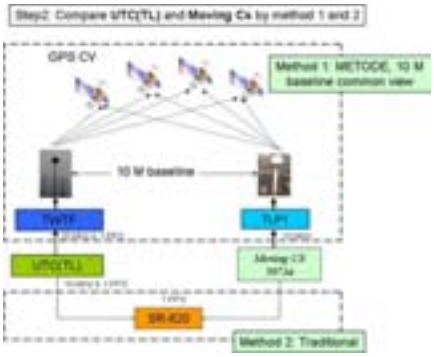

Figure 5. The 10 meter baseline between the UTC(TL) and the mobile Cs. The CCD are measured continuously by both METODE and a TIC SR 620

Two CCD setups were made during 56394-56404 at OP as depicted in Figure 6. The reference receiver at OP is the Z12T OPMT. The last BIPM calibration was carried out in May and June in 2008 between OPMT and BP0C. Repeated calibrations show that OPMT is very stable. This experience is hence also providing a comparison with the calibration of 2008.

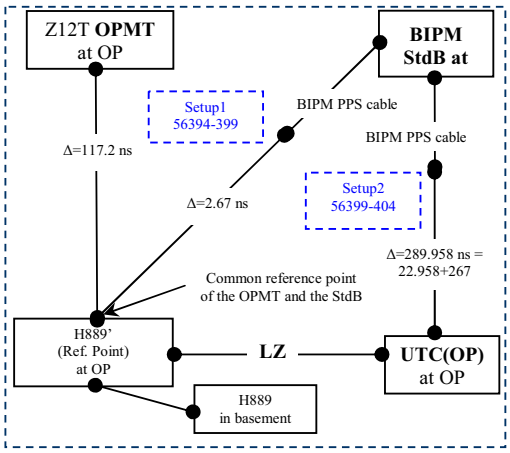

Figure 6. The CCD setups of the Std_B at OP driven by two references: the maser H889 and UTC(OP)

Hourly differences between HM 1400889 and UTC(OP) are given in the LZ file supplied by OP. On the other side, it can also be independently measured by METODE calibrator. The RMS of the differences between the LZ and the METODE PPP is 0.117 ns and that of the P3 is 0.495 ns. This is the maximum static uncertainty of the METODE in a laboratory condition because it contains also the uncertainties in the LZ data (0.2 ns) together with all cable delay measurements.

The reference clock of Setup1 is the HM 1400889 and the reference clock of Setup2 is UTC(OP). Figure 7 shows the difference of the averaging values of the two setups is 0.486 ns, which covers the uncertainties of the METODE calibrator and the LZ as well as the uncertainty in the cable delays between. Again, it covers also all the GPS measurement uncertainties.

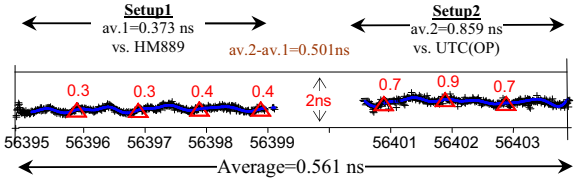

Figure 7. PPP CCD OPMT-Std_B at OP: Setup1 and Setup2

C. METODE vs. mobile Cs clock over a 25 km baseline

A 25km CCD baseline experience was carried out at TL. A mobile Cs clock was transported together with the METODE calibrator developed by TL.

In the 25km baseline test, we replace the absolute reference from the direct SR620 measurement to a linear fitting to the SR620 result. Table II gives the daily average of the differences between the results of the METODE and the mobile Cs clock. It should be pointed out that these differences include, among others, the instability of the mobile Cs clock which may be up to 1 ns depending on various conditions of temperatures, transports and power etc. By the table, the daily RMS are within 1 ns except for 56391 when occurred an earthquake of 6 degree. The RMS of them is 0.92 ns.

TABLE II. DAILY AVERAGES OF THE DIFFERENCES BETWEEN THE RESULTS OF THE METODE AND THE MOBILE CS CLOCK

MJD	RMS/ns
56384	0.454
56391	1.447
56392	0.609
56393	0.849

D. The closures

After 11 days' between 56394 and 56404 staying at OP, the BIPM Std_B was returned. A closure of 0.3 ns on average was found. This should be taken into account in the estimate of METODE uncertainty.

E. METODE calibration vs. classical receiver calibration

BP0C was absolutely calibrated in 2001 [15,16,20]. The related calibration uncertainty u_B is about 2.3 ns. Table III gives the differences of the results by METODE calibration and by the 2008 classical receiver calibrations of OPMT vs. BP0C. By PPP, the difference of the calibration is 0.9 ns between OPMT and BP0C. In the table, u_A is the measurement uncertainty. This is to study the discrepancy between the classic and the METODE calibrations and will not be taken into account in the estimate the reachable uncertainty of METODE.

TABLE III. DIFFERENCES OF THE CALIBRATION RESULTS OF METODE AND THE 2008 CLASSICAL RECEIVER CALIBRATIONS

Receivers	PPP±u_A/ns	P3±u_A/ns
OPMT vs. BP0C	0.929±0.060	0.971±0.068

In summary, above the Sections A, B, C and D give separately the uncertainty estimates about: 0.3 ns, 0.7 ns, 0.5 ns and 1.0 ns. The RMS is 0.7 ns.

V. CONCLUSION

For the *total delay*, we estimate accordingly the U_M, the *total uncertainty* in the METODE link calibration which is composed of:

- Measurement uncertainty (u_A): about 0.1 ns~0.3 ns (u_A of PPP link [2,18]);
- Calibration uncertainty of the calibrator Std_B: 0.3~1.0 ns;
- Instability of the reference and travel receivers: 0.5~1.0 ns;
- Others 1.0 ns (unexpected)

The total uncertainty of METODE U_M is hence 1.1~1.8 ns.

The experiments were carefully designed to investigate the total uncertainty of the METODE link calibration. In conclusion, the reachable uncertainty is ≤ 1.8 ns in the worst case without considering the long-term variations. From [10,21], the later might be up to a few ns.

The BIPM calibrator Std_B appears suitable for such a task. Two DICOM GTR50 GPS time transfer receivers are thoroughly studied for the use of the METODE. It proves the stability, simplicity and precision for UTC time link calibration purpose.

Compared with the 2008 classic calibration result with the BIPM BP0C as the reference, we obtained a total delay calibration correction of 0.9 ns to the OP OPMT.

The UTC/TAI Tsoft software is improved to perform the METODE application. A standard algorithm is under development. A priori, the PPP data will be used for the UTC time link calibration.

A set of Ashtedch Z12-T and Septentrio PolaRx GPS/GLONASS receivers from BIPM and OP participated in the whole campaign between both laboratories. The collected data are currently under analysis. The BIPM Std_B equipment is planned to travel to PTB, AOS, PL and TL to further study the attainable uncertainty in the UTC time links.

ACKNOWLEDGMENT

We thank M. Abgrall, B. Chupin, O. Chiu and I. I. Taïeb of Observatoire de Paris for their technical support.

REFERENCES

[1] Arias E.F. and Z. Jiang, *Considerations on unifying the TWSTFT and GPS Calibration for UTC time transfer*, CCTF WG on TWSTFT Workshop 2008, http://www.bipm.org/wg/AllowedDocuments.jsp

[2] BIPM *Circular T 303*, ftp://ftp2.bipm.org/pub/tai/publication/cirt.303

[3] Esteban H., J. Palacio, F. J. Galindo, T. Feldmann, A. Bauch, D. Piester, *A GPS calibration trip experience between ROA and PTB*, Proc. EFTF 2009

[4] Feldmann T., Bauch A., Piester D., Stefanov A.; Bernier L.G., Schlunegger C., Liang K., *On Improved GPS-Based Calibration of the Time Links between METAS and PTB*, Proc. EFTF 2010

[5] GTR50 - Time and frequency transfer receive, http://www.dicom.cz/en/product/873-time-frequency-transfer-receiver

[6] Jiang Z. et N. A. Niessner, *Calibrating GPS with TWSTFT for Accurate Time Transfer*, Proc. PTTI 2008

[7] Jiang Z., F. Arias, W. Lewandowski, G. Petit, *Toward new procedures in TWSTFT and GNSS delay characterization for UTC time transfer*, Proc. EFTF 2010

[8] Jiang Z., Arias F., Lewandowski W., Petit G., *BIPM Calibration Scheme for UTC Time Links*, Proc. EFTF 2011, pp 1064-1069

[9] Jiang Z., L. Tisserand and G. Petit, Tests of the BIPM portable calibration station - ETODE: MEasurement of TOtal Delay, CD Proc. PTTI 2012

[10] Jiang Z., D. Matsakis, S. Mitchell, L. Breakiron, A. Bauh, D. Piester, H. Maeno and L.G. Bernier, *Long-term Instability of GPS-based Time Transfer and Proposals for Improvements*, Proc. PTTI 2011

[11] Jiang Z., W. Lewandowski, G. Panfilo and G. Petit (2011) *Reevaluation of the Measurement Uncertainty of the UTC Time Transfer*, Proc. PTTI 2011 pp 133-140

[12] Lewandowski W., D. N. Matsakis, G. Panfilo and P. Tavella 2005 *On the Evaluation of the Uncertainties in UTC-UTC(k)*, Proc. EFTF 2005, March 2005, Besançon, France, p. 83

[13] MODEL SR620, Universal Time Interval Counter, http://ilrs.gsfc.nasa.gov/docs/timing/sr620_manual.pdf

[14] Niessner N. A., W. Mache, B. Blanzano, O. Koudelka, J. Becker, D. Piester, Z. Jiang, and F. Arias, *Calibration of the BEV GPS receiver using TWSTFT*, Proc. PTTI 2008

[15] Petit G., Jiang Z., Moussay P., White J., Powers E., Dudle G, Uhrich P., Progresses in the calibration of geodetic like GPS receivers for accurate time comparisons, Proc. 15th EFTF, p.164, 2001a

[16] Petit G., Jiang Z., White J., Beard R., Powers E., "Absolute calibration of Ashtech Z12-T GPS receiver", *GPS Solutions* 4 (4), 41, 2001b.

[17] Petit G., TM116, July 2002, Estimation of the values and uncertainties of the BIPM Z12-T receiver and antenna delays, for use in differential calibration exercise, ftp://tai.bipm.org/TFG/CALIB_GEO/tm116.pdf

[18] Petit G. et al 2011 The time stability of PPP links for TAI, Proc. EFTF 2011

[19] Piester D., Bauch A., Breakiron L., Matsakis D., Blanzano B. and Koudelka O. 2008 Time transfer with nanosecond accuracy for the realization of International Atomic Time *Metrologia* 45 pp 185–98

[20] White J., Beard R., Landis G., Petit G., Powers E., Dual frequency absolute calibration of a geodetic GPS receiver for time transfer, Proc. 15th EFTF, p. 167, 2001

[21] M. Weiss, V. Zhang, J. White, K. Senior, D. Matsakis, S. Mitchell, P. Uhrich, D. Valat, W. Lewandowski, G. Petit, A. Bauch, T. Feldman and A. Proia, « Coordinating GPS Calibrations Among NIST, NRL, USNO, PTB, and OP », Proc. of the Joint Meeting of the 25th European Frequency and Time Forum (EFTF) and the IEEE Frequency Control Symposium, San Francisco, USA, 2-6 May 2011, pp 1070-1075

Research on Precision Measurement of Phase Difference Between Different Frequency Signals

Miao Miao, Wei Zhou, Zhiqi Li, Xueping Zhang, Changsheng Liu
Department of Measurement and Instrument
Xidian University
Xi'an, P.R. China
mmiao@mail.xidian.edu.cn

***Abstract*—Traditional phase comparison must be carried out between the two frequency sources with the same values. However, recent researches have found that phase comparison also can be implemented between frequency sources with different values and obtain higher resolution.**

The paper analyzes the phase difference regularity of arbitrary period signals' comparison. Discuss in detail that fine quantized phase step phenomenon and how the step value to reflect the higher resolution. When two signals with different frequencies are compared, their phase differences are in special order according to the frequency ratio, and, because of small frequency deviation existing, corresponding phase differences in every least common multiple period are different. As for the equivalent phase-discrimination frequency, ABf_{maxc}*, has very high resolution, under the condition of proper reference frequency, the technology in the paper can reach higher measuring resolution. As for the development of present base standard sources and the research on fine quantified phase step phenomenon between period signals, the signal comparison in RF band could reach ps resolution and even fs. Because the hardware used in detecting coincidence information will bring some trigger error and compared signals' own noise will bring some phase uncertainty, the software in connection with algorithm can be used in the technology. On account of instruments' own drift, pulse average method and pulse filling method can be used, and moreover, self-calibration.

***: When the frequency values of compared signals are respectively f_1 and f_2 and their greatest common factor frequency is f_{maxc}, $f_1=Af_{maxc}$, $f_2=Bf_{maxc}$.**

Keywords—phase comparison; phase difference; measuring resolution

I. INTRODUCTION

The phase comparison between periodic signals is the important method to the high resolution measurement technology. The variety of the phase difference between periodic signals reflects a regularity phenomenon of the phase quantization step by step between the frequency signals. The research has a favorable application and development in the field of the time-frequency measurement and control. The periodic signals have the periodic characteristic. Several frequency signals bring about the quantization on time by fine variation of the phase differences for a long time. The phase quantization can provide a theoretical evidence for the technology on the phase comparison, particularly high-precision comparison between random signals. The phase difference between periodic signals varies periodically with the period of their least common multiple[1], while the arbitrary periodical phenomenon can be presented by the phase difference group. On the research of the group theorem, the regularity of the phase difference will be shown properly to get the corresponding characteristics.

This work was supported by the National Science Foundation of China under Grant No. 61201288 and 10978017, and the Fundamental Research Funds for the Central Universities, China (Grant No. K5051304019).

II. CHARACTERISTIC OF PHASE DIFFERENCE BETWEEN DIFFERENT FREQUENCY SIGNAL

The traditional phase comparison is often carried out between the two frequency sources with the same values. The results is a series of phase difference arranged in the order of monotone increasing or monotone decreasing, and the phase variation between two nearby phase differences is constant, which is related to the tiny frequency difference of the two frequency sources. The smaller the additional frequency difference is, the higher comparison it shows and the more difficult the measurement is.

The concept of the phase difference usually aims at the frequency signals with the same value, whose application can show the relationship between the signals more particularly. On the basis the measurement, control, transformation, synthesization and so on can obtain higher precision compared with other methods. But both the phase comparison and the processing usually require the same frequency or the rigorous relationship between the frequencies, which limits its application. In some cases, it is necessary to introduce the complicated frequency transformation for the comparison in the wide frequency range or between the given different frequency signals. It is necessary to discuss whether the phase comparison and processing method can be applied to the different condition.

For the different frequency signals, it is usually difficult to find the variation regularity between the phase differences in a continuous period. At this time, if the period is of the least common multiple T_{minc} between the signals, the several phase difference collections consisting of the two compared signals in a period T_{minc} are called a group. It will not appear the state of the completely same phase difference and the permutation and combination in the different order of the toleration based on the quantitative phase shift resolution $\triangle T$ (just right the equivalent phase cycle). [2]When the relationship on the two frequency signals is constant and no relative variation is present, the value

and arrangement of the corresponding phase difference in each period T_{minc} is completely the same .

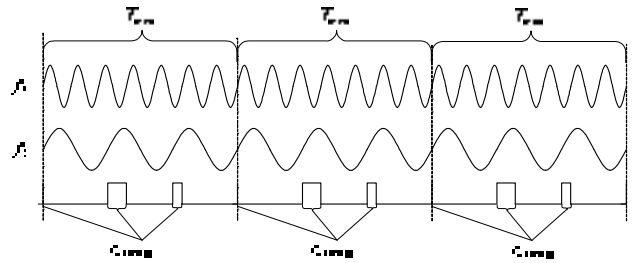

(a) Comparison of the ideal stable signals when the origin phase is zero

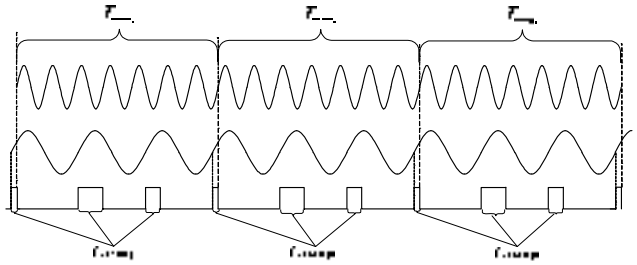

(b) Comparison of the ideal stable signals when there is an origin phase

Fig.1 the phase relationship based on $T_{\min c}$ (without relative frequency variation)

For example, the phase difference collection in two T_{minc} front and back is a group each, and all the phase difference values have the strict relationship based on corresponding group and the distance of T_{minc}. As Fig.1 shown, the results of comparison are expressed in Fig.(a) when the origin phase difference of the comparison signals is zero, and the results of comparison are expressed in Fig.(b) when the origin phase difference of the comparison signals is not zero. It is clear to see the fact that whether there is an origin phase, the group consisting of each phase difference in the period of the least common multiple is the same in the corresponding T_{minc} for the ideal stable signals.

This kind of the phase relationship is more common in practical comparison. The indirect continuous characteristics will appear in the corresponding phase difference for each phase difference group in T_{minc}, when the frequency of the comparison signals is different and there is tiny frequency difference present. The range of each phase difference variation is limited, namely that it monotonically increases to the periodic quantity of less periodic signals (the maximum of the phase difference) and then return to the state of the phase coincidence (the minimum of the phase difference). Each phase coincidence is the critical state of the phase difference from the maximum to the minimum. Otherwise, each of the phase difference monotonically decreases to the state of the phase doublication (the minimum of the phase difference) and then return to less periodic signals (the maximum of the phase difference), as Fig.2 shows.

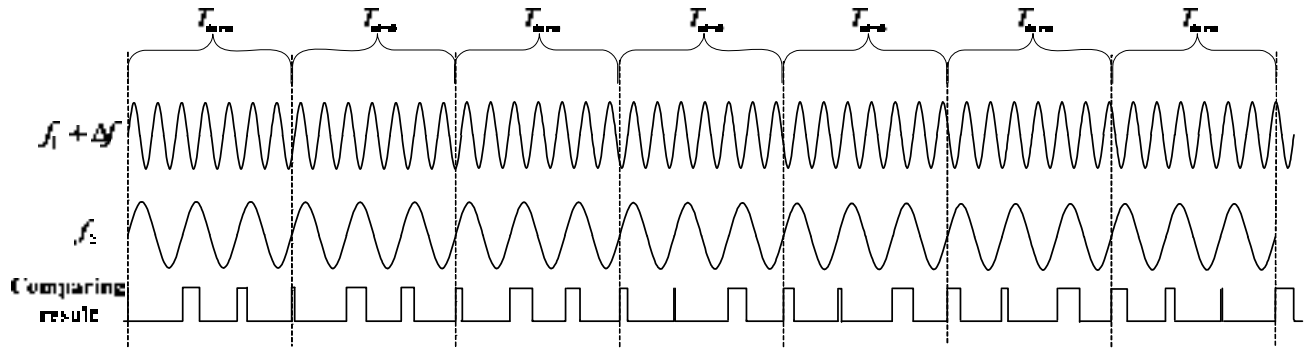

Fig.2 Comparison of the signals with additional frequency difference

Therefore, the consecutiveness of the phase difference variation between the random frequency signals does not appear in each T_{minc}, and it appears in the phase difference group by the interval T_{minc}. With the time going by, the phase difference group that is seemed chaotic can represent the variation of the added relative frequency difference and the phase difference between signals based on the given consecutiveness. In Fig.2, the magnitude and arrangement of the phase difference in the group are both different, but the variation tendency of the corresponding phase difference in each group is of the same discipline. To any phase difference in the group, it only increases the phase variation quantity caused by $\triangle f$ in the next group increasingly or decreasingly in turn.

III. USING OF THE EQUIVALENT COMPARISON FREQUENCY

On the process of the signal comparison, the technology can obtain extremely high resolution on the condition to choose proper referenced frequency, because that the equivalent frequency of phase ABf_{maxc} has the extremely high resolution.

Traditional phase comparison is carried out between the two frequency sources with the same values. The quantitative resolution of the phase difference depends on the relative frequency difference and the named period. If the two compared signals are f_1 and f_2, where $f_1=f_2+\triangle f$, , the n phase differences between the two signals are respectively $\Delta T=nq$, where n=0, 1, 2, 3, ……T1/q. Simultaneously,

$$q = \frac{f_{maxc}}{f_1 f_r}$$

It is of the quantitative phase shift resolution.whose reciprocal is called the equivalent frequency of phase ABf_{maxc}, and f_{maxc} is the greatest common divisor of *f1* and *f2*. T_1 is the period of the signal f_1. The variation of the phase difference is always the integral multiple of q, which can vary from zero to T_0/q. In the other word, the phase difference makes the quantization by the quantitative phase shift resolution and varies monotonously. Therefore, taking advantage of it, the higher measurement resolution will be obtained by choosing the comparison signal properly.

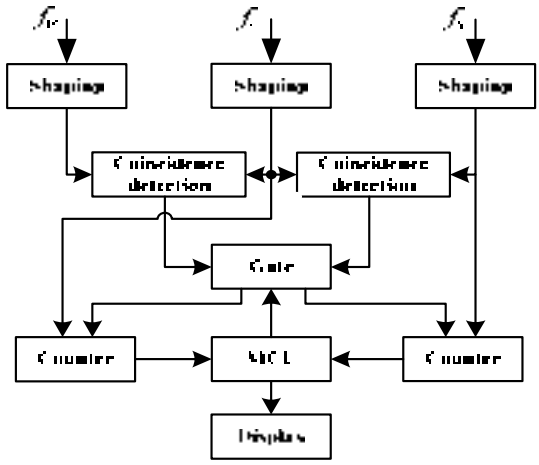

Fig.3 Schematic diagram of phase difference measurement

f_x and f_0 are the two compared signals of the same value or the multiple relationship of the public reference source, and there is the frequency difference or relative frequency difference between the public reference source f_c and the measured frequency signals. The high stable public reference signal f_c makes a detection of phase group superposition with f_x and f_0 respectively, which the frequency of f_c can be changed. Taking the advantage of the comparison between the frequency signals in multiples of each other, it can properly increase the quantitative phase shift resolution between the signals relatively to reduce the measurement requirement of wires.

There are some comparison measurements on the standard of different frequency resource in the experiment. To control the quantitative phase shift resolution between compared signals within 1ns, the public resource should be set with the offset ±1Hz , ±10Hz and ±100Hz after the frequency multiplication, which will make the foundation for the practical measurement of the high resolution. Table 1 shows the corresponding quantitative phase shift resolution after the different frequency multiplication on the mediation source, where f_{equ} is the equivalent frequency of phase between compared signals and is the reciprocal of the quantitative phase shift resolution each other. When the phase difference variation between is within 0º~360º, the corresponding time interval is a period of the low-frequency signal, such as the measured signal of 10M, whose phase difference variation is in 0~100000ps.

Tab.1 the quantitative phase shift resolution

f_x	f_0	f_c	$\Delta T=1/f_{equ}$ (s)
10MHz	10MHz	10MHz±1Hz	1.0×10^{-14}
10MHz	10MHz	50MHz±10Hz	2.0×10^{-14}
10MHz	10MHz	20MHz±100Hz	5.0×10^{-13}
10.23MHz	10.23MHz	10.23MHz±10Hz	9.5×10^{-14}
10.23MHz	10.23MHz	20.46MHz±10Hz	4.7×10^{-14}

Each time, the speed of the frequency shape moving is different causing by the relative acceleration of the real-time phase difference, because of the different small frequency difference Δf between the two compared signals input, namely that the time interval and the slope of the shape are different between the two 0º~360º nearby. The measurement result of the phase comparison of the public oscillator source 2 times the frequency relative to the standard frequency f0 shows in Fig 4 with choosing OSA5585B-CS of 10M as the measured signal, SR625 Rb of 10MHz as the reference signal and 20MHz+100Hz composed by Hp8662A as the public oscillator source.

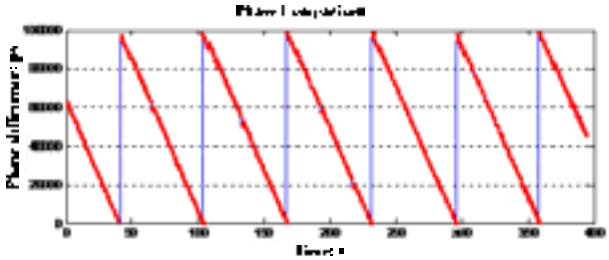

Fig. 4 Phase comparison of the signal of 10MHz （f_c=10MHz+100Hz）

Because of the error of $-T_{minxc}$~ T_{min0c} present between the referential gate and the practical gate, the error between the two practical gates nearby is $-2T_{minxc}$~ $2T_{min0c}$, which lead to the fluctuation between a constant value for the frequency pulse count of f_x and f_c. The practical gate is not constant, and the frequency pulse count of f_x and f_c will increase or reduce at the same time in the practical gate, but it will not influenced on the final calculative result.

The curve described by the frequency pulse count is mainly influenced by the phase difference of f_x and f_c, f_0 and f_c, and the practical gate. The slope of each part depends on the phase difference, and the practical gate leads to the fluctuation of the count value. The hardware detecting signals inside will lead to some triggered errors, which will influence the measurement result; the noise of the compared signal itself can also make it uncertain for the phase difference at the same time. For the influence on the drifting of the device itself, making the calibration itself with the same resource can eliminate the influence on the drifting with the operation simultaneously taking the advantage of the method of pulse on average and pulse filling.

IV. ANALYSIS AND CONCLUSION

This is the conclusion of the quantum mechanics that all the physical quantity is quantized in the most basic sense. For the clearness in math, the quantization property can be ignored

in the macroscopic measurement, and therefore the signals can be expressed in the continuous form. The quantization acts as a technology making the continuous signals dissociated, whose extent leads to the precision. The phase difference variation between periodic signals does be the quantization each other of the phase relationship in nature. The degree of the quantized precision also represents the degree of the mutual compared resolution between the signals, and represents the highest precision measured between the signals. The intrinsic frequency characteristics of the phase of quantum between the frequency signals, namely the quantitative phase shift resolution, can show the high resolution of the comparison, synchronous realization of the phase group , the control and the utilization, which is of important significant. The fundamental theorem on high precision measurement in the phase difference is based on the periodic characteristics between the different frequency signals and the concepts of the phase group synchronization to realize the mutual phase comparison. On the basic of the concepts and theorems of the equivalent frequency of phase, the least common multiple period, the equivalent comparison and so on in the chapter, the public oscillation source is introduced to make the high precision phase comparison and research on the two signals of the same frequency value. The phase difference measurement with high precision can be realized by taking advantage of the phase difference group synchronization, whose resolution of the measurement can be within 10ps.

REFERENCES

[1] Miao Miao, Wei Zhou, Bin Wang, Application of length vernier in phase coincidence detection and precision frequency measurement. Review of Scientific Instruments. Volume: 83, Issue: 2. 2012, Page(s): 024706 - 024706-4

[2] Wei Zhou, Miao Miao, Hui Zhou, Baoqiang Du, Hainiu Zhou, "A novel phase processing approach based on new concept and method" , Frequency Control Symposium, 2009 Joint with the 22nd European Frequency and Time forum. IEEE International, pp.492 - 495

[3] Li Zhiqi, Zhou Wei, Miao Miao, et al, A Super High Resolution Distance Measurement Method Based on Phase Comparison, Chinese Physics Letters, Aug, 2008 Vol. 25,No. 8, pp.2820-2822

Time and Frequency Distribution Improvement in Calern/Geoazur Laboratory for T2L2 Campaigns

Myrtille Laas-Bourez, Etienne Samain, Clément Courde, Jean-Louis Oneto, Pierre Exertier
Géoazur, Université de Nice Sophia-Antipolis, Observatoire de la Côte d'Azur, CNRS (UMR 7329), 250 av Einstein 06560 Valbonne, France
Myrtille.Laas-Bourez@oca.eu

Patricia Fridelance
Phusipus Intégration, 8 allée bellevue, 06460 Saint-Vallier de Thiey, France

Philippe Guillemot
CNES, French Space Agency, Toulouse, France

Daniele Rovera, Michel Abgrall
LNE-SYRTE, Observatoire de Paris, 75014 Paris, France

***Abstract*— The Time Transfer by Laser Link (T2L2)[1] experiment aim to synchronise remote ultra stable clocks over large-scaled distances using two laser ranging stations. T2L2 ultimate time transfer capability can only be demonstrate with a picosecond range ground mastering. We focus this year in knowledge and equipment improvement to perform a T2L2 time transfer with accuracy and stability of a few picoseconds.**

A deep analysis of signals stability has been carried out this year in the time and frequency laboratory in *Plateau de Calern*. The aim was to better understand the limits and hardware configuration and to enhance time and frequency distribution for T2L2 experiment. We showed phase noise and stability problem on our H-maser distribution. Final measures were conducted in October in collaboration with SYRTE. Then a complete equipment reorganisation was done.

This paper focus on the time and frequency laboratory characterization before and after the reorganisation. We introduce our new equipments and present our new H-maser time scale and discuss the performances obtained.

Keywords—Atomic time, time and frequency distribution, T2L2

I. INTRODUCTION

T2L2 is a time transfer technique based on an international collaboration between laser stations and a dedicated space segment implemented on-board the altimeter satellite Jason 2. The project is operational since 2008 [1], [2], [3]. T2L2 relies on the propagation of laser pulses that permit to enhance the performance of time transfer by one or two order of magnitudes as compared to existing microwave techniques such as GPS and Two-Way Satellite Time and Frequency Transfer (TWSTFT).

It provides the capability to compare today's most stable frequency standards with unprecedented stability and accuracy [4]. Ultimate expected T2L2 performances are in the 100 ps range for accuracy, with a time stability of about 1 ps over 1,000 s and 10 ps over one day [5]. These performances can be reach only with a picoseconds ground mastering. This paper presents the new time and frequency laboratory organisation and the new dedicated equipment. It shows the new signal distribution to both laser stations MéO and FTLRS and concludes on the performances reach for T2L2 campaigns.

II. TIME AND FREQUENCY CALERN LABORATORY

In order to reach T2L2 expected performances, we have improved the time and frequency Calern laboratory signals distributions. During 2012, we focused in two points: time scale stability and signal distribution mastering.

Former configuration was relying on two clocks, a cesium clock to generate TA(OCA) and an H-Maser for high performance metrology. This architecture has two drawbacks. First the presence inside the same systems of two different clock signals could generate some cross modulations and thus degrade the performances. Second, such a configuration implied to do some post processing in order to take into account and correct the drift of the H-Maser (To stay synchronised with TA(OCA)).

In this way, we constructed a unique time scale based on our hydrogen maser T4S. It is distributed to both Calern laser stations with new distribution equipment STS and STD. The figure 1 gives a simplified view of the new time and frequency distribution in Calern. The figure 2 shows the overlapping Allan deviation of TA(OCA) before the reorganisation and after. We made the measurement with the Symmetricom 5120A phase noise analysis system. We can conclude from this measurements that we reach the T4S raw performances even after the HROG-10 micro-phase stepper without phase correction ($6{,}13\ 10^{-16}$@4.10^3 seconds). We had also drastically reduced the noise density.

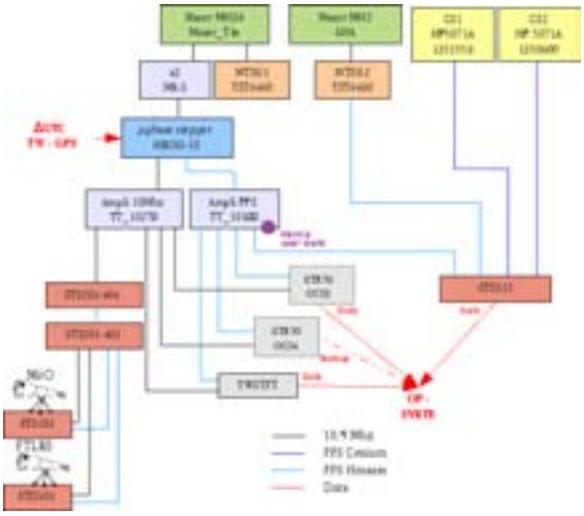

Fig. 1. Simplify diagram of time and frequency distribution from Calern laboratory to both laser stations.

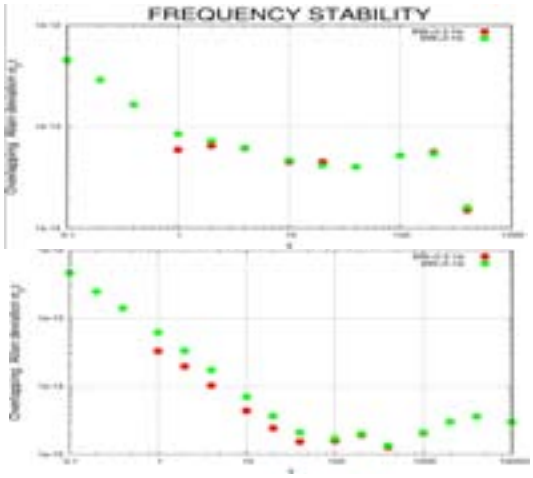

Fig. 2. Overlapping Allan deviation of TA(OCA) before laboratory reorganisation (top) and after in October 2012 (bottom).

The key points of this laboratory optimisation are:

- A single local atomic time scale based on the hydrogen maser T4S MH36.
- Acquisition of a set of ultra stable PPS signal generator: STS and distributor STD.
- Daily and automated maser frequency correction compared to UTC (OP) via GPS and TWSTFT.

Since May 2013 TA(OCA) is steered by applying daily frequency corrections in automated way (Fig. 3). The time difference between TA(OCA) and UTC(OP) is monitored in quasi real time by TWSTFT and by 2 geodetic GPS receiver. After a first period of debug TA(OCA) is expected at less than 20 ns from UTC with a frequency instability of few 10^{-15}. This must be reached by the end of this year.

Fig. 3. Simplify link between OCA time scale and UTC(OP)

III. New Subps Time and signal distribution: STS and STD

If one considers a typical distance between the stations of 100 m, a thermal sensitivity of the cable used to propagate the time reference of 100 fs/m °C and a long term thermal variation in the range 20°, the total delay variation can reach 200 ps which is far away to picosecond objective. To solve this difficulty we designed an ultra stable time signal generator STS201 including an event timer able to monitor the absolute time delay variation in the propagation of the signals between laser station and time and frequency laboratory (Fig. 4). The instrument was developed in the framework of the T2L2 experiment through a collaboration between several partners [6]. This monitoring is made through a double propagation of the signal emitted by the distributor and repeated by the user (laser station). This redistribution can be made through a passive connection if the distance is smaller than a few 10 meters or an active repeater for larger distances. We also designed such a repeater (STD101) well suited for distances of a few 100 meters. It includes an ultra-fast differential comparator connected to a distribution unit.

Fig. 4. Ultra stable time signal generator including a sub-picosecond event timer able to measure the time propagation of the signals.

The repeatability error of the instrument is better than 1 ps rms for the PPS distribution and better than 800 fs rms for the time delay measurement made by the event timer. Figure 5 illustrates the time stability measurement of a PPS signal generated by the instrument and measured by its internal event timer.

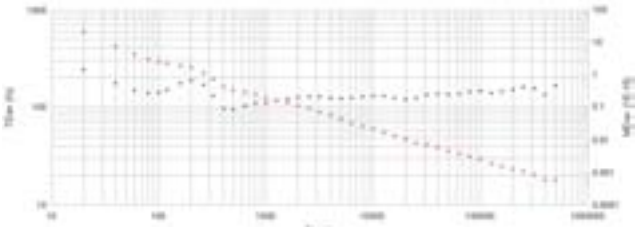

Fig. 5. Time stability of a PPS signal generated by the instrument and measured by its event timer. TDev in black and Mdev in red. The global drift of the measurements is smaller than 1 ps over 10 days. The peak value at 200s is due to the laboratory temperature control.

The STS201 instrument can be slaved with a 1, 5, 10, 100 or 200 MHz external reference. It can generate, through 2 independent channels, a signal between PPS and 100 MHz with an integer division of an internal 400 MHz local oscillator. This functionality permits to generate both PPS signal for time scale synchronization together with a 10 or 100 MHz signal for the time base of any other event timer.

IV. TIME DISTRIBUTION TO LASER STATIONS

Figure 6 is a schematic description of the laser ranging stations of OCA. There are 2 laser stations and a time a frequency lab in the same monument. The laser station on the left (MéO) is based on a 1.54 meter telescope. It was primary designed for laser ranging on the moon and is now the reference station for T2L2. The station on the left (FTLRS) is based on a very small 13 centimeter telescope. It is a mobile station that can be deployed in only 2 days all over the world. The time and frequency laboratory is located between the stations. It is 80 m from MéO Station and 50 m from FTLRS. Each station receives both a PPS signal and a 10 MHz frequency reference. The PPS signal is used to discriminate a zero crossing of a given 10 MHz period for time scale synchronization purpose. The 10 MHz signal is the time reference used by the event timer of the stations. A second STS generator is used at MéO to regenerate another 10 MHz signal coming from the time and frequency laboratory. A STD distributor is used at FTLRS to repeat the 10 MHz signal.

To get a time transfer at the picosecond level it is crucial to have an ultra stable time distribution between the reference clock and the laser stations.

Figure 7 is a typical phase measurement of the double 10 MHz link between laser station and time and frequency lab over 1 week. Phase variations are induced by the thermal variation of the coaxial cables.

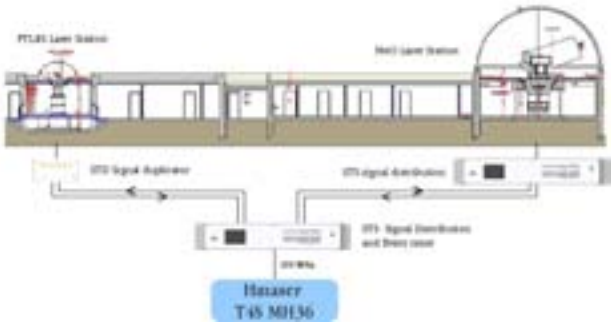

Fig. 6. T2L2 long term stability with MéO and FTLRS in co-location in Calern: simplified experimental setup

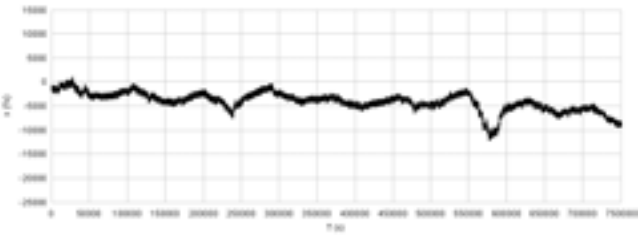

Fig. 7. Typical Phase measurement of the double 10 MHz link between FTLRS station and Time and frequency lab over1 week

Figure 8 shows modified Allan (Mdev in red) and time (Tdev in black) deviations in black of the link between MéO laser station and the Calern time and frequency laboratory. We can see the stability performance of this link is impressive: less than 0,2 ps at 1000 seconds and less than 2ps at one day.

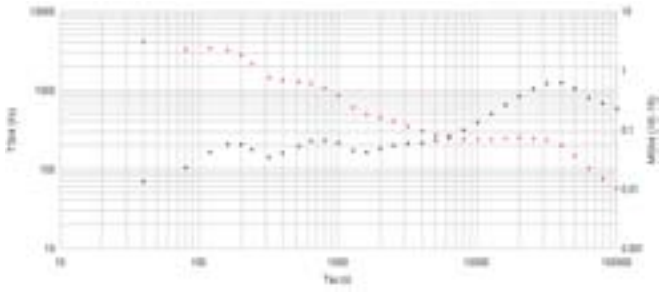

Fig. 8. TDev (black) and MDev (red) of the link between Laser station and Time and frequency lab (50 m)

Data coming from the STS201 event timer are recorded in real time and archived on a server. During the T2L2 data reduction process, start time of the laser events have to be time shifted to take into account the cable time variation measured by STS201. This process will be integrated in the very next future inside the automatic computation of the T2L2 scientific mission center.

V. IMPROVEMENT FOR T2L2 CAMPAIGNS

Today, Calern Time and Frequency laboratory is fully operational. A single local atomic time scale based on the hydrogen maser and corrected compared to UTC(OP) with TWSTFT and GPS is distributed to both laser stations. The signal distribution is monitored to the picoseconds with STS/STD time signal distributors. This is fully compliant for T2L2 experiments and can be transposed to other laser stations.

All the time transfer techniques are calibrated. The laser stations are calibrated with dedicated system (STX301 event time, optical fibre …) [1] with 50ps of global uncertainty. Thanks to the new equipment and time signal distribution, drift and time variation are monitored in real time with 1 ps of uncertainty. The TWSFTF system have been calibrated with SYRTE GPS receivers in March 2013 with a global uncertainty about 3 ns. We will do a new calibration in September-October 2013 with TimeTech mobile station. And our two GTR50 receivers have been calibrated with SYRTE GPS receivers in March 2013 with a global uncertainty about 3 ns. A new calibration will be done in November 2013.

With this new time and frequency architecture, we are organising two main T2L2 campaigns. The first one aims to demonstrate T2L2 stability performance in co-location. We have done it in Calern with both laser stations MéO and FTLRS from December 2012 to June 2013. The results will be published soon. The other one will begin in September 2013 to November 2013. The FTLRS laser station will be in Paris (OP) and this campaign will involve other European Laser Station. The aim will to statue ground to ground T2L2 stability and accuracy ultimate performance.

REFERENCES

[1] E. Samain, "T2L2: ground to ground Time Transfer", EFTF 2012, Goteborg, Sweden, 23-37 may 2012

[2] P. Fridelance, E. Samain and C. Veillet, "*T2L2 - Time transfer by Laser link: A New Optical Time Transfer Generation*", Experimental Astronomy Vol.7 Num.3 Sept.97

[3] Ph. Guillemot, E. Samain, P. Vrancken, P. Exertier, S. Leon, "Time transfer by laser link - T2L2: An Opportunity to Calibrate RF Links", Proceedings of the PTTI 2008, pp 95-106

[4] P. Vrancken, "Characterization of T2L2 (Time Transfer by Laser Link) on the Jason 2 Ocean Altimetry Satellite and Micrometric Laser Ranging", Thesis, Université de Nice - Sophia Antipolis, 2008.

[5] Ph. Guillemot, P. Exertier, E. Samain, F. Pierron, J.-M. Torre, S. Leon, "Time Transfer by Laser Link - T2L2: Results of the First Year of Operation", Proceedings of the PTTI 2009, pp 67-79.

[6] E. Samain, P. Fridelance, Ph. Guillemot, "An ultra stable event timer designed for T2L2", Proceedings of the EFTF, 2011.

Synchronization of Ultrafast Lasers

Huan Zhao, Shengkang Zhang, Jun Ge, Nuanrang Wang
National Key Laboratory of Metrology and Calibration Technology, Beijing Institute of Radio Metrology & Measurement, Beijing, 100039, China

Abstract—**We demonstrate the high precise active synchronization between two independent ultrafast lasers with a RMS timing jitter less than 30fs. With the technique of cavity length monitoring by two PZTs, three PLLs, a motorized translation stage and a computer, this high-precise synchronization remains several hours.**

Keywords- ultrafast laser; active synchronization; phase locked loop; timing jitter

I. INTRODUCTION

Ultrafast laser has important applications in physics, chemistry, biology and advanced manufacture for it could "photograph" the instantaneous actions of atom and molecule. In a typical ultrafast pump-probe experiment, the laser is divided into two beams working as pump and probe light separately. Despite the two beams are synchronized and probably with different power, the key parameters such as central wavelength and pulse width are identical, thus the experiment results are limited. Synchronization of different ultrafast lasers are developed in the last decades and it plays indispensable roles in many researching, e.g. time-resolved measurement, entangled photon pair generation for quantum key distribution, phase-coherent synthesis of multicolor pulses, and far-IR-THz wave generation by means of difference frequency generation(DFG).

This Letter reports our research on highly precise active-synchronization between two independent femtosecond Ti:sapphire lasers. The lasers are firstly synchronized by two phase locked loops(PLL) at relative large timing-jitter, then the sum frequency generation(DFG) signal of the two lasers is fed back to the above PLLs, which acts as the third PLL and improves the precision of the synchronization significantly. Furthermore, by controlling the motion of motorized translation stage inside the ultrafast laser, the synchronization could maintain for several hours.

II. EXPERIMENT TECHNIQUES

A. synchronization based on Two PLLs with DBM

In the experiment, we made two prism-dispersion-controlled KLM (kerr-lens mode-locked) lasers named as TWIN1 and TWIN2[1], which both have about 800nm central wavelength, 100fs pulse width and 80MHz repetition rate. One of the cavity mirrors is attached on A side of the piezoelectric actuator(PZT) which B side is attached on the mirror mount, in order to lighten the load of PZT, this mirror has only a diameter of 6mm and thickness of 1mm.. The PZT inside TWIN1, named as TL PZT, is AE0505D08 made by Thorlabs Inc, its maximal displacement is 6μm@100V voltage, and the resonant frequency is above 10kHz. While the PZT inside TWIN2, named as PI PZT, is PL055.21 made by PI Ltd, its maximal displacement is 2μm@100V voltage, and the resonant frequency is above 100kHz. These two PZTs will be driven by different PLLs and play respective roles in the synchronization.

Essentially, synchronization is achieved by locking the repetition rate of two ultrafast lasers to make them at a fixed value or shift simultaneously. The technique of synchronization includes passive-synchronization[2] and active one[3], the former bases on the cross-phase modulation effect and the latter bases on PLL. In this letter, we focus on the discussion of active synchronization. The PLL for active synchronization is different from electrical one, although the latter could achieve synchronization with timing jitter of picosecond magnitude. There is no real voltage controlled oscillator(VCO), here we call E-VCO, in active synchronization, which is instead by the combination of photodetector, PZT and laser cavity, here we call L-VCO. E-VCO and L-VCO have very different properties. Firstly, the L-VCO has much smaller gain constant less than 1 part in 10^4 of its center frequency, while the E-VCO has the same order to its center frequency. Secondly, the length of laser cavity is susceptible to environment effects, thus there are much more frequency noises in L-VCO, and the amplitude-to-phase conversion is very strong that is hard to be taken off completely. Furthermore, the relationship between frequency and voltage of E-VCO is almost linear, while it is relative more complex in L-VCO, dues to the nonlinear relation between the repetition rate and the laser cavity length.

In general, the feedback error signal for active synchronization is produced by double-balanced mixer (DBM). The photodetectors extract the repetition rate signals of the two ultrafast lasers and import them to the DBM, then the filtered, integral and amplified error signal is loaded on the PZT to adjust the cavity length of the lasers. Since the repetition rate depends on the cavity length of the laser, the PZT can compensate the relative variation of the cavity length and then synchronize the lasers precisely. The DBM could also deal with harmonics of the repetition rate signals, and the higher harmonic, the lower AM-PM phase noise, thus the error signal is more sensitive to the timing jitter of the ultrafast lasers and the synchronization is with higher precision.

Fig.1 shows the schematic diagram of the PLL driving PI PZT inside TWIN2, PIN is a high-speed photodetector D400FC produced by Thorlabs Inc with 100ps rising edge and 1GHz bandwidth, BPF is a 80MHz band-pass filter with 800MHz central frequency and 80MHz bandwidth, OPA is a DC~1GHz wide-band amplifier, DBM is a double-balanced

mixer, LF is a loop filter, OPA227 is a amplifier with high precision and low noise, PA45 is a power amplifier with high voltage and large current.

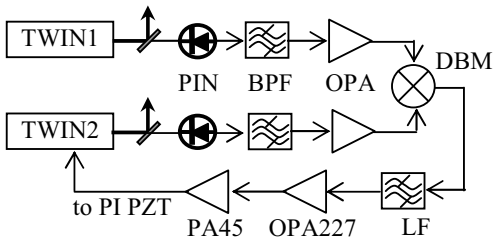

Fig.1 Schematic of PLL1

The BPF extracts the tenth harmonic components of the mode-locked signal of TWIN1[4], i.e. 800MHz, and the DBM works as frequency and phase discriminator. The error signal from the PLL load on PI PZT and drives it to modulate the cavity length rapidly. The loop bandwidth of the PLL is >20kHz, and the operated resonant frequency of PI PZT is >50kHz, so it is defined as a high speed, broadband PLL named as PLL1. It could compensate the relative variations of the cavity length between TWIN1 and TWIN2 and synchronize them with high precision, fast speed response and servo.

Despite of the high speed response, the maximum displacement of PI PZT is less than 0.7μm(the operated voltage load on it is <30V), while the relative cavity length difference of the two lasers maybe much larger than it, so the synchronization could not maintain very long time(more than 10 seconds) just by the PLL1, so we need another PZT with longer displacement to maintain a long-term synchronization.

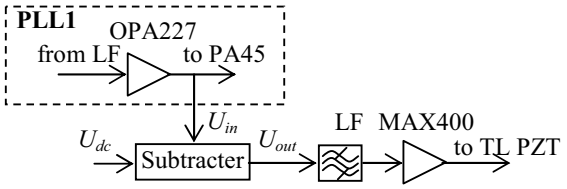

Fig.2 Schematic of PLL2

Fig.2 shows a schematic diagram of another PLL, namely PLL2, which drives TL PZT inside TWIN1. The TL PZT expands a maximum value of 2μm, and it can compensate the relative variation of the cavity length for longer time(>30 minutes generally). In fig.2, U_{in} is from the OPA227 in PLL1, it subtracts a constant voltage U_{dc}(U_{out}= U_{in}- U_{dc}, U_{dc} is a constant), then the difference signal is fed into LF, and the output signal acts on TL PZT after amplified by MAX400(a precise amplifier). The loop bandwidth of LF is about 30Hz, so we define PLL2 as low-speed PLL. The function of PLL2 is to keep U_{out} as zero, that is to keep U_{in} with the same as U_{dc}.

The PLL2 can work together with PLL1 by controlling the loop bandwidth and gain. Once these two PLLs activate normally, TWIN1 and TWIN2 could output synchronized laser pulses trains stably. However, the timing jitter is about hundreds of femtoseconds, which is obviously too large compared to the 100fs laser pulse width, thus we should improve the precision of synchronization further for the practical application.

B. Optical PLL

The template is used to format your paper and style the text. All margins, column widths, line spaces, and text fonts are prescribed; please do not alter them. You may note peculiarities. For example, the head margin in this template measures proportionately more than is customary. This measurement and others are deliberate, using specifications that anticipate your paper as one part of the entire proceedings, and not as an independent document. Please do not revise any of the current designations.

When TWIN1 and TWIN2 are synchronized by the two PLLs mentioned above, we focus two laser beams into a nonlinear crystal to generate sum frequency laser. A photodetector is used to detect the sum frequency laser and convert it into electrical signal. As you know, the signal intensity is very sensitive to the temporal position of the laser pulses, much more sensitive than the output of DBM in PLL1. If feeding this SFG signal back to the above PLLs, it could improve the precision of active synchronization significantly.

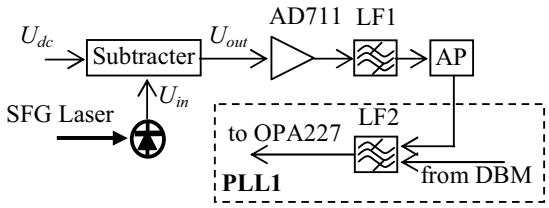

Fig.3 Schematic of PLL3

As indicated in Fig.3, the electrical signal converted from the sum frequency laser pulses firstly subtracts a constant voltage U_{dc}(U_{out}=U_{in}-U_{dc}), then fed into a loop filter(LF1) after amplified by AD711(a fine operational amplifier), the output voltage signal passes through an adjustable potentiometer(AP) and then it is input LF2 together with the error signal from DBM in PLL1, after that LF2 generates the new controlling signal to drive PI PZT. All of these could be regarded as PLL3, an optical phase locked loop.

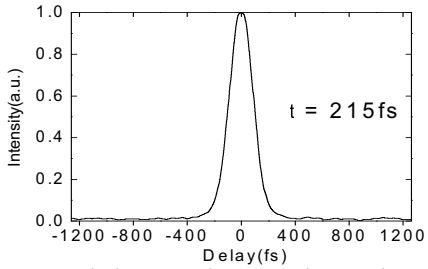

Fig.4 Cross-correlation trace between the synchronized lasers

Once PLL3 activates normally together with PLL1 and PLL2, the timing jitter of TWIN1 and TWIN2 could reduce to tens of femtosecond. We have measured the precision of synchronization with correlation method[5], fig.4 shows the trace of cross-correlation signal with 215fs FWHM, fig.5

shows the time record of the intensity fluctuation of the SFG laser at a fixed time delay when the cross-correlation signal is half of the maximum. Thus the calculated rms timing jitter is about 30fs, which proves that it is very effective using the sum frequency laser pulses as feedback signal to improve the precision of synchronization.

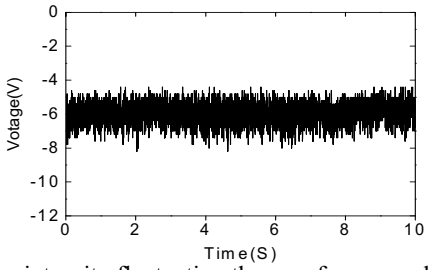

Fig.5 Power intensity fluctuation the sum frequency laser

The PZT control will enable the cavity length to be adjusted finely and quickly for accurate synchronization. The mirror mount, which the PZT is attached on, is fixed on a motorized linear translation stage which controlled by a computer, so the cavity length of the ultrafast laser can also be controlled by the computer in a relatively larger scale, and the controlling speed is much lower compared to PZT. In the experiment， the computer is utilized to monitor the real-time variation of the cavity length difference between these two synchronized lasers. By controlling the motion of the translation stage inside the ultrafast laser, it may compensate the variation of the relative cavity length caused by the surrounding environmental influence. Therefore, once two ultrafast lasers have been successfully locked, they will always keep synchronization with low timing jitter.

III. RESULTS AND DISCUSSIONS

In conclusion, we have demonstrated the active synchronization between two independent femtosecond Ti:sapphire lasers with high precision. There are totally three PLLs playing different roles in the experiment, two PLLs using DBM as phase detector work for preliminary synchronization with relative large timing-jitter, then an optical PLL using the sum frequency laser pulses as feedback signal activates to achieve much higher precision of synchronization, which reduces the timing jitter of the two ultrafast pulse trains from hundreds of femtoseconds to below 30fs measured in 10 seconds.

.

REFERENCES

[1] D. E. Spence, P. N. Kean, and W. Sibbett, “60-fsec pulse generation from a self mode locked Ti:sapphire laser”. *Opt. Lett*. Vol.16, No.1, pp.42-44, Jan. 1991

[2] J. R. Tian, Z. Y. Wei, P. Wang, H. N. Han, J. Zhang, L. H. Zhao, Z. H.Wang and J. Zhang, “Independently tunable 1.3W femtosecond Ti:sapphire lasers passively synchronized with attosecond timing jitter and ultrahigh robustness”. *Opt. Lett*., Vol.30, No.16, pp.2161-2163, Aug. 2005

[3] R. K. Shelton, S. M. Foreman, L. S. Ma, J. L. Hall, H. C. Kapteyn, M. M. Murnane, M. Notcutt, and J. Ye, “Subfemtosecond timing jitter between two independent, actively synchronized, mode-locked lasers”. *Opt. Lett*., Vol.27, No. 5, pp.312-314, Feb. 2002

[4] D. E. Spence, J. M. Dudley, K. Lamb, W. E. Sleat, and W. Sibbett, “Nearly quantum-limited timing jitter in a self-mode-locked Ti:sapphire laser”. *Opt. Lett* , Vol.19, No. 7., pp.481-483, Apr. 1994

[5] Z. Y. Wei, Y. Kobayashi, Z. G. Zhang, K. Torizuka, “Generation of two-color femtosecond pulses by self-synchronizing Ti:sapphire and Cr:forsterite lasers”. *Opt. Lett*. Vol.26, No.22, 1806-1808, Nov. 2001

Multipoint Dissemination of RF Frequency in Delay-Stabilized Fiber Optic Link in a Side-Branch Configuration

Ł. Śliwczyński, P. Krehlik, Ł. Buczek, M. Lipiński
Department of Electronics
AGH University of Science and Technology
Krakow, Poland
krehlik@agh.edu.pl

Abstract— **In this paper we are presenting the concept of the multipoint dissemination of RF frequency signal via a fiber optic network with actively stabilized propagation delays. The idea allows to add tapping nodes and side branches to the main point-to-point frequency transfer link, constituting a tree-like dissemination network. We are demonstrating the experimental results with the 100 km-long side branch starting at the 110th km of the 170 km-long main link. At the end of the side branch we obtained the Allan deviation of a 10-MHz frequency signal of about 4×10^{-17}, and the time deviation not greater than 1.2 ps for 10^5 s averaging.**

Keywords-Frequency dissemination; atomic clock; optical fibers; fiber network.

I. INTRODUCTION

Recently a significant development of fiber-optic based time and frequency (T&F) transfer systems may be observed. A lot of ideas of the frequency (and sometimes also the time) transfer were presented, based on transmission of either a highly coherent optical carrier, or an intensity-modulated light [1]–[5]. The main problem, which should be overcome using any approach is a fluctuation of the propagation delay of the fiber, caused mainly by varying temperature, and on much smaller scale by some mechanical stresses and random fiber birefringence (know also as polarization-mode dispersion).

Our group at the AGH University of Science and Technology is developing the T&F dissemination method based on active electronic stabilization of the propagation delay of the link [4], [5]. Recently we described an idea of point-to-multipoint frequency dissemination, with simultaneous stabilization of all the delays from the common input to all outputs of the system [6]. We demonstrated the experimental results for access nodes located along the main link. In this work we are presenting the new experiments with the side branch configuration, allowing to deliver the frequency reference signal to locations far away from the main link.

II. ACTIVELY STABILIZED SIDE BRANCH

The general concept of our system is depicted in Fig. 1. It comprises the Local and Remote Modules, responsible for stabilization of the propagation delay between the input and the remote output of the trunk link. The Access Module, located at some point along the trunk fiber, taps small portions of the optical signals propagating in both the forward and backward directions and is responsible for stabilizing the propagation delay from the input of the system to the side branch output. The simplest way of tapping the signals propagating along the trunk fiber is to insert the passive directional coupler into the main (trunk) optical path. (When needed the tapping may be combined with optical amplification by means of a bidirectional optical amplifier.)

Ignoring for a moment the Access Module we will recall the core idea of stabilizing the propagation delay of the main (trunk) link. In the Local Module the incoming frequency signal goes through the electronic variable delay line, and then reaches the electro/optic (E/O) converter (the intensity-modulated laser). Next the signal passes the optical circulator and propagates in the forward direction down the trunk optical fiber to the remote location. There it is back-converted to the electrical form and feed to the output, but also turned back to the trunk fiber in the backward direction. The signal coming back to the Local Module is converted to the electrical form, enters the second variable delay line, and reaches the phase detector, which second input is connected to the input port of the module. The phase detector senses the phase difference between the input and feedback signals, and cancels it by varying the delays of both the forward and backward delay lines by the same amount. Thus the round-trip delay in the system is kept constant, unaffected by the fluctuations of the fiber delay. Making the reasonable assumption that the variations of the fiber propagation delay are the same in forward and backward directions, it may be shown that also the input-to-output delay is kept constant. (For more detailed discussion see [4].)

The signal propagating to the side branch output starts at the coupler port marked by letter **A**. After conversion to the electrical form, passing through the variable delay line and being converted again to the optical domain, it reaches the Branch Output Module. There it is redirected back-ward, similarly as in the trunk link, and enters the second variable delay line. The phase detector in the Access Module cancels

This work was supported by Polish National Science Centre under the decision DEC-2011/03/B/ST7/01833.

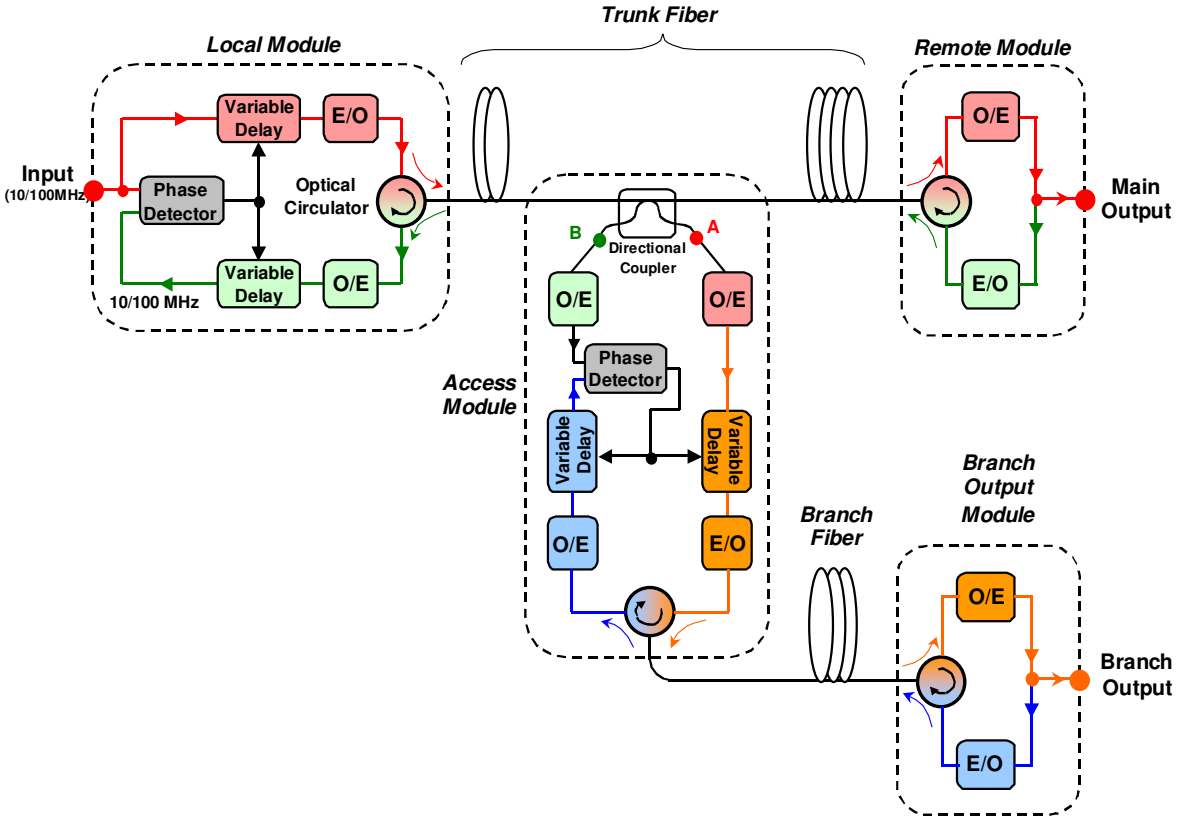

Figure 1. Block diagram of the point-to-multipoint dissemination system.

the phase difference between the signal coming back from the side branch and that coming back from the Remote Module of trunk link (point **B** of the coupler). As we shown in [6], the phase fluctuations observed at both outputs of the coupler (**A** and **B**) are of the same magnitude but opposite sign. Thus the side branch output, being "in the middle" between **A** and **B** points, is not affected by phase fluctuations occurring in the trunk fiber. Also the phase (delay) fluctuations occurring in the branch fiber are canceled similarly as in the basic trunk link [6].

III. EXPERIMENT

The experimental setup is depicted in Fig. 2. The 10-MHz frequency signal was disseminated from the Local Module to two outputs: the Remote Module, terminating the trunk line (173 km of fiber), and Branch Output Module, terminating the 98 km-long side branch. To compensate the attenuation of the optical paths there were three single path bidirectional amplifiers (SPBAs) involved in the setup. Evaluation of the disseminated signals stability was performed using a high-speed, real-time digital oscilloscope (Agilent DSO81004A) and dedicated software built in Matlab. The spooled fibers, SPBAs and Access Module were located in two different, not air-conditioned laboratories, and underwent temperature variations of about 5°C. The two spans of field-deployed fibers were located in Krakow metropolitan area. The rest of the equipment was located in restricted-access laboratory with temperature stability of about 0.5°C.

The results of our measurements are shown in Figs. 3-5, in the form of time-domain plots of the phase fluctuations, as well as the time deviation (TDEV) and the overlapping Allan deviation (ADEV). One set of data was obtained during

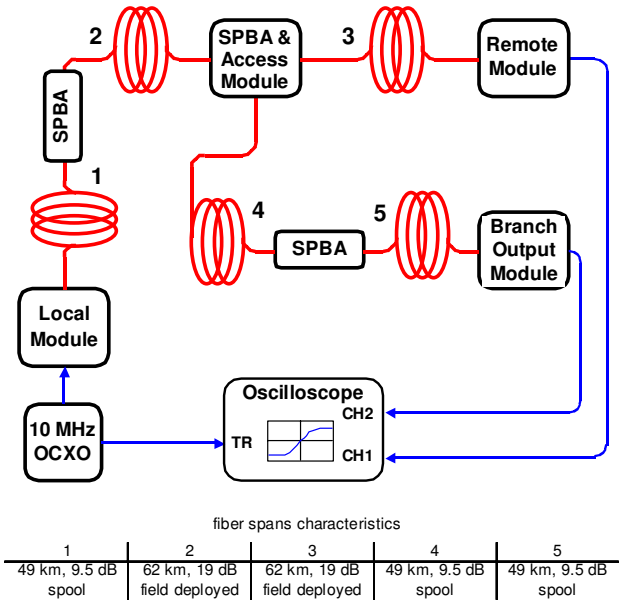

Figure 2. The experimental setup.

12-days long measurement with delay stabilization deactivated (open loop), and during next 12 days in normal (closed loop) configuration.

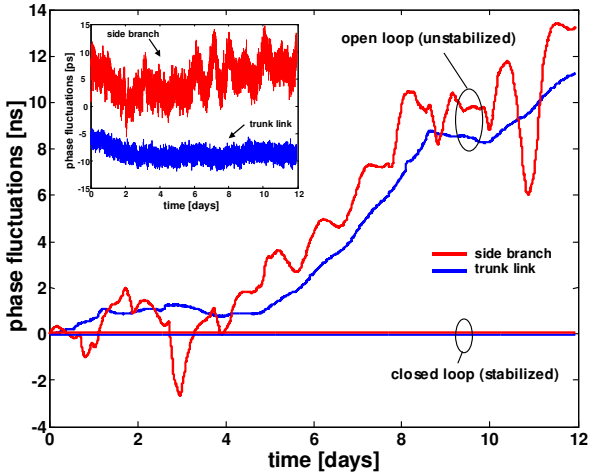

Figure 3. Time-domain phase fluctuations for closed loop and open loop configurations. In the inset the closed-loop fluctuations revealed by picosecond-range vertical scale.

In all figures the expected stabilization feature at both the trunk link and the side branch is clearly visible. The stability obtained in the trunk link is very similar to obtained previously in our other experiments with the basic point-to-point configuration [4], [5], and for the side branch the stability is somehow degraded; ADEV and TDEV is about two times to three times larger. It may be explained noticing that the side branch stability is affected by impairments of all electronic and optoelectronic components present in all modules visible in Fig. 1, whereas the trunk link is not affect by adding of the side branch system (except some optical power tapping). However, the stability obtain at the side branch output is still very good, and significantly outperforms stability of nowadays commercial atomic clocks, especially for longer averaging time.

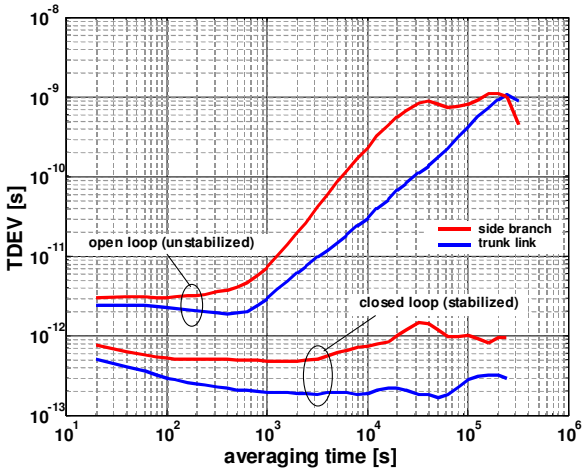

Figure 4. Time deviation for closed loop and open loop configurations.

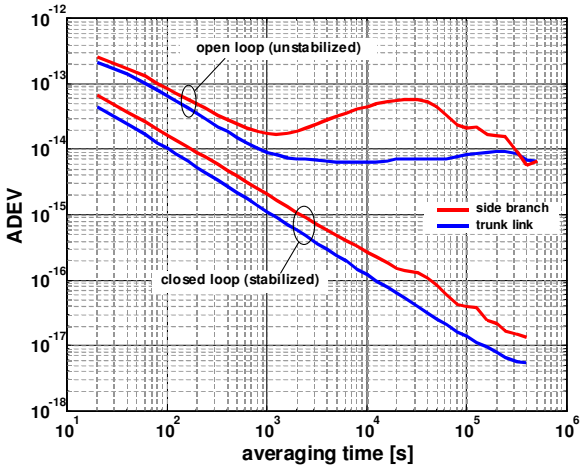

Figure 5. Overlapping Allan deviation for closed loop and open loop

IV. CONCLUSIONS

We experimentally verified the new concept of actively stabilized frequency dissemination system with the side branch connected in some point of the trunk link. Adding of the branch did not affect the trunk link stability, whereas the side branch stability occurred to be two to three time worse comparing to the main (trunk) link, because of much more complicated hardware setup involved in the branch system. Basing of this idea also a more complex, tree-like point-to-multipoint frequency dissemination network may be built.

The natural continuation of this research will be incorporating the time transfer to the point-to-multipoint system, on basis similar to used in our point-to-point system.

REFERENCES

[1] K. Predehl, G. Grosche, S. Raupach, S. Droste, O. Terra, J. Alnis, T. Legero, T. Hänsch, T. Udem, R. Holzwarth, H. Schnatz, "A 920-Kilometer Optical Fiber Link for Frequency Metrology at the 19th Decimal Place", Science, vol. 336, pp. 441-444, 2012.

[2] O. Lopez, A. Amy-Klein, M. Lours, Ch. Chardonnet, G. Santarelli, "High-resolution microwave frequency dissemination on an 86-km urban optical link", Applied Physics B Lasers and Optics, vol. 98, pp. 723-727, 2010.

[3] [1] O.Lopez, A.Kanj, P.E.Pottie, D.Rovera, J.Achkar, Ch.Chardonnay, A.Amy-Klein, G.Santarelli, "Simultaneous remote transfer of accurate timing and optical frequency over a public fiber network", Appl. Physics B, DOI 10.1007/s00340-012-5241-0, 07th October 2012.

[4] Ł. Śliwczyński, P. Krehlik, Ł. Buczek, M. Lipiński, "Active propagation delay stabilization for fiber optic frequency distribution using controlled electronic delay lines", IEEE Transactions on Instrumentation and Measurement, vol. 60, pp. 1480-1488, 2011.

[5] Ł. Śliwczyński, P. Krehlik, A. Czubla, Ł. Buczek, M. Lipiński, "Dissemination of time and RF frequency via stabilized fiber optic link at the distance of 420 km", Metrologia, vol. 50, pp. 133 – 145, 2013, DOI 10.1088/0026-1394/50/2/133.

[6] P. Krehlik, Ł. Śliwczyński, Ł. Buczek, M. Lipiński "Multipoint dissemination of RF frequency in fiber optic link with stabilized propagation delay", IEEE Transactions on Ultrasonics, Ferroelectrics, and Frequency Control, in press.

Evaluation of the AGH-Designed Time and Frequency Transfer System on a 149 km PTB-Hanover-PTB Fiber Link

P. Krehlik and Ł. Śliwczyński
AGH University of Science and Technology
Department of Electronics
al. Mickiewicza 30, 30-059 Krakow, Poland
sliwczyn@agh.edu.pl

G. Grosche, S. Raupach, D. Piester and H. Schnatz
Physikalisch-Technische Bundesanstalt
Bundesallee 100, 38116 Braunschweig, Germany

Harald.Schnatz@ptb.de

***Abstract*— We describe experiments with the AGH-designed fiber optic system for time and frequency dissemination, based on an active stabilization of the fiber delay. The measurements were performed at the Physikalisch-Technische Bundesanstalt, Braunschweig, over a field-deployed optical fiber loop going from PTB to the Magnesium clock laboratory in the Leibniz Universität Hannover and back (149 km, 45 dB attenuation).**

Keywords-time, frequency, dissemination, optical fiber, atomic clock

I. INTRODUCTION

The system for dissemination of time and frequency signals exploiting an electronic stabilization of the propagation delay of the optic fiber link was recently designed and developed at the AGH University of Science and Technology in Krakow, Poland [1]. It allows remote access to 5/10/100 MHz and 1 or 100 pulses per second (PPS) signals generated by atomic sources (e.g. cesium clocks and fountains or hydrogen masers) with the stability and accuracy being at the level of the source producing the signals. Tests performed at AGH showed the Allan deviation (ADEV) around a few times 10^{-17} at one day averaging and the time deviation (TDEV) below 1 ps for 10 MHz and 1 PPS signals, respectively. The system also showed a picosecond-level capability of the calibration of the time transfer. We performed the tests using the fibers spooled in the lab as well as the field-deployed link running from our lab to Skawina near Krakow and back (~120 km) [1], [2].

The purpose of our current work was to perform additional, independent tests of the system stability and calibration accuracy, using various measurement approaches and different fiber optic link, exploiting high-speed real time digital oscilloscope, K+K Phase Recorder [3], dual mixer time difference (DMTD) technique [4] with harmonic trackers and time interval counters (TIC).

II. FIBER OPTIC LINK

To perform the evaluation the time and frequency dissemination system with the stabilization of the propagation delay was installed over a field-deployed fiber optic link running from the Physikalisch-Technische Bundesanstalt (PTB) in Braunschweig to the Magnesium frequency standard laboratory in the Leibniz Universität Hannover (LUH) and back [5]. This link uses standard SMF-28 type fiber with the total length about 149 km, showing the attenuation around 45 dB (estimated from the OTDR measurements). To compensate the attenuation of the fiber we planned to place remotely-controlled single path bidirectional Er-doped amplifier (SPBA) [2], [6] in the middle of the span, in the Magnesium frequency standard laboratory at LUH. The diagram showing the details of the link is presented in Fig. 1a.

After installing all the equipment it appeared that the system could not lock and operate properly. Detailed analysis of the optical paths revealed that although most of the optical connectors used were of APC type, a few ordinary PC

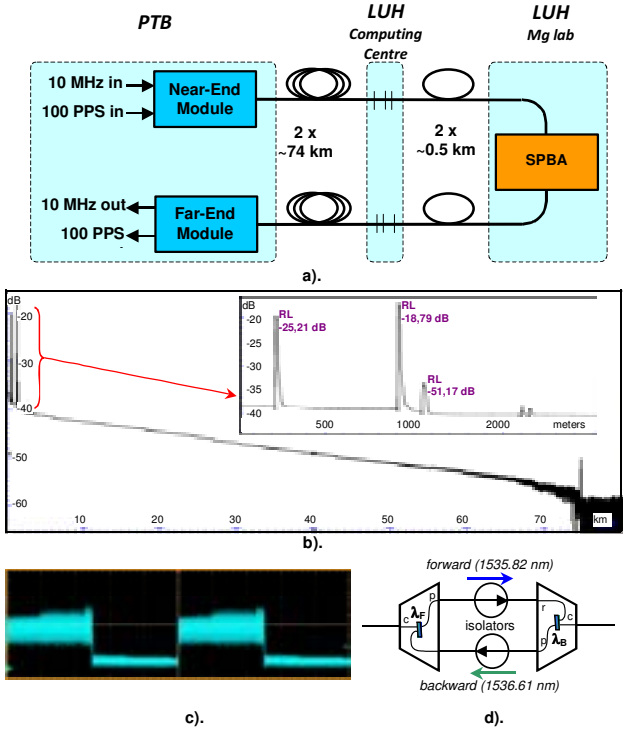

Figure 1. PTB-LUH-PTB fiber optic link: overview (a), PTB-LUH OTDR plot (b), signal observed at the input of the Far-end module and structure of the wavelength-selective isolator (d).

This work was supported by the European Metrological Research Programme EMRP under SIB-02 NEAT-FT. The EMRP is jointly funded by the EMRP participating countries within EURAMET and the European Union. Support by the Centre of Quantum Engineering and Space-Time Research (QUEST) is gratefully acknowledged.

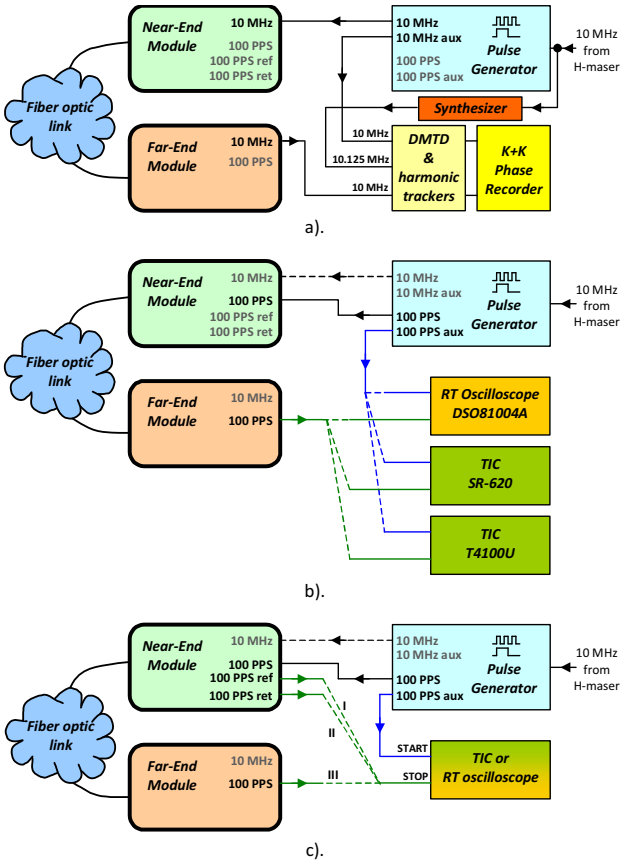

Figure 2. Diagram of test setups used for evaluating time and frequency dissemination system: stability of frequency dissemination (a), stability of time dissemination (b) and time calibration (c).

connectors were also used. They were located close to the SPBA at the LUH Computing Center and showed exceptionally high reflections (between –26 dB and –13 dB accordingly to OTDR measurements – see example OTDR trace in Fig. 1b). As a result the optical signal reaching the receiver of the Far-End Module suffers from both the multiple reflections and noise (generated inside the SPBA from its amplified spontaneous emission - ASE) – see Fig. 1c. This was the reason of malfunction of our dissemination system.

Replacing of suspicious connectors with the APC ones was impossible and cleaning them did not help much so we decided to add a wavelength-selective isolator (see Fig. 1d) at LUH at one side of the SPBA. This module appeared to be very effective in breaking the optical feedback loop around SPBA. After its installation the quality of the signal received by the Far-End module improved to the level allowing for normal operation of our system.

III. Measurement Setup and Evaluation Methods

To evaluate the time and frequency dissemination system we arranged a number of measurements using the setups sketched in Fig. 2. In all these setups we used a pulse generator, having main as well as auxiliary 10 MHz and 100 PPS signals, synchronized to a 10 MHZ signal derived from a hydrogen maser.

For the frequency stability measurement we applied the DMTD technique to increase the resolution of K+K Phase Recorder, using a dedicated hardware developed at PTB, including mixers and PLL-based harmonic trackers, (see Fig. 2a). In this setup 10 MHz frequency signal from the main output of the pulse generator was applied to the input of Near-End Module. The DMTD module received 10 MHz signals from the auxiliary output of the pulse generator and from the Far-End Module, using 10.125 MHz signal, synchronized to the H-maser, as a common reference. Resulting multiplication factor was thus equal to 80.

To measure the time dissemination stability we used the setup shown in Fig. 2b, where the time difference between 100 PPS pulses from the auxiliary output of the pulse generator and output of the Far-End Module was registered by either the oscilloscope or the TIC. For the oscilloscope measurements we exploit the feature of our pulse generator allowing inserting the programmable delay between its main and auxiliary outputs. This allows compensating a long delay of the fiber link (~730 µs), leaving only the residual (below 10 µs) to measure by the oscilloscope, limiting this way the influence of its timebase instability on the measurement results. We decided to use the 100 PPS time signal instead of a standard 1 PPS to reduce the impact of the short-term noise of both the measurement setup and the measured system itself.

The setup we used to measure the accuracy of time dissemination is presented in Fig. 2c. The unique feature of our system is the possibility to accurately determine (calibrate) the propagation delay it introduces between its time reference point (i.e. the 100 PPS_ref point marking the exact moment of transmitting the actual 100 PPS pulse) and 100 PPS output, using only the signals available at the Near-End Module [1], [6]. It is given by the equation:

$$\tau^{C}_{REF\to OUT} = \frac{1}{2}\left[\tau_{REF\to RET} + \Delta\tau_{F\_FB} + \tau_{C}\right], \qquad (1)$$

where $\tau_{REF\to RET}$ is measured round-trip delay, $\Delta\tau_{F\_FB}$ is the difference between the propagation delay in the forward and backward directions of the fiber link and τ_C is the calibration constant determined before installation of the system with a short patchcord in place of the fiber link (this way $\Delta\tau_{F\_FB} \approx 0$). Further $\Delta\tau_{F\_FB}$ may be estimated from the equation:

$$\Delta\tau_{F\_FB} = \Delta\lambda_{FB} D\,, \qquad (2)$$

where D is the total chromatic dispersion and $\Delta\lambda_{FB}$ is the difference of the wavelengths used to transmit the signals in the forward and backward directions. (The correction factor for the Sagnac effect has already been omitted in equation (2) because of loop configuration used in described experiment.)

Performing a measurement of the accuracy of the time dissemination requires a few steps. First, having the START and STOP inputs of the TIC (or two channels of the oscilloscope) connected between the auxiliary output of the

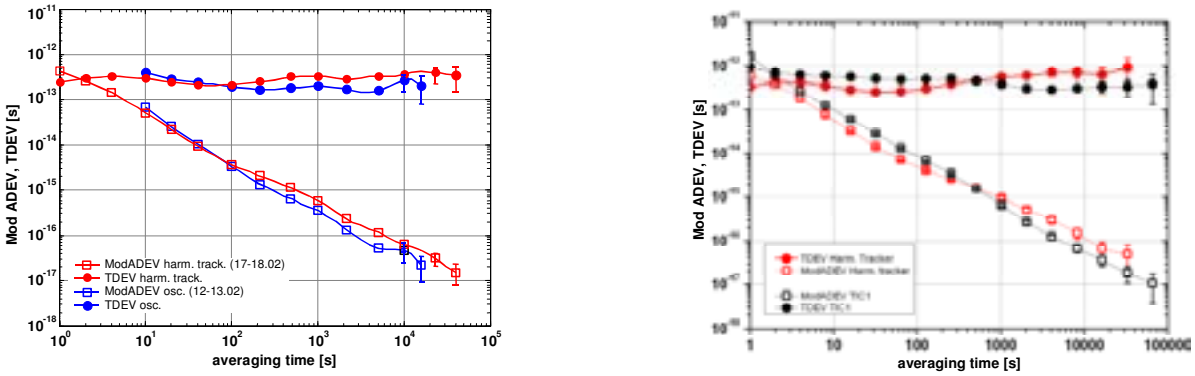

Figure 3. Time and frequency stability comparison: a) - DMTD with harmonic trackers (10 MHz) and oscilloscope (100 PPS), b) - DMTD with harmonic trackers (10 MHz) and SR620 (100 PPS).

pulse generator and the 100 PPS_ref output of the Near-End Module (marked "I" in Fig. 2c) we measure the reference time interval τ_I that takes into account all constant delays (i.e. the propagation delays of the cables, the delay between the main and auxiliary outputs of the pulse generator and the delay between the 100 PPS input and 100 PPS_ref point). In the second step (marked "II" in Fig. 2c) we measure the time interval τ_{II} changing the signal at the STOP input to 100 PPS_ret. Subtracting τ_I from τ_{II} we get the round-trip delay $\tau_{REF\to RET}$ that enters equation (1). The true, directly measured propagation delay $\tau^M_{REF\to OUT}$ may be determined by calculating $\tau_{III}-\tau_I$ according to configuration "III" in Fig. 2c. It may further be compared with the value calculated from equation (1). It is essential to use the same cable connecting the STOP input of the TIC to the source of the signal in all these three steps. For the procedure to be complete we still need the total chromatic dispersion D that may either be known from the fiber link operator or, better, measured using e.g. the procedure described in [6], using a tunable laser transmitter and a TIC.

IV. Results of Evaluation

Using the fiber optic link and the test setups described in two previous sections we arranged a number of measurements to evaluate the stability of time and frequency dissemination as well as time dissemination accuracy. The most important results are summarized below.

A. Time and Frequency Stability

Some representative ModADEV/TDEV curves showing the time and frequency stability are presented in Fig. 3a and b. These are shown jointly because in our dissemination system the 100 PPS signal is recovered from 10 MHz frequency signal so both are phase coherent. Even the structure of output buffers is exactly the same, so both signals should display similar stability. In Fig. 3a comparison of curves registered in two measurement sessions between 12-13.02.2013 and 17-18.02.2013 are shown; the measurement period for Fig. 3b was 22-25.02.2013. The frequency stability was measured using DMTD technique, whereas time stability was measured using DSO81004A oscilloscope (Fig. 3a) and SR620 TIC (Fig. 3b).

Analyzing the results one may observe, as expected, quite close agreement between the stability of time and frequency signals. The slope of the curves, close to τ^{-1}, suggests that the flicker phase noise dominates. For long averaging times the ModADEV approaches values close to 10^{-17} that agrees well with other measurements performed in our lab on the link with comparable length and attenuation. The TDEV is below 1 ps, also being in agreement with our other results.

There are, however, some noticeable differences. In Tab. I the values of ModADEV for a few averaging periods are summarized for different measurement methods. One may notice that DMTD technique gives best results for short averaging times, generally below 100 s. For longer times the DMTD results start to worsen, being even worse than TIC results. An analysis of the data from K+K Phase Recorder revealed some spikes, that are probably related to the temperature variations in the lab caused by human activity (see Fig. 4 as an example). No such effects were noticed in records from the oscilloscope and SR620 TIC. We expect that a better thermal shielding and careful selection of all DMTD components will reduce the sensitivity to environmental temperature fluctuations significantly.

Quite interesting and surprising is a good long-term performance of SR620 TIC, showing ModADEV and TDEV comparable as measured using the oscilloscope. This may be explained noting that when counting of the 100 PPS pulses with the TIC we gained on hundred-fold averaging reducing its

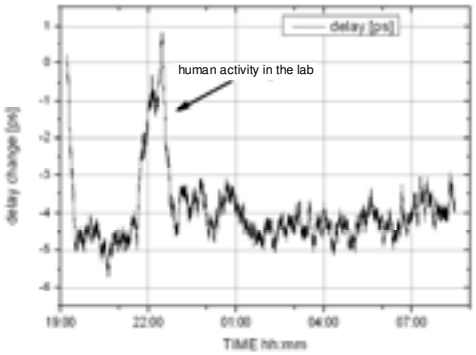

Figure 4. Fragment of the record registered using DMTD technique with harmonic trackers.

TABLE I. MODADEV FOR DIFFERENT MEASUREMENT METHODS

	Averaging time [s]		
	1s	***10^2s***	***10^4s***
DMTD	$4\text{-}6\cdot10^{-13}$	$3\text{-}5\cdot10^{-15}$	$6\text{-}11\cdot10^{-17}$
DSO81004A	-	$3\cdot10^{-15}$	$4.3\cdot10^{-17}$
SR620	$2\cdot10^{-12}$	$8\cdot10^{-15}$	$5.5\cdot10^{-17}$

noise substantially.

B. Time Transfer Calibration

The calibration of time transfer was performed twice – for the first time at 14.02.2013, and further verified at 25.04.2013. During these two months the system was powered off and disconnected from the fibers for some period. After powering on again and reconnecting the fibers no any additional procedures (like tuning or recalibration) were performed. The oscilloscope used for the measurements was transported from Braunschweig to Krakow and back between the two sessions, and all the cabling was rearranged for the second session. The results of these calibrations are summarized in Tab. II.

The value of τ_C includes not only internal differences of the forward and backward propagation delays of the Near- and Far-End Modules but the difference embedded in the wavelength selective isolator as well. It was determined at PTB using the DSO81004A oscilloscope. The value of $\Delta\tau_{F\_FB}$ was measured using the tunable-laser technique [6].

At first calibration performed in February using the oscilloscope the difference between the measured and calculated propagation delays was equal to 18 ps. This is close to expanded uncertainty (i.e. two sigma value giving 95% level of confidence) of both directly measured delay of the link (σ=7 ps) and theoretically calculated delay of 149 km long link using SMF-28 fiber (σ=9 ps) [6]. The calibration was checked again in April, after termination of the link operation mentioned above. This time besides using the oscilloscope we also used a picosecond-accurate T4100U TIC developed at the Warsaw Military University of Technology [7]. The differences between the measured and calculated delays were 19 ps (DSO81004A) and 22 ps (T4100U), being in a very good agreement with the initial calibration performed in February.

TABLE II. RESULTS OF TIME TRANSFER CALIBRATION

Date	February 2013	April 2013
Temperature TX/RX	29,7°C / 23,2°C	28,8°C / 23,7°C
τ_C	52263(±7.2) ps	52270(±7.2) ps
$\Delta\tau_{F\_FB}$	1687(±14) ps	1688(±14) ps
$\tau_{REF\rightarrow RET}$	1457903829(±7) ps (Osc)	1457903828(± 7) ps (Osc) 1457903831(±15) ps (TIC)
$\tau^M_{REF\rightarrow OUT}$ (measured)	728978908(±7) ps (Osc)	728978912(±7) ps (Osc) 728978917(±15) ps (TIC)
$\tau^C_{REF\rightarrow OUT}$ (calculated)	728978890(±9) ps	728978893(±9) ps (Osc) 728978895(±12) ps (TIC)
$\tau^M_{REF\rightarrow OUT} - \tau^C_{REF\rightarrow OUT}$	**Δ = 18(±12) ps (Osc)**	**Δ = 19(±12) ps (Osc)** **Δ = 22(±18) ps (TIC)**

The results confirm that this time transfer technique is reproducible to better than about 5 ps.

V. CONCLUSION

Evaluation of the AGH developed time and frequency transfer system performed at PTB using 149 km long fiber optic link in loop configuration showed ModADEV at the level of $4\text{-}6\cdot10^{-17}$ at 10^4 s and TDEV well below 1 ps. Stability is similar for both 100 PPS and 10 MHz signals. Results obtained with all applied measurement methods are consistent, however for short averaging times the DMTD technique with harmonic trackers prevails, whereas for longer times DSO81004A oscilloscope and SR620 TIC performs better. Good long-term TIC results are mainly because of hundred-fold averaging because of measuring 100 PPS signal instead of usual 1 PPS.

Time transfer calibration of the link was performed twice – the difference between the measured and calculated propagation delay does not exceed 22 ps, even after one month of powering off of the system. Thanks to inserting the wavelength selective isolator it was possible to operate the system even in the presence of unusually strong reflections of optical connectors.

The results obtained confirm that the developed solution for fiber optic time and frequency transfer of microwave signals is reliable and suitable for dissemination of the signals from nowadays atomic sources, like Cs-clocks, H-masers and Cs-fountains.

ACKNOWLEDGMENT

We thank Steffen Rühmann from LUH for his invaluable technical help.

REFERENCES

[1] P. Krehlik, Ł. Śliwczyński, Ł. Buczek and M. Lipiński, "Fiber optic joint time and frequency transfer with active stabilization of the propagation delay", IEEE Trans. Instrum. Meas. 61, 2844–2851, 2012.

[2] Ł. Śliwczyński, P. Krehlik, Ł. Buczek, M. Lipiński, "Frequency transfer in electronically stabilized fiber optic link exploiting bidirectional optical amplifiers", IEEE Trans. Instr. Meas., vol. 61, pp. 2573-2580, 2012.

[3] G. Kramer,W. Klische, "Extra high precision digital phase recorder", 18th European Frequency and Time Forum, pp. 595-602, Guildford, UK, 2004.

[4] W.J. Riley, Handbook of frequency stability analysis, NIST Special Publication 1065.

[5] A. Pape, O. Terra, J. Friebe, M. Riedmann, T. Wübbena, E. Rasel, K. Predehl, T. Legero, B. Lipphardt, H. Schnatz, G. Grosche, "Long-distance remote comparison of ultrastable optical frequencies with 10^{-15} instability in fractions of a second", Optics Express 20, 21477-21483, 2010.

[6] Ł Śliwczyński, P. Krehlik, A. Czubla, Ł. Buczek and M. Lipiński, "Dissemination of time and RF frequency via a stabilized fibre optic link over a distance of 420 km", Metrologia, vol. 50, 133-145, 2013.

[7] R Szplet, Z Jachna, P Kwiatkowski, K. Różyc, „A 2.9 ps equivalent resolution interpolating time counter based on multiple independent coding lines", MST, vol. 24, 035904, 2013

Bi-Directional Optical Amplifiers for Long-Distance Fibre Links

Sebastian M. F. Raupach[1], Andreas Koczwara[1], Gesine Grosche[1], Fabio Stefani[2], Olivier Lopez[2], Anne Amy-Klein[2], Christian Chardonnet[2], Paul-Eric Pottie[3], and Giorgio Santarelli[3,4]
[1]Physikalisch-Technische Bundesanstalt (PTB), Bundesallee 100, 38116 Braunschweig, Germany;
[2]LPL, Université Paris 13, Sorbonne Paris Cité, CNRS, Villetaneuse, France; [3]LNE-SYRTE, Observatoire de Paris, CNRS, UPMC, Paris, France; [4]LP2N, Université de Bordeaux 1, Institut d'Optique and CNRS, Talence, France

***Abstract*—Bi-directional optical frequency links for phase-stabilized frequency transfer require bi-directional amplifiers. Here we present some results from the development and test of two types of bidirectional amplifiers, Er^{+}-doped fiber amplifiers (EDFA) and fibre Brillouin amplifiers (FBA). to be deployed along a fiber link connecting SYRTE/France and PTB/Germany.**

Keywords—frequency metrology, fiber, amplifier

I. Introduction

When transferring an optical signal propagated over hundreds of kilometres in the C-band, the attenuation of the signal is one of the major concerns, as it ranges from .2 to .3 dB/km. This means that amplifiers are needed every hundred of km. For phase stabilised frequency transfer [1-3], the key idea is to partially reflect back the incoming light at the remote end of the link, and to measure and compensate the perturbation of the optical phase after one round-trip. It relies on the strong hypothesis that the noises are identical on the both directions of propagation. As a matter of fact phase-stabilised fibre links need fully bi-directional amplifiers.

II. Development of bi-directional Erbium Doped Fiber Amplifier

A straight forward approach, that complies with Telecom regulations, is to use Er^{+}-doped amplifiers (EDFA). In contrast to standard EDFA, we develop in partnership with IDIL bi-directional EDFA where the optical isolators are removed. It is advantageous that they are well known and reliable equipments, and that they are available now on the market. Largely autonomous in operation, they are almost insensitive in polarisation, what matters, as fibre links don't maintain the input state of polarisation. The maximum gain is +25 dB, for input signal ranging from -45 to -20 dBm. The Noise Figure is below 5 dB. The main drawback comes from the non-immunity to stray reflections as the optical isolators were removed for bi-directional operation. To prevent the amplifier from self-oscillating, the gain is limited to well below +25 dB. On the French link architecture for instance, the average gain over 6 amplifiers is as low as +16 dB/amplifier. They work continuously for more than 2 years without interruptions nor trouble shooting. Remote communications abilities were set up recently, and are now commercially available on the market[4]

The alternative approach that was developed on dark fibre architecture is to take advantage of Brillouin scattering to achieve high gain and wavelength-selective amplifiers.

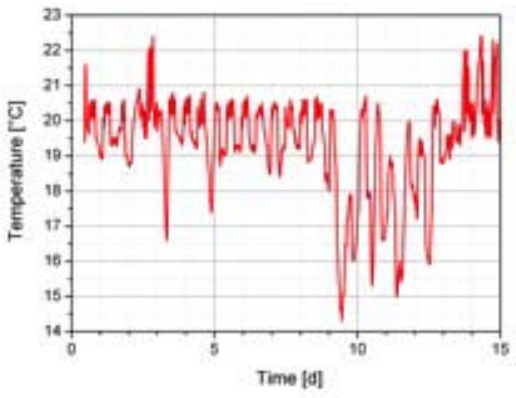

Figure 1 Temperature in a telecommunication hut in rural Germany (spring).

III. Development of Fibre Brillouin Amplifier (FBA) Modules

Fibre Brillouin Amplifiers (FBA) for frequency transfer via phase-coherent bi-directional links have been demonstrated and used in a laboratory environment [3,5]. Main features are a high small-signal gain of more than 40 dB and a narrow gain spectrum [6].

These features make Brillouin amplification a promising technique adapted to bi-directional links.

High amplifier gain allows for a larger distance between amplifier locations, reducing the complexity of the overall setup. Taking advantage of a gain of 40 dB, a transparent link can be set up with distances of around 200 km between the amplifier stations. However, currently Rayleigh backscattering as well as back-reflections prohibit the use of gains in excess of around 20 dB when using broad band bi-directional amplifiers, as uncontrolled lasing may occur.

Brillouin amplification in silica fiber on the other hand has a narrow gain profile with typical widths of around 10 MHz. Hence the amplification of light traveling towards the remote end and of the returning light require different pump frequencies, as the returning light in phase stabilized links typically is marked by a frequency shift of several tens of

Megahertz. In addition selection rule (momentum-conservation) implies that only counter-propagating light with respect to the pump wave-vector is amplified. This allows to discriminate the respective signal light from backscatter light. The main drawback is that the needed pump power is above the standard telecommunication regulation, and hence cannot be implemented so far on shared public network.

In contrast to applications in the laboratory, field-able Brillouin amplifiers require largely autonomous operation under less well-controlled conditions. One challenge are varying temperatures, as experienced in a telecommunication hut during a field test, where a test setup was placed at a distance of about 160 km. While a gain of around 40 dB was observed here and automated locking of the pump frequency to the signal could be achieved, considerable temperature excursions triggered further development of mitigation techniques to keep the pump frequency within the range of operation of the amplifier.

As Brillouin amplification relies on the interaction between signal light and pump laser light, depending on the available power the relative polarization of signal and pump is expected to affect the amplification [6].

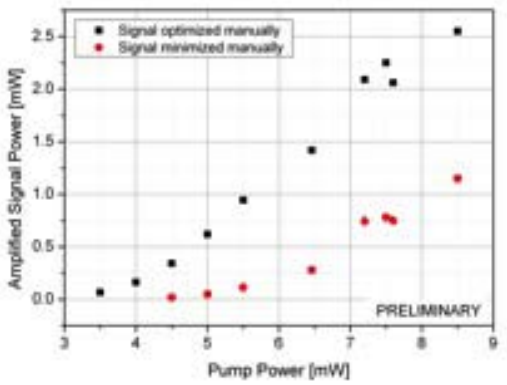

Figure 2 Dependence of the amplified signal power on the relative polarization, set manually, of pump and signal light (31 km fiber spool, signal input power around 80 nW).

We performed a laboratory test employing about 30 km of spooled standard silica fiber, a signal power of around 80 nW and a pump power of around 6,5 mW and automated polarization steps covering the Poincaré sphere.

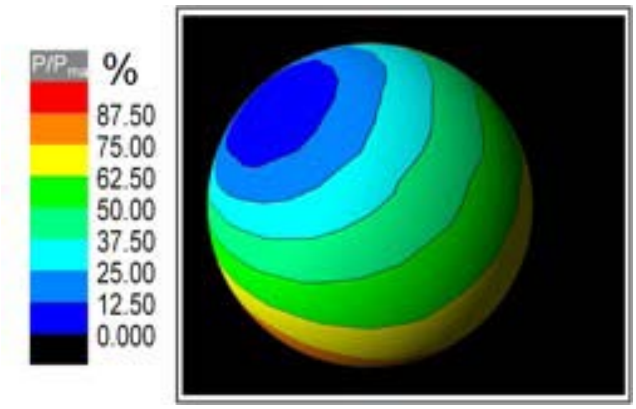

Figure 3 Poincaré sphere of the relative polarization between signal and pump (with an arbitrary offset of the polarization angles; automated steps in polarization) with the colour coded intensity of the signal power relative to the maximum observed power.

Here we found a likelihood of around 10% for losing about 75% of the possible amplified signal power, assuming that all states of relative polarization may occur with equal probability.

To mitigate slow polarization changes, we have developed an automated algorithm for remote polarization optimization upon request or when triggered e.g. by a drop in signal power.

Current and future work includes active mitigation of temperature swings, the development and implementation of remote communication as well as investigating and implementing FBA chains

ACKNOWLEDGMENT

F.S., O.L., A.A.K., C.C., P.-E.P and G.S. gratefully acknowledge IDIL for fruitful collaboration. S.M.F.R. and G. G. gratefully acknowledge helpful discussions and continuous support by H. Schnatz, as well as support concerning the fiber infrastructure by H.-J. Duda (Gasline GmbH), and excellent technical support by A. Koczwara and M. Misera. This work was supported by the European Metrological Research Programme EMRP under SIB-02 NEAT-FT. The EMRP is jointly funded by the EMRP participating countries within EURAMET and the European Union. Support of the work at PTB by the Centre of Quantum Engineering and Space-Time Research (QUEST) is gratefully acknowledged.

REFERENCES

[1] P. A. Williams, W. C. Swann, and N. R. Newbury, J.Opt. Soc. Am. B 25, 2008, pp.1284-1293.

[2] O. Lopez et al., Opt. Ex. 20, 2012, pp. 23518-23526.

[3] K. Predehl et al., Science 336, 2012, pp. 441-444.

[4] IDIL, Rue Claude Chappe, 22300 Lannion (France) http://www.idil-fibres-optiques.com

[5] O. Terra, G. Grosche and H. Schnatz, Opt. Ex. 18, 2010, pp. 16102-16111.

[6] J. Subías et al., Opt. Ex. 17, 2009, pp. 6753-6758.

[7] M. Oskar van Deventer, and A. J. Boot, J. Lightwave Tech. 12, 1994, pp. 585-590.

Tracking DDS for Coherent Optical Links

C.E. Calosso, E. K. Bertacco, D. Calonico,
F. Levi, S. Micalizio, A. Mura
INRIM, Torino, Italy

C. Clivati, G. A. Costanzo.
Politecnico di Torino and INRIM, Torino, Italy

***Abstract*—We report on the design and the realization of a digital architecture based on a tracking direct digital synthesizer (DDS) driven by a Field Programmable Gate Array (FPGA) for the implementation of a coherent optical link for time and frequency dissemination. The realized digital system has been implemented and characterized on a real fiber link on a 47 km metropolitan optical telecommunication network using a Dense Wavelength Division Multiplexing, that is shared with the internet data traffic. We describe the technique, the hardware and the characterization of the link, and we compare the new digital system with the analogic one, that uses common fiber links electronics.**

Keywords—Fiber link, Time and Frequency transfer, Digital Electronics, DDS, FPGA

I. INTRODUCTION

Nowadays, optical fiber links are a key technology for science and metrology. They allow the remote comparison of very accurate clocks, as Cs fountains or optical clocks [1-3]. Their resolution exceeds the state-of-the-art satellite techniques by several orders of magnitude, paving the way for a number of scientific experiments in the fields of high resolution spectroscopy, radio-astronomy, fundamental physics. Using a coherent optical link it is possible to exploit the optical clocks accuracy after few hundreds seconds of measurement over hauls up 1000 km, an unprecedented result. This is a fundamental achievement, as they are the most promising candidates for a forthcoming redefinition of the second. It is possible to achieve frequency dissemination (and comparisons) at the 10^{-16} level of stability [2,3] and time dissemination at the 100 ps level [4] over hauls of 1000 km. This resolution needs the compensation of the phase noise introduced by the fiber due to mechanical stresses and temperature variations, using a bidirectional Doppler cancellation technique [5].

The development of this optical fiber networks is of major interest also for high–tech industries, making available high quality T&F signals in real time, without the need of routine calibration. This research field is growing worldwide, and it is well represented in the European metrology scenario within the EU metrological program EMRP (NEAT-FT project). Among the present challenges for optical links, there is the investigation on new techniques for phase-coherent comparison of remotely located optical clocks, separated by distances of up to 2000 km using optical fiber links. Within this challenge is the development of the equipment necessary for reliable operation of fiber links and all technological steps towards a full and reliable optical link infrastructure. Moreover, these infrastructures should be easily adaptable to perform widespread dissemination of high performance metrological signals towards a larger variety of users, so the development of scalable, modular equipment is needed.

The National Institute of Metrology (INRIM) realizes in Italy accurate T&F signals and disseminates them to a variety of scientific laboratories and industries. Presently, INRIM maintains two Cs fountain primary frequency standards, with an accuracy at the 10^{-16} level [6], and is developing an optical clock based on Yb atoms [7]. To improve the quality of T&F dissemination, INRIM realized together with other major National Institutions, the LIFT project (the Italian Link for Frequency and Time) an optical link along a 642 km fiber that connects Torino to Milano, Bologna, and Firenze, under operation since May 2013 [8]. This optical link is based on a dark fiber architecture, i. e. the fiber is completely dedicated to the experiment. Besides the Torino-Firenze optical link, INRIM has installed a local coherent fiber link in Torino, using a 47 km haul normally used for internet data traffic [9] on a dark channel architecture.

The electronics involved in both links is well established [10] and is based on a frequency mixer used as phase comparator, joined with a frequency divider to extend its phase input and a tracking oscillator or a quartz filter to clean up the beat note of the local laser with the round trip radiation. In addition, a couple of frequency-meters are needed to evaluate the correction to apply to the laser for the link compensation and to monitor the system.

In this work, we propose an alternative digital solution that integrates the whole electronics for detection, compensation and monitoring in a single board based on three DDS driven by an FPGA. The system is compact, flexible and cost effective, providing a complete characterization of the link and the modularity for more complex architectures, such as the multi-point delivering of the ultrastable laser along the haul for real coherent optical fiber networking [11]

II. COHERENT OPTICAL LINK

The optical link allows to transfer an ultrastable laser signal over long distance without appreciable degradation of its phase/frequency by compensating the fiber noise. Fig. 1 shows a particular arrangement suitable for comparing two remote ultrastable lasers. The link is bidirectional and allows to detect potential link anomalies by comparing the measures of the two laboratories. The figure also groups the optical components and the electronics. Here we focus on the electronics involved whose tasks are: 1) detection of the fiber noise φ_e; 2) calculation and applying the correction φ_c; 3) monitoring the link by detecting φ_m. In addition, some phase/frequency meters are necessary to register the main signals, i. e. the correction to the fiber and, primarily, the monitor that, in the figure, is the result of the ultrastable lasers comparison.

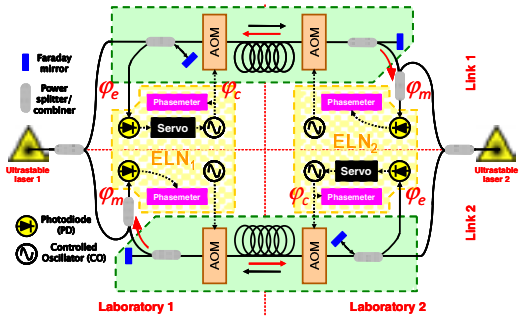

Fig. 1. Bidirectional coherent optical link

In Fig. 2 we also show the experimental set-up.

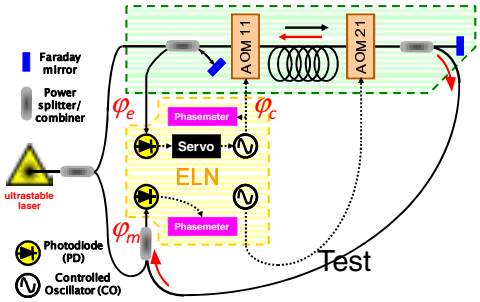

Fig. 2. Experimental setup

A. Traditional analog implementation

The analog implementation (Fig. 3) is well established and proved to allow coherent frequency dissemination over hundreds of kilometers with a residual uncertainty in the 10^{-19} range [1, 2].

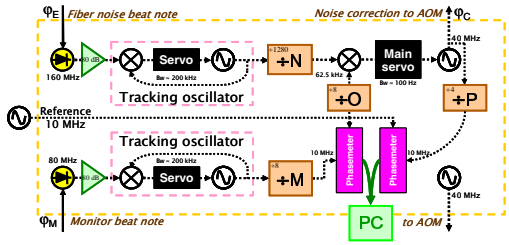

Fig. 3. Analog implementation of the fiber link electronics

In principle, the electronics is very simple: one mixer to detect the beat note that contains the fiber noise, an operational amplifier to generate the correction and a Voltage Controlled Oscillator (VCO) to drive the AOM. In practice, some additional circuitry is necessary: some frequency dividers to extend the mixers input range and a couple of tracking oscillators to clean-up the beat notes in order to properly drive the frequency dividers. The most expensive part is represented by the instruments used to record the signals: phase-meters are the natural choice, being the phase proportional to the optical length, but we often encounter frequency-meters. They are cheaper, but introduce some complications in data analysis due to dead time and to phase noise type.

B. Implementation with Tracking DDS

The proposed implementation can be conceptually obtained by the analog one by simply substituting the VCOs with Direct Digital Synthesizers (DDS) [12, 13] and, consequently the analog servos with digital ones implemented on FPGA (see Fig. 4).

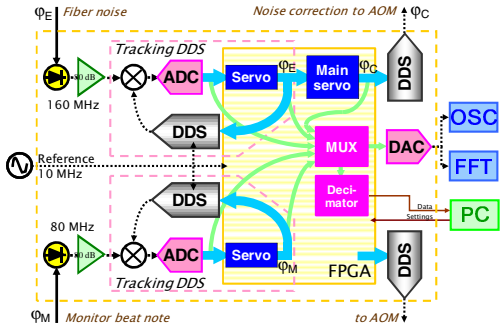

Fig. 4. Fiber link electronics based on Tracking DDS.

The DDS is used in a different manner with respect to the VCO, because the servo drives its phase instead of its frequency. In this manner, by considering the phase imposed to the DDS to track the beat note, we have direct access to the information required φ_e (φ_m). The fiber noise data is then processed by the main servo to calculate the correction that is applied to the AOM by directly driving the phase φ_c (and not the frequency) of the DDS.

The information of interest (φ_e, φ_m and φ_c) is digitally represented and available without the need of any additional

instrumentation. It can be sent to a PC by means of a module implemented in the FPGA that integrates a decimator to reduce data rate and to set the measurement bandwidth that, consequently, is well defined.

In addition, the internal data can be sent to a DAC to have their analog representation that can be observed with the traditional instruments: FFT spectrum analyzer and oscilloscope.

C. Cycle slips

The noise and consequently the required tracking bandwidth is proportional to the length of the link. The actual bandwidth (about 15 kHz) is limited by the time required to write data in the DDS via a serial bus. It is suitable for medium link, up to 50 km. The presence of non-stationary extra noise causes cycle slips. They will be avoided by using in the next design a DDS with parallel data bus that will allow to reach a tracking bandwidth of about 500 kHz. For the moment, we have to remove them for properly analyzing the data.

We tried two algorithms: the first (algorithm A) simply removes discontinuities larger than a suitable threshold; the second (algorithm B) removes discontinuities multiple of half a cycle. The latter can be applied only if the peak-to-peak noise is lower than half a cycle and this can be reached (even for long link) by closing the measurement bandwidth to a few hertz, in order to filter out the big bump from 10 Hz to 1 kHz in the spectrum of the monitor. The second algorithm works much better as shown by the figure below.

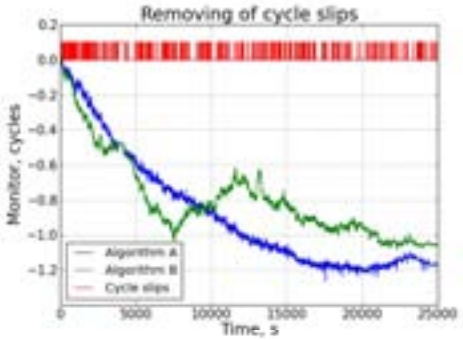

Fig. 5. Comparison of two techniques for cycle slips removing.

III. Results

The electronics based on the Tracking DDS has been tested on a 47 km long loop in Torino. Taking advantage of the loop configuration, it is possible to compare the output of the fiber with the ultrastable laser at the input of the link and get a characterization of the complete system. In addition, it is possible to get the two beat notes and drive the two AOMs with one electronic system.

To demonstrate that the electronics presented is able to fully characterize the link, we report the spectrum up to 100 kHz of the monitor (φ_c) and of the closed loop fiber noise (φ_e). They are obtained by using the DAC output and an FFT spectrum analyzer (Fig. 6 And Fig. 7). We can deduce many informations, such as the bandwidth of the two tracking DDSs, the main loop bandwidth, the one-way and round-trip delays. In particular Fig. 7 shows the easy and fast tuning of the main loop by digitally changing its gain.

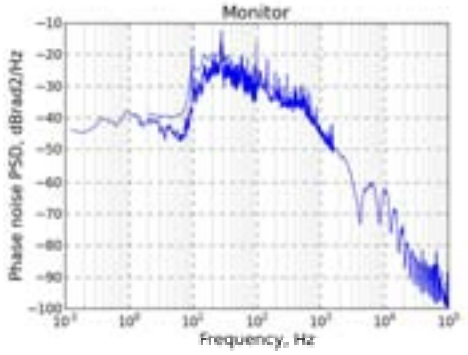

Fig. 6. Monitor PSD from DAC output.

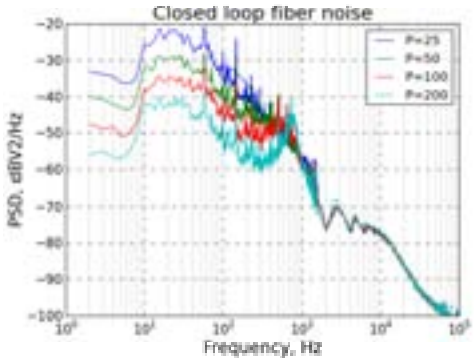

Fig. 7. Closed loop fiber noise (from DAC) with different loop gains

On the other hand, it is possible to directly analyze the downloaded data in the auxiliary PC. The available bandwidth is 4 kHz, and is wide enough to characterize the link. The measurement bandwidth is well defined and can be adjusted by setting the integrated decimator.

The monitor is in the femtosecond range in front of correction to the fiber of hundreds picoseconds (Fig. 8 and 9).

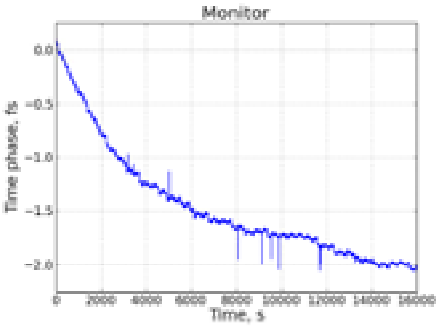

Fig. 8. Monitor signal (φ_m) in time domain.

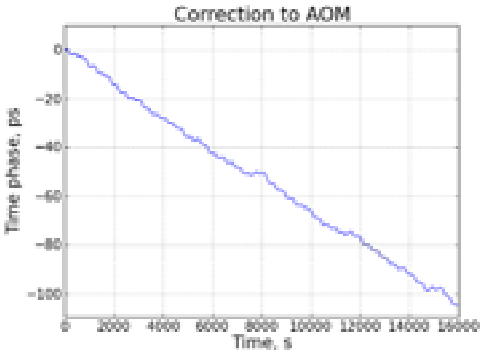

Fig. 9. Correction to the fiber (φ_c).

This allows to disseminate an ultrastable laser with a residual fractional frequency noise of about 10^{-17} at 1 s reaching $4x10^{-20}$ at 1000 s (Fig. 11).

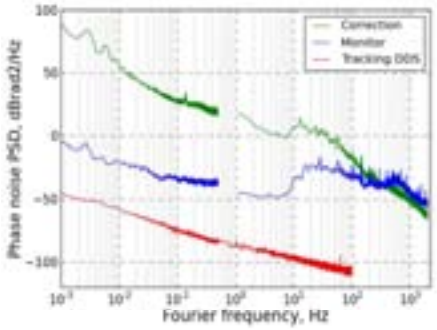

Fig. 10. Phase noise PSD of φ_n, φ_n, and Tracking DDS.

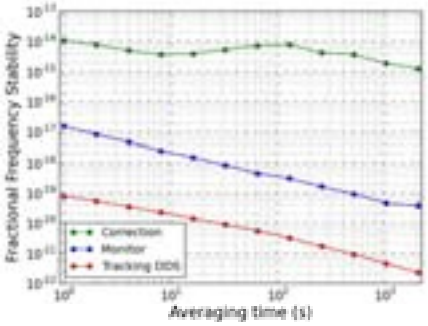

Fig. 11. Allan deviation of φ_n, φ_n, and Tracking DDS. Measurement bandwidth: 0.5 Hz.

IV. CONCLUSIONS

We implemented and characterized the digital electronics for coherent optical link. The digital architecture is based on a tracking DDS driven by an FPGA. The system is very flexible allowing fast and easy tuning as well as monitoring the data of interest, without any external instrumentation. Its digital nature makes it suitable for remote operation, opening new possibilities of application, such as intermediate laser regeneration in very long optical links.

It has been tested on a real urban link exhibiting a frequency stability of 10^{-17} at 1 s and reaching the 10^{-20} region at 1000 s.

We are developing a new version with extended tracking bandwidth that will allow to use this technology in very long optical links.

V. ACKNOWLEDGMENTS

The authors thank E. Rubiola and G. Santarelli for fruitful discussion. The authors acknowledge for funding Compagnia di S. Paolo and the EMRP program (Project SIB02-NEAT-FT). The EMRP is jointly funded by the EMRP participating countries within EURAMET and the European Union. The authors acknowledge GARR for the technical help with the fiber network.

REFERENCES

[1] C. W. Chou, D. B. Hume, J. C. J. Koelemeij, D. J. Wineland, and T. Rosenband, "Frequency Comparison of Two High-Accuracy Al+ Optical Clocks," Phys. Rev. Lett. 104, 070802 (2010).

[2] O. Lopez, A. Haboucha, F. Kefelian, H. Jiang, B. Chanteau, V. Roncin, C. Chardonnet, A. Amy-Klein, G. Santarelli, "Cascaded multiplexed optical link on a telecommunication network for frequency dissemination," Opt. Expr. 18, 16849-16857 (2010).

[3] K. Predehl, G. Grosche, S. M. F. Raupach, S. Droste, O. Terra, J. Alnis, Th. Legero,T. W. Hansch, Th. Udem, R. Holzwarth, H. Schnatz, "A 920-Kilometer Optical Fiber Link for Frequency Metrology at the 19th decimal place," Science 336, 441-444 (2012).

[4] O. Lopez, A. Kanj, P. Pottie, D. Rovera, J. Achkar, C. Chardonnet, A. Amy-Klein, G. Santarelli "Simultaneous remote transfer of accurate timing and optical frequency over a public fiber network" Appl. Phys. B 110, 3–6 (2013).

[5] W. Williams, W. C. Swann, and N. R. Newbury, "High-stability transfer of an optical frequency over long fiber optic links," J. Opt. Soc. Am. B 25, 1284-1293 (2008).

[6] F. Levi, C. Calosso, D. Calonico, L. Lorini, E. K. Bertacco, A. Godone, G. A. Costanzo, B. Mongino, S. Jefferts, T. P. Heavner, E. A. Donley "Cryogenic Fountain Development at NIST and INRIM: Preliminary Characterization", IEEE Trans. UFFC 57, 600-605, (2010)

[7] M. Pizzocaro, G. A. Costanzo, A. Godone, F. Levi, A. Mura, M. Zoppi, D. Calonico, "Realization of an Ultrastable 578 nm Laser for an Yb Lattice Clock", IEEE Trans. UFF C 59, 3, 426431 (2012).

[8] F. Levi, R. Ambrosini, D. Calonico, C. E. Calosso, C. Clivati, G. A. Costanzo, et al., "LIFT: The Italian Fiber Network For Frequency and Time Distribution", this proceedings.

[9] C. Clivati, D. Calonico, G. A. Costanzo, A. Mura, M. Pizzocaro, F. Levi, "Large-area fiber-optic gyroscope on a multiplexed fiber network", Optics Lett., 38, 1092-1094, (2013)

[10] C. Clivati, A. Mura, D. Calonico, F. Levi, G. A. Costanzo, C. E. Calosso, and A. Godone, "Planar-Waveguide External Cavity Laser Stabilization for an Optical Link With 10^{-19} Frequency Stability", IEEE Trans. Ultrason. Ferroelectr. Freq. Contr., 58, 2582-2587 , (2011)

[11] C. Gao, B. Wang, W. L. Chen, Y. Bai, J. Miao, X. Zhu, T. C. Li, and L. J. Wang, Fiber-based multiple-access ultrastable frequency dissemination, Optics Lett., 37, 4690-4692, (2013)

[12] Calosso C. E., Gruson Y., Rubiola E. (2012). Phase noise in DDS. Proc. International Frequency Control Symposium (IFCS) p.777-782, Baltimore, MD, USA, 21-25 May 2012.

[13] Calosso C. E., Bertacco E. K., Micalizio S., Godone A., Calonico D., Costanzo G. A. (2012). OCXO Ensemble As Improved Local Oscillator For Atomic Fountains. In: The European Frequency and Time Forum (EFTF). Goteborg, 23-27 April 2012, pp. 271-274

Distributed Time Transfer Using Optical Fiber Links

Liang Hu, Guiling Wu, Jianguo Shen, Huang Huang, Jianping Chen
State Key Laboratory of Advanced Optical Communication Systems and Networks, Shanghai Jiao Tong University
Shanghai, China
wuguiling@sjtu.edu.cn

Abstract—**This paper proposes a one point to multi-point distributed time transfer scheme using optical fiber links. The corresponding control protocol and adapters for the proposed scheme are designed and implemented. A 1 to 8 experimental system over 20km single-mode fiber with stabilities less than 50ps is demonstrated.**

Keywords-time transfer; optical fiber; distibuted time transfer; one point to multi-point time transfer;

I. INTRODUCTION

Time transfer over optical fiber links [1-9] has attracted extensively interests due to its advantages of broad bandwidth, low loss and so on. Up to now, research on optic-fiber time transfer is mainly focused on the point-to-point transmission [1-9]. However, high precise distributed time transfer is also demanded by many applications like distribution system, locating faults, and scientific experiments [11]. The distributed time transfer can be conducted through coaxial cable or satellite channel [12-13] with electrical distributor. But these schemes have several disadvantages, such as susceptible to transmission interference, high loss, low stability, and so on. J. Laufl et al. has proposed a distributed time transfer over optical fiber link with electrical distributor [10]. Although optical fiber link has better performance than coaxial cable or satellite channel, electrical distributor will lead to extra electrical noise and is complexity since it is an active device and needs O/E/O conversion.

In this paper, we propose a distributed time transfer scheme over a one point to multi-point passive fiber optical network. The distributed control protocol and adapters for the proposed scheme are designed and implemented. A 1 to 8 experimental system over 20km single-mode fiber is demonstrated. The stabilities in different conditions are measured. The results show that stabilities less than 50ps can be reached.

II. DISTRIBUTED TIME TRANSFER SCHEME

Fig.1 illustrates the system architecture of the proposed distributed time transfer over fiber link, where a master node is connected to several slave nodes through an optical distribution network (ODN) made up of passive optical splitters and optical fibers. Different topologies such as star and tree can be adopted on the basis of certain application requirements. Bidirectional optical amplifier can also be used on each sub-link to increase the transmission distance. Slave nodes are accessed to the master node using a time division multiple access (TDMA) mechanism. The clock at each slave node is compared to the high precise reference clock at the master node by two-way time transfer method [5-9] during each assigned sub-period, and is free running on the other time.

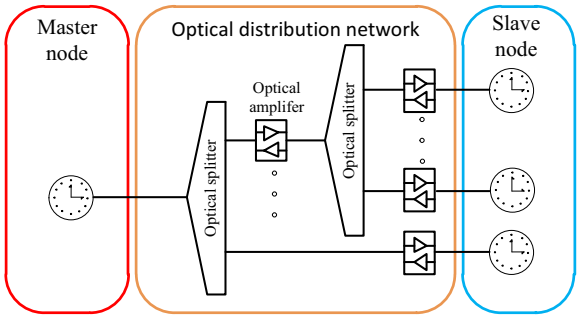

Fig. 1 The architecture of the proposed distributed time transfer over optical fiber

The TDMA control mechanism for the proposed scheme is illustrated in fig. 2 schematically. The whole procedure works periodically under the control of the master node. Each period is divided into a series of sub-period corresponding to slave nodes one by one. The control processing step in each period is as follows.

1) Get current slave node according to certain sequence, and enter the corresponding sub-period.

2) There are three processing phases in each sub-period.

Phase 1: The master node broadcasts a connection request that contains the address of the current slave node to all slave nodes by the optical distribution network. The current slave node, whose address is the same as the destination address in the connection request, replies a connection confirmation to the master node. When the master node receives the connection confirmation, the connection between the master node and current slave node is established.

Phase 2: Two-way time transfer between the master node and the slave node are carried out on the built connection in the phase 1.

Phase 3: When the maximum times of two-way time transfer is reached, the master node sends a disconnection request to the slave node, and the slave node replies a disconnection confirmation to release the connection between them.

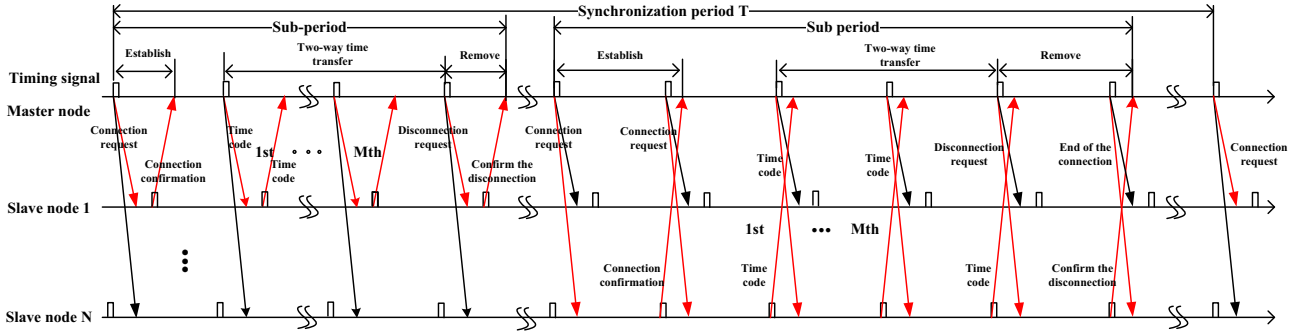

Fig. 2 The TDMA control mechanism for the distributed time transfer scheme

3) If the current slave node is the last one, start a new period. Otherwise, take the next slave node as the current slave node, step into the next sub-period.

III. Experimental System

The experimental setup of the proposed scheme is shown in Fig.3. The system consists of a master node, an ODN made up of a 1 to 8 optical splitter and fibers, and 8 slave nodes. The length of the optical fiber between the master node and each slave node is about 20 km.

Each node contains a Rb clock and an adapter. The Rb clock provides 1PPS and 10MHz to the adapter. Each adapter is used to transmit local time scale to the optical fiber and recover the time scale of remote nodes from received signal. During each sub-period, the difference between the local time signal T_{Si} and the received remote time signal T_{Ri} is measured by a Time Interval Counter (TIC) i at each node. Time difference between the master node and a slave node can be expressed as follows according to the principle of two-way time transfer [5-9].

$$\Delta T_{0i} = \left(TIC_0 - TIC_i\right)/2$$

The i denotes the slave node i $\left(i = 1,2,\cdots 8\right)$.

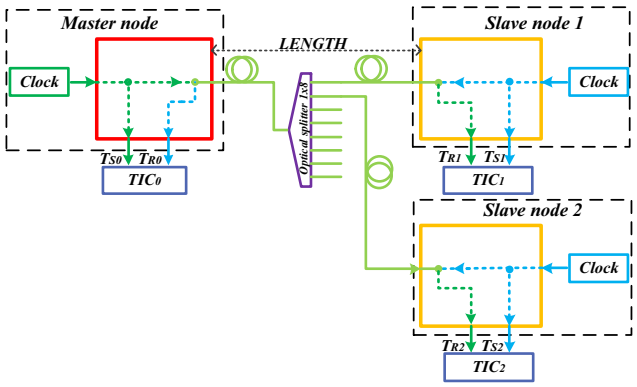

Fig.3 The setup of the proposed distributed time transfer

The picture and the structure of adapter at each node are shown in Fig. 4. It consists of two main components: a FPGA chip and a SFP (Small Form-factor Pluggable) transceiver. In the FPGA, there are four main modules: microprocessor, encoder, decoder, and physical transmit logic unit. The microprocessor is mainly used to carry out the TDMA control protocol proposed in section II. The encoder and decoder are used to complete the encoding and decoding of time code and control protocol frame (Ethernet frame in our experiment), respectively. The physical transmit logic unit is used to implement logic transmission and receive codes. The SFP transmitter is used to implement O/E and E/O conversion.

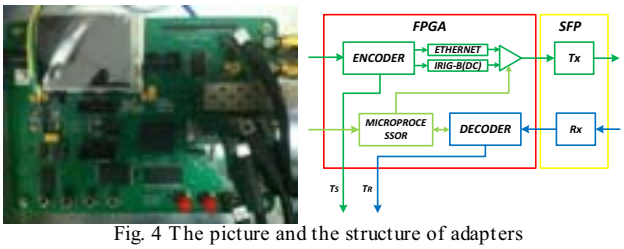

Fig. 4 The picture and the structure of adapters

IV. Results

We performed a set of experiment in order to verify the distributed time transfer via optical fiber links, test developed adapters, and evaluate stability of time transfer in laboratory environment.

Fig. 5 shows the measured results when the sub-period is 1 hour. Blue and Green curves are the measured time difference between the master node and two slave nodes (node1 and node 2), respectively as a function of time. The time division based distributed two-way time transfer with a sub-period of 1 hour can been observed, which is coincident with the TDMA control mechanism in section II. The RMS in every sub-period is also calculated and given as purple and red lines for slave node 1 and slave node 2, respectively. We can see that stability with a standard deviation less than 50ps in each sub-period can be achieved.

Fig. 6 illustrates experiment results when sub-period is 2 hours. We can see that the sub-period of two-way time transfer become 2 hours and the time transfer stability is close to the results in fig. 5.

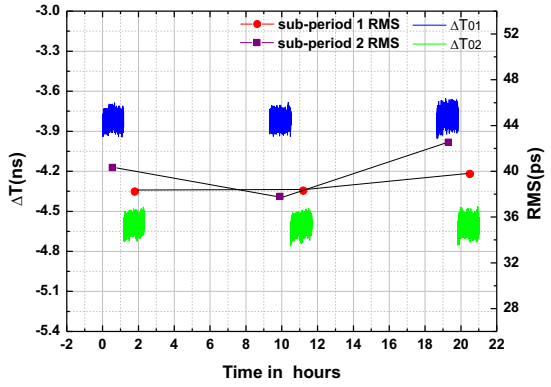

Fig. 5 The measured results when each sub-period is 1 hour. Blue and green are the time difference between the master node and two slave nodes, respectively, and purple and red lines are their RMS in each sub-period

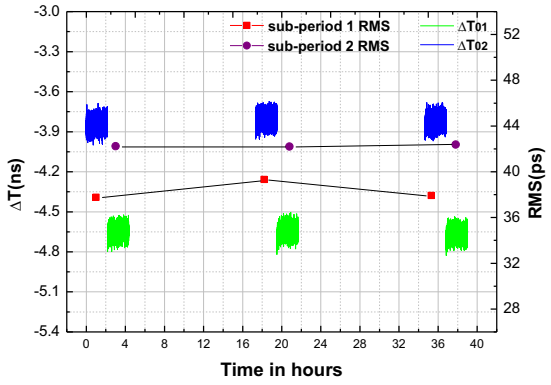

Fig. 6 The measured results when each sub-period is 2 hours. Blue and green are the time difference between the master node and two slave nodes, respectively, and purple and red lines are their RMS in each sub-period

V. CONCLUSIONS

In this paper, a distributed time transfer scheme over a one point to multi-point passive fiber optical network is proposed. A control protocol based on TDMA and adapters for the distributed time transfer scheme are designed and implemented. A 1 to 8 time transfer experimental system over 20km single-mode fiber is demonstrated. The stabilities less than 50ps are reached.

REFERENCES

[1] L. Primas, R. Logan, G Lutes, "Application of ultrastable fiber optic distribution system," Proceedings of the 43rd Annual Symposium on Frequency Control, pp. 202-211, June 1989.

[2] Łukasz Śliwczyński, Przemysław Krehlik and Marcin Lipiński, "Optical fibers in time and frequency transfer," Measurement Science and Technology, vol.21(7), pp.075302, 2010.

[3] Amemiya M, Imae M, Fuji Y, Suzuyama T and Obshima S "Time and frequency transfer and dissemination methods using optical fiber network," Proceedings of the 2005 IEEE International · Frequency Control Symposium and Exposition, pp.914–8, 2005

[4] A. Imaoka and M. Kihara, "Accurate time/frequency transfer method using bidirectional WDM transmission," IEEE trans. On Instrumentation and Measurement, Vol.47, No.2, pp.537-542, 1998.

[5] S.R. Jefferts, M. A. Weiss, S. Dilla and T. Parkeer, "Two-way time and frequency transfer using optical fibers," Conference on precision electromagnetic measurements17-21 Braunschweig, Germany pp. 520-521 IEEE, ISBN 0-7803-3376-4, June 1996

[6] S. R. Jefferts, M. A. Weiss, J. Levine, S. Dilla, E. W. Bell, and T. E. Parker, "Two-Way Time And Frequency Transfer Using Optical Fibers," IEEE Transactions on Instrumentation and Measurement, IM-42, 209-211, 1997

[7] S.C. Ebenhag, P. Jarlemark, R. Emardson, P.O. Hedekvist, K. Jaldehag and P. Löthberg, "Time transfer over a 560 km fiber link," Proceedings of the 22st European Frequency and Time Forum, paper 130 Toulouse France, April 22-25, 2008.

[8] M. Kihara, A. Imaoka, M. Imae, K. Imamura, "Two-Way Time Transfer through 2.4 Gb/s Optical SDH Systems", IEEE Trans. Instr. Meas., vol.50, pp. 709-715, 2001.

[9] Vladimir Smotlacha, Alexender Kuna, Werner Mache, "Time Transfer in Optical Network", 42th Ann. Precise Time and Time Interval (PTTI) Meeting, November 15 - 18, 2010.

[10] J. Laufl, M. Calhoun, W. Diener, J. Gonzalez, A. Kirk, P. Kuhnle, B. Tucker, C. Kirby, R. Tjoelker, "Clocks and timing in the NASA deep space network," Proceedings of the 2005 IEEE International Frequency Control Symposium and Exposition, pp. 830-835, ISBN 0-7803-9053-9 2005.

[11] Lori E. Primas, Ronald T. Logan, Jr. George F. Lutes, "Applications of ultra-stable fiber optic distribution systems," Frequency Control, 1989., Proceedings of the 43rd Annual Symposium on, pp. 202-211, 31 May-2 Jun 1989.

[12] Wlodzimierz Lewandowski, Jacques Azoubib, William J. Klepczynski "GPS:primary tool for time transfer," Proceedings of the IEEE, Volume 87, Issue 1, pp.163-172, 1999.

[13] Ulrich Schmid, Martin Horauer, Nikolaus Kerö, "How to distribute GPS-time over COTS-based LANs," In Proceed- ings of the 31th IEEE Precise Time and Time Interval Sys-tems and Application Meeting (PTTI'99), Dana Point, Cali- fornia, December 1999.

Compass Receiver Positioning Algorithm Under Bad Conditions Based on Unequal Interval Clock Prediction

Jianwei Zhan, Hang Gong, Bo Xu, Guozhu Zhang, Gang Ou
College of Electronic Science and Engineering, National University of Defense Technology, Changsha, 410073, China
sophy_zjw@nudt.edu.cn

***Abstract*—In the typical urban environment where the satellite visibility is limited or the satellite signal is weak due to the blockage or signal jamming, the availability of the navigation satellite system would be degraded, resulting in conventional four-satellite positioning method is very hard to satisfy the requirement of continuous positioning. To solve this problem, a combined prediction model based on the improved polynomial model and the improved grey model is proposed, which adopts a time interval coefficient and a dynamic weighting factor to predict the receiver clock bias (RCB), and then a predicted clock value from the proposed model is introduced to aid positioning. The experimental results based on BeiDou Navigation Satellite System (COMPASS/BDS) observation data demonstrate that the model is more suitable for predicting RCB both under unequal and equal conditions. Moreover, for 50 s RCB predictions duration of the short satellite signal shading outages, the three-dimensional (3-D) position error using the clock-aided position algorithm is slightly larger than about 2.76% than four-satellite 3-D position error, and thus, the availability of positions can be improved efficiently.**

Keywords—satellite navigation; receiver clock bias; clock-aided; combined model; unequal interval

I. INTRODUCTION

It is widely known that at least four code pseudorange measurements are required to determine user three-dimensional (3-D) position and receiver clock bias (RCB). However, in certain applications, such as in the underground traffic routes, the tunnels, and park garages, typically less than four satellites are available due to the blockage to receiver-to-satellite line of sights. In the paper, 3D incomplete condition is defined as the situation where only three satellites are available; and 4D complete condition is defined as the situation where at least four satellites are available [1]. In the typical urban environment, the probability of 3D incomplete condition occurrence is more than 10%, and the average duration of the short satellite signal shading outages statistically is about 50 s [2], which would result in statistically longer time to first fix and time to reacquisition. In this case, a position estimate of the movable object can't be determined by the conventional method using at least 4 satellites signals, such as COMPASS-based PVT method. Thus, the availability would be degraded. To solve this problem, a method using additional measurement information from an external sensor can be adopted to provide 3-D position determination, such as a barometer altimeter, RFID, pseudolites, an electronic map, and so on [3-6]. However, the range of the above method with sensor aiding is limited due to the high-cost devices. In contrast, it is a simple, flexible, and cost-effective way to provide clock-aided PVT services with the RCB prediction model.

Recently, several research in RCB prediction model and corresponding positioning algorithm has been presented. The detailed characteristics and limitations are summarized here [7-10]: (1) previous studies focused on chip-scale atomic clocks or oven controlled crystal operator (OCXO), but the receiver clock is not limited to those. For example, a temperature controlled crystal operator (TCXO) is equipped widely in chip receivers as a clock, the frequency of which is stable or changes in a predictable manner over at least 50 s, (2) conventional RCB prediction model is based on the equal interval RCB series. However, because the intermittent characteristics of the satellite signal shading outages, RCB series obtained under the typical urban environment is unequal interval, and (3) a single RCB prediction model has its own characteristics and scope of applications, and the robustness can not be assured in each instance. So further studies are still necessary.

In order to solve the problem under 3D incomplete condition, taking into account the nonlinear characteristic of the RCB series, an improved polynomial model based on the generalized extended interpolation method and an improved grey model are established. Furthermore, a combined prediction model and the corresponding clock-aided positioning algorithm (CA-PVT) are proposed.

II. RCB PREDICTION MODELS

A. Improved RCB Polynomial Model

Assuming that $x(t_1)$, $x(t_2)$, $\cdots$, $x(t_m)$ is the RCB series obtained from COMPASS pseudorange measurements and the difference between t_i and t_{i-1} is not const. Generally, according to the characteristics, the RCB is modeled using a popular prediction polynomial function [11].

$$x(t_i) = \alpha_0 + \alpha_1(t_i - t_0) + \alpha_2(t_i - t_0)^2 + \cdots + \alpha_n(t_i - t_0)^n + w(t_i),\ i > m \tag{1}$$

where $\alpha_0, \alpha_1, \alpha_2, \cdots, \alpha_n$ are parameters estimated from the available measurements; n is the order of the model determined

by means of the residuals; t_0 is the reference time, generally, normalized to 0; $w(t_i)$ is composed of various noise sources, such as phase noise and measurement noise.

Because the RCB data near the time t_n has the greatest impact on the prediction, $\boldsymbol{\alpha}$ can be estimated by means of the least square method. The estimate is defined as:

$$\begin{cases} \hat{\boldsymbol{\alpha}} = \min\limits_{\boldsymbol{\alpha}} \left\| \boldsymbol{x} - \mathbf{H}\boldsymbol{\alpha} \right\| \\ \boldsymbol{x}(t_n) = \boldsymbol{H}_{\mathbf{n},:}\boldsymbol{\alpha} \end{cases} \tag{2}$$

where $\boldsymbol{H}_{n,:}$ is the n-th row of the matrix **.** Eq. (2) can be solved by Lagrange multiplier [12]. And $\boldsymbol{\alpha}$, $\boldsymbol{x}$, $\boldsymbol{H}$ are defined as follows:

$$\boldsymbol{\alpha} = [\boldsymbol{\alpha}_1, \boldsymbol{\alpha}_2, \cdots \boldsymbol{\alpha}_n]^{\mathrm{T}} \tag{3}$$

$$\boldsymbol{x} = [x(t_1), x(t_2), \cdots x(t_m)]^{\mathrm{T}} \tag{4}$$

$$\boldsymbol{H} = \begin{bmatrix} 1 & t_1 & \dots & t_1^n \\ 1 & t_2 & \dots & t_2^n \\ \dots & \dots & \dots & \dots \\ 1 & t_m & \dots & t_m^n \end{bmatrix} \tag{5}$$

B. Improved RCB Grey Model

Grey system works on the unascertained systems with partially known and partially unknown information, which reduces the effects of noise and obtain the data regularity by bringing accumulated generating operation and inverse accumulated generating operation [13]. Here the most important section in grey model is that it can achieve a high precision with only a few data. Based on these advantages, we attempt to take the RCB series as a grey system.

Conventional GM(1,1) is established based on the equal interval data and thus can not be directly applied to unequal interval RCB series prediction. Fortunately, several method have been explored in other applications, for example, an amendatory metabolism unequal interval grey model (AMUGM (1, 1)) has been proposed [14], which can be used both in linear and unequal interval series through background value optimized. Compared with other methods, it has wider applications. Therefore, it is a very effective way to utilizing it for unequal interval RCB series prediction. In the paper, only the final expression of the predicted RCB estimate is given as

$$\hat{x}(t_{m+p}) = \frac{1}{\Delta t_{m+p}}(1 - e^{\hat{a}(\Delta t_{m+p})}) \left[x(t_1) - \frac{\hat{b}}{\hat{a}} \right] e^{-\hat{a}(t_{m+p} - t_1)} \tag{6}$$

where $\hat{a}$ is the development parameter; $\hat{b}$ is the coordination parameter. And the unequal interval $\triangle t_{m+p}$ is defined as.

$$\Delta t_{m+p} = t_{m+p} - t_{m+p-1}, p \geq 1 \tag{7}$$

C. Dynamic weighted combined model

As discussed in the previous sections, any single prediction model has its own characteristics and applicability. For example, the physical characteristics of the polynomial model is specific, with good short-term prediction performance, while grey model has long-term prediction performance advantage in the case of only a few observation data available. Therefore, it is an effective method by combining of the improved polynomial model and the improved Grey model via the linear weighted equation.

Let $\hat{x}_p(t_i)$ and $\hat{x}_{GM}(t_i)$ are the smoothed estimates of RCB at the instant time t_i, obtained by the improved polynomial model and the improved AMUGM(1, 1) model, respectively, and $\varepsilon_p(t_i)$ and $\varepsilon_{GM}(t_i)$ are the corresponding errors. Then, the new $\hat{x}(t_i)$ and $\varepsilon(t_i)$ can be obtained using the weighted linear combined model, as follows:

$$\begin{cases} \hat{x}(t_i) = w_{\mathrm{p}}\hat{x}_{\mathrm{p}}(t_i) + w_{\mathrm{GM}}\hat{x}_{\mathrm{GM}}(t_i),\ i = 1, 2, \ldots, m \\ w_{\mathrm{p}} + w_{\mathrm{GM}} = 1 \end{cases} \tag{8}$$

$$\begin{cases} \varepsilon(t_i) = w_{\mathrm{p}}\varepsilon_{\mathrm{p}}(t_i) + w_{\mathrm{GM}}\varepsilon_{\mathrm{GM}}(t_i) \\ w_{\mathrm{p}} + w_{\mathrm{GM}} = 1 \end{cases} \tag{9}$$

where the weighting factors w_{p} and w_{GM} could be estimated by means of the least square method and are constrained to

$$\min_{w} I = \boldsymbol{\varepsilon}^{\mathrm{T}}\boldsymbol{\varepsilon} \tag{10}$$

The solution to (10) can readily be found by first differentiating $\boldsymbol{\varepsilon}^{\mathrm{T}}\boldsymbol{\varepsilon}$ with respect to w_{p}.

$$w_{\mathrm{p}} = \frac{2(\boldsymbol{\varepsilon}_{\mathrm{GM}}^{\mathrm{T}}\boldsymbol{\varepsilon}_{\mathrm{GM}} - \boldsymbol{\varepsilon}_{\mathrm{p}}^{\mathrm{T}}\boldsymbol{\varepsilon}_{\mathrm{GM}})}{\boldsymbol{\varepsilon}_{\mathrm{p}}^{\mathrm{T}}\boldsymbol{\varepsilon}_{\mathrm{p}} - 2\boldsymbol{\varepsilon}_{\mathrm{p}}^{\mathrm{T}}\boldsymbol{\varepsilon}_{\mathrm{GM}} + \boldsymbol{\varepsilon}_{\mathrm{GM}}^{\mathrm{T}}\boldsymbol{\varepsilon}_{\mathrm{GM}}} \tag{11}$$

The dynamic weighted combined model established can be used to make short-term RCB prediction with high precision, but the performance will degrade gradually with time due to the fixed parameters. To solve this issue, a sliding window is proposed to lock the latest RCB, and thus the length of RCB data utilized for modeling is fixed, which reduces the storage capacity and computational load.

III. CLOCK-AIDED POSITIONING ALGORITHM

A. Clock-aided Principle

After generating predicted RCB estimate at some time by utilizing the dynamic weighted combined model, we can augment the basic equation with an additional clock-aided equation to be defined below.

$$\omega_x \hat{x}(t_i) = [0 \quad 0 \quad 0 \quad \omega_x][\Delta x \quad \Delta y \quad \Delta z \quad \Delta t]^{\mathrm{T}} + \omega_x \varepsilon(t_i) \quad (12)$$

where ω_x is the standard deviation of pseudorange measurement error σ_s normalized to the standard deviation of predicted RCB error σ_b. It is a weighting factor to scale the Eq. (12) when σ_s is not equal to σ_b.

B. Receiver Clock-aided Positioning Accuracy

In the case of the CA-PVT algorithm, the positioning accuracy is affected by the prediction performance of the RCB. This impact can be expressed as

$$\boldsymbol{P} = \sigma_s^2 (\boldsymbol{H}_3^{\mathrm{T}} \boldsymbol{H}_3)^{-1} + \sigma_b^2 (\boldsymbol{H}_3^{\mathrm{T}} \boldsymbol{H}_3)^{-1} \boldsymbol{H}_3^{\mathrm{T}} \boldsymbol{C}\boldsymbol{C}^{\mathrm{T}} \boldsymbol{H}_3 (\boldsymbol{H}_3^{\mathrm{T}} \boldsymbol{H}_3)^{-1} \quad (13)$$

where $\boldsymbol{H}_3$ is the 3×3 geometry matrix, $\boldsymbol{C}$ is 3 × 1 vector of ones. As observed in Eq. (13), if the error covariance σ_b of the clock bias is greater than the product of the time dilution of precision (TDOP) and the user-range error (URE) σ_s, the positioning accuracy through the clock-aided method performs worse than the one of the unaided method. Therefore, high-precision clock error prediction model will improve positioning accuracy.

$$\begin{aligned} \sigma_b^2 \sigma_s^{-2} &> (\boldsymbol{C}^{\mathrm{T}}\boldsymbol{C} - \boldsymbol{C}^{\mathrm{T}} \boldsymbol{H}_3 (\boldsymbol{H}_3^{\mathrm{T}} \boldsymbol{H}_3)^{-1} \boldsymbol{H}_3^{\mathrm{T}} \boldsymbol{C})^{-1} \\ &= \mathrm{TDOP}^2 \end{aligned} \quad (14)$$

IV. EXPERIMENT RESULTS AND ANALYSIS

A. RCB Prediction Performance Evaluation

To assess the performance of the proposed CA-PVT algorithm, an experiment is carried out in a typical urban environment in the city of Changsha, China, on March 20, 2013. Observation data is collected by using a fixed COMPASS receiver with a sampling rate of 1 Hz, which includes each visible satellite position, pseudorange, dilution of precision (DOP) and RCB. In addition, SOW of the first epoch is 265151 s, and the standard deviations of pseudorange measurement are σ_{GEO} = 6.5 m, σ_{IGSO} = 4.5 m, $\sigma_s = \sigma_{GEO}$, respectively. To model the scenario under 3D incomplete condition, the elevation cutoff angle is set to 30° during some time, thus, the number of visible satellite would less than four. As a simple illustration of clock prediction, the experimental scenario is shown in Fig. 1.

The *x*-axis and *y*-axis represent the relative time and the RCB using satellite signals, and the three segments suffers from the incomplete condition denoted as A, B and C, respectively. Here, we define $\triangle t_A$, $\triangle t_B$, $\triangle t_C$ as the corresponding duration, for Fig. 3, $\triangle t_A$ = 54 s, $\triangle t_B$ = 14 s, $\triangle t_C$ = 14 s.

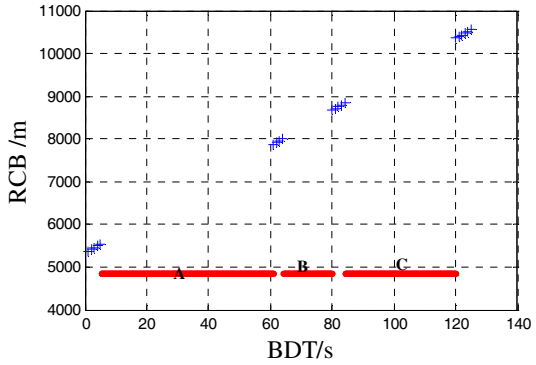

Fig. 1. Experimental scenario in the typical urban environment

B. Comparison of Combined Model to Polynomial Model

To assess the precision of the RCB short-term prediction, a comparison of urban canyon performance for the combined dynamic weighted combined model to the RCB polynomial model is made based on the above experimental scenario. Since the average duration of 3D incomplete condition is 50 s, a prediction time span 155 to 205 epochs is set, and the results are shown in Fig.2.

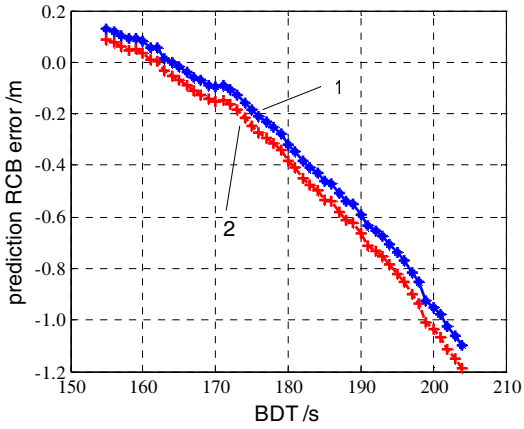

1—the combined dynamic weighted model, s= 13.206 m^2,△= 0. 003%
2—the second-order polynomial model, s=16.3175 m^2,△= 0.003%

Fig. 2. Comparison of the predicted RCB estimates using the combined dynamic weighted model and the second-order polynomial model in typical urban environment

From the comparison results, it shows that both the prediction errors grow with the prediction interval. More specifically, at the 175 epoch, the precision error of the combined model is -0.279 m, and the conventional polynomial model is -0.343 m; at the 200 epoch, the errors of the models reach -1.096 m and -1.187 m, respectively. Moreover, the combined model achieves 1.764 m improvement in RMS error. Therefore, the combined model performs well, and is better than any of the single one by dynamic linear weighting.

C. *Clock–aided Positioning Performance Evaluation*

To evaluate the performance of the proposed CA-PVT algorithm, a comparison of the position accuracy between CA-PVT algorithm and COMPASS-based PVT algorithm o is carried out with 20 epoch observation data. The PRN number of satellites utilized in CA-PVT algorithm is C01, C04, and C07, respectively; while in COMPASS-based PVT algorithm, C01, C04, C07, and C08, respectively; and the sampling rate is 1 Hz. Fig. 3 shows the comparison result, which is our main result.

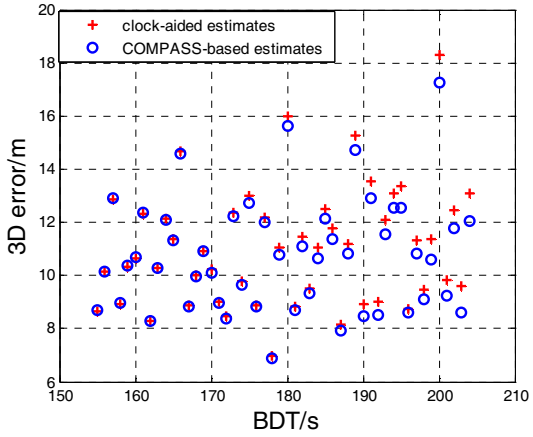

Fig. 3. The positioning result using CA-PVT algorithm and COMPASS-based PVT algorithm

Fig. 3 demonstrates that both the position errors obtained from the two algorithms increase with the prediction time. Note that, because of affected by RCB prediction error, the RMS error with CA-PVT algorithm is 11.263 m, which is slightly larger than the one 10.960 m with COMPASS-based PVT algorithm. However, the level of accuracy with clock-aided remains acceptable for our Standard Positioning Service, and the service is available.

From the comparison in this section, we can come to the conclusion that the PVT performance of CA-PVT algorithm is close to the one provided by COMPASS-based PVT algorithm with four pseudorangement measurement. Therefore, the proposed CA-PVT benefits the continuity and the availability improvement.

V. CONCLUSION

This paper considered the navigation continuity problem of COMPASS receiver equipped with TCXO during short satellite signal shading outages. A combined prediction model and the CA-PVT algorithm have been proposed based on the assumption that the frequency drift rate of TCXO change smoothly and predictably over tens of minutes. The experimental results based on COMPASS observation data show that for 50 s RCB prediction in the urban environment, the 3-D position error using the proposed CA-PVT algorithm is slightly larger than about 2.76% than the one provided by COMPASS-based PVT algorithm with four satellites, and the robustness, the availability and the continuity would be improved efficiently at a low cost.

REFERENCES

[1] P. Misra, "The role of the clock in a GPS receiver," GPS World, vol. 7, no. 4, pp. 60–66, May 1996.

[2] R. Zheng and J. Chen, "New algorithm of GPS positioning in incomplete condition of temporal insufficient signal," Journal of University of Electronic Science and Technology of China, vol. 38, no. 4, pp. 496-500, 2009.

[3] Y. B. Chen and Y. C. Song, "A Bays filter algorithm with non-Gaussian noises based on location of vehicular," Journal of Central South University of Technology (Science and Technology), vol. 41, no. 4, pp. 1462−1466, 2010.

[4] H. Tang and D. Kim, "RFID indoor positioning and navigation using a regularized particle filter integrated with a probability model," Proceedings of the 24th International Technical Meeting of the Satellite Division (ION GNSS 2011), Portland: Oregon Convention Center, 2011: 3470-3479.

[5] J. Peng, F. L. Wu, M. Zhu, F. X. Wang, and K. F. Zhang, "An improved GPS/RFID integration method based on sequential iterated reduced sigma point Kalman filter," IEICE Transactions on Communications, vol. E95-B, no. 7, pp. 2433-2441, July. 2012.

[6] Dah-Jing, Jwo, "Efficient dop calculation for GPS with and without altimeter aiding,". NAVIGATION: The Journal of Navigation, vol. 54, no. 2, pp. 269–279 , 2001.

[7] Chang-Hee, Won, "Regional navigation system using geosynchronous satellites and stratospheric airships," IEEE Transactions on Aerospace and Electronic Systems, vol. 38, no. 1, pp. 271–278, January 2002..

[8] Y. L. Teng, and T. B. Shi, "Clock-based RAIM method and its application in GPS receiver positioning," Journal of Central South University of Technology, vol. 19, no. 6, pp. 1558–1563, June 2012.

[9] S. Bednarz and P. Misra, "Receiver clock-based integrity monitoring for GPS precision approaches," IEEE Transactions on Aerospace and Electronic Systems, vol. 42, no. 2, pp. 636–643, 2006.

[10] R. Ramlall, J. Streeter, and J. F. Schnecker, "Three satellite navigation in an urban canyon using a chip-scale atomic clock," Proceedings of the 24th International Technical Meeting of the Satellite Division (ION GNSS 2011), Portland: Oregon Convention Center, pp. 2937-2945, 2011.

[11] E. D. Kaplan and C. J. Hegarty, "Understanding GPS Principles and Applications," Norwood: Artech House Inc., pp. 304-305, 2006

[12] H. L. Shi and Y. H. Yan, "Extended interpolation method and its applications in piecewise approximations," omputational and Applied Mathematics, Amsterdam: Elsevier Science publishers B.V, pp. 229-236, 1992.

[13] X. W. Zhu, H. Xiao, S. W. Yong, and Z. W. Zhuang, "The Kalman algorithm used for satellite clock offset prediction and its performance analysis," Journal of Astronautics, vol. 29, no. 3, pp. 966−970, 2008.

[14] S. J. Xu, H. Z. Wang, N. S. Wang, and J. P. Yang, "Research on amendatory unequal interval grey model," Mathematics in Practice and Theory, vol. 41, no. 8, pp. 108−114, 2011.

.

Project of Photoassociative Measurements for Determination of the Density Shift of the $^1S_0 - ^3P_0$ Clock Transition in Neutral Strontium

Marcin Bober, Piotr Morzyński, Michał Zawada,
Agata Cygan, Daniel Lisak, Piotr Wcisło,
and Roman Ciuryło
Institute of Physics, Faculty of Physics, Astronomy and Informatics
Nicolaus Copernicus University
Grudziądzka 5, 87-100 Toruń, Poland
Email: bober@fizyka.umk.pl

Jerzy Zachorowski and Wojciech Gawlik
M. Smoluchowski Institute of Physics
Jagiellonian University
Reymonta 4, 30-059 Cracow, Poland

***Abstract*—We present a proposal of determination of the density shift of the $^1S_0 - ^3P_0$ clock transition in neutral cold strontium atoms. Since the direct use of the double forbidden, intercombination clock transition (698 nm) may be difficult we propose to use a three photon photoassociation. The measurement will be performed with the magneto-optical trap set-up designed for the experiments with both ^{88}Sr and ^{87}Sr isotopes.**

I. Introduction

Recent progress in optical atomic clocks with neutral strontium atoms in an optical lattice allows reduction of the clock uncertainty to 10^{-16} level [1]. The most important contribution to the accuracy budget in strontium atomic clock comes from the black body radiation (BBR).

Another important contribution to the accuracy budget comes from cold atoms collisions in the lattice. Cold collisions of neutral atoms lead to the density shift of the measured clock transition. This effect can be reduced by lowering atomic densities but to reach the accuracy below 10^{-16}, cold collisions have to be investigated more precisely.

In this work we report apparatus for determination of the scattering properties of atoms in the $^1S_0$ and $^3P_0$ states. We plan to perform direct measurements with the clock transition (698 nm) or to use a three photons photoassociation with the 689, 688 and 679 nm lasers. The measurement will be performed with the magneto-optical trap which allows one to cool down strontium atoms to few μK. Along with the photoassociative measurements, we are building in our laboratory the second set-up, exclusively designed as the optical lattice atomic clock with strontium atoms. This second set-up will be used as a frequency reference.

II. Photoassociation

Density shift in a cold atomic sample depends on the scattering length a, which is determined by a difference between the energy of collision and the closest bound molecular state (Δ in Fig. 1). Δ can be measured by observation of photoassociation and creation of molecules. For efficient photoassociation, a high density of atoms (high collision rate) is required and can be ensured in a magneto-optical trap operating on the $^1S_0 - ^3P_1$ transition.

Direct measurement with one photon (near the clock transition) may be difficult, since the $^1S_0 - ^3P_0$ transition is very weak. Nevertheless, it may be enhanced by broadening of the transition by the magnetic-field induced mixing of the $^3P_0$ and $^3P_1$ states [2].

Another way to reach a bound state involves three photons. The intercombination $^1S_0 - ^3P_1$ transition at 689 nm (natural width around 10 kHz) can be used together with the $^3P_1 - ^3S_1$ and $^3S_1 - ^3P_0$ transitions at 688 an 679 nm respectively (both with natural width in MHz range).

III. Apparatus

The photoassociation measurement will be done with the existing set-up, consisting of a Zeeman slower [3], blue and red magneto-optical traps [4]. The apparatus allows cooling atoms down to μK temperate.

Atoms are first cooled in the blue MOT. 679 and 707 nm repumping lasers are used in this stage. High magnetic field

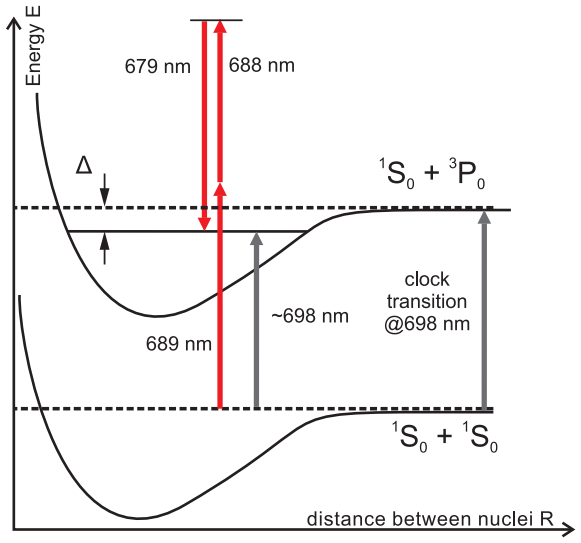

Fig. 1. Two possible ways to photoassosiate atoms close to the clock transition.

gradient (up to 100 G/cm) allows trapping atoms in the triplet state in a magnetic trap [5] which can be used to trap simultaneously several isotopes. In the red MOT we can trap up to 10^7 atoms.

The second cold strontium apparatus is under construction. The set-up is designed exclusively as an optical atomic clock with ^{87}Sr. At the moment the blue MOT is already working. Further cooling in this set-up will be done in an optical lattice by the 689 nm laser. At the moment, the optical lattice at the "magic wavelength" [6] is being installed.

For the photoassociative measurement we will use the 689 nm laser with spectral width below 8 Hz. The laser frequency can be tuned up to 20 GHz. The laser is offset locked to a master laser which is stabilised to the ultra-stable cavity [7]. The 688 nm laser is under construction together with the clock laser for the 698 nm strontium line.

The optical lattice clock together with an optical frequency comb would serve as a frequency reference. The comb is stabilized to a rubidium standard. Long term drift is removed by a lock to the GPS signal.

IV. Plans and conclusion

Presently, we are performing photoassociative spectroscopy with the 689 nm laser. In near future, with the clock and the 688 and 679 nm lasers we want to determine the density shift of the clock transition in strontium. At the same time we are building the second cold strontium set-up which will serve as a frequency reference.

Acknowledgment

The research is part of the program of the National Laboratory FAMO in Torun, Poland and was supported by the Polish MNiSW and the Foundation for Polish Science TEAM Project co-financed by the EU European Regional Development Fund.

References

[1] R. Le Targat et al., "Experimental realization of an optical second with strontium lattice clocks", Nature Communications, vol 4, 2109, 2013.

[2] A. V. Taichenachev et al., "Magnetic field-induced spectroscopy of forbiden optical transitions with application to lattice-based optical atomic clock," Phys. Rev. Lett., vol. 96, 083001, 2006.

[3] M. Bober, J. Zachorowski, and W. Gawlik, "Designing Zeeman slower for strontium atoms - towards optical atomic clock," Optica Applicata, vol. 40, pp. 547555, 2010.

[4] M. Bober et al., "Precision spectroscopy of cold strontium atoms, towards optical atomic clock," Bull. Pol. Ac.: Tech., vol. 60, 707, 2012.

[5] X. Xu, T. H. Loftus, J. L. Hall, A. Gallagher, J. Ye, "Cooling and trapping of atomic strontium," J. Opt. Soc. Am. B, vol. 20, 968, 2003.

[6] H. Katori, M. Takamoto, V. Palchikov, V. D. Ovsiannikov, "Ultrastable optical clock with neutral atoms in an engineered light shift trap," Phys. Rev. Lett., vol. 91, 173005, 2003.

[7] D. Lisak et al., "Ultra narrow laser for optical frequency reference," Acta Phys. Pol. A, vol. 121, pp. 614621, 2012.

Design and Construction of Helical Resonators for Ion Traps

K. Deng, Y. L. Sun, Z. T. Xu, J. Zhang, Z. H. Lu*, and J. Luo

MOE Key Laboratory of Fundamental Quantities Measurement, School of Physics,
Huazhong University of Science and Technology, Wuhan 430074, P. R. China
*Corresponding author: zehuanglu@mail.hust.edu.cn

***Abstract*—High voltage radio frequency (RF) supply is a critical part in the ion trap system. To predict the resonant frequency of the RF supply for the ion trap, we model the helical resonator and the ion trap as a lumped element circuit. Based on the model we present the construction process of a helical resonator. We measured resonant frequency for different loads. The experimental results are in good agreement with our model.**

Keywords- ion trap; helical resonantor; resonant frequency

I. INTRODUCTION

Radio frequency (RF) ion trap has found a wealth application in many fields of fundamental as well as applied physics in recent years. Microwave atomic clocks [1, 2] and optical atomic clock [3, 4] have been built based on several different ions. Ion trap is also an important tool in quantum simulation [5] and quantum information processing [6] since the external degrees of freedom of the ions can be cooled down to the vibrational ground state and the ions feature long coherence time. Ion trap can also be employed in mass spectroscopy[7].

RF drive for ion traps should feature both high voltage and high frequency. High voltage RF for the trap means large trapping depths and longer trapping lifetimes. Commercial RF amplifiers can generate several watts of RF power, however, the amplifiers and their loads should be impedance matched, and otherwise most of the power will be reflected. In order to transmit as much power as possible into the trap, a high Q-factor resonator is used to match the impedance of a RF amplifier and an ion trap. Applying RF voltages via a high Q-factor resonator reduces the power in unwanted frequencies being applied, reduces their contribution to motional heating of ions [8] and also provides higher voltages per input power. It is generally preferable that a predictable driving frequency of ion trap can be given so that high secular frequency can be obtained [9]. Higher secular frequency means higher efficiency in laser sideband cooling.

The high-Q resonator can be realized through a helical resonator. The unloaded resonant frequency and Q-factor of a helical resonator have been studied before [10]. Generally the unloaded helical resonator can achieve rather large resonant frequency and Q-factor. However, when the resonator is connected to a capacitive load, i. e. an ion trap, the resonant frequency and Q-factor will decreased substantially [11]. Less effort has been made on how to predict the loaded resonant frequency.

In this paper we will model the resonator with a lumped element electrical equivalent model and predict the resonant frequency under the realistic condition when the helical resonator is connected to an ion trap. Based on our model, we constructed a helical resonator and experimentally measured the resonant frequency under different loads to confirm our prediction. We also used the resonator to drive a linear Paul trap to test its practical performance.

II. MODEL

A helical resonator consists of a copper can, one main coil and one antenna coil inside. The main relevant parameters of a helical resonator include the shield diameter D, shield height h, coil diameter d, coil height b, winding pitch τ and coil wire diameter d_0. To realize an optimal resonance these parameters can be chosen according to the empirical study of Macalpine and Schildknecht [10]. They also gave an empirical formula to predict the resonant frequency when the resonator is under unloaded operation.

$$f_0 = \frac{\omega_0}{2\pi} = \frac{48300}{ND}\,\mathrm{MHz} \tag{1}$$

N is the total number of windings of the main helical coil and D is the shield diameter in mm. When a load is connected to the resonator, the resonant frequency will decrease. To analysis the resonant frequency of the combined system, Fig. 1 shows a lumped element circuit to model the helical resonator and its load.

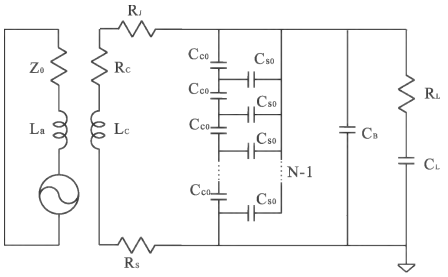

Figure 1. Diagram showing the equivalent circuit.

The resonant frequency of the whole system can be calculated by:

$$f_l = \sqrt{\frac{C}{(C+C_l)}} f_0 \tag{2}$$

Here f_0 is the unloaded resonant frequency of the helical resonator which can be calculated from the above empirical formula (1). Therefore we can use the following equation to calculate the resonant frequency of the loaded system:

$$\omega_l = \sqrt{\frac{C}{(C+C_l)}} \frac{2\pi \times 48300}{ND} \tag{3}$$

Here C_l is the capacitance of the equivalent total load, C is the equivalent capacitance of the resonator without load. The equivalent total load includes the effects of the BNC connector of the output of the helical resonator, the wire between the BNC connector and the ultimate load.

The equivalent capacitance of the resonator without load should include the contribution of two parts: *Cs* and *Cc*. *Cs* is capacitance between the helical coil wire and the surrounding shield. *Cc* is the self-capacitance of the helical coil. The two values can be calculated from the empirical formula.

Here Cc is given by [11]:

$$C_C \approx (0.1126\frac{b}{d}+0.08+\frac{0.27}{\sqrt{\frac{b}{d}}})d\times 10^{-10} \quad (4)$$

Cs is given by [11]:

$$C_S \approx 39.37b\frac{0.75}{\log\left(\frac{D}{d}\right)}\times 10^{-12} \quad (5)$$

When *Cc* and *Cs* are combined to form *C*, it is not a simple relationship of parallel connection or series connection. Figure 1 shows how the equivalent capacitance *C* is composed from *Cs* and *Cc*. Here C_{C0} = (N-1)*Cc* and C_{S0} = *Cs*/(N-1). From Fig. 1 the equivalent *C* can be calculated.

III. CONSTRUCTION

We constructed a helical resonator to confirm our analysis. First we choose the f_0 to be 50 MHz. Then *N* should be about 9.5 according formula (1). Since the coil diameter *d* should be in the range such that 0.45< *d/D* <0.6. We choose it to be 55mm. additionally the axial length of the coil *b* should be restricted in such a way that *b/d* > 1. We choose it to be *b*=83 mm. Furthermore, lengths for the shield should be *h*=*b* + *D*/2=133 mm. The winding pitch is given by τ=*b*/*N*=8.7 mm. The ratio *b/d* here determines the valid range of the wire diameter d_0 to the pitch should be $0.4<d_0/\tau<0.6$. We choose d_0 to be 5 mm. This wire size is expected to be so rigid that it is not susceptible to mechanical vibrations. Diameter of the antenna coil is half of the coil and antenna coil is generally wound into 2-3 turns.

The antenna coil is constructed out of 2 mm wire. For the main helix coil which has a diameter of 5 mm, since it is very important to maintain the winding pitch and the diameter to be constant, we use a specialist machine and a tube to wind the coil. Since it is hard to solder the coil to the shield, the main coil is attached to the shield by soldering it onto a BNC connector. Then a BNC short head is connected to it, which is on the outside of the shield. In order to minimize the coil to shied capacitance the coil is placed centrally inside the shield.

In order to obtain good couple between the antenna coil and main coil, the distance between them is designed to be adjustable. The top hat and the shield are designed with matching thread. Turning the top hat changes the distance between the two coils. Thus the couple of the antenna coil and the main coil can be adjusted. This adjustment can allow an optimal coupling. Figure 2 shows the picture of the helical resonator.

Figure 2. Picture of the helical resonator.

IV. TEST AND RESULTS

We use different loads and measure the resonant frequency as well as the Q-factor when these loads are connected to the resonator. Several different length coaxial lines are used as the capacitive loads of the resonator. The resonant frequency of the helical resonator is analyzed with Agilent E5061B analyzer.

Figure 3 shows a plot of the resonance frequencies as a function of the capacitances of the loads. We are interested in capacitance range from 5 pF to 50 pF since this is the typical range over which the generally used ion trap capacitance can vary. It can be seen from Fig. 3 that the resonance frequencies decrease as the capacitances increase, and the result fit with our model nicely.

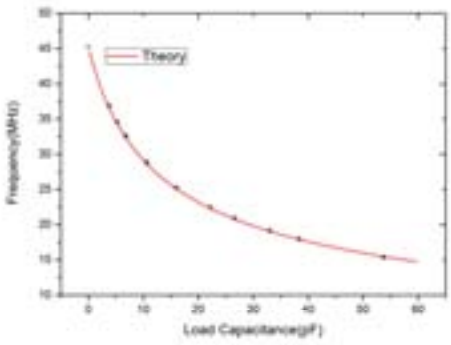

Figure 3. Resonant frequency as a function of the load capacitance.

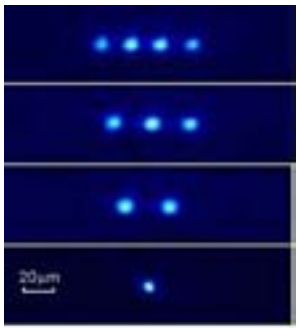

Figure 4. Picture of the trapped ions.

To test the practical performance of the resonator, we used it to drive a linear Paul trap. The Q-factor of the resonator was still about 300 after the trap is connected. A 24.77 MHz RF drive was applied to the blade electrodes through helical resonator. A 280 nm FHG laser from Toptica is used to cool and detect the ions. Pictures of $^{24}Mg^{+}$ are recorded by an EMCCD camera (DU-897D-CS0-UVB, Andor). The result is shown in Fig. 4.

V. CONCLUSION

In conclusion, we have shown a model about the helical resonator and load, predicted the resonant frequency and Q-factor. We constructed a helical resonator and measured its resonant frequency and Q-factor under different loads. The experimental results are in good agreement with our model. Good performance of the RF driver will make it useful for applications of ion trap systems.

REFERENCES

[1] E. A. Burt, S. Taghavi-Larigani, and R. L. Tjoelker, "High-resolution spectroscopy of $^{201}Hg^{+}$ hyperfine structure: A sensitive probe of nuclear structure and the hyperfine anomaly," Phys. Rev. A **79**, 062506 (2009)

[2] J. W. Zhang, Z. B. Wang, S. G. Wang, K. Miao, B. Wang, and L. J. Wang, "High-resolution laser microwave double-resonance spectroscopy of hyperfine splitting of trapped $^{113}Cd^{+}$ and $^{111}Cd^{+}$ ions," Phys. Rev. A **86**, 022523 (2012)

[3] C. W. Chou, D. B. Hume, J. C. J. Koelemeij, D. J. Wineland, and T. Rosenband, "Frequency comparison of two high-accuracy Al^{+} optical clocks," Phys. Rev. Lett. **104**, 070802 (2010)

[4] A. A. Madej, P. Dube, Z. Zhou, J. E. Bernard, and M. Gertsvolf, "$^{88}Sr^{+}$ 445-THz single-ion reference at the 10(-17) level via control and cancellation of systematic uncertainties and its measurement against the SI second," Phys. Rev. Lett. **109**, 203002 (2012)

[5] C. Schneider, D. Porras, and T. Schaetz, "Experimental quantum simulations of many-body physics with trapped ions," Rep. Prog. Phys. **75**, 024401 (2012)

[6] D. J. Wineland and D. Leibfried, "Quantum information processing and metrology with trapped ions," Laser Phys. Lett. **8**, 175 (2011)

[7] P. Wolfgang, "Electromagnetic traps for charged and neutral particles," Rev. Mod. Phys. **62**, 531 (1990)

[8] Q. A. Turchette, D. Kielpinski, B. E. King, D. Leibfried, D. M. Meekhof, C. J. Myatt, M. A. Rowe, C. A. Sackett, C. S. Wood, W. M. Itano, C. Monroe, and D. J. Wineland, "Heating of trapped ions from the quantum ground state," Phys. Rev. A **61**, 063418 (2000)

[9] S. R. Jefferts, C. Monroe, E. W. Bell, and D. J. Wineland, "Coaxial-resonator-driven rf (Paul) trap for strong confinement," Phys. Rev. A **51**, 3112 (1995)

[10] W. W. Macalpine and R. O. Schildknecht, "Coaxial resonators with helical inner conductor," Proceedings of the IRE, **47**, 2099 (1959)

[11] J. D. Siverns, L. R. Simkins, S. Weidt, W. K. Hensinger, "On the application of radio frequency voltages to ion traps via helical resonators," Appl. Phys. B **107**, 921(2012)

Determination of Mode Number Using Two Laser Combs with Large Difference in Repetition Rate

Jin-Long Peng, Tze-An Liu, and Ren-Huei Shu
Center for Measurement Standards
Industrial Technology Research Institute
Hsinchu, Taiwan
jlpeng@itri.org.tw

***Abstract*—Two Er-fiber laser combs with repetition frequency of 500 MHz and 400 MHz are used to measure the frequency of a free-running external cavity diode laser. The mode number is determined by operating the 500 MHz comb at two different repetition rates while keeping the repetition rate of the 400 MHz comb unchanged. A monochromator measures the wavelength of the ECDL to offers an approximate mode number to help determining the mode number shift between the two repetition rates of the 500 MHz comb. The mode number of the beating comb line can be determined with short average time of 1 s.**

Keywords-optical frequency measurement; optical frequency comb; mode-locked laser; mode number; dual-comb

I. INTRODUCTION

Mode-locked (ML) femtosecond laser functioning as an optical frequency comb has revolutionized optical frequency metrology over a decade [1]. To measure the frequency of a laser under measurement (LUM) using a mode-locked laser comb, the mode number of the beating comb line must be determined. Besides using a wavelength meter to offer a precise *a priori* knowledge of the frequency of the LUM, mode number can be determined by measuring the beat frequencies at various repetition rates [2, 3]. Using single comb operated at different repetition rate is limited to measure stable optical frequency with fluctuations of some tens of kHz [3]. Peng et al. developed methods based on two combs with repetition rate difference of kHz to measure the mode number, which can be independent of the frequency fluctuations of the LUM [4-6]. However, the two combs need to have almost the same length of laser cavity or their cavity length be tunable to close to each other. Inaba et al. demonstrated the comb mode determination using two combs with large difference in repetition rate [7]. But, they need long measurement time of 1000 s to average down the uncertainty of the beat frequency. Newbury et al. demonstrated dual-comb spectrometer capable of rapid absolute measurement of a dynamic continuous-wave laser within sub-millisecond [8]. However, they need highly coherent dual-comb system phase-locked to optical frequency reference.

In this paper, we demonstrate method that can determine the mode number in short average time of 1 s using two fiber laser combs with large difference in repetition rate and phase-locked to a microwave frequency reference.

II. THEORY

This method relies on measuring the beat frequencies at two different repetition rates of comb1 while keeping the repetition rate of comb2 unchanged. Furthermore, a monochromator is used to measure the wavelength of the LUM to offer an approximate frequency to help determining the mode number shift of comb1 when its repetition reate is changed. First, the LUM is mixed with comb1 at f_{r11} and comb2 at f_{r2} and two beat frequencies f_{b11} and f_{b21} are generated and measured simultaneously. Then, the repetition frequency of comb1 is changed to f_{r12}, while the repetition rate of comb2 remains to be f_{r2}, and two another beat fequencies f_{b12} and f_{b22} are generated and measured simultaneously. For simplicity, assume that the carrier-envelope-offset (CEO) frequencies of the two combs are zero and the signs of the beat frequencies are determined to be positive. Therefore, the frequency of the LUM can be expressed as:

$$f_L = n \cdot f_{r11} + f_{b11} = k \cdot f_{r2} + f_{b21}, \quad (1)$$

$$f_L = (n+m) \cdot f_{r12} + f_{b12} = k \cdot f_{r2} + f_{b22}, \quad (2)$$

where n and k are the mode number of the beating comb lines for comb1 and comb2, respectively; m is the mode number shift of comb1 when the repetition rate is changed from f_{r11} to f_{r12}. From (1) and (2), the mode number n can be derived as

$$n = \frac{m \cdot f_{r12} + (f_{b21} - f_{b11}) - (f_{b22} - f_{b12})}{f_{r11} - f_{r12}}. \quad (3)$$

Also, m can be expressed as

$$m = \frac{n \cdot (f_{r11} - f_{r12}) - (f_{b21} - f_{b11}) + (f_{b22} - f_{b12})}{f_{r12}}. \quad (4)$$

Since all the beat frequencies in the parentheses of (3) and (4) are simultaneously measured, the frequency fluctuation of the LUM can be subtracted; therefore, the beat frequency difference is equal to the frequency difference of the beating comb lines and is independent of the frequency fluctuation of the LUM. To determine the integer n using (3), the uncertainty of the numerator, which is dominated by the

relative frequency fluctuation between the beating comb lines since the two combs are usually phase-locked to a common microwave frequency standard, must be much less than the value of the denominator. For a usual tracking instability of the repetition frequency of 10^{-13}, the relative frequency fluctuation of the beating comb lines in the visible and near infrared range is less than 100 Hz. Similar to [6], f_{r11}-f_{r12} in the order of kHz is large enough to determine n. For a laser comb with repetition rate of 500 MHz, the comb mode near 1560 nm will change only by 1 if the repetition frequency is changed by 1 kHz. Since m is a small integer and all the other terms in (4) except n can be precisely measured, we can use monochromator to measure the wavelength of the LUM to get an approximate mode number n_{approx} and substituted into (4) to replace n and obtain m first. After m is determined, n can be calculated using (3).

III. Experimental Setup and Results

The experiment is demonstrated using two Er-fiber laser combs with repetition rates of 500 MHz and 400 MHz to measure the frequency of a free-running external cavity diode laser (ECDL) at wavelength of 1560 nm (NewFocus velocity 6328H).

The two Er-fiber laser combs have similar σ-type ring oscillator mode-locked by semiconductor saturable absorber mirror and deliver pulses centered at 1560 nm with bandwidth larger than 10 nm. The other part of the fiber laser comb construction is similar to that one published in [9]. Each comb has three output ports. One port is used to detect the repetition frequency and monitor the fiber laser oscillator. The other two ports are two branches of supercontinua. One branch is used for the CEO frequency detection and the other is used for optical frequency measurement. Each fiber comb is located inside an aluminum box of A3 paper size with 6.5 cm thick. To the best of our knowledge, this is the most compact fiber laser comb with an f-2f interferometer inside.

The power of the ECDL is split into two parts by a 3-dB coupler and then combined with the monitor ports of the two combs with two 3-dB combiners. The outputs from the two combiners pass through two monochromators to filter the beating comb lines. To measure the wavelength of the ECDL, the two combiners are first disconnected from the two combs. The wavelength of the ECDL is determined when maximum power passed through the monochromator is measured. The measured wavelength is 1560±10 nm, which corresponds to an approximate mode number of 384365±0.7%. Then, the two combiners are connected to the two combs again. The beat frequencies are detected by two InGaAs photodiodes. Two polarization controllers are used before the 3-dB combiners to control the polarization of the comb lines and optimize the beat signals. The beat signals are filtered by low pass filter and counted by two universal frequency counters (Agilent Technologies 53132A). The counters are triggered by an external signal generated from a pulse generator and have a gate time of 1s.

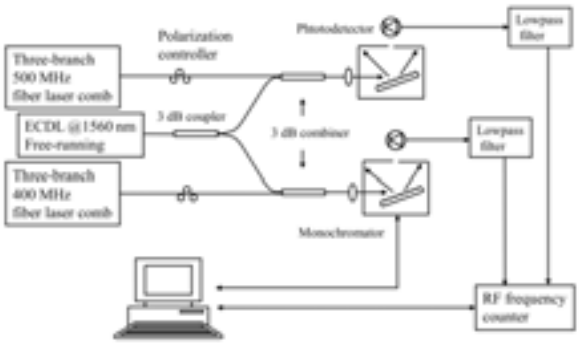

Figure 1. Experimental setup for the optical frequency measurement.

The repetition frequency of comb1 is first controlled to be 500 MHz and that of comb2 is about 400 MHz. The CEO frequencies of the two combs are controlled to be the same value of 140 MHz. The two beat frequencies of comb1 and comb2 mixed with the ECDL are simultaneously counted by the triggered counter and collected by a personal computer through Labview program. The measured beat frequencies are shown in Fig. 2 (a). They are correlated with the frequency drift of the free-running ECDL. The difference of the two beat frequencies is shown in Fig. 2 (b) and not dependent on the drift of the ECDL. Then, the repetition frequency of comb1 is changed to 499.99866 MHz and that of comb2 is not changed. Another two beat frequencies are measured as shown in Fig. 2 (c) and their differences is shown in Fig. 2 (d). The sign of the beat (CEO) frequency is determined by observing the variation of the beat frequency while changing the repetition

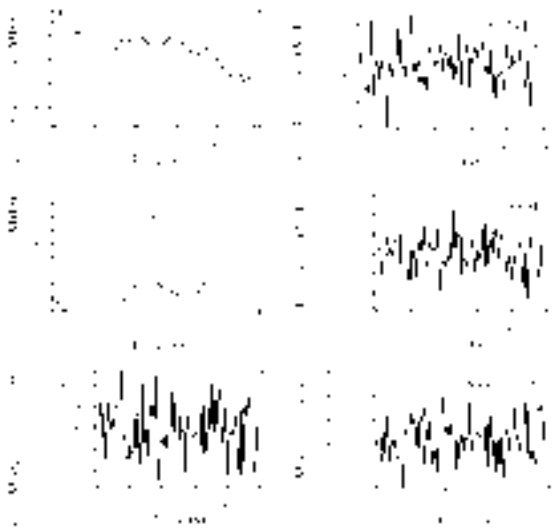

Figure 2. Simultaneously measured beat frequencies f_{b11} and f_{b21} at f_{r11} =500 MHz (a); f_{b12} and f_{b22} at f_{r12}=499.99866 MHz (c); comb2 is fixed at about 400 MHz; dashed line fir of comb1, solid line for comb2. Parts (b) and (d) are the frequency difference of (a) and (c), respectively. Parts (e) and (f) are the calculated m using n_{approx}=384365 and n values, respectively.

(CEO) frequency. All beat frequencies have positive sign. The CEO frequency of comb1 is determined to be negative. The calculated m using n_{approx}=384365 is shown in Fig. 2 (e). The uncertainty of n_{approx} introduces only extra 0.7% uncertainty to the values shown in Fig. 2 (e). It is obviously m=1. The calculated n is shown in Fig. 2 (f). The uncertainty is only 0.09. Clearly, n=384417. The frequency of the ECDL can then be determined to be 384417×500 MHz-140 MHz+f_{b11}.

For average time of 1 s, the maximum fluctuation of the calculated n is only about 0.2; therefore, this method can determine n in short average time of 1 s and is suitable for measuring the frequency of the free-running laser as demonstrated.

IV. Conclusions

We have demonstrated using two fiber laser combs with repetition frequency of 500 MHz and 400 MHz to measure the frequency of a free-running external cavity diode laser. The required average time for the determination of the mode number of the beating comb line is as short as 1s. This method is suitable for measuring the frequency of a free running laser as long as its frequency drift does not interfere the beat frequency measurement.

Acknowledgment

The authors thank Yuh-Chuan Cheng for her contribution to the electronics used in the fiber laser comb.

References

[1] Th. Udem, R. Holzwarth, and T. W. Hänsch, "Optical frequency metrology," Nature, vol. 416, pp. 233-237, March 2002.

[2] L.-S. Ma, M. Zucco, S. Picard, L. Robertsson, and R. S. Windeler, "A new method to determine the absolute mode number of a mode-locked femtosecond laser comb used for absolute optical frequency measurements," IEEE J. Sel. Top. Quantum Electron., vol. 9, pp. 1066-1071, July/August 2003.

[3] J. Zhang, Z. H. Lu, Y. H. Wang, T. Liu, A. Stejskal, Y. N. Zhao, R. Dumke, Q. H. Gong, and L. J. Wang, "Exact frequency comb mode number determination in precision optical frequency measurements," Laser Phys., vol. 17, pp. 1025-1028, July 2007.

[4] J.-L. Peng and R.-H. Shu, "Determination of absolute mode number using two mode-locked laser combs in optical frequency metrology," Opt. Express, vol. 15, pp. 4485-4492, April 2007.

[5] J.-L. Peng, T.-A. Liu, and R.-H. Shu, "Optical frequency counter based on two mode-locked fiber laser combs," Appl. Phys. B, vol. 92, pp. 513-518, September 2008.

[6] T.-A. Liu, R.-H. Shu, and J.-L. Peng , "Semi-automatic, octave-spanning optical frequency counter," Opt. Express, vol. 16, pp. 10728-10735, July 2008.

[7] H. Inaba, Y. Nakajima, F.-L. Hong, K. Minoshima, J. Ishikawa, A. Onae, H. Matsumoto, M. Wouters, B. Warrington, and N. Brown, "Frequency measurement capability of a fiber-based frequency comb at 633 nm," IEEE. Tran. Instru. Meas., Vol. 58, pp. 1234-1240, April 2009.

[8] F. R. Giorgetta, I. Coddington, E. Baumann, W. C. Swann, and N. R. Newbury, "Fast high-resolution spectroscopy of dynamic cintinuous-wave laser sources," Nature Photon., vol. 4. pp. 853-857, December 2010.

[9] J.-L. Peng, T.-A. Liu, and R.-H. Shu, "Self-referenced Er-fiber laser comb with 300 MHz comb spacing," Proceedings of the 2009 IEEE International Frequency Control Symposium jointly with the 22nd European Frequency and Time Forum (IFCS/EFTF), pp. 344-346, 2009.

Long-term Miniaturized Stabilization of Ultrafast Laser based on Rubidium Coherent Population Trapping Atomic Resonator

Jiutao Wu, Dong Hou, Zhong Wang and Jianye Zhao*
Department of Electronics
Peking University
Beijing, China
*Corresponding author email: zhaojianye@pku.edu.cn

Abstract—**Many locking approaches have been exploited to stabilize the mode-locked laser (MLL), helping to generate high-stable microwave sources. We present a novel miniaturized stabilization scheme for MLL, based on a rubidium coherent population trapping (CPT) atomic resonator. By directly frequency-locking the repetition rate of the MLL to a ^{85}Rb CPT resonance, we demonstrate a very small stabilization system (length of 5 cm, width of 5 cm and height of 2.2 cm) for MLL with a long-term instability of ~3×10^{-12}.**

Keywords-ultrafast laser, coherent population trapping; frequency stabilization.

I. INTRODUCTION

Ultrafast lasers, based on the phenomenon of mode-locking, have obtained a considerable attention in many fields [1, 2] these years. There is a considerable interest in achieving both so high and stable repetition rate of a mode-locked laser (MLL) as to synthesize a high-stable and low-noise microwave source [3]. To generate the high-stable microwave from a MLL, the MLL should be stabilized to a frequency standard [4]. Many stabilization approaches have been proposed to achieve this [5-12]. In these approaches, the MLLs were phase-locked to very high-stable external frequency references, including atomic microwave, optical clocks, and narrow optical-linewidth continuous wave (CW) lasers. Many experiments have shown that these approaches can improve the stability and phase noise of the MLL significantly. However, the large physical size and system complexity of these approaches is a problem in practical application. A small stabilization system with long-term stability, therefore, should be proposed to meet the portable requirement of some practical applications. In this paper, we demonstrate a miniaturized MLL stabilization scheme to directly frequency-lock the repetition rate of MLL to an atomic CPT resonance [13, 14], generating a stable microwave with a decent long-term stability. The key point of this approach is that this stabilization system is not simply used as conventional locking technique to synchronize the MLL and a frequency reference, but also acts a self-locking loop in an atomic clock to directly stabilize the repetition rate of a MLL to an atomic resonance, where the MLL is similar in spirit to the electronic oscillators. A Rb CPT resonance is chosen as the atomic resonance here because it is easy to miniaturize the physical parts in CPT atomic clock [15, 16]. We built a small ^{85}Rb physics package with the length of 33 mm, width of 13 mm and height of 18 mm, as the frequency resonator, and integrated a frequency-locking servo-loop circuit to stabilize the repetition rate of a MLL to a ^{85}Rb CPT resonance at a hyperfine frequency. With this technique, we achieve a very small ultrafast laser stabilization system with length of 5 cm, width of 5 cm and height of 2.2 cm, leading to a long-term frequency instability of ~3×10^{-12}.

II. SCHEME OF FREQUENCY STABILITION USING CPT RESONATOR

The miniaturized atomic frequency standard based on CPT has been studied for many years [13]. In this paper, we utilize a ^{85}Rb CPT resonator to achieve a miniaturized stabilization system, for directly frequency-locking the repetition rate of the MLL to a ^{85}Rb CPT resonance. In ^{85}Rb CPT, as the decay rate of the ground state coherence is small, the resonance with a small linewidth forms a high-precision frequency reference.

The setup of this MLL stabilization system based on CPT in ^{85}Rb is illustrated in Fig. 1. It contains a ^{85}Rb CPT resonator, a passive Er-doped MLL with fundamental repetition rate of 144.5 MHz, and a servo-loop circuit. The objective of the stabilization system is to directly frequency-lock the repetition rate (the 21st harmonic) of the MLL to the ^{85}Rb CPT resonance at a hyperfine frequency of 3.035 GHz. The frequency of the vertical cavity surface emitting laser (VCSEL) driven by a high-precise laser current source is tuned to the ^{85}Rb D1 absorption line. A bias-T is used to couple the VCSEL injection current, and a RF signal of 3.035 GHz extracted from the MLL is used to modulate the VCSEL. The laser beam illuminates the vapor cell containing a natural mixture of both Rb isotopes (^{85}Rb and ^{87}Rb) and buffer gas (Ne and Ar) to excite the atomic transition and CPT resonance. The good noise properties of the VCSEL improve the performance of the resonator, allowing accurate detection of narrow CPT resonance. A photodetector (PD) converts the variation of the transmitted laser power to an electronic signal. The electronic signal is delivered into two different lock-in amplifiers. One lock-in amplifier is used to control the laser current and stabilize the VCSEL operating at the wavelength of the ^{85}Rb $5^2S_{1/2}$– $5^2P_{1/2}$ transition (D1 line). The other one generates the frequency-error signal to finely tune the pump source of the MLL [17], and then locks the 21st harmonic repetition rate of

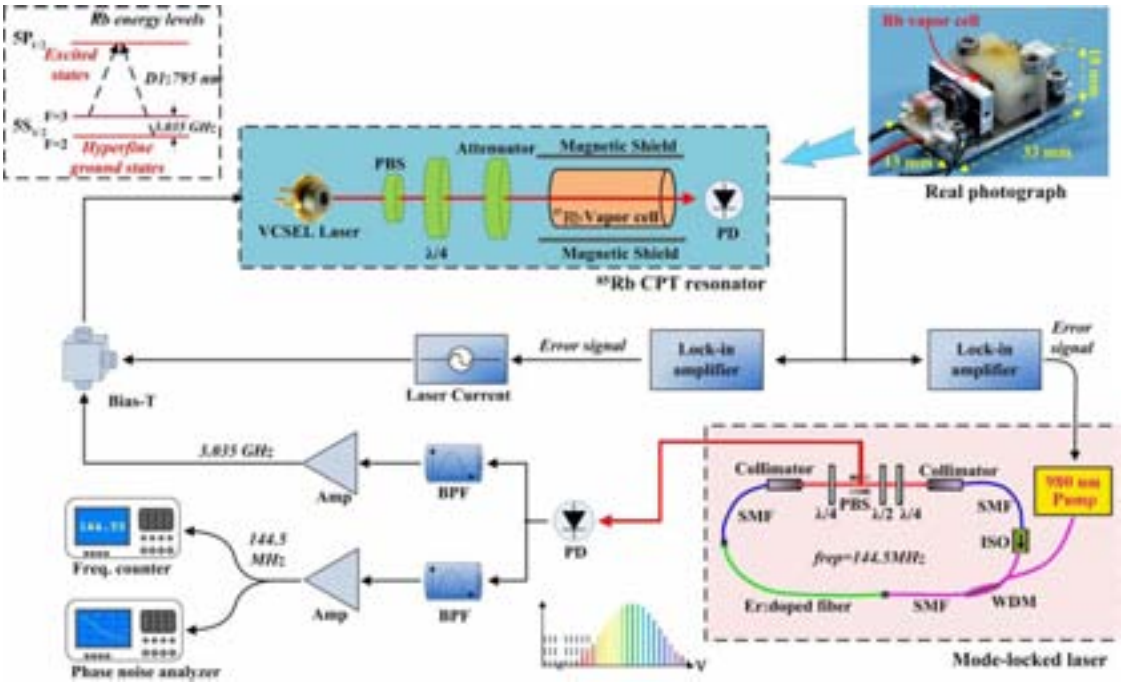

Figure 1. Direct frequency stabilization scheme of MLL with a ^{85}Rb CPT atomic resonator.

the MLL to the Rb CPT resonance. Essentially, these two lock-in amplifiers form two stabilization servo loops. With the help of the servo loops, the VCSEL optical frequency and repetition rate of the MLL are stabilized to the absorption spectrum of ^{85}Rb D1 line and a ^{85}Rb hyperfine frequency of 3.035 GHz respectively. We extracted the fundamental repetition rate of the MLL into a frequency counter and a phase noise analyzer, for measuring the frequency instability and the phase noise.

The key component in our stabilization is the small ^{85}Rb CPT resonator with the length of 33 mm, width of 13 mm and height of 18 mm, and this resonator dominantly determines the physical size of our stabilization. It consists of a VCSEL equipped with integrated microlenses, a small ^{85}Rb vapor cell and a low-noise PD [18, 19]. The schematic of the CPT resonator is also shown in Fig. 1. With the VCSEL laser, phase-coherent first-order sidebands can be generated directly with high efficiency by modulating the laser frequency via injection current. The ^{85}Rb Λ system is used in our resonator because the VCSEL laser operating at the wavelength of the ^{85}Rb $5^2S_{1/2}$– $5^2P_{1/2}$ transition (D1 line) is easily accessible and the modulation bandwidth of VCSEL lasers covers the ground-state hyperfine splitting. In practice, the VCSEL laser emits light close to the 795 nm D1 line in Rb. To tune the wavelength to this line, we adjust the temperature of the VCSEL with a resistive element placed around the laser. The laser beam passes a polarizing beam splitter (PBS), quarter-wave plate and an attenuator lens, where it is circular polarized and attenuated, respectively. Finally, the beam enters a glass blown ^{85}Rb vapor cell, where a PD placed after the cell monitors the transmitted light. The cell is placed at the center of a solenoid which generates a magnetic field to lift the Zeeman degeneracy of the hyperfine states. All physical parts of the resonator are integrated on a magnetic shielded board, and its real photograph is illustrated in Fig. 1.

III. EXPRIMENTAL RESULT

To investigate the performance of proposed stabilization scheme, we conducted a long-term stabilization experiment. The MLL was exposed to the environment with temperature stabilization and air flow control. The 21st repetition rate of the MLL was directly frequency-locked to a Rb CPT resonance at the hyperfine frequency of 3.035 GHz for hours. In addition, to examine the stabilization performance, we compared our direct-stabilized MLL system with a conventional CPT clock (SA.45s, Symmetricom). This clock is a commercial CPT clock, and has a same configuration and physical size of our CPT stabilization loop, where the only difference is that its frequency oscillator is not the MLL but a high-stable electronic crystal oscillator and a microwave synthesizer.

The linewidth of the CPT resonance is a key parameter to determine the short-term instability and the phase noise of the CPT stabilization system [14]. Therefore, we first measured the CPT linewidthes excited by the MLL and an electronic oscillator respectively. Fig. 2 clearly shows that, compared to an electronic oscillator generated from a microwave synthesizer (Agilent N9310), the MLL oscillator excites a narrower linewidth. The linewidth is closely related to the laser light mixed with the microwave at 3.035 GHz, and the purer light will excite the narrower linewidth. Therefore, the

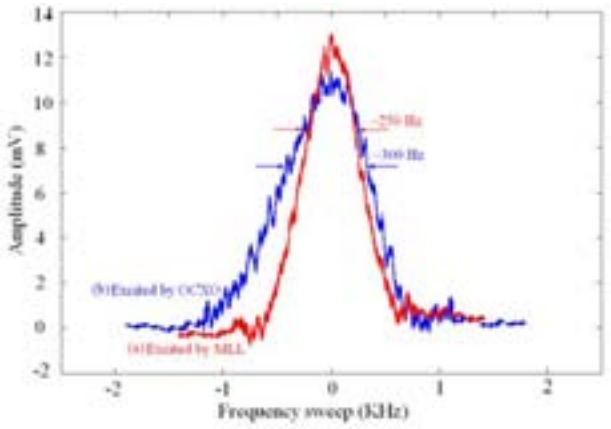

Figure 2. CPT resonance linewidthes are excited by a MLL oscillator and a high-stable electronic oscillator at 3.035 GHz respectively. (a) was excited by the MLL (with the phase noise of ~-110 dBc/Hz at 10 KHz offset). (b) was excited by the high-stable electronic microwave synthesizer (Agilent N9310, with the phase noise of ~-90 dBc/Hz at 10 KHz offset).

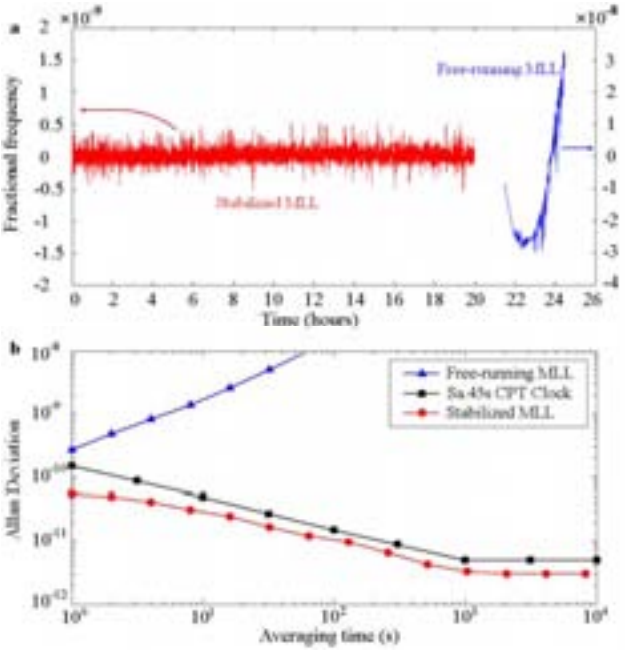

Figure 3. (a) Time records of measured fundamental repetition frequency at 144.5 MHz for stabilized MLL and free-running MLL. The measurements for stabilized MLL and free-running MLL lasted ~20 hours and ~2 hours respectively. (b) Fractional frequency instabilities for stabilized MLL, free-running MLL and a commercial Rb CPT clock.

difference of the linewidthes is primarily due to the qualities of the different microwaves. In fact, with electronic microwave oscillator, it is difficult to obtain a more ultrastable pure microwave than the MLL, because the electronic oscillator and the frequency synthesizer will introduce extra electronic noises and hence deteriorate the quality of the microwave.

We measured the frequency instabilities and phase noises of stabilization system. Fig. 3a shows the frequency drifts of microwaves (fundamental repetition rate of 144.5 MHz) extracted from the free-running MLL and the stabilized MLL. In the figure, we can see that the system using a Rb CPT resonator performs a good stabilization of frequency-locking. The frequency drift of the stabilized MLL shows a flat curve over the measure time (20 hours), for the CPT resonance limits the frequency drifts severely. The frequency instabilities of the microwaves extracted respectively from the free-running and the stabilized MLL are shown in Fig. 3b, and that of a commercial CPT clock (SA.45s, Symmetricom) with the same size as our stabilization system is also illustrated for comparison. The instability of the free-running MLL is 3×10^{-10} for a 1-s gate time and much higher than 10^{-8} for a 100-s gate time (filled triangle in Fig. 3b). The stabilization loop with Rb CPT resonator improves the instability to 5×10^{-11} for a 1-s gate time and about 3×10^{-12} at 1000-s (filled circle in Fig. 3b). The short-term and long-term frequency instability for the stabilized MLL is both a little lower than that of the commercial Rb CPT clock (filled square in Fig. 3b). This shows that the Rb CPT resonator improves the MLL's instability within the whole frequency range, compared to conventional CPT clock with the same physical size.

Fig. 4 shows the phase noises of the microwave extracted from the free-running MLL and the stabilized MLL. A phase noise curve of a microwave signal synthesized from the commercial Rb CPT clock (Sa.45s, Symmetricom) is also illustrated in the same figure. The figure shows that the phase noise of the free-running MLL is ~-45 dBc/Hz at 1 Hz offset and ~-130 dBc/Hz at 1 MHz offset. Compared with the free-running MLL, the stabilization loop with Rb CPT resonance improved the phase noise to ~-67 dBc/Hz at 1 Hz offset. We found the phase noise at 1 MHz offset cannot be improved, because the phase noise at high-frequency off is determined by the MLL in itself. We can see that the stabilized MLL has a lower phase noise than the electronic microwave oscillator at full frequency offset. This implies that the phase noise of the

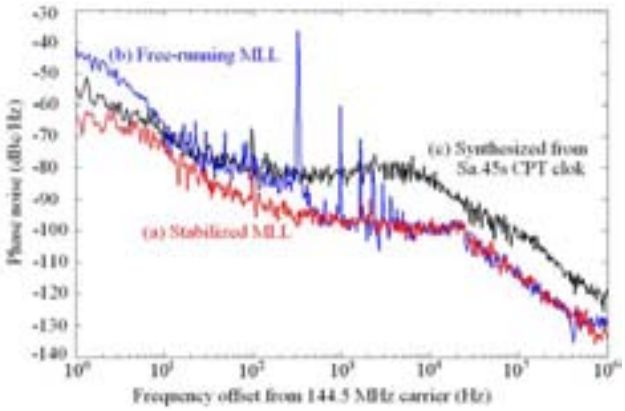

Figure 4. Phase noise spectrum of the generated microwaves for stabilized MLL (a), free-running MLL (b), and microwave signal synthesized from the Sa.45s CPT clock (c).

stabilized MLL using Rb resonance is just limited by the Rb CPT resonance and the optical parts. These experimental results demonstrate that the stabilization scheme using the Rb CPT resonance, with a very small physical size, has a good long-term stabilization performance for the MLL.

IV. CONCLUSION

In summary, the proposed stabilization scheme where the MLL is directly frequency-locked to the Rb CPT resonance is different from the conventional PLL technique. For repetition rate stabilization of MLLs, the most commonly used PLL stabilization schemes [5-7] usually synchronize the MLL to an external frequency standard. Besides, many experiments reported that, with a PID regular, the PLL stabilization technique can perform a good performance of long-term stabilization [5-7]. However, in most case, we find that the frequency instability of a MLL stabilized by the PLL technique is higher than the frequency reference [7]. This implies that the electronic circuits in the PLL will bring the extra stability loss in the stability transfer from the frequency reference to the MLL. In addition, the connection between the external frequency reference and the PLL stabilization system will introduce extra noise in phase and amplitude which reduces the stabilization performance. To avoid the stability loss and the extra noise, an approach which directly stabilizes the MLL to the ^{85}Rb CPT resonance is proposed in this paper. By directly transferring the frequency stability of the atomic hyperfine frequency to the MLL, this approach can improve the frequency stability of the MLL significantly. Besides the improvement in frequency stability, the approach can also simplify the system complexity and dramatically reduce the physical size because of the removal of the PLL servo circuit. Although some PLL stabilization schemes using high-stable Rb or Cs atomic clocks with big physical size have a better instability performance, the miniaturized stabilization scheme with a decent long-term stability is just the advantage of our approach. We believe that the proposed approach have a superior stability to other stabilization techniques with the same small physical size.

ACKNOWLEDGMENT

This work was supported in part by the Nature Science Foundation of China under Grant 60704040 and Grant 11027404, and the National High-tech R&D Program of China. The authors would like to thank Prof. Zhigang Zhang from the department of electronics, Peking University, for helpful discussion and assistance on the experimental setup of ultrafast laser.

REFERENCES

[1] T. Udem, R. Holzwarth, and T. W. Hansch, "Optical frequency metrology," Nature, vol. 416, pp. 233-237, 14 March 2002.

[2] P. Gill, "Femtosecond timing distribution," Nature photon. vol. 2, pp. 711-712, December 2008.

[3] U. Keller, "Recent developments in compact ultrafast lasers," Nature, vol. 424, pp. 831-838, 14 August 2003.

[4] S. T. Cundiff and J. Ye, "Phase stabilization of mode-locked lasers," J. Mod. Opt., vol. 52, pp. 201-219, February 2005.

[5] W. W. Hsiang, C. Y. Lin, N. K. Sooi, and Y. C. Lai, "Long-term stabilization of a 10 GHz 0.8 ps asynchronously mode-locked Er-fiber soliton laser by deviation-frequency locking," Opt. Express, vol. 14, pp. 1822-1828, 6 March 2006.

[6] D. Hayes, D. N. Matsukevich, P. Maunz, D. Hucul, Q. Quraishi, S. Olmschenk, W. Campbell, J. Mizrahi, C. Senko, and C. Monroe, "Entanglement of Atomic Qubits Using an Optical Frequency Comb," Phys. Rev. Lett. , vol. 104, 140501, April 2010.

[7] D. Hou, J. Wu, Q. Ren and J Zhao, "Analysis of Long-Term Phase-Locking Technique for Mode-Locked Laser With PID Regulator," IEEE J. Quantum Electron. , vol. 48, pp. 839-846, July 2012.

[8] J. Rauschenberger, T. M. Fortier, D. J. Jones, J. Ye, and S. T. Cundiff, "Control of the frequency comb from a mode-locked Erbium-doped fiber laser," Opt. Express, vol. 10, pp. 1404-1410, 2 December 2002.

[9] S. A. Diddams, D. J. Jones, J. Ye, S. T. Cundiff, J. L. Hall, J. K. Ranka, R. S. Windeler, R. Holzwarth, T. Udem, and T. W. Hansch, "Direct Link between Microwave and Optical Frequencies with a 300 THz Femtosecond Laser Comb," Phys. Rev. Lett., vol. 84, pp. 5102-5105 , 29 May 2000.

[10] A. Bartels, C. W. Oates, L. Hollberg, and S. A. Diddams, "Stabilization of femtosecond laser frequency combs with subhertz residual linewidths," Opt. Lett. 29, pp. 1081-1083, 15 May 2004.

[11] R. J. Jones and J. C. Diels, "Stabilization of Femtosecond Lasers for Optical Frequency Metrology and Direct Optical to Radio Frequency Synthesis," Phys. Rev. Lett. , vol. 86, pp. 3288-3291, 9 April 2001.

[12] J. Millo, M. Abgrall, M. Lours, E. M. L. English, H. Jiang, J. Guena, A. Clairon, M. E. Tobar, S. Bize, Y. Le Coq, and G. Santarelli, "Ultralow noise microwave generation with fiber-based optical frequency comb and application to atomic fountain clock," Appl. Phys. Lett. , vol. 14, 141105, 2009.

[13] J. Vanier, "Atomic clocks based on coherent population trapping: a review," Appl. Phys. B 81, pp. 421-442, 2005.

[14] J. Vanier, M. W. Levine, D. Janssen, and M. J. Delaney, "The Coherent Population Trapping Passive Frequency Standard," IEEE Trans. Instrum. Meas., vol. 52, pp. 258-262, April 2003.

[15] S. Knappe, V. Shah, PDD Schwindt, L. Hollberg, J. Kitching, L. A. Liew, and J. Moreland, "A microfabricated atomic clock," Appl. Phys. Lett., vol.85, pp. 1460-1462, 30 August 2004.

[16] J. Kitching, S. Knappe, and L. Hollberg, "Miniature vapor-cell atomic-frequency references," Appl. Phys. Lett., vol. 81, pp. 553-555, 15 July 2002.

[17] N. Haverkamp, H. Hundertmark, C. Fallnich, and H. R. Telle, "Frequency stabilization o f mode- locked Erbium fiber l asers using pump p ower contro l," Appl. Phys. B, vol. 78, pp. 321-324, 2004.

[18] K. Deng, T. Guo, D. W. He, X. Y. Liu, L. Liu, D. Z. Guo, X. Z. Chen, and Z. Wang, "Effect of buffer gas ratios on the relationship between cell temperature and frequency shifts of the coherent population trapping resonance," Appl. Phys. Lett., vol. 92, 211104, 2008.

[19] K. Deng, T. Guo, J. Su, D. Z. Guo, X. Y. Liu, L. Liu, X. Z. Chen, and Z. Wang, "Full hyperfine frequency modulation in the implementation of coherent population trapping atomic clocks," Phys. Lett., vol. 373, pp. 1130–1132, 2009.

International Timescales with Optical Clocks (ITOC)

H. S. Margolis, R. M. Godun, P. Gill,
L. A. M. Johnson, S. L. Shemar, P. B. Whibberley
National Physical Laboratory (NPL)
Teddington, UK
helen.margolis@npl.co.uk

H. Denker, L. Timmen, C. Voigt
Institut für Erdmessung (IfE)
Gottfried Wilhelm Leibniz Universität
Hannover, Germany

D. Calonico, F. Levi, L. Lorini, M. Pizzocaro
Istituto Nationale di Ricerca Metrologica (INRIM)
Torino, Italy

S. Falke, D. Piester, C. Lisdat, U. Sterr,
S. Vogt, S. Weyers
Physikalisch-Technische Bundesanstalt (PTB)
Braunschweig, Germany

P. Delva, S. Bize, J. Achkar
LNE-SYRTE, Observatoire de Paris, CNRS and UPMC
Paris, France

J. Gersl
Cesky Metrologicky Institut (CMI)
Brno, Czech Republic

T. Lindvall, M. Merimaa
Mittatekniikan Keskus (MIKES)
Espoo, Finland

***Abstract*—A new collaborative European project "International timescales with optical clocks" (ITOC) aims to tackle the key challenges that must be addressed prior to a redefinition of the SI second. A coordinated programme of comparisons will be carried out between European optical clocks developed in five different laboratories, enabling their performance levels to be validated at an unprecedented level of accuracy. Supporting work will be carried out to evaluate relativistic effects that influence the comparisons, including the gravitational redshift of the clock transition frequencies. A proof-of-principle experiment will also be performed to demonstrate that optical clocks could be used to make direct measurements of the Earth's gravity potential with high temporal resolution.**

Keywords-optical clock; redefinition of the second; international timescales; time and frequency transfer; geodesy

I. INTRODUCTION

The SI second is currently defined in terms of the frequency between the two ground state hyperfine levels of the ^{133}Cs atom. However the most advanced optical atomic clocks have now reached levels of stability and accuracy that significantly surpass the performance of the best caesium primary frequency standards. For example, the Al^+ optical clock at NIST has an estimated systematic uncertainty below 1 part in 10^{17} [1], and several others have reached uncertainties below 1 part in 10^{16} [2–4]. In contrast, the accuracies of the best caesium fountain primary standards are in the range 2 – 5 parts in 10^{16} [5–9]. As a result, an optical redefinition of the SI second is being considered by the international community [10].

The key prerequisite for a redefinition of the second is the integration of optical atomic clocks into the international timescales TAI (International Atomic Time) and UTC (Coordinated Universal Time). This requires a coordinated programme of clock frequency comparisons to be carried out, to validate the uncertainty budgets of the optical clocks, to anchor their frequencies to the present definition of the second, and to establish the leading contenders for a new definition.

Such a comparison programme is planned within a new collaborative European project "International Timescales with Optical Clocks" (ITOC). Since the current satellite link infrastructure used to compare microwave clocks in spatially separated laboratories is inadequate to match the increased stability of optical clocks, several alternatives will be explored, with the emphasis on techniques that could be applied on an intercontinental scale. To support the comparison programme a complete evaluation will also be made of all relativistic effects influencing time and frequency comparisons at the 10^{-18} level of accuracy, including the gravitational redshifts of the clock transition frequencies.

II. CLOCK COMPARISON PROGRAMME

To date, very few direct comparisons of optical clocks have been carried out to verify their estimated performance levels. Frequency comparisons between two Al^+ optical clocks at NIST demonstrate agreement at the 1.8 parts in 10^{17} level, consistent with the estimated uncertainty of the older of the two clocks [1], whilst a recent comparison of two strontium optical

lattice clocks at LNE-SYRTE showed that they agreed to within their uncertainty budget, with a total uncertainty of 1.5 parts in 10^{16} [11]. Both comparisons involved two optical clocks developed in the same laboratory. Almost all information about the reproducibility of optical clocks developed in different laboratories comes from independent absolute frequency measurements made relative to local caesium fountain primary frequency standards. For example, four independent absolute frequency measurements of the optical clock transition in ^{87}Sr agree at the part in 10^{15} level [11–14], whilst similar agreement is observed between two measurements of the electric octupole clock transition frequency in $^{171}Yb^{+}$ [3,15]. However such comparisons are inherently limited by the uncertainties of the primary standards. The ITOC project aims to address this deficiency by carrying out a tightly integrated programme of frequency comparisons between European optical clocks at a level limited only by the accuracies of the clocks themselves.

The proposed clock comparison programme is illustrated in Fig. 1; it involves four different types of measurement and optical clocks in five different laboratories.

Firstly, frequency comparisons will be carried out locally between optical clocks developed in individual laboratories, either by direct beat frequency comparison (for clocks of the same type) or by using femtosecond optical frequency combs to measure optical frequency ratios (for different types of clock). Since it has previously been shown that femtosecond combs do not fundamentally limit optical frequency comparisons at the 10^{-18} level or even lower [16], these types of comparison will lead to the highest levels of stability and accuracy, with the accuracies achieved depending on the limiting systematic shifts for each type of clock.

To compare optical clocks developed in different laboratories, two different techniques will be used. Two comparisons will be performed using transportable optical clocks developed at PTB and MIKES (a strontium optical lattice clock and a strontium ion optical clock). The focus will be on the development and characterization of transportable optical clocks with the best possible levels of accuracy and stability. This is in contrast to other efforts to develop optical clocks for space applications, where these pure metrological goals may be compromised by the restrictions imposed on the mass, size and power consumption of the clocks. Secondly, an improved two-way satellite time and frequency transfer (TWSTFT) technique based on an increased chip rate will be investigated. The goal is a gain in stability by one order of magnitude compared to state-of-the-art frequency comparison techniques via satellite (including various GPS methods) [17], to a stability of 1×10^{-16} after one day of averaging.

Finally, a set of absolute frequency measurements of the optical clocks will be made with uncertainty limited by the caesium primary frequency standards used as the reference. These measurements are essential to allow the frequencies of the optical clocks to be determined relative to the current definition of the second with the lowest possible uncertainty. This will maximize their potential contribution to TAI prior to a redefinition, and also ensure that no discontinuity is introduced at the point of redefinition.

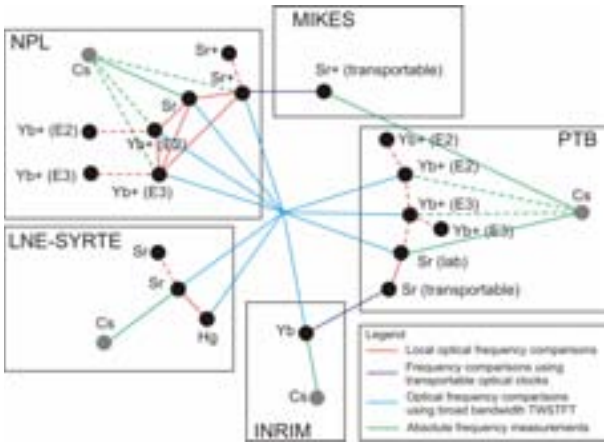

Figure 1. ITOC clock comparison programme. The aspiration for the broad bandwidth two-way satellite time and frequency transfer (TWSTFT) measurement campaign is to compare as many optical clocks as possible in the four participating laboratories. Dotted lines indicated measurements that will be carried out within other projects, but included within the self-consistency analysis performed within the ITOC project.

Within the comparison programme, there will be a sufficient number of cross-checks to allow internal self-consistency checks to be performed. A frequency matrix formalism will be set up and a least-squares analysis procedure developed to perform self-consistency checks on a large body of data for the first time.

When the project was formulated, optical fibre links had already been demonstrated to be suitable for optical frequency comparison at the 10^{-18} level for clocks separated by hundreds of kilometres [18–20], but no links between the laboratories of interest were firmly established. However this situation is soon expected to change and optical clock comparisons performed using such links in other projects will be included in the self-consistency analysis along with other values available in the scientific literature.

The statistical and systematic uncertainties of the optical clocks are not the only important factors when considering their use to derive steering corrections to TAI [21]. Although unattended operation of caesium fountain primary frequency standards with low dead time is now routinely achieved in several laboratories, optical clocks have not yet reached this level of reliability. A local flywheel frequency reference must thus be used to obtain TAI steering data, which results in a significant additional uncertainty contribution. A further uncertainty contribution arises from the performance of available frequency transfer techniques. Whilst currently operational methods offer stabilities which are satisfactory for TAI steering by caesium fountain standards, their performance would significantly degrade the inherent uncertainties achievable with optical clocks. The relevance of these two factors for TAI steering will be quantified, based on the typical performance characteristics of optical clocks, state-of-the-art flywheel oscillators and the expected improvements in frequency transfer techniques.

III. Relativistic Timescales and Geodesy

The levels of stability and accuracy reached by optical clocks are now such that, to derive the maximum benefits from incorporating them into international timescales, relativistic effects influencing the comparison must be evaluated at an improved level of accuracy. These include the Sagnac effect, the velocity of the clocks with respect to an inertial reference frame, and the gravitational redshifts of the clock transition frequencies.

To support the comparison programme outlined in section II, an evaluation will be made of the relativistic effects important in the broadband TWSTFT technique and how these can be corrected or effectively eliminated. The relativistic effects relevant for time and frequency transfer using optical fibre links will also be studied, for which it will be necessary to develop methods to account for signal propagation in a medium with a refractive index larger than unity. Finally, the potential use of continuously operating transportable optical clocks for time transfer will be investigated.

To determine the gravitational redshift corrections for the optical clocks involved in the comparison programme, it is necessary to determine the gravity potential at each clock site. Although only gravity potential differences need to be determined for the frequency comparisons, absolute potential values relative to a defined reference surface are required for future integration of the optical clocks into international timescales. For optical clocks with a projected fractional accuracy of 10^{-18}, an accuracy of about 0.1 m^2s^{-2} in the gravity potential is required, corresponding to about 1 cm in height. This level of accuracy represents a significant improvement on the current state-of-the-art and also requires the evaluation of time-varying effects such as solid Earth and ocean tides due to the effects of the moon and the sun. Setups will be designed to determine the static gravity potential at the clock locations and gravity surveys will be performed around each clock site. These gravity observations will then be included in a re-evaluation of the existing gravity database and used to compute a refined European geoid model. To account for the time-varying effects, tidal potential time series will also be computed for each clock site.

IV. Proof-of-Principle Clock-Based Geodesy Experiment

Although the main focus of the ITOC project is on the future realization of international timescales, we also aim to demonstrate the impact that optical clocks could have on the field of geodesy, by showing that they can be used to measure gravity potential differences over medium–long baselines with sensitivity at the decimetre level.

In contrast to other instruments used for gravity measurements, optical clocks are directly sensitive to the gravity potential, which determines their gravitational redshift. Within the ITOC project we will carry out a proof-of-principle experiment to show that the gravitational redshift of optical clocks can be used to measure the gravity potential difference between two well-defined locations.

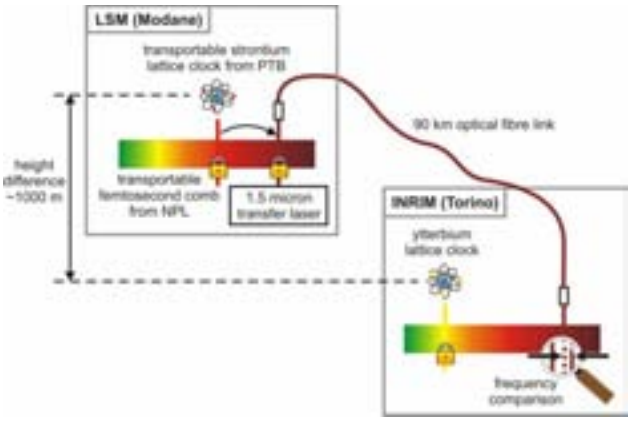

Figure 2. Schematic diagram of one possible configuration for the proposed proof-of-principle clock-based geodesy experiment.

The proposed experiment is illustrated in Fig. 2. One of the optical clocks will be the ytterbium optical lattice clock at INRIM in Turin, Italy. The other will be the transportable strontium optical lattice clock from PTB, which will be taken to the Laboratoire Souterrain de Modane (LSM) in the Fréjus tunnel, just over the France-Italy border. The frequency comparison between the two clocks will be performed using an optical fibre link between the two laboratories. Two optical frequency combs are also required for the frequency ratio measurement between the two optical clocks, because the transmission window of the optical fibre link is at 1.5 μm. Since no frequency comb is available at LSM, a transportable comb from NPL will be used to link the frequency of the transportable lattice clock to that of a 1.5 μm transfer laser.

The INRIM-LSM test-bed offers a large gravity potential difference, with a height difference of approximately 1000 m between the two sites. The expected gravitational redshift is therefore about 10^{-13}, while the target accuracies of the clocks are 5×10^{-17}. Since instability targets are $1\times10^{-15}\,\tau^{-1/2}$ for the clocks and $1\times10^{-14}\,\tau^{-1}$ for the optical link, these accuracies are expected to be reached after a few hours measurement time. Knowing the proper frequency ratio between the two clocks, which will be determined by transferring the PTB transportable lattice clock to INRIM, it should thus be possible to measure the 1000 m elevation difference between two points separated by about 90 km at the decimetre level within a few hours. The value obtained by using the clocks in this way will be compared with the result obtained using standard geodetic methods.

V. Conclusions

The most direct impact of the ITOC project will be on the top-level realization of the SI unit of time, in providing results and procedures to prepare for a future redefinition of the second. This will be achieved by input to the Consultative Committee for Time and Frequency (CCTF) and its associated working groups. In particular, the results will lead to improved frequency values for secondary representations of the second, and independent verification of the performance of optical clocks developed in different laboratories.

The international scientific community will also benefit from validated clock comparisons as a basis for tests of fundamental physical theories. One example is the search for temporal variation of the fine structure constant by comparing transition frequencies in different optical atomic clocks. The demonstrated performance of the ground-based optical clocks will also benefit fundamental science space missions such as ACES (Atomic Clock Ensemble in Space) and STE-QUEST (Space-Time Explorer and Quantum Equivalence Principle Space Test).

The proof-of-principle clock-based geodesy experiment carried out within the project will demonstrate that optical clocks can be used to make direct measurements of the Earth's gravity potential. High-resolution measurements made at selected well-defined locations using transportable optical clocks could bring significant benefits to the geodesy community in terms of achieving a consistent alignment of national height systems within Europe, as well as checks of global and regional geoid models, established by alternative means. Such measurements would also complement the data obtained from satellite missions such as GOCE or GRACE, which provide global coverage but give values that are spatially averaged over length scales of about 100 km.

More generally, accurate time and frequency references underpin numerous technologies that we have come to take for granted in everyday life, particularly in the areas of communication and navigation. Building on the developments realized within the ITOC project, it will be possible to disseminate time and frequency with unprecedented stability to end users of international timescales. In this way, the stability and accuracy of optical clocks, confined today to a few laboratories, will be made available to industry, and can be expected to lead to widespread impact on innovation, science and daily life.

ACKNOWLEDGMENT

The ITOC project is part of the European Metrology Research Programme (EMRP). The EMRP is jointly funded by the EMRP participating countries within EURAMET and the European Union.

REFERENCES

[1] C. W. Chou, D. B. Hume, J. C. J. Koelemeij, D. J. Wineland and T. Rosenband, "Frequency comparison of two high-accuracy Al^+ optical clocks," Phys. Rev. Lett., vol. 104, 070802, February 2010.

[2] A. D. Ludlow et al., "Sr lattice clock at 10^{-16} fractional uncertainty by remote optical evaluation with a Ca clock," Science, vol. 319, pp. 1805–1808, March 2008.

[3] N. Huntemann, M. Okhapkin, B. Lipphardt, S. Weyers, C. Tamm and E. Peik, "High-accuracy optical clock based on the octupole transition in $^{171}Yb^+$," Phys. Rev. Lett., vol. 108, 090801, March 2012.

[4] A. A. Madej, P. Dubé, Z. Zhou, J. E. Bernard and M. Gertsvolf, "$^{88}Sr^+$ 445-THz single-ion reference at the 10^{-17} level via control and cancellation of systematic uncertainties and its measurement against the SI second", Phys. Rev. Lett., vol. 109, 203002, November 2012.

[5] T. P. Heavner, S. R. Jefferts, E. A. Donley, J. H. Shirley and T. E. Parker, "NIST-F1: recent improvements and accuracy evaluations", Metrologia, vol. 42, pp. 411–422, September 2005.

[6] F. Levi, D. Calonico, L. Lorini and A. Godone, "IEN-CsF1 primary frequency standard at INRIM: accuracy evaluation and TAI calibrations", Metrologia, vol. 43, pp. 545–555, November 2006.

[7] R. Li, K. Gibble and K. Szymaniec, "Improved accuracy of the NPL-CsF2 primary frequency standard: evaluation of distributed cavity phase and microwave lensing frequency shifts", Metrologia, vol. 48, pp. 283–289, August 2011.

[8] J. Guéna et al., "Progress in atomic fountains at LNE-SYRTE", IEEE Trans. Ultrason. Ferroelectr. Freq. Control, vol. 59, pp. 391–410, March 2012.

[9] S. Weyers, V. Gerginov, N. Nemitz, R. Li and K. Gibble, "Distributed cavity phase frequency shifts of the caesium fountain PTB-CSF2", Metrologia, vol. 49, pp. 82–87, November 2012.

[10] P. Gill, "When should we change the redefinition of the second?" Phil. Trans. Roy. Soc. London, vol. A369, pp. 4109–4130, October 2011.

[11] R. Le Targat et al., "Experimental realization of an optical second with strontium lattice clocks", Nature Communications, vol. 4, article no. 2109, July 2013.

[12] G. K. Campbell et al., "The absolute frequency of the ^{87}Sr optical clock transition", Metrologia, vol. 45, pp. 539–548, September 2008.

[13] F.-L. Hong et al., "Measuring the frequency of a Sr optical lattice clock using a 120 km coherent optical transfer", Opt. Lett., vol. 34, pp. 692–694, March 2009.

[14] S. Falke et al., "The ^{87}Sr optical frequency standard at PTB", Metrologia, vol. 48, pp. 399–407, September 2011.

[15] S. A. King et al., "Absolute frequency measurement of the $^2S_{1/2} - {}^2F_{7/2}$ electric octupole transition in a single ion of $^{171}Yb^+$ with 10^{-15} fractional uncertainty", New. J. Phys., vol. 14, 013045, January 2012.

[16] L.-S. Ma et al., "Optical frequency synthesis and comparison with uncertainty at the 10^{-19} level", Science, vol. 303, pp. 1843–1845, March 2004.

[17] D. Piester, M. Rost, M. Fujieda, T. Feldmann and A. Bauch, "Remote atomic clock synchronization via satellites and optical fibers", Advances in Radio Science, vol. 9, pp. 1–7, July 2011.

[18] P. A. Williams, W. C. Swann and N. R. Newbury, "High-stability transfer of an optical frequency over long fiber-optic links", J. Opt. Soc. Am. B, vol. 25, pp. 1284–1293, August 2008.

[19] F. Kéfélian et al., "High-resolution optical frequency dissemination on a telecommunications network with data traffic", Opt. Lett., vol. 34, pp. 1573–1575, May 2009.

[20] K. Predehl et al., "A 920-kilometer optical fiber link for frequency metrology at the 19th decimal place", Science, vol. 336, pp. 441–444, April 2012.

[21] T. E. Parker, "The uncertainty in the realization and dissemination of the SI second from a systems point of view", Rev. Sci. Instrum, vol. 83, 021102, February 2012.

A Space-Based Optical Kennedy-Thorndike Experiment Testing Special Relativity

Alexander Milke[†] Deborah N. Aguilera[*] Norman Gürlebeck[†] Thilo Schuldt[*†]
Sven Herrmann[†] Klaus Döringshoff[‡] Ruven Spannagel[*†] Claus Lämmerzahl[†]
Achim Peters[‡] Bernd Biering[*] Hansjörg Dittus[*] Claus Braxmaier[*†]
[*]German Aerospace Center (DLR), Institute for Space Systems, Bremen, Germany
[†]Center for Applied Space Technology and Microgravity (ZARM), University of Bremen, Germany
[‡]Institute for Physics, Humboldt University of Berlin, Germany

***Abstract*—We propose a small satellite mission that aims for testing the foundations of special relativity by performing a Kennedy-Thorndike (KT) experiment. A potential boost dependence of the velocity of light is measured by comparing a length reference (i.e. a highly stable optical resonator) with a molecular frequency reference. By employing clocks with 10^{-16} frequency stability at half orbit time (45 min) and by integration over 5000 orbits (2 years mission lifetime with 50% duty cycle) a 1600-fold improvement in measuring the Kennedy-Thorndike coefficient is targeted, compared to the current best terrestrial test.**

I. Introduction

Many candidates of a quantum theory of gravity, e.g. string theory and loop quantum gravity, predict a violation of the Lorenz symmetry at some scale. In order to test the fundamental assumptions of special relativity, a broader framework – a test theory – has to be considered, in which special relativity is embedded. This framework usually includes a set of parameters. For a specific choice of these parameters special relativity is recovered. The Robertson-Mansouri-Sexl (RMS) theory [9], [11] is such a test theory[1], which allows for a speed of light $c(\vec{v},\theta)$ that depends on the velocity of the frame with respect to some preferred frame[2], $\vec{v}$, and the orientation of the frame, θ:

$$\frac{c(\theta,\vec{v})}{c_0} = 1 + (\alpha - \beta + 1)\,\frac{\vec{v}^2}{c^2} + \left(\beta - \delta - \frac{1}{2}\right)\frac{v^2}{c^2}\sin^2\theta \tag{1}$$

The last term describes the anisotropy of light propagation and is limited by Michelson-Morley experiments to $\beta - \delta - \frac{1}{2} \leq (4 \pm 8)\cdot 10^{-12}$, cf. [6]. The Ives-Stilwell experiment measures the relativistic Doppler effect. The current most precise experiment yields $\left|\alpha + \frac{1}{2}\right| \leq 8.4 \cdot 10^{-8}$, cf [10]. The first term in Eq. (1) describes the velocity dependence of the velocity of light. The current best Kennedy-Thorndike experiments to measure this term were carried out by Tobar et al., see [4], and give for the KT coefficient $\alpha - \beta + 1 = -(4.8 \pm 3.7)\cdot 10^{-8}$. In the framework of the RMS theory, the Kennedy-Thorndike experiment, the Michelson-Morley experiment and the Ives-Stilwell experiment are sufficient to validate special relativity ($\alpha = -\frac{1}{2},\ \beta = \frac{1}{2},\ \delta = 0$).

[1]Other even more general test theories like the Standard Model Extension (SME) can be used as well, see e.g. [2], [7] and in particular [8] for the relation of the SME with the RMS.

[2]The frame in which the Cosmic Microwave Background is isotropic is a natural choice.

Here we propose a space mission that would improve the measurement of the KT coefficient by a factor of 1600. An improvement by a factor 100 is expected solely by going to space. This is due to an orbital velocity $v_{sat} \approx 7.4\frac{\mathrm{km}}{\mathrm{s}}$ of the satellite with 650 km altitude, which is about 25 times higher than that of a ground based laboratory. This would increase the amplitude of the variation of the speed of light in Eq. 1 by that factor. Furthermore, the shorter integration period of 90 min in a low earth orbit compared to 1440 min in a ground based laboratory gives an additional improvement by a factor 4. The rest of the improvement is due to employing better clocks.

Additionally, performing the KT experiment in space offers many advantages. For example, several noise sources like tidal effects and atmospheric pressure effects, which have the same period as the intended measured variation of c due to Lorentz violation are not present in space, and also mechanical distortions due to gravity are eliminated. The latter is especially relevant for the optical cavity described in the next section.

II. Payload configuration

A modern KT experiment is performed by comparing two frequency standards in a beat measurement, where one frequency reference depends on the explicit value of the speed of light - typically an optical cavity - and the second reference is independent of c - typically an atomic or molecular clock. Thus, if c depends on the velocity of the frame as discussed in Sec. I, then a modulation of the laboratory velocity would lead to a modulation of the recorded beat signal. In a satellite, this would yield to a beat signal varying with the orbital motion.

The principle setup is depicted in Fig. 1. In the experiment proposed here, we compare a laser at 1064 nm stabilized to an optical cavity and one laser at 532 nm stabilized to a hyperfine transition in molecular Iodine. In fact, one laser is sufficient if a frequency doubler and an AOM for frequency shifting is used. This would also suppress some common noise effects. However, for redundancy we included two lasers here. The frequency comparison is realized by recording their beat signal in the DMU. A space qualified version of a 1064 nm solid-state laser is available by Tesat Spacecom GmbH.

Laser frequency stabilization using optical cavities is realized in many laboratories worldwide. They utilize cavities made of thermally ultra stable materials such as Ultra Low

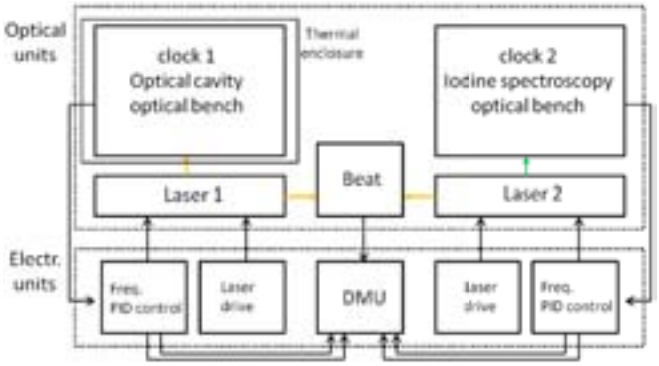

Fig. 1. Schematic representation of a Kennedy-Thorndike experiment. The beat frequency between a cavity stabilized laser and a molecular frequency reference based on Doppler-free Iodine spectroscopy is measured.

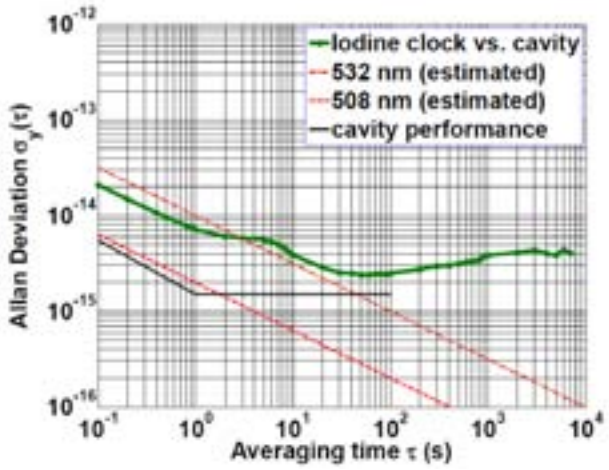

Fig. 2. Frequency stability of the Iodine based frequency reference developed in a collaboration of the University of Applied Sciences Konstanz and the Humboldt University of Berlin. The frequency stability was obtained by a beat measurement with a cavity setup.

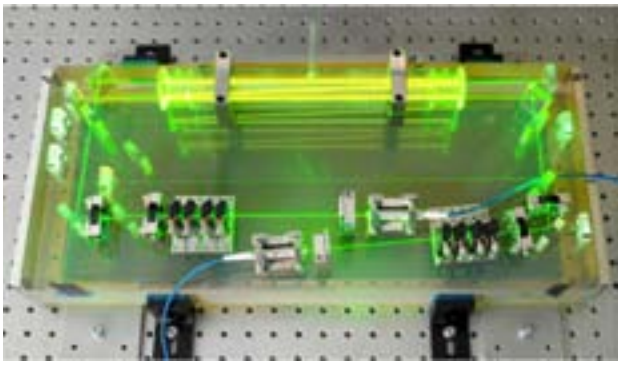

Fig. 3. Photograph of the Iodine based frequency reference realized on elegant breadboard (EBB) level. The baseplate made of OHARA Clearceram has dimensions of 25 cm x 55 cm x 5 cm [12].

Expansion (ULE) glass or Zerodur glass ceramics. State-of-the-art laboratory setups, as e. g. realized at the Humboldt University of Berlin show a frequency stability in the low 10^{-15} range at integration times of 100 s. Currently, several activities are ongoing, in order to develop a space-compatible high-finesse cavity stabilization setup [1], [5].

Also, Iodine based frequency reference is a well known technology, realized in a variety of laboratories. A setup on Elegant Breadboard (EBB) level was developed in a cooperation of the University of Applied Sciences Konstanz and the Humboldt University of Berlin, demonstrating $4 \cdot 10^{-15}$ frequency stability at integration times between 1 s and 10^4 s, cf. the measurement shown in Fig. 2 [3], [12]. The setup is realized using modulation transfer spectroscopy (MTS) and operates at a wavelength of 532 nm. It uses an OHARA Clearceram baseplate where the optical components are integrated using adhesive bonding technology, see 3. The dimensions of the spectroscopy unit are 25 cm x 55 cm x 10 cm. In a current DLR funded activity, a setup on EM (engineering model) level is developed based on the experiences gained with the EBB setup. The EM setup is further improved with respect to compactness and thermal and mechanical stability. After integration it will undergo environmental testing such as thermal cycling and vibration tests.

By switching to a nearby line at 508 nm wavelength an improvement in frequency stability by a factor of almost 10 is expected. However, this makes a development of a space qualified laser operating at that wavelength necessary.

III. Mission overview

The proposed mission housing a KT experiment has been designed to operate in a low earth orbit (LEO). The orbit will be circular and sun-synchronous in order to minimize temperature variations at the optical cavity as well as reducing the needs for radiation and thermal shielding. Meeting the science goals requires the temperature variations of the bus spacecraft interfaces to be < 1K at the orbit period.

The instrument is sensitive to mechanical vibrations in that a perturbation of the spacecraft bus will cause a change in the cavity length increasing the science signal noise. To minimize the spacecraft bus induced vibration, simple spin stabilization is used for attitude control and solar panels used to minimize the impact of thermal snap when transitioning through the eclipse.

The spacecraft will fly at 650 km orbital altitude with a 90 minutes orbital period. The designed mission will have 2 years lifetime with a 50% duty cycle. Therefore, by employing clocks with a 10^{-16} frequency stability at orbit time and by integration over 5000 orbits, a 1600-fold improvement in measuring the KT-coefficient is targeted.

The proposed mission corresponds to a small satellite technology, in which the space vehicle mass (including spacecraft bus and instruments) is estimated to 150 kg consuming 100 W of average power.

IV. Conclusion

The proposed mission with a modern Kennedy-Thorndike experiment is designed to test the symmetry of spacetime by measuring violations to the velocity independency of the speed of light, one of the fundamental postulates of special relativity. The orbital velocity and period will enhance any asymmetry signal 100 times respect to ground, therefore, it is planned to improve the KT coefficient 1600 times compared to previous experiments performed in laboratories.

ACKNOWLEDGMENT

The development of the Iodine frequency references on EBB and EM level is supported by the German Space Agency Deutsches Zentrum für Luft- und Raumfahrt (DLR) with funds provided by the Federal Ministry of Economics and Technology (BMWi) under grant numbers 50QT1102 and 50QT1201.

REFERENCES

[1] B. Argence, E. Prevost, T. Lévèque, R. Le Goff, S. Bize, P. Lemonde, and G. Santarelli. Prototype of an ultra-stable optical cavity for space applications. *Opt. Express*, 20(23):25409–25420, Nov 2012.

[2] D. Colladay and V. A. Kostelecký. Lorentz-violating extension of the standard model. *Phys. Rev. D*, 58:116002, 1998.

[3] K. Döringshoff, M. Reggentin, M. Nagel, E. Kovalchuk, A. Keetman, T. Schuldt, C. Braxmaier, and A. Peters. Iodine based optical frequency reference with 10^-15 stability. *Proceedings of the European Time and Frequency Forum, (EFTF 2012), Gothenburg (Sweden)*, 2012.

[4] M. E. Tobar et. al. *Phys. Rev. D*, 81(2):022003, 2010.

[5] W. M. Folkner, G. deVine, W. M. Klipstein, K. McKenzie, D. Shaddock, R. Spero, R. Thompson, D. Wuchenich, N. Yu, M. Stephens, J. Leitch, M. Davis, J. deCino, C. Pace, and R. Pierce. Laser frequency stabilization for grace-ii. *Proceedings of the Earth Science Technology Forum, Arlington, Virginia, June 22, 2010*, 2010.

[6] S. Herrmann, A. Senger, K. Möhle, M. Nagel, E. V. Kovalchuk, and A. Peters. Rotating optical cavity experiment testing lorentz invariance at the 10^{-17} level. *Phys. Rev. D*, 80:105011, 2009.

[7] V. A. Kostelecký. Gravity, Lorentz violation, and the standard model. *Phys. Rev. D*, 69(10):105009, 2004.

[8] V. A. Kostelecký and M. Mewes. Electrodynamics with Lorentz-violating operators of arbitrary dimension. *Phys. Rev. D*, 80(1):015020, July 2009.

[9] R. Mansouri and R. U. Sexl. *Gen. Rel. and Grav.*, 8:497–513, 1977.

[10] S. Reinhardt, G. Saathoff, H. Buhr, L. A. Carlson, A. Wolf, D. Schwalm, S. Karpuk, C. Novotny, G. Huber, M. Zimmermann, R. Holzwarth, T. Udem, T. W. Hänsch, and G. Gwinner. Test of relativistic time dilation with fast optical atomic clocks at different velocities. *Nature Physics*, 3:861–864, December 2007.

[11] H. P. Robertson. *Rev. Mod. Phys.*, 21:378–382, 1949.

[12] T. Schuldt, A. Keetman, K. Döringshoff, M. Reggentin, E. Kovalchuk, M. Nagel, M. Gohlke, U. Johann, D. Weise, A. Peters, and C. Braxmaier. An ultra-stable optical frequency reference for space applications. *Proceedings of the European Time and Frequency Forum (EFTF 2012), Gothenburg (Sweden)*, 2012.

CMOS-MEMS Resonators and Their Applications

Sheng-Shian Li
Institute of NanoEngineering and MicroSystems, National Tsing Hua University, Hsinchu, Taiwan
Email: ssli@mx.nthu.edu.tw

Abstract—**This paper reports on the recent progress of the high-*Q* integrated micromechanical resonator, oscillator, and filter using the "CMOS-MEMS technology" to enable monolithic integration of MEMS and IC. The paper scope covers three major parts, including (i) the fabrication technologies of the CMOS-MEMS resonators and their associated circuitry; (ii) the performance enhancement of the resonators on motional impedance, quality factor, power handling, thermal stability, frequency tuning, and parasitic feedthrough; (iii) the implementation of the CMOS-MEMS resonators for frequency generation (i.e., oscillators) and frequency selection (i.e., filters) functionalities. In the first part, various fabrication technologies in the 0.35μm and 0.18μm CMOS technology nodes are presented, showing their own features and advantages. In the second part, several strategies in design aspects and material point of views were proposed to enhance the performance of the CMOS-MEMS resonators. In the last part, designs and experimental results of the CMOS-MEMS oscillator and filter are presented. We take full advantage of the IC and semiconductor strength in Taiwan to develop several CMOS-MEMS resonator platforms towards single-chip implementation for timing reference, oscillator, filter, and sensor applications.**

Keywords-CMOS-MEMS; Resonator; Integration; High Q; Power Handling; Motional Impedance; Thermal Stability; Frequency Tuning; Feedthrough Cancellation; Oscillator; Filter

I. Introduction

Mechanical resonators are the key element for frequency control where the high-*Q* tanks implemented by the resonators form crucial building blocks, including frequency generation, frequency selection, and even sensing. Off-chip vibrating components, such as quartz and SAW (surface acoustic wave) devices, have dominated this market for more than fifty years. However, their bulky size and CMOS incompatibility hinders the miniaturization of electronic systems and impedes the cost-down and integration for portable applications. In order to reduce size, power consumption, and increase quality factor, vibrating micromechanical circuits fabricated using IC-compatible MEMS technologies have been developed in the past decade towards the integration with on-chip RF transistor circuits [1]. However, prior approaches for the CMOS-MEMS integration leads to complexity and compromise of fabrication processes, impeding the fast cycling time of product development and causing huge barriers for MEMS design houses. As a solution, the foundry-oriented CMOS-MEMS platform provides ease of use, fast prototyping, and circuit integrated features for vibrating RF-MEMS applications.

As depicted in Fig. 1, this paper reviews several generalized platforms utilizing the foundry CMOS technologies [2], showing several unique features, such as ease of use, low cost, fast turnaround time, and innate MEMS-circuit integration.

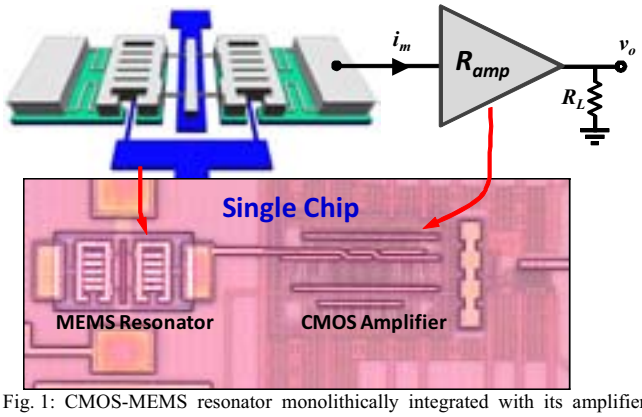

Fig. 1: CMOS-MEMS resonator monolithically integrated with its amplifier circuitry.

With such a resonator platform, various configurations of CMOS-MEMS resonators monolithically integrated with circuits have been demonstrated as shown in Fig. 1.

II. Fabrication Technologies

We have developed several CMOS-MEMS resonator platforms [3][4][5][6] co-fabricating mechanical resonators and their amplifier circuits for MEMS/IC integration. The platforms can be mainly categorized into two different release methods - oxide removal and metal removal maskless post-CMOS processes, implemented in both 0.35μm 2-Poly-4-Metal (2P4M) and 0.18μm 1-Poly-6-Metal (1P6M) CMOS technologies. In the following contents, their pros and cons will be discussed.

A. Oxide Removal Release Process in a 0.35μm CMOS [3]

Fig. 2 presents the cross-section of the 0.35μm CMOS process, clearly showing its two polysilicon layers and four metal interconnect layers, respectively, and the fabricated

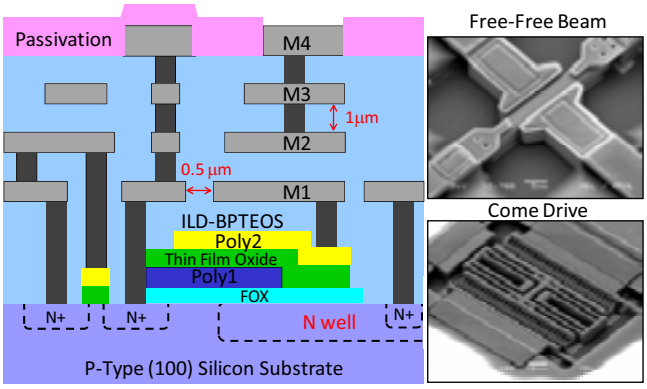

Fig. 2: Chip cross-sectional view and SEM photos of the fabricated resonators using the oxide removal release process in a 0.35μm CMOS technology.

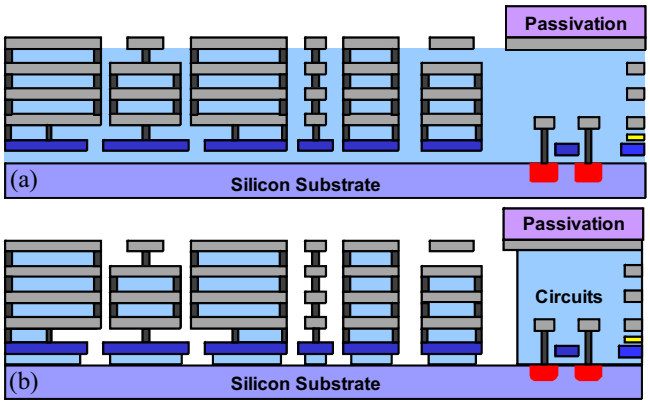

Fig. 3: Fabrication process flow for a CMOS-MEMS resonator in a 0.35µm 2P4M technology under the oxide removal post process. (a) Chip prepared by the CMOS foundry. (b) Device is released by a buffer HF solution.

resonators, such as beam and come-drive resonators, can be seen in the right. The fabrication flow is quite simple as shown in Fig. 3 where the device can be released in a commercially available buffer HF solution, Silox Vapox III. Fig. 3(b) indicates that (i) various resonators, such as in-plane and out-of-plane versions, and (ii) different combinations of the structural materials, such as mere metal and metal/oxide composite, can be realized in this platform to offer more flexible design options. Note that the minimal electrode-to-resonator gap spacing is limited by the feature size of the 0.35µm CMOS technology node such that the motional impedance of the fabricated resonators is in several MΩ due to their low electromechanical coupling coefficient.

B. Oxide Removal Release Porcess in a 0.18µm CMOS [4]

To address the issue of high motional impedance in section II.A, we transfer this oxide removal process into a 0.18µm CMOS where the cross-sectional schematic and physical views are shown in Fig. 4. The electrode-to-resonator gap spacing is reduced via the minimal feature size of the 0.18µm CMOS (1.8X smaller than the 0.35µm CMOS) while the transducer area can be increased by the 6-metal stacking (4-metal stacking in the 0.35µm CMOS). The combined merit of the gap and area contributes to much lower motional impedance as compared to the 0.35µm CMOS-MEMS resonators. Fig. 5 presents the performance comparison between the 0.35µm 2P4M and 0.18µm 1P6M platforms, showing the advanced technology nodes would lower the motional impedance, reduce the dc-bias voltage, and attain

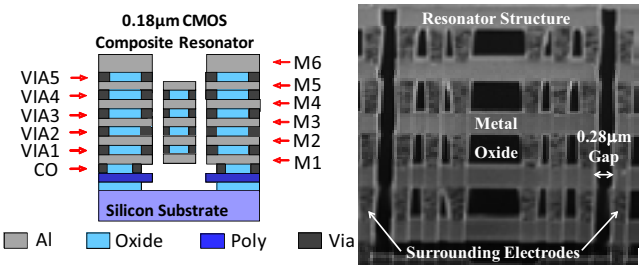

Fig. 4: CMOS-MEMS resonator in a 0.18µm 1P6M CMOS-MEMS platform.

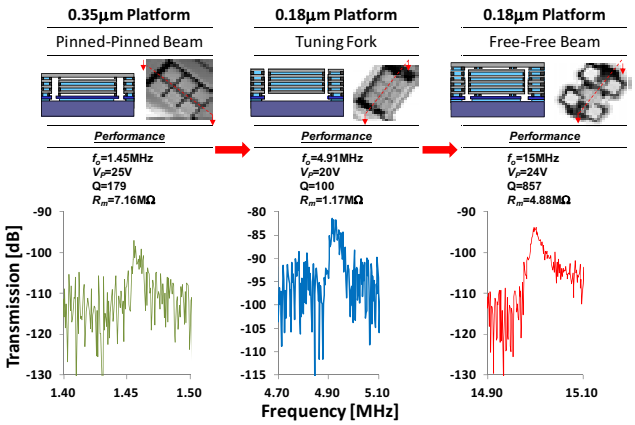

Fig. 5: Performance comparison of the CMOS-MEMS resonators in 0.35µm 2P4M and 0.18µm 1P6M CMOS-MEMS platforms.

higher resonance frequencies.

C. Metal Removal Release Process in a 0.35µm CMOS [5]

Although the oxide removal process only requires one maskless wet etching step, the metal-rich feature of the aforementioned resonators places a bottleneck on quality factor Q since the structural aluminum is often treated as a high-loss acoustic material. As can be seen in Fig. 5, Q is lower than 1,000, which is not sufficient for the later oscillator and filter implementation. To address low-Q issue in the oxide removal process, we proposed a metal removal post process to form low-loss oxide-rich resonator structures to enable high Q.

As indicated in Fig. 6, the device was first prepared by the CMOS foundry using a standard 0.35µm 2P4M CMOS process. Then the etching solution containing H_2SO_4 and H_2O_2 was utilized to remove metal layers. This maskless etching technique provides excellent selectivity between the metal and dielectric layers; therefore, the issues from time-based etching in part II.A and II.B can be greatly alleviated. Finally, Reactive Ion Etching (RIE) was used to remove the passivation layer for the following wire bonding. Fig. 7 presents a resonator SEM view, an integrated CMOS-MEMS

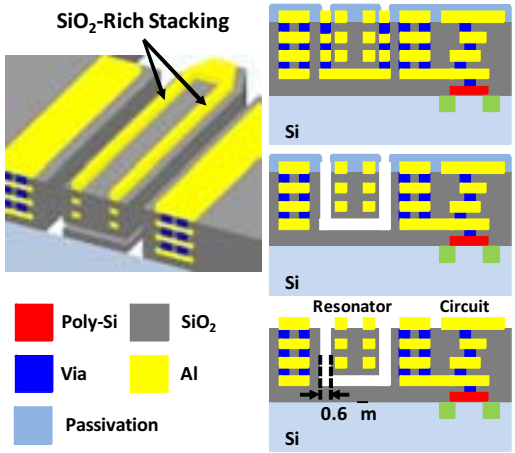

Fig. 6: CMOS-MEMS resonator using the metal removal post process in a 0.35µm 2P4M CMOS-MEMS platform.

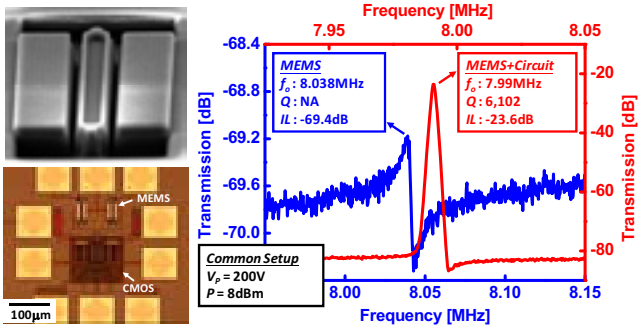

Fig. 7: Performance of a 0.35μm CMOS-MEMS resonator using the metal removal post process.

system, and their frequency characteristics including the standalone resonator and MEMS/IC integrated version. Q of the oxide-rich resonator is greater than 6,000, which is 6X higher than the metal-rich counterparts in Fig. 5.

D. Metal Removal Release Process in a 0.18μm CMOS [6]

The release approach in part II.C has also been transferred into a 0.18μm CMOS node as shown in Fig. 8 to gain the smaller feature size of the advanced CMOS for low motional impedance. To fabricate the CMOS-MEMS double-ended-tuning-fork (DETF) oxide-rich resonator in Fig. 8, chips were manufactured using a standard TSMC 0.18μm 1P6M CMOS process. Then a metal wet etchant was utilized to remove the sacrificial metals, hence providing air gap spacing of around 0.53μm. Finally, the RIE was utilized to open bond pads. Fig. 8 also presents a cross-sectional image of the DETF structure and its measured frequency characteristic, showing Q greater than 4,800 due to its oxide-rich feature. The achievable resonance frequency is higher than that of the device in part II.C (Fig. 5) owing to its smaller gap spacing via the 0.18μm CMOS.

III. Motional Impedance

The major bottleneck of the capacitive resonators comes

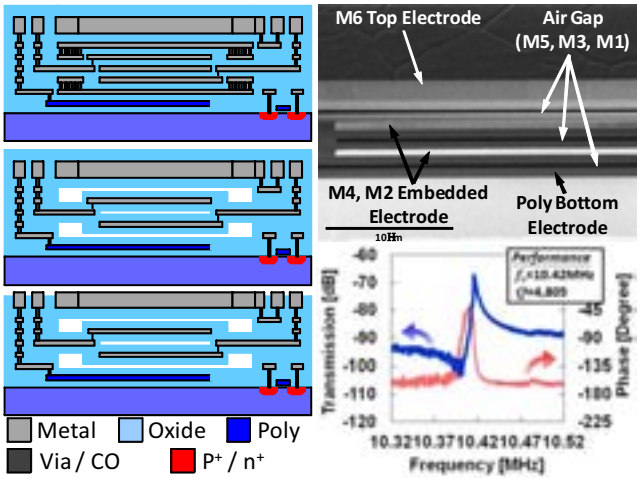

Fig. 8: Fabrication process flow, SEM, and frequency response for a CMOS-MEMS resonator in a 0.18μm 1P6M technology under the metal removal post process.

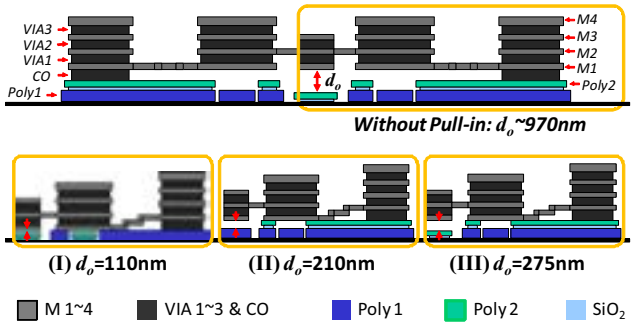

Fig. 9: Pull-in gap reduction mechanism implemented in a 0.35μm CMOS-MEMS resonator for motional impedance reduction.

from the relatively higher motional impedance (often much larger than 50Ω) due to their low electromechanical coupling capability which is several orders of magnitude lower than that of the piezoelectric counterparts. The CMOS-MEMS resonators inherit such a deficiency where the motional impedance is typically several MΩ as indicated in Fig. 5 [3][4]. The limit of the electromechanical coupling stems from the minimum feature size of the CMOS technologies as described in section II, even if advanced technology nodes are utilized. Here, we proposed several approaches in design aspects to greatly reduce the motional impedance of the CMOS-MEMS resonators without pursuing costly, nm-regime CMOS processes.

A. Pull-in Gap Reduction Design

Based on the pull-in mechanism of capacitive transducers, we proposed an effective gap reduction approach [7] in a standard CMOS-MEMS technology to reduce the electrode-to-resonator gap spacing without the need of advanced CMOS nodes, hence providing a cost-effective solution to alleviate performance degradation using conventional CMOS-MEMS platforms. With the well-known electrostatic pull-in effect, various gap-reduction configurations utilizing the existing layers of the 0.35 μm 2P4M CMOS technology have been demonstrated to achieve deep-submicron gaps, significantly lower the motional impedance of the resonators to 100kΩ range suitable for oscillator implementation. Using the gap reduction mechanism depicted in Fig. 9, beam resonators with gaps of 110nm, 210nm, and 275nm, respectively, have been successfully demonstrated that achieves comparable electro-

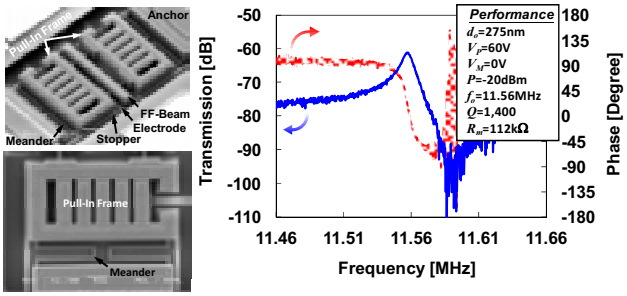

Fig. 10: SEMs and measured frequency characteristic of a 0.35μm CMOS-MEMS resonator under a pull-in gap reduction design to achieve low motional impedance.

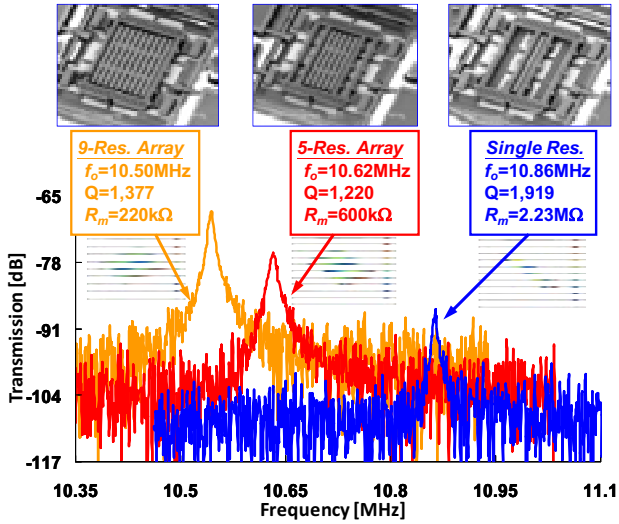

Fig. 11: Comparison of single resonator and 9-resonator array under the same motional impedance and input power.

mechanical coupling [2], as shown in Fig. 10, with their non-CMOS-MEMS counterparts [1].

B. *Mechanically-Coupled Array Design*

Under the same 0.35μm CMOS-MEMS resonator platform, a mechanically-coupled array design [8] offers an efficient approach to reduce the motional impedance which is inversely proportional to the number of the constituent resonators in an array device. More resonators mechanically coupled as an array, the smaller motional impedance. Since the coupled array becomes a multi-degree-of-freedom mechanical system, a high-velocity coupling scheme was used to accentuate the desired mode shape and reject the spurious modes. As shown in Fig. 11, the proposed 9-resonator and 5-resonator arrays [8] have been experimentally characterized to have 10.1X and 3.7X smaller motional impedances, respectively, as compared to a single resonator. In addition, the resonator array is benefitted from the large transduction area to effectively reduce the required dc-bias voltage while maintaining reasonable motional impedance.

IV. Quality Factor

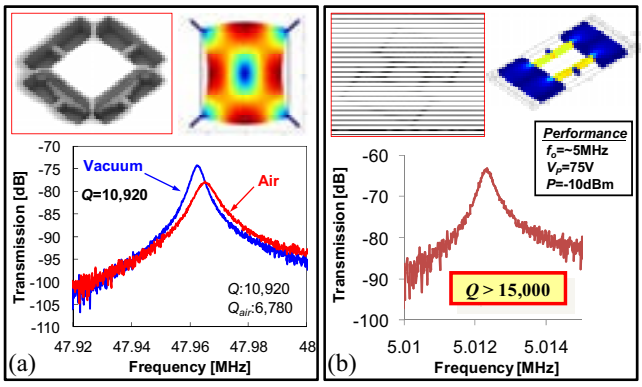

Fig. 12: (a) Lame-mode and (b) longitudinal-mode CMOS-MEMS resonators feature Q > 10,000, verifying high Q of bulk-mode designs.

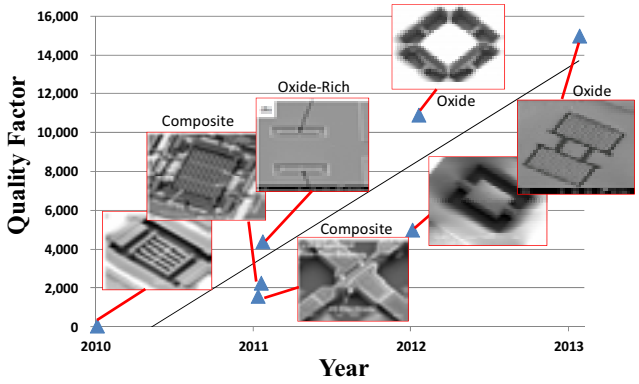

Fig. 13: Progress on quality factor of the CMOS-MEMS resonators developed in our group.

As compared to the single-crystal or polysilicon based MEMS resonators, Q of the CMOS-MEMS resonators becomes a main issue to be used in timing reference and wireless applications. Due to the lossy nature of the metal materials in the CMOS back-end-of-line (BEOF) configuration, CMOS-MEMS metal-rich composite resonators often suffer Q limited to 1,000 as indicated in Fig. 5. We have proposed several approaches to resolve this bottleneck.

A. *Nodal Support Design*

Q in MEMS resonators is often dominated by the support loss once they are operated in vacuum and the thermal elastic damping is avoided by the designed frequencies. We have adopted a nodal support design [8][9] to effectively isolate the vibrating energy of the resonant structure from its anchors, thus verifying Q of the nodal support design is two orders of magnitude higher than that of the conventional designs [7].

B. *Oxide-Rich Design*

In addition to the nodal support design, material loss also plays a significant role on resonator Q. A simple way to overcome this structural loss is to increase the constituent ratio of the SiO_2 (i.e., low-loss material) inside the resonator, thus enabling high Q. We took advantage of the metal removal post process described in section II.C and II.D to form oxide-rich resonators since SiO_2 is treated as high-Q structural material. The oxide-rich CMOS-MEMS resonators [5][6] in Fig. 7 and Fig. 8 feature 3-4X higher Q than that of the metal-rich versions in Fig. 5. Please note the flexural-mode vibration now becomes the limiting factor once the oxide constituent ratio is maximized.

C. *Bulk-Mode Design*

To further boost Q of the CMOS-MEMS resonators, the flexural-mode design can be switched into a bulk-mode vibration. Fig. 12 presents the measured frequency characteristics of Lame-mode [10] and dog-bone like [11] CMOS-MEMS resonators with Q greater than 10,000, indicating the high-Q nature of the bulk-mode resonators. With proper structural materials and resonator designs, we

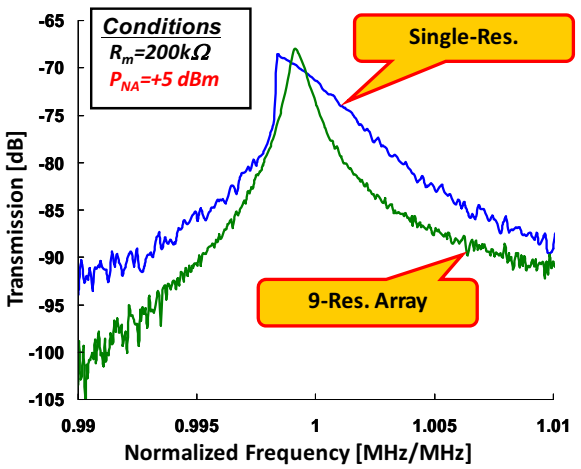

Fig. 14: Comparison of the single resonator and 9-resonator array under the same motional impedance and input power.

have proved Q of the CMOS-MEMS resonators is comparable to the silicon-based resonators.

Fig. 13 finally presents the progress on quality factor of our proposed CMOS-MEMS resonators in the past four years. As can be seen, Q greater 10,000 has been realized by the combination of the nodal support design, oxide-rich structural material, and bulk-mode operation, thus greatly benefiting the future oscillator and filter applications.

V. Power Handling and Linearity

Upon high input power levels, capacitive resonators often suffer the Duffing nonlinearity resulted from both capacitive and mechanical nonlinearities, hence degrading output power and phase noise performance of oscillators implemented using those resonators. The mechanically-coupled array design [8] described in section III.B not only reduces their motional impedance but greatly enhances the power handling capability since the effective stiffness of the N-resonator array ideally is N times higher than that of a single resonator, thus contributing N times larger power handling ability. Fig. 14 presents the frequency characteristics of single resonator and 9-resonator array designs under the same input power, where the former falls into the nonlinear regime while the later still preserves the linear vibration with a symmetrical frequency response and high Q.

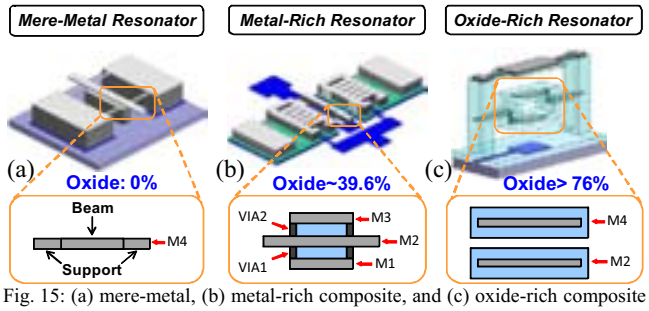

Fig. 15: (a) mere-metal, (b) metal-rich composite, and (c) oxide-rich composite structures of CMOS-MEMS resonators to modulate TC_f.

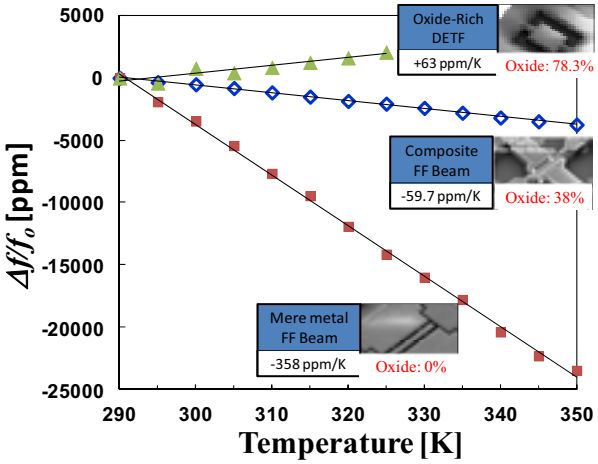

Fig. 16: Temperature coefficient of frequency in CMOS-MEMS resonators can be adjusted by the constituent ratio of SiO_2.

VI. Thermal Stability

A. Passive Temperature Compensation

The CMOS-MEMS resonators mostly composed of metals are sensitive to temperature variation due to the very negative temperature coefficients of Young's modulus (TC_E's) of their constituent metal materials. To improve the thermal stability of those CMOS-MEMS resonators, the silicon-dioxide (SiO_2) in the CMOS back-end-of-lone (BEOL) process with positive TC_E offers a simple "passive" temperature compensation scheme where metal-oxide composite structures can be utilized to build resonators capable of improving their thermal stability [3]. For example, the oxide constituent ratio of the CMOS-MEMS resonators can be adjusted as indicated in Fig. 15 where the mere-metal, metal-rich, and oxide-rich structures would lead to very negative, slightly negative, and very positive temperature coefficients of frequency (TC_f's). Fig. 16 presents the comparison of fractional frequency change versus temperature measurements for mere-metal, metal-rich composite, and oxide-rich composite beam resonators, verifying our design concept in Fig. 15 and indicating the near-zero TC_f is plausible once the ratio between SiO_2 and metal is optimized. Thus, the use of SiO_2 as part of the composite structures in CMOS-MEMS resonators brings an easy and effective temperature compensation scheme [2].

B. Active Temperature Compensation

To further enhance the thermal stability of the CMOS-MEMS resonators down to ppm level, a constant-resistance control [12] was implemented as a low-cost active compensation scheme with which TC_f of the CMOS-MEMS resonators was dramatically improved with a record-low value, -12.5 ppm/K [11], to date among any CMOS-MEMS resonators. Note that the polysilicon layers from the CMOS BEOL process are embedded inside the proposed resonator structures, serving as the key element for the constant-resistant control.

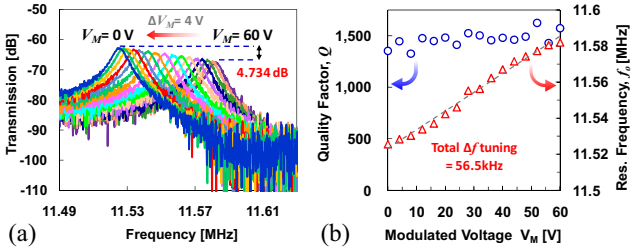

Fig. 17: (a) Frequency tuning capability and (b) steady Q under different modulated voltages.

VII. Frequency Tuning

With enhanced TC_f through the use of both the passive and active temperature compensation approaches mentioned in section VI, the CMOS-MEMS resonators simply demand a linear frequency tuning mechanism with low cost and low power consumption for final temperature compensation. In the high-end applications, frequency tuning capability is necessitated. On the other hand, initial frequency trimming of batch-fabricated resonators is also of great importance for commercialization. The resonance frequency of capacitive-type MEMS resonators can be tuned via their dc-bias voltages through the electrical stiffness; however, the change of motional impedance as well as the parabolic relationship between the bias voltage and frequency makes such a post-fabrication trimming technique not suitable for real implementation. To solve this issue, we proposed a quasi-linear frequency tuning via the adjustment of an independent bias voltage [2] without consuming any dc power, showing 5,000 ppm tuning range and sensitivity of 83.3 ppm/V, as shown in Fig. 17(a). In addition, such resonators under frequency tuning operation still preserve steady quality factor Q with very limited influence on motional impedance as shown in Fig. 17(b), hence ensuring stable resonant performance suited for future oscillator and time-keeping applications.

VIII. Feedthrough

The differential pair of CMOS amplifiers is often used to remove the common-mode noise and to preserve correct transmission and phase even with the presence of the parasitic capacitances. The weak electromechanical coupling makes the capacitive resonators very sensitive to parasitic feedthroughs

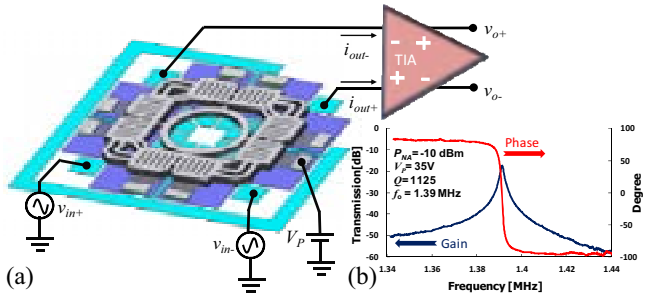

Fig. 18: (a) Fully-differential CMOS-MEMS circuit and (b) its measured frequency characteristic.

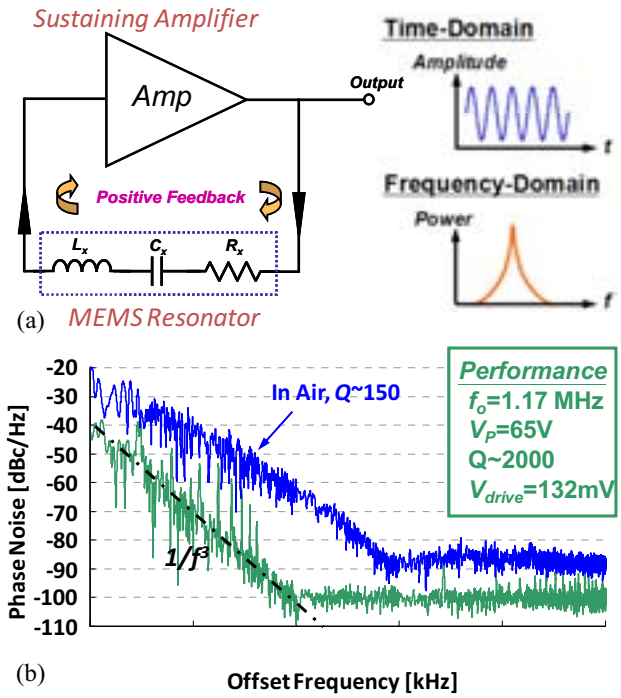

Fig. 19: (a) Closed-loop oscillation and (b) phase noise performance of a CMOS-MEMS oscillator.

since the resonance behavior (i.e., the motional current) is often masked by the feedthrough signals. Therefore, similar concept has been implemented in capacitive resonators to cancel the feedthroughs. A CMOS-MEMS ring resonator featuring differential-mode of mechanical operation was integrated with a fully-differential transimpedance amplifier as shown in Fig. 18, demonstrating a clear resonance behavior where the transmission amplitude is quite symmetric without anti-resonance while its phase is cross 0° at resonance [13]. With the fully-differential configuration applied both on MEMS and IC, Barkhausen criteria can be easily fulfilled for oscillator implementation.

IX. Oscillator Implementation

After addressing the bottlenecks and proposing solutions to enhance performance of the CMOS-MEMS resonators, the oscillator implementation is of great importance for timing and frequency synthesizing applications. As depicted in Fig. 19(a), the micromechanical resonator and its sustaining amplifier can form a closed loop to ensue oscillation once Barkhausen criteria (loop gain >1 and loop phase = 0°) are satisfied. In our group, a single-chip CMOS-MEMS oscillator has been successfully demonstrated in vacuum, exhibiting the phase noise performance, as shown in Fig. 19(b), is comparable to the silicon-based oscillators. Even in air (i.e., large squeeze film damping), the oscillator was still functional, indicating the great potential to be used in gas, chemical, and mass sensing application based on frequency-shift mechanism. The abovementioned approaches to improve quality factor and

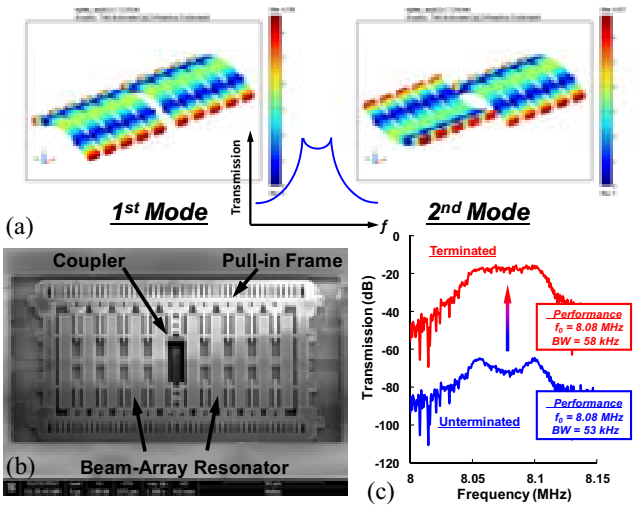

Fig. 20: (a) Simulated filter modes, (b) SEM view, and (c) un-terminated and terminated frequency response of a mechanically coupled CMOS-MEMS filter.

power handling of the CMOS-MEMS resonators would benefit the close-to-carrier and far-from-carrier phase noise performance, respectively, of the implemented oscillators. In addition, the reduction of the motional impedance described in section III would lead to the overall phase noise reduction for the CMOS-MEMS integrated oscillators.

X. Filter Implementation

Another significant building block for frequency control and wireless communication is the frequency selection element. The developed CMOS-MEMS resonators can serve as the fundamental elements for bandpass filters. Since the resonance frequency of the CMOS-MEMS resonators is limited, it is best to be used in sensors front-end with much lower operation frequencies. Fig. 20 presents a CMOS-MEMS filter composed of two CMOS-MEMS resonator arrays mechanically coupled through a quarter-wavelength mechanical link to enable a narrow-bandwidth bandpass filter for channel selection [14]. The in-phase and out-of-phase filter modes shown in Fig. 20(a) form the passband of a filter. The fabrication is the same as the CMOS-MEMS resonators in section II.A and the SEM view of the fabricated filter is shown in Fig. 20(b). After filter termination, a flat passband and real insertion loss can be obtained as shown in Fig. 20(c).

XI. Conclusions

In the past few years, the CMOS-MEMS technology has been thoroughly explored and implemented in vibrating MEMS applications. The CMOS-MEMS resonator fabrication platforms bring low cost, batch production, fast turnaround time, and MEMS/IC integration to the resonator applications. Most of the bottlenecks in CMOS-MEMS resonators, including motional impedance, quality factor, power handling/linearity, thermal stability, frequency tuning, and feedthrough issues, have been addressed using various design and material strategies. In addition, the oscillator and filter implementation is also covered in this paper. This technology is expected to pave a way to realize fully-integrated high-performance CMOS-MEMS oscillators and filters which would benefit future single-chip transceivers for wireless communications.

Acknowledgment

This work was supported by the National Science Council of Taiwan under grant of NSC-101-2628-E-007-008-MY2 and the Toward World-Class University Project. The authors also wish to thank the TSMC and National Chip Implementation Center (CIC), Taiwan, for supporting the IC Manufacturing.

References

[1] C. T.-C. Nguyen, "MEMS technology for timing and frequency control," *IEEE Transactions on Ultrasonics, Ferroelectrics and Frequency Control*, vol. 54, no. 2, pp. 251-270, Feb. 2007.

[2] W.-C. Chen, W. Fang, and S.-S. Li, "High-*Q* integrated CMOS-MEMS resonators with deep-submicron gaps and quasi-linear frequency tuning," *IEEE/ASME J. Microelectromech. Syst.*, vol. 21, no. 3, pp. 688-701, June 2012.

[3] W.-C. Chen, W. Fang, and S.-S. Li, "A generalized CMOS-MEMS platform for micromechanical resonators monolithically integrated with circuits," *J. Micromech. Microeng.*, vol. 21, no. 6, pp. 065012, May 2011.

[4] C.-S. Li, L.-J. Hou, and S.-S. Li, "Advanced CMOS-MEMS resonator platform," *IEEE Electron Device Letters*, vol. 33, no. 2, pp. 272-274, Feb. 2012.

[5] Y.-C. Liu, M.-H. Tsai, W.-C. Chen, M.-H. Li, S.-S. Li, and W. Fang, "Temperature-compensated CMOS-MEMS oxide resonators," *IEEE/ASME J. Microelectromech. Syst.*, in press.

[6] W.-C. Chen, M.-H. Li, Y.-C. Liu, W. Fang, and S.-S. Li, "A fully-differential CMOS-MEMS DETF oxide resonator with *Q* > 4,800 and Positive TCF," *IEEE Electron Device Letters*, vol. 33, no. 5, pp. 721-723, May 2012.

[7] M.-H. Li, W.-C. Chen, and S.-S. Li, "Realizing deep-submicron gap spacing for CMOS-MEMS resonators," *IEEE Sensors Journal*, vol. 12, no. 12, pp. 3399-3407, Dec. 2012.

[8] M.-H. Li, W.-C. Chen, and S.-S. Li, "Mechanically-coupled CMOS-MEMS free-free beam resonator arrays with enhanced power handling capability," *IEEE Transactions on Ultrasonics, Ferroelectrics, and Frequency Control*, vol. 59, no. 3, pp. 346-357, March 2012.

[9] M.-H. Li, W.-C. Chen, and S.-S. Li, "CMOS-MEMS transverse-mode square plate resonator with high Q and low motional impedance," *Dig. of Tech. Papers*, the 16th Int. Conf. on Solid-State Sensors & Actuators (Transducers'11), Beijing, China, June 5-9, 2011, pp. 1500-1503.

[10] W.-C. Chen, W. Fang, and S.-S. Li, "VHF CMOS-MEMS oxide resonators with *Q* > 10,000," *Proceedings*, 2012 IEEE Int. Frequency Control Symp., Baltimore, Maryland, May 21-24, 2012, pp. 581-584.

[11] C.-S. Li, M.-H. Li, C.-H. Chin, C.-Y. Chen, P. X.-L. Feng, and S.-S. Li, "A piezoresistive CMOS-MEMS resonator with high *Q* and low TC_f," to be presented in the 2013 IEEE UFFC Joint Symposia, Prague, Czech Republic, July 21-25, 2013.

[12] C.-C. Chen, H.-T. Yu, K.-H. Lee, and S.-S. Li, "Enhancement of temperature stability via constant structural-resistance control for MEMS resonators," *Proceedings*, 26th IEEE Int. Micro Electro Mechanical Systems Conf. (MEMS'13), Taipei, Taiwan, Jan. 20-24, 2013, pp. 765-768.

[13] V. Pachkawade, M.-H. Li, C. S. Li, and S.-S. Li, "A CMOS-MEMS resonator integrated system for oscillator application," *IEEE Sensors Journal*, in press.

[14] C.-Y. Chen, M.-H. Li, C.-S. Li, and S.-S. Li, "Design and characterization of mechanically-coupled CMOS-MEMS filters," *Dig. of Tech. Papers*, the 17th Int. Conf. on Solid-State Sensors & Actuators (Transducers'13), Barcelona. Spain, June 16-20, 2013.

2DEG Electrodes for Piezoelectric Transduction of AlGaN/GaN MEMS Resonators

Laura C. Popa and Dana Weinstein
Massachusetts Institute of Technology
Cambridge, MA, USA

***Abstract*—A 2D electron gas (2DEG) interdigitated transducer (IDT) in Gallium Nitride (GaN) resonators is introduced and demonstrated. This metal-free transduction does not suffer from the loss mechanisms associated with more commonly used metal electrodes. As a result, this transducer can be used for both the direct interrogation of GaN electromechanical properties and the realization of high *Q* resonators. A 1.2 GHz bulk acoustic resonator with mechanical *Q* of 1885 is demonstrated, with frequency quality factor product (*f*·*Q*) of 2.3×10^{12}, the highest measured in GaN to date.**

Keywords-MEMS Resonator, IDT, Gallium Nitride, 2DEG, Compund Semiconductor, Piezoelectricity

I. INTRODUCTION

Monolithic integration of micro-electromechanical (MEM) resonators can provide basic RF and mm-wave building blocks with high *Q* and small footprint for use in wireless communication, microprocessor clocking, navigation and sensing applications. Direct integration of MEMS with standard integrated circuits (ICs) is motivated primarily by improved size, weight and power (SWaP), and relaxed constraints on IOs and on impedance matching [1]. Moreover, for high frequency applications (UHF band and above), this integration side-by-side with control circuits is critical for the elimination of parasitics associated with bond pads and off-chip routing.

The majority of IC integration efforts for resonators have focused on Si-based and metal-based MEMS in CMOS [2,3,4,5] where transduction mechanisms are limited to electrostatic, thermal, and piezoresistive transduction. However, many opportunities exist for MEMS in piezoelectric III-V materials used for mm-wave ICs (MMICs). Wide band-gap compound semiconductors such as GaN are used increasingly for high power (>10W/mm), high frequency (>100 GHz) applications due to high electron velocity, charge density (1×10^{13} cm^{-2} in AlGaN/GaN), and critical electric field >3 MV/cm. In its Wurtzite crystal structure, GaN also exhibits high piezoelectric coefficients (k_T^2 up to 2%) necessary for low insertion loss, large bandwidth MEMS filters.

The AlGaN/GaN heterostructure used to form High Electron Mobility Transistors (HEMTs) for MMICs is typically grown on SiC, diamond, or sapphire substrates to ensure high quality material [6]. However, the cost of such substrates has prompted the development of GaN on (111) Si. As this is a relatively new technology, material growth optimization is an active field of study. While ample information is available on the electrical properties of GaN on Si, electromechanical characterization is lacking. In this work we demonstrate AlGaN/GaN resonators that can be used to intimately interrogate the electromechanical properties of GaN. These resonators are driven piezoelectrically using 2DEG interdigitated transducers (IDTs). This metal-free transduction allows for the elimination of losses associated with metal electrodes typically used in piezoelectric resonators.

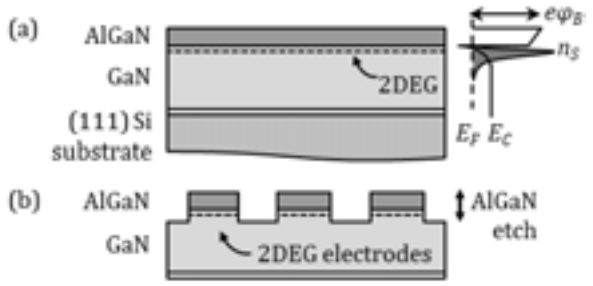

Figure 1. AlGaN/GaN heterostructure on (111) Si. (a) A 2DEG is confined in the conduction band potential well at the interface between AlGaN and GaN. (b) 2DEG electrodes are patterned via a shallow AlGaN etch.

II. DISSIPATION MECHANISMS IN MEMS RESONATORS

In order to isolate the intrinsic mechanical properties of GaN, it is necessary to minimize other loss mechanisms that limit the *Q* of a MEMS resonator. These losses can be classified into extrinsic dissipation mechanisms, which are design-dependent, and intrinsic ones, which depend on the properties and quality of the material [7]. Dominant extrinsic loss mechanisms include anchor loss and air damping. The energy dissipated into the substrate can be minimized through an appropriate anchor design. Meanwhile, air damping is less significant for high frequency bulk modes, and can be eliminated by operation at low pressure. Intrinsic mechanisms include thermoelastic damping (TED), phonon-electron scattering and phonon-phonon scattering. While TED becomes less significant in the case of high frequency bulk modes and phonon-electron interactions are not a limiting mechanism in semiconductors, phonon-phonon scattering defines the fundamental limit of resonator *Q* [8].

A study of this fundamental limit is required to interrogate the acoustic performance of various GaN growth processes. However, most piezoelectric transducers are realized using metal electrodes. Metal electrodes result in added acoustic losses, and contribute to mode distortion through mass loading. In AlN, efforts to minimize losses associated with metal in piezoelectric resonators have included physically separating the

electrodes from the piezoelectric film [9] and segmentation of IDT metal electrodes [10]. In GaN, the standard MMIC platform provides a metal free conductive sheet inherent to the heterostructure, which can be used to define electrodes, eliminating the metal completely from the resonant structure.

III. 2DEG ELECTRODES

The piezoelectric resonator presented here uses 2DEG IDTs to drive acoustic waves in an AlGaN/GaN heterostructure. 2DEG electrodes have previously been demonstrated as IDTs in a SAW AlGaN/GaN filter [11] as well as for piezoelectric actuation of AlGaN/GaN heterostructures [12,13]. However this is the first use of 2DEG IDTs in MEMS resonators. The authors have recently demonstrated a switchable piezoelectric transducer using the 2DEG as a bottom electrode and Schottky metal as a top electrode [14].

The starting AlGaN/GaN heterostructure used in the current work is illustrated in Fig. 1(a). Large spontaneous and piezoelectric polarizations form a sharp potential well confining electrons in a 2D plane just below the interface of AlGaN and GaN [15]. This 2DEG is conductive enough to form electrodes for piezoelectric transduction. The 2DEG can be patterned with a shallow AlGaN etch as shown in Fig. 1(b). To drive acoustic waves in the structure, an AC electric field is applied through the GaN, between the interdigitated 2DEG electrodes.

At resonance, strain fields defined by the mode shape induce a polarization field through the direct piezoelectric effect. For Wurtzite crystal materials such as GaN, the induced polarization field can be written as:

$$\boldsymbol{P_{PE}} = (e_{51}\epsilon_{zx})\hat{\boldsymbol{x}} + (e_{51}\epsilon_{yz})\hat{\boldsymbol{y}} + \left(e_{31}\epsilon_x + e_{31}\epsilon_y + e_{33}\epsilon_z\right)\hat{\boldsymbol{z}} \quad (1)$$

Taking z along the Wurtzite c-axis, ϵ_x, ϵ_y, and ϵ_z are the strains along the x, y and z-axis, respectively, and ϵ_{yz} and ϵ_{zx} are shear strains. Here, e_{31}, e_{33} and e_{51} are the piezoelectric coefficients found in the Wurtzite crystal structure. There are two contributions to the bound charges associated with this polarization field. First, an interface charge σ is generated by a discontinuity in the polarization at the AlGaN/GaN interface:

$$\sigma = (\boldsymbol{P_{PE,AlGaN}} - \boldsymbol{P_{PE,GaN}}) \cdot \hat{\boldsymbol{z}} \quad (2)$$

Second, the polarization generates volume charge ρ throughout the heterostructure:

$$\rho = -\nabla \cdot \boldsymbol{P_{PE}} \quad (3)$$

The overall mechanically induced charge is found by integrating σ along the AlGaN/GaN interface in the region defined by the IDT and integrating ρ over the GaN volume under the IDT. The summed contribution of the interface and bulk charges is compensated by free charge flowing into the 2DEG, which translates into an AC current.

IV. FABRICATION

The ability to form metal-free electrodes is dependent on the presence of a 2DEG, which is an inherent feature of existing GaN MMIC technology. This platform can be leveraged to fabricate 2DEG IDT piezoelectric resonators with only two additional masks as shown in Fig. 2. The starting material is an AlGaN(25nm)/GaN(1.7μm) stack grown by Molecular Beam Epitaxy on a (111) Silicon substrate, using a thin AlN nucleation layer [16]. The growth of the material in this work was performed at Raytheon with subsequent fabrication at MIT. A shallow BCl_3/Cl_2 plasma etch of the AlGaN is used for both electrical isolation between devices and patterning the 2DEG IDTs. The 2DEG is removed from the regions where the AlGaN is etched away, by eliminating the potential well generated by the AlGaN/GaN interface.

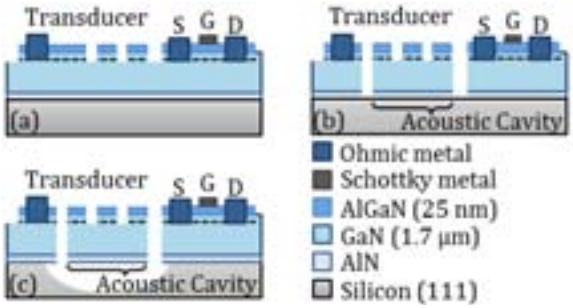

Figure 2. Fabrication involves two additional steps to (a) existing GaN MMIC technology, including (b) a deep GaN etch, and (c) a release step.

A Ti/Al/Ni/Au metal stack is deposited and patterned, followed by a rapid thermal anneal (RTA at 870˚C, 30 sec) to form Ohmic contacts to the 2DEG. While in a typical HEMT process flow these Ohmics are used to access the source and drain of the transistors, in this work they also serve as a means of electrically contacting the 2DEG electrodes. This takes place outside of the resonant cavity to avoid metal loading. From the Ohmic metal contact, the 2DEG forms a conductive path through the suspension beams onto the resonator. At this point, the piezoelectric transducer is completely defined. To extend the process for the inclusion of HEMTs, a Ni/Au/Ni gate metal stack can be deposited and patterned to form Schottky contacts for the gate (Fig. 2(a)). An additional Cl_2 inductively coupled plasma etch of the GaN layer defines the acoustic cavity (Fig. 2(b)). Finally, a XeF_2 isotropic Si etch releases the resonators from the substrate (Fig. 2(c)).

V. RESULTS

A GaN piezoelectric resonator using a 2DEG IDT is shown in Fig. 3(a), with the simulated resonant mode shape shown in Fig. 3(b). This structure corresponds to "Design A", with dimensions 50 by 65 μm and using quarter wavelength suspension beams to minimize anchor losses. For comparison, an identical resonator using Ohmic metal IDTs is also fabricated.

Devices were tested under vacuum to reduce air damping. A 50Ω terminated 2-port measurement was performed. The parasitics of the RF pads were deembedded using an open structure. Since the goal of this work is to isolate the mechanical performance of the AlGaN/GaN resonators, further deembedding needs to be

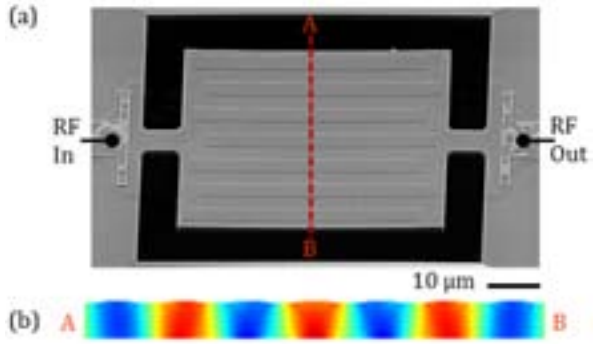

Figure 3. (a) SEM of GaN resonator with 2DEG IDT. The 2DEG electrodes are patterned with a 70 nm deep AlGaN etch. Ohmic contacts are used to access the 2DEG outside of the resonant structure. (b) Strain fields of the bulk contour mode excited using the 2DEG IDT.

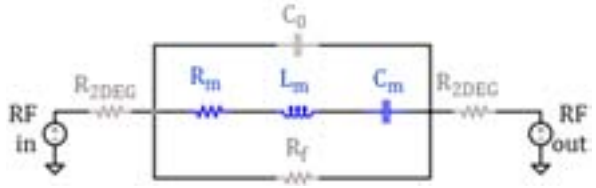

Figure 4. Equivalent circuit model of 2DEG IDT. Elements in blue represent the mechanical resonance while elements in grey are electrical parasitics of the structure and are deembedded from the measurement.

performed to eliminate electrical parasitics, especially the loss associated with feed-through capacitance and the series resistance of the 2DEG. The equivalent circuit describing this device is captured by Fig. 4. After parameter fitting was performed to extract C_0, R_f, and R_{2DEG}, these contributions were deembedded from the admittance of the device, leaving only the mechanical response shown in Fig. 5(a). The measured deembedded frequency response of the resonator with Ohmic metal IDT is shown in Fig. 5(b). The mechanical quality factor of the device with metal electrodes is 3× lower than that of the 2DEG IDT, which can be attributed to the additional damping mechanisms associated with metal electrodes, as discussed in §II.

Table 1 summarizes the extracted mechanical Q and $f{\cdot}Q$ products for two resonator designs, each measured using 2DEG IDTs and metal IDTs. As mentioned above, "Design A" resonators use quarter wavelength suspension beams. In the case of "Design B", a phononic crystal is used to mechanically isolate the resonant mode. In both cases, the Q of the 2DEG IDT device is significantly higher than that of the metal IDT.

TABLE I. COMPARISON OF 2DEG AND METAL IDT RESONATORS

		Extracted Parameters			
		f (MHz)	Q_m	$f{\cdot}Q_m$ (s^{-1})	k_T^2 (%)
Design A	2DEG	523.7	1587	8.3×10^{11}	0.091
	Metal	553.4	476	2.6×10^{11}	0.095
Design B	2DEG	525.3	1193	6.3×10^{11}	0.08
	Metal	516.4	460	2.3×10^{11}	0.05

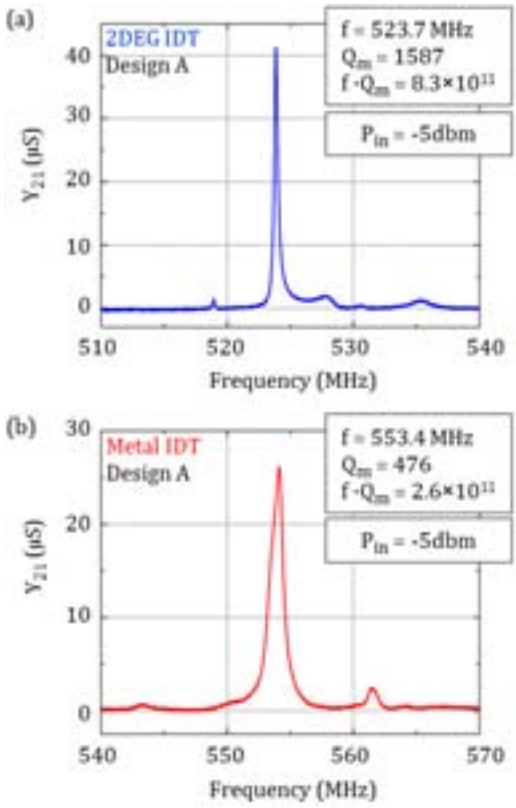

Figure 5. (a) Frequency response of "Design A" resonator using 2DEG IDT after deembedding the electrical parasistics. (b) The deembedded measured response of a metal IDT resonator with equivalent design.

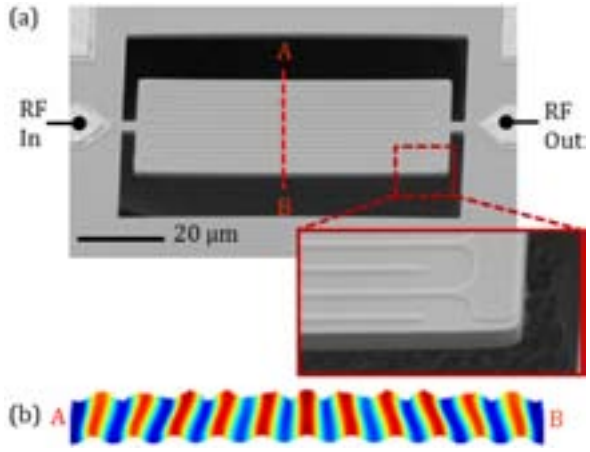

Figure 6. (a) SEM of 1.2 GHz 2DEG IDT resonator. The 2DEG electrodes are patterned with a 90 nm deep AlGaN etch. (b) Mode shape showing the strain fields induced at resonance.

A 2DEG IDT designed to operate at 1.2 GHz is shown in Fig. 6(a), with the simulated mode shape illustrated in Fig. 6(b). This device was tested under vacuum, and the same deembedding technique described above was used to extract the mechanical frequency response. A bulk mode resonance was detected at 1.22 GHz with a Q of 1885, which is the highest measured $f{\cdot}Q$ product in GaN to date.

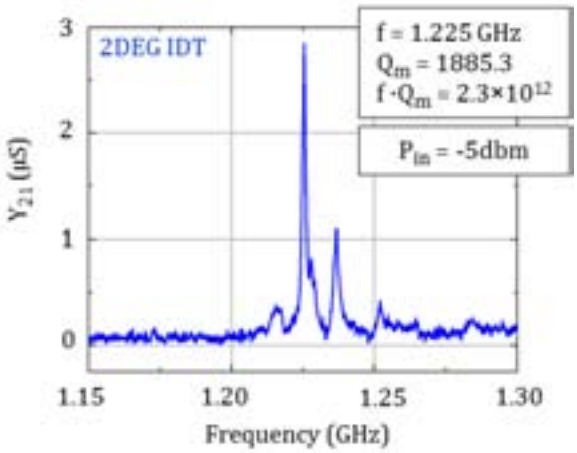

Figure 7. Deembedded frequency response of 1.22 GHz 2DEG IDT resonator. The extracted mechanical resonance has the highest $f \cdot Q$ product measured in GaN to date (2.3×10^{12} at 1.225 GHz).

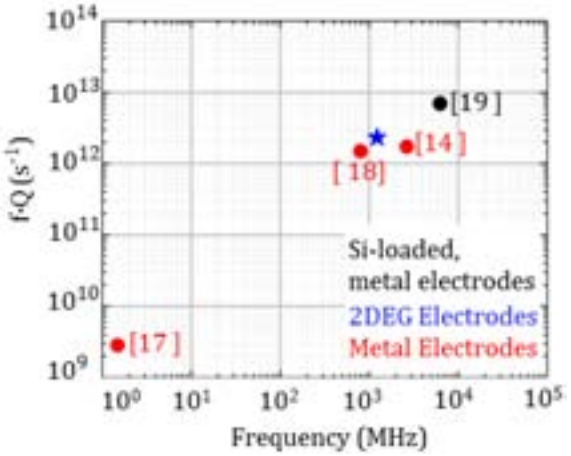

Figure 8. The 2DEG IDT resonator demonstrated here achieved the highest $f \cdot Q$ product in GaN resonators. Ref. 19 shows $f \cdot Q$ of 6.9×10^{12} in a Si-loaded resonator, which does not represent intrinsic GaN properties.

VI. CONCLUSION

We have introduced and demonstrated a GaN piezoelectric resonator that uses 2DEG electrodes to drive and sense acoustic waves. This resonator is metal-free, enabling the highest mechanical $f \cdot Q$ product in GaN to date at 2.3×10^{12}. A benchmarking of this work against state-of-the-art GaN resonators is shown in Fig. 8. Ref. [19] demonstrates an $f \cdot Q$ of 6.9×10^{12} at 6.3 GHz, represented by the black data point. It should be noted that this device uses silicon loading to boost Q, so it is not representative of the fundamental limits of GaN.

This demonstration of metal-free resonators allows for the intimate interrogation of GaN material properties, in the absence of losses and distortions associated with metal electrodes. This work was realized in a standard MMIC heterostructure, with only two modifications to the HEMT process flow. This highlights the potential of 2DEG electrodes for benchmarking the electro-mechanical properties of GaN for material optimization.

ACKNOWLEDGMENT

The authors thank William Hoke and Thomas Kazior (Raytheon) for GaN growth, and process and model discussions. Fabrication took place at MIT's Microsystems Technology Laboratories.

REFERENCES

[1] G. K. Fedder, R. T. Howe, Tsu-Jae King Liu, E.P. Quevy, "Technologies for Cofabricating MEMS and Electronics," *Proceedings of the IEEE* , vol. 96(2), 306-322, (2008)

[2] F. H. Xie, G.K. Fedder et al, "Post-CMOS processing for high aspect-ratio integrated silicon microstructures", *J.Microelectromech. Syst.* vol. 11(2), 93-101 (2002).

[3] W.-C. Chen, C.-S. Chen, K.-A. Wen, L.-S Fan, W. Fang, and S.-S. Li, "A generalized foundry CMOS platform for capacitively-transduced resonators monolithically integrated with amplifiers," *IEEE MEMS,* 204-207 (2010).

[4] J. L. Lopez, J. Verd, J. Teva, G. Murillo, J. Giner, F. Torres, A. Uranga, G. Abadal, and N. Barniol, "Integration of RF-MEMS resonators on submicrometric commercial CMOS technologies," *J.Micromech. Microeng*., vol. 19(1), 13-22 (2009).

[5] R. Marathe, W. Wang, D. Weinstein, "Si-Based Unreleased Hybrid MEMS-CMOS Resonators in 32nm Technology," *IEEE MEMS, (*2011).

[6] O. Ambacher, "Growth and Applications of Group III-nitrides", *J. Phys. D: Appl. Phys.,* vol. 31, 2653-2710 (1998).

[7] F. Ayazi, L. Sorenson, R. Tabrizian, "Energy Dissipation in micromechanical resonators", *Proc. SPIE*, vol. 8031, 803119-9

[8] Braginsky, "Systems with small dissipation", The University of Chicago Press (1985).

[9] L.-W. Hung, Clark T.-C. Nguyen, "Capacitive-Piezoelectric AlN Resonators with Q>12000", *IEEE MEMS* (2011).

[10] C. Casella, J. Segovia-Fernandez, G. Piazza, "Segmented Electrode Excitation of AlN Contour Mode Resonators to Optimize the Device Figure of Merit", *IEEE Transducers*, (2013).

[11] Y. Wong, W. Tang, K.M. Lau, K. Chen, "Surface acoustic wave device on AlGaN/GaN heterostructure using two-dimensional electron gas interdigitated transducers", *Appl. Phys. Lett.,* vol. 90, 213506 (2007).

[12] K. Brueckner, F. Niebelschuetz, K. Tonisch , S. Michael, A. Dadgar, "Two-dimensional electron gas based actuation of piezoelectric AlGaN/GaN microelectromechanical resonators", *Appl. Phys. Lett.,* vol. 93, 173504 (2008).

[13] K. Tonisch, C. Buchheim, F. Niebelschuetz, A. Schober, G. Gobsch, "Piezoelectric actuation of (GaN)/AlGaN/GaN heterostructures", *J. Appl. Phys.,* vol. 104, 084516 (2008).

[14] L.C. Popa, D. Weinstein, "Switchable Piezoelectric Transduction in AlGaN/GaN MEMS Resonators", *IEEE Transducers*, (2013).

[15] O. Ambacher, J. Smart, J.R. Shealy, N. G. Weinmann, K. Chu, et. al., "Two-dimensional electron gases induced by spontaneous and piezoelectric polarization charges in N- and Ga-face AlGaN/GaN heterostructures", *J. Appl. Phys.,* vol. 85**,** 6 (1999).

[16] T.E. Kazior, R. Chelakara, W. Hoke, J. Bettencourt, "High Performance Mixed Signal and RF Circuits Enabled by the Direct Monolithic Heterogeneous Integration of GaN HEMTs and Si CMOS on a Silicon Substrate", *CSICS,* 1-4, (2011).

[17] M. Faucher, B. Grimbert, Y. Cordier, N. Baron, A. Wilk, H. Lahreche, "Amplified piezoelectric transduction of nanoscale motion in gallium nitride electromechanical resonators", *Appl. Phys. Lett.,*vol. 94, 233506 (2009).

[18] A. Ansari, V.J. Gokhale, V. Thakar, J. Roberts, M. Rais-Zahed, "Gallium Nitride-on-Silicon Micromechanical Overtone Resonators and Filters", *IEEE IEDM*, (2011).

[19] A. Muller, D. Neculoiu, G. Konstantinidis, A. Stavrinidis, D. Vasilache, A. Cismaru, et. al., "A 6.3 GHz Film Bulk Acoustic Resonator Structures Based on a Gallium Nitride/Silicon Thin Membrane, *IEEE Electr. Dev. Lett.*, vol 30, no 8, (2009).

Reduction of Anchor Losses by Etched Slots in Aluminum Nitride Contour Mode Resonators

Cristian Cassella, J.Segovia-Fernandez, G.Piazza
Electrical and Computer Engineering
Carnegie Mellon University
Pittsburgh, PA, USA

M.Cremonesi, A.Frangi
Department of Civil and Environmental Engineering
Politecnico di Milano
Milano, Italy

***Abstract*—This paper presents a new technique to increase the quality factor, *Q*, of AlN Contour Mode Resonators (CMRs). The technique uses etched slots in the body of AlN CMRs to reduce energy dissipation through the anchors. The reduction of the energy lost through the supporting anchors improves the device *Q* without altering its electromechanical coupling, k_t^2. An almost 50% improvement in the Figure of Merit, *FoM*, defined as the product between *Q* and k_t^2, has been measured in 220 MHz AlN CMRs.**

I. Introduction

MEMS resonators have been widely researched because they offer the possibility to implement stable frequency references and filtering functions through a CMOS compatible process. The improvement of their quality factor, *Q*, is highly desirable, as it would improve phase noise in oscillators and lower losses in filters.

AlN Contour Mode resonators have shown low motional resistance and moderate *Q* in the radio frequency bands. It has been observed [3,5] that the equivalent damping in AlN CMRs is mostly due to anchor loss and interfacial dissipation. The former is due to acoustic energy lost through the supporting anchors. The latter is due to stress jumps at the interface between different materials in the resonator's body. It has also been shown [3,5] that anchor loss represents the main source of energy dissipation in Very High Frequency (VHF) and low Ultra High Frequency (UHF) bands (up to 500 MHz). In contrast, interfacial dissipation [2,4] represent the main source of energy dissipation above 500 MHz.

This paper presents a new technique to reduce anchor losses in AlN CMRs. The technique has been applied to 220 MHz AlN CMRs and has brought an improvement of *Q* of almost 50%, without any deterioration of the electromechanical coupling coefficient. This approach uses etched slots in the body of the resonator, and close to the anchors, to limit the energy leaking to the substrate through the anchors. The slots behave as acoustic reflectors placed at the edge of the resonator's active region. These reflectors reduce the energy transmitted to the substrate, increasing the acoustic energy trapped in the cavity.

To validate the new design approach, and to verify an analytical model that describes this phenomenon, four different configurations of 220 MHz AlN CMRs with different slot's dimensions have been fabricated and tested. An *ad-hoc* developed finite element code was used to model the effect of the slots in each configuration and predict the resonator *Q*.

The authors would like to thank the DEFYS DARPA contract # FA86501217624 for funding.

II. AlN Contour-Mode Resonators

The principle of operation of AlN CMRs has been already analyzed in previous papers [1]. The devices described in this paper are Lateral Field Excitation (LFE) resonators [1], which are constituted by a piezoelectric layer of AlN sandwiched between two metal plates (Fig.1). The patterned top metal plate has the shape of an interdigitated structure, in which each adjacent finger is biased with opposite polarity to excite the resonator into lateral vibrations. A floating bottom metal is used to confine the electric field in the AlN, ensuring that a high k_t^2 is attained.

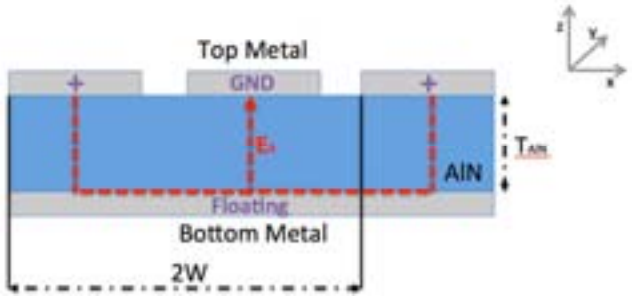

Figure 1: Cross-Section of a 3 fingers LFE AlN CMR.*W* is the finger's width and T_{AlN} is the thickness of the AlN film. The electric field lines, in red, are confined to be mostly in the vertical direction by the floating bottom metal plate. The polarity of the voltage applied to each metal strip is indicated in purple.

The voltage applied to the interdigitated top metal electrode establishes an electric field, E_0, in the AlN film. Considering the limited thickness of the AlN film, the curvature of the electric field lines is negligible. Therefore, to a first order of approximation, E_0 can be considered as oriented exclusively in the z-direction (Fig.1). In CMRs the electric field generates strain through the equivalent piezoelectric coefficient, d_{31}. The generated strain is maximum when the device is excited close to the resonance frequency. The resonance frequency of an AlN CMR is set by the period, $2W$ (Fig.1), of the voltage polarity distribution in the interdigitated top metal electrode and by the acoustic velocity

of the resonator stack. The expression for the resonance frequency of the AlN CMR is given by:

$$f_0 = \frac{1}{2W} \cdot \sqrt{\frac{E_p}{\rho_p}} \qquad \text{[Eq.1]}$$

where E_p and ρ_p are equivalent Young's modulus and mass density, which are a function of the corresponding physical properties of each of the materials that form the resonator stack.

III. Anchor Losses

As shown in [3,5], anchor loss represents the main source of acoustic energy loss for AlN CMRs with resonance frequency in the VHF range. The width-extensional vibrations excited in the AlN film also generate a longitudinal wave that propagates in a direction orthogonal to the main vibration (Fig.2). This longitudinal wave is responsible for the loss of energy through the anchors. As Fig. 2 clearly shows, the anchors and theirs semi-infinite extensions in the substrate represent a path for the longitudinal wave to propagate and dissipate some of the energy generated in the resonator's active region. Although a 2-D analysis should be used to quantify the anchors' dissipations, a simplified 1-D analytical model is adopted here. To a first approximation, the maximum displacement related to the longitudinal wave is proportional to the maximum displacement of the width-extensional mode of vibration and to the AlN Poisson ratio, ν. Therefore, considering a generic point, $P_0(x_0,y_0)$,on the resonator's body (Fig.2), the displacement vector $\vec{\mu}$at P_0 can be seen as the sum of two orthogonal components. In this simplified model, one component represents the desired width-extensional contour-mode, and the other represents the orthogonal mode (Fig.2) that is generated by the main vibration through ν:

$$\vec{\mu}(x_0, y_0) = \mu_x \cdot \hat{x} + \mu_y \cdot \hat{y} = \mu_x \cdot (\hat{x} + \nu \cdot \hat{y}) \qquad \text{[Eq.2]}$$

Hence, for this simple model the displacement function in the y-direction can be attained as a function of the displacement in the x-direction (Fig.2).

The lateral displacement, μ_x, in an AlN CMR is also assumed to be given simply by:

$$\mu_x = A_0 \cdot \cos[kx] \qquad \text{[Eq.3]}$$

where A_0 is the peak-to-peak amplitude of the vibration, k is the wave number associated with the width-extensional acoustic mode, and x is the direction of vibration.

The vicinity of the anchors to the resonator's active region allows assuming the propagation of the longitudinal wave through the anchors to be almost cylindrical. Therefore, in the general case of W_a<W the energy lost through the anchors can be calculated considering the expression of μ_y in -W/2<x<W/2. An expression for the energy lost per unit length of the resonator will be then formulated:

$$W_{lost} \propto \nu^2 \cdot \int_{-W/2}^{W/2} \frac{1}{2}[E_p \cdot T_{AlN}] \cdot (\frac{d\mu_x}{dx})^2 dx \qquad \text{[Eq.4]}$$

where T_{AlN} is the thickness of AlN.

The quality factor, Q, of a resonator is defined as the ratio between the energy stored and the energy lost:

$$Q = \frac{W_{stored}}{W_{lost}} \qquad \text{[Eq.5]}$$

Considering the case of devices with resonance frequency lower than 500 MHz, it is possible to neglect any other source of dissipation in the resonator, except for anchor loss. Q can then be considered to be inversely proportional to W_{lost}. This is clearly an approximation, but it works well with the 220 MHz devices reported here.

The reduction of the energy that escapes from the anchors would results in an increase of the device Q. The increase in Q is electrically modeled as a decrease of the resonator motional resistance R_m[1], and would lead to lower energy dissipation in filters and oscillators.

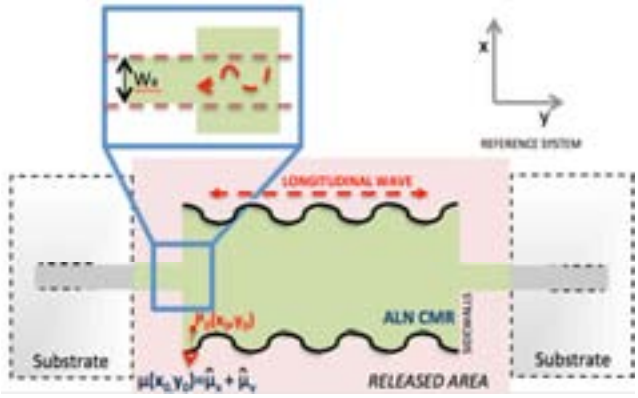

Figure 2:Schematic representation of an AlN CMR used to highlight the existence of a longitudinal mode orthogonal to the main lateral,width-extensional mode of vibration. The device is connected to the substrate through two supporting anchors through which the longitudinal wave escapes the resonator body.

IV. Etched Slots To Reduce Anchor Losses

A new design approach is presented here to reduce anchor losses and, consequently, to increase Q in AlN CMRs. This technique is based on the introduction of etched slots in the AlN film, in close proximity of the anchors (Fig.3). Each slot is effectively an air gap that is created during the etching of the AlN film. The slot's surface represents a free-stress boundary that totally reflects the longitudinal incident wave coming from the resonator's active region. The main design dimensions of the slots are the width, w, and the length, l (Fig.3). w is chosen to have a value close to the minimum feature size that can be defined by the available lithographic equipment (~ 1 μm) . This is done so as to minimize the impact of the slot on the mode of vibration of the resonator. The slot's length, l, directly impacts the amount of acoustic energy that is reflected back after hitting the walls of the slot. This energy, W_{inc}, can be calculated as:

$$W_{inc} \propto v^2 \cdot \int_{-l/2}^{l/2} \frac{1}{2}[E_p \cdot T_{AlN}] \cdot (\frac{d\mu_x}{dx})^2 dx \qquad \text{[Eq.6]}$$

To evaluate Q a new reflection coefficient, Γ is defined. Γ is the ratio between the energy that hits the slot's wall and is reflected back to the cavity, W_{inc}, and the energy that would be lost through the anchor if the slots were to be removed, W_{lost}.

$$\Gamma = \frac{W_{inc}}{W_{lost}} \qquad \text{[Eq.7]}$$

Using (Eq.4) and (Eq.6) it is possible to write the reflection coefficient as:

$$\Gamma = \frac{[\frac{-2\lambda}{2\pi} \cdot \sin(\frac{2\pi}{\lambda} \cdot \frac{l}{2}) \cdot \cos(\frac{2\pi}{\lambda} \cdot \frac{l}{2}) + l]}{[\frac{-2\lambda}{2\pi} \cdot \sin(\frac{2\pi}{\lambda} \cdot \frac{W}{2}) \cdot \cos(\frac{2\pi}{\lambda} \cdot \frac{W}{2}) + W]} \qquad \text{[Eq.8]}$$

where λ is the acoustic wavelength ($\lambda=2W$) (Fig.1). This reflection coefficient permits to readily estimate the Q improvement if we assume that all the losses in the resonator are represented by W_{lost}:

$$\frac{Q_{slot}}{Q_{conventional}} = \frac{1}{(1-\Gamma(l))} \qquad \text{[Eq.9]}$$

where Q_{slot} is the quality factor of the resonator with slots and $Q_{conventional}$ is the quality factor of an identical resonator without slots. The predicted Q as a function of l is plotted in Fig.4. A $Q_{conventional}$ equal to 2000 was assumed for a 220 MHz AlN CMR.

V. Fabrication

The microfabrication process used for making the devices analyzed in this paper is a 3-mask process. 10 nm of Ti and 100 nm of Pt were deposited and patterned on a high resistivity silicon wafer. Subsequently, 1 µm of AlN was sputtered followed by the deposition and patterning of 100 nm of Al. The etching of AlN, followed by the structural release in XeF_2, completed the fabrication process.

VI. Experimental Results

To validate the technique presented in this paper, four different configurations of 220 MHz AlN CMRs have been built (Fig.3). Configuration A represents a device without slots; configurations B, C and D are obtained from A by inserting two slots at a distance of 3.5µm from the edge of the resonator (Fig.3). Configuration B has a slot length (Fig.4) equal to 3.5 µm; configuration C has a slot length equal to 7 µm; configuration D has a slot length equal to 14 µm. The slot width w is about 1µm for all configurations. The anchor's width is 8.6 µm and the anchor's length is 7 µm.

The experimental results are averages of 8 devices for A, 7 devices for B, 6 devices for C and 6 devices for D. The devices were extracted from 8 different dices coming from the same wafer. The reason why not all 8 devices were considered for calculating the averages for B, C and D is that some of these devices were not functional. The reason of the reduced yield is not to be attributed to the introduction of the slot, but issues with wafer processing.

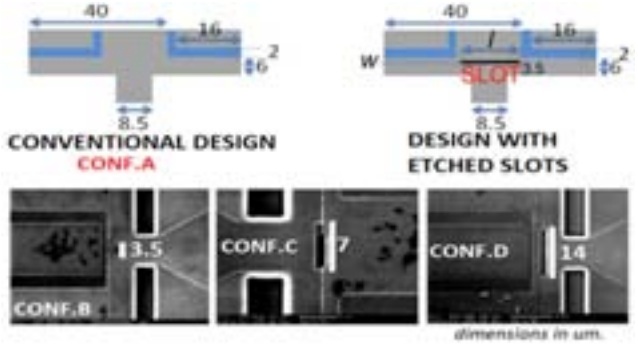

Figure 3: Geometries of configurations A, B, C and D.The slot's length is highlighted in the SEM for configurations B,C and D.

The average measured Q for each configuration is shown in Fig.4. This trend shows that increasing the slot's length with respect to the acoustic wavelength ($\lambda \approx 40\mu m$) results in an improvement of Q. Indeed, configuration D presented the highest quality factor. The measured trend is in line with the analytical prediction (Fig.4 – in green). This validates the design approach and confirms that the use of slots can improve the Q of resonators operating at 220 MHz. As shown in Fig.5, the improvement in Q comes with a proportional decrease of R_m with respect to the conventional configuration. Since this design approach does not deteriorate k_t^2, an almost 50% improvement in the *FoM* of the resonator has been obtained. The measured admittance of the best devices for each configuration is shown in Fig.5.

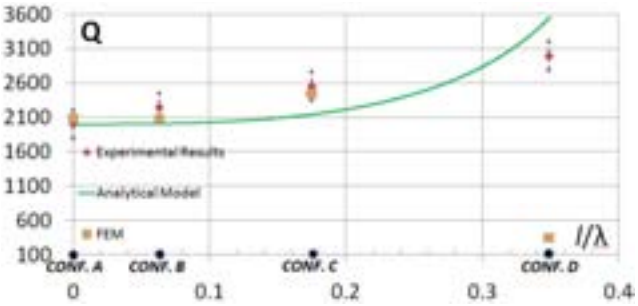

Figure 4:Red diamonds:Experimentally obtained average Q for configurations A,B,C and D. Yellow squares:Q simulated by FEM. Green line: analytical prediction of Q as a function of the slot's length l, according toEqs.7-8.

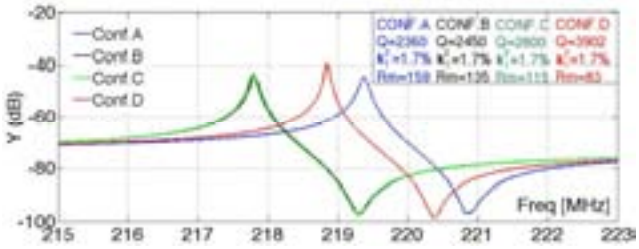

Figure 5: Admittance of the best device measured for each configuration. R_m decreases as we move from configuration A to configuration D. No variation in k_t^2 is measured.

VII. FEM SIMULATIONS

A dedicated 3D finite element (FE) tool has been employed to analyze the impact of the etched slots on the resonator *Q*. The dissipation of elastic waves radiating from the anchor of the resonator into the elastic subspace is simulated via the Perfectly Matched Layer (PML) technique.

Extensive validation of this FE tool for the prediction of Q for MEMS resonators has been previously reported [5,6].

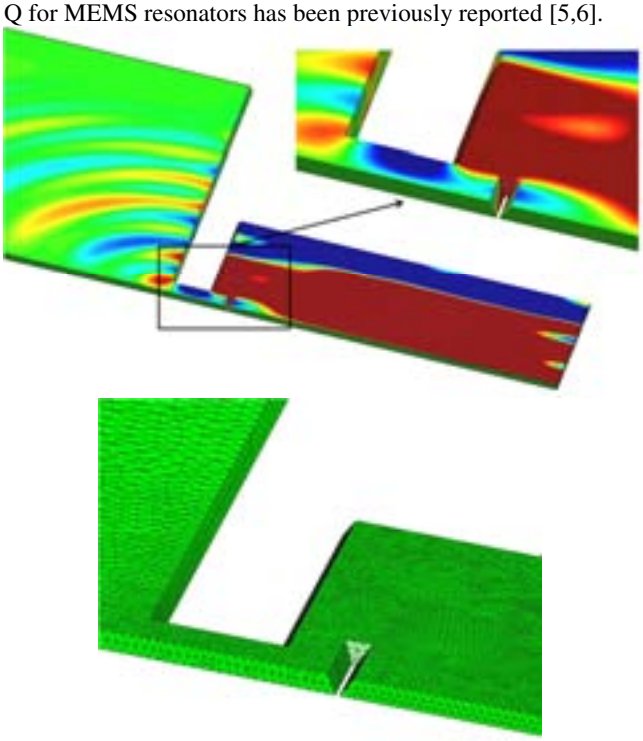

Figure 6: Rapresentation of the waves dissipating into the substrate and mesh used in the FEM simulations.

Figure 6 depicts the geometry of the device used in the numerical simulations. Given the symmetry of the problem, only 1/4 of the resonator has been discretized. To ensure accurate solution, approximately 180000 10-node tetrahedra have been used for the space discretization.

The results of the numerical analyses are reported with the experimental data In Figure 4. The FE data show good agreement with experiments for the first three slot lengths On the contrary, for conf. D the mismatch between numerical predictions and experiments is significant. A careful investigation of the possible cause of this discrepancy is still ongoing. Especially, we have noticed that the FE data continue to follow the analytical values for slot lengths greater than $l/\lambda > 0.35$. Hence, the discrepancy appears to be isolated to this specific data point. The analyses performed to date have shown that the resonator *Q* is greatly affected by a number of geometrical parameters of the resonator. In particular it has been observed that *Q* strongly depends on the sidewall angle and on the shape of the regions where the anchor connects to the substrate and to the resonator. As an example, if the sidewall angle for configuration D is taken as 55° instead of 60°, the quality factor raises from 363 to 1100. Furthermore, since conf. D presents the longest slot (see Figure 3) it is reasonable to assume that it will be mostly affected by the anchor shape (which shows rounded edges) near the resonator. We expect that a more accurate description of the resonator geometry would eliminate the existing discrepancy.

VIII. CONCLUSIONS

In this paper, a new design technique for improving the *Q* of VHF and low UHF designs of AlN CMRs has been presented. The technique uses etched slots in the body of the AlN film close to the anchors. This method reduces anchor losses, and improves *Q*. A 1-D analytical model, and a finite element code have been developed to respectively describe the physical role of the slot and predict the resonator *Q* for different slot's dimensions. Using this approach an average 50% increase in *Q* and in the *FoM* was recorded for 220 MHz AlN CMRs.

REFERENCES.

[1] G. Piazza, P. J. Stephanou, A. P. Pisano, "Piezoelectric Aluminum Nitride Vibrating Contour- Mode MEMS Resonators", *Journal of MEMS*,vol. 15, no. 6, pp. 1406-1418, 2006.J. Clerk Maxwell, A Treatise on Electricity and Magnetism, 3rd ed., vol. 2. Oxford: Clarendon, 1892, pp.68-73.

[2] L.-W. Hung and C. T.-C. Nguyen, "Capacitive piezo transducers for higher Q contour-modeAlN resonators at 1.2 GHz," *Solid-State Sensor and Actuator Workshop*, pp. 463-466, 2010.

[3] J.Segovia, M.Cremonesi, C.Cassella, A.Frangi, G.Piazza,"Experimental Study On The Impact Of Anchor Losses On The Quality Factor Of Contour Mode AlN Resonators", to be published in *Digest Tech. Papers Transducers'13 Conference*, Barcelona, Spain, June 2013.

[4] C.Cassella, J.Segovia-Fernandez, G.Piazza, "Segmented Electrode Excitation of AlN Contour Mode Resonators to optimize the device figure of merit", to be published in *Digest Tech. Papers Transducers'13 Conference*, Barcelona, Spain, June 2013.

[5] A. Frangi, M. Cremonesi, A. Jaakkola, T. Pensala,"Analysis of anchor and interface losses inpiezoelectric MEMS resonators", *Sensors & Actuators: A Physical*, vol. 190, pp. 137-134, 2013.

[6] A. Frangi, A. Bugada, M. Martelo, P.T. Savadkoohi "Validation of PML-based models for the evaluation of anchor dissipation in MEMS resonators", *European Journal of Mechanics - A/Solids,* vol. 37, pp. 256-265, 2013.

IX. CONTACTS

*C.Cassella; ccassell@andrew.cmu.edu

*M.Cremonesi; massimiliano.cremonesi@polimi.it

A 2.8 GHz Combined Mode of Vibration Aluminum Nitride MEMS Resonator with High Figure of Merit Exceeding 45

Yu Hui, Zhenyun Qian, and Matteo Rinaldi
Department of Electrical and Computer Engineering
Northeastern University
Boston, MA, USA
hui.y@husky.neu.edu; qian.z@husky.neu.edu; rinaldi@ece.neu.edu

***Abstract*—This paper presents the first demonstration of a high frequency (2.8 GHz), lateral field excited (simple two masks fabrication process), combined lateral-thickness extensional mode of vibration aluminum nitride (AlN) micro-electro-mechanical systems (MEMS) resonator with unprecedentedly high figure of merit ($k_t^2 \cdot Q > 45$). For the first time, a single interdigital electrode was employed to excite a high frequency mode of vibration in an AlN plate (1.5 µm thick) by making use of both the d_{33} and d_{31} AlN piezoelectric coefficients. The resulting MEMS resonator showed high quality factor, Q~2000, (thanks to the high quality AlN film directly deposit on top of the Silicon substrate) and the highest electromechanical coupling coefficient ever reported for AlN MEMS resonators employing a single electrode, k_t^2~2.5% (thanks to the coherent combination of d_{33} and d_{31} coefficients to transduce one single mechanical mode of vibration).**

Keywords—Aluminum Nitride; MEMS Resonators; Combined Mode; Electromechancial Coupling Coefficient; Figure of Merit

I. INTRODUCTION

The high frequency Aluminum Nitride (AlN) Micro-Electro-Mechanical Systems (MEMS) contour mode resonator (CMR) technology [1] has shown great potential for the implementation of single-chip, multi-frequency RF filters and frequency sources. The CMR technology has the same advantages of thin film bulk acoustic resonators (FBARs) over SAW devices in terms of miniaturization and IC integration capabilities. Nevertheless, the CMR technology employs the d_{31} piezoelectric coefficient of AlN to transduce a lateral-extensional mode of vibration in the micromechanical structure, in contrast to FBARs, which use the d_{33} piezoelectric coefficient of AlN to transduce a thickness-extensional mode. Therefore, the operating frequency of CMRs is lithographically set by the lateral dimensions of the device (rather than by the thickness of the AlN layer as in the FBAR case) enabling the fabrication of multiple frequencies of operation on the same silicon chip. This is a crucial feature for advanced wireless communication systems, for which single-chip, multi-band RF solutions are becoming the dominant trend.

Nevertheless, the performance of an electromechanical resonator is in general evaluated in terms of figure of merit (*FOM*) defined as the product of quality factor (Q) and electromechanical coupling coefficient (k_t^2) of the resonator. High Q>2000 is typically achieved in high frequency AlN CMRs while only limited values of k_t^2<2.5% have been demonstrated for this class of devices due to the relatively small value of the d_{31} piezoelectric coefficient of AlN employed to excite the contour-extensional mode of vibration [2] (in contrast to FBAR devices which show higher values of k_t^2 ~6% [3] being the d_{33} piezoelectric coefficient more than two times larger than the d_{31}). Furthermore, such piezoelectric coefficient-limited values of k_t^2 can only be achieved by maximizing the confinement of the excitation electric field across the thickness of the AlN layer, which requires the use of a thickness field excitation scheme (TFE, shown in Fig. 1(a)) involving a top and bottom electrode (4-mask fabrication process). Lateral field excitation (LFE, Fig. 1 (b)) schemes involving the use of a single interdigital electrode on top of the AlN plate have been proposed [4]. Such LFE configuration greatly simplifies the fabrication of the device (2-mask fabrication process required). Furthermore, operation in the super-high frequency band (up to *9.9 GHz*) [5] and values of Q as high as *2200* [6] have been demonstrated using LFE. Nevertheless, it has been theoretically demonstrated [7] that only relatively low values of k_t^2< 1.5% can be achieved using the LFE configuration due to the reduced confinement of the excitation electric field across the thickness of the AlN layer.

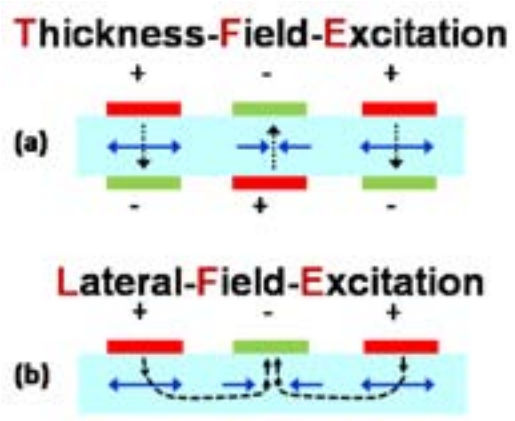

Fig. 1. Schematic illustration of the TFE and LFE schemes of AlN CMRs: the black dash arrows represent the electric field and blue solid arrows represent the in-plane displacement of the AlN plate.

In this work, for the first time high operating frequency (*2.8 GHz*), quality factor (Q~*1855*) and electromechanical coupling coefficient (k_t^2~*2.48%*) were simultaneously

This work was supported by DARPA Young Faculty Award contract No. N66001-12-1-4221.

demonstrated in a LFE AlN MEMS resonator whose thickness and lateral dimension were properly designed to transduce a single mechanical mode of vibration based on the coherent combination of the d_{31} and the d_{33} piezoelectric coefficients of AlN. Such combination of piezoelectric coefficients enhanced the k_t^2 of the device resulting in a *2.8 GHz* LFE AlN MEMS resonator with unprecedentedly high *FOM~46* despite the use of a single interdigital top-electrode (simple 2-mask fabrication process).

II. DESIGN AND FABRICATION

A conventional LFE CMR is composed of a simple two-layer structure in which an interdigital metal electrode is deposited on top of an AlN plate. When an AC signal is applied to the top interdigital electrode a contour-extensional mode of vibration is excited through the equivalent d_{31} piezoelectric coefficient of AlN. Given the equivalent mass density, ρ_{eq}, and Young's modulus, E_{eq}, of the material stack that forms the resonator, the center frequency, f_0, of this laterally vibrating mechanical structure, is set by the pitch, W, of the top interdigital electrode [1]. For the combined mode resonator proposed in this work, the pitch, W, of the interdigital electrode and the thickness, T, of the AlN layer were optimized through FEM simulation in order to excite a single mechanical mode of vibration based on the coherent combination of d_{31} and d_{33} piezoelectric coefficients which maximizes the electromechanical coupling coefficient of the device.

A 2D finite element method (FEM) simulation was performed using CMOSOL Multiphysics to investigate the k_t^2 dependence on the thickness, T, of the AlN resonator for a given value of the interdgital electrode pitch, W, hence wavelength, $\lambda=2W$. The simulation result, reported in Fig. 2, indicates that high values of $k_t^2 > 2.5\%$ (~ two times higher than the best values achievable with conventional LFE AlN CMRs [8]) can be achieved for T/λ values ranging between *0.35* and *0.55* for which the d_{31} and the d_{33} piezoelectric coefficients of AlN are coherently exploited to excite a single combined mode of vibration with enhanced k_t^2.

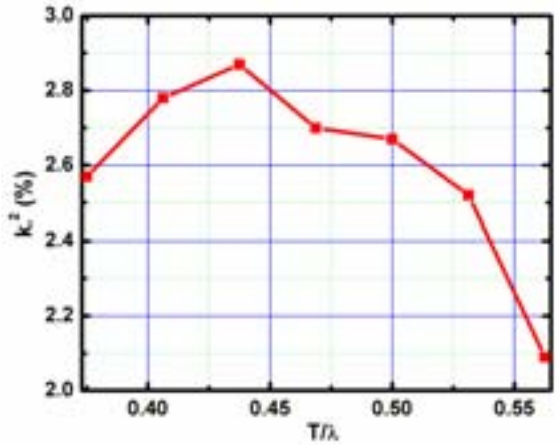

Fig. 2. FEM simulated k_t^2 dependence on T/λ for an AlN LFE resonator employing a single top interdigital electrode ($\lambda=2W$) .

The simulated admittance curve and the corresponding 2D mode shape of vibration for $T/\lambda=0.47$ are shown in Fig. 3. The simulation result clearly shows that, at the resonance frequency, the lateral-extensional and thickness-extensional modes are combined into a single mechanical mode of vibration with enhanced electromechanical coupling coefficient, $k_t^2 \sim 2.78\%$.

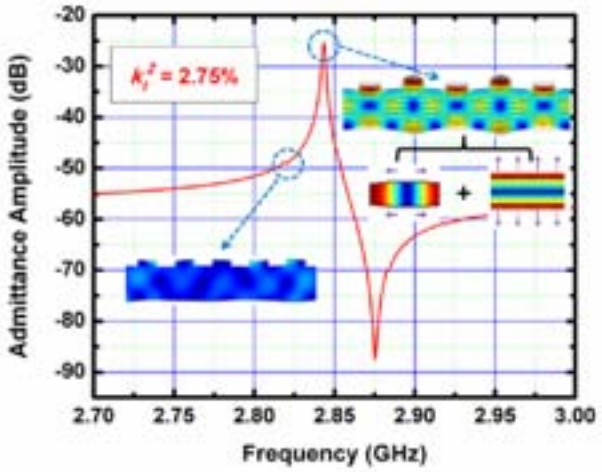

Fig. 3. FEM simulated admittance curve and 2D mode shape of vibration of the LFE combined mode AlN resonator. A single combined mode of vibration is predicted. A spurious mode at a frequency slightly lower than the resonance is also predicted and observed in the experimental data in Fig. 6.

Based on the aforementioned analysis, a device prototype with $T/\lambda=0.47$ was designed and fabricated. The pitch, W, of the interdigital electrode was set to *1.6 μm* and the thickness, T, of the AlN was accordingly chosen to be *1.5 μm.* The proposed AlN resonator was fabricated using a simple two-mask microfabrication process (Fig. 4): 1.5 μm thick AlN film was sputter-deposited on top of a high resistivity Silicon wafer. Then, 200/50 nm thick Al/TiN film was deposited on top of AlN film and patterned by lift-off process to define the top interdigital electrode. Next, the AlN film was etched by ICP in Cl_2 based chemistry to define the shape of the resonator. Finally, the Silicon substrate underneath the AlN resonator was released by XeF_2 isotropic etching. The SEM image of the fabricated device is shown in Fig. 5.

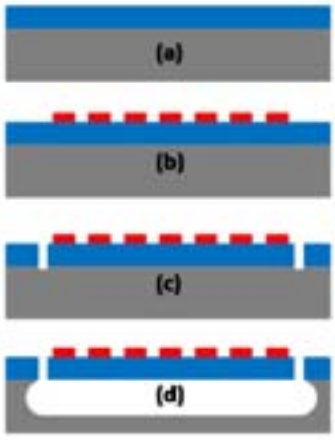

Fig. 4. 2-mask microfabrication process of the AlN combined mode MEMS resonator: (a) AlN thin film was sputter-deposited on top of Si substrate; (b) Al/TiN film was deposited on top of AlN film and patterned by lift-off process; (c) AlN film was etched by ICP in Cl_2 based chemistry; (d) Si substrate was released by XeF_2 isotropic etching.

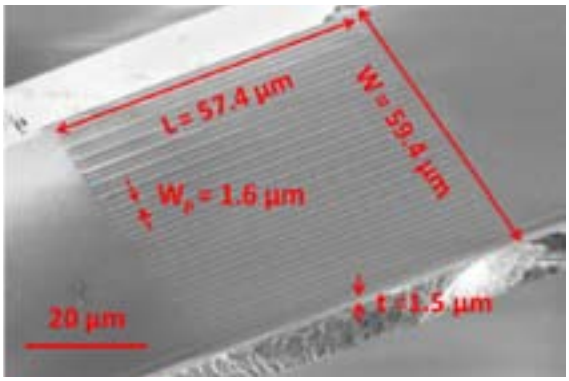

Fig. 5. Scanning Electron Microscope (SEM) image of the fabricated AlN combined mode MEMS resonator.

III. EXPERIMENTAL RESULTS

The electrical performance of the fabricated AlN LFE combined mode MEMS resonator was measured by an Agilent E5071C network analyzer after performing an open-short-load calibration. The measured admittance response versus frequency and the Butterworth-van Dyke (BVD) fitting are shown in Fig. 6. A single resonance peak was measured at *2.82 GHz* in agreement to the FEM simulation. As expected, high quality factor, *Q of 1855* (thanks to the direct deposition of AlN film on a polished Silicon substrate) and high electromechanical coupling coefficient, k_t^2*~2.48%* (thanks to the combined d_{31} and d_{33} piezoelectric coefficients) were achieved. The measured k_t^2 of *2.48%* and the corresponding *FOM~46* are the highest ever reported among LFE AlN MEMS resonators employing a single top interdigital electrode (2-mask fabrication process).

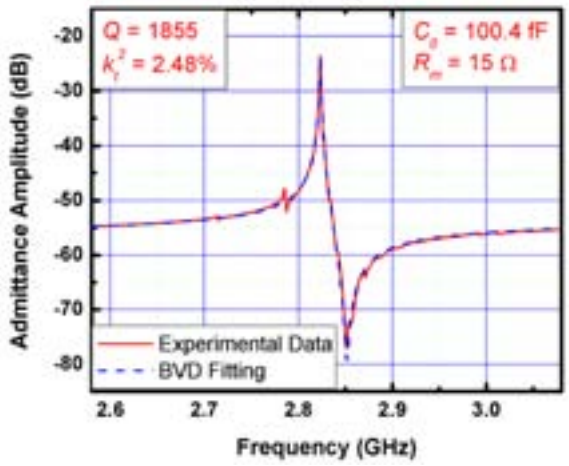

Fig. 6. Measured admittance curve and BVD fitting of the fabricated LFE combined mode AlN MEMS resonator.

IV. CONCLUSION

In this paper, a novel design concept for the implementation of high electromechanical coupling AlN MEMS resonators was experimentally verified. A single interdigital electrode was employed to excite a high frequency mode of vibration in an AlN plate (1.5 µm thick) by making use of both the d_{33} and d_{31} AlN piezoelectric coefficients and a high frequency (*2.8 GHz*), lateral field excited (simple 2-mask fabrication process), combined mode of vibration AlN MEMS resonator with unprecedentedly high figure of merit ($k_t^2 \cdot Q$ ~ *46*) was experimentally demonstrated. The measured figure of merit is the highest ever reported among LFE AlN MEMS resonators employing single top interdigital electrode (2-mask fabrication process).

ACKNOWLEDGMENT

The authors wish to thank Ben Griffin, Peggy Clews and Troy Olsson at Sandia National Laboratory for the fabrication of the device presented in this work. This work was supported by DARPA Young Faculty Award contract number: N66001-12-1-4221.

REFERENCES

[1] G. Piazza, P. J. Stephanou and A. P. Pisano, "Piezoelectric Aluminum Nitride Vibrating Contour-Mode MEMS Resonators",*Journal of Microelectromechanical Systems*, vol. 15, pp. 1406-1418, 2006.

[2] M. Rinaldi, C. Zuo, J. Van der Spiegel and G. Piazza, "Reconfigurable CMOS Oscillator based on Multi-Frequency AlN Contour-Mode MEMS Resonators", *IEEE Transactions on Electron Devices*, vol. 58, issue 5, pg. 1281-1286, 2011.

[3] R. C. Ruby, P. Bradley, Y. Oshmyansky and A. Chien, Thin film bulk wave acoustic resonators (FBAR) for wireless applications, *2001 IEEE Ultrasonics Symposium*, Atlanta, GA, 07-10 Oct 2001, vol.1 pg. 813 - 821.

[4] M. Rinaldi, C. Zuniga, C. Zuo and G. Piazza, "GHz Range Nanoscaled AlN Contour-Mode Resonant Sensors (CMR-S) with Self-Sustained CMOS Oscillator", *Proceedings of the Solid-State Sensors, Actuators and Microsystems Workshop (Hilton Head 2010)*, Hilton Head Island, 06-10 June 2010, pg. 471-474.

[5] M. Rinaldi, C. Zuniga, and G. Piazza, "5-10 GHz AlN Contour-Mode Nanoelectromechanical Resonators", *Proceedings of the 22nd IEEE Conference on Micro Electro Mechanical Systems (MEMS 2009)*, Sorrento, Italy, 24-28 January 2009, pg. 916-919.

[6] C. Zuo, J. Van der Spiegel and G. Piazza, "1.05 GHz MEMS Oscillator Based On Lateral-Field-Excited Piezoelectric AlN Resonators", *2009 Joint Meeting of the European Frequency and Time Forum and the IEEE International Frequency Control Symposium (EFTF-IFCS 2009)*, Besancon, France, 20-24 April 2009, pg. 381-384.

[7] J. H. Kuypers, C. Lin, G. Vigevani and A. P. Pisano, "Intrinsic temperature compensation of aluminum nitride Lamb wave resonators for multiple-frequency references", *2008 IEEE International Frequency Control Symposium*,Honolulu, HI, 19-21 May 2008, pg. 240-249.

[8] C. Zuo, J. Van der Spiegel, G. Piazza, "Switch-Less Dual-Frequency Reconfigurable CMOS Oscillator Using One Single Piezoelectric AlN MEMS Resonator with Co-Existing S0 and S1 Lamb-Wave Modes", *IEEE MEMS 2011*, Cancun, Mexico, 23-27 January, pp. 177-180.

Highly Coupled Resonator Based on Ridge-Shaped Periodically Poled Materials for Radio-Frequency Applications

Fabien Henrot[1], Florent Bassignot[1], Clément Guyot[1], Jean-Yves Rauch[1], Blandine Guichardaz[1], Sylvain Ballandras[2]
[1]FEMTO-ST Institute, 32 avenue de l'Observatoire, 25000 Besançon, France
[2]FreC'N'Sys, 18 rue Alain Savary, 25000 Besançon, France
fabien.henrot@femto-st.fr

***Abstract*— Surface Acoustic Wave (SAW) and Bulk Acoustic Wave (BAW) devices are largely used in telecommunication for radio Frequency (RF) signal processing. Nevertheless, these devices are limited by various factors such as short-circuit between electrodes for SAW and precise thickness control for BAW. This paper shows the interest of a new kind of transducer using Periodically Poled Lithium Niobate (PPLN) developed to overcome SAW and BAW technological limits. A former PPLN-based wave-guide was presented some years ago exploiting planar technologies. The novelty of the present work lies in the 3D structuring of the transducer allowing for very high aspect ratio structures exhibiting a theoretical electromechanical coupling about 20% and a phase velocity up to 20 km.s^{-1}.**

Keywords- Periodically poled transducer; Lithium Niobate; high aspect ratio ridge

I. INTRODUCTION

Surface acoustic wave (SAW) devices using inter-digitated transducer (IDT) are commonly used for passive radio-frequency components such as resonators and filters. This mature technology is particularly addressing RF filter demands, yielding a yearly production of billions of pieces. Although effective and massively produced, SAW devices based on IDTs are limited by various factors when addressing the demand for frequency operation in excess of 2.5 GHz. Among these limitations, the nature of the mode and single crystal acoustic properties do not allow for the excitation of surface waves with phase velocity much higher than 6 km.s^{-1} (leaky-longitudinal SAW on Lithium Niobate – $LiNbO_3$ [1]). Also, currently implemented industrial technologies for SAW devices provide electrode width in the vicinity of 0.3 µm. Such lithography resolution requires high quality control of IDT finger definition to avoid any risk of short-circuit between electrodes (preventing the correct operation of the resulting SAW device).

Many efforts are presently developed to address these issues, along various principles and structures (RF Micro-Electro-Mechanical Systems – RF MEMS – such like Film Bulk Acoustic Resonators, Solidly Mounted Resonators, and a population of locally vibrating parts excited using electrostatic forces [2]). An approach has been identified as an attractive combination of bulk and surface wave transducer characteristics, using ferroelectric polarization to generate an interference grating for acoustic waves. The so-called periodically poled transducer (PPT) is actually taking advantage of a planar definition of the acoustic period (similarly to SAW) and a bulk propagation, allowing for various kinds of mode and acoustic propagation to be exploited. It consists of a periodic polarization of ferroelectric materials such as single crystal $LiNbO_3$, combined with plane electrodes exciting and detecting waves propagating in the bulk of the material [3], providing an alternative to IDT's exhibiting remarkable properties. As shown in [3], assuming a given grating period, the frequency of a PPT is twice higher than the one of IDT, as PPTs do naturally operate on a second harmonic regime, as explained in fig. 1. This kind of PPT was successfully manufactured as shown in [3] and [4], but the best experimental electromechanical coupling remained smaller than 1%. More specifically in [4], a Periodically Poled Lithium Niobate (PPLN) wafer was stacked between two silicon wafers to guide acoustic waves and to reduce the temperature coefficient of frequency [4], allowing for transducer working from 65MHz to 1.3GHz with a TCF of -50 ppm.K^{-1}, i.e. twice smaller than the TCF of PPT on pure $LiNbO_3$ plates.

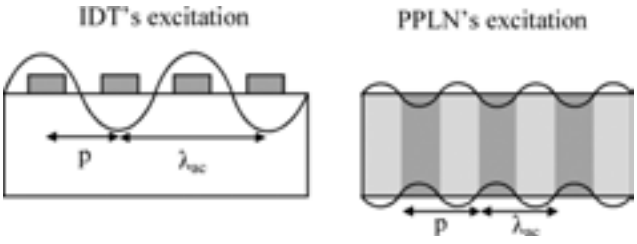

Figure 1. Excitation principle for (left) inter-digitated transducer and (right) periodically poled lithium niobate

As this new device only allows for the excitation/detection of acoustic modes with limited electromechanical coupling (1% in the best case for $LiNbO_3$ and Lithium Tantalate – $LiTaO_3$), they revealed poorly appropriate to modern RF filter challenges, requiring electromechanical coupling up to 10% or even more. However, these two materials are known to allow for much more coupled mode excitation, particularly concerning bulk waves. Even if advanced transducer combinations provide advantageous conditions for wave trapping [4], PPTs based on this basic architecture are not

capable to overcome such coupling values (PZT – Lead zirconate titanate – was found theoretically capable of larger mode coupling, but it poorly suits RF requirements due to excessive intrinsic acoustic losses [5]). To overcome this limitation, various electrode configurations and excitation conditions have been investigated, resulting in a new device architecture based on a high aspect ratio structure (ridge) which allows for coupling higher than 20%. This kind of structure is used for optical waveguides ([6], [7], [8]) allowing to develop new devices requiring highly guided light.

Using a homemade simulation tool [9], different device designs have been studied to determine the best configurations. Ridges are achieved by dicing trenches into $LiNbO_3$ periodically poled wafers [10]. The sides of the ridges are polished during the saw dicing, yielding wave confinement. Electrodes then are deposited on the ridge sides using gold or aluminum sputtering. The characterization of such transducers then is achieved by using a network analyzer. The agreement between theory and experiment has been checked to confirm theoretical predictions, assessing the efficiency of the developed concept and the associated analysis.

Device manufacturing is detailed in the following sections of the paper. The obtained devices are characterized to emphasize the advantages of these ridge-based PPTs.

II. TRANSDUCER MANUFACTURING

The fabrication of the new device based on PPLN ridge is described in this section. Two dicing methods are described to illustrate saw-dicing capabilities for manufacturing high aspect ratio structures.

A. Description of the process flow-chart

For this process, a 500µm thick Z-cut Lithium Niobate wafer was used. First, a photo-lithography process is achieved to pattern the shape of future inverted domains (Fig. 2 a) and 2 b). Lithium Niobate then is wedged between two seals to introduce an electrolyte without leaks. A mechanical system allows for keeping the wafer and seals together (Fig. 2 c). An electric field higher than the coercive field of Lithium Niobate (21kV/cm) is applied between the two sides of the wafer. A photo-resist layer is used as an electric insulator. Consequently, areas covered by the photo-resist are not inverted (Fig. 2 d). For more details about poling steps, the reader should refer to ref. [3]. After the poling step, the wafer is coated with a photo-resist overlay and diced to fabricate ridge shaped transducers. Saw-dicing is performed along X axis over depths ranging from 100µm to 500µm (Fig. 2 e). Aluminum electrodes are then sputtered on the device walls and patterned by lift-off. Electrode deposition method is depending on the saw-dicing depth. In that purpose, the device can be tilted by few degrees to reach ridge bottoms (Fig. 2 f).

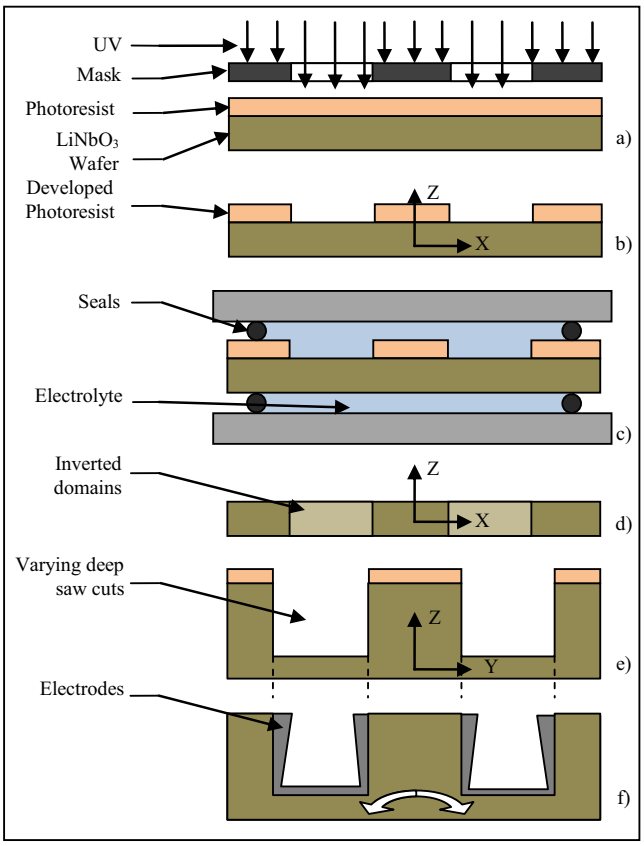

Figure 2. Process steps for Lithium Niobate PPT-ridge fabrication

B. Dicing

Saw-dicing is the main technological process for this kind of PPT-ridges. It also provides the final structure of the device and therefore it conditions the transducer performances which largely depend on dicing quality and precision. This process is achieved using a DISCO saw apparatus, with diamond blade of 400µm width and 5.2cm diameter. Two ridge-width-spaced cuts are achieved to obtain one ridge. Parameters such as feed rate and operating speed have been optimized to get the best side wall quality. A photo-lithography process is first performed on the poled wafer to allow for electrode patterning. Two dicing methods have been investigated to determine the most effective one.

- The first one consists of dicing a ridge to a depth smaller than the wafer thickness (500µm), allowing ridge narrower than 10µm and higher than 100µm. This method allows for very narrow ridges, yielding then high working frequencies (above one GHz) and width over poling period (w/p) ratios of 0.2 and 0.4 – identified as the best working points to reach the highest electromechanical coupling. An example of these ridges is shown on fig. 3. a).
- The second method consists in dicing the whole thickness of the wafer. This method allows for devices

very close to theoretical configurations. However, device width can't be smaller than about 100µm due to technological limits, therefore w/p ratios of 0.2 and 0.4 can be reached only for period larger than 500µm. Figure 3.(b) shows ridges diced through the whole depth of the wafer.

For both methods, the process is developed to achieve polished ridge sides (5 < Ra < 50nm with Ra the average roughness), the better the side quality, the better the wave confinement.

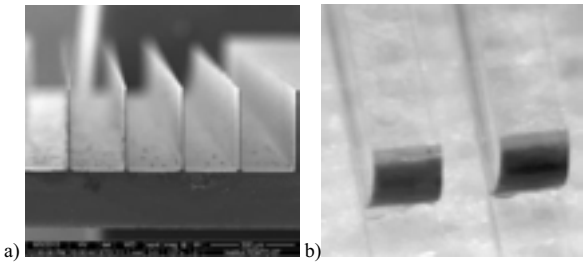

a) b)

Figure 3. Ridges achieved with the dicing first method a) and with the second dicing method b)

For the first method, electrodes are sputtered on ridge sides by tilting device by few degrees (fig. 2 f). A lift-off process then is achieved to pattern the electrodes. The second method allows for a direct sputtering on ridge sides as the device can be tilted by 90° within the sputtering machine.

C. Transducer Characterization

Only the second type of device is characterized here because of simulation model and experimental setup completion. Before achieving the device characterization, electrodes are deposited on its (YX) sides. One electrode is deposited all along the device to ensure the contact between the PCB plate and the device. Another electrode is deposited only on the poled area (see fig. 4), allowing for the excitation of this area only (avoiding any parasite bulk response).

Figure 4 shows one of the experimental devices (λ=600µm, w=120µm), stuck on a PCB with a conductive silver paste. Another device (λ=600µm, w=200µm) has been characterized to check result coherence.

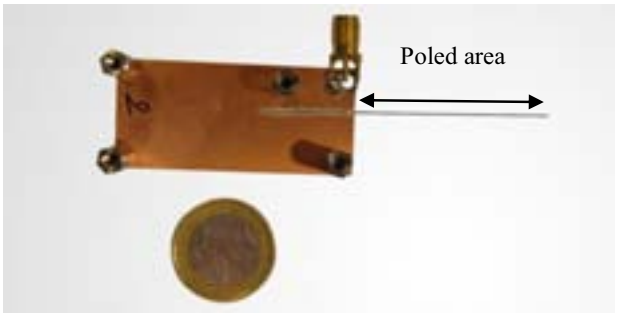

Figure 4. As-prepared ridge-PPT device for characterization.

The SMA port shown in fig. 4 is connected to the network analyzer on one side and to the device by a thin gold wire on the other side allowing for the characterization of the transducer. Device response is recorded for frequencies ranging from 1MHz to 30MHz. Due to their design and dimensions, these devices were particularly suited to check the position of resonance frequencies and confirm the existence of coupling close to 20%. Theoretical investigations show that there are two interesting resonant modes: a longitudinal mode around 10.3MHz (k^2 = 9%) and a shear mode around 16.8MHz (k^2 = 22%). Figure 5 compares the frequency analysis of the device (measured conductance) with simulation results (harmonic conductance).

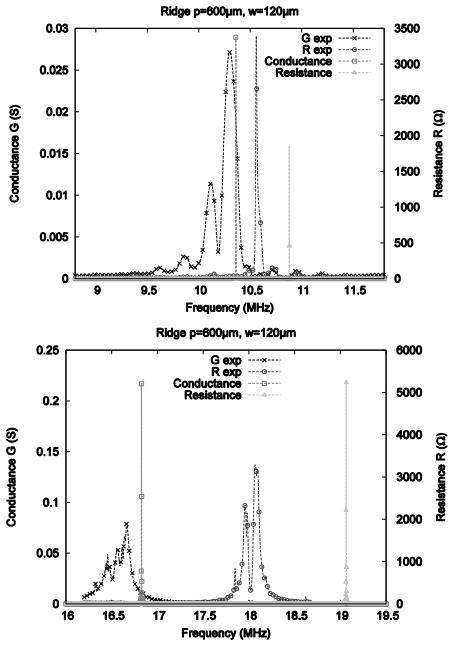

Figure 5. Comparison between experimental (actual conductance) and theoretical (harmonic conductance) device response.

The deviation between theoretical and experimental frequencies of the two investigated modes at 10.3MHz and 16.8MHz respectively is smaller than 1% (fig. 5). This matching is not only explained by the adequacy between the finite element model and the actual device design but also by the accuracy of $LiNbO_3$ physical coefficients used in the computation ([10]). The device was indeed not poled nor excited on its stuck extremity, yielding it very close to a "free-free model". Experimental coupling coefficient of these devices is not as high as predicted but it is found 20 times larger than former $LiNbO_3$ PPTs [4]. Moreover, the experimental electromechanical coupling evolution follows the theoretical prediction, as shown in Table 1. The difference between theoretical and experimental couplings can be explained by the quality of the ridge sides. Due to the indented profile of the ridge, its width is not constant along its length,

leading to resonant mode spreading and electromechanical coupling decreasing.

TABLE I. TRANSDUCERS CHARACTERIZATION RESULTS AT λ =600µm

Length (cm)	Depth (µm)	Width/period ratio (µm)	Resonance frequency (kHz)		Electromechanical coupling (%)	
			Exp.	Theo.	Exp.	Theo.
5	500	0.20	16665	16821	14.95	22.08
			10299	10364	4.88	9.09
		0.33	11468	11553	10.94	18.33
			10316	10093	8.42	10.76

These results confirm nevertheless the existence of the two predicted acoustic resonant modes close to the expected frequencies, and as a side result, the accuracy of our simulation tool. They also confirm that coupling coefficients can reach values larger than 10%, depending of the device configuration.

CONCLUSION

A new type of structures has been successfully manufactured to allow for experimental investigation of waves excited and propagating in ridge-PPTs. The obtained results are encouraging, emphasizing a very good agreement between simulation and experiment. Electromechanical coupling coefficients of about 15% have been experimentally demonstrated, according to theoretical predictions, which is a key-point for the future exploitation of these devices as wide-band filter for telecommunication. Wave velocities in excess of $9km.s^{-1}$ have been also observed, in line with theoretical predictions. This result indicates that waves propagating in the proposed ridge-PPT are capable to largely overcome SAW velocities and may advantageously compete with Lamb waves characteristics. The proposed approach is therefore a serious alternative for high frequency acoustic devices needed for the telecommunication standard of the future.

ACKNOWLEDGMENT

This work was partly supported by the French RENATECH network and its FEMTO-ST technological facility. This work is also supported by the French National Research Agency (ANR) in the MatEtPro Research Program as the CHARADES project under grant#ANR2011RMNP01201.

REFERENCES

[1] Makkonen, T. ; Plessky, V.P. ; Grigorievski, V.I. ; Kopp, L. ; Solal, M. ; Steichen, W. ; Salomaa, M.M. in IEEE Ultrasonics Symp., 2002, vol. 1, pp. 317–320.

[2] R. Ruby, in IEEE Ultrasonics Symp., 2007, pp. 1029–1040..

[3] E. Courjon, N. Courjal, W. Daniau, G. Lengaigne, L. Gauthier- Manuel, S. Ballandras, and J. Hauden, J. Appl. Phys., vol. 102, art. no. 114107, 2007.

[4] F. Bassignot, E. Courjon, G. Ulliac, S. Ballandras, J.-M. Lesage, and R. Petit, J. Appl. Phys., vol. 111, art. no. 064106, 2012.

[5] Muralt, P. ; Antifakos, J. ; Cantoni, M. ; Lanz, R. ; Martin, F. in IEEE Ultrasonic Symp., 2005 vol. 1. Pp. 315–320.

[6] S.W. Kwon, W.S. Yang, H.M. Lee, W.K. Kim, H.-Y. Lee, W.J. Jeong, M.K. Song, D.H. Yoon, Appl. Surf. Sci., vol. 254, no. 4, pp. 1101–1104, 2007.

[7] H. Hui, R. Ricken, and W. Sohler, J. Lightwave Technol., vol. 28, no. 13, pp. 1913–1916, 2010.

[8] Weigand, B. ; Stolze, M. ; Rubel, F. ; L'huillier, J. ; Lenhard, A. ; Becher, C. ; Wolff, S., "Fabrication of ridge waveguides in $LiNbO_3$," in Proc. Int. Symp. Applications of Ferroelectrics, held jointly with European Conf. Applications of Polar Dielectrics and Int. Symp Piezoresponse Force Microscopy and Nanoscale Phenomena in Polar Materials, 2012, pp. 1–4.

[9] S. Ballandras, P. Lardat, M. Wilm, Th. Pastureaud, A. Reinhardt, N. Champavert, W. Daniau, V. Laude, R. Armati, and G. Martin, J. Appl. Phys., vol. 105, art. no. 014911, 2009.

[10] G. Kovacs, M. Anhorn, H. E. Engan, G. Visintini, and C. C. W. Ruppel, "Improved material constants for $LiNbO_3$ and LiTaO3," in Proc. IEEE Ultrasonics Symp., 1990, pp. 435–438.

Recent Progress and Perspectives of Extremely Low Loss Acoustic Cavities: From Frequency Sources to Artificial Atoms

Maxim Goryachev and Michael E. Tobar
ARC CE for Engineered Engineered Quantum Systems
School of Physics
University of Western Australia
35 Stirling Hwy, Crawley, 6009, Australia
Email: maxim.goryachev@uwa.edu.au

Serge Galliou
FEMTO-ST (UMR CNRS 6174), Département Temps Fréquence
ENSMM 26, Chemin de lEpitaphe, 25000 Besançon, France
Email: Serge.Galliou@ens2m.fr

***Abstract*—Bulk Acoustic Wave devices with effective phonon trapping demonstrate extremely low losses superior to any other mechanical systems currently under investigations. It is demonstrated that quality factors of such systems approach the level of 10^{10} at relatively high frequencies approaching one GHz. The record high $Q \times f$ product of 1.6×10^{18} opens a wide range of applications for such devices including testing of fundamental physics, quantum hybrid systems and high precision frequency generation.**

I. Introduction

This work gives a general overview of the recent achievements and future perspectives of the cryogenic quartz Bulk Acoustic Wave (BAW) devices. The work discusses the major issues related to such devices including loss mechanisms and nonlinearities. Identification of loss mechanisms in extremely high quality factor system is an important step in their further development. Characteristics of the state-of-the-art acoustic cavities given in this work open a door for various applications of such systems ranging from frequency standards to tests of fundamental physics.

Section II discusses principles of operation of BAW resonators from the point of view of phononics. The following section discusses various loss mechanisms in detail giving some estimations. Section IV discusses two sources of nonlinearities experimentally observed in cryogenic acoustic cavities. Section V gives characteristics of the most advanced BAW cavities investigated at cryogenic temperatures. Section VI section summarises the progress and problems of possible applications of cryogenic BAW devices in the area of frequency standards. And, finally, Section VII proposes applications of acoustical cavities for various physical experiments.

II. Overview of the Quartz BAW Cavities

In record low loss regimes at low temperatures [1]–[4], Bulk Acoustic Wave quartz resonators could be regarded as an acoustic analogue of well-known optical Fabry-Pérot cavities. Indeed, the former are typically composed of two partially transmitting mirrors aligned to confine the light beam in confined space. Incident photons of the cavity exhibits multiple reflection allowing it to interfere with itself many times. If the wave length of the light is such that interference does occur within the cavity, the resonance conditions are met and the energy is effectively stored in the system. The same operation principles are utilised in BAW plate resonators where the role of photons (real particles defined in the space) is played by phonons (quasi-particles defined in a crystal lattice), quanta of lattice vibration. These quasi-particles exhibit multiple reflection from the vacuum-crystal interfaces playing the role of mirrors. In the same way as in optics, the resonance conditions are met when the phonon wavelength leads to multiple interference of sound with itself.

The number of phonon self-interference events is limited by the cavity quality factor. The quality factors of the acoustic cavities are approaching 10^{10} for the wavelengths approaching 400 μm giving cavity linewidths of orders of tens of miliHz. This parameter is limited by a number of factors that can be classified into two classes: phonon leakage to the environment [5] or material-related loss mechanism. The former class represent phonon losses due to clamping mechanisms which hardly depend on temperature. The latter type groups mechanisms related to the material of the cavity, which includes phonon-phonon dissipation due to the crystal anharmonisity, thermoelastic losses, two-level system absorption, phonon scattering, etc. These mechanisms are discussed in the next section.

For almost all applications of acoustic cavities it is vital to keep the system losses as low as possible. For this purpose, the phonon leakage losses must be engineered to a minimum. For the plate cavity geometry this is achieved by an effective phonon-trapping technique. The solution is to trap acoustic energy in the centre of the disk plate while the disk is clamped from the sides. The trapping is done by introducing curvature into one of the plate surfaces by manufacturing a plano-convex shape [3], [6]. This variable plate thickness increases the local phonon frequency along the plate disk radius closer to the edges. The corresponding energy difference along the radial direction due to this curvature can be considered as an

978-1-4799-0342-9/13/$31.00 ©2013 IEEE

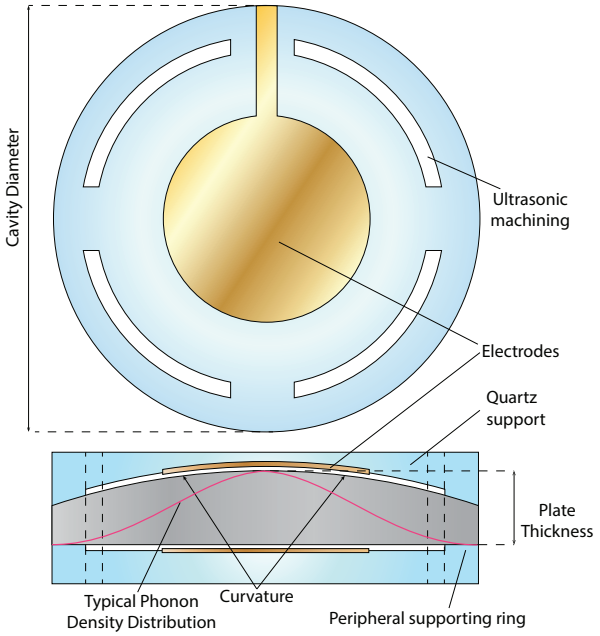

Fig. 1. Acoustic cavity design. The effective phonon trapping reduces phonon density near the disc border preventing losses due to phonon tunnelling to the environment. Phonon density distribution is typically Gaussian for a main overtone mode.

effective potential well. So, phonons are trapped if their total transverse energy (corresponding to in-plane wave numbers) do not exceed the energy difference between the edge and the centre. This situation significantly decreases the probability to find a resonant phonon near the clamping points. Theoretical treatment of the energy trapping problem from the point of view of linear elastodynamics is given in [6]. The calculations predict the mode shape in the form of polynomial-normal distribution. This result has been confirmed by means of X-ray spectroscopy [7], [8]. The cavity design is sown in Fig. 1 demonstrating the typical phonon density for the investigated modes.

An acoustic cavity can exhibit resonance conditions for different phonon polarisations corresponding to different sound velocities. The two quasi-transverse polarizations are known as B (fast-shear) and C (slow-shear) modes. It is demonstrated [1], [2] that the quasi-longitudinally polarised phonons corresponding to the A-mode exhibit the minimum material losses at cryogenic ($\sim$ 4 K) and deep-cryogenic ($\sim$ 20 mK) temperatures. Thus, from this point on, only longitudinally polarised modes are discussed.

The operation of optical cavities require lasers as sources of coherent optical radiation. For acoustical analogues, the cavity may be pumped by an external signal source through effective electromechanical coupling due to the piezoelectric effects of crystals. For this purpose, two conducting electrodes impose a potential difference between two surfaces of the plate that creates a gradient of the electric potential along the plate thickness. The spatial Fourier harmonics of this gradient are coupled to mechanical vibrations through the piezoelectric effect. Frequencies of these vibrations are set by plate dimensions, material properties and the order of the harmonic. This type of vibration is referred as a thickness vibration that has to be distinguish from parasitic flexure vibration modes. Detection of the plate vibration is performed by measuring the displacement current between the surfaces of the plate. To minimise the acoustic losses due to the electrodes, they are separated from the crystal plate by a tiny vacuum gap. This solution is known as the BVA-technology [9]. Electrodes are deposited on two quartz supports placed on each side of the resonator, and in such a way that the gap between electrodes and resonator surfaces is typically between 5 and 10μm [2], [3].

III. Acoustic Losses

Total intrinsic losses of an acoustic cavity apart from phonon tunnelling to the environment are a sum of losses due to different mechanisms:

$$\frac{1}{Q} = \frac{1}{Q_{phonon-phonon}} + \frac{1}{Q_{TLS}} + \\ + \frac{1}{Q_{scattering}} + \frac{1}{Q_{thermoelastic}} + \text{etc}, \quad (1)$$

where the Q-values represent different mechanisms discussed in this section. Temperature and frequency dependancies of these losses are given in [4].

The first phonon loss mechanism in acoustic cavities at low temperatures and relatively high frequencies is loss mechanism due to phonon-phonon scattering over crystal lattice anharmonicity ($Q_{phonon-phonon}$ in equation (1)). This mechanism was first analytically considered by Landau for the case of shear-polarized phonons [10], [11]. The original work discards such losses for longitudinal phonons in the case of two phonon collision, due to significantly higher sound velocity. Later revisions of the theory considered the case of three colliding phonons [12] predicting the following law: $Q^{-1}_{phonon-phonon} \sim T^{-6.5}$. This law is experimentally observed for acoustic cavities between between 6K and 13K [4]. The acoustic wave attenuation α is proportional to the resonance angular frequency ω as long as $\omega\tau_{TH} \gg 1$ where τ_{TH} is the average lifetime of thermal phonons, $\hbar$ the Planck constant, and k_B the Boltzmann constant. So, the $Q_{phonon-phonon}$-factor of an acoustic wave propagating with velocity V

$$Q = \frac{\pi\omega}{V\alpha} \quad (2)$$

would no longer depend on frequency ω. Since these conditions are met in the case of considered systems, the Q-factor tends to be independent of f ($Q = const$ law) and thus independent of the cavity overtone number [4].

It is known the even Top High Quality synthetic crystals are hosts of different kind of impurity ions. In the case of the synthetic alpha quartz material, these ions are Al^{3+}, Na^{+} and Li^{+}, Si^{4+}, H^{+}, etc [13]–[16] studied by various methods. Although the utilised material is premium pure, concentration of these ions could reach $1-3$ ppb. These randomly spread

ions exhibit quantised energy level behaviour and typically appear as two-level systems (TLS) absorbing acoustic phonons. Temperature dependence of associated losses (Q_{TLS} in equation (1)) is predicted to obey the $T^{-0.3}$ [17] scaling law which is also observed in acoustic cavities [3], [4]. Such dependence have been also observed in a various of electromechanical systems [18]–[22].

Despite predictions of the Landau-Rumer theory on frequency-independent losses, the increase of cavity losses at higher frequencies (typically $100 - 220$ MHz) occurs for the most of the experimentally studied devices [1]–[4]. This phenomenon can be explained by phonon scattering on the cavity surfaces ($Q_{scattering}$ in equation (1)). This type of scattering originates from the surface roughness as well as from the presence of a dead layer. The reflection coefficient on a rough surface with a roughness variance σ^2, assuming a gaussian probability density, and can be expressed as $R = e^{-2k^2\sigma^2}$ [23] , for the phonon wave number k.Thus, the reflection is equivalent to a modified path causing an attenuation equal to $\alpha^{'} = \alpha + \ln(R/h)$, where h is the cavity thickness. So, for an overtone number $n = kh/\pi$, the Q-factor is given as:

$$Q_{scattering} = \frac{h^2}{2n\sigma^2} \tag{3}$$

Since the resonant frequency $\omega = 2\pi f$ is almost proportional to the overtone number n, this mechanism results in $Q \times f = const$ scaling law. The highest measured Q-values are close to estimated values of $Q_{scattering}$, demonstrating that the cavity roughness could be a limiting factor for higher frequencies. The surface scattering mechanism explains better performance of the cavities with a better surface polishing grading [4]. The largest observed values of Q-factors correspond to $\sigma = 1$ nm, which is consistent with specification of the fabrication process. For other cavities, the standard deviation varies from 4 or 7 nm, which is also in agreement with used polishing processes.

A cause of the quality dependence on the frequency for even higher resonance frequencies (> 200 MHz) is bulk phonon scattering. At such frequencies, the expected $Q = const$ law is overcame by $Q \times f^3 = const$ dependence. This type of frequency scaling law corresponds to elastic Rayleigh scattering of waves over microscopic particles whose dimensions are smaller than a wavelength. This type of wave scattering is known to be the main mechanism of loss in optical fibres [24]. Rayleigh scattering attenuation is inversely proportional to the forth power of the wavelength, or equivalently directly proportional to the fourth power of frequency: $\alpha \sim f^4$. So, using relation (2), this gives the experimentally observed $Q \sim f^{-3}$ law. Acoustic wave scattering over this quenched randomness is analogous to a light beam scattering in optical fibres. When a phonon hits an impurity or other imperfection of the crystal structure, it can maintain the same direction of propagation without attenuation, or alternatively change the direction of propagation and escape the cavity [5] giving rise to energy loss. Rayleigh scattering of acoustic waves has been theoretically predicted and observed for various polycrystalline and glass materials [25]–[27].

Another loss mechanism that can potentially be observed for quasi-longitudinally polarised phonons is the thermoelastic losses mechanism. So, the $Q_{thermoelastic}$ for longitudinal vibration can be estimated based on the description the coupled equations of motion of the medium and the equation of thermal conduction [28]. Simplified estimations of such losses can be made assuming an isotropic medium and propagation along the Z-axis which is the most experimentally studied case. This analysis implies calculation of a turning-point frequency f^* that shows if a mechanical system works in adiabatic or isothermal regimes:

$$f^* = \frac{V_3^2}{2\pi\chi_3} \tag{4}$$

where χ_3 is the material diffusivity, and V_3 is the wave velocity for a propagation along the Z-axis. The former is calculated based on data on thermal conductivity and heat capacity at cryogenic temperatures [29], [30] giving $1 \leq f^* \leq 5.5$ MHz for $3 \leq T \leq 10$K. Over this temperature range, all the resonant frequencies are always greater than f^*, and acoustic wave propagates in the quasi-isothermal regime. For this regime, the maximum attenuation is:

$$\alpha_\infty = \frac{\epsilon_3 \pi f^*}{V_3} \tag{5}$$

with ϵ_3, where λ_{33} are calculated from the thermal expansion tensor and the tensor of isothermal elastic constants of crystalline quartz. Whereas the thermal expansion coefficients have been measured at low temperatures [29], the elastic constants on the other hand can just be roughly approximated by their values at room temperature. Nevertheless, the corresponding thermoelastic losses estimated from equation (2) remain always at least two orders of magnitude lower than those measured below 10K. Since α_∞ is almost independent of frequency for a given material, these type of losses result in $Q/\omega = const$ law.

IV. Sources of Nonlinearities

The most common source of nonlinearities of acoustic cavities at cryogenic cavities is due to crystal anharmonisity [31] which comes as higher order terms in a crystal Hamiltonian describing atom vibrations. These terms are responsible for mode couplings leading to the Landau-Rumer losses, in particular. As explained above, these losses come when the acoustic phonons of a driven mode are scattered by thermal phonons of the material modes on the crystal anharmonicity. Although the crystal anharmonicty is involved in the loss mechanism, the mode behaviour remains linear until the point where self interaction between acoustic phonons becomes pronounced. So, despite the fact that all Taylor series terms of the Hamiltonian representing the lattice anharmonicity could potentially take part in the loss mechanisms, only the linear losses resulting from the lowest (three-phonon mixing) Hamiltonian terms [12] have been experimentally observed in extremely high-Q acoustic cavities. It is the mixing between acoustic phonons

that leads to the nonlinear effects in BAW devices known as the isochronism defect [32], [33]. This nonlinear phenomenon appears as resonance frequency dependance on incident power and the bistability effect at higher powers. Such effects could be observed with extremely low loss modes for incident powers as low as -45 dBm. This phenomenon at room and cryogenic [34] temperatures is well-described by a Duffing oscillator model both where the nonlinearity is introduced into an equation of motion as a cubic dependance of a resonance frequency on the amplitude of the vibration.

The related effect is due to frequency-temperature relations when due to dissipation injected phonons increase the temperature that causes the resonance frequency shift. This effect typically observed in cryogenic BAW devices at high enough powers (typically above $-30..-25$ dBm) even though frequency-temperature sensitivity of the acoustic modes decreases with temperature.

Another source of nonlinear behaviour in cryogenic acoustic cavities is attributed to various sorts of defects resulting in a high degree of disorder resulting. In the case of high quality factor cavities and large number of defects, the probability of phonon interaction with such impurities is high enough to be detected macroscopically. Such situation arises when an effective phonon-trapping cavity is build of unswept quartz crystal. The main feature of such crystals is comparatively high concentration (up to 10 ppm) of alkali impurities Na^+, Li^+, K^+ trapped in potential-wells near substitutional Al^{3+} [35]. If such potential well is not harmonic, than phonon-impurity interaction leads to a nonlinear loss term in the equations of motion for a macroscopic acoustical mode. This results in anomalously strong nonlinearity that is observed for a cavity incident powers as low as -95 dBm. Such nonlinearity can be modelled by a stable van der Pol oscillator where the nonlinearity is introduced through the power dependent loss term in the equations of motion. Experimentally, the phenomenon is observed by various effects including: 1) frequency sweep discontinuity and related oscillatory instability regions, which manifested as a abrupt response moving away from the resonance with increasing incident power; 2) frequency-power dependence, seen as frequency shift with increasing power; 3) power sweep discontinuity, observed as an abrupt change of the modulus of the reflection coefficient for a given frequency with only a small increase of incident power; 4) self-induced transparency, which was seen as an avoided crossing with incident power causing the doubling of the frequency response extrema at given values of incident power. These nonlinear phenomena in devices at cryogenic temperatures are still a matter of current investigations.

V. Characteristics of State-of-the-Art Acoustic Cavities

Various types of acoustic cavities have been tested at both liquid helium and mili-Kelvin temperatures. Among those types, acoustic cavity design described in Section II demonstrated superior Q-factors and $Q \times f$ products. For such design, the main geometric parameters are the plate disc diameter, plate thickness and curvature radius. Other important parameters are material quality (all cavities are manufactured with Top High Quality alpha synthetic quartz) and surface roughness. The summary of these parameters and corresponding experimental measurements is given in Table. I.

The measured characteristics of these cavities demonstrate that the cavity losses are minimised by improved surface polishing and increased disk radius. The former results in minimisation of surface scattering losses that are believed to be the limiting mechanism in the $100-200$ MHz frequency range. The latter improves decreases phonon-tunnelling to the environment.

VI. Applications to Frequency Standards

Extremely low loss systems of any sort are very attractive for building secondary frequency standards. In the case of cryogenic BAW devices, the goal of building such system is twofold. On one hand, it can result in building a hyper-stable frequency source whose frequency (of the order of tens of Megahertz) is close to the reference frequency of met of laboratory equipment ($5-10$ MHz). Unlike microwave and optical clocks that will not require significant frequency devision that unavoidably leads to losses in frequency stability. On the other hand, it helps to understand whether or not the BAW technology has reached its limits. It is important to predict the frequency stability limits of this quartz oscillators in comparison with other technologies [36].

To improve stability of frequency sources, ultra-narrow linewidths of cryogenic acoustic devices can be utilised by either active [37] or passive methods [34]. The first approach implies building a cryogenic analog of a well-known quartz oscillator with a cryogenic BAW as a frequency selective element. The second solution utilises the resonator as a part of a discriminator in a negative feedback that improves long term stability of a given frequency source. The active solution is more challenging. First, there is a limited choice of electronic components, which exhibit unnatural behaviour and high characteristic dispersion (for devices from the same series) [38]. Moreover, the gap between simulation and experiment remains considerable. This leads to unpredictable results, such as, the inability to excite optimal modes. In addition, long cool down-warm up cycles of cryocoolers make oscillator adjustments almost impossible. Although this approach is potentially, more fruitful since one can benefit not only from high qualities of cryogenic BAW drives but also from low (temperature) noise of electronic components.

The early attempts to build secondary frequency sources based on BAW devices [31], [34], [37], [39] reveal that the main advantage of the cryogenic quartz devices – very high quality factors – is annulled by the absence of a frequency-temperature turnover point, and strong nonlinear effects. Although multiple turn-over points in frequency-temperature characteristics of chosen OTs was observed at temperatures below 1K [3], their utilisation is impractical due to limitations of widely used cryocoolers. Although at the stage of the first realisation, oscillators based on cryogenic BAW quartz

TABLE I
SUMMARY OF CRYOGENIC TESTS OF DIFFERENT ACOUSTIC CAVITIES TESTED AT CRYOGENIC TEMPERATURES.

Experiment	**Frequency, MHz at 300K**	**Thickness, mm**	**Diameter mm**	σ, **nm**	**Separated Electrodes**	Q_{max}**-factor**	$Q \times f$, **Hz**	f_{max}, **MHz**	**Temperature, K**
[2]	10, shear	1.08	13	4..7	yes	3×10^8	5.2×10^{15}		3.8
[3]	10, shear	0.54	13	4..7	yes	2×10^9	7.8×10^{16}		20×10^{-3}
[4]	5, shear	1	30	1	yes	8×10^9	1.6×10^{18}	241.7	3.75
under review	5, shear	1	30	1	yes	$\sim 3 \times 10^9$, loaded	4×10^{17}	517.9	15×10^{-3}
[4]	10, shear	0.54	13	4..7	no	5×10^8	2.3×10^{16}		3.75

technology may result in moderate improvement of the long term frequency stability over their room-temperature counterparts [31], [34], they still cannot compete with the state-of-the-art cryogenic microwave sapphire oscillators. The next generation of quartz frequency sources should be based on specially designed resonators with a frequency-temperature turnover point at 4K, have passive and active vibration compensation system, employ more reliable active devices.

VII. APPLICATIONS IN FUNDAMENTAL AND APPLIED PHYSICS

Low loss mechanical systems play a very important role as instruments in the investigation of a wide variety of fundamental physics problems including quantum measurement and computation [40], spin detection, ultra-sensitive force detection, gravitational wave detection and more. Thus, the demonstrated extremely low losses in BAW cavities have potential applications in a variety of areas of physics including fundamental aspects and applications. Whether the former can emily extremely long coherence times of such devices, the latter can benefit from better understanding of process in crystal solids.

The equilibrium ground state of hybrid mechanical systems has become a topic of interest of many research groups [41]. To achieve the operation of hybrid mechanical systems in their quantum ground state, it is vital to develop resonators with very low losses at temperatures approaching absolute zero. The frequencies accessible using mechanical systems are low, and thus a lower temperature is required (governed by $\hbar\omega > k_B T$) to reach the equilibrium ground state. The average number of thermal phonons is governed by the Bose-Einstein distribution

$$n_{\mathrm{TH}} \sim \frac{1}{e^{\frac{\hbar\omega}{k_B T}} - 1}, \tag{6}$$

which dictates, for example, that a frequency of greater than 144 MHz is required to have $n_{\mathrm{TH}} < 1$ at a temperature of 10 mK. Recent years have seen mechanical resonators developed with frequencies as high as 11 GHz [42], corresponding to $T = 0.53$ K for an average phonon occupation number below unity. But such high frequencies of mechanical systems come at the cost of high losses. For instance, O'Connell et al. [43] demonstrated single phonon control of an FBAR resonator at 6.07 GHz, but exhibiting a quality factor of only 260 making full Wigner state tomography impossible. This low value of Q significantly limits the coherence time of hybrid systems based on these devices. Aside from conventional thermodynamic cooling, the ground state or Standard Quantum Limit could potentially be reached by exploiting an low loss resonance, where the mode can be cold damped through feedback or a parametric processes. In the ideal case, the ratio Q/T remains constant, where the acoustic Q-factor is reduced as the mode amplitude is then damped and electromagnetically cooled to a lower temperature. So, once again, the ground state is achieved by means of degrading loss characteristics. So, BAW cavities have a considerable advantage over these traditional mechanical resonators like micro-toroids and membranes which require additional cooling techniques (parametric, sideband cooling) by having high enough resonance frequencies (now approaching 1 GHz) and over film devices by having much higher quality factors (up to several thousands of millions above 240 MHz at 15 mK). Recently, acoustic modes in the ground state have been observed for a BAW device with a loaded quality factor above half a billion. Comparison of BAW cavities with other mechanical systems near the quantum ground state is shown in Table II. The comparison assumes that the ratio of Q/T remains constant for resonator cooled either parametrically or with a negative feedback. By coupling acoustic cavities to nonlinear elements like Josephson Junctions, quantum bits with extremely high coherence times could be designed. In addition, piezoelectric nature of a cavity can be exploited to create strong photon-phonon coupling regimes of a hybrid systems.

Moreover, unlike nano-scale mechanical resonators used in the majority of quantum mechanics-related experiments, acoustic cavities are macroscopic objects of considerable effective mass varying in the range of $0.1 - 10$ milligrams for modes between 100 and 10 MHz. This fact means that experiments with BAW cavities in the ground state can be a promising approach to unifying quantum mechanics and general relativity in a single experiment [51] by measuring gravitational deviation from the canonical commutation relationship. This implies possibilities to utilise such systems in testing fundamental physics.

Besides applications to quantum hybrid systems, extremely high sensitivity should allow future applications of acoustical cavities to be broadened and be used as an alternative (to optical cavities) experimental base for broad range of physical experiments, including material characterisation [52], quantum cavity electromechanics [53], [54], quantum metrology [51], [55] etc. Indeed, potentially phonon cavities can be considered

TABLE II

COMPARISON OF SOME MECHANICAL RESONATORS, WHICH HAVE BEEN COOLED EITHER TO OR NEAR THE GROUND STATE, OR HAVE ACHIEVED HIGH Q-FACTORS. THE TABLE SHOWS THE FREQUENCY, Q-FACTOR, ENVIRONMENTAL TEMPERATURE, NUMBER OF THERMAL PHONONS (n_{TH}) AND Q-FACTOR IF THE SYSTEM COULD BE COOLED IDEALLY TO $n_{\mathrm{TH}} = 1$ PHONON (ASSUMING $Q/T = \mathrm{CONST}$).

Experiment	**Frequency (Hz)**	Q**-factor**	**Temperature (K)**	$n_{\mathbf{TH}}$	$Q(n_{\mathbf{TH}} = 1)$
Silicon [44]	1.96×10^{4}	2×10^{9}	4	4.3×10^{6}	677
Sapphire [45]	5.33×10^{4}	6×10^{8}	4	1.6×10	554
Silica [46]	7.0×10^{7}	10^{4}	0.6	179	81
FBAR [43]	6.07×10^{9}	260	0.025	9×10^{-6}	260
Al [47]	1.06×10^{7}	3.3×10^{5}	0.015	29.1	1.6×10^{4}
Silicon beam [48], [49]	3.68×10^{9}	4×10^{5}	20	113	5.1×10^{3}
Nb-Al-SiN beam [50]	6.3×10^{6}	10^{6}	0.10	330	4.4×10^{3}
Quartz BAW -21st OT [3]	6.54×10^{7}	1.2×10^{9}	0.021	6.2	2.6×10^{8}
Advanced Quartz BAW			0.015	< 1	0.7×10^{9}

as an alternative to photon cavities in many low-frequency, low-power experiments. The advantages of acoustic devices is the ease of operation and integration into higher-order electronic systems, compact size, natural way of combination of mechanical motion and electromagnetic environment, as well as artificial lattice impurities.

ACKNOWLEDGMENT

This work was supported by the Australian Research Council Grant No. CE110001013 and FL0992016, and the Regional Council of Franche-Comté, France, Grant No. 2008C16215.

REFERENCES

[1] S. Galliou, J. Imbaud, R. Bourquin, N. Bazin, and P. Abbe, "Quartz crystal resonators exhibiting extremely high q-factors at cryogenic temperatures," *Electronics Letters*, vol. 44, no. 14, pp. 889–890, 2008.

[2] S. Galliou, J. Imbaud, M. Goryachev, R. Bourquin, and P. Abbe, "Losses in high quality quartz crystal resonators at cryogenic temperatures," *Applied Physics Letters*, vol. 98, no. 9, p. 091911, 2011.

[3] M. Goryachev, D. L. Creedon, E. N. Ivanov, S. Galliou, R. Bourquin, and M. E. Tobar, "Extremely low-loss acoustic phonons in a quartz bulk acoustic wave resonator at millikelvin temperature," *Applied Physics Letters*, vol. 100, no. 24, p. 243504, 2012.

[4] S. Galliou, M. Goryachev, R. Bourquin, P. Abbé, J. Aubry, and M. Tobar, "Extremely low loss phonon-trapping cryogenic acoustic cavities for future physical experiments," *Nature: Scientific Reports*, vol. 3, p. 2132, 2013.

[5] G. Cole, I. Wilson-Rae, K. Werbach, M. Vanner, and M. Aspelmeyer, "Phonon-tunnelling dissipation in mechanical resonators," *Nature Communications*, vol. 2, 2011.

[6] D. S. Stevens and H. F. Tiersten, "An analysis of doubly rotated quartz resonators utilizing essentially thickness modes with transverse variation," *The Journal of the Acoustical Society of America*, vol. 79, no. 6, pp. 1811–1826, 1986.

[7] B. Tanner, *X-Ray Diffraction Topography*. Oxford: Pargamon, 1976.

[8] S. Slavov, "Prediction of the frequency spectrum of at-cut contoured quartz resonators by means of x-ray diffraction topography," *Applied Physics A*, vol. 52, pp. 184–187, 1991.

[9] R. J. Besson, "A new "electrodeless" resonator design," in *31st Annual Symposium on Frequency Control*, 1977, pp. 147 – 152.

[10] L. Landau and G. Rumer, "Uber schall absorption in festen Körpen," *Physikalische Zeitschrift der Sowjetunion*, vol. 11, no. 18, pp. 18–25, 1937.

[11] P. G. Klemens, *Physical Acoustics*. New York:Academic, 1965, vol. III, no. B, ch. Effect of thermal and phonon processes on ultrasonic attennuation.

[12] H. Maris, *Physical Acoustics*. Academic, 1971, vol. 3, ch. Interaction of sound waves with thermal phonons in dielectric crystals, pp. 279–345.

[13] J. Martin, "Aluminum-related acoustic loss in at-cut quartz crystals," in *Proc. 38th Ann. Freq. Control Symposium*, 1984, pp. 16–21.

[14] W. Mason, "Effects of impurities and phonon processes on the ultrasonic attenuation of germanium, crystal quartz, and silicon," in *Physical Acoustics*. Elsevier Science, 1990, vol. III, no. B, ch. Lattice Dynamics.

[15] F. Euler, H. Lipson, A. Kahan, and A. Armington, "Characterization of alkali impurities in quartz," in *Proc. 36th Ann. on Freq. Contr. Symp.*, 1982, pp. 115–123.

[16] L. Halliburton, M. Markes, J. Martin, S. Doherty, N. Kouvakalis, W. Sibley, A. Armington, and R. Brown, "Radiation effects in synthetic quartz: The role of electrodiffusion and radiation-induced mobility of interstitial ions," *IEEE Transactions on Nuclear Science*, vol. 26, no. 6, pp. 4851–4856, 1979.

[17] C. Seoanez, F. Guinea, and A. H. Castro Neto, "Dissipation due to two-level systems in nano-mechanical devices," *Europhysics Letters*, vol. 78, no. 6, p. 60002, 2007.

[18] H. Jiang, M. F. Yu, B. Liu, and Y. Huang, "Intrinsic energy loss mechanisms in a cantilevered carbon nanotube beam oscillator," *Physical Review Letters*, vol. 93, no. 18, p. 185501, 2004.

[19] A. K. Hüttel, G. A. Steele, B. Witkamp, M. Poot, L. P. Kouwenhoven, and H. S. J. van der Zant, "Carbon nanotubes as ultrahigh quality factor mechanical resonators," *Nano Letters*, vol. 9, no. 7, pp. 2547–2552, 2009.

[20] S. B. Shim, J. S. Chun, S. W. Kang, S. W. Cho, Y. D. Park, P. Mohanty, N. Kim, and J. Kim, "Micromechanical resonators fabricated from lattice-matched and etch-selective gaas/ingap/gaas heterostructures," *Applied Physics Letters*, vol. 91, no. 13, p. 133505, 2007.

[21] G. Zolfagharkhani, A. Gaidarzhy, S. B. Shim, R. L. Badzey, and P. Mohanty, "Quantum friction in nanomechanical oscillators at millikelvin temperatures," *Physical Review B*, vol. 72, no. 22, p. 224101, 2005.

[22] M. Imboden and P. Mohanty, "Evidence of universality in the dynamical response of micromechanical diamond resonators at millikelvin temperatures," *Physical Review B*, vol. 79, no. 12, p. 125424, 2009.

[23] P. Welton, "The potential method formulation of acoustic wave scattering by rough surfaces," *Journal of the Acoustical Society of America*, vol. 54, no. 1, pp. 66–73, 1973.

[24] W. Zhi, R. Guobin, L. Shuqin, and J. Shuisheng, "Loss properties due to rayleigh scattering in different types of fiber," *Optics Express*, vol. 11, no. 1, pp. 39–47, 2003.

[25] W. P. Mason and H. McSkimin, "Attenuation and scattering of high frequency sound waves in metals and glasses," *Journal of Acoustical Society of America*, vol. 19, no. 3, pp. 464–473, 1947.

[26] A. Bhatia, "Scattering of high-frequency sound waves in polycrystalline materials," *Journal of Acoustical Society of America*, vol. 31, no. 1, pp. 16–23, 1958.

[27] E. Papadakis, "Ultrasonic attenuation caused by scattering in polycrystalline metals," *Journal of Acoustical Society of America*, vol. 37, no. 4, pp. 711–717, 1965.

[28] H. Deresiewicz, "Plane waves in a thermoelastic solid," *Journal of the Acoustical Society of America*, vol. 29, no. 2, pp. 204–209, 1954.

[29] T. Barron, J. Collins, T. Smith, and G. White, "Thermal expansion, grüneisen functions and static lattice properties of quartz," *Journal of Physics C: Solid State Physics*, vol. 15, no. 20, p. 4311, 1982.

[30] R. Zeller and R. Pohl, "Thermal conductivity and specific heat of noncrystalline solids," *Physical Review B*, vol. 4, no. 6, pp. 2029–2041, 1971.

[31] M. Goryachev, *Cryogenic BAW Resonators and Oscillators*. Lambert Academic Publishing, 2012.

[32] N. Gufflet, R. Bourquin, and J. Boy, "Isochronism defect for various doubly rotated cut quartz resonators," *IEEE Transactions on Ultrasonics, Ferroelectrics and Frequency Control*, vol. 49, no. 4, pp. 514–518, 2002.
[33] J. Nosek, "Drive level dependence of the resonant frequency in BAW quartz resonators and his modeling," *IEEE Transactions on Ultrasonics, Ferroelectrics and Frequency Control*, vol. 46, no. 4, pp. 823–829, July 1999.
[34] M. Goryachev, S. Galliou, J. Imbaud, R. Bourquin, and P. Abbé, "Recent investigations on BAW resonators at cryogenic temperatures," in *Proc EFTF & IEEE IFCS Joint Meeting*, San Francisco, USA, May 2011.
[35] J. Martin, "Electrodiffusion or sweeping of ions in quartz - a review," *IEEE Transactions on Ultrasonics, Ferroelectrics and Frequency Control*, vol. 35, no. 3, pp. 288–296, 1988.
[36] J. Vig and etc, "Panel discussion: To what extent will quartz be squeezed out by MEMS and CSAC session," in *Proc EFTF & IEEE IFCS Joint Meeting*, San Francisco, USA, May 2011.
[37] M. Goryachev, S. Galliou, J. Imbaud, and P. Abbé, "Advances in development of quartz crystal oscillators at liquid helium temperatures," *Cryogenics*, vol. In press, June 2013.
[38] M. Goryachev, S. Galliou, and P. Abbé, "Cryogenic transistor measurement and modeling for engineering applications," *Cryogenics*, vol. 50, pp. 381–389, 2010.
[39] M. Goryachev, S. Galliou, P. Abbé, P.-Y. Bourgeois, S. Grop, and B. Dubois, "Quartz resonator instabilities under cryogenic conditions," *IEEE Trans. Ultrason. Ferroelect.*, vol. 59, no. 1, January 2012.
[40] V. B. Braginksy and F. Y. Khalili, *Quantum Measurement*. Cambridge University Press, 1992.
[41] A. Schliesser and T. J. Kippenberg, *Advances In Atomic, Molecular, and Optical Physics*. Academic Press, 2010, ch. 5 - Cavity Optomechanics with Whispering-Gallery Mode Optical Micro-Resonators, pp. 207–323.
[42] M. Tomes and T. Carmon, "Photonic micro-electromechanical systems vibrating at x-band (11-ghz) rates," *Physical Review Letters*, vol. 102, no. 11, p. 113601, 2009.
[43] A. D. O'Connell, M. Hofheinz, M. Ansmann, R. C. Bialczak, M. Lenander, E. Lucero, M. Neeley, D. Sank, H. Wang, M. Weides, J. Wenner, J. M. Martinis, and A. N. Cleland, "Quantum ground state and single-phonon control of a mechanical resonator," *Nature*, vol. 464, no. 7289, pp. 697–703, 2010.
[44] D. F. McGuigan, C. C. Lam, R. Q. Gram, A. W. Hoffman, D. H. Douglass, and H. W. Gutche, "Measurements of the mechanical q of single-crystal silicon at low temperatures," *Journal of Low Temperature Physics*, vol. 30, pp. 621–629, 1978.
[45] C. R. Locke, M. E. Tobar, and E. N. Ivanov, "Monolithic sapphire parametric transducer operation at cryogenic temperatures," *Review of Scientific Instruments*, vol. 71, no. 7, pp. 2737–2741, 2000.
[46] R. Rivière, S. Deléglise, S. Weis, E. Gavartin, O. Arcizet, A. Schliesser, and T. J. Kippenberg, "Optomechanical sideband cooling of a micromechanical oscillator close to the quantum ground state," *Physical Review A*, vol. 83, no. 6, p. 063835, 2011.
[47] J. D. Teufel, T. Donner, D. Li, J. W. Harlow, M. S. Allman, K. Cicak, A. J. Sirois, J. D. Whittaker, K. W. Lehnert, and R. W. Simmonds, "Sideband cooling of micromechanical motion to the quantum ground state," *Nature*, vol. 475, no. 7356, pp. 359–363, 2011.
[48] J. Chan, T. P. M. Alegre, A. H. Safavi-Naeini, J. T. Hill, A. Krause, S. Groblacher, M. Aspelmeyer, and O. Painter, "Laser cooling of a nanomechanical oscillator into its quantum ground state," *Nature*, vol. 478, no. 7367, pp. 89–92, 2011.
[49] A. Safavi-Naeini, J. Chan, J. Hill, T. Alegre, A. Krause, and O. Painter, "Observation of quantum motion of a nanomechanical resonator," *Physical Review Letters*, vol. 108, no. 3, p. 033602, 2012.
[50] T. Rocheleau, T. Ndukum, C. Macklin, J. B. Hertzberg, A. A. Clerk, and K. C. Schwab, "Preparation and detection of a mechanical resonator near the ground state of motion," *Nature*, vol. 463, no. 7277, pp. 72–75, 2010.
[51] I. Pikovski, M. Vanner, M. Aspelmeyer, M. Kim, and C. Brukner, "Probing planck-scale physics with quantum optics," *Nature Physics*, vol. 8, pp. 393–397, 2012.
[52] B. Luthi, *Physical Acoustics in Solid State Science*, ser. Solid-State Sciences. Berlin: Springer-Verlag, 2005.
[53] I. Mahboob, K. Nishiguchi, H. Okamoto, and H. Yamaguchi, "Phonon-cavity electromechanics," *Nature Physics*, vol. 8, pp. 387–392, 2012.
[54] R. Ruskov and C. Tahan, "On-chip quantum phonodynamics," *http://arxiv.org/abs/1208.1776*, 2012.
[55] M. Aspelmeyer, T. Kippenberg, and F. Marquardt, "Cavity optomechanics," *http://arxiv.org/abs/1303.0733*, 2013.

A Novel Evanescent-Mode Möbius-Coupled Resonator Oscillators

Ajay K. Poddar
Synergy Microwave Corp, NJ, USA
Technical University Munich (TUM), Germany
Email:akpodar@synergymwave.com

Ulrich L. Rohde
Cottbus University, BTU Cottbus, Germany
Technical University Munich (TUM), Germany
Synergy Microwave Corp, NJ, USA

***Abstract*—A novel evanescent-mode Möbius-coupled resonator oscillator is developed for the applications of synthesized X-band signal sources in RADAR and modern communication systems.**

Keywords-Evanescent-Mode, Mobius Resonator, Oscillator

I. INTRODUCTION

It is important to achieve low phase noise in various applications. The phase noise increases a bit error rate in telecommunication links, degrades stability of beam in particle accelerators and decreases sensitivity of radars. DROs represent an interesting solution to improve the stability by reducing the bit error rate because high quality factor of a Dielectric Resonator (DR) allows for achieving an excellent phase noise performance at microwave and millimeter wave frequencies. Dielectric resonators are ceramic materials which have high dielectric permittivity, high quality factor, and high temperature stability. They have much smaller size compared to cavity resonators; therefore, they are frequently employed in the design of frequency stable RF circuits, especially in oscillators [1]-[5].

When high data-rates have to be transferred, as with M-QAM modulation in LTE, LMDS, and fixed frequency point-to-point digital radio and satellite-links, these systems need low phase noise signal sources either free running or phase-locked. RADAR systems and Research Laboratories also require ultra-low noise sources to generate ultra-low noise carrier signals.

A wide range of military, industrial, medical, test and measurement markets demand these very stable frequency sources with enhanced phase noise performance and low thermal drift. A popular solution in the range of 3 to 30 GHz frequency spectrum is the dielectric resonator oscillator (DRO), recognized for its superiority in ultimate noise floor and spectrum purity when compared to other competing solutions such as multiplied lower frequency fundamental sources [6]-[9].

A novel Mobius-coupled printed resonator oscillator is reported in this paper for the application of synthesized signal sources in RADAR and modern microwave communication systems. The concept of the Mobius strips is based on the fact that a signal coupled to a strip shall not encounter any obstruction when travelling around the loop; enabling compact high Q-factor resonators [10]-[14].

A necessary and sufficient condition for a Mobius surface to be developable is that its Gaussian curvature should everywhere vanish. Given a curve with non-vanishing curvature there exists a unique flat ruled surface (the so-called rectifying developable) on which this curve is a geodesic curve (as shown in Figure 1) is described by [1]

$$\vec{x}(s,t) = \vec{r}(s) + t[\vec{b}(s) + \eta(s)\vec{t}(s)] \quad (1)$$

$$\tau(s) = \eta(s)k(s), \quad s = [0, L], t = [-w, w] \quad (2)$$

Where $\vec{r}$ is a parameterization of a strip with r as centerline and of length L and width 2w, where $\vec{t}$ is the unit tangent vector, $\vec{b}$ the unit binormal, k the curvature and τ the torsion of the centerline, the parameterized lines s = const. are the generators, which make an angle β = arc[tan(1/η)] with the positive tangent direction. Due to the unique properties of Mobius strips, the shape minimizes the deformation energy, which is entirely due to bending, can be described by [1]

$$V = \frac{1}{2} D \int_0^L \int_{-w}^{w} k_1^2 (s,t) dt ds \quad (3)$$

where $D = 2h^3E/[3(1-\nu^2)]$, with $2h$ the thickness of the strip, and E and ν Young's modulus and Poisson's ratio of the material. In this paper, a planar Mobius-coupled resonator oscillator is described, and the method for miniaturization can be applied to tunable filters, antenna and matching networks.

The eigenfunctions of the Mobius resonator form an orthogonal basis set; presents an interesting possibility for the design of metamaterial for the application in tunable oscillators, antenna, and filter circuits [6]. The oscillator's loaded Q factor Q_L is [11]

$$Q_L = \frac{\omega_0}{2} \left| \frac{d\varphi(\omega)}{d\omega} \right|_{\omega=\omega_0} = \frac{\omega_0}{2} \tau_d; \quad \tau_d = \left| \frac{d\varphi(\omega)}{d\omega} \right|_{\omega=\omega_0} \quad (4)$$

$$\tau_d = \left| \frac{d\varphi(\omega)}{d\omega} \right|_{\omega=\omega_0} = \frac{\varphi(\omega_0 + \Delta\omega) - \varphi(\omega_0 - \Delta\omega)}{2\Delta\omega} \quad (5)$$

where $\varphi(\omega)$ is the phase of the oscillator's open loop transfer function at a steady state and τ_d is the group delay of the resonator. From (4)-(5), Q_L is proportional to the group delay; therefore, for low oscillator phase noise application, the design goal is to maximize the group delay of Mobius strip resonator by incorporating phase-injection techniques. The unique characteristic of Mobius strip is self-phase-injection properties along the mutually coupled surface of the strips, which enables higher quality factor for a given size of the printed transmission line resonator [12].

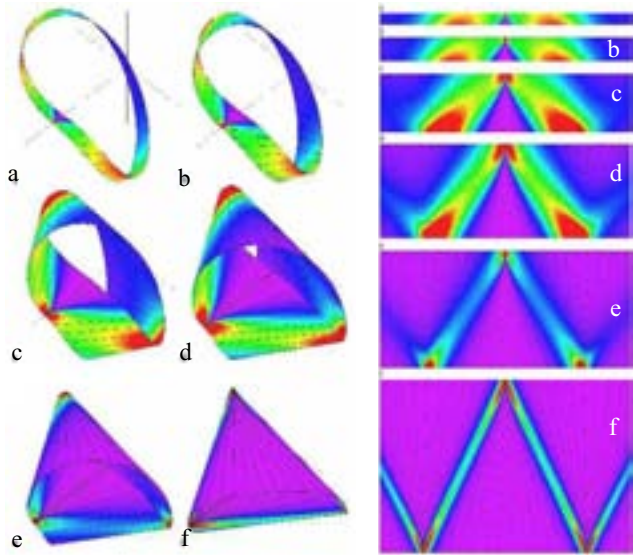

Figure 1: Computed Mobius strips (coloring changes according to the local bending energy density, from violet for regions of low bending to red for regions of high bending). The left panel shows their 3D shapes for w = 0.1 (a), 0.2 (b), 0.5 (c), 0.8 (d), 1.0 (e) and 1.5 (f), and the right panel the corresponding developments on the plane [1]

II. MOBIUS-COUPLED EVANESCENT MODE RESONATOR

The printed coupled resonator based oscillator can overcome problem associated with DRO, except the poor phase noise performance due to inherent low Q-factor associated with printed transmission line resonator. The Q (quality) factor of the coupled planar resonator network can be enhanced by introducing slow wave propagation dynamics, however large physical size and mode-jumping restricts the application especially at lower frequencies [13]. The loaded quality factor Q_L of the coupled resonator network is given in terms of unloaded quality factor Q_o as [14]:

$$[Q_L(\omega_0)]_{electrical-coupling} \cong 2\left[\frac{Q_0}{(1+\beta_e)}\right]_{\beta_e<<1} \cong 2Q_0 \quad (6)$$

$$[Q_L(\omega_0)]_{magnetical-coupling} \cong 2[Q_0(1+\beta_m)]_{\beta\to 1} \cong 2Q_0 \quad (7)$$

$$[Q_L(\omega_0)]_{hybrid-coupling} \cong 2\left[Q_0\frac{(1+\beta_{mh})}{(1+\beta_{eh})}\right]_{\beta_e<<1,\ \beta_{mh}\to 1} \cong 4Q_0 \quad (8)$$

Where coupling factor β (β_e for electric field, β_m for magnetic field, and β_h for hybrid field)

From (8) hybrid coupling (β_h) acts as a Q-multiplier effect, but this phenomena holds good for fixed frequency operation only and very difficult to realize broadband Q-multiplier dynamics which is necessary for wideband oscillators [14]. In addition to this, mode-jumping caused by undesirable higher order mode generation in hybrid coupling makes this structure not suitable for tunable wideband VCO (voltage controlled oscillator) applications. The alternative approach is to tune the coupling factor β_j over the desired operating frequency band in conjunction with higher order mode-suppressing network. But broadband mode-suppression is not an easy task in multi-mode resonator structure. A simplified approach is to use injection-locking and phase-synchronization techniques for broadband applications.

A. Möbius-Coupled Evanescent-Mode resonator Oscillator

A novel mode-coupled self-injection locked oscillator is developed in response to replacing expensive DRO (Dielectric Resonator Oscillator) for reference signal sources for modern communication systems. Figures (2), (3), and (4) show the typical block diagram, layout, and measured phase noise plot of the 10.2 GHz oscillator using a SiGe Hetrojunction-bipolar-transistor (HBT) active device were fabricated on Rogers substrate material with a dielectric constant of 2.2 and thickness of 20mils (microstripline/stripline) for the validation of the approach.

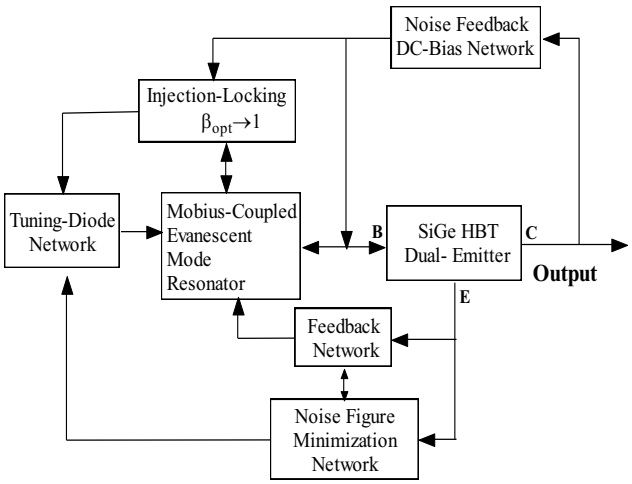

Figure 2: A typical block diagram of X-band MCEMR (Mobius-Coupled Evanescent Mode Resonator) oscillator

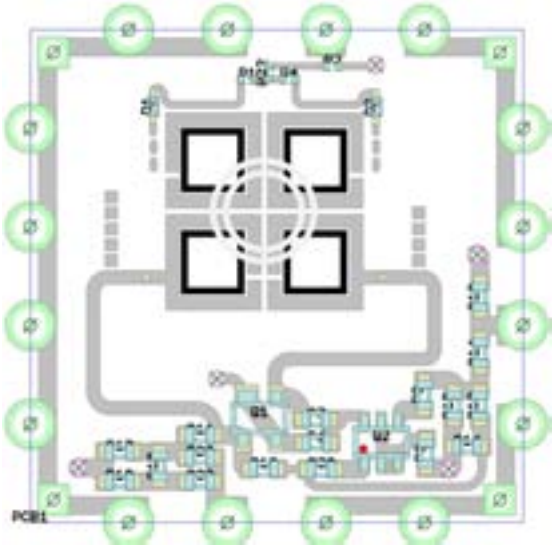
Figure 3: Layout of 10.2 GHz MCEMR VCO (0.9x0.9x0.2 inches)

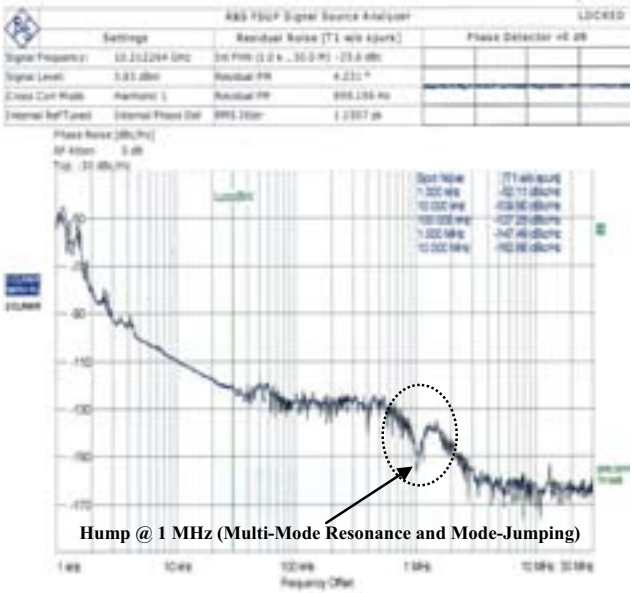

Figure 4: Measured Phase Noise Plot of 10.2 GHz MCEMR VCO

The oscillator works at DC bias of 10 Volt and 30 mA, measured output power exceeds +5 dBm. As shown in Figure 4, there is hump and dip between 100 kHz and 10 MHz offset from the carrier, possibly due to the resonator mode-jumping phenomena. By incorporating multi-mode-injection-locking, mode-jumping can be suppressed and stable oscillation can be guaranteed.

B. Examples: Compact Size MCEMR VCO

The tiny MCEM VCO is designed with rugged construction to minimize vibration noise and microphonic effects to prevent unwanted modulation.. Figure 5 shows the typical printed resonator layout for the realization of MCEMR VCO in 0.5"x 0.5" x 0.08" inches square package. Figure 6 shows the CAD simulated phase noise plots of oscillator circuits using different configurations of planar resonator topologies depicted in Figure 5. This exercise is done for the basic understanding of the SMD (surface mounted device) packages low cost high performance signal source applications. As shown in Figure 5, different possible configurations of MCEMR VCO are built on Rogers substrate material with a dielectric constant of 2.2 and thickness of 20mils (microstripline/stripline). The drawback of these resonator structures (Figure 5) is narrow tuning range and inferior phase noise performance. Figure 6 shows the measured plot of unloaded Q-factor of the printed resonator structures (electrical coupled, magnetic coupled, hybrid or mixed coupled, and Möbius coupled) for giving brief insight about the improvement in quality factor in planar domain.

As shown in Figure 6, the Möbius coupled printed resonator (MCPR) structure act like a Q-multiplier, peaking at 8.6 GHz due to the convergence of evanescent- modes. It can be seen in Figure 6 that Möbius resonator exhibits the undesired multi-mode resonant characteristics, and care must be taken to suppress these spurious modes for low jitter in RADAR applications. The drawback of this approach is multi-mode frequencies and mode-jumping (encircling the resonator characteristics), restricts the broadband operations.

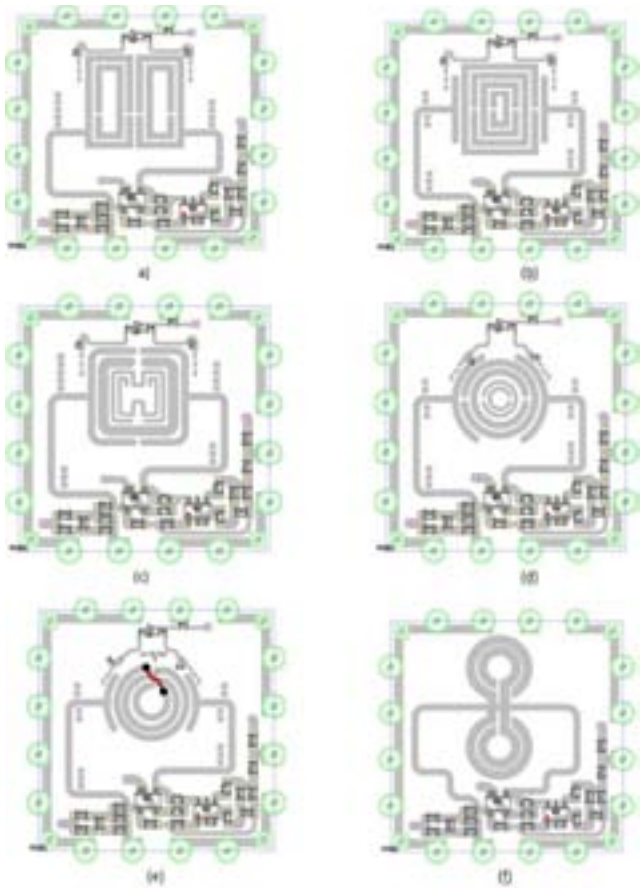

Figure 5: shows the layout of the SMD (surface mounted device) version of 0.5"x 0.5" x 0.08" inches square package are developed for low cost signal source applications: (a) 3.2 GHz Oscillator, (b) 4.7 GHz Oscillator, (c) 8.2 GHz Oscillator, (d) 12.2 GHz Oscillator, (e) 14.2 GHz Oscillator, and (f) 18 GHz Oscillator (20mils substrate height, 2.22 dielectric constant)

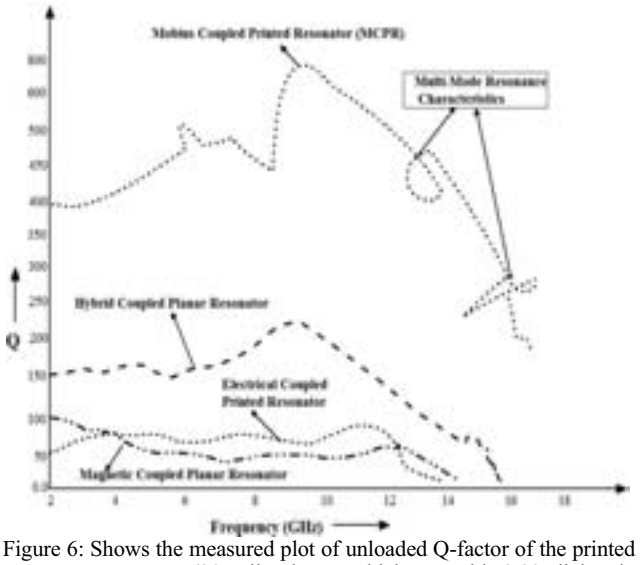

Figure 6: Shows the measured plot of unloaded Q-factor of the printed resonator structures (20 mil substrate thickness with 2.22 dielectric constant, 0.35x0.35x0.18 inches).

To overcome this problem, mode stabilization (injection of higher order modes into the resonant cavity with proper phase shift that improves the stability factor) control circuit is incorporated [15]-[16]. This degrades the Q factor by 10-20% resulting in degradation in phase noise performances by 3-6 dB but overcomes the problem of mode jumping, therefore, stable operation. The mode-injection locked MCEMR VCO using a SiGe Hetro-junction-Bipolar-transistor (HBT) active device, built on 20 mils substrate material with a dielectric constant of 2.2 illustrated in Figure 7 overcomes the limitation of oscillators circuits depicted in Figures 3 and 5.

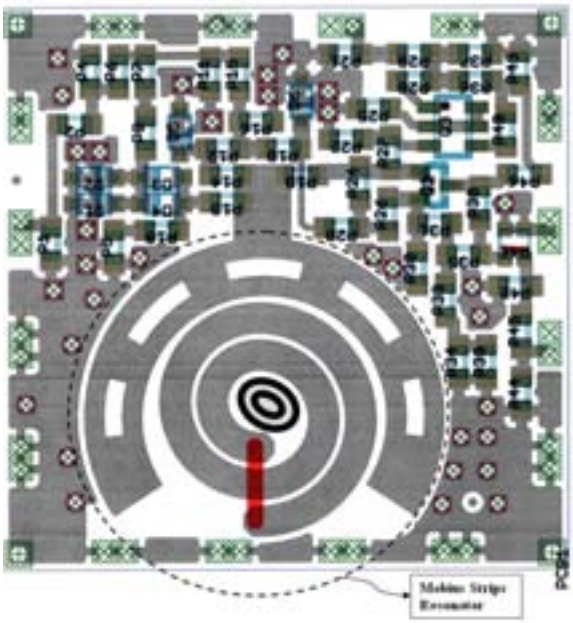

Figure 7: Shows the layout of mode-injection-locked 10.24 GHz oscillator (depicts the Möbius strips resonator used for high Q-factor resonator (PCB layout is done with 20 mil substrate thickness with 2.22 dielectric constant, 0.5x0.5x0.18 inches)

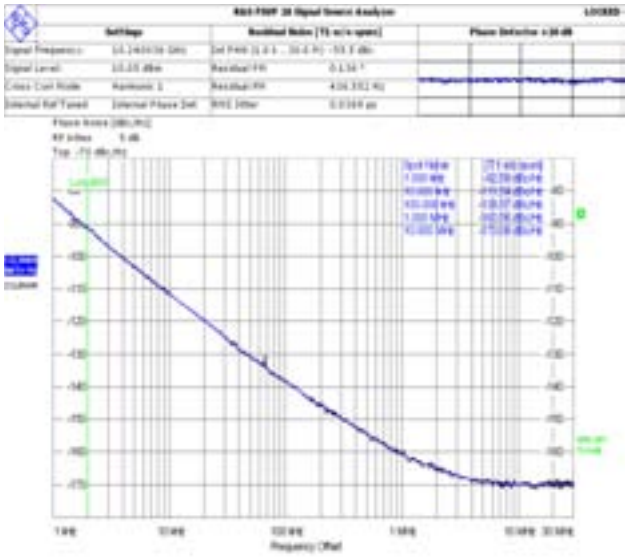

Figure 8: Measured Phase Noise Plot of mode-locked MCEMR VCO

The frequency is set at the fundamental resonance of MCEMR (Mobius-Coupled Evanescent Mode Resonator) and can be electrically tuned by using varactor tuned network (Tuning voltages of 1 to 24 VDC enable variations in the center frequency by ±400 MHz to compensate for frequency drift in phase-locked systems).

Figure 8 shows the measured phase noise plot of 10.24 MCEMR VCO, the measured phase noise @ 10 kHz offset is better than -110dBc/Hz, validates the tuning capability without degrading the phase noise performance in SMD packaged version.

III. CONCLUSION

Mobius-Coupled Evanescent-Mode (MCEM) resonators are attractive due to several reasons: the Mobius effect makes them very compact and can support evanescent mode coupling for obtaining Q-multiplier effect at resonant condition, thus low phase noise signal source solutions. Mobius-Coupled Evanescent-Mode (MCEM) resonator approach described in this paper offers cost-effective and integrable alternative for DRO circuits.

[1] Starostin E.L., van der Heijden G.H.M. (2007). "The shape of a Möbius strip", Nature Materials 6 (8): 563–7. doi: 10.1038/nmat1929.PMID 17632519.

[2] J. M. Pond, "Mobius Dual Mode Resonators and Bandpass Filter", IEEE. Trans. of MTT Vol. 48, Dec 2000, pp 2465-2471.

[3] J.M.Pond, S.Liu, and N.Newman, "Bandpass Filters Using Dual-Mode and Quad-Mode Mobius Resonators," IEEE Trans. on Microwave Theory and Tech. vol.49, pp.2363-2368, Dec.2001.

[4] I. G. Wilson, C. W. Shramm & J. P. Kinzer. "High Q Resonant Cavities for Microwave Testing" Bell System Technical Journal, No.5. (March2005),pp. 1515-1530, doi:10.1364/OPEX.13.001515.

[5] Honkote V., "Capacitive load balancing for Mobius implementation of standing wave oscillator", 5[2nd] IEEE MWSCAS 2009, pp. 232-235

[6] Hoffman, A. J. *et al*. *Nature Mater.* 6, pp. 946–950 (2007).

[7] J-Francois Gravel and J. S. Wight, "On the Conception and Analysis of a 12-GHz Push-Push Phase Locked DRO" IEEE Trans. on MTT, Vol. 54, No. 1, Jan. 2006, pp. 153-159

[8] U. L. Rohde and A. K. Poddar, "Miniaturized VCOs Arm Configurable Synthesizers", IEEE IMS Digest June 2009

[9] J. Clerk Maxwell, A Treatise on Electricity and Magnetism, 3rd ed., vol. 2. Oxford: Clarendon, 1892, pp.68–73.

[10] I. S. Jacobs and C. P. Bean, "Fine particles, thin films and exchange

[11] A. K. Poddar, U.L. Rohde, D. Sundarrajan", Real Time Signal Retention Device using Co-planar Waveguide (CPW) as Mobius strip", 2013 IEEE MTT-S Digest, pp. 1-3, June 2013

[12] A. K. Poddar, U.L. Rohde, D. Sundarrajan", A Novel Mobius-Coupled Printed Resonator Based Signal Sources", 2013 IEEE MTT-S Digest, pp. 1-3, June 2013.

[13] A. K. Poddar and U. L. Rohde, "Slow-Wave Evanescent-Mode Coupled Resonator Oscillator", 2012 IEEE FCS, pp. 01-07, May 2012.

[14] U. L. Rohde and A. K. Poddar, *"Mode-Coupled VCO Replaces Expensive DRO (Dielectric Resonator Oscillator)* 2008 IEEE Int'l Frequency Control Symposium, 296-304, 18-21 May 2008

[15] A. K. Poddar, U. L. Rohde, A. S. Daryoush, "Integrated production of self injection locked self phase loop locked Opto-electronic Oscillators"", US Patent application no. 13/760767 (filed on Feb 06, 2013).

[16] A. K. Poddar, U. L. Rohde, A. S. Daryoush, "Self Injection Locked Phase Locked Looped Optoelectronic Oscillator", US Patent application No. 61/746, 919 (filed on Dec 28, 2012).

Design of a 2.5µW 1GHz Low Phase Noise Pierce Oscillator with Nanowire NEMS Resonator

Hamidreza Zamani, Philip X.-L. Feng
Department of Electrical Engineering & Computer Science, Case School of Engineering
Case Western Reserve University, Cleveland, OH 44106, USA
Email: hamidreza.zamani@case.edu, philip.feng@case.edu

***Abstract*—Nanowire (NW) resonant nanoelectromechanical systems (NEMS) with integrated electronic signal transduction are attractive for realizing ultra-low-power nanomechanical radio-frequency (RF) signal processing. A major challenge lies in the high motional impedances of electrostatically-transduced high-frequency NW NEMS resonators. In this digest paper, we describe a technique for realizing oscillators that can achieve stable and low phase noise oscillations with such characteristic high motional impedances in NW NEMS. The technique is based on the basic theory of designing CMOS Pierce oscillators with low phase noise and low power consumption. We further design an oscillator with 1.5V power supply, which features a phase noise level of -104dBc/Hz at 10kHz offset from a 1GHz carrier, and consumes only 2.5µW power. Cadence circuit simulations on oscillator performance demonstrate the theoretical insights from this study may be important for designing oscillators based on challenging nanoresonators with high motional impedances.**

Keywords—Pierce oscillator; nanoelectromechanical systems (NEMS); nanowire resonator; motional impedance; phase noise; low power; feedback; oscillator circuit

I. INTRODUCTION

Modern communications demand integrated circuits and systems with ever improving spectral purity, efficiency, and power consumption. Wide interests and extensive efforts have been focused on developing alternatives to crystal resonators, *e.g.*, microelectromechanical systems (MEMS), toward chip-scale oscillators [1-3]. Meanwhile, solutions to the present and potential shortcomings of MEMS oscillators, *e.g.*, temperature instability, are being actively investigated [4,5]. While many challenges remain for developing and establishing optimal MEMS-CMOS cointegration processes for various specific applications, system-in-package (SiP) MEMS oscillators with off-chip MEMS have been widely adopted and are prevailing.

Silicon nanowire (SiNW) NEMS resonators are of interest for oscillators due to a number of merits, including ultrasmall dimensions, very high frequencies, ultralow operating power levels, and high quality (Q) factors [6]. These merits and features are expected to translate into promises for interesting oscillator performance. The motional impedance (resistance) R_m, however, is often large at high frequencies, particularly for NW NEMS. Here, instead of discarding and finding ways of avoiding nanodevices with large R_m values, we explore the possibility of embracing the high R_m's in NW NEMS.

This presentation was made possible, in part, through financial support from Case School of Engineering, student travel support from the School of Graduate Studies at Case Western Reserve University, and from the 2013 Joint IEEE UFFC, EFTF, and PFM Symposium.

II. LOW PHASE NOISE PIERCE OSCILLATOR DESIGN

Figure 1a illustrates the scheme of a Pierce oscillator and the equivalent electronic circuit of a NEMS/MEMS resonator with electrostatic transduction. This consists of a series *LCR* circuit (*motional* branch) in parallel with a static capacitor C_g. The oscillator circuit includes three non-resonator-based capacitors C_1, C_2 and C_3', (the latter in parallel with C_g whose parallel combination is called C_3). We shall derive signal-to-noise ratio (SNR) and phase noise equations to gain insights into the design of low phase noise NW NEMS oscillators.

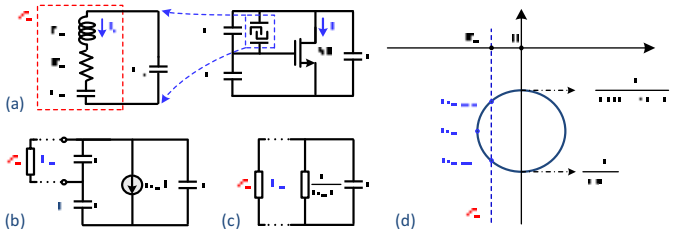

Fig. 1. Illustration of NEMS Pierce oscillator and design principles. (a) Schematic of a Pierce oscillator with equivalent circuit of the NEMS resonator. (b) Small-signal model of the oscillator. (c) Approximate schematic at $C_3 << C_1, C_2$. (d) Negative impedance trajectory of the motional branch ($-Z_m$ line) in Laplace domain with change of frequency-pulling, and the impedance trajectory of the rest of the oscillator with change in G_m (circle).

To find the oscillation frequency f_{osc} of a Pierce oscillator referenced to a nanoelectromechanical resonator, we analyze the small-signal schematic (Fig. 1c), an approximate to that in Fig. 1b if $C_3 << C_1, C_2$ (the latter assumption explained in Section III). Though change of G_m affects f_{osc} (Fig. 1d), in low power designs (small G_m), we have

$$\omega_{osc} \equiv 2\pi f_{osc} \cong 1/\sqrt{L_m C_m}\,, \tag{1}$$

i.e., pulling frequency is not large, since $C_m << C_2$. Thus, with such relative set of oscillator capacitors, f_{osc} will not be much different from the unloaded resonance frequency of the NEMS/MEMS resonator.

To find noise due to loss from the motional resistance, we note that energy stored in the motional impedance (a series tank) can be expressed as $E_m = (1/2) L_m I_m^2$, which helps to write the signal current (squared) in the series tank as

$$I_m^2 = 2E_m / L_m \cong 2E_m \omega_{osc}^2 C_m . \quad (2)$$

Equipartition theorem of thermodynamics [7] states that for a system in equilibrium at temperature T, each independent degree of freedom of the system has a mean energy of $(1/2)k_B T = (1/2)L_m \langle i_{N,m}^2 \rangle$, where $\langle i_{N,m}^2 \rangle = S_{i_{N,m}} \Delta f$, Δf and $S_{i_{N,m}}$ are mean square, bandwidth and power spectral density (PSD) of the current noise due to motional dissipation. Therefore, we have the noise current mean square due to loss in the motional branch (series tank) equals

$$\langle i_{N,m}^2 \rangle = k_B T / L_m \cong k_B T \omega_{osc}^2 C_m , \quad (3)$$

where k_B is Boltzmann constant. From (2) and (3), the ratio of motional noise PSD to power of the signal is

$$\frac{S_{i_{N,m}^2}}{I_m^2} \propto E_m^{-1} \propto \frac{1}{L_m I_m^2} \cong \frac{1}{L_m (C_3/C_1)^2 I_{bias}^2}, \quad (4)$$

where I_{bias} is the oscillator bias current. The above relation does not consider noise due to the active circuit though. Thus, a parameter γ to account for the effect of MOS channel noise (dominant noise of the active circuit) referred to the motional branch [8] is introduced, yielding a total current noise

$$S_{i_{N,tot}^2} = (1+\gamma) S_{i_{N,m}^2} = \left(1 + \frac{S_{i_{N,ch}^2}}{4k_B T R_m (\omega_{osc} C_2)^2}\right) S_{i_{N,m}^2}, \quad (5)$$

where $S_{i_{N,ch}^2}$ and $S_{i_{N,tot}^2}$ are, respectively, the current spectral densities of the MOS channel noise and the total oscillator noise referred to the motional branch. Using linear time-invariant noise theory, the total phase noise spectral density is

$$S_{\varphi_{N,tot}^2} = \frac{1}{2} \frac{(1+\gamma) S_{i_{N,m}^2}}{(|I_m|/\sqrt{2})^2} \propto \frac{\left(1 + \frac{S_{i_{N,m}^2}}{4k_B T R_m (\omega_{osc} C_2)^2}\right)}{L_m (C_3/C_1)^2 I_{bias}^2}. \quad (6)$$

Equation (6) clearly gives very good design intuition to us. In low power designs where I_{bias} is very small, in order to decrease total phase noise, L_m, C_3/C_1 and C_2 should increase. The first two parameters decrease phase noise due to both mechanical and active noise while C_2 only decreases effect of active circuit noise. However, as we will see in the next section, in a contradicting condition with low phase noise requirement, $C_3 << C_1, C_2$ should be met so that the oscillator starts self-sustained oscillation. This makes it inevitable to use large L_m to achieve low phase noise. We will also see trade-offs of using large C_2 on power consumption in Section IV.

There are different methods to increase L_m in mechanical resonators with electrostatic transduction. Reference [9] gives the formulation by which L_m and R_m scale inversely while C_m directly proportional to square of parameter $\eta = V_p \partial C/\partial x$, where V_p is the polarization (DC) voltage and $\partial C/\partial x$ is the change in capacitance between the mechanical resonator and the electrode per unit displacement (x) across the resonator-electrode gap. The parameter η shows how L_m can be increased by decreasing bias voltage across resonator-electrode or some NEMS dimensions and/or increasing initial (static) gap distance where in all cases R_m also increases. This clearly shows the necessity of dealing with high-R_m resonators in design of low phase noise Pierce oscillators.

III. Oscillation Start-Up and Reducing Power

A. Oscillation Start-Up

Impedance of the motional branch can be restated as [8,10]

$$Z_m = R_m + j \cdot 2p/\omega C_m , \quad (7)$$

where p is the frequency pulling defined as $p = (\omega - \omega_m)/\omega_m$, with ω and ω_m denoting the operating frequency and motional-branch resonance frequency. Negative impedance ($-Z_m$) of the motional branch for different frequencies makes up a line trajectory with constant real part ($-R_m$) and variable imaginary part in Laplace plane (Fig. 1d). The input impedance of the rest of Pierce oscillator circuit (see Fig. 1a right panel, between gate and drain nodes), when combined with the parallel static capacitor of the NEMS resonator C_g, can be modeled by Z_c. This impedance changes by change of the transconductance G_m of the driver MOS and makes up a circular trajectory (in case of linear circuit operation) in the Laplace plane (Fig. 1d). Figure 1d depicts that oscillation happens at intersection of the line (impedance $-Z_m$) and the circle (impedance Z_c) assuming both resonator and circuit have linear behavior. In fact, this is a pictorial expression of the Barkhausen criterion [11]. Oscillation occurs for G_m between $G_{m,min}$ and $G_{m,max}$.

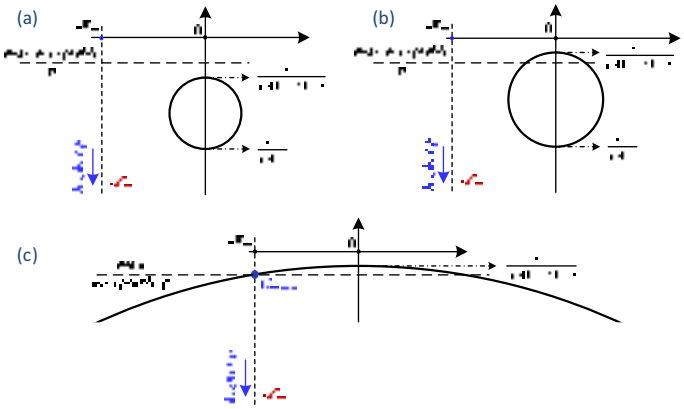

Fig. 2. Trajectories of negative motional impedance ($-Z_m$, vertical lines) and the impedance of the rest of Pierce oscillator (circles). (a) When R_m is high and there is no intersection between the two trajectories for any G_m. (b) When C_{12} is increased to make it potentially possible for the two trajectories to intersect at acceptable pulling frequencies. (c) When C_3 is decreased enough to make the intersection (oscillation start-up) happen.

An important challenge which can be explained through Fig. 2a is with oscillators that are referenced to high R_m and high f_{res} resonators. As (7) shows, for resonators with high ω_m, the absolute value of imaginary part of $-Z_m$ decreases. In other words, for the whole oscillator to oscillate at frequencies near ω_m, the circle should intersect with the line at points very close to the real (horizontal) axis. This necessitates using large $C_{12} = C_1 C_2 / (C_1 + C_2)$. For resonators with high R_m, we need to lower C_3 below what can be currently achieved by off-

chip (or integrated) components. In fact, even the CMOS parasitic capacitances can be larger than the desired C_3.

Therefore, to enable a Pierce oscillator based on high-R_m and high-ω_m resonator to realize stable and self-sustained oscillation, we take two steps, collectively. First, the circle should shift up to cross the line of maximum acceptable p by increasing both C_1 and C_2 (Fig. 2b). Second, the circle diameter should increase by decreasing effective C_3 (Fig. 2c). This way, the circle and the line would intersect.

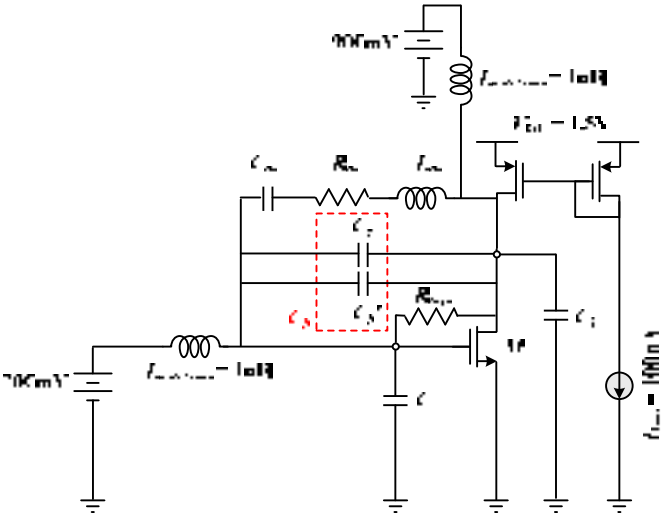

Fig. 3. Circuit schematic of the designed Pierce oscillator referenced to a series L_m- C_m-R_m NW NEMS resonator. Two bonding wire inductors (instead of a single one parallel to the resonator) are employed, between gate or drain at one end and the ac ground at the other end, respectively. DC voltage sources of 700mV and 900mV, and a very large R_{bias} are used to bias the circuit at the correct operting point. The bias current of I_{bias}=100nA is chosen to attain the very low power consumption levels.

To decrease C_3, we need a method as simple as possible so that it does not create unwanted side effects which are quite probable at high operation frequencies. A good solution would be adding a bonding wire inductor parallel to C_3. The value of the inductor should be chosen in such a way that at oscillation frequencies, the inductor cancels out a good portion of C_3, yielding a very small effective C_3.

B. Reduction in Power Consumption

As an alternative to the method suggested, we can use two inductors from gate and drain nodes, respectively, to the ac ground. To compare the two approaches, we note that increasing C_2 as suggested earlier to decrease effect of active circuit noise and also to enable the oscillator to attain stable oscillation at high resonator f_{res} with small p, might lead to a low-impedance path to ground which increases power consumption. Thus, the second approach can cancel out a good portion of C_2 to keep the circuit power consumption low. However, this does come along with the expense of a higher pulling frequency p.

We should also note that decreasing C_3 by any technique decreases the power consumption. From ref. [8], we can determine that that for linear oscillator circuit operation, the real part of Z_c is

$$Z_c = \frac{-G_m C_1 C_2}{\omega^2 (C_1 C_2 + C_2 C_3 + C_3 C_1)^2 + (G_m C_3)^2}. \qquad (8)$$

From (8) we can conclude that for constant G_m and lower C_3, the circuit provides more negative resistance. In other words, instead of increasing G_m to make the circle intersect with the line, we can just decrease C_3.

There is another phenomenon [8] that is worth mentioning. In practice, the oscillator circuit may behave nonlinearly with bias currents even as small as several 10nA if the amplitude of the AC signal I_m is large. In those cases, increase in G_m (by increase in bias current) causes Z_c to be not only a function of bias current, but also a function of the AC signal I_m. The higher amplitude of I_m, the more positive the real part of Z_c will be. This is why increasing R_m has also a good effect that decreases the nonlinear behavior of the oscillator circuit, which in turn makes the resistance of Z_c more negative.

IV. Design Example and Simualtion Results

In this Section, a Pierce oscillator (Fig. 3) is designed and simulated to verify our design intuitions derived earlier in this paper. The mechanical resonator assumed for this simulation is a doubly-clamped SiNW resonator with length (L), width (w), thickness (t) and quality (Q) factor of, respectively, L=419nm, w=20nm, t=80nm and Q=2000. The MOS technology used for this circuit is CMOS 0.35µm process and all simulations are done with Cadence Spectre simulator.

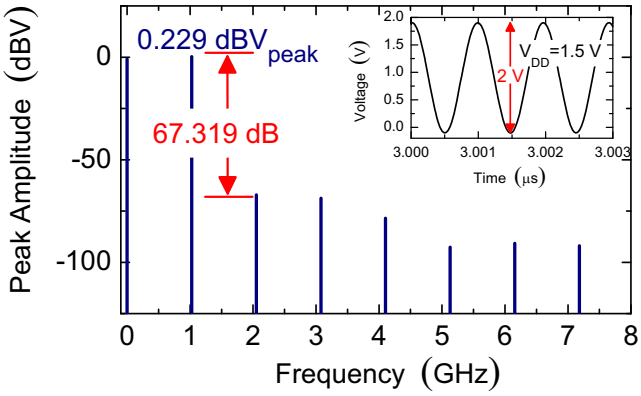

Fig. 4. Cadence simulated steady-state output voltage waveform (between drain and ground) of the fundamental and higher harmonics versus frequency. The large relative difference between the fundamental and the second harmnic demonstrates the linearity of the circuit. *Inset*: The steady-state voltage signal versus time with peak-to-peak amplitude of ~2V when the oscillator is not loaded at the output node.

The bias voltages of 0.7V and 0.9V and a large R_{bias} are used to bias the circuit in the desired operating condition. The bias current of I_{bias}=100nA is also provided using a simple current mirror to make the circuit operate at low power consumption conditions. Such low bias currents are usually used in analog instrumentation front ends (*e.g.*, ref. [12]). Our two-inductors approach is implemented with two 1nH bonding wire inductors (the 2 L_{wirebond}'s in Fig. 3). Figure 4 shows the computed steady-state voltage amplitude of the fundamental and higher harmonic resonances versus frequency at the output (drain of M in Fig. 3).

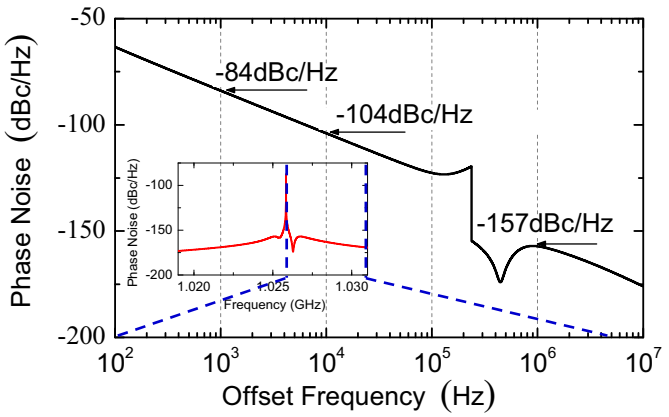

Fig. 5. Phase noise simulation results from Cadence PSS simulator at the oscillator output at different offset frequencies around f_{osc}. Inset shows the phase noise in a wider range versus absolute frequencies. At very small offset frequencies, the phase noise of the wider-range diagram (inset) seems to be smaller which is due to limited frequency resolution in wide-range simulation.

The large relative difference of ~67.32dB between the fundamental and the second harmonic clearly demonstrates the excellent linearity of the circuit. The inset in Fig. 4 shows the voltage *versus* time waveform when the circuit is in steady-state operation. For V_{DD}=1.5V, the output between drain and ground has a peak-to-peak amplitude of ~2V when there is no external circuit loading output of the oscillator.

Figure 5 demonstrates the computed steady-state oscillator phase noise versus offset frequency. The inset to Fig. 5 shows the phase noise performance versus absolute frequency in a wider range. This simulation using the Cadence PSS simulator clearly shows the effectiveness of our design methodology for achieving low phase noise in the designed NEMS oscillator. In order to have an intuition on the performance of our oscillator, phase noise at different offset frequencies as well as power consumption are compared to other prominent recent related works (measurement results) in Table I.

V. Conclusions

In this work, we have first mathematically analyzed the challenges and opportunities of designing low phase noise and low power Pierce oscillators with frequency references based on nanowire electromechanical resonators with high motional impedances. Our analyses on the high-frequency, high-R_m resonators and oscillator requirements provides a set of design insights and implementable guidelines, especially on satisfying oscillation conditions, attaining low phase noise and low power consumption. The design guidelines have been verified by designing a prototype 1GHz nanowire NEMS oscillator, and by computing its performance using Cadence simulator.

TABLE I. Summary of Nanowire NEMS Oscillator Design in This Work, in Comparison with Other Related Works

	R_m	f_{osc}	P_{con}	Phase Noise [dBc/Hz]
This Work	13.1MΩ	1.026GHz	2.5μW	-84 (@ 1kHz), -104 (@ 10kHz), -157 (@ 1MHz)
Ref. [13]	7k Ω	2.0GHz	22μW	-101dBc/Hz (@ 100kHz)
Ref. [14]	22Ω	1.5GHz	6.9mW	-85 (10kHz), -151 (@ 1MHz)
Ref. [15]	25Ω	1.05GHz	3.5mW	-81 (@ 1kHz)
Ref. [16]	750Ω	1.006GHz	1.9mW	-94 (@ 1kHz)

References

[1] M. McCorquodale, S. Pernia, G. Carichner, J. O'Day, E. Marsman, N.D. Nguyen, S. Kubba, S. Nguyen, J. Kuhn, R.B. Brown, "A 0.5–480MHz self-referenced CMOS clock generator with 90ppm total frequency error and spread spectrum capability," *Tech. Digest, IEEE Solid-State Circuits Conf. (ISSCC)*, San Francisco, p. 350-351 & 619, February 2008.

[2] S. Rai., Y. Su, W. Pang, R. Ruby, B. Otis, "A digitally compensated 1.5GHz CMOS/FBAR. frequency reference," *IEEE Trans. Ultrason. Ferroelectr. Freq. Contr.*, vol. 57, pp. 552-560, March 2010.

[3] D. Petit; E. Cesar; E. Bar; S. Joblot; G. Parat; O. Berchaud; O. Barbier; J.-F.Carpentier, "Thermally stable oscillator at 2.5 GHz using temperature compensated BAW resonator and its integrated temperature sensor," *Tech. Digest, IEEE Ultrasonics Symp.* Beijing, China, pp. 895-898, November 2008.

[4] C. Kim, J. Lee, Y. Jun, C. Lee, and B. Kong. "CMOS temperature sensor with ring oscillator for mobile DRAM self-refresh control,". *Microelectronics Journal*, vol. 38, pp. 1042-1049, October 2007.

[5] M. Perrott, J. Salvia, F. Lee, A. Partridge, S. Mukherjee, C. Arft, J-T. Kim, N. Arumugam, P. Gupta, S. Tabatabaei, S. Pamarti, H. Lee, F. Assaderaghi, "A temperature-to-digital donverter for a MEMS-based programmable oscillator with better than ±0.5 ppm frequency stability," *Tech. Digest of IEEE Int. Solid-State Circuits Conf. (ISSCC),* San Francisco, CA, pp. 206-208, February 2012.

[6] X.L. Feng, R. He, P. Yang, M.L. Roukes, "Very high frequency silicon nanowire electromechanical resonators", *Nano Letters*, vol. 7, pp. 1953-1959, July 2007.

[7] F. Reif, *Fundamentals of Statistical and Thermal Physics*, New York, NY: McGraw-Hill, 1985.

[8] E. Vittoz, *Low-Power Crystal and MEMS Oscillators: The Experience of Watch Developments*, New York, NY: Springer, 2010.

[9] C.T.-C. Nguyen, "Frequency-selective MEMS for miniaturized low-power communication devices," *IEEE Trans. Microwave Theory & Techniques*, vol. 47, pp. 1486-1503, August 1999.

[10] W.M.C. Sansen, *Analog Design Essentials*, New York, NY: Springer, 2006.

[11] H. Barkhausen, *Lehrbuch der Elektronen-Röhren*, Chapter 3, Ruckkopplung, Verlag S. Hirzel, Leipzig, Germany, 1935.

[12] J.L. Bohorquez, M. Yip, A.P. Chandrakasan, J.L. Dawson, "A digitally-assisted interface for biomedical applications," *Tech. Digest, IEEE Symp. on VLSI Circuits*, Honolulu, HI, p. 217-218, June 2010.

[13] A, Nelson, J. Hu, J. Kaitila, R. Ruby, B. Otis, "A 22μW, 2.0GHz FBAR oscillator," *IEEE Radio Freq. Integrated Circuits Symp.* (*RFIC*) Baltimore, MD, p. 1-4, June 2011.

[14] C. Zuo, J. Van der Spiegel, G. Piazza, "1.5-GHz CMOS voltage-controlled oscillator based on thickness-field-excited piezoelectric AlN contour-mode MEMS resonators," *Tech. Digest, IEEE Custom Integ. Circuits Conf. (CICC)*, San Jose, CA, p. 1-4, September 2010.

[15] C. Zuo, J. Van der Spiegel, G. Piazza, "1.05-GHz CMOS oscillator based on lateral-field-excited piezoelectric AlN contour-mode MEMS resoantors," *IEEE Trans. Ultrason. Ferroelectr. Freq. Contr.*, vol. 57, pp. 82-87, January 2010.

[16] H.M. Lavasani, W. Pan, B. Harrington, R. Abdolvand, F. Ayazi, "A 76dBOhm 1.7GHz 0.18um CMOS tunable transimpedance ampflier using broadband current pre-amplifier for high frequency lateral micromechanical oscillators," *Tech. Digest, IEEE Int. Solid-State Circuits Conf. (ISSCC)*, San Francisco, CA, p. 318-320, February 2010.

Physical Model of Phase Noise in Feedback Oscillator

Xianhe Huang, Wei Fu, Pingping Chen，Hongyuan Huang
School of Automation Engineering
University of Electronic Science & Technology of China
Chengdu, China
xianhehuang@uestc.edu.cn

***Abstract*-The paper mainly focuses on the effect on the oscillator phase noise by the loaded quality factor Q_L in Classical Leeson Model, derives that the equivalent circuit parameters of resonator and the oscillation circuit parameters have conclusive concern with the loaded quality factor Q_L. And the experimental verification is made on the basis of two kinds of oscillator circuits (Pierce oscillator circuit and Butler common-base oscillator circuit) and three kinds of acoustic resonators (120MHz SC-cut crystal resonator, 315 MHz one- port SAW resonator and 10.7 MHz $LiTaO_3$ BAW resonator). The further experiment shows the changes of the crystal oscillator phase noise with different drive levels and presents that besides some parameters such as Q_L, the crystal resonator amplitude-frequency (AF) characteristics can also affect the oscillator phase noise apparently. And then, the acoustic oscillator phase noise model can be established on the basis of the physics, which contains the resonator equivalent parameters, the oscillator circuit parameters and the affection of the resonator AF characteristics.**

I. INTRODUCTION

With the continuing development of modern communication technology, the need for the high stability crystal oscillators has increased. Phase noise is one of the most important characteristics of crystal oscillators. It is a key factor which limits the performance of electronic system. Therefore, the study of crystal oscillator output spectrum and methods to reduce the phase noise are the primary problems in the process of designing crystal oscillators.

II. CLASSICAL LEESON MODEL ANALYSIS

Leeson formula is as follows:

$$S_{\Delta\phi}(f_m)=[1+\frac{1}{f_m^2}(\frac{f_0}{2Q_L})^2]S_{\Delta\theta}(f_m) \quad (1)$$

Where f_m is offset frequency, f_0 is center frequency, Q_L is loaded quality factor, $S_{\Delta\phi}(f_m)$ is the power spectral density of the output phase noise, $S_{\Delta\theta}(f_m)$ is the power spectral density of the oscillator input phase noise. And

$$S_{\Delta\theta}(f_m)=\frac{FkT}{P_{si}}\left(1+\frac{f_c}{f_m}\right) \quad (2)$$

Where f_c is corner frequency , f_m is offset frequency， F is noise figure, k is Boltzmann constant, T is absolute temperature, and P_{si} is input signal power.

When the oscillator is stable and the signal output from the amplifier, we can get the expression of the single sideband power spectral density of the output phase noise $S_{\Delta\phi}(f_m)$ from the Leeson model:

$$S_{\Delta\phi}(f_m)=\frac{1}{2}\frac{FkT}{P_{si}}(1+\frac{f_c}{f_m})\left[1+\frac{1}{f_m^2}(\frac{f_0}{2Q_L})^2\right] \quad (3)$$

When applying this model to design a feedback oscillator, one should know what key points should be paid more attention to and what drawbacks of this model also should be noted.

As we can see in (3), the distribution of the oscillator phase noise spectrum corresponds with the power-law. According to the relationship between the flicker noise corner frequency f_c and the half-bandwidth $f_0/2Q_L$, we can do a further analysis of the structure of the oscillator phase noise spectrum.

When $f_0/2Q_L > f_c$ (i.e. low Q resonator), the expression (3) of the power spectral density of the output phase noise can be approximated as:

$$S_{\Delta\phi}(f_m)=\begin{cases}\left(1+\frac{f_c}{f_m}\right)\frac{FkT}{P_{si}}\times\frac{1}{f_m^2}\left(\frac{f_0}{2Q_L}\right)^2, & f_m<f_c\\ \frac{1}{f_m^2}\left(\frac{f_0}{2Q_L}\right)^2\frac{FkT}{P_{si}}, & f_c<f_m<\frac{f_0}{2Q_L}\\ \frac{FkT}{P_{si}}, & f_m>\frac{f_0}{2Q_L}\end{cases} \quad (4)$$

When $f_0/2Q_L < f_c$ (i.e. high Q resonator), the expression (3) of the power spectral density of the output phase noise can be approximated as:

$$S_{\Delta\phi}(f_m)=\begin{cases}\left(1+\frac{f_c}{f_m}\right)\frac{FkT}{P_{si}}\times\frac{1}{f_m^2}\left(\frac{f_0}{2Q_L}\right)^2, & f_m<\frac{f_0}{2Q_L}\\ \left(1+\frac{f_c}{f_m}\right)\frac{FkT}{P_{si}}, & \frac{f_0}{2Q_L}<f_m<f_c\\ \frac{FkT}{P_{si}}, & f_m>f_c\end{cases} \quad (5)$$

According to (3) - (5), the quality factor Q_L can not only affect the intensity of the output phase noise, but also affect the structure of the output phase noise power-law spectral density. In order to improve the oscillator phase noise, besides the requirements of a high Q_L, a low noise figure F of the circuit, a low corner frequency f_c of the transistor device and a high input signal power P_{si} are also required.

III. DESIGN EXAMPLES AND ANALYSIS

In the past few papers, determinants between loaded quality

factor Q_L and equivalent parameters of a resonator and that of a oscillation circuit have already tried to be revealed.

Fig. 1 shows the relationship between the Q_L (calculated from the Pierce crystal oscillator circuit) and the circuit parameter C_1 (collector to ground capacitance) [8].

The 120MHz SC-cut 5th overtone resonator is utilized in the calculation in Fig. 1 and the unloaded quality factor Q_0 is about 1.05×10^5, Lq is about 8.8mH.

TABLE I shows the measured phase noise data of the Pierce Oscillator using the above crystal resonator when C_1 is 51pF and 18pF, respectively. (The measured phase noise curves are shown in Fig.2 and Fig.3)

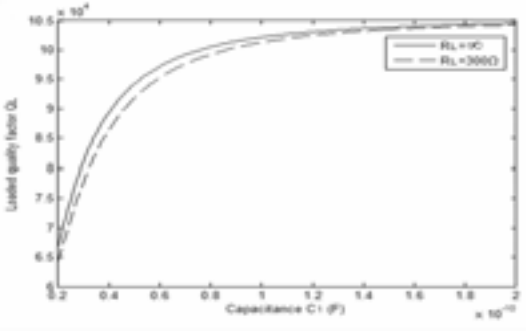

Fig.1.The result of Q_L calculated by MATLAB.

TABLE I. The measured phase noise data

C_1	Offset 10Hz	Offset 100Hz	Offset 10KHz	Offset 100KHz
51 pF	-104.3 dBc	-134.3 dBc	-170 dBc	-175 dBc
18 pF	-100.2 dBc	-132.6 dBc	-171 dBc	-176.5 dBc

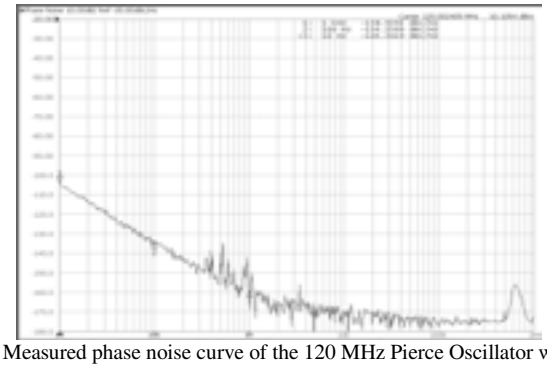

Fig.2. Measured phase noise curve of the 120 MHz Pierce Oscillator when C_1 is 51pF.

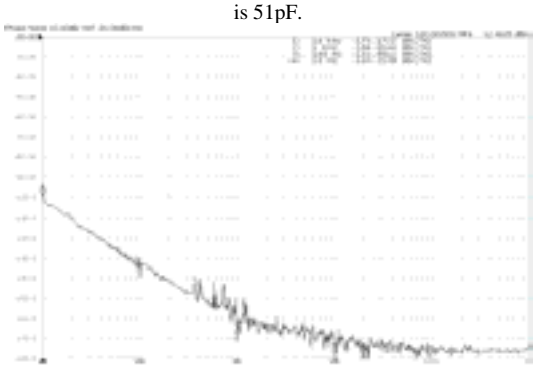

Fig.3. Measured phase noise curve of the 120MHz Pierce Oscillator when C_1 is 18pF.

Fig.4 shows the relationship between the Q_L (calculated from the Butler common-base SAW oscillator circuit) and the circuit parameter C_2 (to ground capacitance) [9].

The 315MHz one-port SAW resonator is utilized in the calculation in Fig.4 and the unloaded quality factor Q_0 is about 1.06×10^4, Lq is about 75μH.

TABLE II shows the measured phase noise data of the Butler common-base Oscillator using the above SAW resonator when C_2 is 30pF and 20pF, respectively. (The measured phase noise curves are shown in Fig.5 and Fig.6)

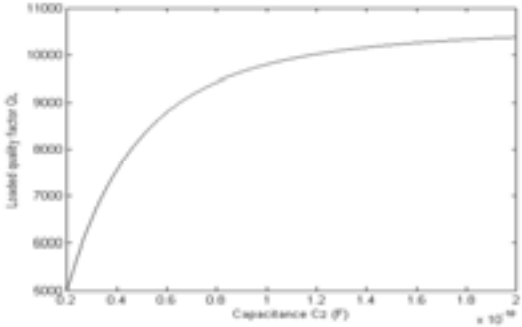

Fig.4.The result of Q_L calculated by MATLAB.

TABLE II.The measured phase noise data

C_2	Output	Offset 100Hz	Offset 1KHz	Offset 10KHz	Offset 1MHz
30 pF	9.9 dBm	-90.0 dBc	-125.5 dBc	-157.0 dBc	-170 dBc
20 pF	10.5 dBm	-88.0 dBc	-123.3 dBc	-155.4 dBc	-170 dBc

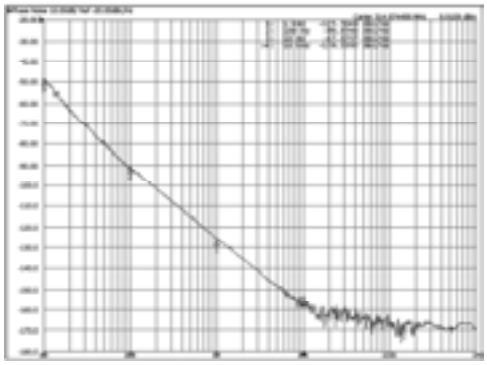

Fig.5.Measured phase noise curve of the 315 MHz Butler common-base Oscillator when C_2 is 30pF.

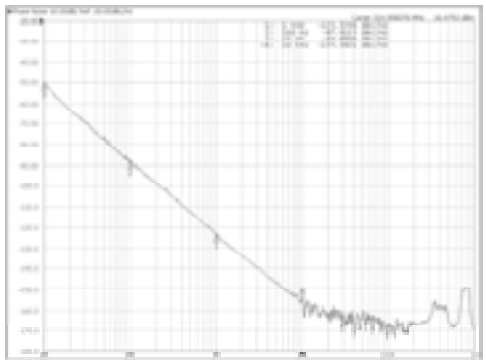

Fig.6 Measured phase noise curve of the 315 MHz Butler common-base Oscillator when C_2 is 20pF

Fig.7 shows the relationship between the Q_L (calculated from the Butler common-base $LiTaO_3$ BAW oscillator circuit) and the circuit parameter C_2 (to ground capacitance) [10].

The 10.7 MHz $LiTaO_3$ BAW resonator is utilized in the calculation in Fig.7 and the unloaded quality factor Q_0 is about

1.24K, Lq is about 3.8×10^{-4} H.

TABLE III shows the measured phase noise data of the Butler common-base Oscillator using the above $LiTaO_3$ BAW resonator when C_2 is 330pF and 160pF, respectively. (The measured phase noise curves are shown in Fig.8 and Fig.9)

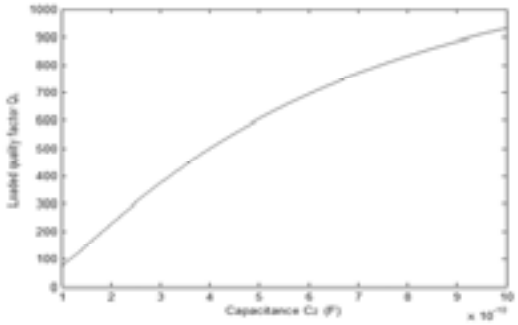

Fig.7.The result of Q_L calculated by MATLAB.

TABLE III.The measured phase noise data

C_2	Output	Offset 10Hz	Offset 100Hz	Offset 1KHz	Offset 100KHz
330 pF	10.3 dBm	-85.2 dBc	-116.7 dBc	-145.5 dBc	-180 dBc
160 pF	11.9 dBm	-81.0 dBc	-113.7 dBc	-143.8 dBc	-180 dBc

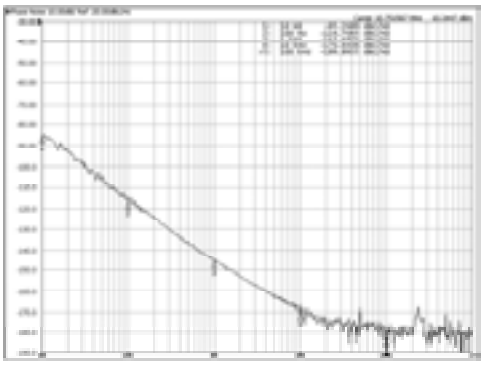

Fig.8. Measured phase noise curve of $LiTaO_3$ oscillator when C_2 is 330 pF.

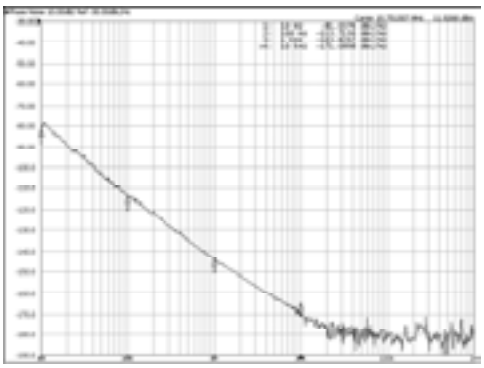

Fig.9. Measured phase noise curve of $LiTaO_3$ oscillator when C_2 is 160 pF.

The initial experimental results show that this method that low phase noise oscillators are designed based on improving Q_L can ameliorate the near carrier frequency phase noise level, and this design is feasible. But, if the value of C becomes larger, the output amplitude will become lower. This is unfavorable for reducing the phase noise. In addition, the derivation of Q_L is just takes into account the passive network, without taking into account the active device and the nonlinear effect produced by active and passive devices. And matching problem exists in the actual circuit. In summary, this design can only be qualitative.

IV. The Effects Of Resonator Amplitude Frequency Characteristics

Further experiments find that one crystal oscillator with different drive levels and output power performs different phase noise level.

TABLE IV and V show the measured phase noise result under the different outputs amplitude. The Pierce oscillator using 100MHz AT-cut 3th overtone crystal resonator is utilized in TABLE IV and C_1 is about 1.2fF, Q is about 130K. In contrast, Pierce oscillator using 10MHz SC-cut 3th overtone crystal resonator is utilized in TABLE V and C_1 is about 0.2fF, Q is about 1160K.

TABLE IV.The phase noise data of 100MHz crystal oscillator with different drive levels

Output amplitude	Output frequency	Offset 10Hz	Offset 100Hz	Offset 1000Hz
-17.9 dBm	100010343 Hz	-97 dBc	-132 dBc	-148 dBc
-15.2 dBm	100010372 Hz	-96 dBc	-130 dBc	-150 dBc
-12.2 dBm	100010432 Hz	-92 dBc	-125 dBc	-152 dBc
-9.0 dBm	100010557 Hz	-83 dBc	-119 dBc	-153 dBc

TABLE V.The phase noise data of 10MHz crystal oscillator with different drive levels

Output amplitude	Output frequency	Offset 10Hz	Offset 100Hz
1.8 dBm	9999628 Hz	-123 dBc	-155 dBc
-0.6 dBm	9999589 Hz	-130 dBc	-154 dBc
-6.4 dBm	9999568 Hz	-134 dBc	-153 dBc

The relationship between the near carrier frequency phase noise and oscillator drive levels is presented clearly in TABLE IV and V. Since this is the same oscillator, it is hard to explain from the point of view of Q_L. However, as the data in both TABLE IV and TABLE V are mainly about the close-in deterioration, it also can't explain from the point of view of the circuit noise factor F in (3) of the Classical Leeson Model. That is because F can make both the close-in noise and the noise floor of the phase noise curve change synchronously, i.e., if the circuit drive are considered raised, since the nonlinear effect of the circuit can result in the increase of F, both the close-in noise and the noise floor of the phase noise curve should deteriorate synchronously with the drive levels.

We can only get the reasonable explanation for this phenomenon from the point of view of the crystal resonator AF (amplitude-frequency) effect [1]-[5]. According to this, the equation (3) of the Classical Leeson Model might add an additional term, which presents the influence of the crystal

resonator AF (amplitude-frequency) effect on the oscillator phase noise.

V. CONCLUSION

Based on the above calculations, experimental results and analysis, the following conclusions are presented:

- What mainly affects the oscillator phase noise in the acoustic resonator is the loaded Q (i.e. Q_L) but the unloaded Q (i.e. Q_0). The Q_L in (3) of the Classical Leeson Model is not only associated with the equivalent parameters of the acoustic resonator, but also related to the circuit parameters of the oscillator.
- On terms of the near carrier frequency phase noise, although the raise of the Q_L is beneficial to the phase noise levels, the oscillator designers shouldn't always raise the Q_L value only, for it can lead to lower output amplitude, and is unfavorable to reduce the oscillator phase noise. In order to achieve a better phase noise level, it's essential to find a reasonable compromise between seeking high Q_L and maintaining output power.
- The equation (3) of the Classical Leeson Model might add an additional term, which presents the influence of the crystal resonator AF (amplitude frequency) effect on the oscillator phase noise, especially the near carrier frequency phase noise.

In a word, according to the conclusion of the initial study, the equation (3) of the Classical Leeson Model should be rewrite as:

$$S_{\Delta\phi}(f_m) = \frac{1}{2}\frac{FkT}{P_{si}}\left(1+\frac{f_c}{f_m}\right)\left[1+\frac{1}{f_m^2}\left(\frac{f_0}{2Q_L}\right)^2\right]+\frac{\tilde{K}}{f^n} \qquad (6)$$

Where $\tilde{K}$ is a dynamic parameter associated with the AF characteristic of the resonator and its value is different with the drive levels. Meanwhile, from experience, the value of n is about 3<n<4.

REFERENCES

[1]. John R. Vig " Quartz Crystal Resonators and Oscillators for Frequency Control and Timing Applications - A Tutorial " http://www.ieee-uffc.org [Online]

[2]. Jeremy Everard "Low Phase Noise Signal Generation, Models and Theory, Oscillators and Their Key Elements, Fractional Regenerative Frequency Division, Teaching",2012 IEEE International Frequency Control Symposium

[3]. Michael Driscoll "Modeling Phase Noise in Multifunction Subassemblies", IEEE Trans. Ultrason. Ferroelectr. Freq. Control, vol. 59, no. 3, pp.373-381,2012

[4]. E. Rubiola and V. Giordano, "On The 1/F Frequency Noise in Ultra-Stable Quartz Oscillators", IEEE Trans. Ultrason. Ferroelectr. Freq. Control, vol. 54, no. 1, pp. 15-22, Jan. 2007.

[5]. R.J. Besson, J.J. Boy, M. Mourey, E.S. Ferre-Pikal, F.L. Walls, "Phase Noise Limitation Due To Amplitude Frequency Effects In State-Of-The-Art Quartz Oscillators" 1996 IEEE International Frequency Control Symposium

[6]. Rodolphe Boudot and Enrico Rubiola, "Phase Noise in RF and Microwave Amplifiers" IEEE Trans. Ultrason. Ferroelectr. Freq. Control, vol. 59, no. 12, pp.2613-2624,2012

[7]. Fabrice Sthal,Serge Galliou,Nicolas Gufflet, "Predicting Phase Noise in Crystal Oscillators", IEEE Trans. Ultrason. Ferroelectr. Freq. Control, vol. 52, no. 1, 2005

[8]. Huang, Xianhe "The Design and Implementation of a 120-MHz Pierce Low-Phase-Noise Crystal Oscillator", IEEE Trans. Ultrason. Ferroelectr. Freq. Control, vol. 58, no. 7, pp. 1302-1306, 2011

[9]. Huang, Xianhe "Optimization and Realization of a 315-MHz Low-Phase-Noise Voltage-Controlled SAW Oscillator", IEEE Trans on Circuits and Systems II-Express Briefs, Vol.59, no.1, pp.16-19, 2012

[10]. Huang, Xianhe "Design of a Wide-Tuning-Range Lithium Tantalate Low-Phase-Noise Voltage-Controlled Oscillator", IEEE Trans on Circuits and Systems II-Express Briefs, Vol.60 no.3, pp.132-136, 2013

Design, Simulation and Test of an Oscillator Suitable for Wafer Level Evaluation of SAW Resonator Phase Noise

Dan Porga, Twinkle Shah, Mike Driscoll (Consultant)
Phonon Corporation
Simsbury, CT, USA
danp@phonon.com

***Abstract*— In a well-designed BAW or SAW oscillator, the primary contributor to near-carrier, flicker-of-frequency noise should be the resonator itself and not the sustaining stage amplifier [1-4]. Determination of resonator short-term frequency stability (self-noise) at the wafer level is highly desirable from both the perspective of resonator selection prior to packaging and evaluation of processing conditions resulting in low noise resonators. The objective of this work was to develop a methodology where the flicker-of-PM noise contributions of the sustaining stage amplifier and the resonator could be reliably and independently determined. In addition, the methodology needed to be compatible with and tolerant of coaxial probe connections to on-wafer resonator arrays. The current status is that the results obtained for evaluation of packaged and on-wafer devices are quite comparable.**

Keywords- SAW Resonator, oscillator, modular amplifier, phase noise, wafer probe

I. INTRODUCTION

To achieve the objective, a 50 ohm loop test oscillator was constructed. Candidate amplifier residual phase noise was determined via operation in an oscillator using an intentionally low delay (low Q) "noiseless" frequency control element in order to very easily identify those amplifiers whose contribution towards oscillator near-carrier noise was about 10dB below the best anticipated SAW resonator noise performance. Next, the test oscillator (using a previously characterized amplifier) was installed in a wafer probe set-up to evaluate SAW resonator self-noise. Extraordinary measures were needed to reduce the effects of acoustic noise, electrical interference and vibration. Finally, the test oscillator was used to evaluate packaged SAW resonators and the results were compared with the wafer probe results.

II. METHODOLOGY

A. Test Oscillator Block Diagram

A 50 ohm oscillator loop consists of an amplifier, power splitter, attenuator, phase shifter and resonator. Fig. 1 shows the basic configuration of the test oscillator. In this figure, a band-pass filter is substituted for the resonator.

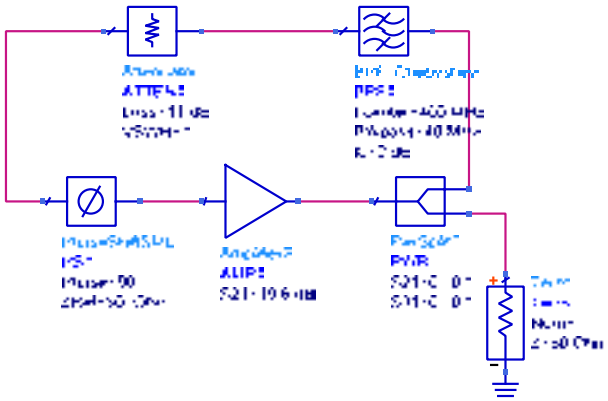

Figure 1. Test Oscillator Block Diagram

B. Leeson's Equation

Single-sideband phase noise (hereon abbreviated phase noise), L(f), is commonly used to characterize oscillators. L(f), is related to the power spectral density of phase fluctuations, $S_\Phi(f)$, as follows.

$$L(f) = 10\log\left[\frac{1}{2}S_\phi(f)\right] \tag{1}$$

Leeson's equation (2) relates oscillator closed loop performance to open loop component characteristics (first bracket) and the effect of closing the loop (second bracket) [6,7].

$$\frac{1}{2}S_\phi(f)_{osc} = \left\{\frac{1}{2}S_\phi(f)_{amp} + \frac{1}{2}S_\phi(f)_{res}\right\}\left\{1+\left(\frac{f_q}{f}\right)^2\right\} \tag{2}$$

$$f_q = \left(\frac{1}{2\pi\tau}\right) \tag{3}$$

$$\frac{1}{2}S_\phi(f)_{amp} = \frac{10^{\left[\frac{Lamp(1Hz)}{10}\right]}}{f} + 10^{\left[\frac{-177-Pin+NF+FF}{10}\right]} \tag{4}$$

$$\frac{1}{2}S_\phi(f)_{res} = \frac{10^{\left[\frac{Lres(1Hz)}{10}\right]}}{f\sqrt{\left(1+\left(f/f_q\right)^2\right)}} \tag{5}$$

Where f=frequency offset from carrier (Hz), f_q=resonator half bandwidth (Hz), τ=loop delay (s) at the carrier frequency, Pin=amplifier input power (dBm), NF=amplifier noise figure (dB) and FF=amplifier noise figure degradation from operating in compression (dB). Also, $L_{amp}(1Hz)$ and $L_{res}(1Hz)$ are the open loop 1 Hz flicker intercepts (dBc/Hz). These are the quantities we wish to measure. 1 Hz intercepts, as opposed to flicker corner frequencies, are chosen because they are independent of the noise floor.

From (2), the effect of closing the loop is a degradation in phase noise performance for $f<f_q$. This is unfortunate for products, but useful for measurements. Since the closed loop noise close to the carrier is much stronger than the open loop noise, it is much easier to measure.

C. Data Fitting

The measured oscillator data was fit to the following model.

$$\frac{1}{2}S_{\phi}(f)_{fit} = \sum_{i=0}^{4} \frac{10^{\left\lceil \frac{Li(1Hz)}{10} \right\rceil}}{f^i} + \frac{L_{5052}(1Hz)}{1+(f/Fc_{5052})^2} \quad (6)$$

Where $L_i(1Hz)$ are closed loop 1Hz intercept points (dBc/Hz) determined by the fitting process. $L_3(1Hz)$, for example, will be referred to as the 3rd order intercept. The measurements presented in this paper were made using an Agilent 5052B Signal Source Analyzer. The measurements exhibit a degradation vs. actual phase noise performance over the approximate frequency range of 2kHz to 500kHz. This is thought to be due to the in-band noise associated with the phase lock loops in the instrument. The last term in the model fits that degradation. $L_{5052}(1Hz)$ is the closed loop 1Hz intercept (dBc/Hz) and Fc_{5052} is a cutoff frequency (Hz). It is included for completeness, but is not important for flicker characterization.

Many fitting strategies were evaluated to minimize the effect of environmental noise on the probe data. These included asymmetric error weighting, windowing to reduce the impact of large errors and frequency masking. The best correlation between wafer and component data was obtained using straight least mean square fitting with a frequency mask for the probe data only.

From Leeson's equation, oscillator performance should be dominated by the 0th and 3rd order intercepts with potential contribution from the 2nd order intercept. 1st and 4th order contributions are not expected. In practice, 1st and 2nd order contributions were not observed in the data and 4th order was used to identify poor quality data. For the resonators evaluated in this paper, probe measurements with 4th order intercepts greater than -30dBc/Hz were considered invalid due to external noise impacts. While poor 4th order intercept indicates poor data, good 4th order intercept does not necessarily indicate good data. Environmental noise can degrade the 3rd order intercept as well. The RMS error between the fit and the data was used as another indication of data quality. In our probe measurements, we observed particular sensitivity in the offset range 100Hz-300Hz. This region was masked during fitting but included when calculating RMS error. Thus, it gave an indication of the severity of the environmental noise impact.

D. Calculate Open Loop Intercepts From Fit Results

From (2), (4) and (5) we see the amplifier and resonator open loop flicker result in 3rd order closed loop phase noise characteristic. Equating the 3rd order terms in (2), (4) and (5) with the model (6) and evaluating at f=1Hz, we get (7).

$$10\log\left\{10^{\left\lceil \frac{Lamp(1Hz)}{10} \right\rceil} + 10^{\left\lceil \frac{Lres(1Hz)}{10} \right\rceil}\right\} = L_3(1Hz) - 20\log(f_q) \quad (7)$$

With (7) we can determine the open loop intercepts $L_{amp}(1Hz)$ and $L_{res}(1Hz)$. Note the 3rd order fit of the measured data, $L_3(1Hz)$, is determined by the strong closed loop phase noise close to the carrier. It is not affected by the oscillator noise floor, the measurement system noise floor nor the 5052B degradation mentioned earlier. Since the noise is strong, it can be measured without cross-correlation. This speeds up the measurement and is helpful in reducing environmental noise impact during wafer probing. The f_q term is easily obtained by measuring the loop delay on a network analyzer.

III. AMPLIFIER CHARACTERIZATION

Equation (7) suggests desired conditions for measuring $L_{amp}(1Hz)$. The contribution of SAWR self noise can be removed from the oscillator signal via resonator removal and replacement by an L-C resonator or band-pass filter. Enhancement of the resulting oscillator closed loop phase noise allows simple and accurate measurement. This is accomplished by making f_q in (3) large or, equivalently, the oscillator loop group delay small. Both of these were achieved by substituting a rather wide band-pass LC filter (low Q) for the resonator in the loop. Fig. 2 illustrates the setup used. Here the amplifier was soldered to a connectorized PCB. For production testing, a fixture for the amplifier would be used to enable rapidly testing multiple devices.

In this work we characterized the amplifiers at 400MHz. The loop components consist of an amplifier (MMIC, 19.6 dB), a power splitter (-3.5 dB), a band pass filter (-2.5 dB, 40MHz bandwidth, 17.3nsec group delay) and a variable phase shifter. After subtracting the loop loss, we will have 13.5 dB excess gain in the loop. For oscillation to occur, the loop gain must be 0dB and the loop phase 0 degrees at the frequency of oscillation. We establish these conditions by measuring the open loop S21 on a network analyzer and make adjustments as necessary. Using a low level stimulus to avoid compressing the amplifier, the loop gain is set to about 2dB. For the above loop, we used an 11dB RF attenuator in the path to achieve 2.5dB excess gain. The network analyzer stimulus level is increased until the amplifier compresses to the point of 0dB loop gain. Finally, the phase shifter is adjusted to 0 degrees loop phase at the desired frequency of oscillation. The data presented below was obtained at 400MHz.

Figure 2. Low Q Phase Noise Measurement Set Up

Several amplifiers were evaluated, including inexpensive, tape-and-reel type MMIC amplifiers containing darlington pair configurations with resistive feedback as well as SMP modular amplifiers [5]. A reasonably large spread in 1/f PM noise was observed for different model tape-and-reel MMIC amplifiers purchased from the same vendor. The same method was used in a discrete component sustaining stage, and in that case, resonator loading was both measured and successfully simulated via determination of the $1/(2\pi\tau)$ corner frequency in the amplifier phase noise plots.

Fig. 3 shows phase noise measurements of a MMIC amplifier, an SMP modular amplifier and a discrete NPN amplifier using the low Q oscillator technique described above. The data was fit to the model (6) and (7) was used to determine the open loop 1Hz intercept: $L_{amp}(1Hz)$. The results are presented in Table I. The discrete NPN amplifier exhibits the best flicker performance of the three presented and is significantly better than the expected SAW resonator flicker performance at this frequency.

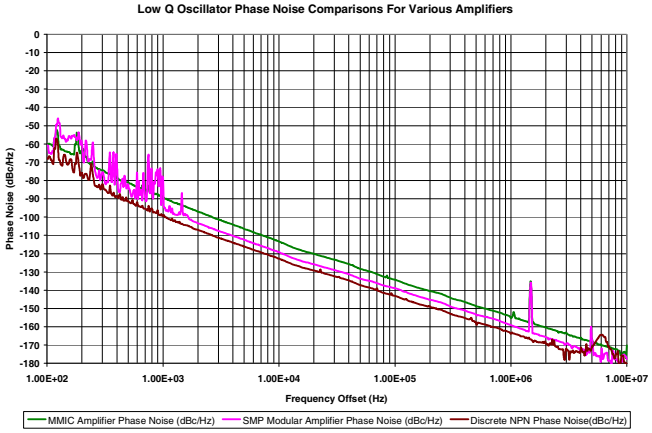

Figure 3. Low Q Oscillator Phase Noise

TABLE I. COMPARISON OF AMPLIFIER $L_{AMP}(1Hz)$

Amplifier	Open Loop 1 Hz Flicker Intercept (dBc/Hz)
Discrete NPN	-150
SMP Modular	-143
MMIC	-140

IV. RESONATOR CHARACTERIZATION

Since we are now interested in characterizing resonators, the amplifier contribution should be minimized. Good practice would be to select an amplifier whose 1Hz flicker intercept is at least 10dB better than the resonator under test. Once a suitable amplifier is selected and characterized, it is used for all resonators under test; Thus $L_{amp}(1Hz)$ in (7) is known. The test oscillator can be used to characterize packaged or on-wafer resonators. The setup to test packaged resonators is similar to Fig. 2, except the band-pass filter is replaced with a resonator in a test fixture.

At wafer probe, the oscillator's short term frequency stability can be significantly affected by ambient acoustic noise and vibration. Measures have been taken in this experiment to reduce the ambient noise as well as reduce the measurement sensitivity to noise. This is challenging since the noise we are trying to suppress is low frequency (10Hz-1kHz). The measures discussed below have improved data quality significantly, but more work remains to be done. To reduce ambient vibration, the prober (Electroglass 1034) was located on an outside wall of the facility. Currently, it is located on the second floor; moving to the ground floor should provide additional benefit. Additionally, the prober is mounted on a two stage vibration isolation table. To reduce ambient acoustic noise, the prober is located in a quiet room as removed from people and equipment as possible. Measurements were performed at night when activity in and around the building is minimal and unused equipment, particularly roof-top air handlers, could be powered off. The prober was also shielded by an acoustic enclosure; however, it did not provide much benefit below 500Hz. Measures were required to reduce acoustic noise generated by the prober itself. Fans were either located remotely (power supply relocated) or computer controlled to turn off during measurements. The prober employs a linear motor that rides on an air bearing which was a significant source of ambient noise. The compressed air was shut off via computer control during measurements. Similarly, any vacuum leaks holding the wafer to the chuck degraded the data. It was observed that the probe tip to wafer interface was particularly sensitive. Robust micro-positioners and probe tips helped as did securing all cabling. Fortunately, the probe electronics did not seem to impact the data; however, the AC power to the microscope light did. Turning the light off after setup alleviated the problem.

SAW resonators at 320MHz were selected to evaluate the methodology. Fig. 4 illustrates example on-wafer and packaged data with the resulting fits. Wafer data was collected with no cross-correlations and three averages. This wafer run exhibited the least degradation due to environmental noise obtained so far, yet degradation is still observed between 100Hz and 400Hz. A frequency mask from 100Hz to 300Hz

was applied to the wafer data during the fitting process. The packaged resonator was much less susceptible to environmental noise as can be seen in the figure. This data was collected with 10 cross-correlations and no averages.

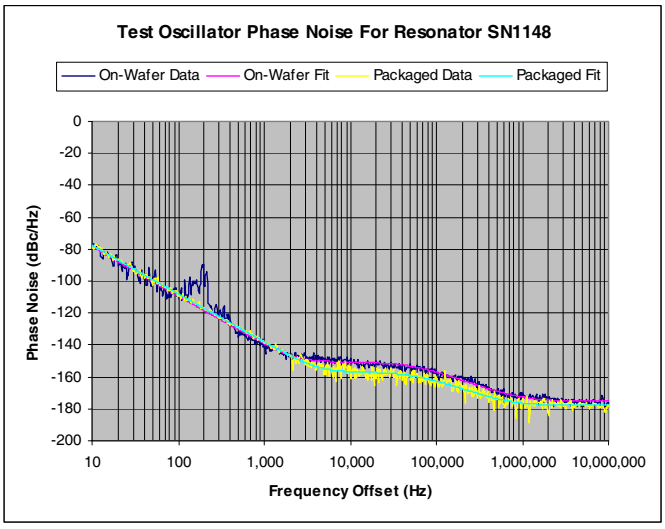

Figure 4. Example Resonator On-Wafer Data and Fit

Linear regression was performed on the wafer and packaged resonator data. The regression was statistically significant with an adjusted R^2 value of 95%. The resulting equation, $L_{res}(1Hz)_{pkg}=0.9996L_{res}(1Hz)_{wafer}$, was the desired result. Fig. 5 illustrates the data and the resulting fit. The relation does not perfectly predict packaged data performance from probe data, but it is useful for ranking resonator die for assembly. Table II presents summary statistics on the difference $L_{res}(1Hz)_{pkg}$- $L_{res}(1Hz)_{wafer}$. The average difference is close to 0dB. This allows accurate comparison of wafers, with different process conditions for example, by comparing the average performance of many die on each. Large data sets are needed to reduce the impact in the variability in the data. This was previously not practical without automated data collection and processing.

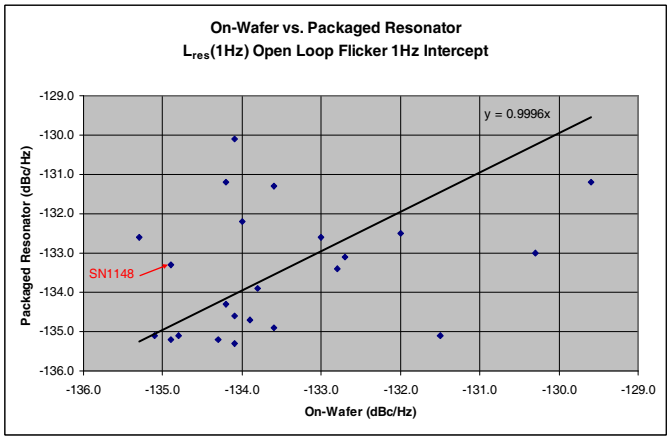

Figure 5. On-Wafer vs. Packaged Resonator $L_{res}(1Hz)$

TABLE II. PACKAGED MINUS ON-WAFER $L_{RES}(1Hz)$

Difference Between Packaged and On Wafer Resonator 1Hz Flicker Intercept (dBc/Hz)	
Count	23
Average	0.04
Stdev	1.81
Min	-3.6
Max	4

V. SUMMARY AND CONCLUSIONS

The goal of this project, the successful development and demonstration of a technique to accurately determine SAW resonator on-wafer phase noise performance, has been accomplished.

The in-oscillator technique uses a sustaining stage amplifier whose phase noise contribution is 10dB below that of best-measured resonators and allows determination of the noise contribution of devices with further improved noise level through design and processing optimization.

Determination of probe oscillator sustaining stage amplifier 1/f PM noise, was greatly facilitated via use of a low group delay filter substituted for the SAW resonator.

The most challenging aspect of this effort involved the minimization of vibration and acoustic induced oscillator phase noise degradation.

ACKNOWLEDGMENT

The authors would like to thank Dr. Tom Martin for many helpful technical discussions.

REFERENCES

[1] M. M. Driscoll and B.W. Kramer, "Spectral Degradation in VHF Crystal-Controlled Oscillators due to Short-term Instability in the Quarts Resonator", Proc. 1985 IEEE Ultras. Symp., Oct. 1985, pp. 340-344.

[2] F. L. Walls and A. E. Wainwright, "Measurement of the Short-term Stability of Quarts Crystal Resonators anfd the implications for Crystal Oscillator Design", IEEE Trans. Instrum. Measmt., Vol. IM-24, no. 1, March 1, 1975, pp. 15-20.

[3] T. E. Parker, "1/f Frequency Fluctuations in Acoustic and Other Stable Oscillators", Proc. 39th IEEE Freq. Contr. Symp., May, 1985, pp. 97-106.

[4] M. M. Driscoll, "Low Noise Oscillator Design and Performance", Tutorial presented at the 2003 IEEE Freq. Contr. Symp., accessible at http://www.ieee-uffc.org/frequency_control/teaching.

[5] M. M. Driscoll, "Low Noise Crystal Oscillators Utilizing 50-Ohm Modular Amplifier Sustaining Stages", Proc. 40th IEEE Freq. Contr. Symp., May, 1986, pp. 329-335.

[6] D. B. Leeson, "A Simple Model of Feedback Oscillator Noise Spectrum", Proc. IEEE, vol. 54, no. 2, Feb. 1966, pp. 329-330.

[7] T. E. Parker, "Characteristics and Sources of Phase Noise in Stable Oscillators", Proc. 41st IEEE Freq. Contr. Symp., May, 1987, pp. 99-110.

The Sampling Theorem in Pi and Lambda Digital Frequency Dividers

Claudio E. Calosso
Division of Optics
INRIM
Torino, Italy
e-mail: c.calosso@inrim.it

Enrico Rubiola
Department of Time and Frequency
CNRS FEMTO-ST Institute
Besancon, France
e-mail: rubiola@femto-st.fr
web page http://rubiola.org

Abstract*— It is a common belief that a noise-free frequency divider by *D* scales down the input phase by a factor of 1/*D*, thus the phase-noise power spectral density (PSD) by $1/D^2$. We prove that the behavior described *does not apply to digital dividers.

Instead, the digital divider scales the white phase-noise PSD down by 1/*D*. Phase downsampling and aliasing, inherent in digital frequency division, is the reason. However the $1/D^2$ law holds asymptotically for flicker, where the aliases can be neglected.

We propose a new de-aliased divider, which scales the input phase-noise PSD by approximately $1/D^2$. The scheme is surprisingly simple and suitable to CPLD and FPGA implementation.

Keywords*— *aliasing; digital frequency divider; phase noise; white noise; flicker

I. Introduction

The noise-free frequency divider can be assimilated to an ideal gearbox that divides the input frequency by *D*, transferring the total jitter $x(t)$ – better referred to as `phase time' or `phase-time fluctuation' – from the input to the output. Accordingly, the output phase noise is $\varphi_{out}(t) = \varphi_{in}(t)/D$, and its power spectral density (PSD) $[S_\varphi(f)]_{out} = [S_\varphi(f)]_{in}/D^2$. So, a modulo-10 divider reduces the input phase noise by 20 dB.

Unfortunately, the output *white* noise of the classical digital divider (Π divider) is ruled by $[S_\varphi(f)]_{out} = [S_\varphi(f)]_{in}/D$. Since the denominator is *D* instead of D^2, a modulo-10 divider reduces the input noise by 10 dB instead of 20 dB. This is due to aliasing, thus it is inherent in the square-wave frequency division (Π divider), and independent of technology.

This article stands on [1], clarifies some issues, and introduces the Λ-type divider. This divider fixes the aliasing by adding shifted square waves with resistors, which results in a triangular-wave output (Fig. 2). Therefore, the noise of the Λ divider is ruled by $[S_\varphi(f)]_{out} = [S_\varphi(f)]_{in}/D^2$, which outperforms the phase noise of the Π-type divider by a factor of 1/*D*.

The $1/D^2$ and 1/*D* laws result from simple mathematical properties of white noise. Of course thermal noise, shot noise, and flicker noise add up, and the noise due to the technology as well.

II. Sampling and Aliasing

It is well known that the spectrum around all multiples of the sampling frequency is down-converted to baseband, and overlaps to the main part of the spectrum. This is the essence of aliasing, fully explained by the sampling theorem. The same fact can be interpreted as a consequence of energy conservation, as the sampling process preserves the total noise power. The power is by virtue of the Parseval theorem equal to the noise PSD integrated over the full bandwidth. Therefore, band compression results into white-noise enhancement by the same factor.

Real-world white noise has constant PSD spanning from 0 to the bandwidth *B* of the system. In the presence of white noise, aliasing deteriorates the SNR by a factor of B/f_N, where f_N is the Nyquist frequency (half the sampling frequency).

By contrast, flicker results in little and generally negligible degradation of the SNR. This happens because the PSD is proportional to $1/f$, so the aliases are small as compared to the base band.

A. Input stage

In digital circuits, the input stage converts the sinusoidal clock input into a square wave. As a relevant consequence, phase noise shows up only at the rising and falling edges, while the signal is saturated in between. This means that phase noise is *sampled* at the frequency 2ν, hence the Nyquist frequency is $f_N = \nu$. Denoting the bandwidth of the input stage with *B*, aliasing increases $S_\varphi(f)$ by a factor of B/ν. For instance, a 100 MHz sinusoid processed by a 300 MHz logic circuit results into a degradation of the input noise by approximately 4 dB.

B. Π-type divider

The classical digital divider is called Π-type divider from the graphical similarity of the output pulses with the Greek letter Π.

In a modulo-*D* divider, one edge every *D* edges propagates from input to output (Fig. 1). This is a hard decimation process, with no low pass (anti-aliasing) filter. In this condition, aliasing increases the white noise by a factor of *D*. Since the pure gearbox scales $S_\varphi(f)$ down by $1/D^2$ and alias enhances it by a factor of *D*, overall the input white noise is governed by the $[S_\varphi(f)]_{out} = [S_\varphi(f)]_{in}/D$ law.

Oppositely, flicker ($1/f$) noise is well approximated by the $[S_\varphi(f)]_{out} = [S_\varphi(f)]_{in}/D^2$ law because the aliases are comparatively small.

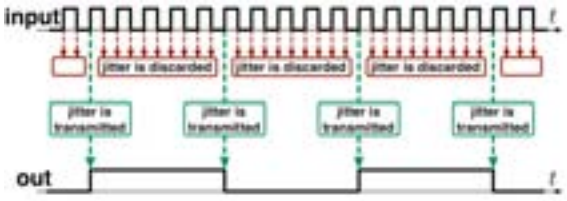

Fig. 1. Output sampling mechanism in Π divider.

C. Λ-type divider

The Λ divider generates a triangular wave signal by combining D square-wave signals shifted by half cycle of the input clock. Figure 2 shows an example of implementation for $D = 10$. Alternate topologies are also possible.

In Fig. 2, two ÷10 Π dividers are used, one driven by the rising edge of the input clock, and one driven by the falling edge. The outputs are delayed by 5-bit shift register, so that 10 phases of the intermediate square wave at $\nu/10$ are available, spanning over 180º. The sum of these intermediate signals is a triangular-wave like staircase (Fig. 3). Of course, the Greek letter Λ in the name derives from the graphical analogy with the triangular waveform.

The relevant feature of the Λ divider is that the output is sampled at the frequency 2ν, i.e., twice the input frequency, instead of $2\nu/D$, which fixes the alias of the Π divider. An alternate interpretation is that the white random signals at the intermediate outputs are statistically independent. Adding D of them results in facror-of-$1/D$ lower phase noise. As a consequence, the Λ divider is governed by the $1/D^2$ law, which is the theoretical limit for the noise-free divider.

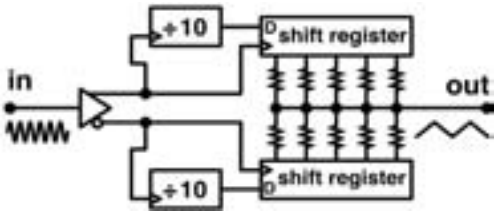

Fig. 2. Λ divider block diagram.

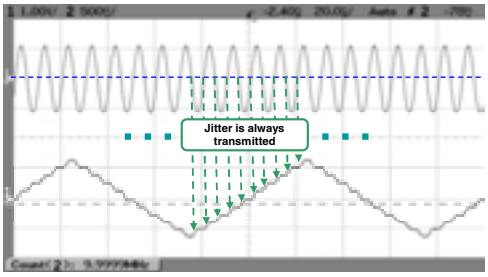

Fig. 3. Waveform at the input and at the output of a Λ divider.

III. Experiments and Results

The Divider Under Test (DUT) is implemented in a CPLD Altera EPM3064A [2], a simple 64-cell device with 10 ns speed grade, kind of the `ancestor' of the FPGA, which for our purposes can be programmed in three ways:

- The simple Π-type divider,
- A multi-buffer Π-type, which is the scheme of Fig. 2 with the `shift registers' re-configured as buffers, i.e., with no shift at all,
- The Λ divider, as it is in Fig. 2.

The resistor network is a SMD array mounted close to the CPLD.

The phase-noise test instrument [3] implements the cross-spectrum technique described in [4].

A. Aliasing

The first experiment is the demonstration of the aliasing phenomenon in the Π and Λ dividers, and of the benefit of the Λ topology. In order to isolate the aliasing effect from other phenomena in the divider, we work with an artificially – and unrealistically – high level of white noise. This is done by attenuating and re-amplifying the clock signal (Fig. 4).

Flicker noise cannot be obtained in the same way. So, we use the phase-modulation feature of a commercial synthesizer driven by an audio-frequency flicker-noise generator.

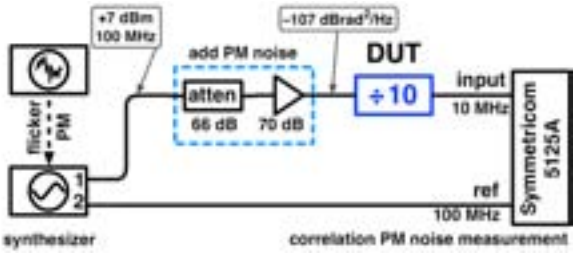

Fig. 4. Experimental setup.

The results of this first experiment are shown in Fig. 5. After waveform shaping, the phase noise is 4 dB higher. This is exactly what expected from the bandwidth of the front end.

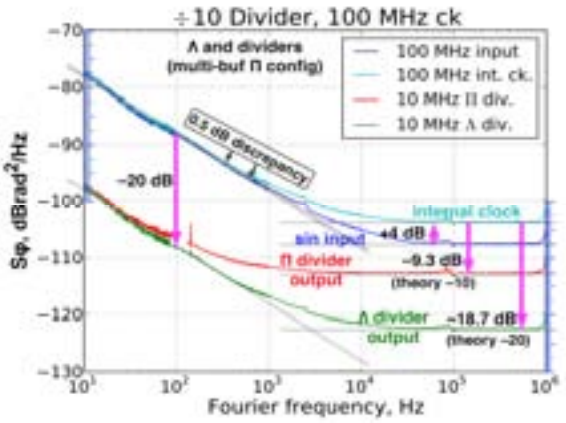

Fig. 5. Result on aliasing in case of flicker and white phase noise.

The flicker noise is scaled down by 20 dB in all cases. This confirms the theoretical prediction that the aliases of $1/f$ noise are too low to be visible on the output spectrum. At 100-1000 Hz, the spectrum differs by 0.5 dB from the straight-line approximation. This is still not explained, and left for future investigation.

The Π divider reduces the phase noise by 9.3 dB, which is close to the expected value of 10 dB. Similarly, the Λ divider reduces the input phase noise by 18.7 dB, close to the value of 20 dB predicted by the theory.

B. Residual Phase Noise of the Dividers

The second experiment is the measurement of the divider phase noise in real-life conditions, in order to demonstrate the practical usefulness of our solutions. The synthesizer is now replaced with a low-noise OCXO, manufactured by Wenzel Inc. [5]. The phase noise spectrum is shown in Fig. 6.

The 1-Hz phase-noise coefficient is $b_{-1}=10^{-12}$ rad^2/Hz (–120 dB rad^2/Hz) for the Π divider, and $b_{-1}=9\times10^{-14}$ rad^2/Hz (–130.5 dB rad^2/Hz) for the Λ divider. Beyond 10 Hz, the flicker noise is 2–3 dB higher. This discrepancy could be an artifact, however the phenomenon is still unexplained.

The white noise is $b_0=2.5\times10^{-16}$ rad^2/Hz (–156 dB rad^2/Hz) for the Π divider, and $b_0=3.2\times10^{-17}$ rad^2/Hz (–165 dB rad^2/Hz) for the Λ divider.

The Allan deviation of the Λ divider is of 2×10^{-14} at 1s. This is equivalent to that of a DDS [6], yet at a way lower cost, complexity, size, and electrical power.

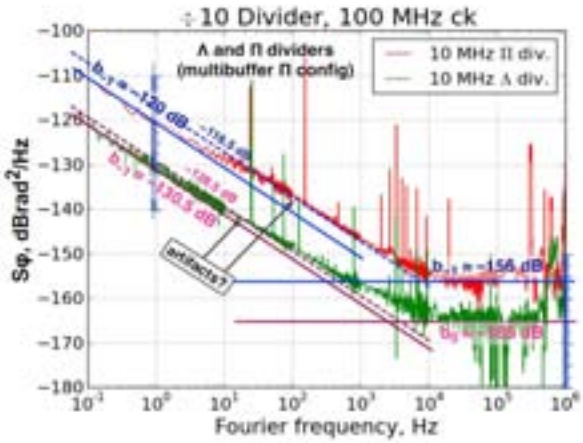

Fig. 6. Residual phase noise of the Π and Λ dividers we tested.

IV. Conclusions

We demonstrated theoretically and experimentally that the white noise of traditional digital frequency dividers (Π topology) is affected by aliasing, and that the new Λ topology fixes the problem.

The phase noise of the Λ divider sets the state of the art for digital dividers. Only the regenerative divider [7] performs lower noise. However, the Λ divider is a fully digital circuit, therefore simple, reproducible, and requires no tuning or adjustment. Thus it is suitable to straightforward integration in larger blocks.

Acknowledgments

This work is partially funded by the ANR (Oscillator IMP project and First-TF network) and by the Région Franche Comté.

We thank Vincent Giordano, Marco Siccardi, Jean Michel Friedt, Marcello Chiaberge for fruitful discussions.

References

[1] W. F. Egan, "Modeling phase noise in frequency dividers", IEEE T UFFC 37(4), July 1990.

[2] http://www.altera.com

[3] http://www.symmetricom.com

[4] E. Rubiola, F. Vernotte, "The cross-spectrum experimental method", arXiv:1003.0113

[5] http://www.wenzel.com

[6] C. E. Calosso, Y. Gruson, E. Rubiola, "Phase noise in DDS", Proc. 2012 IFCS p. 777-782

[7] A. Hati, C. W. Nelson, C. Barnes, D. Lirette, J. DeSalvo, D. A. Howe, "Ultra-low-noise regenerative frequency divider", IEEE T UFFC 59(11), November 2012

Trim Effect Compensation Using an Artificial Neural Network

John C. Esterline
Greenray Industries
Mechanicsburg, PA USA
jesterline@greenrayindustries.com

Abstract— **Trim effect is a skewing of the frequency versus temperature performance of a crystal oscillator as the frequency is pulled (trimmed) away from the oscillator's nominal frequency. As TCXO (Temperature Compensated Crystal Oscillator) frequency versus temperature stabilities have improved to ppb (part per billion) levels trim effect has become more of a concern. Even though unwanted, the degradation of performance from trim effect is something generally accepted as a characteristic of TCXOs. This paper focuses on a method of compensating crystal oscillator trim effect. Through the use of an artificial neural network, trim effect compensation of AT cut crystal oscillators can be achieved with better than +/-15ppb stability over the industrial temperature range (-40 to +85 °C). This is more than a 10 fold improvement over the inherent trim effect found using state of the art polynomial function generator compensation. The theory of this compensation method with be discussed, and data showing the results of trim effect compensation on actual oscillators will be presented.**

I. INTRODUCTION

Trim effect is a skewing of the frequency versus temperature performance of a crystal oscillator as the frequency is pulled (trimmed) away from the oscillator's nominal frequency. This effect is well known, but mostly ignored, due to an inability to reduce or eliminate the skewing. Trim effect manifests because the compensation voltage for the Temperature Compensated Crystal Oscillators (TCXOs) is derived with the control voltage (or EFC) at a fixed value (generally ½ of the supply voltage) and applied to a varactor. The varactor's reactance varies with the voltage applied, which results in a change in load capacitance (C_L). The frequency versus C_L relationship is nonlinear.

This nonlinear relationship leads to degradation in frequency versus temperature performance when the TCXO's control voltage is changed to a value that is different than what it was compensated with. In practical use TCXO's are commonly adjusted for aging drift. The recalibration of the TCXO for aging will inadvertently cause the TCXO's frequency versus temperature performance to be degraded.

The following paper will discuss a trim effect compensation scheme using an Artificial Neural Network (ANN). The method developed by Greenray Industries, has successfully compensated Statek AT-cut strip crystals to stabilities of better than +/- 15 ppb over the industrial temperature range of -40 to +85 °C (including a +/-5ppm trim range).

Using an ANN for temperature compensation has been discussed in literature [2-4]. [2] is a review of the subject matter and asserts that ANN technology would be suited for environmental compensation of crystal oscillators. [3] describes an attempt to compensate the temperature performance of a crystal oscillator using an ANN. The oscillator in [3] was only compensated over a 6 °C range (21 - 27 °C), and the training of the network took 21 days. The conclusion drawn in [3] was that the technology could achieve compensation but the training time at that time (1994) was prohibitive for manufacturing. [4] describes preceding work from Greenray Industries, that compensated a TCXO to better than +/- 10ppb over the industrial temperature range of -40 to +85 °C.

Trim effect has been covered extensively in literature, however compensation of trim effect has been covered to a much lesser extent. [5] describes a TCXO compensation incorporated into a custom TCXO ASIC

In Section II, the basics of ANN technology and how this can be implemented as a curve fitter will be discussed. Section III describes the configuration of the Greenray Industries oscillator employing the ANN temperature compensation and trim effect compensation schema. Section IV summarizes the performance of the ANN compensated oscillator over temperature and trim. Section V, concludes with a discussion of the new compensation methodology.

II. ARTIFICIAL NEURAL NETWORK OVERVIEW

The following is a very brief overview of ANN theory. It is intended to give the unfamiliar reader enough understanding of the topic to comprehend the remainder of this text. For a more in depth discussion of neural network technology, [7] is an excellent source. Being the preceding work to this text, [4] is also a good source as it describes the ANN temperature compensation being employed in this work.

A neural network can be described in general as a "machine that is designed to model the way in which the brain performs a particular task or function of interest [7]." This "machine" achieves this modeling through the interconnections of many simple processing units or neurons. In nature the neurons are biological nerve cells which have electrical and chemical responses to given stimuli. In an artificial neural network the neuron is modeled in hardware and/or software. Figure 1 below shows a non-linear model of a neuron.

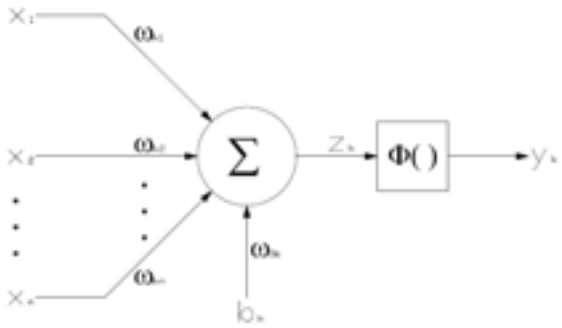

Figure 1: Nonlinear model of a neuron [4]

Starting at the left side of Figure 1, one can see the input vector of input(s) x_1 through x_n. These inputs are then multiplied by the individual synaptic weights ω_{k1} through ω_{kn}. There is a bias b_k, which can have its own weight ω_{0b}. These products are summed together, before being subjected to the activation function. The activation function (Φ) can be nearly any function the designer sees fit to use, and are often chosen to suit the application. The purpose of the activation function is to limit the amplitude of the output to some finite value [7]. Equations (1) and (2) show the neuron in mathematical terms.

$$z_k = \left(\sum_{i=1}^{n} \omega_{ki} x_i \right) + \omega_{0b} b_k \qquad (1)$$

and

$$y_k = \Phi(z_k) \qquad (2)$$

For simplicity, many times Figure 1 is condensed so that the summation and the activation function are both contained in the bubble as can be seen in the remainder of neural network figures in this text.

Activation Function

As mentioned above the activation function (Φ) can be any function the designer desires. The activation function selected for the task of oscillator temperature compensation is the unipolar sigmoid function, shown in (3). In equation (3), α is a slope control variable, and z_k is defined in (1).

$$\Phi = \frac{1}{1 + e^{-\alpha(z_k)}} \qquad (3)$$

For a two input network the sigmoid function becomes a three dimensional sigmoid sheet as seen in Figure 2. The variables affect the three dimensional sigmoid in the same way as its two dimensional counterpart except that there are now two inputs each with independent weights. These two independent weights can rotate or twist the sigmoid sheet in three dimensional space.

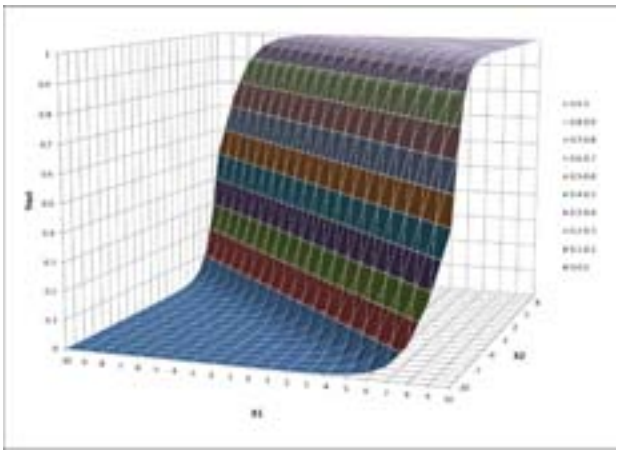

Figure 2: Three dimensional sigmoid

For trim effect compensation the ANN needs to have two inputs, x_1 and x_2. The input x_1 is a voltage that corresponds to the temperature of the oscillator. The input x_2 is the user applied control voltage. This two input network is shown in Figure 3 below.

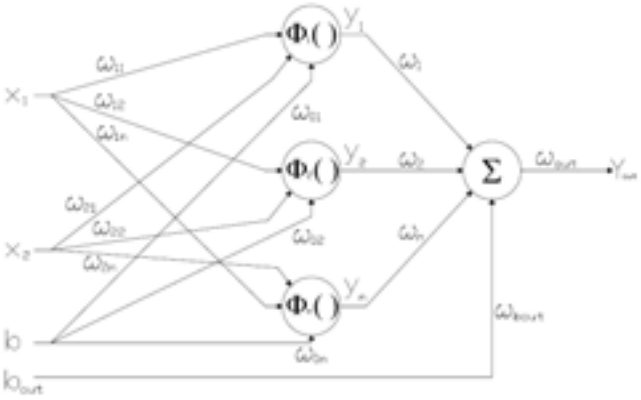

Figure 3: Two input network for trim effect compensation

The network structure in Figure 3 can be described by (4).

$$Y_{out} = \omega_{out} \left[\left(\sum_{i=1}^{n} \omega_i y_i \right) + \omega_{bout} b_{out} \right] \qquad (4)$$

Each neuron (y through y_n) in the input layer has a sigmoid activation function as shown in (3). The input x is a voltage representing temperature, and the output will be a representation of the deviation in ppm.

Network Training/Learning

The weights of the ANN structure are what ultimately determines its response and therefore must be determined in some fashion. In the neural network field the process of

"solving" for these weights is referred to as learning or training. The learning can be defined as "a process by which the free parameters of a neural network are adapted through a process of stimulation by the environment in which the network is embedded [7]." There are many different ways to "train" neural networks and most have applications where one method is preferred over another. For this application, the well-known method of least squares was implemented using a gradient reduction search.

III. ANN OSCILLATORTRIM EFFECT COMPENSATION

To implement trim effect compensation using an ANN two neural networks are implemented. The first network is responsible for compensating the oscillator at center control voltage. The second network is responsible for the trim effect compensation. The trim effect compensation network is placed in parallel to the temp compensation network, and the two compensation voltages are summed together. Figure 4 shows the block diagram of this dual network configuration. Theoretically speaking both the center temperature compensation and the trim effect compensation could be accomplished by the same ANN, however in practical application the complexity of the network to solve the higher deviation three dimensional trim effect solution space makes it more impractical. The gradient reduction solver can easily become "stuck" in a local minima, degrading the level of fit for the solution. Better results have been achieved by first compensating the oscillator at center control voltage, and then applying a secondary trim effect compensation ANN.

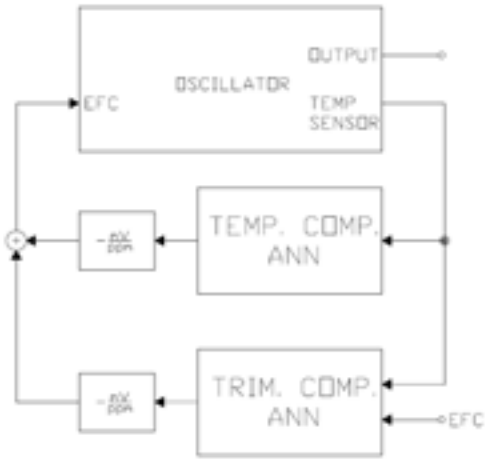

Figure 4: ANN trim effect compensation block diagram

The hardware needed to accomplish the temperature and trim compensations can be seen in Figure 5. The trained weights for the ANN are stored in the EEPROM. Each neuron has 4 variables that are being trained (ω_1, ω_2, b, and α). However from the equation of the sigmoid in (3), one can see that α is distributed in the quantity z_k . After training, this distribution can be done so that what is stored in the EEPROM are the quantities $\alpha\,\omega_1$, $\alpha\,\omega_2$, and α b. This reduces the storage requirements for each neuron down to three quantities. The network as a whole will have a ω_{bout} and ω_{out} that also need to be stored.

The microprocessor samples the temp sensor using the ADC. It then applies that input to the microprocessor which calculates the ANN's response, and the output is converted back into a voltage using the DAC. With the current hardware, seven corrections a second can be applied to the oscillator providing excellent tracking under fast temperature ramp conditions. The low pass filter is to prevent the output frequency from having a step function response to the corrections.

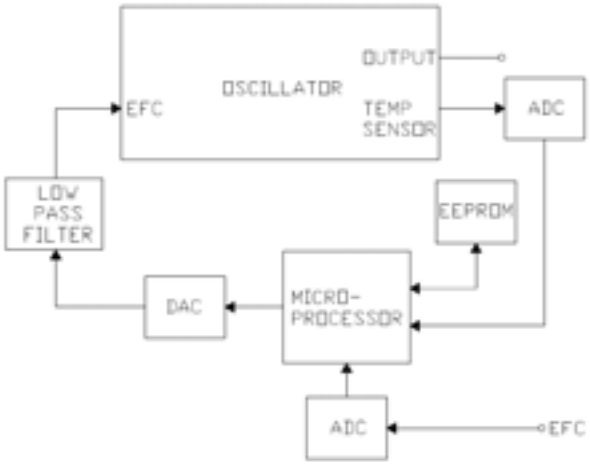

Figure 5: Block diagram of hardware for ANN trim effect compensation

Prototype Testing

Two different compensations were performed in the initial evaluation of the technology. The first compensation was to use one of Greenray Industries 10MHz ANN100-1 oscillator. This oscillator was designed around the ANN hardware in Figure 5. The ANN100 series uses a Greenray Industries T70 TCXO as the oscillator. The T70 was chosen because the oscillator die is in a ceramic package with a Statek AT strip crystal, which is also in a ceramic package, mounted on top. This construction provides a very good thermal design, which has excellent thermal coupling between the temperature sensor on the die and the crystal. Also the Statek AT Cut crystals have proven to be very good for low perturbations and low thermal hysteresis.

The first compensation done in evaluation of the hardware was to use the TCXO's internal compensation followed by a secondary compensation using the ANN methodology described above(with the control voltage set to ½ V_{cc}). This was done to provide a low deviation frequency versus temperature performance at center control voltage, which makes the solution space for the trim effect compensation easier to fit. The second compensation employed was another ANN to provide the trim effect compensation as described in Figure 4 above.

IV. ANN COMPENSATION RESULTS

The below section details the results of the trials described above. Figure 6 below shows the results of the center control voltage frequency versus temperature compensation and the resulting trim effect.

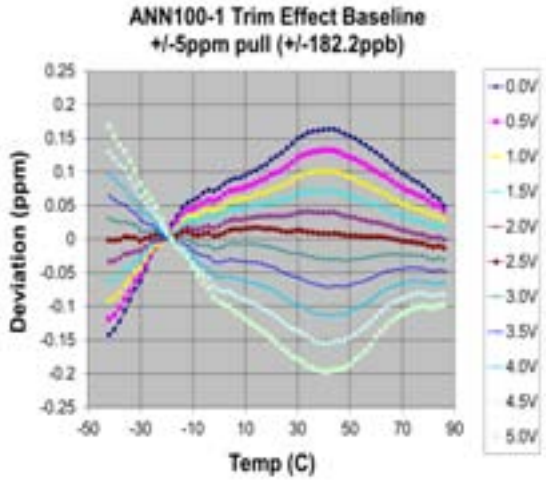

Figure 6: ANN100 frequency versus temperature compensation

In Figure 6 it can be seen that the center control voltage of +2.5V provides a very flat response over temperature and as the voltage is trimmed the deviation becomes increasingly worse. Figure 7 shows the results after implementing the trim effect compensation ANN. It can be seen that the deviation after the ANN trim effect compensation is applied is +/- 10.7ppb including trim effect. This is a compensation of 17 to 1. To achieve this compensation 10 neurons were used.

By implementing these two compensations, a TCXO has been created that has a frequency versus temperature performance of +/- 10.7ppb over the industrial temperature range (-40 to +85 C). This is inclusive of the trim effect generated by trimming the oscillator +/- 5ppm. This performance rivals that of many OCXOs, however the power consumption of the ANN100 is less than 100mW.

The addition of the trim effect compensation to the ANNCXO demonstrates the technology's robustness as a curve fitter improves the performance of the oscillator beyond what is achievable with other traditionally employed compensation methods.

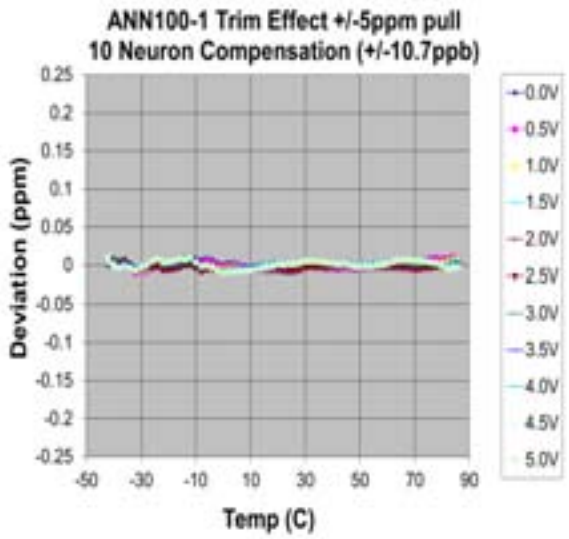

Figure 7: ANN trim effect compensation

V. CONCLUSION

The approach shown above outlines a means for using an ANN to provide temperature compensation and trim effect compensation for a crystal oscillator. From the above data it can be seen that the ANN provides a medium with which to fit very complex multidimensional data. This allows for an embeddable compensation schema to be employed that can improve the frequency versus temperature performance beyond what is achievable with traditional methods. It also allows for the compensation of trim effect which is present in all TCXOs (that have a control voltage).

ANN compensation provides greater than an order of magnitude improvement over the 5th order polynomial compensation. This realized performance improvement over the polynomial style of compensation allows a very low power consumption and relatively small device to have temperature stabilities that rival many OCXOs. A drawback to this approach is that the phase noise performance is that of a TCXO. This could limit the applications that it is ultimately suitable for. However, the advantage in footprint and power consumption (<100mW) will allow the ANNCXO to replace OCXO's in applications that are primarily concerned with temperature performance and not necessarily phase noise.

Building on the ANN temperature compensation described in [4], the trim effect compensation demonstrates how more complex multidimensional environmental effects can be compensated. This insight would allow ANNs to be designed that could compensate for thermal hysteresis, warm-up, and possibly aging. The superior curve fitting nature of the ANN effectively allows the designer to fit and compensate for any frequency deviation that can be sensed. The limit on this statement would be memory for storing weights. As the solution space becomes more complex and spans more dimensions the number of neurons needed to effectively fit that space will grow drastically.

REFERENCES

[1] Raymond L. Filler et al., "Specifiaction and Measurement of the Frequency Versus Temperature Characteristics of Crystal Oscillators," *43rd Annual Symposium on Frequency Control, 1989*

[2] B. Hivert, R. Brendel, "Neural Networks Trends For Frequency Control: A Review," *1995 IEEE International Frequency Control Symposium*, pp. 10-19.

[3] D. B. Opie, "Operation of a Neural Network Controlled Crystal Oscillator,"*1994 IEEE International Frequency Control Symposium*, pp. 600-603.

[4] Esterline, J.C.; , "Temperature compensation of crystal oscillators using an Artificial Neural Network," *Frequency Control Symposium (FCS), 2012 IEEE International* , vol., no., pp.1-7, 21-24 May 2012

[5] Ward, K.R.; , "A novel approach to improving the stability of TCVCXO temperature performance," *Frequency Control Symposium and PDA Exhibition Jointly with the 17th European Frequency and Time Forum, 2003. Proceedings of the 2003 IEEE International* , vol., no., pp. 473- 477, 4-8 May 2003

[6] Steve Fry, "The Design and Performance of Minuature TCXOs," RF Design, September 2006

[7] Simon Haykin, Neural Networks a Comprehensive Foundation. Second Edition, New Jersey, Pretence Hall, 1999, pp. 1-10

Status of the Flight Model of the Cold Atoms Space Clock PHARAO

Igor Moric, Philippe Laurent
Observatoire de Paris, SYRTE
Paris, FRANCE

***Abstract*—PHARAO (Projet d'Horloge Atomique par Refroidissement d'Atomes en Orbite), which is being developed by the French space agency CNES, is the first Primary Frequency Standard (PFS) specially designed for operation in space. PHARAO is a main instrument of the ACES (Atomic Clock Ensemble in Space) mission. ACES is being developed by ESA and the payload will be installed on-board the International Space Station. The mission is based on comparisons with ground based clocks to perform fundamental physics experiments: gravitational redshift measurements, analysis of the stability of the fundamental constants and anisotropy of light. Planned duration of the mission is 18 months with a possible extension to 36 months. The frequency accuracy requirement for PHARAO is less than 3 x 10^{-16} and the expected frequency stability is $10^{-13}\tau^{-1/2}$. An engineering model of PHARAO has been constructed and fully tested to validate the clock architecture. Two sub-systems for the flight model FM) have been delivered: the cesium tube where the atoms are manipulated and the microwave source which generates the 9.2 GHz signals. The other sub-systems, the laser source and the computer, will be delivered this year. Some performances tests have been performed on the microwave source and on the cesium tube assembled with the other EM sub-systems. The whole FM clock will be assembled in 2013.**

I. INTRODUCTION

ACES (Atomic Clock Ensemble in Space) [1] is an ESA mission in fundamental physics which is based on time and frequency comparisons between high performances space clocks and ground based clocks. The space segment will operate a new type of atomic clocks in microgravity environment. The payload (Figure 1.) will be installed on the NASA developed External Payload Facility pallet of the Columbus laboratory (CEPF) on-board the ISS (International Space Station). The station is orbiting at a mean elevation of 400 km with about a 90 min rotation period and an inclination angle of 51.6 degrees. The Number of ISS passes over a European ground station is 5 per day.

The clock signal is obtained from the combination of two atomic clocks: a cold cesium clock PHARAO as a primary frequency standard [2] and an active hydrogen maser [3] as a freewheel oscillator. The comparison with earth based clocks is performed by two way time transfer links operating in the microwave domain (MWL) [4] and in the optical domain (ELT) [5]. Ground terminals will mainly be located in time and frequency laboratories, while the mission will be operated from the ACES User Support and Operation Center (USOC), installed at CADMOS (Centre d'Aide au Developement de la Micrograviteet aux Operations Spatiales) in France.

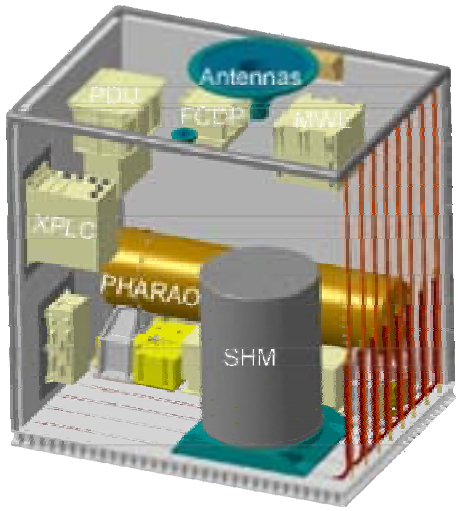

Fig. 1. – Scheme of the ACES payload. PHARAO: the cold cesium clock. SHM: the active hydrogen maser. FCDP: the frequency comparison and distribution package. MWL: the microwave link. ELT: the optical link. GNSS receiver, a computer (XPLC) and a power supply (PDU). The ACES payload has a volume of about $1m^3$, a total mass of 227 kg and a power consumption of 450 W.

The launch is scheduled on 2016. Planned duration of the mission is 36 months. First 6 months are reserved for functionality verification of instruments and performances evaluation. The first objectives are to study the performances of this first cold atom space clock and reach a frequency accuracy lower than 3 x10^{-16} and deliver a timescale with a 25ps/day stability. The microwave link will have to demonstrate the capability to perform phase comparisons between space and ground clocks with a resolution at the level of 0.3 ps over one ISS pass (300s), 7 ps over 1 day, and 23 ps over 10 days.

II. THE COLD ATOM CLOCK PHARAO

CNES is the prime contractor of the PHARAO clock. The clock architecture is shown in Figure 2. It is composed of 4 connected sub-systems. Diagram of the cesium tube is shown in Figure 3.

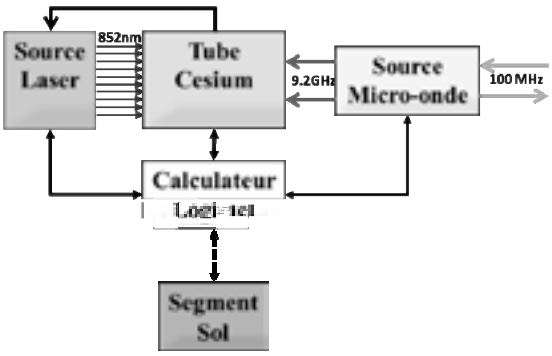

Fig. 2. – The PHARAO clock includes 4 sub-systems: the laser source provides laser beams to the cesium tube to manipulate the atoms. The microwave source provides two 9.2 GHz signals to the cesium tube and a 100MHz signal to the ACES payload. It can also receive a 100 MHz to generate the microwave signals. The computer manages the clock operation, sends data and receives telecommand from the ground segment.

The cold atoms are manipulated inside a titanium vacuum chamber. The pressure of 10^{-8} Pa is maintained by an ion pump and 6 getters. A reservoir with adjustable temperature and aperture provides the cesium flux to the capture zone. The atoms are captured and cooled at the intersection of 6 laser beams that have a diameter of 21 mm (capture cavity). The atomic cloud is then launched at a velocity which can be adjusted between 5 to 500 cm/s.

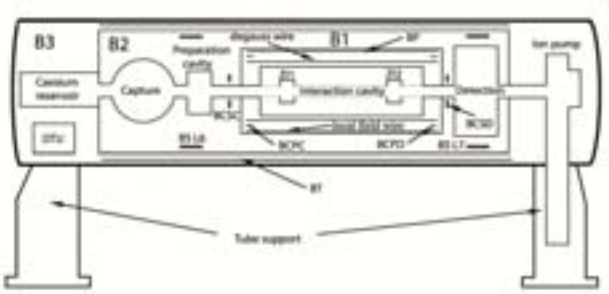

Fig. 3. – Diagram of the PHARAO cesium tube. Labeled are the external shields B1, B2, B3, the DTU magnetometer, ion pump, cesium reservoir, different cavities and coils. From the reservoir cesium atoms are released towards detection passing the capture cavity (where they are cooled), preparation cavity (where F = 3 atoms are selected) and interaction cavity (where the Ramsey interrogation is performed). In the detection zone, ratio of the two populations is obtained. The three Mumetal shields are used to reduce the magnetic oscillations the atoms experience in flight due to the Earth orbit field. The coils are used to improve field homogeneity, separate magnetic Zeeman levels by providing a static magnetic field and for active compensation (BT).

Next, two laser beams inside a microwave cavity (preparation cavity) select the atoms in a pure quantum state and can slice the atomic cloud to reduce the longitudinal expansion. The atoms enter in the interrogation region (interrogation cavity) where they are submitted to a Ramsey interaction inside a ring cavity. The temperature of the cavity is measured by using two calibrated probes placed on the vacuum chamber. After the microwave interaction, the atomic cloud passes through 4 laser beams in order to calculate the population in each hyperfine level from the measurement of the fluorescence signals.

The vacuum chamber is surrounded by 3 magnetic shields where a solenoid and 5 coils provide the magnetic field bias. A second solenoid and a magnetic probe are used for an active magnetic compensation. Two wires pass through the inner shield. One is used to degauss the shields and the other to induce Zeeman transitions in the atoms in order to deduce the local magnetic field. The cesium tube weighs 46 kg, the volume is 47 L and the power consumption is 5W.

A. The microwave source

The microwave source synthesizes two independent 9.2 GHz signals from an ultra stable quartz oscillator. One signal feeds the preparation cavity and the second feeds the Ramsey cavity. Both signals can be tuned over 10 kHz with a 10^{-7} Hz frequency resolution. The power can be adjusted between -20 to -80 dBm with a resolution of 0.02 dB. The signals can also be switched off by 80dB. The switching is mainly used to only feed the preparation cavity when the atoms are inside. In nominal operation the USO is phase locked on the 100 MHz H-maser signal. The microwave source can also use an external 100 MHz signal to generate the microwave signals. The weight of the microwave source is 7 kg, volume is 8 L and the power consumption is 25W.

B. The laser source

The laser source provides 6 laser beams to capture the atoms, 2 laser beams to select the atoms and two laser beams to detect the atoms. It contains two extended cavity diode lasers (with backup) frequency locked on cesium lines. One ECDL injects locked two slave diode lasers (with backup). Each slave laser beam is split in 3 to provide the capture beams. 2 acousto-optic modulators are used to change the laser frequencies and 4 are used to control the laser power. In addition, 6 mechanical shutters switch off the laser powers. The laser beams are injected into maintaining polarizing optical fibers. In order to ensure an optimum coupling or to balance the laser power for the capture beams, the beam alignment can be changed by means of mirrors mounted on PZT transducers. The optical set-up takes place on a double sided optical bench fixed by four 4 damped supports. All electronic drivers are mounted on the baseplate underneath the optical bench.

C. The computer and software

The computer is based on a 32 bits, 20MHz processor with 8 Mo flash memory and 8 Mo RAM memory and on a programmable microcontroller which provides 24 digital lines

to trigger the events of the clock cycle. The computer drives the servo-loops for thermal stabilization, the active magnetic compensation, the degaussing and Zeeman process. A multiplexed analogic digital converter reads physical values for housekeeping and for the determination of the transition probability of the cesium hyperfine transition. The computer also has several serial lines to command the sub-systems and to exchange data and telecommands with the ACES computer XPLC. The weight is 5 kg, the volume is 7 L and the power consumption is 30W. The software is based on 350 sequences dedicated to specific task.

Three different models of the clock have been constructed: the mechanical and thermal model (MSTH) to test the environments (vibrations 20g rms and temperature -40, +60°C), the engineering model to test the operation and the performances, and the flight model which has the benefits of the improvements deduced from the previous results.

D. The performances of the Engineering model

The phase noise and the spectral purity of the microwave source signals are in agreement with the expected performances of the clock. To complete these measurements the microwave source has been used by the SYRTE fountain F02 and the resulting frequency stability is $7.2 \times 10^{-14}\ \tau^{-1/2}$. During these measurements we have detected a transient effect on the 100 MHz signal due to the switching of the preparation cavity signal. As this signal is phase locked to the H-maser, this transient which is a phase jump of 10 µrd leads to a phase drift of the 9.2 GHz interrogation signal. The clock frequency shift can reach 6×10^{-16}.

Among all the optical performances of the laser source, only two are not in agreement with our requirement: the power of each capture laser beam is low, 5mW and the laser spectra are widened by a too large modulation index used by the frequency servo loops. In addition, although the vibration tests on the MSTH have been successful, the thermal tests have shown a sensitivity of the optical alignment with the temperature.

Concerning the cesium tube, the MSTH vibration and thermal tests have demonstrated the robustness, but without sufficient margins. The tests have also highlighted an inaccuracy in the temperature determination of the Ramsey cavity (to evaluate the blackbody frequency shift). The uncertainty can reach 400mK (100mK is required).

The tests of the clock have given a frequency stability of $3.3 \times 10^{-13}\ t^{-1/2}$. The frequency stability is obviously degraded by the ground operation since the interrogation time is only 90 ms. The Ramsey fringes are shown in the Figure 4. and the result is in agreement with a Monte-Carlo simulation. The main systematic effects have been studied. The second order Zeeman shift uncertainty is limited by an inhomogeneity of the magnetic field shown in the Figure 5. Consequently, the Ramsey pattern of the hyperfine resonance between m = 1 sub-levels shown in Figure 6. has a low contrast. Another issue comes from the magnetic field attenuation. In orbit, the magnetic field fluctuations due to the Earth field have an amplitude of about 30µT. The attenuation of the shields is 12000 in the interrogation zone and the active compensation adds a gain of about 5. The total attenuation (60000) is far too low to be sufficient to evaluate the second order Zeeman shift with a required accuracy.

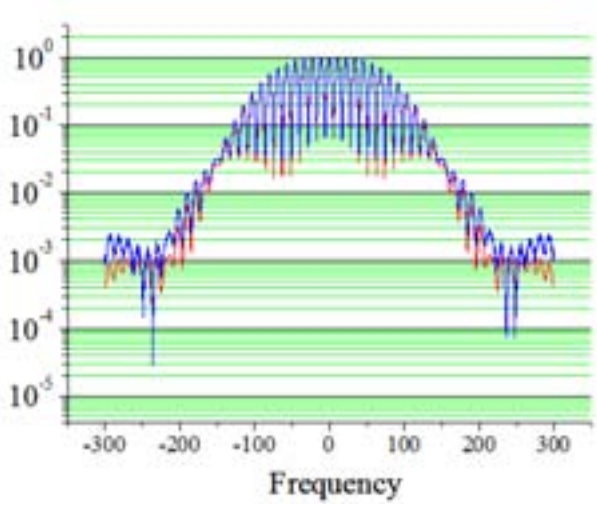

Fig 4. The Ramsey fringes for m = 0 transition in log scale. In blue are the experimental results, in red the simulation.

The frequency accuracy of the engineering model is evaluated at 1.6×10^{-15}. By comparing the clock with the FOM primary frequency standard of SYRTE we obtain frequency differences within 2.10^{-15}, in agreement with the evaluation budget.

From all these tests some modifications have been made on the clock design to build the flight model.

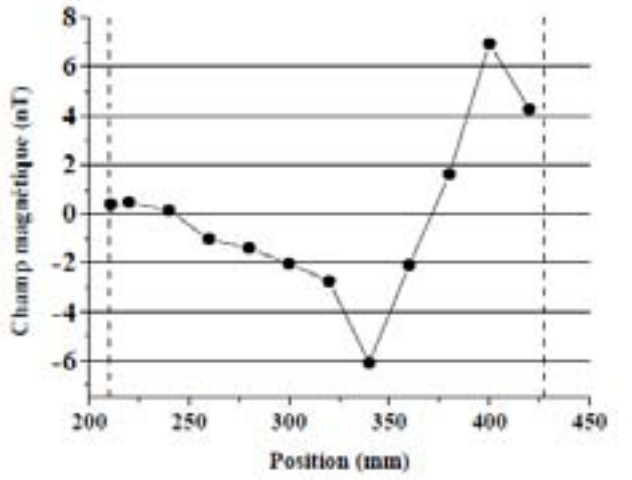

Fig 5. The EM magnetic field inhomogeneity inside the interrogation cavity obtained using a wire placed parallel to the atom path that invokes m = 1 transitions.

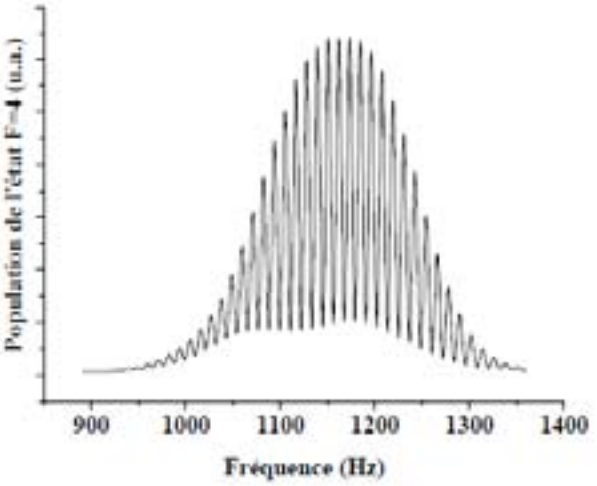

Fig 6. The EM Ramsey fringes for m = 1 transition. Observe the shape dissymmetry.

III. FM STATUS

Based on the experience gathered from the MSTH and EM, various improvements have been made on the FM. Mechanical structure and design improvements have been performed for the laser source and the cesium tube. As a result, the power of the laser source was increased to 15 mW/beam (a factor of 3 improvement over the EM) and a better optical alignment stability was ensured. Cesium tube has a better robustness and temperature accuracy. In order to improve the field homogeneity magnetic shield design was changed. Additionally, the assembly process and software were modified.

Change in the microwave synthesis reduced the transient effect present on the EM microwave source by a factor of 10 (Figure 7.). The phase noise spectral density and spectral purity are as per specification.

The cesium tube was qualified and delivered in March 2013. The laser source is now fully assembled and is to be qualified in August 2013.

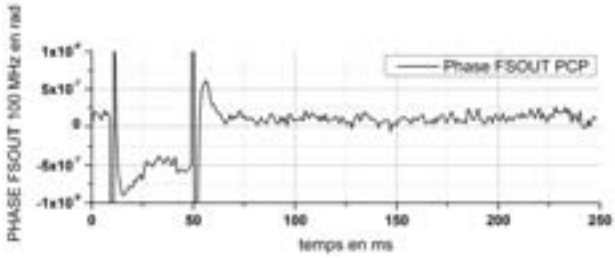

Fig 7. Microwave source transient effect on the FM microwave source. The amplitude jump caused by the turning on and off of the device was reduced by a factor of 10 compared to the EM.

IV. FM PRELIMINARY RESULTS

The FM cesium tube has been assembled with the EM subsystems to verify its operation and magnetic homogeneity improvements. Figure 8. shows the m = 1 hyperfine transition for the FM. The shape is much more symmetrical than on the EM indicating better homogeneity. This has been confirmed by using the Zeeman wire.

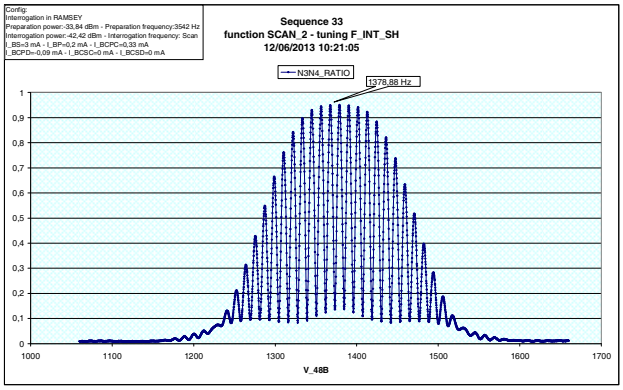

Fig 8. The FM Ramsey fringes for m = 1 transition. Compared to Fig 6. the shape is much more symmetric indicating better homogeneity.

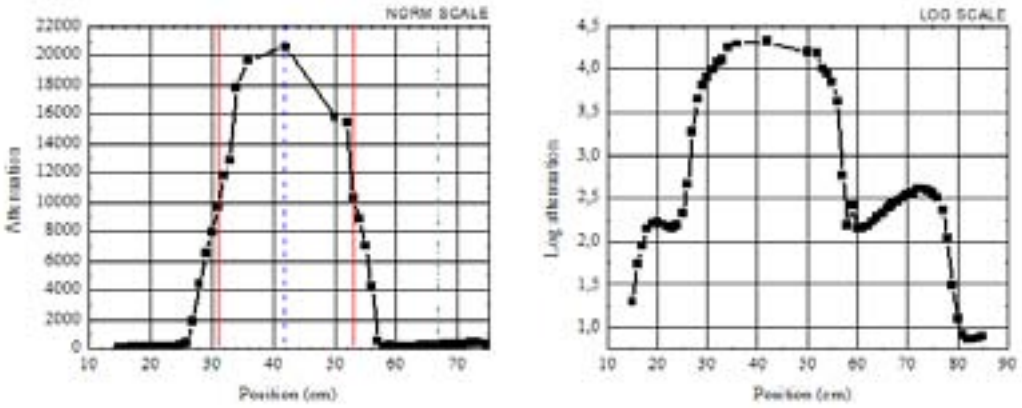

Fig 9. Summary of attenuation results as a function of position along the atom path inside all three shields combined in normal scale (left) and log scale (right). Values were obtained using the peak to peak method. Full vertical lines (red) represent the position of the interaction zones, dashed line (blue) is the center of interaction cavity and the dash-dotted line (green) is the center of preparation cavity. An external field with amplitude of ± 31 μT was used (representing the real peak to peak variation the shield will experience in orbit) and the period was 100 s. An attenuation of 9633 was measured at ZI2, 20550 at the center, 10275 at ZI1 and 250 inside preparation zone.

V. MAGNETIC SHIELDS IMPROVEMENTS

Experiments have been performed to verify the attenuation improvements of the FM shields. Two Helmholtz coils were used to simulate an axial external field around the shields positioned in the center and a fluxgate Mag-01 magnetic probe manufactured by Bartington Instruments was used to measure the internal field. The measurements show an improvement of the EM by a factor of 1.5. The attenuation is 20 550 at the center, 10 250 at the ZI1 (zone interaction 1) and 9650 at the ZI2 (zone interaction 2). On average, the attenuation in the interaction zone is around 18 000 (compared to 12 000 on the EM). For more detail see Figure 9.

Additionally, a new active attenuation system was implemented. It is a feed-forward system composed of a magnetometer (DTU) and a compensating coil (BT). Using the DTU measurements and a model, the field inside the interrogation cavity is calculated. Current is then sent inside the coil to compensate this field. Development of a model was necessary due to a presence of a position dependent hysteresis inside the B3 shield.

Experimental results show that the model performs as expected. The attenuation for the axial component of the orbital field inside the interrogation cavity reaches a value of 100. This can be seen on Figure 4. However, due to the transverse component of the orbital field, the total attenuation is reduced by a factor of around 5. The problem is that the magnetometer installed in the cesium tube cannot separate the axial and the transverse component of the orbital field and the transverse component has a different effect on the device and on the atoms. Additionally, a temperature dependency of the magnetometer has been noticed further reducing the attenuation. Therefore, to reach the required attenuation in order to reduce the quadratic Zeeman effect and have the required frequency accuracy another system composed of measuring the magnetic field (m = 1 transition) every 300s for 10s will be added.

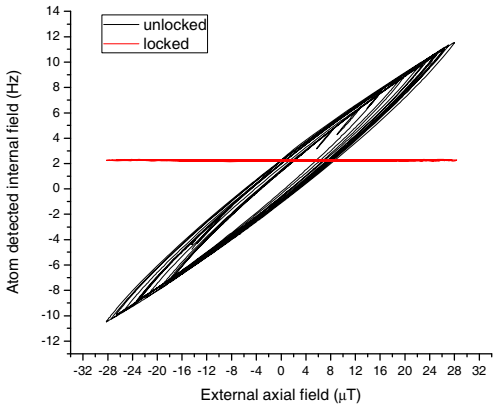

Fig 10. m = 1 hyperfine transition frequency fluctuation with (in red) and without the active attenuation (in black) for an axial component of the orbit field as the external field.

VI. CONCLUSION

In conclusion, the microwave source is ready. The cesium tube magnetic homogeneity and static and active attenuation achieved combined with the m = 1 field measuring system is enough to evaluate the effect of the second order Zeeman effect to a required accuracy.

What remains is to perform the cesium tube thermal analysis and verify the temperature determination accuracy. After the FM laser source is delivered in November 2013, the FM clock will be assembled with all the FM subsystems. During 2 months cold atoms number and temperature, cavity phase shift and cold collision will be evaluated with an objective to reach the total frequency accuracy of 3×10^{-16} . Finally, ACES will be assembled in spring of 2014. The launch is envisioned in 2016 by SpaceX.

REFERENCES

[1] L. Cacciapuoti et al.,Nuclear Physics B, 166, 2007, 303-306.

[2] P. Laurent et al., Appl. Phys. B 84, 683 (2006).

[3] D. Goujon et al., Proceedings EFTF Conference, Noordwijk, The Nederlands, 2010.

[4] M.P. Hess et al., Proceedings IEEE-FCS and EFTF Joint Conference, San Francisco, USA, 2011.

[5] I. Prochazka et al., Proceedings EFTF Conference, Noordwijk, The Nederlands, 2010.

Lifetime of Space Passive Hydrogen Maser

Qinghua Wang, Pierre Mosset, Fabien Droz, Pascal Rochat
Orolia Switzerland Inc.
Neuchâtel, Switzerland
qinghua@spectratime.com

Abstract—**Accurate and ultra-stable space qualified atomic clocks represent critical equipment for the precision Global Navigation Satellite Systems (GNSS). The Passive Hydrogen Maser (PHM), with its excellent frequency stability performance, is the master clock for European Navigation satellite payload, and is the most stable clock ever flown for GNSS. Nine PHMs have been flying onboard Galileo satellites (GIOVE-B and four IOV satellites) since Apr. 2008. More than 35 PHM flight Physics Packages (PP) have been manufactured and characterized by Orolia Switzerland SA (Spectratime), under the industrial consortium led by Selex ES S.p.A.**

Besides radiation effects on electronic components, lifetime on PHM depends mainly on which of PP. In the frame of the "Lifetime Qualification of the PHM" supported by ESA, two Qualification Model (QM) units had been subjected to test under vacuum since 2008. After the first 1.5-year test period as reported in previously published papers [1][2], one QM has been extended for another 2-year lifetime test. This paper provides test results over the overall period of QM1, and gives further comparison and analysis of key PP parameters over 3.5 years of operation (or 4.1 years including the stay-alive period). The extended test enhances the on-ground test statistics and provides better confidences in the PHM lifetime evaluation, which shows the instrument capability to comply with the lifetime requirement of 12 years.

Keywords-Hydrogen maser; lifetime; space atomic clock; GNSS

I. INTRODUCTION

Accurate and ultra-stable space qualified atomic clocks represent critical equipment for the precision Global Navigation Satellite Systems (GNSS).

The Rubidium Atomic Frequency Standard (RAFS) and Passive Hydrogen Maser (PHM) are the baseline clock technologies for the European Navigation satellite payload. The adoption of a "dual technology" for the onboard clocks is dictated by the need to insure a sufficient degree of reliability (technology diversity) and to comply with the lifetime requirement of 12 years. The PHM with its excellent frequency stability performance has been chosen as the master clock.

After almost 10 years of continuous development in Europe the first space PHM has been launched onboard GIOVE-B (Galileo In-Orbit Validation Element) spacecraft on 27 April 2008. The mission of GIOVE-B has proved that PHM is the most stable clock ever flown in space for navigation applications and this clock technology is suitable for the harsh environment of space [3]. Four IOV (In-Orbit Validation) satellites were launched by pair on 21.10.2011 and 12.10.2012, each carrying two PHMs.

II. DEVELOPMENT HISTORY OF PHM

The development of the PHM has been funded continuously by ESA. The first space PHM development activity tailored to navigation applications was kicked off in 2000, led by Observatory of Neuchatel with Selex ES (SES) as subcontractor for Electronics Package (EP).

The industrialization activity aimed at PHM design consolidation for flight production was started in 2003. The industrial consortium is led by SES in charge of the instrument integration and EP design, and Spectratime is responsible for redesign and manufacturing the Physics Package (PP) [4][5]. The overall structure and design were reviewed in order to increase compactness and robustness. Strong efforts have been devoted to further improve both performances and manufacturing processes of the PHM from GSTB-V2 to IOV phases.

From 2009, the production and tests capability have been set up to 2 space PHM PPs per month at Spectratime. More than 35 flight PPs have been delivered, 9 of them have been flying onboard Galileo satellites.

A further development of a miniaturized PHM has been carrying out in the frame of the ESA European GNSS Evolutions Program. The main target is to preserve the excellent PHM frequency stability performance with reduction of the overall mass from present 18 kg down to 12 kg [6]. To achieve this goal, the physics package weight has been realized by Spectratime at 8 kg and demonstrated very similar performance [7].

III. LIFETIME TEST AND EXTRAPOLATION

Besides radiation effects on electronic components, lifetime on PHM depends mainly on which of PP. In order to highlight potential lifetime limitations, in the frame of the "Lifetime Qualification of the PHM" supported by ESA, two Qualification Model units (QM1 and QM2) were subjected to test continuously under vacuum from 05.06.2008 to 04.12.2009. The 1.5-year test results were published in papers [1] and [2], in which the comparison with related telemetries from the early 690-day in-orbit operation of GIOVE-B PHM demonstrated the consistency between the on-ground and in-orbit observations.

Seven months later QM1 was extended for a second 2-year lifetime test period (14.07.2010 – 13.07.2012). A third 1-year lifetime test on QM1 initiated on 06.02.2013 is in progress.

This paper provides test results over the first two test periods on QM1. Further analysis of key PP parameters over 3.5 years (1280 days) of operation (or 4.1 years if including the Stay-Alive period) is presented, which improves the statistical confidence for the lifetime extrapolation.

Fig. 1 illustrates the overall layout of the test bench. In addition to frequency stability performances, about 30 parameters have been measured. Most of them do not present measurable ageing effects. In this paper PP telemetries (Microwave cavity frequency, hydrogen supply tank temperature, high vacuum pressure), and master oscillator frequency, which are more relevant or affected by long term operation, therefore on which the lifetime of the PHM is more dependent, are discussed. The overall characteristics (atomic signal level, frequency stability) are also provided,

A. Microwave Cavity Frequency Drift

The cavity varactor, as part of Automatic Cavity Tuning (ACT) servo loop, is aimed at tuning the microwave cavity resonance frequency to the atomic transition frequency. For an easy and reliable comparison between the PHM units, the varactor voltage has been converted to the equivalent cavity frequency shift wrt the initial frequency.

Fig. 2 shows the cavity frequency shift observed on PHM QM1 during 1280 days (3.5 years) of operation, two curve fittings, and corresponding extrapolations over 12 years.

The least squares fitting of the cavity frequency shift consists in an exponential function of time, which has been also demonstrated during the PHM PP final tests. A square root fit is performed as well in the whole period in an attempt to estimate the drift trend in worse case.

It has to be noted that according the on-ground PHM PP acceptance tests, lifetime tests on QM1&QM2, and in-orbit data from GIOVE-B, the frequency drifts in all cases decease with time reaching an asymptotic value.

By two fitting models, the extrapolated values reach around 60 to 85 kHz in 12 years, which are within the maximum adjustable cavity frequency tuning range, equal to 150 kHz. This considerable margin, with respect to the measured and predicted cavity drift, can be achieved by the combination of the ACT and the fine adjustment of the cavity temperature (by tiny steps of few mK each). Such approach, as demonstrated by test, does not affect the PHM frequency stability.

B. Hydrogen Consumption

Another key aspect that has been monitored is the hydrogen consumption over the time. PHM uses the hydride to store in a tank of 0.1 liters 25 bar*liter of hydrogen, with internal pressure below 5 bars. During the instrument operation, the hydrogen is consumed and the tank temperature is automatically increased by a servo control loop in order to maintain the internal hydrogen pressure at a constant level required for maser operation. Therefore, the temperature

Figure 1. PHM QM Lifetime test bench

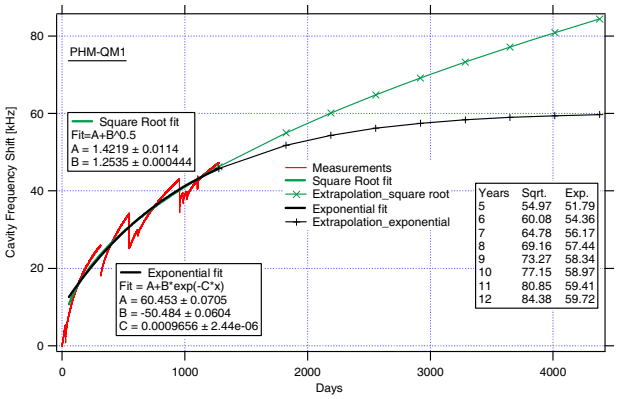

Figure 2. Cavity frequency shift measured during 3.5 years, curve fitting, and extrapolation over 12 year

variation over the time is a good indication of the Hydrogen consumption.

Fig. 3 shows the hydrogen tank temperature variations observed on PHM QM1 during 1280 days (3.5 years) of operation, the curve fitting and the trend extrapolation over 12 years. A square root fit has been used, which is a realistic approach based on hydride properties and its characterization. It can be noticed that the container temperature increasing rate is higher during first few weeks after the switch-on, which could be interpreted by the solid-state hydride transition phase.

The predication based on 3.5 years' data is remarkably similar as the results obtained during first 1.5-year period, which confirms the consistent behavior of the hydrogen tank.

As having highlighted in [1] and [2], the maximum reachable hydrogen tank temperature is limited to 50°C due to the available heating power. A recovery action has been carried out on all PHM models from QM2 on. A new type of hydride (higher purity LN5) achieving lower maximum pressure and more constant pressure plateau has been adopted. Thanks to this, the end of life temperature needed to keep the constant pressure is considerably lower than in the QM1, as demonstrated in the QM2 lifetime test [2].

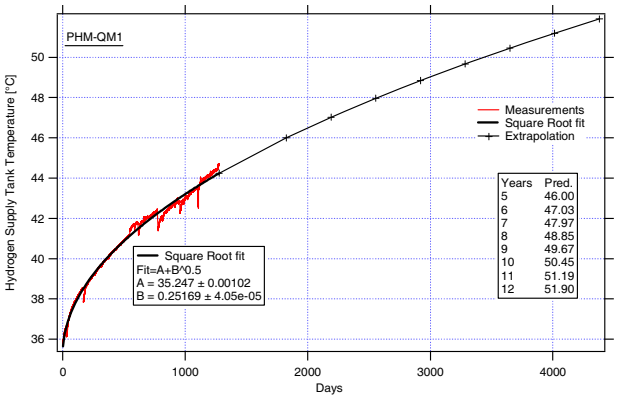

Figure 3. Hydrogen tank temperature measured during 3.5 years, curve fitting, and extrapolation over 12 year

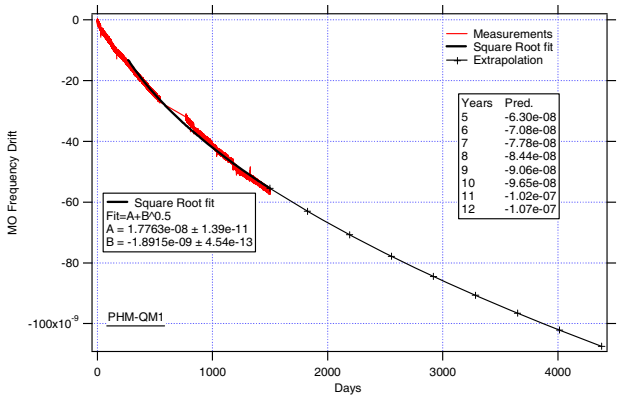

Figure 4. Master oscillator frequency drift measured during 3.5 years of operation (plus 7 months of Stay-Alive in-between), curve fitting, and prediction over 12 years

C. *Master Oscillator Frequency Drift*

The PHM 10 MHz output signal is provided by a crystal Master Oscillator (MO), whose frequency is locked to the atomic hyperfine transition by the varactor voltage. Therefore it is possible to assess the crystal frequency drift and servo loop capability in maintain the oscillator locked for the whole mission lifetime.

As done for the microwave cavity frequency drift, the varactor voltage change is converted to the MO fractional frequency drift.

Fig. 4 shows the MO frequency drift observed on PHM QM1 during 4.1 years, including the stay-alive period when the PHM QM1 was not operating. It's very interesting to note that even during this 7 months, the frequency drifting of the MO was still following the same trend. The figure shows also the simple square root fitting, which allows a very good confidence. The prediction over 12 years indicates the frequency change around -1e-7 in the end of the life.

The worst case analysis performed at PHM instrument level considers an overall frequency drift of the MO equal to ± 2.1e-7. As shown above, this limit is respected with almost 100% of margin. Besides such margin, further 2~3e-7 compensation can be achieved by telecommand. Therefore, the risk to lose a PHM as consequence of unexpected MO frequency drift is negligible.

D. *High Vacuum Pressure*

Fig. 5 shows the high vacuum pressure during 4.1 years (including the 'no-record' 7 months between two test periods). In this STAY-ALIVE mode, only external power was provided to the ion pump to prevent PHM performance degradation during long storage/ OFF periods. The high vacuum pressure had maintained at a reasonable level between 3.4e-7 to 3.6e-7 mbar over 4.1 years.

E. *Atomic Signal Amplitude*

The atomic signal amplitude telemetry provides the most relevant indication of PHM healthy operation.

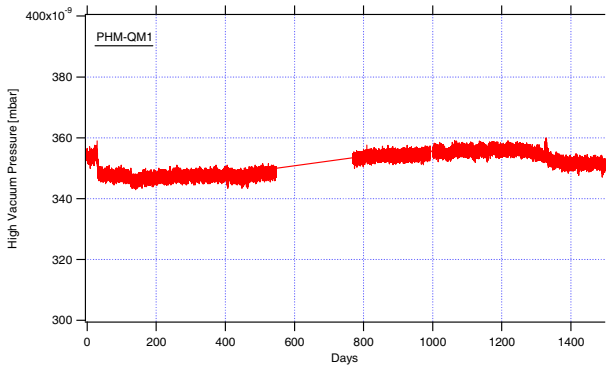

Figure 5. High vacuum pressure measured during 3.5 years of operation (plus 7 months of Stay-Alive in-between)

This telemetry is sensitive to any degradation as internal coating, out-gassing, leakage, dissociation efficiency, quality factor of the microwave cavity, interrogation power instability, receiver electronic degradation, temperature instability, etc. It is therefore of primary importance to verify that its decay over the life time stays below acceptable limits.

Fig. 6 shows the atomic signal amplitude measured during 3.5 years of operation under the same operation condition. The data show a fairly stable behavior as expectation.

F. *Frequency Performances*

Frequency stability and trend evolution is the most fundamental aspect for a clock assessment. Fig. 7 reports the frequency data and the frequency drift evolution over 4.1 years. The frequency offset due to the cavity temperature change experiment during the 1st period [1][2] is corrected in order to compare the overall data under same operation condition. The values show that the frequency drift is improving with the continuation of the operation, finally stabilized below 1e-16/day.

Fig. 8 compares the frequency stabilities for every 3-month, which demonstrates the excellent flicker floor around 3e-15 from 1 day to more than 10 days.

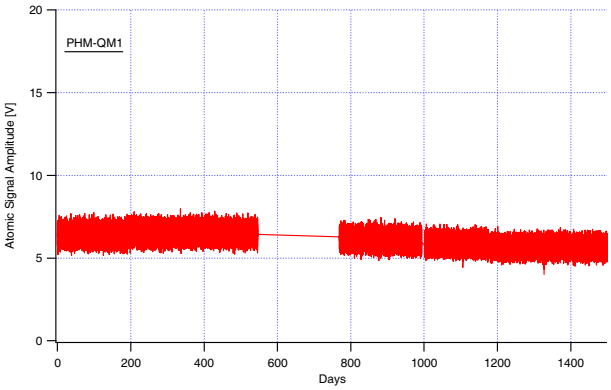

Figure 6. Atomic signal amplitude measured on OM1 during 3.5 years of operation (plus 7 months of Stay-Alive in-between)

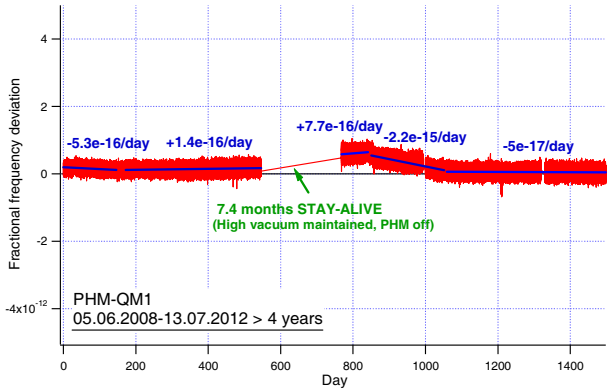

Figure 7. PHM frequency data and drift evolution during during 3.5 years of operation (plus 7 months of Stay-Alive in-between)

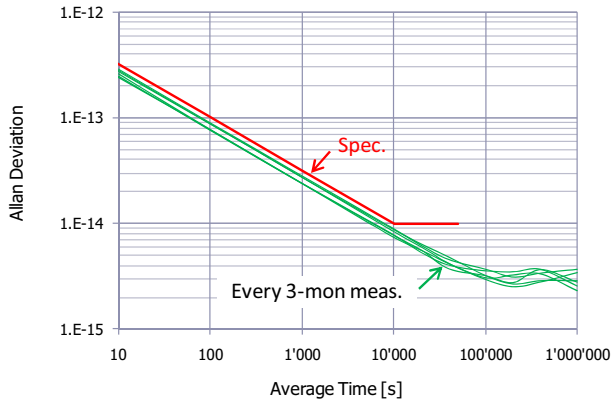

Figure 8. Frequency stabilities of every 3-month

IV. Conclusions

The extended 24-month test enhances the first 18-month test statistics. The comparison and correlation with previous data provides improved confidence in the PHM lifetime evaluation.

The life-demonstration testing on ground is confirming the capability of the PHM to operate in vacuum over the required life time of 12 years. The operational data so far collected for 30'700 h show no appreciable degradation.

Acknowledgment

The authors wish to thank all their colleagues at Spectratime, Selex ES, and ESA for their substantial contributions to these achievements.

References

[1] F. Droz, P. Mosset, Q. Wang, P. Rochat, M. Belloni, M. Gioia, et al. "Space passive hydrogen Maser – performances and lifetime data", Proceedings of the Joint 2009 European Frequency and Time Forum & 2009 IEEE Frequency Control Symposium, 20-24 April, 2009, Besançon (France), pp 393-398.

[2] M. Belloni, M. Gioia, S. Beretta, F. Droz, P. Mosset, Q. Wang, et al. "Space passive hydrogen maser - performances, lifetime data and GIOVE-B related telemetries", Proceedings of the 24th European Frequency and Time Forum, 13-16 April, 2010, ESA/ESTEC, Noordwijk (Netherlands).

[3] Birth of the European satellite navigation constellation. European Space Agency publications, BR-297, Sep. 2011.

[4] F. Droz, P.Mosset, G.Barmaverain, P.Rochat, Q.Wang, M.Belloni, et al. "The on-board Galileo clocks: rubidium standard and passive hydrogen maser current status and performance," Proceedings of the 20th Europen Frequency and Time Forum, 27-30 Mar. 2006, Braunschweig (German).

[5] Q. Wang, P. Mosset, F. Droz, P. Rochat, and G. Busca, "Verification and optimization of the physics parameters of the onboard Galileo passive hydrogen maser," Proceedings of 38th Precise Time and Time Interval (PTTI) Systems and Applications Meeting, 5-7 Dec. 2006, Reston, Virginia (USA), pp 81-94.

[6] M. Belloni, M. Gioia, S. Beretta, F. Droz, P. Mosset, P. Waller, et al. "Space mini passive hydrogen maser - a compact passive hydrogen maser for space applications," Proceedings of 2011 Joint Conference of the IEEE Frequency Control Symposium & European Frequency and Time Forum, San Frnsisco (USA), 1-5 May, 2011, pp 906-910.

[7] P. Rochat, F. Droz, Q. Wang, and S. Froidevaux, "Atomic Clocks and Timing Systems in Global Navigation Satellite Systems," Proceedings of 2012 European Navigation Conference, 25-27 Apr. 2012, Gdansk (Poland).

Piezoelectric Acceleration Sensors Based on LGX and ReCOB Crystals for Application above 645ºC

Yanqing Zheng, Xiaoniu Tu, Jianjun Chen, Pan Gao, Erwei Shi
Shanghai Institute of Ceramics, Chinese Academy of Sciences
588 Heshuo Road, Jiading
Shanghai, 201800 China

***Abstract*-In the field of aviation and aerospace engine, monitoring of the vibration of the engine in situ directly in the high temperature part is of great importance for the safe and performance of the engine. So there is demanding for sensors that can stand for high temperature of 645ºC or above temperature. Recently, the crystals of langasite and ReCOB family are found to be good candidate for this application through the study of basic properties of crystals at high temperature. But there is few reports about the acceleration sensors made of these crystals. In this work, the single crystals of $La_3Ga_5SiO_{14}$ (LGS), $La_3Ga_{5.5}Ta_{0.5}O_{14}$ (LGT), $YCa_4O(BO_3)_3$ (YCOB) and $SmCa_4O(BO_3)_3$ (SmCOB) were grown by Czochralski method respectively, and the basic properties of these crystals were characterized. The acceleration sensors with LGT as sensitive components were successfully made and characterized up to 700ºC. The results show that sensors made by these crystals can be used at the high temperature circumstance above 645ºC and under the vibration with frequency in the range of ten Hz to several thousands Hz.**

I. INTRODUCTION

Piezoelectric acceleration sensors that could stand environment temperature above 645ºC (1200ºF) are of great important to the field of vibration monitoring of aviation and aerospace engine. The traditional piezoelectric materials used in this area include lithium niobate crystal, bismuth layer structure system piezoelectric ceramics. But the issue of the lower electric resistivity limits their application of temperature higher than 645 ºC. $GaPO_4$ crystal which is grown by hydrothermal method could be used up to 900 ºC. However, the difficulty in crystal growth of $GaPO_4$ crystal makes it very expensive and limits its application [1].

ReCOB (Re= La, Y, Sm, Nd, Lu) crystals and LGX crystals including LGT, LGN and LGS are piezoelectric crystals with high melting points above 1400ºC and without phase transition from room temperature to their melting points. All of these crystals can be grown by common Czochralski method up to 4 inches. They are all good candidates for high temperature application. This work is aim to explore the possibility of LGS, LGT, YCOB and SmCOB crystals for application for high temperature acceleration sensors by characterization the basic properties and sensors performance after crystals being grown.

II. EXPERIMENTAL

A. Single Crystal Growth

The raw materials of LGS crystals are the mixing of powders of La_2O_3, Ga_2O_3, SiO_2 in the ration of stoichiometry, while LGT are of La_2O_3, Ga_2O_3 and Ta_2O_5, YCOB are of Y_2O_3, $CaCO_3$, H_3BO_3, SmCOB are of Sm_2O_3, $CaCO_3$, H_3BO_3. All these powders are of purity of 99.99%. Then the raw materials were mixed by 3D mixing machine and pressed into cylindrical blocks and sintered in the oven under the temperature of 1200~1300ºC. After that, the blocks of raw materials were put into iridium crucible and heated to the temperature dozens degrees higher than their melting temperature in vacuum Czochralski furnace with the growth atmosphere of 99% nitrogen and 1% oxygen. The growth rate and rotation rate of the crystals were 0.5~2 mm/hr and 5~20 rpm respectively.

The LGS and LGT crystals had strong growth habits, i.e., the facet faces of specific crystallographic face appeared in the shape. And they were in red brown. The diameter of LGS boule was of 4 inches and that of LGT was 3 inches. YCOB and SmCOB crystals had weak growth habits and were apt to crack along cleavage plane of (20-1) or (202). YCOB was transparent and colorless, while SmCOB was in light-yellow. The former can be grown into 4 inches boule in diameter. The later can be grown into 2 inches boule. The pictures of these four crystals are shown in Fig 1.

(a) LGS (b) LGT (c) YCOB (d) SmCOB

Fig. 1. The as-grown LGS, LGT, YCOB and SmCOB single crystals.

B. Crystals Processing and Characterization

For LGS and LGT crystals, the rectangular plates with the planes perpendicular to X-axis and Z-axis were cut and fine grinded. For YCOB and SmCOB crystals, the rectangular plates with the planes perpendicular to Y-axis were cut and fine grinded. The two sides were coated with Ag or Au platings.

Also the rings with outer diameter of 10 mm and inner diameter of 5 mm and thickness of 1.0 mm were processed for using as the sensitive components. The two sides were coated with Cr-Au films of about 200 nm thick by CVD.

The resistance was measured using a source meter (Keithley 2410C, MetricTest, Hayward, CA) and the dielectric properties were determined using a multifrequency LCR meter (HP 4284A, Hewlett-Packard, Palo Alto, CA). The piezoelectric coefficient was obtained from a Berlincourt type d33 meter (ZJ-2, Institute of Acoustic, Chinese Academy of Sciences, Beijing, China). The resonance and anti-resonance frequencies were obtained from an Impedance-Phase Gain Analyzer (HP4194A, Hewlett-Packard). The effective electromechanical coupling factors and mechanical quality factors were calculated according to IEEE standards. Based upon the potential to operate YCOB crystals at very high temperatures, it was worthy to explore the properties as a function of temperature. In this work, the properties were measured as a function of temperature up to 777ºC, above which, the Au electrodes were subject to degradation.

C. Sensors Fabrication and Characterization

The acceleration sensors were fabricated according to the standard compress mode design. In order to improve the sensitivity of the sensors, multi-piece of piezoelectric rings were used in each sensors.

The acceleration sensors were characterized in a standard acceleration sensors evaluation system. The sensors were put into a temperature controlled oven which can be vibrated in high acceleration and frequency. The sensitivity vs different temperature from 20 to 777ºC and acceleration from 0 to 40 g was tested. The phase of the sensors under different temperatures was also characterized.

III. RESULTS

A. Basic Properties

Table I lists some data of the electrical properties of YCOB and LGT crystals between room temperature and 800ºC, respectively. The dielectric loss were measured at a frequency of 100kHz for Y– cut YCOB samples and found to be on the order of 11 and <0.1% at room temperature, respectively. The piezoelectric strain coefficient d_{26} was measured to be about 7.8 pC/N, comparable to the values of other piezoelectric crystals. It is shown that the crystal YCOB is promising for applications requiring a large voltage output of piezoelectric sensors. The mechanical quality factor Q was found to be on the order of 9000 for YCOB crystals at room temperature, comparable to other piezoelectric crystals.

TABLE I BASIC PROPERTIES OF YCOB AND LGS CRYSTALS

YCOB	20ºC	300 ºC	500 ºC	600 ºC	800 ºC
Resistivity (Ω• cm)	1×10^{17}		1.2×10^{11}	4×10^{9}	2×10^{8}
Dielectric Loss	<0.1%	0.01	0.01	0.01	0.03
d_{26} (pC/N)	7.8	5%	8%	12%	9.0
Q	~9000				
LGS	20ºC	300 ºC	500 ºC	600 ºC	800 ºC
Resistivity (Ω• cm)	1×10^{14}	8.0×10^{8}	9.0×10^{6}		3.6×10^{4}
Dielectric Loss	0.001	0.002	0.13	0.46	27
d_{11} (pC/N)	5.6	6.2	6.9	7.4	8.4
Q	14000	7300	500	450	5000

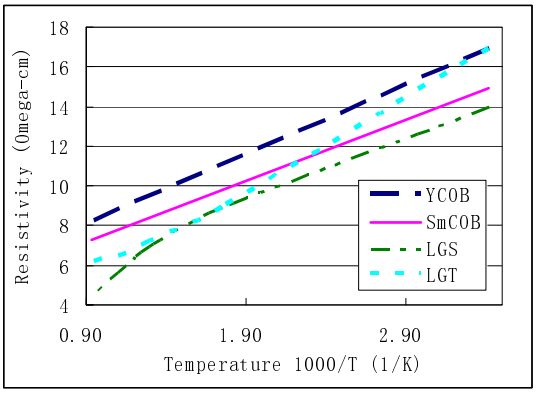

Fig.2 The electric resistivity of four crystals

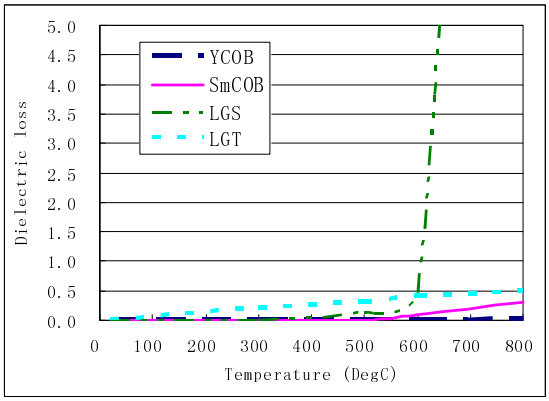

Fig.3 The dielectric loss of four crystals under different temperatures

Fig. 2 shows electrical resistivity as a function of temperature for all these four crystals. The resistivity value of YCOB at 800ºC was found to be $2x10^{8}$Ohm.cm, two order higher than LGT crystals ($1.8x10^{6}$Ohm.cm) and more

than three orders higher than the value of LGS crystals ($3.6x10^4$Ohm.cm). The oxyborate crystals of YCOB and SmCOB exhibited similar slopes, demonstrating they have similar activation energies, which was found to be on the order of 1.6eV. The high electrical resistivity at elevated temperature is desirable for the possible application of BAW resonator and sensors. Similarly, the dielectric loss for YCOB crystal was found to be 3% at 800ºC, while the value of LGT at the same temperature was on the order of 50%, demonstrating that YCOB crystals possess stable dielectric behavior at elevated temperature. The dielectric loss of these four crystals in the temperature range of 20 to 800ºC was shown in Fig. 3.

B. The Properties of the Acceleration Sensors

Fig. 4 and Fig. 5 shown the sensitivity and phase stability of the acceleration sensors made of LGT crystals. It is found it could work until 649ºC with the sensitivity of 1.046 pC/g by less than 5% deviation. And also the sensitivity is quite stable under various vibration frequencies from 10 Hz to 2500 Hz and acceleration from 0 to 40 g.

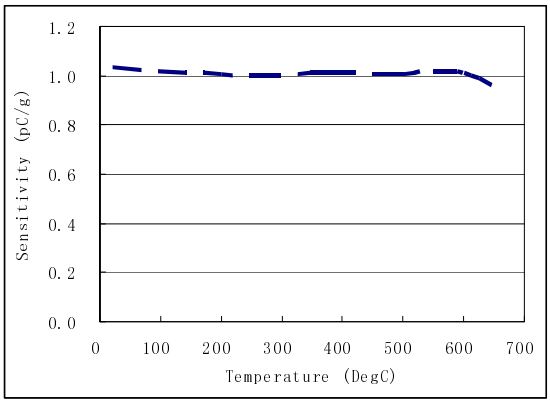

Fig.4 The sensitivity of the sensors under different temperatures

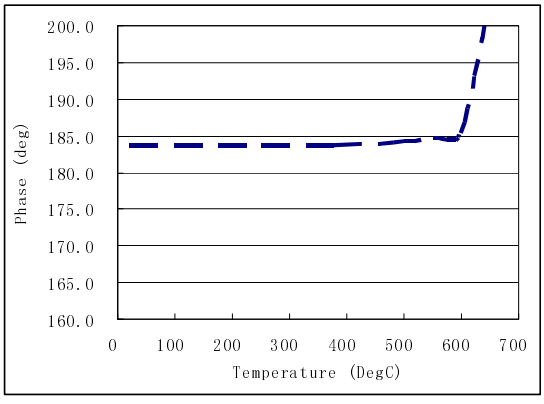

Fig.5 The phase of the sensors under different temperatures

IV. DISCUSION

The acceleration sensors made of LGT crystals can be used up to temperature of 649ºC. It is shown that the ReCOB family crystal has more high stability than LGX crystals. So they may be used under higher temperature. More work has to be done to explore the much high temperature application of these excellent crystals.

V. CONCLUSIONS

LGT, LGS, YCOB and SmCOB were grown successfully, LGS and YCOB with diameter of 4 inches, LGT of 3 inches and SmCOB of 2 inches. The rocking curve of high-resolution X-ray diffraction (HRXRD) of these crystals shown that they were of high quality. Piezoelectric acceleration sensors used the X-cut rings of 10 mm diameter based on these crystals were fabricated and tested. It was shown that our as-grown LGT crystal could be used up to 645 ºC with very steady sensitivity. YCOB and SmCOB crystals could be used to higher temperature up to 900 ºC after overcoming the issue of pyroelectric effect..

ACKNOWLEDGMENT

This work was supported by the Knowledge Innovation Project in Chinese Academy of Sciences under Grant No YYYJ-1117 and the National High-tech R&D Project under Grant No 2013AA031603.

REFERENCES

[1] S.J. Zhang, X. N. Jiang, M. Lapsley, et al, "Piezoelectric acelerometers for utrahigh temperature aplication", Appl. Phys. Lett., vol. 96(1), p.013506, 2010.

[2] F. Yu, S.J. Zhang, X. Zhao, et al. "Dielectric and electromechanical properties of rare earth calcium oxyborate piezoelectric crystals at high temperatures", Ultrasonics, Ferroelectrics and Frequency Control, IEEE Transactions on, vol 58(4), pp. 868-873, 2011.

[3] S.J. Zhang, H.K. Kong, R. Xia, Y.Q. Zheng, J. Xin, T.R. Shrout, "Growth and high-temperature electromechanical properties of $Ca_3NbX_3Si_2O_{14}$ (X = Ga and Al) piezoelectric crystals:, Solid State Comm., vol 150 (9-10), pp. 435-438, MAR 2010.

[4] S.J. Zhang, Y.Q. Zheng, H.k. Kong, J. Xin, E. Frantz, and T. R. Shrout, "Characterization of high temperature piezoelectric crystals with an ordered langasite structure", J. Appl. Phys., vol 105, pp.114107, 2009.

SAW Pressure Sensor Based on Single-Crystal Quartz Layer Transferred on Silicon

S. Grousset, E. Augendre, L. Benaissa,
T. Signamarcheix
CEA LETI MINATEC Campus
17 rue des Martyrs, F-38054 Grenoble Cedex 9, France
E-mail: sebastien.grousset@cea.fr

T. Baron, E. Courjon, S. Ballandras
FEMTO-ST, UMR CNRS 6174
Time & Frequency Dept.
Besançon, France

***Abstract*—In this paper, we present a wafer level approach to fabricate SAW pressure sensors on a single crystal AT-cut Quartz film transferred onto a bulk Silicon substrate. The final thickness of the quartz active layer was obtained using a combination of coarse mechanical thinning and fine polishing. Isolated Quartz membranes with a controlled thickness were then released by DRIE of the Silicon substrate. Details of the sensor fabrication process, modeling and electrical measurements are presented. In addition, theoretical considerations in good agreement with experimental results are disclosed.**

Keywords: Quartz-On-Silicon (QOS); direct wafer bonding; Surface Acoustic Wave; SAW resonator; pressure sensor

I. INTRODUCTION

Surface Acoustic Wave (SAW) devices are extensively used for high frequency wireless telecommunications and various other applications such as high quality resonators, IF bandpass filters and similar RF signal processing [1-2]. Nowadays, they are becoming increasingly popular for passive sensing applications. Indeed, SAW resonators are particularly well adapted for sensing applications since their resonance frequency is directly affected by external parameters such as pressure [3], strain/stress [4], temperature [5] or mass load of chemical species adsorption [6]. By estimating the shift of resonance frequency, one can easily assess the value of the monitored physical parameter. The accuracy of the measurement for its part depends on the quality factor of the resonator. Despite remarkable characteristics SAW devices implementation is limited to essential applications. Indeed, most of available commercial solutions are discrete, implying a significant rise of fabrication cost or complex integration [7].

In this paper, we depict a wafer level approach to transfer single-crystal Quartz layer onto a Silicon substrate. This allows the batch production of SAW resonators for pressure sensing. The process relies on low-temperature direct wafer bonding technology and customized thinning processes. Utmost care was taken to ensure the homogeneity and the integrity of the Quartz film. Thereby, in addition to the benefits of collective fabrication such as cost reduction and high throughput, a silicon based technology simplifies the integration and guarantees a perfect control of all the sensors characteristics. As a first proof of concept, we fabricated a 100mm diameter quartz/silicon hybrid wafers hosting SAW resonators with a quality factor exceeding 12500 when operating at 430 MHz. A linear pressure sensitivity of 25.8 kHz/bar of the sensor was experimentally observed.

This paper is organized as follows: section II of this work presents the clean-room fabrication process to achieve collective realization of SAW pressure sensors. Section III details a previously developed model of inhomogeneous stress distribution in the resonator when pressure is applied on the Quartz membrane. Measurements of the resonators are presented in section IV and compared with theoretical analysis. Section V focuses on conclusions and perspectives.

II. SENSOR FABRICATION

The use of a direct wafer bonding technology for piezoelectric substrates like Quartz material is of great interest as this approach allows for a collective and precise production of sensors which sensitivity is being controlled by the membrane thickness and diameter. The SAW pressure sensors and wafer bonding process are schematically summarized in Fig. 1.

The sensor is composed of a Quartz wafer and a Silicon oxidized wafer. An (*YXl*)/37° AT-cut Quartz substrate was chosen because of its well-known temperature stability. The wafers are cleaned to remove any kind of organic or particular contaminants.

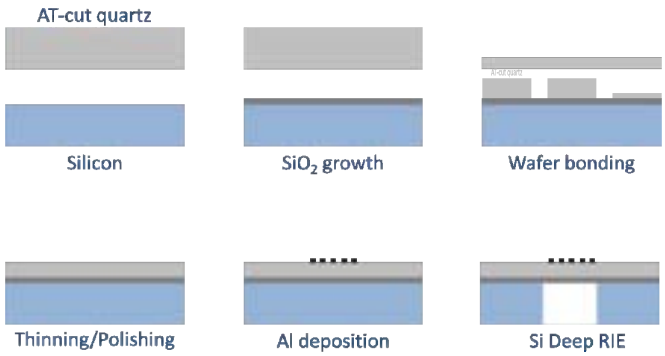

Fig. 1. SAW pressure sensor fabrication process flow

This work was partly supported by the French Direction Générale pour l'Armement (DGA).

We developed a low-temperature direct bonding process based on chemical surface hydrophilization followed by plasma activation. The Quartz wafer is then bonded onto the oxidized Silicon wafer at room temperature and atmospheric pressure. This process was already employed in a previous work [8] and leads to a homogenous and high quality bonding. After bonding, the assembled wafers are annealed at 200°C for 2 hours to strengthen the bond. Figure 2 shows optical and infrared images of the bonded wafer after annealing. It reveals an excellent bonding quality without bonding defect apparition during processing, implying an adequate surface preparation before direct bonding.

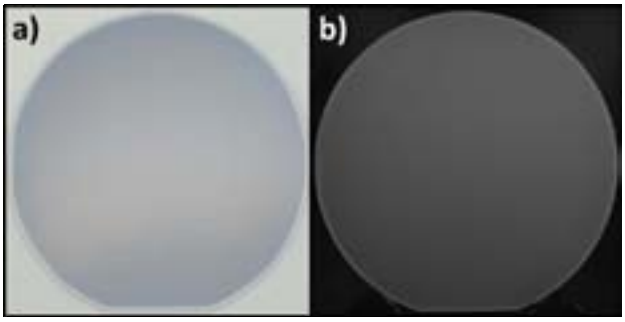

Fig. 2. Optical (a) and InfraRed (b) images of the Quartz-On-Silicon hybrid wafer

The Quartz wafer is then subsequently thinned by coarse mechanical thinning step to an overall thickness of 100 µm, followed by a final polishing step. Aluminum electrodes are deposited on the thinned Quartz plate surface using a lift-off process to achieve single-port SAW resonators. Inter Digitated Transducers (IDT) were designed to generate Rayleigh waves at 430 MHz. Finally, a Deep Reactive Ion Etching (DRIE) of the Silicon wafer is achieved to form the membranes. Figure 3 shows the resonators obtained on the hybrid Quartz/Silicon wafer at the end of the process. Sensors are then cut in individual parts. A photo of a tested SAW pressure sensor is shown in fig. 4.

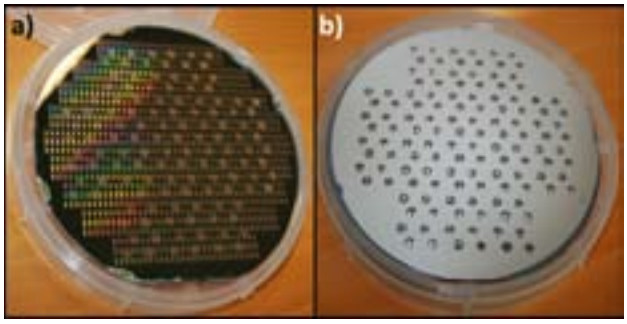

Fig. 3. SAW pressure sensor based on Quartz/Silicon direct wafer bonding: a) top side of the wafer showing SAW resonators; b) back side of the wafer showing the membrane locations

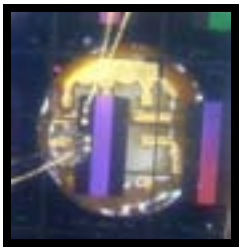

Fig. 4. A SAW pressure sensor ready to be tested

III. SENSOR MODELING

The fabrication of membrane-based SAW pressure sensors has received a strongly interest due to the wave frequency dependence versus stress at the surface of the membrane when bent by pressure [9-11]. The purpose of this section is to model the behavior of surface acoustic waves under stress.

A. Sensor description

The sensor consists of a clamped Quartz circular membrane that is free to move and suspended over on a bulk micromachined silicon wafer. A SAW resonator is then placed on top of it and its resonance frequency is a measure of the tensile stress produced by the membrane bending under pressure effect [11].

B. The Perturbation Method

The behavior of surface acoustic wave under static stress can be modeled using the celebrated Sinha-Tiersten perturbation method [12]. It consists in determining the velocity change of surface acoustic waves under static stress. Frequency variation due to stress is given by (1).

$$\left(\frac{\Delta f}{f_0}\right) = S_{\alpha_{ij}} T_{ij} = S_{\alpha_{11}} T_{11} + S_{\alpha_{33}} T_{33} \qquad (1)$$

where $S_{\alpha 11}$ and $S_{\alpha 33}$ represent the linear sensitivity stress coefficients (in ppm.MPa^{-1}) for radial and ortho-radial stress seen by Rayleigh waves. These coefficients depend only on the Quartz cut choice and are intrinsic characteristics of the material. T_{11} and T_{33} correspond to the in-plane stress associated to these directions (in Pa).

C. Stress and Sensor

We now consider the case where the stress is completely inhomogeneous under the resonator and where the membrane of the sensor is assumed as an isotropic material [13]. Locally, tangential and radial stress to the surface of the membrane are given by (2) and (3) [14].

$$\sigma_r(p) = \frac{p}{h^2} \cdot \frac{3}{8}[R^2(1+\nu) - r^2(3+\nu)] \qquad (2)$$

$$\sigma_\theta(p) = \frac{p}{h^2} \cdot \frac{3}{8}[R^2(1+\nu) - r^2(1+3\nu)] \qquad (3)$$

In these equations, P is the pressure applied on the membrane, h corresponds to the thickness, R is the membrane radius, r the distance from the center and ν is the Quartz Poisson's ratio.

One can note that the induced stress field is linear with the applied pressure P, which means that the resonant frequency shift seen by the resonator is also linear with the applied pressure. The thickness of the Quartz plate as well as the radius of the membrane will also directly influence the pressure sensitivity of the sensor. Thus, these two parameters must be controlled precisely during the fabrication process. A schematic structure of an individual pressure SAW sensor is shown in figure 5.

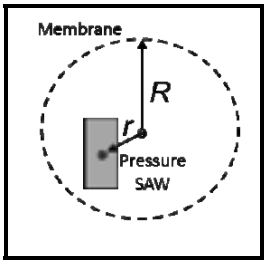

Fig. 5. Schematic structure of the modeled device

IV. ELECTRICAL RESULTS

The electrical characterization was achieved by measuring the reflection coefficient S_{11} of the SAW resonator. The Figure 6 shows the evolution of the electrical conductance and susceptance of a single-port SAW resonator. It exhibits a quality factor around 12500 at 430 MHz, yielding Q×f product of about 0.5×10^{13}. This high Q-factor attests the preservation of the single-crystal quartz bulk material properties through all the steps of our developed process. The design of the resonator did not exhibit enough electrodes, yielding a weak dynamic of the S_{11} parameter.

We also studied the temperature sensitivity of the Rayleigh fundamental mode. The resonator was measured for temperatures ranging from -5 to +70°C. Figure 7 shows the relative frequency drifts as a function of temperature. A first order TCF_1 of -4ppm/°C and a second order TCF_2 of -62ppb/°C² were obtained. This non-zero temperature coefficient of frequency could be attributed to an excessive metal thickness from the electrodes.

A test chamber was used in order to measure the sensor response under pressure effects. It allows for applying pressure (from 0 to 4.8 bar) directly to the membrane. Figure 8 compares theoretical and experimental shifts of the SAW sensor versus the applied pressure. As predicted, the frequency shift dependence is linear versus pressure. The measured pressure sensitivity is about 25.8 kHz/bar and is in excellent agreement with the theory developed in section III. It means that a very good control in term of radius and diaphragm has been achieved during the process, matching the expected geometric values.

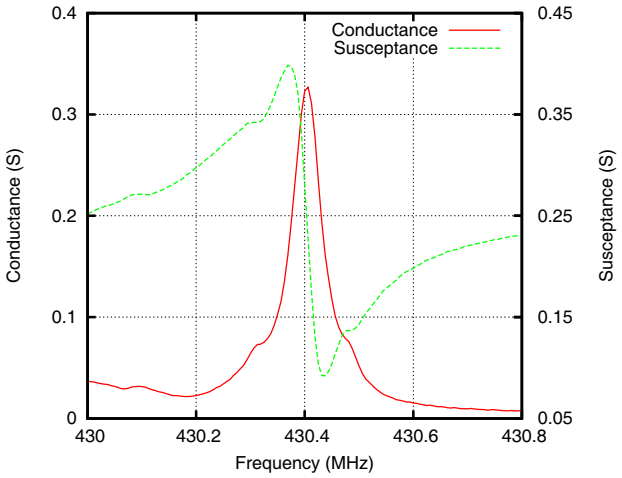

Fig. 6. Admittance measurement of a single-port SAW resonator

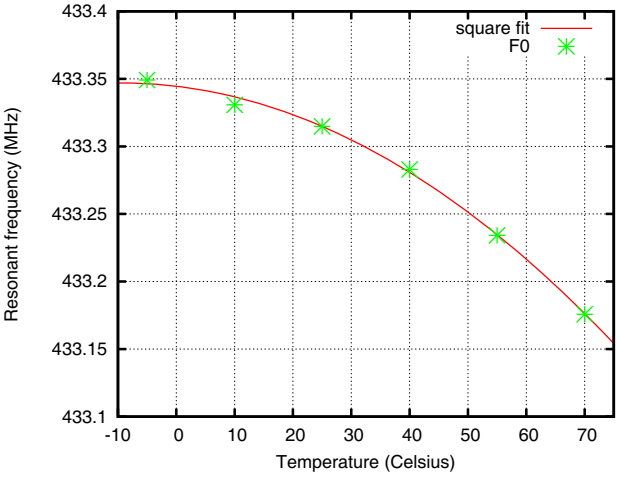

Fig. 7. Variation of the SAW resonance frequency according to the temperature change. The square fit indicates a TCF_1 value of -4ppm/°C and a TCF_2 value of -63ppb/°C²

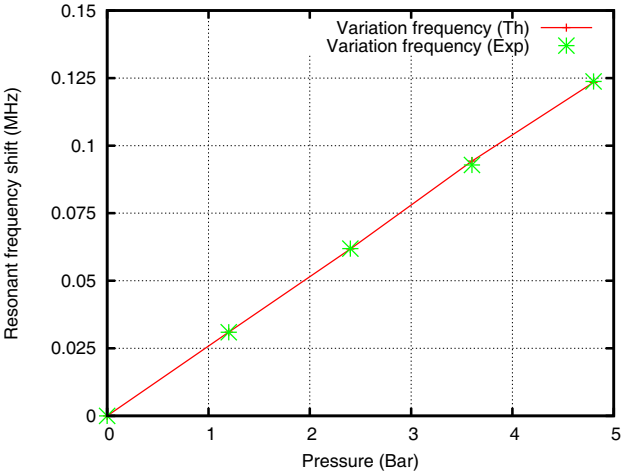

Fig. 8. Comparison of frequency shift under pressure with developed model and experimental data

V. CONCLUSIONS

This work reports the transfer of a thinned Quartz layer onto a Silicon substrate through low-temperature direct wafer bonding and thinning process for a collective manufacturing of Quartz crystal/Si-based SAW pressure sensors. A quality factor as high as 12500 was measured at 430 MHz and a first order temperature dependence of frequency of -4ppm/°C. Notably, a pressure sensitivity of 25.8 kHz/bar was measured and fits very well the expected theory value. Our developed process is generic enough to be applied to different Quartz crystal orientations to satisfy a large variety of applications.

Further developments now will be dedicated to estimate the pressure sensitivity of the sensors depending on their position on the membrane and to compare theoretical optimization with experimental measurements.

ACKNOWLEDGMENT

The authors would like to thank J.-M. Friedt and Sébastien Alzuaga for electrical measurements under pressure and Alexandre Reinhardt for fruitful discussions. This work was partly supported by the French Renatech network and its FEMTO-ST technological facility.

REFERENCES

[1] D.E. Cullen and T.E. Reeder, "Measurement of SAW velocity versus strain for YX and ST Quartz", 1975 IEEE Ultra. Symp. Proc.

[2] D.E. Cullen and G.K. Montres, "Progress in th development of SAW resonator pressure transducers", 1980 IEEE Ultra. Symp. Proc.

[3] H. Scherr, G. Scholl, F. Seifert, and R. Weigel, "Quartz pressure sensor based on SAW reflective delay line," in IEEE Ultrasonics Symposium, San Antonio, TX, USA, 1996, pp. 347–350.

[4] A. Pohl, R. Steindl, and L. Reindl, "The "intelligent tire" utilizing passive SAW sensors – mesurement of tire friction," IEEE Transactions on Instrumentation and Measurement, vol. 48, no. 6, pp. 1041–1046, December 1999.

[5] W. Bulst, G. Fischerauer, and L. Reindl, "State of the art in wireless sensing with surface acoustic waves," IEEE Transactions on Industrial Electronics, vol. 48, no. 2, pp. 265–271, April 2001.

[6] Y. Dong, W. Cheng, S. Wang, Y. Li, and G. Feng, "A multi-resolution passive SAW chemical sensor," Sensors and Actuators B, vol. 76, pp. 130–133, 2001.

[7] V. Yantchev, and I. Katardjiev, "Micromachined thin film plate acoustic resonators utilizing the lowest order symmetric lamb wave mode", IEEE Transactions on Ultrasonics, Ferroelectrics and Frequency Control, 54(1), pp. 87–95, 2007.

[8] S. Grousset, E. Augendre, J. Dechamp, A. Reinhardt, "Single-crystal quartz thin layer transferred on silicon by low-temperature direct wafer bonding and thinning process", 2013, unpublished.

[9] T. Baron, E. Lebrasseur, J. P. Romand, S. Alzuaga, S. Queste, G. Martin, D. Gachon, et al., "Temperature compensated radio-frequency harmonic bulk acoustic resonators pressure sensors", IEEE International Ultrasonics Symposium, pp. 2040–2043, 2010.

[10] T. Baron, D. Gachon, J. P. Romand, S. Alzuaga, S. Ballandras, J. Masson, L. Catherinot, et al., "A pressure sensor based on a HBAR micromachined structure", IEEE International Frequency Control Symposium, pp. 361–364, 2010.

[11] T. Baron, D. Hermelin, J. P. Romand, S. Alzuaga, S. Queste, J. Rauch, S. Ballandras, et al., "SAW pressure sensor on quartz membrane lapping", 10ème Congrès Français d'Acoustique, 2010.

[12] S. Ballandras and E. Bigler, "Precise modelling of complex SAW structures using a perturbation method hybridized with a finite element analysis", IEEE Trans. UFFC, vol 45 no 3, 1998.

[13] D. Hermelin, W. Daniaux, S. Ballandras, B. Belgacem, "Fabrication of surface acoustic wave wireless pressure sensor", IEEE International Frequency Control Symposium Joint with the 22nd European Frequency and Time forum, pp. 96–99, 2009.

S. Timoshenko, "Theory of plates and shells", McGraw-Hill, Inc. Second edition, 1980.

Acoustic Properties of Carbon Nanotube Electrodes in BAW Resonators

E. Iborra, J. Sangrador, M. Clement, T. Mirea, M. DeMiguel-Ramos, J. Olivares, J. Capilla

GMME-CEMDATIC, ETSIT,
Universidad Politécnica de Madrid,
Madrid, SPAIN
eiborra@etsit.upm.es

L. García-Gancedo, S. Esconjáuregui, A. J. Flewitt, W. I. Milne

Electrical Engineering Division, Department of Engineering,
University of Cambridge
Cambridge, UNITED KINGDOM

***Abstract*— In this paper the acoustic characterization of a layer of carbon nanotubes (CNT) deposited on AlN solidly mounted resonators is described. The structure of the CNT layer is analyzed by scanning electron microscopy and Raman spectroscopy. The electrical sheet resistance is derived from 4 point probe measurements and from the fitting of the electrical response of the resonators. Values of sheet resistance around 100 Ω/□ are measured. The longitudinal acoustic velocity is derived from the fitting of the electrical response of the resonators using Mason's model, by adjusting the overtones produced in the CNT layer. A mean value of 62000 $m \cdot s^{-1}$ is obtained, although some devices show values around 90000 $m \cdot s^{-1}$, close to the theoretical value of 100000 $m \cdot s^{-1}$. Some results on the deposition of CNT layers on metallic top electrodes and their influence on the performance of the resonator are also presented.**

Keywords*— Carbon nanotubes (CNT); bio-chemical sensors; BAW resonators; top electrodes

I. INTRODUCTION

During the last few years, the increasing demand for highly sensitive biosensors for real-time monitoring has boosted the development of new devices and materials. Most of the studies have especially focused on the functionalization of sensors and the improvement of their performances [1]. Due to the recent progress achieved in the field of the piezoelectric resonators for communication electronics, acoustic wave devices have become one of the most promising technologies for sensing applications. In particular, bulk acoustic wave (BAW) sensors have been shown to have excellent potential in diagnosis applications [2]. Despite the progress made in this type of resonators, additional work is still required to improve their quality factor (*Q*) and to optimize the sensing layer needed for specific detection.

The top electrode of BAW resonators intended for sensing applications needs special attention, since it strongly affects both their electrical performance and sensing ability [3]. From an electrical perspective, the desired properties for the top electrode material are low mass, high conductivity, and high acoustic impedance. Carbon nanotubes (CNTs) have emerged as good candidates to act as biosensors electrodes or sensing layer. Since their discovery in 1991 by Sumio Iijima [4], they have been widely investigated due to their ultra-light weight, mechanical strength, high chemical resistance, high thermal conductivity, high surface to volume ratio and high electrical conductivity [5]. Among their many applications, CNTs can be used in the microelectronics field as vertical interconnections, conductive flexible composites, low-k dielectrics or as part of transistors, diodes [6] or bio and chemical sensors [7].

The use of CNTs in sensors can be found in many recent studies [8-10]. The main advantage they offer is the possibility of being functionalized to act both as sensing layer and electrode. Their high conductivity is an encouraging prospect to act as a good electrode; additionally, they can be treated to make them sensitive to specific molecules by an adequate functionalization, which can be achieved by chemical methods [11].

Carbon nanotubes are commonly grown by catalytic vapor phase deposition of carbon, being iron and nickel, among others [12], the most frequently used catalysts [8]. The choice of the substrate to grow CNTs is another interesting issue that has been studied recently. It has been demonstrated that CNTs can grow on different materials [13], but the possibility of an optimal growth on metals is still a pending matter.

The final motivation of this work is to develop high sensitive sensors using BAW resonators. To achieve this, CNTs are proposed as sensing top electrode, since they possess an effective surface area which is much greater than that of the standard metallic electrodes. Their light weight also provides advantages to the electrical performance of the resonator. In this paper, the growth of CNT layers on different types of substrates (insulators and metals) using Fe as catalyst has been studied. We have assessed their acoustic, electric and structural properties and evaluated the improvement of their sheet conductivity when grown on metallic surfaces.

II. EXPERIMENTAL

The CNT layers were deposited at temperatures ranging from 600ºC to 750ºC by the pyrolytic decomposition of acetylene (C_2H_2) diluted in ammonia (NH_3) using Fe nanoparticles as catalyst agent. The process was carried out at a total pressure of 300 mTorr. The reaction chamber was evacuated with a two stages mechanical pump and cleaned

before deposition by several purges with high purity nitrogen to ensure very low oxygen content. After the cleaning, NH_3 was fed to the chamber. The substrates, which were previously pre-coated with an evaporated Fe layer, were then heated to the process temperature by a pyrolytic carbon heater at a rate of 5ºC/s. Fe nanoparticles were formed in this step by annealing the substrates in the reducing atmosphere of NH_3. Their size depended on the thickness of the Fe layer, which ranged from 3 nm to 7 nm. After the formation of the nanoparticles, C_2H_2 was fed to the chamber without stopping the NH_3 supply. After the deposition, the samples were cooled down under vacuum at a rate of 1ºC/s.

CNT layers were deposited as top electrode of solidly mounted resonators (SMR) composed of an acoustic reflector, an iridium bottom electrode and a 2 µm-thick piezoelectric AlN layer. All the layers of the piezoelectric stack were deposited by pulsed-DC reactive sputtering in an UHV system. The acoustic reflectors were made of five alternating layers of low acoustic impedance porous-SiO_2 [14] and high acoustic impedance Mo, with thicknesses adjusted for a center resonance frequency of 2.5 GHz. These had been carefully designed to withstand the high temperatures required for CNTs deposition without delamination. The area of the resonators was set by defining the Fe layer through a photoresist lift-off process before the formation of the nanoparticles, which provided the substrate areas for the selective growth of the CNT-top electrode. In some samples, a Mo or Al layer was deposited before the Fe and CNTs layers. Figure 1 shows a SEM image of a typical device after being measured. The indentations in the contact pads are due to the RF test probes.

The electrical impedance spectra of the resonators, measured with an Agilent network analyzer PNA N5230A between 100 MHz and 10 GHz, were fitted with Mason's model to determine the acoustic velocity of the CNT layers. The acoustic properties of the different materials used for the simulations are summarized in Table I.

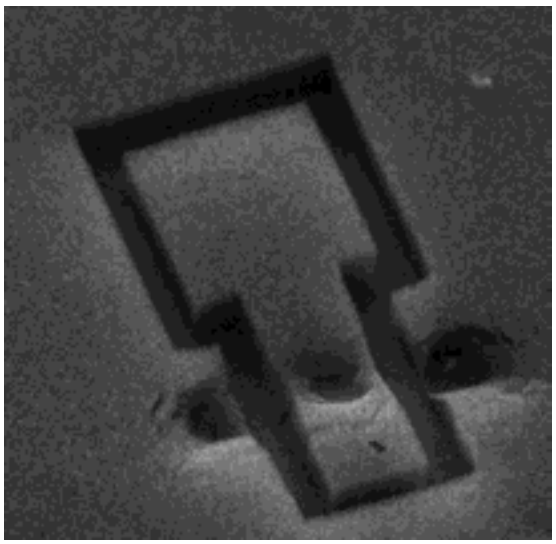

Figure 1. Plan view of a typical test resonator after being measured.

TABLE I. Acoustic impedance of the materials used in this work.

MATERIAL	MASS DENSITY ($kg \cdot m^{-3}$)	SOUND VELOCITY ($m \cdot s^{-1}$)	ACOUSTIC IMPEDANCE ($kg \cdot m^{-2} \cdot s^{-1}) \times 10^{-6}$
Al	2700	5100	13.77
p-SiO_2	1800	5450	9.81
AlN	3300	11000	36.30
Mo	10300	6190	63.76
Ir	22500	5300	119.25

The dimensions of the resonators (thicknesses and areas) were carefully assessed. The thickness of the CNT layers was measured on cleaved samples in a scanning electron microscope (SEM). Mass density was calculated by weighting large substrates before and after deposition of the CNT layer. The structure of the CNTs was assessed by Raman spectroscopy using B&BTek S415-532S spectrometer. The sheet resistance of the CNT carpet was measured by the four point probe method.

III. RESULTS AND DISCUSSION

The Raman spectrum of a typical CNT layer is depicted in figure 2, which indicates that the CNT layers are composed by multiwall nanotubes with relatively high defect content, as determined by the ratio between D and G bands, which is around 1.

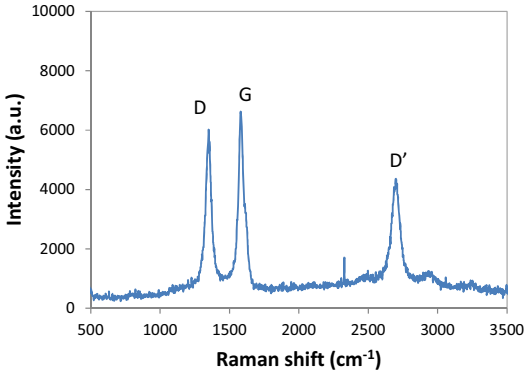

Figure 2. Raman spectrum of a typical CNT layer.

Figure 3 shows a SEM image of the cross section of a typical stack, showing the sequence of the different layers composing the resonator: i) the CNT layer (top layer), ii) the AlN active layer, iii) the Ir bottom electrode and 4) the acoustic reflector.

Firstly, in order to investigate the effect of the high temperature needed to grow the CNTs on the integrity of the piezoelectric stack, the frequency response of conventional SMRs (without CNTs) was assessed before and after a thermal treatment in NH_3 atmosphere similar to that used to deposit the CNT layers; the variations of the coupling factor and the resonant frequency were negligible. However, the parasitic

series resistance slightly increased. We attribute this effect to an increase of the resistivity of the Mo top electrode used in these test devices during the high temperature process. The possibility of some diffusion of the metal atoms into the AlN film was discarded as the resonant frequency did not vary.

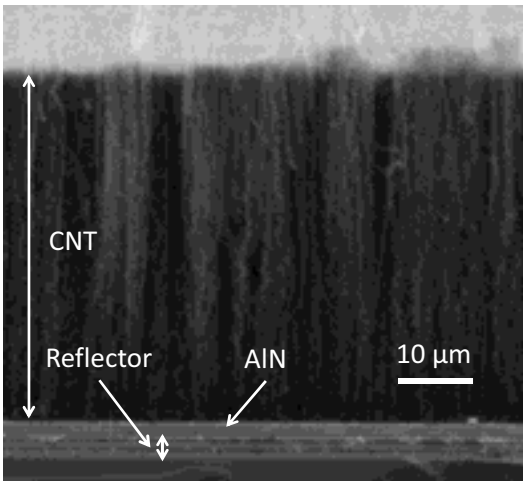

Figure 3. Cross section image of a typical device.

The sound velocity of the CNTs was assessed trough the frequency response of SMRs containing CNTs as top electrode. The frequency response of a typical test device with a 30 µm-thick CNT top electrode is shown in figure 4(b). The frequency response exhibits three clear resonances associated to the main λ/2 longitudinal mode in the AlN film and two secondary overtones in the acoustic reflector. These features also appear in resonators without CNT electrode. In addition, some tiny resonances due to overtones in the CNT layer can also be observed. The fact that these resonances appear so weak can be attributed to a loss of coherence in the reflection of the acoustic waves in the interface between the CNT layer and the air, because of its roughness, which makes it difficult to detect them in some devices. Figure 5 shows the SEM images of two CNT layers with very different roughness. The electrical response of samples with roughness similar to that of figure 5(top) corresponds to figure 4(a) spectrum, which does not show any feature attributable to overtones in the CNT layer.

The fitting of the electrical response of the test devices using Mason's model allowed us to obtain the acoustic velocity in the CNT layer, providing that its density and the properties and thicknesses of all the materials involved in the device are well known. The density of the CNT layers was derived by weighting, with a precision of 10^{-4} g, large substrates (2x3 cm^2) before and after the deposition of the CNTs, and dividing the weight change by the volume of the layer whose thickness was obtained through the SEM picture. The resulting mean density was 100 kg/m^3 with a dispersion of ±30 kg/m^3.

The overtones in the CNT layer could be fitted by varying the sound velocity. The frequency response of the thinner samples did not exhibit overtones, even the smoother ones, but, if the thickness of the layer was large enough (more than 20 µm), the number of overtones was sufficient to determine the sound velocity. The average value obtained after analyzing more than 30 samples is around 62000 $m \cdot s^{-1}$ with a dispersion of around 10% attributable to the dispersion in the value of the mass density and in the thickness of the layers. A few samples exhibited velocity values up to 90000 $m \cdot s^{-1}$, but we cannot attribute these high values to any special feature.

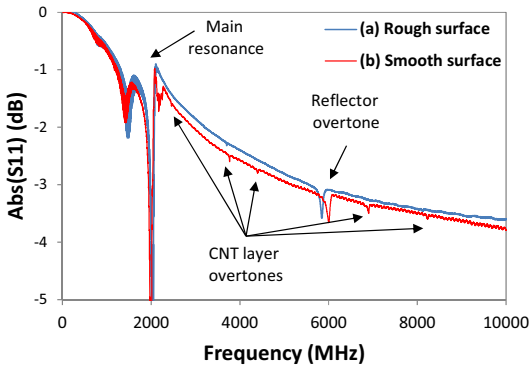

Figure 4. Electrical response of typical devices with CNT exhibiting (a) rough (a) and smooth (b) surfaces

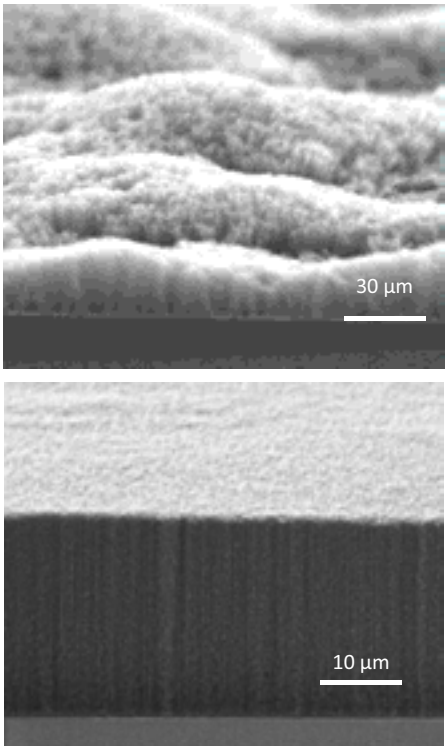

Figure 5. SEM images of two CNT layers with different roughness. The picture on top corresponds to significantly rough layer, in which overtones are barely detected.

Theoretically, the sound velocity can be estimated as the square root of the ratio between the stiffness coefficient and the mass density. The stiffness coefficient of a single CNT is around 1TPa [15] and the resulting velocity is 100000 $m \cdot s^{-1}$ considering a density of 100 $kg \cdot m^{-3}$. There is an interesting

issue that should be set out. The mass density considered above is that of the propagating medium. However, in a CNT carpet, the waves should travel along the nanotubes. Therefore the mass density to be considered would be that of the tubes, regardless of their surface density, which fixes the mass density of the entire film. Thus, the previous theoretical prediction could be incorrect since the measured density depends greatly on the number of CNTs per unit area.

One of the main drawbacks of using CNTs top electrodes is that the devices show large parasitic series resistance, which can rise tens of ohms. The origin of this high sheet resistance is the lateral interconnections between the carbon nanotubes. It is well-established that MWCNT have a very large conductivity in the axial direction [16]. However, the sheet resistance shown by a carpet of well-aligned CNTs appears to be very high. The assessment of a continuous CNT layer using the four point probe method yields a sheet resistance of 100 Ω/□, which represents around 200 Ω of series resistance in a resonator with an area of 15000 μm^2. However, the fitting of the frequency spectra yields a parasitic resistance of only 25 Ω. This aspect, which should be improved in practical devices, is not a drawback for characterizing test devices such as those used in this work.

To prevent the high parasitic series resistance that worsens the resonator response, CNT layers were deposited on a metal layer acting as top electrode. The deposition of CNT on metals is not straightforward because the metals used as catalytic agent (iron or nickel) can diffuse into the substrate during the heat treatments, thus inhibiting the nanoparticles formation. This is the case of Mo, which is the typical top electrode used in BAW devices. CNT layers have been deposited on different metallic thin films, such as Mo, Ti, Au, and Al, but only Al substrates thinner than 70 nm did provide good results. The use of Al reduced the series resistance of the BAW resonators from 25 Ω to 10 Ω, which is still not sufficiently low. More work is required to optimize this aspect.

IV. Conclusions

The acoustic characteristics of CNT layers have been derived from the electric characterization of BAW resonators containing CNT layers as top electrode. The overtones generated in this layer were fitted with Mason's model, which allowed us deriving the CNT's sound velocity. A mean value of 62000 $m \cdot s^{-1}$ ±10% was obtained. The error arises from inaccuracies in the determination of the mass density and the thickness.

The sheet resistance exhibited by the CNT layers suggests that, in their present form, they are not suitable as top electrode for BAW resonators. However, their low density and hence, low mass, provide very thick layers (30 µm) that do not disturb the response of the resonators, since they barely load them. Therefore, CNTs can be very useful as sensing layers on top of BAW resonators, as long as they are grown on metallic electrodes of low sheet resistance. CNT carpets have been successfully grown on thin Al substrates although additional work is still required to achieve optimally-performing devices.

Acknowledgment

The authors acknowledge Prof. Jose de Frutos (ETSIT-UPM) for Raman characterization. This work was partially supported by the European Comission through the 7th Framework Programme by the *RaptaDiag* project HEALTH-304814 (http://www.raptadiag.eu/) and by COST action IC1208 and by the Ministerio de Economía y Competitividad del Gobierno de España through project MAT2010-18933.

References

[1] H. Kang, S. Lim, N. Park, K.-Y. Chun, and S. Baik, "Improving the sensitivity of carbon nanotube sensors by benzene functionalization," *Sensors and Actuators B: Chemical*, vol. 147, no. 1, pp. 316–321, May 2010.

[2] I. Katardjiev, V. Yantchev, "Recent developments in thin film electro-acoustic technology for biosensor applications", Vacuum, vol. 86, pp. 520-531, 2012.

[3] T. Yokoyama, T. Nishihara, S. Taniguchi, M. Iwaki, and Y. Satoh, "New Electrode Material for Low-loss and High-Q FBAR Filters," vol. 00, no. c, pp. 429–432, 2004.

[4] Sumio Iijima, "Helical microtubules of graphitic carbon," *Nature*, vol. 56, no. 354, pp. 56–58, 1991.

[5] V. Popov, "Carbon nanotubes: properties and application," *Materials Science and Engineering: R: Reports*, vol. 43, no. 3, pp. 61–102, Jan. 2004.

[6] F. Kreupl, Q. Ag, and T. Innovations, *Carbon Nanotubes in Microelectronic Applications*, vol. 8. 2008.

[7] C. I. L. Justino, T. a. P. Rocha-Santos, A. C. Duarte, and T. a. P. Rocha-Santos, "Advances in point-of-care technologies with biosensors based on carbon nanotubes," *TrAC Trends in Analytical Chemistry*, vol. 45, pp. 24–36, Apr. 2013.

[8] L. García-Gancedo, Z. Zhu, E. Iborra, M. Clement, J. Olivares, a. J. Flewitt, W. I. Milne, G. M. Ashley, J. K. Luo, X. B. Zhao, and J. R. Lu, "AlN-based BAW resonators with CNT electrodes for gravimetric biosensing," *Sensors and Actuators B: Chemical*, vol. 160, no. 1, pp. 1386–1393, Dec. 2011.

[9] Z. Zhu, L. Garcia-Gancedo, A. J. Flewitt, H. Xie, F. Moussy, and W. I. Milne, "A critical review of glucose biosensors based on carbon nanomaterials: carbon nanotubes and graphene.," *Sensors (Basel, Switzerland)*, vol. 12, no. 5, pp. 5996–6022, Jan. 2012.

[10] M. Dragoman, a. Muller, D. Neculoiu, D. Vasilache, G. Konstantinidis, K. Grenier, D. Dubuc, L. Bary, R. Plana, and E. Flahaut, "High performance thin film bulk acoustic resonator covered with carbon nanotubes," *Applied Physics Letters*, vol. 89, no. 14, p. 143122, 2006.

[11] L. Meng, C. Fu, and Q. Lu, "Advanced technology for functionalization of carbon nanotubes," *Progress in Natural Science*, vol. 19, no. 7, pp. 801–810, Jul. 2009.

[12] L.-L. Tan, W.-J. Ong, S.-P. Chai, and A. R. Mohamed, "Growth of carbon nanotubes over non-metallic based catalysts: A review on the recent developments," *Catalysis Today*, Dec. 2012.

[13] C.-C. Su and S.-H. Chang, "Comparison of the efficiency of various substrates in growing vertically aligned carbon nanotube carpets," *Carbon*, vol. 49, no. 15, pp. 5271–5282, Dec. 2011.

[14] J. Olivares, E. Wegmann, J. Capilla, E. Iborra, M.Clement, L. Vergara, and R. Aigner, "Sputtered SiO_2 as low acoustic impedance material for Bragg mirror fabrication in BAW Resonators", IEEE Trans.Ultrason. Ferroelec. Freq. Contr. Vol. 57 pp. 23-29, 2010.

[15] M. M. J. Treacy, T. W. Ebbesen, and J. M. Gibson, "Exceptionally high Young's modulus observed for individual carbon nanotubes," Nature, vol. 381, no. 6584, pp. 678–680, 1996.

[16] M.P. Anantram and F. Léonard, "Physics of carbon nanotube electronic devices", *Rep. Prog. Phys.*, vol. 69, pp. 507–561, 200

Properties of Piezoelectric Single Crystals $Ca_3TaGa_3Si_2O_{14}$ at High Temperature and High Vacuum Conditions

Hongfei Zu, Huiyan Wu, Yizhong Wang, Q.-M. Wang
Department of Mechanical Engineering & Materials Science
University of Pittsburgh, Pittsburgh, USA
qiw4@pitt.edu

Shujun Zhang, T.R. Shrout
Materials Research Institute
The Pennsylvania State University
University Park, USA

***Abstract*—In this paper, a kind of fully ordered langasite family crystals $Ca_3TaGa_3Si_2O_{14}$ (CTGS) were grown by the Czochralski pulling method and cut into lateral mode. The dielectric, elastic and piezoelectric properties of them were investigated as functions of temperature (up to 1073.15 K) and pressure (up to E-7 torr). It was found that all the crystals exhibited pressure stability properties and temperature dependent characteristics. According to the calculation, the dielectric permittivity, elastic coefficient and piezoelectric coefficient were about 17.66, 9.06 pm^2/N and 3.77 pC/N, respectively. The good properties make CTGS promising candidates for sensing applications at high temperature and high vacuum conditions.**

Keywords—langasite; high temperature; high vacuum

I. INTRODUCTION

High temperature sensors for harsh environments are of major importance to the aerospace and energy industries [1]. For example, high temperature sensors that could bear high vacuum and high radiation of the space environment and work in a wide temperature range are needed for the health monitoring of the aerospace industry.

To date, many kinds of materials have been investigated for the application at elevated temperatures. However, most of them are restricted in use. Currently, quartz (α-SiO_2) crystals are widely used in sensing applications, due to its thermally stable properties (zero temperature coefficient of frequency (TCF)), high mechanical Q, and high electrical resistivity. However, the maximum operating temperature of quartz-based devices is limited by the low α-β phase transition temperature at 573 °C and further restricted by the crystal twinning occurring at 300 °C [1]. Similar to quartz, $GaPO_4$ has been reported to be an excellent candidate for high temperature sensors due to the relatively high resistivity, low dielectric loss and high mechanical Q with α-β phase transition temperature at ~970 °C [2-7]. Unfortunately, the costly raw materials and achievable small crystal size limit the applications [8]. The disordered langasite family crystals (general formula $A_3BC_3D_2O_{14}$) exhibit no phase transitions prior to their respective melting points T_m (T_m = 1300 ~ 1500 °C) and can be readily grown using the Czochralski (CZ) method. Moreover, their piezoelectric coefficient d_{11} and electromechanical coupling factor k_{26} are significantly higher than those of quartz (7.0 pC/N versus 2~3 pC/N) and comparable to $GaPO_4$. However, their electrical resistivity is several orders of magnitudes lower than those of quartz and GaPO4 [9-11].

Recently, a kind of fully ordered langasite family crystals $Ca_3TaGa_3Si_2O_{14}$ (CTGS) have attracted considerable attention for high-temperature applications. Compared to disordered langasite family crystals, CTGS crystals have greatly improved resistivity. At the same time, they exhibit thermal stability of dielectric and electromechanical properties [12-13]. However, the properties of these crystals under high-vacuum conditions have not been studied.

In this paper, we investigated CTGS lateral mode resonators, by looking into the properties of the resonators as functions of temperature (from room temperature to 1073 K) and vacuum condition (from E-2 torr to E-7 torr).

II. EXPERIMENTAL

CTGS piezoelectric crystals were grown by the Czochralski (CZ) technique using iridium crucibles with an atmosphere of N_2 plus 1 vol% O_2. The combination of N_2/O_2 was used to protect the Ir crucibles while avoiding oxygen defects in the grown crystals. The crystals were grown along the crystallographic <100> direction [12]. The crystals were cut into lateral mode (XY-cut).

All the samples were with the dimensions of 0.64 × 3.99 × 13.99 mm^3 and polished using 15-μm SiC powder. The electrodes of the samples were vacuum-sputtered Au thin film (200 nm) and the surfaces of the electrodes were perpendicular to the thickness (0.64 mm) direction. The relative dielectric permittivity $\varepsilon^T/\varepsilon_0$ was determined from capacitance measurements using a multi-frequency LCR meter (Agilent 4284A, precision LCR meter, 20 Hz – 1 MHz). The elastic compliance s and the electromechanical coupling factor k were calculated based on the resonance/anti-resonance frequencies,

measured using an Agilent 4294A precision impedance analyzer (40 Hz – 110 MHz). The piezoelectric coefficient d was calculated using the dielectric, elastic and coupling parameters. During measurement, the samples were put in the chamber of a sputtering system (ATC 1300-F, AJA International, Inc.) with different temperatures (from room temperature to 1073.15 K) and different vacuum conditions (from E-2 torr to E-7 torr).

III. Methods of Calculating Parameters of Lateral Mode Resonators

CTGS is a trigonal crystal belonging to the space group 32. So the dielectric, piezoelectric and elastic constants matrices are as follows:

$$\varepsilon_{ij} = \begin{bmatrix} \varepsilon_{11} & 0 & 0 \\ 0 & \varepsilon_{11} & 0 \\ 0 & 0 & \varepsilon_{33} \end{bmatrix}$$

$$d_{ij} = \begin{bmatrix} d_{11} & -d_{11} & 0 & d_{14} & 0 & 0 \\ 0 & 0 & 0 & 0 & -d_{14} & -2d_{11} \\ 0 & 0 & 0 & 0 & 0 & 0 \end{bmatrix}$$

$$s_{ij} = \begin{bmatrix} s_{11} & s_{12} & s_{13} & s_{14} & 0 & 0 \\ s_{12} & s_{11} & s_{13} & -s_{14} & 0 & 0 \\ s_{13} & s_{13} & s_{33} & 0 & 0 & 0 \\ s_{14} & -s_{14} & 0 & s_{44} & 0 & 0 \\ 0 & 0 & 0 & 0 & s_{44} & 2s_{14} \\ 0 & 0 & 0 & 0 & 2s_{14} & s_{66} \end{bmatrix}$$

From the above matrices, it is easy to obtain the following relationships:

$$\varepsilon_{11} = \varepsilon_{22}, d_{11} = -d_{12}, s_{11} = s_{22} \quad (1)$$

Where ε_{11} and ε_{22} are dielectric permittivity, d_{11} and d_{12} are piezoelectric coefficient and s_{11} and s_{22} are elastic coefficient.

According to d-type piezoelectric equations:

$$S_2 = s_{22}^E T_2 + d_{12} E_1, \; D_1 = d_{12} T_2 + \varepsilon_{11}^T E_1 \quad (2)$$

In (2), S_2, T_2, E_1, D_1, s_{22}, $d_{12,}$ and ε_{11} are strain, stress, electric field, electric displacement, elastic constant, piezoelectric constant and dielectric constant, respectively. And the electric admittance can be given by:

$$Y = j\omega C^T [(1 - k_{12}^2) + k_{12}^2 \frac{\tan(kl/2)}{kl/2}] \quad (3)$$

And:

$$C^T = \frac{wl\varepsilon_{11}^T}{t}, \quad k = \frac{\omega}{v}, \quad v = \sqrt{\frac{1}{\rho s_{11}^E}}, \quad k_{12}^2 = \frac{d_{12}^2}{s_{22}^E \varepsilon_{11}^T} \quad (4)$$

Where w, l, t and ρ are the width, length, thickness and density (= 4.63 g/cm^3) of the CTGS crystal sample, respectively. ω, k, v, and k_{12} are angular frequency, wave number, acoustic velocity and electromechanical coupling factor, respectively. C^T is the low frequency capacitance (measured at 1KHz).

From (3), when tan(kl/2) goes to infinity, Y goes to infinity. Thus, it could be obtained:

$$f_r = \frac{v}{2l} \quad (5)$$

Where fr is the resonant frequency.

In (3), if Y=0, the following relationship could be got:

$$\frac{k_{12}^2 - 1}{k_{12}^2} = \frac{\tan(kl/2)}{kl/2} \quad (6)$$

That means:

$$\frac{k_{12}^2 - 1}{k_{12}^2} = \frac{\tan[\frac{\pi}{2}(f_a / f_r)]}{\frac{\pi}{2}(f_a / f_r)} \quad (7)$$

In (7), fa is the anti-resonant frequency.

Thus, from equations (1), (4) and (5), the following relationships can be calculated:

$$\varepsilon_{11}^T = \varepsilon_{22}^T = \frac{C^T t}{wl} \quad (8)$$

$$s_{11}^E = s_{22}^E = \frac{1}{4\rho(lf_r)^2} \quad (9)$$

$$d_{11}^2 = d_{12}^2 = k_{12}^2 \varepsilon_{11}^T s_{22}^E, \quad d_{11} = -d_{12} \tag{10}$$

Therefore, if t, w, l, ρ, C^T, fr and fa are known, the dielectric constants, piezoelectric constants, elastic constants and electromechanical coupling factor can be obtained by using (7) - (10).

IV. Results and Discussion

Fig. 1 shows that at the same temperature, with the change of pressure, the resonant frequency of CTGS lateral mode crystal stayed stable.

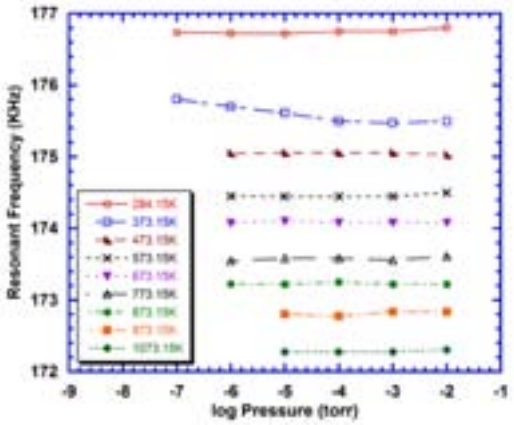

Fig. 1. Resonant frequency as a function of pressure for CTGS lateral mode crystal at different temperatures.

From Fig. 2, it can be seen that the resonant frequency as a function of temperature exhibited linear temperature/frequency characteristics over a wide temperature range. The temperature coefficient of the resonant frequency was found to be -5.1Hz/K. The inset in Fig. 2 presents the impedance as a function of temperature when the pressure is 1.0 E-4 torr, from which it can be seen that the resonant frequency (together with anti-resonant frequency) shifted downward with increasing temperature.

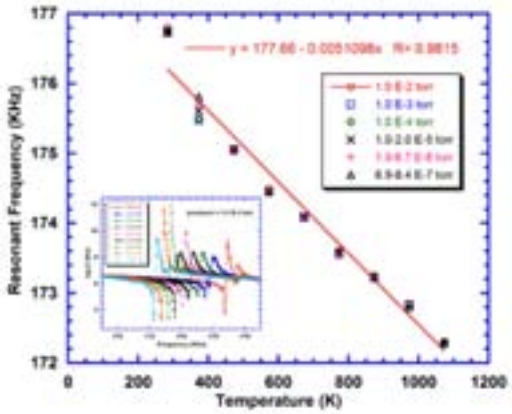

Fig. 2. Resonant frequency as a function of temperature for CTGS lateral mode crystal at different pressures.

Fig. 3 gives the elastic constant (s_{11}^E, s_{22}^E) as a function of temperature. It was found that the values increased almost linearly with the increasing temperature. It was 9.29 pm^2/N at 1073.15K and the temperature coefficient was found to be 0.00053 $(pm^2/N)/K$.

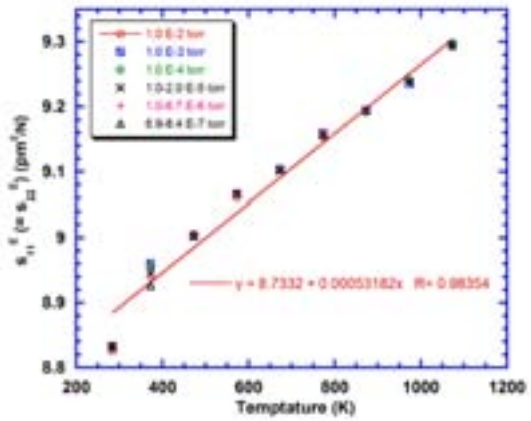

Fig. 3. Elastic constant variation as a function of temperature for CTGS lateral mode crystal at different pressure.

It was observed from Fig. 4 that the dielectric permittivity ($\varepsilon_{11}^T / \varepsilon_0, \varepsilon_{22}^T / \varepsilon_0$) and piezoelectric constant (d_{11}, d_{22}), to some extent, exhibited thermal stability and the values were within the range of ±3.57% around 17.66 and ±2.11% around 3.77 pC/N, respectively. According to the measurement, pressure almost didn't affect the capacitance. So, the dielectric permittivity didn't change with pressure.

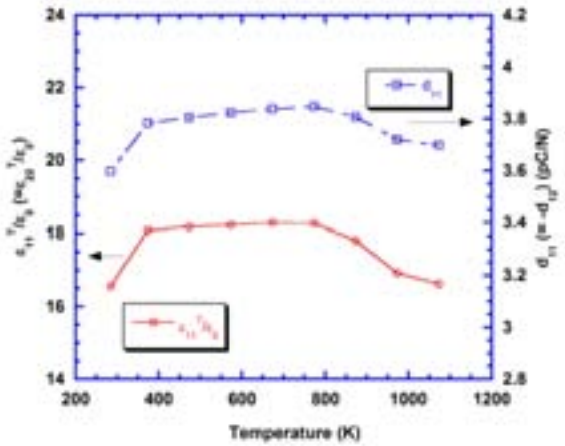

Fig. 4. Dielectric and piezoelectric constant variation as a function of temperature for CTGS lateral mode crystal.

V. Conclusion

In summary, high-quality piezoelectric single crystals CTGS were grown using the Czochralski pulling technique. By specially cut, we obtained lateral mode CTGS resonators

and investigated the dielectric, elastic and piezoelectric properties of them as functions of temperature and pressure. It was found that all the samples exhibited pressure stable properties (up to E-7 torr), which means that the crystals could work well under very high vacuum condition. Moreover, the crystals showed temperature dependent characteristics (up to 1073.15K). According to the calculation, the dielectric permittivity, elastic coefficient and piezoelectric coefficient were about 17.66 (±3.75%), 8.83~9.29 pm^2/N and 3.77 (±2.11%) pC/N, respectively. Thus, the CTGS crystals are promising candidates for sensing applications under high-temperature and high-vacuum conditions.

ACKNOWLEDGMENT

The authors thank Shujun Zhang for help on sample preparation and experiments.

REFERENCES

[1] Fapeng Yu, Shujun Zhang, Xian Zhao, Duorong Yuan, Lifeng Qin, Qing-ming Wang and Thomas R. Shrout, "Investigation of $Ca_3TaGa_3Si_2O_{14}$ piezoelectric crystals for high temperature sensors," Journal of applied physics 109, 114103, 2011.

[2] H. Thanner, P. W. Krempl, R. Selic, W. Wallnofer, and P. M. Worsch, "$GaPO_4$ high temperature crystal microbalance demonstration up to 720°," J. Therm. Anal. Calorim. Vol. 71, pp. 53, 2003.

[3] C. Reiter, H. Thanner, W. Wallnofer, and P. W. Krempl, "Properties of $GaPO_4$ Thickness shear Resonators" Ann. Chim. Sci. Mat. vol. 22, pp. 633-636, 1997.

[4] Holger Fritz, "High temperature piezoelectric materials: Defect chemistry and electro-mechanical properties" J. Electroceram. vol. 17, pp. 625-630, 2006.

[5] E. Philippot, A. Ibanez, A. Goiffon, M. Cochez, A. Zarka, B. Capell, J. Schwartzel, and j. Detaint, "A Quartz-Like Material: Gallium Phosphate (GaPO4); Crystal Growth and Characterization," J. Cryst. Growth, vol. 130, pp. 195-120, 1993.

[6] P. Krempl, G. Schleinzer, and W. Wallnofer, "Gallium phosphate, $GaPO_4$: A new piezoelectric crystal material for high-temperature sensories," Sens. Actuators, A: Physical, vol. 61, pp. 361-363, 1997.

[7] J. Haines, O. Cambon, N. Prudhomme, and G. Fraysse et al, "High-temperature, structural disorder, phase transitions, and piezoelectric properties of $GaPO_4$," Physical review B 73, 014103, 2006.

[8] Fa-peng YU, Duo-rong YUAN, Xian ZHAO, Shu-jun ZHANG, "Investigation of langanite and langatate single crystals for high temperature sensing," IEEE, pp. 564-569, 2010.

[9] Holger Fritze, "High-temperature bulk acoustic wave sensors," Meas. Sci. Technol. 22, 012002, 2011.

[10] Shujun Zhang, Yiting Fei, Eric Frantz, David W. Snyder, Bruce H. T. Chai, and Thomas R. Shrout, "High-temperature piezoelectric single crystal $ReCa_4O(BO_3)_3$ for sensor applications," IEEE Tran, Ultrason. Ferroelectri. Freq. Control. vol. 55, pp. 2703-2708, 2008.

[11] Shujun Zhang, Akira Yoshikawa, Kei Kamada, Eric Frantz, Ru Xia, David W. Snyder, Tsuguo Fukuda, and Thomas R. Shrout, "Growth and characterization of high temperature $La_3Nb_{0.5}Ga_{5.3}Al_{0.2}O_{14}$ (LNGA) and $La_3Ta_{0.5}Ga_{5.3}Al_{0.2}O_{14}$ (LTGA) piezoelectric single crystals," Solid State Communication. vol. 148, pp. 213-216, 2008.

[12] S. J. Zhang, Y. Q. Zheng, H. K. Kong. J. Xin, E. Frantz, and T. R. Shrout, "Characterization of high temperature piezoelectric crystals with an ordered langaste structure," J. Appl. Phys. 105, 114107, 2009.

[13] Fapeng Yu, Xian Zhao, Lihu Pan, Fei Li, Duorong Yuan, and Shujun Zhang, "Investigation of zero temperature compensated cuts in langasite-type piezocrystals for high temperature applications," J. Phys. D 43, 165402, 2010.

High Overtone Bulk Acoustic Resonators for High Temperature Sensing Applications

Emilie Courjon, Bruno François, Gilles Martin, William Daniau, Thomas Baron
FEMTO-ST Institute, UMR 6174 CNRS-UFC-ENSMM-UTBM, Besançon, France
emilie.courjon@femto-st.fr

Leonard Reindl
Albert Ludwigs Universität – IMTEK
Freiburg-im-Breisgau, Germany

Marc Loschonsky, Jean-Michel Friedt, Brahim Belgacem
SENSeOR SAS,
Besançon – Mougins, France

Sylvain Ballandras
frec|n|sys SAS
Besançon, France

Abstract — **High overtone Bulk Acoustic Resonators have been developed for radio-frequency application such as oscillator stabilization, but also as an alternative to surface acoustic wave resonator for sensor development. In the present work, the possibility to operate such devices at temperature up to 800°C is investigated experimentally. Devices built using Aluminum Nitride deposited on Silicon with Platinum electrodes have been manufactured and resonance frequencies near the 434-MHz centered ISM band have been characterized from room conditions to 800°C. Although the exposition to such a temperature yields changes in the device response, it turns out that the operation is partly reversible and that these HBARs could operate without major defects for several tens of hours at such regimes. The development of wireless temperature sensors on this base then reveals accessible.**

Keywords-Sensor; BAW; High overtone Bulk Acoustic Resonator – HBAR; High temperature; AlN; Silicon; Sapphire

I. INTRODUCTION

The development of elastic wave sensors capable to be remotely interrogated without on-board energy has yield new markets rise. The corresponding users challenge these sensors for several extreme applications such as operation at temperature above 500°C. Although the use of Langasite was the most promising approach, Aluminum Nitride (AlN)-based structures were also considered as a potential solution [1]. It was demonstrated that high overtone bulk acoustic resonators (HBARs) can be applied for wireless sensing as an alternative to SAW resonators [2]. As AlN is well-suited for such devices and exhibit a melting point in excess of 2000°C, the idea to exploit AlN-based HBAR for high temperature operation was considered in the present work.

AlN-based HBARs have been manufactured in a Sigma-Trikon sputtering machine, depositing 1µm thick layers onto a (111) Ti/Pt backside electrode deposited atop 530µm thick Sapphire and 400µm thick Silicon substrates. The classical figure of HBAR response was observed, with a frequency separation of about 8 to 9 MHz depending on the substrate and a maximum resonance of the layer alone near 2 GHz. The resonances between 400 and 500 MHz (close to the 434 MHz centered ISM band) have been focused for assessing the operation of the devices at temperature larger than 500°C.

These devices have been submitted to temperature cycles up to 600°C for 48 hours in an oven developed at IMTEK for calibrating acoustic devices [3], and their electrical response were monitored at various frequencies during the experiment. The observation of the device showed minimal de-wetting effects in form of single droplets atop the surface, as it is currently the case for inter-digitated-based transducer devices. The material lattice was found stable enough to withstand the temperature induced tensions as the thermal grooving and the resulting forming of droplets leaving micro cavities in the metallization layer is observed but limited and do not prevent the device operation. The experiments then were extended successfully up to 800°C.

In the first section of the paper, basic considerations on materials and sensor structure are discussed. The fabrication of the test vehicles then is described and finally test results of the HBAR under temperature ranging from room to 600°C and 800°C are reported.

II. HBAR MATERIALS AND STRUCTURE FOR HIGH TEMPERATURE APPLICATION

A. *Materials*

Quartz, Lithium Tantalate ($LiTaO_3$) and Lithium Niobate ($LiNbO_3$) are currently the most common piezoelectric crystals for the development of acoustic wave sensors. However, their maximum admissible operation temperature is limited by intrinsic properties, i.e. phase transitions and material decomposition (see for instance [4]). Gallium Orthophosphate and Langasite have both been used for high temperature purposes and revealed their robustness at temperature in excess of 800°C. The main point is that the SAW devices built on such materials suffer from important degradation when exposed for several tens of hours to temperature in excess of 600°C [3][4].

On the other hand, Aluminum Nitride (like all III-V nitrides) exhibits a high thermal conductivity and a high stability at elevated temperatures. Patel et al. [1] were able to measure an ultrasonic response of AlN at temperatures up to 1150°C, whereas a constant signal strength was observed up to 900°C. AlN exhibits the highest bulk acoustic wave velocity of all known piezoelectric materials, as well as an electromechanical coupling high enough for the generation of high overtones in HBAR structures. The basic idea then is to use such a structure which does not suffer from electrode fragility as it is the case for SAW to operate it at temperature in excess of 600°C. Platinum was considered specifically here as top and bottom electrodes because of its compatibility with high quality AlN deposition and its well known resilience to temperature.

B. Device characteristics

The schematic cross section with the specific stack details of this kind of HBAR is given in Figure 1 as well as the metallization layers and thicknesses. For the processing of the layers themselves, standard processes as described in section III where the buried electrode and top electrode layers were vapor deposited and the transducer layer was sputtered. A standard (100) silicon substrate was used for this type of HBAR. The main electrode layouts are also depicted in Figure 1. The top electrode was not protected anyhow as there were no fine electrode design structures but only plain surface area.

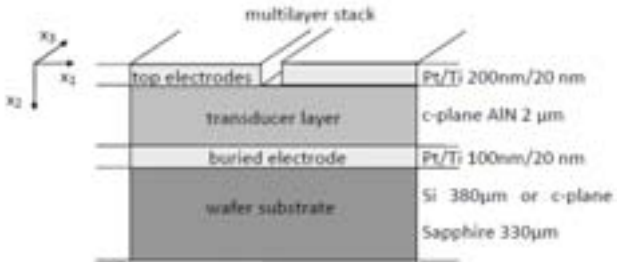

Figure 1 Scheme of HBAR stack structure with design and material parameters for the specific stack used in this work

III. FABRICATION OF THE RESONATORS

AlN-based HBARs have been manufactured in a Sigma-Trikon sputtering machine, depositing 1µm thick layers onto a (111) Ti/Pt backside electrode deposited atop 530µm thick Sapphire and 400µm thick Silicon substrates. The qualitative observation of the layer (**Figure 2**) indicates a dense layer with the expected textured columnar structure.

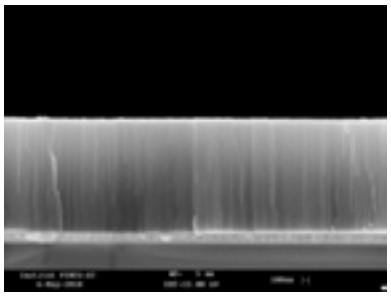

Figure 2 SEM observation of the trench of an AlN layer deposited on a Ti/Pt electrode on silicon

The Ti/Pt bottom electrode was deposited by sputtering and then thermally annealed to obtain proper orientation promoting the AlN deposition. This thermal process was achieved in the sputtering machine just before the AlN deposition to minimize potential surface pollution. Figure 3 shows a view of the devices after top electrode patterning. Although these devices were built for double-port laterally coupled HBAR application, they could be used without difficulties as single port resonators by simply leaving one of the port open.

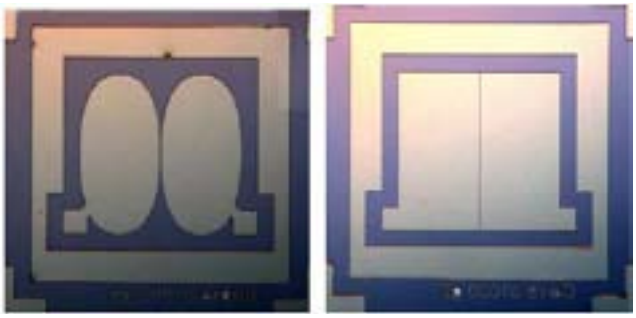

Figure 3 Photos of two top electrode designs for the manufactured HBAR devices, here, devices processed atop c-plane AlN on (100) silicon

IV. EXPERIMENTAL CHARACTERIZATION OF HBAR AT HIGH TEMPERATURE

The classical figure of HBAR response was observed, with a frequency separation of about 8 to 9 MHz depending on the substrate and a maximum resonance of the layer alone near 2 GHz. The resonances between 400 and 500 MHz (close to the 434 MHz centered ISM band) have been focused for assessing the operation of the devices versus temperature. The devices were first exposed to 500°C for tempering the platinum layer and for the following high-temperature measurements at 600°C and 800°C (along the profile of **Figure 4**), the different devices and their frequency characteristics were measured afterwards and evaluated in comparison to un-tempered devices.

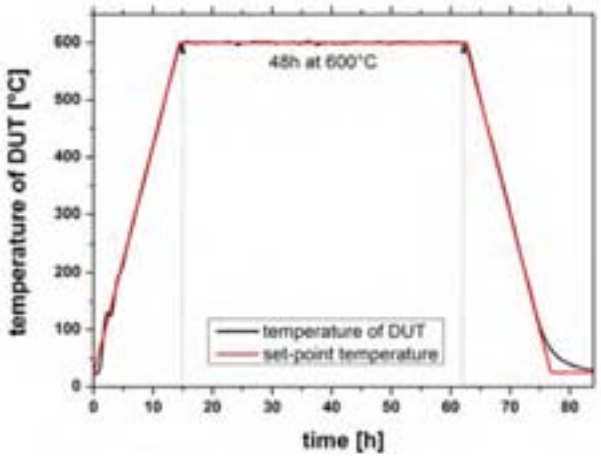

Figure 4 Temperature profile for the characterization of the temperature behavior and stability, the set-point temperature measured by a PT100 is the oven temperature

The on-wafer level measured conductance of the two test designs of HBARs are shown in Figure 5. In the frequency band of interest from 400 to 450 MHz (including the 433MHz-centered ISM band), five well-defined longitudinal mode signatures are observed as well as six very weak signals attributed to shear polarized modes. The resonance frequency of the different modes of one device at one frequency clearly does not change before and after being exposed to 600°C for 48h. Only the amplitude as a figure for the quality factor decreased, possibly due to thermal induced defects at the interfaces between the transducer, layer adhesion and the device surface degradation (not protected during the tests).

During the this first temperature test up to 600°C, the devices were continuously measured by acquiring the resonance frequency measuring the S_{11} parameters automatically every 15 min. using a specific but un-calibrated high-temperature resistant device holder. Therefore one recognizes a varying frequency dependant offset of electrical parasitic effects (see Figure 6).

As the devices did operate well during the whole thermo cycle, the characterization experiment has been extended to 800°C. The devices were heated-up to 800°C and hold at this temperature again for 48h and cooled-down to room-temperature. Comparing the linearity of the frequency of the heating-up phase to the cooling down phase, the frequency shift is about 110 kHz. This corresponds to relative aging rate of 5.3 ppm per hour at 800°C. The linearity during heat-up and cool-down phases and the steadiness of the resonance frequency at the maximum temperature during the hold phase were also evaluated. The results are shown in Figure 7. The temperature coefficient of the frequency (TCF, in some way the sensor "sensitivity") was measured as shown in Figure 8. The TCF then is estimated between -40 and -42 ppm/K for the complete temperature range and -49 ppm/K at 800°C.

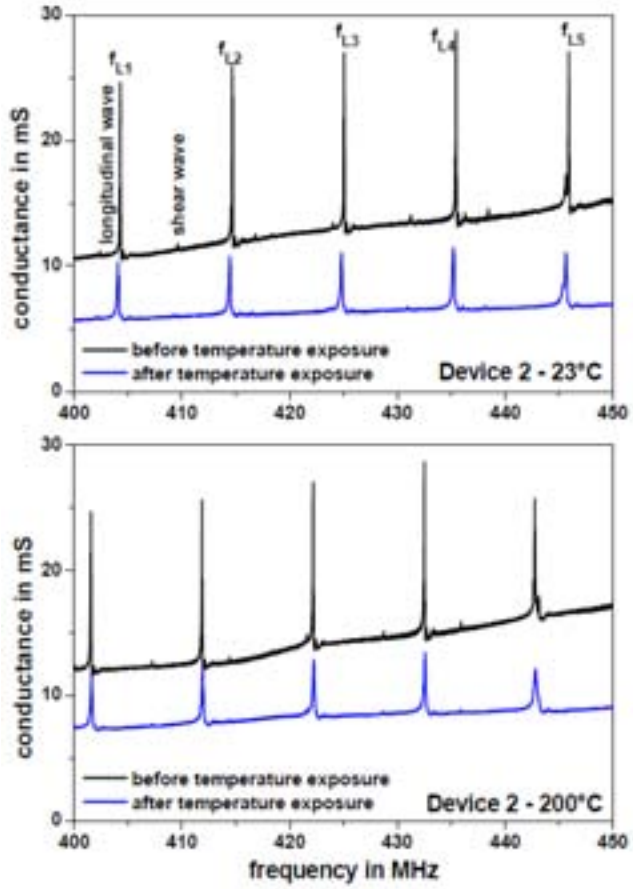

Figure 5 On-wafer measured conductance of the tested HBARs before and after being exposed to 600°C for 48h at room condition and 200°C

At platinum surfaces, as shown in Figure 9, minimal de-wetting effects in form of single droplets atop the surface are observable, showing that the (111) orientation is not fully homogeneous but the lattice is stable enough to withstand the temperature induced tensions as the thermal grooving and the resulting forming of droplets leaving micro cavities in the metallization layer is limited.

VI Conclusion

It has been demonstrated that AlN/Si-based HBARs with Ti-Pt electrodes are capable to operate at temperature up to 800°C for several tens of hours. Some signal characteristics are of course observed as the direct observation of the device reveals obvious but limited defects compared to SAW devices operated at such temperature. The importance of an initial tempering process (electrode annealing) has been emphasized to keep a stable device response on the whole temperature range. An almost linear average TCF was measured near -45 ppm.K^{-1} representative of Silicon thermal sensitivity. Furthermore, as the use of HBAR for wireless applications was already reported, future work will be engaged to develop remotely controlled passive sensors based on the presented principles.

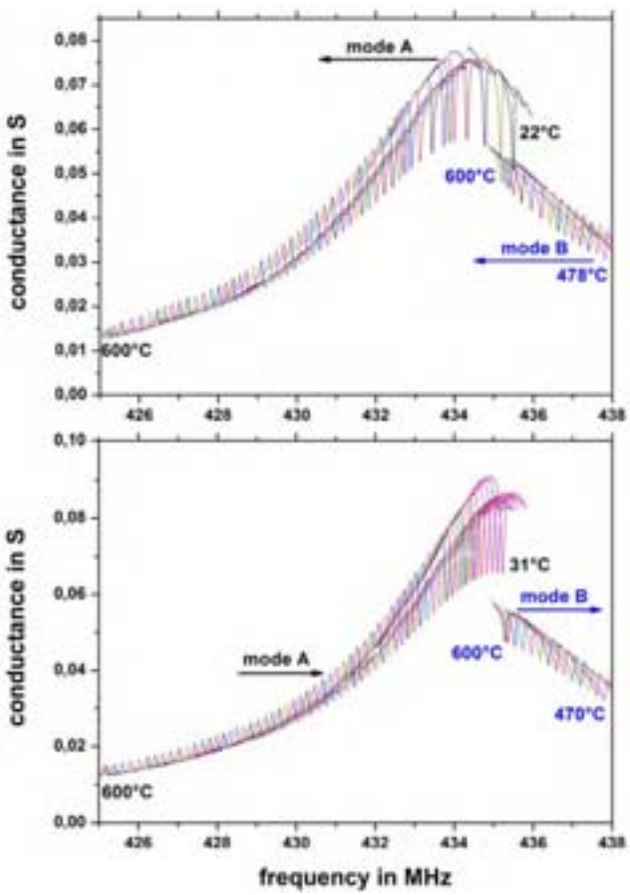

Figure 6 Measured conductance of a test HBAR during heating-up to 600°C (upper graph) Measured conductance of a test HBAR during heating-up to 600°C (upper graph) and cooling down again to room temperature (lower graph) around the 433 MHz ISM band showing two different modes marked as A and B. The flashes indicate the direction in dependence of the temperature gradient

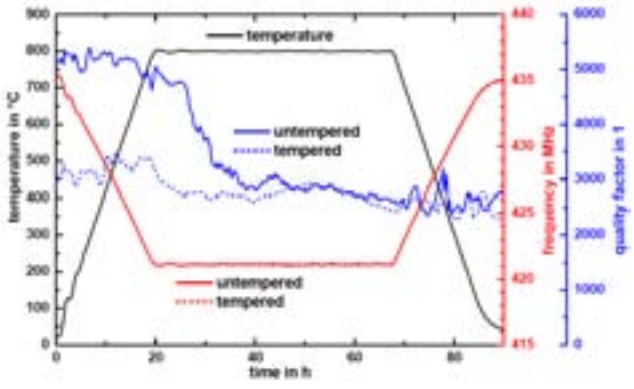

Figure 7 Frequency response and quality factor of un-tempered and tempered HBAR test devices versus time during a measurement cycle of 90 hours with a rising temperature up to 800°C. The quality factor of the tempered devices decreases by a value of about 800 whereas for the un-tempered device the value decreases by 2500

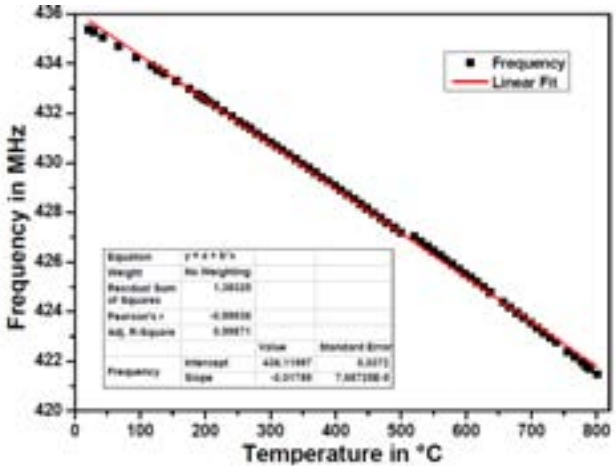

Figure 8 Measured device frequency characteristics of the test device up to 800°C resonance frequency in dependence of temperature with the corresponding linear fit, evaluating the frequency-temperature behavior and its linearity

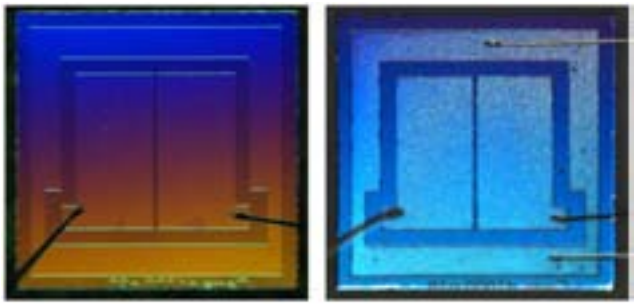

Figure 9 Differential interference contrast LM-micrographs for a visualized surface topography of test devices exposed to temperature. Left-hand side: after being exposed for to 600°C for 48h. Right-hand side: after being exposed to 800°C for 48h.

ACKNOWLEDGMENT

The authors are grateful to Prof. Paul Muralt (Ceramic Laboratory – EPFL) for his advices when developing the AlN deposition process at FEMTO-ST.

This work was partly supported by the french RENATECH network and its FEMTO-ST technological facility.

REFERENCES

[1] N. D. Patel, P. S. Nicholson, "High-frequency, high-temperature ultrasonic transducers," Ndt International, vol. 23, pp. 262–266, 1990.

[2] S. Ballandras et al, "High overtone Bulk Acoustic Resonators built on single crystal stacks for sensors applications" Proc. of IEEE Sensors Conference, pp.516-519, 2011

[3] I. Shrena et al, "SAW-relevant material properties of langasite in the temperature range from 25 to 750 °C: New experimental results," Proc. of the Ultrasonics Symposium, pp.209-212, 2008

[4] R. Fachberger et al, "Applicability of LiNbO3, langasite and GaPO4 in high temperature SAW sensors operating at radio frequencies," IEEE Transactions on UFFC, vol. 51, no. 11, pp. 1427–1431, 2004.

Langatate Temperature-Compensated BAW Orientations Identified Using High-Temperature Constants

Peter Davulis, Mauricio Pereira da Cunha
Electrical and Computer Engineering Dept., University of Maine, Orono, ME, USA
Email: mdacunha@maine.edu

***Abstract*— LGT BAW orientations are investigated up to 900°C for temperature-compensated orientations targeting harsh-environment applications. The study utilizes recently published LGT elastic, piezoelectric, and dielectric constants extracted by the authors using resonant ultrasound spectroscopy (RUS) up to 900°C based on the resonances of bulk crystal samples. Temperature-compensated LGT BAW orientations have been identified for operation at high temperatures. The orientations disclosed in this work have turnover temperatures between 100°C and 550°C for the one quasi-shear mode and up to 150°C for the other quasi-shear mode. Additionally, orientations were identified with pure transverse-shear modes that are selectively excitable and have temperature compensation up to 550°C. These orientations can be readily applied for both frequency control and sensor applications in harsh environments.**

Keywords—Langatate, BAW, high temperature, temperature compensation

I. INTRODUCTION

There is a growing demand for high-temperature (>200°C) sensors and frequency control devices. Langatate (LGT) crystal is a prime candidate substrate for surface acoustic wave (SAW) and bulk acoustic wave (BAW) devices to address high-temperature sensing applications due to demonstrated harsh-environment operation and the availability of recently published acoustic wave constants up to 900°C [1]-[4]. While prior work by the authors on LGT has focused on orientations for high-temperature SAW devices [1], LGT BAW devices capable of operating in harsh-environments also have very attractive applications, such as deposition rate monitoring; high-temperature timing devices; gas, chemical, and physical sensors.

While temperature compensated langasite (LGS) BAW orientations have been reported using extracted LGS constants up to 900°C [5], no such study has been reported on LGT due to the absence of high-temperature constants. Langatate orientations were investigated in [6] for temperature-compensated length extensional, flexural, and torsional cylinder resonators up to 250°C, although the study utilized constants extracted below 150°C from [7], [8] for their predictions. Temperature-compensated thickness shear BAW orientations were predicted to several hundred degrees Celsius in [9] using constants extracted below 150°C [8]. Selected rotated Y-cut BAW orientations were fabricated using LGT crystals grown by Yu, et al., with experimentally identified turnover temperatures as high as 350°C [9], [10].

In this work, LGT BAW orientations are investigated up to 900°C for temperature-compensated orientations targeting harsh-environment applications. In order to predict the high-temperature properties of BAW devices, this study utilizes recently published LGT elastic, piezoelectric, and dielectric constants extracted by the authors using resonant ultrasound spectroscopy (RUS) up to 900°C [3], [4] and the thermal expansion and density up to 1200°C from [11]. These constants and temperature coefficients were validated by high-temperature SAW device measurements in [1], [3], [4], thus suggesting adequate prediction of the BAW properties including turnover temperatures.

Temperature-compensated LGT BAW orientations were investigated based on the analysis of the temperature coefficient of frequency (TCF), the turnover temperature (TCF=0) and the piezoelectric coupling for both thickness-field and lateral-field excitation of the three bulk wave modes. Turnover temperature orientations were identified for both quasi-shear (*QS*) BAWs. Turnover temperatures up to 150°C have been predicted in this work for one of the QS modes, and identified between 100°C and 550° for the other. For this second quasi-shear mode the turnover temperatures are mapped with respect to the crystallographic angles, thus allowing the selection of an orientation with a particular turnover temperature within the range mentioned above. In addition, pure-shear (*PS*) orientations, important for sensor and frequency control applications, are also reported with turnover temperatures up to 550°C.

The LGT BAW properties investigated and the calculation method used are described in Section II. Section III presents LGT BAW orientations and respective properties for high-temperature harsh-environment applications. Section IV discusses pure-shear LGT orientations that are temperature compensated at high temperature. Section V concludes the paper.

II. CALCULATION PROCEDURE & NOMENCLATURE

The identification of BAW orientations for high-temperature operation involved the calculation and analysis of the phase velocity, temperature coefficient of frequency (TCF), thickness field excitation (TFE) piezoelectric coupling (k_{TE})

This work is supported by U.S. Department of Energy Award #: DE-FE0007379TDD. A disclaimer statement is included in the Acknowledgement Section as required by the sponsor.

using the process described in [12], [13], and lateral field excitation (LFE) piezoelectric coupling (k_{LE}) using the procedure outlined in [14]. For each mode there is a single value of k_{TE} but k_{LE} depends on the angle of the lateral electric field [14]. Therefore the lateral-excitation coupling is calculated by rotating the electric field around the cut plane. For the rotated Cartesian coordinate system, using Euler Angles nomenclature, and assuming propagation along the X''' axis, the angle of the lateral electric field, $\Psi_E = 0°$, is defined as coincident with the rotated Y''' axis, and Ψ_E increases in going from the positive Y''' axis towards the positive Z''' axis in the plane normal to propagation. In this work, unless otherwise specified, the k_{LE} given for a particular mode is the maximum lateral field coupling for the orientation found by sweeping Ψ_E.

The BAW properties were calculated for each of the three BAW modes: (*QL*) quasi-longitudinal, (*QS1*) first quasi-shear, and (*QS2*) second quasi-shear. The denomination "quasi" (*Q*) is dropped along orientations where pure shear or pure longitudinal modes take place. The modes are ordered in this work by the eigenvectors (particle polarization) [12], [13], and not by velocity [15]. For this reason the nomenclature "first" and "second" quasi-shear modes were selected, since *QS1*, for instance, can start as the fast shear mode in a plane sweep and then turn into the slow shear mode, after the mode velocities cross each other (mode degeneracy orientation).

The BAW orientations can be given by (YXwl)φ,θ in the BAW rotated plate nomenclature [15], [16] or by [φ, θ, ψ] = [φ, θ, 90°] in Euler angle notation [16]. The BAW properties were calculated in this work for a range of orientations by sweeping the angles 0°≤φ≤60° and −90°≤θ≤90°. These calculations were performed at every 100°C between 100°C and 900°C, and sometimes at smaller temperature intervals. The TCF was numerically determined from the discrete derivatives calculated 5°C above and below the target temperature.

III. LGT BAW High-Temperature Performance

The BAW TCF calculations for the three BAW modes from 100°C to 900°C along LGT [φ, θ, 90°] revealed temperature-compensated orientations for modes *QS1* and *QS2*, but not for the *QL* mode. The *QS2* mode was found to have TCF=0 orientations as high as 550°C and the *QS1* mode had TCF=0 orientations up to 150°C. The k_{TE}, k_{LE}, and TCF are plotted for the *QS1* mode at 150°C in Fig. 1, and for the *QS2* mode at 550°C in Fig. 2.

For the *QS1* mode, LGT orientations in the range [0°≤φ≤5°, −15°≤θ≤0°, 90°], and [55°≤φ≤60°, 0°≤θ≤15°, 90°] were identified with TCF=0 at 150°C, the highest turnover temperature found for this mode. Along these orientations, k_{TE} is less than 0.04. However, k_{LE} reaches values between 0.06 and 0.08 for this same region.

The k_{TE} and k_{LE} coupling and TCF are plotted for the *QS2* mode at 550°C in Fig. 2. The *QS2*-mode shows values of TCF=0 with k_{TE} of 0.04 to 0.14 and k_{LE} up to 0.1 for each temperature investigated between 100°C and 550°C. The turnover temperatures of the LGT *QS2*-mode are plotted in Fig. 3, showing the orientations with TCF=0 between 100°C and 550°C. This particular plot can be used to select an LGT BAW orientation for a desired turnover temperature. The value k_{TE} and k_{LE} decreased by about 15% from 25°C to 550°C for the orientations shown. Therefore, Figs. 2a and 2b can also be used as a guide for the TFE and LFE coupling at lower temperatures.

For the *QS2* mode, orientations in the range [0°≤ ϕ≤10°, −58°≤θ≤−40°, 90°], and [50°≤φ≤60°, 40°≤θ≤58°, 90°], were identified with TCF=0 at 550°C. These orientations have coupling $0.04 \le k_{TE} \le 0.1$ and $k_{LE} \approx 0.1$; for comparison, SC-cut quartz has coupling of $k_{TE} = 0.051$ and AT-cut quartz can coupling of $k_{TE} = 0.063$ [13], [17] at room temperatures. There are also 550°C turnover temperature orientations in the range [25°≤φ≤35°, 5°≤θ≤5°, 90°] with coupling $k_{LE} \approx 0.14$ and $k_{LE} \le 0.02$.

In addition, the temperature compensated orientations identified experimentally in [9], [10] for the *QS2*-mode on (YXl)θ plates, orientations [0°, θ, 90°], were consistent with predictions made in this work. Measurements of a LGT (YXl) −30° plate, Euler angle [0°, −30°, 90°] in [10] found a turnover temperature at between 350°C and 400°C [10, Fig. 7], slightly lower than turnover temperature of around 450°C predicted in this work (Fig. 3). Additionally, the measured turnover temperature LGT (YXl) −10° plates in [10] were found to be around 250°C, whereas the predicted turnover temperature in this work is 300°C. While the measurements from [10] confirm the existence of the predicted LGT orientations with TCF=0 at high temperature made in this work, the identified discrepancies between the predictions in this work and the reported values from [10] are around 15% and call for investigation to identify the source of these differences. Possible causes for the discrepancies include: constants and temperature coefficients inaccuracies; crystal differences due to different suppliers; crystals or wafers being under stress, crystal cut precision, and measurement inaccuracies.

IV. LGT BAW Orientations with Transverse-Shear Modes

Bulk acoustic wave devices that utilize pure-shear BAW, also labeled as transverse-shear modes (TSM), are useful for frequency control and sensor applications, since this mode is selectively excited without exciting the other BAW modes [17]. In addition, the *PS* BAW is important for sensor applications in which the sensor is exposed to viscous media, since these modes have purely shear particle displacements parallel to the device's surface (no longitudinal component), thus not suffering significant attenuation due to the presence of the media.

The LGT orientations [0°, θ, 90°] are Symmetry 4 orientations [18], where a pure shear stiffened BAW mode (*PS2*) exists and uncouples from the unstiffened *QL* and *QS1* modes. Orientations along this plane can be selected with turnover temperatures between 100°C and 550°C, as observed in Fig. 3. For the LGT BAW orientations [0°, −50°→25°, 90°], the *PS2* mode also possesses $0.06 \le k_{TE} \le 0.14$ at 550°C. For lateral field excitation, the *PS2* mode has maximum k_{LE} when $\Psi_E = 90°$, assuming values $0.05 \le k_{LE} \le 0.1$ at 550°C. Therefore the *PS2* can be strongly and selectively excited on LGT with

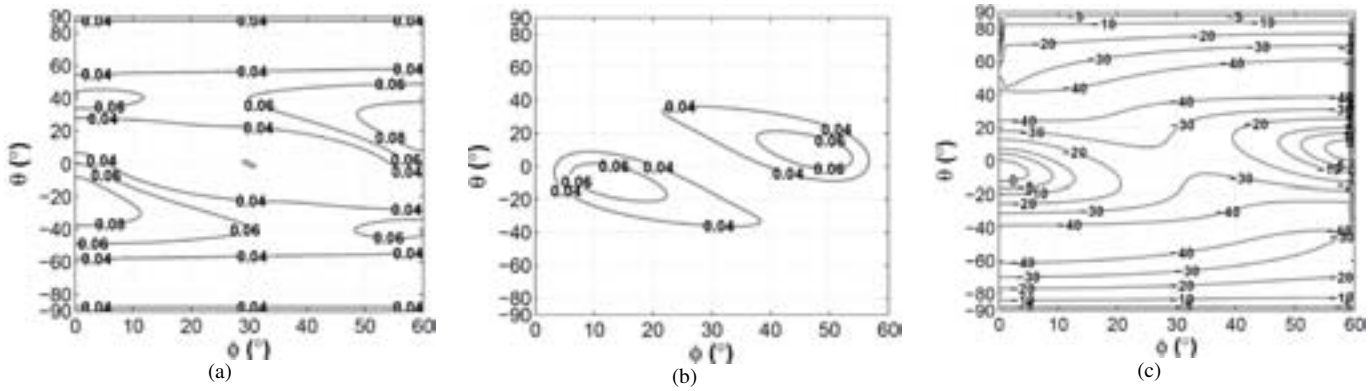

Fig. 1. LGT BAW *QS1* properties at 150°C: (a) max k_{LE} *of the orientation*, (b) k_{TE}, (c) TCF (ppm/°C).

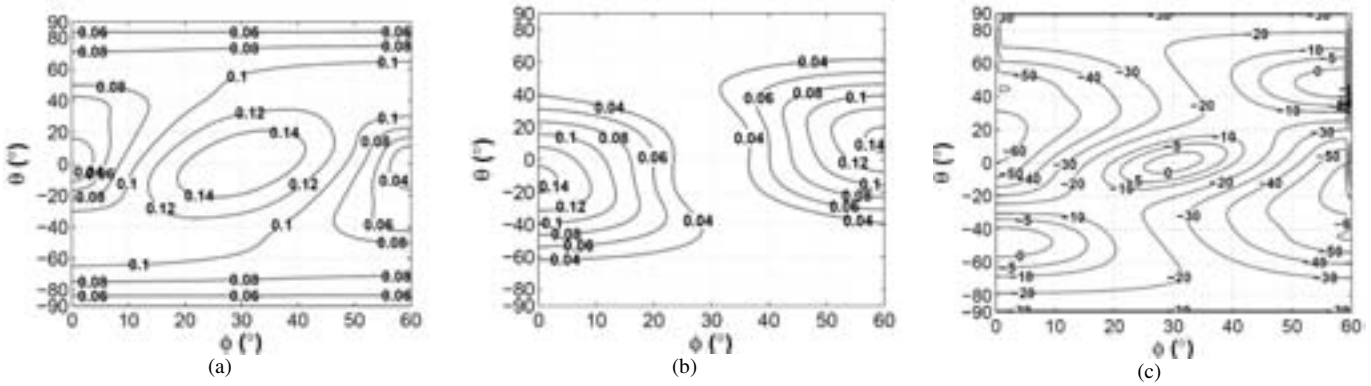

Fig. 2. LGT BAW *QS2* properties at 550°C: (a) max k_{LE} *of the orientation*, (b) k_{TE}, (c) TCF (ppm/°C).

either thickness or lateral electric field excitation along orientations with turnover temperature between 100°C and 550°C.

In addition, modes with a predominantly pure shear particle polarization can be found by searching for quasi-shear modes for which the longitudinal component of the normalized eigenvector is less than 0.01 (i.e. less than 1% of the shear component). Fig. 4 plots the ratio of longitudinal to shear eigenvector components for both *QS1* and *QS2* at room temperature, noting that the eigenvector components do not significantly change for the investigated LGT orientations over the temperature range of 25 to 900°C. Fig. 4 reveals the existence of additional close-to-pure-shear mode orientations with turnover temperatures between 100°C and 550°C. An important observation is that, differently from the Symmetry 4 orientations previously mentioned, these orientations may have significant coupling to more than one mode.

V. CONCLUSIONS

Temperature-compensated LGT BAW orientations have been identified for operation at high temperatures, based on the use of constants extracted up to 900°C and validated by SAW measurements. Orientations with turnover temperatures up to 550°C for the *QS2* mode and up to 150°C for the *QS1* mode have been presented and discussed. Pure transverse-shear mode orientations with temperature compensation up to 550°C have also been disclosed. In addition, the coupling coefficients for both TFE and LFE have been presented at high temperatures. For the *QS2*, in particular, turnover temperature orientations have been mapped between 100°C and 550°C to allow the selection orientations for a targeted turnover temperature. The identified orientations are expected to enable new and diverse high-temperature applications in sensing and frequency control, due to the identified existence of appropriate temperature compensated orientations to suit the particular harsh environment application.

ACKNOWLEDGEMENTS

Disclaimer: This report was prepared as an account of work sponsored by an agency of the United States Government. Neither the United States Government nor any agency thereof, nor any of their employees, makes any warranty, express or implied, or assumes any legal liability or responsibility for the accuracy, completeness, or usefulness of any information, apparatus, product, or process disclosed, or represents that its use would not infringe privately owned rights. Reference herein to any specific commercial product, process, or service by trade name, trademark, manufacturer, or otherwise does not necessarily constitute or imply its endorsement, recommendation, or favoring by the United States Government or any agency thereof. The views and opinions of authors expressed herein do not necessarily state or reflect those of the United States Government or any agency thereof.

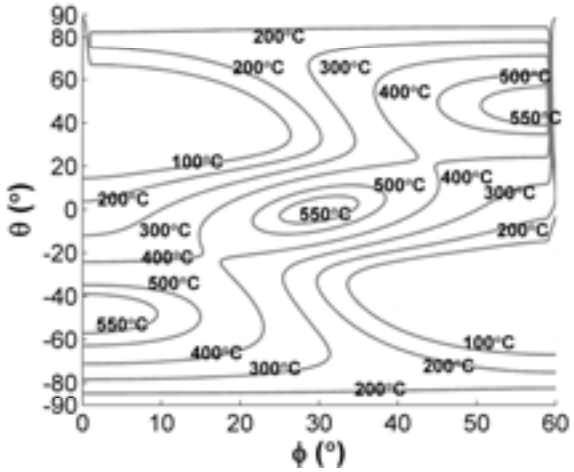

Fig. 3. LGT BAW *QS2* turnover temperatures (°C)

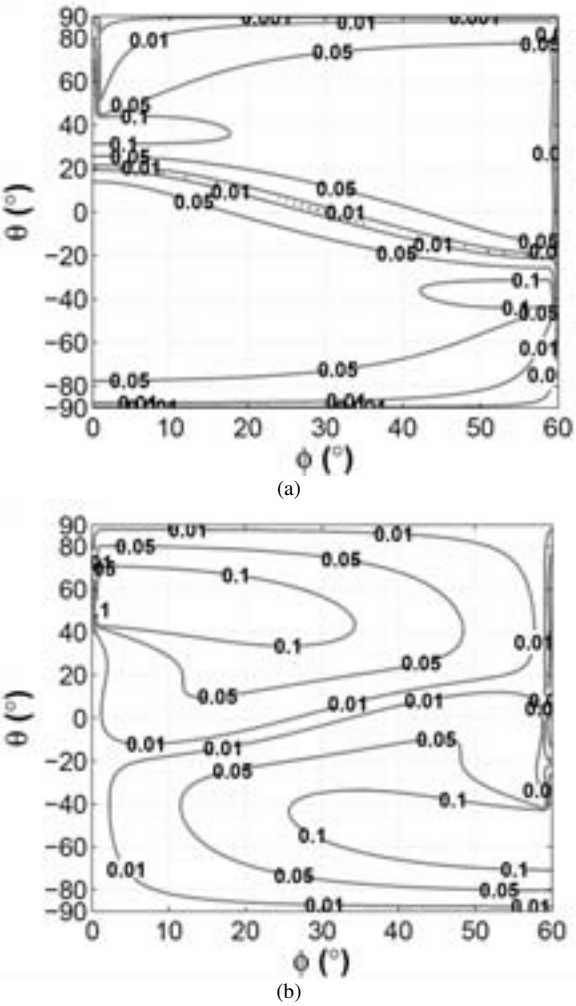

Fig. 4. LGT BAW ratio of longitudinal to shear eigenvector components for (a) QS1 and (b) QS2

REFERENCES

[1] P. Davulis, and M. Pereira da Cunha, "Determination and experimental verification of high-temperature SAW orientations on langatate," *IEEE Trans. on Ultrasonics, Ferroelectrics, and Frequency Control*, vol. 59, no. 2, pp. 287-294, 2012.

[2] P. Davulis, and M. Pereira da Cunha, "Temperature-compensated BAW orientations over 500°C on LGT for frequency control and sensor applications," *Electronics Letters*, vol. 49, no. 3, pp. 170 – 171, 2013.

[3] P. Davulis, and M. Pereira da Cunha, "A full set of langatate high-temperature acoustic wave constants: elastic, piezoelectric, dielectric constants up to 900°C," *IEEE Trans. on Ultrasonics, Ferroelectrics, and Frequency Control*, vol. 60, no. 4, pp. 824-833, 2013.

[4] P. Davulis, "Characterization of the elastic, piezoelectric, and dielectric properties of langatate at high temperatures up to 900°C," Ph.D. dissertation, University of Maine, 2013.

[5] M. Schulz and H. Fritze, "Electromechanical properties of langasite resonators at elevated temperatures," *Renewable Energy*, vol. 33, no. 2, pp. 336 – 41, 2008.

[6] G. Douchet, F. Sthal, E. Bigler, and R. Bourquin, "A comparison of vibrating beam resonators in quartz, GaPO4, LGS and LGT," *Solid State Sciences*, vol. 12, no. 3, pp. 325–332, 2010.

[7] D. C. Malocha, M. Pereira da Cunha, E. Adler, R. C. Smythe, S. Frederick, M. Chou, R. Helmbold, and Y. S. Zhou, "Recent measurements of material constants versus temperature for langatate, langanite and langasite," *Proc. of the 2010 IEEE Int'l Freq. Control Symp.*, pp. 200–205.

[8] R. Bourquin and B. Dulmet, "Thermal sensitivity of elastic coefficients of langasite and langatate," *IEEE Trans. on Ultrasonics, Ferroelectrics, and Frequency Control*, vol. 56, no. 10, pp. 2079–2085, 2009.

[9] F. Yu, X. Zhao, L. Pan, F. Li, D. Yuan, and S. Zhang, "Investigation of zero temperature compensated cuts in langasite-type piezocrystals for high temperature applications," *Journal of Physics D: Applied Physics*, vol. 43, no. 16, p.165402, 2010.

[10] F. P. Yu, D. R. Yuan, X. Zhao, and S. J. Zhang, "Investigation of langanite and langatate single crystals for high temperature sensing," *in 2010 Symp. on Piezo., Acoustic Waves and Dev. App. (SPAWDA)*, pp. 564–569.

[11] T. R. Beaucage, E. P. Beenfeldt, S. A. Speakman, W. D. Porter, E. A. Payzant, and M. Pereira da Cunha, "Comparison of high temperature crystal lattice and bulk thermal expansion measurements of LGT single crystal," *in Proc. of the 2006 IEEE Int'l Freq. Control Symp.*, pp. 658-663.

[12] C.-K. Jen, G. Farnell, E. Adler, and J. Oliverira, "Interactive computer-aided analysis for bulk acoustic waves in materials of arbitrary anisotropy and piezoelectricity," *IEEE Trans. on Sonics and Ultrasonics*, vol. 32, no. 1, pp. 56 –60, 1985.

[13] M. Pereira da Cunha, E. Adler, and D. Malocha, "BAW temperature sensitivity and coupling in langanite," *IEEE Trans. on Ultrasonics, Ferroelectrics and Frequency Control*, vol. 49, no. 5, pp. 656–663, 2002.

[14] J. F. Rosenbaum, *Bulk Acoustic Wave Theory and Devices*. Boston: Artech House, 1988.

[15] A. Ballato, "Doubly rotated thickness mode plate vibrators," in *Physical Acoustics*, New York: Academic, vol. 13, pp. 115–181, 1977

[16] *IEEE standard on piezoelectricity*, ANSI/IEEE Standard 176-1987 Std., 1988.

[17] D. McCann, J. McGann, J. Parks, D. Frankel, M. Pereira da Cunha, and J. Vetelino, "A lateral-field-excited $LiTaO_3$ high-frequency bulk acoustic wave sensor," *IEEE Trans. on Ultrasonics, Ferroelectrics, and Frequency Control*, vol. 56, no. 4, pp. 779–787, 2009.

[18] G. Farnell and E. Adler, "Elastic wave propagation in thin layers," in *Physical Acoustics*, New York: Academic Press, vol. 9, pp. 35 – 127, 1972

A 30-km-long Optical Fiber Link for Frequency Comparison Between Distant Strontium Optical Lattice Clocks

Tomoya Akatsuka[1,2], Hitomi Ono[1,3], Keitaro Hayashida[1,3], Kuniya Araki[1,3], Masao Takamoto[1,2], Tetsushi Takano[1,3], and Hidetoshi Katori[1,2,3]

[1] Innovative Space-Time Project, ERATO, JST, Tokyo, Japan

[2] Quantum Metrology Laboratory, Advanced Science Institute, RIKEN, Saitama, Japan

[3] Department of Applied Physics, Graduate School of Engineering, The University of Tokyo, Tokyo, Japan

Abstract—**We demonstrate a 30-km-long optical fiber link for frequency comparison between two strontium optical lattice clocks being developed at Riken and the University of Tokyo. We use a transfer laser at 1397 nm which is twice the wavelength of the clock transition of strontium clocks. The link stability is estimated to be 1×10^{-17} for an averaging time $\tau = 1$ s, which is in good agreement with the theoretical limit calculated from the fiber noise spectrum. We discuss a remote clock comparison with stability of $10^{-17}(\tau/s)^{-1/2}$ by synchronously operating the two distant clocks.**

I. Introduction

Recently, frequency comparison between two Sr optical lattice clocks demonstrated the quantum projection noise (QPN) limited stability of a few times $10^{-16}(\tau/s)^{-1/2}$ for an averaging time τ either by operating two clocks synchronously [1] or by using stable clock lasers [2]. Such a high clock stability enables to probe the relativistically-curved space-time in real time. Because of its sensitivity to the gravitational potential, frequency comparison between two clocks operating at distant sites allows monitoring temporal fluctuation of the gravitational potential difference, which can lead to new applications in relativistic geodesy [3,4].

Coherent optical frequency transfer via optical fibers [5] serves as an essential technique for frequency link of accurate optical clocks operating at distant sites, though the link stability may deteriorate as the fiber length increases. The limit of stability is mainly because the actual phase noise in the forward and return paths are not equal due to a finite time delay [6]. The residual one-way phase-noise power spectrum density (PSD) for a stabilized fiber is given by [6]

$$S_\phi^{\mathrm{stab}}(f) = (1/3)\,(2\pi f\tau_d)^2\, S_\phi^{\mathrm{free}}(f) \qquad (1)$$

for the Fourier frequency $f < 1/(4\tau_d)$. Here $S_\phi^{\mathrm{free}}(f)$ is the one-way phase-noise PSD for a free-running fiber. Assuming the fiber noise to be uncorrelated with position, $S_\phi^{\mathrm{free}}(f)$ is estimated to be [7]

$$S_\phi^{\mathrm{free}}(f) = \{2[1+\mathrm{sinc}(4\pi f\tau_d)]\}^{-1}\, S_\phi^{\mathrm{free,RT}}(f) \qquad (2)$$

by measuring the round-trip phase-noise PSD with free-running fiber $S_\phi^{\mathrm{free,RT}}(f)$. As the free-running fiber noise is proportional to the fiber length L [7], the residual fiber noise with stabilization $S_\phi^{\mathrm{stab}}(f)$ increases as L^3 by (1).

In order to demonstrate frequency comparison between distant clocks at the stability of $10^{-17}(\tau/s)^{-1/2}$, we have developed a 30-km-long optical fiber link between Riken and the University of Tokyo. According to the fiber noise spectrum measurement, the theoretical limit of the link stability is calculated to be 1×10^{-17} at 1 s. We partly confirm the link stability by implementing a 60-km-long fiber link which includes the 30-km-long fiber. We discuss about the synchronous operation of two distant clocks that will allow measuring clock shift with $10^{-17}(\tau/s)^{-1/2}$ stability.

Since we focus on frequency comparison between two Sr optical lattice clocks operating with 698 nm clock lasers, we implemented a novel scheme utilizing a 1397 nm transfer light which directly links to the clock frequency by the second harmonic generation (SHG) without the help of optical frequency combs. The water-peak attenuation due to the presence of OH radical in the fiber core material centers at around 1383 nm [8] and is not a serious problem for fiber length up to ~60 km (typically 0.2 dB/km at 1397 nm). OH-free fiber is expected to become more popular for coarse wavelength division multiplexing (CWDM) applications [8], which allows extending the frequency transfer at 1397 nm to longer distances. Our transfer scheme will provide a convenient and simple platform for networking Sr optical lattice clock which has become the most widespread optical clock around the world.

II. Experiment

A. 30-km-long optical fiber link between Riken and UT

A schematic of the experimental setup of 30-km-long optical fiber link is shown in Fig. 1. Two clock lasers at 698 nm for Sr optical lattice clocks were developed at Riken (local site) and the University of Tokyo (UT, remote site), a line-of-sight distance between which is 15 km. They were stabilized to high finesse cavities made of ultralow-expansion (ULE) glasses. A transfer laser at 1397 nm was phase locked to the clock laser via SHG by a periodically poled lithium niobate (PPLN) waveguide at the local site (a) and sent to the remote

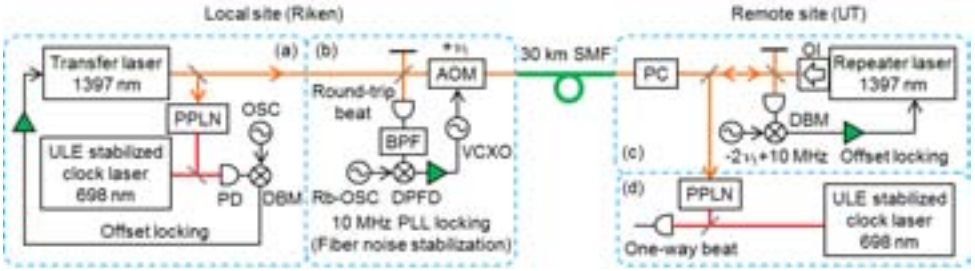

Figure 1. Experimental setup of 30-km-long optical fiber link. A transfer laser at 1397 nm was phase locked to the clock laser at the local site (a) and sent to the remote site. At the remote site, a repeater laser was offset locked to the received signal (c) and was sent back to the local site to measure round-trip fiber noise by a Michelson interferometer (b). A part of the repeater laser is frequency doubled to measure a beat signal with a clock laser at the remote site (d). PPLN, periodically poled lithium niobate waveguide; AOM, acousto-optic modulator; SMF, single-mode optical fiber; PD, photo diode; DBM, double balanced mixer; DPFD, digital phase-frequency discriminator; BPF, band-pass filter; OSC, RF oscillator; OI, optical isolator; VCXO, voltage controlled crystal oscillator; PLL, phase-locked loop; and PC, polarization controller.

site through the 30-km-long telecom fiber. The optical transmission loss of the fiber was 30.4 dB, which was 7 dB larger than that measured at 1550 nm partly due to the water-peak attenuation centered at 1383 nm [8]. To compensate the fiber transmission loss, we used a repeater laser at the remote site (c), by which we boosted and sent back the signal to the local site to measure the round-trip fiber noise by a Michelson interferometer (b). The round-trip beat signal was phase compared with a rubidium oscillator by a digital phase-frequency discriminator (DPFD). The obtained phase error signal was fed back to a voltage controlled crystal oscillator (VCXO) that drove an acousto-optic modulator (AOM) to compensate the round-trip fiber noise. The servo bandwidth was limited to $1/(4\tau_d)$ = 1.7 kHz given by the one-way light propagation time τ_d = 0.15 ms for the 30-km-long fiber. A part of the repeater laser is frequency doubled to measure a beat signal with the clock laser at the remote site (d), which can be used to phase lock the clock laser to the repeater laser for synchronous operation of the two optical lattice clocks.

B. 60-km-long optical fiber link

The one-way beat signal obtained in Fig. 1(d) includes phase noise of two clock lasers, which prevents accessing the potential stability of the frequency link. In order to evaluate the link stability experimentally, we implemented a 60-km-long fiber link by connecting two 30-km-long fibers in series at the remote site as shown in Fig. 2 so that we received the transferred light at the local site where we operated the repeater laser. The total optical transmission loss of the fiber was 61 dB. The propagation time of 0.3 ms limited the servo bandwidth of the fiber noise stabilization by about 800 Hz. With the stabilization, the beat signal between the transfer and repeater lasers was measured to evaluate the link stability. The theoretical limit of the stabilized one-way fiber noise should be 8 times larger than that of 30-km-long fiber by (1).

III. RESULTS AND DISCUSSIONS

A. Performance of the optical fiber link

The round-trip phase noise for the 30-km-long fiber was measured by the phase error signal of the round-trip beat signal

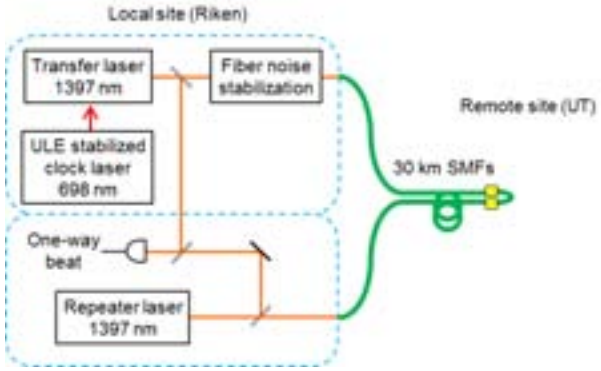

Figure 2. A schematic of a 60-km-long optical fiber link using two 30-km-long fibers connected at the remote site. Both the transfer and repeater laser were operated at the local site, and the link stability was evaluated by measuring a beat signal between them.

(see Fig. 1(b)) as shown in Fig. 3. The $S_\phi^{\text{free,RT}}(f)$ measured at 3 am (b: solid blue line) was an order of magnitude better than that measured at 3 pm (a: solid red line) especially around 100 Hz, which decreased as $S_\phi^{\text{free,RT}}(f) \sim 2\text{x}10^3 f^{-2}$ up to $f < 100$ Hz and decreased even rapidly as f^{-4} for higher frequencies in agreement with observations elsewhere [6]. By activating the PLL for the fiber noise stabilization, the round-trip phase noise was suppressed to the level indicated by the solid black line (c). The residual one-way fiber noise for the stabilized fiber $S_\phi^{\text{stab}}(f)$ at 3 pm and 3 am were calculated by applying (1) and (2) and are shown by dashed red (d) and blue (e) lines, respectively. The solid green line (f) shows the residual one-way fiber noise measured with stabilized 60-km-long fiber at 3 am, which is consistent with the calculation which should be 8 times larger than (e). The dashed green line (g) represents the phase noise of the clock lasers $S_\phi^{\text{laser}}(f) = 0.15\, f^{-3} + 0.02\, f^{-2}$ assuming a thermal noise of the ULE cavities, which corresponds to a frequency stability of $1\text{x}10^{-15}$ at 0.1 s.

Figure 4 shows the fiber link stability evaluated by the modified Allan deviation (MDEV) [9], which was calculated from the one-way beat note (see Fig. 1(d) and Fig. 2) measured by a Λ-type frequency counter with zero dead time (Agilent, 53230A). The open squares (red) and circles (blue) represent

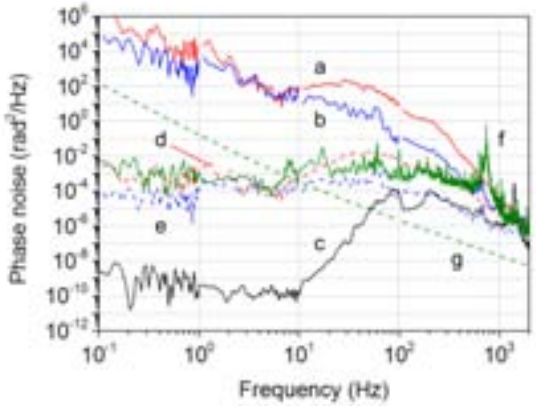

Figure 3. Power spectrum density of the free-running round-trip fiber noise $S_\phi^{\text{free,RT}}(f)$ at 3 pm in the daytime (a: solid red) and at 3 am in the night (b: solid blue) and that of the stabilized round-trip fiber noise (c: solid black). The stabilized one-way fiber noise $S_\phi^{\text{stab}}(f)$ at 3 pm (d: dashed red) and at 3 am (e: dashed blue) were calculated from $S_\phi^{\text{free,RT}}(f)$. The one-way fiber noise measured with stabilized 60-km-long fiber at 3 am (f: solid green) was consistent with the culculation. Phase noise of the clock laser $S_\phi^{\text{lasr}}(f)$ operated at $1\text{x}10^{-15}$ frequency stability at 0.1 s is shown by green dashed-line (g).

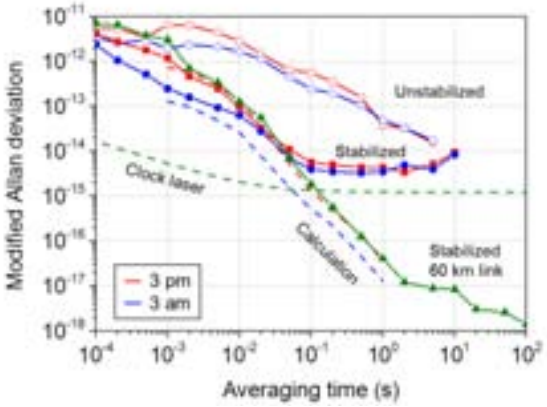

Figure 4. Modified Allan deviations (MDEV) for the fiber link stabilities. Open squares and circles show stabilities of the one-way beat frequency measured with the 30-km-long free-running fiber, while closed ones show that for the stabilized fiber, which include noise of the clock lasers. Those measured at 3 pm and 3 am are shown in red and blue, respectively. Corresponding MDEVs calculated from the one-way fiber noise $S_\phi^{\text{stab}}(f)$ are shown by dashed lines. Closed triangles (green) show the stability of the 60-km-long fiber link at 3 am. The thermal noise limit of clock lasers calculated from $S_\phi^{\text{laser}}(f)$ is shown by a dashed green line.

the stabilities for the free-running 30-km-long fiber at 3 pm and 3 am, respectively, while the closed ones represent those for the stabilized fiber. The MDEV calculated from the estimated one-way fiber noise $S_\phi^{\text{stab}}(f)$ at 3 pm and 3 am (as given in Fig. 3(d) and (e)) are shown by the dashed red and blue lines, which have $\tau^{-3/2}$ slopes for the averaging time $\tau > 0.01$ s because of their white phase noise features for $f < 100$ Hz and reached a few times of 10^{-17} at 1 s. The measured stabilities deviate from the calculated ones for $\tau > 0.1$ s and reach a floor, which is mainly set by the thermal noise of the clock lasers especially for $f < 10$ Hz as shown in Fig. 3(g). The dashed green line in Fig. 4 shows the stabilities of the two clock lasers assuming $S_\phi^{\text{laser}}(f)$, which reasonably explains the measured stability floor. The closed green triangles represent the stability of the 60-km-long fiber link at 3 am, which decreases as $4\text{x}10^{-17}\tau^{-3/2}$ for the averaging time up to $\tau < 2$ s. It corresponds to $1.4\text{x}10^{-17}\tau^{-3/2}$ for the 30 km one-way stability and is in good agreement with the calculation (dashed blue line). For longer averaging time $\tau > 2$ s the MDEV has $\tau^{-1/2}$ slope, which is possibly responsible for the white frequency noise caused by mechanical instability of the heterodyne interferometer.

B. Application to remote clock comparison

We have established a frequency link as stable as $1\text{x}10^{-17}$ at 1 s. The actual stability for clock comparison, however, may be severely limited by the stability of atomic clocks that is about $10^{-16}(\tau/\text{s})^{-1/2}$ even with the best clocks available to date [2]. Here we discuss about synchronous operation [1] of two remote clocks to fully exploit the link stability. We speculate that frequency comparison with stability of $10^{-17}(\tau/\text{s})^{-1/2}$ will be achievable with a clock laser having $1\text{x}10^{-16}$ stability at 1 s. The scheme, therefore, allows comparing two remote clocks at 10^{-18} uncertainty in about 100 s, which will find applications in relativistic geodesy to measure 1 cm height differences every 100 s.

Consider a clock operation with an interrogation time $T_\text{i} = 0.5$ up to 2 s that is well supported by a clock laser having $1\text{x}10^{-16}$ stability at 1 s. Correspondingly, we assume a cycle time $T_\text{c} = T_\text{i} + 0.5$ s, where 0.5 s includes atom loading and state manipulation time. Allan deviation (ADEV) for the clock stability at the QPN limit is given by

$$\sigma_\text{y}^{\text{QPN}}(\tau) = (\gamma/\nu_0\kappa)(T_\text{c}/N\tau)^{1/2}, \quad (3)$$

where $\gamma = 0.8/T_\text{i}$ is the full-width at half-maximum (FWHM) linewidth of the Rabi spectrum, N is the number of interrogated atoms in a cycle, and κ is a coefficient around 1 for Rabi excitation.

In optical lattice clocks that interrogate a large number of atoms, the most severe constraint on the clock stability is imposed by the Dick effect [1]. ADEV for the Dick effect limit is given by [10]

$$\sigma_\text{y}^{\text{Dick}}(\tau) = \Sigma_\text{n}\,[(g_n^{\text{s}}/g_0)^2 + (g_n^{\text{c}}/g_0)^2]\,S_y(n/T_\text{c})\,(\tau/\text{s})^{-1}]^{1/2} \quad (4)$$

where $g_n^{\text{s,c}}$ and g_0 are the Fourier coefficients for sine and cosine components and the mean value of the sensitivity function for the clock sequence, and $S_y(n/T_\text{c})$ is the PSD of fractional frequency noise of the clock laser sampled at frequencies n/T_c with integer n. As both the QPN and the Dick effect introduce white frequency noise on the clock frequency, the clock stability shows $\tau^{-1/2}$ dependence on averaging time τ either in ADEV or MDEV but with a factor of 2 difference [9].

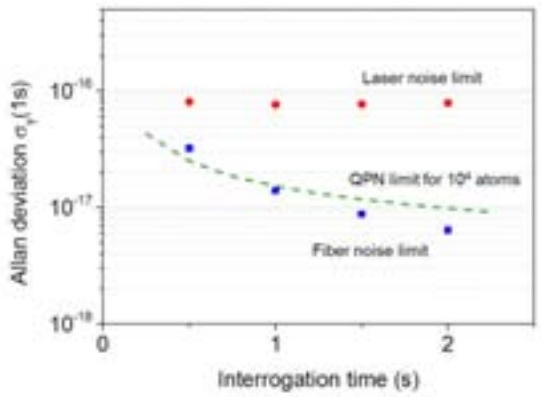

Figure 5. Clock stabilities at an averaging time of 1 s as a function of the interrogation time T_i, assuming a cycle time $T_c = T_i + 0.5$ s. Dick effects are calculated for a laser noise with frequency stability of 10^{-16} (circles) and for the white phase noise of the fiber (squares). Dashed line indicates QPN limit with $N = 10^4$ atoms.

Figure 5 shows the clock stability at $\tau = 1$ s as a function of the interrogation time T_i. Red circles assume a laser nose corresponding to the laser stability of $1\text{x}10^{-16}$ at 0.1 s. It is noteworthy that the clock stability of $0.8\text{x}10^{-16}$ is nearly independent of the interrogation time as frequency noise components lower than $1/T_i$ predominantly determine the Dick effect limit. Blue squares show the Dick effect limit assuming the white phase noise $S_\phi = 1.5\text{x}10^{-4}$ (see Fig. 3(e)) of the fiber at 3 am. As a result of the white phase noise character of the fiber, the longer T_i successfully improves the stability, which reaches $6\text{x}10^{-18}$ for $T_i = 2$ s. It would, therefore, be ideal if we could compare the clocks by rejecting the frequency noise of the clock laser. In addition, in order to set the QPN limit below the Dick effect limit of the fiber, $N = 10^4$ atoms need to be interrogated in a cycle, which is well within the reach of the experiments.

Figure 6 depicts a schematic of the frequency comparison between synchronously operated clocks. A clock laser at a remote site is generated by frequency doubling the repeater laser. Atoms at both sites are thus synchronously interrogated by the local clock laser $f_0(t)$ by taking a time delay τ_d at the remote clock, then the two clocks are independently stabilized by steering AOMs by applying correction frequencies $\delta f_{LO}(t_n)$ and $\delta f_{RE}(t_n+\tau_d)$ for local and remote clocks, respectively, after n-th interrogation period at $t = t_n$. By communicating data series $\delta f_{LO}(t_n)$ and $\delta f_{RE}(t_n+\tau_d)$ via a global area network, the clock shift is obtained as $\Delta\nu(t_n) = \delta f_{RE}(t_n+\tau_d) - \delta f_{LO}(t_n)$. In this scheme, stability of the frequency comparison is solely limited by the Dick effect originating from the residual fiber noise as shown by blue squares in Fig. 5 as long as the QPN (dashed line) is small enough. The stability improves as $\sim 1/T_i$ and can be better than $10^{-17}(\tau/\text{s})^{-1/2}$ for $T_i > 1.5$ s.

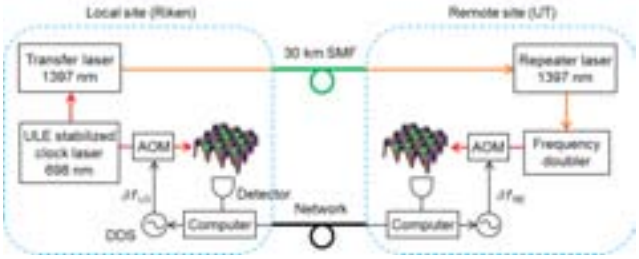

Figure 6. A schematic of frequency comparison of synchronously operated optical lattice clocks via fiber link. A clock laser at the remote site is phase locked to that in the local site. Correction frequencies for AOMs, $\delta f_{LO}(t_n)$ and $\delta f_{RE}(t_n+\tau_d)$, are exchanged via a global area network. Clock shift is given by $\Delta\nu(t_n) = \delta f_{RE}(t_n+\tau_d) - \delta f_{LO}(t_n)$. DDS, direct digital synthesizer.

ACKNOWLEDGMENT

This research was supported in part by the Photon Frontier Network Program of the Ministry of Education, Culture, Sports, Science and Technology and by the Japan Society for the Promotion of Science through its FIRST program.

REFERENCES

[1] M. Takamoto, T. Takano, and H. Katori, "Frequency comparison of optical lattice clocks beyond the Dick limit," Nat. Photon. vol. 5, pp. 288–292, 2011.

[2] T. L. Nicholson, M. J. Martin, J. R. Williams, B. J. Bloom, M. Bishof, M. D. Swallows, S. L. Campbell, and J. Ye, "Comparison of two independent Sr optical clocks with $1\text{x}10^{-17}$ stability at 10^3 s," Phys. Rev. Lett. vol. 109, pp. 230801, 2012.

[3] A. Bjerhammar, "On a relativistic geodesy," Bull. Géod. vol. 59, pp. 207–220, 1985.

[4] H. Katori, "Optical lattice clocks and quantum metrology," Nat. Photon. vol. 5, pp. 203–210, 2011.

[5] L.-S. Ma, P. Jungner, J. Ye, and J. L. Hall, "Delivering the same optical frequency at two places: accurate cancellation of phase noise introduced by an optical fiber or other time-varying path," Opt. Lett. vol. 19, pp. 1777–1779, 1994.

[6] N. R. Newbury, P. A. Williams, and W. C. Swann, ``Coherent transfer of an optical carrier over 251 km," Opt. Lett. vol. 32, pp. 3056–3058, 2007.

[7] P. A. Williams, W. C. Swann, and N. R. Newbury, "High-stability transfer of an optical frequency over long fiber-optic links," J. Opt. Soc. Am. B vol. 25, pp. 1284–1293, 2008.

[8] Y. Chigusa, Y. Yamamoto, T. Yokokawa, T. Sasaki, T. Taru, M. Hirano, M. Kakui, M. Onishi, and E. Sasaoka, "Low-loss pure-silica-core fibers and their possible impact on transmission systems," J. Lightw. Technol. vol. 23, pp. 3541–3550, 2005.

[9] E. Rubiola, "On the measurement of frequency and of its sample variance with high-resolution counters," Rev. Sci. Instrum. vol. 76, pp. 054703, 2005.

[10] G. Santarelli, C. Audoin, A. Makdissi, P. Laurent, G. J. Dick, and A. Clairon, "Frequency stability degradation of an oscillator slaved to a periodically interrogated atomic resonator," IEEE Trans. Ultrason. Ferroelec. Freq. Cont. vol. 45, pp. 887–894, 1998.

Optical Frequency Transfer Over a Single-Span 1840-km Fiber Link

Stefan Droste, Thomas Udem,
Theodor W. Hänsch, Ronald Holzwarth
Max-Planck-Institut für Quantenoptik
Hans-Kopfermann-Str. 1
85748 Garching, Germany
Email: stefan.droste@mpq.mpg.de

Filip Ozimek, Sebastian Raupach,
Harald Schnatz, Gesine Grosche
Physikalisch-Technische Bundesanstalt
Bundesallee 100
38116 Braunschweig, Germany

***Abstract*—We demonstrate optical frequency transfer over an 1840 km underground optical fiber link using a single-span stabilization. To compensate for more than 420 dB of optical attenuation of the light we use twenty Erbium doped fiber amplifiers along the entire link and two additional fiber Brillouin amplifiers. The good passive stability of our fiber link allows us to reach short term instabilities expressed as the modified Allan deviation of 3×10^{-15} for a gate time τ of 1 s reaching 4×10^{-19} in just 100 s. By comparing the sent and transferred frequencies we find no systematic offset within the statistical uncertainty of about 3×10^{-19}. The spectral noise distribution of our fiber link at low Fourier frequencies leads to a τ^{-2} slope in the modified Allan deviation.**

I. Introduction

The development of optical frequency standards [1], [2] raises a demand for transferring highly stable optical signals over continental distances. Such transfer would enable new experiments in fundamental physics such as in quantum electrodynamics or to verify the constancy of fundamental constants. Also applications in navigation or relativistic geodesy will strongly benefit from those stable frequency references. Besides this, the transfer of highly stable optical signals will be mandatory for a future redefinition of the SI-second based on an optical atomic transition. Well-established satellite-based techniques for frequency comparisons and dissemination do not reach the required stability and accuracy to compare optical clocks. In recent years, optical fiber links have been investigated extensively [3]–[7] and are considered as a possible transfer medium for stable optical signals.

II. Experimental Setup

We investigate an optical frequency transfer over an 1840 km fiber link connecting the Max-Planck-Institut für Quantenoptik (MPQ) and the Physikalisch-Technische Bundesanstalt (PTB). The link spans a significant part of Germany and consists of a dedicated fiber which is set up in a loop configuration with sender and receiver being located at MPQ. We use a commercial cw fiber laser emitting at 1542.5 nm that is stabilized to a high-finesse optical reference cavity made from ultra-low expansion (ULE) material to transfer an optical carrier at 194 THz over the fiber link. To overcome the optical attenuation of more than 420 dB of the light in the fiber we use twenty Erbium-doped fiber amplifiers (EDFA) that are distributed equally along the entire link and a fiber Brillouin amplifier (FBA) [8] at each institute. The EDFAs are remotely controlled by using an amplitude modulated 1310 nm communication signal that is sent simultaneously through the same fiber. Additionally, the EDFAs are fully bi-directional and specially designed for low input signal powers. The fiber link is subject to temperature induced optical path length variations and acoustic noise that impose Doppler frequency shifts on the transmitted signals. An interferometric stabilization scheme similar to the one described in [9] is used to detect and compensate for those Doppler shifts.

In contrast to cascading multiple fiber links where each section is phase stabilized separately [4], [10] we investigate a long-distance fiber link by using a single-span stabilization of the whole 1840 km link. While the latter approach comprises a simpler setup as no stable lasers or intermediate regeneration stations have to be installed and operated along the link, the large propagation delay of the light in the fiber yields a strongly reduced bandwidth for the suppression of fiber-induced noise. The round-trip time of the light for the 1840 km loop is close to 18 ms, limiting the noise suppression bandwidth to < 27 Hz.

To characterize the performance of the frequency transfer over the fiber link we generate a heterodyne beat note at MPQ between the sent light and light that has been transferred through the fiber link. To record the beat note we use dead time free frequency counters [11], that can operate in two different modes: the so called Π- and Λ-modes [12]. In contrast to a Π-type counter, a Λ-type counter averages many frequency samples within a gate time, thus noise is effectively suppressed and more accurate data is produced.

III. Results

Figure 1 shows the stability of the transferred frequency after 1840 km of fiber when the link transfer is stabilized. The stability is expressed as the Allan deviation (ADEV) measured with a Π-type counter as well as the modified ADEV measured with a Λ-type counter. Despite the severely reduced servo bandwidth for the suppression of fiber-induced noise, the low intrinsic noise of the fiber link together with active noise cancellation allows for 1-s instabilities of a few parts in 10^{15} and about 4×10^{-19} after 100 s of measurement time. It can be seen that even todays most stable optical clocks can be compared over the distance of 1840 km within a few minutes

978-1-4799-0342-9/13/$31.00 ©2013 IEEE

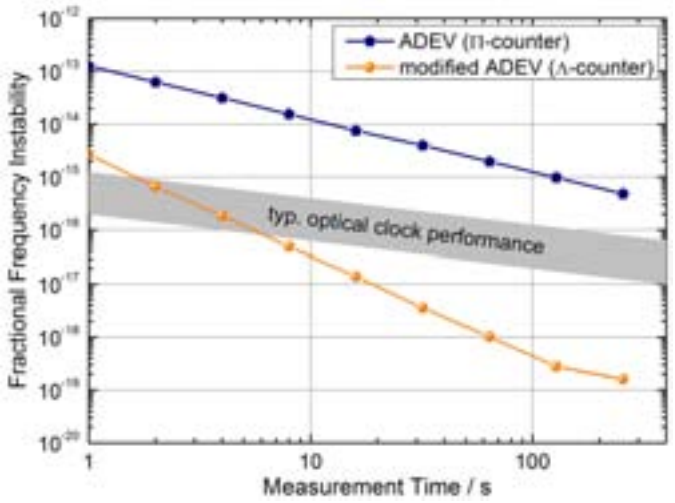

Fig. 1. Fractional frequency instability of the 1840 km fiber link. ADEV measured with a Π-type counter and modified ADEV measured with a Λ-type counter when the link transfer is stabilized. For comparison the instability of state-of-the-art optical clocks is depicted.

of measurement time using our fiber link. The noise of our link peaks at around 15 Hz and is lower at smaller frequencies which leads to a τ^{-2} dependency in the modified ADEV as shown in Figure 1. We attribute the noise maximum around 15 Hz to building and ground vibrations.

To assess potential systematic frequency shifts, we analyzed the mean deviation of the transferred frequency from the input frequency, and found agreement within the statistical uncertainty of 2.6×10^{-19}. The results illustrate that for a remote comparison of state-of-the-art optical clocks, the short-term instability contribution of the stabilized $\approx$ 2000 km link is negligible within one minute of measurement time.

IV. Conclusion

We demonstrated optical frequency transfer along an 1840 km optical fiber link with an instability of 2.7×10^{-15} at 1 s reaching 4×10^{-19} after 100 s of measurement time. The residual uncertainty exceeds the requirements for a comparison of todays most stable clocks by more than one order of magnitude. Our fiber link is provided by a commercial telecommunication supplier and passes several metropolitan areas and computing centers. Despite these environmental conditions active noise cancellation and carefully adjusted in-line amplification can yet provide high-performance frequency transfer over continental distances. We demonstrate that remote comparisons of state-of-the-art optical clocks are possible even if the clocks are separated by nearly 2000 kilometers. This work can be seen as a testbed for a European wide fiber link network to connect metrology institutes across Europe. The ability to compare those modern optical frequency standards opens a variety of applications, including relativistic geodesy [13], tests of the constancy of fundamental constants and quantum electrodynamics.

Acknowledgment

This work was supported by the European Metrology Research Programme (EMRP) under SIB-02 NEAT-FT. The EMRP is jointly funded by the EMRP participating countries within EURAMET and the European Union. We thank K. Predehl for establishing the fiber link; J. Alnis and Th. Legero for setting up the ultra-stable reference cavities; O. Terra for his work on the fiber Brillouin amplifiers and the members of Deutsches Forschungsnetz in Berlin, Leipzig, and Erlangen, Germany, as well as Gasline GmbH for a fruitful collaboration. We also thank the excellence cluster QUEST for financial support. T.W.H. acknowledges support by the Max Planck Foundation.

References

[1] N. Huntemann, M. Okhapkin, B. Lipphardt, S. Weyers, C. Tamm, and E. Peik, "High-accuracy optical clock based on the octupole transition in $^{171}Yb^{+}$," *Phys. Rev. Lett.*, vol. 108, p. 090801, Feb 2012. [Online]. Available: http://link.aps.org/doi/10.1103/PhysRevLett.108.090801

[2] A. A. Madej, P. Dubé, Z. Zhou, J. E. Bernard, and M. Gertsvolf, "$^{88}Sr^{+}$ 445-thz single-ion reference at the 10^{-17} level via control and cancellation of systematic uncertainties and its measurement against the si second," *Phys. Rev. Lett.*, vol. 109, p. 203002, Nov 2012. [Online]. Available: http://link.aps.org/doi/10.1103/PhysRevLett.109.203002

[3] K. Predehl, G. Grosche, S. M. F. Raupach, S. Droste, O. Terra, J. Alnis, T. Legero, T. W. Hänsch, T. Udem, R. Holzwarth, and H. Schnatz, "A 920-kilometer optical fiber link for frequency metrology at the 19th decimal place," *Science*, vol. 336, no. 6080, pp. 441–444, 2012. [Online]. Available: http://www.sciencemag.org/content/336/6080/441.abstract

[4] O. Lopez, A. Haboucha, B. Chanteau, C. Chardonnet, A. Amy-Klein, and G. Santarelli, "Ultra-stable long distance optical frequency distribution using the internet fiber network," *Opt. Express*, vol. 20, no. 21, pp. 23 518–23 526, Oct 2012. [Online]. Available: http://www.opticsexpress.org/abstract.cfm?URI=oe-20-21-23518

[5] M. Fujieda, M. Kumagai, S. Nagano, A. Yamaguchi, H. Hachisu, and T. Ido, "All-optical link for direct comparison of distant optical clocks," *Opt. Express*, vol. 19, no. 17, pp. 16 498–16 507, Aug 2011. [Online]. Available: http://www.opticsexpress.org/abstract.cfm?URI=oe-19-17-16498

[6] G. Marra, R. Slavík, H. S. Margolis, S. N. Lea, P. Petropoulos, D. J. Richardson, and P. Gill, "High-resolution microwave frequency transfer over an 86-km-long optical fiber network using a mode-locked laser," *Opt. Lett.*, vol. 36, no. 4, pp. 511–513, Feb 2011. [Online]. Available: http://ol.osa.org/abstract.cfm?URI=ol-36-4-511

[7] L. Sliwczynski, P. Krehlik, L. Buczek, and M. Lipinski, "Frequency transfer in electronically stabilized fiber optic link exploiting bidirectional optical amplifiers," *Instrumentation and Measurement, IEEE Transactions on*, vol. 61, no. 9, pp. 2573 –2580, sept. 2012.

[8] O. Terra, G. Grosche, and H. Schnatz, "Brillouin amplification in phase coherent transfer of optical frequencies over 480 km fiber," *Opt. Express*, vol. 18, no. 15, pp. 16 102–16 111, Jul 2010. [Online]. Available: http://www.opticsexpress.org/abstract.cfm?URI=oe-18-15-16102

[9] L.-S. Ma, P. Jungner, J. Ye, and J. L. Hall, "Delivering the same optical frequency at two places: accurate cancellation of phase noise introduced by an optical fiber or other time-varying path," *Opt. Lett.*, vol. 19, no. 21, pp. 1777–1779, Nov 1994. [Online]. Available: http://ol.osa.org/abstract.cfm?URI=ol-19-21-1777

[10] O. Lopez, A. Haboucha, F. Kéfélian, H. Jiang, B. Chanteau, V. Roncin, C. Chardonnet, A. Amy-Klein, and G. Santarelli, "Cascaded multiplexed optical link on a telecommunication network for frequency dissemination," *Opt. Express*, vol. 18, no. 16, pp. 16 849–16 857, Aug 2010. [Online]. Available: http://www.opticsexpress.org/abstract.cfm?URI=oe-18-16-16849

[11] G. Kramer and W. Klische, "Multi-channel synchronous digital phase recorder," in *Frequency Control Symposium and PDA Exhibition, 2001. Proceedings of the 2001 IEEE International*, 2001, pp. 144 –151.

[12] S. Dawkins, J. McFerran, and A. Luiten, "Considerations on the measurement of the stability of oscillators with frequency counters," *Ultrasonics, Ferroelectrics and Frequency Control, IEEE Transactions on*, vol. 54, no. 5, pp. 918 –925, may 2007.

[13] C. W. Chou, D. B. Hume, T. Rosenband, and D. J. Wineland, "Optical clocks and relativity," *Science*, vol. 329, no. 5999, pp. 1630–1633, 2010. [Online]. Available: http://www.sciencemag.org/content/329/5999/1630.abstract

Distributed Raman Amplification for Long-Haul Optical Frequency Dissemination

C. Clivati*, D. Calonico, F. Levi, A. Mura
Istituto Nazionale di Ricerca Metrologica
strada delle cacce 91,Torino, Italy
*also with Politecnico di Torino,
corso Duca degli Abruzzi,Torino, Italy

G. Bolognini
IMM Institute, National Research Council CNR
via Gobetti 101, Bologna, Italy

S. Faralli,
Istituto TECIP, Scuola Superiore Sant'Anna
via G. Moruzzi 1, Pisa, Italy

N. Poli
Dip. Fisica e Astronomia and LENS, Università di Firenze
and Istituto Nazionale di Fisica Nucleare, sez. Firenze
via Sansone 1, Sesto Fiorentino (FI), Italy

***Abstract*— This work describes the use of Distributed optical Raman Amplification for the realization of coherent optical fiber links for frequency dissemination. The main advantages of this technique are high gain and feasibility of long fiber spans with a simple apparatus, without degrading the link stability.**

Keywords-fiber links, optical amplifiers, Raman amplification

I. INTRODUCTION

In recent years, phase-compensated optical links proved to be the most performing technique to disseminate optical frequencies on a continental scale [1,2]. Most National Metrology Institutes are thus cooperating to realize a pan-European fiber network, that will enable optical clocks comparisons at unprecedented levels of accuracy and stability. The ultrastable frequency transfer via optical fiber requires that the fiber phase noise is compensated. This is done by reflecting a portion of the transferred light from the user end back to the transmitter end, and by comparing it to the original light. The double pass allows to cancel the phase noise accumulated along the fiber, provided that the optical path is exactly the same in both directions.

Dedicated amplification systems are thus needed, that must be fully bidirectional and symmetrical in the two directions. Bidirectional Erbium Doped Fiber Amplifiers are typically used, but their gain is limited by the back-reflections along the path, that may lead the amplifier to oscillate and may limit the achievable gain to about 20 dB. Distributed amplification is quite promising from this point of view, and offers several advantages compared to BEDFA. Distributed Brillouin Amplifiers (DBA) have recently been demonstrated and fruitfully used in coherent optical links [3]. We demonstrate that Distributed Raman Amplification (DRA) is a reliable technique as well: it does not degrade the transfer of the optical carrier at the 10^{-19} level of stability, and allows to bridge hauls of up to 60 dB losses without intermediate stations [4].

Raman amplification is based on the power transfer between two optical beams, the pump and the signal, through stimulated scattering of light with optical phonons [5]. Since the power transfer is distributed along the fiber, with an effective length of about 20 km, DRA can provide a very high gain without the onset of lasing or oscillations, even for high pump powers [6]. The gain is maximum when the signal is downshifted ~13.2 THz from the pump light, and the bandwidth is several THz wide around the gain peak. DRA requires pump power levels on the order of ~1 W, that is rather high, especially if compared to those required in DBA (~10 mW). On the other hand, DRA is intrinsically bidirectional, i.e. it amplifies signals that propagate in the opposite or in the same direction as the pump (hereafter indicated as counter- and co-pumped), whilst DBA only amplifies counter-propagating signals. Also, thanks to the large gain bandwidth, DRA does not require a frequency control of the pump laser to ensure a stable gain. Thus, DRA technology could help to simplify long haul optical links and to increase the reliability of the whole infrastructure.

In this work, we propose an analysis of the gain, the optical signal to noise ratio (OSNR) and the phase noise of the amplified optical carrier, and report on the use of DRA in a coherent optical link based on 200 km of fiber spools, both in a counter-pumped and in a co-pumped scheme.

II. THE EXPERIMENT

A. Optical Instrumentation and Experimental Apparatus

The laboratory test-bed we used is sketched in Fig. 1. An ultrastable laser radiation at 1542 nm is generated by locking a fiber laser through the Pound-Drever-Hall technique to a Fabry-Perot high finesse (120,000) cavity made of Corning Ultra Low Expansion (ULE) glass. The resulting laser linewidth is smaller than 30 Hz (details in [7]), with OSNR~56 dB in 0.1 nm resolution bandwidth. Light is coupled into a standard SMF-28 single mode fiber, with a total length of up to 200 km. The light power at fiber input is 0.5 mW; total losses due to fiber and connectors amount to ~45 dB. To

achieve phase noise cancellation, two acousto-optic modulators (AOM) are employed. AOM1 is placed before the fiber link and used as actuator to compensate the fiber phase noise. AOM2 is placed after the fiber link to shift the back-reflected radiation and allows to distinguish the real signal from stray reflections. Photodiode PD1 detects the fiber noise from an interferometric scheme [7] and a phase-locked-loop (PLL) feeds AOM1 with the correction signal. The bandwidth of the PLL loop filter is 20 kHz, and a minimum round-trip optical signal power of at least -70 dBm has to combine to the original light on PD1 to phase-lock the optical carrier. Photodiode PD2 is used to compare the phase noise of the radiation transferred through the fiber to that injected at the input.

We tested both co-and counter-pumped DRA, by coupling the pump light into the fiber trough wavelength-division multiplexers WDM1 or WDM2 respectively. Two different pump lasers at 1450 nm were used. The first is a depolarized fiber Raman laser (FRL) delivering up to ~800 mW into the fiber (OSNR >50 dB in 0.1 nm resolution bandwidth). The other Fabry-Pérot laser (FPL) depolarized pump is composed of two polarization-multiplexed Fabry-Perot diode lasers at the same wavelength, providing ~260 mW (OSNR ~58 dB in 0.1 nm resolution bandwidth) at the fiber input [8]. The depolarization of the pump laser is mandatory, as the Raman gain is maximum for co-polarized pump and signal, whilst it is minimum when pump and signal are orthogonally polarized. Therefore, care must be devoted to minimize gain fluctuations associated to polarization mode dispersion in the fiber.

Also, to avoid the transfer of Relative Intensity Noise (RIN) from pump to signal, we used the higher-RIN (~-110 dB/Hz) FRL pump at frequencies lower than 10 MHz) for counter-pumping, and the lower-RIN (~-140 dB/Hz) FPL for co-pumping. Indeed, counter-pumped DRA is known to be less affected by pump-to-signal RIN transfer than co-pumped DRA [9], since the RIN transfer is averaged out by the large difference in the group velocities of counter-propagating pump and signal. Being the signal RIN level <-141 dB/Hz, Raman amplification leads to an expected added signal RIN of ~-134.7 dB/Hz in co-pumping, and ~ -95.3 dB/Hz in counter-pumping, whose cross-talk values are extremely low when integrated over the narrow signal bandwidth (30 Hz).

B. Measurements and Discussion

We initially evaluated the DRA impact with a counter-pump scheme. On-off gain, OSNR and the phase noise of the amplified radiation have been measured by performing on PD2 the heterodyne beatnote between the signal travelling along the link and the light from the short reference arm. Fig. 2 (circles) shows the measured gain after 200 km propagation, versus the fiber-coupled pump power. The gain increases with pump power and attains the maximum value of 23 dB, limited by the effective power available with the FRL (800 mW). The measured OSNR is 106 dB/Hz, and is limited by the amplified spontaneous emission at pump powers higher than 600 mW, whilst it is degraded at lower pump powers due to the electrical noise of PD2.

This work has been partly funded by Compagnia di San Paolo, by the Italian Ministry of Research, contract PRIN09, and by Ente Cassa di Risparmio di Firenze.

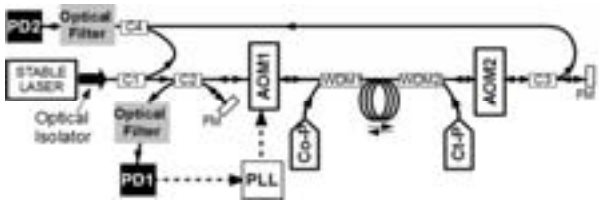

Fig. 1. Set up of the coherent fiber link with DRA. PD Photodiodes, C Couplers, FM Faraday Mirrors, WDM Wavelength Division Multiplexers, Co-P Co-propagating Pump, Ct-P Counter-propagating Pump, AOM Acousto-Optic Modulators, PLL Phase Locked Loop.

To investigate the maximum link length achievable without intermediate stations, the FPL as well was coupled into the fiber as a co-pump. The overall gain then increased to 32 dB, equivalent to a single stage DRA with a 1 W single counter-pump [8], limited by the power available with our FPL. The double stage pump allows to phase-compensate a link with up to 60 dB losses in a single span with our setup.

To test the flexibility of the amplifiers chain, we tried the high-power FRL as co-pump and the low-power FPL as counter-pump. We measured the co-propagating signal gain, as a function of the pump power while keeping a constant counter-pump gain of 9 dB, and with an input signal of ~0.5 mW. At high co-pump power levels, we observed degrading effects on the signal, and a strong gain reduction, as shown in Fig. 2 (squares). This is expected to be due to the power level of the amplified signal, that increases beyond the SBS threshold in the co-pumped scheme. When the gain reaches ~13 dB, the amplified signal achieves 10 mW, i.e. the SBS threshold. The net gain is then reduced by almost 10 dB with respect to the counter-pump scheme. This did not happen in the previous scheme, in which the signal amplified by the counter-pumped FRL was much weaker due to the fiber losses. As a result, in that scheme, the amplified signal never exceeded the SBS threshold [5]. Such detrimental effects can be reduced by a careful design of the amplifier chain whenever intermediate stations are required along the path.

Figure 3 shows the phase noise power spectral density $S_\phi(f)$ of a 100 km compensated link without (dashed grey line) and

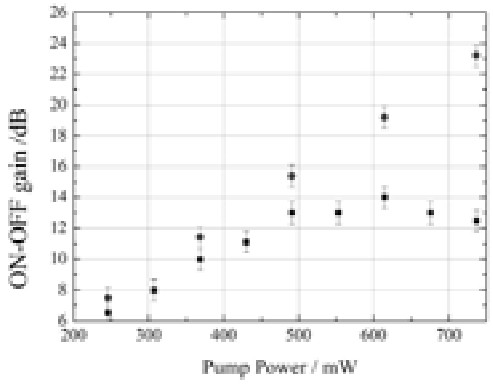

Fig. 2. Raman gain versus pump power in an optimized counter-pumped scheme (circles) and in a not optimized co-pumped scheme (squares).

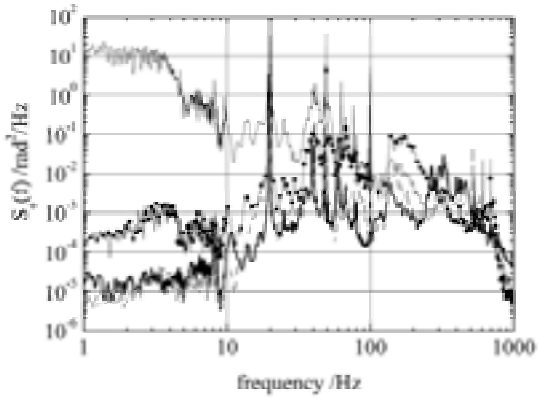

Fig. 3. Phase noise density $S_\phi(f)$ of the free running (thin black line) and compensated link (black line, filled circles) at 200 km, and $S_\phi(f)$ of a 100 km link without amplification (dashed grey line) and with an amplification of 22 dB (thick black line).

with (solid black line) an optical amplification of 22 dB. The spikes observed at frequencies within the link servo bandwidth (500 Hz) are mainly due to acoustic noise on the spooled fiber. The residual noise of the compensated link agrees with the expected limit due to the fiber delay [10], and there is no evidence of phase noise degradation due to DRA. Fig. 3 also shows the phase noise power spectral density of the free-running link at 200 km (thin black line) and of the compensated link (black line, filled circles). Again, the noise of the 200 km agreed with the expectations, considering the phase noise of the free running link and the fiber delay [10].

Link stability over long averaging times was calculated by counting the beatnote on PD2 with a high resolution Λ-type counter [11]. The data frequency instability $\sigma_\Lambda(\tau)$ obtained by processing data from Λ-counters can be converted into the Modified Allan deviation for common phase noises [11]. Fig. 4 shows $\sigma_\Lambda(\tau)$ of the link at 100 km (circles), at 200 km (squares) and of the interferometer without fiber spools (diamonds, grey line). Up to 20 s the link noise is dominant,

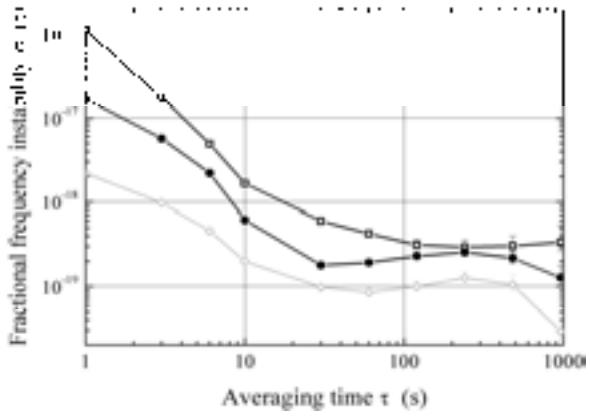

Fig. 4. Fiber link frequency instability on a 100 km link(filled circles), on the 200 km link using ROA (empty squares), and the interferometer noise floor (grey line, empty diamonds).

whilst at longer times the stability reaches a floor of $\sigma_\Lambda(\tau) \sim 3 \cdot 10^{-19}$. We attribute this limit to random, not reciprocal phase variations related to the fiber birefringence. Nevertheless, these results show that DRA enables coherent amplification in phase-compensated optical links.

III. Conclusions and Outlooks

We demonstrate that DRA is suitable for amplification in phase coherent optical links, allowing to bridge hauls of 200 km with a single fiber span, with a frequency instability of $3 \cdot 10^{-19}$ at 100-1000 s. DRA offers several advantages in terms of link maintenance and reliability with respect to discrete amplification techniques, providing a high gain with a simple apparatus. However, care should be devoted to the design of links involving both counter- and co-pumping, to avoid nonlinearities affecting the ultimate performances of the amplifier. We plan to investigate the use of DRA on a 650 km optical link that is under development between INRIM in Turin and LENS-UNIFI in Firenze, Italy [12]. DRA could improve the present design, reducing the number of amplifiers, as nine BEDFA amplifiers are used at the moment.

References

[1] K. Predehl, G. Grosche, S. M. F. Raupach, S. Droste, O. Terra, J. Alnis, et al., "A 920-Kilometer Optical Fiber Link for Frequency Metrology at the 19th decimal place," Science vol. 336, pp. 441-444, April 2012.

[2] O. Lopez, A. Haboucha, F. Kefelian, H. Jiang, B. Chanteau, V. Roncin, et al., "Cascaded multiplexed optical link on a telecommunication network for frequency dissemination," Opt. Expr. vol. 18, pp. 16849-16857, August 2010.

[3] O. Terra, G. Grosche, and H. Schnatz, "Brillouin amplification in phase coherent transfer of optical frequencies over 480 km fiber," Opt. Expr. vol. 18, 16102-16110 , July 2010.

[4] C. Clivati, G. Bolognini, D. Calonico, S. Faralli, F. Levi, A. Mura, N. Poli, "Distributed Raman optical amplification in phase coherent transfer of optical frequencies," IEEE Photonics Technol. Lett., in press.

[5] G. Agrawal, Nonlinear Fiber Optics, 3rd ed. San Diego: Academic Press, 2001.

[6] M. Islam, "Raman Amplifiers for Telecommunications" IEEE J. Sel. Top. Quantum Elect. , vol. 8, pp. 548-559, May/Jun. 2002.

[7] C. Clivati, D. Calonico, C. E. Calosso, G. A. Costanzo, F. Levi, A. Mura, A. Godone, "Planar-waveguide external cavity laser stabilization for an optical link with 10-19 frequency stability," IEEE Trans. Ultrason. Ferroel. Freq. Contr., vol. 58, pp. 2582-2587, Dec. 2011.

[8] G. Bolognini, S. Faralli, A. Chiuchiarelli, F. Falconi and F. Di Pasquale, "High-power and low-RIN lasers for advancedfirst- and higher-order Raman co-pumping," IEEE Photonics Technol. Lett., vol.18, pp. 1591-1593, Aug. 2006.

[9] C. R. S. Fludger, V. Handerek, and R. J. Mears, "Pump to Signal RIN Transfer in Raman Fiber Amplifiers," IEEE J. Lightwave Technol., vol. 19, pp. 1140-1148, Aug. 2001.

[10] W. Williams, W. C. Swann, and N. R. Newbury, "High-stability transfer of an optical frequency over long fiber optic links," J. Opt. Soc. Am. B, vol. 25, pp. 1284-1293, Aug. 2008.

[11] S. T. Dawkins, J. J. McFerran, A. N. Luiten "Considerations on the Measurement of the Stability of Oscillators with Frequency Counters," IEEE Trans. Ultrason. Ferroelectr. Freq. Control, vol. 54, pp. 918-925, May 2007.

[12] F. Levi, R. Ambrosini, D. Calonico, C. E. Calosso, C. Clivati, G. A. Costanzo, et al., "LIFT: The Italian Fiber Network For Frequency and Time Distribution", this proceedings.

Two Color One-Way Frequency Transfer in an Urban Optical Fiber Network

S.C. Ebenhag*, P.O. Hedekvist* and K. Jaldehag
Measurement Technology, Time and Frequency Lab
SP Technical Research Institute of Sweden
Borås, Sweden
*also with Chalmers University of Technology
Göteborg, Sweden
sven-christian.ebenhag@sp.se

***Abstract*—SP Technical Research Institute of Sweden has previously presented results with a two color one- way method. This method is an alternative method to two-way time and frequency transfer that is useful if there are unknown asymmetries in the connection. The method is possible to use in existing infrastructure and is able to coexist with data channels for example in WDM systems, which make it possible to broadcast to multiple users and enables the user to be anonymous to the time or frequency transfer.**

This paper will present the results from the analysis when implementing the technique in an urban commercial optical fiber data communication WDM network between two clock labs in Sweden connecting two cesium clocks to each other for frequency comparison. The evaluation is performed with two wavelengths 8 nm apart on 6 km of installed fiber in an urban city network.

The transmitter and the receiver are installed in an electromagnetically shielded room several meters below ground, and the fiber runs to a building at a distance of 3 km, and then back again. The comparison will be within the laboratory, eliminating any errors from a reference system. Results and conclusion from this evaluation reveals the propagation delay variations in the propagation distance and will display the need of compensation for these variations

Keywords — Optical fiber network, optical fiber, frequency transfer, two color.

I. INTRODUCTION

The last decade has the need for high accuracy frequency and time transfer has significantly increased and due to that has the users with the most demanding requirements for comparisons of remotely located frequency and time standards been investigating the use of optical fibers.

Recent work in the field of optical frequency transfer shows results with potential accuracies below 10^{-17} obtained in less than a day, demonstrating that the technique is useful for the comparison of optical frequency standards [1, 2].

Several of the optical frequency transfer methods focus on two-way frequency transfer, whether it uses the optical phase or intensity modulation at microwave frequencies, dark fiber, or wavelength division multiplexing channels [1 - 14]. When two-way frequency transfer methods are used, there is a presumption that the signal delays are equivalent (symmetrical) in both directions, but in several cases the two transmission paths are asymmetrical and this introduces a varying error. Solutions that use bidirectional signals in a single fiber results in a close to perfect match, but other limitations still occur [11]. For a solution utilizing one-way frequency transfer, it is therefore beneficial if the delay variations can be sufficiently compensated. Recent results have been presented using either a fiber based pre-compensation [15 - 17], or an electronic post-compensation [18]. The pre-compensation uses a temperature controlled fiber as a part of the transmission and a feedback signal that adjusts the temperature to keep the phase difference constant between two propagated frequencies. The electronic post-compensation utilizes a model of the fiber to translate a phase difference between the two wavelengths into the corresponding delay in the fiber, and then adjusts an in-line delay unit accordingly.

The results section of this paper presents three different setups of measurement and the first presents the frequency stability of measurements using signals with two wavelengths separated by 8 nm propagated through a 3-km fiber in a commercial metropolitan fiber network. The frequency stability is presented for transmission time using both compensated and uncompensated optical fiber. The second part presents measurements of the varying transmission time due to varying ambient temperature, and for this setup the 3 km optical fiber was looped to a distance of 6 km, which includes that the transmitter and receiver are located at the same place in an electromagnetically shielded room several meters below ground. The last measurements of the result section present measurements performed in a controlled laboratory environment for evaluation of error sources.

A Cesium beam frequency standards were used as primary source to evaluate the system.

II. Method Description

The successful distribution of a proposed phase stabilized frequency over a one-way fiber optic connection relies on the unambiguous correlation between the dispersion and the group velocity in a single mode optical fiber. The variation in dispersion, as is detectable at the receiver, can be transformed to a corresponding change in delay through the fiber. When distance increases, and especially when a significant amount of the transmission media is outdoors, the temperature variations will affect the propagation properties of the media.

Polarization mode dispersion and polarization dependent losses are small and the influence is minimized when using a polarization scrambler. Furthermore, the waveguide dispersion is negligible in standard single mode fiber, even though this also could be added if implemented in networks of dispersion shifted fiber.

The proposed method to solve for constant and varying transfer time (τ and $\tau_{det}(t)$) is to transmit two wavelengths through the same fiber and then detect the propagation delay differences between them [19 - 21]. The difference is then applied as a correction term for the delay variations in $\tau_{det}(t)$.

Furthermore, the proposed method operates within the C-band of commercial Dense Wavelength Division Multiplexing (DWDM) networks. The motive for using the C-band is that the commonly used Erbium Doped Fiber Amplifier (EDFA) has a flat gain spectrum between 1530 nm and 1560 nm that includes the C-band frequencies. The effect is larger when the two transmitted wavelength are far apart, while the availability to access channels in bright DWDM-fibers improves when the spacing is narrow.

In a fully operational solution, the time or frequency from the master clock can be distributed to a network of slave clocks, with an uncertainty smaller than what would be the case if only a single wavelength was transmitted.

The feasibility of this transfer technique is supported by previous presented experimental results [16 - 18].

III. Frequency transfer setup

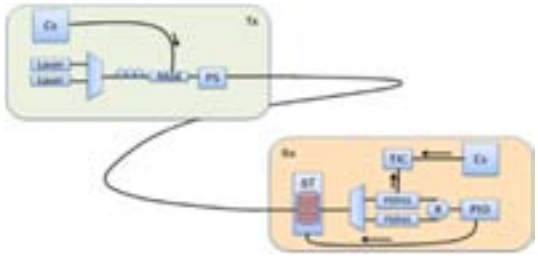

Fig. 1. Frequency transfer setup. The transmitter includes a Cesium standard (Cs), two tunable lasers, a WDM multiplexer, a Mach-Zehnder optical modulator (Mod) which is preceded by a polarization controller (three circles) and followed by a polarization scrambler (PS). At the receiving end, *ΔT* illustrates a temperature controlled fiber spool, followed by a WDM demultiplexer, photo-detection, filter, amplification and splitting (PDFAS). The two outputs are mixed to achieve a difference signal for the PID regulator (PID) which controls the temperature box. The output characterizes the local Cs utilizing a time interval counter (TIC).

This paper is based on a previous experiment with the following setup presented in Fig. 1 and further in the text.

Two tunable lasers emitting light at different wavelengths 8 nm apart (1551 nm and 1559 nm) are combined in a WDM multiplexer and modulated by a 10 MHz sinusoidal signal from the Cesium clock (Cs). The modulated light is transmitted through a polarization scrambler, which varies the output polarization state controlled by four uncorrelated frequencies. The 3 km fiber between the transmitter and receiver is installed in tubing a few meters below city streets. At the receiver, the light is propagated through a 500 m standard single mode fiber (SMF) placed in a thermally controlled box. At the output of this fiber, the light is split in a WDM demultiplexer and connected to P-I-N photodiodes for conversion to electrical signals. These signals are connected in parallel paths at equal length and attenuation to amplifiers and power splitters (PDFAS), and finally combined in a mixer to generate phase-difference detection (PDD) signal.

If the fiber in the temperature controlled box has the same characteristics as the fiber used in the transmission, the phase of the transferred signal is stable when the PDD signal is constant. The PDD signal is therefore connected to a proportional-integral-derivative (PID) regulator which controls the temperature of the box.

Both the master oscillator and slave oscillator are cesium beam frequency standards with high-performance beam tubes. The PDD signal emits a phase corresponding to the difference in the arrival time of the two signals.

To further evaluate the sources of error and the need for transfer time compensation the fiber was looped to begin and end in the same place with a total distance of 6 km and the transfer time was measured continuously. The results are presented in Fig.3.

Since the experiment is based on a field environment a similar setup was mounted in a controlled environment with a few minor changes that the distance was changed to 16 km of which 8 km located outdoors and 8 km in a temperature cabinet and the frequency was increased to 100 MHz, all this to further evaluate the error sources.

IV. Results

The frequency stabilities of the previous transfers in an urban fiber network, as estimated with the Overlapping Allan deviation, is shown in Fig. 2.

Time interval measurements for the compensated and uncompensated frequency transmissions are assembled with an existing multi-channel TIC with the measurement interval of 1 s at the receiver end. External temperature influence of an optical fiber is a slower process than 1 s, which means that if the time between measurements is in the 60 s range is it enough to create good propagation variation compensations.

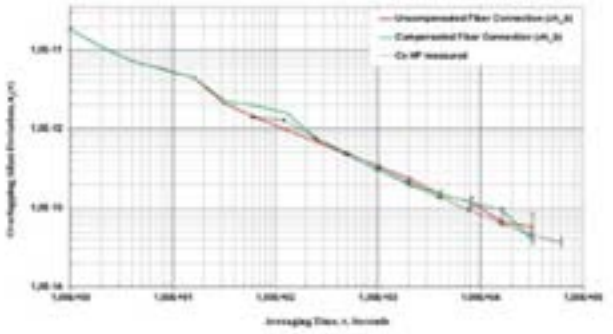

Fig. 2. The frequency stability of the uncompensated frequency transfer utilizing fiber is presented in red and the real-time compensated frequency transfer utilizing fiber is presented in green. The black Overlapping Allan Deviation line presents data sampled every 60 s between two high performance Cesium standards of the same type as used in the experiment.

From the Overlapping Allan deviation graph shown in Fig. 2, it is evident that improving the stability of the compensated fiber connection is small. A small degradation at an averaging period of 100 s is expected, caused by the bandwidth of the feedback loop. The frequency stability of the link is approximately 3×10^{-13} for an average period of about 1000 s. The main improvement is expected over 10 000 s, which is slightly indicated in Fig. 2, but measurements over a longer period will be necessary to prove the full performance of the technique and would also serve the same purpose as more stable clocks to some extent.

The fiber network is placed in tubes below the surface which makes the network less affected by temperature changes but nevertheless is it still affected.

For an evaluation of the temperature impact on the urban fiber network the transit time was measured through a 6 km roundtrip fiber path and is shown in Fig. 3. The used frequency is measured and distributed through a frequency distribution amplifier (FDA) and its impact on the measurement is also presented in Fig. 3.

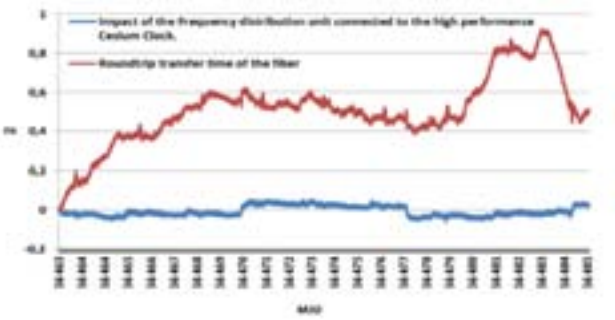

Fig. 3. In red the varying transfer time through 6 km of fiber in tubing below ground during 22 days in June and July is presented and as can be seen it does vary more than 900 ps. For these measurements a FDA is used and it s impact on the measurements is shown in blue. The impact of the FDA regarding the measurement is neglible. The small steps in the FDA data is due to change of climate control of the room. There are redundant climate control and every 7th day master system is changed.

To evaluate most of the error sources an equal system was setup in a controlled environment with the exception that the modulation frequency and distance was increased. In this case the distance was 16 km of which 8 km was located outdoors and the other 8 km was placed in the Peltier regulated temperature chamber. The modulation frequency was increased to 100 MHz.

In this setup the signal was optical split after 8 km to be used as reference of the outdoor temperature impact of the fiber. Transfer time measurements of the compensated fiber and the reference fiber are presented in Fig. 4.

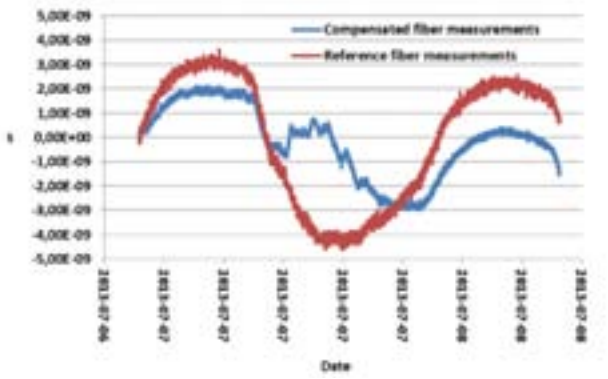

Fig. 4. In red is the varying transfer time through 8 km of fiber located in a box oudoors during 1.5 day and as can be seen it does vary more than 7 ns. In blue are the same measurements performed but through the whole compensated distance of 16 km and as can be seen the variation is reduced. The reason for the short dataset is that the used temperature chamber is limited to work in a region of ± 10˚C from it initial value which limits the compensation algorithm and measurements for proof where only performed. The slightly less short term noise for the compensated measurements are to some extemt due to the use of filtered Avalanche Photo Diodes for conversion between optical and electrical domain instead of P-I-N photodides.

The stability of the frequency for both the reference and the compensated are presented in Fig. 5.

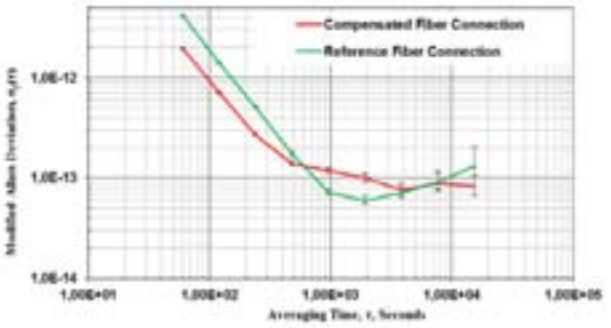

Fig. 5. The data from Fig. 4 are used to plot he frequency stability both the reference and compensated measurements. It is a short dataset, but still do the the compensated fiber (red) perform better than the uncompensated (green) for short term but perform worse for average times between 600 – 4000 s.The data set is too short to be able to perform a fair evaluation of the daily variations, but idicates that with a good temperature regulation the system should be sufficiently stable to support a stable output phase for clocks that perform better than cesium beam frequency standards.

V. CONCLUSION

Measurements in urban optical fiber network as well as in controlled environment are performed. One major conclusion is that even though your fiber is placed in tubing below the ground it is still affected by temperature changes (Fig. 3). For short distances as 3-6 km the transfer time is varying in the region of 900ps during three weeks.

In conclusion, the experiment has been successful and has shown that the compensated one-way way fiber solution can be implemented in an existing metropolitan data network. Future improvements are related to size-reduction of the hardware and increased reliability of the transmitter, receiver and temperature tuning.

ACKNOWLEDGEMENTS

This project was initiated and made possible thanks to the valuable support of The Swedish Defense Material Administration and electronics constructions from Br. Voss Engineering Company AB.

REFERENCES

[1] C. Cliviati, D. Calonico, C. Calosso, G. Costanzo, F. Levi, A. Mura, and A. Godone, "Time Transfer on Optical Fiber Development at INRIM," *Proceedings of the 26th European Frequency and Time Forum*, Gothenburg, Sweden, 2012.

[2] O. Lopez, A. Amy-Klein, C. Daussy, Ch. Chardonnet, F. Narbonneau, M. Lours, and G. Santarelli, "86-km Optical Link With a Resolution of 2 × 10^{-18} for RF Frequency Transfer," *Eur. Phys. J. D,* vol. 48, no. 1, pp. 35-41, 2008.

[3] F. Kéfélian, H. Jiang, P. Lemonde, and G. Santarelli, "Ultralow-Frequency-Noise Stabilization of a Laser by Locking to an Optical Fiber-Delay line," *Opt. Lett.*, vol. 34, no. 7, pp. 914-916, 2009.

[4] A. Imaoka and M. Kihara, "Accurate Time/Frequency Transfer Method Using Bidirectional WDM Transmission," *IEEE T. Instrum. Meas.*, vol. 47, no. 2, pp. 537-542, 1998.

[5] H. Jiang, F. Kéfélian, S. Crane, O. Lopez, M. Lours, J. Millo, D. Holleville, P. Lemonde, A. Amy-Klein, Ch. Chardonnet, and G. Santarelli, "Progress to a Full Optical Link on a Telecom Network," *Proceedings of the 22nd European Frequency and Time Forum*, Toulouse, France, 2008.

[6] N. Newbury, P. Williams, and W. Swann, "Coherent Transfer of an Optical Carrier over 251 km," *Opt. Lett.*, vol. 32, pp. 3056-3058, 2007.

[7] P. Williams, W. Swann, and N. Newbury, "High-Stability Transfer of an Optical Frequency over Long Fiber-Optic Links," *J. Opt. Soc. Am. B,* vol. 25, no. 8, pp. 1284-1293, 2008.

[8] G. Grosche, B. Lipphardt, H. Schnatz, G. Santarelli, P. Lemonde, S. Bize, M. Lours, F. Narbonneau, A. Clairon, O. Lopez, A. Amy-Klein, and Ch. Chardonnet, "Transmission of an Optical Carrier Frequency over a Telecommunication Fiber Link," *Proceedings of Conference on Lasers and Electro-Optics (CLEO)*, CMKK1, Baltimore, Maryland, 2007.

[9] O. Terra, G. Grosche, K. Predehl, R. Holzwarth, T. Legero, U. Sterr, B. Lipphardt, and H. Schnatz, "Phasecoherent Comparison of Two Optical Frequency Standards over 146 km Using a Telecommunication Fiber Link," *Appl. Phys. B*, vol. 97, no. 3, pp. 541-551, 2009.

[10] O. Terra, G. Grosche, and H. Schnatz, "Brillouin Amplification in Phase Coherent Transfer of Optical Frequencies over 480 km Fiber," *Opt. Express*, vol. 18, no. 15, pp. 16102-16111, 2010.

[11] F. Narbonneau, M. Lours, S. Bize, A. Clairon, G. Santarelli, O. Lopez, C. Daussy, A. Amy-Klein, and C. Chardonnet, "High Resolution Frequency Standard Dissemination via Optical Fiber Metropolitan Network," *Rev. Sci. Instrum.*, vol. 77, no. 6, pp. 064701 - 064701-8, 2006.

[12] S. Jefferts, M. Weiss, J. Levine, S. Dilla, and T. Parker, "Two Way Time Transfer Through SDH and Sonet Systems," *Proceedings of the 10th European Frequency and Time Forum*, Brighton, United Kingdom, pp. 461-464, 1996.

[13] M. Kihara, A. Imaoka, M. Imae, and K. Imamura, "Two Way Time Transfer Through 2.4 Gb/s Optical SDH Systems*," IEEE T. Instrum. Meas.*, vol. 50, no. 3, pp. 709-715, 2001.

[14] R. Emardson, P. Hedekvist, M. Nilsson, S. Ebenhag, K. Jaldehag, P. Jarlemark, C. Rieck, J. Johansson, L. Pendrill, P. Löthberg, and H. Nilsson, "Time Transfer by Passive Listening over a 10 Gb/s Optical Fiber," *IEEE T. Instrum. Meas.,* vol. 57, no. 11, pp. 2495-2501, 2008.

[15] J. Hanssen, S. Crane, and C. Ekstrom, "One way Temperature Compensated Fiber Link," *Proceedings of the Joint Conference of the IEEE Frequency Control Symposium and the 25th European Frequency and Time Forum*, San Francisco, California, pp. 1-5, 2011.

[16] S. Ebenhag and P. Hedekvist, "Two Color One Way Time and Frequency Transfer in an Urban Optical Fiber Data Communication WDM Network," *Proceedings of the 44th Precise Time and Time Interval Systems and Applications Meeting*, Reston, Virginia, 2012.

[17] S.C. Ebenhag, P.O. Hedekvist and K. Jaldehag, "Two-Color One-Way Frequency Transfer in a Metropolitan Optical Fiber Data Network", *NCSLI Measure J. Meas. Sci.,* vol. 8, no. 2, 2013.

[18] S. Ebenhag, P. Hedekvist, and K. Jaldehag, "One Way Time Transfer Utilizing Active Detection of Propagation Delay Variations of Dual Wavelengths in an Optical Fiber Network," *Proceedings of the 43rd Precise Time and Time Interval Systems and Applications Meeting*, Long Beach, California, pp. 9-16, 2011.

[19] P. Vella, P. Garrel-Jones, and R. Lowe, "Measuring Chromatic Dispersion of Fibers," *United States Patent 4551019*, 1985.

[20] W. Hatton and M. Nishimura, "Temperature Dependence of Chromatic Dispersion in Single Mode Fiber," *J. Lightwave Technol.*, vol. LT-4, no. 10, pp. 1552-1555, 1986.

[21] L. Cohen and J. Fleming, "Effect of Temperature on Transmission in Lightguides," *Bell Syst. Tech. J.*, vol. 58, no. 4, pp. 945-951, April 1979.

Fiber-Based Multiple-Access Ultrastable Radio and Optical Frequency Dissemination

Y. Bai,[1,3] B. Wang,[1,2] C. Gao,[1,3] W.L. Chen,[4] J. Miao,[1,3] X. Zhu,[1,3] and L.J. Wang[1,2,3,4]
[1]Joint Institute for Measurement Science, Tsinghua University, Beijing 100084, P. R. China
[2]The State Key Lab of Precision Measurement Technology and Instrument, Department of Precision Instruments and Mechanology Tsinghua University, Beijing 100084, P. R. China
[3]Department of Physics, Tsinghua University, Beijing 100084, P. R. China
[4]National Institute of Metrology, Beijing 100013, P. R. China
Email: bo.wang@tsinghua.edu.cn

***Abstract*—We demonstrate a fiber-based multiple-access ultra-stable frequency dissemination scheme for both radio frequency modulated on the optical carrier and optical frequency. Relative frequency stabilities of 7×10^{-14}/s and 5×10^{-18}/day for radio frequency, 3×10^{-16}/s and $4 \times 10^{-18}/10^4$s for optical frequency have been obtained, respectively. Using this method, highly synchronized radio-frequency modulation signal or the optical signal itself can be regenerated along the entire fiber link and it is expected to have potential applications.**

I. Introduction

Along with the significant progress of modern atomic frequency standards in recent years[1], the transfer and synchronization of ultra-stable frequency signals is required by more and more applications. Due to its properties of low attenuation, high reliability and continuous availability, frequency dissemination via fiber link has been actively studied[2]. Different schemes, such as fiber based radio frequency (RF) dissemination[3], [4], optical frequency dissemination[5], [6], [7], and even optical frequency comb signal dissemination[8], [9] have been proposed and demonstrated, respectively. All of these schemes have much higher dissemination stability than that of the conventional frequency dissemination via satellite link, which has a limited stability of 10^{-15}/day[10], [11]. Ultra-long distance frequency dissemination has also been demonstrated by cascaded frequency dissemination method[7], [12], [13]. However, at present, almost all of the frequency dissemination fiber links are built between precision laboratories and used for atomic clock comparisons[14]. Most of the application areas, such as distributed synthetic aperture radar[15], very-long-baseline interferometry (VLBI)[16], and particle accelerators[17], still use satellite links to synchronize time and frequency. It is mainly due to the frequency accessing limitation of the fiber link. For satellite link, it can disseminate time and frequency signal to cover essentially the entire globe; for fiber link, the point to point frequency dissemination protocol limits its coverage area.

In this paper, we demonstrate a multiple-access dissemination scheme which can reproduce the stably disseminated radio or optical frequency signal at arbitrary node along the entire fiber pathway. For the radio frequency dissemination, we build up a time and frequency dissemination system via a 80 km urban telecommunication fiber network between Tsinghua University (THU) and the National Institute of Metrology (NIM)[4]. We reproduce the disseminated 9.1GHz modulation signal at an arbitrary node[18]. For the optical frequency, Grosche proposed a technique for multiple access optical frequency dissemination in 2010[19]. However, the user at an arbitrary node along the pathway needs a highly stable laser source of same wavelength to reproduce the disseminated signal, which makes the system costly and technically complex. We propose a more convenient and efficient idea to solve this problem[20]. Relative frequency stabilities of 7×10^{-14}/s and 5×10^{-18}/day for radio frequency, 3×10^{-16}/s and $4 \times 10^{-18}/10^4$s for optical frequency have been obtained, respectively. Optical frequency transfer can provide better stability while the RF dissemination is relatively simple for practical applications. Using this method, we can regenerate the highly synchronized radio-frequency modulation signal or the optical signal itself along the entire fiber link and it is expected to have potential applications such as a large area branching fiber network for frequency synchronization.

II. Multiple-access radio frequency dissemination

The schematic diagram of the multiple-access radio frequency dissemination system based on 80 km urban fiber link is shown in Figure 1. During the performance test, for the convenience of phase difference measurement, we connected two parallel 40 km fiber links at the NIM site. Consequently, the local and remote sites of the 80 km fiber link are both placed in the same lab at THU. The experimental setup is almost the same as that of [4], except that a 3 km fiber spool is connected to the 80 km urban fiber link at the local site, which is used to demonstrate the multiple-access frequency dissemination. A 9.1 GHz frequency signal $V_r = cos(\omega t + \phi_r)$ (without considering its amplitude) from an oscillator referenced to an atomic clock is used as the reference frequency signal. The phase noise compensation system is composed of a voltage controlled crystal oscillator (VCXO), electro-absorption modulated 1547 nm diode laser, erbium-doped fiber amplifiers (EDFA), optical circulator, fast photo-detector, and a feedback locking loop. It generates a 9.1 GHz phase-compensated frequency signal $V_0 = cos(\omega t + \phi_0)$ and modulates the amplitude of the 1547 nm laser carrier. Through round-trip phase noise detection and active phase noise compensation, the phase of the transmitted signal, $\phi_0(t)$,

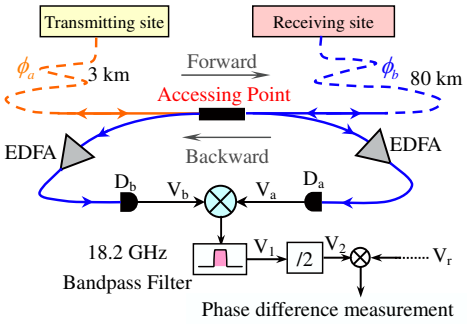

Fig. 1. Schematic diagram of the multiple-access RF dissemination system.

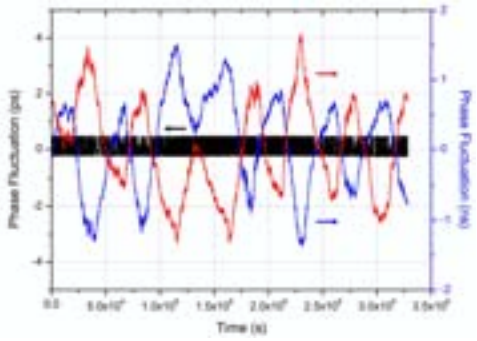

Fig. 2. Measured relative phase fluctuations of the reproduced frequency signals at an arbitrary accessing node of the fiber link.

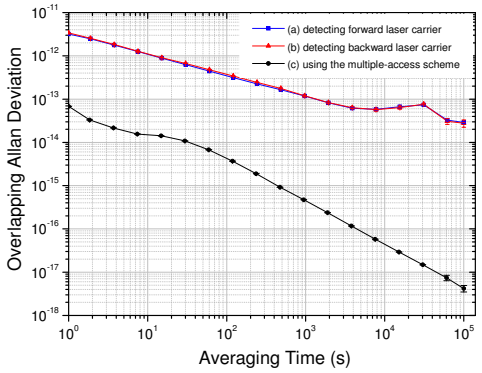

Fig. 3. Measured relative frequency stability of the reproduced frequency signal at an arbitrary accessing node of the fiber link. (a) forward signal; (b) backward signal; and (c) signal obtained using the multiple-access rf dissemination method.

will follow the phase offset of the reference frequency signal ϕ_r, together with the phase fluctuation $\phi_p(t)$ introduced during transmission in the 83 km fiber link, giving the relation,

$$\phi_0 = \phi_r - \phi_p. \quad (1)$$

Here, to maintain consistency with the published papers[3], [4] and for the convenience of presentation, we neglect the time item of phase part. Consequently, the received frequency signal at the receiving (remote) site becomes $V_1 = cos(\omega t + \phi_0 + \phi_p) = V_1 cos(\omega t + \phi_r)$, which is phase-locked to that of the reference signal, V_r.

From the principle of the applied phase noise compensation scheme, the highly stable 9.1 GHz microwave signal can only be reproduced at the "remote" end without any degradation in frequency stability. We take the connecting point (marked by a red star in Fig. 1) of a 3 km fiber spool and the 80 km urban fiber link as the example of an arbitrary accessing node. One can splice a 2×2 fiber coupler to couple out the 1547 nm laser carrier transferring forward and backward in the fiber link. The frequency signal modulated on the laser carrier can be detected and reproduced by two fast photo-detectors D_a and D_b, and can be expressed as $V_a = cos(\omega t + \phi_0 + \phi_a)$, and $V_b = cos(\omega t + \phi_0 + \phi_a + 2\phi_b)$, respectively. Here, ϕ_a and ϕ_b are the phase fluctuations induced by transits in the 3 km fiber spool and the 80 km urban fiber link, respectively. They have the relationship of $\phi_a + \phi_b = \phi_p$. When the round-trip phase noise compensation loop is closed, considering Eq. (1), the two received signals can be written as:

$$V_a = cos(\omega t + \phi_0 + \phi_p - \phi_b) = cos(\omega t + \phi_r - \phi_b) \quad (2)$$

$$V_b = cos(\omega t + \phi_0 + \phi_p + \phi_b) = cos(\omega t + \phi_r + \phi_b). \quad (3)$$

They both carry the phase fluctuation ϕ_b of the 80 km fiber link which is located between the accessing node and the remote end.

To demonstrate it, we measure the relative phase fluctuations and frequency stability of the intermediate signals V_a and V_b compared with the frequency reference V_r, simultaneously. The results are shown in Fig. 2 and Fig. 3. From Fig. 2, we can see that their phase fluctuation terms are complementary to each other. Therefore, a summing operation on phase terms of these two rf signals will cancel out this fluctuation. From Fig. 2, we can see that they show very similar behaviors and stabilities of 3.5×10^{-12}/s and 3×10^{-14}/day, respectively. Consequently, if we directly access the dissemination channel at a given point in the fiber link, even if using the round-trip phase noise compensation method, the reproduced frequency signal will carry the phase fluctuations of the remainder of the fiber link. That is to say, the closer to the local site, the more noise it will have gathered. For this reason, we choose a node very close to the sending site, and therefore having maximal noise, as a typical case for a demonstration. Figure 1 shows the schematic diagram of the multiple-access rf dissemination scheme we implemented. The out-coupled 1547 nm laser carriers received from both directions are amplified by two EDFAs and detected by two fast photo detectors D_a and D_b, respectively. Two intermediate signals V_a and V_b, with power of 5 dBm and 10 dBm respectively, are then mixed by a frequency mixer and filtered by a 18.2 GHz bandpass filter. An 18.2 GHz (2ω) frequency signal

$$V_2 = cos(2\omega t + 2\phi_r), \quad (4)$$

is generated. It does not carry the phase fluctuation term ϕ_b and is phase-locked to the frequency reference V_r. Using a divide-by-2 pre-scaling frequency divider, V_2 is down-converted to

$$V_3 = cos(\omega t + \phi_r). \quad (5)$$

This way, an rf signal V_3 whose phase and frequency are locked to the reference signal V_r, is reproduced at the accessing node. We measure the relative frequency stability of V_3 compared to V_r (with 3Hz effective measurement bandwidth), and the relative frequency stabilities of 7×10^{-14}/s and 5×10^{-18}/day have been obtained (Fig. 3). We emphasize that there are several orders of magnitude in improvement on

the relative stability compared to those of directly obtained frequency signals V_a and V_b. Furthermore, we note that a 10^{-18}/day fiber-based, multiple-access rf dissemination system can fulfill the needs of essentially any practical applications of present time.

III. Multiple-Access Optical Frequency Dissemination

Figure 4 shows the schematic diagram of the fiber based multiple-access optical frequency dissemination experiment. The whole system is separated into three parts, which are the local site, remote site and download site, respectively. For the convenience of phase stability measurement, they are located in the same lab. The arbitrary frequency accessing point is chosen as being 1.5 km away from the sending site. As a performance test, a commercial 1550nm laser module (RIO ORION Laser Module) is used as the reference resource at the local site. Its frequency signal can be expressed as $E_0 = V_0 cos(\omega t + \phi_0)$. After passing a circulator and an 80MHz fiber-couple acoustic optical modulator AOM1 (+1st order Bragg shift), the 10 mW laser signal is coupled into the fiber link. A phase fluctuation ϕ_p of the signal E_0 will be induced during its propagation. At the remote site, another 80MHz AOM2 (+1st order Bragg shift) is employed as a frequency shifter for optical beating at the download site. The received signal E_1 at the remote site can be expressed as

$$E_1 = V_1 cos(\omega t + \Omega_1 t + \Omega_2 t + \phi_0 + \phi_p + \phi_{AOM1}). \quad (6)$$

Here, $\Omega_1 \approx \Omega_2 \approx 2\pi\times 80$ MHz are the frequency offsets induced by AOM1 and AOM2, ϕ_{AOM1} is the correction phase modulated on AOM1, and the fixed phase shift induced by AOM2 is neglected. To compensate the phase fluctuations induced during fiber dissemination, at remote site, a fraction of the received optical signal is sent back (via an optical circulator) to beat with E_0 at the local site. The round-trip signal E_2 can be expressed as

$$E_2 = V_2 cos(\omega t + 2\Omega_1 t + 2\Omega_2 t + \phi_0 + 2\phi_p + 2\phi_{AOM1}), \quad (7)$$

and the beating signal is proportional to $cos(2\Omega_1 t + 2\Omega_2 t + 2\phi_p + 2\phi_{AOM1})$. The beating signal is processed by the phase noise compensation system, and the generated error signal is fed to control the phase of AOM1. It is the same way as that of conventional optical-stabilization techniques[21]. Once the phase-locking loop is closed, without loss of generality, we can get:

$$\phi_p + \phi_{AOM1} = 0. \quad (8)$$

Consequently, the phase noise compensation is accomplished and the received frequency signal E_1 is phase locked to E_0 at the local site. To overcome the phase fluctuations induced by the single trip elements in local and remote sites, these elements have been temperature controlled.

In order to download the disseminated frequency signal at an arbitrary accessing point, using a 2×2 fiber coupler (80/20 ratio), we can easily couple out the forward and backward propagating optical signal from the fiber link. Due to the existence of AOM2, there is a frequency difference of 160 MHz between the two signals. Consequently, they can be

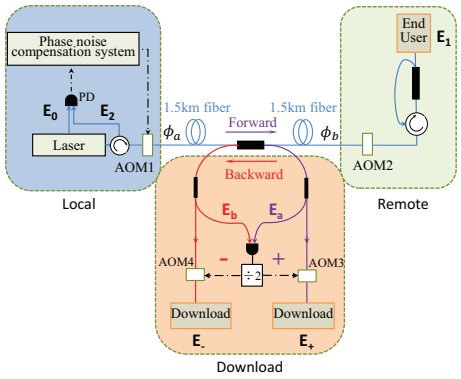

Fig. 4. Schematic diagram of the fiber based multiple-access optical frequency dissemination system.

expressed as

$$\begin{aligned} E_a &= V_a cos(\omega t + \Omega_1 t + \phi_0 + \phi_a + \phi_{AOM1}) \\ &= V_a cos(\omega t + \Omega_1 t + \phi_0 - \phi_b), \end{aligned} \quad (9a)$$

$$\begin{aligned} E_b &= V_b cos(\omega t + \Omega_1 t + 2\Omega_2 t + \phi_0 + \phi_p + \phi_b + \phi_{AOM1}) \\ &= V_b cos(\omega t + \Omega_1 t + 2\Omega_2 t + \phi_0 + \phi_b). \end{aligned} \quad (9b)$$

Here, ϕ_a and ϕ_b are the phase fluctuations induced by the fiber links before and behind the accessing point, respectively. They obviously have the relationship of $\phi_a + \phi_b = \phi_p$. From Eq. (9), we can see the phase fluctuation terms of these two directly accessing frequency signals E_a and E_b are complementary to each other. By beating E_a and E_b with E_0 respectively, we can get the relative frequency stabilities of the directly accessing signals. As shown in Fig. 5(curve (a), (b)), they are $1\times 10^{-14}/s$, $6\times 10^{-15}/10^4 s$ for the forward signal and $1\times 10^{-14}/s$, $4\times 10^{-15}/10^4 s$ for the backward signal. To cancel the phase fluctuations ϕ_a and ϕ_b of the two directly accessing optical signals, we simply beat 20% of the forward and backward transmitted signals E_a and E_b, and get

$$V_{beat} \propto cos(2\Omega_2 t + 2\phi_b). \quad (10)$$

Two more accousic optical modulators AOM3(+1st order Bragg shift) and AOM4(-1st order Bragg shift) are further employed as shown in Fig. 4. The beat signal V_{beat} is discriminated and digitally divided by 2. The resulting 80MHz RF signal with phase ϕ_b is then bandpass filtered, amplified, and fed to AOM3 and AOM4. The modulated, download signals of the forward and backward directions can be written as:

$$E_+ = E_- \propto cos(\omega t + \Omega_1 t + \Omega_2 t + \phi_0). \quad (11)$$

Therefore, the reproduced signals E_+ and E_- have exactly the same form as E_1 received at the remote site. As shown in Fig. 5(curve (c), (d)), relative frequency stabilities can be improved to $3\times 10^{-16}/s$, $4\times 10^{-18}/10^4 s$ for the forward signal, and $2\times 10^{-16}/s$, $4\times 10^{-18}/10^4 s$ for the backward signal. As a preliminary demonstration, we emphasize the advantages of this method - there is no requirement of any additional laser source at the download site, and the apparatus is as simple as that of remote site. This feature will greatly improve the feasibility of a branching fiber network for optical frequency dissemination. However, there are still many challenges ahead to realize its practical application in

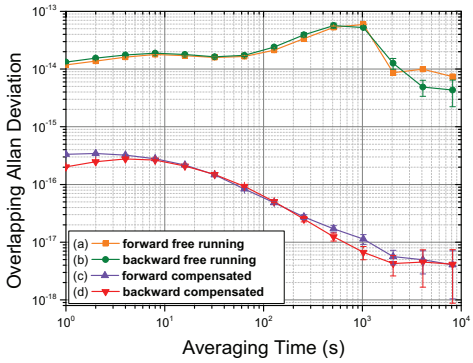

Fig. 5. Measured relative frequency stabilities of frequency signals at the download site with and without phase noise compensation. (a) forward signal directly accessing; (b) backward signal directly accessing; and (c) forward signal with compensation; (d) backward signal with compensation.

non-dedicated telecommunication networks, such as a reliable Hertz-level narrow linewidth laser module, universal interface of the download module, and automatic parameter optimization of the compensation system.

IV. Conclusion

In summary, we have demonstrated a fiber-based, multiple-access optical frequency dissemination scheme for both radio and optical frequency. Using the method, ultra-stable, distributed radio and optical frequency signals can be accessed conveniently at an arbitrary point along the entire fiber link of the dissemination system. The relative frequency stability is at the same level with the dissemination stability of the whole fiber link. A branching fiber network for high-precision synchronization of frequency standards is thus enabled by this method, which will not only cover the research labs with high quality frequency resources, but also cover different industrial users which need precision time and frequency service.

Acknowledgment

The authors would like to thank funding supports from the Major State Basic Research Development Program of China (No.2010CB922901) and Tsinghua University Scientific Research Initiative Program (No.20131080063).

References

[1] C.W. Chou, D.B. Hume, J.C.J. Koelemeij, D.J. Wineland, and T. Rosenband, "Frequency Comparison of Two High-Accuracy Al^{+} Optical Clocks," Phys. Rev. Lett., vol. 104, p. 070802, 2010.

[2] B. Warrington, "Two Atomic Clocks Ticking as One," Science, vol. 336, pp. 421-422, 2012.

[3] M. Kumagai, M. Fujieda, S. Nagano, and M. Hosokawa, "Stable radio frequency transfer in 114 km urban optical fiber link," Opt. Lett., vol. 34, pp. 2949-2951, 2009.

[4] B. Wang et al. "Precise and continuous time and frequency synchronisation at the 5×10^{-19} Accuracy Level," Sci. Rep., vol. 2, 2012.

[5] P.A. Williams, W.C. Swann, and N. R. Newbury, "High-stability transfer of an optical frequency over long fiber-optic links," J. Opt. Soc. Am. B vol. 25, pp. 1284-1293, 2008.

[6] O. Lopez, A. Haboucha, B. Chanteau, C. Chardonnet, A. Amy-Klein, and G. Santarelli, "Ultra-stable long distance optical frequency distribution using the Internet fiber network," Opt. Express. vol. 20, pp. 23518-23526, 2012.

[7] K. Predehl et al. "A 920-Kilometer optical fiber link for frequency metrology at the 19th decimal place," Science, vol. 336, pp. 441-444, 2012.

[8] G. Marra et al. "High-resolution microwave frequency transfer over an 86-km-long optical fiber network using a mode-locked laser" Opt. Lett. vol. 36, pp. 511-513, 2011.

[9] D. Hou, P. Li, C. Liu, J. Zhao, and Z. Zhang, "Long-term stable frequency transfer over an urban fiber link using microwave phase stabilization," Opt. Express, vol. 19, pp. 506-511, 2011.

[10] A. Bauch et al. "Comparison between frequency standards in Europe and the USA at the 10^{15} uncertainty level," Metrologia, vol. 43, 109, 2006.

[11] J. Levine, "A review of time and frequency transfer methods," Metrologia, vol. 45, S162, 2008.

[12] M. Fujieda, M. Kumagai, and S. Nagano, "Coherent microwave transfer over a 204-km telecom fiber link by a cascaded system," IEEE Trans. Ultrason. Ferroelectr. Freq. Control., vol. 57, pp. 168-174, 2010.

[13] O. Lopez et al. "Cascaded multiplexed optical link on a telecommunication network for frequency dissemination," Opt. Express, vol. 18, pp. 16849-16857, 2010.

[14] F.L. Hong et al. "Measuring the frequency of a Sr optical lattice clock using a 120 km coherent optical transfer," Opt. Lett., vol. 34, pp. 692-694, 2009.

[15] Wen-Qin Wang, "GPS-Based Time Phase Synchronization Processing for Distributed SAR," IEEE Transactions on Aerospace and Electronic Systems, vol. 45, pp. 1040-1051, 2009.

[16] C. E. Dunn, S. M. Lichten, D. C. Jefferson, and J. S. Border, "Sub-nanosecond GPS-based clock synchronization and precision deep-space tracking." The Telecommunications and Data Acquisition Progress Report 42-111., July-September, pp. 1-10, 1992.

[17] A Norman, R Kwarciany, G Deuerling and N Wilcer, "The NOvA Timing System: A system for synchronizing a long baseline neutrino experiment," J. Phys.: Conf. Ser., vol. 396, p. 012034, 2012.

[18] C. Gao et al. "Fiber-based multiple-access ultrastable frequency dissemination," Opt. Lett., vol. 37, pp. 4690-4692, 2012.

[19] G. Grosche, "Verfahren zum Bereitstellen einer Referenz-Frequenz," DPMA Patent application, DE 10 2008 062 139, 2010.

[20] Y. Bai et al. "Fiber Based Multiple-Access Optical Frequency Dissemination," Opt. Lett., submitted.

[21] L. Ma, P. Jungner, J. Ye, and J. Hall, "Delivering the same optical frequency at two places: accurate cancellation of phase noise introduced by an optical fiber or other time-varying path," Opt. Lett., vol. 19, pp. 1777-1779, 1994.

On the Importance of Time and Frequency in Geodesy

Karl Ulrich Schreiber
Technische Universitaet Muenchen
Geodaetisches Observatorium Wettzell
Bad Kötzting, Germany
Email: schreiber@fs.wettzell.de

Urs Hugentobler
Technische Universitaet Muenchen
Forschungseinrichtung Satellitengeodaesie
München, Germany
Email: urs.hugentobler@bv.tum.de

***Abstract*—According to Friedrich Robert Helmert geodesy is the science of the measurement and mapping of the figure of the Earth. With the advent of the space age it was possible to establish a global reference frame, which can relate different locations across the entire Earth with an accuracy of currently about 1 cm with respect to each other. A rapid development of highly precise and stable frequency standards took place at the same time and is an important prerequisite for the actual quality of this global terrestrial reference frame. In fact all measurement techniques in modern space geodesy are based on precise time and frequency. Growing demands for the monitoring of global change as one of several examples of the importance of a highly resolved reference frame require more than one order of magnitude improvement over the existing level of quality. Optical clocks, optical frequency combs and near lossless time and frequency transfer have the potential to provide significant improvements of the individual techniques of space geodesy. This talk reviews how time and frequency impacts space geodesy and how the observation techniques may benefit from the recent progress in this field.**

I. Introduction

With the advent of the space age, the tool box of geodesy has changed considerably. With the classical methods, such as triangulation, distance measurements and astronomical observations a consistent reference frame on a global scale remained a dream. With the help of dedicated satellite missions, highly precise time and frequency standards and broadband data acquisition techniques, an entirely new scenario emerges, which allows to reference any event on the body of the Earth to another location with 1 cm of accuracy in a global scale. Space geodesy today contributes to Earth sciences in several ways by

- providing 3-D coordinates in a local, regional and global scale (terrestrial reference frame).
- measuring the precise coordinates of extra galactic radio sources (quasars) and their structure as a function of time (celestial reference frame).
- the determination of the rotation rate of the Earth and polar motion, in order to provide the transformation between these two frames of reference.
- establishing the gravity field of the Earth precisely.

In order to gain access to the continuous evolution of the Earth from variations of the global mass transport, tectonic motion and other mechanisms, the geodetic measurements are repeated frequently. The most prominent measurement concepts are the Very Long Baseline Interferometry (VLBI), Satellite Laser Ranging (SLR), the Global Navigation Satellite System (GNSS) and Doppler Orbitography and Radiopositioning Integrated by Satellite (DORIS). A network of continuously operating globally distributed observing stations forms the backbone of space geodesy.

Apart from high precision navigation, the establishment of a highly precise terrestrial reference frame and for that matter also an equally precise celestial reference frame serves as an underlying metric for models and measurements on climate change, sea level rise, seismic activity and mass loss in the cryosphere of the Earth. For the lithosphere the rate of change reaches from highly dynamic earthquake activities with velocities of km/s to the very slow tectonic plate motions over millions of years with velocities of a few cm per year. The extreme positions of the rate of change for the hydrosphere are given by the current rate of sea level rise of 3 mm per year up to highly dynamical tsunamis with velocities of up to 300 m/s. While weather patterns are typically changing over hours up to days, variations in the global climate are happening over secular periods down to decades. These requirements between very small and slow processes and highly dynamic realtime events are placing severe constraints on the measurement techniques of space geodesy, demanding a terrestrial reference frame of extremely high resolution and stability over at least 9 orders of magnitude of dynamic range and with high spatial and temporal resolution. The Global Geodetic Observing System (GGOS), an initiative within the International Association of Geodesy (IAG), has formulated these requirements in order to integrate GGOS as an important contributor into the Earth System research, which attempts to measure and model the ongoing physical, chemical and biological processes [1].

II. The role of time and frequency in geodesy

In order to establish a maximum in sensitivity and stability all precise ranging techniques in space geodesy are based on the measurement of intervals of time. GNSS, VLBI and DORIS are one-way measurement techniques, while SLR uses a two-way approach. The advantage of SLR is the fact, that the range measurement is based on a precisely detected interval of time on the same clock. The one-way measurement techniques on the other side always rely on the precise synchronization of the two clocks, one at each end of the distance of interest.

978-1-4799-0342-9/13/$31.00 ©2013 IEEE

The process of synchronizing the two sensor clocks therefore is an integrated part of the data reduction procedure in space geodesy. As a matter of fact, one-way geodetic measurement techniques are well suited for precise time and frequency transfer.

The need for precise time as an independent geodetic observable in itself is not given so far. To realize accurate ephemerides of fast moving satellites as part of the data reduction process, an accuracy of the applied timescale of the order of 1 μs is required. The reason for not using precise absolute time is the inherent difficulty of transfering and comparing time experimentally due to the finite velocity of electromagnetic signals, acting as the carrier of time and the difficulty of controlling the entire delays on the signal path up to the point of reference of time. In this context we are not even touching any aspects of the theory of relativity, which will need additional careful consideration for a complete treatment of the time transfer. Time transfer in the microwave regime requires some sort of code measurements in order to transfer time tags and to resolve the ambiguity inherently related to phase measurements. For the GNSS technique, as an example, the code measurement is about a hundred times less precise than the phase measurement, requiring extended filtering techniques to reach a high accuracy. On top of that and even more important, time transfer requires calibrated and temperature stable antennas, cables as well as electronic circuits, such as signal conditioners and amplifiers, of similar quality. Compared to the desirable level of performance of $\Delta t \approx 1$ ps, a viable concept has not yet been demonstrated.

The situation is very different for time transfer in the optical regime, both for the ground to space application as well as for the actively controlled fiber links on the ground. Both applications are utilizing a two-way measurement concept, using essentially a single local timescale to establish the round-trip time as a precisely determined time interval. An additional detector at the single path distance is then used for the timescale comparison, while the round-trip measurement determines the delays, or in the case of the fiber link is used to stabilize the transit delay to a constant value. Neither the optical two-way time transfer from ground to space, nor the two-way compensated fiber link from ground to ground are common or well established techniques in space geodesy today. This may change with the advent of highly precise optical clocks, demonstrating a relative stability approaching $\delta f/f \approx 10^{-18}$ and making gravity field estimates based on exploiting the gravitational redshift by clock comparisons possible in the future. If we are taking the current GGOS goals as the baseline for the requirements for today's space geodesy, this would mean that a remaining uncertainty of 1 mm in the position accuracy from phase measurements would require $\Delta_c = 1$ mm/$c = 3$ ps for the granularity of the applied clocks and $\Delta_v = 1$ mm/$v_{sat} = 0.3$ μs for the accuracy of the applied timescale. In summary time itself needs to be 5 orders of magnitude less precise than the measured time intervals for a given observable. This is another way to express the difficulties that come about with actually measuring time itself as a quantity. How is space geodesy dealing with these difficulties?

All one-way measurement techniques require clocks on both ends of the measured distance that are synchronized at the ps-level in order to derive accurate signal travel times. For GNSS a typical measurement scenario means that every receiver observes more than one satellite that are measured simultaneously. At the same time every satellite is observed by more than one permanent receiving station. As a result one can synchronize all clocks for each measurement epoch from this redundancy, so that no stable clocks are required within the network. However this does not preclude, that the geodetic products would gain, if the clocks would be stable and this stability would be exploited in the data analysis.

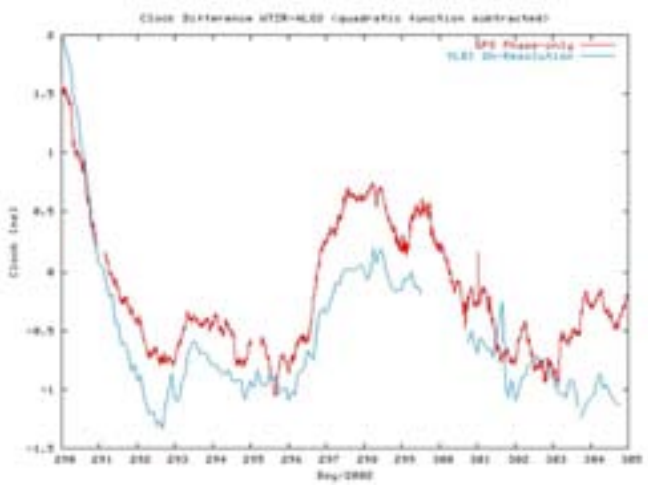

Fig. 1. Transatlantic Clock comparison between the Algonquin and Wettzell observatory. The diagram shows the residual clock drift between the GNSS and VLBI clock synchronization after a common linear and quadratic trend has been removed.

For the VLBI operations a similar situation is given. There is more than one quasar observed and a redundant number of telescopes are participating in the measurement campaign. As the quasars are, however, measured by the parabolic dishes one after the other, the station clock needs to be modeled for an observation session. In the processing procedure usually one set of clock corrections is computed for all systems after every 2 hours in addition to a quadratic clock drift. The clock of one of the stations is selected as the reference clock. Figure 1 shows an illustrating example for a clock comparison based on data of the CONT'02 campaign during which a network of VLBI instruments were operated continuously during two weeks. The VLBI stations, namely Algonquin (Canada) and Wettzell (Germany) are operated from a H-maser each. The same masers are also used as a timing reference in the GNSS permanent receivers simultaneously operated on these observatories. In the absence of any other error source one would expect that the two one-way measurement techniques would provide the same relative clock drift. Once a linear and a quadratic trend, describing the relative drift between the two masers, has been removed, a small time varying discrepancy of the order of up to 1 ns remains. This indicates that small variable systematic biases from the station delays are contaminating the clock synchronization process and hence the measurement resolution.

DORIS is a one-way microwave technique, too. Ultra stable oscillators operated at the ground beacons as well as in the Earth observation satellites have to be synchronized

with master beacons equipped with H-masers. Also for DORIS the absolute timing requirement is at some 1 μs. One beacon observes in general only a single satellite while only the second generation satellite DORIS receivers are capable of observing up to seven beacons at the same time. As a consequence the satellite clocks have to be modeled and the beacon oscillator frequencies have to be estimated per satellite pass. In order to mitigate clock instabilities the phase measurements are converted to Doppler measurements. Precise synchronization of the ground beacon oscillators in conjunction with second generation DORIS satellites would allow to use the high precision phase measurements.

The two-way technique SLR observes time intervals and determines system delays from calibration measurements to local targets of known distance. The requirements for the correct epoch of measurements are comparatively low, since an error in time shifts the measurement along the track of the satellite orbit with the velocity of the satellite. Epoch corrections and range offsets are computed for all systems from a redundant number of observing stations.

III. Common Clock Concept

A clock comparison over large distances as shown in the above example for VLBI and GNSS is limited by a combination of errors. For the microwave techniques we find a high correlation between the refraction correction, phase center variation in the antenna, unaccounted for signal delays in the receiver chain and potentially geometrical instabilities of the entire measurement system. These accumulative error sources are exacerbated by additional delays in the process of synchronizing the clock to the VLBI and the GNSS receiver system independently. Usually the H-maser for the VLBI system is located in a temperature stabilized environment some distance away from the detection system. The same is normally true for the GNSS system. Since all the mentioned error sources are technique specific, part of the high correlation between all contributors can possibly be broken up, if all techniques would be operated on a common clock with lossless time and frequency distribution within each observatory. The lossless time and frequency distribution on the observatory however requires a closed loop locking scheme, where the variable delay on the transmission line is actively controlled and compensated.

For this purpose the classical two-way transfer concept can be employed, where an optical frequency travels back and forth on the identical optical fiber [2], [3]. The phase delay accumulated over this double pass is detected interferometrically and is subsequently stabilized in a closed loop by adjusting the outgoing frequency to provide a stable interferogram at the source at all times. In this way a de facto common clock can be realized for a distributed ensemble of instrumentation in space geodesy, removing the local clock error from the inter-technique comparison. While the viability of this frequency transfer concept has been demonstrated over distances of nearly 1000 km, the same concept does not work for the transfer of time to the same extend, because the frequency dispersion of the fibers do not support the necessary bandwidth for sub-picosecond laser pulses to travel large distances without decomposition. However the closed loop distribution of time over several hundred meters can be achieved with uncertainties of far less than 1 ps, which is enough to synchronize an entire observatory.

Precise optical time transfer over large distances with an accuracy of far less than a nanosecond has been proposed for the Atomic Clock Ensemble in Space (ACES) onboard the International Space Station (ISS) and the concept is currently under construction [4] with an expected launch date in 2015. The time transfer is based on SLR, where two-way time of flight measurements are used to establish the orbit of the ISS. Since the laser pulses are also detected and time tagged on the ACES timescale during the SLR measurement process, the timescale on the ground and the timescale of ACES can be synchronized with an expected accuracy of 100 ps [5]. The inherent high stability of the ACES clocks will also allow a non-common view time comparison, thus allowing to synchronize geodetic observatories over intercontinental baselines for demonstrating the common clock concept.

IV. Conclusion

Modern space geodesy has reached a point where the international terrestrial reference frame allows to relate globally distributed positions with about 1 cm of accuracy with respect to each other. While this falls short of the GGOS goals by about one order of magnitude, it is desirable to improve the situation by providing a lossless distributed common frequency source to all instrumentation on a geodetic Fundamental station. Closed loop fiber links for optical frequency distribution have been demonstrated to provide the necessary phase stability. They are also suitable for accurate time transfer over short distances. Eventually optical laser time transfer via satellites and stable clocks in space may demonstrate an improved accuracy for clock synchronization supporting the generation of highest-accuracy and long-term stable geodetic reference frames.

Acknowledgment

The authors acknowledge support from the German National Science Foundation DFG within the Forschergruppe FOR1503.

References

[1] H.-P. Plag and M. Pearlman (Eds.), *Global Geodetic Observing System – Meeting the Requirements of a Global Society on a Changing Planet in 2020*, Springer, 2009, ISBN 978-3-642-02687-4.

[2] S. M. Foreman, A. D. Ludlow, M. H. G. de Miranda, J. E. Stalnaker, S. A. Diddams and Jun Ye; *Coherent Optical Phase Transfer over a 32-km Fiber with 1 s Instability at* 10^{-17} PRL **99**, 153601 (2007)

[3] O. Terra, G. Grosche, K. Predehl, R. Holzwarth, T. Legero, U. Sterr, B. Lipphardt and H. Schnatz; *Phase-coherent comparison of two optical frequency standards over 146 km using a telecommunication fiber link*, Appl. Phys. B, **97** (3), 541-551, (2009)

[4] M. P. Heß, L. Stringhetti, B. Hummelsberger, K. Hausner, R. Stalford, R. Nasca, L. Cacciapuoti, R. Much, S. Feltham, T. Vudali, B. Leger, F. Picard, D. Massonnet, P. Rochat, D. Goujon, W. Schäfer, P. Laurent, P. Lemonde, A. Clairon, P. Wolf, C. Salomon, I. Prochazka, U. Schreiber, and O. Montenbruck; *The ACES mission: System development and test status* Acta Astronautica, **69** (11), 929–938, (2011)

[5] K. U. Schreiber, I. Prochazka, P. Lauber, U. Hugentobler, W. Schäfer, L. Cacciapuoti, and R. Nasca *Ground-based demonstration of the European Laser Timing (ELT) experiment*, IEEE Transactions on Ultrasonics, Ferroelectrics and Frequency Control, **57** (3), 728-737, (2010)

A Fiber Optic Gyroscope on Multiplexed Telecommunication Network with a Large Enclosed Area

C. Clivati, G. A. Costanzo, M. Pizzocaro
Istituto Nazionale di Ricerca Metrologica
Strada delle Cacce 91, Torino, Italy
and Politecnico di Torino,
corso Duca degli Abruzzi 124,Torino, Italy

D. Calonico, A. Mura, F. Levi
Istituto Nazionale di Ricerca Metrologica
Strada delle Cacce 91, Torino, Italy

Marco Olivieri
Istituto Nazionale di Geofisica e Vulcanologia, sez. Bologna
Via Creti 12, Bologna Italy

Giorgio Spada
Dipartimento di Scienze di Base e Fondamenti
Urbino University "Carlo Bo"
Via Santa Chiara 27, Urbino (PU) Italy

***Abstract*—This work describes the realization of a fiber optic gyroscope with a sensitivity of 10^{-8} (rad/s)/√Hz. Such a high sensitivity is obtained using a 47 km long single mode fiber of the urban optical telecommunication network, that is shared with other users and encloses an area of 20 km^2. This setup has been used to investigate ground motion in occurrence of earthquakes.**

Keywords-fiber optic gyroscope, optical links,fiber optics

I. INTRODUCTION

In recent years, the study of the rotational components of seismic events has received a great attention in seismology, as it can provide a deep insight in the investigation of ground motion. The key tools used to perform this research are optical gyroscopes based on the Sagnac effect. These instruments are the most performing rotation sensors available, and their reading is not corrupted by translational motion as in the rotation sensors based on inertial masses.

There are basically two kinds of optical gyroscopes: Ring Laser Gyroscopes (RLGs) are complex experiments, that require careful maintenance and sophisticated instrumentation, such as free-space optics and ultrastable lasers; they have a high sensitivity, that allows detection of rotation signals well below 10^{-9} (rad/s)/√Hz, such as those occurring during large teleseismic events [1-3]. On the converse, rotation sensors based on passive Fiber Optic Gyroscopes (FOGs) are not suitable for such demanding applications, as their sensitivity varies between 10^{-4} rad/s and 10^{-6} rad/s [4], with a single relevant exception in the 10^{-8} rad/s range [5]. However, they have a broader dynamic range, are transportable, and require only commercial components [6].

We realized a FOG that aims to combine the high sensitivity of RLGs with the robustness of FOGs. This has been done by implementing a Sagnac interferometer on a multiplexed telecom fiber that encloses a 20 km^2 urban area [7]. Our instrument can detect signals that exceed 10^{-8} (rad/s)/√Hz, without the need of ultrastable lasers or complex optics, and may offer new possibilities for the investigation of the rotational component of seismic events.

II. THE EXPERIMENT

A. How the fiber optic gyroscope works

Optical fiber gyroscopes are based on the Sagnac effect, i. e., two optical beams propagate in opposite directions over a closed fiber path enclosing an area; if the platform rotates with respect to an inertial frame, the two beams accumulate a phase difference φ_{nr}. To realize this interferometer and detect φ_{nr}, an optical source is split into two beams that are injected in a fiber loop in opposite directions, and are recombined on a photodiode PD after a round trip. φ_{nr} is related to the rotation rate of the platform $\boldsymbol{\Omega}$ through the relation::

$$\varphi_{nr}=8\pi(\nu/c^2)N\mathbf{A}\cdot\boldsymbol{\Omega} \quad (1)$$

where **A** is the area enclosed by one loop of the fiber spool, N the number of turns of the spool, c is the speed of light in vacuum, and ν is the optical frequency.

To improve the sensitivity of this scheme, we realized an interferometer that has one single loop enclosing a wider area rather than just increase the number of turns. In our setup, the beams are then injected in a 47 km single mode commercial fiber located in the urban area around the city of Turin (Italy, colatitude ~45°). This fiber is used for the Internet data traffic and is implemented on a Dense Wavelength Division Multiplexed (DWDM) architecture, with about 25 dB of optical losses. The 44th channel of the International Telecommunication Union (ITU) grid is dedicated to our

experiment, while Internet data are transmitted on the 21st and 22nd channels, 2 THz away. There is no evidence of any crosstalk between the channels. The shape of the fiber loop is an elongated triangle with an enclosed area of 20 km^2: the resulting phase due to the Earth rotation should be about 55 rad. The optical signal is a laser radiation at 1542 nm provided by a fiber laser with a linewidth of about 10 kHz and optical power of 6 mW . The beam polarization is randomized through a polarization scrambler PS, that reduces

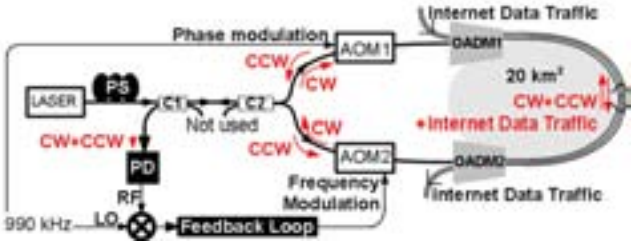

Fig. 1: The large area FOG setup: PS polarization scrambler, C couplers, AOM acousto-optic modulators, OADM Optical Add&Drop Multiplexers, CW (CCW) clockwise (counter clockwise) propagation direction

the effect of polarization mode dispersion along the fiber, i.e. a source of phase shifts between the two beams. Two Optical Add and Drop Multiplexers, OADM1 and OADM2, are used to inject and extract the two beams from the urban loop. In Figure 1, the experimental setup is sketched, in the typical minimum configuration scheme. This setup ensures that the two beams travel exactly the same optical distance [8]. A phase modulation stage is inserted in the loop in a position such that one of the two beams is phase-modulated at the beginning of the loop, whilst the other is modulated after a round trip. In our setup, the phase modulation is performed through an acousto-optic modulator AOM1. The delay in the phase modulation of the two beams enables the detection of an ac photocurrent on the photodiode PD, that varies with time at the phase modulation rate f_m:

$$I = I_0 + I_1 \sin \varphi_{nr} \cos[2\pi f_m t - \varphi_0] + f_m \text{ harmonics} \qquad (2)$$

where I_0 and I_1 are the amplitudes of dc and first harmonic signal; I_1 depends on the phase modulation depth and on the fiber length, and φ_0 is an arbitrary phase. We implemented a closed-loop system [8] in which the non-reciprocal phase shift φ_{nr} is compensated by a proper frequency offset Δ_f between the two counter-propagating beams, according to the relation:

$$\Delta_f = c/(2\pi L\eta)\Delta\varphi_{nr} + c/(L\eta)\kappa, \qquad (3)$$

being η the refractive index of the fiber and κ an integer. As actuator, we use another acousto-optic modulator, AOM2. The variations of the Earth rotation rate can be related to those of Δ_f, through the relation:

$$\Delta_f = 4(\eta v/c)\mathbf{A}\cdot\boldsymbol{\Omega} \quad . \qquad (4)$$

In principle, this interferometer is sensitive to the variations of both the orientation and the magnitude of $\boldsymbol{\Omega}$. However, the sensitivity to variations of tilt is ~10^4 times lower than the sensitivity to variations of spin, and can thus be neglected. Also, with this detection scheme there is an ambiguity in the definition of Δ_f and, for these reason, this setup is better suited to measure the variations of $\boldsymbol{\Omega}$, rather than its accurate value.

B. Measurements and Discussion

Several contributions may affect the phase reading, by inducing a phase noise that pollutes the Sagnac phase. The most relevant comes from the mechanical noise of the fiber originated by acoustic vibrations, human activity and temperature drifts. At first order, the interferometer is not sensitive to mechanical noise, since the optical length variations perturb the phase of the two beams of the same amount. However, the uncorrelated part of the noise $S_{\varphi,nr}(f)$ leads to a residual contribution, and this clearly depends on the Fourier components of the disturbance. We evaluated it by considering the phase noise of the fiber itself, its power spectral distribution $S_\varphi(f)$ and the round trip time of the radiation in the fiber. We estimated this contribution to be

$$S_{\varphi,nr}(f) = 1/3(2\pi fL/c)^2 S_\varphi(f), \qquad (5)$$

assuming that the noise is uniformly distributed along the fiber. It is interesting to note that the sensitivity of the gyroscope should improve using longer fibers, since $S_\varphi(f)$ scales as the fiber length L [9], and thus $S_{\varphi,nr}(f) \sim L^3$. In addition, the ratio A/L should be maximized in order to take full benefit from the available fiber loop. For instance, a factor 9 of improvement in our setup could be obtained simply by reshaping our triangular fiber loop into a circle, without changing the fiber length.

Fig. 2 shows the spectral density of the frequency correction signal Δ_f, that can be converted into the power

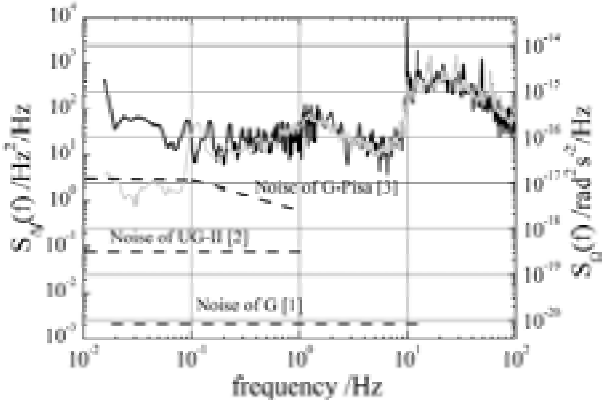

Fig. 2: Sensitivity of our FOG: black line, noise power spectral density of the frequency correction signal (left-hand axis) and of the equivalent rotation signal (right-hand axis); grey line, limitation by the mechanical noise of the fiber; dashed lines: sensitivity of some state-of-the-art RLGs.

This work has been partly funded by Compagnia di San Paolo

spectral density of the Earth's spin variations using eq. (4). The graph also shows the ultimate noise that can be obtained (grey line), considering the mechanical noise of the fiber loop used and the round-trip time. For comparison, the background noise of some state-of-the art RLGs is shown as well. The background noise of our FOG nicely agrees with the predictions down to Fourier frequencies of 0.1 Hz. The stability of our setup over longer averaging times was evaluated by counting Δ_f with a frequency counter and converting it into variations of the Earth rotation rate. It is shown in Fig. 3. On the medium and long term, the Sagnac phase instability is degraded due to linear or circular birefringence of the optical fiber (for instance, induced by stresses and Faraday effect), that varies with time due to slow and unpredictable drifts in the beams' polarization. This noise contribution should be averaged out if the two beams were completely depolarized, thus an improvement in our depolarization stage could help to decrease the long term noise. Nevertheless, the ultimate sensitivity already achieves $2 \cdot 10^{-9}$ rad/s for integration times of 1000 s.

Other noise contributions that may affect FOGs stability [6] are below our present noise. These include: backscattering, Kerr-based nonlinearities, and scale factor instability (i.e. variations in the length L or in the area A of the loop).

Backscattering occurs at the connectors and in the fiber itself; however, backscattered light passes two times through either AOM1 or AOM2, whilst the coherent signal passes only once in both AOMs. By adjusting the frequency difference between AOM1 and AOM2, the backscattered light can be overimposed to the coherent signal or pushed at a different frequency. We performed measurements both with a small (< 2 kHz) and with a large (>200 kHz) frequency offset, and could not detect any difference in the background noise. We conclude that this effect is still below the present sensitivity.

Variations of the optical power could affect the phase difference of the two beams through the Kerr effect. To quantify this contribution we changed the optical power of one of the two beams by about 20%, that is much higher than in normal operation (<5%), and looked for related variations in the non-reciprocal phase. We did not detect any difference, therefore we estimate this effect as well to be below the noise.

The detrimental effects of scale factor instability are more difficult to model. Nevertheless we can make some realistic assumptions based on the sensitivity of our interferometer: the dependence of the correction frequency Δ_f on variations of the fiber length is about 0.8 Hz/m, whilst the dependence on variations of the area is 2 mHz/m^2. Therefore, the response of the FOG to any reasonable geometrical variation of the loop should be negligible at the present state.

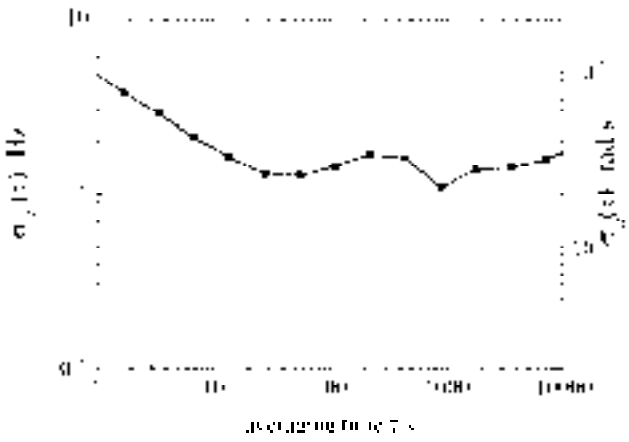

Fig. 3. Allan deviation of the correction frequency sDf(t) (left-hand y axis) and the equivalent instability sW(t) of the spin variations (right-hand y axis).

Location	UTC Time	coordinates	Distance from Turin	Magnitude
Italy (Sicily)	2013-01-04 07:50:06	37.81°N, 14.80° E	~ 9°	M_w=4.3
France (Alps)	2013-01-07 04:20:24	44.76°N 6.75° E	<1°	M_l=3.5
Alaska	2013-01-05 08:58:19	55.28°N 134.67°W	~ 71°	M_w=7.5

Table 1. Earthquakes occurred while the FOG was measuring.

C. *Earthquakes detection*

We let the gyroscope collect data uninterruptedly for several days, from December 23rd 2012 to January 8th, 2013. During acquisition some relevant seismic events happened, that are summarized in Table 1. They include one large and far earthquake and two small but close ones. In all cases, the estimated rotational sensitivity of our gyroscope was too low

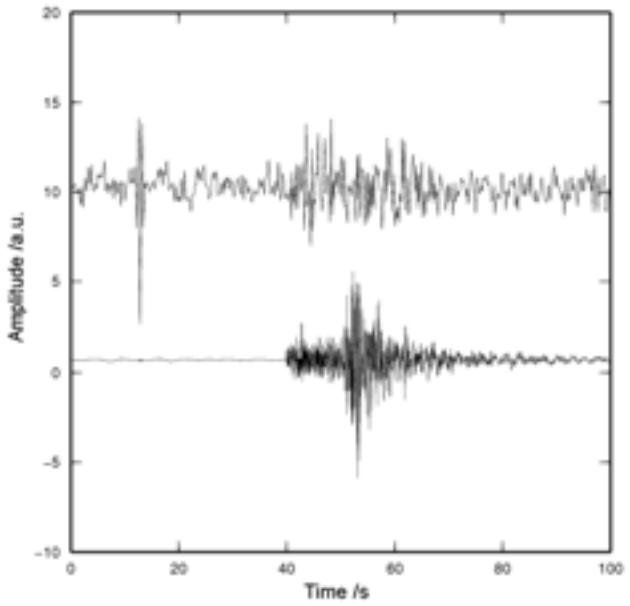

Fig. 4: The Gyroscope signal (top) and the seismometer signal (bottom) for the January 7th, 2013 earthquake in France (M_l = 3.5). Amplitudes have been arbitrarily scaled to compare. Seismogram (in velocity) has been recorded by station GU.LSD (Lago di Serrù, Latitude 45.4595°, Longitude 7.1343°) about 60 km North East from Torino.

to detect such events; however, our analysis was based on the model for small gyroscopes, as we still lack a model that predicts what kind of signal we should expect with this distributed sensor. Actually we could not detect any signal from the earthquakes of Italy and Alaska, but the FOG detected the earthquake occurring on January 7th in France.

In Fig. 4 both the signal from the gyroscope (top) and the signal from the closest available seismometer (GU.LSD) from the location of the gyroscope (bottom) related to this event are shown. The spectral components of the signal are between 0.1 Hz and 0.7 Hz. However, still we have no elements to conclude that this is a rotational signal rather just an increase of the background noise. This event was indeed very close to Turin (less than 100 km distance from the epicenter) and the seismic noise associated to the earthquake could have increased the fiber noise, with a subsequent increase in the noise of the instrument, that would lower the detection capability. Because of high frequency shaking, this would occur only for local earthquakes. This issue is still under investigation.

III. Conclusion and Outlooks

We realized a FOG on a multiplexed commercial fiber network that is 47 km long and has an enclosed area of 20 km^2. Its sensitivity is high enough to detect variations of the Earth rotation rate larger than 10^{-8} (rad/s)/√Hz without using complex optics nor ultrastable lasers; the potential of this technique is however not fully exploited yet. A better depolarization and a spectrally broader laser source could reduce the noise on the long term, whereas the sensitivity in the short and medium term (i.e. for frequencies higher than 0.1 Hz) is limited by the mechanical and temperature noise of the fiber. This could be improved on one hand by increasing the dimensions of the fiber loop, and on the other hand, by maximizing the area enclosed by the loop. For instance, the sensitivity could be improved of a factor 9 in our setup if the loop had not been an elongated triangle but a circle, with the same fiber length.

More sophisticated techniques have recently been proposed and can be implemented to improve the sensitivity [11].

We demonstrate that fiber networks used for the Internet data traffic could be suitable to realize optical fiber gyroscopes. An increasing number of telecom fiber loops are currently being used not only for telecommunications, but also for the coherent transfer of optical phase, and this could support the realization of a grid of such optical sensors distributed over large geographical areas [12, 13]. This setup could be helpful for the detection of teleseismic rotational signals, but novel applications could be envisaged as well, that could in principle support the research in rotational seismology. However, a deeper investigation on how the ground motion is detected over such a large area, and on the potential and feasibility of a distributed grid of such FOGs is still needed.

Acknowledgments

The authors acknowledge J. Belfi, N. Beverini, G. Carelli and L. Sambuelli for useful discussions; the GARR Consortium for technical help with the fiber infrastructure. Earthquake locations in Table 1 have been extracted from the EMSC website (http://www.emsc-csem.org), while magnitudes have been extracted respectively from the Quick RCMT catalog (http://www.bo.ingv.it/RCMT), from the INGV catalog (iside.rm.ingv.it) and from the USGS NEIC catalog (http://earthquake.usgs.gov/) . Station GU.LSD is part of the RSNI SEISMIC NETWORK maintained by the Dipster, Università di Genova. Data have been retrieved from the website http://eida.rm.ingv.it.

References

[1] K.U. Schreiber, A. Velikoseltsev, G. E. Stedman, R. B. Hurst, T. Klugel, "New applications of very large ring lasers" Symposium Gyro Technology , p. 8.0 (Sorg H, ed. 2003).

[2] R. B. Hurst, G. E. Stedman, K. U. Schreiber, R. J. Thirkettle, R. D. Graham, N. Rabeendran, and J.-P. R. Wells, "Experiments with an 834 m^2 ring laser interferometer" J. Appl. Phys vol. 105, pp. 113115-113115-10, June 2009.

[3] J. Belfi, N. Beverini, G. Carelli, A. Di Virgilio, E. Maccioni, G. Saccorotti, F. Stefani, A. Velikoseltsev, "Horizontal rotation signals detected by "G-Pisa" ring laser for the M=9.0, March 2011, Japan earthquake" J. Seismol. vol. 16 , pp. 767-776, Febr. 2012.

[4] A. Velikoseltsev, K. U. Schreiber, A. Yankovsky, J.-P.R. Wells, A. Boronachin, A. Tkachenko, "On the application of fiber optic gyroscopes for detection of seismic rotations", J. Seismol. vol. 16, pp. 623-637, Febr. 2012.

[5] L. R. Jaroszewicz, Z. Krajewski, H. Kowalski,G. Mazur, P. Zinowko, J. Kowalski, "AFORS: Autonomous Fibre-Optic Rotational Seismograph: Design and Application" Acta Geophysica vol. 59, pp. 578-596, June 2011.

[6] B. Culshaw, "The optical fibre Sagnac interferometer: an overview of its principles and applications" Meas. Sci. Technol. vol. 17, pp. R1-R16, Nov. 2005.

[7] C. Clivati, D. Calonico, G. A. Costanzo, A. Mura, M. Pizzocaro, F. Levi, "Large-area fiber-optic gyroscope on a multiplexed fiber network",Opt. Lett., vol. 38,, pp. 1092-1094, March 2013.

[8] J. L. Davis, S. Ezekiel, "Closed-loop, low-noise fiber-optic rotation sensor", Opt. Lett. vol. 6 , pp. 505-507, Oct.1981.

[9] W. Williams, W. C. Swann, and N. R. Newbury, "High-stability transfer of an optical frequency over long fiber optic links," J. Opt. Soc. Am. B vol. 25, pp. 1284-1293, Aug. 2008.

[10] H. Igel, A. Cochard, ∗ J. Wassermann, A. Flaws, U. Schreiber, A. Velikoseltsev, and N. Pham Dinh, "Broad-band observations of earthquake-induced rotational ground motions", Geophis. J. Int., vol. 168, pp. 182–196, Jan. 2007.

[11] S. Schiller, "Feasibility of giant fiber-optic gyroscopes", Phys. Rew. A vol. 87, 033823-033823-7, March 2013.

[12] O. Lopez, A. Haboucha, F. Kefelian, H. Jiang, B. Chanteau, V. Roncin, C. Chardonnet, A. Amy-Klein, G. Santarelli,"Cascaded multiplexed optical link on a telecommunication network for frequency dissemination," Opt. Expr. vol. 18, pp. 16849-16857, Aug. 2010.

[13] K. Predehl, G. Grosche, S. M. F. Raupach, S. Droste, O. Terra, J. Alnis, Th. Legero,T. W. Hansch, Th. Udem, R. Holzwarth, H. Schnatz, "A 920-Kilometer Optical Fiber Link for Frequency Metrology at the 19th decimal place," Science vol. 336, pp. 441-444, Apr. 2012.

s-Wave Collisional Frequency Shift of a Fermion Clock

Eric L. Hazlett, Yi Zhang, Ronald W. Stites, Kurt Gibble and Kenneth M. O'Hara
Department of Physics
The Pennsylvania State University
University Park, USA

***Abstract*—We have experimentally observed a collisional frequency shift of trapped ultracold fermions. We probe the distinguishing features of s-wave collisional frequency shifts of fermions by stepping the atomic interactions through zero near an s-wave Feshbach resonance.**

Keywords—atomic clock, fermion, collision, frequency shift

I. SUMMARY

This paper summarizes our recent observations of an s-wave collisional frequency shift of an atomic clock based on fermions [1]. As the temperature of a gas is lowered to zero, collisions become *s*-wave, with no relative angular-momentum of the two particles. While *s*-wave collisions are allowed for bosons and are the most important limitation for the operation of Cs fountain clocks [2-6], they are forbidden for identical fermions. Even when dephasing made fermions distinguishable, collision shifts were absent [7]. Thus, fermions were thought to be immune to *s*-wave collisional frequency shifts (*s*CFS's), making them ideal for metrology. However, recent theoretical work predicted that fermions have *s*CFS's because the inhomogeneity of the excitation field makes particles distinguishable [8].

Here we experimentally observe *s*-wave collisional frequency shifts in a thermal gas of ultracold ^{6}Li fermions. Working near a Feshbach resonance, we tune the *s*-wave scattering length through zero around 528G to conclusively demonstrate that the shifts we observe are due to s-wave collisions. We show that Ramsey spectroscopy clearly distinguishes the novel behaviors of the *s*CFS, via unique dependences on the first and second Ramsey pulse areas, θ_1 and θ_2. We observe that the shift is insensitive to θ_1 and thereby the difference of the spin populations [8], in stark contrast with the shifts for bosons and the often-used mean-field expression. Instead, the fermion *s*CFS depends strongly on θ_2, which reads out the interaction-induced phase shifts of each atom. The shift is canceled if the atoms' phases are detected, on average, with equal sensitivity at $\theta_2=\pi/2$ [8]. Interestingly, we show that correlations in the sample perturb the null of the *s*CFS to θ_2 slightly greater than $\pi/2$. We explicitly see that the *s*CFS increases as expected with the independently characterized inhomogeneity of the clock excitation field. The fermion *s*CFS we observe in the resolved sideband regime is analogous to those for optical lattice clocks. Recently, the fermion *s*CFS was simulated with an ^{87}Rb Bose gas [9]. They observed the predicted dependence on θ_2, but an unexpected dependence on θ_1. They elegantly showed a direct link between spin-waves and the fermion *s*CFS, which we observe in the resolved sideband regime.

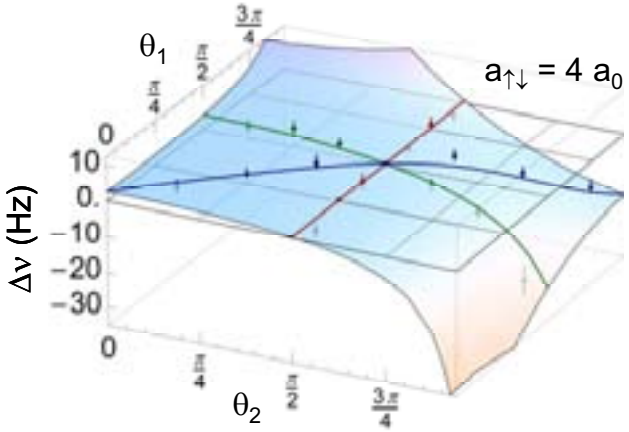

Fig. 1. Collisional frequency shift of ^{6}Li fermions as a function of the Ramsey pulse areas, θ_1 and θ_2 [1,8]. In contrast to bosons, the collision shift of fermions is not proportional to the difference of partial densities $n_\uparrow - n_\downarrow$, which would imply a strong dependence on θ_1. The shift depends strongly on the second Ramsey pulse area θ_2, going to 0 if the second pulse is a $\pi/2$ pulse.

ACKNOWLEDGMENT

We gratefully acknowledge discussions with W. Maineult and P. Rosenbusch.

Financial support from the NSF, AFOSR, ARO, DARPA, the Sloan Foundation (E. L. H.), and Penn State.

REFERENCES

[1] E. L. Hazlett, Y. Zhang, R. W. Stites, K. Gibble and K. M. O'Hara, "s-Wave Collisional Frequency Shift of a Fermion Clock," Phys. Rev. Lett. vol. 110, 160801 (2013).

[2] K. Gibble and S. Chu, "Laser-Cooled Cs Frequency Standard and a Measurement of the Frequency Shift due to Ultracold Collisions," Phys. Rev. Lett. vol. 70, p. 1771-1774, 1993.

[3] F. P. DosSantos H. Marion, S. Bize, Y. Sortais, and A. Clairon, C. Salomon, ”Controlling the Cold Collision Shift in High Precision Atomic Interferometry,” Phys. Rev. Lett. vol. 89, 233004 (2002).

[4] K. Szymaniec, W. Chałupczak, E. Tiesinga, C. J. Williams, S. Weyers, and R. Wynands, ”Cancellation of the Collisional Frequency Shift in Caesium Fountain Clocks,” Phys. Rev. Lett. vol. 98, 153002 (2007).

[5] R. Li, K. Gibble and K. Szymaniec, “Improved accuracy of the NPL-CsF2 primary frequency standard: evaluation of distributed cavity phase and microwave lensing frequency shifts,” Metrologia vol. 48, p. 283-289, 2011.

[6] J. Guéna, M. Abgrall, D. Rovera, Ph. Laurent, B. Chupin, M. Lours, G. Santarelli, P. Rosenbusch, M. E. Tobar, R. Li, K. Gibble, A. Clairon, and S. Bize, "Progress in Atomic Fountains at LNE-SYRTE," IEEE Trans. Ultrasonics, Ferroelectrics, and Freq. Control vol. 59, 391-410 (2012).

[7] M. W. Zwierlein, Z. Hadzibabic, S. Gupta, and W. Ketterle, “Spectroscopic insensitivity to cold collisions in a two-state mixture of fermions,” Phys. Rev. Lett. vol. 91, p. 250404, 2003.

[8] K. Gibble, “Decoherence and Collisional Frequency Shifts of Trapped Bosons and Fermions,” Phys. Rev. Lett. vol. 103, p. 113202, 2009.

[9] W. Maineult, C. Deutsch, K. Gibble, J. Reichel, and P. Rosenbusch, “Spin waves and Collisional Frequency Shifts of a Trapped-Atom Clock,” Phys. Rev. Lett. vol. 109, p. 020407, 2012.

Laser Dynamics Effects on the Systematics of Large Size Laser Gyroscopes

Davide Cuccato
Dept. of Information Engineering,
University of Padova, Italy
Email: davidecuccato@dei.unipd.it

Jacopo Belfi, Nicolò Beverini, Massimo Calamai
Dept. of Physics, University of Pisa, Italy
Email: belfi@df.unipi.it,
beverini@df.unipi.it,
massimo.calamai@gmail.com

Angela Di Virgilio
INFN Section of Pisa, Italy
Email: angela.divirgilio@pi.infn.it

Antonello Ortolan
INFN National Laboratories of Legnaro, Italy
Email: ortolan@lnl.infn.it

***Abstract*—We present the results of the experimental investigation of ring lasers dynamics obtained by operating the G-Pisa gyroscope with the laser plane oriented almost perpendicularly to the local North direction. In this configuration, the Earth's rotation contribution to the Sagnac frequency is less sensitive to orientation errors, and more precise observations of the laser dynamical parameters can be achieved. Cavity losses and scattering parameters are monitored by observing the single beams intensity modulation at the Sagnac frequency while the active medium parameters are identified by a dedicated spectroscopic analysis of the plasma dispersion function. A summary of the performances of both the identification and the frequency denoising algorithm.**

I. Introduction

Active Sagnac interferometers, based on He-Ne ring laser technology [1], find applications in different areas of science as very sensitive gyroscopes. Depending on their scale-factor they can be used as inertial sensors for navigation, rotational seismometers, accurate detectors of geodetic signals modulating the Earth rotation vector. The outstanding stability of the large ring laser G [2], located at the geodetic observatory of of Wettzell, has recently triggered a collaboration for realizing an experiment for testing general relativity on ground, using an array of ultra sensitive ring lasers [3]. The project foresees the construction of a tri-axial gyroscope for the measurement of the Earth's rotation vector with an accuracy goal of at least 10^{-9}. This goal requires a strict control of all the systematics connected to the geometrical scale factor and to the nonlinear dynamics of the laser [6]. The frequency shift δf_S determined by the Sagnac effect on the two beams resonating on the same mode of wavelength λ in an optical cavity of area vector $\vec{A}$ side-length L, rotating at speed $\vec{\Omega}$ (see Fig.1) is:

$$\delta f_S = \frac{4\vec{A}}{L} \cdot \vec{\Omega}(1+\delta_S) + \delta f_{1-2} + \delta f_0 \qquad (1)$$

δ_S is a scale factor correction, due to geometry irregularities, δf_{1-2} is a frequency shift due to the coupling between the counter-propagating beams and the active medium, and δf_0 is a null-shift error coming from non-reciprocities of the active cavity.

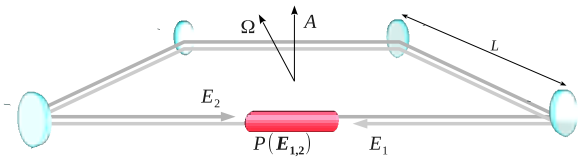

Fig. 1: Basic scheme of a square-cavity ring laser model. The nonlinear polarization $P_(E_{1,2})$ is the coupling function between the two counter-propagating beams 1 and 2.

A. Basics of the model

At the basis of the model we consider the Lamb-Aronowitz theory of ring laser [4], [5]. The electric fields resonating in the cavity are driven by a complex atomic polarization determining amplitudes and frequencies of the two counterpropagating modes. In their treatment the polarization $P(E_1, E_2)$ is expanded to the third order in the field amplitudes $E_{1,2}$:

$$P^{(3)}(E_{1,2}) = -\frac{2i|\mu_{ab}|^2}{\gamma_{ab}} \int_0^\infty \chi_{1,2}(v)\rho^{(2)}(v, E_{1,2})dv, \qquad (2)$$

where $|\mu_{ab}|$ is the atomic dipole amplitude of the laser transition, γ_{ab} is the homogeneous linewidth normalized to the Doppler linewidth, $\chi_{1,2}(v)$ is the complex susceptibility of the medium as a function of the atomic velocity class v, $\rho^{(2)}$ is the second order population inversion distribution. The calculation of the polarization is performed by means of the plasma dispersion function of the gas mixture which is typically composed by He, ^{20}Ne and ^{22}Ne at partial pressures of 7.3 mbar, 0.1 mbar and 0.1 mbar, respectively. In the model two kind of parameters can be distinguished: cold cavity parameters and active medium parameters. Relevant cold cavity parameters consist in the total losses of the two beams μ_1 and μ_2 and the backscattering coupling coefficients $r_1 e^{i\epsilon_1}$ and $r_2 e^{i\epsilon_2}$. The active medium parameters to be calibrated are related to the laser gain and dispersion. According to the Lamb formalism, the laser parameters to be calibrated and identified are:

$$\begin{aligned} \alpha_{1,2} &= G\frac{\Im[kZ(\xi_{1,2}) + k'Z(\xi'_{1,2})]}{\Im[Z(0)]} - \mu_{1,2} \\ \beta_{1,2} &= \alpha_{1,2} + \mu_{1,2}, \end{aligned} \qquad (3)$$

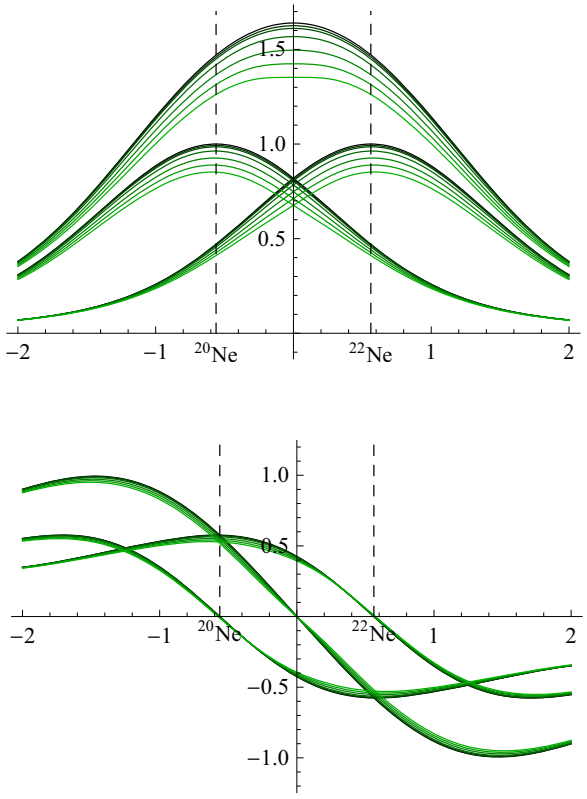

Fig. 2: Imaginary (upper) and real (lower) part of the plasma dispersion function versus normalized detuning. The two isotopic contributions ^{20}Ne and ^{22}Ne are also shown. Different curves correspond to different transition saturation parameters ranging from zero to 0.1 times the transition saturation intensity.

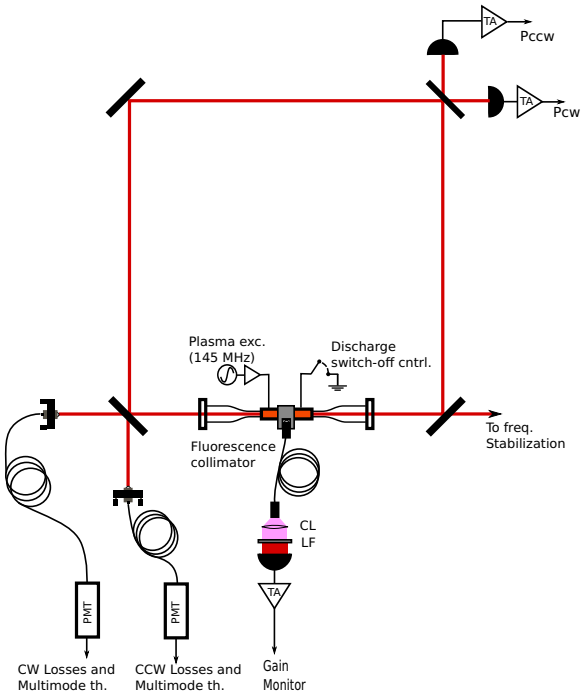

Fig. 3: The experimental setup for the calibration of the ring laser parameters. PMT: photomultiplier tube. TA: transimpedance Amplifier, LF:Line Filter. CL: Collimating Lens. TA Gain for G-Pisa is 1 GOhm.

where G is the single pass gain, $Z(\xi)$ is the plasma dispersion function of the detuning ξ, k and k' are the relative concentration of the two Ne isotopes.

B. Calibration of the ring laser parameters

The complete setup for the calibration of the laser parameters is presented in Fig. 3. The setup allows to perform essential observations on the active medium by accessing the plasma trough the laser capillary. By observing the single beams exiting one of the four cavity mirrors and the intensity of the spontaneous emission from the upper laser level in the plasma fluorescence, one can estimate the "cold cavity" parameters: cavity total losses, backscattering coupling amplitudes and backscattering phases. Other quantities related to the active medium, like the plasma temperature can be estimated by laser Doppler spectroscopy of a strong dipole transition (see Fig.4) by probing the plasma through the discharge capillary.

II. Experimental results

The information about rotation and laser systematics are obtained by sampling three optical outputs of the system: the Sagnac interferogram $S(t)$ and the two monobeams $V_1(t)$ and

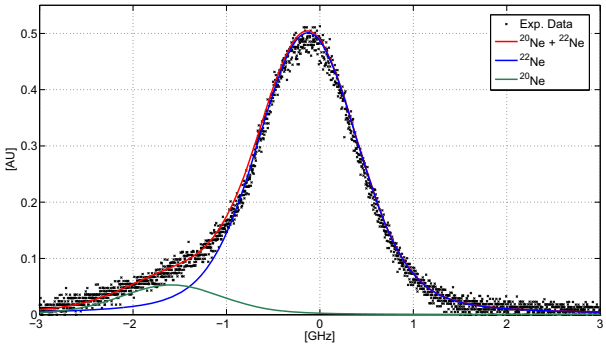

Fig. 4: Doppler profile of the closed optical transition in Neon at 640.2 nm, allowing for the Neon temperature estimation. The measurement is taken in typical operation conditions for a plasma of He-Ne standard mixture at 4.5 mbar. From the fit results, we get $T_{Ne} = \sqrt{\frac{\Gamma_{20}^2 * 20 m_p}{\lambda ln 2 K_B}} = (360 \pm 12) K$.

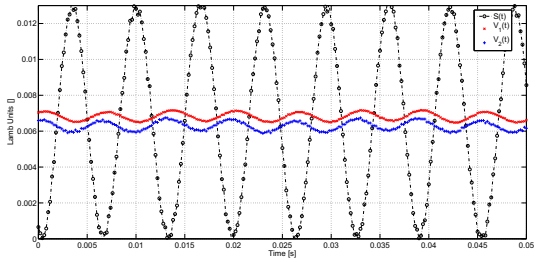

Fig. 5: Typical acquisition of the three main optical signals from G-Pisa. All the signals are sampled at 5kSample/s.

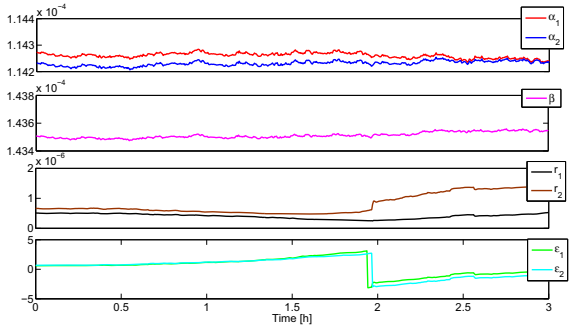

Fig. 6: Lamb parameters tracking obtained from 3 h of experimental data of G-Pisa. After about 2h of acquisition, one of two modes of the ring undergoes a multimode transition. The net effect on the laser dynamics is a sudden change in the amplitude and phases of the backscattering.

$V_2(t)$:

$$\begin{aligned} S(t) &= |a_1 E_1(t) + a_2 E_2(t)|^2 \\ V_1(t) &= |b_1 E_1(t) + c_{21} E_2(t)|^2 \\ V_2(t) &= |b_2 E_2(t) + c_{12} E_1(t)|^2 \end{aligned} \tag{4}$$

where the coefficients a_i, b_i, c_{ij} depend on the optical alignment, backscattering and electronics. Typical acquisition of the three optical signals are shown in Fig. 5.

A. Identification

After the initial calibration of the instrument, the laser parameters are estimated once per 10 second. The tracking of the main laser parameters for a run of 1 hour of operation of the gyro is sketched in Fig.6.

B. Rotation rate estimation

The parameter estimation procedure, based on the perturbative solutions of the laser dynamics, allow us to apply Kalman Filter theory for the estimation of the angular velocity. This method, already presented in [6] makes it possible to remove large part of the fluctuation of the measured Sagnac frequency.

In Fig. 7 is presented a preliminary result of the noise filtering.

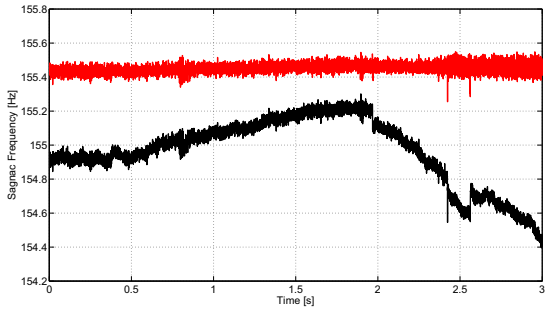

Fig. 7: Sagnac frequency estimation obtained from 3 h (same period of Fig.6) of experimental data of G-Pisa. The uncorrected frequency is plotted in comparison to demonstrate the effectiveness of the method.

III. Conclusion

We proposed a method for the cancellation of the laser dynamic induced drift from the Sagnac frequency of a large ring laser gyro. The method is based on the initial calibration of both passive cavity and active medium parameters. The parameters exhibiting the largest fluctuation are tracked along acquisition of the Sagnac frequency and subsequently exploited for the rotation rate estimation. A sensitive increment in rotation rate resolution and stability has been demonstrated. In order to set the actual limits of the method, further investigations have to be conducted over longer acquisition time periods.

Acknowledgment

The authors would like to thank K. U. Schreiber, A. Gebauer and A. Velikoseltsev for the usefull discussions and suggestions.

References

[1] K. U. Schreiber, J-P. Wells, "Invited Review Article: Large ring lasers for rotation sensing", Rev. Sci. Instrum. **84**, 041101, (2013).

[2] K. U. Schreiber et al.,"The large ring laser G for continuous Earth rotation monitoring", Pure Appl. Geophys. **166**, 14851498, (2009).

[3] F. Bosi et al., "Measuring Gravito-magnetic Effects by Multi Ring-Laser Gyroscope", Phys. Rev. D, **77**, 122002, (2011).

[4] L. N. Menegozzi and W. E. Lamb, "Theory of a ring laser", Phys. Rev. A **8**, 21032125, (1973).

[5] F. Aronowitz, "Fundamentals of ring laser gyro", in Optical Gyros and their Applications, RTO AGARDograph 339, pp. 2330, (1999).

[6] A. Beghi et al., "Compensation of the laser parameter fluctuations in large ring-laser gyros: a Kalman filter approach", Applied Optics, **51** (31), (2012).

Towards a New Clock Laser System Using a Ceramic Cavity and Laser Linewidth Transfer Technique

Kazumoto Hosaka, Hajime Inaba, Daisuke Akamatsu, Masami Yasuda, Atsushi Onae, and Feng-Lei Hong
National Metrology Institute of Japan (NMIJ),
National Institute of Advanced Industrial Science and Technology (AIST),
Tsukuba, Japan
kazu.hosaka@aist.go.jp

Jun Sugawara
Ceramics Division,
Krosaki Harima Corporation,
Kitakyushu City, Japan

***Abstract*— We propose employing an ultra-low thermal expansion ceramic for long cavity spacers that can reduce thermal noise effect on ultra-stable optical cavities relatively, since the high-rigidity ceramic should be insensitive to vibration. Thermal expansion properties are investigated using a prototype ceramic cavity. Simulation results show that responses of a long ceramic cavity to the vertical acceleration are similar to that of a short ultra-low expansion (ULE) glass cavity. Linewidth transfer technique based on an optical frequency comb combining with the narrow linewidth laser stabilized to the ceramic cavity would serve as a useful ultra-stable local oscillator for optical clocks.**

Keywords—ultra-stable laser, optical cavity, thermal noise, ultra-low expansion ceramic

I. INTRODUCTION

Lasers with high frequency stability and a narrow linewidth have been indispensable tools in various scientific fields. In the case of optical clocks, lasers locked to a longitudinal mode of an ultra-stable cavity are used to drive narrow-linewidth clock transitions in atoms/ions with a sub-hertz linewidth. Theoretical study shows that the frequency stabilities of ultra-stable lasers at a short averaging time are close to being limited by mechanical thermal fluctuations of the optical cavities [1]. To improve the short-term stabilities of the clock lasers, new high finesse cavities that reduce thermal noise should be necessary.

Thermal noise can be reduced by using an alternative mirror material with extremely low mechanical losses and cooling the optical cavity itself in a relatively large cryogenic system [2]. Furthermore, a large beam size on the highly reflective mirrors and a long spacer for the cavity should help to reduce the thermal noise relatively [3]. However, a long cavity could be sensitive to the vibration. To surmount the problems, there is a need for a new material, such as ceramic, with high specific rigidity and very low thermal expansion at room temperature.

As another important technique for the new clock laser system, laser linewidth transfer using high-speed controllable frequency comb stabilized to an ultra-stable laser is absolutory useful, because the ultra-stable optical cavity does not have to be operated at required wavelengths for optical transitions in atoms/ions [4-6]. Furthermore, it can be used to stabilize plural lasers with different wavelengths simultaneously using phase lock technique. In this case, even small frequency fluctuation of the resonant frequency of the ultra-stable cavity could be canceled, when the frequency ratio of the lasers stabilized to the same cavity via the comb is used for some experiments, such as frequency ratio measurements between ytterbium and strontium optical clock transitions.

In this proceeding, first we describe properties of the ceramic that will be employed as a spacer of the new long cavity. And then, laser linewidth transfer technique using our high-speed controllable fiber-based frequency comb is briefly explained.

II. DEVELOPMENT OF CERAMIC CAVITY

We have applied an ultra low thermal expansion ceramic based on poly-crystalline cordierite ceramics (‘NEXCERA’ Krosaki Harima [7]), which has a Young's modulus of ~ 130 GPa and a Poisson's ratio of ~ 0.30, to an optical cavity spacer. The ceramic is composed of cordierite grains with grain size of 0.5 to 2.0 μm and slight amorphous phases along the grain boundary. For manufacturing the cavity spacer, mixed raw powders were wet milled together with organic binder and deionized water. The slurry thus obtained was dried using a spray dryer and then isostatically pressed at room temperature into a cylindrical green compact. The green compact was annealed once in air to burn out the organic additives and then sintered at high temperature which is close to its melting point in an Ar-gas flow atmosphere. The sintered body was precisely ground and its both ends were polished to extremely smooth surfaces, thus enabling it to be connected to other materials, such as ULE glass, using the optical contact technique.

A. Thermal propertties of the ceramic

We produced a prototype optical cavity consisting of two ULE mirrors in optical contact with the ceramic spacer. The reflectivity of these mirrors was 99.5(1)% at 1064 nm, giving the cavity a finesse of about 600. The length and diameter of

the ceramic spacer were 75 and 25.4 mm, respectively. A Nd:YAG laser operated at 1064 nm was stabilized to the ceramic cavity and the resonant frequency of the cavity was measured by a fiber-based frequency comb system. We found that the ceramic cavity had a zero cross temperature at 16.4 (1) °C where the thermal expansion coefficient crosses zero [8].

We found that the thermal expansion coefficient of the ceramic cavity at around the zero cross temperature is about 5 times more sensitive to a temperature change than that of the ULE cavity. However, it should be possible to overcome this disadvantage by using a well-designed temperature controller.

B. Design of long ceramic cavities

A finite element based analysis has been employed to calculate the ceramic cavity deformation when loaded. A typical result is shown in figure 1. In this simulation, axial displacements at the end-face centre of the spacer are calculated, when a cut-out type long cavity spacer supported by four points is deformed by the gravity. A reduction in the response of the ceramic cavity to the vertical acceleration by a factor of 2 comparing with an ULE cavity has been shown (Fig. 1.). The estimated sensitivity of 13.6 kHz/(g mm) is same order to that of short (~ 0.1 m) cut-out cavities made by ULE glass [9].

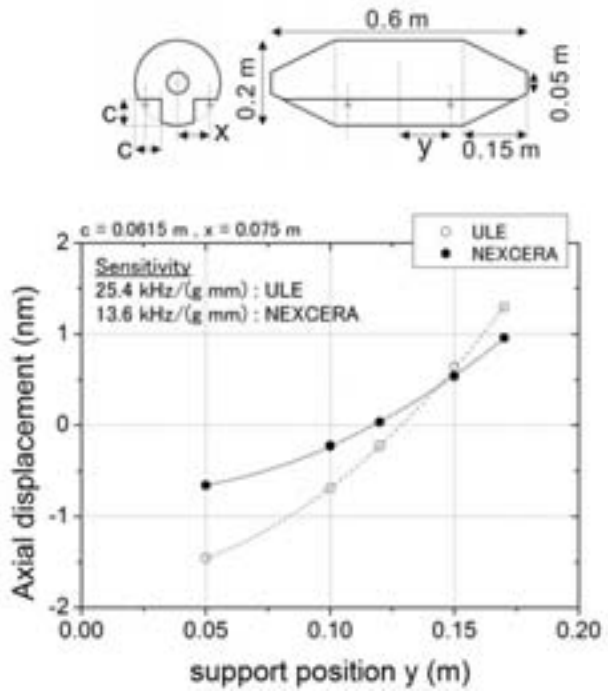

Fig. 1. A design of a long cavity and a calculated result of cavity length change under vertical acceleration as a function of the support position. In the figure of the assumed cavity spacer shape, gray triangles show support positions. In the graph, solid and open circles represent axial displacements of NEXCERA and ULE cavity spacers, respectively. This result shows that the NEXCERA cavity spacer is insensitive to the vibration in comparison with the ULE cavity spacer due to the high specific rigidity.

III. LASER LINEWIDTH TRANSFER TECHNIQUE

Recently, a high-speed controllable fiber comb has been developed at NMIJ. We have demonstrated that the fiber comb can transfer a linewidth of highly stable laser to other wavelength with mHz level [4,5]. The comb is composed of a mode-locked erbium-doped fiber laser with an intra-cavity electro-optic-modulator (EOM), which is inserted into a free space section of the cavity to change the effective cavity length with fast response. Output power from the mode-locked Er fiber oscillator is split into three branches. The first branch is used to stabilize the carrier-envelop offset (CEO) phase of the comb by controlling pump power for the oscillator. Using the second branch, a beat note between a component of the fiber comb and the ultra-stable laser at 1064 nm is observed. Repetition rate frequency of the comb is stabilized by locking the beat frequency to a reference through feedback to the EOM, so that the comb is stabilized to the reference laser. The third branch is used to observe a beat between the comb and light at 578 or 698 nm for our ytterbium or strontium optical lattice clocks [10, 11], respectively. To generate the comb at around 578 or 698 nm, periodically poled lithium niobates (PPLNs) were used. Then, these beat signals are used to stabilize the 578 or 698 nm light sources to the comb. If one would like to use the system for the optical clocks, the system needs to work continuously for a long time. That is one of the reason, why we employ the fiber comb in the experiment. The system has been working continuously for more than weeks. We have used the clock laser system for atomic spectroscopy and successfully observed the Zeeman components of ^{171}Yb and ^{87}Sr in a homogeneous magnetic field.

IV. SUMMARY

We have developed a ceramic cavity to investigate the thermal properties. Experimental results show that the ceramic has a zero cross temperature at room temperature. The sensitivity of the thermal expansion coefficient of the ceramic to temperature change is about five times greater than that of ULE glass at around the zero cross temperature. Furthermore, to calculate the ceramic cavity deformation, a finite element based analysis has been used. Simulation results show that responses of a long ceramic cavity to the vertical acceleration are similar to that of a short ULE glass cavity [9]. Owing to the high specific rigidity and relatively low thermal expansion at room temperature, the ceramic should be a promising material for long optical cavities that can reduce the effect of the thermal noise relatively. The new clock laser system with linewidth transfer scheme is absolutely attractive, because any ultra-stable lasers that would be easy to achieve narrow linewidth and great short-term stability can be used to stabilize other lasers operated at different wavelengths via the comb. By combining the long ceramic cavity with laser linewidth transfer technique, short-term stabilities and linewidth of clock lasers for ytterbium and strontium optical lattice clocks should be further improved.

ACKNOWLEDGMENT

This research is supported by the MEXT/JSPS through its FIRST Program and Grants-in-Aid for Scientific Research Program (KAKENHI Grant Number: 22540415).

REFERENCES

[1] K. Numata, A. Kemery, and J. Camp, "Thermal-Noise Limit in the Frequency Stabilization of Lasers with Rigid Cavities", Phys. Rev. Lett., vol. 93, pp. 250602(4 pages), December 2004.

[2] T. Kessler, C. Hagemann, C. Grebing, T. Legero, U. Sterr, F. Riehle, M. J. Martin, L. Chen and J. Ye, "A sub-40-mHz-linewidth laser based on a silicon single-crystal optical cavity", Nature Photonics, vol. 6, pp. 687 − 692, October 2012.

[3] Y. Y. Jiang, A. D. Ludlow, N. D. Lemke, R. W. Fox, J. A. Sherman, L.-S. Ma and C. W. Oates, "Making optical atomic clocks more stable with 10^{-16}-level laser stabilization", Nature Photonics, vol. 5, pp. 158 − 161, March 2011.

[4] Y. Nakajima, H. Inaba, K. Hosaka, K. Minoshima, A.Onae, M.Yasuda, T. Kohno, S. Kawato, T. Kobayashi, T. Katsuyama and F.-L.Hong, "A multi-branch, fiber-based frequency comb with millihertz-level relative linewidths using an intra-cavity electro-optic modulator", Opt. Express, vol. 18, pp. 1667 − 1676, January 2010.

[5] K. Iwakuni, H. Inaba, Y. Nakajima, T. Kobayashi, K. Hosaka, A. Onae, and F.-L. Hong, "Narrow linewidth comb realized with a mode-locked fiber laser using an intra-cavity waveguide electro-optic modulator for high-speed control", Optics Express, vol. 20, pp. 13769 − 13776, June 2012.

[6] H. Inaba, K. Hosaka, M. Yasuda, Y. Nakajima, K. Iwakuni, D. Akamatsu, S. Okubo, T. Kohno, A. Onae, and F.-L. Hong, "Spectroscopy of ^{171}Yb in an optical lattice based on laser linewidth transfer using a narrow linewidth frequency comb", Opt. Express, vol. 21, pp. 7891 − 7896, April 2013.

[7] J. Sugawara, H. Unno, N. Kosugi, Y. Kuma, and K. Abe, " NEXCERA" zero thermal expansion ceramics for aptical applications", Proceedings of ASPE 2010 Annual Meeting, vol. 50, pp. 405 − 407, 2010.

[8] K. Hosaka, H. Inaba, D. Akamatsu, M. Yasuda, J. Sugawara, A. Onae, and F.-L. Hong, "A Fabry–Pe´rot etalon with an ultralow expansion ceramic spacer", Jpn. J. Appl. Phys., vol. 52, pp. 032402(4 pages), February 2013.,

[9] S. A. Webster, M. Oxborrow, and P. Gill, "Vibration insensitive optical cavity", Phys. Rev. A, vol.75, pp. 011801(R) (4 pages), January 2007..

[10] M. Yasuda, H. Inaba, T. Kohnoy, T. Tanabe, Y. Nakajima, K. Hosaka, D. Akamatsu, A. Onae, T. Suzuyama, M. Amemiya, and F.-L. Hong, "Improved absolute frequency measurement of the ^{171}Yb optical lattice clock towards a candidate for the redenition of the second", Appl. Phys. Express, vol. 5, pp. 102401(3 pages), September 2012.

[11] D. Akamatsu, Y. Nakajima, H. Inaba, K. Hosaka, M. Yasuda, A. Onae, and F.-L. Hong, "Narrow linewidth laser system realized by linewidth transfer using a fiber-based frequency comb for the magneto-optical trapping of strontium", vol. 20 , pp.16010 − 16016, June 2012..